SB3C

biomechanics.
bioengineering.
biotransport.

2021 Summer Biomechanics, Bioengineering, and Biotransport Conference

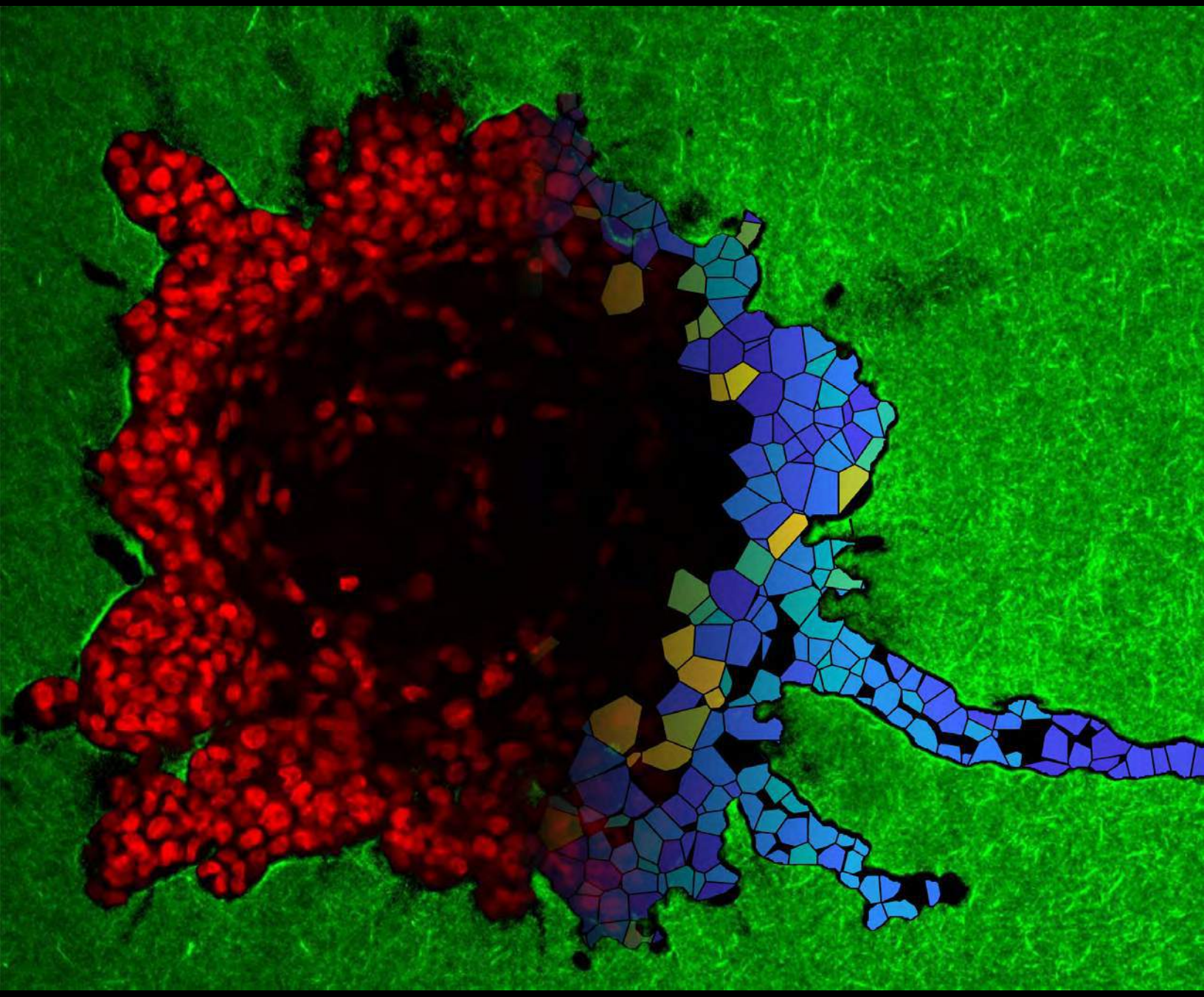

Virtual Meeting

June 14-18, 2021

Proceedings Book

Funding for this conference was made possible (in part) by the National Science Foundation's Civil, Mechanical and Manufacturing Innovation Division (Biomechanics and Mechanobiology) #2017872. Funding for this conference was also made possible (in part) by 1R13EB028126-01 from the National Institute of Biomedical Imaging and Bioengineering. Prizes and other support for the Student Paper Competition were provided by the Bioengineering Division of the American Society of Mechanical Engineers. The views expressed in written conference materials or publications and by speakers and moderators do not necessarily reflect the official policies of the Department of Health and Human Services; nor does mention of trade names, commercial practices, or organizations imply endorsement by the U.S. Government. The conference organizers gratefully acknowledge Aletea vanVeldhuisen from Purdue University for her help with the Program Book and Proceedings.

The 2021 Summer Biomechanics, Bioengineering, and Biotransport Conference (SB^{3}C) organizers gratefully acknowledge the support of the National Science Foundation, the National Institutes of Health, and American Society of Mechanical Engineers.

Congratulations to the 2021 Cover Art Contest Winner:

Jacopo Ferruzzi, University of Texas at Dallas/Boston University
Title: Jamming and Unjamming Transitions Govern the Invasion of Tumor Spheroids within 3D Extracellular Matrices
Description: Metastatic MDA-MB-231 breast cancer spheroids undergo a jamming transition during collective migration in high density collagen. The image displays the equatorial cross-section of an MDA-MB-231 spheroid (initially comprising $\sim$ 1000 cells) invading in a 4 mg/ml collagen matrix for 48 hours. The entire spheroid volume is captured in the image stack by combining optical clearing and multiphoton imaging. DAPI-stained cell nuclei are shown in red and collagen fibers from second harmonic generation signal (SHG) are shown in green. Cell shapes are estimated using a bounded Voronoi tessellation of the cell nuclei and subsequent calculation of the shape index (SI) as the normalized surface area: $SI = \frac{S}{\sqrt[3]{V^2}}$, where S and V represent, respectively, the surface area and the volume of the Voronoi tile approximating each cell within the spheroid. The 2D cross-section of the 3D cell shapes are color coded according to their respective SI value and show a decreasing radial gradient, consistent with the presence of an unjammed fluid-like phase in the spheroid bulk and a jammed solid-like phase while cells invade collectively under confinement from the dense collagen matrix. The field of view has a size of 824.57 x 824.57 μm^2. Fading between Voronoi tiles and cell nuclei was included for artistic e
ect.

Permission to download, print, and photocopy a single, individual copy of any of the works contained in this file for personal use in research and/or educational pursuit is granted by the SB3C Foundation, Inc. For other uses,contact the Board of the SB3C Foundation, Inc., 20 South Duke Street, #1, Lancaster, PA 17602.

ISBN 978-1-7351808-2-3

Copyright 2021 SB^{3}C Foundation, Inc.

SB³C 2021 Virtual Meeting Table of Contents

Monday, June 14	12:30PM – 2:00PM EDT

Advances in Biomedical Engineering Education

Alpine Drift

Session Chair: Debanjan Mukherjee, University of Colorado Boulder
Session Chair: Zhongping Huang, West Chester University

12:30PM **Efficacy of Teaching Biomedical Engineering Laboratories Using Virtual Reality**
Anita Singh[1], Arun Ramakrishnan[2], Sriram Balasubramanian[2]
[1]Widener University, [2]Drexel University

12:43PM **"Hands-On, Minds-On, and Science-Up": A Concept-Based Learning Laboratory With a Taste of Research Experience for an Undergraduate Biomedical Engineering Course**
Cyrus Fiori[1], Taisiya Sigaeva[1], Maria Jose Pino Alban[2], Youssef Beauferris[2], Donovan Stagg[2], Elena Di Martino[2]
[1]University of Waterloo, [2]University of Calgary

12:56PM **Developing Community to Support First Generation Freshman in an Engineering Programming Course**
Sara Wilson[1], Molly McVey[1], Nolan Norton[1]
[1]University of Kansas

1:09PM **Development and Implementation of an Engineering Research Course for a College-In-Prison Program**
Julie Speer[1], Zain Clapacs[1]
[1]Washington University in St. Louis

1:22PM **Incorporating Engineering Standards into a Biomechanics Laboratory Course**
Kristen Billiar[1]
[1]Worcester Polytechnic Institute

1:35PM **Virtual Research Mentoring Between Graduate and Undergraduate Students During the Covid-19 Pandemic**
Julie Speer[1], Max Lyon[1], Julia Johnson[1]
[1]Washington University in St. Louis

Monday, June 14	12:30PM – 2:00PM EDT

Bone Mechanics

Saddle Ridge

Session Chair: Arun Nair, University of Arkansas
Session Chair: Lindsey Westover, University of Alberta

Copyright 2021 SB³C Foundation, Inc.

12:30PM **Multi-Scale Cortical Bone Morphology Varies Across Mice of Different Genetic Backgrounds**
Nicole Migotsky[1], Matthew Silva[1]
[1]Washington University in St. Louis

12:43PM **Investigation of Elastic Moduli of Mineralized Collagen Fibril and Extrafibrillar Matrix in Bovine Cortical Bone Using Peakforce Tapping Atomic Force Microscopy**
Yuxiao Zhou[1], Jing Du[1]
[1]Penn State University

12:56PM **Understanding Mechanisms of Load Transfer in the Tendon-To-Bone Attachment**
Mikhail Golman[1], Jonathan Almer[2], Stavros Thomopoulos[1], Alix Deymier[3]
[1]Columbia University, [2]Argonne National Laboratory, *[3]University of Connecticut Health Center*

1:09PM **Determining Tibial Stress and Strain During the Stance Phase with 3D Finite Element Modeling in a Healthy Running Population**
Patricia Butler[1], Ali Vahdati[1], Stacey Meardon[1], Stephanie George[1]
[1]East Carolina University

1:22PM **Digital Volume Correlation Using Deep Learning-Denoised Synchrotron Micro-CT Images to Study Bone Mechanical Behavior**
Yoshihiro Obata[1], Michael Sieverts[1], Daniel Pelt[2], Claire Acevedo[1]
[1]University of Utah, [2]Centrum Wiskunde & Informatica, Amsterdam, Netherlands

1:35PM **Tendon Enthesis Toughness Relies on Position-Dependent Fiber Recruitment and Bony Attachment Geometry**
Mikhail Golman[1], Victor Birman[2], Stavros Thomopoulos[1], Guy Genin[3]
[1]Columbia University, [2]Missouri University of Science and Technology, [3]Washington University in St. Louis

Monday, June 14	**12:30PM – 2:00PM EDT**

Emerging *In Vitro*, Experimental, Computational and Visualization Methods in Biofluid Mechanics

Mud Springs

Session Chair: Jimmy Azarnoosh, Marquette University
Session Chair: John LaDisa, Marquette University

12:30PM **Rapid Automatic Reconstruction of Heart Valves and Cardiac Structures from CT Images for Pre-TAVR Evaluations Using a Parametric Leaflet Model**
Huang Chen[1], Beom Jun Lee[1], Sri Krishna Sivakumar[1], Breandan Yeats[1], Vinod Thourani[2], Venkateshwar Polsani[2], Lakshmi Dasi[1]
[1]Georgia Institute of Technology, [2]Marcus Valve Center, Piedmont Heart

Copyright 2021 SB³C Foundation, Inc.

12:43PM **A Computational Fluid Dynamics Formulation with Solute Transport Derived from Mixture Theory and its Finite Element Implementation in FEBio**
Jay Shim[1], Steve Maas[2], Vijay Vedula[1], Clark Hung[1], Jeffrey Weiss[2], Gerard Ateshian[1]
[1]Columbia University, [2]University of Utah

12:56PM **Comparison of Nonlinear Membrane, Shell, and 3D Formulations for Vascular Biomechanics**
Nitesh Nama[1], Miquel Aguirre[2], Rogelio Ortigosa[3], Antonio Gil[4], Jay Humphrey[5], C. Alberto Figueroa[1]
[1]University of Michigan, [2]Mines Saint-Etienne, [3]Technical University of Cartagena, [4]Swansea University, [5]Yale University

1:09PM **The Effect of Hematocrit on the Thickness and Asymmetry of the Cell-Free Layer in Arterial Bifurcations**
Sayan Roychowdhury[1], Peter Balogh[1], Amanda Randles[1]
[1]Duke University

1:22PM **Potential Biofluidic and Geometrical Biomarkers of Thoracic Aortic Aneurysm Outcome in the Fbln4SMKO Mouse**
Marisa S. Bazzi[1], Ramin Balouchzadeh[2], Shawn N. Pavey[2], Jessica E. Wagenseil[2], Victor H. Barocas[1]
[1]University of Minnesota, [2]Washington University

1:35PM **A Platform for Studying the Effects of Nanotopography and Reactive Chemical Species on Integrin Selection**
Ryan Fasse[1], Novella Bates[2], Alex Guerra[3], Joe Baio[1], Monica Hinds[2], Patrick Jurney[3]
[1]Oregon State University, [2]Oregon Health & Science University, [3]San Jose State University

Monday, June 14	**12:30PM – 2:00PM EDT**

PhD Student Paper Competition 1: Biotransport, Biosensors and Biomaterials

Mogul Madness

Session Chair: Sara Roccabianca, Michigan State University
Session Chair: Guy Genin, Washington University in St. Louis

12:30PM **Sophorolipids Demonstrate Promising Anti-Cancer Efficacy in 2D, 2.5D, and 3D Breast Cancer Models**
Cassandra Roberge[1], David Kingsley[1], Lillian Murphy[1], Filbert Totsingan[1], Rebecca Miceli[1], Richard Gross[1], David Corr[1]
[1] Rensselaer Polytechnic Institute

12:45PM **Fibrous Microenvironments Regulate Nuclear Shape in a Diameter-Dependent Manner**
Aniket Jana[1], Amrinder Nain[1]
[1]Virginia Tech

Copyright 2021 SB³C Foundation, Inc.

1:00PM **Conductive Polypyrrole-Encapsulated Silk Fibroin Fibers for Myocardial Regeneration**
Yeshi Liang[1], James Goh[1]
[1]National University of Singapore

1:15PM **Diamond: Digital Plasmonic-Nanobubble Detection for Homogeneous Assay with Enhanced Sensitivity**
Yaning Liu[1], Haihang Ye[1], Zhenpeng Qin[1]
[1]University of Texas at Dallas

1:30PM **Successful Cryopreservation of Rabbit Jugular Vein Using Magnetic Nanoparticles Enhanced Single-Mode Electromagnetic Resonance Rewarming System**
Shen Ren[1], Zhiquan Shu[2], Ziyuan Wang[1], Ye Jin[1], Ruidong Ma[1], Shaohang Hao[1], Dayong Gao[1]
[1]University of Washington, [2]University of Washington Tacoma

1:45PM **Modulating the Blood-Brain Barrier by Picosecond Laser Stimulation of Molecular-Targeted Nanoparticles**
Xiaoqing Li[1], Vamsidhara Vemireddy[2], Qi Cai[1], Hejian Xiong[1], Peiyuan Kang[1], Xiuying Li[3], Monica Giannotta[3], Heather Hayenga[1], Edward Pan[2], Shashank Sirsi[1], Celine Mateo[4], David Kleinfeld[4], Chris Greene[5], Matthew Campbell[5], Elisabetta Dejana[3], Robert Bachoo[2], Zhenpeng Qin[1]
[1]University of Texas at Dallas, [2]University of Texas Southwestern Medical Center, [3]FIRC Institute of Molecular Oncology Foundation, [4]University of California San Diego, [5]Trinity College Dublin

Monday, June 14	**2:30PM – 4:00PM EDT**

Biofluids Mechanobiology and Pathology I

Mud Springs

Session Chair: Claudio Chiastra, Politecnico di Torino
Session Chair: Mette Olufsen, North Carolina State University

2:30PM **T Cells from Cadherin-11-Deficient Mice Promote Neointima Formation Following Vascular Injury**
Matthew Bersi[1,2], Matthew Madden[1], Tessa Huffstater[1], Lance Riley[1], Ethan Joll[1], Michael Raddatz[1], Victoria Le[3], Aaron Baker[3], Jeffrey Rathmell[1], David Merryman[1]
[1]Vanderbilt University, [2]Washington University in St Louis, [3]University of Texas at Austin

2:43PM **Linking Gene Expression, Hemodynamics and Cellular Dynamics in a Patient-Specific Multiscale Model of In-Stent Restenosis**
Anna Corti[1], Monika Colombo[1], Stefano Casarin[2], Jared M Rozowsky[3], Yong He[3], Sara Bridio[1], Francesco Migliavacca[1], Jose F Rodriguez Matas[1], Scott A Berceli[3], Claudio Chiastra[1]
[1]Politecnico di Milano, [2]Houston Methodist Hospital, [3]University of Florida

Copyright 2021 SB³C Foundation, Inc.

2:56PM **Multiscale Computational Model Predictions of Shear Stress and Cyclic Stretch in the Pulmonary Vasculature**
Michelle Bartolo[1], Nicholas Hill[2], Naomi Chesler[3], Mette Olufsen[1]
[1]North Carolina State University, [2]University of Glasgow, [3]University of California Irvine

3:09PM **Multiscale Hemodynamic Predictions in Chronic Thromboembolic Pulmonary Hypertension**
Mitchel Colebank[1], Mette Olufsen[1]
[1]North Carolina State University

3:22PM **Elucidating the Role of Wall Shear Stress in Aortic Wall Remodeling in Ascending Thoracic Aortic Aneurysms**
Selene Pirola[1], M Yousuf Salmasi[1], Serena M Fisichella[1], Sumesh Sasidharan[1], Omar A. Jarral[1], Declan P O'Regan[1], James E. Moore Jr[1], Thanos Athanasiou[1], Xiao Yun Xu[1]
[1]Imperial College London

3:35PM **Effects of Prolonged, Altered Hemodynamics on Zebrafish Embryonic Heart Development**
Yoke Yin Foo[1], Efthymios Motakis[2], Zenia Tiang[3], Shuhao Shen[1], Peiyuan Kang[1], Jason Kuan Han Lai[1], Wei Xuan Chan[1], Hadi Wiputra[1], Nanguang Chen[1], Ching Kit Chen[1], Christoph Winkler[1], Roger Foo[3], Choon Hwai Yap[4]
[1]National University of Singapore, [2]Jackson Laboratory, [3]Agency for Science Technology and Research, [4]Imperial College London

Monday, June 14	**2:30PM – 4:00PM EDT**

Biomechanics of Joints and Tissues

Saddle Ridge

Session Chair: Corinne Henak, University of Wisconsin-Madison
Session Chair: Andrew Kemper, Virginia Tech

2:30PM **Effect of Total Ankle Arthroplasty Implantation and Adaptive Gait on Ankle and Adjacent Joint Kinematics During Simulated Gait**
Jeffrey Hoffman[1], Jaeyoung Kim[1], Brett Steineman[1], Rogerio Bitar[1], Daniel Sturnick[1], Jonathan Deland[1]
[1]Hospital for Special Surgery

2:43PM **Additional Distal Femoral Resection Increases Mid-Flexion Laxity of Posterior Stabilized TKA with Flexion Contracture: A Computational Model**
Shady Elmasry[1], Brian Chalmers[1], Cynthia Kahlenberg[1], Peter Sculco[1], Timothy Wright[1], David Mayman[1], Geoffrey Westrich[1], Michael Cross[1], Carl Imhauser[1]
[1]Hospital for Special Surgery

2:56PM **Influence of Chondrolabral Damage and Labral Repair on Hip Joint Mechanics With Cam Fai Morphology**
Jocelyn Todd[1], Travis Maak[1], Gerard Ateshian[2], Andrew Anderson[1], Jeffrey Weiss[1]
[1]University of Utah, [2]Columbia University

Copyright 2021 SB³C Foundation, Inc.

3:09PM **Physiological Loading Conditions to Simulate Standing**
Stephanie Rossman[1,2], Eric Meyer[1], Jorge Isaza[3], Steven Rundell[2]
[1]Lawrence Technological University, [2]Explico Engineering, [3]Spine Specialist of Louisiana

3:22PM **Role of Muscle Activation on Lumbar Spine Force in Frontal Impact Loading**
Sagar Umale[1], John Humm[1], Narayan Yoganandan[1]
[1]Medical College of Wisconsin

3:35PM **PID Controlled, Finite-Element Simulation of Bipolar Radiofrequency Ablation of Porcine Spinal Muscle**
Hanife Tugba Kumru[1], Anilchandra Attaluri[1], Daniel H Cortes[1]
[1]The Pennsylvania State University

Monday, June 14	**2:30PM – 4:00PM EDT**

Image-based Characterization of Soft Tissues

Mogul Madness

Session Chair: Jacopo Ferruzzi, University of Texas - Dallas
Session Chair: Colleen Witzenburg, University of Wisconsin-Madison

2:30PM **Lamina Cribrosa Deformations Induced *In Vivo* by Acutely and Chronically Elevated Intraocular Pressure**
Fuqiang Zhong[1], Yi Hua[1], Junchao Wei[1], Manik Bansal[1], Juan Reynaud[2], Brad Fortune[2], Ziyi Zhu[1], Ian Sigal[1]
[1]University of Pittsburgh, [2]Devers Eye Institute, Legacy Health Research Institute

2:43PM ***Ex-Vivo* Local Plaque Rupture Analysis of Atherosclerotic Human Carotid Arteries Through Nano-Indentation, Tensile Testing and Digital Image Correlation**
Su Guvenir[1], Pablo de Miguel[2], Ali C. Akyildiz[1]
[1]Erasmus Medical Center, [2]Delft University of Technology

2:56PM **On the Relative Sensitivity of AAA Rupture Potential Index to Sex, Intraluminal Pressure, and Familial History**
Balaji Rengarajan[1], Satish Muluk[2], Mark Eskandari[3], Ender Finol[1]
[1]University of Texas at San Antonio, [2]Allegheny Health Network, [3]Northwestern University School of Medicine

3:09PM **Damage Modeling of the Human Meniscus: Validating Finite Element Models with Digital Image Correlation**
Derek Nesbitt[1], Trevor Lujan[1]
[1]Boise State University

3:22PM **The Effect of Age-Related Advanced Glycation End-Products on Tissue Mechanics Depends on Underlying Collagen Organization**
Austin Gouldin[1], Jennifer Puetzer[1]
[1]Virginia Commonwealth University

Copyright 2021 SB³C Foundation, Inc.

3:35PM **Polarized Spatial Domain Imaging for Simultaneous Tissue Strain and Fiber Orientation Measurements**
Coinneach Mackenzie Dover[1], Will Goth[2], James Tunnell[1], Michael Sacks[1]
[1]University of Texas at Austin, [2]SpectraWAVE, Inc.

Monday, June 14	**2:30PM – 4:00PM EDT**

Multi-Scale Modeling and Characterization of Soft Tissues

Alpine Drift

Session Chair: Pim Oomen, University of Virginia
Session Chair: Sara Roccabianca, Michigan State University

2:30PM **A Novel Three-Layered Model of Mouse Distal Colon and Rectum Capturing Through-Thickness Biomechanics**
Yunmei Zhao[1], Bin Feng[1], David M. Pierce[1]
[1]University of Connecticut

2:43PM **Protein Spreading Patterns in Alzheimer's Disease: Exploring the Difference Between a Connectivity-Based and Proximity-Based Connectome Model**
Shima Jalalian[1], Johannes Weickenmeier[1]
[1]Stevens Institute of Technology

2:56PM **Fiber Network-Based Multiscale Models Predict Experimentally Measured Volume Reduction of Stretched Mouse Skin**
Nathan Witt[1], Alan Woessner[2], Kyle Quinn[2], Edward Sander[1]
[1]University of Iowa, [2]University of Arkansas

3:09PM **The Mechanical Similitude of Positive- Versus Negative-Pressure Ventilation in Mouse Lungs**
Kathrine Anduaga[1], Talyah Nelson[1], Samaneh Sattari[1], Crystal Mariano[1], Arzu Ulu[1], Tara Nordgren[1], Mona Eskandari[1]
[1]University of California Riverside

3:22PM **Cortical Thickness Distribution of the Human Cerebral Cortex Identified by Curvature at Local Scales**
Nagehan Demirci[1], Maria Holland[1]
[1]University of Notre Dame

3:35PM **Interaction Mechanisms of Peptoid and Neuronal Cell Receptors and its Dependence on Peptoid Sphere Size and Chain Length**
Mohan Yasodharababu[1], Shannon Servoss[1], Arun Nair[1]
[1]University of Arkansas

Copyright 2021 SB³C Foundation, Inc.

Tuesday, June 15	11:00AM – 12:30PM EDT

Biofluids Mechanobiology and Pathology II

Mud Springs

Session Chair: Ryan Pedrigi, University of Nebraska-Lincoln
Session Chair: Atefeh Razavi, Georgia Institute of Technology

11:00AM **Leveraging Endothelial Glycocalyx Integrity in Atherosclerotic-Relevant Flow Conditions for Targeted Intravenous Nanoparticle Delivery**
Ronodeep Mitra[1], Ming Cheng[1], Gerard O'Neil[1], Praveen Kulkarni[1], Rajiv Kumar[1], Srinivas Sridhar[1], Craig Ferris[1], James Hamilton[2], Hanjoong Jo[3], Eno Ebong[1]
[1]Northeastern University, [2]Boston University School of Medicine, [3]Emory University

11:13AM **Regulation of TXNIP and the Role of ER Stress in the Anti-Inflammatory Effect of Empagliflozin to Glycocalyx Degradation**
Marc-Antoine Campeau[1], Richard Leask[1]
[1]McGill University

11:26AM **Computational Models to Evaluate the Impact of Coronary Collateral Artery Flow in Adult and Postnatal Mice**
Suhaas Anbazhakan[1], Kristy Red-Horse[1], Alison Marsden[1]
[1]Stanford University

11:39AM **Mean and Transverse Wall Shear Stress Correlate with Enos Expression in Endothelial Cells Under Orbital Flow**
Jaideep Sahni[1], Glenn Richardson[1], Ryan Pedrigi[1]
[1]University of Nebraska-Lincoln

11:52AM **Wall Shear Stress Topological Skeleton Variability Predicts Myocardial Infarction**
Maurizio Lodi Rizzini[1], Alessandro Candreva[2], Claudio Chiastra[1], Takuya Mizukami[2], Diego Gallo[1], Jean-Paul Aben[3], Olivier Muller[4], Bernard De Bruyne[2], Carlos Collet[2], Umberto Morbiducci[1]
[1]Politecnico di Torino, [2]OLV-Clinic, [3]Pie Medical Imaging BV, [4]Lausanne University Hospital

12:05PM **Designing a High-Throughput Water Channel to Assess Bone Tissue Development *In Vivo* Under Different Mechanical Environments**
Gina Georgadarellis[1], Craig Albertson[1], Juan Jiménez[1]
[1]University of Massachusetts Amherst

Tuesday, June 15	11:00AM – 12:30PM EDT

Brain and Injury Mechanics I: Kinematics

Saddle Ridge

Session Chair: Amanda Esquivel, University of Michigan-Dearborn
Session Chair: Songbai Ji, Worcester Polytechnic Institute

Copyright 2021 SB³C Foundation, Inc.

11:00AM **The Effect of Head Impact Exposure in NCAA Division I Football on Concussion Symptom Severity**
Jack Seifert[1,2], Alok Shah[2], Jared Muench[2], Jaroslaw Harezlak[3], Steve Rowson[4], Jason P. Mihalik[5], Stefan Duma[4], Paul Pasquina[6], Steve P. Broglio[7], Thomas M. McAllister[3], Michael McCrea[2], Brian D. Stemper[1,2]
[1]Marquettte University, [2]Medical College of Wisconsin, [3]Indiana University, [4]Virginia Tech, [5]University of North Carolina, [6]University of Health Sciences, [7]University of Michigan

11:13AM **Investigating the Effect of Sports Helmets on the Frequency Response of the Human Brain**
Fargol Rezayaraghi (R. Araghi) [1], Javid Abderezaei[1], Efe Ozkaya[1], Colleen E. Shea[1], Mehmet Kurt[1]
[1]Stevens Institute of Technology

11:26AM **Statistical Interpretation of Predictive Factors of Kinematics in Traumatic Brain Injury from Head Impacts**
Ylheng Li [1], Xianghao Zhan[1], Yuzhe Liu[1], David Camarillo[1]
[1]Stanford University

11:39AM **Biomechanics of Headers in Youth and Collegiate Female Soccer**
Tanner Filben[1], Nicholas Pritchard[1], Logan Miller[1], Christopher Miles[1], Jillian Urban[1], Joel Stitzel[1]
[1]Wake Forest School of Medicine

11:52AM **A Strategy for Validating the Kinematics of a Vehicle-Specific MADYMO Model of A Low-Speed Rear-End Collison**
Dominic Demma[1], Keith Button[1], Elizabeth Kappler[1], Stephanie Rossman[1], Steven Rundell[1]
[1]Explico Engineering Company

12:05PM **Effects of Aggressiveness, Confidence, and Perceived Coach Support on Head Impact Exposure Metrics in Youth Football**
Madison Marks[1], William Flood[2], Joel Stitzel[1,2], Jillian Urban[1,2]
[1]Virginia Tech, [2]Wake Forest School of Medicine

Tuesday, June 15	**11:00AM – 12:30PM EDT**

Device, Design and Rehabilitation I

Alpine Drift

Session Chair: Michael Moreno, Texas A&M University
Session Chair: Anita Singh, Widener University

11:00AM **Biomechanical Effects of Cycling Crank Length on Resultant Hip and Knee Joint Forces and Range of Motion**
Avery Newman[1], Abigail Fisk[1], Christiane O'Hara[1], Reymil Fernandez[1], Robert Clark[1]
[1]California Polytechnic State University

Copyright 2021 SB³C Foundation, Inc.

11:13AM **Measuring Prosthetic Foot Use by Activity Level with Step Activity Monitoring**
John Chomack[1], Alexis Sidiropoulos[1], Michael Poppo[1], Jason Maikos[1]
[1]Veteran Affairs New York Harbor Healthcare System

11:26AM **Three Different Office Postures: Determining Pelvic Tilt, Torso Openness, Ground Reaction Forces and Blood Perfusion**
Archana Lamsal[1], Garrett Weidig[1], Teresa Bellingar[2], Tamara Reid Bush[1]
[1]Michigan State University, [2]Haworth Inc.

11:39AM **Wearable Sensor Validation for Tasks Requiring High Acceleration**
Sarah Moudy[1], Yein Lee[1], Shelby Alfred[1], Rita Patterson[1]
[1]University of North Texas Health Science Center

11:52AM **Evidence of Sex Bias in Finite Element Modeling of Hip Arthroplasty**
Syeda Lamia[1], Chien-Yu Lin[2], Richard Hughes[1], Elizabeth Dailey[1], Megan Killian[1]
[1]University of Michigan, [2]University of Texas

12:05PM **Development and Validation of an Ultra-High Field Compatible MR Elastography Actuator**
Emily Triolo[1], Aymeric Pionteck[1], Akbar Alipour[2], Oleksandr Khegai[2], Paul Kennedy[2], Priti Balchandani[2], Mehmet Kurt[1]
[1]Stevens Institute of Technology, [2]Icahn School of Medicine at Mount Sinai

Tuesday, June 15	**11:00AM – 12:30PM EDT**

PhD Student Paper Competition 2: Bladder, Lung, and Ocular Biomechanics

Mogul Madness

Session Chair: Rebecca Heise, Virginia Commonwealth University
Session Chair: Joseph Sherwood, Imperial College of London

11:00AM **Lung Mechanics of Positive- and Negative- Pressure Ventilation Under Varied Inflation Volumes**
Samaneh Sattari[1], Crystal Mariano[1], Mona Eskandari[1]
[1]University of California, Riverside

11:15AM **Deformation of Peripapillary Sclera and Retina in Response to Elevated Intraocular Pressure**
Sunny Kwok[1], Manqi Pan[1], Yanhui Ma[1], Xueliang Pan[1], Jun Liu[1]
[1]The Ohio State University

11:30AM **Assessing the Comparative Strains Between Positive and Negative Pressure Ventilation Using Digital Image Correlation**
Crystal Mariano[1], Samaneh Sattar[1], Mona Eskandari[1]
[1]University of California, Riverside

Copyright 2021 SB³C Foundation, Inc.

11:45AM **Integrating Capillary Flow Modeling and Geometric Quantification Into Reconstructed 3D Capillary Networks of the Optic Nerve Head**
Po-Yi Lee[1], Jason Walker[1], Yi Hua[1], Bryn Brazile[1], Ian A. Sigal[1]
[1]University of Pittsburgh

12:00PM **Investigating the Effect of Varied Breathing Rates and Volumes on the Mechanics of Murine Lungs**
Talyah Nelson[1], Kathrine Anduaga[1], Samaneh Sattari[1], Crystal Mariano[1], Arzu Ulu[1], Tara Nordgen[1], Mona Eskandari[1]
[1]University of California, Riverside

12:15PM **Inflammasome Nlrc4 Gene Knockout Increases Stiffness of Bladder Wall in Rat Model**
Eli Broemer[1], Christina Chan[1], Sara Roccabianca[1]
[1]Michigan State University

Tuesday, June 15	**1:00PM – 2:30PM EDT**

Cartilage Mechanics: Measurement and Injury Biomechanics

Saddle Ridge

Session Chair: Deva Chan, Purdue University
Session Chair: Chris Price, University of Delaware

1:00PM **Vibrometry as a Nondestructive Alternative to Dynamic Mechanical Testing in Cartilage**
Gabriela Espinosa[1], Gaston Otarola-Pezzani[1], Jerry Hu[1], Kyriacos Athanasiou[1]
[1]University of California, Irvine

1:13PM **Crosslinking of Cartilage Collagen Via Nonlinear Femtosecond Laser Activation of Riboflavin**
Jiashuai Fan[1], C.V. Sise[1], Kimberly R. Kroupa[1], Clark T. Hung[1], Gerard A. Ateshian[1], Sinisa Vukelic[1]
[1]Columbia University

1:26PM **Manipulating the Initiation and Propagation of Microcracks in Collagen Networks of Cartilage**
Stephany Santos[1], Corey P. Neu[2], Bryanna Samolyk[1], David M. Pierce[1]
[1]University of Connecticut, [2]University of Colorado Boulder

1:39PM **Crosslinking of Collagen Across Cartilage Tears for Improved Interface Strength**
Kimberly Kroupa[1], C.V. Sise[1], Clark Hung[1], Sinisa Vukelic[1], Gerard Ateshian[1]
[1]Columbia University

1:52PM **Transition from Stress-Governed Fracture to Pressure-Induced Fragmentation in Cartilage Failure**
Dipul Chawla[1], Guebum Han[2], Melih Eriten[1], Corinne Henak[1]
[1]University of Wisconsin-Madison, [2]University of Minnesota

Copyright 2021 SB³C Foundation, Inc.

2:05PM **Articular Cartilage Geometry and Material Properties Predict Functional Tribomechanics Across Species**
Meghan E. Kupratis[1], Ahmed E. Gure[2], Jamie M. Benson[1], Kyla F. Ortved[3], David L. Burris[1]
[1]University of Delaware, [2]University of Texas Arlington, [3]University of Pennsylvania New Bolton Center

Tuesday, June 15	**1:00PM – 2:30PM EDT**

Device, Design and Rehabilitation II

Alpine Drift

Session Chair: Michael Moreno, Texas A&M University
Session Chair: Anita Singh, Widener University

1:00PM **Motor Evoked Potential Recruitment Curves Indicate Neuroplasticity of the Biceps Brachii in Cervical Spinal Cord Injury**
Thibault Roumengous[1], Yasmina Zeineddine[1], Carrie Peterson[1]
[1]Virginia Commonwealth University

1:13PM **Balloon Forming Machine for Customizing Treatment of Coronary Artery Disease**
Kaitlyn Elmer[1], Maxwell Bean[1], Barry Uretsky[1], Morten Jensen[1]
[1]University of Arkansas

1:26PM **An Evaluation of Interface Pressure and Shear Force Patterns in Injury Prone Regions While Seated in an Articulating Chair**
Justin Scott[1], Tamara Reid Bush[1]
[1]Michigan State University

1:39PM **Identifying Key Parameters for Multiobjective Shape Optimization of a Double-Walled Aortic Stent-Graft**
Shannen B. Kizilski[1], Rumi Faizer[1], Victor H. Barocas[1]
[1]University of Minnesota

1:52PM **Change in Knee Joint Mechanics After ACL Transection During Simulated Gait: a Human Cadaveric Model**
Amanda Wach[1], Joseph Ruzbarsky[1], Ashley Pekmezian[1], Tony Chen[1], Russell Warren[1], Peter Torzilli[1], Suzanne Maher[1]
[1]Hospital for Special Surgery

2:05PM **Flow Visualization and Aerosols in Performance**
Abhishek Kumar[1], Tehya Stockman[1], Jean Hertzberg[1], Shelly Miller[1], Donald Milton[2], Jelena Srebric[2], Shengwei Zhu[2], Lingzhe Wang[2], Marina Vance[1], Darin Toohey[1], Sameer Patel[1]
[1]University of Colorado Boulder, [2]University of Maryland

Copyright 2021 SB³C Foundation, Inc.

Tuesday, June 15	1:00PM – 2:30PM EDT

Patient Specific Flow and Physiology I

Mud Springs

Session Chair: Zahra K. Motamed, McMaster University
Session Chair: Alejandro Roldan-Alzate, University of Wisconsin-Madison

1:00PM **Assessment of Sex Differences in Ventricular Vascular Coupling of Left Ventricular and Aortic Flow Derived from 4D Flow MRI in Healthy, Young Adults**
Cody Johnson[1], Ryan Pewowaruk[1], David Rutkowski[1], Amanda Wolfinger[1], Alejandro Roldan-Alzate[1]
[1]University of Wisconsin-Madison

1:13PM **Comparing Tissue-Engineered Vascular Grafts in Fontan Patients to the Standard of Care Using Computational Fluid Dynamics**
Erica Schwarz[1], John Kelly[2], Stephanie Lindsey[1], Kan Hor[2], Aekaansh Verma[1], Ethan Kung[3], Jay Humphrey[4], Christopher Breuer[2], Alison Marsden[1]
[1]Stanford University, [2]Nationwide Children's Hospital, [3]Clemson University, [4]Yale University

1:26PM **Computational Assessment of Renal Hemodynamic Disturbances in a Canine Model of an Abdominal Aortic Coarctation**
Christopher Tossas-Betancourt[1], Yunus Ahmed[1], Petrus van Bakel[1], Drew Braet[1], William Sherk[1], Luis Hernandez-Garcia[1], David Williams[1], Daniel Myers[1], Thomas Wakefield[1], Dawn Coleman[1], Jonathan Eliason[1], James Stanley[1], C. Alberto Figueroa[1]
[1]University of Michigan

1:39PM **Effect of Surgery on Coronary Flow Hemodynamics in Children with Anomalous Aortic Origin of a Coronary Artery (AAOCA): A Patient-Specific Computational Study**
Atefeh Razavi[1], Jayanthi Parthasarathy[2], Yasaman Farsiani[2], Silvana Molossi[3], Carlos Mery[4], Rajesh Krishnamurthy[2], Lakshmi Prasad Dasi[1]
[1]Georgia Institute of Technology, [2]Nationwide Children's Hospital, [3]Baylor College of Medicine, [4]University of Texas at Austin

1:52PM **Virtual Treatment Planning in Williams and Alagille Patients with Peripheral Pulmonary Artery Stenosis**
Ingrid Lan[1], Weiguang Yang[1], Jeffrey Feinstein[1], Thomas Collins[1], Alison Marsden[1]
[1]Stanford University

2:05PM **Tracheomalacia Affects Neonatal Respiratory Airflow in the Upper Airway**
Chamindu Gunatilaka[1], Erik Hysinger[1], Andreas Schuh[2], Deep Gandhi[1], Nara Higano[1], Qiwei Xiao[1], Daniel Ignatiuk[1], Andrew Hahn[3], Sean Fain[3], Robert Fleck[1], Jason Woods[1], Alister Bates[1]
[1]Cincinnati Children's Hospital Medical Center, [2]Imperial College London, University of Wisconsin-Madison

Copyright 2021 SB³C Foundation, Inc.

Tuesday, June 15	1:00PM – 2:30PM EDT

PhD Student Paper Competition 3: Bone and Head Injury Biomechanics

Mogul Madness

Session Chair: Mariana Kersh, University of Illinois at Urbana-Champaign
Session Chair: Richard Debski, University of Pittsburgh

1:00PM **Comparison of Head Impact Exposure Across Common Training Activities in Youth Soccer**
Nicholas Pritchard[1], Tanner Filben[1], Sebastian Haja[1], Logan Miller[1], Mark Espeland[1], Joel Stitzel[1], Jillian Urban[1]
[1]Wake Forest School of Medicine

1:15PM **Investigation of the Hindbrain Motion in Chiari Malformation I Patients Through 3D Amplified MRI**
Javid Abderezaei[1], Aymeric Pionteck[1], Ya-Chen Chuang[1], Itamar Terem[2], Leo Dang[3], Miriam Scadeng[3], Peter Morgenstern[4], Raj Shrivastava[4], Samantha Holdsworth[3], Yang Yang, Mehmet Kurt[1]
[1]Stevens Institute of Technology, [2]Stanford University, [3]University of Auckland, [4] Icahn School of Medicine at Mount Sinai

1:30PM **The Structure-Function Relationships of the Human Vertebral Endplate**
Yuanqiao Wu[1], Elise Morgan[1]
[1]Boston University

1:45PM **Maternal Bone Adaptation to Mechanical Loading During Pregnancy, Lactation, and Post-Weaning Recovery**
Yhan Li[1], Chantal de Bakker[1], Hongbo Zhao[1], Ashutosh Parajuli[2], Wei-Ju Tseng[1], Shaopeng Pei[1,2], Tan Meng[1], Rebecca Chung[1], Liyun Wang[2], X. Sherry Liu[1]
[1]University of Pennsylvania, [2]University of Delaware

2:00PM **Solution Composition Affects Dissolution-Recrystallization Mechanisms of Biomimetic Apatite**
Stephanie Wong[1], Mikayla Moynahan[1], Alix Deymier[1]
[1]University of Connecticut

2:15PM **The Skeletal Response to Varied Models of Metabolic Acidosis**
Mikayla Moody[1], Anna Peterson[1], Brian Wingender[1], Katya Morozov[1], Iris Nakashima[1], Tannin Schmidt[1], Alix Deymier[1]
[1]University of Connecticut Health Center

Copyright 2021 SB³C Foundation, Inc.

Poster Session

Poster Session I	Tuesday, June 15, 2:30PM – 4:00PM EDT

Posters: Cardiovascular Biomechanics

Aspen Glade

Session Chair: Thao (Vicky) Nguyen, Johns Hopkins University
Session Chair: Kristin Myers, Columbia University

Theoretical Assessment of Focused Septal Hypertrophic Growth in Hypertrophic Cardiomyopathy
Sandra Hager[1], Will Zhang[2], Renee Miller[1], Jack Lee[1], David Nordsletten[1,2]
[1]King's College London, [2]University of Michigan

Right Ventricular Strain Estimation in Rodents from High-Frequency Ultrasound
Conner Earl[1], Frederick W. Damen[1], Melissa Yin[2], Kristiina Aasa[2], Sarah Burris[2], Craig J. Goergen[1]
[1]Purdue University, [2]FUJIFILM VisualSonics

Aortic Valve Dynamics Coupled with Growth and Remodeling Due to Aging and Calcification
Mohammadreza Soltany Sadrabadi[1], Mona Eskandari[2], Amirhossein Arzani1
[1]Northern Arizona University, [2]University of California, Riverside

A Multiscale Computational Model for Cell-Signaling Driven Growth and Remodeling of Arteries
Linda Irons[1], Marcos Latorre[1], Jay Humphrey[1]
[1]Yale University

Effect of Arterial Wall Inclusions on Failure Mechanics of Intracranial Aneurysm Tissue
Ronald Fortunato[1], Anne Robertson[1], Chao Sang[1], Spandan Maiti[1]
[1]University of Pittsburgh

Biomechanics of Human Fetal Hearts with Critical Aortic Stenosis and Evolving Hypoplastic Left Heart Syndrome
Chi Wei Ong[1], Meifeng Ren[2], Hadi Wiputra[2], Joy Mojumder[3], Wei Xuan Chan[2], Andreas Tulzer[4], Gerald Tulzer[4], Martin Buist[2], Citra Nurfarah Zaini Mattar[2], Lik Chuan Lee[3], Choon Hwai Yap[5]
[1]Agency for Science Technology and Research, [2]National University of Singapore, [3]Michigan State University, [4]Kepler University Hospital, [5]Imperial College London

Effects of Cardiac Geometric Remodeling During Heart Failure on Cardiac Function
Yu Zheng[1], Wei Xuan Chan[1], Choon Hwai Yap[2]
[1]National University of Singapore, [2]Imperial College London

Determination of an Appropriate Strain Energy Density Function for the Tricuspid Heart Valve Leaflets Using Constant Invariant-Based Mechanical Testing
Devin Laurence[1], Chung-Hao Lee[1]
[1]The University of Oklahoma

Copyright 2021 SB³C Foundation, Inc.

Design and Fabrication of a Novel Polymeric Transcatheter Aortic Valve
Hieu Bui[1], Susan James[2], Lakshmi Prasad Dasi[1]
[1]Georgia Institute of Technology, [2]Colorado State University

Embryonic Aortic Arch Material Properties by Optical Coherence Tomography Guided Micro-Pipette Aspiration
S.Samaneh Lashkarinia[1], Gursan Coban[2], Erhan Ermek[1], Merve Celik[1], Hummaira Siddiqui[1], Yap Choon Hwai[3], Kerem Pekkan[1]
[1]Koc University, [2]Istinye University, [3]Imperial College London

Measuring the Anisotropic Mechanical Properties of Single Neonatal Mouse Cardiac Myocytes
Taylor Rothermel[1], Patrick Alford[1]
[1]University of Minnesota - Twin Cities

Transcatheter Heart Valve Leaflet Design Affects Local Leaflet Strain: An *In-Vitro* Study
Beatrice Ncho[1], Katelynne Berland[1], Vahid Sadri[1], Jillian Ortner[1], Ajit Yoganathan[1]
[1]Georgia Institute of Technology

Stress Analysis of Intracranial Aneurysm Based on *In Vivo* 3D Model and Intraoperative Image: A Case Study
Yuanming Luo[1], Xiaodong Zhai[2], Peng Hu[2], Hongqi Zhang[2], Yadong Wang[2], Lan Cao[3], Jia Lu[1]
[1]University of Iowa, [2]Xuanwu Hospital Capital Medical, [3]Boea Wisdom (Hangzhou) Network Technology Co., Ltd.

Model-Directed Design of Kink-Resistant Vascular Grafts with High Compliance
David Jiang[1], Andrew Robinson[1], Elizabeth Cosgriff-Hernandez[1], Lucas Timmins[1]
[1]University of Utah

Myofibril Disarray Decreases Peak Stress & Efficiency in a Finite Element Model of Muscle Fiber
Charles Mann[1], Hossein Sharifi[1], Alexus Rockward[1], Joy Mojumder[2], Lik Chuan Lee[2], Kenneth Campbell[1], Jonathan Wenk[1]
[1]University of Kentucky, [2]Michigan State University

The Effect of Hematocrit on the Viscoelastic Behavior of Embolus Analogs
Bryan Good[1]
[1]University of Tennessee

Optimizing Transcatheter Heart Valve Use in Mitral Annular Calcification
Breandan Yeats[1], Huang Chen[1], Pradeep Yadav[2], Venkateshwar Polsani[2], Vinod Thourani[2], Lakshmi Dasi[1]
[1]Georgia Institute of Technology, [2]Piedmont Hospital

High-Speed Simulation of the 3D Behavior of Myocardium Using a Neural Network PDE Approach
Wenbo Zhang[1], David Li[1], Tan Bui-Thanh[1], Michael Sacks[1]
[1]The University of Texas at Austin

Copyright 2021 SB³C Foundation, Inc.

The Effect of Endothelial Dysfunction on Aortic Mechanics and Extracellular Matrix Microstructure During Age-Related Vascular Remodeling
Liya Du[1], Jeffrey Rodgers[1], Tarek Shazly[1], John Eberth[1], Susan Lessner[1]
[1]University of South Carolina

Nanoparticle-Mediated Controlled Myocardial Delivery for Hypertrophic Cardiomyopathy
Jun Liao[1]
[1]University of Texas at Arlington

Development of a Fully Degradable Heart Valve for Implantation *In Utero*
Hieu T. Bui[1], Sanchita S. Bhat[1], Christopher K. Breuer[2], Aimee Armstrong[2], Martin Bocks[3], Ajit P. Yoganathan[1], Lakshmi Prasad Dasi[1]
[1]Georgia Institute of Technology, [2]Nationwide Children's Hospital, [3]Case Western Reserve University School of Medicine

A Comparative Biomechanical Study of Porcine Epicardial Layer and Endocardial Layer
Jun Liao[1]
[1]University of Texas at Arlington

Biomechanical Characterizations of Acellular Neonatal Porcine Ventricles
Jun Liao[1]
[1]University of Texas at Arlington

Optimization of Perivascular Region Geometry and Material Properties for Application in Patient-Specific Model of a Coronary Artery
Caleb Berggren[1], David Molony[2], Habib Samady[2], Lucas Timmins[1]
[1]University of Utah, [2]Emory University School of Medicine

Fiber-Gel Coupling in Coated Elastomeric Scaffolds for Replacement Heart Valves
Shruti Motiwale[1], Madeleine Russell[1], Megan Wancura[1], Andrew Robinson[1], Elizabeth Cosgriff-Hernandez[1], Michael Sacks[1]
[1]University of Texas at Austin

***In-Vivo* Estimation of Myocardial Elasticity in HFpEF Using Four-Dimensional Ultrasound Imaging**
Maziyar Keshavarzian[1], Sunder Neelakantan[1], Lilly McAllister[1], Carl Tong[1], Reza Avazmohammadi[1]
[1]Texas A&M University

Developing a Reduced Order Modelling Methodology for Simulating Transcatheter Aortic Valve Replacement Procedures
Imran Shah[1], Milad Samaee[1], Atefeh Razavi[1], Alessandro Veneziani[2], Lakshmi Dasi[1]
[1]Georgia Institute of Technology, [2]Emory University

Patient Specific Modeling and 3-Dimensional Printing for Planning of Redo Transcatheter Aortic Valve Replacement
Sri Krishna Sivakumar[1], Huang Chen[1], Breandan Yeats[1], Sarah Tucker[1], Scott Hollister[1], Pradeep Yadav[2], Venkat Polsani[2], Vinod Thourani[2], Lakshmi Dasi[1]
[1]Georgia Institute of Technology, [2]Piedmont Atlanta Hospital

Copyright 2021 SB³C Foundation, Inc.

Modelling Collagen Fiber Recruitment in Aortic Tissue Using Kinetic Average
Xuehuan He[1], Jia Lu[1]
[1]University of Iowa

Patient Specific Computational Modeling Towards Planning of Valve in Valve Transcatheter Aortic Valve Replacement
Sri Krishna Sivakumar[1], Breandan Yeats[1], Venkateshwar Polsani[2], Pradeep Yadav[2], Vinod Thourani[2], Lakshmi Dasi[1]
[1]Georgia Institute of Technology, [2]Piedmont Atlanta Hospital

A Semi-Automatic Approach for Aortic Wall Segmentation to Improve Rapid and Repeatable Assessments of Regional Wall Strain Using Dense MRI
Patrick Jones[1], John Wilson[1]
[1]Virginia Commonwealth University

Stress-Driven Fiber Remodeling in a Finite Element Model of Cardiac Tissue
Alexus Rockward[1], Charles Mann[1], Hossein Sharifi[1], Joy Mojumder[2], Lik Chuan[2], Kenneth Campbell[1], Jonathan Wenk[1]
[1]University of Kentucky, [2]Michigan State University

Categorization Based on *In-Vivo* Imaging and Histological Data Improves Prediction Capability of a Structured-Based Constitutive Model for Aneurysmal Aortic Tissue Mechanics
Tuan Thinh Tong[1], Miriam Nightingale[1], Michael Scott[2], Alex Barker[3], Taisiya Sigaeva[4], Paul Fedak[1], Elena Di Martino[1]
[1]University of Calgary, [2]Northwestern University, [3]University of Colorado Anschutz Medical Campus, [4]University of Waterloo

Collagen Microstructural Organization Contributes to Neovessel Guidance During Angiogenesis
Jason Manning[1], Adam Rauff[1], Jeffrey Weiss[1]
[1]University of Utah

Posters: Computational Biofluid Mechanics I

Aspen Glade

Session Chair: John LaDisa, Marquette University
Session Chair: Alejandro Roldan-Alzate, University of Wisconsin-Madison

Enhanced Hemodynamic Predictions in a Calcified Aortic Valve Geometry Using the Quemada Model
Asad Mirza[1], Amanda Barreto[1], Tisha Boodooram[1], Sharan Ramaswamy[1]
[1]Florida International University

Dynamics of Morphological Remodeling and Impact of Hemodynamics on Restenosis in Human Stented Superficial Femoral Arteries
Monika Colombo[1], Yong He[2], Anna Corti[1], Diego Gallo[3], Federica Ninno[4], Stefano Casarin[5], Jared M Rozowsky[2], Francesco Migliavacca[1], Scott Berceli[2,5,6], Claudio Chiastra[1,2]
[1]Politecnico di Milano, [2]Politecnico di Torino, [3]University of Florida, [4]University College of London, [5]Houston Methodist Hospital, [6]Malcolm Randall VAMC

Copyright 2021 SB³C Foundation, Inc.

Investigating Structural Covariance Networks by Using Graph Measures to Analyze Brain Connectivity for Schizophrenia
Madison Lewis[1], Nicholas Theis[1], Brendan Muldoon[1], Konasale Prasad[1]
[1]University of Pittsburgh

A General Protocol for Simulating Resting Cardiovascular Physiology Using a Closed-Loop Lumped Parameter Model
Akash Gupta[1], Aseem Pradhan[1], Surya Prakash Sharma[1], Tyler Schmidt[1], Ethan Kung[1]
[1]Clemson University

Developing a New Surrogate Model for Computational Fluid Dynamic Simulation of Aorta Using Statistical Shape Modeling and Deep Neural Networks
Pan Du[1], Xiaozhi Zhu[1], Jianxun Wang[1]
[1]University of Notre Dame

Numerical Investigation of Hemodynamics at Initiation of Pulmonary Arterial Hypertension Associated with Congenital Heart Disease
Melody Dong[1], Ingrid Lan[1], Weiguang Yang[1], Marlene Rabinovitch[1], Jeffrey Feinstein[1], Alison Marsden[1]
[1]Stanford University

Development of a Computational Platform to Evaluate a Positive End-Expiratory Pressure in Patients with Tracheostomy
Shiori Kageyama[1], Naoki Takeishi[1], Hiroki Taenaka[1], Takeshi Yoshida[1], Shigeo Wada[1]
[1]Osaka University

Development on a Computational Framework to Express Patient-Specific Intracranial Cerebrospinal Fluid Flow Based on Phase-Contrast Magnetic Resonance Images
Syusaku Maeda[1], Tomohiro Otani[1], Shigeki Yamada[2], Yoshiyuki Watanabe[2], Selin Ilik[1], Naoki Takaishi[1], Shigeo Wada[1]
[1]Osaka University, [2]Shiga University of Medical Science

Modelling Mechanical Feedback Mechanisms in Multiscale Sliding Filament Model of Lymphatic Muscle Pumping
Peter Xie[1], Christopher Morris[1], James Moore[1]
[1]Imperial College London

Junction Modeling in Patient-Specific Blood Flow Simulations
Elena Martinez[1], Martin Pfaller[2], Jonathan Pham[2], Alison Marsden[2]
[1]Loyola Marymount University, [2]Stanford University

Posters: Design Dynamics and Rehabilitation and Education

Aspen Glade

Session Chair: Michael Moreno, Texas A&M University
Session Chair: Anita Singh, Widener University

Copyright 2021 SB³C Foundation, Inc.

Using Dragonfly Imaging Software for Transmission Electron Microscopy Analysis
Connor Leek[1], Megan Killian[1]
[1]University of Delaware, [2]University of Michigan

Carbon Nanotube Infiltration Effects in Thermal Properties of Shape Memory Polymer Foams – Design of a Triggering Mechanism for Endovascular Devices
Sergio Andres Pineda-Castillo[1], Bradley N. Bohnstedt[2], Yingtao Liu[1], Chung-Hao Lee[1]
[1]University of Oklahoma, [2]Indiana University School of Medicine

Design of a MRI-Compatible Pipette Simulator to Study How Pipette Design Affects Joint Forces and Contact Pressures
Nolan Norton[1], Kenneth Fischer[1]
[1]University of Kansas

Comparative Ankle-Foot Rollover Shape Analysis of Powered and Unpowered Prosthetic Feet in Individuals with Transfemoral Amputation
Michael Poppo[1], Andrew Hansen[1,2], John Chomack[1], Jason Maikos[1]
[1]Veterans Affairs New York Harbor Healthcare System, [2]University of Minnesota

Thumb and Index Finger Motions Coupled with Pilot Work on an Octopus Toward the Development of Smart Prosthetics
Garrett Weidig[1], Chris Sadler[1], Tamara Reid Bush[1]
[1]Michigan State University

A Preliminary Framework for Computational Flow Diverter Design Optimization at Scale
Matthew Gunther[1], Brian Chong[2], David Frakes[1]
[1]Georgia Institute of Technology, [2]Mayo Clinic

A Low-Cost, Open-Source Robot Hand-Wrist System for Tactile-ASL Based Communication for the Deaf Blind
Samantha Johnson[1], Gaogeng Gao[2], Minas Liarokapis[2], Chiara Bellini[1]
[1]Northeastern University, [2]The University of Auckland

Connexone: A Medical Application for Protection Against Opioid Overdose
Hirschel Nambiar[1]
[1]Food and Drug Administration

Non-Invasive System to Synchronize Aerosol Delivery with Inhalation in Neonates
Franklin Briones[1], Athena Chien[1], Hope Fa-Kaji[1], Samantha McClendon[1], Pujita Munnangi[1], Rithika Proddutoor[1], Sabia Abidi[1]
[1]Rice University

Wireless Intracranial Pressure Sensing and Mobile Application Transmission for Ventriculoperitoneal Shunts
Madison Belyea[1], Erik Jaklitsch[1], Levon Rodriguez[1], Alexandra Silverman[1], Halyn Valley[1], Michael Jaeggli[1], Yasmeen Elsawaf[2]
[1]Northeastern University, [2]University of Central Florida

Copyright 2021 SB³C Foundation, Inc.

Ultrasonics - Tracking Full-Thickness Skin Deformations for a Biophysics-Based Evaluation of Skin Health
Kyra Bednarski[1], James Brown[1], Edward LaGrassa[1], Mary McNeil[1], Kyle Shepitka[1], Ahsanul Torza[1], Johannes Weickenmeier[1]
[1]Stevens Institute of Technology

LEAR ISP: Automotive Seat Comfort Analysis System
Brittany Wieland[1], Bethany Balint[1], Juan Jaramillo[1], Drake Barry[1], Eric G. Meyer[1], Wu Pan Zagorski[2]
[1]Lawrence Technological University, [2]Lear Corporation

Phantom Limb Pain Strap
Camara L. Casson[1], Angel E. Collins[1], Dina Dragoljic[1], Alexis R. Hopkins[1], Marissa A. Jordan, Camara Casson[1], Ted Conway[1]
[1]Florida Institute of Technology

Posters: Morphology, Development and Emerging Topics in Tissue and Cellular Engineering

Aspen Glade

Session Chair: Chung-Hao Lee, University of Oklahoma

Extracellular Matrix Regulation of Breast Cancer Cell Invasion in a 3D Tumor Model
Jacob Heiss[1], Hossein Tavana[1]
[1]The University of Akron

Acoustic Radiation Force on Eukaryotic Cell Due to Standing Surface Acoustic Wave
Xiangjun Peng[1], Guy Genin[1]
[1]Washington University

Continuum-Based Interpretations of Mechano-Adaptation in Epithelial Micro-Tissues
Bernard Cook[1], Patrick Alford[1]
[1]University of Minnesota

Fgf-10-Mediated Buckling Morphogenesis of the Embryonic Airway Epithelium
Kara Peak[1], Victor Varner[1]
[1]The University of Texas at Dallas

Identification of Adipocyte Secreted Factors Responsible for Myofibroblast Conversion
Mariam El-Hattab[1], Francoise Gourronc[1], Jesse Liszewski[1], Brandon Davies[1], Aloysius Klingelhutz[1], James A. Ankrum[1], Edward A. Sander[1]
[1]University of Iowa

CFD Analysis of Fluid Flow Shear Stress on the Osteocyte Lacuno-Canalicular Network
Mohammadmehdi Niroobakhsh[1], Loretta Laughrey[1], Mark Johnson[1], Sarah Dallas[1], Ganesh Thiagarajan[1]
[1]University of Missouri-Kansas City

Copyright 2021 SB³C Foundation, Inc.

Contractile Perpendicular Lateral Protrusions Facilitate Myofibroblastic Expansion
Abinash Padhi[1], Edna Cukierman[2], Klaus Hahn[3], Rakesh Kapania[1], Amrinder Nain[1]
[1]Virginia Tech, [2]Fox Chase Cancer Center, [3]University of North Carolina Chapel Hill

Mechano-Transcriptomic Analysis of Migratory Phenotypes of Glioblastoma Patient Cells
Jay Hou[1], Mariah McMahon[1], David Odde[1]
[1]University of Minnesota

Copyright 2021 SB³C Foundation, Inc.

Wednesday, June 16	11:00AM – 12:30PM EDT

Brain and Injury Mechanics II: Soft Tissue Mechanics

Saddle Ridge

Session Chair: Jillian Urban, Wake Forest School of Medicine
Session Chair: Haojie Mao, Western University

11:00AM **Studying the Variation of Biomechanics During Myelination Using an *In Vitro* Neuron-Oligodendrocyte Co-Culture Model**
Ya-Chen Chuang[1], Mehmet Kurt[1], Carmen V. Melendez-Vasquez[2], Ace Alcantara[2]
[1]Stevens Institute of Technology, [2]Hunter College

11:13AM **Effects of Pia-Arachnoid Complex Constitutive Formulations on Predictions of Concussion**
Nikolaus Benko[1], Brittany Coats[1]
[1]University of Utah

11:26AM **Head Impact Simplification Using Effective Kinematic Triplets to Preserve Brain Strain**
Kianoosh Ghazi[1], Shaoju Wu[1], Wei Zhao[1], Songbai Ji[1]
[1]Worcester Polytechnic Institute

11:39AM **Time Course of the Cumulative Strain Damage Measure for Frontal and Lateral Impacts**
Tyler F Rooks[1], John Humm[1], Jamie Baisden[1], Narayan Yoganandan[1]
[1]Medical College of Wisconsin

11:52AM **Development and Multi-Level Validation of a Human Aorta Model for Traumatic Injury**
Wei Zeng[1], Adrian Caudillo[1], Sayak Mukherjee[1], Matthew Panzer[1]
[1]University of Virginia

12:05PM ***In Vivo* Injury Thresholds of Neonatal Brachial Plexus Nerves When Subjected to Stretch**
Virginia Orozco[1], Rachel Magee[1], Mitali Sahni[1], Sriram Balasubramanian[1], Anita Singh[2]
[1]Drexel University, [2]Widener University

Wednesday, June 16	11:00AM – 12:30PM EDT

Development and Morphogenesis

Alpine Drift

Session Chair: Yubing Sun, University of Massachusetts, Amherst
Session Chair: Victor Varner, University of Texas, Dallas

11:00AM **Modulating Epithelial Fluid Secretion and Transmural Fluid Pressure to Regulate Proliferation and Branching Morphogenesis in the Embryonic Lung**
Shelby Mohr-Allen[1], Victor Varner[1]
[1]University of Texas at Dallas

Copyright 2021 SB³C Foundation, Inc.

11:13AM **Heterogenous Expression of Long Non-Coding RNA Regulates Vascular Smooth Muscle Cell Adhesion Strength and Phenotype**
Jaimie Mayner[1], Aditya Kumar[1], Pranjali Beri[1], Valentina Lo Sardo[2], Ali Torkamani[1], Kristen Baldwin[2], Adam Engler[1]
[1]University of California San Diego, [2]Scripps Research Institute

11:26AM **Cell-Cell Adhesion Modulates Tissue Fluidity During Epithelial Morphogenesis**
Xun Wang[1], Christian Cupo[1], Karen Kasza[1]
[1]Columbia University

11:39AM **Myosin Network Architecture During Convergent Extension Tissue Morphogenesis**
Christian Cupo[1], Cole Allan[1], Annie Lin[1], Marisol Herrera-Perez[1], Karen Kasza[1]
[1]Columbia University

11:52AM **Quantification of Neuron Morphological Development Using the Change Point Test**
Ashlee Liao[1], Victoria Webster-Wood[1], Yongjie Zhang[1]
[1]Carnegie Mellon University

12:05PM **Assessing Umbilical Vessel Structural Effects on Contraction-Induced Buckling Using Computational Modeling**
Jason Szafron[1], Sae-Il Murtada[1], Sumeda Nandadasa[2], Suneel Apte[2], Jay Humphrey[1]
[1]Yale University, [2]Cleveland Clinic Lerner Research Institute

Wednesday, June 16	**11:00AM – 12:30PM EDT**

Patient Specific Flow and Physiology II

Mud Springs

Session Chair: Amir Arzani, Northern Arizona University
Session Chair: Hoda Hatoum, Michigan Technological University

11:00AM **Exploring the Link Between Wall Shear Stress Topological Skeleton and Near-Wall Mass Transport in Cardiovascular Flows Using a Eulerian-Based Method**
Giuseppe De Nisco[1], Valentina Mazzi[1], Karol Calò[1], Maurizio Lodi Rizzini[1], Claudio Chiastra[1], Jolanda J. Wentzel[2], David A. Steinman[3], Diego Gallo[1], Umberto Morbiducci[1]
[1]Politecnico di Torino, [2]Erasmus MC, [3]University of Toronto

11:13AM **Simulation of Cryoballoon Ablation for Pulmonary Vein Isolation**
Tejas Patel[1], Tong Gao[1], Lik Chuan Lee[1]
[1]Michigan State University

11:26AM **Examination of Prospective and Retrospective Gated 4D Flow MRI Acquisitions to Evaluation Fluid Velocities in the Carotid Bifurcation**
Elliott Hurd[1], Jason Mendes[1], Edward DiBella[1], John Oshinski[2], Lucas Timmins[1]
[1]University of Utah, [2]Emory University School of Medicine

Copyright 2021 SB³C Foundation, Inc.

11:39AM **Computational Modeling of Borderline Left Ventricular Circulation for Clinical Decision-Making**
Yurui Chen[1], Isao Anzai[1], David Kalfa[1], Vijay Vedula[1]
[1]Columbia University

11:52AM **Tracking of the Left Atrial Appendage Motion in Time Resolved CT**
Sophia Bäck[1], Lilian Henrikson[1], Carl-Johan Carlhäll[1], Anders Persson[1], Matts Karlsson[1], Tino Ebbers[1]
[1]Linköping University

12:05PM **Focal Enhancement in Intracranial Aneurysms – Effects of Local Hemodynamics On VW-MRI Signals**
Franziska Gaidzik[1], Mariya Pravdivtseva[2], Jana Korte[1], Naomi Larsen[2], Sylvia Saalfeld[1], Gábor Janiga[1], Philipp Berg[1]
[1]University of Magdeburg, Germany, [2]University Hospital Schleswig-Holstein Kiel, Germany

Wednesday, June 16	**11:00AM – 12:30PM EDT**

PhD Student Paper Competition 4: Soft Tissue Biomechanics

Mogul Madness

Session Chair: Liyun Wang, University of Delaware
Session Chair: Joel Boerckel, University of Pennsylvania

11:00AM **A High-Fidelity 3D Micromechanical Model of Ventricular Myocardium**
David Li[1], Emilio Mendiola[1], Reza Avaz[2], Frank Sachse[3], Michael Sacks[1]
[1]The University of Texas at Austin, [2]Texas A&M University, [3]The University of Utah

11:15AM **Novel Multiscale Structure-Based Model of the Bovine Caudal Disc Motion Segment**
Minhao Zhou[1], Grace O'Connell[1]
[1]University of California, Berkeley

11:30AM **Measuring *In Situ* Lumbar Facet Capsular Ligament Strains Due to Joint Pressure and Residual Stress**
Elizabeth Gacek[1], Arin Ellingson[1], Victor Barocas[1]
[1]University of Minnesota - Twin Cities

11:45AM **From Microstructure to Micromechanical Properties of Soft Tissues**
Amir Ostadi Moghaddam[1], Woowon Lee[2], Zixi Lin[3], Heidi Phillips[1], Mayandi Sivaguru[1], Barbara McFarlin[4], Kimani Toussaint[3], Amy Wagoner Johnson[1]
[1]University of Illinois at Urbana Champaign, [2]University of Colorado Boulder, [3]Brown University, [4]University of Illinois at Chicago

12:00PM **Actomyosin Contractility Regulates Multi-Scale Mechanobiology of Nucleus Pulposus Cells in Inflammation**
Timothy Jacobsen[1], Paula Hernandez[2], Nadeen Chahine[1]
[1]Columbia University, [2]University of Texas Southwestern Medical Center

Copyright 2021 SB³C Foundation, Inc.

12:15PM **Mechanical Response of Mouse Cervices Lacking Decorin and Biglycan During Pregnancy**
Nicole Lee[1], Lei Shi[1], Mariano Caraballo[2], Shanmugasundaram Nallasamy[2], Charles Jayyosi[1], Mala Mahendroo[2], Kristin Myers[1]
[1]Columbia University, [2]University of Texas Southwestern Medical Center

Wednesday, June 16	**1:00PM – 2:30PM EDT**

Biotransport in Tumor Microenvironment and Immunotherapy

Mud Springs

Session Chair: Kunal Mitra, Florida Tech
Session Chair: Fateme Esmailie, Georgia Institute of Technology

1:00PM **Re-Engineering the Mechanical Tumor Microenvironment with Dexamethasone Enhances Efficacy of Cisplatin-Loaded Nanocarrier in Metastatic Breast Cancer**
Fotios Mpekris[1], John D. Martin[2], Myrofora Panagi[1], Thahomina T. Khan[2], Margaret R. Martin[2], Chrysovalantis Voutouri[1], Jumpei Norimatsu[2], Triantafyllos Stylianopoulos[1], Kazunori Kataoka[3], Horacio Cabral[2]
[1]University of Cyprus, [2]University of Tokyo, [3]Kawasaki Institute of Industrial Promotion

1:13PM **Spatiotemporal Progression and Modulation of the Blood-Brain-Tumor Barrier**
Qi Cai[1], Xiaoqing Li[1], Hejian Xiong[1], Xiaofei Gao[2], Robert Bachoo[2], Zhenpeng Qin[1]
[1]The University of Texas at Dallas, [2]University of Texas Southwestern Medical Center

1:26PM **Targeted Heating of Mitochondria Greatly Augments Nanoparticle-Mediated Cancer Chemotherapy**
Jiangsheng Xu[1], Xiaoming He[1]
[1]University of Maryland, College Park

1:39PM **A Novel Local Tumor Progression Prediction Method for Multi-Mode Thermal Ablation**
Xinyi Wang[1], Jianlong Yang[1], Aili Zhang[1], Lisa X. Xu[1]
[1]Shanghai Jiao Tong University

1:52PM **Mechanotherapeutics Combined with Cytotoxic Nanomedicine Overcomes Vessel Compression and Resistance to Immunotherapy in Triple Negative Breast Cancer**
Myrofora Panagi[1], Fotios Mpekris[1], Chrysovalantis Voutouri[1], John D. Martin[2], Kazunori Kataoka[3], Horacio Cabral[2], Triantafyllos Stylianopoulos[1]
[1]University of Cyprus, [2]The University of Tokyo, [3]Kawasaki Institute of Industrial Promotion

2:05PM **Quantitative Assessment of the Effects of Interstitial Flows, Macrophage Polarization and Immunotherapy on Tumor Immune Cell Infiltration**
Huu Tuan Nguyen[1], Nadia Gurvich[2], Christie Zhang[2], Giovanni Offeddu[1], Mark Gillrie[1], Sharon Lee[1], Seng-Lai Tan[2], Roger Kamm[1]
[1]Massachusetts Institute of Technology, [2]Elstar Therapeutics

Copyright 2021 SB³C Foundation, Inc.

Wednesday, June 16	1:00PM – 2:30PM EDT

Growth and Remodeling Mechanics I: Growth and Remodeling

Mogul Madness

Session Chair: Kyoko Yoshida, University of Virginia
Session Chair: Adrian Buganza Tepole, Purdue University

1:00PM **3D Growth and Remodeling in Ascending Thoracic Aortic Aneurysms**
Joan Laubrie[1,2,3], Jamaleddin Mousavi[1,2,3], Stéphane Avril[1,2,3]
[1]Mines Saint-Etienne, [2]University of Lyon, [3]University of Jean Monnet

1:13PM **Remodeling of the Thoracic Aorta Due to Ageing in Mice**
Yasmeen Farra[1], Jacqueline Matz[1], Chiara Bellini[1]
[1]Northeastern University

1:26PM **Computational Modeling of Stress-Mediated Vascular Remodeling in Pulmonary Arterial Hypertension**
Reza Pourmodheji[1], Zhenxiang Jiang[1], Christopher Tossas-Betancourt[2], C. Alberto Figueroa[2], Seungik Baek[1], Lik Chuan Lee[1]
[1]Michigan State University, [2]University of Michigan

1:39PM **Alterations to the Maternal Bony Pelvis and Pelvic Floor Muscle Complex During Pregnancy: a Statistical Shape Analysis**
Megan Routzong[1], Liam Martin[1], Ghazaleh Rostaminia[2], Pamela Moalli[1], Steven Abramowitch[1]
[1]University of Pittsburgh, [2]University of Chicago

1:52PM **Effect of Elastase Digestion and Maternal Age on Murine Vagina Wall Biaxial Mechanics**
Shelby White[1], Laurephile Desrosiers[2], Leise Knoepp[2], Kristin Miller[1]
[1]Tulane University, [2]Ochsner Clinical School

2:05PM **A Hybrid Discrete-Continuum Multiscale Kinematic Growth Model**
Elizabeth Gacek[1], Ryan Mahutga[1], Victor Barocas[1]
[1]University of Minnesota - Twin Cities

Wednesday, June 16	1:00PM – 2:30PM EDT

Ligament and Tendon Mechanics: Modeling and Measurement

Saddle Ridge

Session Chair: Megan Killian, University of Michigan
Session Chair: Babak Safa, Georgia Institute of Technology

1:00PM **An Inverse Mechanics Approach to Determine Changes in the Mechanical Heterogeneity of the Lumbar Facet Capsular Ligament**
Jill Middendorf[1], Victor Barocas[1]
[1]University of Minnesota

Copyright 2021 SB³C Foundation, Inc.

1:13PM **Tuning Shear Wave Tensiometry to Improve Subject Specificity in Achilles Tendon Loading Measurements During Walking**
Stephanie Cone[1], Dylan Schmitz[1], Darryl Thelen[1]
[1]University of Wisconsin

1:26PM **Sensitivity of the Shear Wave Speed-Stress Relationship to Ligament Fiber Alignment – A Probabilistic Finite Element Study**
Jonathon Blank[1], Darryl Thelen[1], Joshua Roth[1]
[1]University of Wisconsin-Madison

1:39PM **Fatigue Loading of Mouse Achilles Tendon Explants Does Not Induce Collagen Denaturation**
Krishna Pedaprolu[1], Spencer Szczesny[1]
[1]Pennsylvania State University

1:52PM **Signal to Noise Ratio of Polarization Imaging Parameters Is Dependent on Light Intensity and Microstructural Anisotropy of Soft Tissues**
Leanne Iannucci[1], Yingkai Chen[2], Viktor Gruev[2], Spencer Lake[1]
[1]Washington University in St. Louis, [2]University of Illinois at Urbana-Champaign

2:05PM **Label-Free Quantification of Soft Tissue Alignment by Polarized Raman Spectroscopy**
Hui Zhou[1], Janny Pineiro[1], Malisa Sarntinoranont[1], Ghatu Subhash[1], Chelsey Simmons[1]
[1]University of Florida

Wednesday, June 16	**1:00PM – 2:30PM EDT**

Tissue Engineering and Regeneration

Alpine Drift

Session Chair: Brendon Baker, University of Michigan
Session Chair: Alix Deymier, University of Connecticut Health Center

1:00PM **Sustained Il-10 Delivery Enhances Recovery from Volumetric Muscle Loss Injury Through Immunoregulatory Factors**
Tai Huynh[1], Cassandra Reed[1], Zain Blackwell[1], David Zaharoff[2], Jeffrey Wolchok[1]
[1]University of Arkansas – Fayetteville, [2]University of North Carolina - Chapel Hill

1:13PM **Mechanosensing as a Therapeutic Target in Synovial Fibrosis**
Edward Bonnevie[1], Carla Scanzello[1], Robert Mauck[1]
[1]University of Pennsylvania

1:26PM **Mechanosensitive Notch Signaling Regulates Phenotypic Changes in Vascular Smooth Muscle Cells**
Cansu Karakaya[1], Valery Visser[1], Tommaso Ristori[1], Carlijn Bouten[1], Cecilia Sahlgren[1,2], Sandra Loerakker[1]
[1]Eindhoven University of Technology, [2]Åbo Akademi University

Copyright 2021 SB³C Foundation, Inc.

1:39PM **Reversible Inhibition of Myofibroblast Activity to Improve Elbow Range of Motion After Capsulectomy**
Jordan A Jensen[1], Venkat Ganesh[1], Mariam Y El-Hattab[1], Jaidev Chakka[1], Juliana C Quarterman[1], Timothy P Fowler[1], Emily Petersen[1], Douglas Fredricks[1], James A Martin[1], Aliasger K Salem[1], Edward A Sander[1]
[1]University of Iowa

1:52PM **Stiffness and Anisotropy Dependent Proangiogenic Potential of Mesenchymal Stromal Cells**
Michael Nguyen-Truong[1], Seungil Kim[2], Courtney Doherty[1], Megan Frederes[1], Samantha Kaonis[1], Soham Ghosh[1], Peiman Hematti[3], William Wagner[2], Zhijie Wang[1]
[1]Colorado State University, [2]University of Pittsburgh, [3]University of Wisconsin, Madison

2:05PM **Fibril Strain Promotes Addition of Type I Collagen Molecules to Single, Native Collagen Fibrils *In Vitro***
Seyed Mohammad Siadat[1], Jeffrey Ruberti[1]
[1]Northeastern University

Poster Sessions

Poster Session II	**Wednesday, June 16, 2:30PM – 4:00PM EDT**

Posters: Biotransport

Aspen Glade

Session Chair: Joanna Dahl, University of Massachusetts, Boston
Session Chair: Zhenpeng Qin, University of Texas, Dallas

Peristaltic Pumping in Sub-Wavelength Perivascular Models
Jessica Shang[1], John Brennen Carr[1], Caroline Cardinale[1], Delin Zeng[1]
[1]University of Rochester

A Continuum Mechanics Approach to Model Stiffness Sensing by Smooth Muscle Cells
Ali Akbar Karkhaneh Yousefi[1,2], Claudie Petit[1,2], Stephane Avril[1,2]
[1]Mines Saint-Etienne, [2]University of Lyon

Excess collagen deposition in diabetic kidney disease enhances cellular communication: A mathematical model
Haryana Thomas[1,2], Ashlee Ford Versypt[1,2]
[1]Oklahoma State University, [2]University at Buffalo

Pulsatile Perfusion Optimization within a Multi-Organ Preservation Device
Daniel Portillo[1], Stephen Rivas[1], Gabriela Pineda[1], Sukhwinder Kaur[1], Lauren Bayliss[2], Leon Bunegin[3], R. Lyle Hood[1]
[1]The University of Texas at San Antonio, [2]The University of Texas - Rio Grande Valley, [3]Vascular Perfusion Solutions

Copyright 2021 SB³C Foundation, Inc.

Differentiating Nanoscale Confined and Collective Heating by Plasmonic Nanoparticle Arrays
Chen Xie[1], Peiyuan Kang[1], Zhenpeng Qin[1]
[1]University of Texas at Dallas

Effect of Convection on Cellular Sensing Precision for Directed Cell Migration
Hye-ran Moon[1], Soutick Saha[1], Andrew Mugler[2], Bumsoo Han[1]
[1]Purdue University, [2]University of Pittsburgh

The Role of Eye Movements in the Process of Silicone Oil Emulsification After Vitrectomy
Irene Nepita[1], Alessandro Stocchio[1], Libero Liggieri[3], Francesca Ravera[3], Eva Santini[3], Mario R. Romano[4], Rodolfo Repetto[1]
[1]University of Genoa, [2]Hong Kong Polytechnic, [3]Institute for Condensed Matter Chemistry and Technologies for Energy, CNR, Genoa, [4]Humanitias University, Milan

Study on Heating Capability of New Radiofrequency Angioplasty Balloon
Hongying Wang[1], Shiqing Zhao[1], Jincheng Zou[1], Aili Zhang[1]
[1]Shanghai Jiao Tong University, Shanghai, China

Estimation of Clinical Size of Breast Tumour Lesions Using Contrast Enhanced Magnetic Resonance Imaging: Delineation of Tumour Boundaries
Manpreet Singh[1], Manjesh Dalal[2], Gurasis Singh Sodhi[2]
[1]University of Maryland, [2]Government Medical college and Hospital, Sector 32B, Chandigarh

Biofluid Mechanics of Surfactant Delivery in Bioengineered Three-Dimensional Lung Airway Model
Hannah Combs[1], Hossein Tavana[1]
[1]The University of Akron

A High Performance, Low-Cost Approach to Ventilation to Increase Global Capacity for Covid-19
Daniel J. Watson[1], Jennifer Frattolin[1], Michael Madekurozwa[1], Willy V. Bonneuil[1], Axel C. Moore[1], James E. Moore Jr.[1], Jakob Mathiszig-Lee[1,2], Joseph van Batenburg-Sherwood[1]
[1]Imperial College London, [2]Royal Marsden Hospital

Effect of Curvature on the Thermal Interface Conductance Between Nanoscale Gold and Water
Blake Wilson[1], Jaona Randrianalisoa[2], Steven Nielsen[1], Zhenpeng Qin[1]
[1]The University of Texas at Dallas, [2]University of Reims Champagne-Ardenne

Bioinspired 3D Culture in Nanoliter Core-Shell Hydrogel Microcapsules Isolates Highly Pluripotent Human IPSCS
Jiangsheng Xu[1], James Shamul[1], Xiaoming He[1]
[1]University of Maryland, College Park

Stroma Affects the Intratumoral Transport of Bacteria-Based Drug Delivery Agents
Ying Zhan[1], Richey Davis[1], Bahareh Behkam[1],
[1]Virginia Tech

Copyright 2021 SB³C Foundation, Inc.

Enhancing Transscleral Delivery of a Drug Surrogate Using Ultrasound in Porcine Eyes
Grayson Bockman[1], Jr. Jiun Liou[1], Jonathan Vande Geest[1]
[1]University of Pittsburgh

Interactive Program Development for Analysis of Hemodynamic Data in Patients with Pulmonary Hypertension
Jordan Elliott[1], Franz Rischard[1], Rebecca Vanderpool[1]
[1]University of Arizona

Posters: Experimental Biofluid Mechanics I

Aspen Glade

Session Chair: John LaDisa, Marquette University
Session Chair: Alejandro Roldan-Alzate, University of Wisconsin-Madison

Prevalence and Risk Factors for Blebs in Intracranial Aneurysms
Seyedeh Fatemeh Salimi Ashkezari[1], Fernando Mut[1], Juan Cebral[1]
[1]George Mason University

Association Between Aneurysm Local Hemodynamics and Wall Enhancement on 7T-MRI
Sara Hadad[1], Fernando Mut[1], Bong J Chung[2], Jorge A Roa[3], Anne M Robertson[4], David M Hassan[3], Edgar A Samaniego[3], Juan R Cebral[1]
[1]George Mason University, [2]Mount Saintclair University, [3]University of Iowa, [4]University of Pittsburg

Evolution of the Hemodynamic Properties and Arterial Wall Remodeling in Pulmonary Arterial Hypertension
Hao Mu[1], Daniela Valdez-Jasso[1]
[1]University of California, San Diego

Frequency Characteristics of Elastic Patient-Specific Aneurysm Model
Ryuhei Yamaguchi[1], Naoki Ikeya[2], Nadia Shafii[3], Kahar Osman[3], Atsushi Saito[4], Gaku Tanaka[2], Makoto Ohta[1]
[1]Institute of Fluid Science, Tohoku University, [2]Chiba University, [3]Universiti Teknologi Malaysia, [4]Sendai Medical Center

A Combined Microfluidic Device and Numerical Simulation Technique for the Evaluation of Red Blood Cell Shear Induced Damage
Ratul Paul[1], Mehdi Nikfar[1], Yuyuan Zhou[1], Meghdad Razizadeh[1], Yaling Liu[1]
[1]Lehigh University

Analysis of Hemodynamics in Aneurysm Blebs with Thin and Atherosclerotic Walls
Seyedeh Fatemeh Salimi Ashkezari[1], Fernando Mut[1], Juan Cebral[1]
[1]George Mason University

Wall Shear Stress (WSS) Values in a Pig Model of Carotid Stenosis Based on Free-Running 5D MRI and CFD
Yinghan Xu[1], John N. Oshinski[1], Murali Padala[1], Keshav Kohli[2], Zhenglun Alan Wei[2], Alison Marsden[3]
[1]Emory University, Georgia Institute of Technology, University of Massachusetts Lowell

Copyright 2021 SB³C Foundation, Inc.

Differential Nanoparticle Accumulation in a Mouse Model of Atherosclerosis May be Driven by Smooth Muscle Cells
Morgan Schake[1], Ian McCue[1], Hunter Miller[1], Badrul Alam Bony[1], Evan Curtis[1], Connor Gee[1], Forrest Kievit[1], Ryan Pedrigi[1]
[1]University of Nebraska-Lincoln

Blood Flow in a Retina Capillary Vascular Network with Explicit Blood Cells
Kacper Ostalowski[1], Jifu Tan[1]
[1]Northern Illinois University

***In Vitro* Validation of a Real-time 3D MRI Urodynamics Protocol**
Colin Kim[1], Cody Johnson[1], James Rice[1], Alejandro Roldan-Alzate[1]
[1]University of Wisconsin-Madison

The Effect of Shear Stress on Human Lung Microvascular Endothelial Cell Glycocalyx
Camden Holm[1], Natasha Cruz-Calderon[1], Solomon Mensah[1]
[1]Worcester Polytechnic institute

Posters: Injury, Bone, Joint and Musculoskeletal Biomechanics

Aspen Glade

Session Chair: Thao (Vicky) Nguyen, Johns Hopkins University
Session Chair: Kristin Myers, Columbia University

Brain Strain at Skull Frame of Reference
Yuzhe Liu[1], Xianghao Zhan[1], August G. Domel[1], Michael Zeineh[1], Gerald Grant[1], David Camarillo[1]
[1]Stanford University

Prediction of Brain Strain Across Head Impact Subtypes Using 18 Brain Injury Criteria
Xianghao Zhan[1], Yiheng Li[1], Yuzhe Liu[1], David Camarillo[1]
[1]Stanford University

Larger Muscle Fibers and Fiber Bundles Manifest Smaller Elastic Modulus in Paraspinal Muscles of Rats and Humans
Masoud Malakoutian[1], Marine Theret[1], Shun Yamamoto[1], Iraj Dehghan-Hamani[1], Michael Lee[1], John Street[1], Fabio Rossi[1], Stephen Brown[2], Thomas Oxland[1]
[1]University of British Columbia, [1]University of Guelph

Finite Element Analysis for Carpal Arch Under Varying Thenar Muscle Force Magnitudes and Directions
Hui Zhang[1], Zong-Ming Li[1]
[1]University of Arizona

Studying the Mechanical Effect of Human Talus Bone Implants on the Surrounding Articular Cartilage
Maha Ead[1], Tao Liu[1], Kajsa Duke[1], Nadr Jomha[1], Marwan El-Rich[2], Lindsey Westover[1]
[1]University of Alberta, [2]Khalifa University

Copyright 2021 SB³C Foundation, Inc.

Modeling the Effect of Bighorn Sheep Horn Shape on Post-Impact Accelerations
Benjamin Wheatley[1], Aaron Drake [2], Luca Fuller[2], Seth Donahue[2]
[1]Bucknell University, [2]University of Massachusetts Amherst

The Differential Impact of Heterogeneity on Trabecular Plates and Rods in Finite Element Models of Human Vertebral Bone
Jason Cox[1], Jacqueline Cole[1]
[1]University of North Carolina at Chapel Hill / North Carolina State University

The Evolution of Heterogeneous Parameters for Modeling Cartilage During the Progression of Osteoarthritis
Xiaogang Wang[1], David Pierce[1]
[1]University of Connecticut

An Electromagnetic Actuator for Brain Magnetic Resonance Elastography
Suhao Qiu[1], Zhao He[1], Runke Wang[1], Ruokun Li[2], Fuhua Yan[2], Yuan Feng[1]
[1]Shanghai Jiao Tong University, [2]Ruijin Hospital

Fatigue-Induced Damage Accretion of the Elbow AMCL Due to Repetitive Valgus Cycling
David Jordan[1], Alexander Kharlamov[2], Patrick Schimoler[1], Mark Miller[1]
[1]University of Pittsburgh, [2]Allegheny General Hospital

Estimation and Assessment of Sagittal Spinal Curvature and Thoracic Muscle Morphometry in Different Postures
Anoosha Pai S[1], Thomas R. Oxland[1], David R. Wilson[1], Stephen H.M. Brown[2], John Street[1], Honglin Zhang[1], Sidney Fels[1]
[1]The University of British Columbia, [2]University of Guelph

Mechanical Function of Fan-Like Extension and Midsubstance Fibers of Porcine Anterior Cruciate Ligament
Satoshi Yamakawa[1], Konsei Shino[2], Tatsuo Mae[1], Ken Nakata[1], Hiromichi Fujie[3]
[1]Osaka University, [2]Yukioka Hospital, [3]Tokyo Metropolitan University

On the Clinical Diagnosis of Acromioclavicular Joint Arthritis
Bethany Arn[1], Mohamed Samir Hefzy[1], Brian Trease[1], Abdulazim Mustapha[1]
[1]The University of Toledo

Clinical Evaluation of a Novel Fastening Device for a Scoliosis Brace
Denis DiAngelo[1], Chloe Chung[1], Daniel Hoyer[1], Derek Kelly[2], Jeffery Sawyer[2]
[1]The University of Tennessee Health Science Center, [2]Campbell Clinic Orthopaedics

Multi-Directional Flexibility Endurance Testing of Four Different Cervical Total Disc Replacement Prostheses
Denis DiAngelo[1], Chloe Chung[1], Daniel Hoyer[1], Tyler Carson[2], Kevin Foley[2]
[1]The University of Tennessee Health Science Center, [2]Semmes Murphey Clinic

Shear Expulsion Testing of Four Different Cervical Total Disc Replacement Prostheses
Denis DiAngelo[1], Chloe Chung[1], Daniel Hoyer[1], Tyler Carson[2], Kevin Foley[2]
[1]The University of Tennessee Health Science Center, [2]Semmes Murphey Clinic

Copyright 2021 SB³C Foundation, Inc.

Influence of Physiologically Informative Average Contact Stresses on Cartilages' Tribological Rehydration
Shamimur Akanda[1], Meghan Kupratis[1], David Burris[1], Christopher Price[1]
[1]University of Delaware

Effect of Seat Orientation on the Lumbar Response to FAA-Longitudinal Crash Pulse: A Parametric Modeling Study
Karthik Somasundaram[1], John Humm[1], Prashant Kandelwal[1], Narayan Yoganandan[1], Frank Pintar[1]
[1]Medical College of Wisconsin

Implementing an Artificial Neural Network to Study Brain Strain and Mild Traumatic Brain Injury Metrics
Luke Patterson[1], Yanir Levy[1], Haojie Mao[1]
[1]University of Western Ontario

Bone Biomechanics Advances Animal Welfare in Egg-Laying Hens
Glynn Gallaway[1], Brittney Emmert[1], Thomas Siegmund[1], Darrin Karcher[1]
[1]Purdue University

Development of an Anatomically Accurate Non-Human Primate Finite Element Head Model
Tyler Rooks[1], John Humm[1], Jamie Baisden[1], Narayan Yoganandan[1]
[1]Medical College of Wisconsin

A Computational Digital Twin Methodology for Understanding Biomechanics of Vertebroplasty
Hossein Ahmadian[1], Prasath Mageswaran[1], Dukagjin Blakaj[1], Ehud Mendel[1], Soheil Soghrati[1], Wiiliam Marras[1]
[1]The Ohio State University

Presence of Greater Tuberosity Facets Significantly Altered in Subjects with Symptomatic Isolated Supraspinatus Tendon Tears
Luke Mattar[1], Rachel Martello[1], Adam Popchak[1], Volker Musahl[1], James Irrgang[1], Richard Debski[1]
[1]University of Pittsburgh

Accelerated Acquisition of Displacements and Strain in Tibiofemoral Joint Cartilage by Spiral DENSE MRI and Compressed Sensing
Woowon Lee[1], Emily Miller[1], Corey Neu[1]
[1]University of Colorado Boulder

Alteration of Intrinsic Brain Motion After Endoscopic Third Ventriculostomy Treatment in Neonatal Hydrocephalus
Aymeric Pionteck[1], Manasa Rao[2], Peter Morgenstern[2], Mehmet Kurt[1]
[1]Stevens Institute of Technology, [2]Icahn School of Medicine at Mount Sinai

Copyright 2021 SB³C Foundation, Inc.

Toward the Translation of 3D-Printed Flexible-PLA Intervertebral Discs in Small Animal Rodent Models
Samantha Marshall[1], Jennifer Pilamunga[1], Joseph Lombardi[1], Nadeen Chahine[1]
[1]Columbia University

***In Vivo* Quantification of Brain Morphologies Via Mechanics-Informed Deep Learning Approach**
Shuolun Wang[1], Nagehan Demirci[1], Vicente Castro Solar[2], Maria Holland[1], Francisco Sahli Costabal[2]
[1]University of Notre Dame, [1]Pontificia Universidad Catolica de Chile

Analyzing Suture Fixation Techniques for Tibial Eminence Avulsion Fractures
Yulia Yatsenko[1], Nyaluma Wagala[1], Calvin Chan[1], Volker Musahl[1], Richard Debski[1]
[1]University of Pittsburgh

Effect of Helmet on Gender-Based Cervical Spine Segmental Responses in Rear Impact
Yuvaraj Purushothaman[1], John Humm[1], Hoon Choi[1], Deepak Rajasekaran[1], Narayan Yoganandan[1]
[1]Medical College of Wisconsin

Altering Surface Curvature of Patellar Osteochondral Allografts Through Subject-Specific Modification of Subchondral Bone
Katherine Spack[1], Courtney Shaeffer[1], Peter Shyu[1], James Cook[2], Clark Hung[1], Melvin Rosenwasser[1], Gerard Ateshian[1]
[1]Columbia University, [2]University of Missouri

Wave Transmission and Bone Growth in Bioinspired Scaffolds
Marco Fielder[1], Arun Nair[1]
[1]University of Arkansas

Sitting MRI Study of Lumbar Spinal Musculature
Vicky Varghese[1], Hoon Choi[1], Jamie Baisden[1], Anjishnu Banerjee[1], Ulrich Kemmo[1], Sagar Umale[1], John Humm[1], Narayan Yoganandan[1]
[1]Medical College of Wisconsin

Head Impact Biomechanics of Ice Zone and Athlete Intent in Youth Ice Hockey
Abigail Swenson[1], N. Stewart Pritchard[1,2], Logan Miller[1,2], Jillian Urban[1,2], Joel Stitzel[1,2]
[1]Wake Forest University School of Medicine, [2]Virginia Tech

Mechanical Environment of Supraspinatus Tendon During Functional Reach: A Finite Element Study
S. Cyrus Rezvanifar[1], John Looft[2], Anna Spracklin[3], Mohab Eid[1], Justin Staker[1], Arin Ellingson[1], Paula Ludewig[1]
[1]University of Minnesota - Twin Cities, [2]Minneapolis VA Health Care System, [3]Northwestern University

Segmental Loads in Male and Female Necks Under Helmeted Condition in Frontal (G-X) Impacts
Yuvaraj Purushothaman[1], Sagar Umale[1], John Humm[1], Narayan Yoganandan[1]
[1]Medical College of Wisconsin

Copyright 2021 SB³C Foundation, Inc.

Effects of Impact Position, Muscle Activation and Posture on Head Injury Risk
Jonathan Mortensen[1], Nikolaus Benko[1], Brittany Coats[1], Andrew Merryweather[1]
[1]University of Utah

Evaluating Flexor Digitorum Superficialis Tendon Fatigue Using High-Frequency Ultrasound Based Strain Algorithms
Andrew Darling[1], Conner Earl[1], Fredrick W. Damen[1], Nan Chen[1], Travis Mendoza[2], Denny Yu[1], Grace O'Connel[2], Carisa Harris Adamson[3], Craig J. Goergen[1]
[1]Purdue University, [2]University of California, Berkeley, [3]University of California, San Francisco

Machine Learning Segmentation for Densitometric Phantom CT Data
Ashley Pernsteiner[1], Carla Winsor[1], Heidi-Lynn Ploeg[2], Corinne Henak[1]
[1]University of Wisconsin – Madison, [2]Queen's University

Youth Pitching Kinematics: Associations with Body Overweight Parameters
Christina Fong[1], Ryan Sax[1], Rafael Escamilla[2], Arnel Aguinaldo[3], Scott Hazelwood[1], Stephen Klisch[1]
[1]California Polytechnic State University, [2]California State University, Sacramento, [3]Point Loma Nazarene University

A Methodology to Measure the True Flexural Strength of Brittle Cylinders
Michael MacIsaac[1], Ghatu Subhash[1], Salil Bavdekar[1]
[1]University of Florida

Measurement of Mechanical Properties of Iberian Ribbed Newt Tendon Toward Establishment of Complete Tendon Regeneration Model
Fumiya Sato[1], Daisuke Suzuki[2], Toshinori Hayashi[3], Takeo Matsumoto[1], Eijiro Maeda[1]
[1]Nagoya University, [2]Hokkaido Chitose College of Rehabilitation, [3]Hiroshima University

Micromechanical Comparison Between Hydrogel and Silicone Gel Used for Studying Stiffness Sensing by Adherent Cells
Kathleen Heusser[1], Nikhil Mittal[1], Mohanish Chandurkar[1], Zhongtian Zhang[1], Karrar Alofari[1], Jeffrey Allen[1], Bruce Lee[1], Fei Long[1], Sangyoon Han[1]
[1]Michigan Technological University

Posters: Mechanobiology in Tissue and Cellular Engineering

Aspen Glade

Session Chair: Solomon Mensah, Worcester Polytechnic Institute

Structural and Non-Structural Determinants of Speed and Timing of Conduction in Auditory Neuronal Axons
Jun Xu[1]
[1]Tarleton State University

Role of the Extracellular Environment in Achieving Stable Epithelial Morphogenesis *In Vitro*
Marjan Hagelaars[1], Carlijn Bouten[1], Sandra Loerakker[1]
[1]Eindhoven University of Technology

Copyright 2021 SB³C Foundation, Inc.

Melanoma Tumour Formation in 3D Collagen *In Vitro* Matrices is Regulated by Intracellular Mechanics and Tbx3 Content
Ghodeejah Higgins[1], Faatiemah Higgins[1], Jade Peres[1], Tamer Abdalrahman[2], Muhammad Zaman[3], Sharon Prince[1], Thomas Franz[1]
[1]University of Cape Town, [2]Charité Medical University of Berlin, Germany, [3]Boston University

Myosin-Independent Mechanotransmission for Sensing Stiffness of Extracellular Matrix
Nikhil Mittal[1], Sangyoon Han[1]
[1]Michigan Technological University

Role of Substrate Stiffness on Pluripotency and Differentiation of Human Embryonic Stem Cells
Jasmeet Kaur Virdi[1], Prasad Pethe[2]
[1]SVKM's NMIMS Deemed-to-be University, [2]Symbiosis International University

Male and Female HUVEC Differ in Extracellular Matrix, Inflammation, and Vascular Function-Related Gene Expression
Callie Weber[1], Nicole Arnold[2], Douglas Dluzen[1], Alisa Clyne[1]
[1]University of Maryland, [2]Morgan State University

Acute Remodeling of a Tissue Engineered Vascular Graft Is Influenced by Compliance and Transforming Growth Factor Beta 2
Kenneth Furdella[1], Shinichi Higuchi[1], Kang Kim[1], Tom Doetschman[2], William Wagner[1], Jonathan Vande Geest[1]
[1]University of Pittsburgh, [2]University of Arizona

In Airway Epithelial Cells, Unjamming Transition Involves Basal Cell Elongation and Stress Fiber Accumulation
Thien-Khoi Phung[1], Jennifer Mitchel[1], Michael O'Sullivan[1], Jin-Ah Park[1]
[1]Harvard T.H. Chan School of Public Health

Notochord Eccentricity and its Relation to Cell Packing
Emma Sorrell[1], Sharon Lubkin[1]
[1]North Carolina State University

Intercellular Coupling Among Smooth Muscle Cells Changes While Undergoing Agonist-Induced Constriction
Suzanne Stasiak[1], Dhananjay Tambe[2], Harikrishnan Parameswaran[1]
[1]Northeastern University, [2]University of South Alabama

Directional Cell Migration Guided by a Strain Gradient
Feiyu Yang[1], Yubing Sun[1]
[1]University of Massachusetts, Amherst

Copyright 2021 SB³C Foundation, Inc.

Wednesday, June 16	5:00PM – 6:30PM EDT

Engineered *In Vitro* Models

Alpine Drift

Session Chair: Arun Nair, University of Arkansas
Session Chair: Jingjie Hu, Mayo Clinic

5:00PM **Evaluation of the Seeding Efficiency of a Custom-Designed Seed-and-Culture Perfusion Bioreactor for Engineered Tissue Vascular Grafts**
Sarah Saunders[1], Joao Soares[1]
[1]Virginia Commonwealth University

5:13PM **A 3D Macromolecular Modeling Framework for Collagen Fibril Mechanics and Plasticity**
Lauren Bersie-Larson[1], Paolo Provenzano[1], Victor Barocas[1]
[1]University of Minnesota, Twin Cities

5:26PM **Changes in Fiber Level Strains & Calcium Activity after Exposure to Bacterial Collagenase in Neuron Collagen Constructs Mimicking Ligaments Suggests Possible Mechanisms for Pain Associated with Joint Degeneration**
Sagar Singh[1], Beth Winkelstein[1]
[1]University of Pennsylvania

5:39PM **Development of a Deformable Microfluidic Chip to Replicate Tissue Strains *In Situ***
Andre Montes[1], Jonathan McKinley[1], Grace O'Connell[1], Mohammad Mofrad[1]
[1]University of California, Berkeley

5:52PM **Substratum Stiffness Modulates the Morphology and Proliferation of Primary Corneal Keratocytes in Response to PDGF-BB**
Krithika S. Iyer[1], David W. Schmidtke[1], W. Matthew Petroll[2], Victor D. Varner[1]
[1]University of Texas at Dallas, [2]University of Texas at Southwestern

6:05PM **Towards Controlling Arterial Growth and Remodeling Via Cell-Cell Signaling: A Multiscale Computational Model**
Jordy van Asten[1], Marcos Latorre[2], Jason Szafron[2], Tommaso Ristori[1], Frank Baaijens[1], Jay Humphrey[2], Sandra Loerakker[1]
[1]Eindhoven University of Technology, [2]Yale University

Wednesday, June 16	5:00PM – 6:30PM EDT

Growth and Remodeling Mechanics II: Mechanobiology

Mogul Madness

Session Chair: Colleen Witzenburg, University of Wisconsin-Madison
Session Chair: Johannes Weickenmeier, Stevens Institute of Technology

Copyright 2021 SB³C Foundation, Inc.

5:00PM **Modeling the Three-Way Chemo-Mechanical Feedback between Cellular Contractility, Actin Polymerization, and Adhesion Turnover in the Remodeling of Endothelial Junctions**
Eoin McEvoy[1], Tal Sneh[2], Emad Moeendarbary[3], Xingyu Chen[2], Tatyana Svitkina[2], Roger Kamm[4], Vivek Shenoy[2]
[1]National University of Ireland Galway, [2]University of Pennsylvania, [3]University College London, [4]Massachusetts Institute of Technology

5:13PM **Multiscale Model of Heart Growth During Pregnancy: Integrating Mechanical and Hormonal Signaling**
Kyoko Yoshida[1], Jeffrey Saucerman[1], Jeffrey Holmes[2]
[1]University of Virginia, [2]University of Alabama at Birmingham

5:26PM **Modeling Wound Healing Mechanobiology: Multi-scale Coupling of a Cell Adhesion Model to a Finite Element Model of Tissue**
Yifan Guo[1], Julian Jimenez[1], Sarah Calve[2], Adrian Buganza Tepole[1]
[1]Purdue University, [2]University of Colorado Boulder

5:39PM **Force Transmission within the Migrating Endothelium Regulates Shunt Formation during Angiogenic Remodelling**
Lowell T. Edgar[1], Miguel O. Bernabeu[1]
[1]University of Edinburgh

5:52PM **Local Tissue Heterogeneity Surrounding Neurons May Modulate Their Responses Via Altered Axonal Strain Fields**
Jill Middendorf[1], Meagan Ita[2], Beth Winkelstein[2], Victor Barocas[1]
[1]University of Minnesota, [2]University of Pennsylvania

6:05PM **Evolving structure-function relations in aortic maturation and aging**
Cristina Cavinato[1], Sae-Il Murtada[1], Alexia Rojas[1], Jay D. Humphrey[1]
[1]Yale University

Wednesday, June 16	**5:00PM – 6:30PM EDT**

Multiscale Biotransport in Drug Delivery

Mud Springs

Session Chair: Jifu Tan, Northern Illinois University
Session Chair: Zhiquan Shu, University of Washington

5:00PM **The Impact of Injection Timing and Location on Microparticle Delivery for Tumor Targeting in a Patient-Specific Liver**
Tim Bomberna[1], Charlotte Debbaut[1], Geert Maleux[2], Chris Verslype[2], Lawrence Bonne[2]
[1]UGent, [2]UZ Leuven

5:13PM **Constant Pressure CED Infusions with Controlled Catheter Movement in Agarose Gel Brain Tissue Phantoms**
Jason N. Mehta[1], Brianna E. Morales[1], Christopher G. Rylander[1]
[1]The University of Texas at Austin

Copyright 2021 SB³C Foundation, Inc.

5:26PM **Mechanism of Enhanced Thermal Transport and Photoacoustic Effect for Silica-Coated Gold Nanoparticles**
Peiyuan Kang[1], Jonghae Youn[1], Zhenpeng Qin[1]
[1]University of Texas at Dallas

5:39PM **Design and Evaluation of Faciliflow: A Lymph Node Prosthetic for Prevention of Surgically Induced Lymphedema**
Jennifer Frattolin[1], Arushri Swarup[1], Alain Vella[1], Fatima Al-Khal[1], Anaös Schaschkow[2], Pierre Gianello[2], Guido Giacalone[2], James E. Moore Jr.[1]
[1]Imperial College London, [2]Université Catholique de Louvain

5:52PM **A Mechanistic Study of the Interstitial Transport of Collagenase-secreting Tumor-targeting Salmonella Typhimurium Toward Improving Tumor Colonization**
Eric Leaman[1], Bahareh Behkam[1]
[1]Virginia Tech

6:05PM **Enhancement of Drug Delivery to Pancreatic Cancer Targeting Fibrin Matrix**
Sae Rome Choi[1], Hye-ran Moon[1], Yi Yang[2], Matthew J. Flick[2], Bumsoo Han[1]
[1]Purdue University, [2]University of North Carolina

Wednesday, June 16	**5:00PM – 6:30PM EDT**

Ocular and Reproductive Mechanics I: Form and Function

Saddle Ridge

Session Chair: Katrina Knight, University of Pittsburgh
Session Chair: Hamed Hatami-Marbini, UIC

5:00PM **Changes in Vaginal Shape Throughout the Lifespan**
Liam Martin[1], Megan Routzong[1], Pamela Moalli[1], Ghazaleh Rostaminia[2], Victoria Martin[1], Katherine Lebrun[1], Steven Abramowitch[1]
[1]University of Pittsburgh, [2]Northshore HealthSystems

5:13PM **Effects of Maternal Geometry and Gestational Age on Loading of the Gravid Human Uterus and Cervix**
Erin Louwagie[1], Lindsey Carlson[2], Joy Vink[1], Timothy Hall[2], Helen Feltovich[1], Kristin Myers[1]
[1]Columbia University, [2]University of Wisconsin-Madison

5:26PM **The Effects of Fetal Head Size on Maternal Coccyx Rotation During a Vaginal Delivery**
Sheng Chen[1], Megan Routzong[2], Steven Abramowitch[2], Michele Grimm[1]
[1]Michigan State University, [2]University of Pittsburgh

5:39PM **Effect of Osmotic Loading on Vaginal Viscoelastic Mechanical Properties**
Gabrielle Clark-Patterson[1], Laurephile Desrosiers[2], Leise Knoepp[2], Raffaella De Vita[3], Kristin Miller[1]
[1]Tulane University, [2]Ochsner Clinical School, [3]Virginia Polytechnic Institute and State University

Copyright 2021 SB³C Foundation, Inc.

5:52PM **The Impact of Tissue Property Variations on Optic Nerve Head Deformation Under Physiological and Supra-Physiological Loading**
Andrew Feola[1,2], C. Ross Ethier[2], Brian Samuels[3]
[1]Atlanta VA Medical Center, [2]Georgia Institute of Technology, [3]University of Alabama at Birmingham

6:05PM **Factors Influencing Minimum Lamina Cribrosa Oxygen Concentration**
Yi Hua[1], Jason Walker[1], Po-Yi Lee[1], Fengting Ji[1], Haiden McDonald[1], Pedro Pallares[1], Bryn Brazile[1], Ian Sigal[1]
[1]University of Pittsburgh

Poster Session

Poster Session III	Wednesday, June 16, 6:30PM – 7:30PM EDT

Posters: BS Finalists Poster Session

Aspen Glade

Session Chair: Megan Killian, University of Michigan

Proposed Injury Threshold for Drone Blade Lacerations
Lauren Duma[1], Mark Begonia[1], Barry Miller[1], Stefan Duma[1]
[1]Virginia Tech

3D Image Correlation of Porcine Adipose Tissue Under Compression
Dari Samson[1], Bryce Chapman[1], Brenda Burke[1], Dr. Lakiesha Williams[1]
[1]University of Florida

Engaging Biomedical Engineering Students with Gamification in Online Learning
Nina Dorfner[1], Rana Zakerzadeh[1]
[1]Duquesne University

Simulation of Oxygen Mass Transport in a Complaint Abdominal Aortic Aneurysm Model
Alexis Throop[1], Burton Carbino[1], Alexander Guy[1], Nina Dorfner[1], Rana Zakerzadeh[1]
[1]Duquesne University

The Effect of Stenosis Severity and Arterial Wall Mechanics on Functional Diagnostic Parameters
Angelica Alday[1], Talha Lone[1], Rana Zakerzadeh[1]
[1]Duquesne University

Whitewater Helmet STAR: Evaluating the Biomechanical Performance and Risk of Head Injury for Whitewater Helmets
Brock Duma[1], Mark Begonia[1], Stefan Duma[1]
[1]Virginia Tech

Copyright 2021 SB³C Foundation, Inc.

Data Acquisition System to Quantify Bone Viscoelasticity in Hindfoot and Midfoot Arthrodesis
Melissa Requist[1], Amanda Rugg[1], Brooks Johnson[1], Michelle Son[1], Alicia Alvarez[1], Daniel Latt[1]
[1]University of Arizona

Location Dependent Mechanical Behavior of Aponeurosis Tissue Under Uniaxial Tensile Stretch
Emily Tully[1], Benjamin Wheatley[1]
[1]Bucknell University

Loss of Endothelin-1 May Offer Pulmonary Vascular Protection After Myocardial Infarction
Hailey Frye[1], Diana Tabima[1], David McCulley[2], Naomi Chesler[3]
[1]University of Wisconsin – Madison, [2]University of California, San Diego, [3]University of California, Irvine

The Synoviocyte Response to Physiologic Shear Under Culture Conditions Simulating Diabetic Insulin Resistance and Osteoarthritis Joint Inflammation
Neeraj Sakhrani[1], Lance Murphy[1], Andy Lee[1], Eric Semler[2], Roshan Shah[1], Gerard Ateshian[1], Clark Hung[1]
[1]Columbia University, [2]MTF Biologics

The Impact of Pregnancy and Childbirth on Vaginal Dimensions and Curvature
Victoria Martin[1], Megan Routzong[1], Steven Abramowitch[1]
[1]University of Pittsburgh

Pharmaceutical Intervention Helps but does not Prevent Proteoglycan Loss in the Meniscus Following Traumatic Knee Injury
Ashley Herrick[1], Gerardo Narez[1], Loic Dejardin[2], Wei Feng[2], Roger Haut[2], Tammy Haut Donahue[1]
[1]University of Massachusetts Amherst, [2]Michigan State University

Metabolism of Chondrocytes After Traumatic Overloading Determined by Click Chemistry Techniques
Annie Porter[1], Liyun Wang[1], X. Lucas Lu[1]
[1]University of Delaware

Can Exercise-Based Load Prevent or Reduce Age-Related Advanced Glycation End-Product Accumulation in Tendons?
Panth Doshi[1], Kelly Ott[1], Jennifer Puetzer[1]
[1]Virginia Commonwealth University

Parametric Patient-Specific Model Simulating Human Cervix Deformation During the First Stage of Labor
Arielle Feder[1], Erin Louwagie[1], Joy Vink[1], Kristin Myers[1]
[1]Columbia University

Copyright 2021 SB³C Foundation, Inc.

Layer-Specific Mechanical and Collagen Microstructural Characterizations of Tricuspid Valve Leaflets
Katherine Casey[1], Mulan Tang[1], Devin Laurence[1], Chung-Hao Lee[1]
[1]The University of Oklahoma

MR Image-Based Characterization of Medial and Lateral Meniscal Geometries for Patient-Specific Finite Element Modeling
Kathryn Colone[1], Madison Lang[1], Kate Lindsey[1], Sofia Guarnieri[1], Amy Lerner[1]
[1]University of Rochester

Carbon Nano-onion-mediated Dual Targeting of P-selectin and P-glycoprotein to Overcome Cancer Drug Resistance
Yutong Liang[1], Hai Wang[1], Xiaoming He[1]
[1]University of Maryland, College Park

Computational Modeling of Arterial Hemodynamics in Pediatric Pulmonary Arterial Hypertension
Nathan Li[1], Christopher Tossas-Betancourt[1], C. Alberto Figueroa[1]
[1]University of Michigan

Efficacy of Poloxamer 188 in Mitigating Changes to Subchondral Bone Composition and Architecture Following Traumatic ACL Injury and Reconstruction
Gabriel Brown[1], Gerardo Narez[1], Loic Dejardin[2], Wei Feng[2], Roger Haut[2], Tammy Haut Donahue[1]
[1]University of Massachusetts Amherst, [2]Michigan State University

A Computational Model of the Impact of Cerebral Amyloid Angiopathy on Vaso-Responsiveness of Cerebral Arteries
Cole Theobald[1], Ryan Mahutga[1], Patrick Alford[1], Victor Barocas[1]
[1]University of Minnesota - Twin Cities

Using 4D-Flow MRI to Quantify Left Atrial Flow and WSS to Better Understand Atrial Remodeling and Stretch in Atrial Fibrillation Patients
Cody Johnson[1], Morgan Parks[1], Riley Parks[1], Matthew Kalscheur[1], Alexey Glukhov[1], Alejandro Roldan-Alzate[1]
[1]University of Wisconsin-Madison

Simulating Structural Covariance Networks in Schizophrenia Patients
Katherine Dash[1], Brendan Muldoon[1], Konasale Prasad[1]
[1]University of Pittsburgh

Magnetic Resonance Imaging (MRI) of Brain Motion: Phase Contrast Velocity Versus Displacement Encoding
David Bat[1], Blaise Simplice Talla Nwotchouang[2], Maggie Eppelheimer[2], Daniel Barrow[3], Francis Loth[2], John Oshinski[3]
[1]Georgia Institute of Technology, [2]University of Akron, [3]Emory University

Characterization of Glycocalyx Core Proteins in Human Endothelial Cells
John Mwangi[1], Theodora Stanley[1], Selina Banerjee[1], Ronodeep Mitra[1], Eno Ebong[1]
[1]Northeastern University

Copyright 2021 SB³C Foundation, Inc.

Knee Contact Forces in Transtibial Amputees: Implications for Rehabilitation and Lifelong Fitness Exercises
Reymil Fernandez[1], Shaida Biglari[1], Scott J. Hazelwood[1], Stephen M. Klisch[1]
[1]California Polytechnic University, San Luis Obispo

A Repeatable Method for *In-Situ* Joint Alignment of Disarticulated Human Knees During *In-Vitro* Mechanical Testing
Zachary Pinkley[1], Kate Benfield[1], Trevor Lujan[1]
[1]Boise State University

The Relationship Between Perceived Confidence and Writing in a Biomedical Engineering REU Site
Elisabeth Reed[1], Donna Kain[1], Stephanie George[1]
[1]East Carolina University

A Computational Tool to Automate the Analysis of Stress-Strain Data from Tensile Tests of Soft Tissues
Miranda L. Nelson[1], Derek Q. Nesbitt[1], Trevor J. Lujan[1]
[1]Boise State University

The Relation Between Cortical Thickness and Morphology: A Study of Nonhuman Primate Brains
Mia Hoffman[1], Nagehan Demirci[1], Maria Holland[1]
[1]University of Notre Dame

Effect of Stress-fiber Contraction on the 3D Shape of the Aortic Heart Valve Interstitial Cell
Quan Nguyen[1], Alex Khang[1], Xinzeng Feng[1], Michael Sacks[1]
[1]University of Texas at Austin

Analysis of Boundary Conditions in Numerical Assessment of Paravalvular Leakage in Transcatheter Aortic Valve Replacement
Kyra Halbert-Elliott[1], Zhenglun Wei[2], Huang Chen[1], Sri Krishna Sivakumar[1], Breandan Yeats[1], Ajit Yoganathan[1], Prasad Dasi[1]
[1]Georgia Institute of Technology, [2]University of Massachusetts Lowell

Raman Needle Arthroscopy Towards *In Vivo* Monitoring of Engineered Cartilage Growth
Juncheng Zhang[1], Tianbai Wang[1], Magnus Jensen[2], Mark Grinstaff[1], Brian Snyder[1], Mads Bergholt[2], Michael Albro[1]
[1]Boston University, `[1]King's College of London

Stress-Relaxation Response of Porcine and Human Synovium in Confined Compression
Benjamin Johnston[1], Young Guang[1], Alexandra Davis[1], Lori Setton[1]
[1]Washington University in St. Louis

Quantification of the Flexural Rigidity of Peripheral Arterial Endovascular Catheter and Sheaths
Chase Hartquist[1], Vinay Chandrasekaran[1], Halle Lowe[1], Eric Leuthardt[1], Joshua Osbun[1], Mohamed Zayed[1], Guy Genin[1]
[1]Washington University in St. Louis

Copyright 2021 SB³C Foundation, Inc.

Identifying Hemodynamic Predictors of Cerebral Aneurysm Growth Using Computational Fluid Dynamics
Allyson Weiss[1], Aaron Panduro[2], Ingrid Lan[1], Erica Schwarz[1], Alison Marsden[1], Nicholas Telischak[1]
[1]Stanford University, [2]California State University, Fresno

In Silico Modeling of Embolic Particle Drug Delivery for Liver Cancer
Autumn Zemlicka[1], Andrew Beiter[1], Premal Trivedi[2], Debanjan Mukherjee[1]
[1]University of Colorado Boulder, [2]University of Colorado Anschutz Medical Campus

Biaxial Mechanical Properties of Right Ventricular Myocardium in Advanced Pulmonary Arterial Hypertension
Michael Bennington[1], Daniela Valdez-Jasso[1]
[1]University of California, San Diego

Contrasting the Mechanics of Healthy and Asthmatic Airway Development Using *In Silico* Modeling
Neftali Lau, Mona Eskandari[1], Mohammad Ganjeh[1]
[1]University of California, Riverside

Collagen V Promotes Cell Contractility Compared to Collagen I
Shaina Royer[1], Nikhil Mittal[1], Sangyoon Han[1]
[1]Michigan Technological University

Exploration of the Impact of Blood Viscosity in the Development of Embolisms at the Pulmonary Artery of High-Risk Covid-19 Patients
Ifti Hossain[1], Diana Alatalo[1], Fatemeh Hassanipour[1]
[1]University of Texas at Dallas

Posters: MS Finalists Poster Session

Aspen Glade

Session Chair: Kristin Miller, Tulane University

Effects of Marathon Training on Male and Female Femoral Stress Fracture Risk
Clara Lin[1], Scott Hazelwood[1]
[1]California Polytechnic State University San Luis Obispo

Quantifying Euler-Bernoulli and Timoshenko Beam Theory Accuracy of Finite Element Analyses for Estimating Flexural Rigidity of a Bone Surrogate in Three-Point Bending with Finite Element Analysis
Mahsa Zojaji[1], Heidi-Lynn Ploeg[1], Baixuan Yang[1], Caitlyn J. Collins[2]
[1]Queen's University, [2]ETH Zürich

A Physics-Informed Machine Learning Model for the Identification of Active Contraction Properties in the Ventricular Myocardium
Igor Augusto Paschoalotte Nobrega[1], Wenbin Mao[1]
[1]University of South Florida

Copyright 2021 SB³C Foundation, Inc.

Understanding the Effects of Long-Duration Spaceflight on Fracture Risk in the Human Femur Using Finite Element Analysis
Keyanna Henderson[1], Scott Hazelwood[1]
[1]California Polytechnic State University, San Luis Obispo

***In Vitro* Method to Quantify and Visualize Mechanical Wear in Human Meniscus Subjected to Joint Loading**
Kate Benfield[1], Zachary Pinkley[1], Katherine Hollar[1], Kirk Lewis[2], Trevor Lujan[1]
[1]Boise State University, [2]Idaho Sports Medicine Institute

On the Relation between Computational Fluid Dynamics-Derived Biomarkers and Coronary Artery Bypass Remodeling
Nhien Tran-Nguyen[1], Francesca Condemi[2], Stephen Fremes[3], Piero Triverio[1], Laura Jimenez-Juan[4]
[1]University of Toronto, [2]CorWave, [3]Sunnybrook Health Sciences Centre, [4]St. Michael Äôs Hospital

Sensitivity of the Shear Wave Speed-Stress Relationship to Properties of Ligament-Mimicking Mechanical Phantoms
Lesley Arant[1], Joshua Roth[1]
[1]University of Wisconsin - Madison

Maximum Ventricular Wall Loading Coincides with Periventricular White Matter Hyperintensity Locations
Valery Visser[1,2], Andreia Cacoilo[2], Johannes Weickenmeier[2]
[1]Eindhoven University of Technology, [2]Stevens Institute of Technology

A Comparative Study of Regular- and High-Fidelity Finite Element Algorithms for the Prediction of Aortic Flows
Yiyang Fu[1], Mehdi Najafi[1], Stephen Fremes[1], Laura Jimenez-Juan[1], David Steinman[1], Piero Triverio[1]
[1]University of Toronto

Load-Dependent Microstructural and Biomechanical Properties of Porcine Pulmonary Valve Cusps
Luke Hudson[1], Arshid Mir[1], Harold M. Burkhart[1], Chung-Hao Lee[1]
[1]University of Oklahoma

Macroscale and Microscale Responses of the Rat Lumbar Facet Capsular Ligament to Subfailure Repeated Cyclic Loading and a Ramp-and-Hold
Jonathan Marcelin[1], Sagar Singh[1], Beth Winkelstein[1]
[1]University of Pennsylvania

Role of Coherent Structures in Airflow Mediated Infectious Disease Spread with Expiratory Particles
Sara Meschi[1], Amirhossein Arzani[1]
[1]Northern Arizona University

Copyright 2021 SB³C Foundation, Inc.

Characterizing and Modeling Adolescent Pectus Excavatum Anatomy to Inform Surgical Planning and Device Design
Delanie Lynch[1], Katelyn Greene[1], Ashley Weaver[1]
[1]Wake Forest School of Medicine

Transition to Turbulence Downstream an Eccentric Stenosis with Flexible Walls Under Steady Flow Using Laser Doppler Vibrometry for Whole Blood and a Newtonian Fluid
Rayanne Pinto Costa[1], Blaise Simplice Talla Nwotchouang[1], David A. Steinman[2], Francis Loth[1]
[1]The University of Akron, [2]University of Toronto

Improved Efficiency in Biomedical Modeling with Automated Removal of Mounting Hardware from Soft Tissue 3D Imaging Datasets
Sam Stephens[1], Neil Ingels[1], Jonathan Wenk[2], Morten Jensen[1]
[1]University of Arkansas, [1]University of Kentucky

Passive Leg Raise as a Simple and Robust Maneuver to Measure Pulmonary Vascular Distensibility
Callyn Kozitza[1], Farhan Raza[1], Naga Dharmavaram[1], Diana Tabima[1], Naomi Chesler[2]
[1]University of Wisconsin – Madison, [2]University of California, Irvine

Collagen Damage in Arteries - Choice of Analysis Technique Matters in Identifying Rate Dependence
William Anderl[1], Noah Pearson[1], Michael Yu[1], Kenneth Monson[1]
[1]University of Utah
Wavy Fiber Structure Improves Contractile Phenotype of Vascular Smooth Muscle Cells
Chun-Yu Lin[1], Pen-hsiu Grace Chao[1]
[1]National Taiwan University

Size-Dependent Solute Diffusivity in Synovial Explants Parallels Solute Transport Following Intra-Articular Delivery *In Vivo*
Alexandra Davis[1], Young Guang[1], Thomas McGrath[1], Benjamin Johnston[1], Christine Pham[1], James Fitzpatrick[1], Lori Setton[1]
[1]Washington University in St. Louis

A Viscodamage Model to Simulate Both Fatigue and Static Failures in Soft Fibrous Tissue
Bradley Henderson[1], Katelyn Cudworth[1], Danielle Siegel[1], Madison Krentz[1], Estefania Pena[2], Trevor Lujan[1]
[1]Boise State University, [2]University of Zaragoza

Computationally Enhanced 4D Flow MRI for the Assessment of Pre- and Post-Coarctation Repair Aorta Flow Dynamics
Labib Shahid[1], James Rice[1], Haben Berhane[2], Cynthia Rigsby[2], Joshua Robinson[2], Lindsay Griffin[2], Michael Markl[3], Alejandro Roldán-Alzate[1]
[1]University of Wisconsin-Madison, [2]Ann & Robert H. Lurie Children's Hospital of Chicago, [3]Northwestern University

The Effect of Header Characteristics on Head Kinematics of Women's Soccer Players
Gabriella Milef[1], Tanner Filben[1], Jordan Hemmen[2], Jillian Urban[1], Joel Stitzel[1]
[1]Wake Forest School of Medicine, [2]Virginia Tech

Copyright 2021 SB³C Foundation, Inc.

Rheological Analysis of the Mechanical Properties of Murine Lungs Over the Lifespan
Olajumoke Harrison[1], Henry Rozycki[1], Rebecca Heise[1]
[1]Virginia Commonwealth University

Patient-Specific, *In-Vitro* Modeling of Aortic Coarctation Using 4D Flow MRI and Particle Image Velocimetry
James Rice[1], Labib Shahid[1], Haben Berhane[2], Cynthia Rigsby[3], Joshua Robinson[3], Lindsay Griffin[3], Michael Markl[2], Alejandro Roldán-Alzate[1]
[1]University of Wisconsin-Madison, [2]Northwestern University, [3]Ann & Robert H. Lurie Children's Hospital of Chicago

3D Visualization of the Podocyte Actin Network Using Integrated Membrane Extraction, Electron Microscopy, and Deep Learning
Chengqing Qu[1], Guy Genin[1], Hani Suleiman[1], Shumeng Jiang[1], Robyn Roth[1], Jeffrey Miner[1]
[1]Washington University in St. Louis

Finite Element Modeling of the Long Head of the Biceps Tendon
Miles Wing[1], Arin Ellingson[1], Paula Ludewig[1], Aaron Hellem[1], Victor Barocas[1], S. Cyrus Rezvanifar[1]
[1]University of Minnesota

Effect of Stimulus Waveform on Transcranial Magnetic Stimulation Metrics in Proximal and Distal Arm Muscles
Christopher Lynch[1], Thibault Roumengous[1], Carrie Peterson[1]
[1]Virginia Commonwealth University

Patient-Specific Artery Geometry and ABM/FEA/CFD Computational Framework
John Yoo[1], Jeremy Warren[1], Heather Hayenga[1], Clark Meyer[1]
[1]University of Texas at Dallas

Development of an Automated, Machine Learning-Based Methodology for Yield Point Identification from Tensile Testing Data of Soft Tissues
Joseph Kim[1], Timothy Chung[2], David Vorp[2], Madhavan Raghavan[1]
[1]University of Iowa, [2]University of Pittsburgh

D33 Characterization of Porous Polyvinylidene Fluoride Polymer for Biosensor Applications
Matthew Danley[1], Jack Kloster[1], Zhaolin Gao[1], Ping Zhao[1], Victor Lai[1]
[1]University of Minnesota Duluth

Comparison of Anabolic Osteoporosis Treatments: PTH Vs. PTHRP on the Activation of New Bone Formation and Improvements in Bone Microarchitecture
Tala Azar[1], Wenzheng Wang[1], Wei-Ju Tseng[1], Hongbo Zhao[1], Jing Du[1]
[1]University of Pennsylvania

Design, Construction, and Testing of a Differential Resistance Elliptical Exercise Machine
John Easton[1], Christopher Hurt[1], David Brown[2], Alan Eberhardt[1]
[1]University of Alabama at Birmingham, [2]University of Texas Medical Branch

Copyright 2021 SB³C Foundation, Inc.

Toll-like Receptor-4 Modulates Inflammatory Response of Intervertebral Disc to Static but not Dynamic Injurious Loading

Hagar Kenawy[1], Samantha Marshall[1], James Rogot[1], Clark Hung[1], Nadeen Chahine[1]
[1]Columbia University

Live-Cell, Dynamic Imaging of Matrix Assembly in an *In Vitro* Model of Human Corneal Development

Alexandra Silverman[1], Seyed Mohammad Siadat[1], Jeffrey Ruberti[1]
[1]Northeastern University

Assessing the Hemodynamic Influence of Pulse Flow Modulation for Left Ventricular Assist Devices

Akshita Sahni[1], Jay Pal[2], Debanjan Mukherjee[1]
[1]University of Colorado Boulder, [2]University of Colorado Anschutz Medical Campus

Copyright 2021 SB³C Foundation, Inc.

Thursday, June 17	11:00AM – 12:30PM EDT

Emerging Topics in Cardiovascular Mechanics

Alpine Drift

Session Chair: Danny Bluestein, Stony Brook University
Session Chair: Ender Finol, University of Texas at San Antonio

11:00AM **Development of an Abdominal Aortic Aneurysm Prognosis Classifier to Predict Patient Outcomes**
Timothy Chung[1], Nathan Liang[1], David Vorp[1]
[1]University of Pittsburgh

11:13AM **Polymeric Pediatric Heart Valve Replacements**
Sanchita S. Bhat[1], Hieu T. Bui[1], Milad Samaee[1], Subhadra Shashidharan[2], Susan P. James[3], Ajit P. Yoganathan[1], Lakshmi Prasad Dasi[1]
[1]Georgia Institute of Technology, [2]Emory University School of Medicine, [3]Colorado State University

11:26AM **Role of Mitral Valve Leaflet Pre-Strain in an Integrated Left Ventricle-Mitral Valve Model**
Hao Liu[1], Harshita Narang[1], Joseph Gorman[2], Robert Gorman[2], Michael Sacks[1]
[1]University of Texas at Austin, [2]University of Pennsylvania

11:39AM ***In Vivo* Analysis of Aortic Hemodynamics by Combining 4D Flow MRI and Complex Networks Theory**
Karol Cale[1], Andrea Guala[2], Diego Gallo[1], Jose Rodriguez-Palomares[2], Stefania Scarsoglio[1], Luca Ridolfi[1], Umberto Morbiducci[1]
[1]Politecnico di Torino, [2]Universitat Autonoma de Barcelona

11:52AM **Development of Predictive Model of Ischemia in Anomalous Aortic Origin of Coronary Artery**
Yasaman Farsiani[1], Jayanthi Parthasarathy[1], Silvana Molossi[2], Carlos Mery[3], Rajesh Krishnamurthy[1], Lakshmi Dasi[4]
[1]Nationwide Children's Hospital, [2]Texas Children's Hospital, Baylor College of Medicine, [3]Dell's Children's Medical Center, University of Texas at Austin, [4]Georgia Institute of Technology

12:05PM **Platelet Adhesion Dynamics: Machine Learning-Assisted Analysis of Adult and Cord Platelets and Development of a Multiscale Model**
Jawaad Sheriff[1], Peineng Wang[1], Peng Zhang[1], Ziji Zhang[1], Wadie Bahou[1], Yuefan Deng[1], Danny Bluestein[1]
[1]Stony Brook University

Copyright 2021 SB³C Foundation, Inc.

Thursday, June 17	11:00AM – 12:30PM EDT

Multiscale Detection and Diagnosis in Biotransport

Mud Springs

Session Chair: Lyle Hood, University of Texas at San Antonio
Session Chair: Haishui Huang, The Ohio State University

11:00AM **An *Ex Vivo* Platform for Testing Diagnostic and Thrombolytic Capabilities of Ultrasound-aided Nanoparticles**
Connor Watson[1], Janna Sloand[1], Eric Rokni[1], Julianna Simon[1], Keefe Manning[1], Scott Medina[1]
[1]Penn State University

11:13AM **Deep Learning-enabled Label-free On-chip Detection and Selective Extraction of Cell Aggregate-laden Hydrogel Microcapsules**
Alisa White [1], Yuntain Zhang[1], James Shamul[1], Xiaoming He[1]
[1]University of Maryland

11:26AM **Whole brain perivascular space network reduces mean transport distance between**
Parenchyma and cerebrospinal fluid
Julian Rey[1], Uzair Farid[1], Christopher Najjoum[1], Kulam Magdoom[2], Thomas Mareci[1], Malisa Sarntinoranont[1]
[1]University of Florida, [2]National Institutes of Health

11:39AM **Group Refractive Index of Nanocrystalline Yttria-Stabilized Zirconia Transparent Cranial Implants**
David Halaney[1], Nitesh Katta[2], Hamidreza Fallah[3], Guillermo Aguilar[1], Thomas Milner[2]
[1]University of California, Riverside, [2]University of Texas, [3]University of Isfahan

11:52AM **Microfluidics Layout Design for Improved Circulating Tumor Cell Capture Efficiency**
Michael Hood[1], Jifu Tan[1]
[1]Northern Illinois University

12:05PM **Probing Neuropeptide Volume Transmission *In Vivo by* a Novel All-optical Approach**
Hejian Xiong[1], Hui Ouyang[1], Xueqi Xu[1], Emre Lacin[2], Tyler Kern[2], Daniel Kircher[2], X Xiuying Li[1], Celin Mateo[3], David Kleinfeld[3], Paul Slesinger[2], Zhenpeng Qin[1]
[1]University of Texas at Dallas, [2]Ichan School of Medicine at Mount Sinai, [3]University of California, San Diego

Thursday, June 17	11:00AM – 12:30PM EDT

Ocular and Reproductive Mechanics II: Structure and Function

Saddle Ridge

Session Chair: Andrew Feola, Georgia Institute of Technology
Session Chair: Kyoko Yoshida, University of Virginia

Copyright 2021 SB³C Foundation, Inc.

11:00AM **A Convolutional Neural Network Algorithm for 3D Super-resolution of Pelvic Floor MRI Based on Low Inter-slice Resolution Data**
Fei Feng[1], James A. Ashton-Miller[2], John O.L. DeLancey[2], Jiajia Luo[3]
[1]Shanghai Jiao Tong University, [2]University of Michigan, [3]Peking University

11:13AM **Biomechanical Properties of Post-Menopausal Vaginal Samples in Relation to Pelvic Organ Prolapse**
Elvis Danso[1], Laurephile Desrosiers[2], Leise Knoepp[2], Kristin Miller[1]
[1]Tulane University, Ochsner Clinical School

11:26AM **A High-Accuracy Digital Volume Correlation for Soft Tissue Biomechanics Characterization Using Optical Coherence Tomography**
Fuqiang Zhong[1], Yi Hua[1], Junchao Wei[1], Manik Bansal[1], Juan Reynaud[2], Brad Fortune[2], Ian A. Sigal[1]
[1]University of Pittsburgh, [2]Devers Eye Institute, Legacy Health Research Institute

11:39AM **The Curvature and Collagen Network of the Human Lamina Cribrosa in Glaucoma and Control Eyes**
Cameron Czerpak[1], Yik Tung Tracy Ling[1], Joan Jefferys[1], Harry Quigley[1], Thao Nguyen[1]
[1]Johns Hopkins University

11:52AM **Assessment of the Poroelastic Mechanical Properties of Porcine Optic Nerve Head Using Micromechanical Testing and Biphasic Mixture Modeling**
Babak N. Safa[1], A. Thomas Read[1], C. Ross Ethier[1]
[1]Georgia Institute of Technology

12:05PM **Do Glycosaminoglycans Act as a Structural Constituent of the Scleral Tissue?**
Hamed Hatami-Marbini[1], Mohammad Pachenari[1]
[1]University of Illinois at Chicago

Thursday, June 17	**11:00AM – 12:30PM EDT**

PhD Student Paper Competition 5: Cardiovascular Fluid Biomechanics

Mogul Madness

Session Chair: Rana Zakerzadeh, Duquesne University
Session Chair: **Anne Robertson,** University of Pittsburgh

11:00AM **Spectral Bandedness in High Fidelity CFD Predicts Rupture Status in Intracranial Bifurcation Aneurysms**
Daniel MacDonald[1], Mehdi Najafi[1], Lucas Temor[1], David Steinman[1]
[1]University of Toronto

11:15AM **A Deep-Learning Approach for Direct Whole-Heart Mesh Reconstruction**
Fanwei Kong[1], Shawn Shadden[1]
[1]University of California, Berkeley

Copyright 2021 SB³C Foundation, Inc.

11:30AM **Unraveling the Etiology of Discrete Subaortic Stenosis: Focus on Hemodynamics**
Jason Shar[1], Sundeep Keswani[2], K. Jane Grande-Allen[3], Philippe Sucosky[4]
*[1]*Wright State University*, [2]*Texas Children's Hospital*, [3]*Rice University, [4]Kennesaw State University

11:45AM **Wall Shear Stress Topological Skeleton Analysis in Image-Based Stented Coronary Bifurcation Models**
Valentina Mazzi[1], Claudio Chiastra[1], Diego Gallo[1], Umberto Morbiducci[1]
[1]Politecnico di Torino

12:00PM **Harmonic Distortion as a Noninvasive Means to Assess Blood Pressure Waveform and Arterial Stiffness**
Nicholas Milkovich[1], Anastasia Gkousioudi[1], Francesca Seta[1], Bela Suki[1], Yanhang Zhang[1]
[1]Boston University

12:15PM ***In Vitro* Assessment of the Effects of Cardiac Output and Valve Orientation on Bioprosthetic Pulmonary Valve Hemodynamics**
Nicole K. Schiavone[1], Christopher J. Elkins[1], Doff B. McElhinney[1], John K. Eaton[1], Alison L. Marsden[1]
[1]Stanford University

Thursday, June 17	**1:00PM – 2:30PM EDT**

Cardiac Function and Modeling

Saddle Ridge

Session Chair: Jonathan Wenk, University of Kentucky
Session Chair: **Anna Grosberg,** University of California, Irvine

1:00PM **Multiscale Model of Heart Growth During Pregnancy: Integrating Mechanical and Hormonal Signaling**
Kyoko Yoshida[1], Jeffrey Saucerman[1], Jeffrey Holmes[2]
[1]University of Virginia, [2]University of Alabama at Birmingham

1:13PM **ATP Utilization During Generation and Maintenance of Contractile Stress in Striated Muscle**
Andrew Schmidt[1], Alexander Grosberg[2], Anna Grosberg[1]
[1]University of California, Irvine, [2]New York University

1:26PM **Multiscale Modeling of LV Growth Under Autonomic Regulation of Baroreflex Feedback Loop**
Hossein Sharifi[1], Charles Mann[1], K Alexus Rockward[1], Kenneth Campbell[1], Jonathan Wenk[1]
[1]University of Kentucky

Copyright 2021 SB³C Foundation, Inc.

1:39PM **Histo-Mechanics of the Passive Right Ventricular Myocardium**
Sotirios Kakaletsis[1], Gabriella P. Sugerman[1], Tomasz Jazwiec[2], Marcin Malinowski[2], Tomasz A. Timek[2], Manuel K. Rausch[1]
[1]University of Texas at Austin, [2]Cardiothoracic Surgery Spectrum Health

1:52PM **Sex Differences in Right Ventricular Functional Remodeling in an Animal Model of Pulmonary Arterial Hypertension**
Ethan Kwan[1], Daniela Velez-Rendon[2], Hao Mu[1], Daniela Valdez-Jasso[1]
[1]University of California San Diego, [2]University of Illinois at Chicago

2:05PM **Evaluation of Constrained Mixture Theory on Cell-Sparse Systems: Application to Cerebral Aneurysms**
Elizabeth Shih[1], Victor Barocas[1], Patrick Alford[1]
[1]University of Minnesota – Twin Cities

Thursday, June 17	**1:00PM – 2:30PM EDT**

Cardiovascular Design, Devices and Imaging

Mud Springs

Session Chair: Choon Hwai Yap, Imperial College London
Session Chair: **Caitriona Lally,** Trinity College Dublin

1:00PM **Annular Holding Strength and Microstructure in a Diseased Animal Model: An *Ex Vivo* Study**
Sanchita Bhat[1], Beatrice Ncho[1], Md. Tausif Salim[1], Emma Hazenberg[1], Dharani Balakumar[1], Andrew Siefert[1], Robert Gorman[2], Joseph Gorman[2], Ajit Yoganathan[1]
[1]Georgia Institute of Technology, [2]University of Pennsylvania

1:13PM **Made to Measure: 3D Printing Patient Specific Paediatric Stents**
Orla McGee[1], Sam Geraghty[1], Celia Hughes[1], Parastoo Jamshidi[2], Damien Kenny[3], Moataz Attallah[2], Caitriona Lally[1]
[1]Trinity College Dublin, [2]University of Birmingham, [3]Our Lady's Hospital, Crumlin

1:26PM **Hemodynamic Diversities Between Four Stent Graft Systems Via Patient-Based Simulations**
Anastasios Raptis[1], Michalis Xenos[2], George Kouvelos[3], Konstantinos Spanos[3], Athanasios Giannoukas[3], Miltiadis Matsagkas[3]
[1]Institute of Vascular Diseases, Larissa, [2]University of Ioannina, [3]University of Thessaly, Larissa

1:39PM **Experimental Framework for MRI-Based Measurement of Myocardial Stiffness in 3D-Printed Heart Phantoms**
Fikunwa Kolawole[1], Tyler Cork[1], Michael Loecher[1], Seraina Dual[1], Marc Levenston[1], Daniel Ennis[1]
[1]Stanford University

Copyright 2021 SB³C Foundation, Inc.

1:52PM **Factors Explaining the Differences in 2D and 3D Fetal Echocardiography Strain Measurements**
Meifeng Ren[1], Wei Xuan Chan[1], Aimee Armstrong[2], Andreas Tulzer[3], Gerald Tulzer[3], Martin Lindsay Buist[1], Choon Hwai Yap[4]
[1]National University of Singapore, [2]The Heart Center, Nationwide Children's Hospital, Columbus, Ohio, [3]Dept of Pediatric Cardiology, Kepler University Hospital, Linz, [4]Imperial College London

2:05PM **Hypertrophic Cardiomyopathy Progression Characterized via Spatiotemporal Strain Mapping from 4D Ultrasound**
Frederick W. Damen[1], Daniel P. Gramling[1], Craig J. Goergen[1]
[1]Purdue University

Thursday, June 17	**1:00PM – 2:30PM EDT**

PhD Student Paper Competition 6: Mechanobiology and Musculoskeletal Tissue Engineering

Mogul Madness

Session Chair: Brianne Connizzo, Boston University
Session Chair: **Ryan Pedrigi**, University of Nebraska-Lincoln

1:00PM **Slow Stretch Mirroring ACL Growth Rates Drives Zonal Ligament-To-Bone Enthesis Maturation**
Ethan Brown[1], Jennifer Puetzer[1]
[1]Virginia Commonwealth University

1:15PM **Unilateral, Daily Bouts of Muscle Loading Leads to Mineral and Extracellular Adaptation of the Immature Achilles Enthesis in Mice**
Elahe Ganji[1], Bill Duncan[1], Angela Livingston[1], Noelle Whyte[2], Matthew Stepanovich[2], Megan Killian[2]
[1]University of Delaware, [2] University of Michigan

1:30PM **Mechano-Regulation of Embryonic Meniscus Development**
Tonia Tsinman[1], Xi Jiang[1], Saima Ahmed[2], Aurelie Levillain[2], Yuming Huang[2], Eiki Koyama[3], Niamh Nowlan[2], Nathaniel Dyment[1], Robert Mauck[1]
[1]University of Pennsylvania, [2]Imperial College of London, [3]Children's Hospital of Philadelphia

1:45PM **Targeting Hedgehog Signaling to Improve Zonal Tendon-to-bone Repair**
Timur Kamalitdinov[1], Keitaro Fujino[1], Xi Jiang[1], Mary Kate Evans[1], Miltiadis Zgonis[1], Andrew Kuntz[1], Nathaniel Dyment[1]
[1]University of Pennsylvania

2:00PM **Curvature Sensing IRSp53 Is Critical for Migrational Persistence in Cells Crawling On Suspended Nanofibers**
Apratim Mukherjee[1], Bahareh Behkam[1], Shiro Suetsugu[2], Amrinder Nain[1]
[1]Virginia Tech, [2]Nara Institute of Science and Technology

Copyright 2021 SB³C Foundation, Inc.

2:15PM **Mechanical Stimulation Mediates the Changes in Multiscale Tendon Mechanics Observed During Embryonic Development**
Benjamin Peterson[1], Spencer Szczesny[1]
[1]Pennsylvania State University

Poster Session

Poster Session IV	Thursday, June 17, 2:30PM – 4:00PM EDT

Posters: Computational and Experimental Biofluid Mechanics II

Aspen Glade

Session Chair: John LaDisa, Marquette University
Session Chair: Alejandro Roldan-Alzate, University of Wisconsin-Madison

Validation of Hepatic Factor Computational Fluid Dynamics Simulations for Pre-Surgical Planning
Reza Rasooli[1], K. Banu Kose[2], S. Samaneh Lashkarinia[1], Kerem Pekkan[1]
[1]Koc University, [2]Istanbul Medipol University

Automated Estimation of Patient-Specific Boundary Conditions for Cardiovascular Simulations: An Optimal Control Approach
Elisa Fevola[1], Francesco Ballarin[2], Laura Jimenez-Juan[3], Stephen Fremes[3], Piero Triverio[4], Stefano Grivet-Talocia[1], Gianluigi Rozza[2]
[1]Politecnico di Torino, [2]SISSA - International School for Advanced Studies, [4]St Michael's Hospital and Sunnybrook Research Institute, [4]University of Toronto

Computational Assessment of a Novel Design of Trileaflet Mechanical Heart Valve Implanted in Aortic Position
Syed Samar Abbas[1], Iman Borazjani[1]
[1]Texas A&M University

Characterizing the Local Resistance and Inertance of Aneurysm Segment to Study the Changes Induced by Flow Diverters in 0D Brain Model
Sara Hadad[1], Fernando Mut[1], Juan R. Cebral[1]
[1]George Mason University

Effect of Blood Pressure Conditions on Transcatheter Aortic Valve Performance and Coronary Flow
Brennan Vogl[1], Rajat Gadhave[1], Mohamad Alkhouli[2], Scott Lilly[3], Hoda Hatoum[1]
[1]Michigan Technological University, [2]Mayo Clinic, [3]The Ohio State University

A Computational Investigation of the Impact of Graft Geometry on Hemodynamic Performance for a Right-Heart Pump Anastomosis
Nicolas Tobin[1], Bryan Good[1], William Weiss[2], Keefe Manning[1]
[1]The Pennsylvania State University, [2]Penn State Hershey Medical Center

Copyright 2021 SB³C Foundation, Inc.

Effect of Postural Adjustment and Repositioning on Contact Penetrations in Human Body Models
Juliette Caffrey[1], Casey Costa[1], Wade von Kleeck[1], Ashely Weaver[1], Jason Hallman[2], F. Scott Gayzik[1]
[1]Wake Forest University, [2]Toyota Motor Eng. & Mfg.

Pre-Surgical Planning of Femoropopliteal Bypass Operation Based on Patient Specific *In Silico* Simulation
K. Banu Kose[1], Muhammed Bayram[2], Cagdas Topel[2], Senol Piskin[3]
[1]Medipol University, [2]Istanbul Mehmet Akif Ersoy Thoracic and Cardiovascular Surgery Training and Research Hospital, [3]Istinye University

The Effect of Aorta Shape on Type a Dissection Risk
Jessica Williams[1], David Marlevi[2], Marie Billaud[1], Thomas Gleason[1], Elazer Edelman[2]
[1]Brigham and Women's Hospital, [2]Massachusetts Institute of Technology

Computational Analysis of Quantitative Echocardiographic Assessments of Functional Mitral Regurgitation: Vena Contracta Area (VCA) Method
Tongran Qin[1], Andres Caballero[1], Rebecca Hahn[2], Raymond McKay[3], Wei Sun[1]
[1]Georgia Institute of Technology, [2]Columbia University Medical Center, [3]The Hartford Hospital

Significance of Gags in Unconfined Compression Response of Posterior Porcine Sclera
Anshul Bhardwaj[1], Hamed Hatami-Marbini[1]
[1]University of Illinois at Chicago

Posters: Soft Tissue Biomechanics

Aspen Glade

Session Chair: Thao (Vicky) Nguyen, Johns Hopkins University
Session Chair: Kristin Myers, Columbia University

The Effect of Permeability Boundary Conditions on the Reserve Zone Chondrocyte Subjected to Different Loading Rates
Masumeh Kazemi[1], John Williams[1]
[1]University of Memphis

A Continuum Mechanics Approach to Model Stiffness Sensing by Smooth Muscle Cells
Ali Akbar Karkhaneh Yousefi[1], Claudie Petit[1], Stephane Avril[1]
[1]Mines Saint-Etienne, Université de Lyon

Tissue Growth and Resorption Finite Element Model to Evaluate Expanders That Aid in Cleft Palate Repair
Tyler Gathman[1], Katherine Brought[2], Robert Tibesar[1], Arthur Erdman[1], David Nedrelow[1]
[1]University of Minnesota, [2]Iowa State University

Mechanical Testing of Type II Collagen Networks: Towards Modulating Mechanics, Identifying Single-Fiber Properties, and Establishing Multiscale Models
Phoebe Szarek[1], David M. Pierce[1]
[1]University of Connecticut

Copyright 2021 SB³C Foundation, Inc.

Spatial Heterogeneity of the White Matter Stiffness in the Corpus Callosum of the Mouse Brain
Xuesong Zhang[1], Johannes Weickenmeier[1]
[1]Stevens Institute of Technology

A Volumetric Growth and Remodeling Framework Towards Predicting the Progression of Osteoarthritis in Articular Cartilage
Muhammed M. Rahman[1], Thomas S. E. Öst[2], Corey P. Neu[3], David M. Pierce[1]
[1]University of Connecticut, [2]FOI Swedish Defense Research Agency, [3]University of Colorado Boulder

Lung Lobar Sliding Helps Reduce Parenchymal Distortion During Breathing
Adam Galloy[1], Ryan Amelon[1], Joseph Reinhardt[1], Madhavan Raghavan[1]
[1]University of Iowa

Numerically Modelling Skin-PPE Interaction to Reduce Injury in Healthcare Workers During the COVID-19 Pandemic
Rikeen Jobanputra[1], Sravani Royyuru[1], Jack Hayes[1], Marc Masen[1]
[1]Imperial College London

On the Characterization of Embryonic Curvatures Using Bezier Curves
Ashok Ramasubramanian[1]
[1]Union College

Specimen-Specific Fiber-Based Modeling and Simulation of Sclera Collagen Fiber Microstructure and Biomechanics
Fengting Ji[1], Manik Bansal[1], Bingrui Wang[2], Yi Hua[1], Felix Matuschke[3], Markus Axer[3], Ian Sigal[1]
[1]University of Pittsburgh, [2]Southwest Jiaotong University, [3]Forschungszentrum Jülich GmbH

The Anisotropic Mechanical Properties of Human Uterus
Shuyang Fang[1], James McLean[1], Joy Vink[1], Christine Hendon[1], Kristin Myers[1]
[1]Columbia University

Implementing Variable-Stiffness Springs for Modeling the Viscoelastic Behavior of the Porcine Urinary Bladder
Tyler Tuttle[1], Sara Roccabianca[1]
[1]Michigan State University

A Nonlinear Fibrous Viscoelastic Model Describes the Experimental Tensile Material Behavior of Human Cervix
Lei Shi[1], Joy Vink[1], Ronald Wapner[1], Kristin Myers[1]
[1]Columbia University

Investigating Conforming and Nonconforming Meshes in Human Lamina Cribrosa Subdomain Simulations
Hirut Kollech[1], Jonathan Vande Geest[1]
[1]University of Pittsburgh

Copyright 2021 SB³C Foundation, Inc.

A Two-Scale Homogenization Scheme for Saturated Porous Media in Three Dimensions
Ashkan Almasi[1], Tim Ricken[2], David M. Pierce[1]
[1]University of Connecticut, [2]University of Stuttgart

Probing the Mechanical Properties of Chick Embryos Using Atomic Force Microscopy
Joel Lefever[1], Jack Edson[1], Ashok Ramasubramanian[1]
[1]Union College

Changes to Micturition Patterns and Urinary Bladder's Extracellular Matrix Mechanical Behavior in an Animal Model of Radiation Cystitis
Marissa Grobbel[1], Bernadette Zwaans[2], Elijah Ward[2], Laura Lamb[2], Sara Roccabianca[1]
[1]Michigan State University, [2]Beaumont Health

Modeling the Human Lens Capsule with Implanted Accommodative Intraocular Lens
Kurt Ameku[1], Ryan Pedrigi[1]
[1]University of Nebraska-Lincoln

Crosslinks and Toughness of Gelatin Hydrogels for Tissue Engineering
Anshul Shrivastava[1], Namrata Gundiah[1]
[1]Indian Institute of Science, Bengaluru

Ocular Biomechanics due to the Ground Blast Reinforcement of an Improvised Explosive Device at Various Heights
Alireza Karimi[1], Reza Razaghi[2], Christopher A Girkin[1], J. Crawford Downs[1]
[1]University of Alabama at Birmingham, [2]Research Department, Heel of Scene Ltd., Tokyo

Parallel Stage Mechanism for Image Guided and Targeted MR Elastography
Efe Ozkaya[1], Waiman Meinhold[2], Derek Petti[1], Emily Triolo[1], Paul Kennedy[3], Lazar Fleysher[3], Jun Ueda[2], Mehmet Kurt[1]
[1]Stevens Institute of Technology, [2]Georgia Institute of Technology, [3]BioMedical Engineering and Imaging Institute

Development of a Method to Quantify Elastin Content in Large Datasets of Bladder Tissue Histology with Machine Learning Algorithm
Eli Broemer[1], Sara Roccabianca[1]
[1]Michigan State University

Effect of Stent Orientation on Aortic Root Stress during Transcatheter Aortic Valve Deployment: A Computational Study
Atefeh Razavi[1], Srikrishna SivaKumar[1], Breandan Yeats[1], Vinod Thourani[2], Venkateshwar Polsani[2], Pradeep Yadav[2], Lakshmi Prasad Dasi[1]
[1]Georgia Institute of Technology, [2]Piedmont Heart Institute

Decoupling Hydrostatic and Deviatoric Strain Energy Density in Biomaterials with Poisson's Ratio Larger Than 0.5
Amevi Semodji[1], Katherine Hollar[1], Gunes Uzer[1], Trevor Lujan[1]
[1]Boise State University

Copyright 2021 SB³C Foundation, Inc.

Effect of Region and Direction on Meniscus Elasticity as Measured by Atomic Force Microscopy
Kevin Orton[1], Wyndham Batchelor[1], Noel Ziebarth[1], Francesco Travascio[1], Alicia Jackson[1]
[1]University of Miami

Stress and Strain Distribution Analysis of Specimen-Specific Interweaved Fiber Sclera Model Under Equi-Biaxial Strain
Manik Bansal[1], Fengting Ji[1], Yi Hua[1], Fuqiang Zhong[1], Ian A. Sigal[1]
[1]University of Pittsburgh

Effect of Temperature on Equilibrium Compressive Modulus of Immature Bovine Articular Cartilage
C.V. Sise[1], Kimberly Kroupa[1], Jiashuai Fan[1], Clark Hung[1], Sinisa Vukelic[1], Gerard Ateshian1
[1]Columbia University

Inverse Finite Element Modeling of *Ex-Vivo* Organ-Scale Porcine Lung Based on 3d Digital Image Correlation and Controlled Pressure-Volume Loading
Mohammad Maghsoudi-Ganjeh[1], Crystal Mariano[1], Samaneh Sattari[1], Mona Eskandari[1]
[1]Univeristy of California-Riverside

Energy Dissipation in the Meniscus: A Parametric Study on Tissue Properties and Mechanical Loading Conditions
Massimiliano De Rosa[1], Alicia Jackson[1], Francesco Travascio[1]
[1]University of Miami

Efficacy of Combinational Therapy on Bone Restoration and Compensation After Contusion Spinal Cord Injury
Valerie Lallo[1], Michael Feeley[1], Anita Singh[1]
[1]Widener University

The Role of Glycosaminoglycans in Anterior and Posterior Scleral Swelling and Tensile Behavior
Mohammad Pachenari[1], Hamed Hatami-Marbini[1]
[1]University of Illinois at Chicago

Effects of Covid-19 Inflammation on the Regional Behavior of the Lung: A Computational Study
Sunder Neelakantan[1], Hamed Babaei[1], Reza Avazmohammadi[1]
[1]Texas A&M University

It Takes Both: on the Protein Interactions of Neurofibrillary Tangles and Amyloid Beta Plaques in Alzheimer's Disease
Trisha Gollamudi[1], Shima Jalalian[1], Johannes Weickenmeier[1]
[1]Stevens Institute of Technology

Development of a Novel Testing System to Evaluate Microscale Mechanics at the Vitreoretinal Interface
Joseph Phillips[1], Brittany Coats[1]
[1]University of Utah

Copyright 2021 SB³C Foundation, Inc.

Posters: Tissue Engineering

Aspen Glade

Session Chair: Feng Xu, Xi'an Jiaotong University

Methacrylated Recombinant Collagen Peptide (RCP-MA) As Collagen Mimicking 3D Hydrogel Model for Cardiac Tissue Engineering
Dylan Mostert[1], Ignasi Jorba[1], Leda Klouda[1], Nicholas Kurniawan[1], Carlijn Bouten[1]
[1]Eindhoven University of Technology

Characterization of Oxidatively Responsive Thiol-Ene Networks for Tissue Engineering Applications
Tyler Touchet[1], Samuel Briggs[1], Lance Graul[1], Duncan Maitland[1]
[1]Texas A&M University

Characterization of an Electrospun Polyurethane with Tunable Chemistry and Thiol-ene Crosslinking for Biomedical Applications
Samuel Briggs[1], Scott Herting[1], Grace Fletcher[1], Mary Beth Browning Monroe[2], Duncan Maitland[1]
[1]Texas A&M University, [2]Syracuse University

Image Based Evaluation of *In Vivo Degradation* for Shape Memory Polyurethane Foam in Embolic Applications
Lance Graul[1], Thomas Cheung[1], Staci Jessen[1], Landon Nash[2], Duncan Maitland[1]
[1]Texas A&M University, [1]Shape Memory Medical Inc.

Investigating the Role of Patterned ECM Stiffness and Proliferation During Branching Morphogenesis in the Embryonic Kidney
Somdutta Chakraborty[1], Thomas Carroll[2], Victor Varner[1]
[1]The University of Texas at Dallas, [2]University of Texas Southwestern Medical Center

Computer-Aided Molecular Design of Water Compatible Monomer for Dental Application
Yonas. Rufael[1], Ruben Molina[1], Farhana Abedin[1]
[1]California State Polytechnic University Pomona

A Microfluidic Approach to Create Gradients in Collagen Fiber Anisotropy
Indranil M. Joshi[1], Mehran Mansouri[1], Adeel Ahmed[1], Steven W. Day[1], Vinay V. Abhyankar[1]
[1]Rochester Institute of Technology

Fabrication of 3D Printer Associated Rotatory Bioreactor for Vascular Tissue Engineered Structures
Khemraj Deshmukh[1], Arindam Bit[1], Esther Beltran[2], Kunal Mitra[3]
[1]National Institute of Technology, [2]University of Central Florida, [3]Florida Tech

Macroscale Mechanical Characterization of Heterogeneous Fibrin Gels with Varying Density
Julian Jimenez[1], Yifan Guo[1], Adrian Buganza-Tepole[1], Sarah Calve[2]
[1]Purdue University, [2]University of Colorado, Boulder

Copyright 2021 SB³C Foundation, Inc.

An *In Vitro* Model of Bone Ingrowth in a Porous Titanium Scaffold
Alyssa Oberman[1], Brett English[2], Weidong Tong[2], Glen Niebur[1]
[1]University of Notre Dame, [2]DePuy Synthes

Development of a 3D *In Vitro* Vascularized Human Skin Equivalent Utilizing Collagen/Keratin Hydrogels
Kameel Zuniga[1], Neda Ghousifam[1], Mark Van Dyke[2], Marissa Rylander[1]
[1]University of Texas at Austin, [2]University of Arizona

Development and Utilization of a Vascularized 3D-Printed *In Vitro* Physiologically Representative Skin Tissue Platform for Burn Injury Investigation
Sean Brocklehurst[1], Neda Ghousafim[1], Kameel Isaac[1], Danielle Stolley[1], M. Nichole Rylander[1]
[1]University of Texas in Austin

Accelerated Degradation of Electrospun Polycaprolactone Tissue Engineering Scaffolds Under Dynamic Loading Conditions
Emily Clement[1], Johane Bracamonte[1], Joao Soares[1]
[1]Virginia Commonwealth University

Thursday, June 17	**4:00PM – 5:30PM EDT**

Computational and Experimental Modeling of Cardiovascular Interventions

Mud Springs

Session Chair: Luke Timmins, University of Utah
Session Chair: **Jessica Oakes,** Northeastern University

4:00PM ***In Vivo* Estimation of Regional Mechanical Properties of the Aortic Wall Accounting for the Active and Passive Effect of Periaortic Structures with an Inverse Finite Element Approach**
Johane Bracamonte[1], John Wilson[1], Joao Soares[1]
[1]Virginia Commonwealth University

4:13PM **Engineering Analysis of Aortic Wall Stress and Root Dilation in the V-Shape Surgery for Ascending Aortic Aneurysms**
Hai Dong[1], Minliang Liu[1], Tongran Qin[1], Liang Liang[2], Bulat Ziganshin[3], Hesham Ellauzi[3], Mohammad Zafar[3], Sophie Jang[3], John Elefteriades[3], Wei Sun[1]
[1]Georgia Institute of Technology, [2]University of Miami, [3]Yale University

4:26PM **Impact of Flow Rate on High Frequency Flow Instabilities in Intracranial Aneurysms, with Implications for Wall Vibration**
David Bruneau[1], Mehdi Najafi[1], Thangam Natarajan[2], Kristian Valen-Sendstad[2], David Steinman[1]
[1]University of Toronto, [2]Simula Research Laboratory

4:39PM **Hemodynamic Simulations to Predict Successful vs. Unsuccessful Catheter Interventions: Proof-of-Concept and Experimental Validation in Swine**
Ryan Pewowaruk[1], Luke Lamers[1], Alejandro Roldan-Alzate[1]
[1]University of Wisconsin - Madison

Copyright 2021 SB³C Foundation, Inc.

4:52PM **A Novel Dynamic Blalock-Taussig Shunt Regulator: An *In Vitro* Study**
Milad Samaee[1], Subhadhara Shashidharan[2], Kevin Maher[3], Ajit Yoganathan[1], Lakshmi Prasad Dasi[1]
[1]Georgia Institute of Technology, [2]Emory University School of Medicine, [3]Children's Healthcare of Atlanta

5:05PM **Haemodynamic Analysis of Branched Endografts for Complex Aortic Arch Repair**
Sampad Sengupta[1], Yu Zhu[1], Mohamad Hamady[1], Yun Xu[1]
[1]Imperial College London

Thursday, June 17	**4:00PM – 5:30PM EDT**

Mechanobiology in Tissue and Cellular Engineering

Alpine Drift

Session Chair: Eno Ebong, Northeastern University
Session Chair: **Spencer Szczesny,** Penn State University

4:00PM **Tensional Homeostasis Regulates Chromatin Accessibility and Represses Matrix Degradation Pathways Through Yap/Taz**
Dakota Jones[1], Xi Jiang[1], Eddie Bonnevie[1], Elisabeth Lemmon[1], Mary Kate Evans[1], Su-Jin Heo[1], Nathaniel Dyment[1], Robert Mauck[1]
[1]University of Pennsylvania

4:13PM **Long-Term Effect of TBI-Like Shear Stimuli on Astrocytes**
Tasnim Shireen[1], Susan Hua[1]
[1]University at Buffalo SUNY

4:26PM **The Primary Cilium Regulates Mechanoresponsive Pathways in Tenocytes**
McKenzie Sup[1], Fei Fang[1], Stavros Thomopoulos[1]
[1]Columbia University

4:39PM **Mechanical Stiffness Regulates Chromatin Remodeling in Mesenchymal Stem Cells**
Samantha Kaonis[1], Soham Ghosh[1]
[1]Colorado State University

4:52PM **On the Relation Between 3D Aortic Valve Interstitial Cell Shape and Contractile Behavior**
Alex Khang[1], Quan Nguyen[1], Xinzeng Feng[1], Michael Sacks[1]
[1]The University of Texas at Austin

5:05PM **Escaping the Stiffness Trap: Adhesion Strength and Contractility Enable Metastatic Cells to Become Adurotactic**
Benjamin Yeoman[1], Gabe Shatkin[1], Pranjali Beri[1], Afsheen Banisadr[1], Parag Katira[2], Adam Engler[1]
[1]University of California, San Diego, [2]San Diego State University

Copyright 2021 SB³C Foundation, Inc.

Thursday, June 17	4:00PM – 5:30PM EDT

Undergraduate Design Competition Live Session

Mogul Madness

Session Chair: Michael Moreno, Texas A&M University
Session Chair: **Ted Conway,** Florida Institute of Technology

4:00PM **The Development of a Mechanized Stepped Tension Brace for Treatment of Achilles Tendonitis in Collegiate Athletes**
Sneha Jeevan[1], Jack Latella[1], Mary Murray[1]
[1]University of Pittsburgh

4:15PM **Ventilators for the Developing World**
Grace L. Bugara[1], Taylor A. Corpuz[1], Maeve X. Enright[1], John B. Fortescue[1], Laurie A. Trainer[1], Vanessa S. Zighelboim[1], Michael Jaeggli[1], Lee Makowski[1], Marc Fuller[1]
[1]Northeastern University

4:30PM **Haptic Feedback to Aid the Visually Impaired**
John C. Tereck[1], Carter M. Roper[1], Peyton D. Duersel[1], Brandon M. Jackson[1], Matthew J. Kamin[1], Dario Martelli[1]
[1]The University of Alabama

4:45PM **Automatic Reclining Car Seat**
Md Joynal Abedin[1], Mohammad Shah Jalal[1], Alex Sullivan[1], Ahmee Cho[1], El Mokhtar Majdoub[1], Ahmed Ahmed[1], Parisa Saboori[1]
[1]The City College of New York

5:00PM **DynaCon PLS**
Robert Anhalt[1], Brooke Towns[1], Peter DiNapoli[1], Sebastian Moreno[1], Warren Dixon[1], Sean Niemi[1], Kimberly Stubbs[1]
[1]University of Florida

5:15PM **The MultiFlex Catheter - A Variable Stiffness Endovascular Catheter**
Halle R. Lowe[1], Vinay D. Chandrasekaran[1], Chase M. Hartquist[1], Jin V. Lee[1], Mohammed Zayed[1], Joshua W. Osbun[1], Eric C. Leuthardt[1], Michael Talcott[1], Guy M. Genin[1]
[1]Washington University in St. Louis

Thursday, June 17	4:00PM – 5:30PM EDT

Vascular Functioning and Modeling

Saddle Ridge

Session Chair: Hai-Chao Han, University of Texas, San Antonio
Session Chair: **Chiara Bellini,** Northeastern University

Copyright 2021 SB³C Foundation, Inc.

4:00PM **Computational Modeling on Transmural Distribution of Coronary Perfusion and Myocardial Work**
Lei Fan[1], Ravi Namani[1], Jenny Choy[2], Ghassan Kassab[2], Lik Chuan Lee[1]
[1]Michigan State University, [2]California Medical Innovation Institute

4:13PM **A Probabilistic and Anisotropic Failure Metric for Risk Assessment of Ascending Thoracic Aortic Aneurysm**
Minliang Liu[1], Liang Liang[2], Qing Zou[1], Yasmeen Ismail[1], Xiaoying Lou[3], Glen Iannucci[3], Edward Chen[3], Bradley Leshnower[3], John Elefteriades[4], Wei Sun[1]
[1]Georgia Institute of Technology, [2]University of Miami, [3]Emory University, [4]Yale University

4:26PM **Bent Buckling of Arteries with Non-Circular Cross Section**
Yasamin Seddighi[1], Hai-Chao Han[1]
[1]University of Texas San Antonio

4:39PM **Differential propensity of dissection along the aorta**
Ehsan Ban[1], Cristina Cavinato[1], Jay Humphrey[1]
[1]Yale University

4:52PM **AI-Accelerated Multiscale Modeling for Multi-Platelet Aggregation at Millisecond And Molecular Resolutions**
Peng Zhang[1], Yicong Zhu[1], Changnian Han[1], Jawaad Sheriff[1], Yuefan Deng[1], Danny Bluestein[1]
[1]Stony Brook University

5:05PM **Coupling NO-cGMP-PKG Chemical Pathway with Hemodynamics Model to Understand Regulation of Vascular Tone in the Pulmonary Vascular Tree**
Haritha Mullagura[1], Vasilina Filonova[2], Hamidreza Gharahi[2], C. Alberto Figueroa[2], Seungik Baek[1]
[1]Michigan State University, [2]University of Michigan

Copyright 2021 SB³C Foundation, Inc.

Friday, June 18	11:00AM – 12:30PM EDT

Bioprinting and Biomanufacturing

Alpine Drift

Session Chair: Lijie Grace Zhang, George Washington University
Session Chair: **David Corr,** Rensselaer Polytechnic Institute

11:00AM **Mechanical Cues Drive the Robust Assembly of Microfabricated Stem Cell-Derived Cardiac Tissues**
Samuel DePalma[1], Austin Stis[1], Domenica Passariello[1], Christopher Davidson[1], Adam Helms[1], Brendon Baker[1]
[1]University of Michigan

11:13AM **Silk-Based Bio-ink with Interpenetrating Network for Extrusion Bio-printing**
Xuan Hao (Ernest) Tan[1], Wen Xin Tan[1], Cho Hong James Goh[1]
[1]National University of Singapore

11:26AM **3D Printed Microstructures for Regenerative Osteochondral Implants**
Kevin Eckstein[1], Camila Uzcategui[1], Stephanie Bryant[1], Robert McLeod[1], Virginia Ferguson[1]
[1]University of Colorado at Boulder

11:39AM **Migration Patterns of Contractile Cell Fragments on ECM Mimicking Suspended Fibers**
Abinash Padhi[1], Brooke Danielson[2], Deema Alabduljabbar[3], Ji Wang[1], Daniel Conway[2], Rakesh Kapania[1], Amrinder Nain[1]
[1]Virginia Tech, [2]Virginia Commonwealth University, [3]University of California Davis

11:52AM **Tunable Physical and Soluble Microenvironmental Cues Synergistically Enhance Tenocyte Migration**
Robert Kent[1], Mohamed Said[1], Megan Busch[1], Daniel Matera[1], William Wang[1], Samuel DePalma[1], Harrison Hiraki[1], Megan Killian[1], Adam Abraham[1], Jae-Won Shin[2], Ariella Shikanov[1], Brendon Baker[1]
[1]University of Michigan, [2]University of Illinois Chicago

12:05PM **Single Cell Analysis of VCAM-1 Protein Expression by Micropatterned Endothelial Cells**
Meghan Fallon[1], Monica Hinds[1]
[1]Oregon Health & Science University

Friday, June 18	11:00AM – 12:30PM EDT

Cardiovascular Tissue Engineering and Mechanobiology

Saddle Ridge

Session Chair: Emma Lejeune, Boston University
Session Chair: **Daniela Valdez-Jasso,** University of California, San Diego

Copyright 2021 SB³C Foundation, Inc.

11:00AM **Lymphocyte Nanomechanics in Response to Stent Implantation**
Konstantinos Kapnisis[1], Andreas Stylianou[2], Despoina Kokkinidou[1], Marianna Prokopi[1], Andreas Anayiotos[1]
[1]Cyprus University of Technology, [2]European University Cyprus

11:13AM **SarcGraph: Automated Segmentation, Tracking, and Analysis of Sarcomeres in Human Induced Pluripotent Stem Cell Derived Cardiomyocytes**
Bill Zhao[1], Emma Lejeune[1]
[1]Boston University

11:26AM **Post-Stretch Recovery of Vascular Smooth Muscle Cells is Strain Rate Dependent**
Samuel Boland[1], Patrick Alford[1]
[1]University of Minnesota

11:39AM **Microenvironmental Determinants of Organized Stem Cell-Derived Cardiac Tissues on Synthetic Fibrous Matrices**
Samuel DePalma[1], Christopher Davidson[1], Austin Stis[1], Adam Helms[1], Brendon Baker[1]
[1]University of Michigan

11:52AM **Changes in Right Ventricle Viscoelasticity with Maturation**
Wenqiang Liu[1], Michael Nguyen-Truong[1], Kevin Labus[1], Jeremiah Easley[1], Christian Puttlitz[1], Zhijie Wang[1]
[1]Colorado State University

12:05PM **Signaling Network Model of TSC1 Knock-Out Recapitulates a Degradative Vascular Smooth Muscle Cell Phenotype**
Ana Estrada[1], Jay Humphrey[1]
[1]Yale University

Friday, June 18	**11:00AM – 12:30PM EDT**

Valvular Modeling I

Mud Springs

Session Chair: Michael Sacks, University of Texas at Austin
Session Chair: **Manuel Rausch,** University of Texas at Austin

11:00AM **Functional Mechanics of the Murine Pulmonary Heart Valve**
Xinzeng Feng[1], Yifei Liu[2], Hao Liu[1], Christopher Breuer[3], David McComb[2], Michael Sacks[1]
[1]University of Texas at Austin, [2]The Ohio State University, [3]Nationwide Children's Hospital

11:13AM **Pressure Drop and Recovery with MitraClip: An *In Vitro* Study**
Shelley Gooden[1], Breandan Yeats[1], Vinod Thourani[2], Konstantinos Boudoulas[3], Lakshmi Dasi[1]
[1]Georgia Institute of Technology, [2]Piedmont Heart Institute, [3]The Ohio State University Wexner Medical Center

Copyright 2021 SB³C Foundation, Inc.

11:26AM **Evaluation of Affine Fiber Kinematics in Porcine Tricuspid Valve Leaflets**
Colton Ross[1], Arshid Mir[1], Harold Burkhart[1], Chung-Hao Lee[1]
[1]The University of Oklahoma

11:39AM **The Tricuspid Valve (Mal)adapts in Ovine Models of Ventricular Heart Disease**
William Meador[1], Artur Iwasieczko[2], Tomasz Jazwiec[2], Mrudang Mathur[1], Marcin Malinowski[2], Tomasz Timek[2], Manuel Rausch[1]
[1]University of Texas at Austin, [2]Spectrum Health

11:52AM **Comparative Computational Analysis of PASCAL and MitraClip Implantation in a Patient-Specific Left-Heart Model**
Ryan Errthum[1], Andres Caballero[1], Wei Sun[1]
[1]Georgia Institute of Technology

12:05PM **Polymeric TAVR Durability and Hydrodynamics Testing, Enhanced by Machine Learning for Tracking Leaflets Motion**
Brandon Kovarovic[1], Steven Crimarco[1], Ziji Zhang[1], Oren Rotman[1], Marvin Slepian[2], Danny Bluestein[1]
[1]Stony Brook University, [2]University of Arizona

Friday, June 18	**1:00PM – 2:30PM EDT**

Emerging Solid Mechanics Topics in Mechanobiology

Saddle Ridge

Session Chair: Edward Sander, University of Iowa
Session Chair: **Chiara Bellini,** Northeastern University

1:00PM **Modeling the Astrocytic Lamina and its Response to Increase in Intraocular Pressure**
Yik Tung Tracy Ling[1], Arina Korneva[1], Harry Quigley[1], Thao Nguyen[1]
[1]Johns Hopkins University

1:13PM **Oral All-Trans Retinoic Acid Treatment Alters Scleral Biomechanics and Induces Myopia**
Dillon Brown[1], Machelle Pardue[2], Ross Ethier[1]
[1]Georgia Institute of Technology, [2]Atlanta VA

1:26PM **Intraarticular MMP-1 in the Facet Joint Modifies the Capsular Ligament's Response to Load & that Response Correlates with the Extent of Degraded Collagen**
Meagan Ita[1], Sagar Singh[1], Beth Winkelstein[1]
[1]University of Pennsylvania

1:39PM **Effect of ECM Heterogeneity on Cell Mechanosensing**
Maria Proestaki[1], Jacob Notbohm[1]
[1]University of Wisconsin-Madison

Copyright 2021 SB³C Foundation, Inc.

1:52PM **Mechanical Stress in Pancreatic Cancer: Signaling Pathway Adaptation Activates Cytoskeletal Remodeling and Enhances Cell Migration**
Maria Kalli[1], Ruxuan Li[2], Gordon B. Mills[3], Triantafyllos Stylianopoulos[2], Ioannis Zervantonakis[2]
[1]University of Cyprus, [2]University of Pittsburgh, [3]Oregon Health & Science University

2:05PM **Computational Analysis of the Role of Collagen Network Viscoelasticity in Rapid-Stretch *In-Vitro* Axon Injury Models**
Maryam Nikpasand[1], Jill Middendorf[1], Jonathan Marcelin[2], Beth Winkelstein[2], Victor Barocas[1]
[1]University of Minnesota, [2] University of Pennsylvania

Friday, June 18	**1:00PM – 2:30PM EDT**

Emerging Topics in Cell and Tissue Engineering

Alpine Drift

Session Chair: Will Richardson, Clemson University
Session Chair: **Soham Ghosh,** Colorado State University

1:00PM **Rapid Formation of 3D Tumor Model with Tumor-Stroma Interface at Extremely High Cell Density**
Cih Cheng[1], Bumsoo Han[1], George T Chiu[1]
[1]Purdue University

1:13PM **Nanomechanical Signature of Sarcomas Can Be Predictive of Response to Chemotherapy**
Andreas Stylianou[1,2], Fotios Mpekris[2], Chrysovalantis Voutouri[2], Triantafyllos Stylianopoulos[2]
[1]European University Cyprus, [2]University of Cyprus

1:26PM **Characterization of Thermal and Optical Properties of Porcine Pancreas Tissue for Plasmonic Photothermal Therapy**
Forhad Akhter[1], Santiago Manrique-Bedoya[1], Chris Moreau[1], Andrea Smith[1], Kathryn Mayer[1], Yusheng Feng, Lyle Hood[1]
[1]University of Texas at San Antonio

1:39PM **An *In Vivo* Demonstration of Adhesion Strength as a Predictive Measure of Metastatic Potential**
Katherine Birmingham[1], Pranjali Beri[1], Jerry Tuler[1], Benjamin Yeoman[1], Adam Engler[1]
[1]University of California San Diego

1:52PM **Contact Guidance During Breast Cancer Dissemination**
Kristen Loesel[1], Harrison Hiraki[1], Brendon Baker[1], Carole Parent[1]
[1]University of Michigan

Copyright 2021 SB³C Foundation, Inc.

2:05PM **The Role of Ligand Density and Degradability in Hydrogel Induced Breast Cancer Dormancy**
Cindy Farino[1], Shantanuq Pradhan[1], John Slater[1]
[1]University of Delaware

Friday, June 18	**1:00PM – 2:30PM EDT**

Valvular Modeling II

Mud Springs

Session Chair: Wei Sun, Georgia Institute of Technology
Session Chair: **Lakshmi Dasi,** Georgia Institute of Technology

1:00PM **Clinical Risk Assessment of Post-TAVR Cardiac Conduction Abnormality Using Patient-Specific Bicuspid Aortic Valve Models**
Salwa Anam[1], Matteo Bianchi[1], Brandon Kovarovic[1], Ram Ghosh[1], Ashraf Hamdan[2], Rami Haj-Ali[2], Danny Bluestein[1]
[1]Stony Brook University, [2]Tel-Aviv University

1:13PM **Neo-Sinus and Sinus Flows After Transcatheter Aortic Valve Implantation of Evolut, SAPIEN 3, Accurate Neo and Allegra**
Hoda Hatoum[1], Shelley Gooden[2], Yasaman Farsiani[2], Milad Samaee[2], Janarthanan Sathananthan[3], Scott Lilly[4], Abul Rahman Ihdayhid[5], Vinod Thourani[6], Lakshmi Prasad Dasi[2]
[1]Michigan Technological University, [2]Georgia Institute of Technology, [3]St Paul's and Vancouver General Hospital, [4]The Ohio State University, [5]Monash Health, [6]Piedmont Hospital

1:26PM **Frequency Effect on Transcatheter Valve Motion and Fluid Dynamics in an Accelerated Environment**
Sailahari Ponnaluri[1], Keefe Manning[1], Michael Sacks[2]
[1]Penn State University, [2]University of Texas at Austin

1:39PM **Fluid-Structure Interaction Modeling of Patient-Specific Bicuspid Aortic Valves**
Tongran Qin[1], Andres Caballero[1], Wenbin Mao[2], Brian Barrett[1], Norihiko Kamioka[3], Stamatios Lerakis[3], Wei Sun[1]
[1]Georgia Institute of Technology, [2]University of South Florida, [3]Emory University

1:52PM **Patient-Specific Prediction of IMR Recurrence After Mitral Valve Surgical Repair**
Harshita Narang[1], Bruno Rego[1], Robert Gorman[2], Joseph Gorman[2], Michael Sacks[1]
[1]The University of Texas at Austin, [2]University of Pennsylvania

2:05PM **Towards Non-Invasive Computational-Mechanics and Imaging-Based Diagnostic Framework for Patients with Transcatheter Aortic Valve Replacement**
Vahid Khodaei[1], Zahra K. Motamed[1]
[1]McMaster University

Copyright 2021 SB³C Foundation, Inc.

CONFERENCE ABSTRACTS

Copyright 2021 SB³C Foundation, Inc.

RE-ENGINEERING THE MECHANICAL TUMOR MICROENVIRONMENT WITH DEXAMETHASONE ENHANCES EFFICACY OF CISPLATIN-LOADED NANOCARRIER IN METASTATIC BREAST CANCER

Fotios Mpekris[1], John D. Martin[2], Myrofora Panagi[1], Thahomina T. Khan[2], Margaret R. Martin[2], Chrysovalantis Voutouri[1], Jumpei Norimatsu[2], Triantafyllos Stylianopoulos[1], Kazunori Kataoka[3] and Horacio Cabral[2]

(1) Cancer Biophysics Laboratory,
Department of Mechanical Engineering,
University of Cyprus, Cyprus

(2) Department of Bioengineering,
Graduate School of Engineering,
University of Tokyo, Tokyo, Japan

(3) Innovation Center of NanoMedicine,
Kawasaki Institute of Industrial Promotion,
Kawasaki, Kanagawa, Japan

INTRODUCTION

Nanocarriers (NCs) accumulate in tumors through the enhanced permeability and retention (EPR) effect [1]. As NCs and other nano-sized therapies are in clinical practice, translatable strategies that increase the magnitude of their accumulation and penetration while reducing heterogeneity of microdistribution may improve treatment outcomes. One such strategy to increase and conform NC penetration and accumulation involves re-engineering the non-cancerous components of the tumor, which collectively are known as the tumor microenvironment (TME), to reach normal levels [2]. Without normalization of TME, tumor vessel function is compromised because the TME promotes vessel leakiness and compression [2]. Dexamethasone is a glucocorticoid steroid with anti-inflammatory properties used to treat many diseases, including cancer, in which it helps manage various side effects of chemo-, radio-, and immunotherapies. Here, our research objective was to investigate the TME re-engineering effects of dexamethasone in metastatic murine breast cancer (BC). We found that low dose dexamethasone normalizes vessels and the extracellular matrix, thereby reducing interstitial fluid pressure, tissue stiffness, and solid stress [3]. Also, dexamethasone increases the tumor accumulation and efficacy of ~30 nm polymeric micelles containing cisplatin (CDDP/m) against murine models of primary BC and spontaneous BC lung metastasis, which also feature a TME with abnormal mechanical properties. These results suggest that pretreatment with dexamethasone before NC administration could increase efficacy against primary tumors and metastases.

METHODS

Orthotopic models for murine mammary tumors were generated by implantation of $5x10^4$ 4T1 and 4T1-luc cancer cells in 40 µl of serum-free medium into the third mammary fat pad of 6-week old BALB/c female mice. Treatment was initiated when tumors reached ~90mm^3. Dexamethasone at 3mg/kg was administered daily from days 0 through 8. CDDP/m at 1mg/kg was administered by retro-orbital injection during sedation with isoflurane on days 2, 5, and 8. The tumors were measured every 1-2 days using calipers by an investigator blind of the treatment groups.

RESULTS

Vascular endothelial growth factor (VEGF) is the major driver of the pathophysiology of tumor vessels and blocking it promotes vascular normalization [4]. Dexamethasone reduces VEGF expression in murine models of brain cancer [5], so we hypothesized it would do so in BC. We treated immunocompetent BALB/c mice bearing orthotopic 4T1 BC daily for 4 days with 3 or 30 mg/kg dexamethasone. Dexamethasone reduced the levels of VEGF as assessed by immunofluorescence staining of tumor sections (Figure 1A,B). We next tested the effect of dexamethasone on vessel structure by using histology. Dexamethasone at 30 mg/kg reduced the microvessel density (Figure 1C,D), whereas dexamethasone at 3 mg/kg avoided pruning yet increased vessel maturity, as indicated by the association of NG2+ pericytes with CD31+ endothelial cells (Figure 1E,F).

We then tested whether dexamethasone re-engineers the tumor extracellular matrix (ECM). We focused on collagen I and hyaluronan because they have been identified as matrix components that contribute to solid stress accumulation and vessel compression. With histological staining we found that dexamethasone reduced levels of hyaluronan (Figure 2A,B) and not collagen I (Figure 2A,C) in the tumors. Based on these results, we tested whether the mechanical TME was normalized. We found that 30 mg/kg dexamethasone reduced tissue stiffness, whereas 3 mg/kg only produced a trend (Figure 2D). On the other hand, by using the "tumor-opening" assay, which indicates the amount of

Copyright 2021 SB³C Foundation, Inc.

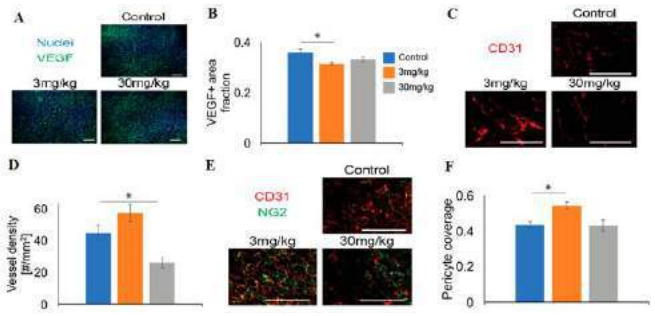

Figure 1: Dexamethasone induces vascular normalization. (A) Representative images of VEGF (green) with nuclear counterstain (blue) immunofluorescence. (B) Quantification of area fraction positive for VEGF immunofluorescence staining. (C) Representative images of CD31 (red) immunofluorescence marking tumor vessels. (D) Immunohistological quantification of the tumor vessel density, as assessed by the number of vessels normalized to the image area. (E) Representative images of CD31 (red) and NG2 (green) immunofluorescence marking endothelial cells and pericytes, respectively. Yellow areas indicate colocalization of both cell types. (F) Quantification of the pericyte coverage of microvessels, as assessed by the fraction of CD31-positive staining area that is also positive for NG2.

residual solid stress held within the tumor tissue by the amount it opens after cutting, we confirmed that both doses reduced solid stress (Figure 2E). A larger opening is associated with more solid stress. Furthermore, we found that dexamethasone reduces interstitial fluid pressure in 4T1 tumors (Figure 2F). Thus, the results from the histology, and mechanical experiments suggest that dexamethasone re-engineers the ECM in tumors by reducing hyaluronan levels.

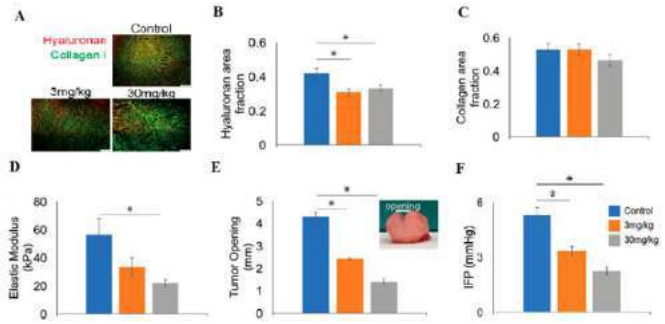

Figure 2: Dexamethasone induces ECM normalization. (A) Representative images of hyaluronan (red) and collagen I (green) immunofluorescence. Yellow areas indicate colocalization of both ECM components. (B) Quantification of area fraction positive for hyaluronan immunofluorescence. (C) Quantification of area fraction positive for collagen I immunofluorescence. (D) Tumor tissue elastic modulus, which is a measure of stiffness. (E) Solid stress levels, which was assessed by length of the tumor opening after cutting the tissue. (F) Interstitial Fluid Pressure levels.

After confirming that dexamethasone normalizes vascular structure, ECM, and vessel function, we next hypothesized that dexamethasone would affect the rate NCs transport across tumor vessels and penetrate toward cancer cells. Thus, to test our hypothesis, we used CDDP/m, which are ~30 nm. Firstly, we tested the therapies in a primary tumor growth delay study against orthotopic 4T1-luc tumors, with an end point of days until 1000 mm^3 tumor volume. We found that CDDP/m (1 mg/kg) monotherapy increased the number of days for the tumors to reach 1000 mm^3 compared to control (Figure 3A). Combining dexamethasone (3mg/kg) with CDDP/m (1 mg/kg) significantly increased this time period compared to that with CDDP/m monotherapy (Figure 3A). Thus, dexamethasone enhances the efficacy of CDDP/m against 4T1 primary tumors.

Next, we investigated the effects of the combination of dexamethasone and CDDP/m on lung metastases. To mimic the clinical treatment protocol of metastatic disease and produce spontaneous metastases, we surgically removed 4T1 primary BC tumors when they reached ~300 mm^3. Then, after waiting 2 days post-surgery for the mice to rest and metastases to develop further, we administered two cycles of CDDP/m with daily dexamethasone. In these mice, we found that only the combination of dexamethasone (3mg/kg) and CDDP/m (1mg/kg) provided a survival advantage (Figure 3B). Thus, dexamethasone increases the efficacy of CDDP/m against BC pulmonary metastasis.

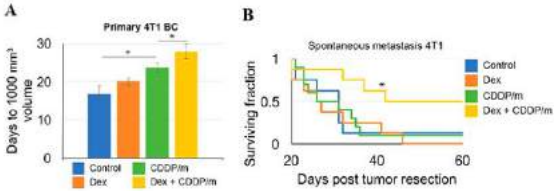

Figure 3: Dexamethasone increases the efficacy of 30 nm CDDP/m in 4T1 tumors. (A) Quantification of tumor growth rate. Graph of the number of days between treatment initiation and 1000 mm^3 tumor volume. When tumors reached ~90 mm^3, they were size- and time-matched into control, dexamethasone monotherapy, CDDP/m monotherapy, and dexamethasone and CDDP/m combination. (B) Animal survival in mice with spontaneous metastases, which developed after surgical primary tumor resection at 300 mm^3. Mice were size- and time-matched into control, dexamethasone monotherapy CDDP/m monotherapy, and dexamethasone and CDDP/m combination.

DISCUSSION

Our results demonstrate the value of TME normalization in improving the efficacy of NCs. By identifying dexamethasone as a therapy that re-engineers both the ECM and vessels, we confirm that the combination of normalization strategies is effective in potentiating the efficacy of cytotoxic NCs in models of metastatic BC.

ACKNOWLEDGEMENTS

[1] European Research Council under the European Union's Seventh Framework Programme (FP7/2007-2013) / ERC grant agreement no 336839-ReEnginneeringCancer.
[2] Research and Innovation Foundation of Cyprus, (POST-DOC/0718/0084): Optimizing immunotherapy in triple-negative breast cancer by normalizing the tumor microenvironment.
[3] Research and Innovation Foundation of Cyprus, New Strategic Infrastructure Units – Young Scientists, (CancerNanoMED): Center for Preclinical Evaluation and Optimization of Cancer Nanomedicines.

REFERENCES

[1] Stylianopoulos, T. et al., *Nanomedicine* 11(8): 1893-1907, 2015.
[2] Stylianopoulos, T. et al., *Trends in cancer* 4(4): 292-319, 2018.
[3] Martin, J.D. et. al, *ACS Nano* 13(4): 292-319, 2018.
[4] Goel, S., et al., *Physiol Rev* 91(3): p. 1071-121, 2011.
[5] Heiss, J.D., et al., *J Clin Invest* 98(6): 1400, 1996.

Copyright 2021 SB³C Foundation, Inc.

SB³C2021
Summer Biomechanics, Bioengineering and Biotransport Conference
June 14-18, Virtual

TOWARDS NON-INVASIVE COMPUTATIONAL-MECHANICS AND IMAGING-BASED DIAGNOSTIC FRAMEWORK FOR PATIENTS WITH TRANSCATHETER AORTIC VALVE REPLACEMENT

Seyedvahid Khodaei (1), Zahra Keshavarz-Motamed (1,2,3)

(1) Department of Mechanical Engineering, McMaster University, Hamilton, Ontario, Canada

(2) School of Biomedical Engineering, McMaster University, Hamilton, Ontario, Canada

(3) School of Biomedical Engineering, McMaster University, Hamilton, Ontario, Canada

INTRODUCTION

Transcatheter aortic valve replacement (TAVR) is an emerging minimally invasive intervention for patients with aortic stenosis (AS) *across a broad risk spectrum* (1). Despite recent improvements in the design of transcatheter valves and implantation techniques, paravalvular leak (PVL, leak around the prosthesis) remains a foremost complication and an independent predictor of mortality (2). As Pibarot (2019) stated *"Paravalvular regurgitation is considered the main Achilles' heel of transcatheter aortic valve replacement"* (3). It is important to note that mild PVL arises in 20% to 80% of patients, whereas moderate and severe PVL happen in 5% to 22% of them (4). As use of TAVR increase, we must advance our understanding of its interactions with diseases of other valves and the ventricular state. However, despite the prevalence of PVL, the quantitative understanding of the interplay between pre-existing valvular pathologies, PVL, LV and post-TAVR recovery is inadequate.

"Cardiology is flow"(5). Abnormal fluid dynamics lead to initiation and advancement of cardiovascular disease. Such abnormalities are often displayed by disturbed flow, altered biomechanical forces, and in some cases a rise in the heart workload. There has thus been an emergent call by many for quantitative investigations of hemodynamics that take into account the interactive coupling of the valves, left ventricle, and the arterial system (6–8). This is what we seek to do.

In this study, we developed a Doppler-based and patient-specific lumped-parameter modeling framework, that takes interactions of the valves, left ventricle and arterial system into account, to estimate the LV workload (*global hemodynamics)* non-invasively. In addition to the global hemodynamics, we quantified the effect of PVL on the 3-D flow structures in the LV and LV outflow tract (*local hemodynamics*) using a computational fluid mechanics and lumped parameter modeling framework based on and correlated with clinically measured hemodynamic metrics and images in both pre and post-TAVR states.

METHODS

Global hemodynamics (LV workload). We developed a patient-specific lumped-parameter model that considers interactions of the aortic valve, LV and arterial system to estimate the LV workload non-invasively in both pre and post intervention states. The model uses a limited number of input parameters all of which can be reliably obtained using Doppler echocardiography and a sphygmomanometer (9).

Local hemodynamics (blood flow dynamics). We developed a fluid-solid interaction and lumped parameter modeling framework to calculate 3-D blood flow dynamics in the LV. As described above, the lumped parameter model in this framework used few input parameters all of which can be measured using Doppler echocardiography and a sphygmomanometer.

RESULTS

LV workload (global hemodynamics). The LV workload is an effective metric of the LV load and clinical state and represents the energy that the ventricle delivers to the blood during ejection plus the energy necessary to overcome the viscoelastic properties of the myocardium itself. Pre-TAVR, untreated AS increased the load on the LV due to the augmented flow resistance which caused a LV pressure overload. Although the flow resistance and consequently the LV pressure decreased greatly post TAVR, the LV workload did not improve because PVL contributed to a switch from a ventricular pressure overload to a ventricular volume overload (Figure 1).

SB³C2021-003
Copyright 2021 SB³C Foundation, Inc.

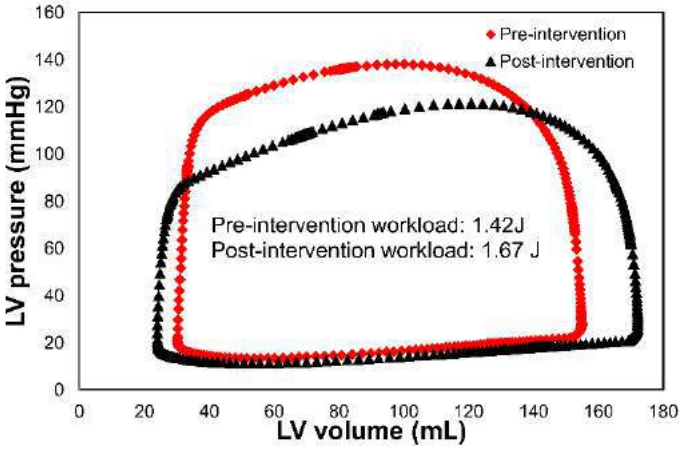

Figure 1. LV workloads in a sample patient between baseline and 90 days post-TAVR. *Pre-TAVR:* brachial pressures: 75 - 141 mmHg, aortic valve effective orifice area: 1.4 cm^2, no aortic regurgitation, moderate mitral regurgitation, LV stroke volume: 85 mL; *Post-TAVR*: brachial pressures: 60 - 123 mmHg, aortic valve effective orifice area: 2.3 cm^2, mild-moderate PVL, moderate-severe mitral regurgitation, LV stroke volume: 100 mL. *LV workload did not improve by TAVR.*

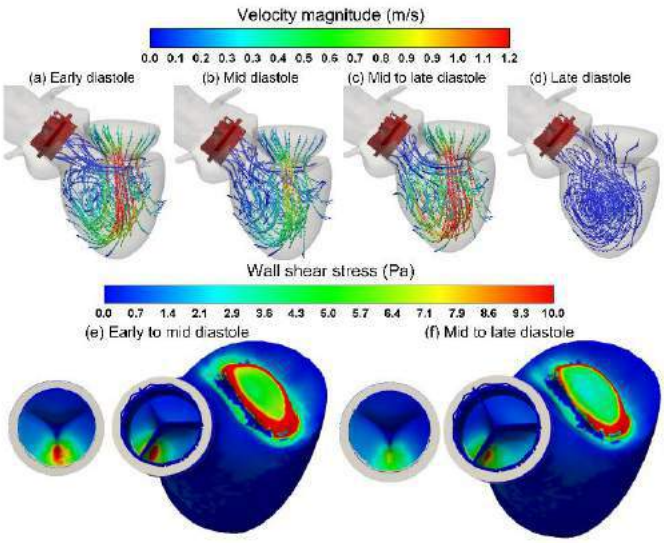

Figure 2. Flow modeling in a LV with mild PVL in a sample patient. (a) Velocity vector during diastole. (b) Wall shear stress during diastole.

LV fluid dynamics (local hemodynamics). During filling of the healthy heart, the blood entering the LV through the mitral valve forms a vortex that minimizes energy dissipation and optimizes the pumping efficiency. The vortical structure in the LV is altered in presence of valvular and ventricular diseases. In such cases the vortex dynamics becomes less synchronized with the heart contraction than the healthy vortex ring is, and other vortices may emerge and interact with one another. PVL following TAVR substantially alters the vortical structure in the left ventricle outflow tract and LV, creating disturbed flow (Figure 2). The jets emerging from PVL orifices diverge within the LV. This unfavorable flow condition leads to high shear stresses on TAV and mitral valve leaflets (Figure 2) which can cause tissue inflammation which can ultimately lead to the mitral valve failure. Moreover, PVL, characterized by multiple jets, enters the LV chamber, directly interacts with the mitral inflow, hinders formation of normal fluid vortical structures in the LV and may worsen the mitral regurgitation post-TAVR. We observed similar flow characteristics in other patients with mild, moderate, and severe PVL.

DISCUSSION

PVL limits the benefit of TAVR: may increase the LV load, may potentially worsen MR, and worsens heart failure. MR and its exacerbation by PVL will likely play an important hindering role in success of TAVR. The findings of this study suggest that beyond routine clinical indices for hemodynamic evaluation of the valvular disease (e.g, Doppler pressure gradients), valvular and ventricular hemodynamics and their interactions should be clinically quantified and considered to better conduct the aortic valve management and treatment planning.

ACKNOWLEDGEMENTS

ZKM and SK were supported by NSERC Discovery Grant (RGPIN-2017-05349).

REFERENCES

1. Padala M, Sarin EL, Willis P, et al. An Engineering Review of Transcatheter Aortic Valve Technologies. Cardiovasc. Eng. Technol. 2010;1:77–87.
2. Pibarot P, Hahn RT, Weissman NJ, Monaghan MJ. Assessment of paravalvular regurgitation following TAVR: a proposal of unifying grading scheme. JACC Cardiovasc. Imaging 2015;8:340–360.
3. Pibarot P. Paravalvular Regurgitation Following Transcatheter Aortic Valve Replacement: Is it Still an Issue in 2018? Struct. Heart 2019;3:31–33.
4. Sannino A, Stoler RC, Vallabhan R, et al. Assessment of the Severity of Paravalvular Regurgitation and its Role on Survival After Transcatheter Aortic Valve Replacement. Struct. Heart 2019;3:24–30.
5. Richter Y, Edelman ER. Cardiology is flow. Circulation 2006;113:2679–2682.
6. Dweck MR, Boon NA, Newby DE. Calcific aortic stenosis: a disease of the valve and the myocardium. J. Am. Coll. Cardiol. 2012;60:1854–1863.
7. Pibarot P, Dumesnil JG. Improving assessment of aortic stenosis. J. Am. Coll. Cardiol. 2012;60:169–180.
8. Ben-Assa E, Brown J, Keshavarz-Motamed Z, et al. Ventricular stroke work and vascular impedance refine the characterization of patients with aortic stenosis. Sci. Transl. Med. 2019;11.
9. K. Motamed Z. A diagnostic, monitoring, and predictive tool for patients with complex valvular, vascular and ventricular diseases. Nat. Sci. Rep. 2019;Under review.
10. Gharib M, Rambod E, Kheradvar A, Sahn DJ, Dabiri JO. Optimal vortex formation as an index of cardiac health. Proc. Natl. Acad. Sci. 2006;103:6305–6308.

Copyright 2021 SB³C Foundation, Inc.

DEFORMATION OF PERIPAPILLARY SCLERA AND RETINA IN RESPONSE TO ELEVATED INTRAOCULAR PRESSURE

S. Kwok (1), M. Pan (1), Y. Ma (2), X. Pan (3), J. Liu (1,2)

(1) Department of Biomedical Engineering
The Ohio State University
Columbus, OH, USA

(2) Department of Ophthalmology and Visual Sciences
The Ohio State University
Columbus, OH, USA

(3) Department of Biomedical Informatics
The Ohio State University
Columbus, OH, USA

INTRODUCTION

Glaucoma is the second leading cause of blindness worldwide [1]. Glaucomatous damage initiates at the optic nerve head (ONH) with characteristic cupping of the ONH in advanced stages of pathology [2]. Elevated intraocular pressure (IOP) has been identified as a primary risk factor for glaucoma onset and progression. IOP-related mechanical damage of neural and connective tissues [3] play a central role in glaucoma pathophysiology. Therefore, characterization of the biomechanical response of the ONH and its surrounding tissues in response to IOP elevation may serve to further our understanding of the biomechanical contributors to glaucoma damage.

We have developed and validated a technique applying high frequency ultrasound to measure tissue deformation in the posterior eye [4] and reported ONH and peripapillary sclera (PPS) strains during IOP elevation [5]. In this study, we aimed to characterize the deformation of the peripapillary retina (PPR) to gain insights into the biomechanical response of this critical neural tissue to IOP elevation.

METHODS

Ten donor globes (20 – 74 years old, 4 male and 6 female) were obtained within 12 h postmortem from the Lion's Eye Bank of West Central Ohio (Dayton, OH, USA) in accordance with the Declaration of Helsinki.

Before inflation, extraocular tissue was removed from the globe and the optic nerve was trimmed close to the surface of the sclera for ultrasound imaging from the posterior side. Two spinal needles were inserted through the equator of the globe to secure the eye to a custom-built holder (Fig. 1A). Two 20G needles were inserted into the anterior chamber of the eye, one connected to an infusion pump (Ph.D. Ultra, Harvard Apparatus, MA) and the other to a pressure sensor (P75, Harvard Apparatus, MA) to control and record IOP.

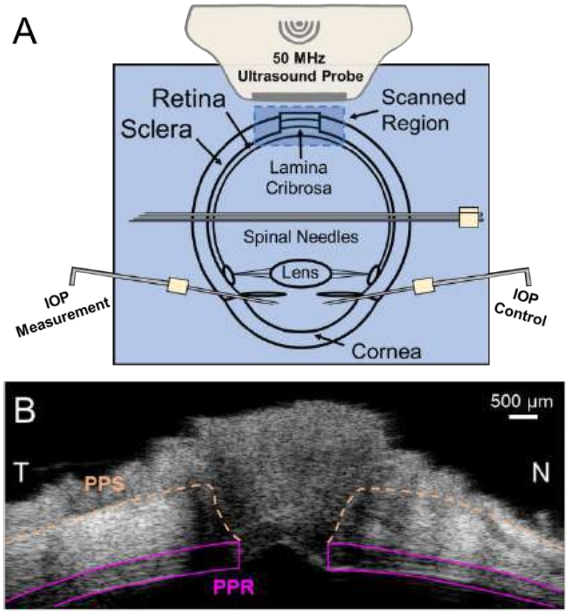

Figure 1: A) Experimental setup of human donor globe inflation with high-frequency ultrasound imaging of the ONH and peripapillary region. B) A representative ultrasound image of the scanned region along the nasal-temporal (NT) axis. PPS (dashed tan) and PPR (solid pink) segmentation are shown.

The globes were first preconditioned with 20 cycles from 5 to 30 mm Hg at 2 seconds per cycle before equilibrating at 5 mm Hg for 30

Copyright 2021 SB³C Foundation, Inc.

minutes. The inflation tests were then performed by increasing IOP from 5 to 30 mm Hg with 0.5 mmHg steps. The IOP was held constant at each IOP level for 30 seconds before ultrasound scans were acquired using a 50MHz ultrasound probe (Vevo2100, VisualSonics). Each eye was inflated twice to capture 2D scans (approximately 4 mm × 10 mm) of the posterior eye centered at the ONH along the nasal-temporal (NT) and superior-inferior (SI) axes.

A correlation-based ultrasound speckle tracking algorithm was used to compute tissue displacements [4]. Briefly, the ultrasound radiofrequency (RF) data were sampled at 1.5 µm × 19 µm (axial × lateral). A region of interest (ROI) was manually defined to include the PPS, PPR, and ONH at the reference/initial IOP. Within the ROI, the RF data were divided into kernels (75 µm × 570 µm, 50% overlap). The displacement of each kernel was computed by cross-correlation between successive RF frames within a search window. The cumulative displacement vectors were calculated with respect to the kernel location at the initial IOP.

Strains were calculated using least squares estimation based on the local displacement gradient [4]. Radial, tangential, and shear strain was obtained by coordinate transformation. PPS and PPR were defined by manual segmentation based on tissue boundaries visible in ultrasound images (Fig 1B). Strain maps were generated for each region with spline interpolation to the pixel level. Average strains in each region were obtained at IOP = 30 mmHg.

RESULTS

The average radial strain within the PPR was -0.55±0.25%, while the shear and tangential strains were 1.49±0.65% and 0.29±0.19%, respectively, at 30 mmHg. In comparison PPS had greater radial strain (-2.32±0.74%, p<0.001), less shear strain (1.13±0.32%, p=0.029), and similar levels of tangential strain (0.38±0.19%, p=0.13, Fig 2A). Exploratory analysis showed no significant differences in strains between quadrants in either PPR or PPS (Fig 2B).

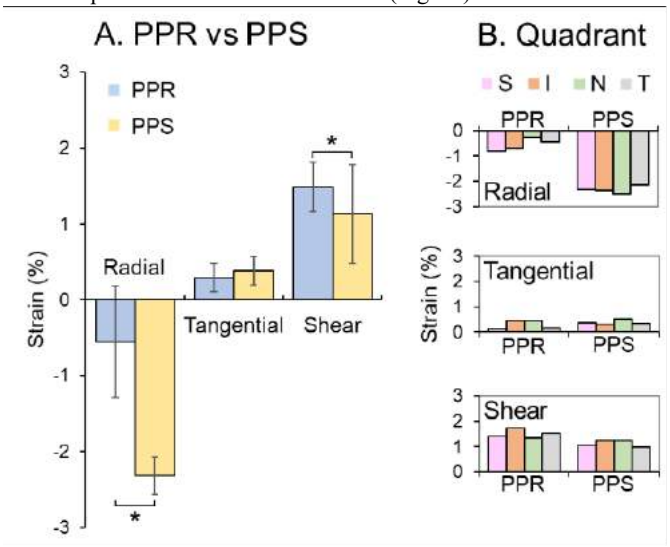

Figure 2: A) Comparisons of the radial, tangential, and shear strains between PPR and PPS at 30 mmHg (* denotes p<0.05). B) PPR and PPS strains showed no significant differences across quadrants. S: superior, I: inferior, N: nasal, T: temporal.

Localized high shear strains were observed in PPR in the region close to the ONH (up to 10%, Fig 3). In some cases, higher tangential strains were also seen in the same location of high shear, especially along the anterior boundary of the PPR.

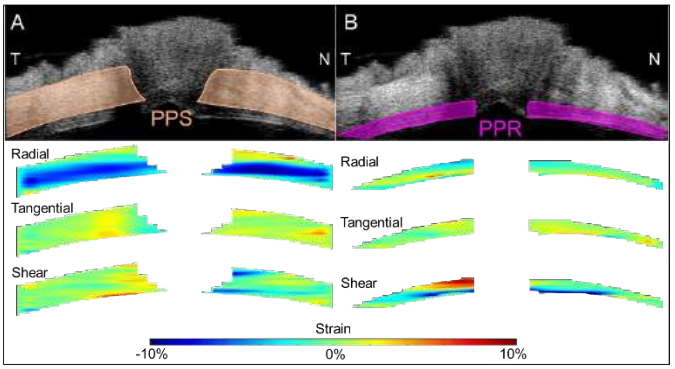

Figure 3: Radial, tangential, and shear strain maps of A) PPS (shaded in tan) and B) PPR (shaded in pink) in a representative eye at 30 mmHg.

DISCUSSION

Our results suggest that the PPR tissue mostly experienced shear strains in response to IOP elevations, with minimal radial compression and tangential stretch. Furthermore, high shear appeared to concentrate in the region close to the ONH. Although the overall PPR tangential strain was low, localized higher tangential strain was observed along the anterior surface of PPR, which may correspond to the retinal nerve fiber layer (RNFL) consisting of axons. These localized high strains could contribute toward mechanical vulnerability in these regions to IOP-related glaucomatous damage.

Interestingly, although PPR experienced minimal radial compression, the PPS had high radial compression, especially in the more anterior region adjacent to the PPR. The ability of the PPS to compress may serve as a protection for the neural PPR against large compressive impact during acute IOP rise. In contrast, PPR deformation was dominated by shear in the region close to the ONH. PPS also displayed localized shear in the ONH-PPS conjunction, suggesting that this region is likely more susceptible to mechanical damage during IOP elevation.

This study has a few limitations. The ex vivo inflation model does not fully represent the complexities of the in vivo system. Although several other mechanical stressors such as blood or cerebrospinal fluid pressure affect the ONH, IOP has been shown to be the dominant load affecting ONH stresses and strains [6]. The small sample size may also warrant future studies to verify the results.

Optic neuropathy, most notably within and around the ONH, is characteristic of glaucoma. High-frequency ultrasound has enabled us to capture the deformations of the PPR and PPS in the same eye, showing a similar shear response but different radial response. These findings may provide new insights into IOP-related mechanical insults to the neural and connective tissues in and around the ONH, where glaucomatous damage initiates.

ACKNOWLEDGEMENTS

This work is supported by the National Institute of Health R01EY025358.

REFERENCES

[1] Quigley, HA, *Br J Ophthalmol*, 80(5):389-393, 1996.
[2] Nickells, RW et al, *Annu Rev Neurosci*, 35(1):153-179, 2012.
[3] Burgoyne, CF et al., *Prog Retin Eye Res*, 24(1):39-73, 2005.
[4] Tang, J & Liu, J, *J Biomech Eng*, 134:091007, 2012.
[5] Ma, Y et al., *Invest Ophthalmol Vis Sci*, 60:913-920, 2019.
[6] Hua, Y et al., *Invest Ophthalmol Vis Sci*, 59(1):154-165, 2018.

Copyright 2021 SB³C Foundation, Inc.

NOVEL MULTISCALE STRUCTURE-BASED MODEL OF THE BOVINE CAUDAL DISC MOTION SEGMENT

Minhao Zhou (1), Grace D. O'Connell (1,2)

(1) Department of Mechanical Engineering
University of California, Berkeley
Berkeley, CA, United States

(2) Department of Orthopaedic Surgery
University of California, San Francisco
San Francisco, CA, United States

INTRODUCTION

Failure of the annulus fibrosus (AF) due to mechanical overload can accelerate intervertebral disc (IVD) degeneration and cause debilitating pain. Previous studies suggested that fiber mechanics could largely determine AF and thus disc failure behaviors.[1-2] However, directly measuring *in situ* AF fiber mechanics (*e.g.* fiber stress and strain distributions) is challenging due to experimental limitations and can result in contradicting reported data with large variations.[2-4] Earlier joint-level studies that measured AF fiber strains under physiological axial compressions reported fiber strains that varied considerably from 3 to 55%.[3-5] Thus, despite recent advancement in experimentations, *in situ* AF fiber mechanics at joint level remains poorly understood.

Finite element models have been used to complement experimental studies, providing a powerful tool for predicting hard-to-measure, fiber-reinforced tissue mechanics. However, most IVD models employ homogenization theory and describe every AF element as a combination of fibers and matrix and are thus not capable of explicitly examining subtissue-level mechanics, such as interfibrillar stress and strain distributions.[6] To address the limitation, we previously developed a multiscale structure-based AF model, where fiber bundles and the extrafibrillar matrix were explicitly modeled to occupy separate volumes. Parameter calibration was conducted at the subtissue level using tissue subcomponent mechanical testing data (*e.g.* fiber bundles and matrix). The model was then validated at tissue level under uniaxial tension, biaxial tension, and shear.[7-8] In this study, we will employ this modeling-validation framework to evaluate *in situ* AF fiber mechanics by developing and validating a joint-level model based on discs.

METHODS

We developed the model based on bovine caudal discs using the reported geometry data.[9] The multiscale structure-based modeling-validation framework used for our tissue-level AF tissue-level models was employed (**Fig. 1A**).[7-8] Gradients in fiber orientation and solid volume fraction from inner to outer AF were described based on literature data (**Fig. 1A**–**B**).[10] The current model was created at 1:5 scale for computational efficiency; thus, preliminary work was performed to ensure that scaling did not alter model validation results. All model parameters were directly linked to physical or biochemical tissue properties, including modulus, Poisson's ratio, and fixed charge density (**Fig. 1C**), and were determined based on data in the literature.[11-14]

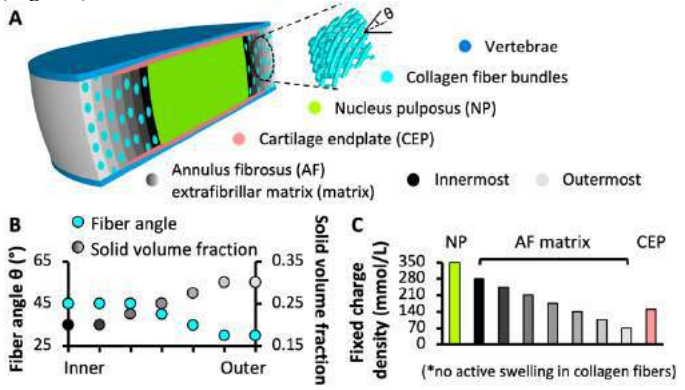

Fig. 1: (A) Disc model at 1:5 scale. (B) Annulus fibrosus structural parameters. (C) Disc fixed charge density distribution.

The model was loaded in two steps: first, the disc was allowed to swell (triphasic) in 0.15 M saline. Intradiscal pressure (IDP) was assessed as the average nucleus pulposus pressure and was compared to human IVD experimental IDP data for validation, due to the lack of IDP data from bovine discs. The second step was one of the three cases: 0.5 MPa axial compression (**Case *A***), 10 N·mm axial rotation (**Case *B***), or 0.5 MPa axial compression followed by 10 N·mm axial rotation (**Case**

Copyright 2021 SB³C Foundation, Inc.

C). Average AF fiber stretch and stress distributions were assessed at 0.5 MPa axial compression for **Case *A*** and at 10° axial rotation for **Case *B*** and ***C*** to represent the higher rotation of bovine discs, where the post-swelling configuration was considered as the reference configuration. Model-predicted compressive and torsional stiffness were normalized by geometry and validated with experimental data.

RESULTS

Across models of three different scales (1:4, 1:5, 1:6), the predicted intradiscal pressure was 0.18±0.006 MPa post-swelling and 0.48±0.006 MPa under 0.5 MPa axial compression. The predicted normalized compressive stiffness was 8.12±0.28 MPa and the predicted normalized torsional stiffness 36±8 kPa/°. These model predictions agreed well with literature (**Fig. 2**). Thus, we considered the current model valid for describing swelling, axial compression and rotation behaviors.

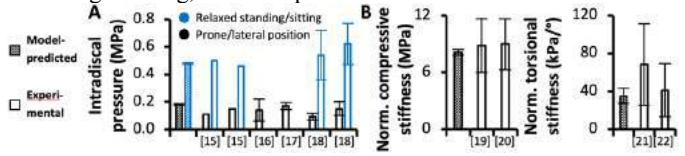

Fig. 2: Model-predicted (A) intradiscal pressure and (B) normalized (norm.) compressive and torsional stiffness vs. experimental data.

Under pure axial compression (**Case *A***), the average AF fiber stretch was ~1.05 and was consistent throughout the AF (**Fig. 3A**–black circles). Fiber stretch was comparable under pure rotation (**Case *B***), but a linear increase was observed from 1.04 in the innermost AF layer to 1.07 in the outermost layer (**Fig. 3A**–blue circles). Under combined loading (**Case *C***), the average fiber stretch nearly doubled, increasing from ~1.05 (**Case *A*** & ***B***) to ~1.10 (**Fig. 3A**–red circles).

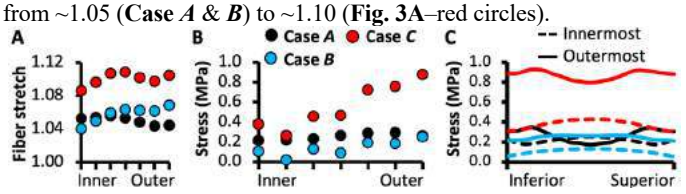

Fig. 3: Average annulus fibrosus (AF) post-loading fiber (A) stretch and (B) stress. (C) AF post-loading fiber stress profiles along the fiber length in the inner- and outermost AF layers.

Strain concentrations were observed near cartilage endplates in inner AF (**Fig. 4A**). Under pure compression, average AF fiber stress was relatively consistent throughout the AF (0.22–0.29 MPa; **Fig. 3B**–black circles). The rotation-only loading (**Case *B***) reduced fiber stress in the inner-middle AF by ~60% but did not alter the fiber stress in the outer AF (**Fig. 3B**–blue vs. black circles). Under combined loading (**Case *C***), the average fiber stress increased linearly from inner to outer AF, where the combined compression rotation resulted in a more than 1.5-fold increase in inner AF fiber stress and a more than 3-fold increase in the outer AF fiber stress (**Fig. 3B**–red; **Fig. 4**).

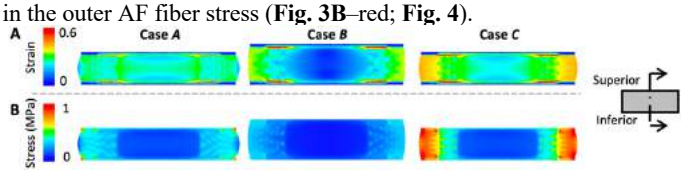

Fig. 4: Post-loading disc (A) strain and (B) stress distributions.

Fiber stress profiles were tracked along the fiber length from the superior to inferior vertebra. In all cases, peak fiber stress was observed near the vertebrae in outer AF (**Fig. 3C**–solid lines). Pure axial compression or rotation generated comparable fiber stresses across AF. However, the combined loading amplified the difference between outer and inner AF fiber stresses (**Fig. 3C**–red vs. black & blue lines).

DISCUSSION

The recent shift towards multiscale modeling is important for understanding the IVD subtissue-level degeneration-induced changes that act to preserve the joint-level properties. Our previous multiscale joint-level model assessed disc swelling behaviors and proved that a computational model developed with parameters directly representing tissue physical or biochemical properties (*e.g.* fiber modulus or fixed charge density) was capable of replicating morphological changes of degenerated discs, such as the decrease in disc height and the inward bulging of inner AF.[23] This study expanded upon that work by further validating the joint-level mechanics under axial compression and rotation. Additionally, we further expanded the model's capability by modeling AF fiber structure to evaluate fiber mechanics and assess the ability to predict disc failure. Lastly, the multi-scale model-validation framework further expanded our previous tissue and subtissue-level work,[7-8] as results of this study proved that the framework is still valid at the joint level, demonstrating its robustness and predictive power.

Physiological disc-joint loadings resulted in a fiber stretch ranging from 1.04 to 1.10, agreeing with previous *in vitro* photogrammetry-based studies, [4-5] and indicating a low likelihood of failure based on experimental AF fiber bundle failure stretch data (1.14±0.03).[24-25] The structure-based modeling technique partially addressed the prior concern about homogeneous models overestimating fiber stretches and thus predicting premature disc failure under physiological loads.[5] In a previous study, a fiber stretch of ~1.13 was observed under physiological axial rotation; the stretch reached up to ~1.20 under combined loading configurations, indicating a high likelihood of tissue failure under physiological loading.[6] We will use the current model to examine more combined loading modalities to strengthen this finding.

Disc failure has been shown to occur through endplate fracture, AF damage in the outer AF, or inward bulging starting from the inner AF. Under all loading conditions, strain concentrations (**Fig. 4A**) and peak fiber stresses (**Fig. 3C**) were located near the AF-endplate-vertebrae interfaces, which might help explain the large likelihood of endplate rupture during *in vitro* joint-level tests.[26] Interestingly, compared to the pure compression or rotation case, the increase in outer AF stresses result from the combined loading was disproportionally larger than the increase in outer AF strains (**Fig. 4**). These results agree with observations of AF-only failures that occurred in the outer AF with multiaxial loading applied to ovine lumbar discs.[27] Taken together, these findings suggest that disc failure might be driven more by peak stresses than strains, which could serve as an important reference when modeling disc tissue damage.

Concentric and radial annular tears, rim lesions, and annular fissures are common in degenerated discs. Thus, a comprehensive understanding of *in situ* fiber mechanics is essential for predicting AF damage initiation and accumulation, which can be applied to development of workplace loading limits (*e.g.* factory workers). The modeling framework described here provides a powerful tool for investigating multiscale disc mechanics with degeneration and can be used to develop clinically relevant models that use noninvasive imaging to determine biochemical composition. Ongoing work is leveraging this framework to evaluate changes in biochemical composition on stress distributions between tissues and within tissues to assess how the disc preserves joint-level mechanics during early degeneration.

ACKNOWLEDGEMENTS The work was supported by the National Science Foundation (CMMI: 1760467).

REFERENCES [1] Iatridis+, *JBM*, 2004; [2] Rausch+, *BMMB*, 2016; [3] Shah+, *J Bone Jt Surg*, 1978; [4] Stokes, *JOR*, 1987; [5] Heuer+, *JBM*, 2008; [6] Schmidt+, *Spine*, 2007; [7] Zhou+, *BMMB*, 2020 [8] Zhou+, *JMBBM*, 2021; [9] O'Connell+, *Spine*, 2007; [10] O'Connell+, *BioRes ope accs*, 2015; [11] Goel+, *JBME*, 1995; [12] Cortes+, *JBM,* 2014; [13] Bezci+, *JOR Spine*, 2019; [14] Périé+, *JBM*, 2005; [15] Wilke+, *Spine*, 1999; [16] Nguyen+, *J Bone Jt Surg Am,* 2008; [17] Urban+, *Spine*, 1988; [18] Sato+, *Spine*, 1999; [19] Beckstein+, *Spine*, 2008; [20] Bezci+, *JBME*, 2015; [21] Showalter+, *Spine,* 2012; [22] Bezci+, *JMBBM*, 2018; [23] Yang+, *Acta Biomater*, 2020; [24] Skaggs+, *Spine*, 1994; [25] Isaacs+, *JMBBM*, 2005; [26] Adams+, *Spine*, 1985; [27] Berger-Roscher+, *Spine*, 2017

Copyright 2021 SB³C Foundation, Inc.

PROPOSED INJURY THRESHOLD FOR DRONE BLADE LACERATIONS

Lauren A. Duma, Mark T. Begonia, Barry Miller, Stefan M. Duma

Institute for Critical Technology and Applied Science (ICTAS)
Virginia Tech
Blacksburg, Virginia, United States

INTRODUCTION

As the use of drones becomes increasingly popular and more widespread, the number of drone related injuries is increasing. Drone accidents have caused a variety of injuries, including head injuries, open globe eye lacerations, and skin lacerations, which are the most common observed injury [1-3]. The objective of this study was first to examine the different properties of drone propellers that cause skin lacerations, and second to propose an injury threshold that can be used to design drones that reduce the risk of these injuries.

METHODS

A total of 17 experiments were performed using nine different drones. The selected drones were the Phantom 4 Advanced (A), Air Hogs Axis 200 (B), Air Hogs Battle Tracker (C), Air Hogs 4T2010 (D), Star Wars X-Wing Fighter (E), Gyroscopes System (F), Syma FPV Real-Time (G), Holy Stone HS-Series (H), and Air Car A380 (I). For each drone, the blade tip thickness and blade length were measured, and angular velocity (rpm) was recorded using a laser tachometer. Blade tip velocity was then calculated using the angular velocity and blade length.

For each experiment, the skin surrogate made full contact with the drone blade (Figure 1). The skin surrogate, second trimester fetal bovine skin, was selected due to its ability to accurately model drone blade laceration injuries in human skin [4]. The skin was mounted on gelatin and held in place by hemostats [5]. The skin was harvested and tested within 24 hours according to approved IRB procedures. The skin mount was placed on a slide system to contact the drone blades. The observed injury caused by the drone was then assigned a level of injury severity: 0 for no injury, 1 for a minor abrasion, and 2 for a minor laceration. A new skin sample was used for each test.

Figure 1: Testing configuration with fetal bovine skin mounted on a slide moved into the Phantom 4 blade.

RESULTS

Five of the 17 experiments resulted in no injury (Table 1). Minor abrasions were observed in eight tests at blade tip speeds higher than 80 ft/s. Minor lacerations were observed in four tests at blade tip speeds higher than 200 ft/s. For example, the Air Car A380 caused no injury, minor abrasion, and minor laceration in three different tests depending on blade tip speeds ranging from 66.9 ft/s to 104.0 ft/s to 313.1 ft/s accordingly (Figure 2).

Copyright 2021 SB³C Foundation, Inc.

Overall, injury severity had the strongest correlation to tip speed (r^2=0.79). There was separation from no injury to minor abrasion at 80 ft/s, and also separation between minor abrasion and minor laceration at 200 ft/s (Figure 3).

However, injury severity did not correlate as strongly to angular velocity (r^2=0.56), which ranged from 1,526 rpm to 33,226 rpm. Blade length also did not correlate to injury severity (r^2=0.03), and ranged from 1.08 in to 4.70 in. Blade tip thickness correlated the least to injury severity (r^2=0.01), and ranged from 0.015 in to 0.035 in.

Table 1: Test configuration, data, and injury results.

Test - Drone	Blade tip thickness (in)	Blade length (in)	Angular Velocity (rpm)	Blade tip Speed (ft/s)	Observed Injury
1-A	0.035	4.70	8115	332.8	Minor laceration
2-B	0.020	2.52	2181	48.0	No injury
3-C	0.016	3.77	1526	50.2	No injury
4-D	0.016	3.08	3330	89.4	Minor abrasion
5-E	0.018	2.38	4605	95.6	Minor abrasion
6-F	0.021	3.82	2569	85.6	Minor abrasion
7-G	0.027	2.63	2719	62.4	No injury
8-G	0.027	2.63	5730	131.5	Minor abrasion
9-H	0.021	2.86	2971	74.2	No injury
10-H	0.021	2.86	6125	152.9	Minor abrasion
11-H	0.021	2.86	6072	151.5	Minor abrasion
12-I	0.015	1.08	7099	66.9	No injury
13-I	0.015	1.08	8658	81.6	Minor abrasion
14-I	0.015	1.08	11030	104.0	Minor abrasion
15-I	0.015	1.08	24960	235.2	Minor laceration
16-I	0.015	1.08	30493	287.4	Minor laceration
17-I	0.015	1.08	33226	313.1	Minor laceration

Figure 2: The fetal bovine skin surrogate showing no injury in test 12-I (top), a minor abrasion in test 14-I (middle), and a minor laceration in test 16-I (bottom).

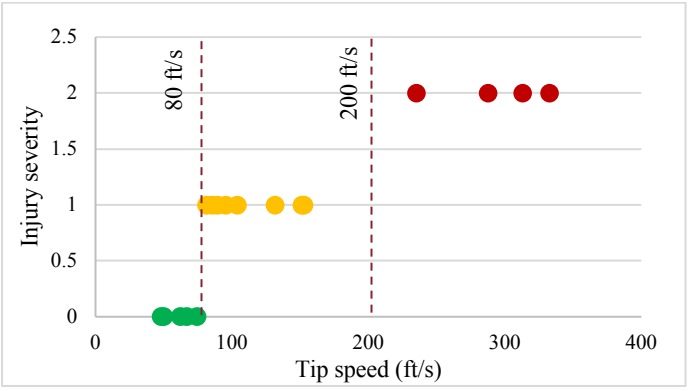

Figure 3: Injury severity vs tip speed for all tests with proposed injury thresholds. Green represents no injury, yellow represents minor abrasions, and red represents minor lacerations.

DISCUSSION

Blade tip speed proved to correlate the most to laceration injuries caused by drone blades, with speeds above 80 ft/s causing minor abrasions and speeds above 200 ft/s causing minor lacerations. In order to avoid severe injuries caused by drone propellers, maximum blade tip speed should stay below the threshold of 200 ft/s, especially for drones designed for toy use.

Interestingly, all other parameters (blade tip thickness, blade length, and blade angular velocity) did not seem as critical to injury risk. This implies that manufacturers can create drones with many different blade designs as long as they evaluate blade tip speed as the injury criteria.

The nine different drones were selected to represent a broad range of commercial and toy drones that are most likely to be handled and flown in close proximity to people. Seven of the nine drone types produced injury with a range of blade designs. The two drones that did not result in injury were tested at their maximum speed. The minor abrasions represented damage to the epidermis while the minor lacerations included damage through the epidermis to the underlying dermis skin layer.

There are two limitations of this study. First, the skin surrogate is not human skin. While previous researchers utilized human volunteer testing, the unknown severity prevented this option [6,5]. Second, there are countless drone blade configurations and additional testing could provide additional insight into their safe design.

ACKNOWLEDGEMENTS

I would like to acknowledge and thank the Federal Aviation Administration (FAA), the Mid-Atlantic Aviation Partnership (MAAP), and the Institute for Critical Technology and Applied Science (ICTAS) for supporting this research.

REFERENCES

[1] Campolettano, E.T. et al, *Ann Bio Eng,* 45:2733, 2017
[2] Moskowitz, E.E. et al, *Am J of Ophth.,* 10:35-37, 2018.
[3] Ranamukhaarachchi, S.A. et al., *Nature*, 6:32074, 2016.
[4] Duma, Lauren A. et al., BMES, 2019.
[5] Papy, Alexandra et al., *IRCOBI*, 2012.
[6] Reed, Matthew P. et al., *SAE*, paper 942217, 1994.

SB³C2021
Summer Biomechanics, Bioengineering and Biotransport Conference
June 14-18, Virtual

BRAIN STRAIN AT SKULL FRAME OF REFERENCE

Y. Liu (1), X. Zhan (1), A. Domel (1), M. Zeineh (2), G. Grant (3), D. Camarillo (1)

(1) Department of Bioengineering
Stanford University
Stanford, CA, 94305

(2) Department of Radiology
Stanford University
Stanford, CA, 94305

(3) Department of Neurology
Stanford University
Stanford, CA, 94305

INTRODUCTION

Mild traumatic brain injury (mTBI) is mainly caused by the rapid rotation of the head impact. Because of the inertia, the brain will be deformed. Both angular velocity and angular acceleration can be used to describe the head rotation. However, how each parameter decides brain strain is unclear because of the interdependency between them (angular acceleration is the derivative of the angular velocity). Previous studies based on statistical analyses found that angular velocity peaks correlated better with the brain strain peaks [1], and the brain injury models based on angular velocity peaks were found to have higher predictability of brain strain [2,3]. However, these findings contradict with the volunteer experiment [4]: volunteers experienced angular velocity higher than the injury threshold [5], but had no brain injury and low brain strains. The classification of the head kinematics according to the impulse duration gave an explanation [6]: the brain strain peak depends on angular velocity peak in short-duration impacts, on angular acceleration peak in long-duration impacts and on both in moderate-duration impacts. However, the mechanism underlying this classification is still unclear.

Different from previous studies, we propose to describe the head impact in the skull frame of reference (FoR). In the skull FoR, the effects of angular acceleration and angular velocity are represented by the inertial force. In this way, we can separate the brain strain caused by each kinematic parameter. We use the rigid-body rotation of brain (RRB) as a bridge to explain how the inertial force associated by each kinematics parameter causes brain strain. Furthermore, we also provided an explanation of the classification according to the impact duration. [6]

.

THEORETICAL ANALYSIS

Different from the description in ground FoR (**Fig.1A**), in the skull FoR (**Fig.1B**), the skull does not move and the brain is deformed the inertial forces as,

$$\begin{aligned}\boldsymbol{F}(\boldsymbol{r}) &= \rho(\boldsymbol{r})\boldsymbol{a} - \rho(\boldsymbol{r})\boldsymbol{\omega}\times(\boldsymbol{\omega}\times\boldsymbol{r}) - \boldsymbol{\beta}\times\boldsymbol{r} \\ &= \boldsymbol{F}_{\mathrm{LinAcc}}(\boldsymbol{r}) + \boldsymbol{F}_{\mathrm{AngVel}}(\boldsymbol{r}) + \boldsymbol{F}_{\mathrm{AngAcc}}(\boldsymbol{r}) \qquad (1)\end{aligned}$$

Where $\boldsymbol{F}(\boldsymbol{r})$ is the inertial force per unit mass at the location $\boldsymbol{r}$; $\boldsymbol{a}$, $\boldsymbol{\omega}$ and $\boldsymbol{\beta}$ are the linear acceleration at the coordinate origin, the angular velocity, and the angular acceleration of the head, respectively. Here we assume the Coriolis force can be neglected. $\boldsymbol{r}$ is the position vector, and the coordinate origin of $\boldsymbol{r}$ is set at the center of gravity (CoG) of the brain (**Fig.1A**). The inertial force by each kinematics are,

$$\boldsymbol{F}_{\mathrm{LinAcc}}(\boldsymbol{r}) = \rho(\boldsymbol{r})\boldsymbol{a} \qquad (2)$$

$$\boldsymbol{F}_{\mathrm{AngVel}}(\boldsymbol{r}) = -\rho(\boldsymbol{r})\boldsymbol{\omega}\times(\boldsymbol{\omega}\times\boldsymbol{r}) \qquad (3)$$

$$\boldsymbol{F}_{\mathrm{AngAcc}}(\boldsymbol{r}) = -\rho(\boldsymbol{r})\boldsymbol{\beta}\times\boldsymbol{r}(1) \qquad (4)$$

Then, the inertial torque associated with each kinematic parameter can be calculated by integrating Eqs. (2-4) over the whole brain,

$$\boldsymbol{T}_{\mathrm{LinAcc}} = \iiint \rho(\boldsymbol{r})\boldsymbol{r}\mathrm{dv}\times\boldsymbol{a} = \boldsymbol{0} \qquad (5)$$

$$\boldsymbol{T}_{\mathrm{AngVel}} = \iiint \rho(\boldsymbol{r})(\boldsymbol{\omega}\cdot\boldsymbol{r})\boldsymbol{\omega}\times\boldsymbol{r}\mathrm{dv} \qquad (6)$$

$$\boldsymbol{T}_{\mathrm{AngAcc}} = \iiint \rho(\boldsymbol{r})\left(\boldsymbol{r^2}\boldsymbol{\beta} - (\boldsymbol{r}\cdot\boldsymbol{\beta})\boldsymbol{r}\right)\mathrm{dv} \qquad (7)$$

Assuming the brain shape is close to a sphere with r_0, Eqs.6 and 7 are,

$$\boldsymbol{T}^{\mathrm{sphere}}_{\mathrm{AngVel}} = \boldsymbol{0} \qquad (8)$$

$$\boldsymbol{T}^{\mathrm{sphere}}_{\mathrm{AngAcc}} = \frac{8}{15}\rho_0\pi r_0^5\boldsymbol{\beta} \qquad (9)$$

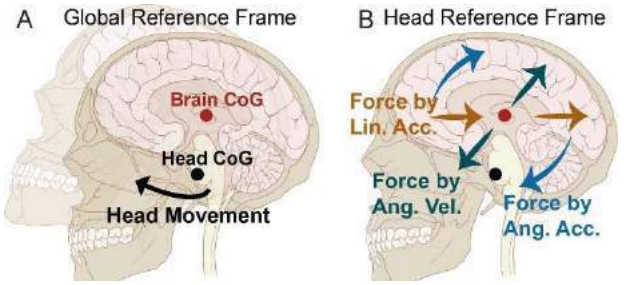

Figure 2. The diagrams of how head impact causes the brain strain at (A) the ground frame of reference (FoR) and (B) the skull FoR.

For the actual brain,

$$\boldsymbol{T}_{\mathrm{AngVel}} \ll \boldsymbol{T}_{\mathrm{AngAcc}} \quad (10)$$

According to the conservation of angular momentum, the angular momentum ($\boldsymbol{L}$) at skull FoR is only decided by $\boldsymbol{T}_{\mathrm{AngAcc}}$. We define the equivalent angular velocity of brain ($\dot{\boldsymbol{\phi}}$) as,

$$\boldsymbol{L} = I_C \dot{\boldsymbol{\phi}} \quad (11)$$

Then, the equivalent angle $\boldsymbol{\phi}$ can be calculated by quaternion integrating $\dot{\boldsymbol{\phi}}$. $\boldsymbol{\phi}$ describes the RRB and has the same variation of brain strain. Since $\boldsymbol{\phi}$ is decided by $\boldsymbol{L}$, which is further decided by $\boldsymbol{T}_{\mathrm{AngAcc}}$, the angular acceleration is the kinematic parameter that decides the brain strain.

VALIDATION

We simulated 118 head impacts collected by Stanford Instrumented Mouthguard using KTH head model [7]. The simulations were performed at both ground FoR and skull FoR, and the brain strain was very close. (difference in the peak of 95th percentile maximal principal strain (95% MPS) <0.0009).

Then, we gave $\boldsymbol{F}_{\mathrm{LinAcc}}$, $\boldsymbol{F}_{\mathrm{AngVel}}$, $\boldsymbol{F}_{\mathrm{AngAcc}}$ separately and compared the brain strains with the simulation with all inertia. As shown in **Fig.2**, the brain strain caused by angular acceleration is almost the same as that by all inertia force, and the brain strain caused by other kinematic parameters can be neglected.

DISCUSSION

The theoretical analysis is limited by that the 95% MPS and $\boldsymbol{\phi}$ are only linearly correlated in simulation. Although the correlation coefficient is high, we do not know the exact corresponding relationship. The idea of using the rotation of the brain respected to the skull was adopted in the reduced-order models [8,9] and these models manifest high predictability of the brain strain. Future studies about this relationship should be performed with more detailed head models.

ACKNOWLEDGEMENTS

This research was supported by the Pac-12 Conference's Student-Athlete Health and Well-Being Initiative, the National Institutes of Health (R24NS098518), Taube Stanford Children's Concussion Initiative. We also want to thank Dr. Svein Kleiven for sharing the finite element head model, and Dr. Yue Gao for the insightful discussion.

REFERENCES

[1] X. Zhan, Y. Liu, S. J. Raymond, H. V. Alizadeh, A. G. Domel, O. Gevaert, M. Zeineh, G. Grant, and D. B. Camarillo, arXiv preprint arXiv:2010.08527 (2020).

[2] S. Kleiven, International Journal of Crashworthiness **11**, 65 (2006).

[3] E. G. Takhounts, V. Hasija, S. A. Ridella, S. Rowson, and S. M. Duma, in *Proceedings of the 22nd enhanced safety of vehicles conference. Paper*2011), pp. 1.

[4] F. Hernandez and D. B. Camarillo, Journal of neurotrauma **36**, 1125 (2019).

[5] E. G. Takhounts, M. J. Craig, K. Moorhouse, J. McFadden, and V. Hasija, Development of brain injury criteria (BrIC), 2013.

[6] L. F. Gabler, H. Joodaki, J. R. Crandall, and M. B. Panzer, Journal of biomechanical engineering **140** (2018).

[7] S. Kleiven, Predictors for traumatic brain injuries evaluated through accident reconstructions, 2007.

[8] K. Laksari *et al.*, Journal of Neurotrauma **37**, 982 (2020).

[9] L. F. Gabler, J. R. Crandall, and M. B. Panzer, Annals of biomedical engineering **47**, 1971 (2019).

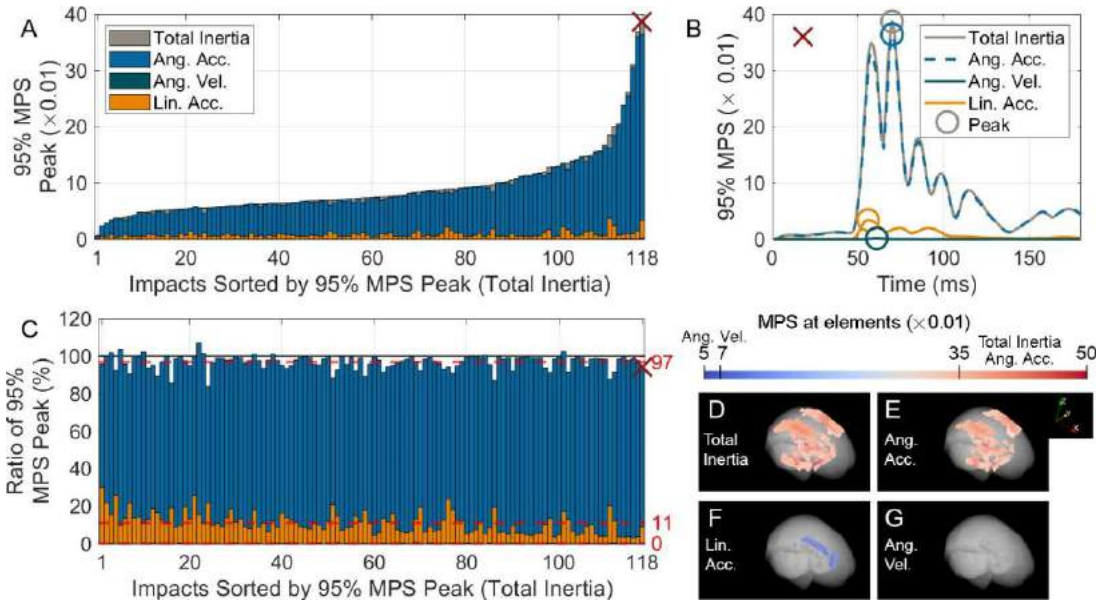

Figure 1. (A) The 95% MPS peak calculated by simulation with inertial force by all kinematics (Total Inertia), angular acceleration, angular velocity and linear acceleration. (B) The 95% MPS traces calculated with different inertial forces in the case with highest 95% MPS peak (according total inertia). This case is denoted by red cross in (A, C). (C) The ratio of 95% MPS peak by individual kinematic parameter to 95% MPS peak by all kinematics. The mean ratio over 118 head impacts for angular acceleration, linear acceleration and angular velocity are 97%, 11% and 0%. (D-G): The MPS distribution when 95% MPS peak reach the maximum with total inertia (D), angular acceleration (E), linear acceleration (F) and angular velocity (G). The orientation of the brain is shown by the coordinates on the right of (E), X: back to front, Y: right to left, Z: bottom to top.

THE EFFECT OF PERMEABILITY BOUNDARY CONDITIONS ON THE RESERVE ZONE CHONDROCYTE SUBJECTED TO DIFFERENT LOADING RATES

M. Kazemi (1), J. L. Williams (1)

(1) Biomedical Engineering Department
University of Memphis
Memphis, TN, USA

INTRODUCTION

The growth plate consists of a thin layer of hyaline cartilage trapped between the epiphysis and metaphysis and is responsible for longitudinal growth through an endochondral ossification process. Histologically, growth plate cartilage has three zones reflecting the activities of the chondrocytes from the epiphysis toward the metaphysis: a reserve, proliferative and hypertrophic zone. Mechanical loading modulates chondrocyte activity in the proliferative and hypertrophic zones. As growth continues the growth plate develops into a three-dimensional interlocking interface of hills and valleys, called mammillary processes, and a layer of compact subchondral bone and calcified cartilage arises at the border of the reserve zone and epiphysis. The undulations on the metaphyseal side of the growth plate are formed by endochondral ossification. However, the mechanism by which the subchondral bone plate forms to create an epiphyseal interface parallel to the metaphyseal one has not been investigated. Recent discoveries of stem-like cells in the reserve zone suggest that reserve zone cells close to the subchondral bone border may modulate growth under mechanical loading and contribute to epiphyseal mammillary processes development [1][2][3]. Experimental findings indicate that the morphology of mamillary processes and the thicknesses of subchondral bone and calcified cartilage along the border of the reserve zone changes during skeletal development [4][5], resulting in changes in the permeability of the reserve zone-epiphyseal bone interface. Such changes may affect the microenvironment of reserve zone cells close to the subchondral bone border and thereby change the cells' response to applied mechanical loading. The main objective of this study was to develop a poroelastic multiscale finite element model of bone/growth plate/bone to investigate the microenvironment of reserve zone cells close to the subchondral bone and evaluate the effect of permeability boundary conditions on the reserve zone cell response close to epiphyseal border.

METHODS

A poroelastic multiscale axisymmetric finite element model of bone/growth plate (GP)/bone (radius of 2.5 mm) was developed using Abaqus (CAE 2019, USA). A stress relaxation test in unconfined compression was simulated by applying a ramp displacement function to the macroscale model of 0.025 mm (5% strain of the height of growth plate) at four strain rates of 0.18%/s, 5%/s, 50%/s, and 200%/s, after which the displacement was held constant. The material properties and dimensions of different regions within the macro- and micro-scale models are summarized in Tables 1&2.

Table 1. Material properties of different layers in the macroscale model

Tissue	E (MPa)	ν	K_0 (mm⁴/N.s)	e_0	M	Thickness (mm)
Subchondral bone (SB)	2000[6]	0.200[6]	90[7]	0.176 [6]	-	0.6
Calcified cartilage (CC)	300	0.200[8]	90 [9]	1.1[9]	-	0.06
Reserve zone (RZ)	0.98[10]	0.125[11]	1.41×10^{-3} [12]	4.25[11]	5.48 [9]	0.25
Proliferative/Hypertrophic zone (PZ/HZ)	0.49[10]	0.125[11]	5.8×10^{-3} [12]	3.6 [11]	6.43 [9]	0.25
Provisional calcification (PC)	100	0.200	22.5× 1	3.5	-	0.15
Epiphysis (EP) Metaphysis (MP)	1000 1000	0.200 0.200	45.3× 10^5 45.3× 10^5[7]	3.7[9]	- -	0.5 0.5

Table 2. Material properties used for the microscale model

Region	E (MPa)	ν	k_0 (mm4/N.s)	e_0	$Radius$ (μm)
Cell	0.002 [10]	0.04 [13]	4.2× 10-3 [6]	4.88 [6]	5 [14]
Cell membrane	4× 10-2 [6]	0.04 [13]	3× 10-9 [6]	3 [6]	0.1 [6]
Pericellular matrix (PCM)	0.265 [10]	0.04 [13]	4× 10-5 [15]	4 [15]	0.5 [14]

The microscale model included one cell close to the reserve zone (RZ)-calcified cartilage (CC) border. The strain-dependent hydraulic permeability was defined for GP regions in the macroscale model and for cell, cell membrane and pericellular matrix in the microscale models using equation (1) [4][9].

$$k = k_0 \left[\frac{e}{e_0}\right]^2 exp\left(\frac{M}{2}\left(\left(\frac{1+e}{1+e_0}\right)^2 - 1\right)\right), \quad (1)$$

where k_0 is the initial hydraulic permeability (mm^4/N.s), e_0 and e are initial and current void ratios, and M is a non-dimensional constant. To get the hydraulic conductance (mm/s) used in Abaqus, the hydraulic permeability (mm^4/N.s) was multiplied by the specific weight of the wetting fluid (9.81×10^{-6} N/mm^3) [9]. CAX4P elements were used for all regions. Mesh convergence was confirmed for the cellular maximum principal strain and fluid velocity. To study the effect of the permeability boundary conditions at the calcified cartilage (CC) interface on the transient response of the cell and fluid flow across the cell membrane, another model was developed with very low CC permeability ($k_0 = 5.8\times 10^{-3}$ mm^4/N.s). Intracellular maximum principal strain (logarithmic) and fluid pressure, transmembrane effective fluid velocity (mm/s) and cell membrane maximum tensile strain (logarithmic strain) were calculated at 95% of the peak applied displacement to avoid any possible numerical artifact due to the transition to fixed displacement following ramp loading.

RESULTS

Figs.1a&b compare the intracellular maximum principal strain and fluid pressure between the permeable and impermeable boundary conditions for cells located at the CC border at four strain rates. The highest strain value of 9% is related to the 5%/s strain rate, indicating a 2-fold amplification of applied tissue strain. In contrast, the smallest value of strain occurs at 200%/s. Decreasing the permeability of the CC drops all the strain values, however, it does not change the overall cellular strain pattern. The highest maximum principal strain still occurs for a strain rate of 5%/s, but is closer in magnitude to the applied tissue strain. Intracellular fluid pressure increases with the applied strain rate. The pressure is greatest (0.58 MPa) at 200%/s when the fluid has less time to move through the tissue, thereby providing higher fluid resistance. Preventing fluid exchange across the CC results in a slight increase in cell fluid pressure for all strain rates as the fluid cannot flow across the CC border (Fig. 1b).

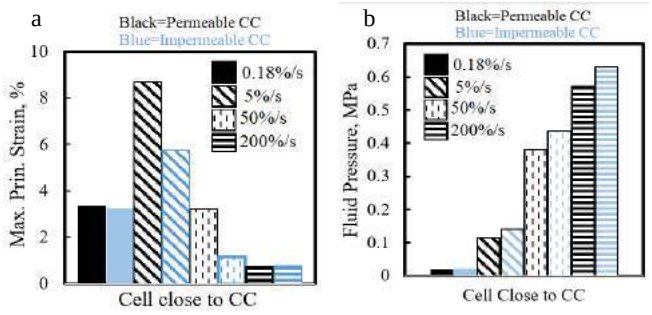

Fig. 1. Comparing maximum principal strain (logarithmic strain) and intracellular fluid pressure between permeable and impermeable calcified cartilage (CC) properties, at the 4.5% strain time point and 0.18%/s, 5%/s, 50%/s, and 200%/s strain rates for reserve zone cells close to CC.

Fig. 2a shows the percent decrease in transmembrane fluid velocity due to employing the impermeable boundary condition. The greatest change occurs for the two faster strain rates (70%), while at the slowest strain rate the transmembrane fluid flow changes slightly by 4%. Tangential tensile membrane strain follows a similar trend to that of maximum principal strain at each equivalent strain rate. Restricting fluid from crossing the CC decreased the tangential membrane strain for the three slower strain rates, however it has an opposite effect at the fastest applied load, and impermeability of CC increases the tangential tensile membrane strain slightly by 10% (Fig. 2b).

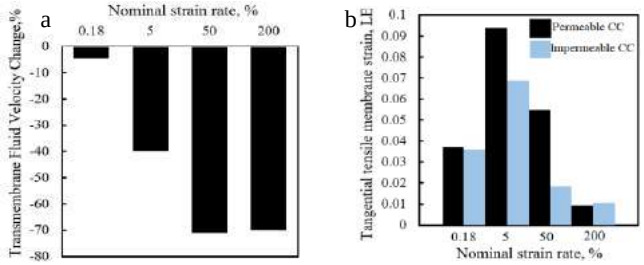

Fig. 2. a) Change in the peak fluid velocity across the cell membrane close to calcified cartilage (CC) due to impermeable CC properties. b) Comparison of peak tangential tensile membrane strains for a permeable and an impermeable CC.

DISCUSSION

The results of this study revealed that the magnitudes of cellular maximum principal strain and peak tangential membrane strain are highly dependent on the applied loading rate and also the permeability of the CC between the subchondral bone (SB) and RZ. The effect of increasing loading rates on cellular strains shows a different pattern which can be explained by the transmembrane effective fluid velocity, which itself depends on intracellular fluid pressure. Fluid pressure provides a pressure gradient within the fluid phase of the porous solid and determines the directions and values of fluid velocity. The highest cellular strain value at the slower loading rate (5%/s) can be attributed to the higher fluid flow out of the cell across the cell membrane which results from higher cellular fluid pressure and higher-pressure gradient across the cell membrane.

In this study, we investigated quantitatively how changing the permeability of CC at the border of the RZ can change the microenvironment of RZ cells. During skeletal development, epiphyseal subchondral bone (SB) and CC, located between the RZ and epiphysis, undergo fundamental changes in their thickness, morphology and porosity. Such morphological changes can act to provide a barrier to fluid flow and decrease the permeability across the border of RZ-CC/SB. Decreasing the permeability changes the micromechanical environment of RZ cells and that may act to signal the RZ cells to stop growth and begin the process of growth plate fusion.

REFERENCES

[1] Hallett, S et al., *Int. J. Mol. Sci.*, 20.23: 6009, 2019.
[2] Lui, JC., *J. Endocrinol*., 246.1: R1-R11, 2020.
[3] Kazemi, M et al., *J. Cartilage*, p.1947603520924776, 2020.
[4] Mow, V et al., *Annu. Rev. Biomed. Eng*., 4.1: 175-209, 2002.
[5] Wosu, R et al., *Biomech. Model Mechanobiol*., 11.3-4: 303-312, 2012.
[6] Moo, E et al., *J. Biomech*., 47.5: 1004-1013, 2014.
[7] Hwang,J et al.,*Official J. Ameri. College of Rheuma*.,58.12: 3831-3842, 2008.
[8] Fan, C et al., *J. Bone*, 44.1: 61-70, 2009.
[9] Stender, ME et al.,*Comput. Methods. Biomech. Biomed. Eng*.,20.3:319-331, 2017.
[10] Gao, J et al., *PloS one*, 10.4:e0124862, 2015.
[11] Sakai, N et al., *J. Biomech. Eng.*, 10.4: 15-00228, 2015.
[12] Sergerie, K et al., *J. Biomech*., 42.4: 510-516, 2009.
[13] Alexopoulos, LG et al., *Acta Biomat*.,1.3: 317-325, 2005.
[14] Kazemi, M et al., *Int. Sym. Comput Methods Biomech. Biomed, Eng*.,Cham, 2019.
[15] Wu, JZ et al., *J. Med. Eng. Phys.*, 22.1: 1-12, 2000.

STRUCTURAL AND NON-STRUCTURAL DETERMINANTS OF SPEED AND TIMING OF CONDUCTION IN AUDITORY NEURONAL AXONS

J. Xu

Department of Engineering and Computer Science
Tarleton State University
Stephenville, TX, USA

INTRODUCTION

The speed of action potential conduction in the myelinated auditory axon is fundamental to information processing in the brain. However, its regulatory mechanisms are not fully understood. Here we report findings from a computational study to examine both structural and non-structural factors in the Ranvier nodes and internodes of auditory axons. The structural element we looked at included mainly the internode length. The non-structural factors included three main ionic currents and a leak current.

METHODS

The model of Ranvier nodes includes the potassium current I_K, the fast sodium I_{Na}, the hyperpolarization-activated cation current I_h, and a leak current I_{Leakn}. While only the leak current I_{Leaki} is included in the myelinated axon. The propagation of the electrical signal through axons is modeled by cable theory [1, 2]. The computational task is to numerically solve the following transient cable equation.

$$C\frac{\partial V}{\partial t} = \frac{\partial^2 V}{\partial x^2} - (I_{Na} + I_K + I_h + I_{Leak}) \quad (1)$$

where C is the membrane capacitance. Spatial discretization of above equation produces a family of ordinary differential equations of the form

$$C_k\frac{dV_k}{dt} = \sum_l \gamma_{l,k}(V_l - V_k) - (I_{Na} + I_K + I_h + I_{Leak})_k \quad (2)$$

where k and l index compartments, C_k is the capacitance for compartment k, V is the transmembrane voltage, $\gamma_{lk} = 2/(\rho_k+\rho_l)$ is the coupling conductance between adjacent compartments, and the sum is over all compartments l connected to compartment k. The capacitance of a compartment k is defined as $C_k=C_m\pi dk\Delta x_k$ and the axial resistance is defined as $\rho_k=Ra\Delta x_k/\pi r_k^2$. C_m is the specific capacitance of the membrane, R_a is the axoplasmic resistivity, r_k is the radius, and Δx_k is the length of the compartment, respectively. Currents injected through a simulated microelectrode are added to the first node of Ranvier. Sealed end boundary conditions are used.

All the channels are expressed in the nodes of Ranvier except for myelinated axon where only internode leak current I_{Leaki} is included. Except where otherwise noted, the ion channel kinetics were taken from published models [3-6]. The peak conductances are: G_{Na}=0.588 S/cm^2, G_K=0.04 S/cm^2, G_h=0.095×10^{-3} S/cm^2, internode leak conductance G_{Leaki}=0.1×10^{-3} S/cm^2, and nodal leak conductance G_{Leakn}=1.76×10^{-3} S/cm^2. The simulation programs was written in C/C++ programming language and run in MS Visual Studio Academic 2019.

RESULTS

Figure 1a shows that conduction velocity indeed decreases as the K conductance increases (without h channels). Furthermore, with only Na channel presents, the conduction velocity is about 14.4 m/s, corresponding to the zero conductance data point on the left in Figure 1a. Figure 1b shows the conduction velocity increases as the h channel conductance increases, indicating that h channels facilitate AP conduction along the axon. Please note that the conduction velocity was calculated from the time needed for the AP to travel from the 71st to the 90th internode.

Figure 2a shows the axonal current that would be conducted into cell body to depolarize the cell body. The bigger the current, the easier the cell body is depolarized. The result shows that this is indeed the case. In addition, the result shows that the depolarization would happen faster as the current travels faster compared with the constant-spaced model. In Figures 2a and 2b, the internode length linearly decreases from 197.7

micron to about 53.5 micron before injecting into the cell body (soma). Please note that the distal end length varies from 197.7 to 1 micron. In addition, the all internode lengths are linearly decreasing from the first to last internodes.

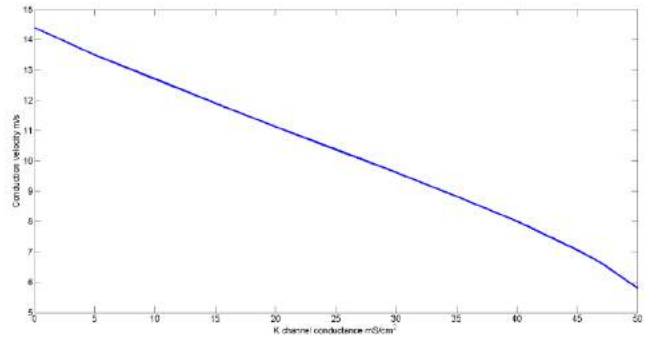

(a)

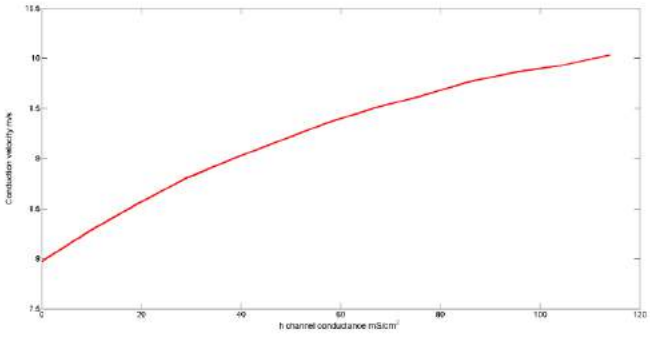

(b)

Figure 1: Effects of ion channel K+ and h conductances on Conduction Velocity (CV).

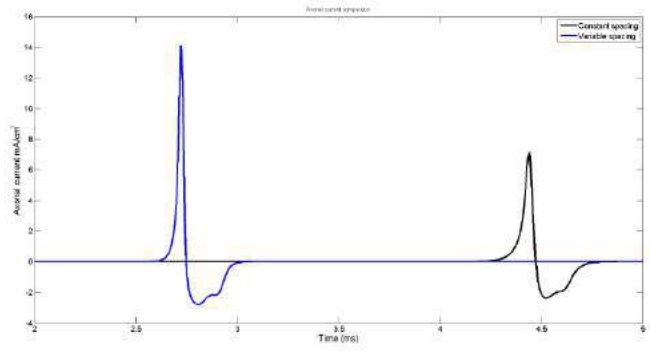

(a)

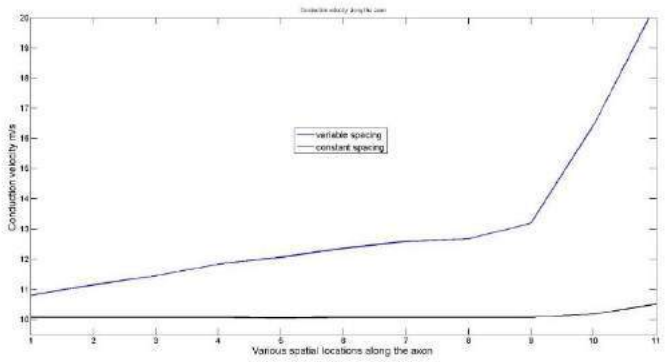

(b)

Figure 2: Effects of Internode spacing on CV and axonal current.

DISCUSSION

Simulations predicted that the internode length helps to adjust the conduction speed and timing of action potentials. The spatial properties of the myelinated axon deviated significantly from the traditionally assumed structure. Previous studies showed internode length decreased and Ranvier node diameter increased progressively along with the distal axon segments, which our simulations show this special structural arrangement leads to a higher axonal current that would be conducted into a cell body to depolarize the cell body. The bigger the current, the easier the cell body is depolarized. The result confirms that this is indeed the case. In addition, the results show that the depolarization would happen faster as the current travels faster compared with the traditionally assumed constant-length internode model. Moreover, our simulations show that conduction velocity decreases as the k conductance increases and increases as the h channel conductance increases indicating that h channels facilitate AP conduction along the axon. The spatial arrangement of internodes and ionic currents can be the potential temporal regulatory mechanism of the auditory signals.

ACKNOWLEDGEMENTS

The author wishes to gratefully acknowledge the financial support provided by the Tarleton State University Faculty-Student Research and Creative Activity Internal Grants (FSIG).

REFERENCES

1. Traub, R.D., et al., *A branching dendritic model of a rodent CA3 pyramidal neurone.* J Physiol, 1994. **481 (Pt 1)**: p. 79-95.
2. Rall, W., *Branching Dendritic Trees and Motoneuron Membrane Resistivity.* Experimental Neurology, 1959. **1**(5): p. 491-527.
3. Ford, M.C., et al., *Tuning of Ranvier node and internode properties in myelinated axons to adjust action potential timing.* Nat Commun, 2015. **6**: p. 8073.
4. Halter, J.A. and J.W. Clark, Jr., *A distributed-parameter model of the myelinated nerve fiber.* J Theor Biol, 1991. **148**(3): p. 345-82.
5. Rothman, J.S., E.D. Young, and P.B. Manis, *Convergence of auditory nerve fibers onto bushy cells in the ventral cochlear nucleus: implications of a computational model.* J Neurophysiol, 1993. **70**(6): p. 2562-83.
6. Spirou, G.A., et al., *Heterogeneous Ca2+ influx along the adult calyx of Held: a structural and computational study.* Neuroscience, 2008. **154**(1): p. 171-85.

ENHANCED HEMODYNAMIC PREDICTIONS IN A CALCIFIED AORTIC VALVE GEOMETRY USING THE QUEMADA MODEL

Asad M. Mirza, Amanda Barreto, Tisha Boodooram, Sharan Ramaswamy

Department of Biomedical Engineering
Florida International University
Miami, Florida, United States of America

INTRODUCTION

When conducting computational fluid dynamics (CFD) simulations around the aortic valve, blood is often assumed to be a Newtonian fluid [1]. This assumption is supported through previous studies of similar large vessels in arteries where shear rates are relatively large, (>1000 s^{-1}), which is the case in the region surrounding the aortic valve [2]. However, for more tortuous arterial geometries [3], the Newtonian assumption fails to properly quantify the wall shear stress (WSS) which results in false identification of regions prone to thrombogenesis [4]. These inaccuracies could also occur when this assumption is applied to the aortic valve geometries, where leaflet flexure and calcifications can induce regions of very low shear rates on the fibrosa side. The following study investigated and compared three viscosity models: Newtonian, Carreau, Quemada on a calcified aortic valve geometry to determine which model would facilitate maximum accuracy in hemodynamic predictions.

METHODS

A construction of a human aortic heart valve, taken from an 82-year-old patient at the early diastolic phase, was purchased (Valve – 012 - Heart Print catalog, Materialize Inc, Plymouth MI). Geometry was then imported into a commercial modeling software (ANSYS Spaceclaim; ANSYS Inc, Canonsburg, PA) for mesh repair, smoothing, shrink-wrap, labelling, and fluid volume extraction. A mesh independence study was done on the valve and calcifications resulting in a finalized mesh with 1.7 x 10^6 and 5 x 10^5 elements, respectively, with an average mesh quality of .82. Inlet velocity of 1 cm/s along with an 80-mmHg pressure condition on the outlet were prescribed.

Blood flow was assumed to be incompressible and modeled using the Navier-Stokes equations (Eq 1 and 2)

$$\rho\left(\frac{\partial \vec{u}}{\partial t} + (\vec{u}\cdot\nabla)\vec{u}\right) = \nabla p + \rho g + \mu\Delta\vec{u} \quad \text{(Eq 1)}$$

$$\nabla\cdot\vec{u} = 0 \quad \text{(Eq 2)}$$

where $\vec{u}$ and p represent, respectively, the fluid velocity vector and the pressure. ρ is the density of blood, which was set to 1060 kg/m^3.

Blood viscosity, μ, was defined using three different models. Newtonian model used a constant viscosity of 3.3 cP. A non-Newtonian Carreau model given in (Eq 3) with μ_∞ = 3.2 cP; μ_0 = 45.6 cP; λ = 10.03 s; n = 0.344.

$$\mu = \mu_\infty + (\mu_0 - \mu_\infty)\left(1 + (\lambda\gamma)^2\right)^{\frac{1-n}{2}} \quad \text{(Eq 3)}$$

And the non-Newtonian Quemada model given in (Eq. 4) with μ_p = 0.001123 Pa; μ_0 = 3.9 cP; μ_∞ = 1.766 cP; γ_c = 5 cP s; and Hct = 48%.

$$\mu = \mu_p\left(1 - \frac{1}{2}\frac{\mu_0 + \mu_\infty\sqrt{\dot{\gamma}/\gamma_c}}{1 + \sqrt{\dot{\gamma}/\gamma_c}}Hct\right)^{-2} \quad \text{(Eq 4)}$$

All parameter values were found by curve fitting experimental blood data (Fig 1) using a non-linear least squares algorithm in MATLAB (MathWorks, Natick, MA, USA).

Simulations were conducted on an MSI GT73EVR 7RE Titan with 64 GB RAM, 2.90 GHz Intel i7, and a NVIDIA GeForce GTX 1070. Simulation was done in ANSYS Fluent with ANSYS Mosaic Meshing, using the SST k-ω model. Steady state convergence criterion was set to 1x10^{-6}.

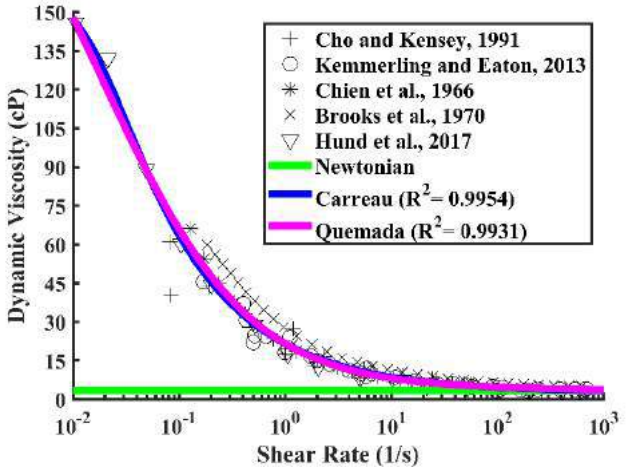

Figure 1. Viscosity model fittings for Newtonian (green), Carreau (blue), and Quemada (purple). Experimental data taken from whole blood from 5 different sources.

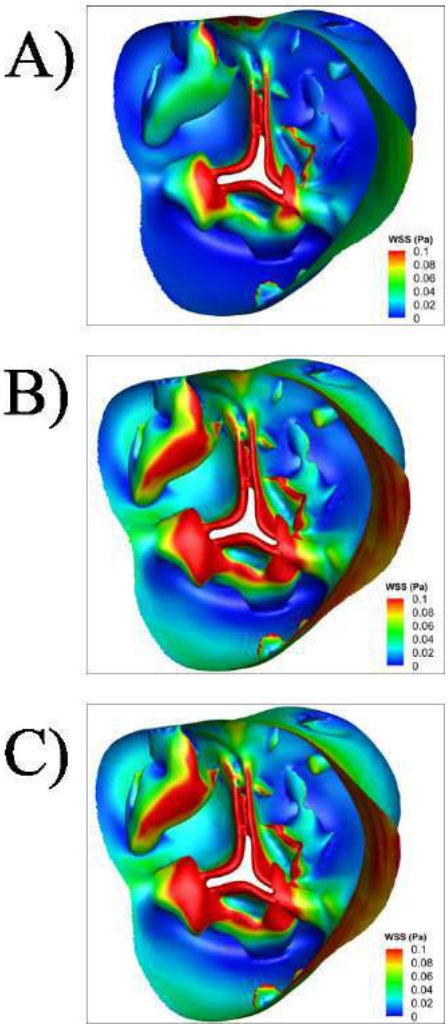

Figure 2. Wall shear stress distribution on the calcified fibrosa side of the aortic valve under three different steady state viscosity model conditions: A) Newtonian B) Carreau C) Quemada.

RESULTS

Model fittings (Fig 1) showed great agreement with experimental data (R^2 > .99) for both Carreau and Quemada models. On the other hand, the Newtonian model only partially fit the data (shear rates > 100 s^{-1}).

Simulations under all three viscosity conditions showed drastically greater WSS on the ventricularis side of the aortic valve (>1000 s^{-1}) compared with the fibrosa (< 1 s^{-1}). Along the free edge of the leaflets there was similar agreement in shear rates and WSS between all three models. For the majority of the fibrosa side, the Newtonian model (Fig 2A) greatly underestimated WSS when compared with both Carreau (Fig 2B) and Quemada (Fig 2C) models. Within the cusp regions or in pocket regions formed by the calcifications WSS was often greater under both non-Newtonian models (> 0.4 dynes/cm^2), than in the same area under the Newtonian model.

DISCUSSION

Many previous works in large arterial vessels have been justified in their use of the Newtonian model for blood viscosity due to the large shear rates present in them [5-7]. However, applying this assumption to a calcified aortic valve is suspect as, on the fibrosa side, shear rates can be below 1 s^{-1} during diastole. This results in low WSS, < 1 dynes/cm^2, which are primarily found in the inner regions of the cusps, which have been noted as being sites prone to thrombosis [8]. The Quemada and Carreau models exhibit an excellent response across a wide range of shear rates. However, the Quemada model has the added benefit of accounting for changes in blood hematocrit, a parameter that has been noted to vary with both age and gender of patients [9]. We conclude that that the Quemada model is most applicable for calcified aortic valve geometries so as to more accurately capture leaflet WSS and to identify regions of flow stagnation, which are vulnerable to thrombosis.

REFERENCES

1. Spuhler, J.H., et al., Front Physiol, 2018. **9**: p. 363.
2. Hasler, D. and D. Obrist, PLoS One, 2018. **13**(3): p. e0194384.
3. Rahman, M.M., et al., AIP Conference Proceedings, 2018. **1980**(1): p. 040017.
4. Buck, A.K.W., et al., ASAIO journal (American Society for Artificial Internal Organs : 1992), 2018. **64**(2): p. 211-217.
5. Xu, X.Y. and M.W. Collins,. Proceedings of the Institution of Mechanical Engineers, Part H: Journal of Engineering in Medicine, 1994. **208**(3): p. 163-175.
6. Bluestein, D., et al., J Biomech Eng, 1996. **118**(3): p. 280-6.
7. Steinman, D.A., et al., Magn Reson Med, 2002. **47**(1): p. 149-59.
8. Demirozu, Z.T. and O.H. Frazier, Tex Heart Inst J, 2012. **39**(5): p. 618-20.
9. Houssein, H.A.A., et al. 2011. Berlin, Heidelberg: Springer Berlin Heidelberg.

SB³C2021
Summer Biomechanics, Bioengineering and Biotransport Conference
June 14-18, Virtual

PERISTALTIC PUMPING IN SUB-WAVELENGTH PERIVASCULAR MODELS

Jessica K. Shang (1), J. Brennen Carr (1), Caroline D. Cardinale (1), Delin Zeng (1)

(1) Department of Mechanical Engineering
University of Rochester
Rochester, NY, USA

INTRODUCTION

Cerebrospinal fluid (CSF) flows through the annular perivascular spaces (PVSs) surrounding the surface arteries of the brain. One hypothesis is that the flow is peristaltically driven by traveling-wave pulsations of the arterial walls, a mechanism termed "perivascular pumping" [1]. The hypothesis has been supported by *in vivo* measurements, which show an unsteady movement of CSF that is correlated with the cardiac cycle and modulated by varying arterial pulsation [2,3].

Idealized models of the PVS have been employed in theoretical and computational studies of perivascular pumping (see [4] for a review). These studies have reached differing conclusions on the feasibility of perivascular pumping. One variable between studies is the the choice of domain length, which can be of integer wavelength, or shorter than a wavelength. The peristaltic wavelength is expected to be about 0.1 m, but each PVS segment is short, 10^{-4} to 10^{-3} m [2, 3], so a sub-wavelength domain may be more realistic. Simulations showed that mean flow rate is orders of magnitude smaller in sub-wavelength models compared to integer-wavelength models, and only applying a small pressure difference across its length can increase the net flow rate to a physiologically relevant value [5, 6].

In this study, we extend the lubrication approximation of peristalsis employed by others [7-9] to sub-wavelength planar channels ($n < 1$). Non-integral wavelengths were previously studied by [9] for cylindrical tubes greater than a wavelength. Here, analytically explore the regime where the domain is sub-wavelength in length, which is relevant to perivascular flow. Our model demonstrates a significant effect of domain length on mean and instantaneous flow rate, and sheds light on the appropriateness of simple peristaltic models to describe perivascular pumping.

METHODS

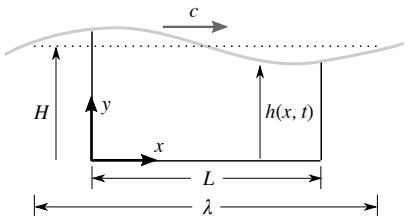

Figure 1. Peristaltic model.

The channel is modeled as a two-dimensional, rectangular domain of height H and length $L = n\lambda$, where λ is the wavelength of the peristaltic wave (Figure 1). The peristaltic wave propagates along the upper wall in the longitudinal (x) direction, and its position is given by $h(x,t) = H\big(1 + G(x - ct)\big)$, where c is the wavespeed, t is time and G is a waveform that is continuous and periodic over $x = [0, \lambda]$. The bottom wall is fixed. The channel is filled with an incompressible, Newtonian fluid of density ρ and dynamic viscosity μ, and is open, not porous. The upper and lower walls are impermeable.

In the lubrication approach [7-9], non-dimensionalization of the Navier-Stokes equations shows that inertial effects are negligibly small, resulting in the lubrication equations:

$$0 = -\frac{\partial p}{\partial x} + \mu\frac{\partial^2 u}{\partial y^2};\ 0 = \frac{\partial p}{\partial y}. \qquad (1)$$

where u and v are the x- and y- components of velocity, respectively, and p is the pressure. We also note that the average Reynolds number calculated from experiments is also small, $Re = \frac{\rho \overline{u} H}{\mu} \approx 10^{-2}$, where $\overline{u}$ is the mean velocity. No-slip boundary conditions are applied at $y = 0$ and $y = h(x,t)$ to solve for the velocity profile

$$u(x,y,t) = \frac{1}{2\mu}\frac{\partial p}{\partial x} y(y-h). \quad (2)$$

We can integrate continuity $\frac{\partial u}{\partial x} + \frac{\partial v}{\partial y} = 0$ with respect to y. Substituting the velocity profile u, we obtain

$$\frac{\partial}{\partial x}\left(\frac{h^3}{12\mu}\frac{\partial p}{\partial x}\right) = \frac{\partial h}{\partial t}. \quad (3)$$

We can integrate this to obtain $p(x,t)$. For brevity, we consider the case where there is no applied pressure difference over the channel, $p(x=0) = p(x=L)$. The flow rate q is determined by integrating u:

$$q = \int_0^h u\, dy = -\frac{h^3}{12\mu}\frac{\partial p}{\partial x} \quad (4)$$

and substituting the pressure,

$$q = -\int_0^x \frac{\partial h}{\partial t} dx' + \frac{\int_0^L \frac{\int_0^{x'} \partial h/\partial t\, dx''}{h^3(x',t)} dx'}{\int_0^L h^{-3}(x',t)\, dx'}. \quad (5)$$

We can apply a transformation of variables (see [8] for details) and substitute our definition for $h(x,t)$ to manipulate q into the form

$$\frac{q}{cH} = 1 + G(x,t) - \frac{\int_0^L \{(1+G(x,t)\})^{-2}\, dx}{\int_0^L \{(1+G(x,t)\})^{-3}\, dx}. \quad (6)$$

RESULTS

We calculate flow rates using Eq. 6 and prescribe an experimental *in vivo* arterial wave [3] as our wall wave $G(x,t)$, as shown in Fig. 2. We also show $q(x,t)$ at various locations and $n \leq 1$. For $n = 1$, q has the same amplitude for all x, and is in phase with $G(x,t)$. In contrast, for smaller values of n, q varies with x in amplitude and phase shift, and the flow rates are not in phase with G.

In particular, for $n << 1$, the flow rates at the inlet and outlet are of opposite sign and mimic the wall velocity dG/dt, and the flow in the middle of the channel is small. The local slope of the wall wave is small (the wavelength is much larger than the amplitude), so a short channel contracts and expands nearly uniformly as the wave passes through. When the channel contracts, fluid is squeezed out of the ends, and when the channel expands, fluid rushes back in. Hence the inlet and outlet flow oppose each other and follow the wall velocity. As the channel length increases to a wavelength, the velocity-like behavior fades, and $q(x,t)$ favors the wall displacement function $G(x,t)$.

For the mean flow rate, we integrate over the period $\tau = \lambda/c$:

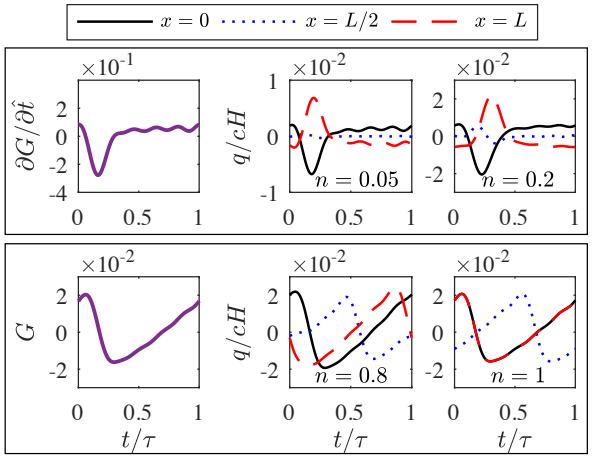

Figure 2. Instantaneous flow rates for varying channel length and at different channel positions.

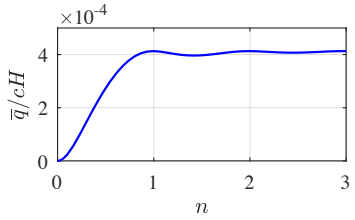

Figure 3. Mean flow rate as a function of n.

$$\bar{q} = \frac{1}{\tau}\int_0^\tau q(x,t)\, dt. \quad (7)$$

The mean flow rate is shown in Fig. 3, and is very small for $n << 1$. The mean flow rate varies periodically with n, and is maximized when n is an integer. For non-integer $n > 1$, the mean flow rate is slightly less than for integer n, which was also noted by [9] for finite tubes.

DISCUSSION

We have examined the flow rate produced by a peristaltic wave in sub-wavelength channels. While our model is 2D and does not mimic the PVS-specific annular geometry, our observations can be extended to 3D geometries, since the lubrication approximation will apply.

At low values of n, the fluid predominantly oscillates in and out of the ends, synchronous with the wall velocity. This wall velocity-like behavior was observed in simulations [5, 6, 10], though they did not explicitly show velocity profiles at locations other than the inlet or outlet. However, *in vivo* measurements did not show significant changes in amplitude and phase along a perivascular segment [3].

In agreement with previous studies, the mean flow rate at low n is very small compared to n = 1 [5, 6, 10]. Applying a pressure difference can increase the mean flow rate [5, 6]. However, even if the applied pressure is pulsatile, its unsteady component does not vary spatially, so the instantaneous flow rate is still unphysiologically spatially inhomogeneous in phase and amplitude at small n. A full-wavelength model is spatially homogeneous, but as noted by [5], the flow amplitude is unrealistically large compared to mean flow rates.

In conclusion, idealized models of perivascular pumping thus far do not adequately represent the desired flow. The inclusion of additional physics through complex boundary conditions coupled to perivascular flow models are a rich area for future study, that can be improved with expanded *in vivo* measurements.

ACKNOWLEDGEMENTS

This work was supported by the National Institute of Aging (RF1 AG057575-01), and the Office of Naval Research (N0001-18-1-2456). We are grateful for constructive discussions with J. H. Thomas, D. H. Kelley, and J. Tithof.

REFERENCES

[1] Hadaczek P et al., *Brain. Mol. Ther.* 14(1): 69-78, 2006.
[2]Bedussi B et al., *J Cerebr Blood F Met* 38(4):719-726, 2017.
[3] Mestre H et al., *Nat. Comm.* 9(1):4878, 2018.
[4] Thomas JH,. *J. Roy. Soc. Int.* 16(159):20190572, 2019.
[5] Kedarasetti R et al., *Fluids Barriers of the CNS*, 17(1):1-25, 2020.
[6] Daversin-Catty C et al., *bioRxiv*, 2020.06.17.157917.
[7] Shapiro AH et al., *J. Fluid Mech.*, 37(4):799-825, 1969.
[8] Schley D et al., *J. Theor. Biol.* 238(4):962-974, 2006.
[9] Li J and Brasseur JG, *J. Fluid Mech*. 248:129-151, 1993.
[10] Asgari M et al., *Sci. Rep*., 6: 38635, 2016.

DEVELOPMENT OF A DEFORMABLE MICROFLUIDIC CHIP TO REPLICATE TISSUE STRAINS IN SITU

Andre R. Montes (1), Jonathan P. McKinley (1), Grace D. O'Connell (1), Mohammad R.K. Mofrad (1,2)

(1) Department of Mechanical Engineering
University of California, Berkeley
Berkeley, CA, USA

(2) Department of Bioengineering
University of California, Berkeley
Berkeley, CA, USA

INTRODUCTION

Cells respond to mechanical and biochemical stimuli to maintain homeostasis; changes in the magnitude or type of stimuli can lead to various diseases. For example, the heart and lung tissue stiffen over time potentially leading to cardiovascular disease and lung fibrosis, respectively [1,2]. In this study, we focus on back and spine pathologies that affect ~8 million people in the United States and cost over $100 Billion annually [3,4]. The most identifiable and widely studied source of back pain is due to degeneration or failure of the intervertebral disc [5,6]. Disc degeneration, stemming from disruption of the annulus fibrosus (AF), leads to increased pain and reduced mobility [7,8]. To enable regenerative medicine strategies, a better understanding of AF cell mechanobiology during tissue development is needed. A method is required to quantitatively and reliably replicate intradisc loading to test potential disease mitigators at the cellular and nascent tissue levels. Advancements in microfluidics have enabled micromechanical testing of small cohorts of cells [9,10]. However, a chip that emulates more physiological strains observed in the AF is needed. Therefore, we present a deformable chip that emulates the AF's cyclical and multiaxial strains. We demonstrate a method to evaluate the effects of these strains on the initiation and propagation of AF tissue degradation. We bolster development of the chip by using the Finite Element Method (FEM) to validate lab measurements and examine strains within a cell monolayer.

METHODS

We designed a deformable microfluidic chip using principals of beam mechanics to target clinically relevant, multiaxial loads in the AF. Our previous work created a polydimethylsiloxane (PDMS) chip that enclosed a single microchannel (Figure 1A) [11]. The chip was deformed over a rigid cylinder (radius = 10.6 mm) to create uniform depth-dependent strains, due to bending. A microscope slide was positioned beneath the chip to help visualize cells throughout loading (Olympus CKX31 microscope; Figure 1B). When the chip is bent around the cylinder, uniform depth-dependent strains, ε, are assumed to follow the mechanics of a beam in pure bending: $\varepsilon = Y/\rho$, where Y is the vertical distance from the Neutral Axis (NA), and ρ is the radius of curvature [12]. We assumed that the NA bisects the chip. Two configurations of the chip were fabricated with differing Y-positions of the microchannel relative to the NA: 5% target strain (Y=0.63mm) and 10% target strain (Y=1.26mm) conditions as measured in the X direction. These represent the intradiscal radial strains observed in the AF during compression and bending [13,14]. We measured strain in the X direction by tracking the 1D displacements of the chip's channel walls using edge detection in MATLAB (MathWorks, Inc).

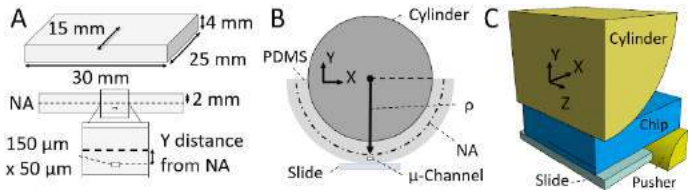

Figure 1: Schematic of (A) chip design with the microchannel, (B) loading setup, and (C) quarter computational model.

A solid model of a quarter symmetrical chip was created in Solidworks (Dassault Systemes) with the channel positioned for three configurations (0%, 5%, and 10% target strain). We imported geometries into GMsh [15] to construct meshes with tetrahedral elements. Then, the meshes were individually imported into Finite Elements for Biomechanics (FEBio) Preview 2.1.1 [16]. We then added the cylinder, the microscope slide, and a "pusher" (Figure 1C). All parts

except the chip used a rigid material model and were meshed using hexahedral elements. The PDMS chip used a Neo-Hookean material model with a Poisson's ratio of 0.45 and a Young's Modulus of 1.7 MPa [17]. We added symmetry boundary conditions and defined frictionless contacts between contacting surfaces. We applied a Y-displacement of 7 mm on the "pusher" to enforce the chip's curvature during the test cycle. The cycle is defined as when the chip starts to bend until it reaches its maximum curvature. We verified the curvature match between the model and the setup by comparing radii of curvature using ImageJ [18] (data not shown). Lab-based strain measurements at the chip's center were compared to beam-theory estimates and model predictions.

For the 10% target configuration, we placed an idealized bovine chondrocyte monolayer, in the shape of a rectangular prism, at the base of the channel to model the strain transfer from the chip to the cells. We filled the channel with a 9 µm tall monolayer and applied a Neo-Hookean material model with a Young's Modulus of 14 kPa and a Poisson's ratio of 0.34 [19]. We added a no-slip contact between the channel bed and the monolayer. We neglected any adhesion between the channel walls and the monolayer. Lastly, we applied a structured hexahedral mesh to the monolayer. We compared the monolayer model's strains to those observed in the AF via magnetic resonance imaging (MRI) [20]. X and Y direction strains in the model correspond to radial and axial strains reported in the AF, respectively. We ran all models in FEBio 2.9.1, then analyzed outputs in FEBio Postview 2.5.

RESULTS

A linear fit of the model results ($\varepsilon = 8.8*Y+1.74$) showed that the NA was 0.198 mm above the midline and not at the midline as predicted by beam mechanics (Figure 2). Compared to the measured strains, the beam mechanics and model predictions had a 24.1% and 4.55% average percent error, respectively. The range of radial and axial strains in critical locations of the AF, as measured by MRI [20], are approximately -4 to 10% and -10 to 0%, respectively (Figure 3). The monolayer model covered a range of 0 to 15.1% and -6.9 to 0% strain in the radial and axial directions, respectively. The monolayer model overshot the positive radial strains by 5.1%. The model was unable to cover -10 to -6.9% axial strain or any negative radial strain.

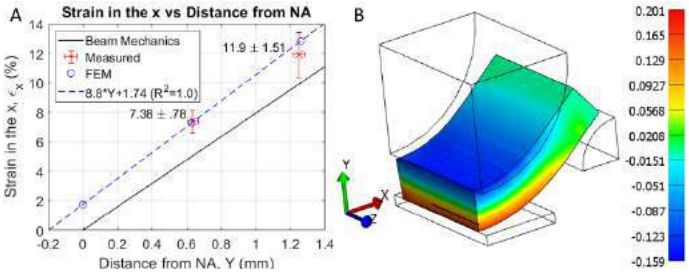

Figure 2: (A) Comparison plot of models to measurements. (B) The model strain results for the 10% target strain chip.

DISCUSSION

The work presented here builds upon our previous development of a deformable organ-chip system that aims to replicate strains experienced by AF cells *in situ*. Results from this study indicate that the computational model provided a more accurate approximation of chip strains than simple beam theory. To cover the full range of axial and radial strains observed *in situ*, we can use modeling to inform us how to scale our chip, position our channel, and alter the chip's bending magnitude.

While many microfluidic platforms exist to evaluate the effects of fluid shear stress on cell behavior [9,10], evaluation of physiologically relevant applied multiaxial strains on AF cells remains unexplored. Our chip provides a controllable method of applying these strains. Since the applied strain in the monolayer model follows a predictable curve over the test cycle (Figure 3), we can adjust bending amplitude to meet target strains. Also, while modeling is often used to characterize factors like mechanical or fluid loading applied by the chip onto the cells, modeling of the cells themselves is often missing. By modeling the cellular mechanics and confirming them empirically, we can estimate internal cellular stresses and strains in three dimensions which otherwise would be difficult to observe. While the current application of our chip is for the AF, biological systems that undergo similar stretching patterns, such as cardiovascular walls, the cervix, or the bladder, can also be investigated by altering the chip geometry to represent healthy or diseased loading conditions. For example, the maximum absolute strain in the left ventricle is 20% in healthy tissues but decreases to 15% right before heart failure [1]. Ongoing work is focused on directly measuring strains in the monolayer to validate model predictions. We will also evaluate cellular responses to different applied strain conditions representative of healthy and degenerated discs.

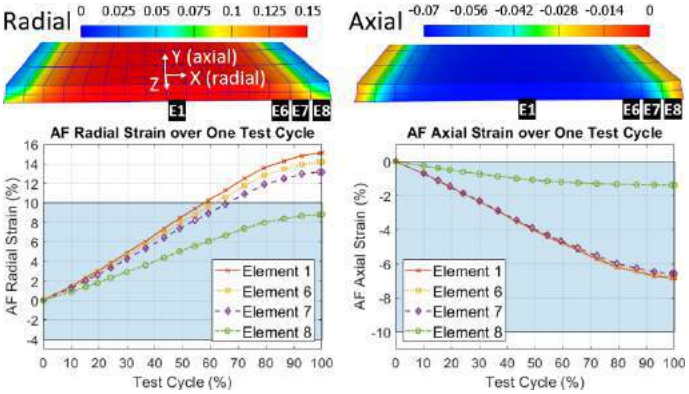

Figure 3: (Left) Radial and (Right) axial direction strains in the chip model were compared to the range of strains reported during AF flexion and extension (shaded region) [20].

ACKNOWLEDGEMENTS

Thank you Minhao Zhou for the FEBio tutorial and guidance.

REFERENCES

[1] Smiseth, O et al., *European Heart Journal.*, 37: 1196-1207, 2016. [2] Guenat, O. and Berthiaume, F., *Biomicrofluidics*., 12: 042207, 2016. [3] Centers for Disease Control and Prevention (CDC), *MMWR Morb Mortal Wkly,* 58(16):421-426, 2009. [4] Katz, J et al., *The J. of Bone and Joint Surgery,* 88(2):21, 2006. [5] Pattappa, G et al., *J. of Anatomy,* 221(6):480-496, 2012. [6] Torre, O et al., *Annals of the NY Acad of Sci,* 1442(1):61-78, 2018. [7] Blankenbaker, D et al., *American J. of Roentgenology,* 186(3):795-799, 2006. [8] Guteri, C et al., *European Cells and Materials,* 25:1-21, 2013. [9] Chou, P et al., *Stem Cell Research & Therapy*., 7(1):34, 2016. [10] Dai, J et al., *ACS Biomater. Sci. Eng.,* 5: 2041-2051, 2019. [11] McKinley, J et al., *BMES Annual Meeting*, 2020. [12] Shigley, R et al., *Mech. Eng. Design,* 7:125, 2004. [13] O'Connell, G et al., *Spine.* 32:2860-2868, 2007. [14] White III, A et al., *Clin. Biomech. of the Spine.* 2(14):7, 1990. [15] Geuzaine, C. et al., *Itnl J. Num. Met. in Eng.* 79(11):1309-1331, 2009. [16] Maas, S et al., *J. of Biomech Eng.,* 134(1): 011005, 2012. [17] Johnston, I et al., *J. Micromech. and Microeng.,* 24: 035017, 2014. [18] Schneider, C et al., *Nature Methods.,* 9(7): 671-675, 2012. [19] Nyugen, B et al., *J. R. Soc. Interface.,* 7: 1723-1733, 2010. [20] O'Connell, G et al., *J. of Orthopaedic Res.*, 29(4):547-555, 2010.

LEVERAGING ENDOTHELIAL GLYCOCALYX INTEGRITY IN ATHEROSCLEROTIC-RELEVANT FLOW CONDITIONS FOR TARGETED INTRAVENOUS NANOPARTICLE DELIVERY

R. Mitra (1), M. Cheng (1), G. O'Neil (3), P. Kulkarni (4), R. Kumar (5), S. Sridhar (5), C. Ferris (4), J. Hamilton (6), H. Jo (7), E. Ebong (1,2)

(1) Department of Chemical Engineering
Northeastern University
Boston, MA, USA

(2) Department of Bioengineering
Northeastern University
Boston, MA, USA

(3) Department of Biology
Northeastern University
Boston, MA, USA

(4) Department of Psychology
Northeastern University
Boston, MA, USA

(5) Department of Physics
Northeastern University
Boston, MA, USA

(6) Department of Physiology and Biophysics
Boston University School of Medicine
Boston, MA, USA

(7) Department Biomedical Engineering
Georgia Tech and Emory University
Atlanta, GA, USA

INTRODUCTION

The cell surface-attached extracellular glycocalyx (GCX) layer, a heterogeneous polysaccharide chain, is a major contributor to endothelial cell (EC) function and EC-dependent vascular health, acting as a first line of defense against vascular diseases including atherosclerosis [1]. It largely consists of cell-linked sialic acid and glycosaminoglycans including heparan sulfate, hyaluronic acid, and chondroitin sulfate. The endothelial GCX acts as a buffer between the endothelium surface and blood-flow derived shear forces and contributes to vascular barrier functionality [2]. Endothelial surface GCX shedding plays a role in endothelial dysfunction, compromising endothelial barrier function and increasing vascular permeability [2]. This GCX degradation increases lipid flux thereby promoting lipid deposition in the vessel walls and cascading to an inflammatory response, a hallmark of atherosclerosis.

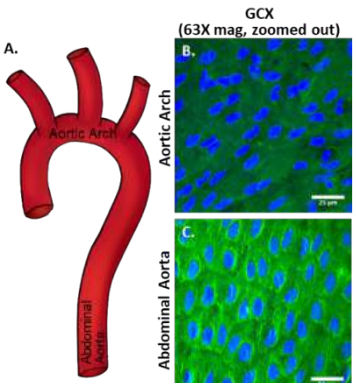

Fig. 1. Flow-dependent regulation of GCX (green) is confirmed in vivo, showing a decrease in GCX expression in aortic arch in comparison to abdominal aorta of mice. (Adapted from Harding et al. *J Transl Med,* 2018.)

The impact and influence of flow on the GCX have been conducted in previous studies. For instance, it provides protection of the endothelium along vessel walls exposed to uniform blood flow and relatively good health [3]. However, in geometrically complex vasculature structures, such as the aortic arch or carotid bifurcation, vessel walls exhibit non-uniform flow patterns with low wall shear stresses due to blood recirculation, attributing to GCX shedding (Figure 1). Van den Berg et al. [4] demonstrated a thinned endothelial GCX at the bifurcation region of a mouse internal carotid artery compared to the common carotid artery with impaired barrier properties of the GCX, contributing to enhanced pro-atherogenic low density lipoprotein accumulation in the intima at the carotid artery bifurcation.

A unique surgical procedure was developed by Nam et al. [5] to perform partial left carotid artery ligation in mice. This was characterized as a model of disturbed flow with characteristics of low and oscillatory wall shear stress. However, this study did not examine GCX expression after acutely inducing disturbed blood flow. The first part of our study sought to elucidate the impact on GCX integrity post-one week of partial left carotid ligation in mice to validate endothelial GCX shedding and correlate that to endothelial dysfunction.

The second part of this study examined vessel wall permeability after GCX shedding by examining resultant macrophage infiltration, related to atherosclerosis onset, as well as nanoparticle infiltration, related to targeted drug delivery for early atherosclerosis intervention. In mice, the left carotid artery (LCA) that was partially ligated to acutely induce disturbed blood flow exhibit both enhanced macrophage infiltration as well as enhanced infiltration of 10-nm polyethylene-glycol (PEG) coated gold nanospheres (GNS) after they were intravenously administered.

METHODS

For the first study, six to seven week-old C57Bl/6-background apolipoprotein (ApoE-KO) male mice were subjected to a partial (LCA) ligation procedure [5] to induce disturbed blood flow patterns in the LCA while the right carotid artery of each mouse was not surgically intervened, to provide a control in each mouse (Figure 2). Ultrasound was performed immediately and magnetic resonance imaging (MRI) was performed on days 1, 5, and 7 post-ligation to demonstrate changes in blood flow in ligated LCAs along with counterpart RCAs. Mice were sacrificed post-one-week ligation surgery and the LCA and RCA were dissected and immunohistochemically stained for GCX to determine percent coverage and thickness. Values of GCX coverage and thickness in LCA vessel walls were normalized to their RCA counterpart. Macrophage infiltration similarly detected, measured, and normalized. The normalized results were expressed as mean ± standard error of

mean (SEM). Normalized data sets were compared using Graph Pad Prism software and a two-way ANOVA test to analyze statistical significance between groups with an alpha value of 0.05.

For the second study, C57Bl/6 male mice at four weeks of age underwent partial LCA ligation surgery. Ultra-small gold nanospheres (GNS) coated with PEG were fabricated. At day 26 post-ligation, anesthetized mice intravenously received 25 mg of biotin-conjugated PEGylated GNS in 150 uL of sterile phosphate buffer solution (PBS). GNS were then allowed to circulate in the mice for 48 hours. The animals were euthanized, fixed, and dissected after 28 days post-ligation surgery, 2 days after GNS treatment. The carotid arteries were then extracted. Fluorescent staining of biotinylated GNS uptake in vessel wall, and GCX expression on the inner surface of the vessel wall, were performed. Measurements were reduced to mean ± SEM. Graph Pad Prism software was used to perform ANOVA statistical analysis to determine statistical significance.

RESULTS

The initial analysis was intended to ensure that partial ligation surgeries were conducted correctly, by qualitatively and quantitatively collecting data through MRI and ultrasound, respectively (Figure 3).

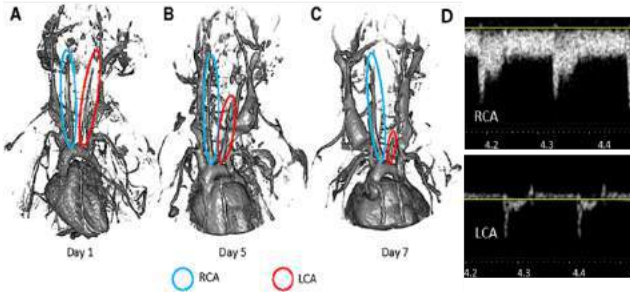

Fig. 3. A, B, and C. Representative MRI images detecting ferumoxytol flowing through mice vessels. Blue circles indicate RCAs and red circles indicate LCAs. Over time, reduction of detectable ferumoxytol in LCA suggests reduced blood flow, corresponding to lower shear stress along LCA wall. **D.** Depicts ultrasound of mouse blood flow velocity in RCA and LCA, demonstrating low shear and oscillation of blood in LCA in comparison to RCA.

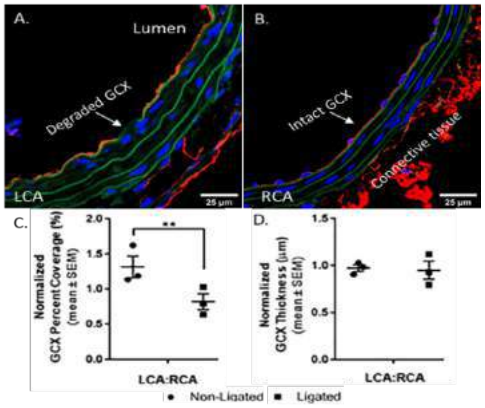

Fig. 4. Partial ligation surgery did cause GCX shedding after one week, in correlation to endothelial dysfunction. There was no change in GCX thickness.

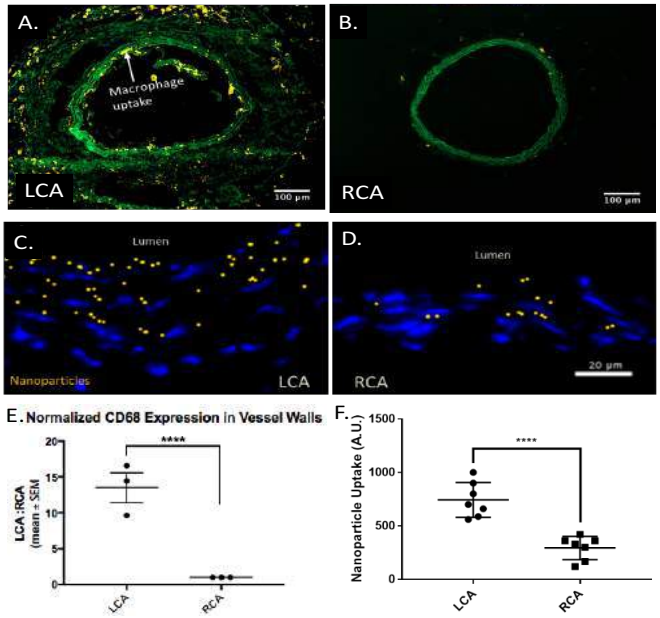

Fig. 5. Histology of mouse LCA and RCA. Elastin (green), Macrophage CD68 (A. & B. yellow), Cell nuclei (blue), and GNS (C. and D. yellow). Data indicates a higher infiltration of macrophages (A.) with a 14-fold increase (E.) and nanoparticles (C.) with a 4-fold increase (F.) in the LCA in comparison to the RCA (B. & D.) due to lower expression of GCX in LCA in comparison to RCA.

DISCUSSION

In summary, we successfully performed a partial LCA ligation to acutely disturbed blood flow in a mouse vessel and we observed subsequent blood vessel remodeling, particularly with respect to GCX, and endothelial dysfunction, both associated with atherosclerosis and cardiovascular disease. We also observed passive targeting of GNS to affected areas. The GCX is often neglected even though it acts as a first line of defense against atherosclerosis, demonstrating that targeting dysfunctional vessels based on GCX shedding offers an innovative approach in early cardiovascular disease therapy and prevention.

ACKNOWLEDGEMENTS

Funding: National Institutes of Health (KO1 HL125499) and National Science Foundation (DGE-0965843 and CMMI-1846962).

REFERENCES:

1. Mitra, R., et al., *Glycocalyx in Atherosclerosis-Relevant Endothelium Function and as a Therapeutic Target.* Curr Atheroscler Rep, 2017. **19**(12): p. 63.
2. Mitra, R., et al., *The comparative effects of high fat diet or disturbed blood flow on glycocalyx integrity and vascular inflammation.* Transl Med Commun, 2018. **3**.
3. Zeng, Y. and J.M. Tarbell, *The adaptive remodeling of endothelial glycocalyx in response to fluid shear stress.* PLoS One, 2014. **9**(1): p. e86249.
4. van den Berg, B.M., et al., *Atherogenic region and diet diminish glycocalyx dimension and increase intima-to-media ratios at murine carotid artery bifurcation.* Am J Physiol Heart Circ Physiol, 2006. **290**(2): p. H915-20.
5. Nam, D., et al., *Partial carotid ligation is a model of acutely induced disturbed flow, leading to rapid endothelial dysfunction and atherosclerosis.* Am J Physiol Heart Circ Physiol, 2009. **297**(4): p. H1535-43.

SB³C2021
Summer Biomechanics, Bioengineering and Biotransport Conference
June 14-18, Virtual

ALTERATIONS TO THE MATERNAL BONY PELVIS AND PELVIC FLOOR MUSCLE COMPLEX DURING PREGNANCY: A STATISTICAL SHAPE ANALYSIS

Megan R. Routzong (1), Liam C. Martin (1), Ghazaleh Rostaminia (2), Pamela A. Moalli (3), Steven D. Abramowitch (1)

(1) Department of Bioengineering
University of Pittsburgh
Pittsburgh, PA, USA

(2) Division of Urogynecology
University of Chicago
Skokie, IL, USA

(3) Department of Obstetrics, Gynecology & Reproductive Surgery
University of Pittsburgh
Pittsburgh, PA, USA

INTRODUCTION

During pregnancy, maternal pelvic organs and tissues undergo dramatic remodeling due to hormone-induced biochemical changes and the altered mechanical environment created by the growing fetus [1]. In the levator ani muscles, reduced active force and less shortening during contraction have been detected during pregnancy [2,3]. Meanwhile, the stiffnesses of pelvic connective tissues decrease, corresponding with pelvic organ descent and increased mobility [1,4,5]. These alterations purportedly prepare the maternal pelvic soft tissues for vaginal delivery as a mechanism to prevent stretch-related tissue injury [6].

Evidence suggests that this maternal remodeling and response to a changing mechanical environment alters the shape of the maternal pelvic floor and bony pelvis. Imaging studies have identified increased levator hiatal dimensions during pregnancy, while statistical shape modeling has identified midsagittal pelvic floor shape differences in late pregnancy [5,7]. With robust quantification, maternal pelvic shape could be used to determine the extent of remodeling undergone during pregnancy, which, in turn, could contribute to prediction models estimating risk for stretch-related injury during vaginal delivery.

The aim of this study was to quantify maternal bony pelvis and pelvic floor muscle complex shape variation in pregnancy and to determine relationships between shape and gestational age, maternal age, and parity (i.e. the number of times a woman has given birth). We hypothesized that in the levator plate and coccyx we would see inferior-posterior motion towards a more vertical orientation and straightening with increased gestational age, maternal age, and parity.

METHODS

This was a retrospective study approved by the Institutional Review Board at the University of Pittsburgh and considered exempt at Northshore University HealthSystem. Pregnant women age 20-49 who underwent pelvic MRI without contrast as instructed by their physician for medical indications at Magee-Womens Hospital or Northshore University HealthSystem between 2005 and 2018 were included.

The pelvic floor and bony pelvis were segmented. In this study, the pelvic floor muscle complex included the coccygeus, levator ani, anal sphincter complex, perineal body, and superficial perineal structures (including the bulbocavernosus and transverse perineal muscles and the perineal membrane) all segmented as a continuous structure (Figure 1). To reduce computational costs and improve point correspondence, the perineal membrane and other superficial tissues were segmented as one instead of leaving gaps in between individual structures. The bony pelvis included the coccyx, sacrum, and left and right innominate bones.

To smooth the segmentations and calculate corresponding points, a template pelvic floor and bony pelvis were generated and deformed onto the patient-specific segmentations. Because the coccyx bones are geometrically less complex, an ellipse was used as the template. Once corresponding points were determined, each patient's pelvic floor, bony pelvis, and coccyx were recombined into the correct positions. Then these combined bony pelvis-pelvic floor geometries were imported into Mathematica™ to carry out the remaining statistical shape modeling (SSM) workflow previously established by our lab [7]. This process involves a Procrustes analysis to align the shapes; a principal component (PC) analysis to identify modes of variation; and a parallel analysis to determine significant modes (i.e. those that explain more variance than noise). This results in PC scores—projections of patient-specific data onto eigenvectors—for each patient and significant mode which become the dependent variables in ensuing statistical analyses.

A multiple linear regression was performed to determine which modes were significant predictors of gestational age. Subsequently, t-tests and ANOVAs were used to evaluate potential shape differences associated with age (< 35 vs ≥ 35) and parity (0 vs 1 vs >1).

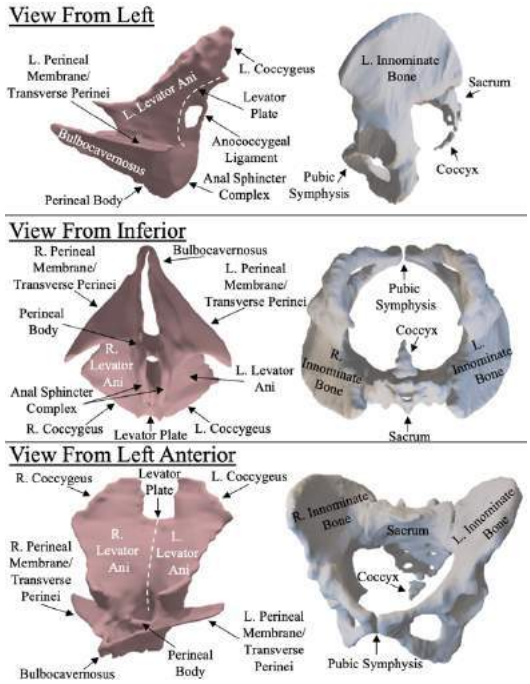

Figure 1: A pelvic floor muscle complex (left) and bony pelvis (right) from multiple views with relevant labels.

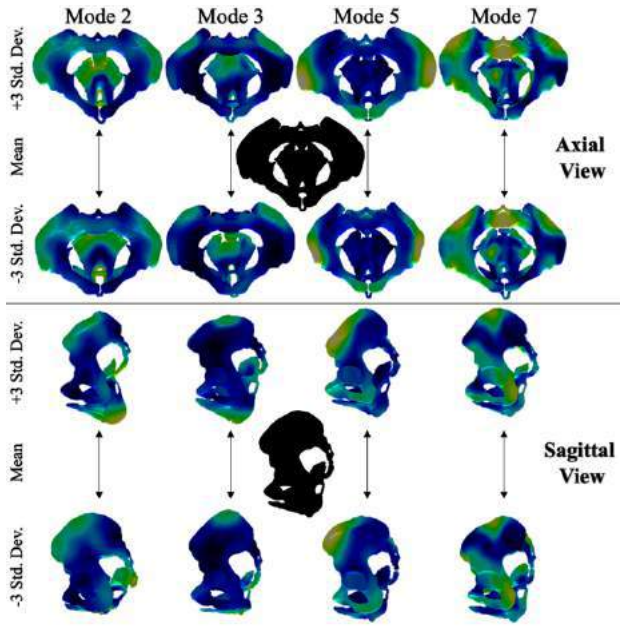

Figure 2: Visualization of relevant modes. Dark to light colors signify regions with minimal to maximal variation from the mean shape.

RESULTS

A total of 25 pregnant anatomies were included with gestational ages ranging from 5 to 36 weeks, maternal age from 21 to 41 years, and parity from 0 to 3. Three women were in the 1st trimester, 10 in the 2nd trimester, and 12 in the 3rd trimester of their pregnancy.

There were 7 significant modes of variation that explained 22%, 20%, 8.4%, 6.8%, 6.3%, 5.3%, and 4.3% of the total shape variance, respectively. Note that across all modes, only 4 PC scores were further than 2 standard deviations from the mean shape. The linear regression revealed that modes 2, 5, and 7 were significant predictors of gestational age (β=0.408, 0.345, and -0.453 and p=0.016, 0.038, and 0.008, respectively) with a model significance of 0.002. Qualitatively, mode 2 indicates perineal descent, levator plate straightening in a more vertical orientation, and coccyx straightening; mode 5 a more anterior pubic symphysis and flatter iliac crest; and mode 7 a more platypelloid shaped (proportionally wider) pelvis with increased gestational age (Figure 2).

Younger vs older shapes significantly differed for mode 2 (p=0.001), with older shapes corresponding with more positive mode 2 PC scores as also seen with increased gestational age. Shapes of varying parity significantly differed across mode 3 (p=0.040), with those with a parity of 1 demonstrating shorter superior-inferior pelvic floor muscle complex length (more negative mode 3 PC scores).

DISCUSSION

These results indicate that pregnancy, age, and parity significantly influence specific aspects of maternal bony pelvis and pelvic floor muscle complex shape. The hypothesized levator plate and coccyx straightening and more vertical levator plate were observed, though a more vertically oriented coccyx was not directly associated with gestational age. This supports the idea that in pregnancy the maternal pelvis remodels to generate shape alterations that would reduce the amount of stretch experienced by pelvic soft tissues during delivery, thereby preventing acute, childbirth-related injuries. Additionally, mode 2 suggests that some of the shape changes observed during pregnancy may also be observed with age.

The findings agree with previous studies that evaluated pregnancy-related changes to the levator plate and perineal body in 2D but build upon these studies with the creation of objective, continuous definitions of bony pelvic and pelvic floor shape variation [4,7]. SSM delivers robust shape quantification while providing shapes that can be used as geometric inputs for finite element models. This will improve computational simulations of, in this case, vaginal delivery, which are currently limited by the frequent use of single, patient-specific anatomy from non-pregnant women. The modes of variation from this study will allow for the generation of anatomies representative of a population of pregnant women to create more generalizable simulation results.

This study was limited by the small number of subjects in subgroups of interest, making it hard to isolate certain relationships—such as those of young, nulliparous women during their first pregnancy specifically. Due to its retrospective design, we only had images at a single time point for each woman. Future steps will include collecting prospective data in order to evaluate women multiple times within a single pregnancy and to correlate shape with delivery outcomes.

ACKNOWLEDGEMENTS

We acknowledge use of the University of Pittsburgh Center for Research Computing advanced computing resources. This material is based upon work supported by the NSF GRFP under Grant #1747452.

REFERENCES

[1] Alperin, M, Impact of Pregnancy and Delivery on Pelvic Floor Biomechanics. In *Biomechanics of the Female Pelvic Floor*, 229-238, 2016.
[2] Davidson, MJ et al., *Int Urogynecol J,* 31:2345-2351, 2020.
[3] Siafarikas, F et al., *BJOG An Int J Obstet Gynaecol,* 122:1083-1091, 2015.
[4] Van Geelen, H et al., *Int Urogynecol J,* 29:327-338, 2018.
[5] Shek, KL et al., *Int Urogynecol J,* 23:1561-1567, 2012.
[6] Catanzarite, T et al., *Am J Obstet Gynecol,* 218:512.e1-512.e9, 2018.
[7] Routzong, MR et al., *Comput Methods Programs Biomed,* 194, 2020.

MECHANOTHERAPEUTICS COMBINED WITH CYTOTOXIC NANOMEDICINE OVERCOMES VESSEL COMPRESSION AND RESISTANCE TO IMMUNOTHERAPY IN TRIPLE NEGATIVE BREAST CANCER

Myrofora Panagi[1], Fotios Mpekris[1], Chrysovalantis Voutouri[1], John D. Martin[2], Kazunori Kataoka[3], Horacio Cabral[2] and Triantafyllos Stylianopoulos[1]

(1) Cancer Biophysics Laboratory, Department of Mechanical Engineering, University of Cyprus, Cyprus

(2) Department of Bioengineering, Graduate School of Engineering, The University of Tokyo, Japan

(3) Innovation Center of NanoMedicine, Kawasaki Institute of Industrial Promotion, Japan

INTRODUCTION

Recent advances in cancer nanomedicine have led to the development of several new systemically administered nanoparticles to treat various tumor types. However, the efficacy of those nanomedicines to highly desmoplastic tumors such as breast is hindered by abnormalities in the structure of the tumor vasculature, which can reduce drastically tumor perfusion and subsequently drug delivery. To overcome these obstacles, two strategies, which have been traditionally used separately, are applied in the clinic: vascular normalization and normalization of the tumor stroma [1]. The former involves the judicious use of anti-angiogenic agents to target vessel permeability, while the second is based on the use of mechanotherapeutic drugs exerting anti-fibrotic properties to alleviate intratumoral mechanical forces and thus, decompress tumor blood vessels and improve perfusion [2–4]. The scope of this study is to explore the potential of the anti-fibrotic drug tranilast to act as mechanotherapeutic and improve antitumor efficacy of the nanomedicine Doxil and immunotherapy in murine breast tumors.

METHODS

Animal tumor models. 4T1 and E0771 tumor models were generated by orthotopic implantation of either 5×10^4 4T1 or E0771 mouse breast cancer cells in serum-free medium into the mammary fat pad of BALB/c and C57BL/6 female mice, respectively. Animals were treated with saline (Control), tranilast (200mg/kg, daily, orally), Doxil (3mg/kg, intravenously, once a week) and tranilast-Doxil. Immunotherapy was intraperitoneally applied as a cocktail of 5mg/kg cytotoxic T lymphocyte-associated protein 4 (anti-CTLA-4) and 10mg/kg programmed cell death 1 (anti-PD1).

Immunohistochemical assessment of TME. Vascular perfusion and functionality: Prior to primary tumor removal, animals were anesthetized and intracardially injected with biotinylated lycopersicon esculentum lectin (4mg/kg). Harvested tumors were fixed, sectioned and immunostained accordingly. Blood vessel number was measured from the positive staining of the endothelial marker CD31 while the area fraction of perfused vessels was determined as the ratio of lectin and CD31 overlapping staining to CD31 positive staining. Pericyte coverage of perfused vessels was determined by the co-localization of CD31 and lectin with the pericyte marker, αSMA. Hypoxia: Mice bearing E0771 tumors were injected with pimonidazole HCl (60mg/kg) 2hr prior to tumor removal. ECM content: Fixed tissue cryosections were incubated with anti-collagen I and anti-hyaluronan antibodies. Fluorescence signal was quantified using an in-house MATLAB code.

Biomechanical analysis. Interstitial fluid pressure was measured *in vivo* using the wick-in-needle method just before tumor harvesting. Characterization of the mechanical properties and calculation of the elastic modulus were determined using an unconfined compression experimental protocol.

RESULTS

Re-purposing of tranilast as a mechanotherapeutic agent enhances antitumor efficacy of Doxil by producing a more than 3-fold increase in tumor doubling time, while tranilast or Doxil monotherapies do not have any impact on the growth of either syngeneic mammary tumor model, 4T1 or E0771 (Figure 1A, B). Consistent with this pertinent delay in tumor growth was the prolonged survival of animals treated with tranilast-Doxil combination. Tranilast alone had no effect on animal survival, whereas Doxil monotherapy produced a modest effect (Figure 1C).

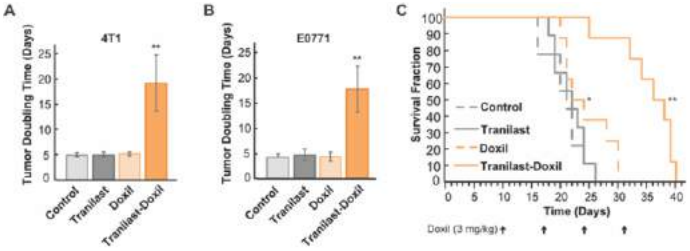

Figure 1. Tranilast potentiates anti-tumor efficacy of Doxil nanomedicine. Quantification of tumor growth rate, based on the time to reach double the initial volume, for 4T1 (A) and E0771 (B) tumors. (C) Kaplan-Meier survival curves for E0771 tumors treated as indicated.

As tranilast has been previously found to modulate TME by altering the expression of the two abundantly found extracellular matrix components (ECM), collagen and hyaluronan, we sought to examine whether its combination with cytotoxic nanomedicine may yield to a more efficient normalization phenotype. To address this question, we performed immunofluorescence staining and found that Doxil potentiates tranilast's effects in terms of ECM remodeling resulting to a further reduction in collagen and hyaluronan levels (Figure 2A-C).

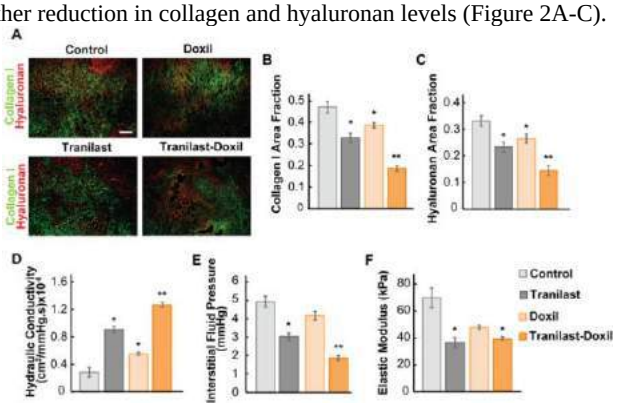

Figure 2. Nanomedicine promotes tranilast-mediated normalization effects. (A-C) Fluorescence images and quantification of collagen I (green) and hyaluronan (red) of 4T1 tumors. (D) Hydraulic conductivity, (E) interstitial fluid pressure and (F) elastic modulus measurements.

To further explore the additive effects of cytotoxic nanomedicine in reducing the mechanical forces and stiffness, we assessed tumor hydraulic conductivity, interstitial fluid pressure (IFP) and elastic modulus. Both tranilast and Doxil increased tumor hydraulic conductivity, while the most prominent effect (6-fold increase) was observed following their combination, in both 4T1 and E0771 tumors (Figure 2D). Tranilast-Doxil also produced a 2-fold decrease in IFP (Figure 2E) and tumor elastic modulus similarly to tranilast (Figure 2F).

Since ECM constituents develop reciprocal interactions with tumor blood vessels, we next investigated the impact of the combinatorial treatment on vascular perfusion. We found that the percentage of perfused vessels was increased by 66% after tranilast-Doxil co-administration compared to control (Figure 3A,B). This improvement in vascular functionality is explained by an analogous increase in vessel diameter and pericyte coverage (Figure 3D). Normalization of the tumor vasculature also improved tissue oxygenation as indicated by the reduction in hypoxic fractions (Figure 3C).

Moreover, we studied the antitumor effects of normalization combined with the immune checkpoint blockers (ICB) cocktail consisting of a mixture of anti-CTLA-4 and anti-PD1 to treat 4T1 and E0771 tumors.

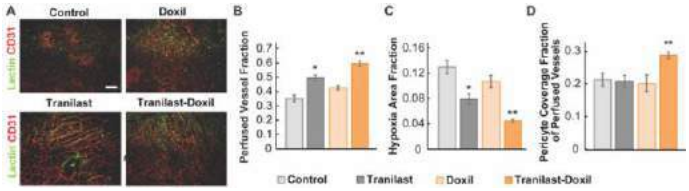

Figure 3. Enhanced tumor normalization by tranilast-Doxil improves vascular functionality, perfusion and oxygenation. (A) Fluorescence images of 4T1 sections stained for lectin (green) and CD31 (red). (B) Quantification of CD31 and lectin co-expression indicating vascular perfusion. (C) Quantification hypoxic fraction in E0771 tumors and pericyte coverage of perfused vessels (D).

We first employed an overall survival study and found that animals receiving the tranilast-Doxil-ICB combination displayed a significant survival benefit compared to all other groups for both tumor models (Figure 4A). To investigate the mechanism of the improved therapeutic outcome of the triple therapy, we repeated the experiment in 4T1 tumors and excised the lungs 10 days after resection of primary tumors. Our findings indicate a significant decrease in the macrometastases following tranilast-Doxil-immunotherapy treatment (Figure 4B).

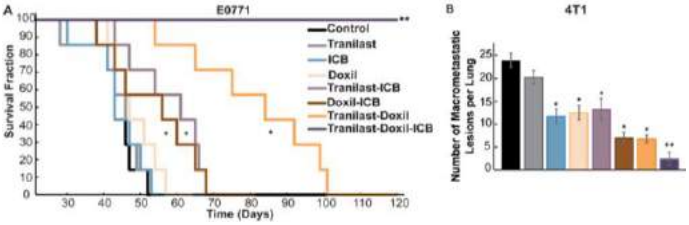

Figure 4. Tranilast increases the efficacy of nano-immunotherapy by prolonging survival (A) and reducing metastasis formation (B).

DISCUSSION

Our findings suggest that tranilast enhances drug efficacy in both primary and metastasis site and acts with Doxil to further reduce ECM and alleviate tumor mechanical stresses. Stress alleviation promotes tumor vessel decompression and functionality leading to improved perfusion. Subsequently, the increased tumor oxygenation potentiates immune stimulation and therapeutic outcome of immunotherapy extending animals survival and inhibiting metastasis. Our results demonstrate the potential of mechanotherapeutic agents to improve the efficacy of standard-of-care cancer therapies.

ACKNOWLEDGEMENTS

European Research Council Grants: StG-336839, PoC-838414, CoG-863955 and the INFRASTRUCTURE/1216/0052 grant co-financed by the European Regional Development Fund and the Research Promotion Foundation of Cyprus (to T.S.) and partially supported by Grants-in-Aid for Scientific Research B (JP16H03179; Research Promotion Foundation of Cyprus, New Strategic Infrastructure Units – Young Scientists, (CancerNanoMED): Center for Preclinical Evaluation and Optimization of Cancer Nanomedicines.

REFERENCES

[1] Stylianopoulos, T et al., *PNAS*, 110:18632–7, 2013.
[2] Chauhan, VP et al., *Nat Commun*, 4:1–11, 2013.
[3] Papageorgis, P et al., *Sci. Rep*, 7:46140, 2017.
[4] Polydorou, C et al., *Oncotarget*, 8:24506, 2017.

SB³C2021
Summer Biomechanics, Bioengineering and Biotransport Conference
June 14-18, Virtual

A CONTINUUM MECHANICS APPROACH TO MODEL STIFFNESS SENSING BY SMOOTH MUSCLE CELLS

A. Karkhaneh Yousefi (1), C. Petit (1), S. Avril (1)

(1) Mines Saint-Etienne, Université de Lyon
INSERM, U 1059 SAINBIOSE
F - 42023 Saint-Etienne France

INTRODUCTION

Aortic Smooth Muscle Cells (SMCs) play a vital role in maintaining homeostasis in the aorta by sensing and responding to mechanical stimuli. In the healthy aorta, SMCs are essential for the regulation of the wall stiffness as they can maintain mechanical homeostasis through variations of their active tone [1, 2]. Therefore, missensing of mechanical stimuli by SMCs can alter the maintenance of mechanical homeostasis and induce impaired adaptations that are responsible for the progression of the aortic aneurysm [3]. However, the mechanisms that underlie the ability of SMCs to sense and respond to stiffness change are still partially unclear.

Recent studies have highlighted the significant role of contractile acto-myosin units in the cytoskeleton that can act as stiffness sensors [4]. In the present study, we investigate stiffness sensing through the contractile acto-myosin units. We develop a new computational model based on the principles of thermal strains for the contractile behavior of SMCs that can account for the variations of cellular Traction Forces (TFs) with the surrounding stiffness [5]. To account for the inherent variability of cellular responses, large populations of SMCs are modeled with the Finite Element (FE) method, each cell having a random number and a random arrangement of Stress Fibers (SFs) as they are the main contributor to the force-generating capacity inside a cell.

METHODS

We assume that SFs uniformly shorten after myosin activation. As SMCs are attached to the substrate at focal adhesions, shortening results in a deformation of the substrate. If the substrate is sufficiently compliant, the deformation is large and SFs only withstand a small tensile force, but if the substrate is rigid, the deformation becomes negligible and SFs have to withstand large tensile forces. Therefore, TFs tend to increase with the substrate stiffness, which is consistent with recent Traction Force Microscopy (TFM) results [5]. However, for too stiff substrates, TFs can potentially reach a certain elastic limit, which corresponds to sliding between actin and myosin filaments [6].

To model shortening of SFs induced by myosin activation, we introduced an eigenstrain, denoted $\alpha\Delta T$, analogously to a thermal contraction: α is the contraction coefficient and ΔT represents the level of myosin activation, satisfying $0 \leq \Delta T \leq 1$, in which $\Delta T = 1$ corresponds to the maximal activation and $\Delta T = 0$ to no activation. Let us consider a SMC on the surface of a substrate. After some myosin activation $\Delta T > 0$, the actual shortening of SFs satisfies $\epsilon_a < \alpha\Delta T$ as they are adherent to the substrate. Therefore, we assumed that SFs have a stress-strain response that is composed of two parts (Figure 1):

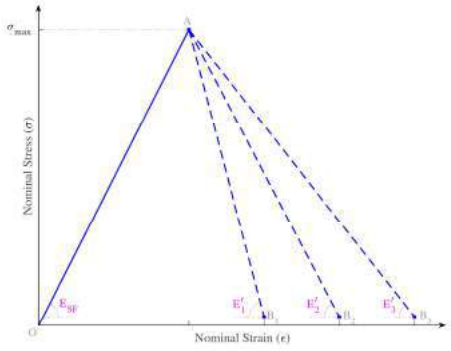

Figure 1: Schematic stress-strain behavior of a SF.

$$\sigma = E_{SF}(\alpha\Delta T - \epsilon_a), \qquad \epsilon \leq \epsilon_{max} \qquad (1)$$

$$\sigma = \sigma_{max} + E'_{SF}(\epsilon - \epsilon_{max}), \qquad \epsilon > \epsilon_{max} \qquad (2)$$

in which E_{SF} is the Young's modulus and E'_{SF} is the softening coefficient. It was also assumed that the strain threshold satisfies: $\epsilon_{max} = \xi\alpha\Delta T$, where $0 < \xi < 1$. For the FE modeling, we assumed that the stiffness of a SF was a constant, with $E_{SF} = 50$ MPa and the cross-section being circular with a diameter 0.2 µm [7]. The model parameters α, ΔT, ξ, and E'_{SF} need to be determined by experimental data.

Aortic SMCs usually exhibit a spindle shape with focal adhesions at both ends. In our model, we consider a semi-spindle of dimensions 250 x30 µm^2 which corresponds to the average size of SMCs [5]. The model includes the cell membrane, cytoplasm, nuclear envelope, and nucleus. We assumed that the cytoplasm of SMC includes a random number of SFs (mean = 25, standard deviation = 6.05). At least half of the SFs were connected to focal adhesions on both sides, the others being connected to the nuclear envelope at one end.

This single SMC and the underlying substrate (0.4x5x5 mm^3) were meshed and computed with the Abaqus software. A tie constraint was assigned between the cell membrane and the substrate surface at the focal adhesion (surface of 148.84 µm²). We assumed that the sum of reaction forces at a focal adhesion area was a prediction of the TFs measured in the TFM. The cell membrane and the nuclear envelope were modeled as neo-Hookean materials with a shear modulus of 600 kPa [8]. The same behavior was also assumed for both the cytoplasm and the nucleus with a shear modulus of 100 Pa. Equivalent Poisson's ratios of 0.45 and 0.49 were assigned to the substrate and to all the cell components, respectively.

RESULTS

To identify the model parameters, we confronted its predictions with the TFM results of SMCs on the surface of substrates with different elastic modulus 4, 8, 12, and 25 kPa [5]. By fitting an exponential probability distribution function to the experimentally measured TFs, we estimated the average activation level $\Delta T = 0.132$. Then, 300 cells were generated for FE simulation. Each cell had a random arrangement, a variable number of SFs, and an exponential distribution of the activation level. By fitting the FE results to experimental data, we obtained $\alpha = 0.034$, $\xi = 0.68$, and $E'_{SF} = -19.9$ MPa.

In Figure 2a, we show the strain field around the focal adhesions on the surface of the substrate simulated for one of the randomly generated SMC with the FE model, using 25 SFs, in which 13 of them connect one focal adhesion to the other one. The predicted force was $TF = 15.9$ nN for the 12 kPa stiffness substrate. Figure 2b also shows the experimentally measured strain field on the surface of the same substrate for a SMC. The strain field patterns in both figures are similar.

In Figure 3, we compare the measured TFs with the average values among 300 random SMC predicted by the numerical model. It can be observed that the identified model with the softening behavior is in very good agreement with the experimental results, whereas the absence of softening in the material model misses reproducing precisely the stiffness sensitivity for substrates of large stiffness.

DISCUSSION

In the current study, we have developed the first continuum mechanics model of SMCs accounting for stiffness sensing through the contractile acto-myosin units. Model predictions were in very good agreement with cellular tractions measured on different substrates. One of the most important aspects of the proposed model is to account for the intercellular variability of acto-myosin contractility. The variability is modeled through a random arrangement of SFs, a variable number of SFs, and an exponential distribution of activation levels.

The predictability of the model combined to its relative simplicity are promising assets for further investigation of stiffness sensing in 3D environments. Eventually, this could contribute to decipher the effects of mechanosensitivity impairment, which are known to be at the root of aortic aneurysms. In addition, our future studies will be extended to investigate changes in the load applied to the nucleus in different environments as it can affect gene expression [9].

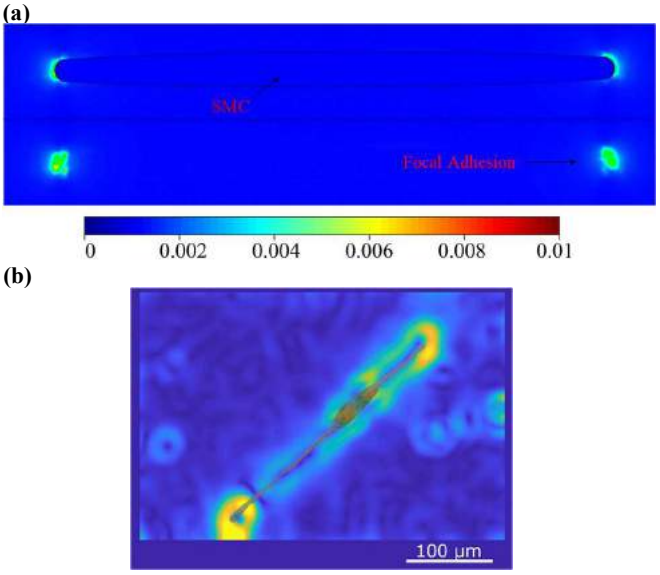

Figure 2: Predicted (a) and experimental (b) strain fields

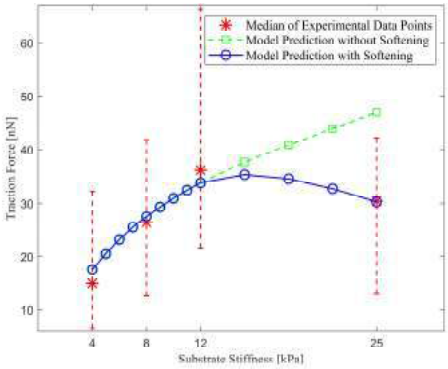

Figure 3: Model prediction of traction forces

ACKNOWLEDGEMENTS

The authors are grateful to the ERC for financial support through ERC-2014-CoG BIOLOCHANICS grant.

REFERENCES

[1] Humphrey, J, *Cardiovascular solid mechanics: cells, tissues, and organs*, 2013.

[2] Mao, N et al., *Interactive cardiovascular and thoracic surgery,* 21.1: 62-70, 2015.

[3] Locally, P et al., *Cardiovascular research,* 114.4: 513-528, 2018.

[4] Elosegui, A et al., *Trends in cell biology,* 28.5: 356-367, 2018.

[5] Petit, C et al., *Molecular and Cellular Biomechanics,* 2019.

[6] Chan, E et al., *Science,* 322.5908: 1687-1691, 2008.

[7] Gouget, LM et al., *Biomechanics and modeling in mechanobiology,* 15.2: 331-344, 2016.

[8] Sleep, J et al., *Biophysical journal,* 77.6: 3085-309, 1999.

[9] Wang, N et al., *Nature reviews Molecular cell biology,* 10.1: 75-82, 2009.

SB³C2021
Summer Biomechanics, Bioengineering and Biotransport Conference
June 14-18, Virtual

HETEROGENEOUS BLOOD PERFUSION MAPPING IN CANCEROUS LESIONS

Manpreet Singh

Department of Mechanical Engineering,
University of Maryland Baltimore County,
Baltimore, MD, USA

INTRODUCTION

Perfusion mediated heat-sink impede the treatment efficacy of cancer treatments. The heat-sink effect is detrimental to thermally-driven ablation therapies as it induce cooling with its functional blood supplying vessels which carries away heat via thermal convection mode of heat transfer. It has profound implications within zones of conductive heat transfer while designing an effective cancer treatment protocols for thermal ablation therapies. With the recent advancements in medical imaging and computational resources, patient- or tumour specific extraction of heterogeneous perfusion is feasible. Dynamic contrast-enhanced sequences-Magnetic Resonance Imaging[1] (DCE-MRI) and Doppler ultrasound demonstrates such extraction of heterogeneous blood perfusion rates in human malignancies which varies very widely i.e. in the range of 5-15 mL per 100 g per min. Furthermore, tumours exhibit dead necrotic core region having zero perfusion, and intermediate and peripheral blood flow regions which may have low, moderate or high perfusion depending on shape, size and the growing stage of tumour.

Due to the large density variations of soft healthy tissues than diseased tissues, the tumour appears with brighter voxels in MRI slices after contrast injections. For the breast tumour reported discussions, only homogeneous blood perfusion (isotropic) is considered to perform any kind of computational simulation. As per our understanding, there is no reported work in context of breast cancer that has considered the heterogeneous blood perfusion (anisotropic) on spatial co-ordinates of the computational domain to compute results for clinical relevance.

METHODS

Clinical breast MRI examination was performed at Post Graduate Institute of Medical Education and Research, Chandigarh, India with Siemens MAGNETOM Aera at magnetic field of 1.5T using a standard and consistent clinical breast MRI protocol. MRI uses magnetic fields instead of x-rays to produce very detailed, cross-sectional images of the body. One Woman was imaged in the prone position using a dedicated multichannel surface array breast coil. After the native scan was obtained, DCE were acquired in axial plane employing 3D T1-weighed fast gradient echo-based DCE series with one pre and three post-gadolinium contrast-enhanced sequences. Gadodiamide (Omniscan GE Healthcare) at a dose of 0.01 mmol/kg was injected manually. Technical parameters employed were Plane: axial, multichannel (8 channel) breast coil, 3-D mode, SPIR fat suppression, parallel imaging factor 1.5 R/L, TR-5.6 ms, TE-3 ms, slice thickness of 1 mm and a flip angle of 10 degrees. MRI exams for breast imaging use a contrast material (usually gadolinium-DTPA) that was injected into a vein in the arm before or during the exam to improve the ability to capture detailed images of breast tissue.

MRI Dicom data has information about both breasts including other organs such as lungs but only breast tumour specific information is extracted as part of this analysis. Therefore, available Dicom images (.dcm format) are first converted into (.tiff format) with IrfanView 64 software in order to successfully import into NRecon®; Reconstruction software package provided by Microphotonics to select the region of interest i.e. left breast only. We have used NRecon software to remove all other information except region of interest i.e. breast tumour tissue located in fibro-glandular tissue compartment. All necessary information like slice thickness for MRI scan were noted through MIMICS v. 19.0. The resultant reconstructed images were greyscale images where the pixel intensities are between 0-255 where 0 being black and 255 being white. All the voxels represents the coordinates for the generated mesh through 3-matic software. A Matlab® (Natick, MA)

code is written to convert all 108 reconstructed images into similar number of text files (.txt format) which contains information about the co-ordinates of breast tumour anatomy. The brighter pixels from individual slices represents some values against co-ordinates which we have used to identify the tumour irregular boundaries as extracted through MIMICS software 19.0. These co-ordinates will be mapped with the Comsol-multiphysics 5.2 co-ordinates of the three-dimensional geometry of tumour. Thereafter, all text files generated through Matlab will now be merged into single Excel file (.csv format) through software SAS® (SAS Institute, Cary, NC) which is widely used for data analysis and statistics. This large excel file is successfully used to define heterogeneous tissue blood perfusion on mesh co-ordinates. Volumetric linear interpolation function and constant extrapolation is used between elements to achieve smooth distribution without incurring singularities while loading the .txt file/spreadsheet for blood perfusion.

The present computation uses image-based mesh generation and interpolation features of Comsol Multiphysics 5.2 to define blood perfusion based on nearest neighbor method and then using these interpolation functions to define blood perfusion as a function of mesh coordinates. The nearest neighbor of tumour (subpart node T) node corresponds to the node *i* in the breast (object) mesh having the minimum Euclidean distance (ED) to the tumour node via eq. 1 as:

$$ED = \sqrt{(x_{nodeT} - x_i)^2 + (y_{nodeT} - y_i)^2 + (z_{nodeT} - z_i)^2} \quad (1)$$

where *x, y, z* represents the nodal coordinates. It is ensured that tumour offers a higher level of refinement compared with the mesh for the breast anatomy as a single unit.

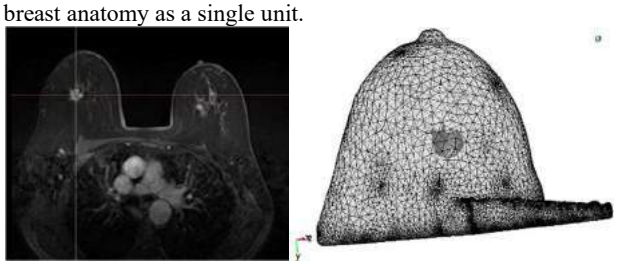

(a) (b)

Figure 1: DCE-MRI slice of breast cancerous lesion in axial plane and extraction of three-dimensional breast anatomy[2].

RESULTS

Fig. 1 illustrates one slice from a set of 108 images of DCE-MRI acquisition. Three-dimensional model of female breast is generated using imaging segmentation tools. It is ensured that each individual pixel location must be mapped through mesh coordinates to visualize the pronounced heterogeneity. One experimental study[3] based on positron emission tomography reports the values of mean blood flow of tumour as 29.8±17.2 (SE) ml/dl/min in comparison to healthy breast tissue blood flow of 1.4 ml/dl/min. Thus, the perfusion metrics shown in fig. 2 for a breast malignancy shown in present scenario is in agreement and typically follows similar order of magnitude[4] i.e. 5.3×10^{-3} to 5.3×10^{-2} m^3s^{-1} m^{-3} as reported and used in estimation of temperature fields through priori-simulations[2]. It is to note that the experimental and histological studies on breast tumours suggests existence of a delicate vasculature than normal surrounding tissue, thus one would suspect to have lower prevailing perfusion micro-environment but the findings from in-vitro and in-vivo studies reveals counterintuitive higher mean blood flow. Such an inference is an indicative reflection of increased metabolic demand by the tumour.

DISCUSSION

The present study is expected to unveil a deeper understanding on inclusion of heterogeneous perfusion source maps in computation of temperature fields during thermal ablation treatments. We have presented means to generate anistropic perfusion maps which were simply ignored over homogeneous perfusion assumptions and thus, may results in the suboptimal treatment efficacy of breast cancer treatments. Our present study reveals the need of inclusion of such heterogeneities into computational experiments to understand the thermal variations within tumour parenchyma. The computational approach we propose here will open new avenues to further develop the therapeutic strategies that specifically target cancerous lesion. This can successfully be deployed with unprecedented accuracy in clinics to better understand the physics behind in-vivo results, rather than simply relying on purely experience driven repetitive clinical trials. It is still the choice of the medical practioner/physicist which computational model to use and usually such selection is restricted based on purpose, and available imaging details. We believe that the extracted blood perfusion rate would be useful to improve accuracy of theoretical simulation, especially when the simulations are used to design heating treatment protocols. Future work should extend our computational framework to patient-specific complex irregular tumour anatomies in the near vicinity of blood vessels.

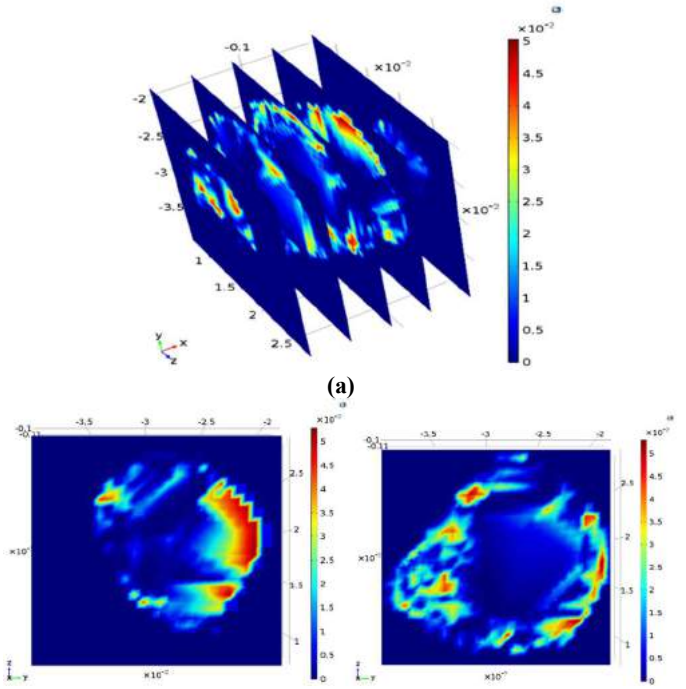

(a)

(b) (c)

Figure 2: Three-dimensional spatial perfusion heterogeneity for a breast tumour in Sagittal Plane (Y-Z plane) with the clear illustration of presence of necrotic core. It possess regions of no perfusion, low perfusion, moderate perfusion, high perfusion respectively. Spatial coordinates can be mapped with eucledian distance approach.

ACKNOWLEDGEMENTS

Manpreet Singh is appreciative of the Graduate School, University of Maryland, Baltimore County for conferring the award of Dissertation Fellowship towards the progress of Doctorate degree.

REFERENCES

[1] Wust, P et al., *Lancet Oncol.*, 3:487-497, 2002.
[2] Singh, M et al., *Comp. Meth. & Prog. in Biomed.*, 198:105781, 2021.
[3] Wilson, H et al., *Cancer Research,* 52:1592-1597, 1992.
[4] Vaupel, P et al., Pathophysiol. of solid tumour, *Springer* 51-92, 2009

SB³C2021
Summer Biomechanics, Bioengineering and Biotransport Conference
June 14-18, Virtual

EXPERIMENTAL FRAMEWORK FOR MRI-BASED MEASUREMENT OF MYOCARDIAL STIFFNESS IN 3D PRINTED HEART PHANTOMS

Fikunwa O. Kolawole (1,2,3), Tyler E. Cork (1,2,4), Michael Loecher (1,2), Seraina A. Dual (1,2,3), Marc E. Levenston (1,3), and Daniel B. Ennis (1,2)

(1) Department of Radiology
Stanford University
Stanford, CA, USA

(2) Division of Radiology
Veterans Administration Health Care System
Palo Alto, CA, USA

(3) Mechanical Engineering
Stanford University
Stanford, CA, USA

(4) Bioengineering
Stanford University
Stanford, CA, USA

INTRODUCTION

A significant consequence of ventricular remodeling, which contributes to both decreased cardiac function and heart failure (HF), is increased passive (diastolic) myocardial stiffness [1]. However, there exists no accepted clinical method to measure changes in myocardial stiffness. Myocardial stiffness can be measured by *ex vivo* mechanical testing which is not feasible for clinical applications. Passive myocardial stiffness can also be inferred from the left ventricle (LV) end diastolic pressure-volume (*P-V*). However, *P-V* relationships inherently depend on ventricular geometry and boundary conditions. Hence, this method does not extract intrinsic myocardial stiffness.

Constitutive modeling is one method of obtaining *in vivo* myocardial stiffness. Constitutive models provide stress-strain relations that describe the material's response to different loading conditions, and the model parameters define the material stiffness. Hence, the material stiffness can be deduced from measured deformation and loading conditions. Cardiac magnetic resonance imaging (MRI) combined with measured loading pressures and a finite element modeling (FEM) framework has been used to obtain patient-specific myocardial stiffness [2]. However, quantifying the accuracy and precision of these MRI and FEM-based stiffness estimation techniques is understudied due to the challenge of obtaining ground-truth measures of *in vivo* myocardial stiffness. Validation of these methods necessitates the development of a highly controlled *in vitro* stiffness estimation framework that incorporates a ventricular phantom of known stiffness properties.

The aims of this study were: (1) to develop 3D-printed heart phantoms with myocardium-mimicking materials of known mechanical and MRI properties; and (2) to demonstrate the feasibility of an MRI compatible *in vitro* diastolic filling setup for estimating phantom ventricular mechanics and stiffness.

METHODS

Tissue-Mimicking Material Selection: Uniaxial tensile testing samples of Silicone elastomer (Sylgard) were developed and mechanically characterized according to the ASTM D412 standard [3] using an Instron 5848 Microtester (100N load cell). MRI relaxation properties were measured using T1-mapping (MOLLI 5-3-3, spatial resolution $1.00\times1.00\times5.0\text{mm}^3$) and T2-mapping (T2-prep FLASH; flip angle 12º; spatial resolution, $1.00\times1.00\times5.0\text{mm}^3$).

Heart Phantom Development: High-resolution images from a healthy *ex vivo* porcine heart (geometrically restored to its *in vivo* mid-diastasis geometry) [4] were used to generate a 3D geometric mesh model of the heart. The geometric model was modified (Fusion 360, Autodesk) to incorporate ventricular ports and an apical anchor. The LV and right ventricular (RV) blood pools were segmented and converted into sterolithography (STL) files, then 3D printed (Ultimaker 3 Extended) with water-soluble polyvinyl acid (PVA). An STL negative for casting was created from the whole heart segmentation, then 3D printed using polylactic acid (PLA). A heart phantom was then cast using a blend of 20% Sylgard 184 and 80% Sylgard 527.

Inflation Flow Loop: The final model was embedded within a flow loop (Figure 1) controlled by a programmable MRI-compatible linear motion stage (MR-1A-XRV2, Vital Biomedical Technologies). The loop was designed to reproduce *in vivo* diastolic LV filling. MRI-compatible pressure transducers (Micro-Tip SPR 350S, Millar) in the ventricular cavities enable acquisition of filling pressures.

Imaging Methods: All *in vitro* images were acquired on a 3T (Skyra, Siemens). First, a static reference imaging volume of the entire phantom was acquired (3D SPGR; TE/TR = 2.17/5.5ms; FA = 20º; isotropic 1.00mm^3), then a cardiac-like late-diastolic filling cycle (sinusoidal flow: 13 mL/cycle mean, 1s period) was induced. Phantom motion was imaged with an externally triggered cardiac tagging

sequence (TE/Tres=3.1/53.0ms; FA=10º; spatial resolution, 1.0×1.0×8.0mm^3; 17 phases per cardiac cycle, 5mm grid tags) with slices spanning the whole phantom.

Geometric Accuracy: Phantom geometric accuracy was assessed qualitatively using landmark-based rigid registration of *in vivo* MR images (bSSFP; TE/TRes=1.6/17.9ms; flip angle, 38º; spatial resolution, 1.2×1.2×8.0mm3; mid-diastasis cardiac phase) to *in vitro* 3D SPGR images at their native voxel resolution (MITK, German Cancer Research Center). Landmarks used for registration consisted of four points in the most basal slice (septal wall center, anterior papillary muscle, free wall center, posterior papillary muscle) and four similar points at a slice near the apex.

Quantitative Strain Analysis: Tag lines were tracked with a neural-net based algorithm, which produced displacement curves for tag line intersections [5]. Circumferential strain (Ecc) was calculated from displacements with a radial basis function interpolant [6].

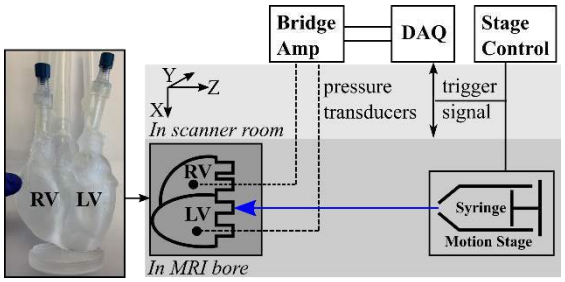

Figure 1: MRI compatible experimental setup

RESULTS

Mechanical and MRI properties of Sylgard blends are reported in Figure 2 and Table 1. Reference values for healthy myocardium are shown. Blends with 10% and 20% Sylgard184 exhibit comparable mechanical and MRI properties to myocardium. The 20% Sylgard184 blend was chosen as heart phantom material for easier workability.

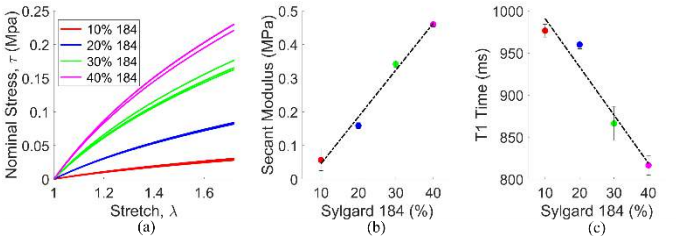

Figure 2: (a) Stress-Stretch curves for Sylgard 184 and 527 blends (b) Secant modulus at stretch of 1.05 (c) T1 relaxation time

Table 1: Sylgard material properties (chosen blend highlighted). Reference values for Myocardium shown in last row

Sylgard 184	Sylgard 527	Secant Modulus (MPa)	T1 time	T2 time
10 %	90 %	0.057±0.032	976.5±7.7	434.8±18.0
20 %	80 %	0.159±0.009	959.9±5.0	313.8±12.3
30 %	70 %	0.342±0.010	866.2±20.3	232.7±10.7
40 %	60 %	0.460±0.007	816.5±11.5	214.7±14.1
Myocardium		0.06 to 0.412 [7]	1158.7 [8]	45.1 [8]

Heart phantom development procedure adequately reproduces the *in vivo* and *ex vivo* geometry as shown by the comparison of registered *in vitro* (phantom), *in vivo* and *ex vivo* (porcine) images (Figure 3).

Tagged image acquisition and analysis demonstrate the feasibility of obtaining quantitative strain measures during late diastolic inflation. Recorded pressures were sinusoidal (peak 28mmHg; mean 14 mmHg) (Figure 4). Strain also followed a sinusoidal pattern (like the filling flow pattern) with peak global LV E_{cc} of 0.0076 (Figure 5) and 1.05mm of peak displacement which accords with magnitude expected *in vivo*.

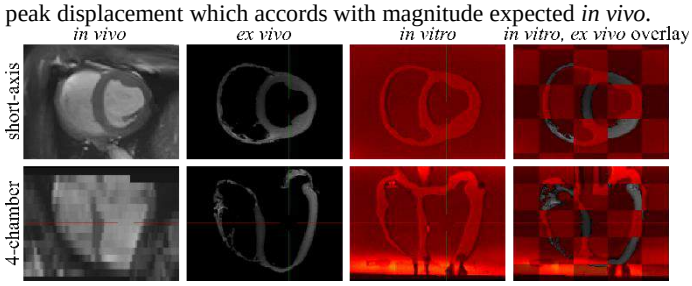

Figure 3: Direct image comparison of *in vivo* (porcine subject) bSSFP, *ex vivo* GRE (geometrically restored to *in vivo*), and *in vitro* (phantom) 3D SPGR after landmark-based rigid registration

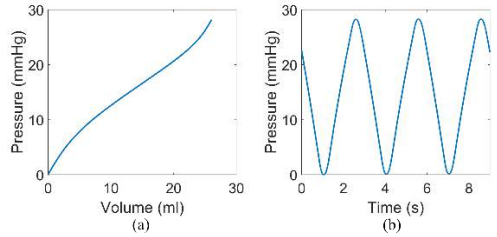

Figure 4: (a) LV Pressure-Volume (b) Pressure-time (three cycles)

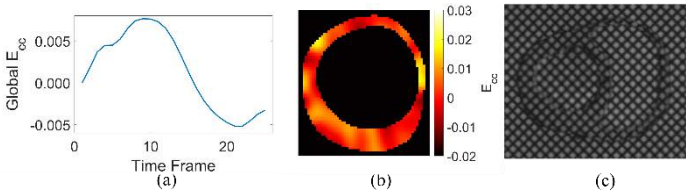

Figure 5: (a) Global LV Circumferential Strain (Ecc). (b) LV Ecc map at peak Global LV Ecc (c) Tagging slice used to calculate strain

DISCUSSION

This work demonstrates that subject-specific heart phantoms with diastolic myocardium-mimicking properties can be developed and incorporated within an MRI-compatible diastolic filling setup for estimating phantom material stiffness. Though phantom properties are comparable to myocardium, *in vivo* heart anisotropy was not replicated.

Tensile testing of samples allows for ground-truth phantom material stiffness estimates. Future work will use this system to estimate the phantom's material stiffness as proof-of-principle that material stiffness estimation is feasible *in vivo*. Different subject-specific heart phantoms based on *in vivo* images can be manufactured, with phantom stiffness tuned to a known value. This enables characterizing the accuracy and precision of the stiffness estimation framework.

ACKNOWLEDGEMENTS

This project was supported by NIH R01 HL131823 to DBE.

REFERENCES

[1] Azevedo, P.S. et al., *Arquivos Brasileiros de Cardiologia*, 106:62-69, 2016. **[2]** Wang, V.Y., et al., *Annual Review of Biomedical Engineering*, 17: 351-83, 2015. **[3]** ASTM Standard D412-16, 2016 **[4]** Cork, T.E., et al., *Functional Imaging and Modeling of the Heart*, 177-86, 2019. **[5]** Loecher, M., et al., *Cardiac Tag Tracking with Deep Learning Trained with Comprehensive Synthetic Data Generation.* ISMRM 28th Annual Meeting, 2020 **[6]** Bistoquet, A., et al., *Medical image analysis* 12.1:69-85, 2008. **[7]** Demer, L.L., et al., *The Journal of Physiology* 339:615–30, 1983. **[8]** Von Knobelsdorff, F., et al., *Journal of Cardiovascular Magnetic Resonance* 15:53, 2013.

VALIDATION OF HEPATIC FACTOR COMPUTATIONAL FLUID DYNAMICS SIMULATIONS FOR PRE-SURGICAL PLANNING

R. Rasooli (1), K.B. Kose (2), S.S. Lashkarinia (1), K. Pekkan (1)

(1) Department of Mechanical Engineering
Koc University
Istanbul, Turkey

(2) Department of Biomedical Engineering
Istanbul Medipol University
Istanbul, Turkey

INTRODUCTION

10 in 1000 babies are born with a clinically significant congenital heart defect each year in the US and 8 in 1000 in the world [1]. Univentricular heart defects are among the most serious pathologies which lead to death without neonatal treatment. A series of palliative surgical courses including the Fontan procedure is typically performed for these patients to utilize the single ventricle solely for pumping the oxygenated blood to the systemic and pulmonary circulation arranged serially. Despite the efficacious lifesaving feature of Fontan for the patients undergoing the operation, there is a growing rate of patients with failed Fontan physiology in a long-term postoperative run. For example, pulmonary arteriovenous malformations (PAVMs) can occur after the Fontan procedure and lead to decreased systemic oxygenation.

Transporting pulmonary growth factors, the uneven distribution of hepatic flow from inferior venous return to both lungs in total cavopulmonary connection (TCPC) is believed to play a key role in the cause of PAVMs [2]. While hepatic flow distribution can only be predicted by computational fluid dynamics (CFD), to our knowledge no experimental validation has been performed in the literature. Therefore the primary aim of the present study is to provide an experimental protocol and series of *in-vitro* data to validate patient-specific simulations performed in pre-surgical planning with complex vascular connections. The validation approach is demonstrated in a very complex patient-specific model as well as in two standard idealized TCPC geometries with different caval offsets. Three key performance parameters including power loss (PL), hepatic flow distribution (HFD) and total pulmonary flow split (TPFS) are experimentally quantified at different SVC/IVC (Superior/Inferior Vena Cava) flow ratios (FR). Furthermore, CFD simulations employing different turbulence and solver settings are performed for the proposed models and the final results are compared with the obtained experimental values.

METHODS

Two ideal TCPC geometries having half-diameter and one-diameter offset (DO) for inlets (IVC and SVC) were designed using SolidWorks (Dassault systemes, Waltham, Massachusetts, USA). The inner diameter was considered to be 7 mm with a 10D extension from each inlet/outlet to eliminate the entrance effects on the impingement zone as depicted in Figure 1.a and 1.b. For the patient-specific anatomy, the IRB approved image and PC-MRI data for a complex single ventricle patient having interrupted IVC and azygous (AZY) vein continuation was obtained by 1.5-Tesla scanner (SignaHDx; GE Medical Systems, Milwaukee, WI, US). The average velocity values were calculated to be used as boundary conditions inputs for CFD analysis. The final patient geometry was scaled with a factor of 0.58 to fit the 3D printer platform (Figure 1.c). The inlet boundary condition values were accordingly scaled to keep the Reynolds number identical to the clinical conditions.

The models were 3D printed using Formlabs (Somerville, Massachusetts, US) followed by a post-curing process to enhance model rigidity and reduce water absorbability. Figure 2 represents the schematic of the *in vitro* setup for the patient-specific prototype. Distilled water was used as the working fluid and loaded with tracer fluid for IVC inlet. The tracer fluid (Pelikan 4001 Royal blue ink) concentration measurements were performed using Multiscan FC microplate reader (ThermoFisher, Waltham, Massachusetts, US). A calibration process was carried out to identify the linear regression relation between the absorbance data obtained from the microplate reader and the tracer fluid concentration. The boundary condition for right and left pulmonary arteries (RPA and LPA) was considered zero

gauge outlet pressure. IVC and SVC inlet flowrates were 40 and (20,30,40) L/hr respectively in ideal model. IVC, RSVC,LSVC and AZY flowrates were 60, 15, 24 and 40 L/hr respectively in patient-specific model.

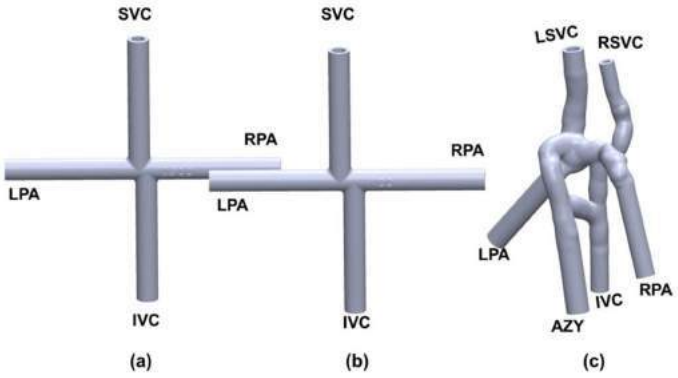

Figure 1: Geometrical representation of experimental prototypes. a: 0.5DO ideal TCPC, b: 1DO ideal TCPC and c: real patient-specific TCPC model

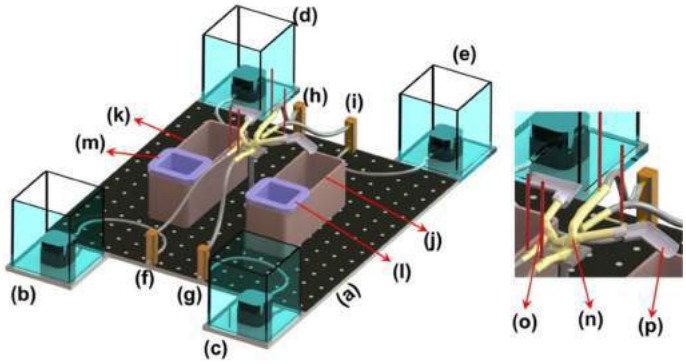

Figure 2: Schematic representation of the *in vitro* experimental setup. (a) Anti-vibration optical table. (b)-(e) RSVC, LSVC, AZY IVC reservoirs respectively. (f)-(i) LSVC, AZY IVC flowmeters respectively. (j)-(k) LPA and RPA waste reservoirs. (l)-(m), LPA and RPA sample collectors. (n) Model prototype, (o) pitot tube pressure probes and (p) flow guidance extension.

For each case, experiment was repeated three times to account for repeatability and the averaged values were considered for the final report. Outlet samples from RPA and LPA were collected for duration of 180 secs and the flowrates were calculated by measuring the collected sample volume with a resolution of 10 mL. The static pressure measurements were accomplished by the pre-integrated pitot tubes at each inlet wall. PL was calculated based on total pressure which was obtained by adding the dynamic part using the averaged inlet/outlet velocities. The CFD simulations were carried out in Star ccm+ (Siemens, Melville, NY, USA). Four different CFD solvers were considered as: CFD1: second order implicit unsteady laminar, CFD2: RANS Standard k-ε two-layer, CFD3: RANS Realizable k-ε and CFD4: RANS Realizable k-ε two-layer.

RESULTS

Discretization error for CFD simulations was analyzed by performing a mesh independent study at three different grid resolutions of 153K, 455K and 830K elements. The absolute difference for domain averaged velocity and concentration was found to be less than 1% for all grid levels. In addition to the residual reduction of 10^{-5} as the convergence criterion, we monitored the integral quantities such as mass flowrate at the outlets and continued the iteration until a steady state is achieved in RANS simulations. In transient simulations, the temporal iteration was continued until a convergence in ensemble average is achieved for all quantities. Table 1 summarizes a part of experimental and computational data for both ideal and patient-specific TCPCs. The flowrate and concentration values are presented for LPA. HFD and TPFS present the LPA's share. HFD was calculated using the continuity equation for the tracer fluid. The error for the tracer fluid continuity equation in experimental data was found to be less than 2% for all cases which shows the reliability of the data.

Table 1: Experimental and computational data for both ideal and patient-specific TCPC. Q: flowrate (L/hr), C: concentration. PL unit is mW. Except PL, other data are provided for LPA outlet.

	1 DO ideal TCPC (FR = 0.5)				
	Q	C	% HFD	% TPFS	PL
EXP	32.0	0.364	29	53	1.57
CFD1	33.0	0.398	33	55	1.72
CFD2	31.1	0.358	28	52	1.49
CFD3	31.9	0.374	30	53	1.81
CFD4	31.1	0.357	28	52	1.50
	Patient-specific TCPC				
	Q	C	% HFD	% TPFS	PL
EXP	77.3	0.230	29	56	19.67
CFD1	77.5	0.260	34	56	19.17
CFD2	79.9	0.237	31	57	19.43
CFD3	79.3	0.248	32	57	19.90
CFD4	80	0.239	32	58	19.38

DISCUSSION

Flow dynamics and mixing inside a TCPC have been mostly considered laminar for computational simulations throughout literature; however, impingement of jet flow streams inside TCPC can create turbulent behaviors. Our earlier studies [3,4] on jet flow in cardiovascular cannulae revealed that a RANS simulation can excellently capture the flow features in line with PIV experiments at transitional flow regimes. Our results in the present study showed that turbulent models can predict the three key parameters (HFD, TPFS and PL) in TCPC anatomies with more than 100 times faster performance and a better level of accuracy as compared to unsteady laminar solver. This is of paramount importance in Fontan pre-surgical planning with different surgery scenarios where a fast decision needs to be made. More importantly, our proposed ideal TCPC geometries can be reliably used for a thorough validation of computational solvers trying to simulate the flow dynamics in real patient complex vascular anatomies since they delivered the same level of accuracy in both cases.

ACKNOWLEDGEMENTS

Financial supports provided by TUBITAK grant numbers 118M369 and 118S108 (PI: Kerem Pekkan) are highly appreciated.

REFERENCES

1. Hoffman JI et al, J Am Coll Cardiol, 39:1890–900, 2002.
2. Pike NA et al, Ann. Thorac. Surg, *78*(2), 697-699, 2004.
3. Rasooli R et al, Artif. Organs, *43*(10), E233-E248, 2019.
4. Rasooli R et al, J Biomech Eng, *142*(5), 051002, 2020.

ROLE OF THE EXTRACELLULAR ENVIRONMENT IN ACHIEVING STABLE EPITHELIAL MORPHOGENESIS IN VITRO

Marjan J. Hagelaars (1,2), Lisanne W. Kuntz (1,2), Carlijn V.C. Bouten (1,2), Sandra Loerakker (1,2)

(1) Department of Biomedical Engineering
Eindhoven University of Technology
Eindhoven, the Netherlands

(2) Institute for Complex Molecular Systems
Eindhoven University of Technology
Eindhoven, the Netherlands

INTRODUCTION

Epithelial morphogenesis is a crucial aspect in the development of three-dimensional (3D) membrane-like tissue structures, such as tubes or cysts. In the case of normal organ development, these 3D structures are polarized monolayers surrounding an open lumen. Tight regulation of the mechanical force balance involved in controlling lumen size and shape is necessary to obtain well-functioning tissues *in vivo*.

The mechanical forces that play a role in lumen growth and its potential stabilization are displayed in Figure 1. The inflation of the lumen can be imposed by an increase in intraluminal hydrostatic pressure. Water passively follows the created osmotic pressure by the secretion of ions in the opening aperture [1]. Tension by the cytoskeleton is able to restrict the expansion created by hydrostatic pressure. Proliferation of the cells can relieve the cytoskeletal forces and thus favors lumen growth [2]. Lastly, the properties of the extracellular matrix surrounding the tube or cyst define the resistance the expanding structure experiences [3]. While the lumens of 3D epithelial structures *in vivo* grow until the appropriate diameter to fulfill their physiological functions is reached, 3D structures *in vitro* have not shown any stabilization of the lumen in time [4].

To understand the individual and combined contributions of these forces in lumen expansion and stabilization, we designed *in vitro* experiments where the hydrostatic pressure, cellular tension, and extracellular matrix resistance are systematically varied. The insights gained could then help mechanically control this process for regenerative or tissue engineering purposes. Madin Darby Canine Kidney cells (MDCKs) serve as an excellent *in vitro* cell model to study lumen formation and growth in the context of kidney morphogenesis, as these cells spontaneously form cysts with a single lumen when cultured in a 3D environment. Here, we varied the extracellular environment composition to possibly increase its resistance to the growth of the central lumen formed in MDCK cysts. Furthermore, preliminary efforts were undertaken to quantify cyst geometry over time.

METHODS

To change ECM resistance to luminal growth, 3D collagen-I gels created with different concentrations of collagen (1, 2 and 3 mg/ml) were fabricated from rat-tail collagen (Corning). The collagen solution was first mixed with culture medium and neutralized with 1M NaOH solution (Sigma-Aldrich). The gel mixture was then placed at 37°C for

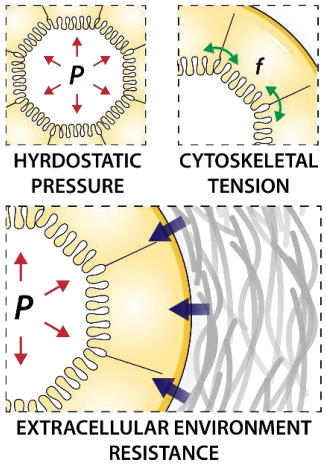

Figure 1: Illustration of the three mechanical forces that influence lumen development: (i) the intraluminal hydrostatic pressure (ii) the cytoskeletal tension on the apical surface of the membrane and (iii) the resistance provided by the extracellular matrix.

45 minutes. After full gelation, culture medium was added on top. Cell-free gels were characterized with SEM to quantify fiber density and orientation, and with micro-indentation to determine pristine gel stiffness.

MDCKs were incorporated in the gel mixture with a density of approximately $2 \cdot 10^5$ cells/ml. The cell-gel constructs were fixed at either a fixed time point (10 days) or monitored over time using fixation times of 2, 4, 7, 10, 14 and 21 days. Immunofluorescent (IF) staining was used to characterize the formed cellular aggregates. Cyst diameter, lumen diameter, circularity and cell number were obtained from the IF images using a custom-built Python script. Using micro-indentation, the gel stiffness of the cell-gel constructs was also measured at the given time points.

RESULTS

The fabricated gels consistently contained dense collagen fiber networks, where fiber density increased with increasing collagen concentration (Fig. 2 - SEM). Cysts were formed in the lower collagen concentrations of 1 and 2 mg/ml (Fig. 2). These cysts were heterogeneous in terms of size and cell number. The circularity however was concurrent in both concentrations. Interestingly, the 1 mg/ml collagen gels seemed to stiffen when comparing the stiffness of cell-free gels with cell-laden gels after 10 day of culture. The 2 mg/ml on the other hand showed no change. The 3 mg/ml concentration collagen gel contained essentially no cysts after 10 days of culture and were excluded from further analysis.

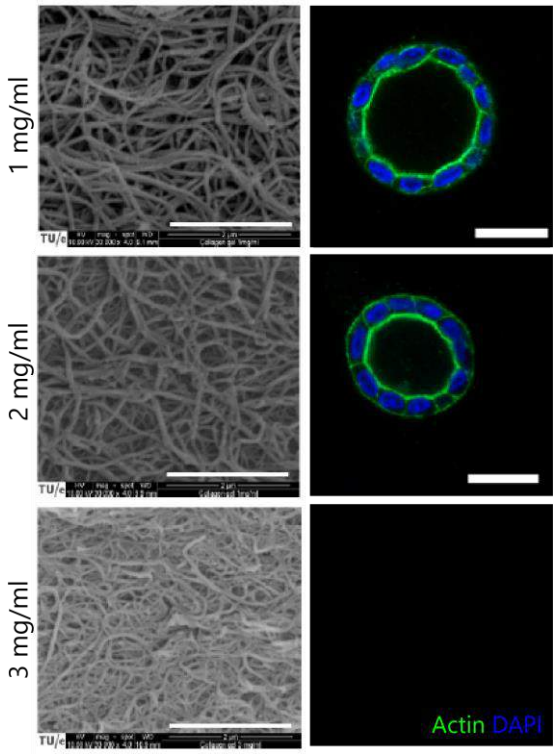

Figure 2: MDCKs grown in different concentrations of collagen gels (1, 2 and 3 mg/ml). The SEM images (left) display the formed fiber networks. Scale bars represent 2 µm. In the IF images, cells stained for DAPI and actin visualize the cyst formation in the different conditions. Scale bars represent 25 µm.

Cyst growth did not stabilize in 21 days, when cultured in a 2 mg/ml collagen gel (Fig 3a). The cyst growth was accompanied by both lumen growth (Fig 3a) as well as cell proliferation (Fig 3b). The results exhibit a high inter- and intra-sample variability.

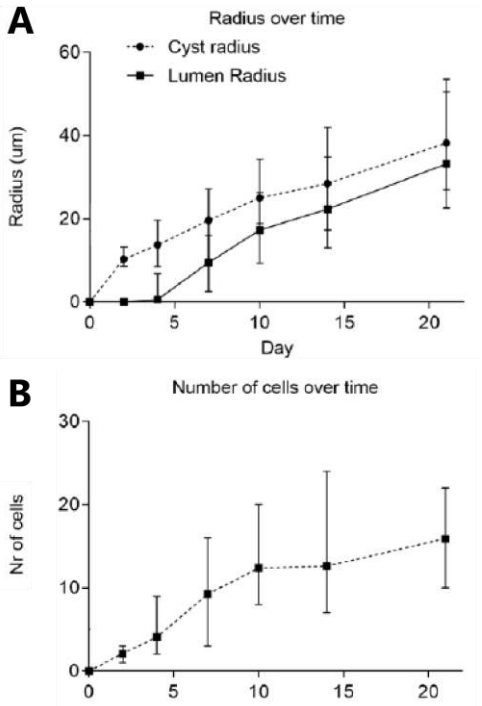

Figure 3: Characterization of MDCK cysts grown in a 2 mg/ml collagen gel concentration over time. (A) Quantification of the cyst and lumen radius over time and (B) the number of cells per cyst over time.

DISCUSSION

Our initial results suggest that the composition of the environment could be one of the mechanical forces that play a role in lumen growth and possible stabilization. Quantitative measurements of cyst geometry over time for the other two collagen concentrations are necessary to investigate to what extent the resistance posed by the environment composition is able to control lumen growth. The found heterogeneity in the experiments could be explained by local differences in matrix composition. In the future, the influence of the other morphogenetic processes should be investigated to obtain a full understanding of their interplay and identify conditions that could enable the stabilization of lumen growth. Furthermore, implementation of these processes in a computational model could further help to explain the individual as well as combined mechanical effects these processes have on lumen growth.

ACKNOWLEDGEMENTS

This study is supported by the partners of Regenerative Medicine Crossing Borders (RegMed XB). It is financed by the Dutch Ministry of Economic Affairs by means of the PPP Allowance made available by the Top Sector Life Sciences & Health to stimulate public-private partnerships.

References

[1] Sigurbjörnsdóttir, S. et al. *Nat Rev Mol Cell Bio* 15:665-676, 2014.
[2] Gupta, K. et al. *J. Hepatol.* 66:1231-1240, 2017.
[3] Luschnig, S. et al. *Curr. Biol.* 16:186-194, 2006.
[4] Engelberg, J. et al. *PLoS Comp. Biol.* 7:e1002030, 2011.

3D GROWTH AND REMODELING IN ASCENDING THORACIC AORTIC ANEURYSMS

J. Laubrie (1), J. Mousavi (1), S. Avril (1)

(1) Mines Saint-Etienne, Univ Lyon,
Univ Jean Monnet, INSERM, U 1059
Sainbiose, Centre CIS, F - 42023
Saint-Etienne France

INTRODUCTION

Mechanoregulation in blood vessels tends to maintain homeostasis of mechanical stresses. As a result, given a change of the stress state in the arterial wall, growth and remodeling (G&R) will induce mass changes at the tissue scale to recover its homeostasis. If a localized lesion appears, the artery may not always recover homeostasis and have a degenerative expansion. A number of authors have developed computational models of aneurysm progression using the G&R theory. However, they usually considered straight tubes [1,2]. In this work, we developed a G&R computational model to study aneurysm progression in patient-specific curved arteries, like ascending thoracic aortic aneurysms (ATAA) in the aortic arch (Figure 1).

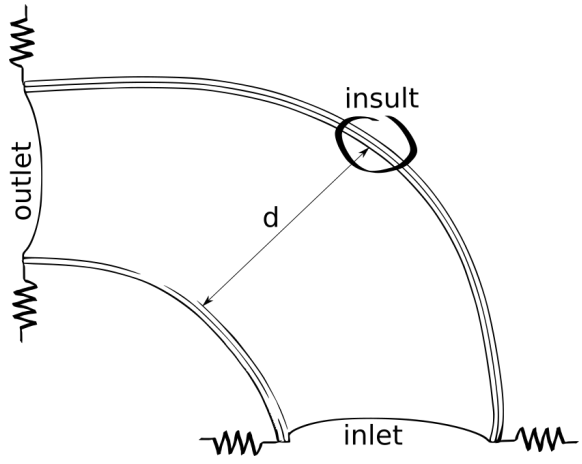

Figure 1: Scheme of simulation conditions.

METHODS

Our G&R framework is based on the homogenized Constrained Mixture Models (hCMM) [1]. The aorta is modeled as a bilayer. The material is composed of three constituents (elastin, collagen, smooth muscle cells) giving a mixture where each constituent has an individual elastic and inelastic deformation such as

$$F = F^j_e F^j_{gr} \tag{1}$$

with F as the deformation gradient of the mixture, F^j_e is the elastic deformation gradient and F^j_{gr} is the inelastic deformation gradient for the jth constituent, ($j = e, c_i, m$).

The strain energy function (SEF) per unit volume for each layer is written such as

$$W = \varrho^e_R \Psi^e + \varrho^m_R(\Psi^m_{pas} + \Psi^m_{act}) + \varrho^{c_i}_R \Psi^{c_i} \tag{2}$$

where Ψ^j and ϱ^j_R are the SEF per unit mass and the density (in reference volume) for each constituent, respectively. The elastin is modeled as an isotropic neo-Hookean material, the collagen and passive smooth muscle cells with anisotropic Fung quadratic material. Moreover, the smooth muscle cells have an active model as presented in [2]. Different mass densities are assigned for every single constituent of the mixture.

The G&R scenario considered for ATAA progression is a localized insult with a loss of elastin inducing a ballooning around the lesion, running up to 5500 days. In these simulations we assessed the sensitivity to the gain parameter, which is the parameter relating the rate of collagen mass change to the deviation of stress homeostasis.

This parameter translates into how fast mechanoregulation is achieved in the tissue.

The simulations were performed over three geometries: cylinder (straight tube), half arch and patient-specific arch. The cylinder is the benchmark case published in [2] with the same material properties and elastin loss. The half arch has a similar shape (lumen diameter and arch radius) as the patient geometry. Then, mechanical properties for arch and patient-specific were calibrated against data obtained on human aortic tissue [3]. In Figure 1, we show how the lumen diameter is measured throughout the aneurysm progression, following deformations induced by G&R. The insult point is located at the right hand side of the diameter arrow. The conditions at the inlet and outlet boundary only allow radial displacements with some stiffness modeled with springs (penalization of the radial displacements). Moreover, for the half-arch and the patient-specific geometries, spatially variable deposition stretches were assigned to elastin as initial conditions to ensure homeostasis.

RESULTS

We first verified that our model was in good agreement with previously existing studies on straight tubes [2]. The effect of the gain parameter is significant as the diameter change varies from 13% to 153% just by varying the gain parameter of a factor 3 (Table 1).

Table 1: Growth under localized elastin loss.

Gain	Straight tube	Arch	Patient
0.05/T	153.8%	292.5%	77.7%
0.09/T	45.8%	103.1%	22.3%
0.11/T	27.0%	55.4%	13.6%
0.15/T	13.0%	20.9%	7.2%

For the same gain parameters, the half-arch shows larger diameter increase than the straight tube. The diameter increase becomes very large for gains from 0.05/T to 0.11/T. The deformation of the arch with a gain of 0.05/T is extrapolated to 5500 days from the simulation until 3860 days.

The patient specific case showed lower diameter changes. Actually, with a gain of 0.15/T, the diameter change is almost half of the deformation obtained on the straight tube. Moreover, a 77.7% growth in the diameter was obtained for 0.05/T (extrapolated from a simulation stopped at 4220 days). Figure 2 shows the von Mises stress distribution of the patient at 4220 days where in some regions the stress reaches 350[kPa] in the adventitia at the left side of the picture. This shows a transfer of stress from the media to the adventitia that occurred during aneurysm progression.

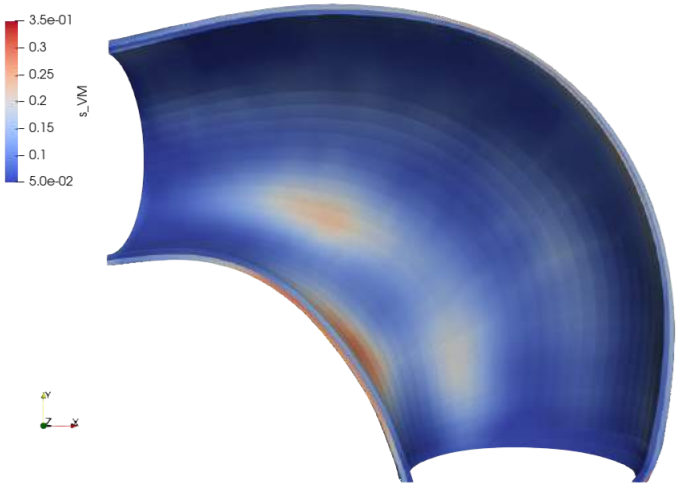

Figure 2: Patient ascending thoracic aorta with von Mises stress.

DISCUSSION

We successfully implemented the hCMM approach into a 3D G&R model of ATAA progression.

After a localized insult, geometries showed a diameter increase above 50% with low gain parameters. Usually the condition to declare an aneurysm is a diameter 50% bigger than the initial one. This shows that the initial insult that we considered can effectively lead to an aneurysm.

The development of the numerical models for the arch and for the patient-specific geometry had to overcome several convergence issues, which were related to the initial deposition stretches and the boundary conditions at the inlet and outlet of the artery. The initial deposition stretch is needed to ensure a homeostatic stress state in the initial geometry. The boundary conditions at the inlet and outlet were set to penalize radial displacements. The spring stiffness can induce stress concentrations which were avoided here by tuning the stiffness appropriately.

Future work will focus on comparing the model predictions to real ATAA geometries on a cohort of patients. The long-term goal is to enable patient-specific predictions of ATAA progression during clinical assessment.

ACKNOWLEDGEMENTS

The authors are grateful to the European Research Council for grant ERC-2014-CoG BIOLOCHANICS (grant number 647067) and to the CONICYT.

REFERENCES

[1] Cyron, C et al., *Biomech Model Mechanobiol*, 15:1389-1403, 2016.
[2] Braeu, F et al., *Biomech Model Mechanobiol*, 16(3):889-906, 2017.
[3] Mousavi, J et al., Int *J Numer Meth Biomed Engng*, 34:e2944, 2018.

MELANOMA TUMOR FORMATION IN 3D COLLAGEN IN VITRO MATRICES IS REGULATED BY INTRACELLULAR MECHANICS AND TBX3 CONTENT

Ghodeejah Higgins (1), Faatiemah Higgins (2), Jade Peres (2), Tamer Abdalrahman (1,3), Muhammad H. Zaman (4,5), Sharon Prince (2), Thomas Franz (1,6)

(1) Division of Biomedical Engineering
Department of Human Biology
University of Cape Town
Observatory, South Africa

(2) Division of Cell Biology
Department of Human Biology
University of Cape Town
Observatory, South Africa

(3) Julius Wolff Institute for Biomechanics and Musculoskeletal Regeneration
Charité Universit□tsmedizin
Berlin, Germany

(4) Department of Biomedical Engineering
Boston University
Boston, MA, USA

(5) Howard Hughes Medical Institute
Boston University
Boston, MA, USA

(6) Bioengineering Science Research Group
Engineering Sciences,
University of Southampton,
Southampton, UK

INTRODUCTION

Metastatic spread requires the biomechanical adjustment of cell volume and hence, altered biochemical cascades and cell mechanical properties [1]. It is known that melanoma cells have a predilection for distant metastasis, such as the lung, liver, brain, and bone [2]. However, little is known about why melanoma cells may favor specific distant organs over others. Even less is known about melanoma cell's inherent biomechanical and biochemical properties that coordinate tumor formation in changing 3D environments. Recently, cell stiffness and the oncogenic factor TBX3 have been identified as potential mechanical and molecular biomarkers of metastasis, respectively [3, 4]. Therefore, this study sought to determine how cell stiffness and TBX3 levels change in melanoma cells before tumor formation compared to after tumor formation in 3D *in vitro* collagen matrices of varying rigidity.

METHODS

ME1402 vertical growth phase (VGP) and WM1158 metastatic (MET) human melanoma cells were embedded in Type I rat tail collagen matrices at final collagen concentrations of 2 and 4 mg/ml. Isolated cells and cell clusters were assessed after 1 day (24 hrs) and 7 days. Cells were stained with Mitotracker Green. Mitochondrial fluctuations were captured using time-lapse confocal microscopy (100 s), mitochondrial trajectories constructed using TrackMate, and the ensemble-averaged mean-square displacement (MSD) $\langle \Delta r^2(\tau)_{xy} \rangle$ determined, where the delay time τ is the time between first and last image frame used for the analysis. The MSD-dependent diffusivity α was calculated as a measure of intracellular fluidity (deformability) as:

$$\alpha = \frac{\partial \ln\langle \Delta r^2(\tau) \rangle}{\partial \ln(\tau)} \quad (1)$$

TBX3 content was assessed with immunofluorescence techniques. Data were assessed with multi-factorial ANOVA, with $p < .05$ indicating statistical significance.

RESULTS

The MSD and deformability α of isolated cells were larger for VGP than for MET in 2 mg/ml (MSD: $p < .001$, α: $p = .002$) and 4 mg/ml collagen matrices (MSD and α: $p < .001$), see Fig. 1.

Cluster formation in 2 mg/ml collagen did not affect the intracellular mechanics of VGP cells (MSD and α: $p > .05$) and α of MET cells ($p = .154$) but increased MSD of MET cells ($p < .001$). In 4 mg/ml collagen, cluster formation increased the MSD of VGP and MET cells ($p < .001$ for both cases) whereas α decreased for VGP ($p = .001$) but increased for MET cells ($p = .045$).

TBX3 was equally overexpressed in isolated VGP and MET cells in 2 mg/ml collagen ($p = .987$), see Table 1. In 4 mg/ml collagen, the TBX3 level decreased by 57% ($p = .007$) in VGP and by 87% ($p < .001$) in MET cells compared to 2 mg/ml collagen. TBX3 was still present in VGP but nearly depleted in MET cells.

Cluster formation of VGP cells did not alter TBX3 levels for 2 mg/ml collagen ($p = .731$) but increased the TBX3 content for 4 mg/ml collagen ($p = .028$). TBX3 was overexpressed in VGP clusters. For MET, cluster formation slightly decreased TBX3 levels in 2 mg/ml collagen ($p = .201$) but increased TBX levels in 4 mg/ml collagen ($p = .032$).

DISCUSSION

Mitochondrial fluctuations decreased and cell stiffness increased as VGP progressed to MET stages in 2 mg/ml (soft) and 4 mg/ml (stiff) collagen matrices. The increase in cellular stiffness contrasts with several studies that reported decreased stiffness [3, 5] whereas reports of increased stiffness with increased metastatic potential in melanoma are limited [6]. The Warburg effect may explain smaller mitochondrial fluctuations. Mitochondria of cancer cells produce insufficient ATP;

hence cells switch to a glycolytic metabolic pathway, which has strongly been associated with the metastatic potential, to meet the energy demands [7].

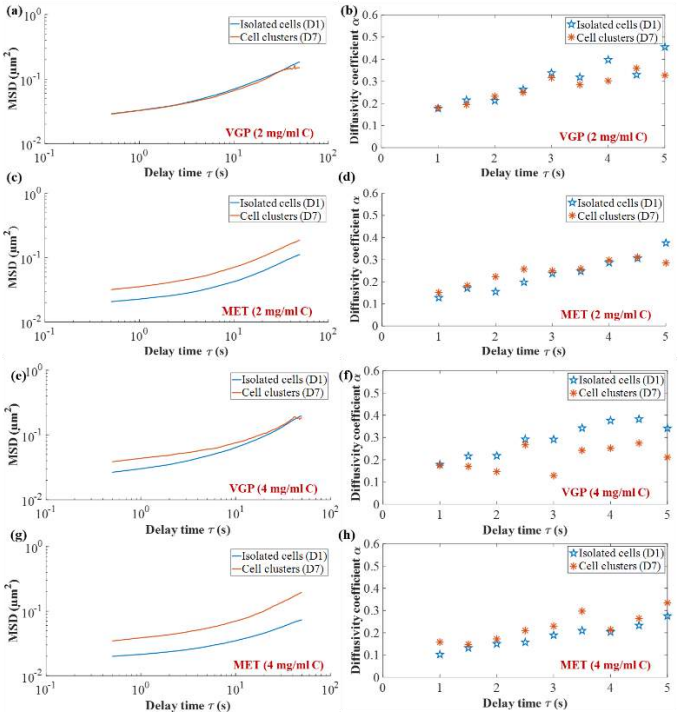

Figure 1: Mean square displacement (MSD) and diffusivity of isolated cells (at day 1: D1) and cell clusters (at day 7: D7) for VGP and MET disease stage in 2 and 4 mg/ml collagen (C) matrices.

Table 1: TBX3 expression in nuclei of isolated cells (at day 1) and cell clusters (at day 7) for VGP and MET disease stage in 2 and 4 mg/ml collagen matrices.

	Collagen concentration (mg/ml)	VGP	MET
Isolated cells	2	0.60 ± 0.41	0.61 ± 0.44
	4	0.26 ± 0.21	0.54 ± 0.35
Cell clusters	2	0.51 ± 0.16	0.32 ± 0.13
	4	0.07 ± 0.07	0.10 ± 0.06

Values are given as mean ± standard deviation

Glycolysis is primarily mediated and enhanced by the PI3K/AKT biochemical cascade [7]. Interestingly, PI3K/AKT signaling has been implicated in melanoma formation and invasion [4]. Further, TBX3 has emerged as a substrate of AKT3, an isoform of AKT, and therefore plays prominent roles in the PI3K/AKT pathway [8]. TBX3 has been reported to promote tumor formation and metastasis [9]. TBX3 was overexpressed in isolated VGP and MET cells in soft matrices, but TBX3 content decreased in stiff matrices. Considering that VGP cells quickly formed cell clusters whereas MET cells remained mainly isolated, it is suggested that overexpressed TBX3 promotes tumor formation in VGP cells and migration but not tumor formation in MET cells.

Decreased TBX3 expression in stiff matrices indicates that TBX3 expression is partially governed by the cells' mechanical interaction with the environment in addition to TBX3 upregulation by signaling molecules [9]. It is proposed that increased matrix rigidity increases actomyosin contractility, which in turn stimulates signaling molecules that have overlapping functions in cytoskeletal remodeling and the PI3K/AKT signaling pathway, such as activation of Cdc42. Cdc42 activity was shown to decrease with increased 3D collagen rigidity [10], and decreased Cdc42 levels were associated with increased PI3K/AKT signaling [11].

Mitochondrial bioenergetics are crucial for tumorigenesis [7]. However, for VGP cells, cluster formation led to an adjustment of intracellular mechanical properties in stiff but not soft matrices. It is proposed that VGP cluster formation in soft matrices do not require increased mechanical or bioenergetic fortification. Instead, isolated VGP cells are innately endowed with suitable mechanical properties to form clusters. This is supported by the findings that TBX3 expression was similar in VGP isolated cells and VGP cell clusters.

VGP cluster formation in stiff matrices was associated with increased mitochondrial fluctuations and cell stiffness. Increased proliferation is common in stiff matrices [12] and associated with increased mitochondrial bioenergetics [13]. The increased mitochondrial fluctuations observed here may result directly from the increased mitochondrial metabolism required for proliferation during VGP cluster formation in stiff matrices. Furthermore, cluster growth through proliferation amplifies the compressive conditions that VGP cells experience, thereby stiffening them.

For MET cluster formation, mitochondrial fluctuations increased in soft and stiff matrices. Conceivably, the formation of MET clusters is an energy-exhaustive process, regardless of matrix rigidity. Noting that mitochondria are regarded as dysfunctional in isolated metastatic cells, cluster formation was not automatic. Instead, cells remained isolated to invade 3D matrices.

Increased mitochondrial dynamics downregulates the PI3K/AKT pathway, thereby limiting glycolytic-mediated metabolism [7]. Although overexpressed in isolated cells, TBX3 decreased during MET cluster formation in soft matrices, alluding to increased mitochondria-mediated metabolism. Furthermore, VGP and MET cell clusters exhibited higher TBX3 levels than isolated cells in stiff matrices, demonstrating that TBX3 is indispensable during cluster formation in 3D cellular environments.

ACKNOWLEDGEMENTS

This study was supported financially by the National Research Foundation of South Africa (grant IFR14011761118) and the South African Medical Research Council (grant SIR328148).

REFERENCES

[1] Northcott, J.M., et al., *Front Cell Dev Biol*, 6:17, 2018
[2] Damsky, W.E., L.E. Rosenbaum, and M. Bosenberg, *Cancers*, 3:126-63, 2010
[3] Pachenari, M., et al., *J Biomech*, 47:373-9, 2014
[4] Peres, J. and S. Prince, *Mol Cancer*, 12:117, 2013
[5] Xu, W., et al., *PLoS One*, 7:e46609, 2012
[6] Weder, G., et al., *Nanomedicine*, 10:141-8, 2014
[7] Weinberg, S.E. and N.S. Chandel, *Nat Chem Biol*, 11:9-15, 2015
[8] Peres, J., S. Mowla, and S. Prince, *Oncotarget*, 6:1821-33, 2015
[9] Khan, S.F., et al., *Gene*, 726:144223, 2020
[10] Kim, S.J., et al., *Biochem Biophys Res Commun*, 443:1280-5, 2014
[11] Arias-Romero, L.E. and J. Chernoff, *Expert Opin Ther Targets*, 17:1263-73, 2013
[12] Mih, J.D., et al., *J Cell Sci*, 125:5974-83, 2012
[13] Cheng, G., et al., *Br J Cancer*, 111:85-93, 2014

PREDICTION OF BRAIN STRAIN ACROSS HEAD IMPACT SUBTYPES USING 18 BRAIN INJURY CRITERIA

Xianghao Zhan (1), Yiheng Li (2), Yuzhe Liu(1), David B. Camarillo (1)

(1) Department of Bioengineering
Stanford University
Stanford, CA, USA

(2) Department of Biomedical Informatics
Stanford University
Stanford, CA, USA

INTRODUCTION

To evaluate the mild traumatic brain injury (mTBI) risk associated with a head impact, multiple brain injury criteria (BIC) have been developed [1-6]. Physiologically, the brain's mechanical strain is often considered the key parameter of brain injury [7]. To evaluate the accuracy of predicting brain injury risks of the BIC, typically Pearson correlation between the BIC and the brain strain (particularly 95% MPS), as well as the coefficient of determination of the linear regression of brain strain on the BIC, have been used [1-3].

Although the BIC are typically designed for specific types of head impacts, many BIC are widely used, regardless of their development background [8]. However, when applied to different impact subtypes, even for the same values of MPS some BIC give different values. That the different BIC may indicate potentially similar brain strain across impact subtypes, poses a risk to using the BIC across the mTBI field.

To better understand the risk of using one BIC for a general metric across impacts subtypes, 5 datasets from various head impact subtypes are used for analysis. Linear regression models were built with 18 BIC as predictors for 95% MPS (MPS95), 95% MPS at corpus callosum (MPSCC95) and cumulative strain damage (CSDM 15%, the volume fraction of brain with MPS exceeding the threshold of 0.15), to analyze the regression slopes and the brain strain prediction generalizability.

METHODS

Data from 6 sources were used to construct 5 datasets: dataset 1 contained 2183 football-type lab head impacts: 2130 were simulated by a validated finite element analysis (FEA) model of hybrid III anthropomorphic test dummy (ATD) headform [9] and 53 were reconstructed impacts in National Football League [10]; dataset 2 contained 302 on-site college football impacts [11, 12]; dataset 3 contained 457 on-site mixed martial arts (MMA) impacts [7,13]; dataset 4 contained 48 impacts in automobile crashworthiness tests from the National Highway Traffic Safety Administration (NHTSA) [14]; dataset 5 contained 272 numerically reconstructed head impacts in National Association for Stock Car Auto Racing (NASCAR) by hybrid III ATD headform. Finite element (FE) modeling based on the KTH model [15] was used to calculate the MPS95, MPSCC95, CSDM. The accuracy in predicting the MPS95/MPSCC95/CSDM was used to evaluate the brain strain predictability of the BIC.

The 18 BIC studied included Severity Index (SI), Head Injury Criterion (HIC), Generalized Acceleration Model for Brain Injury Threshold (GAMBIT), Head Impact Power (HIP), Principal Component Score (PCS), Kinematic rotational Brain Injury Criterion (BRIC), Power Rotation Head Injury Criterion (PRHIC), Kleiven's Linear Combination (KLC), Rotational Injury Criterion (RIC), Brain Injury Criterion (BrIC), Combined Probability of Concussion (CP) [6], Rotational Velocity Change Index (RVCI), Damage [2], Convolution of impulse response for Brain Injury Criterion (CIBIC) [4], Brain Angle Metric (BAM) [3], the peak values of the magnitudes of the linear acceleration at the brain center of gravity (lin_acc_CG_max), angular velocity (ang_vel_max) and angular acceleration (ang_acc_max).

Linear regression models were built with each BIC as the predictor and the MPS95/MPSCC95/CSDM as the outcomes. The regression slopes were analyzed to investigate the relationship between BIC and brain strain on different datasets. 1000 bootstrapping experiments were done. One-way ANOVA and Wilcoxon signed rank tests were used to test the statistical significance of the regression slopes across datasets. Additionally, the predictability was tested on the single-dataset (80% of a dataset to train the model and predict the MPS95/MPSCC95/CSDM of the remaining 20% data) and across-dataset (a dataset used to fit the model and predict the brain strain of another dataset) with the R^2 as the regression metric. To ensure robust results, the mean R^2 was calculated in 100 iterations of bootstrapping resampling on the training data.

RESULTS

Firstly, the regression slopes were analyzed. One-way ANOVA shows statistical significance of the different slopes across datasets on all three outcomes ($p<0.001$). **Fig. 1** show the pairwise comparison Wilcoxon test p-values of regression slopes across datasets (MPS95, with similar results for MPSCC95/CSDM). The results show 535 out of the 540 pairwise comparisons manifested statistical significance ($p<0.05$), and 527 out of the 540 pairwise comparisons manifested statistical ($p<0.001$), which indicates that the exact relationship between the BIC and the brain strain vary with different types of head impacts.

Then, the accuracy of predicting MPS95/MPSCC95/CSDM on the single-dataset or across datasets was analyzed. The MPS95 prediction accuracy is shown in **Fig. 2**. The diagonal elements generally showed higher R^2 in single-dataset prediction tasks than the off-diagonal elements representing the cross-dataset prediction. Similar results were found on MPSCC95/CSDM regressions.

P<0.001 0.001≤P<0.01 0.01≤P<0.05 P≥0.05

MPS95 Regression Slope (Pairwise Rank Sum Test P-values)										
BIC \Data set Pair	1-2	1-3	1-4	1-5	2-3	2-4	2-5	3-4	3-5	4-5
SI	<0.001	<0.001	<0.001	<0.001	<0.001	<0.001	<0.001	<0.001	<0.001	<0.001
HIC	<0.001	<0.001	<0.001	<0.001	<0.001	<0.001	<0.001	<0.001	<0.001	<0.001
GAMBIT	<0.001	<0.001	<0.001	<0.001	<0.001	<0.001	<0.001	<0.001	<0.001	<0.001
HIP	<0.001	<0.001	<0.001	<0.001	<0.001	<0.001	<0.001	<0.001	<0.001	<0.001
PCS	<0.001	<0.001	<0.001	<0.001	<0.001	<0.001	<0.001	<0.001	<0.001	<0.001
BRIC	<0.001	<0.001	<0.001	<0.001	<0.001	<0.001	<0.001	<0.001	<0.001	<0.001
PRHIC	<0.001	<0.001	<0.001	<0.001	<0.001	<0.001	<0.001	<0.001	<0.001	<0.001
KLC	<0.001	<0.001	<0.001	<0.001	<0.001	<0.001	<0.001	<0.001	<0.001	<0.001
RIC	<0.001	<0.001	<0.001	<0.001	<0.001	<0.001	<0.001	<0.001	<0.001	<0.001
BrIC	<0.001	<0.001	<0.001	0.288	<0.001	<0.001	<0.001	<0.001	<0.001	<0.001
CP	<0.001	<0.001	<0.001	<0.001	<0.001	<0.001	<0.001	0.538	<0.001	<0.001
RVCI	0.442	<0.001	<0.001	<0.001	<0.001	<0.001	<0.001	<0.001	<0.001	<0.001
CIBIC	<0.001	<0.001	<0.001	<0.001	<0.001	<0.001	<0.001	<0.001	<0.001	<0.001
Damage	<0.001	<0.001	<0.001	<0.001	<0.001	<0.001	<0.001	<0.001	<0.001	<0.001
BAM	<0.001	<0.001	<0.001	<0.001	<0.001	<0.001	<0.001	<0.001	<0.001	<0.001
fit_acc_CG_max	<0.001	<0.001	<0.001	<0.001	<0.001	<0.001	<0.001	<0.001	<0.001	<0.001
avg_vel_max	<0.001	<0.001	<0.001	<0.001	<0.001	<0.001	<0.001	<0.001	<0.001	<0.001
avg_acc_max	<0.001	<0.001	<0.001	<0.001	<0.001	<0.001	<0.001	<0.001	<0.001	<0.001

Figure 1 The p-values of pairwise comparison of regression slopes on different datasets based on Wilcoxon signed rank tests.

DISCUSSION

Different BIC have been developed on different head impact subtypes, but the predictability of the BIC across head impact subtypes has not been investigated. To study the BIC predictability across different head impact subtypes, this study investigated the regression slopes in linear regressions of MPS95/MPSCCC95/CSDM on 18 BIC and the generalizability of brain strain prediction if the regression models fitted on an impact subtype, with five datasets of different head impact subtypes (lab impacts, college football impacts, MMA impacts, NHTSA impacts, NASCAR impacts). This study found statistically significantly different slopes in most regression models across datasets in **Fig. 1**, indicating that the underlying relationship between BIC and brain strain varies with head impact subtypes. A potential explanation is that the characteristics of the kinematics used by BIC to predict brain strain are different. The differences in the relationship between BIC and brain strain suggest that the risks of brain injury even predicted by the same BIC value vary with head impact subtypes.

The influence of the datasets on the accuracy of the brain strain prediction were shown in **Fig. 2**. The bars were generally higher on the diagonal than off diagonal, indicating the single-dataset predictions generally showed higher mean R^2 than those in the cross-dataset predictions. In other words, the model was more accurate in the prediction of MPS95/MPSCC95/CSDM if it was fit on the same head impact subtype. Exceptions did exist when the off-diagonal prediction accuracy was higher, and the potential reasons may be the insignificant slope difference in the regression between datasets and the randomness in a small dataset. This finding suggests that the accuracy of the BIC should be evaluated according to head impact subtypes. In previous BIC studies, the evaluation of the accuracy in brain strain prediction has been mainly done on the same dataset. Although different head impact subtypes have been combined to develop BIC, it was until recently that researchers started to study the declining accuracy of the brain strain prediction models when applied to a different head impact subtype. Zhan et al [16] developed a deep learning head model for predicting whole-brain strain and showed that the model accuracy deteriorates when the model was trained on a dataset with mainly simulated impacts and applied to MMA. According to this study, concerns arise when a BIC is used to evaluate brain strain if the BIC regression model is fit on a different head impact subtype. The BIC and any other computational head model for predicting brain injury risks need validation across head impact subtypes if they are ever intended to be used in that way.

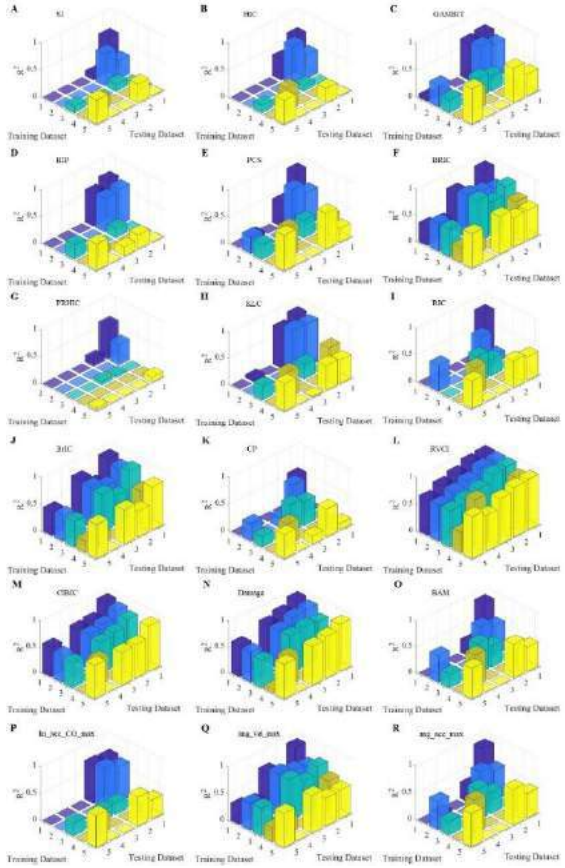

Figure 2 The mean R^2 in the single-dataset prediction and cross-dataset prediction of MPS95 based on 18 BIC.

ACKNOWLEDGEMENTS

The study is supported by PAC-12 Conference's Student-Athlete Health and Well-Being Initiative, National Institutes of Health (R24NS098518).

REFERENCES

[1]Gabler, L. et al., J Biomechanics, 140.3 (2018).
[2]Gabler, L. et al., Ann. Biomed. Eng., 47.9 (2019): 1971-1981.
[3]Laksari K. et al., J Neurotrauma, 37.7 (2020): 982-993.
[4]Takahashi, Y. et al. 25th Int. Tech. Con. On the ESV NHTSA. 2017.
[5]Greenwald, R. et al. Neurosurgery. 62.4 (2008): 789-798.
[6]Rowson, S. et al. Ann. Biomed. Eng. 41.5 (2013): 873-882.
[7]O'Keeffe, E. et al. J Neurotrauma. 37.2 (2020): 347-356.
[8]Pellman, E. et al. Neurosurgery. 53.4 (2003): 799-814.
[9]Giudice, J. Ann. Biomed. Eng., 47.2 (2019): 464-474.
[10]Sanchez, E. et al. Clin. Biomechanics, 64 (2019): 82-89.
[11]Camarillo, D. et al., Ann. Biomed. Eng. 41.9 (2013): 1939-1949.
[12]Liu, Y. et al., arXiv: 2008.01903 (2020).
[13]Tiernan, S. et al., J Eng. In Med. (2020): 0954411920947850.
[14]NHTSA. United States. https://www.nhtsa.gov/data
[15]Kleiven S. et al., SAE Tech. Paper, 2007. No. 2007-22-0003.
[16]Zhan X. et al., arXiv: 2010.08527

VIRTUAL TREATMENT PLANNING IN WILLIAMS AND ALAGILLE PATIENTS WITH PERIPHERAL PULMONARY ARTERY STENOSIS

Ingrid S. Lan (1), Weiguang Yang (2), Jeffrey A. Feinstein (1,2), R. Thomas Collins II (2), Alison L. Marsden (1,2)

(1) Bioengineering
Stanford University
Stanford, CA, USA

(2) Pediatric Cardiology
Stanford University
Stanford, CA, USA

INTRODUCTION

Peripheral pulmonary artery stenosis (PPAS) is a congenital heart disease found in isolation or in association with Williams and Alagille syndromes. PPAS is characterized by stenoses in the central and peripheral pulmonary arteries (PAs) and results in lung perfusion disparity, right ventricular (RV) hypertension, RV hypertrophy, and ultimately RV failure [1]. No clinical consensus exists regarding the optimal treatment strategy for Williams and Alagille patients with PPAS. Hanley et al. at Lucile Packard Children's Hospital (LPCH) demonstrated that surgical PA reconstruction (PAR), involving comprehensive homograft patch augmentation of all stenoses from the central to lobar and segmental PAs, effectively normalizes RV pressures and provides excellent long-term outcomes with low rates of morbidity, mortality, and reintervention [1-3]. However, patch augmentation of lobar and segmental stenoses is a challenging surgical procedure requiring long hours in the operating room and specialized expertise. Transcatheter interventions thus remain the standard of care for PPAS at most centers despite evidence of unfavorable outcomes, including persistent RV hypertension, pulmonary hemorrhage, vessel dissection, aneurysm formation, rupture, in-stent restenosis, and even death [4-6].

To our knowledge, no prior studies have investigated hemodynamic conditions following transcatheter interventions in Alagille or Williams patients. While previous computational fluid dynamics (CFD) studies modeled the post-operative hemodynamics following surgical PAR in Alagille patients [7-8], these models were not validated against post-operative PA pressures, the primary indicators of success in PPAS repair. Autoregulation of blood flow was considered in response to perturbations in wall shear stress (WSS), yet did not include other factors of known importance to pulmonary vascular adaptation, such as intraluminal pressure and metabolite concentrations [9-11]. Furthermore, adaptation of pulmonary inflow was not considered in response to changes in pulmonary vascular resistance (PVR) [12]. In this study, we aim to predict post-stent PA hemodynamics for Williams and Alagille patients with PPAS using physiologically sound methods to adapt both the cardiac output and downstream PVR. We validate our methods on two patients who underwent stent placement, and subsequently assess the hemodynamic consequences of virtual stenting in four patients who underwent surgical PAR. We further develop the foundations of a virtual treatment planning platform by identifying lesions most responsible for the elevated PVR.

METHODS

The open-source software SimVascular (simvascular.org) was used to construct patient-specific pre- and post-stenting 3D anatomical finite element PA models for n=2 patients who underwent PA stent placement at outside institutions and n=4 patients who underwent surgical PAR at LPCH. Under the guidance of interventional cardiologists, virtual stenting was performed by modifying the lumen segmentations of stented vessels. **Figure 1** shows catheter angiograms most representative of the disease burdens, the CTA/MRA-based pre-stent models, and the modified segmentations for the post-stent models. Hemodynamic simulations were performed with a backflow-stabilized 3D Navier-Stokes solver, and fluid-structure interaction was incorporated via the coupled momentum method [13] with prescribed elastic moduli of 2.5×10^6 dyn/cm^2 for the unstented PAs and 2.5×10^8 dyn/cm^2 for the stented regions. The MPA inlet and PA outlets were coupled to lumped parameter networks (LPNs) representing the upstream right heart and downstream vasculature, respectively (**Figure 2A**). An automated tuning framework was developed to iteratively identify boundary conditions (BCs) that best achieve patient-specific pre-stent systolic, diastolic, and mean pressures at the main PA (MPA), proximal left PA (LPA), and proximal right PA (RPA) measured via cardiac catheterization. To leverage numerical optimization, we designed a high-fidelity nonlinear 0D surrogate of the 3D PA domain (**Figure 2B**). In progressing from the pre- to post-stent simulation for

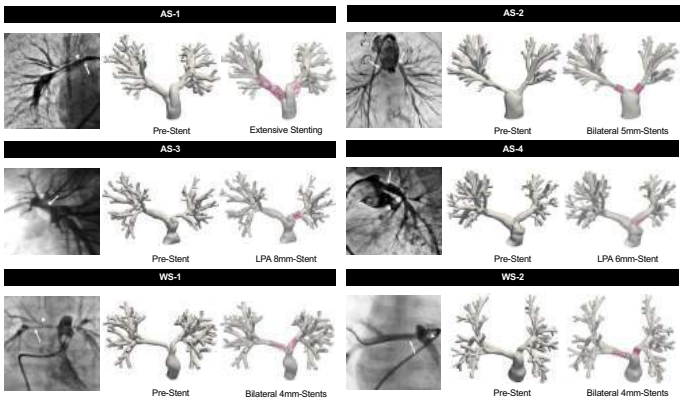

Figure 1: Catheterization angiograms, pre-stent models, and virtual stenting for Williams (WS) and Alagille (AS) patients.

each patient, parameters in the right heart LPN were maintained, as the governing equations offer an automatic approach for adapting the cardiac output in response to altered PA pressures and PVR. To capture vascular adaptation in response to changing hemodynamics, arterial resistances downstream of the PA outlets were adapted with an empirical model for stable autoregulation in response to perturbations in WSS, intraluminal pressure and metabolite concentrations [10-11]. Specifically, the pre-stent arterial network downstream of each PA outlet was modeled with a structured tree [14]; vessel diameters in the structured tree were subsequently adapted. Post-stent predictions of PA pressures were validated on the stenting cohort (n=2) prior to application to the surgical cohort (n=4). To facilitate treatment planning, pre-stent vessel segment resistances were computed to identify the most critical lesions for repair.

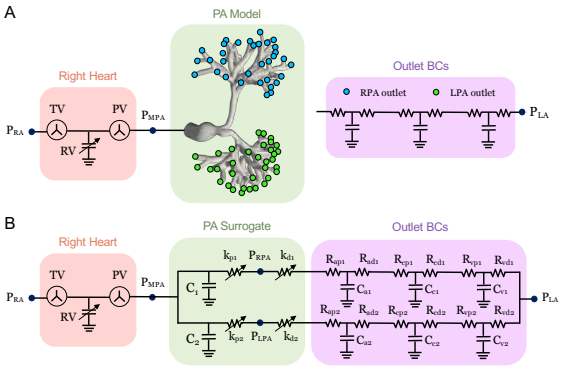

Figure 2: (A) LPNs coupled to the 3D PA model as inlet and outlet BCs and (B) the LPN used for automated BC tuning.

RESULTS

For all six patients, the automated tuning framework successfully identified parameters in the coupled inlet and outlet LPNs that achieved all pre-stent target pressures within 5 mm Hg. Correspondingly, the severe pre-stent pressure drops across the proximal stenoses were accurately captured. While PA flow distributions were not available for all patients and thus were not included as tuning targets, the simulated RPA flow fractions fell within 4% for the 3 patients with available data. Furthermore, we successfully validated our predictions of post-stent pressures for the stenting cohort (within 5 mm Hg of catheterization measurements), suggesting that our numerical methods offer physiological means for adapting the cardiac output and downstream PVR. While most patients were virtually stented only in the proximal PAs to reflect the standard of care, patient AS-1 underwent extensive stenting into the lobar PAs as a bridge therapy to liver transplantation.

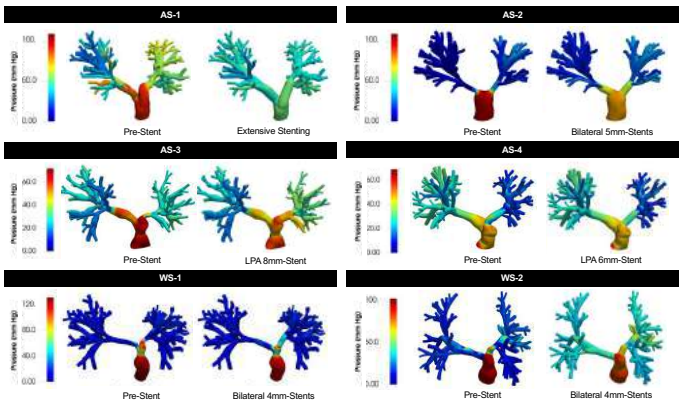

Figure 3: Pre- and post-stent systolic PA pressures.

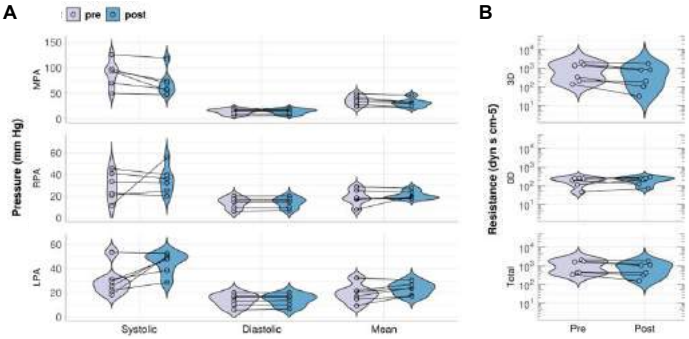

Figure 4: Pre- and post-stent PA pressures and PVR.

Stent placement did not sufficiently normalize PA pressures in any patient but yielded the largest improvement in AS-1, with decreases in systolic and mean MPA pressures by 41% and 26%, respectively. In addition, our pre-stent vessel segment resistance maps effectively identified lesions contributing the most to the elevated PA pressures. We therefore plan to perform additional virtual stenting procedures informed by these segment resistance maps, such that both proximal and extensive stenting are assessed per patient.

DISCUSSION

While surgical PAR has been found to normalize long-term PA pressures at LPCH, transcatheter interventions remain the standard of care for PPAS repair despite its associated complications in Williams and Alagille patients. CFD simulations provide a unique platform for virtual patient-specific treatment planning, in which anatomical models are altered to represent different interventions. Accurate predictions of post-interventional hemodynamics are critical to the success of such a platform, and we have indeed incorporated the relevant autoregulatory physiology and successfully validated our predictions for post-stent hemodynamics. Our results suggest that while lobar stenting reduces pressures beyond the limits of proximal stenting, stenting remains ineffective for normalizing PA pressures in Williams and Alagille patients with PPAS. We note that our methods are broadly applicable to CFD investigations of other cardiovascular interventions.

ACKNOWLEDGEMENTS

This study is supported by the NSF Graduate Research Fellowship and the Stanford Graduate Fellowship in Science and Engineering. CFD simulations were performed using Stanford Research Computing Center's Sherlock and the Extreme Science and Engineering Discovery Environment (XSEDE) under NSF grant number ACI-1548562.

REFERENCES

[1] Monge, MC et al., *J Thorac Cardiovasc Surg*, 145:476-481, 2013.
[2] Collins, RT et al., *Ann Thorac Surg*, 108:146-153, 2019.
[3] Luong, R et al., *J Pediatr* In press, 2020.
[4] Adamson, GT et al., *Catheter cardiovasc Interv* 95:262-269, 2020.
[5] Cunningham, JW et al., *Circ Cardiovasc Interv* 6:460-467, 2013.
[6] Hallbergson, A et al., *Am J Cardiol*, 113(3):541-545, 2014.
[7] Yang, W et al., *Biomech Model Mechanobiol*, 15:1345-1353, 2016.
[8] Yang, W et al., *Congenit Heart Dis*, 13:241-250, 2018.
[9] Carlson, BE et al., *Am J Physiol Heart Circ* 295:H1572-1579, 2008.
[10] Pries, AR et al., *Am J Physiol* 275:H349-360, 1998.
[11] Pries, AR et al., *Am J Physiol Heart Circ* 281:H1015-1025, 2001.
[12] Pennati, G et al., *Interface Focus* 1:297-307, 2011.
[13] Figueroa, CA et al., *Comput Methods in Appl Mech Eng*, 195:5685-5706, 2006.
[14] Olufsen, MS, *Am J Physiol*(1 Pt2):H257-268, 1999.

REVERSIBLE INHIBITION OF MYOFIBROBLAST ACTIVITY TO IMPROVE ELBOW RANGE OF MOTION AFTER CAPSULECTOMY

Jordan A. Jensen (1), Venkat Ganesh (1), Mariam Y. El-Hattab (1), Jaidev Chakka (2), Juliana C. Quarterman (2), Timothy P. Fowler (3), Emily Petersen (3), Douglas Fredricks (3), James A. Martin (3), Aliasger K. Salem (2), Edward A. Sander (1,3)

(1) Roy J. Carver Department of Biomedical Engineering
University of Iowa
Iowa City, IA, USA

(2) Department of Pharmaceutical Science
University of Iowa
Iowa City, IA, USA

(3) Department of Orthopedics and Rehabilitation
University of Iowa
Iowa City, IA, USA

INTRODUCTION

Post-traumatic joint contracture in the elbow results in reduced range of motion (ROM), primarily due to thickening, stiffening and contracture of the joint capsule. When nonsurgical interventions, such as physical therapy and splinting, are ineffective, surgical capsular release is performed. However, capsular release generally only improves ROM but does not restore it to its normal range. In addition, the surgical procedure itself often initiates additional fibrosis and contraction that reduces ROM gains. Consequently, better treatment methods are needed.

A common feature of fibrotic tissue is the chronic presence of activated myofibroblasts. Myofibroblasts are a fibroblast phenotype distinguished by the expression of alpha smooth muscle actin (α-SMA) in the cytoskeleton and their ability to generate large traction forces and deposit collagen and other extracellular matrix (ECM) proteins. These cells are also highly responsive to their mechanical environment and the presence of biochemical factors, such as TGF-β1. These components interact dynamically and reciprocally with the myofibroblasts in a mechano-chemical feedback loop that can resolve with either normal or pathological healing. We hypothesize that one can control this feedback loop so that myofibroblast activity is reduced, healing proceeds normally, and ROM is improved/restored. One strategy we are exploring is to temporarily block non-muscle myosin II (NMMII)-actin engagement in myofibroblasts with the drug blebbistatin (or one its derivatives). Previously, we demonstrated that blebbistatin-loaded poly(lactide-co-gylcolide) (PLGA) particles could safely inhibit myofibroblast contractile forces and reduce collagen synthesis *in vitro* [1]. We are now exploring whether the controlled-release of blebbistatin or para-nitro blebbistatin can limit elbow joint contracture in an established Long-Evans rat model [2]. We are also exploring the kinetics of drug release and its activity on cells as a function of drug formulation parameters, such as the use of PLGA microparticles versus pellets, in a force measuring bioreactor. This bioreactor allows quantification of myofibroblast force generation and downstream collagen production, data that are used to help evaluate and inform the complimentary animal studies.

METHODS

Drug Encapsulation and Characterization

6 g of 50:50 PLGA polymer was finely grounded into a powder and well-mixed with 100 mg of blebbistatin. The polymer-drug mix was hot-melt extruded at into a long filament 1 mm in diameter and cut by hand into ~5 mm long pellets. Pre-weighed blebbistatin loaded PLGA pellets were incubated at 37 ºC with 1 mL of PBS and 1% Tween-80. 1 µL samples were drawn regularly to quantify drug release via HPLC-UV. The blebbistatin-loaded PLGA microparticles were fabricated as detailed in [1] and characterized the same way as the pellets.

In Vitro Cell Response

Rabbit joint capsule fibroblasts (RJCFs) obtained from medial synovial tissues were used to evaluate the drug and its action *in vitro*. RJCFs were homogeneously dispersed in 0.5 mL fibrin gels that were detached from the wells of 24-well plates after 24 hours, imaged for an additional 24 to 48 hours, and then analyzed for area reduction. Additionally, rectangular fibrin gels were polymerized within a custom force measuring bioreactor. A rigid glass rod and a calibrated, bendable Nitinol wire were embedded at each end of the gel. Contractile force was calculated from the amount of wire deflection observed over time using an overhead microcontroller-based time-lapse imaging system. Functional relationships between drug release and myofibroblast contractility were evaluated under conditions that included no blebbistatin, 50 µM blebbistatin in DMSO, 50 µM blebbistatin-loaded

PLGA microparticles, and 50 μM blebbistatin-loaded PLGA pellets. After 10 days, the fibrin gels were imaged for collagen visualization and assayed for collagen content.

Long-Evans Rat Contracture Model

Following the contracture model developed by Lake *et al.* [2], Long-Evans rat left elbows will be subjected to an anterior capsulotomy, transection of lateral collateral ligament, and immobilization for 6 weeks to produce a contracted elbow. Injured and non-injured controls will be compared with blebbistatin treatment groups at days 7, 21 and 42. Differences will be assessed with histology and mechanical testing. A flexion-extension device was built to interface with an ElectroForce® Planar Biaxial Test Bench Instrument. It has been used to assess uninjured joint total ROM, neutral zone length, and ROM midpoint from torque-angle curves and will be applied to the other groups soon.

RESULTS AND DISCUSSION

Previously, we characterized the release properties of blebbistatin-loaded PLGA microparticles [1]. However, the encapsulation efficiency of those particles was only ~30%. In addition, ~75% of the drug was released within 120 hours (Fig. 1A). To increase encapsulation efficiency and the reservoir of implanted drug, blebbistatin-loaded PLGA pellets were also made.

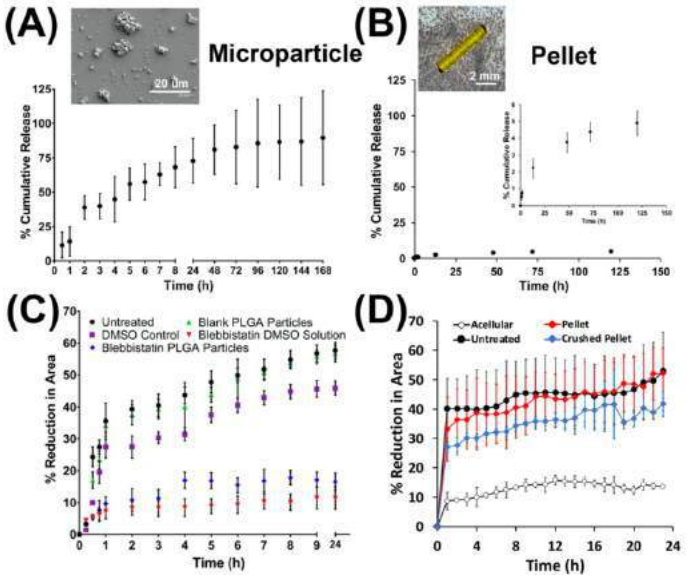

Fig. 1: (A) 75% of the blebbistatin in PLGA microparticles was released after 120 hours [1]. (B) Only 5% of the blebbistatin was released from the pellets over the same period. (C) Microparticles inhibited myofibroblast gel compaction almost to the same degree as blebbistatin in solution [1]. (D) Blebbistatin released from intact pellets did not impact myofibroblast activity. Less compaction was observed when crushed pellets were used due to the increase in available surface area for drug diffusion.

The release of drug from pellets was much slower (~ 5%) after 120 hours compared to microparticles (Fig. 1B). The two formulations variably changed myofibroblast activity. In microparticles (Fig. 1C), the drug activity was similar to adding the drug (dissolved in DMSO) directly to solution. In contrast, the amount of drug released from intact pellets (Fig 1D) was too low to have an impact over the short-term. Crushed pellets, which provided more surface area for drug release, did reduce gel compaction, though not to the same extent as microparticles.

Addition of blebbistatin dissolved in DMSO to the force bioreactor (Fig. 2A) resulted in a 30% reduction in myofibroblast traction forces, which were quantified from wire deflection recovery (Fig. 2B, C)). Additional data for the response to drug delivery via microparticles and pellets is ongoing.

Fig. 2: (A) Schematic showing the main components of the force bioreactor and measurement of the amount of wire deflection, δ. (B) An overhead camera images each of 6 bioreactors every hour. The bioreactors slowly rotate under the camera via a turntable. (C) Gel compaction and wire deflection generally reach equilibrium after 48 hours. Addition of blebbistatin in DMSO temporarily reduced cell traction forces by ~ 30%.

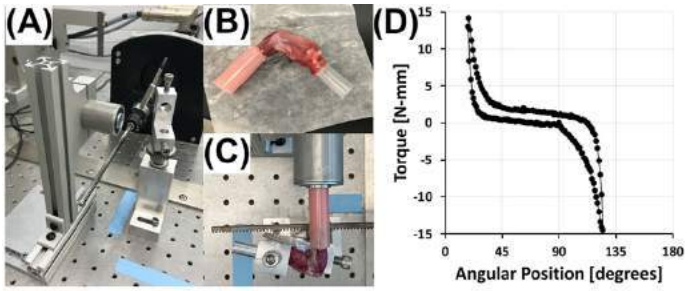

Fig. 3: (A) The fixtures for mechanical testing, (B) an excised Long-Evans rat arm potted for testing, (C) a representative image of the flexion-extension test, and (D) mechanical data for an uninjured rat elbow.

Load-controlled flexion-extension testing on uninjured rat elbows were completed successfully comparable with the results of Lake *et al.* [2]. The total ROM, neutral zone length, and ROM midpoint for the representative sample depicted in Fig. 3D was 107°, 76.4°, and 68.2°, respectively. Additional mechanical testing of injured and injured/treated arms is ongoing.

The combination of detailed *in vitro* studies with an animal model of the elbow contracture is providing complementary and unique data on mechano-chemical components responsible for contracture and on the feasibility of targeting NMMII with small molecules as an alternative/adjunctive treatment for elbow contractures. The knowledge gained here should also have broad applicability to other fibrotic conditions.

ACKNOWLEDGEMENTS

Support for this work was provided by the National Institutes of Health (NIH 1R21AR075137-01A1). We also acknowledge assistance provided by Dr. Spencer Lake, Alex Reiter, Dr. Sathivel Chinnathambi, and Dr. Keerthi Atluri.

REFERENCES

[1] Atluri *et al.* ACS Biomaterials Science & Engineering 2 (7), 1097-1107 (2016)

[2] Lake *et al.* Journal of Orthopaedic Research 34 (2). 354-364 (2016)

LARGER MUSCLE FIBERS AND FIBER BUNDLES MANIFEST SMALLER ELASTIC MODULUS IN PARASPINAL MUSCLES OF RATS AND HUMANS

Masoud Malakoutian (1), Marine Theret (2), Shun Yamamoto (3), Iraj Dehghan-Hamani (1), Michael Lee (3), John Street (3), Fabio Rossi (2), Stephen Brown (4), Thomas Oxland (1,3)

(1) Department of Mechanical Engineering
University of British Columbia
Vancouver, BC, Canada

(2) Department of Medical Genetics and School of Biomedical Engineering
University of British Columbia
Vancouver, BC, Canada

(3) Department of Orthopaedics
University of British Columbia
Vancouver, BC, Canada

(4) Department of Human Health and Nutritional Sciences
University of Guelph
Guelph, ON, Canada

INTRODUCTION

Passive elastic modulus of muscles is important for biomechanical functioning of the musculoskeletal system. While most studies assume that the size of a muscle fiber bundle (i.e. a number of muscle fibers ensheathed in their connective tissue) does not influence elastic modulus after normalizing for cross sectional area, elastic modulus of muscle fibers has been shown to be size-dependent [1]. The objectives of this study were to determine the degree to which this size effect was evident in muscle fiber bundles and to examine the validity of the frequent assumption of a circular cross section of muscle fiber bundles.

METHODS

Muscle fibers and fiber bundles were extracted from lumbar spine multifidus and longissimus of three cohorts: group one (G1) and two (G2) included 13 (330±14g) and 6 (452±28g) Sprague-Dawley rats, while Group 3 (G3) comprised 9 human degenerative spine patients. A minimum of six muscle fibers and six muscle fiber bundles from each muscle underwent cumulative stretches, each of 10% strain followed by 4 minutes relaxation. Elastic modulus was calculated as tangent at 30% strain from the resulting stress-strain curve. Linear correlations between the fiber/fiber bundle cross sectional area and elastic moduli in each group were performed. Major and minor axis diameters of fibers and fiber bundles were measured and their ratios were calculated. The results were contrasted against the theoretical median of 1 (for cylindrical shape assumption) using Wilcoxon signed rank test.

RESULTS

In total, 391 fibers (192 in G1, 112 in G2, 87 in G3) and 570 bundles of fibers (262 in G1, 137 in G2, and 171 in G3) were tested. Bundles contained 14±7 fibers. The correlations showed that increasing specimen cross sectional area resulted in lower elastic modulus for both rats and humans, muscle fibers and fiber bundles (all $p<0.05$ except for G2 longissimus bundles with $p=0.21$, Figures 1-2). The median ratio of major to minor axis exceeded 1.0 for all groups, ranging between 1.15 and 1.29 for fibers and 1.27 and 1.44 for fiber bundles (Figure 3).

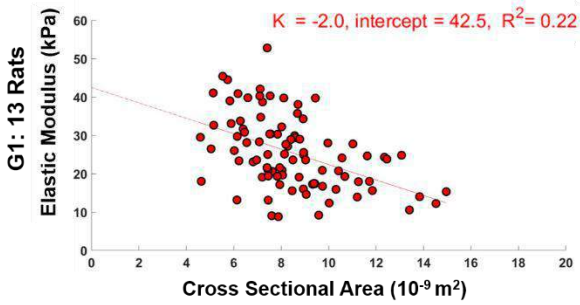

Figure 1: Correlation between elastic modulus and cross sectional area of G1 multifidus single fibers.

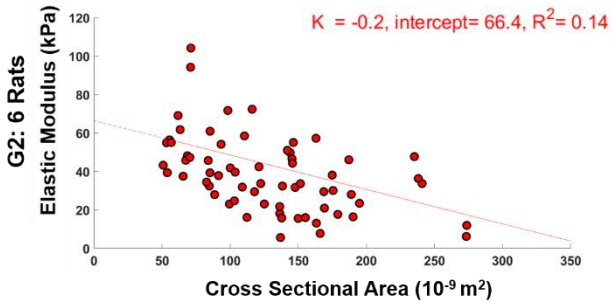

Figure 2: Correlation between elastic modulus and cross sectional area of G2 multifidus fiber bundles.

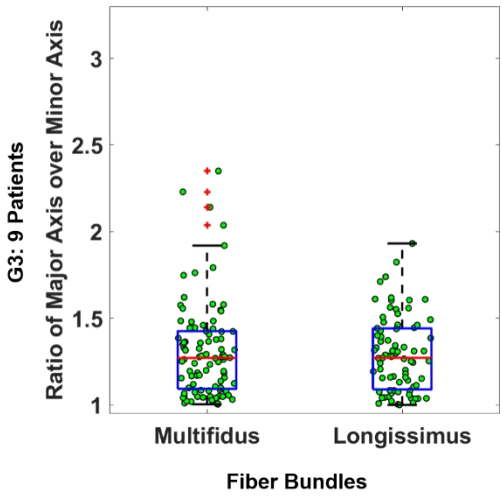

Figure 3: Ratio of major over minor axis diameters of fiber bundles tested in G3.

DISCUSSION

The results of this study demonstrated that the size matters and in general, larger sizes were associated with lower elastic moduli in muscle fibers and bundles of muscle fibers. Therefore, future studies should consider maintaining consistent bundle sizes for measurement of passive properties especially when comparing different groups against each other.

The lower elastic moduli with increasing size can be explained by relatively less collagenous extracellular matrix (ECM) in the large fiber bundles (Figure 4). It is well established that bundles of fibers have a larger elastic modulus than single fibers due to the high stiffness of ECM [2][3][4][5][6]. Assuming that the ECM and fibers within a bundle are both homogenous, the elastic modulus of a bundle can be calculated following the rule of mixture for composites as:

$$E_{Bundle} = f_{ECM}E_{ECM} + (1 - f_{ECM})E_{Fiber} \quad (1)$$

where E_{Bundle}, E_{ECM}, and E_{Fiber} are the elastic moduli of the bundle, the extracellular matrix, and fibers, respectively; and f_{ECM} denotes the percentage of the extra cellular matrix within the bundle. For example, the elastic modulus of a bundle containing 5% ECM (i.e. $f_{ECM} = 0.05$) with a fiber elastic modulus of 20 kPa and ECM elastic modulus of 1MPa [6] is calculated as 69 kPa. The predicted bundle elastic modulus would be 79 kPa or 59 kPa had the ECM percentage been changed to 6% or 4%, respectively.

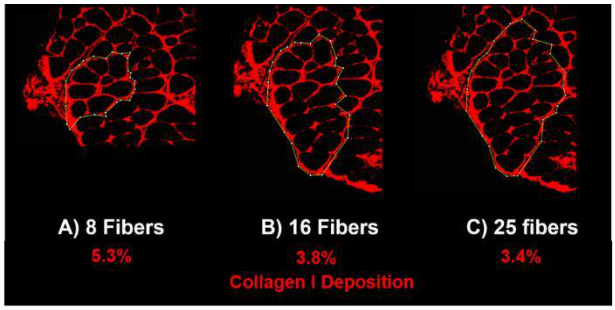

Figure 4: Inverse correlation between collagen I area fraction and size of three bundles of different sizes from multifidus of one rat in G1. Yellow lines represent the borders of selected bundles.

In a recent study, Ward et al. [7] measured the elastic modulus of rabbit muscles at multiple levels, i.e. single fibers, fiber bundles (~20 fibers), fascicles (~300 fibers), and whole muscles. They found that elastic modulus increases nonlinearly with these size scales as does the collagen content. The results of the current study demonstrated that larger bundles were associated with lower elastic moduli. These results are not in conflict, but rather they are complementary. Our results suggest that for fiber bundles of less than ~50 fibers larger sizes will be associated with smaller elastic moduli. However, beyond a certain size (e.g. ~300 fibers), bundles will transition to true fascicles, including the presence of perimysium and higher amounts of collagenous tissue, thereby leading to larger elastic moduli compared to bundles. In conclusion, the findings of our study suggest that future studies of passive property measurement should aim for consistent bundle sizes and measuring diameters of two orthogonal axes of the muscle fibers and fiber bundles.

ACKNOWLEDGEMENTS

The authors would like to acknowledge the support and funding received from Medtronic Canada and Natural Sciences and Engineering Research Council of Canada.

REFERENCES

1. Noonan AM, Zwambag DP, Mazara N, et al (2020) Fiber Type and Size as Sources of Variation in Human Single Muscle Fiber Passive Elasticity. J Biomech Eng 142:. https://doi.org/10.1115/1.4047423
2. Brown SHM, Gregory DE, Carr JA, et al (2011) ISSLS prize winner: Adaptations to the multifidus muscle in response to experimentally induced intervertebral disc degeneration. Spine (Phila Pa 1976) 36:1728–1736. https://doi.org/10.1097/BRS.0b013e318212b44b
3. Prado LG, Makarenko I, Andresen C, et al (2005) Isoform diversity of giant proteins in relation to passive and active contractile properties of rabbit skeletal muscles. J Gen Physiol 126:461–480. https://doi.org/10.1085/jgp.200509364
4. Zwambag DP, Gsell KY, Brown SHM (2019) Characterization of the passive mechanical properties of spine muscles across species. J Biomech 88:173–179. https://doi.org/10.1016/j.jbiomech.2019.03.036
5. Ward SR, Tomiya A, Regev GJ, et al (2009) Passive mechanical properties of the lumbar multifidus muscle support its role as a stabilizer. J Biomech 42:1384–1389. https://doi.org/10.1016/j.jbiomech.2008.09.042
6. Meyer GA, Lieber RL (2011) Elucidation of extracellular matrix mechanics from muscle fibers and fiber bundles. J Biomech 44:771–773. https://doi.org/10.1016/j.jbiomech.2010.10.044
7. Ward SR, Winters TM, O'Connor SM, Lieber RL (2020) Non-linear Scaling of Passive Mechanical Properties in Fibers, Bundles, Fascicles and Whole Rabbit Muscles. Front Physiol 11:. https://doi.org/10.3389/fphys.2020.00211

THE IMPACT OF INJECTION TIMING AND LOCATION ON MICROPARTICLE DELIVERY FOR TUMOR TARGETING IN A PATIENT-SPECIFIC LIVER

Tim Bomberna (1), Chris Verslype (2), Lawrence Bonne (3), Geert Maleux (3,4), Charlotte Debbaut (1)

(1) IBiTech-bioMMeda
Ghent University
Ghent, Belgium

(2) Department of Clinical Digestive Oncology
University Hospitals Leuven, KU Leuven
Leuven, Belgium

(3) Department of Radiology
University Hospitals, KU Leuven
Leuven, Belgium

(4) Department of Imaging and Pathology
University Hospitals, KU Leuven
Leuven, Belgium

INTRODUCTION

Hepatocellular carcinoma (HCC), the most common form of primary liver cancer, is one of the leading causes of cancer-related deaths worldwide. In 80-90% of HCC patients, cirrhosis is present [1].

The preferred treatment for unresectable HCC is transarterial chemo- or radioembolization (TACE or TARE). During these therapies, microparticles are injected in the hepatic arteries to selectively damage tumor tissue through a combination of embolization and a secondary chemotherapeutic effect (TACE), or through emission of high-intensity beta radiation (TARE) [2]. The goal of these transarterial therapies is to maximize the dose delivered to tumor tissue and limit the offsite-toxicity delivered to healthy tissue.

However, the impact of clinical parameters (e.g. the injection's location and timing) and microparticle characteristics (e.g. size and density) on the particle distribution is unclear. Therefore, computational fluid dynamics (CFD) may help to understand this impact and potentially use these parameters to improve the clinical outcome [3].

To date, Childress et al. [4] studied the impact of injection timing during the cardiac cycle in two simplified literature-derived hepatic arterial geometries. However, Aramburu et al. [3] noted that the geometry has a significant impact on the particle distribution. Therefore, we previously studied the impact of particle size, density and injection location in two patient-specific hepatic arterial geometries [5].

In this study, the impact of injection timing will be investigated for two axial injection locations in a patient-specific geometry.

METHODS

Geometry & meshing. The liver geometry was obtained by combining vascular corrosion casting and micro-CT imaging of a cirrhotic human liver (see [6] for more details). The hepatic network was segmented and 3D reconstructed using Mimics and 3-matic software (Materialise, Leuven, Belgium). A volume mesh containing $9 \cdot 10^6$ tetrahedral elements and three prism boundary layers was created in ICEM CFD (Ansys Inc., Canonsburg, USA).

CFD. Blood flow (continuous phase) was modeled using a density of 1060 kg/m³ and a modified Quemada model for viscosity. The mass transport of particles (discrete phase) in the fluid phase was calculated in a Lagrangian framework using the Discrete Phase Model (DPM) in Ansys Fluent (Ansys Inc., Canonsburg, USA). The presence of a moderate tumor (565 ml) was modeled in liver segment IV (outlets 1-6, see Fig. 1) using outflow percentage boundary conditions (ranging between 1.25 and 27.75%) based on the arterial perfusion distribution methodology proposed by Aramburu et al. [7]. At the inlet, a transient flow waveform was specified, with a cycle length of 0.8 s and cycle-averaged flow of 481.2 ml/min. The fluid time step was alternated between $1 \cdot 10^{-3}$ and $5 \cdot 10^{-4}$ s depending on convergence conditions. Particles with a diameter of 40 µm and a density of 1600 kg/m³, mimicking SIR-Spheres (Sirtex Medical Australia) used for TARE, were released from the inlet (see '1' in Fig. 1; simulation 1 (Sim1)), and from a second axial injection location near the second bifurcation (see '2' in Fig. 1; Sim2). Seven (Sim1) or six (Sim2) cardiac cycles were run, and particles were released every 0.01 s during the third cycle (1.6 s-2.4 s).

RESULTS

For each injection timing, Particle Release Maps (PRMs) were generated. As shown in Fig. 1, PRMs are visualizations of the injection plane cross-section, showing where particles should be injected to reach certain exit branches (ideally, the tumor-perfusing branches (TPB)). In Composite Particle Release Maps (CPRMs), particles are colored according to their target specificity throughout the cycle, where *e* indicates for which % of the selected injection timings particle fates

corresponded with exit through a TPB (see Fig. 2B & 3B). Here, 16 evenly-spaced injection timings between 1.60s and 2.35s were selected, comparing particle fates from one injection timing to their nearest-neighbor fates at other timings.

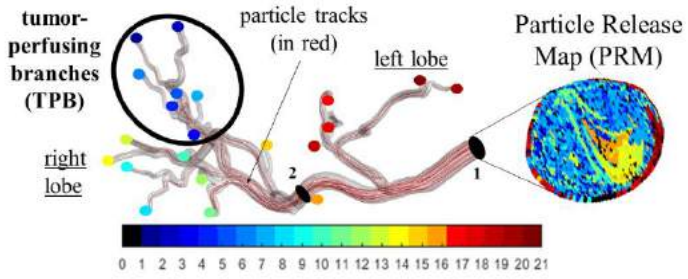

Figure 1: A Particle Release Map (PRM) shows where particles should be injected to reach the tumor.

In Fig. 2A-3A, the PRMs are given for injections at several injection timings (t = 1.60s, 1.80s, 2.00s, 2.20s) at the inlet and at the second bifurcation, respectively. As is clear, the PRM patterns vary significantly between the two axial locations. Moreover, the tumor targeting zone (shown in blue, outlets 1-6 in Fig. 1) varies significantly throughout the cycle. However, injection typically lasts for several cardiac cycles. Therefore, in Fig. 2B-3B, the corresponding CPRMs are given, with the green cells (e > 80%) indicating the cross-sectional injection locations where particles exit through a TPB for >80% of the cycle. These zones can be considered as ideal zones to position the catheter tip throughout the whole cycle.

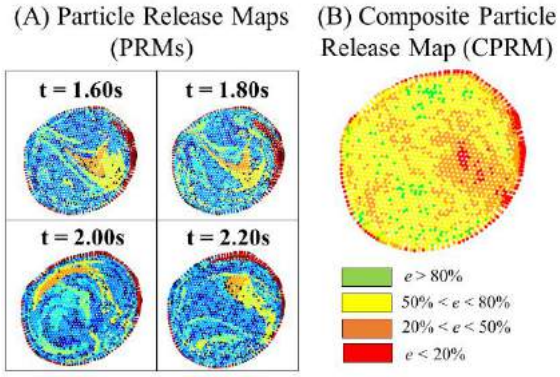

Figure 2: (A) PRMs and (B) CPRM for the inlet injection.

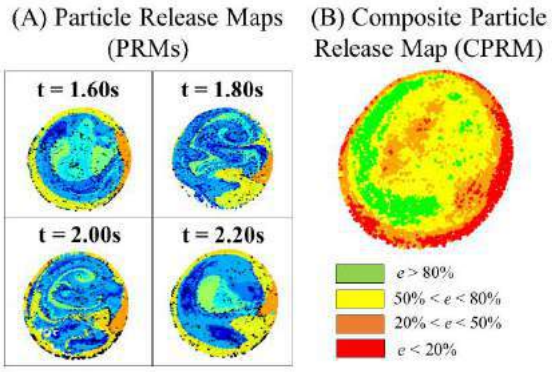

Figure 3: (A) PRMs and (B) CPRM for injection near the second bifurcation.

For the inlet, these ideal locations are distributed over the whole cross-section (4% of total particles displayed). However, for the injection location near the second bifurcation, the ideal cross-sectional injection locations are less spread out and form a much larger, more clearly delineated injection zone (16.8% of total particles).

DISCUSSION

Childress et al. [4] constructed CPRMs for their two idealized hepatic arterial geometries (with only 5 and 3 outlets, no tumors modeled). They noted that for their basic 5-outlet geometry there was little variation between the PRMs for different injection timings, and that clear targeting zones could be distinguished in the CPRM for each exit branch. Interestingly, they noted that the variation was much higher for their 3-outlet geometry, and that there were no clear targeting zones in the CPRM. This implies the importance of the arterial geometry.

In this study, a much more complex, patient-specific arterial geometry was considered (with 21 outlets). As shown in Fig. 2, the variation between the PRMs was large for different injection timings. The CPRMs in Fig.2B & 3B show that for inlet injections there was no clear tumor targeting zone (green), while for injections at the second bifurcation the targeting zone was much clearer. This suggests that the results do not only depend on the arterial geometry, but also on the axial injection location. These results support our hypothesis that injection locations closer to the tumor make it easier to target the tumor.

The strengths of the study lie in (i) the consideration of a complex, patient-specific cirrhotic liver geometry, (ii) the direct comparison of two axial injection locations, and (iii) the modeling of a realistic cancer scenario with increased arterial perfusion in the TPB.

The limitations lie in considering only surface injections. The next step in the workflow includes modeling of the catheter, releasing a targeted injection from the suggested targeting zone (green, Fig. 2B-3B) and investigating the impact of catheter presence on the local hemodynamics and downstream particle distribution. Moreover, a wider range of axial injection locations and particle properties (i.e. size, density) should be studied for their impact on the CPRMs.

Judging from Fig. 2B-3B, there might be a trade-off between the choice of axial and cross-sectional location: far away from the tumor, the ideal targeting zones are minimal, implying that the cross-sectional injection location needs to be very precise; while, closer to the tumor, the ideal targeting zones are larger, and the location of the catheter tip matters less. Since accurate intra-arterial positioning of the catheter tip may prove to be a complex task, the ideal targeting zone should be maximized as much as possible.

In conclusion, the CPRM, studied on a wider scale of injection locations and particle properties, can be a helpful tool in selecting the most optimal injection conditions (i.e. those which maximize the ideal targeting zone) for efficient patient-specific tumor targeting.

ACKNOWLEDGEMENTS

This research was supported by the strategic basic FWO grant 1S10421N.

REFERENCES

[1] Tang, A et al., *Abdom Radiol*, 43:13–25, 2018.
[2] Salem, R et al., *Clin Gastroeneterol Hepatol*, 11:604–611,2013.
[3] Aramburu, J et al., *Curr Med Chem*, 25:1–15,2018.
[4] Childress, EM et al., *J Biomech Eng*, 134:051005,2012.
[5] Bomberna, T et al., Expert Opin Drug Deliv, 2020. [published online]
[6] Debbaut, C et al., *J Anat*, 224:509–517,2014.
[7] Aramburu, J et al., Int J Numer Method Biomed Eng, 32: e02764,2016.

EXCESS COLLAGEN DEPOSITION IN DIABETIC KIDNEY DISEASE ENHANCES CELLULAR COMMUNICATION: A MATHEMATICAL MODEL

Haryana Y. Thomas (1, 2), Ashlee N. Ford Versypt (1, 2)

(1) School of Chemical Engineering
Oklahoma State University
Stillwater, OK, USA

(2) Dept. of Chemical & Biological Engineering
University at Buffalo, SUNY
Buffalo, NY, USA

INTRODUCTION

Diabetes is a significant burden on public health in the U.S. and worldwide. In the year 2015, over 400 million people were diagnosed with diabetes worldwide—a number that is expected to rise to over 600 million in the year 2040 [1]. One-third of these diabetic patients are expected to develop diabetic kidney disease, the leading cause of end stage renal disease [1]. Our lack of understanding of how diabetic kidney disease progresses and affects cellular and tissue function has led to the shortage of effective treatment methods and thus our inability to mitigate the rapidly rising burden of diabetic kidney disease. Diabetic kidney disease, characterized by proteinuria and a loss in glomerular filtration rate, is induced by biochemical perturbations and morphological changes such as excess collagen deposition in the kidney [2,3]. Although excess collagen deposition is a hallmark of diabetic kidney damage, its impact on cellular and tissue function is still not well understood. Thus, our aim is to use a modeling approach to fill this gap in knowledge.

Collagen deposition occurs in the mesangium, a tissue located at the center of the filtration unit of the kidney, the glomerulus. The mesangium is composed of a collagenous matrix and is the region that separates the three key glomerular cells: mesangial, endothelial and podocyte cells. Studies have shown that these three cell types are in constant communication and that interference in this communication can lead to dysfunction within the glomerulus [4-8]. During diabetic kidney damage, the collagen deposition that occurs in the mesangium changes the transport property of the matrix, and, therefore, the ability of signaling molecules to traverse through that medium. The extent to which collagen deposition impacts the ability of glomerular cells to communicate has not been previously investigated. Using established models, we investigate whether collagen deposition impacts glomerular cell communication. We hypothesize that the pathological deposition of collagen decreases the ability of glomerular cells to communicate.

Method

We first mathematically derive a property, the effective signaling distance (ESD), to quantify cell-cell communication in a similar manner to Francis et al. [9] with some changes. In our model, we consider a single mesangial cell that is secreting signaling molecules that diffuse from the cell surface through the extracellular matrix toward podocyte cells. The mass balance for the signaling molecules is

$$\frac{\partial c}{\partial t} = D\frac{1}{r^2}\frac{\partial}{\partial r}\left[r^2\frac{\partial c}{\partial r}\right] \tag{1}$$

where c represents the concentration of the signaling molecules, D is the diffusion coefficient of signaling molecules through the matrix, and r represents the radial distance from the center of the cell. The first boundary condition imposed is

$$-D\frac{\partial c}{\partial r} = F_o \quad \text{at} \quad r = \rho \tag{2}$$

where F_o is a constant secretion rate at the cell surface located at position ρ. The second boundary condition imposed is

$$c \to 0 \quad \text{as} \quad r \to \infty \tag{3}$$

We also postulate that initially there are no signaling molecules present in the matrix, representing the onset of pathological disturbed secretion of signaling molecules. The analytical solution is

$$c = \frac{F_o\rho}{D}\varphi(r,t) \tag{4}$$

where $\varphi(r,t)$ is a function composed of exponential and error functions that depend on r and t [9]. The steady state value of φ is $1/r$. Substituting k_m for c as the minimum concentration required to induce a response in the receiving cell, we can solve for the position for ESD

$$ESD = r = \frac{F_o\rho}{Dk_m} \tag{5}$$

which we define as the steady state propagation distance of k_m.

Secondly, we use an experimentally validated, empirical model to quantify how collagen deposition in the matrix affects the diffusivity of signaling molecules [10]

$$D = D_o \exp\left(-\pi\Phi^b\right) \exp\left(-0.84 f^{1.09}\right) \quad (6)$$

where D is the effective diffusion coefficient, D_o is the free diffusion coefficient, Φ is the volume fraction of collagen in the matrix, and b and f are parameters that depend on the solute radius and the matrix fiber radius. The Stokes-Einstein equation is used to estimate D_o.

RESULTS

The concentration profile of the signaling molecule diffusing through a healthy matrix (Figure 1) shows that over time the signaling molecules accumulate until a steady state concentration of twice the threshold concentration is reached at the cell surface.

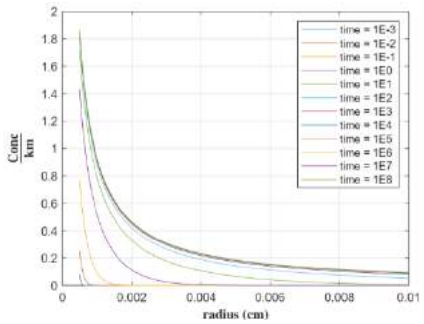

Figure 1. Concentration profile of signaling molecule over time (s)

The propagation of the threshold concentration through the spatial domain clears shows the approach to steady state (Figure 2).

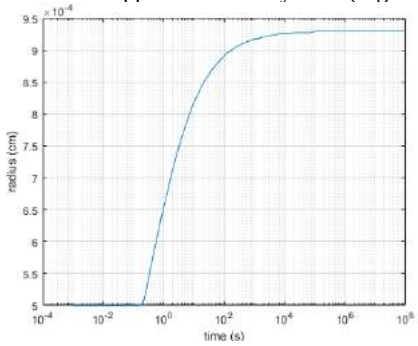

Figure 2. Propagation of the threshold concentration k_m

Unlike Francis et al. [9], we define the ESD at the steady state because steady state is approached much faster in the glomerular anatomy than the generalized infinite domain. The dependence of ESD on the diffusivity of signaling molecules through a diseased matrix is also explored (Figure 3). As the matrix volume fraction increases due to collagen deposition, the effective signaling distance for small signaling molecules increases by over two-fold from an initial signaling distance of 2.5 cell radii. This is surprising, because we had hypothesized that as the matrix becomes diseased, the ability of cells to communicate would decrease; however, we see from these results that a diseased matrix actually enhances the ability of a cell to signal rather than diminishing it if the secretion rate is kept constant. The results also show that larger signaling molecules have greater signaling distances than smaller signaling molecules and that their signaling distance is further increased in diseased conditions with larger volume fraction (Figure 3).

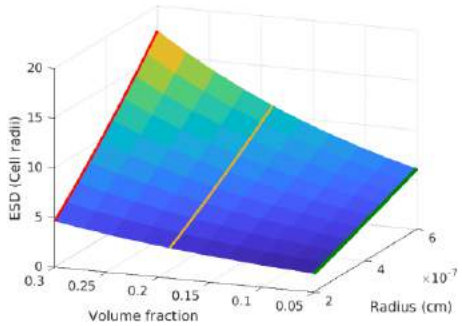

Figure 3. ESD increases with increased collagen deposition

DISCUSSION

As shown in our results, pathological collagen deposition during diabetic kidney disease actually enhances the ability of glomerular cells to communicate, counter to our hypothesis. The unexpected result is due to the counterintuitive nature of diffusion, where a slower diffusivity results in a larger propagation distance. This unusual behavior of diffusion has been observed and documented by others in other contexts [11,12].

Our predicted values for the ESD in the healthy case is within the expected range. Using experimental methods, Bagnall et al. found that the signaling distance for fibroblast cells is on the order of a few cell diameters [13], similar to our model prediction of 2-5 cell radii. Our predictions regarding the changes in ESD due to collagen deposition, however, need experimental validation.

In our model, we assume that there is no breakdown and no self-consumption of the signaling molecules, which leads to an overestimate of ESD, and that no convective transport of signaling molecules occurs, leading to an underestimate of ESD. Although we cannot say the extent to which each assumption impacts the ESD, their opposing influence on ESD could nullify any individual impact. Regardless, this is a potential area for future work. In conclusion, the model provides quantitative insight into the impact of collagen deposition on cellular communication and thus expands our understanding of how diabetic kidney damage affects cellular function.

ACKNOWLEDGEMENTS

This material is based upon work supported by the National Science Foundation under Grant No. 1845117 and resources from Oklahoma State University and the University at Buffalo.

REFERENCES

[1] Jitraknatee, J et al., *Scientific Reports*, 10:1-10, 2020
[2] Ban, C. R. et al., *Vascular Health and Risk Management*, 4:575–96, 2008
[3] Mason, M. R et al., *JASN*, 14:1358-1373, 2003
[4] Leveen, P et al., *Genes and Development*, 8:1875-1887, 1994
[5] Lindahl, P et al., *Development*, 15:3313-3322, 1998
[6] Soriano, P, *Genes and Development*, 8:1888-1896, 1994
[7] Bjarnegard, M et al., *Development*, 131:1847–1857, 2004
[8] Schlondorff, D et al., *JASN*, 20:1179-1187, 2009
[9] Francis, K et al., *PNAS*, 94:12258-12262, 1997
[10] Hunt et al., *Physiol Renal Physiol*, 310:222-229, 2015
[11] Lander A, *Cell*, 128:245-256, 2007
[12] Saha K, *Development*, 133:889-900, 2006
[13] Bagnall J, *Science Signaling*, 11(540), 2018

METHACRYLATED RECOMBINANT COLLAGEN PEPTIDE (RCP-MA) AS COLLAGEN MIMICKING 3D HYDROGEL MODEL FOR CARDIAC TISSUE ENGINEERING

D. Mostert[1, 2], I. Jorba[1, 2], L. Klouda[1], N.A. Kurniawan[1, 2], C.V.C. Bouten[1, 2]

[1] Soft Tissue Engineering and Mechanobiology
Eindhoven University of Technology
Eindhoven, the Netherlands

[2] Institute for Complex Molecular Systems (ICMS)
Eindhoven University of Technology
Eindhoven, the Netherlands

INTRODUCTION

The myocardium is a mechanically active tissue environment. Following cardiomyocyte death, for instance due to an ischemic insult, the response to injury induces a phenotypical switch from cardiac fibroblast (cFB) to myofibroblast. This will lead to excessive collagen deposition and extracellular matrix (ECM) remodeling, eventually resulting in a stiff fibrotic tissue (E = 35 – 70 kPa), as opposed to undamaged myocardium (E = 5 - 10 kPa) [1]. Presently, it is not well documented how cardiomyocyte progenitor cells (CPCs) perceive alterations in the stiffness of the myocardial microenvironment. Three dimensional (3D) ECM mimicking model systems with tunable stiffness and native-like adhesion sites may shed light on cardiac cell behavior under these circumstances to potentially design strategies to halt adverse remodeling.

Collagen is the most abundant protein in the ECM. It not only provides structural support for cells and tissues, but also mediates many important biological processes through interactions with various binding partners [2]. Up to now, animal-derived collagen and gelatin have often been used to mimic human collagen in 3D scaffolds for disease modeling and tissue engineering purposes. However, increasing concerns associated with animal derived materials in healthcare, batch-to-batch differences, and the inability to tune the stiffness of collagen in a well-controlled manner result in a strong need for an alternative, preferably synthetic, material. Methacrylated Recombinant Collagen Peptide (RCP-MA, Fujifilm) is a collagen mimicking peptide based on human collagen I, produced by a yeast fermentation process, containing no animal-derived components. The peptide is highly reproducible and enriched with arginine-glycine-aspartic acid (RGD) sequences to allow control over its cell-adhesive properties. Moreover, RCP-MA is modified to contain methacrylic groups that enable chemical crosslinking and hydrogel fabrication with a stiffness ranging from 1 kPa to ~300 kPa.

In this study, we explore the usage of RCP-MA as a 3D *in vitro* mechanobiology study platform. With this model, we aim to exploit the tunability of RCP-MA to study how normal and pathology-mimicking myocardial stiffness affects CPC behavior and stiffness perception. To do this, we investigate the expression of cell-specific markers and YAP localization, an important component of the Hippo pathway that conveys mechanical signals from the ECM to intracellular signals that guide cell fate.

METHODS

RCP-MA hydrogels were fabricated by solubilizing RCP-MA (kindly provided by Fujifilm Manufacturing Europe B.V.) with 20% and 50% degrees of methacrylation (%DS) in sterile cell culture medium and chemical crosslinking with UV (Omnicure) at 365 nm in sterile Teflon molds, using lithium phenyl-2,4,6-trimethylbenzoylphosphinate (LAP) as photo-initiator. In this project, RCP-MA was used with 20% DS and 50% DS. Cell-free hydrogel constructs were physicochemically characterized by micro-indentation (Microtester G2, CellScale, Canada) and swelling experiments.

To allow cell encapsulation in separate experiments, pelleted CPCs were resuspended at a concentration of 1×10^6 $cells/ml$ in RCP-MA prepolymer solution before crosslinking. For cell encapsulation experiments, hydrogels were fabricated from prepolymer solutions of a) a 1:1 mixture of 20% DS and 50% DS and 2) 50% DS, and illuminated for 30 s at 2.5 mW/cm^2. Hydrogel biocompatibility was assessed with live/dead staining (calcein AM/propidium iodide) and the phenotype and YAP localization were determined using whole mount immunofluorescence staining.

RESULTS

Micro-indentation experiments were performed to determine whether the different number of photo-crosslinkable methacrylations for RCP-MA had an influence on the final mechanical properties of the crosslinked hydrogels. As expected, a clear difference was observed between the 20%, the 20/50% (1:1), and 50% RCP-MA precursor mixtures (Figure 1A), demonstrating a higher Young's modulus (E-modulus) with increasing number of photo-crosslinkable moieties that can be chemically crosslinked with UV irradiation. A 30s exposure at 2.5 mW/cm^2 of 20/50% (1:1) and 50% RCP-MA resulted in hydrogels that mimic the stiffness of normal and pathological myocardium, respectively (Figure 1B).

Cell viability assays of CPCs encapsulated inside the RCP-MA hydrogel constructs showed viable cells (>70%) up to ten days of culture. Starting from three days of culture inside the hydrogel constructs, live cell imaging (calcein AM) of CPCs displayed an elongated morphology and cellular network formation, allowing cell – cell contact between individual CPCs (Figure 2). After 48 hours of culture on top of the RCP-MA hydrogel constructs, the CPCs produced and deposited fibronectin (data not shown).

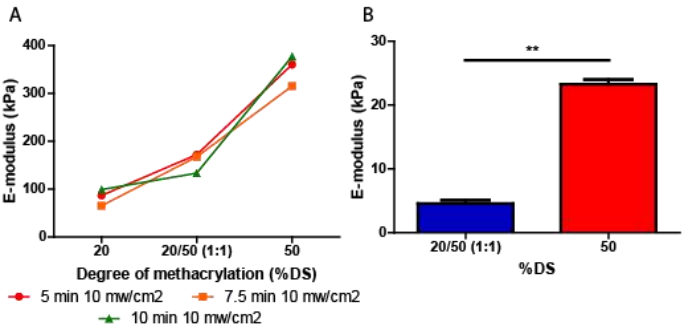

Figure 1: A) Young's modulus (E-modulus) of RCP-MA hydrogels upon varying degree of methacrylation (%DS). B) RCP-MA hydrogels with normal and pathology mimicking stiffness for myocardial disease modelling. $^{**}p < 0.01$.

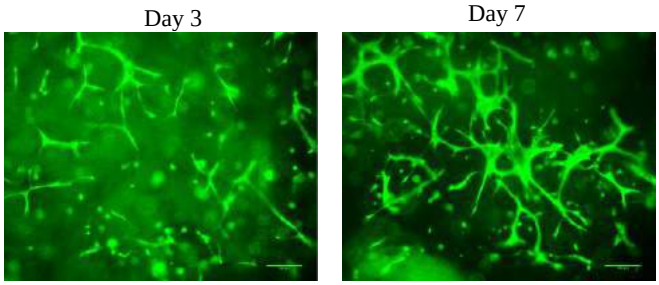

Figure 2: Cardiac progenitor cells (CPCs) demonstrate an elongated morphology and network formation in RCP-MA hydrogels. Calcein AM staining of CPCs (green) after 3 and 7 days of culture inside 20/50% (1:1) RCP-MA. Scale bar indicates 100 µm.

DISCUSSION

The present study reports on the mechanical behaviour of RCP-MA hydrogels as well as the biocompatibility with cardiac cells. The results show that the mechanical behaviour of the RCP-MA hydrogels is affected by the crosslinking of methacrylic functionalities with UV, leading to a range of mechanical properties that can be tuned in a well-controlled manner. Our results indicate that 20/50% (1:1) DS and 50% RCP-MA precursor solutions can be crosslinked into hydrogels that mimic the stiffness of normal and pathological myocardial tissue. *In vitro* biological evaluation demonstrated that RCP-MA is biocompatible towards CPCs, showing elongated cell morphologies and cell – cell contact up to ten days of culture inside the 3D hydrogel constructs. Taken together, these results indicate that RCP-MA is an attractive synthetic alternative to animal-derived collagen or gelatin constructs for cardiac disease modelling. Further studies will focus on the effect of myocardial stiffness on the behaviour and YAP signalling of CPCs. Moreover, the biocompatibility of RCP-MA towards other cardiac cell types, such as cFBs and cardiomyocytes, will be studied.

ACKNOWLEDGEMENTS

This project is funded by the Gravitation Program 'Materials Driven Regeneration' subsidized by the Netherlands Organization for Scientific Research (024.003.013).

REFERENCES

[1] Engler, A. J. et al., Bergmann, G et al., *J of Cell Science*, 121, 22,11, 2008.
[2] Ghazanfari, S. et al., *Biomaterials*, 97, 74-84, 2016.

MECHANICAL STIMULATION MEDIATES THE CHANGES IN MULTISCALE TENDON MECHANICS OBSERVED DURING EMBRYONIC DEVELOPMENT

Benjamin E. Peterson (1), Spencer E. Szczesny (1,2)

(1) Department of Biomedical Engineering
Pennsylvania State University
University Park, PA, USA

(2) Department of Orthopaedics and Rehabilitation
Pennsylvania State University
Hershey, PA, USA

INTRODUCTION

Despite significant efforts, no tissue engineered construct has successfully replaced a tendon or ligament in a human patient[1]. Clues on how to advance current tissue engineering approaches may lie in understanding how tendons form during embryonic development. In particular, chick tendons undergo rapid changes in macroscale mechanics during late embryonic development that produce a tissue with high tensile load-bearing capabilities[2]. Previous work suggests that this mechanical transformation is due to increases in collagen fibril length[3] and mechanical stimulation via muscle activity[4]. However, no study has investigated the multiscale tensile mechanics of embryonic chick tendons or their dependence on mechanical stimulation. Therefore, **the objective of this study was to measure the changes in multiscale tendon mechanics during late embryonic development and identify the effect of skeletal muscle paralysis**. We hypothesized that the increase in tendon macroscale mechanical properties with development will coincide with an increase in the fibril strains and a reduction in interfibrillar sliding, which is consistent with increasing fibril lengths[5]. Additionally, we hypothesized that skeletal muscle paralysis will prevent the developmental changes in both the fibrillar deformations (i.e., strains and sliding) and the macroscale tissue properties observed during late embryogenesis. This information will provide a deeper understanding of the mechanisms driving tendon development, which will guide the development of tissue engineered constructs that can successfully replicate tendon function.

METHODS

Fertilized chicken eggs obtained with IACUC approval were set within a benchtop egg incubator. At embryonic day 3 (E3), eggs were windowed according to established procedures[6]. At day 15 (E15), eggs were treated to induce rigid or flaccid skeletal paralysis via injection with either 100 µl of 0.02% decamethonium bromide (DMB) or pancuronium bromide (PB), respectively. Control samples were injected with 100 µl of saline. Subsequent injections of 50 µl were then administered daily from E16 – E19. Embryonic motility (events/2 min) was examined daily from E15 – E19 following established protocols[6]. Embryos were sacrificed at E16, E18, and E20 for testing.

Mechanical testing was conducted using a custom uniaxial microtensile device mounted atop a confocal microscope[7]. For each test, the flexor digitorum longus tendon was dissected and stained with 5 µg/ml DTAF. Samples were loaded within custom grips at a gauge length of 10 mm and preloaded to 0.1 g. The tendon major/minor diameters were measured from z-stack images and the cross-sectional area was quantified assuming an elliptical cross-section. Three sets of photobleached lines (PBL) (4 lines, 80 µm apart) were bleached at the sample center and ± 1.5 mm from the center. Samples were loaded to failure in 2% grip-to-grip strain increments. At each strain increment, z-stack images were acquired at all PBL locations. The stage positions of the two peripheral PBL sets were used to calculate the macroscale tissue strain. Fibril strains and sliding were calculated at each PBL site by measuring the displacement between the photobleached lines and their tortuosity, respectively[5]. The fibril:tissue strain ratio was calculated by dividing the mean fibril strain by the tissue strain at each increment.

A two-way ANOVA was used to test for differences in motility with regards to age and paralysis. A one-way ANOVA with a Dunnett's or Tukey's correction was used to measure differences in modulus due to paralysis or development, respectively. An ANCOVA with Bonferroni post-hoc tests was used to determine if the fibril:tissue strain ratio or fibril sliding was dependent on age or paralysis. Linear regressions determined the correlation between the fibril:tissue strain ratio and the applied tissue strain, and t-tests determined if the average fibril:tissue strain ratio was significantly less than 1. Significance was set at $p < 0.05$.

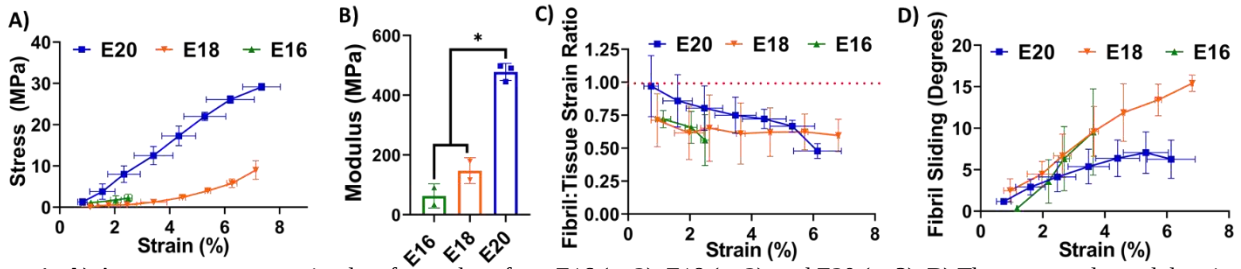

Figure 1: A) Average stress vs. strain plots for tendons from E16 (n=2), E18 (n=2), and E20 (n=3). **B)** The macroscale modulus significantly increased with developmental age. **C)** The fibril:tissue strain ratio in only the E20 samples was negatively correlated with the applied tissue strain but was significantly different from one for all ages. D) There was a significant decrease in fibril sliding with increasing developmental age.

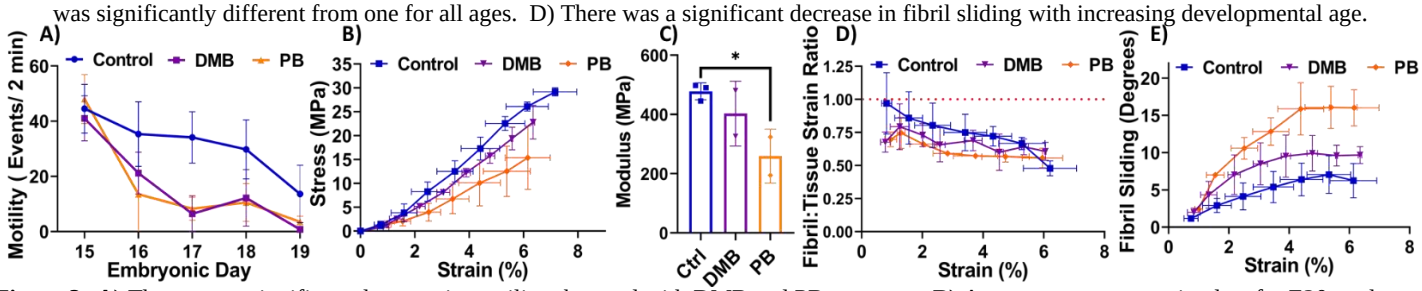

Figure 2: A) There was a significant decrease in motility observed with DMB and PB treatment. **B)** Average stress vs. strain plots for E20 tendons with vehicle control (n=3), rigid paralysis (DMB, n=2), and flaccid paralysis (PB, n=2). **C)** There was a significant decrease in modulus with PB treatment. **D)** The fibril:tissue strain ratio was significantly different from one in all samples and was negatively correlated with applied tissue strain for control and PB tendons. **E)** There was a significant increase in fibril sliding with PB treatment but not with DMB.

RESULTS

Tendons at E20 had a significantly greater macroscale modulus compared to earlier developmental ages ($p < 0.05$) (**Fig. 1A-B**). While the average fibril:tissue strain ratio was less than one for all ages ($p < 0.05$) (**Fig. 1C**), ANCOVA analysis indicated a significant effect due to age ($p < 0.05$) and only the E20 samples displayed a negative correlation with applied tissue strain ($p < 0.001$). Furthermore, there was a significant decrease in fibril sliding comparing E16 versus E20 ($p < 0.01$) and E18 versus E20 ($p < 0.001$) (**Fig. 1D**).

While both DMB and PB significantly reduced motility during development ($p < 0.05$) (**Fig. 2A**), a significant drop in modulus was only observed with PB treatment ($p < 0.05$) (**Fig. 2B-C**). The average fibril:tissue strain ratio was significantly less than one for all samples ($p< 0.01$) (**Fig. 2D**) and no treatment effects were observed from ANCOVA analysis. However, only the control and PB treated samples were negatively correlated with the applied strain ($p < 0.01$). Compared to control tendons, there was a significant increase in fibril sliding with PB treatment ($p < 0.001$) but not DMB ($p = 0.07$) (**Fig. 2E**).

DISCUSSION

This study demonstrated that there is a shift in tendon multiscale mechanics during late embryonic development that is consistent with increasing fibril lengths. Specifically, the increase in the macroscale modulus observed with development (**Fig. 1B**) is accompanied by an increase in the fibril:tissue strain ratio at low applied tissue strains leading to a negative correlation with increasing strain (**Fig. 1C**). Additionally, there was a decrease in fibril sliding with increasing developmental age (**Fig. 1D**). Together, these data suggest that more of the applied tissue strain is being transmitted to the collagen fibrils at later embryonic ages, which is consistent with our hypothesis and previous work suggesting that collagen fibrils fuse and rapidly elongate during late embryonic development[3,5]. While further work involving multiscale modeling and direct measurement of fibril lengths through ultrastructural imaging is necessary to confirm this interpretation, our findings suggest that collagen fibril elongation is the key structural change driving late embryonic tendon development.

Our findings additionally found that mechanical stimulation was necessary to induce the multiscale mechanical changes observed during tendon development. Flaccid paralysis reduced the increase in macroscale modulus seen during normal development (**Fig. 2C**). Furthermore, while not statistically significant due to a low sample size, there appeared to be a small drop in the fibril:strain ratio at low applied tissue strains for the PB samples (**Fig. 2D**). This suggests that flaccid paralysis retards tendon development by preventing fibril elongation and inhibiting strain transmission to the fibrils, which is supported by the increased fibril sliding with PB treatment (**Fig. 2E**). Interestingly, there was a similar but muted effect on the multiscale tendon mechanics with rigid paralysis (i.e., DMB treatment). Since previous work demonstrated that DMB reduces the compressive modulus of embryonic chick tendons[4], the lack of statistical significance in our DMB data may be due to a small sample size. Still, the smaller effect size of DMB compared to PB treatment suggests that while rigid paralysis prevents dynamic muscle activity, it still produces static tension (and hence some mechanical stimulation). This suggests that cyclic mechanical stimulation is critical for proper tendon development.

Altogether, our multiscale tensile testing of embryonic tendons supports the hypothesis that fibril elongation is essential for producing a robust tensile load-bearing tissue and that this structural change is mediated by cyclic rather than static mechanical stimulation. Future work will investigate whether these findings translate into improved approaches to produce tissue-engineered constructs that can successfully replicate tendon and ligament function.

ACKNOWLEDGEMENTS

This work was funded by the NIH (R21 AR075941).

REFERENCES

[1] Shearn et al., *JMNI*, 2011; 1**1(2)**: 163-73
[2] McBride et al., *Int. J. biol. Macromol*., 1998; **10(4):**194-200
[3] Birk et al., *Dev. Dyn*., 1995: **202(3)**:229-43
[4] Pan et al., *Phil. Trans. R. Soc B.*, 2018; **373**: 20170325
[5] Szczesny et al. *Acta Biomat*., 2014; **10(6):**2582-2590
[6] Wu et al., *JEZB:MDE*, 2001; **291**:186-194
[7] Peterson et al., *Acta Biomat.*, 2020; **117**:302-3

AUTOMATED ESTIMATION OF PATIENT-SPECIFIC BOUNDARY CONDITIONS FOR CARDIOVASCULAR SIMULATIONS: AN OPTIMAL CONTROL APPROACH

Elisa Fevola (1), Francesco Ballarin (2), Laura Jimenez-Juan (3), Piero Triverio (4), Stefano Grivet-Talocia (1), Gianlugi Rozza (2)

(1) Department of Electronics and Telecommunications
Politecnico di Torino
Torino, Italy

(2) mathLab, Mathematics area
SISSA – International School for Advanced Studies
Trieste, Italy

(3) St Michael's Hospital and Sunnybrook Research Institute
University of Toronto
Toronto, Canada

(4) Department of Electrical & Computer Engineering, Institute of Biomaterials & Biomedical Engineering
University of Toronto
Toronto, Canada

INTRODUCTION

In recent years, large advancements have been made in the development of patient-specific cardiovascular models for blood flow simulations. In these simulations, the choice of appropriate boundary conditions is a crucial step, since they have a large influence on the resulting flow rates and hemodynamic parameters of clinical relevance, such as wall shear stress (WSS). In-vivo measurements, if available, can be used to guide the selection of boundary conditions, such that simulation results better match clinical data. A common approach is to split a given inlet flow rate among all outlets according to their area by means of Murray's law [1]. From the obtained flows and an estimate of pressure, the resistance to be placed at each outlet is obtained. However, manual tuning is required to match in-vivo data, which is time consuming and operator dependent. More systematic methods have been proposed based on optimal control [2], Bayesian estimation [3], and Kalman filtering [4].

With optimal control, a rigorous Lagrangian approach [5] is used to determine the optimal value of resistance boundary conditions that match the given in-vivo measurements. Optimal control was applied to a glass replica of cardiovascular models [6] and to coronary artery bypass grafts [2], but using less realistic Neumann-type boundary conditions. In this work, we propose an optimal control framework for determining resistance-type boundary conditions in patient-specific aortic models, starting from flow measurements obtained with 4D-Flow MRI. We show the validity of the proposed framework on a real clinical case, and investigate the influence of the obtained boundary conditions on WSS and oscillatory shear index (OSI).

METHODS

We present the proposed method by considering the aortic arch represented in Fig. 1, with the goal of determining the values of the resistance R_i imposed at each outlet. The anatomy of the vessels was derived from the computed tomography (CT) images acquired with a 320 multidetector scanner (Aquilion ONE, Canon Medical Systems). From the CT images, the vessels surface was reconstructed using SimVascular (www.simvascular.org). A computational mesh was generated with Tetgen. After CT imaging, blood velocity was acquired in-vivo with 4D-Flow magnetic resonance imaging (MRI) with a 3T MRI scanner (MAGNETOM Aera, Siemens Healthineers).
Blood flow in the vessels is modelled with the steady Stokes equations

$$\begin{cases} -\eta\Delta v + \nabla p = f\,, & in\ \Omega \\ \nabla \cdot v = 0, & in\ \Omega \end{cases} \tag{1}$$

At the ascending aorta inlet Γ_{in}, a Poiseuille flow was imposed, whose average value was extracted from the 4D-Flow MRI data of the patient.

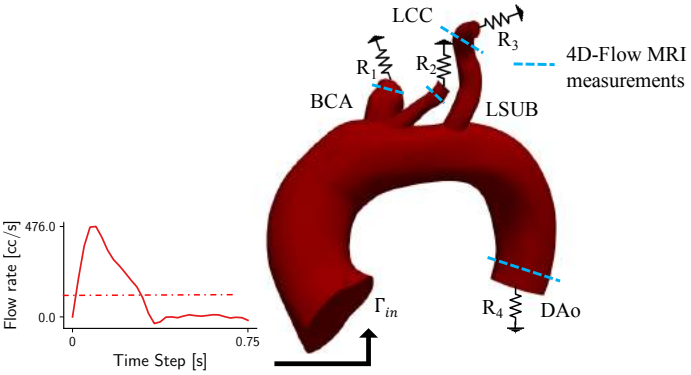

Figure 1: General setting of the proposed framework on a patient's aortic arch.

A no-slip condition was imposed at the vessel walls, assumed to be rigid. At the four outlets, corresponding to descending aorta (DAo), brachiocephalic artery (BCA), left common carotid artery (LCC) and left subclavian artery (LSUB), a resistive-type boundary condition was imposed following the coupled multidomain method proposed in [7]. The unknown resistance values R_i were then determined solving an optimal control problem. Optimal control estimates unknown parameters by minimizing a cost functional constrained by the governing equations of the system.

We defined a cost functional J with the following form:

$$J = \alpha_p \frac{\int_\Omega ||p - p_d||^2 d\Omega}{2\int_\Omega ||p_d||^2 d\Omega} + \sum_{i=1}^{4} \alpha_i \frac{\int_{\Gamma_i} ||v - v_i||^2 d\Gamma_i}{2\int_{\Gamma_i} ||v_i||^2 d\Gamma_i} + \sum_{i=1}^{4} \beta_i \frac{\int_{\Gamma_i} ||R_i||^2 d\Gamma_i}{2\int_{\Gamma_i} ||R_{i,M}||^2 d\Gamma_i} \quad (2)$$

where α_p is set to 100, α_i and β_i to 1, and $R_{i,M}$ is the resistance value at the outlet Γ_i obtained with Murray's law. The first term in (2) represents the difference between the pressure p obtained from (1) and the patient's average aortic pressure p_d derived from clinical data. The second term relates to the difference between the velocity v from (1) and the average velocity v_i measured at each outlet Γ_i. The third term consists of the norm of the control variables R_i, and acts as a regularization term. For solving the optimal control problem, we adopted an adjoint-based Lagrangian approach [5], first deriving the optimality system containing the first-order optimality conditions, and then recasting it to saddle-point form to obtain a monolithic algebraic system for easier computations. The obtained system was then solved with the open-source libraries FEniCS [8] and multiphenics [9].

RESULTS

The results obtained for the case of Fig. 1 are detailed in Table 1. On the first row, Table 1 reports the patient's average pressure measured non-invasively after MRI, and flow rates measured in-vivo with 4D flow MRI. The second and third row of the table report the values obtained with the boundary conditions estimated with Murray's law and with the proposed method. The pressure and flow values obtained with optimal control match the patient measurements quite closely, indicating a proper assimilation of in-vivo information. While a perfect match would be ideal, this is often not possible in practice, due to the noise and uncertainty affecting in-vivo measurements, and due to the assumptions of the adopted mathematical model (1). By minimizing (2), the proposed approach finds the set of boundary conditions that comes as close as possible to the given in-vivo information.

We also observe that the solution from the proposed method is not too far from the one obtained with Murray's law, where boundary conditions are set on the basis of purely anatomical information [1]. This observation further confirms the physiological validity of the boundary conditions selected by the proposed method. Table 2 reports the resistance values obtained with the two methods, Murray's law and optimal control. The values are similar, except for the LSUB resistance, which differs substantially (23%). To investigate how this difference may affect clinically-relevant hemodynamic parameters, we used the two sets of boundary conditions reported in Table 2 to run two unsteady high-fidelity Navier-Stokes simulations, using SimVascular. Resistance values were used to set three-element Windkessel models at each outlet, assuming a total capacitance of 0.001 cm^5/dyne, distributed among the various outlets with an area-based criterion. Fig. 2 depicts the absolute difference between the OSI computed with the two sets of boundary conditions. While the difference is negligible for the most part of the geometry, the difference reaches 40% of the OSI range (0÷0.5) in the region past the left subclavian artery.

Table 1: Comparison of average aortic pressure and outlet flow rates obtained with Murray's law and with the proposed method.

	Pressure (mmHg)	Flow rates (cm^3/s)			
		BCA	LCC	LSUB	DAo
Patient measurements	98.7	15.9	5.98	8.48	73.1
Murray's law	98.8	19.2	6.19	7.48	86.2
Proposed	95.2	19.8	6.10	9.41	83.9

Table 2: Resistance values obtained with Murray's law and with the proposed method (all values in dyn·s·cm^{-5}).

	DAo	BCA	LCC	LSUB
Murray's law	1,526	6,837	21,241	17,591
Proposed	1,513	6,409	20,801	13,467

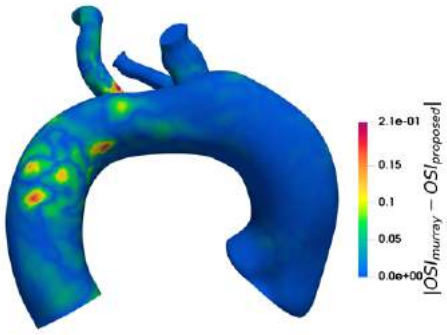

Figure 2: Absolute difference of OSI between Murray's law and the proposed method (back view of the aorta).

DISCUSSION

We proposed a computational framework for the determination of resistance-type outlet boundary conditions based on the assimilation of 4D-Flow MRI measurements by means of optimal control. Our study documents the application of such framework to a real clinical case and shows the influence that the choice of outlet boundary conditions has on OSI, one of the hemodynamic quantities of potential clinical interest. The presence of regions with a considerable difference from Murray's law-based results confirms the crucial role of boundary conditions in hemodynamic modeling, and suggests the need for further research on determining appropriate boundary conditions for computational hemodynamics.

REFERENCES

[1] Murray C.D, *Proc. of the Ntl Acad of Sciences USA*, 1926, 12.3: 207.
[2] Zainib. Z. et al., *Int J for Num Methods in Bio Eng,* 2020, e3367.
[3] Schiavazzi DE et al, *Int J for Num Methods in Bio Eng,* 2017; 33(3): e02799.
[4] Arthurs CJ et al, *Adv Mod Sim Eng Sciences,* 2020; 7(1): 1-37.
[5] Gunzburger MD, *Perspectives in Flow Control and Optimization,* SIAM, 2003.
[6] Koltukluoglu T. S. et al., *J Fluid Mech.,* 2018; 847: 329-364.
[7] Vignon-Clementel IE. et al., *Computer methods in applied mechanics and engineering,* 2006; 195(29-32): 3776-3796.
[8] Alnaes MS. et al., *Arch Numer Softw.,* 2015; 3(100): 9-23.
[9] https://mathlab.sissa.it/multiphenics. 2019

MODULATING THE BLOOD-BRAIN BARRIER BY PICOSECOND LASER STIMULATION OF MOLECULAR-TARGETED NANOPARTICLES

XQ. Li (1), V. Vemireddy (2,3), Q Cai (4) H. Xiong (4), X. Li (4), M. Giannotta (5), H. Hayenga (1), E. Pan (6), S. Sirsi (1), C Mateo (7), D Kleinfeld (7), C Greene (8), M Campbell (8) E. Dejana (5), R. Bachoo (2,3,6), Z. Qin (1,4,9,10)

(1) Department of Bioengineering, University of Texas at Dallas, Richardson, TX 75080, USA

(2) Department of Internal Medicine, University of Texas at Southwestern Medical Center, Dallas, TX 75390 USA

(3) Harold C. Simmons Comprehensive Cancer Center, University of Texas at Southwestern Medical Center, Dallas, TX 75390 USA

(4) Department of Mechanical Engineering, University of Texas at Dallas, Richardson, TX 75080 USA

(5) FIRC Institute of Molecular Oncology Foundation (IFOM), 20139 Milan, Italy

(6) Department of Neurology, University of Texas Southwestern Medical Center, Dallas, TX75390, USA

(7) Department of Physics, University of California San Diego, La Jolla, CA92093 USA

(8) Smurf Institute of Genetics, Trinity College Dublin, Dublin 2, Ireland

(9) Department of Surgery, University of Texas Southwestern Medical Center, Dallas, TX75390, USA

(10) Center for Advanced Pain Studies, University of Texas at Dallas, Richardson, TX 75080, USA

INTRODUCTION

Formed by the endothelial tight junction (TJ) and adherent junction complexes, the blood-brain barrier (BBB) plays a crucial role in protecting the brain parenchyma from the toxic effects of plasma proteins but also poses a formidable challenge to the delivery of therapeutics[1]. High osmotic mannitol to increase BBB permeability has mostly been abandoned due to procedure-related neurotoxicity[2]. While the use of focused ultrasound to increase BBB permeability have progressed to early-phase clinical trial, safety issues such as sterile inflammation[3] and loss of vasoreactivity[4] have been raised.

There is increasing evidence that a dysfunctional BBB is an integral component of many primary neurological brain diseases (e.g., Alzheimer's disease). Therefore, it is critical that the strategies used to disrupt the BBB in at-risk brains do so in a highly selective manner to minimize the risk of unintended injury. To address these challenges, we present a novel method that modulates the BBB with picosecond (ps) laser excitation of TJ-targeted plasmonic gold nanoparticles (**Fig. 1A**). This method increases permeability through the TJ without compromising its structural integrity or inducing any discernable neuronal injury. The increase in BBB permeability allows immunoglobulins (IgG), adeno-associated viral (AAV) vectors, and liposomes to enter the brain parenchyma.

METHODS

Nanoparticle synthesis and functionalization: Gold nanoparticles (AuNPs) were synthesized by previous reported method[5]. Then, the AuNPs were functionalized with antibody (BV11: anti-mouse JAM-A) for targeting JAM-A[6], one of the TJ proteins (**Fig. 1B**).

In vivo experiments: C57BL/6 mice were injected 18.5 μg/g AuNPs functionalized with BV11. We then applied ps laser pulse (532 nm, full width half maximum = 28 ps), through mouse skulls to excite the AuNPs on blood vessels. To mearsure BBB permeability, we intravenously (I.V.) inject tracer (980 Da Evans blue, or 660 Da EZ-link biotin and 70 kDa fluorescein isothiocyanate (FITC) labeled dextran) at different time points post laser stimulation. After 0.5 hr circulation, the mice were transcardially perfused with 25 ml PBS and 25 ml 4% PFA for tracer leakage study, or with 25 ml 2% lanthanum nitrate and 25 ml 2% PFA mixed with 2% glutaraldehyde for electron microscopy (EM) imaging. The brain tissue was extracted for tracer extravasation imaging and analysis.

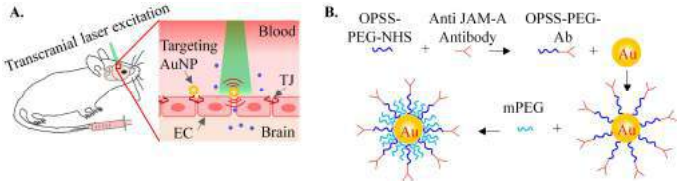

Fig.1. Methods of BBB modulation *in vivo*. (A) Schematic for laser excitation of TJ-targeted AuNP. (B) Synthesis of TJ-targeting AuNPs[7]. Ab: Antibody, EC: endothelial cell.

RESULTS AND DISCUSSION

Nanoparticle targeting and light modulation of the BBB by paracellular diffusion

We examined the targeting of AuNP-BV11 with intravenous injections. Silver enhancement staining of AuNP along brain capillaries was only seen in the case of AuNP-BV11, but not for non-targeting AuNP-PEG (PEG: polyethylene glycol) (**Fig. 2A**). EM imaging showed that AuNP-BV11 co-localizes with the TJ (**Fig. 2B**), indicating that AuNP-BV11 recognizes and targets TJ *in vivo*. Ps laser excitation of the TJ-targeted AuNP-BV11 temporarily increases BBB permeability, as indicated by Evans blue (albumin-bound, 66 kDa in total, **Fig. 2C**). Next, we co-administered tracers of different molecular weights. Leakage of the 660 Da EZ-link biotin was detected up to 6 hr, while 70 kDa FITC-dextran was only detected up to 1 hr after laser excitation (**Fig. 2D**). A size-selective temporal pattern of tracer entry into the brain parenchyma would be consistent with a gradual closing of a paracellular route. No leakage of the two tracers was observed 24 hr after laser excitation, suggesting that the BBB recovers within this time period.

To study the BBB modulation route, we performed transcardial perfusion with 2% lanthanum (La) nitrate after ps-laser stimulation. EM imaging reveals that BBB modulation leads to complete La filling in half of the TJ cleft (51%), while 49% showed partial filling (**Fig. 2E top**). In contrast, in control tissue near 100% of the TJ clefts showed La partial lining the luminal portion of the TJ cleft. Most strikingly, in the former, La was seen to line the basement membrane and diffuse into the interstitial space of the brain parenchyma (**Fig. 2E bottom**).

These results provide clear evidence to suggest that the increased BBB permeability involves the paracellular pathway to allow the passage of luminal tracers through the TJ cleft and into the brain interstitial space.

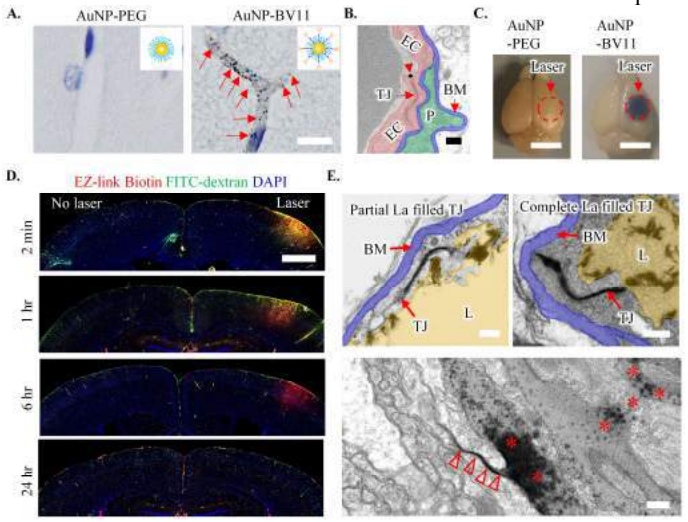

Fig. 2. Picosecond laser stimulation of TJ-targeted nanoparticles reversibly modulates BBB permeability by paracellular route. (A) AuNPs are visualized by silver enhancement staining. (B) AuNP-BV11 (arrow head) co-localizes with TJ detected by EM. (C) BBB modulation visualized by the leakage of albumin-binding Evans blue (25 mJ/cm^2, 1 pulse). (D) BBB permeability probed by molecular tracers (660 Da EZ-link biotin and 70 kDa FITC-dextran, 5 mJ/cm^2, 1 pulse). (E) EM imaging of La infused TJ of brain capillaries, and diffused into basement membrane (*) and interstitial space (empty arrow head). Pseudocolours: endothelial cell (EC: red), basement membrane (BM: blue), pericyte (P: green), Lumen (L: yellow). Scale bar: 10 µm (A), 200 nm [(B), (E)], 4 mm (C), 1 mm (D).

Impact of BBB modulation on brain parenchyma

To investigate the effect of BBB modulation on brain parenchyma post laser excitation (25 mJ/cm^2, 1 pulse, 72 hr post laser stimulation), we performed inmunohistochemry (IHC) staining. The change was not observed in neurons and their axonal processes (NeuN, Ankyrin-G) (**Fig. 3A**), nor in astrocyte end-foot process (AQP4), and pericyte (NG2) as mural support of the BBB (**Fig. 3B and C**). This suggests the BBB modulation doesn't affect the cellular architecture of the brain parenchyma.

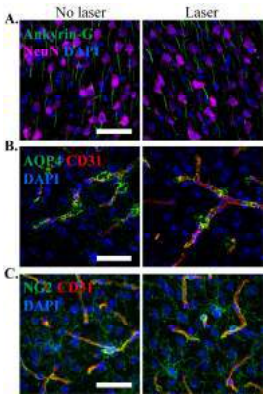

Fig. 3. BBB modulation preserves the cellular architecture. The IHC stianing of neuronal nucleus and axon indicated by NeuN and Ankyrin-G (A), water transporter of astrocyte endfeet indicated by AQP4 (B) and pericyte indicated by NG2 (C). Scael bar: 40 µm.

Antibody, gene, and nanoparticle delivery to the brain

Lastly, we demonstrate that the temporary BBB modulation allows successful delivery of functional molecules and particles, including IgG (**Fig. 4A**), gene therapy vector AAV (**Fig. 4B**) and liposome (**Fig.4C**), which indicates significant therapeutic potential.

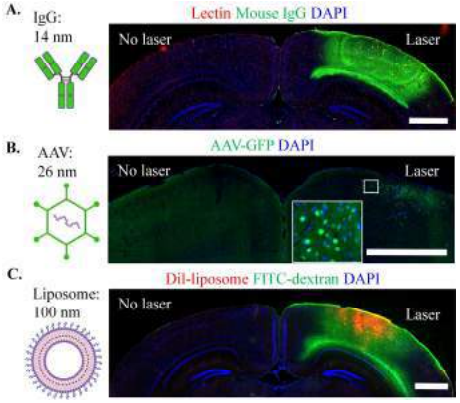

Fig. 4. BBB modulation enables delivery of functional molecules and particles. Delivery of mouse IgG antibody (A, 25 mJ/cm^2, 1 pulse), AAV-CamKII-GFP (B, 10 mJ/cm^2, 1 pulse), and liposome (C, 25 mJ/cm^2, 1 pulse) into the brain. Scale bar: 1 mm.

CONCLUSION

Picosecond-laser stimulation of TJ-targeted AuNPs temporarily increases the BBB paracellular permeability allowing macromolecules to diffuse through the TJ cleft into the interstitial space, including immunoglobulins, AAV particles and liposomes. The ps-laser induced increase in BBB permeability doesn't affect the brain parenchyma. Focal brain delivery of therapeutic agents through the BBB following systemic administration has important translational implications.

ACKNOWLEDGEMENTS

We acknowledge funding support from Cancer Prevention & Research Institution of Texas (RP160770, RP180846).

REFERENCES

1. Arvanitis, C.D., *et al*. *Nat Rev Cancer* **20**, 26-41 (2020).
2. Marchi, N., *et al. Epilepsia* **48**, 732-742 (2007).
3. Kovacs, Z.I., *et al. Proc Natl Acad Sci U S A* **114**, E75-E84 (2017).
4. Todd, N., *et al. J Control Release* **324**, 450-459 (2020).
5. Perrault, S.D. *et al. J Am Chem Soc* **131**, 17042-17043 (2009).
6. Bazzoni, G. *et al. Physiol Rev* **84**, 869-901 (2004).
7. Dai, Q., *et al. Angew Chem Int Ed Engl* **53**, 5093-5096 (2014).

LINKING GENE EXPRESSION, HEMODYNAMICS AND CELLULAR DYNAMICS IN A PATIENT-SPECIFIC MULTISCALE MODEL OF IN-STENT RESTENSOSIS

A. Corti (1), M. Colombo (1), S. Casarin (2,3,4), J. M. Rozowsky (5), Y. He (5), S. Bridio (1),

F. Migliavacca (1), J. F. Rodriguez Matas (1), S. A. Berceli (5,6), C. Chiastra (1,7)

(1) LaBS, Department of Chemistry, Materials and Chemical Engineering "Giulio Natta", Politecnico di Milano, Milan, Italy

(2) Center for Computational Surgery, Houston Methodist Research Institute, Houston, TX, USA

(3) Dept. of Surgery, Houston Methodist Hospital, Houston TX, USA

(4) Houston Methodist Academic Institute (HMAI), Houston, TX, USA

(5) Dept. of Surgery, University of Florida, Gainesville, FL, USA

(6) Malcom Randall VAMC, Gainesville, FL, USA

(7) PoliTo^{BIO}Med Lab, Dept. of Mechanical and Aerospace Engineering, Politecnico di Torino, Turin, Italy

INTRODUCTION

Although percutaneous transluminal angioplasty with stenting is widely used for treatment of peripheral artery disease, in-stent restenosis (ISR) is still a serious drawback, compromising the long-term success of the procedure. ISR consists in a maladaptive arterial response to the intervention, which leads to lumen re-narrowing through an abnormal increase of cellular proliferative and synthetic activities [1].

There are different factors contributing to ISR and, among them, the inflammatory response activated by the damage due to the angioplasty, and the abnormal hemodynamics, induced by the stent presence, are thought to play a major role [2]. Specifically, monocyte gene expression data were used as the marker of the inflammatory cues triggered by vascular interventions and were found to correlate with an unfavorable post-surgical outcome [3],[4]. In addition, the low wall shear stress (WSS) was identified as an indicator of disturbed local hemodynamics that contributes to ISR by delaying the endothelial recovery and modulating smooth muscle cell (SMC) activity [5].

Given the complex multifactorial and multiscale nature of ISR, computational modeling, based on a systems biology approach, is deemed to provide a better understanding of the mechanobiological processes. Moreover, patient-specific in-silico models are being established as means that can support the biomedical research and guide towards new therapeutic solutions in the context of personalized medicine.

Accordingly, in the present work we propose an innovative patient-specific multiscale model of ISR that integrates the effects of the local hemodynamics and monocyte gene expression on the cellular dynamics. To do this, computational fluid dynamics (CFD) simulations are coupled with an agent-based model (ABM) of cellular dynamics, replicating arterial wall remodeling in response to local WSS and gene expression inputs.

METHODS

The CFD-ABM computational framework simulated the arterial response following stenting procedure in patient-specific stented superficial femoral artery (SFA) models through the four steps schematized in the central panel in Fig.1. The framework and the ABM scheme were based on our previous work on atherosclerosis [6].

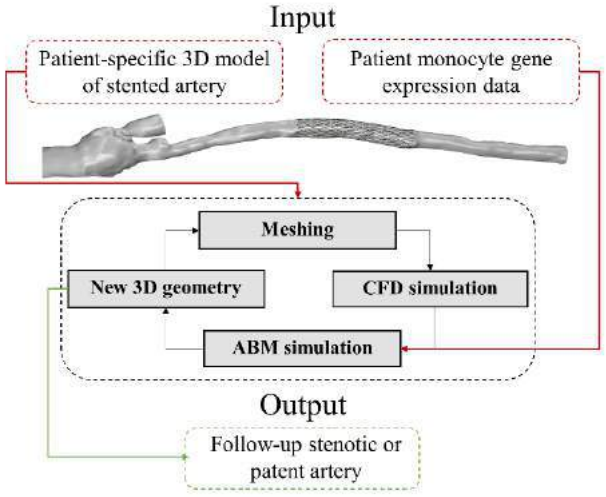

Figure 1: CFD-ABM computational framework of ISR.

The 3D patient-specific stented SFA, reconstructed from CT images, was meshed using polyhedral elements with five layers of prism elements near the wall. A steady-state CFD simulation was performed to compute the average hemodynamics in the stented area and the WSS

was extracted in 9 cross-sectional planes (one every two stent rings). Both the meshing step and the CFD simulations were performed in Fluent (Ansys Inc., Canonsburg, PA, USA). For each cross-section, a 2D ABM was implemented in Matlab (MathWorks, Natick, MA, USA) and, being initialized with the CFD-derived WSS profile and the gene expression data, it simulated the arterial wall remodeling by replicating cell and extracellular matrix (ECM) dynamics. Patient monocyte gene expression was measured at 1 hour before, and 2 hours, 1, 7 and 28 days after the intervention. Only those genes that were found to significantly correlate with the intervention outcome were used as input of the ABM [3],[4].

The 2D ABM of arterial cross-section was generated on a hexagonal grid and filled with SMC and fibroblasts, ECM and stent strut agents. While the patient geometry was used to define the arterial lumen, a circular external border and literature derived wall thickness were set, due to the lack of patient-specific information [7],[8].

The behavior of each cell and ECM agent was simulated by assigning probabilistic rules to the events of interest, namely cell mitosis/apoptosis and ECM production/degradation. While constant activities in the media and adventitia layers were set to preserve homeostasis [6], cell mitosis and ECM production in the intima depended on the local WSS and patient gene expression.

After one simulated month, the ABM simulations were stopped in order to update the fluid dynamics in the modified vessel geometry. Thus, a new geometry was reconstructed from the ABM outputs and the cycle was repeated for a specified follow-up period.

Due to the stochasticity of the model, 5 ABM simulations were run for each plane and the lumen configuration closest to the average of the 5 simulations was selected to reconstruct the new vessel geometry.

As preliminary evaluation of the framework, the lumen area of the stented portion obtained at one month was computed and compared with that measured from patient's CT images at one-month follow-up. The individual distributions were examined through the Mann-Whitney U test and statistical significance was assumed for p-value < 0.05.

RESULTS

Figure 2 shows the ability of the framework to capture the process of intimal growth in the stented region at one-month follow-up. Specifically, after one month all planes showed an increased intima thickness with coverage of the stent struts, due to perturbed cell and ECM activities, while media and adventitia preserved their initial areas. Moreover, the results obtained by the multiple runs were consistent between each other and a good reproducibility of the outputs was confirmed by the small interquartile range of the one-month lumen area (Fig. 2). Finally, no significant differences were observed between the patient's lumen area of the stented portion at one month and the model prediction (Fig. 3). In both cases, a significant lumen area reduction was found with respect to the condition immediately after stenting intervention.

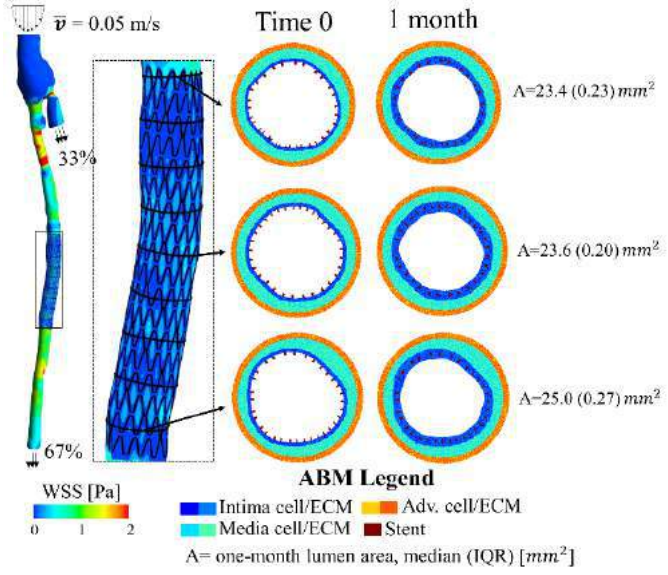

Figure 2: one-month results of the ISR framework for three explanatory planes.

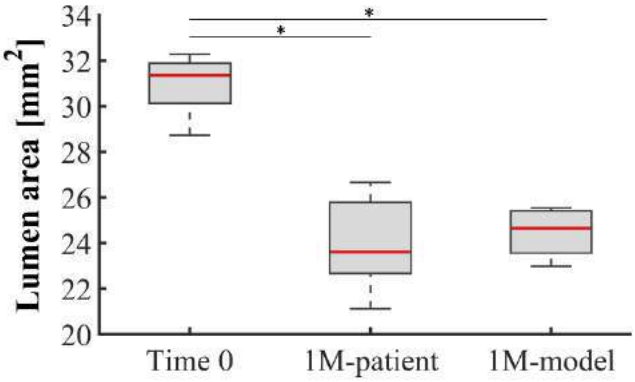

Figure 3: Comparison of the lumen area of the stented portion at one-month follow-up between the patient data (1M-patient) and the model (1M-model). *: p-value < 0.05.

DISCUSSION

In this work, a novel multiscale CFD-ABM framework of ISR was developed and applied to a patient-specific case of stented SFA. The important innovation was the integration of patient's monocyte gene expression as the driver of the cell and ECM dynamics. Accordingly, herein ISR was modeled at cell scale as the arterial response to the gene-weighted systemic inflammation and the stent-induced hemodynamic alteration, through the replication of the ABM cellular and ECM dynamics.

In the near future, a proper calibration of the ABM parameters will be performed based on the available follow-up data. Furthermore, the CFD-ABM framework will be applied to other patient-specific cases to elucidate the role and the interdependence of the different factors promoting ISR, with the ultimate goal to build a multiscale model being able to predict ISR in human SFAs.

ACKNOWLEDGEMENTS

The work has been supported by Fondazione Cariplo, Italy (Grant number 2017-0792, TIME).

REFERENCES

[1] Mitra, A. K. et al. *J. Clin. Pathol.* 59: 232–239, 2006.
[2] Chaabane, C. et al. *Cardiovasc. Res.* 99: 353–363, 2013.
[3] DeSart, K. et al. *J. Vasc. Surg.* 64: 766-778.e5, 2016.
[4] Rehfuss, J. P. et al. *Circ. Genomic Precis. Med.* 11: e001970, 2018.
[5] Koskinas, K. C. et al. *J. Am. Coll. Cardiol.* 59: 1337–1349, 2012.
[6] Corti, A. et al. *Comput. Biol. Med.* 118: 103623, 2020.
[7] Hafner, N. M. et al. *Cardiovasc. Ultrasound* 14: 1–9, 2016.
[8] Wong, M. et al. *Arterioscler. Thromb.* 13: 482–486, 1993.

DYNAMICS OF MORPHOLOGICAL REMODELING AND IMPACT OF HEMODYNAMICS ON RESTENOSIS IN HUMAN STENTED SUPERFICIAL FEMORAL ARTERIES

M. Colombo (1), Y. He (2), A. Corti (1), D. Gallo (3), F. Ninno (1,4), S. Casarin (5), J.M. Rozowsky (2), F. Migliavacca (1), S. Berceli (2,6), C. Chiastra (1,3)

(1) LaBS, Department of Chemistry, Materials and Chemical Engineering "Giulio Natta", Politecnico di Milano, Milan, Italy

(2) Department of Surgery University of Florida, Gainesville, FL, USA

(3) PoliTo^{BIO}Med Lab, Department of Mechanical and Aerospace Engineering, Politecnico di Torino Turin, Italy

(4) Department of Medical Physics and Biomedical Engineering, University College of London, London, UK

(5) Department of Surgery Houston Methodist Hospital Houston, TX, USA

(6) Malcom Randall VAMC Gainesville, FL, USA

INTRODUCTION

Self-expandable stents are commonly implanted to treat atherosclerotic superficial femoral arteries (SFAs). Though, this minimally-invasive treatment is widely affected by in-stent restenosis (ISR), one of the major drawbacks usually requiring a new revascularization [1]. Despite the incidence of this pathology, little is known about its initiation and progression. A combination of clinical (diabetes, smoking) and biomechanical factors (arterial wall injury provoked by the endovascular procedure and the altered hemodynamics due to stent presence) is deemed to promote ISR. In particular, the altered hemodynamics seems to play an important, but still not fully understood, role [2, 3].

In the present work, the progression of ISR over time is studied in human stented SFAs by detailing the morphological lumen remodeling in vessel models. Furthermore, the impact of altered hemodynamics on ISR initiation and progression is analyzed by performing computational fluid dynamics (CFD) simulations at multiple follow-ups within the first post-interventional year.

METHODS

Ten lesions of seven patients presenting with stenotic SFAs were considered (with the written consent). The lesions were treated with stents of different length (range [40÷300] mm) and in some cases in multiple overlapping configurations. The SFA models were obtained from computed tomography (CT) images using a validated reconstruction method [4]. To investigate the ISR progression, the data at four follow-ups (i.e. 1-week (1W), 1-month (1M), 6-months (6M) and 1-year (1Y)) were analyzed.

Transient CFD simulations were carried out for the first three follow-ups, employing the patients' Doppler ultrasound data to impose patient-specific boundary conditions [4].

The morphological remodeling was described by quantifying the lumen area change (ΔA) every 1 mm along the vessel length at each follow-up, and by analyzing the trajectory over time in the whole stented region. As regards the hemodynamics, several wall shear stress (WSS)-based descriptors, including those accounting for the WSS multi-directionality, were quantified. In particular, the time-averaged WSS (TAWSS), oscillatory shear index (OSI), relative residence time (RRT), the axial and secondary components of WSS averaged in time (TAWSSax and TAWSSsc), the transverse WSS (transWSS), the cross-flow index (CFI), and the ratio of the secondary and axial WSS components (WSSratio) were calculated [5]. Hemodynamic data were averaged circumferentially and every 1 mm axially to match the morphological data.

To obtain spatial independent data, the computed local morphological and hemodynamic results were preliminarily processed by calculating a decorrelation length based on surrogate data analysis, as previously described [3, 6]. The most conservative, patient-specific decorrelation length (range [2÷10] mm) was determined.

Following the normality test, the morphological data were examined by comparing the groups at consecutive follow-ups and time intervals (1W-1M, 1M-6M and 6M-1Y) using Kruskal Wallis test. The individual distributions were examined through the Mann-Whitney U test. Moreover, the linear regression between the lumen area change occurring in each time interval and the lumen area at the beginning of that time interval was quantified. The Spearman's correlation was computed between the WSS-based descriptors and the lumen area change. The results were analyzed at a global (i.e. considering one point per lesion) and local level (i.e. collecting all the results together). Statistical significance was assumed for $p\text{-value} < 0.05$.

RESULTS

As emerges from the trends of lumen area over time (Fig. 1-A,B), the first time interval (1W-1M) was the most dynamic in terms of lumen remodeling and was characterized by the largest lumen area change. Overall, in the intermediate time interval (1M-6M), the lumen area reduction was smaller as compared to the first time interval In the last time interval (6M-1Y), short portions of the lesions were characterized by severe, focal lumen re-narrowing, as also observable from the SFA reconstructed anatomies at 1Y (Fig. 1-C).

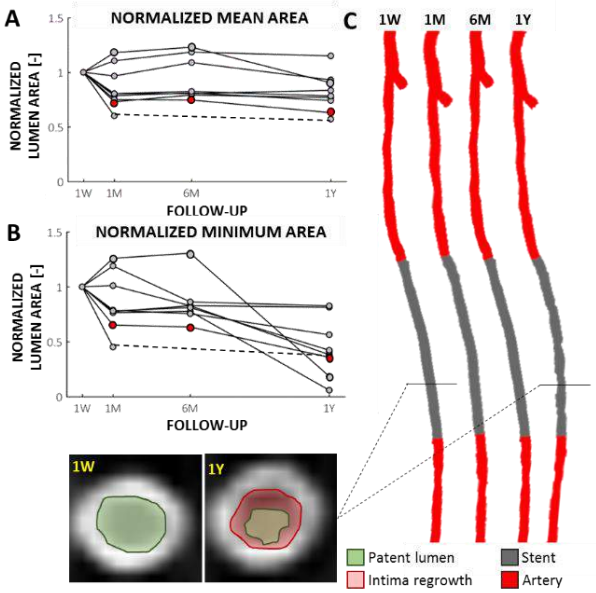

Fig. 1: Remodeling trajectory over time of all cases, reported as A) mean and B) minimum lumen area normalized with respect to the 1W lumen area. C) Reconstructed SFA models and CT images of one explanatory case.

Differences between the lumen area distributions at 1W and 1M ($p=0.0539$) and between those at 1W and 1Y ($p=0.0140$) were present (Fig. 2A). The fractional rate of lumen area change, computed as the lumen area change normalized by the time interval length, was largely different between the first (1W-1M) and the last time interval (6M-1Y, $p=0.0434$) (Fig. 2B). Moreover, a strong positive linear association emerged between the lumen area change in the first time interval (1W-1M) and the lumen area at 1W, indicating that for larger initial lumen area, a larger immediate lumen reduction occurs ($R^2=0.501$, $p<0.0001$).

Regarding the analysis of the association between hemodynamics at the beginning of the time interval and the lumen area change in that time interval, a strong positive correlation was found at the global level between CFI_{1W} and lumen area change $\Delta A_{1W:1M}$ ($\rho=0.6970$, $p=0.0311$), and between $WSSratio_{1W}$ and lumen area change $\Delta A_{1W:1M}$ ($\rho=0.6606$, $p=0.0440$). Moreover, for low TAWSS, high OSI and high RRT, high remodeling occurred in the subsequent time intervals (even if the global results were not significant). The previous global results were confirmed by the local level of analysis (Fig. 3). All the WSS-based descriptors at 1W but the TAWSSsc were correlated with the lumen area change $\Delta A_{1W:1M}$. No significant associations were found in the second time interval (1M-6M). OSI_{6M}, RRT_{6M} and CFI_{6M} were positively correlated to $\Delta A_{6M:1Y}$ ($\rho=0.2233$ with $p=0.0004$, $\rho=0.2277$ with $p=0.0006$, $\rho=0.2019$ with $p=0.0024$, respectively), while the $TAWSSax_{6M}$ was negatively associated with $\Delta A_{6M:1Y}$ ($\rho=-0.1573$, $p=0.0185$).

DISCUSSION

To the best of authors' knowledge, this is the first study quantifying the morphological remodeling occurring in human SFAs after stenting over 1Y follow-up period. The findings of this study showed that in this vascular region the lumen remodeling is a dynamic process characterized by high lumen area change during the first post-interventional month and possible focal re-narrowing in the time interval 6M-1Y. The lumen remodeling was similar along the lesion length, with only slight regional-specific differences (results not shown).

Furthermore, the hypothesis that ISR progression is promoted by abnormal hemodynamics seems to be confirmed. Interestingly, the direction of the correlations between morphological remodeling and WSS-based descriptors was aligned with previous works [2, 3]. Thanks to the longitudinal nature of this study, more quantitative results were here presented, suggesting that the multidirectional WSS is an important biomechanical factor involved in the ISR process, especially in the time interval 6M-1Y, subjected to focal re-narrowing.

In conclusion, despite the limited number of investigated lesions, the methodology adopted in this study enabled to widen the knowledge of ISR progression in human stented SFAs, showing the importance of considering long-term follow-ups in the investigation of ISR and giving insights on the role of hemodynamics.

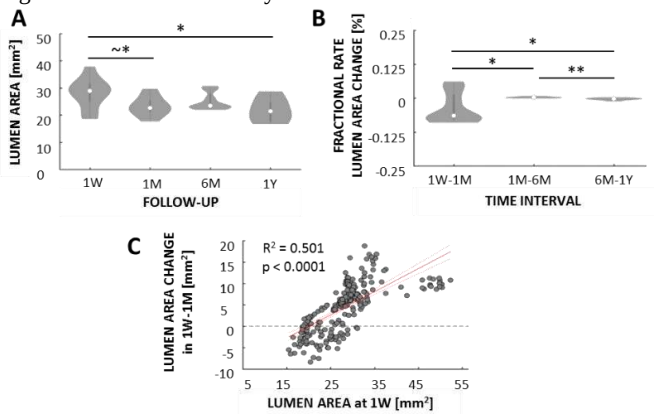

Fig. 2: Local morphological results in terms of A) lumen area distributions, B) fractional rate of lumen area change and C) linear regression of 1W lumen area and lumen area change in the time interval 1W-1M. ~*: p~0.05; *: p<0.05; **: p<0.01.

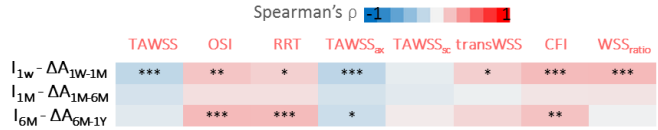

Fig. 3: Local Spearman's correlations between the lumen area change in the current time interval and the WSS-based descriptors computed at the beginning of that time interval. *: p<0.05; **: p<0.01; ***: p<0.001.

ACKNOWLEDGEMENTS

This work has been supported by Fondazione Cariplo, Italy (Grant number 2017-0792, TIME).

REFERENCES

[1] Schlager O et al. *Atherosclerosis*, 233: 76-82, 2014.
[2] Gökgöl C et al, *Biomec & Mod Mechan*, 18(6): 1883-93, 2019.
[3] Colombo M et al., *Sci Rep*, In press, 2021.
[4] Colombo M et al., *Med Eng & Phy*, 75: 23-35, 2020.
[5] De Nisco G et al. *Ann. Biomed. Eng.* 47:425–438, 2019.
[6] Pfeiffer V et al., *J Biom Eng*, 135(2), 2013.

MYOSIN-INDEPENDENT MECHANOTRANSMISSION FOR SENSING STIFFNESS OF EXTRACELLULAR MATRIX

Nikhil Mittal (1), Sangyoon Han (1)

(1) Department of Biomedical Engineering
Michigan Technological University
Houghton, MI 49931, USA

INTRODUCTION

Mechanical stiffness of the extracellular matrix (ECM) plays a critical role in proliferation, differentiation and migration of adherent cells (1). While it is well-known that stiffness sensing is mainly mediated by integrin-based focal adhesions (2), its exact mechanism has been still unclear. In order for different stiffness to be sensed differently, different 'force' should be transmitted through the focal adhesions in which the force triggers conformational opening of mechanosensitive proteins such as talin and vinculin (2). Indeed, a substantial number of studies have shown an increasing traction force in response to increasing substrate stiffness (3-5). To explain the relationship between the stiffness and the traction, a 'molecular clutch' model has been successfully implemented and used (6). In the clutch model, F-actin's retrograde flow dynamically 'clutches' with the cell-ECM adhesion that results in the transmission of the force to the substrate. Myosin II contractility has been the only source of the retrograde flow where myosin's muscle-like behavior of force-velocity could nearly explain the observed traction in response to stiffness (7, 8). However, evidence shows that cells are able to transmit small but significant traction force even in the absence of myosin activity with also increasing trend with increasing substrate stiffness (9). Given myosin as a 'result' of mechano-signaling, identifying how cells transmit differential force without myosin would shed light on the very initial stiffness sensing event by a cell without complication by myosin's effect. As an alternative power source, actin assembly at the barbed end of F-actin can contribute to the retrograde flow by pushing the membrane and being pushed by the membrane (10). Actin Related Protein 2/3 complex (arp2/3) and formin homology protein are the two main actin nucleators (11, 12). Here, we hypothesize that myosin-independent traction comes from the actin-polymerization-driven retrograde flow and its two main mediators regulates the force transmission in a distinct manner.

METHODS

TFM experiments were performed on a high refractive index silicone gel (Q-gel, Quantum Silicones) substrate of different stiffnesses (0.3, 0.8, 1.5, 5 and 12 kPa) coated with 40nm diameter, far-red carboxylated beads as fiducial markers (13). The stiffness of gels with different mixing ratio was measured with parallel disk-based rheometry. 3T3 fibroblast cells stably expressing paxillin-mRuby (gift from Ginsberg lab) were treated with 1) blebbistatin, a myosin inhibitor, only, 2) blebbistatin with smifh2, a formin inhibitor or 3) blebbistatin with CK666, an arp2/3 inhibitor. In addition, cells without treatment were used as a control. Cells and beads on the gel, 4 hours after seeding, were imaged under a total internal reflection fluorescence (TIRF) microscope, after which another bead image, a reference image, was collected after lysing cells using 10% bleach. Traction reconstruction was done using our own MATLAB-based TFM software (13). Briefly, the displacement field was calculated by particle tracking velocimetry and corrected using the outlier filtering. A regularized-Fourier Transform Traction Cytometry (regFTTC) was used for the inverse problem solution. The regularization parameter was chosen by an L-curve, L-optimal method using FastBEM (13).

RESULTS

First, we assessed how the traction of control 3T3s behaves in response to a range of gel stiffness. We quantified the total force at the cell perimeter, which is an integration of traction over a 2 um-thick inner-band along each cell perimeter, as our metric. As expected, the total force increased with the gel stiffness (Fig. 1a-e). Specifically, a linear increase was observed up to 5 kPa, after which the total force plateaued at stiffer regime (Fig. 1u). When treated with myosin inhibitor, blebbistatin, the overall magnitude of the traction force reduced (Fig. 1f-j, note the reduced color limit), but there was still non-zero,

concentrated traction located mostly near cell edges. Furthermore, the differential transmission was still observed, i.e., a linear increase in traction with increasing stiffness (Fig. 1u, v). This result suggests that the differential traction against varying stiffness is myosin-independent. To investigate the role of actin polymerization in stiffness sensing, in addition to myosin inhibition, either of two actin nucleators, formin or arp2/3, was inhibited with smifh2 or CK666, respectively. Cells treated with these double-inhibitions exhibited a reduced traction overall (Fig. 1k-t). However, the traction trends were observed to be no longer increasing. First, cells treated with blebbistatin and smifh2 showed a sharp increase in force at the soft stiffness regime (up to 0.8 kPa) but plateaued at intermediate regime then slightly reduced at stiff regime (Fig. 1k-o, v). Second, cells treated with blebbistatin and CK666 showed a biphasic behavior in traction with a peak at intermediate (1.5 KPa) stiffness after which traction dropped with the higher stiffness (Fig. 1p-t, v). The force transmission was hampered at stiffer (5-12 kPa) regime by both formin and arp2/3 inhibitions. While the arp2/3 inhibition frustrates the force transmission further than formin inhibition but the cells experience 'frustration point' in formin-inhibited cells earlier at soft regimes (Fig. 1v).

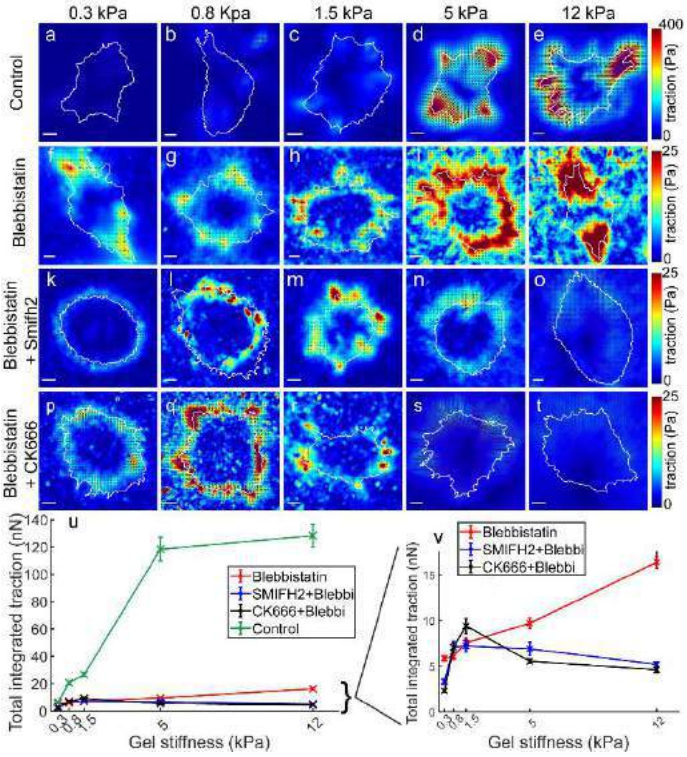

Figure 1: Myosin-independent traction transmission is hampered by further inhibition of actin nucleators. (a-t) High-resolution traction maps with traction vectors of 3T3s in control, blebbistatin, blebbistatin with smifh2, blebbistatin with CK666 conditions on a gel with 0.3 kPa (a,f,k,p), 0.8 kPa (b,g,l,q), 1.5 kPa (c,h,m,r), 5 kPa (d,i,n,s) and 12 kPa (e,j,o,t) as Young's modulus, respectively. (u) Total traction integrated over cell perimeter in all four conditions. Scale bar: 10 µm. (v) Total traction integrated over cell perimeter in all conditions except for control condition. Here, n= 45 (0.3 kPa), 33 (0.8 kPa), 57 (1.5 kPa), 57 (5 kPa), 70 (12 kPa) for control; n= 72 (0.3 kPa), 69 (0.8 kPa), 31 (1.5 kPa), 53 (5 kPa), 60 (12 kPa) for blebbistatin; n= 32 (0.3 kPa), 40 (0.8 kPa), 33 (1.5 kPa), 32 (5 kPa), 35 (12 kPa) for blebbistatin with smifh2; n= 39 (0.3 kPa), 37 (0.8 kPa), 40 (1.5 kPa), 42 (5 kPa), 28 (12 kPa) for blebbistatin with CK666 are the number of independently imaged cells.

DISCUSSION

In this work, we have shown using high-resolution TFM that cells in the absence of myosin activity can still transmit more traction when they are on a stiffer matrix. This trend is abolished upon further inhibition of the two actin-binding proteins that facilitate actin polymerization (Fig. 1v), demonstrating the importance of actin polymerization's active role in stiffness sensing.

The traction trend of the control cells as a function of the stiffness (Fig. 1a-e) is consistent with previously reported data (4, 6). The increase in traction in response to increasing stiffness can be explained by a molecular clutch model where more adhesion proteins are engaged in the complex via fast force development (6). In both formin- and arp2/3-inhibited conditions, cells show a plateauing trend in traction at intermediate-to-high stiffness, but at low stiffness regime, cells exhibit a linear increase in the traction. We speculate that this traction behavior is due to small but significant 'clutching' actin flow by the actin polymerization promoted by the other actin nucleator. Indeed, a work by Pollard group has shown that upon arp2/3 inhibition only, the actin flow becomes even faster, but with additional inhibition of myosin, the flow speed was significantly reduced but still non-zero (14). As actin is linearly polymerized by formin, formin-mediated actin assembly can confer fast-enough actin flow speed, but it can be 'slipped' when not assisted by Arp2/3. Thus, the slowed actin flow might not be enough to effectively clutch against, and unfold, mechanosensitive molecules such as talin, resulting in less force transmission. In contrast, arp2/3-mediated actin retrograde flow might be slower than one by formin, but it can be 'stickier', i.e., interacting better with adhesion molecules and clutch better for traction transmission. Our immediate next plan is to develop an actin polymerization-powered molecular clutch model, by which we will recapitulate the experimental results in Fig. 1. To validate our control cell experiment, we will perform make-up experiment on cells treated with DMSO. We will also quantify the actin flow speed using actin speckle microscopy with qFSM at each condition. We anticipate these experiments/simulations will deepen our understanding on myosin-free mechanotransmission. Together, our results suggest that both arp2/3 and formin synergistically modulate stiffness sensing, possibly by contributing to retrograde actin flow.

ACKNOWLEDGEMENTS

This work was funded by NIH R15GM135806. We thank Dr. Mark Ginsberg and Dr. Hosup Lee (both at UCSD) for stable cell line.

REFERENCES

[1] Discher, D. E. *et al.*, *Science*, 310:1139-1143, 2005.
[2] Hoffman, B. D. *et al.*, *Nature*, 475:316-323, 2011.
[3] Han, S. J. *et al.*, *Biophys J*, 103:640-648, 2012.
[4] Ghibaudo, M. *et al.*, *Soft Matter*, 4:1836-1843, 2008.
[5] Oakes, P. W. *et al.*, *Biophys J*, 107:825-833, 2014.
[6] Elosegui-Artola, A. *et al.*, *Nat Cell Biol*, 18:540-548, 2016.
[7] Mitrossilis, D. *et al.*, *Proc Natl Acad Sci U S A*, 106:18243-18248, 2009.
[8] Chan, C. E. *et al.*, *Science*, 322:1687-1691, 2008.
[9] Zhou, D. W. *et al.*, *Mol Biol Cell*, 28:1901-1911, 2017.
[10] Ji, L. *et al.*, *Nat Cell Biol*, 10:1393-1400, 2008.
[11] Johnson, H. E. *et al.*, *J Cell Biol*, 208:443-455, 2015.
[12] Pollard, T. D. *et al.*, *Science*, 326:1208-1212, 2009.
[13] Han, S. J. *et al.*, *Nat Methods*, 12:653-656, 2015.
[14] Yang, Q. *et al.*, *J Cell Biol*, 197:939-956, 2012.

THEORETICAL ASSESSMENT OF FOCUSED SEPTAL HYPERTROPHIC GROWTH IN HYPERTROPHIC CARDIOMYOPATHY

Sandra P. Hager (1), Will Zhang (2), Renee M. Miller (1), Jack Lee (1), David A. Nordsletten (1,2)

(1) School of Biomedical Engineering and Imaging Sciences
King's College London
London, UK

(2) Department of Biomedical Engineering and Cardiac Surgery
University of Michigan
Ann Arbor, Michigan, USA

INTRODUCTION

Hypertrophic cardiomyopathy (HCM), affecting 1 in 200 people [1], is a genetic disease impacting key sarcomeric proteins in the myocyte. The histological phenotypes for HCM include hypertrophied and disarrayed myocytes, interstitial fibrosis, and cardiac hypertrophy. On a macroscale, the clinical phenotype includes regional growth despite no obvious change of the loading conditions in the heart. HCM growth patterns are heterogeneous, but around 1/3 of patients experience growth in the basal interventricular septum region [2]. In addition to tissue hypertrophy, an HCM patient's heart is at higher risk for cardiac arrhythmias, sudden cardiac death, and heart failure [3].

The following study aims to identify essential factors for regional growth patterns in HCM with the help of modelling. This abstract will investigate two theories for growth drivers in HCM. The first test accounts for the histological change of the fiber orientation in the hypertrophic area of HCM due to disarray. In contrast, the second test investigates the influence of inflammation and the tissue's resulting isotropic swelling in the region of HCM. Inflammation is common in severe HCM cases, particularly those with regional and diffuse fibrosis [4].

METHODS

The general setup for the growth problem is described through a mechanical problem, by solving for the linear momentum balance and the mass conservation equation, such that

$$\int_{\Omega_X} \mathbf{P}(\mathbf{F}, p) : \boldsymbol{\nabla}_X \mathbf{w} + \left(\rho J \ddot{\mathbf{U}} - J\mathbf{b}\right) \cdot \mathbf{w} + q(J-1)dX = 0, \qquad (1)$$

where $\mathbf{w} \in \mathcal{U}_0$ and $q \in \mathcal{P}$ represent the arbitrary test functions of the system for the displacement and the pressure, respectively. Ω_X defines the domain over which the growth problem is solved; ρ is the mass density in the stress-free reference configuration; **P** represents the first Piola-Kirchhoff stress tensor, which is dependent on the overall deformation gradient **F** of the continuum body. The subscript X of $\boldsymbol{\nabla}$ indicates that the derivatives of the gradient are defined with respect to the material coordinates. **b** refers to the body forces acting on the continuum body and was neglected for the below shown simulations. J denotes the determinant of the deformation gradient **F** and gives information about the volume change during the growth process. The system solves the problem with respect to the physical displacement **U** and the initial pressure p.

The theory of kinematic growth is one of two common approaches to model growth, the other being the constrained mixture theory [5,6]. The main advantage and disadvantage of the kinematic growth method is that the whole domain is assumed to be one continuum, which allows for easy parameterization of the material and the use of a phenomenological rate equation for the growth process. The existence of an intermediate configuration as a grown reference state is accepted by researchers in this field [7]. This assumption justifies a multiplicative decomposition (Fig. 1) of the overall deformation gradient into an elastic and an inelastic deformation gradient, such that

$$\mathbf{F} = \mathbf{F}_e \cdot \mathbf{F}_g, \qquad (2)$$

where $\mathbf{F}_g$ describes the growth from an initial stress-free reference configuration, $\Omega_X \subset R^3$ to a new intermediate locally stress-free state $\Omega_Y \subset R^3$. This new state may vary from the intact physically grown configuration $\Omega_t \subset R^3$. The elastic part ($\mathbf{F}_e$) of the deformation gradient maps the intermediate state to the physical configuration and ensures continuity of the body. By doing so, residual stress may be introduced into the body.

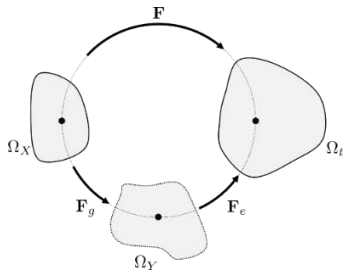

Figure 1: Schematic overview of the multiplicative decomposition of F into an inelastic deformation gradient $\mathbf{F}_g$ and an elastic deformation gradient $\mathbf{F}_e$ (adapted from [8]).

From this assumption, it is possible to map the integral from Eq. 1, which was defined on the reference domain, to the intermediate state. This is done by substituting the overall deformation gradient in this formulation with its multiplicatively-decomposed parts.

In this study, growth was modelled in a patient-specific biventricular geometry. Simulations utilized a Neo-Hookean material law and a boundary condition was applied to constrain the center of mass, ensuring no rotation nor translation of the body in space. As a global growth trigger, an arbitrary spatial constant growth stimulus was introduced that induced an increase in the wall thickness (concentric growth), which is a typical response to an elevated afterload in the heart. The implementation of this type of growth was achieved by using an orthotropic growth tensor $\mathbf{F}_g$, such as

$$\mathbf{F}_g = \mathbf{f}_0 \otimes \mathbf{f}_0 + \vartheta^{\perp}\mathbf{s}_0 \otimes \mathbf{s}_0 + \vartheta^{\perp}\mathbf{n}_0 \otimes \mathbf{n}_0. \quad (3)$$

Here $\mathbf{f_0}$ specified the cell's long axis and was defined using a rule-based method [9]. $\mathbf{s_0}$ described the sheet vector of the cell bundles, and $\mathbf{n_0}$ was the sheet plane normal direction. $\vartheta^{\perp}$ reflects as a growth factor for the change of fiber thickness. Remodeling, however, results in a reorientation of the microstructure.

Two tests were used to try to recreate growth patters observed in HCM. In the first, concentric growth was applied with and without disarray in the basal interventricular septal region. Fiber disarray was introduced by adding stochasticity to the mean fiber and sheet direction in the predefined HCM region. Applying a spatial constant concentric growth tensor $\mathbf{F}_g$ (Eq. 3) that causes the fiber to grow in thickness might result in the typical HCM growth pattern. In the second test, isotropic growth, such as occurs during inflammation, in addition to concentric growth, was introduced in the septal region. Applying equal amounts of growth in all microstructural directions of the myocytes allows a reformulation of Eq. 3, such that

$$\mathbf{F}_g{}^{\mathrm{iso}} = \vartheta^{\mathrm{iso}}\mathbf{f}_0 \otimes \mathbf{f}_0 + \vartheta^{\mathrm{iso}}\mathbf{s}_0 \otimes \mathbf{s}_0 + \vartheta^{\mathrm{iso}}\mathbf{n}_0 \otimes \mathbf{n}_0, \quad (4)$$

where ϑ^{iso} the growth multiplier for isotropic growth is. In this specific test, the overall growth tensor is a weighted function of the concentric growth tensor (Eq. 3) applied on the entire geometry except for the HCM region and the isotropic growth tensor (Eq. 4) solely in the predefined septal area prescribed.

RESULTS

Both geometries in Fig. 2 show the same displacement magnitude over the entire body with no clear manifestation of a typical HCM growth pattern. Therefore, fiber disarray in the basal interventricular septal region did not result in regional hypertrophy as seen in HCM. In comparison, the addition of a regional isotropic growth term exhibited growth patterns typical of HCM, as illustrated in Fig. 3. The right panel with regional isotropic growth shows an extensive amount of growth in the septal region (as indicated by the yellow arrow), leading to an extrusion of the wall while the left image shows more homogeneous growth throughout.

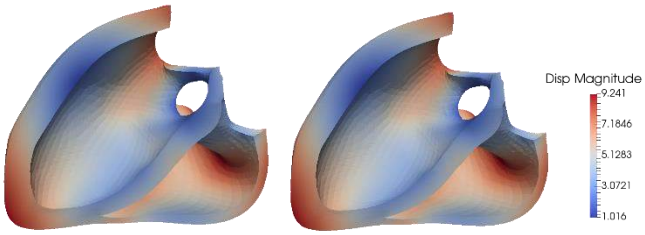

Figure 2: Comparison of the displacement magnitude in concentric growth applied to a bi-ventricular geometry with (right) and without (left) a fiber disarray in the basal interventricular septal region (dimensions in mm).

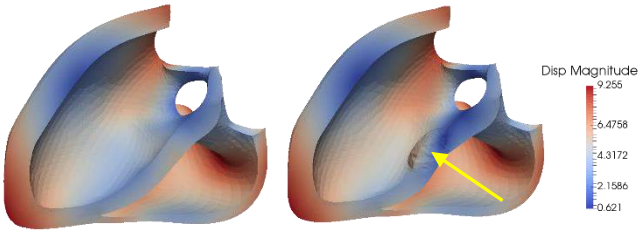

Figure 3: Comparison of the displacement magnitude in concentric growth applied to a bi-ventricular geometry with (right) and without (left) regional isotropic growth in the basal interventricular septal region (dimensions in mm).

DISCUSSION

Under constant growth scenarios, local myofiber disarray does not yield the heart's phenotypical response, while regional isotropic growth does. This supports the idea that septal hypertrophy is not driven by disruption of the fiber structure but could be a consequence of fibrosis and inflammatory responses.

Future work will focus on implementing physiological growth law, with a growth rate dependent on local stress and strain values in the tissue to identify the individual impact on HCM growth pattern. As an alternative approach, we will additionally investigate the effect of constant heterogeneous growth in the heart. In this case, the theory is that myocytes in the septum's hypertrophic region experience higher growth stimuli than the surrounding tissue while the entire geometry experiences the same growth type. By reproducing HCM in the heart, it is possible to study residual stresses in the grown area and further develop patient-specific models for HCM patients.

ACKNOWLEDGEMENTS

This work was also supported by the Wellcome ESPRC Centre for Medical Engineering at King's College London (WT203148/Z/16/Z) and the British Heart Foundation (TG/17/3/33406).

REFERENCES

[1] Semsarian, C et al., *JACC*, 65:1249-1254, 2015.
[2] Marian, AJ and Braunwald, E, *Circ Res.*, 121:749-770, 2017.
[3] Maron, B, *JAMA*, 287:1308-1320, 2002.
[4] Fang, L et al., *Am. J. Transl. Res.*, 9:5063-5073, 2017.
[5] Rodriguez, EK et al., *J. Biomech*, 27:455-467, 1994.
[6] Humphrey JD and Rajagopal KR, *Math. Mod. Meth. Appl. S.*, 12:407-430, 2002.
[7] Goodbrake, C et al., *Proc. R. Soc. A*, , 2021.
[8] Goriely, A, *The mathematics and mechanics of biological growth.* Vol. 45. Springer, 2017.
[9] Doste, R et al., *Int. J. Numer Meth. Biomed. Engng.*, 35:e3185, 2019.

SB³C2021
Summer Biomechanics, Bioengineering and Biotransport Conference
June 14-18, Virtual

INVESTIGATING STRUCTURAL COVARIANCE NETWORKS BY USING GRAPH MEASURES TO ANALYZE BRAIN CONNECTIVITY FOR SCHIZOPHRENIA

Madison T. Lewis (1), Nicholas D. Theis (2), Brendan M. Muldoon (2) Konasale M. Prasad (2)

(1) Department of Bioengineering
University of Pittsburgh Swanson School of Engineering
Pittsburgh, Pa, United States

(2) Department of Psychiatry
University of Pittsburgh School of Medicine
Pittsburgh, Pa, United States

INTRODUCTION

Schizophrenia (SZ) is a chronic brain disorder that affects ≈1% of the population. Clinical symptoms include delusions, hallucinations, disorganized thought process, and neurocognitive impairments [1]. Antipsychiatric medications have many side effects, are not curative, and only minimally affect the core neurocognitive deficits [1]. Precise understanding of pathophysiology in SZ – such as brain network dysconnectivity – would help in designing more efficacious treatments. The structural covariance network (SCN), constructed from regional morphometric measures from structural MRI data [2], offers a method to quantify connectivity between brain regions. We examined SCNs built using the Human Connectome Project (HCP) parcellation atlas which includes 358 regions based on functional and structural connectivity, on 81 SZ in comparison with 76 healthy controls. Prior studies used atlases have <100 regions and are based on anatomical landmarks or structural data.

METHODS

Using the volume, surface area, and cortical thickness MRI data, the SCN was constructed using the Pearson correlation coefficients between each of the 358 atlas regions. We examined thickness and surface area because volume is the product of these measures. This creates a 358x358 matrix which holds values for strength of the edge (correlation coefficients between two regions), producing one SCN for each group along with a random graph for each of these groups. A random graph is constructed from the group data, but after 100 permutations of randomization. These graphs were used to compare SZ and HC SCNs. First, we examined the distribution of graph measures with threshold sweep using both an intensity threshold and a density threshold. An intensity threshold is computed by choosing a strength and eliminating any of the edges below that value. A density threshold uses a proportion of edges and eliminates in the order of the lowest valued edge. The density threshold keeps the number of edges consistent across groups. Intensities from 0 (includes all edges) to 1 (excludes all edges) are examined at intervals of 0.025. Densities are examined across 0.025-0.95 at intervals of 0.025. At each threshold value, the graph measures modularity, characteristic pathlength, clustering coefficient, and betweenness centrality were calculated using the Brain Connectivity Toolbox [3]. These measures were chosen to evaluate community structure, efficiency, and centrality of the SCN. Additionally, the strength of the network was calculated at three different thresholds for each thresholding method and using all three morphometrics. For the intensity threshold, 0.3, 0.5, and 0.7 were chosen based on the intensity threshold sweep as the approximate location of the maximum values of the SZ measures for modularity (≈0.7), pathlength (≈0.3), and betweenness centrality (≈0.5). The three density thresholds chosen were 0.15, 0.2, and 0.25 based on the small worldness of the networks. Small worldness (σ) is calculated by comparing the clustering coefficient and the pathlength of the SCN with the random SCN [4]:

$$\sigma = \frac{C/C_R}{L/L_R} \qquad (1)$$

where C is the clustering coefficient and L is the pathlength. When calculating pathlength, the connection distance was estimated by using the Euclidian distance. Using the small worldness calculation, a range of thresholds was chosen for the analyses. The minimum (0.15) was chosen when the graphs were fully connected and the maximum (0.25) was chosen when σ asymptotically approached 1. For further investigation into the biological meaning, the hubs, or highly connected regions, was calculated for each group. A region was defined as a hub if the regional degree, betweenness centrality, or

eigenvector centrality was > 2 standard deviations from the network average [4]. The hubs were calculated over the threshold range stated above and if the hubs were found in over 50% of the threshold values, it was considered a network hub.

RESULTS

The threshold sweep for the intensity shows the same shape of the curve for both groups but the SZ tends to be show lower threshold values and the HC is more resilient (Fig 1). The density threshold sweep shows more similar values between the SZ and HC, but at later thresholds, the SZ begins to deviate from the HC curve. In figure 3, Volume, cortical thickness, and surface area are the x labels 1, 2, and 3 respectively. The strength of the FEAP network drops significantly as the intensity threshold increases when compared to the healthy control. The strength using the density threshold showed no significant difference between FEAP and HC. SZ SCN shows smaller number of hubs than the HC (table 1). The two networks share one common hub, Left Area 9 Middle.

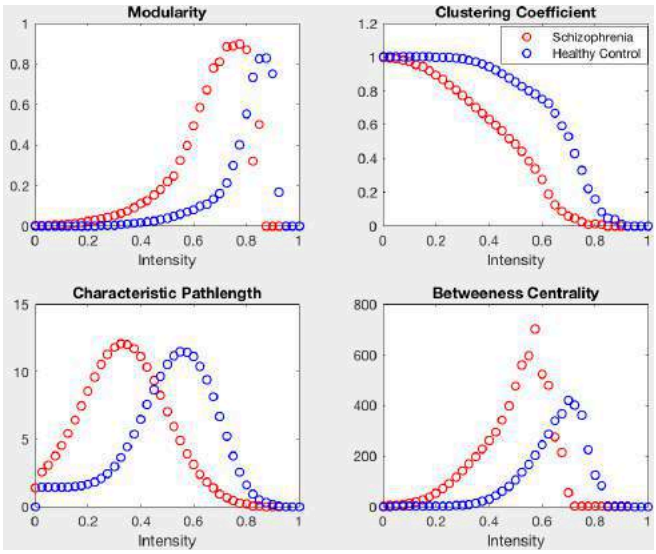

Figure 1: Threshold sweep using an intensity threshold and volume morphometric.

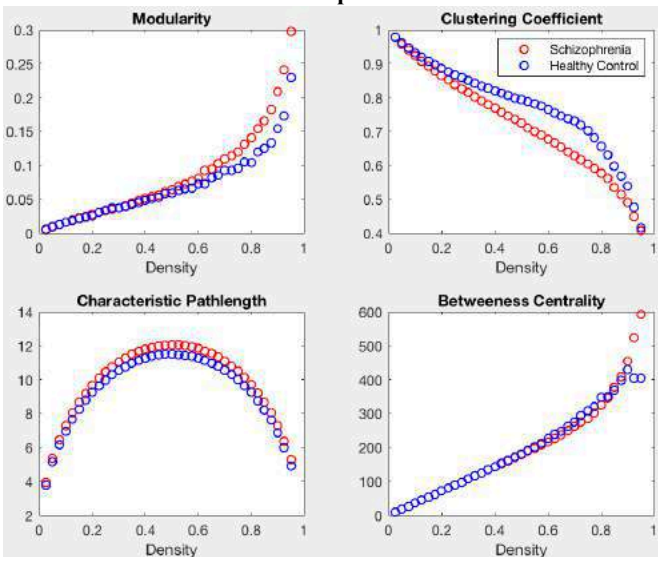

Figure 2: Threshold sweep using a density threshold and volume morphometric.

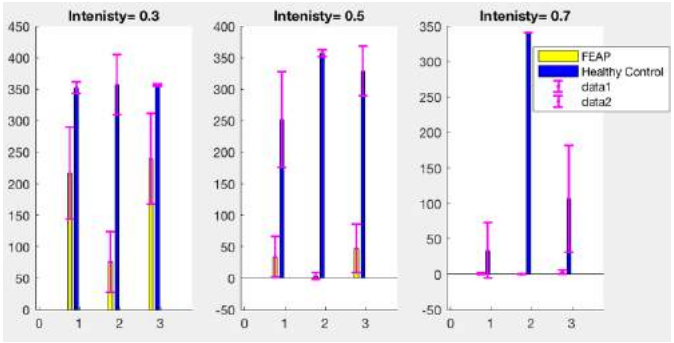

Figure 3: Strength of the SCN at intensity thresholds of 0.3, 0.5, 0.7.

Schizophrenia	Healthy Control
Left Area 9 Middle	Left Area 9 Middle
Left Area 47s	Left Area TG Dorsal
Right Area TF	Left Area PHT
Right Anterior Agranular Insula Complex	Right Area 7 Middle
	Right Area 23 Center
	Right Area 47 Lateral
	Right Area TG Dorsal
	Right Area Posterior Insula 1
	Right Auditory 5 Complex

Table 1: Regional hubs for Schizophrenic and healthy control groups.

DISCUSSION

The intensity threshold sweep shows that the SZ SCN is not as resilient as the HC because it deviates from fully connected network before the HC. Similar results for the SZ and HC SCN strength is shown in Figure 3. The HC SCN has a higher strength throughout all thresholds while the regional connection strength for SZ were not as strong because they were eliminated at lower thresholds. The density threshold for SZ deviated more from HC suggesting that the SZ SCN may be less resilient. A lower number of hubs in the SZ SCN supporting network disarray of SZ SCN. The higher spatial resolution of the HCP atlas allows for a better understanding of the precise circuitry involved in the SZ SCN. Since some of the hub regions are connected either functionally or structurally, it further supports that the schizophrenia network may be disrupted, adding more evidence to suggest schizophrenia is a network disconnection disease.

ACKNOWLEDGEMENTS

This work was supported through grants from NIMH (RO1 MH1152806 and RO1 MH112584 (Prasad)), of the CONCEPT lab.

REFERENCES

[1] West, Joyce et al. “Patterns and Quality of Treatment for Patients with Schizophrenia in Routine Psychiatric Practice.” 2005.

[2] Prasad, Konasale “Aberrant modularity and decreased diversity of cortical morphology in first-episode antipsychotic-naïve psychoses.”

[3] Rubinov M, Sporns O (2010) NeuroImage 52:1059-69.

[4] Basset, Danielle. “Hierarchical Organization of Human Cortical Networks in Health and Schizophrenia.” 2008.

EVALUATION OF AFFINE FIBER KINEMATICS IN PORCINE TRICUSPID VALVE LEAFLETS

Colton J. Ross (1), Arshid Mir (2), Harold M. Burkhart (3), Chung-Hao Lee (1,4)

(1) Biomechanics and Biomaterials Design Laboratory
School of Aerospace and Mechanical Engineering
The University of Oklahoma
Norman, OK, USA

(2) Department of Pediatric Cardiology,
(3) Department of Surgery,
The University of Oklahoma Health Sciences Center (OUHSC)
Oklahoma City, OK, USA

(4) Institute for Biomedical Engineering, Science and Technology (IBEST)
The University of Oklahoma
Norman, OK, USA

INTRODUCTION

The mechanics and material anisotropy of soft collagenous tissues are often facilitated by the underlying collagen fiber architecture (CFA). Specific to the atrioventricular heart valve (AHV) leaflets, the unloaded collagen fibers were found in a crimped state, with a preferential alignment along the circumferential tissue direction of the tissue [1]. When loads are applied to the tissue, the collagen fibers tend to reorient towards the primary loading direction, which manifests as a low-stress "toe-region" in the tissue-level nonlinear stress-stretch behaviors. After reorientation, the fibers are recruited and elongated that contribute to the mechanical behaviors in the asymptotic high-stress regime. Collagen fiber kinematics forms the basis of constitutive models to represent the mechanics of tissues; however, some researchers assume that the *affine fiber kinematics* (AFK) is sufficient for accurately modeling the AHV leaflet biomechanics, while others claim that the *non-affine fiber kinematics* is necessary. Herein, the AFK describes elastic elongations of collagen fibers in conjunction with rigid-body rotations, whereas the non-AFK considers the fiber uncrimping process together with elastic elongations of collagen fibers. In the previous work by Lee *et al*. (2015), they performed biaxial testing of the mitral valve anterior leaflet together with small angle X-ray scattering and found that the AFK theory requires correction by including the fiber crimp into the model formulation [2]. While that study provides insight into the mechanics of the mitral valve leaflets, there has not yet been any work to verify the AFK assumption for the tricuspid valve (TV) leaflets, which are subjected to a lower pressure gradient and a distinct functional and mechanical environment and may have different tissue microstructures compared to their mitral valve counterparts.

The goal of this study is to evaluate the AFK assumption for the TV leaflets using an integrated biaxial testing-polarized spatial frequency domain imaging (pSFDI) system to analyze the load-dependent CFA of the tissues. Our approach is advantageous, as the pSFDI device does not require tissue fixation, allowing for the observation of more accurate collagen fiber kinematics. Findings from this study will be useful for TV leaflet *in-silico* modeling that will eventually lead to improved TV simulations with future applications in therapeutic refinements.

METHODS

Porcine hearts were obtained from a commercial vendor (Animal Technologies, TX) and dissected to retrieve the three TV leaflets: anterior leaflet (AL, n=11), posterior leaflet (PL, n=14), and septal leaflet (SL, n=12). The belly region of the TV leaflets were sectioned into a 10x10 mm specimen and mounted to a biaxial testing device (CellScale, Canada) combined with an in-house pSFDI device (**Fig. 1a**) [3]. Tissues were mounted with the circumferential (Circ) and radial (Rad) directions aligned with the X- and Y-directions of biaxial testing, respectively. After mounting, a 2x2 fiducial marker array was glued on the tissue surface using glass beads for determination of tissue strains. Then, tissues were submerged in the phosphate-buffered saline solution at 32 °C. Submerged tissues were preconditioned to a physiologically emulating membrane tension (T) of 50 N/m in both directions, and then tested with 4 displacement-controlled cycles at various ratios of the targeted tension: T_{Circ}:T_{rad}=1:1, 1:0.66, 1:0.33, 0.66:1, and 0.33:1.

After mechanical testing, the pSFDI device was used to capture the tissue CFA of the tissues at the post-preconditioned (PPC) and different peak loading states, based on the birefringent and diattenuating properties of the tissue [3]. Briefly, the procedure consists of: (i) a DLP projector shining light through a polarizer; (ii) the polarized light cast on the specimen at an angle, $\theta_{\text{polarizer}}$; (iii) the light reflected from the tissue with an intensity, I; (iv) the reflected light passing through the polarizer and captured by a CCD camera. The above sequence is

repeated for $\theta_{polarizer}$=0°-180° at 5° increments. The measured fiber orientation angle, θ_{fiber}, at each pixel location is determined as the polarizer angle $\theta_{polarizer}$ corresponding to the maximum reflected *I*. Further details, regarding the pSFDI theory, can be found in [3].

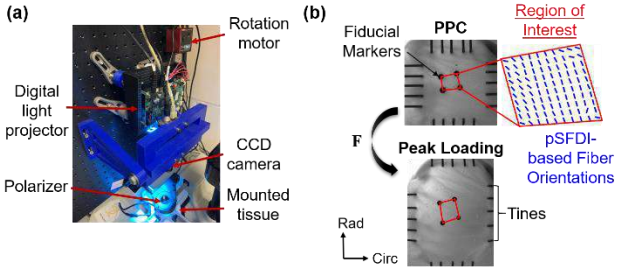

Figure 1: (a) Biaxial testing-pSFDI device. (b) Fiducial marker region of interest for the 100x100 parametric grid.

Based on the pSFDI-derived CFA, the AFK theory was employed to predict the collagen fiber reorientations for a 100x100 parametric grid constructed within the fiducial marker domain (**Fig. 1b**). In brief, the deformation gradient **F** was determined using the locations of the four fiducial markers. Then, the orientation vector at the PPC configuration, $\mathbf{N}=[\cos(\theta_{PPC,j}), \sin(\theta_{PPC,j})]^T$, was determined from the pSFDI-measured fiber orientation at the PPC state, where *j* denotes each query point in the 100x100 grid. The AFK-predicted fiber orientation $\mathbf{n}=[\cos(\theta_{pred.,j}), \sin(\theta_{pred.,j})]^T$ associated with different loading states was computed via $\mathbf{n}=\mathbf{F}\cdot\mathbf{N}/|\mathbf{F}\cdot\mathbf{N}|$. The error between the predicted and the experimentally measured fiber angles was calculated as $\theta_{error}=|\theta_{pred.}-\theta_{exp.}|$. Pearson correlation coefficients (*r*) were calculated to discern trends between metrics. Values are reported as mean ± standard error of the mean.

RESULTS

Results of a representative TVPL specimen are shown in **Figure 2**, including the biaxial stress-stretch responses (**Fig. 2a**) and comparisons of the pSFDI-measured and AFK-predicted CFA (**Fig. 2b-g**).

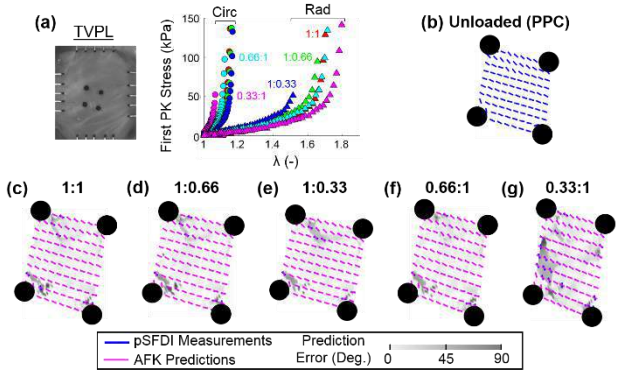

Figure 2: (a) Biaxial testing results for a TVPL specimen. (b) PPC CFA, as measured from pSFDI. (c-g) pSFDI- and AFK-derived CFAs from the five loading states, with vector lines denoting the orientations for selected points, and the color map denoting θ_{error}.

Tissue mechanics-wise, the PPC stretches (λ_{PPC}) were similar for all three leaflets: circumferential direction, 1.17±0.03 (TVAL), 1.17±0.03 (TVPL), and 1.17±0.03 (TVSL); radial direction, 1.31±0.05 (TVAL), 1.36±0.04 (TVPL), and 1.32±0.04 (TVSL). Meanwhile, the TVAL was found to be the least extensible leaflet under *equibiaxial* loading: TVAL, λ_{Circ}=1.31±0.04, λ_{Rad}=1.48±0.06; TVPL, λ_{Circ}=1.38±0.07, λ_{Rad}=1.62±0.07, and TVSL, λ_{Circ}=1.49±0.07, λ_{Rad}=1.72±0.08, whereas the TVPL was found to be the most anisotropic leaflet, as quantified by the anisotropic index (AI)=$\lambda_{Rad}/\lambda_{Circ}$: TVAL, 1.13±0.04; TVPL, 1.21±0.07; TVSL, 1.16±0.05.

In general, we observed that the AFK theory under-predicts the collagen fiber reorientations for the investigated TV leaflet specimens, especially with larger errors in the *non-equibiaxial* loading protocols. Specifically, the average θ_{error} was determined as follows: 10.5°±1.3° (TVAL), 13.3°±2.3° (TVPL), and 17.4°±2.5° (TVSL). Meanwhile, in loading protocol T_{Circ}:T_{Rad}=1:0.33, θ_{error} was found to be: TVAL, 14.6°±1.8°; TVPL, 17.4°±3.4°; TVSL, 23.0°±3.6°.

DISCUSSION

In this study, we have a performed a *first-of-its-kind* evaluation of the AFK theory for the TV leaflets using the pSFDI technique. We found that the AFK theory tended to under-predict the rotations of the collagen fibers, especially in non-equibiaxial loading scenarios. To elaborate, in equibiaxial loading we observed θ_{error} increased with increasing fiber reorientations, suggesting that the AFK theory may be better suited for smaller changes in θ_{fiber} (r=0.66). We also noted the tissue anisotropy, denoted by AI, was weakly, negatively correlated with the collagen fiber reorientations (r=-0.22); however, it was not correlated with θ_{error} (r=-0.01). This observation may be counterintuitive, as more isotropic tissues should exhibit smaller fiber reorientations due to a more disperse fiber network. Our pSFDI device can directly quantify the *optical anisotropy*, however this imaging modality requires more research to quantify the *structural* fiber dispersion. Nevertheless, it is possible the preferential alignment of the fiber network may affect the accuracy of the AFK theory, as noted in a previous tendon study in which more disperse fiber networks correlated to increased AFK errors [4]. The trends in our study may also be explained by the influence of fiber crimp, as reported in Lee *et al*. (2015) [2]. Additionally, we found a weak correlation between λ and θ_{error} (Circ, r=0.16; Rad, r=0.20) under equibiaxial loading, suggesting that larger stretches may attribute to larger errors from the AFK theory, which was also noted in a previous vasculature testing study [5].

The implications of our results suggest the necessity for cautious use of or making adjustment to the AFK theory, such as by including fiber crimping, and/or the incorporation of the non-AFK into the TV leaflet constitutive model forms. The AFK corrections made in the prior studies result in a more robust and computationally inexpensive modeling method; however, the morphological differences in the CFA (fibrillar density, dispersion, etc.) of the TV leaflets may render this option inviable. Thus, our results necessitate an in-depth investigation of the appropriate computational implementation of the TV leaflet collagen fiber kinematics. The refinement of TV leaflet model forms will result in enhanced valve simulations, which will lay the foundation for patient-specific cardiac modeling and guidance for clinical diagnostics and disease treatment.

ACKNOWLEDGEMENTS

This work was supported by the American Heart Association Scientist Development Grant (16SDG27760143), the Presbyterian Health Foundation Team Science Grant, and the National Science Foundation Graduate Research Fellowship (GRF 2020307284).

REFERENCES

[1] Kunzelman, K. *et al*., *J Heart Valve Dis*, 2:236-244, 1993.
[2] Lee, C.-H., *et al*., *Biophys J*, 108:2074-2087, 2015.
[3] Jett, S., *et al*., *Acta Bio*, 102:149-168, 2020.
[4] Lake, S., *et al*., *Biomech Model Mechanobiol*, 11:197-205, 2012.
[5] Cavinato C., *et al*., *J Mech Behav Biomed Mater*, 74:488-498, 2020.

SINGLE CELL ANALYSIS OF VCAM-1 PROTEIN EXPRESSION BY MICROPATTERNED ENDOTHELIAL CELLS

Meghan E. Fallon (1), Monica T. Hinds (1)

(1) Department of Biomedical Engineering
Oregon Health & Science University
Portland, Oregon, USA

INTRODUCTION

Atherosclerosis, the leading cause of cardiovascular disease, is characterized by the thickening and hardening of arterial walls due to chronic plaque accumulation. The initial step of the atherogenic process is the adhesion of circulating monocytes and lymphocytes to the endothelial surface followed by their subsequent transmigration into the intimal layer. Endothelial dysfunction and the upregulated surface expression of adhesion molecules, including E-selectin, intercellular adhesion molecule-1 (ICAM-1), and vascular cell adhesion molecule-1 (VCAM-1), predominantly mediate these early processes [1]. Atherosclerotic development has been correlated to regions within the native vasculature exposed to disturbed flow, which primarily occurs at bifurcations and curves [2]. As fluid shear stress acts on the vessel wall, endothelial cells (ECs) alter their morphology, cytoskeletal alignment, and phenotype in response. It has been shown that ECs exposed to low, oscillatory shear stress maintain a rounded cobblestone morphology with an unaligned cytoskeleton, upregulate adhesion molecules, thus, induce a pro-atherosclerotic phenotype. In contrast, ECs exposed to high laminar shear stress maintain an elongated morphology, alignment of the cytoskeleton, and downregulation of adhesion molecules resulting in an athero-protective phenotype [2].

The differential response of ECs to various flow regimes has been extensively studied within literature, but it is still largely unclear exactly how ECs convert mechanical stimuli into biochemical responses. Various mechanotransduction pathways have been proposed, and the cytoskeleton has been implicated to play a significant role in the decentralized model of endothelial mechanotransduction. This theory proposes that the cytoskeleton is able to transmit signals from the luminal surface of ECs via spatial stress distribution throughout the cell, suggesting that cell shape and cytoskeletal structure may regulate EC function and phenotype [2]. Previous studies have suggested the effects of endothelial shape and cytoskeletal alignment on population-based VCAM-1 gene expression [3]. However, a majority of these studies were performed in the absence of a confluent monolayer and lacked the single cell analysis needed to isolate the effect of cytoskeletal alignment on EC phenotype, resulting in the need for further investigation. In this study, we investigated the effects of endothelial shape and cytoskeletal alignment on VCAM-1 regulation independent of fluid shear stress. Topographic micropatterning techniques were used to generate a distribution of EC elongation in a confluent monolayer. Single cell image analysis techniques were employed to correlate EC morphology with VCAM-1 protein expression. We hypothesized that an elongated morphology and cytoskeletal alignment would downregulate VCAM-1 expression, resulting in an athero-protective phenotype.

METHODS

Substrate Fabrication: Topographical micropatterned culture substrates were fabricated as previously described [4]. Briefly, PDMS submasters with both planar and parallel ridge and groove areas with a pitch of 6 μm were fabricated using soft lithography. Polyurethane was then dispensed on top of the PDMS patterns and covered with glass coverslips. Culture substrates were cured with 2 J of long-wave UV light, demolded, and sterilized.

Cell Culture: Human umbilical vein endothelial cells (HUVECs) were cultured in complete endothelial growth medium (Lifeline) and were used in experiments at passage 6. HUVECs were seeded on substrates for 24 hrs and then stimulated with TNF-α (100 U/mL) for 24 hrs to upregulate adhesion molecules. Cells stained for VE-cadherin, VCAM-1, and nuclei. Samples were imaged on a Zeiss 880 inverted confocal microscope (20X, NA = 0.8). Three images per pattern per replicate were collected for quantitative image analyses.

Single Cell Analyses: Images were loaded into FIJI (SciJava) and color channels were automatically split. A 4x4 grid overlaying the VE-cadherin color channel was used to randomly select individual cells to be traced (n=6-12 per image). Cells closest to grid points were measured for cell area (A_S), perimeter (P), and major and minor axis lengths. Whole cell morphology was determined by calculating the shape index (SI, with 0 equal to a straight line and 1 to a circle):

$$SI = \frac{4\pi(A_S)}{P^2} \quad (1)$$

Deviance angle of the cell relative to the pattern was determined as the absolute value of the major axis of the cell minus the angle of the pattern. The deviance of planar cells was calculated using the pattern angle on the same substrate. Cell deviance angles of 0° is reported as perfectly aligned to the pattern and 90° as perpendicular to the pattern. VCAM-1 protein expression was determined using the VCAM-1 color channel only. Mean intensities within previously traced regions of interest were measured. Values were then corrected for background noise and normalized by individual cell area.

Statistics: Correlations were performed by linear regression between SI, cell deviance, and VCAM-1 expression and confirmed with QQ plots. Data was analyzed using one-way ANOVA and Tukey's HSD post hoc test against substrate type. Data is presented as mean ± SD.

RESULTS

Micropatterned HUVECs showed a significant downregulation of VCAM-1 protein expression compared to planar cells (Fig. 1). Normalized VCAM-1 expression on micropatterns and planar regions was 1.20 ± 1.12 ABUs and 2.10 ± 2.51 ABUs, respectively ($p = 0.01$).

Topographical micropatterning induced significant elongation for micropatterned cells with SIs of 0.52 ± 0.15 compared to or planar regions with SIs of 0.69 ± 0.15 ($p < 0.001$). Cells were also significantly aligned to the pattern compared to planar cells with whole cell deviances of 12.87 ± 9.64° and 40.25 ± 24.25° ($p < 0.001$), respectively (Fig. 2).

Single cell VCAM-1 protein expression was significantly correlated to SI for micropatterned cells ($p = 0.02$, Pearson's Coefficient = 0.294) but was not significant for planar cells (Fig. 3). Similarly, single cell VCAM-1 protein expression was significantly correlated to cell alignment for micropattemed cells only (data not shown, $p = 0.03$, Pearson's Coefficient = 0.297).

DISCUSSION

Topographical micropatteming techniques were shown to align and elongate an endothelial monolayer compared to planar substrate regions. Cellular alignment was shown to downregulate the protein expression of VCAM-1, as shown in other studies [3,5-6]. By using single cell image analysis techniques, the correlation between elongation and VCAM-1 expression was found to be significant. This quantitative data suggests that cytoskeletal alignment has a role in the mechanotransduction of VCAM-1, an inflammatory surface marker, independent of shear stress and supports the cytoskeleton is an active regulator of EC phenotype and function.

ACKNOWLEDGEMENTS

Work was supported by NIH R01HL130274 and R01HL144113.

REFERENCES

[1] Ross, R. et al., *Diabetologia*, 35:S34-S40, 1992.
[2] Davies, P.F., *Physiol Rev.*, 75(3):519-560, 1995.
[3] Vartanian, K.B. et al., *BBRC*, 371:787-792, 2008.
[4] Hagen, M.W. et al., *Tissue Eng A*, 2020.
[5] VandenBerg, E. et al., *J Cell Biochem*, 91:926-937, 2004.
[6] Kato, S. et al., *J Biomed Mat Research*, 54(3):366-372, 2000.

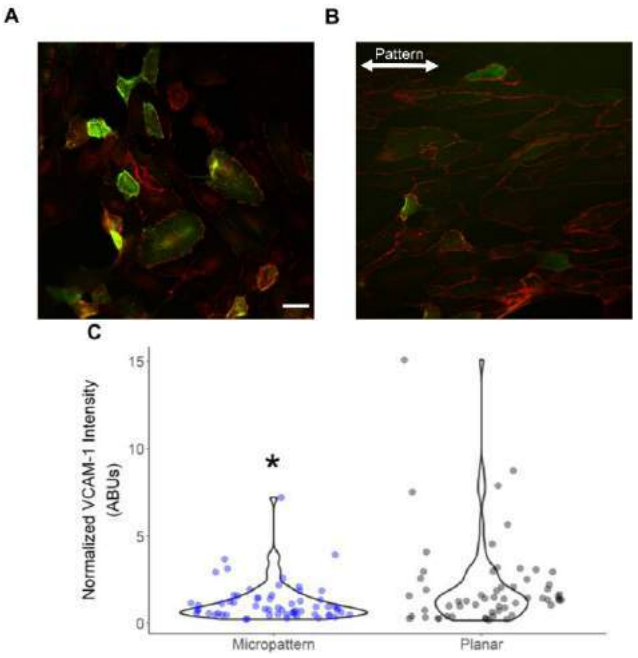

Figure 1: Fluorescent images of planar (A) and micropatterned (B) HUVECs. Scale bar is 10 µm. VCAM-1 intensity is significantly downregulated for micropatterned cells compared to planar cells (C).

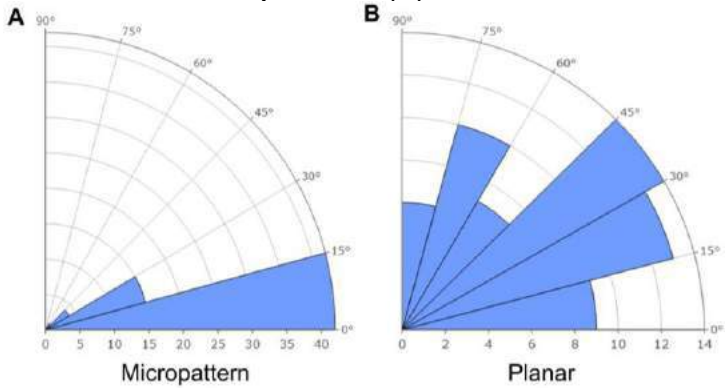

Figure 2: Topographical micropatterning drives alignment of an endothelial monolayer independent of shear stress. Distribution of alignment is shown for cells on micropatterned (A) and planar (B) substrates.

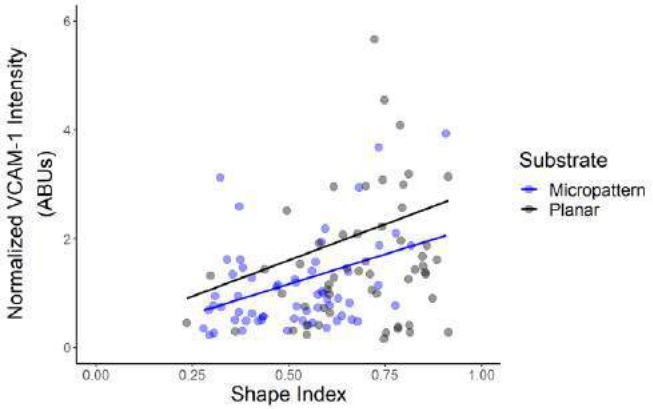

Figure 3: Single cell correlation between shape index and normalized VCAM-1 intensity.

SB³C2021
Summer Biomechanics, Bioengineering and Biotransport Conference
June 14-18, Virtual

TRACHEOMALACIA AFFECTS NEONATAL RESPIRATORY AIRFLOW IN THE UPPER AIRWAY

Chamindu C. Gunatilaka (1,2), Erik B. Hysinger (3), Andreas Schuh (4), Deep B. Gandhi (1,5), Nara S. Higano (1), Qiwei Xiao (1), Daniel A. Ignatiuk (1), Andrew D. Hahn (6), Sean B. Fain (6), Robert J. Fleck (5), Jason C. Woods (1,2,3,5), Alister J. Bates (1,3)

(1) Center for Pulmonary Imaging Research, Cincinnati Children's Hospital Medical Center, Cincinnati, OH, USA

(2) Department of Physics, University of Cincinnati, Cincinnati, OH, USA

(3) Department of Pediatrics, Cincinnati Children's Hospital Medical Center, Cincinnati, OH, USA

(4) Department of Computing, Imperial College London, London, UK

(5) Department of Radiology, Cincinnati Children's Hospital Medical Center, Cincinnati, OH, USA

(6) Department of Medical Physics, University of Wisconsin–Madison, Madison, WI, USA

INTRODUCTION

Many pre-term newborns have airway or lung defects due to prematurity. Tracheomalacia is the narrowing of the largest airway, most often with dynamic collapse during breathing. Newborns with tracheomalacia have breathing difficulties and often require positive-pressure support for breathing. We have previously shown that with tracheomalacia require more energy to move air through the trachea compared to the subjects without tracheomalacia, due to the dynamic tracheal motion [1]. However, the effect of tracheomalacia on airflow in the upper airway (nasopharynx to glottis) during breathing in this patient population has not been studied.

Ultrashort echo time (UTE) magnetic resonance imaging (MRI) is a non-invasive, non-ionizing, and free-breathing imaging technique that can capture the 3D dynamic motion of the airway [2]. This imaging method also allows the reconstruction of high-resolution, respiratory-gated images at different phases of breathing, which can be used to model airway motion via registration [3,4]. Computational Fluid Dynamics (CFD) is a well-known method to model respiratory airflow via medical imaging and it can quantify airway parameters such as work of breathing, pressure loss, and airway resistance that cannot currently be derived clinically. In this study we performed patient-specific CFD simulations with airway motion and investigated the effect of neonatal tracheomalacia on airflow parameters elsewhere in the upper airway.

METHODS

This study included 10 non-intubated newborns (5 non-tracheomalacia, 5 tracheomalacia) from the neonatal intensive care unit of Cincinnati Children's Hospital. Eight subjects were clinically diagnosed with lung disease of prematurity (i.e. bronchopulmonary dysplasia), and 2 term subjects had no respiratory defects. All subjects were imaged using a neonatal sized MRI scanner (1.5 T) while on clinically-indicated respiratory support (room air, high flow nasal cannula, and non-invasive pressure ventilation) [2]. The k_0 waveform obtained from the center of the MRI raw k-space data was used to monitor breathing and to reconstruct 4 MR images, which represent different phases during breathing (end expiration, peak inspiration, end inspiration, and peak expiration) [1,4,5].

All airway surfaces were semi-automatically segmented and registered to obtain airway motion during a breath [3,6]. The k_0 waveform and the segmented lung volumes were used to generate airflow waveforms for the left and right bronchi [1]. Airway motion and airflow waveforms of each subject were used as boundary conditions to perform patient-specific CFD simulations to model airflow from the nasopharynx to the main bronchi.

The commercial CFD package, STAR-CCM+ 14.04.011-R8 was used to run CFD simulations. The CFD mesh consisted of two million cells with polyhedral cells in the interior and nine prism layers on the wall [7]. The Large-Eddy Simulation (LES) turbulence model and the no-slip condition were applied. The pressure at the nasopharynx was assumed to be at atmospheric pressure. An unsteady CFD simulation was performed for each subject for the breathing cycle with a temporal resolution of 0.8 ms [7].

The regional daily work of breathing, the total pressure loss at peak inspiration and peak expiration during breathing, and airway resistance integrated with respect to time across one breathing cycle were calculated for the upper airway (nasopharynx to glottis), (Figure 1). A two-tailed, unpaired, and unequal variance t-test was used to compare results between subjects with tracheomalacia and without tracheomalacia.

RESULTS

On average, the daily work of breathing of the upper airway of the subjects without tracheomalacia (yellow) was 29.9 ± 16.7 J and with tracheomalacia (blue) was 382.4 ± 242.3 J (p = 0.03, Figure 1A). The average total pressure loss of the upper airway at peak inspiration in the subjects without tracheomalacia was 6.5 ± 3.4 Pa; in contrast, subjects with tracheomalacia showed 100.1 ± 77.8 Pa (p = 0.05, Figure 1B). Similar results were also observed at peak expiration. On average, the total pressure loss at peak expiration in the subjects without tracheomalacia was 23.7 ± 14.1 Pa and 247.3 ± 151.4 Pa in the subjects with tracheomalacia in the upper airway (p = 0.03, Figure 1C). The integrated upper airway resistance with respect to time over the breathing cycle also showed a significant difference between the two study groups (p = 0.02, Figure 1D); the average upper airway resistance was 0.2 ± 0.1 Pa.s^2/ml and 2.0 ± 1.1 Pa.s^2/ml in the subjects without tracheomalacia and with tracheomalacia, respectively. Similar results were found after normalizing results based on weight, height, and body surface area of each subject.

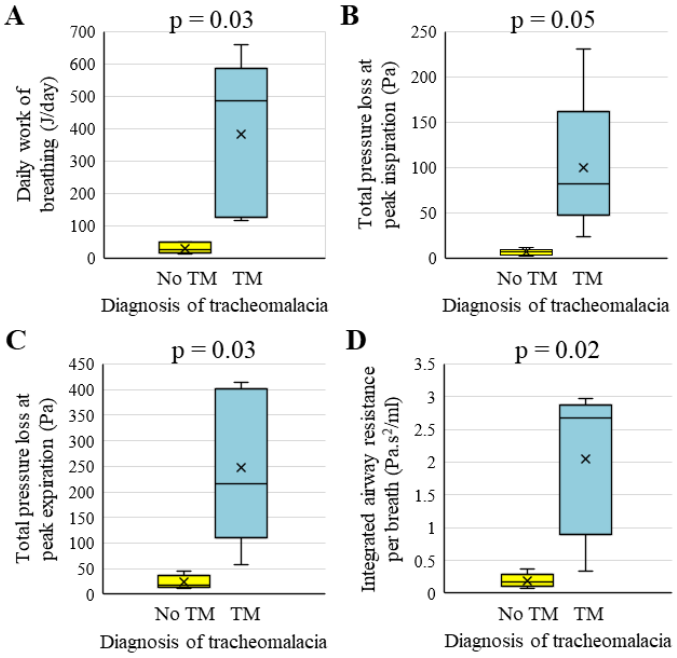

Figure 1: Daily work of breathing (A), total pressure loss at peak inspiration during the breathing cycle (B), total pressure loss at peak expiration during the breathing cycle (C), and integrated airway resistance with respect to time over a breath (D) in the upper airway of the subjects with tracheomalacia (TM) and without TM.

In order to understand the significant differences of the respiratory airflow parameters among the two groups, Figure 2 illustrates the airflow velocity during peak expiration in a subject without tracheomalacia (A) and with tracheomalacia (B). There is a strong jet at the glottis in the subject with tracheomalacia. However, the jet at the glottis in the subject without tracheomalacia is much weaker compared to the subject with tracheomalacia. As a result, the daily work of breathing was 115 J per day for the subject with tracheomalacia and 48 J per day for the subject without tracheomalacia.

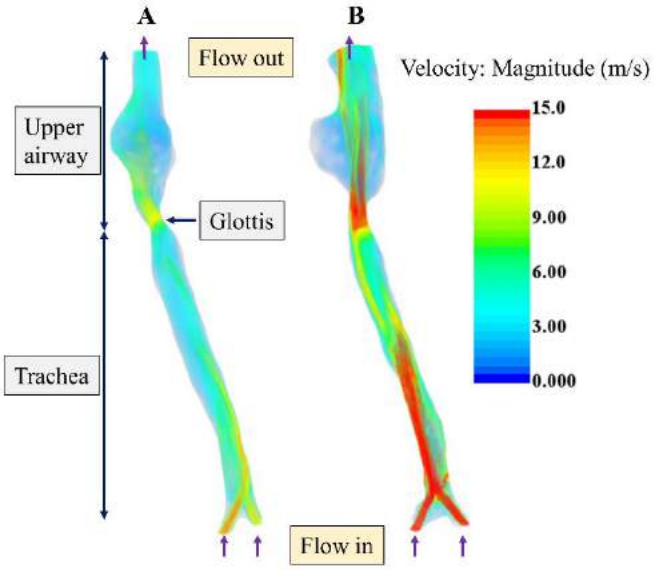

Figure 2: The velocity distribution at peak expiration of a subject without tracheomalacia (A) and a subject with tracheomalacia (B).

DISCUSSION

Tracheomalacia is known to affect the flow specifically in the tracheal region. However, this is the first study to demonstrate that tracheomalacia also significantly affects the flow in the upper airway in neonates (Figure 1). Figure 2 indicates that the laryngeal jet at the glottis affects airflow parameters by creating flow instability in the upper airway, and that neonates with tracheomalacia lose 10 times more pressure in the upper airway than the subjects without tracheomalacia. It is noted that subjects with tracheomalacia were receiving respiratory support at the time of MRI. Without this support, the values would likely be even higher. This study included only non-intubated subjects, since the endotracheal tube can bypass the motion.

The patient-specific CFD simulations with prescribed MRI-based wall motion have shown clinically important information, which may be used in the future to improve patient care and growth. One of the limitations of this study was the image coverage. MR images covered the lungs and the central airway and did not include the upper region of the nasopharynx and through to the nostrils. Another limitation was the CFD run time. Each simulation took approximately 1000 core-hours to complete. The techniques used in this study can also be applied to other airway diseases such as sleep apnea and can be used for older patient populations. Future work will be focused on quantifying regional effects through the entire airway.

ACKNOWLEDGEMENTS

This study was supported by the National Institutes of Health (NIH) K99 HL144822, NIH T32 HL007752, and NIH R01 HL146689.

REFERENCES

[1] Gunatilaka, C C *et al., Ann Am Thorac Soc,* 17:1247–1256, (2020).
[2] Hahn, A D *et al., J Magn Reson Imaging,* 45:463–471, (2017).
[3] Bates, A J *et al., Int j numer method biomed eng,* 34:e3144, (2018).
[4] Higano, N S *et al., Magn Reson Med,* 77:1284–1295, (2017).
[5] Bates, A J *et al., J Magn Reson Imaging,* 49:659–667, (2019).
[6] Yushkevich, P A *et al., Neuroimage,* 31:1116–1128, (2006).
[7] Gunatilaka, C C *et al., Comput Biol Med,* 127:104099, (2020).

SB³C2021
Summer Biomechanics, Bioengineering and Biotransport Conference
June 14-18, Virtual

TISSUE GROWTH AND RESORPTION FINITE ELEMENT MODEL TO EVALUATE EXPANDERS THAT AID IN CLEFT PALATE REPAIR

Tyler J. Gathman (1), Katherine M. Braught (2), Robert J. Tibesar (3), Arthur G. Erdman (4), David S. Nedrelow (4)

(1) School of Medicine
University of Minnesota
Minneapolis, Minnesota, USA

(2) Department of Computer Science
Iowa State University
Ames, IA, USA

(3) Department of Otolaryngology
University of Minnesota
Minneapolis, MN, USA

(4) Earl E. Bakken Medical Devices Center
University of Minnesota
Minneapolis, MN, USA

INTRODUCTION

Orofacial clefts are the third most common congenital anomaly, with cleft palate having an incidence rate of 1 in 800 births [1]. Currently, surgery remains the definitive treatment for orofacial clefts, however, revision operations from infection, fistulas, or abscess formation are common thereby increasing cost and overall risk [2]. Surgeries to repair large clefts may result in tension across the sutured soft tissue which impairs wound healing [3]. Hence, a method of producing additional graft tissue is needed to reduce the rate of complications and other morbidities.

Inflatable tissue expanders have previously been used in large skin defects, such as severe burns and congenital nevi, to produce additional grafted tissue [4]. Studies have experimented with the use of anisotropic hydrogel expanders in palatal tissue expansion with porcine animal models. An important limitation of tissue expanders are deformities in the underlying bone [5].

The purpose of our study was to formulate a mucosa growth and bone resorption finite element model to examine whether tissue expanders, with the limitations of boney defects, may assist in cleft palate repair procedures. If tissue expanders can produce sufficient mucosal growth for tension-free repair without excessive bone loss, then overall costs for cleft palate repair and risks from primary and revision surgeries may be significantly reduced.

METHODS

Mucosa growth and bone resorption algorithms were developed to model tissue expansion with FEBio. Tissue growth was based on a phenomenological growth model with a multiplicative decomposition of the deformation gradient as shown in Eq. (1) [6].

$$\boldsymbol{F} = \boldsymbol{F}^{(e)} \cdot \boldsymbol{F}^{(g)} \tag{1}$$

The elastic component, $\boldsymbol{F}^{(e)}$, was reversible whereas the growth component, $\boldsymbol{F}^{(g)}$, was not [6]. Ateshian and Ricken proposed a multigenerational material composed of a collection of constrained porous bodies [7]. Here, the multigenerational framework was used to generate a new body when the criteria for growth were satisfied. Our model's rate of mucosa generation was based on a literature value of 4.2 days [8]. In addition to time, an elastic area stretch ratio, $\vartheta^{(e)}$, greater than a critical threshold of 1.10 was required for growth which has been suggested to activate mechanoreceptors and amplify growth factors [6]. Each (fully grown) generation was assigned the same constitutive parameters as the initial body. The mucosa's area stretch ratio, ϑ, was computed with two orthonormal basis vectors, $\overrightarrow{e_0}^{(1)}$ and $\overrightarrow{e_0}^{(2)}$, that were parallel to the tissue surface. The orthonormal stretch ratios, $\lambda^{(1)}$ and $\lambda^{(2)}$, were calculated with Eq. (2) from the corresponding orthonormal basis vector.

$$\lambda^{(k)} = \sqrt{\overrightarrow{e_0}^{(k)} \cdot \boldsymbol{C} \cdot \overrightarrow{e_0}^{(k)}} \tag{2}$$

Where $\boldsymbol{C}$ is the right Cauchy Green tensor. Then, the orthonormal stretch ratios were used to determine the area stretch ratio.

$$\vartheta = \lambda^{(1)}\lambda^{(2)} \tag{3}$$

It is noteworthy that Eq. (1) allows area stretch ratios to be calculated as total, $\vartheta^{(t)}$, elastic, $\vartheta^{(e)}$, and growth, $\vartheta^{(g)}$ quantities.

Boundary conditions included a biphasic contact between the expander, bone, and mucosa surfaces. Mucosal and bone outer edges were fixed. Expander nodes were fixed in the contact plane but allowed to move in the direction normal to the bone surface. To simulate expansion, mucosa was initially placed above the expander, and then translated against the bone. Bone was modeled as a mesh free thin shell with nodes fixed in the contact plane directions, but freely moving (resorption) in the direction normal to the surface. The growth configuration was calculated after generating a new body in the affected elements by translating the mucosa away from the bone thereby isolating the growth deformation component.

Bone resorption was modeled as a pressure-threshold phenomenon initiated above a critical pressure of 1.96 kPa [9]. The rate of bone resorption was assumed to be proportional to pressure in the time period examined here as suggested by previous studies [9]. To quantify the pressure-resorption relationship, our model was fit to a recent *in-vivo* study conducted by Swan *et al.* for bone loss. Swan *et al.* reported about 450 mm^3 of bone resorption [10]. Our fit determined an approximate linear constant of 1.61 µm per kPa-day.

To our knowledge, previous studies have not provided mechanical properties for palatal mucosa under tension. We performed strip biaxial testing of porcine mucosa specimens in the anterior-posterior and medial-lateral directions. Fresh mucosa specimens (12x 5 x 2 mm) were stretched to ~1.25 at a rate of 1 mm per minute (n = 4). Negligible differences in stress were found in each direction. Thus, the tissue was assigned isotropic properties. A least-squares method was used to fit a Holmes-Mow constitutive model to the data (Table 1).

Table 1: Palatal mucosa and expander mechanical properties [11].

Material	Model	E (kPa)	ν	β
Palate Mucosa	Holmes-Mow	386	0.30	9.97
Hydrogel Expander	Neo-Hookean	5800	0.30	N/A

For the purposes of soft tissue expansion, the geometric and mechanical properties have a significant impact on mucosal growth and bone loss. A set of 45 expanders with varying heights, bone-contact areas, and expansion angles were examined. A multiple regression analysis of geometric parameters was used to guide the patient-specific expander design that we applied to a 1-year-old male cleft palate case.

RESULTS

In a patient-specific finite element model, expansion over a 42-day duration resulted in a mucosal area gain of 40 mm^2, or mean growth area stretch ratio of $\langle \vartheta^{(g)} \rangle = 1.18$ as shown in Fig. 1.

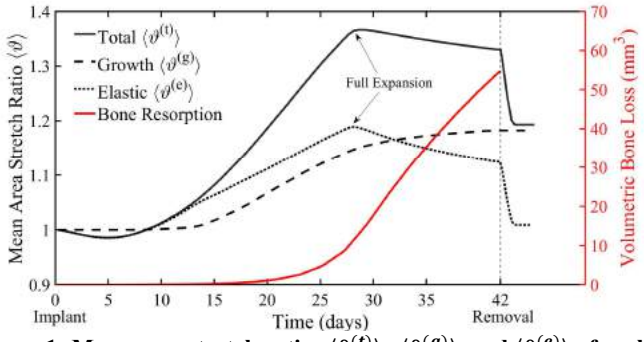

Figure 1: Mean area stretch ratios $\langle \vartheta^{(t)} \rangle$, $\langle \vartheta^{(g)} \rangle$, and $\langle \vartheta^{(e)} \rangle$ of oral surface mucosal elements and volumetric bone loss during tissue expansion.

Full expansion occurred at day 28 which was accompanied by the maximum total and elastic mean area stretch ratios. The volumetric bone loss was approximately 55 mm^3 (Fig. 1) with a depth, demonstrated in Fig. 2, that peaked at 0.70 mm.

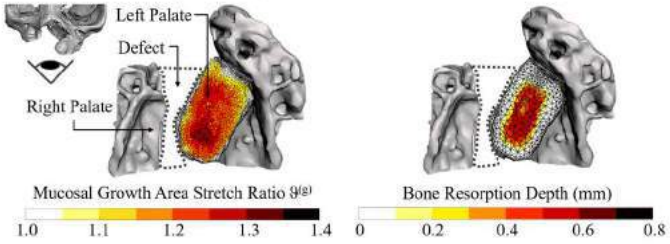

Figure 2: Mucosa growth area stretch ratio and bone resorption depth varied across the palate surface after expander removal.

The model suggested that bone perforation will not occur as greater than 20% of the bone thickness was preserved upon device removal (0.90 mm initial thickness). With a defect area of approximately 70 mm^2 (Fig. 2 dashed lines), the model provided evidence that the amount of tissue growth, visualized in Fig. 3, would aid in a tension-free closure.

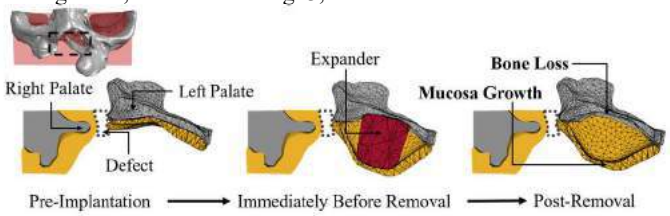

Figure 3: Frontal cross-section view showing bone resorption and mucosa gain that can be grafted to close large defects.

DISCUSSION

Swan *et al.* demonstrated anisotropic hydrogel expanders may improve cleft palate repairs in an animal study. Our patient-specific model suggested that with careful design considerations, significant mucosal tissue from expanders can aid in closing a cleft defect without perforating the underlying bone. Hence, the use of tissue expanders could be a promising adjunct to large cleft palate repair surgeries that may result in less complications than surgeries performed without tissue expansion.

Bone resorption and possible perforation remain a major limitation of tissue expanders for cleft palate repair. Our bone resorption constant that was fit to data from Swan *et al.* used a linear relationship with pressure. Nonetheless, the relationship between load and bone resorption is complex and may be non-linear in other time regimes or dependent on biological factors. For simplicity, the bone resorption process was calculated with contact-pressure rather than stress through the bone. We recognize that bone mechanotransduction has been examined with respect to density and stress, but for the purposes of our simulation's limited time period, we considered a linear assumption to be applicable. Recent literature pertaining to skull bone demonstrated that bone deformities from expanders or other load-inducing devices were reversible within 3 to 9 months post-removal [5]. Additional studies will be required; however, this may indicate an absence of long-term consequences from expander induced bone resorption.

Considering the drastic cost and quality-of-life concerns with cleft palate defects, our results indicated palatal expansion devices can aid surgeons in improving surgical outcomes for large or complex cleft defects.

ACKNOWLEDGEMENTS

This work was supported by the University of Minnesota's Earl E. Bakken Medical Devices Center with gifts from the Frank J. and Eleanor A. Maslowski Charitable Trust and the Pediatric Devices Innovation Consortium.

REFERENCES

[1] Mai, C et al., *Birth Defects Res.*, 111:1420-1435, 2019.
[2] Mahboubi, H et al., *Int J. Pediatr. Otohino.,* 79:803-807, 2015.
[3] Eberlink, A et al., *Cleft Palate Craniofac J.,* 49:643-648, 2012.
[4] LoGiudice, J et al., *J. Craniofac. Surg.,* 14:866-872, 2003.
[5] El-Saadi, M et al., *J. Plast. Reconstr. Aesthet.,* 61:413-418, 2008.
[6] Zollner, A et al., *Biomech Model. Mechanobiol.,* 11: 855-867, 2012.
[7] Ateshian, G et al., *Biomech Model. Mechanobiol.,* 9:689-702, 2010.
[8] Cutright, D et al., *Oral Surg, Med., Path.,* 23:249-259, 1967.
[9] Sato, T et al., *J. Dental. Res.,* 77:387-392, 1998.
[10] Swan, M et al., *Plast. Reconstr. Surg.,* 129:79-88, 2012.
[11] Nagaoka, S., *Polymers*, 21:847-850, 1989.

SB³C2021
Summer Biomechanics, Bioengineering and Biotransport Conference
June 14-18, Virtual

A GENERAL PROTOCOL FOR SIMULATING RESTING CARDIOVASCULAR PHYSIOLOGY USING A CLOSED-LOOP LUMPED PARAMETER MODEL

Akash Gupta (1), Aseem Pradhan (1), Surya Prakash Sharma (3), Tyler Schmidt (1), Ethan Kung (1,2)

(1) Department of Mechanical Engineering
Clemson University
Clemson, South Carolina, The United States

(2) Department of Bioengineering
Clemson University
Clemson, South Carolina, The United States

(3) Department of Electrical and Computer Engineering
Clemson University
Clemson, South Carolina, The United States

INTRODUCTION

Lumped Parameter Network (LPN) models are one of several mathematical modelling techniques used to simulate the hemodynamics of the human cardiovascular system. These models are capable of simulating cardiovascular physiology with closed-loop cardiac feedback at minimal computational expense. Their applications in surgical planning, medical device design, education, and training are well documented. However, the inverse problem, i.e., the determination of appropriate LPN input parameters, remains a challenge. Investigators often resort to manual tuning procedures where reasonable ranges for LPN inputs are established, and then different combinations of LPN inputs are tested until the LPN output matches the desired response. Such a process is not only time-intensive, but also requires invasive clinical measurements that are not always available. To our best knowledge, there exists no protocol that can automatically provide appropriate LPN parameter values based on subject characteristics such as age, height, and weight (henceforth collectively referred to as "attributes").

In this work, we address this gap by describing our protocol which provides suitable parameter values for an LPN model that reflects typical, hemodynamics of a healthy subject at rest with specific attributes. Furthermore, the tuned LPN can serve a basis with which minor adjustments can be tuned to match patient-specific characteristics.

METHODS

Our proposed protocol is a procedure which derives a full set of input parameters for an existing closed-loop LPN model (Ref [1] - Figure 1.1) that is derived from previous work modeling uni-ventricular resting and exercise hemodynamics. We will refer to the full set of input parameters, which are necessary to execute the LPN model, as the "LPN inputs" henceforth. For this LPN, we start with a set of inputs which produce a nominally realistic simulation of resting hemodynamics; this particular set of inputs will be referred to as the "reference LPN inputs". For a detailed explanation of the LPN, the circuit diagram, and the reference LPN inputs, please refer [1]. We will refer to hemodynamic quantities such as aortic pressures, pulmonary artery pressures, ventricular volumes, etc., which are the LPN simulation results as "LPN outputs".

We obtain physiologically realistic target values of critical LPN outputs from literature that correspond to a generic subject with the particular set of attributes to be simulated[1]. These attribute-specific critical LPN outputs include hemodynamic parameters such as the systolic and diastolic values of aortic pressure, pulmonary artery pressure, ventricular volumes, mean atrial pressures, etc. Next, we calculate the target Systemic Vascular Resistance (SVR) and Pulmonary Vascular Resistance (PVR) based on these critical LPN outputs.

We have divided the LPN inputs into three categories based on how these values are arrived at. The values of the LPN inputs in the first category are constants, equal to the reference values. We use an Artificial Neural Network (ANN) to estimate the LPN inputs in second category, while the values of the LPN inputs of the third category are arrived at using a scaling procedure.

The LPN inputs in the second category consist of parameters which model the ventricles, i.e., the maximum and minimum elastances for both ventricles, as well as the capacitance of the aorta, and a factor by which all the initial pressures and volumes in the circuit are scaled. The neural network architecture we have employed has been specifically designed for non-linear regression [2]. The neural network operates as a limited inverse model of the LPN. When target values of critical LPN outputs as well as the SVR and PVR are provided to the ANN, it

estimates the values of the LPN inputs in the second category. To generate the data for training the neural network, we used a Uniform Latin Hypercube sampling algorithm to generate 500,000 combinations of the LPN inputs in the second category, within specified limits. The LPN outputs generated by executing the LPN with the 500,000 combinations of the LPN inputs, and the corresponding LPN inputs were used to train the ANN.

The LPN inputs in category 3 are determined by the scaling procedure. These LPN inputs include all of the systemic and pulmonary resistors and capacitors, excluding the thoracic aortic capacitance. Using the values of SVR, and PVR determined from the attribute-specific critical LPN outputs mentioned previously, we can calculate SVR and PVR scaling factors. To account for body size, all capacitors in the third category are scaled using an allometric scaling factor in a manner similar to previous work [3]. Using the ANN's predictions of ventricular elastance values, estimates for the end systolic pressure, and trigonometric relations, we determine the ventricular reference volumes. Finally, the heart rate is prescribed based on Ref [1].

For validation purposes, we have tested the protocol 100 realistic combinations of ages (range: 20 - 70 years), heights (range: 155 – 188 cm) and weights (range: 56 – 100 kg), and have compared the protocol output against literature predictions from Ref [1].

RESULTS

Comparisons of the hemodynamic parameters simulated by the protocol and the corresponding literature predictions are shown in Figure 1. The mean bias, maximum absolute deviation of the protocol test results from the literature predictions, and the corresponding 95% confidence intervals[1], are described in Table 1. In the protocol test results, the mean pulmonary artery (PA) pressure in 96 cases ranged between 14.5 and 19mmHg, with 4 outliers greater than 20 mmHg. Mean right atrial pressures ranged between 3.9 and 5.7 mmHg, whereas mean left atrial pressures ranged between 6.3 mmHg and 17 mmHg.

DISCUSSION

All the simulated hemodynamic parameters in the protocol test set, when compared against literature predictions, exhibit non-zero bias on average (Table 1). However, other than the systolic aortic pressure, and the systolic right ventricular volume, the magnitude of the mean bias is small when compared to their corresponding nominal values. In the case of the systolic aortic pressure and the systolic right ventricular volume the deviation grows near the low end of the range (Figure 1). Despite this, all hemodynamic parameters exhibit deviations within the 95% confidence intervals of literature predictions. In 96 of 100 test cases, the mean PA pressure is below the clinically accepted threshold of 20mmHg for pulmonary hypertension. In all test cases, both mean atrial pressures lie within clinically normal ranges.

Therefore, we conclude that given the attribute information, our proposed protocol can provide the full set of input parameters for the LPN such that it reflects a realistic hemodynamic response under resting conditions for healthy adults across a range of age, height, and weight. In future work, we will expand the scope of this protocol to include exercise hemodynamics, given the same attribute information and the exercise intensity.

ACKNOWLEDGEMENTS

This work is supported by an award from the National Science Foundation (1749017) and by the department of Mechanical Engineering at Clemson University. Clemson University is also acknowledged for their generous allotment of compute time on the Palmetto cluster.

REFERENCES

[1] Pradhan, A. M., 2020, "Delineating the Relationship Between Cardiovascular Physiology And Subject Characteristics Using Computational Modeling and Systematic Review,", Thesis, Mechanical Engineering, Clemson University.

[2] Chen, D., et al., 2020, Entropy, **22**(2).

[3] Kung, E., et al., J. Biomech. Eng., **136**(8), p. 081007.

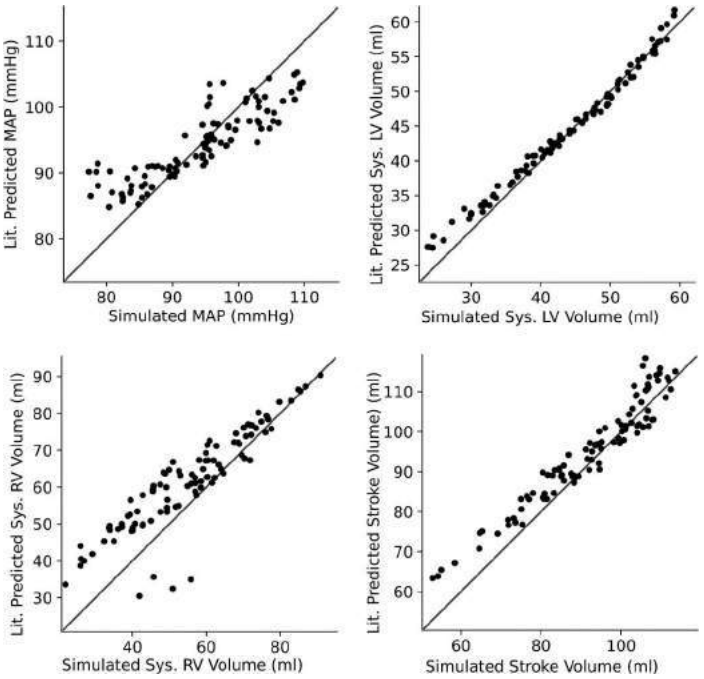

Figure 1: Protocol output validation against literature data [1]. The line that appears in all plots is the unity line. LV, Left Ventricle; RV, Right Ventricle; Sys., Systolic; MAP, Mean Arterial Pressure.

Hemodynamic Parameter	Mean Bias (absolute)	Max. Absolute Deviation	Lit. 95% CI
Mean Aortic Pressure	0.78	12.81	NA
Sys. Aortic Pressure	9.88	34	± 40.3
Dia. Aortic Pressure	2.95	9.5	± 19.9
Sys. LV Volume	0.16	4.5	± 34.8
Sys. RV Volume	5.28	20	± 32.3
Stroke Volume	2.22	15	± 156

Lit., Literature; LV, Left Ventricle; RV, Right Ventricle; Sys., Systolic; Dia., Diastolic

Table 1: Bias and deviations of hemodynamic parameters output by the protocol against literature predictions[1]**. All pressures are in mmHg, volumes in ml, and stroke volume in ml/beat.**

PULSATILE PERFUSION OPTIMIZATION WITHIN A MULTI-ORGAN PRESERVATION DEVICE

Daniel J. Portillo (1), Stephen Rivas (1), Gabriela Pineda (1), Sukhwinder Kaur (2), Lauren Bayliss (3), Leonid Bunegin, R. Lyle Hood (1,2,4)

(1) Department of Mechanical Engineering
The University of Texas at San Antonio
San Antonio, Texas, U.S.A.

(2) Department of Biomedical Engineering
The University of Texas at San Antonio
San Antonio, Texas, U.S.A.

(3) Department of Internal Medicine
The University of Texas – Rio Grande Valley
School of Medicine
Edinburg, Texas, U.S.A.

(4) Graduate School of Biomedical Sciences
The University of Texas Health Science Center
San Antonio
San Antonio, Texas, U.S.A.

INTRODUCTION

Over 110,000 people are currently on the waitlist to receive a life-saving organ transplant, and only 36,000 organs were successfully transplanted in 2020 [1]. A leading cause for the organ shortage is a lack of adequate preservation methods, evidenced by the fact that thousands of organs are discarded every year after being harvested and preserved [2]. The current gold standard for organ preservation is static cold storage, where the organ is bathed in a preservation solution maintained at hypothermic temperatures. However, research has shown that hypothermic and normothermic machine perfusion are superior to static cold storage, as they increase both preservation quality and preservation time [3, 4]. This improved preservation capability allows organs to be transported over longer distances, which ultimately increases the number of organs available to waitlisted patients.

Currently, there are preservation devices specifically designed to maintain individual organs, including kidneys, livers, hearts, pancreases, and lungs [5]. Unfortunately, these devices are typically expensive, bulky, and difficult to operate without proper training. Additionally, the current devices are focused on single organs, which severely limits their utility and, in the event of a donor capable of donating multiple organs, would necessitate multiple devices from multiple companies. Thus, our objective is to develop a frugal, compact, and easy-to-use device that can provide machine perfusion for a variety of organs.

A prototype device was designed and fabricated with the storage capacity needed to preserve a human kidney, liver, heart, or pancreas. Utilizing a modified diaphragm pump, the device is designed to deliver oxygenated and pulsatile perfusion to the organ being preserved. The device is also designed to be compatible with preservation solutions and preservation temperatures that are commonly used for preserving various organs. An image of the device can be seen in Figure 1.

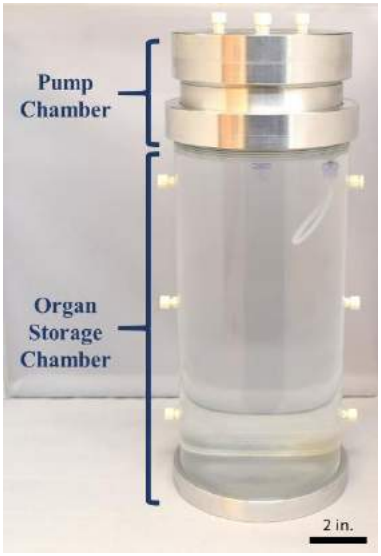

Figure 1: Fabricated preservation device prototype

Two of the most critical machine perfusion parameters for any preservation device are the perfusion pressure and the perfusate flow rate, both of which depend on the organ being preserved. The focus of this work was to validate and optimize the device's perfusion capabilities within the ranges necessary for multiple organs. Specifically, we hypothesized that our device would supply a perfusion pressure and flow rate that would satisfy the perfusion requirements of a human kidney (<30 mmHg, ~140 mL/min) and a human pancreas (<30 mmHg, ~30 mL/min).

METHODS

The device is approximately 6 inches in diameter and 15 inches tall and weighs approximately 16 lbs. when operating. The diaphragm-style pump within the prototype device was driven by pulsed compressed oxygen. Thus, the variables dictating the pump's performance include the size of the diaphragm, the pressure of the oxygen, the frequency of oxygen pulses, and the duty cycle of oxygen pulses. While the size of the diaphragm was kept constant throughout all tests, the oxygen pressure was varied from 2 – 20 psi at increments of 2 psi. Unlike previous work focused on nonelectronic oxygen regulation [6], the compressed oxygen was regulated by a three-way pinch valve (Masterflex®, Cole-Parmer Instrument Company, LLC) programmed to operate at a frequency of 0.25 Hz and a 50% duty cycle. Pressure transducers (U5244-000005-005PG, Measurement Specialties, Inc.) and a flow rate sensor (2PXL-TS410, Transonic Systems Inc.) were used to measure the perfusion pressure and flow rate of the perfusion solution in real time. The perfusion solution (deionized water) was diverted from its normal path into a flow loop so that it could be measured with the flow sensor. The hydraulic resistance created by the flow loop was tuned to 0.5 mmHg/mL/min, which is roughly analogous to the vascular resistance of a kidney and pancreas [7, 8].

The data was collected with a custom LabVIEW virtual interface (NI 9221, NI USB-9162, National Instruments) and exported to MATLAB for processing. The pulsatile flow rate profiles were averaged together (for each individual pressure) and the area under their curves at each progressive time step (0.001 s) was calculated to determine the frequency and duty cycle that would maximize the cumulative flow rate.

RESULTS

Any data from a trial whose peak perfusion pressure exceeded 60 mmHg was discarded, as that perfusion pressure would damage the vasculature of a kidney or pancreas. The average perfusion pressure for the remaining trials varied between 5 – 15 mmHg. Pulsatile flow rate data was averaged (n=30) at various oxygen pressures, and Figure 2 shows the flow profiles of single pulses (with the shaded areas representing the standard deviation). It can be observed that the pulsatile flow rate increased as the oxygen pressure increased.

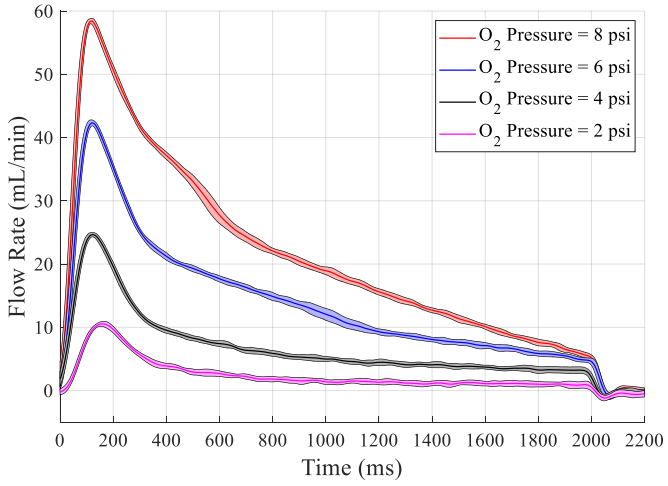

Figure 2: Raw pulsatile flow rate data

The data presented in Figure 2 was used to tune the pulse frequency and duty cycle of the pulsed oxygen and those results can be seen in Figure 3, which displays the experimentally measured cumulative flow rate and the estimated maximized cumulative flow rate. The error bars on the optimized flow rates stem from the deviations of the pulsatile flow profiles shown in Figure 2. The best identified pulse frequency ranged from 1.5 – 2.5 Hz and the best identified duty cycle ranged from 70 – 80%. As oxygen pressure increased, the best identified pulse frequency decreased, and the best identified duty cycle increased.

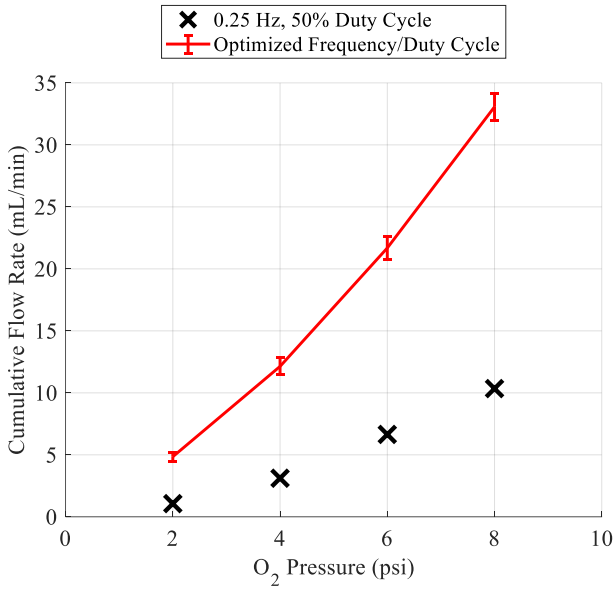

Figure 3: Cumulative flow rates of perfusate

DISCUSSION

The analysis of the diaphragm pump conducted in this study demonstrates that the device can provide adequate perfusion for a human pancreas. However, the device does not provide the cumulative flow rate required by a human kidney. Future work will include altering the size of the diaphragm pump, which will directly influence the response time of the pump. A faster response time will allow for higher pulse frequencies and lower peak perfusion pressures, which will ultimately increase the cumulative flow rate. The device also needs to be evaluated against alternative vascular resistances, preservation solutions, and preservation temperatures. Once the device's performance has been fully characterized, *ex vivo* human organ preservation studies will be conducted to validate the device's ability to preserve a variety of organs.

ACKNOWLEDGEMENTS

This work was funded through a Department of Defense PRMRP Award Number: W81XWH-18-1-0640. The authors would like to thank David Kuenstler for assisting with the fabrication of the device.

REFERENCES

[1] U.S. Department of Human and Health Services, Organ Procurement and Transplantation Network, National Data.
[2] Giwa, S et al., *Nat Biotechnol*, 35(6):530-542, 2017.
[3] Tingle, SJ et al., *Cochrane Database of Sys Reviews*, (3), 2019.
[4] Guarrera, J et al., *Am J of Transplantation*, 10(2):372-381, 2010.
[5] *TransMedics, Inc.*, OCS Liver, Lung, and Heart Information, 2020.
[6] Portillo, DJ et al., SB^{3}C Conference, 2020.
[7] Stratta, RJ et al., *Journal of the American College of Surgeons*, 204(5):873-882, 2007.
[8] Kumar, R et al., *Int J Surg*, 54(A):206-215, 2018.

SB³C2021
Summer Biomechanics, Bioengineering and Biotransport Conference
June 14-18, Virtual

MECHANICAL TESTING OF TYPE II COLLAGEN NETWORKS: TOWARDS MODULATING MECHANICS, IDENTIFYING SINGLE-FIBER PROPERTIES, AND ESTABLISHING MULTISCALE MODELS

Phoebe Szarek (1), David M. Pierce (1,2)

(1) Department of Biomedical Engineering
University of Connecticut
Storrs, CT, USA

(2) Department of Mechanical Engineering
University of Connecticut
Storrs, CT, USA

INTRODUCTION

Articular cartilage and other collagenous soft tissues rely heavily on their internal networks of collagen for mechanical strength. When placed in tension, e.g. due to external loading or osmotic swelling, collagen fibers contribute to the mechanical response and stiffness of these tissues. Collagen networks also provide a foundation for many applications in tissue engineering. We seek to establish a robust methodology and platform for testing isolated collagen networks to aid researchers in investigating the effects of mechanical loading (e.g. repeated, damage-inducing, rate-dependence) and biochemical modifications (e.g. temperature, +/- crosslinking, cell products) on this essential mechanical constituent within tissues and biomaterials. Such understanding may aid in the development and testing of therapeutics aiming to heal damaged tissues, specifically those developed to treat diseases of articular cartilage, i.e. osteoarthritis. Furthermore, isolating collagen networks from the tensile forces generated by osmotically induced pretension may aid in understanding intra-constituent interactions and their roles in tissue biomechanics. Testing of isolated networks of collagen fibers may lead to understanding of the mechanics of individual fibers that can inform multiscale mechanical models.

METHODS

We sequentially focused on sourcing, preparing, and testing networks of type II collagen and sought to optimize each step. We first established a method for isolating collagen networks from bovine articular cartilage. Additionally, cartilage contains a collagen network with through-thickness heterogeneity, a factor that we can include as a variable or control for with specific protocols. We extracted full-thickness cartilage from the patellofemoral groove and femoral condyles attached to the subchondral bone in 1×2 cm pieces. We then sliced the cartilage pieces into 200 μm thick sheets (the thickness of the well-aligned superficial zone of cartilage [1]) using a microtome, before digesting out the proteoglycan (PG) constituents using trypsin [2]. We used the most superficial two or three sheets of cartilage to control for variability in the fiber alignment through the thickness of cartilage [3].

We determined the appropriate trypsin concentration and the duration of digestion using another set of specimens extracted from the tibial plateau and patella for 24 or 48 hours in 0.25, 0.5, 1.0, or 2.0 mg/mL enzyme in phosphate buffered saline (PBS). We quantified the PG remaining and the collagen loss using glycosaminoglycan and hydroxyproline assays. We chose the enzyme concentration and duration that removed the most PG with minimal loss of and damage to collagen, also aiming to minimize the digestion time and the amount of enzyme required. We also investigated the volumetric effects of digestion by imaging specimens before and after digestion and computed the deformation gradients associated with the digestion.

We then established the appropriate specimen dimensions. We used the ASTM D1708 standard dimensions for microtensile testing as a baseline and scaled these down to reduce the amount of tissue required for each test [4]. We performed finite element analyses to ensure that the geometry of the specimen we selected did not create problematic stress concentrations and that the stress distribution in the gauge region remained homogenous. We then varied the specimen thicknesses starting at a maximum of 200 μm, aiming to create sheets of collagen as thin as possible, but thick enough to manipulate during testing and while minimizing undesirable edge effects from damage sustained during specimen preparation. We selected the thinnest specimens that did not present obvious loss of stiffness in the bulk network.

We next determined the displacement rate for tensile testing to eliminate strain-rate dependence while still achieving a reasonable test duration. We started at 75 μm/min (previously determined to be quasi-static [5]) and increased the rate until we noted rate dependence in the

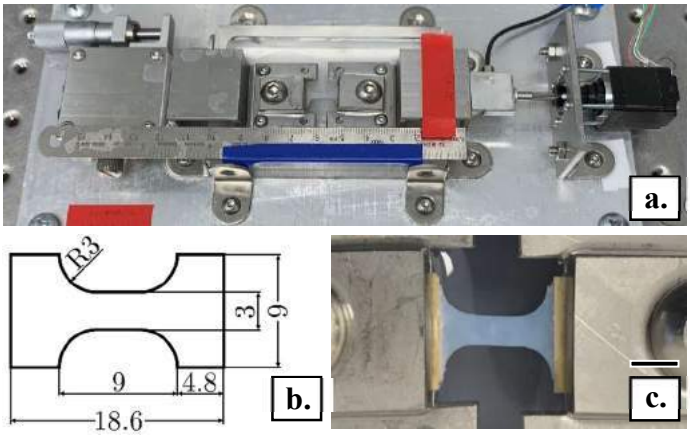

Figure 1. Mechanical testing of collagen networks: a. microtensile testing device; b. dimensions of our tensile specimen in mm; c. specimen mounted within the microtensile device, bar = 5 mm.

mechanical results. Aiming to create a test platform for efficient research, we chose the highest displacement rate that did not increase the apparent stiffness of the collagen network.

We performed all tensile tests on a custom-built microtensile device (**Fig. 1a**) with a displacement range of 12.5 mm (resolution: 2.5 µm) and force capacity of 20 N (resolution: 0.3 mN). We kept tissues hydrated in a PBS bath at 25°C and aligned specimens with the principal fiber orientation, but designed the device to fulfill requirements and constraints of future studies on collagen networks (e.g. visualizing fiber structures, quantifying damage during loading, studying temperature effects). We secured the specimens using cyanoacrylate glue and sandpaper (**Fig. 1c**) and monitored testing to ensure tissue failure occurred within the gauge region.

RESULTS

Table 1 shows the preliminary results of testing our protocols for enzymatic digestion. We will finalize a digestion protocol to reduce the PG in the tissue to less than 2% of the original PG mass with less than 1% collagen mass lost or damaged, while still aiming to reduce the cost and time needed for the specimen preparation. **Fig. 1b** shows the dimensions of our specimens that reduce the required tissue but still maintain a gauge region with homogenous stresses to simplify subsequent mathematical analyses of fiber networks under loading. Preliminary tests also show this level of digestion and PG removal does not cause considerable changes in specimen geometry, i.e. deformation that should be included in interpreting the resulting mechanical data.

Table 1. Mass Percent PG Remaining Post Digestion (Mean ± Standard Deviation, n = 6 per test group)

	Trypsin Concentration (mg/mL)				
Duration	0	0.25	0.5	1	2
24 hr	87.4 ± 4.8	2.2 ± 0.4	1.3 ± 0.8	1.1 ± 1.3	1.6 ± 0.5
48 hr	84.2 ± 4.9	1.2 ± 0.8	1.3 ± 0.6	1.5 ± 0.4	1.1 ± 0.4

Preliminary tests show that digested specimens have a stiffness less than that of intact specimens and that extreme digestion can over soften tissue by damaging the collagen network during removal of PG (**Fig. 2**). Preliminary results show loss of collagen (and thus network damage) at the higher concentrations shown in **Table 1**. Additionally, increasing the strain rate stiffens the tissue response due to the viscoelastic response of collagen fibers [6]. Finally, preliminary tests show that there is a minimum thickness (threshold) below which the stiffness of the tissue decreases due to edge effects from damage.

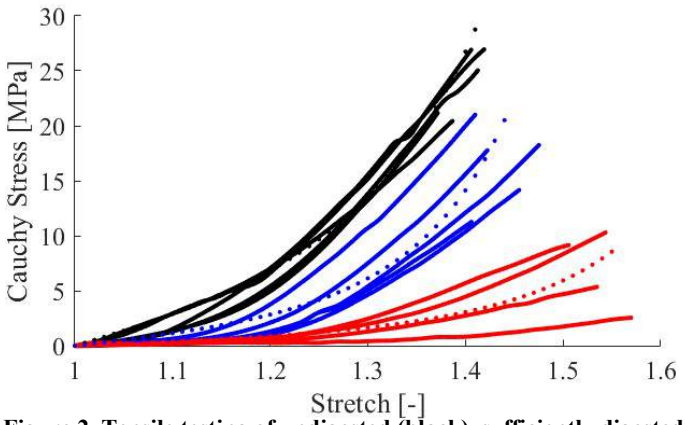

Figure 2. Tensile testing of undigested (black), sufficiently digested (blue), and overly digested (red) cartilage specimens as a source of type II collagen networks. The dashed lines show the prediction based on the average parameters fit from each test type (n = 5).

DISCUSSION

Variability within cartilage and collagen networks arises from many factors. With this protocol, we aim to create a process that is repeatable so that effects presenting in future tests reflect the independent variable of interest and not the innate variability between tissue specimens. We also aim to quantify intra-specimen variability to inform future research.

Preliminary results show that the test parameters we are investigating are relevant in altering the apparent mechanics of collagen networks, speaking to the effects of chemical and mechanical damage as well as the strain-dependent response of collagen networks and possibly fibers, yet we will also evaluate our testing protocol further. We plan to visualize potential damage to the collagen network using collagen hybridizing peptide (CHP) to ensure internal damage without loss of collagen is not present. We also plan on using digital image correlation (DIC) to confirm that strain is homogeneous within the gauge region and investigate the mechanism of failure.

While establishing a testing platform, we needed to make decisions to transform a theoretical test into a practical experiment. Conflicting constraints and aims limit the optimization of these methods, e.g. an ideally thin (<200 nm) sheet of a single layer of collagen fibers would be nearly impossible to handle and mount for tensile testing. We also established arbitrary (but practical) cutoffs for acceptable levels of remaining PG and lost/damaged collagen since we cannot reasonably perform a complete digestion of PG with no effect on the collagen.

Future work using this test platform will characterize the mechanical response of individual type II fibers by analyzing the network structure using a host of tools including second harmonic generation microscopy, transmission electron microscopy, and micro-digital image correlation. Mechanical characterization of individual collagen fibers and isolated collagen networks will also inform models aiming to include micro-mechanics into models of bulk tissues.

ACKNOWLEDGEMENTS

NSF 1662429, GAANN P200A160323, GE Fellowship. Christopher Lemay, Zachary Ohayon, Anthony Rivera.

REFERENCES

[1] Mow, V et al., *Basic orthopaedic biomechanics & mechanobiology*, 180-258, 2005. [2] Torzilli, P et al., *J. Biomech.,* 30:9, 1997. [3] Kempson, G et al., *Biochim. Biophys. Acta*, 297, 1973. [4] ASTM Intl., *D1708-18*, 2018. [5] Maier, F et al., *J. Mech. Behav. Biomed.,* 65, 2017. [6] Li, L.P. et al., *Biorheology,* 41, 2004.

COMPUTATIONAL ASSESSMENT OF A NOVEL DESIGN OF TRILEAFLET MECHANICAL HEART VALVE IMPLANTED IN AORTIC POSITION

Syed Samar Abbas (1) and Iman Borazjani (1)

(1) J. Mike Walker ’66 Department of Mechanical Engineering
Texas A&M University
College Station, Texas, USA.

INTRODUCTION

The native aortic valve is characterized by three cusps (or leaflets) and regulates the unidirectional flow of blood from the left ventricle into the aorta. It may malfunction in children and young adults due to congenital heart defects or rheumatic diseases. In such case, it is widely replaced by a Bileaflet Mechanical Heart Valve (BMHV), having two prosthetic leaflets. The commercially available BMHVs are albeit durable, however, they are known to generate non-physiological blood flow patterns [1-4] which can result in thrombus formation [5]. Consequently, recipients of these valves should take anticoagulant drugs for the rest of their lives, which can have fatal consequences if not monitored properly. For this reason, novel mechanical heart valves are required to be designed, tested, and implanted to ascertain physiological blood flow inside the human aorta. This study numerically investigates the hemodynamics of a novel Trileaflet Mechanical Heart Valve (TMHV), designed with three leaflets to replicate the flow field generated by a native aortic valve.

METHODS

The computational simulations were carried out by using Curvilinear Immersed Boundary (CURVIB) method for solving the blood flow field, governed by 3D Navier Stokes equations [6]. The employed CURVIB solver has been well-validated in the past research [6, 7]. The excursion of the TMHV leaflets in response to the cardiac flow is determined by coupling the leaflet equations with the flow through a strong-coupling fluid-structure interaction (FSI) algorithm [6]. The boundary conditions included the incorporation of a physiological flow curve at the inlet of the computational domain and a ‘no-slip’ condition at the leaflet/blood interface. Triangular mesh elements were used to discretize the three leaflets and housing of the TMHV as required by the CURVIB for the classification of the background domain into fluid, boundary, and solid nodes by using an efficient ray-tracing algorithm [6]. To provide high spatio-temporal resolution, the computational fluid domain was discretized with around 10 million cells. The hemodynamics of the TMHV was the output of the numerical solver and have been visualized in Paraview. The scalar viscous shear stresses were evaluated as the major hemodynamic load on the blood constituents, and were calculated by using the formulation proposed by Apel et al. [8].

RESULTS

The leaflet kinematics, velocity field, and the viscous shear stresses have been analyzed to evaluate the hemodynamic performance of the TMHV, as done in the past research [1-4]. Figure 1 shows the leaflet kinematics in response to the prescribed flow curve (also illustrated).

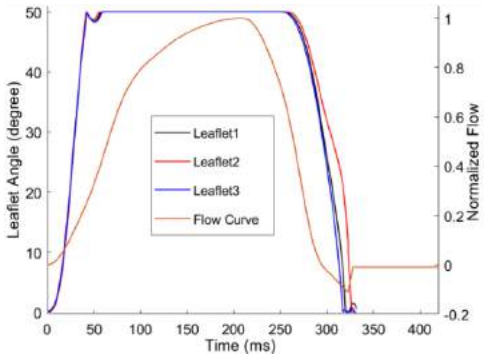

Figure 1: Leaflet kinematics and imposed flow curve

The three leaflets opened synchronously and did not noticeably keep fluttering after having reached to their fully opened position. They

started to close slightly asynchronously during the late forward deceleration phase of the cardiac cycle and fully closed, contrary to BMHVs that start to close by the backward flow [6], without any pronounced rebound. The early closure and absence of leaflet rebound are desirable characteristics that might aid in reducing the regurgitation flow volume.

Figure 2 presents the velocity profile at the peak systolic phase of the cardiac cycle, where the leaflets are fully opened, and the flow is dominantly characterized by a strong 'central-jet' with a triangular cross-section. The central jet could be observed to be void of eddies and vortical structures, in contrast to the flow field observed in conventional BMHVs [5, 7, 9, 10]. Three narrow 'side-jets', one from each leaflet, were also observed with a crescent-shaped structure and a similar maximum velocity as that in the central jet. In the same figure, weak flow recirculation zones with low velocity magnitudes could also be observed in the bulbous sinus region of the aorta.

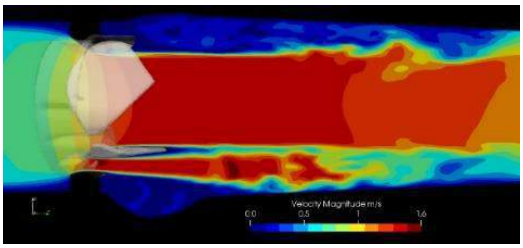

Figure 2: Velocity profiles at peak systolic phase

Figure 3(a-c) presents the scalar viscous shear stresses during three cardiac instants of early, peak and late systole, respectively, in the region located in the vicinity of the TMHV leaflets. Figure 3(a) shows the development of shear layers near the leaflet surfaces, which strengthen as the peak systolic phase of the cardiac cycle is reached as shown in Figure 3(b). At peak systole, the maximum viscous shear stresses in the shear layers around the leaflets exceed a magnitude of 10 Pa, however, the blood constituents will be advected with the high-velocity flow, as previously illustrated by the velocity profile in Figure 2, thereby washing out the mentioned regions. For other regions of the domain, the shear stresses are within the threshold magnitude reported to initiate platelet activation [2, 3, 11] but considerably lower than those previously observed for BMHVs [1, 3, 7]. Additionally, there are no large regions of high shear stresses in the bulbous sinuses. During the valve closure phase, the maximum shear stresses only occur in the shear layers formed around the leading edges of the closing leaflets, as illustrated in Figure 3(c).

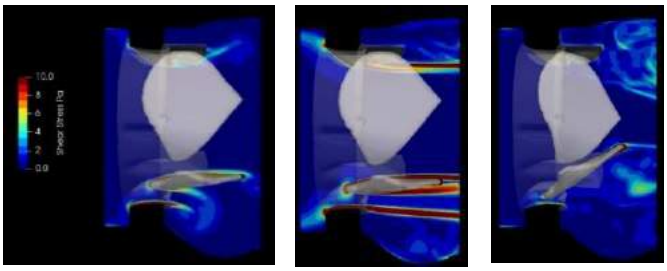

(a) (b) (c)

Figure 3: Viscous shear stresses at various cardiac instants

DISCUSSION

The current numerical study provides insights into the unprecedented details of TMHV hemodynamics with high spatial and temporal resolution. The TMHV demonstrates a physiological opening and closing kinematics of the leaflets, being contrary to that reported for BMHVs [3, 7]. The central jet generated by the TMHV during the peak systolic phase of the cardiac cycle has a triangular cross-section, which replicates the native aortic flow field. The maximum viscous shear stresses are significantly low in magnitude and do not occupy large regions in sinuses, which contingent with the fact that there exists weak flow recirculation in this region, can drastically reduce the possibility of platelet activation [3]. It could be concluded that the novel design of TMHV analyzed in this study has great potential of circumventing the hemodynamic problems associated with the use of BMHVs.

ACKNOWLEDGEMENTS

The authors gratefully acknowledge the financial support from Novostia SA, and the computational resources provided by the High Performance Research Computing (HPRC) group at Texas A&M University. The authors thank Mohammadali Hedayat who carried out the initial simulations.

REFERENCES

1. Hedayat, M. and I. Borazjani, *Comparison of platelet activation through hinge vs bulk flow in bileaflet mechanical heart valves.* Journal of biomechanics, 2019. **83**: p. 280-290.
2. Hedayat, M., H. Asgharzadeh, and I. Borazjani, *Platelet activation of mechanical versus bioprosthetic heart valves during systole.* Journal of Biomechanics, 2017. **56**: p. 111-116.
3. Abbas, S.S., et al., *Numerical investigation on the effect of bileaflet mechanical heart valve's implantation tilting angle and aortic root geometry on intermittent regurgitation and platelet activation.* Artificial Organs, 2020. **44**(2): p. E20-E39.
4. Abbas, S.S., et al., *Numerical investigation on the relationship of cavitation initiation in bileaflet mechanical heart valves (BMHVs) with the aortic root geometry and valve's implantation rotation angle.* Journal of the Brazilian Society of Mechanical Sciences and Engineering, 2020. **42**(1): p. 23.
5. Zakaria, M.S., et al., *Review of numerical methods for simulation of mechanical heart valves and the potential for blood clotting.* Medical & Biological Engineering & Computing, 2017: p. 1-30.
6. Borazjani, I., L. Ge, and F. Sotiropoulos, *Curvilinear immersed boundary method for simulating fluid structure interaction with complex 3D rigid bodies.* Journal of Computational physics, 2008. **227**(16): p. 7587-7620.
7. Borazjani, I., L. Ge, and F. Sotiropoulos, *High-resolution fluid–structure interaction simulations of flow through a bi-leaflet mechanical heart valve in an anatomic aorta.* Annals of biomedical engineering, 2010. **38**(2): p. 326-344.
8. Apel, J., et al., *Assessment of hemolysis related quantities in a microaxial blood pump by computational fluid dynamics.* Artificial Organs, 2001. **25**(5): p. 341-347.
9. Dasi, L., et al., *Vorticity dynamics of a bileaflet mechanical heart valve in an axisymmetric aorta.* Physics of Fluids, 2007. **19**(6): p. 067105.
10. Ge, L., et al., *Flow in a mechanical bileaflet heart valve at laminar and near-peak systole flow rates: CFD simulations and experiments.* Journal of biomechanical engineering, 2005. **127**(5): p. 782-797.
11. Alemu, Y. and D. Bluestein, *Flow-induced platelet activation and damage accumulation in a mechanical heart valve: numerical studies.* Artificial organs, 2007. **31**(9): p. 677-688.

FROM MICROSTRUCTURE TO MICROMECHANICAL PROPERTIES OF SOFT TISSUES

A. Ostadi Moghaddam (1), W. Lee (2), Z. Lin (3), H. Phillips (4), M. Sivaguru (5), B. L. McFarlin (6), K. C. Toussaint (3), A. J. Wagoner Johnson (1,5,7)

(1) Mechanical Science and Engineering University of Illinois at Urbana-Champaign Urbana, IL, USA

(2) Mechanical Engineering University of Colorado Boulder Boulder, CO, USA

(3) School of Engineering Brown University Province, RI, USA

(4) College of Veterinary Medicine University of Illinois at Urbana-Champaign Urbana, IL, USA

(5) Carl R. Woese Institute for Genomic Biology, University of Illinois at Urbana Champaign, Urbana, IL, USA

(6) College of Nursing University of Illinois at Chicago Chicago, IL, USA

(7) Carle Illinois College of Medicine University of Illinois at Urbana Champaign Urbana, IL, USA

INTRODUCTION

The organization and composition of the tissue constituents, i.e., tissue structure, dictate the mechanical behavior and function of the tissue. A range of diseases, such as tendinosis and osteoporosis, and conditions, such as pregnancy, influence the tissue structure and mechanical behavior [1]. To diagnose and treat the diseases and understand the influence of biological processes on tissue condition, it is necessary to evaluate the structure and mechanical function of healthy, diseased, abnormal, and damaged tissue.

The characterization of the tissue structural and mechanical properties, and the relationship between them, is experimentally challenging. Many tissues are small, spatially heterogeneous, and elastically anisotropic, and traditional mechanical tests are unsuitable for such samples. Analysis of the tissue structure through the use of optical microscopy and exogenous stains is time-consuming and limited to 2D. Therefore, the 3D structural heterogeneity of the tissue cannot be directly measured from these methods, yet it is important to understanding function.

The measurement limitations are particularly important for complex tissues like the cervix. The cervical tissue is of interest because it has an important biomechanical role during pregnancy; it should stay firm to retain the fetus yet undergo dramatic changes through pregnancy and birth. Both cervix microstructure and micromechanical properties change during this remodeling process.

Advanced imaging technologies and mechanical property testing methods, such as second-harmonic generation (SHG) microscopy and nanoindentation (NI), respectively, can help to overcome these challenges. NI can quantify the local elastic, viscoelastic, and poroelastic mechanical properties of tissues. SHG imaging is suitable for quantifying the microstructural organization of biological materials due to its specificity to collagen and high spatial resolution in 3D.

Previous studies provided valuable insights on the microstructural and micromechanical properties of soft tissues, but the correlation between these properties on the microscale is still poorly understood. We used the combined approaches of NI and quantitative SHG (qSHG) microscopy [1] to evaluate the spatially heterogeneous mechanical properties and 3D microstructure of the cervix, as a model system. We observed a strong correlation between the indentation modulus (E) measured from NI and the qSHG parameters related to the 3D collagen organization. The results contribute to understanding the relationship between the 3D collagen microstructure and mechanical function of the cervix as well as other collagenous tissues.

METHODS

Sample preparation: Non-pregnant (n=5) and 21-days pregnant (n=3) rat cervices (Sprague Dawley's) were harvested and stored at −80°C. Thawed samples were embedded in optimal cutting temperature (OCT) compound, then cryosectioned (−20°C) at mid-cervix, perpendicular to the cervical canals. OCT was washed out after sectioning. Samples were indented and imaged immediately.

SHG microscopy: A custom SHG microscope was used for imaging the non-pregnant cervices. A 10x objective lens imaged the entire cross-section of the samples. Higher resolution images were obtained on selected regions using a 60x water immersion objective lens. The pregnant cervices were imaged with a commercial confocal microscope (Zeiss LSM 710, Oberkochen, Germany) using a 40x objective lens. Two parameters collectively quantified the 3D organization of collagen fibers: average out-of-plane fiber angle (φ) relative to the imaging plane and spherical variance (SV). SV is a measure of the fiber dispersion in 3D.

NI: A Piuma nanoindenter (Optics11, Amsterdam, Netherlands) with a spherical probe indented samples submerged in PBS along a

continuous medial-lateral line every 25 µm. Indentation modulus, E, was calculated using the Hertz model [2]. The tip radius and stiffness were 41.75 ± 22.98 µm and 0.26 ± 0.33 N/m, respectively. The protocol for co-registering the NI and SHG data is in [3].

Statistical analysis: A one-way ANOVA with a post hoc Tukey test compared the data from different cervical regions. A student's t-test compared the pregnant and non-pregnant data. Pearson's r assessed correlation between E and SHG parameters.

Modified SV for fibers: A set of vectors, $\hat{X}_i$, representing collagen fibers, can be equally represented by another set of vectors with the opposite directions, i.e., $-\hat{X}_i$. The following modified SV definition was introduced to take this into account.

$$\hat{R}_1 = \hat{X}_m\,,\ m = \underset{i}{argmax}\,\frac{1}{n}\sum_{j=1}^{n} cos\,(A_{ij}) \quad (1)$$

$$\hat{R}_{i+1} = \hat{R}_i + \hat{X}_m\,,\ m = \underset{i}{argmax}\left(cos\,(tan^{-1}\frac{\|\hat{R}_i \times \hat{X}_j\|}{\hat{R}_i.\hat{X}_j})\right) \quad (2)$$

$$SV = 1 - \|\hat{R}_n\| \quad (3)$$

where A_{ij} is the angle between the i^{th} and j^{th} input vectors.

RESULTS

SHG microscopy: Figure 1 compares the qSHG parameters of three regions in the non-pregnant cervix samples (ring, septum, near septum). The fibers in the near-septum had a significantly larger φ ($p<0.02$) compared to the two other regions, which were statistically similar. The 3D dispersion of collagen fibers, reflected in SV, was also significantly higher in the near-septum, but the ring and septum were again statistically similar.

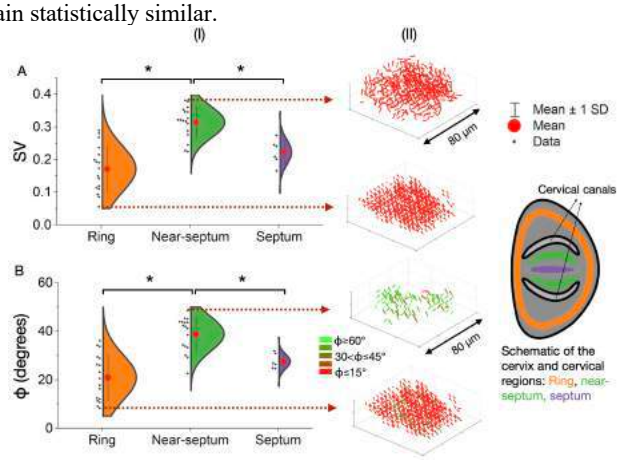

Figure 1: qSHG parameters in the ring, near-septum and septum (I). Representative results illustrate the physical meaning of the parameters (II).

Correlation of E and SHG parameters for non-pregnant cervix: Pearson's r showed a significant correlation ($p<0.02$) between E and both SV (Figure 2-A) and φ (Figure 2-B).

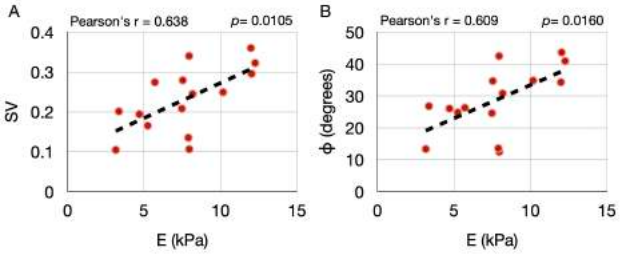

Figure 2: Correlation between qSHG parameters A: SV and B: φ and indentation modulus, E, from NI for non-pregnant cervix.

Comparison between pregnant and non-pregnant rat cervices: Figure 3 compares preliminary results of the 2D microstructural and micromechanical properties of day 21 pregnant cervices to those obtained from the non-pregnant samples. The circular variance (CV), a measure of in-plane fiber dispersion, was significantly higher in the pregnant samples ($p<0.001$), indicating more disorganized fibers. E was significantly higher in the non-pregnant samples, compared to the pregnant ones ($p<<0.001$). Both the quantitative microstructural measures and E differentiated the pregnant vs non-pregnant tissues.

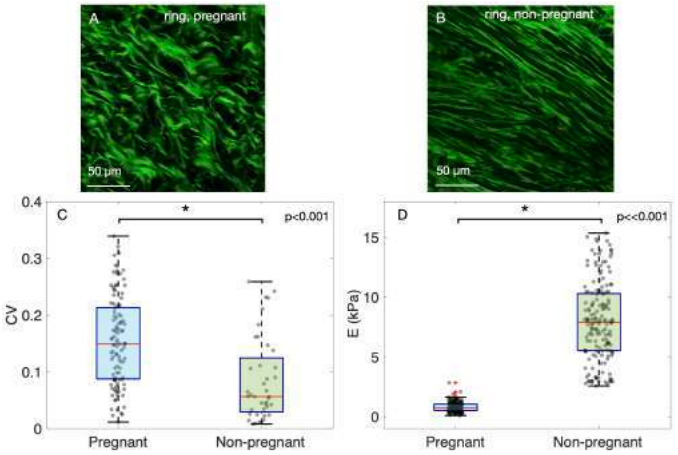

Figure 3 Comparison between the pregnant and non-pregnant cervices. A and B: representative images of ring, C: CV, D: E

DISCUSSION

Physiological changes, such as hormonal changes during pregnancy, alter the tissue microstructure and mechanical properties and affect the tissue function. We co-registered the microstructural and micromechanical properties of rat cervix using SHG microscopy and NI, respectively, and found significant correlations between the measurements. Such correlations can help to explain the underlying principles of biological processes such as cervical remodeling.

An accurate quantitative description of tissue microstructure is a prerequisite for the investigation of structure-mechanical properties relationships. The qSHG parameters used in this study successfully described the collagen fiber organization of the cervix and revealed a link between tissue micromechanical properties and microstructure. The modified definition of SV provides a more accurate description of the 3D dispersion of collagen fibers (data not shown).

There were several limitations to this study. We measured E, but not other properties such as poroelasticity. Further, we did not yet quantify the region-specific 3D structural properties of the pregnant samples. Future work includes a comprehensive 3D microstructural analysis at multiple gestational ages.

To our knowledge, this is the first work that co-registers and identifies a direct correlation between the 3D microstructural and micromechanical properties of the pregnant and non-pregnant cervix. The results contribute to understanding the 3D collagen microstructure and its relation to the mechanical function of the cervix tissue. While we focused on cervix, the findings are useful for understanding the underlying mechanobiology of other collagenous tissues.

ACKNOWLEDGEMENTS

This work was supported by the Burroughs Wellcome Fund, North Carolina, USA (#1017300) and the National Institute of Biomedical Imaging and Bioengineering (#T32EB019944).

REFERENCES

[1] W. Lee et al. IEEE Trans Med Imaging, 4425-4435, 2020
[2] K. L. Johnson, Cambridge University Press, 1985.
[3] A. O. Moghaddam et al. SB3C, Vail, Colorado, 2020

TRANSITION FROM STRESS-GOVERNED FRACTURE TO PRESSURE-INDUCED FRAGMENTATION IN CARTILAGE FAILURE

Dipul Chawla (1), Guebum Han (2), Melih Eriten (1), Corinne R. Henak (1,3,4)

(1) Department of Mechanical Engineering
University of Wisconsin-Madison
Madison, WI, USA

(2) Department of Mechanical Engineering
University of Minnesota
Minneapolis, MN, USA

(3) Department of Biomedical Engineeri
University of Wisconsin-Madison
Madison, WI, USA

(4) Department of Orthopedics and Rehabilitation
University of Wisconsin-Madison
Madison, WI, USA

INTRODUCTION

Osteoarthritis (OA) is a multifactorial disease, which includes mechanical failure of cartilage in the form of fracture and fibrillation. Cartilage is poro-viscoelastic (PVE), with intrinsic viscoelastic responses from the collagen, glycosaminoglycans (GAGs), and proteoglycans (PGs) solid matrix, and poro-elastic responses from the fluid phase moving through the solid [1–6]. Because energy dissipation is central to fracture initiation, PVE relaxations are important in delaying fracture [7-8]. Because PGs and GAGs are responsible for maintaining tissue hydration by balancing the charge concentration with the surrounding fluid, changing the osmolarity of the surrounding fluid will induce cartilage swelling or shrinking, thereby affecting mechanical properties [9-10]. Therefore, the objectives of this study were to determine the influence of osmolarity on fracture initiation under micro-indentation under extremely slow and extremely fast loading rates, then to estimate where cartilage transitions failure regimes from stress-governed fracture to pressure-induced fragmentation.

METHODS

Experimental Methods

Micro-indentation fracture tests were conducted. Eighty-seven full-thickness cartilage samples from 16 patellae of 5-6 months old pigs were obtained from a local abattoir (sex unknown and assumed random). Patellae were stored at -20° C prior to testing. Cylindrical cartilage cores of 6 mm diameter were obtained using a biopsy punch and scalpel blade. Three different osmolarity sodium chloride solutions were made: 0.0015 M NaCl (hypo-osmolarity), 0.15 M NaCl (normal-osmolarity), and 2 M NaCl (hyper-osmolarity). All solutions contained protease inhibitor (Protease Inhibitor, EDTA-Free, Thermo Scientific, Waltham, MA). Three groups of 29 cylindrical core samples were immersed in each of the above sodium chloride solutions for 1 hour before testing. The equilibrium time was selected to achieve constant thickness based on our preliminary studies. Cartilage thickness was measured using digital calipers at three to four locations per sample, and average cartilage thickness was calculated. Samples were fixed to a custom loading well using cyanoacrylate (Loctite 495, Henkel, Germany).). Fluid was added to the well up to the top of the sample.

Analysis of Experimental Measures

Micro-indentation tests were performed using a diamond sphero-conical indenter with tip radius of R = 100 μm and tip angle of θ_{tip} = 90° (Anton Parr, Austria) on tabletop test machine equipped with a 1000 g load cell (3230-AT series III test ElectroForce, TA Instruments, New castle, DE). Tests were conducted at two loading rates to capture pre- and post-relaxation regimes: slow loading rate (SLR, 0.005 mm/s, n = 16 per osmolarity) and fast loading rate (FLR, 5 mm/s, n = 13 per osmolarity). Critical work, W_c, critical load, L_c, and critical displacement, D_c, were evaluated at the first decrease in load of more than 29.4 mN, which was identified as the point of fracture initiation (Fig. 1). Optical crack images were studied at SLR and FLR (Fig. 1 Insets). W_c was calculated as the area under the load-displacement curve using trapezoidal integration in Origin 2019 (OriginLab, MA).

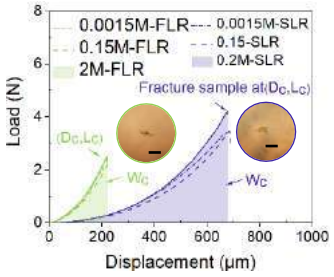

Figure 1: Cylindrical samples were tested using micro-indentation in three osmolarity groups at two loading rates to induce cracks (bar = 400 μm).

Strain Energy Density and Contact Pressure Calculations

Contact pressure (CP) and strain energy density (SED) were calculated to evaluate different failure regimes [12]. First, the contact radius a was determined for the sphero-conical indenter [13]. CP was approximated as the critical load divided by a circular projection of the contact radius

($CP \approx \frac{L_c}{\pi a^2}$). SED was approximated as the critical work divided by a spherical effected volume under the indentation tip ($SED \approx \frac{W_c}{a^3}$). Here, πa^2 is the projected contact area; L_c, and W_c were calculated from the fracture experiments. The normalized thickness (a/t), ratio of the contact radius to the sample thickness, was calculated to evaluate the CP and SED variation zone on the cartilage sample during indentation to eliminate any thickness bias because of large variation in cartilage's thickness in animal studies. The approximations helped in estimating a linear relationship between the CP beneath the indenter tip and the SED responsible for fracture.

Statistical Analysis

Differences between response variable with different osmolarities and loading rate were evaluated statistically. The Shapiro test was conducted to confirm the normality of the data for each loading rate and osmolarity. An ANOVA was used to determine the dependence of CP, SED, W_c, L_c, and D_c on osmolarity for each loading rate. Post-hoc pairwise comparisons were made using Tukey's test. Significance was set at $p \leq 0.05$, and $0.05 < p \leq 0.10$ indicated a trend.

RESULTS

The effect of osmolarity on critical displacement, critical load and critical work trended towards significance at the SLR but not at the FLR (Fig. 2). While not tested statistically, rate-dependent results were consistent with the findings of previous study [18]. CP and SED were not significantly different by osmolarity.

A greater difference in the magnitude of CP and SED vs normalized thickness (a/t) (Fig. 2D, and E) between FLR and SLR was observed, stratifying the cause of fracture into two failure regimes shown by a vertical stratification line drawn at a location where the transition is evident (Fig. 2D, E, and F). On the left side of the line, CP and SED have values that vary with normalized thickness, suggesting a region where neither CP nor SED provides a failure criterion and failure is instead governed by pressurization. On the right side of the line, CP and SED remain roughly constant across normalized thickness, suggesting a regime where failure is stress-governed. Overall, the CP at FLR was 4.87 times larger than at SLR, whereas SED was 4.83 times larger demonstrating a transition from stress-governed failure regime to pressure-induced failure regime (Fig. 2D, E, and F).

DISCUSSION

This study examined the effect of osmolarity on the fracture behavior of articular cartilage and estimated the transition between stress governed fracture and pressure induced fragmentation. Energy dissipation decreased with decrease in Na^+/ NaCl concentration (hypo-molarity) because of increased electrostatic repulsion between charged PGs and tensed collagen fibrils due to Donnan osmotic pressure [13-17] resulted in lower L_c, W_c, and D_c under SLR. On the contrary, we did not observe any noticeable trend in L_c, W_c, and D_c under FLR, thereby demonstrating possible dominance of pre-relaxation time scale over the osmolarity effect. The current set of indentation experiments were consistent with our previous results, which showed a dramatic difference between FLR, in the pre-relaxation regime, and SLR, in the post-relaxation regime [17]. As per Hertz's contact solution [19], CP could be determined by $CP \approx \frac{L_c}{\pi a^2}$. Numerically, a, L_c, W_c, and D_c were higher at SLR than FLR consistent with our previous study [18], hence the CP and SED at FLR were higher than CP and SED at SLR. CP versus normalized thickness (a/t) (Fig. 2D), SED versus normalized thickness (a/t) (Fig. 2E), and CP versus SED (Fig. 2F) showed a transition depicted by a vertical line, from lower values at SLR indicating dissipation of energy via fractures with multiple branches (post-relaxation regime) to higher values at FLR because of localized.

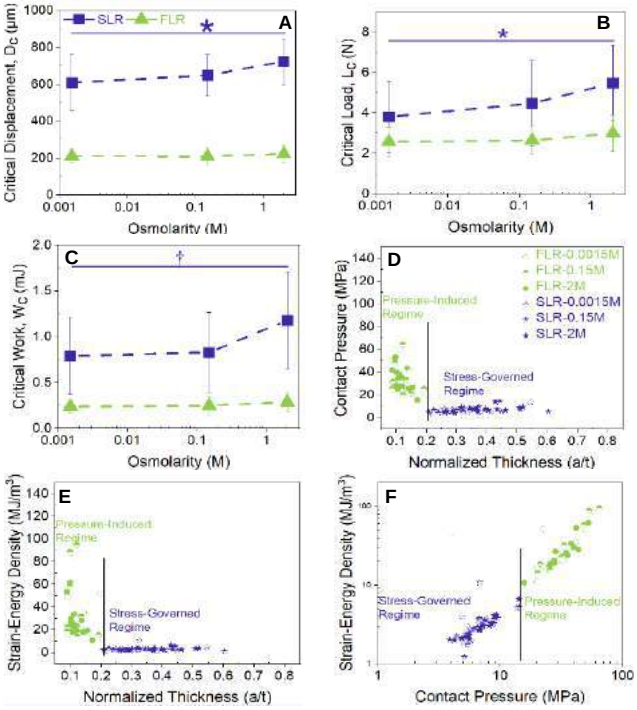

Figure 2: Experimental results: critical displacement, Dc (A), critical load, Lc (B), critical work, Wc (C) (n =13-16), and CP vs normalized thickness (a/t) (D), SED vs normalized thickness (a/t) (E), and CP vs SED scatter plot (F) * = significant, † = trend, and vertical line in (D), (E), and (F) depicts the stratification line for two failure regimes.

envelope near the indenter tip (pre-relaxation regime). The crack morphology studied with optical images during the experiments (Fig. 1 insets), details not reported here, showed line-shaped cracks at FLR and multiple cracks at SLR like the studies performed on balloons [20] and fragmentation aggregation process [21]. Overall, these findings provided new insight into the effects of osmolarity and loading rate, and thereby PG concentration and collagen fiber configuration on fracture nucleation in articular cartilage.

ACKNOWLEDGEMENTS: NSF (CMMI-DCSD-1662456).

REFERENCES: [1] Mow, V. C. et al., *Biomaterials*, 13(2): 67–97, 1992; [2] Zhu, W. et al., *J. Biomech.*, 29(6): 773–783, 1996; [3] Nia, H. et al., *Biophys. J.*, 101(9): 2304–2313, 2011; [4] Chiravarambath, S. et al, *J. Biomech. Eng.*, 131(1): 011004, 2009; [5] Mak, A. F. et al., *J. Biomech. Eng*., 108(2): 123–130, 1986; [6] Edelsten, L. et al., Soft Matter, 6(20): 5206–5212. 2010 [7] Edelsten, L. et al., Soft Matter, 6(20): 5206–5212. 2010; [8] Chin-Purcell et al., J. Biomech. Eng., 118(4): 545–556,1996; [9] Torzilli, P. A. et al., *J. Orthop. Res.*, 3(4): 473–483, 1985; [10] Maroudas, A. et al., *BBA - Gen. Subj.*, 1073: 285–294, 1991; [11] Shergold, O. A. et al., *J. Biomech. Eng.*, 127(5): 838–848, 2005; [12] Briscoe, B. J. et al., *J. Phys.D.: Appl Phys.*, 27: 1156–1162, 1994; [13] Han, E. et al., *Biophys. J.*, 101(4): 916–924, 2011; [14] Urban, J. P. G. et al., *Biorheology*, 16(6): 447–464, 1979; [15] Eisenberg, S. R. et al., *J. Orthop. Res.*, 3(2):148–159, 1985; [16] Myers, E. R. et al., *J. Biomech. Eng.*, 106(2): 151–158, 1984; [17] Wachtel, E. et al., *Biochim. Biophys. Acta - Gen. Subj.*, 1381(1): 37–48, 1998; [18] Han, G. et al., *J. Mech. Behav. Biomed. Mater.*, 96: 186-192, 2019; [19] Johnson, K. et al., *Contact Mechanics*, Cambridge University Press, 1985; [20] Moulinet, S. et al., *Phys. Rev. Lett.*, 115(18), 2015; [21] Vledouts, A. et al., *Proc. R. Soc. A.*, *471*, 2015.

SPATIAL HETEROGENEITY OF THE WHITE MATTER STIFFNESS IN THE CORPUS CALLOSUM OF THE MOUSE BRAIN

Xuesong Zhang (1), Johannes Weickenmeier (1)

(1) Department of Mechanical Engineering
Stevens Institute of Technology
Hoboken, NJ 07030, United States

INTRODUCTION

Multiple sclerosis (MS) is one of the primary non-traumatic neurological disabilities in young adults. MS is a demyelinating disease that causes a neuroinflammatory response which leads to the demyelination of axons, neuronal and axonal degeneration, and ultimately death. Breakdown of healthy axon functions leads to deficient nutrient transport around white matter lesions and defunct ion homeostasis, which eventually results in cell death. White matter axon fibers are wrapped by myelin sheaths that provide not only structural integrity to the fiber but also leads to a 10-fold increase in signaling speed along the fiber. Beirowski et al. reported that myelin sheaths can significantly increase the conduction speed of electric impulses [1]. In addition to the electrical importance of myelin in CNS, myelin has been suggested as an important factor causing change of mechanical environment which can further influence neuronal growth and development [2]. For example, Garbern et al. reported that a lack of myelin results in axonal degeneration in CNS [3]. Moreover, Weickenmeier et al. studied white and gray matter of fresh bovine brain and found a proportional relation between myelin density and tissue stiffness [4].

Previous work used experimental methods to quantify white matter stiffness. Koser et al. studied white and gray matter stiffness in fresh tissue using atomic force microscopy (AFM) and concluded that the stiffness of gray matter (159±26Pa) is much higher than white matter (60±7Pa) [5]. Melendez et al. conducted studies on 4% paraformaldehyde (PFA) fixed mice brains and reported that demyelinated corpus callosum (CC) shows a lower stiffness in comparison to control mice [6]. While both studies provided an average stiffness value for local CC subregions, the spatial heterogeneity of white matter stiffness across the entire CC remains unclear. The objective of this study is to address this knowledge gap using nanoindentation experiments in coronal brain slices from healthy mice.

METHODS

Sample Preparation. A total of six female 8-week-old C57BL/6 mice were obtained from Jackson Laboratory and fed with normal chow for six weeks. As outlined in Figure 1A, all mice were sacrificed by cervical dislocation and the brain was harvested. We submerged all brains in 4°C phosphate-buffered saline solution and used a vibratome (VT-1200S, Leica Co.) to cut a 500µm thick coronal slice 0.7mm from Bregma. We subsequently glue the resulting slice into a petri dish and submerge the sample in contact lens solution (Opti-free, Alcon) for measurements. All experiments are completed within 4 hours of death.

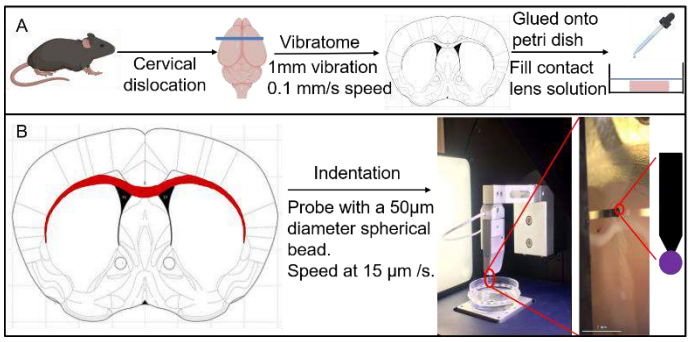

Figure 1. Graphical illustration of the methods. (A) Sample preparation. (B) Indentation measurements.

Indentation Measurements. All indentation measurements were conducted using our FT-MTA03 Micromechanical Testing System (FemtoTools AG). An FT-S200 (FemtoTools AG) microforce sensing probe with a ±200µN force range and a resolution of 0.0005µN at 10HZ. As shown in Figure 1B, we glue a 50µm-diameter polystyrene microsphere (Alpha Nanotech) to the tip of the sensor probe. Our indentation protocol works as follows: we move the probe towards the sample surface at a speed of 100µm/s; when we detect a contact force of 0.3µN, the sensor is automatically moved back to a distance of 40µm in preparation of the actual indentation test. A single indentation measurement is conducted at a constant speed of 10µm/s until we reach an indentation depth of 15µm. To map tissue stiffness of the whole CC section, we repeat individual measurements and move the probe head in

horizontal and vertical increments of 75μm in-between from the left bottom corner along the CC to the right bottom corner, as outlined in Figure 1B. Single force-displacement data at each location is automatically recorded by the testing system.

Data Analysis. All measurement data was processed with customized algorithms. Specifically, each force-displacement curve is fitted to Hertz's model to obtain Young's modulus as following:

$$F = \frac{4}{3}\left(\frac{E}{1-\nu^2}\right)^2 \sqrt{R}\delta^{3/2}, \quad (1)$$

where F is the indentation force, E is Young's modulus, R is the radius of the bead, δ is the indentation depth, and ν is Poisson's ratio which we set to 0.5. To compare the result from each brain, we implement a registration algorithm that maps each brain onto a reference CC shape. Once registered, we interpolate in the reference grid and determine mean and standard deviation (std) at each grid point. A Student's T-test was used to determine the statistical significance between groups, where * means $p < 0.05$, ** means $p<0.01$, and *** means $p<0.001$.

RESULTS

The resulting mouse CC stiffness was plotted as a heatmap in Figure 2, where the relative X is the horizontal position of the tested location to the symmetry line, and the relative Y is the vertical position of the tested location to the lowest location. It is clear the stiffness is heterogeneous in CC. Specifically, the closer the X position to the symmetry line, the softer the tissue.

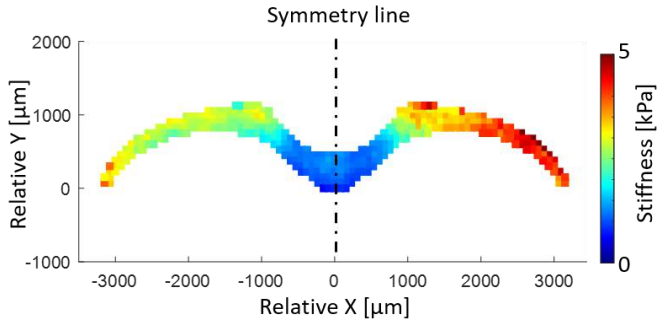

Figure 2 Stiffness heatmap of mouse corpus callosum. We registered all brains onto a reference geometry and report the mean stiffness value at each grid point.

To further study the spatial dependence of white matter stiffness, we calculated mean and std with respect to the same horizontal position, as shown in Figure 3A. We observe that stiffness is lowest at the center and increases as we move outwards, which results in a 'U'-shaped stiffness profile. Moreover, we differentiate between three distinct regions of interest (ROIs) and analyze the center (ROI 2) and two wings (ROI 1 and 3), separately. In Figure 3B, we show the boxplot of each ROI. Mean±std stiffness of ROI 2 is 1.52±0.6 kPa which is significantly lower than ROI 1 (2.80±0.31 kPa) and ROI 3 (3.77±0.62 kPa). Interestingly, ROI 3 is consistently stiffer than ROI 1, as well.

DISCUSSION

The stiffness variation pattern in mouse CC has been investigated in this study. The results suggest a spatial heterogeneity of mouse CC stiffness, which provide significant new insight following previous reports of more localized arrays [5,6]. The spatial heterogeneity in white matter stiffness is likely caused by heterogenous distribution of myelin, cell density, and fiber orientation, and is subject to further analysis. In view of work by Min et al. local variation of fiber orientation and their corresponding angle map in the CC are strong indicators for a structurally motivated reason for stiffness variations [7].

Future works will show whether and how these parameters can be linked to the spatial heterogeneity of mouse CC stiffness. Also, the idea of combining mechanical characterization and immunohistology, as shown in Figure 3C, could serve as a robust method in other soft tissue studies, including tumor, tissue regeneration, and other diseases.

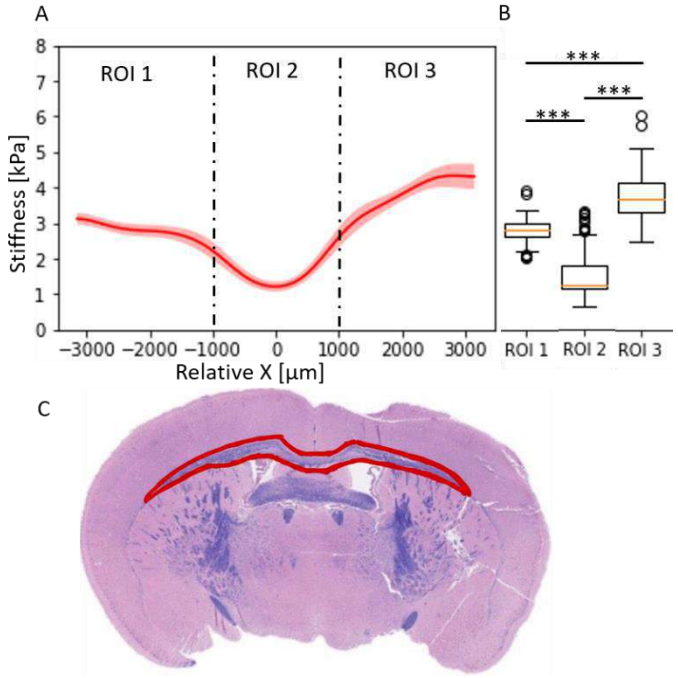

Figure 3 Stiffness variation pattern with respect to relative X. (A) Mean±std stiffness from all measurements with respect to relative X. (B) Boxplot of our three ROIs showing. (C) Combined H&E and Luxol Fast Blue histology image of a coronal mouse brain slice; we outline the blue-appearing corpus callosum which is indicates the presence of myelin sheaths wrapped around axons (* p < 0.05, ** p<0.01), *** p<0.001).

In summary, we demonstrate spatial heterogeneity of white matter stiffness in the corpus collosum of the mouse brain. Our results have significant implications for brain injury mechanisms in traumatic brain injury and multiple sclerosis in terms of tissue regeneration following inflammation.

ACKNOWLEDGEMENTS

None. No funding to declare.

REFERENCES

[1] Beirowski et al. *J. Cell Biol.* 215 (2016).
[2] Franze et al. *Development* 140 (2013).
[3] Garbern et al. *Brain* 125 (2002).
[4] Weickenmeier et al. *Acta Biomater.* 42 (2016).
[5] Koser et al. *bioRxiv* (2018).
[6] Urbanski et al. *Sci. Rep.* 9 (2019).
[7] Min et al. *Sci. Rep.* 6 (2016).

DEVELOPING A NEW SURROGATE MODEL FOR COMPUTAIONAL FLIUID DYNAMIC SIMUALTION OF AORTA USING STATISTICAL SHAPE MODELING AND DEEP NEURAL NETWORKS

Pan Du (1), Xiaozhi Zhu (2), Jianxun Wang (1)

(1) Department of Aerospace and Mechanical Engineering
University of Notre Dame
Notre Dame, IN, U.S.

(2) Department of Applied and Computational Mathematics and Statistics
University of Notre Dame
Notre Dame, IN, U.S.

INTRODUCTION

Due to the rising demand for acquiring comprehensive hemodynamic flow information for the diagnosis of cardiovascular diseases, image-based Computational Fluid Dynamics (CFD) has been widely employed to enable the derivation of functional information that is not accessible by medical images alone (e.g., pressure distribution, shear stress contour, velocity vector field), facilitating quantitative analysis and risk assessment in clinical therapy [1-2]. However, such modeling requires solving mesh-based discretization of partial differential equations numerically, which is computationally expensive, particularly for complex flow or when considering fluid-structure interaction. This has largely limited the translation of image-based CFD to clinical treatments that require timely feedback for further therapeutic assessment and treatment planning [3-4]. Moreover, it has posed a significant challenge to many-query applications, including uncertainty quantification, parameter estimation, and optimization problems arising in cardiovascular modeling. To enable efficient cardiovascular hemodynamic simulations, reduced-order or surrogate models have received increased attention and been developed as an alternative to predict functional information with a significantly less computational cost. For example, Lumped Parameter or 1-D reduced-order models are widely used to rapidly predict volumetric flow rate and have been an area of intense investigation [5-7]. However, those approaches only focus on global information and are incapable of providing local flow information such as spatiotemporal fields of velocity or wall shear stresses, which is more crucial to advancing cardiovascular research/healthcare. Deep neural network (DNN) is renowned for its capability of approximating complex nonlinear functions and fast online inference speed. As a result, trained DNN shows a great potential of serving as a surrogate model for high-dimensional CFD simulations. Recently, Liang *et al*. [8] developed an innovative DNN-based surrogate model that substitutes traditional structural finite-element analysis (FEA) by mapping the shape of the aorta to the corresponding stress contour. The results show good agreement between the original FEA and the DNN-surrogate model, which shows the promise of developing machine learning-based surrogate models for cardiovascular systems. In this work, we propose a novel deep learning surrogate modeling framework for image-based computational fluid simulations, enabling fast predictions of hemodynamics given complex 3-D patient-specific geometries.

METHODS

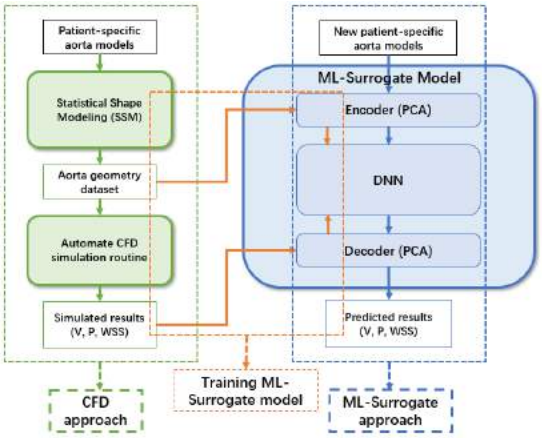

Figure 1: Diagram of the CFD approach and ML-Surrogate model approach

As shown in figure 1, our workflow consists of three steps: (i) build a stochastic shape model (SSM) that generates a synthetic aorta geometry dataset as training data; (ii) establish an automatic CFD

routine that takes in an arbitrary aorta geometry and outputs simulated results including velocity field, pressure distribution, and wall shear stress contours; (iii) feed the aorta geometry and corresponding simulated results as training pairs into the ML-surrogate model and train it. Once our ML-surrogate model is trained, test samples will be fed into the ML-surrogate model for validation.

1). The SSM that generates a synthetic aorta geometry dataset is constructed based on the LDDMM algorithm [9], where the "mean shape" of a set of shapes and the "best" deformation from the mean shape to each shape in the dataset are estimated. The detailed procedure of building the SSM is summarized as follows:

1. Firstly, the correspondence between the different aorta shapes is identified. With the input of N shapes referred to as $\{X_i\}_{i=1,\dots,N}$ where $X_i \in R^{n\times 3}$, the template X_{mean} and approximate shapes $\{\hat{X}_i\}_{i=1,\dots,N}$ deformed from the template can be computed.
2. Each approximate shape $\hat{X}_i$ is flattened into a vector $\tilde{X}_i$ and then squeezed into a data matrix $X = (\tilde{X}^T{}_1, \dots, \tilde{X}^T{}_N)^T$. Subsequently, Principal Component Analysis (PCA) is applied to X, from which one can obtain $\{W_k\}$ and $\{\lambda_k\}$ that represent eigenvectors and eigenvalues of covariance matrix respectively.
3. Each surface can be approximated as follow:

$$X^* \approx X_{mean} + \sum_{k=1}^{K} \alpha_k \sqrt{\lambda_k} W_k \quad (1)$$

where $\alpha_k$is the projection of the variance to the k[th] eigenvector.

2). The CFD routine that produces the simulated flow is built using python which incorporates meshing, setting up models, executing simulations, and extracting results of interest. The meshing step utilizes the Vascular Modeling Toolkit (VMTK) [10] which generates volumetric triangular mesh for each aorta. Next, OpenFOAM simulations are automatically set up and solved using the pimpleFoam solver. For each simulation, a periodic flow is assumed at the inlet and a pre-tunned Windkessel model is applied at the outlet such that the aorta pressure range is within 80~120 mmHg. Every simulation runs for 4~7 cardiac cycles to reach convergence. Finally, the flow vector field, pressure, and wall shear stress distribution of the aorta at systolic pressure are extracted as labeled training data for the ML-surrogate model.

3). The ML-surrogate model that yields the predicted flow includes three components: an encoder, a deep neural network, and a decoder. The encoder and decoder are constructed based on PCA or proper orthogonal decomposition (POD). For example, by reformatting equation 1 the shape encoder is obtained that encodes the nodes for the geometry to principal component values α_k:

$$\alpha_k = \frac{W_k{}^T (X^* - X_{mean})}{\sqrt{\lambda_k}} \quad (2)$$

The velocity vector fields, pressure, and wall shear stress are encoded separately using their POD modes, which can be decoded as full-field solutions in the backward direction. The vascular shapes and simulated flow solutions are encoded and the mappings in-between are captured by a DNN. Eventually, three decoupled sub-DNNs are trained and serve as the surrogate model that maps the input geometry to the corresponding velocity, pressure, and wall shear stress, respectively.

RESULTS

In this work, the initial dataset contains ten samples. The upper branches of the aorta are trimmed off for simplicity. Only the first three principal components are kept, representing over 90% of the variance. Since $X_{mean}, \{W_k\}$ and $\{\lambda_k\}$ are provided by the SSM, one only need to sample $\{\alpha_k\}$ to generate an aorta surface. Thus, A synthetic aorta geometry dataset with 200 aorta shapes is generated by sampling α_k from a normal distribution $\alpha_k \sim N(0,1)$. Figure 2 shows five selected samples, where one can see that the deformation of the showed samples fully occupies the variance of 3D space, hence the synthetic dataset can be considered as a good representation of the input space.

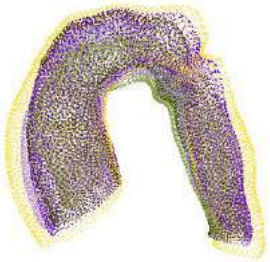

Figure 2: Synthetic geometry created by SSM using LDDMM.

Currently, we are still in the progress of generating CFD simulated training data using the geometry collection sampled by SSM. Once it's done, a cross-validation process will be performed to train and test the ML-surrogate model. We expect close agreement between the ground truth and predicted especially for pressure and shear stress distribution since both of the results are located at the same vertices as the input geometry. For the velocity, the flow pattern in the descending aorta is more likely to have a large discrepancy because the current surrogate model has limitations in capturing local features due to the linear nature of the PCA algorithm.

DISCUSSION

In this work, a synthetic aorta geometry dataset is created by SSM that represents the input space very well. Later, a Machine Learning based Surrogate model is developed to predict hemodynamic flow information within the aorta given its geometry. The author expects the ML-surrogate model can rapidly predict flow solutions close to those generated by CFD simulation. Among the flow information, the author infers that the velocity vector field will have a certain discrepancy due to the current surrogate model's incapability of capturing local details. Local-preserved learning such as geometric DNN will be explored in the future work.

ACKNOWLEDGEMENTS

I would like to express my gratitude to my advisor Prof. Jianxun Wang for providing insights and guidance in building up the workflow. I am also grateful to Xiaozhi Zhu's help in developing the SSM model and building the PCA algorithm for geometry parameterization. I would also like to thank all my colleagues including Han Gao, Luning Sun, and Xinyang Liu who shared their thoughts and suggestions with me.

REFERENCES

[1] Romarowski, Rodrigo M., et al. *International journal for numerical methods in biomedical engineering*, 34.11: e3134, 2018

[2] Dillon-Murphy, Desmond, et al. *Biomechanics and modeling in mechanobiology*, 15.4: 857-876, 2015.

[3] Bäumler, Kathrin, et al. *Biomechanics and Modeling in Mechanobiology*: 1-22, 2020.

[4] Campobasso, Rossella, et al. *Cardiovascular engineering and technology*, 9.4: 707-722, 2018.

[5] Kokalari, Isidor, Theodhor Karaja, and Maria Guerrisi. 2013.

[6] Shimizu, Shuji, et al. *The Journal of Physiological Sciences* 68.2: 103-111, 2018

[7] Mirramezani, Mehran, and Shawn C. Shadden. *Annals of Biomedical Engineering*, 48.12: 2870-2886, 2020

[8] Liang, Liang, et al. *Journal of The Royal Society Interface*, 15.138: 20170844, 2018.

[9] Bône, Alexandre, et al. *International Workshop on Shape in Medical Imaging*. Springer, Cham, 2018.

[10] Izzo, Richard, et al. *Journal of Open Source Software*, 3.25: 745, 2018

FINITE ELEMENT ANALYSIS FOR CARPAL ARCH UNDER VARYING THENAR MUSCLE FORCE MAGNITUDES AND DIRECTIONS

Hui Zhang (1,2), Zong-Ming Li (1)

(1) Hand Research Laboratory
Departments of Orthopaedic Surgery and Biomedical Engineering
University of Arizona
Tucson, AZ, United States

(2) Department of Chemical and Biomedical Engineering
Cleveland State University
Cleveland, OH, United States

INTRODUCTION

The transverse carpal ligament not only constitutes the palmer boundary of the carpal tunnel but also serves as the primary origin for the thenar muscles (abductor pollicis brevis, flexor pollicis brevis, opponens pollicis). The thenar muscles biomechanically interact with the ligament during manual activities involving the thumb. Shen and Li (2013) demonstrated that thenar muscle contraction during pinching increased the area in the ligament-formed carpal arch [1]. The muscle's biomechanical effects exerted on the carpal arch are dependent on several factors including magnitude, direction, and location of the muscle force. Thenar muscle contraction level can be voluntarily changed from low to high force magnitude (e.g., picking up a small object vs. forceful grasping). And the direction of force application of the thenar muscles on the ligament is also adjustable by changing thumb positions (e.g., key pinch vs. tip pinch). The purpose of this computational study was to examine the effects of various force magnitudes and directions of the thenar muscles on the carpal arch. We hypothesized that the carpal arch area would (1) enlarge with increasing force magnitude, and (2) increase as force rotated from radial to volar directions.

METHODS

A validated finite element model of the distal carpal arch previously developed in our laboratory [2] was utilized (Figure 1). A cadaveric hand (male; left; age 74 years; BMI 30.3 kg/m^2) was imaged by ultrasonography at the distal carpal tunnel to obtain a cross section at the hook of hamate level. The image was segmented to obtain the geometrical information of the hamate, trapezium, thenar muscles, skin, fat, and transverse carpal ligament. The cross section was extruded with 1-mm thickness for a pseudo three-dimensional model. Material properties of these structural components were based on and shown in literature [2]. In particular, the ligament's anisotropic modulus was implemented by adding tension-only nonlinear springs to strengthen the transverse modulus. Structural stiffness parameters of carpal arch were defined according to a previous study [3]. A tie constraint was set for interfaces with an assumption of ''no-slip" contact. All components had displacement boundary condition free in-plane but fixed out-of-plane. The hamate was rigidly fixed.

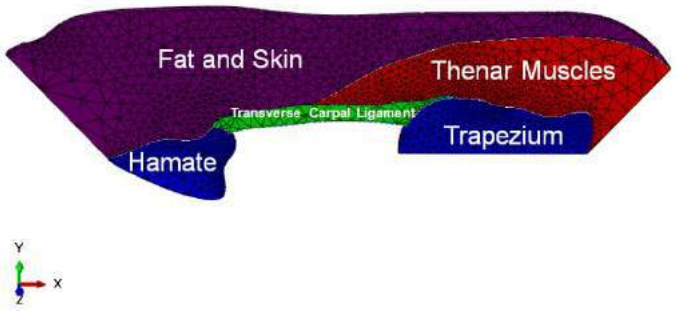

Figure 1: Finite element model of the distal carpal tunnel with components of the hamate, trapezium, thenar muscles, skin and fat, and transverse carpal ligament.

Thenar muscle contraction was simulated by applying force on the muscle-ligament interface. Only the abductor pollicis brevis and opponens pollicis were included in this study as the flexor pollicis brevis has negligible attachment to the ligament [4]. The maximal force by the combined two muscles at distal tunnel cross section was set as 9.09 N according to their force generation capabilities [5]. Three force levels (15%, 30%, and 45%) were simulated, and each force level was evenly distributed on the 95 nodes at the muscle-ligament

interface. The force directions were varied from 0 to 90 degrees (i.e., radial to volar) with an increment of 15 degrees.

RESULTS

The initial arch area without thenar muscle force was 12.1 mm^2. Force applications at any direction and magnitude led to increases of the arch area (Figure 2). The greatest arch area (48.4 mm^2) occurred at the 45% force and 90 degrees. For a given force direction, the area increased as force magnitude increased; for a given force magnitude, the area increased as force rotated from radial to palmar direction. For example, at the force direction of 0 degrees, the areas were 14.0, 16.7, and 20.2 mm^2 under 15%, 30%, and 45% of force, respectively; at 90 degrees, the areas were 29.6, 40.0, and 48.4 mm^2 under 15%, 30%, and 45% of force, respectively. At the 45% force, areas were 20.2, 43.2, 48.4 mm^2 with force directions at 0, 45, 90 degrees, respectively.

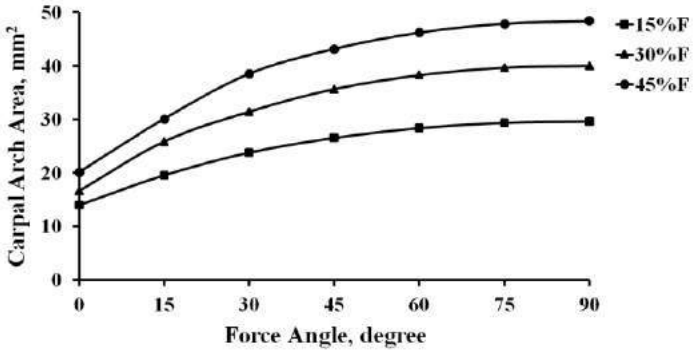

Figure 2: Carpal arch area under various force magnitudes and directions

DISCUSSION

This simulation study demonstrated carpal arch enlargement by thenar muscle forces—the larger the force magnitude, the greater the carpal arch space. The findings are consistent with previous studies involving *in vivo* thenar muscle contractions or *in vitro* force application [1,6]. The amount of carpal arch area increase was also dependent on muscle force direction. The muscle force exerted by the thenar muscles on the transverse carpal ligament can be decomposed into radial and volar directions. The volar component plays the role in decreasing the arch width and/or ligament elongation leading to palmar bowing and increased arch area. In the model, as the force angle changed from radial (0 degree) to volar (90 degrees) directions, the volar component increased from 0 N to full force magnitude, which explains the results in Figure 2 showing the increased arch area with direction change for any given force magnitude.

For *in vivo* condition, direction of force applied on the transverse carpal ligament by thenar muscle contraction is associated with thumb position. As the thumb moves from extension/supination to flexion/pronation positions, the thenar muscle orientation changes from radial to more volar directions, which make the muscle forces more effective in enlarging the carpal arch. On the other hand, thumb positioning may also change the relative distance between muscle origins and insertions, which may affect force generating capabilities of the thenar muscles. Further studies are needed to understand the interactive effects of thumb position, voluntary muscle contraction, and carpal arch changes. Our findings suggest thenar muscle contraction can be considered as means to increase carpal arch space which could be potentially applied to increase carpal tunnel space for median nerve decompression.

ACKNOWLEDGEMENTS

The study was funded by NIAMS/NIH R01AR068278.

REFERENCES

[1] Shen, Z. L., and Li, Z-M., 2013, "Biomechanical Interaction between the Transverse Carpal Ligament and the Thenar Muscles," J. Appl. Physiol., **114**(2), pp. 225–229.

[2] Yao, Y., Erdemir, A., and Li, Z.-M., 2018, "Finite Element Analysis for Transverse Carpal Ligament Tensile Strain and Carpal Arch Area," J. Biomech., **73**, pp. 210–216.

[3] Gabra, J. N., and Li, Z-M., 2016, "Three-Dimensional Stiffness of the Carpal Arch," J. Biomech., **49**(1), pp. 53–59.

[4] Loss, J., and Li, Z-M., 2020, "Biometry of Thenar Muscle Origins on the Flexor Retinaculum," Clin. Anat., **33**(8), pp. 1176–1180.

[5] Brand, P. W., Beach, R. B., and Thompson, D. E., 1981, "Relative Tension and Potential Excursion of Muscles in the Forearm and Hand," J. Hand Surg. Am., **6**(3), pp. 209–219.

[6] Li, Z-M., Tang, J., Chakan, M., and Kaz, R., 2009, "Carpal Tunnel Expansion by Palmarly Directed Forces to the Transverse Carpal Ligament," J. Biomech. Eng., **131**(8).

PREVALENCE and RISK FACTORS for BLEBS in INTRACRANIAL ANEURYSMS

Seyedeh Fatemeh Salimi Ashkezari (1), Fernando Mut (1), Juan R. Cebral (1)

(1) Bioengineering Department
George Mason University
Fairfax, VA, USA

INTRODUCTION

Intracranial aneurysmal blebs are focal bulges that are commonly observed on the surface of original aneurysm walls. Several clinical studies have identified aneurysm blebs as a risk factor for future rupture, probably because bleb walls are usually weaker than the original aneurysm walls [1-5]. The presence of blebs has been included as a risk factor in scoring scales to assess the risk of rupture of intracranial aneurysms (IAs) [6, 7], and recently has been studied independently from aneurysm size and location [8].

Despite few studies about prevalence of blebs in IAs [9, 10], strong statistical associations between presence of blebs and clinical, morphological, and hemodynamic factors have not yet been established. The purpose of this study was to statistically confirm previous results about prevalence of blebs and factors associated to their development. Another objective of this study was to validate trends relating aneurysm hemodynamic and geometric characteristics to the formation of blebs by using image-based CFD analysis in a large database of IAs.

METHODS

A total of 1704 patients with 2515 intracranial aneurysms and imaged with 3D rotational angiography (3DRA) or computed tomographic angiography (CTA) were studied. Patients ranged from 12 to 100 years of age, with a mean of 57.1 years. There were 1090 females and 423 males (information was unavailable for a subset of patients), and the mean aneurysm size was 6.7mm (range=1.1 – 39.3mm).

Using previously described methods [11], patient-specific vascular models were constructed from 3DRA or CTA images. In these aneurysms, blebs were identified by visual inspection of corresponding volume rendered 3D images, reconstructed vascular models, and aneurysm Gaussian curvature maps, and interactively marked on the vascular models, using a tool called ChePen3D, as detailed in [9].

In order to characterize the local hemodynamic conditions at bleb sites prior to their formation, the bleb regions were first projected to the model with virtually removed blebs and then hemodynamic variables were calculated over these regions.

A total of 13 hemodynamic variables were computed that measure different properties of the intra-aneurysmal flow, including strength and concentration of the inflow jet, speed, viscous dissipation, complexity and stability of the flow pattern, and strength, concentration and spread, and oscillation of the wall shear stress (WSS). In addition, the mean number of critical points were calculated.

Similarly, the geometry of the aneurysm was characterized by computing 10 variables that capture different aspects of the aneurysm geometry, including aneurysm sac size, aneurysm neck size, aneurysm elongation, and aneurysm shape distortion relative to a spherical shape and surface irregularity.

Associations between categorical variables and presence of blebs were analyzed using contingency tables and the Pearson's Chi-squared test. The mean values of continuous variables (hemodynamic and geometric characteristics) were compared between the group of aneurysms with and without blebs using the two-sample unpaired Wilcoxon (Mann-Whitney) test.

The p-values were adjusted for multiple testing using the Benjamini & Hochberg (BH) method available in R. All statistical analyses were performed in R and associations were considered statistically significant if $p<0.05$ after adjustment.

RESULTS

A total of 1176 blebs were identified in 765 (30%) aneurysms in of the 2515 aneurysms studied. The remaining 1750 (70%) aneurysms were classified as having no blebs. The mean bleb size was 2.85 ± 1.40

mm. Of the 765 aneurysms with blebs 450 had a single bleb, while 315 had multiple blebs (two or more).

No significant associations were observed between bleb presence and patient sex (p=0.8988) and age (p=0.5983). The presence of blebs was significantly associated with aneurysm rupture status (p<0.0001), in agreement with several previous studies. Also, significant associations were observed between bleb presence and aneurysm multiplicity (p<0.0001), aneurysm type (p<0.0001), and aneurysm location (p<0.0001).

Hemodynamic and geometric differences between aneurysms with blebs (virtually removed) and aneurysms without blebs are presented in Table 1. As presented in this table, most of the hemodynamic and geometric variables were significantly different between the two groups of aneurysms, even after adjustment for multiple testing.

Table 1: Hemodynamic and geometric characteristics of aneurysms with blebs and aneurysms without blebs. Statistically significant differences are indicated with a "*".

Characteristic	Variable	Aneurysms with deleted blebs	Aneurysms without blebs	Adjusted p-value
		Mean ± SD	Mean ± SD	
Hemodynamics				
Inflow jet	Q (ml/s)	1.93 ± 28.5	0.57 ± 0.72	<0.0001*
	ICI	1.23 ± 6.56	0.61 ± 0.73	<0.0001*
Flow pattern	VE (cm/s)	29.1 ± 5.04	8.79 ± 6.73	<0.0001*
	VD	1708 ± 1725	1579 ± 6396	0.8451
	corelen (mm)	2.17 ± 2.50	1.25 ± 2.02	<0.0001*
	podent	0.21 ± 0.15	0.17 ± 0.13	<0.0001*
Wall shear stress pattern	WSSmax (dyn/cm^2)	384 ± 395	225 ± 205	<0.0001*
	WSSmean (dyn/cm^2)	95.1 ± 19.9	20.9 ± 21.8	0.0895
	LSA (%)	49.9 ± 33.1	50.6 ± 33.5	0.4064
	SCI	6.05 ± 7.45	4.14 ± 5.10	<0.0001*
	OSImax	0.32 ± 0.11	0.25 ± 0.14	<0.0001*
	OSImean	0.02 ± 0.02	0.01 ± 0.02	<0.0001*
	nCrPoints	2.34 ± 1.02	1.55 ± 1.12	<0.0001*
Geometry				
Size	Asize (mm)	8.1 ± 3.6	6.1 ± 4.1	<0.0001*
	Nsize (mm)	4.9 ± 2.1	4.2 ± 2.2	<0.0001*
	SR	2.43 ± 1.19	1.76 ± 1.26	<0.0001*
	GAA (cm^{-1})	9.31 ± 8.08	21.8 ± 24.2	<0.0001*
Elongation	AR	1.19 ± 0.62	0.90 ± 0.62	<0.0001*
	VOR (mm)	9.83 ± 17.9	6.35 ± 15.1	<0.0001*
	BF	1.34 ± 0.43	1.15 ± 0.41	<0.0001*
Shape distortion	NSI	0.22 ± 0.05	0.20 ± 0.05	<0.0001*
	CR	0.81 ± 0.11	0.76 ± 0.13	<0.0001*
Irregularity	UI	0.19 ± 0.11	0.24 ± 0.13	<0.0001*

To illustrate these differences, examples of flow visualizations in two aneurysms at the middle cerebral artery (MCA) bifurcation are presented in figure 1, one without a bleb (left) and another with a bleb (right, in this case flow simulation corresponds to the aneurysm prior to bleb formation—that is, with the bleb virtually deleted).

DISCUSSION

Consistently with one previous study [9], it was found that blebs are relatively common and happen in about 30% of all aneurysms.

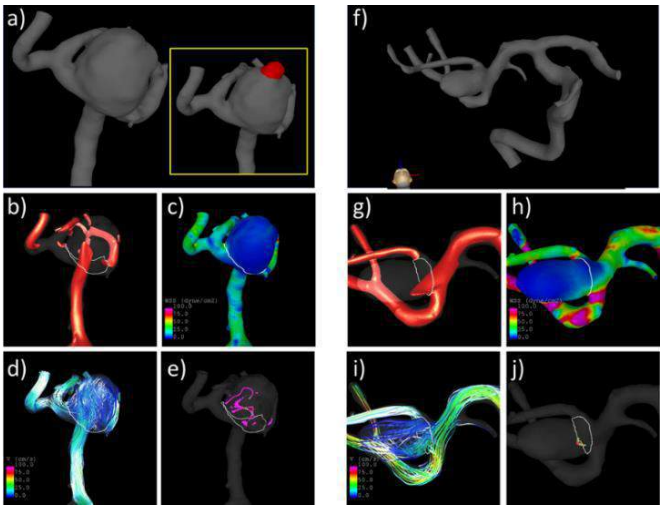

Figure 1. Examples of hemodynamics (at peak systole) for MCA-bifurcation aneurysms with and without blebs. Left panel – aneurysm with bleb removed: a) geometry of aneurysm after removal of one bleb (marked in red), b) inflow jet (iso-velocity surface), c) WSS magnitude, d) flow pattern (streamlines), e) vortex corelines. Right panel – aneurysm without bleb: f) geometry of aneurysm without bleb, g) inflow jet, h) WSS magnitude, i) flow pattern, and j) vortex corelines.

We verified and validated the results associating the presence of blebs in aneurysms, presented in previous studies [9, 10] with more cases and using a different data selection.

New associations between presence of blebs in aneurysms and aneurysm location, type, and multiplicity were found. Blebs are more likely to form in large, elongated, and irregularly shaped aneurysms, and in aneurysms at certain locations such as the ACoA and PCoA.

Hemodynamic conditions characterized by strong and concentrated inflow jets, high speed, complex and unstable flow patterns, and concentrated, oscillatory and heterogeneous wall shear stress patterns favor the formation of blebs in intracranial aneurysms.

Bleb formation seems to be a highly localized phenomenon, and the flow conditions identified here as favorable for bleb formation are characterized by strong and concentrated flow characteristics. Therefore, it seems reasonable to propose that these adverse flow and geometric characteristics may be signs of aneurysm instability and could be used to better understand which aneurysms are more likely to develop blebs and progress to a more fragile and rupture-prone status.

ACKNOWLEDGEMENTS

This work was supported by NIH grant R01NS097457.

REFERENCES

[1] Beck J, et al., *Acta Neurochir*, 145:861–865, 2003.
[2] Sonobe M, et al., *Stroke*, 41:1969–1977, 2010.
[3] Morita A, et al., *N Engl J Med*, 366:2474–2482, 2012.
[4] Burkhardt J-K, et al., *J Neurol Surg*, 78:521–524, 2017.
[5] Yamano A, et al., *J Surg Case Rep*, 117, 2018.
[6] Greving JP, et al., *Lancet Neurol*, 13:59–66, 2014.
[7] Etminan N, et al., *Neurology*, 85:881–889, 2015.
[8] Lindgren AE, et al., *Stroke*, 47:1219–1226, 2016.
[9] Salimi Ashkezari SF, et al., *J Neurointerv Surg*, Jul 2020.
[10] Salimi Ashkezari SF, et al., *J Neurointerv Surg*, Jul 2020.
[11] Cebral JR, et al., *IEEE Trans Med Imaging*, 24:457–467, 2005.

SB³C2021
Summer Biomechanics, Bioengineering and Biotransport Conference
June 14-18, Virtual

EXTRACELLULAR MATRIX REGULATION OF BREAST CANCER CELL INVASION IN A 3D TUMOR MODEL

Jacob Heiss (1), Hossein Tavana (2)

(1) Department of Biomedical Engineering
The University of Akron
Akron, OH, USA

INTRODUCTION

The extracellular matrix (ECM) is a key regulator of tumorigenesis.[1] ECM provides structural support for tumors and signaling cues to cancer cells through various binding sites. Despite important roles of ECM in cancer, many tumor models do not incorporate the ECM and its compositional complexity. Animal models that are also frequently used in cancer research are not suitable to mechanistically study the ECM roles in tumors. The lack of a physiologic tumor model has been a roadblock in understanding interactions of cancer cells with the tumor stroma, including the ECM, and developing drugs against tumor-stromal interactions.[2] The goal of this study is to use our recently-developed 3D breast tumor model and examine the role of ECM in regulating invasiveness of cancer cells.

METHODS

Tumor spheroids were made in 384-well plates using a cell micropatterning technology based on an aqueous two-phase system of polyethylene glycol and dextran.[3] Two different triple negative breast cancer cell lines, MDA-MD-231 and SUM159, were used to form spheroids with 7.5×10^3 cells in four days. Both cell lines stably expressed a green fluorescent protein. After spheroids formed, they were encapsulated in a hydrogel of human-derived type I collagen alone, or also containing fibronectin (FN) or hyaluronic acid (HA) at 10% by weight, or both. Four days after encapsulation, the spheroids were imaged using confocal microscopy and the invasion pixel area in each image was measured. Using a Prestoblue assay, the metabolic activity of spheroids was measured across all four different ECM conditions as a surrogate for cell proliferation.

RESULTS

Breast tumors have a complex ECM with type I collagen being the predominant component followed by FN and HA, and few other proteins. These proteins interact with cancer cells through specific binding sites. We aimed to evaluate effects of these ECM proteins on breast cancer invasiveness. Both TNBC cells significantly invaded from the spheroids into the collagen ECM (Fig 1A&2A), with MDA-MB-231 cells showing higher invasiveness than SUM159 cells. Addition of FN to the ECM further and significantly promoted invasion of both cell lines (Fig 1B&2B). The largest invasion occurred in the system where the ECM comprised of collagen and HA (Fig 1C&2C), which resulted in 1.7-fold and 3.5-fold increase in matrix invasion of MDA-MB-231 and SUM159 cells (Fig 3), respectively, compared to collagen only. Nevertheless, when both FN and HA were incorporated, the invasion of both cell lines significantly decreased almost to the level of the base system that only had collagen as the ECM (Fig 1D&2D). The quantified invasion data for both TNBC cells are shown in Fig 3. Our measurements of metabolic activities of cells in the tumor models showed small changes across different ECM conditions (Fig 4). Although some of these changes were significant, e.g., MDA-MB-231 cells in collagen only or in collagen and FN, the changes are relatively small.

DISCUSSION

Our study demonstrates that addition of FN or HA to the collagen matrix significantly promotes cancer cell invasion. The TNBC cells have high expression of integrin $\alpha_5\beta_1$ that enables them interact with FN in the ECM. This interaction is known to activate kinase pathways that regulate cell invasion.[4] Similarly, expression of CD44 receptors on the TNBC cells enables them to interact with HA in the ECM. This interaction axis also converges on pathways that promote cell motility and invasion. Inhibiting $\alpha_5\beta_1$, a primary biding site for FN, and CD44 receptor, a primary binding site for HA, is necessary to confirm these data. Paradoxically, addition of both FN and HA to the collagen matrix generated an antagonistic effect and led to a significant decrease in cancer cell invasion. We are currently conducting morphological imaging of the different ECM compositions to study whether this effect is caused by disruption of assembly of collagen fibers and also conducting a Western blot analysis to understand the underlying mechanisms. Small changes in proliferation of cells in different ECMs is also likely because invading cancer cells do not actively proliferate. A more direct analysis of cell proliferation is needed to complement this result.

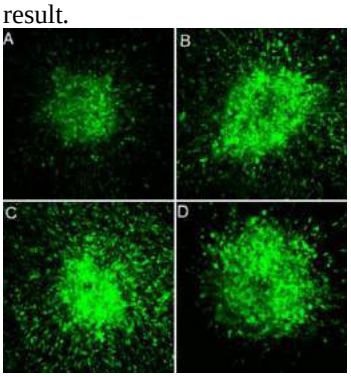

Figure 1: Confocal images of MDA-MB-231 spheroids in different ECM compositions – (a) Collagen only, (b) Collagen + FN, (c) Collagen + HA, and (d) Collagen + FN + HA

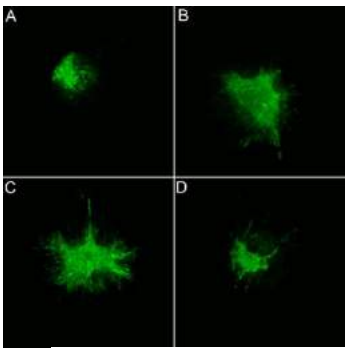

Figure 2: Confocal images of SUM 159 spheroids in different ECM compositions – (a) Collagen only, (b) Collagen + FN, (c) Collagen + HA, and (d) Collagen + FN + HA

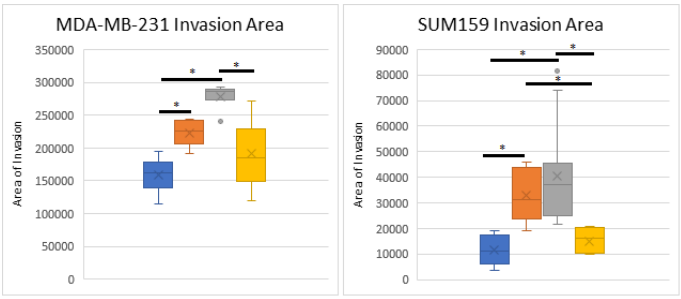

Figure 3: Box and whisker plot of day 4 area of invasion of MDA-MB-231 and SUM159 cells. The boxes represent the 25th and 75th percentiles with the median shown with a horizontal line inside each box. The mean is shown with a cross symbol inside each box. The whiskers represent the 10th and 90th percentiles of the data. Blue: Collagen only, Orange: Collagen + FN, Grey: Collagen + HA, Yellow: Collagen + FN + HA. * $p < 0.05$ (ANOVA with a posthoc Tukey's test).

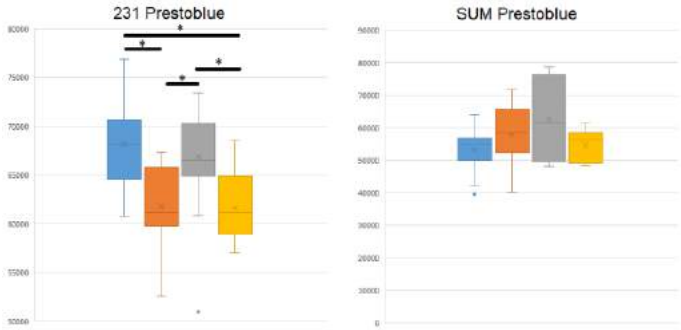

Figure 4: Box and whisker plot of day 4 Prestoblue reading of MDA-MB-231 and SUM159 cell lines. Blue: Collagen only, Orange: Collagen + FN, Grey: Collagen + HA, Yellow: Collagen + FN + HA. * $p < 0.05$ (ANOVA with a posthoc Tukey's test).

ACKNOWLEDGEMENTS

This project is funded by grants CA225549 from NIH and 1801591 from NSF..

REFERENCES

[1] Winkler, J., Abisoye-Ogunniyan, A., Metcalf, K.J. *et al*. Concepts of extracellular matrix remodelling in tumour progression and metastasis. *Nat Commun* **11,** 5120 (2020). https://doi.org/10.1038/s41467-020-18794-x

[2] Reticker-Flynn, N. E., Malta, D. F., Winslow, M. M., Lamar, J. M., Xu, M. J., Underhill, G. H., Hynes, R. O., Jacks, T. E., & Bhatia, S. N. (2012). A combinatorial extracellular matrix platform identifies cell-extracellular matrix interactions that correlate with metastasis. *Nature communications*, *3*, 1122. https://doi.org/10.1038/ncomms2128

[3] S. Lemmo, E. Atefi, G.D. Luker, H. Tavana, "Optimization of aqueous biphasic tumor spheroid microtechnology for anti-cancer drug testing in 3D culture" *Cell. Mol. Bioeng.* 7 (2014) 344-354.

[4] Meng, X. N., Jin, Y., Yu, Y., Bai, J., Liu, G. Y., Zhu, J., Zhao, Y. Z., Wang, Z., Chen, F., Lee, K. Y., & Fu, S. B. (2009). Characterisation of fibronectin-mediated FAK signalling pathways in lung cancer cell migration and invasion. *British journal of cancer*, *101*(2), 327–334. https://doi.org/10.1038/sj.bjc.6605154

[5] Toole, B. P. "Hyaluronan-CD44 Interactions in Cancer: Paradoxes and Possibilities." *Clinical Cancer Research*, vol. 15, no. 24, 2009, pp. 7462–7468., doi:10.1158/1078-0432.ccr-09-0479.

CHARACTERIZING THE LOCAL RESISTANCE AND INERTANCE OF ANEURYSM SEGMENT TO STUDY THE CHANGES INDUCED BY FLOW DIVERTERS IN 0D BRAIN MODEL

Sara Hadad (1), Fernando Mut (1), Juan R. Cebral (1)

(1) Department of Bioengineering
George Mason University
Fairfax, VA, USA

INTRODUCTION

Flow diverters (FDs) are one of the most popular cerebral aneurysm (CA) treatments, especially for complex aneurysms [1]. Although many aneurysms have been treated successfully with FDs, several studies have reported delayed aneurysm rupture and intraparenchymal hemorrhage (DIPH) after treatment with FDs [2]–[4]. These complications are often life-threatening. The rate of occurrence of delayed rupture aneurysm is about 1% [5] and the rate of DIPH is up to 3% [4]. Many studies [6]–[8] have tried to find a mechanism or explanation for DIPH; however, they could not explain some clinical observations or have been rejected by future research.

A promising method to inspect the reason of DIPH can be studying the effect of local changes after FD deployment in the entire brain circulation. However, modeling the fluid dynamics of blood in the entire brain circulation is complicated. Lumped parameter model, which is based on electrical circuit analogy, can provide a simple model for the entire circulation. Characterizing the local changes of aneurysm segment after FD implantation and using these local changes in the 0D model of brain circulation can help researchers study the effect of those changes on the entire brain blood circulation and the mechanism of DIPH. This study characterizes the resistance and inertance of aneurysm segment to simulate the changes due to FD device deployment.

METHODS

In this study, a total of 27 patient-specific aneurysm models constructed from the 3D images were used to perform CFD simulations. Navier-Stokes equations were numerically solved while assuming rigid vessel walls. Two cardiac cycles with a timestep of 0.01 second were performed and the results of the second cycle were used to calculate the pressure difference.

Local Resistance Changes Two models were made for each aneurysm to calculate the local resistance of the aneurysm segment. In each case, the first model was the original model with aneurysm and the second one without aneurysm. In the second model, the aneurysm was removed virtually to simulate the condition of flow divertor implantation when aneurysm occludes completely.

To calculate the pressure drop due to aneurysm, the skeleton of the parent artery was created where two groups of points were defined (Figure 1): one group before the aneurysm (proximal points) and the other one after the aneurysm (distal points). Then three steady state CFD simulations were performed with three different inflow rates as the inflow boundary conditions. The pressure drop for each inflow rate for both models (the original model and the model without the aneurysm) were calculated between the proximal and distal points (Equation (1)).

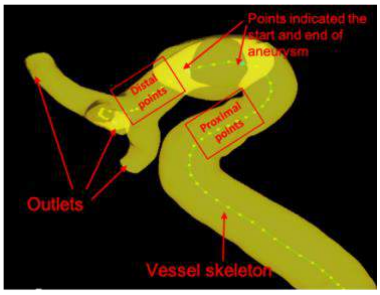

Figure 1: Skeleton made along the parent artery for calculating the local resistance and inertance of aneurysm segment.

The pressure drop along the aneurysm segment was plotted against the inflow rate for both models, and the slope of the linear regression fitted to both curves was calculated — Figure 2 shows the process for the original model. This slope shows the resistance, as Equation (2) indicates.

$$\Delta P = P_{proximal} - P_{distal} \quad (1)$$

$$\frac{\Delta P}{Q} = R \quad (2)$$

The change in the resistance of the aneurysm segment between the two models was calculated based on Equation (3).

$$\Delta R = \frac{R_{without\ CA} - R_{original}}{R_{original}} \times 100 \quad (3)$$

where $R_{original}$ is the resistance of the original model and $R_{without\ CA}$ is the resistance of the model with removed aneurysm. All these steps were repeated for the 27 patient-specific aneurysm geometries among which the maximum change in resistance (ΔR in Equation (3)) was found.

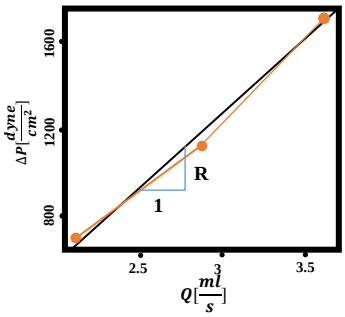

Figure 2: Pressure drop vs. inflow rate for the original model, the slope equals the resistance.

Local Inertance Changes To calculate the local inertance change of aneurysm segment, unsteady CFD simulations were performed. A sinusoidal flow rate (Equation (4)) was considered as the inflow boundary condition.

$$Q(t) = Q_0 + q\, e^{i\omega t} \quad (4)$$

where q is the amplitude of the flow wave, Q_0 is the mean steady state flow rate, ω is the angular frequency of the wave, and t is the time. The pressure drop also was broken into steady and unsteady parts as Equation (5) shows.

$$\Delta P(t) = \Delta P_0 + p\, e^{i\omega t} \quad (5)$$

where p is the magnitude of the pressure wave, and ΔP_0 is the mean steady state pressure drop.

Equation (6) shows the lumped parameter equation.

$$\Delta P = R\,.\,Q + L\frac{dQ}{dt} \quad (6)$$

After inserting Equations (4) and (5) into Equation (6), the result can be broken into two parts: the mean steady state pressure (Equation (7)) and the unsteady contribution of pressure (Equation (8)).

$$\Delta P_0 = R.\,Q_0 \quad (7)$$

$$p\, e^{i\omega t} = R\,.q\, e^{i\omega t} + L\,.\,i\omega q e^{i\omega t} \quad (8)$$

by simplifying Equation (8), Equation (9) was derived. Then $p - R.\,q$ was renamed as ΔP_l (Equation (10)).

$$p = R\,.q + L\,.\,i\omega q \quad (9)$$

$$\Delta P_l = p - R\,.\,q \quad (10)$$

Three CFD simulations with different flow amplitudes (q) and with resistances calculated in the previous part were performed. Then, ΔP_l vs. ωq was plotted for both models. The slope of the linear regression fitted to the plots gave the inertance of the aneurysm segment.

Equation (11) was used to calculate the inertance change between the two models.

$$\Delta L = \frac{L_{without\ CA} - L_{original}}{L_{original}} \times 100 \quad (11)$$

where $L_{original}$ is the inertance of the original model and $L_{without\ CA}$ is the inertance of the model without the aneurysm. This process was repeated for 27 patient-specific geometries among which the maximum inertance change was found.

RESULTS

Analysis of 27 patient-specific aneurysm geometries showed that removal of aneurysm because of FD devices leads to 15.6% and 19% maximum changes in, respectively, the resistance (ΔR) and inertance (ΔL) of the aneurysm segment.

The results also showed that ΔR and ΔL are linearly correlated with an R^2 of 0.91 and a p-value less than 0.001. This study also showed that ΔR and ΔL have no clear relationship with aneurysm size and shape. However, R and L seem to be related to flow domination in shear-driven or inertia-driven flows [9].

DISCUSSION

In this study, the change in pressure due to aneurysm removal (i.e. aneurysm occlusion after FD treatment) was consistent with the previous studies [10][11] that showed the pressure changes after FD deployment. The magnitude of ΔR and ΔL were calculated here from 27 patient-specific aneurysm geometry. There seemed to be an association between these changes and intra-aneurysmal flow as also reported by previous studies [12][13]. The maximum changes of local resistance and inertance of aneurysm were 15.6% and 19%, respectively. These results can be used in the 0D model of the entire brain circulation to study the effect of local hemodynamic changes – because of the FD – and to study the mechanisms of DIPH. The flow condition before and after FD treatment can be modeled by changing the local resistance and inertance. The maximum changes of the resistance and inertance calculated in this study can show the maximum possible change in these parameters in other parts of the brain circulation model.

A limitation of this study comes from assuming Poiseuille flow in the parent artery segment. This is the basic assumption of the lumped parameter model. Future studies can use more realistic methods to calculate the local changes.

In summary, this study calculated the magnitude of maximum changes of the resistance and inertance of aneurysm segment. These changes were up to 15.6% and 19%, respectively, for the local resistance and inertance.

Reference:

[1] Pierot, L et al., *J. Neuroradiol.*, 43:167–175, 2016.
[2] Arrese, I et al., *Neurosurgery*, 73:193–200, 2013.
[3] Brinjikji, W et al., *Stroke*, 44:442–447, 2013.
[4] Rouchaud, A et al., *Neuroradiology*, 58:171–177, 2016.
[5] Kulcsár, Z et al., *EJMINT*, 2012:1244000088, 2012.
[6] Hu, YC et al., *J. Neurosurg.*, 120:365–374, 2014.
[7] Tomas, C et al., *Neuroradiology*, 56:155–161, 2014.
[8] Cruz, JP et al., *Am. J. Neuroradiol.*, 33:603–608, 2012.
[9] Meng, H et al., *Am. J. Neuroradiol.*, 27:1861–1865, 2006.
[10] Yu, H et al., *Int. J. Numer. Method. Biomed. Eng.*, 35:e3256, 2019.
[11] Cebral, JR et al., *Am. J. Neuroradiol.*, 35:1567–1573, 2014.
[12] Larrabide, I et al., *J. Neurointerv. Surg.*, 7:272–280, 2015.
[13] L. Augsburger, L et *al.*, *Clin. Neuroradiol.*, 19:204–214, 2009.

ROLE OF SUBSTRATE STIFFNESS ON PLURIPOTENCY AND DIFFERENTIATION OF HUMAN EMBRYONIC STEM CELLS

Jasmeet Kaur. Virdi (1), Prasad. Pethe (2)

(1) Sunandan Divatia School of Science, SVKM's NMIMS Deemed-to-be University, Mumbai, Maharashtra, India

(2) Symbiosis Centre for Stem Cell Research, Symbiosis International University, Pune, Maharashtra, India

INTRODUCTION

Pluripotent stem cells (PSCs) have the potential to differentiate into any cell types but, to differentiate them into specific lineage continues to be a challenge for researchers. While signaling molecules are well known to initiate lineage specific differentiation, recent studies using various biomaterials have shown that the stem cells respond to the biophysical cues from extracellular matrix which in turn modulates specific differentiation [1-3]. Substrate stiffness alone has been shown to regulate cellular adhesion, cell spreading, proliferation and differentiation [4,5]. Specifically, substrates with the stiffness mimicking that of biological tissue induces differentiation in adult and pluripotent stem cells towards the corresponding lineage. MSCs when cultured on soft and stiff substrates differentiate into adipogenic and osteoblastic lineage respectively [6-9].

Hippo pathway regulated transcriptional co-activators YAP and TAZ mediates substrate-dependent stem cells behavior via cytoskeletal tension [10]. YAP is known to integrate several signals from soluble biomolecules as well as insoluble cues from microenvironment (such as substrate stiffness, topology, cell polarity etc.) [11,12]. Numerous studies in mesenchymal stem cells (MSCs) have shown YAP activation and nuclear localization on stiff substrate depends on reorganization of F-actin bundles. Conversely on soft substrate, since there is less tension created on cytoskeleton, YAP remains in the cytoplasm in phosphorylated and inactive state [6,13-14]. However, the role of biochemical cues in stiffness-dependent YAP/TAZ regulation still remains unclear. Whether the differentiation is triggered by YAP/TAZ or by the varying the substrate stiffness alone still remains a question. Comparatively to MSCs, the effect of mechanical cues on human PSCs have received less attention.

The above considerations and the fact that embryonic stem cells in the early embryo development experiences soft environment a contrast to the stiff environment of *in vitro* culture conditions, motivated us to investigate whether the change in the substrate stiffness induces differentiation of human embryonic stem cells (hESCs).

To achieve this, we cultured hESCs on varying substrate stiffness with pluripotency maintaining media and with differentiation inducing media. Since the response of human MSCs to substrate stiffness is well established were used them as control. The expression of pluripotency markers OCT4 and NANOG, and lineage specific markers *SOX17* (endoderm), *PAX6* (ectoderm) and *BRACHYURY* (mesoderm) was checked by western blot and qRT PCR respectively. We also looked at the expression of Hippo pathways proteins YAP, TAZ, MST1, MOB1, LATS and SAV1 by western blot.

METHODS

Cell culture

KIND1 (hESCs cell line) and hMSCs were cultured on tissue culture treated plates (TCP) and CytoSoft® (CS) substrates having stiffness of 0.2kPa (kilopascal), 0.5kPa, 2kPa, 8kPa, 16kPa, 32kPa and 64kPa for four days over three passages. 0.2kPa-8kPa is considered as soft substrate and 16-64kPa as stiff substrate for the study. For maintaining pluripotency KIND1 cells were maintained in Essential 8 (E8) media. For differentiating conditions KIND1 cells were maintained in Advanced DMEM media with 2% FBS. hMSCs were cultured in IMDM media with 10% FBS and 1% GlutaMax.

mRNA expression analysis

Gene expression studies were carried out by qRT PCR. For each sample, normalized threshold cycle (ΔCt) was calculated by subtracting Ct values of each gene with the corresponding Ct value of the sample of 18S rRNA (housekeeping gene). The relative fold change in global expression was obtained by $2^{-\Delta\Delta Ct}$ method. Each PCR was carried out in

duplicates by samples from three biological replicates, with 3 technical replicates each.

Protein expression analysis

Protein expression was studied by western blot. An equal concentration of protein was loaded on SDS-PAGE. Primary antibodies were labelled to target proteins, then HRP-conjugated secondary antibody was added for visualization. Each fold change was plotted against cells cultured on different substrate with respect to the cells on TCP after normalizing with GAPDH.

Statistical analysis

All statistics were performed using ImageJ software (National Institute of Health, USA) and GraphPad Prism software. Multiple comparisons were assessed using two-way ANOVA variance analysis and Turkey's Multiple Comparison Test.

RESULTS

To investigate the matrix-induced changes in stem cells we cultured hESCs and hMSCs on CS substrates of different stiffness. We observed that hESCs on CS substrates did not show any morphological difference compared to cells on TCP in Essential 8 and Advanced DMEM medium. hESCs were in compact colonies with proper cell spreading. hMSCs showed less cell spreading and less number of cells on soft substrates compared to stiff substrate and TCP. hMSCs on stiff substrates showed elongated fibroblast like morphology similar to hMSCs on TCP. Other than visual observation, the proliferation was also checked by the Cyclin D1 protein expression in hESCs on all the substrate.

Pluripotency and Differentiation study

We investigated the expression of pluripotency markers OCT4 and NANOG in hESCs cultured in E8 and Advanced DMEM media on all the substrates. Surprisingly, hESCs cultured on soft as well as stiff substrates did not show any change in the expression of pluripotency markers OCT4 and NANOG as seen by the western blot (Figure 1,2). No expression of lineage specific markers *SOX17*, *PAX6* and *BRACHYURY* was seen by qRT PCR in hESCs cultured in E8 media, however, when cultured in Advanced DMEM, *BRACHYURY* expression was seen in more in soft substrate than stiff substrates. This suggests that the hESCs maintained their pluripotency despite the stiffness change but differentiated into mesoderm lineage on soft substrate due to differentiating media.

Relationship between Hippo pathway and substrate stiffness

Since Hippo pathway is the main regulator of YAP/TAZ we wanted to study the effect of substrate stiffness on Hippo pathway proteins. First, we studied the expression of MST1, SAV1, LATS, MOB1, YAP, pYAP and TAZ in hESCs cultured in E8 media by western blot. MST1 and SAV1 expression was drastically reduced on soft and stiff substrate when compared to TCP. No expression of LATS was seen in any of the substrates except TCP, MOB1 expression did not change significantly in either of the substrates when compared with TCP. YAP expression was lower on soft substrate, however stiff substrate showed high expression of YAP than TCP. Alternatively, pYAP showed high expression on soft substrates whereas almost no expression was seen on stiff substrates as compared to TCP (Figure 1,2). This suggests that substrate does affect the Hippo signaling pathway. Other than F-actin, Hippo pathway might be involved in regulating the expression of YAP on soft substrate. However, this needs to be explored further. Next, we changed the media to Advanced DMEM to check whether adding differentiation media change the expression of YAP and pYAP. YAP expression was less in all the other substrates however the expressions were high than E8 media. pYAP expression increased gradually from soft substrate to stiff substrate.

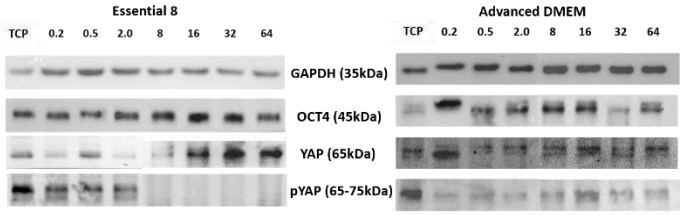

Figure 1: Protein expression in hESCs when cultured with (A) Essential 8 media and (B) Advanced DMEM.

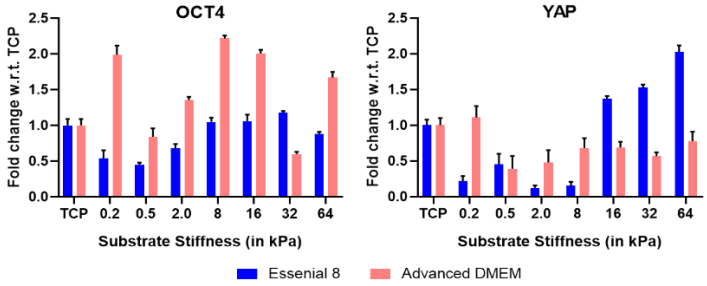

Figure 2: Western bot analysis of OCT4 and YAP shows no statistical difference between each stiffness.

DISCUSSION

Most of the published literature has shown that mouse ESCs and hMSCs differentiate in response to substrate stiffness. However, our findings suggest that substrate stiffness alone does not induce differentiation in hESCs. This suggests that there is some fundamental difference between these stem cells and the way they respond to changes in their environment. hESCs did not differentiate in response to stiffness exclusively, however, once differentiation inducing media was added it led to differentiation, thus it implies that biochemical cues play an important role in cell differentiation that substrate stiffness. It has been previously reported that decrease in YAP expression causes loss of pluripotency in stem cells however, our findings suggests that hESCs maintain a basal level of YAP expression and did not corelate directly with pluripotency. Thus, we show that the correlation of the YAP and pluripotency in hESCs on varying substrate stiffness needs to be explored further.

ACKNOWLEDGEMENTS

The authors gratefully acknowledge the Department of Biotechnology (DBT), Govt of India, BT/PR28474/MED/31/393/2018 for funding and Senior Research Fellowship to JKV from Human Resource Development Group, Council of Scientific and Industrial Research (CSIR-HRDG).

REFERENCES

[1] Murphy, WL et al., *Nat Mater*, 13:547-57, 2014.
[2] Vining, KH et al., *Nat Rev Mol Cell Biol*, 18:728-742, 2017.
[3] Smith, LR et al., *Physiology*, 33:16-25, 2018.
[4] Pelham, RJ et al., *Proc Natl Acad Sci U.S.A*, 13661–13665, 1997.
[5] Engler, AJ et al., *Surface Sci*, 570:142-154, 2004b.
[6] Engler, AJ et al., *Cell*, 126:677-689, 2006.
[7] Rowlands, AS et al., *Am J Physiol Cell Physiol* 295:C1037-1044, 2008
[8] Gilbert, PM et al., *Science*, 329:1078-1081, 2010.
[9] Musah, S et al., *ACS Nano*, 6(11):10168-77, 2012.
[10] Dupont, S et al., *Nature*, 474:179-183, 2011.
[11] Halder, G et al., *Nat Rev Mol Cell Biol*, 13:591, 2012.
[12] Piccolo, S et al., *Physiol Rev*, 94:1287-1312, 2014.
[13] Musah, S et al., *Proc Natl Acad Sci USA*. 111:13805-13810, 2014.
[14] Aragona, M et al., *Cell*, 154:1047-1059, 2013.

EFFECTS OF MARATHON TRAINING ON MALE AND FEMALE FEMORAL STRESS FRACTURE RISK

Clara Lin, Scott J. Hazelwood

Department of Biomedical Engineering
California Polytechnic State University
San Luis Obispo, CA, USA

INTRODUCTION

Marathon runners are prone to femoral stress fractures due to high magnitudes and frequencies of loads during training. Stress fractures result from bone fatigue and insufficient bone toughness caused by microcracks in bone tissue [1]. Bone has a cellular remodeling response to remove damaged tissue, but accumulation of microcracks may propagate into stress fractures if the rate of removal cannot keep up with damage accretion. In addition, bone remodeling temporarily reduces bone density and load-bearing ability as damaged bone tissue is removed by osteoclasts creating resorption cavities.

Femoral fractures are common in runners yet difficult to diagnose and treat [1]. Understanding the mechanisms behind this injury and preventing fracture is ideal. Females runners tend to have a higher incidence of stress fractures compared to males [2]. This discrepancy in injury rate may be influenced by sex-specific differences in hip geometry, joint pressure, and muscle activation patterns that affect bone remodeling. Prior studies have found that females have a proportionally wider pelvis, higher hip joint pressure, and greater gluteal muscle activation during running with respect to body weight [3]-[8].

The purpose of this study was to develop a 3D finite element model of the male and female femur during marathon training. This model builds upon prior bone remodeling and finite element studies by focusing on how sex-specific differences observed in female athletes affect bone remodeling during marathon training [9], [10]. This model tested the hypothesis that female marathon runners have lower density and more bone damage at sites of interest after marathon training, which may contribute to greater stress fracture risk compared to males.

METHODS

Finite Element Model Development

A 3D femur finite element model integrated with a mechanistic bone remodeling algorithm [10] was used for the analysis. The finite element mesh was derived from a CT-scan of a male cadaveric femur and consisted of 29,175 quadratic tetrahedral elements. Briefly, the bone remodeling algorithm simulated bone adaptation by cellular activity responding to the level of loading and fatigue microdamage. Bone was assumed to have evolving elastic moduli for cortical (Eq. 1) and trabecular (Eq. 2) bone dependent on porosity, *p*.

Elastic Modulus for Cortical Bone (for $p < 9.7\%$)

$$E_{cortical}\ (MPa) = 23440(1-p)^{5.74} \quad (1)$$

Elastic Modulus for Trabecular Bone (for $p \geq 9.7\%$)

$$\mathrm{E_{trabecular}}(MPa) = 14927(1-p)^{1.33} \quad (2)$$

Microdamage formation in bone was assumed to be proportional to strain and the number of load cycles. Damage removal was a function of the osteoclast activity and the area resorbed. A remodeling period of 24 days for bone resorption followed by 64 days for formation was used. All finite element analyses were performed in Abaqus 2020 (Dassault Systems, Rhode Island, United States).

Baseline Model and Validation

First, a baseline model with properties representative of a mature, active adult femur was established. Hip joint contact and muscle forces for the gluteus medius, gluteus minimus, adductor longus, adductor brevis, psoas, vastus lateralis, and vastus medialis muscles were incorporated based on a 725 N body weight male and 556 N body weight female. To model sex differences in hip structure, the angle of the abductor muscle forces (Male: 24.2°, Female: 19.4°) and magnitude of the hip joint contact pressure (Male: 250% body weight, Female: 313% body weight) were modified for the male and female models respectively [5]-[8]. 5,000 cycles per day (per leg) of heel-strike and toe-off loading conditions were applied to model daily activity.

The baseline model was run to achieve steady state values of porosity, damage, and cell activity and then validated by comparing axial strain at four femoral locations in the model to experimental strain gauge results from a previous study [11].

Marathon Training Simulation

After the validated baseline model was achieved, a 16-week marathon training schedule with mileage ranging from 28-45 miles and two rest days per week was simulated. The training schedule culminated with running a 26-mile marathon. Daily running mileage was converted to cycles per day by assuming 85 cycles per minute at a 7.5-minute mile pace. To simulate running conditions, joint pressure was increased to 520% body weight for males and 651% body weight for females [12]. Gluteus medius and minimus muscle forces increased to 180% of baseline in the male model [12]. Increased muscle activation was modeled in the female gluteus medius (240% of baseline) and vastus lateralis (125% of baseline) [6]. Axial strain, bone mineral density (based on porosity), and damage were analyzed at regions of interest (superior femoral neck, inferior femoral neck, proximal diaphysis, and trochanter) at the end of the training/marathon period.

RESULTS

Increased damage and strain, and decreased bone mineral density, were predicted at all regions of interest after marathon training except for the male trochanter (Table 1). The inferior neck had the highest strain in all models, the greatest increase in strain after marathon training, and the most damage (Table 1, Fig 1a).

Females were predicted to have weaker bone at the superior neck, trochanter, and proximal diaphysis after marathon training compared to males. A greater increase in damage was predicted at these regions, as well as 53% more superior neck damage (Fig 1b) in the female compared to the male model. Strain at the superior neck and trochanter were predicted higher for females, despite their lower body weight.

Table 1: Predicted changes in femur parameters of interest following marathon training

	Superior Neck	Inferior Neck	Proximal Diaphysis	Trochanter
Strain				
Male:	↑ 45%	↑ 92%	↑ 32%	↓ 2.4%
Female:	↑ 44%	↑ 85%	↑ 39%	↑ 30%
Density				
Male:	↓ 0.23%	↓ 23%	↓ 5.7%	↑ 0.2%
Female:	↓ 0.7%	↓ 21%	↓ 4.4%	↓ 0.1%
Damage				
Male:	↑ 97%	↑ 97%	↑ 43%	↑ 29%
Female:	↑136%	↑ 91%	↑ 50%	↑ 43%

DISCUSSION

Weaker baseline bone and increased gluteal muscle activation may have increased strain and damage more in the female model. Since the female model had baseline muscle and joint pressure loads scaled to a lower body weight, the femur may have been less able to bear the higher volume and magnitude of marathon training loads. Closer analysis at the trochanter and superior neck show that females have lower bone mineral density than males at these regions (Fig 2). A scaled-up gluteus medius muscle force was applied to the female model, but this increase may not have been large enough to counterbalance high loads from running, causing more load to be transferred to bone. The gluteus medius insertion point is also located at the trochanter, which was predicted to have greater strain and damage in females.

Stress fracture risk depends on interactions among microdamage, the remodeling response, and resulting bone strength. A small increase in microdamage may significantly impact strength if bone has already reached a level of reduced bone mineral density [13]. While it is not clear if the greater strain and damage predicted for females is significant enough to increase fracture risk compared to males, these predicted model trends suggest that bone becomes weaker, which could potentially increase likelihood of stress fracture for females over time.

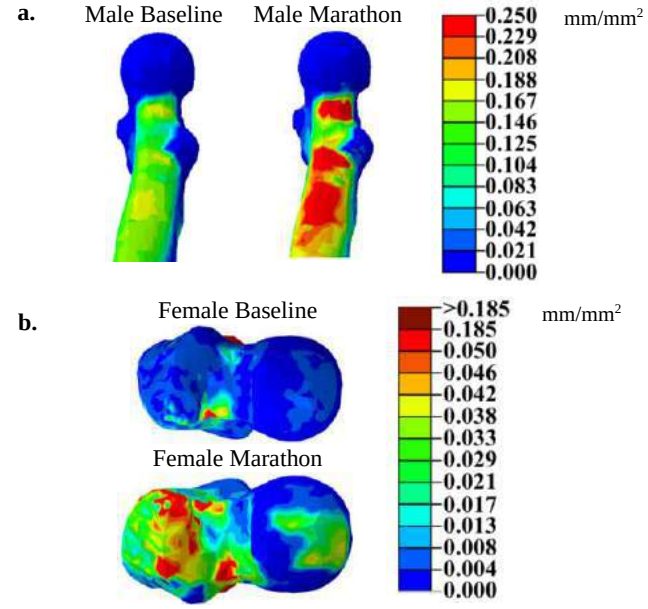

Figure 1: Predicted damage (total crack length (mm) per section area of bone (mm²)) at the (a) inferior and (b) superior neck

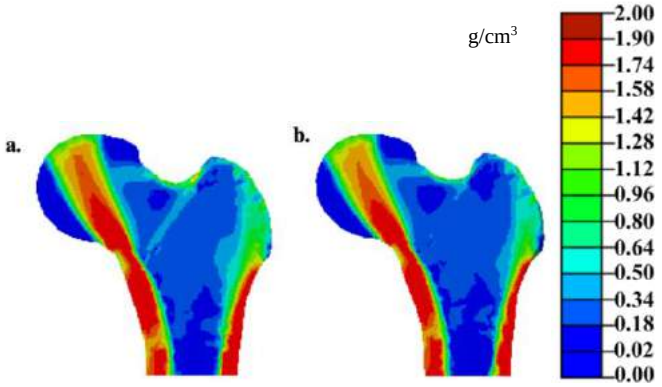

Figure 2: Bone mineral density in the (a) male marathon model and (b) female marathon model

ACKNOWLEDGEMENTS

The authors gratefully acknowledge Christopher Deuel for development of the finite element mesh used in the analysis of this study.

REFERENCES

[1] Astur, D.C. et al., *Rev Bras Orto*, 51:3-10, 2015. [2] Callahan, L.R., *Clin Sports Med*, 19:313-314. 2000. [3] Iglic, A. Et al., *J Musculoskelet Surg Res*, 5:17-21, 2001. [4] Kersnič, B. Et al., *Arch Orthrop Trauma Surg*, 116:345-347, 1996. [5] Kralj-Iglič, V. *Osteoarthritis*, Ch 7, 2015. [6] Chumanov, E.S. et al., *Clin Biomech*, 23:1260-1268, 2008. [7] Woyski, D. *Surg Radiol Anat*, 35:713-719, 2013. [8] Willson, J.D. et al., *Clin Biomech*, 27:1052-1057, 2012. [9] Hazelwood, S.J., Castillo, A.B., *Int J Fatigue*, 29 :1057-1064, 2006. [10] Hazelwood, S.J. et al., *J Biomech*, 34:299-308, 2001. [11] Deuel, C.R. et al., *J Bone Joint Surg*, 91 :124-130, 2009. [12] van den Bogert, A.J. et al., *Med Sci Sports Exerc*, 31:131-142, 1998. [13] Burr, D.B. et al., *J Bone Miner Res*, 12:6-15, 2009.

MECHANICAL STIFFNESS REGULATES CHROMATIN REMODELING IN MESENCHYMAL STEM CELLS

Samantha M. Kaonis (1,3), Soham Ghosh (1,2,3)

(1) School of Biomedical Engineering
Colorado State University
Fort Collins, Colorado, United States

(2) Department of Mechanical Engineering
Colorado State University
Fort Collins, Colorado, United States

(3) Translational Medicine Institute
Colorado State University
Fort Collins, Colorado, United States

INTRODUCTION

Multipotent mesenchymal stem/stromal cells (MSC) from different sources such as bone marrow and adipose tissue are highly promising candidates for tissue engineering and regenerative medicine. Despite having multi-differentiation ability, immunomodulatory and trophic properties, scalable application of MSC at the clinical endpoint is limited. To achieve a clinically relevant number of MSC, a small amount of autologous MSC must be expanded to millions of MSC. During the *in vitro* expansion process, MSC gradually lose their stemness and regenerative capability. Mechanics of the culture substrate is a potential candidate among several factors that might promote loss of the MSC phenotype [1,2]. Recently, we and other groups found that the mechanics of the cellular environment can define the tissue specific cellular phenotype through the modulation of intranuclear mechanics and chromatin architecture via epigenetic mechanisms [3,4]. Our objective in this work is to understand how the mechanics affects the MSC phenotype, specifically the deviation from the MSC-like characteristics in culture through chromatin remodeling and epigenetic mechanisms. We investigated how the substrate mechanical stiffness affects the nuclear morphology, intranuclear chromatin architecture and the epigenetic hallmarks using bone marrow derived human MSC.

METHODS

Cell culture: Primary human MSC derived from bone marrow were cultured (PT-2501, Lonza). Passage 3 cells were cultured on either a soft PDMS substrate (Sylgard 527, Dow) with a type I collagen coating or a stiff substrate, which was standard tissue culture plastic. Imaging of the soft substrate required a thin PDMS gel to be made using our optimized protocol.

Imaging and analysis of nuclear and cell morphology: Cells were fixed with 4% PFA, washed in 1X PBS, and stained with DAPI and phalloidin (Thermo Fisher) then imaged using a confocal microscope (Zeiss LSM 980). ImageJ was used to compute the nuclear aspect ratio and roundness.

Imaging and analysis of chromatin architecture: DAPI stained fixed cell nuclei were imaged using a confocal microscope (Olympus IX83). Chromatin segregation index was calculated using a previously published code [5].

Imaging and analysis of epigenetic marker H3K27me3: Cells were fixed in 4% PFA and immunostained to visualize H3K27me3 (CST). Imaging was performed using a laser scanning confocal microscope (Zeiss LSM 980). For high resolution immunofluorescence imaging with a 63× oil objective, the Airyscan 2 modality was used. Low magnification images were used to quantify the relative intensity of the H3K27me3 normalized to the DAPI channel fluorescence intensity, where all imaging parameters were the same for the different groups. ImageJ was used to apply a FFT filter and subsequent thresholding using the same parameters on each image for spatial characterization of H3K27me3 from high magnification nuclei images.

Gene expression study: Total RNA was extracted from cells (Qiagen), reverse transcribed into cDNA and subsequently real time quantitative PCR was performed using QuantStudio 3 (Thermo Fisher). GAPDH was the control gene and primers were custom designed.

Statistics: Student's t-test was used to compare different groups. *p value of < 0.01 represents statistically significant difference.

RESULTS

As reported in numerous previous studies, the cells better maintained their MSC phenotype on the soft substrate, indicated by the spindle-like shape (Figure 1) and diffuse actin in the cytoskeleton. Cells showed relatively more flattened, fibroblast-like phenotype with actin stress fiber formation when cultured on the stiff substrate.

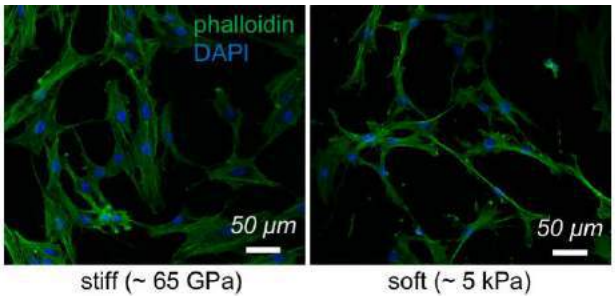

Figure 1. MSC cultured on stiff and soft substrates show different cellular and nuclear shape. Soft substrate promotes a spindle like cell phenotype and elongated nuclear phenotype, along with lower amount of cytoskeletal stress fiber formation.

Cells cultured on soft substrate promoted an elongated nucleus in the subsequent subculture (passage 4) as characterized by the higher aspect ratio and lower roundness values (Figure 2). However, subculture on the soft substrate better preserved the MSC specific chromatin architecture even though they were previously cultured (primed) on a stiff substrate. Open chromatin architecture and therefore, a higher value of chromatin segregation is a hallmark of stem cells.

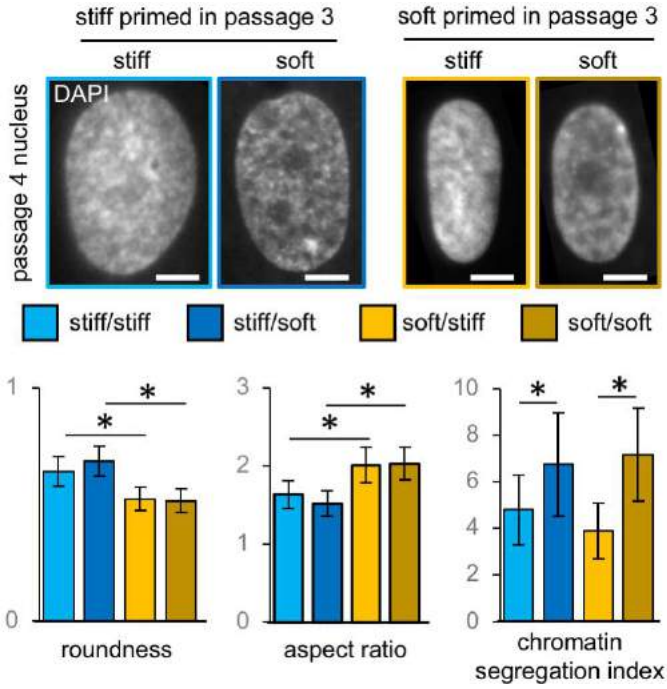

Figure 2. Nuclear morphology and chromatin architecture are different for MSC cultured on substrate with different stiffness. Soft priming of cells promotes more elongated nuclei. Subculture on soft substrates promote chromatin segregation and open chromatin, a hallmark of MSC. Scale bar: 10 μm. Error bar: SD.

To understand whether the chromatin architecture might be potentially associated with the transcriptional status of the genes, we quantified the expression of the transcriptionally repressive histone modification marker H3K27me3. We found that the expression of H3K27me3 is lower in cells cultured on soft substrates (Figure 3), in line with the previous finding that epithelial cells showed lower intensity of H3K27me3 in mechanically strained cells [4]. To further understand how the epigenetic marker is related with the MSC chromatin architecture, we visualized the spatial distribution of H3K27me3 in the nuclei at high resolution. We found that for MSC on soft substrate H3K27me3 is mostly localized near the nuclear periphery thus opening the nuclear interior, whereas on the stiff substrates they are homogeneously distributed in the nucleus, in accordance with a diffuse chromatin architecture (Figure 4a). Interestingly, the gene ARID1A which makes the BAF250A protein (a key component of chromatin remodeling mechanism) was highly expressed in cells cultured on stiff substrates (Figure 4b).

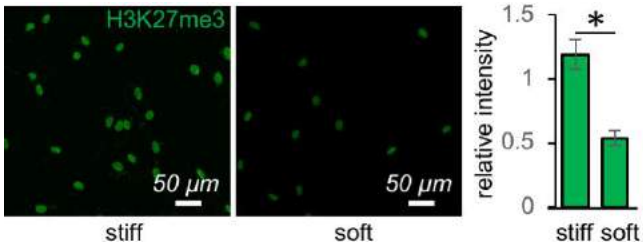

Figure 3. Soft substrate promotes lower amount of H3K27me3, an epigenetic marker for transcriptional repression. Error bar: SD.

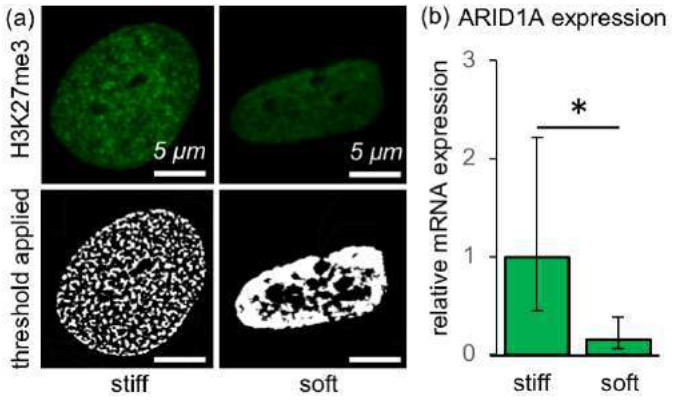

Figure 4. (a) Stiff substrate is associated with a homogeneous distribution of H3K27me3. Soft substrate is associated with a more distinct localization of H3K27me3 clusters at the nuclear periphery. (b) Gene related to chromatin remodeling protein BAF250A is more expressed in cells cultured on stiff substrates (error bars are based on maximum and minimum values, not standard deviation).

DISCUSSION

Our findings suggest that mechanics affects the chromatin architecture and the distribution of the epigenetic marker through possible mechanosensitive mechanism associated with chromatin remodeling. It has been recently found that in response to mechanical strain, the emerin-actin-non muscle myosin IIA complex functions as a nuclear force sensor that controls H3K27me3 occupancy [4]. Stiffer substrates, resulting in higher strain, promote a diffuse chromatin architecture, higher transcriptional repression and more homogenous distribution of the transcriptionally repressive histone modifier. These chromatin remodeling patterns are possibly aided by the chromatin remodeler BAF250A. Further mechanistic studies will reveal how the mechanics functionally alters the MSC resulting into the loss of MSC phenotype, opening novel possibilities to intervene such mechanism.

REFERENCES

[1] Levy, O et al., *Sci Adv*, 6:eaba6884, 2020.
[2] Killaars, A.R. et al., *Adv. Sci*, 6:1801483, 2019.
[3] Seelbinder, B. et al., *bioRxiv*, 2019.
[4] Le, H.Q., et al., *Nat. Cell Biol.*, 18:864-875, 2016.
[5] Irianto, J. et al., *Med. Engr. Phys.*, 36: 412-417, 2014.

RIGHT VENTRICULAR STRAIN ESTIMATION IN RODENTS FROM HIGH-FREQUENCY ULTRASOUND

Conner C. Earl (1), Frederick W. Damen (1), Melissa Yin (2) Kristiina L. Aasa (2), Sarah K. Burris (2), Craig J. Goergen (1)

(1) Weldon School of Biomedical Engineering
Purdue University
West Lafayette, IN, USA

(2) FUJIFILM VisualSonics Inc.
Toronto, Ontario, Canada

INTRODUCTION

Right ventricular (RV) strain measurements from speckle tracking echocardiography (STE) are being used more frequently as a non-invasive diagnostic tool for cardiopulmonary pathologies, including pulmonary embolism, heart failure, acute respiratory distress syndrome, pulmonary hypertension, and even SARS CoV-2 [1-7]. Despite the clinical utility of RV STE, previous attempts to quantify RV strain in rodent models have been limited due to ultrasound-based artifacts and non-standardized imaging procedures [8-11]

Here we present a simple method for *in vivo* estimations of RV strain using high frequency ultrasound and automated speckle tracking. We demonstrate that reliable RV strain values can be obtained in rodents with modified imaging and analysis techniques that optimize the echocardiographic view of the RV free wall while limiting lung and rib artifacts. A small number of groups have successfully estimated RV strain in rats using STE [8, 10], yet this is the first time to our knowledge that a method for the estimation of RV strain in mice has been described.

METHODS

Twenty-five-week-old female wild-type CD-1 mice (n=5; Charles River, Wilmington, MA), ten-week-old female C57BL/6J (B6) mice (n=5; Jackson Laboratories, Bar Harbor, ME) , eleven-week-old male B6 mice (n=5; Jackson Laboratories, Bar Harbor, ME), and six-week-old male Sprague Dawley wild-type rats (n=5; Charles River, Wilmington, MA) were used for RV imaging and analysis.

For ultrasound imaging, we used the Vevo3100 system (FUJIFILM VisualSonics Inc., Toronto, Ontario Canada) with a 21 MHz center frequency linear array ultrasound transducer probe (15-30 MHz bandwidth; MX250) for rats and a 40 MHz center frequency linear array ultrasound transducer (25-55 MHz bandwidth; MX550D) for mice. The probes for both mouse and rats were positioned just lateral to the sternum at approximately a 30° angle from the midline in order to obtain a modified parasternal long axis view of the right ventricle (Figure 1). By adjusting the ultrasound probe angle, we optimized our view of the RV free wall and limited anatomical image artifact. We then used a speckle tracking algorithm (VevoStrain, FUJIFILM VisualSonics Inc.) to quantify wall motion and calculate mechanical parameters such as longitudinal strain, strain rate, displacement, and wall velocity for both the endocardial and epicardial borders.

Additionally, we estimated the 2D Green-Lagrange full strain tensor using the endocardial and epicardial boundaries and displacement information provided by the speckle tracking algorithm. For each time point, the 2D version of the deformation gradient tensor ($\boldsymbol{F}$) was calculated [12, 13]. The deformation gradient tensor was then used to estimate the Green-Lagrange strain tensor ($\boldsymbol{E_{2D}}$; eq.1) using the following equation where $\boldsymbol{I}$ is the identity matrix, E_{zz} is the component of the strain tensor that corresponds to the longitudinal strain, E_{rr} is the component that corresponds to the radial strain, and the E_{zr} and E_{rz} components correspond to the shear strain.

$$\boldsymbol{E_{2D}} = \frac{1}{2}(\boldsymbol{F^T F} - \boldsymbol{I}), \quad \boldsymbol{E_{2D}} = \begin{bmatrix} E_{zz} & E_{zr} \\ E_{rz} & E_{rr} \end{bmatrix} \tag{1}$$

RESULTS

We estimated peak RV free wall endocardial longitudinal strain values in female CD-1 (-10.7±0.1%), female C57BL/6J (-10.1±1.0%), and male C57BL/6J (-10.4±0.8%) mice (mean±SEM; n=5/group). As there was no statistical difference between the strain measurements from each mouse group (ANOVA, p=0.85) a combined analysis was also performed with estimated peak RV free wall endocardial longitudinal strain of -10.4±0.4% in mice (n=15, Figure 1). Another group of male Sprague Dawley rats had an average peak RV free wall strain of -4.85±0.42% (n=5). We further demonstrated a full-wall strain analysis approach by estimating the longitudinal component of the Green-Lagrange strain tensor to be -5.7±0.48% in mice and -2.1±0.28% in rats. Finally, we found that the RV estimated parameters were not significantly different in mouse groups when stratifying by age (10-25 weeks), sex, or genetic strain (CD-1 vs. B6).

DISCUSSION

From these results we found that it is possible to estimate RV free wall strain in rodents. Additionally, we found that our RV estimated parameters were not significantly different between mouse groups with different age (10-25 weeks), sex, or genetic strain (CD-1 vs. B6).

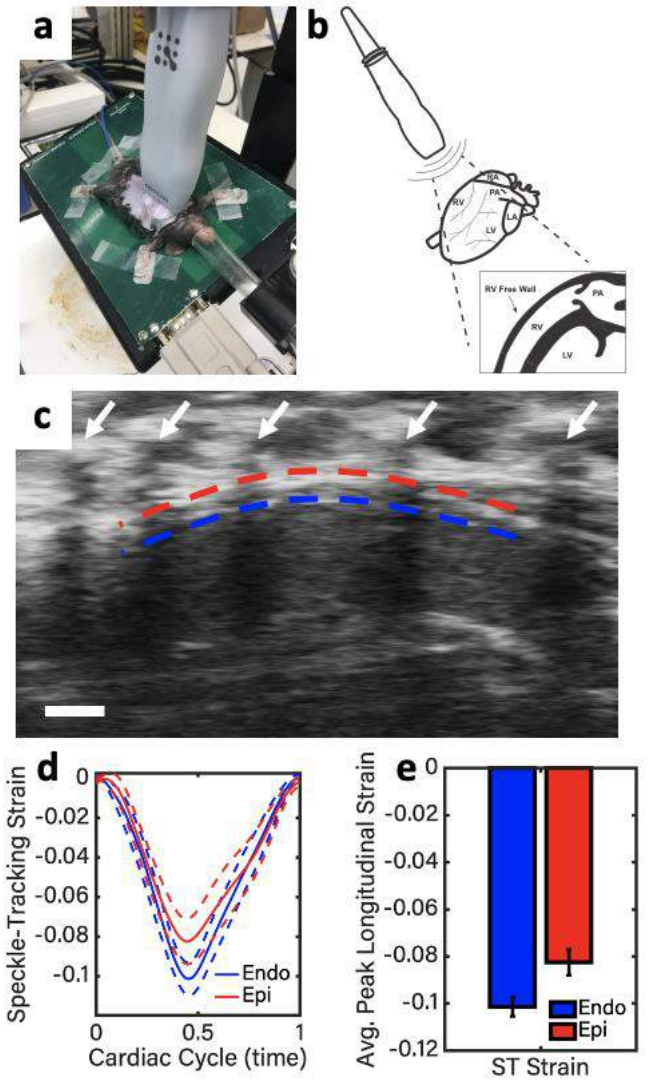

Figure 1: Right ventricular strain estimation in wild-type mice (n=15) (a) A 40 MHz center frequency linear array transducer was used to acquire right ventricular images. (b) A depiction of the unique parasternal long-axis imaging window used to maximize RV free wall visualization. (c) Representative ultrasound image where the red dotted line indicates RV free wall epicardial border, the blue dotted line indicates RV free wall endocardial border used in the analysis, white arrows indicate rib shadow artifacts. Scale bar = 1mm. (d) Average RV endocardial (blue) and epicardial (red) free wall longitudinal strain with 95% CI (solid and dashed lines) over a normalized cardiac cycle. (e) Average peak longitudinal strain for RV endocardial (blue) and epicardial (red) free wall longitudinal strain with error bars (mean±SEM).

While the absolute values of RV wall motion parameters presented in this work may need additional validation, the ability to estimate *in vivo* strain consistently in a non-invasive manner is a strength of this approach. This method of strain estimation allows for longitudinal assessments in the same animal, allowing for the characterization of strain differences over time or between control and diseased models. This non-invasive method also allows for a reduction in total animals used in longitudinal studies of RV function as each animal can be imaged at multiple time points without necessitating terminal procedures for data collection. Additional benefits include cost-savings compared to other non-invasive imaging modalities such as magnetic resonance or computed tomography. As with any method, consideration of these limitations and benefits in the context of study design will be important for optimal results.

Measurement of RV strain in a mouse model is of particular interest as mice are so ubiquitously used and studied in the field of translational medicine. For example, genetic, chemical, and surgical models of RV pathology already exist in mice [14-16]. Studying these pathologies in a small animal preclinical model can be helpful to save costs, evaluate novel treatments, and improve translational potential before moving to large animal and human studies. This may be of particular interest or importance in disease models such as pulmonary hypertension or the cardiopulmonary sequela of SARS-CoV-2.

Murine models of heart disease have been and continue to be of paramount importance to the development of our understanding and treatment of cardiopulmonary disease. While ultrasound analysis of the RV has been limited with these models in the past, continued improvements in technology and methods may allow us to utilize these models to their full potential by improving image quality and reproducibility. Additionally, a standardized approach such as the one presented in this work will help with reproducibility and provide valuable metrics for non-invasive longitudinal assessment of diseased models.

ACKNOWLEDGEMENTS

We acknowledge Bret Hawkins and Stephen Buttars (FUJIFILM VisualSonics, Inc., Toronto, Ontario, Canada) for their scientific advice and expertise regarding the use and application of the VevoStrain software.

REFERENCES

[1] Labombarda, F., et al., *Pediatric Cardiology*, 10.1007/s00246-020-02320-3, 2020.
[2] Lemarié, J., et al., *Annals of Intensive Care*, 10.1186/s13613-020-0636-2, 2020.
[3] Malik, N., et al., *Journal of the American Heart Association*, 10.1161/jaha.119.015016, 2020.
[4] Padiyath, A., et al., 10.1111/echo.12016, 2013.
[5] Sciaccaluga, C., et al., *Current Heart Failure Reports*, 10.1007/s11897-020-00455-1, 2020.
[6] Shukla, M., et al., *Canadian Journal of Cardiology*, 10.1016/j.cjca.2018.04.016, 2018.
[7] Trivedi, S.J., et al., *The International Journal of Cardiovascular Imaging*, 10.1007/s10554-020-01779-8, 2020.
[8] Bernardo, I., et al., *PloS one*, 2017.
[9] Espe, E.K.S., et al., *American Journal of Physiology-Heart and Circulatory Physiology*, 10.1152/ajpheart.00357.2019, 2020.
[10] Kimura, K., et al., *Int Heart J*, 10.1536/ihj.14-367, 2015.
[11] Kohut, A., N. Patel, and H. Singh, *Journal of Cardiovascular Ultrasound*, 10.4250/jcu.2016.24.3.229, 2016.
[12] Ligas, M., M. Banaś, and A. Szafarczyk, *Reports on Geodesy and Geoinformatics*, 10.2478/rgg-2019-0007, 2019.
[13] Humphrey, J.D., R.K. Strumpf, and F.C.P. Yin, *Journal of Biomechanical Engineering*, 10.1115/1.2891193, 1990.
[14] Ciuclan, L., et al., *American Journal of Respiratory and Critical Care Medicine*, 10.1164/rccm.201103-0412oc, 2011.
[15] Maarman, G., et al., *Pulmonary Circulation*, 10.1086/674770, 2013.
[16] Stenmark, K.R., et al., *Am J Physiol Lung Cell Mol Physiol*, 10.1152/ajplung.00217.2009, 2009.

EVALUATION OF CONSTRAINED MIXTURE THEORY ON CELL-SPARSE SYSTEMS: APPLICATION TO CEREBRAL ANEURYSMS

Elizabeth D. Shih (1), Victor H. Barocas (1), Patrick W. Alford (1)

(1) Department of Biomedical Engineering
University of Minnesota – Twin Cities
Minneapolis, MN, USA

INTRODUCTION

Arteries undergo multiscale growth and remodeling (G&R), including morphological changes and apoptosis of cells during cerebral aneurysm (CA) formation. Despite such changes, vascular smooth muscle cells (VMSCs) contribute to G&R via mechanoadaptation, either remedying or exacerbating the disease state. A commonly used framework to model the mechanics of vascular tissues during G&R is the constrained mixture model (CMM), which captures the mechanisms of microscale constituents responsible for tissue-scale behavior (**Fig. 1A**) (1). In our models, VSMC stress drives cell-mediated G&R, where VSMCs internally remodel, deposit, or degrade surrounding matrix to return to a homeostatic target stress (3). In a cell-sparse tissue, we hypothesize that the CMM assumption that constituents strain equally is less likely to represent the tissue appropriately and the calculated cell stress governing G&R is subsequently less accurate (**Fig. 1B-C**). Here, we simulate cell-sparse systems using finite element (FE) modeling to explore thresholds of cell loss and density where CMM may require modifications to more precisely characterize microscale behavior in disease states.

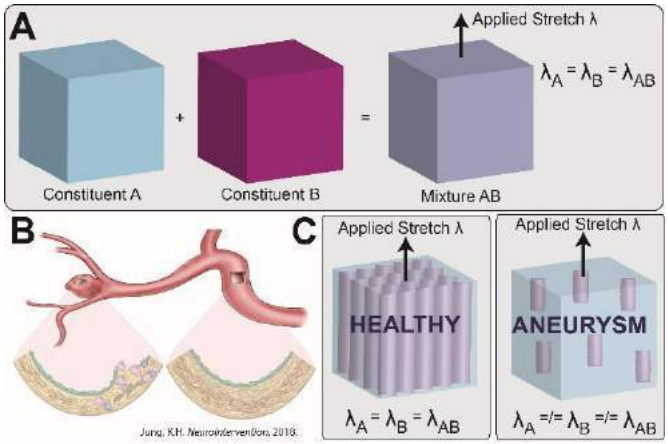

Figure 1. A. Behaviors of constituents undergo the same deformation and are summed to estimate mixture behavior. B. Illustration of CA versus healthy arterial structure (2). C. Presumed deformations of VSMCs in healthy arteries and CAs.

METHODS

Model Geometry. A cubic geometry was created in FEBio with a cell modeled in the center of a box, representative of matrix (4). Eighth symmetry was imposed for simplification (**Fig. 2A**). Multiple geometries, including various volume fractions, aspect ratios, and shapes were created to simulate a wide variety of cellular configurations and morphologies. The model was meshed with hexahedron elements.

Boundary Conditions and Constraints. A uniaxial stretch up to a stretch ratio of 1.33 was applied to the model on the top surface on axis 1 (**Fig. 2A**). The inner faces of the matrix were fixed in their normal directions, while the outer faces on axes 2 and 3 were set to deform inwards, reflective of the Poisson effect in incompressible materials.

Variables and Controls. In the first set of simulations, the cell and the matrix were modeled as incompressible Neo-Hookean (NH) materials with the cell as a cylinder. Different cell volume fractions (VFs) from 0.03 to 0.275 were investigated with changing cylinder heights, influencing a height fraction (HF) varying from 0.1 to 1. The latter HF corresponds to a control cell at its maximum height, completely percolating through the system, thus deforming the same amount as the matrix under applied stretch. Additionally, different ratios of the effective stiffnesses of the cell and the matrix (C/M) were modeled. The second set of simulations investigated the same VFs, HFs, and C/M ratios, but the matrix was modeled as an incompressible

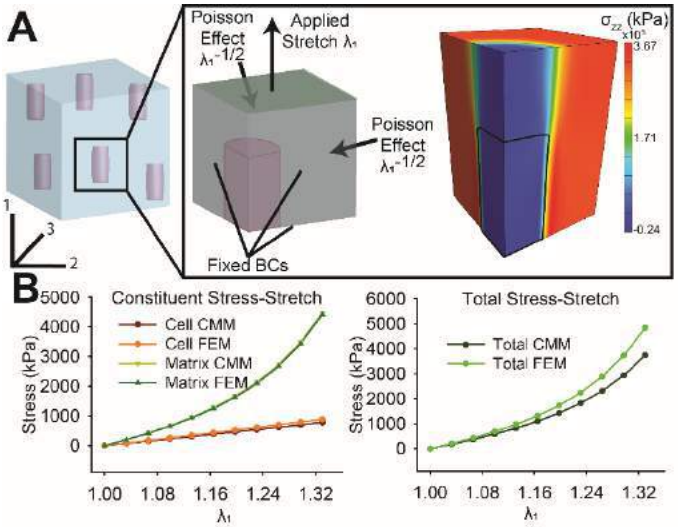

Figure 2. A. Schematic of cell in a box model, with boundary conditions and constraints. Example FE modeled Cauchy stress in 1-direction of deformed configuration. B. Example FE and CMM stress-stretch curves of linear cell in a nonlinear matrix.

Holzapfel-Gasser-Ogden (HGO) material with fibers in the 1-direction (5). The cell was modified to a sphere in the third set of simulations.

Error Analysis. Total, cell, and matrix Cauchy stresses in the 1-direction were calculated at each time step (**Fig. 2B**). A corresponding analytical CMM solution was calculated at each step by

$$\sigma_{tot} = VF_{cell}\sigma_{cell} + (1 - VF_{cell})\sigma_{mat} \quad (1)$$

where σ_{cell} and σ_{mat} are the derived Cauchy stresses of the cell and matrix from their respective material models. The error was defined as the absolute value percent difference of the FE solution from the CMM solution. The percent errors at each step were averaged to obtain single error values for the cell, matrix, and system for all simulations.

RESULTS

The cell stress is the primary value in question for G&R of cell-sparse tissues and is investigated here. Average percent errors against the CMM solution for the simulated cell are plotted across HFs for the first two sets of simulations at different VFs (**Fig. 3A-B**). Additionally, the cylindrical cells at different VFs, fixed at a HF of 0.6, were modeled across different C/M stiffness ratios (**Fig. 3C-D**). Percent errors were plotted across VFs for the third set of simulations at different C/M stiffness ratios (**Fig. 3E**).

NH Cylindrical Cell in NH Matrix. In the first set of simulations, the cell stress error was minimized for HF=1, where the cell fully percolated through the system, undergoing the same deformation as the matrix. As HF decreased, reflective of shortening cells, errors increased, reaching maxima at different HFs for each VF. As C/M ratios were altered, the simulated cell had minimum errors at ratios (~1) where both constituents had similar material properties. Errors increased between the simulated cell and the CMM solution as VFs decreased, indicative of smaller, less dense cells.

NH Cylindrical Cell in HGO Matrix. In the second set of simulations where the matrix was modeled as an incompressible HGO material with fibers in the 1 direction, similar trends as seen in the first set were observed, but with higher percent errors.

Neo-Hookean Spherical Cell in HGO Matrix. In the third set of simulations in which the cell was modeled as a sphere, different C/M stiffness ratios were modeled across increasing cell VFs. Like the former sets, cell error increased as VF decreased. Errors also decreased as C/M stiffness ratios increased, reflective of increasing similarity between the apparent stiffnesses of the cell and matrix, though it must

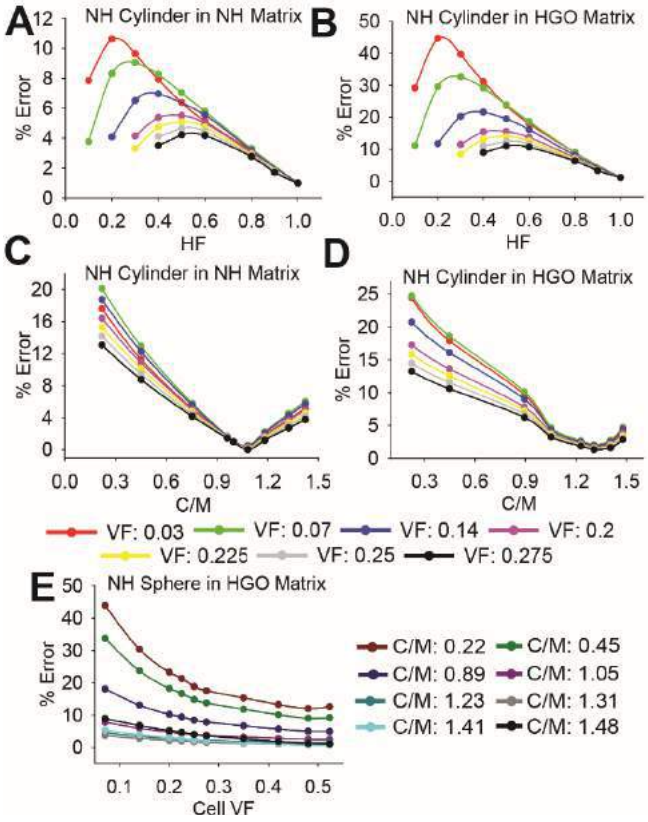

Figure 3. A. NH cylindrical cell in NH matrix (set 1) over cell HFs. B. NH cylindrical cell in HGO matrix (set 2) over cell HFs. C. NH cylindrical cell in NH matrix (set 1) over C/M ratios. D. NH cylindrical cell in HGO matrix (set 2), over C/M ratios. E. NH spherical cell in HGO matrix (set 3), over various cell VFs.

be noted that towards the highest C/M ratios (1.23 and up), the errors start to slowly increase as the cell becomes stiffer than the matrix.

DISCUSSION

The results show that in denser systems with higher cell VFs, simulated cell stresses closely match those of the CMM solution. Additionally, CMM is accurate in sparse systems, but only where cells percolate through their matrix at higher cell heights. Such findings demonstrate that cell shape alongside cell sparsity influence cell behavior to deviate from the assumptions followed in CMM (1). This is consistent with our proposition that increased system heterogeneity in diseased arteries may warrant a different or modified mixture law.

We will modify CMM to capture distributions in constituent deformations as a function of their geometries and the applied deformation. However, continued simulations are required to thoroughly elucidate the efficacy of the existing form on sparse systems. Our future work will include modeling systems where the fiber distribution is localized around the vicinity of the cell and is a function of the distance from the cell. This will recapitulate phenomena in which cells deposit and remodel surrounding matrix, contributing to increased system heterogeneity that may further affect the robustness of CMM.

ACKNOWLEDGEMENTS

We acknowledge financial support by NSF (CMMI 1553255).

REFERENCES

[1] Humphrey, J. et al., *Math Models Methods Appl Sci.*, 12(3). 2002. [2] Jung, K.H. *Neurointervention*, 13(2). 2018. [3] Alford, PW. et al., *BMMB.*, 7(4). 2008. [4] Maas, S., et al., *J Biomech Eng.*, 134(1). 2012. [5] Holzapfel, G., et al., *J Elasticity.*, 61(1). 2000.

ASSOCIATION BETWEEN ANEURYSM LOCAL HEMODYNAMICS AND WALL ENHACEMENT ON 7T MRI

Sara Hadad (1), Fernando mut (1), Bong J. Chung (2), Jorge A. Roa (3), Anne M. Robertson (4), David M. Hasan (5), Edgar A. Samaniego (3), Juan R. Cebral (1)

(1) Department of Bioengineering
George Mason University
Fairfax, VA, USA

(2) Department of Applied Mathematics and Statistics
Mount Saintclair University
Montclair, NJ, USA

(3) Department of Neurology, Neurosurgery and Radiology
University of Iowa
Iowa, IA, USA

(4) Department of Mechanical and Material Science
University of Pittsburgh
Pittsburgh, PA, USA

(5) Department of Neurosurgery
University of Iowa
Iowa, IA, USA

INTRODUCTION

Aneurysm wall enhancement (AWE) measured by high-resolution vessel wall imaging (HR-VWI) has been used to assess wall inflammation and insatiability of cerebral aneurysm (CA) in recent years [1]. Physicians can manage patient treatment strategies based on AWE assessment. Stable aneurysms based on evaluation of AWE may be monitored over time without considering an immediate surgical or endovascular treatment with their life-threatening complications [2].

However, the mechanisms of AWE are still unknown. A study indicated an association between AWE and intramural thrombus of ruptured aneurysms and suggested that rapture points could be identified by AWE [3]. Other studies have studied relationships between AWE and known rupture risk factors such as size, aneurysms location, and shape irregularity [4,5,6]. Recently, another study showed that aneurysms with AWE had lower wall shear stress (WSS), lower velocity, and larger size compared to the aneurysms without AWE [7].

This study aims to investigate the association between local flow conditions and AWE regions of aneurysm to better understand AWE mechanisms. Here, 7T-MRI is used to segment AWE and then to calculate the local flow conditions in different regions of CA by computational fluid dynamics (CFD) simulations.

METHODS

In this research, twenty patients with 23 unruptured cerebral aneurysms were studied. The CAs imaged by 7T-MR included a TOF-MRA and a 3D T1-weighted MRI before and after gadolinium (Gd) injection.

Patient-specific aneurysm models constructed from the 3D images were used in this work to perform CFD simulations. Navier-Stokes equations with pulsatile inflow conditions were numerically solved. Outflow boundary conditions were defined based on Murray's law and the vessel walls were assumed rigid. Two cardiac cycles with a timestep of 0.01 second were performed and the results of the second were used to calculate the local hemodynamics parameters of aneurysms and AWE regions.

To map the segmented AWE regions to CFD models of aneurysms, we followed a specific methodology. First, 3D models were constructed from available 3D images. Second, the image processing software Amira was used to align a rough segmentation of TOF-MRA to the 3D model. Third, AWE regions were segmented from the subtraction of pre- and post-Gd T1-weighted images. The AWE regions were determined based on the consensus of two experienced teams of investigators (Samaniego and Roa, and Hadad and Cebral, the authors). The high resolution of 7T-MRI allows us to determine the AWE regions visually. The surfaces of segmented AWE region were projected onto the 3D model and were labeled "enhanced'' regions and the rest of the aneurysm area was labeled "non-enhanced".

We computed the region-average of some hemodynamics parameters such as mean (average over time) and peak systole of wall shear stress magnitude (pWSS, mWSS), mean gradient oscillatory number (GON), mean WSS divergence and gradient (WSSDIV, WSSGRAD), and oscillatory shear index (OSI).

We divided the aneurysm sac – based on the geodesic distance to the defined neck line [8,9] –into three regions: neck, body, and dome (Figure 1). Then the locations of AWE regions were determined based on the maximum percentage of overlap between the AWE regions and one of the aneurysm regions (neck, body, and dome). We also classified the location of AWE regions into two groups, "close" and "far", based on their distance to the aneurysm inflow (details in Ashkezari et al. paper [10] in the 'Bleb Location' section).

To analyze our data statistically, we considered three approaches. In the first approach, the means of hemodynamics parameters of

enhanced regions were compared with non-enhanced regions. All parameters were normalized by the corresponding values of the entire aneurysm. Also, all the AWE regions of each aneurysm were considered as a single region (some aneurysms had more than one AWE region). In the second approach, each AWE region located at the neck, body, or dome of the aneurysm was compared with the non-enhanced regions of the aneurysm. In the final approach, hemodynamic parameters of AWE regions at different locations (neck, body, and dome) and their distance to the inflow (far, close) were compared.

In all statistical tests — Wilcoxon tests — differences with $p<0.05$ were considered significant for two-sided test and marginally significant for one-sided tests.

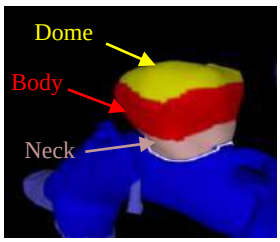

Figure 1: Aneurysm regions: neck (pink), body (red), and dome (yellow).

RESULTS

A total of 72 AWE regions were defined in the 23 aneurysms. Most of the AWEs were at the body of the aneurysms (n=40, 56%) and the rest of them were distributed almost equally at the dome (m=18, 25%) and neck (n=14, 19%).

Results of the first approach showed that on average the mWSS of enhanced regions was lower than non-enhanced regions (p=0.0493). The WSSDIV was larger negative in enhanced regions (p=0.0255). Results of the second approach indicated that AWE regions at neck had higher WSSDIV (p=0.0494), smaller GON (p=0.494), and higher WSSGRAD (p=0.0494) in comparison to the non-enhanced regions. AWE regions located at the body had lower mWSS (p=0.0120), pWSS (p=0.0159), and WSSGRAD (p=0.0086) than non-enhanced regions. Additionally, AWE regions that were far from the inflow had lower mWSS (p=0.006) and pWSS (p=0.037) than non-enhanced regions. Finally, the results of the third approach demonstrated that the AWE regions close to the inflow had larger pWSS (p=0.0147) and mWSS (p=0.0799) compared to AWE regions far from the inflow. Also, the AWE regions located at the neck had larger WSSGRAD than the regions at the body (p=0.0018) and dome (p=0.0070).

DISCUSSION

In our study, the normalized mWSS of AWE region was lower than the non-enhanced regions which was consistent with the previous studies [3,11]. Khan et al. [3] and Xiao et al. [11] and have also reported lower WSS in AWE regions. In our work, most of AWE regions were seen at the body of the aneurysm and fewer were at the dome and neck. Further, different local flow conditions were observed at AWE regions located at different locations. These different flow conditions show the different microenvironments of the aneurysm. These microenvironments have different stages of histological reaction to the blood flow, and thus AWE can indicate the different stages of them. Based on our observations, we hypothesized that hemodynamic conditions are different in AWE regions at different locations. To test this hypothesis, AWE regions were classified according to their locations (neck, body, and dome) and their distance from the inflow (far or close). The results indicate that AWE regions at the neck and close to the inflow have higher WSS, larger negative WSSDIV, and higher and less oscillatory WSSGRAD than the non-enhanced regions. However, AWE regions far from the inflow have lower WSS and WSSGRAD. These results suggest that different mechanisms can be responsible for the AWE regions at different locations.

Despite many studies on the topic, the mechanism responsible for AWE is still unclear. One of the possible mechanisms is the infiltration of Gd through the wall because of increased endothelial permeability. This increased permeability can lead to wall inflammation [1,11,12]. The correlation between circumferential AWE and contrast enhancement in the parent artery [13] shows this inflammation can lead to aneurysm formation. Endothelial dysfunction, caused by abnormally low WSS or high WSS, may also lead to wall inflammation [14] and the leakage of Gd to the wall. Further research needs to understand the AWE mechanisms completely and their potential use as biomarkers for aneurysm inflammation.

The small sample size and lack of follow-up data limited the scope of this work. The small sample size did not allow us to have a specific threshold to identify AWE regions objectively. Further studies with a larger sample size should be done to approve our findings.

Our results showed that AWE regions have lower WSS than non-enhanced regions, and AWEs at the neck and near the inflow have higher WSS and WSSGRAD. These results suggest different mechanisms for AWE at different locations.

ACKNOWLEDGEMENTS

The 2019 Brain Aneurysm Research Grant from The Bee Foundation, a Pilot Research Grant from the Society of Vascular and Interventional Neurology (SVIN), and a part of NIH grant R01NS097457 – granted to Drs. Samaniego, Robertson, and Cebral – supported this work. Also, an MRI instrument funded by 1S10RR028821-01 was used in this study.

REFERENCES

[1] Larsen, N et al., *AJNR Am J Neuroradiol*, 39:1617–1621, 2018.

[2] Rouchaud, A et al., *Neuroradiology*, 58:171-7, 2016.

[3] Matsushige T et al., *World Neurosurg*, 127:e578-84, 2019.

[4] Liu, P et al., *Interventional Neuroradiol*, 22:501-05, 2016.

[5] Lv, N et al., *Neurosurgery*, 84:E385-91, 2019.

[6] Wang, GX et al., *J Neuroradiol*, 46:25-28, 2019.

[7] Khan, MO et al., *J Neurosurg*, 2020.

[8] Ashkezari, SF et al., *J Neurointerv Surg*, 2020.

[9] Mut, F et al., *Int J Numer Method Biomed Eng*, 37:822-39, 2011.

[10] Xiao, W et al., *AJNR Am J Neuroradiol*, 39:2082-87, 2018.

[11] Shimonaga, K et al., *Stroke*, 49:2516-19, 2018.

[12] Matsushige, T et al., *Neuro Med Chir*, 59:407-14, 2019.

[13] Samaniego, EA et al., *J Neurointerv Surg*, 12:1018-22, 2020.

[14] Frösen, J et al., *Neurosurg Focus*, 47:E21, 2019.

ACOUSTIC RADIATION FORCE ON EUKARYOTIC CELL DUE TO STANDING SURFACE ACOUSTIC WAVE

Xiangjun Peng (1), Guy M. Genin (1,2)

(1) Department of Biomedical Engineering
Washington University
St. Louis, MO, USA

(2) Bioinspired Engineering and
Biomechanics Center (BEBC)
Xi'an Jiaotong University
Xi'an, P.R. China

INTRODUCTION

Standing surface acoustic wave-based (SSAW-based) acoustic tweezers are widely integrated with microfluidics for this purpose [1], and 3D (three-dimensional) SSAW acoustic tweezers have been proposed [2]. Theoretical analysis of acoustic manipulation with SSAW is crucial for understanding the underlying mechanisms of acoustic tweezers and for refining the technique.

However, a theoretical study to establish a foundation for developing this technology has not yet been undertaken. We therefore undertook such a study with the aim of improving SSAW technologies by revealing the mechanisms underlying acoustic tweezer manipulation of heterogeneous bodies like cells. Conventional theories for estimating ARF are based upon planar standing waves, and therefore fail to consider the transmission of energy from solid to fluid, and the associated influence of the Rayleigh angle, as is needed for the study of surface standing waves [3]. Moreover, theories for planar standing waves cannot predict the component of ARF acting perpendicular to substrate, as is needed for modeling and controlling particles or cells (Fig. 1a).

We therefore developed a spherically symmetric, three-layered model and calculated the ARF vector induced by a SSAW incident on a three-layered cell using the partial wave expansion method (Fig. 1). Results revealed significant effects of the Rayleigh angle and of the geometrical and acoustic parameters of the nucleus.

METHODS

SSAWs can be generated by two identical interdigital transducers (IDTs), fabricated on a piezoelectric substrate, that generate two progressive surface acoustic waves traveling towards one other with phase velocity c_s (Fig. 1a). When surface acoustic waves travel along the substrate-fluid boundary, part of the vibrational energy transports into the fluid medium, yielding two compressional waves. Each wave travels with velocity c_f at a Rayleigh angle θ_R with respect to the *x*-axis:

$$\theta_R = \arcsin(c_f/c_s) \quad (1)$$

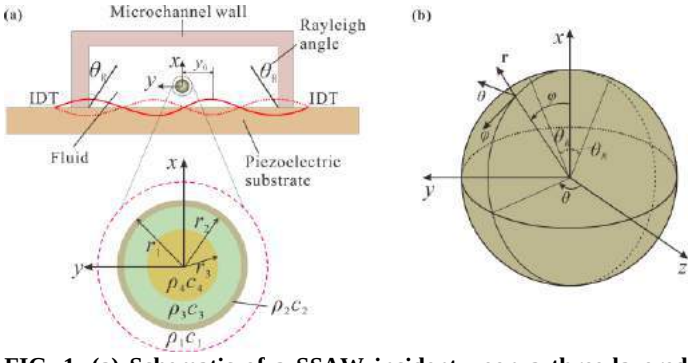

FIG. 1. (a) Schematic of a SSAW incident upon a three-layered model of a eukaryotic cell. (b) The origin of the local spherical coordinate system $(\boldsymbol{r}, \boldsymbol{\theta}, \boldsymbol{\varphi})$ resides at the instantaneous center of the eukaryotic cell.

For a continuous SSAW travelling in an ideal fluid, the total ARF, $\boldsymbol{F}$, can be determined by integrating the excess of pressure $(p - p_0)$ generated by the sound field over the instantaneous surface $S(t)$ of the eukaryotic cell, as:

$$\boldsymbol{F} = -\int\int_{S(t)} (p - p_0)\boldsymbol{n}dS \quad (2)$$

where $\boldsymbol{n}$ is the outward normal to $S(t)$. For proper evaluation of the ARF, the excess of pressure should be taken up to second-order terms in the velocity potential [4]. For a periodic wave, the ARF is defined as a time-averaged quantity over period T of the sound field. The time-

averaged force acting on a sphere immersed in an infinite ideal fluid is given by:

$$\langle \boldsymbol{F} \rangle = -\left\langle \int\int_{S_0} \rho \langle (u_n \boldsymbol{n} + u_t \boldsymbol{t}) u_n \rangle \boldsymbol{n} dS \right\rangle + \int\int_{S_0} \left[\frac{1}{2}\frac{\rho}{c^2} \left\langle \left(\mathrm{Re}\left[\frac{\partial \phi_1}{\partial t} \right] \right)^2 \right\rangle - \frac{1}{2}\rho \langle |\nabla \mathrm{Re}[\phi_1]|^2 \rangle \right] \boldsymbol{n} dS \quad (3)$$

where $\langle \cdot \rangle$ is represents the time average, $\boldsymbol{t}$ is the outward-pointing unit tangential vector of S, S_0 is the surface of the target at its equilibrium position, $dS = rdrd\theta$, and the parameters $u_n \boldsymbol{n}$ and $u_t \boldsymbol{t}$ are the radial and tangential components of the velocity at the surface, respectively. In the following study, we will mainly focused on the normalized ARF in x-direction, Y_{px}, which has been ignored by previous studies.

RESULTS

For illustration, with reference to Fig. 3(a), we consider the effect of the acoustic impedances of the cortical layer and cell nucleus while keeping the position parameter set to $y_0 = \lambda_s/2$, so that the cell is centered at the pressure antinodes; the Rayleigh angle was set to $\theta_R = 20°$. The theoretical and the finite element predictions of the dimensionless ARF Y_{px} were within a few percent for all cases and for acoustic excitation frequencies studied. As the SSAW frequency increases, the curve describing the dimensionless ARF Y_{px} exhibits a series of prominent peaks and dips, due mainly to resonant vibrations of the cell, and the magnitude of the peaks decreases. The presence of either a nucleus or a cortical layer can significantly affect the ARF on the cell, with an especially strong effect of the nucleus. This is due to the strong mismatch in acoustic impedance of the nucleus relative to other components, which results in significantly effect on the scattering field.

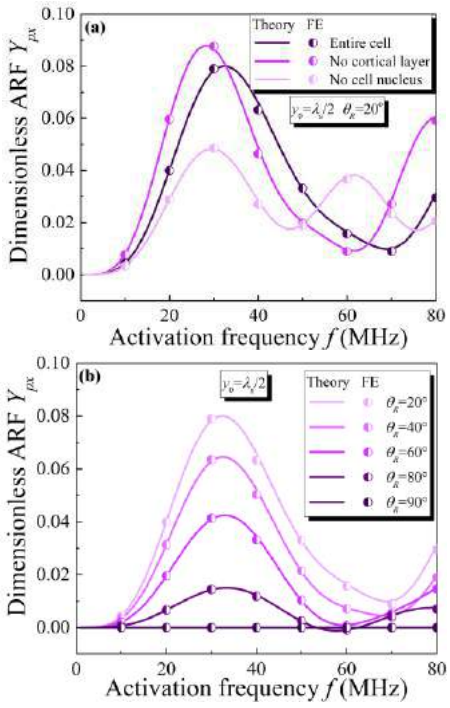

FIG. 3 (a) Dimensionless acoustic radiation force, Y_{px}, versus frequency for an entire cell, a cell lacking a cortical layer, and a cell lacking a nucleus. For the case shown, the cell position parameter is $y_0 = \lambda_s/2$ so that the cell is centered at the pressure antinodes, and the Rayleigh angle is $\theta_R = 20°$. (b) Dimensionless ARF, Y_{px}, versus frequency for an entire cell with several different Rayleigh angles. For the case shown, the position parameter is $y_0 = \lambda_s/2$ so that the cell is centered at the pressure antinodes. For certain frequency ranges at higher Rayleigh angles, the cell is drawn back towards the substrate.

We next consider the effect of the Rayleigh angle (Fig. 3b), with the cell position again fixed at $y_0 = \lambda_s/2$. The dimensionless ARF Y_{px} is largest at around 32 MHz for all values of the Rayleigh angle below 90° with the magnitude of the peak at 32 MHz increasing with decreasing Rayleigh angle. This is expected because more energy will emerge in the *x*-direction with decreasing Rayleigh angle. This suggests a preferred frequency for manipulating eukaryotic cells when a large ARF is needed. Further inspection of Fig. 3b reveals that Y_{px} can become negative for certain frequencies at larger Rayleigh angles, indicating that the ARF in the *x*-direction points back towards the substrate.

DISCUSSION

We have shown that the design of SSAW microfluidic devices to manipulate cells is strongly dependent upon the Rayleigh angle of the system and the heterogeneous mechanics of the cells, neither of which had previously been explored theoretically. Our results extend the state of the art analysis to include waves other than plane standing waves, and to assess the effects of the Rayleigh angle and of cell mechanics. The theoretical model we derived reduced to earlier, simpler solutions for planar standing and planar traveling waves. It provided exact solutions for scattering coefficients, and a near-field approximation for the ARF.

These exact solutions have some limitations that bear mention. For example, the mechanical properties of cells depend strongly upon the way that they are loaded. The numbers used in the studies here are all derived from experiments that involve large perturbations of cells, but the application of ultrasound involves minimal deformation and relatively low stresses. The results presented may enable the estimation of mechanical properties at very low levels of cell deformation based upon motion in response to ARF.

ACKNOWLEDGEMENTS

This work was supported in part by the National Natural Science Foundation of China (11972185), the China Scholarship Council (201906280470), the US NSF Science and Technology Center for Engineering Mechano-Biology (CMMI 1548571), and the National Institutes of Health (R01AR077793).

REFERENCES

1. Ding, X., et al., *Surface acoustic wave microfluidics.* Lab on a Chip, 2013. **13**(18): p. 3626-3649.
2. Guo, F., et al., *Three-dimensional manipulation of single cells using surface acoustic waves.* Proceedings of the National Academy of Sciences, 2016. **113**(6): p. 1522-1527.
3. Kim, M., et al., *Acoustic trap-and-release for rapid assessment of cell motility.* Soft Matter, 2019. **15**(21): p. 4266-4275.
4. Hasegawa, T. and K. Yosioka, *Acoustic ‐ radiation force on a solid elastic sphere.* The Journal of the Acoustical Society of America, 1969. **46**(5B): p. 1139-1143.

SB³C2021
Summer Biomechanics, Bioengineering and Biotransport Conference
June 14-18, Virtual

VIBROMETRY AS A NONDESTRUCTIVE ALTERNATIVE TO DYNAMIC MECHANICAL TESTING IN CARTILAGE

M. Gabriela Espinosa (1), Gaston A. Otarola-Pezzani (1), Jerry C. Hu (1), Kyriacos A. Athanasiou (1)

(1) Biomedical Engineering
University of California, Irvine
Irvine, CA, United States

INTRODUCTION

Physiological loading of knee articular cartilage is highly dynamic. Excessive strains occurring with cyclic compression are mitigated by cartilage's dynamic mechanical properties. Without this protective behavior, mechanical fatigue often results in the onset of osteoarthritis [1]. Therefore, measurement of cartilage's dynamic mechanical properties is critical for functional assessment of native tissue and is strongly recommended by the Food and Drug Administration (FDA) for any knee cartilage repair or replacement product [2].

Mechanical testing of cartilage tissue is common, but dynamic measurements are infrequently performed compared to quasi-static methods. This may be partly due to the destructive nature of these tests, thus preventing researchers from performing more comprehensive investigations. The possibility of a nondestructive form of dynamic mechanical testing would be a boon to cartilage research, enabling the field to further explore cartilage tissue dynamics.

Vibrometry, a nondestructive measurement modality, has been extensively used to determine dynamic properties of engineering materials. We hypothesized that vibrometer-based measurements of cartilage dynamic mechanical properties would correlate with quasi-static mechanical properties and biochemical composition. We also hypothesized that the vibrometer would detect differences in the dynamic and viscoelastic properties among various knee cartilages. The results from this work will enable nondestructive dynamic characterization of native, repaired, and replacement cartilage to determine their ability to withstand physiological mechanical demands.

METHODS

Cartilage punches (5mm dia.) were obtained from the tibiofemoral condyle, trochlear groove, patella, and meniscus of juvenile bovine knees. Each punch was placed on a piezoelectric actuator which excited the bottom surface of the tissue. Two forms of excitation were used: a frequency sweep ranging from 10Hz to 100kHz and a 500Hz sinusoidal. Deformation of the tissue's top surface was measured by a PSV-500-B Xtra Laser Scanning Vibrometer (Polytec). Each sample's first and second resonant frequencies were identified in response to the frequency sweep. ASTM guidelines were used to calculate the dynamic modulus (G*) based on these resonant frequencies [3]. Additionally, phase shifts between the tissue response and applied sinusoidal were then used to calculate storage (G') and loss (G'') moduli. Linear perturbation frequency analysis in ABAQUS was used to predict and compare to the resonant frequencies and bending modes of the cartilage samples. Modeled and experimentally observed frequencies were correlated using a Pearson's test.

Following vibrometry, the punches were divided into portions to be used for stress relaxation tests (at 10% and 20% strains), creep indentation, and biochemical assays. Biochemical assays measured collagen, pyridinoline, and GAG content per wet weight and dry weight. Quasi-static mechanical and biochemical parameters were correlated to vibrometry-based measures (G*, G', and G'') using Spearman's ρ test. Statistical differences between cartilage groups were determined using a one-way ANOVA and Tukey's post hoc test.

RESULTS

Distinct bending mode shapes were identified for each group's first and second resonant frequencies and were closely matched with model predictions (Fig. 1). First resonant frequencies ranged between 2kHz and 9kHz, while the second resonant frequencies ranged between 5kHz and 15kHz. Measured and modeled resonant frequencies significantly and strongly correlated across all cartilage groups (R^2=0.93). Dynamic moduli (Fig. 2) were not significantly different among the condyle, patella, and trochlear groove groups, but the meniscus dynamic modulus

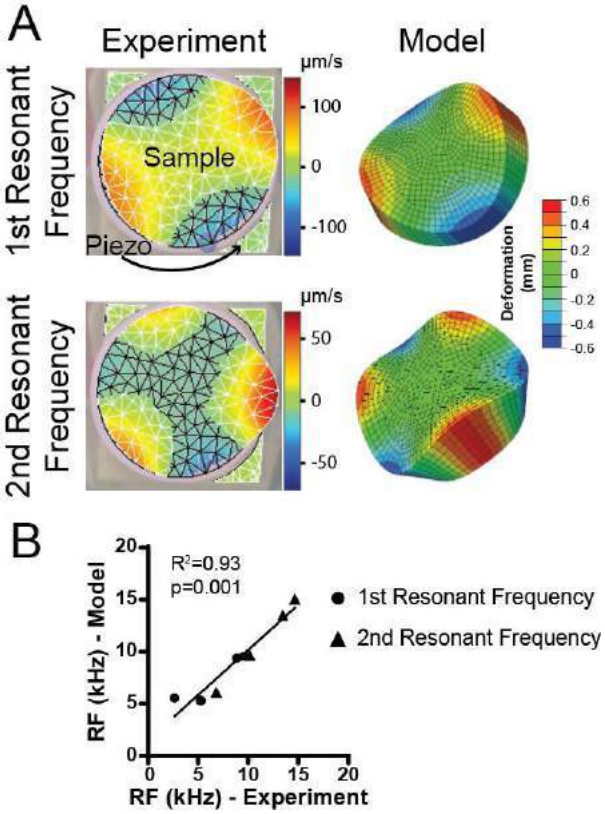

Figure 1: (A) Velocity plotted over the tissue and piezo platform (left) with corresponding modeled bending modes (right) at the first and second resonant frequencies. (B) There is a strong correlation between measured and predicted frequencies (R^2=0.93).

(6.1±0.5MPa) was significantly lower than that of the patella (46.7±11.0MPa) and trochlear groove (56.4±29.9MPa).

The storage modulus, G', mirrored the pattern observed in the dynamic modulus and significantly correlated with the instantaneous moduli from stress relaxation tests (Fig. 3). There were significant differences in the loss modulus, G'', even among the hyaline cartilage groups. The meniscus values were significantly lower than that of the condyle group (78% decrease). G'' was most strongly correlated with the aggregate and shear moduli from creep indentation tests. A similar correlation between G'' and GAG content was also observed (not shown).

DISCUSSION

The dynamic mechanical properties of cartilage are critical for the daily function of the knee joint. However, the destructive nature of most dynamic testing and tissue scarcity often preclude this form of characterization. We found that vibrometry was a novel, nondestructive alternative. Cartilage deformation at resonance was well represented by finite element modeling. Our high frequency vibrometer-based results were not only comparable to previously reported dynamic properties using other methods [1,4], but also correlated with various mechanical properties obtained through quasi-static methods. This is further reinforced by similar correlations to biochemical composition.

Vibrometry is well poised to make significant contributions to cartilage research. For example, the present data show that the meniscus has a significantly lower loss modulus than condylar cartilage, which supports recent calls to reconsider meniscus function as energy absorbing [5]. Future work includes the development of a fluid-filled sample chamber amenable to vibrometry to reduce drying effects and enable time-course measurements. These efforts may present new opportunities for studying the mechanical maturation of engineered cartilage.

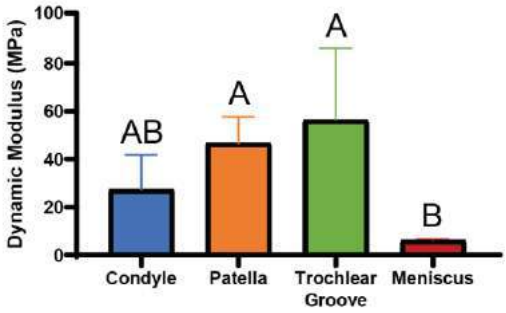

Figure 2: Dynamic moduli are determined from the resonant frequencies. The values significantly differ among the cartilages of the knee. Capitalized letters not shared between groups denote significant differences. Error bars represent standard deviation.

ACKNOWLEDGEMENTS

National Institutes of Health (R01 AR067821 and R01 AR071457), NIH Diversity Supplement (for MGE), Fulbright Chile scholarship (for GO), and Becas Chile scholarship (for GO). We also thank Polytec, Inc. for their technical support.

REFERENCES

[1] Park, S et al., *Osteoarthr. Cartil.*, 12:65-73, 2004.
[2] Food and Drug Administration, Preparation of IDEs and INDs for Products Intended to Repair or Replace Knee Cartilage, 2011.
[3] ASTM International, E1876-15, 2015.
[4] Laasanen, M et al., *Biorheology*, 40:133-140, 2003.
[5] Gaugler, M et al., *Knee Surg. Sports Traumatol. Arthrosc.*, 23:1141-1146, 2015.

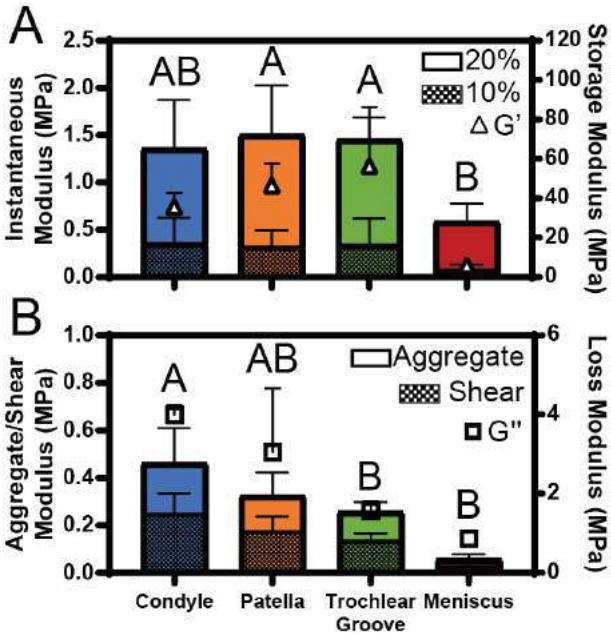

Figure 3: (A) Instantaneous moduli correlate with storage moduli. (B) Aggregate and shear moduli also significantly correlate with the loss moduli. Capitalized letters denote statistically significant differences in storage and loss moduli among groups.

SB³C2021
Summer Biomechanics, Bioengineering and Biotransport Conference
June 14-18, Virtual

A VOLUMETRIC GROWTH AND REMODELING FRAMEWORK TOWARDS PREDICTING THE PROGRESSION OF OSTEOARTHRITIS IN ARTICULAR CARTILAGE

Muhammed M. Rahman (1), Thomas S. E. Öst (2), Corey P. Neu (3), David M. Pierce (1,4)

(1) Department of Mechanical Engineering, University of Connecticut, Storrs, Connecticut, USA

(2) Department of Weapons, Protection and Security, FOI – Swedish Defense Research Agency, Stockholm, Sweden

(3) Department of Mechanical Engineering, University of Colorado Boulder, Boulder, Colorado, USA

(4) Department of Biomedical Engineering, University of Connecticut, Storrs, Connecticut, USA

INTRODUCTION

Articular cartilage, a soft tissue covering the bone ends in joints, provides support for bearing load and movement by the virtue of unique structural composition and very low coefficient of friction at the surface. Osteoarthritis (OA) is a disease of the synovial joint, with degeneration and loss of articular cartilage as one hallmark change. Despite the multifactorial nature of OA, mechanical stresses, e.g., tension, compression, shear, hydrostatic pressure, play a key role in the destructive evolution of the disease [1-4]. Both overloading (e.g. trauma) and reduced loading (e.g. immobilization) of cartilage induce molecular and microstructural changes that lead to mechanical softening, fibrillation, and erosion.

In response to mechanical and chemical stimuli, chondrocytes (the cells within cartilage) express and degrade components of extra-cellular matrix (ECM) including structural constituents such as collagen, proteoglycan, and other proteins. To facilitate better understanding of the mechanobiology of cartilage and chondrocytes we seek functional relations between the type and magnitude of mechanical stimuli and the resulting cell-driven mass/density changes within cartilage, which affects the subsequent mechanics.

Here we established a novel framework to incorporate the evolution of constituents generating volumetric changes in cartilage, i.e., volumetric growth and remodeling (VG&R), by leveraging our established constitutive model of cartilage [5-6]. Experimental evidence indicates that application of strain at varying physiological frequencies facilitates chondrocytes expressing PG and collagen at different rates and total quantities [7-10]. We curated the available literature and established functional relations between the loading conditions and normalized expression of constituents. To validate our proposed VG&R framework for cartilage we reproduced the experiment of Kraft et al. [11] and predicted the production of collagen and PG.

METHODS

Constitutive Model. We modeled articular cartilage as a biphasic (swelling) continuum $\phi = \phi^{\mathrm{S}} + \phi^{\mathrm{F}}$ consisting of a porous solid phase ϕ^{S} saturated with an interstitial fluid phase ϕ^{F}. We defined the Helmholtz free-energy function of the solid ψ^{S} as [5-6]

$$\psi^{\mathrm{S}} = \psi^{\mathrm{S}}_{\mathrm{OP}}(J_{\mathrm{S}}) + (1-\nu)\psi^{\mathrm{S}}_{\mathrm{IM}}(J_{\mathrm{S}}, I_1) + \nu\psi^{\mathrm{S}}_{\mathrm{FN}}(\mathbf{C}_{\mathrm{S}}, \mathbf{M}), \quad (1)$$

where $\psi^{\mathrm{S}}_{\mathrm{OP}}$, $\psi^{\mathrm{S}}_{\mathrm{IM}}$, and $\psi^{\mathrm{S}}_{\mathrm{FN}}$ are the contributions of the osmotic pressure, isotropic matrix, and network of collagen fibers, respectively; ν is the volume fraction of collagen to total solid; J_{S}, $\mathbf{C}_{\mathrm{S}}$, and $\mathbf{M}$ are Jacobian, the right Cauchy-Green tensor, and the reference fiber orientation, respectively; and $I_1 = \mathrm{tr}(\mathbf{C}_{\mathrm{S}})$. We modeled the contribution from osmotic pressure as [6]

$$\psi^{\mathrm{S}}_{\mathrm{OP}} = \frac{1}{\rho^{\mathrm{S}}_{0\mathrm{S}}} R\theta c^{\mathrm{fc}}_{0\mathrm{S}} n^{\mathrm{F}}_{0\mathrm{S}} \left[\frac{2\bar{c}_{\mathrm{m}}}{c^{\mathrm{fc}}_{\mathrm{m}}} - \frac{\sqrt{4(\bar{c}_{\mathrm{m}})^2 + (c^{\mathrm{fc}}_{\mathrm{m}})^2}}{c^{\mathrm{fc}}_{\mathrm{m}}} + \sinh^{-1}\left(\frac{c^{\mathrm{fc}}_{\mathrm{m}}}{2\bar{c}_{\mathrm{m}}}\right) \right], \quad (2)$$

where $R = 8.314$ MPa mm^3/mmol K, $\theta = 310.2$ K, $\rho^{\mathrm{S}}_{0\mathrm{S}}, c^{\mathrm{fc}}_{0\mathrm{S}}, n^{\mathrm{F}}_{0\mathrm{S}}, c^{\mathrm{fc}}_{\mathrm{m}}, \bar{c}_{\mathrm{m}}$ are the initial solid partial density, initial concentration of fixed charges, the initial fluid volume fraction, initial concentration of fixed charge and the ion concentration of the external solution, respectively. We modeled the contribution from densely packed proteoglycan as [2,3]

$$\psi^{\mathrm{S}}_{\mathrm{IM}} = \frac{1}{\rho^{\mathrm{S}}_{0\mathrm{S}}} \left[U(J_{\mathrm{S}}) + \frac{1}{2}\mu^{\mathrm{S}}(I_1 - 3) \right], \quad (3)$$

including compaction effects via $U(J_{\mathrm{S}})$ and with shear modulus μ^{S}. We modeled the contribution from the network of collagen fibers as [5-6]

$$\psi^{\mathrm{S}}_{\mathrm{FN}} = \frac{1}{\rho^{\mathrm{S}}_{0\mathrm{S}}} \int_{\Omega} \rho(\mathbf{M}) \frac{k_1}{2k_2} \left\{ e^{[k_2(I_4-1)]^2 - 1} \right\} \mathcal{H}(I_4 - 1)\, \mathrm{d}\Omega, \quad (4)$$

where $\rho(\mathbf{M}), k_1, k_2$ are a voxel-wise orientation distribution function, a stress like parameter and dimensionless parameter, respectively, $I_4 = \mathbf{M} \cdot \mathbf{C}_{\mathrm{S}}\mathbf{M}$, and $\mathcal{H}$ is a Heaviside function.

We modeled the corresponding permeability of cartilage matrix as [5-6]

$$\mathbf{K}_{\mathrm{F}} = k_{0\mathrm{S}} \left(\frac{n^{\mathrm{F}}}{1 - n_{0\mathrm{S}}^{\mathrm{S}}} \right)^{m} \frac{1}{4\pi} \int_{\Omega} \frac{\rho(\mathbf{M})}{I_4} \mathbf{m} \otimes \mathbf{m} \, \mathrm{d}\Omega \,, \tag{5}$$

where $\mathbf{m}$ is the current fiber orientation, n^{F} and $n_{0\mathrm{S}}^{\mathrm{S}}$ are the volume fractions of fluid and solid, and $k_{0\mathrm{S}}$ is the initial Darcy permeability.

Volumetric Growth and Remodeling Framework. We defined the target volume change due to VG&R as $\hat{v} = \sum_{i=\mathrm{PG,CO}} \hat{m}_i \phi_i$, where $\hat{m}_i$ and ϕ_i are the individual normalized mass productions and volume fractions, respectively. We defined the modified Jacobian, and right and left Cauchy-Green tensors as $\hat{J} = \hat{v}^{-1} \det(\mathbf{F}) = J/\hat{v}$, $\hat{\mathbf{C}} = \hat{v}^{-2/3}\mathbf{C}$ and $\hat{\mathbf{b}} = \hat{v}^{-2/3}\mathbf{b}$, respectively. We also defined the modified invariants as $\hat{I}_1 = \hat{v}^{-2/3} I_1$, $\hat{I}_2 = \hat{v}^{-4/3} I_2$, $\hat{I}_3 = \hat{v}^{-2} I_3$, and $\hat{I}_4 = \hat{v}^{-2/3} I_4$. The density changes of the individual constituents are $\hat{\rho}_i = \hat{m}_i / \phi_i$. Finally, we express the total Cauchy stress of the solid constituents as,

$$\boldsymbol{\sigma}^{\mathrm{S}} = \boldsymbol{\sigma}_{\mathrm{OP}}^{\mathrm{S}} + (1 - \nu) \hat{\rho}_{\mathrm{PG}} \boldsymbol{\sigma}_{\mathrm{IM}}^{\mathrm{S}} + \nu \hat{\rho}_{\mathrm{CO}} \boldsymbol{\sigma}_{\mathrm{FN}}^{\mathrm{S}} \,, \tag{6}$$

Normalized PG and Collagen Production. Experiments confirm that chondrocytes synthesize components of PG and collagen at different rates under different treatments with cyclic compression [7-10]. Therefore, we proposed a generalized function of normalized production of PG and collagen dependent on applied stretch (λ) within the tissue, loading rate or frequency (f), and the time (τ), i.e for the duration of loading. We proposed a linear relation,

$$\hat{m}_i = \alpha_i \lambda + \beta_i f + \gamma_i \tau + \omega_i \,, \tag{7}$$

where α_i, β_i, γ_i, and ω_i are fitting parameters for $i \in \{\mathrm{PG}, \mathrm{CO}\}$.
To facilitate general loading we converted the frequency to strain rate and stretch to principal stretches and maximum shear stretches, and implemented these within our VG&R framework.

Cartilage under Hydrostatic Pressure. To validate our established numerical framework, we simulated cartilage undergoing cyclic hydrostatic pressure [11] and predicted both proteoglycan and collagen production. We created a quarter-symmetry model of a cylindrical specimen of cartilage (10 mm Ø, 182 µm thickness) with 582 linear hexahedral elements. We first allowed the model to swell and achieve equilibrium. We then applied cyclic hydrostatic pressure from 0.5 MPa to 5 MPa at 0.1 Hz frequency following the experiment [11]. Exploiting the very different time scales between daily activities, e.g. walking (sec), and progression of OA (days to years), we used iterative rather than simultaneous solutions. We simulated the loading conditions for 21 days. We present the model properties for our analyses in **Table 1**. We performed our simulations using FEBio (University of Utah, USA).

Table 1: Model parameters for cartilage

Parameter			
$\boldsymbol{\mu^{\mathrm{S}}}$	0.25 MPa	$\boldsymbol{k_{0\mathrm{S}}}$	9.6×10^{-4} mm^4/Ns
$\boldsymbol{k_1, k_2}$	0.43 MPa, 8.0 [-]	$\boldsymbol{m}$	3.3 [-]
$\boldsymbol{n_{0\mathrm{S}}^{\mathrm{S}}}$	0.15 [-]	$\boldsymbol{c_{0\mathrm{S}}^{\mathrm{fc}}}$	0.50×10^{-6} mol/mm^3
$\boldsymbol{\nu}$	0.82 [-]	$\boldsymbol{\bar{c}_{\mathrm{m}}}$	0.15×10^{-6} mol/mm^3
$\boldsymbol{J_{\mathrm{cp}}^{\mathrm{S}}}$	0.37 [-]		

RESULTS

The fitted parameters for our normalized PG and collagen production, i.e. (7), are $\alpha_{\mathrm{PG}} = 0.0850, \beta_{\mathrm{PG}} = 0.0294, \gamma_{\mathrm{PG}} = 0.0206,$ and $\omega_{\mathrm{PG}} = 0.852$ for PG, and $\alpha_{\mathrm{CO}} = -5.03, \beta_{\mathrm{CO}} = 0.0215, \gamma_{\mathrm{CO}} = 0.0531,$ and $\omega_{\mathrm{PG}} = 5.53,$ for collagen. We present the fitted multilinear equations as contour surfaces with the experiment data used for fitting in **Fig. 1**.

We predicted the normalized production of cartilage constituents for each day of the experiment, see **Fig. 2**. **Fig. 2(a)** shows a comparison between the predicted (normalized) production of PG vs. the corresponding experiment from Kraft et al. [11], while **Fig. 2(b)** illustrates the same comparison for collagen type II.

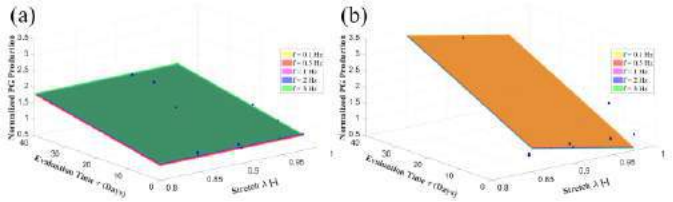

Figure 1: Normalized production of (a) proteoglycan (PG) and (b) collagen type II under general loading conditions.

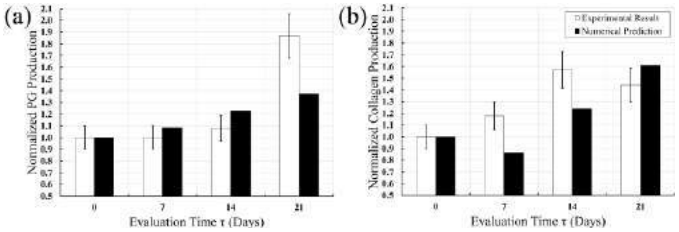

Figure 2: Normalized production of (a) proteoglycan (PG) and (b) collagen type II predicted versus experiment [11].

DISCUSSION

We introduced a VG&R framework considering the mechanobiologically induced turnover of constituents in articular cartilage resulting from mechanical loading. Our simulations of the cartilage successfully predict the production proteoglycan and collagen determined experimentally [11]. In predicting the evolution of PG, our simulation reasonably approximates the experimental results except for day 21. Our prediction of collagen follows the trend determined in the experiment; but the numerical values differ. Nevertheless, the difference between the prediction and experiment is in a narrow range of the normalized scale.

Unfortunately, the experimental data available for calibrating our framework i.e., formulate and fit (7), are quite sparse. In this light we selected the most simple (linear, not nonlinear) relationship among stretch, frequency, and time. Moreover, we formulated (7) based on experiments under uniaxial cyclic loading, while we predicted the evolution of constituents under cyclic hydrostatic pressure. Despite of the difference in loadings, we successfully predicted the evolution of constituents to test our novel VG&R framework for articular cartilage.

Limitations and outlook. We must improve the correspondence between predictions and experiments [11]. By leveraging more experimental data we could extent (7) to include nonlinearity and likely improve the fitting. In our simulations, we considered the number of chondrocytes as constant, while this may evolve with cell death or proliferation. Our framework is the first step towards a new class of computational tools that will facilitate, for the first time, patient-specific modeling of OA progression considering the biomechanics and kinetics of cell ECM turnover and production, both *in vitro* and *in vivo*.

ACKNOWLEDGEMENTS

NSF 1662429; X. Wang; V. Strbac.

REFERENCES

[1]Andriacchi, TP et al., *Ann Biomed Eng*, 32:447-457, 2004. [2] Goldring, MB and Marcu, KB, *Arthr Res Ther*, 11:224, 2009. [3] Polur, I et al., *Histol Histopath*, 25:599-608, 2010. [4] Loeser, RF et al., *Arthritis Rheum*, 64:1697-1707, 2012. [5] Pierce, DM et al., *Biomech Model Mechanobiol*, 15:229-244, 2016. [6] Wang, X et al., *J Mech Behav Biomed Mat*, 86:409-422, 2018. [7] Mauck, RL et al., *Tissue Eng*, 9:597-611, 2003. [8] Kisiday, JD et al., *J Biomech*, 37:595-604, 2004. [9] Tsuang, YH et al., *Int J Art Organs*, 31:439-449, 2008. [10] Wang, PY and Tsai, WB, *J Bio Sci*, 24:507-519, 2013. [11] Kraft, JJ et al., *Cartilage*, 2:254-264, 2011.

SB³C2021
Summer Biomechanics, Bioengineering and Biotransport Conference
June 14-18, Virtual

LUNG LOBAR SLIDING HELPS REDUCE PARENCHYMAL DISTORTION DURING BREATHING

Adam E. Galloy (1), Ryan Amelon (1), Joseph M. Reinhardt (1), Madhavan L. Raghavan (1)

(1) Roy J Carver Department of Biomedical Engineering
University of Iowa
Iowa City, Iowa, United States of America

INTRODUCTION

Many lung diseases, such as chronic obstructive pulmonary disease, initially affect only a small region of the lung tissue. However, these diseases are diagnosed and characterized based on pulmonary function tests that only capture the total function of the lungs. When only the total function of the lungs is considered, healthy tissue can obscure the effects of small regions of unhealthy tissue that need medical attention. Patients may receive better diagnoses and treatment plans if regional lung mechanics metrics are used to characterize lung health. However, regional mechanics information is difficult to interpret because of a poor understanding of its role in breathing and because of variability within and between patients.

One source of both inter and intra patient variability arises from the sliding motion of the lung lobes. Lung lobes slide against each other along lobar fissures throughout the respiratory cycle [1]. However, some patients have missing or incomplete lobar fissures which can limit or prevent lobar sliding and change how the lung deforms [2]. In addition, patients can have different fissure orientations and lobe geometries [3].

We previously reported on a method for quantifying lobar sliding [1]. The objective of this study is to test the hypothesis that lobar sliding helps reduce directional distortion in the lung tissue during breathing using finite element analysis (FEA). Understanding how lobar sliding, or the lack thereof, affects regional lung deformation will improve our understanding of lung physiology and help us account for some of the variability between patients.

METHODS

Image Acquisition and Segmentation We acquired 4DCT scans from eight subjects with lung cancer using a protocol approved by the institutional review board. Patients were scanned in the supine position during gaited tidal breathing using a 40-slice CT scanner (Siemens Biograph, Hoffman Estate, IL) operating in helical mode.

The chest wall boundary and lung lobes were segmented for each subject from CT images at end of inhalation using Slicer4 and converted to smooth surface geometries using Mimics (Materialise). From the chest wall boundary, a 3-node triangular shell mesh was generated for each subject using Gambit (Ansys). Also using Gambit, 4-node tetrahedral solid meshes were generated for each lung lobe. Only the left lung was considered for this study.

Finite Element Analysis We used FEBio (University of Utah) for the FEA simulation. For both lung lobes of the left lung, we assigned a neo-Hookean material model with the parameters $E = 3$ kPa and $\nu = 0.30$. We applied nodal displacements to the chest wall shell to simulate the motion of the chest wall as it moves from end of inhalation to end of exhalation. These displacements were derived from deformable image registration of the end inhalation and end exhalation segmentations of the lung/chest wall boundary. We also applied contact boundary conditions between the chest wall shell and lobes as well as contact boundary conditions between lobes. These boundary conditions ensured that the lung tissue deformed with the chest wall. Contact between each interface was enforced using FEBio's sliding elastic formulation with augmented Lagrangian constraint enforcement. To compare lung deformation with lobar sliding to lung deformation without lobar sliding, we generated two models for each subject: one model with a friction coefficient of 1.5 between lobes to prevent lobar sliding, and one model with no friction between the lobes to allow for lobar sliding (Figure 1).

Post-Processing In order to quantify the directional distortion at a point in the lung tissue we used the anisotropic deformation index (ADI) [4]:

$$ADI = \sqrt{\left(\frac{\lambda_1 - \lambda_2}{\lambda_2}\right)^2 + \left(\frac{\lambda_2 - \lambda_3}{\lambda_3}\right)^2} \quad (1)$$

Where λ_i^2 are the eigenvalues of the right Cauchy-Green tensor. For each left lung model, ADI was calculated at each element and a volume-weighted average of ADI was calculated for the entire lung, the lower lobe, and the upper lobe. To determine if the differences in mean ADI between sliding and non-sliding models for the left lung as a whole and in each of the lobes were significant, we performed a Wilcoxon signed-rank test with $p<0.05$ as the criteria for significance.

In addition, the FEA mesh and displacements were interpolated onto a voxel grid. To quantify the amount of sliding that occurred at a voxel element, we used our sliding metric [1]:

$$\gamma_{max} = \frac{\lambda_1 - \lambda_3}{2} \quad (2)$$

The mean sliding metric of all fissure elements was calculated to quantify the amount of sliding on the entire fissure for each subject.

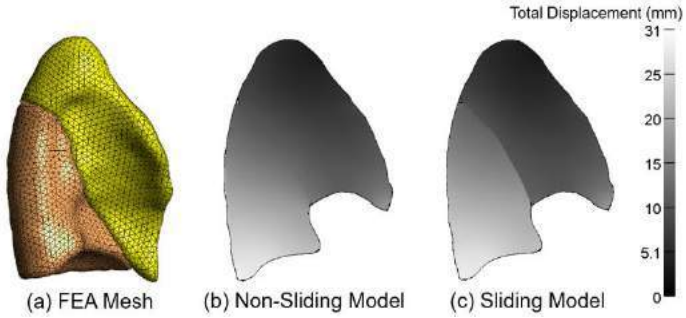

Figure 1: Finite element mesh of a lobe-specific CT segmentation from a representative subject (a). Displacement map on sagittal slice for FE simulation when lobar sliding was disallowed (b) and when friction-free lobar sliding was allowed (c). Note the displacement discontinuity at the lobar fissure in the latter, and the smooth transition in the former.

RESULTS

Using the ADI within the lung tissue calculated from the FEA results as a measure of directional distortion, we compared the mean ADI between the left lung models that restricted sliding to the models that allowed sliding (Figure 2). Mean ADI was calculated in the whole lung and within each lobe. We found that mean ADI significantly decreased in the lungs (5.3% average difference, $p < 0.01$). This supported our hypothesis that the additional degrees of freedom provided by lobar sliding allow the lungs to inflate with less directional distortion. A more pronounced mean ADI decrease between sliding and non-sliding models was observed when only the lower lobe was examined (9.4% average difference, $p < 0.01$); however, in the upper lobe there was no significant difference (2.0% average difference, $p = 0.11$). The lower lobe is closer to the diaphragm which is one of the largest sources of directional distortion in the lungs. This could be why the lower lobe is better positioned to decrease directional distortion with lobar sliding.

In addition to looking at differences between models from the same subject, we also looked at trends between subjects. In Figure 3 we plotted the reduction in ADI between the non-sliding models and the sliding models against the mean sliding metric along the lobar fissure for each subject. We found a positive correlation between the mean sliding metric and the mean ADI drop, further indicating that lobar sliding decreases directional distortion in the lungs. The five-fold difference in the smallest and largest mean sliding metric demonstrates the degree of variability in different subjects' sliding motion.

DISCUSSION

The inter and intra subject trends of this study are consistent with the hypothesis that lobar sliding allows the lungs to deform with less directional distortion. Lobar sliding is an often neglected cause of mechanical variation within and between subjects. Many FEA studies model the lungs as continuous solids, but this could lead to inaccurate deformation results such as larger directional distortions. Future work will consider the right lung and explore the relationship between fissure geometry and the amount of sliding that occurs to help us better account for inter-subject variability in lung mechanics.

One limitation to our study is that we only simulated scenarios where each lobe was free to slide frictionlessly or where sliding was almost completely prevented by a large friction coefficient. However, the lobes may be coupled to each other at certain locations, or a moderate friction coefficient may govern the sliding behavior. Future work comparing model predicted displacement fields to displacement fields computed from image registration of the original CT images can test these assumptions.

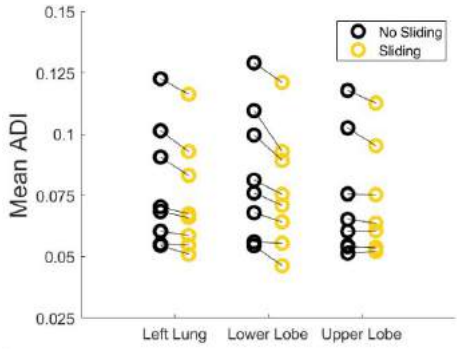

Figure 2: Change in spatial mean ADI in each subject's lung and in lobes when sliding was allowed. Models that allowed lobar sliding had significantly less directional distortion. This difference was more pronounced in the lower lobe of the lung.

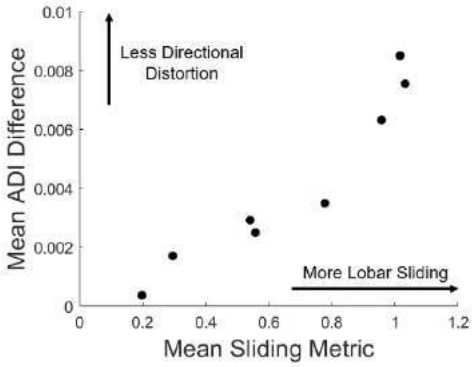

Figure 3: Subjects that had more sliding along the lobar fissure had a greater decrease in directional distortion.

ACKNOWLEDGEMENTS

This research was supported by training grant T32 HL144461 from the National Institutes of Health.

REFERENCES

[1] Amelon, R et al., *Ann Biomed Eng*, 42:642-650, 2014.
[2] Koster, T and Slebos, D, *Int. J. Chron. Obstruct. Pulmon. Dis.*, 11:765-773, 2016.
[3] Chan, H et al., *J. Biomech. Eng.*, 137:0510101-0510107, 2015.
[4] Amelon, R et al., *J Biomech*, 44:2489-2495, 2011.

MECHANICAL STRESS IN PANCREATIC CANCER: SIGNALING PATHWAY ADAPTATION ACTIVATES CYTOSKELETAL REMODELING AND ENHANCES CELL MIGRATION

M. Kalli (1), R. Li (2), G. B. Mills (3), T. Stylianopoulos (1) and I. K. Zervantonakis (2)

(1) Cancer Biophysics Laboratory, Department of Mechanical Engineering University of Cyprus Nicosia, Cyprus

(2) Tumor Microenvironment Engineering Laboratory, Department of Bioengineering, University of Pittsburgh, Pittsburgh, USA

(3) Knight Cancer Institute, Oregon Health & Science University, Oregon, USA

INTRODUCTION

Pancreatic ductal adenocarcinoma (PDAC) is responsible for over 90% of pancreatic cancer cases and is the seventh leading cause of cancer-related deaths in the United States[1]. New treatments for pancreatic cancer are urgently needed as it is highly resistant to all forms of chemotherapy and radiotherapy. Complete surgical resection is currently the only curative treatment, however, patients with advanced or metastatic pancreatic cancer are ineligible for surgical removal, and even following resection, the tumor usually relapses a year after surgery[1]. Current studies focus on targeting or restoring the microenvironment of PDACs that exhibit biomechanical abnormalities. These abnormalities include a dense tumor-associated stroma composed of extracellular proteins such as collagen I and hyaluronan that are remodeled to create a stiffer Extracellular Matrix (ECM), a condition known as desmoplasia. Increased matrix stiffness serves as a diagnostic marker and is associated with poor prognosis. These altered mechanical properties of the ECM, trigger signaling cascades resulting in increased cell motility, migration and invasion[2]. Moreover, tumor growth within a physically-restricted environment, surrounded by dense stroma, leads to the development of compressive forces in the tumor interior, generating intracellular *solid stress* that can reach up to 75mmHg (10kPa)[2]. This type of stress has been shown to activate signaling pathways that promote tumorigenesis and invasiveness. *However, the molecular mechanisms that enhance metastatic potential via mechanical stress remain elusive.* We hypothesize that mechanical compression, and hence solid stress, overstimulates several signaling pathways that have been shown to be consistently activated in pancreatic tumors. These pathways include the PI3K/Akt and Ras/MAPK signaling cascades that are involved in the regulation of cell survival and motility [2]. Specifically, Ras genes (*K-Ras, N-Ras, H-Ras*) are frequently mutated in several tumor types, including pancreatic tumors, whereas K-Ras is found to be the most frequently mutated gene in invasive pancreatic tumors with a rate of 95%[3]. One of the main targets of the K-Ras pathway is the MAPK signaling cascade, that includes the Jun N-terminal kinase (JNK) and p38 MAPK. These kinases are known to be activated by environmental and genotoxic stresses and have key roles in the regulation of cell proliferation, survival and migration and could possibly be implicated in solid stress-induced signal transduction[3]. In our previous studies, we showed that mechanical stress promotes GDF15-induced cancer cell migration through activation of PI3K/Akt and MEK1/Erk1 signaling cascades in pancreatic and brain cancer cell lines, respectively [4, 5]. Based on these findings, we comprehensively profiled mechanical stress-induced signaling cascades that drive the motility of pancreatic cancer cells using a large-scale proteomic assay. Our results elucidate mechanical stress-induced signaling mechanisms and provide novel information to prioritize therapeutic targets for pancreatic cancer metastasis.

METHODS

Cell Lines*:* MIA PaCa-2 cells were purchased from the American Type Culture Collection (ATCC, Manassas, VA, USA) and cultured according to manufacturer's guidelines.

Application of mechanical compression: The application of a defined and controlled compressive solid stress on cancer cells was achieved using a piston with adjustable weight, which was placed on the top of a cell monolayer that was covered with an agarose cushion and placed in a transwell insert. 4.0 mmHg of compressive stress was applied to the cell monolayer. Control cells were covered with an agarose cushion only.

Wound Healing: To characterize migration, a wound healing assay was performed on cancer cells growing in 2% FBS-containing medium by introducing a scratch wound on a cell monolayer[4]. Images were taken at 0 hours and 16 hours post-compression. The cell-free area was quantified using the ImageJ software. Quantification was performed for each condition using the following formula: (Width of the wound at 0 hours – Width of the wound at 24 hours) / (Width of the wound at 0 hours).

Protein Extraction for Reverse Phase Protein Array (RPPA): Pancreatic cancer cells were compressed by 0.0 or 4.0 mmHg in 2%-FBS containing medium for 16 hours and then were washed twice with cold PBS. Cells were then lysed using 150µl of cold lysis buffer. Proteomic analysis using reverse-phase protein arrays (RPPA) was performed at the RPPA core facility (MD Anderson Cancer Center, Houston, TX). For pathway analysis, scores were used to evaluate the activity of the pathways after compression. RPPA data was normalized and grouped by compression (n=3). Pathway scores were calculated as the average sum of expression level of all protein members in each pathway, and then normalized to the uncompressed expression level. Heatmaps for pathways were generated to show the alteration of each protein member. Proteins and cell samples were grouped with a two-way hierarchical clustering based on the column-normalized z-scores. (Only Ras/MAPK heatmap is shown in this submission).

RESULTS

To examine the effect of compression on the migration of pancreatic cancer cells, we performed a scratch wound assay and found that compressed MIA PaCa-2 exhibited increased migratory ability as compared to the uncompressed cells (**Figure 1A**). To also determine whether mechanical compression impacts cell shape after compression, we performed a phalloidin staining and we observed increased stress fibres, filopodia and lamellipodia formation in compressed compared to the uncompressed cells (indicated with white arrows in **Figure 1B**).

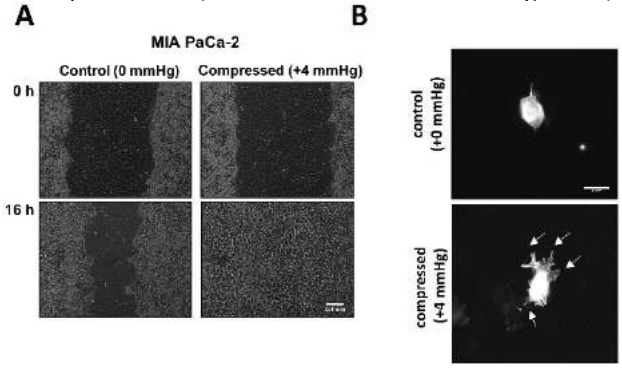

Figure 1. Mechanical stress induced the migration of pancreatic cancer cells. A, Wound healing assay of compressed MIA PaCa-2 cells[4]. Scale bar: 0.1 mm. B, Phalloidin staining of compressed MIA PaCa-2 cancer cells. Scale bar 0.1 mm.

Next, to tease out the signaling pathways that are associated with increased migratory ability of cells caused by mechanical compression, we further analysed MIA PaCa-2 protein extracts using a Reverse Phase Protein Array (RPPA). Pathway score analysis of the RPPA data, that incorporates both positive and negative regulators of signaling pathways, revealed that proteins implicated in cell cycle progression and TSC/mTOR pathway were decreased upon compression. Contrary to that, the PI3K/Akt and Ras/MAPK signaling cascades were activated (**Figure 2A and Figure 2B**). By validating selected RPPA hits in MIA PaCa-2 and PANC-1 pancreatic cancer cells using Western Blotting and by modulating expression levels using inhibitors and siRNAs, we revealed that mechanical stress can activate JNK/ c-Jun and p38 MAPK signaling. We showed that c-Jun and p38 MAPK regulated cell survival and the expression of genes implicated in epithelial-to-mesenchymal transition (EMT), including Slug, Twist and Snail. Moreover, compression can activate HSP27, a stress response element that is downstream of p38 MAPK, and Rac1 and cdc42 that altogether regulate actin cytoskeleton remodeling for the formation of cell protrusions necessary for cell motility. Rac1 and cdc42 can also activate PAK1 to stabilize actin filaments and mediate actomyosin contractility, resulting in enhanced pancreatic cancer cell migration under compression.

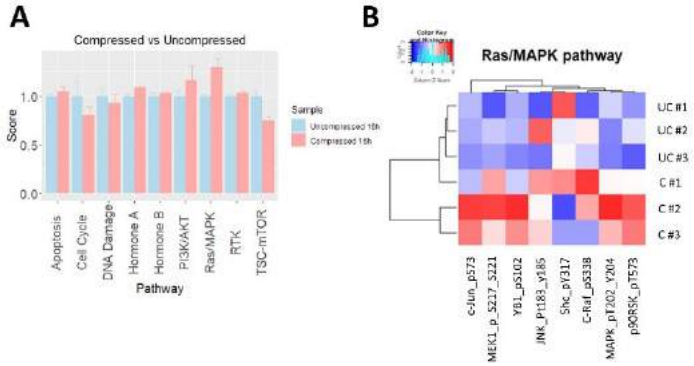

Figure 2. A, Pathway score analysis of proteomic data in MIA PACA-2 cells 16 hours after exposure to 4 mmHg (n=3). B, Heatmap of Ras/MAPK pathway shows the alteration of each pathway member in uncompressed (marked as "UC") and compressed (marked as "C") cells derived from 3 independent experiments. Red shows high protein expression compared to the median and blue shows low protein expression.

DISCUSSION

Although mechanical stress has already been associated with pancreatic tumor progression, little is known about the molecular mechanisms involved. Here, we used for the first-time proteomic profiling to examine signaling pathway adaptation of compressed pancreatic cancer cells and monitor multiple signaling pathways, regulating processes including cell cycle progression, actin cytoskeleton remodelling and migration. Specifically, we revealed that mechanical compression reduced TSC/mTOR pathway activity, while activating the RAS/MAPK signaling pathway to regulate cell motility. The high expression of these pathways in pancreatic tumors could eventually be used as a novel marker for the presence of mechanical forces in the tumor interior. Furthermore, these mechanical stress-induced signaling pathways could be targeted, in combination with conventional treatments, to improve treatment responses in pancreatic tumor patients.

ACKNOWLEDGEMENTS

European Research Council Proof of Concept (ERC-2018-PoC-838414 CancerFingerPrints) to T.S. Startup funds from the Department of Bioengineering (University of Pittsburgh) and National Cancer Institute (R00CA222554) to I.K.Z.

REFERENCES

[1]. Aier, I et al., *Cancer Epidemiol.* **58**, 104-110 (2019).
[2]. Nia, H.T et al., *Science* **370**, eaaz0868 (2020).
[3]. Wagner, E.F. & Nebreda, Á.R. *Nat. Rev. Cancer* **9**, 537-549 (2009).
[4]. Kalli, M. *et al. Sci. Rep.* **9**, 978 (2019).
[5]. Kalli, M. *et al*. *Front. Oncol.* **9**, 992 (2019).

TRACKING OF THE LEFT ATRIAL APPENDAGE MOTION IN TIME RESOLVED CT

Sophia Bäck (1,2), Lilian Henrikson, (1,2), Carl-Johan Carlhäll (1,2), Anders Persson (1,2), Matts Karlsson (2,3), Tino Ebbers (1,2)

(1) Department of Health, Medicine and Caring Sciences, Link□ping University Link□ping, Sweden

(2) Center for Medical Image Science and Visualization (CMIV), Link□ping University Link□ping, Sweden

(3) Department of Management and Engineering, Link□ping university, Link□ping, Sweden

INTRODUCTION

The left atrial appendage (LAA) is an anatomical structure in the left atrium that influences the blood pressure and flow in the left atrium (LA). Its function was long unknown, but recent research suggests that its active contraction and high concentration of atrial natriuretic peptide are important for cardiovascular hemodynamics, thrombogenesis and arrhythmogenesis [1]. The contraction pattern of the LAA seems to vary largely between individuals and is challenging to investigate.

Clinically, the contraction is commonly assessed by measuring the peak velocities of the blood in the LAA orifice with doppler ultrasound, but this method is limited to the measurement of the velocity components along the ultrasound beam and does not provide high quality 3-dimensional information. Alternatively, the blood velocity in the LA can be measured with 4D-flow MRI. Markl et al. measured the blood flow in LA of patients with atrial fibrillation and found lower velocities in patients compared to healthy controls [2].Though they analyzed the general flow in the LA, it is challenging to identify the LAA in 4D flow MRI images.

In recent years, assessment of the cardiac structure and function with time resolved computed tomography (CT) has become more common. Using iodine-based contrast agents, the blood pool in the heart can be distinguishable in CT images. Using modern CT systems, 3D images can be obtained over the cardiac cycle at a relatively low radiation dose. Tracking the motion of the LA and the LAA in CT is challenging. Commonly in time resolved CT, the cardiac motion is reconstructed to 10-20 frames per cardiac cycle. The LAA contracts very quickly and its motion might not be fully captured with this temporal resolution. A few tracking algorithms have been proposed[3], [4],but these have not been evaluated against other measurement modalities.

We aimed to develop and validate a motion tracking algorithm that can capture the quick motion of the LAA, facilitating clinical assessment of LAA motion from CT and possibly LA and LAA hemodynamics using Computational Fluid Dynamics (CFD) simulations, similar to [5]. To validate our algorithm, we compared the motion tracked in time resolved CT images with velocities measured in 4D flow MRI of the same individual.

METHODS

Study Population In this study we included 9 patients that received a clinical coronary CT angiography examination for diagnosis of chest pain. The participants agreed to take part in an additional 4D flow MRI examination. The study was approved by the local ethics board and written informed consent was obtained by all patients.

CT and MRI acquisition The CT images were acquired on a third-generation Siemens dual-source CT scanner (Somatom Force, Siemens Healthineers, Forchheim, Germany) during sinus rhythm and inspiration. The images were reconstructed to 20 temporal phases, equivalent to 0% to 95% of the R-R interval. The in-plane resolution was 0.353×0.353 mm ± 0.035 mm and the slice thickness was 0.5 mm with a 0.25 mm increment.

After the CT examination, 4D flow MRI images were acquired on a clinical 3.0-T Philips Ingenia MRI unit (Phillips Healthcare, Best, the Netherlands) during sinus rhythm and free breathing. The cardiac cycle was reconstructed to 40 phases and the spatial resolution was 2.9×2.9×2.9 mm.

Wall tracking The blood bool was segmented in the 4D CT data using ITK-SNAP (www.itksnap.org) and MeVisLab (www.mevislab.de). Thereafter, motion of the endocardium was tracked from the blood pool surfaces using an algorithm based on the optimal step nonrigid iterative closed point algorithm developed by Amberg et al. [6]. This algorithm deforms a source surface onto a target surface by reducing the distance between the surfaces while keeping the topology of the source. To obtain more accurate tracking of the LA and LAA, these regions were tracked separately, allowing for different tracking settings.

Evaluation To validate this approach, the flows though the LAA orifice and thought the mitral valve (MV) were derived from the registration and from 4D flow MRI measurements. To calculate the mitral valve flow based on the wall tracking, the volume of the ventricle was calculated for each of the 20 phases and then differentiated with

respect to time. Negative volume changes equate to the flow through the mitral valve. The flow thought the LAA orifice was measured similarly, by deriving the volume of the LAA over time.

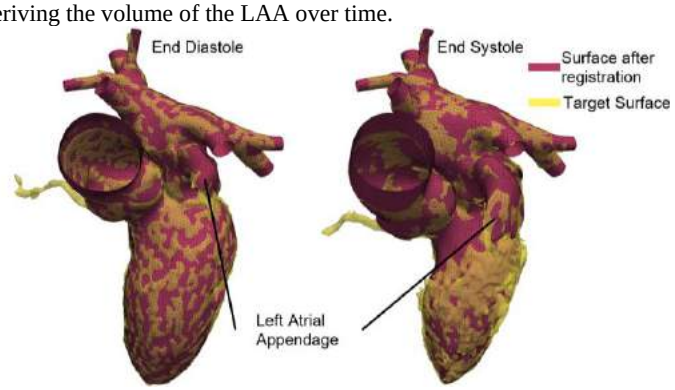

Figure 1: Surface of endocardium after registration and target surface at end diastole and end systole

In the 4D flow MRI images, the mitral valve flow was quantified by tracking the valve over the cardiac cycle and integrating the flow over the mitral valve orifice. Measuring LAA flow from 4D flow MRI was challenging, as the LAA cannot be clearly defined over the whole cardiac cycle. Therefore, the flow rate was measured in three parallel planes, that were set during LAA peak outflow phase and kept at the same position though the cardiac cycle. In every plane the flow over the cardiac cycle was obtained by integrating the flow in a manually drawn region of interest. The flow curves in the LAA orifice were defined by averaging the volume flow from the three planes.

RESULTS

Visual inspection showed a good agreement between the surface of the endocardium after the wall tracking and the target surface, as shown for a typical patient at end diastole and end systole in Figure 1. The average distance between the tracked surface and the target surface for all patients over all time steps was 0.62 mm with a standard deviation of 0.49 mm.

The flow through the mitral valve is characterized by two flow peaks, the first one during early ventricular filling and the second one during the late filling. Both peaks are clearly visible in Figure 2 a). The timing of the peaks is similar in both imaging modalities. The average early diastolic mitral flow was 494.4 ±183.1 ml/s and 283.1 ±67.7 ml/s for CT and MRI, respectively. The average late diastolic mitral flow was 309 ±66.9 ml/s and 283.1 ±67.7 ml/s for CT and MRI, respectively, see Figure 2 b). While the magnitude of the peak flow during late filling was similar, the average peak flow during early filling was 1.74 times higher for CT.

The flow though the LAA orifice calculated from time-resolved CT followed a similar pattern as the mitral valve flow, but with a lower magnitude. This bi-phasic characteristic was less obvious in the in 4D flow MRI, in which the early diastolic peak often not could be recognized. The average late diastolic LAA flow was 40.2 ±17.9 ml/s and 60.8 ±30.2 ml/s for CT and MRI, respectively, see Figure 2 d).

DISCUSSION

We developed a surface-based algorithm to track the LA motion including the LAA from CT data. The results are in good agreement with automatically segmented geometries and results from 4D flow MRI data.

Previous studies [3], [4] have assessed the motion of the LA in CT images, but these have not been validated against other measurements in the same individual. Our algorithm could successfully track the motion even with noisy target surfaces that contained holes.

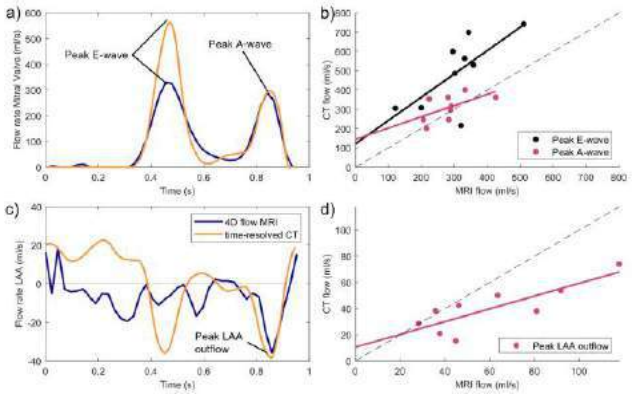

Figure 2 a),c): Flow through Mitral Valve and LAA measured with CT and 4D flow MRI over time for 1 example patient. b),d): linear regression of peak flow for all 9 patients.

The blood flow though the mitral valve showed a similar pattern in both measurements. However, the magnitude of the early wave was higher in the CT measurement than in 4D flow MRI. This could be due to that the MRI data are averaged over many cardiac cycles and synchronized at end-diastole. Fluctuations in the length of the cardiac cycle could lead to less accurate results during early diastole

Similar to Al-Issa et al. [4], there are two peaks in the flow through the LAA orifice measured in CT. The late peak agrees well between CT and MRI, while the early peak is only apparent in the CT measurement. Besides the temporal averaging of the MRI data, another reason for the difference could be that the signal-to-noise ratio for MRI is relatively low in the range of LAA outflow velocities and therefore the early wave might not be apparent in the MRI data.

Our study is limited by the relatively small group of 9 individuals. In the future, it would be beneficial to include more individuals and analyze the blood flow with respect to different cardiac pathologies such as atrial fibrillation and heart failure. Additionally, we noted a trend for individuals with high LAA contraction at late diastole, in which the velocities in MRI where slightly higher than in CT. This might indicate that the temporal resolution of the time-resolved CT is not fully sufficient to capture the complete motion of the LAA, leading to an overestimation of the minimal LAA volume and an underestimation of peak outflow rates. Future developments in CT technology leading to higher temporal resolutions could improve this disagreement. However, from a clinical perspective, accurate assessment of LAA in patients with moderate and weak LAA contraction is most interesting, since this might promote thrombus formation.

In conclusion, our surface-based algorithm could successfully track the endocardium and the wall of the LAA. The resulting LAA outflow was in good agreement to flow rates measured in the same individual with 4D flow MRI.

ACKNOWLEDGEMENTS

The authors acknowledge funding from the Swedish Research Council, the Swedish Heart Lung Foundation, Vinnova and the County Council of Östergotland.

REFERENCES

[1] Karim, N et al., *Europace*, vol. 22, no. 1, pp. 5–18, 2020.
[2] Markl, M. et al., *J. Cardiovasc. Magn. Reson*., 18 O90, 2016.
[3] Otani, T. et al., *Comput. Biol. Med*., 114:103454, 2019.
[4] Al-Issa, A et al., *Eur. Heart J. Cardiovasc. Imaging*, 17:7:788–796, 2016.
[5] Lantz, J. et al., *Radiology*, 289:1:51–58,2018.
[6] Amberg, B. et al., *IEEE Conference on Computer Vision and Pattern Recognition, Minneapolis*, MN, USA, 2007

POTENTIAL BIOFLUIDIC AND GEOMETRICAL BIOMARKERS OF THORACIC AORTIC ANEURYSM OUTCOME IN THE FBLN4^{SMKO} MOUSE

Marisa S. Bazzi (1), Ramin Balouchzadeh (2), Shawn N. Pavey (2), Jessica E. Wagenseil (2), Victor H. Barocas (3)

(1) Department of Chemical Engineering and Material Science
University of Minnesota
Minneapolis, MN, USA

(2) Department of Mechanical Engineering and Materials Science
Washington University
St. Louis, MO, USA

(3) Department of Biomedical Engineering
University of Minnesota
Minneapolis, MN, USA

INTRODUCTION

Thoracic aortic aneurysms (TAAs) are bulging enlargements of the aorta. They affect approximately 15,000 people in the US per year and can be fatal in 80% of the cases when ruptured[1]. Surgical intervention criteria are defined primarily in terms of the maximum diameter and growth rate, but it has been shown that about 60% of the patients present complications before the intervention criteria are reached[2].

Formation and growth of TAAs are often associated with genetic connective tissue disorders (CTDs), which are mutations that affect extracellular matrix (ECM) proteins[3]. Similarly, blood flow dynamics features, such as altered luminal pressure, wall shear stress, and intramural stress, have also been linked to the disease[4]. Further, it has been found recently that the aortic tortuosity index (ATI) correlates with the disease outcome[5]. The long life cycle of the human and the need to protect patients place limits on our ability to study aneurysm growth and failure mechanisms in humans. Mouse models of CTD provide an opportunity to explore the in-vivo progression of aneurysms.

In this study, we used blood flow dynamics features to explore better predictive indicators of aneurysm outcomes. To perform the study, we used a combination of mouse-specific fluid-structure interaction (FSI) models and aortic shape measurements to characterize aortic aneurysms in a CTD mouse model, and we compared the various measurements and calculations with the lifespan of the individual mice.

METHODS

Mouse models: Mouse models with TAA caused by deletion of the ECM fibulin-4 gene in smooth muscle cells (Fbln4^{SMKO}) were used. TAA growth in each animal was monitored throughout the early disease stages by magnetic resonance angiography (MRA). The scans were collected at two, four, and six months of age. After the mice died naturally or were sacrificed at least 24 months of age, biaxial mechanical testing was performed to obtain the material properties of the aortic tissues. Table 1 shows the results of the biaxial measurements, as well as wall thickness, lifespan, and ATI for each mouse.

Table 1. Mouse-specific parameters.

Mouse	Elastic modulus [MPa]	Wall thickness [mm]	Lifespan [months]	ATI
1	2.23	0.129	17.8	45.34
2	1.16	0.122	18.2	59.53
3	1.22	0.109	22.4	37.87
4	0.88	0.112	21.9	53.57
5	1.59	0.110	25.1*	39.86
6	0.93	0.123	24.9*	38.78
7	0.64	0.119	24.9*	22.80

* Sacrificed after reaching at least 24 months of age

FSI simulations: MRA images of mice at 6 months of age were used to generate mouse-specific models for the FSI simulation. Wall thickness was treated as constant over the length of the aorta and based on experimental measurement as shown in Table 1. The aortic wall was described as neo-Hookean and incompressible, with each mouse specified based on the elastic modulus measured post mortem.

Blood was treated as Newtonian with a viscosity of 3.5 cP. A waveform from an earlier mouse study[6] was used as the inlet boundary condition and assumed to be the same for all mice. For the outlet arteries, windkessel models with values based on literature[6] were used as boundary conditions for all mice. Simulations were performed for five cardiac cycles using SimVascular[7] at the Minnesota Supercomputer Institute (MSI).

Data Analysis and Statistics: A Tobit model[8] was used to analyze the data assuming linear effects with lifespan data censored to a maximum value of 25 months (i.e., the three mice that were sacrificed were specified to have a lifespan of at least 25 months). A pseudo-r^2 estimate[9] was used to assess goodness-of-fit for each Tobit model fit.

RESULTS

We performed FSI simulation for seven Fbln4^{SMKO} mice all at 6-months of age, and at different stages of aneurysm formation. Figure 1 shows the geometry and von Mises stress distribution at peak systole for each aortic model. High-stress regions are concentrated in the ascending aorta, close to the branches for all the models.

Using the results obtained from the simulations, we investigated the correlation between mouse lifespan and the features of the blood flow dynamics. Figure 2 shows the pseudo-r^2 correlation matrix for results from the FSI simulation and experimental measurements. Red circles highlight the parameters that have the highest correlation with mice lifespan (LS). Among those, oscillatory shear index (OSI) shows a very high value (r^2=0.95), suggesting it is the best parameter to be used as a predictor of the outcome of an aortic aneurysm in these mice. Surprisingly, the calculated OSI correlated *positively* with lifespan.

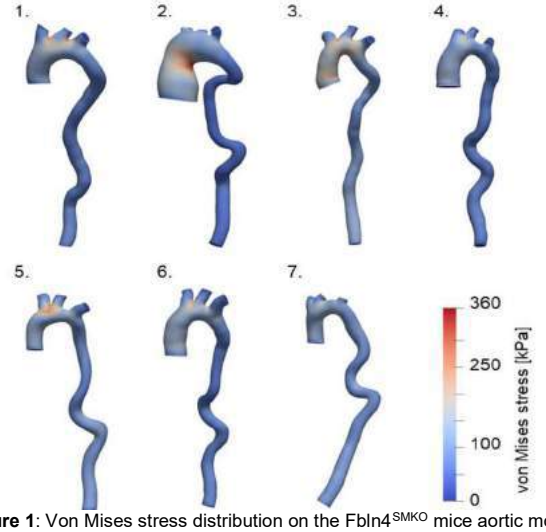

Figure 1: Von Mises stress distribution on the Fbln4^{SMKO} mice aortic models.

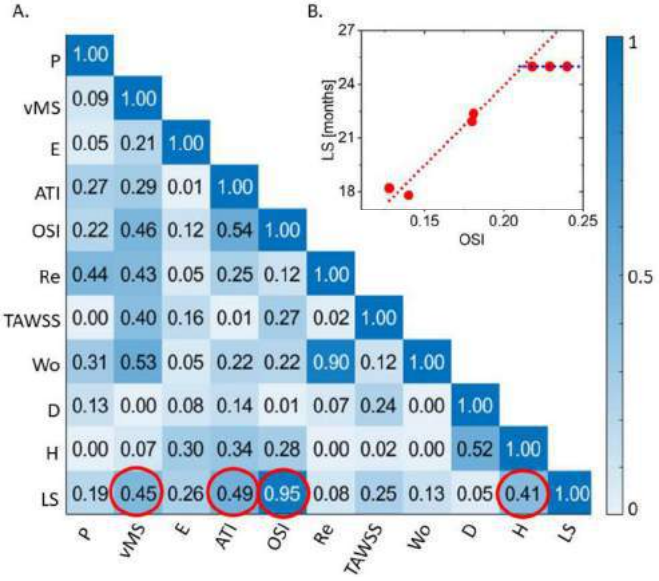

Figure 2: A) Correlation matrix for maximum luminal pressure (P), maximum von Mises stress (vMS), maximum velocity (V), elastic modulus (E), aortic tortuosity index (ATI), oscillatory shear index (OSI), Reynolds number (Re), time averaged wall shear stress (TAWSS), Womersley number (Wo), maximum aortic diameter (D), maximum aortic thickness (H), and lifespan (LS). Red circles highlight the parameters with high correlation with LS. B) Correlation plot between LS and OSI from Tobit model. Blue line represents the maximum value of the censored data.

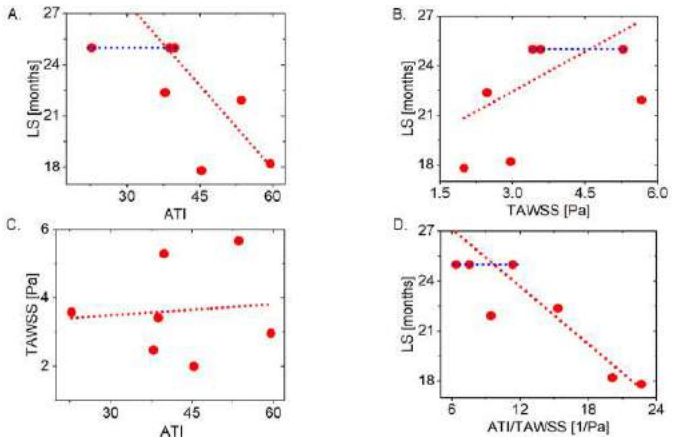

Figure 3: Correlation plots for **A)** LS and ATI, **B)** LS and TAWSS, **C)** TAWSS and ATI and **D)** LS and the ratio of ATI and TAWSS. Solid circles are the measurements for each one of models, the dashed line is the linear fitting from Tobit model, and blue line represents the maximum value the censored data.

Additionally, we notice that extra information could be collected by combining ATI and TAWSS: both have a fair correlation ($r^2 \geq 0.25$) with LS, as shown in Figs. 3A and 3B, but are largely uncorrelated with each other ($r^2 \leq 0.01$, Fig. 3C), suggesting that a combination of the two could provide additional information. The ratio ATI/TAWSS shows a high negative correlation with LS ($r^2 = 0.79$, Fig. 3D).

DISCUSSION

We created seven aortic models for Fbln4^{SMKO} mice at the age of 6 months. The mice were at different stages of the aneurysm formation and exhibited different degrees of aortic tortuosity. Mouse-specific material properties and wall thickness were combined with generic boundary conditions for blood flow in the FSI simulations. Results for von Mises stress distribution along the wall show a high-stress region concentrated at the ascending aorta for all the models.

Mouse lifespan was correlated to vMS, ATI, H, and especially OSI, suggesting that OSI estimated from patient-specific flow simulations could serve as a biomarker for aneurysm outcome. The combination of ATI (a geometric measure) and TAWSS (a biofluids measure) also showed a high r^2, suggesting that a hybrid measurement may be used to improve the prediction of aneurysm outcome.

This was a small study (n = 7) of only one mouse model. Further study is needed to determine which, if any, of the effects observed here are general, how those effects change with different CTDs, and how the ideas suggested can be extrapolated to humans. Nevertheless, as it becomes more and more possible to acquire geometric and mechanical data from patients[10], multi-physics, multi-information models will provide new insight into aneurysm disease and its outcomes.

ACKNOWLEDGEMENTS

This work was supported by NIH U01HL139471 and by the Marfan Foundation. Special thanks to Dr. Vijay Vedula from SimVascular for his help. We appreciate the support from the Minnesota Supercomputing Institute (MSI) at the University of Minnesota.

References

1. Zhou, B. *et al.* W *Lancet* **389**, 37–55.
2. Pape, L. A. *et al. Circulation* **116**, 1120–1127 (2007).
3. Kim, J., *et al. Am. J. Physiol. Heart Circ. Physiol.* **309**, H103.
4. Howard, D. P. J. *et al. Br. J. Surg.* **102**, 907–915.
5. Franken, R. *et al. Int. J. Cardiol.* **194**, 7–12 (2015).
6. Cuomo, F., *et al.*. *Ann. Biomed. Eng.* **43**, 1555–1570 (2015).
7. Lan, H. *et al. J. Biomech. Eng.* **140**, 1–11 (2018).
8. Tobin, B. Y. J. E. *Econometrica* **26**, 24–36 (1985).
9. Veall, M. & *et al.*. *Oxf. Bull. Econ. Stat.* **56**, 485–99 (1994).
10. Farzaneh, S., *et al.*. *Ann. Biomed. Eng.* **47**, 1038–1050 (2019).

UNRAVELING THE ETIOLOGY OF DISCRETE SUBAORTIC STENOSIS: FOCUS ON HEMODYNAMICS

Jason A. Shar (1), Sundeep G. Keswani (2), K. Jane Grande-Allen (3), Philippe Sucosky (4)

(1) Mechanical and Materials Engineering
Wright State University
Dayton, Ohio, United States

(2) Division of Pediatric Surgery
Texas Children's Hospital
Houston, Texas, United States

(3) Department of Bioengineering,
Rice University,
Houston, Texas, United States

(4) Department of Mechanical Engineering,
Kennesaw State University,
Marietta, Georgia, United States

INTRODUCTION

Discrete subaortic stenosis (DSS) is an obstructive cardiac disease characterized by the formation of a thin fibromuscular ring of tissue in the left ventricular (LV) outflow tract (LVOT). Risk factors promoting DSS include morphological LVOT abnormalities such as a steep aortoseptal angle (angle between the long-axis of the aorta and the septal wall), subphysiologic aortic annulus diameter, and large aortic valve-mitral valve separation distance [1]. Without intervention, the lesion can lead to an array of secondary pathologies including aortic regurgitation, LV hypertrophy, infective endocarditis, and death [2]. Treatment consists of invasive membrane resection, but many patients require additional surgeries due to the lesion's high recurrence rate (8-34%) [2].

Although the etiology of DSS is unknown, the strong association between DSS and morphological LVOT abnormalities suggests that the lesion could result from a biological cascade initiated by endocardial cells and triggered by flow alterations in the LVOT [2]. The assessment of this hypothetical pathway requires elucidating the LV wall shear stress (WSS) abnormalities caused by the aberrant LVOT anatomy. Therefore, the aim of this study was to utilize 3D computational fluid dynamics to quantify the LVOT WSS environment in representative LV models reconstructed from patient data.

METHODS

LV images were obtained from a healthy 21-year-old adult female volunteer using a 3T MRI scanner (GE Medical Systems MR 750w). 20 total temporal phases per cardiac cycle were acquired within the short-axis plane with a slice thickness of 8 mm. Manual segmentation and 3D reconstruction were done using Segment v3.0 R7568 [3] to generate a template LV geometry (Fig. 1), and intermediate displacements between frames were generated using cubic spline interpolation.

Echocardiographic data taken from recent DSS resection patients (DSS-prone; n=40) and healthy individuals (control; n=40) between May 1997 and June 2020 at Texas Children's Hospital were used to generate additional LV geometries. Variations in LV and LVOT anatomy were parametrized by segregating the patient data into four age ranges (1-2 yrs., 3-5 yrs., 6-8 yrs., and >9 yrs.; n=8 total cases), from which representative LV geometries were generated (Fig. 1). Briefly, the LV template was first globally scaled to match patient-averaged blood volumes, and the LVOT anatomy was recreated using patient-averaged aortic/mitral annuli dimensions and aortoseptal angles. Finally, the averaged location of DSS development was identified and

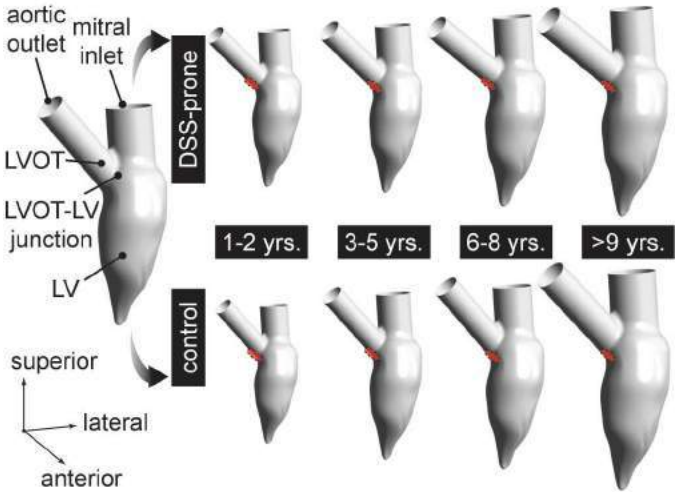

Figure 1. Age-matched representative LV geometrical models with averaged location of DSS development (highlighted in red).

specified as a region of interest in both study groups (Fig. 1).

LV motion was implemented via a one-way fluid-structure interaction (FSI) technique in ANSYS 2019 R3 [2]. Following a mesh sensitivity analysis, each fluid domain was meshed with a characteristic cell length of 0.8 mm and a near-wall resolution of 10 μm. The cycle-averaged LV WSS environments were characterized in terms of the temporal shear magnitude (TSM, cycle-averaged WSS magnitude) and oscillatory shear index (OSI, quantifies WSS oscillatory nature; 0: unidirectional, 0.5: bidirectional). The WSS topological skeleton was also computed to map the complex features of the WSS vector field [4].

RESULTS

Global blood flow characteristics between the DSS-prone and control groups were similar despite differences in local LVOT geometry and global hemodynamic parameters across the age groups. Interventricular filling generated an asymmetric vortex ring during diastole, which redirected blood flow towards the LVOT and out the LV during systolep. Systolic volume-averaged velocity and vorticity magnitudes, averaged among all age ranges, indicated no substantial differences between the DSS-prone and control groups (8.4% and 1.7% difference, respectively).

Cycle-Averaged Hemodynamic Stress Characteristics

Pair-wise comparisons of the global cycle-averaged hemodynamic stress spatial distributions did not substantially vary between the DSS-prone and control groups; however, local value differences were detected primarily in the LVOT. Regions of high TSM were observed at the LVOT-LV junction, which were augmented on the LVOT anterior-inferior area in the DSS-prone anatomies (Fig. 2). Conversely, OSI values captured at the LVOT-LV junction were uniformly low, highlighting strong unidirectional flow behavior leading into the outflow tract. A region of high OSI value, indicating flow recirculation, was detected downstream on the anterior LVOT surface, which trailed further into the LVOT in the DSS-prone models.

The cycle-averaged WSS topological skeleton was computed by taking the divergence of the normalized cycle-averaged WSS vector field (WSSdiv_{Norm}) to characterize fixed points (i.e., locations where the WSS vector field disappears) and the WSS contraction/expansion regions that connect them (contraction: $\mathrm{WSSdiv}_{Norm} < 0$; expansion: $\mathrm{WSSdiv}_{Norm} > 0$) [4]. All models exhibited fixed points primarily on the superior LVOT-LV junction, with the DSS-prone group revealing additional points lining the anterior-inferior areas of the junction (Fig. 2). Both groups predicted concentric regions of WSS expansion with similar normalized magnitudes upstream the LVOT-LV junction. Though all models displayed similar concentric regions of WSS contraction at the LVOT-LV junction, the DSS-prone LVs predicted stronger WSS contraction on the anterior-inferior region of the junction, which colocalized with areas of high TSM (> 80th percentile).

WSS Characteristics in Regions Prone to DSS

The averaged site of lesion development showed substantial differences in WSS characteristics between the study groups. When compared against the age-matched controls, a threshold was observed in the DSS-prone LVs in which patients younger than 5 years exhibited lower WSS magnitudes (up to 6.5 % decrease in TSM vs. control) and older than 6 years exhibited WSS overloads (>30% increase in TSM vs. control). Although no such threshold was identified when evaluating WSSdiv_{Norm} , increased age was associated with stronger WSS contraction in both DSS-prone and control LVs. Further, age-matched comparison indicated that DSS-prone LVs generated substantial decreases in WSSdiv_{Norm} especially in the youngest age range (up to 11.2-fold decrease vs. age-matched control), suggesting strong WSS luminal contraction. Despite this, multidirectionality characteristics between both study groups were similar (less than 0.05-point difference in OSI between age-matched LVs), and indicated strong pulsatile/unidirectional flow overall (OSI <0.2).

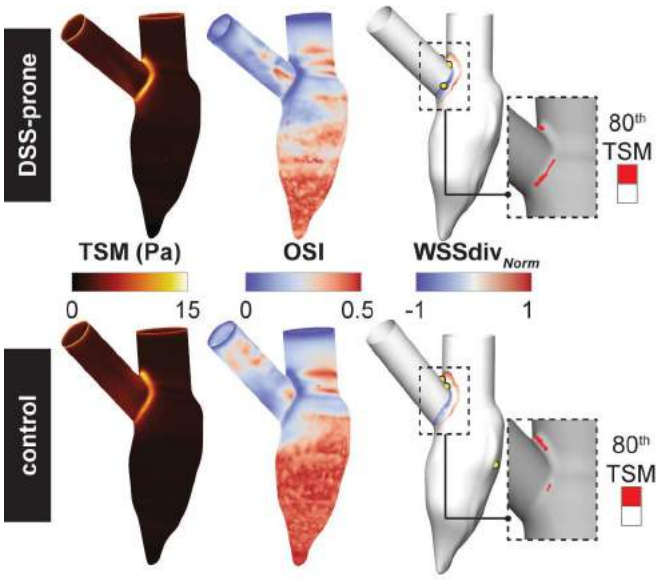

Figure 2. 3D contour mapping on the > 9 yrs. LV model (yellow dots: saddle points). Insets denote colocalized regions of high TSM (> 80th percentile) and WSS contraction ($\mathrm{WSSdiv}_{Norm} < 0$).

DISCUSSION

3D simulations of representative LV models with realistic wall motion were performed to assess the effects of anatomic variation on blood flow patterns and hemodynamic stresses. Though predicted hemodynamics did not substantially vary between the study groups, small changes in LVOT morphology heavily impacted the WSS environment and resulted in WSS overloads and increased local contraction action in regions susceptible to DSS development. Consistent with the literature which suggests such mechanistic impacts could promote lesion formation, the results, therefore, provide compelling evidence for (1) the existence of a mechano-etiology for DSS, and (2) the potential role played by abnormal WSS colocalizations in DSS lesion development.

Although exclusion of the cardiac valves is a limitation, this study demonstrates the existence of significant WSS abnormalities in LVs prone to DSS formation, which may play a key role in the pathogenesis of the lesion. Further biological studies are needed to assess the effects of such abnormalities at the tissue and cellular levels.

ACKNOWLEDGEMENTS

This work was supported in part by the National Institutes of Health (NIH) grant R01HL140305. The authors would like to acknowledge Dr. Roldán-Alzate and Asela Liu for their assistance in acquiring the patient data used in this study.

REFERENCES

[1] Shar, J et al., *Front. Bioeng. Biotechnol.,* 8: 1-14, 2020.
[2] Kleinert, S et al., *J. American College Cardio*, 22: 1501-1508, 1993
[3] Heiberg, E et al., *BMC Medical Imaging*, 10:1-13, 2010.
[4] Mazzi, V et al., *Biomech Model in Mechano,*19:1403-1423, 2019

SB³C2021
Summer Biomechanics, Bioengineering and Biotransport Conference
June 14-18, Virtual

AN EVALUATION OF INTERFACE PRESSURE AND SHEAR FORCE PATTERNS IN INJURY PRONE REGIONS WHILE SEATED IN AN ARTICULATING CHAIR

Justin Scott and Tamara Reid Bush PhD

Department of Mechanical Engineering
Michigan State University
East Lansing, MI, USA

INTRODUCTION

Pressure Injuries (PIs) are soft tissue wounds that affect an enormous number of wheelchair users, especially those with spinal cord injuries (SCIs). This population has an 80% lifetime incidence [1]. Not only are PIs prevalent, but treatment costs $35,000 on average [2]. As such, the United States spends $11 billion annually to treat them [3]. It is imperative to reduce PI occurrence to improve quality of life and decrease the societal financial burden.

The buttocks and lower back are regions of the body that are especially prone to PIs. This is due to large interface loads, both normal and shear, while seated. Around half of PIs occur in the buttocks or lower back, and thus, prevention efforts have focused on these regions [4]. In particular, wheelchairs include back recline and whole-body tilt to reduce pressure on the buttocks and lower back. Unfortunately, results are inconclusive regarding the effectiveness of these approaches, despite being the most used pressure relief positions [5]. PIs in the buttocks and lower back have persisted to be a common medical issue.

Determining effective PI prevention strategies often includes modeling of PI prone regions. Finite element models connect external loads to tissue stresses, and ultimately to PI formation. However, many finite element models used to study PI formation in wheelchair users relied on inputs from able-bodied individuals [6]. As wheelchair users experience larger external loads while seated relative to able-bodied individuals, load data from wheelchair users are needed to create more representative models [7].

Therefore, the goals of this work were to design an accessible articulating chair and to collect data from both able-bodied individuals and wheelchair users that 1) evaluate back recline and seat pan tilt for their effectiveness in reducing normal interface pressure in the buttocks and lower back, and 2) evaluate a custom nylon cushion cover for its ability to reduce shear interface load on the buttocks while seated.

METHODS

30 individuals volunteered for this study (IRB #15-889). 20 able-bodied individuals (10 male, 10 female) and 10 male wheelchair users participated. An articulating chair was built with independently rotating seat pan and chair back. Thorax and pelvis supports were mounted on the back (Fig. 1). The seat pan, pelvis, and thorax surfaces were mounted on six-axis load cells and covered by pressure mats.

Force and interface pressure data were obtained in 9 seated positions for all participants. Positions were described by **all the combinations** of back recline angles and seat pan tilt angles described in Table 1. Recline and seat pan tilt were the chair back's and seat pan's angles from the vertical and horizontal, respectively. Whole-body tilt positions were those with both nonzero back recline and seat pan tilt. Interface pressure and force data were collected in each position with two cushion covers on the seat pan. One was a standard vinyl cover, while the second was a custom cover constructed from two layers of nylon fabric designed to reduce shear.

Pressure data were then segmented by region of the body. The inferior third of the back pressure mat was considered the lower back, and the posterior half of the seat pan pressure mat was considered the buttocks (Fig. 1). The maximum pressure recorded in each of these regions is reported in the results.

A three-way repeated measures ANOVA and subsequent Tukey tests were used to determine the effects of back recline and seat pan tilt, and group differences on the buttocks and lower back on maximum pressures of able-bodied individuals and wheelchair users. A two-way repeated measures ANOVA and subsequent Tukey tests were used to determine the effects of back recline and inter-group differences in shear force on the buttocks.

Table 1. Angles of rotation for chair supports in all positions, given in degrees

Back Recline	Seat Pan Tilt
0°	0°
10°	15°
20°	30°

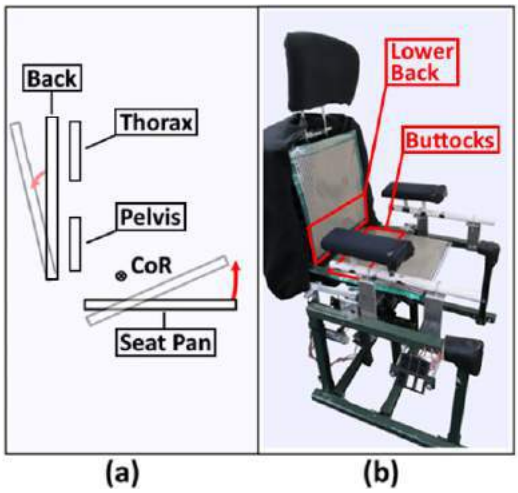

Figure 1. a) Articulating chair schematic, where seat pan and chair back rotate about point 'CoR' b) pressure mats attached to chair with regions of interest in red boxes

RESULTS

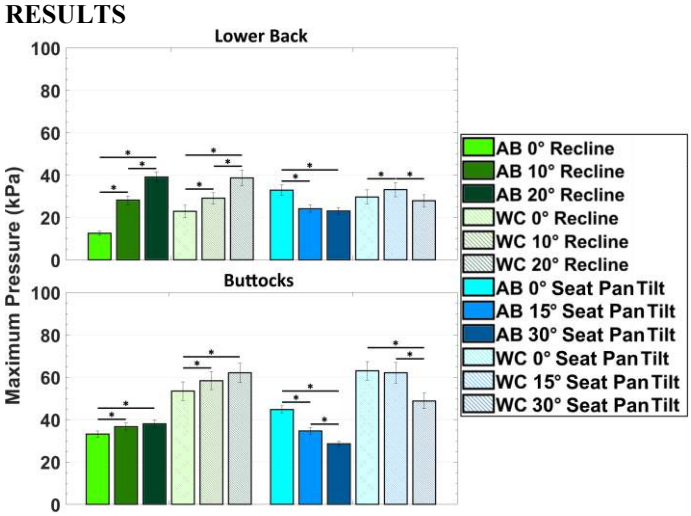

Figure 2. Average maximum interface pressure in the lower back (top) and buttocks (bottom) regions for each level of each articulation. Able-bodied (AB) participants are darker bars, and wheelchair users (WC) are light bars. In general, pressures on both regions increased with increased recline and decreased with seat pan tilt. Significant differences are indicated by asterisks (*)

Normal interface pressure data in the lower back and buttocks are presented in Figure 2 for both able-bodied participants and wheelchair users. Data are shown for every level of recline and seat pan tilt. Both chair articulations and wheelchair use were found to affect maximum normal pressures. The normal pressure data indicated that recline increased the maximum normal pressure in the lower back and buttocks of both groups, while seat pan tilt decreased it. The maximum pressures in the buttocks of the wheelchair users were significantly larger than the maximum pressures of the able-bodied group, but there were no significant inter-group differences in the lower back.

A majority of the effects of recline angle, cushion cover, and group on shear force were significant. Shear force on the seat pan increased with recline angle in both groups regardless of cover. Overall, the custom nylon cover reduced shear force on the seat pan relative to the vinyl cover. The nylon cover reduced the shear force on the seat pan by approximately 10% for all back recline angles for both groups, except for the 0° recline position for wheelchair users. Lastly, wheelchair users tended to have higher shear forces than able-bodied individuals, but there were no significant differences between groups ($p = .069$).

DISCUSSION

This project characterized normal pressure and shear force patterns in PI prone regions of seated individuals across several seated positions and with two cushion covers. Both wheelchair users and able-bodied participants were included, and common pressure relieving positions, recline and whole-body tilt, were tested as well as isolated seat pan tilt.

The primary goal of this work was to assess the efficacy of different seated positions at reducing interface pressure in PI prone regions. Changes in seated position affected the normal pressure and shear force patterns in all participants. Of particular importance was the finding that increasing recline angle increased both the normal pressure and shear force in the buttocks region of the seat pan. This is important because recline is the most common pressure reducing position in wheelchair users, but our results do not support its use [5]. Both normal pressure and shear force are associated with the formation of PIs; and therefore, another chair articulation could be more effective at PI prevention. As whole-body tilt was a combination of back recline and seat pan tilt, it did not have a definitive effect on the maximum pressure in the lower back or buttocks. Instead, seat pan tilt alone was actually found to decrease the maximum normal pressure on the buttocks and lower back and thus shows potential as a PI prevention strategy. Though trends in shear force relative to seat pan tilt have yet to be established, it has shown promise as a pressure reducing articulation that can help prevent PIs.

The custom nylon cushion cover reduced shear force on the seat pan, providing a non-repositioning based option for reducing factors associate with PI risk. The nylon cover may be used in conjunction with other PI prevention strategies, such as seated repositioning or specialized cushions, to further reduce the risk of PI formation.

The data and trends observed in this study can be used to inform processes, such as design of components and model development, in the future. Wheelchairs can be designed with an isolated seat pan rotation to allow individuals to relieve the pressure on their buttocks and lower backs. Cushion covers can be designed to minimize shear force on the buttocks. Moreover, since these data include interface pressure data from wheelchair users, they can be used to model how seated repositioning affects the tissue stresses in wheelchair users in more representative models.

ACKNOWLEDGEMENTS

Funding for this project was provided by NSF grant CBET-1603646

REFERENCES

[1] Hubli, M., et al., *Spinal Cord.*, 2020.
[2] Chan, B., et al., *J. Wound Care*, 26, 2017.
[3] Sen, C., et al., *Wound Rep & Reg*, 17, 2009.
[4] Boyko, T., et al., *Adv Wound Care*, 7, 2018.
[5] Ding, D., et al., *J. Reh. Res.*, 45, 2008.
[6] Wagnac, E., et al., *IEEE on Biomed Eng.*, 55, 2008.
[7] Hobson, D., *J Rehab Research*, 29, 1992.

SB³C2021
Summer Biomechanics, Bioengineering and Biotransport Conference
June 14-18, Virtual

WALL SHEAR STRESS TOPOLOGICAL SKELETON ANALYSIS IN IMAGE-BASED STENTED CORONARY BIFURCATION MODELS

Valentina Mazzi (1), Claudio Chiastra (1), Diego Gallo (1), Umberto Morbiducci (1)

(1) Polito[BIO]Med Lab, Department of
Mechanical and Aerospace Engineering
Politecnico di Torino
Turin, Italy

INTRODUCTION

Coronary stents are tube-shaped devices expanded inside an atherosclerotic coronary artery aiming to restore the correct blood flow to the heart. In studying the hemodynamics in stented coronary arteries, a large body of literature has highlighted that local blood flow disturbances may play a key role in the pathophysiological trajectories leading to stent failure, e.g., in-stent restenosis [1,2]. Notwithstanding the growing research interest in stented artery hemodynamic features as predictors of stent failure, how local hemodynamics influence flow-related processes leading to in-stent restenosis is still not completely understood.

In this context, to improve and extent the current understanding of the association between local hemodynamics and vascular diseases, a marked interest recently has emerged on Wall Shear Stress (WSS) vector field topological skeleton, composed by fixed points and their connections, called stable/unstable manifolds [3,4]. A fixed point is a focal point where the WSS vanishes, and unstable/stable manifolds are contraction/expansion regions linking fixed points [4]. Such an interest arises from the ability of WSS topological skeleton features to reflect cardiovascular complexity, with direct links to near-wall flow stagnation, separation, and recirculation, flow features associated with in-stent restenosis in coronary arteries [3].

The present study explores the WSS topological skeleton features in image-based computational fluid dynamics (CFD) stented coronary artery models replicating the complete clinical procedure of stent implantation performed in clinical practice [2]. The final aim is to investigate the possible involvement of WSS topological skeleton features in the processes leading to stent failure. To do that, a recently proposed Eulerian-based method for the analysis of the topological skeleton of the WSS vector field [4] is applied.

METHODS

Computational hemodynamics. The two cases (i.e., CASE A and B) of pathologic Left Anterior Descending (LAD) artery with bifurcations treated with the provisional stenting technique considered here have been already partially presented elsewhere [2]. In CASE A, a Xience Prime stent by Abbott Vascular (nominal diameter of 3 mm, length of 28 mm and strut thickness of 81 μm), was implanted. In CASE B, two Endeavor Resolute stents by Medtronic (nominal diameter of 2.75 mm, length of 15 mm and strut thickness of 91 μm) were implanted. Pre-operative vessels were reconstructed combining conventional angiography and computed tomography angiography data [2], and structural finite element analyses replicating the clinical stenting procedures were used to obtain the post-operative, stented fluid domains [2]. A hybrid discretization strategy using both tetrahedral and hexahedral elements was adopted [2]. Transient CFD simulations were performed using a finite-volume based code, applying a pulsatile flow waveform representative of the human LAD as inflow boundary condition. Additionally, two transient simulations in the two non-stented geometries were performed. Exhaustive details on the computational settings are provided elsewhere [2].

WSS topological skeleton. The WSS topological skeleton analysis was performed by considering a recently proposed Eulerian-based method [4]. Briefly, based on Volume Contraction theory, it has been demonstrated that the divergence of the normalized WSS vector field can be used to easily identify the connections between WSS fixed points, i.e., WSS manifolds [4]:

$$DIV_W = \nabla \cdot \left(\frac{\boldsymbol{\tau}}{\|\boldsymbol{\tau}\|_2}\right) = \nabla \cdot (\boldsymbol{\tau}_u) \quad (1)$$

where $\boldsymbol{\tau}_u$ is the WSS unit vector. Technically, DIV_W negative values identify *contraction regions* approximating *attracting manifolds*, while positive values identify *expansion regions* approximating *repelling*

manifolds. To complete the WSS topological skeleton analysis, WSS fixed points were identified and classified by computing Poincaré index and eigenvalues of the Jacobian matrix respectively, according to the scheme proposed in [4].

In addition, a quantity based on WSS divergence, named Topological Shear Variation Index (*TSVI*) [5], i.e., the root mean square deviation of the divergence of the normalized WSS with respect to its average over the cardiac cycle:

$$TSVI = \left\{\frac{1}{\mathrm{T}}\int_0^{\mathrm{T}}\left[\nabla\cdot(\boldsymbol{\tau}_u) - \overline{\nabla\cdot(\boldsymbol{\tau}_u)}\right]^2\ dt\right\}^{1/2} \qquad (2)$$

where T is the cardiac cycle duration, was here adopted. Roughly speaking, $TSVI$ measures the local amount of variation in WSS contraction/expansion action exerted along the cardiac cycle on Endothelial Cells (ECs) lining the luminal surface of a vessel.

RESULTS

The cycle-average WSS topological skeleton and the $TSVI$ distribution along the luminal surface for stented CASE A and B are displayed in Figures 1 and 2, respectively. In both cases, WSS fixed points were mostly located at the luminal surface in correspondence with stent peaks. Moreover, WSS fixed points were located at the luminal surface close to all strut connectors in CASE A (Figure 1) and in the overlapping region between the two stents in CASE B (Figure 2). Both stented cases were characterized by WSS contraction regions, identified by negative DIV_W values, located at immediately upstream struts regions and WSS expansions regions, identified by positive DIV_W values, located at immediately downstream struts regions. Interestingly, a completely reverse DIV_W distribution can be observed in the stent malapposition region for CASE A (Figure 1) and in the overlapping zone between two stents for CASE B (Figure 2).

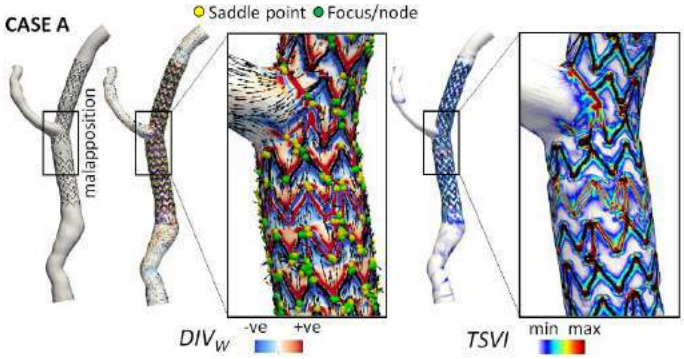

Figure 1: Cycle-average WSS topological skeleton and *TSVI* distribution on the luminal surface for CASE A with stent. Regions where the stent struts are in contact with the wall are black colored.

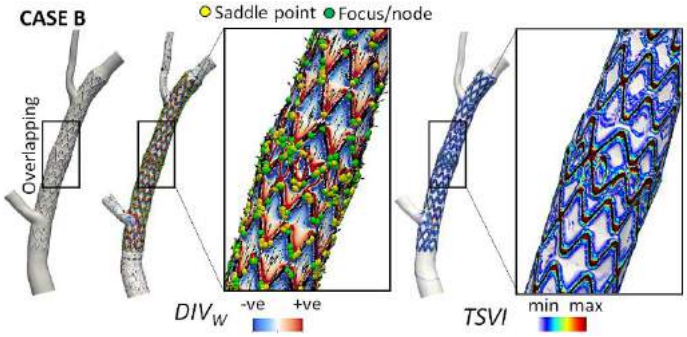

Figure 2: Cycle-average WSS topological skeleton and *TSVI* distribution on the luminal surface for CASE B with stent. Regions where the stent struts are in contact with the wall are black colored.

TSVI maps highlighted that marked variations in the WSS contraction/expansion action exerted on the endothelium along the cardiac cycle were mainly located at the luminal surface in correspondence with stent peaks and close to all the struts in both models. The highest *TSVI* values were located at the bifurcation, in the stent malapposition region and close to stent connectors for CASE A (Figure 1), and at the stents overlapping region for CASE B (Figure 2).

To appreciate the hemodynamic impact of the stenting procedures, the cycle-average WSS topological skeleton and the *TSVI* distribution along the luminal surface of the non-stented models are displayed in Figure 3. In non-stented models WSS saddle points, WSS contraction/expansion regions and high *TSVI* values were located only at the bifurcation regions, and in the proximal region CASE A, where the vessel presents marked curvature and tortuosity.

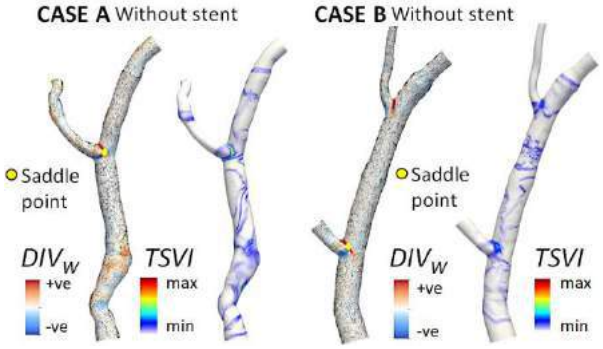

Figure 3: Cycle-average WSS topological skeleton and *TSVI* distribution on the luminal surface for CASE A and for CASE B without the presence of stent.

DISCUSSION

The present study investigated for the first time the role of the WSS topological skeleton features in processes leading to in-stent restenosis in coronary arteries by applying a Eulerian-based WSS topological analysis on two image-based stented coronary artery models. The findings of this analysis suggest that WSS topological skeleton features could represent a hemodynamic cue promoting coronary in-stent restenosis, in addition to the well-established low WSS. In detail, the luminal exposure to the high variability in the contraction and expansion action exerted by WSS (biomechanically described by *TSVI*) could induce a recurring variation in intracellular tension (acting e.g., on cell roundness) [6] and intercellular tension (e.g., increasing propagation of tension acting on junctions directionality) [7], with consequences on the endothelium permeability. Moreover, WSS contraction and expansion regions surrounding the stent struts could be linked to the EC migration and accumulation process observed in experimental studies [8], with WSS contraction action co-localized with ECs migration upstream from stent struts and WSS expansion action co-localized with ECs accumulation immediately downstream from stent struts [8].

In conclusion, the presented approach might contribute to a deeper understanding of the hemodynamics-driven processes underlying in-stent restenosis in coronary arteries.

REFERENCES

[1] Ng, J. et al., *Arterioscler Thromb Vasc Biol*, 37:2231-2242, 2017.
[2] Chiastra, C. et al., *J R Soc Interface*, 10: 20130193, 2013.
[3] Arzani, A. et al., *J Biomech*, 73: 145-152, 2018.
[4] Mazzi, V. et al., *Biomech Model Mechanobiol*,19:1403-1423,2020.
[5] De Nisco, G. et al., *Med Eng Phys*, 82:119-129, 2020.
[6] Longest, P. W. et al., *J Med Eng Technol*, 24:102-110, 2000.
[7] Melchior, B. et al., *Am. J. Physiol. Cell Physiol.*, 299, 2010.
[8] Hsiao, T.S. et al., *Cardiovasc Res.*, 3:689-701, 2016.

IN VIVO ANALYSIS OF AORTIC HEMODYNAMICS BY COMBINING 4D FLOW MRI AND COMPLEX NETWORKS THEORY

Karol Calò (1), Andrea Guala (2), Diego Gallo (1), Jose Rodriguez-Palomares (2), Stefania Scarsoglio (1), Luca Ridolfi (1), Umberto Morbiducci (1)

(1) PolitoBIOMed Lab, Department of Mechanical and Aerospace Engineering, Politecnico di Torino, Turin, Italy

(2) Hospital Universitari Vall d'Hebron, Department of Cardiology, CIBER-CV, Vall d'Hebron Institut de recerca (VHIR), Universitat Autonoma de Barcelona, Barcelona, Spain

INTRODUCTION

Ascending aorta (AAo) aneurysm is a common aortic disease which consists of a localized dilation of the AAo and which carries a considerable risk of life-threatening events, such as aortic dissection. Since a dilation of the AAo usually presents with altered hemodynamics and aortic insufficiency, an accurate knowledge of the aortic blood flow is required to reveal possible links between hemodynamic features, dilation progression and related risks. In this exploratory study, the Complex Networks (CNs) theory was applied for the first time to an *in vivo* dataset of 4D flow MRI acquisitions of human aorta, aiming at exploring the spatiotemporal heterogeneity of large scale/dominant aortic flow features, as well as its association with AAo dilation. A total of ten patients, five presenting with no AAo dilation and five with dilated AAo, underwent 4D flow MRI [1], covering the thoracic aorta with a spatial resolution of 2.5x2.5x2.5 mm. The time-resolved phase velocity data were used to build a correlation-based CN for each subject [2]. The persistence length of the correlation of velocity data along the cardiac cycle was quantified and its association with AAo dilation, kinetic energy, flow jet angle, and pulse wave velocity was explored.

METHODS

The study population comprises five patients presenting with AAo dilation (one of them with bicuspid aortic valve, BAV), and five with no AAo dilation (one with BAV). All the enrolled patients also present with mild-to-severe aortic valve dysfunction. Full details on 4D flow MRI acquisition protocol and data processing are exhaustively reported elsewhere [1,3]. The study was approved by the ethics committee of the Vall d'Hebron Hospital and informed consent was obtained from all participants. The lumen of each thoracic aorta was semi-automatically segmented from an angiography derived from 4D flow MRI data using ITK-Snap and its centerline was computed using VMTK (www.vmtk.org). Anatomical landmarks were identified from co-registered 2D cine images and used to ensure a consistent spatial extent across all cases. For each patient and each voxel pertaining to the aorta, time-resolved velocity magnitude waveforms were obtained, as reported elsewhere [1]. 3D velocity data were exported using in-house Matlab code (MathWorks Inc, USA) and used to build a CN.

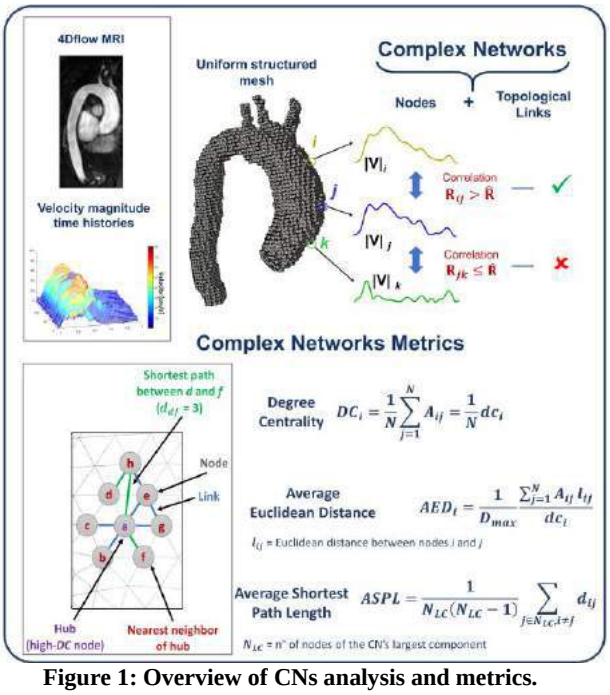

Figure 1: Overview of CNs analysis and metrics.

In detail, each node of the CNs is defined by the voxel where the velocity magnitude |**V**| time history along the cardiac cycle is acquired and two nodes are connected by a topological link $\{i, j\}$ if the Pearson correlation coefficient R_{ij} between the time histories at nodes *i* and *j* is greater than a threshold value $\hat{R}$ (**Fig. 1**) [2]. In this study, the median value of the correlation coefficients between |**V**| time histories derived from patient-specific CFD simulations carried out on a dataset of healthy aorta models was adopted as threshold value ($\hat{R}$=0.87). Each patient's network was characterized by its adjacency matrix A_{ij} containing the information on each node connections [2]. The topological structure of the networks built from *in vivo* data was characterized by three CNs metrics [2] (**Fig. 1**): (1) the *degree centrality* (DC_i) of node *i*, defined as the number of nodes of the CN connected to node *i* expressed as a percentage of the number of voxels in the model; (2) the *normalized average Euclidean distance* (AED_i) between node *i* and all its nearest neighbors, expressed in terms of number of maximum patient-specific AAo diameters D_{max}; (3) the *average shortest path length* ($ASPL$) of the network, defined as the average length of the shortest path d_{ij} connecting two generic nodes *i* and *j* in the CN (**Fig. 1**). DC is a measure of the homogeneity/heterogeneity of |**V**| time history acquired at each voxel with respect to the whole fluid domain, whereas AED and $ASPL$ quantify for each patient the anatomical and topological persistence length of the correlation between |**V**| time histories in the aorta, respectively [2]. The impact of clinically-relevant features on the heterogeneity of the aortic hemodynamics was evaluated by exploring the existence of associations between CNs metrics and kinetic energy (KE), flow jet angle (FJA) [4], pulse wave velocity (PWV) [5] and AAo maximum diameter (D_{max}).

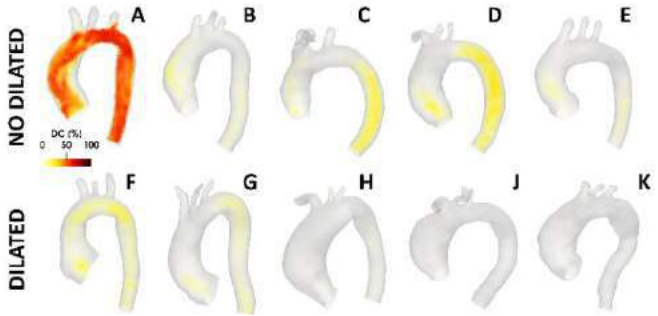

Figure 2: DC volumetric maps.

RESULTS

The volumetric maps of DC in **Fig. 2** clearly highlight a large interindividual variability in the heterogeneity of |**V**| time history shapes. The CN built on patient A is characterized by a dense pattern of connections between nodes in the entire aortic domain, confirmed by the DC values around 50%. The other patients present sparse, scarcely connected networks, reflecting from very poor (as in dilated patients H, J and K, **Fig. 2**) to moderate homogeneity (in particular no dilated patients C and D). The AED maps (data not shown) highlight that, in general, the anatomical length of the correlation of |**V**| time histories is higher in the descending aorta, whereas it reaches a minimum the ascending aorta, especially in patients with dilated AAo. A significant, negative correlation emerges between AED median values and D_{max} (**Fig. 3a**), suggesting that AAo dilation can play a major role in disrupting hemodynamic similarity in velocity magnitude waveforms not only in the AAo, but involving the entire thoracic aorta. In parallel, a near significant positive trend (p_{value}=0.06) emerges between KE and AED, suggesting that high peak kinetic energy values might contribute to increase the anatomical length of the correlation persistence (**Fig. 3b**).

The opposite effects of aortic dilation and blood flow kinetic energy also emerge in the moderate but significant associations with the topological correlation persistence length, expressed by $ASPL$ (**Fig. 3c** and **3d)**. Finally, CNs metrics were not significatively correlated with FJA and PWV at this stage of the investigation, probably because of the scarcely stratified dataset.

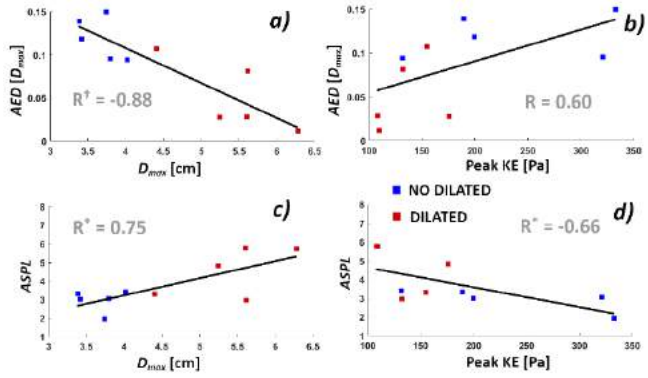

Figure 3: Associations between CNs metrics and clinically-relevant features. For each CN, AED is expressed as the median value of all nodes. (*p_{value} < 0.05; †p_{value} < 0.001)

DISCUSSION

In this study, the CNs theory is applied to *in vivo* 4D flow MRI velocity data to investigate the spatiotemporal heterogeneity of aortic velocity magnitude waveforms shape along the cardiac cycle, and the existence of possible associations between CNs metrics and quantities of clinical interest is explored. The main findings suggest that the physiological Euclidean and topological length of persistence, which are supposed to characterize the physiological aortic intravascular hemodynamics, might be more markedly disrupted in patients with larger maximum AAo diameter (high D_{max} values reduce the anatomical extension of the correlations, AED, and increase the topological separation between nodes, $ASPL$). This is consistent with a recent study on CFD models of ascending thoracic aorta aneurysms, highlighting how the aortic dilation disrupts the correlation persistence of velocity-based waveforms, breaking the topological connections between nodes, especially in the region where a marked change in the mechanical properties of the aortic wall occurs [6]. Conversely, it is suggested that the amount of fluid kinetic energy, representative of the large scale flow features, might play a beneficial role in preserving physiological homogeneity in blood velocity magnitude waveforms shape. In conclusion, this first *in vivo* application of CNs theory to cardiovascular flows looks promising in disentangling the complex 4D aortic hemodynamics. The combined use of D_{max} and CNs distance metrics may allow a finer risk stratification for AAo disease in future applications on larger datasets.

ACKNOWLEDGEMENTS

Guala A. has received funding from the Spanish Ministry of Science, Innovation and Universities (IJC2018-037349-I).

REFERENCES

[1] Dux-Santoy, L et al., *Eur Hear J-Cardiovasc Imaging*,34:1-11,2019.
[2] Calò, K et al., *IEEE Trans Biomed Eng*, 67:1841-53, 2020.
[3] Johnson, KM et al., *Magn Reson Med*, 60, 1329-1336, 2008.
[4] Sigovan, M et al., *J Magn Reson Imaging*, 34.5:1226-1230, 2011.
[5] Guala, A et al., *JACC: Cardiovasc. Imaging*, 12.6:1020-1029,2019.
[6] De Nisco, G et al., *Med Eng Phys*, 82: 119-129, 2020.

USING DRAGONFLY IMAGING SOFTWARE FOR TRANSMISSION ELECTRON MICROSCOPY ANALYSIS

C. Leek (1,2), M.L. Killian (2)

(1) Department of Biomedical Engineering
University of Delaware
Newark, DE, USA

(2) Department of Orthopaedic Surgery
University of Michigan School of Medicine
Ann Arbor, MI, USA

INTRODUCTION

Tendons are highly organized and fibrous tissues that transmit the mechanical load from muscle onto bone.[1–3] Common measurements of tendon quality are the quantification of collagen fibril size, shape, and organization.[4,5] Often mutants with compromised tendons have smaller and irregularly shaped collagen fibrils.[6]

As fibril diameters are measured in nm, observation requires highly sophisticated imaging techniques. Transmission electron microscopy (TEM), which is a high magnification and high resolution imaging technique which generates a greyscale image that assigns pixel value based on scattered electrons. However, TEM is limited by the noise associated with high magnification images and can be difficult to quantify automatically. That is why there is a need for quick, accurate, and repeatable technique for TEM analysis. Dragonfly (Object Research Systems, Montreal, Quebec, Canada) high performance software is a great for analysis of data based on pixel value. Here, we designed a protocol for the quantification of TEM image date using Dragonfly and compared the repeatability and time-requirements of our methodology to ImageJ[7], which is commonly used for tendon. We hypothesized that our Dragonfly technique would be quicker and yield similar results to ImageJ quantification.

METHODS

For TEM, right Achilles tendons of adult wild type mice (6-8 months of age; n = 2) were dissected and fixed for 2 weeks in a 2% glutaraldehyde, 2% paraformaldehyde (PFA) solution buffered to PH 7.4 with 0.1M sodium cacodylate. Tendons were cut in the transverse plane from the proximal tendon and imaged to visualize collagen fiber diameters and tendon ultrastructure (Zeiss Libra 120 Transmission Electron Microscope; 120kV, 0.34nm point to point resolution, and Gatan Ultrascan 1000 CCD camera, Pleasanton, CA).

From a single 10 x 10 µm TEM image, five separate 2 x 2 µm regions of interest (ROIs) were extracted. Partial fibrils that were cut off by the perimeter of the ROI were omitted from the study. Two separate rounds of quantification were completed to test for repeatability. To avoid bias, data was not reviewed until both rounds were completed. Minimal fibril size in the second round was larger than the first round. During the round 2, a timer was run during quantification to see how long each method took. The timer began after file was uploaded and the timer ended once data was exported. On the second round of Dragonfly quantification, window leveling was adjusted for sake the figure 1 to make fibrils stand out better.

Files were first uploaded into ImageJ[7]. Using the freehand selection tool, fibrils were outlined, measured, and saved. Per ROI, average fibril area and fibril number were calculated.

Original ROIs were uploaded into Dragonfly. A histogram of pixel values was generated, dark fibrils were highlighted while the light space around the fibrils were omitted. These highlighted fibrils were separated into a sperate ROI. Using a combination of morphological operations and the ROI painter tool, fibrils were filled in and non-connected pixels were removed (Fibril ROI). The highlighted ROI was duplicated and inverted to select the surrounding space (NonFibril ROI). From the NonFibril ROI a distance map was generated which assigned a pixel value based on the distance from the ROI. Thus, the center of the fibrils was the brightest, and the fibril edges were the darkest. The distance map was then inverted so dark represented the center of the fibrils. The same define range tool was used on the inverted distance map. A range of pixel values was selected that separated each fibril (New ROI). Using the painter tool on New ROI, we removed highlighting between fibrils and filled in small fibrils that might have been lost. The result was each fibril having a separate highlight. On the New ROI channel, we generated a new multi-ROI which gives each fibril highlight a unique

color. We then did a watershed transform based on multi-ROI, inverted distance map, and Fibril ROI to expand the ROI highlight to the full area of the fibril. The filled multiROI was then exported into a file which listed each fibril and corresponding area. Per ROI, average fibril area and fibril number were calculated.

Statistical analyses were performed using Prism 8.0 (GraphPad, LaJolla, CA). Student's t-tests were used to compare time and measurement rate. Two-way ANOVAs were used to compare fibril area and fibril count repeatability. Z score was calculated per method, based on average and standard deviation of separate rounds.

RESULTS

Both ImageJ and Dragonfly come with their advantages and disadvantages for fibril analysis (Table 1). Both provide easily identifiable and reviewable data. Qualitatively, these techniques provided very similar results between separate rounds of quantification (Figure 1).

Table 1: Comparisons by fibril quantification techniques

	ImageJ	VS	Dragonfly
Learning Curve	Mild	<	Steep
Fibrils/ min	8.68	<	15.80
Area StDev	3.00E-04	≈	6.00E-04
Area Repeatability (Z test)	0.30	≈	0.81
Count StDev	8.26	≈	5.87
Count Repeatability (Z test)	0.12	≈	0.90
RAM requirement	≈ 150 MB	<	≈ 300 MB
File size relative to original	≈1X	<	≈10x

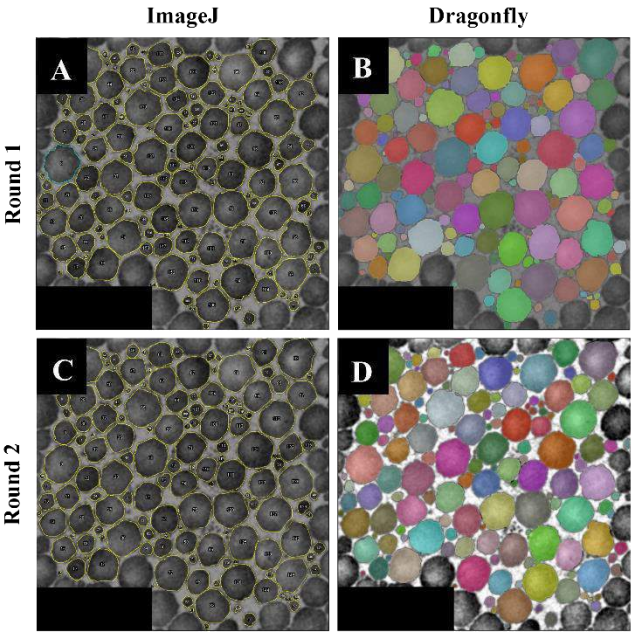

Figure 1: Both ImageJ and Dragonfly allow quantification and observation of collagen fibrils. Each ROI = 4μm^2.

Data was expected to be similar between technical replicates since all technical replicates came from the same TEM image. A larger minimal fibril size was set during the second round of quantification. For quantifying fibril area and fibril count, both ImageJ and Dragonfly similar data between two separate rounds (Figure 2A,B). However, Dragonfly data better reflected the changes to minimal fibril size as average fibril area increased (Figure 2A) and fibril count decreased (Figure 2B) from round 1 to round 2. Between the two techniques, ImageJ was more repeatable (Figure 2B). Dragonfly took less time to quantify each image (Figure 2C), with more fibrils counted per minute (Figure 2D).

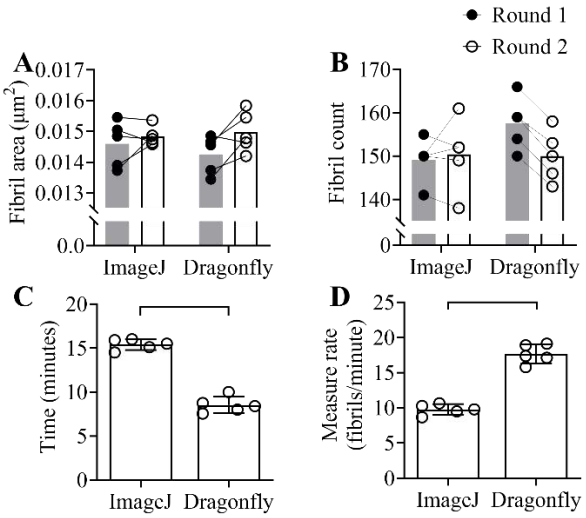

Figure 2: Dragonfly offers a quicker alternative to manual measurements in ImageJ. Both ImageJ and Dragonfly quantification shows an insignificant difference in repeatability of (A) fibril area measurement and (B) fibril count measurement. (C) Dragonfly is the faster method for fibril quantification with (D) more fibrils counted per minute. Data are technical replicates, mean ± SD. Lines in C and D indicate significance ($p < 0.05$).

DISCUSSION

Here, we have established a repeatable, reliable, and fast method for quantifying collagen fibril properties from TEM. When compared with manual ImageJ methods, our Dragonfly method is quicker with similar repeatability in fibril area measurements. Since our ROIs are 4 μm^2 pieces of a 100 μm^2 image, this difference in time would be immensely different in a TEM analysis with multiple technical and biological replicates. Although ImageJ is the "ground truth" method for counting, Dragonfly is better as handling differences in methods as seen between round 1 and 2 where different minimal fibral size was set. This may be attributed to the automatic nature of Dragonfly which eases any user bias. Though quicker, this Dragonfly method comes with a slower learning curve and a higher computational demand. This technique remains promising as it does not take full advantage of the power of Dragonfly, and we hope to advance these steps soon.

ACKNOWLEDGEMENTS

This research was supported by the Eunice Kennedy Shriver National Institute of Child Health & Human Development of the National Institutes of Health under award numbers K12HD073945 (MLK), R03HD094595 (MLK), and R01HD049808 (DMO); an Institutional Development Award (IDeA) from the National Institute of General Medical Sciences of the National Institutes of Health under award number P30GM103333; the National Institute of Arthritis and Musculoskeletal and Skin Diseases under award number P30AR057235; and the University of Delaware Research Foundation.

REFERENCES

[1] Apostolakos J et al., *Muscles, Ligaments and Tendons Journal*. 4(3):333, 2014. [2] Benjamin, M et al., *Comp Biochem Physiol, Part A Mol Integr Physiol*, 133(4):931-945, 2002. [3] Murchison, ND et al., *Development*, 134(14):2697-2708, 2007. [4] Michna, H et al., *Cell Tissue Res*, 236(2), 1984. [5] Michna, H et al., *International Orthopaedics*, 13(3):161-165, 1989. [6] Edom-Vovard, F et al., *Dev Dyn*, 229(3):449-457, 2004. [7] Schneider, CA et al., *Nat Methods*. 9(7):671-675, 2012.

HYPERTROPHIC CARDIOMYOPATHY PROGRESSION CHARACTERIZED VIA SPATIOTEMPORAL STRAIN MAPPING FROM 4D ULTRASOUND

Frederick W. Damen (1), Daniel P. Gramling (1), Craig J. Goergen (1)

(1) Weldon School of Biomedical Engineering
Purdue University
West Lafayette, Indiana, USA

INTRODUCTION

Murine models play a critical role in uncovering the underlying mechanisms of cardiac disease and progression[1, 2]. Complementary to these mouse models, high-frequency ultrasound has become an integral tool for noninvasively quantifying cardiac function (ejection fraction, stroke volume, etc.)[3], thus helping to characterize disease stage. Here we demonstrate how we can leverage recently developed high-frequency four-dimensional ultrasound (4DUS) techniques[4, 5] to provide comprehensive characterizations of left ventricular (LV) function. Using mice with pathological cardiac hypertrophy and litter-mate controls, we quantify spatiotemporal maps of regional circumferential and longitudinal strain, and demonstrate how those maps change due to both normal aging and disease progression.

METHODS

Animal Models: 4DUS data was collected on 24 male mice with genetically induced cardiac hypertrophy (n=12; *Nkx2-5*$^{183P/+}$)[6] and control littermates (n=12; wild-type). Six mice from each cohort were euthanized at week 8 and had hearts excised for proteomic analysis. Remaining animals were subsequently imaged at week 12 and 16, after which they were similarly euthanized for proteomics analysis.

Ultrasound Imaging: All data was collected using a Vevo2100 high-frequency ultrasound system (FUJIFILM VisualSonics Inc.) with a 40 MHz center frequency transducer (MS550D). 4DUS data was created by collecting cardiac- and respiratory-gated planar images from serial short-axis views across the LV and then spatiotemporally sorting images in MATLAB (MathWorks Inc.).

4DUS Left Ventricle Kinematics: 4DUS data were loaded into an in-house MATLAB GUI and analyzed using a standardized procedure (Figure 1), resulting in a structured point cloud that tracked regional kinematics of the endocardial boundary across a representative cardiac cycle. A 4D mesh was then interpolated from the analysis-derived point cloud with a set number of interpolation points around (60) and down (60) the LV, as well as across the cardiac cycle (60).

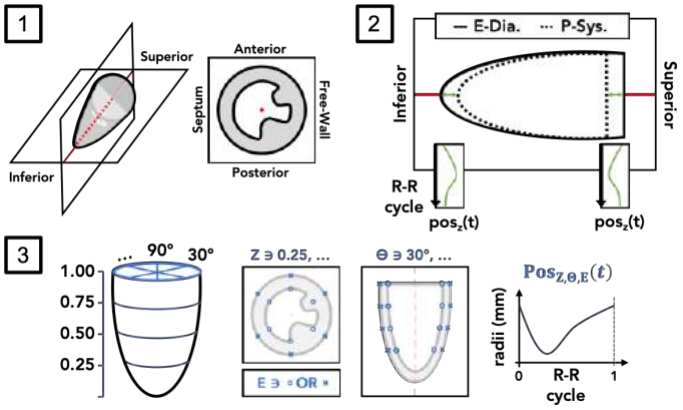

Figure 1. Schematic of 4DUS analysis procedure demonstrating: (A) standardization of orientation, (B) definition of LV base and apex displacement, and (C) tracking of regional wall kinematics.

Spatiotemporal maps of circumferential strain were then compiled from strain curves computed at each slice down the 4D LV mesh, using the Green-Lagrange strain tensor definition[7]:

$$E_{\theta\theta}(z,t) = \frac{1}{2}\left(\left(\frac{C(z,t)}{C_D(z)}\right)^2 - 1\right) \quad [1]$$

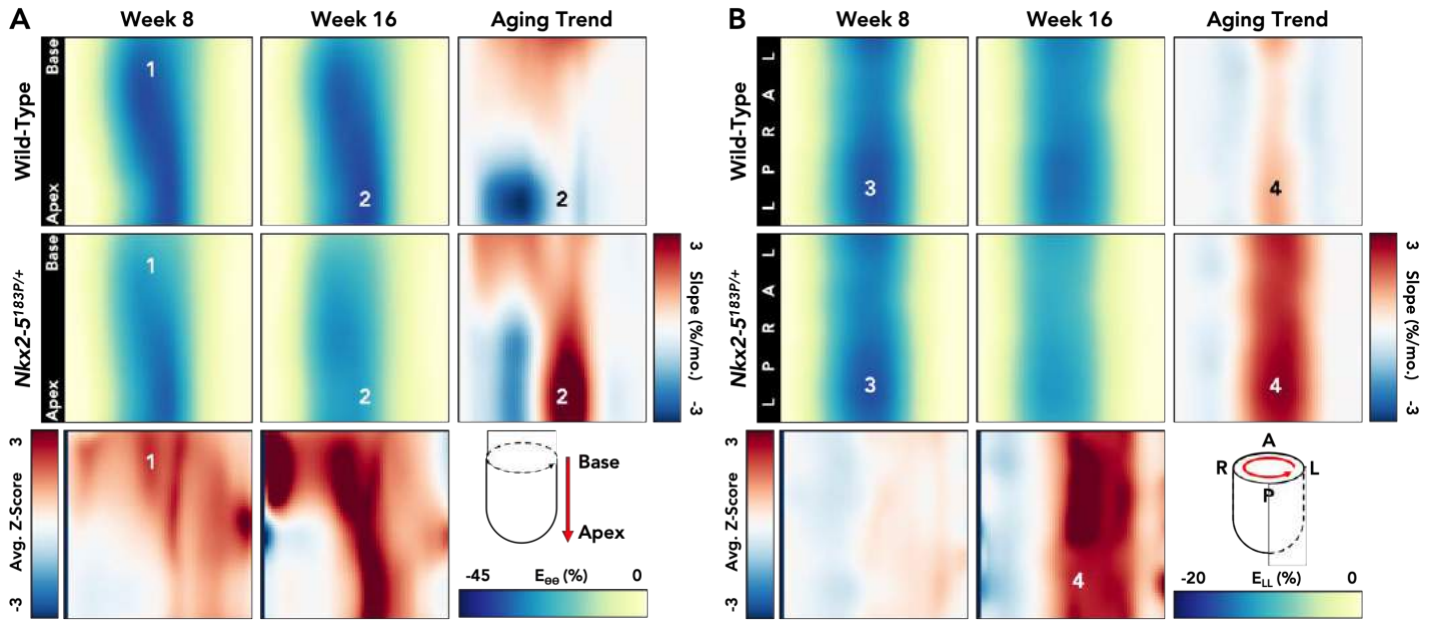

Figure 2. Spatiotemporal colormaps of circumferential (A) and longitudinal (B) strain across a representative cardiac cycle (x-axis = R-peak to R-peak; y-axis relative spatial position). Cohort averaged maps are shown for week 8 and 16. Z-score maps (bottom row) visualize how the mean *Nkx2-5*$^{183P/+}$ maps compare pixelwise to the wild-type distribution (i.e., standard deviations from the wild-type mean) at weeks 8 and 16. Additionally, trend maps (right column) visualize pixelwise per-month changes in strain for each cohort.

where C represents the relative circumference at slice z and time position t in the cardiac cycle; C_D is the circumference at end-diastole (t=0). Comparable spatiotemporal maps of longitudinal strain were derived using the linear small strain approximation (i.e., proportional length change from end-diastole) at each rotation around the center axis.

RESULTS

Since spatiotemporal strain map matrix sizes were standardized during analysis (60 locations x 60 time-points), resultant maps could be overlaid by cohort and age, allowing for pixelwise averaging and comparisons. Figure 2 highlights averaged strain maps at weeks 8 and 16, cross-sectional comparisons using pixelwise z-scores, and trend maps showing strain changes per month of aging. Week 12 data was excluded for clarity. The primary observations from Figure 2, marked 1-4 in the figure, are provided below:

1. At the earliest age imaged, circumferential strain magnitude deficits in the *Nkx2-5*$^{183P/+}$ cohort were primarily observed at the base of the heart during systole, suggesting weakened contractility near the mitral and aortic valves.
2. As both cohorts aged to week 16, a disproportionately lower magnitude circumferential strain was observed apically for the *Nkx2-5*$^{183P/+}$ cohort. Interestingly, both cohorts showed a decrease in strain magnitude in the basal region through aging, suggesting a natural shift of systolic contractility towards the apex over time.
3. In both cohorts, the posterior free-wall observes higher magnitude longitudinal strain throughout systole. Although unlike circumferential strain, negligible differences were observed at week 8, suggesting that circumferential systolic contractility may be more sensitive to the early development of hypertrophy.
4. By week 16, the distribution of longitudinal strain in the *Nkx2-5*$^{183P/+}$ cohort became more uniform around the ventricle and the duration of the systolic contraction wave shortened. Interestingly, both cohorts show a trend of increased early systolic longitudinal strain, suggesting a more rapid response to the cardiac conduction system with aging.

DISCUSSION

We demonstrate here the ability to use 4DUS imaging to produce spatiotemporal maps of both circumferential and longitudinal strain, from which we can quantify changes in cardiac kinematics that correlate with age and phenotype. In this study, we identified when and where kinematic patterns deviate in a genetic model of cardiac hypertrophy (*Nkx2-5*$^{183P/+}$). Our findings suggest that inhibited cardiomyocyte energy handling induced by the *Nkx2-5*$^{183P/+}$ mutation not only induces a hypertrophic myocardium[8], but also alters the systolic contraction kinematics. As research exploring regionally specific strain in mice using 4DUS technology remains limited[9], these findings may provide a framework for how 4DUS can be leveraged to provide more comprehensive characterizations of cardiac function and disease.

ACKNOWLEDGEMENTS

This work was supported by the AHA (14SDG18220010), NIH (F30-HL145980; T32-DK101001), and the Geddes Endowment from Purdue University. The authors acknowledge Mauro Costa at The Jackson Laboratory for access to the *Nkx2-5*$^{183P/+}$ murine model.

REFERENCES

[1] Zaragoza, C. et al., *J Biomed Biotechnol,* 2011:497841, 2011.
[2] Patten, R.D. et al., *Circ Heart Fail,* 2:138-44, 2009.
[3] Lindsey, M.L. et al., *Am J Physiol Heart Circ Physiol,* 314:H733-H752, 2018.
[4] Damen, F.W. et al., *Tomography,* 3:180-187, 2017.
[5] Soepriatna, A.H. et al., *Int J Cardiovasc Imaging,* 2017.
[6] Furtado, M.B. et al., *Jci Insight,* 2:e88271, 2017.
[7] Morrison, T.M. et al., *J Vasc Surg,* 49:1029-36, 2009.
[8] Wilmanns, J.C. et al., *Mol Metab,* 2018.
[9] Soepriatna, A.H. et al., *J R Soc Interface,* 16:20190570, 2019.

THE SKELETAL RESPONSE TO VARIED MODELS OF METABOLIC ACIDOSIS

Mikayla K. Moody (1), Anna K. Peterson (1), Brian Wingender (1), Katya Morozov (1), Iris Nakashima (1), Tannin A. Schmidt (1), Alix Deymier (1)

(1) Department of Biomedical Engineering
University of Connecticut Health Center
Farmington, CT, USA

INTRODUCTION

Metabolic acidosis (**MA**), a disease affecting millions annually, is clinically characterized by a decrease in blood pH and bicarbonate ($\mathbf{HCO_3^-}$) [1-3]. MA can lead to bone loss, fueled by a dissolution of bone mineral that can restore pH homeostasis by yielding the required buffering alkali from bone mineral [1-4]. MA is most commonly observed in chronic kidney disease, diabetes, and critically ill patients; however, western diets may also cause onset acute MA [5-7]. MA is known to increase the risk of bone fractures since acidic environments denature collagen and affect the structure and composition of bone mineral, reducing bone strength, bone volume, and mineral stiffness [8-10].

Despite the prevalence and establishment of the negative effects of MA on the skeletal system, there are limited studies of murine models that recapitulate the clinical blood chemistry and bone phenotype of MA. Previously established methods induced MA in adult mice by administering 0.28M ammonium chloride (NH_4Cl) into their diet. However, these methods do not mimic the MA bone phenotype observed clinically nor maintain long-term acidemia [11-13]. We previously established a method to induce MA in adult mice by administering NH_4Cl into their diet, providing a higher graded dosage every three days. This graded diet mimicked the MA bone phenotype observed clinically and maintained MA over the course of two weeks [14]. To better understand the skeletal response to MA temporally and determine a dosage-dependent response to acid-loading in murine bones, we characterized the bone phenotype resulting from two models of MA over the course of two weeks and characterized the blood gas and bone responses.

Here, we propose a murine MA model with a graded NH_4Cl diet as an alternative to the conventional flat-dose models. We hypothesized that the use of graded acid-loading for MA induction will inhibit excessive compensatory buffering from the kidneys and lungs to exceed dietary acid loading, resulting in a bone phenotype similar to that observed in clinical MA.

METHODS

Induction of MA: All animal experimental procedures were approved by the Institutional Animal Care and Use Committee at UConn Health Center and Columbia University, and comply with the National Institutes of Health guide for the care and use of laboratory animals (NIH Publications No. 8023, revised 1978). Metabolic acidosis was induced in 4-6-month old CD-1 mice by replacing their drinking water with an aqueous solution of ammonium chloride and 5% sucrose. For the flat-dose group, the NH_4Cl dose remained constant at 0.28M for 14 days [11,13]. For the graded group, the NH_4Cl dosing began at 0.2M NH_4Cl and was increased by 0.1M every 3 days for 14 days, with the highest dose at 0.6M [14]. Mice were sacrificed following the time of blood-gas analysis indicated for each group. *Blood chemistries analysis*: For each time period assessed, 200-300 µl of blood was extracted from non-anesthetized mice through submandibular puncture procedures [15]. Blood samples were analyzed using a Heska PoC Epoch blood-gas analyzer (Loveland) to obtain values of blood chemistries. *Whole-bone mechanics:* 3-point bend tests were used to evaluate the mechanical properties of the femurs. Load vs. displacement curves were analyzed using custom programs in MATLAB (MATLAB, R2020a, MathWorks) to determine structural and material mechanical properties. Stress vs. strain curves were calculated by normalizing the force and displacement using the beam span length, the bone centroid distance, and area moment of inertia as determined from micro-computed tomography (µCT). *Structural analysis:* After mechanical testing, the femoral samples were evaluated by µCT to obtain morphological information for the distal trabecular bone. The images were analyzed using the

BoneJ toolbox of ImageJ (U.S. NIH) and the Bruker CTAn software. *Statistical analysis:* Statistical analysis was done using one-way ANOVA on Minitab software. A significance level of 0.05 was used for all tests. Comparisons between time periods were made using post-hoc tests. Both the flat-dose and graded models were compared to independent and concurrently run control groups. Data are mean ± standard deviation.

RESULTS

At day 1 of NH_4Cl administration, the flat-dose model exhibited a significant decrease in blood pH and subsequent increase in Ca^{2+} compared to the control mice (**Figure 1**). However, following this time point, the pH and Ca^{2+} returned to baseline, with Ca^{2+} levels again increased on day 14. HCO_3^- in the flat-dose group was not significantly altered at any time point evaluated. The flat-dose group also did not exhibit any changes in mechanical properties nor the structural metrics. Our graded model of MA showed continuously decreased blood pH and HCO_3^- and increased Ca^{2+} as observed in clinical MA, with the exception of day 3. For the graded group, the femurs exhibited a significant decrease in bone volume (%) for days 1 and 3 compared to the control (**Figure 2**). Additionally, there was a significant increase in toughness from day 1 to day 14 (**Figure 3**). Resilience also increased significantly from days 1 and 3 to day 14 (data not shown). The other structural and material mechanical properties were not altered in the graded model.

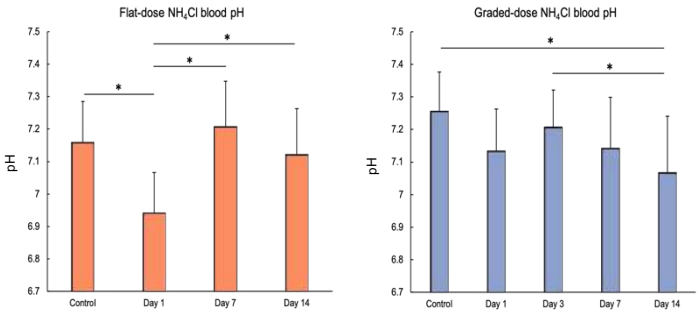

Figure 1. Blood pH data for MA across 14 days. N=16-25/day for flat and N=18-24/day for graded.

DISCUSSION

The flat-dose model of diet-induced MA showed unreliable utility as a model of MA in mice as it did not meet the clinical criteria for MA of low pH and low HCO_3^- but instead only induced "acute" acidemia at day 1. The increase in blood Ca^{2+} at this time point suggests that the onset of acidemia may generate bone dissolution, but phenotypic MA-induced bone loss or altered bone mechanics were not reflected in any metrics from our analysis. This suggests that compensatory buffering mechanisms, likely via the kidneys, were successfully engaged in the flat-dose model. Despite being well-established in the literature, the clinical chemistry and lack of bone phenotype renders this model of MA in adult mice unsuitable beyond an "acute" timepoint.

The graded-dose model effectively induced "chronic" MA across all time points, except on day 3, based on blood pH and HCO_3^-. The return to normal blood-gas pH, Ca^{2+}, and HCO_3^- values at this timepoint implies the onset of the clinically observed phenomena of "eubicarbonatemic MA", whereby bone dissolution reestablishes blood pH and ion homeostasis [7]. Furthermore, a decrease in the percent bone volume at days 1 and 3 illustrates this dissolution. At day 14, an increased toughness and resilience suggests a greater contribution of collagen to the total bone mechanics due to bone mineral dissolution in an acidic environment. Continued bone dissolution due to acidosis could contribute to further compromised mechanics as seen clinically [16]. Future and ongoing studies aim to concretely determine whether bone composition and bone remodeling dynamics are altered in these models of MA independently. We conclude that there is both a dosage-dependent response to acid-loading in bone, and the temporal response to MA in bone drives the clinically observed phenotype. Ultimately, our model of graded MA is characteristic of the bone phenotype observed clinically and can maintain onset of MA for the course of 14 days.

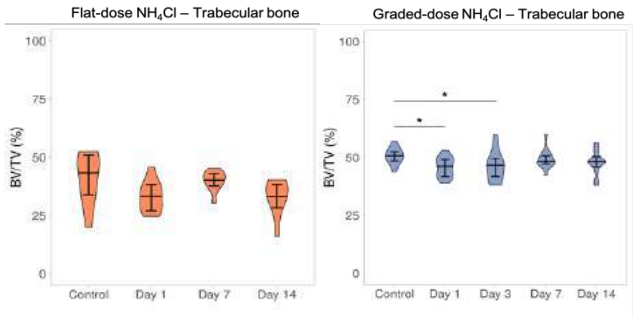

Figure 2. Bone volume (%) for MA across 14 days (N=12-14 /day).

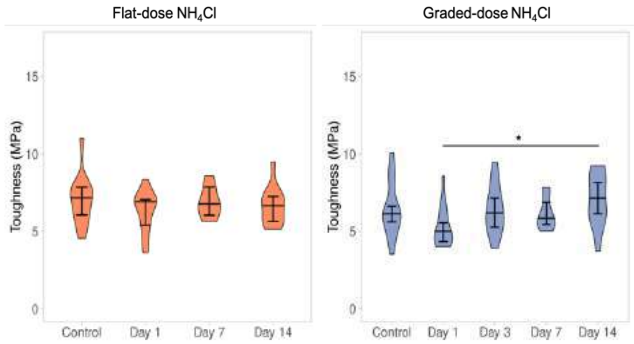

Figure 3. Toughness (MPa) for MA across 14 days (N=10-15/day).

ACKNOWLEDGEMENTS

Funding was provided by Prof. Deymier's Startup Funds at UConn Health, fellowships from the UCHC Graduate School, the GEM Fellowship, and the Harriott Fellowship.

REFERENCES

[1] Kraut, J. et al., *Nat Rev Nephrol,* 6:274-285, 2010. [2] Malluche, H. H., *J Am Soc Nephrol.,* 23:525-532, 2012. [3] Kraut, J. et al., *Kidney Int,* 30:694-700, 1986. [4] Alpern, R. J. et al., *Am J Kidney Dis*., 29:291-302, 1997. [5] Kraut, J. et al., *Am J Kidney Dis*, 67:307-317, 2015. [6] Krieger, N. S. et al., *Curr Opin Nephrol Hypertens*, 13:423-36, 2004. [7] Amodu, A. et al., *Clin J Am Soc Nephrol*, 8:2034-2042, 2013. [8] Zhang, et al., *J Theor Comput Chem*, 10:245-259, 2011. [9] Usha, et al., *J Appl Polym Sci.,* 75:1577-1584, 2000. [10] Deymier, A. et al., *Biomaterials,* 127:75-88, 2017. [11] Nowik, M. et al., *Cell Physiol Biochem*, 26:1059-1072, 2010. [12] Imenez, S. et al., *Kidney Int*, 97:253-255, 2020. [13] Rector, F. C. et al., *J Clin Invest*, 34(1):20-26, 1955. [14] Peterson, A. et al., *Acta Biomater,* In Press. [15] O'Connell, K. et al., *Comp Med*, 65:96–113, 2015. [16] Sellmeyer, D.E. et al., *Am J Clin Nutr,* 73:118-122, 2001.

SB³C2021
Summer Biomechanics, Bioengineering and Biotransport Conference
June 14-18, Virtual

SENSITIVITY OF THE SHEAR WAVE SPEED-STRESS RELATIONSHIP TO LIGAMENT FIBER ALIGNMENT – A PROBABILISTIC FINITE ELEMENT STUDY

Jonathon L. Blank (1), Darryl G. Thelen (1), Joshua D. Roth (1,2)

(1) Department of Mechanical Engineering
University of Wisconsin-Madison
Madison, WI, USA

(2) Department of Orthopedics and Rehabilitation
University of Wisconsin-Madison
Madison, WI, USA

INTRODUCTION

Shear wave tensiometry is an emerging measurement technique used to determine the tension in tendon [1] and ligament [2] noninvasively. Fundamentally, this technique measures the speed of a shear wave propagating along the length of the tissue. Based on an analytical relationship for a shear wave propagating in a tensioned beam, we can determine the axial tissue stress and tension from the measured shear wave speed. In previous ex vivo experiments, we have observed that shear wave speeds measured in axially loaded collateral ligaments [2] are greater than those measured in axially loaded tendon [3] by up to 45% at a similar axial stress level.

While tendons and ligaments both exhibit transversely isotropic material properties, they differ in factors relating to their structure that might affect their loading behavior. For example, ligaments have less well-aligned fibers than tendon [4]. Further, the gradual recruitment of substructural features, such as fiber-fiber bonds, in ligaments can cause nonlinear material behavior to occur during loading, which could be in part due to an increase in shear modulus [5]. Concerning tensiometry, it is well understood that the unloaded shear modulus is the driving factor for changes in shear wave speed at low loads in tendon [1]. However, the interaction between the substructure-dependent shear modulus and shear wave speed remains uninvestigated in ligament.

The purpose of this study was to investigate whether the substructure-dependent shear modulus could alter shear wave speeds. Our hypothesis was that less well-aligned fibers would increase the tissue's unloaded shear modulus, and thus shear wave speed, during axial loading.

METHODS

We modeled a ligament (FEBio v3.0) as a rectangular prism with an aspect ratio of 8 with a similar cross-sectional area as a human MCL. In the static portion of the simulation, we axially loaded the tissue to a constant axial strain and allowed it to settle. During the dynamic portion of the simulation, we applied a transverse ramp displacement to nodes through the depth of the tissue to excite a shear wave and measured the shear wave speed using the time delay in wave arrival at two points downstream from the excitation. We modeled the tissue's material behavior using a Mooney-Rivlin transversely isotropic constitutive model [5,6]. The variation in the tissue's intrinsic fiber alignment was governed by a 2D semi-circular von Mises distribution [7].

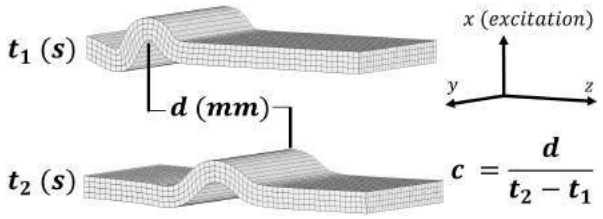

Figure 1: Fiber alignment was modeled in 2D planes parallel (xz) and perpendicular (yz) to the excitation direction (x-direction). Shear wave speed (c) was measured as distance divided by time. For visualization, displacement in the figure was amplified 100x.

We used Monte Carlo probabilistic modeling to determine sensitivities of the shear wave speed-stress relationship to variations in fiber alignment in 2D planes parallel (Figure 2a) and perpendicular (Figure 2b) to the excitation. A fiber concentration factor, k_f, was prescribed to scale the semi-circular von Mises distribution. We varied k_f according to a one-sided normal distribution, with a value of 0 corresponding to an isotropic fiber distribution. As k_f increases, the fibers become more aligned along the preferred fiber orientation (axial loading direction). We varied the axial strain according to a random uniform distribution between 0% and 10%. Using a high-throughput computing grid, we performed 10,000 simulations per analysis.

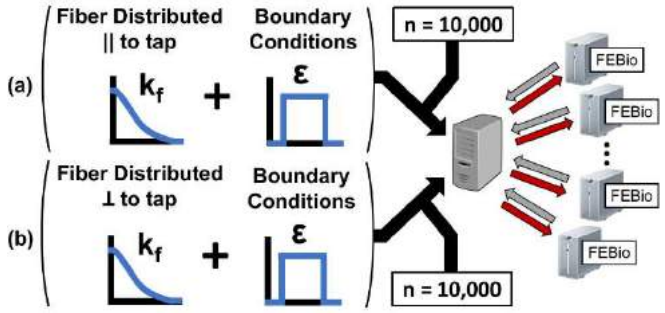

Figure 2: We used Monte Carlo probabilistic modeling in two cohorts of simulations with randomly applied fiber alignment factors (one-sided normal distribution, mean ± standard deviation = 0 ± 25) and axial strains (uniform distribution between 0-10%).

To assess the shear wave speed-stress relationship, we used an analytical relationship (Equation 1) relating the shear wave speed, c, to the axial stress, σ_z, in terms of the shear modulus in the plane of the shear wave (μ_{xz}, scaled by a shear correction factor k') and the tissue density (ρ) [1]:

$$c^2 = \frac{k'\mu_{xz}+\sigma_z}{\rho} \qquad (1)$$

We determined the sensitivity of this analytical relationship to ligament fiber alignment using a linear regression between the squared shear wave speed and axial stress for fiber concentration factors from 0-50+ in increments of 1. The shear modulus of interest (in plane with the shear wave) was determined using the corresponding term in the underlying spatial elasticity tensor.

RESULTS

The shear wave speeds measured using the finite element model agreed closely with predictions using the analytical model ($R^2 > 0.99$). When varying only the fiber alignment, there was a notable difference in shear wave speed for less well-aligned fibers for the cohort of simulations with fibers distributed parallel to the excitation (Figure 3).

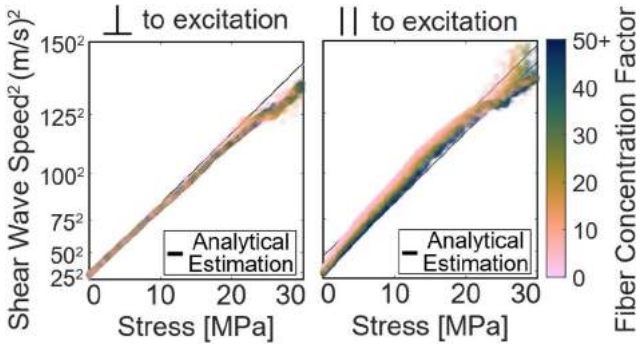

Figure 3: Shear wave speed measured for each cohort of simulations (n=10,000 each). Overall, the shear wave speed was well predicted by the analytical relationship.

Less well-aligned fibers parallel to the excitation resulted in shear wave speeds that were 9.6% higher than the analytical estimation of the shear wave speed for a transversely isotropic material at a given stress level. Despite this, they remained well predicted by the upper and lower bounds (corresponding to the lowest and highest μ_{xz} observed in the entire cohort, see Figure 4b) of the analytical estimation. Overall, there was an average predictive error of 2.68 ± 1.92 and 4.07 ± 2.88 m/s using the analytical model and unloaded shear modulus for fibers distributed perpendicular and parallel to the excitation direction, respectively.

The shear wave speed-stress relationship demonstrated a higher sensitivity for models that had less well-aligned fibers, and this sensitivity was higher for models with fibers distributed parallel to the excitation (Figure 4a). This is likely a result of a higher shear modulus for low fiber distribution factors (Figure 4b), since the shear modulus is a component of the analytical relationship governing the squared shear wave speed-stress relationship (Equation 1).

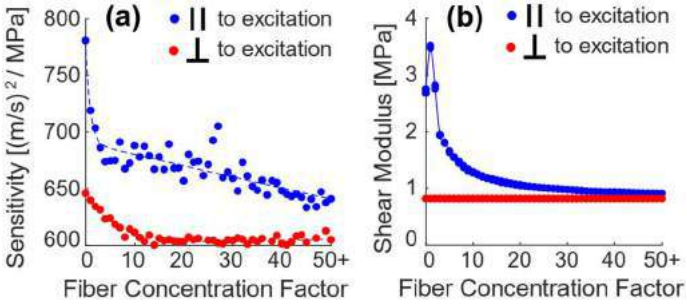

Figure 4: (a) The model was more sensitive to fibers distributed in the direction of the excitation, and the sensitivity to fiber alignment generally decreased as fibers became more aligned. (b) The resulting differences in shear wave speed could be due to the higher unloaded shear modulus in the excitation direction.

DISCUSSION

Our study shows that our dynamic finite element model can predict shear wave speeds in ligaments with distributed fibers that are in the same range as previous studies [1-3]. Further, the analytical relationship between the shear wave speed and axial stress holds for ligament models with different degrees of fiber alignment. The sensitivity between the squared shear wave speed and axial stress decreases as fibers become more highly aligned, and there is a nonlinear trend with low fiber alignment for both cohorts of models (Figure 4a). This is likely due to the nonlinear effect of fiber concentration on the unloaded shear modulus of the tissue (Figure 4b).

This study provides useful insights into how the unloaded shear modulus may affect shear wave propagation. However, the shear modulus for less well-aligned fibers can increase with loading (e.g., 10x and 3x increase in shear modulus for $k_f = 0$ and $k_f = 10$, respectively, at 10% strain, based on pilot simulations). This may be exacerbated in intact ligaments, where the gradual recruitment of microstructural features, such as fiber-fiber bonds, can change material shear behavior during loading [5]. The exact effect that loading may have had on the shear modulus-dependent shear wave speeds and whether the loaded shear modulus may provide a better analytical estimate of the shear wave speed is a focus of our on-going investigation.

The model-based findings of this study suggest that the degree of fiber alignment can affect the shear modulus and measured shear wave speeds in axially loaded ligaments. Practically, these effects should be accounted for when making shear wave speed measurements experimentally. Moving forward, insights from this model will be used to inform and develop methods for the noninvasive characterization of collateral ligament stress using shear wave tensiometry.

ACKNOWLEDGEMENTS

We gratefully acknowledge support from the NIH (R21 EB024957) and NSF (GRFP DGE-1747503).

REFERENCES

[1] Martin, JA et al., *Nat. Commun.,* 9:1592, 2018. [2] Blank, JL et al., *J. Mech. Behav. Biomed. Mat.*, 105:103704, 2020. [3] Martin, JA et al., *J. Biomech.,* 90: 9-15, 2019. [4] Amis, A., in *Sciences Basic to Orthopaedics,* 222-239, 1998. [5] Weiss, JA et al., *J. Biomech.,* 35: 943-950, 2002. [6] Gardiner, JC et al., *J. Orthop. Res.,* 21: 1098-1106. 2003. [7] Gouget, CM et al., *Biomech. Mod. Mechanobiol.,* 11:475-482, 2012.

TOWARDS CONTROLLING ARTERIAL GROWTH AND REMODELING VIA CELL-CELL SIGNALING: A MULTISCALE COMPUTATIONAL MODEL

Jordy G.M. van Asten (1), Marcos Latorre (2), Jason M. Szafron (2), Tommaso Ristori (1,3)
Frank P.T. Baaijens (1), Jay D. Humphrey (2), Sandra Loerakker (1)

(1) Department of Biomedical Engineering
Eindhoven University of Technology
Eindhoven, the Netherlands

(2) Department of Biomedical Engineering
Yale University
New Haven, CT, United States

(3) Department of Biomedical Engineering
Boston University
Boston, MA, United States

INTRODUCTION

Arteries have the ability to grow and remodel in response to alterations in their mechanical environment induced by injury or pathology. It is thought that arteries adapt to these perturbations in an effort to restore levels of stress and/or strain to preferred values, hence maintaining a so-called mechanobiological homeostasis [1]. Multiple computational models have been developed that aim to understand this arterial response to mechanical perturbations and predict the corresponding adaptive growth and remodeling (G&R) [2,3]. These models are often phenomenological and do not consider the biochemical and cellular mechanisms underlying arterial G&R. To better understand arterial G&R and uncover ways to control it, there is therefore a need for more mechanistic models that consider mechano-mediated cellular processes driving tissue G&R across length scales.

It is known that arterial G&R is modulated, in part, by vascular smooth muscle cells (VSMCs) populating the arterial wall. These can switch between a contractile phenotype, characterized by quiescence and muscular tone, and a synthetic one, characterized by increased proliferation and matrix synthesis. This phenotypic switch is regulated by Notch signaling, a mechanosensitive, cell-cell signaling pathway that involves interactions between membrane-bound receptors and ligands of neighboring VSMCs and plays a crucial role in arterial development, homeostasis, and adaptation [4,5]. It has been shown that the Notch pathway in VSMCs is sensitive to strain [6,7] and this has recently been incorporated into a computational model that simulates Notch signaling interactions and predicts the phenotype of VSMCs [6]. However, this model does not include arterial G&R and does not feature a full coupling between events at the tissue and cell scale.

Here, we have developed a multiscale computational model integrating cell-scale Notch signaling, mechanobiology and phenotypic switching with tissue-scale arterial G&R and mechanics. This framework provides a systematic tool to gain a deeper understanding of the role of Notch signaling in arterial G&R. This could ultimately be used to explore methods to control arterial G&R via interventions in the Notch pathway.

METHOD

A computational model was developed that combines a tissue-scale description of arterial G&R with a cell-scale description of Notch signaling in VSMCs (Fig.1). The tissue-scale part is based on the widely adopted constrained mixture theory [8], and describes arterial tissue with constituents collagen, elastin, and smooth muscle, whose production and removal are captured with constitutive equations to simulate the tissue G&R. In addition, biaxial stresses and strains are computed based on arterial geometry and hemodynamic loading conditions using Laplace's law.

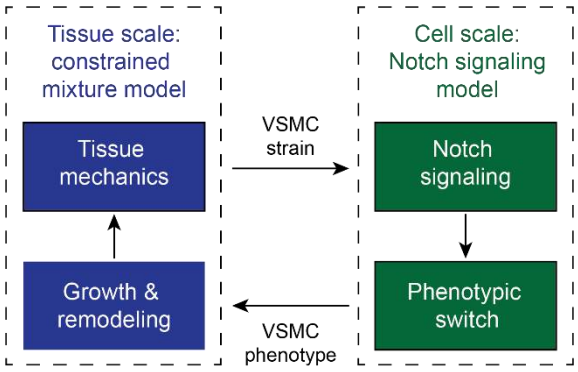

Fig. 1. Schematic overview of the multiscale computational model.

Cell-cell Notch signaling dynamics in the arterial wall are simulated using a recent model [6] in which Notch receptors and ligands of adjacent cells interact, resulting in the release of the Notch IntraCellular Domain (NICD) and, consequently, Notch activation and gene transcription. The production of Notch receptors and ligands decreases with increasing VSMC strain and, for each cell, changes in Notch protein content are described using a system of ordinary differential equations. The NICD content in each cell is used to predict whether that cell adopts a contractile or synthetic phenotype.

Fig.1 illustrates how the two models are coupled. In classic constrained mixture models, the mass production and removal terms of the constituents are governed by phenomenological stimulus functions whose values are based on perturbations from a mechanobiological homeostasis [2,3]. Here, we adapt this method by introducing a Notch stimulus function, which similarly acts as a regulator of the production and removal of tissue constituents and is itself a function of the NICD content and, thus, phenotype of the VSMCs. In particular, we assume that a contractile phenotype causes normal turnover, while a synthetic phenotype leads to increased proliferation and matrix synthesis.

RESULTS

Figure 2 shows the response of the model to a mechanical perturbation, such as a sustained increase in blood pressure, which results in increased inner radius and associated VSMC stretch (Fig.2A). This causes an initial decrease in the expression of Notch pathway proteins and, consequently, a decrease in NICD molecules, representing reduced Notch activation (Fig. 2B), leading to a switch from contractile to synthetic cells. As a result, tissue production is increased and the artery grows, shown by an increase in mass density (Fig. 2C) and wall thickness (Fig. 2D). Over time, thickening of the wall and a decrease in inner radius (not shown) in turn decrease the stretch and, thus, compensate for the initial perturbation leading to the tissue re-establishing its mechanobiological homeostasis as the stretch returns to its original value.

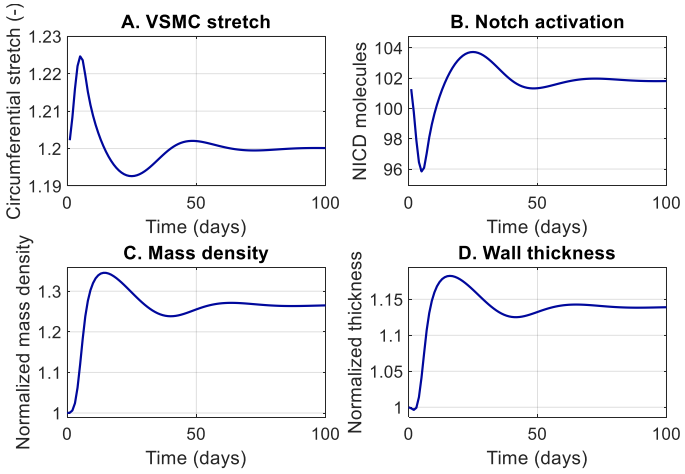

Fig. 2. Predicted adaptation of an artery to a sustained mechanical perturbation starting at day 0.

The model can also be adopted to investigate interventions in the Notch pathway, as shown in Fig. 3, where both over- and under-expression of Notch ligands in VSMCs are simulated. This leads to the phenotypic switch between synthetic and contractile cells occurring at a higher or lower stretch, respectively. As a result, the tissue will reach an altered homeostatic state, accompanied by a different mass density and wall thickness, corresponding to the new homeostatic stretch value.

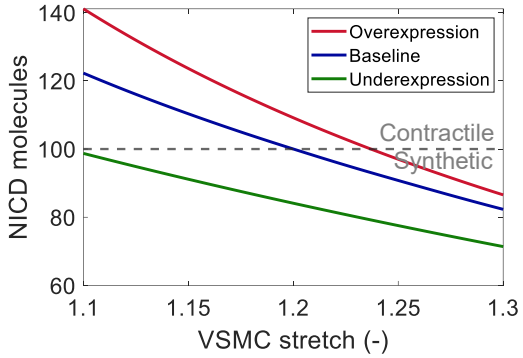

Fig. 3: Over- or underexpression of Notch ligands alters the stretch at which VSMCs reach a contractile phenotype.

DISCUSSION

An increase in arterial wall thickness (Fig. 2D) following increased strain induced by some mechanical perturbation is consistent with previous findings from both computational [2,3] and experimental studies [9]. The underlying changes in Notch activity seen in the model are also in accordance with previous experiments [7,10].

Interestingly, the model results are quite sensitive to interventions in the Notch pathway such as over- or underexpression of ligands (Fig. 3), which leads to the prediction of different homeostatic states. This is in line with experimental findings in which Notch interventions were successful in altering the adaptation of arteries after injury [5] and shows the model's potential to simulate how arterial G&R may be manipulated or controlled using Notch signaling. This potential could be adopted to explore new treatment options or be applied to the field of tissue engineering to examine methods of improving the G&R potential of engineered tissues by manipulating the Notch pathway, for example by functionalizing scaffold biomaterials with Notch ligands, which has recently been shown to be feasible [11].

Taken together, our multiscale model provides a computational framework that integrates mechano-mediated cell-cell Notch signaling with arterial G&R to predict the adaptation of arteries to mechanical perturbations. Our model demonstrates how Notch signaling can act as a key mechanistic player in G&R models, which have previously been mainly phenomenological, and has shown its potential in predicting ways to control tissue G&R via interventions in the Notch pathway. Ultimately, our model may be utilized to gain a better understanding of cell-mediated arterial G&R, explore new therapeutic strategies and aid in the rational design of scaffolds for vascular tissue engineering.

ACKNOWLEDGEMENTS

This project has received funding from the European Research Council (ERC) under the European Union's Horizon 2020 research and innovation programme (Grant agreement No. [802967]).

REFERENCES

[1] Humphrey, JD et al., Hypertension, 52:195-200, 2008. [2] Valentin, A et al., Phil Trans R Soc A, 367:3585-3606, 2009. [3] Latorre, M et al. APL Bioengineering, 2, 026108, 2018. [4] Iso, T et al., Arterioscler Thromb Vasc Biol, 23:543-553, 2003. [5] Zhu, G et al., Ann Vasc Surg, 41:241-258, 2017. [6] Loerakker, S et al., PNAS, 115(16):E3682-E3691, 2018. [7] Morrow, D et al., Am J Physiol Cell Physiol 289: C1188-C1196, 2005 [8] Humphrey, JD et al., Math Models Methods Appl Sci, 12(3):407-430, 2002. [9] Matsumoto, T et al., J Biomech Eng, 118(1):62-73, 1996 [10] Baeten, JT et al., Adv Pharmacol, 78:351–382, 2017. [11] Putti, M et al., ACS Appl Polym Mater, 1:2044-2054, 2019.

CHARACTERIZATION OF OXIDATIVELY RESPONSIVE THIOL-ENE NETWORKS FOR TISSUE ENGINEERING APPLICATIONS

T. Touchet (1,2), S. Briggs (2), L. Graul (2), D. Maitland (2)

(1) Trilliant Surgical, LLC
Houston, Texas, United States

(2) Dept. of Biomedical Engineering
Texas A&M University
College Station, Texas, United States

INTRODUCTION

Type II Diabetes (T2D) affects up to 21 million people in the United States and continues to increase each year[1]. Patients with T2D have a decreased ability to heal after a bone fracture or reconstructive surgery[2]. Delayed healing or non-union can be attributed to several factors, such as reactive oxygen species (ROS) like hydrogen peroxide, that promote osteoclastic activity over osteoblastic[3].

The current standard of care for at-risk patients is to use more hardware to increase fixation to achieve boney fusion. Unfortunately, these methods have not demonstrated clinical success and in the case of extremities, failed fixation in T2D patients often leads to amputation.

The ideal bone graft can be characterized by the ability to promote bone fusion despite the native environment, degrade at a rate complementary to neotissue formation, and maintain mechanical integrity throughout the remodeling process. Specific to T2D, modulation of the biological response to decrease inflammation and oxidative stress could return tissue back to homeostasis. By fabricating a synthetic bone graft with the antioxidant moieties, the shortcomings of current solutions may be addressed.

In this study, we report the preliminary findings on the chemical and oxidative degradation properties of a class of thiol-ene based thermoset polymers for use as bone grafts. Additionally, the thiol-ene polymer networks were assessed in terms of their oxidative responsiveness and ability to scavenge hydrogen peroxide at pathophysiologic levels.

METHODS

Fabrication of Thiol-ene Photopolymers (TPP). Polymer disks approximately 12.0 mm in diameter and 2.5 mm thick or thin films approximately 10.0 mm x 5.0 mm x 2.5 mm (l x w x h) were fabricated by mixing methacrylate macromers, butanediol dimethacrylate (BDMA) and diurethane dimethacrylate (DUDMA), with thiol macromers, pentaerythritol tetrakis3-mercptopropionate (PTMP), PCL4MP, and Glycol Dimercaptoacetate (GMA). The methacrylate and thiol ratio were varied from 50:50 to 70:30. Control compositions without thiol groups were fabricated in the same manner. Resin compositions were made in accordance with Table 1 with 0.5 wt% photoinitiator and cured using UV light at 425 nm for 5 minutes. The disks were then washed with isopropyl alcohol and dried under vacuum (32 mmHg) at 50ºC until a constant weight was achieved.

Table 1: Formula weights of resin composition used to make antioxidant thiol-ene networks.

Formulation Name	Weight Percent (wt %)				
	BDMA	PTMP	PCL4MP	DUDMA	GMA
TPP1a	43.3	21.6	13.0	21.6	-
TPP1b	33.3	16.6	33.3	16.6	-
TPP1c	24.4	12.2	51.1	12.2	-
TPP2	66.3	-	-	33.2	-
TPP3	45.2	22.6	-	22.6	9.0
TPP4	58.5	-	29.3	-	11.7

Chemical Characterization. The chemical structure of the thiol-ene networks was characterized by Attenuated Total Reflectance Fourier Transform Infrared Spectroscopy (ATR-FTIR) using a Bruker Alpha (Bruker).

Thermomechanical Characterization. Dynamic Thermal Mechanical Analysis (DMTA) was conducted with a Q800 DMA (TA Instruments) on neat films approximately 10.0 mm x 5.0 mm x 2.5 mm (l x w x h). Specimens were subject to a temperature ramp from -20°C to 120°C at

a rate of 5°C/min while under a 0.1% cyclic strain at 1 Hz frequency. The storage modulus and glass transition temperature were recorded.

Accelerated Oxidative Degradation. A 20% H_2O_2 solution was used for the accelerated oxidative solution. Disks were submerged in 25 mL of solution in a sealed vial. The vials were placed in a 37 °C oven (± 0.5 °C, measured continually with a thermocouple). Samples were incubated for 7 days before replenishing the solution, checked daily to monitor solution levels, and were weighed every week. At each time point, samples were removed, rinsed thoroughly in RO water, and dried in a 50 °C oven. Vacuum was pulled for 24 hours at 32 mm Hg. After removal from the oven, samples were weighed and returned to the vials, with freshly replenished solution. The mass was converted to remaining mass percentage, and the average change and standard deviation was recorded and plotted.

Hydrogen Peroxide Consumption. A 6.8 ppm (200 µM) H_2O_2 solution was used to simulate pathologic levels of hydrogen peroxide. Polymer disks were submerged in a 25 mL of solution in a sealed vial. The vials were placed in a 37 °C oven (± 0.5 °C, measured continually with a thermocouple). Hydrogen peroxide levels were evaluated using a colorimetric Hydrogen Peroxide Assay Kit (CHEMetrics) upon initial insertion (t=0) and after 72 hours (t=72). A blank vial filled with solution was used as a control. The concentrations were recorded and the average value with the standard deviation was plotted.

RESULTS

All formulations produced optically clear disks or neat films. The structures were confirmed with ATR-FTIR and show a reduction in the free thiol and the (CH2=CH2) bond of methacrylates, indicating successful incorporation of thiols into the network.

DMTA of the thin films for TPP1a, TPP2, and TPP3 displayed a storage modulus at 25˚C in the GPa range, with TPP3 being the highest. Additionally, TPP3 demonstrated a sharp transition likely attributed to the ideal network formation and the influence of hydrogen bonding from the urethane groups. All compositions demonstrated a decrease in storage modulus at 37˚C except for TTP1c because the network was in the rubbery phase. Although the glass transition temperature of TPP3 is near 37˚C, the storage modulus is consistent with the reported values of trabecular bone[4].

Table 2: Summary of mechanical and thermal properties of polymerized thiol-ene networks.

Formulation Name	Modulus at 25˚C	Modulus at 37˚C	Tg
TPP1a	1420 MPa	674 MPa	47°C
TPP1b	50 MPa	28 MPa	11°C
TPP1c	7 MPa	7 MPa	-19°C
TPP2	3015 MPa	2772 MPa	51°C
TPP3	1318 MPa	315 MPa	38°C
TPP4	349 MPa	199 MPa	28°C

In vitro accelerated degradation was performed in an oxidative environment to characterize the oxidative response of the polymer. All thiol containing resins was characterized by rapid changes in mass followed by a plateau for scaffolds that contained sulfide groups (Figure 2). This phenomenon may be attributed to the oxidation of sulfide functional groups, which increases the network's susceptibility to hydrolysis.

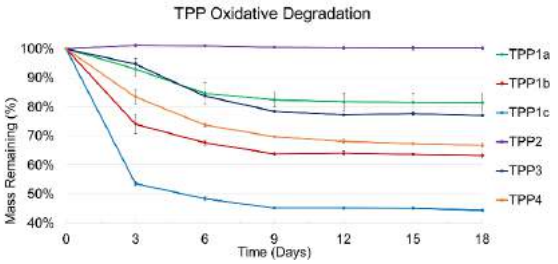

Figure 2: Mass loss of thiol-ene networks in accelerated oxidative media.

Increasing thiol content from 70:30 (methacrylate:thiol) to 50:50, correlated to a decrease in hydrogen peroxide concentration as represented by TPP1, TPP2, and TPP3. Additionally, hydrogen peroxide consumption increases in resin compositions that contain shorter chain thiols such as TPP3 and TPP4. Hydrogen peroxide concentration did not decrease with the thiol free resin, TPP2. The control blank demonstrated that there was slight degradation with the initial hydrogen peroxide which is expected as hydrogen peroxide naturally degrades over time.

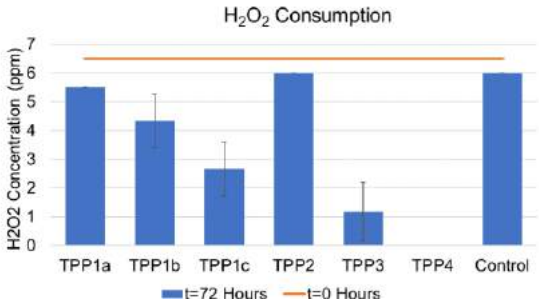

Figure 3: Consumption of hydrogen peroxide at pathophysiologic concentrations.

DISCUSSION

The work presented in this study demonstrates that polymer networks containing sulfide groups successfully sequester hydrogen peroxide at pathologic levels. Hydrogen peroxide responsiveness can be tailored by changing the methacrylate to thiol ratio as well as the molecular weight of the thiol moieties used. The oxidative media converts the sulfide groups to sulfoxides and sulfones. This oxidation increases the hydrophilicity near ester moieties allowing for increased degradation via hydrolysis. The oxidative degradation of the resin composition did not directly correlate with the ability to react with ROS species, indicating that the processes may not be directly related.

This preliminary work shows that thiol-ene polymer networks can reduce the ROS species that contribute to delayed bone healing in T2D. Additionally, the storage modulus of the resin compositions was comparable to native bone. Future work will focus on optimizing the ROS sequestering in addition to biocompatibility assessment and mechanical testing relevant to bone grafting applications.

ACKNOWLEDGEMENTS

This work was supported by funding from Trilliant Surgical, LLC.

REFERENCES

[1] Bullard, K. M., et al., *Morbidity and Mortality Weekly Report*, *67*: 359, 2018.
[2] Jiao, H., et al., *Curr Osteoporos Rep*, *13*: 327-35, 2015.
[3] Fraser, J. H., et al., *Bone*, *19*: 223-6, 1996.
[4] Bouxsein, M. L., et al., *J Bone Miner Res*, *12*: 839-46, 1997.

MOTOR EVOKED POTENTIAL RECRUITMENT CURVES INDICATE NEUROPLASTICITY OF THE BICEPS BRACHII IN CERVICAL SPINAL CORD INJURY.

Thibault Roumengous (1), Yasmina Zeineddine (1), Carrie L. Peterson (1)

(1) Department of Biomedical Engineering
Virginia Commonwealth University
Richmond, VA, USA

INTRODUCTION

Chronic spinal cord injury (SCI) is a condition that involves motor impairment through partial or complete paralysis, reducing the quality of life for individuals with SCI [1]. Understanding injury-induced neuroplasticity following SCI has implications for the development of rehabilitation programs aimed at recovering motor function [2]. Reliable tools and models are needed to provide accurate indicators of neuroplasticity over time in these populations to further aid recovery.

Non-invasive brain stimulation is a promising approach for measuring neuroplasticity. Resulting motor evoked potentials (MEPs) from the different transcranial magnetic stimulation (TMS) intensities represent responses from a variety of neural populations, and demonstrate a graded response with increasing intensities, offering comprehensive insights into the condition of a neuromuscular circuit through metrics such as the slope of the curve [3]. Thus, RCs could enhance our understanding of injury-induced neuroplasticity and recovery when analyzing these changes over time [4]. If RCs are to be used as a metric of neuroplasticity in individuals with SCI, an understanding of RC reproducibility is needed. In particular, proximal arm muscles such as the biceps brachii (BIC), which may be targeted in rehabilitation to grant individuals with SCI greater functional independence, have not been studied with respect to their ability to produce reproducible RCs at a given time point.

This study aims to compare RC slopes between SCI and nonimpaired (NI) individuals and determine the reproducibility of RC slopes across three assessments. Additionally, linear regression and the Boltzmann equation were compared as methods of modeling the MEP RCs. We hypothesized a steeper slope in SCI patients relative to NI subjects, which would correlate to increased excitability in the BIC and imply adaptive neuroplasticity after injury.

METHODS

Experimental Set-up: Eight nonimpaired (F=4, mean age 22.7 ± 2.5 years) and five SCI (F=3, mean age 46.6 ± 7.8 years, levels of injury: C5-C6, ASIA scores: A-D, at least 3 years post injury) participants consented to participate in the study and completed two or three sessions separated by at least a day, a week at most. EMG surface electrodes were placed on the BIC before determining the cortical hotspot and resting motor threshold (RMT) using a double cone TMS coil. To collect RCs, TMS pulses were randomly administered between 80%-160% of a participant's RMT in 10% increments with a 10s inter-stimulus interval. MEPs were excluded if they exceeded ±3 standard deviations of the mean response per intensity to eliminate MEPs that may have been facilitated by low levels of muscle activation.

$$Y = minEMG + \frac{(maxEMG - minEMG)}{1 + e^{\frac{(V50 - X)}{Slope}}} \quad (1)$$

Equation (1), the Boltzmann equation, was used to model the RC data [5]. The variable *minEMG* and *maxEMG* represent the minimal and maximal MEP size, respectively. *V50* represents the stimulus intensity (% MSO) value when the MEP size is half of its maximal size. Simple linear regression was also utilized for curve fitting, and their respective accuracies of prediction (R^2) were calculated for comparison.

Data and Statistical Analysis: Statistical analyses were performed using R (R Core Team (2013)) and GraphPad Prism. Slopes obtained between 110% and 160% RMT from the recruitment curves of SCI and NI participants were compared using an unpaired t test with

Welch's correction to account for unequal standard deviations between the SCI and NI groups.

Inter-session reproducibility was determined by calculating intraclass correlation coefficients (ICCs) of the slope parameter. ICCs were calculated using a two-way random-model with consistency agreement. ICC values > 0.75 were defined to represent good to excellent agreement between sessions [6].

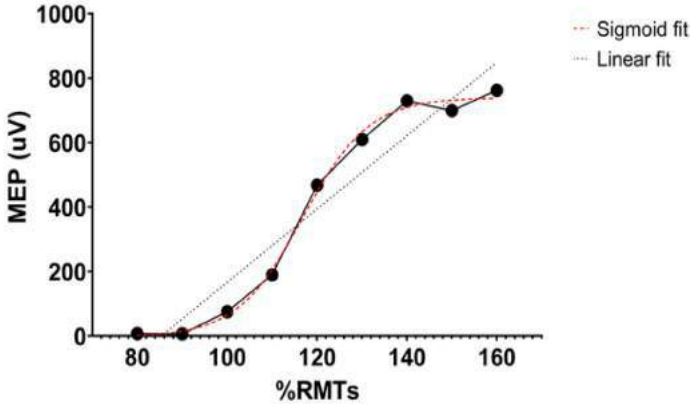

Figure 1: MEP recruitment curve from an individual with SCI. Both curve fitting methods are shown superimposed onto the recorded MEP data (black).

RESULTS

The RC's slopes obtained using linear regression from the SCI group (6.12 mV/%RMT ± 6.82) were significantly higher than the slopes obtained from the NI group (1.34 mV/%RMT ± 1.32) ($p = 0.008$ $t = 2.505$, $df = 13.52$). No significant differences in RMTs were found between the SCI and NI group ($p = 0.557$, $t = 0.5919$, $df = 44$) (Figure 2). Accuracy of prediction (R^2) and inter-session reproducibility data are presented in Table 1.

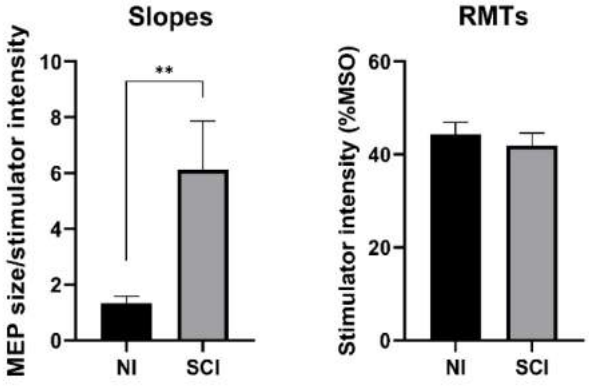

Figure 2: Left: Slopes obtained from linear regression are significantly greater in the SCI group compared to NI. Right: Mean RMTs are not different between SCI and NI. Asterisks represent statistical difference ($p < 0.05$) and error bars represent standard the error of the mean (SEM).

Table 1: Inter-session reproducibility and accuracy of prediction of curve fitting methods (mean ± SEM).

Parameters	NI	SCI
Mean ICC (3, k)	0.83	0.78
Sigmoid fit mean R^2	0.73 ± 0.04	0.95 ± 0.05
Linear fit mean R^2	0.71 ± 0.04	0.82 ± 0.05

DISCUSSION

Our primary aim was to compare MEP RCs of the BIC between nonimpaired participants and participants with chronic cervical SCI and determine the reproducibility of biceps RCs. A secondary aim was to investigate curve fitting methods (linear regression versus sigmoidal function).

Our study results demonstrate that MEP recruitment curves of the BIC analyzed using linear regression revealed significantly higher slopes in the chronic SCI group compared to the nonimpaired group. An increased RC slope indicates greater excitability in the neuromuscular circuit between the motor cortex and the BIC, suggesting a degree of cortical reorganization occurred post-injury in the group with SCI [7]. Potential mechanisms of reorganization include the enlargement of the motor representation of the BIC in the motor cortex, enhanced synaptic transmission, or reduced inhibition [8, 9]. No significant differences in RMTs were found between groups. This suggests that the alteration in excitability after SCI (demonstrated by the RC differences) may be prominently occurring at sub-cortical or spinal levels since RMTs are thought to be related to the membrane excitability of a central core of cortical neurons [10].

The sigmoidal function models the shape of the curve more precisely compared to the linear regression approach, although no differences in accuracy of prediction (R^2) were found in both NI and SCI groups. Linear regression was found to accurately represent the slope of the modeled data. Finally, parameters extracted from the MEP recruitment curves were found to be reproducible across sessions, lending credibility to the utility of RCs in monitoring neuroplasticity in populations undergoing neuromuscular rehabilitation.

Limitations of this work include small sample sizes and heterogeneities in remaining motor function among SCI participants. Additionally, most SCI participants only completed two sessions, limiting the reproducibility analysis across two days.

Future research should determine whether RCs are a sensitive biomarker for the effect of recovery or interventions during acute and chronic stages of SCI.

ACKNOWLEDGEMENTS

This work was supported by VCU's CTSA (UL1TR000058 from the National Center for Advancing Translational Sciences) and the CCTR Endowment Fund of Virginia Commonwealth University.

REFERENCES

[1] Sezer N, et al., *World J Orthop,* 6: 24–33, 2015.
[2] Moxon KA, et al., *Neuroscience* 283: 78–94, 2014.
[3] Devanne H, et al., *Exp Brain Res*, 114: 329–338, 1997.
[4] Nicotra, A, et al., *Eur Spine J* 22, 189–196, 2013.
[5] Kukke SN, et al., *J Clin Neurophysiol,* 31: 246–252, 2014.
[6] Koo TK, et al., *J Chiropr Med*, 15: 155–163, 2016.
[7] Hylin MJ, et al. *Neural Plasticity,* e7125057, 2017.
[8] Freund P, et al., *Eur J Neurosci*, 34: 1839–1846, 2011.
[9] Nardone R, et al., *Spinal Cord* 53: 534–538, 2015.
[10] Ziemann U. Chapter 32 - In: *Handbook of Clinical Neurology*, *Elsevier*, p. 387–397, 2013.

SB^{3}C2021
Summer Biomechanics, Bioengineering and Biotransport Conference
June 14-18, Virtual

HEMODYNAMIC SIMULATION TO PREDICT SUCCESSFUL VS UNSUCCESSFUL CATHETER INTERVENTIONS FOR BRANCH PULMONARY ARTERY STENOSIS – EXPERIMENTAL VALIDATION IN SWINE

Ryan J. Pewowaruk (1), Luke J. Lamers (2), Alejandro Roldán-Alzate (1,3,4)

(1) Biomedical Engineering
University of Wisconsin - Madison
Madison, WI, USA

(2) Pediatrics
University of Wisconsin - Madison
Madison, WI, USA

(3) Mechanical Engineering
University of Wisconsin - Madison
Madison, WI, USA

(4) Radiology
University of Wisconsin - Madison
Madison, WI, USA

INTRODUCTION

Branch pulmonary artery stenosis (bPAS) commonly occurs in congenital heart disease (CHD) [1]. The presence of localized, anatomical bPAS disrupts global distribution of blood flow to the lungs due to obstruction to the lung distal to the bPAS, and an increase in relative flow into the 'unaffected' lung. At many centers catheter based interventions are used to manage patients with bPAS. While catheter interventions successfully relieve the anatomical bPAS with long term favorable outcomes [2], a recent study showed that 1/3 of patients do not improve their pulmonary blood flow (PBF) distributions following interventions [3]. The reasons for the failure of some patients to normalize their PBF distributions, despite catheter-relief of the anatomical bPAS, remains unknown. Failure to improve PBF distributions was associated with lack of improvement of exercise capacity and could be especially problematic in young patients, for whom normal PBF is believed to be essential for lung and PA growth.

There is a clinical need for a non-invasive tool to predict which patients are most likely to benefit from bPAS intervention. The development of such a tool should improve treatment planning for patients and may also suggest novel research directions to better understand the pathophysiology of this disease. Hemodynamic simulations based on patient specific anatomies extracted from non-invasive medical imaging are a promising technology with expanding applications in the clinical management of coronary artery disease and an active area of research in other vascular territories, including bPAS [4]. The goal of this study was to develop a predictive tool leveraging non-invasive MRI measurements to generate hemodynamic simulations using 3D vascular anatomy reconstructions and flow dynamics followed by direct experimental measures and outcomes in a validated swine PAS model.

METHODS

Discrete proximal left PA stenosis (LPAS) was surgically created as in ten 2-week old male swine. Five swine had stent intervention at 5 weeks of age with stent dilation at 10 weeks of age. Five swine had stent intervention at 10 weeks of age. Right heart catheterization and MRI were performed to measure hemodynamics and pulmonary blood flow (PBF) distributions immediately pre- and post- intervention. Further details on the imaging and catheterization techniques can be found in our previous publications [5]. The University of Wisconsin IACUC reviewed and approved this protocol.

We had 13 cases to perform virtual intervention predictions. A recently developed lumped parameter modeling technique was implemented and used for hemodynamic simulations that retains accuracy while significantly improving efficiency compared to traditional computational fluid dynamics [6]. First pre-intervention pulmonary artery anatomies were segmented from medical imaging datasets. The resistance and compliance of the distal right and left pulmonary vasculature were tuned to match measured pre-intervention PBF distributions to within 10% accuracy. The diameter of the proximal LPA was then virtually increased to match the maximum distal LPA diameter. Predictive hemodynamic simulations were then performed, either PBF based simulations or RHC based simulations.

The agreement of simulation predictions with experiments was assessed with standard statistical techniques such as Bland-Altman analysis and ICC. The accuracy and diagnostic value of simulations was evaluated by their capability to predict physiologic intervention success based on whether interventions met three previously defined criteria: 1. an increase in total LPA blood flow greater than 20%, 2. a decrease in the stenotic pressure gradient greater than 50%, and 3. a decrease in systolic MPA pressure greater than 25%.

RESULTS

The variability of the physiological responses to an intervention was large. For further information of the physiological consequences of LPAS and stent interventions in swine the reader is referred to our previous publication [5].

Representative results of pre-to-post intervention changes from a simulation of a 5-week stent intervention are shown in Figure 1. It can be observed that the simulation predicted a decreased MPA pressure, decreased stenotic pressure gradient, and increased PBF to the left lung.

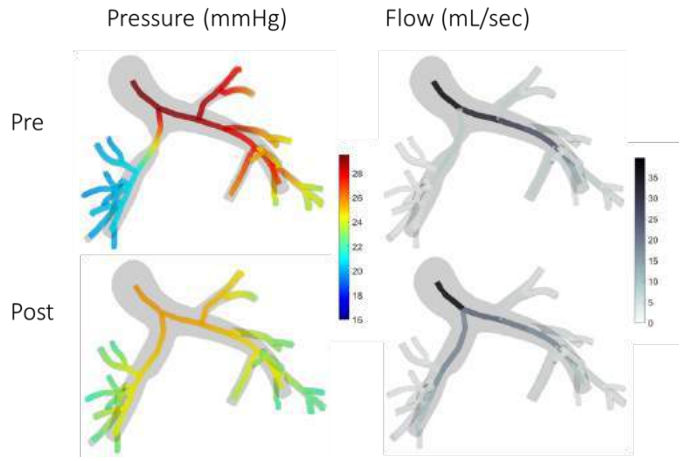

Figure 1: Representative intervention prediction results

Results from Bland-Altman analysis and ICC are presented in Table 2. Simulations predicted a decrease in MPA systolic pressure that was not observed experimentally. Simulations systematically predicted smaller changes to the stenotic pressure gradient compared to experiments. There was a negligible bias between experimentally measured changes in left PBF distribution and simulations. Simulations had moderate agreement and correlation with experimentally measured changes in left PBF %.

Table 1: Statistical comparison of simulations and experiments

	Δ Experiment	Bias	ICC	r
MPA Systolic Pressure (mmHg)	0.5±3.5	-2.9±3.6	0.00	0.29
Stenotic Pressure Gradient (mmHg)	-12.5±4.7	4.5±4.2	0.28	0.57
Left PBF (%)	11.4±15.6	3.4±11.1	0.69	0.71

Predictions of >20% LPA flow increase had excellent accuracy and diagnostic value. Predictions of >50% decrease in pressure gradient were also excellent but diagnostic value could not be calculated as 100% of our experimental interventions successfully decreased the pressure gradient. Predictions of >25% MPA systolic pressure decrease has excellent accuracy but weak diagnostic value.

Table 2: Accuracy and Diagnostic Value

Success Marker		Simulation
>20% Flow Increase to LPA	Accuracy	92%
	Area Under Curve	0.96
>50% Decrease Pressure Gradient	Accuracy	90.9%
	Area Under Curve	--
>25% Decrease MPA Pressure	Accuracy	92%
	Area Under Curve	0.58

DISCUSSION

We investigated the feasibility of hemodynamic models to predict the success of catheter based interventions for branch pulmonary artery stenosis. These predictions were then validated with experimental measurements in a swine model of left PAS with catheter interventions. Overall, there was only weak to moderate agreement between predicted and measured changes in stenotic pressure gradient and pulmonary blood flow distributions. However, simulations showed good diagnostic value for predicting successful vs. unsuccessful bPAS interventions. We believe the results of this proof of concept study are promising and should encourage future development for using hemodynamic models in planning interventions for patients with bPAS.

Catheter interventions to relieve bPAS in patients with CHD have shown long term favorable results [2] and in several centers catheter techniques are first line therapy for bPAS. However, research on catheter based interventions for bPAS has typically focused on immediate procedural technical success measured by the increase in the stenotic diameter rather than physiologic changes in PBF distributions, exercise capacity, or patients' clinical symptoms. A recent study found that for catheter interventions in patients with bPAS immediate technical success was achieved in 100% of patients, but PBF distribution improved in only 67% of patients [3]. Importantly, the patients who did not improve PBF distribution also did not improve their exercise parameters or symptoms.

While we consider the results of the current study promising, improvements could be made to enhance the simulations predicative capabilities. A key area for improvement would be to include changes in distal vascular resistance following interventions. Our simulations predicted that MPA pressures would decrease following intervention which experimentally does not occur in swine or humans [3,5]. Previous simulations of surgical repair for bPAS have assumed that the distal vasculature will vasodilate to maintain wall shear stress homeostasis [4] but this would further decrease MPA pressures. Instead, our results and the cited literature suggest that in patients without significantly elevated PA or RV pressures, the distal pulmonary vascular will vasoconstrict to maintain pre-intervention MPA pressures following an intervention. The hemodynamic and anatomical response of the distal pulmonary vasculature to changes in flow and pressure (both before and after relief of stenosis) is clearly complex. There is potential for these simulations and subsequent direct measures of PBF to support a better understanding of this disease, which should lead to more effective therapies, particularly for the 1/3 non-responder group.

Limitations include a relatively small sample size of only male swine, and that surgically created discrete PAS lesions are likely simpler than the complex lesions often seen in human patients.

In conclusion, this study investigated the feasibility of hemodynamic models to predict the success of catheter based interventions to relieve branch pulmonary artery stenosis. We believe the results of this proof of concept study are promising and should encourage future development for using hemodynamic models in planning interventions for patients with bPAS.

ACKNOWLEDGEMENTS

NCATS UL1TR002373 and NHLBI T32 HL 007936

REFERENCES

[1] Rhodes, J et al., *Am. J. Cardiol.* 81:1217–1219, 1998.
[2] Law, M et al., *Catheter. Cardiovasc. Interv.* 75:757–764, 2010.
[3] Hiremath, G et al., *JACC Cardiovasc. Interv.* 12:289–297, 2019.
[4] Yang, W et al., *Congenit. Heart Dis.* 13:241–250, 2018.
[5] Pewowaruk, R et al., *Catheter. Cardiovasc*, 96: 1454-1464, 2020
[6] Miramezzani, M and Shadden, S, *Ann. Biomed. Eng.* 1–17, 2020

A DEEP-LEARNING APPROACH FOR DIRECT WHOLE-HEART MESH RECONSTRUCTION

Fanwei Kong and Shawn C. Shadden

Department of Mechanical Engineering
University of California, Berkeley
Berkeley, California, USA

INTRODUCTION

Computer models of anatomical structures reconstructed from volumetric medical images are increasingly used for a number of clinical applications. In particular, computer models of the heart, if combined with biophysical simulations, can assist understanding, diagnosis and treatment of cardiac diseases [1-2]. Creating accurate patient-specific models of the heart from image data requires significant time and human efforts; this is arguably the #1 factor limiting clinical applications. Deep learning methods can train neural networks from existing data to automatically process medical images and generate whole heart reconstructions. Such methods may accelerate the model generation process to enable high-throughput, large-cohort analyses of patient-specific cardiac function.

Most deep learning methods have focused on segmentation of the cardiac structures by pixel classification [3-4]. This results in an implicit representation of cardiac structures, however simulation and even some visualization methods require explicit representations—typically as unstructured meshes. Besides requiring additional surface processing techniques to generate meshes from the segmentation, these prior approaches suffer from a number of limitations including disconnected regions or incorrect surface topology due to erroneous segmentation and stair-case artifacts from limited image resolution [3].

We propose a novel approach that directly predicts whole heart surface meshes from volumetric images by predicting deformation on mesh vertices from a pre-defined mesh template using a graph convolutional neural network. We demonstrate promising performance of generating high-resolution and high-quality heart reconstructions from both CT and MR data. Furthermore, our method shows improved robustness to limited data, and can more efficiently produce temporally-consistent and feature-corresponding predictions of heart motion from CT or MR cine sequences, and therefore can potentially be applied for efficiently constructing 4D whole heart dynamics.

METHODS

Dataset Information: Contrast-enhanced CT images or MR images that cover the whole heart were obtained from four existing public datasets: multi-modality whole heart segmentation challenge (MMWHS), orCalScore challenge, left atrial wall thickness challenge and left atrial segmentation challenge. From these data, we used a total of 87 CT images and 41 MR images to train our model, and 15 CT images and 6 MR images to validate the model. The final performance of our model was evaluated on the MMWHS held-out test dataset that contains 40 CT images and 40 MR images. Furthermore, additional time-series CT images were collected to evaluate the performance of our approach on time-series image data.

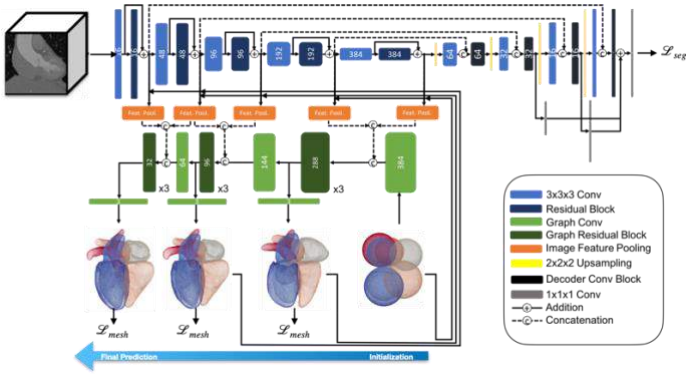

Figure 1: Proposed automatic whole heart reconstruction approach.

Neural Network Architecture: As shown in Fig 2, our framework consists of three components to predict the whole heart meshes from a volumetric input image. For an 3D image volume, our framework uses an image encoding module that extracts and encodes image features. From these image features, we use a mesh deformation module that combines features from images and meshes to predict deformation of mesh vertices from sphere mesh templates. The mesh deformation module consists of three deformation blocks with graph convolutional layers that progressively deform mesh templates to match with the corresponding tissue boundaries. Furthermore, our framework uses a segmentation module that predict a binary segmentation map to enable additional supervision using ground truth annotations.

Neural Network Optimization: The training of the neural network model was supervised by 3D ground truth meshes of the whole heart as well as a binary segmentation representing the occupancy of the heart in the input image. The ground truth whole heart meshes were extracted from the segmentation of cardiac structures using a marching cube algorithm. We considered two categories of loss functions for the mesh predictions, geometry consistency losses and regularization losses in the training process. The geometry consistency losses include point and normal consistency losses while the regularization losses include edge length and Laplacian losses. The parameters in the neural network models were optimized by minimizing the loss functions using the Adam stochastic gradient descent algorithm.

RESULTS

Our method is able to automatically generate high-resolution whole-heart reconstructions (10k surface vertices for each cardiac structure) from an input image within half a second on a modern GPU. We compare the performance of whole-heart reconstructions from our method against two baselines: 2D UNet [5] and a modified 3D UNet [6]. Table 1 shows the average Dice score (a similarity index) of the reconstruction results of both the whole heart and individual cardiac structures for the MMWHS test dataset. For both CT and MR data, our method consistently outperformed our baselines in terms of Dice scores for both whole heart and all individual cardiac structures.

Table 1: A comparison of prediction accuracy on MMWHS MR and CT test datasets from different methods.

		EPI	LA	LV	RA	RV	AO	PA	WH
C T	Ours	**0.899**	**0.932**	**0.940**	**0.892**	**0.910**	**0.950**	**0.852**	**0.918**
	2D UNet	**0.899**	0.931	0.931	0.877	0.905	0.934	0.832	0.911
	3D UNet	0.863	0.902	0.923	0.868	0.876	0.923	0.813	0.888
M R	Ours	**0.797**	**0.881**	**0.922**	**0.888**	**0.892**	**0.890**	**0.816**	**0.882**
	2D UNet	0.795	0.864	0.896	0.852	0.865	0.869	0.772	0.859
	3D UNet	0.761	0.852	0.879	0.866	0.828	0.742	0.764	0.840

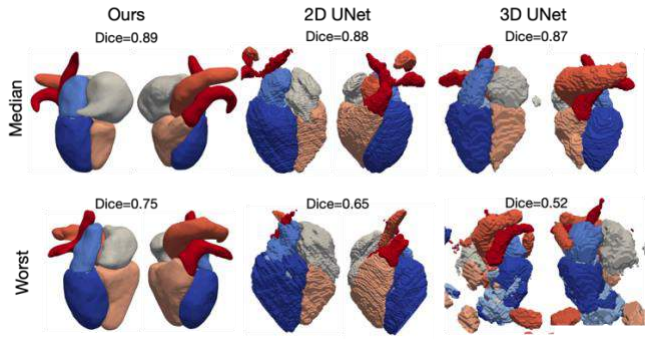

Figure 2: Visualizations of the median and worst reconstruction results among the test dataset in terms of whole-heart Dice scores.

Figure 2 visualize the median and worst results from the different methods for MR images, respectively, from the MMWHS test dataset. As shown, our method is able to construct smooth geometries while segmentation-based methods, such as the 2D UNet or 3D UNet, produced surfaces with staircase artifacts or disconnected regions that would require post-processing to remove or connect.

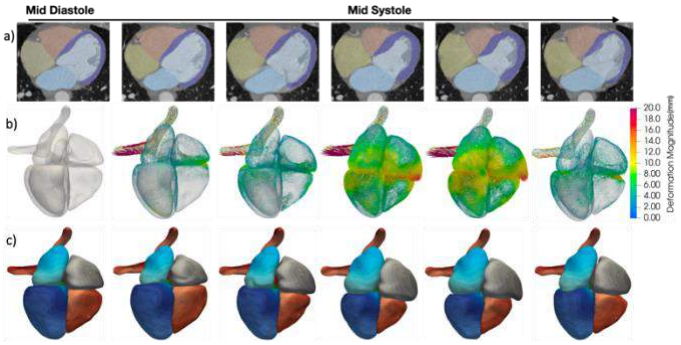

Figure 3: Whole-heart reconstruction results for time-series CT data. A) predicted segmentation b) mesh deformation vectors since late diastole and c) the feature correspondence maps of meshes.

Figure 3 displays example whole-heart reconstructions from our methods on time-series CT data. Although our model predicts mesh reconstructions independently from each time frame, it is able to consistently deform the template meshes so that the same mesh vertices on the template are generally mapped to the same region of the reconstructed geometries across different time frames, as shown by the color maps of vertex IDs in Figure 3. Moreover, as shown, our method is able to capture the minor changes between time frames whereas 2D and 3D UNet results (not shown) often had significant segmentation discrepancies between time frames. Therefore, our method can potentially be applied to efficiently construct 4D dynamic whole-heart models to capture the motion of a beating heart by computing the deformation field on each mesh vertex, as displayed in Figure 3.

DISCUSSION

Automated image-based reconstruction of cardiac anatomy and the concomitant geometric representation using unstructured meshes is important to a number of applications, including visualization of patient-specific heart morphology and computational simulations of cardiac function. We have demonstrated the advantages of this method over prior segmentation-based approaches in terms of both precision and surface quality [4-6]. Namely, the use of a template mesh can introduce topological constraints so that predicted cardiac structure are diffeomorphic to the template. Thus, our template-based approach enables one to eliminated disconnected regions and greatly reduce erroneous topological artifacts often encountered with prior methods. Furthermore, the method produced temporally consistent and feature-corresponding predictions by consistently mapping mesh vertices on the templates to similar structural regions of the heart. While the cardiac structures of interest were diffeomorphic to spheres, the presented method has the potential to be generalized to anatomical structures with a different topology, by using a different template mesh with the required topology.

ACKNOWLEDGEMENTS

This work was supported by the NSF, Award #1663671.

REFERENCES

[1] Prakosa et al., *Nature Biomed Eng*, 2(10), Oct, pp. 732–740, 2018.
[2] Chnafa et al., *Annals of Biomed. Eng.* 44(04), 2016
[3] Kong et al., *J of Biomechanical. Eng.* 142(11), 09. 111011, 2020.
[4] Zhuang et al., *Med Image Analysis*, 58, 101537, 2019.
[5] Ronneberger et al., *MICCAI, Springer*, pp 234-241, 2015.
[6] Isensee et al., *MICCAI, Springer* pp. 287–297, 2017.

SB³C2021
Summer Biomechanics, Bioengineering and Biotransport Conference
June 14-18, Virtual

MALE AND FEMALE HUVEC DIFFER IN EXTRACELLULAR MATRIX, INFLAMMATION, AND VASCULAR FUNCTION-RELATED GENE EXPRESSION

Callie M. Weber (1), Nicole Arnold (2), Douglas Dluzen (2), Alisa S. Morss Clyne (1)

(1) Fischell Department of Bioengineering
University of Maryland
College Park, MD, USA

(2) Department of Biology
Morgan State University
Baltimore, MD, USA

INTRODUCTION

As we move toward personalized precision medicine, understanding the influence of sex on cellular phenotype and disease is becoming increasingly important. Most research on sex-specific effects focuses on lifelong exposure to sex hormones in primary adult cell lines. Human umbilical vein endothelial cells (HUVEC) provide unique insight into innate differences between male and female endothelial cells. Prior studies found that female HUVEC express a more proliferative and migratory phenotype than male [1], and a proteomic analysis of twin pairs demonstrated 88 differentially expressed proteins between male and female HUVEC [2]. Sexual dimorphisms in HUVEC may help parse out hormonal vs. innate effects of sex on endothelial function, and thereby provide novel insight into vascular pathologies and subsequent cardiovascular disease. The goal of this study was to determine the influence of cell sex on endothelial gene expression.

METHODS

Cell culture: Pooled HUVEC (passages 4-9) from 3 male and 3 female donors were cultured in Endothelial Growth Medium-2 supplemented with 10% fetal bovine serum, 1% penicillin-streptomycin, and 1% L-glutamine.

RNA Isolation: Total RNA for RNA sequencing were isolated using TRIzol phenol/chloroform. RNA quantity and quality were assessed using a NanoDrop 2000c. RNA was sequenced by Novogene using the NovaSeq 6000 with 150-bp paired end reads. Data were cleaned and assessed in Galaxy and visualized in Advaita iPathway.

Western Blotting: Protein O-linked β-N-Acetylglucosamine (O-GlcNAc) and endothelial nitric oxide synthase (eNOS) were assessed by Western blot. Cells were scraped and lysed in ice-cold RIPA buffer. Lysates were normalized to protein content, separated using SDS-PAGE in a 4-12% Bis-Tris Gel, and transferred to a nitrocellulose membrane using the iBlot 2 system. Membranes were incubated overnight at 4°C with an O-GlcNAc (CTD110.6) or eNOS (D9A5L) primary antibody diluted 1:1000, and then incubated for 2 hours at room temperature with a horseradish peroxidase-conjugated secondary antibody at 1:2000. Proteins were visualized using an Enhanced Chemiluminescence Substrate in a Fluorchem digital imager. Band intensities were quantified using AlphaView Software.

Statistical analysis: Differential expression of sequenced RNA was assessed using the EdgeR function in Galaxy with a Benjamini-Hochberg p-value correction. Genes with an adjusted p-value of less than 0.05 and a log fold change of at least 0.5 were identified as being significant. Western blots were analyzed using an unpaired two-tailed t-test in Prism (GraphPad).

RESULTS

2,140 of the 37,747 genes identified through RNA sequencing were differentially expressed in male and female HUVEC (Fig. 1A). Pathway analysis in iPathway revealed extracellular matrix (ECM) interactions, vascular function, and inflammation to be among the pathways with the highest degree of differential gene expression between male and female HUVEC. 13 of these genes were related to ECM proteins and adhesion (Fig. 1B). Of the six collagen-encoding genes that were differentially expressed, genes for Collagen I Alpha I, Collagen 4 Alpha 6, and Collagen 6 Alpha 2 and 3 (COL1A1, COL4A6, COL6A2, COL6A3), were downregulated in male, while Collagen I Alpha 2 and Collagen 9 Alpha 3 (COL1A2, COL9A3) were upregulated. Genes coding for integrin subunits Alpha 1, Alpha 10, Alpha 7, and Beta 4 (ITGA1, ITGA10, ITGA7, ITGB4) were upregulated in male cells. Laminin genes encoding for laminin subunits beta 3 and gamma 2 (LAMB3, LAMC2) were downregulated in male cells.

Seven differentially expressed genes were associated with vascular dysfunction and inflammation (Fig. 1C). NOS3, which encodes eNOS, was downregulated in male compared to female HUVEC, confirming previous findings [1]. SDC1, which encodes glycocalyx proteoglycan syndecan-1, was also downregulated in male HUVEC. Genes encoding for ICAM-1, VCAM-1, and E-Selectin (ICAM1, VCAM1, SELE) were all upregulated in male HUVEC. Finally, IL1R1, which encodes for an IL-1 receptor, was upregulated in male HUVEC, while IL1A, which encodes for IL-1α was downregulated in male cells.

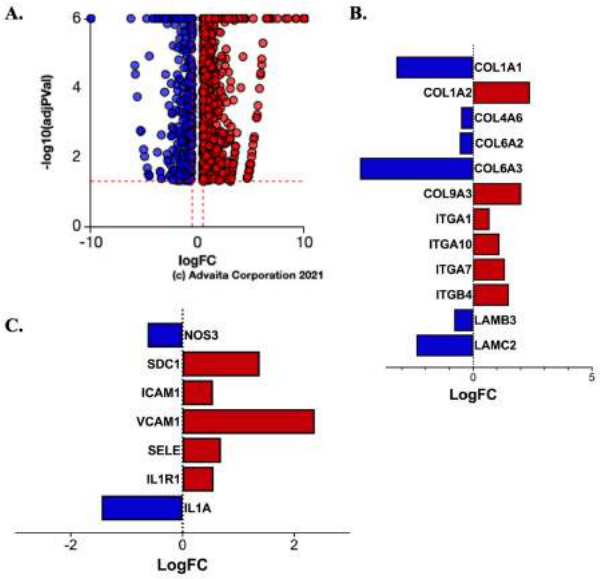

Figure 1. Differential gene expression in male vs. female HUVECs. A. Volcano plot showing significantly up- or down-regulated genes. Genes were categorized as significant for adjusted p<0.05, and a log fold change >0.5. B. Log fold changes of ECM associated genes. C. Log fold change of vascular function associated genes. Red: genes upregulated in male cells compared to female cells. Blue: genes downregulated in male cells compared to female cells.

We confirmed that NOS3 gene upregulation correlated with increased eNOS protein (Fig 2). eNOS O-GlcNAcylation, which is thought to inhibit NO production, is higher in female HUVEC. However, there were no differences in the glycolytic enzymes regulating O-GlcNAc production (glutamine-fructose-6-phosphate aminotransferase; GFAT), attachment (O-Linked N-Acetylglucosamine Transferase; OGT), or removal (O-GlcNAcase; OGA).

DISCUSSION

Sexual dimorphisms identified through RNA sequencing in this project confirm previous findings [1][3] and support innate sex differences in ECM and vascular function and inflammation pathways. Differential ECM gene expression may indicate differences in cell adhesion between male and female cells. Collagen I increases focal adhesion complexes, while laminin decreases endothelial cell doubling and adhesion time and increases adhesion force compared to uncoated glass [4]. ECM composition is also closely linked with vessel stiffening, with collagen, a stiff protein, dominating ECM composition in hypertension [5]. Further examination of ECM sex differences in HUVEC are valuable in determining the influence of cell sex on angiogenesis, response to shear stress, and arterial stiffening.

Increased SDC1 expression in female cells may increase syndecan-1 release from endothelial cells. Syndecan-1 increased angiogenesis and invasion in human dermal microvascular endothelial cells through association with $\alpha_v\beta_3$ and $\alpha_v\beta_5$ integrins [6]. Thus syndecan-1 may be a mechanism by which female HUVEC have increased proliferation and migration compared to male HUVEC [1]. Upregulation of ICAM1, VCAM1, and SELE, all associated with leukocyte adhesion and transendothelial migration, indicate male HUVEC may have a more pro-inflammatory phenotype than female cells. Additionally, IL1R1, upregulated in male cells, binds proinflammatory cytokines IL-1α and IL-1β, and anti-inflammatory IL-1 receptor antagonist (IL-1Ra). Increased binding of proinflammatory cytokines and leukocyte extravasation may make the male endothelium more prone to atherosclerotic lesion development and growth, and arterial stiffening.

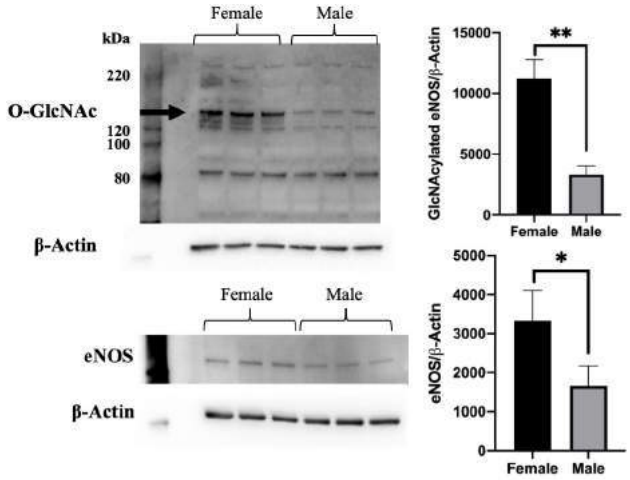

Figure 2. HUVEC O-GlcNAcylated eNOS (~140 kDa) and eNOS (140 kDa), normalized to β-actin, are both higher in female cells than in male cells. *p<0.05, **p<0.01.

eNOS O-GlcNAcylation was found to be increased in female HUVEC, yet others have shown female HUVEC produce more NO in static culture, as measured through eNOS phosphorylation and the citrulline:arginine ratio [7]. Thus, it is possible that female HUVEC have other adaptations that enable them to produce more NO despite eNOS O-GlcNAcylation. Further research is needed to determine why female cells have increased protein O-GlcNAcylation, since we did not observe changes in the related enzymes.

Overall, these data call for further analysis of the influence of sex on endothelial cell-ECM interactions and vascular function. Specifically, the influence of sex on endothelial cell-mediated angiogenesis and vascular stiffening should be examined in greater detail through sex specific *in vitro* and *in vivo* modeling. A greater understanding of the influence of cell sex on the vasculature will improve individualized treatment of cardiovascular disease and other vascular pathologies.

ACKNOWLEDGEMENTS

This research was funded by NIH R01HL140239 to ASMC, NIMHD 5U54MD013376 subproject 8281 to DD, and the National Science Foundation Graduate Research Fellowship Program under Grant No. DGE 1840340 to CW.

REFERENCES

[1] Addis, R. *et al. Biol. Sex Differ.* 5, 1–12, 2014. [2] Witt, E. *et al. J. Proteomics* 201, 48–56, 2019. [3] Huxley, V. H. *et al. J. Physiol.* 596, 3929–3949, 2018. [4] Genge, A. *et al. Clin Hemorheol. Microcirc.* 64, 867-874, 2016. [5] Intengan, H. *et al. Hypertension*. 33, 569-574, 1999. [6] Beauvais, D. *et al. J. Exp. Med.* 206, 691-705, 2009. [7] Cattaneo, M. G. *et al. Sci. Rep.* 7, 1–13, 2017.

SB³C2021
Summer Biomechanics, Bioengineering and Biotransport Conference
June 14-18, Virtual

CLINICAL RISK ASSESSMENT OF POST-TAVR CARDIAC CONDUCTION ABNORMALITY USING PATIENT-SPECIFIC BICUSPID AORTIC VALVE MODELS

S. Anam (1), M. Bianchi (1), B. Kovarovic (1), R. Ghosh (1), A. Hamdan (2), R. Haj-Ali (3), D. Bluestein (1)

(1) Department of Biomedical Engineering
Stony Brook University
Stony Brook, New York, U.S.A

(2) Department of Cardiology, Rabin Medical Center, Faculty of Medicine, Tel-Aviv University, Tel Aviv, Israel

(3) School of Mechanical Engineering
Tel-Aviv University
Tel-Aviv, Israel

INTRODUCTION

Bicuspid aortic valve (BAV) is the most common congenital cardiac anomaly with an incidence of 0.4 – 2.25% in general population [1]. Unlike tri-leaflet aortic valves, BAV is marked by the fusion of two aortic leaflets with a thick, fibrous raphe present at the location of fusion in most cases. In addition to the anomalous valve morphology, BAV is also associated with other structural complications including aortic root dilatation and dissection [2]. The structural malformation and altered hemodynamics result in an early onset of calcific aortic valve disease (CAVD) in most BAV patients, eventually leading to aortic stenosis (AS) and regurgitation, which may require replacement of the valves. A minimally invasive, alternative to surgical aortic valve replacement, transcatheter aortic valve replacement (TAVR) is designed for tricuspid calcific aortic valve and recently adapted for off-label use to treat BAV patients with severe AS due to the presence of CAVD. Despite showing promising performances, TAVR is reported to be associated with various clinical complications including atrioventricular and left bundle branch blockage (LBBB) [3]. Post-TAVR cardiac conduction abnormality (CCA) can occur due to any mechanical damage sustained by the atrioventricular conduction system located near the inter-leaflet triangle region between the non-coronary and the right-coronary leaflet. Conduction disturbances may eventually lead to permanent pacemaker implantation, abnormal cardiac function, and therefore to increased mortality [4]. This is of particular concern among the BAV population since many of them who require aortic valve replacement are young and low risk patients. The structural anomaly of the BAV patients make them susceptible to conduction abnormalities and exacerbates other post-TAVR complications, which prevents the establishment of TAVR as a standard care for BAV patients. In addition, BAV patients had systematically been excluded from TAVR clinical trials due to inherent structural asymmetry, severe leaflet calcification and resulting distorted stent profile. Finite element (FE) modeling is a common research computational method for performing patient-specific simulation of the TAVR procedure, studying post-procedural outcomes and aiding in pre-surgical planning. The number of computational work focusing on modeling conduction disturbances in BAV patients is minimal. This motivates us to perform computational study on 2 BAV patient groups – 1) Control patients and 2) Patients who developed post-TAVR LBBB. The goal of this work is to simulate TAVR procedure in patient-specific BAV models, investigate post-procedural strain development near the atrioventricular conduction region, and analyze for possible strain value threshold that may predict the risk of post-TAVR CCA development in BAV patients.

METHODS

Anonymized cardiac CT scans of 6 type I BAV patients who underwent TAVR, were obtained from Rabin Medical Center, Israel, with IRB approval. Patient- specific surface meshes were reconstructed from DICOM images and optimized for FE analysis using ANSYS SpaceClaim and Fluent Meshing while maintaining their features. Native tissue was modeled using isotropic Ogden hyper elastic material model. Calcium deposits were modeled using linear elastic homogenous isotropic material (E = 12.6 MPa, ν = 0.3) [5]. Self-expandable TAVR stents were modeled using super-elastic nitinol alloy. A cylindrical catheter with cone shaped tip was modeled in order to crimp the self-expandable stent as well as to help the leaflets open during device delivery. A 4-step FE simulation (crimping, insertion, deployment, and relaxation) was performed using Abaqus Explicit 2019, and the implantation depth was chosen based on the clinical data. Clinical data also includes membranous septum (MS) length, which is obtained from the cardiac CT scans, marked by the distance between the hinge point of the non-coronary cusp and the vertex of the muscular septum (Figure 1 A and B) as described by Hamdan et al. [6]. This information along

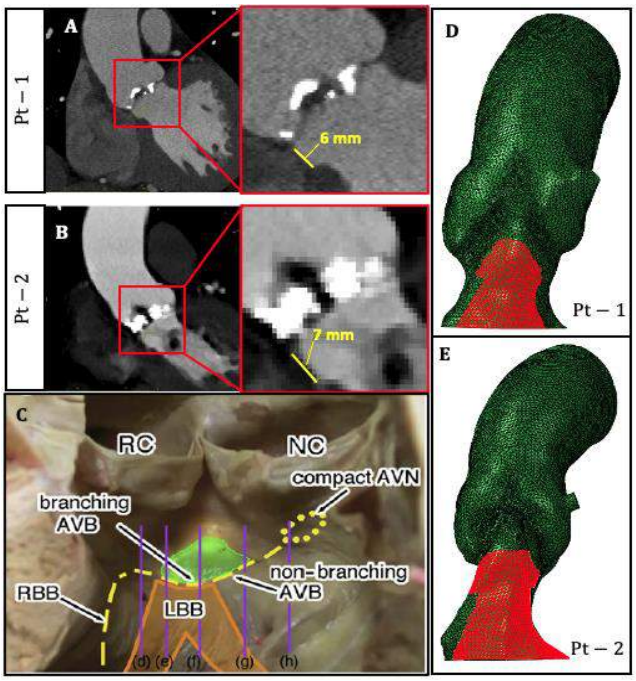

Figure 1: A,B - Measurements of the MS length, obtained from the coronal view of the cardiac CT scans; Patient 1 MS length = 6mm, Patient 2 MS length = 7mm; C - Morphology and location of atrioventricular bundle and left bundle branch (LBB) [7]; D, E – Estimated MS and LBB region in 2 patient specific models (highlighted in red); Patient 1 – control and Patient 2 - LBBB

with a previous report on the anatomical detail and variation of MS and LBB location (Figure 1 C) were then used as a guide to define the MS and LBB region in the patient models (Figure 1 D - E). The area-weighted average logarithmic (LE) strain (%) in the LBB region was calculated in all implantation steps.

RESULTS

A highly eccentric stent deployment was observed in two patient cases (Figure 2 A-B; Patient 1 – control patient, Patient 2 – developed post-procedural LBBB). The distribution of maximum principal LE strain values on the left ventricular outflow tract (LVOT) near the MS and LBB regions was analyzed (Figure 2 C-D). The difference in strain contour between these patients was marked by a region of very high strain located between the non-coronary and the right coronary cusp in patient 2. In addition, the distal end of the LVOT region in patient 1

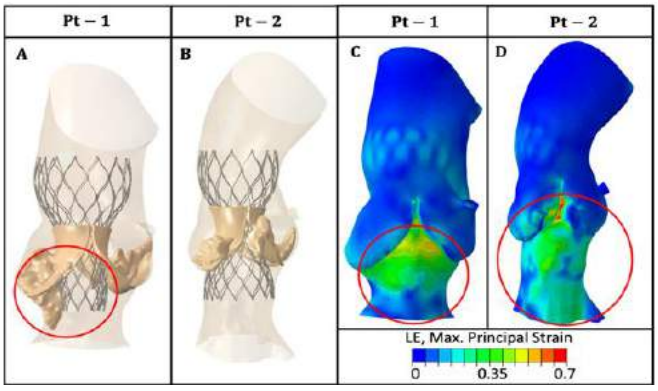

Figure 2: A, B - Post-deployment eccentric stent profile with heavily annular calcification in patient 1 (circled); C, D - Maximum LE strain on ascending aorta and LVOT (circled).

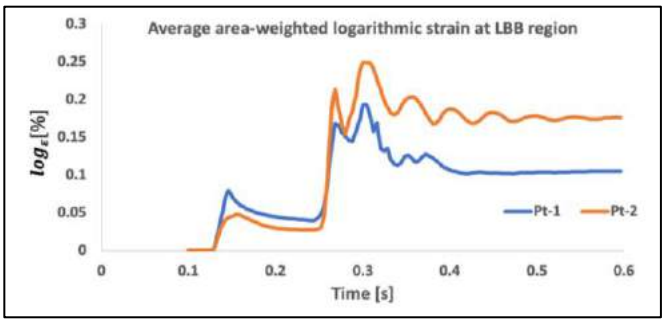

Figure 3: Mean area-weighted average strain at LBB region

exhibited an overall lower strain value. In both patients, the area-weighted average LE strain values at the LBB region (Figure 3) increased until the middle of the deployment phase (0.3 s) and reached a stable value by the end of relaxation phase (0.6 s). The strain value of LBB in patient 1 reached ~ 10 %, whereas in patient 2, it reached a higher value, ~ 17%.

DISCUSSION

The higher strain in the LBB region predisposes patient 2 to the risk of LBBB, which one of the most common post-TAVR complications, especially in BAV patients. This data agrees with the clinical data as patient 2 was reported to have new post-TAVR LBBB. Multiple factors including MS length and calcification are important predictors of post-TAVR conduction disturbances [6]. Non-coronary leaflet calcification that extended downward toward the LVOT along the ventricular wall (Figure 2 A), interrupts the interaction between the distal end of the stent and the part of the lumen that is adjacent to MS and LBB region (Figure 1 A), resulting in an overall lower strain value at the distal end of the LVOT, which is adjacent to LBB. Whereas in patient 2, the distal end of the stent was completely in contact with the LVOT lumen. This trend was also reflected by the area-weighted average LE strain values calculated at the LBB region in both patients. Our current work is focusing on the patients receiving self-expandable valves because self-expandable valves are more likely to cause conduction disturbances due to the constant radial force applied by the nitinol frame, and having a large portion of the device located at the LVOT region increases the risk of mechanical damage to the atrioventricular conduction region. However, we are currently working on extending our study to the balloon-expandable patient group in order to analyze the difference in strain value between self-expandable and balloon-expandable patient populations. As a part of our ongoing study, we are working on additional BAV patient models with a possibility of establishing a strain threshold that could differentiate between the patients who does and the patients who does not develop CCA. By establishing this computational framework, we could strengthen the role of patient-specific modeling as a predictive tool in pre-TAVR planning, which can help identify BAV patients who are at increased risk of developing post-TAVR CCA.

ACKNOWLEDGEMENTS

Funding provided by NIH-NIBIB Phase II-U01EB012487 (DB); NIH-NIBIB 1U01EB026414-01 (DB). Industry Partners: ANSYS, Simulia Living Heart Project.

REFERENCES

[1] Das, R, and Puri, R, *Frontiers in cardio medicine*, 2018, 5:91-91.
[2] Votta, E, et al. *Int J Numer Meth Biomed Engng*. 2017; 33:e2849
[3] Auffret, V., et al., Circulation, 2017,136:1049-1069
[4] Houthuizen, P, et al., *Circulation*. 2012, 126:720–728
[5] Bianchi, M, et al., *Biomech Model Mechanobiol*, 2019, 18:435-451.
[6] Hamdan, A, et al., *J. Cardiovasc. Comput. Tomogr.*, 2020
[7] Kawashima, Tomokazu et al., *Int. J. Cardiol*, 174:1-6

EFFECTS OF PIA-ARACHNOID COMPLEX CONSTITUTIVE FORMULATIONS ON PREDICTIONS OF CONCUSSION

Nikolaus A. Benko (1) and Brittany Coats (1)

(1) Mechanical Engineering
University of Utah
Salt Lake City, Utah, USA

INTRODUCTION

It has been hypothesized that the mechanics of the pia-arachnoid complex (PAC) contribute substantially to the dynamic strain response of the brain during traumatic injury. However, the paucity of experimental data to characterize the human PAC has prevented detailed investigations into the role of the PAC during traumatic brain injury. In this study, we use recent *in situ* measurements of the human PAC modulus in traction to investigate the importance of PAC heterogeneity and anisotropy in computational predictions of brain strain, as well as the relative contribution of PAC constitutive formulations to the prediction accuracy of concussion.

METHODS

To test the effect of PAC constitutive formulations on strain prediction in computational models of traumatic brain injury, a simplified finite element model of the human head was constructed. Four PAC formulations were created and used in a 2-factor 2-level design to isolate the effects of PAC heterogeneity and constitutive model isotropy.

Model geometry was based off of a segmented T1-weighted MRI of a 24-year-old male with no neurological dysfunction, available from the public OASIS dataset [1]. Scan IP (Synopsys, Mountain View, CA) was used to create surface meshes of gross brain parenchyma, meningeal layers, falx cerebri, tentorium cerebelli, and the skull. Surface meshes were loaded into TrueGrid (XYZ Scientific, Pleasant Hill, CA) and used to define the boundaries of a multi-block hexahedral mesh (Figure 1A). The falx cerebri and tentorium cerebelli were represented with 2D shell elements (Figure 1B). 3D elements representing brain matter were roughly divided into seven regions representing the frontal lobe, corpus callosum, brainstem, parietal lobe, temporal lobe, occipital lobe, and cerebellum. All elements used a reduced integration formulation.

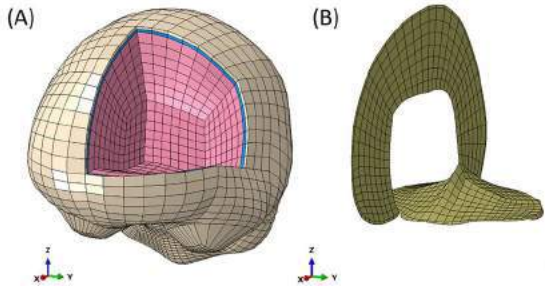

Figure 1: (A) Hexahedral mesh of skull, CSF, and brain matter. (B) Shell elements representing falx and tentorium.

Four versions of the FE model were created with different constitutive formulations for the PAC elements. First, a baseline model, *Model I*, was created representing the PAC as a linear elastic isotropic material that is homogeneous across the surface of the brain. The modulus for the baseline model is defined as the average PAC traction stiffness from previous studies by our lab [2]. The second model, *Model H*, is also a linear elastic isotropic material model, but the PAC modulus is heterogenous across the brain. This model defines a unique modulus for each PAC region (Figure 2) from the average of the regional material properties. All isotropic PAC elements had a Poisson's ratio of 0.4999 corresponding to an average bulk modulus of 21.1 MPa. The final two models were homogeneous (*Model T*) and heterogeneous (*Model HT*) as defined above, but implemented using a transversely isotropic linear elastic formulation for the PAC instead of an isotropic formulation. The

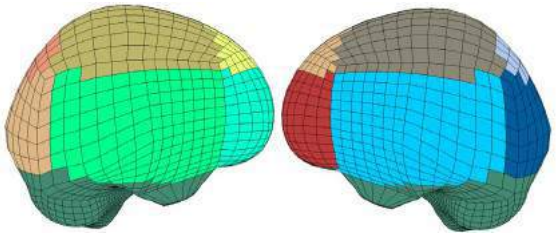

Figure 2: PAC regions assigned unique material properties based on experimental measurements of PAC traction stiffness.

transversely isotropic material models were formulated using the methods described in Scott et al [3].

For injury prediction, we simulated 53 recreated impacts from the National Football League (20 with concussion, and 33 without) [4]. Three-dimensional accelerations from the reconstructions were used as the inputs for the simulations. Strain data were recorded for each element in time increments of 0.0001 seconds for the duration of each simulation. Average 90th percentile peak maximum principal strain (ε_{90}) was calculated for each brain region, as well as the brain as a whole. The 90th percentile value of peak strain taken from each anatomical region were fit to concussion outcomes using multivariate regression. A leave-one-out cross validation scheme was adopted to account for potential overfitting with the limited training dataset. The injury prediction performance of different PAC formulations was compared using area under the curve (AUC), sensitivity, and specificity extracted from ROC curves.

RESULTS

Across the 53 impacts, ε_{90} throughout the whole brain for the homogeneous isotropic model was 32.56%. For the heterogeneous isotropic model, homogeneous transversely isotropic model, and heterogeneous transversely isotropic model, ε_{90} values were 32.60%, 29.32%, and 29.31% respectively. Two-way analysis of variance (ANOVA) showed that PAC heterogeneity had no significant effect on ε_{90} when averaged across the entire brain (p=0.9506) while transversely isotropic models predicted significantly lower ε_{90} than isotropic models (p<0.0001, Figure 3). These trends were persistent within individual anatomical regions of the brain.

Of the four PAC formulations, the Model H performed best in the testing dataset (AUC=0.870, sensitivity=0.85, specificity=0.91). *Model I* performed very similarly to *Model H* (AUC=0.870, sensitivity=0.80, specificity=0.91), while *Model T* and *Model HT* both had a much lower specificity of 0.76 (Figure 4).

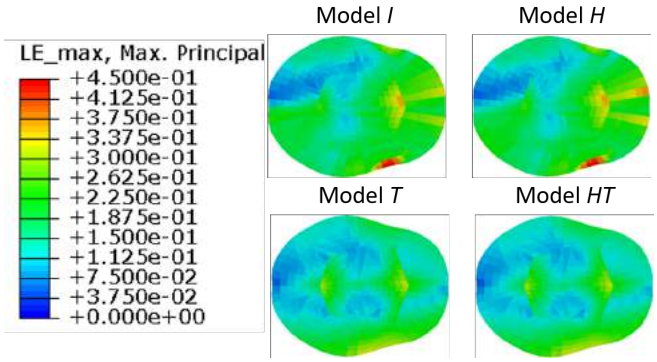

Figure 3: Fringe plots comparing peak maximum principal strain distributions in Case 038HD01 from the impact dataset with each of the PAC constitutive formulations.

DISCUSSION

Simulations of recreated collisions between football players revealed that PAC heterogeneity had no discernible effect on strain estimates. This is likely due to the relatively small regional variability in PAC modulus (12.8±3.2kPa). Transversely isotropic models of the PAC yielded lower estimates of brain strain than isotropic models. The increased stiffness of the transversely isotropic formulations was mostly due to the explicit inclusion of the in-plane tensile modulus which was much greater than the out-of-plane traction modulus.

Isotropic PAC formulations produced better injury predictions than transversely isotropic formulations with increased specificity. The heterogeneous formulation produced marginally higher injury prediction sensitivity, however given the limited size of the injury prediction dataset, this finding should not be considered definitive. The relatively lower performance of transversely isotropic PAC formulations is interesting as the anatomical structure of the space, with trabecular fibers predominantly oriented radially outward from the surface of the brain, would suggest that the PAC would have a directionally dependent strain response. For this study, we relied on our previous measurements of the out-of-plane traction response of the human PAC and derived the in-plane behavior from previous studies of bovine PAC [5]. The findings presented here suggest the importance of further experiments to quantify the in-plane tensile and shear behavior of the human PAC.

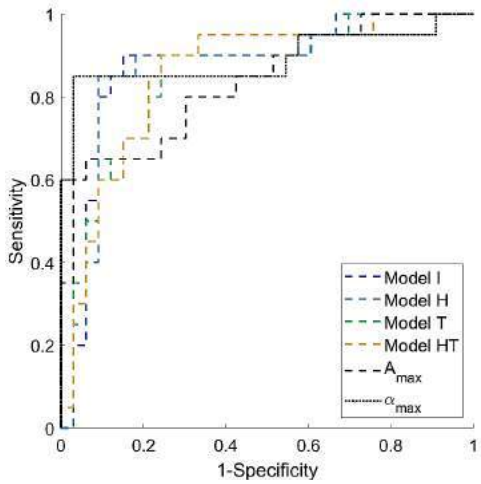

Figure 4: ROC curves for the multivariate injury predictions for *in situ*-based PAC formulations. Univariate injury predictions based off of peak linear (A_{max}) and angular (α_{max}) accelerations have been added for reference. Homogeneous and heterogeneous variations of PAC formulations performed similarly for both isotropic and transversely isotropic variations. Isotropic formulations had higher AUC and specificity compared to transversely isotropic formulations.

ACKNOWLEDGEMENTS

NSF Smart and Connected Health Award No. 1622741.

REFERENCES

[1] Marcus et al. *J Cogn Neurosci*, 19(9):1498–1507, 2007
[2] Benko et al. *J Mech Beh Biomed Mat, in review*
[3] Scott et al. *Biomech.Model Mechanobiol*, 15(5):1101–1119, 2016
[4] Pellman et al. *Neurosurgery*, 53(4):794–799, 2003
[5] Jin et al. *Ann Biomed Eng*, 42(4):812–821, 2014

STUDYING THE MECHANICAL EFFECT OF HUMAN TALUS BONE IMPLANTS ON THE SURROUNDING ARTICULAR CARTILAGE

M. Ead (1), T. Liu (1,2), K. Duke (1), N. Jomha (3), M. El-Rich (2), L. Westover (1)

(1) Department of Mechanical Engineering
University of Alberta
Edmonton, Alberta, Canada

(2) Department of Mechanical Engineering
Khalifa University
Abu Dhabi, United Arab Emirates

(3) Department of Surgery
University of Alberta
Edmonton, Alberta, Canada

INTRODUCTION

The talus bone in the human ankle joint has a limited blood supply with only 40% being supplied by blood vessels and the rest enclosed with cartilage [1]. When the talus is injured or fractured, this limited blood supply makes it vulnerable to osteonecrosis which can cause severe ankle pain [2]. One of the common treatments for talar osteonecrosis is tibiotalocalcaneal arthrodesis, a surgical procedure where the talus bone is fused to the tibia and calcaneus bones [3]. Not only is this procedure technically challenging, but it also inhibits range of motion and function, which significantly impact the quality of life of these patients [4]. Additionally, this procedure may lead to other complications such as nonunion and infection [3,4]. Talar body replacement is an alternative procedure where the talus bone is replaced with an artificial prosthesis, preserving ankle functionality and reducing pain [5]. In this procedure, computed tomography (CT) scan data of the contralateral (uninjured) talus is used to design and create a customized implant [5]. Although this procedure offers good outcomes for patients [5], it is quite expensive and patients are forced to endure delayed treatment as a result of the lengthy surgical planning process. As well, this procedure cannot be used on patients who have injured both tali.

Since the talus bone shape is similar across the population [6], a universal talus implant can be designed and made readily available for surgery. It would be used instead of customized implants and would be manufactured in different sizes to accommodate the various talus sizes within the population. This will enable patients with talar injuries to avoid long wait times and costly procedures while taking advantage of the benefits of talar body replacement surgery.

To design a successful implant, the mechanical effect of the candidate implants on the articular cartilage surrounding the talus bone would need to be examined first. Therefore, the objective of this study is to model the talus bone and surrounding joints and use finite element (FE) simulations to calculate resultant contact pressure and contact area on the articular surfaces.

METHODS

The model geometry is created by taking CT scans of a cadaver ankle in a neutral standing position. These 2D CT scans are imported into Materialise-Mimics® (Materialise, Leuven, Belgium), an image processing software which converts them into a 3D model. The ankle model is then imported into Geomagic® (3D Systems, South Carolina, USA) to isolate all 5 bones in the region: the talus, fibula, tibia, calcaneus, and navicular. Geomagic® is also used to refine the bone models by smoothing and reducing noise. Next, each of the bone models are exported to HyperMesh® (Altair, Troy USA) for meshing and the articular cartilage layers are created by highlighting the contact areas on every bone and extruding the surfaces by 1.5 mm. Adding the cartilage causes adjacent layers to be in an overlapping position. Therefore, all bones and surrounding cartilage are moved slightly away from the talus using HyperMesh®. Finally, the ankle model is exported to ABAQUS® (Dassault Systèmes, Johnston, USA) for conducting the FE simulations.

The talus models included in the simulations are the *biological* model (natural talus with human cortical bone [7] and cartilage [8] mechanical properties to serve as a means of comparison), the *customized* model (same shape as the biological model with no cartilage

layers), the *universal* model (average talus bone shape developed by Trovato et al. [6]) and the *statistical shape* model or SSM (average talus bone shape developed by Liu et al. [9]). For the three implant models, the cartilage thickness is taken into account by scaling the original models using a volume scale factor. The implants are then given mechanical properties of cobalt chrome [10].

The simulations on ABAQUS® occur in three successive time steps: 1) the talus is fixed and initial contact is created by moving the other bones back to their original positions in the CT scans; 2) the talus is unconstrained; 3) the tibia and fibula are given a translational degree of freedom (DOF) in the z-direction and the fibula also a rotational DOF about the z-plane and then a downwards axial load of 2000 N is applied to the tibia (Figure 1) [11]. The simulations are performed on all models and the resulting contact pressure on the talus bone is calculated in the tibiotalar and talocalcaneal cartilage. The contact pressure is displayed in the form of color maps to easily visualize the distribution.

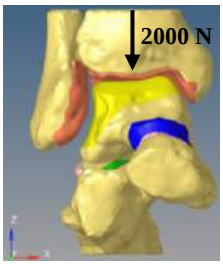

Figure 1: Ankle model with talus implant and cartilage areas colored in yellow, blue, and green. Cartilage layers of surrounding bones are colored in red and pink. The axial load applied is shown.

RESULTS

The contact pressure (MPa) in the tibiotalar region of all four models is displayed in Figure 2a. The maximum contact pressure in each model was also recorded and presented in the figure. Figure 2b includes the contact pressure and maximum values for the talocalcaneal cartilage area. The contact pressure scales were normalized to the maximum values of the biological model in both figures. Therefore, the grey areas represent contact pressure values greater than 10.9 MPa and 13.6 MPa in the tibiotalar and talocalcaneal cartilage areas, respectively.

From the color maps in Figure 2a, it can be deduced that the contact area of the tibiotalar region in all three implant models was less than the biological. The maximum contact pressure was substantially larger in the implant models and there were more areas of stress concentration (red/grey areas). Similar results were found in the talocalcaneal cartilage area. Also, the shape of the contact pattern of the universal and SSM implants were different from the biological model (Figure 2b).

DISCUSSION

The goal of this study was to calculate contact pressure on the articular surfaces of the ankle model when using talus implants and compare the results to that of a natural talus. Results showed that the candidate implants currently result in smaller contact areas and larger values for contact pressure. Areas of stress concentration were identified, as shown in Figure 2. In the future, we will investigate other implant shapes and designs that can reduce the instances and magnitudes of stress concentrations and obtain contact pressure contours similar to the biological model. The customized talus model had the same shape as the biological model and although the contact contours were similar, the maximum contact pressure was considerably higher. This suggests that materials other than cobalt chrome should be investigated and may provide results closer to the biological model.

Future work will focus on including talofibular and talonavicular cartilage areas in the analysis. Two more loading scenarios (dorsiflexion and plantarflexion) will also be simulated along with the neutral standing position. Lastly, more subjects will be included to offer a more definitive conclusion of the impact of these implants on the ankle.

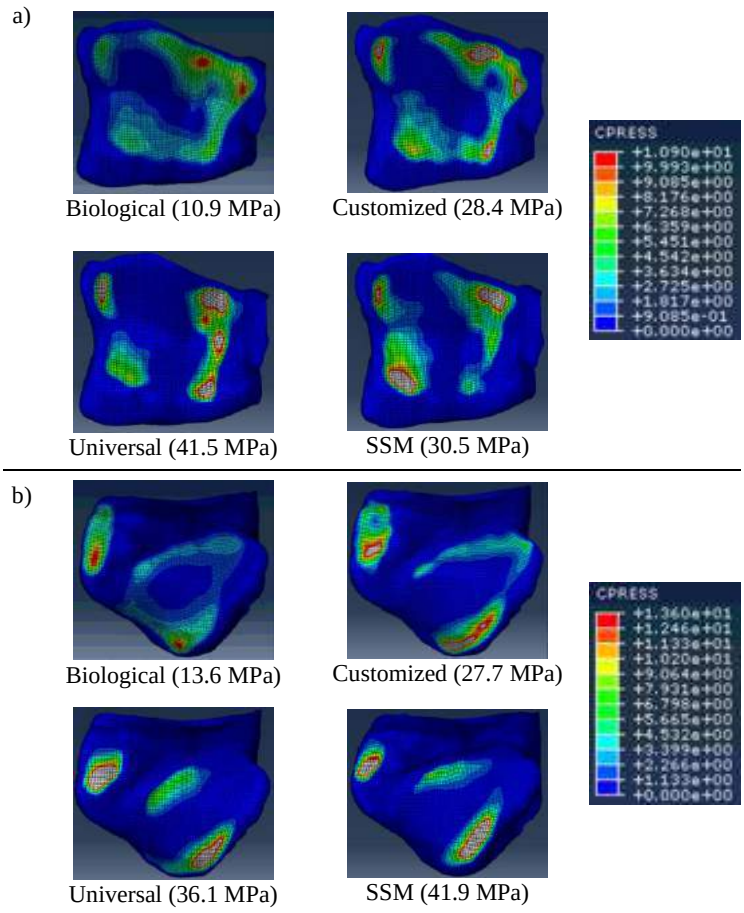

Figure 2: Talus contact pressure color maps at the a) tibiotalar and b) talocalcaneal cartilage areas. Maximum values in brackets.

ACKNOWLEDGEMENTS

We would like to acknowledge the financial support of the Natural Sciences and Engineering Research Council of Canada (NSERC) and the Edmonton Orthopaedic Research Committee.

REFERENCES

[1] Fortin, P T et al., J Am Acad Orthop Surg, 9:114–127, 2001.
[2] Delanois, R E et al., J Bone Jt Surg, 80:529–36, 1998.
[3] Cooper, P S, Clinical Orthopaedics and Related Research, 2001.
[4] Papa, J et al., J Bone Jt Surg - Ser A, 75:1056–1066, 1993.
[5] Taniguchi, A et al., J Bone Jt Surg - Am Vol, 97:1348–1353, 2015.
[6] Trovato, A et al., Foot Ankle Surg, 23:89–94, 2017.
[7] Mondal, S et al., Comput Methods Biomech Biomed Engin, 22:1247–1257, 2019.
[8] Anderson, D D et al., J Biomech, 40:1662–1669, 2007.
[9] Liu, T et al., Front Bioeng Biotechnol, 8:656, 2020.
[10] Al Jabbari, Y S, J Adv Prosthodont, 6:138–145, 2014.
[11] Liu, T et al., (unpublished).

SB³C2021
Summer Biomechanics, Bioengineering and Biotransport Conference
June 14-18, Virtual

LUNG MECHANICS OF POSITIVE- AND NEGATIVE- PRESSURE VENTILATION UNDER VARIED INFLATION VOLUMES

S. Sattari (1), C.A. Mariano (1), M. Eskandari (1,2,3)

(1) Department of Mechanical Engineering
University of California, Riverside
Riverside, CA, USA

(2) Department of Bioengineering
University of California, Riverside
Riverside, CA, USA

(3) BREATHE Center, School of Medicine
University of California, Riverside
Riverside, CA, USA

INTRODUCTION

Pressure-volume curves are classical measures of investigating lung mechanics and deviations caused by disease progression [1]. Studies of pressure-volume curves have been limited to using positive-pressure ventilation (PPV), where the air is directly applied to the lung to cause inflation, as in modern artificial ventilators [2]. Conversely, natural lung function is governed by negative-pressure ventilation (NPV), where the lung inflates due to diaphragm distension, reducing the thoracic cavity pressure which the lung expands to fill. However, despite these drastic loading differences, the mechanical characteristics of the lung in physiological NPV settings is vastly underexplored and its pressure-volume response in relation to PPV is unknown. This knowledge void continues to plague understanding how ventilators should be optimized, a need that can no longer be overlooked as highlighted by the demand to ventilate COVID-19 patients.

To address these fundamental scientific needs, we utilize our custom-designed and validated novel volume-controlled, pressure-measuring, and dual-piston apparatus capable of testing the lung in both PPV and NPV under matched loading conditions [2]. We study the effect of various tidal volumes (one of the key variables in ventilator settings) in ex-vivo porcine lungs. Directly comparing the classical pressure-volume curves of PPV and NPV will enable improved ventilation strategies by understanding how to emulate the loading patterns characteristic of physiological lung mechanics, ultimately helping to mitigate fatalities caused by barotrauma, volutrauma, acute respiratory distress syndrome, and ventilator induced lung injury.

METHODS

Lungs from three pigs (200-250lbs) were collected from a local abattoir. The lungs were tested within 24hrs of sacrifice to minimize tissue damage and were stored in 1X PBS [3]. Specimens were inflated with a preload of 5 cmH_2O to implement a fixed reference state for all specimens regardless of trapped air inside the lung. The inflation-deflation rate was set to a normal frequency of 15 breaths per minute. Applied inflation volumes of 675, 900, and 1350 ml, corresponding to clinical tidal volumes of 6, 8, and 12 ml/kg in PPV were used [4]. The compressed air volume of the lung was measured by controlling and equilibrating the piston-actuator positions in real-time, enabling a valid comparison between PPV and NPV loading mechanisms [2]. The induced peak pressures and lung volume changes were recorded from applied loads under positive-pressures and then analogous negative-pressure loading cycles were applied to the lung such that the peak pressure magnitudes and volumes matched within $\pm 10\%$.

Each test was repeated three times to precondition the lung and followed by the matched test inflation-deflation cycle. The area between loading and unloading curve was used to define the hysteresis. Energy loss was described as the hysteresis area normalized by the total work done. Initial and final slopes of pressure-volume curve were calculated using a bilinear model fitted to two linear portions of curve while the difference between fitted line and experimental data was minimized by setting the coefficient of determination R^2 to 0.9 [5].

Statistical comparison of PPV and NPV results was performed using paired t-test and volume group comparison was done by one-way analysis of variance (MATLAB Statistics Toolbox, MathWorks Inc.). The significance level was set at $p< 0.05$, represented by * and ▲ for PPV-NPV and volume comparisons, respectively. Due to COVID-19 there was a shortage of research available pig lungs, limiting our analysis to the statistical minimum of three specimens.

RESULTS

Representative volume-pressure curves for artificial (PPV) and corresponding physiological (NPV) breathing mechanics for different

inflation volumes are shown in Figure 1. Greater inflation volume had similar effect on both PPV and NPV tests, resulting in increasingly disparate inflation and deflation paths.

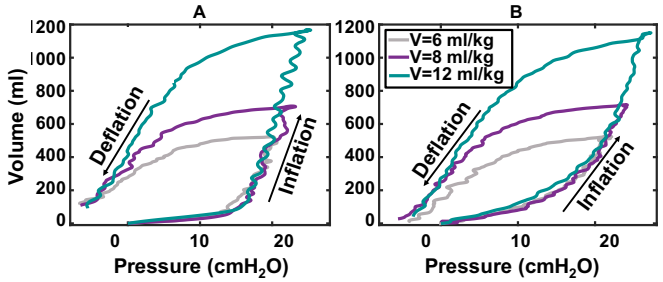

Figure 1: Representative specimen's volume-pressure response for various inflation volumes in PPV (A) and NPV tests (B). Inflation loading response drastically differed while deflation paths were similar between PPV and NPV tests.

Figure 2A illustrates the lung inflation-deflation response in PPV and NPV. Initially, the inflation slope increased incrementally in PPV compared to the greater slope of NPV. The quantitative initial and final slope values obtained from bilinear fitting for three pigs were averaged and represented in Figure 2B and 2C, respectively. Initial slopes were notably higher for NPV compared to PPV, although these differences were found to be statistically significant only in tidal volumes of 6 and 12ml/kg. In contrast, PPV tests inverted the trend for the final slope, surpassing the NPV slope for 6 and 12 ml/kg tidal volumes (Figure 2C). Greater inflation volumes resulted in unidirectionally increasing higher initial slopes in NPV (Figure 2B) which was not observed in PPV; the final slopes of PPV and NPV were instead noted to increase with increasing inflation volumes (Figure 2C).

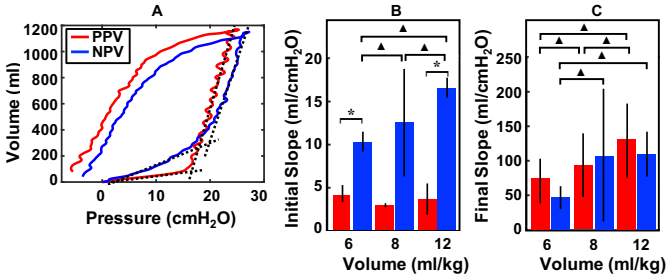

Figure 2: Representative of a volume-pressure response for a tidal volume of 12 ml/kg comparing PPV and NPV tests where dotted lines show bilinear fit (A). Comparison between slopes of fitted lines to initial (B) and final (C) portion of PPV and NPV curves for different inflation volumes.

Lung behavior in PPV and NPV settings, was also examined energetically: hysteresis was noticeably greater in artificial breathing in all inflation volumes although not enough to be statistically significant. Similarly, the lung lost more energy in PPV compared to NPV tests. Variation in maximum inflation volume resulted in an increase in hysteresis in both test settings, however, its effect on energy loss was not unidirectional.

DISCUSSION

This study directly compares the pressure-volume mechanics of the lung in artificial and physiological breathing conditions for the first time and further assesses the comparative response of porcine lung under various tidal volumes. The direct comparison between PPV and NPV shows that despite matching the peak lung pressure and expansion volume, the inflation paths followed to reach each matched tidal load

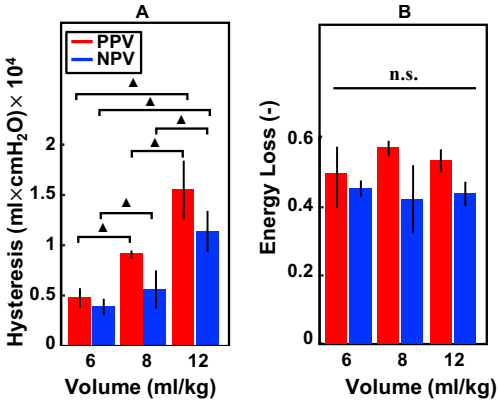

Figure 3: Comparable hysteresis and energy loss for PPV and NPV tests at various tidal volumes where bar graphs represent average and standard deviation for three pigs.

differed significantly in PPV and NPV (Figure 1): during initial inflation, the relative reduced pressure-volume slope in PPV is representative of greater organ stiffness, while lung behaves more compliantly (greater slope) in NPV. This initial part is medically known as the lower inflection point, indicative of airway resistance and the minimum pressure required to recruit alveoli [6]. The notable differences between initial slope of PPV and NPV reveals that the latter the alveoli inflate early on and there is much less airway resistance. This phenomenon can be attributed to the different loading mechanism between PPV and NPV; in PPV, the air must be pushed through each airway before reaching the alveoli whereas in NPV, the lung is inflated by a difference in pressure felt foremost at the distal alveoli pulling air in from the proximal airways. These results are in agreement with previous studies reporting better oxygenation and more homogenous air distribution in NPV tests based on hemodynamics and biochemical responses [7].

In addition to the different loading paths followed in PPV and NPV, the lung exhibits greater hysteresis and energy loss in PPV tests, potentially explaining damages associated with this ventilation method; an increase in hysteresis is associated with an increase in the work of breathing, where the latter phenomena has been reported in chronic obstructive pulmonary disease patients [8].

The effect of lung volume inflation on compliancy and hysteresis has also been examined in this study. Greater inflation volume does not affect initial compliancy in PPV tests (Figure 2B) but results in greater initial compliancy in NPV tests as well as an increase in the final compliancy and hysteresis in both PPV and NPV tests. While these are the first measures for NPV, increase in hysteresis with greater inflation volumes for PPV are in agreement with what has been reported for dog and human lungs [9].

This mechanical study demonstrated that the lung is more energy efficient and compliant in physiological loading compared to artificial breathing conditions. These direct mechanical comparisons between PPV and NPV will inform the improvement of ventilators function and mitigate injury.

REFERENCES

[1] Faffe, DS et al., *Physiol Rev*, 89:759–75, 2009. [2] Sattari, S et al., *Front Bioeng Biotechnol*, 8:578762, 2020. [3] Eskandari, M et al., *J Appl Physiol*, 125:878–88, 2018. [4] Chiumello, D et al., *Am J Respir Crit Care Med*, 178:346–55, 2008. [5] Lynch, HA et al. *J Biomech Eng*, 125:726–31, 2003. [6] Interpreting the shape of the pressure-volume loop [Internet], 2019. [7] Grasso, F et al. *Am J Respir Crit Care Med*, 177:412–8, 2008. [8] Chen, S et al. *J Thorac Dis,* 8:2212–8, 2016. [9] Mead, J et al. *J Appl Physiol*, 10:191–6, 1957.

INTEGRATING CAPILLARY FLOW MODELING AND GEOMETRIC QUANTIFICATION INTO RECONSTRUCTED 3D CAPILLARY NETWORKS OF THE OPTIC NERVE HEAD

Po-Yi Lee (1,2), Jason Walker (3), Yi Hua (2), Bryn Brazile (2), Ian A. Sigal (1,2)

(1) Department of Bioengineering
University of Pittsburgh
Pittsburgh, PA, USA

(2) Department of Ophthalmology
University of Pittsburgh
Pittsburgh, PA, USA

(3) Department of Biological Sciences
University of Pittsburgh
Pittsburgh, PA, USA

INTRODUCTION

Vision loss in glaucoma, the second leading cause of blindness in the world, is due to progressive retinal ganglion cell axon damage. [1] Although it is known that this damage starts in the back of the eye, in a region called the optic nerve head (ONH), the pathogenesis of the disease is still not well understood. Understanding the mechanisms leading to nerve damage will help with early detection and treatment. This is crucial in glaucoma because lost nerve fibers cannot be recovered, and therefore vision is lost forever. One of the leading hypotheses of glaucoma postulates that low blood flow within the ONH may contribute to ischemic death of the retinal ganglion cells. [2] If this is correct, understanding how eye-specific contributes to low blood flow would allow predicting susceptibility to disease.

Our goal in this project was to characterize geometric parameters of the ONH capillaries and determine whether they are associated with blood flow. Specifically, we reconstructed the 3D capillary network of a monkey ONH, and quantified four geometric parameters: capillary length, tortuosity, inclination, and azimuth. We simulated the blood flow throughout the capillary network, and then evaluated the associations between the local flow rate and the four geometric parameters for each capillary segment.

METHODS

3D reconstruction of the ONH capillary network. Serial histological sections (thickness: 16 µm) were obtained from a normal monkey ONH, in which the vasculature had been perfusion-labeled with a fluorescent dye. The sections were imaged with fluorescence microscopy at a resolution of 0.73 µm per pixel. The images were registered to one another as a 3D stack. The capillaries were then identified using a modified 3D Hessian filter and manual segmentation. The result was skeletonized and converted into a graph for simulation of blood flow rate and quantification of vascular geometry.

Simulation of blood flow rate. A fluid mechanics approach was used to predict the blood flow rate within the capillaries. [3] Hemodynamics boundary conditions were defined to simulate blood inflow from the circle of Zinn-Haller in the periphery, drainage through the central retinal vein, and interactions with the pre and retrolaminar regions. Blood was considered as an incompressible Newtonian fluid, and its flow behavior was described by the Hagen-Poiseuille equation.

Quantification of vascular geometry. Each capillary segment was defined as an unbranched vascular tract between two branch points or between a branch point and a terminal point. We quantified four geometric parameters of capillaries: length, tortuosity, inclination, and azimuth. Figure 1 shows the detailed definition of each parameter.

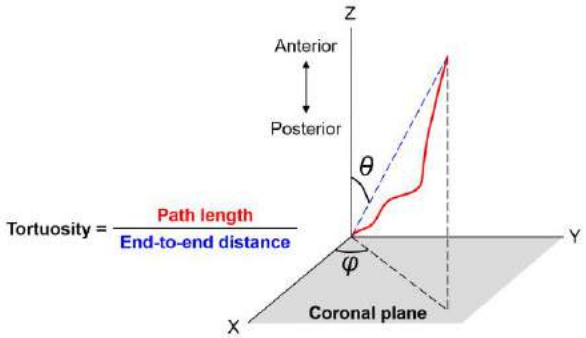

Figure 1: Definition of the capillary geometric parameters. Tortuosity (≥ 1) was the ratio of the path length (red solid line) to the end-to-end distance (blue dashed line). Inclination ($0 \le \theta \le 90^o$) was the angle between the end-to-end line and the z-axis (anterior-posterior axis). θ=90˚ indicates that the capillary is parallel to the x-y plane (coronal plane). Azimuth ($0 \le \varphi < 360^o$) was the angle between the projected end-to-end line and the *x*-axis.

Statistical analysis. As we analyzed the results, we found that neither the blood flow rate nor the four geometric parameters were normally distributed (Figures 2 and 3). To improve the normality of their distributions and residuals, the flow rate, length, tortuosity, and inclination were transformed with a base 10 log. Since the azimuth is circular data, it was transformed with dummy variables. We performed a multivariate linear regression analysis to determine the associations and used $\alpha = 0.001$ to define significance. All statistical analyses were done using R (v4.0.3).

RESULTS

The 3D ONH capillary network architecture and its flow were quite complex. Figure 2 shows the network as reconstructed, and the distributions of the flow rate, capillary length, tortuosity, inclination, and azimuth. Scatterplots of segment flow rate and the four geometric parameters are shown in Figure 3, and the statistical results in Table 1. There was no preferential azimuthal orientation of the capillaries. A majority of the fibers were in the coronal plane.

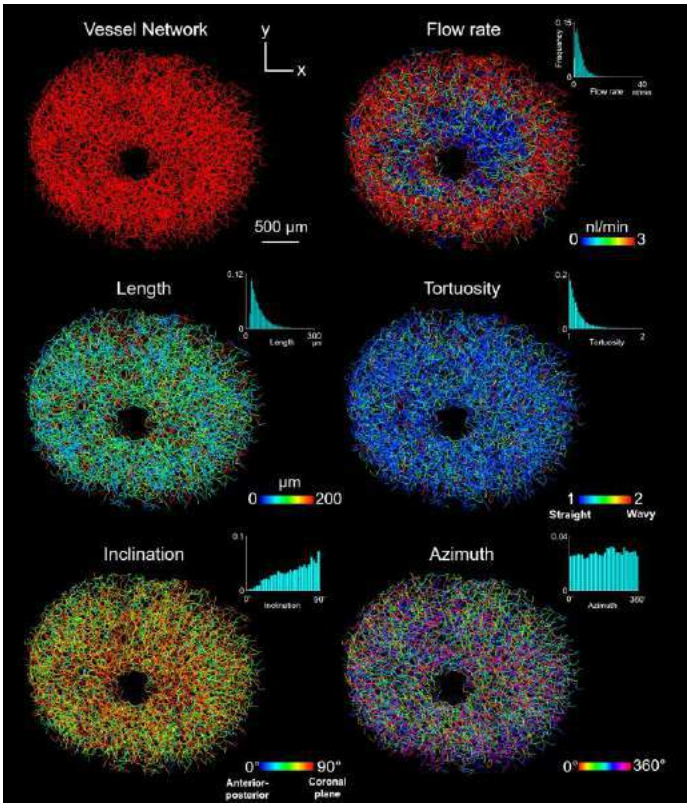

Figure 2: 3D reconstruction of the capillary network of a normal monkey ONH, which included 1100 terminal points, 7989 branching points, and 12966 segments. The network is shown colored by segment flow rate, length, tortuosity, inclination, and azimuth, with histograms showing their distributions.

Table 1: Summary of results from statistical tests.

Parameter	Slope	*P*
Length	-	> 0.01
Tortuosity	-0.06	< 0.0001
Inclination	-0.11	< 0.0001
Azimuth	-	> 0.01

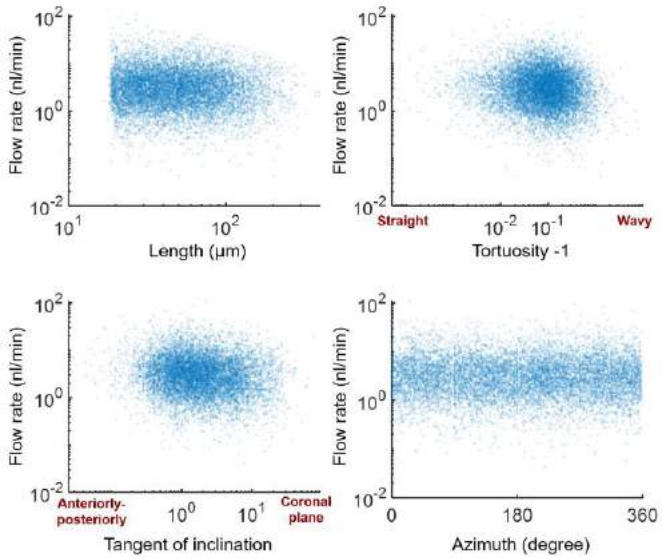

Figure 3: Scatterplots of blood flow rate as a function of the four geometric parameters. Flow rate had a small negative association with tortuosity and inclination (P's < 0.0001). We detected no associations between flow rate and length or azimuth (P's > 0.1).

DISCUSSION

The capillaries in the ONH form an extremely complex interconnected network. Since measuring blood flow experimentally is still not possible, we used computational simulation to estimate blood flow in a specimen-specific ONH capillary network and then determined the associations between the capillary geometric parameters and blood flow.

We found that the flow rate was negatively associated with the capillary inclination. This suggests that the flow rate in capillaries within the coronal plane (θ = 90°) was slightly lower than that in capillaries oriented anteriorly-posteriorly (θ = 0°). Previous models of optic nerve head blood flow used simplified 2D ONH capillary networks, [4] which may reduce the fidelity of the models for representing hemodynamics in the ONH.

We also found that the flow rate was negatively associated with the capillary tortuosity. That is, the flow rate in a tortuous capillary was lower than that in a straight one. However, the slope of the association was very low (*i.e.*, -0.06), indicating that the effects of tortuosity on the flow rate were small. Tortuous capillaries would increase the proximity to tissues and the time the blood is available for nutrient and oxygen exchange, which may be advantageous for the tissues. [5]

In summary, our study revealed associations between the ONH capillary geometric parameters and blood flow rate. The associations, however, were weak. Findings from this study have the potential to be clinically useful in glaucoma management, diagnosis, and risk profiling.

ACKNOWLEDGEMENTS

NIH R01-EY023966, R01-EY028662, P30-EY008098, and T32-EY017271 (Bethesda, MD), the Eye and Ear Foundation (Pittsburgh, PA), and Research to Prevent Blindness.

REFERENCES

[1] Burgoyne C.F., Exp Eye Res. 2010; 93: 120–132.
[2] Osborne NN, et al., Br J Ophthalmol. 2001;85:1252–1259.
[3] Secomb, T.W., et al., Ann Biomed Eng. 2004; 32: 1519-1529.
[4] Chuangsuwanich, T. et al., IOVS. 2016; 57: 6167-6179.
[5] Brazile, B.L., et al., IOVS. 2020; 61: 2.

A NOVEL LOCAL TUMOR PROGRESSION PREDICTION METHOD FOR MULTI-MODE THERMAL ABLATION

Xinyi Wang, Jianlong Yang, Aili Zhang*, Lisa X. Xu

School of Biomedical Engineering,
Shanghai Jiao Tong University,
Shanghai, China

INTRODUCTION

Multi-mode ablation [1] is a new minimally invasive therapy that uses thermal energy to destroy tumors. During the therapy consisting of sequential rapid freezing, thawing and radio-frequency heating, tumors undergo significant cell damage and capillaries rapture, resulting in antigen releasing and triggering of immune responses. Since the ablated lesion remains in vivo, a detailed histological analysis is not available. To avoid potential recurrences, post-operative evaluation becomes extremely important.

Continuous and frequent imaging follow-up is the most common way to track progression that has occurred [2], rather than predicting it in advance. Radiomic attempts to find hidden clues beyond structural differences in images before the event, but is rarely reported in thermal treatment [3]. Based on the thermal history experienced, temperature and thermal dose estimate the extent of local ablation [4]. However, the difficulty in predicting complex changes, such as immune effect and indirect death, dramatically limits the use of long-term assessment.

This work establishes a prediction framework for local tumor progression. We leverage the multi-modal information provided by pre- and early post-operative MRI, intra-operative CT, and especially, a novel thermal dose map, implicitly giving the relationship between the applied heat and the necrosis and immunity within tumors. The information is then inputted into the random survival forest model [5]. In addition to returning the risk score, this model shows the temporal evolution of survival probabilities, an important reference for clinical follow-ups. Its exclusion of static and medical priors also benefits the generalization capability of trained models. To validate our framework, a clinical dataset from Shanghai Cancer Center, Fudan University was used, including 17 patients with colorectal liver metastases and hepatocellular carcinoma. We collected the multi-modality informatics mentioned above in this dataset retrospectively.

METHODS

The proposed framework consists of three major steps (Fig. 1): multi-modal preprocessing, model development and model output (with Comsol 5.4, simpleITK, pyradiomics, pysurvival, survcomp).

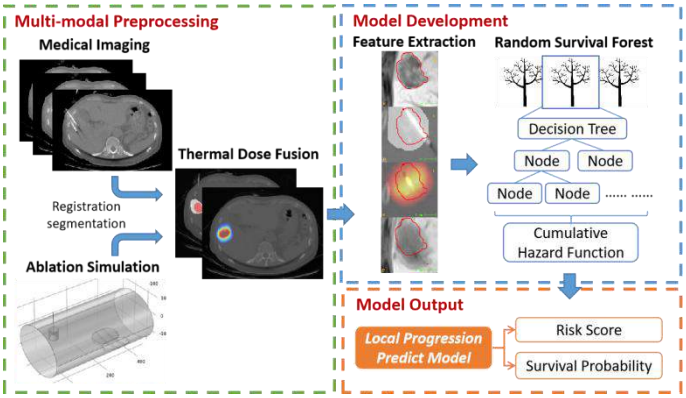

Figure 1: The framework to predict the risk of local progression

Thermal dose mapping was first calculated and only for radio-frequency ablation, since the ice balls in CT scans could characterize the cooling process. We used a numerical simulation model based on the patient's individualized impedance to invert the steady-state temperature field [6]. The initial state and boundary conditions were set according to actual therapeutic parameters. We calculated the equivalent thermal dose during steady state in voxel-scale, the values of which were accumulated if heated more than once. We fused the thermal dose maps with intra-operative images, and registered the pre- and post-operative scans to the same CT series [7]. The segmentation of the region of interest was then implemented.

Table 1: The extraction of radiomic features

Image	Tumor	Ice Ball	Thermal Dose	Ablation Zone
Geometric	√	√		
Grayscale			√	
Texture	√		√	√

We extracted a total of 113 features directly from each sample. The radiomic features were extracted from 2D slices of the region of interest (Table 1), and the texture features consisted of Law features, Tumaru features, and GLCM features in detail. Age, disease type, tumor number and treatment position were added as clinical features. Considering the complex linear and nonlinear relationships in high-throughput features, we applied the group-Lasso and correlation graph to avoid dimensional catastrophes.

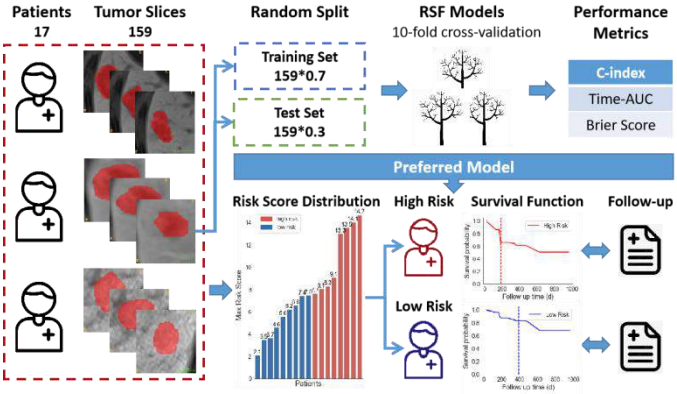

Figure 2: The training and validation of random survival forests

We used the random survival forest to predict the risk of local progression (Fig. 2). A conservation-of-events principle for survival analysis is introduced to define the overall mortality, a interpretable measure used as a predicted risk. We randomly split 159 slices into training and test set by 7:3. Based on the ranked importance of predictors, models with different input combinations were established.

Three performance metrics were measured: the C-index, the Brier Score and the time-dependent AUC, expressed as mean±deviation and confirmed by Wilcoxon rank-sum test. According to the distribution of maximum risk scores, we classified the patients into high- and low-risk groups. Kaplan-Meier curves were used to validate the grouping ability. Randomly selected two patients from each subgroup, we observed the predicted disease-free survival, especially at the event.

RESULTS

Importance ranking was performed for all selected features (Fig. 3a). The clinical (blue), pre-operative (yellow), intra-operative (red) and post-operative (gray) features contributed 18.3%, 29.2%, 34.5% and 18.1%, respectively. Intra-operative features had a higher ranking than post-operative ones, implying an indispensable role in prognostic evaluation. Therefore, the followed two models were compared:

• Model 1: clinical features, pre-operative tumor features, and post-operative ablation zone features.

• Model 2: clinical features, pre-operative tumor features, and intra-operative thermal dose features.

Performance metrics measure the ability of ranking survival times and grouping risk levels, and the error of predicted survival probability (Fig. 3 b-d). The thermal dose in Model 2 improved the C-index by 11% with less deviation, and maintained higher grouping accuracy until the median follow-up (iAUC: P=0.007). It might indicate the reflection for both immediate damage and long-term immunity. Model 2 also reached a lower error for maximum and average (iBS: P=0.004), providing a reliable estimate of individual progression-free survival.

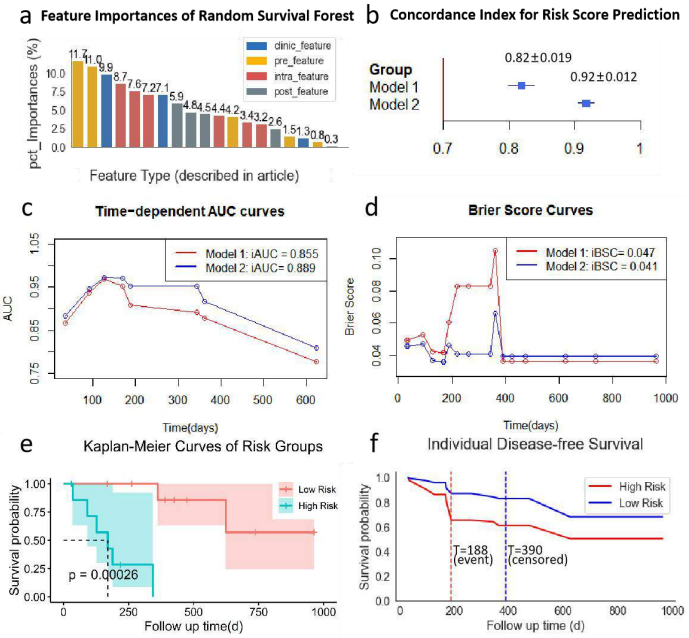

Figure 3: The performance of prediction models

The validation of the preferred Model 2 to clinical data was analyzed (Fig. 3f). The Kaplan-Meier curves for the predicted high-risk and low-risk groups differed significantly. The individual survival probability dropped sharply around the actual event for the high-risk patient, while it kept above 0.8 without progression for the low-risk patient. The predicted risk scores and survival probabilities provide quantitative information to assist early intervention.

DISCUSSION

The purpose of this study is to develop an accurate, timely and instructive prognostic evaluation tool, which allows the immediate evaluation of the progression risk after multi-mode ablation treatment. Our results show the potentiality of thermal dose maps to predict the direct and indirect damage more precisely in long-term, which may be attributed to the high-throughput features rather than a simple specific threshold. The quantitative information, especially individual survival probabilities, advance the potential of this method for clinical applications. In the future, we will explore the associations of immune response with thermal dose and provide personalized treatment for patients. We will also include more patients into our dataset.

ACKNOWLEDGEMENTS

This work is supported by National Natural Science Foundation of China (No. 51890892). The clinical trial in Shanghai Cancer Center, Fudan University is registered No. ChiCTR-INR-16009089.

REFERENCES

[1] Xu, L. X. *et al.*,*Science,* 57-60, 2016.

[2] Appelbaum, L. *et al.*,*Tech Vasc Interv Radiol,* 16:287-295, 2013.

[3] Huang, Y. *et al.*,*Radiology,* 281(3):947-957, 2016.

[4] Hue, Y. K. *et al.*,*IEEE Trans Med Imaging,* 37(2):417-427, 2017.

[5] Ishwaran, H.,*Ann. Appl. Statist,* 2:841-860, 2008.

[6] Fangyu *et al.*,*Conf Proc IEEE Eng Med Biol Soc,* 3232-3235, 2018.

[7] Xu, P. *et al.*,*IEEE Access,* 8:13613 - 13619, 2020.

WALL SHEAR STRESS TOPOLOGICAL SKELETON VARIABILITY PREDICTS MYOCARDIAL INFARCTION

Maurizio Lodi Rizzini (1), Alessandro Candreva (2), Claudio Chiastra (1), Takuya Mizukami (2), Diego Gallo (1), Jean-Paul Aben (3), Olivier Muller (4), Bernard De Bruyne (2,4), Carlos Collet (2), Umberto Morbiducci (1)

(1) PolitoBIOMed Lab, Department of Mechanical and Aerospace Engineering
Politecnico di Torino
Turin, Italy

(2) Cardiovascular Center Aalst
OLV-Clinic
Aalst, Belgium

(3) Pie Medical Imaging BV
Maastricht, The Netherlands

(4) Department of Cardiology
Lausanne University Hospital
Lausanne, Switzerland

INTRODUCTION

Myocardial infarction (MI) is the deadliest complication of coronary artery disease (CAD), with approximately 1 million of cases per year in the United States alone [1]. Coronary atherosclerotic plaques experience a variety of hemodynamic stimuli, such as wall shear stress (WSS) and pressure gradients, linked to plaque progression and destabilization, increasing the risk of an abrupt occlusion [2]. In particular, WSS is purported to play a major role in translating hemodynamic signals to vascular biological phenomena. In this regard, peculiar WSS features obtained from patient-specific computational fluid dynamics (CFD) simulations have been associated with coronary plaque rupture [3]. Therefore, WSS-based quantities may prove to have predictive capability for MI, allowing the identification of lesions prone to rupture improving the medical management of CAD patients.

Accordingly, the present study aims to explore the capability of a comprehensive hemodynamic assessment of coronary lesions to predict MI. To do that, quantitative coronary angiography (QCA), fractional flow reserve derived from angiography (vFFR) and WSS derived from patient-specific CFD simulations were retrospectively tested on a population of patients (N=188 vessels) with future culprit (FC) and non-future culprit (NFC) lesions.

METHODS

Patient population. Patients presenting with acute MI admitted for invasive coronary angiography were retrospectively screened to identify those who had (1) a previous coronary angiography performed between 1 month and 5 years before the event (baseline angiography), (2) a visually identifiable FC mildly stenosed lesion (i.e., $\leq$ 50% diameter stenosis) at the baseline angiography, and (3) at least one additional NFC lesion in the other two major epicardial vessels. This selection resulted in 80 patients and a total of 188 vessels, with 80 FC lesions and 108 NFC lesions.

Computational hemodynamics. The workflow of the study is presented in Figure 1. Three-dimensional QCA vessel reconstructions were performed using two angiographic projections with at least 30 degrees apart, extracting anatomical (percentage area stenosis, %AS) and functional (vFFR) data, using the CAAS Workstation vFFR software (Pie Medical Imaging, Maastricht, the Netherlands). 3D reconstructions were then discretized and transient CFD simulations were performed using a finite element-based code (CAAS Workstation WSS software, Pie Medical Imaging) to obtain the WSS distribution along the luminal surface. Patient-specific mean flow rates were prescribed as inflow boundary conditions scaling a generic Doppler velocity curve, distinctive for the right, left anterior descending, and left circumflex coronary arteries with a diameter-based scaling law [4].

Wall shear stress-based descriptors. The most widely adopted cycle-average descriptors of WSS magnitude, multidirectionality and topological skeleton features were tested. Here, we focused on the two descriptors that emerged as the strongest predictors of MI, as reported in the following. In detail, the cycle-average WSS (TAWSS) was selected as a measure of the WSS magnitude acting on the endothelium. Moreover, the contraction/expansion action exerted by hemodynamic shear forces on the endothelium was quantified according to a recently proposed Eulerian-based method for the analysis of the WSS topological skeleton based on the divergence of the WSS unit vector field (DIV_{WSS}) [5]: negative (positive) DIV_{WSS} values at the luminal surface identify WSS contraction (expansion) regions. Very recent findings demonstrated that the WSS topological skeleton is able to capture hemodynamic features linked to vascular dysfunction [6,7,8]. Here the quantity Topological Shear Variation Index (TSVI) was used as a measure of the variability of the local contraction/expansion action

exerted by the WSS along the cardiac cycle. Technically, the TSVI is defined as [7,8]:

$$TSVI = \left\{\frac{1}{T}\int_0^T [DIV_{WSS} - \overline{DIV_{WSS}}]^2 dt\right\}^{1/2} \quad (1)$$

where T is the cardiac cycle duration.

Statistical analysis. WSS-based descriptors were averaged over the lesion, identified using the standard QCA-based approach. The predictive capacity of WSS-based descriptors was quantified in terms of receiver operating characteristic (ROC) curve and area under the curve (AUC).

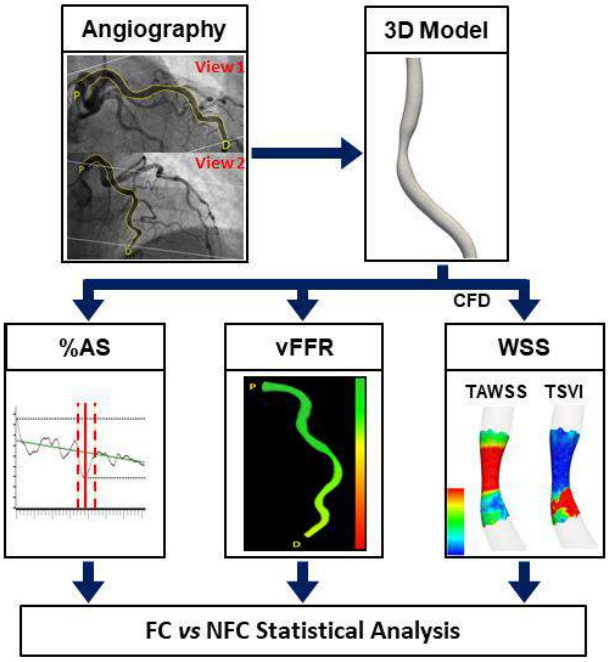

Figure 1: Workflow of the study

RESULTS

The FC and NFC groups were significantly different in terms of both anatomical and functional data ($p<0.001$ and $p=0.009$ for %AS and vFFR, respectively). Significant differences emerged between the FC and NFC distributions of lesion-average values of TAWSS (FC: 3.36 [IQR: 2.51-5.23] Pa; NFC: 2.94 [IQR: 2.36-3.80] Pa, $p=0.011$) and TSVI (FC: 71.08 [IQR: 44.42-116.20] m^{-1}; NFC: 33.21 [IQR: 24.77-60.11] m^{-1}, $p<0.001$), as reported in figure 2. Notably, both TAWSS and TSVI were significantly higher in FC than NFC group, with a more marked statistical significance for TSVI.

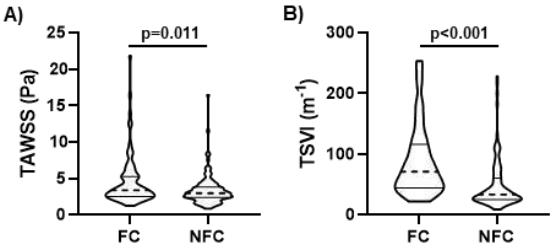

Figure 2: Violin plots of TAWSS (panel A) and TSVI (panel B) averaged over the lesion.

Anatomical and functional data emerged as moderate predictors for MI (AUC=0.65 and AUC=0.63 for %AS and vFFR, respectively). In figure 3, the ROC curves for lesion-average values of TAWSS and TSVI are presented. From the analysis, it emerged that TAWSS was a moderate (AUC=0.61; 95% CI: 0.53 to 0.69, $p=0.011$) but weaker MI predictor than anatomical and functional data. TSVI (AUC=0.77; 95% CI: 0.70 to 0.84, $p<0.001$) emerged as a stronger MI predictor than anatomical and functional data, as well as TAWSS. The best identified threshold values were: (1) 5.01 Pa for TAWSS, resulting in sensitivity equal to 0.34 and specificity equal to 0.89; (2) 40.52 m^{-1} for TSVI, resulting in sensitivity equal to 0.85 and specificity equal to 0.65.

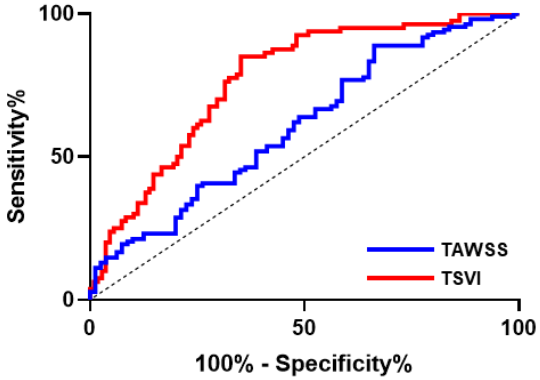

Figure 3: ROC curves based on TAWSS (blue) and TSVI (red) prediction of MI.

DISCUSSION

This study investigated the prediction capability for MI of anatomical, functional, and CFD-derived WSS-based quantities. The main results can be summarized as follows: (1) significantly different anatomical (%AS), functional (vFFR) and hemodynamic quantities (TAWSS and TSVI) characterized FC and NFC groups; (2) vFFR, %AS, and high TAWSS exhibited a moderate MI prediction capability; (3) high TSVI emerged as the strongest MI predictor. The obtained results enforce the hypothesis that (1) endothelial shear stress is a main actor in CAD, and (2) TSVI represents a relevant hemodynamic cue in CAD. The emergent predictive power of TSVI expands its association with long-term restenosis after carotid endarterectomy [7] and ascending aortic aneurysm wall degradation [8]. Physically, TSVI describes the variability of the contraction/expansion action exerted by WSS on the endothelium. Thus, it describes different features of the WSS vector field with respect to TAWSS and it represents a different hemodynamic stimulus to the endothelium. Translating this into mechanistic implications, the variability in the contraction/expansion action exerted by shear forces on endothelial cells reflects on intracellular tension variability that could lead to aggravating biological events [9]. A high temporal variability of WSS contraction/expansion action may result in fibrous cap fragility, accelerated disease progression, plaque fatigue, ending in plaque rupture and subsequent MI. This hypothesis, which needs further investigation, is also supported by the fact that TSVI identifies blood flow stagnation, recirculation and separation regions usually classified as flow disturbances promoting vascular dysfunction.

In conclusion, high TSVI resulted a strong predictor of MI in the analyzed population, encouraging further clinical trials to enforce the presented results and translate this concept into clinical practice.

REFERENCES

[1] Virani SS et al. *Circulation*, 2020.
[2] Lee JM et al., *JACC Cardiovasc Imaging*, 12(6):1032-43, 2019.
[3] Kumar A et al., *J Am Coll Cardiol*, 72(16):1926-35, 2018.
[4] van der Giessen AG et al., *J Biomech*, 44(6):1089-95, 2011.
[5] Mazzi V et al., *Biomech Model Mechanobiol*, 19(5):1403-23, 2020.
[6] Arzani A et al., *J Biomech*, 73:145-152, 2018.
[7] Morbiducci U et al., *Ann Biomed Eng*, 48:2936–49, 2020.
[8] De Nisco G et al., *Med Eng Phys*, 82:119-129, 2020.
[9] Lei M et al., *Med Eng Phys*, 18(4):326-32, 1996.

LYMPHOCYTE NANOMECHANICS IN RESPONSE TO STENT IMPLANTATION

Konstantinos Kapnisis (1), Andreas Stylianou (2, 3), Despoina Kokkinidou (1), Marianna Prokopi (1) and Andreas Anayiotos (1)

(1) Department of Mechanical Engineering and Materials Science and Engineering, Cyprus University of Technology, Limassol, Cyprus

(2) School of Sciences, European University Cyprus, Nicosia, Cyprus

(3) Cancer Biophysics Laboratory, Department of Mechanical and Manufacturing Engineering, University of Cyprus, Nicosia, Cyprus

INTRODUCTION

Changes in the arterial mechanical environment due to stent implantation are the main causes of the initiation of thrombosis and restenosis [1]. The mechanical properties of live cells can affect their physical interactions with the surrounding extracellular matrix, potentially influencing the process of mechanical signal transduction in living tissues. Previous studies have described the infiltration of inflammatory cells and immunocytes (T-lymphocytes) in restenotic tissue. This inflammatory response is characterized by the activation of circulating leukocytes that express adhesion molecules on the cell surface [2]. In this work we investigate stent-induced alterations in the nanostructure, cytoskeleton and mechanical properties of circulating lymphocytes in an effort to establish mechanical biomarkers to access stent-induced inflammation in the adjacent vascular tissue.

METHODS

Animal stenting: Male atherosclerotic ApoE−/− (30±5 g) and male CD1 (40±5 g) mice were used throughout the study (Project license: CY/EXP/PR.L9/2019). Custom made self-expanding nitinol stents (0.7 x 3.3 mm, closed-cell design with a diamond-shaped pattern; Admedes GmbH, Pforzheim, Germany), were implanted following the experimental protocol reported by Simsekyilmaz et al. 2013 [3] which describes a rapid and accessible procedure of stent implantation in mouse carotid artery.

Lymphocyte isolation: Whole blood (0.5-1 ml per animal) was collected from control (non-stented; n=3 per strain) and stented (12 weeks post implantation; n=3 per strain) mice, by direct cardiac puncture using a heparinized syringe. Mononuclear cells (MNCs) were isolated from whole blood using the SepMate™ procedure and highly purified CD4+ T lymphocyte subsets were enriched via the RosetteSep™ protocol (Stemcell Technologies, Vancouver, BC, CA).

Cell culture: Isolated lymphocytes were cultured in RPMI1640 medium, supplemented with penicillin 100 IU/ml, streptomycin 100 mg/ml, L-glutamine and 10% newborn calf serum at 37 8C in a humidified atmosphere of 5% CO2. The cells were cultured either on 35 petri dishes or glass cover slips, both coated for 5 minutes with Poly-L-lysine hydrobromide (Sigma).

Atomic Force Microscopy (AFM): AFM characterization was performed to probe the mechanical properties of live cells using a Molecular Imaging-Agilent PicoPlus AFM system and V-shaped soft silicon nitride probes (MLCT-Bio, probe C, Bruker). Petri dishes with the cultured cells, either for 2h (same day group) or for 24h (next day group), were directly mounded on AFM sample plates. In an area of 1x1μm near the center of the cells, 8x8 points of force curves were collected and analyzed by the freeware software AtomicJ so as to calculate the sample's Young's modulus using the Hertz model (for cells a 0.5 Poisson ratio was used). All mechanical properties measurements were recorded with a set point of 1nN normal force. For the mechanical characterization at least 30 live cells per condition from 3 independent experiments were studied, while attention was paid to always perform the measurements in less than 40min per experiment. Imaging of fixed cells (20 min with 4% paraformaldehyde-PFA) was performed in tapping mode with silicon probes (ACT-Applied Nanostructures). The AFM image processing was performed by using the PicoView software (Agilent) and the freeware scanning probe microscopy software WSxM.

Cell Immunostaining: Cells were first fixed with 4% PFA for 20 min and then a permeabilization buffer containing phosphate buffered saline, 2mg/ml Bovine Serum Albumin, and 0.1% Triton X-100. Then, cells were incubated with phalloidin for 1 hour at room temperature. Finally, cells were washed again three times with the permeabilization buffer and incubated for 2 min with 4',6-Diamidino-2-Phenylindole

(DAPI, Sigma). All coverslips were then mounted on a slide and observed under an Olympus BX53 fluorescent microscope equipped with an Olympus XM10 Monochrome CCD camera.

Stress fibers: For the characterization of the actin stress fibers, the FilamentSensor tool was used. In the reconstructed images each color corresponds to a different fiber orientation. Stress fiber orientation was assessed using the order parameter S=cos2θ, where he higher the value of S is, the more oriented the fibers become.

Cells' shape: Cell elongation was assessed using optical microscopy images. ImageJ software was used to automatically measure factor E from cells. Factor E equals to the long axis divided by the short axis minus one. Thus, E is zero for a circle, and one for an ellipse with an axis ratio 1:2. The cells that presented E values 0–0.5 were considered as spherical, 0.5–1 as ellipsoid, and E values higher than 1 as elongated. We used the optical microscope images from the cells so as to measure the cells circularity.

RESULTS

Firstly, we studied normal lymphocyte morphology. Our data demonstrated that lymphocytes from non-stented (control) ApoE and CD1 mice present typical spherical shape (Fig.1A), while high resolution AFM images showed cellular microvilli at the cells' surface and pseudopodia at the edge of the cell (Fig.1B). Furthermore, stress fibers where mainly located at the periphery of the cells, without any significant orientation pattern (Fig. 1A).

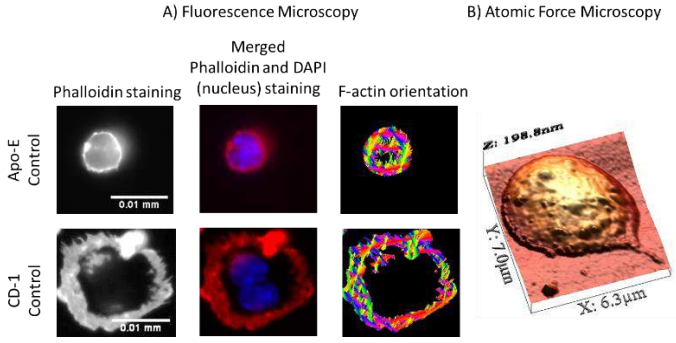

Figure 1: Representative images of lymphocytes (from control ApoE and CD1 mice) via A) fluorescence and B) AFM microscopy.

AFM studies on live cells from stented mice, highlighted that lymphocytes exhibit a significantly higher Young's modulus value. This pattern was observed in cells from both mouse strains, and in lymphocytes that were studied *in vitro* either 2h (same day) or 24h (next day) after isolation (Fig.2).

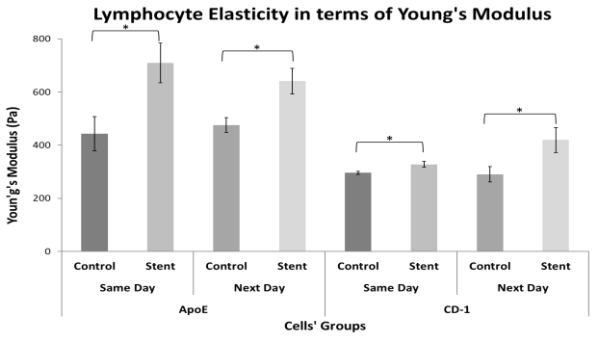

Figure 2: Young's modulus of lymphocytes (2h and 24h after isolation) from control vs stented mice. (* indicates p<0.05)

Subsequently, we used fluorescent microscopy to study whether inflammation alters lymphocytes morphology and F-actin stress fibers characteristics, which are considered to be the major cytoskeleton characteristic responsible for cells' mechanical properties. The results show that lymphocytes morphology was altered, as lymphocytes were becoming more elongated (Fig. 3 A (left) and B). Furthermore, notable cytoskeleton changes were observed, including F-actin stress fibers distribution and orientation (Fig. 3 A (right) and C). Stress fibers were distributed throughout the cell body, and more elongated patterns were formed. We believe that these alterations in F-actin fibers are due to the activation of lymphocytes as a result of the stent-induced inflammatory response. Consequently, cellular remodeling significantly modified the cell's mechanical properties, as assessed with AFM.

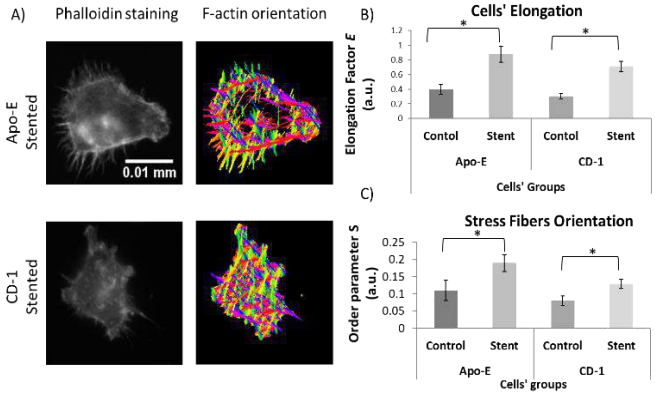

Figure 3: A) Representative images of lymphocytes (from stented ApoE and CD1 mice). Quantification of cell's B) elongation and C) stress fibers orientation. (* indicates p<0.05)

DISCUSSION

Restenosis appears to be associated to inflammatory and immunological activity that persists several months after coronary intervention. AFM has emerged as a powerful tool for studying important dynamic cellular processes in real time and it has been recently demonstrated that it can be used for developing nanomechanical biomarkers from single cells up to tissue samples [4].

Our research results demonstrated that lymphocytes from stented mice present an increase in their stiffness. Cell remodeling was observed in two different mice strains, the most widely used model of atherosclerosis, the ApoE-/- (for which changes due to lymphocyte activation are more profound) and the multipurpose CD1 strain. It is noted that the elevated Young's modulus is accompanied with the cytoskeleton rearrangement. Our findings suggest that the nanomechanical properties of circulating lymphocytes, could potentially be used as a biomarker to access stent-induced inflammation and possibly early stages of in-stent restenosis.

ACKNOWLEDGEMENTS

This work was co-funded by the European Regional Development Fund and the Republic of Cyprus through the Research and Innovation Foundation (Project INTERNATIONAL/USA/0118/0057).

REFERENCES

[1] Wang J. et al., Regenerative Biomaterials, 5(3), 177–187, 2018.
[2] Tabas I. and Lichtman A.H. Immunity. 47(4): 621–634, 2017.
[3] Sakine Simsekyilmaz, et al. J Vis Exp. (75):50233, 2013.
[4] Stylianou, A, et al. Nanoscale (10):20930, 2018.

MULTISCALE HEMODYNAMIC PREDICTIONS IN CHRONIC THROMBOEMBOLIC PULMONARY HYPERTENSION

Mitchel J. Colebank (1), Mette S. Olufsen (1)

(1) Department of Mathematics
North Carolina State University
Raleigh, NC, USA

INTRODUCTION

A compromised pulmonary vasculature can lead to pulmonary hypertension (PH), a disease defined by a mean pulmonary arterial blood pressure (mPAP) $>$ 20 mmHg [1]. Though there have been advances in PH treatments, only chronic thromboembolic pulmonary hypertension (CTEPH) is considered curable. CTEPH is characterized by multiple recurrent or unresolved pulmonary emboli that impede flow to the alveoli. Disease confirmation requires elevated mPAP and at least one lobular perfusion deficit verified by a ventilation-perfusion (V/Q) scan. Severe CTEPH leads to small vessel arteriopathy, affecting pulmonary arterioles in both obstructed and unobstructed territories [2]. CTEPH patients typically undergo pulmonary thromboendoarterectomy (PTE); however, those with lesions in the smaller segmental and subsegmental arteries are deemed inoperable, and represent up to 60% of CTEPH patients [3]. An alternative surgical procedure for inoperable patients is balloon pulmonary angioplasty (BPA), which mechanically disrupts thromboembolic material by inflating a catheter balloon. Patients undergoing BPA receive multiple treatments, and the treatment strategy, i.e., the order in which lesions are targeted, vary with lesion severity and location, making it difficult to prioritize lesions for BPA. To address this, we propose a multiscale model of CTEPH hemodynamics that couples a one-dimensional computational fluid dynamics model (1D CFD) of the large arteries to a linearized 1D model of the small arteries and arterioles. We also integrate two pressure-loss models, mimicking typical CTEPH lesions. Our results show that the model framework predicts common phenotypes of CTEPH, including perfusion deficits, small vessel flow imbalances, and elevated mPAP.

METHODS

The pulmonary arteries and lung tissue from a normotensive, control CT image (from SimVascular, http://simvascular.github.io/) are segmented using 3D Slicer [4] (see **Fig. 1**). The segmented geometry is converted to a centerline network using the Vascular Modeling Toolkit (http://www.vmtk.org/), and then post-processed using custom MATLAB (Natick, MA) software [5], providing the network connectivity and individual vessel length and radii. We assume that the small vessels not captured by imaging follow a fractal, binary structured tree [6]. Each small vessel's length and daughter radii are determined as

$$L = \ell_{rr} r_p, \qquad r_{d_\alpha} = \alpha r_p, \qquad r_{d_\beta} = \beta r_p, \tag{1}$$

where α and β are dimensionless radius scaling factors ($\beta \leq \alpha < 1$), and ℓ_{rr} is the length-to-radius ratio. The small vessel network emanates

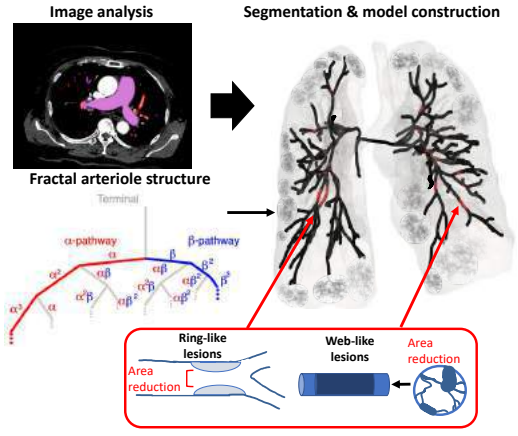

Figure 1: Proposed workflow that integrates medical imaging data, a small vessel fractal network, and two lesion energy loss models to predict multiscale hemodynamics in CTEPH.

from each terminal large artery and ceases after reaching a specified minimum radius, $r_{min} = 75\mu$m.

Large artery hemodynamics are predicted by solving nonlinear 1D CFD equations. Assuming that blood is incompressible, flow is Newtonian and axially dominated with no swirl, and that blood vessels are cylindrical and impermeable, the mass conservation and momentum balance equations are

$$\frac{\partial q}{\partial x} + \frac{\partial A}{\partial t} = 0, \qquad \frac{\partial q}{\partial t} + \frac{\partial}{\partial x}\left(\frac{q^2}{A}\right) + \frac{A}{\rho}\frac{\partial p}{\partial x} = -\frac{2\pi\nu R}{\delta}\frac{q}{A} \tag{2}$$

where x (cm) and t (s) denote space and time, and the dependent variables q (cm^3/s), $A = \pi R^2$ (cm^2), and p (mmHg) are the flow, cross-sectional area, and pressure, respectively. The hemodynamic parameters $\rho = 1.055$ (g/cm^3) and $\nu = 0.032$ (cm^2/s) are the blood density and kinematic viscosity. We assume that the blood velocity profile is flat but linearly decreases from the boundary layer thickness, $r = \delta$ (cm), to the vessel wall, $r = R$, satisfying the no-slip condition [6]. The system of equations is closed under the assumption that vessel walls are linear, elastic, incompressible, and isotropic, giving

$$p = \frac{4}{3}\frac{Eh}{r_0}\left(\sqrt{A/A_0} - 1\right) \tag{3}$$

where E (mmHg), h (cm), and $A_0 = \pi r_0^2$ (cm^2) are the Young's modulus, wall thickness, and reference area, respectively. An inflow profile drives the hyperbolic PDE system, conservation of pressure and flow are enforced at vessel junctions, and a small vessel hemodynamics model provides a terminal boundary condition for the large arteries.

In the small arteries and arterioles, we assume greater viscous forces than inertial, leading to a linearized form of eq. (2). We rewrite pressure and flow as periodic functions, leading to a wave equation with analytical solutions. Here, blood viscosity is modeled as non-Newtonian [6]. We assume pressure and flow conservation at each junction tree and prescribe a terminal impedance Z_{trm} as a resistance boundary condition.

To model CTEPH conditions, we increase both small and large artery stiffness, dilate the proximal arteries, and induce small vessel vasoconstriction. In addition, we employ two pressure loss models to simulate ring- and web-like stenoses common in CTEPH. They are

$$\Delta p_R = \frac{\mu K_v}{2\pi r^3} q + \frac{\rho K_t}{2A^2}\left(\frac{1}{C} - 1\right)^2 |q|q + \frac{\rho K_u L_R}{A}\frac{\partial q}{\partial t} \quad \text{and} \tag{4}$$

$$\Delta p_W = L_W\left(\frac{\mu}{K_p}\frac{q}{A} + \rho K_W\left(\frac{q}{A}\right)^2\right), \tag{5}$$

respectively, where K_v, K_t, and K_u are the viscous, turbulent, and inertial loss coefficients, K_p and K_W are the static and inertial permeability coefficients, L_R and L_W (cm) are the ring- and web-like lesion lengths, and $C \in [0,1]$ is the maximal area reduction of ring-like lesions. Eq. (4) is often used to model coronary artery stenoses [7], whereas eq. (5) is a novel model for web-like lesions. We place 20 lesions throughout the large arteries (see Fig. 1); 9 ring-like lesions ($C = 90\%$) and 11 web-like lesions with ($K_p = 9 \times 10^{-3}$, $K_W = 1.05$).

RESULTS

Fluid dynamic simulations are conducted under normotensive and CTEPH conditions, the latter including large and small vessel stiffening and 20 pulmonary lesions. Systolic pressure predictions in all 226 large arteries are provided in **Fig. 2a**. Results show a pressure increase proximal to CTEPH lesions, while pressure downstream from the lesions is substantially lower. The fractional flow reserve (FFR), defined as the ratio of mean proximal and distal pressure, is 0.37 ± 0.23 and 0.94 ± 0.05 for ring- and web-like lesions, respectively. Hemodynamic predictions in the structured tree are shown in **Fig. 2b** along an obstructed pathway distal to a lesion and an unobstructed pathway. Both mPAP and mean flow decrease in the obstructed pathway in CTEPH,

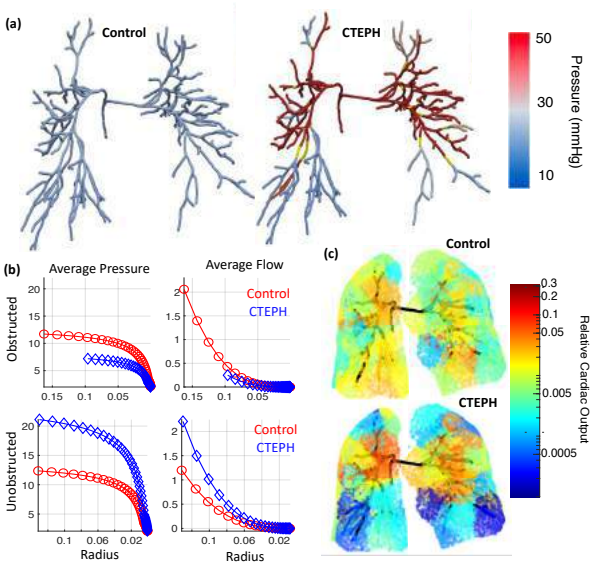

Figure 2: Model simulations in normotensive and CTEPH scenarios. (a) Systolic pressure throughout the large artery network. (b) Mean pressure and flow in the small vessels in both an obstructed and unobstructed pathway. (c) Perfusion map projected from the large vessels to the segmented lung tissue.

while these quantities both increase in the unobstructed pathway. Small vessel vasoconstriction in the obstructed path decreases the radii values in the structured tree relative to control, as shown on the x-axis. Lastly, flow predictions are mapped to the lung tissue in **Fig. 2c** and show increased flow heterogeneity and perfusion deficits in CTEPH.

DISCUSSION

Pulmonary hemodynamics models are underutilized in comparison to their systemic counterparts [7]. However, our model framework provides a useful *in-silico* tool for understanding the progression of CTEPH, and, more broadly, PH. FFR values from the model are consistent with those measured invasively by a catheter wire [8]. CTEPH is known to cause large perfusion deficits, increased mPAP, and small vessel arteriopathy, which is captured in our multiscale results in **Fig 2**. Results show underperfusion in vessels downstream to lesions, while small vessels in unobstructed pathways are overperfused, consistent with clinical hypotheses [2]. This proof of concept study lays the foundation for future investigations into the both the progression of small vessel disease in CTEPH and disease management. Our ultimate goal is to integrate patient specific lesions from CTEPH CT scans, estimate patient biomarkers, and provide an assistive tool in surgical planning, i.e., identifying improved mPAP and perfusion after BPA.

ACKNOWLEDGEMENTS

This research was supported by the AHA (19PRE34380459) and the NSF (NSF-DMS 1615820).

REFERENCES

[1] Simonneau, G et al., *Eur Respir J*, 53:1801913, 2019.
[2] Lang, I et al., *Ann Am Thorac Soc*, 13:215-221, 2016.
[3] Kawakami, T et al., *Circ Cardiovasc Inter*, 9:1-8, 2016.
[4] Fedorov, Andriy et al., *Magn Reson Imaging,* 30:1323-1341, 2012.
[5] Colebank, M et al., *J R Soc Interface,* 16:20190284, 2019.
[6] Chambers, M et al., *I Mech Eng H,* 234:1312-1329, 2020.
[7] Yin, M et al., *Comput Methods Appl Mech Eng*, 353:66-85, 2019.
[8] Ishiguro, H et al., *JACC Cardiovasc Imaging,* 9:324-325, 2016.

CHARACTERIZATION OF AN ELECTROSPUN POLYURETHANE WITH TUNABLE CHEMISTRY AND THIOL-ENE CROSSLINKING FOR BIOMEDICAL APPLICATIONS

S. Briggs (1), S. Herting (1), G. Fletcher (1), MB. Monroe (2), D. Maitland (1)

(1) Department of Biomedical Engineering
Texas A&M University
College Station, Texas, United States

(2) Department of Biomedical and Chemical Engineering
Syracuse University
Syracuse, New York, United States

INTRODUCTION

Many medical procedures today require biomaterials which are both versatile and adaptive in order to treat complex conditions. The aim of this project is to combine the versatility of shape memory polymers (SMPs) with the biocompatibility of the electrospinning fabrication technique. SMPs are often beneficial for medical applications as they allow for significant shape change in difficult to access areas. Additionally, electrospinning is an advantageous fabrication technique for tissue contacting devices due to high porosity, flexibility, and ECM like microstructure. Presented in this study is a thermoplastic polyurethane with tunable chemistry which can be crosslinked via thiol-ene click chemistry post fabrication into the desired geometry via electrospinning. The ability to crosslink these materials post-fabrication enables mechanical properties not usually achievable by thermoplastic electrospun materials. Mechanical, morphological, and shape memory properties are presented. These properties are important in determining appropriate potential biomedical applications for this material. Potential applications include self-constricting tubes for improved support and protection in tendon and anastomosis surgeries, a protective wrap for use in bone defect repair, or as a self-closing bandage for wound healing.

METHODS

Fabrication of Crosslinkable Thermoplastic Polyurethane. A thermoplastic polyurethane was synthesized as described previously by Hearon et al.[1] with changes described hereafter. This polymer system includes pendant vinyl groups by incorporating trimethylolpropane allyl ether (TMPAE) into the backbone with allows for tiol-ene crosslinking post fabrication into the desired geometry. Alterations to the polymer backbone were made as shown in Table 1 to tune material properties.

Table 1: Polymer backbone alterations to tune material properties.

Target Alteration	Isocyanate	Diol	AA Concentration
Molecular Weight	TMHDI	1,3-BD	0.5%
			1%
			2%
Glass Transition Temperature	TMHDI	1,4-BD	1%
		1,3-BD	
		2-DMPD	
Hydrophobicity	TMHDI	1,3-BD	1%
	0.5 HDI 0.5 TMHDI		
	HDI		

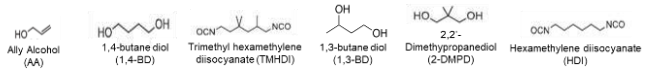

Electrospinning and Crosslinking Process. Electrospinning solutions were prepared by mixing thermoplastic and solvent on a weight basis (g/g) in a glass vial. This solution was then agitated on an orbital shaker until completely dissolved. For crosslinked samples, the desired weight of crosslinker (PETMP) and photoinitiator (DMPA) was then added, vortexed, and allowed to mix of the orbital shaker for 30-40 minutes. The desired volume was then drawn into a syringe which was loaded on the syringe pump and connected to PTFE tubing running into the electrospinning box. The positive end was connected to the dispensing needle via an alligator clip and the ground wire was wound around the rotating collection mandrel. The gap distance was measured as the distance between the end of the dispensing needle and the top of the rotating mandrel. The syringe pump was run until the solution was starting to come out of the dispensing needle and the voltage source was

then started. Samples were allowed to spin for 30 minutes. UV crosslinking of the electrospun mats was performed using a UV floodlight box (Integrated Dispensing Solutions – Intelli Ray 400). Samples were treated for 30 minutes per side at 50% intensity.

Fiber Morphology Characterization. Scanning Electron Microscope (SEM) images of the mats were collected using a JEOL JSM-7500F at magnifications of 100 and 500X for each sample. Prior to imaging, samples where mounted on carbon tape and sputter-coated using an Au target. Fiber diameter was determined using ImageJ software plugin Diameter J.

Mechanical Testing. Tensile testing for both bulk film and electrospun mat samples was performed on an Instron 5965. Samples were tested with a gauge length of 20mm, width of 7.6 mm, and thicknesses between 0.5 and 1 mm. Deformation was applied at a rate of 10 mm/min until sample failure.

Shape Memory Testing. Shape recovery testing was performed on a TA Instruments Q800 Dynamic Mechanical Analyzer (DMA). Samples were heated to 80 °C (well above their Tg's) and elongated to 100% strain. The strain was then locked and the samples were cooled to -10 °C to lock in the elongated shape. The DMA control arm was then allowed to float and the samples were heated to 50 °C and recovery stain was measured.

RESULTS

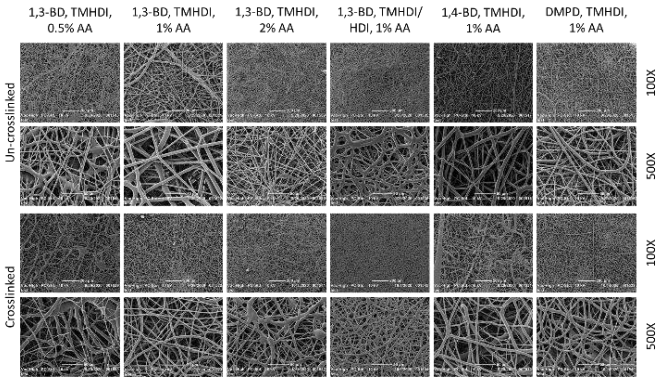

Figure 1: SEM images of electrospun polyurethane. Each column indicates one of each of the formulations presented in Table 1.

With exception of the formulation that used only HDI, all polymer compositions were able to be successfully electrospun into microfibers ranging from 2-20 µm as shown in Figure 1. This includes both un-crosslinked samples, which lacked the addition of crosslinker or photoinitiator, and crosslinked samples which were UV treated.

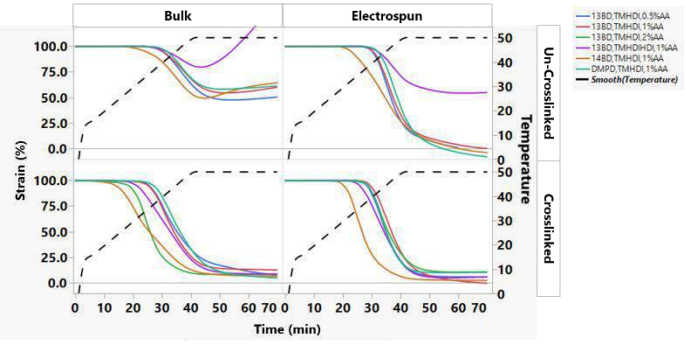

Figure 2: Shape recovery profile for bulk and electrospun samples

Shape recovery data is presented in Figure 2 and demonstrates the shape recovery properties of these materials. When un-crosslinked, bulk samples only achieved about 50% of the applied strain while crosslinked samples achieved 90%+. For electrospun samples, both un-crosslinked and crosslinked samples achieved 90%+ shape recovery with one exception (un-crosslinked 1,3-BD, TMHDI/HDI, 1%AA).

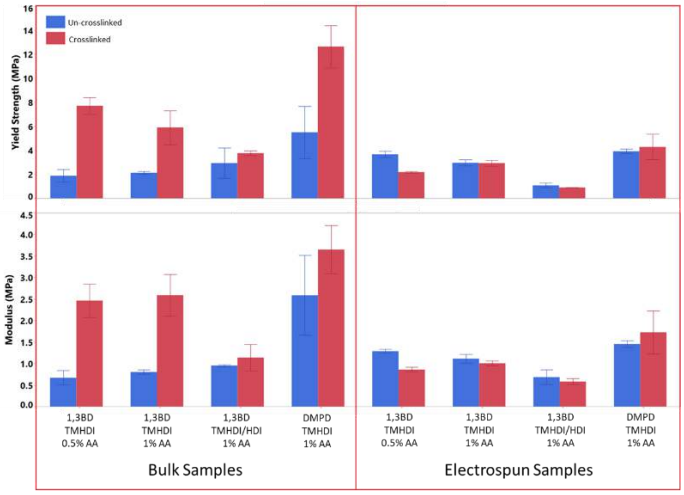

Figure 3: Modulus and yield strength of bulk and electrospun samples when crosslinked and un-crosslinked.

Mechanical testing of both bulk and electrospun materials is presented in Figure 3. Most bulk samples showed marked increases in modulus and yield strength when crosslinked. This indicates the success of the crosslinking process for these samples. The un-crosslinked Electrospun samples had comparable mechanical properties to their un-crosslinked bulk counterparts which is surprising given the inherent porosity and random fiber orientation of the materials. However, the electrospun samples did not show improvement of mechanical properties when crosslinked, indicating either a failure of the crosslinking process for these samples or an inability of this crosslinking to translate into tensile toughness.

DISCUSSION

This study demonstrated the ability to electrospin a shape memory polyurethane with good shape recovery properties and mechanical properties appropriate for biomedical applications. The fibrous nature of this electrospun material makes it an ideal candidate for tissue contacting implants and the shape memory properties enable innovative applications. One such application could be for anastomosis repair applications in which an electrospun SMP sleeve could be used to cover and protect the anastomosis site, helping to prevent dehiscence and leakage which can occur during these procedures [2].

ACKNOWLEDGEMENTS

Thank you to the Biomedical Device Laboratory at Texas A&M.

REFERENCES

[1] K. Hearon *et al.*, "A Processable Shape Memory Polymer System for Biomedical Applications," *Adv. Healthc. Mater.*, vol. 4, no. 9, pp. 1386–1398, Jun. 2015, doi: 10.1002/adhm.201500156.

[2] C. J. Zeebregts, R. H. Heijmen, J. J. van den Dungen, and R. van Schilfgaarde, "Non-suture methods of vascular anastomosis," *BJS*, vol. 90, no. 3, pp. 261–271, 2003, doi: 10.1002/bjs.4063.

MATERNAL BONE ADAPTATION TO MECHANICAL LOADING DURING PREGNANCY, LACTATION, AND POST-WEANING RECOVERY

Yihan Li[1], Chantal M. J. de Bakker[1], Hongbo Zhao[1], Ashutosh Parajuli[2], Wei-Ju Tseng[1], Shaopeng Pei[1,2], Tan Meng[1], Rebecca Chung[1], Liyun Wang[2], and X. Sherry Liu[1]*

[1] McKay Orthopaedic Research Laboratory, University of Pennsylvania, Philadelphia, PA, USA

[2] Department of Mechanical Engineering, University of Delaware, Newark, DE, USA

INTRODUCTION

Although the maternal skeleton undergoes dramatic bone loss during pregnancy and lactation, several innate compensatory mechanisms are initiated to maintain the skeletal mechanical integrity [1,2]. Our previous studies suggest that reproduction-induced adaptations in cortical bone structure compensate for trabecular bone loss to maintain whole-bone mechanics [3]. Moreover, the extent of post-weaning bone recovery highly depends on bone's load-bearing capacity [4]. The above findings lead to our next question: does maternal bone also have a greater response to external loading? Recently, it was found that lactation-induced perilacunar/canalicular remodeling (PLR) may alter the osteocyte microenvironment [5,6], thus affecting skeletal mechanosensitivity. The objective of this study is to investigate the effects of pregnancy, lactation and weaning on maternal bone's mechano-responsiveness and osteocyte microenvironment in a rat model. We hypothesized that alterations in the osteocyte microenvironment through PLR activities during lactation would result in greater responsiveness to external loading, thereby indicating a beneficial effect of weight-bearing exercise on bone health postpartum.

METHODS

All animal experiments were approved by IACUC. *In vivo dynamic loading:* Female SD rats (n=8/group; age 26 weeks when loading started) were assigned to Virgin, Pregnancy (loading from day 7 of pregnancy), Lactation (loading from day 1 of lactation), and Post-weaning (loading from day 1 of post-weaning) groups, and subjected to a 2-week dynamic, compressive loading protocol [7]. A peak load of 45N, corresponding to ~1500 με at the tibial midshaft medial surface as determined by strain gauges, was applied to the left tibia at 2 Hz, at 5 min/session for 2 weeks (5 days/week), while the right tibia remained unloaded. *In vivo μCT imaging:* μCT scans of proximal tibia and tibial midshaft were performed on both tibiae before (week 0) and two weeks after loading (week 2) using VivaCT 40 (Scanco, voxel size 10.5μm). Percent changes between week 0 and week 2 for non-loaded and loaded tibiae were calculated, and the corresponding loading-induced differences in cortical microstructural percent changes between loaded *vs.* non-loaded tibiae were further derived. All rats were sacrificed at the age of 28 weeks after μCT scans. *Dynamic histomorphometry:* All rats were injected with calcein green and alizarin red on day 4 and day 13 of loading. Dynamic histomorphometry analyses were performed to evaluate double-labeled bone formation, and the fold change of bone formation parameters between loaded *vs.* non-loaded tibiae for each rat were calculated to determine the loading-induced bone formation. *Histology and IHC:* Paraffin-embedded non-loaded tibial cortex (n=6/group) was immunostained for MMP13 and CtsK to evaluate PLR enzyme expression. Ploton silver staining were performed on the tibial cortex to assess the lacunar-canalicular network. *Statistics:* Student's paired t-test was used to compare parameters between the loaded and non-loaded limbs in the same animal, while one-way ANOVA with Bonferroni corrections was used to compare loading responses and osteocyte-related parameters in rats with different reproductive status. Significant differences were considered when $p<0.05$.

RESULTS

Reproduction and lactation induced dramatic alterations in trabecular microstructure at the proximal tibia, but minimal changes in cortical bone structure at the tibial midshaft. At the proximal tibia, loading significantly reduced lactation-induced loss in trabecular bone volume fraction and thickness (BV/TV and Tb.Th) in Lactation rats, while minimal loading responses were found in other groups (Fig

1AB). At the tibial midshaft, loading led to significantly increased cortical bone area (Ct.Area) and polar moment of inertia (pMOI) compared to unloaded tibiae in all rats (Fig 1CD). However, loading responses in Ct.Area or pMOI did not differ among groups (Fig 1EF). Dynamic histomorphometry suggested that the 2-week dynamic loading led to significant increase in, and bone formation rate (BFR/BS) in the loaded *vs.* non-loaded tibia in all groups (Fig 2AB). Intriguingly, a higher loading-induced fold change in BFR/BS in Lactation rats was detected when compared to other groups (Fig 2C). Similar results were found in mineralizing surface and mineral apposition rate (data not shown).

Histological assessment at the tibial cortex indicated that Lactation rats had greater lacunar perimeter than all other groups (Fig 2AB) while no difference was detected in number and density of canalicular network (data not shown). Moreover, the investigations of PLR enzymatic expression revealed that Lactation rats had 37% and 40% greater percentage of MMP13+ osteocytes than Virgin and Post-weaning rats, respectively (Fig 2CD). Similarly, the percentage osteocytes that stained positive for CtsK was 50% higher in Lactation than Post-weaning rats (Fig 2EF).

DISCUSSION

While weight-bearing exercise during pregnancy and postpartum improve women's physical and psychological well-being, its effect on bone health remains unclear. By applying a dynamic loading protocol in a rat model, we demonstrated that loading reduced lactation-induced trabecular bone loss and improved cortical bone structure regardless of reproductive status, indicating a beneficial effect of weight-bearing exercise on maternal bone health postpartum. Moreover, loading led to greater periosteal bone formation in lactating rats as compared to rats at other reproductive stages or age-matched virgins, indicating a greater mechano-responsiveness of maternal bone during lactation. Consistent with previous studies in mice [5,6], we further confirmed that lactation led to increased lacunar size and osteocytic PLR enzyme activities in rats, and these transient changes were reverted post-weaning. According to the LCS fluid flow model initiated by Weinbaum *et al.* [8] and developed by Wang et al. [7,9], the enlarged lacunae and canaliculi alone could contribute to the pericellular fluid space, leading to marked increase of fluid drag force on osteocyte body and cell processes under a high frequency (4Hz) loading and an enhanced solute transport through LCS. Moreover, degradation of the PCM fibers, which most possibly would occur in matrix lysis, along with high frequency loading, would synergistically promote flow-mediated mechanical stimulations on osteocytes and their cell processes and enhance solute transport in LCS. Taken together, these factors may partially explain the elevated mechano-responsiveness of female skeleton during lactation observed in the current study.

This study was the first investigation on the effects of dynamic loading on bone health during pregnancy, lactation, and post-weaning recovery in an *in vivo* animal model. Our study provides important insight into the relationship between reproduction and lactation-induced skeletal changes and external mechanical loading, emphasizing the importance of weight-bearing exercise on maternal bone health postpartum.

ACKNOWLEDGEMENTS

NIH/NIAMS P30-AR069619, R03-AR065145, and R01-AR071718.

REFERENCES

[1] Kovacs, *Physiol Rev,* 2015; [2] Liu+, *Biomech*, 2019; [3] de Bakker+, *JBMR*, 2017; [4] de Bakker+, *J Biomech Eng,* 2017; [5] Qing+, *JBMR,* 2012; [6] Kaya+, *JBMR,* 2017; [7] Wang+, *JBMR*, 2014; [8] Weinbaum +, *J Biomech.*, 1994; [9] Price+, *JBMR*, 2011.

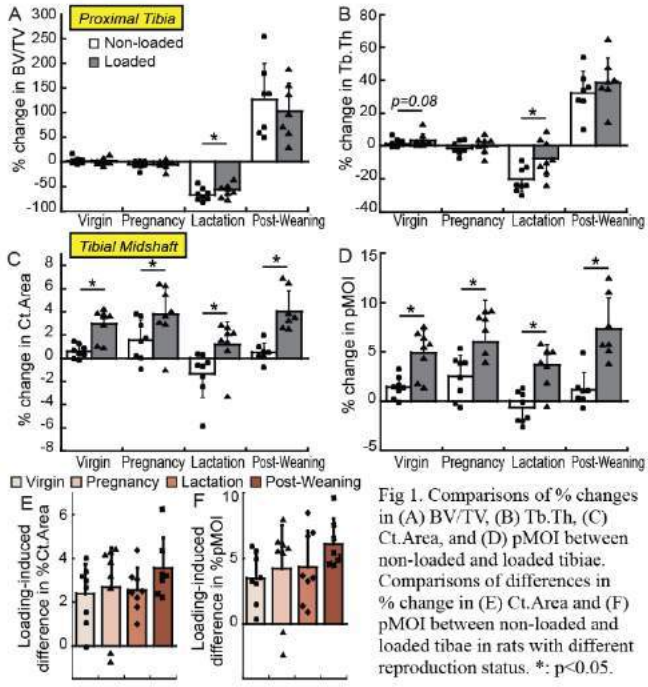

Fig 1. Comparisons of % changes in (A) BV/TV, (B) Tb.Th, (C) Ct.Area, and (D) pMOI between non-loaded and loaded tibiae. Comparisons of differences in % change in (E) Ct.Area and (F) pMOI between non-loaded and loaded tibae in rats with different reproduction status. *: p<0.05.

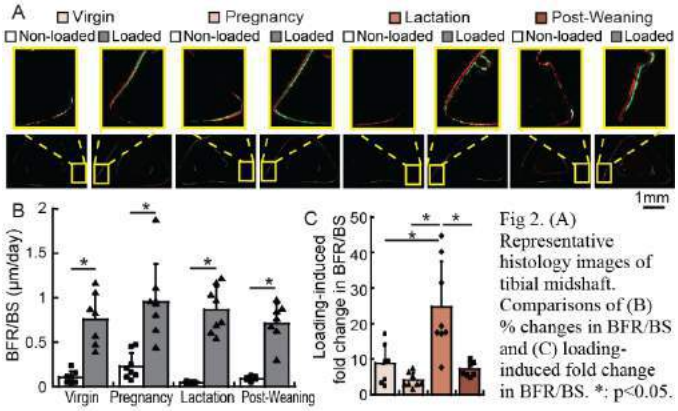

Fig 2. (A) Representative histology images of tibial midshaft. Comparisons of (B) % changes in BFR/BS and (C) loading-induced fold change in BFR/BS. *: p<0.05.

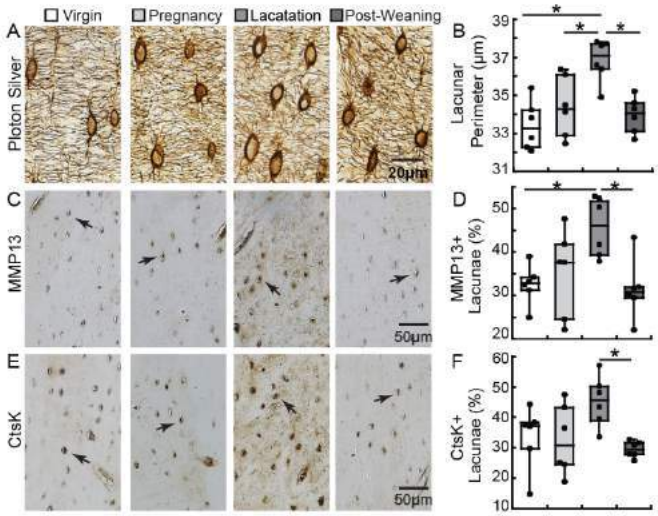

Fig 3. Comparisons of (A-B) lacunar-canalicular structure, (C-D) % MMP13-positive lacunae, and (E-F) % CtsK-positive lacunae. *: p<0.05.

MODELING THE EFFECT OF BIGHORN SHEEP HORN SHAPE ON POST-IMPACT ACCELERATIONS

Benjamin B. Wheatley (1), Aaron M. Drake, Luca H. Fuller (2), Seth W. Donahue (2)

(1) Department of Mechanical Engineering
Bucknell University
Lewisburg, PA, USA

(2) Department of Biomedical Engineering
University of Massachusetts Amherst
Amherst, MA, USA

INTRODUCTION

Male bighorn sheep (Ovis canadensis) engage in repeated ramming bouts and do not exhibit major signs of traumatic brain injury. Previous work has shown that the keratin-rich horn may play an important role in mitigating brain injury through energy dissipating horn-tip oscillations [1]. Specifically, removal of the distal half of the horn increased brain cavity accelerations up to 51% in a dynamic finite element model of ramming [1]. However, the extent to which specific horn shapes may reduce accelerations post-impact remains unclear. The goal of this work was to investigate different tapered horn shapes in reducing post-impact accelerations of a simplified impact model. We hypothesized that the specific tapered horn shape found in male bighorn sheep horns [2] would reduce post-impact payload accelerations when compared to a simplified tapered circular shape or a shape rotated by 90°.

METHODS

A representative male bighorn sheep skull and horns were previously scanned using computed tomography, segmented, and smoothed to produce a skull (bone) and horns (keratin) for the work by Drake et al. [1]. The left horn was imported into computer aided design software (Fusion 360, Autodesk Inc.). A loft defined by the mid center spline and seven cross-sections was created that closely approximated the horn shape and was then attached to a half sphere representing the sheep's skull. Two additional horn shapes of the same approximate volume were created by modifying the distal half of the horn – one with circular cross sections and one with cross sections rotated by 90° counterclockwise (Figure 1).

Each geometric model was imported into finite element software (Abaqus, Dassault Systèmes Inc.) for a 0.05 second dynamic analysis of a symmetric impact with an explicit solver (Figure 2). This model was based on the work of Drake et al., which details a symmetric finite element model of bighorn sheep ramming. Horn and half-sphere were assigned linear elastic keratin material properties E = 2 GPa, ν = 0.3, and ρ = 1.3 g/cm^3 [1]. An initial velocity of 4.7 m/s was applied to the horn and half sphere [1] in the z-direction, and all other degrees of freedom of the symmetric surface were restricted (Figure 2). Model outputs include half sphere center point translational z-acceleration 5 ms head injury criterion (HIC_5) [3], mean horn tip velocity for top 1% of nodes, mean horn von Mises stress for top 1% of elements, and kinetic energy to total energy fraction.

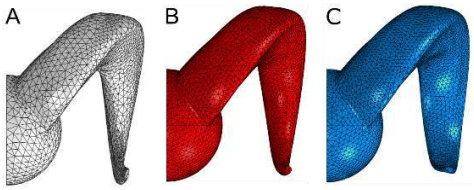

Figure 1. Horn variations A) baseline, B) circular, and C) rotated.

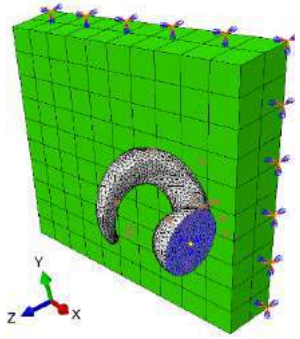

Figure 2. Symmetric finite element model of the baseline shape.

RESULTS

The baseline model exhibited the lowest HIC_5 when compared to the circular model (41% increase) or rotated model (38% increase) (Table 1). This result is mainly attributed to the consistent reduction in after-impact acceleration over the 0.05 sec simulation (Figure 3). The baseline model also exhibited a greater top 1% mean velocity, though this result was less pronounced (Table 1). There were no clear differences between top 1% von Mises stress or kinetic energy to total energy fractions.

Table 1: Simulation results.

Model	HIC_5 [s]	Top 1% Velocity [m/s]	Top 1% VM Stress [MPa]	KE:TE Fraction [-]
Baseline	21,200	28.9	27.4	0.919
Circular	29,900	26.8	26.3	0.903
Rotated	29,300	25.8	28.0	0.892

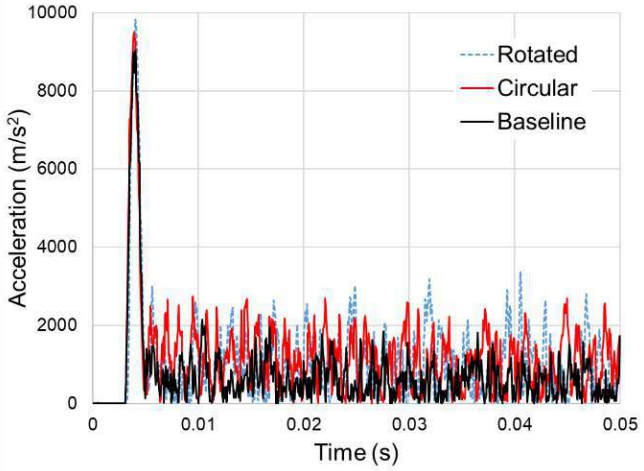

Figure 3. Model center point translational accelerations as a function of time. The center point represents the payload or brain cavity center.

Horn tip velocity vectors showed that the baseline model exhibited the greatest horn tip oscillations in the medial-lateral direction (perpendicular to the direction of impact), while the rotated model exhibited primarily anterior-posterior oscillations (the impact direction) (Figure 4). The circular model exhibited less of a preference in horn tip oscillation direction.

DISCUSSION

This study investigated the effect of bighorn sheep horn tip shape on the mechanics of a simplified impact model. Previous modeling work suggested that oscillations of the horn tip contribute to mitigating brain cavity accelerations during and after impact by directing kinetic energy away from the brain cavity [1]. The goal of this study was to determine the extent to which the cross-sectional shape may play a role in reducing brain cavity accelerations and thus mitigating traumatic brain injury. Such information could be useful in designing a wide range of devices or systems for applications that include automotive impacts, high-impulse athletic events, military applications, or other scenarios where energy dissipation is needed. This study also demonstrated an elastic energy dissipation technique, which could be reusable in comparison to other techniques such as material plasticity or damage.

Our results showed that the anatomically accurate horn model – with a medial-lateral bending preference due to the horn tip shape – exhibited lower center point (payload) accelerations when compared to a circular or rotated cross section. The unique tapered horn shape of adult male bighorn sheep is consistent between animals [2], suggesting that the medial-lateral horn tip oscillations observed after impact [1] (Figure 4) may be observed across animals.

This work showed that medial-lateral horn tip oscillations convert pre-impact kinetic energy into medial-lateral kinetic and strain energy, which has a reduced effect on center point accelerations due to symmetry. The circular and rotated models have less medial-lateral oscillation (Figure 4) and a lower horn tip velocity (Table 1), thus diminishing the mechanism that reduces center point acceleration. Additionally, the ability to reduce payload accelerations did not come at a cost of increased horn von Mises stress (Table 1), thus demonstrating a viable elastic energy dissipation technique.

Previous work has shown that a tapered spiral cylinder exhibits beneficial shockwave reducing properties in comparison to simpler shapes such as a non-tapered spiral cylinder [4]. Comprehensively, our results suggest that carefully designed non-cylindrical tapered structures may provide a further benefit for impact or shockwave applications by employing directed structural oscillations. Future work may explore additional horn shape variations and loading conditions to further explore the properties of these structures and potential applications to human safety systems.

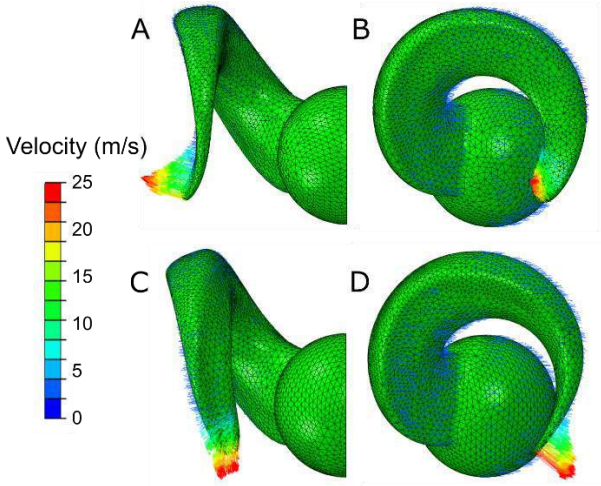

Figure 4. Horn tip velocity vectors after impact, highlighting the differences in oscillation directions between the baseline (A, B) and rotated (C, D) models.

CONCLUSIONS

This study revealed that an anatomically accurate bighorn sheep horn geometry, with a bending preference in the medial-lateral direction, exhibited lower payload acceleration, greater horn tip velocity, and similar material stress in comparison to models with circular or rotated geometries. Thus, horn-like structures could be specifically designed for optimal energy dissipation during and after high-rate impacts through directional oscillations. These findings could help influence the design of structures to prevent injury or damage because of such impacts.

REFERENCES

[1] Drake, A et al., *Acta Biomater*, 44:41-50, 2016.
[2] Gilmore, E. et al., *44th Meeting of the ASB*, 2020.
[3] Hutchinson, J. et al., *Appl Math Comput*, 96:1-16, 1998.
[4] Johnson, K. et al., *J Biomech Eng*, 136:021023, 2014.

SOLUTION COMPOSITION AFFECTS DISSOLUTION-RECRYSTALLIZATION MECHANISMS OF BIOMIMETIC APATITES

S. Wong (1), M. Moynahan (1), A. Deymier (1)

(1) Biomedical Engineering Department
University of Connecticut
Farmington, Connecticut, US

INTRODUCTION

Aging affects bone health and blood chemistry but it is unknown how these are related. As we age, kidney function diminishes, which decreases blood bicarbonate and pH leading to aging-induced metabolic acidosis[1]. In addition, other blood components, such as ionic strength and phosphate levels, change with aging-induced metabolic acidosis[2]. To aid the body in reaching homeostasis, bone mineral dissolution occurs to attempt to increase bicarbonate and pH levels[2]. While it is generally known that acidic pH's can increase bone mineral dissolution[3], it is unknown how these other factors affect bone mineral dissolution. Therefore, the objective of this study is to identify the mechanisms of pH, ionic strength, and phosphate content on the dissolution of biomimetic bone mineral.

METHODS

Biomimetic carbonated apatite (CAP) with either 2, 6, or 12 wt% carbonate was synthesized by an aqueous precipitation. These were exposed to various solutions for 72 hours in order to determine the effects of pH, ionic strength, and phosphate (PO_4^{3-}) content. To evaluate the effect of initial solution pH (pH_i), 6 wt% CAP was exposed to either 0.1M potassium chloride (KCl), water, or 1x phosphate-buffered saline (PBS) all at pH_i 5.5, 7.4, and 8.0. To isolate ionic strength effects, water and 0.1M KCl at pH_i 5.5 was used for 2, 6, and 12 wt% CAP. For PO_4^{3-} content, 0.1M KCl and 0.7x PBS both at pH_i 3.0 was used for 6% CAP in order to have identical ionic strength, pH, and buffering capacity while varying PO_4^{3-} content. After exposure, the powders were weighed, filtered, and dried in a 60°C oven overnight. Then, the powders were analyzed by Raman spectroscopy to identify the change in carbonate to phosphate ratio (ΔCO3/PO4) and X-ray Diffraction (XRD) to analyze the lattice and microstructure. The change in pH (ΔpH) of each solution was measured at 72 hours to obtain buffering information. In addition, calcium (Ca), sodium (Na), phosphorus (P), and potassium (K) levels in the solutions were measured by Inductively Coupled Plasma - Optical Emission Spectroscopy (ICPOES).

RESULTS

pH Effects: In all cases, the ΔpH positively increased as pH_i decreased. Mass loss occurred for all conditions and was not well correlated to pH_i. Generally, PBS and KCl showed a greater loss of carbonate (-ΔCO3/PO4) with decreasing pH_i (Fig. 1). Conversely, water gained carbonate (+ΔCO3/PO4) irrespective of pH_i (Fig. 1). For CAP in PBS, the c-axis decreased and a-axis generally increased as pH_i decreased, however, no trend in pH was observed for the lattice of CAP in KCl and water. Ca in the solution increased for all solutions after exposure with no clear correlation to pH_i. P was increased in water and KCl but decreased in PBS with no relationship to pH_i. Na generally increased as pH_i decreased in water and KCl while PBS exhibited no correlation to pH_i.

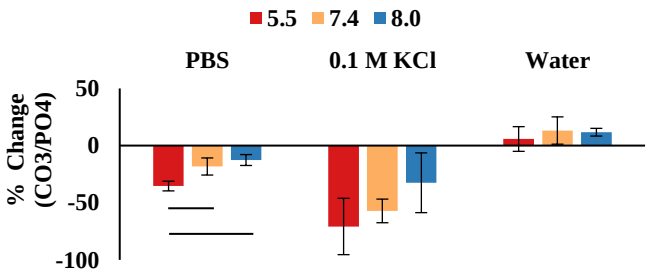

Figure 1: Carbonate decreased in CAP as pH_i decreased after exposure to PBS and KCl.

Ionic Strength Effects: As ionic strength increased, the ΔpH significantly increased while mass loss significantly decreased. ΔCO3/PO4 significantly decreased as ionic strength increased for 2 and 12 wt% CAP with 6% CAP showing similar trends (Fig. 2). The c-axis increased as ionic strength increased for all CAP while there was no trend in the a-axis for ionic strength. Crystallite size increased irrespective to ionic strength as well. Ca, P, and Na in solution decreased as ionic strength increased, while K generally did not change.

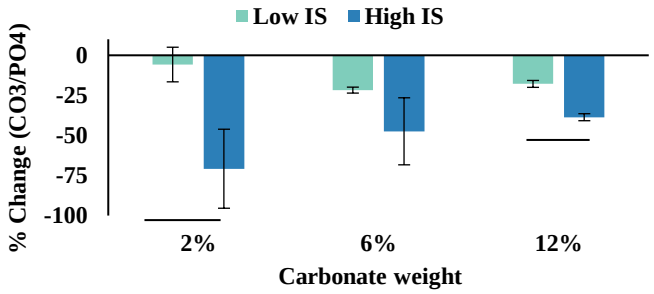

Figure 2: Carbonate decreased in CAP as ionic strength (IS) increased.

PO_4^{3-} Effects: The change in pH and mass loss increased and ΔCO3/PO4 decreased significantly as PO_4^{3-} in the solution decreased (Fig. 3). Ca, K, and Na increased after exposure irrespective of initial PO_4^{3-} content. The c- and a-axis generally do not change with no PO_4^{3-} content in the solution while the c- and a-axis increase with PO_4^{3-} content. Crystallite size increased for both solutions with no association with PO_4^{3-} content. In addition, the amount of P decreased in the solution as initial PO_4^{3-} content increased while P content increased without initial PO4 content.

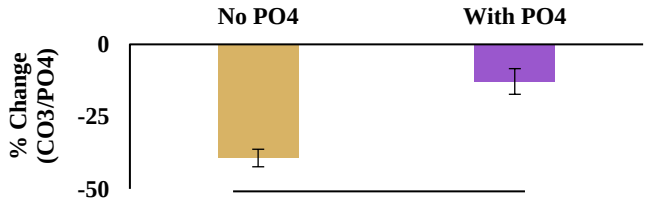

Figure 3: Less carbonate is lost in the presence of PO_4^{3-} in solution.

DISCUSSION

pH Effects: Although decreasing pH is generally believed to increase mineral dissolution, we found that pH effects were solution specific. pH_i was negatively correlated to ΔpH in all solutions indicating that decreased pH promoted the release of buffering ions to raise the pH. The decrease in ΔCO3/PO4 as pH_i decreases for PBS and KCl suggest that low pH's may preferentially release carbonate from CAP for buffering. This is supported by the decrease in c-axis and increase in a-axis for PBS, which are associated with carbonate removal from the lattice[4]. The reduced P in PBS after exposure implies that CAP in PBS experiences a dissolution/recrystallization event where carbonate is released at low pH and then recrystallization of a less carbonated apatite occurs. The inconsistent change in CAP lattice in KCl may indicate the presence of other substitutions, such as K^+ and Cl^-, into the lattice while carbonate is lost during recrystallization[5]. These ionic substitution changes could explain the lack of correlation between pH_i and mass loss as the crystal density may be modified with recrystallization. For CAP in water, the increased ΔCO3/PO4, inconsistent lattice spacing, and increased solution P after exposure suggests the low pH_i in water preferentially releases PO_4^{3-} from CAP or the CAP surface is adsorbing protons due to a lack of proton-accepting ions in solution[6]. Overall, we found that the effects of solution pH_i were highly solution dependent making it necessary to understand the role of other solution factors.

Ionic Strength Effects: Decreased ΔCO3/PO4 with increasing ionic strength suggests that the presence of K^+ and Cl^- increased carbonate removal from CAP into the solution. This is supported by a larger increase in ΔpH in the KCl compared to water. However, both the c- and a-axis increases, which is not reflective of carbonate removal from the apatite lattice[4]. This may again be caused by the substitution of Cl^- for OH^- in CAP. The additional release of OH^- into the solution could further explain the larger ΔpH in KCl. Additionally, Cl^- substitution may explain the smaller mass loss since chlorapatite is denser than carbonated apatite[7]. However, the amount of Cl^- substitutions may be insufficient to induce a phase transition that can be clearly seen on XRD. In conclusion, the increased ionic strength significantly modified the dissolution behavior of CAP; however, this may be specific to the presence of certain ions.

PO_4^{3-} Effects: The presence of PO_4^{3-} significantly decreased ΔpH, mass loss, and increased ΔCO3/PO4 compared to an absence of PO_4^{3-}. This suggests that the presence of PO_4^{3-} in solution is protective against dissolution, reducing mass loss and carbonate loss. To compensate for the carbonate loss, P is up taken for apatite recrystallization, as shown by decreased solution P after exposure. In the process, H^+ may be sequestered to form an HPO4-bearing apatite that may change the lattice spacing as seen in XRD[5,6,8]. Alternatively, in the absence of PO_4^{3-}, the increased ΔpH, mass loss, P in solution and decreased ΔCO3/PO4 in CAP after exposure implies that both carbonate and PO_4^{3-} is being released from CAP into the solution, resulting in heightened dissolution. In general, the presence of PO_4^{3-} may shield CAP from further dissolution.

To fully elucidate the effects of solution type on CAP dissolution, it will be necessary to examine larger variations of ionic strength and phosphate content in solution, ideally with non-substituting ions and controlling for buffer capacity.

This study challenges the notion that pH is a main contributor of apatite dissolution, especially in metabolic acidosis conditions. Acidic pH's generally increase the dissolution of bone mineral. However, in these tested conditions, pH is likely not the sole component affecting apatite dissolution and other factors may take precedence, such as ionic strength and ion substitutions like K^+, Cl^-, and PO_4^{3-}. We found that the presence of PO_4^{3-} was protective against dissolution leading to lower carbonate and mass loss. Conversely, increased ionic strength and the presence of K^+ and Cl^- appear to increase carbonate loss possibly due to substitutions of those ions into the apatite structure. These results will be important in understanding bone dissolution associated with the complex changes in blood chemistry, such as ionic strength and ionic content, as seen in aging-induced metabolic acidosis.

ACKNOWLEDGEMENTS

I would like to acknowledge Mikayla Moynahan's work on the pH and ionic strength data acquisition. This work was supported by Dr. Alix Deymier's startup funds and Mikayla Moynahan's School of Dental Medicine Summer Research Fellowship.

REFERENCES

[1] Frassetto, L. et al., *Journals Gerontol. - Ser. A Biol. Sci. Med. Sci*, 51:91-99, 1996. **[2]** Bushinsky, D. A., *Eur. J. Nutr*, 40:238–244, 2001. **[3]** Dorozhkin, S. V., *J. Colloid Interface Sci.* 191:489–497, 1997. **[4]** Deymier, A. C. *et al. Biomaterials* 127:75–88, 2017. **[5]** Wopenka, B. et al., 25: 131-143, 2005. **[6]** Dorozhkin, S. V. *World J. Methodol.* **2**: 1-17, 2012. **[7]** Ptáček, P. et al., *InTech*, 2016. **[8]** Young, R.A., et al., *Calcif Tissue Int*, 36:60-63, 1984.

TARGETING HEDGEHOG SIGNALING TO IMPROVE ZONAL TENDON-TO-BONE REPAIR

Timur B. Kamalitdinov (1), Keitaro Fujino (1,2), Xi Jiang (1), Mary Kate Evans (1), Miltiadis H. Zgonis (1), Andrew F. Kuntz (1), Nathaniel A. Dyment (1)

(1) Department of Orthopaedic Surgery
University of Pennsylvania
Philadelphia, PA, USA

(2) Department of Orthopedic Surgery
Osaka Medical College
Takatsuki, Osaka Prefecture, Japan

INTRODUCTION

Growth and development studies have defined a critical role for Hedgehog (Hh) signaling in the formation of zonal tendon-to-bone insertions (i.e., entheses). Zonal enthesis formation involves anchoring collagen fibers, synthesizing proteoglycan-rich fibrocartilage, and mineralizing part of this fibrocartilage. Specifically, Hh signaling promotes mineralized fibrocartilage production, leading to the establishment of distinct tissue zones [1]. Despite this important developmental role, it is not known whether the Hh pathway plays a similar function in adult tendon-to-bone repair, representing a significant gap in knowledge. Unfortunately, traditional tendon-to-bone repair surgeries do not recreate a zonal insertion. However, ligament injuries reconstructed with a tendon graft passed through a bone tunnel can result in zonal insertions [2,3]. In this setting, amplifying α-smooth muscle actin (αSMA)-expressing bone marrow stromal cells (bMSCs) contribute to tunnel integration by forming zonal fibrocartilaginous attachments [2]. Our central hypothesis is that the Hh pathway promotes tendon-to-bone integration in the adult, similar to growth and development. Using our established murine anterior cruciate ligament (ACL) reconstruction model, our objective is to modulate the Hh pathway genetically and pharmacologically in these αSMA-expressing cells to determine the effect of Hh signaling on tunnel integration in adult repair.

METHODS

All animals and procedures were approved by UPenn's IACUC. Experimental Design. ACL reconstructions (ACLR) were performed on 93 transgenic mice. *Genetic Hh Inhibition Study*. αSMACreERT2 mice [4] that target the amplifying progenitor pool that gives rise to zonal attachments [2] were crossed with mice containing loxP sites flanking a coding sequence of the central signal transducer of the Hh pathway Smoothened ($Smo^{flox/flox}$) [5] (Smo^{tm2Amc}/J) to yield SMACre;$Smo^{flox/flox}$ (SmoKO) experimental mice to decrease Hh signaling and $Smo^{flox/flox}$ control genotypes. Mice were sacrificed at 28 days post-surgery and assigned to cryohistology (n = 7/group) or biomechanics (n = 9/group). *Genetic Hh Activation Study*: αSMACreERT2 mice were crossed with constitutively active SmoM2 mice [6] ($Gt(ROSA)26Sor^{tm1(Smo/EYFP)Amc}$/J) to yield SMACre;SmoM2 (SmoCA) mice with increased Hh signaling and Cre-negative control genotypes. Mice were sacrificed at 28 days post-surgery and assigned to cryohistology (n = 5-6/group) or biomechanics (n = 5-7/group). Tamoxifen injections (80 mg/kg) were given on the day of surgery then every other day for a total of five injections to ablate Smo or constitutively activate Smo in αSMA-expressing cells. *Pharmacologic Hh Activation Study*: Mice received either Hh agonist (20mg/kg Hh-Ag1.5) or PBS vehicle control injections 5X per week. Mice were assigned to cryohistology (n = 6/group) at 7- or 28-days post-surgery and biomechanics (n = 7/group) at 28 days post-surgery. Demeclocycline and EdU were given 1 day before sacrifice to help define mineralized fibrocartilage (MFC) zones of attachments and label proliferating cells, respectively. ACL Reconstruction. The ACL was excised near the femoral insertion. The tibial and femoral tunnels were drilled with 27G needles. A tail tendon autograft was passed through the tunnels and anchored to outer cortices with stainless steel washers [2,3]. Mineralized Cryohistology. Knees were fixed in formalin, embedded, sectioned undecalcified with cryofilm, and imaged on the Zeiss Axio Scan.Z1 (Fig. 1B-D). Tunnel Pullout Test. Femurs were potted in PMMA and gripped such that the tunnel was parallel to the linear actuator. A suture was passed through the washer and loaded to failure (Fig. 2D). Image Quantification. MFC area/total length was measured to assess the extent of zonal integration (Fig. 2A) while EdU+ cells in expanding marrow were measured to assess amplification of the progenitor pool (Fig. 3A). Statistics. Experimental and control groups

were compared via Student's t-tests ($p < 0.05$). Data presented as Mean ± SD.

RESULTS

SmoKO, SmoCA, and Hh agonist-treated groups did not display any adverse systemic effects throughout the duration of the study. Hh Pathway Positively Regulated Tunnel Integration and Strength. When targeting the αSMA-expressing amplifying progenitor pool, SmoKO mice (53 ± 18μm^2/μm, n = 7) had a 23% decrease in MFC area in the bone tunnels compared to controls (70 ± 32 μm^2/μm, n = 7) at day 28 ($p = 0.2$). SmoCA mice had 36% greater MFC compared to controls at day 28 ($p = 0.07$) (Fig. 2B). Mice that received Hh agonist for four weeks had 35% more MFC at the tunnel interface compared to PBS controls ($p = 0.06$) (Fig. 2C). SmoKO mice (0.9 ± 0.3N, n = 9) possessed comparable pullout strengths with controls (0.8 ± 0.3N, n = 9) at day 28 ($p = 0.4$). SmoCA mice showed a 58% increase in pullout strength compared to controls at day 28 ($p = 0.2$) (Fig. 2E). Mice that received Hh agonist for four weeks had 48% greater pullout strength compared to PBS controls ($p = 0.02$) (Fig. 2F). Hh Pathway Activation Increased Proliferation of the bMSC Progenitor Pool. There were 50% greater EdU+ cells in the expanding bone marrow adjacent to the graft (Fig. 3A) in agonist treated mice after 7 days ($p = 0.1$) (Fig. 3B).

DISCUSSION

Following ACL reconstruction, bMSCs expand and infiltrate the periphery of the tendon graft, then assemble collagen and produce fibrocartilage to anchor the tendon graft to adjacent bone. In the present study, we demonstrated that Hh signaling positively regulated mineralized fibrocartilage formation (Fig. 2A-C) leading to greater pullout strength (Fig. 2D-F), which can partially be explained by increased proliferation of the progenitor pool (Fig. 3). While Hh signaling improves fracture repair via improved osteogenesis and angiogenesis [7], here we found through both genetic and pharmacologic means that Hh signaling improves fibrocartilage formation similar to enthesis development. Since we saw a similar effect with Hh agonist delivery as the SmoCA model where we targeted the αSMA-expressing progenitor pool that gives rise to attachments, it suggests that this cell population is the most important to target. However, it is still unclear if Hedgehog signaling is only important at the progenitor stage of this lineage or if it is also important for the differentiation of these cells into mineralized fibrochondrocytes. Our results indicate that the increased MFC formation may, at least partially, be due to increased proliferation of the bMSCs. A potential mechanism for this increase in MFC could be an increased expansion of the bMSC progenitor pool leading to a higher number of attachments along the tunnel length. However, another mechanism for increased MFC could be that Hh signaling is promoting fibrocartilaginous differentiation and maturation of cells in attachment sites at later stages of the repair process, leading to more MFC per attachment. In future studies, we will deliver the Hh agonist at different stages of the repair process to assess this important proliferation vs. differentiation question.

An improved understanding of the signaling pathways that regulate zonal insertion formation in the adult will be crucial to developing novel therapies to improve repair outcome. If the Hh pathway is harnessed therapeutically, it could result in a paradigm shift in the clinical treatment of these debilitating injuries, especially in more challenging scenarios that require reformation of the enthesis, such as rotator cuff repair.

ACKNOWLEDGEMENTS

Work supported by NIH R00AR067283, NIH P30AR069619, NIH R01AR076381, the Thomas B. McCabe and Jeannette E. Laws McCabe Fund at UPenn, and startup funds from the Department of Orthopaedic Surgery at UPenn.

REFERENCES

[1] Dyment, N et al., *Dev Biol, 405*(1), 96–107, 2015.
[2] Kamalitdinov, T et al., *J Orthop Res*, 38(1), 105–116, 2020.
[3] Hagiwara, Y et al., *Ann N Y Acad Sci*, 1460(1), 57-67, 2020.
[4] Grcevic, D et al., *Stem Cells*, 30(2), 187-196, 2012.
[5] Long, F et al., *Development,* 128(24), 5099–5108, 2001.
[6] Liu, C-F et al., *PLoS ONE*, 8(6), e65411, 2013.
[7] McKenzie, J et al., *J Orthop Res*, *37*(1), 51–59, 2019.

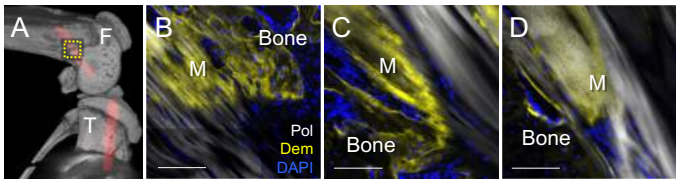

Figure 1: Murine ACL reconstructions result in mineralized fibrocartilage anchoring collagen fibers to bone after 28 days. A) μCT of mouse knee showing tunnel placements (red) in femur (F) and tibia (T). B-D) Representative images of mineralized fibrocartilage (M) with adjacent bone from control (B), SmoCA (C) and Hh agonist-treated mice (D) taken from femoral tunnel (dashed box in A). Pol – polarized light, Dem – demeclocycline, scale bars = 100 μm.

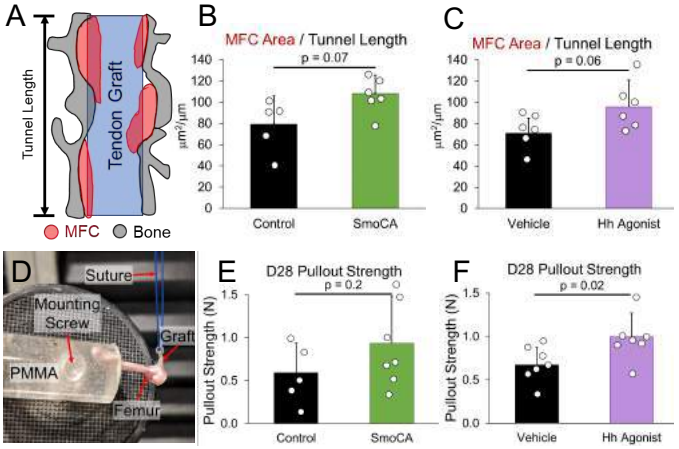

Figure 2: Increased Hh signaling promoted MFC formation and integration strength. A) Schematic of MFC quantification strategy with MFC area (red) normalized by the tunnel length. B-C) MFC area in SmoCA (B) and Hh agonist-treated mice (C) at day 28. D) Tunnel pullout test setup with femur potted in PMMA and suture attached to washer and linear actuator. E-F) Tunnel pullout strength in SmoCA (E) and Hh agonist-treated mice (F) at day 28.

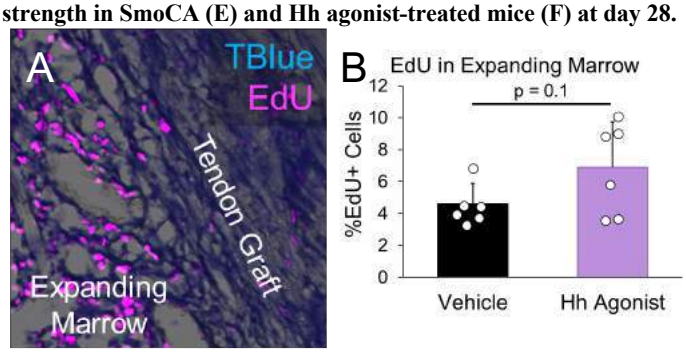

Figure 3. Hh agonist treatment led to more proliferation of the progenitor pool. A) Example toluidine blue and EdU stained section showing cell proliferation in the expanding marrow. B) Percentage of EdU positive cells in the expanding marrow of Hh agonist-treated mice at day 7.

FIBER NETWORK-BASED MULTISCALE MODELS PREDICT EXPERIMENTALLY MEASURED VOLUME REDUCTION OF STRETCHED MOUSE SKIN

Nathan J. Witt[1], Alan E. Woessner[2], Kyle P. Quinn[2], Edward A. Sander[1]

[1]Department of Biomedical Engineering, University of Iowa, Iowa City, IA, 52242, USA

[2]Department of Biomedical Engineering, University of Arkansas, Fayetteville, AR, 72701, USA

INTRODUCTION

The mechanical behavior of skin is complex – it is heterogenous, anisotropic, viscoelastic, and non-linear. Furthermore, its properties are dependent on anatomic location, sex, age, health, and ethnicity, primarily due to differences in microstructural composition and organization of the collagen rich dermal layer [1]. To better understand how changes to the microstructure relate to functional changes in the tissue, we submit that a multi-scale perspective of skin is required, as local microstructural changes impact global tissue function. The ability to simultaneously observe both macro-scale tissue deformation and microscale fiber-level restructuring, however, has been technologically challenging until recently [2]. Now that such data exist, we are interested in using multi-scale mechanical models to help interpret and understand the rich mechanical behavior observed in skin. Ultimately, we envision that these models will be useful for understanding and improving skin health in a variety of scenarios, such as aging, wound healing, disease, long-term interactions with wearable technologies, *etc*.

METHODS

Experiments: Dog-bone shape murine skin was gripped in an ADMET bioreactor mounted on a multiphoton microscope (MPM). These skin samples were preconditioned and then stretched at a rate of 0.2 mm/min to 4 mm of displacement while being imaged. At each mm of displacement, MPM image stacks of the collagen microstructure were acquired in the center of the gauge region while the loading was paused. Quantification of tissue kinematics and changes in microscale volume and directional variance (DV) were also made [3].

Simulation: To-scale image-based multiscale models (MSMs) were created based on the geometry of the sample prior to tensile loading akin to previous work [4]. These MSMs link the macroscopic domain of the model to fiber networks representative of the collagen microstructure using volume averaging theory [5]. A FE mesh of 105 linear hexahedral FEs was then generated (one FE through the thickness). At the microscale, the volume fraction of fibers was set to match experimental values (~25%) for three different network cases: nearly aligned (DV = 0.15), experimentally matching (DV = 0.55), and nearly isotropic (DV = 0.90). For each case, five unique fiber network models were created with the same fiber network throughout the model. To represent the skin's non-collagenous matrix an additive stress from a compressible Neo-Hookean material (G = 3.0 kPa, ν = 0.1) was included. Parameters in the fiber-level constitutive equation were chosen to closely match the experimental loading curve in the DV = 0.55 case and were also applied to the nearly isotropic and nearly aligned cases.

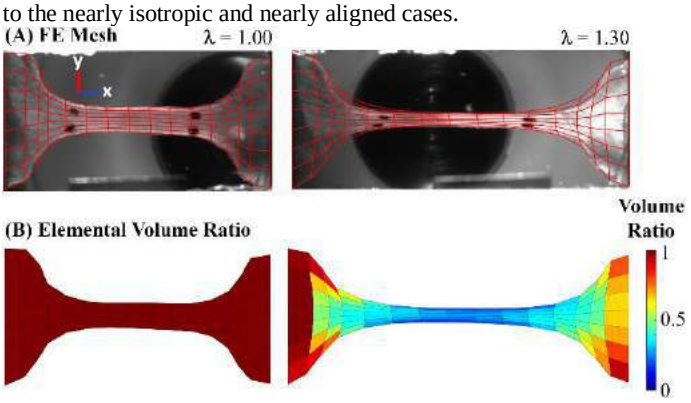

Fig. 1. Macroscale comparison of experiment and simulation. (A) The FE mesh, which initially closely corresponded to the sample geometry, reasonably followed sample stretch (DV = 0.55 model depicted). (B) FE volume decreased substantially with stretch, particularly within the gauge region of the model.

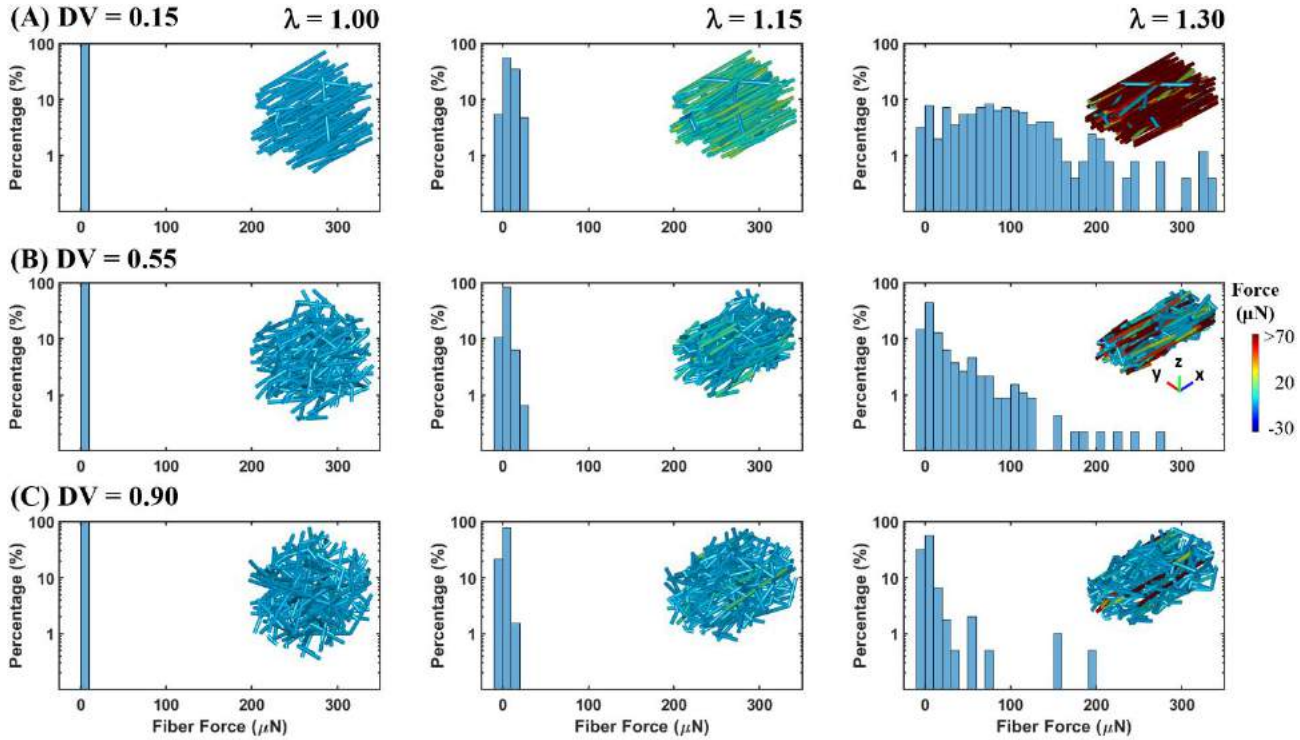

Fig 2. Representative fiber networks from the central element of the gauge region for each DV case. Fiber color corresponds to fiber force. The distribution of force within the network is also indicated in the histograms. In the initial state, λ = 1.0, the forces within each fiber are zero. As stretching progresses, the arrangement and loading of fibers changes to accommodate macroscopic tissue loading.

RESULTS

Macroscopically, the models deformed and decreased in volume similarly to the sample, with the DV = 0.55 case overlapping closest (Fig. 1). Microscopically, a comparison between networks in the central element with MPM volumes indicates that each of the three fiber network models was capable of reproducing the large decrease in skin volume that accompanied stretch observed experimentally (Fig. 3A). However, the network models that were less (DV = 0.90) or more aligned (DV = 0.15) than experimental values did not match changes in DV with stretch ratio as well (Fig. 3B).

An examination of fiber network kinematics in the central part of the gauge region (Fig. 2) highlights the complex restructuring associated with each type of network. Nearly aligned (DV = 0.15) networks remained so and experienced very high forces in comparison to moderately aligned and nearly isotropic cases. In the DV = 0.55 and DV = 0.90 cases, more fibers are able to rotate to accommodate stretch before picking up load, and their volume changes are more substantial, particularly in the directions orthogonal to the direction of tissue stretch. This volume decrease was greatest in the DV = 0.55 case.

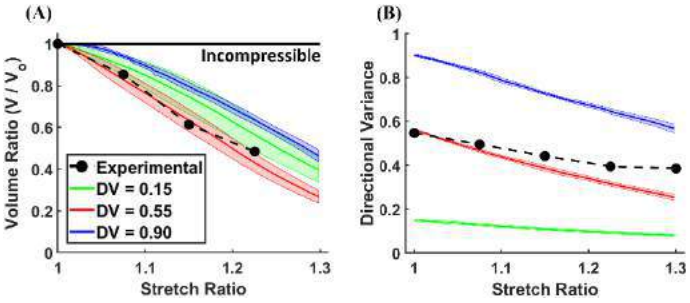

Fig. 3. Comparison of model simulation with experiment. (A) Models including fiber networks decreased in volume with stretch at the MPM imaging and central element location. (B) DV decreased with stretch in the experiment and in all three network models as a function of network capacity for fiber realignment.

DISCUSSION

Our work provides an image-based comparison of the macro- and microscale mechanics of mouse skin using experimental and computational approaches. Our results demonstrate that MSMs consisting of interconnected fiber networks can capture the complex kinematic changes displayed experimentally, such as the large decrease in tissue volume observed under uniaxial tension. Further, the fiber networks presented an increase in fiber level alignment and varied fiber-level force responses due to differences in reorganizational patterns. Future work will investigate how these behaviors change when fiber-level damage is incorporated in addition to analyzing the microstructural changes responsible for the altered mechanics of aged skin.

ACKNOWLEDGEMENTS

Support for this work was provided by R01 AG056560. Computational resources were provided by the University of Iowa Argon HPC Cluster.

REFERENCES

1. Blair, M.J. et al, Adv Wound Care, 9(3):127-143, 2020
2. Woessner, A.E. et al, In Review, 2020
3. Liu, Z et al., J Biomaterials, 116:34-47, 2017.
4. Sander, E.A. et al, PNAS, 106:17675-17680, 2009.
5. Stylianopoulos, T. et al, JCMA, 196: 2981-2990, 2007.

NUMERICALLY MODELLING SKIN-PPE INTERACTION TO REDUCE INJURY IN HEALTHCARE WORKERS DURING THE COVID-19 PANDEMIC

R. D. Jobanputra, S. Royyuru, J. Hayes, M. A. Masen

Department of Mechanical Engineering
Imperial College London
United Kingdom

INTRODUCTION

Due to the COVID-19 pandemic, medical staff wear personal protective equipment (PPE) for much longer than recommended. The extended duration of use has resulted in a range of skin issues including irritation and injuries such as urticaria, skin tears and pressure injuries, ranging from isolated indentation marks at the locations of contact, to deep tissue level bruising across a larger area (Fig. 1). Such device related pressure injuries are caused by the prolonged shear stresses acting on the skin that result from wearing PPE. These shear stresses in the skin are increased when there is high friction in the skin-PPE interface. The occurrence of injury also correlates with heavy sweating and with the use of higher-grades, thus tighter fitting, PPE[1]. Preventing these injures in healthcare workers is critical, as researchers have also found a dermal pathway to COVID-19 infection.

Figure 1: Skin damage following excessive PPE-skin interaction. Source: www.instagram.com/covid_nurses

MATERIALS & METHOD

In this study we aim to reduce the subsurface stresses in the skin and thus reduce the risk of skin injury developing, by optimizing the interface between the PPE and skin. This information will help improve the design of PPE; for example, by modifying geometric and material parameters. A finite element model describing the contact between respirator masks and facial tissue was developed to calculate the stresses in the skin. As skin bruising and damage typically involves the rupturing of blood vessels in the dermis, this skin layer was the focus of the investigation. In line with observations from Oomens[2], we use the local maximum strain energy density (SED) in the dermis as the critical output parameter that is indicative of skin injury developing.

The seal or skin interface of a respirator masks are typically silicone rubbers or various foams of polypropylene, polyester or polyvinylchloride. To establish the ideal material, a parametric study was performed in which the geometric and interfacial properties of the mask against the skin were varied. Parameters altered include the stiffness and Poisson's ratio, the thickness of the material as well as the size. Finally, the adhesive friction coefficient at the PPE-skin interface was also varied to observe the effect on direct shear stresses on the strain energy density in the dermis.

RESULTS

A SED field developing in the skin as the result of contact with PPE is shown in Figure 2. Two areas of elevated SED can be observed in the upper dermis, just under the edge of the contact with the face mask. A larger central area of high strain energy density develops deeper in the skin. The results of the parametric study show that a significant reduction of the maximum strain energy density in the dermis can be achieved through varying the characteristics of the PPE-skin interaction.

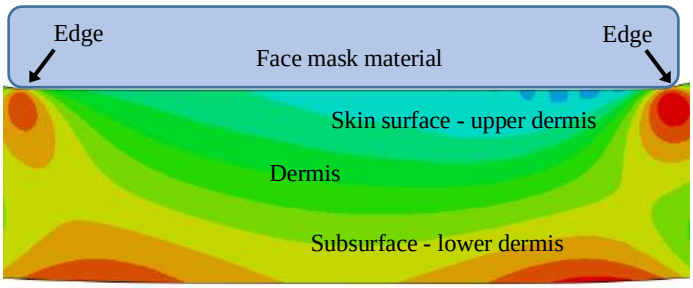

Figure 2: Dermal SED during PPE interaction. Red spots indicate peak SED.

In detail, the following effects were found:

- **Stiffness (E):** The use of softer materials decreases SED in the dermis and results in lower SED peaks in the upper dermis. In contrast, the use of stiffer materials results in the migration of the maximum SED to the upper dermis.
- **Friction (μ):** Reduced interfacial friction in the skin-PPE interface results in lower dermal SED (Fig. 3). Friction directly affects upper dermal SED, whilst having a negligible effect on the lower dermis.

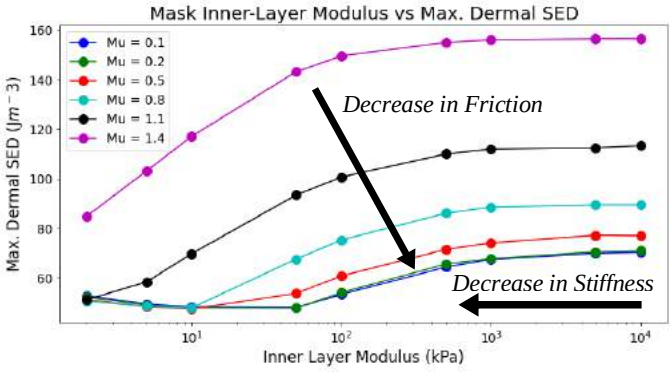

Figure 3: Effect of changing the stiffness and interfacial frictional coefficient of the mask's inner layer on the max. dermal SED.

- **Poisson's ratio (*ν*):** For materials with intermediate levels of stiffness (0.01-1MPa), a lower *ν* results in a significant reduction in maximum SED in the dermis. For soft materials, a lower *ν* results in a lower average SED and a migration SED from the upper dermis to the lower dermis.
- **Thickness (t):** For softer materials, a thicker mask material slightly reduces the average SED in the skin.
- **Size of the contact (S):** By changing the radius of curvature (r) of the edge of the mask, the size of the contact between skin and PPE was altered. Larger sizes resulted in lower dermal SED. However, the effects of changing contact area along with modulus were highly non-linear.

DISCUSSION

In this investigation, dermal shear and deviatoric stresses were found to have similar trends to dermal SED. The locations of the two isolated upper dermal SED peaks and the larger lower dermal central SED peak could respectively represent the indentation and deep tissue bruising marks seen amongst healthcare workers. Soft materials are often used in the interface with skin to reduce the discomfort caused by elevated pressures. In this investigation, reducing the stiffness of the material indeed resulted in a reduction of both the average and maximum SED. However, and possibly counter-intuitively, the use of rubber-like materials may actually result in an increase of the SED in the dermis due to the combination of an intermediate stiffness, high incompressibility (i.e. *ν* approaches 0.5), and high friction against skin that rubber materials show. In addition, mask designs that combine a large interface with skin with the use of soft materials show elevated SED as the increased area results in a reduction of the pressure but also a disproportionally large increase of the friction. Finally, dermal SED increases with increasing friction and this effect is particularly pronounced at elevated levels of friction. Therefore, decreasing the interfacial adhesive frictional coefficient should be a priority. This can be done by material selection or by directly modifying the skin-PPE interface, for instance using creams, lubricants or dressings[3].

The obtained results enable the specification of an ideal material to minimize skin injury. Such a material would have a sufficiently low stiffness (e.g. < 1 MPa) and a Poisson's ratio smaller than 0.45. In addition, the surface of the material should have a frictional coefficient against skin, not exceeding about 0.3. In addition, the material should be breathable and reduce the impact of perspiration, to prevent elevated friction[4]. All this may be achieved by employing foams made from PU, PP or PE. Foam materials are frequently used in a variety of skin-contact based applications, from headphones to prosthetic limbs. An outer skin or coating could be added to the material to benefit from the combination of good bulk material properties of the foam (low stiffness and low Poisson's ratio) and optimum interfacial properties, in terms of friction and moisture uptake.

Finally, it should be noted that the simulations presented in this work focus on the local effects of skin-PPE interaction and presume appropriate use and fit of PPE. The properties of facial soft tissue and craniofacial dimensions differ significantly, for instance between ethnicities and sexes and further work is needed to enable differentiation and further optimization of PPE design.

CONCLUSION

The use of close-fitting PPE is essential to prevent exposure to dispersed airborne particles such as the COVID-19 virus. However, the current pandemic led to many healthcare professionals wearing their PPE for prolonged times, causing skin irritation and injury. These injuries can be prevented by optimizing the design of the PPE with respect to its skin interaction characteristics. This should be done by ensuring the PPE interface is designed with a sufficiently low stiffnesses material that shows low friction. This will help reduce the risk of discomfort, skin injury and skin failure.

REFERENCES

1. Jiang Q, Song S, Zhou J, et al. The Prevalence, Characteristics, and Prevention Status of Skin Injury Caused by Personal Protective Equipment Among Medical Staff in Fighting COVID-19: A Multicenter, Cross-Sectional Study. *Advances in Wound Care*. 2020;9(7). doi:10.1089/wound.2020.1212
2. Oomens CWJ, Bader DL, Loerakker S, Baaijens F. Pressure Induced Deep Tissue Injury Explained. *Annals of Biomedical Engineering*. 2015;43(2). doi:10.1007/s10439-014-1202-6
3. Masen MA, Chung A, Dawczyk JU, et al. Evaluating lubricant performance to reduce COVID-19 PPE-related skin injury. *PLOS ONE*. 2020;15(9). doi:10.1371/journal.pone.0239363
4. Klaassen M, Schipper DJ, Masen MA. Influence of the relative humidity and the temperature on the in-vivo friction behaviour of human skin. *Biotribology*. 2016;6. doi:10.1016/j.biotri.2016.03.003

ON THE CHARACTERIZATION OF EMBRYONIC CURVATURES USING BEZIER CURVES

Ashok Ramasubramanian

Department of Mechanical Engineering
Union College
Schenectady, NY, USA

INTRODUCTION

We study morphogenesis (shape changes) that occur during early embryo development. The shape of the early embryo is characterized by a series of well-defined curves. We study here the dorsal curvature of the early chick embryo, which is characterized by two distinct bends – cervical and thoracic flexures (Fig.1). We study the formation and deepening of these flexures starting at about Hamburger and Hamilton (HH) Stage 14 and following the development 9 or 10 hours of incubation later, when the embryo reaches HH Stage 15 or 16 [1].

The deepening of flexures is a significant morphogenetic event in the early embryo and usually they are described imprecisely and using adjectives. Reference [1], for instance, describes cervical flexure as "a broad curve". We need a mathematically precise way to quantify flexures and precise criteria that can be used to distinguish between normal and abnormal flexures. Prior research indicates that correct flexure formation is important for the development of major organs, including the heart [2]. In that study, we quantified the cervical flexure by fitting a circle and here we expand on those results, by fitting a parametric curve to the entire dorsal wall. We use Bezier curves, which are widely used in computer graphics and to precisely define font shapes, to describe the shape of the dorsal wall in early embryonic development.

METHODS

The dorsal wall was "sampled" by selecting closely-spaced points using ImageJ. We used a total of 7 embryos (n=7). Measurements were taken at t=0 and at t=9h (n=2) or 10h (n=5). The cubic Bezier curve is a parametric curve where $t \in [0,1]$ is a parameter that varies from 0 (start of the curve) to 1 (end of the curve).

$$\mathbf{B}(t) = (1-t)^3\mathbf{a_0} + 3(1-t)^2 t\mathbf{a_1} + 3(1-t)t^2\mathbf{a_2} + t^3\boldsymbol{a_3} \qquad (1)$$

where $\mathbf{a_0}$, $\mathbf{a_1}$, $\mathbf{a_2}$, and $\mathbf{a_3}$ are the Bezier control points in 2D space. The line joining the Bezier control points is called the Bezier Polygon (Fig. 1). Unlike polynomial fits, wherein the coefficients do not convey insight about the shape of the curve, the Bezier control points, which are the curve parameters, are rich in meaning. To begin with, the first (last) control point is simply the first (last) point in the data set. The middle two control points ($\mathbf{a_1}$, $\mathbf{a_2}$) were fit using an optimization procedure in MATLAB. Also, the line joining the first two control points ($\mathbf{a_0}$, & $\mathbf{a_1}$) is tangent to the initial curve direction and the line joining the last two control points ($\mathbf{a_2}$, & $\mathbf{a_3}$) are tangent to the final curve direction. Note also that the movement of the middle control points from t=0 to t=9 or 10h quantifies the deepening of flexures and the movement of the first and last control points shows the increase in curve length (Fig. 1A,B). Bezier curves are also invariant under affine transformations.

The single cubic fit is unable to capture fully the sharpness of the thoracic flexure at the later time point (Fig. 1C). In this case, it is possible to fit a piecewise Bezier curve where the last control point of the first curve becomes the first control point of the second curve, i.e., $\mathbf{a_3} = \mathbf{b_0}$ (Fig. 1C). Also, we impose a constraint for geometric continuity, i.e., $\mathbf{a_2}$, $\mathbf{b_0}$, and $\mathbf{b_1}$ are colinear. The ability to break up larger curves into smaller ones, each with its own control polygon, is a significant advantage to using Bezier curves to characterize complex shapes.

RESULTS

The length of the curve, as measured by a numerical line integral using the selected data points, increases from 3.46±-0.27 mm at t=0 to 5.43±0.42 at t=9 or 10h. These values are similar to the Bezier curve lengths (data not shown).

Once a parametric curve is fit, we can measure the curvature using techniques from Differential Geometry. Fig. 1D shows the curvature for a single embryo (done in MATLAB and verified in Mathematica). Note that the composite curve fit is able to precisely capture the thoracic flexure, enabling us to calculate the curvature more accurately (Fig. 1C,D). For the composite fit, the curvature is very nearly straight for the first half of the curve (arrow in Fig. 1D), indicating that the cervical flexure portion can be approximated by a circle. For the embryo in Fig.1C, the radius for cervical flexure is about 2.5 mm ($\kappa \cong 0.4$, Fig. 1D), which is consistent with the results from our earlier study [2].

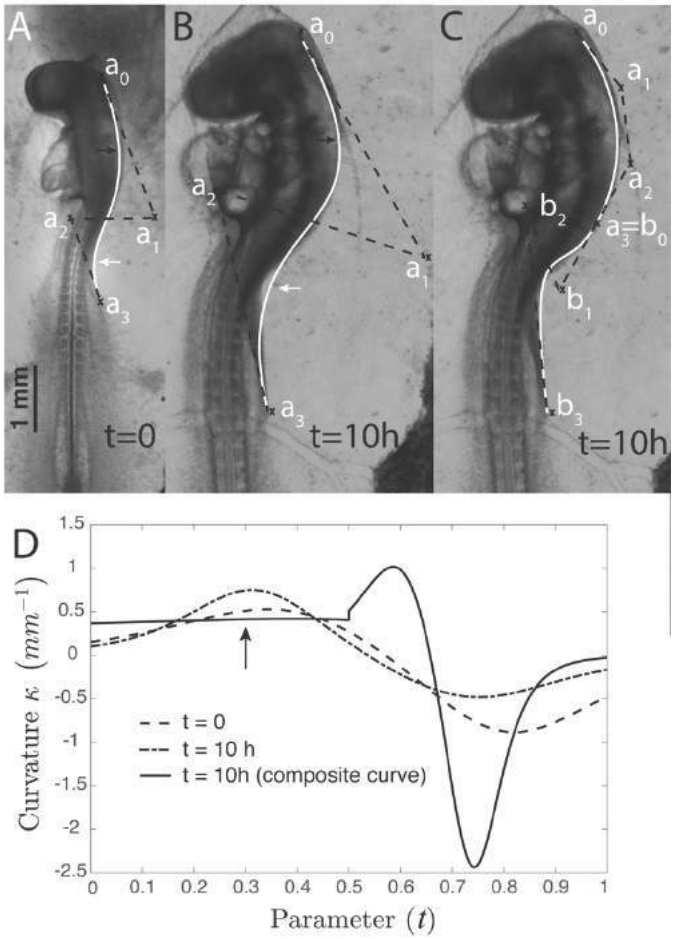

Figure 1: Chick embryo at stage HH 14 (A) and 10 hours later (B, C), along with Bezier curve fits and curvatures (D). Black and white arrows in A & B indicate cervical and thoracic flexures, respectively; note the deepening of flexures at t=10h (B). A—C show the Bezier curve (white) and Bezier polygon (black dashed). In (A) & (B), a_0, a_1, a_2, a_3 are the four control points (marked by "x") of the single cubic Bezier curve. The middle control points move farther from the embryo (compare locations of a_1 & a_2 in B & C), indicating the deepening of flexures. The fit for the thoracic flexure is poor in (B), a situation remedied by the composite Bezier curve fit in (C). Curvatures for the curves shown in (A—C) are reported in (D). The curvature information can be used to develop finite element models (Fig. 2B) that give insight into the mechanisms driving flexure formation. The reader is cautioned not to confuse the parameter *t* (*italic*; used in the horizontal axis in D) with the time stamp t used to denote progression of embryo development.

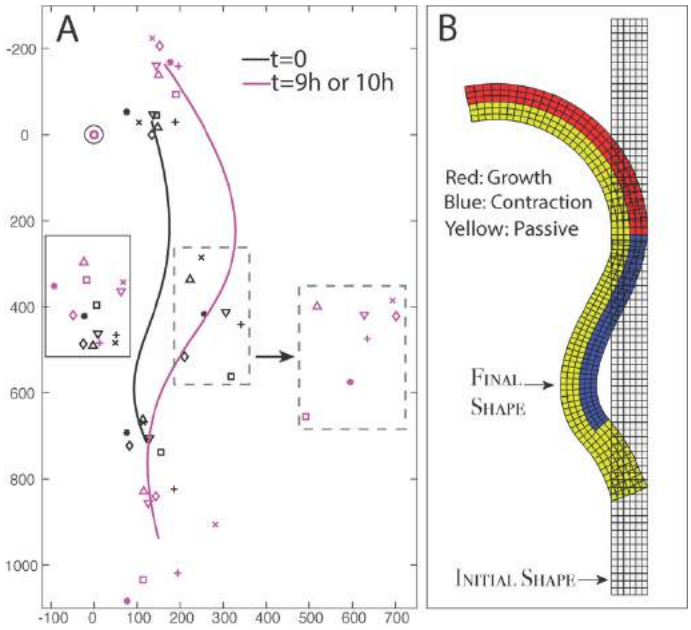

Figure 2: (A) Bezier control points "constellation" from curve fits on 7 embryos, each shown by a different marker (+,* etc.). Pixel dimensions are used (225.696 pixels = 1 mm). An affine transformation (translation) is carried out with the embryo eye as the origin (denoted by the bull's eye symbol at 0,0). Black markers denote t=0 while purple markers denote t=9 or 10h. Solid curves show the average Bezier curve fit based on the Bezier control points presented. Note that the second control points (enclosed in the dashed boxes; again, black and purple symbols denote t=0 and t=9 or 10h respectively) move farther (black arrow), indicating a deepening of cervical flexure. There is not a similarly large shift in the third control point location (solid box), which corresponds to the thoracic flexure; hence we use a composite curve to better capture the thoracic flexure (Fig. 1C). (B) Results from a finite element model (done in ABAQUS) of the dorsal wall with growth (contraction) specified in regions of positive (negative) curvature. Undeformed (black) and deformed (color) shapes are shown.

DISCUSSION

Cubic Bezier curves have a number of elegant properties which make them ideal to quantify shape changes during morphogenesis. We found that a single cubic Bezier curve captures the overall features of the dorsal wall. The control points (Fig. 2) and the control polygon (Fig. 1) are useful tools to broadly characterize shapes. Composite curves can be used to fit cubic curves for smaller sections when more precision is desired (Fig. 2C). Tools from differential geometry such as curvature, arc length, and velocity of curves can be used to develop finite element models and investigate mechanisms driving morphogenesis. Bezier curves can be used to compare curvatures across different time points, control vs. perturbation conditions, and also for comparing embryo shapes from different species at the same developmental period.

ACKNOWLEDGEMENTS

This research was supported by the NSF (Award #1936733)

REFERENCES

[1] Hamburger, V & Hamilton, H L, *J. Morph*, 88:49-92, 1951.
[2] Ramasubramanian, A et al., *J Biomech Eng*., 141:1-12, 2019.

ORAL ALL-TRANS RETINOIC ACID TREATMENT ALTERS SCLERAL BIOMECHANICS AND INDUCES MYOPIA IN MICE

Dillon M. Brown (1,2), Machelle T. Pardue (1,2), C. Ross Ethier (1)

(1) Coulter Department of Biomedical Engineering
Georgia Institute of Technology and Emory University
Atlanta, GA, USA

(2) Atlanta Veterans Affairs Healthcare System
Atlanta, GA, USA

INTRODUCTION

The prevalence of myopia (nearsightedness) is rapidly increasing, with predictions of approximately 50% of the global population affected by 2050 [1]. Myopia is a refractive error, *i.e.*, a mismatch between eye geometry and optical power, predominately caused by excessive axial elongation of the eye. Evidence implicates remodeling of the sclera, the outermost white coat of the eye, and the resulting altered biomechanics as obligate to myopic axial elongation. Scleral biomechanics are consistently observed to change with myopia development, and altering scleral biomechanics, e.g., through surgical scleral reinforcement or collagen crosslinking, has been used to combat myopia progression in humans and animal models.

Certain light stimuli can be myopigenic, meaning that retinal sensing and processing of such stimuli result in axial elongation. This implies the existence of signal(s) capable of both traversing the vascular choroid that separates the retina and sclera (**Fig. 1**) and directing scleral remodeling processes. While the specifics of this retinoscleral signaling cascade are still poorly understood, retinoic acid (RA) has emerged as a promising candidate molecule central to the process. RA is found in all tissues between retina and sclera, and in increased concentrations in mammalian eyes developing myopia. Additionally, guinea pigs given exogenous all-trans RA (atRA) developed myopia [3]. Here, we feed mice atRA to test the hypothesis that exogenous atRA treatment will mimic the effects of sustained myopigenic visual stimulation, including alteration of scleral biomechanical properties.

METHODS

Male C57BL/6J mice (n=10) were trained to voluntarily ingest sugar pellets at 4 weeks of age (2.5 g pellet/kg). Mice were fed either sugar pellets with a 25 mg/kg dose of atRA (atRA: n=6) or plain sugar pellets (Ctrl: n=4) once daily for 2 weeks. Groups were chosen to ensure presence of littermate controls. Refractive errors (RE) of eyes were measured weekly until 6 weeks of age using a photorefractor, with baseline measurements made the day prior to starting atRA treatment. Reported refractive errors are the average of both eyes of each animal.

Animals were sacrificed and one eye each was randomly selected for biomechanical testing from a subset of animals (Ctrl: n=4, atRA: n=4). Eyes were enucleated and stored in 4 °C PBS (1X) until mechanical testing. Scleral samples (1 mm diameter) were taken ~0.5 mm from the optic nerve head and coated in graphite powder. Unconfined compression stress-relaxation experiments were performed on samples submerged in a 37 °C PBS bath using the Microsquisher (CellScale, Waterloo, Canada). Samples were compressed to 15% strain in three incremental steps (5% strain each), allowing stress to relax and equilibrate before application of the next step. A compressive modulus was obtained for each strain step as the ratio of equilibrium stress to strain. The conewise linear elastic biphasic model was independently fit to each strain step to determine the tensile modulus and hydraulic conductivity [4,5]. Generalized linear mixed models were used to test statistical significance of differences in biomechanical properties.

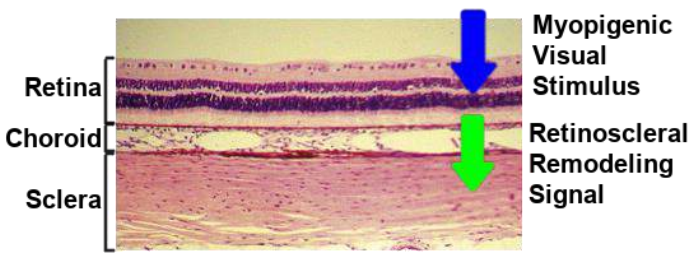

Figure 1: Structure of the posterior eye wall [2]. Signal(s) directing scleral remodeling originate in the retina after exposure to

myopigenic stimulus (blue arrow) and are believed to traverse the choroid (green arrow) to reach the sclera.

RESULTS

All animals voluntarily ingested the pellets with or without atRA. Control mice fed sugar pellets displayed a typical hyperopic refractive development that was significantly disrupted by oral atRA treatment (Interaction: treatment*age, $F(2,16) = 42.9$, $p<0.001$; **Fig. 2**). Relative myopia developed after 1 week of atRA treatment in atRA-fed mice vs controls (mean±STD: 0.3±2.7 vs 4.3±0.4 D, $p=0.024$) with the difference increasing after an additional week of treatment (mean±STD: -1.0±2.6 vs 6.3±0.1 D, $p<0.001$).

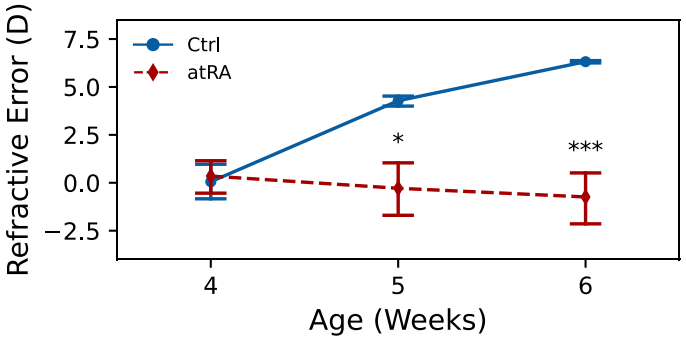

Figure 2: Development of refractive error (in diopters) of mice fed sugar pellets (blue, n=4) and sugar+atRA (red, n=6). Error bars represent 95% confidence interval. Statistical significance is indicated as: * p < 0.05, ** p <0.01, *** p < 0.001.

Changes in RE were accompanied by significantly altered scleral biomechanical properties, indicative of scleral remodeling. In-plane tensile stiffness of sclerae from atRA-fed animals was significantly decreased compared to control sclerae on average (95% CI, atRA: [83.8, 118] kPa, Ctrl: [131.6,186] kPa, Main effect: atRA, $\chi2(3)=13.5$, $p=0.004$; **Fig. 3**). The effect of atRA on in-plane scleral tensile stiffness was more evident at the larger compressive strain steps (Interaction: atRA*Strain, $\chi2(2)=9.9$, $p=0.007$), with sclera from atRA-treated eyes being only about half as stiff as controls at 15% compressive strain (95% CI, atRA: [109.6,168.2] kPa, Ctrl: [224.5,344.5] kPa, $p<0.001$).

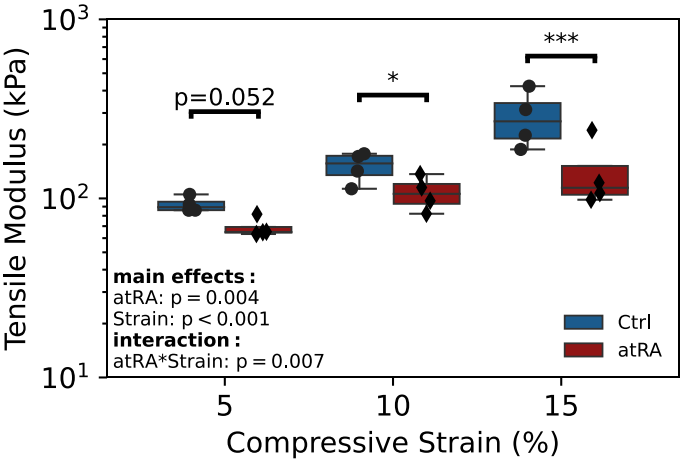

Figure 3: Scleral tensile modulus at 3 strain steps. Sclerae from control animals were stiffer than atRA-fed animals (n=4 each). Statistical significance indicated as: *p<0.05, ***p< 0.001.

Permeability was highly compressive-strain dependent (Main effect: Strain, $\chi2(4)=36.9$, $p<0.001$), with values spanning an order of magnitude over the range of compressive strains used. On average, sclera from atRA-fed animals trended towards being more permeable than the contralateral control sclera (95% CI, atRA: [5.6,10.6] $m^4/Ns*10^{-15}$, Ctrl: [4.1,7.8] $m^4/Ns*10^{-15}$, Main effect: atRA, $\chi2(3)=13.5$, $p=0.36$; **Fig. 4**) with the largest difference observed in the final strain step (95% CI, atRA: [2.6,6.2] $m^4/Ns*10^{-15}$, Ctrl: [1.4,3.3] $m^4/Ns*10^{-15}$, $p=0.05$). There was no significant change in compressive stiffness due to atRA treatment (95% CI, atRA: [5.9,8.2] kPa, Ctrl: [6.7,9.3] kPa, Main effect: atRA, $\chi2(3)=3.4$, $p=0.33$).

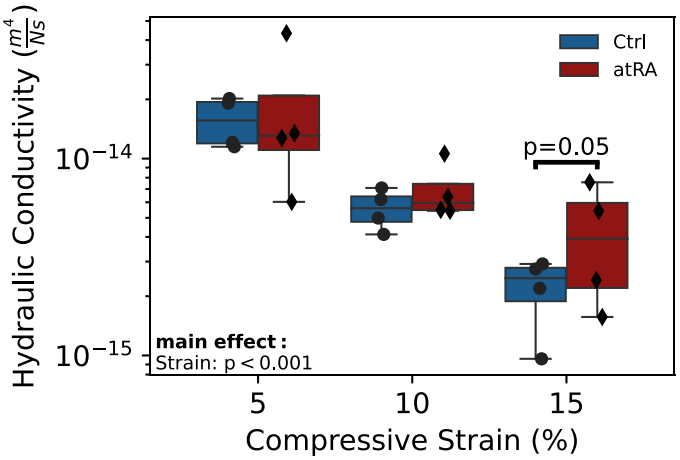

Figure 4: Scleral hydraulic conductivity at 3 strain steps. atRA-fed animals showed a trend towards more permeable sclerae than controls (n=4 each).

DISCUSSION

We have shown that exogenous atRA is highly myopigenic in mice, a novel result that corroborates previous findings in guinea pigs and is consistent with other correlational data in mammalian models of myopia. Further, we show for the first time that oral delivery of atRA affects scleral biomechanics by decreasing in-plane tensile stiffness of the sclera, suggesting that systemic atRA reaches and acts upon the sclera to influence remodeling processes. Scleral proteoglycans and collagen are known to remodel during myopia development, both of which may influence tensile stiffness. Both the rate of the atRA-induced myopia development (~7D of myopia in 2 weeks) and the decrease in scleral tensile stiffness are comparable to that seen in the mouse model of form deprivation myopia [5], consistent with a role for atRA in retinoscleral signaling of myopigenic visual cues.

Future work will study ocular tissue retinoid concentrations and how they compare between exogenous atRA treatment and myopigenic visual cues. Further, with atRA identified as myopigenic in the mouse, the power of transgenic animals can be exploited to elucidate the role of atRA in myopia development, e.g., by knocking out specific retinoid receptors or retinoid binding proteins.

ACKNOWLEDGEMENTS

NIH T32 EY007092 (DMB), Georgia Research Alliance (CRE), NIH R01 EY04635 (MTP), Dept. of Veterans Affairs Research Career Scientist Award (MTP).

REFERENCES

[1] Holden, B et al., *Ophthalmology*, 123:1036-1042, 2016.
[2] Remington, *Butterworth-Heinemann*, 2012.
[3] Li et al, *Molecular Vision*, 16:689-697, 2010
[4] Soltz, A and Ateshian, G, *J. Biomech. Eng*., 122:576–586, 2000.
[5] Brown et al, *Invest. Ophthalmol. Vis. Sci*, 61(7):3410, 2020

IMAGE BASED EVALUATION OF *IN VIVO* DEGRADATION FOR SHAPE MEMORY POLYURETHANE FOAM IN EMBOLIC APPLICATIONS

L.M. Graul (1), T.B. Cheung (1), S.L. Jessen (1,2), L.D. Nash (3), F.J. Clubb (1,2), and D.J. Maitland (1)

(1) Dept. of Biomedical Engineering
Texas A&M University
College Station, Texas, United States

(2) Dept. of Veterinary Pathobiology
Texas A&M University
College Station, Texas, United States

(3) Research and Development
Shape Memory Medical Inc.
Santa Clara, California, United States

INTRODUCTION

Degradation quantification techniques have been employed for various polymer systems, primarily for *in vitro* degradation kinetics [1]. Gravimetric analysis serves as the gold standard when possible. However, the quantification of *in vivo* degradation for polymer systems requires in-depth images or scans of the material. Image-based techniques offer the ability to combine pathological analysis and degradation quantification, as well as spectroscopic analyses [2,3]. The earliest non-destructive degradation evaluation techniques for implanted polyurethane foams were semi-quantitative [4]. Modern techniques rely on several imaging modalities, including magnetic resonance (MR), computed tomography (CT), optical coherence tomography (OCT), and microscopy (light and electron) [5-7]. However, these modalities often require some modification to the polymer system (e.g. metallic additives) for visibility. Spectroscopy is another common technique but fails to determine an exact quantitative mass loss [8]. The process becomes especially challenging when the polymer system is a porous implant for vascular occlusion applications, where tissue encompasses the material.

A Shape Memory Polyurethane (SMP) foam system has been developed and optimized for vascular occlusion applications [9-11]. From this platform material, two primary devices have been developed for clinical use. The peripheral embolization device (PED) is intended for the treatment of vascular insufficiency and is typically deployed in the designated vessel. The neurovascular embolization device (NED) is intended for the treatment of intracranial aneurysms. Both devices have been tested thoroughly for FDA clearance. Specifically, these devices have been implanted in animals for safety testing. The performance and lifetime of the implants *in vivo* served as the motivating factors for this work.

The porous foams allow blood to perfuse the scaffold, inducing microclots throughout the volume that transition into a complete embolized clot. Via the wound healing response, inflammatory cells remove the clot/foam matrix and scar tissue replaces the clot [9]. These devices are thus intended to rapidly occlude the region of interest, induce wound healing at the site, and gradually degrade to make way for pseudo-neointimal tissue for permanent occlusion. As reported in previous work, the SMP foam system is hydrolytically stable but oxidatively degradable, making the foam susceptible to cellular processes. A unique degradation profile has been identified in the foams, with scalloping events along the edges of struts (Figure 1).

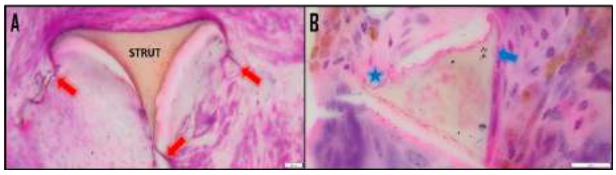

Figure 1: (A) strut of the SMP foam in histological section with membranes attached at vertices (red arrows). (B) strut with visible scalloping along edges (star) and isolated pits (blue arrow).

The SMP foam system is not inherently tuned for live imaging such as OCT, making *in vivo* gravimetric analysis a post-implantation process. Moreover, these implants had already been processed for histological assessment, limiting the method to trans-sectional evaluation. Thus, a method for quantitatively and qualitatively evaluating *in vivo* degradation will be presented in this work. It is critical that the degradation be quantified for the purpose of toxicity assessments and understanding device performance, especially as it relates to regulatory submissions. This paper will report out the degradation rates *in vivo* and the character of the observed degradation.

METHODS

SMP Foam Synthesis and Device Fabrication. PEDs were fabricated as detailed by Jessen et al, and NEDs were fabricated as described by Herting et al. and Boyle et al. [11-13]. Specifically, the PED implants are composed of a SMP foam (HH30/40) pledget attached to a bare nitinol anchor coil. HH30/40 foams range in pore size from 800-1500μm, and are comprised of hexamethylene diisocyanate (HDI), 30/40% N,N',N'-tetrakis(2-hydroxypropyl) ethylenediamine (HPED), and 70/60% 2,2',2"-nitilotriethanol (TEA). NED implants are composed of SMP foams (TH60) threaded over bare Pt-W coils. TH60 foams are comprised of trimethylhexamethylene diiscoyanate (TMHDI), 40% HPED, and 60% TEA.

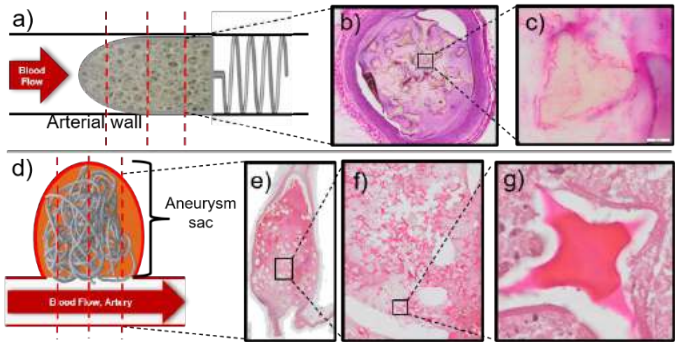

Figure 2: Device implants (a,d) in vivo were processed (b,e) for histology. High magnification and resolution images were used from these sections to evaluate degradation (c,f,g).

Gravimetric and Microscopic Analysis of SMP Foams. The mass ratio between struts and membranes in the SMP foams was determined through gravimetric analysis. Cold plasma reticulation was used to remove membranes from the foams according to the process outlined by Nash et al. [14]. Masses were taken before and after plasma treatment to determine the mass of membranes. All foams were imaged under light microscopy to ensure foam struts were not destroyed in the process.

Device Implantation and Explantation. The devices were implanted in their respective environments, with PEDs implanted in porcine arteries (n=3 animals per timepoint) and NEDs implanted in rabbit right common carotid aneurysms (n=10, 5, and 14 animals per timepoint) [12,13]. PEDs were explanted at 30, 60, and 90 days from different animals. NEDs were explanted at 30, 90, and 180 days. Explanted tissues were then fixed and sectioned according to previously reported methods [12,13].

Quantitative and Qualitative Analysis of Degradation. Histological sections were scanned at high resolution and magnification using OLYVIA Olympus software. Scans were then prepared for degradation analysis through detailed imaging of the remnant foam in the scans. Membranes of the foam were tallied as present, disrupted, or missing to form the relative membrane loss (RML). Visible struts were counted in the sections across the different timepoints to establish a relative strut loss (RSL). Struts that presented quantifiable degradation were imaged at high resolution. The images were imported to FIJI (ImageJ), scaled accordingly, and the regions of pitting and scalloping were measured using the Freeform tracing tool. These measurements formed the second part of the strut analysis: measured strut loss (MSL). Using the mass ratios from the gravimetric analysis of struts (k_s) and membranes (k_m), the following equation was used to determine the estimated mass loss for the section evaluated:

$$Deg_{Section} = RML * k_m + (RSL + MSL * (1 - RSL)) * k_s \quad (1)$$

RESULTS

Gravimetric Analysis of Struts and Membranes. Membranes accounted for 28.6 ± 9.8%; 26.8% ± 4.5%; and 22.9 ± 2.6% mass ratio for HH30, HH40, and TH60 foams, respectively. Struts subsequently accounted for the remaining mass percent. These values were incorporated into the equation for calculating the mass loss per section.

Quantitative and Qualitative Analysis of Device Mass Loss. For the PED studies, degradation was observed to steadily increase with increasing implantation time (Table 1). Relative strut loss was non-existent within the sections for all timepoints. Relative membrane loss dominated the degradation profile. Membranes were steadily disrupted and isolated through cellular activity and tissue ingrowth. Struts presented with increasing volumes of pitting along edges. For NED studies, 30-day timepoints showed near total membrane loss. Struts did not show evidence of dissolution and relative counts were high. 90-day timepoints showed drastic mass loss, with near total strut loss observed. Pockets of foam struts were located near the osteum of the aneurysm. 180-day sections showed a similar progression of degradation with one outlier section.

Table 1: PED/NED Mass Loss Rates per Explant Timepoint

Device	Timepoint (d)	Mass Loss (%)
PED [12]	30 (n=11)	3.22 ± 3.90
	60 (n=12)	6.91 ± 4.97
	90 (n=17)	9.42 ± 7.05
NED [13]	30 (n=10)	13.6 ± 2.75
	90 (n=5)	98.5 ± 0.22
	180 (n=14)	97.3 ± 3.08

DISCUSSION

The method presented expands on previously published image-based degradation quantification techniques by estimating a true polymer mass loss. Additionally, the qualitative assessment, coupled with the known pathological assessment of the devices, adds another dimension to the devices' performance. PEDs in porcine arteries showed a slower mass loss rate than observed *in vitro* and especially slower than NEDs in the rabbit elastase aneurysm models. The marked difference in the device lifetimes (90 days versus 3 years) have initiated an investigation into the wound healing responses of porcine models versus rabbit models. The degradation rates reported here will guide toxicity threshold assessments. The data presented has been used in FDA submissions for device clearance.

ACKNOWLEDGEMENTS

Special thanks to the Biomedical Device Laboratory and Shape Memory Medical Inc. for iterative feedback on method development.

REFERENCES

[1] Weems et al., *Acta Biomater*, 59:33-44, 2017
[2] van Tienen et al., *Biomat*, 23:1731-1738, 2002
[3] McGough et al., *Tissue Eng. A*, 00:1-15, 2018
[4] Sinclair et al., *Plast Reconstr Surg*, 92:1003-13, 1993
[5] Sweedy et al., *JBMR B*, 106:1567-1577, 2018
[6] Iakovlev et al., *JBMR B*, 105:237-248, 2017
[7] Costello et al., *JBMR B*, 83:44-49, 2007
[8] Lattuati-Derieux et al., *J Chromatogr A*, 1218:4498-4508, 2011
[9] Rodriguez et al., *JBMR A*, 103:1577-1594, 2015
[10] Landsman et al., *JBMR B*, 63:195-206, 2016
[11] Boyle et al., *JBMR B*, 104:1407-1415, 2016
[12] Jessen et al., *ACS Biomater Sci Eng*, 6:2588-2599, 2020
[13] Herting et al., *JBMR B*, 107:2466-2475, 2019
[14] Nash et al., *Macromol Rapid Comm*, 37:1945-1951, 2016

DIAMOND: DIGITAL PLASMONIC-NANOBUBBLE DETECTION FOR HOMOGENEOUS ASSAY WITH ENHANCED SENSITIVITY

Y. Liu (1), H. Ye (1), Z. Qin (1,2,3,4)

(1) Department of Mechanical Engineering
University of Texas at Dallas
Richardson, TX 75080, U.S.

(2) Department of Bioengineering
University of Texas at Dallas
Richardson, TX 75080, U.S.

(3) Center for Advanced Pain Studies
University of Texas at Dallas,
Richardson, TX 75080, U.S.

(4) Department of Surgery
University of Texas Southwestern Medical Center
Dallas, TX 75390, U.S.

INTRODUCTION

The ability to rapidly detect diseases is of paramount importance as evidenced by the current COVID-19 pandemic.[1] Homogeneous assays are simple and rapid detection methods without the need for immobilizing, separating or washing reagents, and are promising for POC diagnostic applications. For example, homogeneous assays utilizing plasmonic gold nanoparticles (AuNPs) have been widely used in chemical and biological detection for proteins, nucleic acids, and virus particles.[2] Due to their localized surface plasmon resonance and coupling, AuNPs in the visible wavelengths provide intense color signals that can be conveniently read out by naked eyes. However, the performance of colorimetric and other ensemble measurements has been largely limited by the high background signal, resulting in poor sensitivity. The limitation makes such assays inadequate to be standalone diagnostic platforms.

In this work, we report a novel strategy, based on digital plasmonic-nanobubble detection (DIAMOND), to achieve the compartment- and label-free homogeneous assay with dramatically enhanced sensitivity. Specifically, the plasmonic-nanobubble (PNB) refers to the transient vapor bubble generated around a plasmonic NP by the laser heating and can be readily detected by the optical scattering (**Figure 1A**). Importantly, the PNBs are highly dependent on the light absorption and heat generation, and thereby are sensitive to the NPs' sizes and concentration. Due to their transient structure, the PNB events have lifetime up to several hundred nanoseconds and allow signal confinement within a detection zone, bypassing the conventional sample partitioning (e.g., microwells or droplets). As a result, the integrated DIAMOND platform measures "on" and "off" signals digitally in a flow channel and has the capability of single-particle enumeration (**Figure 1B**). With its ability to differentiate PNB signals from individual NPs and their clusters, DIAMOND is suitable to implement on homogeneous assay for rapid diagnostic fashion (<2 min). We demonstrated the DIAMOND technique enhanced the sensitivity of homogeneous assay by more than 300 times using respiratory syncytial virus as a model.

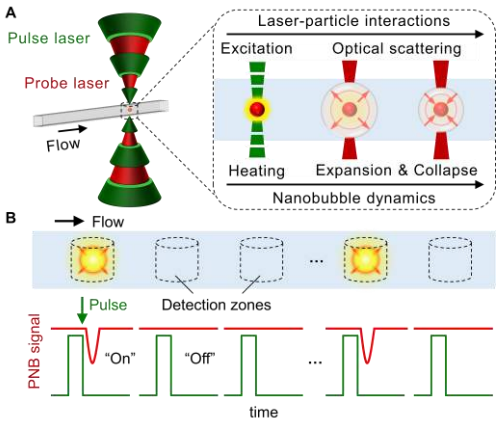

Figure 1. Schematic illustration of DIAMOND platform. (A) The major courses involved during a transient plasmonic-nanobubble (PNB) event. Pump-probe laser configuration allows PNB generation and detection simultaneously. (B) The digital counting of "on" and "off" PNB signals in the presence and absence of target of interest.

METHODS

DIAMOND platform. Briefly, ultrafast 532 nm laser pulses (28 ps, 50 Hz) were applied to activate the NPs and induce PNBs. The continuous probe laser of a 633 nm was used to monitor the PNB signals by a high-

speed photodetector (FPD510-FV, Thorlabs) and an oscilloscope (LeCroy WaveRunner204Xi-A). Data processing and analysis were automatically performed through a MATLAB script.

DIAMOND-based Single-Particle Detection. We prepared AuNPs solutions according to Frens' methods with slight modification.[5] The 70 nm AuNP suspensions were pumped through a micro-capillary (200 μm×200 μm) for the signal generation and data acquisition in DIAMOND system.

DIAMOND-enhanced RSV detection. We conjugated Synagis (RSV specific antibody) to AuNPs using DTSSP as crosslinkers to prepare RSV probes. The AuNP probes were incubated with RSV and other respiratory viruses at room temperature (RT) for 30 minutes before absorbance measurements and DIAMOND test.

RESULTS

DIAMOND-based Single-Particle Enumeration

First, we evaluated the performance of DIAMOND technique in single-particle enumeration. **Figure 2A** shows the typical PNB signal traces recorded from the 70 nm AuNPs suspensions with different concentrations. The concentrations were converted into expected number (λ) of NPs considering the 16 pL detection zone. Apparently, the different number (k=0, 1, 2…) of AuNPs passing through the detection zones caused the signal variations. At high concentration (λ=40), the number of AuNPs being detected was more than 15 in the detection zones, resulting in consecutive "on" signals. Decreasing the concentration led to the increasing probability of NPs in absence (k=0), causing the discrete signal traces and in turn, allowing the digital counting of "on" and "off" signals. Taking the AuNPs of λ=0.4 as an example, **Figure 2B** shows the bivariate plot of amplitude and area-under-curve (AUC) extracted from the signal traces. The as-counted frequencies, f_{off} and f_{on}, were close to the theoretical probabilities (P) of none (k=0) and a number (k>0) of AuNPs being detected, based on Poisson statistics. A close inspection of the data based on a gating algorithm using the theoretical P allowed us to sort the scatters representing for a number (k=0, 1, 2, and >2) of AuNPs being detected (**Figure 2C**). Clearly, the DIAMOND technique detects NPs at single-particle resolution.

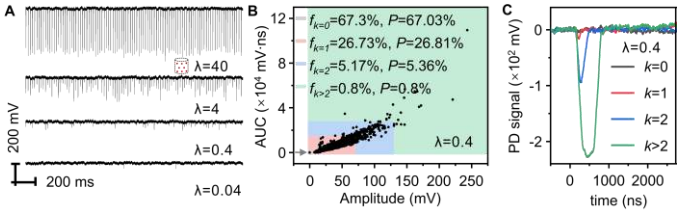

Figure 2. **DIAMOND technique for the single-particle enumeration.** (A) PNB signal traces recording of 100 pulses for 70 nm AuNPs with different particle concentrations at fluence of 8 μJ. Schematics show the expected number (λ) of AuNPs per detection zone correspondingly. (B) Bivariate plot of amplitude and AUC for the case of λ=0.4. f is the counting frequency of specific number (k) of AuNPs in detection zone and P is the corresponding Poisson probability. (C) The representative PNB signals for a number (k=0, 1, 2 and >2) of AuNPs being detected.

DIAMOND-Enhanced Homogeneous Assay

Next, we evaluated the DIAMOND technique for homogeneous assay of respiratory syncytial virus (RSV). RSV is the major respiratory pathogen in infants and children worldwide.[6] AuNPs conjugated with antibodies as probes could specifically target to RSV and were ready for detection (**Figure 3A**). The TEM images in **Figure 3B** confirmed the effective target-probe binding, while the spectra measurements shown in **Figure 3C** revealed the good detection selectivity among different respiratory viruses, including Parainfluenza viruses (PIV), Influenza A (IVA), Human metapneumovirus (hMPV) and sensitivity around 3.6×10^4 PFU/mL. We then carried out the DIAMOND test for the sensitivity enhancement. **Figure 3D** shows the bivariate plot of the detection results at different RSV titers in the borate buffer solution, where the thresholds were determined as five times standard deviation above the mean of control groups and assigned for the "on" signal counting. The calibration curve that plotted the counted frequency (f_{on}) against the RSV titers was shown in **Figure 3E**. In particular, a linear relationship (R^2 = 0.995) in the range of 10^2-10^4 PFU/mL was observed and the limit of detection (*LOD*) was calculated to be 108 PFU/mL (inset of **Figure 3E**). Clearly, DIAMOND improved the detection limit by more than 2 orders of magnitude.

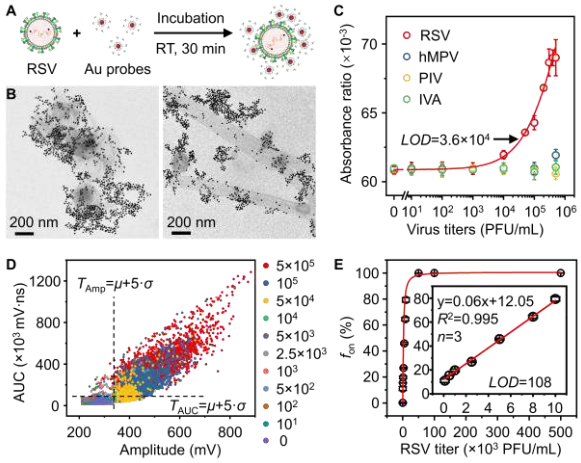

Figure 3. **Applying DIAMOND technique for the homogeneous assay of RSV**. (A) The schematic illustration of homogeneous assay. (B) TEM images of AuNPs targeting RSV of different shapes. (C) Colorimetric analysis of the assay. (D) Bivariate plot extracted from PNB signal traces of assay solutions. The thresholds were highlighted in grey and dash lines. (E) Quantification of RSV titers as a function of frequency counting (f_{on}). Error bars indicate the standard deviations of three independent measurements. The inset shows the linear detection range and *LOD* was calculated as 3 times standard deviation of the control dividing the slope of regression line.

DISCUSSION

In this study, a novel method based on the digital plasmonic nanobubble detection (DIAMOND) was developed to detect NPs and RSV. The results suggested the DIAMOND technique could detect NPs at single-particle level and RSV at 108 PFU/mL. This work will have a broader impact on addressing the technological challenges of conventional digital assays and providing a diagnostic platform for rapid and ultrasensitive tests. Further optimization of the DIAMOND system allows high throughput data acquisition and portable and even handheld POC prototype.

ACKNOWLEDGEMENTS

This research is partially supported by National Institute of Health grants R21AI140462 and R01AI151374, and DOD grant PR192581.

REFERENCES

1. Tang, Y., et al. *J. Clin. Microbiol*. **2020**, *58*.
2. Godakhindi, V.S., et al. *ACS Sens*. **2017**, *2*, 1627-1636.
3. Lukianova-Hleb, E., et al. *ACS Nano* **2010**, *4*, 2109–2123
4. Basu, A.S. *SLAS. Technol*. **2017**, *22*, 369-386.
5. Kimling, J., et al. *J. Phys. Chem. B* **2006**, *110*, 15700-15707.
6. Shi, T., *Lancet* **2017**, *390*, 946-958.

NUMERICAL INVESTIGATION OF HEMODYNAMICS AT INITIATION OF PULMONARY ARTERIAL HYPERTENSION ASSOCIATED WITH CONGENITAL HEART DISEASE

Melody L. Dong (1), Ingrid S. Lan (1), Weiguang Yang (2), Marlene Rabinovitch (2), Jeffrey A. Feinstein (1, 2), Alison L. Marsden (1, 2)

(1) Bioengineering
Stanford University
Stanford, CA, USA

(2) Pediatrics – Cardiology
Stanford University
Stanford, CA, USA

INTRODUCTION

Pulmonary arterial hypertension (PAH) is characterized by elevated pulmonary artery (PA) pressure >25 mmHg, dilation of the proximal PA vessels, distal PA remodeling resulting in occlusion of the PA vasculature, and right heart failure. Although the exact biological mechanisms of PAH initiation are unknown, PAH associated with congenital heart disease (CHD), PAH-CHD, is likely to develop in patients with untreated systemic-to-pulmonary shunts, especially for large shunts with pulmonary to systemic flow ratios (Qp:Qs) >2 [1]. Ventricular septal defects (VSDs) are the most common type of CHD where a hole exists in the interventricular septum between the two ventricles resulting in systemic-to-pulmonary, or left-to-right, shunts which are an indicator of severity and VSD size.

Although previous studies have investigated PA hemodynamics and its effect on cellular function in PAH, most have only focused on the disease progression and on the larger PAs [2, 3]. Few have investigated PA hemodynamics in the small, distal PAs, which are most severely affected by the remodeling process in PAH, and in the context of CHDs. Difficulties in assessing the hemodynamics in the small, distal PAs include the lack of *in vivo* flow and morphometry measurements, specifically in the pediatric population. We hypothesize that unrestricted left-to-right shunts alter PA hemodynamics and mechanical stimuli on vessel walls leading to initiation of dysfunctional cellular pathways in the small PAs contributing to the initiation of PAH.

In this study, we performed computational fluid dynamics (CFD) simulations to study the hemodynamics of the entire PA tree in different VSD conditions to understand the mechanical conditions present at initiation of PAH. We used a patient-specific geometry of the pediatric proximal PA vessels to simulate large PA hemodynamics (>1mm diameter vessels) in a 3D model. To model small PAs (<1mm diameter), we used scaling laws of PA morphometric somatic growth and PA resistance approximations to optimize a distal PA tree geometry and estimate hemodynamics in a 0D model. To our knowledge, this is the first study investigating the hemodynamics at the initiation of VSD-induced PAH that quantifies hemodynamics in the entire PA tree.

METHODS

To model the hemodynamics in the proximal PAs (>1mm diameter) in VSD conditions, we created a 3D geometric model of the healthy PAs of a 1-year-old male subject (BSA=0.49m^2, Ht=75.6cm, Wt=11.3kg) from a CT scan using the open-source software package, SimVascular (simvascular.org). Hemodynamics were simulated using SimVascular's stabilized finite-element solver [4] with backflow stabilization [5] and coupled Windkessel boundary conditions [6]. To model PA wall deformability, we used the coupled momentum method [7] for fluid-solid interaction with external tissue support [8] where PA walls were modeled as deformable linear elastic membranes with variable wall thickness. An elastic modulus of 126 kPa, 163 kPa, and 291 kPa was used for the normal and small VSD, moderate VSD, and large VSD simulations, respectively, based on previous studies showing stiffer PA material properties at higher pressures [9, 10].

To simulate increasing VSD severities, we prescribed a generalized normal PA inflow waveform at the main PA, scaled to mean flows of 2.5, 3.7, 4.9, and 7.4 L/min to represent the left-to-right shunt quantified by the Qp:Qs ratios found in a healthy control (1:1) [11], small VSD (1.5:1), moderate VSD (2:1), and large VSD (3:1). For all simulations (healthy and VSD conditions), we prescribed the same 3-element Windkessel model to all 3D PA outlets to represent a healthy downstream pulmonary vascular resistance and compliance. These Windkessel models were tuned to achieve a healthy target main PA pressure in the control simulation and subsequently used for all VSD simulations to represent conditions before vascular remodeling and the

initiation of PAH. The 3D PA simulation setup is shown in Figure 1a. From the proximal PA simulation, we extracted pressure, velocity, wall shear stress (WSS), oscillatory shear index (OSI), and strain measurements at each PA segment in the 3D PA model.

To model the distal PAs (<1 mm diameter), we used an optimized PA morphometric geometry to extrapolate 3D PA simulated flows to the distal geometry in a 0D model. The distal PA geometry was constructed using scaling laws of the PA morphometry for the 1-year-old BSA [12], the vessel connectivity of previous PA morphometric studies [13, 14], and optimization of the distal PA dimensions to achieve a target PA resistance of 33% of the entire healthy pulmonary vascular resistance [15]. Distal PA hemodynamics were calculated by extrapolating the outlet flows from the proximal PA model to the optimized distal PA morphometric model (Fig 1b). To extrapolate flows down to 50 μm diameter vessels and calculate wall shear stress (WSS), we applied Poiseuille assumptions in a 0D model with a diameter-dependent viscosity exponential function [16] to account for non-Newtonian effects from the Fahreus-Lindqvist effect in the small PAs.

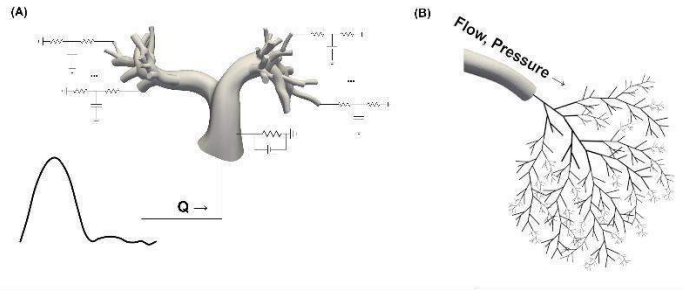

Figure 1: (a) Proximal PA model simulation setup with a prescribed inlet flow waveform, Windkessel outlet boundary conditions, and external tissue support. (b) Distal PA mathematical model setup with extrapolated outlet flows from the proximal 3D PA simulation to an optimized distal 0D PA tree.

RESULTS

In the proximal 3D model, pressure, flow, vessel strain, and WSS increased with increasing VSD size. OSI decreased with increasing VSD size in the larger PA vessels. WSS in the proximal 3D model increased from the main PA to the smaller PA vessels in the model in all conditions. In the distal PA 0D model, WSS increased with increased VSD size and increased in the smaller, distal PA vessels exceeding 100 dyn/cm^2 in the smallest pre-acinar PA vessels. Figure 2 shows WSS increasing from the proximal PAs in the 3D model to the distal PAs in the 0D model and with increasing VSD size. Due to differences in model assumptions between the 3D proximal and 0D distal PA models, WSS varies largely at this transition.

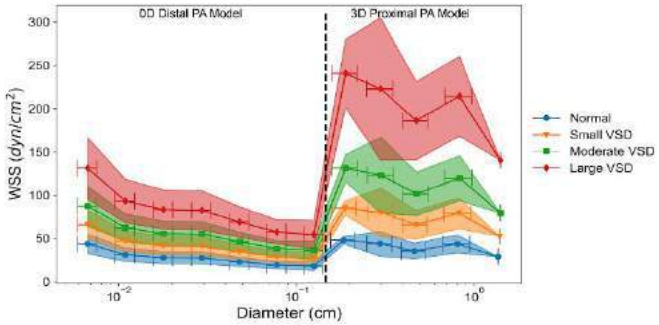

Figure 2: WSS increased from the proximal PAs (~1cm-1mm) to the distal PAs (~1mm-50μm) and increased with VSD size.

DISCUSSION

Knowledge of the hemodynamics in the small, distal PAs is significant in our understanding of the remodeling process that occurs in PAH. We estimated several hemodynamic markers with significant WSS differences between the normal and large VSD conditions with small distal PAs exhibiting >100 dyn/cm^2 WSS values. This is significant in informing mechanotransduction studies investigating the initiation of PAH, specifically as a result of the mechanical stimuli involved in untreated CHD patients who later develop PAH. Previous shear stress related gene expression studies on PAH have used lower WSS values of 5-20 dyn/cm^2 [2, 17], which correspond mostly to the largest PAs where dilation and remodeling usually occur in late stages of PAH, not initiation or early stages.

This is the first study to estimate the hemodynamics of the entire pediatric PA tree with VSD conditions before initiation of PAH, showing much higher WSS estimates in the small PAs than previously believed. These results have implications for the design of future biological studies assessing the effects of mechanical stimuli on endothelial cells as well as vascular wall mechanics that may occur during the initiation of PAH.

ACKNOWLEDGEMENTS

This work was supported by the National Science Foundation Graduate Research Fellowship and the Benchmark Capital Fellowship through the Vera Moulton Wall Center at Stanford University. Simulations were performed using Stanford supercomputer resources (Sherlock).

REFERENCES

[1] Kulik, T.J, *Pulm Circ*, 2(3):327-339, 2012.
[2] Li, M., et al., *J Vasc Res*, 46(6):561-71, 2009.
[3] Tang, B.T., et al., *Pulm Circ*, 2(4):470-6, 2012.
[4] Taylor, C.A., et al., *Comput Methods in Appl Mech Eng*, 158(1-2), 1998.
[5] Esmaily Moghadam, M., et al, *Comput Mech*, 48:277-291, 2011.
[6] Vignon-Clementel, I.E., *Comput Methods Biomech Biomed Eng*, 13(5):625-640, 2010.
[7] Figueroa, C.A., et al., *Comput Methods in Appl Mech Eng*, 195(41-43), 2006.
[8] Moireau, P., et al, *Biomech Model Mechanobiol*, 11:1-18, 2012.
[9] Forouzan, O., et al, *J Cardiovasc Magn Reson*, 17:109, 2015.
[10] Long, C.C, et al, *Int J Numer Meth Bio*, 28(5):513-527, 2012.
[11] Cattermole, G.N., et al., *Physiol Rep*, 5(6), 2017.
[12] Dong, M, et al, *Am J Physiol Heart Circ*, 319(2): H432-H442, 2020.
[13] Huang, W., et al., *J Appl Physiol*, 81(5): 2123-33, 1996.
[14] Spilker, R.L., et al., *Ann Biomed Eng*, 35(4):546-59, 2007.
[15] Raj, J.U., Chen, P, *Circ Res*, 59(4):398-404, 1986.
[16] Secomb, T.W., *Annu Rev Fluid Mech*, 49:443-61, 2017.
[17] Szulcek, R., et al., *Am J Respir Crit Care Med*, 193(12), 2016.

UNILATERAL, DAILY BOUTS OF MUSCLE LOADING LEADS TO MINERAL AND EXTRACELLULAR ADAPTATION OF THE IMMATURE ACHILLES ENTHESIS IN MICE

E. Ganji (1,2), B. Duncan (3), A. Livingston (3), N. S. B. Whyte (2), M. T. Stepanovich (2), M. L. Killian (2)

(1) Department of Mechanical Engineering
University of Delaware
Newark, DE, USA

(2) Department of Orthopaedic Surgery
University of Michigan
Ann Arbor, MI, USA

(3) Department of Biomedical Engineering
University of Delaware
Newark, DE, USA

INTRODUCTION

The tendon-to-bone attachment (i.e., enthesis) is a functionally graded tissue that translates muscle-generated force from tendon to bone. The enthesis matures during postnatal growth and is susceptible to overuse injuries. Repeated loading of the adult enthesis induces mineralization and causes abnormalities such as bony spur formation and calcification of the distal tendon. Increased activity during periods of rapid growth, such as in children and during adolescence, can lead to micromotion at the enthesis and apophysis, resulting in inflammation and the clinical presentation of Sever Disease [1]. However, the temporal effect of training on the growth and remodeling of the enthesis remains unclear.

The use of small animal models allows for mechanistic exploration of the effect of loading on the growth and structural remodeling of the enthesis. Previously, muscle unloading has been shown to disrupt the structural and mechanical properties of the growing postnatal enthesis [2-4]. In the present study, we aimed to determine the effect of repeated daily bouts of increased muscle loading (using optogenetically-controlled muscle contractions) on the growth and adaptation of the immature and mature enthesis. We hypothesized that the mechanoadaptation differs between the immature and mature enthesis, and we compared the mineralization and structural changes of the enthesis in response to *in vivo* loading-induced remodeling. To do this, we used non-invasive optogenetic control of muscle contraction, which relies on the expression of light-responsive microbial opsins (e.g., Channelrhodopsin-2, ChR2) in activatable cells to translocate ions across the cell membrane for cell-specific, fast optical control of the membrane potential [5]. We and others have previously used optogenetics to control muscle contraction *in vivo* in mice and we have demonstrated the feasibility of eliciting sustained muscle contractions in the triceps surae muscle group [6-8]. In this study, we used optogenetics to induce isometric muscle contraction for non-invasive loading of the Achilles tendon enthesis daily, for three weeks, in Immature (3-week old) and Mature (6-month old) mice. We used microcomputed tomography (microCT) and histology to evaluate the effect of repeated mechanical loading on the mineralization and structural changes of the Achilles enthesis between repeatedly loaded and contralateral entheses.

METHODS

All procedures were approved by our Institutional Animal Care and Use Committee. Doxycycline-inducible ACTA1-rtTA;tetO-cre mice (Acta1-Cre; C57BL6J background) were crossed with Ai32 reporter mice (C57BL6J background) to generate Acta1-Cre; Ai32 offspring that expressed ChR2 blue light-sensitive opsin (455nm sensitivity) in skeletal muscle when treated with tetracycline. Dams were treated with doxycycline chow at the time of mating until weaning. Offspring were genotyped using PCR (Transnetyx), and Acta1-Cre; Ai32 homozygous mice (Immature group: 3-week old, n = 6 ; 2 females and 4 males; Mature group - 6-month old: n = 4; 2 females and 2 males) were used for blue light-induced stimulation. In addition to contralateral within animal controls (right: stimulated, left: control), external age-matched littermates heterozygous and homozygous Ai32 offspring (n = 7; 4 females and 3 males) were used as non-stimulated controls for the Immature group. Mice were anesthetized with isoflurane, hair was removed from their right triceps surae muscles to expose the skin, and animals were placed on a heating pad at 37°C. Right limbs were stabilized at the knee joint and feet were placed on a foot pedal connected to a servomotor shaft (Aurora Scientific) to induce isometric muscle contractions. For light stimulation, a collimated LED light (455 nm, 900 mW, M455L3, Thorlabs) and a high-power LED driver (DC2200, Thorlabs) were used for pulse modulation [6]. Muscles were stimulated using 10Hz pulsed light (70ms on, 30ms off; 10 cycles)

followed by 4 seconds of rest for 20 minutes (240 consecutive loading cycles), for 5 consecutive days per week for (3 weeks). Ankle torque measurements were collected throughout loading bouts. Maximum ankle torque at the start of each bout of stimulation was compared after normalizing to body weight. Contralateral limbs of the Loaded group were used as paired controls for microCT. Knee and ankle placement was also repeated for non-stimulated control immature group for 20 minutes under anesthesia. After 3 weeks of unilateral loading, mice were euthanized using carbon dioxide asphyxiation. Hindlimbs were dissected and fixed overnight in 4% paraformaldehyde and then scanned using microCT (Bruker SkyScan 1276; 59kV, 175µA, 10.58µm voxel size, 930ms exposure, 0.5mm aluminum filter). Digital reconstructions were analyzed using CTAn (Bruker) and Dragonfly (Object Research Systems) for: calcaneal total and bone volume; apophyseal total and bone volume; apophyseal bone mineral density (BMD); and calcaneal length. After microCT, tissues were decalcified in 14% EDTA and paraffin processed for histology. Sagittal plane sections of the Achilles enthesis (6µm) were stained using Toluidine Blue and Hematoxylin and Eosin (for enthesis morphology) and DAB immunohistochemistry (IHC) for markers of enthesis tissue transition (Aggrecan, Collagen Type II, Collagen Type III). *Statistical analysis*: maximum measured torque was normalized to the measured body weight for each bout of loading and repeated measures ANOVA was used to compare the variation of normalized torque for each mouse for the duration of the experiments. Paired Student t-test was used to compare BMD, BV, TV, and BV/TV between contralateral limbs.

RESULTS

All mice tolerated the daily loading bouts well and were included in analyses. Normalized maximum torque did not fluctuate for the duration of the experiment for each mouse and between mice of each group (Immature and Mature) at each bout (data not presented here). After 3 weeks of unilateral loading in the Immature group, the Achilles enthesis showed increased vascular infiltration in the calcaneal apophysis and at the calcified fibrocartilaginous border of the enthesis in stimulated limbs compared to contralateral limbs (Fig. 1A, shown with arrows). In 50% of the Immature mice, repetitive loading resulted in the formation of an enlarged and irregularly shaped apophysis compared to unloaded controls (Fig. 1A). We also saw a smaller fibrocartilage zone, with less Collagen II staining, in the Loaded compared to control entheses of Immature mice and adaptation to compressive loading at the wrapping site of the enthesis (Fig. 1C).

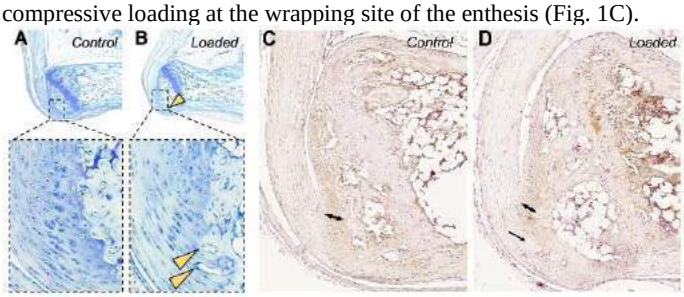

Figure 1: Morphology of the Achilles enthesis of (A) Control and (B) Loaded Immature mice after 3 weeks of daily bouts of optogenetic muscle contraction. Yellow triangles show misshapen apophysis near the enthesis and increased vascularity. (C, D) Loaded Immature mice have thinner entheses, indicated by less Collagen II (black arrow).

Bone loss visualized histologically in the loaded Immature group was confirmed following microCT analysis, both qualitatively and quantitatively. The apophysis was "pulled" in the posterior direction in the Immature group enthesis (dotted line, Fig. 2A), but not in the Mature group. Bone quality, measured as BMD, was lower in Loaded compared to contralateral Control apophyses in the Immature group (Fig. 2B). However, the total apophyseal volume did not differ between loaded and control groups in the Immature group. In the Mature group, the morphology of the Achilles enthesis and apophysis appeared histologically normal and there were no significant differences in BMD or apophysis volume between loaded and control sides (Fig. 2 E, F).

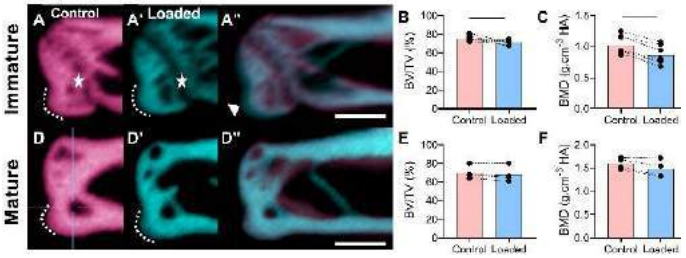

Figure 2: Sagittal microCT view of representative calcanei of Immature (A-A") and Mature (D-D") (Achilles attachment site outlined with dashed line). After 3 weeks of daily loading, Immature mice had posteriorly pulled apophyses (white triangle in A'') with growth plate opening (stars in A, A'). Apophyseal bone volume fraction and BMD (B, C) were reduced in the Loaded Immature group compared to contralateral apophyses. No structural differences were observed in the Mature group (D-F). Scale bar: 500 µm, bars indicate $p < 0.05$.

DISCUSSION

Using high-resolution three-dimensional imaging techniques (microCT) and histology, we found irregular apophyseal bone formation and increased vascularization, with smaller fibrocartilage and decreased bone quality, following repetitive loading in the Immature but not Mature enthesis. Vascular infiltration may be an indicator of bone and fibrocartilage remodeling in the immature entheses [9]. These findings model the structural and mechanical changes similar to those occurring during overuse activities in the young athlete and are generally associated with pediatric apophyseal pathologies [9-12].

Significance/clinical relevance: Pediatric sports-related injuries, such as Sever disease, Little Leaguer's elbow, and Osgood-Schlatter disease, all represent common clinical apophyseal pathologies in the young athlete. Increasing clinical evidence demonstrates the link between prolonged overuse activities and repetitive loading with other diagnostic (e.g., magnetic resonance imaging) and clinical abnormalities in skeletally immature athletes [10-13]. Our non-invasive, repeatable model for *in vivo* muscle loading enables mechanistic investigation of the effect of loading on the structure of developing and mature enthesis in order to improve clinical interventions for overuse injuries in children and adults.

ACKNOWLEDGEMENTS

NSF CAREER 1944448, National Institutes of Health (R03HD094594; P30AR069620), University Doctoral Fellowship Award.

REFERENCES

[1] Doung MM et al., *J Pediatr Orthop*., 40(2):93-96, 2020; [2] Killian ML, Thomopoulos S, *FASEB J.*, 30(1):301-11, 2016; [3] Schwartz AG et al. *Bone*, 55(1):44-51, 2013; [4] Thomopoulos S et al., *J Orthop Res*. , 25(9):1154-63, 2007; [5] Towne C et al., *PLoS One*., 8(8):e72691, 2013; [6] Ganji E et al., *Connect Tissue Res.*, 62(1) 15-23, 2020; [7] Magown P et al., *Nat Com., 6, 8506, 2015;* [8] Bruegmann T et al., *Nat Com.*, 6, 7153, 2015; [9] Binks DA et al., *Ann Rheum Dis.*, 74(1):196-203, 2015; [10] Holt JB et al., *Am J Sports Med*., 48(2):466-472, 2020; [11] Pennock AT et al., *J Bone Joint Surg Am.*, 98(9):761-7, 2016; [12] Pennock AT et al., *Orthop J Sports Med*., 6(2):2325967118756825, 2018; [13] Holt JB et al. *J Pediatr Orthop.*, 40(1):e19-e24, 2020.

SARCGRAPH: AUTOMATED SEGMENTATION, TRACKING, AND ANALYSIS OF SARCOMERES IN HUMAN INDUCED PLURIPOTENT STEM CELL DERIVED CARDIOMYOCYTES

Bill Zhao (1), Emma Lejeune (1)

(1) Mechanical Engineering
Boston University
Boston, MA, USA

INTRODUCTION

Heart disease is the leading cause of death worldwide [1]. Because of this pressing societal challenge, cardiac drug discovery and cardiac tissue engineering are highly active areas of research. There is not only a pressing need to discover new treatments for cardiac disease, but also a pressing need to understand unintended cardiac-related adverse effects of drugs used for other purposes [2]. Recently, there has been a growing focus on human induced pluripotent stem cell derived cardiomyocytes (hiPSC-CMs). This technology presents a feasible approach to acquiring human cells and future patient-specific treatment plans [3]. However, hiPSC-CMs are both morphologically and functionally distinct from mature cardiac tissue (Fig. 1).

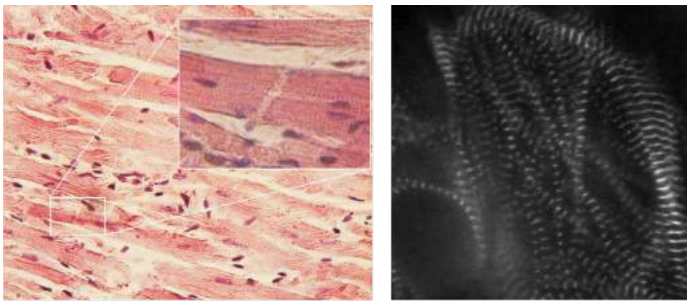

mature cardiac tissue hiPSC-CMs

Figure 1. Contrast between mature tissue and hiPSC-CMs.

The immature and non-linear structure of hiPSC-CMs makes it difficult to extract quantitative information from image-based assays. Recently, there has been significant work in this direction where z-disks in hiPSC-CMs are fluorescently labeled (Fig. 1) and advanced image processing and analysis software is used to segment and track sarcomeres and approximate their length with respect to time [3]. However, these state-of-the-art computational methods have room for improvement in both the efficacy of sarcomere segmentation and tracking under laboratory conditions, and strategies for comprehensive data analysis. Here we present our recent step forward in automated quantitative analysis of beating hiPSC-CMs.

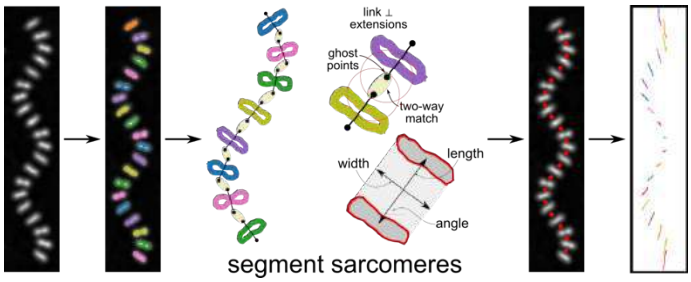

Figure 2: Z-disk and sarcomere segmentation and tracking.

METHODS

Here we introduce "Sarc-Graph," a computational framework to segment, track, and analyze sarcomeres in fluorescently tagged immature and non-linear hiPSC-CMs. Our framework includes functions to segment z-disks and sarcomeres, track z-disks and sarcomeres in movies of beating cells, and perform automated spatiotemporal analysis and data visualization. Here we briefly note a few key features of our framework. First, we created an algorithm to segment z-disks and sarcomeres (Fig. 2). Of note, our algorithm does not require any input parameter tuning, and is able to reliably capture non-linear sarcomeres in the presence of noise. Then, we track z-disks

and sarcomeres independently using the Python package trackpy which is based on the Crocker–Grier algorithm [4]. Finally, we use Gaussian process regression to interpolate data between lost movie frames when necessary and feasible [5]. The segmentation and tracking process takes only a few minutes to run on a laptop computer.

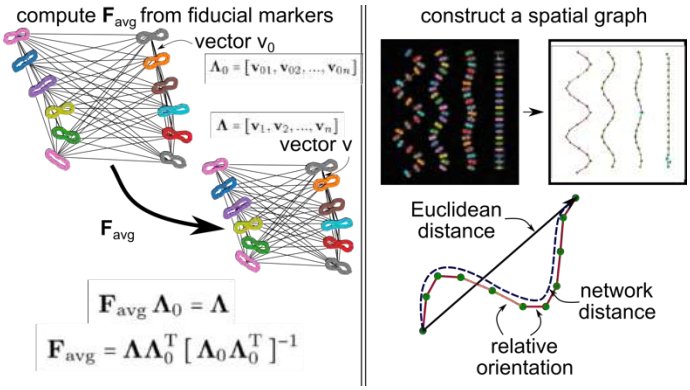

Figure 3: Analyzing average and local sarcomere behavior.

Next, we introduce two novel analysis approaches. First, we treat tracked and segmented components (i.e., sarcomeres and z-disks) as fiducial markers and use them to compute the approximate deformation gradient of the entire tracked population. This represents a new quantitative descriptor of hiPSC-CM function (Fig. 3). Second, we construct spatial graphs where z-disks correspond to nodes and sarcomeres correspond to edges. This makes measuring the network distance between each sarcomere straightforward and makes it possible to compute statistics that include information about the network structure (Fig. 3). We showcase and validate our approach with both synthetic and experimental movies of beating hiPSC-CMs. The Sarc-Graph software can be freely accessed through GitHub: https://github.com/elejeune11/Sarc-Graph. Example data and code to generate and analyze synthetic data with a known ground truth are also included on GitHub. We encourage anyone interested to try it out.

RESULTS

Here we show two examples of Sarc-Graph run on movies of beating hiPSC-CMs (Fig. 4, raw data first published with [3]). For Example E1, we are able to segment ≈500 sarcomeres per frame and successfully track 74 sarcomeres. The time series plot of normalized sarcomere length with respect to frame number shows three distinct contraction events during the movie. Though the individual sarcomeres are clearly not perfectly in sync, there is enough of a unifying pattern for these three peaks to emerge. These three distinct contraction events are also reflected in the average deformation plot. For Example E2, we are able to segment ≈500 sarcomeres per frame and successfully track 60 sarcomeres. The time series plots of absolute sarcomere length change and average deformation with respect to frame number also show three distinct peaks. We also show the spatial graph representation of each example and a plot of normalized cross-correlation between pairs of individual sarcomere time series curves with respect to network distance. We note briefly that additional information, including movies, more experimental data examples, and validation examples on synthetic data, are available both on GitHub and in our forthcoming manuscript.

DISCUSSION

Qualitatively, Examples E1 and E2 are different in that the sarcomeres in Example E1 appear vertically aligned throughout while the sarcomeres in Example E2 appear radially aligned around the edge of the cell and unaligned in the center. By segmenting the sarcomeres and analyzing their individual un-tracked properties, we can quantitatively confirm this morphological description. In addition, we can use our tracking results and our computed average deformation metric to go beyond morphology alone and quantify the function of the observed hiPSC-CMs. For example, we can show that the contraction-driven deformation in Example E1 is quite anisotropic while the contraction-driven deformation in Example E2 is nearly isotropic.

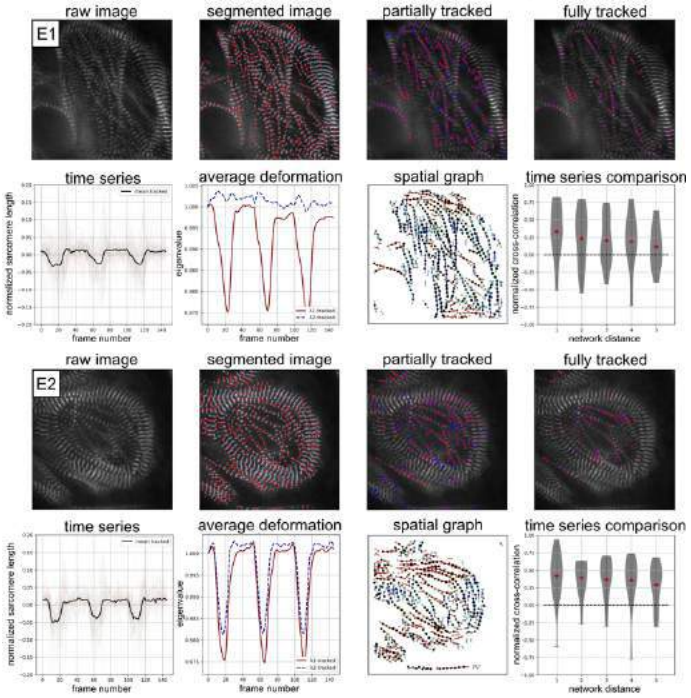

Figure 4: Two example results from running SarcGraph.

The objective of this work was to provide an open source computational framework to quantitatively analyze movies of beating hiPSC-CMs. With our framework, we are able to automatically segment and track a higher number of sarcomeres than other state of the art tools, and we introduce two important new approaches for the analysis of beating hiPSC-CM: a method for computing an average deformation gradient based metric, and a method for treating the hiPSC-CMs as spatial graphs. Looking forward, we see this work as an important tool for substantial future study of hiPSC-CM behavior with applications ranging from drug discovery to tissue engineering.

ACKNOWLEDGEMENTS

This work was supported by the CELL-MET Engineering Research Center NSF ECC-1647837, the Boston University Hariri Junior Faculty Fellowship, and the David R. Dalton Career Development Professorship.

REFERENCES

[1] Murphy, Sherry L., et al. "Mortality in the united states, 2017," 2018.
[2] de Korte, Tessa, et al. *Annu Rev Pharmacol Toxicol.* 60: 529-551, 2020.
[3] Toepfer, Christopher N., et al. *Circ Res.* 124.8: 1172-1183, 2019.
[4] Allan, et al. soft-matter/trackpy: Trackpy v0.4.2 (Version v0.4.2). Zenodo. http://doi.org/10.5281/zenodo.3492186
[5] Pedregosa et al., *JMLR* 12:2825-2830, 2011.

HEAD IMPACT SIMPLIFICATION USING EFFECTIVE KINEMATIC TRIPLETS TO PRESERVE BRAIN STRAIN

Kianoosh Ghazi (1), Shaoju Wu (1), Wei Zhao (1), Songbai Ji (1,2)

(1) Biomedical Engineering
Worcester Polytechnic Institute
Worcester, Massachusetts, USA

(2) Mechanical Engineering
Worcester Polytechnic Institute
Worcester, Massachusetts, USA

INTRODUCTION

Traumatic brain injury (TBI) is a major public health problem in the world (Peden *et al.*, 2004; CDC, 2015). It is caused by rapid brain deformation (strain) resulting from sudden head acceleration or deceleration events. Numerous studies attempt to translate impact kinematics to brain injury risk by defining kinematics based injury metrics (Hernandez *et al.*, 2015). Their effectiveness is usually assessed by how well they represent the peak maximum principal strain of the whole brain. However, an important limitation is that these metrics are scalar and do not consider the anatomical location where the peak strain occurs. For example, peak rotational acceleration/velocity do not account for the directionality or the temporal shape of the impact profile, which are important for spatially detailed brain strains.

To overcome this limitation, finite element (FE) models of the head provide valuable insight into the induced brain strain spatial distributions. However, unlike kinematic injury metrics, FE model simulations are slow and resource intensive. They are infeasible for real-time injury risk assessment (Zhao and Ji, 2019). Methods to circumvent the computational cost of FE models include pre-computation (Ji and Zhao, 2015) and more recently, deep learning (Wu *et al.*, 2019; Ghazi *et al.*, 2020b). The former simplifies an arbitrary head impact to an idealized acceleration impulse to interpolate strain, while the latter directly transforms an arbitrary head impact to detailed brain strains.

In this study, we explores a concept of "effective impact kinematics", which inversely determines a set of simple kinematics variables while preserving spatially detailed brain strains.

METHODS

We used an impact database (N=3069) drawn from contact sports, which were previously simulated using the Worcester Head Injury Model (WHIM) V1.0 (Wu *et al.*, 2019). For each simulated impact, a corresponding simplified impact was identified from the previous pre-computed brain response atlas (pcBRA) (Zhao *et al.*, 2017). The pcBRA consists of idealized, acceleration-only impacts about different rotational axes and velocity magnitudes, which allows real-time strain estimation *via* interpolation. For each arbitrary impact, simplified pcBRA impacts that had "similar" brain strains based on elementwise linear regression slope and correlation were first identified. Their rotational axes were weight-averaged to produce a rotational axis to represent that of the arbitrary impact (Fig. 1).

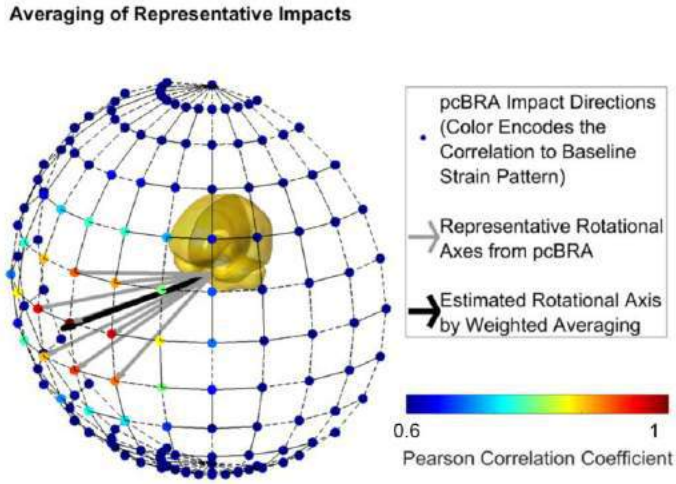

Figure 1: Wireframe and scatter plot illustrating the pcBRA data structure, where each dot represents an impact with a prescribed rotational axis. A cluster of representative impact of similar strain

patterns are identified and weight averaged to produce an effective rotational axis for the arbitrary real-world impact.

The peak rotational velocity magnitude was next determined that would produce a linear regression slope of 1.0 between its corresponding brain strains with respect to those from the arbitrary impact. This process generated three unique scalar values, which were referred to as the "effective kinematic triplets" to describe the impact: peak rotational velocity (v_{rot}), azimuth (θ) and elevation (α) angles.

In order to bypass this "analytical" process, a convolutional neural network (CNN) was further developed to transform an arbitrary head impact profile directly into the effective kinematics triplets. To verify the accuracy of the CNN, the estimated triplets were translated into brain strains *via* the pcBRA and were compared to those directly from the actual impact simulation. The whole process is illustrated in Fig. 2.

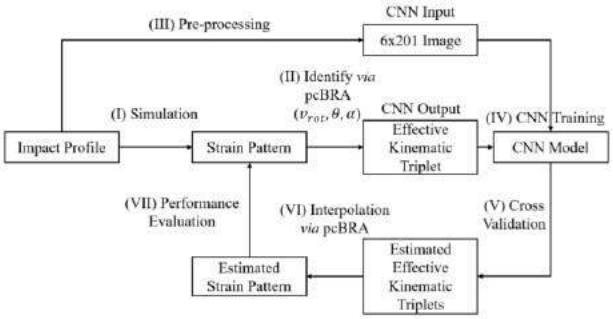

Figure 2: Flowchart of the study. Impact profile is first simulated. The resulting brain strains are used to determine a close representative in pcBRA, from which "effective kinematic triplets" are determined. Then, a CNN is trained to predict the triplets based on arbitrary impact profiles. Its prediction accuracy is evaluated by translating the triplets into brain strains using the pcBRA and to compare strains from the direct simulation.

RESULTS

For the set of arbitrary impacts, 66.1% of the impacts (N=2030) were able to be simplified into a triangulated rotational impulse based on pcBRA. From these, CNN was able to successfully predict effective impact triplets for 74.5% of the impacts (Fig. 3). An example impact is further illustrated in Fig. 4.

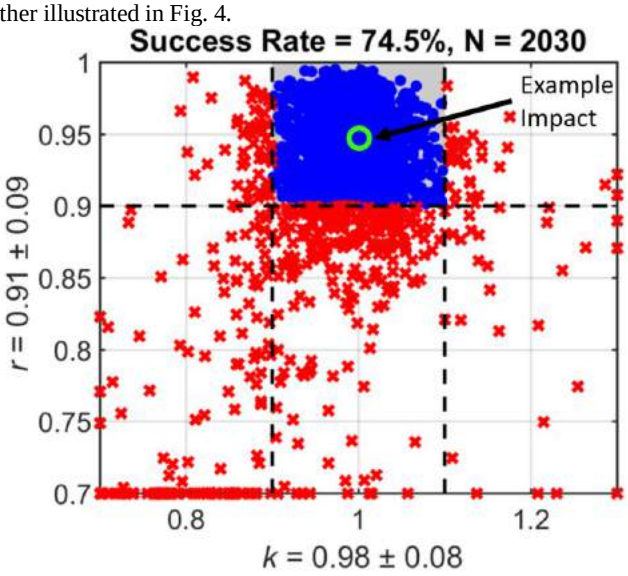

Figure 3: Pearson correlation coefficient (*r*) vs. regression slope (*k*)

of elementwise comparison between brain strains based on CNN-predicted effective kinematic triplets and the baseline simulation.

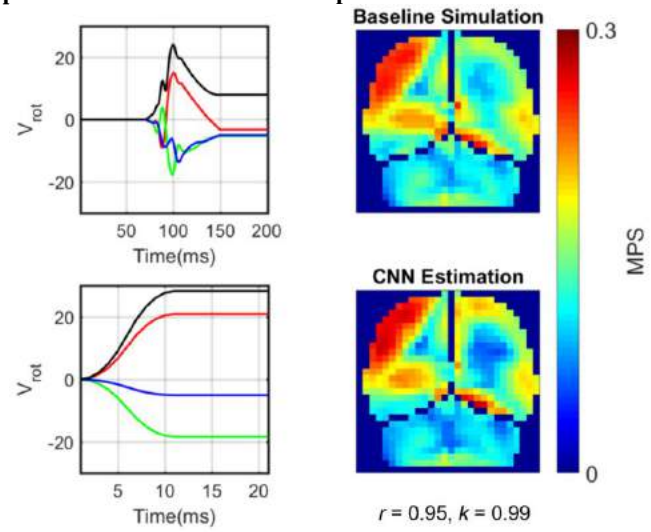

Figure 4: An example of a simplified impact and the corresponding strain distribution.

DISCUSSION

Impact kinematics-based injury metrics are ubiquitously used. In this study, we explore the concept of "effective kinematic triplets" to simplify an arbitrary real-world head impact into an idealized head rotational impulse to preserve spatially detailed brain strains. Essentially, the idea is to inversely map brain strains based on the pcBRA. The triplets consist of peak rotational velocity magnitude and the azimuth and elevation angles that characterize the impact severity and rotation directionality, respectively. The impact simplification may facilitate intuitive understanding and comparison of real-world impacts.

The pcBRA is restricted to acceleration-only impacts. This limits the range of brain strains that can be used to approximate real-world impacts. About two thirds of impacts from the dataset were successfully represented. Using a CNN, effective kinematic triplets for ~75% of the impacts were successfully predicted (Fig. 3). It is worth exploration whether inclusion of more head rotation "modes" could improve the performance, e.g., to include head impacts with both acceleration and deceleration in the pcBRA to expand variations in brain strains.

To conclude, we show that it is possible to use a simplified head impact to represent a complicated, real-world impact while preserving spatially detailed brain strains. The "effective kinematic triplets" repurpose existing kinematic variables, which may facilitate better comparisons among arbitrary real-world head impacts in the future.

ACKNOWLEDGEMENTS

Funding is provided by the NIH grant R01 NS092853 and the Ford University Research Program.

REFERENCES

[1] CDC, Report to Congress on Traumatic Brain Injury in the United States: Epidemiology and Rehabilitation, 2015. [2] Ghazi, K. *et al. Journal of Neurotrauma*, 13, p. in press., (2020b). [3] Hernandez, F et al., Ann. Biomed. Eng. 43, 1918–1934, 2015. [4] Ji, S and Zhao, W, Ann. Biomed. Eng. 43, 1877–1895, 2015. [5] Peden, M et al., World report on road traffic injury prevention, 2004. [6] Wu, S et al., Sci. Rep. 9, 1–11, 2019. [7] Zhao, W et al., Ann. Biomed. Eng. 47, 475–486, 2019. [8] Zhao, W. and Ji, S., *Ann. Biomed. Eng.*. Springer US, 47(2), pp. 475–486, (2019).

EVOLUTION OF THE HEMODYNAMIC PROPERTIES AND ARTERIAL WALL REMODELING IN PULMONARY ARTERIAL HYPERTENSION

H. Mu (1), D. Valdez-Jasso (1)

(1) Bioengineering
University of California, San Diego
La Jolla, CA, United States

INTRODUCTION

Pulmonary Arterial Hypertension (PAH) is a progressive vasculopathy characterized by sustained elevation of mean pulmonary arterial pressure. As the disease progresses, the stiffening and thickening of the large pulmonary arteries increases pulse wave velocity and decreases vascular compliance, further exacerbating the pressure overload and adversely impairing perfusion and hemodynamics. [1,2] To understand how the remodeling of the arterial wall alters pulmonary hemodynamics during disease progression, a one-dimensional fluid dynamic model is used to examine *in-vivo* pressure and flow measurements from the main pulmonary artery (MPA) and *ex-vivo* mechanical properties of the left and right pulmonary arteries (L/RPA) measured at different stages of PAH in rats. Herein, we present our work on establishing a baseline of the hemodynamic properties of the pulmonary vasculature in early and advanced PAH stages.

METHODS

Male Sprague-Dawley rats weighing about 200 grams (Charles River Lab) were injected with monocrotaline (MCT) to induce PAH. Timepoints studied were one and four weeks post-disease induction to mimic the early and advanced stages of the disease. Aged-matched rats injected with saline were added as the control group. Rats underwent an open-chest surgery to simultaneously measure pulmonary arterial flow and pressure with a 1.6F dual-pressure sensor catheter and a flow probe (Transonic Science), respectively (Figure 1). The data were collected and pre-processed in LabChart Software (ADInstruments Inc.). After hemodynamic measurements, pulmonary arteries from LPA and RPA were harvested, cannulated, and mounted into the BioDynamic chamber (ElectroForce Systems Group) to perform tubular biaxial mechanical testing. The circumferential forces and displacements were used to calculate the stress and strain, respectively, and thus the elastic modulus of the LPA and RPA at each stage of the disease. [3]

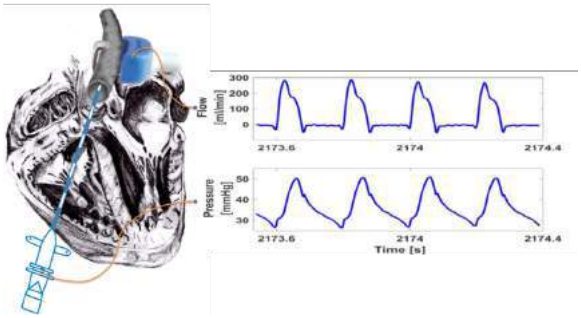

Figure 1: *In-vivo* blood pressure and flow measurements taken from male Sprague-Dawley rats. [5]

Our one-dimensional fluid model spans the first three branches coming out from the right ventricle: MPA, LPA, and RPA. The arteries are assumed to be the tapering right cylinders with no-slip and impermeable walls. We assume blood to be incompressible and Newtonian, and blood flow is described as axisymmetric, inviscid, and laminar. The partial differential equations relating flow Q, pressure P, and cross-sectional area A as function of time t and space x are the Euler equations with conservation of mass (Equation 1) and momentum (Equation 2). A linear thin-wall equation (Equation 3) describes the pressure-area relation of the vessel wall.

$$\frac{\partial A(x,t)}{\partial t} + \frac{\partial Q(x,t)}{\partial x} = 0 \quad (1)$$

$$\frac{\partial Q(x,t)}{\partial t} + \frac{\partial}{\partial x}\left(\frac{Q(x,t)^2}{A(x,t)}\right) + \frac{A(x,t)}{\rho}\frac{\partial P(x,t)}{\partial x} + \frac{2\pi\upsilon}{\delta} r(x,t)\frac{Q(x,t)}{A(x,t)} = 0 \quad (2)$$

$$P = P_0 - \frac{4Eh}{3r_0}\left(1 - \sqrt{\frac{A_0}{A}}\right) \quad (3)$$

In these equations, ν kinematic viscosity, δ boundary layer thickness, r outer radius of the vessel; E circumferential elastic modulus, h the thickness of vessel wall, and A_0 and r_0 are the *ex-vivo* area and radius of the individual arteries.

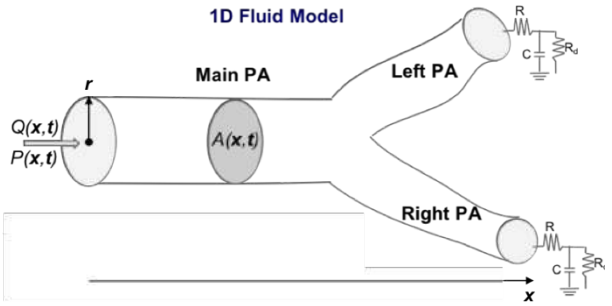

Figure 2: One-dimensional fluid model of the large pulmonary arteries initiated with flow *Q* and pressure *P* measured invasively that simulates flow and pressure propagation along the vasculature.

The model is initialized with the *in-vivo* flow and pressure data measured at the inlet. At the bifurcation, flow exiting MPA equals the sum of flow entering LPA and RPA, and pressure is the same for the three arteries. At the outlet boundary conditions of LPA and RPA, three-element Windkessel models are applied to account for the effect of all downstream vessels (Figure 2), where R is the proximal resistance, R_d is the distal resistance, and C is the compliance. [4,5]. Windkessel model parameters are determined from *in-vivo* flow and pressure measurements offline. The elastic moduli of LPA and RPA are obtained by fitting the stress-strain data from the tubular biaxial testing to a quasi-linear viscoelasticity model of the arterial wall. [3] The MPA elastic modulus is assumed to be the average of LPA and RPA values and is tuned to fit the measured *in-vivo* pressure.

RESULTS

Simulations using data from MCT animals reproduce the shape of measured *in-vivo* pressure, including the ratio of systole and diastole duration, the slope of diastolic pressure decay, and timing of peak pressure (Figure 3). Wave propagation is shown as the delay of systolic peak pressure along the arteries. The difference between the flow and pressure waveforms show the presence of wave reflection, indicating that our model mimics features of the blood waveforms.

The tuned MPA elastic modulus increased from 0.52×10^6 g/(cm•s^2) in the control, to 1.7×10^6 g/(cm•s^2) in the early PAH, and 3.4×10^6 g/(cm•s^2) in the advanced PAH. By inspecting the first cardiac cycle, the peak pressure is about 23 mmHg in the control, 47 mmHg in the early PAH, and 57 mmHg in the advanced PAH, while the *in-vivo* measurements have the peak pressure in the same cycle as about 19 mmHg in the control, 40 mmHg in the early PAH, and 53 mmHg in the advanced PAH. The peak pressure of the simulation results matches with the measurement in the control and advanced PAH. The early and advanced PAH groups have pressure elevation in both diastolic and systolic phases. The PAH groups also have an increased pulse pressure. The peak cross-sectional area of the first cardiac cycle is about 9.5 cm^2 in the control, 11 cm^2 in the early PAH, and 9.5 cm^2 in the advanced PAH.

DISCUSSION

The reflected wave superimposes with the forward-traveling wave, and the wave speed determines the timing of this superposition, given the wave is reflected from the same location. [7] As in shown in our simulations, there was an increase in wave speed due to arterial wall stiffening from the control to the advanced PAH, so the reflected wave returned early at systole, increasing the pulse pressure as we observed in the simulation.

The peak cross-sectional area of MPA increases from the control to the early PAH, and then the value returns to the original in the advanced PAH. This finding does not match with the persistent increase in peak pressure, but it can be explained by the almost 7 folds increase in the MPA stiffness. The different trends of area and pressure changes imply the presence of structural remodeling (stiffening of the arterial wall) in the proximal pulmonary arteries. According to [6], the stiffening and thickening of the arteries reduce the stress and strain experienced by the vessels, thus returning the system to homeostasis.

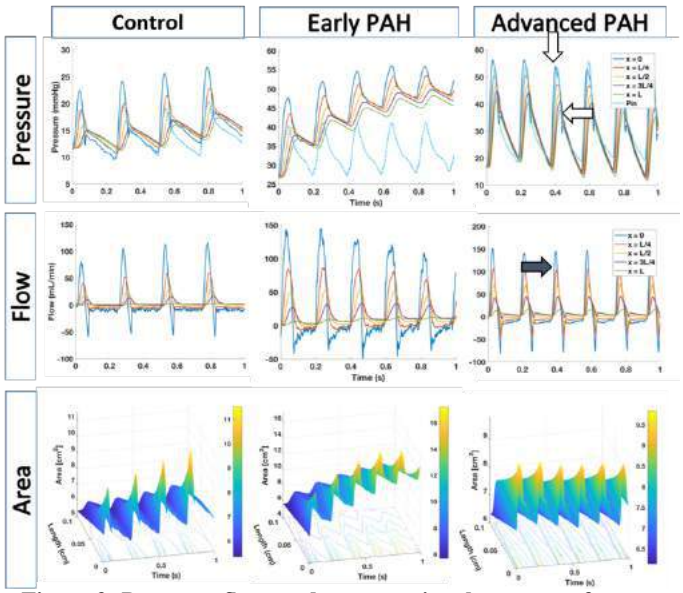

Figure 3: Pressure, flow, and cross-sectional area waveforms simulations across the MPA, where P_{in} is the measured *in-vivo* pressure. The simulated pressure is generally in the same range of measured pressure in the control and the advanced PAH groups. White arrows indicate the delay of peak pressure, and the black arrow indicates the difference in flow and pressure waveforms.

The major advantage of our framework shown here is the animal-specific *in-vivo* flow data along with the mechanical properties of the downstream vessels LPA and RPA. We can run these simulations to test the hypothesis that the stiffening of proximal pulmonary arteries is an important determinant in PAH. Current limitations include the high computational cost due to small step sizes and lack of MPA elastic modulus measurements due to the geometry of the MPA that is short and curved for tubular biaxial testing.

ACKNOWLEDGEMENTS

This work was funded by the American Heart Association Scientist Development Grant 16SDG29670010. The authors would also like to acknowledge the discussions with Yasser Aboelkassem.

REFERENCES

[1] Zambrano BA, et al. *J Biomech*, 2018.
[2] Lai, YC et al. *Circ Res*, 1:115, 2014.
[3] Pursell, ER et al. *J Biomech Eng*, 11:138, 2016.
[4] Olufsen, MS. *IMFUFA* 345:98, 1998.
[5] Gerringer, JW et al. *Physiol Rep,* 3:6, 2018.
[6] Tsamis, A et al. *J Biomech Eng*.131:101004, 2009.
[7] Westerhof, BE et al. *Hypertension*. 48:595-601, 2006.

SPECIMEN-SPECIFIC FIBER-BASED MODELING AND SIMULATION OF SCLERA COLLAGEN FIBER MICROSTRUCTURE AND BIOMECHANICS

Fengting Ji (1, 2), Manik Bansal (2), Bingrui Wang (3), Yi Hua (2), Felix Matuschke (4), Markus Axer (4), Ian A. Sigal (1,2)

(1) Department of Bioengineering
University of Pittsburgh
Pittsburgh, PA, USA

(2) Department of Ophthalmology
University of Pittsburgh
Pittsburgh, PA, USA

(3) Department of Mechanical Engineering
Southwest Jiaotong University
Chengdu, Sichuan, China

(4) Institute of Neuroscience and Medicine (INM-1)
Forschungszentrum J□lich GmbH
52425, J□lich, Germany

INTRODUCTION

Modeling and simulation are widely used to study scleral biomechanics and the effectiveness of the models depends on the accuracy of the assumed microstructure [1, 2]. However, most models use continuum approaches which do not incorporate some potentially critical characteristics of the fibers, such as fiber-fiber interactions, in-depth fiber distributions and fiber interweaving [3]. Our goal was to build a specimen-specific fiber-based model of sclera and use it to determine the fiber mechanical properties.

METHODS

General strategy: A model was created and optimized to match fiber orientation data obtained using polarized light microscopy (PLM). Fiber mechanical properties were estimated through inverse modeling by matching model's prediction to experimental measurements (stress-strain curves) obtained from biaxial tensile tests of human sclera [4].

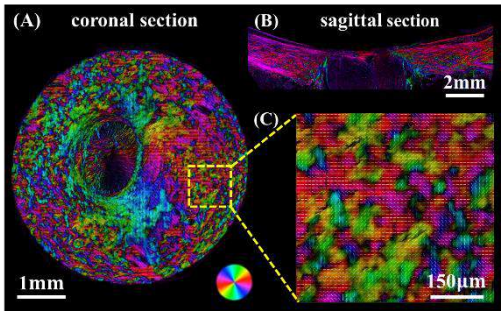

Figure 1. (A) Coronal and (B) sagittal ONH sections were imaged using PLM. The colors indicate the local fiber orientation in the section plane, whereas pixel intensity is proportional to collagen fiber density. (C) Example of selected region of a coronal section.

Image acquisition: Two optic nerve heads (ONH) were sectioned, one coronally and the other one sagittally, both at 30 µm thickness. The sections were imaged using PLM to obtain local collagen fiber density and orientations (Figure 1) [5].

Model construction: Images of 17 consecutive coronal sections were registered to form a volume. A rectangular region (721x691 µm) in the nasal sector was selected to build the fiber model.

To initialize the fiber structure, orientations from the images were sampled in a grid, with grid cell edge length (24 pixels) equal to the average width of small fiber bundles in images (Figure 2). In each grid cell, a straight fiber extending the full span of the volume was traced in the direction of the local PLM orientation. Fibers were thus traced in all images. Fibers were defined in linear truss elements (T3D2) and their locations characterized by Cartesian coordinates X, Y, Z of nodes p_i. Initially, all fibers from an image were in the same plane. To match fiber in-depth positions with PLM data, we first meshed fibers into small elements which were subjected to merge and split in a further step. Then we adjusted Z coordinates of fiber elements based on their visibilities in PLM images. A fiber segment with an orientation that was in good agreement with the PLM orientations (within 45deg) in the images was kept at that level. A fiber segment that disagreed with the local orientation (more than 45deg), was "moved" in Z. This process implies the assumption that fibers are continuous. Fibers were created and processed for each image in the stack.

To resolve fiber overlaps, we used an iterative algorithm that refines and displaces them [6]. Briefly, if the smallest distance between two elements was less than fiber diameter, a collision was detected. All the elements were then moved apart iteratively to resolve collisions. Fiber elements were re-meshed and smoothed to maintain pre-defined average length and fiber radius of curvature.

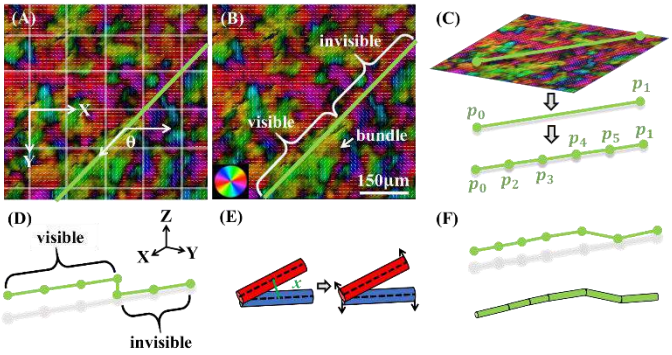

Figure 2. Workflow of creating and processing fibers. (A) grid (shown enlarged) was defined and used to sample orientation θ at a grid cell center, in turn used to trace a straight fiber. (B) In this case, the fiber follows the direction of a yellow-green bundle. Fibers are "visible" or "invisible" if they are in agreement, or not (within 45deg), with the local orientations. (C) (top) Isometric view of the image and the fiber. (middle) The fiber initially had one element and 2 nodes p_1 and p_2 and (bottom) split into five elements and six nodes. (D) The visible elements (p_0-p_2, p_2-p_3, p_3-p_4) were assigned a higher Z coordinate value than invisible elements (p_4-p_5, p_5-p_1), effectively "pushing" the invisible elements to another section. (E) Elements were moved apart if the shortest distance x between them was smaller than fiber diameter, indicating a collision. During the process, elements were combined or split to maintain a pre-defined average length and fiber curvature was adjusted for smoothing. (F) (top) the fiber after processing (bottom) fiber 3D rendering. Fiber diameter was assumed to be 2.98 μm.

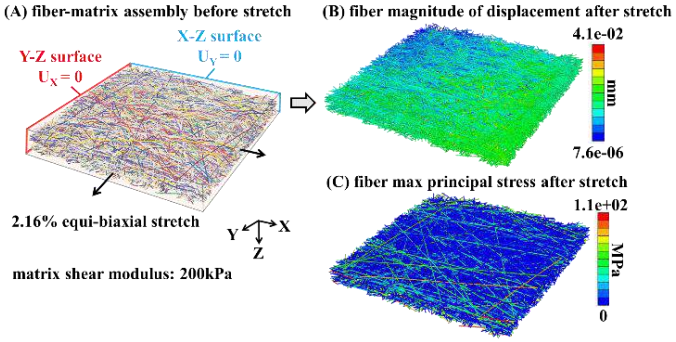

Figure 3. (A) Model as reconstructed, before test. (B, C) After stretch, the fiber mechanics were highly variable.

Model validation and optimization: In-depth fiber orientations of the model were adjusted in an inverse process to match the orientation distribution and anisotropy from the PLM data of the sagittal sections. Wilcoxon rank sum tests were used to compare distributions.

Inverse fitting: Fibers were embedded in a matrix and were assigned a hyperelastic Mooney-Rivlin material property (Figure 3) [7]. The matrix was meshed with linear eight-node, hybrid hexahedral elements (C3D8H) and modeled as a neo-Hookean material. Fiber interactions were approximated by preventing fiber interpenetrations and were defined as general contact with no friction.

Extraction of fiber material properties: To be consistent with the experiment [4], we assigned an equi-biaxial stretch of 2.16% as displacement boundary conditions to the fiber-matrix assembly. The model stress-strain behaviors were calculated, where the stress was computed as the total force along that direction divided by the normal cross-sectional area. The two material constants (C_{10} and C_{01}) of the fiber model were identified which yielded the closest match to the experimental stress-strain curves.

RESULTS

There were no significant differences in fiber orientation distributions between the model and the PLM images, in both coronal ($p>0.7$) and sagittal ($p>0.6$) directions (Figure 4).

The fiber model material constants were C_{10}=5746.9MPa and C_{01}=-5002.6MPa. The resulting model's stress-strain curves fit closely the experimental data in X and Y directions simultaneously (Figure 5).

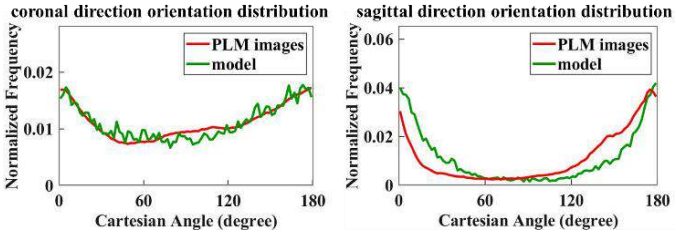

Figure 4. There was excellent agreement between the fiber orientation distributions in the reconstructed model and PLM data in both (left) coronal and (right) sagittal directions.

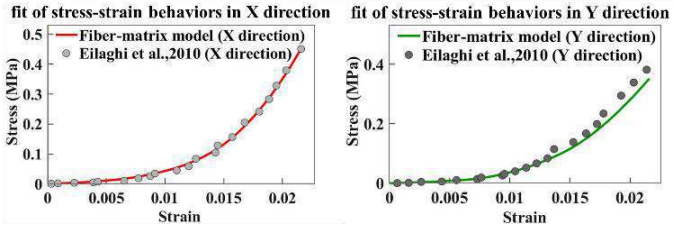

Figure 5. An excellent fit of stress-strain response was achieved between the model and the experiment in both (left) X and (right) Y directions (R^2=0.9978 and R^2=0.9585 for X and Y, respectively).

DISCUSSION

We developed a fiber-based scleral model that explicitly simulated collagen fiber architecture. The fiber orientations of the model matched both in-plane and in-depth high-resolution PLM data. The model accounts for fiber-fiber interactions and long-distance load transfer, previously ignored. The model mechanical behavior fits very well with experimental data. The predicted fiber stiffness is higher than in previous studies [8]. This difference may be due, in part, to the relatively low fiber volume fraction of this model compared with previous ones. The PLM data were from both pig and sheep ONHs, which can be improved in further study. This modeling approach provides unprecedented details of fiber-level tissue behaviors, such as microscale variations in deformations and stresses, which are crucial to understanding tissue remodeling and cell activation.

ACKNOWLEDGEMENTS

Supported in part by National Institutes of Health R01-EY023966, R01-EY028662, P30-EY008098 and T32-EY017271 (Bethesda, MD), the Eye and Ear Foundation (Pittsburgh, PA), and Research to prevent blindness.

REFERENCES

[1] Coudrillier B et al., *Biomech. Model Mechano*.,12(5):941-963,2013.
[2] Zhou, D et al, *J. R. Soc. Interf.*, 16 (154), Article 20180685, 2019.
[3] Wang, B et al., *Acta Biomater.*, 113: 429-437, 2020.
[4] Eilaghi, A et al., *J Biomech*, 43(9): 1696-1701, 2010.
[5] Gogola, A et al., *IOVS*, 59(12): 4763-4774, 2018.
[6] Matuschke, F, *Fiber Architecture Simulation Toolbox for PLI*, 2020.
[7] Holzapfel, G A, *Handb. Mater. Behav. Models*, 3:1049-1063, 2001.
[8] Grytz, R et al., *IOVS*, 54.15: 79-79, 2013.

SB³C2021
Summer Biomechanics, Bioengineering and Biotransport Conference
June 14-18, Virtual

MEASURING IN SITU LUMBAR FACET CAPSULAR LIGAMENT STRAINS DUE TO JOINT PRESSURE AND RESIDUAL STRESS

Elizabeth Gacek (1), Arin M. Ellingson, PhD (2), Victor H. Barocas, PhD (1)

(1) Department of Biomedical Engineering
University of Minnesota – Twin Cities
Minneapolis, MN., USA

(2) Department of Rehabilitation Medicine
University of Minnesota – Twins Cities
Minneapolis, MN., USA

INTRODUCTION

The lumbar facet capsular ligament (FCL) plays a potential role in the development of low-back pain (LBP) due to its role of sending proprioceptive and nociceptive signals to the brain[1-2]. LBP affects 70-85% percent of Americans at some point in their lifetime, with almost a quarter of cases resulting in chronic LBP without a clinically identifiable trigger[3-4]. The FCL fully encases the facet joint space between two adjacent articulating vertebrae, with ligament insertion into both the superior and inferior facet joint of the vertebra. The FCL's structural matrix consists of collagen and elastin fibers. The collagen fibers are highly aligned and primarily oriented bone-to-bone, resisting loads parallel to their orientation and preventing painful motions from occurring. The FCL also encapsulates synovial fluid within the joint space that lubricates the articulating joint surfaces as well as pressurizes the FCL *in vivo*. Given the complicated anatomical structure of this joint, mechanical testing of the FCL is limited to planar off-bone samples. Excised, off-bone FCL samples have been well characterized with many previous studies capturing its structural-mechanical relationship via uniaxial[1], biaxial[5] and shear[6] testing.

Little is known, however, about the state of the FCL and its constituent collagen and elastin fibers *in situ*. Two factors to consider are (1) the ligament's residual stress due to its attachment to the vertebrae, and (2) the pressurization of the joint space via the encapsuled synovial fluid. These constraints can cause the FCL to be under strain *in vivo*, even when the joint is unloaded, and cutting the FCL off the bone for planar mechanical testing releases the ligament from these constraints, altering the rest state prior to experimentation. Therefore, both residual strain and inflation of the ligament due to pressurization must be considered when relating the mechanics of planar off bone FCL samples back to its *in situ* state. In this study, we conducted inflation and residual strain tests to capture the *in situ* strain state of the FCL.

METHODS

Sample Preparation

One donor lumbar spine (F, age 41), without a history of spinal pathologies, was obtained through the Anatomy Bequest Program at the University of Minnesota Twin-Cities. The spine was cleared of superficial tissue to expose the posterior region of a left L3L4 FCL. The FCL sample was speckled with dried Verhoeff-Van Geison stain that had been crushed into a fine powder prior to speckling.

Inflation Testing

The cadaveric FCL was injected with roughly 0.55 mL of 1% PBS at a rate of 1 mL/min into the joint space between adjacent facet pairs. The pressure within the joint space was measured using a pressure transducer (Harvard Apparatus), and a baseline pressure drop due to flow through the needle was established prior to insertion into the joint space. At the conclusion of the inflation test, the PBS was withdrawn from the joint space to return the FCL to its original, undeformed state prior to residual strain testing.

Residual Strain Testing

The FCL was released of its residual stress by cutting a rectangular sample from the center of the ligament. Careful consideration was taken to fully release the underside (anterior) of the ligament off the bone.

3D Strain Tracking and Analysis

Over the course of the inflation and residual strain tests, FCL motion was tracked in 3D using a two-camera stereo system. Surface ligament deformations were analyzed using MultiDIC[7], where a region of interest (ROI) was selected to include the released area and the area immediately surrounding it. The residual and elastic deformation, or deformation due solely to inflation of the joint space, were obtained for each discretized element on the tracked ROI. The total deformation gradient tensor was calculated using equation 1:

$$\boldsymbol{F} = \boldsymbol{F}_{\boldsymbol{I}} * \boldsymbol{F}_{\boldsymbol{R}}^{-\boldsymbol{1}} \quad (1)$$

where $\boldsymbol{F}$ is total deformation, $\boldsymbol{F_R}$ is the deformation due to releasing the residual stresses, and $\boldsymbol{F_I}$ is the inflation-induced deformation (Fig 1).

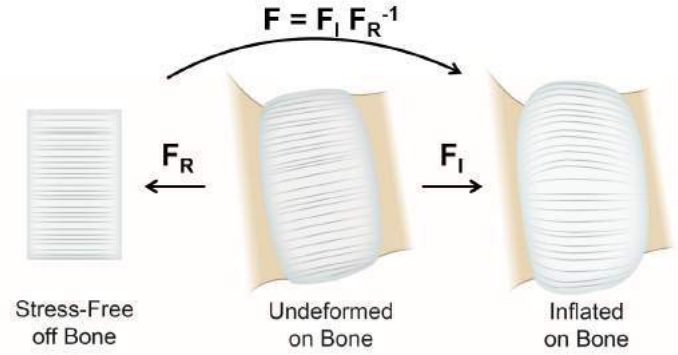

Figure 1: Posterior view and deformation of the FCL in a stress-free (F_R) and inflated state (F_I). The total deformation (F) of the ligament is considered to be the combined deformation of the residual and inflated states.

The maximum first principal strain was calculated as the max eigenvalue of the Green-Lagrangian strain tensor, as calculated from **F** using equation 2:

$$\boldsymbol{E} = \frac{1}{2}(\mathbf{F}^{\boldsymbol{T}}\mathbf{F} - \boldsymbol{I}) \quad (2)$$

where $\boldsymbol{E}$ is the Green-Lagrangian strain tensor, and $\boldsymbol{I}$ is the identity.

RESULTS

A relationship between joint pressure and volume of injected PBS is shown in Fig. 2a. Initially, the pressure increases linearly before a non-linear pressure response is observed, which may suggest that the joint space was initially filling with PBS before the ligament was loaded and contributing to the observed phenomenon. The residual strain is shown in Fig 2b with an average max 1st principal strain of 13.3% across 287 ROI elements.

The inflation strain, as measured from inflation testing, and the total max 1st principal strain was calculated for three points along the pressure-volume curve (Fig. 2c-h). Within the 287 ROI elements tracked during the residual strain test, the average of the inflation max 1st principal strain was 4.1%, 7.7%, and 10.7% for the strain distribution shown in Fig. 2 c, e, and h, respectively. Subsequently, the average of the calculated total max 1st principal strain was 14.7%, 16.1%, and 23.2%, respectively (Fig. 2 d,f,h).

DISCUSSION

In this work, we paired an inflation test with a residual strain test to decouple ligament strains from either inherent residual stresses and inflation stress due to pressurization of the joint space. We obtained ligament strain distributions when the ligament was inflated and then released from its residual strain, which allowed us to calculate the contribution of each to the total observed strain. To our knowledge, this is the first mechanical characterization of the *in situ* state of the FCL.

An accurate characterization of the local mechanics of the FCL is crucial to understanding the influence of the FCL on spinal motions, and the deformations that may result in nerve strain and pain signaling. Overlapping regions of similar tensile or compressive strains in the inflation and residual strain distribution compound to give localized regions of high total strain, indicating that these may be regions capable of triggering a pain signaling cascade (Fig. 2). An average max residual strain of 13.3% would significantly lengthen collagen fibers that become crimped in off bone FCL samples. Due to experimental limitations, there is no known record of pressure within the *in vivo* lumbar FCL joint space, but inner capsular pressure is essential for healthy fluid movement in joints[8] so we can assume the pressure is non-

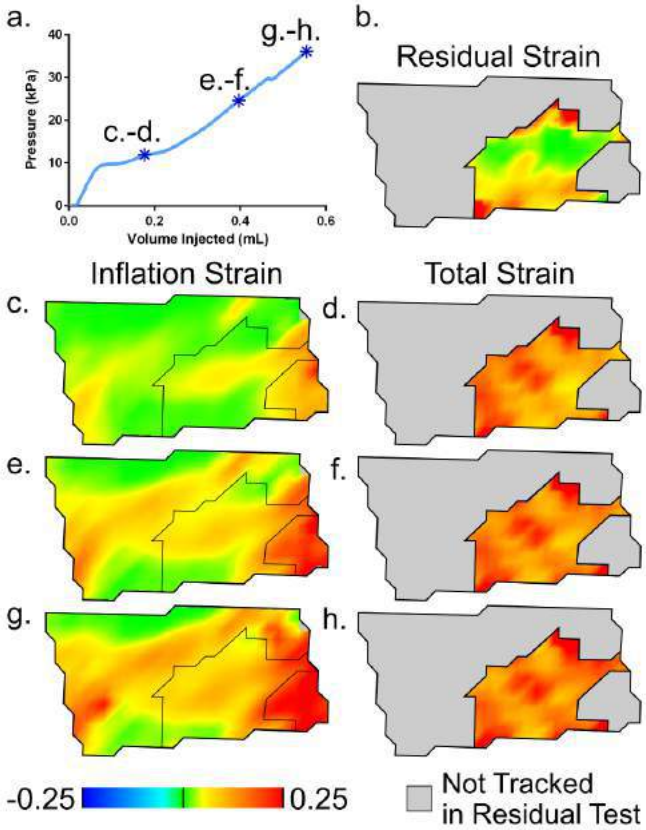

Figure 2: (a.) FCL pressure-volume relationship with three analysis points marked (*). (b.) The max 1st principal strain of the residual as observed when a portion of the ligament was removed from the bone. The max 1st principal strain observed during inflation with low (c.), medium (e.), and (g.) high volume of fluid injection and the corresponding calculated total max 1st principal strain (d.), (f.), and (h.), respectively. Outline in c, e, and g corresponds to tracked area in d, f, and g. A portion of the ROI mesh elements (gray) were not tracked due to either their location outside the portion of the ligament cut during the residual strain test or due to high correlation coefficient between the tracked stereo images.

negligible. Therefore, we can use these experimental results to establish a baseline strain distribution for undeformed, pressurized FCLs and, using residual strains, can relate the mechanics of planar FCL samples back to their on-bone state, furthering our understanding of *in vivo* FCL mechanics.

ACKNOWLEDGEMENTS

Funding provided by NIH/NCCIH U01-AT010326, NIH/NICHD K12HD073945, and NIH/NIAMS T32 AR050938. The authors thank the Anatomy Bequest Program at the University of Minnesota and Elizabeth Shih for their assistance.

REFERENCES

[1] Little, JS et al., J. Biomech. Eng., 127:15, 2005. [2] Yamashita, T et al., Spine, 21:538-43, 1996. [3] Andersson, GBJ, The Lancet, 354:581-585,1999. [4] Belague, F et al.,The Lancet,379:482-91, 2012. [5]Claeson, AA, et al.,J. Mech. Behav. Biomed. Mater.,65:127-136, 2017. [6] Bermel, EA, et al., J. Biomech.,105, 2020. [7] Solav, D. et al., IEEE Access 6: 30520–30535, 2018. [8] Levick, JR, et al. Ann Rheum Dis, 54:417-23,1995.

AORTIC VALVE DYNAMICS COUPLED WITH GROWTH AND REMODELING DUE TO AGING AND CALCIFICATION

Mohammadreza Soltany Sadrabadi (1), Mona Eskandari (2), Amirhossein Arzani (1)

(1) Department of Mechanical Engineering
Northern Arizona University
Flagstaff, AZ, USA

(2) Department of Mechanical Engineering
Department of Bioengineering
BREATHE Center, School of Medicine
University of California, Riverside
Riverside, CA, USA

INTRODUCTION

Aortic stenosis (AS) is a prevalent form of aortic valve disease. In AS, the leaflets become thickened, stiffened, and calcified. In general, calcification and aging contribute to AS. Calcific aortic valve disease (CAVD) is a form of AS where the calcium deposits produced in the valve leaflets accelerate the natural stiffening and thickening process due to aging, and ultimately the valve dynamics is impaired [1]. CAVD is a multistage process. The first phase of CAVD shares similarities with atherosclerosis. However, the major distinction between atherosclerosis and CAVD is in the second phase; in this propagation phase, valvular interstitial cells (VICs) differentiate to a pro-calcific phenotype, and the resulting apoptotic bodies create nucleation sites for calcium deposition. The outcome is a stiffer and thicker valve structure that compromises valve functionality. Calcification is more likely to occur on the aortic side of the leaflets [2], which has been linked to the complex hemodynamic environment in this region.

Conversely, aging has an inevitable effect on biological systems. Aortic valve leaflets are known to become thicker and stiffer due to aging [3]. Consequently, aging affects the dynamic of the valve. Given the large time-scale for CAVD progression, aging also needs to be considered in CAVD growth models.

Modeling CAVD is a multiscale problem. Although the stiffening and thickening of leaflets due to aging and calcification take place over the time-scale of months/years, the valve opening and closing occurs over one cardiac cycle. This demonstrates the temporally multiscale nature of CAVD. In this study, we have developed a multiscale model that can couple the transient dynamics of aortic valve with long-term growth and remodeling (G&R) due to calcification and aging. Specifically, we propose a multiscale continuum growth framework and couple transient aortic valve dynamics with *global* tissue thickness growth and stiffening due to aging, and *local* tissue thickness growth and stiffening due to calcification. Subsequently, we study the transient dynamics of the aortic valve during these processes using measures such as the geometric orifice area (GOA), which are of clinical interest.

METHODS

An idealized 3D aortic valve was the assumed geometry. The model included the valve leaflet, the aortic root, the sinus, and the ascending aorta. To simplify the model, the three leaflets were considered to have the same size, and symmetry was used where only half of one leaflet was considered to reduce the computational cost required in performing several cycles of nonlinear transient structural mechanics simulations. The baseline valve dimensions were collected for a healthy 35 years old subject [4]. The model was discretized into 360K tetrahedral elements with higher resolution in the leaflet. The model was meshed in SimVascular. The aortic wall was assumed as a linear hyperelastic material with a single term Mooney-Rivlin constitutive equation (Eq. 1a). The leaflet was considered as anisotropic hyperelastic material with the strain energy defined in Eq. 1b [5].

$$W_{wall} = c_{wall}(I_1 - 3), \tag{1a}$$

$$W_{valve} = c_1\left(e^{c_2(I_1-3)} - 1\right) + c_3\left(e^{c_4\left(\sqrt{I_4}-1\right)^2} - 1\right), \tag{1b}$$

where I_1 is the first invariant of the right Cauchy-Green strain tensor and I_4 models the anisotropic behavior due to collagen fibers in the circumferential direction. A density of 1100 kg/m^3 was used for all tissues. A transient nonlinear structural mechanics solver was implemented in FEniCS using quadratic elements. Namely, Cauchy's equation of motion was formulated in the reference configuration for a nearly incompressible material

$$\rho_0 \frac{\partial^2 U}{\partial t^2} - \nabla.(\mathrm{F_e} S) = \rho_0 b_0, \quad \text{where } F_e = F_t F_g^{-1}. \tag{2}$$

In Eq. 2, F_t is the total deformation gradient, F_e is the elastic part, and F_g is the growth part of the deformation gradient [6]. Boundary conditions (BCs) include fixing the vessel wall in the circumferential and axial directions at the ends (zero Dirichlet BC) and pulsatile pressure waveforms applied at the vessel wall and leaflet (Neumann BC) driving the tissue dynamics. An algorithm was developed to couple the dynamics of the valve in a cardiac cycle with the local/global growth and stiffening effects due to calcification/aging. Our proposed algorithm

has six components and simulates calcification and aging for a person between 35 to 85 years old. The calcification growth pattern was pre-assumed in this study based on clinical data. In total, we simulated 10 cardiac cycles sampled within 824 growth stages that spanned between the above ages. Our model includes several key mechanisms: *1- Global growth of the aortic valve leaflet due to aging:* Aging-related valve thickness changes were modeled. The direction of the growth was assumed to be normal to the surface of the leaflet. The total leaflet thickness growth over these 50 years (35 to 85 years old) was assumed to be 81 percent. *2- Global stiffening of aortic valve due to aging:* The valve stiffness was globally increased linearly due to aging during these 50 years such that the final stiffness was 2.3 times the baseline. *3- Local growth of aortic valve due to calcification:* The calcification pattern was assumed to be around the coaptation area based on prior clinical studies. The calcification process was assumed to start from 60 years old. The tagged band for local growth was the first two layers of elements in the aortic side of the leaflet. 100 percent local growth for these two layers was prescribed from 60 to 85 years old. *4- Local stiffening of aortic valve due to calcification:* The stiffness of the elements corresponding to local growth (calcification) was increased to the level reported for calcium deposits [7]. *5- Global stiffening of the aortic wall due to aging:* The aortic wall stiffness was increased during the 50 years based on clinical data. *6- Dynamics of the valve:* global and local growth and stiffening were considered to happen in the timescale of years. However, each heartbeat is about one second. In Cauchy's equation of motion (Eq. 2), the first left-hand-side term (acceleration term) was assumed zero when each growth step was first being prescribed. However, during the corresponding transient cardiac cycle simulation, the acceleration term was considered. Finally, the transvalvular pressure gradient was increased with age based on clinical data.

RESULTS

GOA was calculated by projecting the leaflet surface to the plane perpendicular to the aortic root. For the healthy case (35 years old), the intra-cardiac temporal variation of GOA and displacement for a point at the leaflet tip were verified with previous studies [4,8]. Subsequently, GOA results for different ages (35 years old to 85 years old) were computed, which are shown in Fig. 1. The model shows a heterogeneous reduction in GOA during early years where aging is only applied and later years (after 60 years old) where aging and calcification are applied.

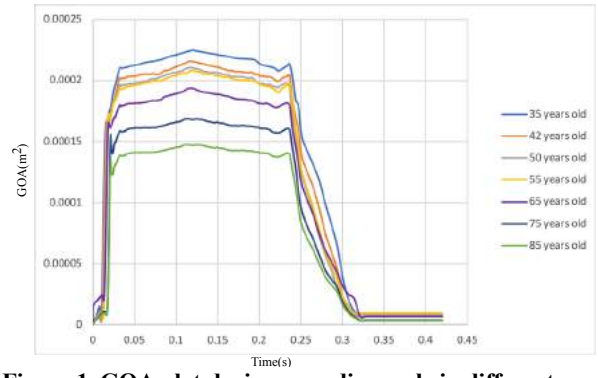

Figure 1. GOA plot during a cardiac cycle in different ages.

In Fig. 2, the displacement patterns for 3 different ages are shown. In the top row, the maximum valve open position in systole is shown for 35, 55, and 75 years. In the bottom row, changes in the valve thickness due to aging/calcification can be observed. Our model simulates the concurrent effect of aging and calcification (prescribed a priori) on the transient valve dynamics throughout 50 years.

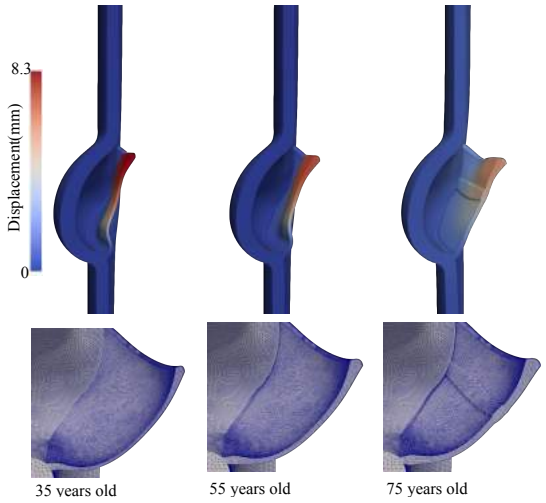

Figure 2. Top row: Peak systolic displacement patterns. Bottom row: Aortic valve thickness growth for different ages.

DISCUSSION

We developed a novel model to investigate how calcification and aging influence the transient dynamics of aortic valves. We simulated global stiffening/growth due to aging (based on population-averaged data) and local stiffening/growth due to calcification (based on a common calcification pattern). Our model demonstrates the substantial effect of calcification on aortic valve dynamics in comparison to aging.

Our study has several limitations. First, we have used an idealized geometry. Second, the calcification and aging patterns were prescribed a priori. Additionally, the thickening in the aortic wall and changes in aortic diameter were deemed negligible. While we validated our baseline model with clinical data (results not shown), validation of long-term results is expected to be challenging and remains to be performed. Nevertheless, our goal was to demonstrate how local (pathological) and global (aging) growth and stiffening could be simulated and coupled to transient nonlinear structural mechanics simulations of valve dynamics.

Our model is an early step towards a comprehensive multiscale continuum model of CAVD. Our model simulated the temporal multiscale process in CAVD based on a "pre-assumed" calcification model. In future work, we plan to extend our model to consider hemodynamics-driven calcification using a mechano-sensitive systems biology model of calcification [9]. The ultimate goal is to develop a spatiotemporally multiscale model that can capture the two-way coupling between aortic valve hemodynamics and calcification.

ACKNOWLEDGEMENTS

This work was supported by NSF grant No.~1947559.

REFERENCES

[1] Otto, C. M. *et al.*, Circulation, 95(9):2262–2270, 1997.
[2] Yip, C.Y.Y. and Simmons, C. A. Cardiovascul. Pathol. 20(3):177-182, 2011.
[3] Sahasakul, Y. *et al.*, The A. J. of Cardiology, 62(7):424–430, 1988.
[4] Weinberg, E. and Mofrad, M. R. K., Cardio. Engineering, 7(4):140–155, 2007.
[5] Humphrey, J. D. and Yin, F. Biomech. Eng. 109 (4), 298–304, 1987.
[6] Eskandari, M. *et al*, Ann. Biomed. Eng, 43(10):2538-2551, 2015.
[7] Arzani, A. and Mofrad, M. R. K. J. Biomech. 65:216-220, 2017
[8] Lee, J. H. *et al*, Ann. Biomed. Eng., 48(5):1475-1490, 2020.
[9] Arzani, A. *et al.* ACS Biomater. Sci. Eng, 3(11): 2922-2933, 2017.

FOCAL ENHANCEMENT IN INTRACRANIAL ANEURYSMS – EFFECTS OF LOCAL HEMODYNAMICS ON VW-MRI SIGNALS

F. Gaidzik (1,3), M.S. Pravdivtseva (2), J. Korte (1,3), N. Larsen (2), S. Saalfeld (3,4), G. Janiga (1,3), P. Berg (1,3)

(1) Laboratory of Fluid Dynamics and Technical Flows
University of Magdeburg
Magdeburg, Germany

(2) Department of Radiology and Neuroradiology
University Hospital Schleswig-Holstein
Kiel, Germany

(3) Research Campus *STIMULATE*
University of Magdeburg
Magdeburg, Germany

(4) Department of Simulation and Graphics
University of Magdeburg
Magdeburg, Germany

INTRODUCTION

The assessment of intracranial aneurysm (IA) rupture risk still remains challenging due to its complex nature [1]. Patient-specific remodeling processes, driven by the local hemodynamics and the individual wall properties, might lead to the formation of a stable dilation or a vulnerable, rupture-prone aneurysm shape. Apart from advanced analyses of morphologic and hemodynamic parameters [2], the acquisition of IA wall imaging becomes more and more feasible [3]. Aneurysm wall enhancement on vessel wall MR imaging (VW-MRI) after administration of Gadolinium-based contrast agents has been proposed as a surrogate marker for wall inflammation and aneurysm instability. Thus, advanced quantitative analyses were carried out, e.g., using image-based blood flow simulations, to associate wall enhancement with specific hemodynamic conditions. In the most recent study, Hadad et al. [4] found that IA wall enhancement regions tend to have lower wall shear stress than nonenhanced regions. Similar findings were reported by Larsen et al. [5], demonstrating that focal wall enhancement is colocalized with lower wall shear stress, lower maximum oscillatory shear, and increased low shear areas.

Besides those observations, it must be noted that flow artifacts occurring in the vicinity of the aneurysm wall can additionally contribute to the signal enhancement based on VW-MRI measurements. In this regard, Cornelissen et al. [6] showed in *in vitro* experiments that insufficient slow-flow suppression can result in enhancements similar to those attributed to vessel wall inflammation on VW-MRI sequences.

To further quantify this effect, this study investigates the role of local hemodynamics on the intensity of VW-MRI signal in three patient-specific IA models.

METHODS

To allow for extensive quantitative analysis of the VW-MRI enhancement, three representative, patient-specific IAs were selected. Specifically, one basilar tip aneurysm, one case located at the carotid terminus, and one originated at the middle cerebral artery bifurcation were chosen. The corresponding image datasets, acquired using digital subtraction angiography (Allura XperFD 20/10, Philips, Best, the Netherlands), were processed according to Pravdivtseva et al. [7]. The resulting three precise flow models were used to obtain flow *in vitro*.

VW-MRI and Phase-Contrast Magnetic Resonance Imaging (PC-MRI) were performed for all models to acquire the luminal signal enhancement and the corresponding time-resolved, three-dimensional velocity fields. The measurements were performed on a 3T MR system (Ingenia CX, R5 V6.1, Philips Healthcare, Best, the Netherlands).

In addition to the PC-MRI measurements, image-based blood flow simulations were carried out, enabling analyses at the highest temporal and spatial resolution (Δt=1 ms, Δx=0.1 mm). Here, numerical results were obtained using the fluid dynamics solver STAR-CCM+ 14.04 (Siemens Product Lifecycle Management Software Inc., Plato, TX, USA). Corresponding boundary conditions (time-dependent flow and pressure waveforms, fluid properties) were derived from the measurements to establish an identical flow setup.

RESULTS

As demonstrated in Figure 1, the signal enhancement drastically deviates throughout the different IA models. Higher inflow velocities lead to less signal intensity, while regions of slow flow correspond to intra-luminal enhancement. The highly-resolved blood flow simulations further confirm this observation and are capable of reproducing visible inflow jet phenomena (e.g., Figure 1, Model 3).

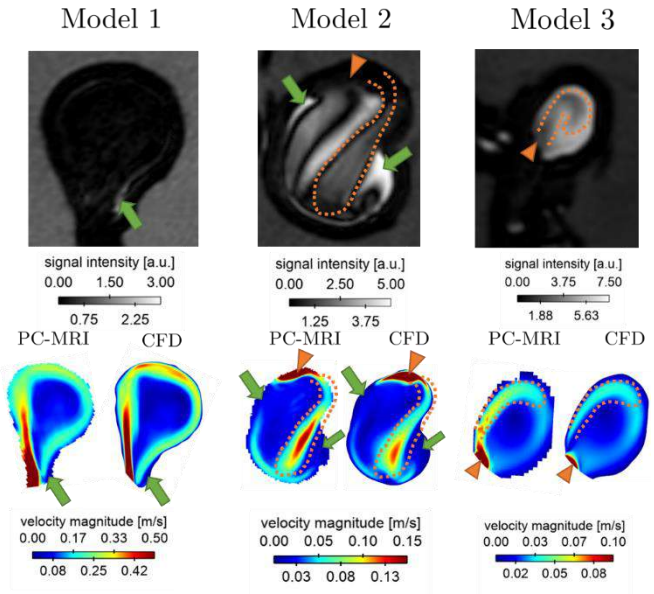

Figure 1: Illustration of the signal enhancement based on VW-MRI measurements (top) and the local hemodynamics (bottom) in the lumen of three IA models. Enhanced regions are marked green (arrows), and signal void zones are represented in orange (triangles, dashed lines)

To further quantify the underlying flow structures, Figure 2 contains the results of a cluster analysis. Here, regions of similar VW-MRI signal intensity values are compared to the corresponding velocity values. It can be noticed that almost identical trends are visible. Specifically, an exponential relationship between the local velocity value and the associated extent of enhancement exists in all cases. Hence, the strongest signal intensity appears in regions where the blood flow is very low (i.e., smaller than 3 cm/s).

DISCUSSION

The role of wall enhancement on VW-MRI as a potential surrogate marker for the assessment of IA rupture risk is a recent research question awakening the interest of many neurointerventionalists [8]. Although its clinical use for IA stage evaluation remains currently uncertain, an increasing number of observations inficate that aneurysms at risk could be identified with these modified MR-sequences [3]. However, in addition to wall enhancement, increased signal intensity attributable to slow flowing blood was observed within the aneurysm lumens [9]. To quantify the luminal enhancement, this study demonstrated the relationship between local flow velocities and the corresponding MR signal intensity. Based on three patient-specific IA models, it was shown that low flow results in strong enhancement.

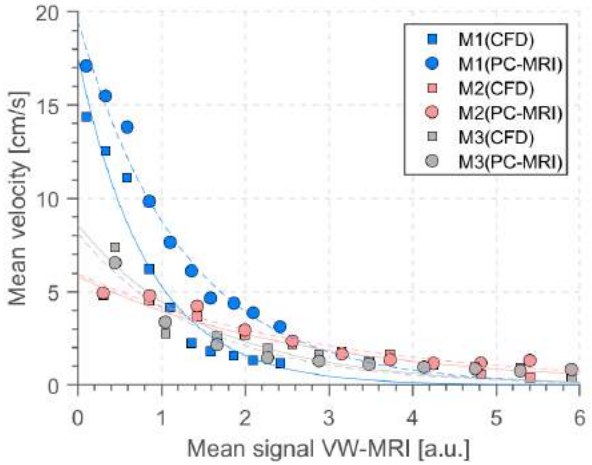

Figure 2: Cycle-averaged velocity values measured using PC-MRI and CFD over mean signal intensity for all IA models.

Therefore, VW-MRI can be used to assess potential inflammatory processes within the aneurysm wall and to detect regions of slow flow inside the lumen. This could be especially of interest for identifying thrombotic regions after endovascular treatment or detecting a recurrence.

Finally, it is important to outline several existing limitations regarding the investigations. First, due to enormous efforts with respect to the measurements and simulations, only three IA cases were considered. For generalizable conclusions, further observations with more aneurysms varying in size and morphology have to be carried out. Second, a blood-mimicking fluid was used instead of real blood, and the fluid-dependency of VW-MRI needs to be further investigated.

ACKNOWLEDGEMENTS

This study was funded by the Federal Ministry of Education and Research in Germany within the Forschungscampus *STIMULATE* (13GW0473A), the German Research Foundation (BE 6230/2-1) and the international graduate school MEMoRIAL at University of Magdeburg, Germany (ESF, project number ZS/2016/08/80646). Furthermore, we are grateful for the financial and intellectual support by the Research Training Group “Materials4Brain” (GRK2154; P2, P10).

REFERENCES

[1] Wiebers, DO et al., *Lancet*, 362:103-110, 2003.
[2] Detmer, FJ et al., *Neuroradiology*, 61:275-284, 2019.
[3] Samaniego, EA et al., *J Neurointerv Surg*, 11:1105-1112, 2019.
[4] Hadad, S et al., *Am J Neuroradiol*, 10.3174/ajnr.A6927, 2020.
[5] Larsen, N et al., *Neuroradiology*, 62:1627-1635, 2020.
[6] Cornelissen, BMW et al., *Neurosurg Focus*, 47:E19, 2019.
[7] Pravdivtseva, MS et al., *Med Phys*, accepted, 2021. DOI: 10.1002/mp.14714
[8] Lv, N et al., *Neurosurgery*, 84(6):E385-E391, 2019.
[9] van den Berg, R, *Neuroradiology*, 62:269-270, 2020.

MECHANOSENSITIVE NOTCH SIGNALING REGULATES PHENOTYPIC CHANGES IN VASCULAR SMOOTH MUSCLE CELLS

Cansu Karakaya (1,2), Valery L. Visser (1), Tommaso Ristori (1,2,3), Carlijn V.C. Bouten (1,2), Cecilia M. Sahlgren (1,2,4), Sandra Loerakker (1,2)

(1) Department of Biomedical Engineering
Eindhoven University of Technology
Eindhoven, The Netherlands

(2) Institute for Complex Molecular Systems
Eindhoven University of Technology
Eindhoven, The Netherlands

(3) Department of Biomedical Engineering
Boston University
Boston, Massachusetts, USA

(4) Faculty of Science and Engineering
Åbo Akademi University
Turku, Finland

INTRODUCTION

Cardiovascular diseases are among the major causes of morbidity and mortality worldwide. Surgical interventions are often needed to replace diseased vessels with autologous tissues or synthetic grafts. However, autologous tissue sources are limited, and synthetic grafts often have complications affecting long-term patency, particularly for small-diameter vascular grafts. *In situ* cardiovascular tissue engineering, which aims to transform biodegradable scaffolds into living tissues at the implantation site, has the potential to overcome these limitations. Currently, there are still many questions related to how the engineered tissues remodel after implantation, and how the native-like organization can be achieved to enable proper functionality. To answer these questions, a mechanistic understanding of the processes regulating functional vessel growth and remodeling is needed.

Vascular growth and remodeling are mediated by vascular smooth muscle cells (VSMCs), in turn influenced by mechanical cues and cell-cell signaling. VSMCs demonstrate a quiescent contractile phenotype in mature vessels, and switch towards a more proliferative and migratory synthetic phenotype when growth and remodeling is needed. These phenotypic changes are regulated by Notch, a juxtacrine signaling pathway [1]. Increasing evidence suggests that Notch signaling is mechanosensitive [2], and computational modeling has recently predicted that this Notch mechanosensitivity can regulate the phenotypic switch in VSMCs and explain the establishment of homeostasis [3]. Nevertheless, these computational findings are scarcely validated and the combined effects of strain and Notch on VSMCs of different phenotype are poorly characterized. Validating this prediction and understanding the complex interaction between mechanical cues and Notch signaling in VSMCs will provide an opportunity to steer this interaction and control vascular growth and remodeling in engineered tissues. The outstanding question is therefore: '*Does Notch signaling regulate strain-mediated changes in VSMC phenotype?'*.

METHODS

Human coronary artery smooth muscle cells (Lonza) were cultured for 7 days in Medium 231 (Gibco) supplemented with either smooth muscle growth supplement (Gibco) to obtain synthetic VSMCs, or smooth muscle differentiation supplement (Gibco) to obtain contractile VSMCs. In addition, the Jagged1 ligand was immobilized on the culture surface in static conditions to investigate if activation of Notch signaling can directly lead to differentiation in synthetic VSMCs.

Bioflex culture plates (Flexcell) were coated with bovine fibronectin (Gibco) in the center of the wells. One day after cell seeding on the Flexcell, cells were either treated with the γ-secretase inhibitor DAPT (Sigma) to inhibit Notch signaling, or with the vehicle DMSO at a similar concentration as a control. Furthermore, cells were either cultured statically or equibiaxially stretched with the Flexcell Tension System at 1 Hz for 48 hours. The membranes of each well were marked and tracked with a camera. The displacement was analyzed, and the corresponding strain was calculated via digital image correlation.

Immunofluorescence (IF) imaging and quantitative polymerase chain reaction (qPCR) were conducted to characterize the changes in cell phenotype, ECM production and Notch signaling upon stretch. In particular, cells were stained for the contractility marker α-smooth muscle actin (αSMA), vinculin, F-actin and collagen. The gene expression of phenotypic markers αSMA, calponin and Ki67; Notch-related genes Notch1, Notch2, Notch3 and Jagged1 were compared in static and stretched conditions, as well as the control and Notch-inhibited cells. One-way ANOVA and post-hoc Tukey HSD were used to determine statistically significant differences between experimental

groups (GraphPad Prism v8). The qPCR data were plotted as boxplot and differences were considered statistically significant for $p<0.05$.

RESULTS

Synthetic and contractile VSMCs showed differences in their morphology and gene expression. Contractile VSMCs were larger in size, had more and elongated focal adhesions, and they expressed more αSMA (Figure 1) and calponin compared to synthetic VSMCs. Moreover, αSMA was organized as fibers in contractile VSMCs, differently than synthetic VSMCs (Figure 2A&C).

The initially synthetic cells cultured on the immobilized Jagged1 coating showed similar trends as the contractile VSMCs, in terms of organized stress fibers and gene expression, confirming a role of Notch in determining VSMC phenotype. In agreement with this, the expression of proliferation marker Ki67 was increased in synthetic VSMCs compared to the contractile and Jag1-stimulated groups.

The contractile phenotype required Notch signaling to be active. In fact, the stress fiber organization observed in contractile VSMCs disappeared when Notch signaling was inhibited (Figure 2C-D). αSMA (Figure 1), calponin, and Jagged1 expressions also decreased in Notch-inhibited contractile VSMCs. On the other hand, Notch inhibition hardly affected synthetic VSMCs (Figure 1&2A-B).

Upon strain application for 48 hours, our results showed that αSMA expression in contractile VSMCs decreased to the level of synthetic VSMCs (Figure 1). In addition, stress fibers were not detected in stretched contractile VSMCs (Figure 2G), and Jagged1 expression was reduced. This suggests a transition of contractile VSMCs towards a more synthetic state mediated by Jagged1 reduction upon stretch. In agreement with this, the expression of αSMA did not change in synthetic VSMCs upon stretch (Figure 1). Moreover, Notch inhibition in stretched contractile VSMCs did not have a synergistic effect on αSMA expression.

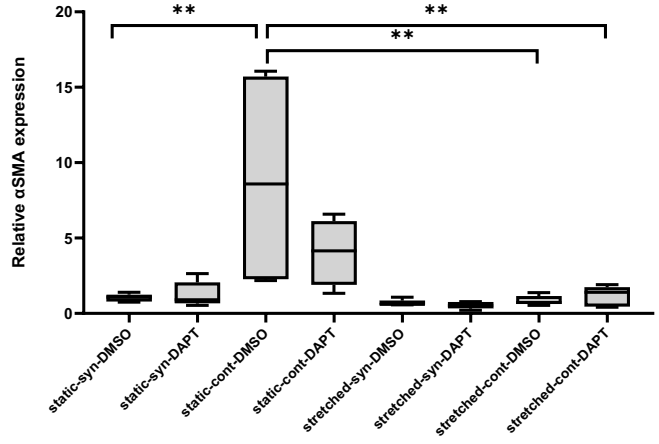

Figure 1: The gene expression of αSMA was compared in static and stretched (10% strain for 48 hours at 1 Hz) VSMCs. DMSO was added as a control to Notch-inhibited (DAPT) groups. All expression values were normalized to static synthetic control group (syn: synthetic VSMCs, cont: contractile VSMCs) ($p<0.01$, $n=5$).**

DISCUSSION

Our results so far indicate that Notch signaling might have a key role in regulating strain-mediated changes in VSMC phenotype. Contractile VSMCs obtain stress fibers (Figure 2C) and increase their Notch activity. Notch induction promotes a contractile-like phenotype, whereas Notch inhibition leads to a synthetic phenotype in VSMCs. Similarly, strain decreases Notch signaling and induces a shift towards a synthetic state in contractile VSMCs. In addition, Notch inhibition in stretched VSMCs has a similar effect. To better understand the role of Notch in strain-mediated changes, future efforts will be directed to analyze Notch-stimulated VSMCs. Unravelling this complex interaction is an important step towards controlling functional growth and remodeling in engineered vessels.

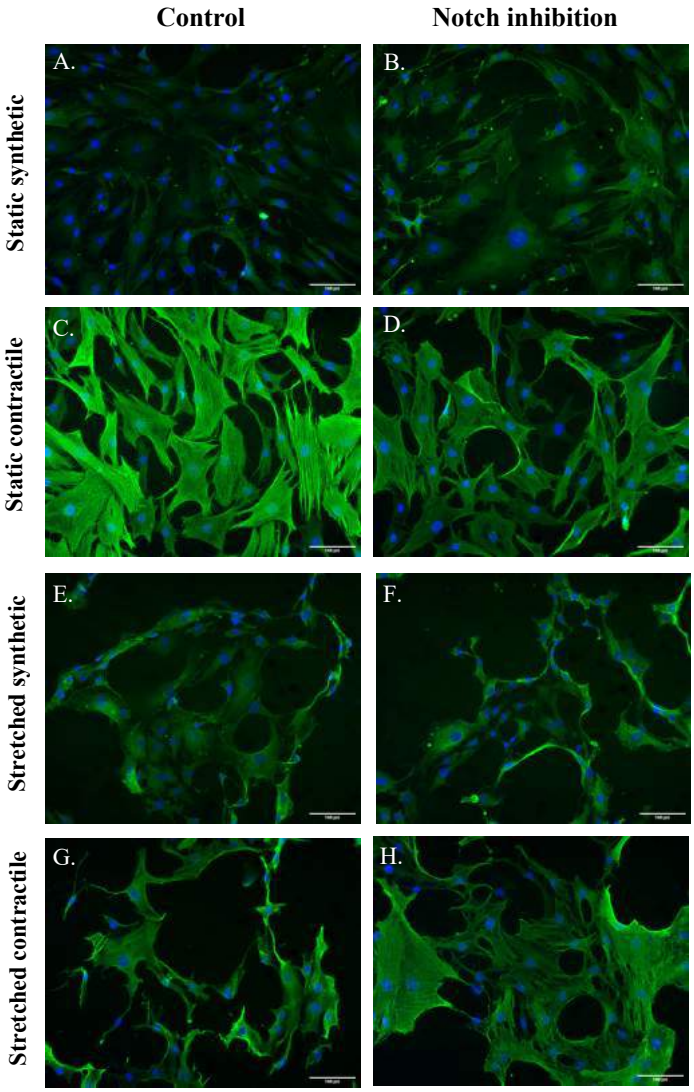

Figure 2: IF staining of αSMA was visualized for synthetic and contractile VSMCs treated with either DMSO as a control or DAPT for Notch inhibition. The cells were radially stretched at 10% strain, 1Hz, for 48 hours (E-H) and compared with the static controls (A-D). (green: αSMA, blue: DAPI. Scale bar: 100 um)

ACKNOWLEDGEMENTS

This project has received funding from the European Research Council (ERC) under the European Union's Horizon 2020 research and innovation programme (Grant agreement No. [802967]).

REFERENCES

[1] Doi, H et al., *J Biol Chem*, 281:28555-28564, 2006.
[2] Beamish J et al., *Tissue Eng Part B Rev,* 16:467-491, 2010.
[3] Loerakker S et al., *PNAS*, 115:E3682–E3691, 2018.

A MULTISCALE COMPUTATIONAL MODEL FOR CELL-SIGNALING DRIVEN GROWTH AND REMODELING OF ARTERIES

Linda Irons (1), Marcos Latorre (1), Jay D. Humphrey (1)

(1) Department of Biomedical Engineering
Yale University
New Haven, CT, USA

INTRODUCTION

Soft biological tissues adapt, remodel, and repair in response to diverse mechanical and biochemical stimuli, which are sensed by cell surface receptors. Downstream signaling leads to altered gene expression and gene products, and many such transcriptional changes alter extracellular matrix composition and organization, orchestrating changes in tissue geometry and biomechanical properties, thereby affecting tissue functionality. Cell signaling is mechanosensitive, and tissue-level biomechanical changes induce further changes in cell signaling in the form of a feedback loop. This feedback is crucial to understand, since tissue homeostasis requires negative feedback, whereas positive feedback is considered a potential driver of disease.

Although there has been much progress in modeling cell signaling networks and tissue-level growth and remodeling (G&R) separately, a continuing challenge has been coupling computational models across these disparate scales to enable modeling from transcript to tissue. Coupled models capturing the feedback between cell signaling and tissue mechanics promise to provide improved mechanistic insight into remodeling by allowing studies of the role of specific signaling proteins and pathways. In addition, they uniquely allow for studies of targeted interventions or disrupted signaling and the resulting effects on potential tissue maladaptations. Here, we present our new multiscale modeling framework for cell-signaling driven growth and remodeling of arteries [1]. We have coupled of a logic-based cell signaling model and a constrained mixture model of soft tissue G&R, motivated by the fundamental need to capture changes in cell phenotype and associated changes in deposition and degradation of individual components of the extracellular matrix. We view a mixture-level balance of mass equation as central to coupling outputs of the cell signaling model to inputs in the constrained mixture model. For illustrative purposes, we focus on homeostatic control of arterial G&R in response to sustained changes in blood pressure and flow.

METHODS

We couple two previously developed modeling frameworks to capture associated multiscale interactions: one for vessel-level growth and remodeling and one for cell-level signaling. At the vessel level, we use a constrained mixture model [2] to model evolving wall mechanics, considering three primary load-bearing constituents: elastin-dominated, collagen-dominated (with four families of fibers), and smooth muscle cell-dominated. Such models have proven useful in predicting diverse adaptations as well as disease progression using phenomenological constitutive relations. Nevertheless, we now seek an improved mechanistic understanding of these processes and we replace phenomenological relations for stress-driven production and removal of mass with outputs of a logic-based signaling model [3] which directly predicts changes in collagen synthesis, matrix metalloproteinases, and cell proliferation in response to altered intramural stress, wall shear stress, and exogenous angiotensin II.

The signaling model accounts for activation and inhibition reactions across 52 species of interest, focussing on six main pathways (Smad, p38, ERK, JNK, PI3K/mTOR, RhoA/ROCK), with relations inferred from the literature. Central to the multiscale coupling are the widely separated timescales between G&R (days, weeks, months) and signaling processes (seconds, minutes, hours). Relatively, the stress inputs to the signaling network change slowly, thus it is reasonable, and computationally efficient, to assume steady state cell signaling within G&R timesteps (1 day). Thus, ordinary differential equations (ODEs) for cell signaling reduce to nonlinear algebraic equations.

The coupled model is outlined schematically in Fig 1. Under imposed changes in blood pressure and flow, we calculate tissue-level changes in intramural and wall shear stresses, which depend on material properties, wall geometry, and fold-changes in applied loads. These stresses form inputs to the cell signaling model, outputs of which govern phenotypic modulation of cells and associated turnover of extracellular matrix. The resulting tissue turnover affects the stresses, which feedback to the cell signaling model, and so forth.

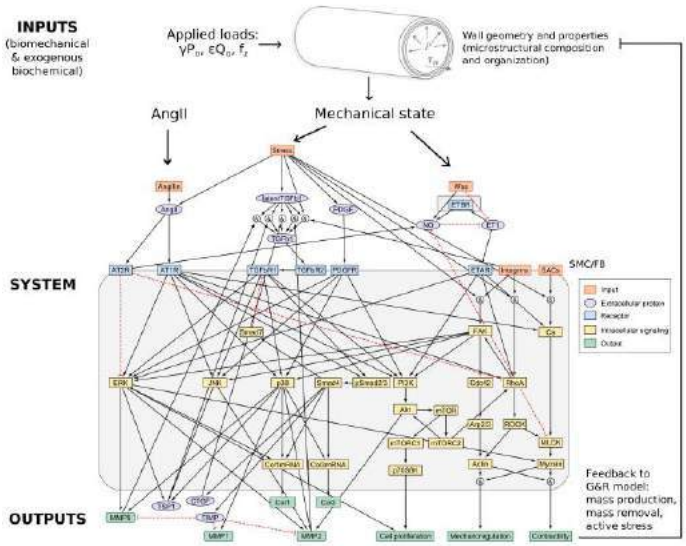

Fig 1. Schematic outline of multiscale coupling. Vessel-level changes in intramural and wall shear stresses feed into the logic-based cell signaling model, the outputs of which govern constituent turnover (collagen, smooth muscle cells) in the vessel-level constrained mixture model. Figure first published in [1] by Springer Nature.

RESULTS

We first verified our model predictions against previously published data from the hypertensive murine infrarenal abdominal aorta in apolipoprotein-E null (ApoE-/-) mice in response to 28 days of AngII infusion [4]. Material parameters were determined previously from pressure-diameter and axial force-length curves from vessels subject to biaxial loading [5], and network parameters were fit to capture the evolved collagen and smooth muscle cell mass densities (calculated from histological data at day 28). Our model then predicted well the evolving vessel geometry, stresses, and composition at intermediate timepoints (0, 4, 7, 14, 21 days).

Next, we verified the model against a broader range of synthetic results generated by a phenomenological model. Such models have long captured diverse experimental datasets, and we aimed to ensure that our model could produce similar behavior over a broad range of pressure and flow perturbations. We considered 15 combinations of pressure and flow perturbations, and fit the coupled model to results for one intermediate combination (a 30% increase in pressure and 5% increase in flow). Using the best-fit parameters for this case, we ran coupled model predictions for the remaining 14 combinations and found the results to be consistent with those from the phenomenological model.

To challenge this new framework, we considered effects of noisy signaling parameters, and replicated the network 100 times to represent heterogeneous cells. Cell signaling networks are inherently noisy, yet robust in function, and we used the coupled framework to investigate the sensitivity of tissue-level outputs to perturbed signaling parameters. We do this in two ways: firstly, with uniformly distributed noise applied identically across each network, and secondly, with uniformly distributed noise applied individually to the 100 networks (simulating cell heterogeneity). We find that higher levels of noise can be withstood when applied heterogeneously, and that the averaged signaling outputs with moderate noise ($\pm$20%) yield robust tissue-level results.

DISCUSSION

Phenomenological models have provided, and continue to provide, considerable insight into the G&R of biological soft tissues. However, given the continually increasing information available on transcriptional changes (e.g. bulk and single-cell RNAseq) and associated cell signaling, there is now an opportunity, and necessity, to incorporate such information into models that predict tissue-level clinical phenotypes. We have now developed a multiscale framework for coupling cell signaling and constrained mixture G&R [1], which will enable myriad future studies in diverse areas. We first verified the implementation and validated tissue-level predictions for the hypertensive murine abdominal aorta, and then for a larger synthetic dataset generated by a previously validated phenomenological model. We also tested the effects of noisy signaling parameters and found tissue-level outputs to be robust to mild signaling perturbations, as must be in the case in real biological systems. To represent cell heterogeneity, we then simulated parallel identical networks with different parameters, and similarly found robust tissue-level responses in the presence of moderate noise. Our results highlight the importance of collective behavior and the protection it offers from the noise, individual fluctuations, and disruptions inherent to cell signaling networks. Within this new modeling framework, the same principles used to simulate heterogenous cells could be extended to support multiple cell types with unique network structures, and be used to better understand associated paracrine signaling. Accordingly, now that the basic framework for coupling is in place, the current tissue-level model can be extended and refined, for example to a bilayered wall model.

ACKNOWLEDGEMENTS

This work was supported by grants from the US NIH (R01 HL105297, P01 HL134605, R01 HL139796, U01 HL142518, R01 HL146723).

REFERENCES

[1] L. Irons, M. Latorre and J. D. Humphrey. From transcript to tissue: multiscale modeling from cell signaling to tissue remodeling. *Annals of Biomedical Engineering*. doi.org/10.1007/s10439-020-02713-8. 2021.

[2] J. D. Humphrey and K. R. Rajagopal. A constrained mixture model for growth and remodeling of soft tissues. *Mathematical Models and Methods in Applied Sciences*, 12(03):407-430, 2002.

[3] L. Irons and J. D. Humphrey. Cell signaling model for arterial mechanobiology. *PLoS Computational Biology*, 16(8):e1008161, 2020

[4] M. R. Bersi, *et al*. Differential cell-matrix mechanoadaptations and inflammation drive regional propensities to aortic fibrosis, aneurysm or dissection in hypertension. *Journal of The Royal Society Interface*, 14(136):20170327, 2017.

[5] M. Latorre, M. R. Bersi, and J. D. Humphrey. Computational modeling predicts immuno-mechanical mechanisms of maladaptive aortic remodeling in hypertension. *International Journal of Engineering Science*, 141:35-46, 2019.

SB³C2021
Summer Biomechanics, Bioengineering and Biotransport Conference
June 14-18, Virtual

FREQUENCY CHARACTERISTICS OF ELASTIC PATIENT-SPECIFIC ANEURYSM MODEL

Ryuhei Yamaguchi (1), Naoki Ikeya (2), Nadia S. Shafii (3), Kahar Osman (3), Atsushi Saito (4), Gaku Tanaka (2), Makoto Ohta (1)

(1) Institute of Fluid Science
Tohoku University
Sendai, Miyagi, Japan

(2) Graduate School of Engineering
Chiba University
Chiba, Japan

(3) Faculty of Biomedical Engineering
Universiti Teknologi Malaysia
Skudai, Johor Bahru, Malaysia

(4) Department of Neurosurgery
Sendai Medical Center
Sendai, Miyagi, Japan

INTRODUCTION

The middle cerebral artery (MCA) is one of predilection vessels of aneurysm. In hemodynamics of cerebral aneurysm, a lot of researchers assumed to be rigid wall in CFD. A few numerical approaches were carried out for the cerebral aneurysm with elastic wall in FSI [1]. However, the frequency characteristic of elastic cerebral aneurysm model has not been clarified [2]. In the present study, the effect of wall elasticity on frequency characteristics was experimentally investigated the comparison of deformable with non-deformable models using PIV.

METHODS

Phantom model

The morphology constructed from a patient-specific aneurysm at apex of bifurcation at human middle cerebral artery (MCA) in full-scale is shown in Figure 1. Two outlet vessels M2 and M3 bifurcate from the inlet vessel M1. The left and right morphology show the front (median plane) and the right-side views shown in Figure 1, respectively. The diameter of inlet vessel M1 is d_1= 2.8 mm, and the diameters of each outlet M2 and M3 are d_2 = 2.3 mm and d_3 = 1.8 mm, respectively.

The current phantom model was fabricated in silicone elastomer of Sylgard 184 (Dow Chemical Co.) using a special technique. The wall elasticity is E = 0.67 MPa which was measured in the tensile machine.

Flow circuit

The flow circuit is shown in Figure 2. To reproduce pulsatile flow waveform through human cerebral vessel, the high reproducibility pulsatile pump (Alfa Flow EC-1, FUYO Co.) was employed. The phantom model was immersed in the acrylic bath (40×50×120 mm³). After passing through the phantom model, the flow rates through both outlet vessels were measured by flow meter (Keyence, FD-XS8). The pressure at inlet and two outlets was measured in pressure transducer (Keyence, AP-12S).

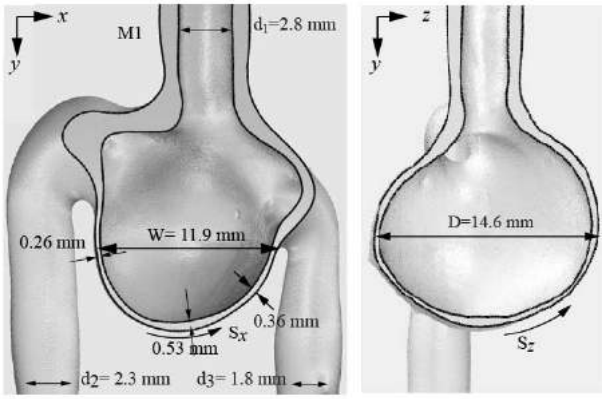

Figure 1: Phantom morphology of front and right side views.

The working fluid is aqueous Glycerol with potassium iodide solution, i.e. Water of 47.38 %, Glycerol of 36.94 %, NaI of 15.68 % [3]. The physical properties are as follows: the density of ρ = 1188 kg/m³, the kinematic viscosity of ν= 3.57×10⁻⁶ m²/s and the refractive index of n=1.412. The maximum and minimum Reynolds numbers are 510 and 255, respectively. The mean Reynolds number of 310 is referred as the flow rate of Q_{mean}= 146 mL/min [4]. One period of pulsatile flow is set to be 1.0 s, the peak flow phase is at t= 0.28 s and the Womersley number is α= 1.86.

RESULTS

At peak systole, the velocity contours in non-deformable and deformable models are shown in Fig. 3. Although both flow patterns are

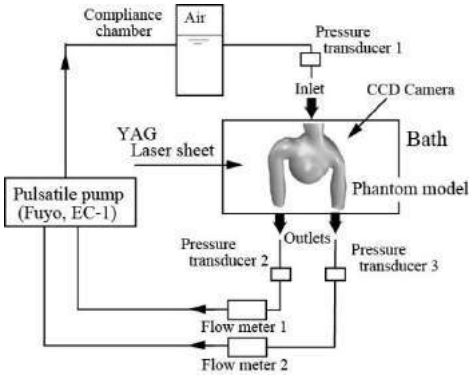

Figure 2: Current flow circuit.

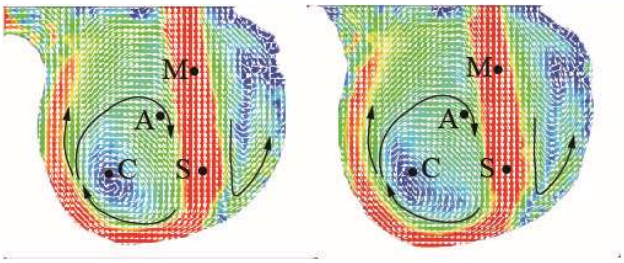

(a) Non-deformable (b) Deformable

Figure 3. Velocity contour at peak systole.

similar and the large clockwise circulating flow appears in left side, the velocity in non-deformable velocity is slightly larger. At typical points C, A, M and S, the frequency characteristic is examined using a SpeedSense M camera (Dantec SYSTEM 8) in PIV. For power spectral density (PSD), velocity data were analyzed over four cardiac cycles at sampling rate of 2000 fps.

Figure 4 depicts PDS at three points C, A & S. At each point at low frequency range, the gradient of PSD decrease in deformable is larger than that in non-deformable models. Furthermore, at high frequency range, PSD reaches constant value for each point and PSDs in deformable are lower than those in non-deformable models.

DISCUSSION

Asymptotical decrease of PSD from 10 to 100 Hz in Fig. 4(a) denotes laminar flow around point C. Also, there was another difference between constant PSD (1×10^{-7}) at >70 Hz in non-deformable and constant PSD (1×10^{-8}) at >100 Hz in deformable models. Furthermore, at low frequency range, the gradient PSD of 2.6 in deformable is larger than that of 1.7 in non-deformable models. Except for point M (not shown here), the gradient PSD in deformable model is larger than that in non-deformable model. In other words, PSD in deformable model steeply decreases. At point M, although there is little gradient of PSD in both models and PSDs are constant over 15-100 Hz because velocity around this point is like uniform flow and there is little velocity gradient. Around points A and S, this trend is similar to that around point C as shown in Figs. 4(b) and (c). Generally, at higher frequency rangePSD in deformable model asymptotically approaches lower constant PSD and it is also by approximately 10-fold lower than that in non-deformable models. So, the small displacement of wall might absorb flow instability.

ACKNOWLEDGEMENTS

This research was partially supported by Grant-in-Aid for Scientific Research JSPS K19K041630, 2019 Bilateral Joint Research JSPS and Collaborative Research Project J20I040 of IFS, Tohoku University. Also, this research was partially supported by grants of the Ministry of Education Malaysia and Research Management Centre, Universiti Teknologi Malaysia with vote number R. J130000.7851.5F385 Parametric Analysis of Intracranial Aneurysm Coil Porosity for Blood Coagulation Potential.

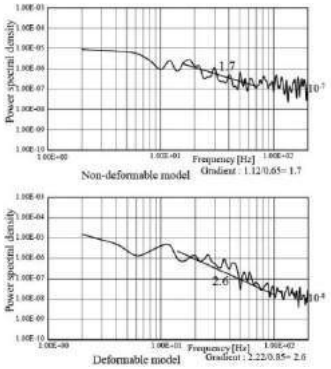

(a) Point C (Circulation region separating around point C)

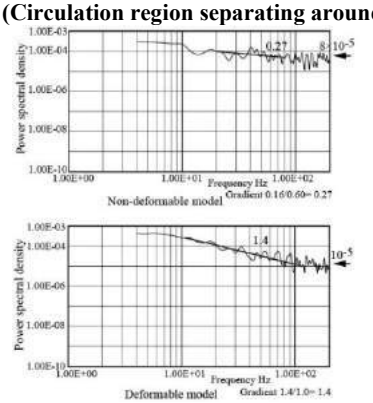

(b) Point A (Adjacent to main flow)

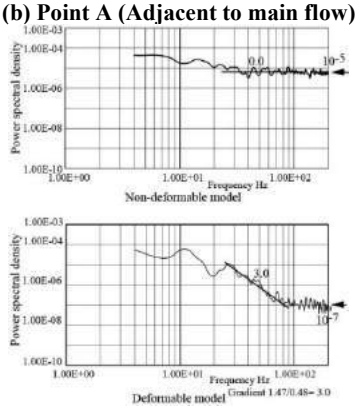

(c) Point S (Around stagnation point)

Figure 4. Comparison of PSD in non-deformable with deformable models.

REFERENCES

[1] Torii, R., et al., Computer & Fluids, 36:160-168, 2007.
[2] Lee, C.J., et al., J Biomech, 46:14; 2402-2410, 2013.
[3] Yazdi, S. G., et al., Annals Bio Med, 46;1697-1721, 2018.
[4] Laleh Z,, et al., JCBFM. 35(4), 648–654, 2015.

ARTICULAR CARTILAGE GEOMETRY AND MATERIAL PROPERTIES PREDICT FUNCTIONAL TRIBOMECHANICS AROSS SPECIES

Meghan E. Kupratis (1), Ahmed E. Gure (3), Jamie M. Benson (1), Kyla F. Ortved (4), David L. Burris (2), Christopher Price (1,2)

(1) Biomedical Engineering
University of Delaware
Newark, DE, USA

(2) Mechanical Engineering
University of Delaware
Newark, DE, USA

(3) Bioengineering
University of Texas Arlington
Arlington, TX, USA

(4) Clinical Studies
University of Pennsylvania
Kennett Square, PA, USA

INTRODUCTION

Healthy articular cartilage withstands complex, repeated loading patterns while maintaining low strains (5-20%) and vanishingly low friction coefficients ($\mu_k < 0.02$).[1] These remarkable capabilities occur primarily through *interstitial lubrication*, whereby pressurized interstitial fluid carries the bulk of applied loads (>95%). How variations in cartilage properties influence these important tribomechanical behaviors remains an unresolved, yet fundamentally important question. While a number of preclinical animal models have been used to study cartilage's compositional and biomechanical variability in health and disease *ex vivo*,[2-4] similar comparative approaches have seen limited application to cartilage lubrication. Moore and Burris showed that improved fluid load support and equilibrium friction behaviors were associated with increased equilibrium contact modulus, increased tensile modulus, and lower permeability in bovine stifle cartilage.[5] To our knowledge, similar studies had not been performed in other model species. Therefore, comparative assessment of healthy cartilage's material properties and tribological performance across model species may serve as a basis for interpreting the functional consequences of disease-related changes in cartilage composition.

We recently performed a comparative analysis of cartilage tribology across five common mammalian models (equine/horse, bovine/cow, porcine/pig, ovine/sheep, and caprine/goat) using our convergent stationary contact area (cSCA) configuration.[6] In the cSCA, hydrodynamic pressurization at the edges of the contact drives, through *tribological rehydration*, the restoration of tissue lubrication, sustaining a sliding environment on the benchtop that is both physiologically consistent and informative. This study revealed incredible consistency in many sliding speed-dependent characteristics of tribological rehydration, despite the presence of noted inter-specimen/species variabilities. In the present study, we sought to uncover predictive correlations that inform critical relationships between tissue geometry, material properties, and tribological behaviors. Importantly, the presence of inherent variability within our study populations allows us to define relationships between tissue properties and biphasic lubrication with bearing on both healthy and diseased tissue function.

METHODS

Osteochondral explants were harvested from the centerline of femoral condyles of five model species.[6] A static loading experiment with optical measurement of *in situ* contact areas was performed for each species to determine the normal loads necessary to generate contact pressures of 0.25 ± 0.05 MPa. Each tribological test began with static compression to drive fluid exudation from the cartilage, enabling the facile observation of tribological rehydration upon initiation of sliding at different speeds. The duration of static compression was calculated from the classical relationship between cartilage's characteristic stress relaxation time and the square of the contact radius.[7] Compression (δ), strain (ε), and kinetic friction coefficients (μ) were measured during bouts of reciprocal sliding at 10-80 mm/s.

A custom microtribometer was used determine cartilage material properties using rate-dependent indentation.[5] Moore and Burris's analytical model based on Hertz biphasic theory was used to calculate compressive modulus (E_{y-}), tensile modulus (E_{y+}), intrinsic permeability (k_0), and the nonlinear flow limiting constant (M).[8]

After tribological and indentation testing, the average cartilage thickness across the center of the bisected cSCA contact and the contact radius-of-curvature were determined.[6] Species-specific explant geometries and material properties were compared using the nonparametric Welch's ANOVA in Prism 9 (significance set at $p <$

0.05). All outcome measures were then correlated using Pearson's method (significance set at $p < 0.01$).

RESULTS

Cartilage thickness increased proportionally with body size (**Fig. 1A**). Equine specimens were the thickest (1.31 ± 0.17 mm), while ovine and caprine samples were the thinnest (0.49 ± 0.09 mm, and 0.40 ± 0.08 mm, respectively). Interestingly, cSCA explant radius of curvature did not vary significantly among species (**Fig. 1B**).

Each species' material properties are shown in **Fig. 1C**. As expected, all specimens exhibited significant tension-compression nonlinearity ($p < 0.0001$, Student's *t*-test; $E_{y+} \approx 10E_{y-}$). Significant differences in compressive moduli were not observed among species ($p = 0.15$). However, tensile moduli of larger species were greater than those of smaller species ($p < 0.05$). Intrinsic (k_0) and strain-dependent (M) permeability values were greatest in smaller species ($p < 0.001$).

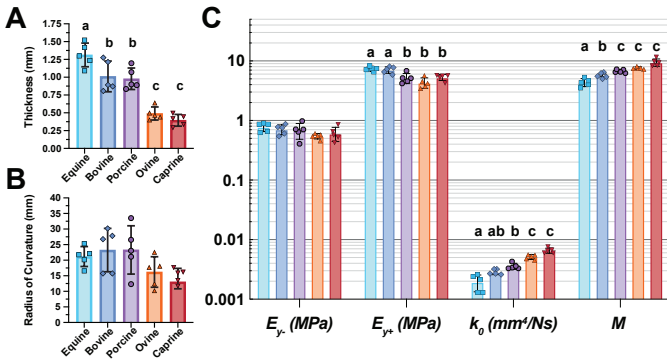

Fig. 1. Geometric (A-B) and material properties (C) of cartilage explants from each model species. Dissimilar letters indicate significant differences ($p < 0.05$, Welch's ANOVA).

The thinnest cartilage explants (ovine and caprine) had the highest intrinsic permeabilities (R = -0.85). Similarly, thicker cartilage had greater compressive moduli (R = 0.63); tensile moduli and intrinsic permeability were inversely correlated with one another (R = -0.61). Correlative analyses also revealed pathlength-dependent characteristics of tribological rehydration: time-averaged compression (δ_{TA}) during static loading (R = 0.62) and compression recovery (δ_{rec}) during high-speed sliding (R = 0.78) were cartilage significantly correlated with tissue thickness. As anticipated from the strong inverse relationship between thickness and permeability, increasing k_0 was associated with decreased ∂_{rec} during high-speed sliding (R = -0.79).

Between static loading and high-speed sliding, δ_{TA} values were strongly correlated (R = 0.97; **Fig. 2A**); as were δ_{TA} between static loading and slow sliding (R = 0.98). Importantly, δ_{TA} under static conditions exceeded δ_{TA} under all sliding conditions ($p < 0.001$, paired *t*-test). **Fig. 2B** shows that slow speed sliding behaviors are predictive of high-speed behaviors, and vice versa; e.g., end-of-sliding compression (δ_{EoS}) at 10 mm/s was strongly correlated with that at 80 mm/s (R = 0.91).

We extrapolated the sliding speeds at which load-induced fluid exudation and sliding-induced fluid recovery matches (i.e., *tribological rehydration threshold speed*, v_{TR}) as well as the minimal speed needed to suppress increases in friction (i.e., *friction recovery threshold speed,* $v_{\mu rec}$) for each specimen. More permeable explants required faster sliding speeds to sustain fluid recovery (R = 0.41, v_{TR} vs. thickness) and lubrication (R = 0.57, $v_{\mu rec}$ vs. thickness). The strong correlation between these parameters highlights the phenomenal and universal lubricating properties of tribological rehydration (R = 0.77; **Fig. 2C**). Similar to the compression behaviors, kinetic friction coefficients under recovery conditions were strongly correlated with those under exudation conditions (R = 0.66; **Fig. 2D**). Importantly, high-speed sliding facilitated a ~50% suppression of time-average friction vs. slow sliding.

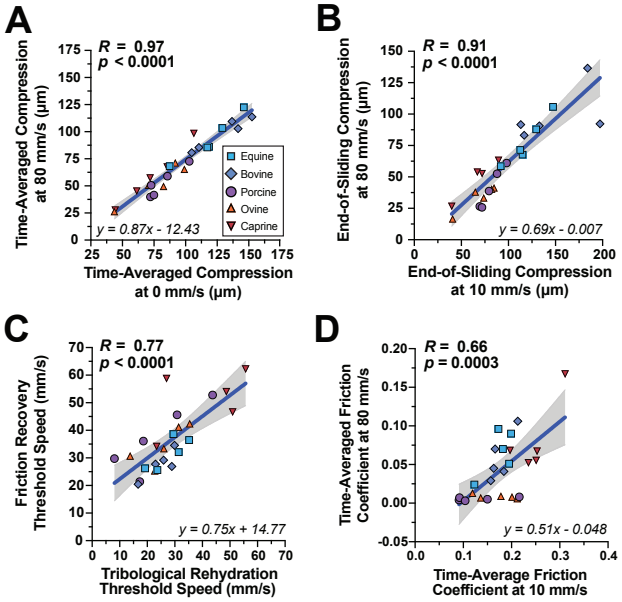

Fig. 2. Compressive behavior under static load was predictive of compression in response to sliding (A-B). Strain and friction showed similar speed dependencies (C), and slow-speed friction behavior was predictive of high-speed friction (D).

DISCUSSION

Our findings demonstrate that cartilage's ability to recover and sustain fluid load support under hydrodynamic sliding conditions are dependent upon tissue material properties, and more importantly, can be extrapolated from their static compression behaviors. More permeable tissues, with lower compressive and tensile moduli, exhibited increased relative exudation and rehydration, but required faster sliding speeds for recovery. Similar predictive relationships were identified among static exudation behaviors and slow cSCA sliding responses, and among slow- and high-speed sliding responses. An imperfect relationship between time-averaged compression under static and slow sliding conditions (i.e., *slope* ≠ 1) indicates the even slow speed sliding (10 mm/s) is capable of partially 'buffering' load-induced fluid exudation. Taken together, these results provide further context for cSCA-based studies of tribological rehydration within the broader cartilage tribology literature, the bulk of which comprises classical SCA tests under slow sliding speeds (0.1-10 mm/s) and show that cartilage's compressive response under hydrodynamic conditions can be surmised from its behavior in other widely used 'non-hydrodynamic' testing regimes. Additional relationships among structural and functional properties have been identified and will be explored in future work. Collectively, these findings provide a framework with which to interpret the effect of disease-associated changes in tissue properties on their subsequent hydration and tribomechanical responses during articulation.

REFERENCES [1] Ateshian, *J Biomech*, 42:1163-76, 2009. [2] McCoy, *Vet. Pathol.*, 52: 803-818, 2015. [3] Moore & Burris, *OA&C*, 23: 161-169, 2015. [4] Mancini *et al., Bone*, 127: 664-673, 2019. [5] Athanasiou *et al., JOR*, 9: 330-340, 1991. [6] Kupratis *et al.*, *Biotribology*, 2020 (*in press*). [7] Armstrong *et al., J Biomech Eng*, 106: 165-173, 1984. [8] Moore & Burris, *J Biomech,* 47: 148-153, 2014.

SILK-BASED BIO-INK WITH INTERPENETRATING NETWORK FOR EXTRUSION BIO-PRINTING.

Xuan Hao (Ernest) Tan (1), Wen Xin Tan (2), Cho Hong, James, Goh (2)

(1) NUS Graduate School of Integrative Sciences and Engineering, National University of Singapore, Singapore, Singapore.

(2) Biomedical Engineering Department National University of Singapore, Singapore, Singapore.

INTRODUCTION

Bio-printing is an emerging tissue engineering technique that has gained prominence in recent times. It's rising prominence is due to its ability to create 3-dimensional (3D) structures that not only help provide embedded cells with the appropriate 3D biological environment, it also recapitulates physiologically relevant structures that capture complex architectural details that could not be re-created using other tissue engineering methods [1]. Bio-printing can be performed using three main techniques, namely extrusion, inkjet and light-assisted printing [2]. Of these, extrusion bio-printing has proven to be the most popular technique, given its versatility in using a wide range of bio-inks affordability and ease of modification [3].

While bio-printing has gained prominence amongst the tissue engineering community, the main challenge is in developing bio-inks that are both printable and bio-functional. These two properties are often conflicting with each other and is adequately captured in the 'biofabrication paradigm' [4]. As such, much effort has been placed in the bio-printing community to develop bio-inks that push the biofabrication paradigm boundary. An exciting bio-ink candidate is silk fibroin (SF) which has garnered the interest of research groups around the world in recent years. Due to its superior mechanical properties, degradability and simple processibility, research groups are looking at using SF bio-inks to push the biofabrication paradigm. However, one major challenge of using SF bio-inks is in its poor viscosity characteristics when the protein is dissolved [5]. The challenge becomes even more prominent in relation to extrusion bio-printing, which requires shear-thinning bio-inks.

This paper describes the development of a silk-based bio-ink, containing an interpenetrating network between its constituents, that allows the bio-ink to be printed using extrusion bio-printing at room temperatures. This is done by functionalizing SF solutions with methacrylate groups (SilMA) and adding gelatin methacryoyl (GelMA) to form SilMA-GelMA (SG) bio-ink. This paper serves as a proof of concept that the SG bio-ink is suitable for extrusion bio-printing at room temperature. Structures can then be thermally stabilized using the appropriate photo-initiator and light exposure to allow bio-printed structures to be incubated at physiological *in vitro* conditions. The SG bio-ink demonstrates a simple way to functionalise SF for extrusion bio-printing, which has the potential to push the biofabrication paradigm, allowing for more detailed structures to be printed with greater bio-functionality.

METHODS

Organic silk fiber yarns were obtained from Chul Thai Co. Ltd., which were then degummed using 0.02M Sodium Carbonate solution to remove the hydrophilic sericin outer coating. The degummed fibers were left to dry in a fume hood overnight, at which point 9.3M Lithium Bromide solutions (LiBr) was used to dissolve the degummed fibers at 60^{o}C. Glycidyl Methacrylate (GMA) was added during the dissolution process to functionalise the SF protein chains with methacrylate groups, to confer photocrosslinkability. After dissolution, the resulting SilMA solution was then dialysed in DI water over 4 days to remove LiBr and unreacted GMA. The solutions were then dialysed in PEG solutions with average molecular weight of 10,000 MW to obtain the appropriate concentration. After dialysis, they were then stored at 4^{o}C until further use. GelMA was synthesized using protocols well established in other papers. Briefly, Type A gelatin was dissolved in DI water to form 10% w/v solutions. Methacrylic Anhydride (MeAH) was added drip-wise to the solution at 50^{o}C, and allowed to react for 3 hours. The resulting solution was then centrifuged, decanted, and dialysed in DI water to remove un-reacted MeAH for one week. The solution was then syringe

filtered under sterile conditions, lyophilized and stored in -20ºC until further use.

The SG bio-inks were made by first syringe filtering the SilMA solutions under sterile conditions. The required lyophilized GelMA was then added to the sterile SilMA solutions and stirred at 50ºC until complete dissolution. Lithium phenyl-2,4,6 trimethylbenzoylphosphinate (LAP) measuring to 0.2% w/v was also added to the solution as the photo-initiator. The resulting bio-ink was then left in 4ºC to form an extrudable hydrogel that can be used for subsequent experiments. Single Sweep Rheology was performed using TA Instruments RH-2 Discovery with 20mm flat disc attachment to obtain the Viscosity against Shear Rate profile. Briefly, the SG bio-inks were loaded onto the rheometer platform and measured between 1/100 to 1000 rotations per second. This was performed under 25ºC with 1 minute of soak time. Viscosity and shear stress against shear rate was then measured accordingly.

Bio-printing was performed using Cellink Inkredible+ Bio-printer, in which porcine Nasal Chondrocytes (pNCs) were mixed in SG bio-inks at a cell density of 1 x 10^7 cells per ml. The cell-laden SG bio-inks were then bio-printed at approximately 50-70kPa, exposed to UV light (of 365nm and 405nm) for 2 minutes and subsequently incubated in either control culture medium or chondrogenic medium. Live/dead viability assays were performed at various timepoints to assess if pNCs could survive within the bio-printed constructs. After 14 days, the constructs were fixed with formalin, and immunohistochemistry (IHC) was performed with anti-rabbit AP-polymer and rabbit Col II antibodies to assess if pNCs could express appropriate phenotype.

RESULTS

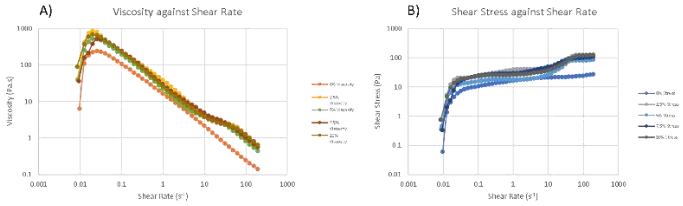

Figure 1: Rheological properties of SG Bio-Ink. A) Viscosity against Shear Rate profile. B) Shear Stress against Shear Rate profile.

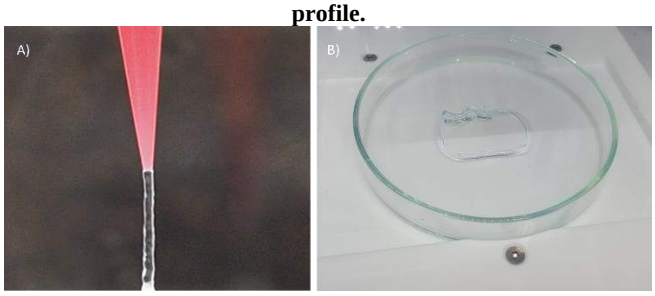

Figure 2: Printability demonstration of SG Bio-ink. A) Close-up photo of extruded filaments. B) Shape retention of bio-printed cat structure using SG Bio-ink.

Single sweep rheology showed that the SG bio-inks possess shear thinning properties as shown by the downward slope of the viscosity against shear rate graphs of all SG bio-ink compositions as seen in figure 1. This indicates that as shear rate increases, viscosity decreases, which is favorable for bio-printing applications. This was also confirmed by the shear stress vs shear rate graph as shown by figure 1B. The printability of the SG bio-ink was also confirmed as shown by figure 2. Figure 2A shows the extrusion of SG bio-inks as a single, continuous filament, with little deviation from the exit nozzle. Figure 2B also shows that the extruded filaments could retain its bio-printed shape.

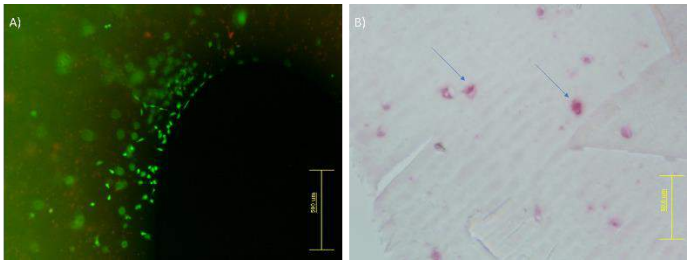

Figure 3: Bio-functional properties of SG Bio-inks. A) Live/Dead image of embedded pNCs. Note that pNCs towards the edge show cell elongation. B) IHC of SG Bio-ink using Col II antibodies. Red indicating positive stain.

The bio-functional properties of SG bio-inks were also demonstrated by the live/dead assay and IHC results as shown in figure 3. Figure 3A shows the live/dead image captured at day 7. The interesting thing to note about figure 3A is the elongation of pNCs at the edge of the SG bio-ink, which indicates that pNCs at the edges are experiencing proliferative activity. Figure 3B shows the IHC images of SG bio-inks that were formalin fixed at 14 days and stained for Col II antigens. Red stains indicate positive Col II antigen expression. One thing to note is that the pericellular area shows some signs of degradation, which indicates that the embedded pNCs could be re-modelling the bio-ink matrix surrounding it.

DISCUSSION

Because extrusion bio-printing is one of the most affordable and versatile bio-printing techniques, it is crucial that novel bio-inks are developed for extrusion methods so that there is greater adoption of bio-printing techniques around the world. The main challenge, however, is in developing bio-inks that also push the boundaries of the biofabrication paradigm, with a balance between the printability and bio-functionality characteristics. SF, being a recent entrant as a bio-ink candidate, also must be functionalized to push the boundaries of the paradigm.

In this paper, we present a simple method of functionalizing SF for extrusion bio-printing. By leveraging on GelMA's ability to form gel-like structures at room temperature [6], the combination of both SilMA and GelMA to form SG bio-inks results in a bio-ink that can be easily used in extrusion bio-printing applications. Furthermore, the methacrylate functional group that exist on both SilMA and GelMA allows both to photocrosslink to form an interpenetrating network, further enhancing the mechanical properties of the final structure.

Further development of the SG bio-ink needs to be done to characterize the mechanical properties of the bio-printed structure, and its degradation profile. Also, more work needs to be done to examine if other cell types can be used in conjunction with the SG bio-ink and whether these cells can still maintain its phenotypic expression.

ACKNOWLEDGEMENTS

This study was supported by a Ministry of Education (MOE) Academic Research Fund Tier 2 grant (Grant number: MOE2017-T2-2-150).

REFERENCES

[1] Dey M et al. *Nature S. Reports,* 10:14023, 2020
[2] Ibrahim T,O et al, *Additive Manufacturing,* 13:179-200, 2017
[3] Wei S et al, *Biofabrication,* 12: 022002, 2020
[4] Malda J et al. *Advanced Materials,* 36:5011-5028, 2013
[5] Chawla S et al, *A. Healthcare M.*, 8:1701204, 2018
[6] Loessner D et al, *N. Protocols,* 11:727-746, 2016

COMPARISON OF HEAD IMPACT EXPOSURE ACROSS COMMON TRAINING ACTIVITIES IN YOUTH SOCCER

N. Stewart Pritchard, MS (1,2), Tanner M. Filben, MS (1,2), Sebastian Haja, BS (1), Logan E. Miller, PhD (1,2), Mark A. Espeland, PhD (3), Joel D. Stitzel, PhD (1,2), Jillian E. Urban, PhD, MPH (1,2)

(1) Department of Biomedical Engineering
Wake Forest School of Medicine
Winston-Salem, NC, USA

(2) School of Biomedical Engineering and Sciences
Virginia Tech – Wake Forest University
Winston – Salem, NC, USA

(3) Department of Internal Medicine
Wake Forest School of Medicine
Winston-Salem, NC, USA

INTRODUCTION

Soccer is a popular sport in the United States, but the nature of the sport exposes players to repetitive head impacts and increased risk of concussion.[1] Repetitive head impacts in soccer have been associated with deficits in clinical outcomes such as reduced processing speed[2] and neuro-ophthalmological function,[3] which may be the result of microstructural changes occurring in the brain.[4] In response to the growing concern over the potential short- and long-term effects of head impacts in soccer, the United States Soccer Association banned heading for youth athletes age 10 and younger and added restrictions for athletes age 11-12.[5]

Head motion sensors coupled with time-synchronized video have been used to characterize the frequency and magnitude of head impacts in youth soccer.[6–8] Associations between head impact magnitude and frequency and athlete-specific factors such as sex and age have been observed as well as mechanistic factors such as ball delivery method and impact type. Yet, it is unclear how head impact exposure may vary by the activities the athlete engages in during training. In sport, practice sessions are a compilation of unique training activities designed to improve skill and performance that may also affect head impact exposure.[9] Characterizing head impacts across common activities performed in soccer can help to inform meaningful interventions that aim to reduce head impact exposure through changes in training regimens. Therefore, the objective of this study was to compare head impact exposure across common training activities in soccer.

METHODS

Eight youth soccer players (13.5 ± 0.11 yr, 166.8 ± 5.57 cm, 60.1 ± 9.28 kg) from a single U14 soccer team were recruited to participate in this study. To assess head impact exposure, a combination of film review (to assess head impact frequency) and kinematic sensor analysis (to assess head impact magnitude) was utilized. Head kinematic data was collected using a custom mouthpiece instrumented with a tri-axial accelerometer and gyroscope. Players wore the mouthpiece sensor during all practices and games during the study period. Data was collected from the accelerometer and gyroscope at 4,681 Hz and 800 Hz, respectively for 60 ms (15 ms pre-trigger, 45 ms post-trigger) whenever the device recorded linear acceleration above 5 g (season 1) or 3.5 g (season 2) for at least 3 ms. Sensor thresholds were adjusted in the second season to increase the number of video-verified head impacts recorded by the sensor. Kinematic data was processed following the steps of Rich et al.[10] Briefly, the data was calibrated to standard units (g and rad/s), filtered, rotated to align with a conventional coordinate system and zero-offset. Rigid body dynamics were used to transform the measured linear acceleration to the center of gravity of the head. A time-synchronized camera was used to film each practice and game. Events without head contact were excluded from the present analysis. The film collected from each practice and game was reviewed to identify all head contact events that occurred from each player enrolled in the study and to video-verify all sensor recorded events. Reviewers recorded the time and impact type of each head contact event. Possible impact types included: ball-to-head impacts, player-to-player collisions, ground contact, and other impacts (e.g., player's head touches the ground during core conditioning).

During each session, research staff recorded all activities performed by each enrolled player. The start and end time and description of each activity was recorded. If a player was inactive during any part of the activity (i.e. on the bench), the time the player was inactive was subtracted from the total time of the activity to obtain the player-specific exposure time. Each activity was characterized as one of 16 drill types under the advisement of the coach. Each drill was further categorized into one of 5 activity types: technical training, team

interaction, position specific, set pieces, and other (e.g., conditioning). The time of each mouthpiece recorded and film reviewed head contact event was used to pair the event with a corresponding drill/activity type.

Peak resultant linear acceleration, rotational velocity, and rotational acceleration were computed from kinematic data corresponding to a video-verified event. Impact rate was computed from the head impacts observed in the film review. Mixed effects models were used to compare peak kinematic metrics across activity types while controlling for the session date and season. All kinematic metrics were log-transformed prior to analysis and back-transformed to report results. A generalized linear model using a negative binomial link function was used to identify differences in impact rate across activity types. Activities with fewer than 20 total head impacts and/or less than 5 hours of total exposure were excluded from statistical comparisons of kinematics and impact rate, respectively.

RESULTS

The eight players enrolled in the study were monitored over 110 sessions (n=72 practices, n=38 games) across two seasons. Only 6 players were monitored in the second season as two players declined to continue with the study. Each player was exposed to an average of 106.0 hours of soccer activities throughout the two seasons of soccer. This consisted of an average of 31.6 hours of team interaction, 31.3 hours of technical training, 23.8 hours of game play, 16.0 hours of other activities, 0.3 hours of set pieces, and 0.3 hours of position specific activities for each player. A total of 4,329 head impacts (n=2,583 season 1, n=1,746 season 2) were observed from film review of which 2,001 head impacts (46%; n=990 season 1, n=1,001 fall) were recorded by the mouthpiece. Most head impacts (film reviewed [mouthpiece recorded] occurred during technical training activities (86%, n=3,736 [1,737]) followed by other activities (5%, n=225 [96]), game play (4%, n=188 [96]), team interaction activities (4%, n=167 [61]), and position-specific activities (<1%, n=13 [9]). No head impacts occurred during set pieces.

Overall, mean head impact rates were greater during practice (4.09 per player per practice) than games (2.53 per player per game). Technical training activities were associated with the highest head impact rate across activity types. Overall, mean peak kinematic magnitudes were 9.57 g, 4.30 rad/s, 0.69 krad/s^2. For each kinematic variable, a significant main effect was observed for activity type (all $p<0.0001$) and drill type (all $p<0.0001$). Figure 1 compares the mean head impact magnitude and frequency across activity types. Head impacts occurring during game play were associated with the greatest mean peak linear acceleration and mean peak rotational acceleration compared with all activity types. A total of 30 (31%) head impacts >20 g were observed during game play compared with 27 (1.6%) during technical training. Head impacts occurring during team interaction activities resulted in significantly greater peak rotational acceleration than technical training and other activity types (all $p<0.001$). Peak rotational velocity during team interaction and game play activities had significantly greater mean kinematic magnitudes compared with other and technical training activity types (all $p<0.0001$). A total of 1,389 (80%) head impacts occurring during technical training activities were below 10 g. Ball-to-head impacts were the most common type of impact across activity types except position-specific activities where falls and dives were most common. A small number of player-to-player collision related head impacts were reported in technical training (n=4), team interaction (n=7), and game play (n=3) activities.

DISCUSSION

This study compared head impact exposure across common activities in youth soccer. To the best of the researcher's knowledge this is the first study to characterize head impact exposure across common activities in soccer. Technical training activities exposed players to significantly greater impact rates than all other activity types but mean head impact kinematics were significantly lower than other activity types. Moreover, game play and team interaction activities exposed players to the greatest mean peak head impact kinematics but at much lower frequencies than other activity types. Although mean kinematics were greater in game play and team interaction activities, a similar number of head impacts greater than 20 g were experienced in both technical training activities and game play activities. These events may be attributed to increased ball velocity and/or use of poor header technique. Soccer balls with reduced mass and/or ball pressure have been shown to reduce impact forces, and the use of these soccer balls during technical training activities may help to reduce head impact magnitudes[11]. Interventions designed to reduce head impact frequency may benefit from targeting technical training activities, whereas interventions designed to reduce head impact magnitude in soccer may benefit from targeting team interaction and game play activities.

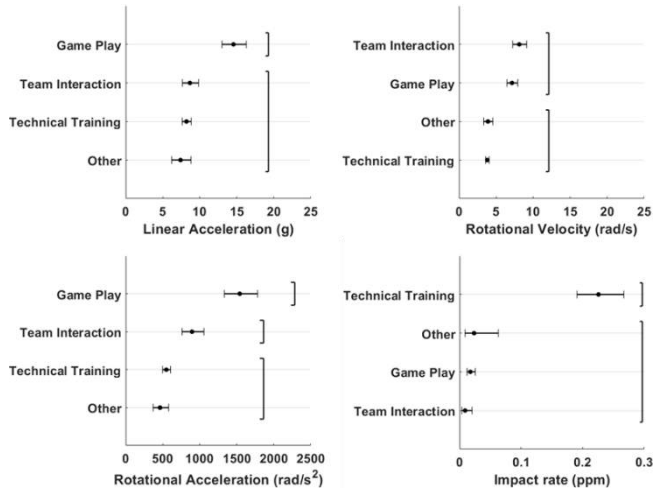

Figure 1. Head impact exposure across activity types in soccer. Markers represent the mean and lines represent the 95th% confidence interval. Mean values of activity types not bounded by the same bracket were significantly different.

ACKNOWLEDGEMENTS

The authors received support from the Childress Institute for Pediatric Trauma at Wake Forest Baptist Medical Center to complete this study. The authors would like to thank the athletes, coaches, and club who participated in this study for their generous support. They would also like to thank Konstantia Strates for her efforts in coordinating the study and Megan Hayden and Kathryn Romano for their efforts in collecting and processing data.

REFERENCES

[1] Langhorst P. EngageSports. [2] Levitch CF et al. *J Int Neuropsychol Soc*. 2020;26:633-644. [3] Nowak MK et al. *JAMA Ophthalmol*. 2020;138(4):350-357. [4] Lipton ML et al. *Radiology*. 2013;268(3). [5] *US YOUTH SOCCER POLICY ON PLAYERS AND PLAYING RULES As Of*.; 2020. [6] Miller LE et al. *Res Sport Med*. 2019;0(0):1-17. [7] Chrisman SPD et al. *Clin J Sport Med*. 2019;29(1):1. [8] Reynolds BB et al. *Orthop J Sport Med*. 2017;5(4):1-10. [9] Kelley ME et al. *J Neurosurg Pediatr*. 2019;23(3):381-389. [10] Rich AM et al. *Ann Biomed Eng*. 2019;47(10):2109-2121. [11] Auger J et al. Useche SA, ed. *PLoS One*. 2020;15(10):e0240162.

MECHANICAL RESPONSE OF MOUSE CERVICES LACKING DECORIN AND BIGLYCAN DURING PREGNANCY

Nicole A.L. Lee (1), Lei Shi (1), Mariano C. Caraballo (2), Shanmugasundaram Nallasamy (2), Charles Jayyosi (1), Mala Mahendroo (2), Kristin M. Myers (1)

(1) Department of Mechanical Engineering
Columbia University
New York, NY, USA

(2) Department of Obstetrics and Gynecology and Green Center for Reproductive Biology Sciences
University of Texas Southwestern Medical Center
Dallas, TX, USA

INTRODUCTION

Proper cervical function, acting as a barrier between the fetus and the external environment, is critical to a healthy pregnancy. The tissue must stay closed throughout gestation and remodel sufficiently at the appropriate time to allow for an at-term delivery [1]. Premature remodeling of the cervix is a final common pathway for premature birth (PTB), defined as birth before 37 weeks of gestation, and PTB prediction and prevention remains a significant clinical challenge [2]. Murine models are therefore used to understand the evolution of the gravid cervix. Remodeling of the mouse cervix over the 19 days of gestation has been previously characterized and attributed to changes in the extracellular matrix and collagen turnover [3,4]. This study will explore the role of extracellular proteins in cervical mechanics over pregnancy using genetic knockout mouse models.

Small leucine rich proteins (SLRPs) are one of many components found in the extracellular matrix (ECM) of biological tissues, including cervical tissue [5]. Decorin and biglycan are SLRPs found in the mouse cervix, and their roles have been studied previously in many other tissue types, including tendon and heart [6,7]. Both SLRPs have been implicated in the formation and assembly of ECM structural components, mainly the collagen fibers [8,9]. TEM imaging studies of cervical tissue demonstrated a gestation-dependent effect of decorin loss on the microstructure, in which aberrant collagen fibrils are observed only in early pregnancy [4]. Also, previously unpublished data shows abnormal elastic fibers in cervical tissue with a loss of these proteoglycans. Due to the high homology between the 2 SLRPs, it is of interest to study the two proteoglycans together and their possible compensatory behaviors. Furthermore, mice lacking decorin and bigylcan (DKO) manifest complications in pregnancy, but cervical function has not yet been studied [10]. The goal of this study was to characterize the mechanical behavior of mouse cervices lacking decorin and/or biglycan through pregnancy and understand how they may contribute to cervical dysfunction. With the motivation to observe the hyperviscoelastic behavior typical of hydrated, soft tissue, we develop a mechanical test that would elicit these mechanical behaviors and examine the role of SLRPs in instantaneous and viscoelastic properties, their evolutions being a key feature of tissue softening in pregnancy [11].

METHODS

A viscoelastic testing protocol was developed to assess the role of decorin and biglycan in cervical mechanics. Six mouse genotypes were tested in this study, as shown in Table 1. Cervix samples were collected from non-pregnant (NP) mice and mice at day 18 (d18) of gestation, with 19 days considered term. Five of each genotype was tested, except DKO, for which two were tested. Samples were prepared for whole-specimen ring tensile loading, as previously described [12].

Table 1: 6 genotypes for NP and d18 time points.

Name	Genotype
Wildtype (WT)	Dcn +/+ Bgn +/+
Decorin Knockout (DcnKO)	Dcn -/- Bgn +/+
Biglycan Knockout (BgnKO)	Dcn +/+ Bgn -/-
Decorin Knockout, Biglycan Heterozygous (DB)	Dcn -/- Bgn +/-
Biglycan Knockout, Decorin Heterozygous (BD)	Dcn +/- Bgn -/-
DKO	Dcn -/- Bgn -/-

Samples were first allowed to swell for 2 hours in phosphate-buffered saline with 2 mM ethylenediaminetetraacetic acid. The loading protocol consists of 2 main sections: 1) strain rate sensitivity cyclic load-unloads and 2) stress relaxation ramp- holds (Fig.1). Different load levels were applied for NP and d18 to ensure each sample could sustain a majority of the test without breaking. Between each loading, the sample was held at zero displacement for 20 minutes to recover.

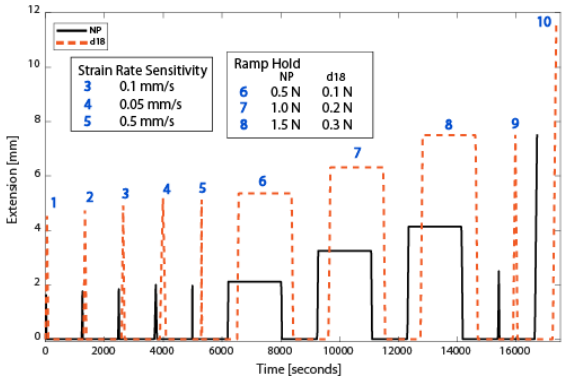

Figure 1: Viscoelastic Loading Regimen for NP and d18 samples.

Sample geometry was tracked and used to generate stress-stretch curves from which structural parameters were determined. A 2-term exponential decay function was fit to each ramp hold to characterize the time-dependent behavior. A microstructurally-inspired material model was fit to the equilibrium behavior of the ramp hold section using inverse finite element methods (IFEA). The model consists of fibers embedded in a compressible ground substance. The fiber component is a free joint chain and, in a configuration, inspired by the Arruda-Boyce 8 chain model [13]. The free energy density is:

$$\psi(I_1,J) = n\theta kN\left[\frac{\sqrt{I_1}}{\sqrt{3N}}\beta + \ln\left(\frac{\beta}{\sinh\beta}\right)\right] - \frac{nk\theta}{3}\sqrt{N}\beta_0 \ln J + \frac{1}{2}\kappa(\ln J)^2 \qquad (1)$$

where N is the locking stretch of the chain, ξ=nkθ is strength coefficient, and κ is the bulk term. A genetic algorithm was applied to optimize the three material parameters for each sample [Under Review]. The force-displacement and final thickness-displacement data were used for fitting. The width-displacement and length-displacement were used for validation. A non-parametric ANOVA with a posthoc t-test (p-value <0.05) was used to assess significance.

RESULTS

The cervix indeed exhibited hyperviscoelastic behavior. The model captured the equilibrium force and thickness data and provided a good match to the width and length data (Fig.2).

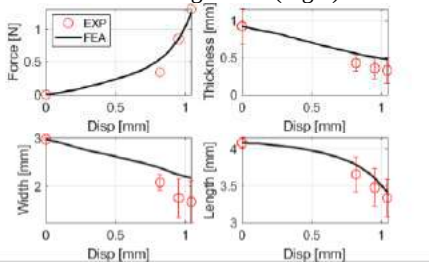

Figure 2: Representative fitting from IFEA. Fit Force-Disp. and final Thickness-Disp. Validate with Width-Disp and Length-Disp.

An increase in N was observed in late pregnancy, indicating an increase in stretchability of d18 samples (Fig3A-B). A decrease in ξ and κ with d18 samples indicates a decrease in stiffness and resistance to compression consistent with softening (Fig3C-F). Surprisingly, for NP, no difference between parameters for genotypes was observed, but after cervical remodeling, this model describes a material difference between knockouts and WT. BgnKO, BD, and DKO exhibited a decreased N compared to WT, indicating a loss of stretchability (Fig3B). Remarkably, DcnKO and DB had a similar N to WT. Although not significant, the knockouts' ξ increased compared to WT, with DKO being the stiffest of the genotypes (Fig3D). In comparing structural parameters of cycles 3-5 (Fig. 1), strain rate dependency was not observed. The time constants of the exponential fit were higher in knockouts than WT, indicating a slower stress dissipation.

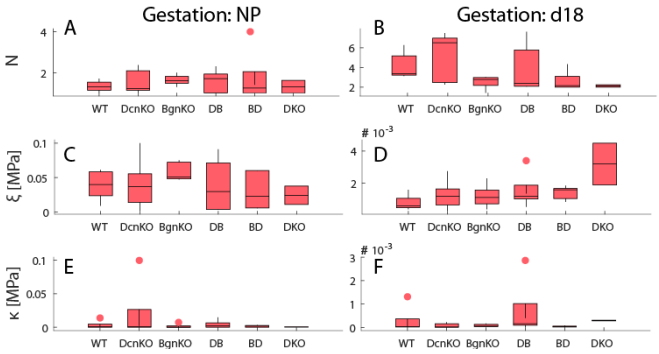

Figure 3: Optimized material parameters by gestation and genotype. A-B) Locking stretch N, C-D) Strength coefficient ξ, E-F) Bulk term κ

Decreased rupture stress and stretch highlight the mechanical insufficiency of the knockout models.

DISCUSSION

The material model captures the equilibrium material behavior of cervical tissue, describing force and 3D tissue deformation. Moving from a phenomenological model, this relatively simple microstructure-based model with three parameters can capture large deformation behavior of both NP and d18 mouse cervices. The change in parameters between NP and late pregnant mouse cervix was also reflected in the human cervix [Shi et al, In Preparation]. The d18 DKO fiber was less stretchable (lower N). An essential characteristic of a correctly remodeled d18 cervix is its high extensibility without breaking, indicating a possible mode of cervix mechanical failure. The material model and changes in rupture and stress relaxation between genotypes indicate the role of decorin and biglycan is gestation dependent as some deficiencies are recovered, while others augmented through cervical remodeling. Ultimately, these modeling efforts are towards our goal of modeling the viscoelastic material response of cervix.

Limitations of this experiment include simplified cervical geometry. The small sample size limited statistical power, but trends are still evident. The data indicates the crucial role of decorin and biglycan in the proper remodeling of cervical tissue during pregnancy and offers insight into how proteoglycans support its proper mechanical function.

ACKNOWLEDGEMENTS

Research in this abstract was supported by the National Science Foundation CAREER award (CMMI 1454412) to KMM and the Eunice Kennedy Shriver National Institute of Child Health & Human Development under Award R01HD088481 to KMM and MM.

REFERENCES

[1] Timmons, B. et al., *Trends in Endocrinology & Metabolism*, 21(6): 353-361, 2010.
[2] Vink, J. et al., *Seminars in Perinatology*, 41:427-437, 2017.
[3] Yoshida K. et al. *PLOS One*, 9(11): e112391, 2014.
[4] Nallasamy S. et al., *Endocrinology*, 158(4):950-962, 2017.
[5] House M. et al. *Seminars in Perinatology*, 33(5): 300-307, 2009.
[6] Gordon JA et al., *J Biomech*, 48(10):2110-2115, 2015.
[7] Weis S. et al. *Matrix Biology*, 24(4):313-324, 2005.
[8] Danielson K.G. et al. *J Cell Biol*. 136(3): 729-743. 1997.
[9] Young, MF.et al. *Glycoconjugate J*, 19(4-5):257-262, 2002.
[10] Calmus M. et al. Reproduction, 124(1): 183-194, 2011.
[11] Yoshida K. et al. *Interface Focus*, 9(5).
[12] Jayyosi C. et al., *Acta Biomaterialia*, 78:308-319, 2018.
[13] Arruda et al. *Journal of the Mechanics and Physics of Solids*, 41(2): 389-412, 1993.

SB³C2021
Summer Biomechanics, Bioengineering and Biotransport Conference
June 14-18, Virtual

SPECTRAL BANDEDNESS IN HIGH FIDELITY CFD PREDICTS RUPTURE STATUS IN INTRACRANIAL BIFURCATION ANEURYSMS

Daniel E. MacDonald, Mehdi Najafi, Lucas Temor, David A. Steinman

Department of Mechanical & Industrial Engineering
University of Toronto
Toronto, ON, Canada

INTRODUCTION

Recent studies using high-fidelity computational fluid dynamics (CFD) in patient-derived cerebrovascular geometries have revealed high-frequency flow instabilities, which have been speculated to contribute to the growth and rupture of intracranial aneurysms (IAs) **[1, 2]**. Various techniques have quantified the power of these instabilities, such as fluctuating kinetic energy and spectral power index (SPI) **[3]**, but these metrics have yet to show association with IA rupture.

In experimental studies, IAs have been observed to emit acoustic *bruits,* which are thought to result from "turbulence"-induced wall vibration **[4]**. These vibrations are difficult to measure in-vivo and have not been a reliable source of diagnostic information, but hint at intriguing associations between acoustic harmonics and IA stability.

Spectrograms of cardiovascular CFD data have been demonstrated as a method for summarizing spectro-temporal hemodynamic trends over a spatial domain. In **[5]**, sac-averaged spectrograms reveal coherent harmonic banding, suggesting the presence of vortex-shedding phenomena in the IA sac, as distinct from more broadband spectra associated with turbulent-like flow. The hemodynamic implications of such narrowband harmonic flow structures, which could preferentially trigger IA wall vibrations **[6]**, have yet to be studied in detail.

Spectrograms are a common audio representation for which a broad array of quantification and decomposition tools exist **[7]**. In this paper, we make novel use of this audio-processing literature to present a method for quantifying narrowband harmonics from CFD spectrograms, and explore them for possible associations with rupture in a cohort of 48 patient-derived IA geometries.

METHODS

We propose a method based on spectral chroma features, which are a cyclical representation of frequency commonly used in musical audio processing for identifying similar pitches across octaves of an equal-tempered scale **[7, 8]**. For example, the consecutive doubling of a given frequency (e.g., 100, 200, 400, 800 Hz) are all considered to have the same pitch class and thus chroma value, c, as given by:

$$c = log_2 f + \lfloor log_2 f \rfloor$$

where f is the frequency and $\lfloor \cdot \rfloor$ indicates the floor function. Each frequency has a unique chroma value $c \in [0, 1)$.

To calculate a chroma power spectrum from a frequency power spectrum, power is integrated over frequency bins with equivalent chroma values. Broadband chroma power may suggest noise, while power concentrated into narrow regions of chroma suggest harmonic structure. A *chromagram* depicts the chroma power as a function of time. To quantify the concentration of chroma power in a chromagram derived from a sac-average spectrogram, we compute the time-varying dynamic range of chroma power and normalize by the range of the final time frame; this ratio is termed the *narrowbandedness ratio* (NBR).

To assess the possible relationship between NBR and rupture status, we used a dataset of 48 high-fidelity *pulsatile* CFD simulations of patient-derived bifurcation IA geometries from the AneuriskWeb project database **[9]**. Simulation details, including meshing strategy and solver settings, are as described in **[10]**. The methodology for generating sac-averaged spectrograms of hemodynamic velocity is detailed in **[5]**. Chromagrams were generated from the sac-averaged spectrograms using the chroma_stft module of the Librosa 0.8.0 audio toolkit in Python **[7]**. From these chromagrams, we calculated NBR.

To assess relationship with rupture status, we performed univariate logistic regression for previously established geometric and hemodynamic factors (IA size; size ratio (SR); time-average wall shear stress (TAWSS); oscillatory shear index (OSI)) **[11]** with time-averaged NBR. For each model, we computed significance tests using Student's t-test for normally distributed data and the Mann-Whitney U test for

non-normally distributed data using a critical value of p=0.05 to reject the null hypothesis of equivalent populations. Standard clinical receiver operating characteristics (ROC) analysis was performed to compare the performance of each regression model, as quantified by the area under each ROC curve (AUC).

RESULTS

Results from three representative high-fidelity CFD cases are shown in Figure 1. The spectrograms of (Aneurisk case IDs) C0029 and C0078 demonstrate narrowband harmonic structures. The respective chromagrams show energy concentrated within narrow chroma bands, and the time-varying histograms of chroma power show periods of high dynamic range. The spectrogram of C0052 demonstrates the presence high-frequency flow instabilities, but exhiibits little banding in the spectrogram or chromagram. The chroma dynamic range contracts near peak systole, suggesting characteristics of broadband noise, i.e. turbulent-like flow.

Figure 2 shows the ROC analysis using all 48 cases, summarizing various performance metrics for the univariate logistic regression models. Only the proposed NBR was found to be a significant predictor of rupture for this dataset (p=0.008); however, owing to the relatively wide CIs, none of the AUCs themselves were significantly different.

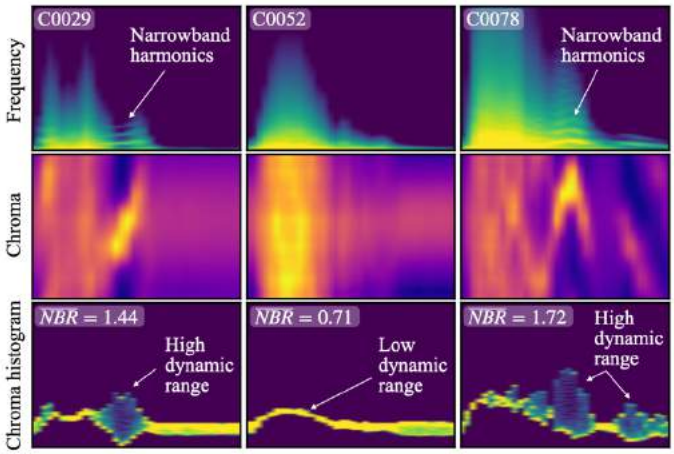

Figure 1: Representative results from 3 of 48 cases, showing: (top) sac-averaged spectrograms (frequency 0-1314 Hz), (middle) chromagrams; (bottom) histograms of chroma power, with corresponding NBR value. X-axis is time (one cardiac cycle).

DISCUSSION

The harmonic quality of blood flow instabilities may be an important feature in the search for predictors of IA rupture. In this cohort of 48 cases, narrowband chroma power of sac-averaged chromagrams was shown to have stronger association with rupture compared to established geometric and hemodynamic predictors. The presence of multiple harmonic bands in a sac-average spectrogram is speculated to result from vortex-shedding in the IA sac, and thus supports further research of IA vibration and its potential mechanobiological effects on aneurysm wall integrity.

The associations of IA size, SR, TAWSS, and OSI with rupture status were weaker than previously reported in **[11]**. This may be due to our use of a smaller cohort (n=48 vs n=204 cases). On the other hand, it might be due to or our focus on bifurcation IAs compared to their cohort of both bifurcation and sidewall IAs, since morphological and hemodynamic predictors of rupture have previously been shown to differ significantly in bifurcation vs. sidewall IAs **[12]**.

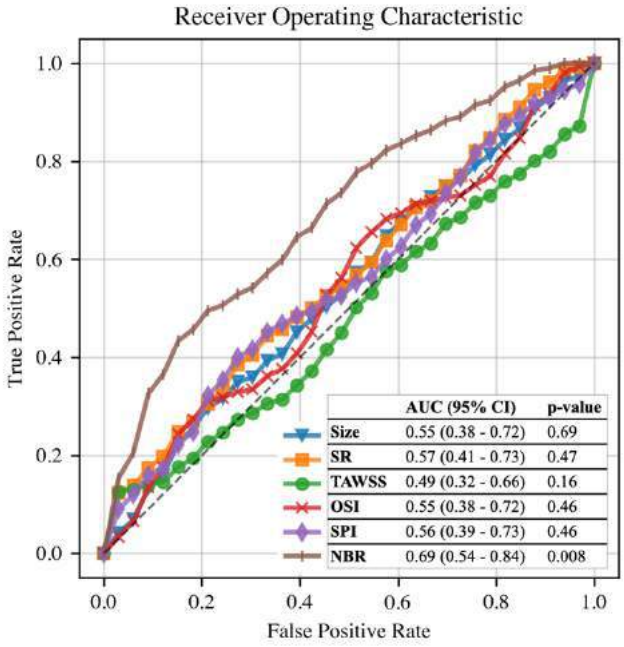

Figure 2: ROC curves of probabilities from each univariate logistic regression. CI = confidence interval

As noted in the Methods, the chroma equation maps frequencies according to a geometric progression given by the consecutive doubling of a fundamental frequency. Flow-induced harmonics may behave more closely to integer multiples of a fundamental frequency, as suggested by the evenly spaced banding in the spectrograms of C0029 and C0078. Nevertheless, since spectral power tends to decay with frequency, we expect the chromagram to be dominated by low-frequency spectral power and, in the presence of integer harmonics, by the low-integer harmonics.

Patient-specific flow rates were not available for the Aneurisk cases, so we used a well-validated power-law **[13]** to estimate pulsatile flow conditions for each case. As flow instabilities are likely more sensitive to inflow rates than other hemodynamic factors [**3**], sensitivity of NBR to such uncertainty must still be explored and quantified. Further work will also focus on better understanding the fluid dynamical phenomena implicated by these narrowband harmonics.

ACKNOWLEDGEMENTS

Supported by a grant from the Natural Sciences & Engineering Research Council of Canada.

REFERENCES

[1] Valen-Sendstad K et al., *J Biomech*, 44:2826-32, 2011.
[2] Cebral JR et al., *Am J Neuroradiol*, 38:119-26, 2017.
[3] Khan MO et al., *J Biomech*, 52:179-82, 2016.
[4] Ferguson GG et al., *J Neurosurg*, 33:485-97, 1970.
[5] Natarajan T et al., *J Biomech*, 110:109977, 2020.
[6] Aaslid R & Nornes H., *J Neurosurg*, 60:32–36, 1984.
[7] McFee B et al., *Proc of 14th Python in Science*, 8:18-25, 2015.
[8] Bartsch MA et al., *IEEE Trans on multimedia*, 7:96-104, 2005.
[9] AneuriskWeb, http://ecm2.mathcs.emory.edu/aneuriskweb, 2012.
[10] Natarajan T et al., *CMBBE Imaging Vis*, 8:182-93, 2020.
[11] Xiang J et al., *J Neurointerv Surg*, 8:104-10, 2014.
[12] Baharoglu MI et al., *J Neurosurg*, 116:871-81, 2012.
[13] Chnafa C et al., *J Biomech*, 26:159-65, 2018.

VIRTUAL RESEARCH MENTORING BETWEEN GRADUATE AND UNDERGRADUATE STUDENTS DURING THE COVID-19 PANDEMIC

Julie E. Speer (1), Max Lyon (2), Julia Johnson (3)

(1) Setton Laboratory
Department of Biomedical Engineering
Washington University in St. Louis
St. Louis, MO, USA

(2) Santi Laboratory
Center for Reproductive Health Sciences
Washington University School of Medicine in St. Louis
St. Louis, MO, USA

(3) Center for Teaching and Learning
Washington University in St. Louis
St. Louis, MO, USA

INTRODUCTION

Participating in research as an undergraduate student has been associated with beneficial outcomes such as increased GPA, retention in STEM majors/careers, and the development of a scientific identity[1]. Serving as a mentor to undergraduate researchers is a common feature of graduate training and offers an opportunity for graduate students to gain experience in teaching and research management[1]. In STEM, these mentorships typically occur through face-to-face interactions in the laboratory where both the undergraduate mentee and graduate mentor have access to laboratory equipment, reagents, and other research samples. The onset of the COVID-19 pandemic and associated stay-at-home orders and social distancing measures meant that many research mentorships were required to transition to a work-from-home model and use virtual platforms to accomplish research goals.

Virtual mentoring (also referred to as e-mentoring or digital mentoring) has been used for over two decades and has been shown to promote many of the same benefits as face-to-face interactions, such as social and academic support and professional development[2]. Virtual mentoring has several advantages including increased flexibility in meeting times and locations comparted to in-person mentoring[2]. However, virtual mentoring also has challenges (e.g. technology and privacy) and adjusting to the format can be difficult[2]. When campuses shut down due to COVID-19 and transitioned to online learning, many resources were made available to educators to assist with using synchronous and asynchronous classrooms, setting new guidelines for students, and altering attendance/grading policies. In contrast, at some institutions relatively little guidance was provided to graduate students on how to maintain their own research productivity and how to continue mentoring undergraduate researchers.

The objective of the present study was to understand how undergraduate mentees and graduate mentors at one private R1 institution (Washington University in St. Louis) adjusted research mentorships to the virtual environment at the onset of the COVID-19 pandemic (Spring 2020 semester). Here we seek to determine if there were changes in the mentoring relationships, communication, and productivity when switching to virtual mentoring and to identify the benefits and challenges mentors and mentees experienced.

METHODS

A survey was developed using Qualtrics software (Qualtrics, Provo, UT) that included multiple choice, Likert scale, and short response questions, and asked students to reflect upon their virtual mentorships during the COVID-19 pandemic. In June 2020, an email was sent to undergraduate and graduate students in six departments at Washington University in St. Louis where research is largely conducted in wet laboratories (Biology, Chemistry, Physics, Biomedical Engineering, Mechanical Engineering and Materials Science, and Earth and Planetary Sciences). Undergraduate students who had been mentored by a graduate student ("mentees") or graduate students who had mentored an undergraduate student ("mentors") during the Spring 2020 semester were invited to participate in the survey.

Survey participants were required to state their research role (mentor or mentee) but otherwise were permitted to leave other questions blank. Subsequent questions asked students to rank their overall research experience (occurring from January to May 2020) and to indicate how virtual research (March to May 2020) compared to their face-to-face interactions prior to the onset of the pandemic (January – March 2020). At the end of the survey, students were asked to indicate their academic department and year of study. This research study was conducted with approval from the Washington University in St. Louis Institutional Review Board.

117 total respondents participated in the survey (79 undergraduate mentees and 38 graduate mentors) and these individuals represented all academic years and departments surveyed. Analysis of the qualitative

and quantitative data was considered in aggregate (all responses) and according to mentorship role (mentor or mentee). The multiple choice and Likert scale responses were tabulated and presented as percentage of total responses. The answers from the free-response questions were assessed using an open coding, two-pass, approach to identify emergent themes. First, categories of responses were generated and then answers were assigned to categories which were altered, combined, or generated as necessary.

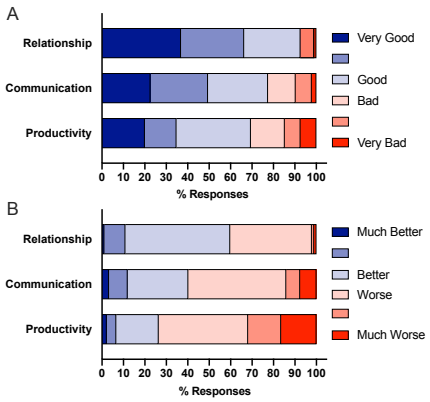

Figure 1: Ratings from undergraduate and graduate students in aggregate showing perceptions of mentoring relationship, communication, and productivity overall (A) or indicating how these measures changed with the shift from face-to-face to virtual mentoring (B).

RESULTS

The responses from undergraduate mentees and graduate mentors revealed that the quality of the mentored research experience during the Spring semester of 2020 was perceived as positive overall. 92% of respondents indicated positive relationships with their mentor/mentee, 77% rated their communication as good to very good, and 69% said their mentorships had above-average productivity (Fig. 1A). 60% of respondents rated their mentoring relationship as improved following the switch to virtual research. However, only 40% and 26% indicated improvements to communication and productivity respectively (Fig. 1B).

Qualitative analysis of the text-based answers corroborated and expanded on trends in the quantitative data. Reponses from both mentors and mentees suggested that the increased informality of virtual mentoring improved the mentoring relationship (““I get to see [pet] photos and learn more about my mentee and her life”). Additionally, this insight into the personal lives of the mentees prompted many mentors to take greater consideration for their mentees’ mental health and wellbeing. However, not all mentoring relationships were improved using the virtual format, and many respondents had challenges with maintaining communication. Mentors utilized a variety of platforms to accomplish research remotely including email and video conferencing which were employed by 40% and 34% of respondents, respectively (Fig. 2). Respondents who indicated their communication improved utilized a combination of communication modalities to achieve distinct goals. Two common trends were observed in responses that indicated worsened communication, 1) response times became much slower or communication halted completely following campus shut downs, or 2) individuals were speaking directly with their mentor but were not communicating with the lab group as a whole. Lastly, decreased ratings of productivity by both mentors and mentees were generally related to an inability to conduct hands on research in the wet lab. Many undergraduates also indicated that that research activities other than data collection were perceived as inherently less productive (e.g. data analysis, data visualization, or literature review). Conversely, there were undergraduates who indicated that, “…the remote work [was good] because it forced me to think about my work more conceptually and engage with the material.”

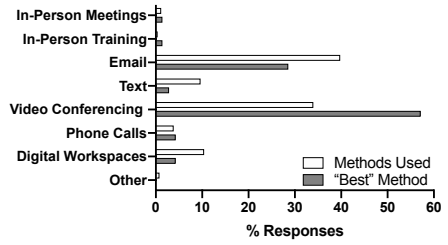

Figure 2: Communication modalities survey respondents indicated they used and those they perceived to be “best.”

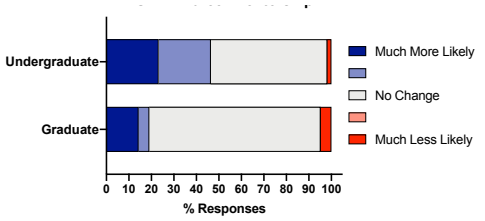

Figure 3: Interest of respondents in future STEM careers (undergraduate students) or mentoring opportunities (graduate students).

Although the data indicate ways in which the benefits of virtual research differed from in-person mentorships, undergraduate respondents indicated that their interest in future STEM careers had either increased (46%) or remained unchanged (52%). Similarly, 19% of graduate student mentors said their interest in serving as a mentor had increased and for 76%, their interest remained unchanged (Fig. 3).

DISCUSSION

The responses of both undergraduate and graduate researchers at Washington University in St. Louis reveal ways in which virtual platforms were able to support research mentorships during the COVID-19 pandemic. The majority of mentors and mentees noted benefits to virtual mentoring such as improved relationships, opportunities to emphasize scientific theory, and increased consideration of the emotional and mental wellbeing of researchers. However, challenges arose when mentors and mentees did not work effectively together to define research and learning objectives or did not communicate with each other efficiently. The finding that neither undergraduate nor graduate students altered their future plans following this experience may speak to the ability of virtual mentoring to support professional/academic development but may also reflect how many students felt this was a temporary situation. Additional studies including those with longitudinal components will be required to determine and assess the efficacy of virtual mentoring in STEM research. These data also demonstrate the necessity of providing researchers with support and training in how to effectively engage in research mentorship remotely as well as face-to-face. Best practices will need to be defined to optimize virtual mentoring as a tool for research mentorships while the COVID-19 pandemic continues and beyond. If implemented well, virtual mentoring can positively supplement in-person mentoring and increase access to STEM research for populations traditionally underrepresented in laboratories.

ACKNOWLEDGEMENTS

The authors wish to express thanks to all the survey participants and the administrations of the Chemistry, Biology, Physics, Biomedical Engineering, Mechanical Engineering and Materials Science, and Earth and Planetary Sciences departments (particularly Dr. Buhro, Dr. Larsen, Dr. Olsen, Dr. Ferrrer, Dr. Setton, Dr. Bayly, Dr. Bradley, and Dr. Skemer) for their assistance in distributing the survey. Additional thanks to the Center for Teaching and Learning for their support. JES has received financial support from the Spencer T. and Ann W. Olin Fellowship for Women in Graduate Study.

REFERENCES

[1] Dolan E. and Johnson D, *J Sci Educ Tech,* 18(6):487-500. 2009.
[2] Ensher, E et al., *J Vocat. Behav,* 63(2):264-288. 2003.

MULTISCALE COMPUTATIONAL MODEL PREDICTIONS OF SHEAR STRESS AND CYCLIC STRETCH IN THE PULMONARY VASCULATURE

MA Bartolo (1), NA Hill (2), NC Chesler (3), MS Olufsen (1)

(1) Department of Mathematics
North Carolina State University
Raleigh, NC, USA

(2) School of Mathematics and Statistics
University of Glasgow
Glasgow, UK

(3) School of Engineering
University of California Irvine
Irvine, CA, USA

INTRODUCTION

Pulmonary hypertension caused by left heart failure (PH-LHF) is a progressive disease that contributes to increased morbidity and mortality in millions of adults in the United States [1]. PH-LHF begins as a passive process called isolated post-capillary PH (Ipc-PH) and is diagnosed by elevated mean pulmonary artery pressure (mPAP) with normal pulmonary vascular resistance (PVR). Mortality in patients increases significantly once Ipc-PH transitions to combined pre-/post-capillary PH (Cpc-PH). Clinical and experimental hypotheses suggest that pathological wall shear stress (WSS) and cyclic stretch (CS) are key regulators of pulmonary vasoconstriction and remodeling, yet the exact mechanical stimuli of PH-LHF are unknown due to the difficulty associated with estimating these quantities.

In this study, we develop a one-dimensional (1D) fluid mechanics model predicting blood pressure, blood flow, area deformation, WSS, and CS in the pulmonary arterial and venous system. This work extends a previous study [2] by adding a capillary model allowing us to compute WSS and CS in the complete network. Our extended model includes large arteries and veins with geometry extracted from computed tomography (CT) data, small pulmonary arteries and veins, modeled as structured trees with fractal dimensions extracted from data, as well capillaries, which are modeled using a sheet model inspired by previous work by Y.C. Fung [4]. Combining these three submodules allows us to capture dynamics at multiple scales ranging from centimeters to nanometers. This multiscale approach allows quantification and exploration of system dynamics and mechanistic relationships at several levels of the pulmonary circulation, and under different hemodynamic conditions of the left heart.

Large vessel hemodynamics are predicted in a reconstructed geometry from CT imaging using 1D Navier-Stokes equations, while small vessel predictions occur in an empirically driven, bifurcating fractal tree using a linearized version of the large vessel equations. The arterial and venous trees are connected by pulmonary capillaries whose network geometry is characterized by a sheet of fluid flowing between two membranes. This approach provides a novel way to investigate hypotheses related to disease progression in PH-LHF.

METHODS

Large Vessels. Vessel-dimensions and network connectivity are extracted from CT chest images from a healthy human adult. We used 3DSlicer to reconstruct three generations of arteries and one generation of veins and subsequently used the vascular modeling toolkit (VMTK) to obtain cartesian loci tracing each vessel's centerlines and measure associated radii. Each large vessel is modeled as an axisymmetric tube with a circular cross-section and impermeable wall. We assume that the blood is Newtonian and the flow is incompressible, irrotational, and laminar. We consider a Stokes velocity profile discussed in [2] and obtain reduced 1D conservation of mass and momentum equations

$$\frac{\partial A}{\partial t}+\frac{\partial q}{\partial x}=0, \qquad \frac{\partial q}{\partial t}+\frac{\partial}{\partial x}\left(\frac{q^2}{A}\right)+\frac{A}{\rho}\frac{\partial p}{\partial x}=-\frac{2\pi\nu}{\delta}\frac{q}{A}, \tag{1}$$

where $A(x,t)$ is the cross-sectional area, $q(x,t)$ is the volumetric flow, $p(x,t)$ is blood pressure, ρ is blood density, η is kinematic viscosity, and $\delta=\sqrt{\nu T/2\pi}$ is the boundary layer thickness with T denoting the length of a cardiac cycle. In the large vessels, WSS is $\tau=-\mu\frac{\partial u}{\partial r}$.

Small Vessels Arterioles and venules are represented by asymmetrical bifurcating structured trees (Figure 1a) generated using physiology-based scaling laws. The structured trees are connected to the large vessels via an admittance matrix [2]. At each junction, the daughter vessel radii and lengths are scaled by factors α and β to the parent vessel based on computations found in [3]. Scaling parameters, along with a prescribed minimum radius determine the number of generations and vascular bed density encompassing the small arteries, arterioles, veins, and venules.

Since viscous effects are dominant in small vessels, we can ignore nonlinear inertial terms in equation (1) yielding the following momentum and continuity equations

$$\frac{\partial u_x}{\partial t}+\frac{1}{\rho}\frac{\partial p}{\partial x}=\frac{\nu}{r}\frac{\partial}{\partial r}\left(r\frac{\partial u_x}{\partial r}\right), \qquad C\frac{\partial p}{\partial t}+\frac{\partial q}{\partial x}=0 \tag{2}$$

where $u_x(x,t)$ is the axial velocity, r is the radial coordinate, and $C=\partial A/\partial p$ is the compliance.

As the fluid moves back and forth due to an oscillatory pressure gradient, the WSS exerted by the fluid on the tube wall is given by

$$\tau_\phi(t)=\frac{\Lambda}{\pi R^3}\frac{J_1(\Lambda)}{J_0(\Lambda)-\frac{2}{\Lambda}J_1(\Lambda)}q, \tag{3}$$

where $\Lambda=\left(\frac{i-1}{\sqrt{2}}\right)\Omega, \Omega=R\sqrt{\frac{\rho\omega}{\mu}}$, R is the tube radius, J_0 and J_1 are Bessel equations. To find the percentage of CS in vessel we divide the area deformation by the maximum area and multiply by 100.

Capillaries. The dense network of pulmonary capillaries can be modeled as a sheet of fluid flowing between two membranes held apart by

equally spaced posts. Based on work by Fung [4], the flow within a capillary sheet can be expressed as

$$\left(\frac{d^2}{dx^2}+\frac{d^2}{dy^2}\right)h^4 = 0, \quad (4)$$

where $h = h_0 + a(p - p_{alv})$ is the average sheet height where p is the blood pressure, p_{alv} is the pressure of the air in the alveoli, a is the compliance constant, and h_0 is a constant such that $h = h_0$ when $p = p_{alv}$. Extending the WSS calculation for arterioles and venules will allow us to predict this quantity in the capillaries.

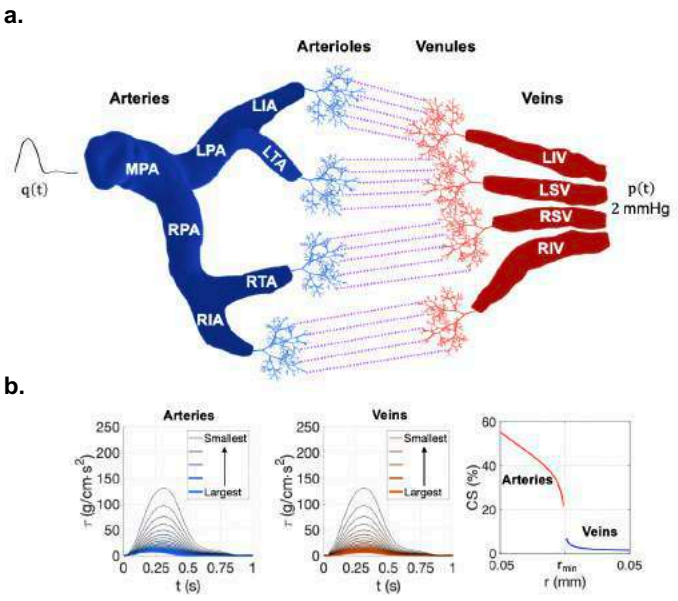

Figure 1: Schematic of the pulmonary circulation arranged in order of large arteries, arterioles, capillaries, venules, and large veins (a). Imposed inflow profile and imposed left atrial pressure are found using a structured tree model for experimental conditions of left atrial pressure of 2 mmHg and typical cardiac output. Predicted WSS and CS for small arteries and veins in the structured tree (b).

RESULTS

Large Vessels. Pressure in the large vessels ranges between 8 and 30 mmHg with pressure in arteries being more dynamic than that of the veins. The mean flow decreases as it is distributed to the downstream vasculature with large arteries having a higher volumetric flow rate of blood than veins. The area in arteries is more dynamic over a cardiac cycle than veins. The area for large veins does not fluctuate as much as the large arteries throughout a cardiac cycle and is less than that of the arteries. This is due to the fact that veins are twice as stiff as arteries in our model. For large vessels, we use a Stokes boundary layer formation along the large arteries and large veins. The mean pulmonary artery (MPA) has the largest shear stress of the large arteries. In general veins have higher shear stress than arteries. Shear stress for veins ranges from 0-7 g/cm^2s whereas shear stress for arteries ranges from 0-5 g/cm^2s.

Small Vessels. In the small arteries and veins, arterioles and venules the pressure decreases with decreasing vessel radius with a maximum pressure of about 30 mmHg and minimum pressure of about 2 mmHg. By contrast, for venules, smaller vessels have larger pressure. For both arterioles and venules, the flow decreases with decreasing vessel radius. For the small vessels, shear stress is predicted along the structured tree. We see that in both small arteries and veins, smaller vessel radius results in higher shear stress (Figure 1b). We find that the arterioles have a higher percentage of CS than venules due to differences in stiffness. Generally, CS decreases with decreasing vessel radius (Figure 1b).

DISCUSSION

The objective of this study is to model pressure and flow propagation and calculate WSS and CS in the pulmonary circulation by setting up a network that includes large and small arteries and veins. This is an extension of several studies that utilized structured tree models to simulate the pulmonary circulation, but it is the first to develop a multiscale model predicting WSS in both large and small arteries and veins. Through our model simulations, we find that large arteries have higher pressure and flow than large veins, as well as more pronounced changes in area throughout the cardiac cycle. In small vessels, we see that as vessel radius decreases, pressure decreases for arterioles but increases for venules. As vessel radius decreases, we also find that volumetric flow decreases.

Our results for pressure, flow, and area in the large arteries and veins generally agree with results found in literature [2]. Several previous studies [5,6] used computational fluid dynamics models to predict WSS in large arteries. While our WSS results for large arteries agree with literature, we are the first to predict WSS in both large and small arteries and veins. This is a significant development because PH begins in the left ventricle and propagates to the left ventricle through the pulmonary veins, venules capillaries, arterioles, and large pulmonary arteries. Thus, by studying both the pulmonary macrovasculature and microvasculature, we are able to advance our understanding of PH pathogenesis.

Results presented here report WSS and CS in the large arteries and veins for a healthy subject and we are currently working on extending these results to a) study how shear stress changes in patients with PH-LHF and b) expanding the model to also include predictions in the capillaries. To simulate LHF-PH, we are working on generating sub-models to progressively increase disease severity by increasing left-atrial pressure, increasing stiffness, and decreasing flow. To capture dynamics in the capillaries, we will couple the structured tree models to the sheet model in [4]. Analyzing results that correspond to disease progression will allow us to further understand the mechanistic quantities that are involved in PH pathogenesis. In addition, we do not yet account for the gravitational gradient that impacts hemodynamics in the veins. Despite these noted limitations, the in-silico computational fluid dynamics model presented in this study is an important tool that provides a new way to analyze and investigate hypotheses related to understanding the physiological mechanisms underlying the progression of pulmonary diseases.

ACKNOWLEDGEMENTS

This work was supported in part by the NIH-HL147590-01 and NSF-DMS 1615820.

REFERENCES

[1] Lam, C et al., *J Am Coll Cardiol,* 53: 1119-1126, 2009.
[2] Qureshi, MU et al., *Biomech Model Mechan*, 13: 1137-1154, 2014.
[3] Chambers, MJ et al., *J Eng Med,* 234: 1312-1329, 2020.
[4] Fung, YC et al., *J Appl Physiol,* 26: 472-488, 1969.
[5] Zambrano, B et al., *J Biomech,* 68:84-92, 2018.
[6] Yang, et al. *Biomech Model Mechan,* 18: 779–796, 2019.

DEVELOPMENT AND IMPLEMENTATION OF AN ENGINEERING RESEARCH COURSE FOR A COLLEGE-IN-PRISON PROGRAM

Julie E. Speer* (1) and Zain Clapacs* (2)

(1) Setton Laboratory
Department of Biomedical Engineering
Washington University in St. Louis
St. Louis, MO, USA

(2) Rudra Laboratory
Department of Biomedical Engineering
Washington University in St. Louis
St. Louis, MO, USA

*Authors contributed equally

INTRODUCTION

As of the 2018-2019 academic year there were approximately 300 higher education programs in prisons across the United States.[1] These programs offer varying modes of instruction (e.g. face-to-face, online, correspondence), degree offerings, and curricular and extracurricular activities[1]. Data has demonstrated a role for prison education programs to reduce recidivism and increase the rates of employment for people who have been formerly incarcerated, but the programs may also serve a role in addressing structural racism in both the education and justice systems[2]. The number of higher education programs in prisons have been increasing over the past decade[1] as has the availability of STEM programs for incarcerated students[3,4]. Technology companies including Slack have begun to offer internships/training programs in coding to formerly incarcerated individuals[3] while other programs such as The Last Mile work with currently incarcerated scholars to learn business and technology skills[4]. Other STEM programs outside of formal classroom settings have been shown to promote development of scientific identities, ideas of being "science-capable" and an interest in participating in further scientific education[5]. These effects are similar to the known benefits of participating in undergraduate research as demonstrated for non-carceral students[6]. In contrast, there is less known about the impact of engaging incarcerated students in academic STEM research as knowledge creators.

Washington University's Prison Education Project (PEP) PEP began teaching college-level, for-credit courses to incarcerated students and correctional staff at Missouri Eastern Correctional Center (Pacific, Missouri) in 2014[7]. Since then, PEP has awarded both Associate in Arts and Bachelor of Science in Integrated Studies degrees and offers programs for intellectual engagement outside of the classroom including tutoring services, lecture series, and reading groups which are available to both PEP students and other individuals at MECC[7]. Here we present a model (Fig. 1) for an engineering research independent study course designed to promote the documented benefits of traditional undergraduate research experiences for currently incarcerated students. Through this new course, PEP students were invited to participate in engineering research, an offering previously unavailable to PEP students through Washington University in St. Louis.

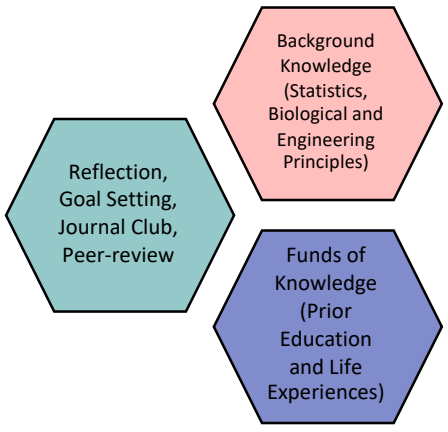

Figure 1: The core components of this course (leveraging funds of knowledge, creating opportunities for reflection, and introducing scientific theory) were integrated and applied in context of engineering research.

METHODS

PEP academic advisors and administrators provided information about the course offering to PEP students at MECC pursuing a Bachelor of Science in Integrated Studies with a STEM focus. Five students with

varying levels of experience in technical fields enrolled in the 2-credit pass/fail course which began in September 2020. Due to the COVID-19 pandemic, this course was offered entirely virtually. Additionally, the course was specifically designed to allow students to conduct research activities using the technology already available to the students and without necessitating access to laboratory equipment. Each PEP student has access to a tablet with word processing and spreadsheet software. The tablets also allow students to utilize a proprietary learning management system (LMS) but do not allow students to directly access the internet. Therefore, all course materials were made available to students directly through the LMS and students submitted assignments through the same mechanism. Lastly, all communication between instructors and students was conducted through the messaging feature within the LMS.

During the first section of the course, students reflected on their personal learning goals and engaged in modules which provided overviews to topics such as research statistics, data visualization, scientific communications, data literacy, and experimental planning. These modules provided a framework for subsequent course activities and established necessary background information so that the course could engage all students without requiring prerequisites of either coursework or technical experience. Each module consisted of a PowerPoint presentation and/or a pre-recorded lecture video, a worksheet, and supplementary materials as needed (e.g. manuscripts or textbook chapters).

In the next section of the course students explored the scientific literature through mediated journal club discussions, analyzed research data, and interpreted the findings. Background information on the research topic was provided to the students through a video recording and/or PowerPoint slideshow. Additionally, students were given access to the manuscript, a glossary of terms/concepts, and two worksheets. The first worksheet guided students through reading the manuscript and asked students to answer questions related to the scientific theory, data as it was presented and interpreted by the authors, and the organization of the manuscript. Because the course was offered asynchronously, and the learning management system did not offer discussion boards, the second worksheet was used to facilitate journal club discussions. Using this second document, students reflected on the experience of reading the paper, aspects of the manuscript they enjoyed, elements they found confusing, and a future direction for the research they think could be interesting to explore. Once students submitted their own journal club sheet, they were sent a document from one of their peers and asked to read it, compare and contrast their experience of reading the manuscript to those of their peer, and to identify something they learned from their peer's response.

This virtual journal club was conducted in order to foster scientific community and to promote some of the most beneficial aspects of in-person journal clubs where scientists are able to learn from one another, share and hear differing experiences or perspectives, and discuss ways to apply the results to future experimentation. Additionally, this activity helped to acclimate the students to reading scientific literature as well as serving the important function of modeling that conducting research requires collaboration and benefits from diversity of perspectives and backgrounds. The instructors also demonstrated this by providing detailed feedback to the students on all the submitted assignments or questions sent via email. These communications were used to address not only the scientific theory and to provide clarifications or corrections but also allowed the instructors to offer messages of encouragement and to share their own research and educational experiences.

In the final course section, students identified an area of their own scientific interest and applied the skills they developed earlier in the course to generate a testable hypothesis, plan a theoretical experiment, propose hypothetical research data, interpret these results, describe limitations of the study, and cite opportunities for future work. For the final deliverable, students compiled these efforts and wrote a 1-page abstract or designed a scientific poster (both based on templates from biomedical engineering conferences held in 2020). The students were given the option of presenting their work in the more text-based or more visual format (scientific abstract or poster, respectively). As with the prior assignments, both instructors served as mentors to the students as they worked on the independent projects by providing scientific literature to the students (who didn't have internet access), helping to workshop the research plans, and assisting with formatting and editing the final documents.

RESULTS

This course was offered for the first time during the Fall 2020 semester (September – December 2020). The impact of this program will be assessed through anonymized student feedback and future iterations may employee pre- and post-tests to quantitatively track student gains. Informal feedback from students has indicated that they found the course to be interesting and that they benefitted from the opportunity to apply previous knowledge in an engineering research context, learn new scientific skills, and gain experience with scientific writing. Students also noted ways in which this experience contributed to gains in self-confidence, interest in future STEM learning and careers, and development of a scientific identity. Given student interest, a second iteration of the course will be offered during the Spring 2021 semester and all students who participated in the first semester have chosen to enroll in the course again.

DISCUSSION

This course represents the first opportunity for students pursuing a Bachelor of Science in Integrated Studies through PEP at Washington University in St. Louis to engage in academic research as knowledge creators. The design of this course emphasized a holistic approach to research that included data collection and analysis along with literature review, experimental planning, and engaging in a scientific community. Additionally, the course combined elements of both classroom instruction as well as mentored research experiences. This model requires validation using both qualitative and quantitative data, but the available feedback from the students demonstrates the value of this asynchronous, virtual research-based course. The use of a similar model may be applicable to other contexts of academic research or in different higher education settings as a method of providing mentored experiences to students who are either incarcerated or otherwise are underserved by traditional programs, however, optimization of the curriculum should be conducted in partnership with the students in order design a system that best meets their personal, professional, and educational goals.

ACKNOWLEDGEMENTS

The authors wish to thank the students who have participated in this course and the Prison Education Project at Washington University in St. Louis and Missouri Eastern Correctional Center (particularly Dr. Barbara Baumgartner and Natasha Narayanan). Additional thanks to Drs. Lori Setton and Jai Rudra for their support of this course. JES has received financial support from the Spencer T. and Ann W. Olin Fellowship for Women in Graduate Study.

REFERENCES

[1] Royer, C.E. et al., Alliance for Education in Prison, 2020.
[2] Castro, E.L., *Critical Education,* 9(17): 1-14. 2018.
[3] https://slack.com/blog/news/next-chapter-a-pilot-program-aiming-to-help-formerly-incarcerated-individuals-find-work-and-succeed-in-tech
[4] https://thelastmile.org/
[5] Horns, J.J. et al., *PLoS ONE*, 15(5): e0233083, 2020.
[6] Dolan E. and Johnson D, *J Sci Educ Tech*, 18(6):487-500. 2009.
[7] https://prisonedproject.wustl.edu/

HARMONIC DISTORTION AS A NONINVASIVE MEANS TO ASSESS BLOOD PRESSURE WAVEFORM AND ARTERIAL STIFFNESS

Nicholas Milkovich (1), Anastasia Gkousioudi (1), Francesca Seta (2), Béla Suki (3), Yanhang Zhang (1,3)

(1) Department of Mechanical Engineering
Boston University
Boston, Massachusetts, USA

(2) Department of Medicine
Boston University
Boston, Massachusetts, USA

(3) Department of Biomedical Engineering
Boston University
Boston, Massachusetts, USA

INTRODUCTION

Blood pressure (BP), the pressure of circulating blood within the arteries, is routinely used as a measure of cardiovascular system's function. Parameters derived from BP and artery dimensions, such as distensibility, have been broadly used as indicators of mechanical properties of arteries. However, they rely solely on systolic and diastolic pressure values, and the mechanical information associated with the blood pressure waveform (BPW) is not well understood. For example, there is a marked difference in BPW measured in central and upper limb (brachial) arteries between young and older individuals, and this mainly arises from the phase difference between the blood pressure downstream wave and the upstream reflected wave[1]. Stiffening of central elastic vessels, such as the aorta and the carotid arteries, results in a pressure augmentation from the propagating and reflected waves, which increases the peak of the waveform in the systolic phase of the cardiac cycle[2]. Therefore, the BPW is also associated with arterial stiffness. The purpose of this study is to assess changes in BPW in the settings of diet-induced hypertension and establish the relationship between BPW and arterial stiffness.

METHODS

Animal model: All procedures were approved by the Boston University Institutional Animal Care and Use Committee. Male (n = 20) C57Bl/6J mice were purchased from the Jackson Laboratory (Bar Harbor, ME). After acclimation, 2-mon-old mice were fed a control normal diet (ND: 4.5 % fat, 0% sucrose) or high fat, high sucrose diet (HFHS: 35.5 % fat, 16.4 % sucrose). This is a well-established model of diet-induced obesity which develops hyperinsulinemia, glucose-intolerance, increased arterial stiffness and hypertension within 8 months on diet, closely mimicking the human metabolic syndrome[3].

In vivo blood pressure measurements: BP was measured using radiotelemetry[3] (Data Sciences International, St Paul, MI, USA). Briefly, mice were kept anesthetized (1% isofluorane) as a gel-filled catheter was inserted in the aortic arch via catheterization of the left carotid artery. After recovery from surgery (1-2 weeks), BPW recordings were acquired for 20 secs every hour over a 24 hour period (Fig. 1). *In vivo* BP measurements were made when the mice were 2-14 months old in the following 5 groups: 2mon ND (n = 6), 10-14mon ND (n= 5), 3mon HFHS (n = 6), 4mon HFHS (n = 5), and 10-12mon HFHS (n = 4).

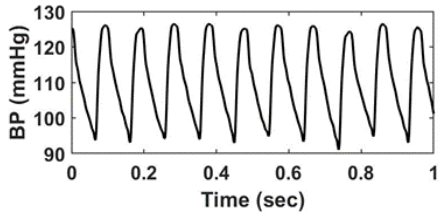

Figure 1: Representative *in vivo* blood pressure waveform over 1 sec time period measured using radiotelemetry.

Harmonic distortion: To quantify the shape of BPW, we introduced a parameter, harmonic distortion (HD), defined as:

$$HD = \frac{\sum_{k=2}^{n} A_k^2}{A_1^2} \quad (1)$$

where A_i are the BPW's Fourier coefficients obtained via discrete Fourier transform. Thus, HD is essentially the ratio of energy above the fundamental frequency and energy at the fundamental frequency of the waveform. For an ideal sinusoidal wave (no distortion), the HD is 0. To obtain HD, individual heartbeat cycles isolated from the 20 sec BP recordings were analyzed using a custom MATLAB code according to

Equation (1). The HD value and the corresponding heartbeat's systolic BP (SBP) was then recorded.

In vitro biomechanical measurements: Carotid arteries were excised from the following mice: 4mon ND (n = 3), 4mon HFHS (n = 2), 10mon ND (n = 3), and 10mon HFHS (n = 2). Biaxial tension-inflation tests were performed using a pressure myograph (Danish Myo Technology, Denmark). From the circumferential Cauchy stress-stretch curve, tangent modulus (TM) was determined at every 10 mmHg between 100 and 140 mmHg transmural pressure. HD vs. TM curves were then plotted at the corresponding transmural pressure.

Statistical analysis: Paired student t-tests were performed on the HD data contained within defined BP bins for the age and diet groups. A two-way analysis of variance (ANOVA) test was performed on the slopes of linear regressions of TM vs. HD. A p-value of 0.05 or lower was considered significant ($^{*}P<0.05$).

RESULTS

Figure 2 shows the HD vs. luminal SBP obtained from BPWs over a 24-hour period for a 10mon ND mouse. HD shows a negative linear relationship with SBP. To further resolve relationship between HD and luminal SBP for the mouse groups, for each mouse, the maximum and minimum SBPs were identified and 12 equally spaced SBP bins were used to average the HD and SBP values within each bin. The average HD vs. SBP were then plotted. A linear regression between HD vs. SBP was performed on the 5 age and diet groups (Fig. 3).

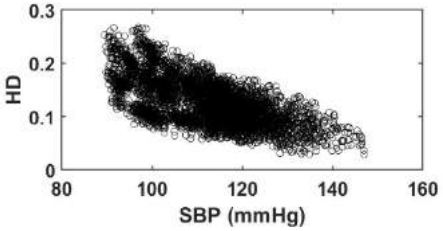

Figure 2: Harmonic distortion vs. luminal systolic blood pressure for a 10mon ND mouse.

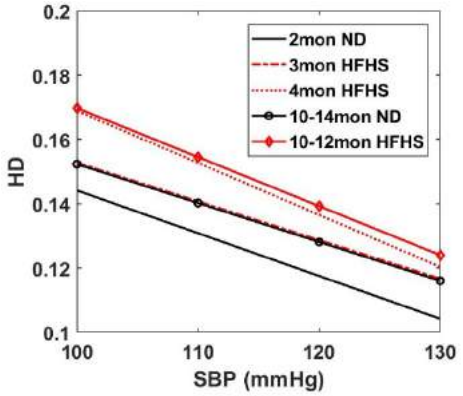

Figure 3: Linear regressions between HD and luminal SBP for the 5 age and diet groups

One-way ANOVA showed that there was a significant difference among the group means for both the slopes (p=0.046) and the intercepts (p=0.007). Pairwise, the slopes were not different, but the intercepts between 4mon HFHS and 3mon HFHS as well as between 4mon HFHS and 10-14mon ND were different. HD values within transmural BP bins ranging from 100-130 mmHg were also found to be statistically significant from one another. This suggests that the linear relationships between HD and transmural BP follows a linear trend for all age and diet groups with a similar slope, however aging and diet results in a significant upward shift of the linear curves.

HD obtained from *in vivo* BPW and tangent modulus from *in vitro* biomechanical measurements at the corresponding transmural BP was found to be linearly related, i.e., as the tangent modulus increases, HD decreases consistently (Fig. 4a). Note that in order to pair HD and TM at the corresponding transmural pressure, *in vivo* perivascular pressure needs to be accounted for[4]. This value was found to be 13.25 mmHg and was subtracted from the *in vivo* luminal SBP. The slopes of the linear relationships were found to be significantly different between ND and HFHS diet groups (p=0.024).

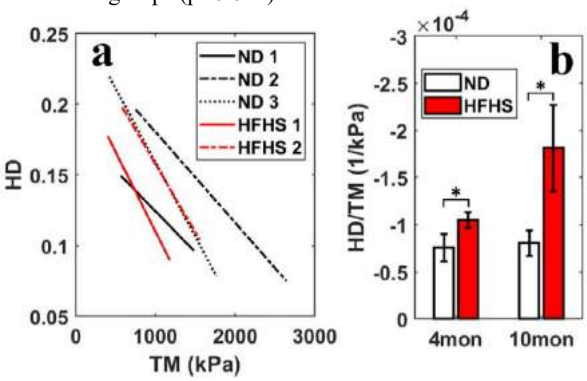

Figure 4: (a) Harmonic distortion vs. tangent modulus for 4mon ND and HFHS mice. (b) Average slopes of the harmonic distortion vs. tangent modulus linear fits for age and diet groups ($^{*}P<0.05$).

DISCUSSION

BPW contains information from the coupled interactions among the forward propagation wave, reflected wave, as well as the arterial wall mechanics. The inverse linear *relationship* between HD and SBP (Fig. 2) suggests that HD is sensitive to changes in arterial stiffness, since with higher BP, the arterial stiffness increases. This is further confirmed by Fig. 4a, in which HD is directly related to the tangent modulus. These findings suggest that HD of BPW shows promises in assessing arterial wall stiffness. Our results further suggest that for the HFHS and the aging groups, HD is more sensitive to changes in arterial wall stiffness (Fig. 4b). The linear relationships between HD and SBP appear to be similar for the 3mon HFHS and the10mon ND groups (Fig. 3), suggesting accelerated changes in BPW with HFHS diet. Interestingly, the 4mon HFHS group is not significantly different from 10mon, suggesting changes in the arterial wall mechanics have already occurred in the 4mon HFHS group. However earlier studies suggested that hypertension was not developed in the 4mon HFHS groups[3], thus HD can potentially be used as a noninvasive predictor of hypertension which warrants further studies.

ACKNOWLEDGEMENTS

This research was supported in part by Translational Research in Biomaterials Fellowship Program (TRB) at Boston University T32 EB006359, and 2R01HL098028 to Y.Z.

REFERENCES

[1] Hirata, K et al., Pulse wave analysis and pulse wave velocity, *Circulation journal*, 70(10):1231-9, 2006.

[2] Van Varik, B et al., Mechanisms of arterial remodeling: lessons from genetic diseases. *Frontiers in genetics*, 3:290, 2012.

[3] Weisbrod, RM et al., Arterial stiffening precedes systolic hypertension in diet-induced obesity, *Hypertension*, 62(6):1105-10, 2013.

[4] Ferruzzi, J et al., Combining in vivo and in vitro biomechanical data reveals key roles of perivascular tethering in central artery function, *PLOS ONE,* 13:e0201379, 2018.

THE ANISOTROPIC MECHANICAL PROPERTIES OF HUMAN UTERUS

S. Fang (1), J. McLean (2), J. Vink (3), C. Hendon (2) K. Myers (1)

(1) Department of Mechanical Engineering
Columbia University
New York, NY, USA

(2) Department of Electrical Engineering
Columbia University
New York, NY, USA

(3) Department of Obstetrics and Gynecology
Columbia University Medical Center
New York, NY, USA

INTRODUCTION

The mechanical function of the uterus is critical for a successful pregnancy. During gestation, uterine tissue grows and stretches to many times its size to accommodate a growing fetus; it is hypothesized that uterine tissue stretch triggers the onset of contractions. Early contractile activation (defined as ≤ 37 weeks) of uterine tissue can lead to preterm labor and birth (PTB) [1]. In 2015, more than 10% of pregnancies globally ended in PTB. It is also the leading cause of death in children under five years of age [2]. Therefore, characterizing the uterine tissue's mechanical properties and responses during pregnancy is essential for understanding the mechanical failures' mechanisms and causes of PTB.

A previous study found the fibers' orientation and dispersion in biological tissue greatly impact its mechanical responses [3]; this likely holds for uterine tissue, as well [4]. Spherical indentation and uniaxial tension have been combined with inverse finite element analysis (IFEA) to study fibrous biological tissues including the human cervix [5]. In this study, we apply indentation, tension, and video extensometry to capture material responses under compression and tension. We translate previously reported fiber architectures [6] into a constitutive model to describe material responses. We then use IFEA with a genetic algorithm to characterize uterine tissue's anisotropic mechanical properties.

METHODS

Specimen preparation: 27 uterine specimens were collected from consenting a non-pregnant (NP) patient and a pregnant (PG) patient who underwent hysterectomy. Specimens were collected across the full uterine wall thickness (15 to 25 mm) from three anatomical locations: anterior, posterior, and fundus (Fig. 3a). The approximate dimensions of each specimen are 12, 12, and 4 mm in width, length and thickness. Specimens were stored in a –80°C freezer immediately after sectioning. Before testing, the specimens were thawed at 4°C for 12 hours in phosphate buffered saline (PBS) to equilibrate.

Fiber distribution characterization: We developed a hybrid method in R 4.0.2, and fitted a π-periodic von Mises distribution (or a mixture of them) to a fiber orientation previously determined by OCT. A single π-periodic von Mises is defined as:

$$f(x|\mu,\kappa)\frac{1}{\pi}\frac{e^{\kappa\cos(2(x-\mu))}}{I^0(\kappa)} \quad (1)$$

where μ is mean orientation (preferential fiber direction); κ is concentration (the reciprocal of dispersion, where small κ denotes a less concentrated [more dispersed] distribution about the angle μ); and I^0 is the modified Bessel function of order of zero.

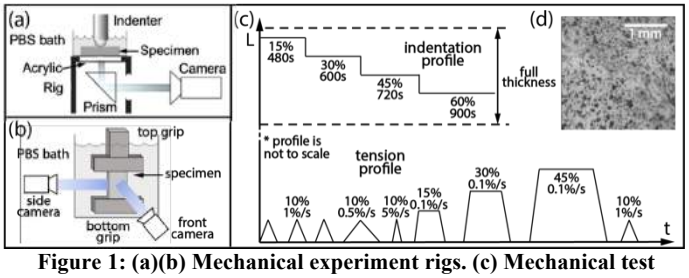

Figure 1: (a)(b) Mechanical experiment rigs. (c) Mechanical test profiles. (d) A representative specimen speckle pattern.

Mechanical testing and digital image correlation (DIC): Specimens were speckled with Verhoeff's stain on one surface for DIC. For indentation, the specimen was positioned in the PBS bath (Fig. 1a) with an acrylic bottom surface. A 90º prism was fixed under to reflect the speckled surface into a camera to capture the full-field displacement. A four-level ramp-hold indentation test was performed (Fig. 1c) on a universal testing machine (Instron, Inc., Norwood, MA) using a 6-mm diameter spherical indenter attached to a 5N load cell. The ramping rate was 1%/s for all specimens. The holding time following each ramp was

480, 600, 720, and 900 seconds, respectively. For tension, the specimen was sectioned three ways: with the preferential fiber orientation at 0º, 45°, and 90º to the uniaxial tension direction. The sectioned specimen was held vertically in PBS (Fig. 1b) with the speckled surface facing forward. Two perpendicular cameras captured the tissue's deformation and displacement from the front and side. The test protocol includes six load-unload cycles with different strain rates (0.5%/s ~ 5%/s) and three incremental load-hold-unload cycles (0.1%/s). The holding time was 30, 45, and 60 minutes for the three levels, respectively (Fig. 1c). Force-time data were collected using material test software (Instron, Inc., Blue Hill). For both testing scenarios, images were taken and processed using Vic-Snap (Correlation Solutions, Irmo, SC). The first (e_1^{DIC}) and second (e_2^{DIC}) Lagrangian principal strains were calculated using a 90% centered Gaussian filter and extracted.

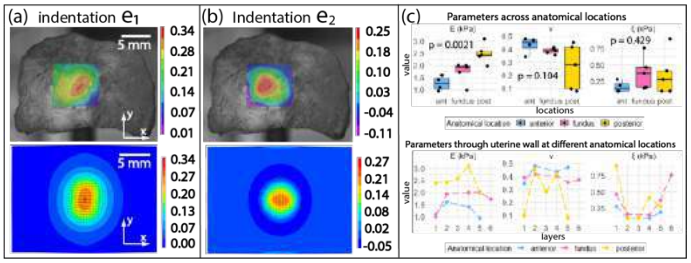

Figure 2: (a)(b) Indentation and tension DIC and FEA first Lagrangian principal strain comparisons show good match. (c) Optimized NP tissue parameters plotted across anatomical locations and uterine layers (1 = outermost, 6 = innermost).

Finite element analysis (FEA) and constitutive model: FEA was performed for comparison with mechanical tests (Fig. 2ab) using FEBio Suite (Salt Lake City, Utah). A rectangular cuboid represented the specimen, a 6-mm diameter sphere represented indenter, and two small rectangular cuboids represented the tension grips (not shown). All geometries were meshed with HEX-8 elements. Uterine tissue was modeled using a previously verified constitutive model [5], described by five material parameters including Young's modulus E, Poisson's ratio ν, fiber stiffness ξ, and OCT-informed preferential fiber direction θ and fiber concentration κ (reciprocal of dispersion).

Inverse finite element analysis (IFEA): An IFEA method using a genetic algorithm optimized the constitutive model's parameters to fit our experimental data. Three material parameters (E, ν, and ξ) were optimized with the objective function:

$$\Xi(E,\nu,\xi) = \sum_{i=1}^{N}\left|\frac{e_1^{FEA^i}-e_1^{EXP^i}}{e_{norm}^{EXP^n}}\right| + \sum_{i=1}^{N}\left|\frac{e_2^{FEA^i}-e_2^{EXP^i}}{e_{norm}^{EXP^n}}\right| + \sum_{i=1}^{N}\left|\frac{F^{FEA^i}-F^{EXP^i}}{F^{EXP^n}}\right| \quad (2)$$

where i is number of mechanical test levels, e is the equilibrium principal strains of the specimen, and F is the equilibrium force recorded by the testing machine. "FEA" and "EXP" denote the data of the finite element model and experiment, respectively.

Statistical analysis: One-way ANOVA ($p \le 0.05$) was performed in R. Optimized parameter set (E, ν, and ξ) were compared in groups according to (1) patient gravidity (NP, PG), (2) anatomical locations (anterior, posterior, and fundus), and (3) relative specimen depth in the uterine wall (outermost, mid, and innermost layers).

RESULTS

Human uterus' compressive are reported in this abstract. Further research is underway to complete its tensile counterpart.

Fiber distributions are significantly different between the NP and PG tissue, both anisotropic (Fig. 3). Each line represents a fiber family, and the concentration κ about the preferential direction θ is indicated by the color bar. Blue denotes a concentration factor equal to zero for a uniform distribution; while red for a more anisotropic distribution.

The best-fit material parameters under indentation are averaged and listed in Table 1. Values reflect data of all 27 indentation tests.

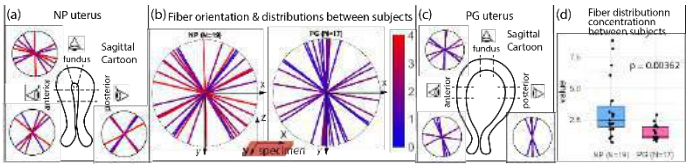

Figure 3: (a)(c) NP & PG tissue fiber distributions by locations. (b) The dominant fiber directionality of NP tissue appears to be at around π/4 & 3π/4 while PG is at π/2. (d) PG tissue show smaller concentration factors, indicating a more uniform distribution.

Heterogeneous mechanical properties are seen in human uterine tissue at different anatomical locations and across different uterine wall layers (Fig. 2c). Specially for NP tissue, Young's modulus E appears to be significantly different between anatomical locations. When comparing the middle layers of NP uterine wall to its most outer and inner layer, the Young's modulus E is larger and fiber stiffness ξ is smaller. For PG tissue, its Poisson's ratio ν is larger at the outer uterine wall for anterior and fundus locations (not shown).

Table 1: IFEA & von Mises fitted material parameters.

Parameter	Mean value	Standard deviation
E [0.1, 100] kPa	1.756 kPa	0.685 kPa
ν [0, 0.499]	0.329	0.124
ξ [0.1, 10] kPa	0.393 kPa	0.347 kPa
κ [0 $\propto$]	2.46	1.99

DISCUSSION

In this study, we aim to characterize the material behavior of human uterus under compression and tension with a single set of mechanical properties. While results reported in this abstract only reflect compression, the tension counterpart is underway; asymmetries in material behavior between compression and tension may change our estimate of fiber stiffness ξ. Both NP and PG tissue have anisotropic material properties, but PG tissue fibers are more dispersed than NP tissue fibers. NP tissue exhibits a basket-weaving or circularly arranged fiber architecture (Fig. 3a), consistent with prior work [3]. PG tissue exhibits a longitudinally or meridionally arranged architecture (Fig. 3c) as the uterus undergoes a sixfold increase in length during pregnancy. Similar to the human cervix [5], the force response of the human uterus under indentation is time-dependent and non-linear, and uterine fiber architecture dictates 2-D principal strain fields. Human uterine tissue also shows heterogeneous mechanical properties at different locations.

The research and conclusions described here have the following limitations: compared to ground substance, fiber stiffness is less sensitive to compressive loads and so will be better informed by the ongoing tensile data analysis; for obvious reasons, specimens collected from hysterectomy are usually pathological, and this may reduce our study's external validity; racial differences in uterine material properties have been demonstrated elsewhere but not explored here.

ACKNOWLEDGEMENTS

Research reported in this publication was supported by the NIH R01HD091153 to KM and R01HD072077 to TJH, HF & KM. The content is solely the responsibility of the authors and does not necessarily represent the official views of the NIH.

REFERENCES

[1] Cook, JL et al., *Endocrinology*, 141(5):1718-28, 2000.
[2] Liu, L et al., *Lancet*, 388(10063):3027-35, 2016.
[3] Weiss, S et al., *Anat Rec*, 288(1):84-90, 2006.
[4] Holzapfel, GA et al., *Proceedings of the Royal Society*, 475, 2019.
[5] Shi, L et al., *J Biomech*, 141(9):0910171-1713, 2019.
[6] McLean, JP et al., *Biom Opt Exp*, 11:5518-41, 2020.

MODELING THE MOUSE ASTROCYTIC LAMINA AND ITS RESPONSE TO INCREASE IN INTRAOCULAR PRESSURE MODELING THE MOUSE

YTT. Ling (1), A. Korneva (1,2), H. Quigley (2), T. Nguyen (1)

(1) Department of Mechanical Engineering
Johns Hopkins University
Baltimore, MD, USA

(2) Wilmer Eye Institute
Johns Hopkins School of Medicine
Baltimore, MD, USA

INTRODUCTION

Glaucoma is an ocular disease characterized by degeneration of retinal ganglion cell axons [1], and increase in intraocular pressure (IOP) is associated with the progressive loss of the axons at the optic nerve head (ONH) [2]. The axons are mechanically supported by a connective tissue called lamina cribrosa (LC) at the ONH. The human LC consists of a network of collagen beams with astrocyte cells spreading along the beams and across the pores to form passages for the axons [3]. In rodent lamina, the astrocytic processes also surround the axonal bundles despite the absence of collagen beams. Thus, the astrocytic lamina (AL) in rodents is functionally comparable to the human LC. Confocal images revealed that 3-day ocular hypertensive (OHT) nerves have larger coverage of actin cytoskeleton, lower area fraction of the astrocytic intermediate filament, GFAP, and thinner astrocyte processes [4]. Previous inflation tests of mouse eye explants showed that pressure-induced strains in 3-day OHT nerves were greater than those in the controls [5]. Therefore, it is hypothesized that the changes in the astrocytic structure may affect the local strain response.

The objective of this study was to develop a computational model for the mouse AL and investigate the effect of the AL network structure on the local stress and strain responses. Understanding the relationship between structure and strain variations will elucidate how glaucoma-induced remodeling affects mechanical insult to the axons and astrocytes in the AL.

METHODS

Specimen preparation: Seven intact eye globes from mice expressing the green fluorescent protein in all astrocytes (FVB/N-Tg(GFAP-GFP)14Mes) were used for inflation tests [5]. The eyes were glued to a plastic holder, cannulated at the cornea and connected to a fluid reservoir for control of IOP. IOP was elevated from a baseline of 10 to 30 mmHg and the ONH was imaged with two-photon laser source at an excitation wavelength of 895 nm (Zeiss, LLC) at both pressures. Displacement fields between baseline and deformed images were calculated using digital volume correlation (DVC) [6,7].

Optic nerve of a 6-month old GFP-GLT1 transgenic mouse was excised and cryosectioned for immunolabeling of GFAP and staining of actin and nuclei [4]. Confocal fluorescent images were obtained at an in-plane resolution of 0.104 μm/pixel (Fig. 1a). The non-actin and non-GFAP regions were segmented as axonal compartments (ACs). The area of ACs and width of actin and GFAP combined processes were recorded for structure-strain comparisons.

Finite Element Model: The AL geometry was created using the segmentations of the GFAP, actin and AC structures. The segmented image was down-sampled to a resolution of 1.13μm/pixel and extruded to a thickness of 11.3μm. The geometry was meshed with trilinear hexahedral elements (HEX8) in the Gibbon Toolbox (Fig. 1b, [8]) and imported into FEBio 3.0 [9]. Nodal displacements were prescribed to the side surface of the AL using boundary displacements from the aforementioned inflation test. In addition, a pressure of 20 mmHg was applied to the anterior surface of the AL to simulate the increase in IOP (Fig. 1c). All three materials were assumed to be incompressible Neo-Hookean materials. Shear modulus (G) of 2.4MPa for GFAP was obtained from existing measurement of intermediate filament vimentin [10], and G for actin was found to be 8.8 times larger than that for vimentin [11]. The AC was assigned a G of 1.9 kPa [12] as measured from white matter of brain tissues. Bulk modulus for each material was set to 100 times larger than its G.

Statistical Analyses: Comparisons among the strain outcomes and among the 3 materials were conducted using 1-way analysis of variance (ANNOVA). Correlations between structural properties and simulated strains in the AC and astrocyte processes were analyzed using a linear regression model in MATLAB.

RESULTS

In the control ONH, preliminary results showed that the average nasal-temporal strain (E_{xx}= 0.033) in the AL was higher than the inferior-superior strain (E_{yy}= 0.026), while the anterior-posterior strain was compressive (E_{zz}= -0.021, p<0.01). The result of higher E_{xx} compared to E_{yy} was consistent with that measured in the inflation tests (0.029 and 0.012 respectively). The maximum principal stress (σ_{max}) was lower in the ACs (0.002 MPa) when compared to that in the GFAP (0.021 MPa) and actin structures (1.83 MPa, p<0.01, Fig. 1e & 2a). However, the ACs have larger maximum principal strain (E_{max}, 0.25 ± 0.25) than that experienced by GFAP (0.07 ± 0.04) and actin (0.03 ± 0.02, p<0.01, Fig 1f and 2b). Similarly, tensile strain E_{xx} and E_{yy}, and compressive strain E_{zz} were highest in the ACs (p<0.01 for all).

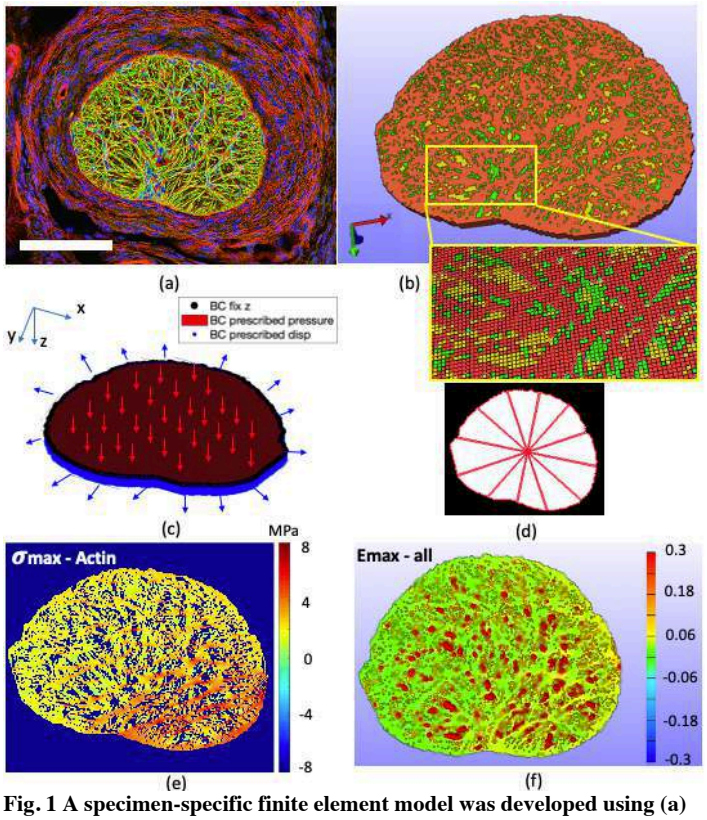

Fig. 1 A specimen-specific finite element model was developed using (a) image acquired from the unmyelinated zone of a mouse optic nerve that was labeled for GFAP (green), actin (red) and nuclei (blue). Non-actin and non-GFAP labelled regions were marked as axonal compartments (ACs). (b) The actin (red), GFAP (green) and ACs (yellow) were then converted to a finite element model with HEX8 elements using Gibbon toolbox and imported into FEBio 3.0. (c) Pressure was applied on the anterior surface to simulate increase in IOP and nodal displacements were applied on the side surface using average of experimental results from previous inflation study. (d) AL was divided into 12 sectors for calculation of pore volume fraction in each region. (e) Color map of maximum principal stress (σ_{max}) in actin and (f) of maximum principal strain (E_{max}) experienced in all 3 materials. Scale bar = 100 µm.

The average area for ACs was 5.4 ± 7.6 µm^2 and the average process width was 5.7 ± 2.1 µm for this specimen. Greater tensile strains E_{max}, E_{xx} and E_{yy}, and greater compressive strains E_{zz} were associated with larger ACs (Fig. 2c, p<0.01). In addition, thicker processes were more inclined to have lower strain magnitudes**.** When divided into 12 sectors (Fig. 1d), AL sectors with higher volume fraction of AC had higher average Emax in the corresponding actin and GFAP processes (Fig. 2d, p<0.01). Other structural measurements such as tortuosity and aspect ratio of the processes will also be analyzed for their effects on local stress and strain responses.

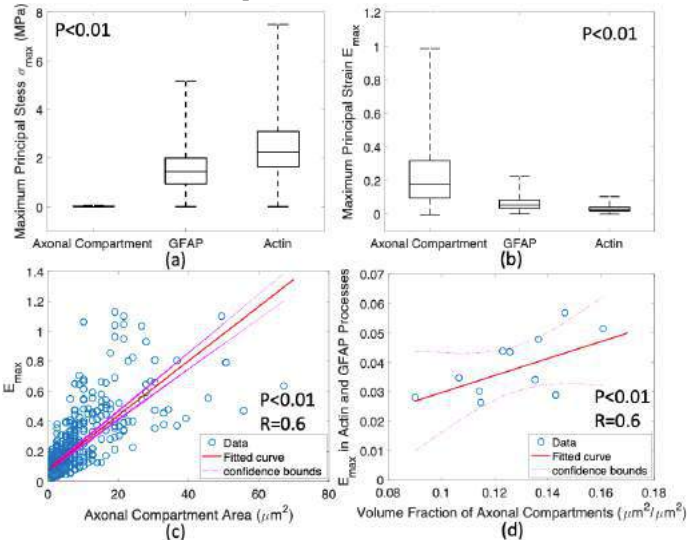

Fig. 2 Results from the specimen-specific finite element model of the mouse astrocytic lamina, showing (a) higher maximum principal stress in actin than in ACs and GFAP, while (b) ACs experienced higher strain Emax than in GFAP and actin. (c) ACs with larger area had larger E_{max}, and (d) sectors with higher volume fraction of ACs is correlated with higher E_{max} in their corresponding actin and GFAP processes.

DISCUSSION

Models of the human lamina cribrosa have been developed for investigation of structural effects in pressure induced strains [13, 14]. However, there have not been models that directly incorporate both experimentally-derived boundary displacements and applied pressure on a specimen-specific model of the AL. The model presented in this abstract included both boundary conditions and simulated strain response in the ACs. The result of E_{xx} larger than E_{yy} agreed with the results from the inflation tests. Further, local strain response was found to be associated with variations in structural properties.

Studies in brain injuries have shown that a strain of 0.05 - 0.3 causes moderate to severe diffuse axonal injury [15]. Our model showed that larger ACs experienced strains much higher than this threshold and may be more susceptible to axonal insult in glaucoma. We are currently developing more specimen-specific models of both control and 3-day OHT samples to further investigate the relationship between structural properties and local strains in the AL. The models will be validated by comparing to experimental measurements of the strain-structure relationships [16]. We will also examine the sensitivity of the predicted structure-strain and stress relationships to model assumptions for the material properties and for the segmentation and reconstruction of the astrocytic lamina.

ACKNOWLEDGEMENTS

NSF Award 1727104; NIH EY001865, Wilmer Core Grant (EY01765); EY02120 (Dr Quigley); and the Croucher Foundation (YTTL).

REFERENCES

[1] Quigley, H. and Green, W., *Ophthalmol,* 86(10):1803–1827, 1979. [2] Quigley, H et al., *Invest Ophthalmol Vis Sci,* 16:640–646, 1977. [3] Trivino, A et al., *Vis Res,* 36.14:2015-2028, 1996. [4] Ling, YTT et al., *Invest Ophthalmol Vis Sci,* 61.11:14-14, 2020. [5] Korneva, A et al., *J R Soc Interface,* 17.173:20200708, 2020. [6] Midgett, D et al., *Acta Biomater*, 53:123–139, 2017. [7] Bar-Kochba, E et al., *Exp Mech*, 55:261–274, 2015. [8] Moerman, K., *J Open Source Softw*, 3(22), 506, 2018. [9] Maas, S et al., *J Biomech Eng*, 134(1), 2012. [10] Guzman, C et al., J *Mol Biol*, 360.3:623-630, 2006. [11] Janmey, P et al., *J Cell Biol*, 113.1:155-160, 1991. [12] Budday, S et al., *J Mech Behav Biomed,* 46:318-330, 2015. [13] Voorhees, A et al., *Invest Ophthalmol Vis Sci,* 58.12:5336-5346, 2017. [14] Voorhees, A et al., *Invest Ophthalmol Vis Sci,* 61.13:15-15, 2020. [15] Wright, R and Ramesh K., *Biomech Model Mechanobiol*, 11.1-2:245-260, 2012. [16] Ling, YTT et al., *Invest Ophthalmol Vis Sci,* 60.7:2406-2422, 2019.

CONTINUUM-BASED INTERPRETATIONS OF MECHANO-ADAPTATION IN EPITHELIAL MICRO-TISSUES

Bernard L. Cook (1), Patrick W. Alford (1)

(1) Department of Biomedical Engineering
University of Minnesota
Minneapolis, MN, USA

INTRODUCTION

During development, epithelial tissues, such as the endocardium that lines the lumen of the developing heart, undergo morphogenesis, or shape change, which gives mature structure to amorphous tissue. It has been suggested that this shape change is driven by the epithelia mechano-adapting to rapidly changing loading conditions experienced during development [1]. Though progress has been made towards understanding short-term epithelial mechanics, long-term mechano-adaptation in epithelial tissue has yet to be systematically characterized.

Here, we use Cellular Microbiaxial Stretching (CμBS) to show that stresses in micro-tissues consisting of Madin-Darby Canine Kidney (MDCK) cells evolve at the tissue scale following a sustained stretch, a phenomenon captured with a continuum-based architecture dependent growth law that attributes stress evolution to cytoskeletal remodeling.

METHODS

Stretching device. The CμBS device [2] is comprised of a silicone membrane secured between metal clamps fastened to linear actuators (Fig. 1A). Bead-doped polyacrylamide gels are chemically bonded to the membrane, onto which cells are micropatterned into designated geometries (Fig 1B). The device is fixed above an inverted confocal microscope (Fig. 1C) and housed within a chamber maintained at physiological conditions. The linear actuators are used to precisely stretch micropatterned cells, while the confocal microscope is used to quantify cell-generated forces and cellular architecture (Fig 1D).

Substrate preparation. For all stretching experiments, MDCKs were micropatterned into square "micro-tissues" (8000 μm^2) (Fig. 1D, i) and cultured in standard cell growth medium.

Micro-tissue stretching protocol. A stretching protocol used to assess single-cell mechano-adaptation was adapted from a previous study [3]. MDCK micro-tissues were uniaxially strained to 30% (applied stretch ratios λ_x=1.3, λ_y=1) at a rate of 2%/s and held in this configuration for 24 hrs (Fig. 1D-E). For stress experiments, brightfield

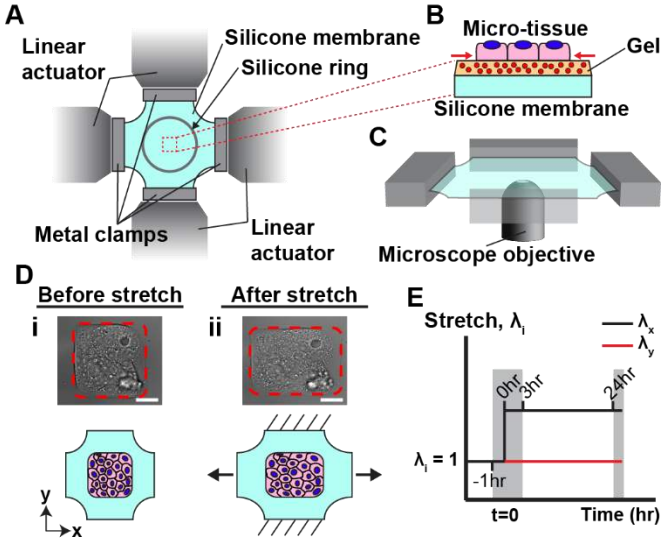

Figure 1. CμBS device is used to assay cell-scale mechano-adaptation. A) Stretching device. Silicone ring contains cells. B) Micropatterned cells. Cell forces deform the gel (arrows); this deformation is captured using C) a confocal microscope. Traction stresses are quantified from these deformations using traction force microscopy. D) MDCKs micropatterned into micro-tissues before (i) and after (ii) uniaxial stretch. E) Mechano-adaptation stretch protocol. Data is captured in regions boxed in grey. Scale: 30 μm.

and bead images were captured before and after stretch (Fig. 1E). After the experiment, cells were lysed with 0.1% SDS and microbead images were captured in both the deformed and undeformed configuration to quantify bead displacements used to determine traction and midplane Cauchy stresses. For architecture experiments, MDCKs were stained with CellMask Deep Red and imaged before and after stretch.

Cell stress and structure. Traction stresses (Fig. 2A) and midplane Cauchy stresses (Fig. 2B) were calculated as previously described [2]. Midplane cross-sectional areas were estimated with monolayer height [4] and micro-tissue geometry. Architecture alignment was quantified from images of stained MDCKs and quantified (Fig. 2C-D) with a ridge-detection algorithm [5].

Modeling mechano-adaptation. Micro-tissues were assumed to be incompressible, and undergo shear-free, axisymmetric deformation. Micro-tissues were taken to be comprised of a population of discrete actin fibers embedded in a surrounding matrix, representing non-fiber components of the cell. Micro-tissue strain energy density was taken to be comprised of a term that represents the cellular matrix and a second term that represents fiber contributions as in Eq.1,

$$W = \frac{\mu}{2}(I_1 - 3) + \frac{1}{n}\sum_{i=1}^{n}\frac{C_f}{2}\left(\left(\frac{\lambda_{fi}}{\lambda_{gfi}}\right)^2 - 1\right)^2 \quad (1)$$

where shear modulus μ and fiber stiffness C_f and are material parameters, $I_1=\lambda_x^2 + \lambda_y^2 + \lambda_z^2$, where λ_i is the elastic stretch in the i^{th} direction, λ_{fi} and λ_{gfi} are the fiber stretch and growth of the i^{th} fiber, respectively, and n is total number of fibers. Fiber stretch is related to elastic stretch through $\lambda_f^2 = \lambda_x^2 cos^2\theta + \lambda_y^2 sin^2\theta$. Midplane stresses were calculated assuming cells were unconstrained (i.e., stress-free) in z. Single-fiber stress was calculated assuming fibers to be 1-dimensional.

Here, we explored two models of mechano-adaptation. In a targeted growth formulation, we assumed cytoskeletal fibers grew following stretch according to Eq. 2,

$$\frac{\dot{\lambda}_{gf}}{\lambda_{gf}} = \frac{1}{T_f}(\sigma_f - \sigma_{f0}) \quad (2)$$

Where $\dot{\lambda}_{gf}$ is the rate of change of λ_{gf}, T_f is a time constant, and σ_f and σ_{f0} are the current and homeostatic fiber stress, respectively. In a hyper-restoration formulation, we assumed that fibers grew according to Eq. 2; however, fiber target stress σ_{f0} was taken to evolve according Eq. 3,

$$\dot{\sigma}_{f0} = -\frac{1}{T_s}(\sigma_f - \sigma_{f0}) \quad (3)$$

where $\dot{\sigma}_{f0}$ is the rate of change of σ_{f0} and T_s is a time constant.

Model optimization. To fit each model to experimental stress data, micro-tissues were assumed to be comprised of an incompressible matrix embedded with 2000 discrete actin whose orientations were randomly sampled from experimentally measured PDFs of fiber alignment (see Fig 2C). Before stretching, it was assumed that $\lambda_x=\lambda_y=\lambda_z=\lambda_f=1$. Micro-tissues were stretched ($\lambda_x=1.3$), stresses solved, and growth and homeostatic stress evolution evaluated with finite differences. Constants C_f, μ, λ_{g0}, and T_f and T_s were optimized using least squares minimization between experimental and model stresses.

RESULTS

Before stretch, micro-tissues had architecture aligned primarily at 0° and ±90°. Following stretch, architecture was passively realigned in the direction of stretch (Fig. 2C-D).

Following stretch, micro-tissue traction stresses spatiotemporally evolved (Fig. 2A), suggesting an active response to stretch. At the tissue scale, stresses increased following stretch; over time, however, stresses decreased. By 25 hrs post-stretch, stresses fell below pre-stretch magnitudes, indicating that MDCKs adapted to the loading (Fig. 2E). Both mechano-adaptation models captured early stress behavior (Fig. 3D-E); however, the hyper-restoration model more aptly captured the stress overshoot observed 24 hrs post-stretch (Fig. 3E).

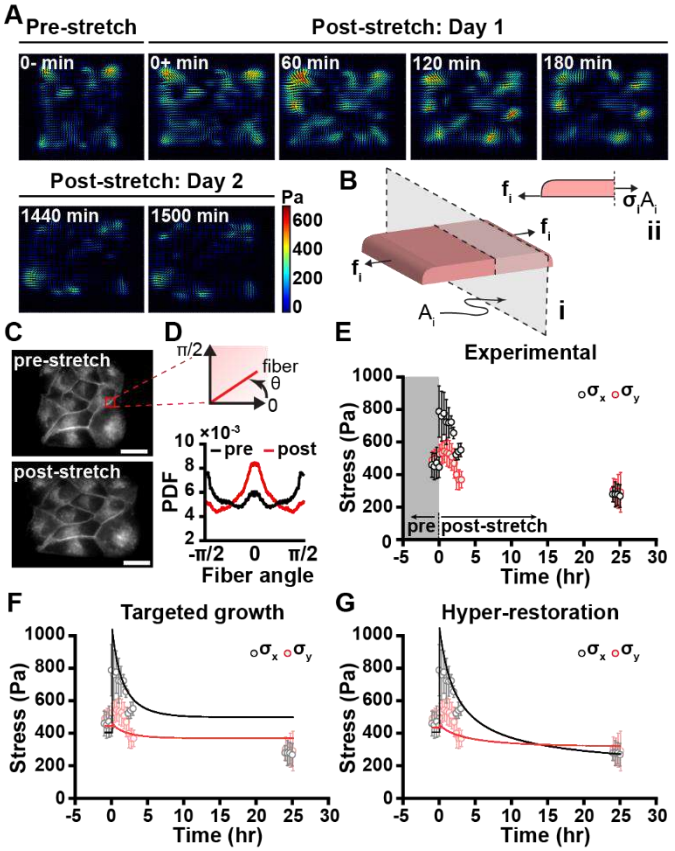

Figure 2. Epithelial micro-tissues mechano-adapt. A) Traction stresses before and after stretch. B) Cauchy stress calculation, where f_i is cell force (calculated from traction stresses), A_i is midplane cross sectional area, σ_i is midplane Cauchy stress, and i = x, y. C) A) The same micro-tissue stained with CellMask DeepRed, shown before and after stretch. B) Coordinate system used to determined orientation of cell architecture (top), from which probability density functions for architecture alignment are quantified (bottom). C) Experimental Cauchy stresses. D-E) Models fit to experimental data. Scale: 30 μm.

DISCUSSION

Here, we used our CμBS device to measure and characterize mechano-adaptation in epithelial micro-tissues. We find that tissue-scale stress evolution can be captured with a continuum-based formulation of mechano-adaptation that attributes changes in stress to cytoskeletal remodeling. The present work is a first step towards creating stronger models of morphogenesis that investigate the role of forces in shaping developing tissues, and elucidating which forces lead to maladaptive changes in shape. Ultimately, this work will serve as a framework that will be applied towards understanding mechano-adaptation in specific developing tissues, such as the embryonic heart.

ACKNOWLEDGEMENTS We acknowledge support from the NSF CMMI-156319 (PWA) and the UMN CSE Fellowship (BLC). **REFERENCES**

[1] Taber L, *Biomech Model Mechanobiol*, 7:427-441,2008. [2] Win Z et al., *J Biomech Eng*, 139(7):0710061-07100610,2017. [3] Steucke K et al., *J Biomech Eng*, 139(7):0710051-0710059,2017. [4] Zehnder S et al., *Biophys J*, 108(2):247-250,2015. [5] Alford et al., *Biomaterials*, 31(13):3613-3621,2010.

AN EX VIVO PLATFORM FOR TESTING DIAGNOSTIC AND THROMBOLYTIC CAPABILITIES OF ULTRASOUND-AIDED NANOPARTICLES

C. Watson (1), J. Sloand (1), E. Rokni (2), J. Simon (2), K. Manning (1,3), S. Medina (1)

(1) Department of Biomedical Engineering
The Pennsylvania State University
University Park, PA, USA

(2) Graduate Program in Acoustics
The Pennsylvania State University
University Park, PA, USA

(3) Department of Surgery
Penn State Hershey Medical Center
Hershey, PA, USA

INTRODUCTION

Deep vein thrombosis (DVT) is a pressing clinical issue that requires further investigation into both the disease pathway and clinical intervention. DVT is characterized by slow clot formation over months, with symptoms beginning as mild pain and swelling in the afflicted area and growing to pulmonary embolisms and strokes **[1]**. Complications associated with DVT are estimated to result in between $5-8 billion in annual domestic medical spending [**2]**. Anticoagulants are a common treatment, but often either fail to stifle thrombosis sufficiently or result in severe side effects such as excessive bleeding **[3]**. Due to a lack of accessibility and poor clot visualization, clinical diagnostic practices are ripe for improved imaging resolution and alternate approaches.

The mechanics by which clots form in the venous circulation are still not fully understood. Certainly, the venous valves serve as a nidus for clot formation due to flow stagnation and recirculation within the sinus region. However, how procoagulant conditions arise are not clear **[4]**. Venous thrombosis is markedly different from arterial clots, as thrombus composition is predominately red blood cells and fibrin. Knowing that clot formation can be interpreted through the lens of Virchow's Triad, it is important to target the appropriate pillars, namely hemostasis and increased thrombogenicity.

Combining therapeutic innovation with improved diagnostic methods would therefore serve a pressing clinical purpose. Ultrasound (US) is both a common diagnostic method for DVT and a prospective delivery method for thrombolytic agents. The use of ultrasound has the advantage of localized drug delivery over the current method of systemic anticoagulation **[3]**. B-mode imaging displays a grayscale visualization of physical structures while Doppler imaging assesses flow magnitude and direction **[5]**. Combining the two elements of ultrasound imaging allows for analysis of both clot location and structure, as well as the alteration in flow regimes that arise due to the growing thrombus. A method of increasing imaging resolution at the boundary of deep veins and the internal site of clot formation would be an important step in *in vivo* diagnosis of DVT.

A novel nanoparticle, described as a nanopeptisome, acts as an ultrasound sensitive scattering agent. This nanoparticle serves the dual purpose of increasing the imaging depth of contrast US and competitively inhibiting clot formation. The Arginine-Glycine-Aspartate (RGD) ligand incorporated within the self-assembling peptide shell of the nanopeptisome targets the $\alpha_{IIb}\beta_3$ binding site, limiting platelet-platelet adhesion. This nanoparticle is designed with the intention to localize to activated platelets, limiting further aggregation via competitive inhibition, and aiding in detection by scattering acoustic signals. The development of an *ex vivo* platform will allow for the testing of these properties.

METHODS

Blood was obtained from a bovine jugular vein the same day as experiments, into an CPDA-anticoagulated blood bag. After checking the hematocrit and platelet count, the blood was recalcified to 20mM prior to flow loop circulation in order to restore coagulability. Bovine carotid vessels were obtained from Lampire Biological Lab LLC (Everett, PA) and sectioned into 15 cm strips for insertion into the flow loop. The vessels were untreated and used one day after harvesting while shipped in a refrigerated DMEM suspension. The vessel was trimmed and secondary outlet vessels were ligated to prevent leakage. Both the proximal and distal ends of the sectioned vessel were attached to the flow loop with barbed connectors and sealed using a plastic clamp. A 2000IU/mL solution of bovine lung thromboplastin (BioPharm LLC, UT) was prepared from frozen stock on the day on experimentation. A 26.5g needle was inserted into the vessel so that the angled tip was flush with the vessel wall, serving as an injection port for

the thromboplastin. After operation of the flow loop, the clamps were unfastened, and the vessel was removed from the connectors for dissection and clot observation.

Nanoparticles were fabricated via an emulsification procedure utilizing perfluoropentane and a fluorinated amphiphilic peptide containing an RGD binding motif, as previously described **[6].** The nanopeptisome solution was diluted 1:20 within the blood and circulated throughout the loop.

In vitro clotting studies were performed in both static and dynamic conditions. Nanoparticles were diluted in recalcified bovine blood within 24 well plates on a rocker, or within a Chandler loop operating at 1 Hz and allowed to clot overnight at 37˚C. A flow loop was designed to create a closed-loop system for initiation and localization of thrombosis within the *ex vivo* platform. A centrifugal pump, was used to drive flow at Reynolds number 200. Flow rate was confirmed to be steady by an ultrasonic flow probe downstream of the vessel platform. A tissue analogue model was fabricated of 2% agarose within a plastic container with a channel bore for the vessel. Agarose was suspended in water and cured overnight at 0˚C**.** The loop was operated for 30 minutes or until complete occlusion. After flow cessation, the vessel was removed from its tubing attachments and dissected longitudinally to observe the clot. A Verasonics (Kirkland, WA) research ultrasound system was used to collect B-mode and Doppler signals. The 5MHz ultrasonic transducer was aligned with the longitudinal axis of the vessel.

RESULTS

In vitro clotting experiments yielded data regarding the efficacy of clotting inhibition via nanopeptisomes as a function of both hematocrit and nanoparticle concentration. The nanoparticle demonstrated an ability to localize activated platelet binding sites at a significantly higher rate than nonspecific binding in similar conditions (**Fig 1A and 1B).** The activation of platelets causes a change in conformation that exposes additional binding sites. Clot mass was shown to be significantly reduced with blood samples of 40 and 60% HCT (**Fig 2)**, indicative of venous blood composition.

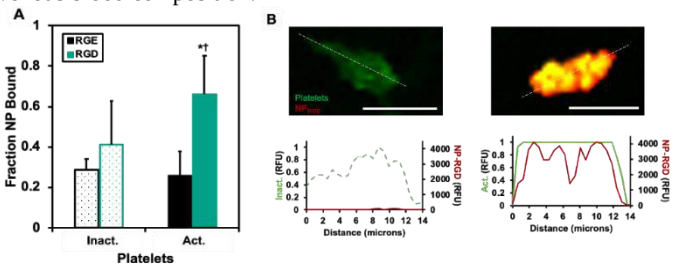

Figure 1: (A) Increase in ligand binding affinity and specificity as a result of platelet activation
(B) Specific localization of nanoparticles to platelet binding sites

Within the *ex vivo* flow loop, case studies (n=6) showed a similar ability of the nanoparticles to inhibit clotting on the vessel test surface under physiological conditions. The ultrasound system was able to detect and measure clot growth within the deep tissue analogue with sufficient resolution for identification and measurement (**Fig 3)**.

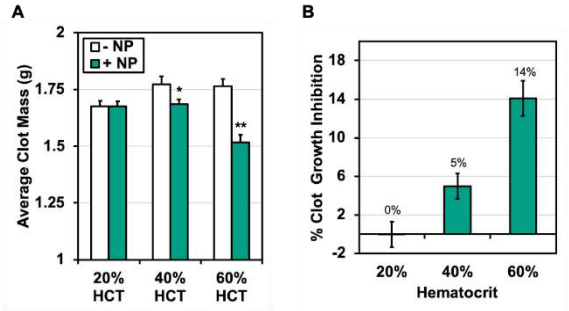

Figure 2: (A) Mean clot mass at varying hematocrit conditions
(B) Nanoparticle effect on *in vitro* clot mass with respect to HCT

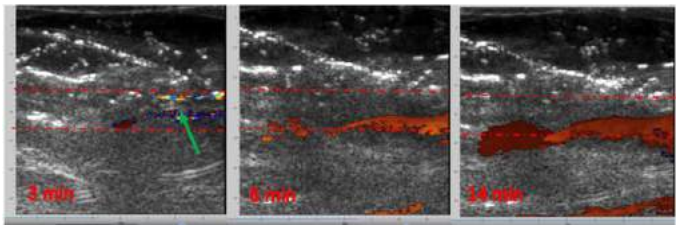

Figure 3: Clot growth within vessel visualized with Doppler US. The red outline denotes the vessel region while the green arrow points out the initial clot location

DISCUSSION

This study consisted of a two-pronged approach in developing an *ex vivo* platform for initiating, visualizing, and inhibiting thrombus formation. Nanopeptisomes were fabricated to be used as both an acoustic marker and a competitive inhibitor for platelet binding. Due to the embedded RGD motif within the peptide shell, nanoparticles were shown to effectively inhibit platelet-platelet binding at $\alpha_{IIb}\beta_3$ sites at both the *in vitro* and *ex vivo* levels. *In vitro* clotting was significantly inhibited at 40% and 60% hematocrit. In both static and dynamic conditions, clot inhibition was most pronounced at higher hematocrits and nanoparticle concentrations, suggesting an effect caused by the ratio of nanoparticles to platelets. This is likely due to increasing availability of nanoparticles, and the decrease in total platelets to be suppressed as this ratio shifts. As hematocrit decreases, total platelet count is increased and available nanoparticles are distributed more sparsely throughout the binding sites, indicating that it might be possible there is a minimum effective threshold for clot inhibition. *Ex vivo* experiments were conducted as a series of case studies, in which each case demonstrated reduced clot growth in the presence of nanoparticles relative to absence. Additional studies are currently being conducted on preformed clots within the *ex vivo* platform to further investigate the acoustic properties and thrombolytic capability of the nanoparticles.

ACKNOWLEDGEMENTS

This study was generously supported by **the Pennsylvania State University, College of Engineering Multidisciplinary Seed Grant.**

REFERENCES

[1] Goldhaber, S et al., *The Lancet*, 279 (9828) 1835-1846 2012
[2] Ashrani, A et al., *Journal of Thrombosis and Thrombolysis*, 28 (4) 463 2009
[3] Schattner, A et al,. *QJM An International Journal of Medicine*, 90 (4) 283-7 1997
[4] Carrier, M et al., *Annals of internal medicine*, 152 (9), 578-9 2010
[5] Mangi, M et al., *Cureus*, 9 (7) 2017
[6] Medina S, et al., *Angewandte Chemie International Edition*, 56 (38), 11404-8 2017

MYOSIN NETWORK ARCHITECTURE DURING CONVERGENT EXTENSION TISSUE MORPHOGENESIS

Christian M. Cupo (1), Cole J. Allan (1), Annie Lin (1), Marisol Herrera-Perez (1), Karen E. Kasza (1)

(1) Department of Mechanical Engineering
Columbia University
New York, NY, USA

INTRODUCTION

Epithelial tissue sheets undergo dramatic changes in shape and structure to build organs during development. These tissues comprise collections of cells whose behaviors must be coordinated to generate complex structures (1-3). Mechanical forces generated by cells are a major driver of tissue shape changes and movements (4-5) and of tissue mechanical properties (6). The mechanical forces driving tissue morphogenesis have been largely attributed to cellular actomyosin networks (7-13), which are mechanically coupled across the tissue through cell adherens junctions. Contractile forces generated by the myosin II motor protein (myosin) are essential to tissue morphogenesis (10), and the localization pattern of myosin in a specific tissue tends to correlate with how the tissue changes shape (11-15). For example, during *Drosophila* axis elongation, myosin accumulates at cell junctions in a planar polarized pattern (higher accumulation at "vertical" contacts between cell neighbors along the AP axis), driving cell intercalation that narrows the tissue along one axis (converges) and elongates it along the other axis (extends) in a flow that doubles the length of the tissue in 30 min (Fig. 1). In contrast, a more isotropic pattern of myosin is observed during *Drosophila* ventral furrow formation. Recent studies of ventral furrow formation reveal a myosin network spanning the tissue that increases in density over time to form a robust network that is resilient to perturbation (13). Yet, it is not well understood how specific properties of myosin network architecture contribute to tissue mechanical behavior in other contexts, such as in convergent extension, or how myosin networks are regulated to promote fluid-like tissue flow in some regions of the embryo and solid-like behavior in others.

To understand how myosin network architecture contributes to convergent extension tissue flows, we identified and analyzed the myosin network in the germband during *Drosophila* body axis elongation. To visualize myosin, we used existing *Drosophila* lines expressing an mCherry-tagged myosin and imaged the embryos by confocal microscopy. To extract the myosin network, we developed a custom MATLAB-based code designed to trace myosin fluorescence intensity. We find that convergent extension coincides with myosin network reorganization, suggesting that myosin network architecture may play a key role in this fluid-like tissue flow.

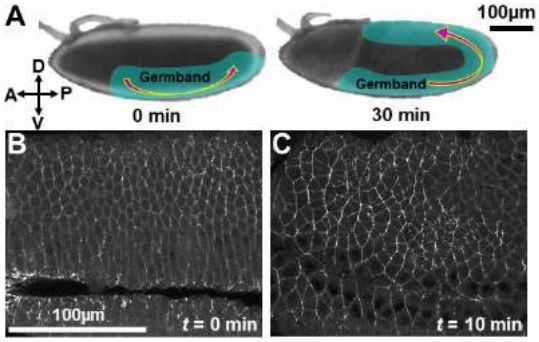

Figure 1. During *Drosophila* body axis elongation, the germband epithelium rapidly extends to twice its length in a convergent extension movement. This tissue flow (A) is thought to be driven by a planar polarized pattern of myosin that produces anisotropic stresses. Planar polarized myosin localization at $t = 0$ (B) and $t = 10$ min (C).

METHODS

Fly Stocks. Fly stocks were from the Bloomington *Drosophila* Stock Center (BDSC). Myosin II was visualized with an mCherry-tagged myosin regulatory light chain (sqh-mCherry).

Time-Lapse Imaging. Collected embryos were dechorionated for 2 min in 50% bleach and washed with distilled water for 2 min. Embryos were mounted between a glass slide and an oxygen-permeable

membrane in halocarbon oil. Confocal imaging was performed with a Zeiss LSM880 laser-scanning confocal microscope on the ventrolateral region of the embryo at 15µm z-steps and 15 s time intervals.

Image Processing and Quantification. Analysis was performed on maximum intensity projections of 3 z-slice images at the apical side of the tissue at the level of adherens junctions. Myosin networks were mapped by combining a watershed algorithm (16) with a mask in MATLAB. Tortuosity and intensity measurements were performed in MATLAB. Tortuosity is the ratio of total segment length to linear node-node distance, with values ≥1. The time point $t = 0$ represents the start of body axis elongation.

RESULTS

The myosin network we identified spans the tissue and dynamically changes during convergent extension. The myosin network predominantly comprises segments connected to the network at both ends (Fig. 2); these segments correspond to myosin at cell junctions as well as in the cell medial-apical domain. The network contains more dendritic strands (not connected to the network at both ends) when the tissue is rapidly flowing at $t = 10$ min (Fig. 2B) compared to at the onset of tissue flow (Fig. 2A).

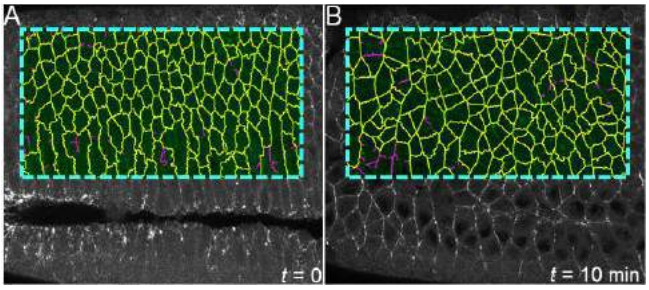

Figure 2. Analyzing the myosin network in the flowing germband epithelium during *Drosophila* convergent extension. The network at the onset of axis elongation $t = 0$ (A) and during rapid tissue flow $t = 10$ min (B). Color map represents connectivity of segments in the network. Yellow segments are connected to two nodes and fully connected to the network. Magenta segments are not connected at both ends to the network and might not robustly transmit forces. Cyan rectangles denote regions used for analyses.

To further characterize the identified myosin network, we quantified the tortuosity (Fig. 3A,B) and orientation (Fig. 3C) of each network segment. We find 2-3 times more segments oriented vertically (along the DV axis) than horizontally (along the AP axis).

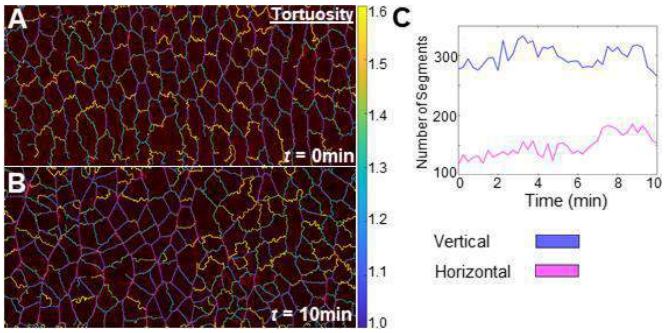

Figure 3. Tortuosity and orientation of myosin network segments during convergent extension. Segments color-coded by tortuosity at $t = 0$ (A) and $t = 10$ min (B). (C) Number of myosin segments oriented vertically (along DV axis) or horizontally (along AP axis) over time.

The average tortuosity of segments decreased over time, but the tortuosity of "horizontal" segments was consistently higher than for "vertical" segments (Fig. 4A). Consistent with the planar polarized pattern of myosin in this tissue (Fig. 1), we observed higher myosin intensities at "vertical" compared to "horizontal" segments (Fig. 4B). The trends for tortuosity and myosin intensity were inversely correlated.

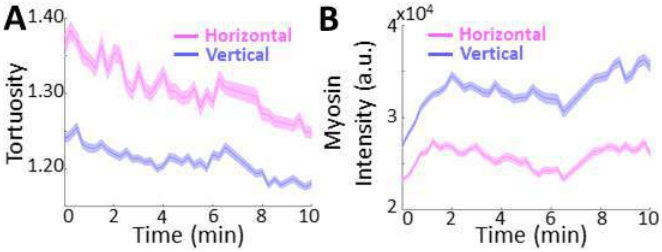

Figure 4. Tortuosity and myosin intensity of network segments show opposite trends during convergent extension. (A) Mean tortuosity of "vertical" and "horizontal" segments over time. (B) Mean myosin intensity of "vertical" and "horizontal" segments over time. Error bars, standard error.

DISCUSSION

In this paper, we identified and analyzed the myosin network spanning the converging and extending germband epithelium during *Drosophila* axis elongation. We quantified how the orientation, tortuosity, and intensity of network segments changed over time. We found fewer segments in the horizontal orientation, possibly reducing resistance to tissue extension along the AP axis during tissue flow. Additionally, we found opposing trends in network segment tortuosity and myosin intensity. Segments displayed increased myosin accumulation and decreased tortuosity over time, with vertical edges having the highest intensity and lowest tortuosity. Overall, these results show that there is a myosin network spanning the germband tissue during convergent extension and that the network architecture changes during this process. These changes in network architecture are likely to alter the mechanical properties and force transmission in the tissue, which may contribute to rapid convergent extension and tissue flow. In future work, we will directly compare these myosin network properties of the flowing germband to the myosin networks present in tissues that show more solid-like behavior, such as during ventral furrow invagination (13), which will help link myosin network architecture and tissue mechanical behaviors, such as tissue fluidity versus solidity.

ACKNOWLEDGEMENTS This work was supported by a Columbia Blavatnik Fellowship to CMC and the NSF CMMI-1751841, a Burroughs Wellcome Fund Career Award at the Scientific Interface, and a Packard Fellowship to KEK.

REFERENCES [1] Bryant, D, et al. Nature Reviews. Molecular Cell Biology. 9.11 (2008): 887-901. [2] Chung, S, et al. Wiley Interdisciplinary Reviews: Developmental Biology 3.4 (2014): 281-300. [3] O'Brien, L.E., et al. Nature Reviews Molecular Cell Biology 3.7 (2002): 531-537. [4] Patwari, P, et al. Circulation Research 103.3 (2008): 234-243. [5] Sadati, M, et al. Differentiation 86.3 (2013): 121-125. [6] Kasza, K, et al. Current Opinion in Cell Biology 19.1 (2007): 101-107. [7] Kasza, K, et al. Current Opinion in Cell Biology 23.1 (2011): 30-38. [8] Heisenberg, et al. Cell 153.5 (2013): 948-962. [9] Zallen, J, et al. Developmental Cell 6.3 (2004): 343-355. [10] Streichan, S.J., et al. eLife 7, e27454 (2018). [11] Mongera, A, et al. Nature 561, (2018): 401–405. [12] Tetley, R.J., et al., Nat. Phys. 15, 1195–1203 (2019). [13] Yevick, H, et al. Developmental Cell 50.5 (2019): 586-598. [14] Wang, X, Merkel, M, et al. Proceedings of the National Academy of Sciences 117 (2020): 13541-13551. [15] Venkatesan, I, et al. Current Biology 29.4 (2019): 578-591. [16] Vincent, L, et al. IEEE 13(6), (1991): 583–598.

IMPLEMENTING VARIABLE-STIFFNESS SPRINGS FOR MODELING THE VISCOELASTIC BEHAVIOR OF THE PORCINE URINARY BLADDER

Tyler G. Tuttle (1), Sara Roccabianca (1)

(1) Mechanical Engineering Department
Michigan State University
East Lansing, Michigan, United States

INTRODUCTION

The lower urinary tract is composed of the urinary bladder, internal and external urethral sphincters, and urethra. During urine storage, a healthy bladder maintains a low pressure through relaxation of the bladder wall as the organ fills. The bladder wall consists of smooth muscle cells (SMCs) and extracellular matrix (ECM). The ECM, which is comprised of proteins, proteoglycans, and glycosaminoglycans, acts as a support structure that gives strength and compliance to the bladder. Because of the prevalence of lower urinary tract pathologies that are associated with tissue mechanical dysfunction, such as decrease or increase in distensibility, it is important to understand the mechanical characteristics of the bladder wall.

An effective way to analyze and quantify mechanical behavior is through the use of constitutive models. These can be either phenomenological or microstructurally motivated, and can give insight into mechanical behavior that is not possible to observe from purely experimental data. Soft-tissue mechanical behavior is generally modeled as hyperelastic or viscoelastic. In this study, we utilize a combination of experimental testing and viscoelastic constitutive modeling to describe the stress-relaxation behavior of the porcine bladder wall.

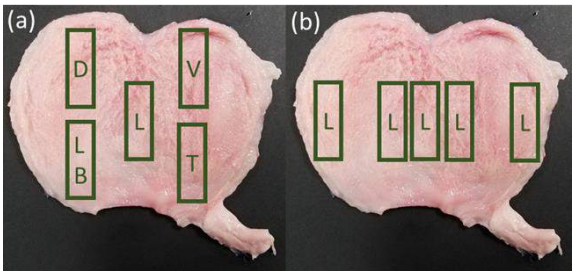

Figure 1: Representative bladder depicting sample locations for (a) location experiments, and (b) osmolarity experiments.

Mechanical characteristics of the bladder have been shown to differ between anatomical locations[1]. However, no study has evaluated location dependent viscoelastic behavior in the bladder. Furthermore, inflammatory response to pathological conditions is seen in many tissues, including the bladder[2], and this can lead to increased tissue swelling. Hence, in this study we also aim to evaluate the effect of swelling on the viscoelastic response of the bladder wall.

METHODS

Porcine bladders (n=6) were obtained at time of slaughter and then were cut along the lateral edge and flattened. A 10mm × 30mm rectangular punch was used to create rectangular samples from the bladder wall in the longitudinal (apex-to-base) direction. The stress-relaxation experiments were split into two separate sets of experiments – i.e., to identify location-specific behaviors (n=3), and the effect of solution osmolarity (n=3). For the location experiments, one sample was taken from each of the five anatomical locations, namely dorsal (D), ventral (V), lateral (L), lower-body (LB), and trigone (T), Figure 1a. For the osmolarity experiments, five samples were taken from the lateral location, Figure 1b.

For the swelling procedure, samples were submerged in 10 mL of modified Krebs-Henseleit buffer solution for 18 hours. For the location experiments, all samples were soaked in solution with an osmolarity of 300 mOsm/L. For the osmolarity experiments, samples were soaked in solutions of either 100, 300, 600, or 900 mOsm/L to induce different levels of swelling.

Uniaxial stress-relaxation experiments were performed with samples fully submerged in modified Krebs-Henseleit buffer solution.

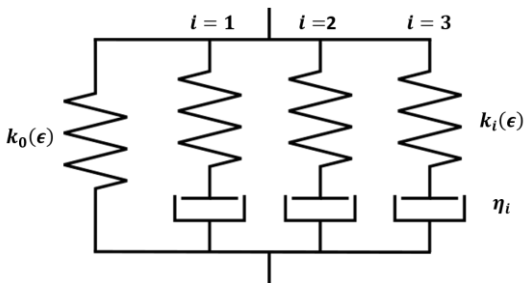

Figure 2: Modified Maxwell-Wiechert model with strain dependent spring stiffness.

For the osmolarity experiments, one sample from each bladder was tested dry to observe the difference in submerged and open-air experiments. Multi-step stress-relaxation was performed at strains of 0.25, 0.5, 1.0, 1.5, and 2.0 with a displacement rate of 50 mm/s, and relaxation times of 30 minutes for the first step, and 45 minutes for all subsequent steps. Sample images were taken at each step to estimate cross-sectional area.

Stress, σ, as a function of time, t, was calculated as follows,

$$\sigma(t) = F(t)/A_\epsilon \quad (1)$$

$$A_\epsilon = b_\epsilon h_\epsilon \quad (2)$$

where $F(t)$ is the force as a function of time; A_ϵ, b_ϵ, and h_ϵ are the cross-sectional area, width, and the thickness for the sample, respectively, measured at each strain level.

For this study we employed a modified Maxwell-Wiechert model[3] with three Maxwell elements (see Figure 2). Nonlinear spring elements were used to capture the nonlinear mechanical behavior of the bladder. Specifically, the standalone spring has a stiffness, $k_0(\epsilon)$, that increases exponentially with stretch,

$$k_0(\epsilon) = c_a e^{c_b \epsilon}\,, \quad (3)$$

where c_a and c_b are spring stiffness parameters with units of stress and nondimensional, respectively. Additionally, the Maxwell element springs have stiffness, $k_i(\epsilon)$, that increases linearly with stretch,

$$k_i(\epsilon) = c_i \epsilon\,, \quad (4)$$

where c_i (units of stress) is a spring stiffness parameter for the given Maxwell element. All dashpots in this model are standard dampers where stress is proportional to rate of strain. The relaxation function for this model, $G(t)$, is as follows,

$$G(t) = \epsilon c_a e^{c_b \epsilon} + \sum_{i=1}^{3} \frac{4\eta_i}{\left(2t\sqrt{c_i} + \frac{2\eta_i}{\epsilon\sqrt{c_i}}\right)^2}\,, \quad (5)$$

where η_i represents the dashpot constants. Time constants, τ_i, for the modified Maxwell elements in this model are as follows,

$$\tau_i = \frac{\eta_i}{8 c_i \epsilon}. \quad (6)$$

Due the strain-dependent stiffness of the springs in the modified Maxwell elements, the time constants are also strain dependent.

The parameter estimation has been performed in two steps, to lower the uncertainty in parameter values by lowering the number of simultaneously estimated parameters. First, we quantified the exponential spring parameters (c_a and c_b) by minimizing the sum of squared error between the relaxed model stress response at each level of strain, and the stress-strain data resulting from using the final stress point in each relaxation step. Second, the remaining parameters are estimated using the time dependent stress-relaxation data. Parameter estimation for this step is done using sum of absolute error, which lessens the impact of short-time stress response deviation from model prediction. Figure 3 shows a representative model fit to experimental data. Statistical analysis for estimated model parameters consisted of 2-way ANOVA's, followed by Tukey-Kramer multiple comparisons tests.

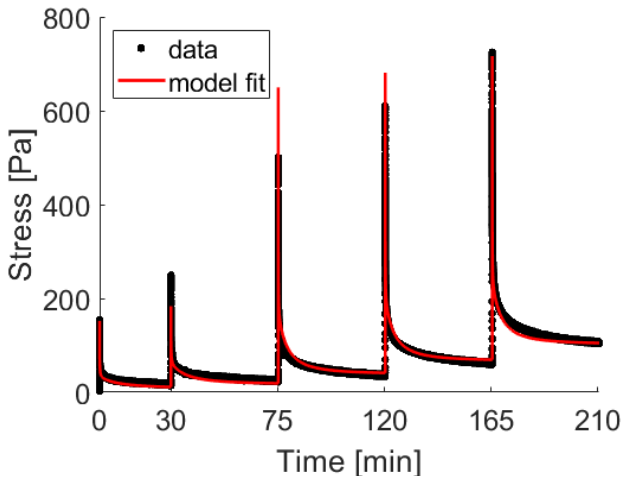

Figure 3: Model fit to experimental data from a representative sample.

RESULTS

For the location-specific experiments, no significant differences were seen between any groups for the viscoelastic parameters (i.e. parameters associated with the modified Maxwell elements). In fact, for many combinations of groups and parameters, p-values are greater than 0.9. When looking at the elastic parameters (i.e., exponential spring), c_a is significantly higher in the lateral location compared to the trigon, and c_b is significantly higher in the trigone compared to all other locations.

For the osmolarity experiments, c_a is significantly higher for 900 compared to all other osmolarities and c_b is significantly lower in 900 compared to dry. For c_3, dry is significantly lower than 100, 600, and 900, and 300 is significantly lower than 900. For η_2, dry is significantly lower than all osmolarities, and η_3 is significantly lower in 300 than 900. τ_2 and τ_3 are significantly higher for dry samples compared to all osmolarities.

DISCUSSION

The differences seen in elastic parameters for the location experiments supports previous work[1] that shows the trigone region having different mechanical properties than other regions of the bladder. However, the lack of differences seen in viscoelastic parameters suggests that all regions may behave similarly in terms of time-dependent behavior.

The differences in viscoelastic parameters based on solution osmolarity suggest that tissue swelling in the bladder wall could change the time-dependent behavior of the bladder. It is possible that this may be a driving factor for remodeling that is seen in diseases and disabilities that are associated with inflammation or changes in urine osmolarity.

Differences in parameters between dry and submerged samples underscores the importance of tissue hydration in mechanical testing. Likewise, it is important to consider differences in protocol when attempting to compare mechanical data from different studies.

REFERENCES

[1] Korossis, S et al., Biomaterials, 30(2):266–275, 2009.
[2] Geppetti, P et al., Int. Suppl., 101:2–6, 2008.
[3] Roylance, David, *Cambridge MA* 2139 (2001): 14-15.

A HIGH-FIDELITY 3D MICROMECHANICAL MODEL OF VENTRICULAR MYOCARDIUM

David S. Li (1), Emilio A. Mendiola (1), Reza Avaz (2), Frank B. Sachse (3), Michael S. Sacks (1)

(1) Oden Institute for Computational Engineering and Sciences & Department of Biomedical Engineering
The University of Texas at Austin
Austin, TX, USA

(2) Department of Biomedical Engineering
Texas A&M University
College Station, TX, USA

(3) Department of Biomedical Engineering
The University of Utah
Salt Lake City, UT, USA

INTRODUCTION

Many cardiac diseases ranging from myocardial infarction (MI) to pulmonary arterial hypertension (PAH) lead to substantial adaptations in cardiac tissue structure and mechanical behavior, often including hypertrophy or degradation of the myofibers, remodeling of the collagen fiber network, and dilation of the ventricles. While the tissue-scale (~1-cm) structure and mechanics of normal and diseased myocardial tissue have been studied previously [1], the mechanical contributions of and interactions between myofibers and the surrounding extracellular matrix (ECM) remains incomplete. In particular, although there has been evidence that the arrangement of myofibers and ECM collagen in myocardium gives rise to unique tissue-level coupling behavior observed for myocardium, such coupling has yet to be characterized at the scale of individual myofibers.

To this end, multiscale computational modeling of the heart has become an important tool for understanding cardiac function. However, there is a need to develop models that are faithful to the microstructure of the myocardium in order to gain insight into the cellular-level mechanical environment, especially to identify mechanisms driving adaptations to structural heart disease. Thus, in this study, we developed a microanatomically realistic finite element model for ventricular myocardium. For this first study, we based our model on a high-resolution 3D imaging dataset from the murine right ventricular free wall (RVFW) to study fiber-specific interactions under planar deformations, with the aim to match the results of our previous tissue-level model [1].

METHODS

Finite element mesh construction

A 3D imaging dataset was acquired from a ~200x200x60-μm section of murine RVFW via confocal microscopy, with tissue components labeled using antibodies and fluorescent markers [2]. The resulting geometry, including myofibers, ECM, myofibroblasts, and coronary blood vessels, was used to generate a volumetric finite element (FE) layer model consisting of myofiber and ECM elements (Fig. 1).

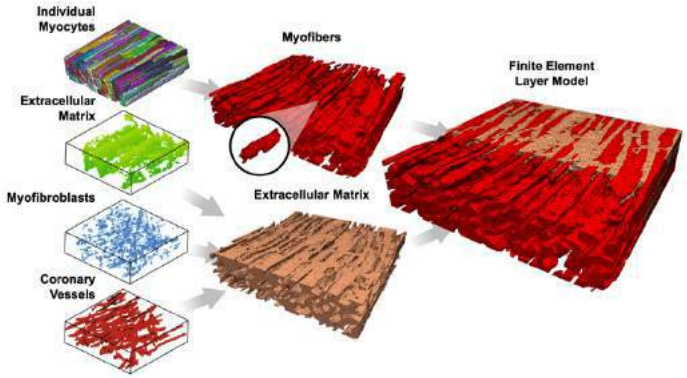

Figure 1: FE layer model developed from 3D geometry [2].

Material modeling

The passive behaviors of the myofiber and ECM phases were modeled with nearly incompressible, nonlinear anisotropic materials derived from our previous studies [1]. The myofibers were represented using a locally orthotropic constitutive form [3], consisting of an isotropic matrix stiffened by mutually orthogonal fiber families in the myofiber (f) and cross-fiber (s) directions within the layer, given by

$$\psi_{\mathrm{myo}} = \frac{\mu_{\mathrm{m}}}{2}(I_1 - 3) + \sum_{i=\mathrm{f,s}} \frac{a_i}{2b_i}\{\exp[b_i(I_{4i} - 1)^2] - 1\}, \qquad (1)$$

where I_1, I_{4f}, and I_{4s} are the first, fourth, and sixth invariants of the right Cauchy-Green tensor, respectively. The ECM was modeled as an isotropic matrix reinforced by a distribution of undulated, linearly stiffening collagen fibers, described by the orientation distribution function Γ_θ and recruitment function Γ_s, given by

$$\psi_{\mathrm{ECM}} = \frac{\mu_c}{2}(I_1 - 3) + \frac{\eta_c}{2}\int_\theta \Gamma_\theta(\theta)\int_1^{\lambda_\theta}\Gamma_s(\lambda_s)\left(\frac{\lambda_\theta}{\lambda_s} - 1\right)^2 \mathrm{d}\lambda_s \mathrm{d}\theta, \quad (2)$$

where θ is the fiber angle, λ_θ is the fiber stretch in the θ direction, and λ_s is the fiber slack stretch at which collagen fibers begin contributing to the ECM stress. Fiber splay and slack stretch were determined based on previous modeling results [1], which also indicated the collagen fiber distribution was aligned with the myofibers (f) in the FE mesh.

FE simulations

The FE layer model was used to simulate planar deformations in order to reproduce previous tissue-level studies [1]. Myofiber and ECM elements were assigned their corresponding material models and assumed to be perfectly bonded. Deformations were applied in E_{11}:E_{22} = 0.30:0.30, 0.15:0.30, and 0.30:0.15 configurations. The material parameters for myofibers and ECM were calibrated to match the stress-strain response predicted by our previously developed tissue-scale structural model [1]. All simulations were performed on the Stampede2 supercomputer at the Texas Advanced Computing Center using FEniCS (fenicsproject.org). Finally, the FE layer simulation was extended to simulate the full-thickness transmural RVFW by stacking 15 individual layer models, each rotationally positioned to capture the reported transmural variation in fiber orientation.

RESULTS

The stress response FE layer microanatomical model successfully reproduced the tissue-scale structural model prediction (Fig. 2). As the FE layer model contained highly aligned myofibers oriented along the f direction, the model showed exponentially stiffening myofiber stress in E_{11} with negligible stress along E_{22}. The ECM exhibited nonlinear stiffening during collagen fiber recruitment ($0.17 < E < 0.20$), after which fibers were fully recruited and the ECM response became linear, as demonstrated previously [1]. Comparing the stress profiles of the myofiber and ECM phases indicated that total response was governed by myofiber behavior in the low-strain regime (below $E < 0.17$). At higher strains, the ECM collagen fibers became the major contributor to the RVFW stress.

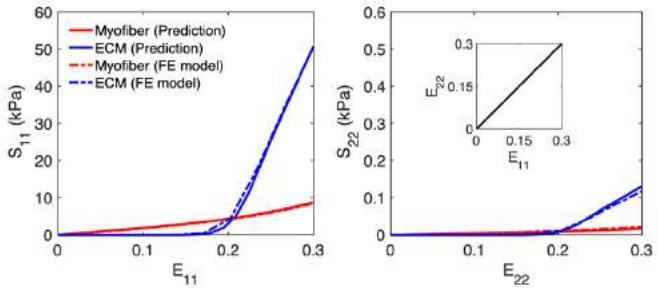

Figure 2: Contributions of myofibers and ECM to the total stress in response to equibiaxial strain. Solid lines: predictions from tissue-scale structural model. Dotted lines: fitted response of microanatomical FE layer simulation.

At maximum deformation, the stress state at the myofiber-ECM interface was visualized via projection of the myofiber stress onto the boundary of selected myocytes, which indicated that the myofiber stress was transferred outward from the myocytes, preferentially along the fiber axis of the layer, but with a persistent cross-fiber component in regions further away from the myocyte ends (Fig. 3).

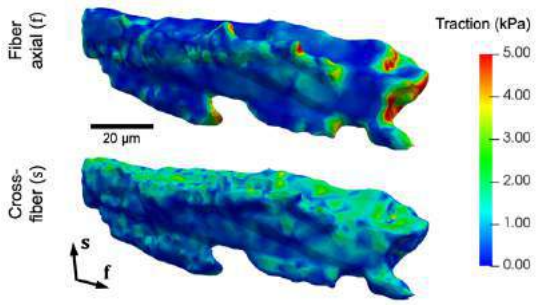

Figure 3: Myofiber-ECM traction magnitudes in fiber axial (f) and cross-fiber (s) directions for a representative myocyte.

The full transmural simulation also demonstrated the effect of transmural variation in fiber orientation through the generation of significant cross-fiber stress in both the myofiber and ECM phases, resulting in stress-strain behavior showing qualitative similarity to tissue-level studies [1] (Fig. 4).

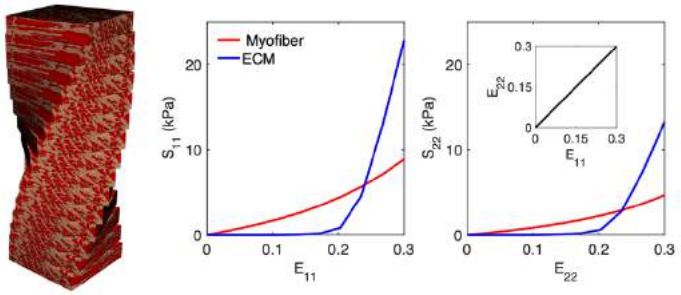

Figure 4: Full-thickness RVFW simulation (left) and equibiaxial stress-strain response (right).

DISCUSSION

To the best knowledge of the authors, this study constitutes a major first step in the development of microanatomically-based computational models of cardiac tissue. The fiber axis-focused profile of stress transfer from myofibers to ECM provides insight into possible mechanisms for the coupling interactions hypothesized in previous work. Through this microanatomical approach, exploration of cellular-scale stress transfer between myocytes and their surroundings can be integrated into larger-scale models and used to further probe the effect of micro-level events on organ-level function. Ultimately, our microanatomical model will allow us to investigate fiber-specific remodeling of the cardiac microstructure in response to structural heart disease.

ACKNOWLEDGEMENTS

NIH (T32 EB007507, F31 HL139113 to D.S.L., K99 HL138288 to R.A.) Specimen imaging was performed at the University of Utah.

REFERENCES

[1] Avazmohammadi, R et al., *APL Bioeng*, 16:561-581, 2017. [2] Seidel, T et al., *Ann Biomed Eng*, 44(5):1436-1448, 2016. [3] Holzapfel, G et al., *Philos Trans Royal Soc A*, 367:3445-3475, 2009.

DIGITAL VOLUME CORRELATION USING DEEP LEARNING-DENOISED SYNCHROTRON MICRO-CT IMAGES TO STUDY BONE MECHANICAL BEHAVIOR

Yoshihiro Obata (1), Michael Sieverts (1), Daniël M. Pelt (2), Claire Acevedo (1,3)

(1) Department of Mechanical Engineering
University of Utah
Salt Lake City, UT, USA

(2) Centrum Wiskunde & Informatica
Amsterdam, The Netherlands

(3) Department of Biomedical Engineering
University of Utah
Salt Lake City, UT, USA

INTRODUCTION

To facilitate understanding of how bone's hierarchical structure naturally resists fracture, it is necessary to examine the morphology of bone and crack propagation at the micro-scale. One advantageous modality for examining bone at this scale is synchrotron radiation micro-computed tomography (SRμCT). This technique uses high flux x-rays to reconstruct an image stack corresponding to the three-dimensional (3D) structure and material composition of a scanned sample. With SRμCT, the crack path of a fractured bone sample can be revealed, and new research has been focused towards determining the stress state during loading and crack propagation using a technique known as digital volume correlation (DVC). In bone, this technique tracks the speckle-like osteocyte lacunae features between different SRμCT scans to determine strain and stress fields. Combining *in situ* mechanical testing with SRμCT and DVC to obtain datasets of crack propagation with near real-time stress and strain states would elucidate crack growth mechanisms at the micro-scale.

This process poses one key challenge: the over irradiation of bone during SRμCT, which damages its mechanical properties [1]. To address this issue, we propose acquiring low-quality scans at a reduced radiation dose to maintain mechanical properties at the cost of reducing the signal-to-noise ratio. Features in these noisy scans cannot successfully be segmented, however, eliminating the possibility of performing DVC. Our solution is to use deep learning to denoise low-quality images. Deep learning has shown promise in learning to remove noise and enhance the signal of images [2]. In this work, a convolutional neural network called a mixed-scale dense network (MS-D net) will be used to denoise low-quality SRμCT scans acquired during *in situ* mechanical testing to obtain internal strain values via DVC without over-irradiation of bone samples.

METHODS

***In Situ* Mechanical Testing at the Synchrotron Microtomography Beamline.** Mechanical testing was performed at the ALS beamline 8.3.2. at Lawrence Berkeley National Laboratory. Pre-notched bovine bone samples of dimensions 1-mm x 2-mm x 10-mm were prepared prior to testing and stored in Hank's Balanced Salt Solution (HBSS) for at least 12 hours prior to testing. Testing is performed in a custom three-point bending chamber with a span of 6-mm. Samples are submerged in HBSS at room temperature during testing to mimic physiological conditions.

A reference high- and low-quality scan are taken of each sample before testing with 3937 and 657 projections respectively. An incident X-ray energy of 24 keV was selected with an exposure time of 100 ms. Final spatial resolution was 1.6-μm/voxel. The three-point bending test was performed at a constant displacement while simultaneously monitoring the recorded force-displacement output of the load cell in the testing chamber. Low-quality scans of the sample are acquired after each drop in load until complete material failure. Reconstruction of SRμCT data was performed in Python open-source package Tomopy and visualization was performed in Dragonfly (ORS) [3].

Mixed-Scale Dense Network. The MS-D net is a convolutional neural network that combines aspects of mixed-scale networks (efficient at resolving features of images at multiple length scales via convolved dilations) and densely connected networks (a network whose feature maps are connected to feature maps of all other layers) [4]. The network used has 100 layers and used Adam as the optimization algorithm with a learning rate of 0.001.

Training was performed on a workstation with an Nvidia GeForce GTX 1080Ti GPU. SRμCT images for each sample at each load step were cropped to a dimension of 1024 x 1024 pixels and approximately 650 images. A training, validation, test split of about 70-15-15 was used

from viable samples, yielding 3240 training images, 680 validation images, and a holdout test dataset (not included in training or validation sets) of 662 test images. Training was performed for 44 epochs using mean-squared error (MSE) as the loss function.

Digital Volume Correlation. DVC was performed using TomoWarp2, a Python based digital volume correlation code [5]. Denoised output from the MS-D net was segmented into a binary image, separating the features of bone (lacunae, canals, and crack) from the matrix. These features were tracked during DVC. For each sample, a correlation window of 25 voxels in all directions and a node spacing of 10 voxels in all directions were chosen. An appropriate search window was selected for each scan.

RESULTS

Network output of the MS-D net for a single image of an SRμCT scan are shown below (Figure 1) compared to the low-quality and high-quality slice accompanied by the Otsu segmentation and image stack grey value histogram.

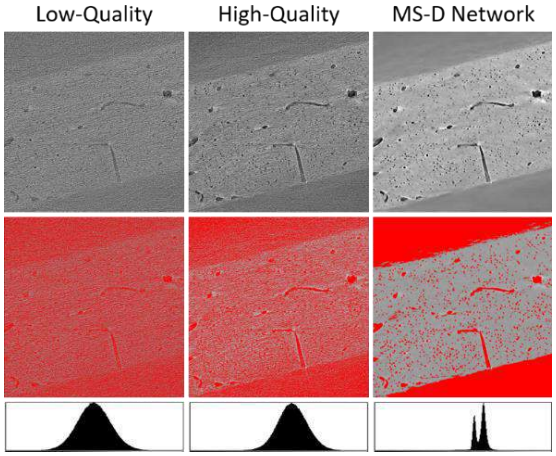

Figure 1: Denoised MS-D network output (right) compared to low-quality scan (left) and high-quality scan (middle)

In both the low- and high-quality images, the image stack histogram is unimodal, meaning the background and bone grey values belong to the same distribution with no clear separation between the two. This is also evident in the corresponding Otsu segmentation for each where bone's background is segmented and colored red. This segmentation does not show a clear distinction from the bone. The output from the MS-D net possesses two clear peaks in the image stack histogram corresponding to bone and background. Segmentation of the image slice shows separation of bone from background, with clear outlines for the bone, notch, canals, and osteocyte lacunae present.

Assessment of network results was performed by examining the MSE and peak signal-to-noise ratio (PSNR) of the network on the validation dataset as well as the DVC results. Metrics compare the MS-D net output and low-quality images to the high-quality images. MSE of the MS-D net output was 9.75, reduced from the low-quality data's MSE of 63.36. This is an expected, positive result because the network minimizes MSE, the loss function. PSNR was increased from the low-quality images compared to the MS-D net with values of 17.43 and 25.52 respectively, indicating a clearer image and reduced noise.

TomoWarp2 was used to correlate the data from loading steps to the reference configuration (0 N load). Shown (Figure 2) is the x-direction strain calculated from the DVC output at the first step of crack growth (20.7 N). Strain in the x-direction is highest for regions of bone around and ahead of the crack path, with strain values varying from 0.05-0.2. The strain field further from the crack path is approximately 0. Two correlations were performed in the preliminary work here, one for a load step with no crack (8.7 N, not shown) and one for a load step with a crack (20.7 N, Figure 2) with mean correlation values of 0.717 and 0.669 respectively. For comparison, DVC was also performed using two high-quality scans with a crack present instead of the MS-D net output, resulting in a mean correlation value of 0.656.

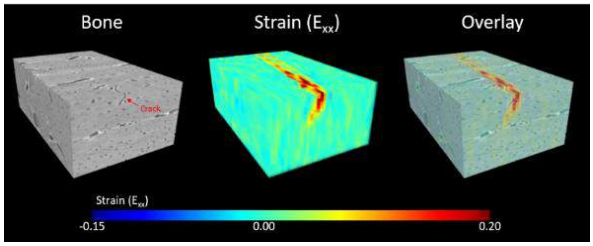

Figure 2: Strain (x-direction) from digital volume correlation on bone sample with a crack.

DISCUSSION

The images denoised by the MS-D net show clear segmentation of bone from background during the *in situ* mechanical test, even more pronounced than the high-quality scan. The implications of this result are twofold; 1) low-quality scans can be taken of a bone sample during SRμCT to limit radiation dose and thus preserve mechanical properties if a denoising method such as the MS-D net used and 2) the resulting network output is clearer in terms of recognizing microstructural features than high-quality scans for the same sample.

While the network output is more easily segmented, the grey values of the bone matrix, directly corresponding to volumetric tissue mineral density (vTMD) and Young's modulus, may be obscured from its true value. Further investigation is required to understand the effects of the MS-D net on vTMD values. Despite this, using SRμCT in conjunction with deep learning has enabled acquisition of *in situ* data at an appropriate time scale for crack propagation to be resolved in near-physiological conditions for use in assessment of features without deterioration of mechanical properties due to over-irradiation.

Performing DVC on time dependent *in situ* data while adhering to guidelines for non-detrimental radiation dose is presently a major limitation of the technique when applied to biological samples such as bone [6]. The presented method yielded promising results, but further validation and analysis of DVC results are required. Preliminary results from DVC have not been validated with data from tests performed without synchrotron radiation and error metrics have yet to be exhaustingly examined. If successful, the proposed method can be used for safely determining the stress/strain state of bone and other biological materials during loading and crack propagation.

ACKNOWLEDGEMENTS

This work received support from the University of Utah seed grant (VPR Research Incentive 51900367 for YO). This work also used resources from the Advanced Light Source at beamline 8.3.2., a U.S. DOE Office of Science User Facility under contract no. DE-AC02-05CH11231.

REFERENCES

[1] Barth, Holly D. et al., *Biomaterials* 32, 34:8892-8904, 2011
[2] Yang, Xiaogang et al., *Scientific reports* 8, 1:1-13, 2018
[3] Gürsoy, Doga et al., *J. of synchrotron rad.* 21, 5:1188-1193, 2014
[4] Pelt, Daniël M., and James A. Sethian, *PNAS* 115, 2:254-259, 2018
[5] Tudisco, Erika et al., *SoftwareX*, 6:267-270, 2017
[6] Palanca, Macro et al., *Journal of biomechanics*, 58: 27-36, 2017

DIFFERENTIATING NANOSCALE CONFINED AND COLLECTIVE HEATING BY PLASMONIC NANOPARTICLE ARRAYS

C. Xie (1), P. Kang (1), Z. Qin (1, 2, 3, 4)

(1) Department of Mechanical Engineering
University of Texas at Dallas
Richardson, Texas, USA

(2) Department of Bioengineering
University of Texas at Dallas
Richardson, Texas, USA

(3) Department of Surgery
University of Texas at Southwestern
Medical Center
Dallas, Texas, USA

(3) Center for Advanced Pain Studies
University of Texas at Dallas
Richardson, Texas, USA

INTRODUCTION

Nanomaterials have been designed to efficiently absorb optical or magnetic energy and convert to heat, and have found wide applications[1]. These studies use two modes of nanoparticle (NP) heating[2]. The first involves continuous excitation (seconds to minutes) of nanomaterials and collective tissue heating, the second involves using a short energy pulse to introduce nanoscale confined heating. However, there have been significant debate over past few years on the existence of significant heating by nanoscale and microscale objects, and on how to differentiate between the heating modes[3].

The fate of nanoscale confined and collective heating depends on spatiotemporal evolution of heating by large number of nanoparticles. Keblinski et al. was among the first to demonstrate that the duration of energy excitation drives the transition of heating modes[4]. Baffou et al. illustrated the importance of geometry of nanoparticle distribution on the temperature confinement or delocalization regime under continuous laser excitation[5]. Despite these efforts, it remains unclear on how the spatiotemporal evolution of nanoparticle heating determines the transition from nanoscale heating to collective macroscale heating.

In this report, we investigated the critical transition from nanoscale confined and collective heating by analyzing the heating of NP arrays, and the corresponding biological responses of the heating. We found that heating time and NP area density determine whether a nanoscale confined and collective heating is established. Next, we analyzed the biological responses corresponding to NP array heating, we demonstrate the feasibility for nanoscale selective protein denaturation, whereas it is unlikely to achieve nanoscale selective TRPV1 based on our current understanding of its kinetics[6]. Furthermore, we introduced dimensionless parameter to describe the transition of heating modes. Our work provides a guideline to design innovative approaches that harvest the nanoscale confined and collective heating to modulate molecular or tissue specific activities under realistic physical constraints.

METHODS

For NP array heating, we solve the problem by superposition of the analytical solution of single nanoparticle heating:

$$\Delta T_{multi}(\boldsymbol{r},t) = \sum_{i=1}^{N} \Delta T_{single}^{i}(\boldsymbol{r},t) \quad (\text{~~3~~}1)$$

Here the ~~Wh~~ΔT_{multi} is temperature raise for multi NP heating, and ΔT_{single}^{i} is the temperature raise for ith NP heating. The single spherical particle heat conduction model in spherical system was analytically solved by Laplace transform [7]. The analytical solution was calculated in Matlab 2019b software.

The dimensionless parameter is based on mathematical description for temperature raise in the center point for circular NP array heating (ΔT_{array}). Using the idea of superposition method, the expression for ΔT_{array} of 2D and 3D NP array are as following:

$$\Delta T_{array,2D} = \frac{qd}{2k}\left[R \cdot erfc\left(\frac{R}{2\sqrt{Dt}}\right) + \frac{2\sqrt{Dt}}{\pi}\left(1 - e^{-\left(\frac{R}{2\sqrt{Dt}}\right)^2}\right)\right] \quad (2)$$

$$\Delta T_{array,3D} = \frac{qd}{2k}\left[R^2 \cdot erfc\left(\frac{R}{2\sqrt{Dt}}\right) - \frac{2\sqrt{Dt}}{\sqrt{\pi}} R \cdot e^{-\left(\frac{R}{2\sqrt{Dt}}\right)^2} + 2Dt \cdot erf\left(\frac{R}{2\sqrt{Dt}}\right)\right] \quad (3)$$

Here, q is heating power, d is NP density, P is interparticle distance, for 2D array, $d = P^{-2}$, for 3D array, $d = P^{-3}$. R is the radius of NP array, k and D are thermal properties, t is the heating time.

RESULTS

Firstly, we investigated the effect of the heating time and NP area density on the heating overlap. Here we compared the thermal responses of NP array heating with different heating times and different NP area densities (Fig. 1 A). The nanoscale confined heating can be achieved for

cases with short heating time (Fig. 1 A Case 1) and low NP area density (Case 3), whereas heating overlaps for cases with longer heating time (Fig. 1 A Case 2) and higher NP area density (Case 4). In order to quantify the transition of the two heating modes, wo introduced $\Delta T_{overlap}$ which is defined by the discrepancy between ΔT_{multi} with ΔT_{single} (Eqn. 2). We define the heating condition as no overlap for $\Delta T_{overlap} \leq$ 3 K, and overlap for $\Delta T_{overlap} >$ 3 K. Fig. 1 B demonstrates 3D map for $\Delta T_{overlap}$ = 3 K in terms of heating time, NP area density and heating power, this surface also serves as the boundary between two heating modes.

$$\Delta T_{overlap} = \Delta T_{multi}(\hat{r}, t) - \Delta T_{single}(\hat{r'}, t) \quad (4)$$

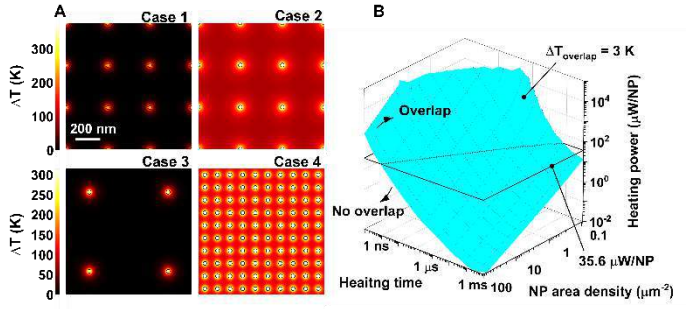

Figure 1. Effect of heating time and NP area density on heating modes. A) Temperature raise (ΔT) profile for 2D NP array heating, Diameter of NP (D_{NP}): 30 nm, heating power (q): 36 μW/NP, case 1: 10 ns heating, 9 NP/μm^2; case 2: 1000 ns heating, 9 NP/μm^2; case 3: 20 ns heating, 2.6 NP/μm^2; case 4: 20 ns heating, 100 NP/μm^2. B) 3D map for $\Delta T_{overlap}$ = 3 K.

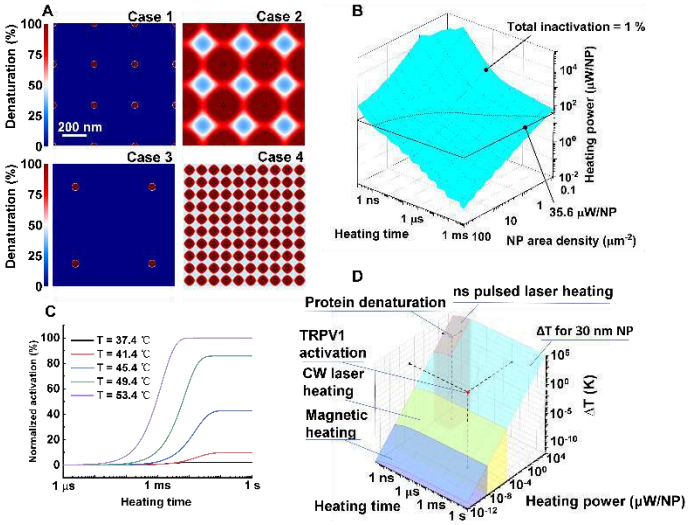

Figure 2. Biological responses for corresponding NP array heating cases. A) Protein denaturation profiles for case 1-4 (α-chymotrypsin). B) 3D map for *total denaturation* = 1 %. C) Kinetic activation for TRPV1 [6]. D) ΔT for 30 nm single NP heating.

Next, we investigated the corresponding biological responses for the NP array heating. Protein denaturation and TRPV1 channel activation are two main biological applications for NP array heating[8]. For protein denaturation, Fig. 2 A shows the protein denaturation profile corresponding to case 1-4. Fig. 2 B illustrates that the 3D map for *total denaturation* = 1% corresponds with 3D map for $\Delta T_{overlap}$ = 3 K. Here we demonstrate the feasibility for nano scale selective protein denaturation, and we found the critical transition from nanoscale confined and collective heating closely matches the shift from minimal and widespread transmembrane protein denaturation. For TRPV1 channel activation, Yao J, et al. demonstrated the TRPV1 channel is activated within 37 – 53 ℃[6]. It takes milliseconds continuous heating for TRPV1 activation (Fig. 2 C). The ns pulsed laser is too short for TRPV1 activation. CW laser and magnetic heating can last for milliseconds, yet they are too weak to heat up single NP to thermally activate TRPV1 (Fig. 2 D). Therefore, it is unlikely to achieve nano scale selective TRPV1 activation with traditional heating methods.

Lastly, we introduced dimensionless parameter to describe the heating modes based on the mathematical description for ΔT_{array} of circular NP array heating (Eqn. 2&3) Fig. 3 A illustrates $\Delta T_{array,2D}$ (temperature raise in center point) in terms of R. For any finite t, when $R \rightarrow \infty$, $\Delta T_{array,2D}$ is finite due a finite heat transfer speed ($\Delta T_{array,2D,R\rightarrow\infty} = \frac{qd}{2k}\frac{2\sqrt{Dt}}{\pi}$). When $\Delta T_{array,2D}$ is close to this $\Delta T_{array,2D,R\rightarrow\infty}$, further increasing R has negligible effect on $\Delta T_{array,2D}$, indicating the heating of NPs located further than R from the center point have negligible effect to $\Delta T_{array,2D}$. Therefore we consider this critical R as a limitation of heat transfer distance in 2D NP array. Based on this idea, we define a Dimensionless parameter (ξ) to describe heating modes by comparing ΔT_{array} with $\Delta T_{array,R\rightarrow\infty}$ and replace R by $P/2$ (half interparticle distance):

$$\zeta_{2D} = \frac{\left(\frac{p}{2}\right)\cdot erfc\left(\frac{p}{4\sqrt{Dt}}\right)+\frac{2\sqrt{Dt}}{\sqrt{\pi}}\left(1-e^{-\left(\frac{p}{4\sqrt{Dt}}\right)^2}\right)}{\frac{2\sqrt{Dt}}{\sqrt{\pi}}} \quad (5)$$

$$\zeta_{3D} = \frac{\left(\frac{p}{2}\right)^2\cdot erfc\left(\frac{p}{4\sqrt{Dt}}\right)-\frac{2\sqrt{Dt}}{\sqrt{\pi}}p\cdot e^{-\left(\frac{p}{4\sqrt{Dt}}\right)^2}+2Dt\cdot erf\left(\frac{p}{4\sqrt{Dt}}\right)}{2Dt} \quad (6)$$

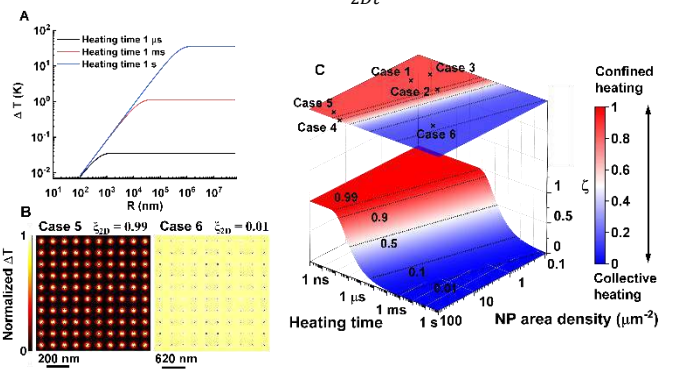

Figure 3. Dimensionless parameter (ξ) for differentiating confined *versus* collective heating. A) ΔT_{array} in terms of NP array radius (R). B) ξ_{2D} for case 5&6; case 5: 2.6 ns heating, 64 NP/μm^2; case 6: 1 ms heating, 12.8 NP/μm^2. C) 3D map for ξ_{2D}.

When $\xi \rightarrow 1$, the heating is confined, while $\xi \rightarrow 0$, a collective heating is established. Fig. 3 B&C shows that ξ_{2D} nicely captures the level of heating overlap between nanoparticles.

ACKNOWLEDGEMENTS

We acknowledge the support from National Science Foundation (1631910), National Institute of Health (R35GM133653).

REFERENCES

[1] Park J, et al., *J. Phys. Chem. C*, 116:26335-26341,2012.
[2] Qin Z, et al., *Chem. Soc. Rev.*, 41:1191-1217, 2012.
[3] Huang H, et al., *Nat. Nanotechnol*., 5:602-606,2010.
[4] Keblinski P, et al., *J. Appl. Phys.*, 100:054305,2006.
[5] Baffou G, *et al.*, *ACS Nano*, 7:6478-6488,2013.
[6] Yao J, et al., *J. Biophys*., 99:1743-1753,2010.
[7] Goldenberg H, et al., Br. *J. Appl. Phys.*, 3:296,1952.
[8] Nelidova D, et al. *Science*, 368:1108-1113,2020.

THE DIFFERENTIAL IMPACT OF TISSUE HETEROGENEITY ON TRABECULAR PLATES AND RODS IN FINITE ELEMENT MODELS OF HUMAN VERTEBRAL BONE

Jason M. Cox (1), Jacqueline H. Cole (1)

(1) Joint Department of Biomedical Engineering
University of North Carolina-Chapel Hill and North Carolina State University
Raleigh, NC, United States

INTRODUCTION

The microarchitecture of cancellous bone is related to its load-bearing ability [1], varies with anatomic site [2], and can be decomposed into trabecular rods and plates [3]. Because they have differing geometry and preferential orientation, plates and rods may have unique mechanical roles in the microarchitecture [4]. Recently, a powerful topology classification algorithm known as individual trabecular segmentation (ITS) enabled trabecular plates and rods to be studied separately in micro-computed tomography (micro-CT) data [5]. Moreover, micro-CT-derived finite element (micro-FE) models of cancellous bone can be used to estimate mechanical properties [6]. Combining ITS and finite element analysis (FEA) allows separate digital manipulation and mechanical analysis of trabecular plates and rods in ways that are impossible with physical specimens [5].

Besides microstructure, the composition of cancellous bone also contributes to its mechanical performance [7]. Varying degrees of mineralization are present throughout trabeculae [8], arising from the continual remodeling of surface bone to repair microdamage [9]. Since bone mineralizes as it matures, mineralization is correlated with both distance from the trabecular surface and tissue age [8], producing a tissue density gradient that increases the amount of microdamage in early loading [10]. Thus, the mineral distribution in trabecular bone contributes to remodeling in a feedback system that ultimately forms the plate-rod microstructure [9], suggesting that the roles of plates and rods may be determined in part by tissue heterogeneity.

Despite the importance of heterogeneity in the processes of tissue damage and remodeling, previous studies implementing ITS and FEA used homogeneous models [5,11]. Therefore, the objective of our study was to examine the effect of tissue heterogeneity on the distinct mechanical roles of trabecular plates and rods through ITS and FEA in human cancellous bone.

METHODS

Cancellous bone cores were extracted from the 12th thoracic and 2nd lumbar vertebral bodies of cadaver spines from 19 Caucasian donors (10 female, 9 male, 58-92 yrs). The cylindrical cores were scanned using quantitative micro-CT and reconstructed at an isotropic voxel size of 17 μm. Tissue mineral density was calibrated using a cortical bone mineral standard. Scans were oriented to align with the vertebral superior-inferior axis and cropped to a diameter of 8.25 mm and length of 17 mm. Specimen-specific thresholds were applied using the Otsu method [12] to segment the bone volume, and the bone voxels were converted to 8-noded linear brick elements in a finite element mesh in MATLAB.

Two sets of finite element models were created. For models with physiological tissue heterogeneity, the elastic modulus (E) for each element was assigned based on the mineral density (ρ) of the associated CT voxel using a power law relationship [7]. For homogeneous models, a single specimen-specific E was assigned to all elements based on the mean tissue ρ for each bone core. For boundary conditions, a compressive strain of 0.25% was applied to the top face of each model, and the bottom face was constrained to prevent bulk translation and rotation. A single-step linear FEA was conducted for all models, and principal strains were obtained for each element using Abaqus. The principal strain with the greatest magnitude was chosen to represent that element, and values surpassing 410 microstrain in tension or -830 microstrain in compression were indicative of failed elements [11].

Individual trabecular segmentation was performed on micro-CT scans of all cores to identify trabecular plates and rods, their relative fraction of total bone tissue, and orientations relative to the core central axis. Orientations (φ) were categorized as longitudinal for $0° < \varphi < 30°$, oblique for $30° < \varphi < 60°$, and transverse for $60° < \varphi < 90°$ [11]. For both FE model sets, plate and rod apparent failed tissue fractions (AFTF) were computed for each core as the total number of failed

elements in plates and rods, respectively, divided by the total number of elements in the model [11]. AFTF was also computed separately for plates and rods within each trabecular orientation group and for elements under tensile and compressive strain in each trabecular core.

Mixed linear models were used to evaluate the effect of material distribution, trabecular orientation, and strain direction on AFTF. Spine donor ID was treated as a random effect to account for repeated measures (2 vertebral levels for each spine), and the Hochberg adjustment was used to correct for multiple comparisons. A significance level $\alpha = 0.05$ was used for all statistical comparisons.

RESULTS

The relative fraction of total bone volume represented by plate-like trabeculae was 70±16%, substantially greater than that represented by rods ($p<0.0001$). Plates were oriented more longitudinally (26±22°, $p<0.0001$), whereas rods were oriented obliquely (55±24°, $p<0.0001$).

Material distribution. Apparent failed tissue fractions did not differ between plates and rods for homogeneous ($p=0.65$) or heterogeneous ($p=0.053$) models, although rod AFTF was higher for both. Total AFTF was 1.63x higher in heterogeneous than homogeneous models (0.160% vs. 0.098%, $p < 0.0001$), for both trabecular plates (0.071% vs. 0.045% $p=0.0012$) and rods (0.089% vs. 0.053%, $p<0.0001$).

Trabecular orientation. For trabecular plates (Fig. 1A), AFTF was higher in longitudinal trabeculae compared to oblique and transverse trabeculae in homogeneous models, and the same trends were observed for plates in heterogeneous models ($p<0.0001$ for all). While AFTF did not differ between heterogeneous and homogeneous models for transverse ($p=0.99$) or oblique ($p=0.97$) plates, AFTF for longitudinal plates was 1.56x higher in heterogeneous than homogeneous models ($p<0.0001$). For trabecular rods (Fig. 1B), AFTF was higher in transverse trabeculae compared to oblique and longitudinal trabeculae in homogeneous models, and the same trends were observed for rods in heterogeneous models ($p<0.0001$ for all). While AFTF did not differ between heterogeneous and homogeneous models for oblique ($p=0.77$) or longitudinal ($p=0.64$) rods, AFTF for transverse rods was 1.69x higher in heterogeneous than homogeneous models ($p<0.0001$).

Strain direction. For longitudinal plates and transverse rods, the apparent fraction of tissue failed in tension was higher than that in compression for both homogeneous and heterogeneous models ($p<0.0001$ for all, Fig. 2A-B). Tissue heterogeneity did not impact the compressive AFTF for these trabeculae ($p>0.99$ for both) but increased the tensile AFTF 1.67x for longitudinal plates ($p<0.0001$, Fig. 2A) and 1.71x for transverse rods ($p<0.0001$, Fig. 2B).

DISCUSSION

Heterogeneous mineral distribution increased bone tissue failure, specifically for longitudinally aligned plates and transversely aligned rods with tensile strains. Plate and rod tissue fractions and orientations in our study agreed with findings from other studies in human vertebrae [5]. Because trabecular plates comprised a greater fraction of vertebral tissue on average, the similar AFTF between plates and rods indicates disproportionately more tissue failure in rods, agreeing with previous findings in human vertebrae [11]. The increase in failed tissue due to tensile strain and lack of change due to compressive strain associated with heterogeneity points to increased trabecular bending. Based on beam theory, a trabecula with material heterogeneity in bending has a strain gradient that runs counter to the mineralization gradient (i.e., highest strains at the surface where mineralization is lowest) [8]. This relationship decreases the bending stiffness but leaves the uniaxial stiffness unchanged relative to a homogeneous trabecula [10].

Because remodeling creates mineralization gradients for all trabeculae, heterogeneity alone cannot explain the disproportionate

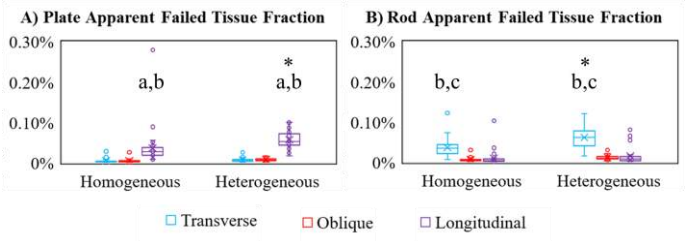

Figure 1: A) Plate and B) rod AFTF by trabecular orientation and material distribution. Symbols denote $p<0.05$ vs. *homogeneous, [a]transverse, [b]oblique, and [c]longitudinal.

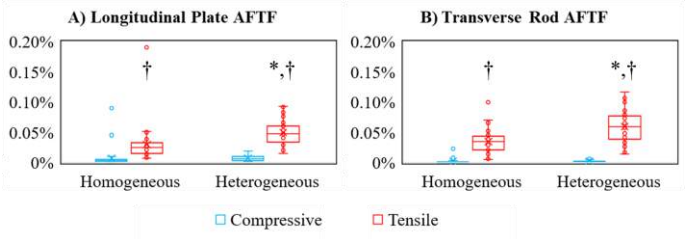

Figure 2: AFTF for A) longitudinal plates and B) transverse rods by element strain direction and material distribution. Symbols denote $p<0.05$ vs. *homogeneous and †compressive.

failure of rods or the different effects on rods and plates by orientation. Other factors promoting trabecular bending also contribute, including a greater trabecular load and transverse alignment to this load. Longitudinal trabeculae bear most of the bulk vertical loading, as shown in previous studies [4,5], and were plate-dominated in the current study, whereas transverse trabeculae were rod-dominated. The compounding effects of orientation and heterogeneity on promoting bending may explain why heterogeneity only increased tissue failure in longitudinal plates and transverse rods. Furthermore, the disproportionate failure of rods in both homogeneous and heterogeneous models indicates that the transverse alignment of rods promotes bending more than the longitudinal alignment of plates. This suggests a possible role for rods as sacrificial elements, protecting the structurally essential plates [5] and converting the energy of loading into reparable tissue damage.

A limitation of the current study was the use of linear FEA that did not directly incorporate element failure. In nonlinear FEA, failed elements weaken the model, increasing the likelihood of additional element failure. Therefore, the values of AFTF we report are likely underestimated. Overall, our results show that heterogeneity is a possible underlying mechanism driving the differential roles of trabecular plates and rods and is important to include in modeling-based approaches for studying cancellous bone tissue failure.

REFERENCES

[1] Hodgskinson, R et al., *Proc Inst Mech Eng H*, 204:115-121, 1990.
[2] Laib, A et al., *J Bone Miner Res*, 14:1167-1174, 1999.
[3] Hildebrand, T et al., *Comput Methods Biomech Biomed Eng*, 1:15-23, 1997.
[4] Ding, M et al., *J Bone Joint Surg*, 84:900-907, 2002.
[5] Liu, X et al., *J Bone Miner Res*, 23:223-235, 2008.
[6] Feldkamp, L et al., *J Bone Miner Res*, 4:3-11 1989.
[7] van der Meulen, M et al., *Bone*, 29:101-104, 2001.
[8] Paschalis, E et al., *Calcif Tissue Int*, 61:480-486, 1997.
[9] Mullender, M et al., *J Orthop Res*, 13:503-512, 1995.
[10] van der Linden, J et al., *J Biomech*, 34:1573-1580, 2001.
[11] Liu, X et al., *J Biomech*, 42:249-256, 2009.
[12] Otsu, N et al., *IEEE Trans Sys Man Cyb*, 9:62-66, 1979.

COMPUTATIONAL ASSESSMENT OF RENAL HEMODYNAMIC DISTURBANCES IN A CANINE MODEL OF AN ABDOMINAL AORTIC COARCTATION

Christopher Tossas-Betancourt (1), Yunus Ahmed (2,3), Pieter A.J. van Bakel (2,3), Drew Braet (2), William Sherk (4), Luis Hernandez-Garcia (1), David Williams (4), Daniel D. Myers (2), Thomas W. Wakefield (2), Dawn M. Coleman (2), Jonathan L. Eliason (2), James C. Stanley (2), C. Alberto Figueroa (1,2)

(1) Department of Biomedical Engineering
University of Michigan
Ann Arbor, MI, USA

(2) Department of Surgery
University of Michigan
Ann Arbor, MI, USA

(3) Department of Vascular Surgery
University of Utrecht
Utrecht, The Netherlands

(4) Department of Radiology
University of Michigan
Ann Arbor, MI, USA

INTRODUCTION

Abdominal aortic coarctation (AAC) is a rare pediatric vascular disease, characterized by a narrowing of the abdominal aorta often with renal and splanchnic arterial involvement. An AAC restricts blood flow causing inadequate perfusion of the kidneys that leads to activation of the renin-angiotensin-aldosterone system (RAAS), which results in vasoconstriction, elevated blood pressure, and significant increases in morbidity and mortality [1].

In severe cases of AAC, renal blood flow may be restored operatively with performance of a thoracoabdominal bypass (TAB) [2]. Although a TAB in these cases may restore renal perfusion, long-term antihypertensive medications are often required post-operatively to maintain normal levels of blood pressure [3,4].

To better understand the cause of these suboptimal surgical outcomes, we previously conducted a computational fluid dynamics (CFD) study of a 9-year-old AAC patient who underwent a TAB repair, and required two antihypertensive drugs to treat her post-operative hypertension [5]. Preoperative CFD analysis revealed high-frequency hemodynamic disturbances in the abdominal aorta and renal arteries (**Fig. 1**). These disturbances were also present in the post-operative 14 mm TAB repair model. Based on these findings, we hypothesize that although a TAB may restore renal perfusion to normal levels, persistent high-frequency hemodynamic disturbances in renal artery hemodynamics may be responsible for increased renin release and persistent RAAS mediated post-operative hypertension.

To test our hypothesis, we propose to investigate the relationship between altered hemodynamics and elevated renin production by combining a computational analysis with a longitudinal experimental study of a canine model of AAC treated with a TAB. The computational results presented in this document will be used to guide the design of suitable experimental AAC and TAB repair models that can reproduce the altered hemodynamics observed in pediatric AAC patients, specifically the disturbed renal waveforms pre- and post-TAB repair of the AAC.

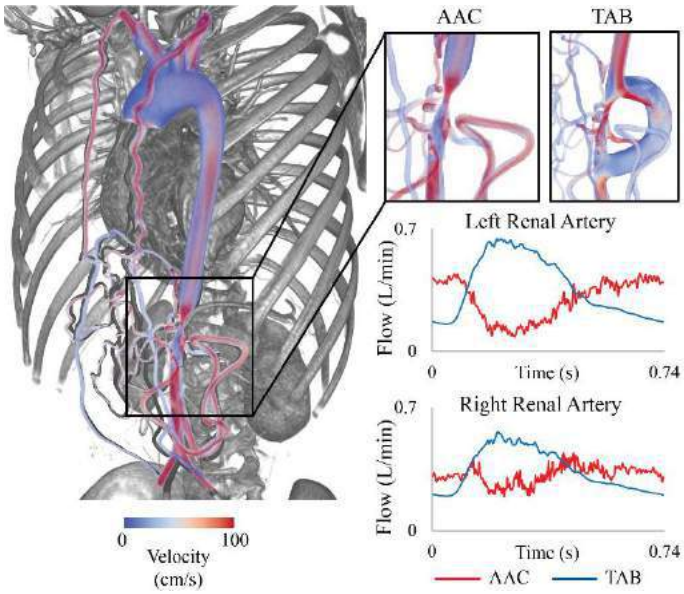

Figure 1. Left: 3D map of AAC peak systolic velocity. Right: High-frequency disturbances are present in the velocity maps and the flow waveforms of both the AAC (red) and TAB repair (blue) models in both renal arteries [5].

METHODS

An arterial fluid-structure-interaction (FSI) model of a 20-30 kg dog was constructed with population-based anatomical data (**Fig. 2**) [6] using the cardiovascular hemodynamics simulation software CRIMSON [7]. This dog weight (20-30 kg) was chosen because the aortic lumen diameter is comparable to that of a 9-year-old child (the subject from our previous study [5]). The ascending aortic flow waveform (**Fig. 2**) [8] was imposed on the inlet face of the model (**Fig. 3**). Spatially-varying mechanical properties – stiffness and thickness – for the aorta were assigned from literature values [9]. Windkessel boundary conditions were prescribed at each outlet face of the model and their parameters tuned to match the available data on experimental pressure [10] and flow splits within 5%. Following calibration, this pre-operative AAC model was modified to introduce varying degrees of coarctation 1 cm above the celiac trunk: 50, 60, 70, and 80% diameter reductions. For each of these geometries, we investigated the degree of disturbance in the renal artery waveforms. Lastly, we simulated surgical repair of the AAC with a 12-mm TAB graft.

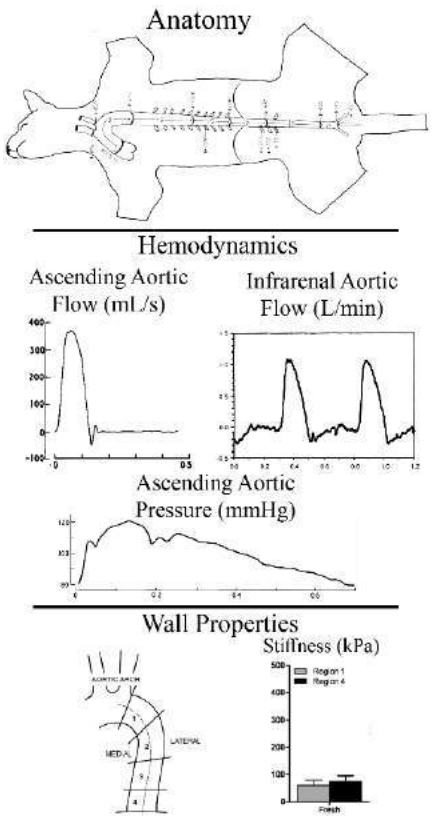

Figure 2. Population-based canine data for anatomy [6], hemodynamics [8,10] and arterial wall properties [9] used in the computational FSI model.

RESULTS

All degrees of AAC diameter reductions led to high-frequency oscillations in the renal artery waveforms. Mesh independence studies were performed to verify that the oscillations were not due to poor mesh resolution. The largest high-frequency content corresponded to the 60% diameter reduction. Highly disturbed velocity patterns were observed in the aorta distal to the AAC and propagating into the renal arteries in both the AAC and TAB models (**Fig. 3**). Computational results also confirmed that while the TAB repair restored mean levels of renal flow and pressure (relative to preoperative conditions), high-frequency disturbances persisted in the renal waveforms, especially in systole.

DISCUSSION

We constructed and calibrated a computational model of a 20-30 kg dog using population-based literature data to investigate the effects of introducing an AAC and TAB repair on hemodynamics within the abdominal aorta and renal arteries. The computational models of AAC and TAB repair confirmed high-frequency disturbances in renal hemodynamics similar to those observed in the human AAC models [5], confirming that the proposed canine model captures the hypothesized biomechanical stimuli triggering elevated renin production.

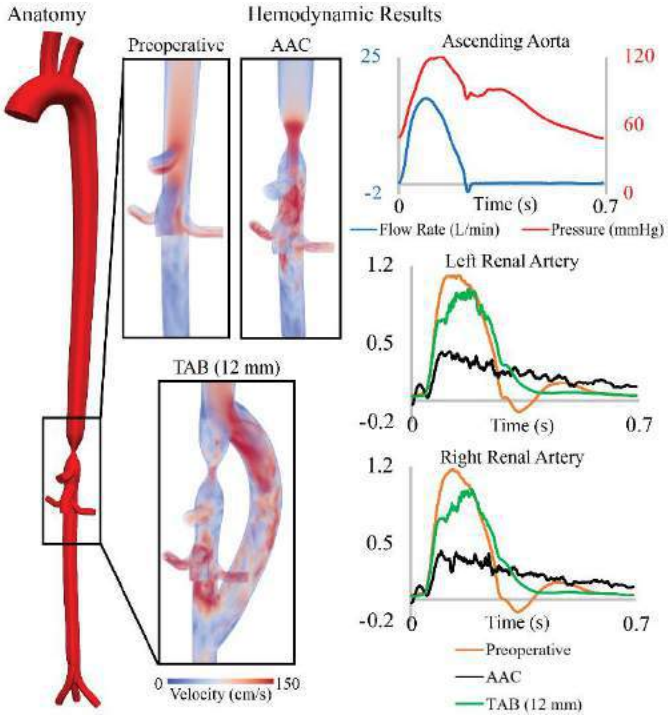

Figure 3. CFD results of preoperative, 60% diameter reduction AAC model, and TAB repair models. Velocity maps and renal waveforms show highly disturbed flow in AAC and TAB models.

Moving forward, a longitudinal prospective study has been designed to combine 20-30 kg canine models, experimental data acquisition, and CFD modeling to investigate the relationship between altered renal hemodynamics and renin production. Given the present study's computational results, a 60% AAC will be created with aortic banding. Data on anatomy, local and global hemodynamics, and renin activity will be acquired at different time points: pre-operatively, following the AAC creation, after the TAB repair, and in long-term follow-up after TAB. This investigation will improve our understanding of the driving mechanisms of RAAS activation. Furthermore, efforts to minimize these hemodynamic disturbances could influence the design of future surgical interventions for AAC repair.

ACKNOWLEDGEMENTS

This work was supported by the NSF (Grant 1531752) Acquisition of Conflux; the National Institutes of Health (U01 HL135842); the NSF Graduate Research Fellowship Program (DGE1256260); the Bob and Ann Aikens Aortic Grants Program; the Frankel Cardiovascular Center; and the University of Michigan Rackham Merit Fellowship.

REFERENCES

[1] Sparks, MA et al., *Compr Physiol*, 4(3): 1201-28, 2014.
[2] Stanley, JC et al., *J Vasc Surg*, 44(6): 1219-28, 2006.
[3] Coleman, DM et al., *J Vasc Surg*, 72(6): 2035-46, 2020.
[4] Rumman, RK et al., *Am J Hypertens*, 31(6): 687-65, 2018.
[5] Tossas-Betancourt, C et al., *J Vasc Surg*, 71(2): 505-16, 2020.
[6] Patel, DJ et al., *J Appl Physiol*, 18: 1111-7, 1963.
[7] Arthurs, CJ et al., *bioRxiv*, 2020.10.14.339960.
[8] White, KC et al., *Circ Res*, 75(4): 637-49, 1994.
[9] Rouleau, L et al., *Cardiovasc Pathol*, 21(5): 390-7, 2012.
[10] Noble, MIM et al., *Cardiovac Res*, 1(1): 9-20, 1967.

SEX DIFFERENCES IN RIGHT VENTRICULAR FUNCTIONAL REMODELING IN AN ANIMAL MODEL OF PULMONARY ARTERIAL HYPERTENSION

Ethan D. Kwan (1), Daniela Vélez-Rendón (2), Hao Mu (1), Daniela Valdez-Jasso (1,2)

(1) Department of Bioengineering
University of California San Diego
San Diego, CA, United States

(2) Department of Bioengineering
University of Illinois Chicago
Chicago, IL, United States

INTRODUCTION

Right ventricular function is an important predictor of morbidity and mortality in patients with pulmonary arterial hypertension (PAH). The RV remodels in response to increased pulmonary pressure, including myocardial hypertrophy and RV geometric remodeling, but PAH commonly results in intractable right heart failure[1]. Furthermore, there are marked sex differences in PAH incidence (2-4x more in females) and outcome (females fare better)[2]. To investigate these disparities, we sought to characterize sex differences in RV remodeling in the well-established sugen-hypoxia (SuHx) rat model of PAH, using invasive RV blood pressure and volume timeseries measurements and ventricular morphologic measurements to assess chamber function. To distinguish the relative contributions of RV geometric remodeling from myocardial material remodeling to changes in RV function, a biomechanics model was fitted to measured RV pressure-volume relations and morphology after 5-6 weeks of sugen injections. While male SuHx rats demonstrated significant myocardial passive stiffening corresponding with increases in diastolic chamber stiffness, there were no changes in the myocardium from female SuHx rats, pointing to acute differences in the remodeling response in PAH.

METHODS

Seven-week old male and female Sprague-Dawley rats (Charles River Labs) were treated with a subcutaneous injection of 20mg/kg sugen (SU5416, Sigma-Aldrich), a vascular endothelial growth factor receptor inhibitor, and then placed in a hypoxia chamber (10% oxygen) for 3 weeks to induce PAH. After 3 weeks, treated rats were returned to normoxic conditions and studied at 5 and 6 weeks post-injection. Control groups of age-matched and sex-matched rats were kept in normoxic conditions for the same time. During terminal surgeries, a 1.9F admittance catheter catheter (Transonic, Ithica, NY) was used to take invasive pressure-volume (PV) measurements during steady state and during occlusion of the inferior vena cava. From the pressure-volume time series, end-systole (ES) and end-diastole (ED) points were identified from maximum RV pressure to volume ratio and highest volume and lowest volume rate change (dV/dt ~0), respectively. RV blood pressure, myocardium wall mechanics, and ventricular morphology were related by a RV biomechanics model developed by Velez-Rendon *et al.* [3] that assumed the RV to be a fraction of a sphere of radius R and thickness h consisting of RV chamber, free-wall (V_w), and septal (V_{sw}) volumes. Assuming a thin-walled sphere, RV blood pressure was related to myocardial circumferential wall stress T by Laplace's Law with mid-wall radius $r = R - h/2$. Total wall stress was modeled as passive stress (T_p) at ED, and passive plus active stress (T_a) at ES.

$$T_p(l) = k_1(e^{k_2(\lambda-1)} - 1) \quad (1)$$

The active stress T_a was modeled as:

$$T_a(l, k_3) = T_{max}\frac{k_3^2}{{k_3}^2 + \frac{C^2}{e^{B(l-l_o)}-1}} \quad (2)$$

where l_o is the constant sarcomere length at which zero active tension is developed, $Tmax$ is the constant maximal isometric tension achieved at normal activation, and the exponent B modulates the shape of peak isometric tension-length relation. The adjustable material parameters were determined by fitting PV data at ED (k_1, and k_2) and ES (k_3) during changes in preload. The model-generated pressure-volume curves were used to partition the contributions of altered RV volume, geometry and material properties to the differences in end-systolic or end-diastolic pressure between control and SuHx rats. Fitted model parameters were used to predict and analyze resting and active sarcomere length-stress relations per animal.

Descriptive statistics were performed in JMP Pro Statistical software (SAS Institute Inc., NC, USA) with non-parametric Wilcoxon-Kruskal-Wallis tests used for non-normally distributed data to identify differences between treatment groups. The Dunn post-hoc test was used when statistical significance was reached, determined by a significance level of $\alpha = 0.05$.

RESULTS

Male and female SuHx-treated rats reached hypertension (mean pulmonary arterial pressures were above 25mmHg). RV free-wall mass increased in both male and female SuHx rats ($p<0.05$) and RV wall thickness increased in male SuHx, ($p<0.05$) but it did not increase in the females. In fact, female RV wall thickness (1.3±.1mm) was almost 70% greater at baseline than male RV wall thickness (0.7±.2mm). While male and female animals had similar end-systolic pressures at baseline (ESP_{CNT-M} = 24±1 mmHg *vs.* ESP_{CNT-F} = 24±1) and pressures significantly increased with SuHx, males ESP was 35% higher than the females (ESP_{SuHx-M} = 66±3 mmHg *vs.* ESP_{SuHx-F} = 49±3 mmHg). Both male and female SuHx groups preserved stroke volume ($p<0.05$). On the other hand, while male and female animals showed similar end-diastolic pressures at baseline (EDP_{CNT-M} = 1.6±.2 mmHg *vs.* EDP_{CNT-F} = 1.2±.2), there was only a significant increase in end-diastolic pressures in the male SuHx rats (EDP_{SuHx-M} = 4.9±.7 mmHg *vs.* EDP_{SuHx-F} = 1.7±.3 mmHg).

The biomechanical model closely fitted the PV measurements at ES and ED for male and female animals and allowed us to discern the relative contributions of geometric changes (black) and myocardium material properties (blue) (Figure 1). Increase ES pressure was largely sustained by hypertrophy in both male (**A**) and female (**B**) SuHx animals. While male SuHx hemodynamic remodeling significantly increased diastolic chamber stiffness (blue line is significantly higher than green and black lines), female chamber stiffness remained largely unchanged (blue line is close to green line).

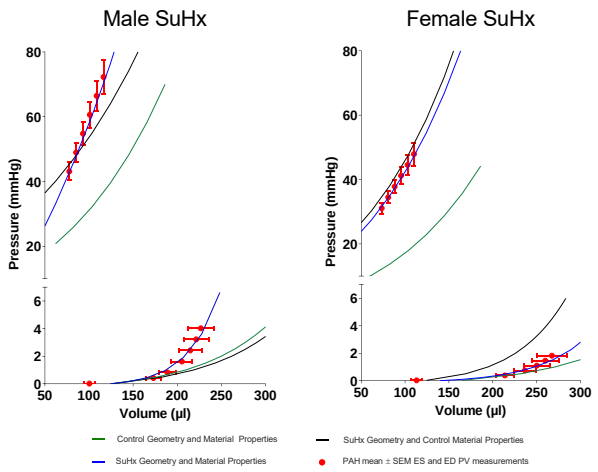

Figure 1. Model predictions of pressure-volume relations using control geometry and mechanical properties (green line), SuHx geometry and control mechanical properties (black line), and SuHx geometry and mechanical properties (blue line) at measured mean ± standard error pressures and volumes at end-diastole and end-systole (red).

From the rat-specific models fitted to pressure-volume data, sarcomere length-stress relations show a significant increase in passive stress in male SuHx rats ventricles, but not in the female SuHx animals (**Figure 2**). While the slope of the active sarcomere length-stress relation increased in the female SuHx animals, no statistical significance was reached ($p = .16$).

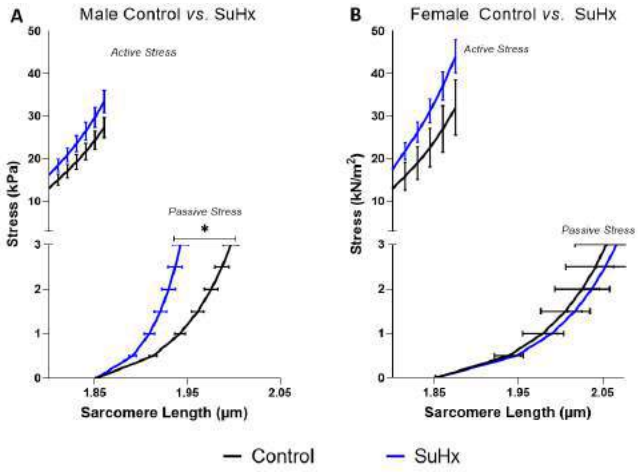

Figure 2. Model predictions of active (top) and passive (bottom) RV free wall stress *vs.* sarcomere length in control (black) and SuHx-treated (blue) male (A) and female (B) rats.

DISCUSSION

In this study, the sugen-hypoxia treatment successfully induced pulmonary arterial hypertension 5 and 6 weeks post-injection. Hemodynamic and morphologic measurements showed associated right ventricular hemodynamic remodeling. Model predictions of sarcomere length-tension relations found significant passive myocardial stiffening in male SuHx rats but not in the female SuHx rats. RV hypertrophic wall thickening maintained end-systolic PV relations in both males and females, whereas myocardial passive stiffening explained end-diastolic PV relations in male rats. Diastolic stiffness may be associated with extracellular matrix stiffness previously identified in male PAH rats [4] and may prevent RV dilation but could also contribute to RV diastolic dysfunction and thus contribute to worse outcome as seen in male patients [5]. In contrast, SuHx-treated female rats showed a maintained ED PV relation with no significant change in passive sarcomere length-stress relations compared to female controls. Instead, greater RV wall thickness at baseline may have helped maintain ED PV relations and prevented material remodeling in the myocardium of female SuHx rats. This study emphasizes the importance of investigating the ventricular adaption to PAH in both male and females and proposes mechanisms that would explain sex-dependent outcomes.

ACKNOWLEDGEMENTS

This work was funded by the American Heart Association Scientist Development Grant 16SDG29670010, and the National Heart, Lung and Blood Institute 1R25HL145817-01 and T32 HL 105373.

REFERENCES

[1] Van de Veerdonk MC *et al*, *Heart Failure Reviews*, 21:259-271, 2016.
[2] Lahm T *et al.*, *Am J Physiol Lung Cell Mol Physiol*, 311(2), 2016.
[3] Velez-Rendon D *et al.*, *Pulmonary Circulation*, 8(4), 2018.
[4] Velez-Rendon D *et al.*, *J Biomech*, 141(9), 2019.
[5] Rain S *et al.*, *Circ Heart Fail*, 9(7), 2016

A NONLINEAR FIBROUS VISCOELASTIC MODEL DESCRIBES THE EXPERIMENTAL TENSILE MATERIAL BEHAVIOR OF HUMAN CERVIX

L. Shi (1), J. Vink (2), R. Wapner (2), K. Myers (1)

(1) Department of Mechanical Engineering
Columbia University
New York, NY, USA

(2) Department of Obstetrics and Gynecology
Columbia University Medical Center
New York, NY, USA

INTRODUCTION

The timely remodeling of the human cervix from a rigid state into a compliant stretchable state is essential for a safe delivery. This dramatic remodeling has been quantified as a 2-order of magnitude decrease in the cervical initial stiffness and the compressive resistance, and a significant increase of the locking stretch using an anisotropic elastic fibrous entropy-chain model [1]. Preterm birth (PTB), defined as birth before 37 weeks of gestation, is believed to be related to premature cervical remodeling and softening. The mechanism of normal and premature cervical remodeling, however, is still understudied. The cervix is a soft tissue mainly composed of a cross-linked collagen fibers embedded in a compressive groundsubstance formed by the negatively charged proteoglycans and glycosaminoglycans [2]. The cervix tissue exhibits complex material properties such as anisotropy and viscoelasticity, due to its complex biological composition.

Cervical viscoelasticity is an important factor in pregnancy because the tissue must be viscoelastic so it does not break in large deformation. The cervical viscoelasticity evolves significantly in cervical remodeling as shown in mouse mechanical studies [3]. To date, limited studies have been conducted on the time-dependent material response of the human cervical tissue, and it is partly due to its strong nonlinearity. The aim of this work is to describe the viscoelastic behavior of the human cervix under uniaxial tensile tests by proposing a nonlinear continuous fibrous viscoelastic constitutive model. Multiple-level-load-hold and load-break uniaxial tensile experiments, coupled with video extensometry, were conducted on human cervical tissue samples. Inverse finite element analysis (IFEA) was utilized to fit the fibrous viscoelastic constitutive model to tensile force responses. Differences in material properties between pregnant and nonpregnant samples are reported.

METHODS

Sample Preparation 4 non-pregnant and 3 pregnant cervical tissue samples were obtained from several consented hysterectomy patients at Columbia University Irving Medical Center. For each cervix, two slices were cut from the upper cervix (UC) and lower cervix (LC), respectively, to conduct an indentation test. For each slice sample, strips were cut along and perpendicular to the preferential fiber direction after the indentation test, where the preferential fiber direction was determined by the displacement response [1]. The samples were stored in a -80^{o}C freezer immediately after the indentation test.

Uniaxial Tensile Experiments Before each test, the tensile sample was swelled in the PBS solution for 24 hours. Then each sample was gripped tightly on both ends and put in the PBS solution. Two cameras were placed perpendicular to each other to capture the front- and side-view deformation during the test (Fig. 1 (a, b, c)). In the load-hold experiment, a displacement-controlled, several-stage ramp-hold uniaxial tensile test was conducted with a ramp rate = 0.1 %/s (Fig. 1 (d)) until the sample broke. In the load-unload test, the sample was loaded and unloaded for several times with a hold between each cycle for sufficient recovery. Two ramp rates (0.1 %/s and 5%/s) were applied sequentially (Fig. 1 (e)). Samples in these two studies were different.

Constitutive Equations The viscoelasticity model in this work is based on the continuous fibrous framework to account for the anisotropy and dispersion of fibers. The continuous fibrous framework is constructed by integrating the contributions of fiber families oriented along all directions emanating from a point in a continuum. The constitutive laws of all fiber families are assumed to be the same and proposed based on the reputation-type tube mechanism and the transient network

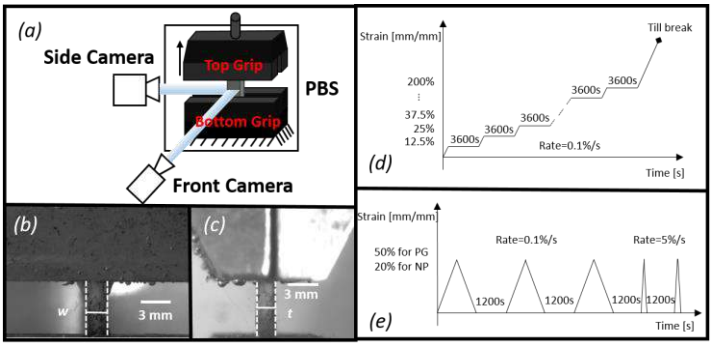

Figure 1: (a) The uniaxial tensile experiment setup. The representative image captured via (b) front and (c) side cameras. Loading profiles of (d) the several-step load-hold tensile test and (e) the load-unload tensile test

mechanism, where a portion of fibers are assumed to be constrained to travel only inside the bounded tube by Brownian motion in a combination of the reptation motion [4]. In this framework, the total stress is the addition of the pure elastic part $\mathbf{T}_{\mathrm{E}}(\mathbf{C},\ \mathbf{n}_0, b)$ (see [1]) and the viscoelastic part $\mathbf{T}_{\mathrm{V}}^r(\mathbf{C}, \mathbf{n}_0, b)$.

$$\mathbf{T}(\mathbf{C}, \mathbf{n}_0, b) = \mathbf{T}_{\mathrm{E}}(\mathbf{C}, \mathbf{n}_0, b) + \int_0^{2\pi}\int_0^{\pi} H(I_n - 1)\frac{1}{\pi}\sqrt{\frac{b}{2\pi}}\frac{e^{2(\mathbf{n}^2-1)}}{\mathrm{erfi}(\sqrt{2b})}\mathbf{T}_{\mathrm{V}}^r(\mathbf{C}, \mathbf{n}_0, b)\sin\phi d\phi d\theta \tag{3}$$

where b is the concentration parameter, $\mathrm{erfi}(\cdot)$ is the imaginary error function, $\mathbf{C}$ is the right Cauchy-Green deformation tensor, $\mathbf{n}_0$ is the original direction of the fiber family, H is the Heaviside function and $I_n = \mathbf{n_0}\cdot\mathbf{C}\cdot\mathbf{n_0}$. For the fiber family r, $\mathbf{T}_{\mathrm{V}}^r(\mathbf{C}, \mathbf{n}, b) = \mathbf{T}_{\mathrm{V}_e}^r\mathbf{T}_{\mathrm{V}_i}^r$, where e and i denotes the elastic and inelastic parts. $\mathbf{T}_{\mathrm{V}_e}^r$ here adopts the form as same as $\mathbf{T}_{\mathrm{E}}(\mathbf{C},\ \mathbf{n}_0, b)$ (see [1]). The total stretch λ could be separated into the elastic and inelastic parts

$$\lambda = \lambda_e\lambda_i \tag{4}$$

The flow rule is as the following form

$$\widetilde{\mathbf{D}}_i = \dot{\gamma}\mathbf{n}\otimes\mathbf{n} \tag{5}$$

where $\widetilde{\mathbf{D}}_i$ is the symmetric part of $\mathbf{L}_i = \dot{\mathbf{F}}_i\mathbf{F}_i^{-1}$ pulled back with $\mathbf{F}_e$, and $\mathbf{n}$ is the current direction of the fiber family. $\mathbf{F}_e$ and $\mathbf{F}_i$ are deformation tensors corresponded to the elastic and inelastic parts. $\dot{\gamma} = \eta(\lambda_i - 1 + \epsilon)^C\left(\frac{\mathbf{T}_{\mathrm{V}}^r}{T_0}\right)^m$. η, T_0, ϵ, C, and m are material parameters with physical meanings related to the microstructure. Specifically, η is the original shear rate, T_0 is the initial flow stress, ϵ is a small constant to guarantee the numerical stability (kept as 0.001 in simulations in this work), m is the hardening coefficient, and C is the reputation stretch coefficient. Other material parameters in $\mathbf{T}_{\mathrm{V}_e}^r$ is also needed, including the viscous initial stiffness ξ_V, the viscous locking stretch N_V, and a dispersion coefficient b.

The "return-mapping" algorithm was applied to numerically achieve the constitutive model, and the Newton method was used to solve for the ordinary differential equations. The constitutive model was coded as a plugin of FEBio (V2.9.1, url: febio.org) and the FEA analysis was done in FEBio to simulate the uniaxial tensile experiments. Then the model was hand-fit to the tensile force responses to get the optimal material parameters.

RESULTS

The load-unload experimental results show the force response is dependent on strain rate, where a higher strain rate produces a larger force response. The load-hold experimental results show the pregnant samples relax more and faster than the nonpregnant samples.

Currently, only the samples from the internal os of one nonpregnant and one pregnant cervix were fitted for each kind of test (load-hold test and load-unload test). The force-relaxation responses of both the load-hold and load-unload tensile experiments are captured well using the proposed nonlinear viscoelastic model (Fig. 2 (a, b)). The best-fit viscous parameters of the load-hold tests are $\eta = 0.0008$, $T_0 = 23\mathrm{kPa}$, $C = -0.2$, $m = 2$, $\xi_V = 3.9\mathrm{kPa}$, $N_V = 1.9$ for the nonpregnant sample and $\eta = 0.0015$, $T_0 = 3.8\mathrm{kPa}$, $C = -0.3$, $m = 1.3$, $\xi_V = 0.23\mathrm{kPa}$, $N_V = 5.5$ for the pregnant sample. The best-fit viscous parameters of the load-hold tests are $\eta = 0.0004$, $T_0 = 52\mathrm{kPa}$, $C = -0.2$, $m = 1.8$, $\xi_V = 3.9\mathrm{kPa}$, $N_V = 2.1$ for the nonpregnant sample and $\eta = 0.0006$, $T_0 = 0.058\mathrm{kPa}$, $C = -0.3$, $m = 1.3$, $\xi_V = 0.53\mathrm{kPa}$, $N_V = 5.5$ for the pregnant sample.

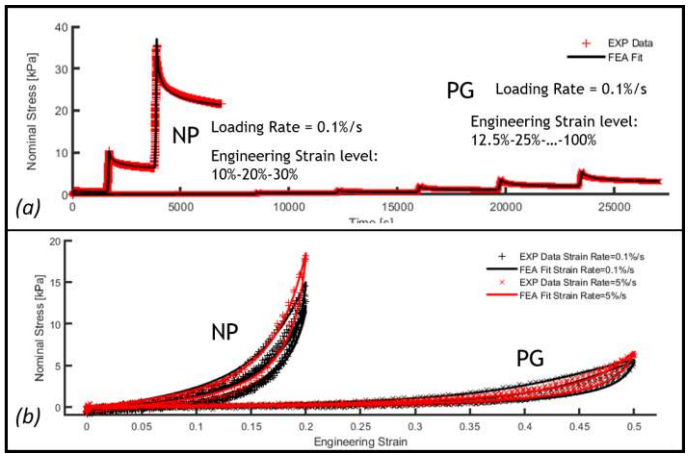

Figure 2: Results: A representative fitted force response of (a) the load-hold tensile test and (b) the load-unload tensile test

DISCUSSION

The main objective of this study was to report tensile viscoelastic material parameters for nonpregnant and pregnant human cervical tissue using a proposed fibrous nonlinear viscoelastic model. Here, we present our experimental data and the load-unload and load-hold uniaxial tensile tests on human cervical samples. Additionally, we prove the constitutive model to fit the experimental data well, though currently only one nonpregnant and one pregnant sample are studied.

Our preliminary results show the cervix remodels to relax more and faster during pregnancy and this change is related to the reduction of the initial flow stress and the viscous initial stiffness, and the increase of the original shear rate and the viscous locking stretch. This demonstrates the ability of our model to capture the intrinsic changes in the microstructure. Next, we will run an automatic IFEA [1] of all of the remaining tensile force data and validate the model by predicting the shape changes obtained from the images captured during the experiments. We will also fit the model to the indentation experimental data. The final goal will be to describe the material behavior of the human cervix under both the tensile and indentation tests.

ACKNOWLEDGEMENTS

Research reported in this publication was supported by the NIH R01HD091153 to KM. The content is solely the responsibility of the authors and does not necessarily represent the official views of the NIH.

REFERENCES

[1] Shi, L et al, 2021, Submitted.
[2] House, M et al., 2009, S. Perinatol, 33, 300-307.
[3] Yoshida, K , et al., 2019, Interface focus 9.5.
[4] Bergstrom, B., & Boyce, C.M., 1998, J. Mech. Phys. Sdids.

IN VIVO ESTIMATION OF REGIONAL MECHANICAL PROPERTIES OF THE AORTIC WALL ACCOUNTING FOR THE ACTIVE AND PASSIVE EFFECT OF PERIAORTIC STRUCTURES WITH AN INVERSE FINITE ELEMENT APPROACH

J. Bracamonte (1), J.S. Wilson (2), J. Soares (1)

(1) Department of Mechanical and Nuclear Engineering
Virginia Commonwealth University
Richmond, VA, USA

(2) Department of Biomedical Engineering
Pauley Heart Center
Virginia Commonwealth University
Richmond, VA, USA

INTRODUCTION

Displacement Encoding with Stimulated Echoes Magnetic Resonance Imaging (DENSE-MRI) is a technique that allows for the non-invasive, patient-specific quantification of regional arterial wall kinematics. This technique has been applied to the aorta, demonstrating that its *in vivo* deformation is circumferentially heterogeneous at different locations along the aorta.[1] Perivascular support and tethering are likely a relevant factor in vascular mechanics and one of the possible causes of deformational heterogeneity.[2] Nevertheless, most models of aortic function assume a homogeneous adventitial boundary condition, leading to an axisymmetric distribution of strain.[3] In a previous work, we developed an inverse Finite Element Method (iFEM) approach using DENSE-MRI data as target displacement and a heterogeneous Elastic Foundation Boundary Condition (EFBC) at the adventitia to model the effect of different perivascular structures that successfully reproduced the patient-specific *in vivo* deformation of the infrarenal abdominal aorta (IAA). We also showed that the inclusion of periaortic structures affects the image-based estimation of aortic wall properties.[4] However, this method can only account for the passive response of static periaortic tissues. A different approach is needed for active interactions of aorta with the heart and other large arteries (Figure 1b, 1c). In this work, we develop a generalized approach that allows for modeling the effect of active and passive perivascular structures on the *in vivo* function of the aorta, while maintaining a low computational expense. To achieve this, we incorporate a moving EFBC using DENSE-MRI derived displacement data as target for an iFEM.

METHODS

Anatomic model and discretization. Steady state free precession (SSFP) cine and 2D DENSE MRI were taken on 25 healthy volunteers from which we analyzed one of three locations of the aorta distal aortic arch (DAA), descending thoracic aorta (DTA) or IAA (Figure 1a). DENSE-MRI derived displacements were estimated as previously described.[1] Diastolic images were segmented and smoothed to obtain an anatomic model of the cross-section of the aortic wall. The model was discretized into quadratic tetrahedral mesh. A single layer of elements was used in the axial direction to enforce a plane-strain 2D problem.

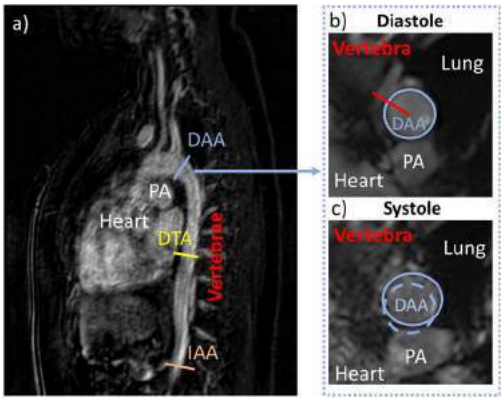

Figure 1. a) Sections of study on sagittal view. b) DAA and surroundings at diastole. Red line: circumferential reference pointing to the vertebra.c) DAA and surroundings at systole. PA: pulmonary artery. Dashed blue line: location of diastolic reference configuration. Solid blue line: current location of aortic wall.

Material model. Fung's orthotropic pseudo-elastic constitutive equation is used as the material model. Assuming orthotropic symmetry and negligible contributions of shear components in the axial direction, the number of material constants is reduced to four. The resulting constitutive equation is given by [2]

$$\Psi = \frac{c}{2}(e^{Q} - 1) + \frac{k}{2}(\ln J)^2, \quad (1)$$

$$Q = a_{rrrr}E_{rr}E_{rr} + a_{\theta\theta\theta\theta}E_{\theta\theta}E_{\theta\theta} + a_{rr\theta\theta}E_{rr}E_{\theta\theta}. \quad (2)$$

To enforce thermodynamic consistency of the material model, material parameters were constrained by following relations:

$$c > 0; \quad a_{ijkl} > 0; \quad a_{iiii} > a_{iijj}. \quad (3)$$

Nearly incompressible behavior was imposed by enforcing $k \gg c$.

Boundary conditions and loads. An EFBC was applied to the outer wall as a distribution of radially-oriented linear springs. Stiffness of each individual spring was calculated as a function of spring density such that the effective stiffness per unit area is set to 10^{-5} times the material constant c. The process is simulated in two quasi-static time-steps. In the first step, the spring ends are fixed and a uniform pressure load of Δp =40 mmHg is prescribed in the lumen. In this step, the aorta expands into an approximately regular-shaped cylinder while compressing all the springs. On the second step, the ends of the springs are displaced on the radial direction to fit the aortic wall to its target shape and position; moving away from the centroid to relax the springs, or moving in and pushing against the adventitial surface to increase the load (Figure 2). The heterogeneous radial displacement (d_n) is set as a piece-wise constant function of a finite number of regions (n) depending on the circumferential position with smooth cubic transitions. Four regions (n = 4) were adequate to obtain good correspondence to DENSE-derived displacement. The angles ϕ_n, representing the boundaries of each region, are measured from a line projected from the luminal centroid to the nearest point of the vertebra, such that the analysis is independent of MRI frame of reference and patient position (Figure 1b).

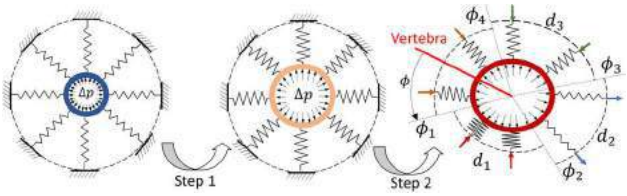

Figure 2. Generalized approach to model active and passive aortic wall interaction with periaortic active and passive structures.

Optimization algorithm. Pixel displacement information from DENSE-MRI was interpolated to the nodes of the FEM mesh as target data. An optimization algorithm, using the *Trust Region Reflective Method* from *Python Scipy* library, was employed to iterate over material model constants $(c, a_{rrrr}, a_{\theta\theta\theta\theta}, a_{rr\theta\theta})$ and EFBC parameters (d_n, ϕ_n) to fit the simulated nodal displacement to the targeted displacement field. The algorithm employs *FEBio 2.9* to solve the FEM forward problem for each iteration until a minimal error is found. To make sure results are not local minima, all cases were run with three sets of starting parameters.

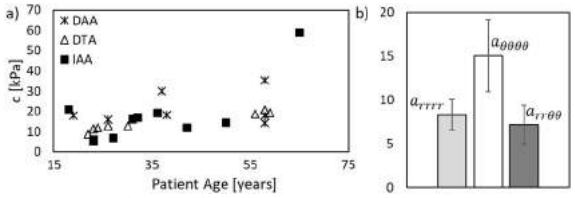

Figure 3. Estimated material parameters: (a) c as a function of patient's age, (b) average anisotropic constants a_{ijkl}.

RESULTS

Displacement fields. Results show a close match between the simulated and targeted deformed geometry converging to averaged nodal displacement errors below pixel size resolution. On average displacement errors were 0.28 ± 0.35, 0.44 ± 0.25 and 0.65 ± 0.33 mm for the IAA, DTA and DAA respectively.

Material properties. Material constant c resulted in the same order of magnitude of those previously reported.[2,4] Standard ANOVA was carried showing significant proportional correlation of c to patient's age (p=0.049), which agrees with the expected increase of artery stiffness with age (Figure 3a).[5] It is important to highlight that other factors not accounted here, such as patient's life-style, also affect arterial stiffness. No significant correlation (p>0.05) was found between mechanical properties and location along the aorta. The circumferential anisotropic term $(a_{\theta\theta\theta\theta})$ was approximately double the radial term (Figure 3b).

Adventitial load distribution. The range and location of the four elastic displacement regions (ϕ_n) showed reasonable correspondence to interactions of the aortic wall to its surroundings. For regions corresponding to rigid structures (vertebra), springs move in towards the aortic wall pushing it to its original position, compensating with a spring compression force equivalent to the resistance of the rigid structure to aortic expansion. Springs move further in to push the aorta beyond its original position to model moving structures pushing the aorta, such as the heart at the DTA or the PA at the DAA. For regions corresponding to soft structures, springs move away from the aortic wall reducing the resistance to expansion. As a consequence, the net transmural force (adventitial minus luminal force) peaks in regions corresponding to stiff or inwardly pushing boundaries. In regions with soft periaortic tissues, net transmural force is lower, and the soft tissues along with the aortic wall absorb a larger share of the pressure pulse energy (Figure 4).

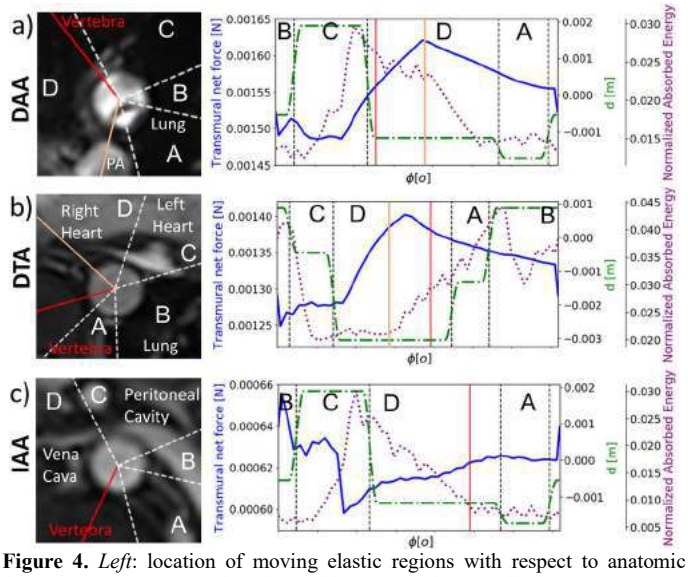

Figure 4. *Left*: location of moving elastic regions with respect to anatomic features. *Right*: transmural net force (blue), optimal EFBC displacement (green), and EFBC stored energy normalized to total aortic wall deformation energy (purple) for (a) DAA from 19 y.o. (b) DTA from 23 y.o. and (c) IAA from 23 y.o. Red line: circumferential reference pointing to the vertebra. Orange line: circumferential reference pointing to moving boundary.

DISCUSSION

Results suggest that modeling the passive and active mechanical effects of periaortic structures can reproduce the *in vivo* heterogeneous deformation and translation of the aortic wall and provide reasonable quantification of *in vivo* patient-specific aortic stiffness at specific locations along the aorta. This method provides an estimation of the distribution of adventitial load and the share of mechanical energy absorbed by the periaortic structures, which could improve our understanding of aortic mechanics and tissue growth and remodeling. The proposed approach has relatively low computational costs as it relies on unidimensional linear springs to model the periaortic structures, while keeping the model parameters to a minimum.

ACKNOWLEDGEMENTS

We thank John Oshinski for the use of DENSE data acquired at Emory University Dept. of Radiology & Imaging Sciences.

REFERENCES

[1] Wilson, J. S et al. *J. Biomech. Eng.* **141**, (2019). [2] Humphrey, J. D. et al. *Ann. Biomed. Eng.* **30**, 509–523 (2002). [3] Ferruzzi, J.et al. *PLoS One* **13**, e0201379 (2018). [4] Bracamonte, J. et al. *J. Biomech. Eng.* **142**, (2020). [5] Roccabianca, S. et al. *J. Mech. Behav. Biomed. Mater.* **29**, 618–634 (2014).

EFFECT OF BLOOD PRESSURE CONDITIONS ON TRANSCATHETER AORTIC VALVE PERFORMANCE AND CORONARY FLOW

B. Vogl (1), R. Gadhave (1), M.A. Alkhouli (2), S.M. Lilly (3) and H. Hatoum (1)

(1) Biomedical Engineering Department
Michigan Technological University
Houghton, Michigan, USA

(2) Department of Cardiovascular Medicine
Mayo Clinic
Rochester, Minnesota, USA

(3) Division of Cardiovascular Medicine
The Ohio State University
Columbus, Ohio, USA

INTRODUCTION

Transcatheter aortic valve (TAV) replacement (TAVR) emerged initially as an alternative procedure to the traditional and highly invasive surgical aortic valve replacement surgery (SAVR). TAVR consists of percutaneously deploying using a catheter, a bioprosthetic valve that can be reduced to a few millimeters in diameter in the aortic annulus, and subsequently, expanding it in the position of interest.

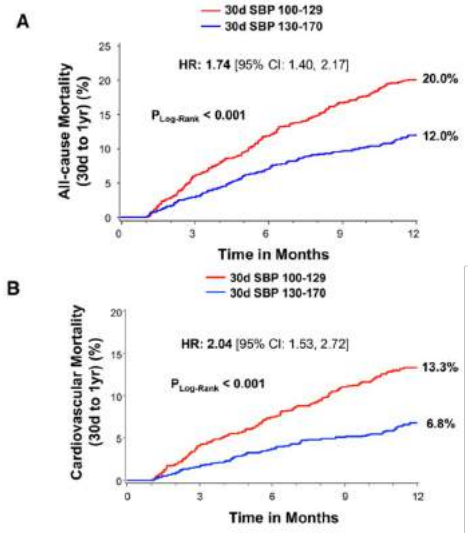

Figure 1: 30 day to 1-year all cause and cardiovascular mortality after TAVR with stable and increased SBP. Image from Ref. 1.

It was reported that more than 50% of aortic stenosis patients (with and without previous history of hypertension) developed hypertensive conditions that proved to be associated with better prognosis[1]. Several studies reported that sustained lower aortic blood pressures post-TAVR were associated with higher incidence of cardiovascular mortality along with alterations in coronary perfusion. In addition, higher arterial elastance (AE), systemic arterial compliance (SAC) and pulse pressure post-TAVR were correlated with increased cardiovascular mortality[2]. These findings, counterintuitive in nature, raised a multitude of questions as they associate typically harmful outcomes with better prognosis. Moreover, coronary perfusion highly depends on the aortic pressures. Studies have shown that the implantation of a TAV alters the sinus flow dynamics leading to potential impairment of coronary perfusion. The goal of this work is to evaluate the impact of various afterload conditions notably blood pressure, resistive and pulsatile load on the performance of TAVs, sinus flow changes, and coronary perfusion.

METHODS

The hemodynamic assessment of a 26mm SAPIEN 3 transcatheter aortic heart valve was performed in a left heart simulator under pulsatile conditions of various aortic pressure, heart rate and flow rate conditions as shown in Table 1. The experimental setup schematic diagram is shown in Fig.2. The fluid used in the experiments was a mixture of water-glycerin with properties similar to those of blood (density of 1060Kg/m^3 and a kinematic viscosity of 3.5cSt). Fifty consecutive cardiac cycles of aortic pressure, ventricular pressure, and flow rate data were recorded at a sampling rate of 100 Hz. The coronary flow was tuned for the experiments at 120/80 mmHg and any variation was recorded as varying from that point. The coronary flow was calculated as varying between 4 – 5% of the total cardiac output. The mean

transvalvular pressure gradient (ΔP) is defined as the average of positive pressure difference between the ventricular and aortic pressure curves during forward flow.

The effective orifice area (EOA) is an important parameter to evaluate valve performance through estimating the available area for flow. EOA was computed using the Gorlin's equation:

Table 2: Experimental and Derived Afterload Conditions

Experimental Conditions				
Transcatheter Aortic Valves	Heart Rate (bpm)	Cardiac Output (L/min)	Conditions of aortic pressure (mmHg)	
26 mm SAPIEN 3 Balloon-Expandable Valve	60, 90 and 120	3.5, 5, and 6.5	Fixed Diastolic Pressure	100/80
				110/80
				120/80
				130/80
				140/80
			Fixed Systolic Pressure	140/40
				140/60
				140/80
				140/100

$$EOA\ (cm^3) = \frac{Q_{rms}\ (cm^3/s)}{51.6\sqrt{\Delta P\ (mmHg)}} \quad (1)$$

The results are presented as mean standard deviations. Statistical analysis was performed using JMP Pro version 13.0.0 (SAS Institute Inc, Cary, NC). For data distributed normally, ANOVA was used followed by the Tukey test for pairwise comparison. For data with non-normal distribution, a Wilcoxon/ Kruskal-Wallis test with a post-hoc Dunn method was performed.

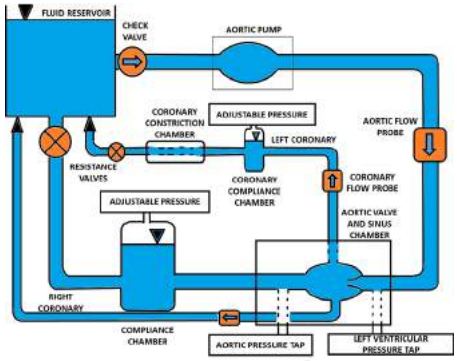

Figure 2: Left heart simulator with coronary flow in-vitro

RESULTS

The EOA variations with increasing systolic blood pressures from 100 to 140 mmHg are shown in Fig.3A and those with increasing diastolic blood pressures from 40 to 100 mmHg are shown in Fig.3B. The variations were shown to be non-monotonic with non-uniform trends depending on the heart rate and the cardiac output. For example, a significant ($p < 0.0001$) decrease in EOA of 1.22 ± 0.06 to 1.08 ± 0.01cm^2 was observed at a CO of 3.5L/min and HR of 60bpm as SBP increases from 100-140mmHg. Whereas, at a CO of 5L/min and HR of 90bpm, a significant ($p < 0.0001$) decrease in EOA of 2.29 ± 0.05 to 1.34 ± 0.01cm^2 going from a SBP of 100-120mmHg, a significant increase of EOA of 1.34 ± 0.01 to 2.14 ± 0.05cm^2 from 120-130mmHg, and a significant ($p < 0.0001$) decrease of EOA of 2.14 ± 0.05 to 1.49 ± 0.18cm^2 from 130-140 mmHg. With varying diastolic blood pressures, a similar observation of non-uniformity in trends was noted. However, for most of the cases, the EOA was found to be decreasing as the diastolic pressures increase.

The coronary flow was found to increase with increasing systolic and diastolic pressures independently from cardiac output and heart rates as shown in Fig.4A and 4B. At the lower pressures (<120mmHg), there was no observed drop in the total coronary flow below the calculated lower acceptable thresholds of 140, 200 and 260 mL/min.

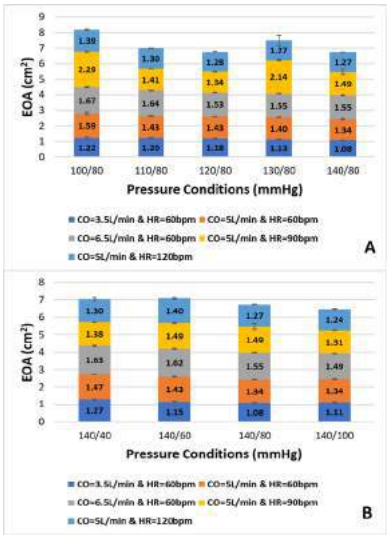

Figure 3: Average EOA variations with varying systolic and diastolic pressures

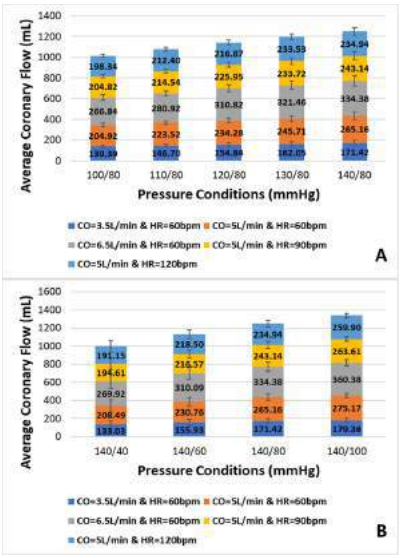

Figure 4: Average coronary flow variations with varying pressures.

DISCUSSION

The TAVR performance parameters vary significantly with various aortic blood pressure conditions. While the variations of the effective orifice area – a crucial parameter to evaluate valve performance – were not monotonic, the data suggest an overall decreasing trend with increasing systolic and diastolic pressures. This suggests the need for additional flow studies such as particle image velocimetry (PIV) to understand the flow dynamics downstream of the aortic valve and in the sinus. In addition, these additional studies would help identify the ideal blood pressure range post-TAVR and further understand the basis of worsening outcomes with lower blood pressure conditions in hypotensive patients. Ongoing work includes computing the variation trends of the valvulo-arterial impedance, a measure of global afterload that theoretically accounts for effects of resistance and compliance, as a function of the total arterial, compliance and resistive loads in addition to PIV experiments.

REFERENCES

[1] Perlman G et al. JACC: Cardiovascular Interventions. 2013;6:472-478.

[2] Lindman B et al. Circulation: Cardiovascular Imaging. 2017;10:e006308.

ACUTE REMODELING OF A TISSUE ENGINEERED VASCULAR GRAFT IS INFLUENCED BY COMPLIANCE AND TRANSFORMING GROWTH FACTOR BETA 2

Kenneth J. Furdella (1), Shinichi Higuchi (2), Kang Kim (1,3,4,5), Tom Doetschman (6)
William R. Wagner (1,2,3,5), Jonathan P. Vande Geest (1,2,5)

(1) Department of Bioengineering
University of Pittsburgh
Pittsburgh, PA, USA

(2) McGowan Institute for Regenerative Medicine
University of Pittsburgh
Pittsburgh, PA, USA

(3) Department of Medicine
University of Pittsburgh
Pittsburgh, PA, USA

(4) Department of Cardiology
University of Pittsburgh
Pittsburgh, PA, USA

(5) Vascular Medicine Institute
University of Pittsburgh
Pittsburgh, PA, USA

(6) Cellular and Molecular Medicine
University of Arizona
Tucson, Arizona, USA

INTRODUCTION

Two core requirements of a functional tissue engineered vascular graft (TEVG) are the recruitment of host vascular smooth muscle cells (SMCs) into the implant and compliance matching to the native vasculature. Compliance has been shown to have an effect on vascular smooth muscle cell phenotype, inflammatory response, and overall patency of the vessel [1]. Specifically, stiff or hypocompliant grafts change the hemodynamic environment of the vessel leading to stenosis and loss of vessel patency [2]. SMCs are the major muscular component of the vessel responsible for extracellular matrix production and the regulation of vascular tone. The recruitment of host SMCs to the TEVG requires migration, proliferation and its long-term function will require the replacement of the biodegrading TEVG with host extracellular matrix (ECM).

The composition of the TEVG also offers a unique ability to encourage SMC manipulation through the integration of biomolecules into the scaffold. One factor of particular interest is transforming growth factor beta 2 (TGFβ2) which has been shown to modulate SMC phenotype depending on concentration [3]. This growth factor is a pleiotropic cytokine that has been shown to regulate cell cycle, cell differentiation, cell growth, cell death, and ECM deposition and organization. On a larger scale, TGFβ2 has also been shown to have a role in ECM remodeling in vascular, cardiac, and embryogenesis [4]. For SMCs specifically, these cells can be recruited by a low TGFβ2 concentration (0.1 ng/mg) from the scaffold to promote cellular migration, while higher concentrations of TGFβ2 (>5 ng/mg) can arrest cellular proliferation/migration to promote ECM production over the course of a 5-day in vitro experiment [5].

The goal of this study was to modulate the release of TGFβ2 (0 ng/mg, 10 ng/mg, and 100 ng/mg) from a compliance matched (CM) TEVG and evaluate cellular infiltration into the scaffold and ECM deposition. The acellular CM grafts were designed using our tightly coupled computation and experimental approach, electrospun, and compliance matched to rat aorta. Next, these grafts were implanted into Sprague Dawley rats for 5 days, imaged in vivo using ultrasound, and explanted to evaluate cellular infiltration of SMCs, macrophages, and collagen.

METHODS

The composition of compliance matched TEVGs consisted of six alternating layers (A+B) of varying ratios of gelatin to polycaprolactone. The layer thickness and ratio was determined using a computational/experimental optimization scheme to match rat aorta thickness and compliance [6]. TGFβ2 concentrations of 0, 10, and 100 ng/mg were added to electrospinning solution to create the three experimental groups. The constructs were fabricated from these solutions using a commercial electrospinning device and crosslinked in 0.5% w/v genipin at 37ºC. After 24 hours, the constructs were washed,

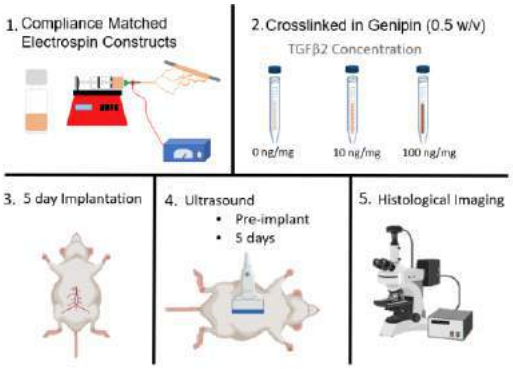

Figure 1: General experimental approach to assess TGFβ2 elution of TEVGs in-vivo.

measured for compliance, and implanted (n=3) into the abdominal aorta of a Sprague Dawley rat for 5 days.

After implantation, the constructs were imaged using in vivo ultrasound at 5 days to determine construct compliance and maximum luminal velocity in relation to the native vessel using a one-way ANOVA. Compliance was calculated using the outer diameter (OD) 120 and 70 as follows:

$$\text{Compliance} = ((OD_{120} - OD_{70})/OD_{70})/50 \text{ mmHg}$$

Each experimental group (0, 10, and 100 ng/mg) was sacrificed at 5 days and evaluated using histology. The 5-day time point was chosen to assess the acute response of the host to various levels of TGFβ2 [5]. For histology, each graft was evaluated cross sectionally in the middle axial region of the graft for SMCs (myosin heavy chain-MHC), macrophages (total-CD68 & M1-CD86), and collagen content. Each group was compared using image processing in MATLAB® and differences were determined using a one-way ANOVA. A general overview of this study is shown in **Figure 1**.

RESULTS

The compliance of CM TEVGs (0, 10, 100ng/mg) matched that of excised rat aorta tissue prior to implantation and were successfully implanted (data not shown). All the rats survived the duration of the study with no known complications.

In vivo compliance measurements showed a general decrease in compliance as TGFβ2 concentration was increased in the TEVG. Specifically, the 100 ng/mg group showed a decrease in compliance compared to native rat aorta, **Figure 2**, while the maximum blood velocity showed no differences.

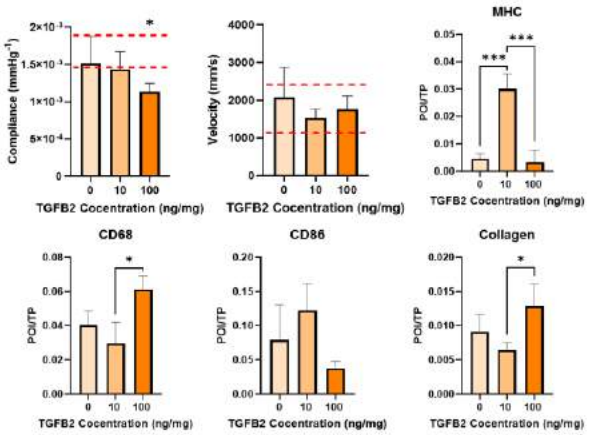

Figure 2: In vivo graft compliance and velocity. Immunohistochemistry of myosin heavy chain, CD68, CD86, and collagen. POI/TP = Pixels of Interest/ Total Pixels *, p<0.05, **, p<0.01, ***, p<0.001

Immunofluorescence of the 5-day explants of 0, 10, 100 ng/mg is shown in **Figure 3** with the implant in green and cell nuclei in blue. For all groups, cells were able to successfully infiltrate the construct and the surrounding tissue regions.

For histology, the majority of the differences were seen from the 10 ng/mg to 100 ng/mg group (**Figure 2**) with increases in the overall immune response in CD68 and collagen in the 100ng/mg constructs, $p<0.05$. No differences were found between all experimental groups for the M1 macrophages marker (CD86). Myosin heavy chain (MHC) expression had the most dramatic differences with an increase in the 10 ng/mg compared to 0 ng/mg and 100 ng/mg groups, $p<0.001$.

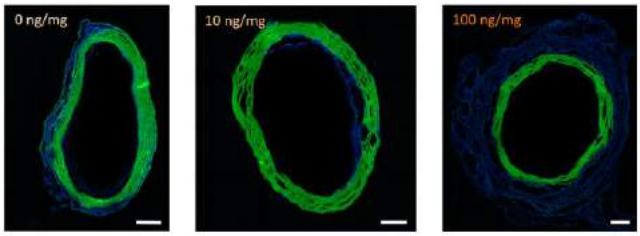

Figure 3: Immunofluorescence images of 5-day explants. Cell nuclei are in blue and the implant is green. Scale bar is 100 µm

DISCUSSION

Our preliminary immunohistochemistry results suggest that the incorporation of TGFβ2 into a compliance matched TEVG promotes increased SMC infiltration and collagen production at an acute 5-day time point. Specifically, the data showed that the low concentration (10 ng/mg) of TGFβ2 will increase smooth muscle cell recruitment (MHC marker). While a higher concentration (100 ng/mg) of TGFβ2 will increase collagen production in the TEVG and create an overall larger immune response. The in vivo ultrasound data also showed that an increase in TGFβ2 concentration will lead to an increase in TEVG stiffness.

Moving towards a functional TEVG, the incorporation of SMCs are vital. In this work, the results suggest the incorporation 10 ng/mg TGFβ2 to the TEVG promotes more positive MHC cells and agrees with past in vitro work. Specifically, Ardila et al. has shown that exogenous low TGFβ2 concentrations (<0.01 ng/ml) increase cellular proliferation while higher concentrations (>5 ng/ml) promote collagen formation [3]. The low concentration of TGFβ2 in this study promoted more MHC positive cells and the higher concentration promoted more collagen development. While the concentrations used in vitro are different, this difference in concentration would most likely be related to in vivo differences seen in the rat.

Given that our implant was only implanted for 5 days, one of the most surprising results from this study was the increase in TEVG stiffness as TGFβ2 concentrations increased. Our groups prior 4 week implantations of non-TGFβ2 eluting TEVGs has been able to maintain host compliance [7]. These two results in combination may be useful in our future work for longer term implantation where delated release of large amounts of TGFβ2 can be used to maintain in-vivo TEVG compliance as our graft fully degrades.

Some important limitations of note in this work include the acute time point of 5-days and the small sample size. As this work is continued, longer time points will be added to this study as well as the incorporation of a hypocompliant (stiffer) TEVG.

ACKNOWLEDGEMENTS

This research was funded by the NIH R56 (1R56HL136517-01) and Biomechanics in Regenerative Medicine Fellowship (T32EB003392).

REFERENCES

1. Peyton, S.R., et al., *The effects of matrix stiffness and RhoA on the phenotypic plasticity of smooth muscle cells in a 3-D biosynthetic hydrogel system.* Biomaterials, 2008. **29**(17): p. 2597-607.
2. Stewart, S.F. and D.J. Lyman, *Effects of an artery/vascular graft compliance mismatch on protein transport: a numerical study.* Ann Biomed Eng, 2004. **32**(7): p. 991-1006.
3. Ardila, D.C., et al., *TGFbeta2 differentially modulates smooth muscle cell proliferation and migration in electrospun gelatin-fibrinogen constructs.* Biomaterials, 2015. **37**: p. 164-73.
4. Goumans, M.J. and P. Ten Dijke, *TGF-beta Signaling in Control of Cardiovascular Function.* Cold Spring Harb Perspect Biol, 2018. **10**(2).
5. Ardila, D.C., et al., *Modulating smooth muscle cell response by the release of TGFbeta2 from tubular scaffolds for vascular tissue engineering.* J Control Release, 2019. **299**: p. 44-52.
6. Tamimi, E.A., et al., *Computationally Optimizing the Compliance of Multilayered Biomimetic Tissue Engineered Vascular Grafts.* Journal of Biomechanical Engineering, 2019. **141**(6).
7. Kenneth J. Furdella, S.H., Ali Behrangzade, Kang Kim, William R. Wagner, Jonathan P. Vande Geest, *In-vivo assessment of a tissue engineered vascular graft computationallyoptimized for target vessel compliance.* Acta Biomaterialia, 2021: p. In Press.

FIBROUS MICROENVIRONMENTS REGULATE NUCLEAR SHAPE IN A DIAMETER-DEPENDENT MANNER

Aniket Jana (1), Amrinder S. Nain (1)

(1) Department of Mechanical Engineering
Virginia Tech
Blacksburg, VA, USA

INTRODUCTION

Proper cellular functions during fundamental biological process like cell migration, differentiation and tissue morphogenesis, are often associated with a tight control on nuclear shape and size. Aberrant nuclear morphologies are implicated in various diseased states like muscular dystrophy, progeria and cancer metastasis. Additionally, nuclear shape remodeling has been associated with various downstream effects, including, nucleo-cytoplasmic shuttling of transcription factors[1] like YAP/TAZ, MKL1 and alterations in transcriptional activity. Previous studies on flat continuous substrates have demonstrated nucleus shape control through a special class of apical actin stress fibers; the perinuclear actin cap[2]. However how such shape regulation occurs in fibrous microenvironments like those commonly observed in skeletal muscle tissue and around highly metastatic tumors, remain poorly understood. In this study, we utilize our previously reported[3] non-electrospinning Spinneret Tunable Engineered Parameters (STEP) technique to manufacture aligned and suspended fiber networks with a wide range of diameters (~150 nm-7 µm) and tunable fiber density to investigate their role in modulating nuclear shape and translocation of YAP/TAZ during cell spreading. We observe that contrary to flat substrates, in suspended fibers which mimic the native extracellular matrix (ECM), the cell cytoskeleton is arranged as a symmetric cage without any apico-basal polarity. Our results also indicate that larger fiber diameters result in increased cytoskeletal tension leading to higher levels of nuclear compression and nuclear translocation of the mechanosensitive transcription factor YAP. Such cytoskeletal mediated force transmission can also result in deep (~1.5-3 µm) nuclear invaginations near the cell-fiber interface. Overall, we demonstrate how physical characteristics of the fibrous ECM, can regulate cell contractility, leading to an exquisite control over nuclear shape.

METHODS

Suspended fiber networks were manufactured from solutions of polystyrene (MW: 2,000,000 g/mol; Scientific Polymer Products and MW: 15,000,000 g/mol, Agilent Technologies) was dissolved in xylene (Thermo Fisher Scientific) using the non-electrospinning STEP technique. C2C12 mouse myoblasts (ATCC) were cultured in Dulbecco's modified Eagle's medium (Invitrogen) supplemented with 10% fetal bovine serum (Gibco) in T25 flasks (Corning). Immunofluorescent staining was performed in paraformaldehyde (4%) fixed cells. Images were taken using a confocal microscope (LSM 880, Carl Zeiss Inc.) with 0.3-0.36 µm z-slice thickness. Image processing was performed in Zen Blue software (Carl Zeiss Inc) or Image J (NIH). *,**,***,**** represent $p< 0.05$, 0.01, 0.001 and 0.0001 respectively.

RESULTS

Here, we utilized force-measuring nanonets composed of horizontal arrays of densely spaced (~10-12 µm spacing) small diameter (200 nm, 350 nm and 800 nm) fibers deposited on top of orthogonal large diameter (~2 µm) support fibers (Fig. 1a). Cells usually adopted symmetric parallel-cuboidal morphologies (Fig. 1b) as they spread along fiber doublets. Well-defined focal adhesion clusters (FAC) formed at all 4 cell poles, with FAC sizes increasing with fiber diameters (Fig 1d). Using our previously reported[4,5] Nanonet Force Microscopy (Fig 1c), we quantified the temporal evolution of cell-fiber adhesion forces and observed that spread-state cell contractility was indeed significantly higher for larger fiber diameters (Fig 1e) and in good agreement with higher adhesion sizes observed. To understand how such mechanical forces were transmitted to the cell nucleus we imaged the 3D localization of the cell cytoskeleton surrounding the nucleus. Contrary to the predominantly apical localization of cytoskeletal elements and nuclear envelope proteins (Lamin A/C) on

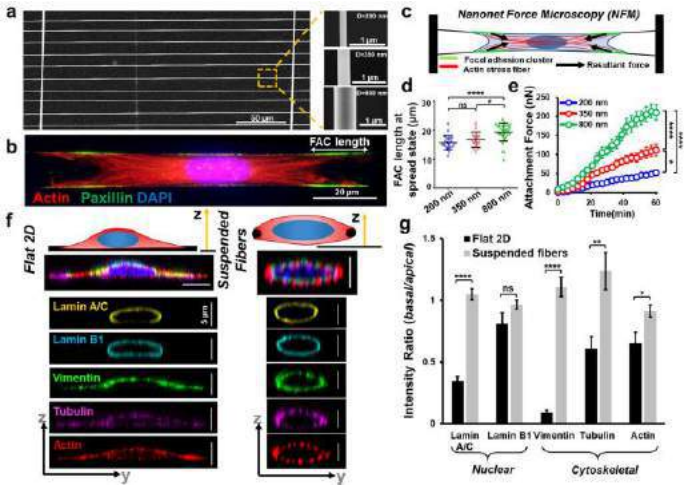

Fig 1: Cells on suspended fibers a) Aligned nanonets with 3 fiber diameter choices, b) Representative immunostained cell on fiber doublet, c) Schematic for nanonet force microscopy d) Comparison of FAC lengths at spread state (60 min. timepoint during spreading) e) Attachment forces during spreading f) Representative confocal side views (yz) of stained cells on Flat 2D and on suspended fibers g) Intensity analysis of apical and basal localization of different proteins in suspended cells and cells cultured on flat 2D glass.

Flat 2D, we observed no such apico-basal polarity on suspended fibers (Fig 1f), with the nucleus surrounded by a symmetric cytoskeletal caging structure (Intensity ratio$_{basal/apical}$~1, Fig 1g).

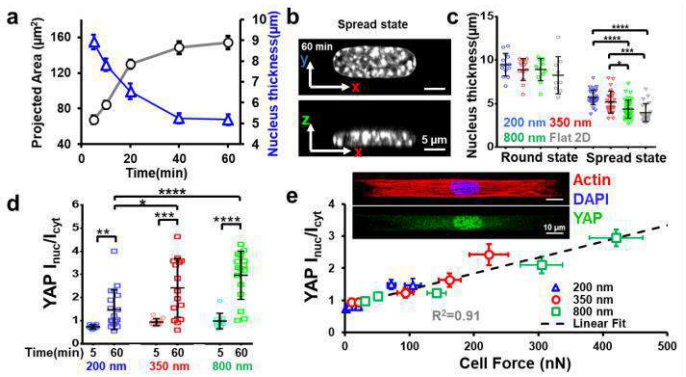

Fig 2: Nucleus shape and YAP localization in cells on fibers a) Evolution of projected area and nucleus thickness during cell spreading b) Representative top and side views of nucleus at spread state (60 min. timepoint) c,d) Comparison of nucleus thickness and YAP localization at round (5 min.)/spread (60 min.) state for different substrates respectively e) Impact of cell force on nuclear entry of YAP

To understand cytoskeletal tension-mediated regulation of nuclear shape, we imaged nuclei fixed at different times (5,10,20,40 and 60 min.) during cell spreading. As cells spread, progressive flattening of the nucleus was observed, characterized by an increase in projected area and reduction in thickness (Fig 2a, b). Interestingly, nucleus thickness in spread cells was found to be significantly lower in larger diameter fiber doublets (Fig 2c). Such higher levels of nuclear compression also resulted in significantly enhanced nuclear translocation of the YAP transcription factor (Fig 2d). In fact, such nuclear entry correlated excellently with the overall cell contractility (Fig 2e), with YAP localization primarily cytoplasmic in the low force regime (Fig 2d, e).

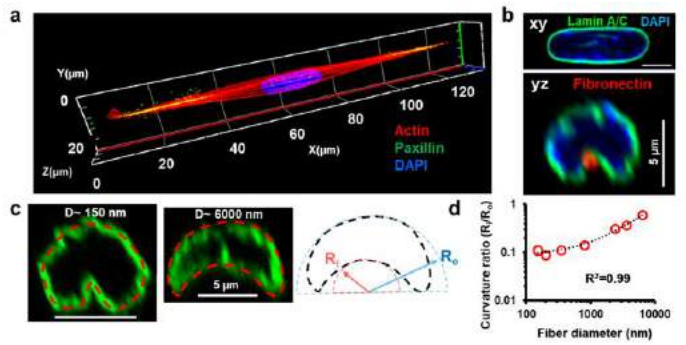

Fig 3: Fiber-mediated nuclear invaginations a) Representative spindle-shaped cell attached to single fibers, b) Stained nuclei showing invagination locally around fiber (red) c) Nuclear invaginations on small and large diameter fibers, R_i and R_o radius of curvature at the invagination side and the apical side respectively, d) Fiber diameter dependence of nucleus invagination curvature ratio (R_i/R_o)

Interestingly, in cells spreading along single fibers (Fig 3a), mechanical forces transmitted by actin stress fibers anchored at FACs at either cell pole can impinge the nucleus against the fiber to cause deep invaginations (Fig 3b). Invaginations were sharp at very low (~150 nm) fiber diameters and smooth on micron-scale (~6-7 μm) fibers (Fig 3c). To quantify such differences in shape, we computed the ratio of the radius of nuclear membrane curvature at the invagination site (R_i) and the radius of curvature at the apical side of the nucleus (R_o). On micron-scale fibers, we observed both radii to be similar, with an almost linear scaling of the curvature ratio (R_i/R_o) with the fiber diameter (Fig 3d).

DISCUSSION

Here, we demonstrate the remarkable mechanosensitivity of cells towards fibrous microenvironments and how ECM fiber geometry and diameter are instrumental in regulating nuclear shape and functions. Our observation of cytoskeletal caging of nucleus is in good agreement with previous studies on 3D microenvironments like microchannels[6] and dense collagen gels, which also show cytoskeletal force transmission from all sides. Higher levels of nuclear compression have been previously associated with nuclear pore complex (NPC) stretching[1] which enhances nuclear entry of various biomolecules. This can potentially explain why cells on larger diameter fibers show enhanced nuclear YAP. ECM–mediated localized nuclear deformations have been previously demonstrated in micropillared substrates[7], but we show for the first time, presence of such deformations in physiologically relevant fibrous matrices. Taken altogether, our findings on nuclear shape control will shed fundamental insights on how the local cellular microenvironment contributes to alterations in the sub-nuclear chromatin organization and overall gene-expression during cell differentiation, myogenesis and cancer metastasis.

ACKNOWLEDGEMENTS

This work is supported by the National Science Foundation (NSF) (Grant 1762634).

REFERENCES

[1] Elosegui-Artola, A et al., *Cell*, 171:1397-1410, 2017.
[2] Khatau, S.B. et al., *PNAS*, 106:19017-19022, 2009.
[3] Nain, A et al., *Macro Rapid Comm*, 30:1406-1412, 2009.
[4] Sheets, K et al., *Biophys J*, 111:197-207, 2016.
[5] Padhi, A et al., *Comm Biol*, 3:1-11, 2020.
[6] Mistriotis, P et al., *J Cell Bio*, 218:4093-4111, 2019.
[7] Davidson, P. M. et al., *Adv Mater*, 21:3586-3590, 2009.

INVESTIGATION OF THE HINDBRAIN MOTION IN CHIARI MALFORMATION I PATIENTS THROUGH 3D AMPLIFIED MRI

Javid Abderezaei (1), Aymeric Pionteck (1), Ya-Chen Chuang (1), Itamar Terem (2), Leo Dang (3), Miriam Scadeng (3), Peter Morgenstern (4), Raj Shrivastava (4), Samantha J. Holdsworth (3), Yang Yang (5,6), Mehmet Kurt (1,6)

(1) Dept. of Mechanical Engineering, Stevens Institute of Technology, Hoboken, NJ, USA

(2) Dept. of Radiology, Stanford University, Stanford, CA, USA

(3) Dept. of Anatomy and Medical Imaging & Centre for Brain Research, University of Auckland, Auckland, New Zealand

(4) Dept. of Neurosurgery, Icahn School of Medicine at Mount Sinai, New York, NY, USA

(5) Dept. of Radiology, Icahn School of Medicine at Mount Sinai, New York, NY, USA

(6) BioMedical Engineering and Imaging Institute, Icahn School of Medicine at Mount Sinai, New York, NY, USA

INTRODUCTION

Chiari Malformation I (CMI) is a common and often debilitating craniocervical junction neurosurgical disease diagnosed in approximately 1% to 4% of patients who receive MRI scans [1,2]. It is often characterized by the structural defects in the cerebellum, and more specifically, the herniation of the cerebellar tonsils 5 mm below the foramen magnum. It is associated with a vast range of symptoms which can include recurrent headaches, nausea, muscle weakness, sleep disorders, and in the most extreme cases, even paralysis [3,4].

So far, the diagnosis of CMI has been based on an assessment of the patient's neurological history combined with the measurement of cerebellar tonsils downward herniation from MRI examination. However, the lack of a uniform and clear symptomatology among subjects is so pronounced that an estimated 33% of the patients affected do not show symptoms significant enough to lead to a diagnosis [3]. Determining which patient to not operate upon, on the other hand, is equally important, as the surgery can carry patient-related morbidity. More recently, the intrinsic motion of the brain during the cardiac pulsation has also been suggested as a potential diagnostic criterion for CMI [5]. Until now, however, the effect of cardiac pulsation and CSF circulation on the subtle motion of the brain tissue has proven difficult to analyze. Conventional imaging techniques such as phase-contrast MRI [6] or DENSE MRI [7] have attempted to study such motions but had certain limitations with scan time and spatial resolution. Recently, a new image processing technique called 3D amplified MRI (3D aMRI) was introduced [8-10]. 3D aMRI allows to selectively amplify the 3D motion in specified frequency bands, thereby making even imperceptible motions visible and quantifiable [8-10]. Having been previously used on against digital phantoms and 3D cine MRI of healthy subjects, in this work, 3D aMRI algorithm was applied to healthy and CMI patients and local distribution of motion in cerebellum and pons were measured and compared.

METHODS

Human subjects and imaging protocol: With IRB approval and informed consent, scans were performed on 4 healthy adult volunteers (2 females and 2 males between 26 and 32 years of age) as well as 4 CMI patients (4 females between 24 and 34 years of age) using a 3T MR imaging system (Skyra, Siemens Healthcare AG, Germany) with a 32-channel head coil at Icahn School of Medicine at Mount Sinai. For each subject, whole-brain 3D cine MRI were acquired using the following imaging parameters: acquisition matrix = 240×173, flip angle = 26◦, FOV = 216×240 mm^2, TR/TE=36.6/1.6 ms, pixel bandwidth = ±990 kHz, 16-23 cardiac phases, and 128 slices with 1.2 mm thickness.

3D aMRI algorithm: The 3D aMRI method is based on the extension of the 2D aMRI algorithm [11-13] to 3D, allowing the visualization and quantification of very subtle voxel displacements in 3 directions ([8-10]; Fig 1). In the first step, a 3D cine MRI data set is used as an input to the algorithm. Then, a 3D steerable pyramid is used to decompose the volumetric data, resulting in local phases of each time frame at different scales and orientations [8-10]. In short, the steerable pyramid is composed of steerable filters with multi-scale decomposition which recursively performs low band-pass filtering and down-sampling of each phase image. The temporal variations of the decomposed phases are then temporally filtered, amplified, and added back to the original phases. Finally, by collapsing the pyramid, the modified video is reconstructed which allows for visualization of the almost imperceptible motion. The schematics of the 3D aMRI algorithm is shown in Fig. 1.

Displacement tracking in the amplified data: Having amplified the 3D cine data in 3-direction, an image registration algorithm based on the Demons [14] was then applied to the amplified data and the overall

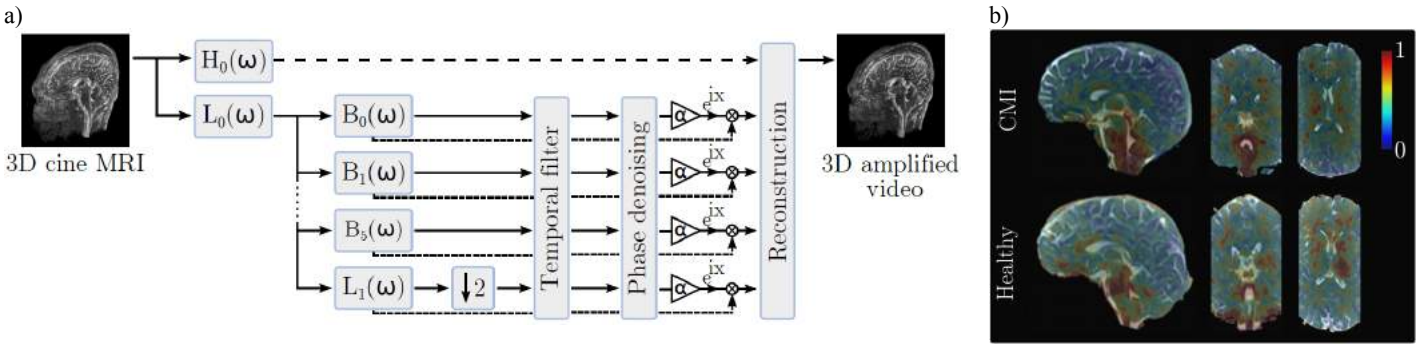

Fig. 1. (a) 3D aMRI algorithm pipeline. (b) Comparison of the CMI and healthy brain displacement between 2 age-matched female cases.

3D brain displacements of the subjects were quantified. We then mapped the acquired displacement fields on a brain atlas and selected a circular region (30 mm^2) at the bottom of the cerebellum and at the bottom of pons near the medulla (Fig. 2). The circular region was further extended to cover 7 adjacent sagittal slices for each subject, and the mean of maximum displacement within this region and across all the slices was then calculated and compared between the healthy and CMI subjects. This region was chosen since previous studies have suggested abnormal motion in the lower parts of the brain in CMI patients [5,9].

RESULTS

Having amplified the 3D cine MRI of the healthy and CMI subjects with an amplification factor of 8, and within the frequency range of 0-4 Hz, the displacement fields of each subject were then measured. In both the healthy and CMI subjects, the maximum displacement was observed to be near the pons and the 4th ventricle (Fig. 1b). When comparing the results between the two groups, we observed that the motion at the bottom of the cerebellum and the pons were significantly higher in the CMI patients as compared to the healthy subjects ($p<0.05$). In the pons, while the mean of the maximum displacement in the region of interest (ROI) was 1.06 ± 0.19 pixels, the ROI_{Pons} of the healthy subjects experienced a displacement of 0.74 ± 0.13 pixels ($p<0.05$, Fig. 2). We also observed a significantly higher displacement of 1.31 ± 0.4 pixels in the selected $ROI_{Cerebellum}$ of CMI patients as compared to the displacement of 1 ± 0.11 pixels in the healthy subjects ($p<0.05$, Fig. 2).

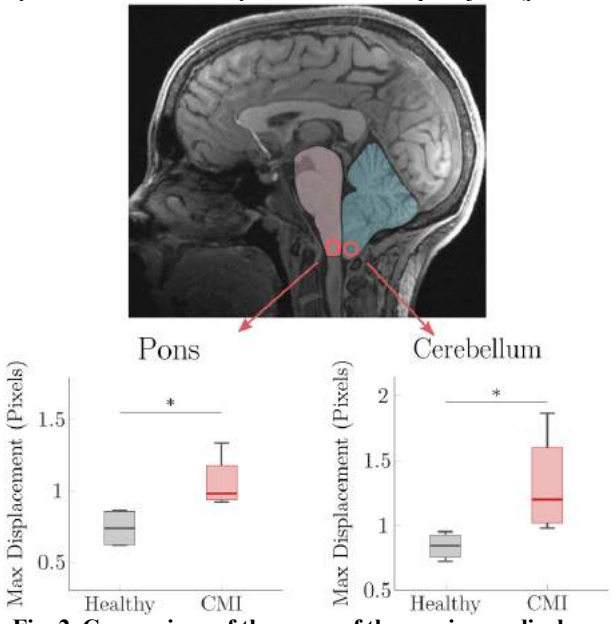

Fig. 2. Comparison of the mean of the maximum displacement between 4 healthy and 4 CMI subjects.

DISCUSSION

In this work, the 3D aMRI method was used to measure the brain's intrinsic motion in CMI patients for the first time. We observed that the highest displacement in both the healthy and CMI subjects is near the pons and the 4th ventricles. Additionally, we demonstrated that the displacement at the bottom of the cerebellum and pons (near the medulla) was significantly higher in the CMI patients as compared to the healthy subjects. Our findings are in line with previous observations that reported abnormal brain intrinsic motion in the lower parts of the brain [5,9,15]. Using the DENSE method, it was recently shown that the displacement in the lower part of the cerebellum and brainstem was much higher in CMI patients [5]. We hypothesize that this difference is mainly due to the geometrical variances between the cerebellum of the healthy and CMI subjects. The morphological changes as a result of CMI could result in partial blockage of the subarachnoid space near the foramen magnum [16]. This could result in the obstruction of the CSF circulation and potentially decrease the CSF volume through there [16]. However, since the driving pressure from the blood flow is higher than the intracranial pressure, the same volume of CSF at a higher velocity would potentially pass through the region, which results in a higher displacement of the lower parts of the cerebellum and pons [16].

Our results show 3D aMRI's capability as a potential diagnostic tool for CMI. 3D aMRI is a post-processing algorithm which is applied on cine MRI data that is already implemented in the standard clinical routine; therefore, it could be used in the current protocols and potentially have an immediate clinical impact.

ACKNOWLEDGEMENTS

This research was partially supported by NSF Grant No. CMMI-1728186 and NIH Grant No. 1R21NS111415-01.

REFERENCES

[1] Strahle, J., et al., J. Neurosurg. Pediatr., no. 2, pp. 205–213, 2011.
[2] Meadows, J., et al., J. Neurosurg., no. 6, pp. 920–926, Jun. 2000.
[3] Taylor, F. R., et al., Curr. Pain Headache Rep., vol. 6, no. 4, pp. 331–337, Aug. 2002.
[4] George, T. M., et al., Neurol. Res., no. 3, pp. 240–246, Apr. 2011.
[5] Nwotchouang, B. S. T., et al., Ann Biomed Eng, 1-15., 2021.
[6] Enzmann, D., et al., Radiology, 178(2):467-474, 1991.
[7] Aletras, A., et al., J Magn Res, 137:247, 1999.
[8] Abderezaei, J., et al., Brain Multiphysics, under review, 2021.
[9] Terem, I., et al., MRM, under review, 2021.
[10] Abderezaei, J., et al., CMBBE, Aug. 14-16th 2019, NY, USA.
[11] Holdsworth, S., et al., MRM, 75(6):2245-2254, 2016.
[12] Terem, I., et al., MRM, 80(6):2549-2559, 2018.
[13] Abderezaei, J, et al., IEEE Trans Med Imaging, 39(12), 4113-4123, 2020.
[14] Vercauteren, T., et al., MICCAI, Springer, pp. 319– 326.
[15] Wolpert, S. MAm. J. Neuroradiol. 15(7):1299–1308, 1994.
[16] Shaffer, N., et al., Neurological research, 33(3), 247-260, 2011.

THE EVOLUTION OF HETEROGENEOUS PARAMETERS FOR MODELING CARTILAGE DURING THE PROGRESSION OF OSTEOARTHRITIS

Xiaogang Wang (1), David M. Pierce (1,2)

(1) Department of Mechanical Engineering
University of Connecticut
Storrs, CT, USA

(2) Department of Biomedical Engineering
University of Connecticut
Storrs, CT, USA

INTRODUCTION

Despite the multifactorial nature of Osteoarthritis (OA), a disease of the synovial joint, mechanical stresses play a key role in the destructive evolution of the disease [1–4]. Both overloading and reduced loading of cartilage induce molecular and microstructural changes that lead to mechanical softening, fibrillation and erosion. Crucially, there is currently no direct method to correlate spatially resolved intra-tissue stresses with progression of OA in individual patients. This unmet need renders us unable to identify the most significant stimuli in the progression of OA, and thus unable to identify reliable targets for treatment or to design new therapies.

Computational models of cartilage and joints have enabled estimates of responses and properties, e.g. distributions of intra-tissue stresses and evolving mechanical properties, especially in the early stages of OA. In this study, we aimed to establish a methodology to calibrate our constitutive models of cartilage by leveraging experimental data we previously published and determine the evolution of material parameters with respect to the severity of OA quantified via the standard OARSI grade [5], especially in early disease stages.

METHODS

We described articular cartilage as a biphasic continuum $\varphi = \varphi^{\mathrm{S}} + \varphi^{\mathrm{F}}$ consisting of a porous solid phase φ^{S}, and saturated with the fluid phase φ^{F}. We calculated the total Cauchy stress tensor as [6]

$$\boldsymbol{\sigma} = -p\mathbf{I} + 2\rho^{\mathrm{S}}\mathbf{F}_{\mathrm{S}}\frac{\partial\Psi^{\mathrm{S}}}{\partial\mathbf{C}_{\mathrm{S}}}\mathbf{F}_{\mathrm{S}}^{\mathrm{T}} = -p\mathbf{I} + \boldsymbol{\sigma}_{\mathrm{E}}^{\mathrm{S}}\,, \tag{1}$$

where p is the fluid pressure, $\mathbf{I}$ is the identity tensor, ρ^{S} is the partial density of solid, $\mathbf{F}_{\mathrm{S}}$ is the deformation gradient of the solid, $\mathbf{C}_{\mathrm{S}}$ is the right Cauchy–Green tensor, and $\boldsymbol{\sigma}_{\mathrm{E}}^{\mathrm{S}}$ is the effective Cauchy stress tensor. We use an additive decomposition of the superimposed solid Helmholtz free-energy function Ψ^{S} into a Donnan osmotic pressure part $\Psi_{\mathrm{OP}}^{\mathrm{S}}$, an isotropic matrix part $\Psi_{\mathrm{IM}}^{\mathrm{S}}$, and a fiber network part $\Psi_{\mathrm{FN}}^{\mathrm{S}}$ as

$$\Psi^{\mathrm{S}} = \Psi_{\mathrm{OP}}^{\mathrm{S}}(J_{\mathrm{S}}) + (1-\nu)\Psi_{\mathrm{IM}}^{\mathrm{S}}(J_{\mathrm{S}},\, I_1) + \nu\Psi_{\mathrm{FN}}^{\mathrm{S}}(\mathbf{C}_{\mathrm{S}})\,, \tag{2}$$

where $J_{\mathrm{S}} = \det\mathbf{F}_{\mathrm{S}}$ is the Jacobian, ν is the volume fraction of collagen to the total solid, $I_1 = \mathrm{tr}\mathbf{C}_{\mathrm{S}}$ is the first invariant of $\mathbf{C}_{\mathrm{S}}$. We model the contribution from the osmotic pressure to the Cauchy stress as

$$\boldsymbol{\sigma}_{\mathrm{OP}}^{\mathrm{S}} = -R\Theta\left[\sqrt{4(\bar{c}_{\mathrm{m}})^2 + (c_{\mathrm{m}}^{\mathrm{fc}})^2} - 2\bar{c}_{\mathrm{m}}\right]\mathbf{I}\,, \tag{3}$$

where $\mathrm{R} = 8.314\times10^3\ \mathrm{mJ/(K\cdot mol)}$, Θ is the absolute temperature, and $\bar{c}_{\mathrm{m}}$ is the ion concentration of the external solution. The concentration of the fixed charge depends on the deformation as

$$c_{\mathrm{m}}^{\mathrm{fc}} = c_{0\mathrm{S}}^{\mathrm{fc}}\left(1-n_{0\mathrm{S}}^{\mathrm{S}}\right)\left(J_{\mathrm{S}}-n_{0\mathrm{S}}^{\mathrm{S}}\right)^{-1}, \tag{4}$$

where $c_{0\mathrm{S}}^{\mathrm{fc}}$ is the initial concentration of fixed charge (within the tissue) and $n_{0\mathrm{S}}^{\mathrm{S}}$ is the initial solid volume fraction, and $J_{\mathrm{S}} = \rho_{0\mathrm{S}}^{\mathrm{S}}/\rho^{\mathrm{S}}$ where $\rho_{0\mathrm{S}}^{\mathrm{S}}$ is the initial solid partial density. We model the (largely) proteoglycan solid matrix $\Psi_{\mathrm{IM}}^{\mathrm{S}}$ using a neo-Hookean function extended with compaction effects. To model the dispersed network of collagen $\Psi_{\mathrm{IM}}^{\mathrm{S}}$ we use $\rho(\mathbf{m_0})$, the orientation distribution function, within

$$\Psi_{\mathrm{FN}}^{\mathrm{S}} = \frac{1}{\rho_{0\mathrm{S}}^{\mathrm{S}}}\int_\Omega \rho(\mathbf{D})\frac{k_1}{2k_2}\{\exp[k_2(I_4-1)^2]-1\}\mathcal{H}(I_4-1)\,\mathrm{d}\Omega\,, \tag{5}$$

where $\Omega = \{\mathbf{m_0}\in\mathbb{R}^3 : |\mathbf{m_0}| = 1\}$ is the unit sphere, $\mathbf{m_0}$ is the reference fiber orientation, $k_1, k_2 > 0$ are fiber parameters $I_4(\mathbf{m_0}) = \mathbf{m_0}\cdot\mathbf{C}_{\mathrm{S}}\mathbf{m_0}$ is the square of the fiber stretch, and $\mathcal{H}$ is a Heaviside step function. We consider the viscoelasticity of both the proteoglycan and collagen solids using two parameters: β [-], a magnitude factor, and τ [s] the associated relaxation time, cf. [6]. The diffusion tensor $\mathbf{D}$ reflects the distribution of collagen fibers and we obtain this from DT-MRI. We calculate the average $\mathbf{D}$ for a representative volume of interest using the Log-Euclidean mean. We modeled the corresponding permeability $\mathbf{K}_{\mathrm{F}}$ as

$$\mathbf{K}_{\mathrm{F}} = \frac{k_{0\mathrm{S}}}{4\pi}\left(\frac{n^{\mathrm{F}}}{1-n_{0\mathrm{S}}^{\mathrm{S}}}\right)^{m}\int_{\Omega}\frac{\rho(\mathbf{m}_0)}{\mathrm{I}_4}\mathbf{m}\otimes\mathbf{m}\mathrm{d}\Omega\,, \tag{6}$$

where $k_{0\mathrm{S}}$ is the initial Darcy permeability and m is a parameter controlling the deformation dependence of the permeability. In order to recover the initial (non-zero) stress distribution resulting from osmotic swelling, we applied the backward displacement method to find an initial equilibrium state before external loading. [7]

In previously published experiments using large-strain shear, we harvested 106 3×3 mm, full-thickness specimens of healthy and OA damaged cartilage from 17 donors [8, 9]. Using standard histological scoring we determined the OARSI grade of each specimen [5]. Prior to shear testing we applied an axial pre-compression of 1% of the undeformed thickness and allowed the specimens to equilibrate for 4000 s. Next, we applied cyclic simple-shear displacements at a rate of 75 μm/min for six cycles. We applied maximum displacements corresponding to shear strains of 5%, 10%, 15%, 20%, and 25%. Many mechanical tests failed at 20% shear strain and here we used data only up to 15% shear strain.

To simulate the shear tests, we modeled the center slice of the specimens under plane strain (**Fig. 1(a)**) and along the shear direction using 20-node hexahedral elements in FEBio (U. of Utah) (**Fig. 1(b)**). We validated our mesh using an *h*-refinement test [6,7]. We assigned three different sets of material parameters corresponding to the superficial zone (SZ), middle zone (MZ), and deep zone (DZ) based on the thickness, which has thickness of 15%, 55% and 35% respectively [7]. In light of the data available, and to minimize the computational burden, we leveraged previous studies to establish some of the parameters (**Table 1)**, where $z^* \in [0,1]$ is the normalized tissue thickness (zero refers to the articular surface and one refers to the interface with subchondral bone). We set $z^*_{\mathrm{SZ}} = 0.075$, $z^*_{\mathrm{MZ}} = 0.425$ and $z^*_{\mathrm{DZ}} = 0.85$.

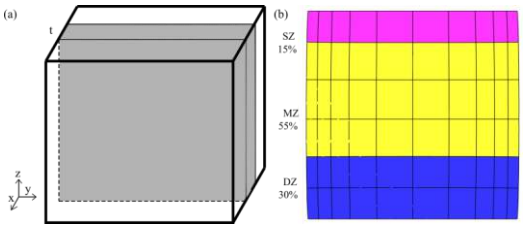

Figure 1: Finite element model of the shear experiment: (a) schematic with center slice in plane strain; (b) mesh with three distinct zones through the thickness.

Table 1: Model parameters from our previous studies [6,7].

Parameter	Value	Unit
$\boldsymbol{\Theta}$	310.15	K
$\boldsymbol{c}^{\mathbf{fc}}_{\mathbf{0S}}$	2.0×10^{-7}	$\mathrm{mol/mm^3}$
$\bar{\boldsymbol{c}}_{\mathbf{m}}$	1.5×10^{-7}	$\mathrm{mol/mm^3}$
$\boldsymbol{\mu}$	0.23	MPa
$\boldsymbol{k_2}$	8	–
$\boldsymbol{n}^{\mathbf{S}}_{\mathbf{0S}}(\boldsymbol{z}^*)$	$0.15+0.15(z^*)$	–
$\boldsymbol{\nu}(\boldsymbol{z}^*)$	$0.43(z^*)^2-0.60(z^*)+0.85$	–
$\boldsymbol{J}^{\mathbf{S}}_{\mathbf{cp}}(\boldsymbol{z}^*)$	$0.36+0.11(z^*)$	–
$\boldsymbol{k}_{\mathbf{0S}}(\boldsymbol{z}^*)$	$(1-0.9)(z^*)\times10^{-3}$	$\mathrm{mm^4/(N\cdot s)}$
$\boldsymbol{m}(\boldsymbol{z}^*)$	$3.0+5.0(z^*)$	–

We fitted the model parameters using the "Levenberg–Marquard" method within FEBio [10]. To fit our constitutive model as a function of OA severity we first extracted target data for fitting each specimen. To eliminate noise and to align the loading state, we used data from the first peak force to the last peak force. In between each pair of peaks, we resampled the data at 24 evenly-spaced intervals. We first assumed cartilage was homogeneous, setting all three zones with the same as the MZ, to fit viscoelasticity of fiber network (β_{FN}, τ_{FN}) and estimate the fiber parameter k_1. We then fixed the viscoelasticity and, using our heterogeneous model, fit fiber parameter k_1 for all three zones.

RESULTS

Figure 2 shows fitted results of two representative specimens: one healthy and one at OARSI grade 3.5. The *x*-axes display the time of the test, including the pre-compression and relaxing periods while the *y*-axes display the reaction force in the direction of shearing. **Table 2** shows the fitted parameters of these two specimens.

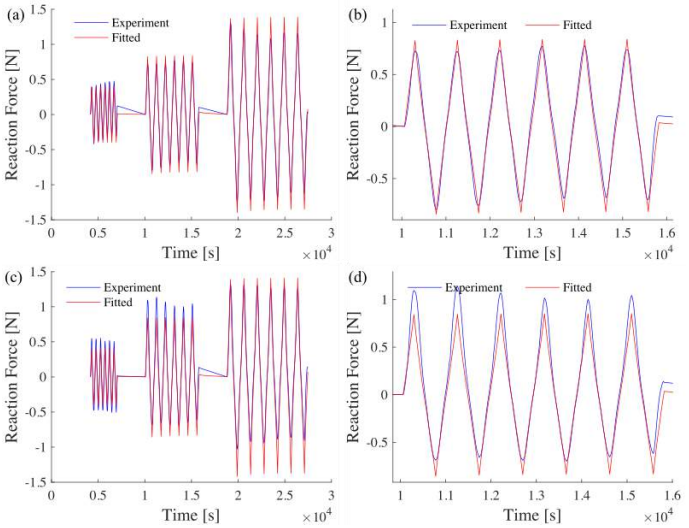

Figure 2: Representative fitting results: (a), (b) are from a healthy specimen while (c), (d) are from an OA specimen (OARSI grade 3.5). (a), (c) are the complete data while (b)(d) focus on 10% shear.

Table 2: Fitted parameters for healthy and OA specimens.

	Parameter	Value	Unit
Healthy Specimen	β_{FN}	1.680	–
	τ_{FN}	1598	s
	$k_1(\mathrm{est})$	2.266	MPa
	$k_1(\mathrm{SZ})$	1.417	MPa
	$k_1(\mathrm{MZ})$	2.890	MPa
	$k_1(\mathrm{DZ})$	3.535	MPa
OARSI Grade 3.5 Specimen	β_{FN}	1.470	–
	τ_{FN}	1697	s
	$k_1(\mathrm{est})$	3.605	MPa
	$k_1(\mathrm{SZ})$	3.363	MPa
	$k_1(\mathrm{MZ})$	4.256	MPa
	$k_1(\mathrm{DZ})$	4.811	MPa

DISCUSSION

Our preliminary results are currently insufficient to yield statistical conclusions, but we do see notable changes in the fitted parameters corresponding to both the through-thickness zones and health conditions of the specimens. The fiber parameter k_1 increases from cartilage surface to the bone interface, indicating stiffer individual fibers in DZ. The decreased β_{FN} in the OA specimen indicates a reduced viscoelastic response that likely reflects degeneration. As we fit more specimens our parameters, and the corresponding statistical analyses, will facilitate new simulation-based analyses and insights.

ACKNOWLEDGEMENTS

NSF CAREER 1653358, 1662429; Franz Maier.

REFERENCES

[1] Goldring, MB et al., *Arthritis Res Ther*, 11:224, 2009. [2] Polur, I et al., *Histol*, 25:599-608, 2010. [3] Loeser, RF et al., *Arthritis Rheum*, 64:1697-1707, 2012. [4] Lawrence, RC et al., *Arthritis Rheum*, 58:26-35, 2008. [5] Pritzker, K. P. H. et al., *Osteoarthritis Cartilage*, 14:13-29, 2006. [6] Pierce, DM et al., *Biomech Model Mechno*, 15:229-244, 2016. [7] Wang, X et al., *J Mech Beh Biomed Mat*, 86:409-422, 2018. [8] Maier, F et al., *J Mech Beh Biomed Mat*, 65:53-65, 2017. [9] Maier, F et al., *Osteoarthritis Cartilage*, 27:810-22, 2019. [10] Wang, X et al., *J Mech Beh Biomed Mat*, 104150, 2020.

AN ELECTROMAGNETIC ACTUATOR FOR BRAIN MAGNETIC RESONANCE ELASTOGRAPHY

Suhao Qiu (1), Zhao He (1), Runke Wang (1)，Ruokun Li (2), Fuhua Yan (2), Yuan Feng (1)

(1) Institute for Medical Imaging Technology
Shanghai Jiao Tong University
Shanghai, Shanghai, China

(2) Department of Radiology
Ruijin Hospital
Shanghai, Shanghai, China

INTRODUCTION

Magnetic resonance elastography (MRE) is a non-invasive method that can measure mechanical properties of brain tissues in vivo [1]. Different from the clinical application of MRE in liver tissue measurements, shear waves must be effectively transmitted through the skull into brain [2]. Therefore, an effective actuator for brain MRE is desired.

Current clinically used actuator is pneumatically driven [3], but studies have shown that it might produce extra peaks in the frequency spectrum [4]. The mechanical actuator can produce accurate frequency but may produce extra noise [4]. Electromagnetic actuator, like the piezo-electric actuator, is convenient to control, and can produce an accurate actuation frequency [5]. However, electromagnetic compatibility [6] and ergonomic design are crucial for the clinical application of the electromagnetic actuator [7].

In this study, we proposed an electromagnetic actuator for brain MRE. A grappler design was used to transmit shear waves to the whole brain efficiently. The performances of the actuator in terms of frequency accuracy, electromagnetic compatibility, and wave generation were evaluated.

METHODS

With a splint-like structure, a support frame held the actuation coil in place on the top of the MR head coil to keep the coil away from the MRE imaging region (Figure 1a). A transmission bar was designed to connect the actuation coil to the vibration plates, transmitting the vibration from the actuation coil to the plate. A curved design was adopted for all vibration plates for ergonomic consideration. The components that were outside of the head coil had a height of 7.5 cm (Figure 1b). Therefore, the whole actuator could fit into the MR bore easily.

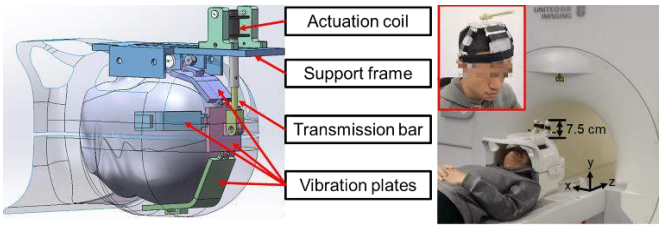

Figure 1: (a) A 3D rendering of the electromagnetic actuator for brain MRE in working position. (b) A volunteer wearing the actuator before moving into the MR bore for MRE. The part of the actuator that extrudes out of the head coil is 7.5 cm in height, leaving enough space for positioning.

We evaluated the performance of frequency actuation of the proposed actuator and compared it with that of a pneumatic actuator. A 3T MRI scanner (uMR 790, United Imaging Healthcare, Shanghai, China) was used for the experiment and all following imaging. Vibrations of the actuator during MRE were recorded using an accelerometer with a gradient echo (GRE) based MRE sequence.

To estimate the magnetic field produced by the actuation coil more precisely, finite element simulations were carried out using COMSOL. In addition, to evaluate the overall influence of the metal components, we tested the electromagnetic compatibility by measuring the signal-to-noise (SNR) ratio of a spherical liquid phantom with T1 weighted (T1W) and T2 weighted (T1W) clinical sequences, respectively.

A cylindrical phantom was manufactured to evaluate the actual shear wave generation performance of the actuator. The phantom was made of glycerol gelatin. The quality of the produced shear wave within

the region of interest (ROI) was assessed by using the octahedral shear strain (OSS) signal-to-noise ratio OSS_{SNR} [8].

$$OSS_{SNR} = \frac{\bar{\epsilon_s}}{\bar{\epsilon_s}^{noise}} \quad (1)$$

where $\bar{\epsilon_s}$ is the average value of OSS over one harmonic cycle and ϵ_s can be calculated as:

$$\epsilon_s = \frac{2}{3}\sqrt{\begin{matrix}(\epsilon_{xx}-\epsilon_{yy})^2+(\epsilon_{xx}-\epsilon_{zz})^2+\\(\epsilon_{yy}-\epsilon_{zz})^2+6(\epsilon_{xy}{}^2+\epsilon_{xz}{}^2+\epsilon_{yz}{}^2)\end{matrix}} \quad (2)$$

where ϵ_{xx}, ϵ_{yy}, ϵ_{zz}, ϵ_{xy}, ϵ_{xz}, and ϵ_{yz} are the components of the Cauchy strain tensor.

RESULTS

The frequency response of the proposed actuator along the x, y, and z axes showed an increased acceleration magnitude with larger vibration frequencies along all three directions (Figure 2a). Compared with the spectrum of the pneumatic actuator, we observed lower frequency offsets for the vibration frequencies, especially at 60 Hz (Figure 2b).

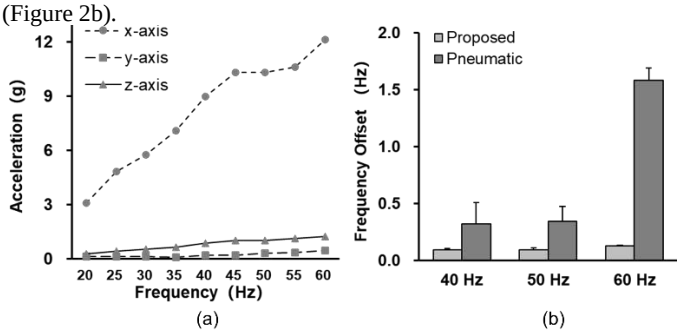

Figure 2: (a) Measured acceleration vs. actuation frequency. The primary motion of vibration was along the x direction. (b) Comparison of frequency offsets between the proposed and the pneumatic actuator at 40 Hz, 50 Hz, and 60 Hz.

The simulated magnetic flux density showed that the ROI of the MRE imaging was outside the 3-G contour (Figure 3), which was less than one part in 10000 compared with the 3-T B_0 field. Therefore, the interference of the fringe field produced by the actuator was at a paltry level.

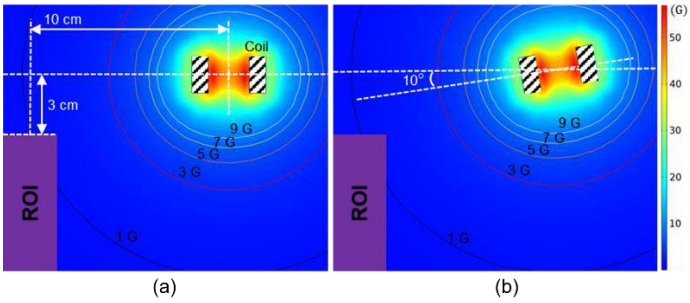

Figure 3: Contour plots of the magnetic flux density for the actuation coil at (a) the horizontal position or (b) the maximum tilt angle. Both cases showed the ROI was outside the 3-G line of the magnetic fringe field.

Analysis of the SNR values from 6 different slices from each set of TIW and T2W images showed no significant differences (Figure 4). This indicated that the proposed actuator did not interfere with the imaging.

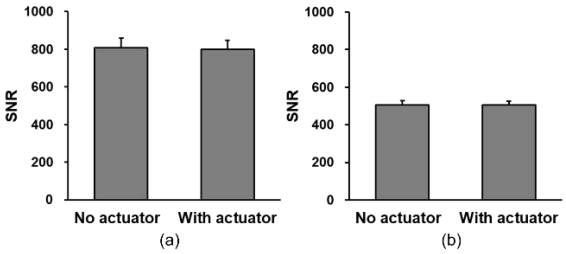

Figure 4: The bar charts showed the mean value and standard deviations of SNR evaluated from 6 different slices for the (a) T1W and (b) T2W images.

For the phantom imaging, we observed an increased stiffness with the frequencies (Figure 5). About 96.9% of the image pixels had $OSS_{SNR} \geqslant 3$ for all actuation frequencies. This indicated that the proposed actuator could generate stable shear waves for stiffness estimation.

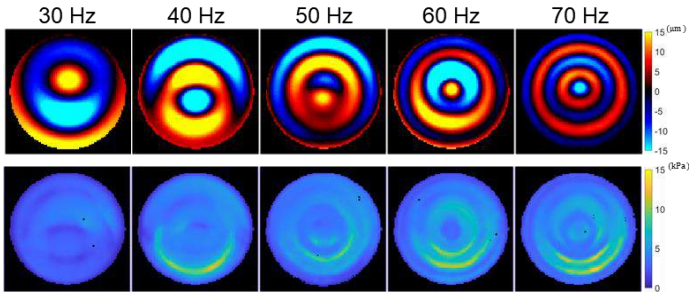

Figure 5: Wave images (top) and the corresponding stiffness maps (bottom) with pixels having OSS_{SNR} > 3 with five different frequencies.

DISCUSSION

In this study, an electromagnetic actuator was proposed for brain MRE. The spectra analysis demonstrated that the proposed actuator could produce waves with accurate frequencies. In addition, the actuator did not interfere with other imaging sequences. Phantom experiments verify the performance of the wave generation.

This study has many limitations. The GRE-based MRE sequence was used for the actuator tests. However, this multi-shot acquisition method may produce a long scanning time and bring potential vibration interference. Therefore, specifically designed and optimized MRE sequence is needed and will be developed in future studies.

ACKNOWLEDGEMENTS

Funding support from grant 31870941 from National Natural Science Foundation of China (NSFC) and grant 1944190700 from Shanghai Science and Technology Committee (STCSM) are acknowledged.

REFERENCES

[1] Murphy, MC et al., *Neuroimage*, 187:176-183, 2019.
[2] Sack, I et al., *NMR Biomed*, 21(3):265-271, 2008.
[3] Johnson, CL. et al., *Dev Cogn Neurosci* , 45:100842, 2020.
[4] Runge, JH. et al., *Phys Med Biol*, 64(4):045007, 2019.
[5] Feng Y et al., *Magn Reson Imaging*, 51:29-34, 2018.
[6] Uffmann, K et al., *IEEE Eng Med Biol Mag*, 27(3):28-34, 2008.
[7] Tse, ZT et al., *Proc Inst Mech Eng H*, 223(4):497-514, 2009.
[8] McGarry MD., *Phys Med Biol*, 56(13):N153-164, 2011.

ACTOYMOSIN CONTRACTILITY REGULATES MULTI-SCALE MECHANOBIOLOGY OF NUCLEUS PULPOSUS CELLS IN INFLAMMATION

T. Jacobsen (1,2), P. Hernandez (3), N. O. Chahine (1,2)

(1) Department of Biomedical Engineering
Columbia University
New York, NY, USA

(2) Department of Orthopedic Surgery
Columbia University Medical Center
New York, NY, USA

(3) U.T. Southwestern Medical Center
Dallas, TX, USA

INTRODUCTION: Disc degeneration is characterized by elevated levels of pro-inflammatory cytokines [1]. Inflammatory stimulation of intervertebral disc nucleus pulposus (NP) cells can lead to a catabolic breakdown of disc extracellular matrix (ECM), acting as a positive feedback of further loss of tissue integrity and inflammation [2]. We have previously shown that pro-inflammatory stimulation significantly alters NP cellular biomechanical properties and morphology [3]. While actomyosin contractility is well known to regulate cell morphology and cell stiffness, its direct role in mediating response of cells to inflammatory stimulation is unknown. In the current study, we investigate the role actomyosin contractility in mediating multiscale mechanobiology in an inflammatory microenvironment. We investigated the gain and loss of function of actomyosin contractility (i.e., effects of myosin-II inhibitor, Blebbistatin, which decreases contractility; CN03, a RhoA activator that increases contractility). We hypothesize inflammatory-induced changes to NP cell biomechanics are driven by a loss of actomyosin contractility. Therefore, increasing contractility can mitigate the degradative effects of inflammatory stimulation of the NP at the cellular and tissue levels.

METHODS: Cell Isolation: Cells were isolated from bovine NP tissue using standard enzymatic digestion and cultured in 3D culture in 1.2% alginate beads to promote round morphology. NP Explant Culture: NP explant tissue punches were isolated from bovine caudal IVDs and cultured in 24 well-plates in a swelling restricted culture system [4]. Treatment: Cells in alginate and NP explants were separately cultured in one of the following groups: (1) untreated, (2) 10ng/ml TNFα, (3) 10µg/ml Blebbistatin, (4) 1ug/ml CN03, or (5) 1ug/ml CN03 + 10ng/ml TNFα. Fluorescence Imaging: Cells were immunostained for pMLC as an indicator of actomyosin contractility, then released from alginate beads and analyzed using an Amnis ImageStream imaging flow cytometer. Cells in explants were stained for actin with Phalloidin and imaged using confocal microscopy. Cell circularity was determined from actin staining in explants. RNA Sequencing: Sequencing of RNA isolated from NP cells was performed on an Illumina NovaSeq 6000 (reference transcriptome: Bos Taurus, ARS-UCD1.2). DESeq2, was used to test for differentially expressed genes between groups. Osmotic properties: Step hyper-(333 to 466 mOsm/L NaCl) and hypo-(466 to 333mOsm/L NaCl) osmotic loads were applied to cells in a custom microfluidic chamber [3]. Volume response was observed using DIC microscopy and analyzed using multiphasic mixture theory [5] to compute hydraulic permeability (Lp) and cell radius. Atomic Force Microscopy (AFM): Force indentation curves were obtained from NP cells using an Asylum MFP-3D BIO AFM with spherical tip probes. Curves were fitted to a Hertzian model to determine cell elastic modulus. GAG Analysis: Explants were fixed, paraffin embedded, sectioned, and stained with alcian blue. Explants digests were assayed for GAG content using DMMB assay. Statistics: Data was analyzed by ANOVA with Fisher LSD post-hoc (Graphpad), $p<0.05$ significant.

RESULTS: TNFα stimulation significantly decreases pMLC staining and alters the expression of genes regulating actomyosin contractility and the cytoskeleton, as indicated by RNA sequencing analysis (Fig1). Decreasing actomyosin contractility with Blebbistatin significantly increases hydraulic permeability and cell size and decreases cell elastic modulus, similar to TNFα stimulation (Fig2). Conversely, increasing actomyosin contractility with CN03 mitigates the effects of TNFα on these same cell biomechanics (Fig2). We confirmed that TNFα increases gene expression of matrix degrading enzymes and decreases expression of ECM genes, and found that CN03 mitigates this catabolic gene expression (Fig3). We found that TNFα altered NP cell morphology in explants, significantly decreasing cell circularity (Fig4).

Increasing actomyosin contractility with CN03 mitigates catabolic effects of TNFα in explants, preventing TNFα-induced GAG loss. Moreover, decreasing actomyosin contractility with Blebbistatin mimicked the catabolic effects of TNFα on explant GAG loss (Fig5).

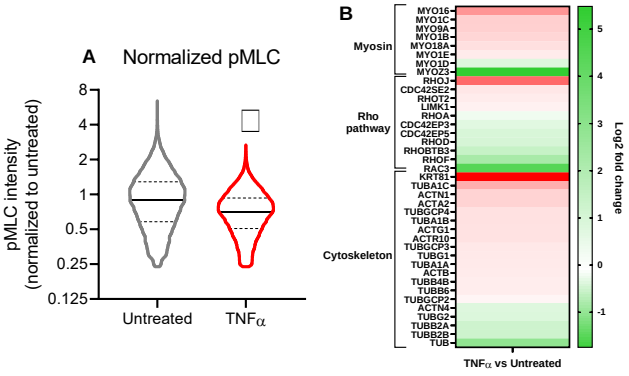

Figure 1: TNFα significantly decreases pMLC staining (A) and alters cytoskeleton gene expression (B). (*p<0.05 vs untreated).

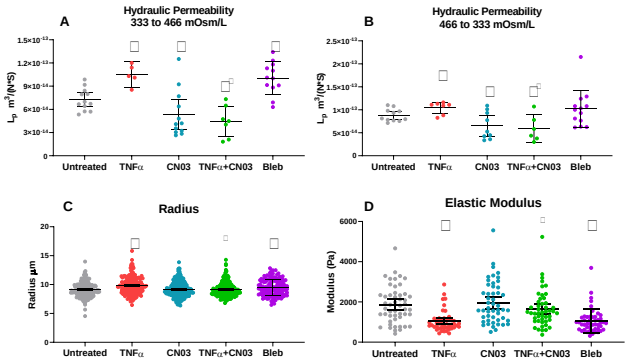

Figure 2: TNFα & Blebbistatin significantly increase cell hydraulic permeability (A,B), size (C), and decrease modulus (D)**.** CN03 mitigates effects of TNFα. (*p<0.05 vs untreated, §p<0.05 vs TNFα).

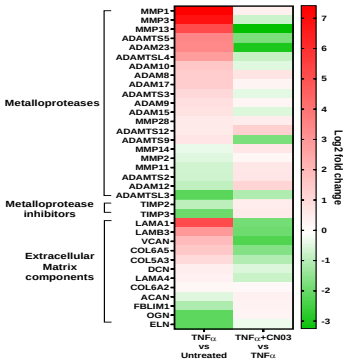

Figure 3: CN03 mitigates effect of TNFα on matrix degrading enzyme and ECM gene expression

DISCUSSION: TNFα stimulation was found to significantly disrupt NP cell mechanobiology, as indicated by altered cytoskeleton gene expression and decreased pMLC staining. Using gain and loss of function approaches, we have shown that actomyosin contractility mediates the effects of TNFα-stimulation on cell biomechanics and tissue level mechanobiology. At the cellular level, decreasing

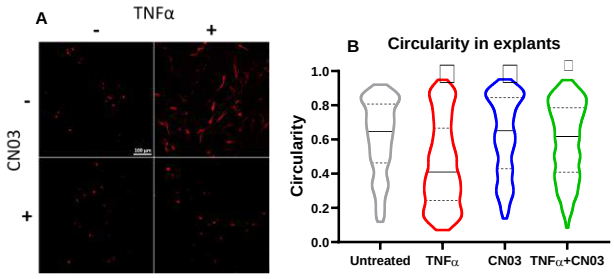

Figure 4: F-actin staining of NP cells in explants (A). Cell circularity quantification (B) . (*p<0.05 vs untreated, §p<0.05 vs TNFα).

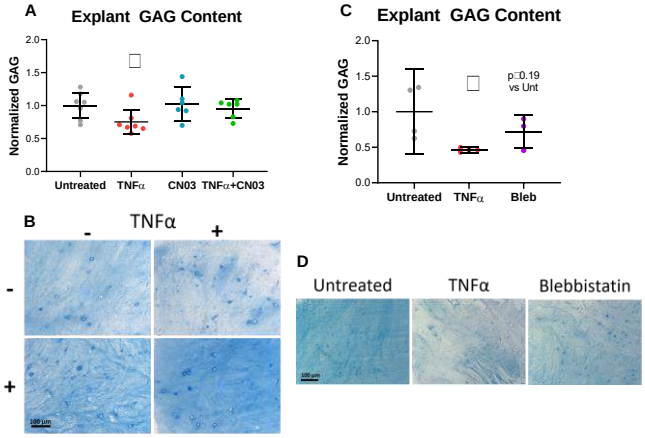

Figure 5: CN03 mitigates TNFα-induced GAG loss as determined by DMMB assay (A) or Alcian blue staining (B). Blebbistatin promotes GAG loss similar to TNFα (C, D). (*p<0.05 vs untreated).

actomyosin contractility mimicked the effects of TNFα on cell stiffness and permeability. At the tissue level, decreasing actomyosin contractility promoted NP GAG loss, similar to the effects of TNFα. We further found that increasing contractility mitigated the effects of TNFα on cell biomechanics and explant ECM, protecting against the deleterious effects of TNFα on NP cell phenotype, mitigating catabolic gene expression, NP cell polarization, and protected against TNFα-induced GAG loss. These findings suggest that cell contractility is critical in the maintenance of tissue integrity. Previously both inflammatory stimulation as well as injurious mechanical loading have independently been shown to lead to similar catabolic responses in disc cells [1,6]. Our findings suggest these responses may share common mechanisms, being mediated through cellular actomyosin contractility. Our results demonstrate that decreased actomyosin contractility mediates the response of NP cells to TNFα-stimulation at both the cellular and tissue levels and highlight actomyosin contractility as a possible point of intervention for the prevention of inflammatory induced degenerative effects in the disc.

ACKNOWLEDGEMENTS

Funded in part by NIH R01AR069668.

REFERENCES

[1] Le Maitre, C et al., *Arth Res Ther*, 7(4):R732-45, 2005.
[2] Millward-Sadler, S et al., *Arth Res Ther*, 11(3):R65, 2009.
[3] Maidhof, R et al., *PLoS ONE*, e99621, 2014.
[4] Hernandez, P et al., *Science advances*, 6(34), 2020
[5] Ateshian et al, *J Biomech*, 39:464-475, 2006.
[6] Fearing, B et al, *JOR Spine*, 1(3), 2018.

COMPARING TISSUE-ENGINEERED VASCULAR GRAFTS IN FONTAN PATIENTS TO THE STANDARD OF CARE USING COMPUTATIONAL FLUID DYNAMICS

Erica L. Schwarz (1), John Kelly (2), Kan Hor (2), Stephanie Lindsey (1), Aekaansh Verma (1), Ethan Kung (3), Jay Humphrey (4), Christopher Breuer (2), Alison L. Marsden (1)

(1) Bioengineering
Stanford University
Palo Alto, CA, USA

(2) General Pediatric Surgery
Nationwide Children's Hospital
Columbus, OH, USA

(3) Mechanical Engineering
Clemson University
Clemson, SC, USA

(4) Biomedical Engineering
Yale University
New Haven, CT, USA

INTRODUCTION

Improved biomaterials promise to reduce the morbidity and mortality associated with congenital heart disease. The common lack of homologous tissue for reconstructive surgery necessitates the use of cadaveric, xenograft, or synthetic materials.[1] These biomaterials have limited durability and particularly relevant to the pediatric population, they lack growth potential and are associated with complications.[2,3] Tissue-engineering offers an alternative to currently available biomaterials by stimulating the growth of autologous tissue for surgical use. Our group has pioneered the use of tissue-engineered vascular grafts (TEVG) in the modified extracardiac Fontan procedure for single ventricle palliation whereby the inferior vena cava is connected to the pulmonary arteries via a vascular graft. This scaffold is implanted directly, and over time, the scaffold degrades and the TEVG develops into a neovessel with the ability to grow and remodel.[4,5]

TEVGs provide several advantages over the traditional choice of material for the extracardiac Fontan procedure, poly(tetrafluoroethylene) (ePTFE). ePTFE grafts engender several known risk factors including stenosis, thrombosis, and calcification, with the additional disadvantage of lack of growth potential.[6-9] This lack of growth potential necessitates delayed insertion and oversizing to ensure long-term functionality. Delayed insertion subjects the patient to a period of progressively worsening cyanosis and hypoxia, whereas oversized grafts may affect the hemodynamic performance of the Fontan circuit until the child grows.[10-14]

Clinical application of our TEVG technology in Fontan patients has shown that these grafts can be successfully implanted without significant long-term risk of thrombosis or calcification.[4,5,12,15,16] The primary graft related complication has been stenosis, or narrowing, of the graft.[16] While the majority of patients with graft stenosis were asymptomatic and the stenosis was successfully treated with balloon angioplasty, stenosis represents a major hurdle to widespread clinical adoption of this otherwise promising technology. Understanding the natural history of TEVG remodeling within the Fontan circulation and how these changes impact hemodynamic performance is critical to the continued use of these grafts.

In this study, we provide insight into TEVG behavior *in vivo* through a detailed analysis of the U.S. clinical trial data. Using a closed-loop lumped-parameter network (CL-LPN), we show how patient-specific changes to conduit geometry and properties affect Fontan hemodynamic performance and compare TEVG, stenotic TEVG, and ePTFE performance.

METHODS

From MRI imaging data, patient-specific CFD models were created for four patients at 6 months and 3 years post-Fontan. The models were virtually modified to mimic varying degrees of stenosed geometry (stenosis defined as the percent decrease in cross-sectional area at the mid-TEVG). To compare against the current standard of care, ePTFE grafts with no growth potential, we investigated both the effects of changing the TEVG MRI compliance to match that of a ePTFE graft and virtually implanting a 16mm diameter ePTFE graft (Figure 1). These are labeled as "Rigid" and "ePTFE" respectively.

Using the flow and deformation measurements from PC-MRI data and estimated pressure outlet boundary conditions, the wall material property values were first tuned to match observed PC-MRI deformation. Then, open-loop boundary conditions were replaced with boundary conditions defined by an LPN based on work by Kung et al.[17,18] We adapted the LPN to model pediatric flows and responses to metabolic rate and further tuned the parameters to match patient-specific clinical values at each time point. In stenosis simulations, max

aortic pressure was matched to the TEVG reference geometry by scaling the total excess blood volume, as an approximation to the body's long-term response mechanism to decreased preload. Wall boundary conditions were defined via elastic moduli that were tuned to match the fractional area change observed *in vivo* over a cardiac cycle.

Patient-specific simulations were run at a youth metabolic equivalent (MET) of 1, 3, and 5 to simulate oxygen consumption states of rest, moderate exercise, and maximum exercise respectively. MET is the ratio of metabolic rate (described as VO_2) used during an activity to the basal metabolic rate (6.5 ml/kg/min in children).[19] MET 5 is a standard maximum metabolic rate found in non-TEVG Fontan children. Oxygenation metrics, systemic/venous metrics, and local hemodynamic metrics describing the *in silico* performance of each model were then calculated from the simulation data.

RESULTS

The oxygen extraction ratio (OER), mixed venous oxygen saturation (sVO2), systemic pressures, venous pressures, and cardiac index calculated from our simulations remained within normal Fontan ranges for stenosis up to 75% at MET 1. At MET 3 and MET 5, performance metrics were more sensitive to stenosis levels, but still showed physiological performance up to 75% stenosis. Energy efficiency also remained with normal ranges up to 75% stenosis. ePTFE performance was nearly identical to TEVG performance up to 25% stenosis, suggesting that even with mild narrowing TEVGs match the performance of the current standard of care (Figure 2).

To determine the risk of thrombosis and quantify the presence of blood recirculation inside the graft, we computed maximum residence time (RT), the maximum time a particle remains in the volume of interest on average, and the oscillatory shear index (OSI). Max RT and OSI were three times larger in ePTFE graft models than in TEVG reference geometries (Figure 2).

To validate our LPN simulations, we compared the velocities predicted by our simulations with the velocities measured via echocardiogram at time points between MRI scans. Each echocardiogram was paired with the simulation that closely matched its post-operative time point and estimated stenosis level. The resulting comparison to the original echocardiograms indicated good agreement between clinically-measured velocity and our simulations.

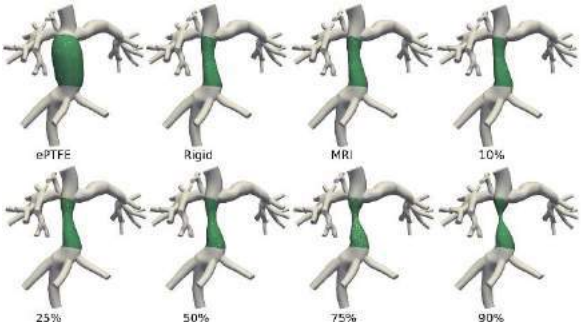

Figure 1. Example of stenosed TEVG and ePTFE models.

DISCUSSION

Our modeling-based evaluation demonstrates that Fontan physiology is robust to large changes in TEVG geometry, including the majority of the narrowing observed clinically in our patient cohort (typically less than 67%). Despite these significant anatomic changes, our models at these timepoints maintained relatively consistent hemodynamic performance metrics, remaining well within the expected physiological range for Fontan patients. The high degree of stenosis required to impact patient hemodynamic performance is in agreement with clinical observation; patients in our study were generally asymptomatic, and rarely reached the levels of stenosis predicted to significantly change performance. One patient in our study did develop stenosis approaching the critical level observed in our modeling. Patient 4 at 5 months post-operation developed stenosis measuring 72% compared to their 6 month MRI geometry or 95% stenosis compared to baseline at implantation. This patient reported symptoms of abdominal pain, in agreement with the computational threshold we identified.

Widening the conduit diameter to 16mm and applying a rigid material property to mimic ePTFE behavior had no effect on the global flow at MET 1 and had minimal impact on simulation results at MET 3 and MET 5. The most striking differences in the ePTFE graft were in OSI and RT. The 3-fold increase in max RT observed in the ePTFE graft models implies the presence of recirculation in the oversized graft that is not present in the integrated TEVG. The higher RT and OSI values also suggest increased thrombotic risk in ePTFE grafts. In particular, average residence times above two cardiac cycles in the coronary/systemic circulation have been linked to higher risks of thrombosis which regions in most of our ePTFE grafts exceed.[20]

In this study, we have confirmed several key advantages of the use of TEVGs as Fontan conduits, including growth potential and potentially reduced thromboembolic risk. We have also quantitatively shown that the primary graft related complication, graft stenosis, is well-tolerated up to most clinically observed levels. Future use of TEVGs in Fontan patients and other forms of congenital heart disease will further our understanding of how TEVGs can be used to replace traditional biomaterials and advance treatment of congenital heart disease as well as other cardiovascular conditions.

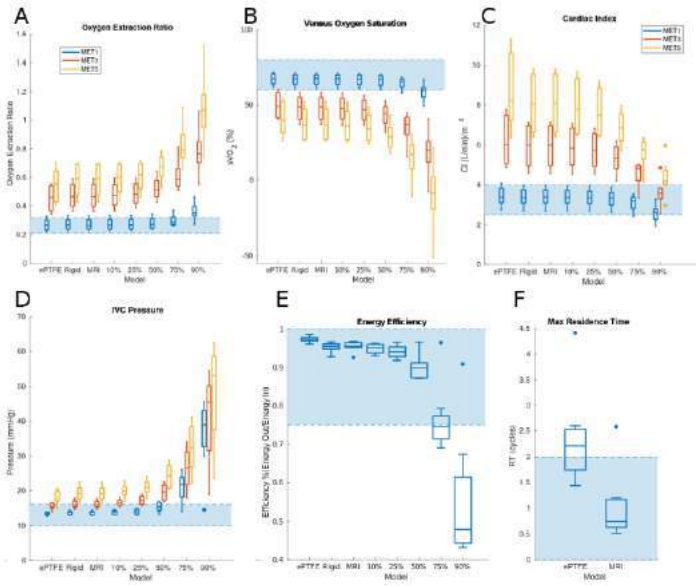

Figure 2. Overview of performance metrics measured from fluid simulations including A-B) oxygenation metrics, C) cardiac index, D) IVC pressure, E) energy efficiency, and F) residence time.

ACKNOWLEDGEMENTS

Funding sources include the NSF GRFP, the department of defence (DoD), and NIH R01HL139796.

REFERENCES

[1] J. Drews et al. *Trends Cardiovasc Med*, 27:8:521–531, 2017.
[2] J. Mayer. *Semin Thorac Cardiovasc Surg*, 7: 130–132, 1995.
[3] E. Tierney. *J Thorac Cardiovascular Surg*, 130:282–286, 2005.
[4] T. Shin'oka. *J Thorac Cardiovasc Surg*, 129:1330–1338, 2005.
[5] N. Hibino, et al. *J Thorac Cardiovasc Surg*, 139:431–436, 2010.
[6] M. Restrepo, et al. *Annals Thorac Surgery*, 97:916–922, 2014.
[7] D. J. Hagler, et al. *Congenit Heart Dis*, 14:571–581, 2019.
[8] C. Deshaies, et al. *J Am Call Cardiology*, 74:1071–1081, 2019.
[9] Y. Hayabuchi, et al. *Am Heart J*, 153:806–e1, 2007.
[10] K. Itatani, et al. *Annals Thorac Surgery*, 88:565–573, 2009.
[11] R. Kannan, et al. *J Biomed Mater Res*, 74:570–581, 2005.
[12] J. Patterson, et al. *Regenerative medicine*, 7:409–419, 2012.
[13] G. J. Gross, et al. *Am J Card*, 74: 705–709, 1994.
[14] P. Madan, et al. *Am Heart J*, 166:365–372, 2013.
[15] T. Sugiura. *Semin Thorac Cardiovasc Surg*, 30:175–179, 2018.
[16] J. Drews, et al. *Science Translational Medicine*, 537, 2020.
[17] E. Kung, et al. *J Biomed Eng*, 136: 081007, 2014.
[18] D. Schiavazzi. *J Thorac Cardiovasc Surg*, 149:689–696, 2015.
[19] N. Butte, et al. *Med Sci Sports Exerc*, 50:246, 2018.
[20] N. Gutierrez, et al. *Int J Cardiol*, 281:15–21, 2019.

COMPUTATIONAL ANALYSIS OF THE ROLE OF COLLAGEN NETWORK VISCOELASTICITY IN RAPID-STRETCH IN VITRO AXON INJURY MODELS

M. Nikpasand (1), J. M. Middendorf (2), J. Marcelin (3), B. A. Winkelstein (3), V. H. Barocas (1,2)

(1) Mechanical Engineering
University of Minnesota
Minneapolis, MN, USA

(2) Biomedical Engineering
University of Minnesota
Minneapolis, MN, USA

(3) Bioengineering
University of Pennsylvania
Philadelphia, PA, USA

INTRODUCTION

Back and neck pain can be associated with excessive strain on the axons embedded in the facet capsular ligament (FCL) [1]. This tension due to this excessive strain is believed to depend on both the magnitude and the rate of strain applied to the tissue [2,3]. The emergence of experimental models involving axons embedded in collagen gels shows a relationship between macroscale tissue strains and nociceptive pain signaling [3–6], but raises the question of how collagen viscoelasticity could affect the rate-dependent response of the system.

We have developed various computational models to analyze load transmission between a collagen gel and an axon [7,8]. In these models, the axon is embedded in a discrete network of nonlinear elastic collagen fibers. In these studies, a purely elastic version examined the effect of heterogeneity and alignment on the axonal deformation but did not address the effect of viscoelasticity and strain rate. Therefore, this study modified a discrete fiber network model to explore how strain rate applied to a fiber network affects the micromechanical environment of an embedded neuron.

METHODS

To model the fibrous environment of an innervated tissue such as the FCL, a 3D discrete fiber network model [7,8] containing a cylindrical representation of an axon embedded in a fiber network was created (Figure 1) and then stretched.

The previous model's connector elements were changed to visco-elastic truss elements to account for rate-dependent behavior of the collagen fibers. Each fiber was modeled as a Prony viscoelastic material with four time constants (2s, 20s, 200s and 2000s), to cover the broad spectrum of collagen fiber relaxation time constants. Parameters were optimized so that stress relaxation results for a $40\times40\times50\mu m^3$ fiber network (without axon) matched the PK1-stress-vs.-time behavior of uniaxial collagen gel measured in a stress relaxation experiment [9].

A 1μm diameter, 30μm long cylindrical idealization of the axon [7] was embedded within the fiber network (Figure 1). The cylinder's bottom surface was placed on the lower *xy*-plane of the network, and its axis was centered within the network. The cylinder was modeled as an elastic matrix (E=43.3MPa) reinforced by longitudinal microtubules (with spring constant of 0.94N/m) and circumferential nonlinear fibers around the perimeter.

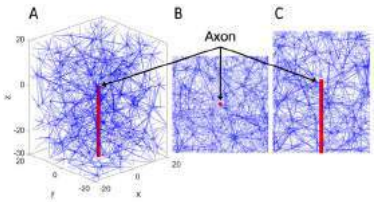

Figure 1: Image of network containing collagen fiber (blue) and axon (red). A) Isometric view. B) Top view. C) Side view.

Next, a series of displacement-controlled stretches were simulated. The network was displaced to 10% macroscopic strain at rates of 0.01 to 500%/s. The top surface of the network (normal to cylinder axis) was displaced in the z direction while the opposite side was kept fixed in all 3 directions. The lower surface of the cylinder was fixed in all directions. To allow network contraction during stretch, fibers with one node attached to the side faces of the network were made to be two orders of magnitude less stiff than the rest of the network. These nodes were free to move in the z direction. The cylinder was fixed to the network at intersections of the cylinder and the network fibers. These intersections included an additional 5 focal adhesion fibers that were half as strong as each network fiber.

Simulations were performed in Abaqus CAE standard using the Visco analysis step. The average and the top 1% maximum principal strain on the axon elements were calculated.

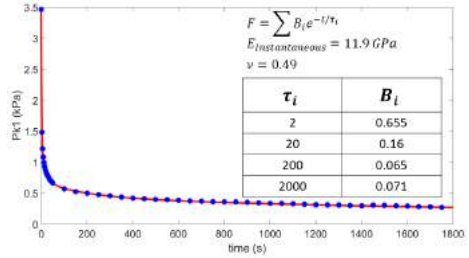

τ_i	B_i
2	0.655
20	0.16
200	0.065
2000	0.071

Figure 2: Parameter optimization by fitting the simulation (red line) to the experiment (blue dots).

RESULTS

A regression of a neuron-free viscoelastic fiber network model behavior to collagen gel stress relaxation data [9], shown in Figure 2, was used to specify the model with four relaxation times from 2 to 2000s. These parameter values were used for all subsequent simulations.

A representative deformed network and the embedded neuron shows relatively homogeneous fiber deformation with a slight bend in the axon (Figure 3A).

Axonal strain maps show heterogeneous strain fields on all axons despite differences in the applied strain rate (Figures 3B). The maximum strain is most noticeable in the zoomed-in view indicated by the red boxes in Figures 3B.

The average max principal strain and the average of top 1 % max principal strain of the axon for different strain rates during their specific stretch periods indicate differences in the rate of increase in the average axon strain (Figure 3C) and top 1% of axon strain (Figure 3D). All strain rates at or above 7% appear to increase axon strain at the same rate.
The max principal strains for all networks rise to different values then relax to similar values after long time periods (Figure 3E, 3F). Increasing the strain rate by two orders of magnitude from 0.01% to 20%/s will increase the average strain by 5%. The top 1% of strains were much more affected by this change in strain rate. The top 1% of strains increased by 15%. All strain rates allow the average max principal strain to reach an average max principal strain of approximately 0.097 after 1800sec of loading. Similarly, all strain rates allow the top 1% of max principal strains to reach approximately 0.4 after 1800sec of loading. Strain rates applied to a network will affect the observed axon strain fields.

DISCUSSION

This study used a computational method to show the effect of strain rate on the axon strain field during gel extensions. Slower strain rates are associated with smaller instantaneous max principal strains in the axon, whereas higher rates lead to higher instantaneous axon strain. These instantaneous axon strains may be important for understanding when and how long an axon will express more signaling molecules. Additionally, the instantaneous strains/stresses that an axon experiences may cause microtubule breakage or other axon damage.

There appears to be an upper threshold for the strain rate at which strain rates do not continue increasing the peak axon strain. In the context of the Prony series model, this case represents most or all of the elastic components of the fibers contributing to load transfer. There should also be a low-strain-rate plateau, corresponding to only the parallel elastic component contributing. Even at 0.01%/s the peak is still higher than the equilibrium so the rate dependency is having an effect.

As seen in Figure 3E and F, the average top 1% max principal strain is approximately 4.5 times the average max principal strain (averaged for different strain rates). This confirms the observation in Figure 3B-F that there is a local hot spot with significantly higher strain.

Incorporating viscoelasticity into a discrete fiber network model provides evidence to understand how changes in network viscoelasticity and applied network strain rate could affect the axon strain field and expression of nociceptive pain signaling molecules.

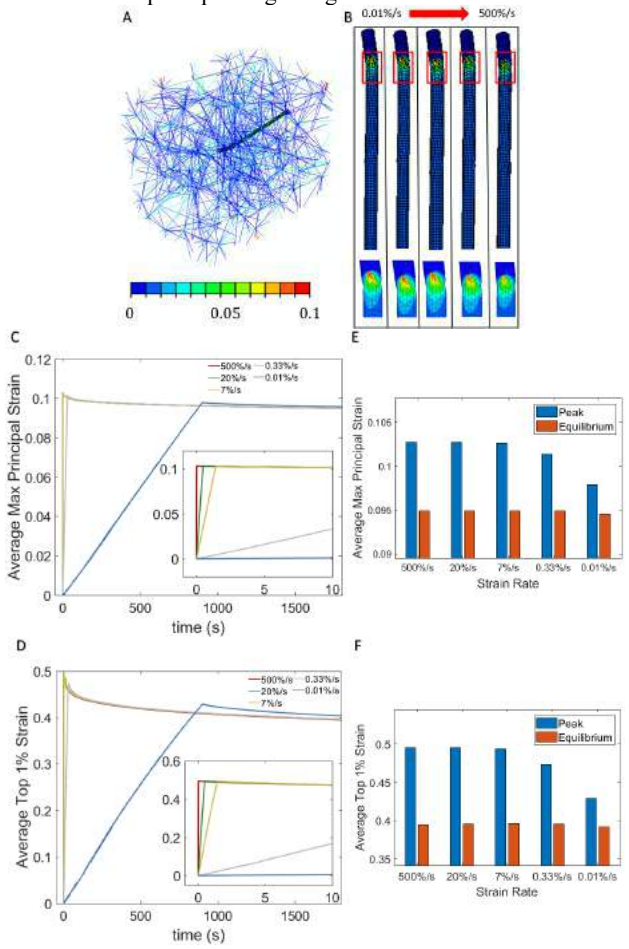

Figure 3: A) Deformed network and axon. B) Representative strain maps for 500%/s, 20%/s, 7%/s, 0.33%/s, and 0.01%/s (the lower row in B is the zoomed-in view of the red boxes). C) Average maximum principal strain and D) Average top 1% principal strain vs time for 0.01%/s to 500%/s. E) Average Max principal strain and F) Average top 1% principal strain at peak stretch and after reaching to equilibrium

ACKNOWLEDGEMENTS

Funding provided by the NIH grant U01 AT010326. We gratefully acknowledge resources and support from the Minnesota Super Computing Institute.

REFERENCES

[1] Jaumard, N. V. et al., J. Biomech. 2011.
[2] Menke, K. H. et al., J. Electromyogr. Kinesiol., 2004.
[3] Zhang, S. et al., J. Biomech., 2016.
[4] Ita, M. E. et al., J. Biomech, 2019.
[5] Dong, L. et al., Neurosci. Lett., 2008.
[6] Lee, K. E. et al., J. Biomech., 2006.
[7] Zarei, V. et al., J. R. Soc. Interface, 2017.
[8] Middendorf, J. M. et al., in preparation"
[9] Korenczuk, C. E. et al., SB3C Conf., 2015.

SLOW STRETCH MIRRIORING ACL GROWTH RATES DRIVES ZONAL LIGAMENT-TO-BONE ENTHESIS MATURATION

M. Ethan Brown (1), Jennifer L. Puetzer (1,2)

(1) Biomedical Engineering
Virginia Commonwealth University
Richmond, VA, USA

(2) Orthopaedic Surgery
Virginia Commonwealth University
Richmond, VA, USA

INTRODUCTION

The anterior cruciate ligament (ACL) is connected to bone via a structurally complex tissue known as the enthesis. Entheses are critical for mechanical function, acting to translate load from elastic ligament to stiff bone via a compliant fibrocartilage region with gradients in collagen organization and biochemical composition. Currently, these gradients are not restored in healing, repair, or engineered replacements, yielding limited repair options and high failure rates [1]. Previously, we developed a novel culture system utilizing compressive boundaries that guide ligament fibroblasts in high-density collagen to develop native-sized collagen fibers by 6 weeks [2]. Further, we demonstrated that the tensile-compressive environment at the clamp interface of this system drives early postnatal enthesis-like development by 2 weeks [3]. This system holds great promise for producing functional engineered bone-ligament-bone replacements but is currently limited by a plateau in properties by 6 weeks and long culture times. Developmental mechanical cues, such as slow elongation from growth, are necessary for enthesis maturation *in vivo*, and if not present the enthesis fails to mature [1,4]. The objective of this study was to leverage these developmental cues to investigate whether continuous slow stretch, mimicking ACL growth rate [5], could significantly improve enthesis maturation in our system. We hypothesize that the addition of slow stretch to our tensile-compressive culture system will significantly improve zonal organization, zonal composition, and mechanical properties compared to statically clamped controls, ultimately producing entheses similar to late postnatal tissue.

METHODS

Engineered constructs were made using rat tail type I collagen, extracted and reconstituted as previously described [2], and bovine ACL fibroblasts, isolated from immature bovine ACLs. Cells and collagen were mixed together prior to gelation, to yield sheet gels at 20 mg/ml collagen and 5x10^6 cells/ml. Rectangles (8 x 30 mm) were cut from the sheet gels and divided between experimental groups. Control samples were cultured statically clamped in our culture device for up to 24 days. Bioreactor samples were cultured for 14 days statically clamped in our culture device to induce early postnatal-like enthesis development [3] and then transferred to a modified CellScale tensile bioreactor and stretched for 10 days at 0.1 mm/day [5]. Constructs were cut into half samples (H.S.) or sectioned into middle (M), transition (T), and clamped (C) regions for analysis of zonal organization, composition, and mechanical properties (Fig 1A). Confocal reflectance was performed to analyze zonal collagen fiber organization. Sectioned regions were characterized for zonal composition of DNA, glycosaminoglycan (GAG), collagen content, and alkaline phosphatase (ALP) activity via PicoGreen, DMMB dye, hydroxyproline (hypro), and paranitrophenol assays, respectively, and normalized to dry weight (DW) or DNA. Mechanical testing of the middle to clamp transition was performed via tensile tests at 0.75% strain rate. All data are expressed as mean±SD. Statistical analysis was performed by 1- or 2-way ANOVA with Tukey's post-hoc ($p<0.05$ significant, $p<0.1$ trending).

RESULTS

Control and bioreactor constructs contracted similarly over 24 days, with bioreactor constructs developing a noticeably smoother transition from middle to clamp (Fig. 1A). Confocal imaging revealed samples begin as an unorganized matrix, and by 14 days in culture, constructs develop early postnatal-like zonal collagen organization with aligned parallel fibers in the mid-section, perpendicular fibers in the transition, and unorganized collagen under the clamp (data not shown). By 24 days, control constructs maintain this organization in the mid and transition section and developed a more porous organization under the clamp. Slow stretch further developed this zonal organization, with more distinct fibers in the mid-aligned section, a shift from perpendicular fibers to isotropic organization in the transition, and a porous clamped section, resembling immature ACL tissue (Fig. 1B).

By 24 days, DNA content significantly increased in the middle zone for control constructs and in the middle and transition zones for bioreactor constructs while it remained constant in clamped zones for both groups (Fig 2A). Collagen content remained steady at ~60% native tissue [2], with no significant differences in any zones for both groups (Fig 2B). GAG normalized to DNA significantly increased under the

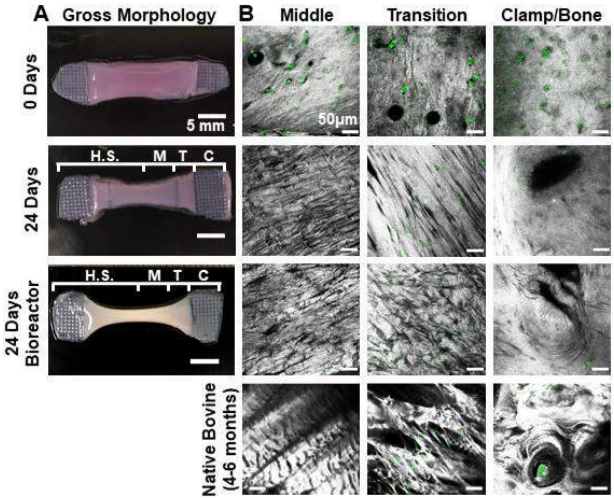

Figure 1: A) Gross morphology of constructs with sections depicted. B) Representative confocal reflectance of collagen organization. Collagen = grey, cells = green.

compressive clamp for both control and bioreactor constructs by 24 days compared to 0 day, middle, and transition zones (Fig. 2C). ALP activity remained relatively constant in control constructs with no differences between zones, whereas slow stretch resulted in zonal ALP activity, with ALP activity significantly increased under the clamp compared to the middle zone at 24 days (Fig 2D).

Continuous slow stretch significantly increased the tensile modulus across the enthesis to ~5 MPa by 24 days, while the control group remained constant at ~1 MPa throughout culture (Fig. 3A). Additionally, slow stretch significantly increased ultimate tensile strength (UTS) and the transition stress 3-fold over control constructs to 1.2 MPa and 120 kPa, respectively (Fig 3B), and led to a trending increase in toe modulus over control samples at 24 days. Slow stretch had no significant effect on the strain properties for both strain at failure and transition strain (Fig 3C).

DISCUSSION

Ten days of continuous slow stretch resulted in enhanced zonal collagen organization, zonal composition, and significantly increased mechanical properties. Both control and slow stretch constructs had significantly elevated GAG accumulation under the clamp, indicating

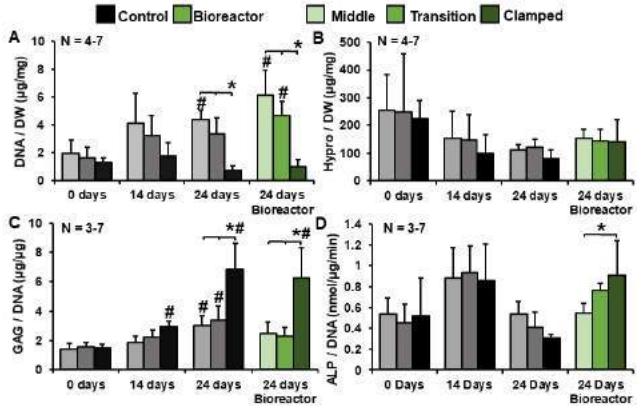

Figure 2: Zonal composition of A) DNA/DW; B) Collagen content (Hypro) /DW; C) GAG/DNA; and D) ALP/DNA for all timepoints. Significance compared to #0 week and *bracket.

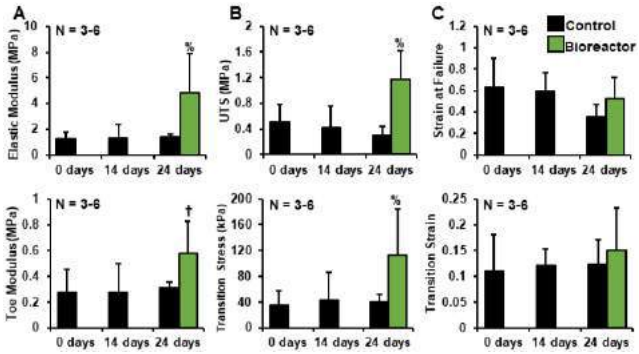

Figure 3: A) Elastic and toe moduli; B) ultimate tensile strength and stress at toe to linear region transition; and C) strain at failure and transition. %Significance compared to all values ($p<0.05$). †Trending compared to all values ($p<0.1$).

that the compressive environment under the clamp drives cells to shift to a more chondrocyte-like phenotype similar to that observed in early postnatal enthesis fibrocartilage [3,6]. This increased GAG content, combined with the increased ALP activity stimulated by slow stretch, signifies further developmental maturation, since ALP is a known marker in formation of mineralized fibrocartilage and bone [7].

Similarly, slow stretch drove significant increases in tensile properties across the enthesis, including increased elastic and toe modulus, UTS, and transition stress. The increased elastic modulus surpassed reported bovine neonatal ACL entheses moduli [1], indicating maturation beyond the neonatal stage. Since the major matrix components, mainly collagen and GAG, did not change with slow stretch, this increase in modulus is most likely attributed to the increased collagen organization in loaded constructs. This maturation in organization closely resembles postnatal development, where collagen fibers in the enthesis shift from being perpendicular to the ligament to more parallel with the ligament, while still maintaining some degree of disorder in mature tissues [8]. This diffuse fiber organization of the enthesis is critical to reducing stress concentrations and allowing for functional transfer of load [9]. Further, with just 10 days of slow stretch, mechanical properties and organization surpassed what was obtained previously with 6 weeks of static culture in our clamping device [3], demonstrating the importance of mechanical stimulation in enthesis formation. On-going work is evaluating collagen I, II, and X distribution and hierarchical organization. This study provides insight into the role that slow stretch elongation from postnatal growth plays in ligament enthesis development and creates an *in vitro* model for further exploration of the mechanical cues that drive enthesis maturation. A better understanding of the mechanical cues that drive enthesis maturation will not only help to develop functional replacements but will shed light on ways to stimulate regeneration after injury.

ACKNOWLEDGEMENTS

This work is supported by the ON Foundation and confocal analysis was performed at the Nanocharacterization Center at VCU.

REFERENCES

[1] Lu, H et al., *Annu Rev Biomed Eng*, 15:201-226, 2013. [2] Puetzer, J et al., *Biomaterials*, 2020. [3] Brown, E et al., *ORS*, 2020. [4] Schwartz, A et al., *Bone*, 55:44–51, 2013. [5] Cone, S et al., *J Bone Jt Surg*, 7(6):e8, 2019. [6] McCorry, M et al., *Stem Cell Res & Ther*, 7:1, 2016. [7] Qu, D et al., *J Orthop Res*, 35:2513-2523, 2017. [8] Wang, I et al., *J Orthop Res*, 24:1745–1755, 2006. [9] Boys, A et al., *ACS App Mat & Int*, 11(30):26559-26570.

MECHANO-REGULATION OF EMBRYONIC MENISCUS DEVELOPMENT

Tonia K. Tsinman (1), Xi Jiang (1), Saima Ahmed (2), Aurélie Levillain (2), Yuming Huang (2), Eiki Koyama (3), Niamh C. Nowlan (2), Nathaniel A. Dyment (1), Robert L. Mauck (1)

(1) Departments of Orthopaedic Surgery and Bioengineering
University of Pennsylvania
Philadelphia, PA, USA

(2) Department of Bioengineering
Imperial Collage of London
London, UK

(3) Department of Orthopaedic Biomedical Research
Children's Hospital of Philadelphia
Philadelphia, PA, USA

INTRODUCTION

The menisci and cruciate ligaments of the knee joint are key fibrous tissues whose specialized extracellular matrices (ECMs) allow for resistance to high mechanical forces during load bearing. In particular, the menisci are semi-lunar wedge-shaped structures that lie between the femur and tibia and distribute forces across the joint. The menisci have a regionally distinct ECM composition that functions to withstand both tensile and compressive loads, with the inner region being proteoglycan (PG) rich and the outer region containing circumferentially aligned collagen fibers. How these tissues establish their unique shape and composite matrix structure, however, is not well understood. It is known that menisci, along with most fibrous knee joint tissues, are formed from interzone cells specified during hindlimb embryonic development [1]. Interestingly, forces generated by limb motion influence meniscus assembly in the chick embryo, suggesting that biophysical cues may play instructive roles in fibrous tissue formation [2]. To further the understanding of mechanobiologic aspects of fibrous tissue formation, this study evaluates the spatiotemporal cellular and ECM patterning and growth of the embryonic meniscus and demonstrates that loss of muscle contraction during this developmental window significantly impacts these processes.

METHODS

Mouse models: Wildtype CD1 mouse embryos were harvested at E13.5, E15.5, E17.5, and P0. Muscle dysgenesis (*mdg)* mutants were harvested alongside littermate wild-type (WT) controls at E15.5 and E17.5. Sample preparation: Knee joints (n=3/timepoint) were harvested, fixed, cryo-embedded, and serially sectioned in the sagittal, coronal and/or transverse planes. Staining: Sections were stained using picrosirius red (collagen), alcian blue (PGs), Lamin A/C (ab133256) antibody, AF546 Phalloidin (actin), and/or DAPI (nuclei). Imaging: Confocal fluorescent microscopy was performed. Multiphoton second harmonic generation (SHG) imaging of transverse sections or explanted whole menisci was performed to visualize collagen fiber organization. Gene expression: Coronal sections at P0 (n=4 animals) were acquired and inner and outer regions were harvested using laser capture microdissection. Extracted RNA was analyzed using a Fluidigm 96.96 Gene Expression Assay for expression of 93 genes [3]. Hierarchical clustering was done with the ClustVis online tool [4]. Quantification: Z-stacks for individual nuclei were acquired (2 animals/genotype/timepoint) and nuclear aspect ratios (NARs) were calculated using Fiji (n=50 nuclei/group). Measurements were pooled per timepoint and compared via a 1-way ANOVA with Bonferroni post-hoc for Fig. 1b and a Student's T-Test for Fig. 3e ($p<0.05$ cutoff). Cell numbers (nuclei) were also counted in the meniscus body region from coronal sections (n=2-3 animals/genotype/timepoint reported).

RESULTS

Between interzone (IZ) specification (E13.5) and joint cavitation (E15.5), the actin cytoarchitecture of IZ and adjacent neocartilage (NC) cells diverged—with E15.5 IZ cells (meniscus and cruciate ligament precursors) obtaining a highly aligned, fibrillar actin cytoskeleton and NC cells adopting a rounded, cortical actin structure (**Fig. 1a**). Within this timeframe, IZ cells also developed more elongated nuclei (higher NAR) compared to NC cells (**Fig. 1b**). IZ nuclear shape change coincided with a dramatic nuclear envelope enrichment of Lamin A/C in fibrous tissue precursors compared to the surrounding NC cells (**Fig. 1c**). These observed differences in cytoarchitecture, nuclear shape, and Lamin A/C abundance persisted in E17.5 formed fibrous tissues (**Fig 1** tendon/ligament data not shown).

While IZ cells were fully patterned by E15.5, no fibrillar collagen could be detected in fibrous tissue condensates by SHG (not shown). By E17.5, however, aligned collagen fibrils percolated through the meniscus cell template (**Fig. 2a**), as well as the patellar tendon and cruciates (not shown). In the meniscus, robust fibrillar collagen matrix was observed at P0 (**Fig. 2a**) but was localized to the outer region (**Fig. 2b-left**). Conversely, the inner zone of the tissue was enriched for proteoglycans (**Fig. 2b-right**), suggesting that regional distinctions in the matrix structure and composition were present by birth. Indeed, this differential matrix accumulation was mirrored by phenotypic divergence of inner and outer cell populations, where hierarchical clustering of gene signatures of P0 cells [3] segregated the profiles based

on tissue region (red line in **Fig. 2c**).

We further analyzed meniscus development in embryos with abrogated hindlimb motion as a result of non-contractile skeletal muscle (*mdg*). Strikingly, anterior horn regions of both menisci—which anchor the tissues to the tibial plateau—failed to condense in *mdg* mutants and were completely missing by E17.5 (**Fig. 3a**). The body regions of the meniscal wedges also had significantly fewer cells (**Fig 3b**), while the posterior horns and their tibial attachments were present but greatly diminished (not shown). Interestingly, cells were correctly positioned at the sites of the patellar tendon (PT) and ACL in E15.5 *mdg* joints, with linear assembly of cells with fibrillar actin structure similar to WT (**Fig. 3c, d-top panel**). However, *mdg* PT and ACL contained cells with hyper-elongated nuclei, (**Fig. 3e**), and by E17.5, both were reduced in size in mutant mice (**Fig. 3d-bottom panel**). Unexpectedly, an ectopic fibrous tissue (**Fig. 3c-arrowhead**) also formed anterior to the cruciates within the *mdg* joint—possibly as a result of abnormal condensation.

DISCUSSION

In all, this work outlines biophysical aspects of the embryonic meniscus microenvironment that may mechano-regulate tissue development. During tissue patterning (E13.5-E15.5), IZ cells adopted an elongated nuclear morphology and fibrillar actin cytoarchitecture, which may indicate increased contractility of fibrous tissue precursors as condensation occurs (**Fig1 a, b**). The nuclear deformation (possibly due to cell tensioning) corresponded with enrichment of Lamin A/C in the nuclear envelope (**Fig. 1c**), consistent with reports of mechano-adaptative nuclear stiffening [5]. Indeed, the severe defects observed in in E15.5 meniscus condensation and cell patterning in muscle mutants indicate that these processes are sensitive to extrinsic mechanical stimuli (**Fig. 3a, b**). Importantly, the fact that anterior regions of the tissue completely failed to form, while posterior portions partially formed, indicates that biophysical and/or molecular factors may influence meniscus assembly in a region dependent manner.

Later stages of embryonic meniscus growth (E15.5-P0) were characterized by a replacement of the E15.5 cellular template with aligned collagen matrix (**Fig. 2a**). In fact, regional variation in matrix composition was apparent by P0 (**Fig. 2b**), suggesting differences in the synthetic activity of inner and outer resident cells arise during embryonic growth, consistent with the distinct gene expression signatures in cells of the two regions at P0 (**Fig. 2c**). Whether these differences are due to differential cell origin or a divergent response to evolving microenvironmental cues remains unclear.

Finally, while mechanobiologic aspects of cell patterning and matrix deposition were similar for menisci and cruciate ligaments and PT (not shown), the latter tissues were able to pattern without muscle contraction, unlike the menisci (**Fig. 3c-e**). Interestingly E15.5, resident cells of the *mdg* PT had very elongated nuclei, which may be reflective of a hyper-contractile cell state. Heightened cell-generated forces, in turn, may have caused the nascent tissues to tear themselves apart, resulting in the reduced tissue size (**Fig. 3d**) and loss of organized fibrillar matrix (not shown) observed at E17.5. Taken together, this study indicates the critical role of extrinsic forces and the local cell mechanical microenvironment in the morphogenesis of dense fibrous tissues of the joint, which may inform future repair strategies.

ACKNOWLEDGEMENTS

This work was supported by ERC Grant #336306, the NIH (R01 AR075418 and R00 AR067283) and the VA (IK6 RX003416).

REFERENCES

[1] Shwartz+, *Cell Rep,* 2016. [2] Mikic+, *J Rehab Res Dev*, 2000. [3] Tsinman+, *ORS,* 2020. [4] Metsalu+, *Nucleic Acids Res.*, 2015. [5] Swift+, *Science*, 2013.

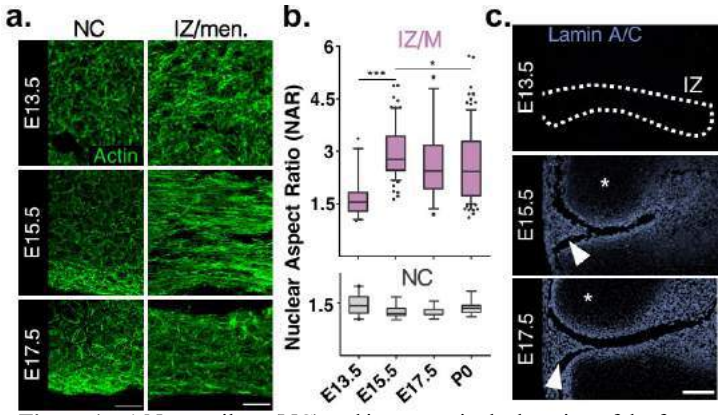

Figure 1: a) Neocartilage (NC) and interzone in the location of the future meniscus (IZ/M) at E13.5 and E15.5 and nascent cartilage and meniscus at E17.5 stained for fibrillar actin. **b)** NAR of NC and IZ/men. cells from E13.5→P0. *:p<0.05; ***:p<0.001. No statistical difference in NC NARs. **c)** Lamin A/C immunostaining showing the IZ/meniscus wedge. Enrichment in the IZ/men.(arrowhead) compared to the NC (star) is marked. SB: 20μm (a), 100 μm (b).

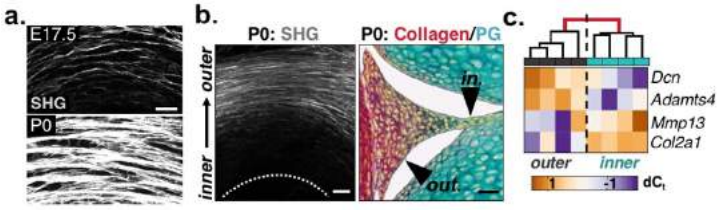

Figure 2: a) SHG of circumferential meniscus sections at E17.5 and P0. **b)** Left: SHG of dissected whole P0 meniscus. White dotted line: inner tissue boundary. Right: Meniscus wedge stained for collagen (red) and proteoglycans (PG, blue). Left and right arrowheads indicate outer and inner tissue regions. **c)** Hierarchical clustering based on delta C_t (dC_t) of 93 genes in 4 inner and 4 outer P0 meniscus samples. Black line denotes sample separation after the first clustering event. dC_t heatmap genes exhibiting differential expression by region. SB: 20μm (a), 25μm (b).

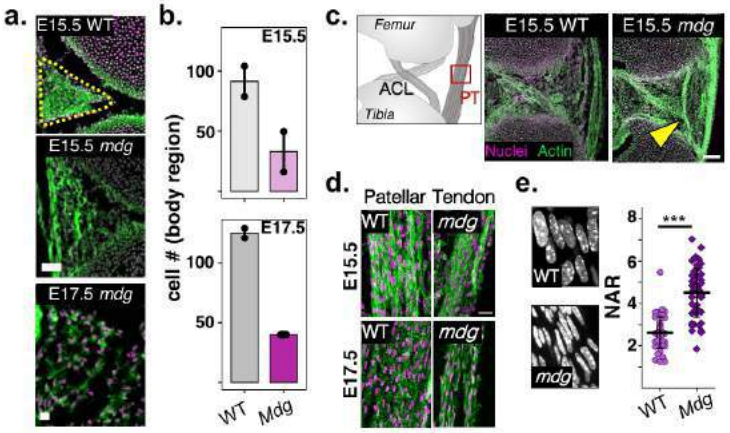

Figure 3: a) WT and *mdg* anterior meniscus region stained for actin and nuclei. Cell condensation is outlined in yellow and is missing in *mdg* samples. **b)** Resident cell number in WT and *mdg* meniscus body regions. **c)** E15.5 WT and *mdg* sections showing the patellar tendon (PT) and ACL. Yellow arrowhead denotes presence of ectopic tissue condensation not observed in WT. **d)** Actin (green) and nuclear (magenta) staining of WT and *mdg* PT tissues. **e)** Measured aspect ratios of E15.5 WT and *mdg* PT cell nuclei. SB: SB: 20μm (a,c), 100 μm (b).

CHARACTERIZATION OF THERMAL AND OPTICAL PROPERTIES OF PORCINE PANCREAS TISSUE FOR PLASMONIC PHOTOTHERMAL THERAPY

F. Akhter (1), S. Manrique-Bedoya (1), C. Moreau (2), A. L. Smith (1), K. Mayer (3), Y. Feng (1), R. L. Hood (1,4)

(1) Department of Mechanical Engineering
University of Texas at San Antonio
San Antonio, TX, US

(2) Gastroenterology & Transplant
UT Health San Antonio
San Antonio, TX, US

(3) Department of Physics & Astronomy
University of Texas at San Antonio
San Antonio, TX, US

(4) Graduate School of Biomedical Sciences
UT Health San Antonio
San Antonio, TX, US

INTRODUCTION

Pancreatic cancer is predicted to be the second leading cause of US cancer deaths by 2030[1]. Current diagnostics and treatment methods are not effective enough to improve the five year mean survival rate >10%[1]. To address this need, our group proposed to apply plasmonic photothermal therapy (PPTT), in which gold nanorods (GNRs) and laser light are used to induce localized thermal ablation in tissue[2]. Delivery of GNRs will be carried out using a fiber optic microneedle device (FMD), which provides enhanced infusion via photothermal heating[3]. The treatment will be delivered endoscopically, and the GNR-infused tumor will be visualized using 3D endoscopic ultrasound. This approach has advantages over other intratumoral therapies as GNRs can be tuned to absorb more light under near infrared (NIR) illumination (high physiological transmissivity), and bioconjugation with tumor tissue can be enhanced by surface functionalization for minimal thermal effect on surrounding healthy tissue[2]. Prior research by this group demonstrated that local photothermal heating by 1064 nm laser energy (higher absorbance by physiological tissue) enhances the volumetric dispersal of macromolecules in rodent cerebral tissue[4]. Similar effects might be evident in pancreas tissue, but this concept is still under investigation. To date, our team has characterized the FMD platform, synthesized GNRs with an absorption peak at 808 nm, developed a Multiphysics computational model to study the optical properties of GNRs, and the subsequent plasmonic heating due to light particle interaction[3, 5]. Tissue specific thermal and optical properties are required to develop the computational model for light-GNR-tissue interaction. Literature review revealed a substantial knowledge gap in the thermal and optical properties of healthy pancreas tissue that prompted many researchers to assume porcine liver properties similar to pancreas tissue[6-8]. We hypothesize that the thermal and optical properties of porcine pancreas tissue differ significantly from porcine liver tissue. Hence, the aim of this research is to investigate *ex vivo* porcine pancreas tissue to evaluate thermal conductivity and optical transmittance, reflectance, and attenuation at both 808 nm and 1064 nm wavelengths in comparison to publish porcine liver data.

METHODS

Fresh pancreas tissue samples were collected from a USDA approved abattoir. Multiple samples were harvested from different size and weight pigs (adult male) and transported to the research facility for immediate use. The method used in this study was modified from Valvano *et al.*[8]. Briefly, a hot plate technique leveraging basic concepts of heat conduction (one-dimensional) and convection was applied. The hot plate temperature was set at 40°C. Two K-type thermocouples were calibrated and maintained against a cold junction prior to the experiment. An approximately (3x3x1) cm^3 porcine pancreas tissue sample was placed on the hot plate while keeping a thermocouple in between the sample and the hot plate (Figure 1A). Another thermocouple was placed on top of the sample. A 3D printed border (high temperature resin, low thermal conductivity at 0.15 $Wm^{-1}K^{-1}$) was used to encompass the periphery of the tissue sample to limit the convection and radiation effects to the outside environment. The following equation was used to measure the thermal conductivity (K) while assuming that at steady state the amount of heat conducted through the thickness of the tissue (1D) is equivalent to the amount of convection at the top surface[9]:

$$K = h * x * \frac{(T_{top} - T_{room})}{(T_{bottom} - T_{top})} \quad (1)$$

Here, h is the convection heat transfer coefficient, x is the tissue thickness (1 cm), and T is the temperature (at top/bottom of the tissue and room). To validate the measurement of h, a control experiment was

conducted using a similar setup with a silicone polymer (Sylgard® 184 elastomer) with known thermal conductivity (0.27 $Wm^{-1}K^{-1}$). Results from this test indicated h was 15 $Wm^{-2}K^{-1}$ at 22°C room temperature. This experiment was replicated with 17 different pancreas tissue samples (n=17).

Tissue optical properties were measured by using two laser sources (808 nm and 1064 nm CW collimated beam) and an integrating sphere for detecting optical power (Figure 1B). Thin sliced tissue samples (thickness 1-8 mm) were placed in between two glass slides. A 3D printed fixture was employed to maintain a consistent gap between the glass slides and to prevent excess force on the tissue sample. The incident laser was aligned vertically with the integrating sphere for the transmittance measurement. Samples were placed on top of the integrating sphere and the output laser power was measured over a range of input powers (0-500 mW). A negative control experiment was first conducted by conducting the experiment with glass slides only (sans tissue sample). The distance between the laser source and the tissue samples (12 mm), as well as the laser intensity (5 mW/mm^2), were maintained consistently for both lasers. The experiment was replicated 18 times for each tissue thickness.

Light reflectance measurement was conducted with similar setup except the integrating sphere was placed in between the laser source and the tissue sample so that the reflected beam from the tissue would be captured by the sphere. First the setup was calibrated against a reflectance standard and the test was repeated 5 times for each sample thickness (thickness 2-4 mm).

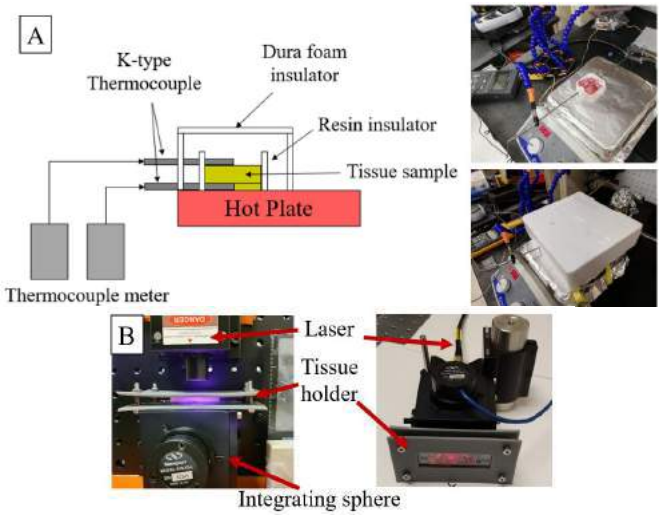

Figure 1: Experimental setup for (A) thermal conductivity measurement, (B) Transmittance and reflectance measurement

RESULTS

Figure 2A exhibits the results of thermal conductivity measurement. Applying Chauvenet's criterion, 3 outliers were eliminated which resulted in an average thermal conductivity of 0.454±0.08 $Wm^{-1}K^{-1}$. Figure 2B shows the exponential decay of light transmittance with respect to the tissue thickness. Applying curve fitting tool, two equations were obtained for both 1064 nm and 808 nm lasers. If the attenuation coefficient is independent of tissue thickness (mean free path of photon propagation inside tissue is constant), then Beer-lambert's can be compared with these equations. Attenuation coefficients (μ) for 1064 nm and 808 nm wavelength were measured as 0.073 mm^{-1} and 0.498 mm^{-1} respectively. Light reflectance measurements were corrected by deducting the reflectance of glass slide and resulted in an average of 0.23±0.05 for 2-4 mm thick tissue samples.

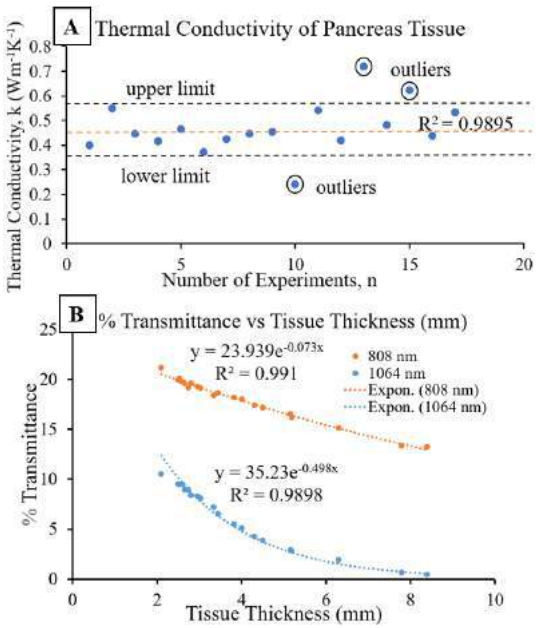

Figure 2: (A) Thermal conductivity, (B) Light transmittance of porcine pancreas tissue

DISCUSSION

The measured thermal conductivity of porcine pancreas tissue was lower than the porcine liver tissue (0.542 $Wm^{-1}K^{-1}$)[7, 8]. The following assumptions were applied that may affect results: only 1D heat conduction was considered, lateral heat convection was omitted due to the use of a boundary insulator, and slight variations in tissue thickness were not considered, among others implicit with the models employed. Light transmission and reflection tests were affected by the variation of physiological properties of the frozen tissue samples. Light transmittance for 808 nm wavelength was found higher than the 1064 nm and thinner tissue samples showed more exponential rise of light transmittance for both wavelengths. This was expected from literature values[2, 10]. Light reflectance measurement could be fine-tuned by using fresh tissue samples with varieties of thickness. In summary, the study hypothesis was verified as both the thermal and optical properties observed in this study were significantly different from the porcine liver tissue as reported in the literature[7, 11]. This is a critical finding with impactful implications for future computational studies and surgical planning around pancreas tissue. Next steps include replicating this study in human tissue, both healthy and malignant.

ACKNOWLEDGEMENTS

The funding support from University of Texas at San Antonio is highly appreciated.

REFERENCES

[1] Rahib, L. et al., *Cancer Res*, 74(11), pp. 2913-2921, 2014
[2] Huang, X., *Lasers in medical science*, 23(3), p. 217, 2008
[3] Akhter, F., *J Mech Behavior of Biomed Materials,* 112, 104042, 2020
[4] Hood, R. L. et al., *Lasers Surg Med*, 45(3), pp. 167-174, 2013
[5] Manrique-Bedoya, S., *J Physical Chemistry,* C 124(31), 17172-17182, 2020
[6] Saccomandi, P., *Lasers in med science*, 31(6), 1041-1050, 2016
[7] Saccomandi, P., *IEEE Trans Biomed Eng,* 59.10: 2958-2964, 2012
[8] Valvano, J. W., *ASME. J Biomech Eng.,* 106(3): 192–197, 1984
[9] Bergman, T. L., *Fund. of Heat & Mass Transfer 7th editon,* 2011
[10] Nussbaum, E. L., *Physiotherapy Canada*, 59(3), 194-207, 2007
[11] Ritz, J. P., *Lasers in Surg. and Med*., 29(3), 205-212, 2001

THE STRUCTURE-FUNCTION RELATIONSHIPS OF THE HUMAN VERTEBRAL ENDPLATE

Yuanqiao Wu (1), Elise F. Morgan (1,2,3)

(1) Department of Mechanical Engineering, Boston University, Boston, MA, USA

(2) Center for Multiscale and Translational Mechanobiology, Boston University, Boston, MA, USA

(3) Department of Biomedical Engineering, Boston University, Boston, MA, USA

INTRODUCTION

The vertebral endplate (VEP), a thin, porous layer of bone tissue between the vertebral centrum and intervertebral disc, has gained increasing attention because of its high relevance in the development of vertebral fractures [1] and other age-related problems, such as disc degeneration [2]. The VEP plays a crucial role in maintaining the structural and mechanical integrity of vertebral body [3,4] and undergoes age-related changes in structure [5] that are not well correlated with those in the rest of the vertebra [6]. VEP mechanical behavior also influences the load distribution within the disc. Study of its structure-function relationships is therefore necessary to understand the development, treatment, and prevention of spinal conditions.

Scant data exist on the mechanical behavior of the VEP. Indentation tests at the microscale suggest that the elastic modulus of the VEP tissue is similar to that of trabecular tissue [7]. Larger-scale (~2-3mm) indentation tests have indicated associations between strength and density [8,9]. Although useful, these studies have not addressed the mechanical behavior of the VEP for the larger length scales and loading conditions that are also relevant to vertebral fracture. Moreover, although vertebral fractures more commonly occur in the superior endplate region [10], whether this arises from differences in mechanical properties of the superior vs. inferior VEP is unknown. Thus, the overall goal of this study is to quantify the mechanical behavior of the VEP in flexion and its association with density and mineral content.

METHODS

Rectangular specimens (n=80; ~30mm×12mm×1.5mm) of VEP were machined from the lumbar central endplates (L1-L4) of fresh-frozen spines (24 males, 15 females; mean ± std age: 77.72 ± 6.50 yrs). Care was taken to remove the cartilage endplate. After using micro-computed tomography (μCT) (μCT40, Scanco Medical; 16μm/voxel, 70kV, 114μA; threshold=510 mg HA/ccm) to quantify bone volume fraction (BV/TV), apparent density (ρ_{app}), and tissue mineral density (TMD), each specimen underwent a four-point bend test (outer span=16 mm; Instron 5565; Canton, MA). Linear elastic beam theory was used to calculate the apparent modulus (E) and lower apparent yield stress ($\sigma_{y,l}$). The latter was measured at the initial yield point. The elasto-plastic beam theory was used to calculate the upper apparent yield stress ($\sigma_{y,u}$), which corresponded to the "fully plastic" point [11]):

$$E = \frac{L^2 \times k}{12 \times I} \quad (1)$$

$$\sigma_{y,l} = \frac{M_l \times h}{2 \times I} \quad (2)$$

$$\sigma_{y,u} = \frac{4 \times M_u}{b \times h^2} \quad (3)$$

In equations (1)-(3), L, b, h and I are the length, width, thickness and moment of inertia of the outer span, k is the maximum slope of the moment-displacement curve, M_l and M_u are the moment at initial yield and ultimate point, respectively. The tissue-level yield stresses corresponding to these upper and lower points were calculated in a similar manner but by using the binarized μCT images, rather than the bulk dimensions of the specimen, to calculate the section modulus [12]. Ultimate strain (ε_u, strain at M_u) and fracture strain (ε_f, strain at which there was both an audible cracking noise and a sharp drop in moment) were calculated from a video recording of each test. After mechanical testing, specimens underwent a sequence of washing, defatting, weighing, drying, and ashing (650 ºC for 16 hours) steps to measure tissue density (ρ_{tissue}), ash fraction (p), and ash density (ρ_{ash}).

Following log transformation where appropriate, linear regression (JMP, SAS Institute) was used to examine the dependence of the

mechanical properties on density and mineral content, and also on age. Multiple regression was used to test for dependence of modulus and strength on both BV/TV and ash fraction [13]. Pearson correlation analysis was used to examine associations between mechanical properties. These statistical analyses were performed separately for specimens from superior (S) vs. inferior (I) VEPs (defined relative to the vertebral body), to avoid having the presence of multiple VEPs from each donor violate the assumption of independence in the regression and correlation analyses. Properties were also compared between superior and inferior VEPs using paired *t*-tests.

RESULTS

Many of the elastic and failure properties were dependent on BV/TV and ρ_{app}. The apparent modulus (S: r^2=0.52, p<0.001. I: r^2=0.51, p<0.001) and both lower (S: r^2=0.43, p<0.001. I: r^2=0.49, p<0.001) and upper (S: r^2=0.44, p<0.001. I: r^2=0.49, p<0.001) yield stresses increased with increasing ρ_{app} (Figure 1). Similar results were found for the dependence of these properties on BV/TV (r^2>0.41, p<0.001). In contrast, none of these three mechanical properties, nor the tissue yield stress, depended on TMD, tissue density, or ash density (r^2<0.09, p>0.16). Adding ash fraction to the regression of apparent modulus and strength against BV/TV moderately improved the fit for the upper yield stress of inferior VEPs (r^2 increased to 0.63, p=0.02) but not for modulus or lower yield stress (p>0.09). The ultimate and fracture strains of inferior VEPs decreased with increasing BV/TV (r^2>0.29, p<0.05) and ρ_{app} (r^2>0.31, p<0.05), while no such dependence was observed for superior VEPs (r^2<0.28, p>0.05).

Correlations were observed between the apparent modulus and many of the failure properties. Apparent modulus was positively correlated with both lower (S: r=0.93, p<0.01. I: r=0.97, p<0.01) and upper (S: r=0.93, p<0.01. I: r=0.98, p<0.01) yield stresses (Figure 2A). In contrast, apparent modulus was negatively correlated with fracture strain for the inferior VEPs (r=-0.67, p=0.02) (Figure 2B).

Superior and inferior VEPs differed from each other in structure but not mechanical properties. When compared across a disc, *e.g.*, inferior L3 vs. superior L4, the inferior VEPs had higher ρ_{app} (p=0.02) and BV/TV (p=0.01). However, when compared within a vertebra, *e.g.*, inferior L3 vs. superior L3, no differences were found (p>0.09).

DISCUSSION

In light of the central role of the VEP in spinal conditions such as vertebral fracture, the goal of this study was to quantify the mechanical behavior of the VEP and its association with density and mineral content. BV/TV and ρ_{app} were each found to be good predictors of the apparent-level elastic and failure behavior of the VEP. With increasing BV/TV and ρ_{app}, VEP specimens were stiffer, stronger, and less ductile. Notably, these structure-function relationships did not extend down to the tissue-level: the tissue yield stress did not depend on TMD, tissue density or ash density, and these three density measures also were not predictive of the apparent modulus or strength.

These results suggest new possibilities for non-invasive assessment of vertebral fracture. Non-invasive estimates of bone stiffness and strength from density measurements is well established, but thus far this approach has not been applied in a data-driven manner for the vertebral endplate. Prior work has shown that the density of the endplate region is poorly correlated with the average density of the vertebral body, particularly in women [6]. Our data suggest that measurement of VEP density can be useful for a more accurate estimate of the mechanical behavior of this biomechanically critical structure and, perhaps by extension, the mechanisms of vertebral fracture.

Our findings also raise new questions. First, although clinical data show that vertebral fractures more frequently affect the superior region of the vertebra [10], we found no difference in mechanical behavior between superior and inferior VEPs. It is possible that a larger sample size is needed to discern differences that may exist or that other factors, such as asymmetry in the shape of the vertebral body, disc loading, or properties of the underlying trabecular bone, contribute to the asymmetry in fracture location. Second, comparison of the VEP data to those for trabecular bone from the vertebral centrum (Figure 2A) suggest that these two tissues, although anatomically adjacent, are mechanically distinct. One reason for the differences seen in Figure 2A may be loading mode, as flexural moduli tend to be lower than compressive and tensile moduli. However, our values of tissue density (mean±std=1.51±0.11g/ccm) and ash fraction (0.60±0.09) in the VEP are lower than those reported in vertebral trabecular bone (1.79±0.04 g/ccm and 0.61±0.02, respectively), and unlike prior reports of correlations between ash fraction and bone stiffness and strength [15], we found no such association for the VEP. Hence, the findings of this study suggest the intriguing possibility that the composition and mechanical behavior of the VEP are different from the rest of the vertebra. Further study of this tissue can lead to better understanding of spine health.

ACKNOWLEDGEMENTS

NIH R01-AR054620, Boston University Micro-Computed Tomography Imaging Core (NIH S10 RR021072)

REFERENCES

[1] Jiang G et al., *Osteoporos Int*, *15*, 887-96, 2004. [2] Wang Y et al., Bone, 48, 804-9, 2011. [3] Benneker, LM et al., *Spine*, 30, 167-73, 2005. [4] Oxland TR et al., Spine, 28, 771-7, 2003. [5] Rodriguez AG et al., *J Orthop Res*, 30, 280-7, 2011 [6] McKay M et al., *Bone*, 131,115-147, 2020. [7] Dall'Ara, E et al., J Mech Behav Biomed Mater, 25, 23-32, 2013. [8] Grant, JP et al., *J Orthop Res*, 20, 1115-20, 2002. [9] Liu, J et al., *J Biomech*, 49, 586-593, 2016. [10] Zhao F-D et al., Bone, 44, 372-9, 2008. [11] Gere et al., *Mechanics of Materials*, 504-10. Seventh edition. [12] Morgan, EF et al., *Bone*, 44, 335-44, 2009. [13] Hernandez CJ et al., *Bone*, 29, 74-78, 2001. [14] Morgan EF et al., *J Biomech*, 569-77, 2001. [15] Keller KS, *J Biomech*, 27,1159-68,1994.

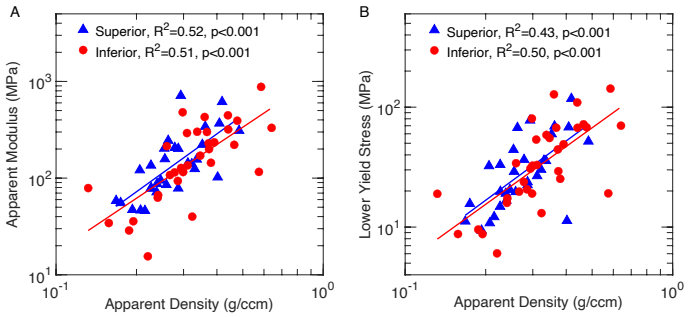

Figure 1. (A) Apparent modulus and (B) yield stress increased with increasing apparent density (shown here is the lower yield stress).

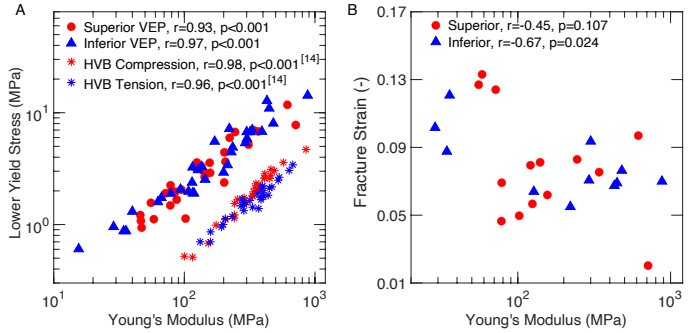

Figure 2. (A) Apparent modulus was highly correlated with yield stress, though in a manner offset to that seen for vertebral trabecular bone (HVB) [14]. (B) In the inferior VEPs, fracture strain was negatively correlated with apparent modulus.

SIMULATION OF CRYOBALLOON ABLATION FOR PULMONARY VEIN ISOLATION

Tejas Patel (1), Tong Gao (1,2), Lik-Chuan Lee (1)

(1) Department of Mechanical Engineering, Michigan State University, East Lansing, Michigan, United States

(2) Department of Computational Mathematics, Science and Engineering, Michigan State University, East Lansing, Michigan, United States

INTRODUCTION

Cryoballoon ablation (CBA) is becoming a promising alternative to radiofrequency (RF) ablation to isolate the pulmonary vein (PV) as a treatment of atrial fibrillation (AF). In CBA, the targeted PV is occluded by inflation of a balloon catheter, and a refrigerant is then sprayed into the balloon to locally freeze the cardiac tissue to create a lesion. Compared to RF ablation, CBA can significantly reduce the treatment time. The effectiveness and safety of CBA, however, depend on multiple factors, such as the cooling rate, leakages, minimal temperature and isotherm distribution. Experimental and a few numerical studies [1,2,3], have been undertaken to investigate CBA. Analysis of tissue damage in CBA [1] have shown that a tissue temperature of -20°C maintained for at least 60s is necessary for creating a lesion in the tissue. If the temperature is held below -40°C, however, the required freeze time for a lesion to form is nearly insignificant because of direct cell damage. In addition, the presence of leakages from the PV ostium may necessitate lower balloon temperatures and unduly increase hold times.

Given these issues, there is a need to investigate factors affecting the temperature (and flow) field in the area surrounding the PV ostium, which may help optimize the treatment. As such, the goal here is to develop a computational modeling framework to investigate blood flow and temperature field during cryoablation. Specifically, we seek to investigate how the presence of a cryoballoon affects hemodynamics in the left atrium (LA) and PV ostium, and how in presence of leakage during PV occlusion affects temperature distribution in the PV.

METHODS

Hemodynamics is simulated in a patient specific 3D model of the LA (including the PV) [4] using the finite element method (FEM). The strong form of the problem's governing equations in non-dimensional form are given as follows:

$$\frac{\partial \boldsymbol{u}}{\partial t} + \boldsymbol{u} \cdot \nabla \boldsymbol{u} = \nabla \cdot \boldsymbol{\sigma} + \boldsymbol{f} \tag{1}$$

$$\nabla \cdot \boldsymbol{u} = \boldsymbol{0} \tag{2}$$

$$\frac{\partial T}{\partial t} + \boldsymbol{u} \cdot \nabla T = \frac{1}{Pe} \Delta T \tag{3}$$

In the above equations, $\boldsymbol{u}$ is the velocity field and T is the temperature field. Blood that is assumed to behave as a Newtonian fluid with stress $\boldsymbol{\sigma}(\boldsymbol{u}, p) = -p\boldsymbol{I} + \frac{2}{Re}\boldsymbol{D}(\boldsymbol{u})$, where $\boldsymbol{D}(\boldsymbol{u}) = \frac{1}{2}(\nabla \boldsymbol{u} + (\nabla \boldsymbol{u})^T)$ is the strain rate tensor. Based on the physical properties of blood, the following dimensionless control parameters are introduced in the problem, namely, Reynold's number $Re = \frac{V_{sc}\, L_{sc}}{\upsilon} = 1047$ and Prandtl number $Pr = \frac{\upsilon}{\alpha} = 27$. The diameter and velocity at the left-superior PV inlet are taken as the characteristic length and velocity scale, respectively. Laminar flow is assumed in the problem.

A closer look at the control parameters reveals that temperature transport is advection dominated, especially in Eq. (3) when the Peclet number is high (i.e., $Pe = Re \cdot Pr \approx 10^4$). Numerical stability to capture sharp spatial gradients at such high *Re* and *Pe* flows is achieved by applying streamline-upwinding (SUPG) and crosswind stabilization schemes to the weak form of the governing equations. Also, apart from Incremental Pressure Correction (IPCS) for velocity-pressure coupling, the following discretization schemes are employed: forward Euler for inertia, two-step explicit Adams-Bashforth for the convection term and Crank-Nicolson velocity for the viscous term. The resultant time-

discretized weak form of the governing equations (with $\boldsymbol{v}$ and w as test functions) is given below:

$$\int_{\Omega} \frac{\boldsymbol{u}^* - \boldsymbol{u}^n}{\Delta t} \cdot \boldsymbol{v} \cdot dx + \int_{\Omega} \frac{1}{2}(3\boldsymbol{u}^n \cdot \nabla \boldsymbol{u}^n - \boldsymbol{u}^{n-1} \cdot \nabla \boldsymbol{u}^{n-1}) \cdot \boldsymbol{v} \cdot dx + \int_{\Omega} \left[-p^n \boldsymbol{I} + \frac{\frac{1}{2}(\boldsymbol{D}^* + \boldsymbol{D}^n)}{2Re}\right] : \nabla \boldsymbol{v} \cdot dx + \int_{\Omega} \tau^1{}_{SUPG} \cdot P(\boldsymbol{u^n}, \boldsymbol{v}) \cdot R_1(\boldsymbol{u}) \cdot dx + \int_{\Omega} (\tau^1{}_{CW} \cdot Q(\boldsymbol{u^n}, \boldsymbol{u})) : \nabla v = 0 \quad (4)$$

$$\int_{\Omega} \frac{T - T^n}{\Delta t} \cdot w \cdot dx + \int_{\Omega} \frac{1}{2}(3\boldsymbol{u} \cdot \nabla T^n - \boldsymbol{u}^n \cdot \nabla T^{n-1}) \cdot w \cdot dx + \int_{\Omega} \left[\frac{\nabla T + \nabla T^n}{2Pe}\right] \cdot \nabla w \cdot dx + \int_{\Omega} \tau^3{}_{SUPG} \cdot P(\boldsymbol{u}, w) \cdot R_3(T) \cdot dx + \int_{\Omega} (\tau^3{}_{CW} \cdot Q(\boldsymbol{u}, T)) : \nabla w = 0 \quad (5)$$

where $\boldsymbol{u}^*$ $(\boldsymbol{u})$ is the intermediate (final) velocity, $P(\boldsymbol{a}, \boldsymbol{b}) = \boldsymbol{a} \cdot \nabla \boldsymbol{b}$ and $Q(\boldsymbol{a}, \boldsymbol{b}) = \boldsymbol{M}(\boldsymbol{a}) \cdot \nabla \boldsymbol{b}$ are the SUPG and crosswind stabilizing operators, $\boldsymbol{M} = \begin{Bmatrix} \boldsymbol{I} - \frac{\boldsymbol{a} \otimes \boldsymbol{a}}{|\boldsymbol{a}|^2} & if\ \boldsymbol{a} \neq \boldsymbol{0} \\ \boldsymbol{0} & if\ \boldsymbol{a} = \boldsymbol{0} \end{Bmatrix}$, and $R, \tau_{SUPG}, \tau_{CW}$[5,6] are the residuals and constants for SUPG and crosswind stabilization respectively.

Taylor hood element is used for spatial discretization of the velocity and pressure fields, while quadratic element is used for discretizing the temperature field. The problem is solved using the open-source FE library FEniCS. Simulations were performed on a patient specific LA geometry (model dimensions [4] are given in Table 1) with a spherical cryoballoon of diameter 23 mm occluding the right-inferior PV inlet (Fig 1). PV isolation was simulated by applying a temperature of -70°C on the cryoballoon. Patient specific PV flow rate measurements [7] (at a heart rate of 63 bpm) was imposed as boundary conditions in the model. Blood temperature was set at 37°C as the initial condition. The problem is solved for 10 heart cycles on an FE mesh consisting of 124238 nodes with a Courant number < 0.15.

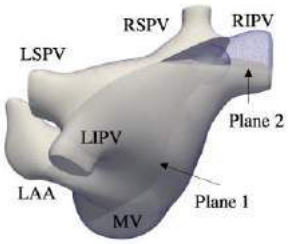

Figure 1: A schematic of the patient specific LA with cryoballoon at the RIPV, mesh and two cross-sections.

Table 1: Areas and diameters of PV's extracted from MRI data

	LSPV	LIPV	RSPV	RIPV
Area (mm^2)	322.5	209.9	188.35	437.6
Av. Dia. (mm)	20.26	16.34	15.48	23.6

RESULTS

Figure 2 shows the velocity and temperature isotherms surrounding the cryoballoon at two different sections of the LA. There is a considerable blood leakage on one side as compared to the other due to the position of the cryoballoon (Fig. 2b). On the side with leakage (with a distance 3.76 mm between the balloon and LA wall), blood accelerates past the cryoballoon, which results in substantial heat convection. As a result, temperature at the wall remains close to 37°C and it is unlikely for lesion to form at the LA wall. We also note that vortices are shed downstream and transported further into the LA on the side with leakage due to the pulsating flow through the PV. However, on the side where the cryoballoon is close to the LA wall (at a distance 0.6 mm), the local wall temperature falls below -20/-40°C, which is below the threshold at which lesion forms.

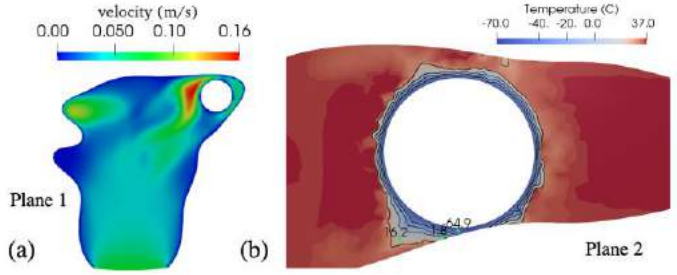

Figure 2: (a) Velocity contours on Plane 1. (b) Temperature isotherms on Plane 2 after 10 heart cycles, four different isotherms correspond to -40, -20, 0, 27 ^{0}C.

DISCUSSION

Here, we have developed a novel computational framework to simulate cryoablation for PV isolation. We show that the LA wall temperature (and effectiveness of PV isolation) is sensitive to the leakage at the PV ostium. Correspondingly, there is a minimum threshold for the distance between the cryoballoon and the LA wall to create a lesion for isolating the PV. Our results suggest that the threshold distance may depend on other factors such as balloon temperature and PV and mitral flow velocity. The developed computer framework may be useful for understanding and optimizing the cryoablation treatment to determine the conditions (e.g., maximum leakage that is permissible) at which lesions will form. Moreover, the framework may be useful for determining the conditions that will avoid phrenic nerve injury (one of the major challenges of CBA) while attaining complete occlusion of the right PV's. There are some limitations associated with this study. First, heat conduction of the LA wall was not taken into account, which may help further reduce the wall temperature. Second, motion of the LA wall is not considered here.

ACKNOWLEDGEMENTS

We acknowledge National Science Foundation grant no. 1702987.

REFERENCES

[1] Yuantong, X. et al., *Appl. Ther. Eng.*, 142: 524-529, 2018.
[2] Getman, M.K. et al., *J. Cardiovas. Electr.*, 30(11): 2274-2282, 2019.
[3] Müssig, R., Hörth, J., *Curr. Dir. Biomed. Eng.*, 4(1): 473-475, 2018.
[4] Fastl T.E., et al. *Medical Image Analysis* 47: 180-190, 2018.
[5] Codina, R., *Comput. Methods Appl. Mech. Eng.*,110: 325-342, 1993.
[6] Volker, J., Knobloch P., *Programs and Algorithms of Numerical Mathematics*, 122-136, 2006.
[7] Lantz, J., et al. *Annals of Biomedical Engineering*, 47(2): 413-424, 2019

SB³C2021
Summer Biomechanics, Bioengineering and Biotransport Conference
June 14-18, Virtual

COMPARATIVE COMPUTATIONAL ANALYSIS OF PASCAL AND MITRACLIP IMPLANTATION IN A PATIENT-SPECIFIC LEFT-HEART MODEL

R. Errthum, A. Caballero, W. Sun

Tissue Mechanics Lab
Georgia Institute of Technology and Emory University
Atlanta, GA, USA

INTRODUCTION

Around 2.5% of the U.S. population is living with a heart valve disease (HVD) [1]. The most common HVD is mitral regurgitation (MR). It is prevalent in 1.7% of the U.S. population and rises to 9.3% prevalence in individuals over the age of 75 [1]. MR is caused by a dysfunctional mitral valve (MV), which is the valve that separates and controls blood flow between the left atrium (LA) and left ventricle (LV). In MR, the MV does not close tightly during LV systole (contraction), which allows retrograde blood flow from the LV into the LA. This may cause death, fatigue, shortness of breath, and other symptoms. There are two types of MR, degenerative MR (DMR), which is caused by intrinsic destruction of the MV tissues, and functional MR (FMR), which is caused by improper LV function and geometry. Most patients living with MR are not candidates for open-heart surgery due to comorbidities. Furthermore, patients with untreated DMR or FMR have a poor prognosis.

Within the last decade, minimally-invasive transcatheter MV repair (TMVRep) devices have been developed. These devices are implanted in the MV and coapt the two MV leaflets, which are the anterior mitral leaflet (AML) and posterior mitral leaflet (PML). The leaflet coaptation mimics the Alfieri Stitch surgical procedure and results in a valve with multiple orifices. The most widely used TMVRep device is the MitraClip (Abbott Vascular) [2]. This device received CE mark in 2008, FDA approval in 2013 for DMR treatment, and FDA approval in 2019 for FMR treatment. The 2019 FMR approval occurred after the COAPT clinical trial showed there was a significant reduction in all-cause mortality and hospitalization for patients treated with MitraClip compared to a control group [3]. However, the results of a separate concurrent trial (MITRA-FR) indicated MitraClip did not improve FMR prognosis [4]. These conflicting results likely stem from patient selection, degree of MR, and surgeon experience [5].

A novel TMVRep device, PASCAL (Edwards Lifesciences), received CE mark in 2019 and has ongoing clinical trails to earn FDA approval for DMR and FMR treatment. Similar to MitraClip, PASCAL mimics the Alfieri Stitch. However, PASCAL has unique design features including a central spacer, broad and curved paddles, a larger size, and a shape-retaining material. These features are designed to plug the regurgitant orifice and decrease the stresses in the MV leaflets. Given the opposing clinical trial results for MitraClip and the short clinical history for PASCAL, a greater understanding of the human host to device interaction and a direct biomechanical comparison between the two devices is needed. To do this, computational simulations will be used to simulate MitraClip and PASCAL implantation in a patient-specific left-heart model. Post-repair cardiac dynamics will be quantified and compared between the two devices.

METHODS

Left-Heart (LH) Model: A patient-specific computational model of a de-identified patient that was diagnosed with FMR was constructed from multi-slice computed tomography (MSCT) images (with IRB approval). The model includes the MV and subvalvular structures, LA, LV, aortic valve, and aortic root. The model was developed and validated using the methods explained in the literature [6].

Material Models: The material properties for the LH structures were obtained by applying hyperelastic models to the mechanical testing data of an age- and gender-matched cadaver heart.

Implant Models: The MitraClip was modeled using methods described in the literature [7]. The PASCAL was modeled by importing and appropriately scaling the images shown in Fig. 1 into Solidworks and using the images as a reference to create a 3-D computer model.

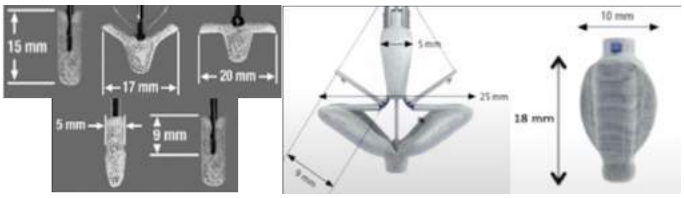

Figure 1: Design of MitraClip (left) and PASCAL (right)

Finite-Element (FE) Simulation: The MV closure dynamics were simulated using methods from the literature [8] and validated by comparing the FE leaflet geometry outputs to systolic CT MV images. In the implantation simulations for both devices, the clips/paddles were opened, positioned in the MV, and closed on the leaflets during systole. After device closure, rough (no separation) contact was applied between the device and leaflets. Systolic and diastolic pressures were applied to the leaflets to simulate post-TMVRep cardiac dynamics. Each device was implanted in a central and lateral MV location, and the max principal stress results from the AML and PML were output during peak systole and compared across devices and implant locations. Elements nearest the mitral annulus (MA) and the highest 1% of peak stress values were ignored to avoid boundary effects and eliminate bias due to local extreme stress-concentration, respectively [9].

RESULTS

The stress results of the FE simulations are shown in Table 1. MitraClip results from the literature were referenced [7].

Table 1: Summary of leaflet stress results

		Pre-TMVR	Central		Lateral	
			MitraClip	PASCAL	MitraClip	PASCAL
AML peak stress	Value (kPa)	564.2	611.0	530.5	924.1	467.7
	Change (%)	0.0	8.3	-6.0	63.8	-17.1
AML average stress	Value (kPa)	112.7	122.5	79.2	167.6	88.5
	Change (%)	0.0	8.7	-29.7	48.7	-21.5
PML peak stress	Value (kPa)	716.9	1163.3	391.4	800.3	736.8
	Change (%)	0.0	62.3	-45.4	11.6	2.8
PML average stress	Value (kPa)	61.2	89.5	39.0	79.1	57.5
	Change (%)	0.0	46.3	-36.3	29.2	-6.0

For the central implant location, the peak and average stress in the AML increased by 8% and 9% post-MitraClip repair, respectively, while that of the PASCAL decreased by 6% and 30%. The peak and average PML stresses had respective increases of 62% and 46% post-MitraClip repair, whereas the corresponding results after PASCAL implantation were a decrease of 45% and 36%, respectively. The lateral results showed similar trends. The peak and average stresses for the AML and PML increased by 64%, 49%, 12%, and 29%, respectively, after MitraClip implantation. In post-PASCAL repair, the peak and average stresses for the AML decreased by 17% and 21%, respectively, and the peak and average stresses for the PML increased by 3% and decreased by 6%, respectively. For both devices, average stresses were higher in both MV leaflets for the lateral location compared to the central location, except for the PML in post-MitraClip repair.

The maximum principal stress distribution in the MV leaflets for post-PASCAL repair is shown in Fig. 2. The implant location site is highlighted in red and the detailed view (top center) shows the stresses surrounding the region of contact between the implant and leaflets. Some elements in the contact region experienced compressive stresses. Additionally, stress concentration is present near the contact region. The stress concentration is reduced compared to the MitraClip, and in general, the PASCAL and MitraClip stress distributions are similar [7].

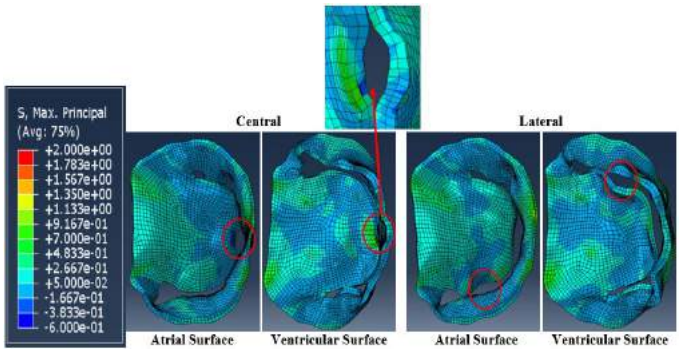

Figure 2: Post-PASCAL repair, distribution of maximum principal stress (MPa) in MV leaflets

DISCUSSION

The results indicate the PASCAL outperforms the MitraClip in terms of limiting/decreasing leaflet stresses. While implantation of the MitraClip results in an increase of peak and average stresses in both MV leaflets, implantation of the PASCAL reduces the leaflet stresses. This is likely due to the central spacer feature of the PASCAL. Since the spacer fills the regurgitant orifice, the PASCAL does not have to pull the MV leaflets as far as the MitraClip in order to coapt the leaflets. Additionally, the PASCAL's contoured paddles and larger size seem to reduce the stress concentration seen at the contact region. With a larger and smoother contact area, the force applied on the leaflets from the paddles is distributed over a larger area which results in a reduction of stress. Furthermore, the MitraClip is a rigid device that locks closed, whereas the PASCAL is made of nitinol, which is a hyperelastic, shape-retaining material. After implantation occurs, the nitinol material allows the paddles to undergo subtle opening and closing motions. As the geometries of the MV leaflets change due to changes in pressure throughout the cardiac cycle, the slight motion of the paddles accommodates the leaflet geometry and limits the stress concentrations.

This study has the limitations of only studying one patient-specific LH model, and the implantation simulations were not validated with clinical data. Future work may include simulating the clip procedure in more patient models, as well as quantifying and comparing other pertinent parameters for characterizing MR reduction such as the regurgitant orifice area and MR hemodynamics. This study shows PASCAL is a viable treatment option for MR. The PASCAL may reduce MR more effectively than the MitraClip, and the information from this study may aid clinical decision-making regarding MR.

ACKNOWLEDGEMENTS

We would like to thank PACE at GT for their computing resources.

REFERENCES

[1] Nkomo, VT et al., *Lancet*, 368:1005-1011, 2006.
[2] Mauri, L et al., *J Am Coll Cardiol*., 62(4):317-328, 2013.
[3] Stone, GW et al,. *N Engl J Med*., 379:2307-2318, 2018.
[4] Feldman, T et al., *N Engl J Med*., 364:1395-1406, 2011.
[5] Goldberg, SL, *Cardiovasc Revascularizat Med,* 20(6):528-529, 2019.
[6] Caballero, A et al., *J. R. Soc. Interf.,* 16:20190355, 2019.
[7] Kong, F et al, *Journal of Biomechanics*, 104:109730. 2020.
[8] Pham, T et al., *Cardiovasc Eng Tech*, 8:3–16, 2017.
[9] Auricchio, F et al., *Med. Eng. Phys.*, 33(3):281–289. 2011.

EFFECT OF ARTERIAL WALL INCLUSIONS ON FAILURE MECHANICS OF INTRACRANIAL ANERUYSM TISSUE

Ronald N. Fortunato (1), Anne M. Robertson (1,2,3), Chao Sang (1), Spandan Maiti (1,2,3,4)

(1) Department of Mechanical Engineering and Materials science
University of Pittsburgh
Pittsburgh, PA, USA

(2) Department of Bioengineering
University of Pittsburgh
Pittsburgh, PA, USA

(3) McGowan Institute for Regenerative Medicine, University of Pittsburgh
And UPMC
Pittsburgh, PA, USA

(4) Department of Chemical and Petroleum Engineering
University of Pittsburgh
Pittsburgh, PA, USA

INTRODUCTION

Intracranial aneurysms (IA), the pathological enlargement of the cerebral arterial wall, and present in about 3.2% of the adult population [1]. Spontaneous rupture of an IA is fatal for approximately 45% of patients, while 50% of the survivors suffer from disabilities that prevent them from returning to work [2, 3]. Currently, it is difficult for clinicians to confidently select aggressive and somewhat risky treatments that can exceed the risks associated with an IA rupture which occurs at an average rate of 1.1% per year [4, 5]. Thus, there is a pressing need for improved evidence-based methods to stratify the aneurysms at a higher risk of rupture and avoid unnecessary risky treatment in others.

As IA rupture is ultimately mediated by structural failure of the aneurysm wall, understanding of structure-failure property relationships for the wall tissue has the potential to reveal mechanisms leading to the loss of IA biomechanical integrity. Indeed, aneurysmal wall structure anomalies such as remodeled collagen architecture, inflammation, and the presence of lipid pools or calcified regions within the wall tissue have been variously implicated as wall-weakening mechanisms leading to the IA rupture. Our group recently reported that wall calcification is more prevalent in human IA wall tissue than previously believed [6]. We also found that physical environment around the calcification is altered compared to the native tissue. For example, calcification could exist within or separate from lipid pools in the wall [6]. Additionally, we found that for ruptured aneurysms, the calcification was never co-localized with lipid pools, suggesting the structural milieu around the calcification is of importance.

In the present work, we computationally investigated the multifactorial nature of IA rupture to understand how the calcification and its surrounding wall tissue environment influence the rupture risk. We hypothesized that the material composition of the Near-Calcification Region (NCR) of the IA wall tissue influences the mechanical stress distribution within the tissue, and thus impacts the overall failure behavior of the calcified IA tissue.

METHODS

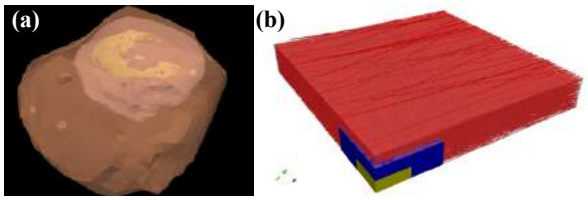

Figure 1. (a) Segmentation of MicroCT data of cerebral aneurysm tissue (orange) with macro-calcification (yellow) embedded in lipid pool (grey) and (b) parametric solid model designed to reproduce cerebral aneurysm tissue with macro-calcification embedded in a lipid pool while limiting the effect of boundary conditions during loading. The computational domain exploits problem symmetry.

We have performed finite element-based stress analysis for a model geometry of the tissue specimen including a central disk-shaped calcified region surrounded by an NCR, see Figure 1. The simplified geometry was chosen to remove the effect of local surface topology of the calcification on the ensuing stress field so that insights gained from the parametric study are general in nature. The diameter of the calcification was motivated from the size of a human aneurysm calcification. The convergence criterion was taken as the change in peak stress, measured from the stress-stretch curve, to be less than 5% between successive mesh refinements. We utilized a recently developed fiber-embedded finite element method, details of which can be found in our previous publications [7, 8]. Briefly, this method models the fibrous soft tissue microstructure as a network of discrete 1D rod elements

embedded within the 3D continuum at the sub-tissue level, while the biaxial testing procedure was simulated at the specimen level by upscaling the information gathered at the lower length scale.

Material parameters, such as matrix and fiber stiffness, for the tissue were regressed from uniaxial experiments on aneurysm tissue with similar dimensions. Other material properties, such as organization and density of the fiber network were motivated by multi-photon imaging of the same tissue using a previously established protocol for aneurysm tissue [9-11] . The calcification properties were taken from literature [12, 13]. Finally, the shear modulus of the NCR was varied parametrically and used to define the shear moduli ratio (SR) of the NCR to tissue matrix ($\frac{\mu_{NCR}}{\mu_{matrix}}$). The range of the SR ratio (0.01-1000) was motivated by published mechanical properties describing soft lipid pools, μ_{NCR}=0.1-1 kPa, to stiff calcification [12, 13].

RESULTS

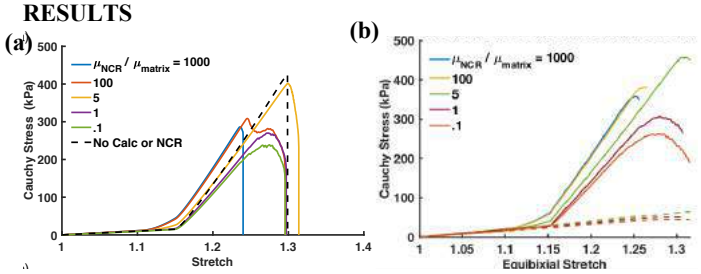

Figure 2. (a) Cauchy stress versus uniaxial stretch curves for an in-situ parametric study of the effect of NCR stiffness relative to the tissue matrix stiffness. For reference a case in which no inclusion was included and displayed as black-dashed line. (b) Cauchy stress versus equibiaxial stretch curves for the same parametric study of NCR stiffness. Solid lines represent circumferential response while dashed lines are corresponding longitudinal responses

Uniaxial stress-stretch curves for the stiffness ratio varying from SR = 0.1 to 1000 are presented in Figure 2 (a). For reference, we also simulated a specimen with without any calcified or NCR. As expected from the rule of mixtures, incorporation of higher modulus NCR resulted in a steady increase in the pre-failure slope of these curves. Peak stress for all cases of NCR stiffness were lower than the "control" tissue, revealing adverse effects of the calcification and NCR on the tissue failure properties. Also, the peak stress varied non-monotonically with the increase in SR. In comparison to the uniaxial case, Figure 2(b), illustrates under equibiaxial stretch the same pattern can be observed in the non-monotonic relationship between SR and peak stress. Also, peak stresses are consistently higher in equibiaxial stress cases. We observed an inversely proportional relationship between the biaxial loading ratio (B) and peak stress. Namely we noticed for all cases of SR, peak stress and stretch at peak stress reduced as B increased from 0.5 to 2.

Stress distribution in the collagen fibers and the non-collagenous matrix of the tissue and NCR before the peak of the stress-stretch curve for SR = 0.1,1,5, and 1000 under equibiaxial stretch is shown in Figure 3. For SR ≤ 5, the fiber stress concentration appears in the vicinity of the NCR orthogonal to the loading axis. For the SR=1000 case shown in Figure 3, the fiber stress concentration can be observed along the loading direction. Subsequently, the tear initiated and propagated from the stress concentration zone observed pre-peak. These stress concentrations and tear patterns were consistent between uniaxial and equibiaxial loading as well as in other loading scenarios B=0.5 and B=2.

DISCUSSION

In the current study, we demonstrated that while the presence of the calcified region elevates the mechanical stress in its vicinity, mechanical properties of the NCR determine how that high stress is propagated and distributed to the rest of the tissue. Our simulations revealed that softer NCR properties, SR≤ 1, allowed for large deformation of the NCR and shielded stress around the NCR along the loading direction but creating high concentrations at the poles of the NCR orthogonal to the loading direction. These highly localized fiber stresses created local micro-tears that propagated at a lower applied stretch, resulting in a low peak of the specimen stress-stretch curve. In contrast, the NCR with shear modulus higher than the tissue matrix (SR>1) distributed the stress to a greater volume of the tissue and failed a higher peak stress.

Our study has the following limitations. In our tissue microstructure model, some of the collagen fibers abruptly ended at the edge of the NCR, while microscopic observations have shown that collagen fibers may also skirt around calcifications. We anticipate that incorporation of such fiber structure will introduce additional stress propagation paths in the vicinity of the calcification. We are currently working on this improvement, but in its current state this study illustrates the role of the calcification and NCR on the IA tissue failure properties contributing to a better understanding of the IA rupture process and assessing rupture risk.

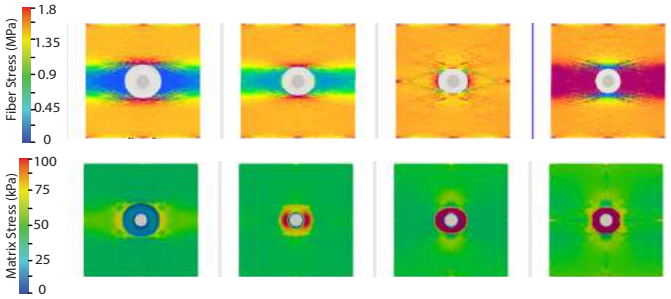

Figure 3. Distribution of collagen fiber nominal stress (top) and non-collagenous matrix Cauchy stress (bottom) before peak stress for four different cases of SR: 0.1, 1 5, 1000 under equibiaxial loading conditions.

ACKNOWLEDGEMENTS

Research reported in this work was supported by the National Institutes of Health under award number 1R01-NS097457-01 and 5T32HL076124-12.

REFERENCES

[1] M. H. M. Vlak *et al.*, *The Lancet Neurology,* 10:626-36, 2011.
[2] P. J. Kelly *et al.*, *Stroke,* 32:530-4, 2001.
[3] A. H. Ropper *et al.,* 60:909, 1984.
[4] S. Juvela *et al.*, *Stroke,* 44:2414-21, 2013.
[5] D. O. Wiebers, *The Lancet,* 362:103-10, 2003.
[6] P. S. Gade *et al.*, *Arterioscler Thromb Vasc Biol,* 39:2157-67, 2019.
[7] J. R. Thunes *et al.*, *J Biomech,* 49:1562-69, 2016.
[8] J. R. Thunes *et al.*, *J Biomech,* 71:84-93, 2018.
[9] C. Sang *et al.*, *J Biomech Eng,* 140:6061010--1--061010--10, 2018.
[10] A. M. Robertson *et al.*, *Ann Biomed Eng,* 43:1502-15, 2015.
[11] M. R. Hill *et al.*, *J Biomech,* 45:762-71, 2012.
[12] L. Cardoso *et al.*, *J Biomech,* 47:870-7, 2014.
[13] A. Ferrara *et al.*, *Comput Methods Biomech Biomed Engin,* 11:553-67, 2008.

THE EFFECT OF HEMATOCRIT ON THE THICKNESS AND ASYMMETRY OF THE CELL-FREE LAYER IN ARTERIAL BIFURCATIONS

S. Roychowdhury (1), P. Balogh (1), A. Randles (1)

(1) Dept. of Biomedical Engineering
Duke University
Durham, NC, USA

INTRODUCTION

In the microcirculation, the migration of red blood cells (RBCs) towards the center of vessels leads to the formation of an RBC core and a cell-free layer (CFL) near vessel walls. This separation directly influences physiological processes such as tissue oxygenation and vasodilation and contraction. Previous works have extensively studied how the CFL develops in microvascular networks both *in vivo* and *in silico* [1-3], noting how geometric characteristics of the CFL such as thickness and asymmetry are linked to changes in downstream cell distributions at branching vessels. Arterial bifurcations disrupt the CFL profile, and the downstream recovery in terms of CFL size and asymmetry can play a crucial role on CFL behavior in a succeeding bifurcation. Although experimental [4] and numerical [5] works have explored the recovery of CFL symmetry downstream of a bifurcation, the role of varying hematocrit (Hct) on CFL recovery has yet to be fully explored.

In this work, we use a 3D computational approach to study the CFL development downstream of bifurcations at two possible hematocrit levels: 15% and 30%. The use of numerical methods allows for the focus on a specific parameter to determine its effect on the quantities of interest while minimizing the effect of other factors. We sample the size of the CFL and its asymmetry in a single-branching bifurcation along several points in the daughter branch to determine where these two quantities to stabilize. Studying the recovery of CFL thickness and asymmetry and comparing across various levels of hematocrit is the first step to linking their effects to CFL development down further branching vessels.

METHODS

To numerically probe the effect of varying hematocrit while holding other hemodynamic parameters constant, we employ the use of HARVEY, a massively parallel computational fluid dynamics solver [6]. The lattice Boltzmann method is used to model the flow of RBCs suspended in plasma, which is treated as a Newtonian fluid. A finite element model is used for the cells and these are coupled via the immersed boundary method.

Fluid and cell simulations. The lattice Boltzmann method is procedure to numerically solve the Navier-Stokes equations; the fluid is treated as a set of discrete particles moving at nodes on a regularly spaced lattice. The probability of particles residing at lattice point $\boldsymbol{x}$ and time t with a discrete velocity $\boldsymbol{c_i}$ is designated by the particle distribution function $f_i(\boldsymbol{x} + \boldsymbol{c_i})$. For a fluid with an external force field, the lattice Boltzmann equation which governs the evolution of these particles is

$$f_i(x + c_i, t + 1) = \left(1 - \frac{1}{\tau}\right) f_i(x,t) + \frac{1}{\tau} f_i^{eq}(x,t) + F_i(x,t) \quad (1)$$

for an external force distribution F_i, equilibrium distribution f_i^{eq}, and relaxation time τ.

RBCs are modeled as biconcave discs with zero-thickness triangulated mesh. The membrane forces are calculated using a finite element model which also includes elasticity and bending stiffness. The Skalak constitutive law governs the shear and dilational elastic responses of the mesh [7].

CFL thickness and asymmetry calculations. To show the development of the average thickness of the CFL and its asymmetry, we present data averaged over time. For each simulation, cell vertices are saved every 10,000 timesteps. For calculations at a radial slice in the vessel, all of the cell vertices laterally located within 5 μm are returned and flattened on the axial plane. Eight wall points are generated along the surface of the vessel. For each wall point, the nearest cell vertex is

identified and a straight-line distance δ from that cell vertex to the wall is stored. To obtain the CFL thickness, this δ is averaged across all of the wall points, while asymmetry is calculated as $\delta_{max}/\delta_{min}$. An example of low and high asymmetry is shown in Figure 1.

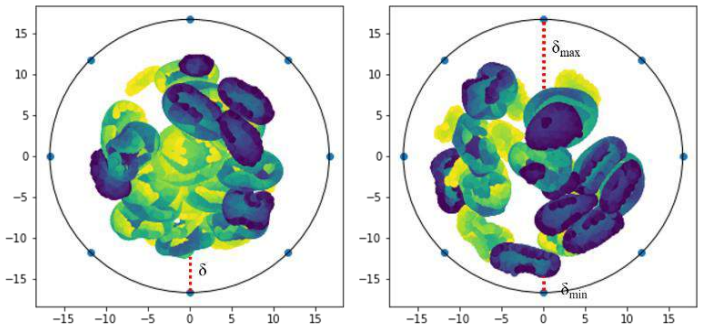

Figure 1: CFL and asymmetry calculations at an instantaneous timepoint in a 2D slice. An example of a low and high asymmetry slice is shown on the left and right, respectively. Recovery of the CFL can be quantitively measured by the CFL thickness and asymmetry reaching a steady state.

RESULTS

Model comparison. Two sets of simulations are performed in straight vessels at diameters of 10 and 20 μm at 15% hematocrit. An external force is generated to match the plasma velocities in a similar computational setup in [8]. Simulations are run with periodic boundary conditions until a relatively steady CFL size is reached. The CFL thickness is calculated to be 2.3 μm and 4.2 μm respectively, in good agreement with the results from [8], where values of 2.4 and 4.3 μm, respectively, were reported.

Single bifurcating channel. A bifurcation geometry is generated using PTC Creo with a daughter arm length of 500 μm. The parent and daughter branch diameters are 40 μm and 33.33 μm, determined from Horton's law to maintain a diameter reduction consistent with that observed in physiology. An input velocity of 8 mm/s is used to generate the flow and initialized with 15% and 30% hematocrit. The average CFL size and its asymmetry are calculated at every 50 μm along the length of the daughter branch; slices are marked in Figure 2a. The time average CFL thickness and asymmetry at each of these slices are presented as a function of distance from the bifurcation in Figure 3.

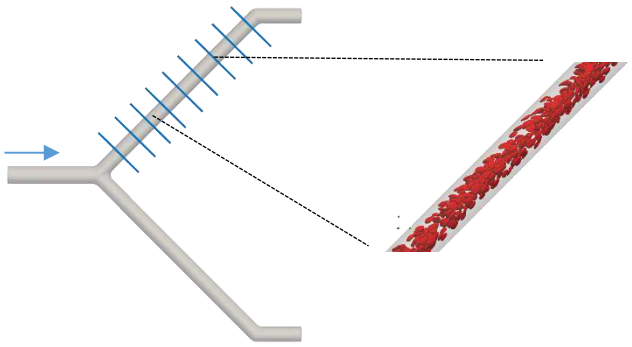

Figure 2: Single bifurcating channel with sample slices taken every 50 μm. CFL thickness and asymmetry are calculated at each slice and averaged over time.

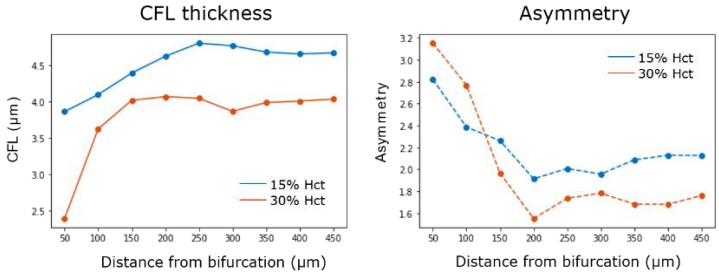

Figure 3: CFL (left) and asymmetry (right) in the daughter branch vs distance from bifurcation. These quantities reach a steady state approximately 250 microns along the vessel.

DISCUSSION

In the single bifurcation simulations, we find that the time average CFL size increases as a function of distance from the bifurcation for both the 15% and 30% hematocrit cases until stabilization. The 15% Hct takes longer to reach a steady CFL thickness at around 250 μm, whereas the 30% maintains its value starting around 150 μm from the bifurcation, shown in Figure 3a. As expected, the lower Hct case has a higher CFL across the board; since there are fewer cells, there will be an increased distance between the RBC core and the vessel wall.

Both Hct cases see a significant drop in asymmetry compared to the beginning of the daughter arm; since the bifurcation changes the motion of flow, we would expect to find a high asymmetry near the beginning of the daughter branch, shown in Figure 3b. Both stabilize roughly 200 to 250 μm into the channel, although the asymmetry of the lower Hct case remains higher; this could be due to the motion of stray RBCs away from the core which results in a lower δ_{min}, which in turn gives a higher asymmetry. There is also a slight rise in asymmetry at both 15% and 30% Hct towards the end of the daughter vessel, which could be influenced by the curve at the end of the channel.

These single bifurcation simulations show that the CFL thickness and skew of RBC distribution stabilizes around halfway through the vessel. The CFL size for the higher Hct equalizes slightly earlier. The lower Hct case stabilizes at a higher CFL thickness and asymmetry than the higher Hct run. Future work can utilize this knowledge to simulate multi-branching vessels and explore the effect of a recovered and non-recovered CFL on further downstream branches.

ACKNOWLEDGEMENTS

Research reported in this publication was supported by the Office of The Director, National Institutes Of Health of the National Institutes of Health under Award Number 1U01CA253511-01. The content is solely the responsibility of the authors and does not necessarily represent the official views of the National Institutes of Health. This work was also supported by NSF award 1943036.

REFERENCES

[1] Balogh, P., & Bagchi, P. *J. Fluid Mech., 864*, 768-806. 2019.
[2] Kim S. *Biorheology. 46I*, 181-189. 2009.
[3] Ong A., et al. *J. Physiol. Heart Circ. Physiol. 298*, 1870-1878. 2010.
[4] Pries A.R., et al. *Microvasc. Res., 38*. 81-101. 1989.
[5] Ye, S. et al. *Microvascular Research, 106*, 14-23. 2016.
[6] Randles, A. et al. *IPDPS* '13. *IEEE CS*, 1063–1074. 2013.
[7] Gounley, J. et al. *Proc. Comp. Sci., 108*. 175-184. 2017.
[8] Fedosov D., et al. *Microcirculation. 17(8).* 615-628. 2010.

FGF-10-MEDIATED BUCKLING MORPHOGENESIS OF THE EMBRYONIC AIRWAY EPITHELIUM

Kara E. Peak (1), Victor D. Varner (1)

(1) Department of Bioengineering
The University of Texas at Dallas
Richardson, TX, USA

INTRODUCTION

Ramified networks form the basic architecture for many organs in the body including the lung, kidney, and salivary gland. In the embryonic lung, these structures are formed via a process known as branching morphogenesis. The lung primordium originates as an out-pocketing of foregut endoderm, which undergoes a series of recursive branching events to build the bronchial tree [1]. This process is regulated by a complex network of signaling pathways, but fibroblast growth factor (FGF) signaling has emerged as a crucial regulator of airway branching. New epithelial branches are thought to arise next to focal regions of FGF-10 expression in the pulmonary mesenchyme, but it is unclear how FGF-10 signaling drives the macroscopic changes in tissue form that shape emerging branches. Here, we used FGF-10-loaded beads to create ectopic sources of FGF-10 to stimulate the formation of supernumerary branches in cultured embryonic lungs. *Ex vivo* organ culture experiments were combined with quantitative fluorescence microscopy, pharmacological modulation of luminal fluid pressure, and computational modeling to determine how cellular behaviors downstream of FGF-10 work in concert with exogenous mechanical forces to sculpt the embryonic airway epithelium.

METHODS

Fertilized White Leghorn chicken eggs were incubated at 37 °C to Hamburger and Hamilton (HH) stage 26. Embryonic lungs were dissected in phosphate-buffered saline (PBS). Small agarose beads, soaked in either PBS or 100 μg/ml FGF-10 in PBS for 2-3 hr at room temperature, were then implanted into the pulmonary mesenchyme along regions of the airway epithelium that normally remain unbranched. The explants were then cultured on Nucleopore membranes at the air-liquid interface in DMEM/F12 medium (without HEPES) supplemented with 5% fetal bovine serum (FBS) and antibiotics. In some experiments, the medium was also supplemented with 1 μM aphidicolin to inhibit cell proliferation, or with either 10 μM forskolin or 200 μM bumetanide to activate or inhibit, respectively, rates of epithelial fluid secretion.

Bright-field images of cultured explants were captured at 0 and 24 hr to quantify the number of ectopic branches, as well as changes in epithelial morphology. Timelapse images were also captured at 30 min intervals to observe the dynamics of supernumerary bud formation. In other experiments, we used the Click-iT EdU Imaging Kit to quantify rates of cell proliferation. These explants were co-stained for LCAM (E-cadherin) immunofluorescence and imaged as whole-mounts using a laser scanning confocal microscope. Other explants were frozen in OCT compound, sectioned into 20 μm slices using a cryostat, and stained for F-actin and phosphorylated myosin light chain (pMLC) immunofluorescence to visualize areas of active actomyosin contractility. In addition, we created a computational model of FGF-10-induced budding morphogenesis using COMSOL Multiphysics and compared our results with *ex vivo* culture data.

RESULTS

Agarose beads containing 100 μg/ml FGF-10 were embedded in the pulmonary mesenchyme of embryonic chicken lungs along regions of the airway epithelium that normally remain unbranched. To our surprise, individual FGF-10-loaded beads stimulated the formation of multiple supernumerary buds after 24 hr of culture. These ectopic buds exhibited a common (or characteristic) wavelength and formed simultaneously, in a manner similar to the buckling morphogenesis of isolated airway epithelial explants cultured in 3D gels of reconstituted basement membrane protein [2]. The formation of these supernumerary buds depended crucially on increased epithelial proliferation, as

determined by EdU quantification and a loss of supernumerary buds in explants treated with aphidicolin.

We also stained explants for phalloidin and pMLC immunofluorescence, which label F-actin and regions of active actomyosin contractility, respectively, since previous studies have suggested that localized regions of contractility can promote the apical constriction of airway epithelial cells and the formation of new branches [3]. The FGF-10-induced supernumerary buds contained no discernible increases in the intensity of either F-actin or pMLC staining, suggesting that apical constriction is not involved in the formation of ectopic branches.

Taken together, these results suggested the possibility that ectopic sources of FGF-10 promote increased proliferation within the airway epithelium, causing it to buckle and form multiple supernumerary buds. To test this more directly, we also modulated rates of epithelial fluid secretion (and thus luminal fluid pressure) to determine if increased epithelial tension could suppress the formation of ectopic branches. Treatment with forskolin, an activator of cAMP activity and epithelial fluid secretion, caused the embryonic airways to inflate dramatically, and suppressed the formation of supernumerary branches in response to an FGF-10-loaded bead (Fig. 1). In other experiments, explants were cultured in the presence of bumetanide, an NKCC1 inhibitor and antagonist of fluid secretion, to determine if decreased epithelial tension might promote buckling, and thereby ectopic branch formation. Indeed, treatment with bumetanide resulted in a greater number of supernumerary buds, which exhibited a shorter wavelength and formed at an earlier timepoint during *ex vivo* culture (Fig. 1).

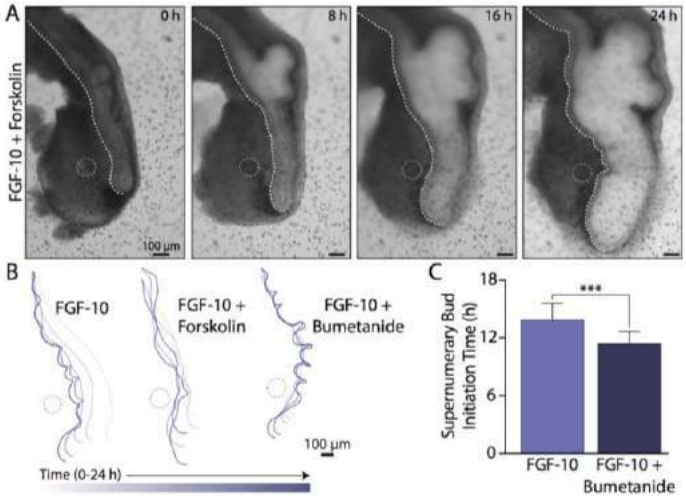

Figure 1: Fluid pressure modulates epithelial buckling and resulting supernumerary bud formation.

Lastly, to more completely understand the mechanics of ectopic bud formation, we also created a nonlinear computational model of the embryonic airway epithelium. Our experimental data suggested that the growth (or expansion) of the epithelium in response to FGF-10 is constrained by the surrounding mesenchyme, which causes the epithelium to buckle and form ectopic branches. To test the plausibility of this mechanism, we modeled the epithelium as a growing bar supported by a spring foundation, to account for the mechanical constraint of the mesenchyme (Fig. 2). The bar was assumed to behave as a hyperelastic material with a Blatz-Ko strain-energy density function, and growth was included by decomposing the overall deformation gradient tensor ($\boldsymbol{F}$) into a component due to growth ($\boldsymbol{G}$) and a component due to elastic deformation ($\boldsymbol{F}^*$) via $\boldsymbol{F} = \boldsymbol{F}^* \cdot \boldsymbol{G}$. Longitudinal growth was included in the epithelium by specifying the components of the growth tensor $\boldsymbol{G}$. As the epithelium elongated, compressive axial forces caused it to buckle, creating numerous epithelial buds, similar to those observed in our FGF-10 bead experiments (Fig. 2). The simulated buds, moreover, formed simultaneously and exhibited a characteristic wavelength, even though the longitudinal growth specified along the epithelium was spatially uniform. Buckling could also be suppressed in the model by stretching the bar longitudinally, in a manner that simulated the dilation of the airway observed upon treatment with forskolin (Fig. 1).

Taken together, these results suggest that ectopic sources of FGF-10 can promote the buckling morphogenesis of the embryonic airway epithelium.

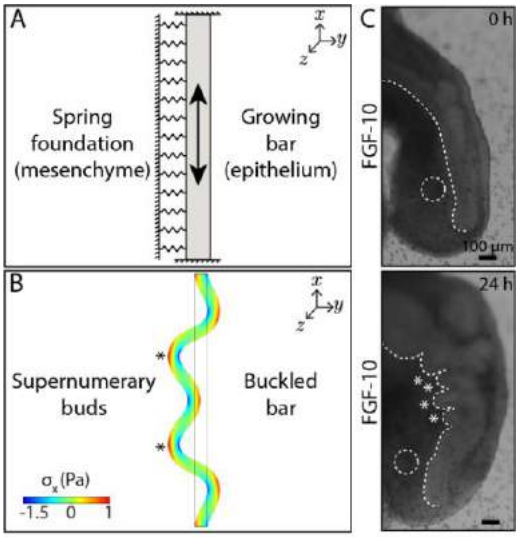

Figure 2: Nonlinear elastic growth-induced buckling model recapitulates experimental supernumerary bud formation

DISCUSSION

The complex network of signaling pathways that regulate branching morphogenesis in the embryonic lung make it difficult to experimentally parse the effects of any individual growth factor. Here, we have used growth factor-loaded beads to isolate the effects of a single growth factor, FGF-10, which is thought to regulate the overall airway branching pattern. Focal sources of FGF-10 are purported to act as chemoattractants that promote the outgrowth of new epithelial branches, with individual buds corresponding to individual domains of FGF-10 expression [4-5]. However, our work has demonstrated that a single focal source of FGF-10 can stimulate the formation of multiple branches via a proliferation-dependent buckling mechanism. Epithelial buckling (and thus branch formation) was modulated by changes in either epithelial proliferation or luminal fluid pressure, suggesting that airway branching is not specified by patterned FGF-10 expression alone. Instead, growth-factor mediated changes in cell behavior act in concert with exogenous mechanical forces to sculpt the bronchial tree.

ACKNOWLEDGEMENTS

This work was supported, in part, by NIH grant R01HL145147 to VDV.

REFERENCES

[1] Metzger RJ, Krasnow MA, *Nature*, 453:745-751, 2008.
[2] Varner VD, et al., *Proc Natl Acad Sci U S A*, 112:9230-9235, 2015.
[3] Kim HY*, Varner VD*, et al., *Development*, 140:3146-3155, 2013.
[4] Morrisey EE, Hogan BLM, *Dev Cell*, 18(1):8-23, 2010.
[5] Hogan BLM, *Cell*, 96:225-233, 1999.

INVESTIGATING THE ROLE OF PATTERNED ECM STIFFNESS AND PROLIFERATION DURING BRANCHING MORPHOGENESIS IN THE EMBRYONIC KIDNEY

Somdutta Chakraborty (1), Thomas J. Carroll (2), Victor D. Varner (1,3)

(1) Department of Bioengineering
The University of Texas at Dallas
Richardson, TX, USA

(2) Departments of Nephrology and Molecular Biology
UT Southwestern Medical Center,
Dallas, TX, USA

(3) Department of Surgery
UT Southwestern Medical Center
Dallas, TX, USA

INTRODUCTION

The kidney is a highly complex organ that filters fluids in the body to regulate their volume and composition. It does so, in part, using a tree-like network of collecting ducts, which forms during embryonic development via a process known as branching morphogenesis. The metanephric kidney initiates when the ureteric bud forms along the Wolffian duct and undergoes a series of repeated branching events to build a tree, the tips of which interact with renal vesicles to direct the formation of developing nephrons [1]. Branching morphogenesis is thus intimately tied to nephron number, and defects in this process can lead to congenital abnormalities that compromise renal function.

Proper renal branching depends crucially on proliferation and elevated levels of proliferation are thought to be localized to the morphogenetically-active tips of the branching ureteric tree [2]. Still, it is unclear how this spatial pattern of proliferation is developmentally patterned. Mechanical forces have been shown to regulate the morphogenesis of other branched organs, such as the lung and mammary gland [3], but the possibility that biophysical cues, such as patterned ECM stiffness, might impact renal branching morphogenesis remains ill-defined.

Here, we used microindentation tests to quantify spatial distributions of stiffness within sagittal sections of developing mouse kidneys. These distributions were then compared with patterns of proliferation along the ureteric tree in 3D reconstructions of embryonic kidneys. We then used a polyacrylamide gel system to determine if changes in substratum stiffness could control the proliferation of cultured collecting duct epithelial cells in vitro. Since disrupted Yap signaling is associated with abnormal renal branching, we also investigated the role of Yap in regulating these stiffness-dependent effects.

METHODS

Microindentation tests: We used the CellScale MicroSquisher to measure tissue stiffness along the cortical-medullary axis in developing mouse kidneys. Briefly, we obtained thick (~500 μm) sagittal sections of postnatal day (P) 4 mouse kidneys (Fig. 1A), and a 70 μm-diameter cylindrical microindenter was used to probe tissue stiffness at different points along the cortical-medullary axis (Fig 1B-C).

Embryonic kidney dissection and culture: Embryonic day (E) 13 mouse embryos were harvested from timed-pregnant CD1 mice (Charles River). Kidneys were dissected in phosphate-buffered saline (PBS) and cultured at 37°C on Nucleopore membranes in DMEM/F12 medium supplemented with 5% fetal bovine serum (FBS) and antibiotics.

Polyacrylamide gel fabrication: Polyacrylamide gels of varying stiffnesses were fabricated on glass coverslips. These gels were then functionalized with 50 μg/ml of either type I collagen, fibronectin, laminin, or type IV collagen [4].

Cell culture: Functionalized PA substrata were plated with immortalized mouse inner medullary collecting duct epithelial cells (m-IMCD3) and cultured for 48 hr at 37°C in DMEM/F-12 medium supplemented with 10% fetal bovine serum and antibiotics. In other experiments, we also used an immortalized line of mutant collecting duct epithelial cells (Lats KO cells) that lack Lats, the kinase that phosphorylates Yap and modulates its subcellular localization.

Quantifying proliferation: Proliferating cells were detected using the Click-iT EdU Imaging Kit.

Confocal microscopy: Samples were fixed using 4% paraformaldehyde and stained for either E-cadherin or Yap immunofluorescence, as well as phalloidin and DAPI. 3D microscopy of fixed samples was

performed on a Zeiss LSM 800, and 3D reconstructions were created using Imaris.

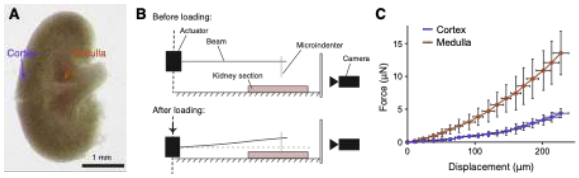

Figure 1: Microindentation tests of P4 mouse kidneys reveal differences in tissue stiffness between cortical and medullary regions of the developing kidney

RESULTS

We performed microindentation tests along the cortical-medullary axis in sagittal sections of P4 mouse kidneys (Fig. 1). We were able to detect reproducible and significant differences in stiffness between cortical and medullary regions of the kidney, with elevated tissue stiffness in more medullary regions. To determine how these regional differences in stiffness compare to distributions of proliferation along the branched network of collecting ducts, we cultured E13 kidney explants ex vivo for up to 96 hr and measured EdU incorporation to quantify spatial distributions of proliferation along the ureteric tree at different stages of branching (Fig. 2). We observed clear differences between cortical and medullary regions of the cultured explants, with substantially increased levels of proliferation in the three most cortical generations of branches.

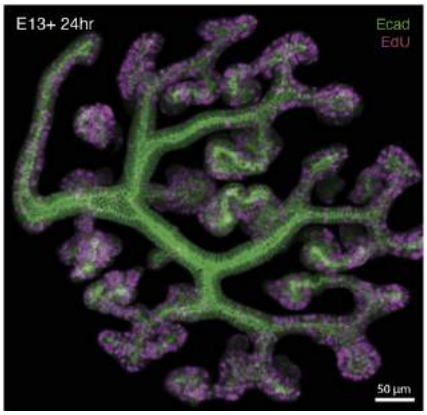

Figure 2: Proliferation is elevated in the a few generations of outermost branches within the kidney.

Taken together, these results suggest the possibility that regional differences in stiffness might regulate the pattern of proliferation within the developing ureteric tree. To test this idea more directly, we cultured collecting duct epithelial cells on PA substrata of different stiffnesses and quantified rates of EdU incorporation to determine if substratum stiffness was sufficient to modulate rates of proliferation. We found that the proliferation of collecting duct epithelial cells depends upon both substratum stiffness and ECM composition, with cells exhibiting higher proliferation on stiffer substrata on either laminin-, fibronectin-, or collagen IV-functionalized gels. On collagen I-coated substrata, however, the cells exhibited no stiffness-dependent differences in behavior. These proliferative phenotypes were accompanied by clear differences in the subcellular localization of Yap. We observed nuclear Yap in cells with elevated levels of proliferation and cytosolic Yap in cells with decreased proliferation.

To determine if Yap activity could be modulating these stiffness-dependent effects, we repeated our PA gel experiments using a mutant cell line (Lats KO), which lacks Lats (the kinase that phosphorylates Yap), resulting in elevated Yap activation. Disrupted Yap signaling altered the observed stiffness-dependent differences in cell proliferation (Fig. 3). Lats KO cells no longer exhibited low levels of proliferation on soft substrata, suggesting that changes in Yap activity underlie the observed stiffness-dependent differences in collecting duct epithelial cell proliferation.

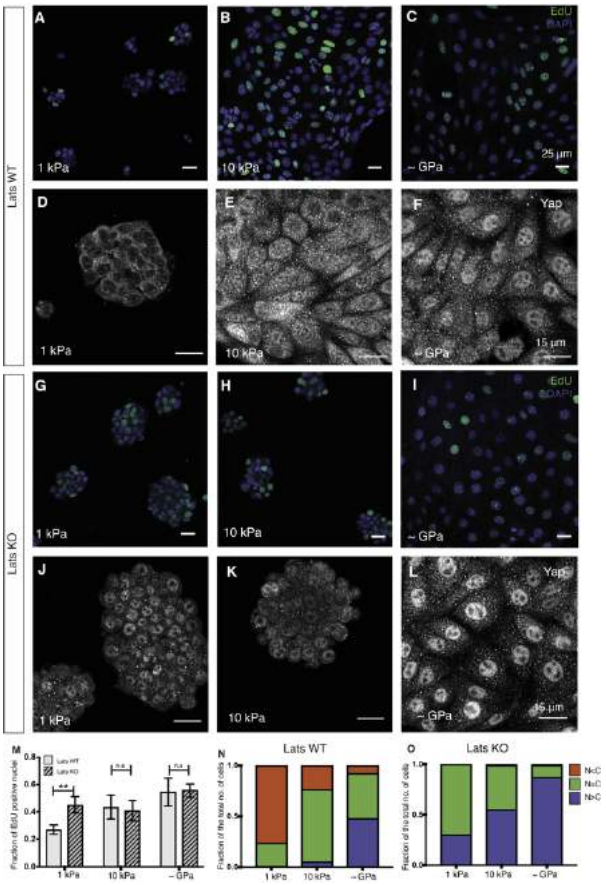

Figure 3: Disrupting Yap signaling disrupts stiffness-dependent cell proliferation for cells cultured on Laminin.

DISCUSSION

Taken together, these data suggest that differences in ECM stiffness may regulate the patterns of proliferation that sculpt the developing network of collecting ducts in the embryonic kidney. Previous work has shown that disrupted Yap activity inhibit branching morphogenesis during renal development [5], but it is unclear how these changes affect either regional differences in tissue stiffness or the patterns of proliferation that are normally present along the ureteric tree. Future work will explore how ectopic stiffening within cultured embryonic kidney explants regulates both the proliferation and branching of the developing collecting ducts.

ACKNOWLEDGEMENTS

This work was supported, in part, by the NIH grant R01HL145147 to VDV.

REFERENCES

[1] Costantini F, Kopan R, *Developmental cell*, 18:698-712, 2010.
[2] Michael L, Davies JA, *Journal of anatomy*, 204:241-255, 2004.
[3] Varner VD, Nelson CM, *Development*, 141:2750-2759, 2014.
[4] Maruri D et al. *Biophysical journal* 119.9 (2020): 1865-1877.
[5] Reginensi, Antoine, et al. PLoS Genet 9.3 (2013): e1003380.

INVESTIGATING CONFORMING AND NONCONFORMING MESHES IN HUMAN LAMINA CRIBROSA SUBDOMAIN SIMULATIONS

Hirut G. Kollech (1), Jonathan P. Vande Geest (2,3,4)

(1) Computational Modeling and Simulation
University of Pittsburgh
Pittsburgh, PA, USA

(2) Department of Bioengineering
University of Pittsburgh
Pittsburgh, PA, USA

(3) Louis J. Fox Center for Vision Restoration
University of Pittsburgh
Pittsburgh, PA, USA

(4) McGowan Institute for Regenerative Medicine
University of Pittsburgh
Pittsburgh, PA, USA

INTRODUCTION

The biomechanics of the optic nerve head region including the lamina cribrosa (LC) and sclera is fundamental for the development and progression of glaucoma. The LC is a porous collagenous disc located in optic nerve head and it undergoes significant remodeling in the presence of the disease [1-2]. Several finite element approaches have been utilized to investigate the biomechanical response and the material properties of this region [3-4]. Although both subdomain and full geometries have been used to model the LC using finite elements, the difference between conforming mesh (based on the geometry and structure) and non-conforming mesh has not been quantified. The purpose of this study is therefore to investigate the differences between a conforming and non-conforming mesh on a small region of a human lamina cribrosa.

METHODS

A non-glaucomatous human eye was imaged using a multiphoton microscope while simultaneously conducting a pressure inflation experiment. Second harmonic generation images were collected and utilized to generate a 3D segmentation geometry of the LC. A small subdomain region was created from the segmented LC (Figure 1) and meshed using a conforming tetrahedral mesh, non-conforming hexahedral and a non-conforming tetrahedral mesh. Representative images of these meshes are shown in Figure 1B for the conforming mesh and Figure 2A & 2B for the nonconforming mesh. Element sizes were varied (coarse to fine) in each group and finite element simulations were run using identical boundary conditions, load (pressure) and material property parameters. A few locations (x, y, z coordinates) were selected to output displacement results after each simulation. These results were compared across the groups and the percent error was calculated.

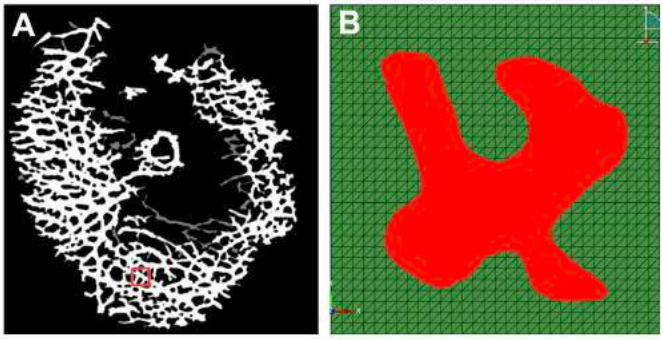

Figure 1 A small subdomain selected from human LC Panel A) a segmented human LC collagen with the subdomain shown in a red box; Panel B) conforming tetrahedral mesh of the subdomain

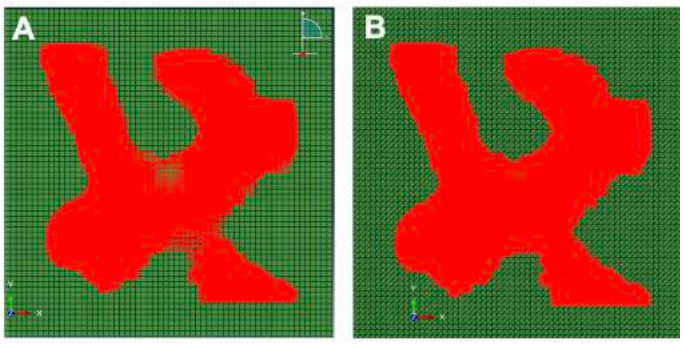

Figure 2 Representative nonconforming mesh of the subdomain Panel A) Hexahedral mesh; Panel B) Tetrahedral mesh of the subdomain

RESULTS

The mesh convergence study within each of the three groups are shown in the following figures. Figure 3 is the conforming tetrahedral mesh, Figure 4 is the nonconforming hexahedral mesh and Figure 5 is the nonconforming tetrahedral mesh. The percent error was calculated using the conforming mesh finest mesh as a reference. The conforming mesh showed the maximum of 6.21 $\pm$ 0.29 % error variation across different element size and the error was smaller than 1% for element sizes greater than 1 million. The hexahedral mesh had a maximum error of 69.76 $\pm$ 8.21% at the coarse mesh size and that of the nonconforming tetrahedral mesh was 57.83 $\pm$ 4.24%.

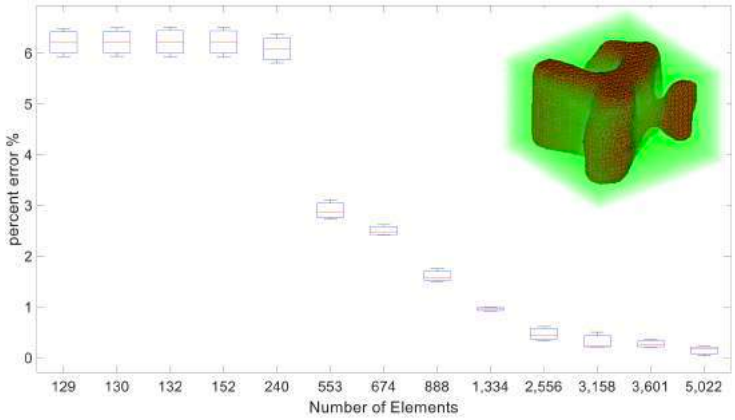

Figure 3) Conforming tetrahedral mesh plots with varying mesh size from coarse to fine. The image in the top right of panel A shows a representative 3D mesh of the LC subdomain region used in the simulations where red indicates the collagen in the LC and green illustrates the non-collagenous extra cellular matrix in the subdomain.

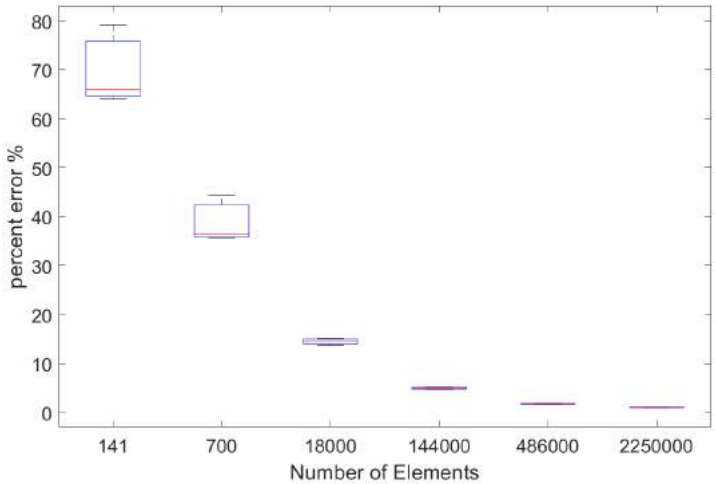

Figure 4) Nonconforming hexahedral mesh plots with varying mesh size from coarse to fine.

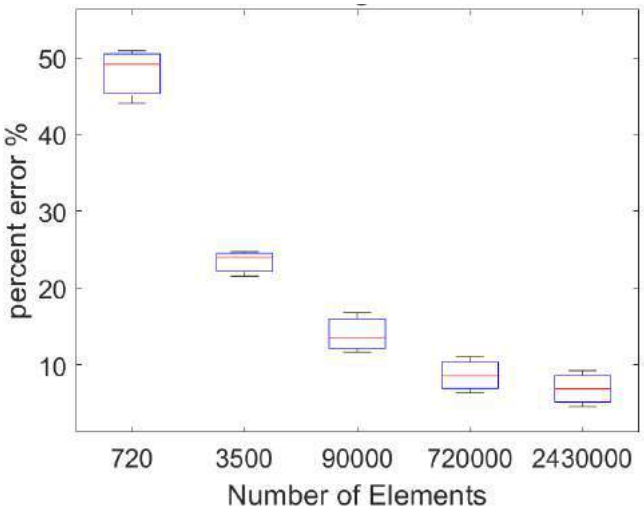

Figure 5) Nonconforming tetrahedral mesh plots with varying mesh size from coarse to fine meshes.

DISCUSSION

The non-conforming mesh simulations results in acceptable percent error values (<5%) at finer mesh sizes. While the geometry in this study was small and the conforming mesh simulations were not computationally demanding, generating conforming mesh finite element simulations for a complex 3D structures such as the LC require large computational resources and time. Therefore, mesh converged nonconforming models that result in small error can be a great alternative. We are currently using these results to estimate the degrees of freedom and total number of elements in our full LC simulations. In addition, these results are utilized to determine the subdomain size to run the full LC finite element analysis.

ACKNOWLEDGEMENTS

Research reported in this abstract was supported by the National Eye Institute under award number R01EY020890 to JPVG and grant number R01FD006582 (JV Co-I, PI: Feinberg and Badylak). The computational resources of this research were supported by University of Pittsburgh Center for Research Computing (CRC) and Pittsburgh Supercomputing Center through NSF-XSEDE award number TG-ENG160035

REFERENCES

[1] Hernanadez, M et al., *J Ophthalmol*, 109(2):180–188, 1990.
[2] Yang H et al., *IOVS*, 52(2):821–829,2011.
[3] Fazio M et al., *IOVS*, 55(11):7189-7198, 2014.
[4] Behkam R et al., *Acta Biomater*, 88:131-140, 2019.

A COMBINED MICROFLUIDIC DEVICE AND NUMERICAL SIMULATION TECHNIQUE FOR THE EVALUATION OF RED BLOOD CELL SHEAR INDUCED DAMAGE

Ratul Paul (1), Mehdi Nikfar (1), Yuyuan Zhou (2), Meghdad Razizadeh (1) , Yaling Liu (1,2)

(1) Department of Mechanical Engineering and Mechanics
Lehigh University
Bethlehem, Pennsylvania, USA

(2) Department of Bioengineering
Lehigh University
Bethlehem, Pennsylvania, USA

INTRODUCTION

Due to the extreme deformability of RBCs, they do not get critically damaged even though experiencing a significant level of shear stress. That is why the deformability of RBC has been extensively studied over the last few decades. Studies have been carried out to associate RBC deformation to several pathological alterations due to malaria [1], sickle cell anemia [2], hereditary disorders [3], diabetes [4], myocardial infarction [5], etc. Changes in the RBC membrane due to these diseases are the reason behind altered deformability. The deformability of RBC can also be altered by shear stress [6]. This is mostly due to the altered association between membrane skeletal proteins and integral proteins that serve as an anchor to connect the skeleton to the lipid membrane. Blood experiences various geometry and flow-induced stresses in blood-wetting devices. These devices include mechanical heart valves, axial and centrifugal blood pumps, ventricular assist devices (VAD), etc. High shear in these devices can damage the RBCs that can potentially be fatal. So, it is important to develop a better understanding of shear-induced damage to RBCs.

Investigating shear-induced damage of RBCs in the single-cell scale is essential for developing a numerical model for predicting cell damage. There have been several efforts to study single-cell shear-induced damage to RBCs. Polycarbonate sieves with micropores have been used to study the resistance of RBCs against mechanical hemolysis during filtration [7]. Abkarian et al. studied the RBC deformation and hemolysis in confined channels and tried to estimate hemolysis based on shear stress and exposure time using empirical correlations [8], [9].

A quantitative study of the changes in the biophysical and mechanical properties of RBC due to shear stress has not been carried out yet. In our previous study, multiscale modeling has been employed to predict hemolysis during microfiltration [10]. But microfilters are not suitable to control the shear stress on a single cell. This method will provide a more quantitative comparison between single-cell shear-induced damage simulation and experiment by utilizing the recently developed light absorption based single-cell hemoglobin, volume, membrane tension, and bending modulus measurement [11].

METHODS

Microfluidic channels with different width and length are used to control the shear stress magnitude and duration while the thickness of the channel is used to control the orientation of the RBC flowing through the channel. The devices have been made with standard photolithography and PDMS molding technique [11]. The squeezing channels have a width ranging from 1 µm to 5µm and length ranging from 10 µm to 200 µm with a fixed thickness of 3 µm to keep the RBCs in a horizontal orientation to the squeezing channel. Another set of squeezing channel has been used to mimic the spleen to check RBC viability. These channels have a high aspect ratio and smaller constriction. The width is only 0.8 µm while the thickness of the channel is 12 µm to fix the RBCs perpendicular to the squeezing channel during squeezing.

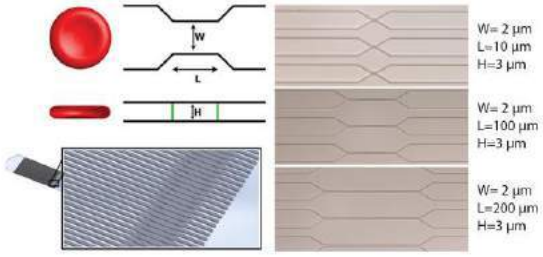

Figure 1: Design of the squeezing channels for the experiment

RBCs are prepared for squeezing by the procedure mentioned in the previous study [11] and inserted in the device with a pressure pump (Precigenome LLC, CA, USA). The RBCs are analyzed in a customized 2 LED (405 nm and 630 nm) illumination with a high-speed CMOS color camera (XIMEA CB120CG-CM). The light absorption due to the RBC has been analyzed to measure the hemoglobin content and volume of the RBC.

The D3Q19 (three dimensions with 19 discrete velocities) version of the Lattice Boltzmann Method (LBM) has been used for the simulation. Spring connected network (SN) is used as the RBC model. The immersed boundary method (IBM) is used for coupling SN and LBM.

RESULTS

The squeezing in a 3 µm wide channel with a velocity of 1.2 mm/s shows that the simulation can accurately predict the deformation and shape of the RBC in high shear flow (**Figure 1**).

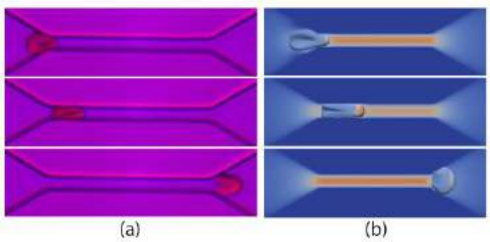

Figure 2: (a) Images captured from the high-speed recording of RBC squeezing through a narrow constriction. (b) Visualization of the numerical model of an RBC squeezing through a narrow channel

The numerical model can be used to determine the areal strain on the membrane that will be used to predict the pore size and hemoglobin release during the squeezing process. For example, **Figure 2** shows the areal strain of the RBC model during theoretical rupture as determined by comparing with the results from Abkarian et al. [8].

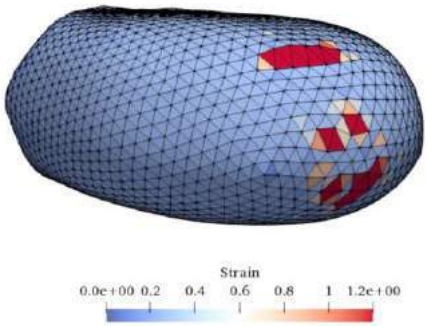

Figure 3: Areal strain predicted by the numerical model

High-speed quantitative light absorption imaging during the squeezing process shows an overall hemoglobin loss by the RBC in the microchannel.

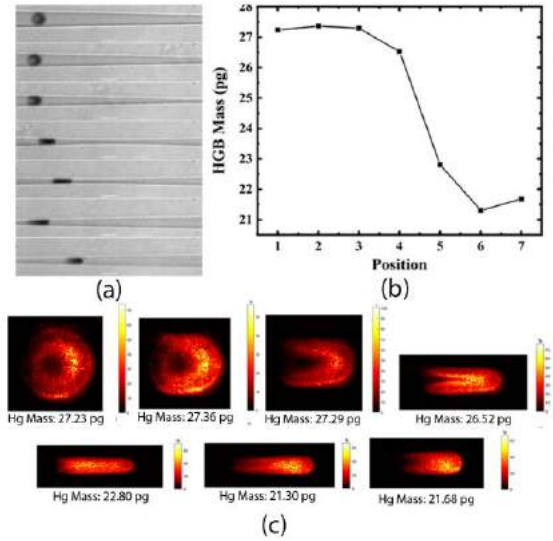

Figure 4:(a) Image sequence of an RBC squeezing through a 3 µm wide and 10 µm long channel. (b) a plot of total hemoglobin mass vs the position of the RBC as measured by quantitative light absorption imaging (c)visualization of the hemoglobin mapping for the RBC at different positions.

Healthy RBCs flowing through the spleen mimicking channel shows that healthy they can pass through them easily.

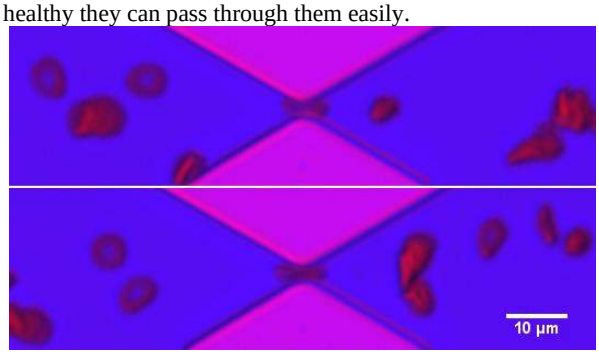

Figure 5: Healthy RBC squeezing through spleen like channel

DISCUSSION

The combined microfluidic and numerical modeling approach can be a powerful tool to predict RBC damage in shear stress. The quantitative light absorption imaging can be further used to calculate the change in RBC volume and membrane tension that will help correlate the mechanical changes to shear stress. If the numerical model can be validated for the hemoglobin loss in high shear rate cases, it can be used to simulate bulk RBC damage in medical devices.

ACKNOWLEDGEMENTS

This work was supported by the National Institutes of Health (NIH) grant number R01HL131750, and the Pennsylvania Infrastructure Technology Alliance (PITA) grant. This project is also funded, in part, under a grant with the Pennsylvania Department of Health. The Department specifically disclaims responsibility for analyses, interpretations, or conclusions. The authors would like to thank the donors participating in this study for providing blood samples. Dr. Zhongjun Wu and Zachary Berk from University of Maryland for coordinating the clinical sample and data collection.

REFERENCES

[1] T. Wu and J. J. Feng, "Simulation of malaria-infected red blood cells in microfluidic channels: Passage and blockage," *Biomicrofluidics*, vol. 7, no. 4, p. 044115, Jul. 2013.

[2] K. D. Barabino GA, Platt MO, "Sickle cell biomechanics.," *Annu Rev Biomed Eng*, vol. 12, no. 345, p. 67, 2010.

[3] L. Da Costa, J. Galimand, O. Fenneteau, and N. Mohandas, "Hereditary spherocytosis, elliptocytosis, and other red cell membrane disorders," *Blood Rev.*, vol. 27, no. 4, pp. 167–178, Jul. 2013.

[4] A. V. Buys, M. J. Van Rooy, P. Soma, D. Van Papendorp, B. Lipinski, and E. Pretorius, "Changes in red blood cell membrane structure in type 2 diabetes: A scanning electron and atomic force microscopy study," *Cardiovasc. Diabetol.*, vol. 12, no. 1, p. 25, Jan. 2013.

[5] A. Vayá *et al.*, "Red blood cell distribution width and erythrocyte deformability in patients with acute myocardial infarction," *Clin. Hemorheol. Microcirc.*, vol. 59, no. 2, pp. 107–114, 2015.

[6] E. Meram, B. D. Yilmaz, C. Bas, N. Atac, O. Yalcin, and H. J. Meiselman, "Shear stress-induced improvement of red blood cell deformability," *Biorheology*, vol. 50, no. 3–4, pp. 165–176, 2013.

[7] S. Chien, S. A. Luse, and C. A. Bryant, "Hemolysis during filtration through micropores: A scanning electron microscopic and hemorheologic correlation," *Microvasc. Res.*, vol. 3, no. 2, pp. 183–203, Apr. 1971.

[8] M. Abkarian, M. Faivre, R. Horton, K. Smistrup, C. A. Best-Popescu, and H. A. Stone, "Cellular-scale hydrodynamics," *Biomed. Mater.*, vol. 3, no. 3, p. 034011, Sep. 2008.

[9] M. Abkarian, M. Faivre, and H. A. Stone, "High-speed microfluidic differential manometer for cellular-scale hydrodynamics," *Proc. Natl. Acad. Sci.*, vol. 103, no. 3, pp. 538–542, Jan. 2006.

[10] M. Nikfar, M. Razizadeh, R. Paul, and Y. Liu, "Multiscale modeling of hemolysis during microfiltration," *Microfluid. Nanofluidics*, vol. 24, no. 5, p. 33, May 2020.

[11] R. Paul, Y. Zhou, M. Nikfar, M. Razizadeh, and Y. Liu, "Quantitative Absorption Imaging of Red Blood Cell to Determine the Physical and Mechanical Properties," *RSC Adv.*, 2020.

IDENTIFICATION OF ADIPOCYTE SECRETED FACTORS RESPONSIBLE FOR MYOFIBROBLAST CONVERSION

M.Y. El-Hattab (1), F. Gourronc (2,3), J. Liszewski (1), B. Davies (2), A. Klingelhutz (2,3), J.A. Ankrum (1,2), E.A. Sander (1)

(1) Roy J. Carver Department of Biomedical Engineering
University of Iowa
Iowa City, Iowa, United States

(2) Fraternal Order of Eagles Diabetes Research Center
University of Iowa
Iowa City, Iowa, United States

(3) Department of Microbiology and Immunology
University of Iowa
Iowa City, Iowa, United States

INTRODUCTION

Aberrant wound healing impacts tens of millions of people in the US annually, with treatment costs over $20 billion dollars [1]. Problems in wound healing can occur from imbalances at any stage of healing, including prolonged and elevated exposure to growth factors and cytokines, increased mechanical tension, and altered rates of matrix degradation and remodeling. Adipose tissues and cells also appear to contribute to multiple wound healing events, both directly and indirectly. Fat grafts, for example, which initially were used to shape and contour tissue defects, were also found to reduce scarring and promote healing. The efficacy of fat grafting, however, remains unclear, as there is little clarity on what components of the graft and what underlying mechanisms are responsible for the reported improvements.

Consequently, we are investigating how the components of fat grafts (*e.g.*, adipocyte derived stem cells, pre-adipocytes, and adipocytes, influence fibroblasts, the major arbiters of matrix remodeling during wound healing. Previously, we found that 3D adipocyte spheroids secreted factors that promoted fibroblast to myofibroblast conversion as evidenced by an increase in human dermal fibroblast collagen production, contractile force generation, and cytoskeletal α-smooth muscle actin (α-SMA) [2]. This conversion appears to be through a mechanism that is independent of TGF-β1, the factor most commonly associated with driving the differentiation of fibroblasts to myofibroblasts. Here, we report on our efforts to identify what adipocyte-secreted factor(s) are responsible for myofibroblast conversion and what the implications to wound healing might be.

METHODS

3D Pre-Adipocyte and Adipocyte Spheroid Culture and Conditioned Medium Collection: Pre-adipocyte and adipocyte spheroids (each containing ~20,000 cells) were generated by growing immortalized pre-adipocyte spheroids using the standard hanging drop method. Spheroids were either maintained or differentiated in pre-adipocyte growth or differentiation medium (PGM2, PDM2) from the Lonza Bullet kit, respectively. After 10 days the growth and differentiation medium were removed, the spheroids were rinsed gently with 1X PBS, then 0.75 mL of Dulbecco's Modified Eagle Medium (DMEM) containing 0.5% fetal bovine serum, 1% penicillin/streptomycin and 0.1% amphotericin B was added to each well. After two days, this medium, termed pre-adipocyte or adipocyte conditioned medium (PCM, ACM) was collected and stored at -80^{o} C.

LEGENDplex Human Adipokine Panel: PCM and ACM were first screened with a multiplex adipokine assay in order to measure levels of common cytokines, hormones, and other factors commonly secreted by adipose tissues. Collected medium was processed and run in triplicate via flow cytometry as described by the manufacturer (Biolegend).

Heat Inactivation & Lipid Inactivation: ACM was heat inactivated by maintaining the medium at 85^{o}C for 1 hour with a benchtop hotplate. Separately, ACM was treated with Cleanascite HC to remove lipid as described by Castro *et al*. [3]. 0.5 mL of Cleanascite HC was added to Eppendorf tubes and centrifuged to remove the saline and the pellet was resuspended in ACM. ACM was then incubated at 4^{o}C overnight with gentle agitation, then centrifuged to remove the pellet of lipid-bound beads. The ACM was decanted into a separate Eppendorf tube and filtered through a 0.45 μm pore size filter to remove residual polymer particles.

Molecular Weight Fractionation of ACM: ACM was fractionated into different molecular weights using cutoff filters of 100 kDa, 30 kDa, 10 kDa, and 5 kDa (Vivaspin and Amicon). Filters were pre-rinsed and

medium was centrifuged sequentially through the filters. Each collected fraction was stored at -80 ^{o}C.

Myofibroblast Conversion Assay: Human dermal fibroblasts were plated at 20,000 cells/cm^2 in 96-well well clear-bottom, black walled plates. In triplicate, the cells were treated for 2-days with ACM that was either heat inactivate, lipid depleted, or fractionated as >100kDa, 30 -100kDa, 10-30kDa, 5-10kDa and <5kDa. Other conditions included control (0.5% FBS DMEM), and positive control (control plus 1 ng/mL TGF-β1 & 50 μg/mL ascorbic acid). After treatment, samples were rinsed, fixed, permeabilized, blocked in 5% BSA-tween solution, and incubated with a primary mouse anti-human α-SMA antibody solution followed by secondary antibody staining using a SuperBoost secondary antibody kit (ThermoFisher). Cell nuclei were labeled with DAPI α-SMA and the proportion of converted myofibroblasts was quantified by measuring fluorescence with a VarioSkan Lux multimode microplate reader.

RESULTS AND DISCUSSION

In order to determine what factor(s) in ACM but not PCM might be responsible for myofibroblast conversion, both types of conditioned medium were subjected first to an adipokine panel (Fig. 1). Differences in the secretion profile of PCM and ACM were found. PCM contained greater amounts of MCP-1, IL-6, and IL-8 than ACM, and ACM contained greater amounts of adiponectin, adipsin, RBP4, and IFN-γ (Fig. 1).

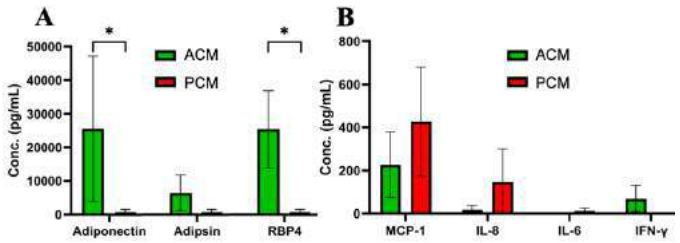

Fig. 1: (A) ACM contained high levels of adiponectin, adipsin, and RBP4, adipokines not present at detectable levels in PCM. (B) Lower levels of MCP-1, IL-8, IL-6, and IFN-γ were present differentially in PCM and ACM. Data is mean ± SD. Two-way ANOVA was conducted * p<0.05.

In parallel, a myofibroblast conversion assay was conducted on heat inactivated, lipid deleted and protein fractionated ACM (Fig. 2). It revealed that the factor(s) responsible for myofibroblast conversion is a protein between 30-100 kDa. The recombination of heat inactivated and lipid depleted fractions also did not lead to myofibroblast conversion, suggesting that lipid soluble co-factors are also not responsible (Fig. 2).

We also fractionated our positive control medium through 100 kDa and 30 kDa molecular weight cutoff filters to confirm that TGF-β1, a 25 kDa homodimer, is not retained in the 30-100 kDa fraction (Fig. 3). We found that α-SMA induction was significantly higher than baseline only in the <30 kDa fraction and not significantly different from the unfractionated positive control. These results provide more evidence that supports the notion that myofibroblast conversion is occurring through a TGF-β1 independent mechanism. Our efforts are now focused on screening several candidate molecules between 30-100 kDa and consistent with our other findings, such as adiponectin. Adiponectin is a 30 kDa protein in abundance in ACM. It also associates into trimers and other multimeric forms that are believed to have differential functions related to cell metabolism. In addition, there is evidence that adiponectin plays a role in wound healing. For example, Ezure *et al.*

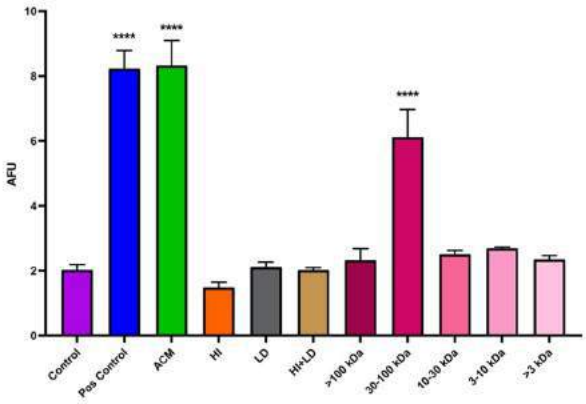

Fig. 2: Myofibroblast Conversion Assay. Fluorescently labeled α-SMA indicates that factor(s) in ACM responsible for myofibroblast conversion are proteins contained in the 30-100 kDa molecular weight fraction. Data presented as mean ± SD, one-way ANOVA conducted with Tukey Multiple comparisons test (** p<0.001).**

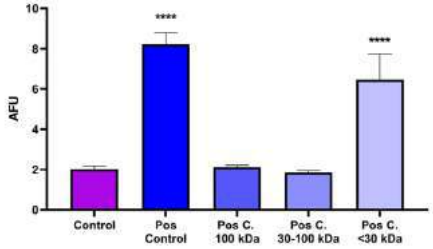

Fig. 3: Positive control fractionated medium shows myofibroblast conversion of fibroblasts from <30kDa protein fraction.

reported that adiponectin upregulates dermal fibroblast matrix production *in vitro* [3]. In contrast, Marangoni *et al.* reported that adiponectin produces anti-fibrotic effects in a mouse model [4]. Regardless, current work is focused on identifying the secreted factor and determining what role it plays in directing fibroblast activity during tissue remodeling. Such information will provide a better understanding of how adipocytes and other components of fat grafts contribute wound healing and how these different components can be optimized to provide maximum therapeutic benefit of fat-related wound healing treatment strategies.

ACKNOWLEDGEMENTS

Support for this work was provided by the National Science Foundation (CAREER 1452728).

REFERENCES

1. Block, L., A. Gosain, and T.W. King, *Emerging Therapies for Scar Prevention.* Adv Wound Care (New Rochelle), 2015. **4**(10): p. 607-614.
2. El-Hattab, M.Y., et al., *Human Adipocyte Conditioned Medium Promotes In Vitro Fibrolbast Conversion to Myofibroblasts.* Sci Rep, 2020. **10**(1): p. 10286.
3. Ezure, T. and S. Amano, *Adiponectin and leptin up-regulate extracellular matrix production by dermal fibroblasts.* Biofactors, 2007. **31**(3-4): p. 229-36.
4. Marangoni, R.G., et al., *Adiponectin is an endogenous anti-fibrotic mediator and therapeutic target.* Sci Rep, 2017. **7**(1): p. 4397.

CONDUCTIVE POLYPYRROLE-ENCAPSULATED SILK FIBROIN FIBERS FOR MYOCARDIAL REGENERATION

Yeshi Liang (1), James Goh (1,2)

(1) Department of Biomedical Engineering
National University of Singapore
Singapore

(2) Department of Orthopaedic Surgery
National University of Singapore
Singapore

INTRODUCTION

Cardiac tissue engineering (CTE) is a promising solution for myocardial infarction. A main strategy in CTE is the scaffold-based approach that aims to recapitulate the native extracellular matrix (ECM) with biomaterials to induce native ECM formation from cells and ultimately regenerate healthy myocardium.[1]

The native myocardium ECM consists of collagen nanofibrils and possesses a DC conductivity around 0.1 S/m.[2] Electrospinning is the most common way to fabricate nanofibrous scaffolds to mimic the ECM's submicron architecture, but the lack of electrical conductivity in most biomaterials restricts the electrical signal propagation between cardiomyocytes (CMs) and hinders tissue contractility restoration. It urges the incorporation of electrically conductive materials, including conducting polymers like polypyrrole (PPy) that possess comparative electrical conductance to metals and semiconductors.[3] Conductive nanofibers containing PPy have been investigated to deliver both the topographical and electrical cues for tissue regeneration. Though PPy-coated electrospun mats showed elevated electrical conductivity, the mechanical properties were too high for CTE. Alternatively, base biomaterials can be blended with PPy to improve the poor spinnability of PPy and balance the overall stiffness of the mat. Kai. *et al.* embedded PPy to Polycaprolactone (PCL)/gelatin electrospun fibers, whose enhanced conductivity promoted CM cardiac gene expression.[4] However, CM's contractility was not reported.

To our knowledge, this study is the first one to blend PPy with natural polymers for electrospinning. Silk fibroin (SF) is naturally derived, which is also relatively easy to be electrospun. We hypothesized that PPy would improve the electrical conductivity of the fibers while SF would increase the spinnability and soften the mechanical properties of the hybrid scaffold for CTE applications. Furthermore, we examined the biofunctional development of CMs on the PPy-SF electrospun mat *in vitro* to evaluate its potential for CTE.

METHODS

Bombyx mori silkworm cocoons were degummed, dissolved and dialyzed against distilled water. Doped-PPy was added to the 7% SF/Hexafluoro-2-propanol solution at three PPy-to-SF ratios (15:85, 30:70, 40:60) and stirred overnight. The spinneret was connected to the negative potential, and fibers were collected with a feed rate of 0.6 mL/h and a voltage of 10.5 kV. Methanol treatment was performed for β-sheet formation. Specifically, mat with PPy-to-SF ratio of 15:85, 30:70, and 40:60 was named 7%PPy15, 7%PPy30 and 7% PPy40, respectively.

Fiber morphology was view by an SEM (JSM-6701F, JEOL Asia). Mat's electrical conductivity was measured using a four-point probe machine (Signatone). The conductivity (mS/cm) is the reciprocal of resistivity as calculated by $\rho=4.25$ V/I. The Young's modulus was calculated from the linear-elastic portion of the stress-strain curve obtained from the tensile test using a table-top tensile tester (Instron).

Neonatal rat CMs (NRCMs) and human induced pluripotent stem cell-derived CMs (hiPSC-CMs) were seeded to fibronectin/gelatin-coated sterilized mats at 100,000 cells/mat. Cell viability was assessed by Live/Dead assay on D2. Cell morphology was observed using SEM. Cardiac-specific protein (Sarcomeric α actinin, Connexin 43 (CX43)) expression was assessed by immunostaining. Fast Fourier transform (FFT) analysis was conducted, where elliptically distributed pixels indicate unidirectional distribution. Mat contraction was evaluated by performing a 'Z-projection' of each beating cycle, where the mat's displacement was defined by the width of the stacked-edges. Contraction frequency was presented in beats per minute (BPM).

All the data are presented as mean ± standard deviation (SD) of the mean. One-way and two-way analysis of variance (ANOVA) was used with Tukey's post hoc correction. P-value less than 0.05 was considered

significant, where *p < 0.05, **p < 0.01, ***p < 0.001. All experiments were performed in at least triplicates.

RESULTS

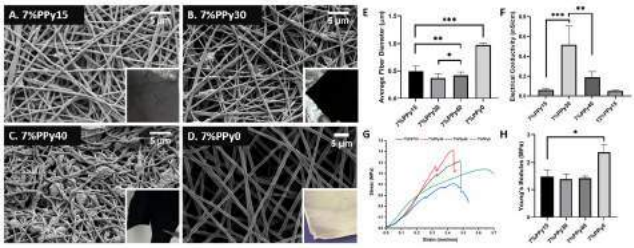

Figure 1: Chacterization of the PPy-encapsulated SF Mats. (A-D) SEM images. (E) Average fiber diameter. (F) Electrical conductivity. (G,H) Mechanical properties.

The electrospun fibers became black with reduced fiber diameters and rougher surface after blending with PPy (Figure 1A-D). A 'U' shape relationship was displayed between PPy amount and fiber diameter, where the smallest fiber diameter was observed in 7%PPy30 (0.375 ± 0.077 μm) (Figure 1E). Surprisingly, Blending PPy reduced the Young's modulus to an average of 1.437 ± 0.044 MPa, which significantly differed from that of 7%PPy0 (Figure 1H). As shown in Figure 1F, the incorporation of PPy remarkably enhanced the mat's electrical conductivity. The highest electrical conductance of 0.520 ± 0.193 mS/cm was detected in 7%PPy30.

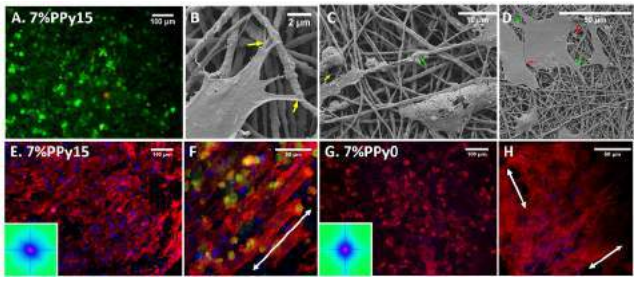

Figure 2: In Vitro Evaluation of the Mats. (A) Live/Dead assay. (B-D) SEM images. (E-H) Immunostaining of cells on mats. Red: Sarcomeric α actinin; Green: CX43; Blue: Nuclei.

PPy-encapsulated SF fibers were biocompatible as high cell viability was observed (Figure 2A). NRCMs anchored cellular process on the PPy-encapsulated SF fibers (Figure 2B yellow arrows). Regarding cell-cell interaction, direct contacts were established between adjacent cells (Figure 2D red arrows), while pseudopodia were developed and bridged remoted NRCMs (Figure 2C green arrows). Though the spindle-like NRCMs on 7%PPy15 had smaller dimensions (Figure 2F) than those on 7%PPy0 (Figure 2H), the sarcomeres were organized anisotropically in 7%PPy15 as a more polarized oval FFT pattern was shown (Figure 2E). In result, the periodic z-lines found on 7%PPy15 were more unidirectional than those on 7%PPy0 (white arrows in Figure 2). CX43 was barely detected from the NRCMs on 7%PPy0 (Figure 2H), but expressed on mats with PPy (Figure 2F).

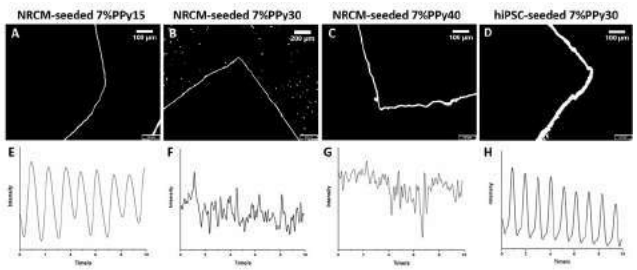

Figure 3: Contraction of the CM-seeded Mats.

All mats did not contract till D5 that 7%PPy15 mat started to show slight consecutive contraction, which became more regular on D7 with a BPM of 45 (Figure 3E). Mats with higher PPy amounts did not show spontaneous contraction but vibrations (Figure 3F,3G). In addition, no contraction was observed from 7%PPy0. Interestingly, for hiPSC-CMs, regular contractions were observed on 7%PPy30 (Figure 3H) with a larger mat displacement than that of NRCM-seeded 7%PPy15.

DISCUSSION

Hybrid electrospun fibers have been gaining interests to advance the scaffold's functionalities. Blending serves as an alternative method to avoid the notable increase of mat's stiffness from coating and the masking of the fiber's nano-topographical cue. To date, PPy has seldom been blended with other biomaterials for electrospinning. Kai *et al.* blended PPy with PCL and gelatin and obtained conductive fibers (0.013~0.37 mS/cm).[4] This study demonstrated that SF as a natural material is another suitable base biomaterial that the hybrid fiber's electrical conductivity was further enhanced to 0.05~0.52 mS/cm (Figure 1F), which falls in the range of that in native myocardium (0.03~6.2 mS/cm).[5] Apart from conductivity, an ideal scaffold should also possess suitable mechanical properties for CMs. Conductive materials are commonly brittle, which could inhibit CM contraction. Our PPy-SF electrospun mats presented an average Young's modulus closer to the desired range for myocardial regeneration than other reported studies (16.8 ± 1.9 ~ 266.7 ± 17.3 MPa). We assumed that the mechanical properties of the composites could be further improved by incorporating softer biomaterials like gelatin.

Though an increased amount of PPy would enhance the electrical property of the scaffold, we found that a moderate amount of PPy (7%PPy15) support CM's functional development better. It is interesting to find that CMs organized anisotropically on 7%PPy15. The alignment of the cardiac tissue regenerated *in vitro* is usually controlled by substrate topography, electrical stimulations, and mechanical loading.[34] Similar to our results, Wang *et al.* reported locally aligned CMs on conductive polyaniline-poly(L-lactic acid) mats.[6] In addition, the most powerful contraction and synchronous electrophysiology were observed from the NRCM-seeded 7%PPy15 mat and hiPSC-seeded 7%PPy30 mat. The different preferences of NRCMs and hiPSCs could be attributed to the species differences. However, both results indicated that the conductive mats would improve CM contraction.

In conclusion, the PPy-encapsulated SF electrospun mats provide nanofibrous features, enhanced electrical conductivity, and suitable mechanical properties for cardiac patches, which supported cell-matrix interaction. CMs from different species showed different preferences on mat that 7%PPy15 best-supported NRCM alignment, enhanced cardiac-specific protein expression, and induced strong contractions, while hiPSC-CMs developed the best contractility in 7%PPy30. Hence, this study demonstrated that PPy-encapsulated SF mat holds great potential as an electroactive scaffold for cardiac tissue regeneration.

ACKNOWLEDGEMENTS

This study was supported by the Singapore Ministry of Education (MOE) Tier 2 Grant MOE2017-T2-2-150.

REFERENCES

[1] Qasim, M et al, *Life Sci,* 229:233-250,2019.
[2] Huyer, L et al, *Biomed. Mater,* 10(3): 034004, 2015.
[3] Shafiee, A at al, Atala, *Annu. Rev. Med,* 68:29-40, 2017.
[4] Kai, D et al, *J. Biomed. Mater. Res. - Part A,* 99(3):376-385, 2011.
[5] Spearman, B. S et al, *Acta Biomater,* 28:109-120, 2015.
[6] Wang, L et al, *Acta Biomater,* 59:68-81, 2017.

EFFECT OF CONVECTION ON CELLULAR SENSING PRECISION FOR DIRECTED CELL MIGRATION

Hye-ran Moon (1), Soutick Saha (2), Andrew J Mugler (2,3), Bumsoo Han (1)

(1) School of Mechanical Engineering
Purdue University
West Lafayette, IN, USA

(2) Department of Physics and Astronomy
Purdue University
West Lafayette, IN, USA

(3) Department of Physics and Astronomy
University of Pittsburgh
Pittsburgh, PA, USA

INTRODUCTION

Directed cell migration is a crucial step in cancer metastasis, a leading cause of death in cancer patients. During this step, cancer cells are capable of sensing and deciphering either chemical or mechanical signals in determining their migratory behaviors in the microenvironment. [1-3] However, the tumor microenvironment is highly complex. Multiple environmental signals are integrated, including upregulated growth factors, reorganized extracellular matrix (ECM) components, and abnormal interstitial fluid pressure (IFP) variance. [2-3] Although the signals to promote directed cell migration have been widely recognized, the integrated effects of the multiple signals are barely understood.

While a concentration gradient of a growth factor such as TGF-β has been widely recognized in guiding the cell movement—chemotaxis, interstitial flow (IF) also plays an essential role in directed cell migration. [2-3] Recent studies recognized that cancer cell directed migration is regulated by interstitial flow through either cell self-secreting chemokine detection or activation of Focal Adhesive Kinases (FAK) pathways. [3] Moreover, interstitial flow also involves the transport of chemical signals, shaping an abnormal signal environment. [4] Due to distinct features of the tumor microenvironment, IFP could be spatially varied, causing absurd interstitial flow. Nevertheless, it is unclear how interstitial flow influences developing the signal environment in the tumor microenvironment and how cells respond to the integrated signals.

In the present study, we investigated the convection-driven signal environment to address how the signal environment is shaped by integrating interstitial flow with TGF-β concentration gradient. Also, we studied how the cells respond to the integrated signal environment. Our driving hypothesis is that cells determine their migration behaviors from a balance between environmental stimulation and a cell's innate ability to sense and process the signal. We evaluated the hypothesis by engineering the microenvironment *in vitro* to develop a TGF-β concentration gradient presenting interstitial flow.

METHODS

In vitro microfluidic platform comprising center, source, and sink channels was used to engineer microenvironment. The harvested cells were mixed with type I collagen and loaded into the center channel, while the source and sink channels were filled with medium. We used KIC cells, a murine pancreatic cancer cell line isolated from a genetically engineered mouse model of pancreatic adenocarcinoma. We engineered the microenvironment by imposing different concentrations of TGF-β between source and sink channels resulting in a concentration gradient in the center channel. Different hydraulic pressure levels were also applied between the source and sink channel, causing interstitial flow in the center channel. While TGF-β concentration at the source channel was consistently higher than the sink channel, interstitial flow direction was applied either 1) source to sink defined as a *parallel flow* or 2) sink to source as a *counter flow*. (**Figure 1**)

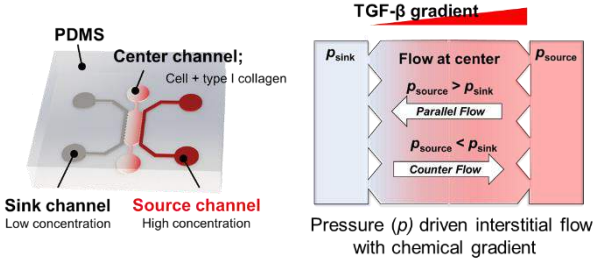

Figure 1: An engineered convection-driven signal environment platform.

We captured migrating KICs using a live-cell time-lapse imaging system inverting a stage top incubator. The directed migration was characterized by directional accuracy represented as directional accuracy index (DAI). We measured DAI = cos θ where θ is an angle between the net displacement of a trajectory and the environmental signal direction. Cells randomly migrate without any signal, showing the spread of DAIs is varied from -1 to 1, where the data points are distributed following cosine shape. The median of the distribution was used as a representative DAI of each control group.

RESULTS

Chemical signals are transported in the tumor microenvironment through both advection and diffusion. [5]

$$\frac{\partial C_i}{\partial t} = \nabla \cdot (D_{eff} \cdot \nabla C_i - v_f \cdot C_i) \quad (1)$$

Here, we considered two different scenarios: i) parallel flow from the source to the sink, and ii) counter flow from the sink to the source, where a chemical signal concentration is higher in the source and lower in the sink. At a steady state, the gradient profiles are non-linear exponential varied by the flow direction and the Péclet number, whereas a linear gradient is developed without the flow. Compared to the linear chemical gradient, two distinct changes were observed in the non-linear chemical gradient. First, the gradient becomes shallower in most regions, except the edge near the boundaries. When the parallel flow was applied, the flow carried the signal molecules and helped to deliver them, increasing the background concentration. Contrarily, the background concentration in the counter flow applied signal environment was relatively low.

The convection-driven signal environment simultaneously exposes both non-linear chemical gradient and interstitial flow to the cells. To interrogate the combined signals' effect, we decoupled those by considering cells' physical detection limit in sensing the chemical gradient. Many types of cells, including cancer cells, are capable of sensing shallow gradients. [6] However, a cell's ability to sense spatial gradient signals is limited due to physical constraints from the cell surface receptor-ligand dynamics and molecule diffusion. Indeed, *Dictyostelium* and cancer cells have recently elucidated to sense as low as ~1% of concentration differences across the cell body. [6-7] Accordingly, we examined the chemical signal environment, whether it satisfies cells' sensing capacity or not. The percent change of the chemical concentration across the cell body was determined as [7]

$$\bar{P}\,[\%] = \frac{ga'}{\bar{c}} \quad (2)$$

Consequently, we decoupled the integrated signal environment by suggesting a region where a chemical gradient effect is negligible with $\bar{P}$ below the cells' physical detection limit (~1%). It implies that the cells cannot sense the chemical gradient to enhance their directional accuracy.

To verify the suggestion above, we investigated cellular response to the integrated signal environment. We analyzed cell trajectories by separating two regions where the percent change is **(i)** above the cell's physical detection limit ($\bar{P}$ > ~1%) and **(ii)** below the limit ($\bar{P}$ < ~1%). (**Figure2A and B**) In the baseline experiments, cells were guided toward either TGF-β gradient (∇T) or upstream direction of interstitial flow (V_f) showing significantly biased DAI distribution toward 1. Remarkably, we observed that KIC cells exposed by the convection-driven TGF-β gradient showed different responses depending on the environmental condition where the physical detection limit for both parallel and counter flow conditions. In both flow directions, cells significantly lost their directional accuracy to the TGF-β gradient at the region (ii) where the TGF-β signal environment does not satisfy the cells' physical detection limit. (**Figure2C and D**) Furthermore, the bias effect induced by the flow signal was eliminated when the background concentration of TGF-β was higher in parallel flow, suggesting that the cell's innate capability in signal processing might compete for chemical and mechanical signals, although further research needs to be performed.

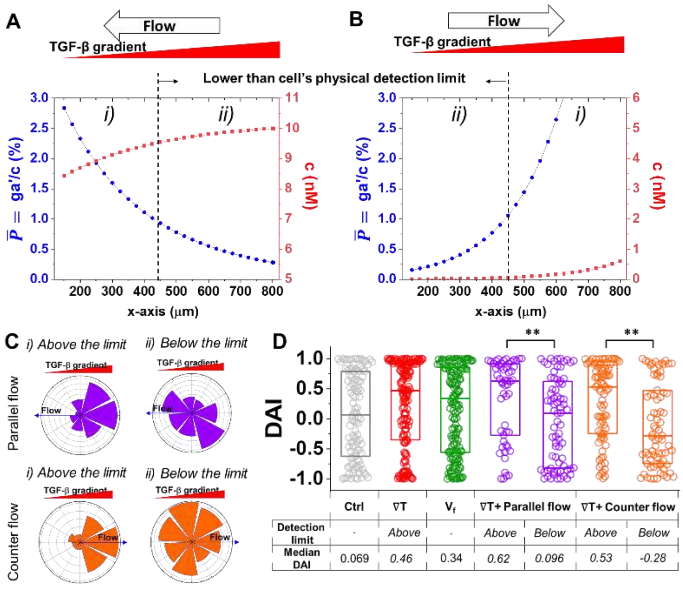

Figure 2: Integrated signal environment with (A) parallel flow and (B) counter flow. (C) Angular distributions (θ) of KIC cell trajectories. (D) Directional accuracy index (DAI) distributions. Box; interquartile range (IQR) with a median line **; p<0.01 (student t-test)

DISCUSSION

The present results elicit an effect of convection on cellular sensing precision for directed cell migration. We evaluated the effect of the complex signal environment by physically decoupling the signals. The flow-applied signal environment alters the TGF-β concentration profiles in non-linear exponentials, where the cells experience the shallow gradient close to the physical detection limit. The cells' movement was highly biased even with the shallow gradient only when they were with the signal above the cells' detection limit. This study provides a novel insight for understanding the complex signal environment inducing directed migration based on quantitative approaches by using an *in vitro* engineered microenvironment.

ACKNOWLEDGEMENTS

This work was partially supported by a grant from the Purdue University Center for Cancer Research, NIH grant P30 CA023168.

REFERENCES

[1] Roussos, E. T., et al., *Nature Reviews Cancer* **11**, 573-587, 2011.
[2] Swartz, M. A., et al., *Cancer Research* **72**, 2473-2480 , 2012.
[3] Polacheck, W.J., et al., *PNAS* **108**, 11115-11120, 2011.
[4] Dewhirst, M.W., et al., *Nature Reviews Cancer* **17**, 738-750, 2017
[5] Ozcelikkale, A., et al., *Wiley Interdisciplinary Reviews: Nanomedicine and Nanobiotechnology* **9**, e1460 2017.
[6] Varennes, J., et al., *Molecular pharmaceutics* **13**, 2224-2232, 2016
[7] Van Haastert, P. J., et al., *Biophysical journal* **93**, 1787-1796, 2007

SUBSTRATUM STIFFNESS MODULATES THE MORPHOLOGY AND PROLIFERATION OF PRIMARY CORNEAL KERATOCYTES IN RESPONSE TO PDGF-BB

Krithika S. Iyer (1), David W. Schmidtke (1), W. Matthew Petroll (2), Victor D. Varner (1)

(1) Department of Bioengineering
University of Texas at Dallas
Richardson, Texas, United States

(2) Department of Ophthalmology
UT Southwestern Medical Center
Dallas, Texas, United States

INTRODUCTION

The cornea is the soft transparent tissue located at the anterior aspect of the eye, which helps bend light towards the retina [1]. It contains three distinct cellular layers, but the stromal compartment accounts for the majority of the thickness. The stroma has a highly organized extracellular matrix (ECM) that consists of lamellae of aligned type I collagen fibrils [2] and promotes the transparent optical properties of the tissue [3].

A population of cells called corneal keratocytes maintain this highly ordered ECM [3], but following injury or refractive surgery, damage to the cornea can cause growth factors, such as transforming growth factor beta-1 (TGF-β1) and platelet derived growth factor-BB (PDGF-BB) to be released into the stromal space [4]. PDGF-BB has been shown to promote the motility and proliferation of corneal keratocytes [5]. However, the cornea also stiffens substantially following an injury [6], and previous work in our group has shown that the TGF-β1-mediated myofibroblastic activation of corneal keratocytes depends on substratum stiffness [7]. But it is unclear if keratocyte behavior in response to other growth factors, such as PDGF-BB, is similarly modulated by changes in stiffness. Here, we used a polyacrylamide (PA) gel system to determine whether changes in substratum stiffness modulate the proliferation and motility of primary corneal keratocytes treated with PDGF-BB.

METHODS

PA substrata with an elastic modulus of either 1 kPa (soft) or 10 kPa (stiff) were fabricated to mimic the mechanical properties of either normal or fibrotic corneal tissue. The gels were then functionalized with unpolymerized type I collagen.

Primary rabbit corneal keratocytes (NRKs) were harvested from rabbit eyes, as described previously [8], plated on either the PA substrata or collagen-coated glass coverslips, and cultured in defined serum-free media in either the presence or absence of PDGF-BB.

We used a freeze injury model to assay changes in keratocyte motility [9]. Briefly, a circular wound, approximately 1.5 mm in diameter, was created by holding a liquid nitrogen-cooled aluminum rod against the underside of the culture dish. In some samples, the media was supplemented with PDGF-BB and samples were then placed in a stage-top incubator, where images were captured at 1-hour intervals for 4 days. In other experiments, keratocytes were treated with PDGF-BB for 72 hours before fixation. Fixed cells were then stained with phalloidin and DAPI, to stain F-actin and nuclei, respectively. We also used the Click-iT EdU Imaging Kit to quantify rates of keratocyte proliferation in both the presence and absence of PDGF-BB. Confocal images of fixed samples were captured on a Zeiss LSM 800, and quantitative image analysis was performed in ImageJ.

RESULTS

To determine if changes in stiffness affect the motility of cultured keratocytes in response to PDGF-BB, we created freeze injuries on both soft (1 kPa) and stiff (10 kPa) PA substrata, as well as collagen-coated glass coverslips (~GPa). In both the presence and absence of PDGF-BB, cells surrounding the decellularized area migrated into the wound over a 96 hr period. PDGF-BB-treated cells migrated further into the wound and exhibited faster migration speeds than their counterparts in serum-free conditions, as assayed by both the tracked displacements of individual cells, as well as the motion of the leading edge of the wound. We did not, however, observe a stiffness-dependent effect in the motility of the PDGF-BB-treated cells.

We also quantified EdU incorporation in NRKs cultured on substrata of varying stiffnesses in both the presence and absence of PDGF-BB (Fig. 1). Cultured keratocytes were pulsed with EdU 72

hours prior to fixation and stained for EdU and DAPI fluorescence. As expected, cells in serum-free conditions exhibited negligible amounts of proliferation on substrata of all stiffnesses (Fig. 1A, 1C). When treated with PDGF-BB, however, the NRKs proliferate at significantly higher rates in a stiffness-dependent manner, with cells on the stiffest substrata proliferating at the highest rate (Fig. 1B, 1C).

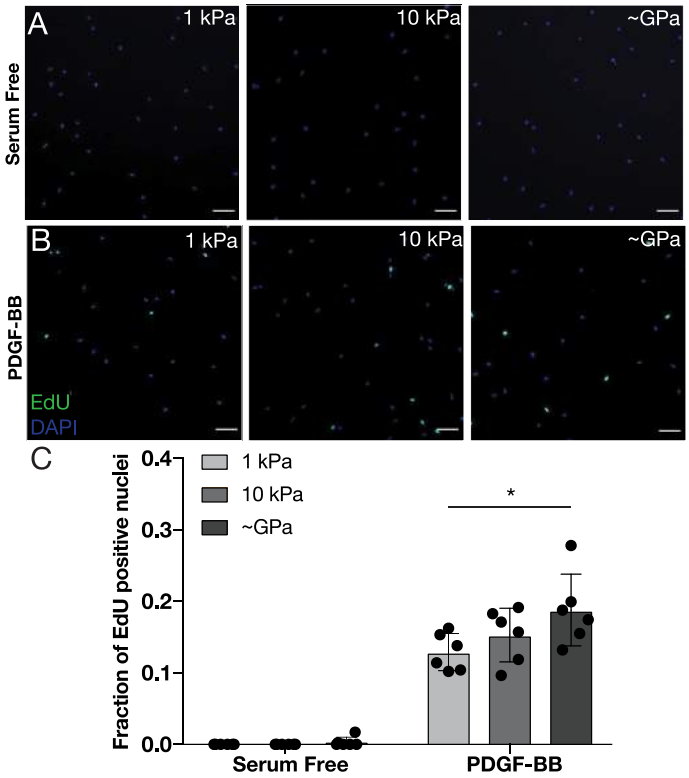

Figure 1: Quantifying keratocyte proliferation on substrata of varying stiffness. Wide-field fluorescence images of NRKs (A) without and (B) with PDGF-BB (C) Quantification of rates of EdU incorporation, scale bar = 100 µm.

Lastly, we analyzed the morphology of PDGF-treated keratocytes cultured on substrata of varying stiffnesses (Fig 2). In serum-free conditions, the NRKs retained a branched, dendritic morphology, indicative of a quiescent keratocyte phenotype (Fig. 2A). Treatment with PDGF-BB, however, promoted striking changes in morphology, as the cells spread out and became more elongated in the presence of this growth factor (Fig. 2B). The PDGF-treated keratocytes also displayed stiffness-dependent differences in morphology, with cells on the stiffest substrata exhibiting the largest cell areas and adopting more highly elongated geometries (Fig. 2C, 2D).

DISCUSSION

Taken together, these data suggest that PDGF-BB-driven changes in keratocyte morphology and proliferation depend on substratum stiffness, in a manner similar to the stiffness-dependent myofibroblastic activation of keratocytes in response to TGF-β1 [7]. PDGF-BB promoted an increase in the motility of cultured keratocytes, consistent with previous studies [5], but we did not detect any stiffness-dependent differences in their ability to repopulate a decellularized wound in vitro. Previous work has suggested that keratocytes treated with PDGF-BB exhibit similar phenotypes in both compressed and uncompressed 3D collagen gels, despite the differences in the mechanical properties of these matrices [5]. Here, however, our use of a polyacrylamide gel

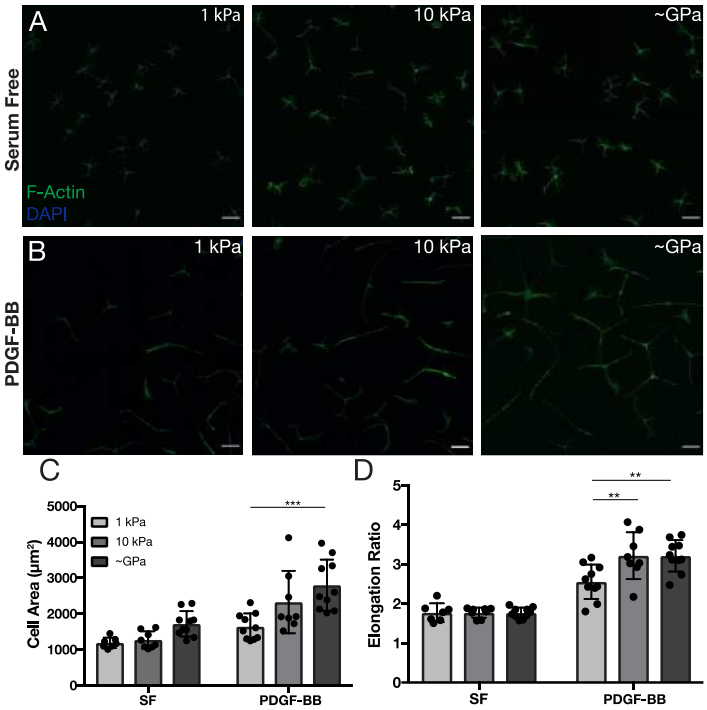

Figure 2: Wide field fluorescence images of phalloidin and DAPI staining in keratocytes cultured on substrata of different stiffness and fixed after 5 days. Cells were cultured either in the (A) absence or (B) presence of PDGF-BB. Scale bar – 100 µm. Quantification of (C) cell area, (D) cell elongation. A two-way ANOVA with a Tukey post-hoc test was used to evaluate significance among groups. (*, p < 0.05; **, p < 0.01; ***, p < 0.001; ****, p < 0.0001; n.s – not significant).

system allowed us to decouple ECM composition from substratum stiffness – two variables that remain coupled in 3D collagen matrices – and we observed striking stiffness-dependent differences in the proliferation and morphology of NRKs treated with PDGF-BB. It is not clear how corneal keratocytes might be detecting these changes in stiffness, and it would be interesting to determine how the traction forces exerted by these cells might (or might not) be regulated by changes in the stiffness of their microenvironment.

ACKNOWLEDGEMENTS

This work was supported by the NIH grants R01 EY030190 and P30 EY030413 and an unrestricted grant from Research to Prevent Blindness to VDV, DWS and WMP.

REFERENCES

[1] Fini, M. E., *Prog Retin Eye Res*, 18:529 – 551, 1999.
[2] Meek, K.M., *Prog Retin Eye Res*, 28:369 – 392, 2009.
[3] Hassell, J. R., *Experimental Eye Research*, 91:326 – 335, 2010.
[4] Torricelli, A. A.M., *IOVS*, 54: 6390 – 6400, 2013.
[5] Lakshman, N., *IOVS*, 53:1077-1086, 2012.
[6] Thomasy, S. M., Acta *Biomaterialia*, 10:785 – 791, 2014.
[7] Maruri, D P., *Biophysical journal*, 119.9: 1865-1877, 2020.
[8] Jester, J. V., *Cornea*, 15:505-516, 1996
[9] Kivanany, P. B., *Journal of functional biomaterials*, 9, 2018.

CURVATURE SENSING IRSP53 IS CRITICAL FOR MIGRATIONAL PERSISTENCE IN CELLS CRAWLING ON SUSPENDED NANOFIBERS

Apratim Mukherjee (1), Bahareh Behkam (1), Shiro Suetsugu (2) and Amrinder S. Nain (1)

(1) Department of Mechanical Engineering
Virginia Tech
Blacksburg, VA, United States

(2) Division of Biological Science and Data Science Center
Nara Institute of Science and Technology
Ikoma, Japan

INTRODUCTION

The Insulin Receptor tyrosine kinase Substrate protein of 53 kDa (IRSp53) is a well-known regulator of cell membrane curvature and is posited to act as an adapter protein, linking the membrane deformations at the cell boundary to changes in the cytoskeletal contractility [1]. Consequently, previous studies have highlighted that the abrogation of IRSp53 leads to impaired protrusive activity at the cell membrane and impeded migration dynamics [2]. However, the role played by IRSp53 in linking the changes in cytoskeletal contractility to the migration cycle remains poorly understood. Additionally, these prior studies have been primarily conducted on flat, 2D surfaces which do not recapitulate the fibrous nature of the extracellular matrix (ECM) *in vivo*.

Here, we used suspended nanofiber matrices to investigate the role of IRSp53 in the migration cycle in IRSp53 knockout (KO) and wild type (WT) U251 glioma cells, which is initiated by the extension of protrusions and subsequent establishment of contractility. We selected two fiber diameters: 135 nm (high curvature) and 500 nm (low curvature) which match reported *in vivo* ECM fiber dimensions [3]. While our results confirmed the role of IRSp53 in limiting both cell protrusive and spreading behavior, we find a surprising association between IRSp53 and cell contractility in mediating the nucleus shape. IRSp53 depletion reduced cell contractility and led to low correlation between nucleus and cell body during migration causing both reduced migration rates and migratory persistence.

METHODS

The non-electrospinning Spinneret based Tunable Engineered Parameters (STEP) method was used to manufacture the fiber networks [4]. Briefly, polystyrene (PS, Scientific Polymer Products, Ontario, NY) of ~2×10^6 g/mol molecular weight was dissolved in xylene (Thermo Fischer Scientific, Pittsburgh, PA) at 6% (w/w) concentration and 10% (w/w) concentration to prepare the solutions for spinning the ~135 nm and ~500 nm diameter fibers respectively.

U-251 cells were obtained from the Japanese Collection of Research Bioresources Cell Bank. The IRSp53 knockout (KO) were generated by the CRISPR/Cas9 system, as described previously [5]. Cells were cultured in high glucose DMEM (Thermo Fisher Scientific) supplemented with 10% bovine calf serum (Thermo Fischer Scientific). Prior to seeding the cells, the fibers were coated with 4 µg/ml Fibronectin (Invitrogen, Carsbad, CA) for 3 hours. Cells were imaged using an AxioObserver Z.1 (with mRm camera) microscope (Carl Zeiss, Germany). Statistical analysis of the data was performed using RStudio (RStudio, Boston, MA) and One-way analysis of variance (ANOVA) with the Tukey test was used to test for statistical significance.

RESULTS

We first investigated the role of IRSp53 in modulating protrusive dynamics on suspended fibers. To this end, we deposited large diameter "base fibers" orthogonal to smaller diameter "protrusive fibers (**Figure 1A**). This configuration of contrasting fiber diameters constrains bulk cell body migration along the base fiber allowing us to investigate individual protrusions along the protrusive fiber. We found that IRSp53 KO cells exhibited protrusions of similar length to the WT cells (**Figure 1B**) but took significantly longer to reach the same maximum protrusion length as the WT cells (**Figure 1C**). Cells sense the suspended fibers by *coiling* (wrapping around the fiber axis) at the protrusion tip [6]. *Coiling* occurs in a cycle with the *coil* width increasing, reaching a maximum value and finally decreasing (**Figure 1D**). We quantified the maximum *coil* width and found that KO cells exhibit diminished *coil* width compared to the WT cells (**Figure 1E**).

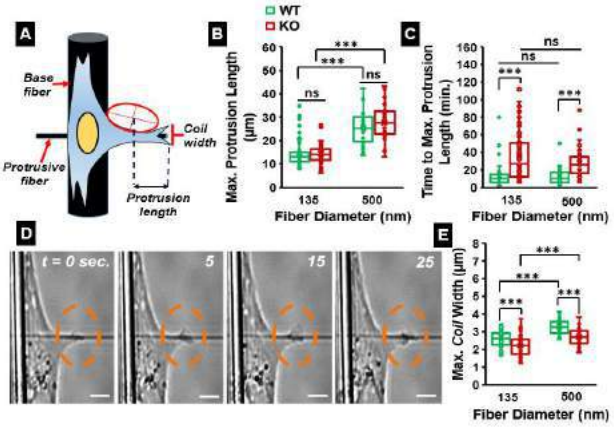

Figure 1: IRSp53 knockout impairs protrusive activity and 3D *coiling* at protrusion tip. (A) Schematic of the fiber network used to quantify protrusive activity. n = 38, 50 for WT and KO cells respectively on each fiber diameter. Quantification of (**B**) maximum protrusion length and (**C**) time taken to reach maximum length**. (D)** Representative phase images showing a typical *coiling* cycle (scale bars are 5 μm). Dashed orange circles show *coiling*. (**E**) Quantification of the maximum *coil* width. n = 30 for both cell types.

We naturally inquired if the altered protrusive activity was connected with cell shape and cytoskeletal contractility. We found that on the flat surface, KO and WT cells both spread at a similar rate and attained equivalent final circularity values (**Figure 2A**). In contrast, on the suspended fibers, the WT cells appeared to spread significantly faster than the KO counterparts and reached a lower steady state circularity signifying elongated cells (**Figure 2B**). Using our nanonet force microscopy (NFM) platform [7, 8] which enables quantification

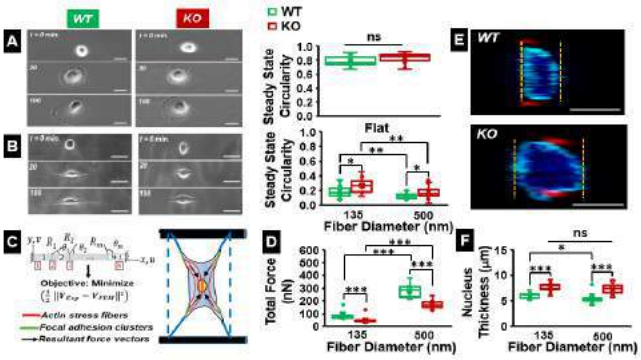

Figure 2: IRSp53 knockout results in impaired contractility. (A) Phase images showing the spreading of WT and KO cells on flat surface and corresponding quantification of steady state circularity on (A) flat surface and (B) suspended 500 nm diameter fibers. Scale bars are 20 μm. n = 18 for each category. **(C)** Schematic depicting the NFM platform. **(D)** Quantification of total forces exerted. n = 15 for each category. **(E)** Confocal images of yz section of the nucleus on 500 nm diameter fiber. Nucleus is in blue, nuclear envelope in cyan, and fiber cross-section in red. Scale bars are 10 μm. **(F)** Quantification of nucleus thickness. n = 18 for each category.

of single-cell forces (**Figure 2C**), we found that the KO cells exerted lower forces than WT (**Figure 2D**) ultimately translating to thicker nucleus (**Figure 2E, F**).

Finally, we investigated if the changes in protrusive activity and contractility resulted in differences in migration dynamics. We found that on both the flat surface and suspended fibers, the KO cells exhibited lower migration speed and persistence of motion (**Figure 3A.i,ii**). Intriguingly, in case of the KO cells, the nucleus displacement lagged behind the centroid whereas in contrast, the WT cells exhibited synchronous nucleus-centroid displacement (**Figure 3B-D**).

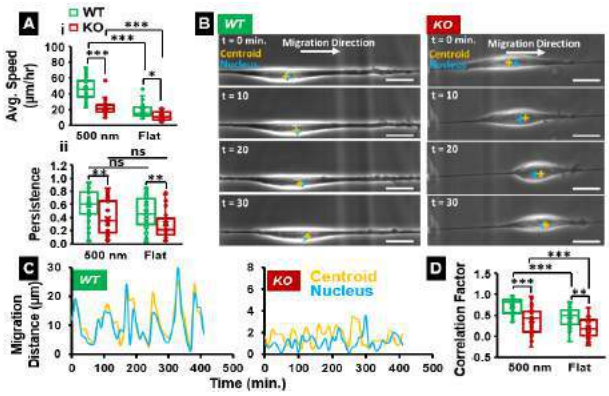

Figure 3: IRSp53 knockout hinders migration dynamics. (A) Quantification of (i) migration speed and (ii) persistence of WT and KO cells on suspended fibers and flat surface. **(B)** Representative phase images showing nucleus (in blue) and centroid (in yellow) tracking for both WT and KO. Scale bars are 25 μm. **(C)** Representative centroid and nucleus profiles during migration for WT and KO cells. **(D)** Quantification of the average correlation factor between nucleus and centroid. n = 35 for each category.

DISCUSSION

In this study, we investigated the role of IRSp53 in linking protrusive activity at the cell membrane to cytoskeletal contractility and resulting migration dynamics on ECM-mimicking suspended fibers.

While previous studies on flat, 2D surfaces have shown that IRSp53 abolishment leads to reduced protrusion length, we find that on ECM-mimicking suspended fibers, the protrusion speed rather than the length is impaired. Furthermore, given that IRSp53 KO has been linked with reduced invasive potential, the lower *coil* width at the protrusion tip concurs with our previous work, in which we have demonstrated a correlation between invasive capacity and *coil* width [6]. Previous studies have also yielded contrasting results regarding the influence of IRSp53 on cell spreading dynamics. Here, we find that IRSp53 KO leads to slower spreading dynamics on suspended fibers and a more rounded steady state morphology compared to WT, differences which are not captured on a 2D substrate. Furthermore, we report, for the first time, that IRSp53 KO results in a change in the nucleus shape which prompts the intriguing possibility of an indirect link between IRSp53 and the gene transcription landscape. In addition to the altered nucleus shape, we find that IRSp53 KO results in an impairment of the nucleus-cytoplasm coupling that alters migration dynamics.

ACKNOWLEDGEMENTS

This work is supported by NSF award #1762634 awarded to Amrinder Nain.

REFERENCES

[1] Miki, H et al., *Nature*, 408:732-735, 2000.
[2] Scita, G et al., *Trends in Cell Biol.*,18:52-60, 2008.
[3] Ushiki, T., *Arch. Of Hist. & Cyt.*, 65:109–126, 2002.
[4] Nain, A. S, et al., *Macromol Rapid Commun*, 30:1406–1412, 2009.
[5] Mashiko, D et al., *Sci. Rep.*, 3:1-6, 2013.
[6] Mukherjee, A et al., *iScience*, 19:905-915, 2019.
[7] Sheets, K et al., *Biophy. J.*, 111:197-207, 2016.
[8] Padhi, A et al., *Comm. Bio.*, 3:1-11, 2020.

SOPHOROLIPIDS DEMONSTRATE PROMISING ANTI-CANCER EFFICACY IN 2D, 2.5D, AND 3D BREAST CANCER MODELS

Cassandra L. Roberge (1), David M. Kingsley (1), Lillian R. Murphy (1), Filbert Totsingan (2), Rebecca T. Miceli (1,2), Richard A. Gross (1,2), David T. Corr (1)

(1) Department of Biomedical Engineering
Rensselaer Polytechnic Institute
Troy, NY, USA

(2) Department of Chemistry
Rensselaer Polytechnic Institute
Troy, NY, USA

INTRODUCTION

Sophorolipids are biosurfactants derived from non-pathogenic yeasts currently being investigated for anti-cancer applications [1]. Synthesis of these drugs is relatively simple, high-yield, and extremely cost-effective, which would make them a promising alternative to traditional chemotherapeutics, pending their success in preliminary drug screening. Traditionally, these screenings are performed in 2D culture systems due to their simplicity and throughput. However, for more advanced screening, sophisticated models are required to capture the complexity of the 3D microenvironment. Indeed, screening with 2D tumor models, lacking a 3D context, has been implicated in the high percentage of investigated drugs that later fail in clinical trials [2]. Multicellular tumor spheroids (MCTSs) are a promising 3D platform that better mimic *in vivo* structure and pathophysiologic gradients. Previously, our lab has used Optical Coherence Tomography (OCT), a non-destructive structural imaging modality, to assess 3D morphologies of MCTSs formed (via liquid overlay) either with or without the addition of Matrigel (solubilized basement membrane derived from mouse sarcoma). We showed that Matrigel addition shifted aggregate morphology from 2.5D disk-like aggregates to more spherical 3D aggregates **(Fig. 1A & B)** [3].

The aim of this study is to assess the anti-cancer activity of two novel sophorolipid candidates in *in vitro* tumor models of increasing dimensionality - 2D monolayers, 2.5D disk-shaped aggregates, and 3D spheroids - to explore the impact of model morphology on drug efficacy. Additionally, the efficacy of these candidate sophorolipids will be benchmarked against a gold standard chemotherapeutic – Paclitaxel. By calculating the half maximal inhibitory concentration (IC_{50}) for each of the tumor models, we hope to decipher how the dosing changes with *in vitro* tumor model dimensionality, as we work toward more predictive *in vitro* tumor models and explore more cost-effective alternatives to traditional chemotherapeutics.

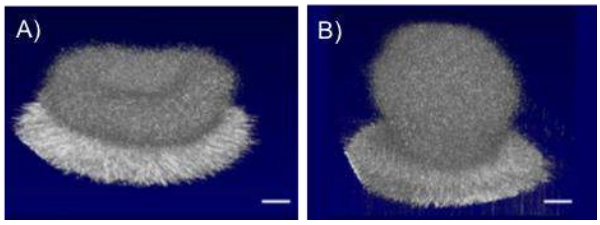

Figure 1: Representative OCT images of (A) Matrigel (-) 2.5D aggregates and (B) Matrigel (+) 3D spheroids, both prepared with M231 cells. Scale bars = 100µm.

METHODS

Sophorolipid ethyl ester diacetate (ESL) and Lactonic/Acidic sophorolipid (LSL/ASL) (ratio 97:3) were synthesized following previously established procedures [4]. Briefly, both sophorolipid mixtures was synthesized by use of *C. bombicola* yeast fermentation under conditions of glucose/oleic acid. ESL was generated from this original mixture via a one-pot reaction with Novozyme 435. To assess cancer specificity, 2D monolayers were prepared using healthy breast epithelial fibroblast controls (CCD-1065Sk) or triple-negative breast cancer cells (MDA-MB-231) by seeding $1x10^4$ cells/well in flat-bottom 96-well plates, and culturing for 24 hours prior to drug-addition. The effect of model dimensionality on drug resistance was assessed by preparing 2.5D aggregates and 3D spheroids using liquid overlay, in which breast cancer cells were seeded ($2.5 x10^4$ cells/well) in non-adherent U-shaped 96-well plates and cultured for 4 days either with or without the addition of 5% Matrigel, respectively [5]. Following 12 hours of drug exposure, samples were treated with

CCK8 metabolic assay and absorbances were measured via spectrophotometer. IC_{50} values were calculated by dividing the absorbance of drugged wells by the absorbance of untreated controls. Next, therapeutic index (TI) was calculated using **Equation 1** to provide a quantitative measure of the efficacy and relative safety of the tested drugs, where a higher TI indicates greater toxicity to cancer cells than neighboring healthy cells.

$$TI = LD_{50}/ED_{50} \qquad \textit{(Equation 1)}$$

The IC_{50} value for the drug on the healthy fibroblasts in 2D monolayer culture was used as the mean lethal dose (LD_{50}), while the IC_{50} value for the drug on a given model was used as the mean effective dose (ED_{50}).

RESULTS

Cell aggregates exhibited higher IC_{50} values in 3D models when compared with both 2.5D and 2D models for all drugs tested, indicating substantially higher drug resistance with greater model dimensionality **(Table 1).** IC_{50} values in 3D were ~4x, 7x, 15x those in 2D monolayers for Paclitaxel, ESL, and LSL/ASL, respectively. ESL was found to be approximately twice as cytotoxic as LSL/ASL in both the 2.5D and 3D MDA-MB-231 models. Both SLs required a ~2-3x higher dose than clinically-used Paclitaxel for nearly all conditions investigated. ESL was the only tested drug that showed cancer-specificity, with a higher IC_{50} value for the healthy fibroblasts than the cancer cells in 2D.

Lastly, we calculated and compared a relative TI for each drug at each model morphology (**Figure 2**). ESL showed the greatest therapeutic index in both 2D and 2.5D models, outperforming LSL/ASL and, notably, Paclitaxel. ESL also showed a comparable TI to Paclitaxel in 3D models, while LSL/ASL showed a poor TI in 3D models.

Table 1: Summarized IC_{50} values for all tested conditions, which revealed increased drug resistance in 3D models, and increased cytotoxicity in ESL over LSL/ASL.

Condition	*Paclitaxel* IC_{50}	*ESL* IC_{50}	*LSL/ASL* IC_{50}
2D monolayer fibroblast control	*15μg/mL*	*36μg/mL*	*14μg/mL*
2D monolayer	*15μg/mL*	*26 μg/mL*	*25 μg/mL*
2.5D aggregate	*54μg/mL*	*48 μg/mL*	*90 μg/mL*
3D spheroid	*65μg/mL*	*180 μg/mL*	*380 μg/mL*

DISCUSSION

Our goal was to provide preliminary data to suggest eventual use of these sophorolipid candidate drugs as a more affordable alternative for clinical interventions. Our data show that synthetically-modified ESL is generally more cytotoxic than LSL/ASL, but its efficacy falls short of clinically-used Paclitaxel, while also demonstrating significant cancer-specificity in 2D models. Taken together, these findings are extremely promising for potential future clinical use of these sophorolipids in cancer treatment.

One of the most striking findings of our study was the influence of model morphology on drug resistance. For all drugs tested, we observed significantly higher IC50 values for 3D models compared to both 2.5D and 2D models, indicating substantially higher drug resistance with increasing model dimensionality. The large IC_{50} differences for the same drug between 2D-2.5D-3D models highlights

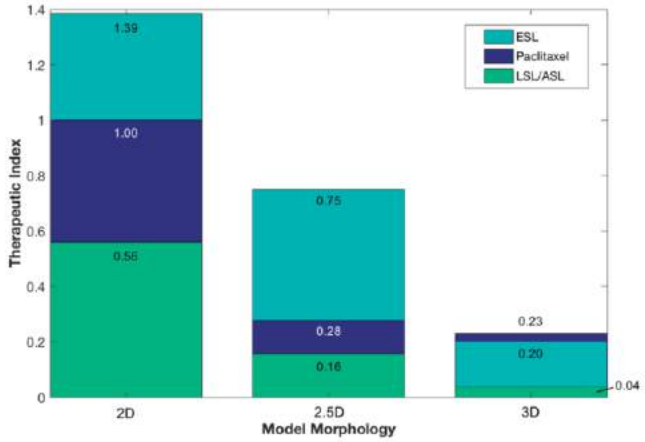

Figure 2: Therapeutic index as a function of model morphology. ESL showed the highest therapeutic index in 2D and 2.5D and was comparable to that of Paclitaxel in 3D models.

the importance of selecting an appropriate model for drug-screening.

Additionally, they indicate that drug toxicity cannot be reliably inferred from 2D models, as the results could differ greatly from *in vivo*-like response, which much more closely mimic the 3D spheroids tested herein (i.e., structure, pathophysiologic gradients). These findings also support the idea that screened drugs' poor success in clinical trials may be attributed, at least in part, to the use of inaccurate drug-screening models [2], such as 2D monolayers, which, despite offering high-throughput capabilities, may greatly overestimate toxicity of a given drug.

Additionally, our 2D testing with a noncancerous cell line showed that the SLs are no more toxic to surrounding cells than our positive control, Paclitaxel. Moreover, Paclitaxel exhibited an identical IC_{50} value for both cell types tested, supporting prior studies which found that Paclitaxel lacks selective cytotoxicity between cancer and normal cells [7, 8]. Interestingly, while the taxol was more toxic to cancer cells than the LSL/ASL, these drugs had comparable IC_{50} values when tested on the fibroblasts, indicating that the LSL/ASL is more toxic to healthy cells than cancer cells. On the other hand, the ESL displayed a higher IC_{50} value for fibroblasts than cancer cells, providing early evidence that this drug formulation may have some cancer-cell specificity. Notably, the TI values are generally lower than similar drug-screening literature, likely due to the heartiness of our selected breast epithelial fibroblast controls compared to weaker healthy cell controls (i.e., immune cells) utilized in those studies. Our future studies will seek to confirm these TI results using additional non-cancerous cells found in the tumor microenvironment (i.e., immune, stromal, and/or endothelial cells), and explore ESL modificaitons to enahance its anti-cancer specificity.

ACKNOWLEDGEMENTS

This work was funded by NIH R01 BRG CA207725 (DTC), NIH R01 CA233188 (DTC), and NIH NIGMS T32GM067545 (RTM).

REFERENCES

[1] Peng Y. et al., *Eur. J. Lipid Sci. Tech.,* 117(1):217–228, 2015. [2] Langhans S., *Front. in pharmac*. 9(6), 2018. [3] Roberge CL et al., *Acta Biomat*. 117:322-334, 2020. [4] Singh SK et al., *J. Org. Chem*. 68(14):5466–5477, 2013. [5] Nagelkerke, A et al., *Anal. Biochem.* 437(1):1719, 2013. [6] Ribeiro IAC et al., *J. Mol. Recognit.* 28(3):155-165, 2015. [7] Filipová A et al., *J. Cell. Mol. Med.*, 23: 5728– 5736, 2019. [8] Ndungu JM et al., *J. Med. Chem*., 53(8):3127–3132, 2010.

LABEL-FREE QUANTIFICATION OF SOFT TISSUE ALIGNMENT BY POLARIZED RAMAN SPECTROSCOPY

H. Zhou(1), J. Piñeiro(2), M. Sarntinoranont(1,2), G. Subhash(1), C. S. Simmons(1,2)

(1) Mechanical & Aerospace Engineering, University of Florida, Gainesville, Florida, United States
(2) J. Crayton Pruitt Family Department of Biomedical Engineering, University of Florida, Gainesville, Florida, United States

INTRODUCTION

Soft tissues like tendons, skin and cartilage support loads and facilitate tissue compliance for functioning of human body. The assessment of structural organization of soft tissue constituents is essential for understanding of their mechanical functionality and for design of surrogates. Polarized Raman spectroscopy (PRS) has been exploited to characterize alignment of collagen in tendon[1] and bone[2] previously. However, Raman data of soft tissue are often noisy due to their intrinsic complex proteins, which hinders the uniform application of PRS to soft tissue with non-collagen extracellular matrix proteins. Here, we apply PRS coupled with principal component analysis (PCA) to provide intuitive quantifiable alignment of proteins in collagen-rich samples (rat tail tendon and fabricated collagen hydrogels) and complex layers of mouse skin. The alignment can be distinguished via PRS without labels and independent of precise tissue proteins, which confirms adaptability of this method to soft tissue containing complex and varying proteins.

METHOD

Biological samples. Bundles of collagen fibers approximately 50 mm long and 200 μm diameter were dissected from the proximal end of rat tails. To make gels, high-concentration rat tail collagen type I (Corning) was used to fabricate 5mg/mL collagen hydrogels polymerized for 30 mins at 37°C, as previously reported[3]. Samples are submerged in phosphate buffered saline (PBS) before measurement. Mouse skin samples were obtained according to protocols approved by Institutional Animal Care and Use Committee at the University of Florida.

Polarized Raman Measurements. Raman spectroscopy was performed in a Renishaw InVia spectrometer with a 532nm argon-ion laser at 50 mW power. The Raman spectra on each sample were recorded with a spatial resolution of approximately 1 μm (20× objective, 200× total magnification). The spectra were collected using WIRE 4.4 workstation software with a resolution less than 0.1cm^{-1}. Measurements were performed at room temperature with samples submerged in PBS, and 10 μm ROI was scanned at a step size of 1 μm, i.e. 11 acquired spectra, with 2 ROIs for each sample. 12 accumulations were used for each location. PRS measurements were conducted while maintaining the Raman polarizer at a fixed angle with both incident and detected laser polarized in the same direction. By rotating the sample, we varied the polarization angle between laser polarization and the sample alignment axis (Figure 1). The polarized angle was varied from 0˚ to 180˚ in 30˚ increments.

Data processing and PCA modeling. The raw spectra were subtracted from background fluorescence in WIRE 4.4 using an eleven-order polynomial fit. The obtained spectra were then truncated from 1400-1800 cm^{-1} and subtracted from background spectra obtained from blank glass slide submerged in PBS. Resulting spectra were further smoothed by Savitzky-Golay filters with polynomial order of 3 and window size of 11 in Matlab. Descriptive and multivariate statistical PCA analysis (Origin2020, OriginLab) of the muscle layer spectra provided a principal component (PC1) that captured differences in the spectra of different polarized angles. The loading curve of this PC1 was treated as a master loading function that was fed into PCA analysis to be applied to spectra of all other tissue samples. The output of PC1 score as a function of polarized angle for each location was fitted with sine function:

$$y = A \cdot \sin[(\pi(x - xc)/90°) \quad (1)$$

The amplitude of sine fit, *A*, was used as a metric for quantifying the alignment level in soft tissue samples via PRS. Tukey's post-hoc test was used to determine the statistically significant differences between the groups in (JMP15 software, JMP Corporation).

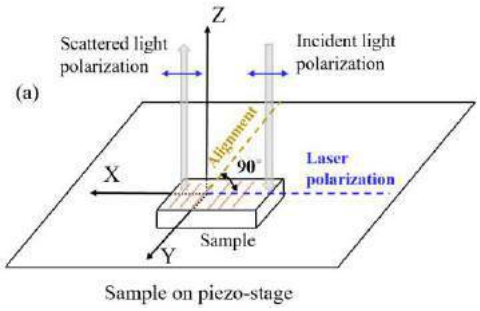

Figure 1: Schematic of the experimental PRS set-up, where the polarized angle is adjusted by rotating the sample counter-clockwise in XY plane with respect the laser polarization axis.

RESULTS AND DISCUSSION

The goal of this work was to leverage PRS to quantify the alignment in soft tissues independent of exact protein composition. To train a loading function that could distinguish the alignment of soft tissue structures, polarized Raman spectra were collected from mouse skin in a region with a known alignment, the paniculous carnosus muscle layer[4] (Figure 2 inset; direction of macroscopic alignment is perpendicular to the visible striations). Generally, intensities of Raman bands acquired in muscle layer were maximal at 0 degree (or 180 degree) and minimal at 90 degree, similar to other reports[6]. PCA was able to distinguish the spectral difference at different polarized angles, with most of the variability (86%) in the data explained by the first principal component (PC1, Figure 3). The PC1 loading curve depicts the Raman bands that exhibit the greatest contribution to the weighted PC1 score, including 1450 cm-1 (ν(CH2)) and 1649 cm−1 (amide I ν(C=O)). This suggests that both CH2 and C=O bonds have orientation-dependent Raman intensities, and indeed, PC1 scores were significantly different among the different polarized angles (Figure 4). Since these bonds are widely present in soft tissue, we hypothesized PC1 could be used to broadly assess alignment of protein structures in tissue.

To establish an analytical method that can quantify alignment in samples within unknown a priori orientation, we analyzed the amplitude of sine fit to the PC1 scores at different polarized angles (Figure 5a). The resulting sine fits reasonably captured the variation in Raman intensity of aligned proteins in tissue (R-square = 0.51±0.17, Figure 5a). Then, we applied the trained PC1 loading function to rat tail fibers (aligned) and collagen gels (unaligned) and obtained the amplitudes of their sine fits. For different structures of similar composition, we found a significantly higher mean amplitude in aligned rat tail tendon compared to the isotropic collagen gel (Figure 5b).

In each case, alignment can be distinguished via PRS without labels and independent of precise protein composition, which confirms adaptability of this method to soft tissue containing different proteins. Future work will focus on confirming utility of trained PCA model on soft tissue samples of different thickness and composition and engineered soft biomaterials, with the ultimate goal of monitoring the evolution of mechanical properties in engineered tissue.

ACKNOWLEDGEMENT

This work was supported by NSF CMMI 1762791.

REFERENCES

[1] Galvis, L et al., *PLoS ONE.* 8(5): e63518, 2013.
[2] Raghavan, M et al., *J Biomed Opt.*15(3):037001, 2010.
[3] Rubiano, A et al., *Tissue Eng. Part C: Methods.* 25: 619-629, 2019.
[4] Craig RW., ed. 2004. Molecular structure of the sarcomere. McGraw-Hill, New York
[5] Pezolet, M et al., *Biophys J.* 53(3): 319-325, 1998.

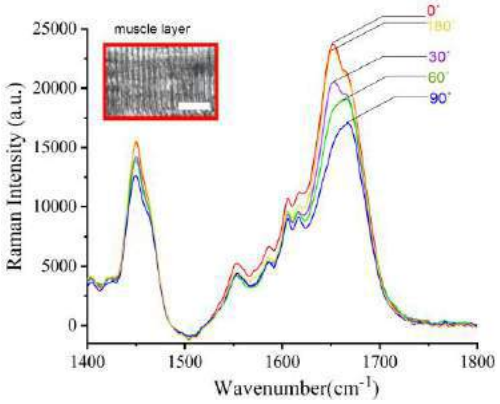

Figure 2: The mean Raman spectra (n = 22 technical replicates) of different laser polarization angles with respect to the muscle layer axis of mouse skin in 1400-1800 cm^{-1} range. Inset: Phase contrast image of muscle layer (scale bar: 10 μm)

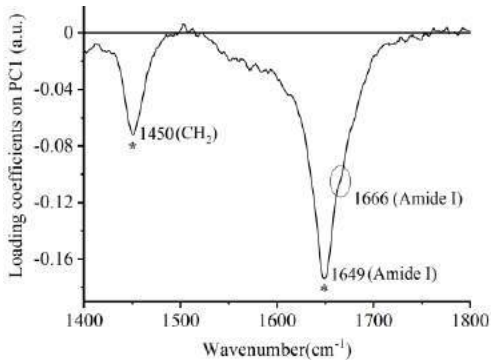

Figure 3: Principal component analysis (PCA) of 22 replicates at 5 angles (110 spectra total) yields a principal loading curve (PC1) that accounts for 86% of the variance among angles. Peaks in the loading curve (e.g., 1450 and 1649 cm^{-1} correspond to CH2 and Amide I bonds).

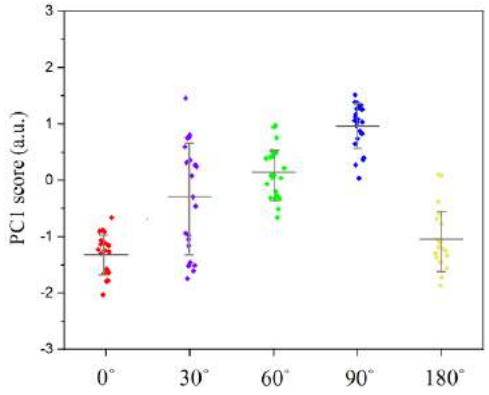

Figure 4: PC1 scores for Raman spectra yield significant differences among polarization angles (p-value ≤ 0.001 for all pairs except 0 ˚and 180˚ [p = 0.64] by Tukey's post-hoc test).

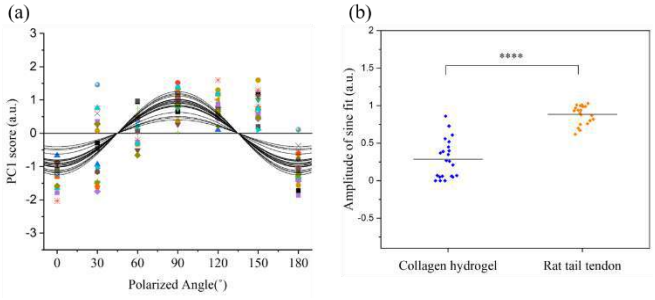

Figure 5 (a) PC1 score as a function of the angle of laser polarization with respect to muscle layer axis was fit by sine Equation 1. The curves show a maximum when the polarization of the laser is perpendicular to the muscle layer axis. (b) This process is translatable to tissues and surrogates with different protein composition than the original training tissue. Here, higher amplitude results for anisotropic tendon compared to the isotropic collagen gels (n=22 technical replicates, p<0.0001).

3D PRINTED MICROSTRUCTURES FOR REGENERATIVE OSTEOCHONDRAL IMPLANTS

**Kevin Eckstein (1), Camila Uzcategui (2),
Stephanie J. Bryant (2,3), Robert McLeod (2,4), Virginia L. Ferguson (1,2)**

(1) Department of Mechanical Engineering
University of Colorado at Boulder
Boulder, CO, USA

(2) Materials Science and Engineering Program
University of Colorado at Boulder
Boulder, CO, USA

(3) Department of Chemical and Biological Engineering
University of Colorado at Boulder
Boulder, CO, USA

(4) Department of Electrical, Computer & Energy Engineering
University of Colorado at Boulder
Boulder, CO, USA

INTRODUCTION

Articular cartilage regenerative scaffolds are typically made from soft hydrogels whose lack of load-supporting ability causes degradation of surrounding tissue [1] and subjects embedded cells to high physiological loads. To overcome the mechanical limitations inherent to these soft gels, we expand upon these scaffolds by integrating a 3D printed microstructure within the gel to support loads and shield cells from high stress (**Fig 1**). Our group recently developed a digital light processing (DLP) projection printing platform that is capable of printing overhanging features and complex geometries, with 1-10 µm printing resolution [2] (**Fig 2.a**). With thermal post-processing, the printed material achieves an elastic modulus of ~39 MPa [2], thus enabling the design of composite structures that feature a stiff framework infilled with a soft (50 kPa), degradable hydrogel for mesenchymal stem cell differentiation [3].

Our goal is to design 3D printed structures that 1) mimic the stiffness of native cartilage (~1 MPa), and 2) deliver precise mechanical cues (strain) to different regions of an osteochondral implant. Our group has demonstrated chondrogenesis in a soft (E = 50 kPa) gel scaffold when subjected to dynamic loading of 10% strain [3] and osteogenesis for strains <1.5% [4]. Using Finite Element Analysis (FEA), we designed a structure (**Fig 2.c**) to mimic these strains under physiological load (100 kPa). We then fabricated (**Fig 2.d**) the design and tested its ability to vary in strain between a top 'cartilage layer' and bottom 'bone layer'. In addition to evaluating strains, we also report the effective Young's modulus, E_{struct}, of each layer to describe load-carrying ability. Finally, we qualitatively evaluate the structure's stability under high deformations to identify presence of unwanted local buckling (**Fig 2.b**) in the framework.

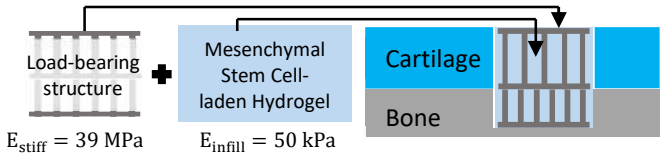

Fig 1. Our approach to creating a mechanically robust osteochondral implant that combines a stiff structure infilled with a soft hydrogel to later serve as a cellular niche.

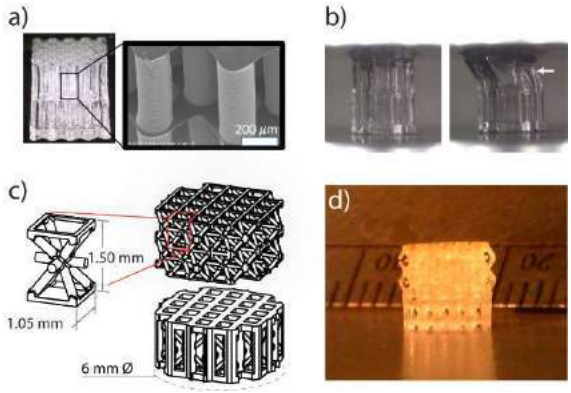

Fig 2. Design evolution of 3D printed structure; a) original design used vertical pillars to support axial load in compression; b) vertical pillars buckled under high (>5%) strains (arrow); c) bilayer design featuring an octet-truss unit cell. Top and bottom geometries differ in stiffness to mimic the osteochondral unit. d) Resulting 3D printed structure, with millimeter ruler in background for reference

METHODS

Design and FEA: We desired a structure that could deliver consistent strains to an infilled gel while bearing physiological load. This approach required a structure capable of resisting buckling under large deformation (>5% strain) while maintaining a stiff, 'structurally efficient' geometry that minimized the volume occupied by the structure. We chose an octet-truss microstructure for the cartilage layer and a simpler arrangement of pillars for the bone layer. Deformation behavior was modeling with FEA in Abaqus, considering non-linear geometric effects. Models used linear elastic material properties ($E = 39$ MPa [4], $\nu = 0.4$), 247k quadratic tetrahedral elements, and displacement-controlled unconfined compression. Thickness of the struts was iteratively changed to achieve the desired stiffness in each layer.

3D printing: The structure was fabricated with authors' custom DLP printer, described in detail in [4]. Materials included an acrylate-based resin, poly(ethylene glycol) diacrylate with pentaerythritol tetrakis(3-mercaptopropionate) (PEGDA:PETMP), and the photoinitiator diphenyl(2,4,6-trimethylbenzoyl) phosphine oxide (TPO). A thermal initiator, 2,2′-Azobis(2-methylpropionitrile) (AIBN) was introduced for post-processing cure.

Mechanical testing: Force-displacement curves were acquired from hydrated structures via displacement-controlled unconfined compression (MTS Insight II), while videos were simultaneously collected with a digital microscope (Dino-Lite) to measure strains in each layer. Tangent modulus was calculated at 10% total nominal strain.

X-ray microscopy (XRM) imaging: Images were collected using X-ray microscopy (Zeiss Xradia 520 Versa; 4×, 40kV, 3W, 4.5s; 801 images, 1.56 μm pixels). Samples were dehydrated in 100% ethanol and air. Unconfined compression was performed in situ with a custom-fabricated device using a micrometer with a non-rotating spindle.

RESULTS

FEA models of the bilayer design predicted the strains for each layer and supported a compressive load of 92 kPa at 5% total strain; E_{struct} was also determined for each layer (**Fig 3.a**). Imaging during compression of fabricated structures resulted in strain measures for each layer (**Fig 3.b**). The peak force was 1.94 N, which was used with the measured diameter (6 mm) and strain to determine each layers' stiffness E_{struct}. Repeated compression cycles resulted in similar force-displacement curves but with softer behavior than predicted by FEA (**Fig 2.c**).

XRM imaging of the dehydrated structure under compression showed no buckling at a strain of 7.7% in the cartilage layer. The bone layer strained to 0.6% (**Fig 4.a**). No buckling was observed during compression (**Fig 4.b**).

DISCUSSION

Our structures were designed to: 1) mimic cartilage stiffness in the top layer and 2) control the distribution of strains in a bilayer scaffold. We were successful in fabricating our bilayer design, and FEA predicts this design will nearly mimic cartilage stiffness in the top layer (0.95 MPa) while delivering a desired strain distribution (10% in cartilage layer [2], <1.5% in bone layer [4] under 92 kPa load. While layer-by-layer strains are reported here, extension of these models is needed to predict the mechanical environment within an embedded soft gel; these models are previously described [5] but require experimental validation.

Mechanical testing of the fabricated structure demonstrated softer behavior than predicted by FEA. Comparisons between XRM scans and the prescribed geometry show discrepancies in the reproduction of horizontal beams. Our next steps will be to optimize printing parameters to better match the exact geometry as designed. The structure was successful in repeatedly deforming without failure and provided two distinct regions of strain; future bioreactor studies may investigate differences in cell behavior between the cartilage and bone regions.

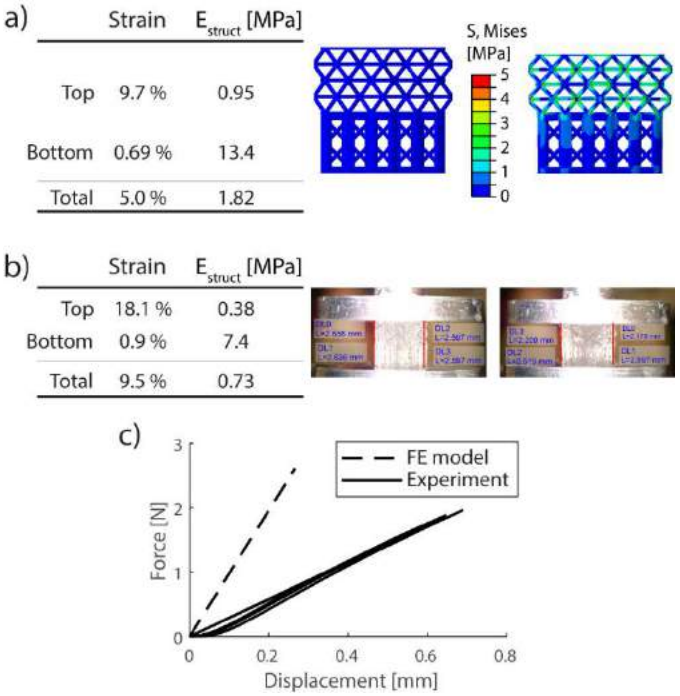

Figure 3: a) FE model results for strain and structural modulus, E_{struct}, in each layer; b) Unconfined compression with imaging results for strain and E_{struct} in each layer; c) force-displacement curves from FE model and experiment.

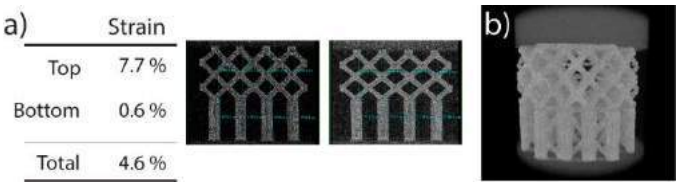

Figure 4: a) Strain in each layer as measured by X-ray Microscopy (XRM); b) 3D image of structure under compression.

XRM of the dehydrated structures under compression revealed a similar strain distribution and showed no evidence of buckling in the cartilage layer at high strain (7.7%). The XRM is a powerful imaging tool for this application as it enables future analysis of 3D printing accuracy as well as microstructure deformation.

The bilayer structure presented here is mechanically robust and offers a new method for controlling the mechanical cues delivered to cells in a scaffold. If successful, these implants could regenerate an osteochondral unit with a strong bone-cartilage interface.

ACKNOWLEDGEMENTS: Funded by NIH 1R01AR069060

REFERENCES

[1] Aisenbrey EA *et al., Biochem Biophys Res Commun*. 514(3):940-945, 2019.
[2] Uzcategui AC *et al.*, *Adv. Eng. Mater.* 20, 1800876, 2018.
[3] Aisenbrey, EA *et al.*, *J. Mater. Chem. B* 4, 3562–3574, 2016.
[4] Aziz, AH *et al.*, *J Tissue Eng Regen Med.* 13, 946–959, 2019.
[5] Eckstein KN *et al.*, BMES Annual Meeting, 2020.

CARBON NANOTUBE INFILTRATION EFFECTS IN THERMAL PROPERTIES OF SHAPE MEMORY POLYMER FOAMS – DESIGN OF A TRIGGERING MECHANISM FOR ENDOVASCULAR DEVICES

Sergio A. Pineda-Castillo (1,2), Bradley N. Bohnstedt (3), Yingtao Liu (2), Chung-Hao Lee (2,4)

(1) Stephenson School of Biomedical Engineering
University of Oklahoma (OU)
Norman, OK, USA

(2) School Aerospace and Mechanical Engineering
University of Oklahoma (OU)
Norman, OK, USA

(3) Department of Neurological Surgery
Indiana University School of Medicine
Indianapolis, IN, USA

(4) Institute for Biomedical Engineering, Science and Technology (IBEST)
University of Oklahoma (OU)
Norman, OK, USA

INTRODUCTION

Brain vessel regions of high shear stress are susceptible to the formation of aneurysms due to progressive thinning of the arterial wall. This risk of aneurysm rupture is mainly attributed to factors such as sex, smoking habits and aneurysm size, as diameters of ≥7 mm are more susceptible to rupture [1]. Currently, treatment techniques include surgical ligation or endovascular embolization, where the latter has exhibited lower in-hospital deaths and morbidity. Among these techniques, endovascular coil embolization aims at occluding the aneurysm space using platinum coils, which are transported and delivered using a detachable micro-catheter. While coiling has been extensively applied since its introduction in 1990's, there are currently several limitations, including incomplete occlusion, mass effect, and aneurysm recurrence [2, 3]. To address some of these challenges, shape memory polymers (SMPs) have arisen as a promising alternative owing to their customizability, tunable properties, and biocompatibility.

We have previously designed pristine polyurethane SMPs, studied their thermomechanical properties, and demonstrated their shape recovery capacity [4]. In this work, we aim to advance the design of SMP-based endovascular devices based on a Joule heating activation mechanism. Specifically, we study the use of carbon nanotubes (CNTs) to enhance the required thermal conductivity in the SMP foams and investigate effects of the CNT addition on the thermal-mechanical properties of the SMP foam material.

METHODS

CNT-infiltrated SMP foams were synthesized using a sugar leaching method. Briefly, CNTs and sugar, as porogen (POR), were mixed in ethanol at different weight ratios (0.50, 0.75, 1.00 and 1.25%). CNT/POR solution was then dried in an oven and molded into blocks. SMP was next synthesized using three monomers: hexamethylene diisocyanate (HDI, ≥98.0%, Sigma-Aldrich), hydroxypropyl ethylenediamine (HPED, ≥98.0%, Alfa Aesar), and triethanolamine (TEA, ≥99.0%, Sigma-Aldrich) with a molar ratio of 1:0.05:0.6 (SMP11), resulting in a glass transition temperature (Tg) of ~38 °C. ~15g of uncured SMP solution was poured onto 30x30x10mm CNT/POR blocks, left in a freezer at -4 °C to allow penetration into the template, and cured at 60 °C and 130 °C (1 hour at each temperature) in a vacuum oven under nitrogen protection environment. Porogen was washed out in deionized water in an ultrasonic bath. CNT-infiltrated SMP foams were then dried in a vacuum oven at 50 °C for 24 hours, cut into different dimensions for each experiment, and stored in vacuum.

A comprehensive assessment of the CNT-infiltrated SMP foam was performed. First, we examined the effects of sugar leaching on the measurement of the T_g of the material, which delimits two mechanical states: (i) a glassy state, below the T_g, with strong polymeric chain interactions, and (ii) a rubbery state, above the T_g, where the material can be deformed. We performed differential scanning calorimetry (DSC) in pristine (solid and porous) SMP specimens at different SMP ratios (**Table 1**) and CNT/POR concentrations to measure their T_g.

Table 1: Other SMP monomer ratios used in the DSC test.

SMP type	HDI	HPED	TEA
SMP8	1.000	0.200	0.400
SMP9	1.000	0.150	0.467
SMP10	1.000	0.100	0.533
SMP11	1.000	0.050	0.600

To investigate the effects of sugar leaching and CNT-infiltration on shape recovery properties, we measured the shape recovery times of the CNT-infiltrated foams. In brief, 10x10x10 mm foam specimens were compressed uniaxially, and shape recovery was triggered with a hotplate above T_g (50 °C). Time from contact to ~90% recovery was recorded as the shape recovery time.

Finally, we assessed the Joule-heating capacity of the material. Direct current (0.50, 0.75, 1.00 and 1.25A) was applied to 5x5x5 mm foams with two copper parallel plates touching the two opposite faces of the SMP foam. Surface temperature of one face of the uncompressed foam was monitored using a thermal camera (ETS320, FLIR Systems).

RESULTS

We successfully synthesized CNT-infiltrated SMP foams (**Fig. 1**) with no significant alteration to the porosity and macrostructural features compared to the pristine foams. We observed a significant reduction in the T_g of the porous SMPs versus the solid SMP specimens (p<0.05), although no monotonic, decreasing trend was observed among various monomer ratios (**Fig. 2a**). We also observed that an increasing concentration of CNTs results in a decreased T_g (**Fig. 2b**). This is due to the reduction of hard segments of the polymeric matrix caused by CNT-infiltration, which ultimately reduces the motility of the polymeric chains and affects its thermal properties [5]. Shape recovery was also affected by CNT-infiltration: a decrease was observed in shape recovery time with an increasing CNT/POR concentration (p<0.05) (**Fig. 3**). These results confirm that CNT infiltration significantly affects the thermal properties of the SMP foams.

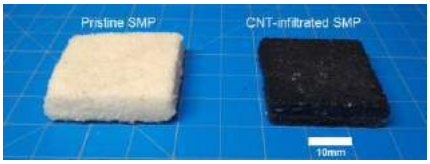

Figure 1: Pristine and CNT-infiltrated polyurethane SMP foams.

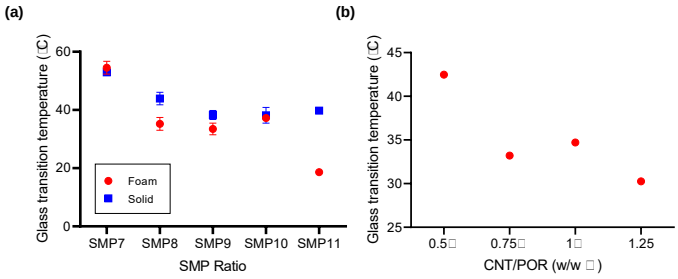

Figure 2: T_g of (a) solid and porous pristine SMP at various monomer ratios, and (b) CNT-infiltrated SMPs with different CNT/POR concentrations.

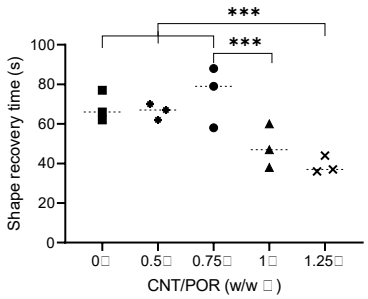

Figure 3: Shape recovery time of CNT-infiltrated SMP foams with different CNT/POR concentrations.

There are several observations from our Joule-heating assessment: (i) CNT-infiltrated foams exhibited Joule-heating when current was applied (**Fig. 4**); (ii) temperature increases faster at the interface between foam and copper plates, due to a high contact resistance; (iii) areas where temperature increased faster were observed, indicate ununiform CNT distribution (**Fig. 4**, dashed circles), and (iv) heating rate is directly related to applied current (**Fig. 4**) and CNT concentration (not shown). This experiment demonstrated the Joule-heating capacity of the proposed CNT-infiltrated SMP foam.

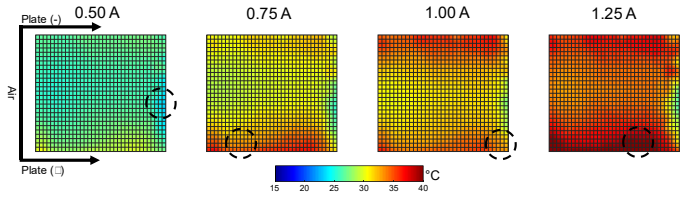

Figure 4: Thermal measurements of CNT-infiltrated foams (0.5% CNT/POR concentration) under Joule-heating activation. Heatmaps at 60s of activation with various applied currents.

DISCUSSION

A Joule-heating triggering mechanism for shape recovery of an SMP foam was designed by means of a CNT infiltration process. This triggering mechanism is key to our design of an endovascular device for brain aneurysm therapeutics, as it will allow timely and accurate triggering of a patient-specific endovascular foam.

In this study, our goal was to quantify the effects of CNT infiltration in the thermal properties of the material. The CNT-infiltrated foams had shape recovery behaviors induced by Joule-heating using parallel copper plates, indicating the promising potential of this triggering method. However, we observed that CNT-infiltration poses new challenges in the design of our endovascular device. First, sugar-leaching significantly reduces T_g, which was also observed as CNT/POR concentration was increased. T_g is a key parameter for shape recovery and foam delivery, as it sets the boundary between thermomechanical states. Special attention should be placed on this parameter due to its importance from a surgical perspective.

In addition, the interface between the foam and the copper plate in the Joule-heating assessment played a key role. We observed a significantly faster heating rate at the interface between the two materials. This is caused by a high contact resistance, that arises from the high dissimilarity between the conductive and thermal properties of the foam and copper tape, as well as a low effective contact surface between the foam and the relatively flat surface of the plate. This observation will play a key role in the design of a catheter that is able to deliver and stimulate the foam into the aneurysm space. Finally, non-uniform heating of the foam was also observed at small areas (**Fig. 4**, dashed circles), indicating the differences in CNT density and the need for improving the process for dispersing CNTs in our future studies.

In conclusion, we determined that CNT infiltration is a promising technique for the design of an SMP endovascular device, as it allows shape recovery in short periods of time with a simple setup. Future studies will address the novel challenges that were presented in this study, which will include the improvement of CNT dispersion methods, design of conductive interfaces to trigger shape recovery and the fine tuning of a surgically relevant T_g that allows *in vivo* implantation.

ACKNOWLEDGEMENTS

This work was supported by Oklahoma Center for the Advancement of Science & Technology (HR18-002), and the IBEST institutional funding for interdisciplinary research. S. P.-C. (first author) was supported in part by OU's Alumni Fellowship. We also thank Dr. Brian Grady for his assistance with the DSC tests.

REFERENCES

[1] G. Toth, et al., *Vasc Med* 2018, 23, 276-288.
[2] G. A. Maragkos, et al., *J Neurosurg* 2019, 1-8.
[3] I. Szikora, et al., *AJNR Am J Neuroradiol* 2013, 34, 935-939.
[4] R. Kunkel, et al., *J Mech Behav Biomed Mater* 2018, 88, 422-430.
[5] F. Askari, et al., *J App. Pol Sci* 2017, 134-143

INVESTIGATING THE EFFECT OF VARIED BREATHING RATES AND VOLUMES ON THE MECHANICS OF MURINE LUNGS

T. Nelson (1), K. Anduaga (1), S. Sattari (1), C. Mariano (1), A. Ulu (2), T. Nordgren (2), M. Eskandari (1, 2, 3)

(1) Department of Mechanical Engineering
University of California, Riverside
Riverside, CA, USA

(2) BREATHE Center, School of Medicine
University of California, Riverside
Riverside, CA, USA

(3) Department of Bioengineering
University of California, Riverside
Riverside, CA, USA

INTRODUCTION

The onslaught of COVID-19 and its victims' need for mechanical ventilation has underscored the need for a better understanding of how the lung's structure is impacted during ventilation. The pressure-volume (PV) curve of a respiratory cycle (measuring transpulmonary pressure and tidal volume) is commonly used to assess how the lung will respond under mechanical ventilation and to evaluate deviations in that response in diseased states [1]. Landmark studies have explored the effects of varied lung inflation pressures and volumes on the PV curve, but have used pressure controlled, non-continuous devices, yielding results that are not as readily comparable to physiological breathing [2]. The effect of varied breathing rates is particularly of recent interest because multifrequency ventilator oscillation shows promise in improving oxygenation [3]; however, such studies have not focused on the mechanical pressure-volume response, rather the downstream biochemical response of the lung due to injury.

To address this need, we investigate the role of breathing rate and inflation volume on lung compliance and the peak pressure response. Compliance is a metric of interest because it is a surrogate measure of pulmonary stress and strain [4]. We hypothesize that, given faster rates and larger volumes, we will see an increase in compliance as well as an increase in peak pressure, indicative of strain-stiffening, a classical biomechanical response of soft tissues [5]. By exploring the dependency of lung mechanics on various breathing rates and inflation volumes, we aim to lend greater understanding of the effects of mechanical ventilation, and ultimately aim to inform physicians of optimal protective ventilation settings and strategies.

METHODS

C57BL/6J mice were obtained from University of California Riverside's School of Medicine BREATHE Center (IACUC approved). Mice were anesthetized, sacrificed, and lungs were excised. A cannula was inserted into the trachea and was inflated to 0.5ml using a syringe to avoid airway collapse. Testing of each lung was completed within 12hrs after sacrifice and kept in 1XPBS before and during testing to minimize deterioration. To achieve statistical significance, three lungs were tested (COVID-19 interfered with tissue supply).

Tests were performed on our custom-designed, continuous volume-controlled, pressure-measuring electro-mechanical device. A predetermined applied volume of air is applied to the lung, and the effect of air compressibility is accounted for in real time [2]. Mice lungs were inflated by pushing air into the lung at increasing inflation volumes of 0.3, 0.5, 0.7, and 0.9ml. At each volume, varying inflation frequencies of 5, 10, and 20 breaths per minute (BPM) were tested. Lungs were inflated with faster frequencies, followed by slower frequencies to avoid air trapping [6]. To ensure a consistent datum state between each test, the lungs were inflated to a preload pressure of 5 cmH_2O. Each specimen was preconditioned three times, and data was collected from a subsequent test cycle.

Lung compliance was calculated as the ratio of volume change over pressure change, the slope of the PV curve [4]. The average compliance and peak pressures for three mice across varied volumes and rates were reported and statistical comparisons were made by one-way analysis of variance (ANOVA) with significance at $p<0.05$ with Bonferroni post-hoc analysis.

RESULTS

The pressure-volume curve (Figure 1) shows the varied rate response for a representative applied inflation volume of 0.7ml. The pressure-volume inflation response was near identical and varying the inflation rates was not found to significantly impact the compliance.

Figure 2A represents the compliance at varying frequencies and at

three applied volumes. The compliance was found to decrease for increasing breathing rates, however, the decrease was not statistically significant. The compliance increased with increasing inflation volumes, notably different between 0.3 and 0.9ml ($p<0.001$) and 0.5 and 0.9ml ($p<0.001$). In Figure 2B, peak lung pressures are compared over a range of inflation/deflation rates at the given applied volumes. The peak pressure unidirectionally increased at faster rates, but this increase was not found to be statistically significant. Across increasing volumes however, the peak pressures were observed to unidirectionally and significantly increase ($p<0.002$).

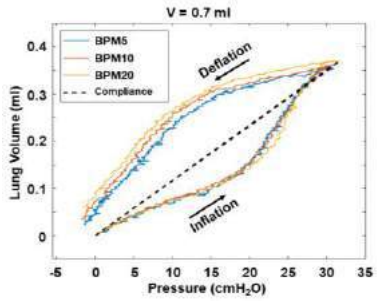

Figure 1: Representative pressure-volume response for an applied inflation volume of 0.7ml, resulting in a compressed lung volume of <0.4ml at breathing rates of 5, 10, 20 BPM.

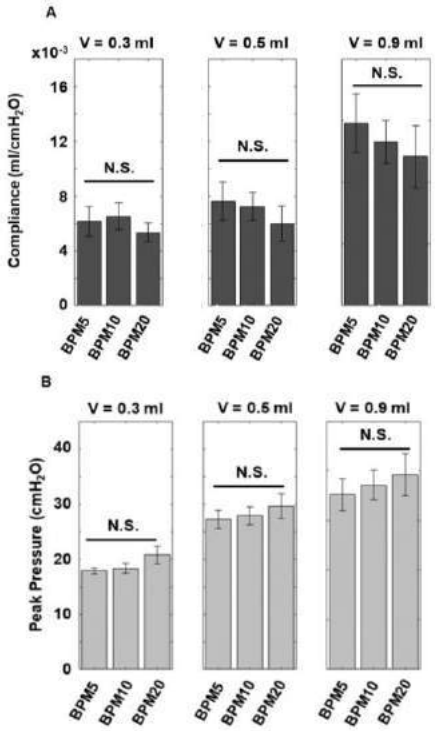

Figure 2: Comparison of mean ± standard deviation of lung compliance (A) and peak pressure (B) at applied volumes of 0.3, 0.5, and 0.9ml, each at three different inflation rates of 5, 10, and 20 BPM. Peak pressure was significantly greater for each applied volume and the compliance was significantly greater for 0.9ml. Neither compliance nor peak pressure was significantly different between any of the breathing rates.

DISCUSSION

In this study the effect of varied inflation volumes and frequencies on the continuous pressure-volume response, compliance, and peak pressure of mice lungs are studied for the first time. Our results show that an increase in breathing frequency does not affect the inflation pressure-volume response, but results in increased peak pressure, decreased compliance, and affects the deflation path.

Various breathing frequencies illustrate near-identical inflation paths and similar inflection points, indicating the shared degree of alveolar opening and airway resistance regardless of breathing rate (Figure 1). However, faster breathing rates resulted in higher peak pressures but lower deflation inflection points. Others have attributed this observed greater pressure drop during deflation to the hyperinflation of the lung; our results show more of these hyperinflated areas in faster frequencies [7].

Furthermore, increased breathing frequency results in increased peak pressures and decreased compliance, which represent increases in lung stresses and mechanical stiffnesses. Similarly, increasing the inflation volume results in greater peak pressure. These findings agree with other studies reporting smaller volumes and slower frequencies reduced ventilator induced lung injury [8]. In line with past work, we also find that compliance significantly increases with greater volumes [9]. This, coupled with our insights on how compliance decreases at faster rates (although not significantly), poses an interesting balancing effect may inform explorations on how to devise protective mechanical ventilation techniques, and lays the foundation for future research.

A limitation to this study is the non-physiological breathing rate, which is challenging given the fast breathing rate of mice. Our rates are in line with that of previous studies [1]. While these rates fall short of representing mice BPM (which can be as high as ten times our fastest rate), choosing physiological rates would no longer allow us to make the quasi-static assumption, because effects of flow would need to be considered [2].

We found that peak pressure significantly increases with larger applied volumes, which is consistent with previous findings [11]. The non-linear pressure-volume relationship is demonstrative of a "strain-limit" in the lungs, beyond which the tissue surpasses physiological thresholds [12]. This is consistent with previous findings suggesting that lowering tidal volumes may be a beneficial protective ventilation method [13]. Additionally, (though not statistically significant), peak pressure unidirectionally increases at faster rates. These trends agree with studies that describe how the lung exhibits strain stiffening at increasing stresses [5], and suggests that faster rates may exacerbate this stiffening.

ACKNOWLEDGEMENTS

Authors would like to thank the University of California Riverside's Dean's Biomed Collaborative Seed Grant awarded to Drs. Mona Eskandari and Tara Nordgren.

REFERENCES

[1] Limjunyawong, N et al., *J Vis Exp*, 95:52376, 2015. [2] Sattari, S et al., *Frontiers in Bioeng and Biotech*, 8:1183, 2020. [3] Kaczka, D W et al., *Anesthesiology*, 123 (6):1394–1403, 2015. [4] Chiumello, D et al., *Am J Respir Crit Care Med*, 178 (4):346–55, 2008. [5] Yan, B et al., *ACS Nano*, 11 (11): 11074–11081, 2017. [6] Frazer, D G & Weber, K C, *J App Physiol*, 40 (6):915–922, 1976. [7] Interpreting the shape of the pressure-volume loop, derangedphysiology.com, 2019. [8] Hotchkiss, J R et al., *Am J Respir Crit Care Med*, 161 (2 Pt 1): 463–468, 2000. [9] Zosky, G R et al., *J App Physiol*, 105 (2):685–692, 2008. [10] Bonnardel, E et al., *Respiratory Research*, 20 (1): 211, 2019. [11] Sprung, J et al., *Anesthesia and Analgesia*, 97 (1): 268–274, table of contents, 2003. [12] Sinclair, S E et al., *Am J Respir Crit Care Med*, 176 (8): 786–794, 2007. [13] Amato, M B, et al., *New Eng J of Med*, 338 (6): 347–354, 1998.

ON THE RELATIVE SENSITIVITY OF AAA RUPTURE POTENTIAL INDEX TO SEX, INTRALUMINAL PRESSURE, AND FAMILIAL HISTORY

Balaji Rengarajan (1), Satish C. Muluk (2), Mark K. Eskandari (3), Ender A. Finol (1)

(1) Department of Mechanical Engineering
University of Texas at San Antonio
San Antonio, TX, U.S.A.

(2) Division of Vascular Surgery
Allegheny Health Network
Pittsburgh, PA, U.S.A.

(3) Division of Vascular Surgery
Northwestern University School of Medicine
Chicago, IL, U.S.A.

INTRODUCTION

Ruptured abdominal aortic aneurysms (AAA) carry an overall mortality rate of 90%, while in clinical practice the maximum transverse diameter is the standard marker utilized for assessing AAA rupture risk. However, wall stress measures have been postulated to be better predictors of rupture risk compared to size alone. Along with wall stress, wall strength has also been proposed to accurately assess AAA rupture risk. The rupture potential index (RPI) is one such measure that accounts for both wall stress and wall strength [1]. Estimation of patient specific wall stress requires knowledge of the patient specific blood pressure. Wall strength requires knowing the patient specific familial history of AAA and the patient's sex. The objective of this study was to assess whether these patient specific metrics (blood pressure, familial history, and sex) have a significant effect on the maximum RPI in a cohort of 64 patients. We hypothesized that peak systolic pressure significantly affected the maximum RPI evaluation relative to the other two metrics (familial history and sex).

METHODS

Retrospectively acquired abdominal computed tomography angiography (CTA) scans were obtained from 64 asymptomatic AAA patients treated at Allegheny General Hospital (Pittsburgh, PA) and Northwestern Memorial Hospital (Chicago, IL) following Institutional Review Board approval at both clinical centers. The CTA images were segmented using our custom segmentation code *AAAVasc* (v1.0.3, The University of Texas at San Antonio, San Antonio, TX) [2]. Using another in house MATLAB®-based meshing code, *AAAMesh* [3], volume meshes were created for each AAA post-segmentation (30,000-90,000 quadratic hexahedral elements). These were used to create triangular surface meshes of the outer AAA wall, which were processed following a nonlinear elastic membrane analysis (NEMA) method to compute wall stress [4]. The proximal and distal ends of the models were fixed and an intraluminal patient specific peak systolic pressure (SP) was applied. The first principal stress component of the stress tensor was calculated using the NEMA technique, while wall strength was calculated [5] following Eq. (1),

$$Wall\ strength = 72.9 - 33.5 * \left(\sqrt{ILT} - 0.79\right) - 12.3 * (NORD - 2.31) - 24 * HIST + 15 * SEX \quad (1)$$

where ILT is the intraluminal thrombus thickness (in cm) at each node on the surface mesh, $NORD$ is the local normalized diameter (a dimensionless parameter) at each node on the surface mesh, $HIST$ is the familial history of AAA (+0.5 for positive family history; -0.5 otherwise), and SEX is the sex of the patient (+0.5 for male; -0.5 for female). The ensuing wall strength is calculated in units of N/cm^2.

The maximum RPI for each AAA models was evaluated as the maximum value of the RPI amongst all the surface elements of the AAA wall. To test the effect of each patient specific metric, 5 groups of data were created. Group 1 consisted of RPI evaluated with the actual patient specific SEX, $HIST$, and SP. Group 2 was created with the patient specific $HIST$ and SP, but using the incorrect SEX. Group 3 was created with the patient specific SEX and SP, but the incorrect $HIST$. Group 4 was created with the patient specific $HIST$ and SEX, but using a SP of 120 mmHg. Group 5 was created with the patient specific $HIST$ and SEX, but using a SP of 180 mmHg.

The maximum RPI calculated for Groups 2-5 was compared to the maximum RPI calculated for Group 1, which is the truly patient specific RPI. A linear regression analysis was used to assess the significance of this comparison based on the magnitude of the coefficient of determination (R^2) characterizing the regression. A series of test of

hypotheses were performed with a Bonferroni-corrected significance level of $\alpha_c = 0.05/4 = 0.0125$ to assess the differences in maximum RPI between Groups 2-5 and Group 1.

RESULTS

The mean maximum RPI for the 64 AAA models was 0.46 (for Group 1). Most patients in the study were males (n = 49) and had a positive family history of AAA (n = 62). The mean systolic pressure for the 64 patients was 144 ± 28 mmHg.

Figures 1-4 illustrate the linear regression analyses of the maximum RPI for Groups 2-5 vs. the maximum RPI for Group 1, respectively. These yielded R^2 values of 0.97, 0.62, 0.93, and 0.93, respectively. The regression analyses for Groups 2, 4, and 5 resemble closely the ideal linear relationship (a slope of nearly 1 and a vertical intercept near 0), shown in each figure by the diagonal line across the graph.

The outcome of the hypothesis tests reveal that the differences between Groups 2 and 1 are not statistically significant ($p = 0.35$), the differences between Groups 3 and 1 are statistically significant ($p = 0.001$), while the differences between Groups 4, 5 and 1 are not statistically significant ($p = 0.22$ and $p = 0.10$, respectively).

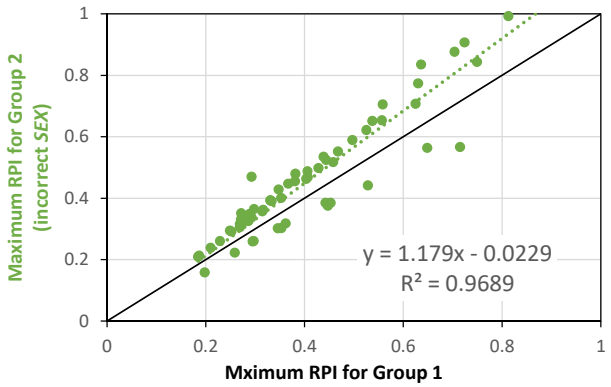

Figure 1: Maximum RPI for Group 2 (incorrect *SEX*) vs. Maximum RPI for Group 1.

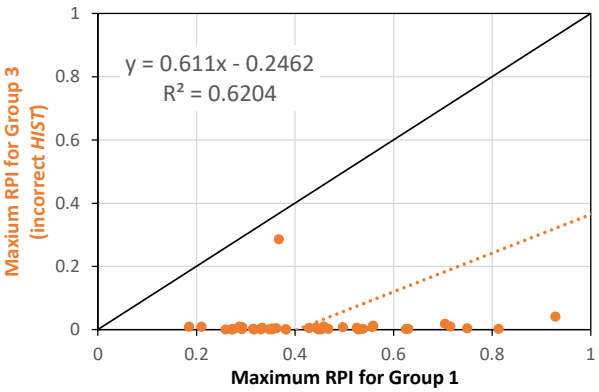

Figure 2: Maximum RPI for Group 3 (incorrect *HIST*) vs. Maximum RPI for Group 1.

DISCUSSION

Maximum RPI evaluated with the incorrect *SEX* or *SP* is statistically similar to the maximum RPI evaluated with the patient specific *SEX* and *SP*. We infer from this outcome that if the sex of an AAA patient is unknown or incorrectly transcribed from the medical records, the uncertainty will not lead to a significantly different prediction of RPI. Similarly, if the peak systolic pressure is assumed to be in the range of 120 to 180 mmHg due to the patient specific *SP* not measured at the time of patient follow up during the CTA exam or otherwise unknown, the predicted RPI is inferred to be similar to the actual RPI. Conversely, using an incorrect familial history of AAA yields a statistically different RPI compared to the actual RPI. We conclude from this analysis that in the estimation of RPI, the family history of the disease plays a far more significant role than sex and peak systolic pressure. Therefore, if *HIST* is unknown or unavailable, it may lead to a significant error in the prediction of maximum RPI.

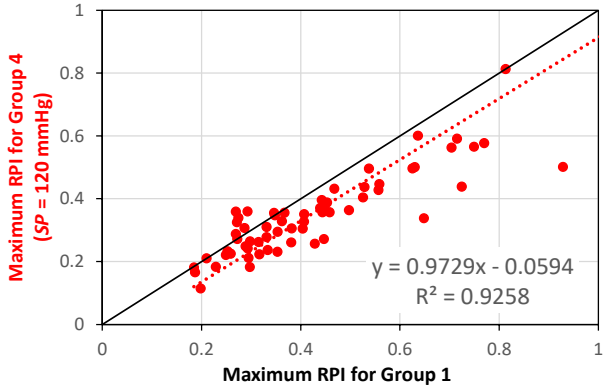

Figure 3: Maximum RPI for Group 4 (*SP* = 120 mmHg) vs. Maximum RPI for Group 1.

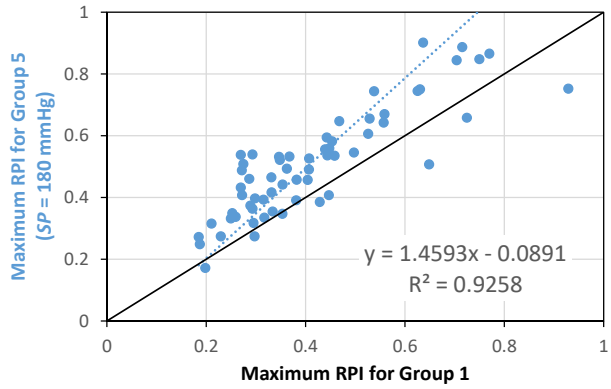

Figure 4: Maximum RPI for Group 5 (*SP* = 180 mmHg) vs. Maximum RPI for Group 1.

ACKNOWLEDGEMENTS

This work was supported in part by National Institutes of Health award R01HL121293.

REFERENCES

[1] Maier, A et al., *Ann Biomed Eng*, 38:3124–3134, 2010.
[2] Shum, J et al., *Medical Physics*, 37:638-648, 2010.
[3] Raut, SS et al., *J Biomech*, 48(10), 53:1972-1981, 2015.
[4] Thirugnanasambandam, M et al., *PhD Thesis*, UTSA, 2018.
[5] Vande Geest, JP et al., *Ann. N.Y. Acad. Sc.*, 1085:11-21, 2006.

CFD ANALYSIS OF FLUID FLOW SHEAR STRESS ON THE OSTEOCYTE LACUNO-CANALICULAR NETWORK

Mohammad Niroobakhsh (1), Loretta E. Laughrey (1), Mark L. Johnson (2), Sarah L. Dallas (2), Ganesh Thiagarajan (1)

(1) School of Computing and Engineering
UMKC
Kansas City, Missouri, US

(2) School of Dentistry
UMKC
Kansas City, Missouri, US

INTRODUCTION

Bone loss and osteoporosis are common with advancing age leading to frailty due to the alteration in bone morphology and mechanical properties [1]. Osteocytes are the bone cells that sense mechanical loading due to physical activity and initiate biochemical signaling (called mechanotransduction), leading to bone formation. It was predicted that osteocytes detect mechanical loads through fluid flow shear stress (FFSS) around the dendritic processes and local strains around the osteocyte cell body [2]. The deterioration in osteocyte dendrite connectivity that occurs with aging may contribute to age-related bone loss, potentially due to impaired mechanoresponsiveness and disruption of osteocyte regulation of osteoblast and osteoclast function [4]. Depending on the cell and lacuno-canalicular network (LCN) morphology, different bone cells receive different FFSS [5]. Inaccessibility of the osteocyte network in the bone matrix limits *in vivo* experiments and the role of LCN morphology in initiating bone signaling and mechanotransduction is not fully understood. Computational fluid dynamics (CFD) models of bones provide an innovative approach to investigate the load-induced fluid flow inside LCN. Realistic image-derived models can imitate the intricate osteocyte microstructure, including LCN shape and canalicular tortuosity, to assess fluid behavior better than idealized geometries [6]. With advancing imaging techniques, cell processes can be captured in image-derived simulations [7]. A single osteocyte dendrite may develop numerous branches, enabling intercommunication between osteocytes. Despite the load-induced flow pattern's reliance on the LCN topology in the pericellular space (PCS), the existence of canalicular branches is mostly neglected in bone modeling [8]. This study aims to predict FFSS behavior in the osteocyte microstructural network, including the contribution of the canalicular branches, which is not conducive to direct measurement.

METHODS

To generate a confocal image-derived LCN model, confocal images of a 4 month-old mouse femur were stained with FITC dye [9]. The staining protocol enables visualization of most of the canaliculi [4]. The collected z-stacks were imported into the MIMICS to make a surface model after defining a light intensity threshold, as shown in Fig1A. The LCN volume was reduced via the smoothing technique to make the cell membrane and dendrites, where the cell body's annular space is greater than the dendrites [10, 11]. The cell membrane was subtracted from the LCN to create PCS for the fluid analysis.

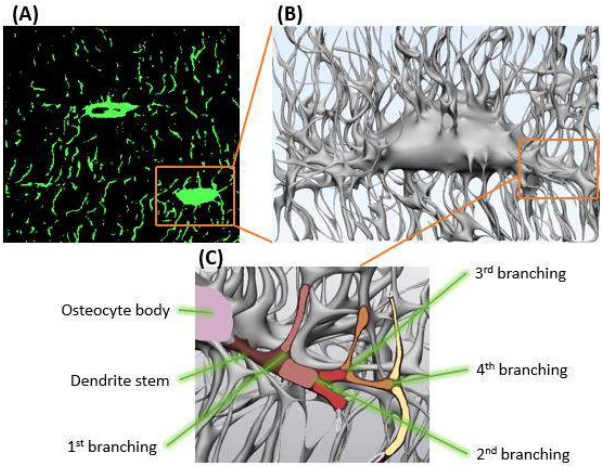

Figure 1: A) 100X confocal scan with a cuboid cropped region of interest (ROI) around the lacuna, B) realistic model of single osteocyte, C) canalicular branching model depicting connected stem process to the cell which forms branches and sub-branches

Fig1B shows the volumetric model of the ROI that was replicated in 3-MATICS software. The dendrites and canaliculi have an average diameter of 0.2 and 0.4 µm, and the annular thickness around the dendrites and the cell are 0.08 and 0.75 µm, respectively. A canaliculus connected to the cell on its left with various branches detached to represent the branching model is shown in Fig1C. These geometries were then imported into the ANSYS CFX for the fluid analysis inside the PCS. They were meshed with CFD preference linear tetrahedral elements, element size of 6e-8 m, and total element number of 10,116,847. To mimic the physiological activity, a fluid pressure gradient of 300 Pa was defined in the inlets while outlets have 0 Pa pressure. The remaining surfaces were considered walls with no-slip condition, and the interstitial laminar fluid was treated as water [10].

RESULTS

Fig2 depicts the wall shear stress distribution of the single-osteocyte model. Dendrites experience higher shear stresses on the walls than the cell membrane on account of an approximately ten times smaller annular space surrounding the dendrites than the osteocyte. The cell body has a maximum FFSS of 0.05 Pa, two orders of magnitude smaller than the maximum FFSS on dendrites, 6.6 Pa, in agreement with previous findings [12].

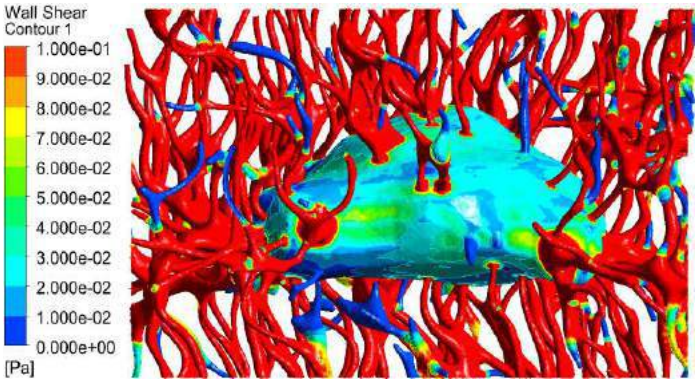

Figure 2: FFSS in PCS surrounding cell membrane

Fig3 shows the range and average FFSS experienced by each branch in the canalicular branching model. The stem has an average FFSS of 0.9 Pa, while the next branches have an average FFSS of 0.5Pa, 0.4 Pa, 0.2 Pa, and 0.07Pa. FFSS distribution and velocity streamlines of fluid flow within PCS is shown in Figs 4A & 4B. It is noticeable that the flow pattern differs in each set of canalicular branches.

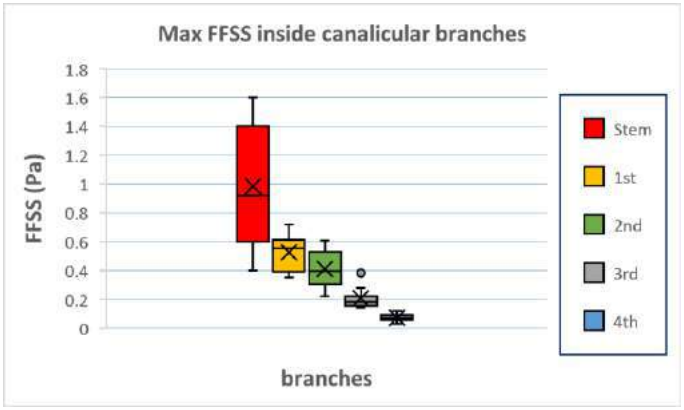

Figure 3: Comparison of FFSS distribution in various canalicular branches

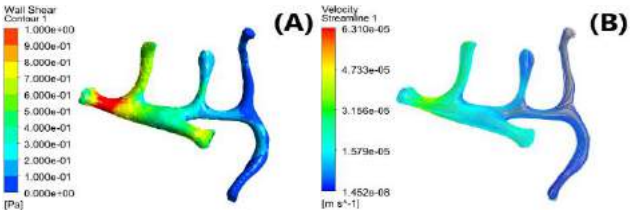

Figure 4: Contour plots of (A) FFSS and (B) velocity streamline in the canalicular branching model

DISCUSSION

Interstitial fluid flow exerts shear stress to the cell membrane besides its other capabilities such as delivering nutrition, eliminating waste, and cell-cell communication through LCN. In the single-cell model, canaliculi have higher shear values (shown in red) than the lacuna. The osteocyte membrane deformation that corresponds to the osteogenic response requires a minimum FFSS of 0.8Pa [13]. The PCS inside the lacuna is much greater than the canaliculi, enabling the lacuna to be a mixing chamber [2]. On the other hand, this large space decreases the fluid velocity and FFSS in the lacuna compared to the canaliculi. Only 18% of the entire domain, specifically canaliculi, reaches 0.8 Pa to bring about intracellular signaling. The canalicular branching model explains that even though all canaliculi experience higher shear values than the lacuna, FFSS differs depending on the branching order. Based on the vicinity of the canaliculus to the cell, FFSS inside the canalicuus is higher. Fluid streams from various branches are merged into the stem canaliculus which is the main route for the fluid enterance to the lacuna. Contributing more canaliculi as fluid inlets drives a higher flow rate and consequently, higher FFSS inside the stem canaliculus attached to the osteocyte. Therefore, the existence of canalicular branches in LCN could be a mechanism to amplify fluid flow and FFSS before entering the osteocyte. It is also apparent that the canalicular diameter decreases by branching, but no data is available for the differences in annular space thickness, so this was kept the same for all branches in this model. All in all, finding a link between the load-induced fluid flow on the osteocytes and its mechano-sensitivity regarding the LCN morphology will bridge the knowledge gap between mechanical load and bone formation.

ACKNOWLEDGEMENTS

NSF, award number NSF-CMMI-1662284 (PI: T Ganesh)
NIH – NIA P01 AG039355 (PI: LF Bonewald)
NIH/SIG S10OD021665 and S10RR027668 (PI: SL Dallas)
The School of Graduate Studies Research Grant Program, UMKC

REFERENCES

[1] Parfitt, A.M., et al., *Clinical Investigation*, 1983.**72**(4):p.1396-1409.
[2] Frotton, S.P., et al., *Annual review of fluid mechanics*, 2009. **41**: p. 347-374.
[3] Tiede-Lewis, L.M., et al., *J Bone*, 2019. **122**: p. 101-113.
[4] Bonewald, L.F., et al., *J Bone*, 2008. **42**(4): p. 606-15.
[5] Van Tol, A.F., et al., *Biomech Model Mechanobio*, 2020.**19**(3): p. 823-840.
[6] You, L.D., et al., *Anat Rec A Discov Mol Cell Evol Biol*, 2004. **278**(2): p. 505-13.
[7] Buenzli, P., et al., *J Bone*, 2015. **75**.
[8] Ganesh, T., et al., *J Bone*, 2020. **137**: p. 115328.
[9] Verbruggen, S.W., et al., *Biomechanics and Modeling in Mechanobiology*, 2014. **13**(1): p. 85-97.
[10] Wang, L., et al., *J Bone*, 2005. **102**(33): p. 11911-11916.
[11] Anderson, E., et al., *Proceeding of National Academy of Sciences of the United States of America*, 2005. **33**: p. 52-62.
[12] Weinbaum, S., et al., *J of Biomechancis*, 1994. **27**(3): p. 339-360.

ELECPHORETIC TRANSPORT OF MOLECULES FOR ENHANCED TISSUE CLEARING.

P. Atsu (1), Z. Nicolella (1), G. Thompson (1)

(1) Department of Chemical Engineering
Rowan University
Glassboro, NJ, USA

INTRODUCTION

The removal of cellular remnants and immunogenic materials from tissue scaffolds is critical to the success of any tissue decellularization process[1]. Removal of immunogenic materials reduces the risk of rejection of the implanted tissue scaffold by the host body. Continuous perfusion has been employed as a tissue clearing method during decellularization over the past decades[2,3]. Though there has been success with clearing tissue with perfusion, the process takes a long time which may lead to tissue degradation. Also, high perfusion fluid pressure can cause disruption of the tissue structure. Electrokinetic transport can be used as an alternate or complementary method for enhanced removal of cell remnants and immunogenic materials from the tissue scaffold[4]. Electrokinetic extraction has the potential of increasing the efficiency of tissue clearing and also shortening the time for the procedure[5].

In this study, the electrophoretic mobility of charged molecules in tissue samples was measured and analyzed using the relative difference of velocities of cationic dyes passing through tissue embedded in agarose gel under an applied electric field. The magnitude of the electrophoretic mobility of the cationic dyes was measured for DC and AC square pulses across the tissue and through the gel. The results demonstrate that pulsed electrophoresis can be used as a method of removing charged cellular remnants during tissue decellularization, with removal rate of the molecules discriminated by their relative sizes.

METHODS

Gels were prepared using 1 mL of 50X Tris-acetate-EDTA (TAE) buffer mixed with 49 mL of deionized water. Once mixed, a 0.5 g agarose tablet was added to the solution to make a 1 % agarose solution. The buffer was prepared using 4 mL of 10X Tris/Borate/EDTA (TBE) and 36 mL of deionized water to create a 1 % TBE solution.

Two dye solutions were prepared, pyronin Y (302.12 Da) and safranin O (350.13 Da). These two dyes bind to nucleic acids and proteoglycans, respectively, and thus were used as their analogues to predict their electrokinetic extraction. Both dyes were prepared by adding 5 mg of the respective dye and 3 mg of sucrose to 7 mL of the previously prepared 1X TBE buffer. Both dyes have a positive N that is ionically bonded to a Cl; so, in an aqueous solution the dyes have a positive charge of 1.

Frozen annulus fibrosus tissues were dissected from whole bovine tails acquired from a local abattoir (Bringhurst Meats, Berlin, NJ, USA). Small pieces of tissue were inserted in wells within the agarose. TBE solution was added on top of the solidified gel, and 7 μL of respective dye solution was added into wells. For data recording purposes, half the wells contained safranin, while the other half had pyronin.

For the DC power supply, the chamber was connected to an Extech (Nashua, NH, USA) DCP60 power supply, and 60 V was applied across the gel for 60 min. The chamber was connected to an A-M Systems (Sequim, WA, USA) 4100 Isolated High Power Stimulator. The chamber was subjected either to DC or to AC waveforms: a pulsed square wave of 60 V on for 10 ms and 0 V for 10 ms. All experiments were run for 60 min.

.

RESULTS

The electrophoretic migration of pyronin Y and safranin O through the annulus fibrosus tissue was driven with DC or AC. All the tested conditions caused migration of each dye within the 60 min duration,

with DC causing the farthest migration of both dyes, as shown in Figures 1 and 2. It is also observed that the distance of migration decreases with increased molecular weight.

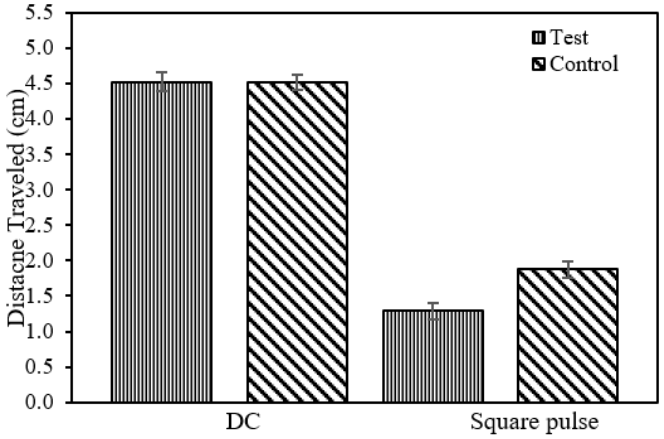

Figure 1. Distance travelled by pyronin Y (302 Da) in AF tissue samples with DC, square pulse and sawtooth pulses as voltage source for electrophoresis.

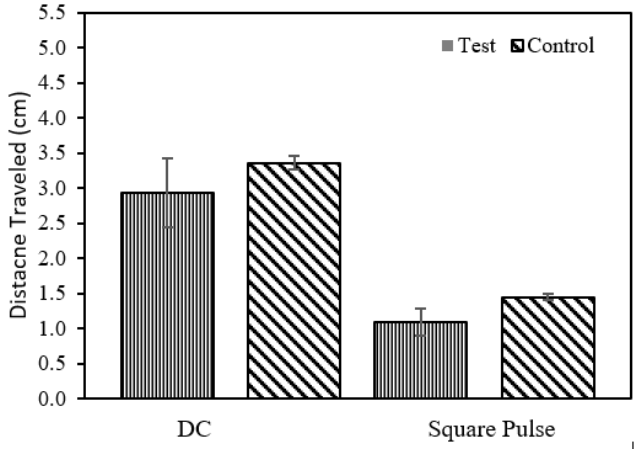

Figure 2. Distance travelled by safranin Y (350.8 Da) in AF tissue samples with DC, square pulse and sawtooth pulses as voltage source for electrophoresis.

DISCUSSION

The applied field being AC or DC affects the mobility of the charged molecules. This is because of the direction and intensity of the electrophoretic flow associated with applied electric fields[4,6,7].When electric field is applied across this medium, the charged molecules experience forces resulting from Columbic interactions, viscous drag, inertia and random thermal motion[7]. The charge relaxation process and associated time scales of the transient motion of the charged particles and ionic cloud can be different for an AC or DC applied field[7,8]. For pulsed electric fields, electrophoretic flow of the charged molecules is instantaneous with the pulse start up, sustained for the duration of the pulse and vanishes almost instantly when the pulse is switched[8]. For DC, the electrophoretic flow is initiated instantaneously when the current is switched and is maintained for the duration of the experiment. This explains the higher distance of dye migration in the DC setup compared to the AC setup as shown in Figures 1 and 2. Other mechanisms such as temperature gradient, fluid convection, and diffusion as a result of concentration gradient also contribute to the transport of molecules in the tissue[5]. The contribution of the individual mechanisms in molecular transport in tissues shall be investigated in our next study.

The electrophoretic mobility of the different dyes were noticeably different. This difference in mobility can be attributed to the molecular weights of the dyes and to specific binding interactions. The measured mobility was inversely proportional to molecular size, as reported in previous gel electrophoresis studies[4]. Pyronin Y ionically binds to the nucleic acids in the tissue whereas safranin O binds to proteoglycans. This makes the transport of safranin through the tissue slower compared to pyronin. The electrophoretic transport of molecules across tissue is therefore limited by the charge and size of the molecule at physiological conditions.

In summary, this was a preliminary study to explore the potential of pulsed electrophoresis as an alternative or complementary method for tissue clearing during decellularization. The study successfully demonstrates the transport of molecules across the tissue sample using pulsed electrophoresis. Our future studies will characterize the electroosmotic flow component from the applied electric fields. Also, a combination of perfusion and electrokinetic transport will be studied for enhanced tissue clearing.

ACKNOWLEDGEMENTS

The authors thank Eunice Nepomceno and Nicholas Brady who worked on the clinic project, Bringhurst Meats for providing the bovine tail; Dr. Tom Christiani and Dr. Andrea Vernengo for training and equipment for tissue harvest; Dr. Vince Beachley and Dave Brennan for training and access to the SEM; and Rob McClernan for equipment installation and maintenance.

REFERENCES

1. Fernandez C, et al. *J Biomed Mater Res - Part A*. 2016;104(12):3093-3106. doi:10.1002/jbm.a.35858
2. Rieder E, et al. *J Thorac Cardiovasc Surg*. 2004;127(2):399-405. doi:10.1016/j.jtcvs.2003.06.017
3. Gilpin A, et al. *Biomed Res Int*. 2017;2017. doi:10.1155/2017/9831534
4. Hunckler MD, et al. *J Biomech*. 2015;48(15):4087-4092. doi:10.1016/j.jbiomech.2015.10.006
5. Garcia AM, et al. *Arch Biochem Biophys*. 1996;333(2):317-325. doi:10.1006/abbi.1996.0397
6. Minor M, et al. *J Colloid Interface Sci*. 1997;189(2):370-375. doi:10.1006/jcis.1997.4844
7. Oddy MH, et al. *J Colloid Interface Sci*. 2004;269(1):192-204. doi:10.1016/S0021-9797(03)00601-5
8. Sadek SH, et al. *Electrophoresis*. 2017;38(7):1022-1037. doi:10.1002/elps.201600368

THE MECHANICAL SIMILITUDE OF POSITIVE- VERSUS NEGATIVE-PRESSURE VENTILATION IN MOUSE LUNGS

K. Anduaga (1), T. Nelson (1), S. Sattari (1), C. Mariano (1), A. Ulu (2), T. Nordgren (2), M. Eskandari (1, 2, 3)

(1) Department of Mechanical Engineering
University of California, Riverside
Riverside, CA, USA

(2) BREATHE Center, School of Medicine
University of California, Riverside
Riverside, CA, USA

(3) Department of Bioengineering
University of California, Riverside
Riverside, CA, USA

INTRODUCTION

Mechanical ventilation has existed for over two centuries and the design of ventilators has changed countless times. Modern day ventilators utilize positive pressure ventilation (PPV), yet studies have shown that PPV induces lung damage [1]. Understanding and amending the causes of ventilated induced lung injury has been a major focus of lung mechanics research in recent years.

PPV does not replicate natural breathing, rather negative pressure ventilation (NPV) is the physiological way many animals, including humans, breathe. The contracting diaphragm produces a pressure gradient resulting in lung expansion. Mechanical ventilators based on NPV, such as the "iron lung," have become historically obsolete due to the inability to access the patient's vital organs during hospitalization. NPV could be employed by a patient for decades whereas PPV risks lung injury in only a few days.

Pressure-volume (PV) curves are a primary focus in lung mechanics research and a wide range of mammalian species have been studied and compared [2]. However, the role of various inflation volumes and breathing rates, and particularly their effect on PPV versus NPV mechanics is unknown. Examining the mechanics of physiological versus artificial ventilation mechanics will establish much needed fundamental scientific insights to better understand how to mitigate respiratory harm. To address these knowledge gaps, we investigate the material response of murine lungs under matched positive- and negative-pressure loading conditions.

METHODS

Three mice lungs, C57BL/6J, were obtained from the University of California Riverside's School of Medicine BREATHE Center (a small number of animal specimens are presented due to COVID-19 supply chain disruptions). After mice were anesthetized and sacrificed, a 20-gauge cannula was inserted into the trachea and secured with thread. A syringe was used to inflate the lung with 0.5ml of air to prevent the collapse of airways. The lung was stored in 1XPBS until testing, which occurred no longer than 4 hours after sacrifice.

The lung was transferred to the tank of our custom-designed apparatus to record pressure changes while continuously controlling volume [3]. Four volumes (0.3ml, 0.5ml, 0.7ml, 0.9ml) at three breathing rates (5, 10, 20 breaths per minute, BPM) were considered, totaling twelve PPV tests. To avoid trapping air, inflation tests were done in order of increasing volumes. A preload pressure of 5 cmH_2O was applied to imitate positive end expiratory pressure (PEEP), followed by three preconditioning cycles of inflation/deflation, and subsequent test cycle which was analyzed for peak pressure and elastance.

After each PPV test, NPV was conducted, matching the actual lung volume (compressed air) from PPV tests, as recorded from the pressure-volume response. PV curves for PPV and NPV for various volumes and BPMs were graphed for comparison.

Hysteresis was defined as the area between the inflation and deflation portions of PV curves. Elastance was defined as the reciprocal of compliance and was calculated as the ratio of peak transpulmonary pressure to volume. For the maximum inflation volume of 0.9ml, each breathing rate's peak pressure and elastance for PPV versus NPV was compared (mean +/- standard deviation). Statistical comparisons were conducted using a paired t-test, with significance defined as $p<0.05$.

RESULTS

The shape of the PV curves for NPV and PPV (Figure 1) resemble that of the PV curve for mice found in literature [4]. For both forms of ventilation, the lowest measured volume had minimal hysteresis and did not exhibit the transitory change in slope during inflation. Conversely,

at higher volumes, the inflation slope of both PPV and NPV greatly increased, with a transition point between 20-30cmH_2O.

The mean +/- standard deviation for peak pressure and elastance is shown in Figure 2 for three breathing rates at an inflation volume of 0.9ml. As the breathing rate increased, peak pressure and elastance increased for PPV as well as NPV. Values of peak pressure and elastance were observably higher for NPV, although the difference was not found to be statistically significant.

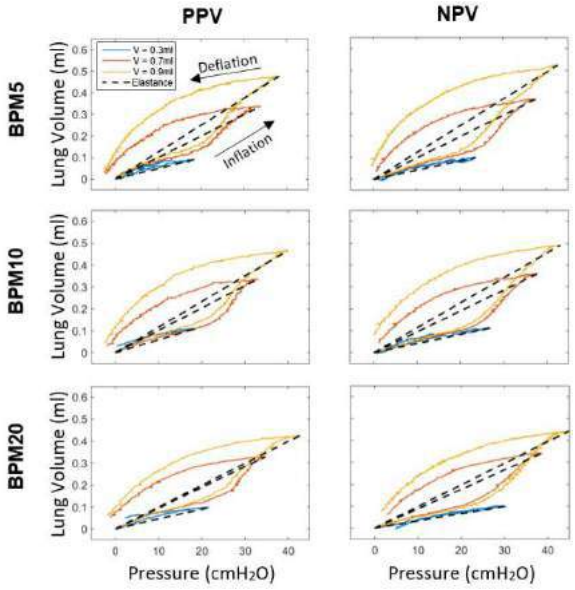

Figure 1: Representative PPV (left) and NPV curves (right) for different inflation volumes. Elastance was calculated as the ratio of peak pressure and peak volume.

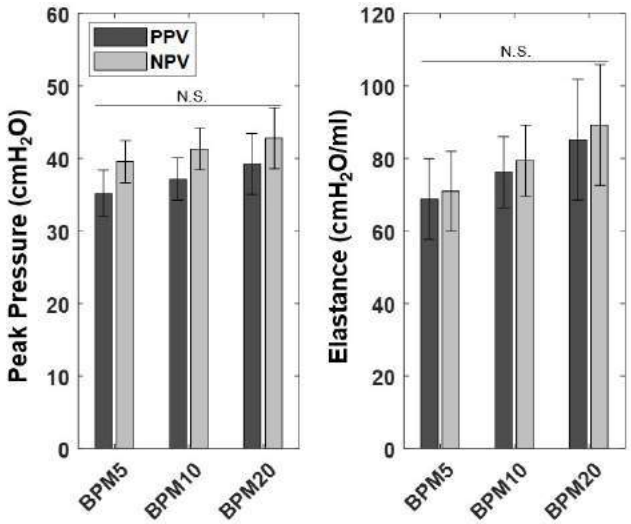

Figure 2: Mean values of peak pressure, left, and elastance, right, at varying BPMs for PPV and NPV at an applied volume of 0.9ml. Error bars are calculated from standard deviation.

DISCUSSION

We hypothesized significant differences between PPV and NPV, in agreement with recent work in our lab on porcine specimens. However, the resultant PV curves show few differences between the two forms of ventilation. This is an unexpected result and does not explain potential reasons for why artificial ventilation causes damage. It is plausible that similarities between PPV and NPV may be isolated to the mouse due to its size and the non-linear scaling of alveoli compared to larger species such as that of the pig or human [5].

One notable difference between PPV and NPV was the sudden pressure drop and resumption during inflation. This sudden alteration in the pressure-volume behavior was observed only during the inflation cycle (not deflation) and only in PPV (not NPV) and may be due to "popping" open the alveoli [6]. Popping may occur because positive-pressure alveolar recruitment is non-physiological. In contrast, NPV appears to inflate the lung through expansion of the distal alveolar regions, resulting in an uninterrupted and continuous PV curve.

In this study lung volume (compressed air) was matched for PPV and NPV. We found that for NPV, a higher transpulmonary pressure was recorded to reach the same volumes as in PPV test counterparts (Figure 1). This divergent behavior between PPV and NPV is most notable at the inflation volume of 0.3ml, where hysteresis is absent, and an elastic response is recorded. Here the PPV pressures were nearly 20cmH_2O, while NPV demonstrated greater pressure values for all breathing rates; NPV pressures collected for 0.3ml inflation in our study reached as high as 30cmH_2O elastically and without hysteresis; however, previous PPV studies, in agreement with our findings, reported hysteresis for pressures reaching 30cmH_2O [7]. The absence of hysteresis for these pressures seen in NPV tests warrants further study.

The observed increase in elastance with increased breathing rate is consistent with a study on excised cat lungs [8]. The stiffening of the whole organ is, in part, due to the local tissue elastance. Studies have shown a logarithmic increase in the dynamic elastance of parenchymal strips as frequency increases [9]. Because this phenomenon occurs in both PPV and NPV, the viscoelastic properties of the lung are a likely attributable cause.

One limitation of this study and of similar studies assessing murine mechanics is the physiological BPM of mice, which is as fast as 250-350, much higher than those tested. Lower BPMs were necessary for the quasi-static assumption, to isolate the lung structure as the main effect of elastance in PV curves [10, 11]. It is possible that the trends observed in this study may not occur at natural breathing rates.

ACKNOWLEDGEMENTS

Authors would like to thank the University of California Riverside Dean's Biomed Collaborative Seed Grant awarded to Drs. Mona Eskandari and Tara Nordgren.

REFERENCES

[1] Bates J, Smith B, *Ann Transl Med*, 6(19):378, 2018.
[2] Bennett FM, Tenney SM, *Respir Physiol*, 49: 131–140, 1982.
[3] Sattari, S et al., *Front Bioeng Biotechnol*, 8:578762, 2020.
[4] Zosky GR et al., *J Appl Physiol*, 105: 685–692, 2008.
[5] Gomes R et al. *J Appl Physiol,* 89: 908–916, 2000.
[6] Namati E et al., *Am J Respir Cell Mol Biol,* 38:572–578, 2008.
[7] Robichaud A et al., *J Appl Physiol,* 123: 746 –756, 2017.
[8] Hildebrandt J, *J Appl Physiol*, 27: 246–250, 1969.
[9] Mijailovich SM et al., *J Appl Physiol*, 76: 773–782, 1994.
[10] Mount LE, *J Physiol*, 127: 157–167, 1955.
[11] Bayliss LE et al., *J Exp Physiol Cogn Med Sci*, 29: 27–47, 1939.

ASSESSING THE COMPARATIVE STRAINS BETWEEN POSITIVE AND NEGATIVE PRESSURE VENTILATION USING DIGITAL IMAGE CORRELATION

C. A. Mariano (1), S. Sattari (1), M. Eskandari (1,2,3)

(1) Department of Mechanical Engineering
University of California, Riverside
Riverside, CA, USA

(2) BREATHE Center, School of Medicine
University of California, Riverside
Riverside, CA, USA

(3) Department of Bioengineering
University of California, Riverside
Riverside, CA, USA

INTRODUCTION

Pulmonary conditions are the predominant cause of morbidity and mortality worldwide with rising concerns due to the novel coronavirus. COVID-19 has necessitated lung biomechanics research due to the increasing number of patients undergoing ventilation and experiencing pulmonary injuries. Modern ventilators use a positive pressure to push air into the lung to deliver oxygenation resulting in overstretching and overstressing of lung tissue [1,2]. Recent investigations seek to compare positive pressure ventilation (PPV) to naturally occurring negative pressure ventilation (NPV) to analyze and mitigate ventilator induced lung injuries (VILI) [3,4]. These previous studies have been limited to evaluating the downstream biochemical response of ventilation instead of characterizing the mechanical strains and pressure-volume behaviors.

Here we introduce novel strain characterization of PPV as compared to NPV through non-contact digital image correlation (DIC) of the whole ex-vivo lung for the first time. Using our custom-designed dual-piston breathing apparatus [5], we subject porcine lungs to various inflation volumes and breathing rates, capturing the altered local strain response at peak inflation to evaluate the mechanics of PPV versus NPV on the same specimens. This investigation yields critical pulmonary mechanics insights for new ventilation schemes, such as high-frequency and multi-frequency oscillatory ventilation [6], aimed at improving patient outcomes, and correlates the bulk global ventilation pressure-volume inputs to the resulting local strain response.

METHODS

DIC was collected using our sealed transparent tank apparatus, applying controlled volumes and measuring the resulting pressure and strain response in both PPV and NPV [7]. PPV was applied by inflating the lung directly, while NPV was induced by removing air from the tank, imitating diaphragm distension. Specimens were inflated in PPV to volumes of 675 ml, 900 ml, and 1350 ml at 10, 15, and 20 breaths per minute (BPM) as clinically relevant [8]; the resulting peak pressure magnitude and change in actual lung specimen volume was measured in real time, enabling NPV loading to directly match the bulk global loading and deformation response in each variable volume and breathing rate test.

Pig lungs were collected from an abattoir and tested on the same day to minimize degradation altering behaviors. The lung was inflated once to open up airways that may have collapsed during transport in 1XPBS, speckled for DIC, and analyzed using Trilion ARAMIS Adjustable 12M system as previously stated [7]. Each lung was preloaded to an inflation pressure of 0.07psi ($5cmH_2O$) to ensure uniform starting states across each specimen and to replicate positive end expiratory pressure (PEEP). Samples were then subjected to three preconditioning cycles at each specified volumes and breathing rate before collecting data from a subsequent test cycle. PPV and NPV lung surface strain contours were analyzed at the peak inflation states. Histograms depicting the relative strain distribution for each sample and resulting mean, range, and median strain values were averaged and compared between PPV and NPV. Three pig specimens were analyzed for statistical significance (despite COVID-19 disrupted tissue supply chains). A paired t-test was used to compare PPV to NPV, and ANOVA with post-hoc Bonferroni was used to compare the breathing rates with defined significance of $p<0.05$.

RESULTS

The qualitative strain contour map of a representative porcine lung at various inflation volumes for PPV and NPV is shown in Figure 1. Local strains increased in response to increased applied inflation volumes. While the lower and upper lobes were noted as the site of minimal and maximal strains respectively in both PPV and NPV, greater

regions of high strain were noted in PPV compared to NPV. Significant changes in strain values and regional distribution were not observed when the breathing rate was varied.

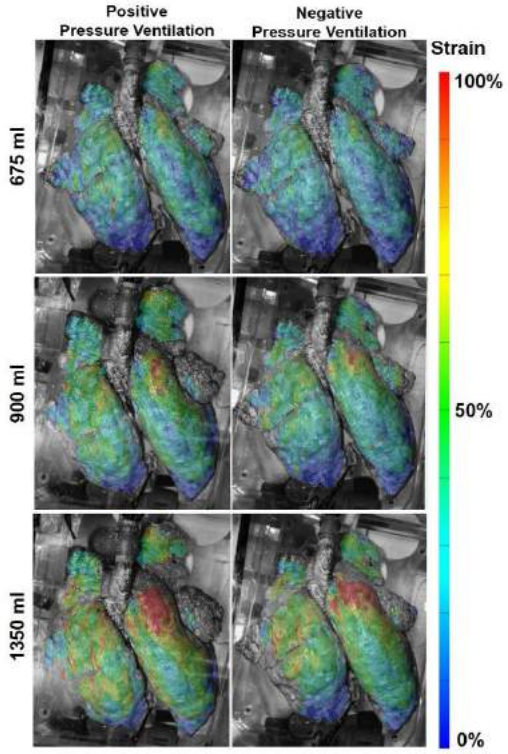

Figure 1: Strain contours of a representative porcine sample inflated at a breathing rate of 10 BPM and at volumes of 675 ml, 900ml, 1350 ml. At each volume, the same lung was inflated using either PPV or NPV.

The resulting strain distribution in PPV and NPV is quantified in Figure 2. The median strains were mainly clustered at <10%. PPV was noted to have statistically significant increased strain ranges relative to NPV across all volumes and breathing rates; NPV peak strains were always much less than peak strains in PPV. While the mean strains in NPV were generally lower than PPV, the decrease was not found to be statistically significant.

DISCUSSION

We expected NPV local strain contours and distribution to significantly differ from PPV but found that the regional behavior did not necessarily differ. In terms of strain distribution, NPV populates lower strain values and has decreased maximum strains compared to PPV; this suggests there are localized strain peaks in artificial ventilation utilizing positive-pressure compared to physiological negative-pressure breathing, underscoring a potential cause of VILI. This finding supports the notion that negative pressure ventilation results in less lung injury [9,10].

The range of strain distribution was not significantly altered for normal (15BPM), slower (10BPM), and faster (20BPM) breathing frequencies in either PPV or NPV. Evaluating if breathing rate could induce varied mean and median strain response for PPV or NPV was inconclusive. While our analysis is restricted to the 3D surface strain profile and ex-vivo specimens, it limits the likelihood of mechanical benefits of varied inflation rates. It may be that multi-frequency oscillatory ventilation improves oxygenation by reducing biotrauma (inflammation) and atelectrauma (opening and closing of alveoli and airways) but not barotrauma and volutrauma [6].

Our recent studies have found that the initial inflation curve of the PPV pressure-volume response (clinically understood as alveoli recruitment) has a significantly smaller slope and is therefore much stiffer compared to NPV [11]; the deflation response was not found to differ. However, the strain analysis performed here was conducted for the matched end-point inflation stage, discounting the temporal evolution and pressure-volume path differences between PPV and NPV. While the end-stage strains for matched peak pressures and applied volumes may minimize differences between PPV and NPV, key physiological and breathing rate distinctions may stem from phases within the inflation cycle. Future studies will consider the strain behavior of PPV and NPV beyond the end-stage inflation state.

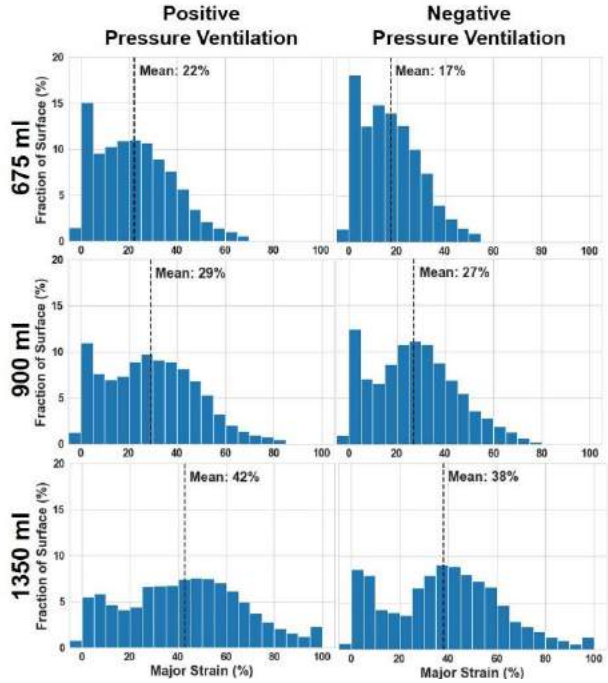

Figure 2: PPV and NPV strain distributions of representative sample inflated at a rate of 10 breaths per minute and at volumes of 675 ml, 900ml, 1350 ml.

ACKNOWLEDGEMENTS

Authors gratefully acknowledge funding support from Dassault Systèmes U.S. Foundation Grant.

REFERENCES

[1] Beitler, J. R., et al., *Clin Chest Med*, 37(4):633-46, 2016. [2] Kneyber, M. C. et al., *Am J Respir Crit Care Med*, 190(3):258-265, 2014. [3] Bruells, C. S. et al., *Anesthesiology*, 119:652-62, 2013. [4] Engelberts, D. et al., *Intensive Care Med*, 38(5):879-85, 2012. [5] Sattari, S. et al., *Front Bioeng Biotechnol*, 8:1183, 2020. [6] Kaczka, D. W. et al., *Anesthesiology*, 123(6):1394-1403, 2015. [7] Mariano, C. A. et al., *Front Physiol*, 11:1536, 2020. [8] Chiumello, D. et al., *Am J Respir Crit Care Med*, 178:346-55 [9] Grasso, F. et al., *Am J Respir Crit Care Med*, 177:412-18, 2008. [10] Raymondos, K. et al., *Critical Care*, 16:R37, 2012. [11] Sattari, S. et al., 2021 in preparation

INFLAMMASOME NLRC4 GENE KNOCKOUT INCREASES STIFFNESS OF BLADDER WALL IN RAT MODEL

Eli Broemer (1), Christina Chan (2), Sara Roccabianca (1)

(1) Mechanical Engineering
Michigan State University
East Lansing, MI, USA

(2) Chemical Engineering
Michigan State University
East Lansing, MI, USA

INTRODUCTION

The urinary bladder is a highly compliant organ with its mechanical behavior largely mediated by smooth muscle and the extracellular matrix (**ECM**) in the bladder wall [1]. The ECM is susceptible to pathological remodeling wherein the structure of its constituents—collagen and elastin—is altered which impacts stiffness and bladder health/function. Loss of healthy bladder function can reduce the affected individual's quality of life: increasing the risk for depression and suicide, or unhealthy coping methods such as reducing fluids and isolation [2]. Annual healthcare cost for treating poor bladder function in the United States is estimated between $9-100 billion [2, 3].

Common urinary dysfunctions have been associated with an inflammatory response including: neurogenic bladder, chronic urinary tract infection, and interstitial cystitis (or, bladder pain syndrome) [4]. Furthermore, inflammation is believed to be involved in the initiation and progression of these dysfunctions. Chronic inflammation within the bladder wall is associated with ECM remodeling which can damage the organ tissue in the long term [5].

Inhibiting pro-inflammatory mechanisms may be a viable approach to prevent bladder wall remodeling and function deterioration. Specifically, inflammasome-mediated pathways has emerged as driving fibrosis in various organs including the bladder [6]. For example, the NOD-like receptor (NLR) inflammasomes NLRP3 and NLRC4 (Pyrin domain-containing protein 3, and Caspase recruitment domain-containing protein 4, respectively) initiate inflammation in response to environmental factors, including gram-negative bacteria such as E. coli [7]. NLRC4 is found throughout the human body, and in the urothelium—the protective layer between urine and bladder tissue—of the bladder wall [8].

Knockout (KO) of the NLRC4 gene may reduce bladder inflammation as it is functional in activating immune response in the bladder wall [8]. In the first stage of this study, we show that NLRC4 KO alone affects mechanical behavior of bladder ECM in rat models.

METHODS

An NLRC4 KO rat model was developed at the MSU Transgenic and Genome Editing Facility by deleting 252 base pairs corresponding to the NLRC4 gene in Sprague-Dawley (SD) rats. Then heterozygous (NLRC4 +/-) and homozygous (NLRC4 -/-) groups were bred. Controls were SD wild-type. Animals were sacrificed at 12-13 weeks, and whole bladders were extracted, imaged, weighed, sectioned into rings, and frozen until testing. Dissection and testing was randomized and blinded.

Fresh tissue geometry was assessed from top-down photos of the flattened whole organ, as shown in **Figure 1a**. Bladder area was measured by thresholding these profile shots with ImageJ, as shown in **Figure 1b**. As the size and weight of the extracted organ is somewhat dependent upon the location of incision at the bladder neck, these measures were normalized by ratio of bladder weight to area.

After thawing, bladder ring samples were decellularized to isolate the ECM, and mounted to a uniaxial testing machine while submerged in Krebs solution. Tests measured force via load cell and length/cross-sectional area via front/side cameras.

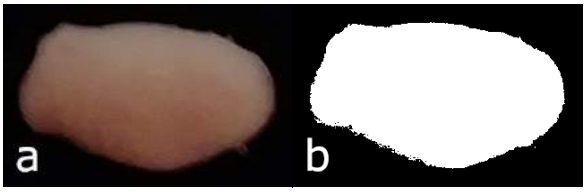

Figure 1: a) Whole fresh bladder after extraction flattened to show profile, b) Threshold applied to measure bladder profile area.

Samples were stretched to four strain levels (5, 10, 15, and 20%). For each of the four tests, the tissue was held at a 2g preload until relaxation diminished, and then cyclically loaded and unloaded at 1% strain/sec. The first test had 10 minute preload and 10 cycles, while the next three tests had 1 minute preload and 5 cycles. This loading protocol ensures each ring is consistently taut and preconditioned so that mechanical behavior becomes repeatable.

Data from the final load cycle at the highest strain level was analyzed and is presented in **Figure 2**. True (Cauchy) stress-strain curves were found using the median cross-sectional area at the preload stage, approximated as a rectangle, and then force and length, recorded continuously, give stress and strain assuming incompressibility. The initial length (reference) used to evaluate stress and strain was each sample's length at the start of the last loading cycle.

RESULTS

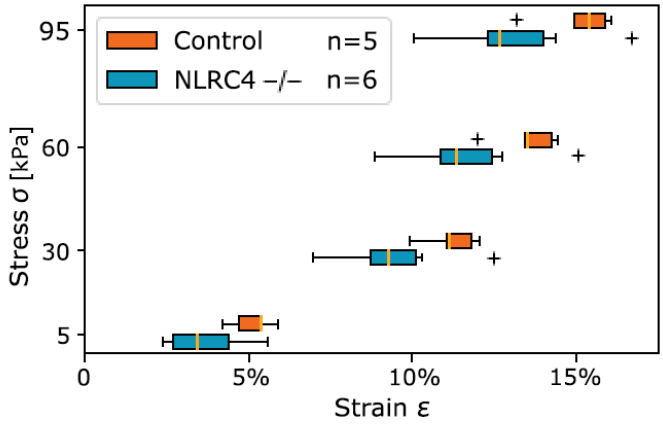

Figure 2: Cauchy stress-strain curve at representative stress levels from bladder ECM tests. Student's t-test of Control v NLRC4 -/- gives P=.049, P=.09, P=.11, and P=.11 at 5, 30, 60, and 95 kPa respectively (no correction).

Figure 2 shows the circumferential mechanical behavior, tested uniaxially, for preconditioned tissue stretched to 20% strain. It should be noted this data is truncated to ~15% strain to better show its non-linear characteristic. The bladder ECM for the KO group (NLRC4 -/-) shows less deformable mechanical characteristics when compared to controls. This difference between control and KO groups was significant at lower values of stress (i.e., 5 and 30 kPa). At higher values of stress (i.e., 60 and 95 kPa), the trend is conserved yet the difference is not significant (P=.11 for both stress values). Heterozygous (NLRC4 +/-) had values of strain in-between control and KO groups for all stress values considered (differences were not significant when compared to either the control or KO animals).

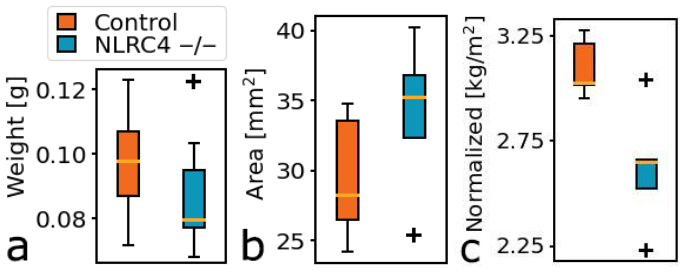

Figure 3: Physical characteristics of fresh whole bladders; a) Weight, b) Flattened area, c) Normalization by weight/area.

Figure 3a shows that whole bladder weight was lower in the KO group compared to controls. Bladder profile area appeared larger in the KO group compared to controls (**Figure 3b)**. Normalization of fresh bladder weight and flattened area (**Figure 3c**) showed marked difference between KO and control groups.

DISCUSSION

These results indicate that NLRC4 KO affects the homeostatic mechanical characteristics of the urinary bladder's ECM. Interestingly, while high distensibility is often problematic and a clinical marker for bladder dysfunction, bladders having comparatively lower distensibility are considered to be stable and healthy [9, 10]. Our data show that NLRC4 KO results in a less distensible ECM and in a lower bladder weight, when compared to controls. This has also been observed in children, where low bladder weight, assessed by ultrasound, was used to predict lower distensibility, as compared to dysfunctional highly distensible bladders [9].

Bladder weight is also considered a marker for bladder inflammation, indeed both NLRC4-driven and bacterial-induced inflammation have shown to double bladder's weight compared to controls [11, 12]. Moreover, bacterial-induced inflammation can trigger detrusor hyperactivity [12], which is compensated for by increased bladder distensibility [13]. Taken together, previously published literature and the results presented here, suggests that the NLRC4 -/- animals had lower levels of inflammation than the control.

Increased bladder area was observed in the KO group vs controls, although reference length (a measure of ECM ring circumference) was similar across groups being 16.8mm +/- 0.5mm. This apparent size discrepancy may be clarified by noting area was measured in relaxed bladders having muscle cells, while reference length was measured in decellularized preconditioned tissue. The difference revealed by normalization may be due to microstructural changes in the detrusor muscle and/or ECM, though that is yet to be determined by histology.

Next steps in this study include histological and immunohistological studies to examine potential microstructural changes between groups as well as the presence and level of inflammatory markers, such interlukin-1β (IL-1β), IL-18 and IL-6. Later steps will include the addition of inflammatory stressors such as a high-fat diet or diabetic predisposition.

ACKNOWLEDGEMENTS

We thank Drs. Elena Demireva and Huirong Xie from the MSU Transgenic and Genome Editing Facility and the Institute of Quantitative Health Science and Engineering for developing the NLRC4 KO rat model. We thank fellow lab members Marissa R. Grobbel and Tyler Tuttle for assistance with mechanical testing protocol. This study was supported by NSF grant CBET 1802992.

REFERENCES

[1] Parekh, A et al., *J Biomech*, 43(9):1708-16, 2010.
[2] Sacco, E et al., *J Urol*, 2:11-24, 2010.
[3] Powell, LC et al., *Neurourol Urodyn*, 37(4):1241-49, 2018.
[4] Liu, HT et al., *Low Urin Tract Symptoms*, 7(2):102-7, 2015.
[5] Kullmann, FA et al., *Front Syst Neurosci*, 12:13, 2018.
[6] Inouye, BM et al., *Curr Urol*, 11:57-72, 2017.
[7] Zheng, D et al., *Cell Discovery*, 6:36, 2020.
[8] Hughes Jr., FM et al., *Int Urol Nephrol*, 47(12):1953-64, 2015.
[9] Ukimura, O et al., *J Urology*, 160(4):1459-62, 1998.
[10] Bauer, SB, *Pediatr Nephrol*, 23:541-51, 2008.
[11] Hughes Jr, FM et al., *Am J Physiol-Renal*, 306(3):F299-308, 2014.
[12] Randich, A et al., *J Pain*, 7(7):469-79, 2006.
[13] Howard, PS, Macarak, EJ, *Adv Exp Med*, 462:215-223, 1999.

IN VITRO ASSESSMENT OF THE EFFECTS OF CARDIAC OUTPUT AND VALVE ORIENTATION ON BIOPROSTHETIC PULMONARY VALVE HEMODYNAMICS

N. Schiavone (1), C. Elkins (1), D. B. McElhinney (2), J. K. Eaton (1), A. L. Marsden (1,3)

(1) Department of Mechanical Engineering
Stanford University
Stanford, CA, USA

(2) Department of Cardiothoracic Surgery
Stanford University
Stanford, CA, USA

(3) Departments of Pediatrics and Bioengineering
Stanford University
Stanford, CA, USA

INTRODUCTION

Tetralogy of Fallot (ToF), the most common type of cyanotic congenital heart defect, affects 1 in every 2500 newborns annually. Typical surgical repair for ToF requires an initial surgery at a few months of age to close the ventricular septal defect and reconstruct the right ventricular outflow tract (RVOT). The defect and repair often leave the patient without a fully functional pulmonary valve and reintervention may be necessary to place an artificial valve in the patient's early teen years. Bioprosthetic xenograft valves, which are commonly used for this procedure, are subject to degradation and dysfunction over time, typically within 15 years of implantation and often leading to additional surgical interventions [1]. However, these valves fail early and unpredictably in as many as 30% of ToF patients and there is currently little understanding of what hemodynamic factors may lead to early valve dysfunction. More comprehensive knowledge of the flow structure local to the valve and leaflet dynamics may aid clinicians in selecting the best placement and size for optimal long-term valve function.

Our prior work analyzed variations in 3D flow fields over the cardiac cycle in both healthy and diseased RVOT geometries *in vitro* [2]. The flows differed significantly, particularly in vortex formation and reverse flow volume, which could have an impact on the valve leaflet function over time. In addition, we found that changing the rotational orientation of the valve further impacted the flow fields. The orientation affected the flow differently depending on the geometry, revealing the compound effect between geometry and orientation.

The current work examines the effect of cardiac output on valve behavior, coupled with continued studies on valve orientation, in a diseased RVOT model. The impact of varying cardiac output can provide insights on valve sizing, which is of particular interest for pediatric patients. We paired measurements of the full flow fields in the model over the cardiac cycle with high speed camera images of the valve leaflet motion to generate a comprehensive picture of the valve environment at different cardiac outputs.

METHODS

The experimental setup consists of a 3D printed model of the RVOT inserted in a flow loop designed to replicate physiological flow and pressure waveforms. The RVOT model was designed based on the centerline measurements of the pulmonary arteries of healthy patients, but with a 150% dilation immediately downstream of the valve to represent a common disease condition seen in ToF (Figure 1). A 25mm St. Jude Medical Epic porcine valve was implanted in the model. The pulsatile flow through the model is pneumatically driven and was adjusted for three different cardiac output cases: 2 L/min, 3.5 L/min, and 5 L/min. The working fluid was a blood analog water-glycerin solution with 40% glycerin resulting in a viscosity of 3.9 centipoise at room temperature.

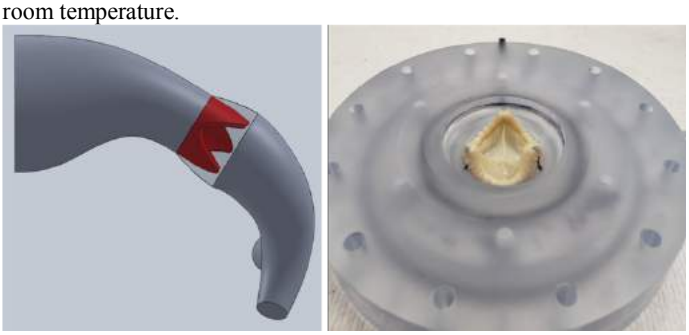

Figure 1: Diseased RVOT model design (left) with 150% vessel dilation in the main pulmonary artery. Bioprosthetic valve inserted in the 3D printed model (right).

For each of the three cardiac outputs, full 3D, three-component, phase-averaged velocity fields were obtained over the cardiac cycle using magnetic resonance velocimetry (MRV) [3]. The experiments were conducted in a whole body, 3 Tesla, General Electric MRI scanner at the Richard M. Lucas Center for Imaging at Stanford University. The MRV sequence was phase-locked, allowing for measurements at different points throughout the cardiac cycle. The spatial resolution of the scans was 0.9mm in the sagittal, axial, and coronal directions. The temporal resolution was 77ms resulting in the direct measurement of approximately 10 phases. For the final results, the resulting data were interpolated to 20 phases throughout the cardiac cycle. The velocity encoding (*venc*) was adjusted for each cardiac output case to account for the differences in maximum velocity.

For all three cardiac outputs, the valve was placed in the native orientation, with a valve leaflet opening along the interior curve. For the 2 L/min and 3.5 L/min cases, the valve was also rotated 180 degrees for additional MRV studies. For the 5 L/min case, the rotated orientation data was only collected with the high-speed camera experiment.

To capture leaflet motion, we took images with a Phantom V2012 Ultrahigh-speed camera with a 105mm Nikkor Lens. The model was submersed in the working fluid to limit distortion due to refraction. The camera was placed downstream of the valve to capture the full leaflet motion over the cardiac cycles. Images were taken at a framerate of 1500Hz, leading to approximately 500 images from valve opening to closing. The MRV and high-speed camera experiments were run with the same experimental parameters and the trigger signal at the start of systole was recorded, allowing us to align the two data sets and examine the relationship between flow fields and leaflet motion.

RESULTS

For 2 L/min, 3.5 L/min, and 5 L/min, the full velocity fields from the MRV scans revealed key differences in flow features due to changes in cardiac output. At peak systole, the shape of the jet through the valve and the formation of vortices are noticeably different for each case. At 2 L/min, the forward flow through the jet is more asymmetric compared to the higher cardiac outputs, and a strong vortex forms, indicating a region of recirculation (Figure 2). The slower overall flow at 2 L/min also produces larger regions of stagnant and reverse flow. At 3.5 L/min, some reverse flow persists as the valves are closing, but at 5 L/min, the faster flow through the valve prevents these reverse flow regions from forming. The valve orientation also has an impact on the flow fields. The rotated orientation results in a large region of reverse flow along the outer curve of the vessel that is not present in any of the native orientation cases. In addition to these differences in the streamwise flow, the radial flow local to the valve was also affected by the cardiac output, with radial flow persisting local to the valve leaflets during diastole only for the low cardiac output cases.

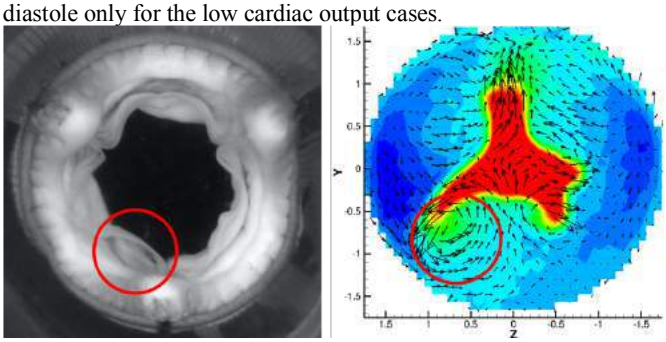

Figure 2: High speed camera image (left) and streamwise velocity contours with in-plane vectors (right) for the 2 L/min case at peak systole. Red circle highlights location where a partially closed section of leaflet influences the velocity fields.

The flow features provide insights into the hemodynamic environment of the valves, while the high-speed camera images capture the instantaneous leaflet motion. The effective orifice area, a key clinical metric in assessing valve performance, changes notably with cardiac output, though the valve orientation has little effect (Figure 3). The largest orifice area occurred at 5 L/min, with an 8.5% decrease for the 2 L/min case, indicating that valve is not operating as effectively at the lower cardiac output. In addition, at 2 L/min, a particular portion of one of the leaflets remains partially closed throughout systole, blocking flow through the valve orifice. This produces the asymmetry seen in the corresponding flow fields from the MRV scans (Figure 2). This connection demonstrates how flow features can reveal valve leaflet behavior.

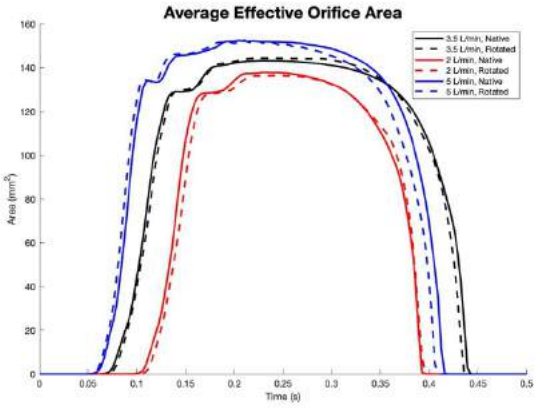

Figure 3: Effective orifice area over the cardiac cycle for 2 L/min (red), 3.5 L/min (black), and 5 L/min (blue)

DISCUSSION

Analyzing both the full flow fields and instantaneous valve motion at different cardiac outputs and valve orientations shows significant differences in stagnant and reverse flow, flow asymmetry, and leaflet behavior. With a 25mm valve, 3.5 L/min represents a normal cardiac output, while 2 L/min represents an oversized valve situation and 5 L/min represents an undersized valve. While some surgeons prefer to oversize the valve in young patients to account for continued growth, the differences in flow features and leaflet function may indicate an adverse environment for long-term valve performance. At 2 L/min, the partial valve leaflet opening produces a recirculation region which may increase risk of calcification. The overall orifice area is also notably lower for the 2 L/min case, which may impair the valve effectiveness. While clinical studies are necessary to fully determine how flow features and valve behavior are correlated with patient outcomes, insights from this study demonstrate that cardiac output significantly affects the valve hemodynamic environment and illustrate connections between the global flow and the instantaneous valve motion. Future work could also use these detailed data for experimental validation of valve fluid structure interaction simulations.

ACKNOWLEDGEMENTS

We gratefully acknowledge funding from the American Heart Association Transformational Project Award. Nicole Schiavone is supported by the Stanford Bio-X Bowes Fellowship and the Stanford Vera Moulton Wall Center.

REFERENCES

[1] McElhinney, D. et al., *Circ – Cardiovasc Interv*, 4:602-U130, 2011.
[2] Schiavone, N. et al., *Cardiovasc Eng Tech*, 2021.
[3] Elkins, C. et al., *Experiments in Fluids*, 43:6:823-858, 2007.

SUCCESSFUL CRYOPRESERVATION OF RABBIT JUGULAR VEIN USING MAGNETIC NANOPATICLES ENHANCED SINGLE-MODE ELECTROMAGNETIC RESONANCE REWARMING SYSTEM

Shen Ren (1), Zhiquan Shu (1,2), Ziyuan Wang (1), Ye Jin (1), Ruidong Ma (1), Shaohang Hao (1), Dayong Gao (1)

(1) Department of Mechanical Engineering
University of Washington
Seattle, WA, USA

(2) School of Engineering and Technology
University of Washington Tacoma
Tacoma, WA, USA

INTRODUCTION

Tissue and organ transplantation remains the most effective treatment for those patients who suffered from acute or chronic organ failures [1,2]. Unfortunately, there is a long waiting list for transplantation due to the lack of an effective organ preservation method. The current hypothermic storage could maintain the viability of hearts and lungs for up to 4 hours, intestine, pancreas, and liver for 8 to 12 hours, and kidney for up to 36 hours [3]. In such a short period, most of the tissues and organs (> 80%) are wasted due to insufficient time to match a recipient or exceeded the maximum storage time during transportation and handling. Cryopreservation, a technology to preserve the biomaterials at low temperatures to pause the biological and chemical reactions, is a potential solution to long-term tissue and organ preservation. To date, successful cryopreservation is limited to small volume biomaterials due to, in part, the challenges remaining in the rewarming process [4]. First, a rapid rewarming rate is needed to avoid fatal ice-recrystallization. Second, this rapid rate needs to be homogeneously distributed within the entire sample (to achieve uniform temperature distribution) to prevent thermal-stress-induced fracture. Therefore, a rapid and uniform rewarming technology is needed.

In this study, we developed a novel single-mode electromagnetic (EM) resonance (SMER) system, successfully converting EM energy into rapid-uniform volumetric heating. A dynamic feedback control loop was embedded to achieve real-time monitoring and adjusting the feeding frequency to maintain the biomaterials' higher absorptivity to the EM power. Thus, the EM cavity associated 'thermal runaway' problem, which is the increasing temperature difference within the sample because of the temperature-dependent EM power absorption, was limited and improved during the warming. Moreover, superparamagnetic nanoparticles (SNPs) were adopted to absorb magnetic field energy to further enhance the energy conversion efficiency.

The SNPs enhanced SMER system achieved ultra-rapid and uniform rewarming for large tissues (> 25 mL) to avoid ice-recrystallization and tissue fracture. The functionality and viability of the cryopreserved rabbit jugular veins using the SMER were comparable to the fresh-tissue control and over 5 times better than using the conventional 37 ℃ water bath (a current gold standard warming method in the clinical settings).

METHODS

Tissue Harvesting and Handling. Rabbit jugular veins were procured from adult male New Zealand rabbits (2-3 kg, N = 26) and immersed in Krebs-Henseleit buffer immediately, then transferred to the research lab within 1 hour. Tissues were sectioned into vein segments with the following dimensions: inner diameter, 2 to 4 mm, wall thickness, 1 to 2 mm, and length, 20 to 40 mm.

Cooling and Rewarming. After loaded with cryoprotective agents (CPAs), tissues with CPA solutions in a sample holder were cooled with liquid nitrogen vapor to -150 ℃ and stored overnight. Three rewarming methods were applied with different warming rates: (1) natural air convection: the cryopreserved tissues were put on the lab bench at room temperature (21 - 23 ℃); (2) water bath heating: the tissues were quickly transferred to 37 ℃ water bath with shaking at 60 RPM in an orbital motion; (3) SMER system: tissues were quickly transferred to the EM resonant cavity with a maximum power of 400 W. Temperature sensors were placed at the center and edge of the tissue holder, the heating was terminated when sample temperature reached 0 ℃.

Viability of tissues. Fresh tissue segments were incubated with growth media plus 10% alamarBlue solution at 37 ℃ and 5% carbon dioxide for 2 hours. The absorbance readings were determined by a

microplate reader at 570 and 600 nm to establish the baseline. The same procedure was repeated to obtain the readings of the warmed tissues.

Biomechanical Assessment of Tissues. Warmed tissues were cut into vein rings in the length of 3-5 mm. Each vein ring was mounted to a high-resolution force transducer in a Falcon tube. After loading the agonist (Histamine) and antagonist (Sodium Nitroprusside), contraction and relaxation response were measured by the transducer.

Tissue cryo-survival data was normalized to fresh tissue controls. Statistical significance is indicated with asterisks:****P <0.0001. The data are presented as the means with SD.

RESULTS

Recorded temperature profiles and thermal gradient between tissue center and edge of three warming methods are shown in Fig 1. The water bath heating achieved an average warming rate at 46.52 ± 4.85 ℃ min^{-1}, with a large temperature difference especially at the beginning of the warming. Natural air heating succeeded in a relatively uniform temperature distribution that confined the temperature difference within 10 ℃, but a slow rate at 4.53 ± 0.14 ℃ min^{-1}. SNPs-enhanced SMER system accomplished the uniform warming while surged the heating rate to 326.91 ± 7.55 ℃ min^{-1}.

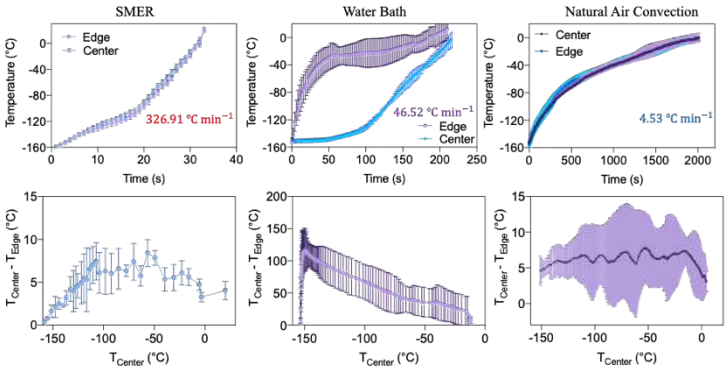

Figure 1. Temperature profiles and thermal gradients of SMER (left), water bath (middle), and natural air convection (right). n = 9.

As shown in Fig 2 left, viability of the vein warmed by SMER showed no statistical difference (P=0.3675) from the fresh samples at $86.54\pm5.63\%$, significantly higher than the convective water bath ($26.73\pm7.75\%$), and air warmed ($32.13\pm11.04\%$). The large decline of tissue viability in water bath and air warmed indicate the cryo-injuries caused by slow and non-uniform warming. The results were supported by Hematoxylin and eosin (H&E) stained histological images. The SMER image (B) demonstrates well-defined intact nuclear morphology

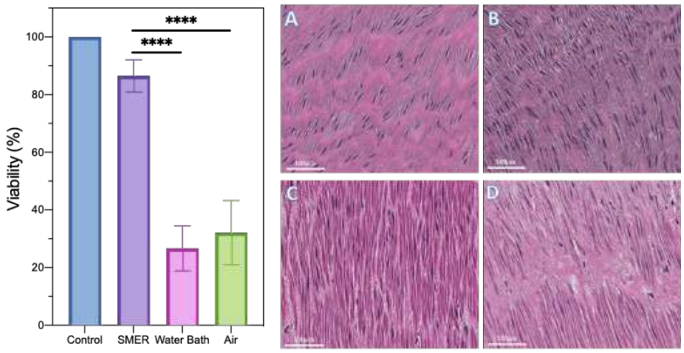

Figure 2. Left, viability of post-thawed vein measured by alamarBlue. **Right,** histological images of H&E stained samples. A, fresh tissue; B, SMER; C, water bath; D, natural air convection.

and structure of the venous smooth muscle cells, and it is comparable to the fresh control group (A). In contrast, the tissue warmed by water bath (C) and air convection (D) showed disruptive structure and dispersed nuclei with apparent hollow space between cells, possibly due to the ice-recrystallization and osmotic injury. The formation of ice could lead to the rupture of the cells and disruptive layered tissues, which could be observed as more hollow space (white area) in the histological images.

Similar to other smooth muscle tissues, contraction and relaxation are the two major biological functions of the jugular veins to maintain blood pressure and transport deoxygenated blood. As shown in Fig 3, fresh tissue and cryopreserved tissue using SMER system indicate the sensitivity of initial contractile and relaxation responses (forces in unit of N) to the agonist and antagonist at a lower concentration. The responses spiked as the concentration increased. Tissues warmed by water bath and air convection show minimal reaction (5 times lower than SMER) to both chemical stimulates and represent the loss of the biological functionalities after the cryopreservation.

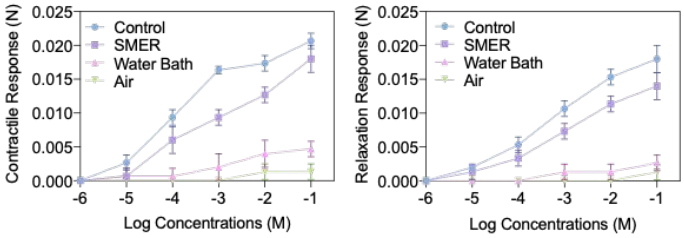

Figure 3. Maximum responses (forces) of post-thawed vein rings to the different concentrations of agonist and antagonist. Left, contractile response. **Right,** relaxation response.

DISCUSSION

In this study, a novel SMER was developed for rapid and uniform rewarming of large biomaterials in cryopreservation. SMER technology were compared with two conventional heating approaches, i.e, water bath heating and room-temperature air heating, respectively, during the cryopreservation of the rabbit jugular veins. Through the systematic examinations of the heating effects on cryopreserved biomaterials, we found that tissue samples rewarmed with slow and non-uniformed methods showed large decline of the viability and damage to the functionality, presumably due to the cell ruptures and tissue facture caused by the lethal ice-crystallization and large temperature gradient. On the other hand, rapid and uniform heating achieved by SMER technology provides a promising approach to the rewarming of large volume biomaterials. All the viability test, histological analysis, and biomechanical assessment results confirmed the successful rewarming of tissues by SNPs enhanced SMER system which maintained the tissue viability and functionality nearly identical to the fresh control. Ongoing and future studies include the further applications of the SMER system for cryopreservation of larger organs like human kidney and heart to meet the increased and urgent needs in organ transplantation.

ACKNOWLEDGEMENTS

This work was support, in part, by the Bill & Melinda Gates Foundation and Origincell Professorship Funds. We thank the Histology and Imaging Core (HIC) at the University of Washington for their technical assistance.

REFERENCES

[1] Bezinover, D et al., *BMC Anesthesiology*, 19(1):32, 2019.
[2] Rall, W et al., *Nature*, 313, 573-575, 1985.
[3] Lweis, J.K. et al., *Cryobiology*, 72(2), 169-182, 2016.
[4] Berendsen, T.A. et al., *Nature Medicine*, 20, 790-793, 2014.

NEO-SINUS AND SINUS FLOWS AFTER TRANSCATHETER AORTIC VALVE IMPLANTATION OF EVOLUT, SAPIEN 3, ACCURATE NEO AND ALLEGRA

H. Hatoum (1), S.C.M. Gooden (2), Y. Farsiani (2), M. Samaee (2), J. Sathananthan (3), S.M. Lilly (4), A.R. Ihdayhid (5), V. Thourani (6) and L.P. Dasi (2)

(1) Biomedical Engineering Department
Michigan Technological University
Houghton, Michigan, USA

(2) Department of Bioengineering
Georgia Institute of Technology
Atlanta, Georgia, USA

(3) Centre for Cardiovascular and Heart Valve Innovation
St Paul's and Vancouver General Hospital
Vancouver, Canada

(4) Division of Cardiovascular Medicine
The Ohio State University
Columbus, Ohio, USA

(5) Monash Heart
Monash Health
Victoria, Australia

(3) Division of Cardiovascular Medicine
Piedmont Hospital
Atlanta, Georgia, USA

INTRODUCTION

Transcatheter aortic valve (TAV) replacement (TAVR) emerged initially as an alternative procedure to the traditional and highly invasive surgical aortic valve replacement surgery (SAVR). TAVR consists of percutaneously deploying using a catheter, a bioprosthetic valve that can be reduced to a few millimeters in diameter in the aortic annulus, and subsequently, expanding it in the position of interest.

Leaflet thrombosis emerged as one of TAVR's adverse effects. The likelihood of leaflet thrombosis ranges between 15 – 40% [1]. Because thrombosis is a flow related phenomenon, more particularly a flow stasis related one, it is important to assess the surrounding flow in the neo-sinus and the sinus [2]. The goal of this work is to evaluate the flow dynamics in the sinus and the neo-sinus after implantation of 3 self-expanding TAVs (Medtronic Evolut, Boston Scientific Accurate Neo, and New Valve Technology Allegra) and a balloon expandable TAV (Edwards SAPIEN 3) in a 23 mm polymeric surgical aortic valve.

METHODS

The hemodynamic assessment of a 26mm Evolut, a 23mm SAPIEN 3, a small Accurate Neo and a 23mm Allegra transcatheter aortic heart valves in a 23mm polymeric surgical valve was performed in a left heart simulator under pulsatile conditions of physiological pressure of 120/80 mmHg, 5L/min and 60 beats per minutes. The fluid used in the experiments was a mixture of water-glycerin with properties similar to those of blood (density of 1060Kg/m^3 and a kinematic viscosity of 3.5cSt). Fifty consecutive cardiac cycles of aortic pressure, ventricular pressure, and flow rate data were recorded at a sampling rate of 100 Hz. Particle image velocimetry (PIV) experiments were performed to assess the flow in the sinus and the neo-sinus of each arrangement. The flow was seeded with fluorescent poly(methyl methacrylate)-rhodamine B particles with average diameter of 10µm. a laser sheet created by pulsed neodymium-doped yttrium lithium fluoride single-cavity diode pumped solid-state laser coupled with external spherical and cylindrical lenses shone on the region of interest while acquiring high-speed images of the fluorescent particles within the sinus region. Lagrangian particle tracking was utilized to estimate sinus and neo-sinus washout. Briefly, the PIV data was exported, and particles were seeded numerically on the neo-sinus and the sinus regions in a uniform grid at the beginning of the cardiac cycle. The updated position of the particles is integrated from the velocity information. At the end of every cardiac cycle, the new locations of the particles are extracted and only those that remain after the cardiac cycle time is over are seeded again. This process is repeated until all the particles have washed out. In addition, shear stress was also computed as per equation 1 and probability density functions were calculated and plotted.

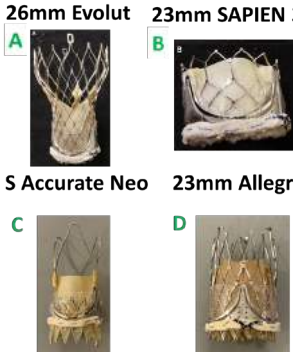

Figure 1: Valves tested. (A) Evolut, (B) SAPIEN 3, (C) Accurate Neo and (D) Allegra

RESULTS

The washout curves in the neo-sinus and the sinus for the 4 self-expanding and the balloon expandable TAVs are shown in Figure 2A and 2B respectively. In the neo-sinus, the Evolut, Accurate and Allegra's washout is nearly 1 cardiac cycle, whereas the SAPIEN 3 washout takes about 3 cardiac cycles.

In the sinus, the Evolut, Accurate Neo and Allegra's washouts are nearly 1 cardiac cycle whereas SAPIEN 3 washout is about 2 cardiac cycles. The results of the shear stress probability density function are

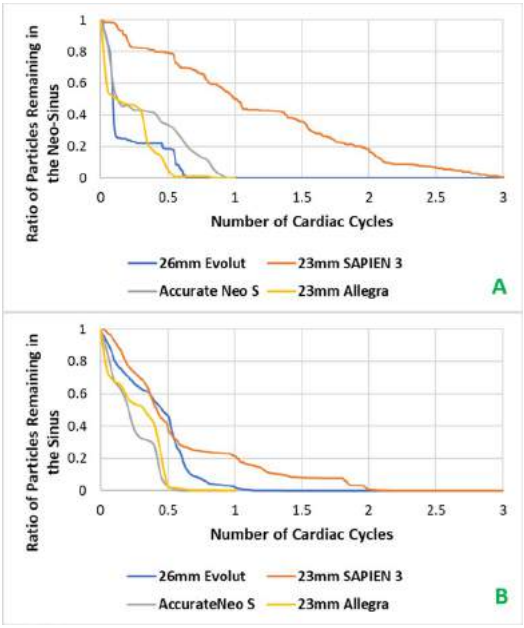

Figure 2: Washout in the neo-sinus and washout in the sinus of the 3 self-expanding TAVs and the balloon expandable TAV.

shown in Figure 3. The range of the shear stress in the neo-sinus and the sinus are shown to be similar (between 1.5 Pa and 3.5 Pa). The Allegra is characterized by the largest shear stress distribution, followed by the SAPIEN 3. In the neo-sinus, the Evolut is characterized by a larger shear stress distribution compared to the Accurate Neo however, in the sinus the Accurate Neo shows a larger distribution with higher likelihoods to develop shear stresses that exceed 1.1 Pa.

The velocity vectors are shown in Figure 4 for the 4 different valve cases. The velocities in the sinus and the neo-sinus were 0.05, 0.078, 0.080 and 0.075 m/s in the Evolut, SAPIEN 3, Accurate Neo and Allegra.

DISCUSSION

The self-expanding TAVs are characterized by a faster washout compared to the balloon expandable TAV, even when the design of the self-expanding valve leaflets was intra-annular and not supra-annular as is the case with the Accurate Neo. The design of the Accurate Neo valve is unique when the frame is considered. Large gaps in the stent show probably allowing more freedom of displacement of the leaflet compared to the SAPIEN 3. The other self-expanding valves are characterized by a supra-annular leaflet design offering a larger and a less confined and restricted neo-sinus area allowing for flow to enter and exit faster. With respect to shear stress in the neo-sinus and the sinus, while larger magnitudes are expected for the self-expanding valves, the balloon expandable SAPIEN 3 shows a larger distribution with larger probabilities compared with the Accurate Neo (with intra-annular leaflet design) and the Evolut (with supra-annular leaflet design). This may be due to the short profile of the SAPIEN 3 that eliminates the potential obstructions for flow to enter the sinus region compared with the other long-frame self-expanding valves.

With the Evolut, given the supra-annular design, it is expected for larger shear stress to occur in the neo-sinus compared with the Accurate Neo (with a smaller neo-sinus, given the intra-annular design). In the sinus

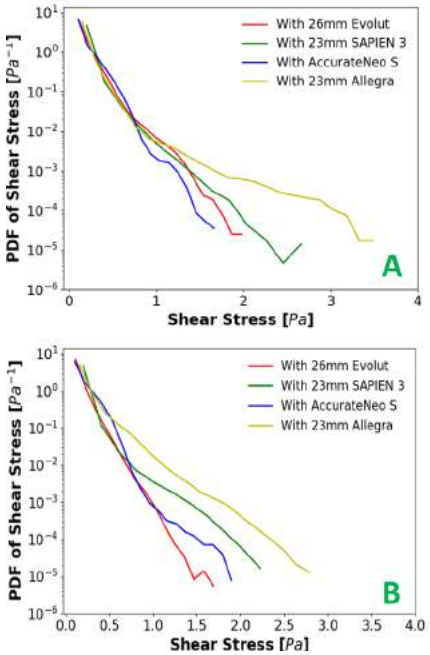

Figure 3: Probability density function of the viscous shear stress in the neo-sinus and the sinus regions of the 3 self-expanding TAVs and the balloon expandable TAV in the (A) neo-sinus and (B) in the sinus over the whole cardiac cycle.

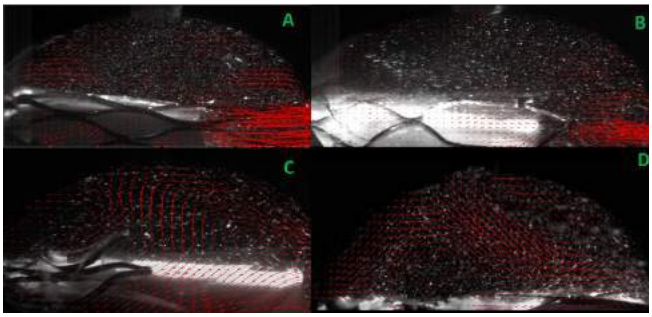

Figure 4: Velocity vectors at peak systole with (A) Evolut, (B) SAPIEN 3, (C) Accurate Neo and (D) Allegra.

however, the Accurate Neo is characterized by a more open frame design allowing for more flow to enter and exit leading to a larger distribution of shear stress there.

In conclusion, Sinus and neo-sinus flow dynamics highly differ between TAVs. Self-expanding supra-annular valves seem to be more advantages compared to an equivalent-size balloon-expandable TAV. We speculate that the data obtained in this study supports the clinical observations where more incidence of leaflet thrombosis is observed with the balloon expandable valves [3].

REFERENCES

[1] Sannino, Anna, et al. AJC 132 (2020): 106-113.
[2] Lowe, Gordon DO. Pathophysiology of haemostasis and thrombosis 33.5-6 (2003): 455-457.
[3] D'Ascenzo, Fabrizio, et al. European Journal of Cardio-Thoracic Surgery 56.3 (2019): 488-494.

QUANTIFYING EULER-BERNOULLI AND TIMOSHENKO BEAM THEORY ACCURACY OF FINITE ELEMENT ANALYSES FOR ESTIMATING FLEXURAL RIGIDITY OF A BONE SURROGATE IN THREE-POINT BENDING WITH FINITE ELEMENT ANALYSIS

M. Zojaji (1), H. Ploeg (2), B. Yang (3), C. Collins (4)

(1,2,3) Mechanical and Materials Engineering Department
Queen's University
Kingston, Ontario, Canada

3) Department of Health Sciences and Technology
ETH Zurich,
Zurich, Switzerland

INTRODUCTION

Bone remodeling is a unique process to bone that continues even after growth. In aging, the balance between bone formation and resorption is not maintained, thus some bones become osteopenic and eventually osteoporotic [1]. Bone quality may be characterized by bone mechanical properties which are estimated by Euler-Bernoulli (EB) and Timoshenko (TI) beam theories. Mechanical testing and image-based finite element analysis (FEA) are commonly used for bone mechanical property assessment; their accuracy is therefore crucial. This study quantified some of the errors in long-bone mechanical property assessments.

In most long bone research studies, Euler-Bernoulli beam theory is typically used, but it is well-established that this beam theory under-estimates the bending deflection of short thick beams [7]. This beam bending theory assumes long slender beams and therefore does not account for shear deformation [2]. Studies on shear deformation in short, thick and non-prismatic beams subjected to bending can be traced back to mid-1800s [2], but few studies in biomechanics have used Timoshenko beam theory (TI) to calculate the elastic modulus from bending tests. Although in bending tests, the main component of bone deformation is bending, shear deflection and roller-indentation also have notable contributions [2]. Previous studies [2, 3, 4] revealed that using the EB to predict the bone mechanical properties like elastic modulus, leads to a considerable underestimation. Consequently, we hypothesized that TI beam theory would be a more accurate analytical method for estimation of bone flexural rigidity (EI). The purpose of this study was to quantify the difference in EI of a short-thick beam in three-point bending using EB and TI beam theories.

METHODS

Three-point bend tests on a bone surrogate [1] were performed with three replicates and six repeats on each using a custom-designed three-point bending apparatus and MTS Bionix 370 Servohydraulic Test System universal materials testing machine. Force was measured by load cell (model# 662-20H-04) while deformation was measured at the crosshead (CH) and midpoint (mid) with extensometer (Epsilon model 3540-001M-ST). Figure 1. Shows the experimental setup. The experimental bending stiffness (K_{CH} and K_{Mid}) were calculated as the slope of the linear portion of their corresponding force-(F) deflection (δ) data (Fig.1).

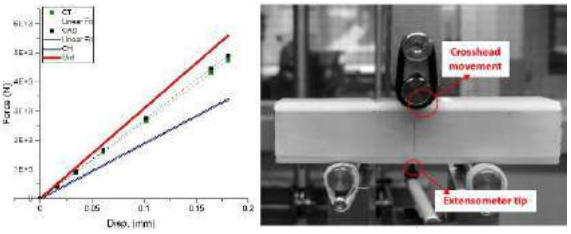

Figure 1: Typical load-displacement curves obtained from a three-point bending test of a bone surrogate. The experimental bending stiffness was calculated as the slope of the linear part of the curve with regression (left). Three-point bend test setup (right)

The same bending test was simulated with FEA (Abaqus CAE/2017) on CAD- and CT-based models. The computational bending stiffness (K_{FEA}) was calculated by dividing the total reaction force at bottom supports over the vertical deflection due to bending at the midpoint. EB and TI beam theories were used to calculate the bone surrogate flexural rigidity (Eq. 1, 2).

$$EI_{EB} = \frac{K_{Exp}(L^3)}{48} \quad (1)$$

$$EI_{TI} = \frac{K_{Exp}l^3}{48(1-\frac{K_{Exp}l}{4kGA})}. \quad (2)$$

Where K_{exp} is stiffness as measured from the bending test; L is the distance between two lower supports (50.8 mm); A is the cross-sectional area from the CAD model of the shell (915.7 mm^2); k shear correction factor for a rectangular cross section (0.83), and G is the shear modulus of the shell (1045.5 MPa) [1]. Theoretical EI value was calculated from the material properties and CAD geometry ($EI_{Theoretical}$= 1.26E+08 Nmm^2) of the bone surrogate shell [1]. Three paired t-tests were conducted to test for statistically significant differences between bone surrogate stiffness determined by different methods (K_{CH}, K_{Mid} and K_{FEA}) (α=0.025, t-critical value=2.45). EI from the bending test with different methods were compared using one-way ANOVA with a Tukey post-hoc test (α=0.05). All statistical analyses were done using OriginPro 2020 and Excel 2013.

RESULTS

Percent error of the bending stiffness was defined in comparison to the three-point bend test results including midpoint deflection data (Figure 2).

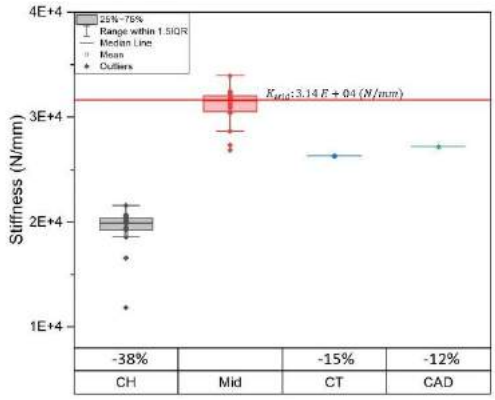

Figure 2: Bone surrogate K and percent error for each method in comparison with midpoint measurements (K_{Mid}), (CH: crosshead displacement, CT: FEA on CT-based model, CAD: FEA on CAD-based model)

Mean K_{CH} was low (-38% error) compared with mean K_{Mid}; and each K_{FEA} was close (-12% and -15% errors) to the mean K_{Mid}. Results were significantly different from the mean K_{Mid} value (p-value< 0.001, α=0.025), (Table 1).

Table 1: Bone Surrogate Bending Stiffness and Percent Errors for each Method. The error was defined with respect to the stiffness obtained from Mid (3.14E+04 N/mm). (CH: crosshead displacement, Mid: midpoint deflection, CT: FEA on CT-based model, CAD: FEA on CAD-based model, TI: Timoshenko beam theory, EB: Euler-Bernoulli beam theory)

	CH	Mid	CT	CAD
Mean (N/mm)	1.87E+04	3.14E+04	2.63E+04	2.72E+04
Std Dev (N/mm)	1.55E+03	8.24E+02	…	…
p-Value	<0.001	…	<0.001	<0.001

In comparison to the theoretical EI (1.26E+08 Nmm^2), Flexural rigidity was under-estimated by EB beam theories (-58% to -32% errors for EI_{CH} and EI_{Mid}), while TI under- and over-estimated the bone surrogate EI (-41% for EI_{CH} and +32% for EI_{Mid}) (Fig. 3). The EI from CT- and CAD-based FEAs as calculated based on TI beam theory had a negligible error (-3% and +2%). In contrast, the EI of the CT- and CAD-based models which were calculated by EB beam theory, had a considerable error (-43% and -41%, respectively) in comparison with the theoretical value ($EI_{theoretical}$= 1.26E+08 Nmm^2).

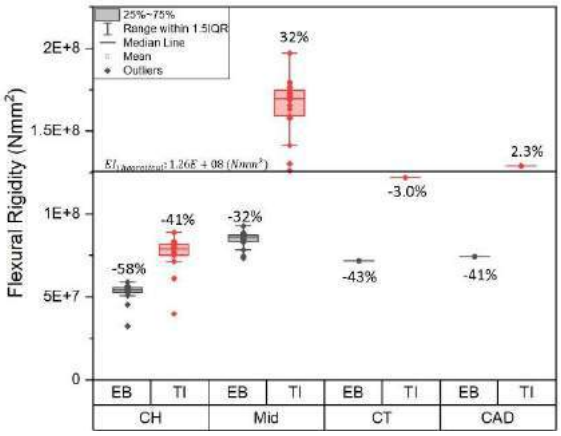

Figure 3: Bone surrogate EI and percent error for each method (CH: crosshead displacement, Mid: midpoint deflection, CT: FEA on CT-based model, CAD: FEA on CAD-based model, TI: Timoshenko beam theory, EB: Euler-Bernoulli beam theory)

DISCUSSION

In this study, K_{Exp} and K_{FEA} of a bone surrogate were measured with a three-point bend test. The corresponding EI for each K was calculated based on EB or TI beam theories. This study confirmed that EB underestimated the bone surrogate EI in all methods and there was statistically significant difference between experimental EI calculated by EB and TI beam theories. EB underestimated EI in comparison to TI beam theory. We found TI beam theory predicted the bone EI more accurately than the EB beam theory for FEA on CT- and CAD-based models. For bone surrogate EI measurements with midpoint deflections, it can be concluded that EB and TI beam theories result in under- and over-predictions, respectively. Future work will include digital image correlation (DIC) to measure the bone surrogate deformation to find the bending stiffness and calculate the corresponding EI. These DIC data would create a gold standard for the comparisons for FEA validation. Limitations of this study were: small sample sizes; not all sources of compliance were not taken into account; and testing was performed on a bone surrogate with simplified geometry and materials. Accurate estimation of bone stiffness and flexural rigidity is crucial for investigations on bone disease, diagnosis, and treatments. The results of this study increase the accuracy of such investigations furthering efforts towards improving bone health.

ACKNOWLEDGEMENTS

We acknowledge the support of the Natural Sciences and Engineering Research Council of Canada (NSERC), Ploeg's Research Initiation Grant, and the Human Mobility Research Centre, Queen's University, Kingston, ON, Canada.

REFERENCES

[1] Collins et al. JMBBM 88(2018):346-351, 2018.
[2] van Lenthe et al., Bone 43:717-723, 2008.
[3] Arias-Moreno et al., J Biomech 101(2020):109654, 2020.
[4] L.C. Kourtis, BMES: 42 (8):1773–1780, 2014.
[5] C. Collins et al., JMBBM.2020.104253

A TWO-SCALE HOMOGENIZATION SCHEME FOR SATURATED POROUS MEDIA IN THREE DIMENSIONS

Ashkan Almasi (1), Tim Ricken (2), David M. Pierce (1,3)

(1) Department of Mechanical Engineering
University of Connecticut
Storrs, CT, USA

(2) Institute of Mechanics, Structural Analysis and Dynamics
University of Stuttgart
Stuttgart, BW, Germany

(3) Department of Biomedical Engineering
University of Connecticut
Storrs, CT, USA

INTRODUCTION

The theory of porous media (TPM) plays an important role in many diverse areas of engineering, including particularly the biomechanics of soft tissues (e.g. liver, brain, and cartilage) [1,2]. The remarkable macro-mechanics of soft tissues derives from the complex micro-mechanics of their constituents, e.g. proteoglycans, collagens, and electrolytic fluid, and their interactions. To facilitate mechanistic understanding and improved analyses (e.g. of experimental results) of the multi-scale mechanics of soft tissues we aimed to establish a computational framework specific to fluid-saturated, fibrous soft tissues and engineered materials. We can apply experiments to quantify mechanical properties and biology of tissues, and imaging to estimate tissue structure and even strains; however, only computational models can estimate intra-tissue stresses in human joints and tissues during daily activities because the required *in vivo* experiments are impossible or unsafe. Here we established a multi-scale framework combining the TPM and the FE^2-method (performing finite element discretizations of boundary value problems (BVPs) on both macro and micro scales) for fluid-saturated porous media within FEBio (University of Utah).

METHODS

FE^2 Modeling Framework For Porous Materials. To solve the partial differential equations governing the macroscopic BVP we used the finite element method twice: we evaluated the macroscopic material tangent $\overline{\mathbf{A}}$ and measures $\overline{\mathbf{P}}$, $\overline{(\mathbf{E}_\mathrm{S})'_\mathrm{S} : \mathbf{C}_\mathrm{S}]_\mathrm{S}}$, $\overline{n^\mathrm{F}\mathbf{w}_\mathrm{FS}}$ (first P-K stress, Green Lagrange strain rate, right Cauchy-Green tensor, Jacobian, fluid volume fraction, and filtration velocity respectively) at each Gauss integration point by a volume averaged solution of the underlying microscopic Representative Volume Element (RVE), as shown in **Fig. 1**.

Constitutive Model. We described a biphasic material model with two material-incompressible constituents $\varphi^\alpha (\alpha \in \{\mathrm{S},\mathrm{F}\})$ constrained

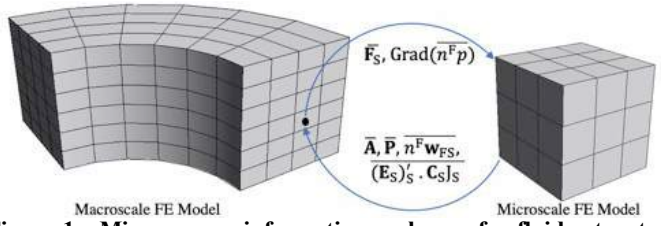

Figure 1: Micro-macro information exchange for fluid-saturated porous media.

by the saturation condition as

$$n^\mathrm{S} + n^\mathrm{F} = 1\,, \tag{1}$$

where n^S and n^F are current solid and fluid volume fractions, respectively. Considering the saturation condition we constrain the material time derivative of the saturation following the solid motion as

$$(n^\mathrm{S})'_\mathrm{S} + (n^\mathrm{F})'_\mathrm{S} = 0\,. \tag{2}$$

We use the balance of mass and the definition of the seepage velocity w_FS to evaluate the entropy inequality of the mixture as [3]

$$\mathbf{d}_\mathrm{S}\left[\boldsymbol{\sigma}^\mathrm{S} + n^\mathrm{S}p\mathbf{I} - 2\rho^\mathrm{S}\mathbf{F}_\mathrm{S}\frac{\partial \Psi^\mathrm{S}}{\partial \mathbf{C}_\mathrm{S}}\mathbf{F}_\mathrm{S}^\mathrm{T}\right] + \mathbf{d}_\mathrm{F}[\boldsymbol{\sigma}^\mathrm{F} + n^\mathrm{F}p\mathbf{I}] + \mathrm{w}_\mathrm{FS}[p\nabla n^\mathrm{F} - \hat{\mathbf{p}}^\mathrm{F}] \geq 0 \tag{3}$$

where p is the fluid pressure, $\mathbf{I}$ is the identity, $\mathbf{F}_\mathrm{S}$ is the solid deformation gradient, $\mathbf{C}_\mathrm{S}$ is the right Cauchy-Green tensor, and $\hat{\mathbf{p}}^\mathrm{F}$ is the interaction force of the fluid. We write partial Cauchy stresses as [4]

$$\boldsymbol{\sigma}^\mathrm{S} = -n^\mathrm{S}p\mathbf{I} + 2\rho^\mathrm{S}\mathbf{F}_\mathrm{S}\frac{\partial \Psi^\mathrm{S}}{\partial \mathbf{C}_\mathrm{S}}\mathbf{F}_\mathrm{S}^\mathrm{T} = -n^\mathrm{S}p\mathbf{I} + \boldsymbol{\sigma}_\mathrm{E}^\mathrm{S}\,, \tag{4}$$

$$\boldsymbol{\sigma}^\mathrm{F} = -n^\mathrm{F}p\mathbf{I}\,, \tag{5}$$

for the solid and fluid, and where $\boldsymbol{\sigma}_\mathrm{E}^\mathrm{S}$ is the effective Cauchy stress.

Validation and Representative Examples. We provide numerical examples demonstrating the performance of our multi-scale approach for fluid-saturated porous material. To validate our implementation we first reproduced 2-D examples from Bartel et al. [6,7] using a neo-Hookean constitutive model for solid the phase [5] and 3-D elements under plane-strain conditions. We first considered a square block of height $H = 10$ mm and width $L = 10$ mm subjected to constant load as shown in **Fig. 2(a)**. We fixed left-bottom corner and used a roller support the right-bottom corner. We used the material properties $\mu = 168$ GPa, $\lambda = 1870$ GPa, $K_d = 0.5$ mm^4/(Ns). We applied a point load $q = 4.55$ N on all nodes at the top surface. We prescribed the fluid pressure $p = 10$ N/mm^2 at top surface and set the pressure to zero on three nodes in the center of the bottom surface. We increased the load and pressure linearly during time ($t = 5$ sec). **Figures 2(b)** and **2(c)** show the corresponding meshes for macroscopic structure (10×10 elements) and the microstructure (5×5 elements), both using eight-node hexahedral elements in plane strain.

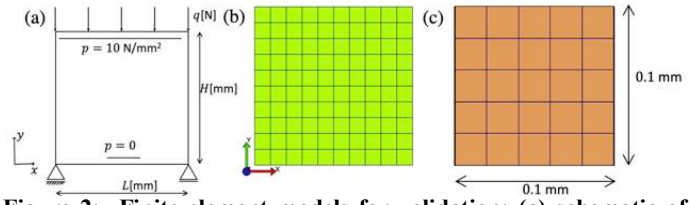

Figure 2: Finite element models for validation: (a) schematic of square block [6]; (b) mesh for macroscopic structure; (c) corresponding mesh for microstructural RVE.

We next considered a cantilever beam of porous material with height $H = 2$ mm and width $L = 10$ mm, as shown in **Fig. 3(a)**. We fixed the left side of beam in all degrees of freedom and prescribed fluid pressure ($p = 10$ N/mm^2) which we increased linearly with time ($t_{\max} = 5$ sec). On the right hand side, we set the pressure to zero. **Figures 3(b)** and **3(c)** show the corresponding meshes for macroscopic structure (40×8 elements) and the microstructure (10×10 elements), using the same elements as above. **Table 1** provides the Lame constants and Darcy permeability of biphasic neo-Hookean used for the RVE.

Table 1: Material parameters of the microstructural RVE.

Material Const	μ [MPa]	λ [MPa]	K_d [mm^4/(Ns)]
Material 1	26	287	0.1
Material 2	16	187	1.0

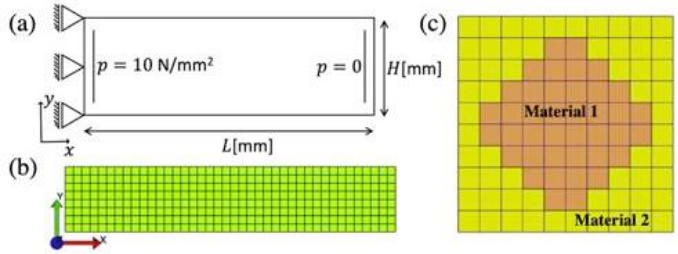

Figure 3: Finite element models for validation: (a) schematic of cantilever beam [7]; (b) mesh for macroscopic structure; (c) corresponding mesh for microstructural RVE.

RESULTS

In **Fig. 4**, we show the results for the macroscopic structure of the first validation case, the square block (**Fig. 2**). **Figures 4(a)-4(d)** show the displacement in the y-direction (u_y), the normal Cauchy stress in the x-direction (σ_{xx}), the fluid pressure (p), and the fluid flux in the y-direction (w_y) for the macroscale model informed by the isotropic microstructural RVE. In **Fig. 5**, we show the results for the macroscopic structure of the second validation case, the cantilevered beam (**Fig. 3**). **Figures 5(a)-5(c)** show the displacement in the y-direction (u_y), the fluid pressure (p), and the fluid flux in the x-direction (w_x) for the macroscale model informed by the heterogeneous microstructural RVE including a hard inclusion. Our macroscopic results from both the square block (**Fig. 4**) and the cantilever beam (**Fig. 5**) match the 2-D results of [6,7], thus validating our multiscale implementation in 3-D.

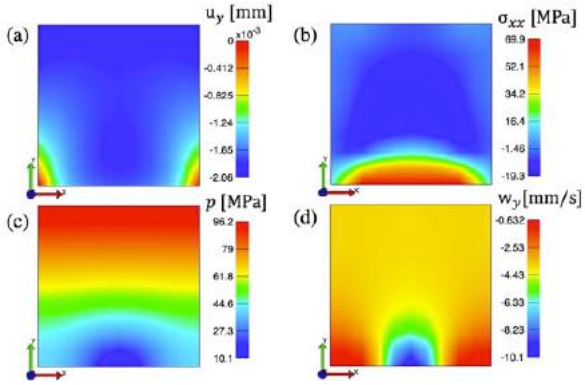

Figure 4: Macroscale results: (a) u_y; (b) σ_{xx}; (c) p; and (d) w_y.

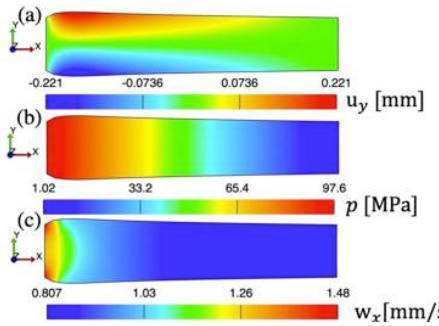

Figure 5: Macroscale results: (a) u_y; (b) p; and (c) w_x.

DISCUSSION

We combined the TPM and the FE^2-method (i.e. the TPM^2 method) to solve two-scale, non-linear, coupled, and time dependent BVPs for materials with a porous microstructures. We considered both isotropic, homogeneous RVEs (**Fig. 2(c)**) and those with inclusions (**Fig. 3(c)**), the latter with relatively stiff and impermeable inclusions. To solve the multiscale BVPs we first provide the microscopic RVEs with macroscopic quantities as boundary conditions (BCs). These BCs must comply with Hill-Mandel homogeneity conditions [7]. The microscopic RVEs must then provide the first Piola-Kirchhoff stress tensors $\bar{\mathbf{P}}$ back to the macroscale model at each integration point. Emerging multi-scale FE^2 methods (FE analyses augmented to derive the material behaviors from a distribution of finer scale FE analyses) are ideally suited to bridge the joint, tissue, and intra-tissue scales, but have not yet been applied to multi-phase, fibrous materials. We will leverage our TPM^2 framework, e.g. to establish how physical activity propagates micro-damage in the collagen network of cartilage.

ACKNOWLEDGEMENTS

NSF CAREER 1653358; Gerard Ateshian; Steve Maas.

REFERENCES

[1] De Boer, R., *Springer*, 2006. [2] De Boer, R., *Springer*, 2012. [3] Ricken, T. et al., *Arch of Appl Mech,* 80:453-465, 2020. [4] Pierce, D.M. et al., *Biomech Model Mechanobiol*,15:229-244, 2016. [5] Bonet, J. et al., *Cambridge University Press*, 1997. [6] Bartel, F. et al., *PAMM*, 15:447-448, 2015. [7] Bartel, F. et al., *PAMM*, 17:577-578, 2017.

EFFECTS OF PROLONGED, ALTERED HEMODYNAMICS ON ZEBRAFISH EMBRYONIC HEART DEVELOPMENT

Yoke Yin Foo[1], Efthymios Motakis[2], Zenia Tiang[3], Shuhao Shen[1], Jason Kuan Han Lai[4], Wei Xuan Chan[1], Hadi Wiputra[1], Nanguang Chen[1], Ching Kit Chen[5,6], Christoph Winkler[6], Roger Sik Yin Foo[3], Choon Hwai Yap[7]

1 Department of Biomedical Engineering, National University of Singapore, Singapore
2 Yong Loo Lin School of Medicine, National University of Singapore, Singapore
3 Genome Institute of Singapore, Agency for Science, Technology and Research
4 Mechanobiology Institute, National University of Singapore, Singapore
5 Department of Paediatrics, Yong Loo Lin School of Medicine, National University of Singapore, Singapore
6 Division of Cardiology, Department of Paediatrics, Khoo Teck Puat-National University Children's Medical Institute, National University Health System, Singapore
7 Department of Biological Sciences, National University of Singapore, Singapore
8 Department of Bioengineering, Imperial College London, London, UK

INTRODUCTION

Previous studies suggested that biomechanical forces play an important role in modulating cardiac morphogenesis, and abnormal biomechanical stimuli may cause congenital heart malformations.

The global effects of prolonged disruption of the hemodynamic environment on morphology and cardiac function have not been fully evaluated. Such analysis can help to improve our understanding of the role of biomechanical environments in cardiac development. Moreover, our understanding of the mechanobiological mechanisms of development is incomplete, and there could be important expression and mechanisms that are yet to be discovered. It would thus be useful to conduct whole transcriptomic analysis of the embryonic heart under heartbeat inhibition to identify candidate expression.

In the current study, we investigated the consequences of administering BDM to 2 dpf zebrafish embryos for a prolonged three-day duration. We characterized changes in cardiac morphology and function caused by the treatment, including using computational fluid dynamics (CFD) simulations to evaluate details of the biomechanical environments during and after the treatment. We also performed whole transcriptomic RNA sequencing of embryonic cardiomyocytes to identify potential pathways for disruption of normal biomechanical environments on the heart development.

METHODS

10 mM of BDM (Sigma, B0753) was used to depress myocardial contractility from 2 to 5 dpf. of a transgenic line, *Tg(phiC31.attP.2A, -0.8myl7: EGFP*), which labels myocardium. BDM was washed out at 5 dpf for two hours, and both control and treated embryos were observed directly thereafter.

The body length, yolk size, cardiac looping angle and ventricular size of control and treated embryos were measured using ImageJ software. Ventricular contractility was also quantified.

CFD simulation of ventricles were performed based on the images taken using line-scan focal modulation microscopy (LSFMM) according to methods established in our previous publication [1]. CFD simulations of three control hearts (Heart I, II & III) and four treated hearts (pre-washout: Treated heart I & II; post-washout: Treated heart III & IV) were completed. Wall shear stresses at the inlet, mid-ventricle and outlet were examined.

GFP-positive cardiomyocytes of control and treated hearts were harvested through fluorescence-activated cell sorting, followed by RNA extraction. The integrity of RNA samples was confirmed (RIN > 7) before RNA sequencing. KEGG pathway analysis was presented.

RESULTS

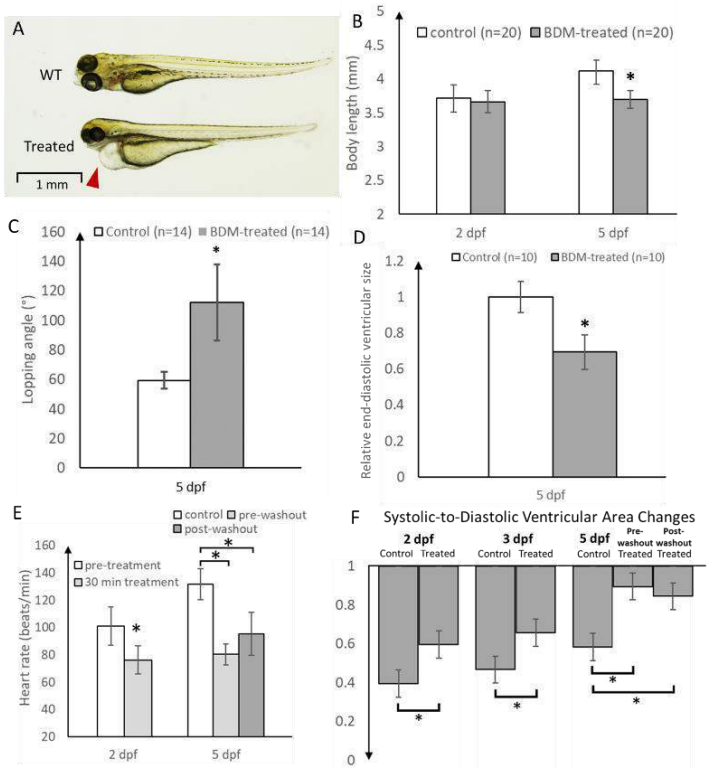

Figure 1. A 5 dpf embryo after 3 days of BDM treatment exhibits

(A) pericardial effusion, (A,B) shorter body length, (C) impaired cardiac looping angle, (D) a smaller ventricular size (relative to normal embryo), (E) decreased heart rate that persisted after BDM washout, and (F) reduced cardiac contractility which also persisted after BDM washout.

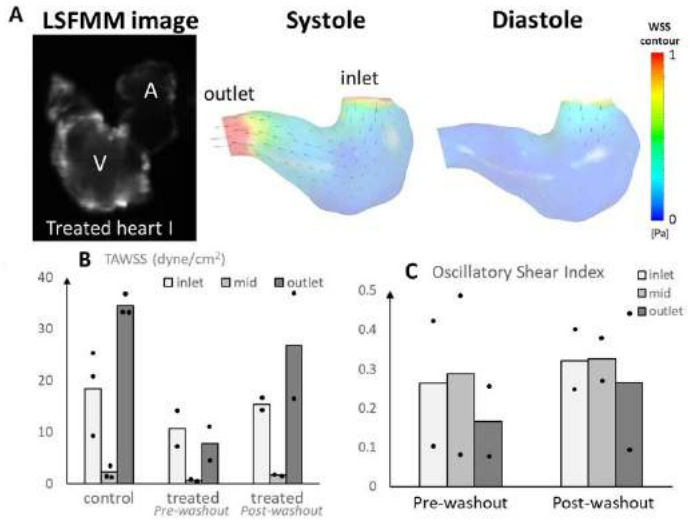

Figure 2. (A) LSFMM image of embryonic heart, and spatial WSS contour results from CFD of a treated heart. A-atria, V-ventricle (B,C)Treated heart retain little function and has low and oscillatory WSS even after BDM washout.

During BDM treatment, most embryos had cardiac contractions completely inhibited, while some had weak and slow contractions. BDM treatment of embryos from 2 to 5 dpf resulted in pericardial effusion, shorter body length and poor cardiac development. Treated hearts exhibit larger looping angle, 30% smaller ventricular chambers (Figure 1), absent ventricular trabeculae and retrograde blood flow.

BDM treatment further resulted in a declined cardiac function, which was determined from embryos after BDM washout. Both heart rate and contractility were significantly reduced (Figure 1E-F). Due to the reduced contractility and regurgitation, cardiac output was significantly reduced, and flow became abnormally oscillatory. This led to reduced and abnormally oscillatory WSS (Figure 2B-C).

RNA sequencing revealed 922 significantly upregulated genes and 1698 significantly downregulated genes, representing alterations to several KEGG pathways in Table 1. First, inflammatory pathways such as the TLR, consisting of several inflammatory genes including *tlr5a*, *tnf-α*, and various interleukins were upregulated. Second, ECM-receptor pathways, ECM remodeling genes including many types of collagen, tenascin and laminin, and cell-adhesion molecule were significantly downregulated. Further, the apoptosis and p53 pathways and a number of apoptosis genes including *fas* and caspases were significantly upregulated. The downregulation of *erbb4a* and *nrg1* suggests perturbations to trabeculation.

Histological investigation confirmed evidence of apoptosis and inflammation in the embryonic hearts.

DISCUSSION

From our results, we propose that BDM treatment has led to disturbed contractile and flow patterns in the heart, leading to inflammation of the endothelium and myocardium, which enhanced apoptosis and reduced growth. Separately, the lack of deformational stimuli decreased ECM-receptor interaction gene responses and ECM remodeling, further impeding growth. The lack of flow stimuli is likely to have prevented trabeculation formations via the notch-neuregulin pathway [2], but interestingly, was found to be accompanied by Erbb4a instead of Erbb2 reduction. A schematic of these pathways is given in Figure 3.

CONCLUSION

Prolonged pharmacologically disruption of the biomechanical environment of zebrafish embryonic hearts resulted in mal-development of cardiac morphology, and significant reduction in cardiac function. These morphological and functional outcomes likely occurred through inflammation and cell-ECM interaction pathways, which enhanced apoptosis and reduced ECM remodeling.

Table 1: Selected list of significant KEGG pathways

Up-regulated	
KEGG Pathways	Corrected P-Value
Toll-like receptor signaling pathway	0.0004
Cytokine-cytokine receptor interaction	0.0008
NOD-like receptor signaling pathway	0.0012
Apoptosis	0.0013
Metabolic pathways	0.0072
p53 signaling pathway	0.0108
RIG-I-like receptor signaling pathway	0.0335
Down-regulated	
KEGG Pathways	Corrected P-Value
Calcium signaling pathway	0.0001
Neuroactive ligand-receptor interaction	0.0004
Cell adhesion molecules (CAMs)	0.0005
ECM-receptor interaction	0.0016
Adrenergic signaling in cardiomyocytes	0.0035
Cardiac muscle contraction	0.0160

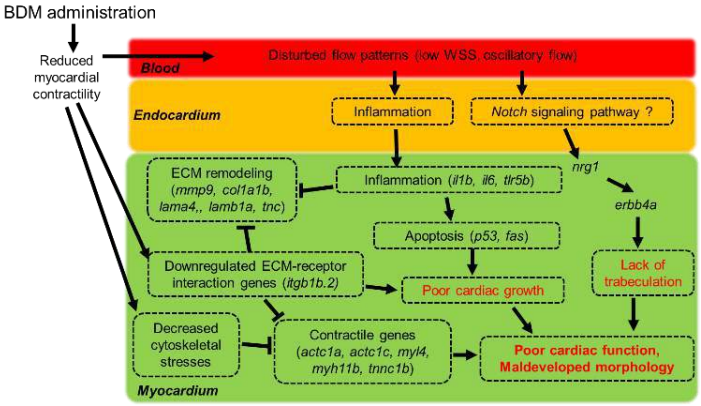

Figure 3. Schematic diagram showing several possible mechano-responsive pathways of a malformed heart after a three-day BDM treatment.

ACKNOWLEDGEMENTS

Funding is provided by the National University of Singapore Young Investigator Award 2015 (PI: Yap), and Imperial College Startup Funding. We would like to thank Ranran Liu and Wen Hui Tan (Department of Biological Sciences, NUS) for helpful guidance in molecular biology techniques.

REFERENCES

[1] Foo, Y.Y., et al., Biomech Model Mechanobiol, 19(1):221-232,2020
[2] Grego-Bessa, J. et al., Developmental cell, 12:415-429,2007

BIOMECHANICS OF HUMAN FETAL HEARTS WITH CRITICAL AORTIC STENOSIS AND EVOLVING HYPOPLASTIC LEFT HEART SYNDROME

Chi Wei Ong(1), Meifeng Ren(2), Hadi Wiputra(2), Joy Mojumder(3), Wei Xuan Chan(2), Andreas Tulzer(4), Gerald Tulzer(4), Martin Lindsay Buist(2), Citra Nurfarah Zaini Mattar(5), Lik Chuan Lee(3) & Choon Hwai Yap(6)

(1) Institute of High Performance Computing, A□STAR, Singapore 138632, Singapore

(2) Department of Biomedical Engineering, National University of Singapore, Singapore

(3) Department of Mechanical Engineering, Michigan State University, United States

(4) Children□s Heart Center Linz, Department of Pediatric Cardiology, Kepler University Hospital, Linz, Austria

(5) Department of Obstetrics and Gynecology, Yong Loo Lin School of Medicine, National University of Singapore, National University Health System,

(6) Department of Bioengineering, Imperial College London, UK

INTRODUCTION

Congenital aortic stenosis has a prevalence of 0.2-0.5 per 1000 live births [1]. It can develop during mid-gestation leading to severe cardiac dysfunction and drastic biomechanical changes. The stenosis results in high LV pressures, the consequent mitral regurgitation, drastically reduced myocardial contraction and stroke volume. Consequently, a substantial proportion of affected fetuses undergo mal-development, and evolve and develop into hypoplastic left heart syndrome (HLHS) by birth [2]. In such cases, fetal aortic valvuloplasty can be used to relief the obstruction, enable better development, and to avoid becoming HLHS at birth [3]. However, neither the biomechanical environments of fetal aortic stenosis nor that introduced by FAV is not well understood, and although FAV produces promising results and statistics, we do not understand why it does not work in many cases. Thus, in this study, we perform image-based finite element (FE) modeling of the biomechanics of the human fetal heart, modelled the various features of critical aortic stenosis, to understand their biomechanical effects.

METHODS

The 3D geometries of three normal human fetal LVs were reconstructed from the 4D (STIC) ultrasound images, and ultrasound measurements in a cohort of 32 fetuses with critical aortic stenosis were acquired, both with IRB approval and patient consent. A validated cardiac motion estimation algorithm [4] was used to track LV motion from an initial segmentation. The FE modelling of the fetal LV was adapted from previous work [5], and featured the Guccione active tension [6], a transversely isotropic Fung strain energy function, epi-to-endo linearly spatially varying fiber orientation, a simplified Windkessel model (Figure 1) [7], and was solved via FEniCS. The fiber angle was adjusted to obtain satisfactory match in LV geometry between FE results and image motion tracking results. Valve flow rate data from the model was translated into valve velocity data via an empirical discharge coefficient formulation, via an iterative solver.

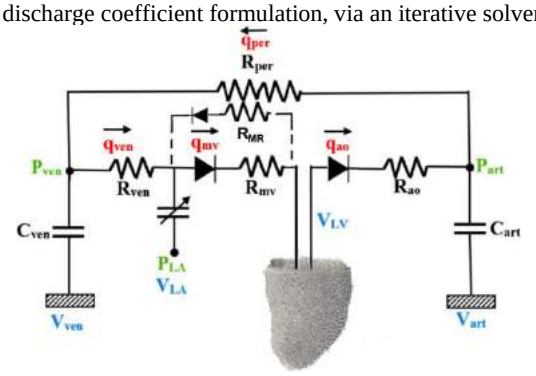

Figure 1. Schematic of the FE model and the simplified Windkessel model.

Subsequently, disease features were modelled as follows.

1. **Aortic Stenosis:** via increasing aortic resistance
2. **Aortic Stenosis and Mitral Regurgitation:** via addition of regurgitation Windkessel element.
3. **Myocardial hypertrophy:** via increasing the wall thickness
4. **Endocardial Fibroelastosis:** via increasing myocardial stiffness.
5. **Cardiomyopathy:** via decreasing active tension magnitude.

RESULTS

The FE modeling was able to produce LV geometries that exhibited a good match with LV geometries from the images, with an average surface distance error of about 1% of the smallest heart's diameter. With aortic stenosis alone (Figure 1), LV pressures were found to elevate by 10-20 mmHg, and stroke volume could be drastically reduced, depending on stenosis severity (leaving the RV to

serve cardiac function alone). With mitral regurgitation in addition to aortic stenosis, LV pressure reduces slightly, and stroke volume increased slightly (Figure 1). Fetal aortic stenosis was further found to extend systolic duration to about 70% of the cardiac cycle, due to an inability to relief pressure, which corroborated with clinical Doppler measurements.

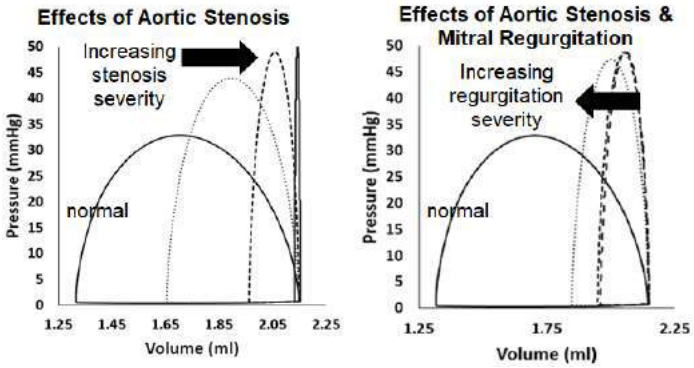

Figure 2. Pressure volume loops of a 28 week old fetal heart with (left) aortic stenosis alone, and (right) aortic stenosis with mitral regurgitation, with various stenosis and regurgitation severity.

With aortic stenosis and mitral regurgitation, aortic valve flow velocity increased to 1.9-2.8 m/s, well above velocities observed in normal fetal hearts (0.6-1.0 m/s). However, we found that aortic valve velocities could not reach high values observed clinically in our diseased cohort (3.4 ± 0.9 m/s). This suggest that myocardial hypertrophy must have occurred to provide greater cardiac power, as our modelling of LV wall thickening demonstrates that significant additional cardiac power can be achieved (Figure 3). A 50% increase in thickness increased systolic pressure by 72% and stroke volume by 54%, and increase aortic valve velocity to 3.9 m/s. Indeed, clinical measurements in 10 our cohort of 32 disease fetuses showed that a 105% increase in wall thickness compared to age-matched normal fetuses, on the average.

However, this typical extent of hypertrophy (100% increase in thickness) was found in our model to generate excessively high LV systolic blood pressures, of about 100 mmHg, which was much higher than invasive clinical measurements of 63 mmHg [8]. This suggested that on top of hypertrophy, typical aortic stenosis fetuses also suffer from reduced contractility. Our model shows that decreased active tension causes a roughly proportional decrease in stroke volume and systolic pressure.

Many fetal aortic stenosis haerts experiences endocardial fibroelastosis, which is a fibrosis of the endocardial layer that is visible in the ultrasound, and which can likely be modelled via increased myocardial passive stiffness. In our modelling, however, stiffness increase of up to 100% demonstrated only modest changes in stroke volume, systolic blood pressure, and myocardial stresses (Figure 3). Thus, contrary to current believes, fibroelastosis is unlikely to impede cardiac function and cause dysfunction, contrary to current clinical beliefs. We hypothesize that fibroelastosis is likely a by-product of the altered biomechanical physiology, rather than a factor impeding function.

DISCUSSION AND CONCLUSION

In this study, we developed and calibrated a FE models of healthy fetal hearts from 4D ultrasound images and then used them to investigate biomechanical changes during disease conditions associated with fetal AS. Our study shed light on how the individual effects of each of the disease features affect the biomechanical environment of fetal heart. We showed that various extent of aortic stenosis, mitral regurgitation, ventricular hypertrophy and cardiomyopathy can cause significant changes to the fetal heart biomechanical environment. These drastic changes are likely to alter the fetal heart growth and remodeling responses, potentially leading to HLHS at birth. We further discovered that changes to the myocardial passive stiffness (fibroelastosis) only had very modest effects cardiac function. Our study thus demonstrated that FE modeling can be a very useful tool in understanding fetal heart diseases. Moving forward, we hope to use the same approach to model the biomechanical effects of the fetal heart intervention in this disease cohort, and develop methods to predict outcomes, such that we can help physicians make clinical decisions. For example, better prognosis can be used to more accurate select patients for intervention, minimizing unnecessary procedural risks and maximizing benefits to the most patients.

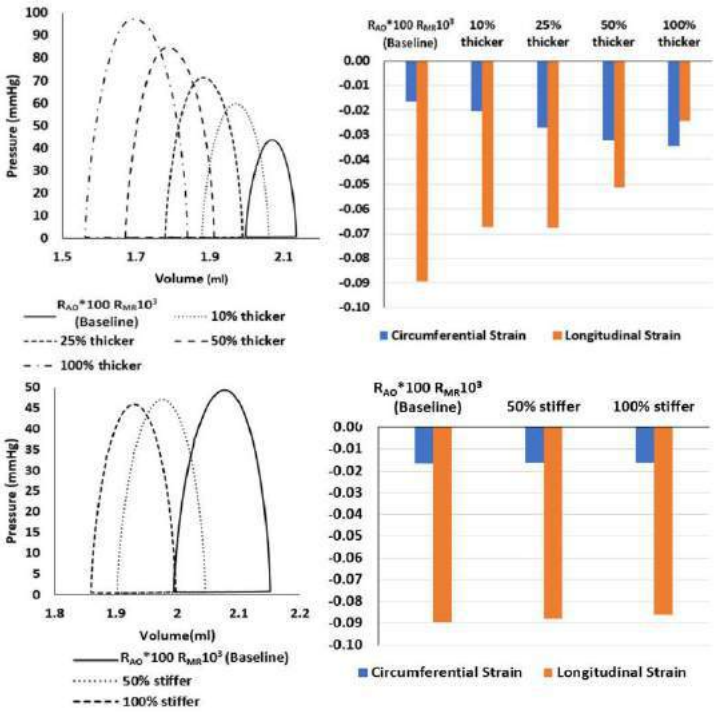

Figure 3 Effect of (top) LV wall thickening, and (bottom) increasing myocardial passive stiffness, on (left) the P-V loop, and (Right) myocardial strains.

ACKNOWLEDGEMENTS

This project is supported by Singapore Ministry of Education Tier 2 Grant (MOE2018-T2-1- 003), and Imperial College startup funding. We thank Felicia Toh and Harshaana Ramlal for coordinating the clinical data collection.

REFERENCES

[1] Freud et al. *Ultrasound Obstet. Gynecol*. 45:326–332, 2015.
[2] Mäkikallio, K., et al. *Circulation*, 113(11), 1401-1405, 2006.
[3] Friedman, K.G., et al. *Ultrasound Obstet Gynecol* 52:212-220, 2018.
[4] Wiputra., *Sci Rep*. 10(1):1-4, 2020
[5] Shavik, S. M. et al. *Physiological reports*, 5(21), e13392., 2017.
[6] Guccione et al. *J. Biomech. Eng*. 113(1):42–55, 1991.
[7] Ong C.W., et al. Biomechanics of Human Fetal Hearts with Critical Aortic Stenosis. *Ann Biomed Eng*. Epub Nov 2020.
[8] Zampi, J., et al. *JACC: Cardiovasc Interv.* 12:1628-1630, 2019.

HAEMODYNAMIC ANALYSIS OF BRANCHED ENDOGRAFTS FOR COMPLEX AORTIC ARCH REPAIR

Sampad Sengupta (1), Yu Zhu (1), Mohamad Hamady (2), Xiao Yun Xu (1)

(1) Imperial College London, London, United Kingdom

(2) Department of Interventional Radiology, St Mary's Hospital, Imperial College London
London, United Kingdom

INTRODUCTION

Aortic arch repair is continually evolving, and clinicians are now equipped with a wide range of methods to tackle diseases arising in the ascending aorta and aortic arch. Unlike conventional surgical procedures, modern methods such as thoracic endovascular aortic repair (TEVAR) provide a minimally invasive alternative which reduces risks and improves the outcome and speed of recovery. Endografts used in TEVAR vary in design depending on the procedure and application. Branched endografts are commonly used to maintain perfusion of blood to the supra-aortic vessels and the haemodynamic performance of these devices is of significant interest [1,2]. These tend to have internal tunnel branches which run through the lining of the graft wall and emerge from the arch to guide the flow into their respective arch branches, thereby maintaining the constant perfusion of blood to essential organs. This reduces the need for both vascular bypass and fenestrations in the graft body [1]. Implantation of a branched endograft alters the geometry of the treated aorta, which could have a profound influence on the local flow patterns and haemodynamic parameters, such as velocity, pressure, and wall shear stress [3]. Changes in these parameters can be determined by computational modelling. Here we present a detailed computational fluid dynamics (CFD) analysis of the effects of branched endografts on blood flow in the arch.

METHODS

The aortic arch has complex anatomical features unique to every individual: namely its curvature, non-planarity, and major branches originating in the region. Since the focus of this study is to investigate the effect of branched endografts on flow in the arch, we used retrospective CT images from patients who underwent TEVAR using similar branched endografts. These multislice images were analysed using a 3D image processing software, Mimics (v20, Materialise,

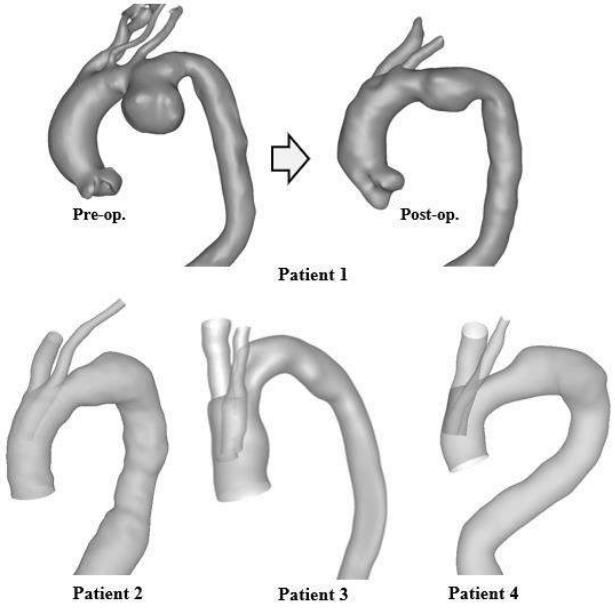

Figure 1: 3D aortic arch reconstructions for patients that have undergone TEVAR using branched endografts: (Top row) showing the aortic arch aneurysm in Patient 1 before and after TEVAR; (Bottom row) other patients that have undergone TEVAR to treat aortic arch aneurysms and Type A aortic dissections.

Leuven, Belgium) to generate anatomically accurate 3D reconstructions of the patient's vasculature, as can be seen in Figure 1. These geometries included the ascending and descending aorta, aortic arch consisting of the supra-aortic vessels, and then internal tunnel branches of the endograft.

Unstructured meshes of approximately 8 million elements, with prismatic boundary layers applied at the walls, were generated using ANSYS ICEM (v15.0, ANSYS Inc., Canonsburg, PA). Physiologically accurate boundary conditions were imposed at the inlet and outlets; these included a 3-element Windkessel model (3-EWM) prescribed at the three outlets and a pulsatile inflow waveform used at the inlet [4]. The wall was assumed to be rigid with a no-slip boundary condition. Numerical solutions were obtained using ANSYS CFX (v15.0, ANSYS Inc., Canonsburg, PA) and the results were analysed using ANSYS EnSight (v10.2) and ANSYS CFD-Post (v15.0) with emphasis being given to haemodynamic parameters such as fluid velocity and pressure, wall shear stress (WSS), displacement forces, and helicity.

RESULTS

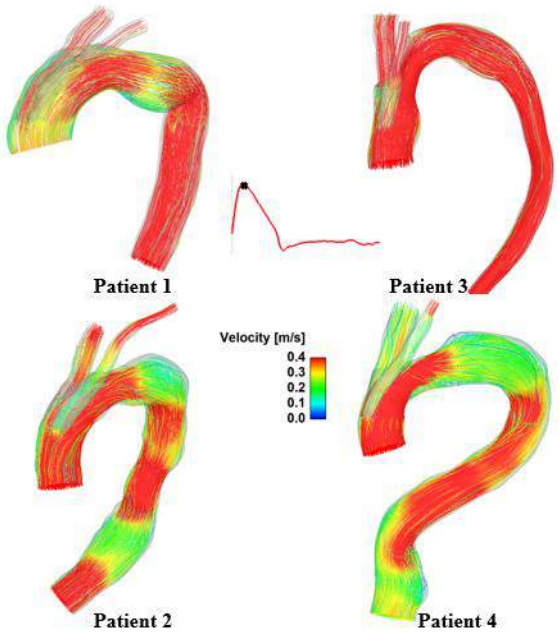

Figure 2: Instantaneous velocity streamlines recorded at peak systole for different patients that have undergone TEVAR.

The effect of branched endografts on flow in the aortic arch is illustrated in Figure 2. Implantation of the endograft results in accelerated flow in the arch, which can be seen more clearly in patients 2 and 4. High velocity flow occurs in the tunnel branches leading into the supra-aortic vessels. The presence of inner tunnels helps guide the flow into the arch vessels, but it also causes significant changes in the local flow patterns in the innominate and left common carotid arteries and in the arch region, that is demonstrated in Figure 2. Structural variations between each patient post-TEVAR also gives rise to varied flow patterns, unique to each patient. To further investigate the effect of tunnel branch diameter, additional models were created with smaller tunnel branch diameters of 10 mm and 8 mm (with the original branches being 12 mm in diameter). Further comparisons were made for WSS-related indices and helical flow index (HFI).

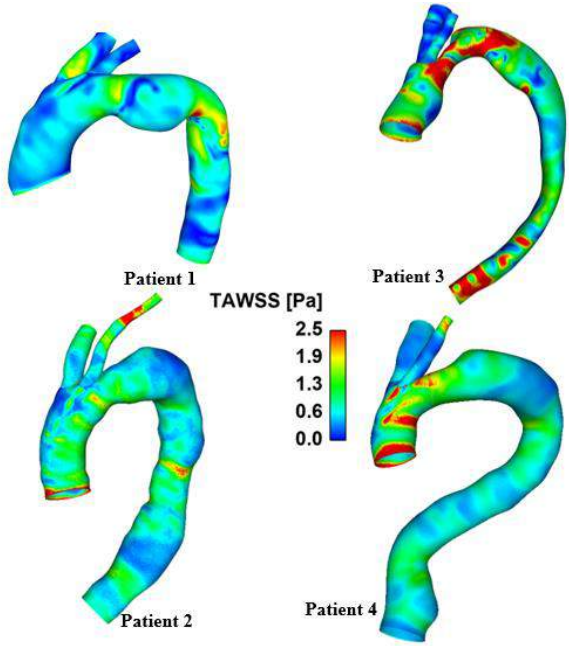

Figure 3: Time-averaged WSS maps showing differing patterns for patients that have undergone TEVAR.

DISCUSSION

Branched endografts have a significant influence on local flow patterns in the arch and the stented supra-aortic branches. Altered flow patterns lead to more spatial variation of WSS (Figure 3), with elevated WSS in the arch where flow is accelerated and low values in regions of flow recirculation. Variations in the endograft position and branch size result in further alterations of the flow in the arch and supra-aortic vessels. Figure 3 further illustrates the geometric variations experienced in different cases, all having undergone TEVAR using the same branched endograft device.

Although double branched endograft implantation offers a minimally invasive approach to the treatment of complex aortic diseases involving the arch, its long-term outcome is yet to be fully assessed. Patient-specific CFD simulations allow for quantitative analysis of haemodynamic parameters which may help predict potential adverse events, such as device migration, endoleaks, or clot formation in the supra-aortic branches.

ACKNOWLEDGEMENTS

This work is funded by the Doctoral Training Programme studentship from the Engineering and Physical Sciences Research Council, UK.

REFERENCES

[1] Bodell, B. D., et al, *Techniques in Vascular and Interventional Radiology, 21*, 137-145, 2018.
[2] van Bakel, T. M., et al, *Annals of Cardiothoracic Surgery, 7*, 406-413, 2018
[3] Zhu, Y., et al, *Medicine in Novel Technology and Devices, 4*, 2019.
[4] Pirola, S., et al, *Journal of Biomechanics, 60*, 15-21, 2017.

NANOMECHANICAL SIGNATURE OF SARCOMAS CAN BE PREDICTIVE OF RESPONSE TO CHEMOTHERAPY

A. Stylianou (1,2), F. Mpekris (2), C. Voutouri (2), T. Stylianopoulos (2)

(1) School of Sciences
European University Cyprus
Nicosia, Cyprus

(2) Cancer Biophysics Laboratory,
Department of Mechanical and
Manufacturing Engineering
University of Cyprus
Nicosia, Cyprus

INTRODUCTION

Solid tumors, such as sarcomas, stiffen as they grow in a host healthy tissue. Stiffening is caused by an increase in the structural components of the tumor, particularly in the density of the extracellular matrix fibers, mainly collagen, and in cancer and stromal cells content. Tumor stiffening can cause blood vessel inefficiency and as a result, it poses major physiological barriers to the effective delivery of drugs. Consequently, there is an urgent need for the development of novel biomarkers, that characterize the mechanical state of a particular tumor so as to support the development of personalized treatments or monitor novel therapeutic strategies, that target the tumor mechanical microenvironment to improve therapy [1].

In this project, Atomic Force Microscopy (AFM) was employed in order to assess unique NanoMechanical FingerPrints of sarcoma during cancer progression [2]. Also, an approved anti-fibrotic drug, tranilast, was re-purposed so as to target the tumor matrix and alleviate stiffness [3]. The AFM data were correlated with *in vivo* ultrasound studies and collagen content measurements with polarized microscopy. The identification of unique AFM-based NanoMechanical FingerPrints can lead to the development of novel biomarkers for treatment perdition and monitoring.

METHODS

Cell culture: Human fibrosarcoma cell line HT1080 was obtained from American Type Culture Collection (ATCC) and were supplemented with 10% Fetal Bovine Serum and 1% antibiotics.

Animal Tumor Models: Orthotopic fibrosarcoma tumors were established by subcutaneous implantation of 5×10^6 human HT1080 cells into the left flank of 6- to 8-week-old NOD/SCID mice (Cyprus Veterinary Services license: CY/EXP/PR.L14/2019).

Animal Treatment: When tumors reach a size of 5 mm, a biopsy (with a semi-automatic biopsy instrument) was obtained. At that point 4 cycles of treatment with a 3-day interval was performed [treatment groups: i) Saline (control), ii) Doxorubicin, iii) Tranilast and iv) Doxorubicin+ Tranilast]. After the first two treatments a 2nd biopsy was obtained. When tumors reached a size of 1200 mm^2, a 3rd biopsy was obtained and the mice were sacrificed via CO_2 inhalation.

Atomic Force Microscopy: The biopsies were transferred into ice-cold PBS supplemented with a protease inhibitor cocktail (Roce Dianostics GmbH). Then each specimen was immobilized on petri dishes and stored at 4°C for 1-72 h. AFM measurements (Molecular Imaging, PicoPlus) were conducted with silicon nitride cantilevers (MLCT-Bio, Bruker). The maximum applied loading force was set to 1.8 nN and 15 different force maps (16×16 point grids over 20x20 μm^2) were recorded per specimen [4]. The force maps were analyzed by AtomicJ using the Hertz model.

Ultrasound elastography and perfusion: Elasticity measurements were performed using the shear wave imaging method (Philips EpiQ Elite Ultrasound, eL18-4 transducer). The average elasticity was acquired from the median elasticity values of 8 regions of interest within the tumor. Also, the vascular status of tumors (microvascular imaging) was assessed using the Color Power Angio imaging mode. Images were analyzed using an in-house MATLAB code.

Polarized Microscopy: Collagen abundance was evaluated via Picro Sirius red staining (Abcam). Briefly, transverse 7μm-thick paraffin sections were produced (SAKURA), deparaffinized and incubated in Picro Sirius red stain for 1h. Then the sections were rinsed with acetic acid and absolute ethanol. Images were acquired at 20x magnification using an Olympus BX53 microscope with linear polarizers. The images were analyzed using custom and built-in algorithms in MATLAB.

RESULTS

First, we studied if AFM can identify unique NanoMechanical FingerPrints in the case of sarcoma tumors. Our results demonstrated that during progression sarcoma tissue presents two distinct characteristics as far as the distribution of elastic modulus is concerned: a lower elasticity peak, due to cancer cell softening, and a higher elasticity distribution, due the collagen overproduction and the desmoplastic reaction (Fig.1A) [2]. During cancer progression, the higher elasticity distribution was significantly increased. In order to correlate the mechanical alterations with collagen content, we performed polarized microscopy on picro sirius red stained samples. With polarized microscopy collagen type I and III fibers are specified in red and green, respectively. The results demonstrated that both collagen type I/ III were increased during cancer progression (Fig.1B).

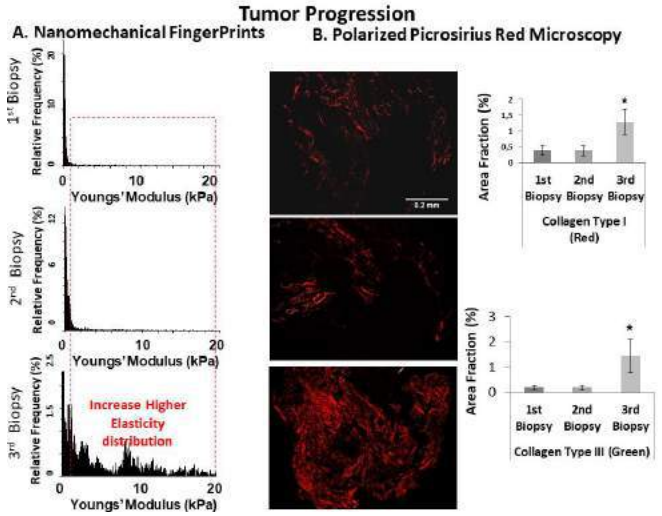

Figure 1: A) AFM Nanomechanical FingerPrints and B) polarized picrosirius red images and analysis during tumor progression.

Next, we studied if tranilast can improve the efficacy of common chemotherapy drugs (i.e., doxorubicin) in the case of sarcoma, as it has been previously found in other tumors [3]. Our results demonstrated that while tranilast itself did not affect tumor growth or mice survival, the combination with chemotherapy improved treatment outcomes (Fig.2A&B). Furthermore, *in vivo* ultrasound studies demonstrated that, both tranilast and the combined treatment, reduced tumor elastic modulus, while tumor perfusion was increased (Fig.2C&D), due to tumor microenvironment remodeling.

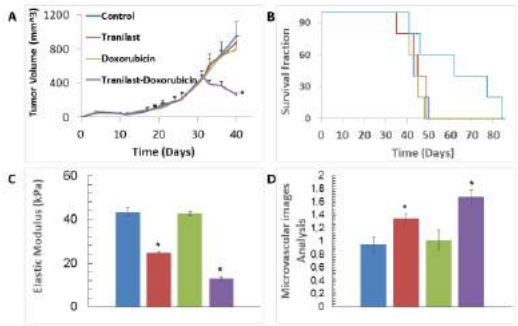

Figure 2: A) Tumor growth curves of tumors. B) Kaplan-Meier survival curves. C) Ultrasound elastography measurments, D) Microvascular image analysis.

Subsequently, we investigated our hypothesis that AFM can access and monitor nanomechanical alterations during microenvironment remodeling as a consequence of external interventions, here drug treatment. Our findings, highlighted that AFM can assess tranilast anti-fibrotic effects tranilast, as the higher elasticity distribution was significantly reduced after treatments (Fig.3A). This decrease was correlated with collagen type I (Fig.3B) and type III (data not shown) reduction. Also, AFM demonstrated that is sensitive enough to distinguish slight nanomechanical alterations between the tranilast and tranilast+chemotherapy groups (Fig.4)

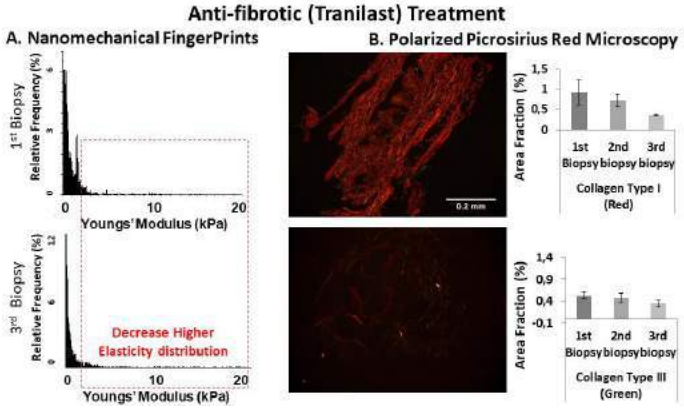

Figure 3: A) AFM Nanomechanical FingerPrints and B) polarized picrosirius red images and analysis during anti-fibrotic treatment.

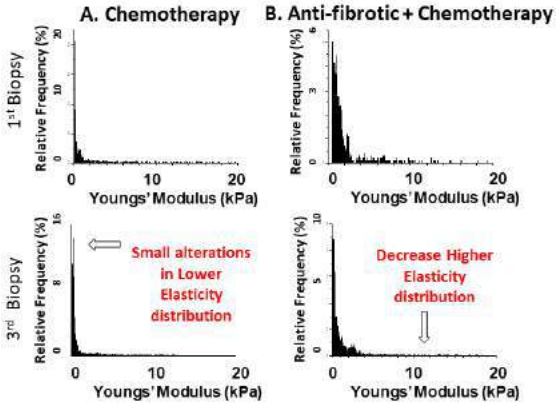

Figure 4: A) AFM Nanomechanical FingerPrints and B) polarized picrosirius red analysis during and after chemotherapy and tranilast+chemotherapy treatment.

DISCUSSION

Our results demonstrated for the first time in the literature that sarcoma tumors present unique NanoMechanical FingerPrints and anti-fibrotic treatment can be used to enhance treatment outcomes. AFM techniques are sensitive to access small nanomechanical modifications after sarcoma treatment with drugs, including chemotherapy and anti-fibrotic agents. Further research in this area will reveal the mechanism of different NanoMechanical FingerPrints for sarcoma and will enable the development of predictive mechanical biomarkers.

ACKNOWLEDGEMENTS

Part of this work was supported by the Cyprus Research and Innovation foundation (CULTURE/AWARD-YR/0119/0012).

REFERENCES

[1] Gkrestsi, V., et al., Front Oncol, 5:214, 2015
[2] Stylianou, A, et al., *Nanoscale*,10:20930, 2018
[3] Papageprgis, P., et al., Sci Rep, 7: 46140, 2017
[4] Plodinec M, et al., *Nat Nanotechnol*,7:757-65, 2012

PROBING THE MECHANICAL PROPERTIES OF CHICK EMBRYOS USING ATOMIC FORCE MICROSCOPY

Joel A. Lefever (1), Jack L. Edson (1), Ashok Ramasubramanian (1)

(1) Department of Mechanical Engineering
Union College
Schenectady, NY 12308, USA

INTRODUCTION

We study early embryonic development in the chick embryo. Two morphogenetic changes occur between Hamburger & Hamilton (HH) Stages 11-15 [1]: the early embryo rotates, and a series of flexures form in the dorsal wall. The underlying forces causing these phenomena are not fully understood [2].

One hypothesis is that an asymmetry develops in the geometry or material properties of the neural tube, which drives flexure and torsion. Prior research has evaluated the mechanical properties of chicken embryos using flat indenters on sectioned embryonic neural tubes [3]. In order to probe the mechanical properties more thoroughly, it is necessary to perform indentation experiments using a technique which can precisely target various locations on the embryo with micron-level precision. In this paper, we discuss how atomic force microscopy (AFM) can be used to probe the material properties of the early neural tube (Figure 1A).

METHODS

Chicken embryos are harvested at Hamburger and Hamilton Stages 10-15 [1], separated from the yolk, and examined in a Petri dish containing phosphate-buffered saline. The sample is fully submerged to protect the tissue and to mitigate surface tension effects. A coverslip serves as a rigid substrate, and filter paper holds the embryo in place. An AFM probe with a 10 μm diameter colloidal tip (sQube) is used to indent the neural tube of the chicken embryo (Figure 1A) in the stages immediately prior to and following rotation. Building on prior research which performed indentation on sectioned embryos [3], the embryos here are tested intact to minimize invasive procedures; however, the vitelline membrane, which covers the dorsal side of the embryo, is removed in order to improve access to the neural tube. The embryos remain submerged during the indentation process. To avoid interference with the indentation measurements, the heart is removed as necessary. The AFM-based indentation technique provides the unprecedented ability to evaluate mechanical properties at a scale of roughly 5 μm, permitting these properties to be mapped over various locations on the embryo. Force-distance curves (Figure 1B) are extracted and various measurements of mechanical properties can be computed, including the stiffness of the neural tube tissue. The stiffness is evaluated as the slope of the retraction portion of the force-distance curve to eliminate plastic effects (arrow in Figure 1B).

RESULTS

Indentation depths are typically observed to be on the order of 2-5 μm, which is limited by the vertical range of travel of the AFM. This indentation depth corresponds with maximum loads on the order of 4-20 nN. The force curves shown in Figure 1B were taken on the neural tube and are typical of several experiments. For this particular embryo, they indicate a stiffness of 7.3 ± 0.2 nN/μm, which is comparable with prior research [3].

As shown in Figure 2, the measured stiffness varies moderately across a single embryo. Figure 2 presents the stiffness data for the 8 embryos investigated to date. On an embryo in which the vitelline membrane was not removed, the stiffness was found to be approximately one order of magnitude greater (data not shown). Using a glass coverslip as a substrate prevents rigid body translation and allows the stiffness of the sample to be evaluated directly after subtracting the compliance of the probe.

DISCUSSION

The greater stiffness observed in the present results (compared to previously-published results in [3]) likely occurs because, unlike the prior study, our procedure maintains an intact neural tube and its

associated pressure (estimated as 30 Pa [4]). This stiffening effect is only partially mitigated by the smaller indenter, which samples a smaller region of tissue and therefore encounters less resistance.

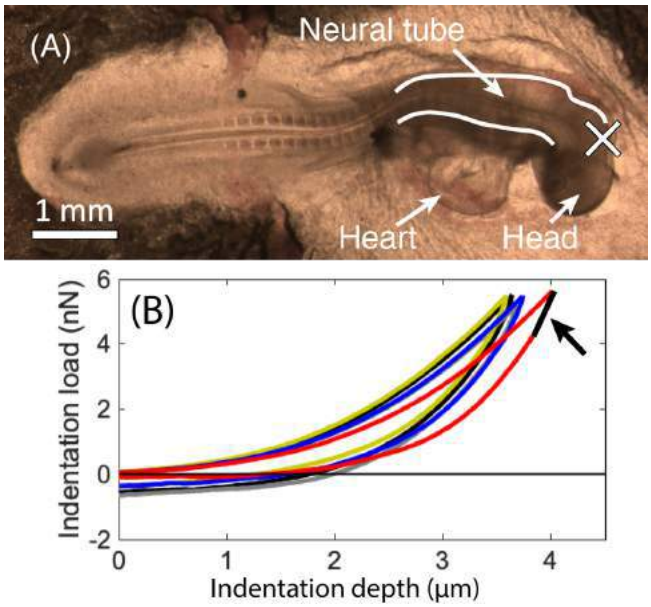

Figure 1: (A) A chicken embryo at HH Stage 14-15 as observed using optical microscopy prior to AFM-based indentation experiments. Major organs are indicated. (B) Five force-displacement curves resulting from a series of indentation experiments in the midbrain region using a colloidal AFM probe, for the embryo shown in (A). The indentations experiments shown in (B) were conducted at the location identified by the X in (A).

The variation in stiffness shown in Figure 2 is likely caused in part by differences in location, the exact stage of development that each embryo was in, and also physical differences between the embryos. Each box and whisker plot represents data from between 2 and 21 locations, as stated on the figure; at each of those locations between 3 and 19 successful indentations were performed. Each of the data points used in the box and whisker plot is an average from these indentations and the standard deviation within each such indentation set is generally small, as evidenced by the minimal scatter in each region in Figure 1(A).

A strong second-order mechanical response was observed in some indents, likely due to fluid flow in the Petri dish and inside the neural tube. This mechanical response affects the linear fit through which the stiffness is calculated; the outliers in Figure 2(B) correspond to the indents where a strong second-order mechanical response was observed.

The methodology described here allows for unprecedented control over the location of the indentation; however, it is not without limitations. The indentation experiment is susceptible to error due to the heartbeat, which cannot be stopped without an invasive operation to remove the heart (which was done for some of the data points) or by stopping the heart using chemicals which may also affect the material response (a chemical inhibitor of heartbeat was not used in this study). In the previous study with which we compare our data, the neural tube was sectioned and removed from the embryo, eliminating the heartbeat as a concern [3]. Experiments must be conducted in the period between heartbeats and it is not possible to confirm whether a heartbeat has occurred except by comparing several indents for uniformity.

Because the material is compliant and highly viscoelastic, it is challenging or impossible in some cases to exactly locate the position at which the indenter makes contact. Therefore, it is challenging to precisely evaluate the indentation depth to compare directly with [3]. We also note that our indenter is spherical, rather than the flat punch used previously [3], which alters the predicted mechanical response from linear to a power-law relationship.

In order to keep the embryos fresh, we attempt to do the indentation experiments as quickly as possible. However, some degradation is visible when the embryos are imaged after the experiments are completed. We notice no strong difference in the measured stiffness or indentation depth from the beginning to the end of the experiments, and therefore believe that this degradation has minimal effect on the measured properties.

The experimental methods described here can be extended to evaluate the mechanical properties across various locations on the embryo, and to determine whether locally stiffer or softer regions are observed. The results of this study will help to elucidate the fundamental mechanisms driving embryonic flexion and rotation.

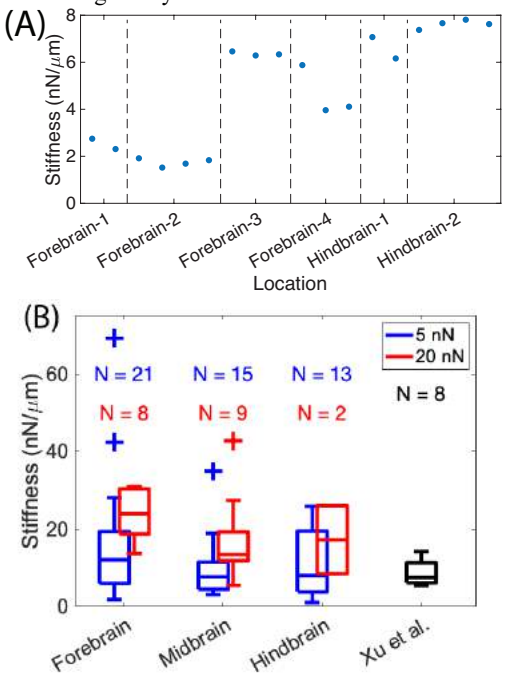

Figure 2: (A) A summary of the stiffnesses measured in six different locations on one embryo and (B) across a total of 68 locations on eight embryos, using AFM. The central mark represents the median, while the top and bottom of the boxes represent the 75th and 25th percentiles; the whiskers represent the range of the data, and crosses represent outliers. Each value of N gives the total number of locations on each section of the brain at which indentations were performed across all embryos. The total number of indentations is much higher. The indentation data in Xu et al. were collected using a custom microindentation device.

ACKNOWLEDGEMENTS

The authors acknowledge funding from the NSF (Award #1936733), and J.E. acknowledges a summer research fellowship and student research grant from Union College.

REFERENCES

[1] Hamburger, V & Hamilton, H L, J. Morph, 88:49-92, 1951.
[2] Ramasubramanian, A et al., J Biomech Eng., 141:1-12, 2019.
[3] Xu, G et al., J Biomech Eng, 132:011005, 2010.
[4] Jelínek, R & Pexiedner, T, Physiologia Bohemoslovaca, 17:297–305, 1968.

A CONVOLUTIONAL NEURAL NETWORK ALGORITHM FOR 3D SUPER-RESOLUTION OF PELVIC FLOOR MRI BASED ON LOW INTER-SLICE RESOLUTION DATA

Fei Feng (1), James A. Ashton-Miller (2), John O.L. DeLancey (3), Jiajia Luo (4)

(1) University of Michigan–Shanghai Jiao Tong University Joint Institute
Shanghai Jiao Tong University
Shanghai, China

(2) Department of Mechanical Engineering
University of Michigan
Ann Arbor, MI, USA

(3) Department of Obstetrics and Gynecology
University of Michigan
Ann Arbor, MI, USA

(4) Biomedical Engineering Department
Peking University
Beijing, China

INTRODUCTION

Magnetic resonance (MR) imaging has played an essential role in the research of pelvic floor disorder mechanism[1], diagnosis of pelvic organ prolapse[2], and measurement of pelvic floor tissue property[3].

Therefore, obtaining high-resolution 3D MR images is crucial in the above tasks. However, the inter-slice resolution is always worse than the intra-slice resolution due to it has high cost in terms of scanning time and expense. It can save the scanning time to ensure a larger field of view for imaging in some cases, such as Valsalva, at the cost of inter-slice resolution deterioration. This introduces difficulties for MR analysis tasks, such as 3D segmentation and geometric model reconstruction. To improve the inter-slice resolution for 3D high-resolution analysis, several digital techniques can be applied. The interpolation method is the most common approach, but it only considers the continuity of pixel values and ignores the structural and semantic continuity. Model-based methods use models to learn the mapping between the low- and high-resolution image pairs, which produces better results.

Several previous studies have demonstrated the use of convolution neural network (CNN) as models for 2D image super-resolution[4]. However, 3D high-resolution images are not available for model training. Therefore, we aimed to develop a 2D CNN-based algorithm for 3D pelvic MR images super-resolution using low inter-slice resolution data in three scanning directions.

METHODS

The pipeline of our algorithm is shown in Fig. 1. We first define the 3D super-resolution task as recovering $I_{(x,y,z)}$ from $\hat{I}_{(x,y,z)}$, where $I_{(x,y,z)}$ denotes high-resolution 3D MR data, $\hat{I}_{(x,y,z)}$ denotes MR data with low-resolution in one or more dimensions, and *x*,*y*,*z* are scanning directions for coronal, sagittal, and axial MR data, respectively. However, as mentioned previously, clinically acquired MR data always have a low resolution in the scanner movement direction. For example, MR data scanned in the coronal plane have a low resolution in the *x*-axis, denoted as $I_{(\hat{x},y,z)}$. Therefore, we need to reconstruct $I_{(x,y,z)}$ based on $I_{(\hat{x},y,z)}$. As shown in Fig. 1, we first performed isotropic analytic interpolation of $I_{(\hat{x},y,z)}$ by spline interpolation algorithm. Then we sliced 2D slices from the *z*-axis and applied the 2D super-resolution model on these slices. After that, the super resolution of the *x*-axis was obtained. As the result was recovered from the *z*-axis, it is denoted as $I_{(x,y,z)}^{SR-z}$. Similarly, we applied the same procedures starting from $I_{(x,y,z)}^{SR-z}$ but from the *y*-axis. Thus, we could obtain the final 3D super-resolution result. As we achieved super-resolution from the axial view (or *z*-axis) and then the sagittal view (or *y*-axis), we denoted it as $I_{(x,y,z)}^{SR-z-y}$. In this framework, no 3D high-resolution MR data was used; instead, it used 2D high-resolution MR data in three views with a 2D super-resolution model.

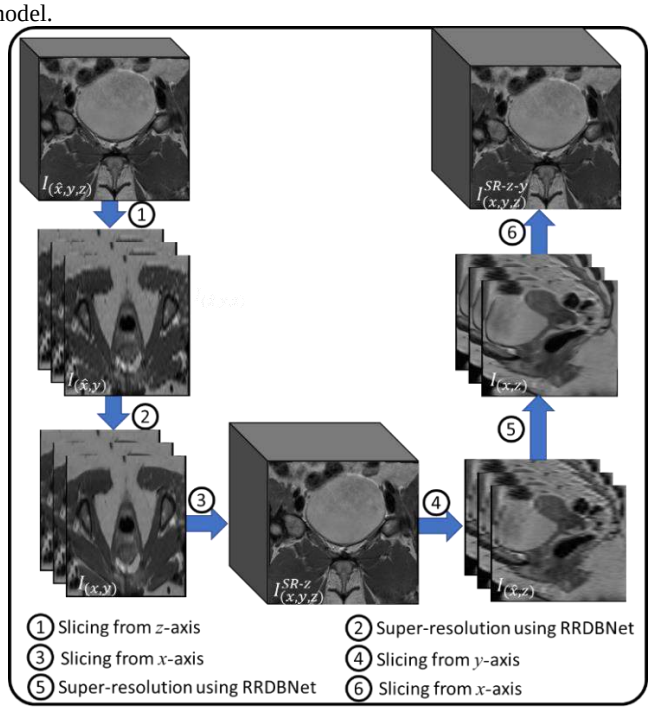

Figure 1: The 3D super-resolution data flow.

The super-resolution was composed of 16 residual in residual dense block (RRDB) modules, so we called it RRDBNet. For the RRDB module, it consists of four residual dense blocks, and in each block there are five convolutional layers connected in a dense way, which ensures efficient feature reuse and better model convergence. Besides, training

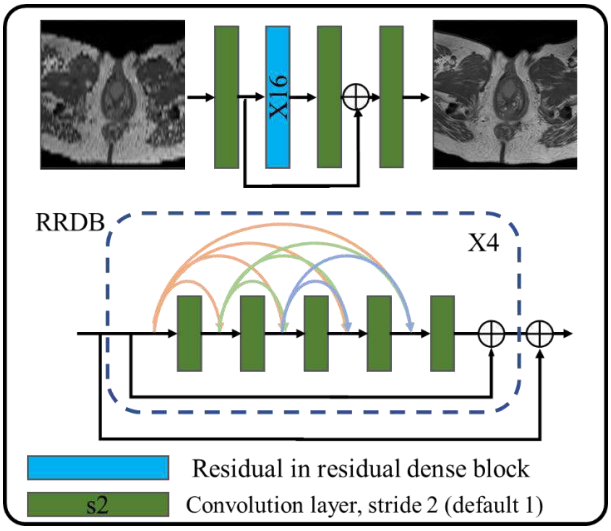

Figure 2: The RRDBNet model structure.

data are important for model training. We simulated the low-resolution training data pairs by downsampling the 2D high-resolution MR images in three views. We used the L1 loss during model training as the cost function and peak signal-to-noise ratio (PSNR) and structural similarity (SSIM) as the evaluation metrics, which are defined as follows.

$$L1 = \frac{1}{MN}\sum_{m,n}^{M,N}|g_{mn} - p_{mn}|\,, \quad (1)$$

where M and N are the lengths for the two image dimensions.

$$PSNR = 20\log\left(\frac{255}{MSE}\right), \quad (2)$$

$$MSE = \frac{1}{MN}\sum_{m,n}^{M,N}(g_{mn} - p_{mn})^2, \quad (3)$$

where MSE is the mean square error between the ground truth and prediction. g_{mn} and p_{mn} are the pixel value for ground truth and prediction, respectively.

$$SSIM = \frac{(2\mu_g\mu_p + 2.55^2)(2\sigma_{g,p} + 7.65^2)}{(\mu_g^2 + \mu_p^2 + 2.55^2)(\sigma_g^2 + \sigma_p^2 + 7.65^2)}, \quad (4)$$

where μ_g and μ_p are the mean values of ground truth and prediction, respectively, σ_g and σ_p are the standard deviations of ground truth and prediction, respectively, and $\sigma_{g,p}$ is the covariance between the ground truth and predicted results.

RESULTS

We used 3D MR data from 48 subjects from the Michigan Pelvic Floor collection with the approval of the institutional ethics review board. For each subject, T2 3D MR data were scanned from coronal, sagittal, and axial views. Each 3D MR sequence had an intra-slice resolution of 0.78 x 0.78 mm and an inter-slice resolution of 5.0 mm. We split this dataset into a training set of 38 subjects' data and a testing set of 10 subjects' data. There were 3037 images in the training set and 796 images in the testing set. We compared our method with the traditional interpolation method. Besides, we also used single-view data for training to explore the difference between single-view data training and three-view data training.

There were 990 coronal, 1020 sagittal, 1027 axial MR images in the training set. When training RRDBNet using single-view data, the final models were named RRDBNet-c, RRDBNet-s, and RRDBNet-a, respectively. We also used all the 3037 images, and the model was named RRDBNet-all. Besides, we performed model evaluation while training with 998 images from 13 subjects and named the model as RRDBNet-partial. All the experiments were performed based on Python (V3.5.2) and Pytorch (V.1.2.0) libraries, using an NVIDIA TITAN RTX graphics card with 24 GB computational memory. The RRDBNet was trained with a batch size of 4 and a learning rate of 2e-4. The testing result was summarized in Fig. 3.

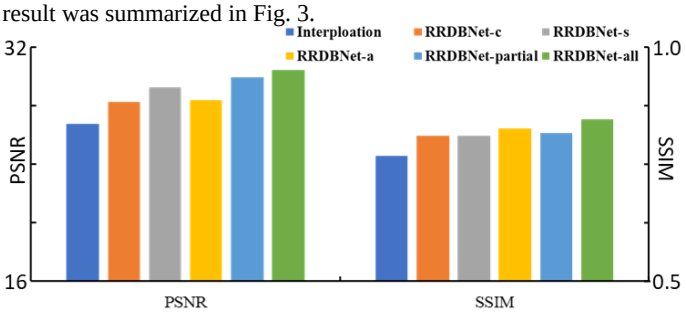

Figure 3: Super resolution performance on the testing set.

Fig.3 indicated that our method has a significant advantage over the interpolation method in terms of both PSNR and SSIM. Besides, RRDBNet-partial obtained higher PSNR and SSIM than RRDBNet-c, RRDBNet-s, and RRDBNet-a. When using all images, RRDBNet-all obtained the best results. We showed the 2D super-resolution and 3D geometric model reconstruction results of the bladder in Fig. 4. From the 2D super-resolution result, we could find that RRDBNet produced results with fewer artifacts and better image fidelity. Small details were also better recovered. In addition, from the bladder reconstruction results, we found that our algorithm produced images with more continuity.

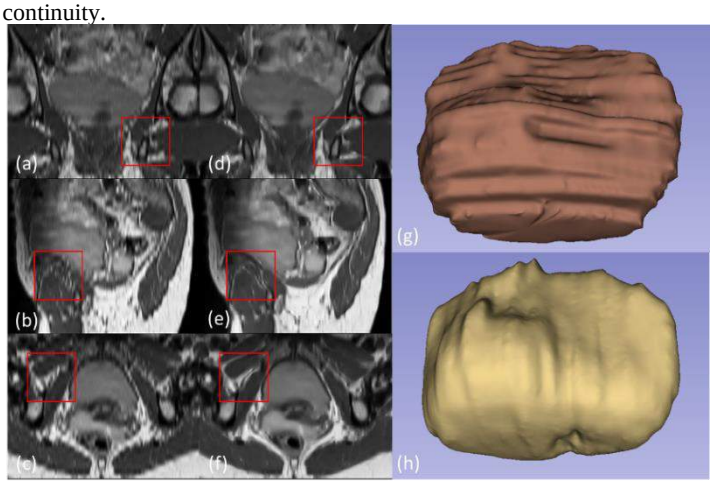

Figure 4: Comparison of super-resolution results. (a)-(c) are results obtained with the interpolation method. (d)-(f) are results obtained with RRDBNet-all. (g) is the geometric model of the bladder with 3D MR images from the interpolation method. (h) is the geometric model of the bladder with super-resolution 3D MR images with RRDBNet-all. (g) and (h) were smoothed in the same configuration.

DISCUSSION

A CNN-based super-resolution algorithm for 3D pelvic MR images was developed, using only low-resolution 3D data. The 3D super-resolution problem was solved as a 2D super-resolution problem using RRDBNet and MR images from three views. We validated that our algorithm outperformed the interpolation method on 2D super-resolution and geometric model reconstruction tasks. In the future, we will validate our algorithm with real high-resolution 3D MR data.

ACKNOWLEDGEMENTS

Thanks for the support of the NSFC General Program grant 31870942, Peking University Clinical Medicine Plus X – Young Scholars Project grant, PKU-Baidu Fund, NIH R01 HD038665, and P50 HD044406.

REFERENCES

[1] J. Luo *et al.*, *J Biomech* 48(9), 1580-1586, 2015. [2] C. Lewicky-Gaupp*et al.*, Am J Obstet Gynecol 202 (5):6, 2010. [3] J. Luo *et al.*, *J Biomech Eng 136 (2):021016, 2014*. [4] C. Dong *et al.*, ECCV, 2014.

EFFECTS OF CARDIAC GEOMETRIC REMODELING DURING HEART FAILURE ON CARDIAC FUNCTION

Yu Zheng[1], Wei Xuan Chan[1], Choon Hwai Yap[2]

(1) Department of Biomedical Engineering, National University of Singapore, Singapore

(2) Department of Bioengineering, Imperial College London, UK

INTRODUCTION

Heart failure with preserved ejection fraction (HFpEF, EF ≥ 50%) and heart failure with reduced ejection fraction (HFrEF, EF ≤ 40%) are two main types of heart failure (HF) with similar prevalence. 88% of HFpEF [1] and 80% of HFrEF [2] undergo heart remodeling, typically concentric hypertrophy (CH) for HFpEF and eccentric hypertrophy (EH) for HFrEF. However, there is substantial heterogeneity, and the concentric remodeling (CR) phenotype as well as an absence of geometric remodeling (normal) has also been observed in HF. It is currently unclear whether these various geometric phenotypes favor or impede function.

Currently, the diagnosis of HFpEF remains clinically challenging due to the preservation of EF and clinical heterogeneity. The inability of EF to indicate disease in HFpEF, and reports that EF can be skewed by cardiac geometric changes [3, 4] demonstrate its ineffectiveness as a indicator of function. However, it remains unclear why this is so.

In the current study, we develop a myocardial numerical model that relates strains to cardiac flow function, as informed by porcine animal data and clinical literature data, to explain why EF is ineffective, and to propose a new corrected EF measure to avoid this problem. We also show that cardiac dilation provides geometric advantages to the heart, allowing better conversion of strains to flow function, while wall thickening does not.

METHODS

CMRI of 5 HFpEF porcine animal model (via gradual constriction of aorta), and 10 HFrEF porcine animal model (via circumflex ligation), and sham/healthy are obtained before intervention (baseline) and at the 28th or 42nd day time point (ending). Cardiac anatomic parameters are measured, as are longitudinal strain (LS) and circumferential strain (CS) at both the endocardial and epicardial boundaries, defined as deformation between end-diastole (ED) and end-systole (ES).

A numerical model of the LV, based on a typical porcine heart anatomic dimensions, is reconstructed as an idealized prolate shape with 3 layers, the epicardial, endocardial and mid-wall layers. The model is discretized, and can undergo specific magnitudes of spatially uniform ED-to-ES strain deformations, in an incompressible way. Geometric changes common during HF remodeling can be modelled, such as wall thickening and dilation, and flow function can be evaluated via EF and stroke volume (SV).

The model is also used to test effects of varying HF geometric phenotypes and strain magnitudes on its flow function, using a population data of 4768 participants [5].

RESULTS

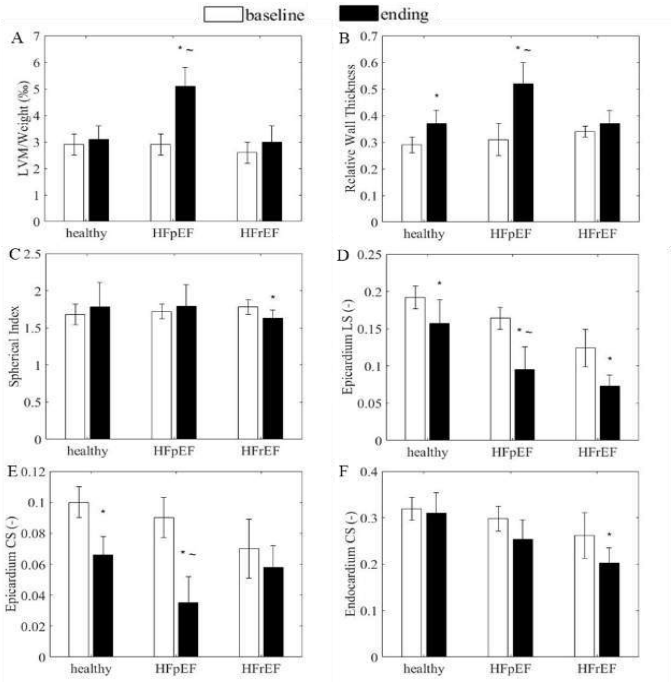

Figure 1. Anatomic characteristics and strain function of the healthy, HFpEF and HFrEF porcine animals. (A) LV mass normalized by weight, (B) relative wall thickness, (C) spherical index. (D-F) Endo- or epicardial longitudinal or circumferential strains. * p<0.05 with baseline. ~ p<0.05 with healthy.

In the porcine animal models, HFpEF and sham EF are above 50%, while HFrEF EF is less than 40%. HFpEF experiences hypertrophy with higher LVM and wall thickness (Fig. 1A-B), suggesting a concentric hypertrophy phenotype. HFrEF has a decreased sphericity index and unchanged RWT, indicating an eccentric hypertrophy phenotype with dilation. Both HF models has decreased strains, but HFpEF endocardial strain is not significantly changed.

With the numerical LV model, increasing wall thickness with no change to strain magnitude (Fig 2A) was found to increase EF but not SV, suggesting that wall thickness changes artificially increased EF when there is no change to flow function. Increasing dilation with no change to strain magnitude (Fig 2B) was found to increase SV, but decrease EF, suggesting that dilation enhances flow function, but EF is not a successful indicator of this.

Our model shows substantial epi-to-endo spatial variability of strain, and this is because during systolic contractions, on top of longitudinal and circumferential strains, there is the radial strain. The radial strain pushes endo-surface inwards, causing further shortening at the endo-surface, but it pushes the epi-surface outwards, causing lengthening at the epi-surface that negate some of the contraction. Epi-strains are thus always lower than endo-strains (Fig 2C, D). Interestingly, wall thickening is found to increase this epi-/endo-difference, as it increases radial displacement during systolic contractions, while dilation reduces the difference, as it reduces the curvature of the LV wall.

The epi- and endo- surfaces are thus not good locations for quantifying strain or volumetric flow function of the heart, and the mid-wall location (in between epi- and endo-) is a better location. Since EF uses the endocardial surface for volume quantification, it becomes skewed by geometric changes of dilation and wall thickening. This explains why it is not a good indicator of function.

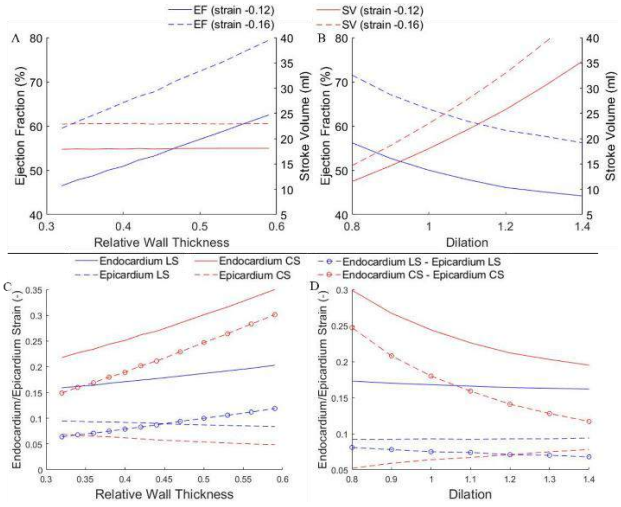

Figure 2. Results of LV myocardial numerical model, showing the dependence of EF and SV on (A) relative wall thickness and (B) dilation at constant strains of -0.12 or -0.16 (at the mid-wall layer), and the dependence of endo- and epicardial strains on (C) relative wall thickness (D) dilation at the same strains.

We thus propose a novel marker, the corrected ejection fraction (CEF), that will not be skewed by cardiac geometric changes:

$$CEF = \alpha \times EF = SV/Vol_{ED,mid} \quad (1)$$

$$\alpha = Vol_{ED,endo}/(Vol_{ED,endo} + LVM/2\rho_{LV}) \quad (2)$$

Where $Vol_{ED,location}$ is the end-diastolic volume calculated at a location, either at the mid-wall or the endocardium, and ρ_{LV} is the myocardium density. The CEF is essentially EF but calculated at the mid-wall layer rather than endocardium layer. When applied to the porcine data, CEF can successfully differentiate between healthy and HFpEF hearts, while EF cannot (Fig. 3). Further, by testing CEF with literature disease data, we can show that CEF is effectively independent of the geometric phenotype, adopting the same value a specific strain magnitude, regardless of the geometric phenotype.

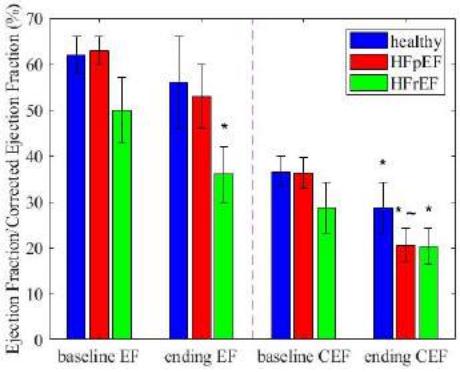

Figure 3. EF and CEF of healthy, HFpEF and HFrEF porcines hearts at baseline and ending time points. * p<0.05 with baseline. ~ p<0.05 with healthy ending. EF cannot differential HFpEF from healthy, but CEF can

With the LV model, we also compared the 4 HF remodeling phenotypes (Norm, CH, CR, EH), in terms of how much increase in strain is needed to achieve a stroke volume of 20% above the normal heart (such as during exercise). Results in Fig 4 shows that the dilated EH phenotype is most geometrically advantageous phenotype in this regard, followed by CH and CR. This suggests that dilation during HFrEF is advantageous to its function, but not the hypertrophic wall thickening during HFpEF.

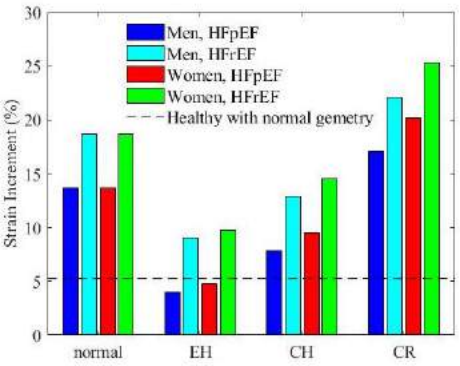

Figure 3. percentage increase in myocardial strain that is required to achieve a stroke volume of 20% higher than a healthy heart, for various HF geometric phenotypes.

CONCLUSION

From our modeling, we find that dilation to be advantageous to cardiac flow function, but not wall thickening. We further find that EF is an imperfect indication of function because it can be modulated by the cardiac geometry changes, such as during HF remodeling, and cannot distinguish some HF phenotypes from normal, and that this is because of its reliance on measurements on the endocardial boundary rather than the mid-wall layer. We proposed a corrected EF measure, the CEF, which we show can remove this geometric dependency and enable a better representation of cardiac contractile function.

ACKNOWLEDGEMENTS

Funding is provided by National University of Singapore Research Scholarship, and by Imperial College startup funding.

REFERENCES

[1] Katz, D. H., et al., *Am J Cardiol*, 112, 1158-1164, 2013.
[2] Nauta, J. F., et al., *Eur J Heart Fail*, 22, 1147-1155, 2020.
[3] MacIver, D. H., et al., *Int J Cardiol Heart Vasc*, 7, 113-118, 2015
[4] Stokke, T. M., et al., *J Am Coll Cardiol*, 70, 942-954, 2017.
[5] Velagaleti, R. S., et al., *Am J Cardiol*, 113, 117-122, 2014

THE ROLE OF EYE MOVEMENTS IN THE PROCESS OF SILICONE OIL EMULSIFICATION AFTER VITRECTOMY

I. Nepita (1), A. Stocchino (2), L. Liggieri (3), F. Ravera (3), E. Santini (3), M.R. Romano (4), R. Repetto (1)

(1) Department of Civil, Chemical and Environmental Engineering, University of Genoa, Genoa, Italy

(2) Department of Civil and Environmental Engineering, Hong Kong Polytechnic University, Hong Kong, China

(3) Institute for Condensed Matter Chemistry and Technologies for Energy, CNR, Genoa, Italy

(4) Department of Biomedical Sciences, Humanitas University, Milan, Italy

INTRODUCTION

The vitrectomy surgical procedure is performed to treat pathological states of the retina and it consists in the removal of the vitreous body from the vitreous chamber. In cases in which the retina is teared, in order to avoid the progression of a retinal detachment, tamponade fluids are inserted in the eye, with the aim to improve the contact between the detached retina and the retinal pigment epithelium, thus facilitating retinal reattachment. At present, the most widely used tamponade fluids are high viscosity silicone oils (SOs). However, SOs cannot be left for very long times in place as they tend to emulsify with the aqueous humor produced by the eye. Emulsion is a highly undesirable event, especially when oil droplets get small enough to move to the anterior segment of the eye where they can block the drainage of the aqueous humor, by accumulating into the trabecular meshwork. This may lead to an increase of the intraocular pressure, which is a significant risk factor for the development of glaucoma.

The release of endogenous molecules from ocular tissues (typically as an inflammatory response to surgery) has a significant role in the generation of an emulsion. The mechanisms behind of the effects of these molecules on the emulsification process depend on their capability to adsorb at the water-oil interface, modifying its mechanical interfacial properties [1, 2]. Furthermore, in order for an emulsion to be generated, mechanical energy must be provided to the system. In this context, some studies have evaluated the role of eye movements in this process in the absence of organic material [3,4]. Recently Wang et al. [5] tried to produce emulsions in a spherical model of the vitreous chamber subjected to a sequence of rotations. Interestingly, the authors never observed the formation of a bulk emulsion, even in the presence of surface-active molecules.

Aim of the present work is to study the effects of mechanical energy provided by periodic eye movements on the emulsion formation in a physical model of the vitreous chamber of the eye in the presence of surfactant biomolecules.

METHODS

A model of a vitreous chamber in Plexiglass with realistic geometry has been employed. The experimental setup composed by an optical diagnostic for monitoring the emulsion, a brushless system controlled by a computer to simulate eye movements and a thermal insulation system to maintain the model at 35°C. In particular, the presence of the lens in the front of the vitreous chamber has been considered, which has a significant influence on the motion of the fluid within the domain [6]. The solutions containing endogenous molecules were prepared using a Dulbecco buffer solution (DPBS) and different concentrations of albumin (0, 1 and 5% of the corresponding concentration in blood). The study involved the characterization of a SO used in ophthalmic surgery (RS-OIL 1000 cSt, Alchimia srl).

Once filled with SO (80%) and aqueous solution (20%), the model is mounted on a support connected to a computer-controlled motor. In this study, harmonic rotations were considered: this choice is suggested by the fact that a harmonic law is the simplest way to represent a sequence of saccadic eye movements in both directions with prescribed amplitude and duration [7]. The model is tested for different values of amplitude (20° – 50°) and with an imposed frequency equal to 5 Hz, for the duration of 1 hour. The temporal evolution of the emulsion has been studied through acquisition of images with a digital camera. An optical microscope (Leica Microsystems, Switzerland) has been used to determine droplets distribution and size. To this aim, acquired images of the emulsions were automatically analyzed by a software developed in MATLAB, able to detect the centers and radii of the drops, based on the concentric circular arrangement (CCA) method [8].

.

RESULTS

Experiments with the sample containing the DPBS alone, did not produce emulsions in the eye model. This result demonstrates that the only presence of a small amount of slightly surface-active impurities in the oil (low molecular weight components) cannot favour the emulsification process. On the contrary, we found formation and persistence of emulsions even when a low concentration of albumin was dissolved in the aqueous solution (1% of the physiological concentration in blood), as shown in Figure 1.

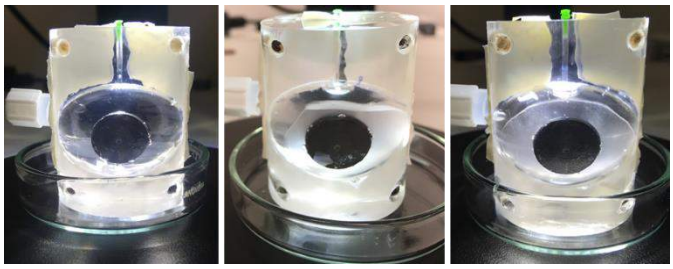

Figure 1: 80:20 volume ratio emulsions between SO and aqueous phases, 1 hour after formation. From left to right: DBPS; albumin 1% in DBPS, amplitude 50°; albumin 1% in DBPS, amplitude 40°.

Moreover, keeping these emulsions on a shelf at room temperature, the situation did not change significantly after 1 week, showing that the emulsions are stable in time.

In order to define a size distribution of the drops for all investigated systems, analysis of the images acquired by the microscope has been carried out considering different ranges of diameters and counting the total number of droplets falling in each range. In general, as shown in the normalized droplets distributions in Figure 2, the majority of the drops has a very small diameter: in the range of 0 – 5 µm. It is interesting to notice that, with 5% albumin solutions, we obtained maximum droplets size of about 55 µm, for all the investigated amplitudes (Fig. 2a). On the contrary, evaluating different amplitudes in the case of 1% albumin solutions, droplets with diameter even above 100 µm have been found (Fig. 2b). For values of amplitude equal to 20° and 30° and 5% and 1% albumin solutions, respectively, the emulsion did not form. A coalescence test has been performed, in order to evaluate the type of the formed emulsion. This allowed us to assess that the continuous phase of the emulsion is the buffer solution and, therefore, we obtained oil-in-water emulsions.

Another important result of this work is represented by the efficiency of the software adopted for image analysis, with an accuracy of 70% of the total droplets within the image.

DISCUSSION

In this work we investigated the effects of surfactant biomolecules and mechanical energy induced by eye rotations on the emulsion formation in a physical model of the vitreous chamber. The considered domain has been developed in order to simulate the real physiological conditions in terms of temperature and geometry. The motion imposed to the eye model by the motor, follows a sinusoidal time law and the imposed values of frequency (5Hz) and amplitudes (20° – 50°) are comparable with those reported in the literature. The experiments have been performed considering a SO in contact with solutions both in absence of proteins and with different concentrations of albumin.

The main result obtained from these experiments consists in the formation of emulsions even when a low concentration of albumin has been dissolved in the aqueous solution (1% of the physiological concentration in blood). The presence of an emulsion did not occur, in absence of proteins, for the same experimental conditions. Moreover, our results confirmed the capability of albumin to form stable SO in water emulsions once formed [1].

Through images analysis acquired by the microscope, we have been able to obtain information about the number of the droplets formed by the emulsification process and their size distribution, for each investigated system. As a result, we found oil-in-water emulsion, in agreement with the Bancroft rule [9], mostly characterized by oil drops with diameter less than 10 µm. This finding has clinical relevance, since droplets of small size can cause occlusion of the trabecular meshwork if they migrate in the anterior segment of the eye and can be swallowed by macrophages that, releasing chemioactive substances, induce inflammatory stimuli.

These experimental results demonstrate that eye movements and the presence of surfactant biomolecules can be considered co-factors of SO emulsification after vitrectomy.

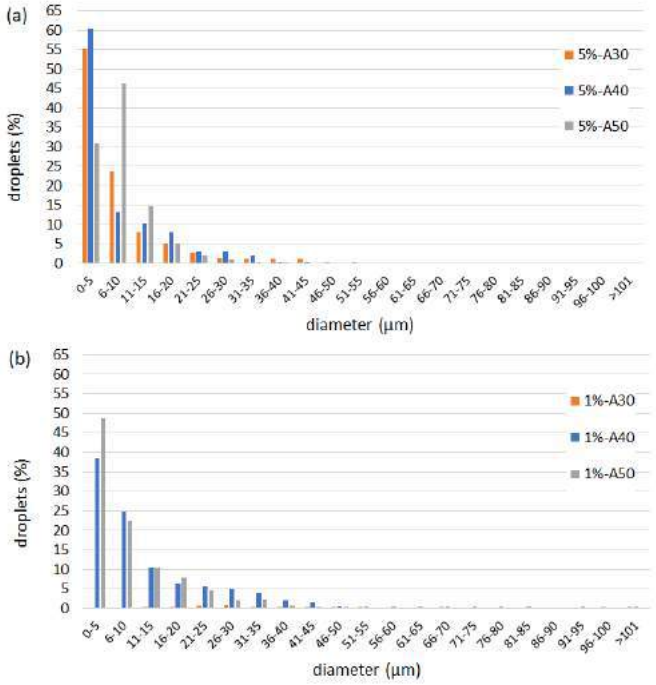

Figure 2: Droplets distributions for all the investigated systems. (a) Solutions containing albumin with concentration of 5%; (b) solutions containing albumin with concentration of 1%. Different color bars correspond to different imposed amplitudes.

REFERENCES

[1] Nepita, I et al., *BioMed Research International*, 2020.
[2] Ravera, F et al., *Adv. Colloid Interface Sci.*, 288, 102344, 2021.
[3] Chan, Y.K. et al., *Investig. Ophthalmol. Vis. Sci*, 56(5), 3314-3319, 2015.
[4] Isakova, K et al., *Physics of Fluids*, 26(12), 124101, 2014.
[5] Wang, R et al., *Acta ophthalmologica*, 2020.
[6] Repetto, R et al., *Biomech. Model. Mechanobiol.*, 9(1), 65-76, 2010.
[7] Bonfiglio, A et al., *Phys Med Biol.*, 58:1969–82, 2013.
[8] Strokina, N et al., *Proceedings of the Proceedings of the 21st International Conference on Pattern Recognition*, 2655-2659, 2012.
[9] Bancroft W.D., *J. Phys. Chem.*, 17, 514, 1913.

FACTORS EXPLAINING THE DIFFERENCE IN 2D AND 3D FETAL ECHOCARDIOGRAPHY STRAIN MEASUREMENTS

Meifeng Ren(1), Wei Xuan Chan(1), Aimee Armstrong(2), Andreas Tulzer(3), Gerald Tulzer(3), Martin L Buist(1), Choon Hwai Yap(4)

(1) Dept of Biomedical Engineering, National University of Singapore, Singapore

(2) The Heart Center, Nationwide Children's Hospital, Columbus, Ohio, USA

(3) Dept of Pediatric Cardiology, Kepler University Hospital, Linz, Austria

(4) Dept of Bioengineering, Imperial College London, London, UK

INTRODUCTION

Fetal echocardiography is increasingly used for assessing fetal cardiac and circulatory function. Echocardiographic myocardial strain measurement is a good way to evaluate fetal cardiac function and to evaluate the severity of cardiac dysfunction, such as during twin-to-twin transfusion syndrome (TTTS) [1] or in congenital heart disease (CHD) [2]. Such evaluation can be important to clinical decisions about treatment, such as endoscopic laser ablation for TTTS or fetal cardiac intervention for CHD.

Echocardiographic strain measurements are typically performed with speckle tracking and can be performed in 2D or 3D. Previous work comparing 2D and 3D speckle tracking strains reported specific biased differences between the two [3]. Mararu et al. found the difference to be statistically significant and suggested that it is due to complex motions of the heart that 2D scans cannot capture [4]. However, the exact mechanism for this has not been elucidated. Further, widely varying fetal heart strain values were reported by different studies, leading to contradictions and confusion during interpretation of measured results [5], but reasons for these discrepancies have not been studied in detail.

Here, we attempt to bridge these literature gaps, using a validated cardiac motion estimation algorithm to track cardiac motion in both 2D and 3D echocardiography images of fetal hearts.

METHODS

Healthy Fetal Echocardiography: The 3D cine ultrasound images were obtained from 10 heathy fetuses at 22 and 32 weeks of gestational age, from the National University Hospital, Singapore, with IRB approval (protocol 2014/00056) and patient consent. Acquisition was performed with the STIC mode (4D scans) aligned with the four-chamber view, using the GE Voluson 730 ultrasound, and with a frame rate of 90 ± 38 frames per second. The 2D cine images were extracted from the 3D images, in order to perform a well-controlled comparison of 2D and 3D strain measurements.

Quantification of Myocardial Strain: A validated cardiac motion estimation algorithm [6] was used to track the motion of the fetal left ventricle (LV) in 3D and 2D. To quantify strains, a line at the middle of the LV wall was traced, both in the longitudinal direction on the long-axis view and in the circumferential direction on the short-axis view, and these lines were motion tracked from end-diastole to end-systole for calculation of shortening and thus strain.

The engineering strain was quantified in line with current clinical practices, and the Green was also quantified to stay relevant to the biomechanics community. The intra- and inter- observer variability was checked to be satisfactory via the intraclass correlation coefficient (ICC), based on measurements by two observers for both 2D and 3D sub-endocardial strains from the same set of 10 fetal hearts for 3 repeat measurements.

Quantification of LV twist and fiber orientation: LV twist was also computed from the 3D motion tracking, by quantifying the differential angular rotation at the apex versus the base and by calculating the maximum minus the minimum of this differential rotation parameters. Myocardial fiber orientation was quantified by seeking the direction in which contraction occurred the most, via the calculation of the eigenvector of the strain tensor.

RESULTS

3D longitudinal strain (LS) was found to be significantly lower than 2D LS by 2.7% (Figure 1). This is due to LV twist causing the longitudinal line in 3D quantification to become diagonal after contraction, thus preserving its length after contraction, and 2D quantification cannot capture this effect (Figure 2a). To understand how much of the 2D vs. 3D difference is caused by this effect, we performed

a 3rd quantification of the projected strain, during which we tracked motion in 3D but projected the final location to the original 2D plane before strain calculations, as a way of negating LV twist motion effects. We found that 1.2% of the difference can be explained by LV twist motion.

In the circumferential direction, 3D strain was found to be significantly higher than 2D circumferential strain (CS) by 2.0% (Figure 1). This can be fully explained by the systolic apical motion of heart, which introduces wider transverse cross-sections of the heart into the imaging plane to negate contractile measurements (Figure 1b).

These results agree with and can explain with findings in adult echocardiography studies. Obokata et al. found in 106 subjects that 3D global LS (GLS) is lower than 2D GLS by 2.0%, while the median 3D global CS (GCS) is higher than 2D GCS by 2.0% [7]. In addition, Reant et al. found in 128 subjects that 3D GLS is lower than 2D by 1.1% [4].

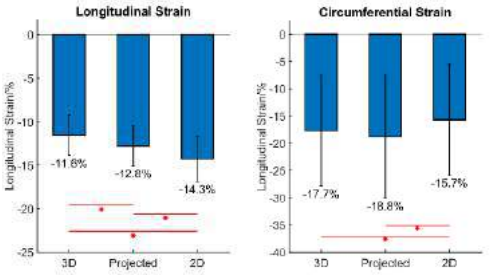

Figure 1. 2D vs 3D strain quantifications from the same ultrasound image.

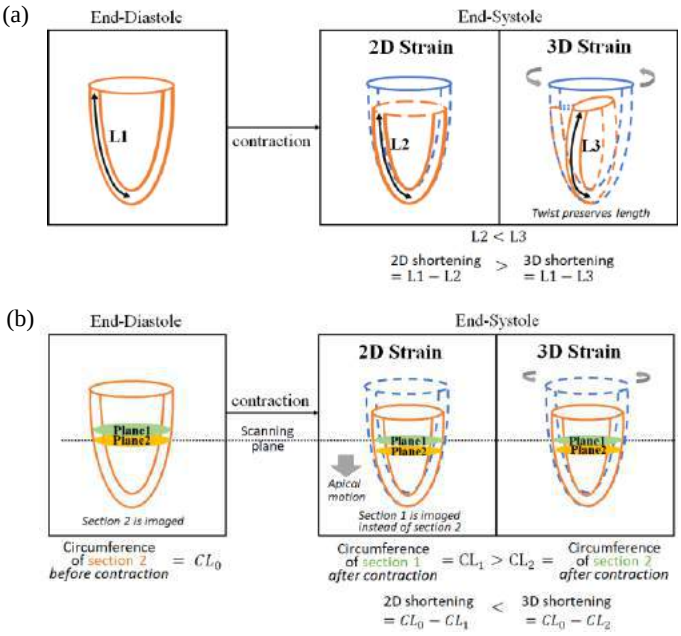

Figure 1: Schematic explanation of differences between 2D and 3D strain in longitudinal (a) and circumferential (b) strain

Further, we observed a timing mismatch between when the longitudinal and circumferential lengths are at their peaks, caused by LV shape changes during the isovolumic contraction period, when the LV momentarily lengthens and narrows [8]. During 2D quantification, strain in each direction is assigned its own zero-strain reference time, but in 3D, a single reference time is necessary for both directions. Thus, in 3D, favoring any one direction when specifying this reference will reduce strain magnitude of the other direction (Figure 3). This accounted for a further 0.7-0.8% difference between 2D and 3D strains.

A spatial variability of strains was also found. Strains at epicardial vs. endocardial locations differed substantially, by 3.6% in the longitudinal direction and 9.3% in the circumferential direction. Since strain quantifications often require manual controls clinically, this can account for wide discrepancies between the different studies mentioned above [5], in which reputable groups reported strain values that differed by 6.3-7.1%. We further found that introducing smoothing during motion tracking can lead to a substantial change in strain values, which can be another reason for wide discrepancies between studies.

Interestingly, 3D motion tracking enabled the quantification of LV twist (7.8 ± 3.3^o from the circumferential axis) and quantification of the myofiber orientations (4.6 ± 4.7^o).

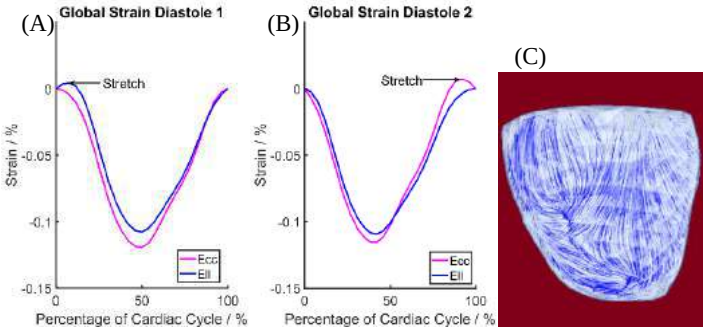

Figure 3. Plots of circumferential and longitudinal strains over time using (A) longitudinal peak as zero-strain reference time, or (B) circumferential peak as reference. (C) Fiber orientation of the heart quantified via eigenvalue of strain tensor

DISCUSSION AND CONCLUSION

In our study, we demonstrate that there are systemic factors that cause specific biased differences between 2D and 3D strain measurements, due to the twisting and apical motion of the LV during systolic contraction and by the timing mismatch between when dimensions in the circumferential and longitudinal directions peaked.

We further found substantial epicardial-to-endocardial spatial variability of strains and significant effects of motion tracking smoothing on strain quantifications, which can explain wide discrepancies in strain values in the literature.

We believe that this calls for caution in interpreting measurements in the literature, until careful standardization of strain measurements can be achieved. Further, although our study was conducted on fetal echocardiography, the results are likely applicable to adult echocardiography as well.

ACKNOWLEDGEMENTS

Funding is provided by Singapore Ministry of Education, Tier 2 Grant (MOE2018-T2-1-003), and Imperial College startup funding.

REFERENCES

[1]J. Rychik et al., Fetal Diagn. Ther. **32**, 131, 2012
[2]T. Ishii et al., Fetal Diagn. Ther. **35**, 18, 2014
[3]P. Reant et al. J. Am. Soc. Echocardiogr. **25**, 68, 2012
[4]D. Muraru, et al. J. Am. Soc. Echocardiogr. **27**, 858, 2014
[5]N. H. M. van Oostrum et al. Eur. J. Obstet. Gynecol. Reprod. Biol. **250**, 178, 2020
[6]H. Wiputra et al. Sci. Rep. **10**, 18510, 2020
[7]M. Obokata et al. Eur. Heart J. – Cardiovasc. Imaging **17**, 525, 2016
[8]W.A. Goetz et al. Am J Physiol – Heart and Circ Physiol. **289**:H196-H201, 2005
[9]D. Muraru et al. Cardiovasc. Diagn. Ther. **8**, 101, 2018
[10]W. A. Goetz et al. Am. J. Physiol. Heart Circ. Physiol. **289**, H196, 2005

INTRAARTICULAR MMP-1 IN THE FACET JOINT MODIFIES THE CAPSULAR LIGAMENT'S RESPONSE TO LOAD & THAT RESPONSE CORRELATES WITH THE EXTENT OF DEGRADED COLLAGEN

Meagan E. Ita (1), Sagar Singh (1), Beth A. Winkelstein (1,2)

(1) Department of Bioengineering
University of Pennsylvania
Philadelphia, PA, United States

(2) Department of Neurosurgery
University of Pennsylvania
Philadelphia, PA, United States

INTRODUCTION

Musculoskeletal pain is the most common type of chronic pain and cause of disability [1]. The spinal facet joints act as pain sensors due to their innervation [2], and their capsule can transmit nociceptive signals under pathologic conditions [3,4]. The interstitial collagenase matrix metalloproteinase-1 (MMP-1) may mediate pathological cascades in painful joints since it increases after trauma and with degeneration [5,6]. It regulates structure and cell-signaling, and degrades Type I collagen that comprises the capsular ligament [7], altering joint biomechanics [6] and possibly mediating signaling in afferents [3]. MMP-1 acts on neuronal receptors and has substrates to neuropeptides and cytokines involved in nociception [7,8]. Despite evidence suggesting MMP-1's involvement in painful diseases, its role in joint pain is undefined.

Injecting intraarticular MMP-1 in the rat C6/C7 facet joint induces immediate and sustained pain and upregulation of the nociceptive peptide substance P [9]. Although MMP-1 may directly mediate facet pain, it is unclear if nociceptive cascades are triggered in afferents by collagen degradation or by MMP-1-mediated signaling pathways [7,8]. Since intraarticular bacterial collagenase also induces pain by inducing microscale degradation of capsular collagen fibers [10], intraarticular MMP-1 may also cause microscale collagen degradation that alters the microstructural kinematics of the fiber network under load. This study investigated isolated C6/C7 facet capsule ligaments from rats at 28 days after bilateral intraarticular administration of MMP-1, when pain persists [9]. One facet from each rat underwent biomechanical testing to define capsular multiscale kinetics and kinematics [11-13]; the other facet underwent a biochemical assay with collagen hybridizing peptide (CHP) to assess the amount of degraded collagen in ligament tissue [14].

METHODS

To assess the effects of intraarticular MMP-1 on ligament macroscale biomechanics, microstructural kinematics, and degraded collagen, spinal columns were harvested from rats (438-532g) after either a bilateral C6/C7 intraarticular injection of either 10μL of human recombinant MMP-1 (n=6) in sterile water (30μg/mL; SRP3117; Sigma) or only sterile water (vehicle; n=5) [9,10], by IACUC-approved procedures. On day 28, spinal columns (occiput-T2) were harvested; the superficial musculature was removed from the facets by fine dissection and the *in situ* length across the C6/C7 facet was recorded [15,16]. A naïve rat was also included for comparison as an un-operated joint.

For biomechanical testing, unilateral C6/C7 facet joints were mounted in an Instron 5865; the *in situ* length was re-established as the unloaded reference position (Fig. 1A) [15,16]. Isolated ligaments underwent tensile loading to failure at 0.08mm/s. Force-displacement data and high-speed images (Phantom v9.1; Vision Research) were acquired at 500Hz. An integrated polarized light imaging system acquired collagen fiber alignment maps before and during loading [11-13]. Force, displacement, and optical data were used to define relevant events during the stretch (Fig. 1B): the first failure, ultimate rupture, and yield (Fig. 1B) [12,15]. Ligament stiffness was also calculated [17].

Collagen fiber alignment maps were generated and used to compute the first occurrence of anomalous fiber realignment [11,12]. Vector correlations generated for every alignment map were used to identify changes between the maps and anomalous collagen fiber realignment (AR) was defined by a decrease of ≥0.35 in the vector correlation [12]. Force, displacement, and collagen fiber alignment maps were extracted at each event. The number of anomalous events [12,16] and the circular variance (CV) were calculated at each event (Fig. 1A), and also at the unloaded reference state [17]. CV quantified the spread of collagen fiber angles (Fig. 1A), with a lower CV indicating a tighter clustering and a higher degree of fiber alignment [17].

To quantify the amount of degraded collagen, the capsular ligament from the other side of the matching facet was isolated and

lyophilized overnight. Ligaments were incubated in 15μM of 5-FAM conjugate of CHP (3Helix) overnight, triple-washed in PBS for 30mins each, and incubated in 1mg/mL Proteinase K for 3hrs at 60ºC [14]. The fluorescence of 200μL duplicates of the homogenate solution was measured [14]; fluorescence values were divided by the wet weight.

Separate repeated-measures ANOVAs with Tukey tests tested differences in CV and AR across events within groups; comparisons in events between groups were tested by Wilcoxon tests. T-tests compared stiffness and CHP fluorescence. Correlations between CHP and CV at events were separately analyzed by linear regressions and ANOVAs.

RESULTS

The force-displacement response of capsules with vehicle injection is similar to that of the naïve rat (Fig. 1B). Yet, the curves for joints with MMP-1 injection are shifted to the right relative to vehicle responses (Fig. 1B), with the yield displacement greater ($p=0.04$) for MMP-1 than vehicle (Fig. 1B). Despite different displacements at yield and nearly a 1.5-fold decrease in stiffness between MMP-1 (1.56±0.87N/mm) and vehicle (2.30±1.28N/mm), stiffness is not different ($p=0.31$).

The microstructural kinematics are different between groups. For vehicle, CV at ligament yield is different ($p<0.03$) from reference (Fig. 2A). However, for MMP-1, collagen fibers do not reorganize until first failure ($p<0.01$) (Fig. 2A). Despite this, the number of AR events increases ($p=0.03$) from the first occurrence to yield after MMP-1 (Fig. 2A). In contrast, the CV of fibers of vehicle capsules is not different between the first occurrence of AR and yield, but differs ($p<0.01$) between yield and first failure (Fig. 2A). MMP-1-injected capsules also experience more events at failure than at yield ($p<0.01$) (Fig. 2A).

Before loading (reference) neither CHP fluorescence ($p=0.84$) nor CV ($p=1.00$) are different between groups. Yet, relationships between CHP and CV differ between groups. The correlation between CHP and CV at reference is significant ($p<0.05$) for all ligaments regardless of group; yet, this relationship is driven by a significant association between CHP and reference CV only with intraarticular MMP-1 ($p=0.02$) and not with vehicle ($p=0.63$) (Fig. 2B). The positive association between CHP and CV with MMP-1 is maintained at both the first occurrence of AR ($p=0.04$) and yield ($p=0.03$) (Fig. 2B).

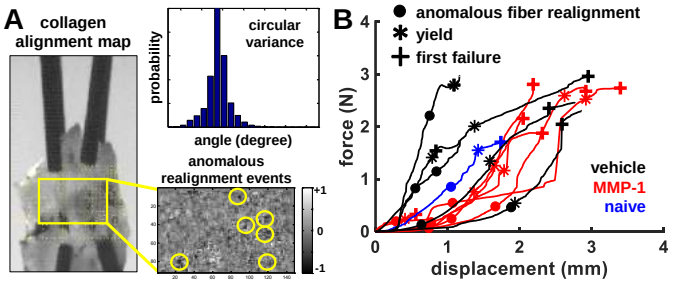

Figure 1: (A) Exemplar image and collagen fiber alignment map at first failure for a vehicle-injected ligament. CV and regions of AR events are computed from the map. (B) Force-displacement responses showing the first occurrence of AR (●), yield (*), and first failure (+). The curves end at ultimate rupture.

DISCUSSION

These findings show that MMP-1, likely via its collagenolytic function [10], alters the biomechanical response and reorganization of the capsular collagen network during its loading (Figs. 1&2). MMP-1 may degrade collagen in several regions of the ligament predisposing it to altered kinematics on the macro- and microscale (Figs. 1&2). That notion is supported by the correlation between degraded and/or partially unwound collagen (CHP) [14] and the spread of collagen fibers (CV) observed for joints in the unloaded state after intraarticular MMP-1 (Fig. 2B). That positive correlation suggests that more damaged collagen fibers correlate to more disorganized fibers. Further, the same correlation at both the first detection of AR and yield (Fig. 2B) supports that the microstructure of the facet capsule is altered by MMP-1 and remains during its loading. A greater displacement at yield for MMP-1 ligaments may indicate laxity in those ligaments [13], which could explain the pain in rats treated with MMP-1 [9]. Ligaments with greater laxity may be more prone to injury during physiologic motions [15,18].

Load mediates the rate of enzymatic breakdown of collagen by protecting strained fibers from degradation [19,20]. Since the capsule's collagen fiber network has varied orientations and undergoes heterogeneous strains with load [21], regions with fibers that are less strained may be preferentially degraded by MMP-1 and could explain the absence of overt structural damage [9]. The occurrence of isolated, yet frequent, AR events that is observed with MMP-1 treatment (Fig. 2A) highlights the possibility that afferents may be more susceptible to activation if they are in regions where the matrix undergoes abnormal kinematics. This study implicates MMP-1 in mediating the structure-function relationships of the capsular ligament and provides a possible mechanism for MMP-1 to induce pain and neuronal dysregulation [9].

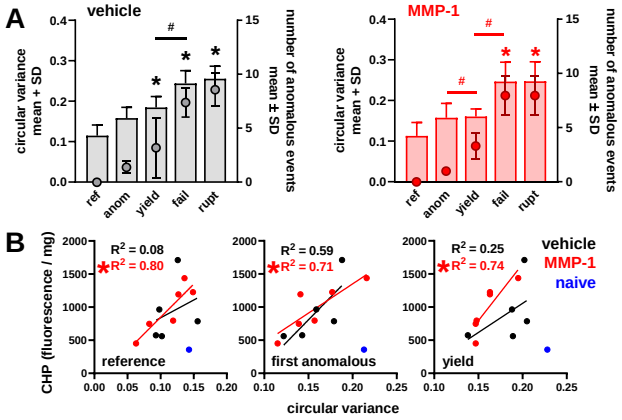

Figure 2: (A) CV (bars; left axis) and number of AR events (points; right axis) at reference (ref), first occurrence of AR (anom), yield, first failure (fail), and ultimate rupture (rupt). CV varies from reference at yield, fail, and rupt with vehicle (*p≤0.03) and at fail and rupt with MMP-1 (*p≤0.01). The pattern of AR events differs between groups (#p≤0.03). (B) CHP and CV are correlated for MMP-1 (*p≤0.04), but not vehicle (p≥0.12). R^2 is goodness-of-fit.

ACKNOWLEDGEMENTS

Funded by NCCIH (AT010326) and Catherine Sharpe Foundation.

REFERENCES

[1] Institute of Medicine, *National Academies Press* 2011 [2] Kallakuri S et al *World J Orthop* 3:10-14, 2012 [3] Sperry M et al *J Biomech Eng* 139:0210031-13, 2017 [4] Manchikanti L et al *BMC Musculoskelet Disord* 5:1-7, 2004 [5] Cohen M et al *J Shoulder Elb Surg* 16:484-90, 2007 [6] Loeser R et al *Arthritis Rheum* 64:1697-707, 2012 [7] Visse R & Nagase H *Circ Res* 92:827-39, 2003 [8] Allen M et al *Sci Rep* 6:35497, 2016 [9] Ita M & Winkelstein B *CSRS Ann Mtg* #40, 2019 [10] Ita M et al *Sci Rep* 10:21965, 2020 [11] Quinn K & Winkelstein B *J Biomed Opt* 14:054010, 2009. [12] Quinn K et al *J Biomech* 43:1870-5, 2010 [13] Quinn K & Winkelstein B *Ann Biomed Eng* 39:2163-73, 2011 [14] Lin A et al *J Ortho Res* 37:431-8, 2019 [15] Quinn K & Winkelstein B *J Biomech* 40:2299-306, 2007 [16] Singh S & Winkelstein B *SB³C* #352, 2020 [17] Ita M & Winkelstein B *J Biomech Eng* 141:0910131-12, 2019 [18] Quinn K et al *Stapp Car Crash J* 51:169-87, 2007 [19] Ruberti J & Hallab N *Biochem Biophys Res Commun* 336:483-9, 2005 [20] Camp R et al *J Am Chem Soc* 133:4073-8, 2011 [21] Ban E et al *J Biomech Eng* 139:0710091-9, 2017.

SB³C2021
Summer Biomechanics, Bioengineering and Biotransport Conference
June 14-18, Virtual

MODELING THE THREE-WAY CHEMO-MECHANICAL FEEDBACK BETWEEN CELLULAR CONTRACTILITY, ACTIN POLYMERIZATION, AND ADHESION TURNOVER IN THE REMODELING OF ENDOTHELIAL JUNCTIONS

Eoin McEvoy (1,2), Tal Sneh (1), Emad Moeendarbary (3), Xingyu Chen (1), Tatyana Svitkina (4), Roger Kamm (3), Vivek B. Shenoy (1)

(1) Center for Engineering Mechanobiology, University of Pennsylvania, Philadelphia, PA, USA

(2) Biomedical Engineering, National University of Ireland Galway, Ireland

(3) Department of Mechanical Engineering, Massachusetts Institute of Technology, Cambridge, MA, USA

(4) Department of Biology, University of Pennsylvania, Philadelphia, PA, USA

INTRODUCTION

The formation and recovery of gaps in the vascular endothelium governs a wide range of physiological and pathological phenomena, from angiogenesis to atherosclerosis and tumor cell extravasation. However, the interplay between the mechanical and signaling processes that drive dynamic behavior in vascular endothelial cells is not well understood. Here, we explore the formation, stability, and failure of endothelial contacts. We propose a model to describe the three-way chemo-mechanical feedback between (i) VE-cadherin bond turnover, (ii) RhoA-mediated actomyosin contractility, and (iii) Rac1-drived actin polymerization, to uncover how endothelial gaps dynamically form and recover. Simulating a 2D monolayer, we resolve the contradictory influence of RhoA and Rac1 signaling on junction stability and demonstrate how a balance and crosstalk between these critical processes is essential in the regulation of homeostatic function.

MODEL DEVELOPMENT

The maintenance of vascular endothelial cell-cell junctions is predominantly governed by VE-cadherin bonding (**Fig 1A**), which exhibit catch-bond behavior at low forces and slip-bond behavior at large forces (1). The dissociation rate of a bond can be described (2) by

$$k_d = \exp\left(\frac{F_b}{F_s} - \phi_s\right) + \exp\left(\phi_c - \frac{F_b}{F_c}\right), \qquad (1)$$

where F_c is the 'catch' force, F_s is the 'slip' force, and ϕ_c and ϕ_s are associated dimensionless catch-slip parameters. The bound cadherin density c_b is then given by $dc_b/dt = (c_{tot} - c_b)k_a - c_b k_d$, where c_{tot} is the total density and the association rate k_a is assumed to be constant. Further, we note a threshold force F_{crit} for unbinding beyond which bonds will rupture. Adherens junctions connect directly to force generating actomyosin networks in the cell cytoplasm which can apply tension to the cadherin bonds and increase their stability. In turn, the forces generated at intercellular junctions trigger a range of biochemical processes (SFK, RhoA) that promote higher cell tension via actomyosin contractility. Our chemo-mechanical feedback model for myosin-dependent force generation ρ (3) is extended here to consider explicit interactions with cell-cell junctions such that

$$\frac{d\rho}{dt} = -k_\rho\left(\varepsilon_{ec} + \beta(\rho - \rho_0) - \sigma_{ec}\alpha_c\left(\frac{c_b}{\gamma_c + c_b}\right)\right), \qquad (2)$$

where ε_{ec} is the cell strain, ρ_0 is a relative myosin motor density in the quiescent state, k_ρ is a kinetic constant, and α_c and β denote chemomechanical coupling parameters relating stress to signaling where γ_c denotes the cadherin concentration for half-strength signaling. The cell stress depends on both active and passive constituents, such that $\sigma_{ec} = \rho + K_{ec}\varepsilon_{ec}$ where K_{ec} is the passive cytoskeletal stiffness. In the event of junction failure, neighboring cells can reconnect as mediated by actin polymerization at the cell periphery (**Fig 1A**). Rac1 activates the WAVE regulatory complex to drive Arp2/3-associated polymerization of branched actin networks (**Fig 1B**). Compressive stress σ_P generated by such polymerization can drive protrusion of the cell membrane. We therefore propose a model to describe the level of branched actin network polymerization P such that

$$\frac{dP}{dt} = -k_P\left(1 - \frac{\sigma_P}{\sigma_{P_0}} - \frac{\rho}{\gamma_\rho + \rho}\right), \qquad (3)$$

where σ_{P_0} is a reference stress induced by actin polymerization. The polymerization-induced stress $\sigma_P = \sigma_{P_0}P$, and k_P is a kinetic constant. The second term describes the antagonistic interactions between RhoA and Rac1 as determined by suppression constant γ_ρ (signaling through ROCK activates Rac1 GAPs, and myosin activation locally prevents recruitment of Rac1 GEFs (4)).

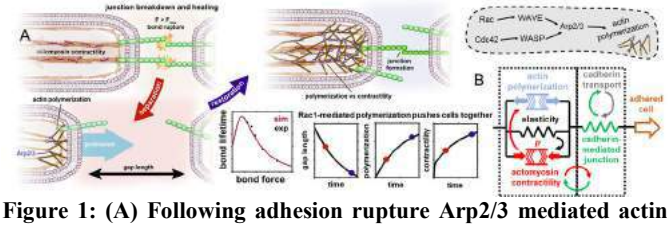

Figure 1: (A) Following adhesion rupture Arp2/3 mediated actin polymerization generates protrusive stress which can ultimately lead to junction restoration; (B) The mechanical model considers stresses induced by polymerization which are opposed by active and passive cell forces. These components couple with cadherin bonds which remodel in response to tension.

This model is implemented in a non-linear 2D spring lattice framework where we discretely consider (i) independent protrusions comprised of active cytoskeletal (polymerizing/contractile) elements, (ii) adherens junction elements that can rupture, remodel, and reform, and (iii) passive membrane/cortical actin elements that connect the protrusions. The system is solved using a Newton-Raphson iterative scheme such that mechanical equilibrium is achieved at every node at every time point in a quasi-static analysis.

RESULTS

Our model predicts that dynamic behavior emerges within a critical feedback strength and polymerization stress range (**Fig 2A**); protrusion facilitates cell-cell contact, enabling spontaneous cadherin bond formation. As the density of bonds increases, the stress-mediated signaling feedback strength also increases which upregulates signaling from SFKs and causes downstream myosin motor phosphorylation and cross-bridge cycling. With higher contractility within a catch regime, bond dissociation is reduced which overall promotes a higher bond density. In conjunction, the polymerization stress is reduced via RhoA-associated Rac1 suppression. However, development of further contractility then drives rapid bond dissociation and rupture, causing cell-cell separation (**Fig 2A**). A loss of adhesion-mediated signaling lowers contractility, in turn facilitating a restoration of the polymerization-induced stress and allowing the cells to reconnect.

Exploring the phase space of α_c and σ_{P_0} facilitates a mapping of the junction state (**Fig 2B**). A high level of Rac1 signaling is predicted to mediate junction weakening, in the form of a closed cell-cell gap but an absence of bond tension and stability. With increasing feedback α_c, the junction strength increases due to higher levels of actomyosin force generation stabilizing cadherin bonds. Impairment of Arp2/3-mediated polymerization is predicted to prevent gap closure, as insufficient stresses are generated to drive development of protrusions. We performed platinum-replica electron microscopy (PREM) on monolayers of cultured HUVECs. This technique permits high resolution imaging of cytoskeletal network organization (5). We observed that the organization of the cytoskeleton was indicative of the junction state at different stages of the rupture/heal cycle. In agreement with model predictions, continuous cohesion of two neighboring cells is characterized by the presence of branched actin networks at the cell-cell junction and actin filament bundles in the junction vicinity (**Fig 2C**). Apparent post-rupture junctions are mainly associated with actin bundles that often form intercellular bridges.

We further cultured a confluent monolayer of HUVECs on collagen gels and studied the evolution of cell-cell junctions (**Fig 2D**). We observed that gaps form at endothelial junctions, grow in size, and heal over time. In agreement, our simulations of monolayer behavior suggest that when a gap forms, separation propagates along the boundary which further increases the gap size (**Fig 2E**). Then, due to the loss in contractility (associated with adhesion rupture and signaling downregulation) and increasing polymerization, the cell membrane protrudes to reestablish contact and bonding. Experimentally, we found that junctions are more frequently disrupted at vertices (multi-cellular junctions) than at borders (bicellular junctions), with quantitative measurements demonstrating that the probability of observing a gap at a vertex is approximately nine-times higher than that at borders (**Fig 2F**). Our model indicates that the forces exerted on cadherin bonds are significantly higher at vertices than at two-cell borders (**Fig 2G**), which can drive bond rupture and junction failure. Gaps were observed to form at the HUVEC vertices approximately once per hour, with ruptures persisting over 30 minutes (**Fig 2H**). Our simulated timescales provide excellent agreement with these data, further supporting the validity of our framework.

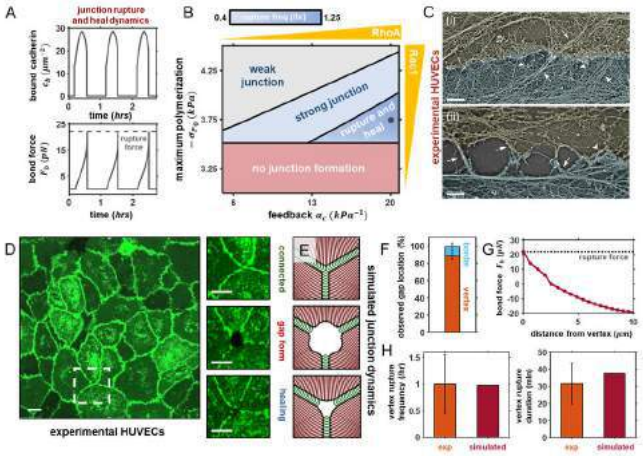

Figure 2: A) Transients in bound cadherin density and individual bond forces during dynamic activity; B) Phase diagram of junction behavior as driven by actin polymerization and adhesion-mediated feedback; C) PREM images showing cytoskeleton organization associated with (i) connected, and (ii) tearing junctions. Arrows and arrowheads mark actin bundles and branch networks, respectively. D) Dynamic behavior of HUVECs expressing VE-cadherin-GFP, showing typical formation and healing of gaps at a multi-cell vertex; E) Gap formation and healing within the simulated monolayer; F) Observed gap locations in the HUVEC monolayer; G) Predicted bond force along the adhered cell edge prior to rupture; H) Rupture frequency at a vertex and duration of rupture.

DISCUSSION

Our chemo-mechanical model provides new insight into how endothelial junctions are regulated by an interplay between mechanical forces and signaling processes, and indicates the mechanisms governing a range of pathophysiological activity. Vascular barrier function can be compromised during inflammation, with thrombin driving endothelial hyper-permeability through RhoA activation (6). Our analysis suggests that this occurs through increased actomyosin contractility driving cadherin bonds into a slip regime and subsequent rupture. Junction dynamics are also critical to cancer progression; tumor cells have been observed to exploit disrupted connectivity at multi-cellular junctions to transmigrate through the endothelium (7). Simulations indicate that gap formation is critically dependent on stress-sensitive adhesion-mediated signaling that upregulates actomyosin contractility, with junction restoration driven by a subsequent recovery in actin polymerization. Overall, our analysis suggests that a critical balance between RhoA and Rac1 expression is required to maintain junction stability and limit endothelial dysfunction. Our proposed model can help guide the development of therapeutics that target the Rho family of GTPases and downstream active mechanical processes.

ACKNOWLEDGEMENTS

NCI Award R01CA232256; NIBIB Awards R01EB017753 and R01EB030876; NSF CEMB Grant CMMI-154857; NSF Grants MRSEC/DMR-1720530 and DMS-1953572; NIH Awards R01 GM 095977 and U01 CA202177; Cancer Research UK Multidisciplinary Award [C57744/A22057];

REFERENCES

(1) Manibog, K. *et al. Nat Commun*. 5, 1–11 (2014)
(2) Novikova, E. *et al. Biophys J.* 105, 1336–1345 (2013)
(3) Shenoy, V.B. *et al. Interface Focus* 6, 20150067 (2016)
(4) MacKay, J.L. *et al. Integr. Biol.* 6, 885–894 (2014).
(5) Svitkina, T.M. *Int. J. Biochem.* Cell Biol. 86, 37–41 (2017)
(6) Amado-Azevedo, J. *et al. PLoS One* 13, e0201231 (2018)
(7) Cao, X. *et al. Biophys. J.* 111, 1541–1552 (2016)

EX-VIVO LOCAL PLAQUE RUPTURE ANALYSIS OF ATHEROSCLEROTIC HUMAN CAROTID ARTERIES THROUGH NANO-INDENTATION, TENSILE TESTING AND DIGITAL IMAGE CORRELATION

Su Guvenir (1), Pablo de Miguel (1,2), Ali C. Akyildiz (1,2)

(1) Department of Biomedical Engineering, Erasmus Medical Center, Rotterdam, the Netherlands

(2) Department of Biomechanical Engineering, Delft University of Technology, Delft, the Netherlands

INTRODUCTION

Atherosclerotic plaque rupture-induced cardiovascular events are the leading cause of mortality and morbidity worldwide [1]. Biomechanically, plaque rupture occurs when the local stresses in the plaque tissue exceeds the local tissue strength. Although plaque tissue is structurally and hence, mechanically highly heterogenous, our current knowledge on the tissue's mechanical (stiffness and failure) properties is limited to average properties, obtained by homogeneity assumption and global deformation measurements in ex-vivo mechanical tests [2]. Yet, local plaque tissue mechanical properties are of paramount importance for accurate rupture risk assessment. In this work, we aimed to capture local mechanical (elastic and failure) properties of carotid plaque tissue. We have performed uniaxial tensile testing on human carotid endarterectomy samples until complete tissue rupture. Then, the local tissue deformation was obtained by using digital image correlation (DIC), and local heterogeneous mechanical characteristics of the tissue by using nano-indentation technique.

METHODS

Local Strength Measurements with Uniaxial Tensile Testing and DIC

Thirty atherosclerotic human carotid artery endarterectomy samples were collected at the Erasmus Medical Center, in Rotterdam. As a preliminary work, three rectangular shape tissue strips, from the common (n=2) and internal (n=1) carotid artery regions, were prepared for the uniaxial tensile testing and DIC. During the tissue preparation, a speckle pattern was applied to the lumen side of the tissues by using a spray paint for the DIC analysis. After a clear speckle pattern was obtained, the tissue strips were tested by using an in-house-built uniaxial tensile testing setup (Fig.1 (A)). The average thickness of the strips was approximately 2 mm. Their width and length (along the circumferential direction of the artery/plaque) sizes were approximately 5 mm and 25 to 30 mm, respectively. Before the tests, the samples were pre-stretched up to 0.05 N. The gauge length was kept approximately 12 mm, and the samples had a length to width ratio of approximately 2.4 after pre-stretching, which falls within the suitable range for the uniaxial testing of soft tissues [3]. Then, preconditioning was performed up to 10% stretch with a speed of 0.05 mm/s for 10 cycles. The tests were performed with the same speed until complete tissue rupture. The initial rupture in this work was defined as the first micro-failure detected on the gauge length-based stress-strain curve (Fig.1 (B)), further confirmed independently by the tensile-testing camera recordings. The engineering stress was calculated from the force measurements and the original cross-sectional area, while the global Green-Lagrange strain was calculated from gauge length measurements. Following the tensile testing, the DIC analysis was performed with an open-source MATLAB based software (Ncorr, version 1.2) for local Green-Lagrange strain measurements.

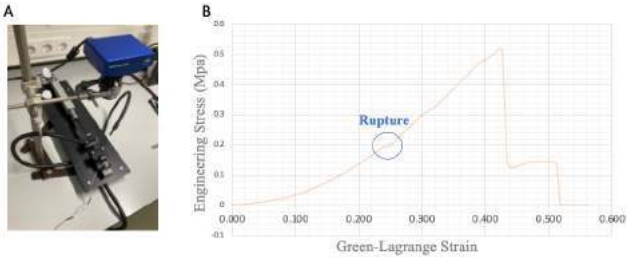

Figure 1: (A) The uniaxial testing setup. (B) Gauge length-based failure detection from the stress-strain curve.

Local Stiffness Measurements with Nano-Indentation

In order to investigate a possible correlation with the local tissue stiffness and the tissue strength, the local mechanical characterization

was performed with a nano-indentation testing. For this purpose, Piuma Nanoindenter (Optics11 Life, the Netherlands) with a 263 micron tip and 0.64 N/m stiff cantilever was used. The ruptured strips were glued to a glass petri-dish from the media side and the petri-dish was filled with a Phosphate-Buffered Saline (PBS) solution (Fig. 2). A total of 10 to 15 measurements were taken from each strip. The testing sites were chosen to be approximately 2 mm apart from each other and the strip edges. The force-indentation displacement curve was fit using a Hertz model to calculate the effective Young's Modulus for each measured location (Fig.2).

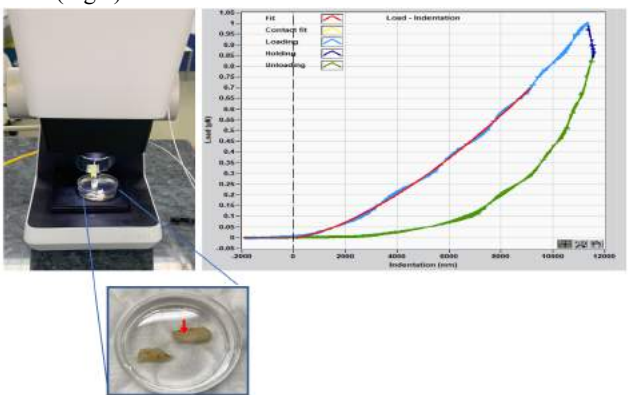

Figure 2: A representative nano-indentation testing, performed near a rupture location indicated by the red arrow. The effective Young's modulus was calculated as 1.21 kPa at this location.

RESULTS

The uniaxial tensile tests of all tissue strips were performed successfully. Speckle patterns were clear and well-captured by the DIC analysis, and local deformation information was obtained. Nano-indentation was successfully performed in total of approximately 40 locations on the three tissue strips, and the Hertz model had a good fit to the load-indentation displacement curves. In total, there were four ruptures in the three plaque strips tested.

By using the gauge length-based analysis, the engineering stress and Green-Lagrange strain at the initial rupture timepoint for the samples were calculated as; 1st strip (at the common carotid): 0.24 MPa and 26%, 2nd strip (at the common carotid): 0.20 MPa and 24%, 3rd strip (at the internal carotid): 0.07MPa and 16%. Then, the DIC based analysis was performed to obtain local deformation measures. The local deformation patterns of Green-Lagrange strain measurements (tensile (E_{yy}) and absolute shear (E_{xy})) are shown in Fig.3. The maximum and mean values obtained for the DIC measurements in the tensile direction are; 1st strip: 84% and 21%, 2nd strip: 59% and 20%, 3rd strip: 53% and 13%.

It was observed that the overall mean values obtained by the DIC analysis were in accordance with the gauge length-based measurements. However, the maximum local measurements obtained by the DIC were much higher than the averaged gauge-length based measurements (65.3% vs 22%). Two of the four rupture sites (1st sample and the 3rd sample, upper left region rupture) were observed at high local tensile strain zones of approximately 84% and 35%. Interestingly, the other two ruptures (2nd sample and 3rd sample, lower right region) were observed at high shear strain regions of approximately 25% and 55%, respectively. The local indentation measures showed a large inter- and intra-sample variation. The stiffness measures obtained for the strips were; 1st strip: 274.8 Pa to 41.8kPa, 2nd strip: 550.9Pa to 53.1kPa, 3rd strip: 968.4Pa to 22.3kPa. The highest stiffness locations of 41.8 kPa, 53.1kPa and 22.3 kPa for the 1st, 2nd and 3rd strips were all observed close to the rupture sites after complete separation.

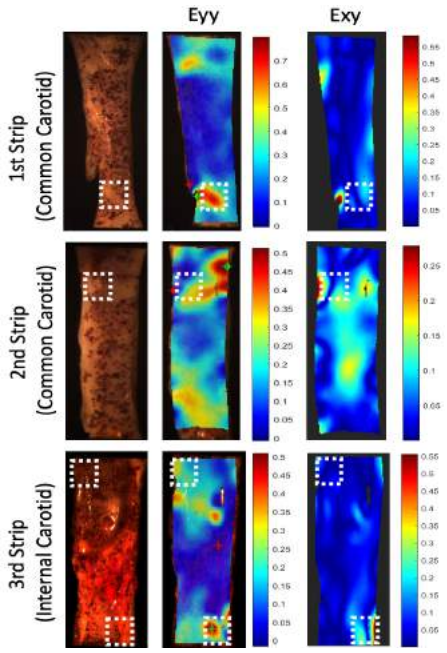

Figure 3: DIC-derived local circumferential Green-Lagrange (E_{yy}) and absolute shear strains (E_{xy}) of the three tissue strips. The rectangular boxes indicate rupture initiation sites.

DISCUSSION

In this work, we have conducted a preliminary research for our new pipeline, which can provide local failure characteristics of highly heterogenous plaque tissue, which is more relevant for real-life plaque rupture than the conventional average ultimate tensile properties obtained by tissue homogeneity assumption. In the developed pipeline, we used uniaxial tensile testing and DIC to obtain local deformation measures at the rupture point, and further, we have used nano-indentation technique to obtain local mechanical properties. First of all, although the test were uniaxial tensile tests, because of the test sample geometries and tissue heterogeneity, DIC measurements showed some high shear strain regions locally, which could not be obtained by traditional, gauge length-derived strain analysis. Furthermore, it was observed that gauge length-derived measurements greatly underestimate tissue rupture strain, due to the inherent homogeneity assumption in the analysis. In addition, DIC measurements demonstrated that the rupture locations were correlated with high tensile and/or shear strain, which implies different failure mechanism due to the tissue's microstructural organization. We plan to address this in the near-future work, by assessing the microstructural (collagen) information with histological examination and correlate that with local mechanical properties. We believe that a possible correlation between the local mechanical and structural tissue properties will provide great insights for the failure mechanisms involved in real-life plaque rupture events.

ACKNOWLEDGEMENTS

This project has received funding from the European Commission's Horizon 2020 research and innovation programme under the Marie Skłodowska-Curie grant agreement # 749283.

REFERENCES

[1] Carr, S et al., *J Vasc Surg*, 23.5:755-766, 1996. [2] Akyildiz A C et al., *J Biomech*, 47.4:773-783, 2014. [3] Mulvihill, J et al., *Biomech Model Mechanobiol.,* 12:975–985, 2013.

A PHYSICS-INFORMED MACHINE LEARNING MODEL FOR THE IDENTIFICATION OF ACTIVE CONTRACTION PROPERTIES IN THE VENTRICULAR MYOCARDIUM

Igor A. P. Nobrega, Wenbin Mao

Department of Mechanical Engineering
University of South Florida
Tampa, FL, USA

INTRODUCTION

Heart diseases are the preeminent cause of death, accounting for over 40% of all human mortality [1]. Advancements in the fields of biomedical engineering, computer science and data mining unraveled bright opportunities to fathom important mechanical properties of soft tissues and their influence over its physiological functions. Early signs of disease or physiological complication can be indicated through the analysis of elastic properties of soft biological tissue [2] as these are intertwined with its internal microstructure [3], which are responsible to govern its macroscopic behavior and mechanical functions.

To better understand the mechanical functions of the heart and support the development of effective treatment and prevention of such heart diseases, it is crucial to define realistic descriptions of myocardium structure with constitutive models. Although several models were developed to represent both passive and active contraction of myocardium tissues, most of them are not desirable; these often require extensive computational resources and time, lessening their usage on clinical applications. Considering the hardship that confines the derivation and application of pure constitutive models, the usage of artificial intelligence and machine learning imposes leading advantages over traditional methods.

Taking this into account, the main objective of this study was to develop a constitutive-based machine learning (ML) method to evaluate and predict the behavior of an active contraction model of the left ventricular myocardium in a cardiac cycle by autonomously selecting the best-fitting material parameters under different clinical conditions.

METHODS

The active and passive reactions of myocardium may be assumed to be coupled as an additive decomposition of the Cauchy stress tensor $\sigma = \sigma_p + \sigma_a$. In this equation, σ_p defines the passive stress component, which characterizes the response of the myocardium when the muscle is inactive. Moreover, σ_a determines the active stress component, which is impelled by the electrical activation of the myocardium tissue [4].

A widely accepted representation of the strain-energy function of the passive myocardium tissue proposed by Holzapfel-Ogden [5] was used as the base model. The key advantage of the selected model is the representation of the fiber distribution along layers on the myocardium wall, considering that the ventricular wall presents a multilayered structure with transmural variation of the direction of its myocytes [5]. The passive strain-energy function is composed of eight material parameters a, b, a_f, a_s, b_f, b_s, a_{fs} and b_{fs}, and is given as follows:

$$\sigma_p = \frac{a}{2b} e^{b(I_1 - 3)} + \sum_{i=f,s} \frac{a_i}{2b_i} \left\{ e^{b_i (I_{4i} - 1)^2} - 1 \right\} + \frac{a_{fs}}{2b_{fs}} \left[e^{b_{fs} I^2_{8fs}} - 1 \right] \quad (1)$$

The active model adopted was proposed by Pezzuto et al. [4]. This model presents benefits over its simplicity, yet effective formulation. By introducing just one additional parameter, γ, the active model takes into account the multiplicative decomposition of the deformation gradient, which preserves the ellipticity of the stress tensor and yields an "active strain" approach [4]. The model is defined by:

$$\sigma_a = (1 - \gamma) \boldsymbol{f}_0 \otimes \boldsymbol{f}_0 + \frac{1}{1-\gamma} (\mathbf{I} - \boldsymbol{f}_0 \otimes \boldsymbol{f}_0) \quad (2)$$

, where $\boldsymbol{f}_0$ denotes the unit vector of fiber axis. The constitutive model was implemented in the open-source Finite Element (FE) solver FEBio [6], and was validated by comparing with the analytical solutions of a solid cube under simple shear and biaxial deformations [4], [5]. In

addition, the mesh independence study was conducted on a truncated ellipsoid geometry (representing an idealized left ventricle) under systolic pressure load (Fig. 1a). We found that 12 layers of elements through the thickness are required for linear elements and 6 layers are required for quadratic elements to reach mesh independence. The idealized and patient-specific geometries are shown in Fig. 1a, representing one of its deformed state, and 1c, respectively; along with a sample fiber orientation illustrated in 1b and 1d. As can be seen, the muscle fiber orientations change with position through the wall: from a positive angle ($\boldsymbol{\alpha_{epi}}$) in the sub-epicardial region to nearly 0◦ in the mid-wall to a negative angle ($\boldsymbol{\alpha_{endo}}$) in the sub-endocardial region. To generate the smooth fiber orientation map, we adopted an rule-based reconstruction algorithm using Poisson interpolation proposed by Wong & Kuhl [7].

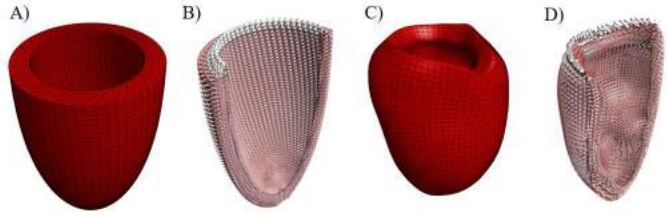

Figure 1: Left ventricular myocardium meshes and fiber orientations: (a) and (b) idealized, and (c) and (d) patient specific.

By conducting a series of FE simulations, we generated an extensive dataset by varying the model's active parameter, **γ**, and fiber's $\boldsymbol{\alpha_{epi}}$ and $\boldsymbol{\alpha_{endo}}$ orientations, while applying pressure load on the endocardium varying from 0 kPa to 16 kPa. Values for endocardium volume, ventricular torsion, wall thickening, longitudinal shortening and radial shortening were computed for each simulation and recorded along with its corresponding **γ**, pressure and fiber orientation. The final dataset consisted of over 4,182,525 sets of datapoints.

Our machine learning model consisted of two main parts: a regressor to find the best combination of $\boldsymbol{\alpha_{epi}}$ and $\boldsymbol{\alpha_{endo}}$ fiber orientations and another regressor to estimate the values for **γ**. Clinically relevant metrics of wall thickening, longitudinal shortening and radial shortening were used as labels for the first regressor, while the values of volume and pressure were used to estimate its corresponding active parameter. To select the best fitting ML model, different methods (Random Forest (RF), Support Vector Machine (SV), Decision Tree (DT), Lasso, Ridge, ElasticNet, SGD, ARD and Bayesian-Ridge regressor models) were used to learn and regress the given dataset and the root-mean-square error (RSME) was used to evaluate their predictions. The best-fitting regressors for each set of input-output were selected and combined into a base model.

RESULTS

For the first part of our ML model, different regressors were tested under different input parameters, the model of "Random Forests Regressor" had the least RSME value, proving to be the most efficient. By the same token, the second part of the ML model was used to predict gamma values for the active contraction under a given PV curve. The "Random Forests Regressor" was again taken as the best-fitting regressor with its RMSE under 10-fold cross validation being 0.0001592.

Furthermore, to test the model's efficiency, we preselected a set of clinical metrics to estimate fiber orientations and a predetermined pressure-volume (PPV) curve in a cardiac cycle to predict a series of γ values (Fig. 2a). The predicted gamma values and fiber orientations were used as the input parameters for the FE model. The model calculated volume waveform was compared with the PPV (Fig. 2b). We can see that the predicted γ value (green line) is highest around peak systole, representing the strongest active contraction. Then it gradually decreases to zero in the end of diastole. The FE calculated endocardium volume waveform matches the predetermined volume very well. As it can be seen, the relative error between these curves is minimal (less than 5%). This process was repeated for different sample PV curves, including one derived from a dataset of heart failure patients. The RMSE was computed for each trial and their average was taken as an indicator of the constitutive-based ML model's efficiency. We found that the averaged RMSE is less than 2.00422 for all testing PV curves.

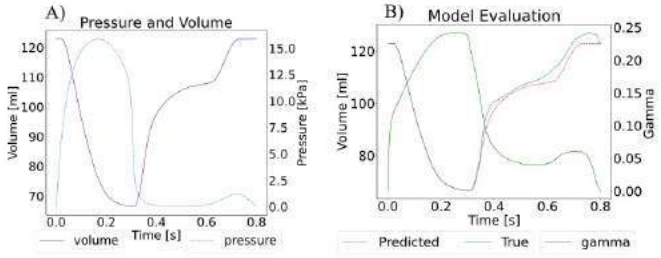

Figure 2: (a) Pressure and volume waveforms of human heart with normal cardiac function (PPV waveform); (b) Model predicted γ values (green line), endocardium volume (solid blue line) and predetermined volume from PPV input (dashed red line).

DISCUSSION

By developing a physics-informed machine learning model, we were able to accurately capture the left ventricular myocardium mechanical response based on a few clinically relevant metrics and prescribed pressure-volume curve. Moreover, our method includes a generation of a sustainable dataset that can be used to train a base ML model capable of selecting a set of epicardium and endocardium fiber orientations and a series of **γ** parameters to represent the contribution of the active contraction. Our model indicates high accuracy for different pressure-volume curves and works well for both idealized and patient-specific geometries of the left ventricle.

The usage of artificial intelligence combined with constitutive-based models allows the autonomously selection of hard to select model parameters. Furthermore, one of the key features that distinguishes machine learning based models is the ability to interactively improve their performance and capabilities when additional data is available. With that in mind, further study will be performed to extend the model to predict detailed deformation of myocardium at different phases in a cardiac cycle.

ACKNOWLEDGEMENTS

This work was supported by the AHA 19CDA34660003 grant.

REFERENCES

[1] Göktepe, S., et al., *Wiley-Blackwells: Great Britain*, p. 1, 2011.
[2] S. Rao., et al., *Clinical Biomechanics*, 69: p. 127-140, 2019.
[3] Gasser, T.C., et al., *J R Soc Interface*, p. 15-35, 2006.
[4] Pezzuto, S., et al., *Eur J Mech A Solids*, 48: p. 83-96, 2014
[5] Holzapfel Gerhard, A., et al., *Philos Trans A Math Phys Eng Sci*, 367(1902): p. 3445-3475 2009.
[6] Maas, S.A., et al., *J. Biomech. Eng.*, 134(1): p. 11005, 2012.
[7] Wong, J., et al., *Computer Methods in Biomechanics and Biomedical Engineering*. 17(11), p.1217-1226, 2014.

ANNULAR HOLDING STRENGTH AND MICROSTRUCTURE IN A DISEASED ANIMAL MODEL: AN *EX VIVO* STUDY

Sanchita S. Bhat (1), Beatrice E. Ncho (2), Md. Tausif Salim (2), Emma Hazenberg (3), Dharani Balakumar (1), Andrew W. Siefert (1) Robert C. Gorman (4), Joseph H. Gorman, III (4), Ajit P. Yoganathan (1,2)

(1) The Wallace H. Coulter Department of Biomedical Engineering
Georgia Institute of Technology
Atlanta, GA, USA

(2) School of Chemical and Biomolecular Engineering
Georgia Institute of Technology
Atlanta, GA, USA

(3) School of Biological Sciences
Georgia Institute of Technology
Atlanta, GA, USA

(4) Gorman Cardiovascular Research Group
Perelman School of Medicine
University of Pennsylvania, Philadelphia, PA, USA

INTRODUCTION

Ischemic Mitral Regurgitation (IMR) is a significant clinical problem that occurs secondary to post-infarction left ventricular remodeling. In this disease, left ventricular enlargement dilates the valve annulus and displaces the papillary muscles, inhibiting the ability of the leaflets to sufficiently close during ventricular contraction and results in valvular regurgitation. [1]. Complications of IMR are recognized to influence the microstructure of the annulus. The extracellular matrix (VECM) within the annulus consists of collagen, elastin and other supplemental proteins that contribute to the structural integrity of tissue [2]. In case of disease, these proteins are shown to degrade or fragment [2,3] potentially altering the biomechanical strength of tissue.

The biomechanical strength of the annular issue is critical to the surgical correction of IMR. In open-heart surgical techniques, sutures are passed through the annular tissue and used to secure prosthetic annuloplasty rings and replacement valves to the annulus [4]. Although usually successful, reports indicate recurrence of moderate to severe regurgitation in approximately one third of treated patients within 12 months of surgery. A recognized cause of recurrent MR is annuloplasty ring dehiscence, which results from sutures pulling through the annular tissue. This deleterious event is estimated to underlie 13-42% of reoperations for failed annuloplasty repairs [5]. Its consequences are often severe, and can include device migration, embolization, endocarditis, patient morbidity, and mortality.

Dehiscence is governed by a balance between the suture holding strength of the annular tissue and the tension required of the suture to hold the device to the annulus. When the suture force magnitude exceeds the local holding strength of the tissue, device dehiscence can occur. In IMR surgery, larger suture forces are required to constrain the large and dilated annulus to a comparably smaller replacement valve or annuloplasty rings. This in the setting of microstructural changes to the valve annulus, elevate the potential risk for dehiscence.

The forces required to pull out these sutures from the annulus vary with circumferential positions around the annulus [5]. These pullout forces are what determine the suture holding strength (HS) of the annulus. Clinical reports [6] and previous studies [5] have indicated dehiscence to be more common along the posterior annulus. As an effort to further investigate the cause of this observation, our group conducted studies using a mitral annulus from healthy ovine subjects [5]. HS and underlying annular microstructure was evaluated at ten positions around the annulus. It was observed that there was sparse collagen content in the posterior annulus, explaining the low holding strength in that region.

Previous studies have been conducted with healthy specimens; however, the relationship of HS and tissue microstructure in a diseased animal model is necessary to understand device failure in case of IMR.

The objective of the study is to develop an improved understanding of suture holding strength and to investigate underlying structural factors that change the biomechanical behavior of the annulus following IMR.

METHODS

IMR Animal Model. The animals used in this work received care in compliance with the protocols approved by the Institutional Animal Care and Use Committee at the University of Pennsylvania in accordance with the guidelines for humane care [7]. Nine ovine subjects received an inferior left ventricular infarction to produce progressive, chronic IMR. This model has been studied extensively and mimics precisely an inferior infarction described in humans [8-11]. Through a sterile left lateral thoracotomy, snares were placed to occlude permanently the proximal second and third obtuse marginal branches of the circumflex coronary artery. After infarction, the thoracotomy was closed and IMR allowed to progress for an 8-week period prior to heart explantation, holding strength, and microstructural assessments.

Assessment of suture holding strength. The mitral valve annulus and leaflets were excised from IMR ovine hearts and mounted to a custom-built testing plate [5]. This custom plate featured a biaxial traverse, allowing freedom for each suture to be pulled perpendicular to the testing arm. Running sutures with Ford interlocking stitch were used along the outer annulus circumference, and the inner circumference (through the basal regions of the leaflets) to secure the annulus on the test plate. Surgically placed sutures at 10 positions corresponding to different locations circumferentially around the annulus (Figure 1A) were pulled using an 858 MiniBionix II (MTS, Eden Prairire, MN) until the suture tore from the tissue. The test plate was fixed to the lower testing arm, in line with a 100 N load cell (Interface, Scottsdale, AZ) on

the upper arm. The tissue was hydrated periodically throughout testing, with 0.75% saline.

HS was defined as the peak recorded force at the time the suture completely ripped out from the tissue. Data was recorded for all 10 suture positions in a clockwise fashion (left trigone (LT), 11, 1, right trigone (RT), 3, 4, 5, 7, 8 and 9 o'clock)

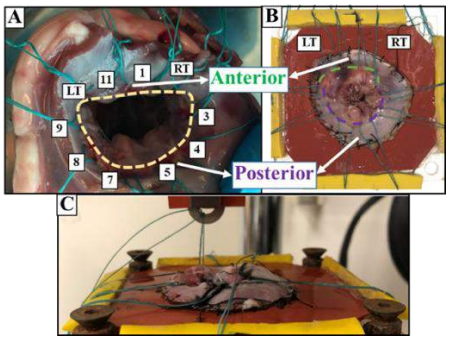

Figure 1: *Ex vivo* mitral annulus excision showing the ten positions around the annulus and setup on custom test plate (A and B). Suture pullout testing shown in C.

Histological analysis of annular microstructure. Following pull out testing, two samples, approximately 3 mm x 3 mm (in the apical-basal and radial directions), were extracted from the LT, 11, 1, RT, 4 and 8 o'clock positions around the annulus. These six representative positions were chosen to represent the anterior, antero-medial, posterior and postero-medial regions. Tissue samples for each position fixed in formalin. Commrcial Van Verhoeff's elastic stain kit (Abcam, Cambridge, UK) was used to visualize, identify and analyze elastin contents in the sample for each position. The stained samples were observed and imaged under a microscope for analysis.

A custom MATLAB (MathWorks, Natick, MA, USA) code was developed to quantify elastin fibers from the microscopic data. The results from the histological analysis were used to compare to both holding strength in the respective positions for each animal.

RESULTS

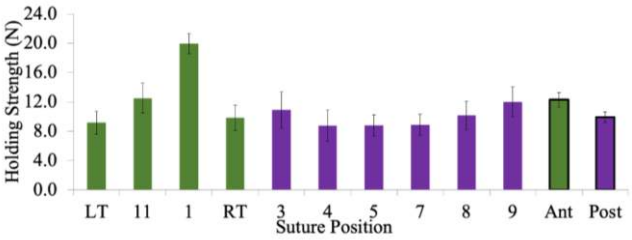

Figure 2: HS in (n=9) diseased subjects at all suture positions. Shown: HS (N). Grouped HS are presented at the right, Left trigone – right trigone, ant (anterior); 3 and 9 o'clock, and 4-8 o'clock, post (posterior).

The average holding strength for all positions in the anterior annulus was observed to be 12.28 N ± 6.02 N, while averaged across all positions along the posterior annulus were 9.94 N ± 5.53 N (Figure 2).

From the elastin histological analysis, the average elastin percentage at the inter-trigonal positions (1 o'clock and 11 o'clock) were observed to be 10% greater than the tested posterior positions (4 o'clock and 8 o'clock). These findings correlate with the lower holding strength observed in the posterior annulus.

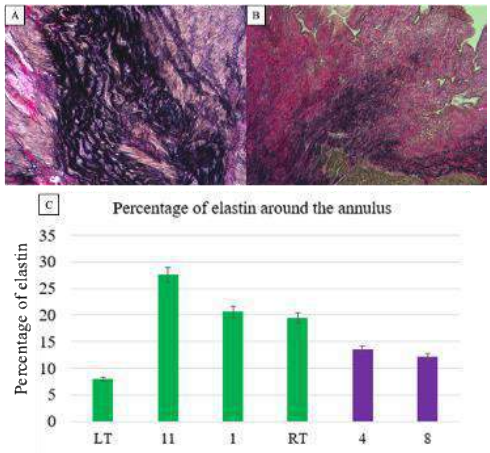

Figure 3: A tissue section taken from the mitral annulus at both the anterior (A) and posterior (B) positions showing elastic fibers (blue/black) embedded in collagen rich (pink) tissue.

DISCUSSION

The posterior annulus exhibited a lower holding strength than the anterior annulus with, the highest holding strength observed at the 11 and 1 o'clock and the lowest at the 3, and 4 o'clock position. The highest holding strength at the inter-trigonal regions is in agreement with prior studies, and could be explained by the higher collagen and elastin content in the anterior annulus [5]. The lowest holding strength positions along the posterior annulus differ from previous investigations in healthy subjects [5]. This could be due to the fact that the infarcted region on the ventricular wall (postero-medial papillary muscle was observed to be closest to the 3, and 4 o'clock region of the annulus. We hypothesize that this ventricular infarct may have contributed to changes in the annular microstructure which led to lower holding strength in that region.

This is the first study to examine the consequences of IMR on both suture holding strength and annular microstructure. Overall, this study aims to investigate the effects of diseased annular tissue on suture holding strength. The current data suggests in that in the diseased tissue region, the holding strength decreases, increasing propensity of suture dehiscence and eventual failure of the device. To understand the basis behind the relationship of cell death due to disease and tissue strength, supplemental histological evidence is being compiled.

ACKNOWLEDGEMENTS

This study was partially supported by the National Heart, Lung and Blood Institute (R01HL147256-01).

REFERENCES

[1] Varma P.K et.al, *Annals of Cardiac Anaesthesia,* 20:432-9, 2017

[2] Hinton, R.B et.al, *Annu Rev Physiol*., 73: 29–46, 2011

[3] Hjortnaes J et.al, *Semin. Thorac Cardiovasc Surg.* 28(4):757-767, 2016

[4] Rabbah, JP et al., et al., *J Biomech Eng*. 135(2): 021007, 2013

[5] Pierce, E.L et.al, *Ann Thorac Surg*, 2:518-526, 2016

[6] Chitwood W.R et.al, J Thorac Surg., 136(2):436-441, 2008

[7] National Research Council (US) Committee for the Update of the Guide for the Care and Use of Laboratory Animals. *Guide for the Care and Use of Laboratory Animals.* 8th ed. 2011.

[8] Gorman JH 3rd, et. al., Ann Thorac Surg. 76(5):1556-63. 2003

[9] Edmunds LH Jr et.al., Cardiac Remodeling and Failure, 2003.

[10]Gorman JH 3rd et. al,.*J Thorac Cardiovasc Surg*.,115:615-22.1998.

[11]Llanera MR, et al, Ann Thorac Surg;57:432-9, 1994.

COMPUTATIONAL MODELING ON TRANSMURAL DISTRIBUTION OF CORONARY PERFUSION AND MYOCARDIAL WORK

Lei Fan[1], Ravi Namani[1], Jenny S. Choy[2], Ghassan S. Kassab[2], Lik Chuan Lee[1],

[1]Department of Mechanical Engineering
Michigan State University
East Lansing, Michigan, USA

[2]California Medical Innovation Institute
San Diego, California, USA

INTRODUCTION

There is a need for intimate balance between the transmural distribution of myocardial demand and supply to maintain normal cardiac function across the heart wall. A mismatch or imbalance between regional myocardial demand and supply is one of the origins of many heart diseases, especially in ischemic heart failure [1]. However, this question is difficult to answer from pure experimental or clinical studies, as in vivo measurements of myocardial blood flow in the deep layer of the heart wall is extremely challenging, and direct measurement of myofiber stress and regional work in the deep layers of the heart wall are currently not amenable to direct observations at the desired resolutions. Besides, there is no model directly considering the interactions among coronary perfusion, cardiac mechanics, and systemic hemodynamics. To address this limitation, a computational framework that couples the systemic circulation consisting of a left ventricular (LV) finite element model (FE) and coronary perfusion in a closed loop manner is developed to investigate the transmural demand (myocardial work)/supply (coronary perfusion) ratio.

METHODS

The computational framework consists of a FE model of the LV and 4 coronary microvascular networks (each network consists 400 vessels) located at different transmural locations across the LV wall (i.e., endocardium, mid-endocardium, mid-epicardium and epicardium) (**Fig. 1a**). The functional relationship between the LV pressure and volume (i.e., $P_{LV} = f(V_{LV}, t)$) is obtained by minimizing a Lagrangian function consisting of myocardial tissue strain energy function and terms associated with the enforcement of constraints on 1) myocardial tissue incompressibility, 2) zero-mean rigid body translation and rotation and 3) cavity volume [2]. The mechanical behavior of the LV is modeled using an active stress formulation, in which the passive and active mechanical behaviors are described by a Fung-type strain energy function and a modified time-varying elastance model, respectively [3]. Coronary flow rate in each vessel of the coronary network is described using a three-element Windkessel model (**Fig. 1b**) consisting of two identical nonlinear resistors and one nonlinear capacitance based on our previous model [4]. Mass conservation is satisfied in the coronary network at each nodal position connecting the vessels, where the number of vessels connected to the node is 3 for a bifurcation and 4 for a trifurcation (**Fig. 1c**). Intramyocardial pressure (IMP), which is the extravascular force applied to the vessel, is prescribed using the local value of the Lagrange multiplier associated with the incompressibility constraint from the FE LV model. We note that the Lagrange multiplier is associated with the hydrostatic pressure of the fluid-like ground matrix in constrained mixture models of the biological tissue, and hence, is assumed here to be the extravascular pressure imposed on the coronary micro-vessels. The FE LV model and coronary arterial network are connected to a lumped parameter representation of the systemic circulation, including the left atrium (LA), proximal peripheral arteries, distal peripheral arteries and peripheral veins each represented by its corresponding electrical analog [4], [5] (**Fig. 1a**). The LA is described by a time-varying elastance model, which relates instantaneous pressure to instantaneous volume.

We first calibrate the model to obtain the waveforms of LV pressure, volume, and strains that are in agreement with those measured in a typical normal human LV or in a large animal under resting conditions. After model calibration, we then vary the parameters from the baseline case to investigate the isolated effects of either the LV's contractility, preload, afterload, or geometry (LV cavity volume and wall thickness) on the LV's chamber pressure, arterial pressure, transmural distribution of IMP, coronary flow, myocardial work and the ratio of myocardial demand and supply.

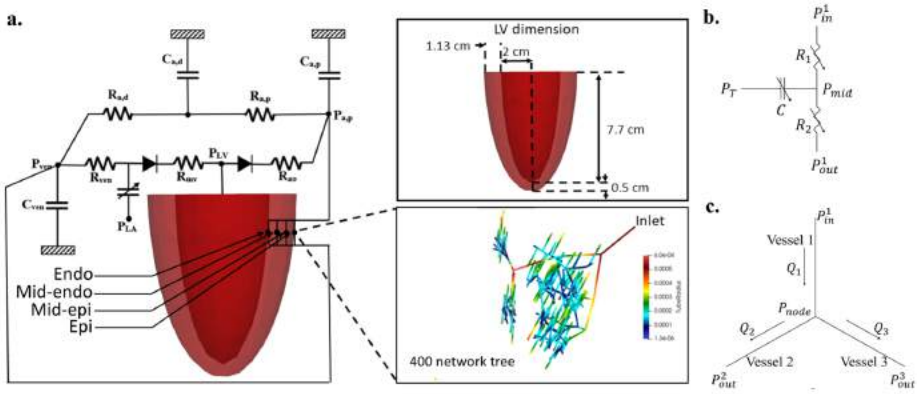

Figure 1a. Schematic of the cardiac-coronary computational framework shows that the LV FE model (with dimension given in the inset) is connected to 4 coronary networks located at different transmural location across the myocardial wall. Each network consists of 400 vessels with different vessel radius (see inset); **b.** Electrical non-linear analog of the segment lumped model; **c.** Single bifurcation three-vessel network.

RESULTS

Waveforms of the pressures in different compartments of the systemic circulation, LV volume, regional IMP, regional coronary flow

rate $q_{cor,i}$, circumferential strain E_{cc}, longitudinal strain E_{ll}, the ratio of the peak IMP and the peak LV pressure, the ratio of the coronary flow normalized with that at the endocardium, regional myocardial work W_f and regional stress-strain curves $S_{ff} - E_{ff}$ at the transmural locations under control condition are presented (**Fig. 2)**. Peak LV pressure, LV's end-diastolic pressure, systolic arterial pressure and diastolic arterial pressure were 131mmHg, 8mmHg, 130mmHg and 73mmHg, respectively (**Fig. 2a)**. Left ventricular ejection fraction, end-diastolic volume, end-systolic volume were 61%, 110ml and 43ml, respectively (**Fig. 2b**). Intramyocardial pressure waveform was highest in the endocardium and decreased transmurally towards the epicardium (**Fig. 2c**). Except in the epicardial and mid-epi regions, coronary flow rate was largely reduced during systole in the inner layers of the myocardium, and was negative at the endocardium (**Fig. 2d**) since the higher IMP during systole in the endocardium impedes most of the flow. Coronary flow rate in the endocardium during systole (t = 0 – 300ms) is dominated by the effects of IMP. At the onset of diastole (t > 300ms), coronary flow rate increased rapidly as IMP fell faster than the reduction rate in arterial pressure (that controls perfusion pressure). In the epicardial and mid-epi regions, coronary flow rate is dominated by the perfusion pressure during systole. Coronary flow rate in the microvascular networks were, however, largely similar in diastole. Peak E_{cc} and E_{ll} were 26% and 21%, respectively, and their waveforms were in agreement with 3D echo measurements from normal humans (**Fig. 2e** and **2f**). From the endocardium to the epicardium, total coronary flow over a cardiac cycle increased while both myocardial work W_f that is the area of regional stress and strain, and IMP decreased transmurally (**Fig. 2g-2j**). The transmural variation of these quantities is approximately linear. Specifically, IMP was approximately 1.1 times of the LV pressure in the endocardium and decreased to around 0 at the epicardium (**Fig. 2g**), which is consistent with experimental measurements. Total coronary flow was largest in the epicardium and approximately 1.7 times of that in the endocardium, which has the smallest total coronary flow (**Fig. 2h**). This result is largely consistent with experimental measurements. Total myocardial work over a cardiac cycle W_f was approximately 1.7 times higher in the endocardium and midwall regions than that in the epicardium, which has the smallest myocardial work (**Fig. 2i**). The larger value of W_f in the endocardial and mid-wall regions is the result of a higher myofiber stress and strain in these regions compared to that in the epicardium (**Fig. 2j**). The myocardial demand and supply balance across the heart wall under normal condition is represented by the ratio of myocardial work and coronary flow. In the parameter study, myocardial work-perfusion mismatch ratio increases with an increase in LV's contractility, preload, wall thickness or cavity volume, with the ratio increasing more towards the endocardium.

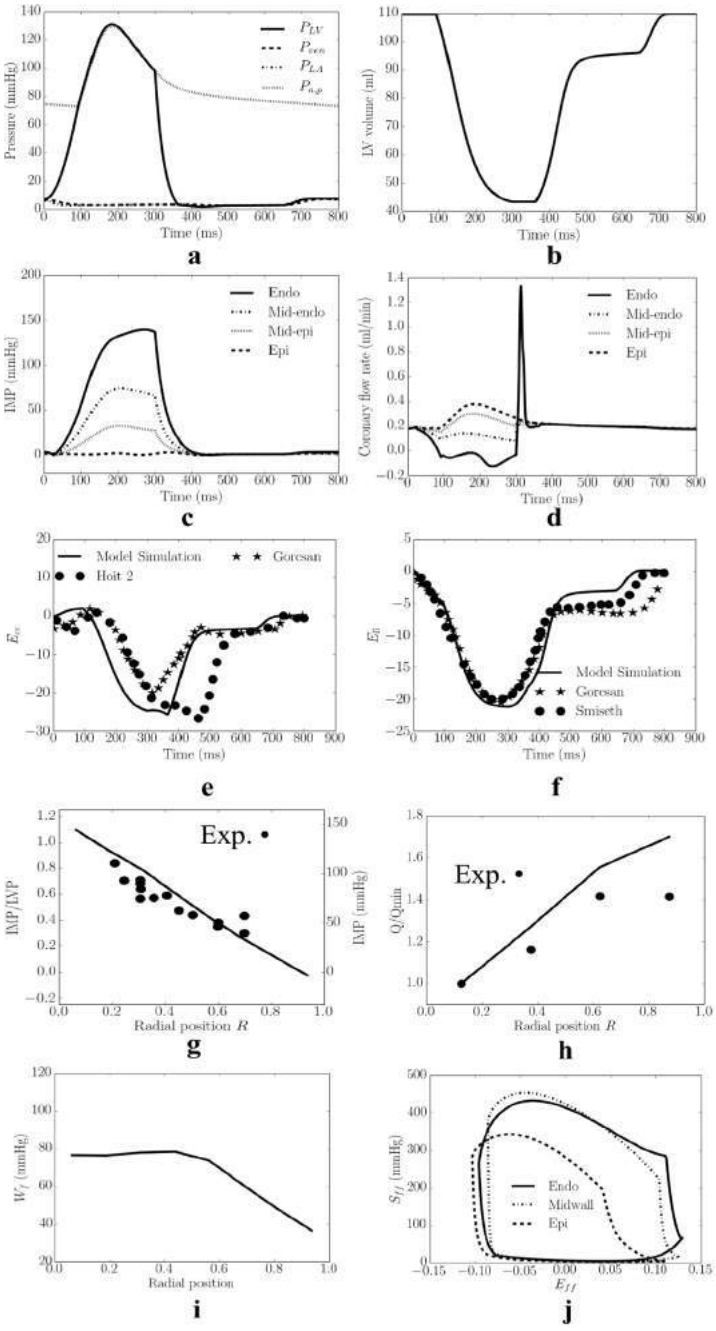

Figure 2a. Pressures; **b.** LV volume; **c.** IMP; **d.** Coronary flow rate; **e.** E_{cc}; **f.** E_{ll} ; E_{cc} and E_{ll} are plotted together with measurements from 3D echocardiography (dots and stars), and were in agreement with clinical measurements . Transmural distribution of **g.** IMP that normalized against LV pressure, is comparable to experimental measurements [6]; **h.** Total coronary flow that is normalized by flow at endocardium, is comparable to the measurements in a canine model under maximal coronary vasodilation [8]; **i.** Work done W_f; **j.** Average $S_{ff} - E_{ff}$ loop at the endocardium, mid-wall and epicardium. • denotes experimental measurements. The radial position R is 0 in the endocardium and 1 in the epicardium.

DISCUSSION

Based on the proposed computational framework, the specific key findings are: **(1)** The model predicted circumferential and longitudinal strains, transmural distribution of IMP and coronary flow under normal condition are able to match the experimental data measured from human and a large animal under resting condition [6]–[8]. **(2)** Transmural distribution of IMP across the LV wall can explain the transmural distribution of passive coronary flow (varying monotonically from endocardium to epicardium) measured experimentally. **(3)** In the parameter study, the model is able to predict the mismatch between myocardial demand and supply, which suggests that endocardium is more vulnerable to ischemia

ACKNOWLEDGEMENTS

This work was supported by NIH grant R01 HL134841.

REFERENCES

[1] Algranati, D et al., *Am. J. Physiol. - Hear. Circ. Physiol.*, 300: 1090-1100, 2011.
[2] Shavik, S. M. et al., *Front. Physiol.*, 11: 2, 2020.
[3] Guccione, J. M. et al., *J. Biomech.*, 28, 1167–1177, 1995.
[4] Fan, L. et al., *Front. Physiol.*, 11: 915, 2020.
[5] Fan, L. et al., *Am. J. Physiol. - Hear. Circ. Physiol.*, (in Press), 2020.
[6] Gorcsan, J. et al., *J. Am. Coll. Cardiol.*, 58: 1401–1413, 2011.
[7] Hoit, B. D. et al., *Circ. Cardiovasc. Imaging*, 4: 179–190, 2011.
[8] Smiseth, O. A. et al., *Eur. Heart J.*, 37: 1196-1207b, 2016.

THE EFFECT OF HEAD IMPACT EXPOSURE IN NCAA DIVISON I FOOTBALL ON CONCUSSION SYMPTOM SEVERITY

J. Seifert (1), A. Shah (2), J. Muench (2), J. Harezlak (3), S. Rowson (4), J.P. Mihalik (5), S. Duma (4), P. Pasquina (6), S.P. Broglio (7), T.W. McAllister (8), M. McCrea (2), B.D. Stemper (1,2)

(1) Biomedical Engineering
Marquette University and
Medical College of Wisconsin
Milwaukee, WI, USA

(2) Department of Neurosurgery
Medical College of Wisconsin
Milwaukee, WI, USA

(3) School of Public Health
Indiana University
Indianapolis, IN, USA

(4) Biomedical Engineering
Virginia Tech
Blacksburg, VA, USA

(5) Matthew Gfeller Sport-Related Traumatic Brain Injury Research Center
University of North Carolina
Chapel Hill, NC, USA

(6) Uniformed Services
University of Health Sciences
Bethesda, MD, USA

(7) Michigan Concussion Center
University of Michigan
Ann Arbor, MI, USA

(8) Department of Psychiatry
Indiana University School of Medicine
Indianapolis, IN, USA

INTRODUCTION

Sport-related concussion results from single or repetitive biomechanical impacts leading to high-rate head rotational accelerations. Incidence of concussion is higher in contact sports than non-contact sports [1]. This is likely attributable to the increased exposure to head impacts that contact sport athletes sustain during routine participation in practices and games. This provides a higher number of opportunities for high magnitude concussive impacts or the possibility of accumulating changes from repetitive head impacts that contribute to decreased concussion tolerance. Head impact exposure (HIE) refers to the accumulation of head impacts and is often quantified as the number and severity of head impacts on a daily, weekly, or season-long basis. Research involving high school and college football athletes indicated that HIE may play a role in incident concussion. For example, the number of head impacts sustained by individual athletes on the concussion date was higher than on other days [2]. Other studies identified more head impacts prior to concussion in injured athletes than matched controls [3]. However, while those studies focused on concussion occurrence, the effect of HIE on concussion severity remains unclear. HIE can be influenced by factors such as the position of an athlete and if the athlete is participating in a game or practice. Positions such as offensive and defensive linemen have been shown to experience more RHI than others [4]. Other studies found that, during competitions, more RHI are logged than in practices [5]. This study focused on the possible correlation of HIE and concussive impact biomechanics, with the severity of acute clinical outcomes. As HIE and concussive acceleration magnitude increases for an athlete, it was hypothesized that concussive symptom severity would increase.

METHODS

During the 2016-2019 NCAA football competition seasons, a total of 39 concussions were sustained by 37 different athletes enrolled in the Head Impact Measurement Core of the NCAA-DoD Grand Alliance Concussion Assessment, Research and Education (CARE) Consortium Advanced Research Core. All athletes were instrumented with the Head Impact Telemetry (HIT) System (Riddell SRS, Riddell, Rosemont, IL), a helmet-mounted accelerometer array for monitoring impact-associated head accelerations, and completed baseline clinical assessments, including the Sport Concussion Assessment Tool 3 (SCAT3) symptom list, which were then repeated at set timepoints after a diagnosed concussion. The SCAT3 symptom severity score is a standardized tool for assessing post-concussion symptom severity in injured athletes. Twenty-two symptoms are scored with a value from zero (none) to six (severe), giving a maximum symptom severity score of 132. SCAT3 symptom severity scores at the twenty-four-hour post-injury time point were analyzed. The concussions were separated into two groups: lower and higher symptom severity. Based on an empirical assessment of the symptom severity scores, two clusters of data were established: 2-31 and 42-87. There were no symptom severity scores between 31 and 42. HIE and concussive impact accelerations were compared between the two symptom severity groups. HIE was evaluated as the number of recorded head impacts (RHI) over the day and week leading up to injury. Concussive impact accelerations were the peak magnitudes of linear and rotational acceleration from the suspected concussive event. The concussive impact was identified using the following steps. If the player was immediately removed from competition, the concussive impact was identified as the highest magnitude impact in the last few seconds of participation. If the player had delayed concussion report, the suspected concussive impact was

identified through post injury interviews and analysis. If available, the identified head impact was compared to video footage of the event.

RESULTS

Results from 39 concussions in 37 athletes showed that the higher symptom group experienced more HIE (median = 17 RHI, 95% CI [10.8, 20.6]) on the day of injury than their lower symptom counterparts (median = 11 RHI, 95% CI [8.2,13.5]) with no significant difference (p = .109). The higher symptom athletes displayed a larger range of HIE on their day of injury compared to the lower symptom athletes (Fig. 1).

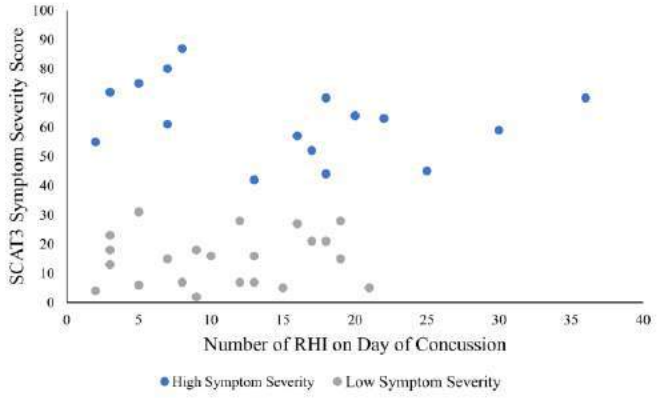

Figure 1. Plot of SCAT3 symptom severity scores versus the number of RHI on day of concussion

Athletes in the higher symptom group did not experience more HIE on the day of injury before the suspected concussive event ($median_{high}$ = 9 RHI, 95% CI [5.2, 12.7], $median_{low}$ = 5 RHI, 95% CI [3.5, 9.0], p = 0.33). For the 31 athletes that also had RHI on the day of injury after their suspected concussive events, the higher and lower symptom groups experienced similar HIE ($median_{high}$= 5 RHI, 95% CI [3.2, 9.9], $median_{low}$ = 5 RHI, 95% CI [3.2, 6.7], p = 0.89). The total number of RHI in the six calendar days prior to injury plus the day of injury ($median_{high}$ = 38 RHI, 95% CI [32.6, 60.8], $median_{low}$ = 40.5 RHI, 95% CI [29.3, 59.9], p = 0.79), and the average ($median_{high}$= 12.9, 95% CI [10.3, 16.5], $median_{low}$ = 11.3, 95% CI [7, 16], p = 0.22) and median ($median_{high}$= 7.5, 95% CI [5.6, 15.7], $median_{low}$ = 11.3, 95% CI [8.6, 16.5], p = 0.2) rates of RHI per session showed no significant difference between the higher and lower symptom groups. Athletes in the higher symptom severity group experienced a longer median symptom resolution time (SRT), $median_{high}$= 9 days (95% CI [7.4, 19.25]) and $median_{low}$ = 6 days (95% CI [5.4, 8.4]), and a longer median time to return to play (RTP), $median_{high}$= 14 days (95% CI [8, 48.6]) and $median_{low}$ = 12 days (95% CI [10.8, 19.2]). There was no apparent correlation between HIE on day of injury and SRT (r=0.168), nor was there a correlation between HIE on day of injury and RTP (r=-0.15). Magnitudes of the concussive linear and rotational accelerations did not show significant variance between the higher and lower symptom groups. Skill players (QB, WR, TE, RB, DB)s, who accounted for 49% of the total population, made up 59% of the concussed players in the lower group, while only accounting for 35% of concussed players in the higher symptom severity group. Skill players, on average, experienced less RHI on the day of injury than other position groups. Competition versus practice environments made no apparent effect in concussion symptom severity; 29% of the concussions in the higher group and 27% of concussions in the lower group occurred during a competition, with the rest of the concussions occurring during a practice. Players concussed during a competition experienced similar HIE (Median = 17 RHI, 95% CI [10.6, 19.2]) to those concussed during practice (Median = 11 RHI, 95% CI [8.9, 15.5]).

DISCUSSION

Head impact exposure was hypothesized to have an influence in the severity of concussion symptoms. The findings of this analysis did not reflect the hypothesized trend. Despite the higher symptom severity group displaying higher median HIE on the day of injury, there was no significant difference between the two populations. Past work found that players who experienced a concussion had more RHI on the day of injury compared to the other practices and competitions where no injury was sustained [2]. Those findings can help guide future work, as the difference in HIE between sessions in which a concussion occurred and sessions in which the athlete left healthy might give insight into the causes of a higher symptom severity score. The lack of significant difference in concussive acceleration magnitudes between the higher and lower groups supports past findings showing their insignificant role in symptom resolution time and time to return to play [6]. This analysis showed a possible correlation between position group and severity of concussion symptoms an athlete may experience. RHI each position group experiences may be the explanation for this trend as skill players are expected to experience less RHI throughout a season based on their roles within a football team [4]. The environment in which a concussion occurred, competition versus practice, showed to have no effect on the symptom severity. This is a surprising trend as athletes concussed during a game had higher median HIE in this analysis, a finding consistent with past studies [5]. As was previously mentioned, the more RHI a player experiences on their day of injury, the higher their respective symptom severity score is expected to be. However, Rowson et al. suggested that individual tolerance plays a large factor in the onset and severity of a concussion [7]. An athlete can have unremarkable HIE and suspected concussive acceleration magnitudes compared to the entire population. However, for the specific athlete the magnitudes they experienced were severe compared to past exposures. Individual tolerance was not explored in this analysis but could possibly explain why the environment does not have an effect, despite more RHI on competition days. More work must be done to quantify the long-term head impact exposure a player experiences throughout a season, and its subsequent role in concussion severity.

ACKNOWLEDGEMENTS

This publication was made possible, in part, with support from the Grand Alliance Concussion Assessment, Research, and Education (CARE) Consortium, funded, in part by the National Collegiate Athletic Association (NCAA) and the Department of Defense (DOD). The U.S. Army Medical Research Acquisition Activity, 820 Chandler Street, Fort Detrick MD 21702-5014 is the awarding and administering acquisition office. This work was supported by the Office of the Assistant Secretary of Defense for Health Affairs, through the Combat Casualty Care Research Program, endorsed by the Department of Defense, through the Joint Program Committee 6/ Combat Casualty Care Research Program – Psychological Health and Traumatic Brain Injury Program under Award No. W81XWH1420151. Opinions, interpretations, conclusions and recommendations are those of the author and are not necessarily endorsed by the Department of Defense.

REFERENCES

[1] Zuckerman et al. *Am J Sports Med* 2015 43(11): 2654-2662.
[2] Broglio, S. P. et al., *J. Neurotrauma*, 34(19): 2675–83, 2017.
[3] Stemper, B. D. et al., *Ann. Biomed. Eng.*, 47(10): 2057–72, 2019.
[4] Crisco J. J. et al., *J. Biomech.*, 44(15): 2673–78, 2011.
[5] Stemper B. D. et al., *Ann. Biomed. Eng.*, 47(10): 2073–85, 2019.
[6] Mihalik J. P. et al., *Ann. Biomed. Eng.*, 48(11): 2555–65, 2020.
[7] Rowson S. et al., *J. Neurotrauma*, 35(4): 681–90, 2018.

FATIGUE- INDUCED DAMAGE ACCRETION OF THE ELBOW AMCL DUE TO REPETITIVE VALGUS CYCLING

David B. Jordan (1); Alexander Kharlamov (2); Patrick J. Schimoler (1,2); Patrick J. DeMeo (2); Mark Carl Miller (1,2)

(1) Mechanical Engineering and Materials Science
University of Pittsburgh
Pittsburgh, PA, USA

(2) Allegheny General Hospital
Pittsburgh, PA, USA

INTRODUCTION

Baseball pitching is an action that generates high magnitudes of rotation and torque at the elbow[1]. The repeated application of high magnitude loads can degrade the mechanical strength of the ligaments at the elbow over time and eventually lead to failure by fatigue.

Failure by fatigue has been documented as one of the primary failure mechanisms of ligaments[2]. One such ligament of the elbow is the anterior bundle of the ulnar collateral ligament (AMCL), which has been shown to be the primary support structure of the valgus motion commonly executed during a baseball pitch[3]. Because the AMCL is in a class of tissue commonly susceptible to fatigue failure and is the primary supporter for high-level loading experienced in baseball pitching, its study is needed.

Fatigue failure is a phenomenon that has been studied for a variety of ligaments and tendons in both animal and human specimens. In studies involving cyclic repetition of the Achilles tendon, it was shown how the stiffness of the tissue progressively degrades[4]. In a study involving repetitive cycling of the ACL in simulated jumping motions, it was shown that the ligament can fail at progressively lower loads for larger number of repetitions[5]. However, these fatigue results are often presented for ranges of loading that may fall out of the observational interests of additional studies.

Critical to defining the fatigue characteristics of a material are the fatigue life and fatigue damage evolution behavior. The fatigue life defines how many repetitions under a given load will fail a particular material and the damage evolution defines how this failure is approached. This study seeks to identify both of these nonlinear characteristics for the AMCL in a non-dimensional formulation for the enhanced applicability to a general baseball pitching scenario, based on the maximum valgus pitching-induced stress/stretch of the AMCL.

METHODS

Twenty-two paired cadaveric elbow specimens were used for testing. All specimens were prepared with the removal of all soft tissue surrounding the UCL, leaving only the distal humerus, proximal ulna and UCL. The transverse and posterior bundles of the UCL complex were then transected, leaving the AMCL as the only connecting tissue between the two bones. The ulna and humerus were set into PVC holsters and secured with polyester resin and steel screws. Black optical markers were placed along the length of the AMCL in three distinct columns of equal spacing for the purpose of camera-assisted measurement of deformation.

Two stages of testing were used to understand the fatigue behavior of the AMCL. The first stage was the elastic elongation and failure testing. The second stage was the fatigue failure testing.

In the elastic testing stage, eleven specimens were secured within a materials testing (MTS) machine using a custom fixture that allows for flexion at angles of 0°–120°. The specimens were elongated to prescribed displacements and MATLAB was used to record measurements of force and displacement. Two cameras were used to record the motion. The specimens were then tested to failure at 90°.

In the fatigue testing, eleven contralateral specimens were secured within a custom fatigue testing device. The device allowed the torque-controlled cycling of the specimens in valgus rotation, with the humerus stationary and the ulna/radius in rotation. The magnitude of the torque applied to each specimen M_f (Equation 1), was a proportion, C, of the product of the respective elongation failure load F_f and the capitellum-to-ligament length L_{cap}, measured with calipers.

$$M_f = F_f L_{cap} C \quad (1)$$

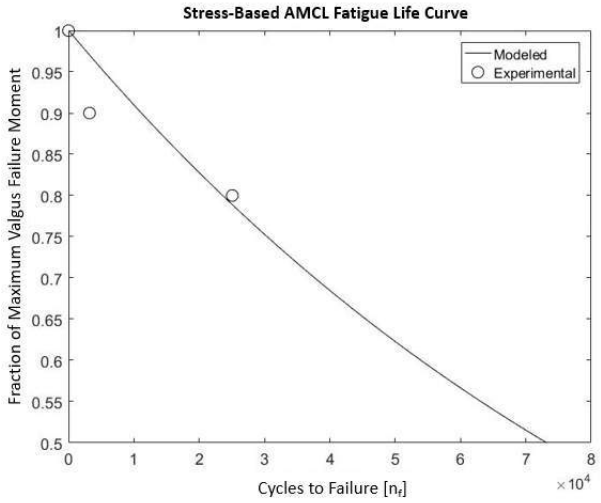

Figure 1: Stress-Based Non-Dimensional AMCL Fatigue Life Curve

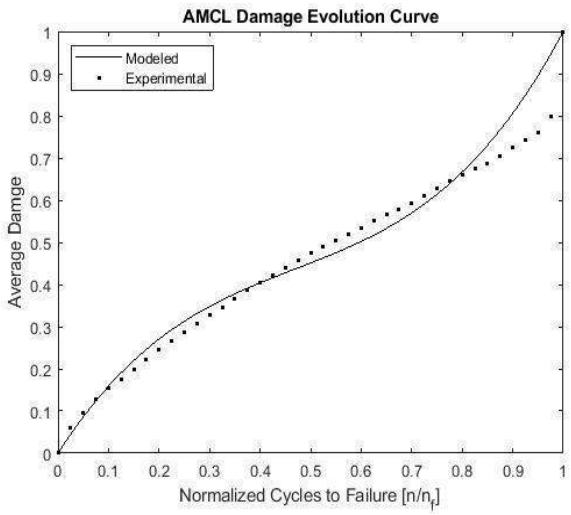

Figure 2: Non-Dimensional Nonlinear AMCL Damage Evolution Curve

Five and six specimens, with magnitudes of C = 0.9 and C = 0.8, were cycled at repeated intervals of 500 valgus cycles until failure was achieved. 500 cycles were chosen to provide enough time for recordings. Saline was manually applied at regular intervals. MATLAB recordings of angular position, torque and cycle number were logged.

RESULTS

For the elongation tests, the average tensile failure load of the AMCL was 595.25 N ± 201.93 N. Using Equation (1), this produced an average value for the theoretical one cycle valgus failure moment of 25.3 Nm ± 8.77 Nm.

For the valgus fatigue experiment, the specimens tested with C = 0.9 and C = 0.8 had an average cycles to failure magnitude of 3211 ± 4721.33 cycles and 25063 ± 30487.58 cycles, respectively.

Two non-dimensional fatigue life curves were generated using the results from the fatigue life test. These were a stress-based curve (Figure 1), where the ordinate gives the respective fraction of the theoretical valgus failure moment M_f. A stretch-based curve was also formulated, where the ordinate is given by the fraction of the experimentally measured average valgus failure stretch. Both data sets were fit with an exponential decay model (Equation 2), where β, γ, and r are constants and n_f is the cycles to failure estimate.

$$S(n) = \beta e^{-\frac{\gamma}{r}n_f} \tag{2}$$

The nonlinear damage evolution curve (Figure 2) was formulated by fitting a cubic model (Equation 3) for the data set representing the average amount of damage D, taken as the relative increase in the maximum angular position, per ratio of current cycles completed n, to total cycle failure life n_f. In Equation (3), A, B, C and E were undetermined constants determined through nonlinear MATLAB regression.

$$D\left(\frac{n}{n_f}\right) = \begin{cases} 0 & \frac{n}{n_f} = 0 \\ A\left(\frac{n}{n_f}\right)^3 + B\left(\frac{n}{n_f}\right)^2 + C\left(\frac{n}{n_f}\right) + E & 0 < \frac{n}{n_f} < 1 \\ 1 & \frac{n}{n_f} = 1 \end{cases} \tag{3}$$

DISCUSSION

The expected trend of increasing cycle life with decreasing valgus torque magnitude was reflected in the results. The high degree of variation in the results can be explained by the complex nature of biological materials, where specimens displayed differing mechanical properties, such as the tensile failure load; and differing geometric qualities, such as the width and thickness.

As expected, the damage accretion curve was nonlinear. As the AMCL is the primary resistor to valgus motion, this curve represents the gradual decrease in the ability of the AMCL to resist the opening of the elbow joint when performing a valgus motion. In the constitutive modeling of the damage behavior of materials[6], this curve describes how the damage variable D, evolves and softens the elastic stress response of the AMCL $\boldsymbol{\sigma_e}$, throughout cycling (Equation 4).

$$\boldsymbol{\sigma} = (1 - D)\boldsymbol{\sigma_e} \tag{4}$$

The non-dimensional formulation of both curves was critical to circumvent the variable characteristics of pitcher-specific pitching properties, such as the magnitude of torque at the elbow. For the same pitch type, different pitchers can generate different torque magnitudes at the elbow and have different resulting fatigue life properties. For any multiple of pitcher-specific torque magnitude, a fatigue life estimate can be made, which then scales the abscissa of the damage evolution curve, providing an estimate of damage for any number of pitches performed.

These estimates of fatigue life and incurred damage, in conjunction with further experimental and computational study, can contribute to the efforts of predicting and mitigating the onset of AMCL fatigue failure in the baseball pitching athlete.

REFERENCES

[1]Werner, S et al., *J Orthop Sports Phys Ther*, 17:274-278, 1993.
[2]Fleisig, G et al., Med Sci Sports Exerc, 33:1803-1810, 2001.
[3]Eygeendaal, G et al., *J Shoulder Elbow Surg*, 8: 612-616, 1999.
[4]Wren, T et al., *Ann Biomed Eng*, 31:710-717, 2003.
[5]Lipps, D et al., *Am J Sports Med*, 41:1058-1066, 2013.
[6]Li, W et al., *J Med Biol Eng*, 36:285-307, 2016.

IN AIRWAY EPITHELIAL CELLS, UNJAMMING TRANSITION INVOLVES BASAL CELL ELONGATION AND STRESS FIBER ACCUMULATION

Thien-Khoi N. Phung (1), Jennifer A. Mitchel (1), Michael J. O'Sullivan (1), Jin-Ah Park (1)

(1) Department of Environmental Health
Harvard T.H. Chan School of Public Health
Boston, MA, USA

INTRODUCTION

The airway epithelium is the first line of defense for external insults such as environmental pollutants or viral infections. Exposure of the airway to these insults causes epithelial injury disrupting the critical barrier integrity that is required to maintain lung homeostasis. After injury, restoration of the disrupted epithelium is initiated by wound healing which requires epithelial cell migration. Migration is traditionally thought to require the epithelial-to-mesenchymal transition (EMT) or partial EMT (pEMT). However, recent work in our lab has revealed a potential alternative mechanism for cell migration, the unjamming transition (UJT) [1]. Unlike in pEMT, during UJT, epithelial markers, cell-cell junctions, and barrier integrity remain intact, while cells become elongated, align into cooperative packs, and migrate collectively [1,2]. UJT has been implicated in various physiological and pathological processes, including airway branching morphogenesis [3,4,13]. However, the role and regulation of UJT in airway epithelial repair and wound healing remain unknown.

Our data indicate that UJT in airway epithelial cells is induced by pathological stimuli linked to lung disease including SO_2 exposure, viral infection, radiation, and mechanical stress. Human bronchial epithelial (HBE) cells grown in air-liquid interface (ALI) culture recapitulate well-differentiated, pseudostratified airway epithelium. Our studies using this system have identified a hallmark of UJT— that cells located at the apical surface elongate and align into cooperative packs [2,4]. However, changes to undifferentiated progenitor (basal) cells located at the basal side have not been studied. Uncovering the role of basal cells may lead to insight into the regulation of UJT. To identify a causal relationship between basal cells and the UJT, we analyzed static images of the mechanically stressed HBE cells— specifically changes to basal cell morphology and the stress fibers within them.

METHODS

Cell Culture

Primary HBE cells isolated from donors with no known lung disease were cultured in transwells first in submerged condition for 4-6 days followed by 14-17 days in ALI in a defined, serum-free media [5]. The cells formed a well-differentiated, pseudostratified epithelium recapitulating the cell architecture and populations of intact human airway. Further details of cell culture are provided in [2].

To induce UJT, cells were exposed to mechanical stress in the form of an apical-to-basal pressure differential of 30 cm H_2O for 3 hours [1]. At 24, 48, and 72 hours after mechanical stress-induced UJT, cells were fixed and stained for F-actin. Two treatment and two control wells were used for each time point. In this study, we examine the cells at a time course across 72 hours because apical cell hallmarks of UJT have been shown to continue evolving over the course of 72 hours [2].

Image Analysis

Five randomly selected fields of view per well were imaged using Zen Blue 2.0 software on a Zeiss Axio Observer Z1 using an apotome module. Across the z-stack from apical to basal-substrate plane, maximum intensity projections were generated at different heights to visualize the apical cell boundaries, basal cell boundaries, and stress fibers (Fig. 1). Cell boundaries were segmented using marker-controlled watershed segmentation in MATLAB. Cell density was quantified as the number of cells per the total cell area. Cell aspect ratio was quantified as the long axis length divided by the short axis from a best fit ellipse to the cell boundary. Stress fibers were segmented using a combination of a tracing algorithm developed by [6] and a fiber reconstruction algorithm developed by [7]. Metrics were quantified and averaged over each field of view. A one-way ANOVA with Bonferroni post hoc test was performed for each metric.

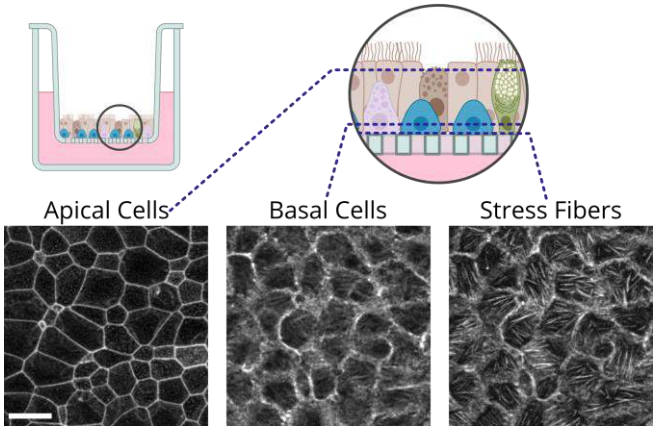

Figure 1: F-actin-stained apical cells, basal cells, and stress fibers were imaged from well-differentiated, pseudostratified human bronchial epithelial cells grown in air-liquid interface culture. Scale bar is 20 µm.

RESULTS

After mechanical stress-induced UJT, apical cells elongated and aligned into cooperative packs similar to our previously published results [2]. The basal cell boundaries were imaged at about 15 µm below the imaging plane of the apical cell boundaries. The basal cell areas increased significantly leading to a decrease in cell density in the field of view (Fig. 2A). The basal cells also significantly elongated as measured by an increase in aspect ratio (Fig. 2B). At the cell-substrate interface about 2 µm below the imaging plane of the basal cells, stress fibers were imaged. Segmented stress fiber lengths significantly increased (Fig. 2C). Total segmented stress fiber length also increased with UJT indicating the accumulation of stress fibers. The increase in basal cell aspect ratio was correlated to stress fiber elongation, $R^2 = 0.81$ (Fig. 2D).

DISCUSSION

In well-differentiated, pseudostratified airway epithelium, apical cell shape changes are a measurable, static hallmarks of UJT [1,2,4]. For the first time, we looked at changes to the basal cells in this layered epithelial system. Basal cells are vital progenitor cells in the human airway epithelium giving rise to and replenishing the specialized differentiated populations including ciliated, goblet, and tuft cells [8-10]. Changes to basal cells have been implicated in pathogenesis of respiratory diseases [11]. From our *in vitro* culture system, mechanical stress-induced UJT decreased the basal cell density and elongated the cell shapes (Fig. 2A and 2B). These data suggest the role of basal cell shape in the UJT.

In monolayer cell culture, cell traction forces have been shown to be regulated by remodeling of stress fibers [12]. Specifically, stress fibers accumulated and aligned in the cells when the monolayer is unjammed. However, the biophysical forces driving migration of the cells in pseudostratified epithelia are not well understood. To determine potential role of stress fibers for UJT in well-differentiated, pseudostratified airway epithelium in ALI culture, we induced UJT and measured accumulation and elongation of stress fibers up to 72 hours after mechanical stress (Fig. 2C). The stress fiber elongation was highly correlated with elongation of the basal cells (Fig. 2D). While it is currently not feasible to measure traction forces in ALI culture, the presence of stress fiber remodeling strongly suggests that basal cells may play a biophysical role in the collective cell migration and apical cell changes observed in the UJT of pseudostratified epithelia. Additionally, basal cells may be an important regulator of the unjamming response to pathological stimuli.

In this study, we presented novel findings demonstrating a positive correlation between basal cell shape elongation and their stress fiber formation in well-differentiated airway epithelium during UJT. Although our results were limited to *in vitro* ALI culture, our data suggest further investigation of the biophysical role of basal cells in regulating collective cell migration seen during epithelial unjamming.

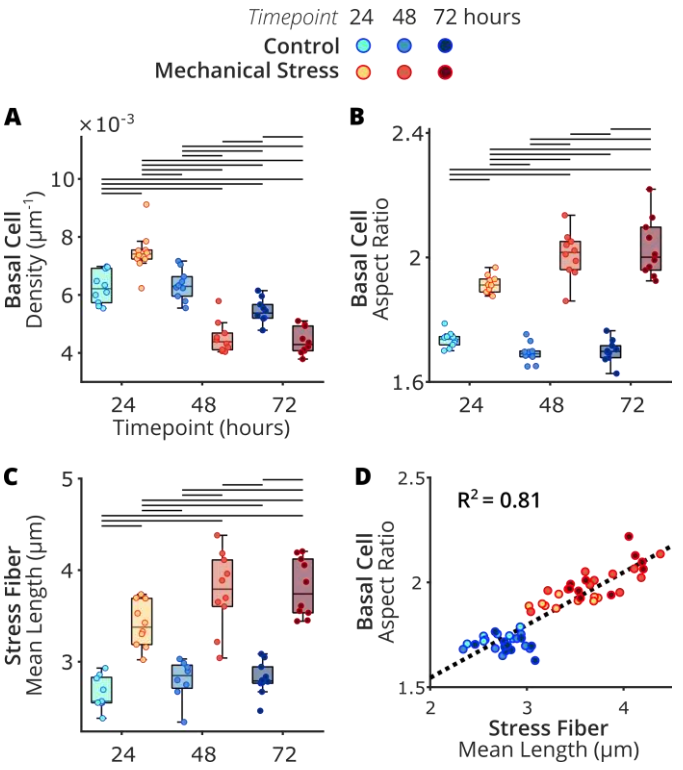

Figure 2: After mechanical stress, (A) basal cell density decreased, (B) cell shapes elongated, and (C) stress fibers elongated. One-way ANOVA with multiple comparisons with significance $p<0.05$. (D) Basal cell elongation was correlated with stress fiber lengthening.

ACKNOWLEDGEMENTS

This work was funded by NIH R01HL148152, T32HL007118, P30ES000002, and the Parker B. Francis Foundation. Part of Fig. 1 was created with BioRender.com.

REFERENCES

[1] Park, JA et al., *Nat Mater*, 14:1040-8, 2015.
[2] Mitchel, JA et al., *Nat Commun*, 11:5053, 2020.
[3] Spurlin, JW et al., *Development*, 146, 2019.
[4] O'Sullivan, MJ et al., *Front Cell Dev Biol*, 8:21, 2020.
[5] Park, JA et al. *J Biol Chem*, 285:29817-25, 2010.
[6] Rogge, H et al. *J Microsc.* 268:129-40, 2017.
[7] Zhang, Z et al. *BMC Bioinformatics*, 18:268, 2017.
[8] Rock, JR et al. *PNAS*, 106(31):12771-5, 2009.
[9] Montoro, DT et al. *Nature*, 560:319-24, 2018.
[10] Walters, MS et al. *Respir Res*, 14:135, 2013.
[11] Rock, JR et al. *Dis Models Mech*, 3:545-56, 2010.
[12] Saraswathibhatla, A et al. *Phys Rev X*, 10:011016, 2020.
[13] Atia, L et al. *Nat Phys*, 14:613-20, 2018.

LOCAL TISSUE HETEROGENEITY SURROUNDING NEURONS MAY MODULATE THEIR RESPONSES VIA ALTERED AXONAL STRAIN FIELDS

Jill M. Middendorf (1), Meagan E. Ita (2), Beth A. Winkelstein (2), Victor H. Barocas (1)

(1) Department of Biomedical Engineering
University of Minnesota – Minneapolis
Minneapolis, MN, USA

(2) Department of Bioengineering
University of Pennsylvania
Philadelphia, PA, USA

INTRODUCTION

Low back pain may be caused by loading innervated fibrous soft tissues such as the facet capsular ligament (FCL)[1]. Specifically, when axons in these collagenous tissues are stretched past a strain threshold the axon will increase expression of nociceptive signaling molecules[2]. However, the relationship between tissue scale loading, collagen network properties, and expression of signaling molecules remains only partially defined.

Recent in vitro experiments have identified how tissue scale loading affects axonal expression of nociceptive signaling molecules[2,3]. Specifically, co-culture experiments with fibroblasts and dorsal root ganglia in stretched collagen gels have shown that axons increase their expression of substance P when accompanied by low concentrations of fibroblasts relative to fibroblast-free cultures. In contrast, high fibroblast concentrations induce little to no increase in axonal expression of substance P compared to fibroblast-free cultures. Although the specific mechanisms responsible for these differences in expression are unknown, fibroblast forces near axons may cause collagen network heterogeneity[4] thus increasing or decreasing axonal strain.

Since axonal strain is difficult to measure experimentally, a discrete fiber network model has been previously created to determine relationships between collagen fiber density and orientation and axonal strain fields[5]. Therefore, our goal was to determine how collagen network heterogeneity surrounding axons can change the axon strain fields using a discrete fiber network model.

METHODS

To represent the various types of collagen networks that could surround an axon, 3 distinct types of Delaunay networks were created: homogeneous networks, heterogeneous networks with a dense center, and heterogeneous networks with a sparse center. The fiber orientation in all networks was isotropic. Homogeneous networks were created with 9 different global collagen volume fractions that ranged from 0.002 to 0.02. The lowest collagen volume fraction was chosen to match the initial collagen concentration found in a 2mg/ml collagen gel[3], while higher collagen volume fractions are expected to occur due to collagen contraction by fibroblasts[4]. Heterogeneous dense center networks (Fig 1A) were created with a dense region (0.02 collagen volume fraction) in the center of the network and a sparse region (0.002 collagen volume fraction) on the periphery. Heterogeneous sparse center networks (Fig 1A) were created with a sparse region (0.002 collagen volume fraction) in the center of the network and a dense region (0.007 collagen volume fraction) on the periphery. To determine if changing the volume of center region in heterogeneous networks affects axons strain, the radius of the center region was set to one of 4 values (3, 5, 10, or 18µm). All collagen fibers in the networks were modeled as nonlinear elastic fibers with the following force displacement relationship.

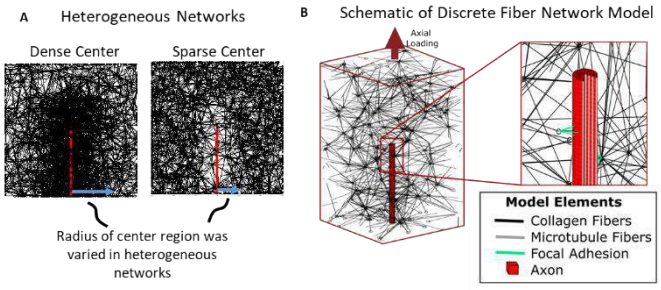

Figure 1: A) Heterogeneous networks showing two distinct network densities. B) Schematic showing the axon embedded in a collagen network.

$$F = \frac{AS}{B\left[\exp\left(\frac{B(\lambda^2-1)}{2}\right)-1\right]},$$

where A, S, and B are set to 43.3MPa, 7854nm^2, and 2.5 respectively. These values were chosen to match previous modeling efforts[5].

Once these networks were created an axon modeled as a composite material was embedded and attached to the center of the network (Fig 1B)[5]. Focal adhesion fibers were used to reduce the effects of point loads on the axon. The axon consisted of microtubules embedded in a linear elastic background modulus. The microtubules were linear elastic with a modulus set to 9.42N/m, which causes the tensile modulus of the axon to match experimental data. The axon background modulus was set to be at much less than the microtubule fibers at 0.433MPa.

Once created, all networks were stretched to 20% axial strain, a strain similar to experiments stretching DRGs embedded in collagen networks[3]. To understand how forces are transmitted through these networks to the axons, we plotted the distribution of forces in each network fiber. To quantify the heterogeneous axon strain fields produced by the networks, the average max principal strain and top 1% of max principal strains were reported.

RESULTS

The distribution of force in each network is dependent on the network architecture. Homogeneous networks have relatively uniform distribution of forces in the fibers throughout the network (Fig 2A). Dense center networks have large forces in fibers on the periphery of the network (Fig 2B). Sparse center networks have large fiber forces in the center of the network (Fig 2C). These fiber force differences may cause changes in the observed axon strain fields.

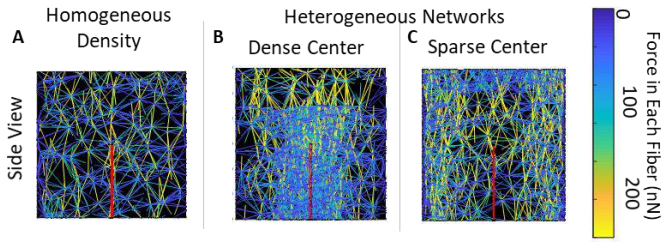

Figure 2: Distribution of fiber forces in networks changes based on the network heterogeneity. A) Homogeneous networks with uniform fiber forces, B) Dense center networks with large fiber forces in periphery, C) Sparse center networks with large fiber forces near the axon.

All axons experience highly heterogeneous strain fields (Fig 3A), but the average and maximum strain in each of these fields is dependent on the network surrounding the axon. Homogeneous networks cause both the average axon strain and the top 1% of axon strains to increase with increasing collagen volume fraction (Fig 3B 3C).

If dense center and sparse center networks are directly compared to homogeneous networks based on their global collagen volume fraction (Figure 3B, 3C), we note differences in the observed strain fields. Specifically, dense center networks increase the average axon strain when compared to homogeneous networks with similar collagen volume fractions. Sparse center networks cause a decrease in the average axon strain when compared to homogeneous networks with similar collagen volume fractions. These differences may be caused by changes in the force transmission from the network boundary to the axon.

DISCUSSION

Heterogeneous networks cause distinct axon strain fields compared to homogeneous networks with similar collagen volume fractions.

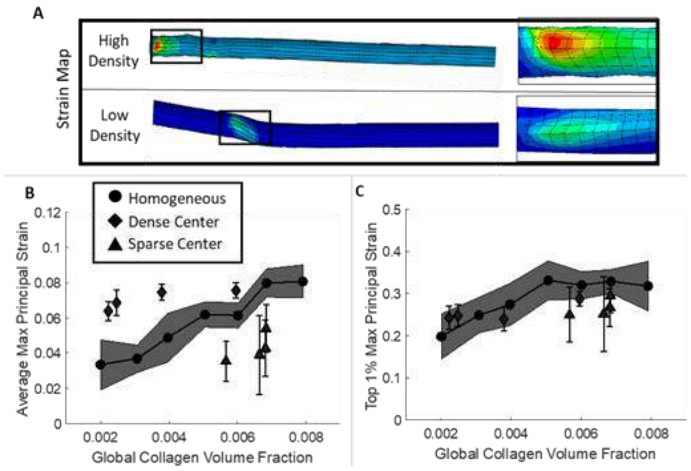

Figure 3: Axon strain fields vary based on network heterogeneity and collagen volume fraction. A) Representative strain maps showing heterogeneous axon max principal strain fields. B) Increasing the collagen volume fraction of homogeneous networks increases the average axon strain. Sparse center networks decrease axon strain, while dense center networks increase axons strains. C) Increasing the collagen volume fraction of networks increases the top 1% of max principal strains. Dense center and sparse center networks cause little to no change in the top 1% of max principal strains on the network.

Interestingly, fiber forces are highest in the sparse regions, but sparse center networks reduced axon strain compared to homogeneous networks. This difference in axon strain may be caused by the large number of fibers transferring force in the peripheral region of the sparse center network and small number of fibers attached to the axon. Since axons tend to grow most readily into regions of low collagen concentration[6], we believe this sparse center network behavior may explain why co-culture experiments with high fibroblast concentrations and DRGs do not cause increased expression of nociceptive signals.

In contrast, the dense center networks show high fiber forces on the network periphery and a large number of fibers attached to each axon. This large number of fibers attached to the axon probably caused the increase in axon strain compared to homogeneous networks with similar collagen volume fractions. Since, aging and disease could cause abnormal collagen formation[7,8], these dense center networks could potentially explain increases in ligament nociceptive signaling.

Local heterogeneity surrounding an axon in a facet capsular ligament can modulate its expression of signaling molecules. Thus, determining the relationships between collagen network heterogeneity, macroscopic loading, and axonal signaling could be critical to understanding pain mechanisms in the spine.

ACKNOWLEDGEMENTS

This work was supported by the Minnesota Supercomputing Institute (MSI), and NIH grant U01 AT010326.

REFERENCES

[1] Kallakuri, S, et al. *World J. Orthop.* 2012
[2] Zhang, S., et al. *J. Biomech.* 2016
[3] Ita, M., et al. *J. Biomech.* 2019
[4] Allen, D., et al. *J. Ultrastructure Res.* 1983
[5] Zarei, V., er al. *J. R. Soc. Interface,* 2017
[6] Cullen, K., et al. *Ann. Biomed. Eng.* 2007
[7] Iida, T., et al. *Spine Journal.* 2002
[8] Martins, G., et al. *Euro. J. of Ortho. Surg. and Traum.* 2018

ON THE RELATION BETWEEN 3D AORTIC VALVE INTERSTITIAL CELL SHAPE AND CONTRACTILE BEHAVIOR

Alex Khang, Quan Nguyen, Xinzeng Feng, Michael S. Sacks

James. T. Willerson Center for Cardiovascular Modeling and Simulation
The Oden Institute for Computational Engineering and Sciences and the
Department of Biomedical Engineering
The University of Texas at Austin
Austin, TX, USA

INTRODUCTION

Aortic valve interstitial cells (AVICs) reside within all layers of the aortic valve and regulate turnover of the extracellular matrix (ECM). AVICs become activated in times of growth and disease and take on a myofibroblast phenotype and increase their contractility. Cell shape is known to correlate closely with stress-fiber geometry and function and is thus a critical feature of cell biophysical state. Previous studies on the AVIC shape-contraction relation have heavily relied on 2D platforms. In this study, we assess the correlation between 3D AVIC shape and contractile behavior using PEG hydrogel matrices to better understand the relation between AVIC shape and local deformation. This body of work lays the foundation for investigations into intrinsic differences in AVIC contractile function in normal and diseased scenarios.

METHODS

3D Traction Force Microscopy. Porcine AVICs and fluorescent microbeads were seeded within peptide-modified, poly (ethylene glycol) hydrogels for 72 hours before experimentation. The sample was incubated in Tyrode's Salt (normal – N state) for 40 minutes before obtaining an image stack of a single AVIC and surrounding fluorescent microbeads. Afterwards, Cytochalasin D (inactive – I state) was added to elicit cell relaxation through actin depolymerization and a second z-stack of the same FOV was obtained. The image sets were analyzed with our software, FM-track [1], which outputted AVIC surface meshes and bead displacements from the I state to the N state.

AVIC principal curvature distribution. Local curvature on the AVIC surface was computed using a surface patch method [3,4]. We generated a local u-v-n tangent-plane coordinate system on the AVIC surface mesh described by a biquadric surface with the following form:

$$S(u,v) = au^2 + 2buv + cv^2, \tag{1}$$

where u and v are local coordinates on the tangent-plane coordinate system, S is the out of plane coordinate, and a, b, and c are fit constants that are determined for each surface node. The principal curvature k_1 is then computed at each node with the following equation [2,3]:

$$k_1 = a + c + \sqrt{(a-c)^2 + 4b^2}. \tag{2}$$

Representation of AVIC shape using Spherical Harmonics. To more completely describe the global AVIC shape, we utilized spherical harmonics (SPHARM) [5,6]. AVIC surface meshes were subjected to spherical parameterization to create a continuous, uniform mapping from the AVIC surface to the surface of a unit sphere. This results in a one-to-one mapping of the cartesian points on the mesh to a pair of spherical coordinates $[x(\theta,\phi), y(\theta,\phi), z(\theta,\phi)]$. Next, the parameterized surface is fit to a set of SPHARM basis functions Y_l^m where l and m denotes the degree and order of the SPHARM, respectively. The SPHARM expansion takes the form:

$$\mathbf{v}(\theta,\phi) = \sum_{l=0}^{L_{max}} \sum_{m=-l}^{l} \mathbf{c}_l^m Y_l^m(\theta,\phi), \tag{3}$$

where $\mathbf{v}(\theta,\phi) = (x(\theta,\phi), y(\theta,\phi), z(\theta,\phi))^T$, $\mathbf{c}_l^m = (\mathbf{c}_{xl}^m, \mathbf{c}_{yl}^m, \mathbf{c}_{zl}^m)^T$ are the SPHARM coefficients, and $Y_l^m(\theta,\phi)$ is the SPHARM function:

$$Y_l^m(\theta,\phi) = \sqrt{\frac{2l+1(l-m)!}{4\pi(l+m)!}} P_l^m(\cos\theta) e^{im\phi}, \tag{4}$$

where $P_l^m(\cos\theta)$ are the Legendre polynomials represented with the following differential equation:

$$P_l^m(x) = \frac{(-1)^m}{(2^l l!)}(1+x^2)^{\frac{m}{2}}\frac{d^{l+m}}{dx^{l+m}}(x^2-1)^l. \quad (5)$$

A SPHARM software from Shen et al. [6] was adapted to compute the SPHARM coefficients at a user specified maximum degree L_{max}. Power spectra were produced by plotting l,m vs $\mathbf{c}_{\mathrm{xl}}^{\mathrm{m}}, \mathbf{c}_{\mathrm{yl}}^{\mathrm{m}}, \mathbf{c}_{\mathrm{zl}}^{\mathrm{m}}$.

RESULTS

AVIC contractile patterns. AVIC contraction produced a complex displacement field with displacements going away and toward the cell surface (Fig. 1). A prominent axis of contraction was observed along with expansion in the orthogonal direction. The majority of appreciable displacements occurred within 60 um of the AVIC surface.

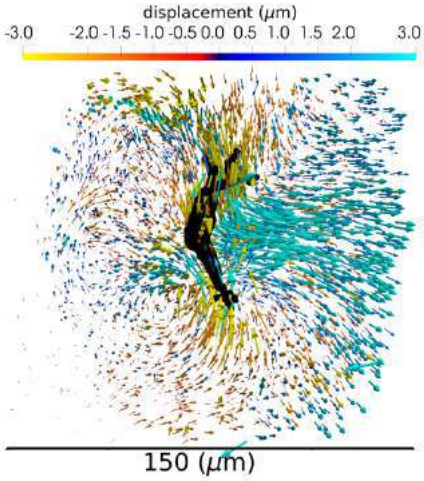

Figure 1: Displacement field produced by AVIC contraction. Displacements that are directed toward the cell surface are represented with warmer colors and negative magnitudes whereas those directed away from the cell surface are represented with cooler colors and positive magnitudes. Vector length is scaled by 3x the magnitude. The AVIC geometry is colored in black.

Curvature-displacement correlation. A statistically significant correlation was observed between curvature and displacement at the nodes of the AVIC surface mesh ($\boldsymbol{\rho} = 0.115$, p-value < 0.001) (Fig. 2). Regions of higher curvature produced larger displacement magnitudes and were localized at the AVIC protrusions.

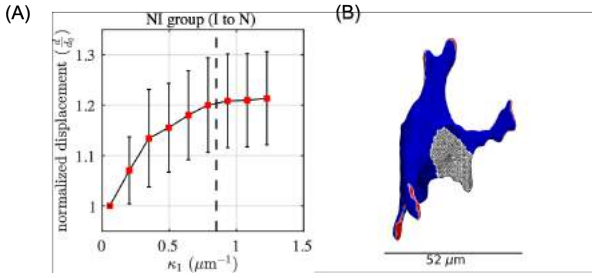

Figure 2: (A) A positive correlation was observed in contractile regions on the cell surface between k_1 and normalized surface displacement. The dashed vertical line denotes the cut-off between regions of high and low curvature. (B) Regions of high (red) and low (blue) curvature mapped onto a representative AVIC. Wireframe denotes expansive regions which were ignored.

SPHARM accurately captures AVIC shape. The AVIC shapes were accurately reproduced with SPHARM (Fig. 3). Increasing the degree of the SPHARM fit resulted in a better representation of the AVIC geometry. A final degree of 47 was used for the fit.

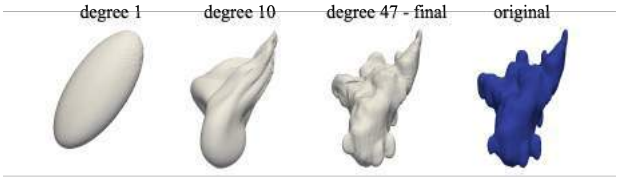

Figure 3: SPHARM representation of an AVIC.

AVIC shape becomes more spherical due to contraction. Power spectra analysis showed that greater SPHARM coefficients were required to fit the I shape than the N shape (Fig. 4). The negative residual of the power spectra, obtained by subtracting the power spectra of the N state by the I state, suggests that AVIC shape is more spherical in the N state than it is in the I state.

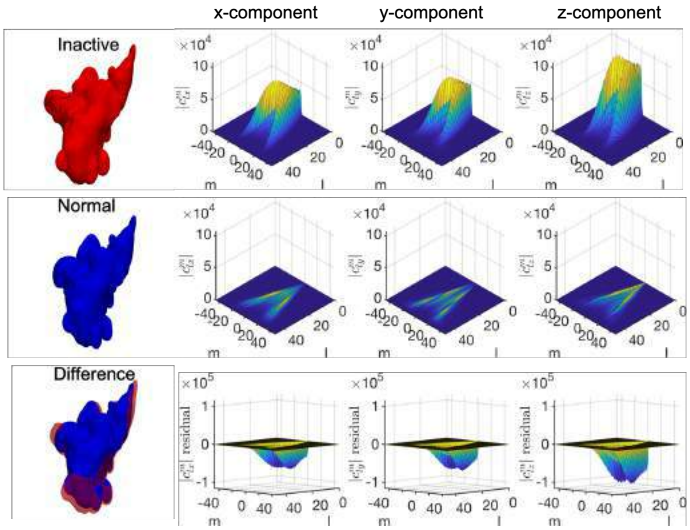

Figure 4: SPHARM fits for each state, the corresponding power spectra, and the difference between the spectra.

DISCUSSION

Here, we present a novel approach to study the 3D relation between AVIC shape and local deformation in high detail. Our findings concur with previous 2D in vitro studies and suggest that in 3D, AVIC shape and function are intimately connected. We successfully reconstructed AVIC shapes with SPHARM at high accuracy and confirm that AVIC shapes become more spherical in a contractile state, which suggests that contraction is mediated by high concentration of stress-fibers localized at cellular protrusions. Future work will involve modeling the sub-cellular components of the AVIC to achieve a mechanistic understanding of the AVIC shape-function relation.

ACKNOWLEDGEMENTS

NSF-GRFP grant no. DGE-1610403, NIH grant no. F31HL154654, NIH grant no. R01 HL142504.

REFERENCES

[1] Lejeune, E et al., *Software X,* 2019.
[2] Pedregosa, F et al., *J. Mach. Learn. Res.* 12:2825-2830, 2011.
[3] Sacks, M et al., *Ann Biomed Eng.* 21:263-275, 1993.
[4] Sander, P et al., *TPAMI.* 12:833-854, 1990.
[5] Brechbühler, CH et al., *Comput Vis Image Und*, 61:154-170, 1995.
[6] Shen, L et al., *Evolution*, 63:1003-1016, 2009.

UNDERSTANDING THE EFFECTS OF LONG-DURATION SPACEFLIGHT ON FRACTURE RISK IN THE HUMAN FEMUR USING FINITE ELEMENT MODELING

Keyanna Henderson (1), Scott J. Hazelwood (2)

(1) Mechanical and (2) Biomedical
Engineering Departments
California Polytechnic State University
San Luis Obispo, CA, USA

INTRODUCTION

Long-duration spaceflight has been shown to have significant, lasting effects on the bone strength of astronauts, and to contribute to age-related complications later in life [1]. The microgravity environment of space causes a decrease in daily mechanical loading, which affects bone remodeling, a biological process carried out by cells to maintain bone mass. This results in a decrease in bone density and an increase in damage, which contribute to bone fragility, creating a risk for fracture [2] [3]. However, there is little information pertaining to the timeline of bone loss and subsequent fracture risk. This study used finite element analysis to model the human femur, one of the bones most adversely affected by spaceflight, to simulate the environments of Earth preflight, a six-month mission on the International Space Station (ISS), and one year on Earth postflight. Inferences were then made on when changes in bone density and damage pose the greatest risk for femoral fracture for astronauts after long-duration spaceflight.

METHODS

To model the effects of spaceflight on the adult femur, a three-dimensional bone, finite element model was integrated with a bone remodeling algorithm [4] through a UMAT user subroutine in Abaqus 2020. In the algorithm, remodeling was activated by the level of loading and by repetitive loads that result in damage. It allowed for remodeling to occur simultaneously for both of these cases in different, local areas of the bone. The algorithm calculated changes at each step in time for nine state variables, one of which was the mechanical stimulus (Φ), the forcing function assumed responsible for driving the remodeling process. Measured in cycles per day, it is a function of principal strain (s) and loading cycles (R_L) of n different daily activities, and is calculated using Equation (1).

$$\Phi = \sum_{i=1}^{n} s_i^q R_{Li} \quad (1)$$

The value of the exponent – assumed to be 4, and the initial mechanical stimulus estimated from the strain needed to maintain bone mass, were based on a study by Whalen and Carter [5]. Remodeling by osteoclasts and osteoblasts was activated by stimulus values less than that of the initial value, and by damage in the bone matrix in the form of microcracks assumed to accumulate based on the stimulus in Equation (1). Changes in porosity were determined from the areas of bone resorbed and formed by osteoclasts and osteoblasts, respectively. Elastic modulus was assumed to have a nonlinear relationship with porosity (p), and was calculated using Equation (2) for cortical bone and (3) for trabecular bone.

$$E = 23440(1-p)^{5.74}\ (\text{MPa}) \quad (2)$$

$$E = 14927(1-p)^{1.33}\ (\text{MPa}) \quad (3)$$

In addition to the implementation of the bone remodeling algorithm, loads were applied to the model that mimic joint and muscle forces experienced during daily activities having the greatest influence on strain and remodeling. Muscles included in the model were the gluteus medius, gluteus minimus, vastus lateralis, vastus medialis, psoas, adductor brevis, and adductor longus.

The femur model was used to conduct a quasi-static analysis of an adult femur before, during, and after traveling to the ISS for six months. This was accomplished by modifying the model and algorithm to produce simulations of Earth preflight, six months of spaceflight, and one year of Earth postflight. Data were then collected from each simulation for changes over time in density (determined as a function of porosity) and damage (determined as crack length per area bone) in the two types of bone in the femoral neck: cortical and trabecular.

The first step of this analysis was to bring the model of the femur to a baseline, preflight form, resembling that of a skeletally mature adult. This was accomplished with an Earth baseline simulation. The joint and muscle forces were applied 5,000 cycles per day (per leg), corresponding to a total of 10,000 steps per day – a fair approximation for the active lifestyle of an astronaut [6]. Data were collected for damage and density in both cortical and trabecular bone. The simulation was validated by comparing its results to a previous strain gage study of cadaveric femurs [7] and to density measurements of cortical and trabecular bone samples in the femoral neck [8] [9].

After the Earth baseline was established and validated, time in space was simulated. The joint force and muscle loads used for the Earth baseline model were scaled to 90% of their original values to simulate the microgravity environment of the ISS and the resistance used during exercise in space [10] [11]. A daily step count of 10,000 was used again to account for the extensive amount of exercise performed by crewmembers in space [6] [12]. The simulation was run for six months to match the average mission to the ISS [13], and data were collected upon completion (i.e. immediately upon return from space). The model was validated by comparing its results for the monthly percent change in density to an experiment measuring cortical and trabecular bone loss of the femur in crewmembers making four to six-month flights on the ISS [1].

Upon completion of the six-month space simulation, a final, postflight simulation was produced to again simulate life on Earth. The joint force and muscle loads were scaled back to their original values and the daily step count was maintained at 10,000. This simulation was run for twelve months to provide the most accurate results and extensive understanding of the femur's behavior upon returning to Earth from space and data were then collected for damage and density of cortical and trabecular bone in the femoral neck once every thirty days.

RESULTS

Cortical and trabecular bone in the femoral neck experienced significant changes in damage as a result of spaceflight (Figure 1). In both types of bone, damage increased significantly after six months on the ISS, and continued to increase after returning to Earth without reaching an equilibrium. After spaceflight, damage in cortical bone had increased by nearly 10%. Upon returning to earth, it continued to increase over the twelve months, achieving an overall increase of 60% from the Earth baseline. The damage in trabecular bone increased by nearly 42% after spaceflight and continued to increase on Earth. By the end of the twelve-month, postflight simulation, damage had increased by 190% from the Earth baseline.

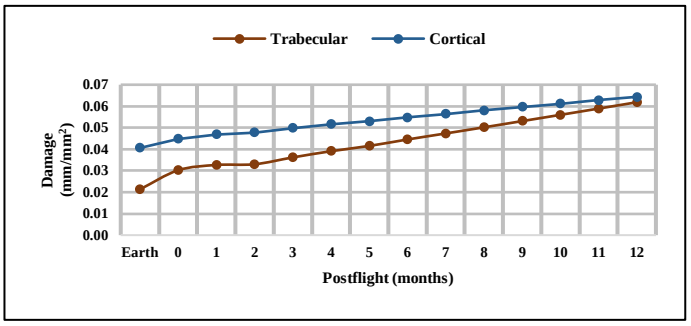

Figure 1: Damage v. Time for Cortical and Trabecular Bone. (0 denotes time immediately after spaceflight)

Changes in density were also seen in both cortical and trabecular bone (Figure 2). The density of cortical bone decreased by approximately 2% after six months of spaceflight. Shortly after returning to Earth, density increased and then leveled off at a value less than that of preflight, remaining at an equilibrium for the remainder of the simulation. Between the Earth baseline and end of the postflight simulation, cortical density experienced an overall decrease of 0.6%. The density of trabecular bone also decreased after spaceflight, but by a much larger magnitude – approximately 18%. At the start of the postflight simulation, density increased slightly, and then leveled off and remained at equilibrium, resulting in an overall decrease of 4%.

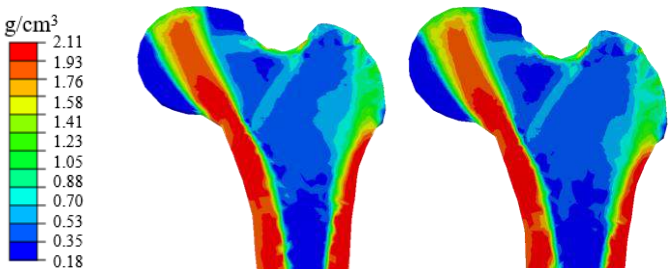

Figure 2: Density After Earth Baseline (left) and Spaceflight (right) Simulations

DISCUSSION

The predicted increases in damage during spaceflight occurred because the microgravity of space resulted in reduced loading altering bone remodeling levels as seen by sharp variations in cellular activity. Although less damage was formed due to the reduced loading, even less damage was removed due to the overall lower activity of the cells, increasing the rate of damage accretion. This suggests that fracture risk is likely to be extremely prominent in the femoral neck and is supported by the fact that naturally, the neck is most prone to fracture due to old age and other medical complications [14]. While the amount of damage required for fracture is unknown, it is reasonable to deduce that higher magnitudes of damage will decrease bone resistance and diminish bone toughness, making it more susceptible to fracture [15].

The higher density loss predicted in trabecular bone was due to the higher accretion rate of damage as well as its naturally high porosity. Because bone loss is the primary effect of long duration spaceflight, it is expected that density will decrease [16]. The greatest decline in density was seen immediately after spaceflight. After returning to Earth, density increased and then oscillated for five months before leveling off. The final predicted value was less than that of preflight, suggesting that bone mass may not recover after one year on Earth. Similar to damage, it is unclear as to what extent density contributes to fracture risk. It is certain however, that loss of bone mass is a risk factor for fracture [17]. Even if a decrease in density is not severe enough to cause fracture immediately upon return from flight, it may lead to health complications later in life [18]. Bone loss may accelerate the onset of osteoporosis, increase its severity, and add to fall risk due to bone fragility in astronauts, long after their time in space.

ACKNOWLEDGEMENTS

The authors are grateful to Christopher Deuel for development of the finite element mesh used in the analysis of this study.

REFERENCES

[1] LeBlanc, A., et al. *J Musculoskel Neuron Interact*, 1: 157–160, 2000. [2] Coulombe, J. C., et al. *Current Osteoporosis Reports*, 18: 1–12, 2020. [3] Johnston, C. C., and C. W. Slemenda. *Ostepoerosis International* 4, 1994. [4] Hazelwood, S. J., et al. *J Biomech*, 34: 299–308, 2001. [5] Whalen, R. T., et al. *J Biomech* 21: 825–837, 1988. [6] Tudor-Locke, C. et al. *Sports Medicine*, 34: 1–8, 2004. [7] Deuel, C. R., et al. *J Bone and Joint Surgery. 9 1-B:* 124–10, 2009. [8] Yeni, Y. N., and T. L. Norman. *Bone*, 26: 499-504, 2000. [9] Morgan, E. F., et al. *J Biomech*, 36: 897-504, 2003. [10] Rogers, M. J. B., et al. *Microgravity*, 1997. [11] Dunbar, B. *NASA*, 2015. [12] Trappe, S., et al. *J App Phys*, 106: 1159–1168, 2009. [13] Garcia, M. *NASA*, 2020. [14] Simon M., MD. *Hopkins Medicine*, 2017. [15] Schaffler, M. B., et al. *Bone, 17:* 521–525, 1995. [16] Lang, T. F. *J Musculoskel Neuronal Interact*, 6: 319–321, *2006.* [17] Sibonga, J. D., et al. *NASA*, 2017. [18] Keyak, J. H., et al. *Bone*, 44: 449–453, 2009.

COMPUTATIONAL MODELS TO EVALUATE THE IMPACT OF CORONARY COLLATERAL ARTERY FLOW IN ADULT AND POSTNATAL MICE

S. Anbazhakan (1), P. Rios (2), B. Raftrey (2), K. M. Red-Horse (2), A. L. Marsden (1)

(1) Bioengineering
Stanford University
Stanford, CA, USA

(2) Biology
Stanford University
Stanford, CA, USA

INTRODUCTION

Coronary collateral arteries are clinically important for shunting blood around a stenosis to protect patients against ischemia [1]. While collaterals have been shown to be beneficial, the number, size and configuration of collaterals that are sufficient to restore flow downstream of a stenosis remains unclear. The functional impact of collaterals is difficult to measure in humans because, generally, collaterals are too small to accurately quantify non-invasively.

Studies of collateral formation have succeeded in promoting the growth of collateral arteries in animal models through various cellular and molecular mechanisms with varying degrees of functional impact [2]. While high resolution data of the vessel geometry typically can be obtained, direct measurements of the collateral function in vivo is usually not possible due to limited accessibility and resolution. In addition, it is not possible to precisely control for the number and size of collaterals, which limits the comparisons that can be made. We also see that adult animal models recover poorly after MI compared to postnatal models, but the role of collateral arteries is not well understood.

Consequently, we use an adult and postnatal mouse model with a combination of computational fluid dynamics (CFD) and light-sheet imaging to systematically quantify flow through virtual collateral arteries in response to varying stenosis levels. These models allow us to control the number, size, and location of the collaterals keeping all other modeling parameters fixed. We hypothesize that collateral arteries in the postnatal heart are more effective in recovering flow downstream of a stenosis than in the adult.

METHODS

Adult and postnatal mice hearts were cleared and stained for smooth muscle actin using the iDISCO method [3]. Then, the hearts were placed in a quartz cuvette filled with DBE and imaged using the Lavision Ultramicroscope II light-sheet microscope.

In SimVascular, we constructed 3D subject-specific models of the mouse coronary vasculature from the light sheet imaging data using the standard workflow [4]. Briefly, we created path lines for each vessel (340 vessels) ignoring vessels that were less than 10um in diameter. Circles were used to approximate the cross-section due to some areas of the vasculature appearing collapsed or deformed. Finally, segmentations were lofted and unioned to create a geometric model that was discretized using a commercial meshing module, MeshSim (Simmetrix, Troy, NY).

Virtual collaterals were strategically added to native coronary vasculature to minimize the initial pressure difference of the two points the collateral was connecting. We did this to ensure that collaterals had virtually zero flow when there was no stenosis. We tested 5 levels of stenosis, and 4 different collateral configurations (0, 3, 6, 12) at 3 different diameters (Figure 1). For the postnatal heart, we tested 12 collaterals at 20um.

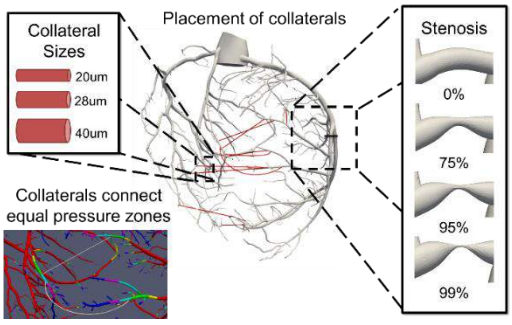

Figure 1: Placement of collaterals.

Pressure and aortic velocity were determined from literature [5]. Using the aortic velocity from literature and the aortic area for each mouse used, a subject-specific pulsatile aortic inflow was applied.

To determine the approximate volume of myocardium each outlet of the coronary model was responsible for perfusing we used a model of the myocardial tissue as the total volume to be perfused and the outlet coordinates as the seed points for the sub-volumes. We used a Voronoi diagram algorithm to assign sub-volumes of the myocardial tissue to each outlet of the coronary model. Resistance boundary conditions were assigned based on these perfusion volumes.

We ran pulsatile flow, rigid wall simulations using a stabilized finite element method in the open-source SimVascular finite element solver svSolver to obtain hemodynamic values, such as pressure, flow, and shear stress [4]. Paraview (Kitware, inc) was used for visualization of the results. Simulations were performed for each collateral configuration and stenosis level (25 cases in total), keeping all other flow parameters and boundary conditions fixed.

RESULTS

To determine the functional recovery for each collateral configuration, we report the total flow at outlets downstream of the stenosis (blue area, Figure 2). Flow downstream of the stenosis decreases non-linearly with stenosis severity with no collaterals (first row, Figure 2). The collateral configurations are ordered from top to bottom based on their functional flow recovery, with 3 collaterals of 40 microns in diameter being the best at stenosis levels greater than 90%.

Flow Recovery Downstream of Stenosis (mm^3/s)

Number of Collaterals	Diameter (um)	Stenosis				
		0%	75%	90%	95%	99%
0	N/A	1.315	1.117	0.685	0.271	0.004
6	20	1.411	1.129	0.731	0.279	0.011
12	20	1.410	1.199	0.719	0.283	0.016
6	28	1.318	1.215	0.699	0.299	0.039
3	40	1.320	1.134	0.711	0.330	0.058

Figure 2: Flow recovery downstream of stenosis. Green, yellow, red colors indicate high, medium, low flow respectively.

To relate the flow recovery with a functional physiological outcome, we estimated the volume of tissue that would be considered "ischemic" based on various thresholds of flow recovery. We found that, for a 99% stenosis, there is a significant reduction in ischemic volume when a very low threshold of 10% flow recovery is used, with 3 collaterals at 40 microns being the optimal configuration (Figure 3).

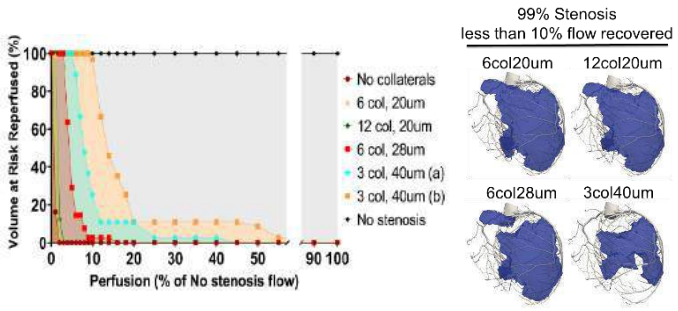

Figure 3: Ischemic volume at 99% stenosis.

In postnatal hearts, collaterals are more numerous and larger than the ones found in the adult after a LCA ligation (Figure 4A). To compare the functional significance of the collateral arteries, we tested the flow recovery downstream of a 99% stenosis in the postnatal coronary vasculature and compared it with the adult. We found that 12 collaterals at 20um in diameter outperformed adult collaterals not only with the same collateral configuration, but even the best possible flow recovery from the adult as indicated by high pressure recovery downstream of the stenosis (Figure 4B).

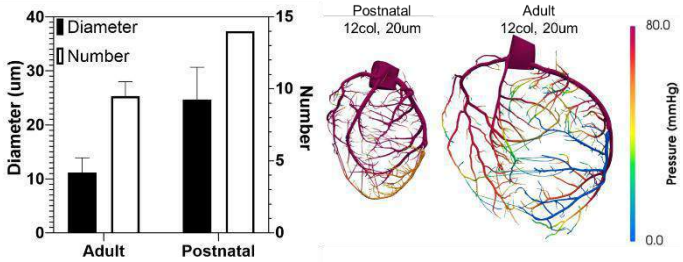

Figure 4: Comparison of adult and postnatal (A) collaterals and (B) pressure recovery downstream of stenosis

DISCUSSION

In this study, we relate the form and function of collaterals by using CFD analysis. This is, to our knowledge, the first time CFD has been used to quantify hemodynamic forces in the adult and postnatal mouse coronary vasculature.

Although we found that fewer, larger collaterals are the most beneficial, that configuration still only recovered about 4% of the unobstructed flow downstream. While we hypothesized that this was due to poor distal pressures, this could also be related to underestimation of pressures at the distal end of the collateral vessels. Future work could address this by accounting for changes in viscosity due to the Fåhræus–Lindqvist effect, which would be relevant at the size of vessels we model [6], however we expect that this would not affect the claims made here regarding the relative functional differences between different collateral configurations and adult vs. postnatal.

In our brief pilot study comparing one collateral configuration between postnatal and adult, we found that collaterals were much more effective, which may be due to higher distal pressures in the postnatal vasculature. We plan to extend the comparisons between adult and postnatal collaterals to include more configurations and detailed volume perfusion differences.

In summary, we present a novel application of CFD analysis to quantify collateral flow in the adult and postnatal mouse coronary vasculature. The findings here suggest the possible benefit of promoting the growth of fewer, larger arteries over many, smaller ones as well as the natural benefit collaterals have in restoring pressure downstream of a stenosis in postnatal hearts. Simulations may also provide mechanical stimulus data to inform mechanobiology studies.

ACKNOWLEDGEMENTS

We acknowledge the Simvascular Open Source project (simvascular.org) and computing resources provided by the Stanford Research Computing Center. Mr. Anbazhakan is a 2018 Stanford Bio-Bowes PhD Fellow.

REFERENCES

[1] Seiler, C et al., *Curr Cardiol Rev*, 10(1):2-16, 2014.
[2] Das, S et al., *Cell*, 176(5):1128-1142, 2019.
[3] Renier, N et al., *Cell*, 159(4):896-910, 2014.
[4] Updegrove, A et al., *Ann Biomed Eng*, 45(3):525-541, 2016.
[5] Hartley, C et al., *Am J Physiol Heart Circ*, 301(2):H269-78, 2011.
[6] Toksvang, L et al., *Adv Physiol Educ*, 37: 129–133, 2013.
[7] Zhang, H et al., *J Mol Cell Cardiol*, 87:4-16, 2015.

LONG-TERM EFFECT OF TBI-LIKE SHEAR STIMULI ON ASTROCYTES

Tasnim Shireen (1), Susan Z. Hua (1,2)

(1) Department of Mechanical and Aerospace Engineering
University at Buffalo
Buffalo, NY, USA

(2) Department of Physiology and Biophysics
University at Buffalo
Buffalo, NY, USA

INTRODUCTION

Traumatic brain injury (TBI) is one of the leading causes of morbidity and death worldwide[1]. Mild TBI results in long-term disruption in the brain and a high risk of developing pathology[2]. In sports, repetitive, often sub-concussive, head injuries increase the risk of chronic traumatic encephalopathy (CTE)[3]. During TBI, an increase in intracellular Ca^{2+} is universally seen in all brain cells[4,5]. Using primary astrocytes model, we have previously reported that shear pulse stimulus induces instant Ca^{2+} influx and the response is accumulative[6]. Cells become more responsive when subjected to multiple low magnitude challenges[6]. We speculate that the external forces during TBI may cause lasting changes in the mechanical environments of Ca^{2+} permeable ion channels, resulting in a long-term dysregulation of Ca^{2+} uptakes.

In this study, we have applied repeated shear stimuli, 6, 12, and 24 hrs apart, and measured Ca^{2+} responses in primary rat astrocytes. We show that the Ca^{2+} response to the second stimulus was significantly higher than the first one. The history of shear stimulus affects the later Ca^{2+} response. This cell memory to early mechanical event lasted ~ 18 hrs. Cells responded to repeated shear stimuli with subsequently increases in Ca^{2+} peak values. These results show that the mechanical forces during TBI may cause long-term deformation in cells, and the cell may store TBI information via a mechanical pathway.

METHODS

The entire experiment was conducted using a high-speed microfluidic chip driving by a fast pressure servo[6]. The pressure servo can generate transient shear stress in the microfluidic channel, mimicking shear forces during TBI. The chip consists of a PDMS flow channel of 1 mm x 100 μm x 15 mm on a cover glass. Holes were punched into both ends of channel as fluid inlet and outlet. The shear stress profile in the channel was pre-calibrated using fluorescent beads[6]. Human Fibronectin was applied into microfluidic channel for 30 mins, which was later washed with culture media.

Adult rat astrocytes (ScienCell) were cultured in petri dish to 95% confluency, then trypsinized. The cell suspension solution was centrifuged and perfused into the microchannel. The cells were cultured on the chip in an incubator for 3-4 days until the confluency reached ~95%, in between every 24 hrs media was changed. Prior to experiments, channel was washed with isotonic solution (1 mM $CaCl_2$, 150 mM NaCl, 5 mM KCl, 2 mM $MgCl_2$ and 10 mM HEPES). The saline solution was used for shear experiments. For repeated shear stimuli, after 1st shear, cells were gently washed with culture media and kept in incubator for designed period. A fresh dye was loaded, and the shear experiment repeated following the same protocol.

Intracellular Ca^{2+} was measured using Fluo-4-AM dye (5 μM, Invitrogen). Fluorescence images were acquired using a Zeiss inverted microscope (Axiovert 200M) and a CCD camera. The normalized change in Ca^{2+} intensity was calculated using:

$$\frac{\Delta F}{F_0} = \frac{F - F_0}{F_0} \quad (1)$$

Where F and F_0 are the intensities at time t and 0, respectively. Ca^{2+}intensity was averaged over 10 cells from each channel. Minimal 4 experiments were performed for each condition. Statistical analysis used the standard error of the mean (s.e.m.). Statistical significance was analyzed from two sample t-test. $p < 0.001$ was considered significant.

RESULTS

Using our high-speed programmable microfluidic chips, we applied repeated square shear pulse of 23 dyn/cm^2 and 10 ms duration and measured Ca^{2+} responses. A conditioning shear pulse was applied at time zero and repeated at 6 and 24 hrs for testing. Figure 2a shows

typical Ca^{2+} responses to conditioning (0 hr) and testing stimuli (6, 24 hrs). Cells appeared more susceptible to shear pulse after a conditioning stimulus. Ca^{2+} responses from selected cells under each condition was plotted in Fig. 1b-d. It was observed that Ca^{2+} response to second shear 6 hrs apart was ~ 30% more than that of conditioning one at 0 hr (Fig. 1b, c). Repeated shear pulse at 24 hrs further increased the amplitude of Ca^{2+} response (Fig. 1d). The Ca^{2+} responses consistently increased with repetition, suggesting that cells have long term memory of previous mechanical events.

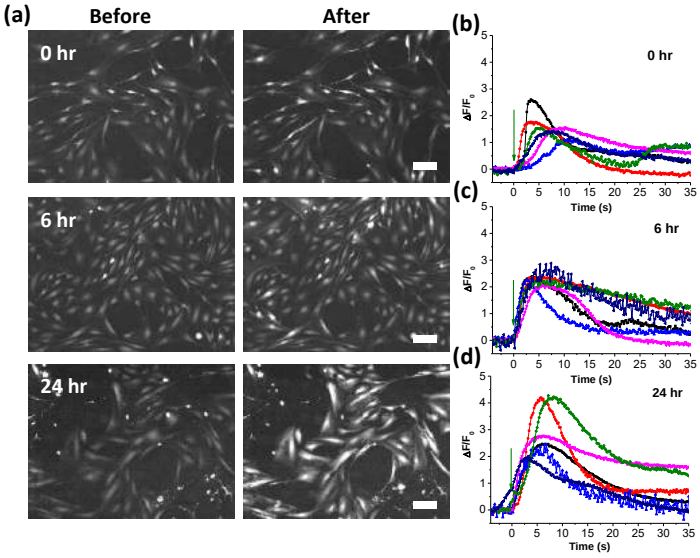

Figure 1. Fluorescence images (a) and time course of Ca^{2+} responses (b-d) to repeated shear pulses at 0, 6, and 24 hrs, showing the responses to repeated stimuli were increased. Each curve was averaged over 10 cells from one experiment. Scale bar = 50 μm.

In controls, cells were not subjected to conditioning stimulus at 0 hr, otherwise was treated the same way (dye loading and imaging), and Ca^{2+} response to testing shear stimuli at 6 and 24 hrs were measured. A comparison between the Ca^{2+} responses with and without conditioning shear stimulus showed that the responses with shear history were consistently higher than the controls (without conditioning shear) (Fig. 2). With conditioning shear, the testing Ca^{2+} intensity at 6 hrs reached to an average of 2.2 (Red curves in figure 3), while without conditioning shear it only reached to 1.55 (Fig. 2a, n = 60). In response to repeated shear at 24 hrs, the response increased to ~3.3 with the conditioning shear, and 2.5 without it (control cells) (Figure. 2c). These results show that cells not only have long term memory of previous mechanical events, but the effect is also accumulative.

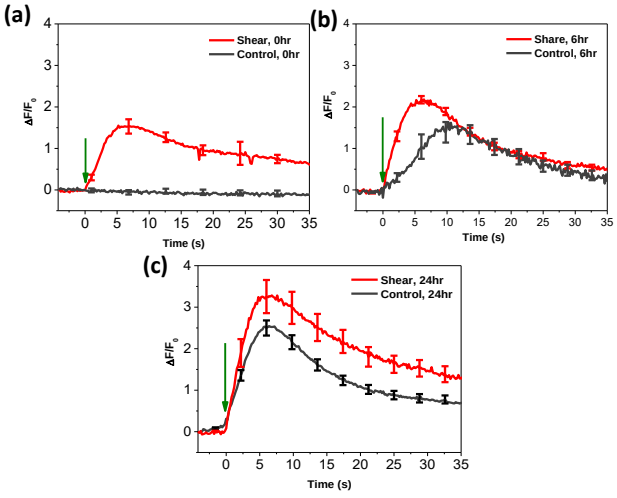

Figure 2. Comparison of Ca^{2+} response with (shear) and without (control) conditioning shear. The conditioning stimulus was applied at 0 hr, test run was conducted at 6 and 24 hrs (n = 60 from 6 runs for each curve). The peak Ca^{2+} value with and without conditioning shear was analyzed using two sample t-test, $p < 10^{-20}$). It shows the response increased significantly with conditioning shear.

To assess the duration of the cell memory, we applied the testing shear stimulus after different time intervals, 6, 12, 18, and 24 hrs. Shear stress of 23 dyn/cm^2 was used for all experiments. We found that longer time interval increased cell sensitivity to the second shear pulse until 18 hrs. For an interval of 6 hrs, the Ca^{2+} intensity in response to second shear pulse was ~50% more than that of first shear pulse. The ratio increased to ~110% for an interval of 18 hrs (Fig. 3a-c). However, the response to shear pulse at 24 hrs showed insignificant difference to the previous one (Fig. 3d). This shows that the limit of memory could be <24 hrs.

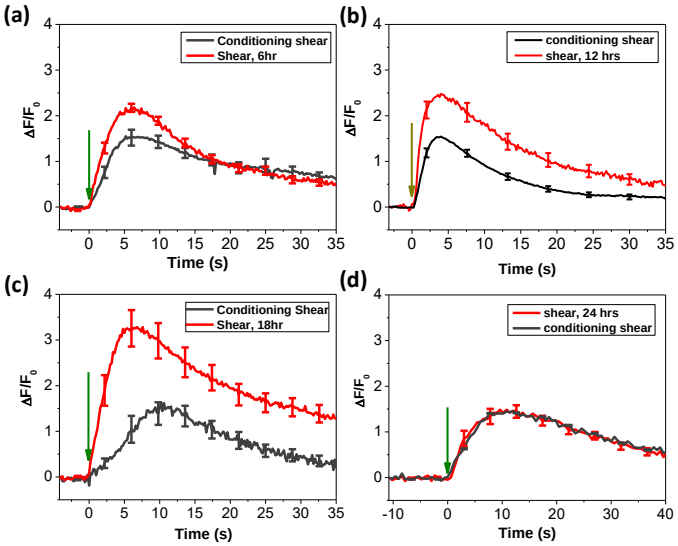

Figure 3. Effect of intervals between stimuli on Ca^{2+} response. The response to conditioning shear at 0 hr (black curves) was compared with testing stimulus at 6 (a), 12 (b), 18 (c), and 24 hrs (d), showing the memory limit is < 24 hrs (n= 50 for each curve).

DISCUSSION

We measured the Ca^{2+} response to repeated shear stress stimuli in astrocytes. We have shown that Ca^{2+} responses to the shear stimulus depend on the stimulus history. The response to subsequent shear stimuli were consistently higher than that to the earlier ones (Fig. 1, 2). The effect of shear stimulus was accumulative. These results show that cells have memory to early mechanical events, and the memory was ~18 hrs (Fig. 3). It is known that TBI causes long-term effects in the brain physiology and pathology. Previous studies have focused primarily on secondary injury that involves biochemical and metabolic dysfunction[7]. Our studies indicate that cells may be able to store TBI information mechanically.

ACKNOWLEDGEMENTS

This work was supported by National Science Foundation (CMMI-2015964).

REFERENCES

[1] Park, E. *et al. CMAJ* **178**, 1163, (2008).
[2] Bell, J. D. *et al. Brain* **130**, 2528, (2007).
[3] Smith, D. H. *et al. Nat Rev Neurol* **9**, 211, (2013).
[4] Shapira, Y. *et al. Neurol Res* **11**, 169, (1989).
[5] Bell, J. D. *et al. Cell Death Differ* **16**, 1665, (2009).
[6] Maneshi, M. M. *et al. J Neurotrauma* **32**, 1020, (2015).
[7] DeKosky, S. T. *et al. Nat Rev Neurol* **9**, 192, (2013).

AI-ACCELERATED MULTISCALE MODELING FOR MULTI-PLATELET AGGREGATION AT MILLISECOND AND MOLECULAR RESOLUTIONS

Peng Zhang (1), Yicong Zhu (1), Changnian Han (1), Jawaad Sheriff (2), Yuefan Deng (1), Danny Bluestein (2)

(1) Department of Applied Mathematics and Statistics
Stony Brook University
Stony Brook, New York, United States

(2) Department of Biomedical Engineering
Stony Brook University
Stony Brook, New York, United States

INTRODUCTION

We have developed and implemented a novel machine learning algorithms for accelerating our multiscale modeling on supercomputers [1]. Our multiscale modeling (MSM) is an all-particle based approach that combines Coarse-Grained Molecular Dynamics (CGMD) model to depict the platelet's biophysical properties at the cellular scales [2] and its dynamic interactions coupled with macroscopic flows modeled by a Dissipative Particle Dynamics (DPD) model [3]. Our MSM can be used to describe the platelet activation mechanotransduction process induced by blood flow [2], simulate shear-induced platelet activation with filopodia formation [4, 5], as well as recruitment aggregation of platelets mediated by fibrinogen via the αIIbβ3 receptors [6]. However, the MSM framework, though successfully handling multiphysics problems at diverse spatial scales occurred in multi-components systems, makes the computation task more complex and less efficient on leadership class computers [7]. We thus introduced a novel artificial intelligence (AI)-guided adaptive time stepping (ATS) algorithm that adapts timestep sizes to underlying biophysical dynamics such as combination of our platelet flipping [2, 3] and aggregating [6] models to multi-platelet aggregation at millisecond-long and molecular-accurate resolutions.

In this work, we for the first time present our AI-MSM framework to overcome the major challenges of simulating 3 aggregating platelets with 3-4 aggregated platelets already deposited to the blood vessel walls in the dynamic shear blood flows. The total simulated time duration is approx. 1.2ms. The molecular events including the flow-platelet dynamic interaction, flow-induced mechanotransduction and αIIbβ3-Fg-αIIbβ3 binding and breaking events are all considered in the simulation [4-6]. The timestep sizes are real-time predicted by our trained AI-ATS method [1] without human interventions. During the simulation, we recorded the trajectory of individual platelets and accumulated mapped flow-induced stresses on the platelet membranes for stress analysis.

METHODS

The platelet model has a total of 140,303 particles at which 67,004 for platelet membrane and integrin αIIbβ3 receptors, as well as 32,853 cytoplasm and 40,446 cytoskeleton particles (Fig. 1). The aggregation force field between the receptors of different platelets is modeled as:

$$\boldsymbol{F}_{ij} = D_0\left(e^{-2\alpha(r_{ij}-r_0)} - 2e^{-\alpha(r_{ij}-r_0)}\right)\boldsymbol{e}_{ij} + f^A(t_{ij})\left(1-\frac{r_{ij}}{d_c}\right)\boldsymbol{e}_{ij}$$

where the experimentally-verified parameters are presented in [6].

The spatial CGMD-DPD interface in this MSM is handled by a hybrid force field in [3] where a Lennard-Jones term is used to maintain platelet incompressibility, while a dissipative and random force term to maintain the flow local thermodynamic and exchange momentum to express interactions between the platelet and the flow particles.

The disparity in temporal scales between DPD and CGMD in this MSM is handled by our novel multiple time stepping (MTS) algorithm [8] that utilized varied timestep sizes for different governing functions. Meanwhile, our new AI-guided ATS algorithm [1] is applied on top of this MTS algorithm to enable adaptivity of timestep sizes to underlying dynamics where the AI guides the omission of multiple redundant time steps without scarifying significant accuracy of the dynamics.

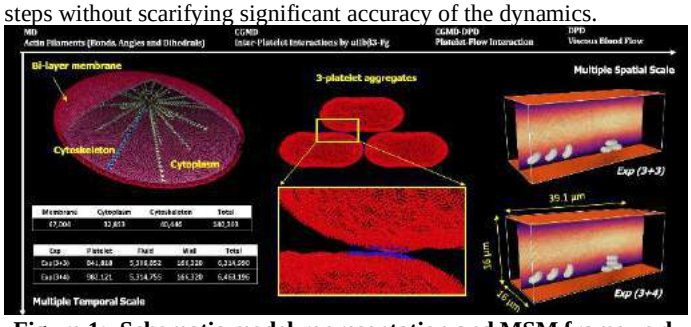

Figure 1: Schematic model representation and MSM framework

RESULTS

Our multiscale model described the biophysical properties of the platelets down to the *nm*-length and *ps*-time scales. Membrane Young's modulus is 31.2 μN/m and shear modulus is 33±9 μN/m. The cytoplasm is modeled by modified Morse potential and its viscosity is 4.1 mPa·s. Actin filament stiffness is 56.3±1.0 pN/nm. [2]

Using this model, we simulated two aggregation numerical experiments: 3 aggregating platelets with 3 and 4 aggregated platelets, as shown in left and right of Fig. 2, named as Exp (3+3) and Exp (3+4) respectively. This simulation studies a microchannel of 39×16×16μm (L×W×H). The pressure-driven Poiseuille flow is modeled with mean velocity of 6 cm/s and flow viscosity of 1.07 dyne/cm^2. During the simulation, our platelet model continuously changes its morphology in response to the dynamic flow stress while flowing and flipping. The aggregated platelets adhered to the blood vessels at the start of simulations. As the flowing platelets approaching, they start to contact the 3-platelet aggregate deposited to the walls. The whole simulated duration is more than 1,250 μs. Fig. 2 shows the velocity magnitude of flowing platelets: initially the flowing platelets flip driven by the flow-induced stresses and there maintains a certain gap between these platelets; after first contacting the aggregated platelets, these flowing platelets are quickly influenced to change their trajectory by climbing up the blood clot in Exp (3+3) and rolling aside in Exp (3+4); after passing the blood clot, these platelets did not firmly aggregate due to the applied strong flow stresses. Clearly, we observed a direct impact of the blood clot size (3 and 4 aggregated platelets) on the dynamics and activities of flowing/aggregating platelets.

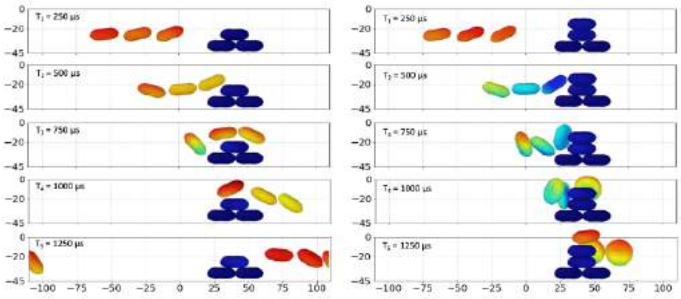

Figure 2: Velocity magnitude distributions on platelet membranes for Exp (3+3) and Exp (3+4) at T = 250, 500, 750, 1000, and 1250 μs

In addition, we studied the accumulated shear stresses on platelet membranes for different cases (Fig 3). We observed that all platelets have larger flow-induced stresses on periphery of their membranes. The flowing platelet has relatively larger flow-induced stress on top/bottom areas than the aggregated platelets as it continues to flip driven by the surrounding flows. The contact region between the aggregated platelets has a relatively smaller flow-induced stresses as this area is hidden from the shear flows. As expected, the bottom platelet (c) has the least flow-induced stresses as it is totally protected by the other two platelets in its front and has no direct contact with the flowing platelets as well. In other words, we can clearly conclude that even under the same flow condition, the relative positions of adhered platelets in a blood clot will lead to a very different accumulated flow-induced stress that may in part respond to different activation states of these adhered platelets [4].

All simulations were conducted on the AiMOS supercomputer using our AI-ATS algorithm on 192 computer nodes, and achieved a speed of 3,077 μs/day using GPUs that are 2.65 times the speed of 1,159 ms/day when using only-CPUs, thus enabling larger-scale, longer simulations.

DISCUSSION

Our approach is the first multiscale numeric method for simulating the platelet flowing, flipping and aggregation under flow that includes bonding and receptors on platelet's membrane. Biophysical properties of a platelet are accurately described down to a nm-length and ps-time scale, and the viscous flow is described at a μm-length and ns-time scale. Platelets are allowed to continuously deform in response to flow stress. In platelet recruitment aggregation, the microscale properties of the receptor-ligand interactions were precisely modeled at molecular scales and correlated well with *in vitro* results, including contact area and detaching force. With this improvement, the aggregation model is able to illustrate the microphenomena that have otherwise been missing.

In addition, our novel AI-ATS method [1] significantly improved the modeling efficiency on leadership-class heterogenous computers and extended our computational capabilities to a billion-scale platelet-fluid system for millisecond-to-second-scale and molecular resolutions.

Ongoing experiments have employed this AI-MSM model to study a second-level aggregation of hundreds of platelets in shear flows for depicting cumulative stress-induced platelet activation (filopodia formation), platelet adhesion to vWF-coated vessels, and activated platelets recruitment aggregation to platelets already adhered to the vessels. Our AI-MSM model can be adopted to other fields, such as drug delivery, by considering the impact of mechanical triggered biochemical events.

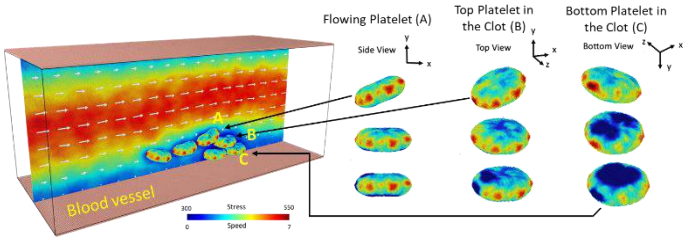

Figure 3: Average stress on platelet membrane for T = 500μs.

ACKNOWLEDGEMENTS

This study was made possible by grants from the National NIH U01 HL131052 (PI: D. Bluestein, Co-Investigators: Y. Deng, M. Slepian). The project is supported by SUNY-IBM Consortium Award, FP00004096 (PI: Y. Deng). The simulations were conducted on the AiMOS supercomputer at Rensselaer Polytechnic Institute.

REFERENCES

[1] C. Han, P. Zhang, Bluestein, D., et al., "Artificial intelligence for accelerating time integrations in multiscale modeling," Journal of Computational Physics, vol. 427, p. 110053, 2021.

[2] P. Zhang, L. Zhang, et al., "A multiscale biomechanical model of platelets: Correlating with in-vitro results," Journal of Biomechanics, vol. 50, pp. 26-33, 2017.

[3] P. Zhang, C. Gao, et al., "Multiscale Particle-Based Modeling of Flowing Platelets in Blood Plasma Using Dissipative Particle Dynamics and Coarse Grained Molecular Dynamics," Cellular and Molecular Bioengineering, vol. 7, no. 4, pp. 552-574, 2014

[4] P. Zhang, J. Sheriff, et al., "A Predictive Multiscale Model for Simulating Flow-Induced Platelet Activation: Correlating In Silico Results with In Vitro Results," Journal of Biomechanics, 2021 (Accept).

[5] S. Pothapragada et al., "A phenomenological particle-based platelet model for simulating filopodia formation during early activation," International Journal for Numerical Methods in Biomedical Engineering, vol. 31, no. 3, p. e02702, 2015.

[6] P. Gupta, P. Zhang, J. Sheriff, et al., "A Multiscale Model for Recruitment Aggregation of Platelets by Correlating with In Vitro Results," Cellular and Molecular Bioengineering, 12(4) 327-343, 2019.

[7] P. Zhang N. Zhang, et al., "Scalability Test of Multiscale Fluid-Platelet Model for Three Top Supercomputers," Computer Physics Communications, vol. 204, pp. 132-140, 2016.

[8] P. Zhang, et al., "A Multiple Time Stepping Algorithm for Efficient Multiscale Modeling of Platelets Flowing in Blood Plasma," Journal of Computational Physics, vol. 284, pp. 668-686, 2015.

IN VITRO METHOD TO QUANTIFY AND VIZUALIZE MECHANICAL WEAR IN HUMAN MENISCUS SUBJECTED TO JOINT LOADING

Kate J. Benfield (1), Zachary A. Pinkley (1), Katherine A. Hollar (1), Kirk J. Lewis M.D. (2), Trevor J. Lujan Ph.D. (1)

(1) Department of Mechanical and Biomedical Engineering
Boise State University
Boise, Idaho, USA

(2) Idaho Sports Medicine Institute
Boise, Idaho, USA

INTRODUCTION

The menisci are fibrocartilaginous soft tissues that absorb and distribute 40-70% of loads across the knee joint.[1] Overtime, repetitive physical activity contributes to meniscus degeneration; a retrogressive breakdown of fibrous tissue that affects over half of individuals above 70 years of age.[2] These microstructural changes to the collagen fiber networks increase the risk of multiplanar tears, pain, joint instability, and progression of osteoarthritis.[1] In order to advance prevention and intervention strategies for meniscal degeneration, it is imperative to characterize the wear behavior of whole meniscus to identify loading conditions and activities that cause rapid meniscus wear.

A challenge in characterizing meniscus wear is the lack of an established technology. Pin-on-plate and pendulum systems are common techniques used to measure wear in biological materials[3], however, these methods are limited to small sectioned specimens and are not suitable for whole complex structures. Alternatively, micro-CT and MRI can image whole soft tissue[1], yet these methods are time consuming, costly, and have insufficient resolution to quantify microscale defects[3]. A novel approach to measuring tissue wear is through 3D optical scanning, which creates 3D reconstructions of complex objects. While 3D optical scanning has successfully measured polymer wear in hip implants[4], no study has developed a method to use this technology to measure wear in meniscus, or any soft tissue. The objective of this study was to develop an in vitro method to characterize volumetric wear in whole human meniscus subjected to joint loading.

METHODS

This study was done in two parts. Part I assessed the accuracy of the proposed methodology for measuring wear in meniscus tissue **(Fig 1A)** through a surrogate model. Part II utilized this method to quantify wear in whole human meniscus subjected to physiological loading.

Scanning Procedure. The 3D optical scanner system consisted of a projector, rotary table, and two high-resolution cameras (LMI Technologies) **(Fig 1B)**. 3D renderings were generated for both surrogate model and human meniscus at three different time points: pre-wear, post-wear, and tibia-only. Five sets of eight scans were taken at 45° increments resulting in a full 360° view of the model. All 40 scans were aligned by common geometry and combined via scanning software, FlexScan3D, to generate the 3D renderings. Open-source software, CloudCompare, was used to evaluate volume loss by aligning tibia-menisci to tibia-only rendered models and preforming common geometry subtraction (CGS) **(Fig 1A)**. The defect volume, V_{defect}, was found by aligning the pre- and post-wear menisci and using CGS to isolate the defect **(Fig 1A)**. For the surrogate model, this process was repeated for the varying wear depths, and the percentage error between known volumes and CloudCompare calculated volumes was determined ($100*|V_{defect}-V_{known}|/V_{known}$). An ANOVA test with Tukey post-hoc was performed for the surrogate model to assess error in measuring wear depth. The human meniscus followed the same scanning procedure; however, volume loss due to tribological behavior (in terms of wear and deformation) was recorded.

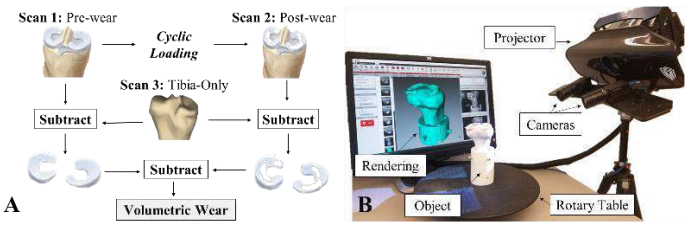

Figure 1. Novel imaging technique to measure tissue wear. A) Flow chart of CGS method, B) 3D scanning setup

Part I: Surrogate. A 3D reconstruction of healthy meniscus (29 yrs, male) was obtained via MR imaging.[5] Both medial and lateral meniscus were 3D printed using polylactic acid material and positioned on a foam replica of a human tibia (Sawbones). Defects in the 3D model were made by applying a wear pattern in meshing software and removing mesh with varying depths of 0.5, 0.025, 0.01, 0.005, and 0 inches to simulate artificially induced wear **(Fig 2A)**. These wear depths corresponded to wear volumes of 412, 206, 79.3, 40.9, and 0 cubic millimeters, respectively. The reference volume, V_{known}, of the 3D defect models was measured using SolidWorks.

Part II: Human. One human cadaveric knee (29 yrs, female) was dissected leaving only menisci and meniscal attachments. The natural reference position of the knee was determined from boney landmarks, mechanical digitizer (Revware Inc), and custom MATLAB code using established Grood-Suntay conventions. Both femur and tibia were potted using Bondo and secured within a custom-made knee fixture **(Fig 3B)** allowing for six degrees of fixed mounting adjustment. Potting alignment was verified through digitizing and kinematic analysis. The potted tibia-meniscus was scanned prior to testing to generate the 'pre-wear' scan **(Fig 1A)**. An Instron E10000 mechanical test system was used to apply combined cyclic axial loading and torsional rotation based on parameters specified by ISO 14243-3 (gait=45%, flexion=10°, axial=2.4 kN, rotation=1.1°). Four loading stages of 250K cycles were run at 2 Hz. Following each stage, the tibia-meniscus was scanned to generate 'post-wear' scans **(Fig 1A)**. After 1 million cycles, the menisci were removed and the 'tibia-only' scan was acquired **(Fig 1A)**.

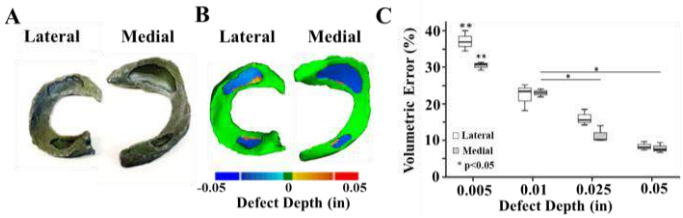

Figure 2. Surrogate: A) real-life, B) color, C) error increases as depth decreases ($p < 0.05$). ** = >all other defect depths ($p < 0.05$)

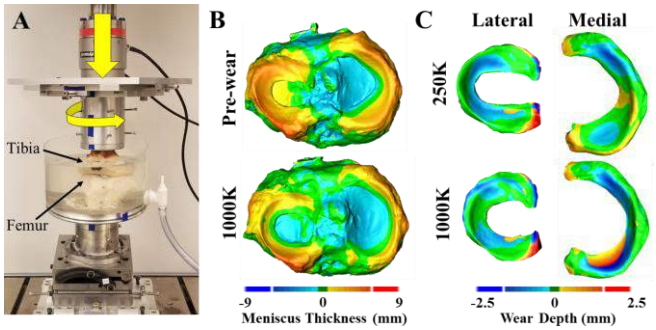

Figure 3. Human: A) Wear testing, Color maps of B) tibia-only to pre-wear and 1000K, and C) pre-wear to 250K and 1000K

RESULTS

Surrogate. Defect patterns were successfully visualized with preservation of detail using the CGS method. The color map shows alignment between two menisci: 0-in control and 0.05-in defect. A tight alignment is indicated by the green regions representing zero difference between the aligned menisci **(Fig 2B)**. The surrogate showed percent error increases as defect depths decrease for both menisci, with errors <7.9% when detecting volumetric changes of 0.4 cm^3 **(Fig 2C)**

Human. Throughout loading, the tibial surface became more prominent **(Fig 3B)** and the inner peripheral regions of the menisci receded **(Fig 3C)**. The CGS method successfully isolated both menisci with overall whole meniscus volume reductions of 52.0% and 31.9% for lateral and medial meniscus, respectively **(Fig 4A)**. Wear volumes increased throughout loading with the lateral meniscus experiencing 25.1% higher wear volume than the medial meniscus **(Fig 4B).**

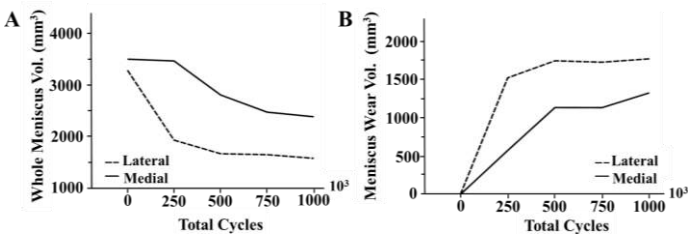

Figure 4. CGS method shows A) whole meniscus volume decreases while B) wear volume increases as the number of cycles increases.

DISCUSSION

For the first time, this study provides a method to characterize in vitro wear in whole human meniscus subjected to physiological loading. Based on our previous work[6], we found that the CGS method we developed has an inherent error of <5% when detecting volumetric changes of 0.4 cm^3 in simple geometry; however, for the complex surrogate analyzed in this study, error increased to <8% **(Fig 2C)**. Using this verified CGS method, we successfully detected and isolated global wear for a human meniscus subjected to joint loading. Wear volumes for both medial and lateral meniscus were shown to increase throughout 1 million cycles of loading. Based on the surrogate analysis, we have confidence that the 42% average measured meniscus volume loss is accurate to within 3%. Additionally, the CGS method yielded average meniscus volumes within +10% of known human meniscus volumes reported from water displacement techniques. This therefore indicates our method can successfully represent whole human meniscus volume.

Colorimetric mapping enabled the detection and visualization of high wear regions in the meniscus structure. A prominent reduction of yellow hue around both menisci from pre- to post-wear **(Fig 3B)** indicates a decrease in meniscus thickness and implies either material loss or hydrostatic deformation. Volume loss mostly occurred in the middle regions of the menisci **(Fig 3C; blue regions)**, matching clinical observations.[7] Additionally, the presence of red regions at 1 million cycles **(Fig 3C)** indicates deviatoric deformation since swelling is unlikely during wear testing. The measured volume loss may therefore be caused by material wear, deformation, or a combination of both.

The CGS method has practical advantages with respect to time, cost, and most importantly, the ability to visualize and quantify meniscus wear and deformation. The method takes 50-125% less time to complete a high-quality 3D model with equipment costs <15 times compared to micro-CT and MRI scanning.[4] Although the absence of synovial lubrication and soft tissue constraints within the joint likely resulted in greater menisci wear than would occur in vivo, the CGS method represents a breakthrough in measuring in vitro volumetric wear under controlled mechanical testing. Therefore, this novel method can provide a fast, accurate, and effective technique to enable researchers to determine meniscal wear rates for specific physiological activities (e.g. running, cutting, stair-climbing) and anatomical variations (e.g. age, BMI, sex) to identify risk factors for whole meniscus degeneration.

ACKNOWLEDGEMENTS: This work was funded by NSF-1154353.

REFERENCES: [1] Howell et al, J. Ortho. (2014) [2] Englund et al, E. Med. (2008) [3] Valigi et al, Mat. (2017) [4] Hollar et al, Wear (2018) [5] Shriram et al, J. Orth. Sur. (2019) [6] Benfield et al, Thesis (2020) [7] Li et al, Am. J. Trans. Res. (2019)

SIGNALING NETWORK MODEL OF TSC1 KNOCK-OUT RECAPITULATES A DEGRADATIVE VASCULAR SMOOTH MUSCLE CELL PHENOTYPE

Ana C. Estrada (1), Jay D. Humphrey (1)

(1) Biomedical Engineering
Yale University
New Haven, CT, United States

INTRODUCTION

Thoracic aortic aneurysms and dissections (TAADs) are severe vascular disorders that can arise due to genetic defects or loss of vessel wall integrity [1]. TAADs are characterized by excessive dilatation of the vessel wall and, in extreme cases, structural failure and rupture of the tissue. These processes inherently depend on the mechanical environment within the vessel and on cellular signaling processes that drive growth and remodeling (G&R) [2]. Vascular smooth muscle cells (VSMCs) are particularly important in vascular G&R given their role in controlling contractility and remodeling of the environment through proliferation and extracellular matrix deposition. In order to study the development and progression of TAADs, we need to understand the interplay between these factors.

In a recent study by Li et al. [3], the authors sought to understand the role of VSMC proliferation on the development and progression of TAADs. To do this, they used a post-natal, conditional, VSMC-specific knock-out (KO) of *Tsc1*, the gene encoding for the mammalian target of rapamycin (mTOR) complex 1 (mTORC1) inhibitor TSC1, and measured the morphological, hemodynamic, and cell signaling changes that occurred. mTOR is responsible for key cellular processes, such as cell growth, protein synthesis, and autophagy [4]. Specifically, mTORC1 is the primary effector of p70 ribosomal S6 kinase (S6K) and eukaryotic initiation factor 4E-binding protein 1 (4EBP1), proteins associated with ribosome synthesis and cell growth. The *Tsc1* KO induced increased activation of mTORC1 in VSMCs and led to higher incidence of TAADs in these KO mice relative to control. Interestingly, the VSMCs in the *Tsc1* mutant mice did not exhibit the characteristics of traditional contractile or synthetic VSMC phenotypes, instead showing decreases in both. The KO mice had significantly lower expression of matrix synthesis transcripts *Eln*, *Fbn1*, and *Col3a1*, as well as decreased elastogenesis, increased susceptibility to elastic fiber damage, and higher expression of matrix metalloproteinase 2 (MMP2). Strikingly, the KO VSMCs expressed high levels of lysosome-related proteins, namely β-catenin, MITF, and LAMP2, and had large numbers of degradative organelles present. These VSMCs notably lacked classic inflammatory cell markers, such as CD45, indicating that they did not undergo dedifferentiation into macrophages. These signaling changes suggested that the VSMCs acquired a novel degradative phenotype in addition to reduced contractile and synthetic capabilities.

The purpose of the current study was to delineate signaling pathways that contribute to the switch of VSMCs from a maintenance phenotype to a degradative phenotype. In order to do so, we constructed a VSMC signaling network model primarily centered on the mTOR pathway and then used it to simulate the *Tsc1* KO and its subsequent phenotypic changes.

METHODS

We built a signaling network model of mTOR signaling in VSMCs by consolidating cell signaling interactions reported in the literature and constructing a system of ordinary differential equations (ODEs) to describe these interactions. The ODEs were based on logic-based Hill-type functions that represent normalized (0-1) activation of each species in the network [5]. For this study, we simulated two conditions: 1) cell signaling in a control VSMC (Baseline) and 2) conditional knock-out of *Tsc1* (KO), in which the maximum activation level of the TSC1/2 species node was set to 0 while keeping all other model parameters constant. For the purpose of tuning the model, we used the steady-state solutions for each model condition to calculate the fold change of species downstream of mTOR (S6K, S6, 4EBP1) and contractile species (AKT, SMMHC, αSMA, SM22). We tuned

model parameters such that these fold changes would fall within one standard deviation of the data reported by Li et al. [4]. We then calculated the fold changes in select synthetic (Col3a1, Elastin, MMP2) and lysosomal species (β-catenin, MITF, LAMP2).

We used our model to describe the phenotypic characteristics in the Baseline and KO conditions. For this purpose, each phenotype (Contractile, Synthetic, and Degradative) is described using a normalized activation, which we calculated as the mean activation of a set of key species. The Contractile phenotype uses SMMHC, αSMA, SM22, and calponin as its primary species. The Synthetic phenotype depends on the levels of Col3a1, Eln, Fbn, and MMP2. The Degradative phenotype is in turn dependent on S6, MMP2, β-catenin, MITF, and LAMP2.

RESULTS

Our VSMC signaling network model consisted of 96 species and 148 reactions. The tuned model used input stress and shear stress values of 0.2404 and Hill-function parameters n = 1.4 and EC50 = 0.52. The weight of cell-surface receptor reactions was set to 0.85 and all downstream reaction weights were set to 1. We tuned the model based on 1) S6K, S6, and 4EBP1 activation at Baseline relative to KO and 2) AKT, SMMHC, αSMA, and SM22 activation at KO relative to Baseline. Our models showed mTOR downstream species relative activations of 0.0334, 0.0128, and 0.0334, respectively, which fall within one standard deviation of the fold changes reported in the experimental data (0.0388 ± 0.0198, 0.0132 ± 0.0040, 0.0498 ± 0.0301, respectively) [Fig. 1a]. The contractile protein species showed relative activations of 0.4294, 0.8005, 0.7617, and 0.7653, respectively, all of which fall within one standard deviation of the reported experimental data relative expression (0.403 ± 0.0324, 0.6912 ± 0.2531, 0.7456 ± 0.0379, 0.7457 ± 0.0599) [Fig. 1b].

Our model was able to capture changes in the synthetic and lysosomal capabilities seen in VSMCs after *Tsc1* disruption. Our model showed reduced levels of synthetic species Col3a1 and Elastin (0.7534 and 0.7986 fold, respectively) in the KO relative to Baseline, while the activation level of MMP2 increased 2.05 fold [Fig. 2a]. In contrast, we saw increased activation levels of β-catenin, MITF, and LAMP2 (1.9596, 4.5341, and 2.5549, respectively) in the KO relative to Baseline, consistent with the increase in lysosomal activity with *Tsc1* disruption [Fig. 2b].

We used our model to describe the phenotypic characteristics in the Baseline and KO conditions based on key species for the Contractile, Synthetic, and Degradative phenotypes. The Baseline condition showed a balance between the Contractile (0.5524) and Synthetic (0.4502) phenotypes and little influence by the Degradative phenotype (0.1419). The KO condition, however, shifted this balance towards a primarily Degradative (0.5308) phenotype, with a decrease in the influence of both the Contractile (0.4202) and Synthetic (0.3096) phenotypes [Fig. 3].

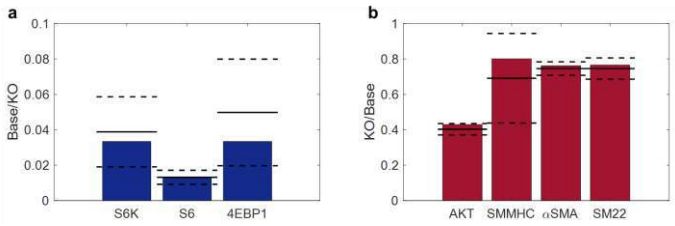

Figure 1: Model relative activation for (a) mTOR downstream species and (b) contractile species fall within 1SD (dashed lines) of the data means (solid lines).

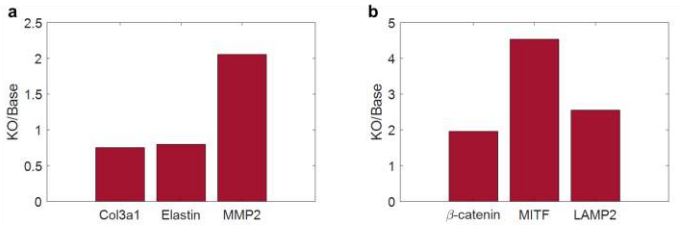

Figure 2: Model relative activations of (a) synthetic and (b) lysosomal species for KO relative to Baseline.

DISCUSSION

One of the key findings by Li et al. [4] was the existence of a degradative phenotype in vascular smooth muscle cells that was previously uncharacterized. This newly-described phenotype challenged the notion that VSMCs operate within a contractile-to-synthetic phenotypic axis. The VSMC signaling network model we presented here recapitulates the phenotypic switch induced by *Tsc1* disruption and captures the signaling changes shown experimentally, specifically increased mTORC1 activity, decreased contractile protein expression, decreased synthetic capabilities, and increased lysosomal activity.

While the simulations presented here used a single network model in isolation, there is potential to use this model in more complex G&R models. Recent work in the Humphrey lab has included coupling a homogenized wall signaling network model to tissue-level constrained mixture G&R modeling [6]. The degradative VSMC network model could also be used in the context of TAAD progression. Eventually, this modeling strategy could be used to simulate the interactions of multiple cell types, such as VSMCs, fibroblasts, and macrophages, and their role in the development and progression of vascular diseases.

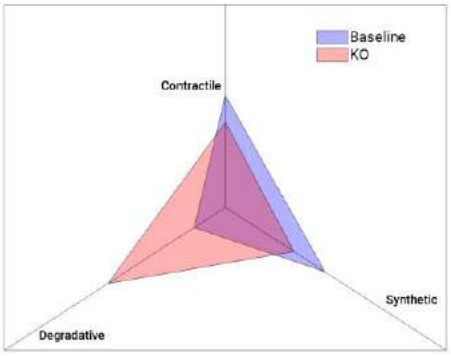

Figure 3: Contractile, Synthetic, and Degradative phenotypes calculated for the Baseline (blue) and KO (red) models.

ACKNOWLEDGEMENTS

This work was supported by NIH Grant (R01 HL146723).

REFERENCES

[1] El-Hamamsy & Yacoub, *Nat Rev Cardiol.*, 6:771-786 2009.
[2] Humphrey et al., *Circ Res.*, 116:1448-1461, 2015.
[3] Li et al., *J Clin Invest.*, 130:1233-1251, 2020.
[4] Laplante & Sabatini, *J. Cell Science*, 20:3589-3594, 2009.
[5] Krauetler et al., *BMC Syst. Biol.*, 4, 2010.
[6] Irons and Humphrey, *PLoS Comp Bio.*, 16, 2020.

CHANGES IN FIBER LEVEL STRAINS & CALCIUM ACTIVITY AFTER EXPOSURE TO BACTERIAL COLLAGENASE IN NEURON COLLAGEN CONSTRUCTS MIMICKING LIGAMENTS SUGGESTS POSSIBLE MECHANISMS FOR PAIN ASSOCIATED WITH JOINT DEGENERATION

Sagar Singh (1), Beth A. Winkelstein (1,2)

(1) Department of Bioengineering
University of Pennsylvania
Philadelphia, PA, USA

(2) Department of Neurosurgery
University of Pennsylvania
Philadelphia, PA, USA

INTRODUCTION

Degeneration of and/or pain from the spinal facet can occur naturally with aging [1,2]. The capsular ligament that encloses the facet joints is comprised of type I collagen fibers and is innervated by afferent neurons [3,4]. Changes to the capsular ligament with joint degeneration also alter its biomechanical properties and induce biochemical cascades, leading to the upregulation of proteolytic enzymes that reorganize and further degrade the extracellular matrix [5-7].

Intraarticular injection of bacterial collagenase, which digests type I collagen fibers, in the rat facet induces pain that lasts up to 3 weeks, absent any visible changes to the ligament's structure [8]. Collagenase treatment also alters neuronal activity and upregulates nociceptive mediators [9]. Collagenase digestion of isolated facets causes greater fiber disorganization and altered fiber kinematics during loading than in native tissues [10]. While microlevel mechanics may be involved in the pain response observed in vivo [8], the relationship between fiber level strains and neuronal activity has not been probed.

This study incorporated fluorescent microspheres in our in vitro model simulating the innervated ligament [11,12] in order to define the microlevel strains and neuronal activity generated with digestion by collagenase. Purified bacterial collagenase was applied for 20 minutes, a time known to alter neuronal activity [9,13]. The number of transient calcium events was measured as an indicator of real-time neuronal signaling and to define effects on neuronal activity [14].

METHODS

NCCs (n=5) were fabricated from 2mg/mL collagen solution and dissociated DRG neurons ($3x10^5$cells/mL) from embryonic day 18 rats [11]. The collagen solution was mixed with fluorescent microspheres (40nm dia; 580nm emission; 1:500 dilution; ThermoFisher). A DRG explant was also plated on each gel to provide a reference. After plating, neurons were cultured with neurobasal medium supplemented by 1% GlutaMAX, 2% B-27, 1% fetal bovine serum, and 10ng/mL 2.5S nerve growth factor (ThermoFisher). On day 2 in vitro (DIV2), neurons were transduced with an AAV expressing GCaMP6f in the feeding media (at 1:6000 dilution) which causes them to transiently fluoresce at 488nm with calcium influx [15,16]. At DIV6, collagen (150μL) with the fluorescent beads was added to encapsulate neurons. At DIV9, NCCs were placed on glass-bottomed dishes (MatTek) in 1.2mL of media.

Two groups of gels were exposed to 1mL of either: 37°C 60U activity bacterial collagenase (Worthington Biochemical) (treated; n=3) or the control of feeding media (untreated; 2 gels). A Leica inverted spinning disc confocal microscope imaged NCCs under a 63x oil-immersion objective, with 4 regions of interest (ROIs) for each gel selected to include 4-11 neurons in each ROI. Images were captured before exposure to define reference positions and baseline neuronal activity and at 20mins after exposure. The DRG explant was also imaged at 4X for each gel and timepoint to capture any gel movement. Image series (1024x1024 pixels^2) were taken at 20fps for 60s and analyzed to calculate strains and capture transient calcium events [8,17].

Displacements of the microspheres were tracked with ProAnalyst (Xcitex) and 4-node elements ($n_{treated}$=415; $n_{untreated}$=180) were generated; maximum principal strain (MPS) for each element at 20mins was calculated using LS-DYNA (LSTC) (Fig. 1). Displacement of the explant was also calculated. Average elemental MPS was calculated for each ROI and compared between groups using a Student's t-test.

The custom MATLAB script, FluoroSNNAP, was used to analyze and quantify the number of calcium events for each segmented neuron in each ROI ($n_{treated}$=94; $n_{untreated}$=44) [8,17]. Care was taken to ensure the same neurons were analyzed for both time points. The frequency of calcium events for each neuron was captured by a template-matching

algorithm [14,18]. The proportions of neurons with no or any calcium activity were calculated, as were the proportions with increased, decreased, or unchanged activity after exposure. Neuronal activity was compared between groups and times for each group by Pearson's chi-squared tests. Frequency distributions of calcium events per neuron were also compared with a Kruskal-Wallis non-parametric test.

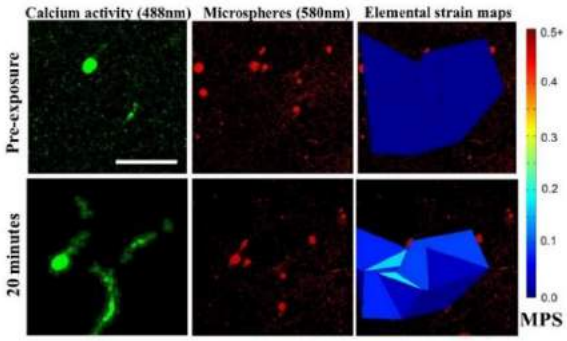

Figure 1: Representative images of a single ROI showing calcium activity (488nm) and microspheres (580nm) at both baseline and 20mins. Also shown are corresponding strains.

RESULTS

Treated NCCs experience strains (10.9±1.6%) nearly twice (p=0.01) those of untreated NCCs exposed to media (5.3±2.6%) (Fig. 1). In contrast, the overall deformation of the gel is not different (p=0.46) between treated (3.5±0.7%) and untreated (2.0±0.9%) cases.

Calcium activity varies with treatment and time (Fig. 2) despite there being similar proportions of inactive neurons in each group before (6.4% in treated; 2.3% in untreated; p=0.34) and after (6.4% in treated; 9.1% in untreated; p=0.57) treatment. Collagenase treatment alters neuron activity at 20mins, with a greater proportion (p=0.03) of neurons exhibiting increased activity (38.3%) compared to those increasing activity in response to media exposure (20.5%) (Fig. 2). Along with that, a greater proportion of neurons decrease (p=0.01) activity after treatment with media (77.3%) than after collagenase exposure (55.3%). These trends are similar for the frequency distributions of calcium events (Fig. 3). Both groups exhibit similar distributions at baseline pre-exposure (p=0.71), and both groups experience a shift to the left at 20mins after exposure, representing overall decreased neuronal activity (p<0.04) (Fig. 3). However, the shift is more pronounced in untreated neurons (p=0.025) than in the collagenase group.

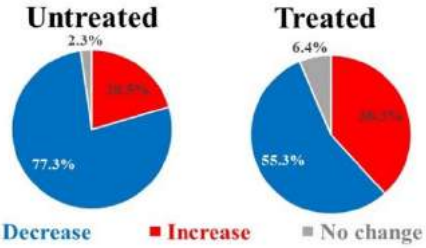

Figure 2: The proportion of neurons with increased activity after collagenase treatment is greater than for media

DISCUSSION

Bacterial collagenase exposure to collagen gels for 20mins generates appreciable microscale strains that can be detected using fluorescent beads embedded in the collagen (Fig. 1). The fact that overall gel deformations are similar across groups (2-4%) and below the collagenase-induced strains (11%) suggests adequate and meaningful measurement resolution in this method. The strains generated by that collagenase exposure are similar to the strains (11.7%) at which anomalous collagen fiber realignment occurs during loading of these same NCCs [12,19]. The similarity of strains and neuronal outcomes suggest collagen degradation may be enough to alter local mechanics of ligaments sufficiently rendering local motions as painful.

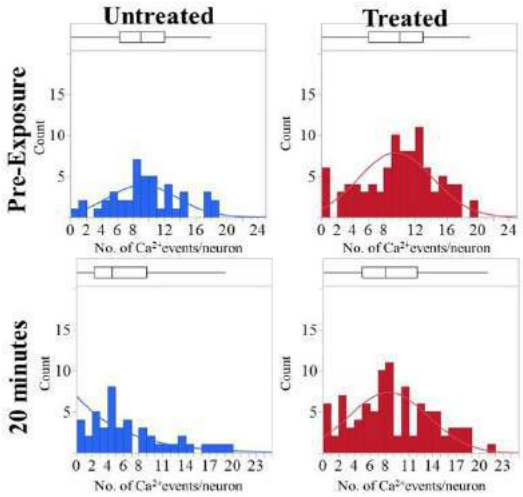

Figure 3: Both groups experience an overall decrease in neuronal signaling with a shift to the left at 20mins. This shift is more pronounced in untreated NCCs with media only.

Both bacterial collagenase and media exposure appear to alter the overall neuronal activity after 20 minutes (Figs. 2 & 3), similar to other reports [8,9]. The increase in firing events in the treated group may provide a mechanism by which those neurons experience local strains large enough to alter their response even absent macroscale deformation [20]. In fact, the strains with collagenase exposure correspond to those inducing upregulation of pERK [12]. The mechanical and biochemical results support microscale mechanics as regulating afferent responses.

Although measurements here were analyzed at the elemental level, mapping local strains to neurons would help to determine the relationships between local strain, neuron activity and even differences between neuronal phenotypes and their responses. Nevertheless, our approach provides a novel experimental platform to study fiber and cellular scale mechanical and functional outcomes.

ACKNOWLEDGEMENTS

Funding from NCCIH (AT010326) and Catharine Sharpe Foundation.

REFERENCES

[1] Kim J et al. *J Cell Physiol* 230(11):2837-47, 2015 [2] Bisson D et al. *J Ortho Res Spine* 1(2):1-11, 2018 [3] Neogi T et al. *Osteoarthr Cartil* 21(9):1145-53, 2013 [4] Yamashita T et al. *Spine* 21:538-43, 1996 [5] Furman B et al. *Arthritis Res Ther* 16(3):R134, 2014 [6] Kim J et al. *Osteoarthr Cartil* 23(12):2242-51, 2015 [7] Ralphs J & Benjamin M. *J Anat* 3:503-9, 1994 [8] Ita M et al. *Sci Rep* 10(1):1-15, 2020 [9] Ita M et al. *SB3C* P123, 2017 [10] Singh S & Winkelstein B. *SB3C* P352, 2020 [11] Zhang S et al. *J Orthop Res* 36(2):770-7, 2018 [12] Zhang S et al. *J Biomech Eng* 138:021013, 2016 [13] Conant K et al. *J Neurochem* 82(4):885-93, 2002 [14] Schultz S et al. *J Neurosci* 29(25):8005-15, 2009 [15] Chen T et al. *Nature*, 499(7458):295-300, 2013 [16] Nguyen J et al. *PNAS USA* 9(33):1074-81, 2015 [17] Patel T et al. *J Neurosci Methods* 243:26-38, 2015 [18] Hadjinicolaou A et al. *Biomaterials* 33(24):5812-20, 2012 [19] Quinn K et al. *J Biomech*, 43(10):1870-75, 2010. [20] Woolf C & Costigan M. *PNAS USA* 96(13):7723-30, 1999.

THE ROLE OF LIGAND DENSITY AND DEGRADABILITY IN HYDORGEL INDUCED BREAST CANCER DORMANCY

C. J. Farino (1), S. Pradhan (1), J.H. Slater (1)

(1) Department of Biomedical Engineering
University of Delaware
Newark, Delaware, United States

INTRODUCTION

While significant advances in cancer treatment have increased survival rate, metastasis persists as the leading cause of cancer associated death. During metastasis, disseminated tumor cells (DTCs) originating from the primary tumor can enter a chemoresistant, dormant state lasting months to decades before returning to an actively proliferative state [1]. However, the underlying mechanisms driving tumor dormancy and reactivation remain elusive.

Towards this goal, we investigated the role tumor microenvironment plays in cancer cell phenotype of four cell lines: the MDA-MB-231 parental line, and three organotropic sublines: BoM-1833 (bone tropic), LM2-4175 (lung tropic), and BrM2a 831 (brain-tropic). Each cell line was encapsulated in three poly (ethylene glycol) (PEG)-based hydrogel formulations composed of a proteolytically degradable PEG, and varying amounts of integrin-ligating RGDS and nondegradable crosslinker N vinyl pyrrolidone (NVP). Dormancy-associated metrics including viability, proliferation, metabolism, morphology, apoptosis, chemoresistance, phosphorylated ERK (p-ERK) and -p38 (p-p38) expression were quantified to classify hydrogel-induced phenotypic state.

METHODS

PEG macromers, PEG-PQ-PEG (PEG-PQ), and PEG-RGDS were synthesized as previously described [2,3]. For cell encapsulation, PEG-PQ was reconstituted in phosphate buffered saline (PBS) to a final concentration of 5% weight/volume (w/v) for all formulations. PEG-RGDS was reconstituted to a final concentration of 10 mM (gel 1), 1 mM (gel 2), or 0 mM (gel 3). Additionally, gel 2 contained 1.0 μL/mL (9.4 mM) NVP. UV-sensitive photocrosslinker, lithium phenyl-2,4,6-trimethylbenzoylphosphinate (LAP) was added to all formulations (3.0 mg/mL (10 mM). Cells cycle was synchronized 48 hr prior to encapsulation using serum-free media. Cells were trypsinized, counted, and re-suspended in pre-polymer solution (10 million cells/mL). Precursor (3 μL) was pipetted, flattened to a height of 500 μm, and photopolymerized by Broad spectrum UV (Blak-Ray flood UV lamp, wavelength: 365 nM, intensity: 10 mW/cm^2). Cell-laden hydrogels were cultured for 15 days with media changes every 4 days.

Hydrogel characterization (compressive modulus, theoretical mesh size, swelling ratio, and degradation) was completed as previously described [2,3]. Dormancy associated metrics were quantified as previously described [2,3]. Briefly, cell viability was measured with a Live/Dead® cell viability kit (Invitrogen), early apoptosis with CF568 Annexin V (Biotium), proliferation via the Click-It® EdU Imaging Kit (Invitrogen), and metabolism via an Alamar Blue assay (Thermo Fisher). For visualizing morphology, cells with fixed, permeabilized, blocked, stained with Alex Fluor 568-F-actin (Invitrogen, 2.6 μg/mL) and counterstained with Hoechst 33342 (10 μg/mL). Drug studies were performed as previously described [3]. For p-ERK and p-38 labeling, cells were fixed, blocked, incubated with the p-p38 primary antibody (1:200), rinsed, and incubated with a secondary goat anti-mouse antibody (IgG-Alexa Fluor 647: 1:500) for 2 hr at room temperature. The protocol was repeated to label cells with the primary p-ERK antibody (1:200) and secondary goat-anti rabbit IgG-Alexa Fluor 488: (1:500) antibody. Hydrogels were counterstained with Hoechst 33342. Expression was measured by quantifying the mean fluorescence intensity of a maximum intensity z-projection. For all imaging, cell-laden hydrogels were placed between two coverslips and fluorescent z-stacks (z-height: 150 μm) were acquired using structured illumination on a Zeiss AxioObserver Z1 inverted fluorescent microscope equipped with a Zeiss Apotome2 imaging system and a Hamamatsu ORCA-Flash 4.0LT camera. FIJI software (NIH).

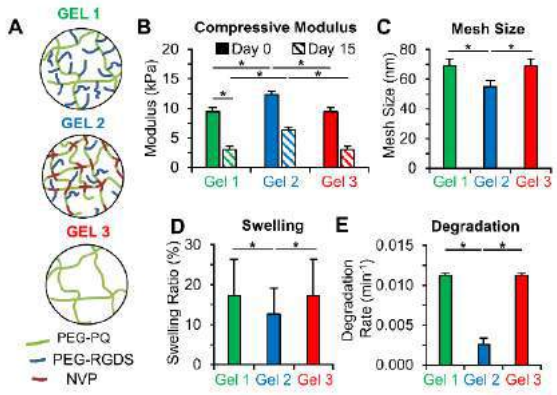

Figure 1: (a) schematic of hydrogel formulations. Quantification of (b) compressive modulus of parental 231 cell laden hydrogels at day 0 (solid) and 15 (striped), (c) swelling ratio, and (e) degradation rate.

RESULTS

To quantify the effect of tuning RGDS and NVP concentrations, elastic modulus of cell-laden hydrogels was measured at day 0 and 15. At day 0, the modulus of hydrogels without NVP (gel 1 and 3) was 9.4 ± 0.8 kPa, while hydrogels with NVP (gel 2) had a modulus of 12.3 ± 0.6 kPa (Fig 1a). NVP incorporation is expected to yield a higher modulus as NVP increases the number of crosslinks. Elastic modulus decreased to 3.0 ± 0.6 kPa (gel 1 and 3), and 6.3 ± 0.5 kPa (gel 2) at day 15, likely due to cell-mediated hydrogel degradation. NVP incorporation also decreased mesh size, swelling, and degradability of gel 2 compared to gel 1 and 3. (Fig 2c-e). Next, we observed how differences in hydrogel composition altered cancer cell phenotype. Parental and organotropic triple negative breast cancer cell lines were individually encapsulated in the three hydrogel formulations for 15 days. First, we measured cell viability at day 0 (6 hr post encapsulation) and 15. In gel 1 and 2 viability remained high at day 15 (>83.3%) for all cell types. In the absence of RGDS, viability dropped to 45.4 ± 3.2% for the parental 231 line in gel 3. Interestingly, viability remained >88.5% for all organotropic cells in gel 3. Temporal changes in viability were quantified by normalizing the number of viable cells at day 15 to the number of viable cells at day 0 (viable cell ratio) (Fig 2). High ligand density and degradability (gel 1) led to a 1.5-1.9-fold increase in the number of viable cells present at day 15. NVP incorporation in gel 2 displayed no significant change in the number viable cells at day 15 compared to day 0 for any cell type. Viable cell density also remained constant for all organotropic cells in gel 3. Quantifying the new number of live cells compared to new number of dead cells at day 15, post day 0 (new live: new dead cell ratio) indicated similar trends (Fig 2).

We also quantified how metabolism, proliferation, and apoptosis changed throughout the culture period. In gel 1, metabolism increased between 5.9-12.5-fold compared to day 0 for all cell types (Fig 2). Additionally, the number of proliferating (EdU^+) cells at day 15 compared to day 0 showed a 3.4-6.1-fold increase. Accordingly, when comparing the number of EdU^+ cells to Annexin V^+ cells at day 15, all cells in gel 1 had significantly more cells undergoing proliferation rather than early apoptosis (Fig 2). In gel 3, all organotropic cells remained a constant state indicated by no significant changes in metabolic activity and the number of proliferating (EdU^+) cells (Fig 2). These cells also indicated a balanced between the number of EdU^+ and Annexin V^+ cells. Furthermore, cells in gel 3 displayed increased drug resistance to doxorubicin and p38 expression, compared to cells in gel 1. Parental cells in gel 3 instead showed decreased metabolic activity, proliferation, and increases apoptosis, alongside increased drug resistance and p38 expression. In gel 2, parental 231s and most organotropic cells displayed a balance in the number of new live and dead cells, metabolic activity, and EdU^+ cells, and increased drug resistance and p38 expression. Interestingly, bone- and brain-tropic cells appeared mostly in clusters, while parental and lung-tropic cells remained as single cells.

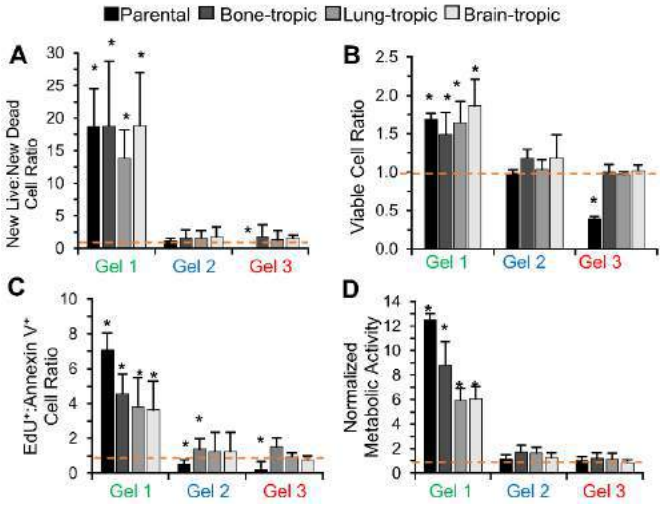

Figure 2: Quantification of (a) the number new live cells compared to new dead cells at day 15, post day 0, (b) the number of viable cells at day 15 normalized to day 0, (c) the number of EdU^+ cells compared to Annexin V^+ cells at day 15, and (d) metabolic activity at day 15 normalized to day 0. * indicates $p<0.05$. n=5. Values represent mean + standard deviation.

DISCUSSION

In this study, we investigated how tuning matrix mechanical and biochemical properties altered cancer cell fate of parental and organotropic 231s. Due to the increases in viable and proliferating cells, metabolic activity, and invasive phenotype, all cells in gel 1 were characterized to be in a growth state. Incorporation of NVP and decreased matrix degradability in gel 2 led to constant viable and EdU^+ cell density, increased chemoresistance, and expression of dormancy marker, p-38. Thus, all cells in gel 2 were in balanced dormancy. Parental and lung-tropic 231s were further characterized as balanced cellular dormancy, while bone- and brain-tropic cells as balanced tumor mass dormancy based on whether cells appeared mostly as single cells or as clusters. Following the same reasoning, organotropic cells in gel 3 were characterized as balanced cellular dormancy. Lastly, in the absence of RGDS, parental 231s were characterized to be in restricted survival dormancy due to its limited viability at in gel 3. Overall, these results show how tuning matrix adhesion and degradability can alter cancer cell fate while simultaneously highlighting how organotropic cells derived from the same parental line can sustain viability in unfavorable conditions. We envision that this this platform may be used in future studies to help identify potential anti-dormancy therapeutic targets for pre-emptive treatment of dormant cancers.

ACKNOWLEDGEMENTS

This work was supported by the National Institutes of Health (R21CA214299) and the W.M. Keck Foundation (15A00396). C.J.F was supported by a University of Delaware Graduate Scholar Award.

REFERENCES

[1] Gomis, R et al, *Molecular Oncology*, 11:62-78, 2017.
[2] Pradhan, S et al, Biomaterials, 215:119177, 2019.
[3] Farino, C et al, *ACS Applied Biomaterials*, 3:5832-5844, 2020.

ON THE RELATION BETWEEN COMPUTATIONAL FLUID DYNAMICS-DERIVED BIOMARKERS AND CORONARY ARTERY BYPASS GRAFT REMODELING

Nhien Tran-Nguyen (1), Francesca Condemi (2), Stephen Fremes (3), Piero Triverio (1), Laura Jimenez-Juan (4)

(1) Institute of Biomedical Engineering
Dept. of Electrical & Computer Engineering
University of Toronto
Toronto, Ontario, Canada

(2) CorWave
Clichy, France

(3) Dept. of Surgery, University of Toronto
Sunnybrook Health Sciences Centre
Sunnybrook Research Institute
Toronto, Ontario, Canada

(4) Dept. of Medical Imaging, University of Toronto
St. Michael's Hospital
Sunnybrook Research Institute
Toronto, Ontario, Canada

INTRODUCTION

In Canada, approximately one person out of eight dies because of coronary artery disease – the leading cause of death in the world [1]. Coronary arteries play a vital role in the body, supplying the heart with oxygenated blood. However, the buildup of atherosclerotic plaques can narrow the lumen of coronary arteries (stenosis), decreasing blood flow to the heart and ultimately contributing to heart failure. In severe cases, coronary artery bypass graft (CABG) surgery can be performed, using a harvested vessel to create an alternative path for blood to reach the myocardium [2]. After grafting, grafts tend to remodel, and sometimes this process degenerates, leading to a complete occlusion of the graft, known as failure. Unfortunately, despite many advancements, failure remains quite common: 25% of vein grafts fail within two years of CABG surgery, affecting 43% of patients [3]. Significantly, the underlying reasons behind graft failure are still unclear.

Altered blood flow dynamics are already known to be involved in the pathophysiological processes behind vascular remodeling. For example, it is well known that low and oscillatory wall shear stress (WSS) can lead to endothelial dysfunction and the initiation of atherosclerosis [4]. More recent studies have also pointed to the potential role of WSS in graft failure [5]. However, while hemodynamics in grafts and coronary arteries likely play a critical role in explaining CABG failure, this information is difficult to obtain non-invasively, even with the latest imaging modalities. The small caliber of coronary arteries and grafts precludes the in-vivo acquisition of blood velocity, which is needed to calculate WSS.

Previous works in other cardiovascular territories show that computational fluid dynamics (CFD) simulations guided by medical images can potentially address this gap [6]. Patient-specific anatomy obtained through coronary CT angiography can be used to guide CFD simulations to provide quantitative information on the blood flow in coronary arteries and grafts [7]. These non-invasive CFD simulations can also be integrated with flow velocity information obtained from 4D-flow MRI to impose patient-specific boundary conditions and improve accuracy [8]. With CFD simulations, a number of relevant hemodynamic biomarkers such as WSS and oscillatory shear index (OSI) can be obtained non-invasively. Such quantities can provide new insights into the root mechanisms behind CABG failure and potentially lead to better treatment plans.

The main objective of this research is to use patient-specific image-guided CFD simulations in the analysis of CABG remodeling. Specifically, we performed a preliminary investigation on the relation between WSS and OSI calculated one month after surgery, and the degree of graft remodeling measured one year after surgery.

METHODS

This prospective study was performed on a cohort of 4 patients who underwent CABG surgery at the Sunnybrook Health Sciences Centre in Toronto, Canada. The cohort includes 10 grafts, 4 of which were left internal mammary artery (LIMA) grafts, 4 were saphenous vein grafts (SVG), and 2 were radial artery (RA) grafts. Both CT and 4D flow MR imaging were performed 1 month after surgery, to obtain anatomical and flow information, respectively. One year after surgery, CT images were acquired again to assess the extent of graft remodeling.

Three-dimensional anatomical models of the aortic arch and associated branches, coronary arteries, and implanted grafts were reconstructed from CT images using SimVascular (Stanford University, Stanford, California) [9]. The generated reconstructions were used for CFD simulations and for measuring the average diameter in each implanted graft. In order to reach a periodic solution, transient CFD simulations were run for 5 full cardiac cycles. Blood flow rate measured using 4D flow MRI was used as an inlet boundary condition in the

ascending aorta, and a lumped parameter model was used as boundary condition at the outlet of descending aorta, aortic branches, and distal coronary arteries [9].

From the velocity computed with CFD simulations, the WSS and OSI distributions in each graft were computed with SimVascular. Post-processing and visualization of CFD results were performed with ParaView (Kitware, Clifton Park, New York) and MATLAB (MathWorks, Natick, Massachusetts). Wall shear stress was time-averaged over a single cardiac cycle. The ratio between the graft wall area exposed to abnormal WSS (<0.5 Pa [10]) and total graft area was computed. Similarly, the ratio between the graft wall area exposed to abnormal OSI (>0.2 [11]) and the total graft area was also computed.

RESULTS

The plots in Figure 1 compare the average graft diameter found 1 month and 1 year post-surgery. Data points below the black dotted line correspond to a reduction in graft lumen diameter after 1 year. Data points are color-coded by graft type. In Figure 1A, the marker size corresponds to the percent graft area exposed to abnormal WSS, while the marker size in Figure 1B corresponds to the percent graft area exposed to abnormal OSI.

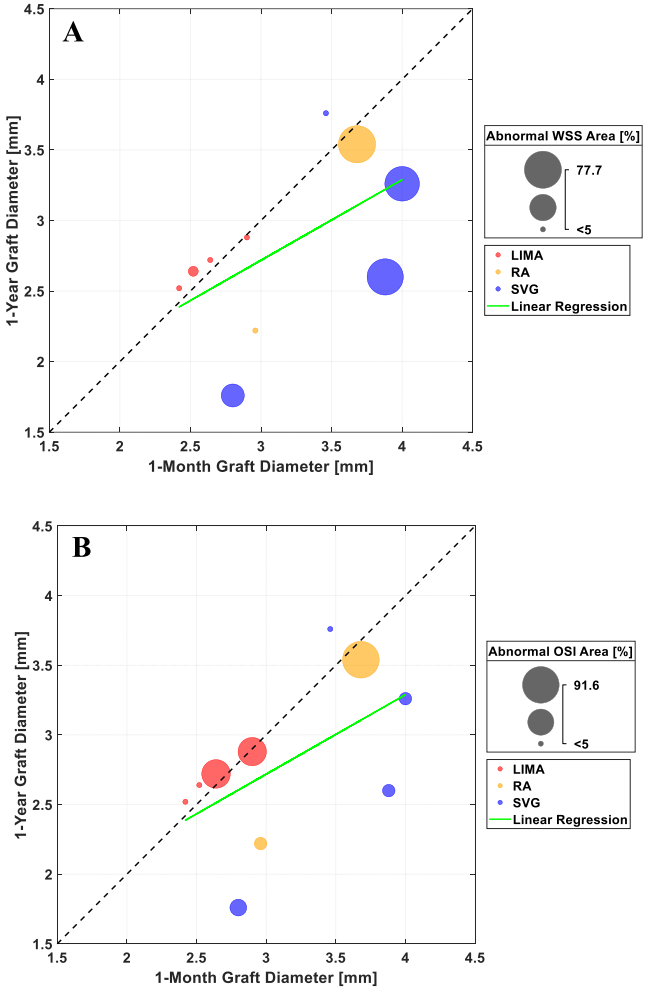

Figure 1: Comparison of average graft lumen diameter between 1 month and 1 year post-surgery. Marker size corresponds to percent graft area exposed to abnormal WSS in (A) and to abnormal OSI in (B).

DISCUSSION

As a whole, the cohort tended towards negative graft remodeling after 1 year, with a linear regression slope of <1. There are also some qualitative differences in the degree of remodeling among the different graft types. None of the LIMA grafts experienced significant remodeling at the 1-year time point, while 3 out of 4 of the SVGs experience a lumen reduction. This observed difference in remodeling for SVG vs. LIMA grafts is consistent with their differential long-term graft patency rates identified in previous studies [12]. The trend for the RA grafts is less clear due to only 2 grafts being included in the analysis.

There are also some qualitative trends between graft remodeling and abnormal WSS area. Figure 1A shows that grafts with lower abnormal WSS area tend to experience less graft remodeling at 1 year than grafts with higher abnormal WSS area. This qualitative observation aligns with what is known about the role of abnormal WSS in vessel remodeling [4]. In particular, we also see that all 4 LIMA grafts have low abnormal WSS area, while 3 out of the 4 SVGs have high abnormal WSS area. This observation seems to align with the clinical observation that LIMA grafts tend to have higher success rate than SVGs [12].

On the other hand, the relationship between abnormal OSI area and graft remodeling is less clear. In Figure 1B, it appears that the grafts with the highest abnormal OSI area did not experience much remodeling at 1 year. The grafts that experienced remodeling were not exposed to much abnormal OSI, while the grafts that did not remodel had mixed exposure to abnormal OSI. Previous studies suggest that abnormal OSI, corresponding to oscillatory WSS, contributes to vascular remodeling [11]. However, others have reported that abnormal OSI alone may not correlate to vascular disease [12]. Our observations regarding the relationship between OSI and bypass graft remodeling are inconclusive.

Overall, the proposed preliminary study revealed some qualitative trends in coronary artery bypass graft remodeling according to graft type and WSS. One limitation of this study is the small sample size, which does not provide enough statistical power to demonstrate significance. Future works will add more patients and grafts to the present study.

ACKNOWLEDGEMENTS

This work was supported by the Radiological Society of North America, the Jean & Lauri Hiivala Research Fund for Heart Health, the Department of Medical Imaging of the University of Toronto, and Compute Canada.

REFERENCES

[1] Statistics Canada, *Table 13-10-0147-01 Deaths, by cause, Chapter IX: Diseases of the circulatory system (I00 to I99)*, 2019. Available: https://www150.statcan.gc.ca/t1/tbl1/en/tv.action?pid=1310014701.
[2] Petrie, M.C. et al., *Circulation*, 134(18):1314-1324, 2016.
[3] Lopes, R.D. et al., *Circulation*, 125(6):749-756, 2012.
[4] Chatzizisis, Y.S. et al., *J Am Coll Cardiol*, 49(25):2379-2393, 2007.
[5] Owida, A.A. et al., *Comput Methods Programs Biomed*, 108(2):689-705, 2012.
[6] Steinman, D.A. et al., *Am. J Neuroradiol*., 24(4):559-566, 2003.
[7] Ballarin, F. et al., *J of Computational Physics*, 315:609-628, 2016.
[8] Numata, S. et al., *Eur. J of Cardio-Thoracic Surgery*, 49(6):1578-1585, 2016.
[9] Updegrove, A. et al., *Ann Biomed Eng*, 45(3):525–541, 2017.
[10] Gijsen, F. et al., *Eur Heart J*, 40(41):3421-3433, 2019.
[11] Chen, Z. et al., *Sci. Rep.*, 7(1):2007, 2017.
[12] Goldman, S. et al., *J Am Coll Cardiol*, 44(11):2149-2156, 2004.
[13] Khan, M.O. et al., *J Cardiovasc Transl Res.*, E-pub ahead of print, 2020. DOI: 10.1007/s12265-020-09982-7.

SIGNAL TO NOISE RATIO OF POLARIZATION IMAGING PARAMETERS IS DEPENDENT ON LIGHT INTENSITY AND MICROSTRUCTURAL ANISOTROPY OF SOFT TISSUES

Leanne E. Iannucci (1), Yingkai Chen (2), Viktor Gruev (2), Spencer P. Lake (1)

(1) Washington University in St. Louis
St. Louis, MO USA

(2) University of Illinois at Urbana-Champaign
Champaign, IL USA

INTRODUCTION

Highly aligned collagen fibers serve as the primary load bearing structure in musculoskeletal soft tissues like tendon and ligament. [1] When this organization is disrupted in periods of disease or damage, it leads to aberrant tissue function, pain, and loss of quality of life. For this reason, rapid, accurate visualization of collagen microstructure in these tissues is essential to diagnose tissue dysfunction, better understand disease pathology, and motivate new repair strategies. [1]

Myriad biomedical optics techniques have been used to evaluate collagenous tissue structure, but many of these modalities lack sufficient (1) spatial resolution to probe microstructural length scales, (2) temporal resolution to see dynamic changes in the extracellular matrix, and/or (3) require excision or destructive processing of tissue prior to analysis. [1] Recently, quantitative polarimetry-based techniques have been used across biomedical applications to overcome some of these limitations. [2] These methods employ the intrinsic birefringence of collagen as a source of endogenous contrast, thus increasing the modalities' sensitivity to fiber structures. Additionally, the minimal instrumentation required to implement these techniques lends itself to endoscopic integration, allowing for exploration into more clinically relevant *in vivo* applications. [2]

When moving towards *in vivo* optical imaging, there is an inherent potential constraint on maximal light intensity available due to a need to minimize heat generation from light sources. [3] As such, there is potential for loss in image quality or data integrity if the signal-to-noise ratio of the measurement in question is not sufficiently high. Additionally, during *in vivo* imaging of non-planar tissues, there are local fluxuations of light intensity that could affect the SNR of particular regions of out-of-plane tissue regions more than others. Therefore, understanding how noise propagates in output parameters calculated during polarimetry under low light conditions is essential for successful clinical translation. [5]

Therefore, the objective of this study was to evaluate low-light imposed noise propagation in common polarimetric calculations of degree of linear polarization (DoLP) and angle of polarization (AoP). These measurements provide information about the strength and orientation of collagen fiber alignment, respectively, when imaging biological tissues. To assess the SNR in these metrics, engineered tissue analogs of prescribed anisotropic or isotropic collagen fiber alignment were fabricated and subjected to reflectance quantitative polarized light imaging (rQPLI) across a gradient of incident light intensities during dynamic loading.

METHODS

rQPLI. As described previously, rQPLI utilizes a polarization-sensitive, division-of-focal plane (DoFP) camera to quantify the first three Stokes parameters, and thus the polarization state of light, on a pixelwise basis for the field of view. A circularly polarized light source is mounted 30° angle to the normal above the sample. The DoFP sensor is directly above the sample. (**Figure 1A)** From the Stokes parameters collected for each sample-spanning pixel, the DoLP and AoP can be calculated. This process is repeated framewise during testing to get dynamic measurements of collagen fiber alignment strength and orientation, respectively.

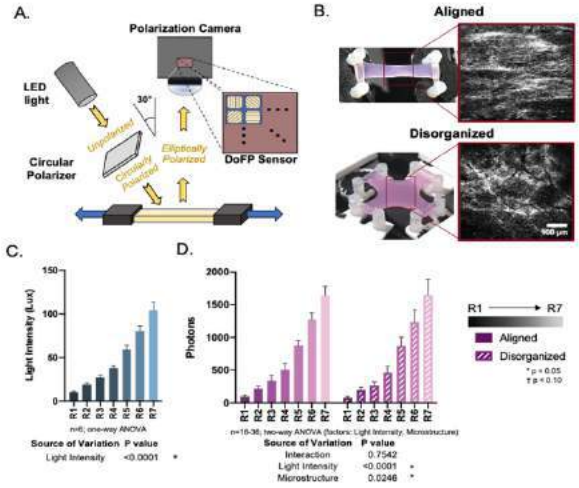

Figure 1. (A) Schematic of rQPLI. **(B)** SHG images indicating anisotropic (Aligned) and isotropic (Disorganized) microstructure of collagen tissue analogs. **(C)** Light intensity measured at plane of sample and **(D)** photons incident on sensor during mechanical testing.

Theoretical Signal-to-Noise Ratio in DoLP and AoP. The theoretical noise within Stokes parameters using DoFP sensors is primarily driven due to photon shot noise and has been previously characterized using standard error propagation techniques. [4] In brief, extending these methods to definitions of the Stokes parameter-derived metrics of DoLP and AoP, the signal-to-noise ratios are defined as:

$$SNR(DoLP) = \frac{DoLP}{\sigma_{DoLP}} = \sqrt{\frac{I}{1+\frac{1}{DoLP^2}}} \quad (1)$$

$$SNR(AoP) = \frac{AoP}{\sigma_{AoP}} = \pi \cdot DoLP \cdot \sqrt{I} \quad (2)$$

where I is the incident light intensity and σ is the noise associated with each polarization parameter.

Tissue Analog Fabrication and Testing. Collagen based tissue analogs of prescribed collagen fiber alignment were generated using previously established methods. [5] Dermal fibroblasts were mixed with Type I collagen and injected into Teflon molds with either a bar- or cruciform-shaped geometry. Rods at the ends of these molds provided static mechanical boundary conditions during 7 days of static culture that stimulated anisotropic (Aligned) or isotropic (Disorganized) collagen fiber alignment in the center of each gel. (**Figure 1B)**

As indicated in Eqs. 1 & 2, the SNR of both DoLP and AoP are dependent on the DoLP of the sample and the intensity of the incident light (I). The baseline DoLP of a sample is determined by its strength of fiber alignment. Creation of tissue analogs with these different microstructures ensured creation of tissues with differing but known baseline DoLP values. To experimentally determine the SNR as a function of changing light intensity, the power of the circularly polarized incident light source was changed to one of seven settings (R1-R7). For each of the prescribed light settings, tissue analogs (n=6-12 per microstructure) were subjected to a mechanical loading protocol (0.1N preload; 10 cycles to 1.25%, 2.5%, 3.75% strain). Samples were cycled at increasing strain amplitudes to assess the ability to discern differing magnitudes of dynamic microstructural realignment due to load in DoLP and AoP at different noise levels (data not shown).

At each light intensity, the average signal and noise were calculated as the mean and standard deviation (STD), respectively, for both DoLP and AoP. Values were calculated for the first 100 frames after preload but before dynamic testing, and then averaged pixelwise within the sample spanning the center region of interest. The ratio of signal (mean) and noise (STD) was then calculated as the SNR for a each sample. Qualitative DoLP and AoP color maps were calculated to visualize signal integrity at each light intensity.

RESULTS

Light Intensity Alteration. Generation of a progressively increasing gradient of light at the plane of the sample was verified via direct luxmeter readings, with values ranging between 10.2 ± 0.9 Lux and 104.0 ± 9.4 Lux from R1 to R7 ($p < 0.05$). (**Figure 1C)** Additionally, a gradient in reflected light onto the sensor after sample interaction was verified by calculating the number of detected photons within the region of interest of the sample ($p < 0.05$); these values ranged between 412.6 ± 110.9 and 7321.4 ± 606.8 photons from R1 to R7 in Aligned samples and between 330.4 ± 78.6 and 7497.1 ± 1049.3 photons from R1 to R7 in Disorganized samples. (**Figure 1D)**

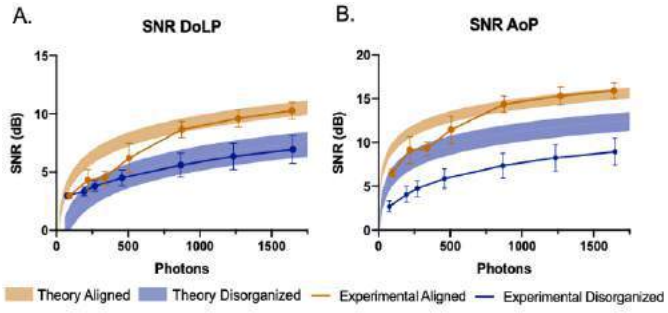

Figure 2. Theoretical solution and experimentally determined signal-to-noise ratio (dB) of **(A)** DoLP and **(B)** AoP. Theoretical bands represent solution to Eq. 1 & 2 at mean ± STD of each microstructure type. Experimental data (n=6-12/microstructure) are mean ± STD.

Theoretical SNR. The baseline DoLP of each microstructure at R7 was considered to be ground truth with which to solve Eqs. 1 and 2 (Aligned 0.28 ± 0.10; Disorganized 0.14 ± 0.03). In these solutions, the higher baseline DoLP resulted in a higher SNR in both AoP and DoLP across all possible light intensities. Additionally, the magnitude of the SNR in AoP is higher across light intensities than that of their respective DoLP SNR counterparts. **(Figure 2)**

Experimental SNR. The SNR of DoLP ranged between 2.97 ± 0.22 dB and 10.25 ± 0.72 dB from R1 to R7 in Aligned and between 2.97 ± 0.23 dB and 6.93 ± 1.21 dB from R1 to R7 in Disorganized. The SNR of AoP ranged between 4.47 ± 0.46 dB and 39.85 ± 7.81 dB from R1 to R7 in Aligned and between 1.88 ± 0.28 dB and 8.28 ± 3.01 dB from R1 to R7 in Disorganized. There was a high degree of congruence between the experimental results and the theoretical solutions, both in magnitude and trend. **(Figure 2)**

DISCUSSION

In this study, the signal-to-noise ratio of DoLP and AoP during rQPLI was explored through imaging of biological tissues of varied anisotropies at graded light intensities. Tissues of known, controlled fiber alignment were fabricated and successfully subjected to a range of incident light intensities resulting in a gradient of photon flux on the surface of the polarization sensor after interaction with the tissues.

Based on the SNR equations of both DoLP and AoP derived from error propagation techniques, we expected SNR to be dependent not only on the incident light intensity, but also the baseline DoLP of the sample. Since the DoLP represents the strength of alignment, this has been shown to be a measurement of the anisotropy of a tissue of interest. [2] Therefore, the SNR of these polarization measurements, and the SNR response as a function of light intensity, should vary based on how aligned a sample is. We confirmed this in both the theoretical solutions to the SNR equations and experimental evaluation of SNR during imaging of biological tissue analogs. The SNR was substantially higher across all light intensities in both DoLP and AoP when imaging the Aligned samples than compared to Disorganized counterparts.

Further, these data show that AoP is more resilient to the noise floor at lower light than DoLP: the magnitude of the SNR AoP is consistently higher both theoretically and experimentally when comparing different microstructures. The DoLP SNR is roughly the same between Aligned and Disorganized at low light intensities (R1-R4, **Figure 2**). At lower light, it is impossible to qualitatively distinguish between microstructures based on the strength of alignment (DoLP) (data not shown) and the signal is effectively lost below the noise floor. This does not occur until much lower lights (R1-R2) when considering the orientation of fibers (AoP).

Overall, these data demonstrate important considerations about SNR when using polarized light to image biological tissues. AoP is more resilient to noise than the DoLP, so it may be of greater use in low light applications like endoscopy, particularly if dynamic range in the sensor of interest is limited. Further, the SNR of DoLP and AoP are both functions of DoLP, and, subsequently, tissue anisotropy. Because of this dependency, low light imaging of highly aligned tissue like tendon may be possible whereas visualization of the disorganized collagen microstructure of other tissues (e.g., skin) might not be visible through noise under the same sensor architecture and conditions of lighting.

ACKNOWLEDGEMENTS

NSF BMMB 1761561 and NIH T32 EB014855-06.

REFERENCES

[1] Goth, W. et al. *Annual Rev. Biomed. Eng.* 18, 357-385, 2016.
[2] York, T. et al. *Proc. IEEE* 102(10), 1450-1469, 2014.
[3] McCallum, R. et al. *Clin. Otolaryngol.* 43(5), 1266-1272, 2018.
[4] Perkins, R. et al. *Optics Express* 12(25), 25815-25824, 2010.
[5] Lake, S. et al. *J Mech. Behav. Biomed.* 13, 25-35, 2012.

AN INVERSE MECHANICS APPROACH TO DETERMINE CHANGES IN THE MECHANICAL HETEROGENEITY OF THE LUMBAR FACET CAPSULAR LIGAMENT

Jill M. Middendorf (1), Victor H. Barocas (1)

(1) Biomedical Engineering
University of Minnesota – Minneapolis
Minneapolis, MN, USA

INTRODUCTION

Recent research has identified a relationship between the lumbar facet capsular ligament (FCL) and sensations of low back pain [1]. This increase in pain may be associated with changes in the mechanical properties of the FCL. Specifically, reduced FCL strength can cause abnormal spinal segment motion [2] or increased strain on axons embedded in the FCL [3], both of which may contribute to low back pain. Global FCL tissue mechanics have been fit to bi-axial force displacement curves [5] providing basic information about FCL mechanical behavior. However, previous work has not determined the heterogeneous mechanical properties of the FCL that could contribute to increased sensations of low back pain.

The FCL has a highly heterogeneous collagen structure [4], but quantification of the mechanics in these heterogeneous regions is unknown. Recent advancements in the use of inverse mechanics methods on soft tissues provide [6,7] an opportunity to directly use experimental data and determine heterogeneous mechanical properties of the FCL. Therefore, to determine differences in FCL mechanical heterogeneity that may cause increased sensations of low back pain, this study coupled experimental data on bi-axially loaded FCLs with an inverse mechanics method.

METHODS

FCLs were obtained from two cadaveric lumbar spines, one with reported low back pain (+LBP) and one with no reported low back pain (-LBP). Prior to dissection, facet joint and IVD health were determined by taking T2 weighted MRI [8]. All scans were performed on a 3T MRI scanner with a Siemens knee coil. The imaging included clinical T2-weighted sequencing in the sagittal plane and the axial plane. We note the articular cartilage in the facet joint of the -LBP spine showed thicker articular cartilage than the facet joint from the +LBP spine (Fig 1). Additionally, both spines contain reduced disc height.

After MRI imaging, the FCL was dissected from the right side of the L3-L4 facet joint in both specimens. Ligaments were cut into approximately a cruciform shape, and then the medial, lateral, interior and superior surfaces were mounted into brackets in a biaxial loading system. A 15-step biaxial loading protocol [6] was applied to the tissue, such that the maximum stretch in both directions was 12%. During loading, videos were taken of the FCL surface, and loads were measured using 6 degree of freedom load cells on each of the 4 loading arms. Once testing was completed, digital image correlation was used to track the

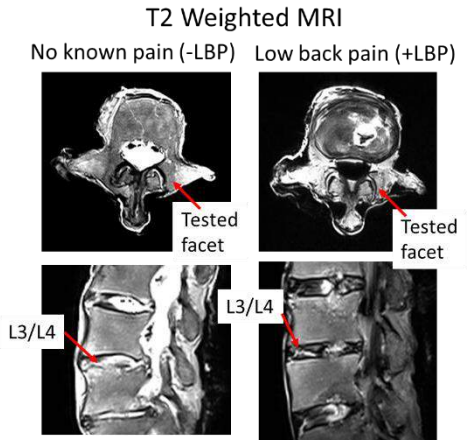

Figure 1: MRI T2 imaging of two different lumbar spines shows variability in the thickness of the facet joint articular cartilage and differences in the IVD height and hydration.

tissue motion and calculate surface strain. These deformation fields were then used partition regions of the FCL into similar and dissimilar regions based on jumps in the deformation gradient, as previously described [7]. Each FCL domain was partitioned until a total of 20 distinct regions were created.

To calculate the local Kelvin moduli of each partitioned region, a previously established generalized anisotropic inverse mechanics (GAIM) approach was used [6,7]. This method solves the weak form of the Cauchy stress balance directly for the mechanical properties of the tissue. The material is assumed to be linear.

RESULTS

Biaxial mechanical testing (Fig 2A) and GAIM analysis reveals differences in the heterogeneous mechanical properties between the two spines. Each FCL exhibits a unique displacement field under the same bi-axial loading scenario (Fig 2B). Visualizations of the maximum Kelvin modulus show large variability across both FCLs (Fig 2C). Quantification of the Kelvin modulus show the FCL from the +LBP spine has a highest average Kelvin modulus (2.1 ± 2.0 MPa, Fig 3A). The Kelvin modulus values for the -LBP spine have a larger relative distribution of values (0.39 ± 0.30MPa, Fig 3A). Interestingly, the +LBP FCL seems to have multiple small regions containing either very large or very low Kelvin Moduli.

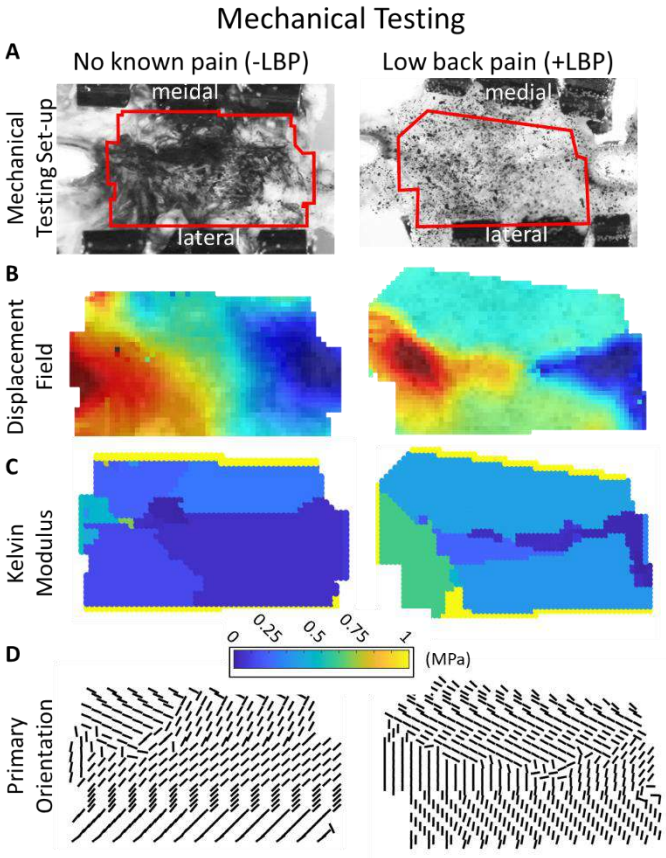

Figure 2: A) Bi-axial testing set-up showing the FCL with a speckle pattern and a region of interest (red). B) Displacement field showing non uniform changes in displacement due to bi-axial loading. C) Kelvin modulus of FCLs show differences in the local mechanical properties. D) The primary orientation of the Kelvin modulus changes between FCLs and between each region in a given FCL.

Finally, the primary orientation of fibers between the two FCL are distinctly different (Fig. 2D). In the -LBP spine, the lumbar FCL's primary mechanical orientation predominately runs 45° from the superior inferior axis (Fig 3B). The +LBP spine has 2 major directions of orientation for the Kelvin modulus. The first is oriented along the medial lateral axis (~90°), while the second major Kelvin orientation is at an angle approximately 150° from the superior inferior axis. Primary orientations in healthy FCLs are expected to occur predominately in the medial lateral axis (90°), so both tested FCLs contain some abnormal changes in the primary orientation.

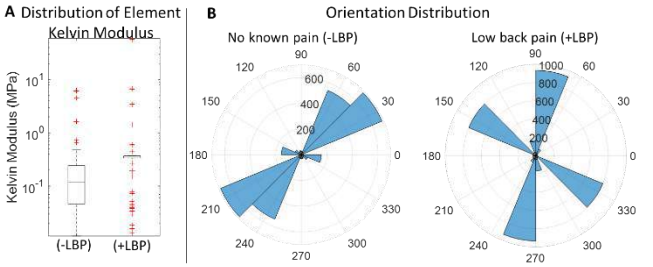

Figure 3: A) Samples from -LBP spines had a larger distribution of Kelvin Moduli. B) The major orientation of Kelvin modulus in FCLs from -LBP spine is about 45° from the medial lateral line, while the orientation of the major Kelvin modulus in the FCL from the +LBP spine is in two different directions.

DISCUSSION

In this study, larger variability in the Kelvin modulus is present in the -LBP spine, while multiple small inclusions of either low or high modulus and a higher average modulus is present in the FCL from the +LBP donor. These differences could affect the axon strain and cause increased expression of nociceptive signaling molecules [3]. Additionally, the changes in fiber orientation between the two FCLs may indicate a process by which collagen fibers change their orientation during disease. These changes could affect both spinal motion and axon strain, which contribute to experienced sensations of low back pain.

Unlike most quantifications of soft tissue material parameters, we did not have to iteratively solve a constitutive model to fit our experimental data [5]. The use of inverse mechanics approaches coupled with an automatic partitioning scheme provides the ability to directly quantify FCL mechanical heterogeneity that may be critical to understanding sensations of pain in the lumbar spine.

ACKNOWLEDGEMENTS

This work was supported by the Minnesota Supercomputing Institute (MSI) and by NIH grant U01 AT010326. Lumbar cadaveric spines were made available through the UMN Anatomy Bequest program.

REFERENCES

[1] O'leary, S. et al. *Annu. Rev. Biomed. Eng.* 2018
[2] Jaumard, N. et al. *J. Biomech. Eng.* 2011
[3] Lee et al *J. Pain* 2009
[4] Zarei, V. et al. *Biomech Model Mechanobio.* 2017
[5] Claeson, A. et al. *J. Mech Behav Biomed Mat.* 2017
[6] Raghupathy, R. et al. *J. Biomechanicl Eng.* 2010
[7] Witzenburg, C. et al. *IEEE Trans Med Imag.* 2016
[8] Foltz, M. et al. *J. Biomechanical Eng.* 2017

SENSITIVITY OF THE SHEAR WAVE SPEED–STRESS RELATIONSHIP TO PROPERTIES OF LIGAMENT-MIMICKING MECHANICAL PHANTOMS

Lesley R. Arant (1), Joshua D. Roth (2, 3)

(1) Department of Biomedical Engineering
University of Wisconsin-Madison
Madison, WI, USA

(2) Department of Mechanical Engineering
University of Wisconsin-Madison
Madison, WI, USA

(3) Department of Orthopedics and Rehabilitation
University of Wisconsin-Madison
Madison, WI, USA

INTRODUCTION

Shear wave tensiometry has recently emerged as a promising method to non-invasively measure tension in load-bearing soft tissues. The driving principle behind shear wave tensiometry is the linear relationship between axial stress (σ) and shear wave speed (SWS) squared [1]:

$$\sigma = \rho(SWS)^2 - k'\mu \quad (1)$$

where μ is the unloaded shear modulus, ρ is the tissue density, and k' is a shear correction factor.

Our research group is developing an intraoperative shear wave tensiometer for the initial application of measuring tension in collateral ligaments in vivo during total knee arthroplasty (TKA). To develop our shear wave tensiometer, we are using ligament-mimicking mechanical phantoms as test specimens because they are made of well-characterized engineering materials that have less variability than biological materials. These phantoms have been shown to have similar mechanical properties [2] and SWS squared–stress relationships [3] to collateral ligaments. However, it is unknown whether and to what extent the properties of these phantoms affect the SWS squared–stress relationship. Furthermore, there have been efforts to use shear wave tensiometers to non-invasively detect differences in the structure and mechanical properties of diseased or damaged tendons [4]. To explore the potential of extending this application to ligaments, a preliminary study in ligament-mimicking phantoms would be informative due to their tunable and well-controlled properties.

Accordingly, the objective of this research was to determine the sensitivity of the SWS squared–stress relationship to the structural and mechanical properties of ligament-mimicking mechanical phantoms.

METHODS

We fabricated ligament-mimicking mechanical phantoms by embedding yarn in silicone, with the yarn aligned parallel to the longitudinal axis of the phantom (Figure 1). During molding of the phantoms, we applied a pretension of 10 N to the yarn to remove slack and align the yarn. We fabricated nine phantoms, which varied in the type of silicone and number of yarn strands used in fabrication following a two-factor face-centered central composite design (Figure 1). We chose to vary the elastic modulus of the silicone and the number of yarn strands to model changes in the ground matrix and collagen content of ligaments, respectively, that may result from ligament pathology or healing [5].

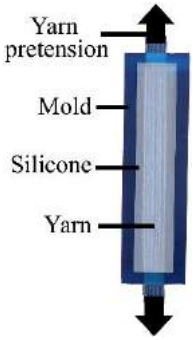

Phantom	Silicone Elastic Modulus [kPa]	Number of Yarn Strands
1	24	8
2	152	8
3	261	8
4	24	10
5	152	10
6	261	10
7	24	12
8	152	12
9	261	12

Figure 1: We embedded longitudinally-aligned, pretensioned yarn in silicone to fabricate ligament-mimicking phantoms (left). Nine phantoms were fabricated following a two-factor face-centered central composite design (right).

To replicate the in situ boundary conditions and ligament length available for making measurements, we fabricated a knee model for testing that includes the femur, tibia, and menisci (Figure 2). A custom clamp attached the phantom to the femur, and a roller at the tibial attachment replicated ligament wrapping over the tibia and allowed for the application of low-friction, controlled loads using an electrodynamic testing system. Following preconditioning, we loaded the phantom using a 0 to 200 N ramp at 20 N/s. During loading, a piezoelectric tapper excited shear waves in the phantom by delivering micron-scale taps at a frequency of 10 Hz. Lasers from two laser Doppler vibrometers were spaced 4-5 mm apart on the phantom to track the shear waves. We computed the SWS using a cross-correlation of the two laser signals to find the time delay in wave arrival at the two points (Δt, Figure 2). We measured SWSs during the ramp load in each phantom for five trials.

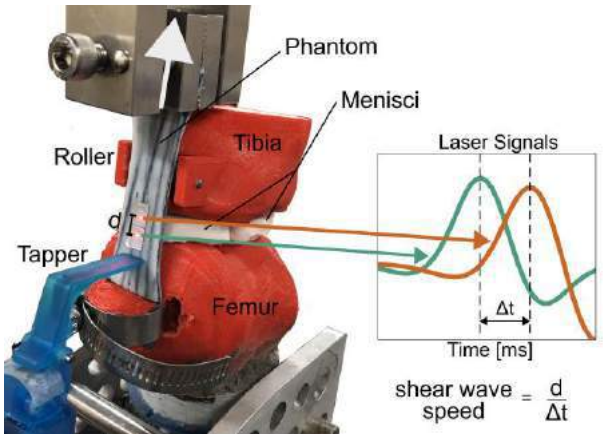

Figure 2: Ligament-mimicking phantoms were placed in a knee model during testing to replicate the in situ boundary conditions.

We extracted the slope, intercept, and R^2 from simple linear regressions between squared SWS (independent) and axial stress (dependent) for each trial of each phantom. We then performed multi-factor regressions to determine the sensitivity of the slope and y-intercept of the SWS squared–stress relationship to phantom properties. The independent variables were the elastic modulus of the silicone and the percentage of the phantom composed of yarn. We chose the latter because we believed yarn content normalized to phantom volume would provide more insight into structure-function relationships than absolute yarn content. We initially fit the models with two-factor interactions, but removed them if they were statistically insignificant ($p > 0.05$).

RESULTS

The axial stress increased linearly with squared SWS for all phantoms (range of R^2 = [0.77, 0.92]). The slope of the SWS squared–stress relationship ranged from 493 to 1304 kg/m^3 across the different phantoms. The multi-factor regression for the slope revealed a significant negative correlation between the yarn percentage and the slope ($p = 0.001$), while the effect of elastic modulus of the silicone was insignificant (Figure 3a). The interaction between the yarn percentage and elastic modulus of the silicone was also significant ($p = 0.046$). The R^2 for this multi-factor regression was 0.26.

The y-intercept of the SWS squared–stress relationship ranged from -764.1 to 13.5 kPa across the different phantoms. In the multi-factor regression for the y-intercept, the interaction term was insignificant, and thus we removed it from the model. The reduced model revealed a significant negative correlation between the elastic modulus of the silicone and the y-intercept ($p = 0.006$), while the yarn percentage was insignificant (Figure 3b). The R^2 for this multi-factor regression with only main effects was 0.18.

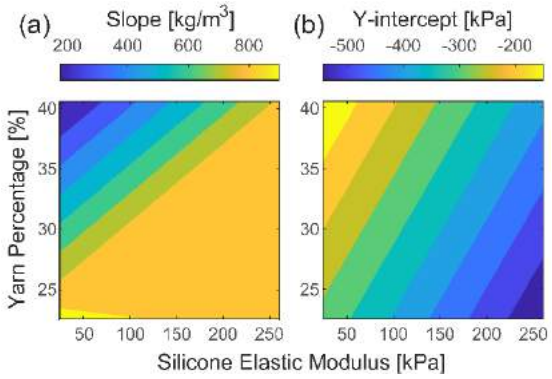

Figure 3: The multi-factor regressions revealed a significant negative relationship between: (a) the yarn percentage and the fitted slopes, and (b) the elastic modulus of the silicone and the fitted y-intercepts.

DISCUSSION

Similar to collateral ligaments [6] and tendons [1], the SWSs in each of the ligament-mimicking phantoms increased linearly with increasing tension. This confirms that the linear relationship between squared SWS and stress holds independent of these fabrication factors.

The slope and y-intercept of the SWS squared–stress relationship were sensitive to properties of the fibrous and isotropic constituents of the phantom, respectively. Since the density is the constant of proportionality between squared SWS and stress (Equation 1), a greater yarn percentage may decrease the slope because yarn has a lower density than silicone. To test the validity of this reasoning, future work will involve repeating this sensitivity analysis with factors that independently alter the density and shear modulus. This should also provide insight into the significant interaction term that was identified in the multi-factor regression model for the slope.

The negative correlation between the elastic modulus of the silicone and the y-intercept is consistent with the structural composition of the phantoms and the analytical model (Equation 1). In transversely isotropic materials with highly aligned fibers, such as ligaments and the phantoms, the transverse shear response is dominated by the isotropic ground matrix [7], for which the shear and elastic moduli are directly proportional. Thus, a higher elastic modulus of the silicone increases the shear modulus of the phantom, which decreases the y-intercept according to the analytical model (Equation 1).

Our results confirm that the properties of the phantoms can be tuned to modulate the SWS squared–stress relationship in a predictable manner. Moving forward, this will allow us to design phantoms that model diseased or damaged ligaments (e.g., contracted and stiffened medial collateral ligaments often encountered in TKA patients [8]). Furthermore, these findings confirm that measurements made using shear wave tensiometry are sensitive to differences in tension, as well as the structural and mechanical properties of the test specimen. This warrants future investigation into the clinical application of shear wave tensiometry to the diagnosis of ligament pathologies.

ACKNOWLEDGEMENTS

We gratefully acknowledge support from the NIH (R21 EB024957).

REFERENCES

[1] Martin, JA et al., *Nat Commun*, 9:1592, 2018. [2] Guzman, RAP et al., in *ORS*, 2020. [3] Arant, LR et al., in *ORS*, 2021. [4] Cone, SG et al., in *ORS*, 2021. [5] Woo, SL et al., *J Biomech*, 39:1-20, 2006. [6] Blank, JL et al., *J Mech Behav Biomed Mater*, 105:103704, 2020. [7] Gardiner , JC et al., *J Biomech Eng*, 123:170-175, 2000. [8] Bellemans, J et al., *Knee Surg Sports Traumatol Arthrosc*, 18:152-156, 2010.

CHANGES TO MICTURITION PATTERNS AND URINARY BLADDER'S EXTRACELLULAR MATRIX MECHANICAL BEHAVIOR IN AN ANIMAL MODEL OF RADIATION CYSTITIS

Marissa R. Grobbel (1), Bernadette M.M. Zwaans (2), Elijah P. Ward (2), Laura E. Lamb (2), Sara Roccabianca (1)

(1) Department of Mechanical Engineering
Michigan State University
East Lansing, MI, USA

(2) Department of Urology
Beaumont Health
Royal Oak, MI, USA

INTRODUCTION

Radiation cystitis is a rare condition that can develop in cancer patients who have undergone pelvic radiation chemotherapy. This condition can cause symptoms such as painful and frequent urination, decreased bladder capacity, nocturia, and blood in the urine. In severe cases blood clots can block urine flow and increase pressure on the kidneys, leading to renal failure [1]. This condition is rare; the American Cancer Society estimates that in 2018, only 5-10% of pelvic cancer patients undergoing radiation chemotherapy actually developed radiation cystitis [2]. However, for these patients, this disease causes painful and frustrating symptoms that ultimately limit their recovery from cancer.

A mouse model of radiation cystitis has been developed in order to understand the changes to the bladder wall following onset of the disease [3]. This model has shown hypervascularization of the bladder as well as significant fibrosis—i.e. increased collagen fiber deposition. Though the remodeling reported in this animal model can provide insight into the tissue mechanics of the urinary bladder affected by radiation cystitis, further studies must be performed to fully understand the alterations to the mechanical behavior of this remodeled extracellular matrix. Additionally, there are several phases of radiation cystitis: an acute phase occurring weeks after treatment, a latent phase occurring within months to years, and a late phase, which is chronic [1]. Because radiation cystitis has several phases, each with their own defining symptoms and remodeling, it is important to study the mouse model in several stages of recovery following radiation treatment. The goal of this study is to identify changes to the mechanical behavior of the mouse urinary bladder extracellular matrix following onset of radiation cystitis at two timepoints of recovery.

METHODS

A single dose of 40Gy radiation was administered to the bladders of 20 8 week-old C57BL female mice via a small animal radiation research platform. Along with 20 age-matched control mice, their weights and micturition data were recorded on a weekly basis, for either 12 or 24 weeks post-treatment—n = 10 control, 10 irradiated for each recovery time. After either 12 or 24 weeks, the mice were placed into a cage with blotting paper for 4 hours, which allowed for measurement of micturition data. After the 4-hour period, the total number of spots, the average spot size, the total volume of urine, and the size of the primary spot were measured from the blot paper.

Following the micturition study, the mice were euthanized and their bladders were isolated. Each bladder was cut laterally into a ring-shaped tissue sample by removing the dome and lower trigone, which were placed into 10% formalin to later be used for histology. The ring-shaped samples were then decellularized via a 48-hour soak in 1% sodium-dodecyl sulfate to isolate and compare the mechanical behavior of the control and irradiated extracellular matrix [4]. Following decellularization, the samples were mounted onto a uniaxial stretching machine using cotton suture. During testing, the samples were kept in a calcium-free Krebs-Hensleit buffer. Once mounted, the samples were subjected to a 2g preload, which was reapplied between each set of cycles. The full test consisted of 10 cycles of 5% stretch (preconditioning) and 5 cycles each of 10%, 15%, and 20% stretch. Throughout the test, the axial force was measured by a load cell (LSB200, Futek) while the height of the sample was measured by a front-facing camera (Fuji). Pictures of the samples were taken between cycles with the preload from the front and side (using an iPhone) to estimate cross-sectional area for stress calculation. Stress and stretch were calculated using the configuration of the sample following preconditioning (with the preload) as a reference. Following the

mechanical test, the bladder ring was placed into formalin with the dome and trigone for 4 days before being moved into 30% ethanol for storage, embedded in paraffin, and stained with Masson's trichrome to calculate each sample's collagen area fraction.

Finally, the last loading curve of the 20% stretch cycles was fitted to a constitutive model to identify differences between the control and irradiated samples. Currently, only the 12-week time point is completed, but once the second time point is finished, the constitutive model will be used to determine effects of time following radiation to the bladder—i.e. disease recovery or progression. For the constitutive model, we use a Demiray-type strain energy function, W [5] that is isotropic and exponential with two parameters, c and k

$$W = c\left(e^{k(I_1(\boldsymbol{C})-3)} - 1\right)$$

where the strain energy function has the following relation to stress, $\boldsymbol{T}$, and deformation via

$$\boldsymbol{T} = -p\boldsymbol{I} + 2\boldsymbol{F}\frac{\partial W}{\partial \boldsymbol{C}}\boldsymbol{F}$$

For a deformation gradient $\boldsymbol{F}$, Cauchy-Green deformation tensor $\boldsymbol{C}=\boldsymbol{F}^T\boldsymbol{F}$, and a Lagrange multiplier p. The experimental data was fitted to the model by minimizing the normalized root mean square deviation (NRMSD) between the model and experimental stresses (t_{th} and t_{exp}) [6]

$$NRMSD = \frac{1}{t_{exp}^{max}}\sqrt{\frac{\Sigma\left(t_{th} - t_{exp}\right)^2}{n}}$$

for n experimental data points.

RESULTS

As the second time point has not arrived yet, the results will be discussed only in terms of the 12-week time point. Radiation was well-tolerated by the animals as denoted by the irradiated group's body weight maintenance and skin health. The volume of urine from each irradiated mouse in the micturition study was significantly lower than that of the control mice (in total, average, and primary spot size), indicating a decrease in bladder capacity, **Figure 1**. There were no changes to the total number of spots. We are still awaiting histology slides in order to estimate collagen area fraction.

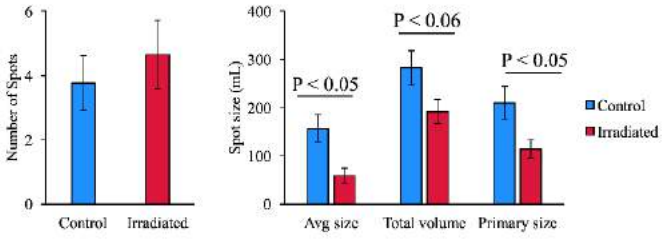

Figure 1. Summary of micturition measurements. No changes in number of urine spots (left), and decreased urine volume (right). Error bars represent standard error.

Mechanical data from one control mouse was not used, as the sample broke early in the test and did not survive the 20% loading. The mechanical data of the remaining samples (n = 9 control, 10 irradiated) showed a stiffening of the urinary bladder extracellular matrix of the irradiated bladders, as compared to the controls. This was noted by a slight left-ward shift of the irradiated experimental data, and a significant increase in one model parameter k (no change in c), **Figure 2**.

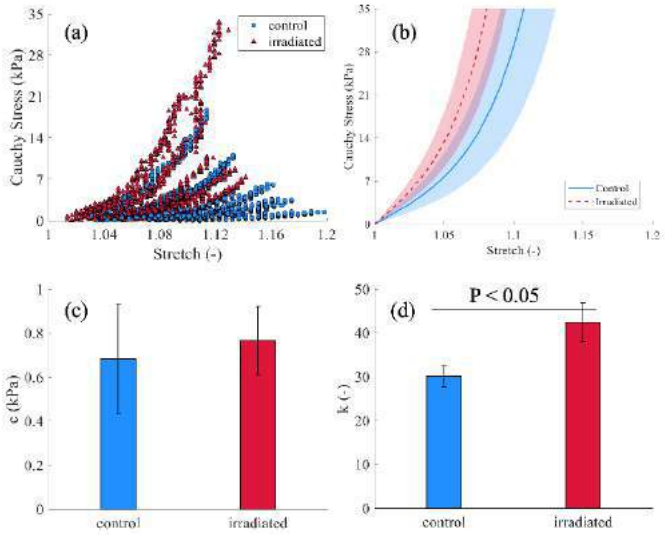

Figure 2. Summary of mechanical measurements. (a) Raw data from all samples, (b) Simulated stretch-stress curves from constitutive model, (c) and (d) constitutive model parameters. Error bars and shaded regions represent standard error.

Following the 24-week time point, we will be able to determine any differences between control and irradiated bladders, but also differences related to either recovery or progression of radiation cystitis.

DISCUSSION

While the radiation was well-tolerated by the mice, there is evidence of the development of radiation cystitis through the diminished bladder capacity, as indicated by the micturition study. The decrease in bladder capacity experienced by these mice is also common in humans who have been diagnosed with radiation cystitis [1]. Though previous studies on this model of radiation cystitis have shown increase collagen area fraction of the bladder [3], our histological analyses are ongoing and we do not yet have values to report.

Following development of radiation cystitis, the extracellular matrices of the irradiated bladders experienced significant stiffening, as was evident in the increased value of parameter k of the constitutive model. Stiffening of the bladder wall of this kind can increase pressure in the bladder, which could pose a threat to renal health and become quite dangerous to radiation cystitis patients. Therefore, it is crucial to understand the changes in bladder wall mechanics and extracellular matrix remodeling related to this disease. To our knowledge, no previous studies have reported changes to the mechanical behavior of the urinary bladder following development of radiation cystitis.

REFERENCES

[1] Zwaans, BMM et al., Urol, 88:14-21, 2016.
[2] American Cancer Society: Cancer Facts and Figures, 2018.
[3] Zwaans, BMM at al., Adv Radiat Oncol, 1:333-343, 2016.
[4] Grobbel, MR et al., BMMB, 17(4):985-999, 2018.
[5] Demiray, H, *J Biomech*, 5(3):309-311, 1972.
[6] Chen, S et al., BMMB 19(1): 275-289, 2020.

MODELING THE HUMAN LENS CAPSULE WITH IMPLANTED ACCOMMODATIVE INTRACOULAR LENS

Kurt A. Ameku and Ryan M. Pedrigi

Mechanical and Materials Engineering
University of Nebraska-Lincoln
Lincoln, NE, USA

INTRODUCTION

Accommodation is a purely mechanical process of the ocular lens, where the lens changes shape to allow a change in focus from distant to near vision. The prevailing theory behind accommodation is that proposed by Helmholtz [1], who suggested that the accommodated state is achieved through contraction of the ciliary body and release of tension in the zonules that connect it with the lens. In youth, the lens can change the power of the eye by up to 14 D, but this ability declines with age in the development of presbyopia, leaving almost no accommodative ability by 55 years of age. Since presbyopia effects nearly everyone, it is an important problem, yet there are no reliable interventional strategies for its restoration.

A promising approach is replacement of the native lens fibers with an intraocular lens (IOL) that can accommodate (AIOL). Currently, restoration of accommodative ability through implantation of an AIOL has low efficacy—on average, AIOLs only restore ~2.5 D of accommodative power [2] and they suffer from substantially increased rates of visually-debilitating capsule fibrosis mediated by inhabiting lens epithelial cells. Such problems make them questionable for implantation during cataract surgery and a non-option for correction of presbyopia (i.e., the risks far outweigh the benefits).

Improving the efficacy of AIOL designs requires computational tools that can predict their interaction with the remnant accommodative apparatus (i.e., the remnant lens capsule, powered by the attached zonules and ciliary muscle) and assess changes to the homeostatic mechanical environment, which may be an important driver of errant lens epithelial cell behaviors after surgery. Numerous studies have examined the native accommodative apparatus, wherein models were typically 2-D, employed linear elastic material properties, and neglected capsule pre-strain in the accommodated state. We recently developed the first finite element model of the remnant lens capsule with implanted IOL, which employed a fully 3-D approach and the Holzapfel anisotropic hyperelastic material model for the lens capsule. Herein, we extended this model to evaluate the efficacy of an implanted AIOL through comparison to a native lens model and reported data.

METHODS

Material Properties. The lens capsule exhibits nonlinear elastic mechanical behavior with regional variations in anisotropy. To model these complexities, we employed the Holzapfel anisotropic hyperelastic constitutive model, the parameters of which were derived from calibration to our group's previously reported inflation data [3] and other previously reported uniaxial stretch data [4]. Material parameters were assessed as a function of meridional position on the lens capsule and prescribed on an element-to-element basis in the finite element model. The lens capsule was assigned a density of 1.05×10^{-3} g/mm^3 and assumed to be incompressible. The crystalline lens was modeled as two separate linearly elastic sections, an inner nucleus and an outer cortex. Both sections were assigned a Poisson's ratio of 0.49. The nucleus was assigned a Young's Modulus of 3 kPa, while the cortex was assigned a Young's Modulus of 3.7 kPa. The AIOL was modeled after a dual-optic Synchrony IOL with a silicone composition and assigned a Poisson's ratio of 0.48 and Young's Modulus of 25.5 MPa.

Finite Element Analysis. All finite element models were developed in Abaqus Standard 2019. C3D8H 3-D continuum hybrid elements were used to model the AIOL and crystalline lens, while S4R shell elements were used to model the lens capsule. The native lens model was simulated in three steps, one to inflate the capsule until the lens was completely contained within it, a second step to release all loads on the capsule so it contacts the lens and achieves the fully

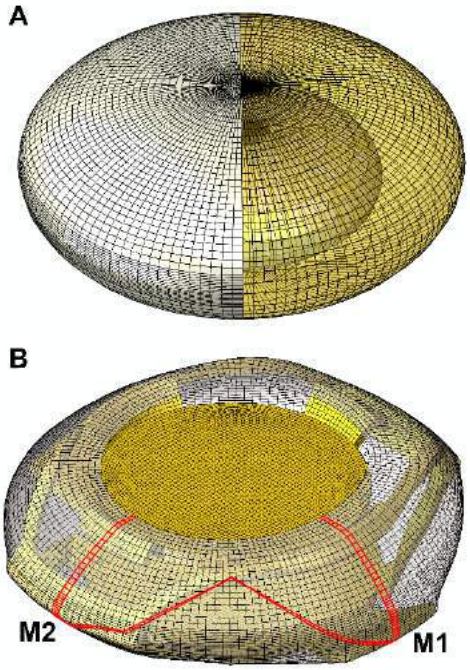

Figure 1: Finite element models of the (A) native lens in the fully accommodated state with the capsule visible on the left and the lens cortex and nucleus visible on the right, and (B) the post-surgical lens capsule with an implanted accommodative IOL in the fully accommodated state with highlighted meridians (M1 and M2) used for radius measurements.

accommodated state (Figure 2A), and a third step to introduce a zonular traction at the equatorial region of the capsule to achieve the fully disaccommodated state (Figure 2B). The post-surgical model was simulated in four steps, one to compress the AIOL and inflate the lens capsule so the whole AIOL was contained within the capsule, a second step to allow the AIOL to unfurl while the capsule was held in place, a third step to release all loads on the capsule to achieve the fully accommodated state (Figure 2C), and the final step to introduce a zonular traction to model the fully disaccommodated state (Figure 2D).

Outputs. Predictions of radius and total thickness were evaluated for the native lens and AIOL models in the fully accommodated and disaccommodated states. Comparisons were also made to the literature.

RESULTS

The model of the native lens *in situ* demonstrated changes in radius and thickness from the accommodated to the disaccommodated state that were comparable to previously reported MRI measurements on 45-year-old human lenses *in vivo*. The radius of the model lens in the fully accommodated state was 4.51 mm and the radius in the fully disaccommodated state was 4.65 mm. These predicted values are similar to empirical values of 4.49 and 4.60 mm, respectively [5]. Likewise, the total thickness of the lens model was 4.14 mm and 4.07 mm in the accommodated and disaccommodated states, respectively, which were similar to empirical values of 4.17 mm and 3.99 mm, respectively [6].

The model of the post-surgical lens capsule with an implanted AIOL demonstrated a significantly different geometry in terms of radius and thickness. Because of the non-axisymmetric design of the AIOL, radius values were measured along two axes where significant contact was made between the capsule and AIOL, labeled M1 and M2 (Figure 1B). In the fully accommodated state, the M1 radius was 4.76 mm, the M2 radius was 4.93 mm, and the total thickness was 2.82 mm. In the

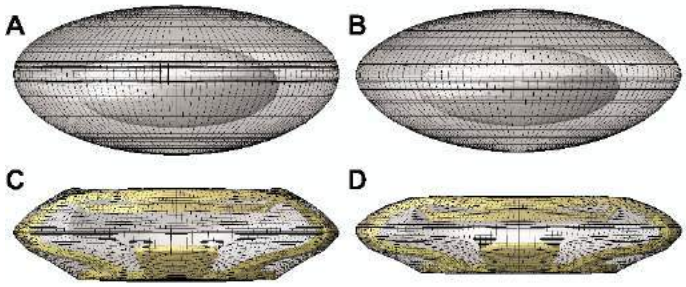

Figure 2: Finite element models of the native lens in the (A) fully accommodated and (B) fully disaccommodated state and the post-surgical lens capsule in the (C) fully accommodated and (D) fully disaccommodated state.

disaccommodated state, the M1 radius was 4.91 mm, the M2 radius was 4.99 mm, and the total thickness was 2.37 mm. This thickness of the AIOL is reasonably close to its intended thickness in the fully disaccommodated state of 2.2 mm [7].

DISCUSSION

Accommodation is a complex process, wherein the mechanical relationships between the ciliary muscle, zonules, and lens determine functionality. This complexity is exacerbated by continuous lens growth and stiffening throughout life, which changes these relationships and ultimately causes presbyopia. The ability to restore accommodative function with reasonable efficacy requires the ability to predict these mechanical relationships with an implanted AIOL. Without mechanical modeling, this task may be out of reach. Indeed, current AIOLs have been hindered by poor performance and the high incidence of capsule fibrosis. To our knowledge, this study reports the first model of the post-surgical lens capsule with an implanted AIOL. The disaccommodated state, which is physiologically induced by relaxation of the ciliary muscle that increases tension in the attached zonules, was incorporated into our model using a traction applied to the equatorial region of the lens capsule. We validated this approach by demonstrating that our native lens model can accurately predict changes in the geometry from the accommodated to the disaccommodated state. We then showed that this model can be extended to assess the functionality of an AIOL, which provides the groundwork for a computational tool that could aid in improving AIOL designs. Although this is an exciting starting point, there is a need for further evaluation of how reported changes in the accommodative apparatus with age, particularly the zonular attachments and ciliary muscle, may impact predicted implant efficacy. Another consideration is the errant cellular response to the procedure. We have previously hypothesized that this fibrotic response is linked to the altered mechanical environment of the lens capsule after cataract surgery. Modeling may be useful in predicting such changes, but this would require growth modeling techniques.

ACKNOWLEDGEMENTS

We gratefully acknowledge support for this work from the National Institute of Biomedical Imaging and Bioengineering of the National Institutes of Health under grant R03EB026837.

REFERENCES

[1] Glasser, A et al., *Ophthalmology*, 106(5):863-872, 1999.
[2] Nishi, O et al., *J Cataract Refract Surg*, 40(2):295-305, 2014.
[3] Pedrigi, RM et al., *Vision Res*, 47(13):1781-1789, 2007.
[4] Krag, S et al., *Invest Ophthalmol Vis Sci*, 38(2):357-363, 1997.
[5] Strenk, SA et al., *Invest Ophthalmol Vis Sci*, 40(6):1162-1169, 1999.
[6] Dubbelman, M el al., *Vision Res*, 43(22):2363-2375, 2003.
[7] McLeod, D, *Trans Am Ophthalmol Soc*, 104:437-452, 2006.

PLATELET ADHESION DYNAMICS: MACHINE LEARNING-ASSISTED ANALYSIS OF ADULT AND CORD PLATELETS AND DEVELOPMENT OF A MULTISCALE MODEL

Jawaad Sheriff (1), Peineng Wang (1), Peng Zhang (2), Ziji Zhang (2), Wadie F. Bahou (3), Yuefan Deng (2), Danny Bluestein (1)

(1) Department of Biomedical Engineering
Stony Brook University
Stony Brook, New York, U.S.A.

(2) Department of Applied Mathematics and Statistics
Stony Brook University,
Stony Brook, New York, U.S.A.

(3) Division of Hematology, Department of Medicine
Stony Brook University
Stony Brook, New York, U.S.A.

INTRODUCTION

Platelet adhesion to blood vessel walls in shear flow is essential in initiating the blood coagulation cascade and prompting clot formation in prosthetic cardiovascular devices and vascular disease processes. In the adhesion process, platelets undergo complex and rapid receptor-ligand binding such as bond association and breakage. Experimental methods have been improved through enhancing the μm-length and ms-time scale results. We have developed a combined Dissipative Particle Dynamics (DPD) - Coarse Grained Molecular Dynamics (CGMD) multiscale model to depict the platelet's biophysical properties at the cellular scales coupled with macroscopic flows, thus predicting platelet motion under flow conditions.[1] However, sparse and noisy raw image data continues to limit the utility of in vitro measurements in validating such computational models. Accurate biological image analysis coupled with rapidly maturing machine learning techniques enable better identification and registration of platelet morphological changes, which can then be rapidly applied in development and validation of platelet multiscale models.

In this study, we apply a semi-unsupervised learning system (SULS), trained and fine-tuned with shear-based in vitro platelet morphological changes, to overcome the major challenges of moving platelet image analysis, including segmentation, in obtaining high-quality outputs without relying heavily on large volume, high velocity, diverse, and hard-to-produce learnable morphological data. This machine learning (ML)-guided approach was applied to flowing adult and cord platelets to explore whether adhesion dynamics is age-specific and dependent on intracellular calcium. We then adapt a DPD-CGMD deformable platelet model to describe flipping and adhesion of platelets via the GPIbα-von Willebrand factor (vWF) bond under physiological flow conditions.

METHODS

Gel-filtered platelets were prepared from blood drawn from consenting healthy adult volunteers, or umbilical cord blood obtained from neonates whose mothers underwent Caesarean sections, under Stony Brook IRB-approved protocol[2], diluted to 150,000/μl and perfused through 100 μm×1 mm microchannels (μ-Slide VI$^{0.1}$ Luer, ibidi USA, Inc., Madison, WI) pre-coated with 100 μg/ml vWF using a syringe pump (Fig. 1a). Platelets were exposed to a wall shear stress of 30 dyne/cm^2. Adhesion events, defined as platelets flipping or sliding on the vWF-coated surface (Fig. 1), were observed at 100× magnification on a DIC microscope (Ti-E, Nikon, Melville, NY) at 1000 fps (Zyla, Andor Technology Ltd., Belfast, UK). To study the role of intracellular Ca2+ on adhesion, platelets were re pre-treated with 20 μM BAPTA-AM at 37°C for 30 min prior to adhesion experiments.

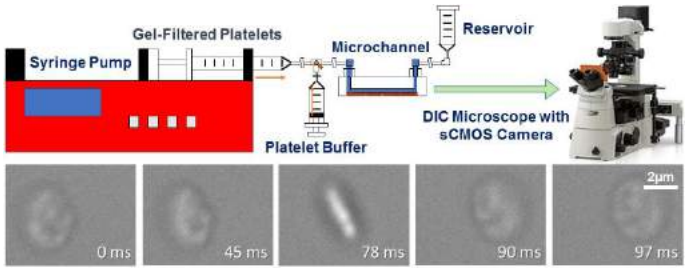

Figure 1: (a) Set-up for adhesion experiments. b) Sequential imaging of platelet adhesion and flipping under flow.

We designed and trained a SULS to extract and classify platelet morphological features from captured images. We selected six agent networks (A-nets) with pre-trained weights for predicting platelet boundaries. A multi-model fusion policy network (P-net) was used to

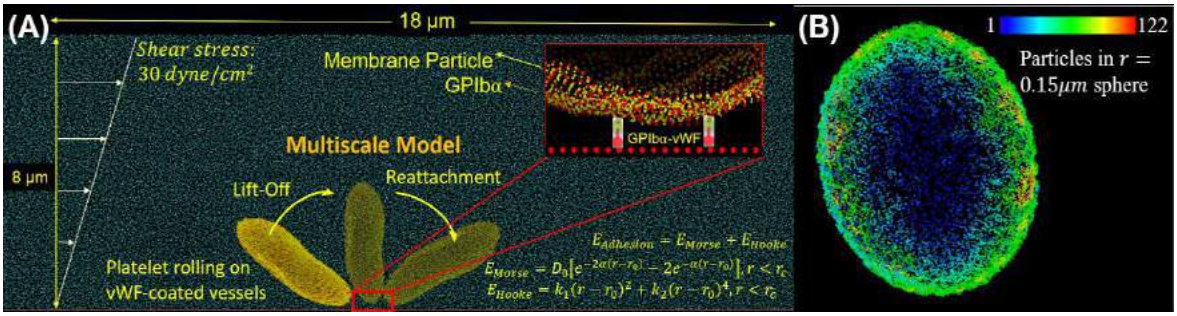

Figure 2. (A) DPD-CGMD multiscale adhesion model schematic. (B) Redistribution of GPIbα receptors.

refine the A-net coarse predictions. Finally, we trained a CNN-based reward network that takes segmentation results from its preceding P-net to produce a scalar score as a quantified indicator for platelet segmentation quality. In vitro platelet adhesion images segmented by the SULS yielded a time series of 2D geometrical data points, which are then input into a mathematical model to calculate platelet major and minor diameters, cross-sectional area, thickness, as well as the platelets' rolling direction. Two periods, Ω_1 and Ω_2, characterizing lift-off and reattachment to the vWF surface during platelet flipping, respectively, were defined. Our observations were compared to models describing such behavior under flow: Jeffery's orbit for (1) rigid ellipsoids and (2) with correction for wall effect.[3] We improved this model by adapting the constant coefficient $\boldsymbol{C}$ as a function of C_1 and C_2, representing the lift-off and reattachment periods, respectively. Constant coefficients within and between adult and cord populations were compared using two-sample t-tests.

We adapted our deformable CGMD multiscale platelet model[1] to describe flipping over vWF in a channel with DPD particles at 30 dyne/cm^2 (Fig. 2A). The platelet's bilayer membrane has a total of 67,004 particles, with 16,751 particles designated as GPIbα receptors, with a density of 585 /μm^2. The vWF, with 506/μm^2 density, is fixed on the blood vessel wall, binds to a platelet GPIbα receptor, and initiates platelet adhesion. The force field between the platelet GPIbα receptor and the vWF ligand is described by a hybrid force field combing Morse and Hooke potentials[4]:

$$E_{Adhesion} = E_{Morse} + E_{Hooke} \quad (1)$$

$$E_{Morse} = D_0\left(e^{-2\alpha(r_{ij}-r_0)} - 2e^{-\alpha(r_{ij}-r_0)}\right) \quad (2)$$

$$E_{Hooke} = k_1(r-r_b)^2 + k_2(r-r_b)^4 \quad (3)$$

We validated our numerical method by correlating simulations and model predictions with in vitro results. In our modeling, we split a whole rotation of an adhered platelet into two periods, wherein disassociation of the GPIbα-vWF bonds in Ω_1 is mimicked and GPIbα-vWF bonds form in Ω_2 as the platelet re-attaches to the vWF-coated wall. In period Ω_1, we adjust the adhesive coefficients of the model to correlate with in vitro measurements. In period Ω_2, we tune the force relaxation distance.

RESULTS

Platelet flipping dynamics at 30 dyne/cm^2 was analyzed from in vitro data using SULS for 2D image segmentation, followed by 3D ellipsoidal reconstruction and calculation of platelet flipping motion. Fig. 3 shows the individual platelet rotation angles for adult (A) and cord (B) platelets, compared with mean rotation angles fit to our modified two-constant Jeffery orbit with constant correction for wall effect. Our observations confirmed two asymmetrical periods, Ω_1 and Ω_2, defining the lift-off and reattachment phases of flipping, for both adult and cord platelets. Cord platelets (C_1=66.81±7.72, C_2=55.54±5.98) flip non-significantly faster than adult platelets (C_1= 70.47±3.54, C_2=59.37±3.23, p>0.05). However, Ω_1 is significantly longer than Ω_2 for both adult and cord platelets (p<0.05). Chelating intracellular calcium in cord platelets with 20 μM BAPTA-AM further reduced these constants (C_1=46.67±20.10, C_2=36.27±11.40), with a corresponding 1.16-fold increase in peak rotational speed (Fig. 3C).

Our initial CGMD-DPD adhesion model indicates that k_1 = 60 and k_2 = 50 can reproduce adult platelet dynamics at 30 dyne/cm^2 prior to GPIbα-vWF breakage during Ω_1. We modified the GPIbα receptor distribution in our CGMD model based on the curvature of the platelet (Fig. 2B), and ongoing simulations are evaluating the effect of this redistribution on GPIbα-vWF bond numbers, forces, and platelet-vWF contact area during both Ω_1 and Ω_2.

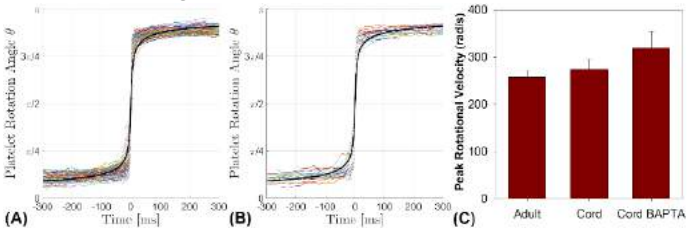

Figure 3. (A) Adult (n=70) and (B) cord (n=21) platelet rotation during adhesion. (C) Peak rotational velocities for adult, cord, and 20 μM BAPTA-AM-treated cord platelets (n=3).

DISCUSSION

We successfully adapted a ML-guided framework that integrates SULS with high-framerate and resolution DIC microscopy for accurate segmentation of flowing and flipping platelets undergoing adhesion. This method provides a critical connection between our experiments and multiscale platelet adhesion models by anticipating dynamics that cannot be captured in vitro. We were able to confirm the heterogeneity of platelet motion during initial adhesion, which is present for platelets from both adult and umbilical cord blood. Furthermore, we show that cord platelets potentially flip faster on vWF-coated surfaces, a phenomenon that is dependent on intracellular calcium. Ongoing multiscale simulations are using our ML-guided segmented platelet images as the ground truth, and we are studying the effect of GPIbα redistribution on flow-mediated adhesion dynamics on vWF. In future studies, the SULS framework will be extended to synthesize large-volume data to build a comprehensive database which can be used to identify physiologically significant platelet dynamics in activation, aggregation, and adhesion. We expect our approach to be adopted by other fields to rapidly and objectively quantify dynamic morphological changes from large datasets.

ACKNOWLEDGEMENTS

The authors thank Dr. Cecilia Avila and Lisa Malone for providing the cord blood samples This project was supported by the NHLBI (5U01HL131052, DB, and 5R01HL119096, WB).

REFERENCES

[1] Zhang, P et al., *J Biomech*, 50:26-33, 2017.
[2] Sheriff, J et al., *Cell Mol Bioeng*, 13: 575-590, 2020.
[3] Mody, N et al., *Biophys J*, 88: 1432-1443, 2005.
[4] Gupta, P et al., *Cell Mol Bioeng*, 12: 327-343, 2019.

THE IMPACT OF TISSUE PROPERTY VARIATIONS ON OPTIC NERVE HEAD DEFORMATION UNDER PHYSIOLOGICAL AND SUPRA-PHYSIOLOGICAL LOADING

Andrew J. Feola (1,2), C. Ross Ethier (2), Brian Samuels (3)

(1) Center for Visual and Neurocognitive Rehabilitation Atlanta VA Medical Center Atlanta, GA, USA

(2) Department of Biomedical Engineering, Georgia Institute of Technology/Emory University, Atlanta GA

(3) Department of Ophthalmology, University of Alabama at Birmingham, Birmingham, AL

INTRODUCTION

The optic nerve head (ONH) in the posterior eye experiences a complex and dynamic biomechanical environment under both physiological and pathological conditions. The ONH is the site of remodeling and/or retinal ganglion cell axon loss in several ocular pathologies, including glaucoma, idiopathic intracranial hypertension (IIH), nonarteritic anterior ischemic optic neuropathy (NAION), and spaceflight-associated neuro-ocular syndrome (SANS) [1,2,3,4]. These pathological conditions are often related to changes in mechanical loads, namely intraocular pressure (IOP), intracranial pressure (ICP), or choroidal volume. However, it is poorly understood how these mechanical loads influence deformation of individual tissue regions within the ONH. Further, it is known that ostensibly pathological loads do not invariably lead to clinical pathology. For example, not all subjects with elevated IOP (30 mmHg) develop glaucoma. This indicates that, even at pathological loading levels, there is likely a range of ONH deformations that lie within a physiological range, possibly due to the natural variability in tissue material properties.

Here, we use finite element modeling to study how physiological and pathophysiological levels of IOP, ICP, and choroidal swelling influence ONH deformation, with specific focus on understanding how variation in tissue material properties lead to variations in ONH deformation.

METHODS

We used our existing geometric model of the eye and finite element approach [5]. In brief, our posterior eye model includes the sclera, peripapillary sclera, annular ring, pia mater, dura mater, laminar cribrosa, prelaminar neural tissue (PLNT), choroid, Bruch's membrane, and optic nerve (Fig 1). The pia mater, dura mater and optic nerve were extended posteriorly 10 mm from the ONH. We also included a single central retinal vessel to approximate the effects of mean arterial blood pressure. We incorporated an anatomically realistic choroid based on OCT scans and average choroidal thickness measurements from the literature at specific distances from the ONH [6].

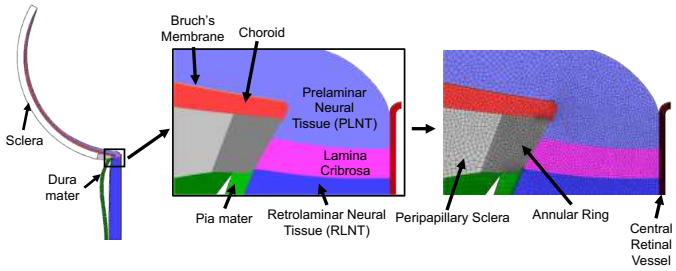

Figure 1: Geometric model of the entire posterior eye (left), zoom of the ONH (center) highlighting each tissue component in the model, and meshed geometry (right).

The model was meshed using Gmsh, and FEBio was used as the finite element solver [7,8]. We assumed axisymmetry, implemented (due to constraints of the FEBio solver) by using a 3° wedge about an axis of symmetry passing though the central retinal vessel. The PLNT, lamina cribrosa, optic nerve, central retinal vessel, and Bruch's membrane were modeled as isotropic linear-elastic. The choroid was treated as a mixture material consisting of a linear-elastic solid capable of swelling based on Donnan equilibrium. This simple approach allowed us to control the degree of choroidal volume change (e.g. swelling) without requiring us to account for the complex geometry of the vascular bed. All other tissues were modeled as neo-Hookean solids with embedded collagen fibers, distributed according to a von Mises distribution. The material properties for each tissue (e.g. Young's

modulus, Poisson ratio, coefficients for collagen fibers) were based on previously reported values [5].

Our baseline condition represented an individual in the upright position: IOP=15 mmHg, ICP=0 mmHg, mean arterial pressure=57 mmHg, and no choroidal swelling (0 uL). We then applied physiological loading conditions including choroidal swelling occurring over a cardiac cycle (ΔV = 2.2 and 14.2 uL), IOP=19 mmHg, which represents normal diurnal variation (ΔIOP = 4 mmHg), and an ICP=10 mmHg, which represents the ICP in a supine position [4,9]. We also examined supra-physiologic, or "pathologic", loading conditions including choroidal swelling (ΔV = 32 and 50 uL), Elevated IOP (30 mmHg), and Elevated ICP (20 mmHg) [4,5,6]. Variation in the tissue material properties at each loading condition were based on an established approach [5,9]. Our outcome measures were the peak 1st and 3rd principal strains (95th percentile and 5th percentile) in the PLNT, lamina cribrosa, and retrolaminar neural tissue (RLNT) relative to our baseline condition.

RESULTS

Peak tensile and compressive strains changed substantially as tissue material properties were varied under physiological and supra-physiological loading conditions (Fig 2 & Fig 3). Under supra-physiological, or pathological, conditions there was a wider range of strains relative to those expected to occur due to physiological choroidal swelling, IOP and ICP

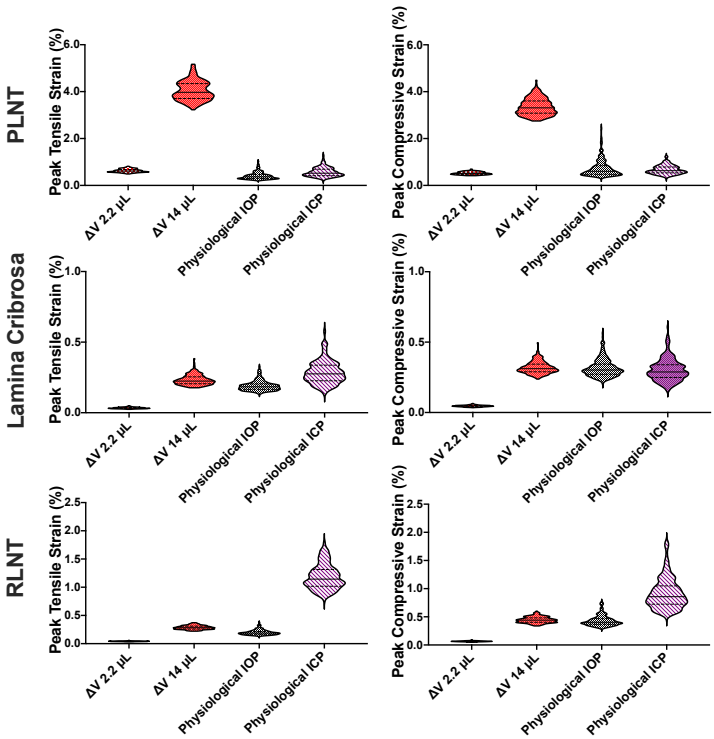

Figure 2: Violin plots of the peak tensile (left) and compressive (right) strains estimated to occur at each physiological condition due to variations in material properties (200 simulations per loading condition). All strain distributions were significantly different within each tissue region (p<0.001).

In the PLNT, median peak strains and the range of peak strains caused by choroidal swelling were significantly greater than those caused by IOP or ICP elevation. Within the lamina cribrosa, elevated IOP caused the highest compressive peak strains; however, choroidal swelling of 50 uL lead to analogous levels of peak tensile strains. Elevated ICP caused major changes in the peak strains in the RLNT.

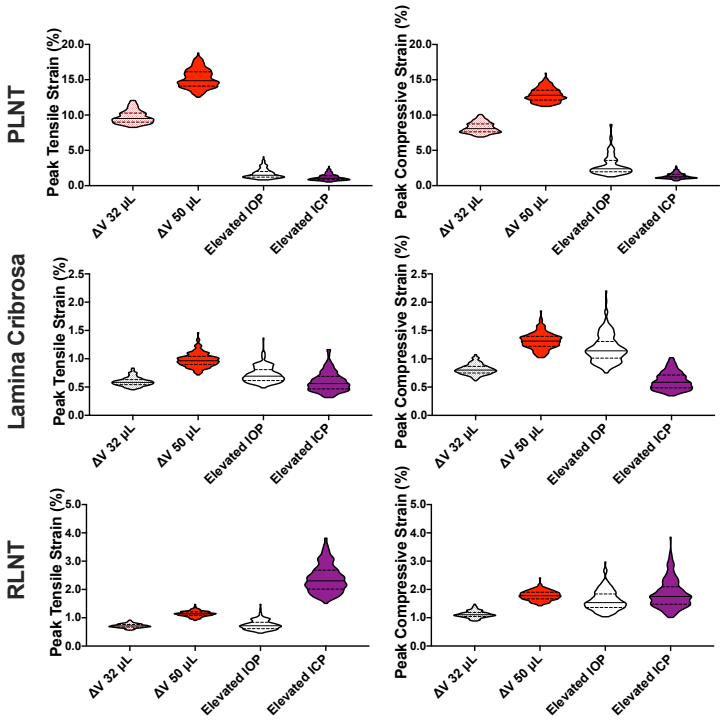

Figure 3: Violin plots of the peak tensile (left) and compressive (right) strains estimated to occur at each supra-physiological condition due to variations in material properties (200 simulations per loading condition). All strain distributions were significantly different within each tissue region (p<0.001).

DISCUSSION

This work is consistent with the hypothesis that certain tissue biomechanical material properties are risk factors for developing ocular pathology, even under physiological (normal) loads. Further, the influence of choroidal swelling on ONH biomechanics is likely underappreciated and deserves further study. While these results are limited to consideration of acute effects, we expect that chronic loading may activate local mechanosensitive cells and result in tissue remodeling.

ACKNOWLEDGEMENTS

This work was supported by a Department of Veterans Affairs RR&D Service Career Development Award (RX002342A; AJF); NASA (80NSSC19K1298; CRE); the NEI (R01 EY030871; AJF), the Georgia Research Alliance (CRE) and an unrestricted grant from Research to Prevent blindness to UAB.

REFERENCES

[1] Barnett, M et al., *BMC pediatrics*. 13:167, 2013.
[2] Burgoyne, C, *Exp. Eye Res,* 93:120-132. 2011.
[3] Nagia, L et al., *IOVS*, 57(11):4679-85, 2016.
[4] Laurie, S et al., ARVO Annual Meeting, 2018
[5] Feola, AJ et al., *IOVS*, 59:4172-81, 2018.
[6] Lee, KM et al., *Acta Ophthalmologica* 94: 697-708, 2016.
[7] Geuzaine, C et al., Int J Num Meth Eng, 79(11):1309-31, 2009.
[8] Maas, SA et al., J Biomech Eng. 134(1):011005, 2012.
[9] Feola, AJ et al., *IOVS* 57(4):1901-11, 2016.

POST-STRETCH RECOVERY OF VASCULAR SMOOTH MUSCLE CELLS IS STRAIN RATE DEPENDENT

Samuel F. Boland (1), Patrick W. Alford (1)

(1) Department of Biomedical Engineering
University of Minnesota – Twin Cities
Minneapolis, MN, USA

INTRODUCTION

During a traumatic brain injury (TBI) event the cerebral vasculature can experience strain rates of up to 1000 s^{-1}. Vascular smooth muscle cells (VSMCs), which encircle blood vessels and modulate blood flow through the cerebral vasculature, experience contractile deficiencies and phenotypic changes in response to mechanical loading characteristic of TBI.[1] Loss of VSMC function may contribute to the development of neurodegenerative diseases such as Alzheimer's disease.[2] Though VSMC function and gene expression have previously been linked to applied stretch[3,4], our understanding of VSMC response to rate of mechanical injury is still fundamentally lacking. Here, we characterize how physiological and trauma-like strain rate loading modifies the contractile properties of VSMCs using traction force microscopy (TFM) and cellular micro-biaxial stretching (CμBS).

METHODS

Substrate Fabrication and Cell Culture. Polyacrylimide (PA) gels of 13.5 kPa stiffness doped with fluorescent microspheres were synthesized onto PDMS membranes using previously described methods.[3] A layer of patterned 32 x 128 μm^2 fibronectin islands was stamped onto the top surface of the PA gel facilitate cell adhesion to the substrate and control cell area. Human umbilical artery VSMCs (Lonza) between passages 5-7 were seeded onto the gel constructs, after which they adhered to the patterned fibronectin. The VSMCs were cultured overnight in supplemented Medium-199 (Gibco) and incubated at 37 °C and 5% CO_2. 24 hours before imaging, the cell culture medium was replaced with a supplemented growth serum-free Medium-199 to induce a contractile phenotype in the cells.

Imaging and Strain Application. The constructs were mounted in a custom-designed CμBS apparatus and the elastomer membranes were stretched to 15% strain at rates of 0.025, 0.1, or 1.0 mm/s (**Fig. 1A**). Following stretch, the constructs were imaged at 40X using a confocal microscope to obtain traction images. VSMCs were imaged once per second in a time-lapse, with the stretch time and imaging time totaling 5 minutes for each condition. For example, for the 0.025 mm/s case, the time to stretch to 15% strain is 2 minutes and cells are imaged for 3 minutes after 15% strain is achieved. Brightfield images were taken of VSMCs at the first timepoint and fluorescent images were taken of the respective underlying bead layer in the PA gel at every timepoint. Constructs were then returned to 0% strain and the same imaging protocol was performed. Three cycles of stretch were performed on each construct. The cells were then lysed with SDS and

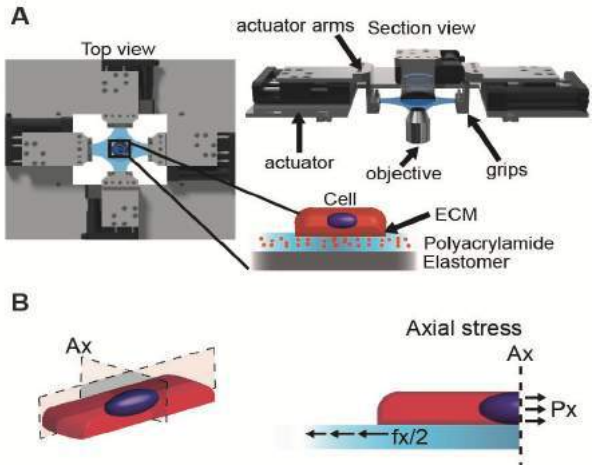

Figure 1: **A**. Schematic of CμBS apparatus. **B**. Calculation of axial PK1 stresses in a single cell. Figure adapted from Win et al.[3]

the bead layer of the gel was imaged again at the location of each cell at 0% and 15% strain. The fluorescent images of the gel layers with the adhered cells were paired with the respective images of the gels without the cells to perform traction calculations.

Traction Calculation. Displacement of the beads due to cellular contraction was tracked and measured using a particle image velocimetry (PIV) ImageJ plugin between paired images with and without the adhered VSMCs.[5] Using the displacement data with the material properties of the PA gel, traction stress vectors throughout the area occupied by the cell were calculated using an unconstrained Fourier transform traction cytometry (FTTC) ImageJ plugin with a filtering regularization factor of 1E-9.[6] Each vector in a specified region of the image was represented by

$$\boldsymbol{T^n} = {T_x}^n \boldsymbol{e_x} + {T_y}^n \boldsymbol{e_y} \quad (1)$$

in which $\boldsymbol{e_x}$ and $\boldsymbol{e_y}$ are the unit vectors along the x and y directions, respectively. From the traction vector field, total force vectors $\boldsymbol{f^n}$ were calculated by

$$\boldsymbol{f^n} = -{T_x}^n a^n \boldsymbol{e_x} - {T_y}^n a^n \boldsymbol{e_y} \quad (2)$$

in which n is the discrete surface and a is the area of the surface. Total force across the cell was calculated by

$$2f_i = \sum_n \frac{{f_i}^n {r_i}^n}{|{r_i}^n|} \quad (3)$$

where r_i is the x or y component of the position vector r^n that maps the surface to the center of the cell such that

$$\boldsymbol{r^n} = {r_x}^n \boldsymbol{e_x} + {r_y}^n \boldsymbol{e_y} \quad (4)$$

From the total force components f_i, x and y components of the First Piola-Kirchoff (PK1) stress P_i of the cell was calculated by

$$P_i = \frac{f_i}{A_i} \quad (5)$$

in which A_i is the axial undeformed cross-sectional area of the patterned VSMC (**Fig. 1B**).

RESULTS

Single cell stress relaxation experiments were performed to investigate how rate of strain impacts VSMC mechanical response immediately following stretch. Representative bright field images and stress maps are shown for a cell stretched at 0.1 s^{-1} for five time points (**Fig. 2A**). Cells were strained according to the protocol described in the methods (**Fig. 2B**).

For cells exposed to a step-change in strain, post-stretch mechanics depended on strain rate during stretch (**Fig. 2C**). Cells that were stretched to 15% strain at a higher rate of 1 s^{-1} demonstrated a comparatively low stress immediately following stretch. Stress decayed exponentially to the pre-stretch value. Cells that were stretched to 15% strain at a lower rate of 0.001 s^{-1} demonstrated a comparatively higher stress immediately after stretch. Stress decayed to a lower value but did not approach the pre-stretch value and remained higher than the stress relaxation plots for faster strain rates. Following compression back to the original configuration, stress recovery behavior was nearly identical for all cells regardless of strain rate. This pattern repeated with increasing cycles.

DISCUSSION

Our results indicate that VSMC stress relaxation behavior depends on strain rate. We found that VSMCs stretched at a higher strain rate exhibit consistently lower contraction stress than cells stretched at a lower strain rate. This implies a strain rate dependency in VSMC stress relaxation that is not captured in conventional models of viscoelasticity. In upcoming experiments, we will propose a new model to more accurately capture VSMC stress relaxation following stretch at high strain rates.

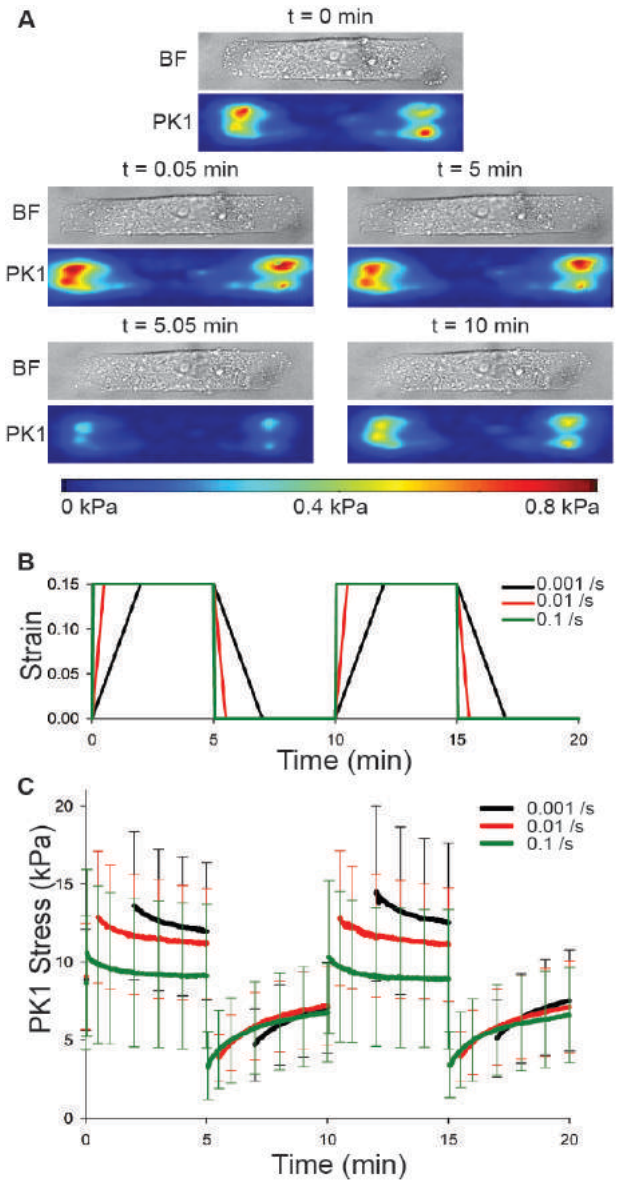

Figure 2: A. Bright field images of VSMC stretched at 0.1 s^{-1} with corresponding PK1 stress map for five time points: t=0 min (prior to stretch), t=0.05 min (immediately after stretch), t=5 min (end of stretched period), t=5.05 min (immediately after compression to original configuration), and t=10 min (end of cycle).. **B.** Strain protocol for stretching and time-lapse periods. **C.** PK1 stress relaxation time lapse for VSMCs stretched to 15% strain at 3 strain rates. n = 18, 16, and 22 for strain rates 0.001, 0.01, and 1.0 s^{-1}, respectively.

ACKNOWLEDGEMENTS

We thank the NSF (CMMI-156319, CMMI-1553255) and the NIH T32 Traineeship in Cardiovascular Engineering for financial support.

REFERENCES

[1] Alford, P et al., *PNAS*, 108(31):12705-12710, 2011.
[2] Zlokovic, B, *Nat Rev Neurosci*, 12:723-738, 2011.
[3] Win, Z et al., *Biophys J*, 115:2044-2054, 2018.
[4] Szczesny, S & Mauck, R, *J Biomech Eng*, 139(2), 2017.
[5] Tseng, Q et al., *PNAS*, 109(5):1506-1511, 2012.
[6] Butler, J et al., *Am J Physiol – Cell Physiol*, 282:C595-C605, 2002.

MECHANISM OF ENHANCED THERMAL TRANSPORT AND PHOTOACOUSTIC EFFECT FOR SILICA-COATED GOLD NANOPARTICLES

P. Kang (1), J. Youn (1), Z. Qin (1, 2, 3, 4)

(1) Department of Mechanical Engineering
University of Texas at Dallas
Richardson, Texas, USA

(2) Department of Bioengineering
University of Texas at Dallas
Richardson, Texas, USA

(3) Center for Advanced Pain Studies
University of Texas at Dallas
Richardson, Texas, USA

(4) Department of Surgery
University of Texas at Southwestern Medical Center
Dallas, Texas, USA

INTRODUCTION

Upon short-pulsed laser irradiation, plasmonic metallic nanoparticles convert light energy into thermal energy and heat up surrounding medium. This sudden heating leads to the thermal expansion in medium and pressure transients known as photoacoustic (PA) effect. PA effect has been developed as imaging tools for noninvasive diagnosis of disease. PA imaging can reach deeper into tissue than optical imaging techniques because light is only used for generating heat not for imaging. Comapred with conventional PA agents such as dye molecules, plasmonic nanoparticles have tunable plasmon resonance and good photostablity. These unique properties make plasmonic nanoparticles be promising contrast agents for PA imaging. Furthermore, the surface engineering of plasmonic nanoparticles, such as coating with polyethylene glycol [1], polymers [2], and inorganic materials [3] can provide advantages, including improved biocompatibility, increased thermal and colloidal stability, and surface functionalization.

Among many coating materials, the silica coating on gold nanoparticles has demonstrated good potential for PA signal enhancemnet [4,5]. Although experimental results were promising, the mechanism of the PA enhancement by thin silica coating of gold nanoparticles is still far from completing. One hypothesize is that silica coatings can change the heat transfer process on the interface of nanoparticle and medium resulting in PA improvement. Although qualitivily describing the experimental observation, this theory remains unresolved and lacks detail. Here, for the first time, we provide a theoretical model to explain how the interfacial heat transfer affects the PA generation with the silica coating in presence. We use experimental method and numerical simulation to investigate two effects on photoacoustic enhancement of silica coating on gold nanosphere, namely the particle structure and the laser duration.

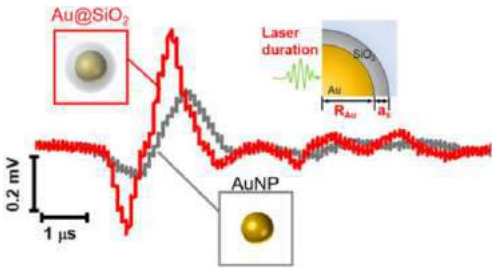

Figure 1. Representative photoacoustic (PA) signal of the silica coated gold nanoparticle (Au@SiO_2) and the bare gold nanoparticle (AuNP). Two important aspects are investigated in this study including laser duration (picosecond vs nanosecond), nanoparticle structure including gold core size (R_{Au}), and silica shell thickness (a_s)

METHOD

Synthesis of nanoparticle: Gold nanoparticles (AuNPs, 15 nm diameter) were synthesized by Turkevich method [6]. AuNPs larger than 15 nm were synthesized by method previously reported [7]. Au@SiO_2 was prepared by following the procedure described by Liz-Marzán et al. [8]. The size of Au core and silica shell thickness (a_s) was determined by JEOL 1400 Transmission electron microscope (TEM).

Photoacoustic signal measurement: To measure the PA signal, samples are diluted to 0.5 OD at 532 nm and loaded in a dialysis cassette. A pulsed picosecond laser (532 nm, full width half maximum (FWHM) = 28 ps) or a pulsed nanosecond laser (532 nm, FWHM = 6 ns) was used to generate PA signal. The PA signal was detected an ultrasound transducer with the central frequency at 0.5 MHz.

Numerical simulation: The numerical simulation was conducted in COMSOL 5.3 software. The PA quantum yield ($\boldsymbol{\phi_{PA}}$) is defined as the ratio of the emitted ultrasound energy ($E_{acoustic}$) to the absorbed photon energy (E_{optic}) from a single nanoparticle and can be calculated by Eq. 1,

$$\phi_{PA} = \frac{E_{acoustic}}{E_{optic}} = \frac{\iint {}^{p^2}/_{R}\, dSdt}{\int \sigma_a I dt} \quad (1)$$

where p is acoustic pressure, R is the acoustic impedance of water, σ_a is the absorption cross section of nanoparticle and I is laser intensity. The area S encloses a large spherical volume containing the nanoparticle [9].

RESULTS

First, we experimentally investigated the effect of particle geometry and laser duration on PA generation. The silica coating is uniformly distributed on the surface of gold and has well-defined thickness (a_s, Fig. 2A). Comparing with the bare AuNP with a diameter of 15 nm, the 1.9 nm silica coating enhances the PA signal more than 100% under ps laser (Fig. 1). The PA enhancement decreases gradually with the shell thickness (Fig. 2B). Importantly, no noticeable PA enhancement by silica coating was observed under the nanosecond laser irradiation. Next, the effect of Au core size on silica coating induced PA enhancement is investigated. Strong PA enhancement can be observed from Au@SiO_2 with 30 nm and 90 nm Au core under picosecond laser. Interestingly, the PA amplification by silica coating only appears when the silica shell thickness is in a certain range. For the 15 nm gold core, the enhancement was observed within a narrow range of shell thickness from 2 ~5 nm. The range for PA enhancement is 5 ~ 10 nm and 3~20 nm for 30 nm and 90 nm Au core, respectively. In the case of 90 nm core, the range is wider than for smaller core AuNPs. The silica thickness range for the signal amplification was wider as the size of the core particle increased.

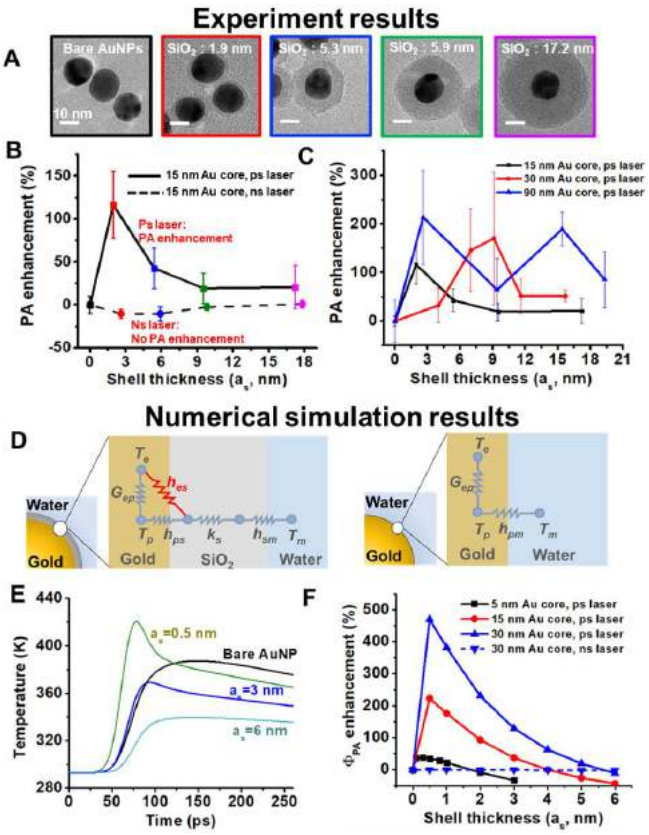

Figure 2. Experiment and numerical simulation results. (A) representative transmission electron microscopy images of bare gold nanoparticles (AuNP) and silica coated gold nanoparticles (Au@SiO_2). (B) Effect of laser duration on PA enhancement. (C) Effect of Au core size on PA enhancement. (D) Schematic of heat transfer model for Au@SiO_2 and AuNP. (E) Temperature of water on the surface of the particle with different silica shell thickness. (F) The enhancement of the PA quantum yield ($\boldsymbol{\phi_{PA}}$) for Au@SiO_2 with different gold core size and silica shell thickness. The silica coating does not enhance PA quantum yield under ns laser.

Second, we numerically investigated the effect of silica coating on PA generation of AuNPs. For Au@SiO_2, besides the phononic heat transfer between gold and silica, the energy will directly be transported from gold electrons to silica phonons (h_{es}, Fig. 2A). This additional transport mechanism enhances the heating rate of adjacent medium under the ps laser irradiation. On the other hand, the interface electron-phonon coupling is absent for the bare AuNP. Compared to the bare AuNP with a diameter of 30 nm, the temperature of water on the particle surface raises faster when a thin silica shell is in presence (a_s<3, Fig. 2E). The enhanced heating rate of water leads to a significant increase of acoustic signal. The PA enhancement is highly dependent on the particle geometry (Fig. 2F). In general, thin silica coatings enhance the PA generation more than thick silica coatings. Furthermore, large Au cores allow larger PA enhancement than smaller Au cores. Importantly, the PA enhancement by silica coating only occurs for ps laser while no obvious enhancement for ns laser. This is because that the direct energy transport through gold electrons to silica phonons is only significant under ps laser pulse in the ps time scale and can be neglected in ns time scale. The numerical simulation results agree with our experimental observations. This indicates that the electron-phonon coupling on gold and silica interface is responsible for PA enhancement by silica coating under ps laser pulse.

DISCUSSION

We systematically studied the effect of the nanoparticle structures and laser duration on photoacoustic signal generation. We observed that silica coating can enhance PA signal by 2 folds compared to bare AuNP under picosecond laser while the signal is unchanged under nanosecond laser. In addition, the core size affects the range of silica thickness range where PA signal is enhanced. These experiment results agree with our theoretical model and suggest that energy transport channel between gold electron and silica phonon contributes to PA enhancement under picosecond laser. This study is an important step towards a better understanding of PA signal generation of plasmonic nanoparticles. For the first time, a clear mechanism was provided to explain the PA enhancement by silica coating on plasmonic nanoparticles and will find many biomedical applications.

ACKNOWLEDGEMENTS

This work is partially supported by NIH grant (R35GM133653). We appreciate helpful discussion with Dr. Samy Merabia, Dr. Ali Alkurdi at Université de Lyon, and Dr. Jaona Randrianalisoa at Université de Reims Champagne-Ardenne.

REFERENCES

[1] Perrault, S. D. et al.. Nano Lett, 9:1909-1915, 2009.
[2] Kreyling, W. G. et al., Nat Nanotechnol, 10:619-623, 2015.
[3] Voss, J. M. et al., ACS Nano, 13:12445-12451, 2019.
[4] Chen, Y. et al., Nano Lett, 11:348-354, 2011.
[5] Jokerst, J. V. et al., ACS Nano, 6:5920-5930, 2012.
[6] Perrault, S. D. et al., J Am Chem Soc, 131:17042-17043, 2009.
[7] Bastús, N. G. et al., Langmuir, 27:11098-11105, 2011.
[8] Liz-Marzán, L. M. et al., Langmuir, 12:4329-4335, 1996.
[9] Chen, Y. et al. Nat Nanotechnol, 14:465-472, 2019.

SUBSTRATE STIFFNESS REGULATES ECM GENE EXPRESSION, AND SIZE OF CELL AND NUCLEUS OF FIBROBLASTS

Brijesh Kumar Verma[1], Aritra Chatterjee[1], Paturu Kondaiah[2] and Namrata Gundiah[1,3]
1. Centre for Biosystems Science and Engineering, 2. Molecular Reproduction, Development and Genetics and 3. Mechanical Engineering,
Indian Institute of Science, Bangalore, 560012, India.

INTRODUCTION

Fibroblasts are mesenchymal in origin and among the most common cell types in the stroma [1]. They are involved in the maintenance of the extracellular matrix (ECM), and synthesize a diverse array of proteins including collagen and proteoglycans; fibronectin; laminins; metalloproteinases (MMPs), among others [2]. Adherent fibroblasts are sensitive to changes in their biochemical and mechanical milieu [3], and induce remodeling of the ECM in skin, lung, heart, kidney, liver and other organs [4,5] in response to these stimuli. Changes to the ECM layout and composition often occurs either through degradation or crosslinking of ECM proteins [6]. Pro-inflammatory cytokines and growth factors, such as Transforming growth factors (TGFs), platelet derived growth factor (PDGF) and tumor necrosis factor (TNF), regulate these behaviors [7]. Maladaptive tissue remodelling requires a switch from inflammatory to pro-fibrotic pathways, thereby triggering fibrosis[8,9]. We work on the preliminary hypothesis that variations in the underlying substrate stiffness result in morphological changes to the cell cytoskeleton and nucleus which alter gene expression levels related to ECM remodeling.

RESULTS

Fig. 1a, shows confocal images of HMF3s cells cultured on substrates of different stiffnesses. Cell areas were significantly smaller on lower substrate stiffness (10:1, 20:1 and 40:1) as compared to tissue culture dish (Fig. 1b). We also found similar observation with regards to nuclear area (Fig.1c). The expression of MMP2, Collagens 1 and III, and TGF-β1was reduced when cultured on 10:1, 20:1 and 40:1 substrate as compared to tissue culture dish. GAPDH expression served as control (Fig.1d). These data suggest that changes in cell and nuclear morphologies of HMF3s cells and ECM associated gene expressions are regulated by changes in substrate stiffness.

METHODS

Substrates of different stiffnesses were prepared by mixing silicone elastomers (Sylgard® 184, Dow Corning) with the cross-linker in different stoichiometric weight ratios of 10:1 (1.58±0.188 MPa), 20:1 (351±24 KPa) and 40:1 (41.89±4.09 KPa)[10.] Substrates were treated with plasma for 2 minutes, followed by incubation with 40 μg/ml of fibronectin (FN) for 1 hour at 37°C, and washed twice with phosphate buffer saline (PBS). Immortalized human mammary fibroblasts (HMF3s)[16], grown in DMEM media supplemented with 10 % fetal calf serum, were cultured on the substrates for 24 hours. Gene expression analysis was performed by RT-PCR. Cellular and nuclear morphologies were analyzed using confocal imaging.

DISCUSSION

Our study provides important insights on the effects of substrate stiffness in combination with changes to the overall cellular and nuclear morphologies that result in ECM associated gene expressions. These results provide useful mechanistic understanding of the ECM remodeling with substrate stiffness changes associated with tissue fibrosis. These finding may be useful in developing a pro-fibrotic molecule in mitigating and facilitating tissue repair due to injuries.

ACKNOWLEDGEMENT

We acknowledge the financial support from Department of Biotechnology, Government of India.

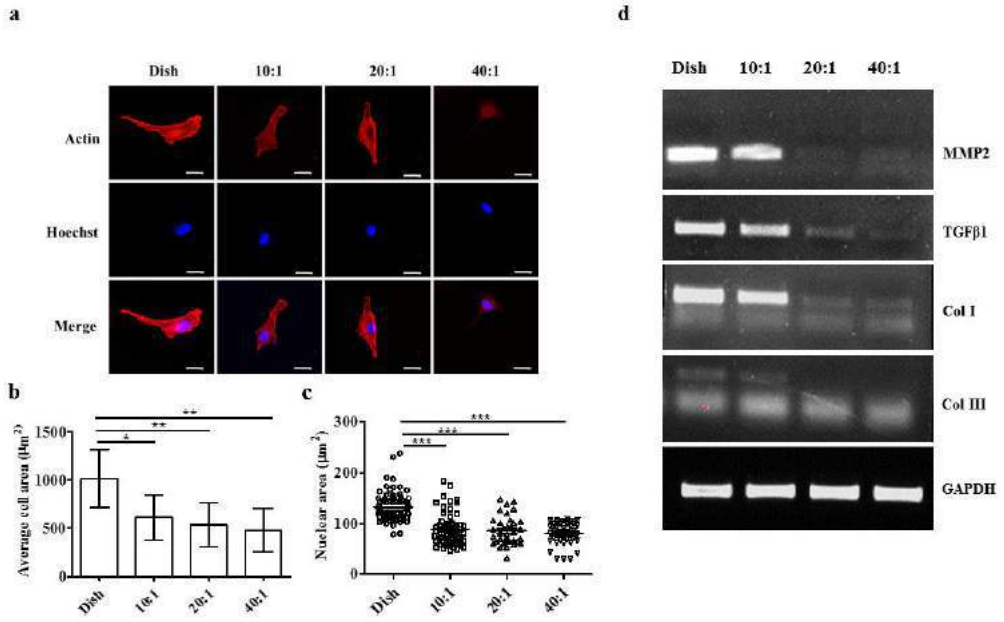

Figure 1 a. Confocal images of HMF3s fibroblasts cultured on substrates of different stiffness (Control tissue culture dish and PDMS membranes of different elastomer to crosslinker ratios of 10:1, 20:1 and 40:1 respectively) stained for F-actin (red) and DAPI nucleus (blue). Scale bar represents 20 µm. **b & c.** Cell and nuclear areas decreased with substrate stiffness. Significant differences are indicated for p<0.001(***), p<0.01 (**) and p<0.05 (*). **d.** RT-PCR products are shown for MMP2, TGFβ1, Col I, Col III and GAPDH genes with RNA collected from HMF3s cells seeded on various substrate stiffness.

REFERENCES

1. Ugurlu, B. & Karaoz, E. Comparison of similar cells: Mesenchymal stromal cells and fibroblasts. *Acta Histochemica* **122**, (2020).
2. Kendall, R. T. & Feghali-Bostwick, C. A. Fibroblasts in fibrosis: Novel roles and mediators. *Frontiers in Pharmacology* **123**, (2014).
3. Ford, A. J., Orbach, S. M. & Rajagopalan, P. Fibroblasts stimulate macrophage migration in interconnected extracellular matrices through tunnel formation and fiber alignment. *Biomaterials* **209**, 88–102 (2019).
4. Desmoulière, A., Chaponnier, C. & Gabbiani, G. Tissue repair, contraction, and the myofibroblast. *Wound Repair and Regeneration* **13**, 7–12 (2005).
5. Darby, I. A. & Hewitson, T. D. Fibroblast Differentiation in Wound Healing and Fibrosis. *International Review of Cytology* **257**, 143–179 (2007).
6. Theocharis, A. D., Skandalis, S. S., Gialeli, C. & Karamanos, N. K. Extracellular matrix structure. *Advanced Drug Delivery Reviews* **97**, 4–27 (2016).
7. Prante, C. *et al.* Transforming growth factor β1-regulated xylosyltransferase I activity in human cardiac fibroblasts and its impact for myocardial remodeling. *J. Biol. Chem.* **282**, 26441–26449 (2007).
8. Rodriguez, E. K., Hoger, A. & McCulloch, A. D. Stress-dependent finite growth in soft elastic tissues. *J. Biomech.* **27**, 455–467 (1994).
9. Robertson, A. M. & Watton, P. N. Mechanobiology of the Arterial Wall. in *Transport in Biological Media* 275–347 (Elsevier Inc., 2013). doi:10.1016/B978-0-12-415824-5.00008-4
10. Babu, A. R. & Gundiah, N. Role of Crosslinking and Entanglements in the Mechanics of Silicone Networks. *Exp. Mech.* **54**, 1177–1187 (2014).

MADE TO MEASURE: 3D PRINTING PATIENT SPECIFIC PAEDIATRIC STENTS

O. M. McGee (1,2), S. Geraghty (1,2), C. Hughes (1,2), P. Jamshidi (3), D. Kenny, (4), M. Attallah (3), C. Lally, (1,2,5)

(1) 1 Trinity Centre for Biomedical Engineering, Trinity Biomedical Sciences Institute, Trinity College Dublin, Dublin, Ireland

(2) Department of Mechanical, Manufacturing & Biomedical Engineering, School of Engineering, Trinity College Dublin, Dublin, Ireland

(3) School of Metallurgy & Materials, University of Birmingham, Birmingham, B15 2TT, United Kingdom

(4) Our Lady's Children's Hospital, Crumlin, Dublin, Ireland.

(5) Advanced Materials and Bioengineering Research Centre (AMBER), Royal College of Surgeons in Ireland & Trinity College Dublin

INTRODUCTION

In the past 30 years, percutaneous therapies for the treatment of congenital heart disease have advanced immensely, however, with the limited investment from industry there is a lack of devices specifically designed for the treatment of congenital heart disease in paediatric patients [1]. There is currently a clear clinical need in the area of stenting for paediatric patients, whereby currently commercially available adult stents are often required to be used off-label for paediatric patients that may lead to suboptimal outcomes [1,2]. The increasingly widespread use of CT and/or MR imaging for pre-surgical assessment, and the emergence of additive manufacturing processes such as 3D printing, could enable bespoke devices to be produced efficiently and cost effectively.

In recent years, research has been carried out into the development of 3D printed metallic stents in an attempt to overcome the disadvantages of the conventional stent manufacturing techniques where stents are laser cut from a tube [3],[4]. Additive manufacturing of metallic stents has the potential to eliminate these challenges in both production and treatment leading the way to 3D printing specialised and unique stent designs. A recent study by Demir & Previtali [3] investigated SLM of cobalt-chromium stents for cardiovascular stenting. That study outlined the need for a selective laser melted stent to be self-supporting and rules on creating such a geometry. This ensures there is no unnecessary damage to the stent in removing supports post-printing. These rules state that struts should be (i) maintained at angles greater than 45° to the horizontal, (ii) have overhangs less than 1mm, and gaps greater than 0.3mm. However, these design rules lead to restrictions in the design of stents available through additive manufacturing. Further to this, Finite Element (FE) models have been used to predict the performance of medical devices [5,7] and can be used to optimise these devices for specific patient anatomies.

The objective of this study is to demonstrate the feasibility of producing patient-specific 3D printed stents for paediatric patients with congenital vascular defects, to investigate the stent designs available through 3D printing, to assess their performance using a combination of FE modelling and experimental bench testing and design an optimised stent for a given paediatric patient.

METHODS

CT Reconstruction: Computer tomography (CT) images of the aortic arch of a paediatric patient with an aortic coarctation, necessitating the placement of a stent were obtained and used to develop 3D models of the coarctation. The aorta geometry is extracted via image segmentation using 3D Slicer [4], a skin surface of the vessel is constructed with ANSYS Spaceclaim (2019 ANSYS. Inc) and a volumetric hexahedral mesh representation of the geometry is finally generated with ANSA-BETA Pre-Processer (BETA CAE Systems, Luzern, Switzerland).

Patient-Specific Silicone Model: Preform (Formlabs Inc., MA, USA) was then used to generate a 3D printed model in elastic resin with varying thickness using a Form 2 Printer (Formlabs Inc., MA, USA). The relationship between the stiffness of the elastic resin and its thickness was investigated by printing 20 mm tubes of different thicknesses and pressurizing them to 80 mmHg and 120 mmHg using a FISO pump and pressure sensor and measuring the change in strain. This was then compared to porcine arterial tissue.

Patient-Specific Stent Design and Processing: A Simple Honeycomb (SH) and a Novel Design (ND) stent geometries were designed based on patient dimensions and design criteria for additive manufacturing based on [5]. These stents were then printed using the ReaLizer Selective Laser Melting (SLM) printer (Realizer GmbH) using Titanium powders. After printing, some of the stents were etched

to reduce the stent strut thickness and improve the surface finish. The samples were immersed into etching solution containing hydrofluoric and nitric acid ((HF: HNO3: H2O = 1:2:3) for approximately 12 minutes and then transferred into distilled water for 5 minutes and rinsed with ethanol. Half of the SH designs were etched, and all three of the ND designs were etched. The finished stent designs can be seen in Figure 2.

Stent Testing: Once printed, these stents were implanted into the patient-specific geometry and underwent an experimental crush test using an Instron 3366 (Instron., MA, USA).

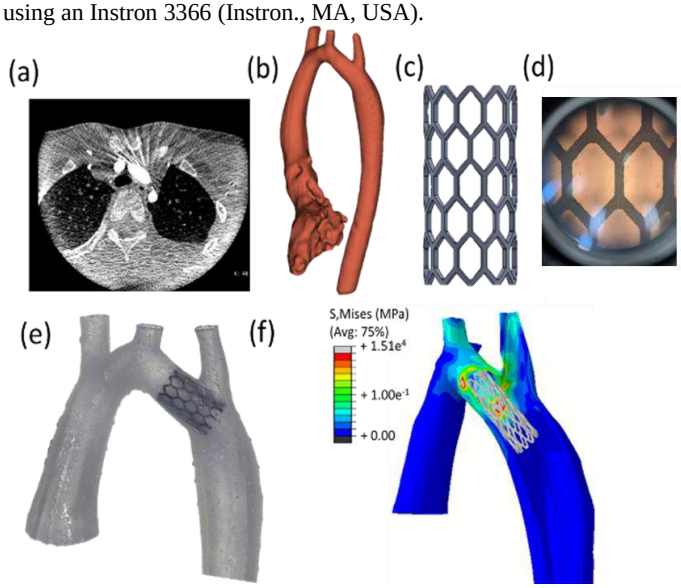

Figure 1. (a) CT scan of a paediatric patient with an aortic coarctation (b) patient-specific model of the aorta (c) STL of stent geometry (d) Stereoscopic image of SLM printed stent geometry (e) our SLM printed stent in the elastic model of the patient-specific aortic root (f) FE model of stent deployment into patient specific geometry.

FE Crush Test: Prior to the experimental crush test measurements of the strut width and thickness of each stent were taken using a stereoscopic microscope. Based on these as etched and as printed measurements the stents were recreated in Solidworks (Dassault Systemes Solidworks Corp, MA, USA). Stents were then prepared for meshing and meshed using Ansys Spaceclaim (2019 ANSYS. Inc) and ANSA BETA (BETA CAE Systems, Luzern, Switzerland) respectively. A FE model was created in ABAQUS and used to replicate the experimental crush test. Using an inverse FE approach the experimental and FE crush tests were compared to calibrate the material properties of the printed and etched stents.

Patient Specific Finite Element Model: Using the generated mesh of the patient's aortic arch from CT images an FE model was used to simulate stent deployment into an isotropic hyperelastic model of the patient specific geometry. This was achieved by crimping the stent inward radially using a cylindrical part (crimper). Hard normal contact with a coefficient of friction of 0.8 was applied between the stent and the crimper [6]. The top and bottom edges of the aortic arch were constrained using displacement boundary conditions in the longitudinal and circumferential directions. The stent was uncrimped and hard normal, frictionless contact was applied between the stent and the aorta [7]. Different stent designs pre- and post-etching were deployed into the patient specific anatomy to analyse and compare stent performance.

RESULTS

Strain measurements from pressurised printed vessels found that the elastic model of the patient-specific aorta demonstrated higher stiffness than native arteries, however, such 3D printed models are a valuable pre-surgical planning tool and offers a means of validation for FE models.

Etching stents was found to reduce the stent strut width and thickness. Alongside this, stent surface finish was improved post-etching. Furthermore, it was found that combining novel designs with etching allows for open stent designs to be printed without the need for additional supports. Such techniques can allow for a greater range of 3D printed stent designs to treat specific patient needs.

Calibration of the stent material properties found that non-etched stents had lower Young's moduli. This is attributed to the fact that increased surface roughness led to overestimation in the stent width and thickness from stereoscopic measurement therefore, led to an overestimation in the stent performance in the FE model.

The patient specific model found changes in stent design combined with etching can reduce aortic stress with minimal loss in lumen gain.

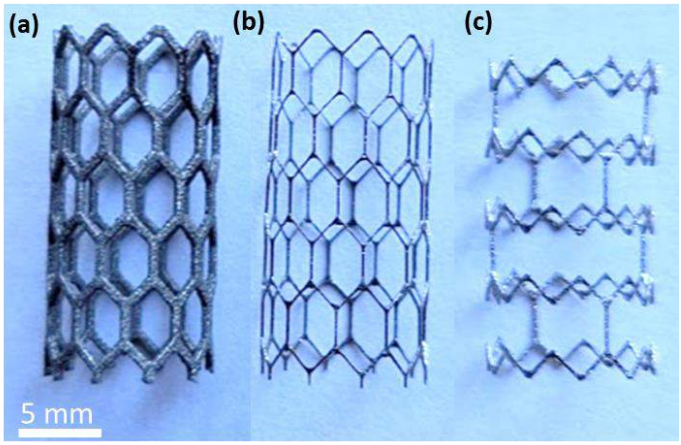

Figure 2. SLM Printed stents; (a) Simple Honeycomb (SH) (b) Simple Honeycomb Etched (SHE) and (c) the Novel Design Etched (NDE).

DISCUSSION

This study demonstrates the feasibility of this in-vivo imaging to product development pipeline that will enable patient-specific stents to be produced for varying anatomies to achieve optimum device performance.

ACKNOWLEDGEMENTS

This study was funded by a National Children's Research Centre Innovation Award and an Irish Research Council Government of Ireland Postdoctoral Fellowship 2019 (GOIPD/2019/222).

REFERENCES

[1] Kenny & Hijazi, Circ. Res., 120; 1015-1026. 2017.
[2] Holzer & Hijazi, Catheter Cardiovasc Interv, 72(6); 848-52. 2008.
[3] A. G. Demir and B. Previtali, Mater. Des., 2017.
[4] V. Finazzi et al., Procedia Struc. Integrity, 15, 16–23. 2019.
[5] McGee et al. Biomech Model Mechanobiol. 18 (1), 79-88. 2019.
[4] https://www.slicer.org/
[5] Demir & Previtali. Mater Design. 119. 338-350. 2017.
[6] T. Y. Qiu et al .Mech. Time-Dependent Mater., 22(2), 273–90,2018.
[7] C. Lally et al., J. Biomech., 38(8),1574–1581, 2005.

A NOVEL THREE-LAYERED MODEL OF MOUSE DISTAL COLON AND RECTUM CAPTURING THROUGH-THICKNESS BIOMECHANICS

Y. Zhao (1,2), B. Feng (2), D.M. Pierce (1,2)

(1) Department of Mechanical Engineering
University of Connecticut
Storrs, CT, USA

(2) Department of Biomedical Engineering
University of Connecticut
Storrs, CT, USA

INTRODUCTION

Our overarching aim is to facilitate mechanistic understanding of visceral nociception by leveraging multiscale models bridging the intra-tissue mechanics within the colorectum and mechanical neural encoding by sensory nerve endings. Mechanotransduction of colorectal distension/stretch plays a critical role in evoking visceral nociception [1]. The colorectum displays strong microstructural hierarchy through the wall thickness, consisting of two major fibrous layers: the inner mucosal-submucosal composite and the outer serosal-muscular composite. We previously conducted mechanical [2,3] and imaging [2-4] experiments to quantify the biomechanics and morphology of the colorectum. Our recent imaging study [4] revealed concentrated collagen in the submucosa relative to other distinct layers, implying that the submucosa serves a specific mechanical role. Furthermore, this mechanical heterogeneity in the colorectum determines the microscale stresses/strains around afferent endings embedded within the collagen-rich regions undergoing noxious mechanical stimuli. We previously separated the colorectal wall into inner and outer composite layers, completed mechanical testing, and fitted constitutive models assuming two layers [5]. In this study we aimed to improve model fidelity, particularly the through-thickness heterogeneity of the colorectum, via a novel three-layered model. We quantified the layer thicknesses and determined parameters for constitutive models of the mucosa and submucosa from three longitudinal locations (colonic, intermediate, and rectal), using nonlinear optimization to fit our mechanical tests [2,3]. We implemented the constitutive equations and created three-layered, 3-D finite element models using FEBio (U. of Utah) [5,6], and simulated three mechanical stimuli commonly used in experiments to study visceral nociception in colorectum *ex vivo*, i.e. circumferential stretching (C. stretch), probing, and shearing [7]. Our models capture the biomechanical heterogeneity in three distinct through-thickness layers and highlight the differential roles of sensory nerve endings in different regions of the colorectum in visceral mechanotransduction.

METHODS

Imaging and Mechanical Testing of Colorectum. We recently conducted nonlinear imaging via second harmonic generation (SHG) to quantify the thickness of each distinct through-thickness layer of mouse colorectum (colonic, intermediate, and rectal), as well as the morphology of the dispersed collagen fibers [4]. The submucosal layer had the largest collagen content with the greatest average diameter of fibers, and presented two principal orientations of alignment. Collagen fibers in muscular layers aligned with the longitudinal and circumferential muscle fibers. In contrast, the mucosa showed no principal orientation of alignment for these fibers. We also performed biaxial extension tests both on bulk composite mouse colorectum and the separated layers of inner and outer composite which provided data for constitutive modeling [2,3]. We identified residual stresses by quantifying the reference configuration of the bulk composite and the separated configurations of inner and outer composites.

Constitutive Modeling and Model Fitting. To model the layers of the colorectum we used the strain-energy function [6,8]

$$\Psi = \mu(I_1 - 3) + \int_\Omega \rho(\mathbf{M}) \frac{k_1}{2k_2}\{\exp[k_2(I_4 - 1)^2] - 1\}\mathcal{H}(I_4 - 1)\mathrm{d}\Omega\,, \quad (1)$$

where μ is the shear modulus of the matrix, $I_1 = \mathrm{tr}\,\mathbf{C}$ where $\mathbf{C}$ is the right Cauchy-Green tensor, k_1 is a stress-like material parameter, k_2 is a dimensionless parameter, $I_4 = \mathbf{M}\cdot\mathbf{CM}$, and $\rho(\mathbf{M})$ is an orientation distribution function characterizing the network of fibers $\mathbf{M}$ with $1/4\int_\Omega \rho(\mathbf{M})\mathrm{d}\Omega = 1$. For the mucosal layer in which collagen fibers showed no principal orientation, we used only the neo-Hookean portion of (1). Guided by our biomechanical and image-based data [2-4], we

established a three-layered square patch of mucosa-submucosa-muscular composite (7.0×7.0 mm^2) which we meshed with eight-node hexahedral elements [6]. To capture the kinematics of the biaxial extension test, we wrote the invariants I_1 and I_4 as

$$I_1 = \lambda_c^2 + \lambda_a^2 + \lambda_r^2 , \quad I_4 = \lambda_c^2 \cos^2\alpha + \lambda_a^2 \sin^2\alpha , \qquad (2)$$

where λ_c, λ_a, and λ_r were the measured principal stretches in the circumferential, axial, and radial directions, respectively; we identified α, representing the angle between the fiber orientation and the circumferential direction, from our SHG imaging data [4]. Consequently, we obtained four parameters (μ,k_1,k_2,α) for the submucosa and one parameter (μ) for the mucosa.

Modeling of Ex Vivo Mechanical Stimuli. We established a three-layered (mucosal, submucosal, and muscular) square patch of colorectum (8.0×8.0 mm^2) (**Fig. 1**) [7]. Specifically, we modeled mechanical stimulation from: (1) homogeneous, circumferential stretch by fixing one edge of the patch and linearly increasing the circumferential displacements, **Fig. 1(a)**; (2) perpendicular probing by applying a cylindrical probe to the mucosa surface including a sliding contact between the surfaces, **Fig. 1(b)**; and (3) mucosal stroking in shear tests by sliding a soft block along the mucosal surface, **Fig. 1(c)**. In cases 2 and 3 we pinned the colorectum flat on a silicone foundation (10.0×10.0 mm^2) by using a tied contact between the interfacing surfaces, consistent with the prior *ex vivo* experimental conditions [7]. We again meshed these models with eight-node hexahedral elements. We included residual stresses between submucosa and muscular layers in the initial configurations using the pre-stretch algorithm in FEBio [6].

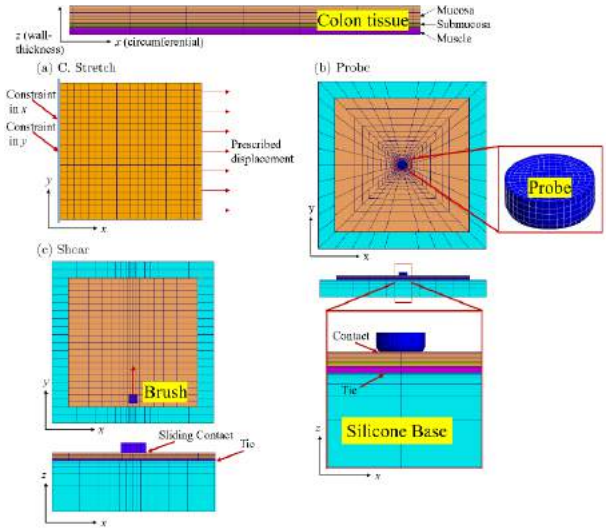

Figure 1: Finite element modeling of mechanical stimuli to the colorectum: (a) circumferential stretch, (b) probe, and (c) shear.

RESULTS

Validating the Constitutive Model. **Figure 2** presents the comparisons between the simulated biaxial extension (finite element models of bulk colorectal patch) versus the experiment data, and **Table 1** summarizes the resulting model parameters for the mucosa and the submucosa along the length of the colon. The relative error is less than 12%. In **Fig. 2**, EXP, FE, cir, and ax are abbreviations for experimental, finite element, circumferential, and axial, respectively.

Modeling of Mechanical Stimuli. **Figure 3** presents the through-thickness distributions of maximum shear stresses in response to three different mechanical stimuli, i.e. circumferential stretching, probing, and shearing. A normalized depth of 0 represents the bottom surface of the muscular layer while 1 represents the top surface of mucosa layer.

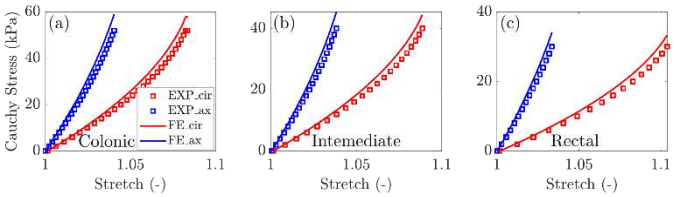

Fig. 2: Model validation for bulk colorectum undergoing biaxial extension: experiment (symbols) with corresponding predictions (solid) for (a) colonic, (b) intermediate, and (c) rectal regions.

Table1: Model parameters for the mucosa and the submucosa.

	μ (kPa)	k_1 (kPa)	k_2 (-)	α (°)
Mucosa-Colonic	29.16	/	/	/
Mucosa-Interm.	19.95	/	/	/
Mucosa-Rectal	14.98	/	/	/
Submucosa-Colonic	47.43	63.41	34.56	60.10
Submucosa-Interm.	32.97	102.9	18.90	50.14
Submucosa-Rectal	21.73	83.54	26.95	46.45

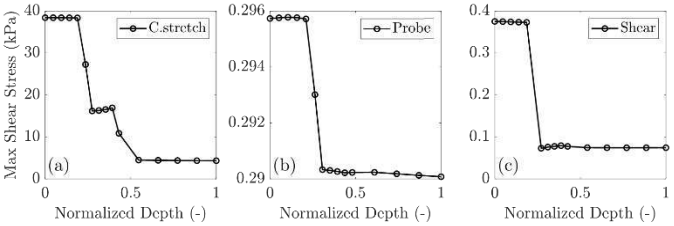

Fig. 3: Maximum shear stresses through the thickness of the colorectum: (a) circumferential stretch, (b) probe, and (c) shear.

DISCUSSION

Combining our experimental data, i.e. the collagen distributions acquired via SHG and the mechanical responses quantified with biaxial extension testing, we improved the fidelity of our computational model of the colorectum by incorporating three layers, i.e., mucosal, submucosal, and muscular layers. Our fitted model shows strong mechanical heterogeneity thought the thickness of the colorectal wall, and indicates that the relatively thin submucosa is the principal load-bearing structure within the colorectum, owing largely to the concentrated, well-aligned network of collagen. The two families of fibers form a dispersed network in the submucosa that informs the micromechanical environment therein, and which is heavily innervated by sensory nerve endings. We compared the maximum shear stresses through the thickness of the colorectum undergoing three experimental mechanical stimuli [8]. Our finite element simulations of intra-tissue stresses/strains within the three-layered colorectum will inform multiscale models exploring the local stress/strain stimuli affecting the individual afferent endings, and ultimately facilitate a mechanistic understanding of visceral nociception and pain.

ACKNOWLEDGEMENTS

NIH R01 DK120824 (BF); NSF 1727185 (BF); S. Siri; F. Maier.

REFERENCES

[1] Feng B, Gebhart GF. *Am J Physiol-Gastr L*, 300:170-180, 2010. [2] Siri S, et al. *Am J Physiol-Gastr L*, 14:473-481, 2019. [3] Siri S, et al. *Am J Physiol-Gastr L*, 3:349-358, 2019. [4] Maier F, et al. *J Mech Behav Biomed Mater*, 113:104116, 2021. [5] Zhao Y, et al. *J Mech Behav Biomed Mater*, 113:104127, 2021. [6] Pierce DM, et al. *Biomech Model Mechan*, 15:229-244, 2016. [7] Feng B, Guo T. *J Neural Transm.* 127:415-429, 2019. [8] Maas SA, et al. *J Mech Behav Biomed Mater*, 61:499-510, 2016.

CROSSLINKS AND TOUGHNESS OF GELATIN HYDROGELS FOR TISSUE ENGINEERING

Anshul Shrivastava[1], Namrata Gundiah[1]

(1) Mechanical Engineering, Indian Institute of Science, Bangalore, 560012, India

INTRODUCTION

Hydrogels are soft materials which can be engineered to mimic the mechanical properties of biological tissues. Gelatin is a promising scaffold material for tissue engineering applications for tissues such as cornea, arteries, etc[1]. Gelatin, though a soft material which is abundantly present, displays failure characteristics of brittle materials which is a severe limitation when used in tissue engineering [2]. We hypothesized that increasing the crosslinks in gelatin will increase the modulus of the gel, measured using monotonic compression, and also improve the fracture properties. Cavitation rheology is a promising method used for the local assessment of the failure behaviors of soft materials and involves the use of needles to initiate cracks of known dimensions in the gel [1][3]. Unstable bubble growth occurs when pressure inside reaches a critical value, related to the Young's modulus of the material, and the initial size of the defect which is associated with a critical pressure due to pressure drop [4]. The objective of this study is to crosslink gelatin gels and measure the failure characteristics using cavitation rheology.

METHODS

We dissolved 0.05 gm/ml of bovine gelatin Type-B powder (Sigma Aldrich, India) in distilled water at 50° C to obtain a clear solution. A 1% v/v of glutaraldehyde (Sigma Aldrich, India, 25% stock) was added as a crosslinking agent which exploits the large number of functional side groups. The uncured mixture was poured into a cylindrical mold of 16 mm diameter and 20 mm height made using polydimethylsiloxane (PDMS, Sylgard ®184, Dow Corning). Gels were cured at 4° C for 6 hours and were soaked in 0.1 M glycine solution to block additional glutaraldehyde action. Specimens were stored in distilled water overnight prior to mechanical tests [2].

The imine bonds in gelatin were crosslinked by placing the gelatin samples in 10ml of 150 mM phosphate buffer (pH = 7.4) and treated with 1% (w/v) $NaBH_4$ solution in 1 mM NaOH at 4° C. This ratio was used to give a substrate: reagent ratio of 30:1 (w/w). The reaction mixture was kept for incubation, with occasional stirring, for 1 hour and washed twice with distilled water after 1 hour to stop the action of $NaBH_4$ [5].

Monotonic compression tests were performed on a Bose Electroforce® 3200 (Bose Corp., USA) instrument equipped with two parallel compression platens. Hydrogel specimens were preloaded to 5 grams and preconditioned for 30 cycles of 10% compressive strain at 0.05Hz to obtain a repeatable material response. Following preconditioning, samples were compressed at a rate of $0.01s^{-1}$ until either the maximum displacement limit of the instrument was reached, or the gels failed catastrophically. Compressive moduli were calculated using the stress-strain data upto 4% strain [2].

Blunt needles with different gauge sizes (CML Supply) were inserted into the gel samples for the cavitation experiments. A syringe pump (model NE1000, New Era Pump Systems) with 20ml syringe was used to introduce an air bubble into the gelatin sample at the rate of 2000 μL/min. A pressure sensor (Honeywell, ASDXAVX015PGAA5) was attached to the outlet of the syringe with the help of a three-way connector, to record the pressure readings inside the cavity in gel. Real time pressure was recorded with the help of Arduino UNO board and the results viewed and analyzed using MATLAB (2020b).

RESULTS

The monotonic compression tests on gelatin gels treated with $NaBH_4$ showed stiffer mechanical response as compared to control gelatin samples that were untreated (Fig. 1a). The schematic of the cavitation rheology experiment is shown in Fig. 1(b) which was used to quantify failure of hydrogels. Fig. 1(c) shows a sequence of high speed videographs of the bubble inflation in the hydrogel which resulted in gel fracture. Variation of pressure with time inside the cavity is shown which clearly shows a sharp drop in pressure. This point occurs upon reaching a critical value of pressure due to rapid growth of the bubble which results in macroscopic rupture of the control hydrogels (Fig. 1d). Ongoing studies are aimed at characterizing the failure of cross-linked gelatin gels to assess improvement in the toughness of the materials which make them attractive for tissue engineering applications.

DISCUSSION

This study aims to provide insights on the role of collagen crosslinks on the mechanical properties of the hydrogels. We aim to use cavitation rheology experiments to assess the fracture toughness of gelatin hydrogels cross-linked using $NaBH_4$. These results will be extended to quantify the toughness of the cornea in keratoconus which is associated with the degradation and disintegration of collagen. These changes result in a progressive change in stiffness of the corneal tissue and corresponding change in the curvature of the cornea leading to progressive loss in vision. Collagen cross-linking chemicals, including riboflavin and UV treatment, will be used to alter the tissue properties in future studies. Cavitation rheology methods developed in this study will be used to quantify the efficacy of such treatment methods in altering the toughness of the corneal tissues.

ACKNOWLEDGEMENTS

We gratefully acknowledges the Department of Biotechnology (BBI2) for project support. We are thankful to Achu Byju who did the pilot cavitation experiments and high speed videography on gelatin failure reported in this study.

REFERENCES

1. Mahmud, K. Al, Hasan, F., Khan, M. I., & Adnan, A. (2020). On the Molecular Level Cavitation in Soft Gelatin Hydrogel. *Scientific Reports*, *10*(1), 9635.
2. Byju, A. G., Kulkarni, A., & Gundiah, N. (2013). Mechanics of gelatin and elastin based hydrogels as tissue engineered constructs. *13th International Conference on Fracture 2013, ICF 2013*, *6*, 4406–4415.
3. Gent, A. N., & Wang, C. (1991). Fracture mechanics and cavitation in rubber-like solids. *Journal of Materials Science*, *26*(12), 3392–3395.
4. Kundu, S., & Crosby, A. J. (2009). Cavitation and fracture behavior of polyacrylamide hydrogels. *Soft Matter*, *5*(20), 3963–3968.
5. Naffa, R., Holmes, G., Ahn, M., Harding, D., & Norris, G. (2016). Liquid chromatography-electrospray ionization mass spectrometry for the simultaneous quantitation of collagen and elastin crosslinks. *Journal of Chromatography A*, *1478*, 60–67.

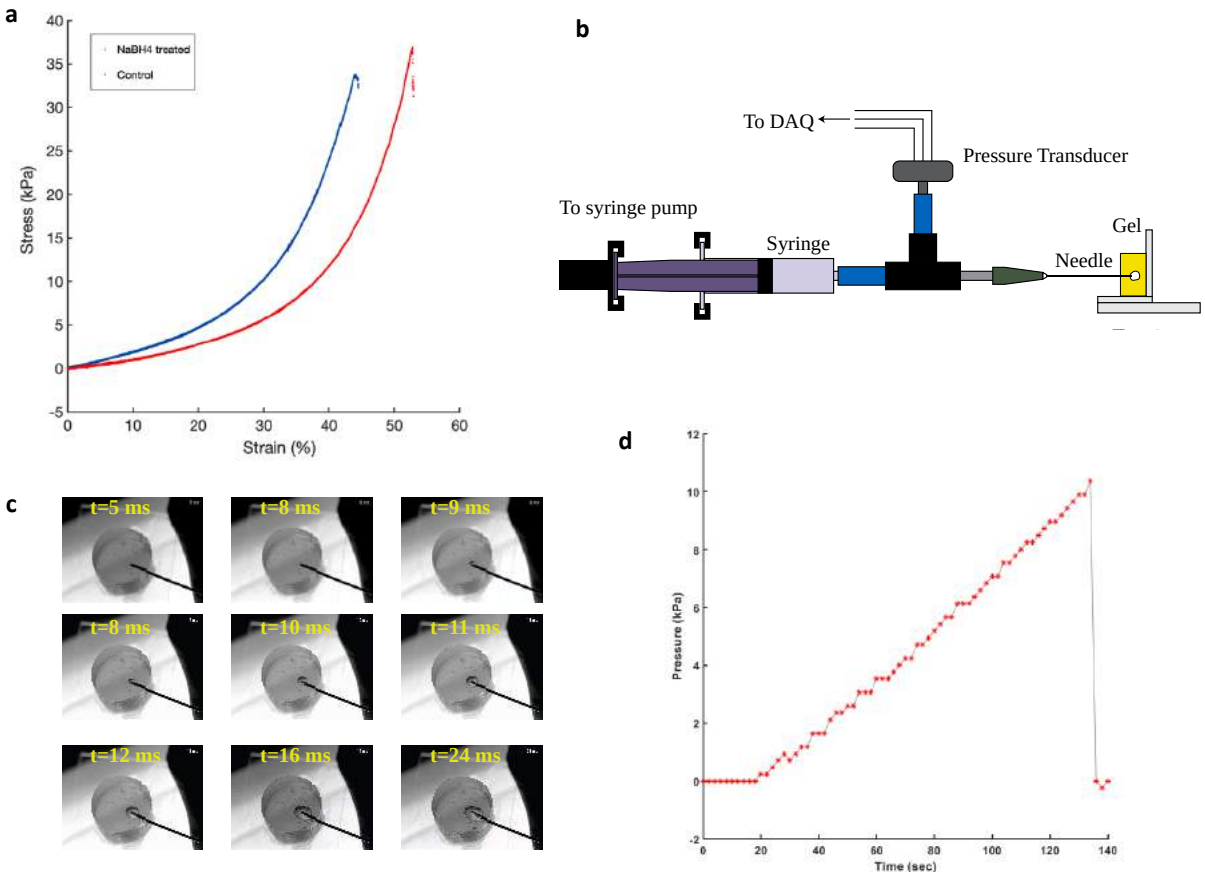

Figure 1 a. Representative traces plotted using monotonic compression tests on gelatin hydrogel samples (control) and gels treated with $NaBH_4$. **b.** Schematic of the experimental setup of cavitation in hydrogels. **c.** Time lapse images showing formation of bubble inside a hydrogel, which ultimately results in fracture of the gel. **d.** Representative plot of variation of pressure with time in the bubble inside hydrogel.

DETERMINATION OF AN APPROPRIATE STRAIN ENERGY DENSITY FUNCTION FOR THE TRICUSPID HEART VALVE LEAFLETS USING CONSTANT INVARIANT-BASED MECHANICAL TESTING

Devin W. Laurence (1) and Chung-Hao Lee, Ph.D. (1,2)

(1) Biomechanics and Biomaterials Design Laboratory
School of Aerospace and Mechanical Engineering
The University of Oklahoma
Norman, Oklahoma, USA

(2) Institute for Biomedical Engineering, Science, and Technology
The University of Oklahoma
Norman, Oklahoma, USA

INTRODUCTION

The tricuspid valve (TV) has often been referred to as the *forgotten heart valve* due to the predominant research focus on the mitral valve and aortic valve within the left side of the heart. However, there has been a shift in attention towards the TV in the past 5 years, focusing primarily on advances in our current understanding of the TV pathologies and improved clinical remedies. Despite the recent advancements, little effort has been devoted to determining the appropriate strain energy density function (SEDF) for the TV leaflets. Typically, a SEDF form is first selected and then fit to available data from planar biaxial mechanical characterizations to determine the model parameters. The resulting SEDF and optimal model parameters often provide a good fit to the experimental data, but *would another SEDF form better represent the mechanical behaviors and directional coupling of the TV leaflets*? This question remains to be answered and has notable implications in predictive modeling of the TV function.

Humphrey *et al.* (1990) [1] previously outlined an experimental technique to determine an appropriate SEDF for hyperelastic transversely isotropic materials using constant invariant protocols. This theory-driven experimental framework has provided promising SEDFs for the left ventricular myocardium tissue [1], the mitral valve leaflets [2], and the jugular vein-derived valves [3]; however, it remains to be investigated for the TV leaflets. The objective of our work is, thus, to determine an appropriate SEDF for the TV leaflets using experimental data acquired from constant invariant experimental characterizations.

METHODS

Theoretical Background: We first assume the TV leaflet is a transversely isotropic material, which can be modeled by a SEDF W that is a function of the first and fourth invariants of $\mathbf{C}=\mathbf{F}^T\mathbf{F}$, i.e., $I_1 = tr\mathbf{C}$ and $I_4 = \mathbf{N}\cdot(\mathbf{CN}) = \lambda^2$, where $\mathbf{F}$ is the deformation gradient tensor, and $\mathbf{N}$ is the unit vector defining the preferred collagen fiber orientation associated with fiber stretch λ. The Cauchy stress $\boldsymbol{\sigma}$ of the material is then computed as

$$\boldsymbol{\sigma} = -p\mathbf{I} + 2W_{,1}\mathbf{B} + W_{,4}\mathbf{F}\cdot\mathbf{N}\otimes\mathbf{N}\cdot\mathbf{F}^T, \tag{1}$$

where $p=2W_{,1}(\lambda_1\lambda_2)^{-2}$ is the penalty term to enforce incompressibility (i.e., $det\mathbf{F}=1$), $\mathbf{I}$ is the identity tensor, $W_{,1}=\partial W/\partial I_1$, and $W_{,1}=\partial W/\partial I_4$. Rearranging the non-zero components of $\boldsymbol{\sigma}$ (i.e., σ_{11} and σ_{22}), we arrive at the following relationships for $W_{,1}$ and $W_{,4}$

$$W_{,1} = \frac{1}{2}\sigma_{22}\xi_2^{-1} \text{ and } W_{,4} = \frac{1}{2\lambda_1^2}\left(\sigma_{11} - \sigma_{22}\xi_1\xi_2^{-1}\right), \tag{2}$$

where $\xi_1 = \lambda_1^2 - (\lambda_1\lambda_2)^{-2}$ and $\xi_2 = \lambda_2^2 - (\lambda_1\lambda_2)^{-2}$. The relationships provided in Eq. (2) can determine $W_{,1}$ and $W_{,4}$ for any planar biaxial data with minimal shear (i.e., $F_{12}=F_{21}=0$).

Constant Invariant-Based Mechanical Characterizations: Equation 2 enables us to determine the values of $W_{,1}$ and $W_{,4}$ for any planar biaxial configuration. However, carefully designed constant invariant protocols are necessary to decouple the contributions from I_1 and I_4. If we ensure $I_4= \lambda_1^2$, constant I_4 protocols can be simply achieved by maintaining a constant value of λ_1 while λ_2 is varied. On the other hand, the complex nature of $I_1 = tr\mathbf{C} = \lambda_1 + \lambda_2 + (\lambda_1\lambda_2)^{-1}$ requires more sophisticated loading paths to maintain a constant value for I_1. For example, given an arbitrary value of λ_1 and a target value for I_1, the required value of λ_2 is

$$2\lambda_2^2 = (I_1 - \lambda_1^2) \pm \sqrt{(I_1 - \lambda_1^2)^2 - 4/\lambda_1^2}. \tag{3}$$

A similar relationship can be established for λ_1. These relationships then guide the displacement paths for the constant I_1 protocols.

Tissue Preparation and Mechanical Characterization: Ten frozen porcine hearts (n=10) were acquired from a regional tissue vendor (Animal Technologies, Inc., Tyler, TX), dethawed, and dissected to obtain the three TV leaflets. The preferred fiber orientation of the leaflet

was first quantified using our in-house polarized spatial frequency domain imaging (pSFDI) apparatus (**Fig. 1a**). Details of this system can be found in [4]. Then, an 8x8 mm specimen was dissected from the leaflet with the *x*-axis of the specimen approximately aligned with the median collagen fiber orientation determined via pSFDI analysis (**Fig. 1b**). Finally, the specimen was mounted to a commercial biaxial tester (CellScale BioTester, Canada) with an effective testing size of 6x6 mm for the subsequent characterizations (**Fig. 1c**).

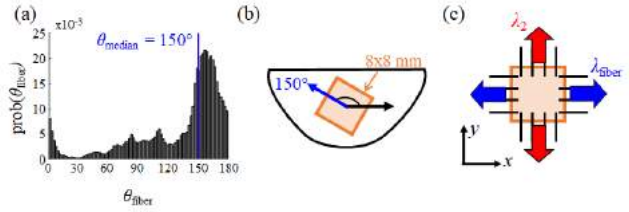

Figure 1. (a) Collagen fiber orientation distribution to inform the (b) excised specimen's orientation. (c) The TV leaflet specimen mounted to the system with the fibers aligned in the *x*-axis.

The TV leaflet specimens underwent eight cycles of force-controlled equibiaxial preconditioning to the approximate *in vivo* forces estimated using the tissue thicknesses and the Laplace's law. The post-preconditioning configurations were taken to be the stress-free reference configurations. Each specimen was then subjected to the comprehensive constant invariant protocols as outlined above. The linear actuator displacements and load cell readings were recorded at 10 Hz throughout the testing. Data from the unloading portion of the last cycle were used to compute the tissue stresses and stretches. Finally, the experimental data was fit with a 3rd-order polynomial surrogate function (**Fig. 2**) to minimize the influence of noise in the subsequent analyses.

SEDFs and Model Fitting: Two general SEDF function forms were fit to the acquired experimental data. The first was a polynomial form:

$$W = \sum_{i=0}^{n}\sum_{j=0}^{n} C_{ij}(I_1-3)^i(I_4-1)^j, \tag{4}$$

whereas the second SEDF was an exponential form

$$W = C_0(I_1-3) + \exp\left(\sum_{i=0}^{n}\sum_{j=0}^{n} C_{ij}(I_1-3)^i(I_4-1)^j\right) - 1. \tag{5}$$

In the above equations, C_0 and C_{ij} are the model parameters, and n denotes the model order. This study considered n=3 for the polynomial SEDF in Eq. (4), and n=2 and n=3 for the exponential SEDF in Eq. (5).

The SEDFs in Eq. (4) and Eq. (5) were fit to the surrogate function curves using nonlinear least squares regression. The fitting was repeated 10 times for each leaflet due to the expected large parameter covariance.

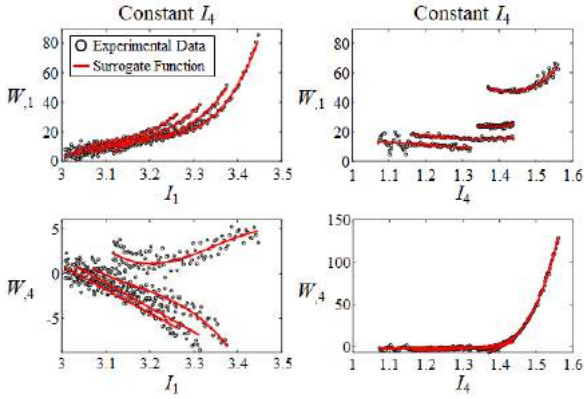

Figure 2. Representative experimental results for one TV leaflet.

Evaluation of the SEDF Forms: The optimal parameters and the corresponding residuals were analyzed to evaluate the candidate SEDFs suitability for the TV leaflets. First, the residuals (i.e., fitting errors) for the three models were compared to understand which form best fits the experimental data. Then, the Hessian **H** of the objective function was calculated using the model parameter set with the lowest residual value for each specimen. The determinant of the Hessian, more commonly known as the D-optimality criterion [5], was calculated to understand the variance of all the model parameters.

RESULTS

Comparison of the SEDF Residual Distributions: The residual values summarized in **Table 1** clearly show the differences in model performance between the polynomial SEDF in Eq. (4) and the exponential SEDF in Eq. (5). In particular, the exponential SEDFs provide noticeably lower residual values compared to the polynomial residual. However, the two exponential SEDFs (i.e., n=2 and n=3) provide similarly excellent fits to the experimental data.

Table 1. Residual values (median ± 0.5*IQR) for the three SEDFs.

Polynomial (n=3)	Exponential (n=3)	Exponential (n=2)
12.64 ± 7.14 kPa	2.99 ± 1.36 kPa	3.33 ± 1.39 kPa

Analyzing the *D*-Optimality Criterion: The *D*-optimality criterion was used to understand the variance in the determined model parameters. **Table 2** summarizes the criterion values for representative leaflet samples, considering the three SEDFs. Larger values of the *D*-optimality criterion, i.e., *det***H**, are indicative of less variance in the model parameters. Thus, it is evident that both exponential SEDFs lead to less variance in the model parameters, with the 2nd-order exponential SEDF outperforming the 3rd-order exponential SEDF.

Table 2. *D*-optimality criterion for three representative TV leaflet samples. AL: anterior leaflet, PL: posterior leaflet, SL: septal leaflet.

	Polynomial (n=3)	Exponential (n=3)	Exponential (n=2)
AL	4.55	$1.7\text{x}10^{18}$	$\mathbf{1.03\text{x}10^{24}}$
PL	4.55	$7.26\text{x}10^{8}$	$\mathbf{6.30\text{x}10^{19}}$
SL	4.55	$6.94\text{x}10^{12}$	$\mathbf{1.77\text{x}10^{22}}$

DISCUSSION

This study has provided the assessment, *first of its kind*, of candidate SEDFs for the TV leaflets using a constant invariant experimental approach. Our results highlighted that the exponential SEDF is likely more suitable than the polynomial counterpart based on the residuals; however, the 2nd- and 3rd-order exponential SEDFs provided similar performance. The commonly-adopted *D*-optimality criterion further elucidated that the 2nd-order exponential SEDF result in less variance in the determined model parameters. Ideally, the reduction in variance would provide a more robust optimization, but this remains to be further investigated. As an extension of this work, we plan to explore the capabilities of the SEDF forms considering different combinations of model parameters beyond those presented herein. The resulting SEDF will then be fit to typical planar biaxial mechanical data and used in *in-silico* computational models of the TV function.

ACKNOWLEDGEMENTS

This work was funded by the American Heart Association Scientist Development Grant and the Presbyterian Health Foundation. DWL was supported in part by the NSF Graduate Research Fellowship.

REFERENCES

[1] Humphrey, J, *et al.*, *J. Biomech. Eng.*, 112(3):333-339, 1990.
[2] May-Newman, K, *et al.*, *J. Biomech. Eng.*, 120(1):38-47, 1998.
[3] Kaul, N, *et al.*, *J. Mech. Beh. Biomed. Mater.*, 75:50-57, 2017.
[4] Jett, S, *et al.*, *Acta Biomater.*, 102:149-168, 2020.
[5] Nathanson, M, *et al.*, *Am. J. Physiol.*, 248:R378-R386, 1985.

IDENTIFYING KEY PARAMETERS FOR MULTIOBJECTIVE SHAPE OPTIMIZATION OF A DOUBLE-WALLED AORTIC STENT-GRAFT

Shannen B. Kizilski (1), Rumi Faizer (2), Victor H. Barocas (3)

(1) Department of Mechanical Engineering
University of Minnesota

Department of Surgery
University of Minnesota
Minneapolis, MN, USA

(3) Department of Biomedical Engineering
University of Minnesota

INTRODUCTION

Endovascular grafting has steadily become a more viable option for patients with aortic aneurysm or dissection [1], [2]. Commercially available stent-grafts are stiff fabric tubes reinforced by wire mesh. Companies and researchers alike are interested in improving upon this design, but most efforts have been dedicated to adding fenestrations for placement in the juxtarenal aorta or the aortic arch [3], [4]. An often-overlooked challenge is that the high stiffness of the device reduces aortic compliance in patients already suffering the effects of high arterial stiffness [5], [6]. Aortic stiffness has independent predictive power for both cardiovascular and all-cause mortality, making it an important parameter to consider when assessing treatment options [7].

We have done proof-of-concept studies on a novel double-walled stent-graft (DWSG), using compressibility of a thin gas layer to introduce compliance [8]. The design balances increasing compliance with minimizing flow disturbance from the reduced lumen area. In the current study, optimization of the longitudinal gas layer profile was conducted to identify designs that best satisfy these competing objectives of increased compliance and minimized flow disturbance.

METHODS

The DWSG gas layer shape was optimized using a multiobjective genetic algorithm through the Platypus optimization package [9] in Python. The objective functions were evaluated with computational fluid dynamics (CFD) simulations [10]. The key components of the routine are described in the sections below.

Model Generation: Although CFD simulations were conducted in 3D, the gas layer profile was axisymmetric, defined by a series of points in the r-z plane (Fig. 1a). The relationship between gas layer volume and DWSG performance was characterized earlier [8], so the present CFD models used a rigid lumen based on the DWSG profile (Fig. 1b).

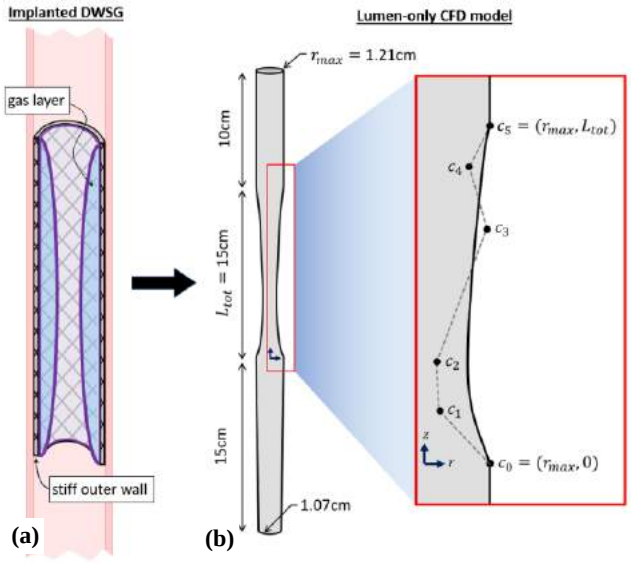

Figure 1: (a) Diagram of the DWSG placed within the descending aorta. (b) Model of the implanted DWSG used for CFD simulations. The DWSG gas layer dictates the profile of the lumen in that region, given by a Bézier curve.

A six-point Bézier curve was used to generate a wide range of profiles by moving the four central control points. The first and last control points were fixed to maintain an overall DWSG length of $L_{tot} = 15cm$ and outer radius of $r_{max} = 1.21cm$. For CFD, the DWSG was placed within a straight segment of the aorta, with 10cm of descending aorta upstream of the device and 15cm of abdominal aorta downstream.

For a given set of control points, a Python script was used to create a file defining the outer wall of the model domain. Using the SimVascular Python API, this contour group file was translated into a 3D model and then a tetrahedral mesh. The mesh was generated with elements approximately 0.3cm long and three boundary layer rings forming a 0.27cm thick region from the wall. To overcome meshing failure, which occurred when the model was very narrow in the DWSG region, the program would automatically attempt to mesh with a second set of parameters with two boundary layer rings in a 0.21cm region.

CFD Simulations: Unsteady flow simulations were conducted to evaluate the impact of each gas layer profile on the hemodynamics in the aorta. Periodic flow for the descending aorta [11] was applied at the inlet of the model, and an RCR boundary condition was applied at the outlet, with parameters taken from Brown et al. [12] Simulations were run for 3 cardiac cycles with a time step of 0.01s, with data collected only from the final cycle.

Optimization Objectives: The optimization was conducted with objectives to minimize: (1) lumen area at the DWSG site, (2) oscillatory shear index (OSI), and (3) mesh area with low time-averaged wall shear stress (TAWSS). Lumen area was a surrogate for gas volume – more gas within the DWSG directly translates to increased compliance. High OSI and low TAWSS are both common measures for atherosclerotic risk [13], so both were evaluated for the unstented regions of the domain. The root mean square (rms) value of OSI and the normalized surface area of the mesh exhibiting $TAWSS < 2\ dyn/cm^2$ were minimized [14]. Restrictive requirements for the system, such as maximum TAWSS not exceeding 200 dyn/cm^2 [15] and the gas layer profile remaining within the bounds of the surrounding vessel wall, were enforced as constraints.

Implementation: The NSGA-II algorithm was implemented through Platypus with a population of 100 individuals. The optimizer called a script that executed a series of Python programs to sequentially generate a new mesh, run the simulation, convert results from the final cycle, and finally evaluate the objective functions and constraints. The simulations were parallelized to four processors on the local machine. Nondominated solutions, which are candidates to lie upon the pareto front, were found via the *ParetoFront()* function in MATLAB [16].

RESULTS

Data were retrieved after the optimizer had completed 564 iterations, or more than 5 evolutionary generations of the algorithm. Figure 2 shows the evaluated objectives over the solution space along with selected gas layer profiles. The lumen volume ranges from 17 to 54 mL, or 25-78% of the total available volume in that region. A strong positive correlation was seen between low TAWSS area and OSI (OSI_{rms}), clearly visible in the 2D projection of the results (Fig. 2, bottom). All of the nondominated solutions showed a gradual tapering of the radius from both the inlet and outlet of the DWSG, leading to the triangular profile depicted in the bottom-right image of Fig. 2.

DISCUSSION

These results show that the shape of the DWSG gas layer has significant impact on local hemodynamics, even for a fixed gas volume. The strong correlation between the two objectives quantifying flow disturbance suggests that future optimization studies may be simplified by replacing those objectives with a single combined value such as relative residence time [17]. Because the flow-based objectives were evaluated only for the unstented regions of the domain, the most optimal designs tended to make the transition between vessel and stent as gradual as possible, leading to sharp discontinuities in the gas layer profile. This behavior can be avoided by including the stented region when evaluating flow behavior. After incorporating the adjustments described here, the next-generation framework will be used to identify a set of optimal potential DWSG designs, which then can be investigated more thoroughly with fluid-structure interaction simulations.

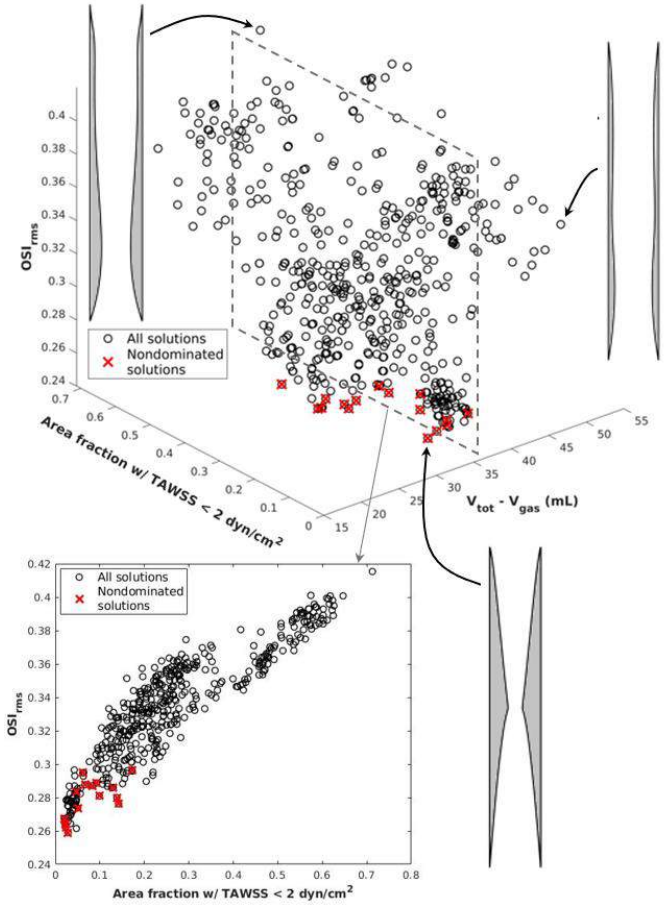

Figure 2: (Top) 3D plot of objectives; nondominated solutions highlighted with an 'x'. Examples of 3 gas layer profiles are shown. (Bottom) The same data in 2D, showing the co-dependence of two objectives: OSI and low TAWSS area.

ACKNOWLEDGEMENTS

This research was supported by NIH NCATS grants TL1R002493 and UL1TR002494, and by NIH NHLBI grant U01HL139471.

REFERENCES

[1] T Sachs et al, *J Vasc Surg*, 52(4):860-6, 2010.
[2] NJ Swerdlow et al, *Circ Res*, 124(4):647-61, 2019.
[3] JT Lee et al, *J Vasc Surg*, 60(4):849-57, 2014.
[4] J Yang et al, *J Thorac Cardiovasc Surg*, 151(4):1203-12, 2016.
[5] HWL De Beaufort et al, *PLoS One*, 12(10):1-7, 2017.
[6] NPE Kadoglou et al, *J Endovasc Ther*, 21(6):850-8, 2014.
[7] S Laurent et al, *Hypertension*, 37(5):1236-41, 2001.
[8] SB Kizilski et al, *J Med Device*, 14(3):031005, 2020.
[9] "Project Platypus", https://github.com/Project-Platypus.
[10] A Updegrove et al, *Ann Biomed Eng*, 45(3):525-41, 2017.
[11] F Cuomo et al, *PLoS One*, 12(3):1-21, 2017.
[12] AG Brown et al, *J Biomech*, 45(3):516-23, 2012.
[13] R Tricarico et al, *Eur J Vasc Endovasc Surg*, 59(1):7-15, 2020.
[14] K Bäumler et al, *Biomech Model Mechanobiol*,19:1607-28, 2020.
[15] FPP Tan et al, *Comput Struct*, 87(11–12):680-90, 2009.
[16] Simone, "Pareto filtering." MATLAB Central File Exch, 2021.
[17] HA Himburg et al, *Am J Physiol Circ Physiol*, 286:H1916-22, 2004.

TUNING SHEAR WAVE TENSIOMETRY TO IMPROVE SUBJECT SPECIFICITY IN ACHILLES TENDON LOADING MEASUREMENTS DURING WALKING

Stephanie G. Cone (1), Dylan G. Schmitz (1), Darryl G. Thelen (1)

(1) Department of Mechanical Engineering
University of Wisconsin -- Madison
Madison, WI, USA

INTRODUCTION

Human motion analysis is a well-established approach for characterizing the joint kinetics that drive an individual's walking pattern [1]. Joint kinetics in turned are often used to infer the timing and magnitude of muscle-tendon forces and joint contact forces [2]. However, redundancies in the musculoskeletal system make it challenging to infer tissue loads from joint level metrics, particularly during swing phase. This challenge highlights the need for a more direct approach to assess muscle-tendon tissue loads during walking.

Shear wave tensiometry is a noninvasive method for assessing tissue loads by exciting and measuring shear waves [3]. A shear wave tensiometer consists of a mechanical tapper that excites a shear wave, and two accelerometers that record the arrival of the wave at downstream locations. Shear wave speed is calculated as the inter-accelerometer distance over wave travel time. A tensioned beam model provides a constitutive relationship directly relating wave speed to tensile load [3]. Indeed, prior studies show that Achilles tendon wave speed closely tracks net ankle torque during stance, but not during swing when tendon load arises from passive stretch [3]. While healthy subjects generally exhibit similar Achilles tendon wave speed patterns during walking [3], there is unexplained variability in wave speed magnitudes. Such inter-subject variability may arise, in part, from design factors and anatomical variability. In this work, we investigated the sensitivity of wave speed metrics to tap excitation patterns across a range of healthy young adults. The first objective was to investigate the dependence of Achilles tendon wave speeds on mechanical tap duration. The second objective was to perform a preliminary assessment of the relationship between tendon wave speed and select anatomical geometry metrics.

METHODS

In a study approved by the University of Wisconsin Institutional Review Board, 16 subjects (8M/8F, 23.5 ± 3.9 years, 71.8 ± 11.2 kg, 1.75 ± 0.10 m) were recruited. A shear wave tensiometer, consisting of a piezoelectric-actuated tapper and two miniature accelerometers (8 mm apart), was secured over each subject's right Achilles tendon. The subject performed a continuous walking trial at 1.34 m/s. Trials consisted of 10 second intervals of pulse wave (50 Hz) taps with varying duty cycles (0.5, 1, 2, and 10 ms pulse durations). Each condition was performed in triplicate in a randomized order. Subjects then stood with their instrumented ankle on a force plate, and static trials of shear wave tensiometry with each pulse duration were collected with 0%, 25%, 50%, 75%, and 100% body weight on the involved limb (Fig. 1).

Transverse B-mode ultrasound images (Verasonics Vantage 64LE) of the Achilles tendon were collected. Imaging was done in a prone position with the ankle passively held in 0° of dorsiflexion.

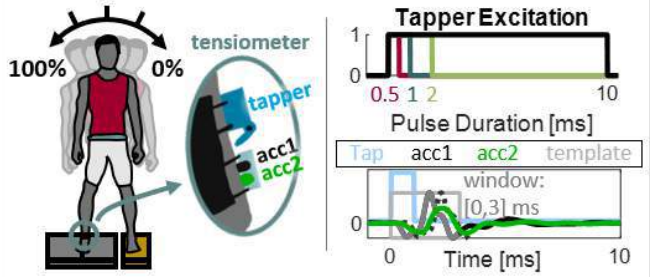

Figure 1: Static loading test methods (left), tap excitation patterns for different pulse durations and wave speed analysis (right).

Shear wave speed was calculated for each tap event. For each tap, wave travel time was computed by finding the time delay that maximized the normalized cross-correlation of accelerometer signals over a 3 ms window following tap onset [3] (Fig. 1). Wave speed signals were re-sampled to 101 points over each gait cycle, and then ensemble

averaged over all gait cycles for each tap duration. Parameters of interest (minimum stance wave speed, maximum push-off wave speed, average standard deviation) were calculated. Repeated measures anova was used to ascertain the effects of tap duration on wave speed metrics ($p<0.05$).

Ultrasound images were used to measure the Achilles tendon thickness and the cross-sectional area (CSA) between the accelerometer locations (Fig. 1). Simple linear regression was used to assess the relationship between peak wave speeds and anatomical metrics.

RESULTS

Pulse duration had a significant effect on the magnitude of shear wave speeds during both stance ($p<0.01$) and swing phase ($p<0.01$). Pulse duration did not have a significant effect on the standard deviation either at peak wave speed ($p=0.42$) or averaged across the gait cycle ($p=0.07$). Additionally, pulse duration had a significant effect on the magnitude of shear wave speeds measured during static loading ranging from 0% to 100% body weight ($p<0.01$), but there was no significant effect of pulse duration on the goodness of fit between calculated tendon load and percent body weight ($p=0.30$).

Table 1: Maximum shear wave speeds and standard deviations averaged across gait for each tap length. Bold represents $p<0.05$.

Tap Pulse Length (ms)	Maximum Push-off Shear Wave Speed (m/s)	Average Standard Deviation (m/s)
0.5	58.6	1.3
1	60.2	0.8
2	59.1	0.9
10	**66.9**	0.9

During walking, the magnitude of shear wave speeds varied by as much as 14% between cases at max push-off across pulse durations averaged across subjects (Table 1). These values were significantly higher with 10 ms pulse durations compared to all other cases ($p<0.01$). At minimum wave speed levels in both stance and swing, 10 ms pulses yielded significantly higher wave speeds compared to other cases by 13% and 11%, respectively ($p<0.01$). At maximum speeds during swing, 2 ms pulses yielded 18% higher wave speeds than other cases ($p<0.01$) (Fig. 2).

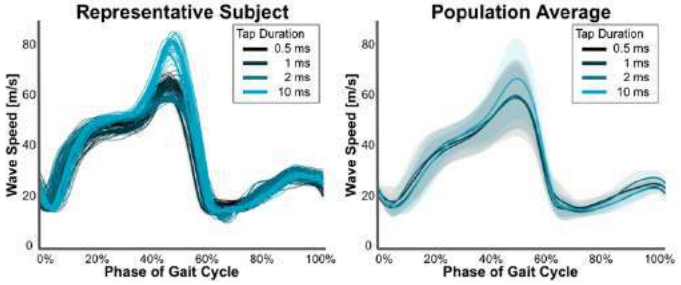

Figure 2: Pulse duration has a significant effect on the overall magnitudes wave speeds in a single subject (left, individual strides) and averaged across subjects (right, mean ± standard deviation).

In static standing trials across loading levels, pulse duration again had a significant effect on shear wave speed magnitudes ($p<0.01$) but not on wave speed variability within a trial ($p=0.30$). Across pulse duration cases, increasing loading led to significant increases in shear wave speeds ($p<0.01$). These increases were on the scale of 55% to 75% increases in shear wave speed as subjects shifted their weight from the non-instrumented to the instrumented limb.

Some significant correlations emerged from the pilot investigation of shear wave speeds and anatomical metrics. Notably, peak wave speed during push-off for the 1 ms pulse was positively correlated with height ($p=0.03$), body weight ($p=0.04$), and anterior-posterior tendon depth ($p=0.04$) (Fig. 3). Similar trends were observed for the other pulse durations (0.5, 2, 5), but did not reach the 0.05 significance level.

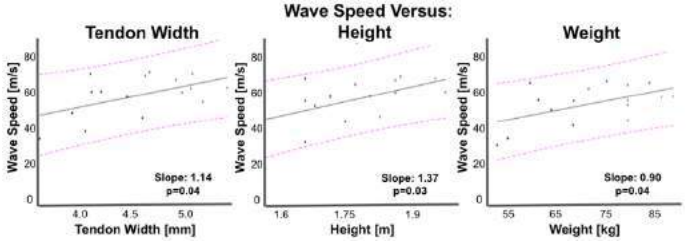

Figure 3: Peak wave speed increased with increasing tendon anterior-posterior depth, height, and weight.

DISCUSSION

This study illuminates the effects that excitation can have on measured tendon wave speeds. Our tensiometer used a transient wave speed measurement approach, in which an impulsive tap is used to induce and measure group wave propagation speed. We varied tap duration which alters the transient wave appearing in the post-tap analysis window (Fig. 1). Tap duration had a non-significant effect on repeatability of the wave speed metrics, though there was a trend for greater variability with the shortest (0.5 ms) duration pulse. This could be a signal-to-noise ratio effect. The shortest impulse doesn't allow for full excitation of the piezoelectric stack we used, hence produced a smaller amplitude wave than pulses under 1 ms.

Wave speed magnitudes were significantly dependent on pulse duration with the longest pulse producing significantly higher peak wave speeds in push-off. This is likely due to the analysis window (3ms) being shorter than the pulse (5 or 10ms) duration. As such, the analysis for the long pulse did not include both the push and release events, which were considered in the shorter duration pulses (Fig. 1). Not including the release event likely alters frequencies inherent to the wave, affecting the wave speed when dispersion is present [4].

There were some intriguing relationships between anthropometry and wave speed that emerged. Notably, peak wave speeds increased with subject height, mass, and tendon size. This may simply reflect the direct dependence between tendon load and wave speed, as propulsion demands increase with body size. The dependence of wave speed on tendon geometry could arise from dispersion effects. Specifically, wave length is greater than the tendon thickness, resulting in guided wave behavior that depends on the relative thickness of tissue layers. Further analysis via computational models and physical experiments are needed to better understand these complex dispersion effects.

This work extends the promising use of shear wave tensiometry to gauge tendon loading during movement. We showed that repeatable results can be obtained with different wave excitation patterns, but that the absolute wave speed is dependent on the duration of excitation and subject anatomy. These observations are important for establishing shear wave tensiometry as a valid sensor of subject-specific tendon loading during locomotion.

ACKNOWLEDGEMENTS

This work was funded by the NIH (NIAMS: F32 AR076276), the Stryker-ORS Women's Fellowship, and the NSF GRFP (DGE-1747503). Images obtained from Servier Medical Art.

REFERENCES

[1] Baker, R, J, Neuroeng Rehab, 2006; [2] Roberts, M +, Phys Ther Rehabil, 2017; [3] Martin, JA +, Nat Comm, 2018; [4] Sadeghi, S +, JMBBM, 2020.

MULTISCALE MODEL OF HEART GROWTH DURING PREGNANCY: INTEGRATING MECHANICAL AND HORMONAL SIGNALING

Kyoko Yoshida (1), Jeffrey J Saucerman (1), Jeffrey W Holmes (2)

(1) Biomedical Engineering
University of Virginia
Charlottesville, Virginia, USA

(2) School of Engineering
University of Alabama at Birmingham
Birmingham, Alabama, USA

INTRODUCTION

Pregnancy stands at the interface of mechanics and biology. Significant mechanical and hormonal changes occur during pregnancy as the growing fetus continuously loads the maternal organs. In response to these changes, maternal soft tissues undergo dramatic growth and remodeling to support the mother and baby for a healthy pregnancy. We focus here on the maternal left ventricle (LV), which increases its cardiac output by 45% [1] and increases in mass by approximately 30% [2] over nine months of pregnancy, only to regress to the nonpregnant size by 3-6 months after delivery. Cardiovascular conditions and heart failure together account for more than 25% of pregnancy-related deaths in the United States. Therefore, there is a critical need to understand how pregnancy hormones and hemodynamic changes interact to affect heart growth during pregnancy. Thus, the objective of this work was to develop a multiscale cardiac growth model that incorporates these interactions.

Towards this objective, we present a novel multiscale cardiac growth model. We coupled a cell-signaling network model of cell-level hypertrophy to an organ-level compartmental growth model of the rat heart and circulation. We first calibrated this multiscale model to LV growth due to experimental volume overload (VO) and infusion of hormones. We then validated the ability of this model to capture interactions between combinations of 2 inputs. Finally, we simulated pregnancy-induced changes in hormones and hemodynamics to predict heart growth during pregnancy.

METHODS

To simulate the influences of hormones and stretch on cell-level hypertrophy, we built an intracellular signaling network model for pregnancy-induced cardiomyocyte hypertrophy (Fig.1A) using previously published methods [3]. This network model consisted of 4 key inputs: the pregnancy hormones progesterone (*P4*) and estrogen (*E2*); Angiotensin 2 (*AngII*), a hormone elevated during both volume overload and pregnancy; and the mechanical signal, *Stretch*. These inputs interacted with each other and nine other intermediate species through 24 reactions. We used normalized Hill-type ordinary differential equations to model signaling reactions. The activity level of each species was represented as a value between 0 and 1, where 0 indicates no signaling activity and 1 represents maximal activation. We based the reactions on a previously published network model of cardiomyocyte hypertrophy by Ryall et al. [3] and adjusted crosstalk interactions to match phosphorylation data from *in vitro* experiments where cardiomyocytes were treated with P4, E2, and/or AngII.

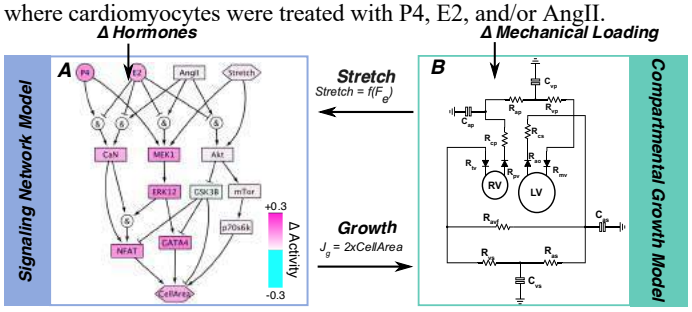

Figure 1: Multiscale cardiac growth model for pregnancy. A) Intracellular signaling network model of cardiomyocyte growth is coupled to a B) compartmental growth model. Growth predicted by the network model is fed into the compartmental model as a growth stretch. Elastic stretches calculated by the compartmental model are fed into the network model to close the loop.

To simulate organ-level heart growth, we modified a previously published compartmental growth model of the canine heart coupled to

a lumped-parameter circuit representation of the circulation [4] (Fig.1B). We used allometric scaling to re-parameterize this model from canine to rat [5]. We then optimized circulatory parameters to match average experimental hemodynamics and reported stretches experienced by the LV during baseline and acute VO states [6]. We used a kinematic growth framework within the compartmental model based on previously published methods [4]. In this framework, the total stretch (F_{tot}) is a product of the growth stretch (F_g) and elastic stretch (F_e): $F_{tot}=F_e*F_g$. We calculated F_g from the signaling network model output, *CellArea,* as $J_g=2*CellArea$, where $J_g=\det(F_g)$. We then input the maximum elastic fiber stretch, $\max(F_{e,f})$, predicted by the compartmental model into the signaling network model input, *Stretch*, as $Stretch=m_{stretch}*\max(F_{e,f})+b_{stretch}$, closing the loop between the two models (Fig.1). Here, $m_{stretch}$ and $b_{stretch}$ are linear transfer function parameters we optimized in the calibration steps outlined below.

We first calibrated the multiscale model parameters by matching the individual effects of VO, AngII, E2, and P4 on heart growth. Next, we simulated the combination of VO+E2 and AngII+E2 to validate the model representation of interactions between inputs. Finally, we simulated pregnancy-induced changes in the hormones and hemodynamics to predict heart growth during pregnancy.

RESULTS

We were able to calibrate the multiscale model to match reported changes in LV mass due to VO in rats and experimental infusion of AngII in rats, E2 in rats, and P4 in mice (Fig. 2). Specifically, we optimized linear transfer function parameters that map hormone concentrations [ug/ml or pg/ml] and $\max(F_{e,f})$ to the appropriate normalized network model inputs for *AngII*, *E2*, *P4*, and *Stretch*. When we simulated the combinations of VO+E2 and AngII+E2, the model correctly predicted attenuated growth as reported in rats [7] and mice [8]. VO+E2 resulted in 4% attenuation in LV mass compared to VO alone, while AngII+E2 resulted in 12% attenuation of LV mass compared to AngII alone.

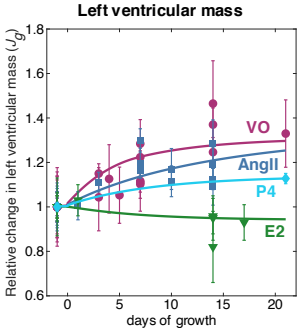

Figure 2: Calibrating the multiscale model. Symbols represent experimental data from volume overload (VO), angiotensin 2 (AngII) infusion, progesterone (P4) infusion, and estrogen (E2) infusion. Solid lines represent model match to data for each experimental condition.

Next, we used the model to simulate pregnancy in rats. We implemented reported changes in circulating concentrations of E2, P4, and AngII from rats during pregnancy for the hormonal inputs. In the circulatory model, we specified the heart rate (*HR*) and systemic resistance (*Ras*) changes calculated from the reported mean arterial pressure (*MAP*), stroke volume (*SV*), and *HR*. To simulate the increase in total blood volume during pregnancy, we allowed stressed blood volume (*SBV*) to change at each growth step to match the reported increase in end-diastolic diameter during pregnancy. When we incorporated pregnancy hormones and these circulation parameter changes, the calibrated multiscale model was able to predict growth (Fig. 3B) and hemodynamic changes that were in good agreement with the experimental data. When we examined the predicted network response for the pregnancy simulation, cell-level growth was primarily driven by species downstream of *P4*. Surprisingly, the network *Stretch* did not increase significantly (Fig.3A), leading to no significant changes in the downstream pathways (Akt, GSK3B, p70s6k).

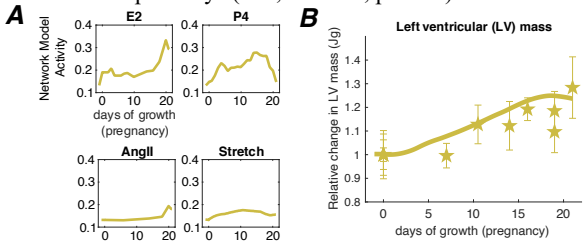

Figure 3: Model predictions for pregnancy. A) activity of input nodes for the network model. B) Solid line demonstrates the predicted relative change in left ventricular mass during pregnancy. Symbols represent experimental data from pregnant rats.

DISCUSSION

The objective of this work was to develop a multiscale cardiac growth model that incorporates hormonal and mechanical signaling for simulating heart growth during pregnancy. We coupled an intracellular signaling network model of cell-level growth to an organ-level compartmental mechanical growth model. We calibrated this model to reported heart growth in response to VO and infusion of AngII, E2, and P4 and validated the interactions between VO+E2 and AngII+E2. When we predicted heart growth during pregnancy by implementing appropriate hormonal and hemodynamic changes, the model produced growth predictions in good agreement with experimental data.

One striking result was the relatively constant level of Stretch throughout pregnancy predicted by the model (Fig. 3A). In this model, the change in network *Stretch* is a function of elastic stretch (F_e), which is dependent on the rate at which LV end-diastolic volume (EDV) increases compared to the rate of ventricular growth. In the model, the rise in P4 during early pregnancy leads to growth that tracks with the increase in EDV as *SBV* gradually increases throughout pregnancy. These results suggest that progesterone stimulation could account for much of the pregnancy-induced heart growth in rats, particularly in the early stages of pregnancy.

An advantage of this model is the ability to validate predictions across multiple length scales from intracellular signaling to organ-level growth. Future work will focus on expanding our network model to incorporate more signaling pathways and validating network model predictions against data. In particular, a better understanding of how *P4* and *Stretch* interact is necessary. An *in vivo* experiment of VO+P4 could provide valuable insights into how Stretch and P4 interact to affect heart growth and intracellular signaling.

ACKNOWLEDGEMENTS

This work was supported by the National Institute of Health (U01 HL127654).

REFERENCES

[1] Hunter, S and Robson, S.C., *Brit Heart J*, 68:540-543, 1992.
[2] Savu O., et al., *Circ: Cardiovasc Imaging*, 5:289-297, 2012.
[3] Ryall K.A., et al., *J Biol Chem*, 287:42259-42269, 2012.
[4] Witzenburg C.W. and Holmes, J.W., *JCTR*, 11:109-122, 2018.
[5] West G.B. et al., *Science*, 276(5309):122-126, 1997.
[6] Holmes, J.W., *J Appl Physiol*, 97(4):1453-1460, 2004.
[7] Voloshenyuk and Gardner, *AJP-Reg., Int., Comp. Physiol.*, 2010.
[8] Pedram et al., *J. Biol. Chem.*, 280(28): 26339-2638, 2005.

COMPUTATIONAL ANALYSIS OF CORONARY PERFUSION IN HEART FAILURE WITH PRESERVED EJECTION FRACTION

Yuexing Sun, Lei Fan, Lik Chuan Lee

Department of Mechanical Engineering
Michigan State University
East Lansing, Michigan, USA

INTRODUCTION

Heart failure with preserved ejection fraction (HFpEF) is a syndrome that accounts for about 50% of heart failure patients [1]. There is, however, no effective treatment for HFpEF. The lack of effective treatment may be partly due to the fact that the mechanisms of the HFpEF are complex and have not been fully elucidated. Specifically, how HFpEF affects the left ventricle (LV) mechanics and coronary perfusion, as well as their interaction remains unclear. This question is difficult to answer from pure experimental and clinical studies since it is impossible to isolate the effects of each confounding factor in HFpEF. In order to overcome this limitation, a computational model that strongly couples the systemic circulation, LV and coronary perfusion with flow regulation in a closed loop system is developed. A key novelty of the model is that myocardial supply and demand are tightly coupled based on a linear relationship between the vasodilator signal F_{meta} and the LV pressure-volume loop area (PVA).

METHODS

The circulatory system is modeled using a closed loop framework consisting of five compartments, namely, LV, left atrium (LA), peripheral proximal and distal arteries, coronary artery and venous networks (**Fig 1(a)**) [2]. The LV and LA are described using a time-varying elastance model that relates instantaneous pressure to instantaneous volume. Coronary flow network consisting of 400 vessels is strongly coupled with the systemic circulation and the LV. Flow in each vessel of the network is described by a three-element Windkessel model that consists of two nonlinear resistors and one parallel capacitance (**Fig 1(b)**) [3]. Intramyocardial pressure (IMP), which is applied to each vessel, is defined as a combination of two mechanisms including time-varying elasticity and ventricular cavity-induced extracellular pressure. Specifically, $IMP = \alpha E_{es} e(t) + \beta P_{LV}$, where α and β are prescribed parameters, P_{LV} is the LV cavity pressure, E_{es} is the maximal chamber elastance of the LV, $e(t)$ is the time-varying elastance function. Flow regulation that includes the myogenic, shear, and flow regulation responses is taken into account in model. Vessel radius under regulated condition can be expressed as $R_{reg} = R_p - A\Delta R_m$, where R_p is the passive vessel radius (under fully dilated condition), ΔR_m is the myogenic activation based on transvascular pressure, and A is the total activation level given as $A = (1 - F_\tau)(1 - F_{meta})$. The total activation A depends on the shear signal F_τ and vasodilator signal F_{meta}. Here, F_{meta} is updated based on a prescribed $F_{meta} - PVA$ relationship, where F_{meta} varies from 0 to 1 linearly with PVA (**Fig 1(c)**), and is saturated when F_{meta} = 1. The gradient of the $F_{meta} - PVA$ linear relationship is controlled by a parameter. The vessel is fully constricted at maximum myogenic response ($F_{meta} = 0$) and fully dilated with the minimum myogenic response ($F_{meta} = 1$).

The model is first calibrated to match the clinical measurements of healthy subjects. These measurements include the blood pressure, LV end systolic pressure (LVESP), LV end diastolic pressure (LVEDP), LV end systolic volume (LVESV), LV end diastolic volume (LVEDV), ratio of E and A waves of the mitral valve flow rate (E/A ratio), LV ejection fraction (LVEF) and total coronary flow over one cardiac cycle under both passive and regulated conditions. The calibrated model is then applied to simulate HFpEF by adjusting parameters that are deemed to change with the condition (e.g., maximal chamber elasticity and LV relaxation) to match clinical measurements in HFpEF patients. The gradient of the $F_{meta} - PVA$ relationship is also determined from these measurements. All simulations are run with a heart rate of 75 bpm for several cardiac cycles until a steady periodic behavior is reached.

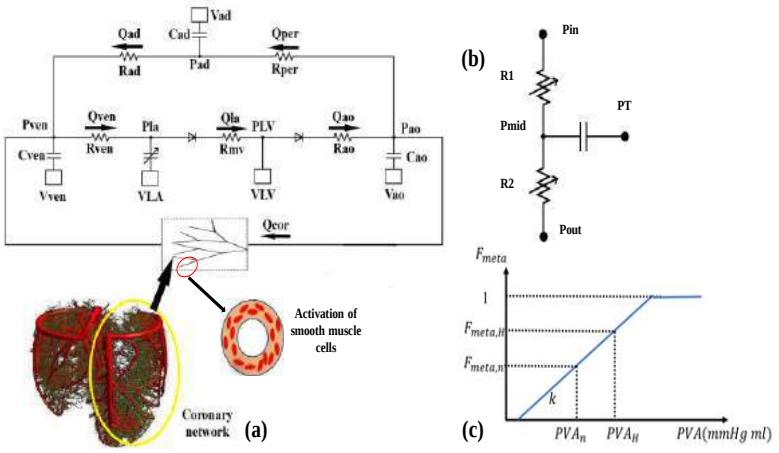

Figure 1(a): Schematic of the LV modeling framework and coronary network; **(b)**: three-element Windkessel model; **(c)**: $F_{meta} - PVA$ relationship.

RESULTS

In the normal case, the calibrated model predicted LVESP, LVEDP, systolic blood pressure (SBP), diastolic blood pressure (DBP), LVESV, LVEDV, LVEF, E/A ratio, and total coronary flow under passive and regulated conditions to be 96mmHg, 13mmHg, 108mmHg, 71mmHg, 42mL, 108mL, 60%, 2.05, 3.15mL and 1.31mL. These values are in agreement with the clinical measurements of healthy subjects, which are in the range of 84-160mmHg, 3-12mmHg, <120mmHg, <80mmHg, 40-54mL, 69-162mL, >45%, 1.4-2.6, 2.144-4.224mL, 0.784-1.9mL, respectively [4]. In order to simulate HFpEF, both maximal chamber elastance E_{es} and relaxation time are increased (based on clinical studies) [5]. Systemic resistances and compliance are also adjusted (to reflect an increase in afterload in HFpEF). In the HFpEF simulation, the model predicted LVEDP, SBP, DBP, LVESV, LVEDV, LVEF, E/A ratio, and total coronary flow under passive and regulated conditions are, 27mmHg, 148mmHg, 84mmHg, 37mL, 103mL, 64%, 0.89, 3.03mL and 1.44mL, matching with the clinical measurements under HFpEF condition, which are 17-31mmHg, 60-90mmHg, 145-165mmHg, 31-59mL, 84-135mL, 53.7-65%, 1.4-2.6, 2.064-4.016mL and 1.056-1.88mL, respectively [6][7]. Since IMP is controlled by LV pressure, the increased LV pressure in HFpEF causes IMP to increase (**Fig 2(a), (e)**), which impedes coronary flow and slows the flow rate in coronary network. Model prediction of E/A ratio is also decreased in HFpEF (**Fig 2(b), (f)**), where the increased A peak is caused by a slow myocardial relaxation rate. In HFpEF, LVEF remains close to a normal value but the heart has less blood inside during the diastolic phase since the LVEDV is slightly reduced compared to normal (**Fig 2(c), (g)**). Comparing the coronary flow rate under passive and regulated conditions from normal to HFpEF cases (**Fig 2(e), (h)**), their values are close to each other. Coronary flow rate in HFpEF, however, is lower in the diastolic phase and higher in systolic phase and the resultant coronary flow reserve (CFR) is lower in HFpEF (2.16) than in normal (2.35). The vessel is fully dilated under passive condition with $F_{meta} = 1$ for both normal and HFpEF cases, but the vasodilator signal is larger in HFpEF ($F_{meta} = 0.55$) than in normal ($F_{meta} = 0.35$) due to the PVA change based on the prescribed relationship, where less myogenic activation applied on the coronary networks, suggesting that the conditions in HFpEF requires more dilation of the vessel.

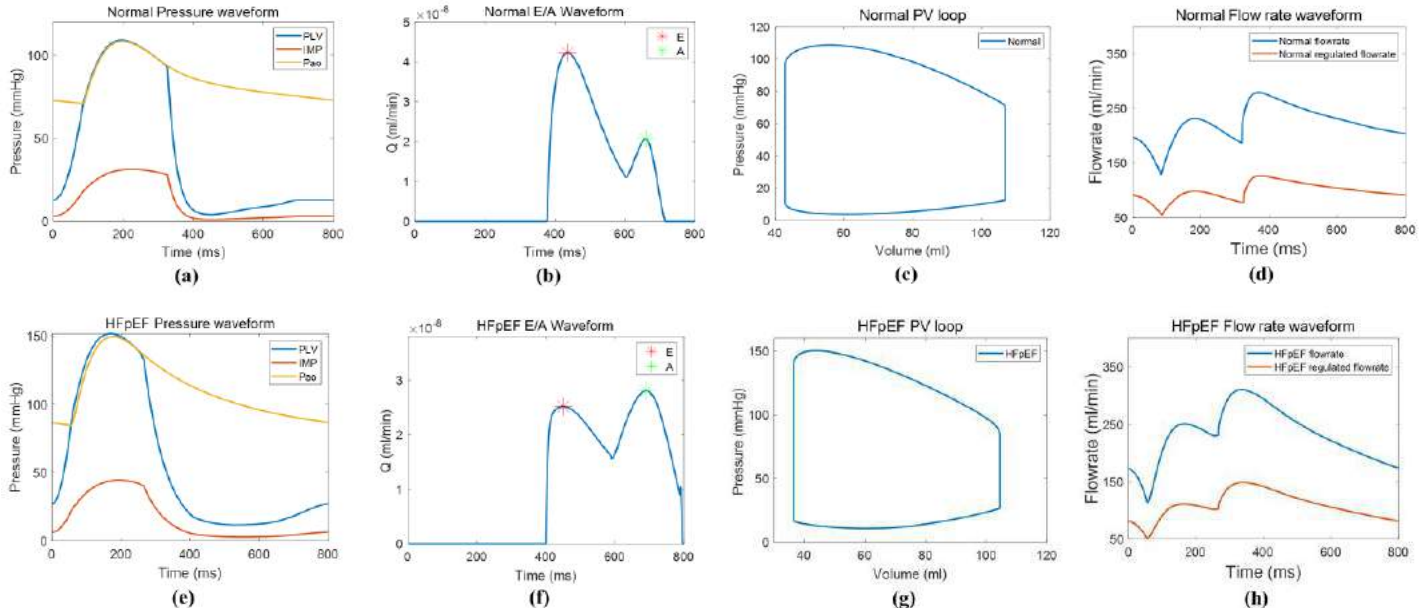

Figure 2(a): LV pressure, arterial pressure, and IMPs waveform under normal condition; **(b)**: E/A ratio of mitral valve flow rate under normal condition; **(c)**: LV pressure volume loop under normal condition; **(d)**: Normal flow rate under passive and regulated conditions; **(e)**: LV pressure, arterial pressure, and IMPs waveform under HFpEF condition; **(f)**: E/A ratio of mitral valve flow rate under HFpEF condition; **(g)**: LV pressure volume loop under HFpEF condition; **(h)**: HFpEF flow rate under passive and regulated conditions.

DISCUSSION

We have developed model coupling LV mechanics and coronary perfusion that is able to quantitatively reproduce clinical measurements in normal and HFpEF patients. The key findings of this study are **1)** from normal to HFpEF, the conspicuously increased LV pressure during the systolic phase led a larger increase of perfusion pressure than that of IMP, which rise more flow rate in systolic. **2)** The vasodilator signal F_{meta} is larger in HFpEF patients than that of the healthy subjects. This results that the vessels are required to be more dilated to accommodate the increase in PVA in HFpEF, which contributes to the slight reduction in CFR. In contrast to previous models [8], we have, for the first time, take into account the coupling between myocardial demand and supply by prescribing a direction relationship between PVA and the vasodilator signal.

ACKNOWLEDGEMENTS

This work was supported by the National Institute of Health (R01 HL134841).

REFERENCES

[1] Owan, Theophilus E et al., *N Engl J Med*, 355(3):251-259, 2006.
[2] Shavik, Sheikh Mohammad et al., *Physiol Rep*, 5(21), 2017.
[3] Fan, Lei et al., *Front Physiol*, 11:915, 2020.
[4] Paulus, Walter J., *Eur Heart J*, 19(7):990-1003, 1998.
[5] Borlaug, Barry A et al., *J Am Coll Cardiol*, 54(5):410-8, 2009.
[6] Srivaratharajah, Kajenny, et al., *Circ Heart Fail*, 9(7), 2016.
[7] Kraigher-Krainer, Elisabeth et al., *J Am Coll Cardio*, 63(5):447-456, 2014.
[8] Namani, Ravi et al., *J Gen Physiol*, 50(1):145-168, 2018.

DESIGN AND FABRICATION OF A NOVEL POLYMERIC TRANSCATHETER AORTIC VALVE

Hieu T. Bui (1), Susan P. James (2), Lakshmi Prasad Dasi (1)

(1) The Wallace H. Coulter Department of Biomedical Engineering
Georgia Institute of Technology
Atlanta, GA, USA

(2) Department of Mechanical Engineering,
Colorado State University
Fort Collins, CO, USA

INTRODUCTION

Transcatheter aortic valve replacement (TAVR) is a minimally invasive procedure that does not require an open-heart surgery. Thus, THVR has been recommended for patients with high surgical mortality risk. The most recent data from clinical trials indicate that TAVR can be extended to patients at intermediate and low risk [1,2]. Unfortunately, THVR faces similar failure mechanisms as bioprosthetic valves where calcification and valvular degeneration are some of the ongoing challenges. The lack of long-term durability data on TAVR further reveals the critical need for improving the design of transcatheter aortic valves (TAV) [3].

Polymeric heart valves show great potential for use in TAVR due to their tunability and cost-effectiveness. Furthermore, enhancing polymers has shown to further improve their durability, hemocompatibility, and hemodynamic properties [4]. TAV with leaflets made of an interpenetrating polymeric network of hyaluronan (HA) and linearly low-density polyethylene (LLDPE) have been shown to be hemocompatible with good hemodynamic performance [5,6]. The objective of this study is to develop a new process of forming the HA-LLDPE TAV that involves a combination of finite element analysis (FEA) and vacuuming forming. The goal is to create a cost-effective fabrication method without sacrificing the performance of the HA-LLDPE TAV.

METHODS

Design optimization. The shape of the cusps was determined via FEA (Abaqus Explicit). Their height and geometry along the fixed edges were predetermined based on an ongoing parametric study. To obtain the desired curvatures and shape of the three leaflets, a mechanical load of 100 mmHg was applied on the aortic side of the predetermined model. The boundary conditions are fixed edges on the outer side of the cusps. In the initial state, the cusps had a cylindrical shape like a tubular film; they were thin (80 um), almost incompressible (Poisson Ratio = 0.45), and linearly elastic with a Young' modulus of 20 MPa. The low modulus creates a compliant material that, when placed under the applied load, causes the cusps obtain the idealized shape that minimizes the stresses for the given loading. The final geometry was exported into a CAD software (Solidworks), and it was used to create a mold for valve fabrication.

Leaflet Fabrication & Valve Assembly. The valve frames (26 mm ID) were 3D printed (uPrint SE Plus, Stratasys) Acrylonitrile butadiene styrene (ABS). The leaflets were shaped using a vacuum forming machine (Formech 300XQ). Briefly, a mold of the idealized leaflet geometry from the design optimization study above was 3D printed. The mold was amounted on the forming machine, which briefly heated a flat LLDPE film (2045G, 80 um thick) for varying durations. Once the polymer sheet is soft, a vacuum is applied and the mold was pressed against the heated LLDPE to obtain the leaflet geometry from the mold. The thermoformed leaflets were then glued onto the valve frames for the in vitro experiment.

Hemodynamic Analysis. The assembled valves were placed in an in vitro model and tested under pulsatile aortic flow conditions. A water-glycerin mixture (40:60 v/v) was used as the blood analog. The aortic pressure, pulsatile rate, and cardiac output were 80/120 mmHg, 60 beats per minute (bpm), and 5 L/min, respectively. The ventricular and aortic pressures were recorded via catheter transducers (Millar Mikro-Tip). The mean pressure gradient (mPG), peak pressure gradient (pPG), effective orifice area (EOA), and the regurgitation fraction (RF) were calculated. Data was averaged over 60 cardiac cycles, and analyzed as described elsewhere [6].

RESULTS

Figure 1 shows the contour plot of the maximum principal strain (left) of the three cusps, which look almost identical. The strain concentration appears highest near the fixed edge. It lowers with decreasing distance along the radial direction towards the coaptation region. The leaflets deformed least near the free edge where the three cusps are seen compressed against each other. The right image shows an example of thermoformed leaflets assembled into a valve. The clear

LLDPE shaped leaflets are seen in the center of the assembly. The yellow portion is the 3D printed ABS frame.

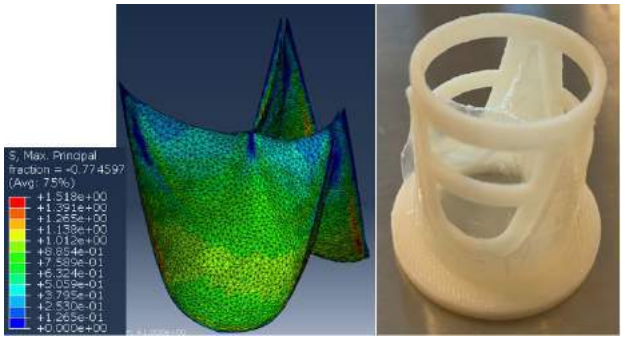

Figure 1: The left image shows idealized shape of the leaflet cusps from the FEM study. Strain unit are dimensionless. The assembled valve is shown on the right side.

Figure 2 shows the results of thermoforming the LLDPE for different durations. The longer durations created more refined shapes of the cusps from the LLDPE film. Shorter heating times, such as 15 and 10 seconds, were not long enough to create the 3D shaped leaflets. The flat LLDPE was also heated to 60 seconds (s) (not shown), and those leaflets were also assembled into a valve.

Figure 2: From left to right, LLDPE films that were thermoformed under different durations of 50, 40, 30, 20, 19, 18, 15, and 10 seconds.

The hemodynamic results are shown in table 1. The EOA does not seem to vary noticeably across all the valves. There is a correlation between heating time and pPG. The TAV with the longest (60 s) and shortest (18 s) heating durations appears to have the most paravalvular leakage with RF of 53.80±0.69 and 36.05±0.71, respectively. The same can be concluded for mPG, which are 11.8 ±0.43 and 9.45±0.26 for 60 and 18 s.

Table 1: Data from the pulsatile flow study showing TAV with LLDPE leaflets heated for 60, 30, 20, and 18 seconds during thermoforming.

Duration (s)	mPG (mmHg)		pPG (mmHg)		EOA		(RF) (%)	
	mean	std	mean	std	mean	std	mean	std
60	11.8	0.43	19.0	0.74	1.76	0.04	53.8	0.69
30	8.77	0.28	13.2	0.24	1.72	0.06	14.4	0.85
20	8.39	0.34	14.6	0.28	1.80	0.07	13.9	0.79
18	9.45	0.26	12.7	0.41	1.69	0.04	36.1	0.71

DISCUSSION

The results show that TAV can be easily assembled through thermoforming. The data also present interesting patterns. For example, long heating time created the 3D shape that may improve the kinematics, but heating too long could lead to a rigid material which could comprise the leaflet kinematics. This may explain why the mPG and pPG increase with longer heating during vacuum forming. Although further improvement is required, the performance of thermoformed TAV is already comparable to FDA approved TAV. For the SAPIEN 3 (Edwards Lifesciences) of the same size, mean EOA is 1.74±0.35 cm^2 with an mPG of 10.59±3.88 mmHg. For the Evolut R (Medtronic) of the same size, mean EOA is 1.69±0.40 cm2 with an mPG of 7.53±2.65 mmHg [7].

Future work will involve more FEA to optimize the shape of the leaflets. The vacuum forming method will be further explored through a series of parametric studies varying the duration, heat, and possibly different grades and thicknesses of LLDPE. Perhaps a parametric study that to analyze the deformation gradient of LLDPE will reveal the localized deformation of the polymer. This would help show the material behavior under heat and further improve the fabrication process. An accelerated wear test will help verify the durability of the thermoformed TAV. Future studies will also include HA-LLDPE IPN formation testing of the thermoformed leaflets and developing a metal stent frame for the novel heart valve.

ACKNOWLEDGEMENTS

We would like to thank the staff at the machine shops from the department of biomedical engineering at Georgia Tech for their advice and equipment. Thank you to Breandan Yeats from the CFM lab in the department of biomedical engineering at Georgia Tech for his guidance in finite element modeling. Funding is provided by National Institutes of Health, National Heart, Lung and Blood Institute, under the Award Number 1R01HL119824-01.

REFERENCES

[1] Fioretta, E et al., *Nature Reviews Cardiology*, 1-25, 2020.
[2] Popma, J et al., *New England Journal of Medicine*, 380(18):1706-1715, 2019.
[3] Rotman, O et al., *Expert review of medical devices*, 15(11):771-791, 2018.
[4] Oveissi, F et al., *Materials Today Bio*, 5:100038. 2020.
[5] Simon-Walker, R et al., *Journal of Biomedical Materials Research Part B: Applied Biomaterials,* 106(5):1964-1975, 2018.
[6] Heitkemper, M et al., *Journal of the mechanical behavior of biomedical materials*, 19:163-174, 2019.
[7] Hahn, R et al., *JACC: Cardiovascular Imaging*, 12(1):25-34, 2019.

SB³C2021
Summer Biomechanics, Bioengineering and Biotransport Conference
June 14-18, Virtual

DESIGNING A HIGH-THROUGHPUT FLOW CHAMBER TO ASSESS BONE TISSUE DEVELOPMENT IN VIVO UNDER DIFFERENT MECHANICAL ENVIRONMENTS

Gina L. Georgadarellis (1), Craig Albertson (2), Juan M. Jiménez (1)

(1) Mechanical Engineering
University of Massachusetts Amherst
Amherst, MA, United States

(2) Biology
University of Massachusetts Amherst
Amherst, MA, United States

INTRODUCTION

It is well established that certain types of physical exercises can serve as a therapeutic treatment to minimize bone loss and decrease the risk of bone fracture [1, 2]. Exercise plays a crucial role in maintaining the skeleton because bone is sensitive to the mechanical forces experienced during physical exercise [3]. Because many molecular and cellular features of mammalian bone are conserved in the zebrafish (Danio rerio) skeleton, such as the major categories of tissues and cells [4, 5], the zebrafish has received increased attention as a vertebrate model in the field of exercise physiology [6] . Furthermore, previous swimming experiments in water tunnels support a role for exercise in increased bone growth and density in adult zebrafish [7].

In humans, the effect of exercise on the skeleton depends on how the skeleton is loaded [2, 3]. This is also true in zebrafish, where results depend on an array of unstandardized swimming parameters (e.g. speed, test duration, number of swimming bouts). For example, swimming exercise studies have reported effects in the growth of the vertebral bodies, with increases in bone volume, mineralization, and the number of bone-forming osteoblasts in zebrafish [7] but has also been shown to induce vertebral lordosis with a dose-response pattern [8]. Further, zebrafish swimming experiments have been conducted in a range of different water tunnel designs, often with uncharacterized fluid flow fields that are assumed to be laminar and thus parabolic [9–12]. Previous work has shown that zebrafish larvae tend to take advantage of this, where they cling to the wall of the test section using their mouth to maintain their position in areas of little to no flow [11]. To address these shortcomings, we designed, built, and characterized a water tunnel with a uniform flow field and small boundary layers near the walls to decrease variability in the experimental outcomes (Figure 1). Additionally, we designed a computer-controlled pump system that allows different types of flow waveforms to be tested. To test our design, we investigate the role of increased swimming speeds on zebrafish bone remodeling.

METHODS

We integrated wind tunnel design methodologies into our testing apparatus to delay boundary layer growth. To achieve uniform flow, a conditioning chamber and a contraction nozzle was incorporated into the design of the water channel. Using established design guidelines [13], the wall curvature, contraction ratio, and the contraction length were carefully chosen. A fifth order polynomial was chosen for the contraction nozzle's wall curvature:

$$Y(X) = H_i - (H_i - H_e)[6(X')^5 - 15(X')^4 + 10(X')^3] \qquad (1)$$

where X'=X/L and L is the contraction length. When aiming for a laminar boundary layer at low Reynolds numbers, minimal boundary layer separation and reasonable flow uniformity at the contraction outlet, this wall shape performed better than those based on third order polynomial, seventh order polynomial, or matched cubics [13]. To drive the flow, our design can either be pump driven or gravity driven to allow for higher speeds if desired. A variety of waveforms can be generated using a computer program we wrote in the LabVIEW software. A voltage signal is exported from a National Instruments data acquisition card and used to control a Watson-Marlow 530U peristaltic pump. The pump propels the water into the water channel and the flow rate at the inlet of the inlet is monitored with a Transonic Systems, Inc. ultrasound flow meter as a feedback control. The testing chamber cross sectional dimensions are 30 mm x 30 mm by a length of 150 mm to allow simultaneous testing of 15-20 juvenile zebrafish (~1 month), enabling high-throughput measurements.

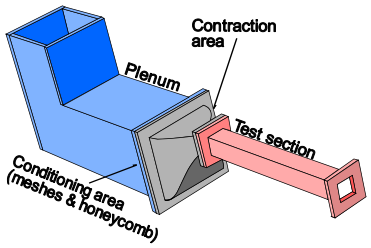

Figure 1: Water channel schematic highlighting the conditioning system (blue), contraction cone (grey) and test section (red).

Water channel experiments are described briefly: 30 days post fertilization (dpf) juvenile zebrafish are exposed to 6h of exercise per day for 7 days with flow rates beginning at 1 body length/sec and increasing by 10% every day. Control fish remain in holding tanks of a similar volume with no flow. For every experiment, increased swimming and control fish are full siblings. Exercise begins with 3h of swimming, followed by 1h of rest, then by another 3h of swimming. Fish are fed a combination diet of newly hatched Artemia and Gemma Micro 300 1h before the first exercise period, during the 1h rest period (test group only), and after the second swimming bout. The night before the experiment, fish are exposed to a green fluorescent bone dye (calcein) to label fish's bones on day 0. After 7 days of swimming, the bones were labeled once more with a red fluorescent bone dye (alizarin red) to label the fish's bones on day 8. The difference in area or length of particular bones is used to assess growth rates

RESULTS

After 7 days of swimming, the growth in 4 superficial bones that represent distinct functional units of the skeleton was calculated: (1) the opercle (OP), which protects the gills and acts in respiration; (2) the cleithrum (CL), which supports the pectoral fin musculature and is involved in stabilization of the body axis; (3) the caudal fin rays (FR), which comprise the caudal fin and are involved in propulsion; and (4) the 3rd infraorbital (ORB), which lines and supports the eye socket. The orb was included as a negative control, as growth in this bone was not expected to be influenced by increased swimming. We found accelerated bone growth in the experimental group compared to the control group in the FR by 19.8%, CL by 43%, and OP by 16%. The negative control, the ORB did not experience a difference in growth (Figure 2). Thus, our water channel can be used to elicit differences in bone growth in a relatively brief period.

DISCUSSION

The design of our water tunnel provided a near uniform flow field that allows for experiments where fish swim for the duration of the experiment. Turbulent flow theory was used to ensure an isotropic and homogeneous flow field void of velocity gradients. Traditional swim studies that utilize laminar flow can be problematic for researchers. This type of velocity profile is parabolic, with zero velocity at the walls and a maximum velocity at the center, and thus zebrafish will experience different velocities and drag forces depending on distance from the test section's wall, adding variability in experimental results. The design of our water tunnel provided a uniform flow field absent of velocity gradients, except at the wall where a very thin boundary layer was present. One minor issue is that the flow rate is limited to 2 L/min (~3 BL/s for juveniles, SL=1.2cm) with the current pump-driven set up, which means some types of experiments are unable to be performed. For example, sprint tests are limited as the critical swimming speed of an adult zebrafish is 18 BL/s [14]. To achieve higher flow rates, the water channel can be driven by using gravity instead. Using our design, we investigated the role of increased swimming speeds on zebrafish bone remodeling. Our preliminary proof-of-concept study resulted in increased bone volume after 7 days. These results show our carefully designed and built water tunnel provides a well-controlled environment where the effects of mechanical forces on skeleton remodeling can be further elucidated.

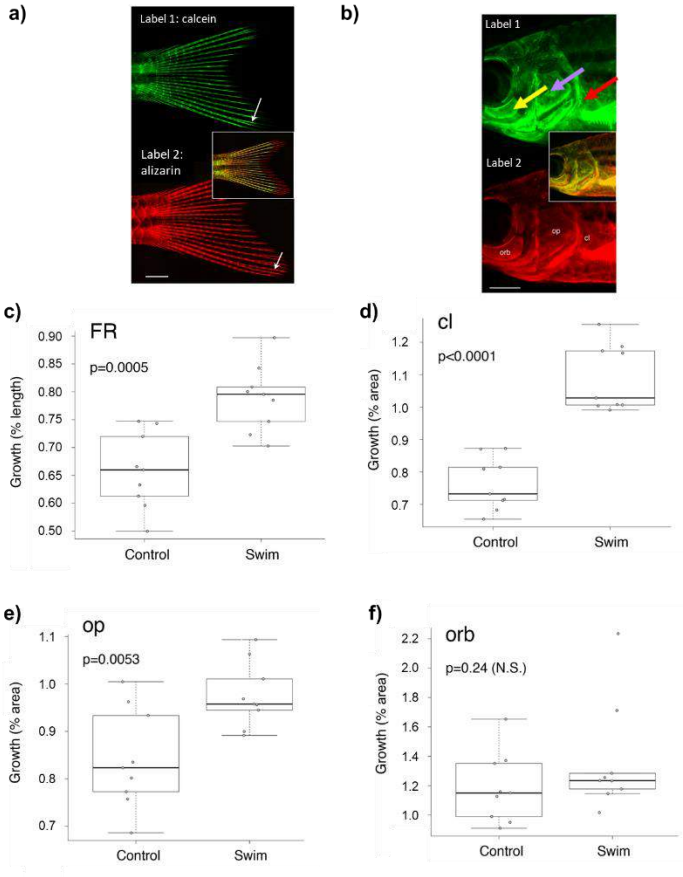

Figure 2: Swim training leads to expanded bone formation in the caudal fin ray (a, c), cleithrum (red arrow b, d), and opercle (purple arrow b, e). There were no differences between groups in the negative control (yellow arrow b, f). Scale bar = 100 µm.

ACKNOWLEDGEMENTS

Special thanks to the Jiménez Lab, Albertson Lab, and Lynch Lab.

REFERENCES

[1] Yuan, Y et al., Prog Biophys Mol Biol, 122(2):122-130, 2016. [2] Hong AR, Kim SW., *Endocrinol Metab (Seoul)*, 33(4):435-444, 2018. [3] Robling, AG et al,. *Med Sci Sports Exerc*, 34(2):196-202, 2002. [4] Apschner, A et al., *Methods Cell Biol*, 105:239-55, 2011. [5] Luderman, LN et al., *Curr Top Dev Biol*, 124:81-124, 2017. [6] Rovira, M et al., *Front Physiol*, 9:1362, 2018. [7] Suniaga, S et al., *Sci Rep*, 8(1):3646, 2018. [8] Printzi, A et al., *J Fish Biol*, published online ahead of print, 2019. [9] Fiaz, AW et al., *J. Appl. Ichthyol*., 30(4):728-739, 2014. [10] Fiaz, AW et al., *PLoS One*, 7(4):e34072, 2012. [11] Bagatto, B et al., *J Exp Biol*, 204(Pt 24):4335-4343, 2001. [12] Pelster, B et al., *Am J Physiol Regul Integr Comp Physiol*, 285(2):R339-R347, 2003. [13] Bell, JH, Mehta, RD., NASA-CR-182747, 1988. [14] Palstra, AP et al., *PLoS One*, 5(12):e14483, 2010.

MAXIMUM VENTRICULAR WALL LOADING COINCIDES WITH PERIVENTRICULAR WHITE MATTER HYPERINTENSITY LOCATIONS

Valery L. Visser (1,2), Andreia Caçoilo (2), Johannes Weickenmeier (2)

(1) Department of Biomedical Engineering, Eindhoven University of Technology, P.O. Box 513, 5600 MB Eindhoven, The Netherlands

(2) Department of Mechanical Engineering, Stevens Institute of Technology, Hoboken, New Jersey 07030, USA

INTRODUCTION

White matter hyperintensities (WMH) are bright appearing lesions in white matter tissue on T2-weighted or fluid attenuated inversion recovery (FLAIR) magnetic resonance imaging (MRI) scans. The prevalence of these lesions strongly increases with age, and has been shown to correlate with cognitive decline and neurodegenerative diseases [1–3]. Even though WMHs are associated with characteristic pathological tissue changes and are commonly observed in elderly, their etiology remains unclear. WMHs are grouped based on their anatomical location into either periventricular WMHs (pWMHs) which are located adjacent to the lateral ventricles (LVs) or deep WMHs (dWMHs) located in diffuse white matter regions throughout the brain [4,5]. Both types of WMH are typically associated with the accumulation of fluid in brain tissue, which induces the hyperintense signal on MRI scans [6]. The interstitial fluid damages surrounding tissue and leads to neuroinflammation and neurodegeneration. This process worsens over time and promotes WMH volume growth. In this study, we pose that the onset location of pWMH originates from ventricular wall failure which causes cerebrospinal fluid (CSF) to leak into adjacent brain tissue [3,7]. Normally, the ependyma, a single layer of cells forming a tight barrier between brain tissue and LVs, prevents CSF to diffuse into the brain tissue [8]. However, after damage of the ependyma this function might be disturbed [9]. Several histological and pathological studies have posed this hypothesis, but none of them has successfully explained what mechanism is responsible for the damage of the ependymal tissue [5,6,9]. Here, we hypothesize that hemodynamically driven LV expansion generates mechanical loading of the ependymal wall, which induces mechanical fatigue in the tight connections between the ependymal cells that line the LVs. This fatigue is thought to induce detachment of the cell-cell connections in the ependyma causing denudation of the LV wall and fluid accumulation in the periventricular space which initiates the onset of pWMH. We use a finite element modeling approach to determine the location of maximum ventricular wall loading and demonstrate that their location matches pWMH locations.

METHODS

From the NYU Langone Alzheimer's Center medical image database, we selected eight healthy subjects (four female, four male) aged 65 through 79. We used FLAIR images of each subject and chose

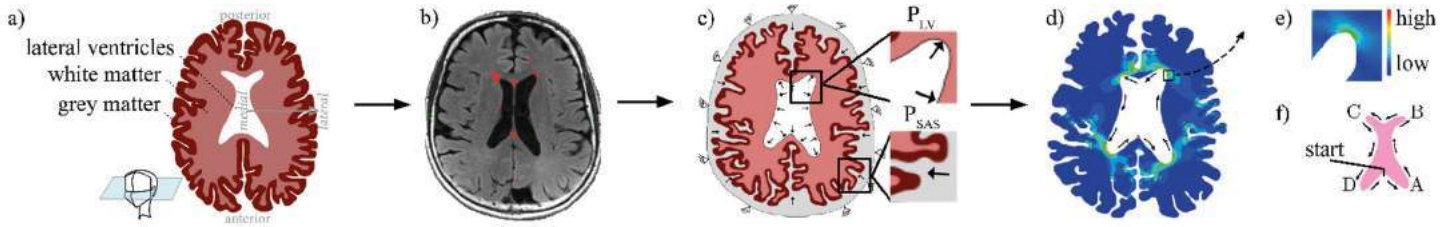

Figure 1: a) Anatomy of axial brain slice, b) FLAIR brain scan with WMH segmentation, c) Boundary conditions 2D FE model, with magnification of pressure in LV and pressure in SAS, d) representative figure of stretch in brain tissue at peak pressure, e) close up of stretch in LV horn, f) parametrization of the location along ventricular wall.

an axial slice that shows a representative cross section of the LV for segmentation using the software Simpleware ScanIP (Synopsis, Mountain View, CA). As shown in Figure 1c, our 2D finite element models differentiate between LV, white matter, gray matter, and CSF. We then imported the meshes into the finite element software Abaqus (Dassault Systèmes, Providence, RI) in order to prescribe Dirichlet and traction boundary conditions. Specifically, a normal pressure of 20 Pa was applied to the wall of the LV, and a normal pressure of 2 Pa to the tissue-CSF interface in the subarachnoid space (SAS) [10]. Grey and white matter tissue was modelled as an Ogden-type hyperelastic material with a Young's modulus of 1 and 2 kPa, respectively. We evaluated our simulations with respect to *maximum* and *minimum principal strain* along the LV, see Figure 1d-e. We further calculated the scalar product between the direction of the maximum principal Green Lagrange (GL) strain and the vector tangential to the LV wall in order to identify regions were cell stretch coincides with maximum GL strain. Finally, we compare the spatial distribution of our measures with WMH location extracted from each subject's WMH mask.

RESULTS

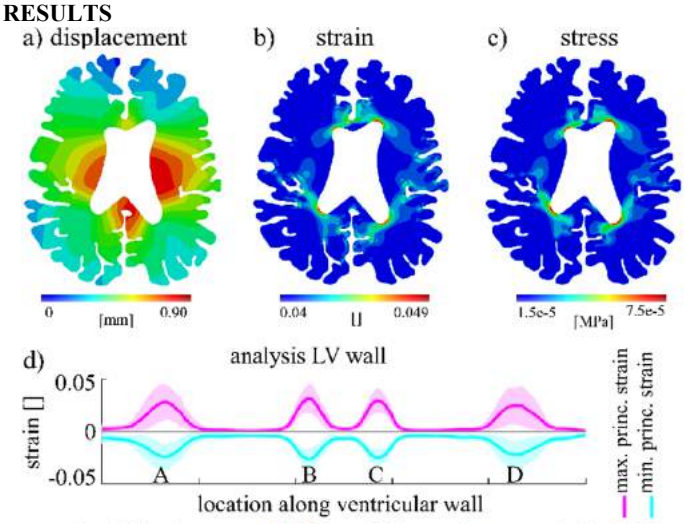

Figure 2: a) Displacement field [mm], b) maximum principal GL strain [-] and c) Von Mises stress [MPa] in one of the models, and d) Mean ± std of the maximum and minimum principal GL strain along LV wall for all eight models [-].

We show in Figure 2 that the LV wall displaces up to 0.9 mm and experiences stretches of up to 5%. From Figures 2b–d it can be derived that strain and stress localize in LV horns. Figure 2d also indicates that max. and min. principal strain show peak values in the anterior (points B and C) and posterior horns (points A and D) for all 8 models.

Figure 3a (3b is a magnification) shows the vector field of the maximum and minimum principal strain directions. From the scalar product between maximum principal strain direction and the vector tangent to the ventricular wall, we show in Figure 3c, that (i) maximum strain projection is predominantly tangential to the wall and that (ii) pWMHs co-localize where maximum principal strain is tangent to the ventricular wall; this is primarily observed in the anterior and posterior horns.

DISCUSSION

The modelling pipeline developed in this study is able to convert MRI scans to patient-specific models to simulate LV expansion. The displacement and strain fields observed in our models are similar to previously reported values for LV wall displacement by amplified MRI studies [10]. This indicates that the model is able to make physiological predictions of stress and strain distributions in the brain tissue due to hemodynamically driven LV expansion.

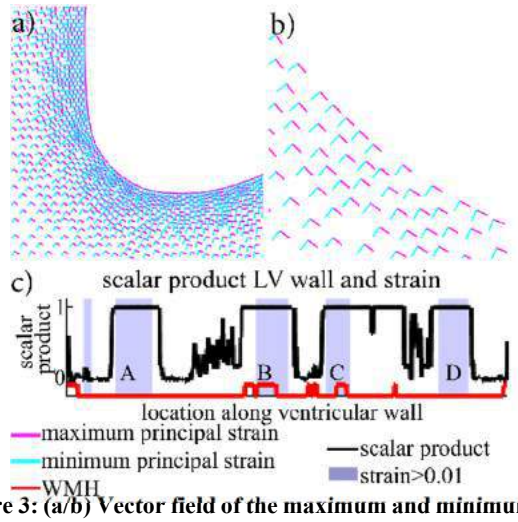

Figure 3: (a/b) Vector field of the maximum and minimum principal strain directions in a representative LV horn; (c) scalar product between maximum principal strain direction and tangent vector of LV wall and pWMH as a function of LV wall location.

The tissue deformation results in peak strains and stresses around the horns of the LV. Analysis of strain along the LV wall shows peak strains coinciding with WMHs found on FLAIR scans. Further analysis of the strains occurring in the ependyma shows that the maximum principal strain is tangential to the LV wall. The local strain state is representative of a cell loading state where cell-cell connections are under tension and cells are compressed. Ependymal cells are considered to be stretched thin which leads to their progressive failure and scar formation of the ependymal wall, as shown in Figure 4. Previous studies have shown that loss of cell-cell connections in the ependyma triggers denudation [11]. This would lead to failure of the tight-barrier function of the ependyma and the onset of pWMH.

This indicates that the locations which have high strains tangential to the LV wall are most prone to develop pWMH. Therefore, strains in ependymal cells could be used to predict the onset location of pWMH. Future studies could analyze how pWMHs grow over time by modeling tissue softening via a constitutive tissue damage model. This could be used to make prognoses of patient specific pWMH development.

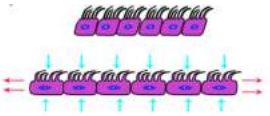

Figure 4: Ependymal cell deformation due to mechanical loading during

ACKNOWLEDGEMENTS

This research was supported by the National Institutes of Health's National Institute on Aging, grant R21AG067442.

REFERENCES

[1] De Groot JC et al. *Ann Neurol* 52(3):335–41, 2002
[2] Prins ND et al. *Nat Rev Neurol*:157–65, 2015
[3] Wardlaw JM et al. *J Am Heart Assoc*:001140, 2015
[4] DeCarli C et al. *Stroke* 36(1):50–5, 2005
[5] Griffanti L et al. *Neuroimage*:174–81, 2018
[6] Kim KW et al. *Biol Psychiatry*:273–80, 2008
[7] Fernando MS et al. *Stroke* 37(6):1391–8, 2006
[8] Jiménez AJ et al. *Tissue Barriers*:1–14, 2014
[9] Milhorat TH et al. *Arch Neurol* 22(5):397–407, 1970
[10] Terem I et al. *Magn Reson Med* 80(6):2549–59, 2018
[11] Oliver C et al. *J Neuropathol Exp Neurol* 72(9):846–60, 2013

A COMPARATIVE STUDY OF REGULAR- AND HIGH-FIDELITY FINITE ELEMENT ALGORITHMS FOR THE PREDICTION OF AORTIC FLOWS

Yiyang Fu (1), Mehdi Najafi (2), Stephen Fremes (3), Laura Jimenez-Juan (4), David A. Steinman (2), Piero Triverio (1)

(1) Dept. of Electrical & Computer Engineering
Institute of Biomedical Engineering
University of Toronto
Toronto, Ontario, Canada

(2) Dept. of Mechanical & Industrial Engineering
Institute of Biomedical Engineering
University of Toronto
Toronto, Ontario, Canada

(3) Dept. of Surgery, University of Toronto
Sunnybrook Health Sciences Centre
Sunnybrook Research Institute
Toronto, Ontario, Canada

(4) Dept. of Medical Imaging, University of Toronto
St. Michael's Hospital
Sunnybrook Research Institute
Toronto, Ontario, Canada

INTRODUCTION

Computational fluid dynamics (CFD) is rapidly gaining ground as a non-invasive way to study blood flow in the cardiovascular system [1]. In the context of cerebral aneurysms, recent studies have shown that the properties of the algorithm used to solve Navier-Stokes equations are as important as the temporal and spatial resolution to obtain accurate hemodynamic predictions [2,3]. For cardiovascular CFD simulations, finite-elements (FEM) algorithms with stabilization schemes, such as streamline upwind Petrov–Galerkin (SUPG) [4], are typically used, due to their robustness, proven track record, and availability in commercial CFD software. While stabilization maximizes numerical robustness, it introduces additional numerical dissipation. We refer to these algorithms as "regular fidelity". This type of algorithm is also used in SimVascular, a comprehensive and open-source suite dedicated to cardiovascular CFD analysis [4].

More recently, it has been shown that more sophisticated algorithms to solve Navier-Stokes equations could offer compelling advantages. In cerebral aneurysms, it was shown that a high order and minimally dissipative FEM solver could attain high accuracy with a temporal and spatial mesh quite coarser than regular-fidelity schemes [2,5]. Furthermore, the high-fidelity approach was able to reveal high-frequency flow instabilities that were suppressed by the regular fidelity approach but may have clinical significance for predicting rupture. We refer to this latter class of algorithms as "high fidelity".

The objective of this study is to compare regular and high-fidelity algorithms in the context of the hemodynamic analysis of the aorta and surrounding branches. The hypothesis is that a high-fidelity approach may offer computational advantages for this type of analysis, which is computationally demanding due to the large caliber of the aorta and the presence of complex flow patterns caused by the relatively high Reynolds number.

METHODS

The study considered the prediction of blood flow in the aorta and supra-aortic branches of a patient admitted to the Sunnybrook Health Sciences Centre (Toronto, Canada) for coronary artery bypass graft surgery. A three-dimensional model was reconstructed from CT images using SimVascular [4]. Blood velocity was acquired in-vivo with 4D-flow MRI and used to set patient-specific boundary conditions to the CFD simulation. The shape of the simulated model is shown in figure 1. At the inlet of the ascending aorta, a pulsatile flow rate was imposed, with a Poiseuille-like velocity profile in the cross-section, and a temporal profile derived from 4D-flow MRI data. As boundary conditions at the outlets, a Windkessel RCR model was used where resistance and capacitance values were calculated based on average aortic pressure and MRI-derived flow rates. Vessel walls were assumed to be rigid to keep computational costs at affordable levels. Blood viscosity and density were assumed to be 0.04 g/(cm·s) and 1.06 g/cm^3, respectively.

Pulsatile flows in the aortic branches were simulated using both the high-fidelity second-order solver Oasis [5], and the regular-fidelity first-order solver available in SimVascular. Four cardiac cycles were simulated to assure that initial transients are washed out and simulation results have converged. All simulations were performed on the SciNet Niagara cluster, using four computing nodes for a total of 160 cores. Various combinations of solver type, mesh resolution, and temporal resolution were tested. Three levels of spatial resolutions (coarse, medium, and fine) were tested using SimVascular. For Oasis, three levels of spatial resolution and three time resolutions (time step of 1ms, 0.5ms, and 0.1ms) were tested, for a total of 9 Oasis scenarios.

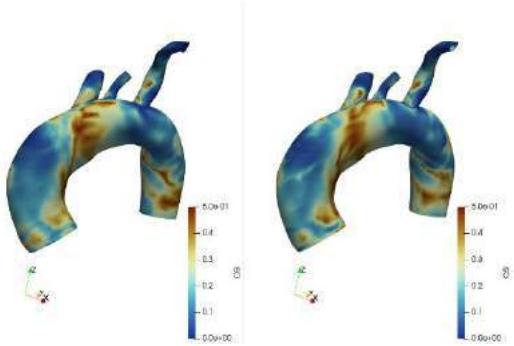

Figure 1: OSI computed by SimVascular (left) and Oasis (right).

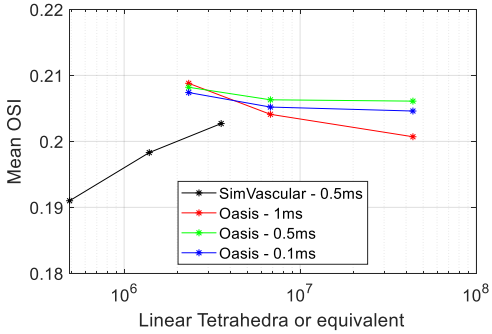

Figure 2: Mean oscillatory shear index vs. number of linear elements of the mesh (or equivalent).

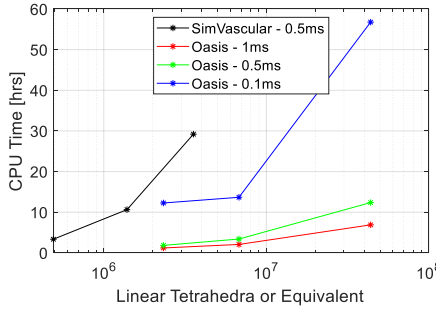

Figure 3: CPU time vs number of linear elements (or equivalent)

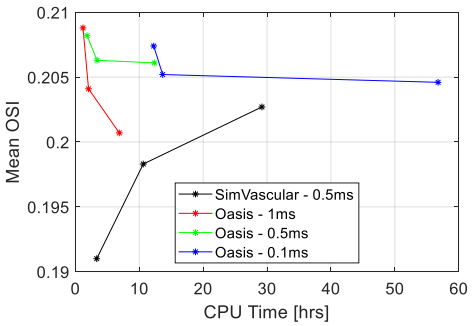

Figure 4: Mean OSI vs. CPU time.

RESULTS

Several hemodynamics indicators were computed to evaluate the simulation results, including mean wall shear stress (WSS), and oscillatory shear index (OSI). Figure 1 compares the mean OSI averaged over the 4th cardiac cycle by SimVascular and Oasis, obtained with the fine mesh and a 0.5-ms time step for both solvers. Figure 2 presents the mean OSI values over the entire model and time-averaged over the fourth cardiac cycle, for all the 12 scenarios examined. Figure 3 shows the CPU time consumed by these simulations as a function of the number of linear tetrahedral elements or equivalent. Since second-order elements were used in Oasis, the number of equivalent linear elements was set to eight times the number of mesh elements. Figure 4 depicts mean OSI as a function of CPU time directly. In figures 2 to 4, each line corresponds to a different combination of solver type and time step. The three points on each line, from left to right, correspond to the three spatial resolution levels (coarse, medium, and fine).

DISCUSSION

From figure 1, it can be seen that the simulation results of OSI given by the two solvers are comparable and agree with each other in terms of general patterns. Similarity is also observed when comparing time-averaged WSS. In figure 2, the mean OSI results of the Oasis solver showed a better converging behavior as mesh refines, compared to SimVascular results which have not yet converged within a 5% tolerance. It is also noted that the coarse temporal resolution setting (1 ms step) may be insufficient for the finest mesh, since its OSI results still show some variation. Figure 3 shows that the high-fidelity solver Oasis generally requires a lower amount of CPU time compared to the regular-fidelity strategy.

By comparing the OSI values vs CPU time in figure 4, it becomes clearer the advantage that a high-fidelity strategy can offer in terms of accuracy and computational efficiency. For the comparison, we take the OSI result of 0.204 obtained with Oasis with the finest settings as the reference result (rightmost point in Fig. 4). We see that the high-fidelity solver Oasis, with any combination of temporal and spatial resolution, yields an OSI prediction within ±2.5% of the reference. On the other hand, the regular-fidelity solver produces an OSI within ±2.5% of the reference value only with the finest spatial mesh, which requires 29 hours of CPU time, compared to the 3.4 hours required by the high-fidelity solver with the same temporal resolution (0.5 ms) and medium spatial resolution. We also observe that the high-fidelity solver delivers a fair OSI estimate even with the coarsest temporal and spatial meshes, while requiring only ~1 h of CPU time.

In conclusion, our study shows that high-fidelity CFD solvers can offer superior accuracy and efficiency in the hemodynamic analysis of large vessels such as the aorta. On par of accuracy, the high-fidelity solver Oasis was shown to reduce CPU time by about eight times compared to a regular-fidelity approach. Furthermore, the high-fidelity strategy seemed able to produce good estimates of hemodynamic indices even with relatively coarse meshes and limited CPU time, an appealing feature for clinical translation.

ACKNOWLEDGEMENTS

We acknowledge the support of the Radiological Society of North America, the Centre for Computational Science and Engineering and the Department of Medical Imaging of the University of Toronto, and Compute Canada.

REFERENCES

[1] Formaggia L et al., Cardiovascular Mathematics: Modeling and simulation of the Circulatory System, Springer, 2010.
[2] Khan MO et al., Am J Neuroradiol 36.7:1310-1316, 2015.
[3] Valen-Sendstad K et al., Am J Neuroradiol 35.3: 536-543, 2014.
[4] Updegrove A et al., Ann Biomed Eng 45.3: 525-541, 2017.
[5] Mortensen M et al., Comput Phys Comm 188: 177-188, 2015.

MULTI-SCALE CORTICAL BONE MORPHOLOGY VARIES ACROSS MICE OF DIFFERENT GENETIC BACKGROUNDS

Nicole Migotsky (1,2), Matthew J. Silva (1,2)

(1) Department of Biomedical Engineering
Washington University in St. Louis
St. Louis, MO, USA

(2) Musculoskeletal Research Center
Department of Orthopaedic Surgery
Washington University in St. Louis
St. Louis, MO, USA

INTRODUCTION

In the United States, more than 54 million people over the age of 50 suffer from osteoporosis or low bone mass,[1] which contributes to an increase in fracture risk. Clinically, fracture risk and osteoporosis are predicted by measuring bone mineral density (BMD). However, fracture risk is not only dependent on BMD, but also bone quality.[2] Patton et al. showed that bone stiffness highly correlates with bone strength, but this relationship varies with sex and age.[3] While both osteoporosis and low bone mass are moderately heritable,[4] little is known about how bone quality and stiffness are genetically regulated.

The micro-architecture of cortical bone is comprised of a porous and highly connected system of intracortical pores, called lacunae, and microchannels, called canaliculi. This system is known to be highly diverse between different bones,[5] but how this system is regulated is still being investigated. It has been shown that higher lacunar density correlates with lower microcrack density,[6] showing the importance of bone properties across length scales.

The goal of this study was to investigate how bone parameters correlate across different length scales and if these properties are genetically modulated. To do this, we analyzed whole-bone and lacunar morphological properties of eight genetically diverse mouse strains and correlated these bone properties to each other and bone stiffness. We hypothesized that bone properties vary between mouse strain and correlate across length scales.

METHODS

Mice. Female and male mice (n = 67) were received from Jackson Laboratory (Jax) at 8 wks and aged in our animal facilities until skeletally mature (22 wks). Mice were sacrificed with CO_2. The eight mouse strains (A/J, C57BL/6J, 129S1/SvImJ, NOD/ShiLtJ, NZO/HlLtJ, CAST/EiJ, PWK/PhJ, and WSB/EiJ) were chosen because they cover 90% of the genetic variation in mice and were used by Jax as the founders for the Diversity Outbred population.

Whole-Bone Morphology. The right tibial diaphysis was scanned on a Scanco vivaCT 40 at 10.5 µm resolution. Total area, bone area, medullary area, cortical thickness, tissue mineral density, polar moment of inertia, and 3D offset of a 1.05 mm long region centered 5 mm proximal to the tibiofibular junction (TFJ) were quantified.

Lacunar Morphology. The left tibia was cut approximately 5 mm proximal to the TFJ and 2 mm distal to the TFJ. A 0.5 mm region was scanned on a Zeiss Xradia Versa 520 X-ray Microscope (XRM) 4 mm proximal to the TFJ, centered halfway between endocortical and periosteal surfaces at the posterial-lateral apex. Scanning parameters were as follows: 40 kV, 3 W, 1601 projections, 20x objective, bin = 2, 4800-5000 projection intensity (7-8 sec exposure), nominal resolution of 0.54 µm. Bones were segmented, filtered, and analyzed using Dragonfly for total lacunar volume, total vessel volume, and individual lacunar properties.

Stiffness Analysis. The right tibia was exposed and cleaned, and a single-element strain gauge was glued to the antero-medial surface 5 mm proximal to the TFJ. The right tibia was axially compressed on a material testing machine (Dynamight 8841) at a peak-to-peak force ranging from 2-10N for 12 cycles at 4 Hz with 3 minutes of rest between each force. The corresponding mechanical strain was measured (LabView), and the force needed to induce a strain of 1500 µε was calculated from the force-strain regression as a proxy of tibial stiffness.

Statistics. Results of cortical bone morphology and stiffness analysis were analyzed using two-factor ANOVA to investigate (mouse) strain and sex effects, and sex-strain interactions. A correlation matrix (Pearson r) of all parameters was created to investigate the relationship between bone properties and bone stiffness.

RESULTS

Most whole-bone parameters vary significantly with (mouse) strain and sex plus have significant strain-sex interaction (Fig 1). Bone properties correlate across length scales with bones with larger area correlating to larger lacunae and more densely spaced lacunae (Fig 3).

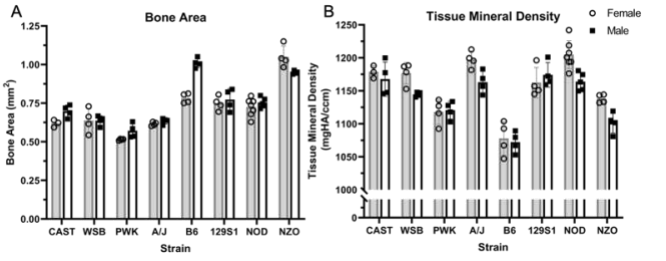

Figure 1: Both bone geometry (A) and composition (B) vary between strain, sex, and have a strain-sex interaction.

On average, 4370 lacunae were analyzed per bone, with the lacunae occupying 0.8-2.4% of the total analyzed bone volume. The lacunar number density (Lc.N/TV) varies from 46,700/mm^3 for A/J males to 84,500/mm^3 for 129S1 female (57% difference). Total porosity (lacunar plus vessel porosity) (Fig 2A) varies significantly between mouse strain, sex, and has a sex-strain interaction. Lacunar volume density and vessel volume density are moderately correlated (r = 0.54) while lacunar number density is independent of vessel volume (Fig 3).

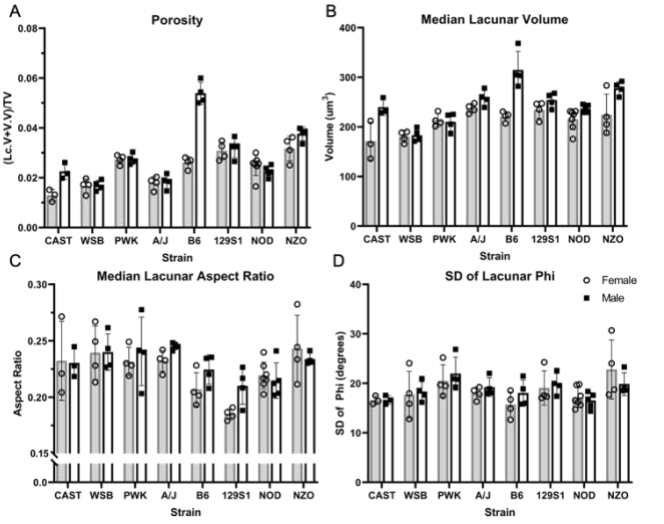

Figure 2: Total porosity (A) varies with mouse strain, sex, and has a strain-sex interaction. (B) Median lacunar volume (size) varies with mouse strain, sex, and has a strain-sex interaction. (C) Median aspect ratio (shape) and (D) SD (standard deviation) of phi (orientation) both vary with mouse strain.

Lacunar size (volume), shape (aspect ratio), and orientation (SD of phi) all vary with mouse strain (Fig 2). The variation of median lacunar volume between strains is sex dependent (Fig 2B). Median lacunar volume is moderately positively correlated with total lacunar volume density (r = 0.65). Shape and orientation are moderately correlated (r = 0.45), with more elongated lacunae (smaller aspect ratio) being more aligned to the loading axis (smaller SD of phi) (Fig 3).

The force to engender and equal strain (1500 με) was calculated and compared as a proxy measurement of stiffness, with stiffer bones requiring more force. Force varies significantly between mouse strains and was moderately correlated with bone size, bone curvature, lacunar size, and lacunar porosity measurements (Fig 3).

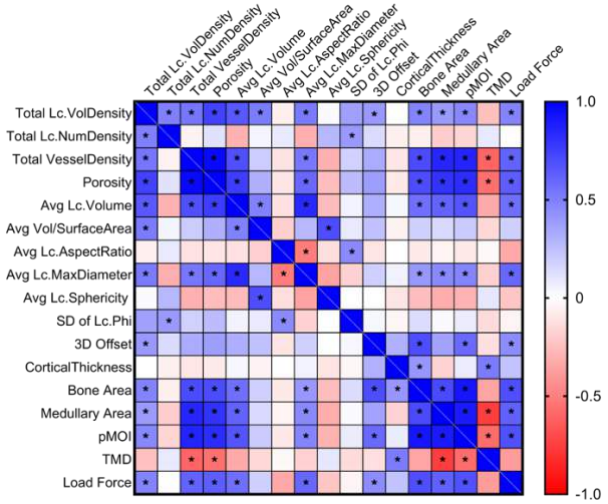

Figure 3: Correlation of Pearson r coefficients for all measurements. * denotes p < 0.001.

DISCUSSION

We showed that bone architecture, at both the whole-bone level and lacunar level, and bone stiffness vary with mouse strain, implicating a genetic contribution. Additionally, we showed that bone properties correlate across length scales with larger bones (higher bone area) having larger lacunae (higher median lacunar volume).

Bone micro-architecture also influences whole-bone tissue mineral density (TMD). Bones with higher porosity and specifically higher vessel volume density, have lower TMD. Therefore, the bone between the pores may have the same mineral density, but when measured at a larger length scale the apparent density is diminished. Therefore, lower TMD measurement in bone may imply more vasculature and not reduced mineralization.

Bones with higher total lacunar volume density tend to have larger lacunae on average, implying an increase in volume density is mainly explained by larger individual lacunae rather than more lacunae. Additionally, as lacunar volume increases, lacunar number density slightly decreases (r = -0.3, p = 0.012), supporting the idea that each lacuna "supports" a certain volume of cortical bone.

Bone micro-architecture also correlates to bone stiffness. Despite lower TMD, bones with higher porosity are stiffer. Larger bones, which also tend to have larger lacunae, are also stiffer. This implies bone size and shape across length scales contribute to bone stiffness and possible fracture risk.

We have shown that bone properties correlate between length scales, and that cortical bone properties vary with genetic background, motivating future studies to investigate the gene loci modulating these relationships.

ACKNOWLEDGEMENTS

R01-AR047867, T32-EB018266, T32-DK108742, P30-AR074992, 1 S10 OD021694-01. We thank Dr. Virginia Ferguson and Jennifer Coulombe for help with the lacunar imaging and analysis.

REFERENCES

[1] Wright, N. C. et al. *J. Bone Miner. Res.* **29**, 2520–6 (2014).
[2] Osterhoff, G. et al. *Injury* **47**, S11–S20 (2016).
[3]Patton, D. et al. *J. Biomech.* **83**, 125–133 (2019).
[4] Richards, J. et al. *Nat Rev Genet* **13**, 576–588 (2012).
[5] Milovanovic, P. et al, *Curr. Osteoporos. Rep.* **17**, 105–115 (2019).
[6] Vashishth, D. et al. *Bone.* **26**, 4 (2000).

SB³C2021
Summer Biomechanics, Bioengineering and Biotransport Conference
June 14-18, Virtual

OCULAR BIOMECHANICS DUE TO THE GROUND BLAST REINFORCEMENT OF AN IMPROVISED EXPLOSIVE DEVICE AT VARIOUS HEIGHTS

A Karimi (1), R Razaghi (2), CA Girkin (1), JC Downs (1)

(1) Department of Ophthalmology and Visual Sciences, University of Alabama at Birmingham, Birmingham, AL, United States

(2) Research Department, Heel of Scene Ltd., Tokyo, Japan

INTRODUCTION

Although the eyes comprise approximately 0.27% of the total body surface area and only 0.1% of the erect frontal profile, eye injuries are found in 10-13% of all combat casualties. Combat eye injuries are often due to unexpected improvised explosive devices (IED), homemade bombs constructed and deployed in ways other than in conventional military action. More than 24,000 injuries to American service members in the military action have been reported (1), and ocular injuries due to IEDs are responsible for ~ 5-13% (2, 3), 29% (4), and 72% (5) of battlefield casualties in prior reports. It is important for ophthalmologists, particularly those working in urban trauma centers, to have knowledge of the mechanisms and spectrum of injury from various IED blast injury patterns (6). However, investigating ocular injuries from IED blasts is difficult experimentally due to complicated experimental setups and variations in the weight, angle, distance of the IED from the victim, and other factors. The finite element (FE) method can be used to estimate the injury to the eye computationally . FE analyses can be used to simulate ocular tissue deformations, stress and strain from IED blast at various IED weights, heights, and angles, which is difficult to achieve experimentally. IEDs are typically placed off the ground to more severe injure the victim through ground blast reinforcement (GBR). However, there is still a paucity of knowledge about the role of the IED height from the ground on ocular biomechanics; and how the GBR can amplify the severity of injury.

METHODS

This study was aimed to establish a 3D fluid structure interaction model of the eye, skull, air, soil, and IED, using a multi-material, arbitrary coupled load blast enhanced and Eulerian-Lagrangian approach to estimate the stresses and deformations in the human eye connective tissues (Fig. 1). An eye-specific FE model of the human eye, including a detailed optic nerve head, was constructed and a generic anterior segment was added. The eye was then incorporated into a 3D FE model of the human skull and the gap between the orbital bone and the eye was filled with extraocular tissue. The skull-eye FE model was then subjected to an IED explosion (IED's weight=2kg) from the front in a way that the blast pressure from the IED hits the frontal bone of the skull. Two different blast formulations, (a) spherical air burst with no amplification (GBR) of the initial shock wave due to interaction with the ground surface; and (b) a hemispherical surface blast from an IED located on or near the ground surface, with GBR, were used to simulate the IED explosion. In the latter case, the initial blast wave is immediately reflected and reinforced by the ground to produce a hemispherical reflected wave from the point of the blast. This reflected wave merges with the initial incident wave, producing overpressures, which are as much as four to eightfold (6) greater than those produced by the initial blast wave alone (7). The simulations were done for a period of 20 ms, much longer than prior studies, which allowed us to simulate the tertiary injury (victim's head translation due to the blast loading) in addition to the full loading of the primary injury. Furthermore, a longer simulation time allowed us to simulate the merging of the GBR and the bomb blast overpressure itself, which finally led to a stronger overpressure in the eye. Prior studies simulated the blast out to ~ 1.6 ms.

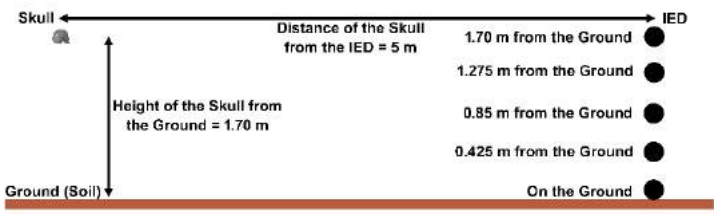

Figure 1: The FSI model of the skull, eye globe, IED, air, and soil. The IED was placed 5 m from the victim at five different heights from the ground. After the explosion, the blast wave from the bomb and its reflection from the ground hit the frontal bone of the skull.

RESULTS

The results revealed that the blast wave from the GBR reached the skull prior to the IED blast itself (Fig. 2).

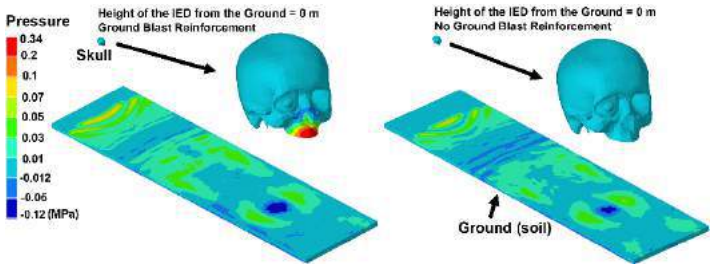

Figure 2: The contours of pressure distribution in the ground (soil) and skull-eye model. The skull-eye model is magnified for each model to better visualize the pressure distribution in the victim.

The GBR also reached the skull ~ 0.6 ms earlier when the IED was on the ground compared to when the IED was at the height of 1.70 m from the ground. The highest and lowest intraocular pressures (IOP) of ~ 17,000 and ~ 15,000 mmHg were observed for the IED heights of 1.70 and 0 m from the ground, respectively, considering the GBR. However, the IOP of ~ 9,000 mmHg was observed when the role of the GBR is ignored, regardless of the IED height from the ground (Fig. 3). The deformation in the apex of the cornea was higher when considering GBR (~ 0.75 cm) compared to the case with no GBR (~ 0.65 cm); no considerable deformation difference was observed at different IED heights from the ground. When the role of the GBR was ignored, the results showed almost the same patterns and magnitudes of stresses and deformations in the skull and eye regardless of the height of the IED from the ground, suggesting the GBR plays a crucial role in ocular blast simulations. Within 1.6 ms after the blast, our results revealed the IOP elevation of 2730 and 1670 mmHg with and without GBR, respectively, which is within the reported ranges of 2625 mmHg (8), 3150 mmHg (9), and 1739±307 mmHg (10). This is consistent with the experimental study on porcine eyes under blast loading by Alphonse (11).

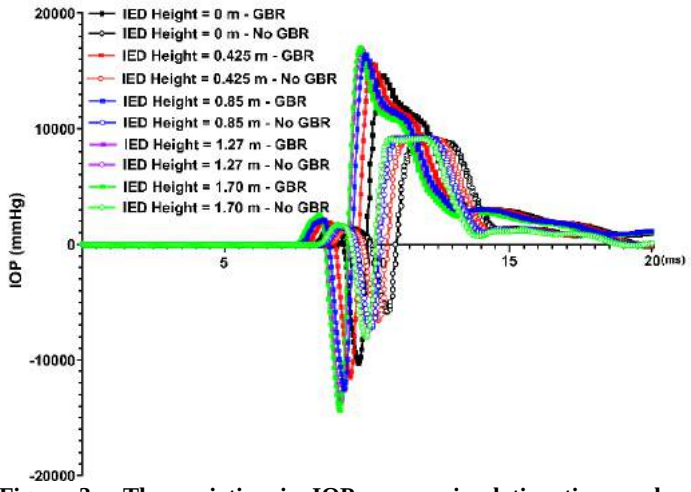

Figure 3: The variation in IOP versus simulation time under various IED heights from the ground as well as ground blast reinforcement.

DISCUSSION

In the cases of the Boston Marathon bombing and the Fertilizer Plant explosion in West, Texas in 2013, blasts were at ground level, and yet they still resulted 13.4% and 14.2% ocular injury rates, respectively (12). This suggests the important role of the IED height from the ground in ocular injury. Our results also showed the importance of the GBR in ocular injury assessment (Fig. 2), as GBR reached skull-eye model prior to the incident IED blast pressure itself. Our results revealed that when the IED was placed on the ground, it took longer for the GBR to reach to the skull compared to when the IED was at the height of 1.70 m. We were able to simulate these differences in the blast wave GBR (7), which is likely important since as it has been shown that the GBR can increase the blast energy by as much as four to eightfold (6). In addition, increasing the height of the IED from the ground led to an increased pressure in the eye and a reduction in the time that took the GBR to reach to the head. This is in agreement with the literature, as IEDs are typically placed at a substantial heights from the ground (*e.g.*, at the height of the vehicle) so as to cause fatal injury (13). This study shows the importance of the IED height and ground blast reinforcement in blast injury assessment using a modified detonation formulation and a multi-material arbitrary coupled load blast enhanced and Eulerian-Lagrangian algorithm, and lays the groundwork for providing ophthalmologists and military medical experts with valuable simulations of IED effects.

ACKNOWLEDGEMENTS

This work was supported in part by the National Institutes of Health Grants R01-EY027924, R01-EY018926, and P30-EY003039 (Bethesda, Maryland); EyeSight Foundation of Alabama (Birmingham, Alabama); and Research to Prevent Blindness (New York, New York).

1. Lehman C. Mechanisms of injury in wartime. Rehabil Nurs. 33:192-205,2008.
2. La Piana FG, Hornblass A. Military ophthalmology in the Vietnam War. Doc Ophthalmol. 93:29-48,1997.
3. Mader TH, Aragones JV, Chandler AC, Hazlehurst JA, Heier J, Kingham JD, Stein E. Ocular and ocular adnexal injuries treated by United States military ophthalmologists during Operations Desert Shield and Desert Storm. Ophthalmology. 100:1462-7,1993.
4. Gataa IS, Muassa QH. Patterns of maxillofacial injuries caused by terrorist attacks in Iraq: retrospective study. Int J Oral Maxillofac Surg. 40:65-70,2011.
5. Ayyildiz O, Hakan Durukan A. Comparison of endoscopic-assisted and temporary keratoprosthesis-assisted vitrectomy in combat ocular trauma: experience at a tertiary eye center in Turkey. J Int Med Res. 46:2708-16,2018.
6. Singh AK, Ditkofsky NG, York CJD, Abujudeh HH, Avery LA, Brunner JF, Sodickson AD, Lev MH. Blast Injuries: From Improvised Explosive Device Blasts to the Boston Marathon Bombing. RadioGraphics. 36:295-307,2016.
7. Le Blanc G, Adoum M, Lapoujade V, editors. External blast load on structures–Empirical approach. 5th European LS Dyna Users Conference, France; 2005.
8. Bhardwaj R, Ziegler K, Seo JH, Ramesh KT, Nguyen TD. A computational model of blast loading on the human eye. Biomech Model Mechanobiol. 2014;13(1):123-40,2014.
9. Tong J, Kedar S, Ghate D, Gu L. Indirect Traumatic Optic Neuropathy Induced by Primary Blast: A Fluid–Structure Interaction Study. J Biomech Eng. 141,2019.
10. Shedd DF. Ocular Injury Following Primary Blast Exposure: The University of Utah; 2017.
11. Alphonse VD, Kemper AR, Strom BT, Beeman SM, Duma SM. Mechanisms of Eye Injuries From Fireworks. JAMA. 308:33-4,2012.
12. Yonekawa Y, Hacker HD, Lehman RE, Beal CJ, Veldman PB, Vyas NM, Shah AS, Wu D, Eliott D, Gardiner MF. Ocular blast injuries in mass-casualty incidents: the Marathon bombing in Boston, Massachusetts, and the fertilizer plant explosion in West, Texas. Ophthalmology. 121:1670-6,2014.
13. Erdurman F, Hurmeric V, Gokce G, Durukan A, Sobaci G, Altinsoy H. Ocular injuries from improvised explosive devices. Eye. 25:1491-8,2011.

A STRATEGY FOR VALIDATING THE KIMEMATICS OF A VEHICLE-SPECIFIC MADYMO MODEL OF A LOW-SPEED REAR-END COLLISION

Dominic R. Demma (1, 2), Keith D. Button (1), Elizabeth H. Kappler (1), Stephanie M. Rossman (1, 3), Steven A. Rundell (1)

(1) Explico Engineering Company, Novi, MI, USA
(2) Wayne State University, Detroit, MI, USA
(3) Lawrence Technological University, Southfield, MI, USA

INTRODUCTION

The mechanical and geometric characteristics of a vehicle's interior contribute to the biomechanics associated with a collision. Specifically, in regard to low speed rear-end collisions, the mechanical properties of the seat play a significant role in the resulting biomechanical response of an occupant. The MAthematical DYnamic MOdeling (MADYMO) software suite provides the capability to simulate such vehicle-specific conditions and corresponding occupant kinematics.

A methodology for analyzing low-speed rear-end collisions using subject-specific simulations has previously been presented [1]. The current study expands upon this methodology to account for the mechanical properties of the vehicle seat. The Insurance Institute for Highway Safety (IIHS) conducts seat rating tests on new vehicles in order to assess the efficacy of seats/headrests in mitigating cervical spine injuries during rear-end impacts. Seat parameters, such as the stiffness of the seat cushions [2,3], seat back stiffness, seat back energy return, cushion energy return, and friction [4], may have an impact on the biomechanical environment experienced by an occupant involved in a rear-end collision.

The objective of the current study was to determine a method for validating a vehicle-specific seat model for studying low speed rear-end collision occupant dynamics. The seat parameters were determined by optimizing computational head and pelvis accelerations to those observed during controlled, physical, rear-end impact sled tests. We hypothesized that utilization of the validated seat properties would allow for accurate computational predictions of occupant head and pelvis acceleration for a range of severities when compared with published physical testing.

METHODS

Seat Validation. The IIHS Dynamic Seat Rating test for the 2013 Honda Accord (SER12031) was utilized to visually construct a seat in MADYMO using a series of ellipsoids and connecting joints. A digital anthropomorphic test device (ATD), specifically a Hybrid III 50th percentile dummy model (Tass International version 2020.1), was placed in the digital environment and positioned to match the precise position of the BioRID II ATD in the sled test (Figure 1). The test acceleration pulse (with a change in velocity, or Delta-V, of 15.6 kph) was taken directly from the IIHS sled test documentation and applied to the MADYMO model. The IIHS also documented the final deflection of the seatback joint along with accelerations of the head and pelvis, and the maximum seatback deflection was determined from the IIHS sled test video. The model seat parameters were based on the seat foam stiffness properties from Cruise et al. (2020) [2] and seatback joint stiffness functions from a Honda Passport in Molino (1998) [4] as a baseline. These properties were iteratively optimized based on the seatback angle and computational ATD head/pelvis accelerations (Figure 2). Optimization of the seatback joint stiffness was conducted by scaling the load vs. displacement functions, as well as adjusting the seat back energy return until the seatback angular position reached the maximum deflection determined from the video and the final angular position recorded in the controlled rear-end collision sled test. The baseline seat foam load vs. displacement functions were scaled, and cushion energy return properties were varied to align the peak timing and peak magnitude of both the head and pelvis accelerations. The friction between the dummy and the seat and the head rest joint damping coefficient were modulated in order to match the computational and physical head kinematics.

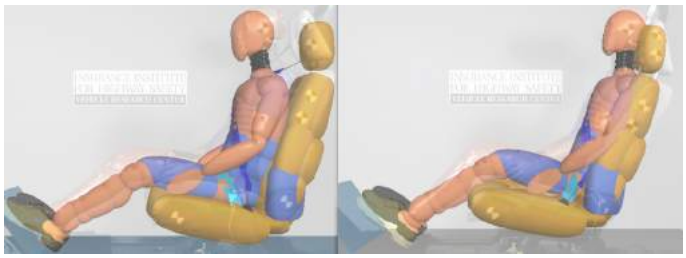

Figure 1: MADYMO seat model overlaid on IIHS test video frames.

Prediction of Varying Severity Impacts. Once the model seat properties were determined, the model was then tested against a previously published rear-end collision testing series [5,6]. This testing consisted of four low- to moderate – speed (Delta-V's ranging from 5.6 kph to 19.5 kph), full-scale, collinear rear-end crash tests [5, 6]. The tests utilized two 2014 Honda Accords which were occupied by restrained and instrumented Hybrid III 50th percentile male ATDs. The crash pulses from this series of testing are reported by Crosby et al.

(2019) [5] and the occupant dynamics results are reported by Toney-Bolger et al. (2019) [6]. Collision acceleration pulses were applied to the vehicle system in MADYMO [5]. Peak resultant linear head acceleration and dynamic pelvis accelerations were compared between the MADYMO simulation and the full-scale testing [6].

RESULTS

Seat Validation. The MADYMO validation simulations matched the results of the IIHS physical sled test in both seat dynamics and ATD kinematics. The IIHS test seat reached a maximum deflection and a final deformed deflection of 4.1 and 1.9 degrees, respectively, as a result of the 15.6 kph rear-end collision. This was the same deflection recorded in the MADYMO simulation. A comparison of the MADYMO ATD pelvis and head acceleration to those of the IIHS test accelerations are depicted in Figure 2. This demonstrates the validation of the computational vehicle specific MADYMO kinetics to those found in the IIHS rear-end sled test, with regards to acceleration magnitude, timing, and duration.

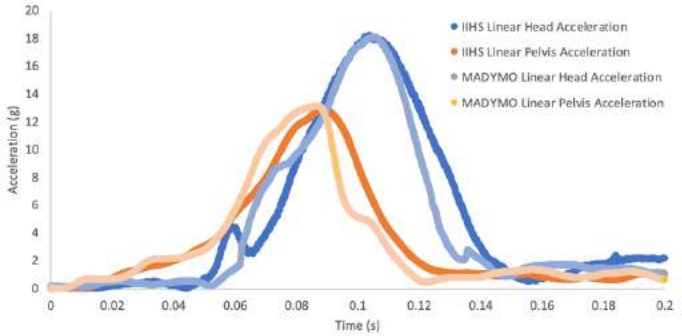

Figure 2: Head and pelvic acceleration comparison between IIHS test and MADYMO validation.

Prediction of Varying Severity Impacts. The peak head accelerations for each physical test of the rear-end test series and MADYMO simulation are compared in Table 1. A graphical comparison of pelvis accelerations are shown in Figure 3. MADYMO predicted peak head accelerations within 3 g's or less of the physical tests for all severities of 13.2 kph and below. However, the peak head acceleration predicted by MADYMO for the 19.5 kph run was 9 g's less than the peak head acceleration experienced by the ATD in the physical test.

Table 1: Head acceleration comparison between Toney-Bolger, M. et al. (2019) rear-end test series and the MADYMO.

Test Series Run – Delta-V	Peak Head Acceleration – Physical Tests	MADYMO Simulation
L1 – 5.6 [kph]	7.9	8.8
L2 – 9.0 [kph]	13.5	12.2
L3- 13.2 [kph]	22.2	19.2
L4 – 19.5 [kph]	28.0	19.0

DISCUSSION

This data demonstrates the efficacy of utilizing standardized crash testing to determine dynamic seat properties for constructing vehicle-specific models of low-speed rear-end collisions in MADYMO. When testing these vehicle-specific seat properties against a published rear-end collision series, the model accurately predicted resultant head and pelvis acceleration at or below the Delta-V of which the validation was performed (5.6 kph to 15.6 kph).

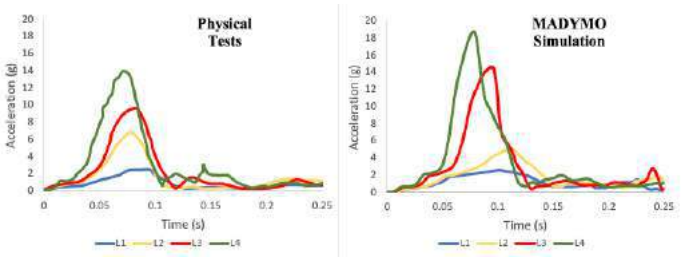

Figure 3: Pelvis acceleration comparison between Toney-Bolger, M. et al. (2019) (Left) rear-end test series and the MADYMO (Right).

A previously presented study outlined a methodology for building a *subject*-specific MADYMO model [1]. In short, the subject driver was imaged using a Faro Focus 3D laser scanner and a scaled ATD was aligned with the 3D laser scan. The methodology presented in the current study can be utilized in conjunction with this previously presented subject-specific methodology in order to create a robust model that incorporates both vehicle and subject-specific geometry and dynamic mechanical properties. These methodologies can be utilized for evaluating real-world collisions that may be less characteristic of generalized testing performed for collinear rear-end collisions with a normally seated driver.

While accurate at lower impact severities, the model overpredicted resultant pelvis accelerations and underpredicted resultant head accelerations at the maximum severity tested (19.5kph Delta-V). This likely occurred because the primary seat properties of a real-world seat differ between low- and mid-speed rear-end collisions due to the excessive amounts of seat cushion penetration and seat back joint deformation experienced at high speeds. While this study is considered successful at validating low-speed rear-end collisions, more severe rear-end collisions likely require additional parameters to account for the non-linear nature of the dynamic seat stiffness characteristics.

While the current study demonstrated the efficacy of a seat-specific model in accurately predicting dummy accelerations, future studies will test the ability of the model to predict kinetic parameters, particularly in the cervical and lumbar spine. Furthermore, in addition to the scalable dummy model used in the present study, MADYMO offers scalable human models [7]. The MADYMO manual indicates that the human models have improved biofidelity in comparison to the dummy models and can be utilized in a wider range of loading conditions. Future work will utilize the human models for a comparison with the current ATD model.

REFERENCES

[1] Sproule, D. et al. (2019) *43rd ASB Meeting.*
[2] Cruise, D.R. et al., *SAE Technical Paper* 2020-01-0524, 2020.
[3] Sieveka, E. et al. (1996). Prepared for NHTSA under Contract DTRS, 57.
[4] Molino, L. *National Highway and Traffic Safety Administration*, 1998.
[5] Crosby, C. et al., *SAE Technical Paper* 2019-01-0415, 2019.
[6] Toney-Bolger, M. et al. *SAE Technical Paper* 2019-01-1220, 2019.
[7] *MADYMO Human Body Models Release 2020.1*. Siemens. 2020.

MODELING BONE MECHANOTRANSDUCTION USING MULTI-SCALE 3D FINITE ELEMENT ANALYSIS FROM CONFOCAL FLUORESCENCE IMAGES

Loretta E. Laughrey (1,2), Nuria Lara-Castillo (2), Yixia Xie (2), Mark Dallas (2), Mohammad Niroobakhsh (1,2), Mark L. Johnson (2), Sarah L. Dallas (2), Thiagarajan Ganesh (1)

(1) Computer Science, Civil and Mechanical Engineering
University of Missouri Kansas City
Kansas City, MO, U.S.A.

(2) Oral and Craniofacial Sciences
School of Dentistry
University of Missouri, Kansas City
Kansas City, MO, U.S.A.

INTRODUCTION

Osteoporosis and low bone mass are estimated by the National Osteoporosis Foundation [1] to affect more than half the U.S. adult population. Predictions indicate that by 2025 fractures due to osteoporosis will cost $25.3 billion per year [2]. Understanding mechanotransduction, the process that transduces bone mechanical strain into biological signals affecting bone remodeling could improve therapeutic methods for reducing the impact of osteoporosis [3]. In particular, it is not known how strain at the microscopic level affects the biological response of individual osteocytes, which are viewed as the mechanosensitive cells. This research tests the hypothesis that osteocytes detect bone strain directly from the strain in the bone matrix, which would mean osteocytes in regions with the highest bone strain would be the ones most likely to respond to loading.

Osteocytic response to loading as measured by increased activation of Wnt/β-catenin signaling pathway was observed to be heterogeneous at the microscopic scale [4]. Preliminary finite element analyses suggest that including lacunae in models of bone loading results in heterogeneous strain distribution[4]. This study aims to find correlations between local bone strain and β-catenin activity in individual osteocytes. This information could be used to develop therapies and medical devices designed to increase strain in regions that will more effectively increase bone formation.

To that end, multi-plexed 3D confocal imaging experiments were performed using stains that allow the lacunocanalicular spaces, osteocyte membranes, and activation of osteocyte β-catenin signaling to be identified in the same bone specimen. The images from these experiments were used to produce models of bone loading for each sample and ascertain where β-catenin activity is strongest.

METHODS

FITC was used to label the lacunocanalicular network (LCN), DiI to label osteocyte cell membranes, and DDAOG, a LacZ substrate, to indicate β-catenin signaling activity in TOPGAL mice.

The tibiae of TOPGAL mice (9 mo male) were loaded with 9.25 N for 100 cycles at 2 Hz to stimulate β-catenin signaling in the osteocytes. The mice were rested for one hour, then sacrificed. Harvested bones were incubated overnight at 37°C in 30 μM DDAOG in X-Gal buffer solution. Transverse sections of the bone were then incubated at RT in 1% FITC in ethanol overnight, rinsed, and incubated in 100 μM DiI in ethanol overnight. Samples were rinsed, polished, and mounted with Permount.

3D confocal fluorescence imaging at 40x with 12-bit depth was used to collect signal from each stain, using 488, 594, and 633 nm laser excitation. The image stacks were imported into the Materialise® Innovation Suite [5] for creation of 3D finite element models, and to calculate osteocyte volume (based on DiI imaging) and total DDAO signal intensity (as a measure of β-catenin activation) for each osteocyte. Relative β-catenin activity was represented by DDAO intensity/Osteocyte volume. The FITC model was inverted to form a volume mesh of the bone matrix for strain analysis.

RESULTS

The image in *Figure 2* shows that the three dyes were clearly distinguished. The LCN fluid space, filled with FITC, is shown in green. The osteocytes labeled with DiI are shown in blue (cyan where signal is colocalized with FITC). DDAO is shown in red (pink or purple where colocalized with other dyes), indicating osteocytes with active β-catening signaling. DDAO was also apparent in a wide-field microscope where activated osteocytes look blue. Resolution is inadequate to

distinguish dendrites from canaliculi. Since regions where DiI dominates must be within the LCN, the LCN and osteocyte signals were combined for modeling the LCN. The LCN model from this image contains about 1.4 million nodes and 5.1 million tet4 elements.

DISCUSSION

The emission spectra for the three dyes, FITC, DiI, and DDAO are shown in *Figure 2*. The 633 nm laser does not excite FITC or DiI, allowing the DDAO label for β-catenin signaling to be distinguished from the other stains. The DDAO signal intensity is a relative measure of osteocyte β-catenin signaling activation[6] when compared with other osteocytes in the same image. DiI can be excited by a 543 nm or 594 nm laser, but to avoid bleed through from FITC, the 594 nm laser was chosen. If any DDAO signal is collected with the DiI signal, it is of no consequence since DDAO is contained within the osteocytes that DiI labels. FITC can also easily be distinguished by selecting an emission range of wavelengths shorter than DiI emissions.

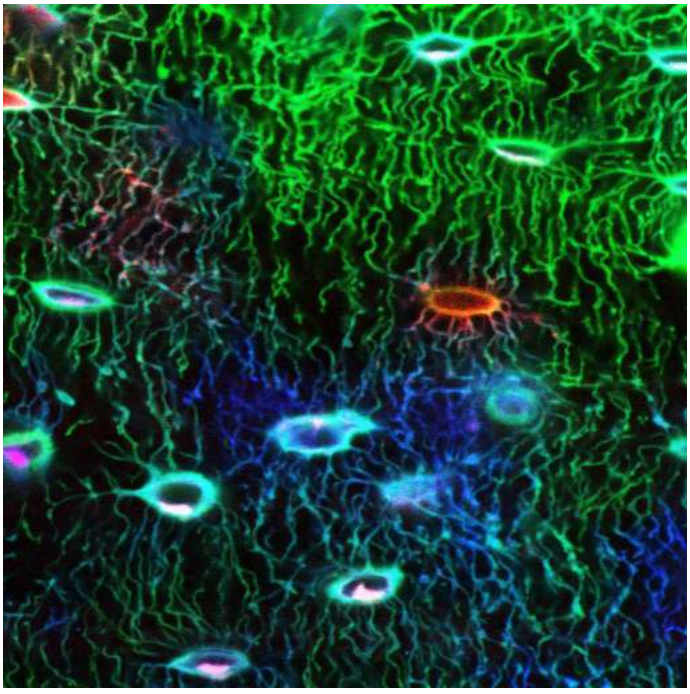

Figure 2: *Confocal fluorescence image of TOPGAL mouse tibia after loading. Green is FITC in the lacunocanalicular extracellular space. Blue is DiI labeling the cell membranes. Red is DDAO in cells with active β-catenin signaling. Notice the heterogeneity of β-catenin signaling activity.*

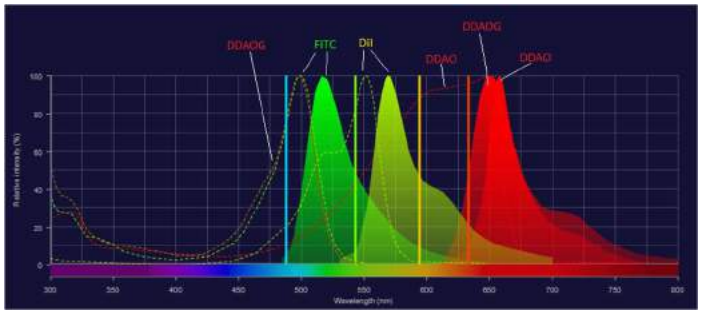

Figure 2:*Spectral graphs for FITC, DiI, and DDAOG/DDAO. The dyes are distinguished from one another by imaging each separately with the 488, 594, and 633 nm lasers. Bleed-through of DDAO signal into the DiI signal is of minimal concern since DDAO is contained within the osteocyte membranes, and the DiI signal is being used for volume measurements only.*

The collected image shown in *Figure 2* demonstrates that the three dyes are compatible when used in combination. Furthermore, the expected heterogeneity of β-catenin signaling in the osteocytes is clearly demonstrated by the different distributions and intensities of DDAO within labeled osteocytes.

An FE model of this image has been constructed to predict the strain distribution. Comparison of the DDAO intensity (β-catenin activation) in and osteocyte and the local strain distribution will provide insight as to whether mechanotransduction is occurring in the immediate vicinity of bone under the highest strains or if it may be due to another phenomenon such as fluid flow shear stress across the cell membranes, which is related more to the volume and architecture of the LCN that affect fluid flow rates.

ACKNOWLEDGEMENTS

- National Science Foundation, NSF-CMMI-1662284 (PI: T Ganesh)
- National Institutes of Health, NIA P01 AG039355 (PI: LF Bonewald)
- UMKC School of Graduate Studies Research Grant Program
- UMKC Women's Council Graduate Assistance Fund: Mary Kay McPhee Award and Betsey Fletcher Award

REFERENCES

1. National Osteoporosis Foundation. *Nof Releases Updated Data Detailing the Prevalence of Osteoporosis and Low Bone Mass in the U.S.* 2014;
2. National Osteoporosis Foundation. *Osteoporosis Fast Facts*. 2015;
3. Bonewald, L.F. and M.L. Johnson, Bone **42**(4) 606-15, 2008
4. Lara-Castillo, N., et al., Bone **76** 58-66, 2015
5. Jamali, A.A., et al., Comput Aided Surg **12**(5) 278-85, 2007
6. Gong, H., et al., Anal Biochem **386**(1) 59-64, 2009

COMPUTATIONAL MODELING OF STRESS-MEDIATED VASCULAR REMODELING IN PULMONARY ARTERIAL HYPERTENSION

Reza Pourmodheji (1), Zhenxiang Jiang (1), Christopher Tossas-Betancourt (2), C. Alberto Figueroa (2,3), Seungik Baek (1), Lik-Chuan Lee (1)

(1) Department of Mechanical Engineering
Michigan State University
East Lansing, MI

(2) Department of Biomedical Engineering
University of Michigan
Ann Arbor, MI

(3) Department of Surgery
University of Michigan
Ann Arbor, MI

INTRODUCTION

Pulmonary arterial hypertension (PAH) is a complex cardiovascular disease characterized by an increase in pulmonary arterial (PA) pressure. Progressive PAH leads to impaired ventricular-vascular coupling and right ventricle (RV) hypertrophy. Pulmonary vascular stiffness (PVS) of the proximal PAs has been recently recognized as an immediate marker of the disease progression [1]. Also, several clinical studies have suggested that PVS is correlated with the mortality of PAH patients [2]. Vascular remodeling in PAH, typically through a mechano-regulatory process, is the direct cause of PVS elevation in both large proximal and small distal PAs. Smooth muscle cell (SMC) hypertrophy and proliferation as well as extracellular matrix (ECM) accumulation such as collagen and elastin have been recognized as common features of PAH remodeling [3]. Due to an increase in the mass of these tissue constituents, the PA wall becomes thicker and stiffer. To investigate the remodeling processes in the large proximal PA due to PAH, we developed a patient-specific computational modeling framework based on the constrained-mixture theory [4]. Specifically, we investigate how an elevation of the mean pulmonary arterial pressure (mPAP) in PAH affects vascular homeostasis. We show that the stress-mediated model predicts an increase in mass production rate, thicker arterial wall and stiffer PA with elevated mPAP.

METHODS

Clinical data and finite element (FE) modeling. Data from a female patient (16 y/o) diagnosed with idiopathic PAH was acquired. Specifically, pressure waveforms in the pulmonary circulation were measured by invasive right heart catheterization. Magnetic resonance images (MRI) were also performed were also performed to acquire the PA anatomy which was used to build the geometric model with CRIMSON [5]. The PA wall was modeled as a membrane structure and the material domain was meshed triangular elements in 3D space (**Figure 1**).

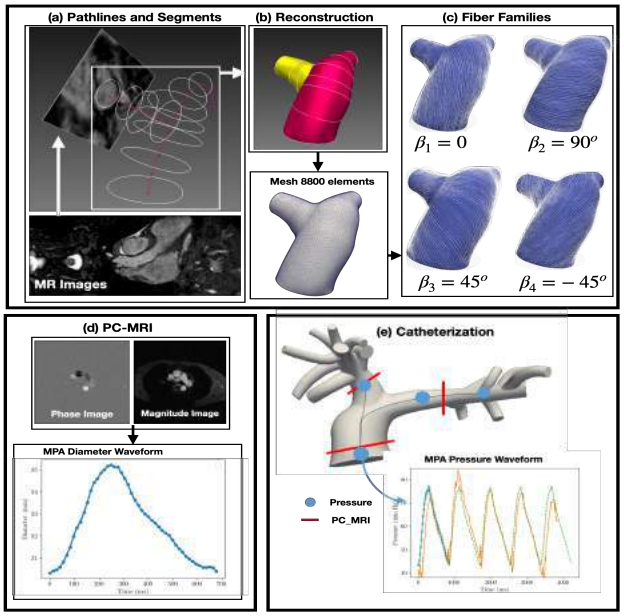

Figure 1: (a-c) Anatomical reconstruction, FE mesh and fiber data. (d-e) Catheterization and waveforms acquirement.

Constrained mixture model of vascular growth. The PA wall was modeled as a mixture of the tissue constituents, which are constrained to deform together. Mechanical contributions of the three primary tissue

structural constituents are considered. These constituents are, namely, collagen fibers ($\alpha = k$) and SMC ($\alpha = m$) whose passive behavior is described by a Holzapfel-type model, as well as elastin $\alpha = e$ that is modeled as a Neo-Hookean solid. Employing the rule of mixture, the collective stored energy function at each G&R timepoint s is given as

$$w^{\alpha}(s) = M^{\alpha}(0)Q(s)\Psi^{\alpha}\left(\mathbf{C}^{\alpha}_{n(0)}(s)\right) + \int_0^s m^{\alpha}(\tau)q^{\alpha}(s-\tau)\Psi^{\alpha}\left(\mathbf{C}^{\alpha}_{n(\tau)}(s)\right)d\tau, \quad (1)$$

where M^{α} and m^{α} are the mass and mass production rate per unit area of the constituent α synthesize at time τ, respectively. $\mathbf{C}^{\alpha}_{n(\tau)}(s)$ is the right stretch tensor of the fiber from its natural stress-free configuration synthesized at time τ that has survived up to time s.

Evolution of constituents' mass. Mass production rate of constituent α is modulated by the deviation from the homeostatic value of its stress:

$$m^{\alpha}(s) = \frac{M^{\alpha}(s)}{M^{\alpha}(0)}\left[k^{\alpha}_{g}(\sigma^{\alpha}(s) - \sigma^{\alpha}_{h}) + m_{basal}\right], \quad (2)$$

where k^{α}_{g} is the non-negative rate parameter governing the constituent stress-driven mass production. k^{α}_{g} scales the production of fibers by cells in response to changes in homeostatic deviation. To have a sensitivity analysis, we picked values in the range of $k^{k}_{g} = k^{m}_{g} =$ 0.5~1.25 for both collagen fibers and SMC and a case of unregulated SMC mass turnover and $k^{k}_{g} = 1.0$.

RESULTS

Simulation was performed by imposing a constant mean pressure of 46.7 mmHg for a 450 days period to reach homeostasis in the PA, following which pressure is then elevated to 56.0 mmHg. The total simulated duration is 800 days (**Fig. 2(a)**). For the first 450 days, the turnover rate and mass density of collagen and SMC reached mass equilibrium (**Fig. 2(b,c)**). The resultant MPA wall thickness also reached homeostasis during this period (**Fig. 2(a), Table 1**). With a 20% increase in PA's pressure at day 450, mass production in collagen fibers and SMC is increased and its rate of increase is controlled by the factor k_g. For the range of k_g considered here, the wall is thickened by 29%-48% (**Fig. 2(a)**) and the PA overall mass is increased by 46%-102% (**Fig. 2(c)**). The larger the regulation factor, the larger the mass of SMC that is produced (**Fig. 2(b,c)**). Collagen mass increase, however, was not affected by k_g (**Fig. 2(b,c)**). When SMC turnover is not regulated, more collagen is produced in comparison to the case where the both constituents are mediated by stress (**Fig 2(b,c)**). Larger local stresses and thickness can be found at the bifurcation points. These quantities are highest at the MPA, followed by LPA and RPA (**Fig. 3**).

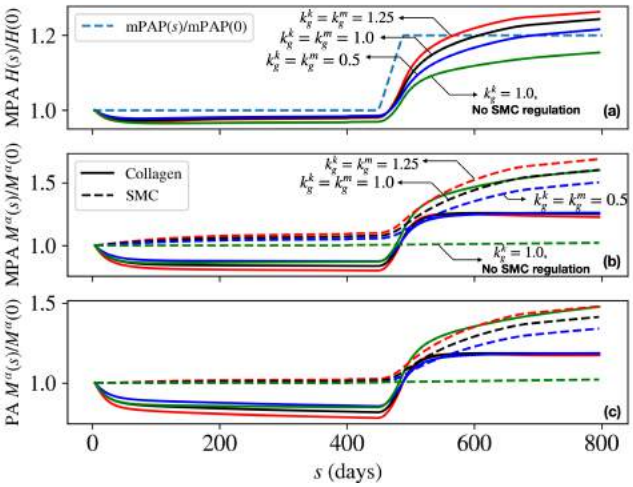

Figure 2: (a) The MPA wall thickness; (b) MPA, (c) PA collagen (-) mass and SMC mass (--).

Mass	Day 450				Day 800			
	MPA	LPA	RPA	PA	MPA	LPA	RPA	PA
Collagen (mg/mm^2)	0.189	0.1516	0.148	0.183	0.283	0.204	0.221	0.265
SMC (mg/mm^2)	0.294	0.284	0.247	0.273	0.442	0.423	0.353	0.384
Thickness (mm)	0.854	0.794	0.729	0.822	1.08	0.977	0.901	1.01

Table 1: Collagen and SMC mass and MPA wall thickness, (0-450)-days 46.7 mmHg and (450-800)-days 56.0 mmHg mPAP.

DISCUSSION

Pressure elevation in the PA causes higher collagen and SMC turnover, mass accumulation, that in turn, produces a thicker arterial wall. An increase in collagen is a common feature of PAH. This increase may be due to adventitial fibroblast activities [3]. Although SMC proliferation is less observed in small animals [6], it is, however, reported to play a role in the remodeling process in larger animals due to the presence of multiple phenotypically distinct SMC populations in the medial layer [7].

The stress-induced growth is controlled by the regulatory factor k_g [4], which affects the SMC growth more significantly. This is because the circumferentially oriented fibers and constituents bear a more significant portion of the additional load. Since SMCs are fully oriented in the circumferential direction (only 10% of collagen fibers are aligned circumferentially) [7], we expect a larger accumulation of SMC in the G&R process (**Fig. 2(c,d)**). Conversely, when SMC is not regulated, the amount of collagen accumulation increases drastically to compensate the absence of SMC response to the pressure elevation (**Fig. 2(b,c)**). A limitation of this study is that elastin was not regulated, even though there are studies indicating altered elastin content factor, e.g. growth [6], fragmentation [3] and no adaptation [9]. There is a need for further studies to have better insight in the role of elastin especially in age-sensitive pediatric PAH which will be a future plan of this work.

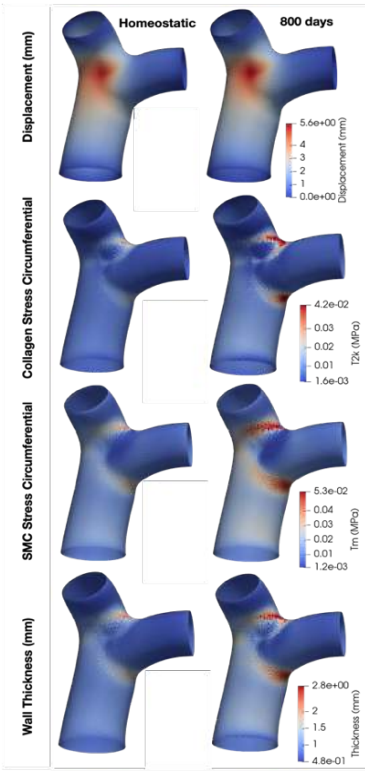

Figure 3: Displacement, circumferential stress in collagen fiber and SMC and thickness distribution in homeostatic and post-insult.

ACKNOWLEDGEMENTS

Supported by NIH (U01 1HL135842)

REFERENCES

[1] Hunter, Kendall S., et al. *J. Appl. Physiol.* 108.4 (2010): 968-975.
[2] Gan, C. Tji-Joong, et al. *Chest* 132.6 (2007): 1906-1912.
[3] Rabinovitch, Marlene. *J. clin. Invest* 122.12 (2012): 4306-4313.
[4] Baek, S. et al. *J. Biomedical Engineering* (2006): 142-149.
[5] Arthurs, CJ et al., *bioRxiv*, 2020.10.14.339960.
[6] Kobs, W., and Naomi C. C. *Biomech. Model. Mechan.* 5.4 (2006): 217-225.
[7] Stenmark, Kurt R., et al. *Circulation research* 99.7 (2006): 675-691.
[8] Zeinali-D, S. et al. *Comput. Methods in Biomech.* 14.9 (2011): 803-817.
[9] Gleason, R. L., and J. D. Humphrey. *J. Vasc. Res.* 41.4 (2004): 352-363

ASSESSING UMBILICAL VESSEL STRUCTURAL EFFECTS ON CONTRACTION-INDUCED BUCKLING USING COMPUTATIONAL MODELING

Jason M. Szafron (1), Sae-Il Murtada (1), Sumeda Nandadasa (2), Suneel S. Apte (2), Jay D. Humphrey (2)

(1) Department of Biomedical Engineering
Yale University
New Haven, CT, USA

(2) Department of Biomedical Engineering
Cleveland Clinic Lerner Research Institute
Cleveland, OH, USA

INTRODUCTION

Umbilical vessels maintain blood flow from the developing mammalian fetus to the placenta throughout gestation [1]. The umbilical vein carries oxygen-rich blood from the placenta to the portal vein and to the inferior vena cava through the ductus venosus, and deoxygenated blood is returned from the internal iliac arteries to the placenta through the umbilical arteries. During this time, it is essential that both sets of vessels maintain patency to allow for normal growth of the fetus [2]. However, shortly after birth, the lumen of the umbilical artery closes rapidly, while the umbilical vein remains patent, which allows for placental transfusion that increases fetal hematocrit [3].

In clinical practice, umbilical venous closure can be caused by clamping of the umbilical cord within a few seconds of birth, though recent studies have found several advantages to delayed cord clamping [4]. Our recent work has shown a natural mechanism that allows for umbilical artery closure, absent in the umbilical vein, that is preserved across many mammalian species [5]. The thick inner layer of the umbilical artery is rich in glycosaminoglycans (GAGs), while circumferentially oriented, contractile smooth muscle cells form the outer layer. Strong contraction by the smooth muscle cells at birth causes circumferential buckling of the inner layer, which protrudes into the lumen and prevents blood from returning to the placenta. Although the vein includes some GAGs in an inner layer and contractile smooth muscle cells, it does not buckle in the same manner as the artery.

We previously developed a computational model of buckling in the umbilical artery to understand the feasibility of the proposed mechanism for closure [5]. Herein, we utilize this model to understand how the structural differences between the umbilical artery and vein can inhibit closure. Parametric studies were performed to assess volume changes in the different layers. Additionally, bifurcation simulations were performed to identify structural effects on buckling.

METHODS

The umbilical vessels were both modeled as thick-walled, bi-layered cylinders with a GAG-rich inner layer and an outer layer including ground matrix, collagenous extracellular matrix (ECM), and contractile smooth muscle cells (Fig. 1A). Stored energy densities for

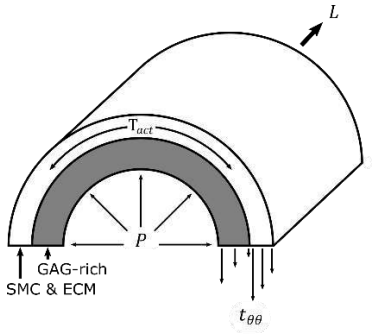

Figure 1. (A) Schematic drawings of the computational model with loading pressure P, axial load L, and active stress contribution T_{act}. Note the GAG-rich inner layer and SMC- and matrix-rich outer layer, which together give rise to the overall biomechanical behavior. Circumferential stress $t_{\theta\theta}$ varies pointwise in each layer.

the GAGs and ground matrix were neoHookean, and the collagenous matrix and smooth muscle cells were given Fung-like exponential forms. Material parameters were fit from biaxial mechanical testing data for the umbilical arteries [5]. As the vessels were observed to exude fluid during contraction, swelling and deswelling were accounted for by prescribing the ratio of the deformed to original volume v/V, and its effect on the stress distribution was enforced via a Lagrange multiplier

[6]. Contraction of the smooth muscle cells was modeled using a Rachev-type active stress in the circumferential component of the Cauchy stress [7]. Vessels were simulated with luminal pressurization and axial extension in a quasi-equilibrated state; the linear momentum balance equations were solved to identify the loaded configuration.

Buckling of the vessels was modeled with an incremental approach to the deformation, where a small perturbation was applied to the finite deformation and the incremental equilibrium equations were then solved to identify bifurcations [8]. A sinusoidal form for the incremental displacements was assumed, which allowed for simplification of the incremental equilibrium equations to a single fourth order ordinary differential equation, which, along with boundary conditions, allowed for a solution using the compound matrix method [9].

RESULTS

To understand better the distinct structures and functions of the umbilical arteries and veins, we modified the structural assumptions used to model the umbilical artery to be like those observed for the umbilical vein. As the loss of volume during contractile testing of the umbilical veins appeared to be greater than the entire volume of their thin GAG-rich inner layer, volume must have also been lost from the layer containing smooth muscle cells and matrix [5]. Therefore, we compared parametric studies where volume changes were constrained to one layer or homogenous across both layers (Fig. 2A and B). In the case with volume loss from the inner layer alone, a decrease in volume ($v/V < 1$) led to a lower active stress required to constrict the vessel, while increases in volume ($v/V > 1$) increased the active stress required for closure. However, with the volume changes occurring across both layers, the trends observed with volume changes in the inner layer alone generally reversed, with smaller lumens at higher values of swelling for all values of active stress.

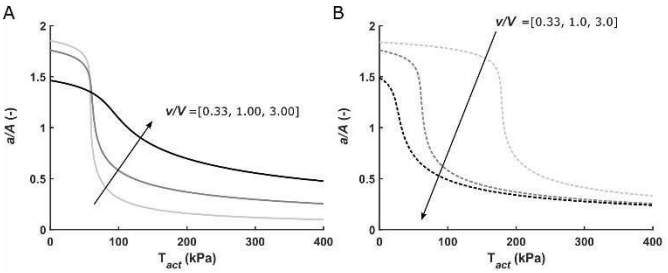

Figure 2. (A) Normalized inner radius a/A as a function of the active stress parameter T_{act} for different fixed values of volume change in the inner layer and (B) for fixed values of volume change in both layers. Arrows depict increasing volume.

We similarly examined the effects of volume changes across both layers on the buckling behavior. When examining the critical value of T_{act} for a vessel with volume changes in both layers, we found that the trends observed for volume changes in the inner layer alone remained the same, with a decrease in volume leading to a decreased active stress required for buckling and increased active stress required for an increase in volume. However, the critical values of T_{act} were lower for swelling in both layers and higher for shrinkage in both layers than in comparable cases for the inner layer alone, that is volume changes in both layers had a larger effect than changes in the inner layer alone. For $v/V = 0.5$, which was observed experimentally for the umbilical artery, the value of T_{act} was increased by nearly 2-fold for volume changes spread across both layers versus in the inner layer alone (Fig. 3A). This is likely because the mean circumferential stress $t_{\theta\theta}$ in the inner layer is less negative when volume is lost from both layers (Fig. 3B), which necessitates additional contraction to generate large enough compressive stress to cause buckling.

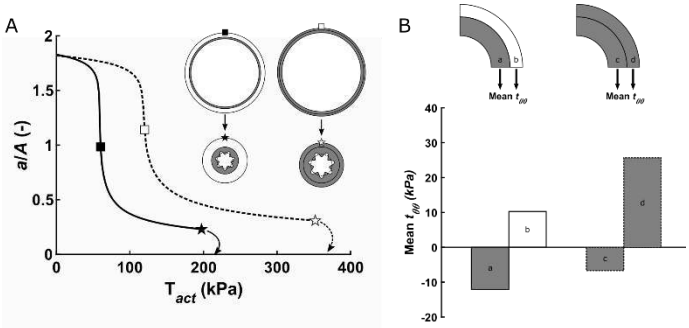

Figure 3. (A) Normalized inner radius a/A as a function of the active stress parameter T_{act} to the critical buckling point for decreased volume of the inner layer alone (solid line) and decreased volume of both layers (dashed line). Inflection points (solid square and open square) and critical points (solid star and open star) are marked and visualized in the corresponding schematics with shading corresponding to volume loss. (B) Mean circumferential stress $t_{\theta\theta}$ across the umbilical vessel wall for varying volume changes for a fixed value of active stress $T_{act} = 200$ kPa: (a) and (b) show circumferential stress for shrinkage of the inner layer alone with $v/V = 0.5$ while (c) and (d) show shrinkage in both layers.

DISCUSSION

Maintaining umbilical vessel patency throughout gestation is critical for ensuring the normal growth and development of mammalian fetuses. The presence of a GAG-rich inner layer, which is generally considered to convey compressive stiffness [10], in both the artery and vein indicates a role during gestation for preventing early narrowing. Indeed, reduction of the stiffness of the inner layer generally reduces the active stress required to reduce the lumen size. However, for buckling to take place, compressive stresses must build within the layer. In the umbilical vein, the propensity for volume losses to occur across both layers reduces the inner layer compressive stresses, which then inhibits buckling (Fig. 3B). Furthermore, stresses are increased in the outer layer of the umbilical vein as additional active stress is required to continue to narrow the lumen. These biomechanical differences arise as a result of the difference in GAG content and are mediated by the differential expression of proteoglycans and proteoglycanases between the vessels [5]. This mechanism provides for a natural method to prevent exsanguination of the newborn, and its ubiquity across mammalian species suggests an evolved role in supporting fetal health.

ACKNOWLEDGEMENTS

This work was supported in part by a Graduate Research Fellowship to JMS (NSF DGE1122492).

REFERENCES

[1] Kiserud, T. *Semin Fetal Neonat M*, 10(6), 2005.
[2] Peyter A.C. et al., *Placenta*, 35:891-899, 2014.
[3] Yao, A.C., Lind, J. *Am J Dis Child*, 127:128-141, 1974.
[4] Bhatt, S. et al., *J Physiol*, 591:2113-2126, 2013.
[5] Nandadasa et al., *eLife*, 9:e60683, 2020.
[6] Demirkoparan, H., Pence, T.J. *Int J Solids Struct*, 44:4009-4029, 2007.
[7] Baek, S., et al., *Comput Methods Appl Mech Eng*, 196:3070-3078, 2007.
[8] Moulton, D.E., Goriely, A., *J Mech Phys Solids*, 59:525-537, 2011.
[9] Haughton, D.M., Orr, A. *Int J Solids Struct*, 34:1893-1914, 1997.
[10] Broom, N.D., Poole, C.A., *Arthritis Rheum*, 26: 1111-1119, 1983.

ESTIMATION AND ASSESSMENT OF SAGITTAL SPINAL CURVATURE AND THORACIC MUSCLE MORPHOMETRY IN DIFFERENT POSTURES

Anoosha Pai S (1), Thomas R. Oxland (2), David R. Wilson (2), Stephen H.M. Brown (3), John Street (2), Honglin Zhang (2), Sidney Fels (4)

(1) School of Biomedical Engineering
University of British Columbia
Vancouver, BC, Canada

(2) Department of Orthopaedics
University of British Columbia
Vancouver, BC, Canada

(3) Department of Human Health and Nutritional Sciences
University of Guelph
Guelph, ON, Canada

(4) Department of Electrical & Computer Engineering,
University of British Columbia,
Vancouver, BC, Canada

INTRODUCTION

Biomechanical models provide a reasonable and relatively inexpensive avenue to analyze spinal pathology. Subject-specific data for such models are obtained from a full-body CT or MRI in supine or prone position [1]. Clinical imaging records, however, do not offer such coherent data of spine and muscle geometry for modelling, as they generally consist of standing x-ray of the entire spine and a supine MRI of only the pathological spinal levels. Hence, there is a need to obtain spinal geometry and muscle line-of-action in positions that is reflect anatomy of the patient's clinical symptom for accurate modeling. Additionally, biomechanical muscle parameters such as cross-sectional area (CSA) and moment-arms measured from imaging modalities, in most cases, are not perpendicular to the scan slices [2] (Fig. 1 A). Hence, they must be corrected to be appropriately used in models.

With an aim to address these literature gaps, our objectives were: i) To develop and validate a method for estimating subject-specific sagittal spinal geometry in different postures (supine, flexion and sitting) from data (vertebral body center (VBC) positions) in a given reference posture (standing) ii) To obtain line-of-actions for two paraspinal muscles-erector spinae and transversospinalis in those postures, and iii) To correct for the cosine between the MRI axial scan plane and dominant fiber line-of-action for muscle parameters (CSA and moment-arm).

METHODS

Imaging

Thoracic Spines of six healthy participants (age 26±6 years, BMI 24±3 kg/m^2) were imaged (0.5T vertical MROpen, Paramed Italy) in four postures (supine, standing, 30° forward flexion, and sitting). VBCs from T1 to T10 were located on sagittal MR images and the intra-rater repeatability was assessed (Fig. 1A). Two muscles— erector spinae and transversospinalis were manually segmented (good/excellent segmentation repeatability [3]) on axial MR images. Muscle parameters, CSA, anterior-posterior (A-P) and medial-lateral (M-L) distances from VBC were computed for each muscle (Fig. 1 D). The unit normal to the MR slice plane was also computed for all postures.

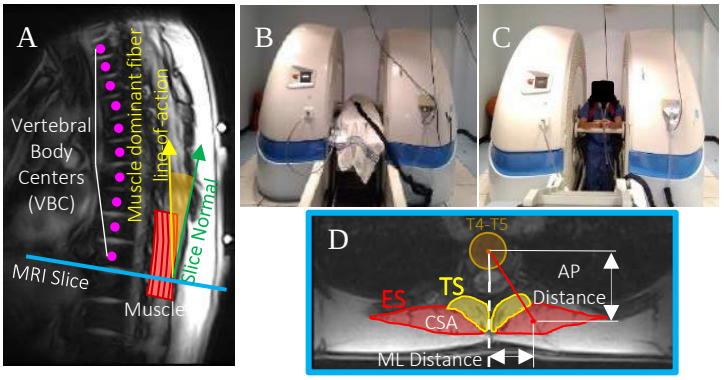

Figure 1: A) Illustration showing direction of muscle line-of-action and scan plane normal. T1 to T10 vertebral body center (VBC) are marked. MROpen image acquisition in B) Supine and C) Standing. D) Illustration to show CSA, anterior-posterior (AP) and mediolateral (ML) distances marked for erector spinae (ES) and transversospinalis (TS) on an axial MR image.

Modelling and Estimation of Sagittal Spine Geometry

Sagittal spine curvature (represented by VBCs) was approximated using a circular arc spline passing through C1, T1, T12 and S1 (Fig. 2 A). The system is constrained such that it has 9 degrees-of-freedom. Assuming the system is hinged at S1, the geometry in any desired posture (supine, flexion, sitting) was be estimated by altering the arc angles, θ (kyphosis and lordosis) and arc lengths (assumed to be constant) of the three segments in the that posture. This data was be obtained from clinical measurements (Cobb Angle), literature and estimations. Furthermore, the position of VBCs in the estimated posture was obtained by normalization with the reference posture (standing).

Validation of the Estimated Spinal Geometry

The VBCs in each estimated posture were rigidly registered to the corresponding MRI data of the thoracic spine, which is the ground truth data, using coherent point drift method [4] (Fig. 2 B).

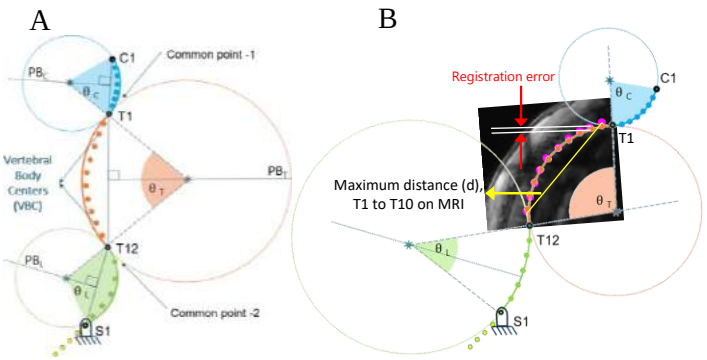

Figure 2: Illustration showing: A) geometric construct of sagittal spinal curvature in the reference posture (standing) B) estimated spine geometry in flexion, rigidly registered to ground truth data (T1 to T10 VBC marked on MRI in flexion) showing registration error. Subscript notations C, T and L refer to cervical, thoracic, and lumbar spine.

Computation of Muscle Line-of-Action and Correction parameter

A generic thoracolumbar model [5] was registered to thus estimated VBCs in different postures in a 3D modelling platform, Artisynth [6]. The dominant muscle fiber line-of-action of erector spinae and transversospinalis for each posture was estimated as the direction vector from the point of origin to insertion. Next, the raw CSA, A-P and M-L distance data obtained from MR images were converted to anatomical CSA and true A-P and M-L distances using the mathematical approach suggested by McGill et al. [7].

RESULTS

Repeatability of Marking T1-T10 VBC on Sagittal MR Images

The intra-rater repeatability for identifying and marking VBCs on MRI scans was found to be excellent (average intraclass correlation coefficient, ICC (3,1) = 0.98).

Goodness of Spinal Posture Estimation

The average maximum registration error between the estimated VBCs and the ground truth data (VBCs marked on MRI) was found to be small (~3.5 mm for supine). The maximum RMSE value for registration (normalized by the maximum distance between T1 and T10 on MR images) was found to be as low as 5.1% (for sitting) (Table. 1).

Table 1: Error assessments (standard deviation) for registration of the VBCs in three estimated postures to corresponding VBCs marked on the sagittal MR images. Max error=Maximum error between corresponding VBCs (mm), Max distance=Distance between two farthest MRI VBC markers (T1 and T10) (mm), RMSE= Root mean square error.

Posture	Max error (mm)	Max distance (d) (mm)	$\frac{\mathbf{RMSE}}{\boldsymbol{D}} * \mathbf{100}$ (%)
Supine	3.5 (0.5)	120.8 (6.7)	2.9 (0.9)
Flexion	3.1 (0.8)	117.8 (9.8)	3.2 (1.3)
Sitting	3.0 (0.5)	111.8 (6.0)	5.1 (1.2)

Corrected Muscle CSA and Distances

The correction factor reduced the muscle parameters (~5% for ES and ~25% for TS) when compared to raw MRI data. While the erector spinae showed most reduction in the flexion, the transversospinalis showed greater decrease in its values for supine (Fig. 3).

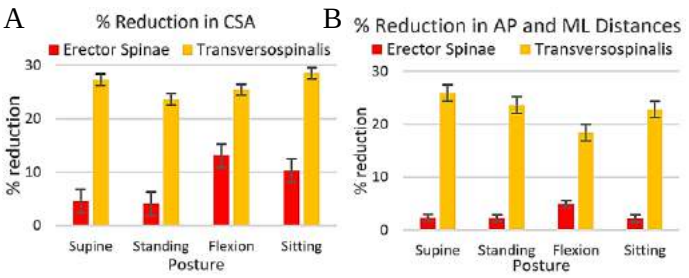

Figure 3: Average (±SD) percentage reduction in magnitudes of A) CSA, B) mean of AP and ML distances, after applying correction factor for MRI slice normal and muscle line-of-action.

DISCUSSION

The spinal curvature, among other factors, is one of the most important parameters for the evaluation of spinal deformities [8]. Although a number of methods exists for quantitative evaluation of sagittal spinal geometry [9], none of these techniques allow for estimations of spinal curvature in different positions from clinically measured parameters (Cobb Angle). Our method is simple, reliable, computationally inexpensive, and easily digitizable for clinical images. Furthermore, the model could be easily modified for different spine geometries by not only changing the number of arcs used to estimate each segment but also the locations of inflection points (T1 and T12 are used in this study). Furthermore, our method could find applications in characterizing spinal deformities not just in the sagittal plane but also in the coronal plane.

Another novelty of this work is reporting trunk muscle properties for postures other than supine. Application of the correction factor demonstrated greater reduction in the parameter values of the transversospinalis than the erector spinae. This is because, transversospinalis is short and obliquely placed to the trunk axis, while the erector spinae, is a long cylindrical muscle spanning several thoracic levels and is usually parallel to the trunk axis in most postures.

Additionally, moment-arm is a sensitive variable in biomechanical models, especially for spinal muscles due to its small magnitude. Small changes in its value could produce large changes in predicted muscle forces. Furthermore, image-based moment-arm data across multiple vertebral levels reported in our study could be used to model the muscle path along the trunk [10]. Overall, our data contributes to the growing literature of trunk geometry evaluation and makes subject-specific biomechanical modelling of the spine clinically more relevant.

ACKNOWLEDGEMENTS

We thank NSERC, CIHR and Medtronic Canada for funding.

REFERENCES

[1] J. Hwang *et al.*, *Ergonomics*, 60(4):577–588,2017
[2] S. M. McGill, *et al*., *Clin. Biomech.*, 8:171–178, 1993
[3] A. Pai S *et al.*, *JOR SPINE*, . 3(3): e1103, 2020
[4] A. Myronenko *et al.*, *IEEE Trans. Pattern Anal. Mach. Intell.*, 32(12):2262–2275, 2010.
[5] A. G. Bruno, *et al.*, *J. Bone Miner. Res.*, 32(6):1282–1290, 2017
[6] J. E. Lloyd, *et al*., *Stud. Mechanobiol. Tissue Eng. Biomater*, 11:355–394, 2012
[7] L. Santaguida, *et al*., *Clin. Biomech.*, 8:171–178, 1993.
[8] S. IA *et al*., *Spine (Phila Pa 1976)*, 19(2):236–248, 1944.
[9] T. Vrtovec, *et al*., *Eur. Spine J.*, 18(5):593–607, 2009
[10] M. J. Jorgensen, *et al*., *Clin. Biomech.*, 16(3):182–193, 2001

LOAD-DEPENDENT MICROSTRUCTURAL AND BIOMECHANICAL PROPERTIES OF PORCINE PULMONARY VALVE CUSPS

Luke T. Hudson (1), Arshid Mir (2), Harold M. Burkhart (3), Chung-Hao Lee (1,4)

(1) Biomechanics and Biomaterials Design Laboratory
School of Aerospace and Mechanical Engineering
The University of Oklahoma
Norman, OK, USA

(2) Department of Pediatric Cardiology
The University of Oklahoma Health Sciences Center
Oklahoma City, OK, USA

(3) Division of Cardiothoracic Surgery
The University of Oklahoma Health Sciences Center
Oklahoma City, OK, USA

(4) Institute of Biomedical Engineering, Science, and Technology (IBEST)
The University of Oklahoma
Norman, OK, USA

INTRODUCTION

The pulmonary valve (PV) anatomically separates the pulmonary artery and the right ventricle, segregating the deoxygenated blood from reaching the pulmonary artery. The PV consists of three cusps attached at the pulmonary root that open and coapt, governing the unidirectional flow of deoxygenated blood into the pulmonary artery, where it can be reoxygenated by the lungs. Collagen, the microstructural component that provides structural integrity to the PV cusps, is vital to tissue's mechanical properties and organ-level function. When the structural integrity of the PV cusps begins to fail (e.g., stenosis), the mechanical properties of the cusps are affected, negating full coaptation, resulting in the retrograde of blood into the right ventricle – a condition known as pulmonic insufficiency. Understanding the relationship between the collagen-dominant microstructure and the tissue mechanics of the PV cusps will not only elucidate the underlying pathology, but also provide the constitutive relations necessary to inform multiscale computational models for improving the treatment of PV disease [1].

Previous investigations of the collagen-dominant microstructure in the PV cusps relied primarily on pressurization systems in conjunction with *destructive* optical imaging techniques [2]. Although these studies yielded valuable relationship between pressure loading and collagen microstructure, those destructive imaging methods require the use of chemical fixatives, limiting their ability to examine the load-dependent collagen fiber architectural changes within *the same tissue specimen*. To overcome this limitation, we employed our in-house opto-mechanical system, capable of observing the realignment and reorientation of collagen fibers under varying biaxial mechanical loads [3], to quantify the load-dependent collagen architecture changes for the PV cusps.

METHODS

Tissue Preparation & Mechanical Testing: Fresh porcine hearts (n=12) were obtained from a local USDA-approved abattoir. Each heart was dissected, and the three PV cusps (i.e., the anterior cusp - *PVAC*, left cusp - *PVLC*, and right cusp- *PVRC*) were extracted. Each extracted cusp was mounted to a commercial biaxial testing system (BioTester – CellScale, Canada) via BioRake tines that penetrate the tissue, creating an effective testing region of 6.5x6.5mm (**Fig. 1a-b**). Fiducial markers were placed on the center region of each tissue specimen to quantify the tissue strain via a digital image correlation (DIC) technique in conjunction with a single bilinear finite element [3]. Pre-conditioning was performed on each specimen with six loading/unloading cycles, prior to biaxial mechanical testing, to return the tissue microstructure to its *in vivo* configuration. After pre-preconditioning, mechanical testing was performed consisting of seven biaxial tension protocols with a target stress of 240 kPa (T_C:T_R=1:1, 1:0.75, 1:0.5, 1:0.25, 0.75:1, 0.5:1, and 0.25:1).

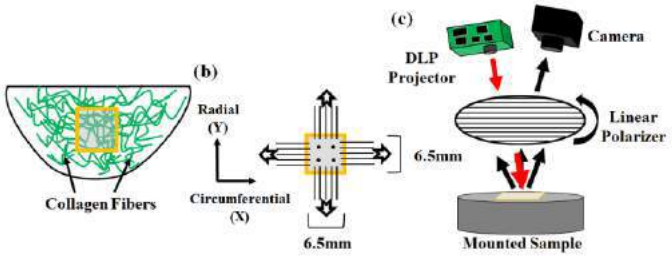

Figure 1. (a) Schematic of a PV cusp, (b) mounted of the tissue to the biaxial mechanical testing system, and (c) examined quantifications of collagen fiber architecture via our in-house collagen imaging system.

pSFDI-based Collagen Microstructural Quantification: Following our developed protocol [3], collagen fiber quantifications were performed utilizing our in-house polarized spatial frequency domain imaging (pSFDI) device integrated with biaxial testing (**Fig. 1c**). In

brief, each tissue was imaged at mounting, after precondition, and at the intermediate and peak loading points of various biaxial tension protocols. Each specimen was imaged to capture the reflected light intensity responses through a rotating linear polarizer (Thorlabs Inc., Newton, NJ, US) at 37 distinct polarization states ranging from 0° to 180°, with a 5° step size. Imaging processing permits the ability to observe the collagen fiber orientation angle θ_{fiber} and the degree of optical anisotropy (DOA) – a metric utilized to quantify the alignment of the collagen fiber architecture – at each individual observed pixel.

RESULTS

Biaxial Mechanical Properties: A non-linear stress-strain relationship was observed for each specimen, exhibiting a low-stress toe region that transitions into high-stress, stiffer region. The high-stress portion of this relationship occurred at a larger stretch for the radial direction then that of the circumferential direction, highlighting the mechanical directional-dependence of collagen fiber architecture in the PV cusps (**Fig. 2a-b)**. For all equibiaxial and non-equibiaxial mechanical loading protocols, the PV cusps displayed greater extensibility in the radial direction, with a much stiffer response shown by the circumferential direction, previously observed heart valve tissues (**Fig. 2c-d**) [3].

Load-Dependent Changes in Collagen Fiber Architecture: Using pSFDI, microstructural reorientation was observed, which exhibits initial collagen fiber orientation in the *radial* direction in the center of the tissue, while displaying *circumferentially*-dominant fibers towards the bottom left of the specimen (**Fig. 2a**).

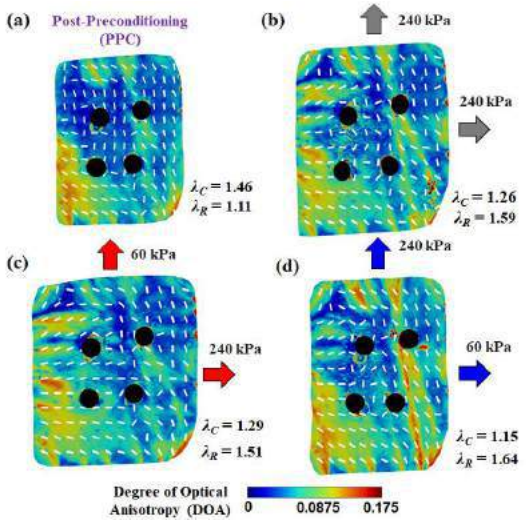

Figure 2. Quantified collagen fiber orientation angle θ_{fiber} (denoted by the white vector plots) and mechanical stretch λ, and degree of optical anisotropy (DOA): **(a)** post preconditioning, and **(b-d)** under various biaxial tensions.

Specifically, under equibiaxial loading, the collagen fiber orientation shifted by 25.9% towards the *radial* direction (**Fig. 2b, Table 1**), whereas under circumferentially-dominant loading, the collagen fiber architecture in the center of tissue shifted in the *circumferential* direction by 28.3% (**Fig. 2c, Table 1**), whereas the radially-dominant loading resulted in a 15.2% shift towards the dominant loading, i.e., *radial*, direction (**Fig. 2d, Table 1**).

Table 1. Percentage changes in the quantified collagen fiber orientation (mean ± SEM) between the mounting configuration and various biaxial loading points for a representative PVLC specimen.

Mount.	PPC	T_C:T_R=0.25:1	T_C:T_R=1:0.25	T_C:T_R=1:1
—	12.5±0.1%	15.2±0.08%	28.3±0.1%	25.9±0.09%

Collagen Fiber Realignment under Equibiaxial Tension: Increasing membrane tension exhibited on the tissue in the equibiaxial state resulted in greater alignment among the collagen fiber architectures. When observing the alignment of the collagen fibers within the mounted configuration (Loading Point 1) yielded DOA values ranging from 0 to 0.04 (**Fig. 3a**). As the membrane tension applied to the tissue increases to $0.3T_{Max}$, greater collagen fiber alignment occurs with DOA values within a range of 0.0875 and 0.1 (**Fig. 3b**). The maximum membrane tension applied (T_{Max}) allowed greater alignment across the entire tissue, although yielding similar DOA values to Loading Point 2 (**Fig. 3c**).

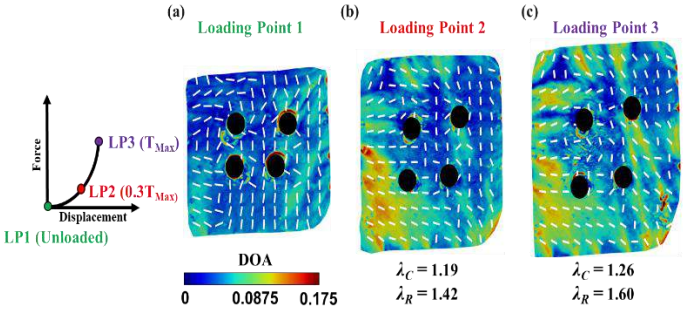

Figure 3. Measured collagen fiber orientation angle (θ_{fiber}) and DOA: (a) mounting configuration, (b) $0.3T_{Max}$ tension, and (c) T_{Max} subjected to the same specimen along the force-displacement curve.

DISCUSSION

This investigation, which is the *first of its kind*, further elucidates the interconnected relationship between the tissue-level mechanics and the load-dependent collagen fiber architecture within PV cusps. Previous studies have relied on destructive imaging techniques to understand the dynamic collagen fiber microstructure within PV specimens, requiring the fixation of tissues under a pressurized load. This approach offers the ability to observe the realignment and reorientation of the collagen-dominant microstructure within the *same specimen*, and allows a systematic examination of the trends across multiple specimens. Employing a non-destructive, opto-mechanical approach allows for the dynamic microstructural changes to be captured within the same tissue, providing novel information regarding the tissue microstructure's ability to adapt to various mechanically-loaded states.

The microstructural-mechanical relationship observed in this study provides unique information that can be implemented into fiber-based constitutive models, establishing the link between local microstructural changes and bulk-tissue mechanical loading [4]. These constitutive models rely on experimental observation that are collected due to the large variations in pressure exhibited on the PV cusps during the cardiac cycle. This combined approach to inform computational models permits future investigations of collagen microstructures of other heart valve, improving the understanding of the collagen-dominant microstructure in response to physiological loading. These potential future computational developments can help elucidate disease pathology and improve the understanding of tissue-engineered prostheses [5].

ACKNOWLEDGEMENTS

This work was supported by the American Heart Association Scientist Development Grant (16SDG27760143), and the Presbyterian Health Foundation Team Science Grant.

REFERENCES

[1] Shen, X *et al*., *PLoS ONE*., 13(6):0199390, 2018.
[2] Joyce, EM *et al*., *Ann. Thorac. Surg*., 87:1240-1249, 2009.
[3] Laurence, DW *et al*., *J Mech. Behav. Biomed.*, 83:16-27, 2019
[4] Jett, SJ *et al*., *Acta Biomater*., 102:149-168, 2020.
[5] Luo, L. *et al*., *Tissue Eng. Part A.*, 2963-2974, 2014.

BALLOON FORMING MACHINE FOR CUSTOMIZING TREATMENT OF CORONARY ARTERY DISEASE

Kaitlyn M. Elmer (1), Maxwell J. Bean (1), Barry F. Uretsky (2), Morten Ø. Jensen (1)

(1) Department of Biomedical Engineering
University of Arkansas
Fayetteville, AR, USA

(2) Department of Internal Medicine
University of Arkansas for Medical Sciences
Little Rock, AR, USA

INTRODUCTION

Coronary artery disease (CAD) often manifests as lesions in the vessel that obstruct blood flow. Percutaneous treatments of CAD involve balloon angioplasty in a predilatation procedure, often followed by stenting of the vessel. Bifurcation lesions, which make up 20% of all percutaneous treatments, are highly complex, and current treatments may cause restenosis [1-3].

Current efforts in improving treatment is including development of tapered balloons in bifurcation lesions [4]. However, tapered balloons are not readily available, and any customization of these balloons are expensive and time consuming to procure. Therefore, the ability to manufacture custom balloon shapes quickly and relatively inexpensively at regional facilities or central locations with access to fast shipping options is needed. In this study, a custom balloon forming machine was developed for immediate and inexpensive balloon creation.

METHODS

The balloon forming machine uses a burst of pressurized air to expand a sealed section of tubing to the desired balloon shape. The sealed section of tubing is in CAD treatment device industry referred to as a "parison".

Parisons were cut to 120mm in length from polyethylene terephthalate (PET) tubing with 0.132" OD and 0.1" ID. Cyanoacrylate glue was used to attach a luer lock to one end of the parison and to seal the other end.

The balloon forming machine's main structure was two halves of an aluminum block (50mm x 50mm x 100mm) that formed a housing for a custom cylindrical mold. Four additional holes were bored to allow space for four 250W cartridge heaters. A sheet of carbon insulation surrounded the block, and a C-clamp was used to hold the two halves of the block together.

The four cartridge heaters were attached to a custom 120V proportional-integral-derivative (PID) controller box using a MyPin TA4 PID (Mypin Electrical Co., Zhongshan, Guangdong, China) to control temperature, with one cartridge heater also containing a thermocouple for sensing temperature. The temperature was assumed to be similar in all heating rods. The custom cylindrical mold was 3-D printed from stereolithography resin to form the desired balloon contour. Two stoppers were created from stereolithography resin and were inserted in the mold to form the desired shape of the balloon ends. The schematic outline of the balloon forming machine is shown in Figure 1.

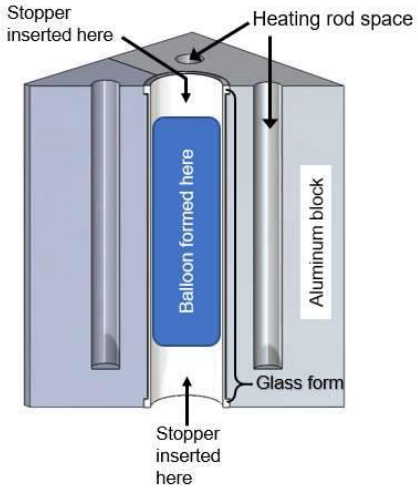

Figure 1: Cross sectional schematic outline of balloon forming machine

To form the balloons, the machine was assembled as shown in Figure 2.

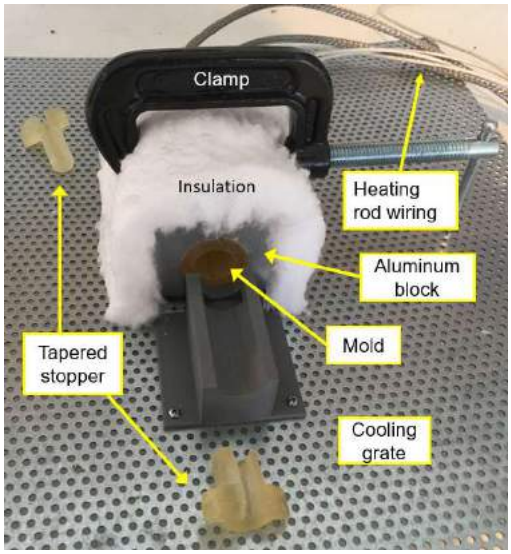

Figure 2: Complete balloon forming machine showing the tapered stoppers that fit inside the glass form.

The system was heated to the desired temperature, and the temperature of the inside wall of the glass form was confirmed with a separate thermometer. The temperature of the interior glass form wall was typically 10-15 C below the temperature settings for the heating rods. Next, the parison was attached to an air compressor via luer lock. The stoppers were inserted into both ends of the glass form mold followed by the insertion of the parison. The parison was heated for 30 seconds, then the air lock on the air compressor was manually opened to form the balloon by inflating the parison. Once inflated, the air lock was closed, and the newly formed balloon was removed from the balloon forming machine and allowed to cool in room temperature air. Additionally, the stoppers were removed and dipped in water to cool before reinserting and forming the next balloon.

In this study, N=104 balloons were made using variations of temperature and pressure. Heating time was kept constant at 30 seconds, and expansion time was 1-2 seconds; both being similar to values indicated in the literature and preliminary testing [5]. Pressure was varied between 55-115 PSI and temperature was in groups of 100 C, 110 C, 120 C, and 130 C.

For ease of handling, balloon dimensions used were much larger than balloons typically used in coronary arteries. The target size for these larger balloons was a diameter of 16mm and a length of 53mm. These values were chosen based on industry balloons created at similar size and shape (10004013EB, Nordson Medical, Westlake, Ohio). Additionally double wall thickness, which is the thickness of the deflated balloon, was targeted to be 0.051-0.061 mm (2-2.4mil). A balloon was considered successful if it exhibited no punctures, was within 20% of intended diameter, and length was greater than 45mm, the length of stent models being used in the lab. An additional criterion called "skew ratio" was created to account for bowing effects observed in balloon formation. The skew ratio calculation was conducted by photographing the balloon with any bowing effect clearly shown. Parallel lines were added to form a box around the balloon. The skew diameter was the width of the box, and the skew ratio is the comparison of the skew diameter to the average diameter of the balloon.

RESULTS

An example of a successful balloon creation is shown in Figure 3.

Figure 3: Completed balloon

104 parisons were used in this study. From the balloons created, a chi-squared test was conducted to determine if pressure, temperature, or a combination of both were significant factors towards balloon creation success. The results from the test are shown in Table 1.

Table 1: Results of Chi-Square Test

Source	G^2	P-value
Temperature	0.479	0.489
Pressure	4.545	0.033*
Temperature and Pressure	7.096	0.008*

A p-value of 0.05 or lower was considered significant. All tests were run using JMP (SAS Institute, Cary, NC).

Pressure alone and pressure and temperature in combination were identified as significant factors towards balloon creation success with p-values less than 0.05. Temperature alone is not a significant factor.

DISCUSSION

For this study, a custom balloon forming machine was created. The balloon forming machine was tested and demonstrates the ability to create viable balloons. Pressure and temperature were both shown to impact balloon creation success, showing that both factors need careful consideration. Temperature alone was not a significant variable for balloon success, which is perhaps due to the temperature chosen being just above glass transition temperature of PET plastic while remaining well below the melting point [6]. The significance of pressure alone seems to correspond to successful balloon creation occurring between 60-85 PSI, though pressures between 55-115 PSI were tested. The significance of both combined indicates an interdependence between pressure and temperature for successful balloon creation.

Future work will involve further optimization of the balloon forming machine. Stretching of balloons during creation is one technique used in industry, which may contribute towards the creation of thin-walled balloons. Additionally, automating parts of the balloon creation process may contribute to less variability in balloon creation.

ACKNOWLEDGEMENTS

Special acknowledgement to the American Heart Association in supporting the funding for this research.

REFERENCES

[1] Lassen, J L et al., *EuroIntervention,* 13: 1540-53, 2018.
[2] Rizik, D et al., *J Invasive Cardiology* 20: 82-90, 2008.
[3] Timmins, L et al., *Lab Invest* 91: 955-67, 2011.
[4] Uretsky, B F (2014) Apparatus and method for treatment of bifurcation lesions. In S. United (Ed.): Barry F. Uretsky
[5] Lalli, D (2006) Cycle to cycle control of the angioplasty balloon creation process. *McGill University, Montreal, Canada.*
[6] Klein P. *Synthesis Lectures on Materials Engineering*. 2009;1(1):1-97.

ANALYSIS of HEMODYNAMICS in ANEURYSM BLEBS with THIN and ATHEROSCLEROTIC WALLS

Seyedeh Fatemeh Salimi Ashkezari (1), Fernando Mut (1), Juan R. Cebral (1)

(1) Bioengineering Department
George Mason University
Fairfax, VA, USA

INTRODUCTION

Many intracranial aneurysms (IAs) have well-defined secondary structures or daughter sacs known as blebs [1]. The presence of blebs is considered a risk factor for rupture [2] and is one of the few aneurysm-specific factors used in aneurysm scoring scales [3, 4].

Blebs can have an effect on the wall stress as well as the local hemodynamics. Mechanisms responsible for bleb development and evolution are not fully understood. Previous studies have shown that aneurysm walls can be extremely heterogeneous. They can have thin translucent regions or thick atherosclerotic walls [5, 6].They can have collagen fiber distributions with unidirectional or bidirectional orientations, and thick wavy fibers or thin fragmented fibers [7]. All of these structural characteristics can affect the strength of the wall and the distribution of intramural stresses [7].

In this study we investigated the relationship between aneurysm blebs with different wall characteristics and their local hemodynamic environment.

METHODS

A total of 32 intracranial aneurysms harboring 41 blebs treated with microsurgical clipping and with available intra-operative videos where the blebs were visible were selected from our database [1]. All these aneurysms were imaged prior to surgery with 3D rotational angiography (3DRA) or computed tomographic angiography (CTA).

Using previously described methods [8], patient-specific vascular models were constructed from 3D images. Blebs have been visually identified and interactively marked on the vascular models for all aneurysms in this database as detailed in [1].

In order to characterize the local hemodynamic conditions at bleb sites prior to their formation, the bleb regions were first projected to the model with virtually removed blebs and then hemodynamic variables were calculated over these regions.

Intra-operative videos were inspected to characterize bleb walls. Blebs that had been previously marked on the 3D vascular models were visually identified in the intra-operative videos. These blebs were classified as: (1) ‘thin’ translucent walls as those with a red appearance, (2) ‘atherosclerotic’ walls as those with a white (hyperplastic) or yellow (fatty) appearance, or (3) ‘unremarkable’ walls as those with a pinkish coloration similar to normal arteries [6].

The blebs identified in each aneurysm were characterized by computing several variables related to strength of the flow stream within the bleb and distribution (magnitude, heterogeneity, oscillations) of the wall shear stress (WSS) distribution over the bleb surface. Hemodynamic variables were computed using the same tools and techniques previously used to characterize the hemodynamics in the entire aneurysm [9].

Hemodynamic characteristics of 'thin' and 'atherosclerotic' blebs were compared using the non-parametric two-sample unpaired Wilcoxon (Mann–Whitney) test. For this purpose, bleb hemodynamic variables were first normalized with their average value over the entire aneurysm. All statistical analyses were performed in R, and differences were considered significant if $P<0.05$.

RESULTS

Average flow characteristics of ‘thin’ and ‘atherosclerotic’ blebs are presented and compared in table 1. This corresponds to 22 thin and 19 atherosclerotic blebs visible in intra-operative videos. Based on these results, maximum oscillatory shear index (OSI) tended to be larger in atherosclerotic blebs ($P=0.0941$) but this association was not significant.

Table 1: Comparison of (normalized) hemodynamic characteristics (prior to virtual bleb removal) of thin (red) blebs and atherosclerotic (white/yellow) blebs.

Characteristic	Variable	Bleb Wall Type		P value
		Thin (Red)	Atherosclerotic (White/Yellow)	
Flow Strength	VEL	0.46 ± 0.41	0.36 ± 0.41	0.3572
	VO	0.89 ± 0.64	0.57 ± 0.54	0.1481
	SR	1.02 ± 0.72	0.65 ± 0.57	0.1271
WSS Distribution	WSS	0.63 ± 0.47	0.47 ± 0.54	0.1557
	OSI(max)	0.38 ± 0.33	0.54 ± 0.29	0.0941
	RRT	1.84 ± 1.64	2.45 ± 1.42	0.1026
	WSSGRAD	0.93 ± 0.65	0.66 ± 0.40	0.1801
	GON	0.99 ± 0.54	0.92 ± 0.41	0.6321

In order to further explore this trend, a subset of aneurysms with multiple blebs of both kinds, thin and atherosclerotic (n=8), was analyzed by computing the ratio of values of thin over atherosclerotic blebs of the same aneurysm, and compared them against one using one-sample Wilcoxon tests. This analysis as presented in table 2 confirmed that thin blebs had lower OSI (ratio OSI=0.38, P=0.0156) than atherosclerotic blebs of the same aneurysm. The WSS tended to be higher (ratio WSS=4.74, P=0.0781) but this association was not significant. An illustrative example is presented in figure 1.

Table 2: Ratio of hemodynamic parameters of thin over atherosclerotic blebs of the same aneurysm. Values are mean ± standard deviation. Significant differences are marked with a "*".

Characteristic	Variable	Ratio (thin/atherosclerotic)	P value
Flow Strength	VEL	4.42 ± 7.64	0.4609
	VO	3.96 ± 4.31	0.1094
	SR	3.78 ± 4.04	0.1094
WSS Distribution	WSS	4.74 ± 5.71	0.0781
	OSI(max)	0.38 ± 0.39	0.0156*
	RRT	0.98 ± 1.57	0.7422
	WSSGRAD	4.40 ± 4.38	0.1094
	GON	1.40 ± 1.95	0.1484

DISCUSSION

Previous observations have led to the common belief that blebs form in regions of slow recirculating flow and that aneurysms rupture at blebs [10]. Conversely, other studies have proposed that blebs could also form at or in the vicinity of flow impingement regions associated with localized high WSS [11]. Moreover, a recent study suggested that blebs are more common in aneurysms exposed to flow conditions characterized by stronger flows and higher WSS compared with aneurysms where blebs did not form [1].

However, in all previous studies, all blebs have been grouped together without distinguishing different kinds of blebs. Therefore, while the conclusions of these studies as well as the common beliefs about blebs may be true for some blebs, they may not be true in general.

Our study has shown blebs with different wall characteristics as reflected in their visual appearance; thin translucent blebs seen red in videos, and atherosclerotic, usually thick-walled, blebs seen white or yellow in videos. The different visual appearances suggest different remodeling processes have led to distinct local wall structures.

In addition, our study found thin red blebs may form in regions exposed to strong flows, flow impingement, and large WSS spatial gradients, while atherosclerotic blebs may form in regions of slow flow and low and oscillatory WSS.

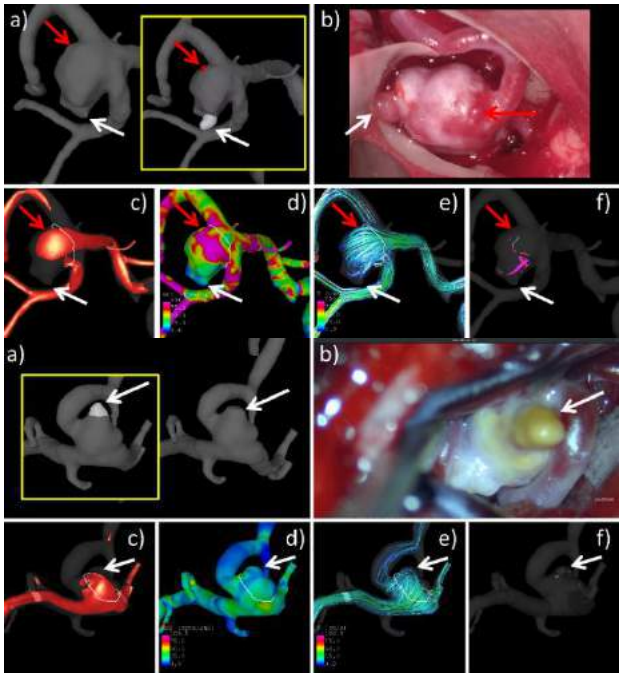

Figure 1. Example of an aneurysm (Top): with a thin bleb (red) and a slightly hyperplastic (white) bleb. (Bottom): with an atherosclerotic (white) bleb. a) anatomical model with blebs removed, b) blebs observed in intra-operative video, c) visualization of inflow stream, d) WSS distribution, e) flow pattern visualized with streamlines, and f) flow structure visualized with vortex corelines. All flow visualizations correspond to peak systole. Arrows point to the regions of bleb formation.

The results and observations of our study suggest that different mechanisms of wall remodeling and degradation in response to locally high- and low-flow conditions may be at play simultaneously in intracranial aneurysms and may be responsible for the development and evolution of blebs with different wall structures.

The trends and hypotheses proposed in this study should be confirmed and further studied with larger datasets. Nevertheless, it is important to highlight the main message of this study, namely that not all blebs are the same and their distinguishing characteristics should be taken into consideration when studying the mechanisms of wall degeneration and when evaluating aneurysms clinically to decide on immediate treatment or conservative observation.

REFERENCES

[1] Salimi Ashkezari SF, et al., *J Neurointerv Surg*, Jul 17 2020.
[2] Lindgren AE, et al., *Stroke*, 47:1219–1226, 2016.
[3] Greving JP, et al., *Lancet Neurol*, 13:59–66, 2014.
[4] Etminan N, et al., *Neurology*, 85:881–889, 2015.
[5] Furukawa K, et al. *PLoS One*, 13:e0191287, 2018.
[6] Cebral JR, et al. *AJNR Am J Neuroradiol*, 40:510–516, 2019.
[7] Robertson AM, et al. *Ann Biomed Eng*, 43:1502–1515, 2015.
[8] Cebral JR, et al., *IEEE Trans Med Imaging*, 24:457–467, 2005.
[9] Mut F, et al. *Int J Numer Method Biomed Eng*, 27:822–839, 2011.
[10] Challa V, et al. *Neurol Res*, 29:569–577, 2007.
[11] Cebral JR, et al. *AJNR Am J Neuroradiol*, 31:304–310, 2010.

COMPUTER-AIDED MOLECULAR DESIGN OF WATER COMPATIBLE MONOMER FOR DENTAL APPLICATION

Yonas. Rufael (1), Ruben. Molina (1), Farhana. Abedin (2)

(1) Electrical & Computer Engineering
California State Polytechnic University
Pomona, California, USA

(2) Electromechanical Engineering Technology
California State Polytechnic University
Pomona, California, USA

INTRODUCTION

Past studies have shown that dentin/adhesive interface is the most vulnerable region for the failure of dental composite restorations [1]. Phase separation, sub-optimal polymerization, water sorption, diffusion of bacteria, and hydrolytic/enzymatic degradation have all been attributed to the failure of the dental adhesive [2]. As the adhesive infiltrates through the wet dentin, it undergoes phase separation into hydrophobic and hydrophilic-rich phases [2]. The cross-linker in the dental adhesive which is hydrophobic in nature accumulates into the hydrophobic-rich phase. This indicates that the hydrophilic-rich phase of the adhesive possesses poor cross-linking density. Moreover, the photosensitizer in the adhesive, camphorquinone is also hydrophobic in nature and resides mostly into the hydrophobic-rich phase, causing poor photopolymerization of this phase [3]. Sub-optimal polymerization and poor cross-linking density in this phase accelerates water sorption and diffusion of bacteria/enzyme which ultimately leads to the failure of this region. It has been proposed that incorporation of water-compatible cross-linker in addition to the current popular hydrophobic cross-linker, will improve the clinical lifetime of composite restorations significantly [3].

In this study, computer-aided molecular design (CAMD) has been employed to design candidate water-compatible crosslinkers for dental adhesive application. The properties based on which the cross-linker was designed were octanol water partition coefficient and degree of conversion.

Computer-aided molecular design (CAMD) utilizes quantitative structure property relationships (QSPRs) and optimization algorithm to propose candidate molecules with optimal properties. QSPRs are mathematical relationships between molecular descriptors and properties [4]. CAMD consists of forward and inverse problems. In the forward problem, a model building set is created which consists of relevant molecules, and properties of interest are determined for these molecules. The structure of the molecules in the model building set is then described quantitatively using the descriptors. Quantitative structure property relationships (QSPRs) are determined by linear regression. In the inverse problem, molecule groups are created which have both ends open for bonding. These groups can be put together to form new molecules. The structure of the newly formed molecule can be optimized for target properties using stochastic optimization algorithm. This method has been used successfully in the past to design hydrophilic photosensitizer for dental application, solvents, catalysts, excipients, polymer etc. [4]. CAMD is a time efficient and inexpensive method which can be used to understand molecular structures with optimal properties for an application.

METHODS

Octanol water partition coefficient and degree of conversion were the properties of interest. Octanol water partition coefficient was selected to tune the hydrophilicity of the cross-linker, and the degree of conversion ensured that the polymerization was substantial giving mechanical strength and providing an intact barrier at the interface. Table 1 and 2 exhibits the cross-linkers that formed the model building set for the octanol water partition coefficient and degree of conversion respectively. The experimental values were obtained from literature. Topological descriptors, connectivity and valence connectivity indices were used to quantitatively describe the molecules in the model building set. Correlations (QSPRs) between the topological descriptors and the properties were obtained by linear regression using the leaps package in the statistical software R. For the degree of conversion connectivity and valence connectivity indices only until first order were used to carry out the regression. The linear regression model with high correlation coefficient was chosen for each property. The predictability of each

selected model was studied by the leave-one-out method. Cross-validation was carried out using the DAAG package in the statistical software R. The predictive squared correlation, Q^2 was calculated to understand the predictive ability of the selected models.

Table 1: Crosslinker molecules in the model building set for logP

Crosslinker	logP	Reference
Tetraethylene glycol diacrylate (TTEGDA)	0.484	[5]
Tryethylene glycol diacrylate (TREGDA)	0.7	[5]
Diethylene glycol dimethacrylate (DEGDMA)	0.81	[6]
Diethylene glycol diacrylate (DEGDA)	0.84	[5]
1,3-propanediol diacrylate (PDDA)	0.946	[5]
Triethylene Glycoldimethacrylate (TEGDMA)	0.96	[7]
Pentaerythritol tetra acrylate (PETA)	2.227	[5]
Neopentyl glycol diacrylate (NPGDA)	2.5	[5]
Hexamethylene glycol diacrylate (HMGDA)	3.08	[5]
(1-methylethylidene) bis (4,1-phenyleneoxy) (1-methyl-2,1-ethanediyl) diacrylate (XDA)	6.1	[5]

Molecular groups with both ends open for bonding were generated based on the molecules in the model building set. These formed the building blocks for generating new molecules. A maximum of six groups were chosen to generate a crosslinker molecule from 42 groups. Properties of the newly generated molecules were determined from the QSPRs. Candidate crosslinker molecule with properties close to the target values were obtained by using the stochastic optimization algorithm, Tabu search. The objective function minimizes the difference between the target property value and that obtained from the corresponding QSPR. Optimization framework proposed by Roughton et al. was modified to perform this task [4]. The optimization formulation is given by the equations below:

$$Minimize\ s = \sum_M \frac{1}{P_M^{Scale}} \left| P_M - P_M^{Target} \right| \quad (1)$$

$$P_M = f_M(\chi) \quad (2)$$

$$\chi = g(a_{i,j}, w_i) \quad (3)$$

$$h_c(a_{i,j}, w_i) \geq 0 \quad (4)$$

Where P_M is the QSPR for M^{th} property, $f_M(\chi)$ is the function to calculate descriptors, χ are the descriptors from the function g, $a_{i,j}$ and w_i are adjacency matrix and identity vector, h_c is structural constraint, P_M^{Target} is the target value of the M^{th} property, P_M^{Scale} is the scaling factor for the M^{th} property, s is the objective function

RESULTS

Equations 5 and 6 exhibits the QSPR for the properties logP and degree of conversion (DC) respectively. The correlation coefficient (R^2) and the predictive correlation coefficient (Q^2) both were greater than 0.95 for logP and DC. Therefore, both the experimental data have a good fit with the respective model, and both have a good predictive ability. The structure of two candidate crosslinker from CAMD is shown in Figure 1. Table 3 summarizes the target values of the properties and the corresponding values for the candidate molecules. It can be seen that the new molecules possessed properties very close to the target values. The logP of the candidate molecules was much lower than that for BisGMA, indicating that these candidate molecules were much more hydrophilic in nature compared to BisGMA. These crosslinkers have approximately 80% DC, showing that they can undergo substantial photopolymerization.

$$\log P = 3.7643 - 1.4099(^1\chi) + 5.4157(^3\chi^v) \quad (5)$$

$$DC = 79.31366 - 0.57471(^1\chi) \quad (6)$$

Table 2: Crosslinker molecules in the model building set for degree of conversion (DC)

Crosslinker	DC	Reference
Urethane dimethacrylate (UDMA)	70.9	[8]
Triethyleneglycol dimethacrylate (TEGDMA)	74.4	[8]
Trimethylol-propane mono allyl ether dimethacrylate (TMPEDMA)	72.6	[8]
1,1,1-tri-[4-(methacryloxyethylaminocarbonyloxy)-phenyl]ethane (MPE)	64	[8]
2,2-bis[4(2-hydroxy-3-methacryloyloxy-propyloxy)-phenyl] (BisGMA)	69.3	[8]

Table 3: Properties of the candidate water-compatible crosslinker

	log P	DC	Objective value
Target	0.80	80%	0.000
Candidate 1	0.80	76%	0.052
Candidate 2	0.76	76%	0.067

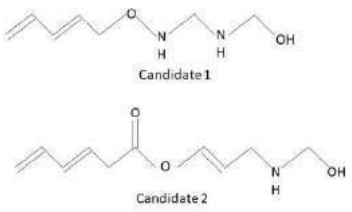

Figure 1. Structure of two candidate crosslinkers

DISCUSSION

Local optimal solutions were obtained by solving the optimization problem related to the structure of dental crosslinkers by using Tabu Search. Molecular structure of two best solutions are proposed here. Both structures have secondary amine group in addition to -C-O-C-. Since both candidates have low octanol water partition coefficient compared to BisGMA they will accumulate in the hydrophilic-rich phase of the dental adhesive in higher concentration, enhancing the crosslinking density. This will reduce the detrimental impact of degradation, water sorption etc., and will improve the clinical lifetime of dental restorations significantly.

ACKNOWLEDGEMENTS

This study was supported by U.S. Department of Education, Title V program.

REFERENCES

[1] Spencer et al., *Ann Biomed Eng*, 38:1989-2003, 2010.
[2] Abedin et al., *Acta Biomater*, 10: 3038-3047, 2014.
[3] Abedin et al., *J Dent*, 99: 103405-103413, 2020.
[4] Roughton et al., *Comput. Chem. Eng.*, 36: 208-216, 2012.
[5] Edelbach et al., *Phy. Chem. Chem. Phy.*, 2: 1763-1771, 2000.
[6] NCBI, https://pubchem.ncbi.nlm.nih.gov/compound/Diethylene-glycol-dimethacrylate, Retrieved 2018, 2021.
[7] Fujisawa et al., *J. Biomed. Mater. Res.*, 15: 787-793, 1981.
[8] Eslick et al., *KU*, 1-47, 2009.

TIME COURSE OF THE CUMULATIVE STRAIN DAMAGE MEASURE FOR FRONTAL AND LATERAL IMPACTS

Tyler F. Rooks, John Humm, Jamie L. Baisden, Narayan Yoganandan

(1) Department of Neurosurgery
Medical College of Wisconsin
8701 Watertown Plank Road
Milwaukee, WI 53226

INTRODUCTION

The Cumulative Strain Damage Measure (CSDM) is one of the most reported and widely used brain injury metrics based on results from computational models. The CSDM metric was theorized as a metric for brain injury in the mid 1990s by Bandak and Dimasi [1], [2]. The CSDM is commonly reported as a peak scalar value with no information relating to the spatial or temporal accumulation of strain resulting from linear and angular kinematics of the head. Similarly, the Maximum Principal Strain (MPS) is reported as a scalar peak value rather than describing the spatial and temporal details of strain accumulation in the brain [3], [4]. Alternative brain injury metrics focus on the product of maximum principal strain and strain rate or more localized axonal strains [5]. None of the above metrics account for the spatial and temporal accumulation of strain in the brain resulting from the linear and angular head kinematics. The purpose of this study was to describe preliminary efforts to understand the spatial and temporal accumulation of strain in the brain by investigating the time-history of CSDM response for anatomical regions specified in two finite element models of the brain.

METHODS

Computational simulations were performed using both the Simulated Injury Monitor (SIMon) head model and version 5 of the Global Human Body Model Consortium (GHBMCv5) head and neck [3], [6]. The SIMon model is symmetric about the midsagittal plane and includes deformable solid elements for the left and right cerebrum, cerebellum, brain stem, ventricles, and cerebral spinal fluid. The GHBMCv5 model is symmetric about the midsagittal plane and includes deformable solid elements for the left and right cerebrum, cerebellum, lateral ventr[7]icles, corpus callosum, thalamus, and brain stem. The cerebrum parts for the GHBMCv5 are further divided into gray and white matter (Figure 1). The GHBMCv5 model is generally stiffer than the SIMon model (Table 1).

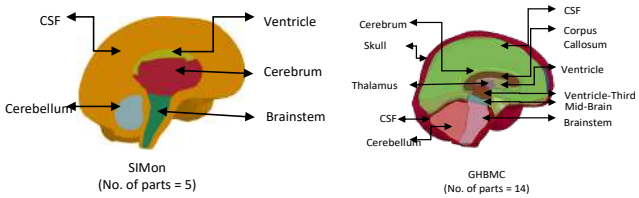

Figure 1: Model overview of the SIMon (left) and GHBMCv5 (right) computational models.

Table 1: Summary of computational model material properties.

	Density (kg/m^3)	Bulk Modulus (GPa)	Go (GPa)	Ginf (GPa)	beta
SIMon*	1040	0.558	1.7e-6	9.3e-7	16.95
GHBMCv5*	1060	2.19	6e-6 to 1.2e-5	1.2e-6 to 2.4e-6	0.0125

*** Model material properties reported for deformable regions of interest. GHBMCv5 shear modulus reported as a range of values for multiple regions.**

Both models were run using LS-DYNA (Livermore Software Technology Corporation, Livermore, CA). CSDM was calculated as the volume fraction of elements within each subpart exceeding a specified strain threshold. For the present analysis, the CSDM threshold was 0.15.

CSDM(15) has been used to validate the second generation SIMon Model. The CSDM was calculated (eq. 1) for each part in the modified model and the original model. Linear and rotational accelerations from experiments were applied at the head center of gravity.

$$CSDM = \frac{Volume\ of\ elements\ >\ Strain\ Threshold}{Total\ Volume} \quad (1)$$

Experimental tests were performed with a rigid arm pendulum striking a helmeted head-neck system. The headform used for all tests was the Facial and Ocular CountermeasUres for Safety (FOCUS) headform [7]. The FOCUS headform is an anthropomorphic test device (ATD) based on anthropometry representative of male military aviators. The FOCUS headform was mounted to a H-III neck and fitted with an Advanced Combat Helmet (ACH) for all tests. Care was taken to ensure that the helmet's bottom rim (near the earcup) was parallel with the Frankfurt plane and was symmetric about the midsagittal plane.. The Frankfurt plane of the head was maintained in a horizontal position for all tests. Impacts from tests conducted at two sites around the helmet, front and left side, are reported for an impact velocity of 6 m/s.

RESULTS

The peak CSDM(15) for the whole brain occurs well after the impact event, indicating that the modeled brain response is slower developing than the impact. CSDM(15) was negligible at the time of the peak resultant acceleration (Table 2) while it reaches between 20% (front impacts) and 40% (side impacts) of the maximum CSDM(15) by the time the rotational velocity peaks.

Table 2: CSDM(15) at peak resultant acceleration (PRA) and peak rotational velocity (PRV) as a percentage of the maximum CSDM(15).

	%Max CSDM(15) at PRA		%Max CSDM(15) at PRV*		Maximum CSDM(15)	
	SIMon	GHBMC	SIMon	GHBMC	SIMon	GHBMC
Front	0%	0%	17%	12%	0.247	0.319
Side	1%	0%	39%	34%	0.399	0.334

*** PRV is reported about Y-axis for front impacts and X-axis for side impacts**

In addition to observing that the whole brain CSDM(15) occurs well after the peak resultant acceleration and peak rotational velocity peak, it was seen in the GHBMCv5 model that the accumulation of strain occurs at different time scales depending on the depth of the brain structures (Figure 2).

DISCUSSION

The present study showed the temporal and spatial brain strain development using two computational models. Both models show similar spatial and temporal strain responses; however, the anatomical accuracy and detail limited the number of additional analyses that could be completed.

The accumulation of strain in different brain regions over time is one potential method to understand further the effects of head impact exposure and the potential effectiveness of protective gear (e.g., helmets). Injury response is dependent on the time of exposure, as evidenced by the incorporation of airbags in motor vehicles reducing the injury rate by lengthening the exposure.

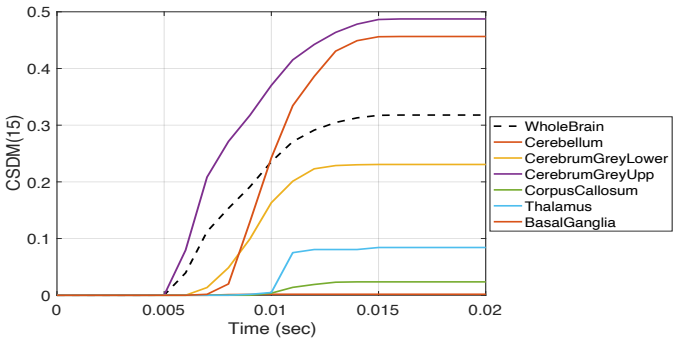

Figure 2: CSDM(15) versus time for multiple GHBMCv5 regions of interest. Figure illustrates the delayed accumulation of strain in the deeper brain structures (e.g., corpus callosum) compared with the surface brain structures (e.g., cerebrum).

Similarly, helmets are intended to extend the time of exposure to reduce the amount of energy transferred to the head. However, while the increased exposure time often results in a reduction in injury, it may also shift the location of the injury. An example of this is the inclusion of knee-bolster airbags in motor vehicles. Rather than eliminating knee-thigh-hip injuries, the airbags shifted the injuries from the knee (at point of impact) to the hip (following mass recruitment allowed by the extended exposure time). This same effect is likely seen in brain response [8]; however, limitations in FE model design (anatomical accuracy), and exposures have limited further investigation in this area using modern models. It is well known that the functional responses of various components of the brain have differing implications from a neurological perspective. Hence, it is important to evaluate at a local/regional/component level, any shift in the location of peak injury metrics with the inclusion of the temporal variable. This study has provided some insights into this aspect of TBI.

The presented study shows the temporal and spatial relationship between exposure (kinematics) and strain response (via CSDM) for a helmeted headform under military-specific exposures. Future work will investigate this relationship further using updated FE models as well as additional kinematic parameters of exposure (e.g., peak severity, length of exposure, total energy, etc.) through parametric analyses.

ACKNOWLEDGEMENTS

This work was supported by the Office of the Assistant Secretary of Defense for Health Affairs, through the Broad Agency Announcement under Award No. W81XWH-16-1-0010. The opinions, interpretations, conclusions, and recommendations are those of the authors and are not necessarily endorsed by the Department of Defense or other sponsors. The authors would like to thank the experimental and computational modeling teams at the Medical College of Wisconsin for their assistance with the work presented. Additionally, the authors would like to thank Dr. Carol Chancey of the U.S. Army Aeromedical Research Laboratory for her support of this work.

REFERENCES

[1] F. P. DiMasi, *SAE Trans.*, pp. 3029–3042, 1995.
[2] F. A. Bandak, *SAE Trans.*, pp. 1708–1726, 1994.
[3] E. G. Takhounts *et al.*, *Stapp Car Crash J.*, vol. 52, 2008
[4] L. F. Gabler, *Ann. Biomed. Eng.*, 44:12:3705–3718, 2016
[5] M. Hajiaghamemar, *J. Biomech. Eng.*, 142:031006, 2020
[6] H. Mao *et al.„J. Biomech. Eng.*, 135:11:111002, 2013
[7] J. S. Crowley, et al., *Aviat. Space Environ. Med.*, 80:9:831 2009
[8] N. Yoganandan et al., *J. Biomech,* 41:10:2253–2262, 2008

HEMODYNAMIC DIVERSITIES BETWEEN FOUR STENT GRAFT SYSTEMS VIA PATIENT-BASED SIMULATIONS

Anastasios Raptis (1), Michalis Xenos (2, 1), George Kouvelos (3), Konstantinos Spanos (3), Athanasios Giannoukas (1, 3), Miltiadis Matsagkas (1, 3)

(1) Laboratory for Vascular Simulations, Institute of Vascular Diseases, Larissa, Greece

(2) Department of Mathematics, University of Ioannina, Ioannina, Greece

(3) Department of Vascular Surgery, Faculty of Medicine, School of Health Sciences, University of Thessaly, Larissa, Greece

INTRODUCTION

During last decades, endovascular aneurysm repair (EVAR) has emerged as the treatment-of-choice for elective and ruptured abdominal aortic aneurysms (AAAs). The evolution of EVAR has brought improvements in efficiency, outcomes, and procedural success. However, the re-intervention rate has been shown to be more common in EVAR than open repair [1].

Computational Fluid Dynamics (CFD) simulations are lately used to identify the hemodynamic impact of endograft installation. The post-EVAR morphology of the lumen, determined by the stent-graft system, could favor regions where disturbed hemodynamics might develop. The initiation of thrombus, immediately after implantation or after months, can be triggered in regions where low wall shear stresses (WSS) prevail [2]. The study of thrombosis in endografts is a high research priority according to the Vascular Surgery Society practice guidelines on the care of AAAs [3].

The current study deals with the post-EVAR flow conditions in 4 stent-graft systems with different design, material and type of fixation. The devices under consideration are: AFX (Endologix, Irvine, California), Endurant (Medtronic, Minneapolis, Minnesota), Excluder (Gore, Newark, Delaware) and Nellix (Endologix, Irvine, California). An endograft-specific approach is applied, analyzing flow statistics based on a sample of patients in each endograft group [4].

METHODS

The cases were EVAR-treated patients with fusiform type of AAA and no signs of diseased common iliac arteries. The preoperative and one-month after EVAR computed tomography (CT) scans of 32 cases (8 cases per endograft group) were used as the raw material for the computational analysis. All patients were on optimal medical treatment (single antiplatelet, statin and hypertension medication) and no event during the early post-operative period was recorded. The screening protocol and the specifications of the CT scanner can be found in [5, 6]. All subjects gave informed consent for the use of their screening data.

Initially, the preoperative CT scans were processed and the following morphological characteristics were calculated using 3mensio (Pie Medical Imaging BV, Maastricht, The Netherlands): neck length, neck diameter, suprarenal and infrarenal angle, aorta length, right and left iliac length, right and left iliac diameter, neck diameter to right iliac diameter, neck diameter to left iliac diameter. The preoperative morphology of the AAAs did not vary significantly between the groups as proven by ANOVA tests in all studied morphological characteristics [4].

Modelling: The methodology involves the reconstruction of postoperative medical imaging data, 3D model refinement, computational mesh generation, CFD simulations, post-processing and statistical analysis, all carried out in a range of commercial and open-source software [5-7]. The 3D postoperative lumen models represent in practice the post-implantation spatial configuration of the endografts (Figure 1). The wall was considered as rigid without thickness or material properties. The computational grids had sufficient resolution to capture complex blood flow dynamics [5-7]. Blood was modeled as a Newtonian fluid with density, $\rho = 1050$ Kg/m^3, and kinematic viscosity, $\nu = 3.2\times10\text{-}6$ m^2/s. A literature-based physiological pulse pressure condition was applied at the inlet and flow rate at the outlets.

Regions of interest (ROI): The zone surrounding the bifurcation of the device: the surface before (1) and after (2) the bifurcation specifically (Figure 1).

Hemodynamic properties: velocity, WSS and helicity. Specifically, i) maximum, ii) maximum WSS on at peak systole, and iii) mean helicity at mid diastole.

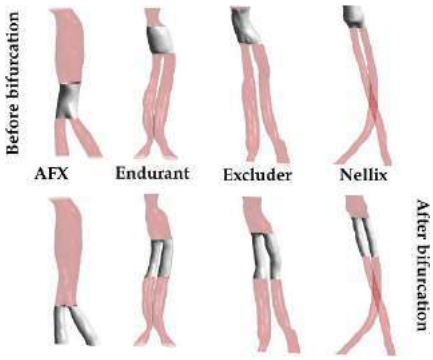

Figure 1: Indicative models and the ROI.

Statistical analysis: Between- and in-group statistical analysis using one-way-ANOVA and t-tests, with $p<0.05$ determining statistical significance.

RESULTS

The velocity is expectedly higher after the bifurcation, as blood flows in smaller diameters. According to Figure 2, the higher blood velocity, in both ROIs, was recorded for Nellix cases, with statistically significant deviation from the AFX ($p=0.03$), Endurant ($p\ll0.01$) and Excluder ($p=0.03$) ones, particularly in the region before the bifurcation. Endurant, on the other hand, is associated with the lowest blood velocity among the endograft groups, before and after bifurcation. The mean value of maximum blood velocity was approximately equal in AFX and Excluder groups before the bifurcation, while after the flow separation, AFX induces the second highest velocity value with Excluder following in the third position.

The highest WSS value was found in Nellix group, before and after the bifurcation (Figure 2). There was a statistical deviation between the Nellix and Endurant groups ($p=0.03$) in terms of maximum WSS before blood flow separation. The order of the endografts in terms of max. WSS is: Nellix, in the first place, followed by AFX and Excluder, while the lowest values were attained in Endurant cases.

Regarding helicity results, the AFX and Nellix follow a different trend than Endurant and Excluder (Figure 2). Specifically, AFX and Nellix exhibit higher mean helicity after the blood stream separation than before while the reverse was evident in the rest 2 endograft groups. In total, the highest helicity value, either before or after the bifurcation, was found for Endurant, followed by Excluder, and Nellix – AFX that are remarkably close in terms of helicity.

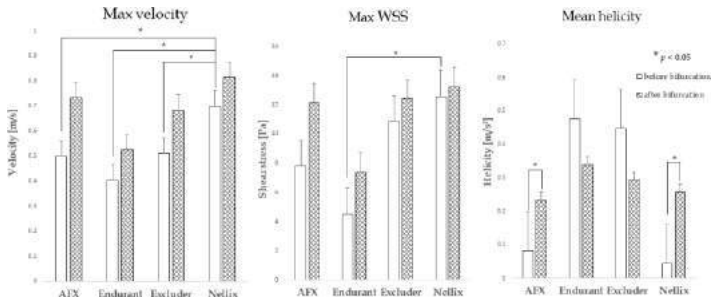

Figure 2: Mean and standard error values of the hemodynamic indexes (velocity, WSS, helicity) in both regions of interest in the 4 endograft groups.

DISCUSSION

The commercial endografts inherently differ in technical specifications and are associated with variable frequency of postoperative adverse events, justifying the need for endograft-specific analysis. Nevertheless, an endovascular device can reduce sac pressure, mechanical stress, pulsatile wall motion, but increased drag forces have also been detected on the device [6]. The material and the design of an endovascular along with the morphology of the AAA are parameters that determine the positioning of the stent-graft inside the aneurysmal sac and the local hemodynamics in large extend.

According to the results, the Nellix distinguishes from the rest devices in terms of velocity and WSS. The special design of Nellix, exploiting the endovascular sealing technology, seems to have a prevalent effect on blood flow. Endurant and Excluder, which incorporate a main body section that bifurcates high in the aneurysmal sac, seem to preserve high-intensity helicity before the flow division. However, the two devices, despite the similar structure, induce distinct blood flow environment in terms of velocity and WSS that might be attributed to their dissimilar material and stent configuration [7, 8]. The AFX device has its main fixation point on the iliac bifurcation such that the post-EVAR lumen morphology resembles physiological anatomy. Previous work has shown that AFX achieves restoration of blood flow indices to physiological levels [5]. In present study, AFX was associated with lower blood helicity values than Endurant and Excluder. It is of interest that similar results occurred for the AFX and Nellix devices regarding helicity, both presenting low helicity before the bifurcation increasing afterwards.

Boersen et al. [9] compared three endografts, Endurant, AFX, and Nellix, visualizing flow with laser particle imaging velocimetry. They suggested that the different stent designs did not influence suprarenal flow. In our study, we found similar results with highest values of velocity and WSS being noted in the Nellix cases, despite not accounting for the suprarenal area. Even, after the flow division, the trend of the results was preserved; Nellix induced the highest velocity and WSS, closely followed by Excluder and AFX.

Loss of limb patency varies between the endografts used in the present study, ranging from 3.4% for the Endurant to 1.1% for the Excluder. Demanget et al. [10] investigated the mechanical performance of 8 different graft limbs without, interferingly, finding significant differences in graft limb complication rates between. More data are needed to affirm whether the differences in flow dynamics found in the present study, may be translated in different graft properties, affecting the clinical outcome. Despite the differences found between the endografts, we must note that the clinical experience with all four devices has demonstrated good results at least during early and mid-term period. The in-stent flow dynamics could reveal the long-term durability of an endovascular device suggesting new ways for the development of complication-resistant stent graft systems.

REFERENCES

[1] Al-Jubouri M, et al., Ann Surg, 258:652-657, 2013.
[2] Shek TL, et al., J Biomech Eng, 134:121002, 2012.
[3] Chaikof EL, et al., J Vasc Surg, 67:2-77, 2018.
[4] Raptis A, et al., *J Vasc & Endovasc Surg*, 58:538-547, 2019.
[5] Raptis A, et al., *Interact Cardiovasc Thorac Surg*, 26:826-833, 2018.
[6] Raptis A, et al., *J Med Device*; 11:021003, 2017.
[7] Raptis A, et al., *Comput Methods Biomec*, 1-8, 2016.
[8] Tasso P, et al., *J Biomech Eng*, 140:111003, 2018.
[9] Boersen JT, et al., *J Vasc Surg*, 66:1844-1853, 2017.
[10] Demanget N, et al., *J Endovasc Ther*, 20:523-535, 2013.

SB³C2021
Summer Biomechanics, Bioengineering and Biotransport Conference
June 14-18, Virtual

A COMPUTATIONAL INVESTIGATION OF THE IMPACT OF GRAFT GEOMETRY ON HEMODYNAMIC PERFORMANCE FOR A RIGHT-HEART PUMP ANASTOMOSIS

Nicolas Tobin (1), Bryan C. Good (1), William Weiss (1,2), Keefe B. Manning (1,2)

(1) Department of Biomedical Engineering
The Pennsylvania State University
University Park, PA, United States

(2) Department of Surgery
Penn State Hershey Medical Center
Hershey, PA, United States

INTRODUCTION

The Fontan operation provides life-saving palliation for children born with a variety of congenital heart defects including tricuspid atresia, mitral atresia, and hypoplastic left heart syndrome. In the Fontan circulation, the inferior vena cava (IVC) and superior vena cava (SVC) are diverted directly to the pulmonary arteries, bypassing the morphological right ventricle so that the systemic and pulmonary circulations are in series with a single functional left ventricle. Patients who have undergone the procedure are increasingly living into adulthood, but many may face heart failure with elevated central venous pressure. The only treatment option for so-called failing Fontans is heart transplantation; however, many are ineligible due to organ failure or other complications. In addition, Fontan patients are more likely to face subsequent right-heart failure after transplantation due to elevated pulmonary vascular resistance.

The Fontan Circulation Assist Device (FCAD) is under development as a destination therapy for failing Fontan patients. *In vivo* evaluation of the pump detailed in Cysyk et al. [1] indicates favorable performance in a sheep model. However, geometric details of the pump anastomosis, such as anastomotic angle onto the aorta, can impact the pump's performance. The purpose of this computational fluid dynamics (CFD) study is to evaluate two surgical options for the FCAD anastomosis to the pulmonary arteries.

METHODS

One MRI-derived patient-specific anatomy, acquired from the Children's Hospital of Philadelphia, is used in the current study. This anatomy is of a 17-year-old girl with an offset total cavopulmonary connection (TCPC). Raw MRI data was used to reconstruct a three-dimensional model of the patient's Fontan conduit, depicted in Figure 1 along with the two surgical anastomosis options considered. Included in the clinical MRI data are the mean flow rates in each of the IVC, SVC, and the left and right pulmonary arteries (LPA and RPA).

Simulations were performed on three separate models. The first model was a simple reconstruction of the patient-specific anatomy. Simulations were also performed of two surgical options for the anastomosis of the pump outlet to the pulmonary arteries. The first was a simple t-junction, whereby the outlet of the pump connected directly to the central pulmonary artery. The second surgical option, the so-called y-graft, directs flow individually to each pulmonary artery through a bifurcated graft. Such a bifurcated graft has previously been shown to improve the energy efficiency and flow distribution of a TCPC conduit [2]. The computational domain in the pulmonary arteries was removed before the presence of any branching.

CFD simulations were performed in OpenFOAM, using a modified version of pisoFoam, a built-in transient, incompressible, low-Mach Navier-Stokes solver. Simulations were run with a Newtonian constitutive model, with a blood density of ρ=1060 kg/m^3 and a kinematic viscosity ν=4.4×10^{-6} m^2/s. To approximately recreate pulsatile flow through the Fontan conduit, the boundary conditions at the IVC and SVC prescribe a sinusoidal flow rate with a period of 1 second, equivalent to a heart rate of 60 beats per minute. The mean flow rates are prescribed based on MRI data. The anastomosis simulations used velocity data from a precursor FCAD simulation for the inlet boundary condition.

Pressures at the pulmonary arteries used a three-element windkessel model, whereby the outlet pressure (p) and flow rates (Q) were linked according to Equation 1. Each lung had its own value of C (capacitance), R (resistance), and Z (proximal resistance) prescribed to match the left-right flow split observed in the MRI.

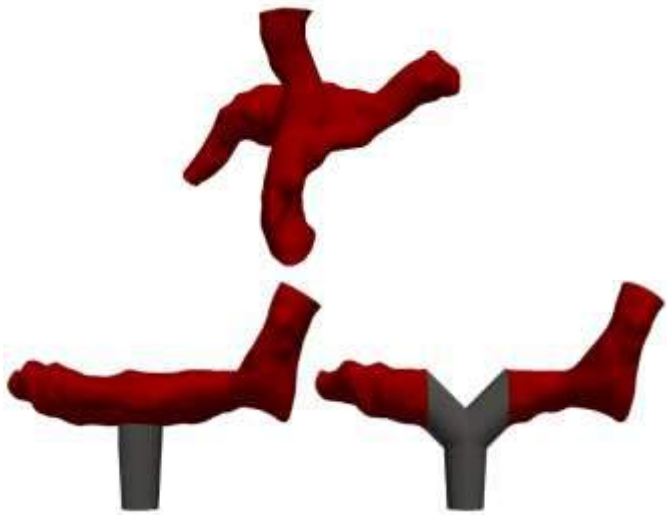

Figure 1. Basic TCPC anatomy (top), and surgical anastomosis options (bottom); t-junction (bottom-left) and y-graft (bottom-right).

$$\frac{dp}{dt} + \frac{p}{RC} = \frac{Q}{C}\left(1 + \frac{Z}{R}\right) + Z\frac{dQ}{dt} \quad (1)$$

All three cases were run on three increasingly fine grids to evaluate grid convergence and provide uncertainty bands by grid convergence index [3] for comparing results. All simulations ran for a start-up time of 4 seconds, and averaging was performed over a subsequent 3 seconds.

RESULTS

The three geometries are evaluated based on several fluid-dynamic metrics, and explicit comparisons are presented between the t-junction and y-graft. Results and statistical significance of difference between t-junction and y-graft are given in Table 1.

Table 1. Fluid-dynamic performance of the three investigated geometries.

	Base	t-junction	y-graft	% reduce Y over T	p-value
E (mW)	14.3	46.8	35.7	23.8%	< 0.0001
$\boldsymbol{\Delta P}$ (mmHg)	2.6	5.0	3.8	25.5%	< 0.0001
$\boldsymbol{A_{OSI}}$ (cm^2)	9.23	6.56	3.30	49.6%	< 0.0001
$\boldsymbol{A_{WSR}}$ (cm^2)	9.98	2.77	1.83	33.9%	< 0.0001
$\boldsymbol{t_r}$ (sec)	2.76	2.41	2.37	1.9%	0.19

In Table 1, E is the rate of energy dissipation, ΔP is the mean pressure drop between the inlets and outlets of the computational domain, A_{OSI} is the area exposed to an oscillatory shear index (OSI) ≥ 0.25, A_{WSR} is the area exposed to a wall shear rate (WSR) less than 200 s^{-1}, and t_r is the maximum residence time in the domain.

DISCUSSION

The primary function of the FCAD is to provide adequate flow to the lungs by overcoming pulmonary hypertension and to reduce central venous pressure, a ubiquitous morbidity in the failing Fontan. Both goals benefit from an energy-efficient placement of the pump, just as previous work has shown more efficient Fontan revisions improve patient outcomes [4]. Both energy loss by viscous dissipation and pressure drop are measures of this efficiency, both of which show significantly better performance in the y-graft as compared to the t-junction. As shown in Figure 2, the impinging jet at the posterior wall of the central pulmonary artery is a significant source of energy loss in the t-junction anatomy, which the y-graft does not suffer from.

Though it is anticipated that the FCAD will improve pulmonary blood flow and central venous pressure, the addition of foreign blood-contacting material is expected to create a thrombosis risk. Hypothetical patients receiving an FCAD would necessarily undergo lifetime anticoagulation therapy, but the fluid dynamics also play a role in thrombosis risk. Thrombosis in this case is primarily a concern of flow stagnation and insufficient washing of adhered platelets by wall shear stress. Although the y-graft shows improvement in area with wall shear rate less than 200 s^{-1}, there is no statistically significant difference in maximum residence time.

The introduction of non-physiological flow patterns in the vicinity of blood vessels creates a risk of vascular injury. The y-graft shows a marked improvement in area with critical OSI. This is primarily due to the lack of impinging jet on the native vessel.

In summary, the y-graft shows improved hemodynamic performance over the t-junction in metrics related to efficiency, thrombosis risk, and vessel damage, and may be a good candidate for connecting the FCAD to the pulmonary arteries.

Figure 2. Dissipation rate (W/m^3) in the t-junction and y-graft geometries, posterior wall visible.

ACKNOWLEDGEMENTS

Research reported in this publication was supported by the National Heart, Lung and Blood Institute of the National Institutes of Health under Award Number R01HL136369. This work was supported by the Office of the Assistant Secretary of Defense for Health Affairs through the Congressionally Directed Medical Research Programs under Award No. (Grant No. W81XWH-16-1-0536). This work used the Extreme Science and Engineering Discovery Environment (XSEDE), which is supported by National Science Foundation grant number ACI-1548562. Thank you to Dr. Mark Fogel of the Children's Hospital of Philadelphia for patient-specific data.

REFERENCES

[1] Cysyk, J., et al., *ASAIO Journal*, 65.6:593-600, 2019.
[2] Marsden, A. L., et al., *J Thorac Cardiov Surg*, 137.2:394-403, 2009.
[3] Roache, P. J., *J Fluids* Eng, 116.3:405-413, 1994.
[4] Trusty, P. M., *J Cardiov Trans Res*, 11.2:133-144, 2018

MACROSCALE & MICROSCALE RESPONSES OF THE RAT LUMBAR FACET CAPSULAR LIGAMENT TO SUBFAILURE REPEATED CYCLIC LOADING & A RAMP-AND-HOLD

Jonathan Marcelin (1), Sagar Singh (1), Beth A Winkelstein (1,2)

(1) Department of Bioengineering
University of Pennsylvania
Philadelphia, PA, USA

(2) Department of Neurosurgery
University of Pennsylvania
Philadelphia, PA, USA

INTRODUCTION

Low back pain is among the top five causes of disability globally [1]. The spinal facet joint is a common source of pain in the neck and low back [2,3]. Repeated loading of joints and their soft tissues can cause repetitive strain injuries and pain, and have a prevalence as high as 22-40% [4,5]. While effects of cyclic and repeated facet loading have been defined for the cervical spine [6,7], little is known about the lumbar facet's response to repeated subfailure loading.

The mechanical response of the spinal facet capsular ligament, like other ligaments, is rate dependent [8]. The facet capsule is primarily comprised of a collagen network [9] and has nerve fibers innervating it [10]. Because collagen networks are viscoelastic and axonal injury has been shown to be rate dependent [11], defining the rate-dependent response of the facet capsule is important for defining relevant pathophysiological mechanisms related to injury and pain.

The goal of this study was to define the effects of repeated loading and a subfailure ramp-and-hold on the lumbar facet capsular ligament's multiscale tissue and collagen fiber alignment responses. The L4/L5 facet capsule of the rat underwent cyclic tension-compression loading to 0.2mm, which is 10% of failure conditions, has been shown to be non-painful in vivo, and to not produce changes in the cervical facet capsular ligament's structure and collagen organization [6,12,13].

METHODS

Lumbar spines (L3-S1) were harvested from male Sprague-Dawley and Holtzman rats (n=3; 360-405gm) according to IACUC-approved procedures [14,15]. The superficial soft tissue was removed to specifically isolate and expose the bilateral L4/L5 facet joints and their capsular ligaments; the *in situ* length of each joint was measured with microcalipers [16,17].

Single facet joints (n=5) underwent mechanical testing using a customized test frame mounted in an Instron 5865 [12,14,15]. Each sample's *in situ* joint position was re-established as the reference gauge length at the start of each test (Fig. 1A). Each sample first underwent 30 cycles of distraction/compression to 0.2mm at 0.4mm/s [18], followed by an additional ramp to 0.2mm at 0.4mm/s with a hold for 90sec (Fig. 1B). Force and displacement data were acquired at 50Hz and filtered [19]. To determine when, during the hold period, the force stabilized, the time when the rate of force change was smaller than twice the resolution of the load cell was calculated (FR0). Quantitative polarized light imaging was integrated with the mechanical set-up and used to acquire collagen fiber alignment maps throughout testing [19]. In particular, the circular variance (CV) was calculated using those data for each sample at: the unloaded reference (ref), first distraction (Cycle

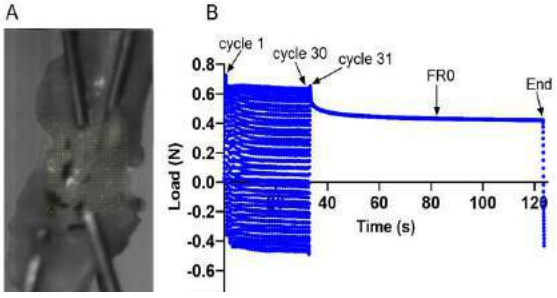

Figure 1: (A) Isolated facet capsule in test set-up showing forceps coupling it to the Instron. (B) Representative load response with each relevant analysis point: cycles 1, 30, and 31, force rate reaching zero (FR0), and the end of the hold.

1), last distraction of the cycling (Cycle 30), peak of the ramp (Cycle 31), FR0, and at the end of the 90sec hold (End) (Fig. 1).

The peak tensile force, peak compressive force, and stiffness were compared between Cycle 1 and Cycle 31. Stiffness was calculated as the slope of the positive portion (tensile) of the loading curve for each cycle. In addition, loads at FR0 and End were also compared to Cycle 31 using separate paired t-tests. CV values were similarly compared between reference and each of those events using separate paired t-tests.

RESULTS

Cyclic loading alters the capsular ligament's mechanical response. The peak tensile force at Cycle 31 (0.59±0.16N) is significantly lower (p=0.0032) than the peak tensile force at Cycle 1 (0.67±0.17N) (Fig. 2). Similarly, the maximum compressive force at Cycle 31 (0.40±0.20N) is larger (p=0.009) than the maximum compressive force from the first Cycle 1 (0.29±0.14N). The stiffness also changes with cyclic loading. The stiffness at Cycle 31 (4.86±1.59N/mm) is significantly larger (p=0.01) than the stiffness at Cycle 1 (3.22±0.8N/mm). During the hold, the force stabilizes after 53.1±7.24sec, decreasing significantly (p=0.0002) by 33.9% to 0.39±0.12N from the peak load at Cycle 31.

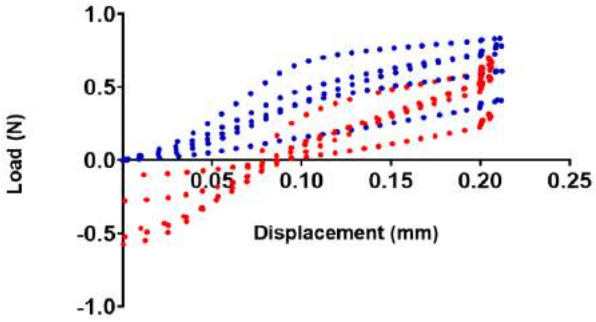

Figure 2: Load-displacement responses for all samples for each of Cycle 1 (blue) and Cycle 31 (red) showing the decrease in peak tensile load and increased stiffness between cycles.

Polarized light data were only available for 4 of the samples but show that one distraction is enough to change the CV (Fig. 3). A single distraction of 0.2mm (Cycle 1; 0.2378±0.0102) significantly (p=0.006) alters CV compared to the reference (0.2289±0.0122) with fiber alignment becoming less organized with increasing CV (Fig. 3). The CV is further increased (p=0.0029) by Cycle 31 (0.2428±0.0107) (Fig. 3). The CV at both the time when force stabilizes (FR0; 0.2438±0.0096) and the end of the hold (End; 0.2473±0.0118) are both significantly different (p<0.0065) from the CV for the unloaded condition (reference). While the CV at End (0.2473±0.0118) is significantly different from that at the peak of Cycle 31 (p=0.0425), the CV at FR0 is not different from either the peak Cycle 31 or at End.

DISCUSSION

The distraction magnitude selected for cyclic loading and the subsequent ramp falls within the toe region of the tensile loading curve for the cervical facet joint loaded to failure [12,15]. Since the collagen fibers in the facet capsular ligament are crimped and overall do not have a preferential orientation, cyclic loading, even at low levels, can reorient and even align fibers in the direction of loading [13,20]. Of note,

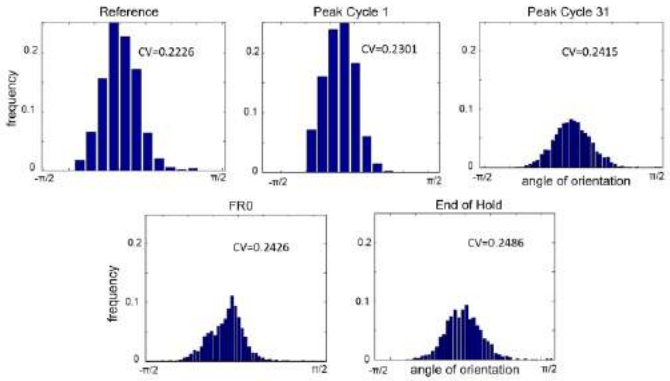

Figure 3: CV (Rat 2LHS) at reference, Cycle 1, Cycle 31, FR0, and the End of the hold, showing changes in fiber alignment

the change in CV after even one cycle at 0.2mm occurs at a lower distraction magnitude than when anomalous realignment of the collagen fibers is detected (0.34-0.68mm) for the rat cervical facet capsule [17]. In addition to varied anatomical levels, differences in sample preparation may account for these discrepancies. These data also indicate that further microstructural changes occur in the collagen network throughout the range of cyclic loading and also during force-relaxation (Fig. 3). Though additional studies are needed to better understand the spatial changes in each test paradigm, the changes in microstructure after cyclic loading are not surprising because repeated distraction of the facet capsule, even below the pain threshold, has been shown to alter capsular mechanics along with pain production [6]. While that repeated loading induced strains that were greater (~8-10%) than those estimated in this study (5%), microstructural changes due to cyclic loading are also supported here by the decrease in load and increase in stiffness (Figs. 1 & 2).

Measuring the local strains along with fiber micromechanics will help to better define and understand this tissues response to its varied loading experienced in the lumbar spine under normal and pathological conditions. Furthermore, defining the rate-dependent response of the facet capsule to mechanical loading will be useful to help refine and develop more realistic computational models of the spinal tissues and ligaments more broadly.

ACKNOWLEDGEMENTS

This study was funded by the NCCIH (AT010326).

REFERENCES

[1] Abbafati C et al, *Lancet*, 396:1204-1222, 2020 [2] Boswell M et al, *Pain Physician*, 10:229-253, 2007 [3] Manchikanti L et al, *Pain Physician*, 5:365-371, 2002 [4] Yassi A et al, *Lancet*, 349:943-947, 1997 [5] Tulder M et al, *Lancet*, 369:1815-1822, 2007 [6] Kartha S et al, *J Biomech Eng*, 140:0.81002-1-0.81002-8, 2018 [7] Lee K et al, *J Pain*, 10:436-445, 2009 [8] Lee K et al, *J Biomech*, 39:1256-1264, 2006 [9] Ban E et al, *J Biomech Eng*, 139:071009-1-079009-9, 2017 [10] Ita M et al, *J Orthop Sports Phys Ther*, 47:450-461, 2017 [11] Ahmadzadeh H et al, *Biophys J*, 106:1123-1133, 2014 [12] Singh S et al, *BMES Ann Mt*, #469, 2019 [13] Quinn K et al, *Stapp Car Crash J*, 51:169-187, 2007 [14] Singh S et al, *SB3C* #352, 2020 [15] Singh S et al, *ORS Ann Mtg*, #1461, 2021 [16] Quinn K et al, *J Biomech*, 40:2299-2306, 2007 [17] Quinn K et al, *J Biomech*, 43:1870-1875, 2010 [18] Quinn K et al, *J Appl Physiol*, 105:1881-1888, 2008 [19] Zhang S et al, *J Biomech Eng*, 138:021013-1-021013-12, 2016 [20] Yahia L et al, *Matrix* 10(1):58-64, 1990.

SB³C2021
Summer Biomechanics, Bioengineering and Biotransport Conference
June 14-18, Virtual

ROLE OF COHERENT STRUCTURES IN AIRFLOW MEDIATED INFECTIOUS DISEASE SPREAD WITH EXPIRATORY PARTICLES

Sara S. Meschi (1), Amirhossein Arzani (1)

(1) Department of Mechanical Engineering
Northern Arizona University
Flagstaff, AZ, USA

INTRODUCTION

Inhalation and contact with virus-laden droplets and aerosols are the main transmission routes of infectious diseases, including COVID-19. Droplets and droplet-nuclei carrying pathogens expelled from the infected person's nose and mouth during expiratory activities transmit the virus to the recipients by coming into contact with their respiratory and eye mucosa [1].

A complex sequence of flow-mediated occurrences, from the formation of infectious droplets, airborne particles, and multi-phase turbulent jets to deposition of the virus on target tissues, makes the disease transmission possible. Thus, the study of the flow physics of respiratory phenomena will lead us toward effective protective solutions. Since the start of the COVID-19 pandemic, a large number of computational and experimental studies have been done to help scientist with understanding the spread of SARS-CoV-2 laden droplets and aerosols in various environmental conditions in terms of ventilation, the distance of the infected person and the recipient, and the type of expiratory event (coughing, sneezing, talking, breathing, singing, etc.) [2]. Studies showed that the expelled content from the nose and mouth contains a multi-phase turbulent gas that carries droplets with a size range of 2-700 μm. Droplets larger than a critical size fall and contaminate surfaces, but smaller droplets evaporate and turn into infectious aerosols, which can stay suspended in the air for hours. Also, it is demonstrated that this multi-phase gas cloud can travel up to 23 to 27 ft depending on environmental and physiological factors, transporting the droplets along with it, which in comparison to the social distancing recommendation (6 ft) is much longer [3].

Considering the above points, it is clear that our understandings of the spread of COVID-19 still have to be evolved, and there are many unanswered questions that remained in the path of establishing more efficient protection guidelines. Additionally, most studies have focused on violent expiratory airflow events such as coughing/sneezing and near-body breathing has received less attention. In this study, we are trying to find out if there is a relationship between the flow topology of the expelled gas cloud from the mouth of the patient and the trajectory of the virus-laden particle traveling toward the recipient. For answering this question, we have employed computational fluid dynamic (CFD) to obtain the flow data during the breathing of two individuals in a confined space. We demonstrate how the Lagrangian coherent structures (LCS) formed in the flow around the two individuals can determine bio-aerosols' destination in the expelled turbulent airflow.

METHODS

A cylindrical confined environment with a diameter of 3 m and height equals 1.5 m is constructed. The heads of the human models are simplified as spheres with a diameter equal to 240 mm to avoid computational complications and are placed 650 mm from each other at the center of the cylinder. Also, the mouth of each model has a diameter of 20 mm. The mesh consisted of 7.3M tetrahedral elements with local refinement between the head models and is generated by the ANSYS Meshing 2019 R3 (ANSYS Inc., Canonsburg, PA) (Fig.1). Pulsatile breathing waveforms are prescribed at both models' mouths with a peak velocity of 2.4 m/s. Two sets of simulations are performed with inlet waveforms with opposite phases (one inhaling and one exhaling) and with inlet waveforms at the same phase (both exhaling and inhaling synchronously) for 5.5 seconds. No-slip boundary condition is prescribed for the model ceiling, floor, and head.

Flow velocity data were obtained using the FEniCS-based open-source finite-element solver Oasis and employing the Large Eddy Simulation (LES) model for solving the turbulent airflow generated by the respiratory events.

Calculation of Finite-time Lyapunov exponent (FTLE) can lead us toward the material surfaces known as LCS. These structures act as transport barriers and have been used in previous studies for investigating the chaotic flow behavior [4]. In this study, we calculated the repelling and attracting LCS, by forward and backward particle integration, respectively. Integrations are performed for integration time lengths of T = 0.2 and 0.5 seconds.

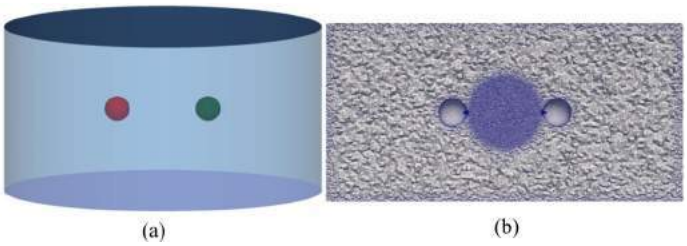

Figure 1: (a) Computational domain consisted of two spheres depicting the human heads. (b) Mesh details in the domain and mesh refinement around the models' mouths.

Furthermore, particle transport was studied by simulating the pathogen-laden droplet nuclei as massless tracers as well as inertial droplets. Approximately 130,000 particles are uniformly seeded at one of the inlets (disease source). Lagrangian particle tracking of tracers is used for tiny aerosols and the Maxey-Riley equation [5] with appropriate force terms for droplets is solved for inertial droplets.

RESULTS

The results of forward and backward FTLE field calculations and the tracers' visualization in the domain are presented in this section. Representative results of the FTLE field calculations for case 1: one person at the exhaling phase and the other one at the inhaling phase and case 2: both human models are exhaling at the same time are shown in Fig. 2 and Fig. 3, respectively.

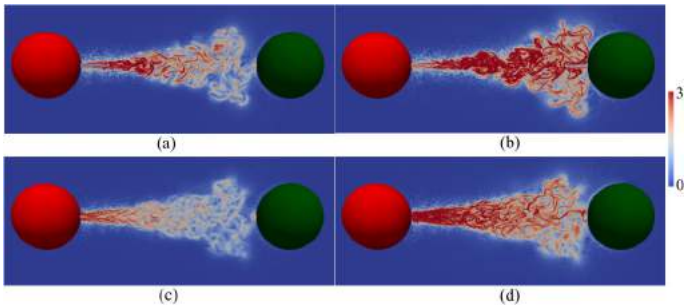

Figure 2: The FTLE field is shown while red model is exhaling and green model is inhaling. Backward FTLE: (a) T=0.2s (b) T=0.5s, Forward FTLE: (c) T=0.2s (d) T=0.5s

For each case, the results for forward and backward integration are presented for integration time of 0.2 s and 0.5 s. The red lines in forward and backward calculations are representatives of repelling and attracting LCS. Furthermore, the tracer/aerosol tracking results along with the corresponding forward FTLE field maps for both simulation cases are shown in Fig. 4, demonstrating the correlation of tracers spread pattern and the Lagrangian coherent structures formed in the turbulent flow around the models' heads.

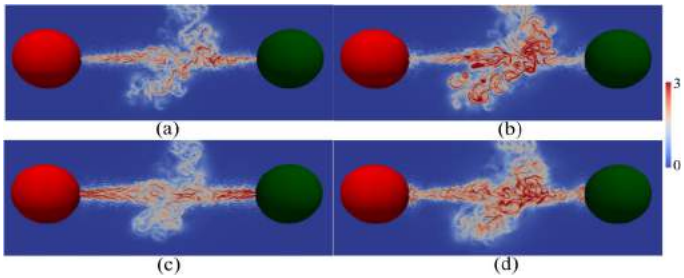

Figure 3: The FTLE field is shown while both models are exhaling. Backward FTLE: Backward FTLE: (a) T=0.2s (b) T=0.5s, Forward FTLE: (c) T=0.2s (d) T=0.5s

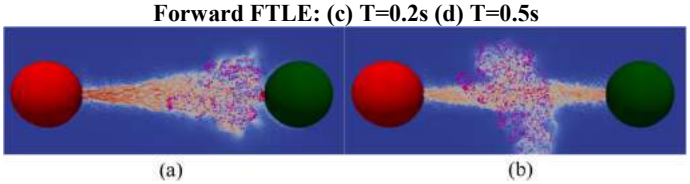

Figure 4: Tracer tracking results shown along with the corresponding FTLE field map calculated forward in time with T=0.5s. Tracers are displayed as massless spheres in magenta.

DISCUSSION

In this study, we have presented a new approach to the investigation of COVID-19 flow physics. We demonstrated that the flow topology of the expelled turbulent gas during breathing carrying expiratory droplets could determine virus-contaminated aerosols fate. This study aims to better understand the spread pattern of virus-laden droplets and aerosols generated by close-contact events such as breathing and talking. We have also performed inertial droplet transport and calculated the corresponding inertial Lagrangian coherent structures (ILCS) [6] to demonstrate the complexity in their trajectory (results not shown). Finally, talking simulations are currently underway and we expect to study the flow topology of small aerosols and large droplets generated in talking using LCS and ILCS, respectively. If we understand how coherent flow patterns influence droplet transport, we can control their spread by modifying airflow. Our proposed framework provides the means to investigate such airflow-mediated protection strategies.

ACKNOWLEDGEMENTS

Partial support from NAU's Office of the Vice President for Research is acknowledged.

REFERENCES

[1] Mittal, R., et al. "The flow physics of COVID-19." Journal of fluid Mechanics 894 (2020).

[2] Alsved, M., et al. "Exhaled respiratory particles during singing and talking." Aerosol Science and Technology 54.11 (2020): 1245-1248.

[3] Scharfman, B. E., et al. "Visualization of sneeze ejecta: steps of fluid fragmentation leading to respiratory droplets." Experiments in Fluids 57.2 (2016): 24.

[4] Haller, G.. "Lagrangian coherent structures." Annual Review of Fluid Mechanics 47 (2015): 137-162.

[5] Maxey, M. R., and James J., "Equation of motion for a small rigid sphere in a nonuniform flow." Physics of Fluids 26.4 (1983): 883-889.

[6] Farghadan, A., et al. "Topological analysis of particle transport in lung airways: Predicting particle source and destination." Computers in Biology and Medicine 115 (2019): 103497.

CHANGES IN RIGHT VENTRICLE VISCOELASTICITY WITH MATURATION

Wenqiang Liu (1), Michael Nguyen-Truong (1), Kevin Labus (2), Jeremiah Easley (3), Christian Puttlitz (1,2), Zhijie Wang (1,2)

(1) School of Biomedical Engineering
Colorado State University
Fort Collins, CO, USA

(2) Department of Mechanical Engineering
Colorado State University
Fort Collins, CO, USA

(3) Department of Veterinary Medicine and Biomedical Sciences
Colorado State University
Fort Collins, CO, USA

INTRODUCTION

Right ventricle (RV) failure contributes significantly to the mortality and morbidity in a variety of cardiovascular disease including pulmonary hypertension, congenital heart disease and heart failure with preserved ejection fraction [1]. The prevalence and clinical significance of RV failure in pediatric and adult patients require a better characterization of this ventricle, including the mechanical changes during cardiac development and maturation. To date, it is unknown how the RV biomechanics alter in post-natal period, when the left and right ventricles start to adapt to different mechanical loads.

The **goal** of the study was to investigate the differences in the passive viscoelastic behavior of the RV between healthy adolescent and fully matured adult sheep. It is documented that the ovine reach sexual maturity at ~6-9 months old [2], whereas other organs like the orthopedic system mature at ~3 years old. Since the full maturation involves multiple organ systems and lasts until 3-4 years old, we **hypothesize** that the RV passive viscoelastic behavior changes during maturation from adolescence to adulthood. To test the hypothesis, *ex vivo* biaxial tensile tests and stress relaxation were performed in adolescent and fully matured adult ovine hearts and the differences in RV passive viscoelastic properties were examined.

METHODS

Fresh ovine hearts (n=3 for 36+ months old and n=4 for 6-8 months old) were obtained with no known cardiovascular diseases from unrelated studies and from the local abattoir, respectively. Within 4~30 hours after harvest, the hearts were placed in cardioplegic solution (CPS) on ice or at 4°C. Prior to the mechanical tests, the tissues were sliced and cut into 3-4 mm thick, 25 mm x 25 mm square samples, and then placed in CPS combined with the 30 mM of 2,3-butanedione monoxime (BDM) solution at body temperature (26-37°C) for at least 10 minutes to ensure that cardiomyocytes were relaxed. The samples were preloaded by approximately 0.1 N and underwent 15 cycles of equibiaxial stretch at the speed of 8 mm/s for preconditioning. Then, cyclic equibiaxial mechanical tests (at 0.02Hz and 1Hz) and stress relaxation (at strain of 9, 12 and 15%) were performed. The outflow tract direction was marked as the longitudinal direction (0°). All samples underwent a maximum displacement of 4 mm to cover the physiological strain range. Deformations of graphite powder speckled samples were tracked with a camera (Nikon, Tokyo, Japan) and the strains were derived by digital image correlation using in-house Matlab codes. Biaxial stretch forces were obtained by 250 lb load cells (Honeywell Sensotec, Columbus, OH).

Cauchy stress (σ) and Green's strain (ε) were calculated from the last cycle of stress-strain data. From the hysteresis loop, the elastic moduli (E) at low and high strain ranges (slopes of the two straight trend lines) of the loading curve (Fig. 1), the transition stress (intersection point of these two lines) of both loading and unloading curves, and the stored energy (W_s) (Fig. 1) were calculated as elasticity measurement. The dissipated energy (W_d), loop width (a) (Fig. 1), and damping calculated as $W_d/(W_d+W_s)$ were derived as viscosity measurement. From the stress relaxation data, the relaxation rates derived from the logarithmic plots at all strains were used to determine the type of the tissue viscoelastic behavior, where a non-linear viscoelastic behavior is indicated if the relaxation curves from multiple magnitudes of input strains are not parallel [3]. Data were presented as mean ± SEM. Student's t-test was performed and $p \leq 0.05$ was considered significant.

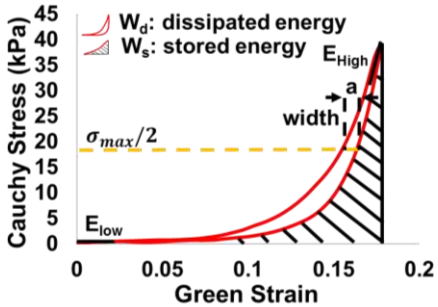

Fig. 1 Various viscoelastic parameters derived from the experimental stress-strain hysteresis loop.

RESULTS

Different frequency-dependent viscoelastic behavior between the adolescent and adult RVs. We firstly compared the viscoelastic behavior of the RV at two frequencies (quasi-static vs. physiological frequency). We found that in both directions, the high-strain E (E_{High}) decreased or tended to decrease as frequency increased, and the two age groups showed similar behavior. But the trends in low-strain E (E_{Low}) were different in these groups: the adult RV tended to stiffen as frequency increased, whereas the adolescent RV showed no frequency-dependent change (Fig. 2A-B). From the viscosity measurement, we found that in both directions, the adolescent RV had higher viscosity with increased frequency, whereas the adult RV had only a mild similar trend in loop width in the circumferential direction (Fig. 2C-D). Our results suggest that adolescent RV had different frequency-dependent viscoelastic behavior than the adult RV.

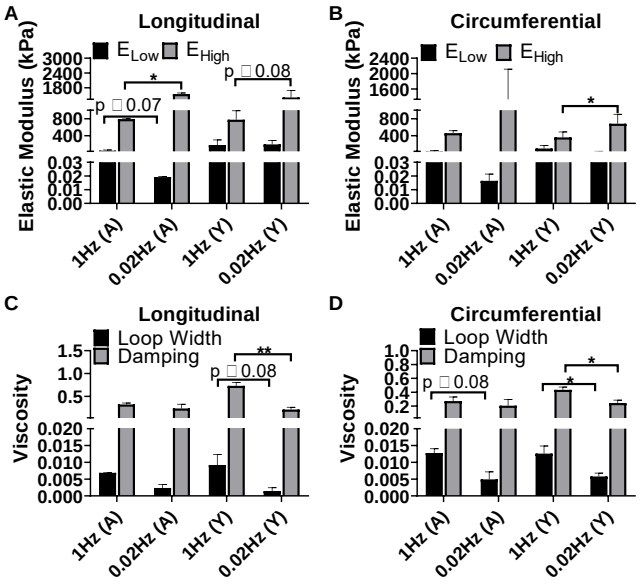

Fig. 2 RV frequency-dependent viscoelastic properties in the longitudinal (L) and circumferential (C) directions from the adult (A) and young (Y) adolescent RVs. (A&B) Local RV elastic moduli at low and high strains; (C&D) RV viscosity measured by loop width and damping. *p<0.05 and **p<0.01.

Different anisotropic viscoelastic behavior between the adolescent and adult RVs. We then further examined the anisotropic viscoelastic behavior of the RV at 1Hz, which mimics the heart rate of sheep. We used storage energy (Ws) to quantify overall RV stiffness and found that with maturation, the RV had increased Ws in both directions, and the increase was significant in longitudinal direction (Fig. 3A). Furthermore, compared to the adult RV, the young adolescent RV exhibit significant anisotropy with larger Ws in the circumferential direction (Fig. 3A). The same trends were observed in the transition stress from the unloading curve (data not shown), another indicator of overall stiffness. As for the viscosity, we found that with maturation the RV became less viscous in both directions, and the decrease was significant in the longitudinal direction (Fig. 3B). Furthermore, compared with the adult RV, the adolescent RV tended to show anisotropic viscous behavior with higher viscosity in the longitudinal direction (Fig. 3B). Overall, our results suggest that after birth, the RV became stiffer and less viscous and was less anisotropic during the cardiac maturation.

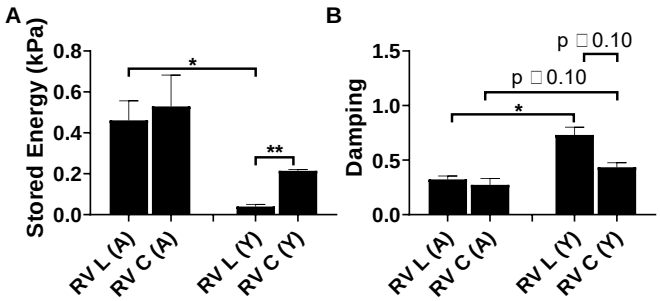

Fig. 3 RV elastic (A) and viscous (B) properties measured in longitudinal (L) and circumferential (C) directions from the adult (A) and young (Y) adolescent RVs (1Hz). *p<0.05 and **p<0.01.

Nonlinear viscoelastic behavior of RV in both age groups. From the stress relaxation data, we observed that the RV exhibited nonlinear viscoelastic behavior in both directions and at both ages (data not shown). This suggests that aging or maturation does not alter the type of RV viscoelastic behavior.

DISCUSSION

Before birth, the RV and left ventricle (LV) are similarly loaded and present similar morphology (e.g. wall thickness). The adaptation of RV after birth is very different than the LV due to the low pressure, low vascular resistance of the pulmonary circulation. But the post-natal cardiac maturation in terms of RV biomechanics is not well known. This study is the first to investigate the changes of RV passive viscoelastic properties between adolescent and fully matured adult sheep. From the pilot data, we found that the adolescent RV showed more pronounced frequency-dependent viscoelastic behavior than the adult RV. Moreover, when examining the viscoelasticity at physiologically relevant frequency (1Hz), we found that the RV became stiffer and less viscous and was less anisotropic during maturation. These age-dependent changes were significant in the longitudinal direction. Myocardial stiffening with aging was reported previously in old adults [4], but the evidence during cardiac maturation is less noted. The main extracellular matrix (ECM) protein in fetal heart is fibronectin, and collagen starts to accumulate after birth and with aging. The age-dependent stiffening may thus be a result of gradual deposition of collagen. But we cannot rule out the role of cardiomyocyte (CM) which stiffens with aging as well [5]. Since microtubules and titin are known to contribute to CM viscoelasticity [6-7], we also speculate that changes in these cellular components during CM maturation lead to increased stiffness and reduced viscosity of RV (as observed here). Such change may be advantageous to enhance RV pumping efficiency. How exactly the ECM deposition and CM adaptation in the RV lead to the viscoelastic changes needs to be further investigated. It also remains unclear whether the changes are unique in the RV. Further study will recruit more hearts and perform biological examinations to fully understand the RV viscoelastic behavior change with maturation. Our study will enhance the understanding of RV biomechanics in pediatric and adult subjects and assist to develop age-dependent RV therapies.

REFERENCES

[1] Konstam, M. A et al., *Circulation*, 137, 578-622, 2018
[2] Price, EO et al., *Calif Agr*, 50(4), 37-40, 1996.
[3] Duenwald, S. E et al., *Ann. Biomed. Eng.*, pp 1131-1140, 2009
[4] Margaret, M et al., *Circulation*, vol. 112, No. 2254-2262, 2005.
[5] Samuel, C et al., *Hear and Cir Physiology*, 645-651, 2004.
[6] Wolfgang, A et al., *J Mus Res and Cell Motlity*, 483-497,2002.
[7] Matthew, A et al., *Biophysical Jour*, 1796-1807,2018.

GROUP REFRACTIVE INDEX OF NANOCRYSTALLINE YTTRIA-STABILIZED ZIRCONIA TRANSPARENT CRANIAL IMPLANTS

David L. Halaney (1), Nitesh Katta (2), Hamidreza Fallah (3), Guillermo Aguilar (1), Thomas E. Milner (2)

(1) Department of Mechanical Engineering
University of California, Riverside
Riverside, CA, USA

(2) Department of Biomedical Imaging
University of Texas
Austin, TX, USA

(3) Department of Physics
University of Isfahan
Isfahan, Iran

INTRODUCTION

Transparent "Window to the Brain" (WttB) cranial implants made from a biocompatible ceramic, nanocrystalline yttria-stabilized zirconia, were recently reported. These reports demonstrated chronic brain imaging across the implants in mice using optical coherence tomography (OCT) [1] and laser speckle imaging [2]. However, optical properties of these transparent cranial implants are neither completely characterized nor completely understood. In this study, we measure the group refractive index of the implant using a swept source OCT system with a spectral range of 136 nm centered at 1300 nm, over a narrow range of temperatures at which the implant may be used during imaging or therapy (20°C – 43°C).

METHODS

The transparent 8 mol% YO1.5 nc-YSZ WttB implant used in this study was fabricated from a precursor yttria-stabilized zirconia nanopowder and densified into a bulk ceramic via Current-Activated Pressure-Assisted Densification (CAPAD) as described previously [3]. The densified sample was polished with diamond slurries to reduce light scattering by the implant surfaces and thus increase transparency. The implant sample was imaged and analyzed using a swept-source OCT system with a mode-locked laser (Axsun, Billerica MA) with central wavelength emission at 1300 nm, 136 nm sweep and an A-scan-rate of 100 kHz. A pixel in the depth dimension was determined to correspond to a real thickness in air of 6.19 µm. The OCT imaging head was placed over a glass dish containing a 100 µm thick coverslip spacer with hole in the center and secured in place with epoxy. The refractive index of the coverslip spacer (made of borosilicate glass) is 1.504 at central wavelength of OCT at 1.31 µm. The glass dish was placed atop a temperature adjustable plate on a tilt and z-stage, allowing for the dish to be positioned with normal incidence to the OCT beam (Figure 1).

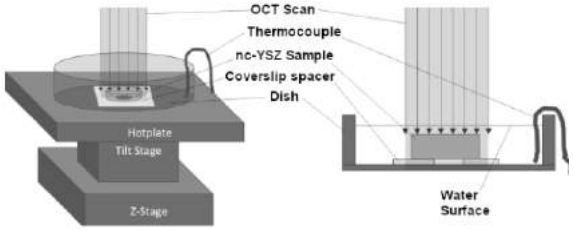

Figure 1: Experimental setup for OCT imaging of nc-YSZ.

A baseline image was acquired, showing the vertical height of the dish and spacer when imaged in air (Figure 2A). Next, the nc-YSZ sample was carefully placed atop the spacer, and water was slowly added to submerge the sample. A thermocouple was used to measure the water temperature as 20.8°C. A room temperature (RT) image was acquired, showing the apparent displacement of the spacer and dish due to non-unity group refractive index of water (at locations F & G) or due to the nc-YSZ and water (at locations A, B, C, D & E) (Figure 2B). The water temperature was increased by heating the temperature adjustable plate to 38°C (near body temperature) (Figure 2C), and then to 43.2°C (the upper limit at which the implant can be used in vivo) (Figure 2D).

The first method of analysis (Method 1) used Image J to quantify distances within the image (in microns and pixels). At locations of interest (A, B, C, D, E, F & G in Figure 2), distances were measured from the top of the image to the following features: top surface of spacer, bottom of dish, top and bottom surfaces of nc-YSZ sample, and surface of water (see colored arrows in Figure 2). From these measurements, and group refractive index values of water at 20.8°C, 38°C, and 43.2°C (1.337, 1.339, and 1.340, respectively), it is possible to separate the total displacement in the image Δ_{total} into apparent displacement $\Delta_{apparent}$ of the dish bottom and/or spacer (due to non-unity

group refractive index of water and nc-YSZ) and the real displacement Δ_{real} of the setup (due to compression and/or expansion of the temperature adjustable plate).

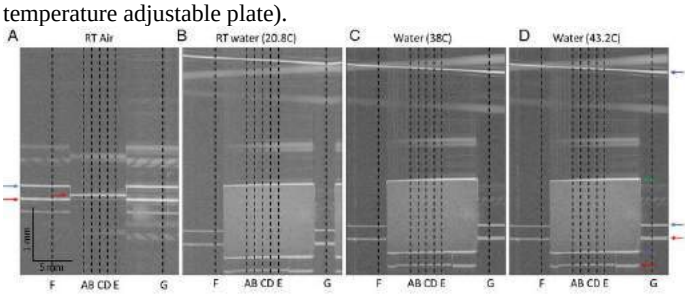

Figure 2: OCT B-Scans of nc-YSZ sample. (A) Dish and spacer in air at room temperature, (B) nc-YSZ sample atop spacer and dish in water at room temperature (20.8°C), (C) nc-YSZ in water at 38°C, (D) nc-YSZ in water at 43.2°C. Horizontal arrows highlight relevant surfaces (red = dish; blue = spacer top/nc-YSZ bottom; green = nc-YSZ top; purple = water surface).

First, the real displacement Δ_{real} of the setup at each temperature is found using the total displacement Δ_{total} of the spacer relative to the baseline image at locations F & G, where $\Delta_{apparent}$ is caused by n_{gwater} only. Subtracting these real displacements from the total displacement Δ_{total} in the images yields the apparent displacement within the image. To calculate the group refractive index of nc-YSZ from the apparent displacement, the method is the same as that used to compute real displacement Δ_{real}, except it is applied at locations A, B, C, D & E, where the apparent displacement $\Delta_{apparent}$ is due to non-unity group refractive index of water and nc-YSZ, using Equation 1:

$$\Delta_{apparent} = (T_{water} - d_{water}) + (T_{nc-YSZ} - d_{nc-YSZ}) = \left(T_{water} - \frac{T_{water}}{n_{g_{water}}}\right) + \left(T_{nc-YSZ} - \frac{T_{nc-YSZ}}{n_{g_{nc-YSZ}}}\right) \quad (1)$$

where T = optical thickness, d = real thickness, and n_g = group refractive index.

The second method of analysis (Method 2) uses the spectral phase function to calculate group refractive index and chromatic dispersion [4]. The spectral phase function describes the relationship between the optical frequencies in the OCT pulse and the difference in phase for each frequency returning from the top and bottom surfaces of the nc-YSZ sample. The spectral phase function may be written as a Taylor series expanded about the central OCT optical frequency, Equation 2:

$$\Phi(\nu) = \Phi^{(0)} + \Phi^{(1)}(\nu_0)(\nu - \nu_0)' + \frac{1}{2}\Phi^{(2)}(\nu_0)(\nu - \nu_0)'' + \frac{1}{6}\Phi^{(3)}(\nu_0)(\nu - \nu_0)''' + \ldots \quad (2)$$

where Φ is phase, ν is optical frequency, ν_0 is the central OCT optical frequency, $\Phi^{(0)}$ is a common phase shift, $\Phi^{(1)}(\nu_0)$ is the group delay (GD), $\Phi^{(2)}(\nu_0)$ is the group delay dispersion (GDD), and higher order terms are higher order dispersion. The group delay of each interface corresponds to the actual optical path length difference between the interface and the OCT reference arm. A subtraction of these GDs for the top and bottom interfaces corresponds to the distance the light experienced within the sample ($T = n_g \cdot d$). Fitting the phase vs. optical frequency data acquired by OCT with a polynomial curve can approximate the spectral phase function. 4th order polynomial fits of the optical phase vs frequency data were performed in MATLAB, and the 1st order terms of these fits give the GD.

RESULTS

Group refractive index of nc-YSZ was determined at each location and each temperature using the image-based analysis (Method 1), shown in Table 1. This method also allowed for determination of real sample thickness $d_{nc\text{-}YSZ}$ at each location and temperature, using the optical thickness T divided by the group refractive index n_g along with a calibration factor of 6.19 microns per pixel in the OCT image. This method is based on whole pixels, and an error analysis shows that the measurement has a 2% error.

Table 1: Group refractive index of nc-YSZ by Method 1:

$ng_{nc\text{-}YSZ}$	20.8°C	38°C	43.2°C
A	2.159	2.159	2.168
B	2.164	2.150	2.165
C	2.176	2.164	2.159
D	2.176	2.174	2.159
E	2.181	2.173	2.176
Average	2.171	2.164	2.165

Next, group delay (GD) of the nc-YSZ sample was obtained using the spectral phase function approach (Method 2). From GD, group refractive index n_g can be calculated using Equation 3 and sample thickness values $d_{nc\text{-}YSZ}$ obtained from Method 1:

$$ng = \frac{GD \cdot c}{4\pi \cdot d} \quad (3)$$

where c = 2.998e+8 m/s. Group refractive index values calculated using Equation 3 are shown in Table 2. Because this method uses sample thickness values determined from Method 1, it also has a 2% error in the calculated values of group refractive index, or an error of ~0.043.

Table 2: Group refractive index of nc-YSZ by Methods 1 and 2:

$ng_{nc\text{-}YSZ}$	20.8°C	38°C	43.2°C
A	2.165	2.156	2.218
B	2.162	2.208	2.202
C	2.182	2.186	2.209
D	2.196	2.196	2.167
E	2.147	2.194	2.202
Average	2.170	2.188	2.200

DISCUSSION

Nc-YSZ cranial implant windows have a group refractive index of 2.1-2.2 for OCT imaging with a spectral range of 136 nm centered at 1300 nm at normal working implant temperatures (20°C-43°C). This is important to consider when interpreting OCT images of underlying brain tissue. Because OCT is a time-based imaging technique, on-axis dimensions in reconstructed OCT images depend on time-of-flight of the OCT pulse. When imaging across the WttB implant with a group refractive index of ~2.1, the implant appears 2.1 times its mechanical thickness, and displaces other features beneath the window downward in the image.

ACKNOWLEDGEMENTS

This work was supported by the National Science Foundation (NSF-PIRE 1545852). The authors acknowledge Gottlieb Uahengo for providing the nc-YSZ sample used in this study.

REFERENCES

[1]. Halaney, DL et al., *Front Bioeng Biotechnol*, 8:659, 2020.
[2]. Davoodzadeh, N., *Bioned Opt Express*, 9 (10):4879-4892, 2018.
[3]. Garay, J.E., *Annu Rev Mater Res*, 40 (1):445-468, 2010.
[4]. Walmsley, I et al., *Rev Sci Instrum*, 72 (1):1-29, 2001.

SB³C2021
Summer Biomechanics, Bioengineering and Biotransport Conference
Virtual Conference, June 14-18, 2021

Embryonic Aortic Arch Material Properties by Optical Coherence Tomography Guided Micro-Pipette Aspiration

S.Samaneh Lashkarinia (1), Gursan Coban (2), Erhan Ermek (1), Merve Celik (1), Hummaira Siddiqui (1), Yap Choon Hwai (3), Kerem Pekkan (1)

(1) Department of Mechanical Engineering, Koc University, Turkey

(2) Department of Mechanical Engineering, Istinye University, Turkey

(3) Department of Bioengineering, Imperial College London, UK

INTRODUCTION

Characterization of material parameters of very soft meso-scale biological tissues is required to understand the cardiovascular biomechanics and governing internal dynamics of a rapidly remodeling vessels. From the mechanobiological perspective, evolution of vessel stiffness and bulk properties of soft tissue can give insights in disease models [1] and predicting in vivo growth and remodeling (G&R) response [2]. G&R is associated with changes in key microstructural constituents like collagen and elastin fibers. Although many techniques have been proposed to determine material properties, determination of the parameters in micro-scale under external stresses in the 0.1-1 kPa range remains a challenging task [3]. A standard approach is through force-displacement measurements, such as the indentation or pipette-aspiration, which are easy to apply for mature vessels, but require careful tool designs. Both methods provide a wide range of stress-strain variation, which is useful to extract mechanical characteristics of the tissue. Tissue aspiration is amiable to simple analytical approximations even for the large strain regimes encountered in very soft gel-like materials.

The aim of this work is to determine the material properties of pharyngeal aortic arch vessels during a critical period of early embryonic development. Present study complements the previous research efforts to describe the properties of embryonic vascular system, which is concentrated on the embryonic heart tube formation and ventricle material properties[4].

METHODS

Measurements are performed in early chick-embryo model at two consecutive Hamburger-Hamilton (HH) stages HH18 (n=4) and HH24 (n=3). Extracted aortic arches (Arch IV – percussor of ascending aorta) are treated with PBS solution. The micro pipette aspiration of the domain is performed by a negatively pressurized glass pipette (WPI Inc, FL, USA) with Rp=30μm tip radius. The cross-sectional tomography of investigated domain during micro pipette aspiration is imaged via cine optical coherence tomography (OCT). We track the pressure displacement data from the calibrated OCT device (Figure 1A). The y- location along the axis of symmetry is a function of the local stretch ratio [5]. Hence, an experimental stretch ratio (λ) for the axis of symmetry is defined by normalizing the aspirated length (L) to the pipette radius $\left(\frac{Rp+L}{Rp}\right)$. The ΔP versus λ curves are fitted to experimental data using the axial Cauchy stress, the incompressibility assumption, and an exponential material law:

$$\Delta P = C * a * \left(\lambda^2 - \frac{1}{\lambda}\right) * \exp\left(a * \left(\lambda^2 + \frac{2}{\lambda} - 3\right)\right) \quad (\mathbf{1})$$

Where, C (mmHg) and a (-) are material parameters [5].

We use an iterative inverse finite element (FE) approach to compute the tissue mechanical properties. Therefore, the best-fit material parameter is found by minimizing the standard error between the FE model estimation and the fitted exponential curve to the experimental measurements. In the model, vacuum

pressure is applied gradually inside the pipette and frictional contact condition are assumed between the pipette and the tissue. The mesh convergence is tested by means of the saturation of Cauchy stress (σ_{yy}) in the specified mesh to achieve less than 5% change in the results (Figure 1B).

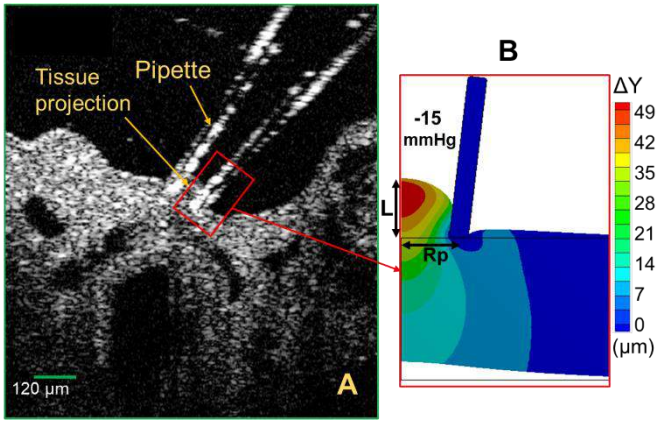

Figure 1: (A) OCT image of the curved aortic arch segment after aspiration *in ovo* (vacuum pressure= -15 mmHg). **(B)** Corresponding simulation from the quasi-static computational finite element model. Directional deformation in Y direction after aspiration is plotted for the embryonic stage HH18.

The goodness of fit is evaluated using the R-squared value. Data are presented as the mean ± standard deviation (Figure 2). The effective modulus, $M= C*a$, is assumed as a stiffness metric for two parameter exponential models [6]. Statistical comparisons between HH18 and HH24 are performed with *t*-test, $*p<0.05$ for n=3.

RESULTS

In the analytical model (Figure 2), statistical tests indicate that the mean value of parameter a increases significantly from a = 0.068± 0.013 (-) at HH18 to a = 0.260±0.014 (-) at HH24 (p= 0.0075). However, effective modulus does not show significant change by M=0.775±0.191(mmHg) at HH18 to M=0.684 ±0.173 (mmHg) at HH24 (p= 0.73).

Optimized neo-Hookean material parameter computed from the FE model are obtained with a standard error < 9%. Assuming incompressible tissue (ϑ=0.49), the optimized initial shear modulus increases from µ=51Pa at HH18 to µ=93 Pa at HH24.

DISCUSSION

Significant changes in the exponential nonlinearity characteristic of embryonic tissue is observed from HH18 to HH24. These differences can be quantified through the load-to-stretch ratio curve (Figure 2) through significant tangential slope increase in the high stretch (λ > 2) region. Stiffening of the stress-strain curve is associated with collagen fiber recruitment in developing vessel wall, in which the fibers straighten with stretch to become recruited and contribute to the local stiffening of the tissue [7]. It can be concluded that significant increase in the non-linearity parameter (a) is due to collagen fiber accumulation in the tissue from HH18 to HH24 [8].The initial shear modulus increases ≈1.8 fold from HH18 to HH24 in the Neo-Hookean material model to capture the stress-strain curve at HH24.

Here, our interpretation for nonlinearity increase in mechanical response of the tissue is increase in collagenous content of tissue, this in agreement with our recent study on embryonic aortic arch microstructure [9] in which the material properties were estimated through loaded and unloaded vessel configurations. However, considering the entire deformation characteristics, effective tissue stiffness (M) in HH24 remains at the same level as HH18. This can be due to the dynamic changes in extra cellular matrix contents in tissue which compensates the stiffness elevation due to collagen fiber accumulation and maintain the effective stiffness of the tissue in the same level.

Our experimental framework is applicable to microscopic tissue systems where extraction of the measurement domain is challenging, or non-invasive in vivo data is desired as in the present application.

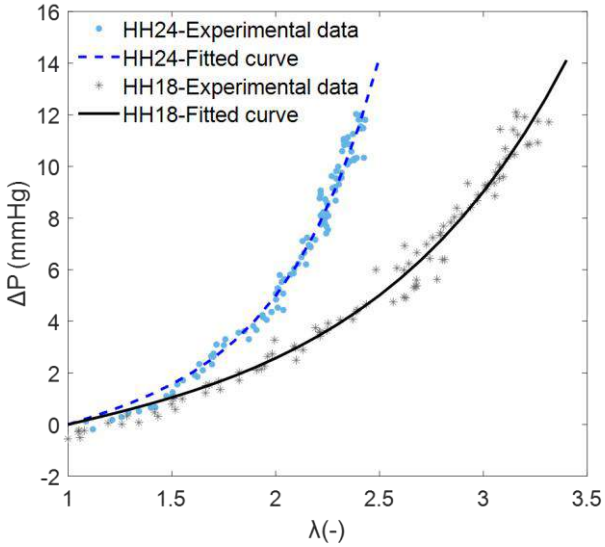

Figure 2: Representative curves that show experimental pressure versus experimental stretch ratio data obtained from aspiration test for samples at HH18 and HH24.

ACNOWLEDGEMENTS

Funding was provided by ERC-Starting Grant 307460, TUBITAK 1003-115E690

REFERENCES

[1] McKee, C.T. et al., Tissue Eng Part B Rev, 2011. **17**(3):155
[2] Ambrosi, D., et al., J. R. S. Interface 2019. **16**(157): 20190233.
[3] Chevalier, N.R., et al., Methods, 2016. **94**: 120
[4]Zamir , E.A., et al., J of Biomechanical Eng, 2005. **126**(6): 823.
[5] Buskohl, et al., Journal of biomechanics, 2012. **45**(5): 895
[6] Butcher, J.T., et al., Circulation R, 2007. **100**(10): 1503
[7] Weisbecker, H., et al., J. R. S. Interface, 2015. **12**(105):111
[8] Celik, M., et al., AJP, 2020. **318**(5): H1208
[9] Lashkarinia, S.S., et al., BMMB, 2020. **19**(5):189

CHARACTERIZING AND MODELING ADOLESCENT PECTUS EXCAVATUM ANATOMY TO INFORM SURGICAL PLANNING AND DEVICE DESIGN

S. Delanie Lynch (1), Katelyn A. Greene (1), Ashley A. Weaver (1)

(1) Center for Injury Biomechanics
Wake Forest School of Medicine
Winston-Salem, NC, U.S.

INTRODUCTION

Pectus excavatum is a common deformity classified by a depression of the anterior chest wall. Pectus excavatum is the most prevalent chest wall deformity in children, constituting over 88% of all chest wall deformities [1]. This deformity has been recognized to have a higher prevalence among males than females [2]. Pectus excavatum can be diagnosed as early as infancy, and most patients present no adverse effects of the deformity until adolescence. As the child experiences growth spurts, they may report symptoms such as decreased exercise tolerance, chest pain, and shortness of breath [2]. It is also common for self-image problems to be associated with pectus excavatum, as the chest can be visibly sunken inwards and lead to a more hunched over posture. To prevent further complications in adulthood, this chest deformity is often surgically repaired during adolescence. Current surgical methods include the Nuss Procedure and the Ravitch procedure [3]. The Ravitch procedure is typically seen in adults and involves cutting the cartilage, manually elevating the sternum before fixing it in place with plates and screws. The Nuss procedure, the most popular procedure in general and for adolescents, involves insertion of a metal bar below the depressed sternum to raise it to a more normal position. However, most cases of the deformity are not uniform in their type and severity, which can make surgical methods challenging. This study aims to create thoracic models of more severe representative adolescent pectus excavatum patients that can be used in surgical planning and device design for chest wall reconstruction.

METHODS

Chest computed tomography (CT) scans of pectus excavatum patients ranging in age from 12-16 were mined from Wake Forest Baptist Health medical records by querying patients with ICD diagnosis codes for pectus excavatum and CPT codes for CT scans covering the chest region. Mined CT scans were acquired from the clinical PACS system. From the 49 scans mined, 7 female and 30 male subjects were selected that had sufficient scan quality. In order to quantify severity of the deformity, measurement tools in TeraRecon (Durham, NC, USA) were used to collect thoracic dimensions and calculate a Haller Index and Correction Index for each subject. Haller Index characterizes the internal dimensions of the thorax and is calculated by dividing the maximal transverse diameter of the chest by the narrowest anterior-posterior (AP) length of chest (Figure 1) [4]. The minimum anterior-posterior distance was measured from the anterior aspect of the spine to the posterior aspect of the sternum. Correction Index represents the percentage of chest depth to be corrected and is computed by dividing the difference of the minimum and maximum anterior-posterior distance by the maximum anterior-posterior distance (Figure 1) [5]. The Haller Index (HI) measurements were used to classify each subject's pectus excavatum deformity as mild (HI 2.0-3.2), moderate (HI 3.2-3.5), or severe (HI > 3.5) [3]. Although, Haller Index was the primary measurement used for classification, the Correction Index measurements provided additional validation of severity and were included to enhance the database of thoracic measurements on the pectus excavatum adolescent subjects.

Based on these data, a severe representative female and male adolescent subject were chosen to create two thoracic models. Severe cases of the deformity were preferred in order to better understand the extent to which pectus excavatum influences all relevant anatomical structures. A more severe case of the defect causes greater impact on other anatomy, such as compression of the lungs or deviation of normal rib morphology. Three-dimensional (3D) models of the entire thoracic region were generated from the CT scans using semi-automated image segmentation in Mimics 23.0 (Materialise, Leuven, BE). All

components of the models were separated to allow for ease of adjustment to the models in subject-specific surgical planning and virtual testing of surgical device designs.

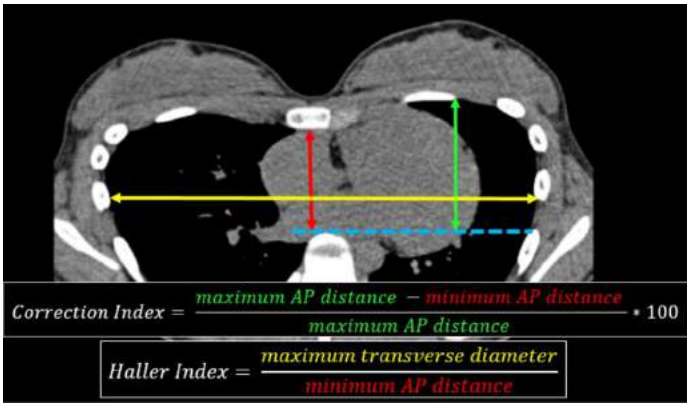

Figure 1: Diagram of Haller Index and Correction Index calculations to characterize severity of pectus excavatum deformity in the axial view of a computed tomography scan.

RESULTS

Of the 37 adolescents analyzed with pectus excavatum, 15 were classified as mild cases, 7 as moderate cases, and 15 as severe cases (Figure 2). The severities were relatively evenly distributed among the male and female subjects. Among male adolescents, pectus excavatum severity was mostly mild (43%, n=13) or severe (40%, n=12), with very few moderate (17%, n=5) cases. Among female adolescents, pectus excavatum severity was mostly severe (43%, n=3), with equal amounts of mild (29%, n=2) and moderate (29%, n=2) cases.

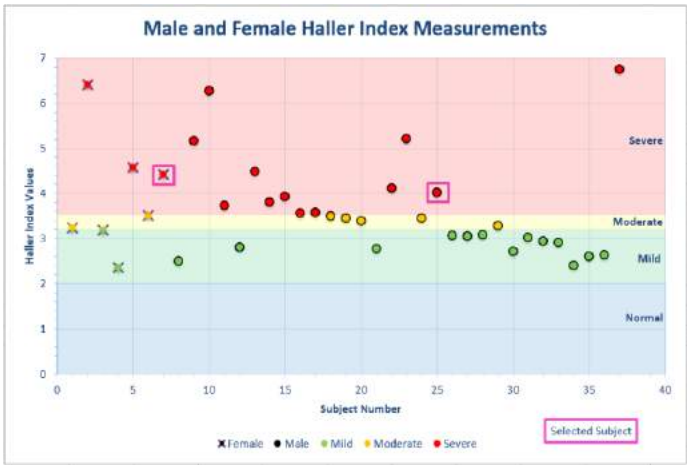

Figure 2: Distribution of Haller Index measurements for the 37 adolescents analyzed with subjects selected for modeling indicated by pink boxes.

From these 37 adolescents, a representative male (age 13) and female (age 15) with severe pectus excavatum deformity was chosen for 3D reconstruction modeling, with Haller Index measurements of 4.02 and 4.43, respectively. 3D reconstructions for the two subjects included models of the individual ribs, sternum, thoracic spine, costal cartilage, lungs, heart, liver, spleen, kidneys, and abdominal cavity (Figure 3).

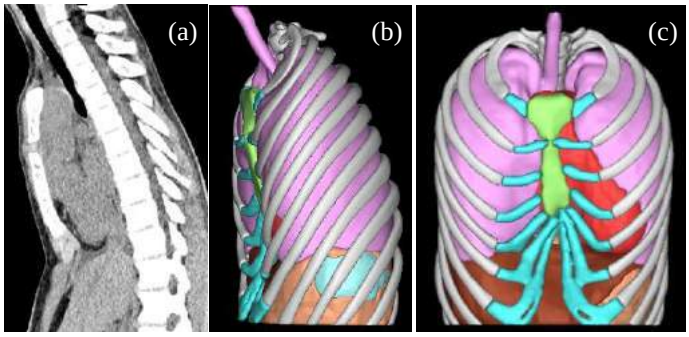

Figure 3: (3a) Original subject CT scan. Completed 15 year old female thoracic model in (3b) lateral view and (3c) anterior view.

DISCUSSION

Medical imaging data were used to characterize pectus excavatum severity and create a male and female thoracic model representative of severe cases of the deformity. The data used in this study is not representative of the entire population with pectus excavatum, but reflective of our hospital's population of these patients with CT scans available. The number of female subjects was very limited, which may be a result of the higher prevalence of the deformity among the male population. Also, this study is limited to subjects 12-16 years of age and does not include any pectus excavatum adult patients or pediatric patients younger than age 12. Of the data available, it can be suggested that adolescent patients with pectus excavatum in our hospital system are more likely to exhibit mild or severe cases of the deformity. This could indicate that moderate cases are less common since they may often progress to severe cases. However, more data is required to conclude definitively.

While the data used in this study may not represent the broader adolescent population with this chest wall deformity, the generated models are clinically valuable because they serve as a tool to inform surgical planning techniques and improve device design for chest wall reconstructions of pectus excavatum on a subject-specific basis. The models representative of severe deformation provide more insight on the range of possible anatomies that may need to be corrected, and helps clinicians both explicitly and intuitively in their assessment of possible solutions with regards to surgical repair. These models can be used to virtually test different device designs for surgical implants and tools used in pectus excavatum chest wall reconstructive surgery.

ACKNOWLEDGEMENTS

Funded by KLS Martin Group (Jacksonville, Florida).

REFERENCES

[1] Obermeyer, R. J., & Goretsky, M. J. (2012). *Surgical Clinics of North America*, 92(3), 669-684. [2] Obermeyer, R. J. et al. (2018). *Seminars in Pediatric Surgery*, 27(3), 127-132. [3] Nasr, A., et al. (2010). *Journal of Pediatric Surgery*, 45(5), 880-886. [4] Robbins, L. P. (2011). *Radiology Case Reports*, 6(1), 460. [5] Peter, S.D. et al. (2011). *Journal of Pediatric Surgery*, 46(12), 2270-2273.

MECHANICAL FUNCTION OF FAN-LIKE EXTENSION AND MIDSUBSTANCE FIBERS OF PORCINE ANTERIOR CRUCIATE LIGAMENT

Satoshi Yamakawa (1), Konsei Shino (2) , Tatsuo Mae (1), Ken Nakata (1), Hiromichi Fujie (3)

(1) Graduate School of Medicine
Osaka University
Osaka, Japan

(2) Sports Orthopaedic Center
Yukioka Hospital, Osaka, Japan

(3) Department of Mechanical Systems Engineering
Tokyo Metropolitan University
Tokyo, Japan

INTRODUCTION

The primary function of the anterior cruciate ligament (ACL) is transmitting tensile forces between the femur and tibia for stabilizing the knee joint. Recent reports focused on medial and lateral fibers, or fan-like extension and mid-substance fibers [2, 3]. Previous anatomical observation reports suggested that the fan-like extension fibers (FLEF) play a role like an anchor and the mid-substance fibers (MSF) transmit tensile force flexibly for changing direction according to the knee position [3], and another report indicated that the failure load of the ACL dramatically drops after transection of FLEF [4]. In addition, the biomechanical investigation indicated that the proximal part of the MSF mainly resists the anterior drawer force [5]. However, these reports did not address the mechanical functions of these fibers under physiological loading conditions and the relationship between the function and magnitude of the loading. Therefore, the objective of the present study was to determine the relationship between the mechanical function of the FLEF and MSF of the ACL, and the magnitude of the anterior drawer force using the robot testing system.

METHODS

A 6-DOF robotic testing system (FR-2010, Technology Service, Japan, Fig.1, [6]) was used to apply loads to knee joints with respect to the knee joint coordinate system [7, 8]. Porcine cadaveric knees (n=3) were used. The knees were dissected down to the joint capsule and fixed to the robotic testing system. The anterior drawer test was performed up to 200 N at maximum extension. During the test, the anterior-posterior (AP) DOF was translated under displacement control at a rate of 0.1 mm/s while all the DOFs except the AP and flexion-extension DOFs were set under force control with prescribed force/moment at zero. The test were repeated at 30, 60 and 90 degrees of knee flexion in intact, fan-like extension fiber transected (FLEFT) and mid-substance fiber transected (MSFT) states. In the present study, the FLEF and MSF were identified based on the femoral attachment region of the ACL referring to the previous report [4] (Fig.2). Anterior tibial translation and *in situ* forces [6] of both FLEF and MSF during the tests were determined at the 50, 100, 150 and 200N of the anterior drawer force application.

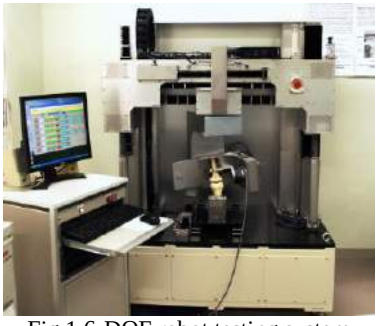

Fig.1 6-DOF robot testing system

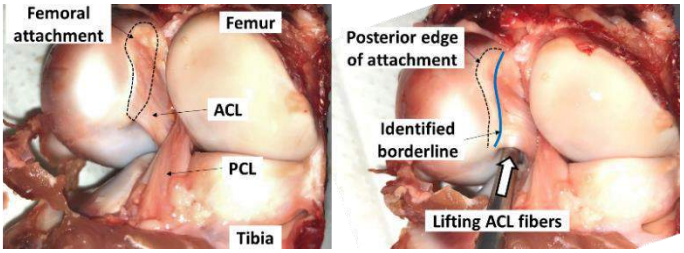

Fig.2 Identifying the borderline (blue line) for dividing the ACL into fan-like extension and mid-substance fibers by lifting the ACL fiber and finding the mid-substance region

RESULTS

At 200 N of the anterior drawer force application, the anterior tibial translation slightly increased after the FLEF transection, the anterior translation was dramatically increased after the MSF transection in all flexion angles (Fig.3). In situ forces of the FLEF at the 200 N of anterior drawer force application were smaller than those in the MSF in all flexion angles.

In maximum extension and 30 degrees of flexion, the *in situ* force of the FLEF gradually increased with the increase of anterior drawer force, and the *in situ* force of the MSF rapidly increased after anterior drawer force application (Fig.4). In 30 and 60 degrees of flexion, the FLEF rapidly responded after anterior drawer force application (Fig.5). The *in situ* force of the MSF rapidly increased at 100 N of the anterior drawer force application and became larger than those in the FLEF.

DISCUSSION

The present study determined the mechanical function of the FLEF and MSF of the ACL in response to more physiological loading and indicated load- and position-dependent function of both fibers.

In maximum extension and 30 degrees of flexion, the MSF rapidly responded to the anterior drawer force application. As the MSF is shorter than the FLEF, the tensile force was assumed to be transmitted earlier in the MSF while the *in situ* force of the FLEF gradually increased in response to anterior drawer force.

The previous study indicated that the FLEF is an important structure for the prevention of structural failure [4], while they were less functional with the increase of the magnitude of anterior drawer force up to 200N. This suggests that 200 N of the anterior force is still *in vitro* load taking the failure load of the ACL into account, and that the MSF is more functional than the FLEF under such a small amount of the loading condition. In other words, the FLEF is afunctional compared to the MSF in the early phase of the load application to the knee. On the other hand, the MSF consists of a lower stiffness structure than those of the FLEF [10, 11]. This suggests that the FLEF consisting of high stiffness structure mainly resists the load under greater loading condition like sports activity, while the MSF of low stiffness allows large deformation.

In 60 degrees of flexion, the FLEF rapidly responded to the anterior drawer force application. This suggests that the FLEF becomes more functional in the flexed knee at early phase of anterior drawer force application, as the femoral attachment of the ACL rotates according to the knee flexion.

CONCLUSIONS

(1) ACL has a site-dependent function, and the function of each site is activated depending on the magnitude of the force.
(2) The site-dependent functions are dependent on the knee flexion angle, as well.

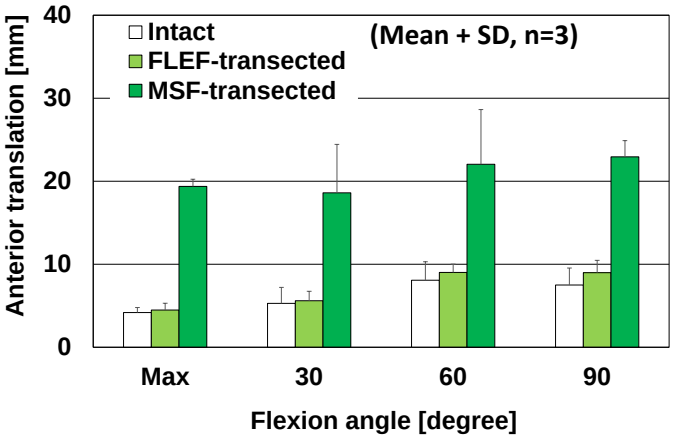

Fig.3 Anterior tibial translation in response to 200 N of anterior force to the knee in each flexion angle

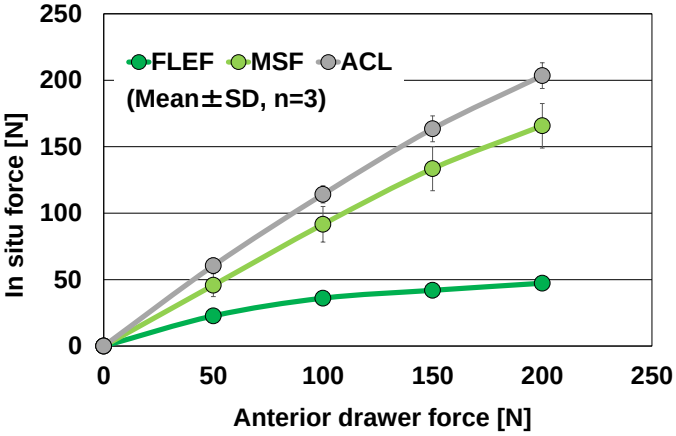

Fig.4 In situ force of fan-like extension and mid-substance fibers and ACL in response to 50, 100, 150 and 200 N of anterior drawer force at 30 degrees of flexion

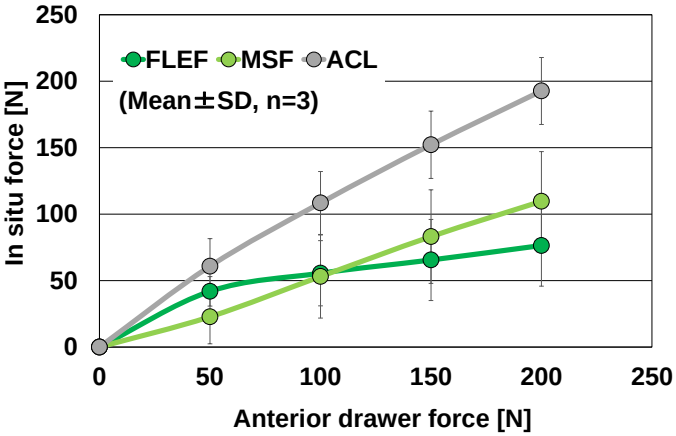

Fig.5 In situ force of fan-like extension and mid-substance fibers and ACL in response to 50, 100, 150 and 200 N of anterior drawer force at 60 degrees of flexion

REFERENCES

[1] Otsubo H. et al., KSSTA, 2012
[2] Mochizuki T. et al., KSSTA, 2014
[3] Sasaki N. Et al., Arthroscopy, 2012
[4] Sabzevari S. et al., KSSTA, 2020
[5] Kawaguchi Y. et al., Arthroscopy, 2015
[6] Debski R.E., et al., JBME, 2017
[7] Grood and Suntay, JBME, 1983
[8] Fujie H. et al., J Biomech, 1996
[9] Fijie H. et al., JBME, 1995
[10] Suzuki D. et al., Clin Anat, 2015
[11] Butler D.L. et al., J Biomech, 1991

STATISTICAL INTERPRETATION OF PREDICTIVE FACTORS OF KINEMATICS IN TRAUMATIC BRAIN INJURY FROM HEAD IMPACTS

Yiheng Li (1), Xianghao Zhan (2), Yuzhe Liu(2), David B. Camarillo (2)

(1) Department of Biomedical Informatics
Stanford University
Stanford, CA, USA

(2) Department of Bioengineering
Stanford University
Stanford, CA, USA

INTRODUCTION

To quantify the risk of Traumatic Brain Injury (TBI) and mild TBI (mTBI), brain strain, particularly maximum principal strain (MPS), is found to be a good predictor for brain injury and assorted pathology and is widely used in mTBI research[1,2]. To quickly evaluate brain injury, many brain injury criteria (BIC) have been developed to approximately quantify brain injury and are often evaluated by the brain strain calculated based on FE modeling. These BIC use different rotational parameters of impact kinematics in the calculation, such as the peak values of angular acceleration.

However, the contribution of different rotational parameters in the calculation of brain strain is not well understood. In addition to the kinematics in their original maximum values, the underlying relationship between the kinematics and MPS may also be high-order. The combination of multiple rotational parameters under mathematical transformations, and the contribution of different parameter components such as angular velocity in different directions in the evaluation of brain strain remain to be further studied. To better develop BIC based on rotational kinematics, we need to systematically study the predictive power of different rotational parameters.

In this study, 5 datasets from various head impact subtypes are used for analysis. With multiple statistical interpretation techniques, we study the predictive power of multiple rotational parameters in the linear regression models of 95% MPS (MPS95). Three aspects of features are focused in this study: the derivative order of the angular kinematics (angular velocity, angular acceleration, angular jerk), the components in three spatial directions and the magnitude, and the power of the kinematics (square root, quadratic, cubic, etc.)

METHODS

The datasets in this study includes 2130 simulated head impacts from a validated finite element model (FEM)[3,4] (dataset HM), 184 college football[5](dataset CF1), 118 college football head impacts[6] (dataset CF2), 457 mixed martial arts (MMA)[2](dataset MMA), 53 reconstructed head impacts by National Football League (NFL) [7] (dataset NFL), 48 car crash dummy head impacts from NHTSA[8] (dataset NHTSA) and 272 numerically reconstructed head impacts in National Association for Stock Car Auto Racing (NASCAR).

To build the regression models of MPS95, various features were extracted. As linear acceleration has been proven to contribute significantly less to MPS compared to angular velocity[9], only angular-velocity-based features are used in our analysis. We extracted features that may contribute to the regression based on three different aspects. 1) derivative order: we took the zero-order, first-order and second-order derivative of angular velocity. 2) spatial component and magnitude: the components of the rotational parameters derived from the components in three spatial directions, which is defined using the right-hand rule. The magnitude of the rotational parameters was also calculated to be the fourth component. 3) power order: power of 1, 0.5, 2, 3, 4, 5, and 6 of those features were calculated and added to the feature set respectively.

Ordinary Least Squares (OLS) was used to build the linear regression models to quantify the contributions of features to MPS95. The OLS model captures the most direct and explicit predicting effect of a feature, and thus is considered the most suitable model in this situation where the purpose of the study is to understand the most directly related features in the prediction. To analyze the relative feature importance from linear models considering the linear correlation among features, four statistical interpretation methods that focus on different perspective of interpreting predictive power were used: zero-order correlation coefficients[10], structure coefficients[11], commonality analysis[12] and dominance analysis[13].

RESULTS

Predictive power of different derivative orders: The predictive power of three factors of derivative orders were analyzed using the four methods mentioned above. According to both zero-order correlation coefficients and structure coefficients, on all datasets but dataset MMA, the first-order features (angular acceleration) were the most predictive features while the second-order features (angular jerk) were the least predictive features ($p < 0.05$). On dataset MMA, both statistical methods showed zero-order features (angular velocity) were the most predictive ($p < 0.05$). Commonality analysis showed that the common information of all three factors had the highest predictive power on datasets HM, CF1, CF2 and NASCAR. On dataset MMA, the common information of zero-order features and first-order features had the highest predictive power. The dominance analysis showed that on dataset HM, CF1, CF2, and NASCAR, the first-order features dominated in every level, and on dataset MMA, the zero-order features dominated in every level.

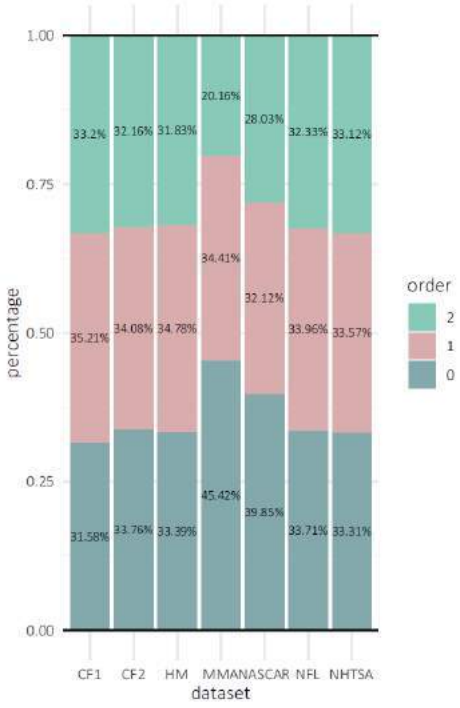

Figure 1. Stacked bar plots of normalized mean R^2 contribution of kinematic factors of 3 different derivative orders in the regression of MPS95 using zero-order correlation coefficients.

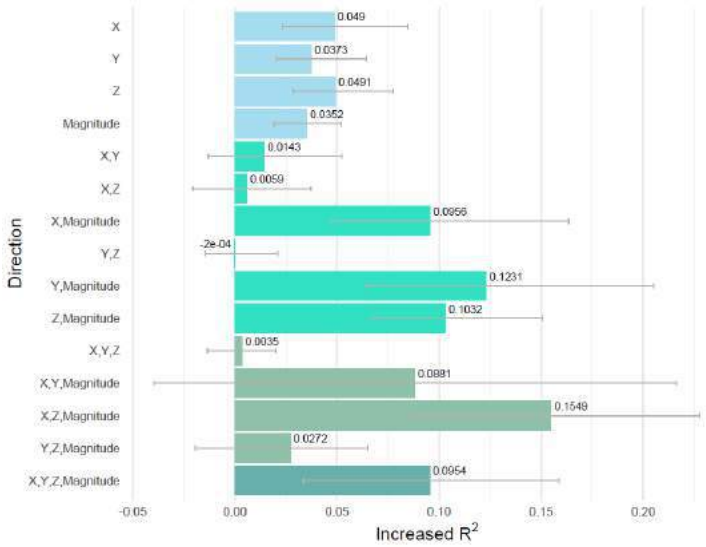

Figure 2. Commonality analysis results for unique or common information of different predictors in the regression of MPS95 from features of 4 different components on dataset MMA.

Predictive power of different kinematic components: The same interpretation methods were used to analyze the four kinematic components: the three spatial directions and the magnitude. According to both zero-order correlation coefficients and structure coefficients, on all datasets but dataset NHTSA, magnitude features were the most predictive features ($p<0.05$). Zero-order correlation coefficients showed the features of z-axis component were the most predictive on dataset NHTSA ($p<0.05$). This result was not statistically significant according to structure coefficients ($p=0.17$). Commonality analysis showed the predictive power varied with different datasets. On dataset HM, the common information of features from y-axis and the magnitude showed the highest predictive power. On dataset CF1 and CF2, the common information of features from x-axis, y-axis, z-axis and the magnitude were the most predictive. On dataset MMA, the common information of features from x-axis, z-axis, and the magnitude was the most predictive. Dominance analysis showed that magnitude features dominated in most levels of analyses with an exception on dataset MMA, where x-axis features dominated over other features on level 3.

Predictive power of different power orders: In the power order analysis, both the zero-order correlation coefficients and the structure coefficients showed that, on all datasets except NHTSA, the first-order-powered features were the most predictive features ($p < 0.05$), while the square-root-features were the most predictive feature on dataset NHTSA ($p < 0.05$). The power orders smaller than 3 were significantly more predictive than the remaining power orders. Besides the power order of 0.5, 1, and 2, as the power order increases, the features showed gradually decreasing predictive power in the regression. According to the results of commonality analysis, the common information of all factors had the highest predictive power, which indicates that changing the power of features does not provide new information in the regression. The dominance analysis showed that the first-order-powered features generally showed dominance, with exceptions on dataset MMA and dataset NASCAR where different factors showed dominance on different levels, which indicates that the predictive power of different factors were not clearly ranked on dataset MMA and dataset NASCAR.

DISCUSSION

This study applied four statistical interpretation methods to analyze the regression of MPS95 to evaluate the predictive power of different factors of rotational parameters of head impact kinematics. In terms of the predictive power among factors when viewed individually (the direct effect defined by Budescu[14]), the zero-order correlation coefficients and structure coefficients manifest that the following kinematic factors generally show the highest predictive power: 1) features based on the first derivative order of angular velocity (angular acceleration), 2) features based on the magnitude of the kinematics and 3) features of power order 1. These findings were generally supported by the dominance analysis in which these three factors dominated in most levels of analyses. Based on the findings in this study, in terms of the feature engineering of brain injury criteria, new mathematical forms can be designed and validated to evaluate the brain injury risk in a more accurate manner. For instance, the brain injury criteria can take into consideration both angular acceleration and angular velocity[9], the magnitude as well as the components in different spatial directions[15], and the first-order-powered and also the square-rooted math forms for better risk evaluation in a wider range of head impacts. In addition to the diagnostic and risk-evaluation development, upon understanding the most predictive features in the head impact kinematics, better concussion-prevention technologies can be developed with focus laid on the features predictive of high brain strain. For instance, in the design process of protective equipment such as the football helmets[16], the peaks of the angular acceleration magnitude can be the metric to guide the design most appropriately.

ACKNOWLEDGEMENTS

The study is supported by Pac-12 Conference's Student-Athlete Health and Well-Being Initiative, National Institutes of Health (R24NS098518).

REFERENCES

1 Wu, S. *et al. Biomech. Model. Mechanobiol.* 19, 927–942 (2020)
2 O'Keeffe, E. *et al. J. Neurotrauma* 37, 347–356 (2020)
3 Kleiven, S. *SAE Tech. Pap.* 2007-Octob, (2007)
4 Giudice, J. S. *et al. Ann. Biomed. Eng.* 47, 464–474 (2019)
5 Camarillo, D. B. *et al. Ann. Biomed. Eng.* 41, 1939–1949 (2013)
6 Liu, Y. *et al. arXiv* 1–45 (2020)
7 Sanchez, E. J. *et al. Clin. Biomech.* 64, 82–89 (2019)
8 NHTSA NHTSA. United States. https://www.nhtsa.gov/data.
9 Gabler, L. F. *et al. J. Biomech. Eng.* 140, 1–13 (2018)
10 Nathans, L. L. *et al. Pract. Assessment, Res. Eval.* 17, 1–19 (2012)
11 LeBreton, J. M. *et al. Organ. Res. Methods* 7, 258–282 (2004)
12 Date, P. U. B. *et al.* (1999)
13 Budescu, D. V. *Psychol. Bull.* 114, 542–551 (1993)
14 Budescu, D. V. *et al. Organ. Res. Methods* 7, 341–350 (2004)
15 Laksari, K. *et al. arXiv* (2018)
16 Vahid Alizadeh, H. *et al. J. Biomech. Eng.* (2020)

PARALLEL STAGE MECHANISM FOR IMAGE GUIDED AND TARGETED MR ELASTOGRAPHY

Efe Ozkaya* (1), Waiman Meinhold* (2), Derek Petti (1), Emily Triolo (1), Paul Kennedy (3), Lazar Fleysher (3), Jun Ueda (2), Mehmet Kurt (1,3)

(1) Department of Mechanical Engineering,
Stevens Institute of Technology,
Hoboken, NJ, USA

(2) Woodruff School of Mechanical Engineering,
Georgia Institute of Technology,
Atlanta, GA, USA

(3) BioMedical Engineering and Imaging Institute,
Icahn School of Medicine at Mount Sinai,
New York, NY, USA

INTRODUCTION

Magnetic Resonance Elastography (MRE) is a developing imaging technique that enables non-invasive estimation of tissue mechanical properties through the combination of magnetic resonance imaging (MRI) and mechanically induced shear waves in the tissue [1]. During MRE imaging of smaller and stiffer tissues, the shear wavelength should not surpass the size of the region of interest (ROI). In other words, enough data having adequate temporal resolution needs to be collected in a single period of cyclic harmonic loading to avoid aliasing. For instance, performing MRE on a small tissue such as the intervertebral disc (IVD) requires the targeting of shear wavefields to maximize the signal-to-noise ratio (SNR) in the ROI [2,3]. Although increased actuation frequency allows placement of shorter wavelengths in a given ROI which can cause an increase in SNR, challenges with attenuation caused multi-driver units to be investigated [4-7]. With multi-driver units, it is aimed to illuminate the ROI in a more uniform fashion through constructive wave interference [6]. Also, past efforts have utilized manual placement of drivers for brain MRE [8], but for more targeted tissue movement, control of driver positioning is needed.

This work details the design and evaluation of an active MRE driver positioning system for image guided MRE that is targeted to be used for the assessment of disc degeneration in the lumbar region in vivo non-invasively. Application of MRE imaging to identifying the degeneration level of the intervertebral disc (IVD) has been performed by multiple research groups primarily on excised IVD tissue [9-11]. The proposed system in this work combines positioning control with MRE actuation and is shown in Figure 1.

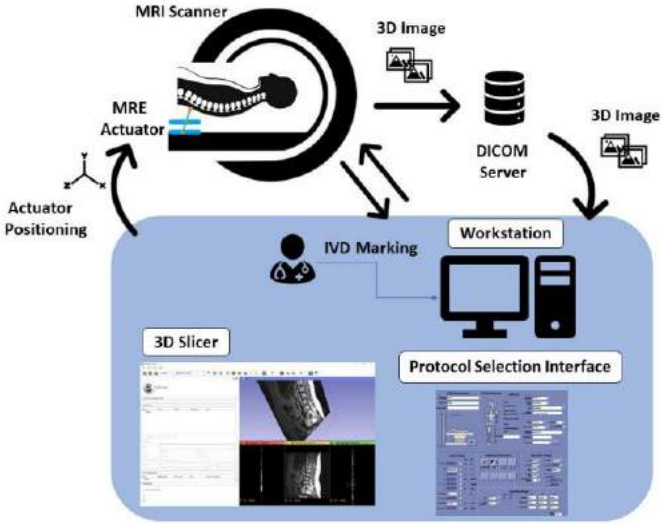

Figure 1: Process flow: Marking of the targeted ROI by MR technician. Image data transfer from DICOM server to local workstation. Bi-directional communication between the local workstation and linear positioners of the parallel stage mechanism. Actuator positioning to the target location through visual servoing.

METHODS

Mechanical Design: A fixed platform was made from two parallel stages distanced by rectangular pillars in between. Both in lower and upper stages, identical carriers were used to provide motion along the y-axis [12]. On top of these y-axis carriers, carriers providing motion along the x-axis were situated (see Fig. 2a). Low surface friction rods

*Contributed Equally

were used as carrier guides. Inside the x-axis carriers, a ring-shaped volume was left empty for contrast agent to be injected. Furthermore, at the center of these x-axis carriers custom cut spherical ball joints were placed. The linear positioning of all the carriers was performed by hydraulic manipulators (syringe-tube-syringe system). As the mechanical vibration source, an MR compatible piezo actuator (APA150M-NM, Cedrat Technologies) was used. This actuator is attached to the tip of a rod which passes through the upper spherical ball joint. The other end of the rod piece was coupled with a syringe that serves as the 5th DOF linear positioner. Inside this rod, a fiducial marker was placed closer to its tip in which the piezo actuator was attached. While the upper spherical ball joint serves as a guide for this rod piece, the lower spherical ball joint holds the syringe tube casing.

Imaging Protocol: A morphological scan was performed to acquire the position and orientation of the piezo actuator attached to the rod piece. Imaging parameters for this 3D morphological scan were acquisition matrix: 96 x 48, TE/TR: 1.26/520.29ms, FOV: 100 mm, flip angle: 38, and slice thickness: 1.6 mm. While performing MRE imaging, the MRE sequence provided TTL triggering was used to drive the piezo actuator in sync with the motion encoding gradients. MRE data was acquired for 19 slices with 3D motion encoding gradients using an echo planar spin echo 2D pulse sequence [13] in the axial plane with the following imaging parameters: acquisition matrix: 96 × 48, TE/TR: 59/2541.4ms, FOV: 240 mm, flip angle: 90, 8 phase offsets, slice thickness: 2 mm, gradient amplitude: 40 mT/m, mechanical vibration frequency: 60 Hz. The experiments were performed on a 3-Tesla Siemens Skyra scanner.

Phantom Preparation: A Knox gelatin phantom was prepared to evaluate the positioning mechanism. Three disc-shaped phantoms made from 100ml-Knox:500ml-water mixture was placed inside of a 35ml-Knox:500ml-water mixture. A plastic pipette was passed through the disc shaped phantoms to hold them in place. During the preparation of both mixtures, Knox dissolved in water was heated in microwave for 80 seconds and then placed in vacuum chamber for 30 seconds before being poured into molds.

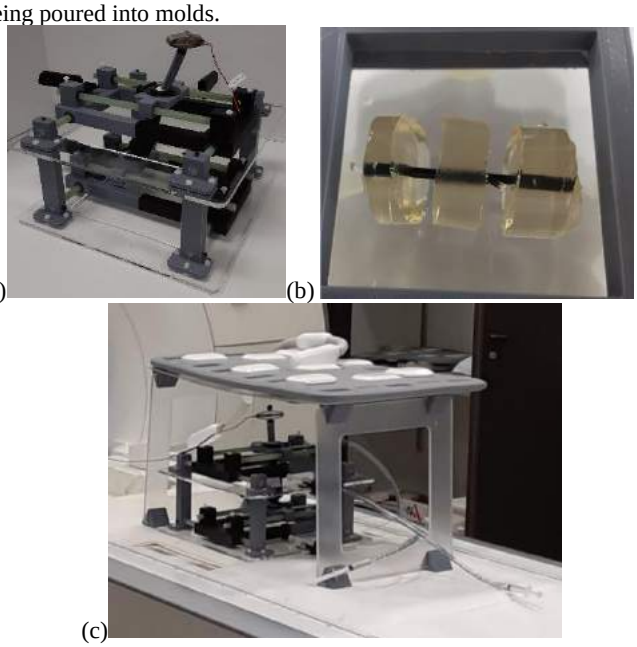

Figure 2: (a) Parallel stage mechanism. (b) IVD mimicking phantom. (c) The whole setup including the hydraulic manipulators. Underneath the body coil, a phantom holder was positioned in which the IVD mimicking phantom resides.

RESULTS

Manual positioning of the piezo actuator was performed by using the hydraulic manipulators (see Fig. 2c). For mechanical wave delivery, a 3D printed rod extension attached to the tip of the piezo actuator was brought in contact with the IVD-mimicking phantom's surface. Wave propagation fields were captured under different harmonic loading angles during MRE imaging (see Fig. 3e-f). The angle of loading for each configuration shown in Figure 3 was calculated through a custom written Python script in 3D Slicer. The harmonic loading angles were 88°, 83°, and 88° with respect to the IVD mimicking phantom's surface (see Fig. 3a-c). The absolute maximum/minimum amplitudes were ±5 microns in all experiments.

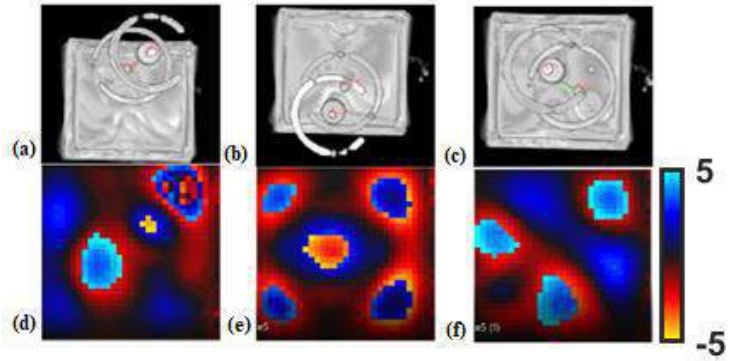

Figure 3: Displacement fields and associated robot configurations for harmonic loading under (a) 88°, (b) 83°, and (c) 88°.

DISCUSSION

Currently elastography imaging of the IVD is not widely available clinically due to limitations of current MRE actuator positioning methods. In this study we have shown that harmonic loading angle has an influence on the acquired wave field data in a phantom model. Our initial prototype's performance will be further evaluated based on the stiffness maps and the propagating wave field profiles acquired of an excised IVD volume. Stiffness maps and wave field profiles can be used to pre-diagnose the onset of a possible tearing on the annulus fibrosus region of an IVD. By having this knowledge at the early stages of degenerative disc disease, precautions can be taken to avoid progression of the disease at early stages. This can prevent a person to go through extensive surgeries in the future.

ACKNOWLEDGEMENTS

This research is funded through DoD CDMRP Discovery Award - W81XWH-20-1-0043.

REFERENCES

[1] Muthupillai, R et al., *Magn Reson Med* , 36(2):266-74, 1996.
[2] Streitberger KJ et al., *Magn Reson Med*, 74(5):1380-7, 2014.
[3] Walter, BA et al., *Radiology*, 285(1):167-175, 2017.
[4] Zheng, Y et al., *Conf Proc IEEE Eng Med Biol Soc*, 1916-9, 2006.
[5] Zheng, Y et al., *Annu Int Conf IEEE Eng Med Biol Soc*, 2611-3, 2007.
[6] Mariappan, YK et al., *Magn Reson Med*, 61(3):678-85, 2009.
[7] Neumann, W et al., *Concepts Magn Reson Part B*, 1-9, 2018.
[8] Anderson, AT et al., *J Mech Behav Biomed*, 34:859-871, 2001.
[9] Cortes, DH et al., *Magn Reson Med*, 72(1):211-9, 2014.
[10] Ephraim, BA et al., *Magn Reson Imaging*, 39:132-137, 2015.
[11] Beauchemin, PF et al., *NMR Biomed*, 31(10):1-8, 2018.
[12] Meinhold, W et al., *IEEE Trans Biomed Eng*, 2020.
[13] Chaze, CA et al., *NeuroImage Clinical*, 22:1-7, 2019.

MEASURING THE ANISOTROPIC MECHANICAL PROPERTIES OF SINGLE NEONATAL MOUSE CARDIAC MYOCYTES

Taylor M. Rothermel (1), Patrick W. Alford (1)

(1) Department of Biomedical Engineering
University of Minnesota – Twin Cities
Minneapolis, MN, USA

INTRODUCTION

Congenital heart defects and subsequent surgical interventions alter the loading conditions on the heart muscle.[1] Biomechanical models of congenital heart defects are useful for understanding disease progression and aiding clinicians in planning treatment. In order to formulate the most predictive tissue and organ level biomechanical models, the mechanical properties of the individual components must also be elucidated. In order to fully understand the mechanical properties of the heart, the mechanical properties of cardiac myocytes, the force generating cells in the heart muscle, must also be characterized. Cardiac myocytes play an important role in remodeling of the heart muscle and are sensitive to mechanical stimuli.[2-3] As cardiac myocytes exist in a dynamic mechanical environment and have a highly organized cytoskeletal architecture, there is a need to understand how complex mechanical loading conditions influence the cell's anisotropic mechanical properties. Here, we measure the stress-strain behavior of cardiac myocytes in response to complex loads.

METHODS

Substrate Fabrication and Cell Culture. Neonatal mouse ventricular myocytes (NMVMs) were isolated from one-day-old mouse pups using standard methods.[4] As previously described,[5] NMVMs were micropatterned with elongated architecture (aspect ratio 7:1 and an area of ~2250 μm^2) on fluorescent-bead-doped polyacrylamide (PA) gel with a Young's modulus of 13.5 kPa (Fig. 1a-b).

Cellular Micro-Biaxial Stretching (CμBS). CμBS experiments were performed using a custom-built microscope-mounted device to perform traction force microscopy (TFM) experiments on cells exposed to biaxial stretching (Fig. 1c). Three types of straining protocols were applied to the micropatterned NMVMs: axial tension, axial compression, and transverse tension where the axial direction is parallel to the short axis of the cell and the transverse direction is parallel to the short axis of the cell (Fig. 1d). Strains were evaluated in 5% increments to a maximum of 15% for all protocols. NMVMs were paced at 1 Hz using an Ionoptix MyoPacer to induce contraction. High temporal resolution (100 Hz) images of the fluorescent bead layer were acquired to capture the full contraction of the cell and used to calculate traction forces of the cardiac myocytes at each applied strain (Fig. 3e).

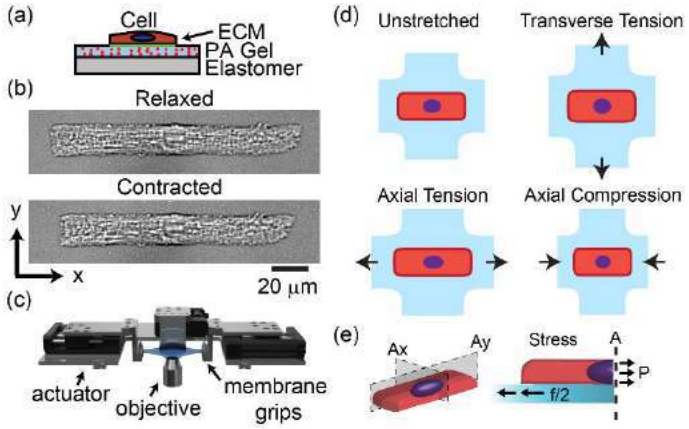

Figure 1: Cellular microbiaxial stretching device and methods for measuring cell stress. (a) Schematic of cell patterned on PA gel,[5] (b) Representative images of a contracting micropatterned NMVM, (c) CμBS device,[5] (d) Schematic of a cell under axial tensile, axial compressive, and transverse tensile strains, (e) Relationship between traction stress, cross-sectional area, and PK1 stress.

Traction forces at each stretch were calculated using standard methods.[5] The first Piola-Kirchhoff (PK1) stresses, represented by $P_x = f_x/(2A_x)$ and $P_y = f_y/(2A_y)$, where f is the traction force and A is the cell cross-sectional area, were calculated at the mid-plane of the cell using the total tensile force and the undeformed cross-sectional area of the cell (Fig. 1c). The PK1 stress was converted to Cauchy stress (σ) by multiplying the PK1 stress by the stretch ratio, λ. The cross-sectional areas of micropatterned NMVMs were estimated to be A_x = 19 μm^2 and A_y = 131 μm^2.[6] Sarcomere spacing during stretching was measured using a fast Fourier transform (FFT) on bright field images of the contracting NMVMs in which the sarcomere structures are visible.

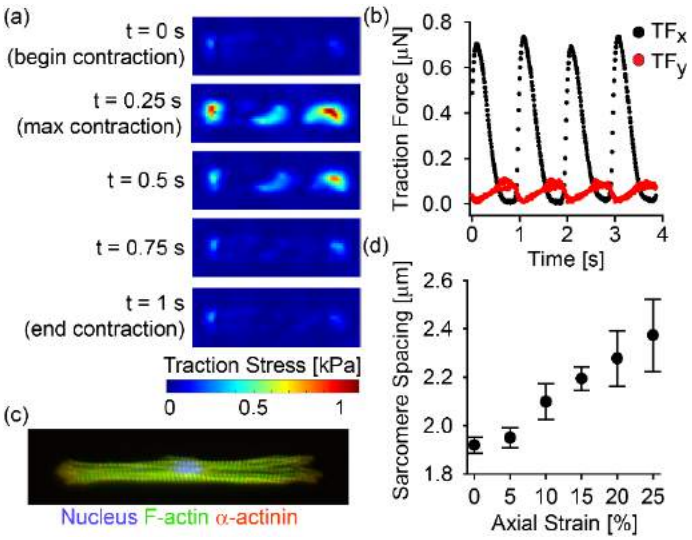

Figure 2: NMVMs are compatible for use with CμBS. (a) Traction stress heat maps during contraction, (b) Trace of the traction forces in a micropatterned NMVM, (c) NMVM stained for nuclei, F-actin and α-actinin, (d) Sarcomere spacing of cardiac myocytes under axial tensile strain.

RESULTS

Traction force of the NMVMs during contraction was measured and was greatest along the long axis of the cell (Fig. 2a-b), which is consistent with the underlying sarcomeric architecture (Fig. 2c). Using FFT, the sarcomere spacing prior to stretch was measured to be ~1.97 μm, which is consistent with measurements from fluorescently stained cells (Fig. 2c) and literature values.[7] When the NMVMs were exposed axial tensile strains, the spacing between sarcomere subunits increased with stretch (Fig. 2d).

In the axial direction, the NMVMs were exposed to tensile or compressive strains using CμBS (Fig. 3a) and the axial Cauchy stress (σ_x) (Fig. 3b) and transverse Cauchy stress (σ_y) (Fig. 3c) were calculated at each deformation. The passive stress was defined as the stress in the cell when the cell is not contracting and the active stress is defined as the difference in cell stress between the fully contracted and non-contracted states. Under axial tensile strains, the active σ_x initially increases with increasing strain before decreasing at the maximum applied strain. Under axial compression, the active σ_x decreased as the cell was compressed. This is consistent with previous understanding of the length-tension relationship observed in striated muscle cells. The passive stress and the stress along the short axis of the cell, σ_y, remained relatively unchanged under both axial tension and compression compared to the active stress in the long axis. Under transverse tensile strains (Fig. 3d), the active σ_x decreased slightly with increasing strains while the passive σ_x was relatively unchanged (Fig. 3e). Both the passive and active σ_y remained relatively unchanged with increasing strains (Fig. 3f).

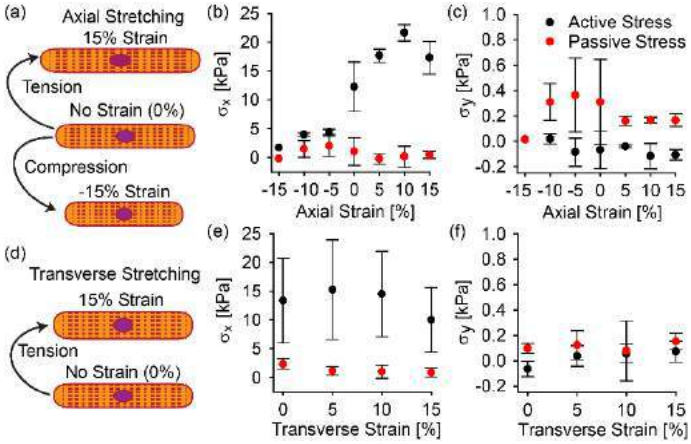

Figure 3: Cauchy stress (σ) measurements in NMVMs under complex loads. Axial Stretching (a-c). (a) Schematic of axial tension and compression, (b) Active and passive σ_x along the long axis of the cell, (b) Active and passive σ_y along the short axis of the cell. Transverse Stretching (d-e). (d) Schematic of transverse tension, (c) Active and passive σ_x along the long axis of the cell, (d) Active and passive σ_y along the short axis of the cell.

DISCUSSION

There is a need to fully characterize the anisotropic mechanical properties of cardiac myocytes in order to develop the best tissue and organ level biomechanical models of the heart. In this study, we used CμBS to measure the stress-strain behavior of NMVMs under complex loads. We found that in the axial direction, the stress-strain behavior is similar to what is described by the length-tension relationship of striated muscle in which changing the sarcomere spacing from an ideal distance decreases the force the cell is able to generate.[8] Additionally, we found that strains applied in the transverse direction also altered cell stress as the active stress appeared to decrease with applied tensile strain. This could be due to inhibiting the interactions of the acto-myosin lattice in the micropatterned cells similar to the axial stretching. Future work will expand the types of stretches performed to include transverse compression and equi-biaxial tension and formulation of a mathematical model to describe the contraction of the cardiac myocytes. Overall, our results suggest that complex loads affect the functional contractility of NMVMs.

ACKNOWLEDGEMENTS

We acknowledge financial support from the National Science Foundation (NSF) CMMI-1553255.

REFERENCES

[1] Petko, C. et al. *J. Am. Soc. Echocardiogr*., 24:1226-1232, 2011.
[2] Taber, L. et al. *Dev. Dyn.*, 203:42-50, 1995.
[3] Ribeiro, A. et al. *Proc. Natl. Acad. Sci*., 112:12705-12710, 2015.
[4] Sakurai, T. et al. *JoVE*, 88:1-9, 2014.
[5] Win, Z. et al. *J. Biomech. Eng.*, 139:1-10, 2017.
[6] Geisse, N. et al. *In Vitro Cell. Dev. Biol. Animal*, 45:343-350, 2009.
[7] Mansour, H. et al. *Circ. Res*., 94:642-649, 2004.
[8] Allen, D. et al. *J. Mol. Cell. Cardiol.*, 17:821-840, 1985.

INFLUENCE OF CHONDROLABRAL DAMAGE AND LABRAL REPAIR ON HIP JOINT MECHANICS WITH CAM FAI MORPHOLOGY

J. Todd (1,2), T. Maak (4), G. Ateshian (5), A. Anderson (1,2,3,4), J. Weiss (1,2,4)

(1) Department of Biomedical Engineering
University of Utah
Salt Lake City, UT, USA

(2) Scientific Computing and Imaging Institute
University of Utah
Salt Lake City, UT, USA

(3) Department of Physical Therapy
University of Utah
Salt Lake City, UT, USA

(4) Department of Orthopedics
University of Utah
Salt Lake City, UT, USA

(5) Department of Mechanical Engineering
Columbia University
New York, NY, USA

INTRODUCTION

Patients with cam femoroacetabular impingement (FAI) morphology are prone to chondrolabral injuries, which often progress to osteoarthritis (OA) [1]. The mechanical factors responsible for initiating and progressing chondrolabral injuries in these patients are not well understood. Additionally, while labral repair is commonly performed during surgical correction of cam morphology, the isolated mechanical effect of labral repair on the labrum and surrounding cartilage is unknown. Using patient-specific finite element (FE) analysis, we asked the following questions: 1) Does cam morphology pose a higher risk of damage to cartilage due to higher stresses and strains, compared to a radiographically normal hip? 2) Do common chondrolabral damage scenarios, including delamination, delamination with rupture of the chondrolabral junction (CLJ), and presence of a chondral defect, experience elevated stress and strain around the damage? 3) How does labral repair affect stresses and strains in the context of the aforementioned chondrolabral damage scenarios?

METHODS

We selected a patient with cam FAI who was representative of a cohort of seven patients in a previous study [2]. The selected patient was a 25-year-old, 90 kg, BMI 24 kg/m^2 male with cam morphology characterized by an alpha angle (AA) of 78°, lateral center edge angle (LCEA) of 28°, Tonnis angle of 7°, femoral neck shaft angle (FNSA) of 131°, no crossover sign, and subspine type I. We selected a control participant from the cohort with similar demographics (male, 23-year-old, 81 kg, BMI 24 kg/m^2) having normal morphology with an AA of 37°, with an LCEA of 27°, Tonnis angle of 7°, FNSA of 130°, no crossover sign, and subspine type I. Patient-specific FE models were created of the cartilage and labrum and meshed with quadratic tetrahedral elements (Figure 1A). The cartilage and labrum were represented as inhomogeneous, biphasic, anisotropic materials. A strain-dependent, anisotropic permeability was used to represent the physiological permeability characteristics of articular cartilage. The mechanical contribution of the collagen fibrils was represented by a continuous fibril distribution constitutive model, which varied in primary orientation through the thickness of the cartilage layers. Material coefficients were set according to a previous study of cartilage mechanics in the hip [3]. Patient-specific kinematics representing one cycle of gait were applied to the patient models. For each scenario analyzed, contact area, contact stress, tensile strain, and shear stress were recorded over the gait cycle and compared.

For the cam FAI model, additional FE models were created to represent delamination, delamination with CLJ rupture, and a full-thickness defect. For each case, a labral tear and labral repair were simulated. The size and location of damage was assigned based on reported clinical prevalence [1].

RESULTS

The cam FAI hip experienced higher magnitudes of all variables compared to the normal hip, and the location of all maximum dependent variables shifted anterosuperiorly. (Fig 1B-D).

Compared to the intact FAI case, the damage cases experienced a more even stress distribution, with 8-10% increases in contact area during heel-strike (Figure 1E). Contact stress during heel-strike for the intact FAI case was concentrated at the CLJ and experienced a peak of 12.3 MPa. The contact stress shifted posteroinferior and, contrary to our expectations, decreased substantially for all damage cases with a peak ranging from 7.5-8.0 MPa, also during heel-strike (Figure 1F, left). Tensile strain and shear stress followed similar trends to contact stress in both location and magnitude, and all damage scenarios followed the same trend; thus, the delamination case was used as a representative

scenario in Figure 1F. Labral repair only marginally affected the cartilage, but subtle increases in contact stress were observed near the CLJ and on the labrum (Figure 1F, right).

DISCUSSION

Our results suggest that patients with cam FAI morphology may be susceptible to chondrolabral damage due to concentrated stress and strain conditions in the anterosuperior region. Shear stress had the largest difference in peak variables between cases, while contact stress and tensile strain also increased for the FAI hip. Shear stress has been implicated as the cause of delamination, which is commonly observed in the anterosuperior location on the CLJ – coincident with the location of peak shear stress predicted in our study. Notably, this result was found without contact or direct impingement between the cam bump and acetabular rim. This finding suggests that, for some patients, chondrolabral damage in the FAI hip could occur due to morphologic femoral and acetabular differences in the central compartment regardless of whether osseous impingement occurs.

Contrary to our hypothesis that varied degrees of chondrolabral damage would result in elevated stress and strain around the damage region, all simulated damage conditions redistributed the load more evenly across the joint compared to intact cartilage in the FAI hip. The redistribution of load seen in damage cases, which increased contact area and decreased contact stress, shifted pressure away from the damage zone. The high shear stress in the intact joint suggest that it is predisposed to damage, but the damage cases relieve that disposition. Regardless of the damage condition, the distribution of contact area during heel-strike also decreased peak strain and shear stresses in the cartilage and labrum. All damage cases experienced concentrations of tensile strain and shear stress around the damage location, but the magnitude may not be high enough to progress damage alone. Larger damage size or other activities may also cause further instability around the damage zone, leading to higher strain conditions. It is also worth noting that the shift in peak stress may cause additional damage in the posteroinferior location. Posteroinferior injuries secondary to anterosuperior damage are reported for patients with femoroacetabular syndrome and were first described by Beck et al in 2005 [4].

Labral repair with delamination shifted peak concentrations of tensile strain from the damage zone border to the CLJ. The repair may cause increased risk for further damage at this location, such as progression to rupture of the CLJ. Additionally, the repaired labrum may be more strained by the repair and cause subsequent labral damage.

It is worth noting that even though we used representative cam FAI patients based on radiographic measurements and average damage data to capture general differences in the groups, further studies including more patients would add confidence to our results. While the patients that we included in this study had similar acetabular morphology and are not dysplastic, differences in acetabular morphology may affect results. Specifically, damage to and around the labrum may have a significantly different effect in borderline dysplastic patients with FAI.

ACKNOWLEDGEMENTS

Financial support from NIH #R01GM083925 and #R21-AR063844, NSF Graduate Research Fellowship, and the LS Peery Discovery Program in Musculoskeletal Restoration is gratefully acknowledged.

REFERENCES

[1] Kapron, A et al., *KSSTA*, 27:3057-3065, 2019.
[2] Atkins, P et al., *J Ortho Res*, 38:823-833, 2020.
[3] Todd, J et al.. *J Biomech,*. 69:113-120, 2018.
[4] Beck M, *JBJS Br*, 87:1012-1018, 2005.

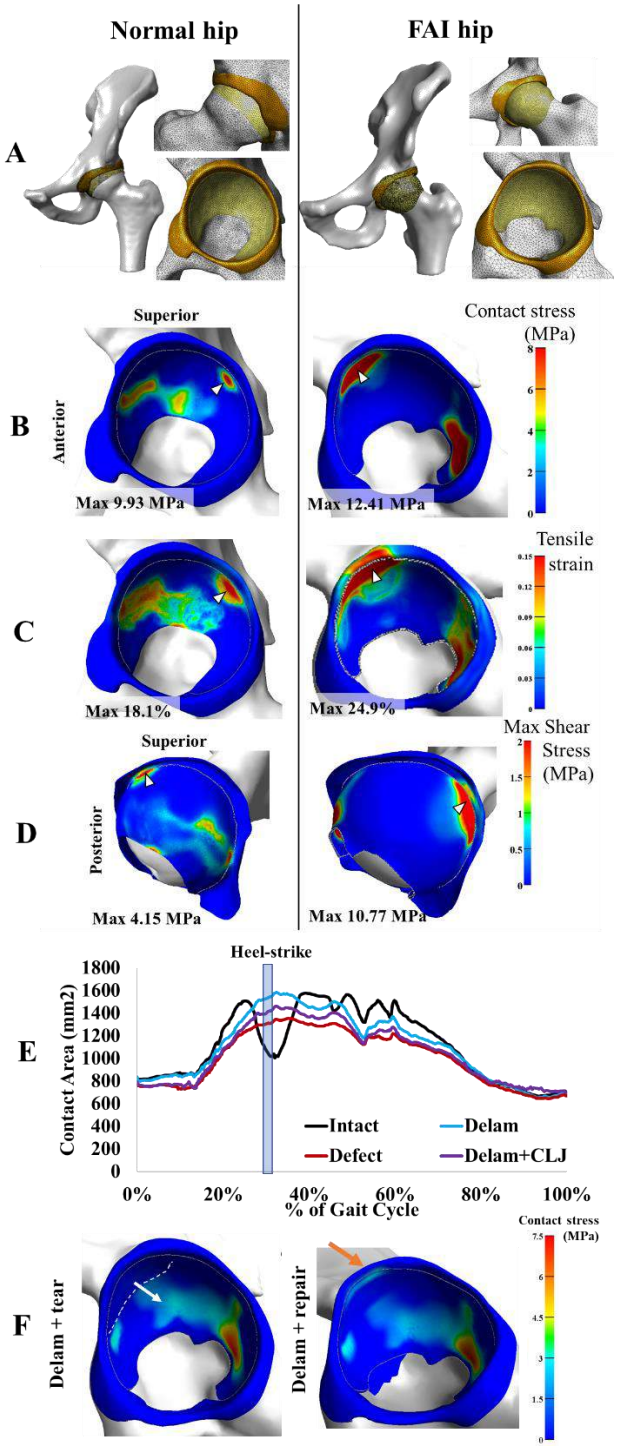

Figure 1 – A) Patient-specific models for the normal (left) and FAI (right) hips. B-D) Comparison of dependent variables between normal and FAI models. Arrows indicate location of maximum value. The FAI model experienced increases in all variables and a shift in maximum location. E) Contact area over time between FAI damage scenarios, with heel-strike (max loading) highlighted to show the decrease in contact area for the intact case. F) Contact stress of delamination model with labral tear and repair. The white arrow indicates shift of contact stress compared to 1B and orange arrow highlights stress near the CLJ with labral repair. Delamination is representative of all damage cases.

ON THE CLINICAL DIAGNOSIS OF ACROMIOCLAVICULAR JOINT ARITHRITIS

Bethany Arn (1), Mohamed Samir Hefzy (1), Brian Trease (1), Abdulazim Mustapha (2)

(1) Mechanical, Industrial, and Manufacturing Engineering Department
The University of Toledo
Toledo, OH, USA

(2) Department of Orthopaedic Surgery
The University of Toledo
Toledo, OH, USA

INTRODUCTION

Osteoarthritis of the acromioclavicular (AC) joint has been said to be a common source of shoulder pain, and is said to be the most common source in patients over the age of 50, with over 50% of the patients showing radiographic signs of degenerative arthritis [1,2]. The pain associated with AC osteoarthritis is thought to be caused by irritation of the subacromial bursa when the AC joint becomes inflamed or had protruding osteophytes and the cross body adduction (CBA) test is a current clinical diagnosis of this pathology [3]. However, recently, another test has been proposed—the Reverse Shoulder Internal Rotation test—that involves placing the hand behind the back, abbreviated HBB for short.

In a clinical setting, it was observed that some patients test negative under the CBA test and positive under the HBB test. These patients were later found to have osteoarthritis of the AC joint through imaging or arthroscopic means. The purpose of this study is to investigate the biomechanics of these two positions in order to determine if the HBB test is a better one.

METHODS

The Zygote Solid 3D Male Homan Anatomy model by ZYGOTE (American Fork, UT) was used to construct a 3D CAD model of an adult 50th percentile male shoulder and chest cavity [4]. This model was created as a SolidWorks file, Dassault Systèmes (Vélizy-Villacoublay, France) [5]. This model was then imported into MSC.ADAMS, Adam View 2017 by MSC Software (Newport Beach, CA) in order to model and study the dynamics of the shoulder in three specified positions – standard anatomical, CBA, and HBB [6]. The model includes the clavicle, scapula, humerus, and the rib cage. The radius and ulna were combined as a single rigid body. Similarly, the 27 bones of the hand were considered as one segment.

Three revolute joints were used to model the glenohumeral joint allowing rotations around three different axes. A spherical joint was used to model the elbow joint. In order to move from one position to another, these six rotations were identified.

Nine springs were used to model five ligaments, with stiffness identified from the literature [7]. Three muscle forces were introduced into the model for the CBA position and two for the HBB position. In order to account for the complexity of the contact constraints of the scapulothoracic contact, normal to the tangent springs were introduced in order to allow scapular motion along the curvature of the thorax.

The shortest distance between the distal clavicle and the acromion process of the scapula was calculated as an indicator of the intensity of the stress at the articulating surfaces, which would indicate the presence of osteoarthritis at the AC joint.

RESULTS

Table 1 shows the seven rotations at the glenohumeral, elbow, and wrist joints that were used to position the skeleton in the CBA position, and the six rotations that were used at the same joints to position the skeleton into the HBB position; both moving from the anatomical position. Figure 1 depicts the skeleton at both final resting positions.

Table 1: Rotations used to position the skeleton in both the CBA and HBB positions

	CBA			HBB		
Step	Angle	Joint	Rotation	Angle	Joint	Rotation
1	90°	GH	Internal Humeral	90°	GH	Internal Humeral
2	100°	GH	Flexion	45°	GH	Extension
3	65°	Wrist	Pronation	20°	GH	Adduction
4	24°	GH	Adduction	40°	Elbow	Pronation
5	90°	Elbow	Flexion	90°	Wrist	Pronation
6	18°	Elbow	Superior	120°	Elbow	Flexion
7	15°	Wrist	Radial Deviation	-	-	-

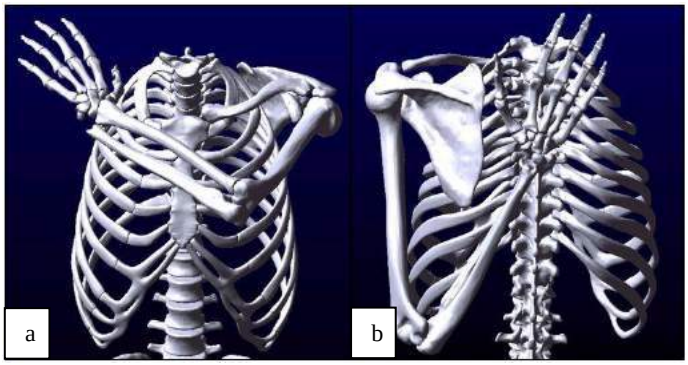

Figure 1: Final resting positions of the (a) Cross Body Adduction (anterior view) and (b) Hand Behind the Back (posterior view) tests.

The shortest distances between the distal clavicle and acromion process of the scapula for these two positions were obtained interactively using MSC.ADAMS and are listed in Table 2. This table also includes the shortest distance in the anatomical position obtained from the literature [8] as well as using MSC.ADAMS and using SolidWorks.

Table 2: Minimum distances between the distal clavicle and acromion process of the scapula.

Source	Distance (mm)
Literature [8]	3.31
Anatomical (SW)	3.14
Anatomical (ADAMS)	3.16
CBA (ADAMS)	2.86
HBB (ADAMS)	1.51

DISCUSSION

Table 2 shows that the acromion process of the scapula moves to different locations relative to the clavicle. With CBA decreasing the distance between the distal clavicle and the acromion process by 0.30 mm there is an indication that the stress level at the joint increases, thus causing irritation of the subacromial bursa. It is then understandable that this is the current method of clinically diagnosing osteoarthritis of the AC joint.

Additionally, Table 2 shows that the spacing at the AC joint is decreased by 1.65 mm from the standard anatomical position in the HBB position, indicating that this is also a valid test for osteoarthritis of the AC joint. Due to the over 5x greater reduction in space, the HBB position may be argued that it is a better test to diagnose earlier stages of osteoarthritis at the AC joint because of the higher degree of irritation that it places upon the subacromial bursa.

In order to validate this anatomical model, the creations of both a kinematic model and a Finite Element Method (FEM) model are needed to complete the three model validation trifecta. The kinematic model would focus upon the placement of the end-effector—the patient's palm—and define the mathematical models that describe the arm's motion regardless of forces or torques—i.e. the muscles and ligaments [9]. Whereas the FEM model would build upon this anatomical model through quantifying the stress at the articulating surfaces as well as the stresses placed upon the ligaments and muscles to ensure that these values stay within their specified reasonable ranges.

REFERENCES

[1] Petersson, C, *Acta Orthopaedica Scandinavica*, 54(3):434-438, 1983.
[2] Horváth, F et al., *Archives of Gerontology and Geriatrics*, 3(3):259-265, 1984.
[3] Buttaci, C et al., *American Journal of Physical Medicine & Rehabilitation*, 83(10):791-797, 2004.
[4] "Solid 3D Male Model." *Zygote*, www.zygote.com/cad-models/collections-products/solid-3d-male-collection.
[5] "3D CAD Design Software: SOLIDWORKS." *Dassault Systèmes*, www.solidworks.com.
[6] "MSC Software Corporation." *Adams – The Multibody Dynamics Simulation Solution*. www.mscsoftware.com/product/adams.
[7] Soslowsky, L et al., *Repair and Regeneration of Ligaments, Tendons, and Joint Capsule*, Humana Press, 2005.
[8] Edwards, S, et al., *Arthroscopy: The Journal of Arthroscopic & Related Surgery*, 23(12):1278-1284, 2007.
[9] Bregler, C, "Kinematic Motion Models." *SpringerLink*, link.springer.com/referenceworkentry/10.1007%2F978-0-387-31439-6_587.

SB³C2021
Summer Biomechanics, Bioengineering and Biotransport Conference
June 14-18, Virtual

DESIGN OF A MRI-COMPATIBLE PIPETTE SIMULATOR TO STUDY HOW PIPETTE DESIGN AFFECTS JOINT FORCES AND CONTACT PRESSURES

Nolan M. Norton (1), Kenneth J. Fischer (1,2)

(1) Bioengineering Graduate Program
University of Kansas
Lawrence, KS, USA

(2) Mechanical Engineering
University of Kansas
Lawrence, KS, USA

INTRODUCTION

The use of manual micropipettes has been associated with a high prevalence of upper extremity and work-related musculoskeletal disorders in laboratory workers [1]. This may be due to a combination of repetitive motions during pipetting and the amplification of forces from the thumb tip to the basilar thumb joint [2] that lead to tendonitis, carpal tunnel syndrome, other musculoskeletal injuries, and may increase risk of osteoarthritis (OA). These pathologies cause substantial physical pain/discomfort, increase health care costs, and cause employees to miss time at work. An investigation into ergonomic pipette design could help to reduce these musculoskeletal pathologies and their consequent negative impacts.

Several methods could be used to investigate the effects of pipetting on the joints in the thumb. These include using a thin-film force sensor underneath the thumb and a kinematic analysis of the motion of the thumb's joints, used in conjunction with computational hand models to predict muscle forces, and tendon displacement [2-4]. While these may be useful in for comparison of movement and muscle forces, this approach requires numerous boundary condition assumptions and assumptions that allow estimation of muscle activation or force distributions. Also, these methods cannot capture nuances of how design features (such as texture) may affect muscle coordination and forces. One method to investigate the effects of pipette design on stresses within joints is through MRI-based modeling. This offers a non-invasive *in vivo* approach to estimate forces, contact pressures, contact area and location(s), and tissue stresses in joints during functional activities. Additionally, MRI-based modeling allows for the use of subject-specific geometries in place of generic geometries and minimizes assumptions for model boundary and loading conditions. This is accomplished through the collection of lower resolution loaded scans (i.e. during simulated pipetting) and higher resolution unloaded scans (i.e. with a relaxed hand) for finite element model building, and image registration to obtain displacement boundary conditions [5-6]. The creation of a MRI-compatible pipette simulator would enable MRI-based modeling of the basilar thumb joint to investigate the effects of different design features on joint forces, contact pressures, and contact area/location(s) within this highly susceptible joint.

OVERALL SYSTEM DESIGN

MRI-compatibility, modularity, and the reproducibility of experimental conditions were primary objectives for the design of the pipette simulator. Ferromagnetic substances could not be included due to safety concerns, and other metals were excluded to avoid image distortion. Therefore, plastic materials were most appropriate, and additive manufacturing allowed straightforward fabrication of the parts (and multiple versions to be tested). Modularity was required so that various different design features could be easily interchanged for testing.

Figure 1. Disassembled pipette simulator

Reproducibility of experimental conditions requires high sensitivity for the sensor and low friction (resistance) in moving parts, so we can assure that the research participants are applying a consistent force.

To achieve modularity, the pipette simulator was divided into multiple parts: a button to be pushed by the thumb, a carbon fiber plunger/rod to transfer force through a handle, an o-ring on the far end of the rod (to prevent the rod and button from falling out of the handle), a two-piece spherical base, and a pneumatic rubber bulb inside the base (Figures 1 & 2). The two parts of the spherical base can be fastened together using plastic nuts and bolts. Each handle set (with button and push-rod) can be screwed onto the spherical base (with rubber bulb).

Figure 2. Fully assembled pipette simulator

The rubber bulb was attached via plastic connectors and tubing to a pneumatic pressure system with pressure regulator to assure consistent pre-pressure (before the pipette plunger is pushed) and a precision pressure transducer. This system provided consistent resistance to plunger depression with minimal friction and a precision of 0.001 psi. Early experiments with plastic and glass syringe designs had substantial friction which increased the force to move the piston from a static position and decreased force to hold the syringe pressure at a fixed level. This behavior was apparent even with lubricants. Other earlier designs experimented with plastic springs within the handle, but these could not provide accurate feedback on the force applied. The aforementioned pressure transducer provides data to the investigators and to the research subject. A custom LabVIEW code provides visual feedback to the subject and allows them to attain and hold the pressure near a specified target during the MRI scan (Figure 3). This also helps assure experimental conditions are consistent across subjects. In addition, subjects wore an MRI-compatible wrist brace with 20º wrist extension, to assure consistent hand/wrist position (and thus more consistent data overall) between subjects.

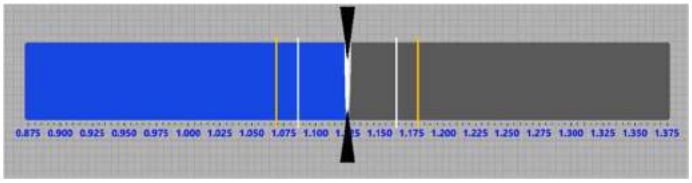

Figure 3. LabVIEW screen visible to the subject during testing.

PIPETTE FEATURES TO EVALUATE

Using 3-D printing, any number of shape parameters and features of the simulated micropipette handle can be easily created and evaluated. Early experiments will examine overall micropipette size (diameter) and the effect of a finger hook/stop on the basilar thumb joint forces required to perform the simulated pipetting task. Future studies could consider additional features, such as cross-sectional shape, stroke length for the plunger, and even texture of the micropipette surface, to determine how these features affect the force and contact mechanics in the basilar thumb joint.

DISCUSSION

The proposed pipette system has been fabricated, tested, and used in a preliminary human subjects study (Figure 4). The system performed consistently through the tests. Changing the handle/features between scans was quick and simple. It is our hope that these studies will identify key design features that can be optimized to reduce risk of overuse injuries and/or osteoarthritis.

Figure 4. Experimental setup for use of pipette simulator

ACKNOWLEDGEMENTS

We would like to thank the University of Kansas General Research Fund for support of this project.

REFERENCES

[1] McKean, ML et al., *G. Ital. Med. Lav. Ergon*, 27(2):240-243, 2005.
[2] Wu, JZ et al., *J. Biomech. Eng.,* 137(8):084501/1-084501/7, 2015.
[3] Wu, JZ et al., *J. Biomech.,* 47(2):392-9, 2014.
[4] Wu, JZ et al., *Med Eng. Phys.,* 35(12):1801-10, 2013.
[5] Johnson, JE et al., *J. Orthop. Res.,* 31(9):1455-1460, 2013.
[6] Johnson, JE et al., *J. Biomech.,* 46:1548-1553, 2013.

FATIGUE LOADING OF MOUSE ACHILLES TENDON EXPLANTS DOES NOT INDUCE COLLAGEN DENATURATION

Krishna Pedaprolu (1), Spencer E. Szczesny (1,2)

(1) Department of Biomedical Engineering
Pennsylvania State University
University Park, Pennsylvania, USA

(2) Department of Orthopaedics and Rehabilitation
Pennsylvania State University
Hershey, Pennsylvania, USA

INTRODUCTION

Tendon overuse (i.e., fatigue loading) is a common cause of injury[1] that results from progressive accumulation of structural tissue damage[2-4] and a reduction in mechanical properties.[2] In order to prevent injury and restore proper tendon function, it is necessary to understand the specific damage mechanisms that are generated by tendon fatigue loading. At a microscopic level, collagen fiber disorganization, kinking, and delamination are seen with fatigue loading[2,5]. At the molecular level, studies show that fatigue induces collagen denaturation in various tendon types, including rat tail tendons[7] and flexor carpi ulnaris tendons.[7-8] Studies of bovine forelimb tendons demonstrate that extensor tendons also experience collagen denaturation during fatigue loading; however, flexor tendons do not, which suggests energy storing tendons are resistant to fatigue damage.[5] Still, it is unknown whether other energy storing tendons (e.g., Achilles tendon) also exhibit a resistance to molecular damage. Since mouse Achilles tendons show similar signs of degeneration with overuse compared to humans[9], the objective of this study was to investigate whether collagen denaturation occurs within mouse Achilles tendon explants during fatigue loading. This information will identify whether degeneration due to fatigue loading is due to tissue damage in the form of collagen denaturation.

METHODS

Mechanical testing:

Three Achilles tendons were extracted from euthanized C57BL/6 mice from an approved IACUC study. The cross-sectional areas of the tendons were determined by a non-contact laser transducer. Mechanical testing of the tendons was performed in culture medium (low glucose DMEM, 1% penicillin and streptomycin, 200 mM Glutamax, 25 mM HEPES, 1 mM magnesium ascorbyl phosphate) at 30°C using a custom bioreactor. The bioreactor applied a cyclical load of 2 MPa (16.8% of the ultimate tensile strength) at 0.5 Hz by offloading hanging weights attached to each sample via a motorized table (**Fig.1**). The samples were loaded until failure.

As a positive control for collagen denaturation, three flexor carpi ulnaris (FCU) tendons were extracted from freshly frozen Long Evans rats from another approved IACUC study. Similar to mouse Achilles tendons, FCUs were cyclically loaded to 20% of the ultimate tensile strength (9 MPa) at 1 Hz either until failure or 158,430 cycles at room temperature in PBS. One of the fatigued FCU samples did not fail after 158,430 cycles. Finally, one mouse Achilles and one rat FCU was gripped in the bioreactor and was statically loaded at a minimal stress value (~0.06 MPa) to act as negative controls.

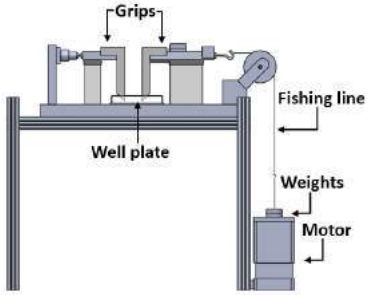

Fig.1. Schematic of the bioreactor design: The bioreactor applies cyclic load to gripped tendon explants by offloading weights from a motorized table

Imaging:

Static controls and fatigue-loaded samples were cryosectioned at a thickness of 20 μm. The sections were stained with fluorescein tagged collagen hybridizing peptide (CHP) at a concentration of 10 μM

overnight at 4°C (3Helix Inc). CHP is a probe that specifically binds to denatured collagen.[10] The sections were washed three times for 10 minutes each with distilled water. Background signal from fatigue loaded samples was removed by using the fluorescence levels of corresponding static samples as a threshold. Percentage area of collagen denaturation was calculated as a ratio of the area of positive signal in to the total area of the tendon section.

Statistical analysis:
A t-test with Welch's correction was used to compare percent area of collagen denaturation between rat FCU and mouse Achilles sections.

RESULTS

Rat FCUs showed significant CHP staining above the threshold intensity value determined from its static control. However, mouse Achilles tendons exhibited minimal CHP staining. The percentage area of collagen denaturation was statistically different between the two tendons. (**Fig. 2**) (p=0.05)

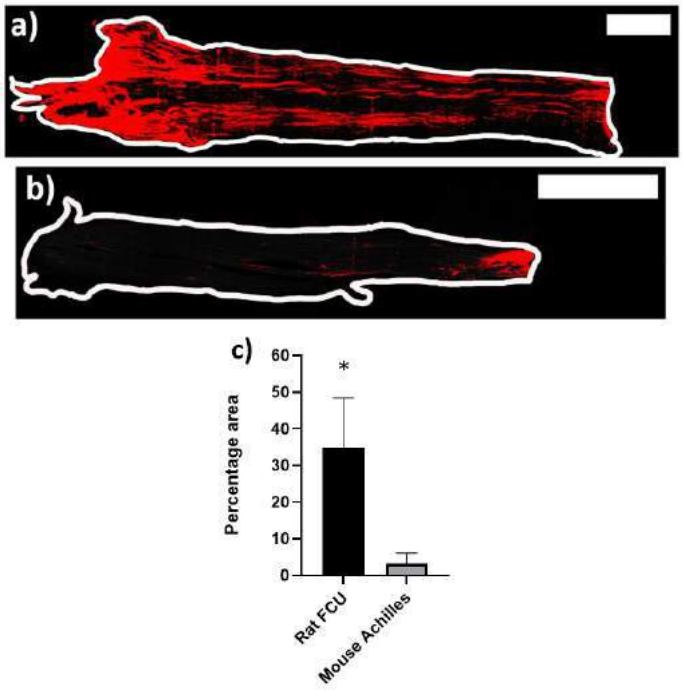

Figure 2 Collagen denaturation via CHP staining. Representative images of thresholded fatigue ruptured (a) rat FCU and (b) mouse Achilles tendons. (c) The percentage of collagen denaturation is higher in rat FCU than mouse Achilles tendons (* p=0.05). Scale bar: 1 mm.

DISCUSSION

We demonstrated that under a similar magnitude of fatigue loading (approximately 20% of the ultimate tensile strength), rat FCUs exhibited significant collagen denaturation in the form of CHP staining, but mouse Achilles tendons show minimal staining. This is in agreement with previous studies demonstrating that energy storing bovine superficial digital flexor tendons (SDFT) do not undergo collagen denaturation when they are cyclically loaded[5] and individual fibrils of such tendons do not show CHP staining when subjected to tensile rupture[11]. While collagen molecules do denature in response to fatigue loading of other flexor tendons, including the FCU in this study and the flexor digitorum longus[6], this may be because these flexor tendons serve different functions than the Achilles tendon and SDFT. Still, our findings confirm that not all tendons, even the same type, will undergo damage the same way. Additionally, our findings suggest that degenerative changes observed with overuse[9] are potentially not due to tissue damage in the form of collagen denaturation.

A limitation to this study is that an explant model does not perfectly replicate in vivo overuse. While a maximums stress of 2 MPa at roughly 20% of the tendon ultimate tensile strength is representative of physiologic loading[12], it is possible that the true in vivo stresses are higher. Additionally, preliminary data show that this level of loading maintained cellular viability, suggesting that tendon cells tolerated the cyclic loading. Future studies will investigate the effect of higher loads on collagen denaturation. Since Achilles tendons are one of the most physiologically relevant tissues to study, these results will help researchers choose an appropriate model to study tendinopathy and determine if degenerative catabolic cellular changes seen in tendinopathic tissues can happen independent of collagen denaturation.

ACKNOWLEDGEMENTS

This work was supported by the Alliance for Regenerative Rehabilitation Research and Training.

REFERENCES

[1] Wilson, JJ et al., *Am Fam Physician*, 72(5), 811-818, 2005
[2] Fung, DT et al., *J Biomech*, 43(2):274–279, 2010.
[3] Gibbon, WW et al., *Br J Sports Med.*, 33(2):129–130, 1999.
[4] Nakama, LH et al., *J Orthop Res*, 23(5):1199–1205, 2005.
[5] Herod, T. W et al., *Acta Biomaterialia*, 42, 296–307, 2016
[6] Lin, AH et al., *Acta Biomater*, 118:153-60, 2020.
[7] Zitnay, JL et al., *Science Advances*, 6(35), eaba2795, 2020.
[8] Szczesny, SE et al., *J Biomech*, 71, 251–256, 2018.
[9] Zhang, J et al., *PLoS ONE*, 8(8), e71740, 2013.
[10] Li, Y et al., Bioconjug. Chem. 24, 9–16, 2013.
[11] Quigley, AS et al., *Scientific reports*, 8(1), 1-14, 2018.
[12] West, JR et al., *J Biomech*, 37(11):1647–1653, 2004.

MANIPULATING THE INITIATION AND PROPAGATION OF MICROCRACKS IN COLLAGEN NETWORKS OF CARTILAGE

Stephany Santos (1), Corey P. Neu (2), Bryanna Samolyk (1), David M. Pierce (1,3)

(1) Department of Biomedical Engineering
University of Connecticut
Storrs, CT, USA

(2) Department of Mechanical Engineering
University of Colorado Boulder
Boulder, CO, USA

(3) Department of Mechanical Engineering
University of Connecticut
Storrs, CT, USA

INTRODUCTION

Macroscale and microscale injury regularly occur in the human knee joint resulting from complex and/or compound motions such as flexion, extension, and rotation, particularly under impact [1]. We previously demonstrated that low-energy mechanical impacts to articular cartilage, usually considered non-injurious, can in fact cause microscale cracks in the collagen network of visually pristine human cartilage [2]. Therein we defined collagen-network microcracks as fractures in the collagen network that are no wider than the diameter of chondrocyte lacunae (<30 μm). Such seemingly minute mechanical trauma may disrupt the microstructure of the extracellular matrix (ECM), altering the critical load-bearing capabilities and fluid retention properties of cartilage. We then quantified the extent to which microcracks initiate and propagate in collagen networks of cartilage during mechanical loading representative of normal activities [3].

Overall we aim to establish therapeutics to slow, stop, or even heal microcrack growth during cyclic loading, and thus minimize the possibility of subsequent cartilage and joint pathologies. Crosslinking of collagen can improve the mechanical stiffness of (especially monomeric) networks through several mechanisms, cf. [4]. Genipin is a well-established cross-linker for proteins and studies confirm that it can improve the mechanical strength of collagen networks [5]. While genipin cannot repair large (mm-scale) fissures [6], its ability to repair micron-scale fissures in collagen remains unknown. In this study we aimed to determine the effects of genipin as a preventative treatment: (1) to mitigate the initiation of microcracks under mechanical impacts; and (2) to mitigate the propagation of microcracks under cyclic compression (and specifically the effects of number and timing of genipin treatments). We hypothesized that treatments with genipin will interrupt initiation and progression of damage in the networks of collagen in cartilage, and thus potentially lead to new treatments.

METHODS

Mechanical Tests and Images via SHG. In total we tested 49 full-thickness, cylindrical osteochondral plugs (specimens) of 3 mm diameter. We pooled specimens from the lateral and medial femoral condyles, and assigned them to one of four different genipin treatment (dosing) groups, which included two time points: (A) before low-energy impact (2.5 mJ/mm^3) and (B) before unconfined cyclic compressions (10% of reference thickness at 1.44 Hz for 12,000 cycles), of either 0 mM (denoted –) or 11 mM (+) of genipin. Our control group (n=10) underwent the same mechanical treatments but no treatment with genipin (and subsequent crosslinking) [3]. We impacted all specimens with the same impact energy density and imaged them via Second Harmonic Generation (SHG) (Zeiss LSM 510, Oberkochen, DE) in Phosphate Buffered Saline (pH 7.4) at three time points, see **Fig. 1**.

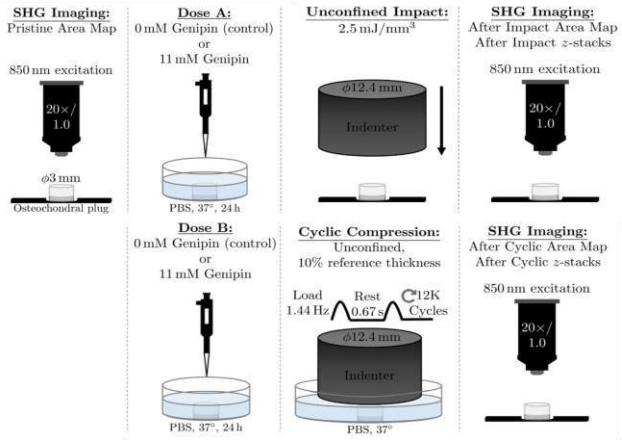

Figure 1: Schematic summary of our experimental protocol.

Analyses of Images. We used Fiji's Grid/Collection stitching plugin to generate images of the full circular cross section at a resolution of 1.2 μm/pixel. Using only the 3 × 3 tile grid centered on the main axis of the cylinder (to avoid edge effects), independent observers measured the length, width, depth, and principal angle (relative to the split-line direction) of each microcrack, cf. [3]. We calculated the length, width, depth, and orientation of all microcracks from both post-impact (PI) and post-cyclic (PC) compression phases of the mechanical experiment, and when possible, used the specific morphologies and orientations to track microcracks between the last two phases.

Statistical Analyses. We used separate mixed regression modeling to evaluate the effects of genipin treatment on microcrack density, and on the length, width, and depth of the microcracks over the course of the experiment. We included genipin treatment (dose) as a fixed effect and the thickness of each cartilage specimen as a covariate. We used post-hoc tests to evaluate differences among treatment combinations. To probe microcrack propagation, we analyzed our data from the tracked microcracks over the course of the experiment using the same mixed-model regressions, but with specimen included as an additional random factor. We completed all statistical analyses using SAS 9.4 (SAS Institute, Inc., Cary, NC) with a significance level $P < 0.05$.

RESULTS

We confirmed that our protocol successfully cross-linked the network of collagen. After 24 hours of incubation, the cartilage transformed from its normal white and glossy state to a dark color produced as genipin reacts with the amino groups. We imaged both treated and untreated specimens via Raman Spectroscopy and confirmed a characteristic fluorescence at 785 nm in only the treated specimens, thus confirming microstructural changes.

Genipin did not have a significant effect on the density and width of microcracks initiated under low-energy impacts, see **Figs. 2(a), (c)**. We did find statistically significant differences in the lengths and depths of microcracks initiated under low-energy impacts, see **Figs. 2(b), (d)**. Microcracks initiated in specimens treated with genipin tended to be longer and penetrate deeper into the cartilage specimens.

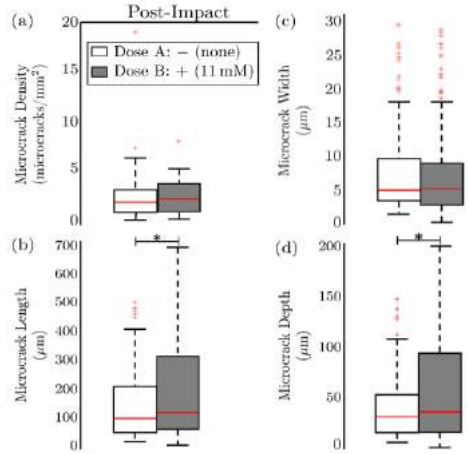

Figure 2: Microcrack Initiation under low-energy impact, untreated (white) vs. treated (gray) specimens. Box plots of the median (red lines) and interquartile ranges (black lines): (a) density, (b) length, (c) width, and (d) depth of microcracks.

Genipin had a significant effect on some aspects of microcrack propagation under cyclic, unconfined compression, see **Fig. 3**. Two treatments of genipin caused significantly greater propagation of microcracks (both longer and wider) than a single treatment of genipin, see **Figs. 3(a), (b)**. A single treatment of genipin did not have a statistically significant effect, but consistently resulted in marginally less propagation. Treatment with genipin had no effect on the depth of microcracks during cyclic, unconfined compression.

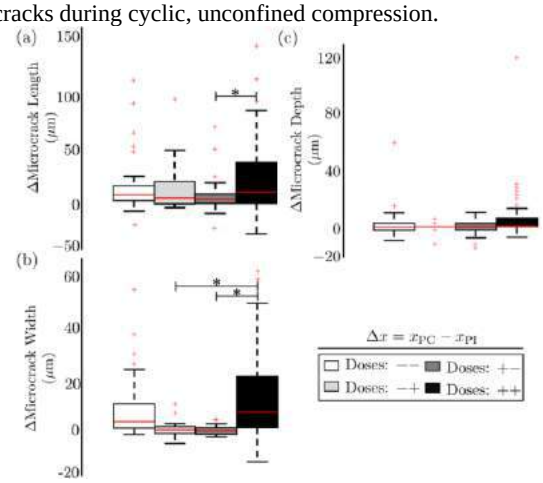

Figure 3: Microcrack Propagation post-impact to post-cyclic, unconfined compression, comparison of untreated (white), and treated (before impact = light gray, before cyclic compression = medium gray, before both = dark gray) specimens. Box plots of the median (red lines) and interquartile ranges (black lines): (a) length, (b) width, and (d) depth of microcracks.

DISCUSSION

In this study, we induced microscale damage to the network of collagen (i.e. collagen network microcracks) using low-energy impacts to cylindrical specimens of cartilage, and propagated these microcracks in unconfined, cyclic compression. The initiation and propagation of microcracks may deteriorate the mechanical function of cartilage and characterize pathogenesis of osteoarthritis, and may suggest therapeutic targets for future studies [3].

Our results do not support our hypothesis that treatments with genipin will improve the damage resistance of cartilage. In the dosing scheme that we tested genipin was not an effective treatment for preventing or repairing damage to the network of collagen in cartilage. Studies show that genipin can enhance the mechanical properties of collagen networks, particularly in engineering constructs. Specifically, genipin treatments to cartilage significantly increased stiffness in specimens treated with 10 mM for 24 hours [5]. In our study, the increased stiffness likely caused a reduction in ductility, which caused the cartilage to be less resistant to damage under impacts. Since crosslinking with genipin did not prevent microcrack initiation, the additional cross-links among collagen fibrils created by treatment with genipin were insufficient to prevent rupture of fibrils. Adding a second treatment of genipin further exacerbated the damage, suggesting that the stiffness may have further increased following the second treatment. While increased stiffness may be desirable in some engineering applications, it may be accompanied by reduced material toughness.

ACKNOWLEDGEMENTS

NSF CAREER 1662429; the Ford Fellowship Foundation.

REFERENCES

[1] Lawrence, RC et al. *Arthritis Rheum*, 58:26-35, 2008. [2] Kaleem, B et al. *Osteoarthritis Cartilage*, 25:544-553, 2017. [3] Santos, S et al. *Osteoarthritis Cartilage*, 27:1392-1402, 2019. [4] Novakofski, KD et al. *Osteoarthritis Cartilage*, 23:1130-1137, 2015. [5] Uquillas, JA et al., *J Mech Behav Biomed*, 15:176-189, 2012. [6] Bonitsky, C et al., *J Orthop Res*, 35:558-656, 2017.

DESIGN AND EVALUATION OF *FACILIFLOW*: A LYMPH NODE PROSTHETIC FOR PREVENTION OF SURGICALLY INDUCED LYMPHEDEMA

J. Frattolin (1), A. Swarup (1), A. Vella (1), F. Al-Khal (1), A. Schaschkow (2), P. Gianello (2), G. Giacalone (3,4), J.E. Moore Jr (1)

(1) Department of Bioengineering
Imperial College London
London, United Kingdom

(2) Laboratory of Experimental Surgery and Transplantation
Institute of experimental and clinical medicine/
Université catholique de Louvain
Belgium

3) De Duve Institute
Université catholique de Louvain
Belgium

(4) Lymfecentrum
AZ Sint-Maarten Hospital
Mechelen, Belgium

INTRODUCTION

Breast cancer-related lymphedema (BCRL) is a chronic and debilitating condition, characterized by an incurable swelling of the arm. Over 70% of patients have surgery during breast cancer treatment, which typically involves removal of at least one lymph node (LN) from the axilla. The removal of LNs disrupts drainage of lymph from the arm, which can lead to permanent swelling. The current standard of care is a management strategy at best, consisting of complete decongestive therapy. While such therapy may help prevent worsening of symptoms, it is only useful in some patients. Autologous lymph node transfer (ALNT) transplants lymph nodes from the groin to the axilla to assist in lymph flow restoration; however, such a specialized procedure is time-consuming and expensive. Improved treatments are necessary to reestablish lymph flow in the affected arm.

We have developed a novel lymph node prosthetic, Faciliflow, that is implanted at the time of breast cancer surgery to prevent the onset of edema. Faciliflow combines physiologically inspired fluid mechanical characteristics in conjunction with a localized release of Vascular Endothelial Growth Factor-C (VEGFC) to encourage lymphatic vessel regrowth. Afferent lymphatic vessels often divide into multiple parallel vessels as they approach the lymph node to decrease the downstream flow resistance to each contracting lymphatic vessel. Similarly, Faciliflow has multiple parallel channels, which encourages both continued interstitial flow and lymphatic vessel regrowth through the implant.

The aim of this study was to demonstrate that Faciliflow enables lymphatic vessel regeneration and reconnection after LN excision.

METHOD

Faciliflow was implanted in rats (n=20), following a modified methodology of Schindewolffs et al. [1], where ALNT is substituted with Faciliflow implantation. This initial Faciliflow design consisted of three parallel channels (Fig. 1A), fabricated through injection molding of medical grade polyurethane (Polymermedics Ltd., St. Astell, United Kingdom). The LNs of one limb of the rat were removed prior to device implantation. At the time of implantation, 6.67μg of exogenous VEGFC was injected intradermally. Vessel reconnections were verified using fluorescent imaging (indocyanine green, or ICG) after 28 days, 2 months, and 4 months. Histology of the implant and surrounding vessels was conducted after sacrifice at 4 months.

Following the *in vivo* investigation in rats, the Faciliflow implant was redesigned to improve ease of use during surgery and to optimize VEGFC release kinetics. Computational fluid dynamics (CFD) modelling (COMSOL Multiphysics 5.3, Burlington, USA) was used to assess Faciliflow 2.0 and investigate the release kinetics of VEGFC over 90 days. The VEGFC release profile was verified experimentally using ELISA to quantify the VEGFC concentration at discrete time intervals.

RESULTS

Successful reconnection of the lymphatic vessels was observed by ICG in 6 of 11 rats in which the correct orientation of the implant was maintained (Fig. 1B). This means that the implant channels remained in the same direction as the afferent and efferent vessels of the excised nodes. This success rate is comparable to that reported by Schindewolffs et al. [1] where rats were treated with ALNT and 6.67μg of VEGFC (55% vs. 53%). The rats implanted with Faciliflow device had a significantly higher success rate than those rats treated with ALNT and a saline-only injection (p=0.01, Fisher's exact test) [1]. The implants in 8 additional rats did not maintain their correct orientation after implantation, with vessel reconnection observed in only one animal. This observation emphasizes that successful vessel reconnection is more easily achieved when the correct channel orientation is

maintained. Histological examination of the tissue after animal sacrifice confirmed the presence of lymphatic vessels, with positive staining of LYVE-1 close to the implant surface (Fig. 1C). One rat died before study completion.

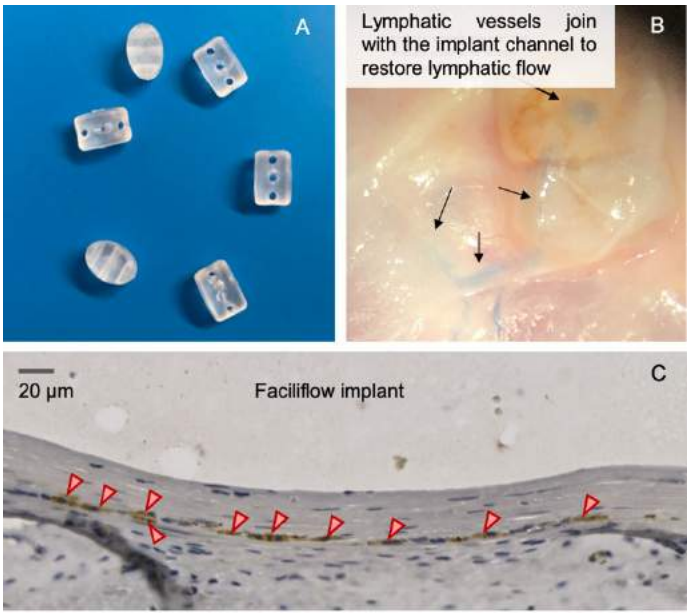

Figure 1: (A) The three-channel design of Faciliflow 1.0 implanted in rats; (B) Successful re-anastomosis of the lymphatic vessels to the implant by ICG in a rat; (C) Histological image indicating positive staining for LYVE-1, confirming presence of lymphatic vessels close to implant surface (indicated by the red arrows).

To prevent Faciliflow from moving after implantation, and thus losing its correct channel orientation, suture tabs were incorporated in the second design iteration of the device, Faciliflow 2.0. This will provide increased device stability and prevent the device from rotating or tilting. In addition, the number of parallel channels was increased to 6, allowing for additional hydrogel volume to be injected and a higher overall VEGFC concentration. CFD modelling indicated a VEGFC release profile of 0.6ng/day per mg of microspheres resulted in a growth factor concentration just below the target therapeutic threshold of 100ng/ml [2]. A rapid initial increase in VEGFC concentration was observed, peaking at approximately 100ng/ml on day 5.5 (Fig. 2). This was followed by a decrease in peak VEGFC concentration of approximately 50% (Fig. 2), which was sustained for the remaining duration of the 90-day simulation period. Experiments are ongoing to verify the VEGFC concentration profile using ELISA.

DISCUSSION

The preliminary *in vivo* investigation in rats demonstrated the efficacy of the Faciliflow implant, with a similar success rate to rats treated with an ALNT and bolus VEGFC injection. However, when the implant did not maintain its correct orientation, lymphatic vessel reconnection was limited to only 1 of 8 rats. This finding confirmed the importance of channel orientation to direct interstitial flow within the channels of the device. It was found by Goldman et al. [3] that VEGFC is more effective in the presence of interstitial flow. Increased lymphatic vessel growth was observed in a mouse tail model with interstitial flow than versus mice with reduced or inhibited flow, after a 4µg dosage of exogenous VEGFC. Therefore, maintaining correct channel orientation in the implant is critical to ensure the therapeutic efficacy of the eluted VEGFC. As a result of these findings and in consultation with clinicians, suture tabs have been added on the lateral sides at the base of the implant, minimizing potential flow disturbances in the vicinity of the channels. The suture tabs provide increased stability and robustness when anchoring the implant.

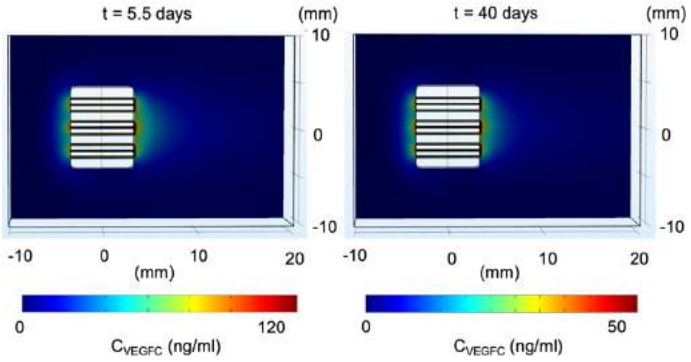

Figure 2: VEGFC concentration at 5.5 days and 40 days after simulated implantation.

The combination of *in silico* modelling and *in vitro* testing allows for a robust evaluation of Faciliflow 2.0 without an immediate need of additional *in vivo* trials. In order to optimize the release of VEGFC from the implant, a dual-release supply of VEGFC is proposed, where the channels of the implant are filled with a type I collagen hydrogel. For short-term release of the lymphatic growth factor, VEGFC is directly incorporated in the hydrogel, with VEGFC-encapsulated PLGA microspheres in the hydrogel for long-term elution. This will allow a therapeutic concentration of growth factor for up to four months. Work is ongoing to quantify the VEGFC concentration over time released from the device, with both free VEGFC and VEGFC encapsulated microspheres, by ELISA.

Secondary lymphedema, surgically induced at the time of breast cancer treatment, is a debilitating condition leaving affected patients with painful arm swelling, chronic infections, and limited treatment options. Faciliflow has the potential to eliminate the risk of BCRL at the time of surgery and improve patient livelihood post-cancer diagnosis.

ACKNOWLEDGEMENTS

The authors acknowledge funding from the National Institute of Health (NIH) and the National Institute of Health Research (NIHR).

REFERENCES

[1] Schindewolffs, L. et al., *Immun Inflamm Dis,* 2(3):152-156, 2014.
[2] Sweat, R.S. et al., *Microcirc*, 21:532-540, 2014.
[3] Goldman, J. et al., *Biomater*, 102:259-267, 2016.

ASSESSMENT OF THE POROELASTIC MECHANICAL PROPERTIES OF PORCINE OPTIC NERVE HEAD USING MICROMECHANICAL TESTING AND BIPHASIC MIXTURE MODELING

Babak N. Safa (1), A. Thomas Read (1), C. Ross Ethier (1)

(1) Wallace H. Coulter Department of Biomedical Engineering
Georgia Institute of Technology/Emory University
Atlanta, GA, USA

INTRODUCTION

Glaucoma is an optic neuropathy and the leading cause of irreversible blindness worldwide. The biomechanics of the optic nerve head (ONH) are a key aspect of the pathogenesis of glaucomatous optic neuropathy [1]; however, there is limited information about the mechanical behavior of the ONH tissue.

Due to their high water-content and biopolymeric structure, many soft tissues behave differently under static vs. dynamic loading (i.e., viscoelasticity). We hypothesized that the ONH also shows viscoelastic behavior, which can be described using mixture theory. A previous study from our lab showed a dependence on loading-rate in the biomechanical response of porcine and murine ONHs [2]; however, no studies report the ONH's viscoelastic properties and underlying structural mechanisms per se. Therefore, our objective was to assess the viscoelastic mechanical properties of the porcine ONH using ex vivo micromechanical testing coupled with biphasic mixture modeling.

METHODS

Animal tissue samples: Eyes were harvested from freshly sacrificed mature female pigs (c. 5 months old). The ONH was dissected from the eye globe within a few hours to 24 hours postmortem (Fig. 1A & B), and from each ONH four samples were isolated using a 1 mm surgical biopsy punch (Fig. 1C). The diameter of each sample (n=13) was then measured using brightfield microscopy (diameter = 1.101 ± 0.043 mm; Fig 1D) followed by mechanical testing (Fig 1E; see below). During all steps of the experiment, hydration was maintained by immersion in phosphate buffered saline (PBS).

Micromechanical testing: We tested the ONH samples using a micromechanical testing device (Microtester; CellScale, ON, Canada), in a 37 °C PBS bath. Samples were subjected to an incremental creep protocol in unconfined compression. They were preconditioned by loading to 200 μN (tare-load) over 60 sec, immediately unloaded to zero force at the same rate, and then loaded to tare-load once more and kept at that force level for 1 minute. The reference height ($h_0 = 0.555 \pm 0.152$ mm) of the tissue was calculated by averaging the distance between the compression plates from the final 20 sec of the last hold at tare-load (Fig.1 E). The incremental creep protocol was imposed as four cycles of loading to 524, 1047, 1470, and 2094 μN, which approximately corresponds to physiological IOPs of 5, 10, 15, and 20 mmHg. At each force level the sample was held for 5 min, and following the fourth creep cycle, the sample was unloaded to the tare-load level over 4 minute and held there for 1 minute.

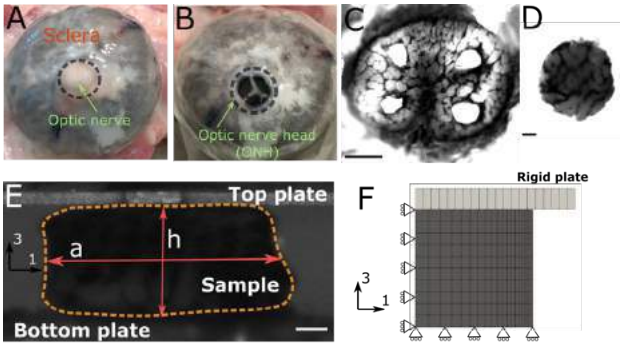

Fig. 1: The experimental procedure used in this study; (A) posterior segment of the eyeball; (B) the optic nerve is removed flush to the scleral surface; from a tangential slice of each ONH (C; bar = 1mm) four samples (D; bar = 0.1mm) are punched out. The sample is tested using a micromechanical tester (E), and the height (h) and width (a) of the sample are measured throughout the test (bar = 0.1mm). (F) An axisymmetric finite element model is used to model the mechanical response of the ONH.

Image analysis and strain calculation: To calculate the axial and lateral strains of the tissue, we used image analysis. During the test, images of the sample were recorded using a CCD camera (Fig. 1E). The images were digitally segmented to obtain a binary mask of the sample, after which we calculated the height of the sample (h) as the distance between the two plates and the width (a) by dividing the area of the binary mask by h. The normal strain in both axial and lateral directions was calculated as $\epsilon_{axial}=h/h_0-1$, and $\epsilon_{lateral}=a/a_0-1$, where h_0 and a_0 were the reference height and width, respectively. We also calculated the apparent Poisson's ratio as $\nu_{app}=-\epsilon_{lateral}/\epsilon_{axial}$.

Finite element model: We used a finite element model with a homogenous constitutive material formulation to model the ONH's mechanical response. Based on the average diameter and height of the experiment samples, we generated an axisymmetric geometry in FEBio (v3.1, febio.org) with linear hexahedral elements (height = 0.55 mm, radius = 0.55, angle = 1°; Fig. 1E). To model compression of the sample with the rigid plate, we used a sliding elastic contact formulation [3]. The tissue was treated as a biphasic poroelastic (solid content 0.22[4]) material with compressible neo-Hookean matrix (matrix material parameters: Young's modulus = E_{NH}, Poisson's ratio = ν_{NH}, and isotropic reference hydraulic permeability = k).

Data fitting: To calculate the model parameters $\{E_{NH}, \nu_{NH}, k\}$, we used multi-start optimization (MSO) [5]. The cost function was designed to fit the axial and lateral strains simultaneously, as:

$$f = \sqrt{\sum_{i=1}^{N} \frac{\left(\epsilon^i_{axial} - \epsilon^i_{axial,0}\right)^2 + \left(\epsilon^i_{lateral} - \epsilon^i_{lateral,0}\right)^2}{2N}} \quad (1)$$

where $\epsilon_{axial.0}$ and $\epsilon_{lateral.0}$ are the experimental axial and lateral strains, respectively. The index i stands for the uniform resampling intervals, which split the time of the test into one hundred equal segments (i.e., N=100).

A constrained nonlinear least squares algorithm was used to perform the optimization (interior-point, *fmincon,* Matlab), where the bounds of the model parameter values were $\{E_{NH}, \nu_{NH}, k\}_{min}$={0.1 kPa, 0, 10^{-4} mm^4/(N.sec)} and $\{E_{NH}, \nu_{NH}, k\}_{max}$={100 kPa, 0.49, 1 mm^4/(N.sec)}. We conducted MSO with 100 random initial guesses, generated using Latin hypercube resampling. The criteria for accepting a fit was as the root mean square of errors (RMSE) of both ϵ_{axial} and $\epsilon_{lateral}$ fits to be less than their respective maximum experimental standard deviation.

RESULTS

The incremental creep protocol showed the expected increasing compressive axial strain as compressive force increased (Fig. 2A). A similar tensile behavior was observed in the lateral strain (Fig. 2A). The peak strain in the axial and lateral directions were -0.29 ± 0.18 (mean ± standard deviation), and 0.13 ± 0.12, respectively. This resulted in an average ν_{app} of 0.41 ± 0.14, which was approximately constant throughout the test (Fig. 2B).

The model successfully fit the experiments in both axial and lateral direction. Out of 100 initial guesses 94 resulted in fits that matched the fit criteria (see summary in Table 1). We used the median response to generate a summary of the fits (dashed lines, Fig.2 A & B). During the incremental creep cycles both the axial and lateral strains, as well as the apparent Poisson's ratio, closely matched between experiment and calculation; however, during the unloading phase (after minute 24) the fits were less accurate.

Table 1: Summary of the model parameter values for the fits.

	E_{NH}[kPa]	ν_{NH}	k [mm^4/(N.sec)]	k [m^4/(N.sec)]
Median	4.26	0.26	5.60×10^{-2}	5.60×10^{-14}
Min.	3.51	0.10	6.19×10^{-4}	6.19×10^{-16}
Max.	4.74	0.33	1.13×10^{-1}	1.13×10^{-13}

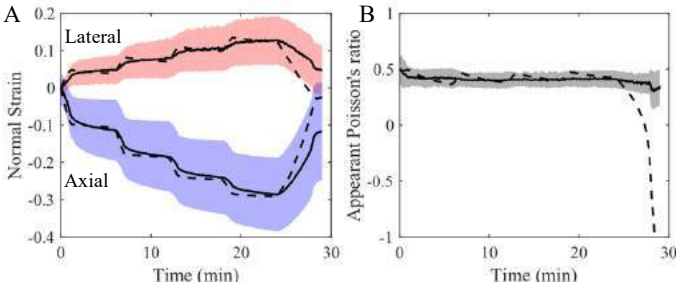

Fig. 2: (A) Axial and lateral strains vs. time, and (B) apparent Poisson's ratio vs. time. The solid line and shaded area show the experimentally determine mean ± 95% confidence intervals. Dashed lines are results of data fitting.

DISCUSSION

We successfully assessed the poroelastic mechanical properties of the porcine ONH using micromechanical testing and biphasic mixture modeling. Our results provide a Young's modulus of 4.26 [3.51, 4.74] kPa (median [min., max.]; Table 1), which closely matches a previous report on the porcine ONH Young's modulus (3.05 kPa [2]), and another study on the human lamina cribrosa (17.2 kPa [6]). Although previous studies assumed incompressibility ([2], [6]), we showed that the ONH is compressible, with a matrix Poisson's ratio ν_{NH} of 0.26 [0.10, 0.33], which was smaller than the apparent Poisson's ratio (Fig. 2B). This difference indicates the role of the fluid component of the ONH in its mechanical properties.

Notably, to the best of the authors' knowledge, for the first time we report the hydraulic permeability of the porcine ONH (k = 5.60×10^{-14} m^4/(N.sec)). A previous study from our lab reported the average k of porcine peripapillary sclera (ppSC), an anatomically adjacent tissue, as being in a similar range but somewhat smaller ($k = 0.86\times10^{-14}$ m^4/(N.sec) [7]). The same study also provided the compressive stiffness as 10 kPa, which is larger than the stiffness we found for the ONH. These differences are consistent with the higher fibrous collagen content of the ppSC compared to the ONH.

Our study was subject to some limitations. As simplifying and practical considerations, we treated the ONH as an isotropic material with non-spatially-varying permeability; however, addition of further modeling considerations, such as strain-dependent permeability, would improve the fidelity of the model. Further, we used an elastic contact to model compression by the rigid plate, which performed well during the loading phases of the mechanical test; however, it was not successful during unloading (Fig. 2), when it is possible that other forms of contact forces are at play, e.g., microscale local fluid pressurization.

In conclusion, this study provides a framework for explaining ONH mechanical behavior using biphasic mixture theory, and the material properties reported herein can be used as benchmarks for future studies aimed at understanding the pathogenesis and role of mechanobiology in glaucomatous optic neuropathy.

ACKNOWLEDGEMENTS

NEI-NIH R01 EY025286, and the Georgia Research Alliance

REFERENCES

[1] Coudrillier *et al.*, *Investigative Ophthalmology and Visual Science*, 53: 1714–1728, 2012. [2] Boazak *et al.*, *Journal of Biomechanics*, 93: 204–208, 2019. [3] Zimmerman and Ateshian, *Journal of Biomechanical Engineering*, 140: 081013, 2018. [4] Albon *et al.*, "Age related changes in the non-collagenous components of the extracellular matrix of the human lamina cribrosa," 2000. [5] Safa *et al.*, *Acta Biomaterialia*, 2021. [6] Braunsmann *et al.*, *Invest. Ophthalmol. Vis. Sci.*, 53: 2960–2967, 2012. [7] Brown *et al.*, *bioRxiv*, 2020.05.21.108936, 2020.

EFFECTS OF MATERNAL GEOMETRY AND GESTATIONAL AGE ON LOADING OF THE GRAVID HUMAN UTERUS AND CERVIX

Erin M. Louwagie (1), Lindsey C. Carlson (2,3), Joy Y. Vink (4), Timothy J. Hall (3), Helen M. Feltovich (2,3), Kristin M. Myers (1)

(1) Department of Mechanical Engineering
Columbia University
New York, NY, USA

(2) Maternal Fetal Medicine Department
Intermountain Healthcare
Provo, UT, USA

(3) Medical Physics Department
University of Wisconsin-Madison
Madison, WI, USA

(4) Department of Obstetrics and Gynecology
Columbia University Irving Medical Center
New York, NY, USA

INTRODUCTION

In 2019, 1 in 10 babies born in the United States was born prematurely [1]. Preterm birth (PTB), which is delivery at a gestational age of fewer than 37 weeks, places infants at an increased risk of many short- and long-term health complications, such as breathing problems, gastrointestinal problems, and cerebral palsy [1,2]. There is currently no accurate method to predict PTB, and current PTB prevention strategies have had little impact on lowering PTB rates [3,4]. A significant barrier to improving PTB prediction and prevention is the pervasive lack of knowledge on normal function and evolution of the human uterus and cervix throughout gestation, making it difficult to demarcate cases that are not normal [3]. Compounding these obstacles is the challenge of conducting in vivo research on pregnant patients. Therefore, this research aims to build computational modeling tools to assess the biomechanical environment of pregnancy and its effect on birthing outcomes. In this work, we use patient-specific parametric computational models to investigate how maternal anatomy affects the uterus and cervix loading in term pregnancies.

The mechanics of pregnancy has been studied previously using computational models. For the most part, these models have used geometry derived from MRI and 3D ultrasound [5,6]. These high-fidelity models provide a wealth of information for a few patients, but since MRIs and 3D ultrasounds are costly to obtain and not commonplace in prenatal care, they are not a viable basis for capturing pregnancy anatomy on a larger scale. To overcome this issue, a method to build parameterized patient-specific models of pregnant anatomy from 2D ultrasound images, which are standard in obstetrics, has been developed and implemented into a longitudinal study of pregnant maternal anatomy [7,8]. This research aims to utilize the existing parametric modeling methods to investigate how maternal geometry impacts the distribution of load throughout gestation. Finite element analysis (FEA) is carried out for pregnant patients with a low-risk for PTB at four time points during pregnancy. The stretch and stress in the uterus and cervix are examined. The FEA results from these models will be used to establish normal patterns of stretch and stress in pregnancies at low-risk for PTB, and in future work will be compared to patients at high-risk for PTB.

METHODS

Trained sonographers took ultrasounds of healthy pregnant patients at four gestational ages (8-14, 14-16, 22-24, 32-34 weeks), and solid models of the uterus and cervix were built using the method described in Louwagie et al. [8]. In Solidworks (Dassault Systemes, Vélizy-Villacoublay, France), the solid modeling process was expanded to include the separation of the cervix from the uterus, and a fetal membrane and supporting abdomen were added. Quarter model geometries were used to decrease computational time, and the resultant solid meshed in Hypermesh (Altair Engineering Inc., Troy, MI). The fetal membrane was meshed with quadratic hexahedral elements, and the cervix, uterus, and abdomen were meshed with quadratic tetrahedral elements. FEBio Studio (v1.1.0) was used for FEA, and the meshed geometry was imported into it [9].

Within FEBio, the material properties, boundary conditions, and contacts were defined. The patients were assumed to have *normal* cervical stiffnesses at each gestational age, where cervical properties were determined using inverse FEA of *in-vivo* cervical aspiration data [10] assuming the cervix is a passive fiber composite material [11]. The uterine tissue was modeled as a passive fiber composite material based on tensile tests of pregnant uterine tissue [12]. The abdominal tissue was considered to be nearly incompressible neo-Hookean. The fetal membrane was modeled as a transversely isotropic fiber-based material with a compressible neo-Hookean ground substance based on existing

literature [13]. The boundary conditions applied were as follows: fetal membranes sliding on the uterine wall and cervix, the uterus tied to the abdomen, the cervix sliding along the abdomen and vaginal canal, and the entire model fixed along the outside surface. A gestational intrauterine pressure was applied to the inner membrane surface [14]. An example of the model setup is shown in figure 1. Patterns of stretch and stress in the uterus and cervix were analyzed, locations of maximum stretch and stress observed, and comparisons made between maternal geometry and FEA results.

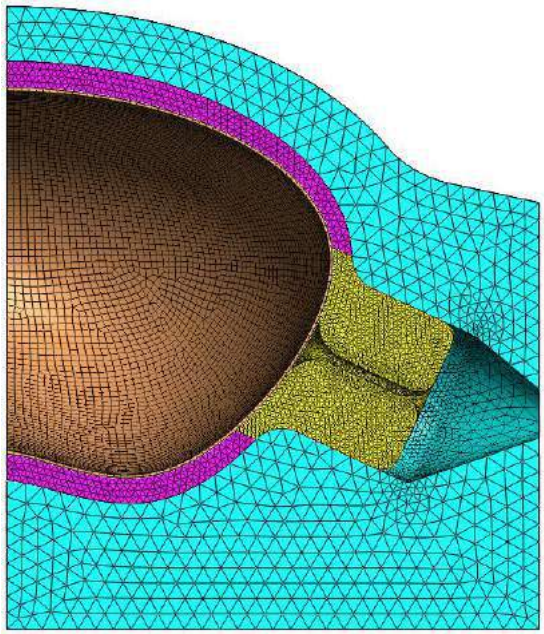

Figure 1: Example of meshed quarter model, including the fetal membrane, uterus, cervix, and supporting abdomen material. Viewed in the sagittal plane.

RESULTS

Model simulation is ongoing for this research. Therefore, we can make limited comparisons between different geometries. In work done thus far, several patterns regarding strain in the uterus and cervix have arisen. In the first trimester and early second trimester, the 1st principal Lagrange strain is most significant at the internal os (opening of the cervical canal into the uterus). Near the end of the second trimester and in the third trimester, the 1st principal Lagrange is similar in magnitude to the uterocervical junction and the internal os. However, the main direction of the 1st principal Lagrange strain changes as pregnancy progresses. In the first trimester, it is in the circumferential throughout the cervix. However, as pregnancy progresses, 1st principal strain is increasingly aligned radially from the internal os, especially near the uterocervical junction. This pattern suggests that, in term pregnancies, there is a progressive shift of loading that the uterus and cervix undergo, where pregnancy advancement brings about the cervix being stretch open and pushed out from the uterus. The 3rd principal Lagrange strain shows the greatest compression of tissue throughout the uterus and at the internal os. As pregnancy progresses, more compression is observed at the uterocervical junction. This pattern makes sense, as the thickness of the lower uterus segment decreases throughout pregnancy [8].

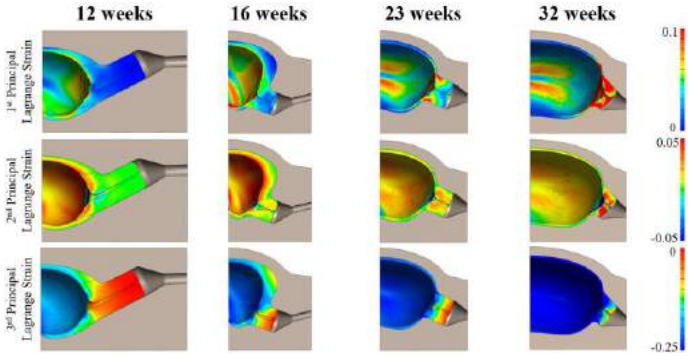

Figure 2: 1st, 2nd, and 3rd principal Lagrange strain heat maps for one patient at 12 weeks, 16 weeks, 23 weeks, and 32 weeks. Models are not to scale.

DISCUSSION

This research shows the evolution of loading patterns in the uterus and cervix throughout pregnancies that will ultimately deliver at term. Thus far, loading has been characterized by a shift in principal strain from being aligned circumferentially throughout the cervix to also be radially aligned from the internal os. This suggests a possible a mode through which the cervix is stretched as pregnancy progresses. Further work will explore how different geometries affect loading in the uterus and cervix.

This study's primary limitations are that the geometries used are derived from measurements already in a loaded configuration, so our reference configurations are not in a stress-free state. Additionally, patient-specific tissue properties and intrauterine pressure are unknown, and we cannot compare our results to in vivo loading results. This means that ultimately, the numerical results' magnitude will not provide an actual measurement of stress and strain for individuals throughout gestation. However, it will provide data on how maternal geometry affects loading on the uterus and cervix during pregnancy and supply a workflow in which patient-specific parameters can be added in future studies.

ACKNOWLEDGEMENTS

This work is supported by the Eunice Kennedy Shriver National Institute of Child Health & Human Development of the National Institutes of Health under award number 1R01HD091153-01. The content is solely the responsibility of the authors and does not necessarily represent the official views of the National Institutes of Health.

REFERENCES

[1] Centers for Disease Control, “Preterm Birth”, 2020.
[2] Mayo Clinic, “Premature Birth”, 2017.
[3] Vink, J and Myers, K, *Best Pract Res Cl Ob*, 52:88-102, 2018.
[4] Singh, N et al., *Placenta*, 98:6-12, 2020.
[5] House, M et al., *Clin Anat*, 26:97-104, 2013.
[6] Fernandez, M et al., *Comput Methods Biomech Biomed Engin*, 19:404-417, 2016.
[7] Westervelt, A et al., *J Biomed Eng*, 139:051004, 2017.
[8] Louwagie, E et al., *PLoS ONE*, In Review.
[9] Maas, S, et al., *J Biomech Eng*, 134(1):011005, 2012.
[10] Badir, S et al., *Prenat Diagn*, 33:737-741, 2013.
[11] Myers, K et al., *J Biomech*, 48:1533-1540, 2015.
[12] Conrad, J et al., *Am J Ob Gynecol*, 96:1055-1059, 1966.
[13] Bürzle, W and Mazza, E., *J Biomech*, 46:1777–1783, 2013.
[14] Fisk, N et al., *BJOG*, 99(1):18-22, 1992.

MUTLI-DIRECTIONAL FLEXIBILITY ENDURANCE TESTING OF FOUR DIFFERENT CERVICAL TOTAL DISC REPLACEMENT PROSTHESES

Denis J. DiAngelo (1), Chloe L. Chung (1), Daniel Hoyer (1), Tyler Carson (2), Kevin T. Foley (2)

(1) Department of Orthopaedic Surgery and Biomedical Engineering
University of Tennessee Health Science Center
Memphis, TN, USA

(2) Semmes Murphey Clinic
Memphis, TN, USA

INTRODUCTION

Motion preservation devices have become increasingly popular in the treatment of spinal pathologies that require biomechanical support following removal of the degenerated tissue [1-3]. As these devices continue to be developed to treat multiple adjacent diseased spinal levels, i.e., using multiple disc prostheses or placing a disc prosthesis adjacent to a fused level, biomechanical data that supports these established surgical methods are needed. The objective was to determine the stability of four cervical disc prostheses tested under low endurance multidirectional loading conditions in a cadaveric cervical spine model.

METHODS

16 (C4-C5) and 16 (C6-C7) functional spinal units (FSUs) were dissected from eight male and eight female cadaveric cervical spines with an average age of 55.9 +/- 9.7 years. Three FSUs were not usable due to poor tissue quality which reduced the sample size to 29 FSUs. Four cervical total disc replacement (TDR) prostheses that had a similar ball and socket type articulation mechanism but varying endplate fixation features were tested (Figure 1): 1. A clinically used and FDA approved single central keel (SCK), 2. Low profile teeth (LPT) with domed endplate shape to allow a better fit in case of concave vertebral endplate, 3. Tripod keel (TK), and 4. Small single keel (SSK). A minimum sample size of 6 implants per prosthesis type was used.

Each specimen was mounted in a robotic testing platform (Figure 2) and tested with a coupled eccentric loading (CEL) protocol that moved the instrumented specimens through a sequence of combined motions of flexion or extension coupled with right and left axial rotation. A compressive load of 50N was applied to the upper mounting pot directly above the midline of the disc implant. End limits of motion were established for load limits of 1.5Nm in flexion, extension and axial rotation resulting in a total applied moment of 2.25Nm. If the specimen reached a total of 15degrees in flexion or extension, or 10 degrees in axial rotation, the corresponding moment value at the end range of motion was used which prevented the resultant target moment from being exceeded. Each specimen was then cyclically tested 2000 times at a rate of 2.5deg/s. Anteroposterior endplate migration of both the upper and lower implant components was measured after 20, 250, 500, 1000, 1500, and 2000 cycles.

Single Central Keel (SCK | Low Profile Teeth | Tripod Keel (TK) | Small Single Keel

Figure 1: Cervical Total Disc Replacement Prostheses.

Implant migration was analyzed by using a digital Vanier caliper set (with 1micron accuracy) to measure the offset distance between a fixed reference plate attached to the front surface of the mounting pot and the outer front face of both upper and lower implant components. Tests were stopped if implant component migration exceeded 3mm or endplate fracture was observed, and migrations less than 0.3mm were defined as clinically stable. A one-way repeated measures ANOVA with a Student Newman-Keuls test was used to compare differences.

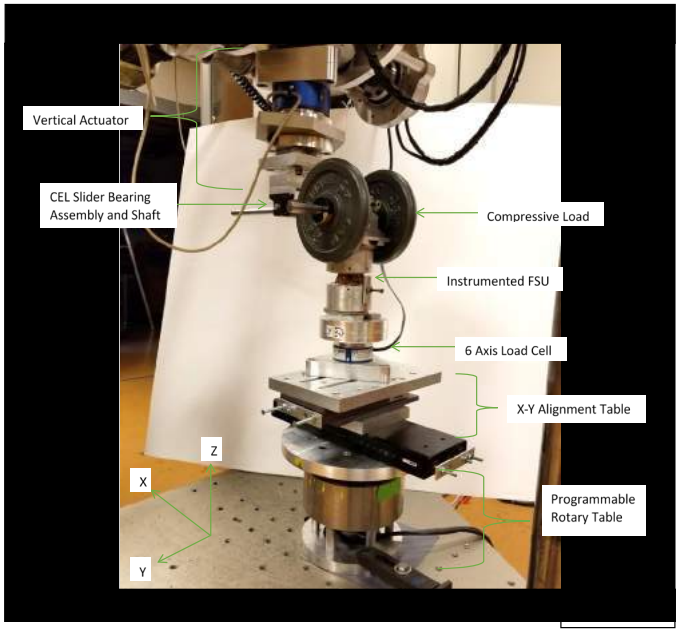

Figure 2: Experimental Setup for Multidirectional Test.

RESULTS

The mean and standard deviations of the combined (flexion plus extension) sagittal plane range of motion or the combined (left plus right) axial motion of the four TDR devices are shown in Figure 3. No statistical differences were found between the ranges of motion (ROM). The anterior-posterior migration of the upper and lower components of the disc prostheses are shown in Figure 4. All but one of the specimen migration values were below 0.3mm. Upper prosthesis component migration ranged between 0.02mm and 0.08mm and between 0.01mm and 0.04mm for the lower components. No significant differences occurred between the upper components or the lower prosthesis components of any implant type.

DISCUSSION

A human cadaveric cervical spine model was used to determine the biomechanical stability properties of four cervical TDR prostheses. Three low profile endplate fixation designs currently in the investigational phase of FDA clearance were found to provide comparable ranges of coupled movements to an existing clinically used and FDA approved central-based keel design. The three investigational prostheses also remained as stable as the FDA approved device following low cyclic testing. More cervical TDR prostheses, having different endplate fixation design features, provides spine surgeons with more options to accommodate anatomical constraints (i.e., varying endplate profiles and shapes) and/or treating multilevel adjacent spinal diseases.

ACKNOWLEDGEMENTS

Research contract from Centinel Spine.

REFERENCES

[1] Bartels RH, et al., Fusion around cervical disc prosthesis: case report. *Neurosurgery* 57:E194, 2005.

[2] Moatz B, et al., Cervical disc arthroplasty: pros and cons. *Surg Neurol Int* 3 (Suppl 3):S216–S224, 2012.

[3] Steinberger J, et al., Cervical Disc Replacement, *Neurosurg Clin N Am*, Jan;31(1):73-79, 2020.

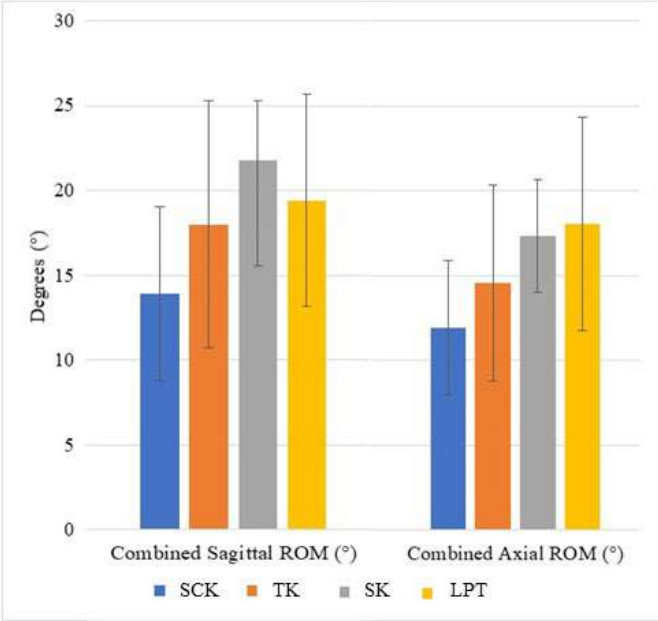

Figure 3: Comparison of ROM Grouped by Implant Type.

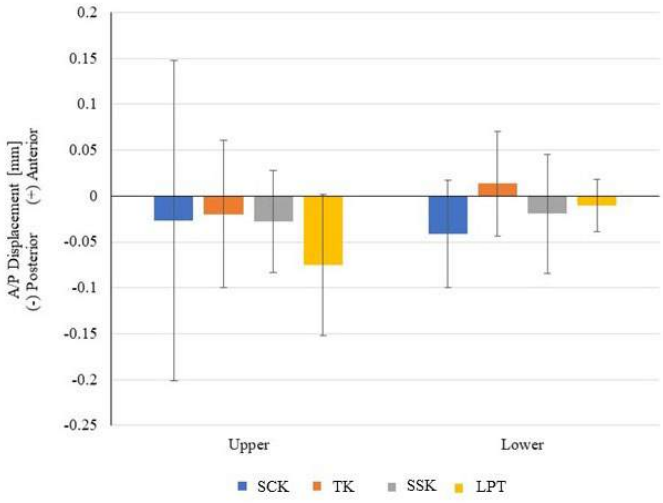

Figure 4: Mean Migration of Upper and Lower Components after 2000 Cycles Grouped by Implant Type.

FREQUENCY EFFECT ON TRANSCATHETER VALVE MOTION AND FLUID DYNAMICS IN AN ACCELERATED ENVIRONMENT

Sailahari V. Ponnaluri (1), Michael S. Sacks (2), Keefe B. Manning (1,3)

(1) Department of Biomedical Engineering
The Pennsylvania State University
University Park, PA, USA

(2) Willerson Center, Institute for Computational and Engineering Sciences, Department of Biomedical Engineering
University of Texas
Austin, TX, USA

(3) Department of Surgery
Penn State Hershey Medical Center
Hershey, PA, USA

INTRODUCTION

As of 2017, approximately 25,000 patients died as a result of heart valve disease (HVD) in the United States annually [1]. For patients with HVD, the native valve presents with severe regurgitation or calcification, increasing the demands on the heart. The primary treatment option for compromised heart valves is to receive either a mechanical or bioprosthetic heart valve replacement. However, 30% of patients with HVD are unable to receive these surgical options due to severe comorbidities and/or age [2]. Transcatheter aortic valve replacements (TAVRs) are a novel approach to treat HVD and are growing in popularity due to their minimally invasive approach, gaining approval in 2019 for low-risk patients [3]. However, despite the increase in interest for TAVR use, the long-term durability is unknown.

To demonstrate heart valve durability for market approval, the U.S. Food and Drug Administration mandates that valves be tested in an accelerated wear tester (AWT) in accordance with ISO:5840. ISO:5840 only specifies biological valves be cycled for at least 200 million cycles while applying a transvalvular pressure, commonly 100 mmHg, across a closed valve for 5% of the cycle [4]. However, no testing frequency is ever specified, which may contribute to differences observed between *in vivo* and AWT cycling. With an increase in testing frequency, porcine heart valve tissue demonstrates a decrease in leaflet stress relaxation. This produces a higher average preload than what is observed *in vivo* [5]. A higher preload could produce a harsher environment with high stresses sustained over the cycle, underestimating the life span of the valve. Alternatively, with a reduced range of stress fluctuations, the durability of the valve may be overestimated. Therefore, this study aims to better understand the influence of frequency within an AWT environment on TAVR motion and fluid dynamics using enface imaging and high-speed particle image velocimetry (HSPIV).

METHODS

To determine the effect of frequency on TAVR valve motion and fluid dynamics, a TAVR was mounted in an Electroforce® Durapulse™ AWT (TA Instruments, New Castle, DE) externally modified for optical access to the valve. The AWT consisted of a proximal chamber, valve holder, distal chamber, and pressure transducers at the base of each chamber (Utah Medical Products, Inc., Midvale, UT) (Figure 1). The AWT head was mounted on a Bose linear motor which developed the ISO:5840 compliant pressure loading conditions at three frequencies (10, 15, and 20 Hz). To provide visual access to the near valve fluid mechanics, the valve stent was trimmed between the upright supports to create windows and was fixed to a custom mount to prevent migration. The Durapulse™ cycled the TAVR in a blood analog comprised of glycerin and saline solution with a density of 1.13 g/ml and a viscosity of 3.99 cP to match the asymptotic viscosity of 40% hematocrit blood.

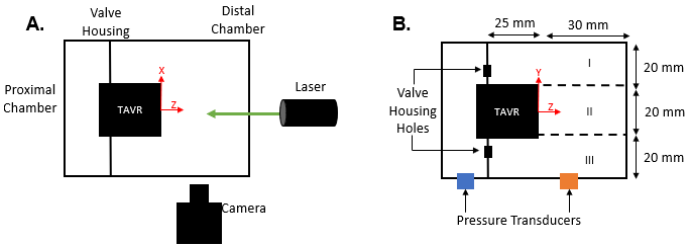

Figure 1: A. HSPIV experimental set-up with the Durapulse, high speed camera and laser. B. Side view schematic of the three regions of interest imaged with HSPIV, with pressure transducers and holes in the valve housing for fluid recirculation indicated.

To quantify the valve motion, the geometric orifice area (GOA) and flow rate was determined using enface imaging. The Phantom Miro-Lab 110 high-speed camera (Vision Research, Wayne, NJ) was mounted to visualize the valve opening and closing behavior. Image contrast was improved with an external light source behind the proximal chamber. Insight 4G (TSI, Inc., Shoreview MN) acquired ten images every 9% of the cycle for each frequency. Images were processed in MATLAB using the workflow shown in Figure 2. The flow rate (Q, ml/s) at each point in the cycle was approximated as a function of the average transvalvular pressure (ΔP, mmHg), fluid density (ρ, g/cm^3), and GOA (cm^2) as shown in Equation 1.

$$Q = 51.6 * \sqrt{\frac{\Delta P}{\rho}} * GOA \qquad (1)$$

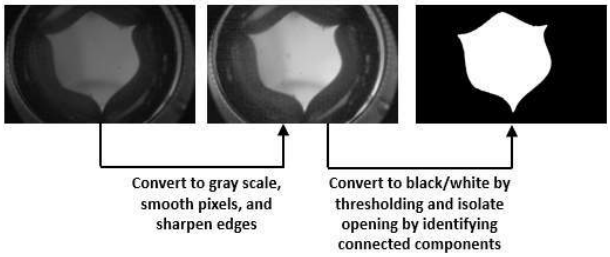

Figure 2: Workflow to process raw valve images in MATLAB to calculate the GOA.

To measure the fluid dynamics, a high-speed camera was mounted to visualize the side of the Durapulse^{TM} chamber (Figure 1B). Three regions were imaged due to large differences in velocity magnitude: Region I above the TAVR, Region II downstream of the TAVR, Region III below the TAVR (Figure 1B). A high-speed Terra PIV laser (Continuum, San Jose, CA) illuminated vertical planes every 1 mm in the x-direction from -10 mm to +5 mm to quantify AWT flow. Two HSPIV data sets were captured: an averaged and an instantaneous set. The averaged set captured 1000 image pairs every 9% of the cardiac cycle to compare between frequencies. The instantaneous set rapidly captured images to visualize random eddies that may develop. Velocity contour plots and streamlines for the averaged and instantaneous data were plotted with Tecplot360 (Tecplot, Bellevue, WA).

RESULTS

For all frequencies, the TAVR opened at the start of the cycle, reached a maximum GOA at 36% of the cycle, and closed until the following cycle. However, differences were observed in GOA and how much the valve leaflets were able to coapt. At 10 Hz, the valve obtained a maximum GOA of 1.54 ± 0.03 cm^2 and a flow rate of 17.13 ± 0.29 L/min (Figure 3A). The 15 Hz valve achieved a maximum GOA of 1.10 ± 0.01 cm^2 and a flow rate of 11.43 ± 0.13 L/min (Figure 3B). Finally, the 20 Hz condition produced a maximum GOA of 0.91 ± 0.02 cm^2 and a flow rate of 8.81 ± 0.15 L/min (Figure 3C).

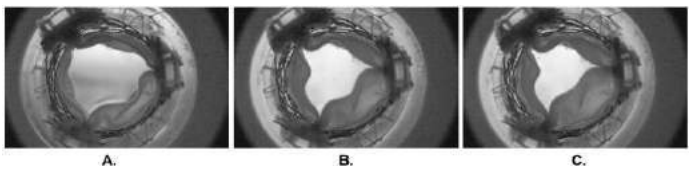

Figure 3: TAVR orifice at 36% of the cycle for A. 10 Hz, B. 15 Hz, and C. 20 Hz.

Additionally, during diastole, leaflet coaptation varied (Figure 4). At 10 Hz, the coapted leaflets curved back on themselves, and the valve was closed for approximately 41% of the 100 ms cycle. For 15 Hz the valve coapted along the entire leaflet, and the valve was closed for approximately 31% of the 66.6 ms cycle. At 20 Hz, the valve leaflets never completely coapted over the 50 ms cycle and opened as soon as the leaflets touched.

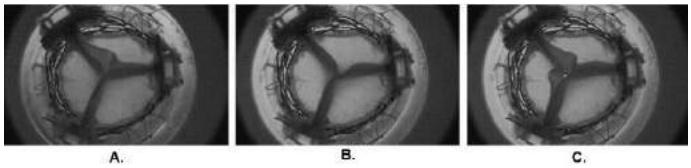

Figure 4: TAVR leaflet coaptation at 90% of the cycle for A. 10 Hz, B. 15 Hz, and C. 20 Hz.

During systole, a jet emerged from the valve and achieved a maximum velocity magnitude at 36% of the cycle for each frequency. As the valve closed, a large recirculation appeared at the base of the valve and dissipated downstream of the valve as the next cycle started. The maximum velocity observed during 36% of the cycle was 0.90 m/s at 10 Hz, 0.66 m/s at 15 Hz, and 0.47 m/s at 20 Hz. During diastole, the jet dissipated further downstream of the valve at lower frequencies.

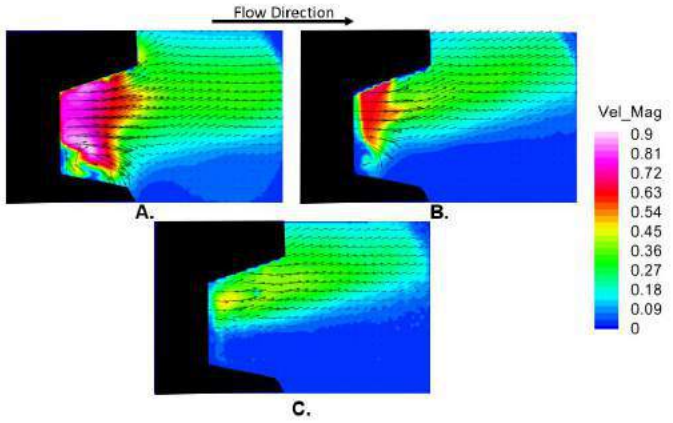

Figure 5: HSPIV data of the maximum jet exiting the TAVR in m/s during 36% of the cycle for A. 10 Hz, B. 15 Hz, and C. 20 Hz.

DISCUSSION

This study demonstrated different valve behavior with increasing frequency. With increasing frequency, the TAVR motion demonstrated a decrease in orifice area and flow rate during peak systole. During diastole, the valve remained closed longer and coapted better at lower frequencies. The fluid mechanics showed a greater jet velocity magnitude during systole and greater dissipation during diastole at the lowest frequency. Therefore, ISO:5840 should specify an AWT frequency due to clear differences in valve loading conditions.

ACKNOWLEDGEMENTS

Research supported by NIH HL129077 and the Penn State Center for Biodevices Leighton Riess Graduate Fellowship in Engineering.

REFERENCES

[1] Benjamin, E., *et al.*, *Circulation*, 135:e146-e603, 2017.
[2] Leon M.B., et al., *N. Engl. J. Med*, 363(17):1597-1607.
[3] Fellerbaum, M., FDA.gov, 2019.
[4] International Standards Organization, ISO:5840:3, 2013.
[5] Vesely, I., et al., *Ann. Thorac. Surg*., 60:S379-383, 1995.

A PLATFORM FOR STUDYING THE EFFECTS OF NANOTOPOGRAPHY AND REACTIVE CHEMICAL SPECIES ON INTEGRIN SELECTION

Ryan Fasse (1), Novella Bates (2), Alex Guerra (3), Joe Baio (1), Monica Hinds (2), Patrick Jurney(2,3)

(1) Chemical, Biological, and Environmental Engineering
Oregon State University
Corvallis, OR, USA

(2) Biomedical Engineering
Oregon Health & Science University
Portland, OR, USA

(3) Biomedical Engineering
San José State University
San Jose, CA, USA

INTRODUCTION

There is an unmet clinical need for small diameter (<6 mm diameter) synthetic vascular grafts. There is strong evidence that the presence of an endothelial cell (EC) layer due to EC migration or endothelial progenitor cell (EPC) capture, known collectively as endothelialization, on the graft luminal surface could increase long term patency of synthetic vascular grafts by inhibiting intimal hyperplasia, the predominant failure mechanism, and by reducing thrombogenicity through an anti-coagulant and anti-inflammatory EC phenotype. ECs attach to surfaces through peptide bonds between the activated N-terminus of various integrins employed by the cell and binding sites on adsorbed proteins or functional groups on the material surface. Researchers in the field of small diameter synthetic vascular graft materials have tried many clever strategies to induce integrin binding on their materials by generating a biofunctional surfaces to recruit EPCs and ECs, which has proven effective in promoting *in situ* endothelialization. However, the molecules typically used to capture and promote the growth of EPCs and ECs are generally expensive, difficult to functionalize on new materials, and lack structural stability, capturing specificity, and biological functionalities which together have limited their applications and clinical potential and wide-spread adoption as platform materials.

Evidence is mounting that nanoscale surface roughness also promotes activation of integrins, and that microscale surface topography can determine the migration propensity and inflammatory phenotype of ECs. Recently our lab has shown that treating a hydrogel graft material poly(vinyl-alcohol) (PVA) with reactive ion plasma (RIP) can increase the attachment and proliferation of EPCs on PVA and reduces both platelet accumulation and fibrin deposition in a clinically relevant model of thrombosis[1]. However, the exact mechanisms of attachment, including which integrins are employed in a given milieu and in response to what substrate properties remains unclear.

Different RIP treatment formulations impart these surface modifications to varying degrees. For example, physical etches such Argon-based RIP treatments introduce more nanoscale roughness than O_2 RIP treatments whereas N_2 RIP treatments impart more surface reactive chemistry than Ar or O_2 treatments at the same power. We have shown that each RIP formulation results in different EPC affinities and that after aging RIP-treated PVA some, but not all, of the surface nitrogen introduced by the RIP degrades after 240 days in storage but the surface topography completely disappears and EPCs no longer adhere or proliferate. We have shown that RIP treatments introduce functional groups such as amines, amides, and carbonyls that we hypothesize allow ECs to attach to the luminal surface of the PVA. Recent data also suggests that there might be a role for the increased surface roughness of RIP-treated PVA in inducing cellular substructures such at filopodia which are necessary for ECs to attach and migrate. Decoupling the effects of surface chemistry and surface roughness by leveraging the differential degradation kinetics of surface reactive chemical groups and nanotopography introduced by RIP treatment would provide an easily adoptable platform to answer longstanding questions about the relative importance of surface chemistry and topography in cell attachment, migration, and proliferation including which integrins are employed in each process and whether specific integrins are typically employed by an EC at the site of cellular substructures such as lamellipodia.

METHODS

Dry PVA films were treated with reactive ion plasma (RIP) using O2, N2, or Ar gas at powers of 50 W or 100 W for 5 minutes. Surface roughness was quantified using Atomic Force Microscopy (AFM),

surface chemistry was determined using X-ray Photoelctron Spectroscopy (XPS) within 14 days or at 240 days after RIP treatment. Endothelial colony forming cells (ECFCs) were isolated from a peripheral venous blood draw. All cells were used between passage numbers 3–4 to seed 8 mm diameter RIP-treated PVA samples and cultured in a standard incubator at 37 °C and 5% CO2. ECFCs were seeded at 100,000 cells per well in 48 well plate. Cells were grown for 48 hours, rinsed and quantified using Quant-iT Picogreen reagent (ThermoFisher, Waltham, MA).

RESULTS

Untreated PVA indicated no surface reactive chemistry, quantified through the atomic percentage of surface nitrogen, and a roughness quotient (R_q) of 6.8 nm. After treating PVA with 100 W Ar RIP the atomic surface nitrogen increased to 2.1% and the roughness quotient increased an order of magnitude to 73.1 nm. After storage for 240 days at standard temperature and pressure the surface nitrogen was measured to be 2.5% and the roughness quotient decreased to a baseline value of 9.6 nm (Figure 1). Importantly, ECFCs (EPC derivatives) adhered on the newly modified PVA surface, but did not adhere to the surface after it was stored for 240 days and allowed to degrade.

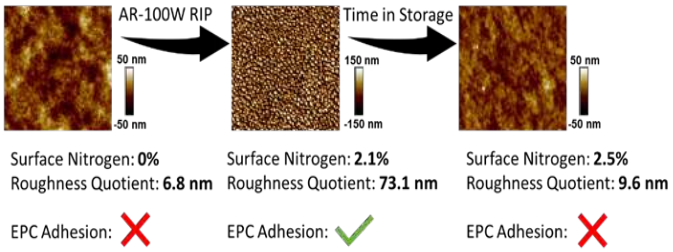

Figure 1: RIP-treating PVA imparts surface roughness and reactive surface chemistry, indicated as the atomic percent nitrogen, onto PVA which corresponds with the adhesion and proliferation of Endothelial Colony Forming Cells. However, after storing RIP-treated samples for 240 days, the surface topography disappears and EPCs no longer adhere, while the surface nitrogen mostly remains.

The roughness quotient (R_q) of RIP treated PVA depends not only on treatment gas and power, but also storage time after treatment. For the RIP treatments at a power of 50 W the roughness quotient was 10.7 nm, 64 nm, and 57.4 nm for O_2, N_2, and Ar gases respectively which increased from the untreated PVA control value of 6.2 nm. For the RIP treatments at a higher power of 100 W, the roughness quotient was 92.4 nm, 69.2 nm, and 73.1 nm for O_2, N_2, and Ar gases respectively. After storage at standard temperature and pressure for 240 days, the R_q for 50 W O_2, N_2, and Ar RIP treatments were 8 nm, 5.8 nm, and 36.7 nm respectively, while the values for 100 W O_2, N_2, and Ar RIP treatments after storage were 15.5 nm, 7.1 nm, and 9.6 nm respectively (Table 1).

Table 1: Roughness quotient (R_q) of PVA films less than 14 days after RIP treatment and 240 after RIP treatment.

Roughness Quotient (R_q)

	<14 days		240 days	
Plasma Treatment	50W	100W	50W	100W
Oxygen	10.7	92.4	8	15.5
Nitrogen	64	69.2	5.8	7.1
Argon	57.4	73.1	36.7	9.6
Untreated		6.2		

DISCUSSION

Aging of RIP-treated PVA samples resulted in a significant decrease in surface roughness, with most samples *relaxing* to the baseline value for PVA, which was never exposed to RIP. Aging of samples tended to have the same effect on the surface nitrogen content, but not to the same degree (data not shown). These results indicate that RIP-treated PVA can be used as a platform to study the attachment and other behaviors of ECs by treating materials with different RIP treatments and allowing each to age until the desired surface properties are obtained. With known underlying surface topography and/or surface chemistry, immunofluorescent imaging and antibody blocking assays can be utilized to determine the specific integrins used by ECs or EPCs in EC behavior. While biofunctional surfaces to recruit EPCs and ECs, have proven effective in promoting *in situ* endothelialization, molecules typically used to capture and promote the growth of EPCs and ECs are generally expensive, difficult to functionalize on new materials, and lack structural stability, capturing specificity, and biological functionalities. Utilizing RIP, which is an inexpensive and widely adopted high-throughput manufacturing technology which is ubiquitous in modern academic, clinical, and industrial laboratories to study the mechanisms of endothelialization of vascular graft biomaterials dramatically increases the utility and potential as a platform system. The system can ultimately be used to increase endothelialization of vascular grafts *in vivo*, which would increase their long-term patency, but might also be used to study the effect of modern medical device sterilization, which often involves RIP, on *in vivo* pathologies and device failure.

ACKNOWLEDGEMENTS

The authors acknowledge the support of NIH R01HL130274 for funding this work.

REFERENCES

[1] Jurney, P. L., Anderson, D. E. J., Pohan, G., Yim, E. K. F. & Hinds, M. T. Reactive Ion Plasma Modification of Poly(Vinyl-Alcohol) Increases Primary Endothelial Cell Affinity and Reduces Thrombogenicity. Macromol. Biosci. 1800132 (2018). doi:10.1002/mabi.201800132

A HIGH-ACCURACY DIGITAL VOLUME CORRELATION FOR SOFT TISSUE BIOMECHANICS CHARACTERIZATION USING OPTICAL COHERENCE TOMOGRAPHY

Fuqiang Zhong (1), Yi Hua (1), Junchao Wei (1), Manik Bansal (1), Juan Reynaud (3), Brad Fortune (3), Ian A. Sigal (1,2)

(1) Department of Ophthalmology
University of Pittsburgh
Pittsburgh, PA, USA

(2) Department of Bioengineering
University of Pittsburgh
Pittsburgh, PA, USA

(3) Devers Eye Institute
Legacy Health Research
Portland, OR, USA

INTRODUCTION

Digital volume correlation (DVC) is a widely used technique to extract the deformation between two image volumes. An increasingly popular way for obtaining volumes of soft tissues, such as eyes, skin and blood vessels, is optical coherence tomography (OCT). The combination of DVC and OCT has thus emerged as a powerful way to characterize the biomechanics of soft tissues **[1-4]**.

We present a new DVC method that overcomes three major challenges to obtaining accurate deformations between OCT volumes. First, because of differences in relative acquisition position and orientation between imaging sessions, OCT volumes acquired at different times often exhibit both deformations and rigid body motion. Rigid body motion increases DVC search area, decreasing computational efficiency. Large rotations reduce correlation **[5]**, affecting the measurement accuracy. Second, OCT image contrast decreases and noise increases with depth. Poor contrast and high speckle noise decrease the convergence of the popular 3D inverse-compositional Gaussian Newton (IC-GN) **[6]**, heavily reducing the DVC measurement accuracy. Third, interpreting the DVC results requires considering simultaneously various aspects of the process, such as local image quality and correlation coefficient. The technique we present overcomes these issues by using a combination of rigid body motion correction, sub-voxel point selection, and a novel scalar measure of "confidence". We demonstrate the technique with optic nerve head images.

METHODS

Rigid body motion correction: A semi-automatic pre-registration technique combining manual operation and automatic phase correlation **[7]** was implemented to correct the rigid-body motion of the tissue in the OCT volumes, especially the rotation angle. An interactive software with a user interface was developed to help 1) monitor the rigid-body motion correction process and 2) manually adjust the position and orientation of the deformed volume to register the reference volume. Manual operation is required if there is a large rotation of the tissue between the two volumes as the large rotation will decorrelate them and may fail an automatic correction. During manual operation, the error tolerance of rotation angles in the X, Y, and Z directions was relatively large: about 2 degrees, decreasing demands on the operator. Thereafter, phase correlation was used to further correct the rigid body motion automatically by maximizing the correlation coefficient in the Fourier domain.

Sub-voxel point selection applied if the 3D IC-GN iteration fails to converge: Commonly, the DVC search process consisted of two steps, a voxel-accuracy coarse search and a sub-voxel registration using 3D IC-GN iteration, among which the latter determined the accuracy of corresponding points searched. To ensure sub-voxel accuracy despite low contrast and high noise, if 3D IC-GN fails to converge, we select the sub-voxel corresponding point when the 2-norm incremental deformation parameter $\|\Delta\mathbf{p}\|$ was minimal; $\|\Delta\mathbf{p}\|$ of each iteration was recorded; $\|\Delta\mathbf{p}\|$ is expressed as,

$$\|\Delta\mathbf{p}\| = [\Delta u^2 + \Delta v^2 + \Delta w^2 + (M\Delta u_x)^2 + \left(M\Delta u_y\right)^2 + (M\Delta u_z)^2 + (M\Delta v_x)^2 + \left(M\Delta v_y\right)^2 + (M\Delta v_z)^2 + (M\Delta w_x)^2 + \left(M\Delta w_y\right)^2 + (M\Delta w_z)^2]^{\mathbf{1/2}} \quad (1)$$

where $\mathbf{p}$ is the deformation parameter: $\mathbf{p} = \{u, v, w, u_x, u_y, u_z, v_x, v_y, v_z, w_x, w_y, w_z\}$. Δ is the incremental operator. M is the half size of subvolume.

Confidence definition: Conventionally, the correlation coefficient $Corr = 1 - C_{ZNSSD}/2$ is assumed directly to reflect the confidence of a tracked point (C_{ZNSSD} represents the coefficient of zero-normalized sum

of square difference **[8]**); with a larger *Corr* indicating higher reliability. However, in practice, this is not sufficient for a reliable result. A point in a region of low contrast may have a large *Corr* without a good result. Average voxel intensity gradient (*AVIG*) is a good indicator of image contrast; a larger *AVIG* **[9]** generally means a higher contrast. We combined both *Corr* and *AVIG* to define a confidence *Conf* of the measured data as follows:

If $Corr_i > T_{corr}$ (a threshold, herein set to 0.7) or $Corr_i < T_{corr}$ & $AVIG_i < Const$:

$$Conf_i = Corr_i \times \left(\frac{AVIG_i}{Const}\right)^2 \quad (2)$$

Otherwise,

$$Conf_i = Corr_i \quad (3)$$

where $Const$ is a constant and set as $\overline{AVIG} \times 0.65$. ($\overline{AVIG}$ denotes the average $AVIG$ of all the reference subvolumes). i is the subvolume number. Greater *Conf* indicates higher reliability. *Conf* can be used to guide the search path of DVC and weigh the points for calculating strain, leading to increased robustness and higher accuracy of DVC measurements.

Test method: We used an OCT volume of the optic nerve head of a non-human primate (NHP) acquired using a Heidelberg Engineering Spectralis system. To test the effectiveness of the pre-registration method, we applied an artificial "synthetic" rigid body motion to the volume (translation vector: [-3.2, 1.8, 9.3] voxels; rotation angle [5.3°, -5.8°, -14.4°]). The pre-registration technique was then used to correct the preset rigid body motion. We compared the presented DVC method with the conventional method by measuring the preset 1) rigid sub-voxel translations ($u = v = w$ = 0.2, 0.4, 0.6, and 0.8 voxels, respectively.) and 2) strained deformation ($[u_x, v_y, w_z]$ = [-0.04, -0.04, 0.1] and [0.04, 0.04, -0.1]; $[u_x, v_y, w_z]$ = [-0.04, -0.04, 0.1] and [0.04, 0.04, -0.1].) In both cases, two rigid body motions were also respectively applied: a translation of [2.6, -3.4, 4.6] voxels (same to both cases); and rotation angles of [2.5°, -3.3°, 3.8°] and [-5.1°, -6.4°, 7.3°], respectively. *u*, *v*, *w* denoted the displacement in the X, Y, and Z directions, respectively; u_x, v_y, w_z were the strains in the three directions. To better mimic real OCT imaging, we also added speckle noise with a standard deviation of 0.05 to the artificially deformed volumes.

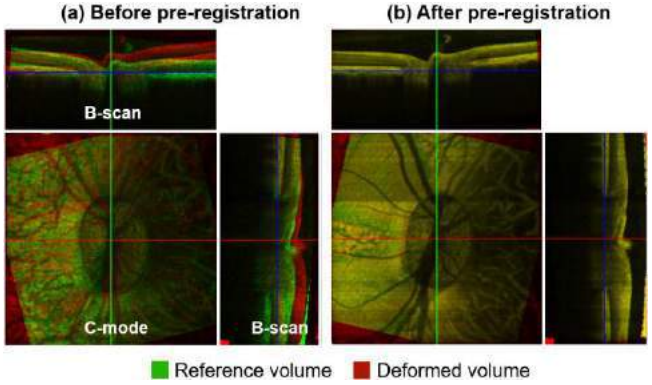

Figure 1. Artificial rigid body motion correction using the presented pre-registration technique. The OCT images are from a NHP optic nerve head. (a) Shown are overlays of the reference volume and the one with artificial rigid body motion before pre-registration; (b) Overlay after pre-registration. The overlays appear yellow if the two volumes register well, and green or red if they do not.

RESULTS

The reference ONH volume registered well with the one with artificial rigid body motion after applying the pre-registration technique (Fig. 1), validating its effectiveness. Absolute differences between the measured rigid body motion and the preset one was a translation of (0.2, 0.2, 0.3) voxels and the rotation angle of (0.25°, 0.26°, 0.36°). For the displacement and strain error comparison (Fig. 2), the presented DVC method had a displacement error of 0.05 voxels, with a strain error under 0.003; whereas, the conventional DVC method exhibited substantially higher displacement error (0.18 voxels) and strain error (more than 0.015). For the rigid body motion with larger rotation angle, the conventional method failed, while the proposed method's accuracy was not affected.

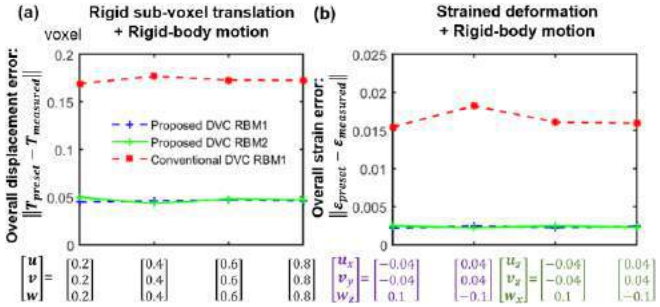

Figure 2. Accuracy comparison between the presented DVC method and a conventional DVC method on displacement and strain measurement accuracy. Two kinds of rigid-body motion (RBM1 and RBM2) are accounted. RBM1: $[T_x, T_y, T_z, \theta_x, \theta_y, \theta_z]$ = [2.6, -3.4, 4.6, 2.5°, -3.3°, 3.8°]; RBM2: $[T_x, T_y, T_z, \theta_x, \theta_y, \theta_z]$ = [2.6, -3.4, 4.6, -5.1°, -6.4°, 7.3°]. (a) The overall displacement errors. (b) The overall strain errors. For RBM2, the conventional DVC method failed, hence, its results were not shown.

DISCUSSION

We developed an improved DVC method that overcomes three important challenges of conventional DVC. We have demonstrated that this method works despite large rigid body motion, ensuring the sub-voxel accuracy even if the convergence of 3D IC-GN iteration fails. Finally, we have defined a novel confidence measure that is a more comprehensive measure of reliability. We have demonstrated that the new DVC method achieves significantly higher accuracy in computing displacements and strains than the conventional method when analyzing OCTs of the NHP optic nerve head.

ACKNOWLEDGEMENTS

Supported in part by National Institutes of Health R01-EY023966, R01-EY028662, R01-EY030590, P30-EY008098 and T32-EY017271 (Bethesda, MD), the Eye and Ear Foundation (Pittsburgh, PA), Research to prevent blindness, BrightFocus Foundation, and Legacy Good Samaritan Foundation.

REFERENCES

[1] Midgett E H, Quigley A, and Nguyen T D, *Acta Biomater*, 96: 385–399, 2019.
[2] Fazio M A, et al., *Sci Rep*, 8(1): 12639, 2018.
[3] Wei J C, et al., *Optical Elastography and Tissue Biomechanics*, *International Society for Optics and Photonics*, 10496, 2018.
[4] Girard M J A, et al., *J R Soc Interface*, 10(87): 20130459, 2013.
[5] Zhong F, and Quan, C, *Opt Laser Eng*, 98: 153-158, 2017.
[6] Wang T, et al., *Exp Mech*, 56(2): 297–309, 2016.
[7] Reddy B S, and Chatterji B N, *IEEE Trans Image Process*, 5(8): 1266–1271, 1996.
[8] Pan B, et al., *Appl Opt*, 49(28): 5501-5509, 2010.
[9] Pan B, et al., *Opt Lasers Eng*, 48(4): 469–477, 2009.

TRANSITION TO TURBULENCE DOWNSTREAM AN ECCENTRIC STENOSIS WITH FLEXIBLE WALLS UNDER STEADY FLOW USING LASER DOPPLER VIBROMETRY FOR WHOLE BLOOD AND A NEWTONIAN FLUID

Rayanne Pinto Costa (1), Blaise Simplice Talla Nwotchouang (1), David A. Steinman (2), Francis Loth (1, 3)

(1) Mechanical Engineering Department
The University of Akron
Akron, OH, USA

(2) Department of Mechanical & Industrial Engineering
University of Toronto
Toronto, ON, Canada

(3) Biomedical Engineering Department
The University of Akron
Akron, OH, USA

INTRODUCTION

Complex geometries such as stenoses can cause turbulence in arterial blood flow. A stenosis is a narrowing of the artery wall, which can cause heart attacks and strokes. Many numerical and experimental studies have been utilized to characterize the turbulence in an arterial geometry. Blood is a non-Newtonian fluid with shear thinning behavior at a lower shear rate and Newtonian behavior at a higher shear rate [1]. Because of this blood behavior, our group has focused on examining the assumption of blood as a Newtonian fluid at higher shear rates with particular emphasis on the impact of the transition to turbulence. This work has revealed a delay (i.e., a slightly higher critical Reynolds number) for whole blood than the Newtonian analog fluid in the transition to turbulence in a straight pipe under steady flow conditions [1]. Similar results were obtained for flow downstream of a stenosis, both experimentally [2,3] and numerically [4]. The stenosis experiments were conducted using a rigid flow model, and it is unclear if the fluid-solid interaction of a flexible wall would alter these results. The present study was conducted to investigate the impact of a flexible wall downstream of a stenosis on the transition to turbulence of blood by measuring wall vibration as an indicator of the level of turbulence.

METHODS

The flow circuit was temperature and flow rate controlled (Figure 1). A centrifugal pump [D] (Sarns Disposable Centrifugal Pump 7850) drove the test fluid from the reservoir [A]. The test fluid was cooled when passing through four glass heat exchangers [B]. The coolant fluid used came from a chiller [J] (RTE-110, Neslab), which was kept at 27ºC and was driven by another pump [G]. The test fluid was warmed using a coil heater [C]. The flow rate and heating/cooling was voltage controlled by three switching DC Power Supplies (BK Precision 1685B, Yorba Linda, CA) based on the feedback of measurements of the temperature and flowrate using an immersion thermistor probe [I] (DP25-TH-A & OL-703, OMEGA Engineering, INC., Stamford, CT), and a transit time ultrasonic flowmeter [H] (TS410 and ME6 PXN, Transonic Systems In., Ithaca, NY), respectively. The data was acquired for 3s with a sampling rate of 250 kHz using a data acquisition of 1.25MS/s (NI USB-6259, National Instrument). Downstream the 5% eccentric stenosis with 75% are reduction geometry [E], a flexible latex tube of length 130mm, inner diameter 6.35mm, and outer diameter 7.94mm [F] (McMaster-Carr, Elmhurst, IL) was used. The circuit flow was located inside an insulated chamber to ensure body-temperature control.

A laser Doppler vibrometer (LDV) was used to measure the velocity of the latex tube downstream of the stenosis. The LDV laser beam was passed through a hole in the insulated chamber. The wall vibration measurement was conducted at three locations downstream of the stenosis: 5D, 10D, and 15D (D-diameter) in the latex tube. In these locations, Polytech A-RET-T010 reflective tape (Polytec, Inc., Dexter, MI) was used to reflect the laser beam. The vibration measurement was acquired data for 3s and 12s with a sampling rate 250kHz. The vibration measurement was conducted at Reynolds numbers: 0, 200, 300, 350, 400, 450, 500, 550, 600, 650, 700, and 750. A total of five experiments were conducted (across all of these Re) with whole porcine blood as well as a water-glycerin mixture. For the whole porcine blood, a mixture of 3.8g of NaCl (Sigma-Aldrich, St. Louis, MO) and 100 ml of distilled water was added for every 900 ml of blood. The water-glycerin mixture had a ratio of 500:460 by volume.

The flowmeter was calibrated using a stopwatch and a 250ml graduated cylinder. The viscosity (at 37ºC and 1000 s^{-1}) and density (at 37ºC) were measured using a rheometer and a scale with a 25ml graduated cylinder, respectively, to define the actual Reynolds number. For the data postprocessing, the amplitude spectrum was calculated by

multiplying the fast Fourier transform by its complex conjugate and then square rooting it. A root mean square was also calculated after a low pass filtering for frequencies above 200Hz.

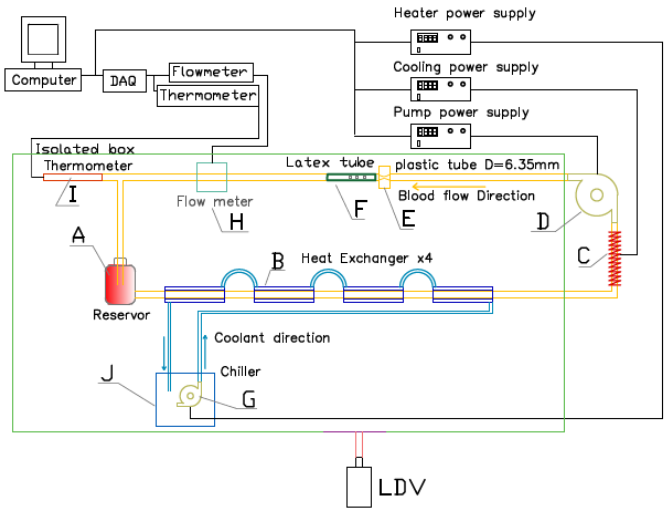

Figure 1: Flow experiment diagram

RESULTS

The average wall root mean square (RMS) velocity for the five samples of blood and water-glycerin are shown in Figure 2. The average wall velocity RMS for blood was slightly smaller than that for water-glycerin. The curves of blood and water-glycerin wall velocity RMS have a similar shape. Their curves rise gradually with an inflection point occurring approximately at Reynolds number ~ 350-500. Most of the measurements had frequencies between 15-19Hz, which is close to the natural frequency obtained by a bump test on the flexible tube when filled with the water-glycerin mixture (19Hz).

DISCUSSION

The results show that whole blood had a similar wall vibration as the Newtonian fluid (water-glycerin) during the transition to turbulence under steady flow within a flexible tube downstream of a 5% eccentric stenosis with a 75% area reduction. This suggests that there is no delay in the transition to turbulence for blood compared to water-glycerin. Blood and water-glycerin had a similar curve pattern for each measurement location near the critical Reynolds number (Re_{cr}~ 350-500) found by Casey and Yao in their rigid wall stenosis model [2,3]. However, they were able to identify a delay in the transition to turbulence by measuring the flow velocity fluctuations using a pulsated Doppler ultrasound probe with a rigid wall model. Yao found a delay of approximately 20% for blood compared to water-glycerin. Yao's experimental study showed Re_{cr}= 473±43 vs. Re_{cr}= 395±20 for blood and water-glycerin, respectively. Casey's results showed that the minimum Re_{cr} for blood was ~ 350-500 and for water-glycerin was ~250.

Note that the measurement of wall vibration is an indirect way to verifying the level of turbulence in the flow, and it was chosen due to the structural sealing limitations for the use of a Doppler ultrasound probe that may affect the wall motion. Thus, it may not have sufficient sensitivity to observe the delay in transition observed by Casey and Yao [2,3]. Nevertheless, the results from our study show that rheology has minimal impact on the wall vibration during the transition to turbulence. The consistency of vibration frequencies clearly indicates wall resonance phenomena, albeit at frequencies lower than expected in vivo. Further research using a more direct measurement of fluid velocity is required to fully understand the impact of a flexible wall on the transition to turbulence, even for simple fluids.

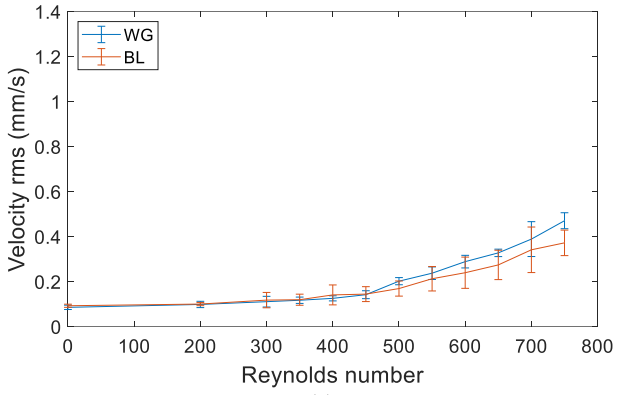

(a)

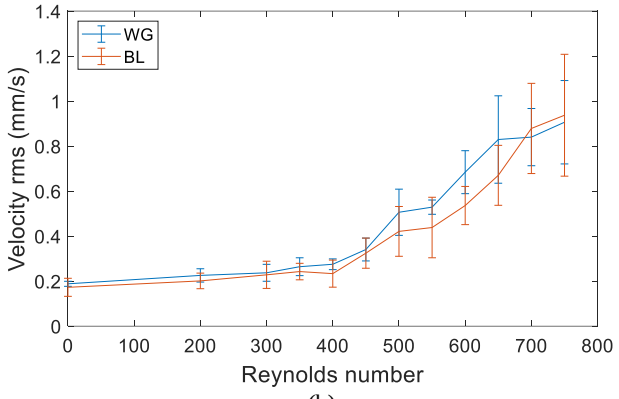

(b)

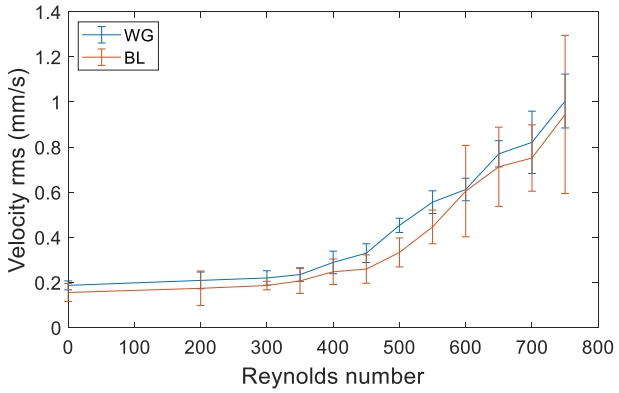

(c)

Figure 2. Wall velocity RMS at locations 5 (a), 10 (b), and 15 (c) diameters downstream of the stenosis.

ACKNOWLEDGEMENTS

We acknowledge the invaluable support of Dr. Dipankar Biswas and Mr. Junyao Yao during this research.

REFERENCES

[1] Biswas, D. et al., *J. of Biomechanical Engineering*, vol.138, 2016.
[2] Casey, D., Master thesis. The University of Akron, Akron, 2014.
[3] Yao, J., Master thesis. The University of Akron, Akron, 2020.
[4] Khan M.O. et al., *Flow Turb Combust*, 102:43-72, 2019.

SB³C2021
Summer Biomechanics, Bioengineering and Biotransport Conference
June 14-18, Virtual

BIOMECHANICS OF HEADERS IN YOUTH AND COLLEGIATE FEMALE SOCCER

Tanner M. Filben (1,2), Nicholas S. Pritchard (1,2), Logan E. Miller (1,2), Christopher M. Miles (1,3), Jillian E. Urban (1,2), Joel D. Stitzel (1,2)

(1) Department of Biomedical Engineering
Wake Forest School of Medicine
Winston-Salem, NC, USA

(2) School of Biomedical Engineering and Sciences
Virginia Tech – Wake Forest University
Winston-Salem, NC, USA

(3) Department of Family and Community Medicine
Wake Forest School of Medicine
Winston-Salem, NC, USA

INTRODUCTION

Concussions occur at a relatively high rate among soccer players, and research suggests that female players may be more susceptible to brain injury than their male counterparts [1]. In addition to concussion, there is increasing concern about the potential consequences of repetitive subconcussive impacts. Although concussions are most likely to occur during player-to-player collisions, the majority of head impacts in soccer are intentional headers [1,2]. Head impact sensors that have been previously used to quantify head impact exposure in soccer may be prone to error resulting from poor coupling with the skull [3]. This has made comparisons across levels of play difficult to adequately assess, and few studies to date have attempted to simultaneously measure head impact exposure in two or more levels of play with the same sensor [4,5]. Further understanding of how head impacts differ across age groups is necessary to inform safety regulations in the sport. Additionally, accurate kinematic measurements are necessary to drive finite element brain models, which have been previously used to estimate tissue-level strain in sport-related impacts [6]. Evaluating the tissue-level strain response of the brain to headers experienced in an on-field setting can help identify factors associated with the biomechanics of repetitive head impacts which, in turn, can inform our understanding of how those impacts relate to neurological deficits and concussion risk. The objective of this study was to evaluate and compare head kinematics and the corresponding tissue-level brain strain of intentional headers across youth and collegiate female soccer players.

METHODS

Soccer players from one U15 girls' team and one National Collegiate Athletic Association Division 1 women's team were recruited to participate in this study over one competitive season. Each participant was instrumented with a previously-validated mouthpiece sensor that contained a tri-axial accelerometer and gyroscope [7]. Kinematic data and time-synchronized video were collected during each game and practice. Sensors were configured to collect 60 milliseconds (ms) of linear acceleration and angular velocity data (15 ms pre-trigger and 45 ms post-trigger) at sampling frequencies of 4,681 Hz and 800 Hz, respectively, when the linear acceleration exceeded 3.5 g (youth) or 5 g (collegiate) for at least 3 ms. Recorded events were processed and transformed to the head center of gravity (CG). Recorded events were video-verified using a custom MATLAB (MathWorks, Natick, MA) graphical user interface that semi-automatically paired event timestamps with corresponding video times. The ball delivery method of each verified header was defined as the method in which the ball was delivered to the player prior to the header and included kicks, throws, and headers (i.e., the player received the ball from another header).

The head kinematics measured from the mouthpiece sensors were used to drive the atlas-based brain model (ABM) [8]. For each header, the measured linear acceleration was numerically integrated to obtain the linear velocity at the head CG. The measured rotational velocity and the calculated linear velocity were applied to the head CG of the model. The maximum principal strain (MPS) in each element was used to calculate two strain-based metrics: the maximum value of the 95th percentile MPS time history curve (MPS95) and the area under the cumulative strain damage measure curve (CSDM area) [6]. Mixed effect models were used to compare head kinematics and strain-based metrics by level of play. Session type and ball delivery method were included in the model as covariates. Because of their right-skewedness, all dependent variables were log-transformed before analysis and back transformed to report the mean and 95% confidence intervals. Statistical analysis was completed in SAS (version 9.4, SAS Institute Inc., Cary, NC).

RESULTS

Six youth girls' and 13 collegiate women's soccer players participated in the study. A total of 567 film-verified headers (n=309 youth, n=258 collegiate) were collected over 88 practices (n=34 youth, n=54 collegiate) and 38 games (n=19 youth, n=20 collegiate). None of the recorded headers resulted in a clinically diagnosed concussion. The mean peak resultant linear acceleration, rotational velocity, rotational acceleration, MPS95, and CSDM area of all 567 headers were 16.3 g, 6.97 rad/s, 1.53 krad/s^2, 0.0649, and 4.50, respectively. Pairwise comparisons of mean head kinematics and strain by level of play and associated summary statistics are provided in Table 1. Compared to youth players, headers experienced by collegiate players had greater mean and 95th percentile peak linear acceleration, peak rotational velocity, peak rotational acceleration, MPS95, and CSDM area.

Table 1 Peak head kinematics and strain metrics by level of play. CI is the 95% confidence interval for the mean.

	Collegiate	Youth
N Headers	258	309
Linear Acceleration (g)	$p < .001$	
Mean	17.1	10.6
[CI]	[15.0, 19.4]	[9.20, 12.1]
Median	22.3	8.93
95th Percentile	44.4	20.6
Rotational Acceleration (krad/s^2)	$p < .001$	
Mean	1.55	0.825
[CI]	[1.35, 1.79]	[0.715, 0.951]
Median	2.23	0.593
95th Percentile	5.09	1.93
Rotational Velocity (rad/s)	$p < .001$	
Mean	7.71	5.09
[CI]	[7.00, 8.50]	[4.62, 5.62]
Median	9.07	4.44
95th Percentile	16.3	9.18
MPS95	$p < .001$	
Mean	0.0728	0.0443
[CI]	[0.0661, 0.0801]	[0.0404, 0.0487]
Median	0.0884	0.0387
95th Percentile	0.166	0.0804
CSDM Area	$p < .001$	
Mean	5.08	3.04
[CI]	[4.62, 5.59]	[2.77, 3.34]
Median	6.22	2.60
95th Percentile	11.6	5.78

DISCUSSION

Collegiate soccer players experienced higher kinematic magnitudes and greater tissue-level brain responses during headers than youth soccer players. The mean linear acceleration, rotational acceleration, rotational velocity, MPS95, and CSDM area were approximately 61%, 88%, 51%, 64%, and 67% greater among the collegiate players compared to the youth players, respectively. The comparison of head kinematics described herein adds to the limited knowledge regarding differences in soccer head impacts experienced across levels of play. The characterizations of brain tissue strain are, to the authors' knowledge, the first comparisons of the brain's response to headers experienced at different levels of play during normal soccer participation.

The increased head kinematics observed in collegiate players compared to youth players in the present study is consistent with two previous studies which observed greater magnitude head impacts among players at higher levels of play. Chrisman et al. reported greater head impact exposure over one month of play among U14 soccer players compared to U12 players [4]. The U14 female players in the study experienced a greater number of head impacts higher than 15 g compared to U12 players (87 vs. 0). McCuen et al. reported that female collegiate soccer players experienced head impacts with slightly greater mean peak linear acceleration (39.3 g vs. 37.6 g) but no significant difference in mean peak rotational acceleration (6.43 krad/s^2 vs. 6.53 krad/s^2) compared to female high school soccer players [5]. Differences in reported mean kinematic magnitudes between studies may, in part, be due to the improved accuracy of the mouthpiece sensors and film verification used in the current study compared with other types of head kinematic measurement devices [3].

The current study contributes to the limited research on the mechanical response of the brain to intentional soccer headers. Kuo et al. evaluated MPS during 14 intentional soccer headers delivered via a ball launcher at 7.0 m/s using the KTH brain model [9]. The resulting median MPS value of 8.5% is similar to our reported median MPS95 of the collegiate headers (8.8%). Allison simulated 111 on-field intentional headers with the Global Human Body Models Consortium head model using kinematic data recorded with the GForce Tracker wireless headband sensor [10]. Interestingly, one of Allison's simulated headers resulted in a concussion and was associated with an MPS value of approximately 18.6%. Four headers in the current study (all from collegiate athletes) had MPS95 values that exceeded that of the concussive impact reported by Allison, but none of them were associated with a diagnosed concussion.

This study was limited by factors associated with the mouthpiece devices, on-field data collection, and the finite element model. First, the devices were configured at different threshold values for the youth (3.5 g along any axis) and collegiate players (5 g along any axis). The youth threshold was lower because previous work found over 40% of youth soccer impacts measured below 5 g [11]. Secondly, the headers recorded during games are biased toward a subset of players who participated in the study. Four of the six youth players and three of 13 collegiate players recorded a header during a game. Thirdly, although the ABM possesses high anatomical accuracy, the model includes several simplifying assumptions [8]. Finally, the ABM was developed from the International Consortium for Brain Mapping brain atlas of adult brains and may not accurately represent brains of the youth participants.

ACKNOWLEDGEMENTS

The authors would like to thank the soccer organizations for participating in the study and Sarah Woods, Megan Hayden, and Sebastian Haja for assistance with data collection and film review. This material is based upon work supported by the National Science Foundation Graduate Research Fellowship under Grant No. 2102417. Any opinion, findings, and conclusions or recommendations expressed in this material are those of the authors(s) and do not necessarily reflect the views of the National Science Foundation. This work was also supported by the Childress Institute for Pediatric Trauma (Winston-Salem, NC, USA).

REFERENCES

[1] Zuckerman, S et al., *Am. J. Sports Med.* 43(11):2654-2662, 2015. [2] Press, J et al., *Clin J Sport Med* 27(2):104-110, 2017. [3] Wu, L et al., *Ann Biomed Eng* 44(4):1234-1245, 2016. [4] Chrisman, S et al., *Clin J Sport Med* 29(1), 2019. [5] McCuen, E et al., *J Biomech* 48(13):3729-3732, 2015. [6] Miller, L et al., *J Neurotrauma* 36(10):1561-1570, 2019. [7] Rich, A et al., *Ann Biomed Eng* 47(10):2109-2121, 2019. [8] Miller, L et al., *Biomech Model Mechanobiol* 15(5):1201-1214, 2016. [9] Kuo, C et al. *J Neurotrauma* 34: 3198-3205, 2017. [10] Allison, W, Master's thesis, The University of Western Ontario, *Electronic Thesis and Dissertation Repository*, 2019. [11] Tomblin, B et al., *J Appl Biomech*, 2020

CORTICAL THICKNESS DISTRIBUTION OF THE HUMAN CEREBRAL CORTEX IDENTIFIED BY CURVATURE AT LOCAL SCALES

Nagehan Demirci (1,2), Maria A. Holland (1,2)

(1) Aerospace and Mechanical Engineering
(2) Bioengineering Graduate Program
University of Notre Dame
Notre Dame, Indiana, USA

INTRODUCTION

The adult human brain has a unique structure and morphology, similar to fingerprints. The complex surface topology of the highly folded cortex, the outermost layer of the brain, consists of asymmetrical outer gyral ridges and inner sulci valleys which emerge during the third trimester of gestation. Although the mechanism of cortical folding is still under investigation, a combination of mechanical and biological factors is thought to affect the buckling of the cortical sheet. Specifically, cellular processes and mechanical forces generated during growth have been shown to lead to consistent regional variations in cortical thickness between gyri and sulci, with gyri being significantly thicker than sulci, both within humans [1-4] and in primates [5]. In this study, we want to investigate how this variation differs across the convoluted surface of the brain beyond just gyri and sulci. This is highly relevant to public health as neurological disorders such as Autism Spectrum Disorder (ASD) [6] and schizophrenia [7] are known to be associated with regional abnormal folding patterns and mean cortical thickness differences of the cortex. Quantification of the typical and atypical folding patterns of the cortex on a local scale, in addition to the regional, is extremely important in order to (1) better understand the causes of diverging folding shapes which are linked to atypical and neuro-typical development of the brain, (2) capture the true variation of cortical folding patterns without loss of valuable local information, and (3) be able to early and objectively diagnose neurological disorders by identifying accurate and reliable biomarkers before clinical symptoms evolve. In this study, we developed an open-source computational toolbox to investigate cortical thickness variations on a local scale (at ~40k points) in order to understand how this varies with the morphology of the folded cortex. The toolbox takes in any cortical surface mesh as an input and calculates the surface measures (curvature, thickness, depth and area) spatially on a local scale (point-wise).

METHODS

The structural MRI of typically developed (TD) human subjects are obtained from a publicly available imaging data set [8]. The outer cortical sheet, i.e. pial surface of the cortex, and the inner cortical sheet, i.e. white surface, are reconstructed from cross-sectional MR images by using an automated open-source neuroimaging pipeline, Freesurfer [9], which outputs a piecewise cortical mesh for both surfaces.

The accuracy of the quantitative surface measures depends on a uniform, smooth mesh, while the original meshes are irregular and uneven. Therefore, we decimated and smoothed both meshes with a user-defined target reduction and smoothing value (Fig. 1). The simplified and uniform surface mesh preserves the original surface topology and geometry for robustness of the calculations. Then, by utilizing the principles of discrete differential geometry, we calculated the curvature measures (mean curvature (H), Gaussian curvature (K), principal curvatures (PCs), Shape Index (SI)), cortical thickness, and sulcal depth at each vertex using our computational pipeline, which will be shared publicly in the future for the use of other researchers. Moreover, we calculated the total folding index (FI) and the total intrinsic curvature index (ICI) for sulcal and gyral regions of the cortex separately. Here, instead of using to an automatic cortical parcellation scheme to distinguish gyral and sulcal regions, such as the Destriuex atlas, we investigated the cortex in its entirety to explore the thickness variations at local scales including the tangential (in-plane) bends of the gyri and sulci. These bends of the cortex have not received much attention previously, but based on our finding that folding directly leads to cortical thickness variations, we expect to observe thickness variations within these folds as well. We attributed convex shaped vertices (negatively signed PCs) as gyral, concave shaped vertices (positively signed PCs) as sulcal and saddle shaped vertices (negatively signed K/oppositely signed PCs) as tangential folds of the cortex.

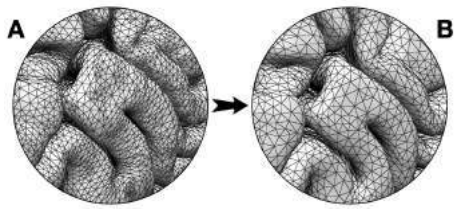

Fig. 1: Representative piecewise mesh of the pial surface. (a) Irregular, dense mesh (b) Simplified, more uniform mesh.

RESULTS

We present the cortical thickness variations throughout the cortex as a Gaussian kernel density distribution with respect to the local morphology identified by the curvature measures (Fig. 2, right). The mean curvature is successful in delineating the gyral and sulcal folds of the cortex (Fig. 2B), while negative Gaussian curvature is an effective measure to highlight the tangential folds (in-plane bends) of the cortex (Fig. 2C). It is important to note that, as it is not possible to distinguish convex from concave by using only the Gaussian curvature, we used principal curvatures additionally to demonstrate the thickness variations of convex (gyral) and concave (sulcal) folds (Fig. 2B-right). Finally, we found that Shape Index by itself is capable of distinguishing gyral, sulcal, and tangential folds of the cortex in a spectrum from cup to cap (Fig. 2D) [10]. From this investigation, we found that gyral folds are consistently thicker than tangential folds and that sulcal folds are the thinnest throughout the cortex.

DISCUSSION

The development of the cortex entails an extensive folding process which engenders characteristic gyral, sulcal and tangential cortical folding patterns and also appears to result in systematic cortical thickness variations throughout the cortex both radially (from sulcus to gyrus) and circumferentially (in-plane folds). In this study, we present the well-organized relationship between the curvature of the cortex and cortical thickness at individual points. Throughout the cortex, the point-wise cortical thickness distribution reveals a continuous spectrum from gyral peaks to sulcal pits, including the tangential folds as well. The curvature measures presented here are useful to investigate these systematic variations.

As part of our future work, we will extend the capabilities of our computational toolbox to extract vertices belonging to outer and inner parts of the tangential folds using the curvature measures presented here or a combination of them. This will allow us to further investigate cortical thickness variations from outer to inner tangential folds of gyri and sulci. Furthermore, we aim to build on recent advances in high-resolution MR imaging [11] and computational neuroimaging tools to investigate the relationship between the local shape (identified by the curvature) and thickness on a laminar scale from gyri to sulci and from inner to outer in tangential folds (in-plane bends). This investigation might not only provide additional insight to understand the consistent relationship between curvature and thickness of the laminar layers but also the role of laminar and major cortical thicknesses in typical development and in abnormal cortical folding seen in neurological disorders such as the ASD.

ACKNOWLEDGEMENTS

This work was supported by NSF Grant No. IIS 1850102.

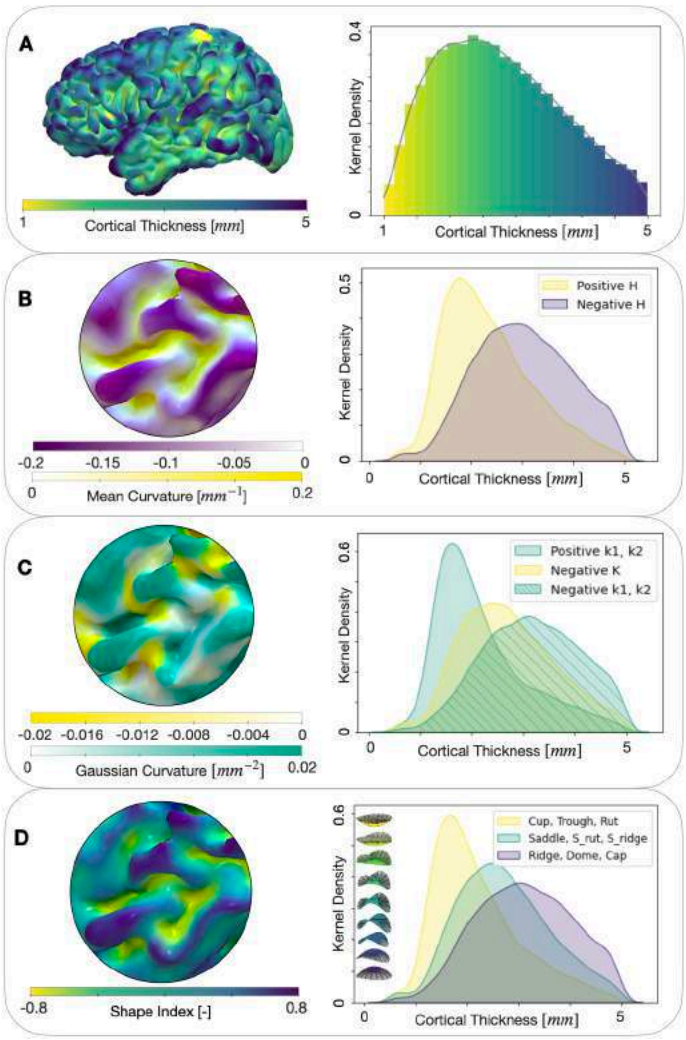

Fig. 2: Cortical thickness Gaussian kernel density distribution with respect to local morphology distinguished by curvature measures. (a) Cortical thickness distribution (b) Mean curvature, $H\ [mm^{-1}]$ (b) Gaussian curvature, $K\ [mm^{-2}]$ (c) Shape Index, $SI\ [-]$. Note that k_1 and k_2 are maximum and minimum principal curvatures respectively.

REFERENCES

[1] Holland, M et al., *Physical Review Letters* 121 (22): 228002, 2018.
[2] Zhang, T et al., *Scientific Reports* 6 (1): 37272, 2016.
[3] Fischl, B., and A. M. Dale, *Proceedings of the National Academy of Sciences* 97 (20): 11050–55, 2000.
[4] Wang, S., et al., *Biomechanics and Modeling in Mechanobiology*, 2020.
[5] Hilgetag, C., and Helen B, *Anatomy and Embryology* 210 (5–6): 411–17, 2005.
[6] Pua, E et al., *Scientific Reports* 9 (1): 1–10, 2019.
[7] Erp, T et al., *Biological Psychiatry* 84 (9): 644–54, 2018.
[8] Di Martino, A et al., *Molecular Psychiatry* 19 (6): 659–67, 2014.
[9] Dale, A. M. et al., *NeuroImage* 9 (2): 179–94, 1999.
[10] [5] Koenderink, J et al., *Image and Vision Comp.* 10 (8): 557–64, 1992.
[11] Wagstyl, K et al., *Cerebral Cortex* 28 (7): 2551–62, 2018.

IMPROVED EFFICIENCY IN BIOMECHANICAL MODELING WITH AUTOMATED REMOVAL OF MOUNTING HARDWARE FROM SOFT TISSUE 3D IMAGING DATASETS

Sam E. Stephens, BS (1); Neil B. Ingels, PhD (1);
Jonathan F. Wenk, PhD (2); Morten O. Jensen, PhD, DrMed (1)

(1) Department of Biomedical Engineering
University of Arkansas
Fayetteville, AR, USA

(2) Department of Mechanical Engineering
University of Kentucky
Lexington, KY, USA

INTRODUCTION

Analysis of three-dimensional (3D) geometry is critical to a wide range of studies in many different disciplines. The proliferation of 3D imaging devices such as magnetic resonance imaging (MRI) and computerized tomography (CT), once out of reach for many researchers, has increased the need for efficient and effective tools with which to perform analysis. Often, particularly within biological studies, samples require support or conditioning from specialized hardware. Examples of such hardware include mounting hardware, pressurized containers, and manipulators. Depending upon the goals of the study, this hardware must frequently be removed from the resulting 3D image dataset prior to further analysis. The most common technique for this relies on removing regions that fall above or below a pixel intensity threshold. Not uncommonly however, situations arise where the contrast between the region of interest and adjacent hardware features is quite low. This generally leads to difficulty with intensity based removal approaches as they tend to under-remove the unwanted areas and more importantly can remove portions of the region of interest. If, however, the specific 3D shapes of the hardware features are already known, it can be removed based purely on geometry. The following presents a new and novel approach for the semi-automatic removal of known-geometry components from a 3D dataset represented by using a 2D image stack.

METHODS

STL File: The algorithm is summarized in Figure 1. Hardware geometry is first input in the form of a binary STL (standard tessellation language) file, which represents the solids as a mesh of triangular facets with associated edges and vertices. Additional inputs include the bottom and topmost image numbers in which the hardware elements are visible, the inter-image spacing and the locations of three (or more) fiducial points. Fiducial points are ideally modeled into the hardware itself in such a way as to allow easy, precise identification.

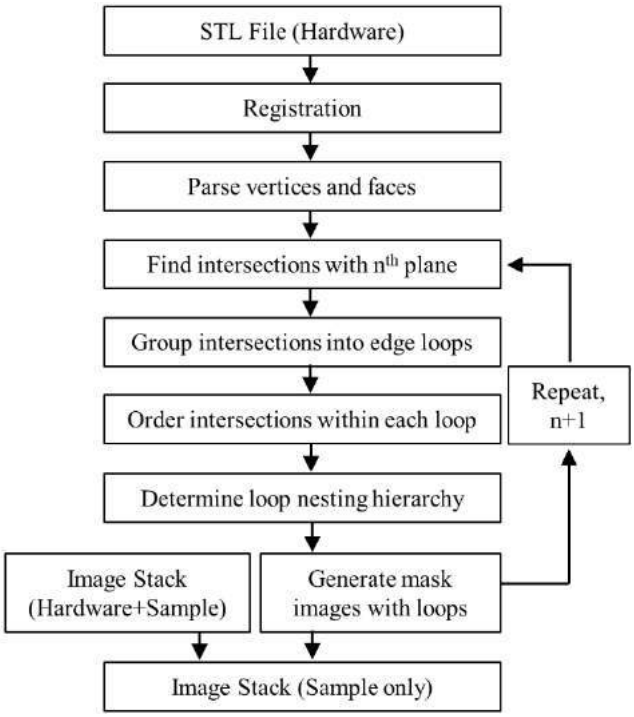

Figure 1 – Flowchart representation of the overall hardware removal process

Registration: A rigid-body transformation is conducted so as to register the three hardware fiducial points (whose positions with respect to one another are known) with their positions within the image stack. The necessary rotation and translation matrices are found through singular value decomposition [1], while scaling is determined from fiducial point-to-point distances.

Find Intersections: A plane is constructed such that it is coincident with the bottom-most image in which hardware is visible. The vertex coordinates from the STL file are parsed into separate faces and associated edges. These faces are evaluated to determine which ones intersect or cross the plane. If the plane is crossed, then the intersection points along the face's edges that cross are found. Any vertices or edges that lie along the plane are also found. All the intersections with the plane, for all STL faces, are compiled into an array.

Group and Order Intersections: These intersections trace out the edges of the model formed by a cross sectional cut taken at the plane. In the event that the hardware element has several branches or internal features, such as holes, then the multiple edges will all be represented by the points within the intersections array. In order to separate the intersection points into individual edge "loops", a connectivity thresholding approach is employed to segment the intersections, whereby all points within a pre-defined radius of an arbitrary base point are considered to occupy the same loop. All similarly "connected" points are grouped until no additional points fall within the connectivity radius, at which point the process is repeated for a new loop. The now grouped intersections must next be ordered within the individual loop arrays such that they would present the smooth, cross-sectional outline of the model if connected in a connect-the-dots manner. This is accomplished through a "nearest neighbor" approach, though other methods may be suitable, such as a traveling-salesman solver [2].

Determine Hierarchy and Generate Masks: Once all loop arrays have been ordered appropriately, the loop hierarchy, or whether the loop represents an interior or exterior edge, must be determined. This may be done by checking whether an arbitrary member from each loop is inside the polygon formed from each of the other ordered loops. The now appropriately ordered sets of intersection points are used to generate polygonal masks that are applied to a template image which is of equal size and resolution to those of the image stack. Mask regions are flood filled white or black according to their hierarchy.

The above procedure is repeated for a new image plane, offset from the first by the data image stack inter-image spacing. This continues until the image plane height matches the uppermost image which displays the hardware to be removed. Masks are finally multiplied pixel-wise by the original images to remove the hardware from the data set.

Mitral Valve Clamp Case Study: A case study was conducted using a portion of a previously described [3] 3D printed, customizable annulus clamp that is utilized in mitral valve scanning studies. The clamp was scanned with a Nikon TH 225 ST CT system with a beam energy and current of 180 kV and 174 µA respectively. An isotropic 32-micron resolution was used. Following reconstruction, the dataset consisted of 1622 images with a pixel depth of 16-bit and a size of 2000x2000 pixels, giving a total dataset size of approximately 12 gigabytes. The clamp piece was mounted atop Styrofoam, which is weakly visible to x-ray, resulting it an isolated clamp against a black field within the resultant image stack. The above described algorithm was performed using the clamp STL and scan imagery, using a Dell XPS 9570 with 16 GB memory, 6 cores and GTX 1050Ti graphics card.

RESULTS

Application of the algorithm to the clamp scan removed more than 96% of the clamp, as measured by the number of pixels before and after removal with an intensity greater than 40,000 (out of 65,536). Total computational time for removal of the 1190 mounting-hardware-containing images was approximately 15 minutes. An example mask, along with its corresponding original image and multiplied result, are shown in Figure 2.

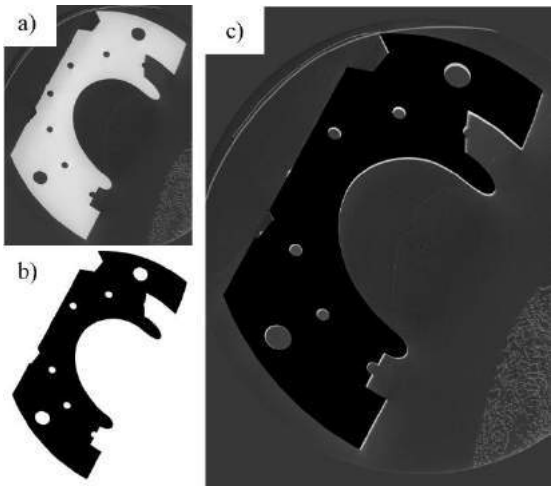

Figure 2 – Example images of a) original image, b) corresponding mask and c) pixel-wise multiplication result showing nearly full hardware removal of scanned mitral clamp

DISCUSSION

The above-described method has been shown to be effective for removing known-geometry hardware elements from imagery. The error preventing total removal was mostly due to imperfect registration with the three fiducial points; this will be improved by using more points. Although the time required to process the image data was relatively short, this can be improved by increasing the number of cores, ram, and graphics on the computation system. In circumstances where low/no contrast is present between mounting hardware and adjacent sample, which would render ineffective many intensity thresholding methods such as Otsu's Method [4], geometry-based removal may well be the only viable option for subtraction of hardware. Another major advantage of this approach over others, such as volume-based subtraction [5], is the vastly reduced computational load. This is primarily due to the image-by-image manner in which masks are generated and applied to the data image stack. Rather than loading into memory the entire dataset, which can often exceed 10Gb for high resolution scans, and then performing operations on each voxel, only a small fraction of the total dataset should be loaded and analyzed at a time with this method.

ACKNOWLEDGEMENTS

This publication was supported by NIH Award R15 HL145585-01 as well as NSF Grant Number NSF BCS-1725925 for the University of Arkansas MicroCT Imaging Consortium for Research and Outreach.

REFERENCES

[1] Arun, K.S. et al., *IEEE PAMI*, vol. PAMI-9, no. 5, pp. 698-700, 1987
[2] Kirk, J, Traveling Salesman Problem - Genetic Algorithm, MATLAB Central File Exchange. 2021
[3] Stephens, S et al., PLoS ONE 12(8): e0184042, 2017
[4] Otsu N,*IEEE Trans Syst Man Cybern Syst*, vol.9,no.1,pp62-66, 1979
[5] Stichting Blender Foundation, *Blender - a 3D modelling and rendering package*., Boolean Modifier, 2021

MUTLI-DIRECTIONAL FLEXIBILITY ENDURANCE TESTING OF FOUR DIFFERENT CERIVCAL TOTAL DISC REPLACMENT PROSTHESES

Denis J. DiAngelo (1), Chloe L. Chung (1), Daniel Hoyer (1), Tyler Carson (2), Kevin T. Foley (2)

(1) Department of Orthopaedic Surgery and Biomedical Engineering
University of Tennessee Health Science Center
Memphis, TN, USA

(2) Semmes Murphey Clinic
Memphis, TN, USA

INTRODUCTION

Motion preservation devices have become increasingly popular in the treatment of spinal pathologies that require biomechanical support following removal of the degenerated tissue [1-3]. As these devices continue to be developed to treat multiple adjacent diseased spinal levels, i.e., using multiple disc prostheses or placing a disc prosthesis adjacent to a fused level, biomechanical data that supports these established surgical methods are needed. The objective was to determine the stability of four cervical disc prostheses tested under low endurance multidirectional loading conditions in a cadaveric cervical spine model.

METHODS

16 (C4-C5) and 16 (C6-C7) functional spinal units (FSUs) were dissected from eight male and eight female cadaveric cervical spines with an average age of 55.9 +/- 9.7 years. Three FSUs were not usable due to poor tissue quality which reduced the sample size to 29 FSUs. Four cervical total disc replacement (TDR) prostheses that had a similar ball and socket type articulation mechanism but varying endplate fixation features were tested (Figure 1): 1. A clinically used and FDA approved single central keel (SCK), 2. Low profile teeth (LPT) with domed endplate shape to allow a better fit in case of concave vertebral endplate, 3. Tripod keel (TK), and 4. Small single keel (SSK). A minimum sample size of 6 implants per prosthesis type was used.

Each specimen was mounted in a robotic testing platform (Figure 2) and tested with a coupled eccentric loading (CEL) protocol that moved the instrumented specimens through a sequence of combined motions of flexion or extension coupled with right and left axial rotation. A compressive load of 50N was applied to the upper mounting pot directly above the midline of the disc implant. End limits of motion were established for load limits of 1.5Nm in flexion, extension and axial rotation resulting in a total applied moment of 2.25Nm. If the specimen reached a total of 15degrees in flexion or extension, or 10 degrees in axial rotation, the corresponding moment value at the end range of motion was used which prevented the resultant target moment from being exceeded. Each specimen was then cyclically tested 2000 times at a rate of 2.5deg/s. Anteroposterior endplate migration of both the upper and lower implant components was measured after 20, 250, 500, 1000, 1500, and 2000 cycles.

Single Central Keel (SCK | Low Profile Teeth | Tripod Keel (TK) | Small Single Keel

Figure 1: Cervical Total Disc Replacement Prostheses.

Implant migration was analyzed by using a digital Vanier caliper set (with 1micron accuracy) to measure the offset distance between a fixed reference plate attached to the front surface of the mounting pot and the outer front face of both upper and lower implant components. Tests were stopped if implant component migration exceeded 3mm or endplate fracture was observed, and migrations less than 0.3mm were defined as clinically stable. A one-way repeated measures ANOVA with a Student Newman-Keuls test was used to compare differences.

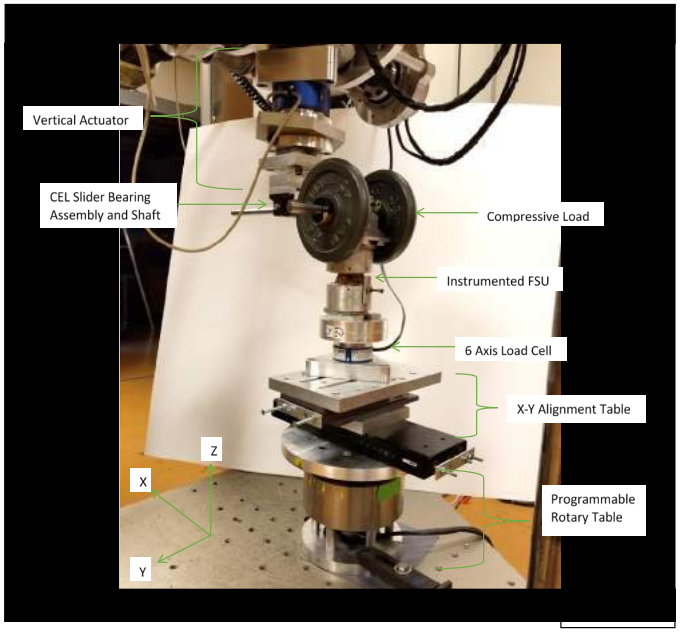

Figure 2: Experimental Setup for Multidirectional Test.

RESULTS

The mean and standard deviations of the combined (flexion plus extension) sagittal plane range of motion or the combined (left plus right) axial motion of the four TDR devices are shown in Figure 3. No statistical differences were found between the ranges of motion (ROM). The anterior-posterior migration of the upper and lower components of the disc prostheses are shown in Figure 4. All but one of the specimen migration values were below 0.3mm. Upper prosthesis component migration ranged between 0.02mm and 0.08mm and between 0.01mm and 0.04mm for the lower components. No significant differences occurred between the upper components or the lower prosthesis components of any implant type.

DISCUSSION

A human cadaveric cervical spine model was used to determine the biomechanical stability properties of four cervical TDR prostheses. Three low profile endplate fixation designs currently in the investigational phase of FDA clearance were found to provide comparable ranges of coupled movements to an existing clinically used and FDA approved central-based keel design. The three investigational prostheses also remained as stable as the FDA approved device following low cyclic testing. More cervical TDR prostheses, having different endplate fixation design features, provides spine surgeons with more options to accommodate anatomical constraints (i.e., varying endplate profiles and shapes) and/or treating multilevel adjacent spinal diseases.

ACKNOWLEDGEMENTS

Research contract from Centinel Spine.

REFERENCES

[1] Bartels RH, et al., Fusion around cervical disc prosthesis: case report. *Neurosurgery* 57:E194, 2005.

[2] Moatz B, et al., Cervical disc arthroplasty: pros and cons. *Surg Neurol Int* 3 (Suppl 3):S216–S224, 2012.

[3] Steinberger J, et al., Cervical Disc Replacement, *Neurosurg Clin N Am*, Jan;31(1):73-79, 2020.

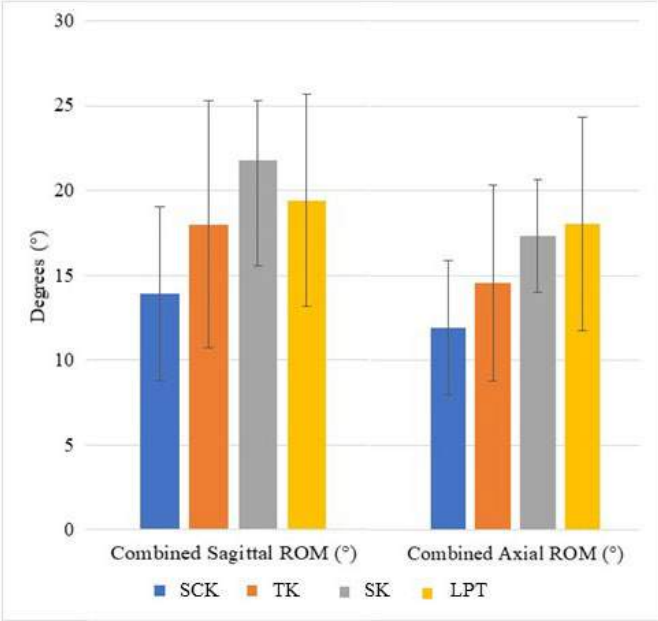

Figure 3: Comparison of ROM Grouped by Implant Type.

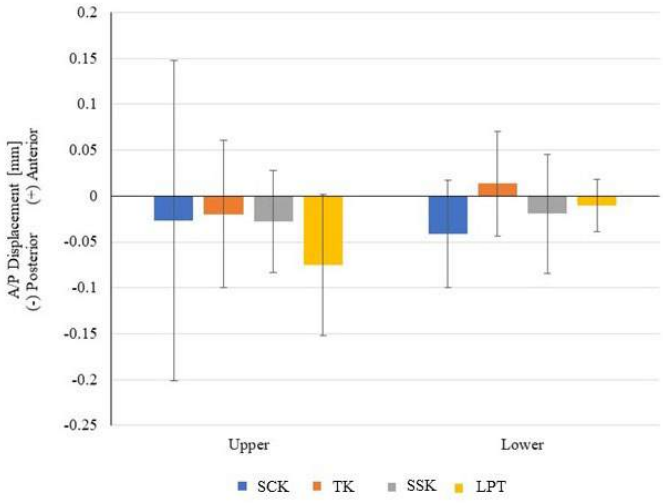

Figure 4: Mean Migration of Upper and Lower Components after 2000 Cycles Grouped by Implant Type.

SHEAR EXPULSION TESTING OF FOUR DIFFERENT CERVICAL TOTAL DISC REPLACEMENT PROSTHESES

Denis J. DiAngelo (1), Chloe L. Chung (1), Daniel Hoyer (1), Tyler Carson (2), Kevin T. Foley (2)

(1) Department of Orthopaedic Surgery and Biomedical Engineering
University of Tennessee Health Science Center
Memphis, TN, USA

(2) Semmes Murphey Clinic
Memphis, TN, USA

INTRODUCTION

Current methods for achieving immediate endplate fixation with cervical total disc replacement (TDR) prostheses include the use of keels or spiked teeth. Non-physiologic push-out or expulsion tests are typically used to measure the distraction force and mechanical work required to expulse the device [1]. The objective of this study was to determine the failure work and load required to expulse the upper and lower components of the four different cervical prostheses after undergoing multi-directional cyclic testing. Endplate configurations included single central keel, tripod keel, and spiked teeth.

METHODS

16 (C4-C5) and 16 (C6-C7) functional spinal units (FSUs) were dissected from eight male and eight female cadaveric cervical spines with an average age of 55.9 +/- 9.7 years. Three FSUs were not usable due to poor tissue quality which reduced the sample size to 29 FSUs. Four cervical total disc replacement (TDR) prostheses that had a similar ball and socket type articulation mechanism but varying endplate fixation features were tested (Figure 1): 1. A clinically used and FDA approved single central keel (SCK), 2. Low profile teeth (LPT) with domed endplate shape to allow a better fit in case of concave vertebral endplate, 3. Tripod keel (TK), and 4. Small single keel (SSK). A minimum sample size of 6 implants per prosthesis type were used. Each instrumented cervical FSU was mounted in a robotic testing platform and cycle 2000 times under combined flexion/extension (up to 1.5Nm) and right/left axial rotation (up to 1.5Nm) at a rate of 2.5deg/s. Following cyclic testing, specimens were disarticulated through the disc space, separated into upper and lower segments, and remounted with different fixtures for expulsion testing (Fig. 1). A custom shear expulsion tool was used to apply a 50N compressive load to the top surface of the implant (Figs. 2 and 3), followed by a downward shear force to the backside of the implant until it was fully expulsed. Shear expulsion force and distraction-displacement were measured and combined to calculate Expulsion Work (area under curve) and Resistive Stiffness (slope of curve) (Fig. 4). Peak Expulsion Force was also obtained. Normality of the expulsion data was tested using the Shapiro-Wilk test (p=0.05). If normality failed, a non-parametric Kruskal-Wallis test with Bonferroni correction was used. An additional test was done to compare the shear expulsion parameters between the upper and lower components of the same implant type. A similar normality test as above was used. If normality failed, a (2 tailed) Mann Whitney test was used.

Single Central Keel (SCK | Low Profile Teeth | Tripod Keel (TK) | Small Single Keel

Figure 1: Cervical Total Disc Replacement Prostheses.

a) b) c)

Figure 2. Shear Expulsion Test Setup. a) Custom shear explusion tool, b) Shear expulsion tool mounted to the upper test assembly, and c) FSU mounted in multi-axis vice with the top surface of disc implant parallel to the shear expulsion tool.

a) b)

Figure 3: Expulsion Protocol. a) Side view showing expulsion tool aligned overtop with the top surface of the disc implant. b) Front view of expulsion tool placed over TDR prosthesis. The shear expulsion tool was displaced downward pushing against the back edge of the prosthesis until the device was fully expulsed.

RESULTS

Mean and standard deviations for Peak Expulsion Forces were 69(41)N, 62(21)N, 110(71)N and 78(36)N, Expulsion Work were 321(225)Nmm, 399(161)Nmm, 463(305)Nmm, and 296(149)Nmm, and Resistive Stiffness were 81(61)N/mm, 44(42)Nmm, 163(207)Nmm, and 150(149)Nmm (Fig. 5). No significant differences occurred between implant types for any of expulsion data. Further, no significant differences were found between the upper and lower components of any implant type except for the Expulsion Work term of the traditional central keel device ($p=0.037$).

DISCUSSION

Using a human cadaveric cervical spine model, the fixation strength of four different cervical TDR prostheses was analyzed. The fundamental premise of the study was to highlight the acute biomechanical fixation properties of prosthetic endplate designs. The findings from the study do not reflect the long-term biological response of osseointegration. Three of the endplate fixation designs studied are currently in the investigational phase of FDA clearance and were found to provide comparable immediate holding strength to an existing clinically used and FDA approved central-based keel design.

ACKNOWLEDGEMENTS

Research contract from Centinel Spine.

REFERENCES

[1] Cunningham BW, et al., Neurosurg Spine 12(2):214-20, 2010.

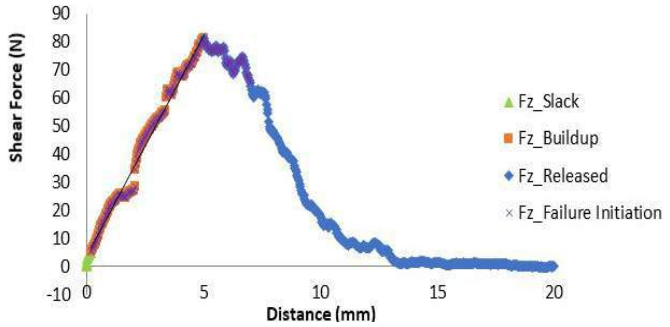

a)

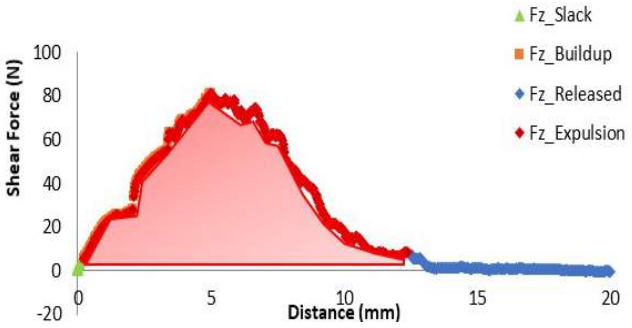

b)

Figure 4: Illustrations of Work Parameters. 2a) Failure Initiation Work: Area under the curve from 5N load to the point after the peak force has dropped off by 20% (i.e., at 80% of peak force). 2b) Expulsion Work Parameter: Area under the curve from 5N load to the point after the peak force has dropped off by 90% (i.e., at 10% of peak force).

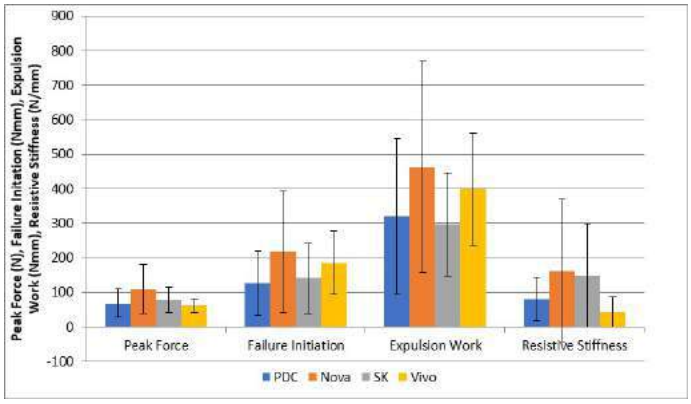

Figure 5: Comparison of the Peak Force, Failure Initiation Work, Expulsion Work and Resistive Stiffness between Implant Types.

SB³C2021
Summer Biomechanics, Bioengineering and Biotransport Conference
June 14-18, Virtual

INFLUENCE OF PHYSIOLOGICALLY INFORMATIVE AVERAGE CONTACT STRESSES ON CARTILAGES' TRIBOLOGICAL REHYDRATION

Shamimur R. Akanda (1), Meghan E. Kupratis (2), David L. Burris (1,2), Christopher Price (2,1)

(1) Mechanical Engineering
University of Delaware
Newark, Delaware, USA

(2) Biomedical Engineering
University of Delaware
Newark, Delaware, USA

INTRODUCTION: Articular cartilage, the remarkable bearing tissue of our joints, can maintain very low coefficients of friction ($\mu<.005$) over millions of annual articulation cycles. Cartilages' phenomenal lubricity arises out of its biphasic structure, which allows it to generate very high levels of interstitial fluid pressure and fluid load support (FLS >90%), shielding the tissue from rapidly applied stresses, and promoting interstitial lubrication.[1] This behavior allows well-hydrated articular cartilage to support rapidly applied peak stresses as high as 20 MPa, which are an order of magnitude higher than its compressive modulus (0.5-1 MPa), without compromising tissue integrity or lubricity.[2]

However, when cartilage is subject to quasi-static loading, it experiences loss of FLS and interstitial lubrication due to time-dependent fluid exudation. As a result, overall articular cartilage function is dictated not by the peak stresses it is subject to but by the average contact stresses it experiences.[3] Within mammalian joints, average contact stresses range from 0.1 - 2.0MPa.[4] As a result of these non-trivial average pressures, cartilage function would be rapidly compromised in our joints if a mechanism for recovering load-induced interstitial hydration and FLS loss did not exist. Fortunately, studies in intact joints suggest that articulation serves as a driver of this requisite fluid recovery,[5] with a number of fluid recovery mechanisms, including free swelling upon contact uncovering/exposure or nominal unloading, having been put forth as potential mediators of fluid recovery, and thus, overall function.

Recently, our team has identified a novel fluid recovery mechanism, termed 'tribological rehydration',[6] that is driven by pure sliding, meaning that it supports the active recovery of cartilage interstitial fluid and FLS without the need for contact migration, unloading, or uncovering. Discovered when we re-interrogated the high-speed sliding behavior of the convergent stationary contact area (cSCA),[6] tribological rehydration represents a competitive process between load-induced fluid exudation and sliding—or hydrodynamic—driven fluid recovery. When hydrodynamic driven fluid recovery exceeds that of pressure-driven exudation, cSCA explants experience the reversal and recovery of interstitial hydration, tissue compression/strain, FLS, and interstitial lubrication loss, and the maintenance of phenomenal lubricity on the benchtop. From these behaviors, it becomes apparent that a critically important influencer of tribological rehydration, and of overall cartilage function, is applied contact stress, with high applied stresses likely contributing to the suppression of sliding-induced tribological rehydration. However, to date, studies utilizing the cSCA have been restricted to a rather small range of applied stresses (<0.3MPa; in bovine tissues).[7] The goal of the present work is to explore the influence of elevated contact stresses on the high-speed sliding behavior of cSCA cartilage using ovine (sheep) stifle explants, which because of their smaller geometry (radius of curvature) enable the application of higher contact stresses using our tribometer.

METHODS: 12 mm diameter osteochondral explants (n = 16) were harvested from previously frozen ovine femoral condyles and stored in 1X PBS at 4°C for no more than 48hrs before tribology test. Tribological rehydration was characterized under six compressive loads (1, 2, 4, 6, 7, and 8N) in a custom reciprocating tribometer[6,8] via a protocol consisted of 20 minutes of compression followed by 10 minutes of sliding at 80mm/s (Figure 1). Samples were 'free swelled' for 30 minutes between each subsequent load level. Compression and friction force/coefficient were recorded throughout.[8] Load dependent contact area was determined optically at the conclusion of the tribology tests.[6] Start- and end-of-sliding compressions and frictions, recovered compression, start- and end-of-static exudation rates and start-of-sliding recovery rate were determined as described previously.[8] Mixed model analysis was

used to quantify tribomechanical parameters as a function of load and stress.

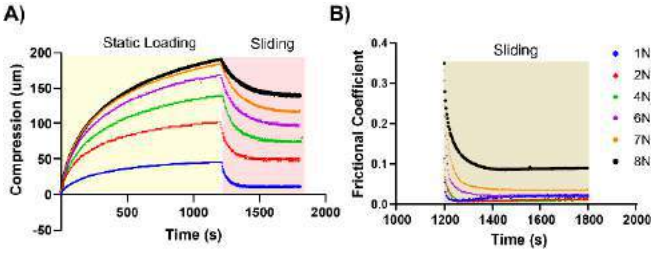

Figure 1: A) Compression and B) Friction traces illustrating the response of a representative ovine cSCA explant to high-speed sliding under six different applied loads.

RESULTS: In the cSCA, both tissue compressions and friction coefficients at the start of sliding and end of sliding increased with increasing loads (Figure 1). The relationship between recovered compression, measured as the difference between start-of-sliding and end-of-sliding compression, and applied load (Figure 2A) was complex, taking the shape of an inverted 'U' that could be fitted with a second-order quadratic equation ($y = ax+bx^2$; Figure 2A). At high sliding speed compression recovery was minimal at low applied loads due to nominal load-induced compression, but these small compressions were almost fully recovered. Compression recovery then increased with moderate applied loads, reaching their peak (34-79um) at intermediate loads (4-8N). Most explants experienced subsequent decreases in compression recovery at higher loads, with one specimen exhibiting zero and/or negative recovered compression (i.e., net exudation) at the highest applied loads. Both start- and end-of-sliding exudation rates increased in proportion to applied load (negative slopes; Figure 2C), whereas fluid recovery rate tended to decrease with increasing load.

When plotted against compressive stress, an inverted 'U' shaped relationship between compression recovery and applied stress was again

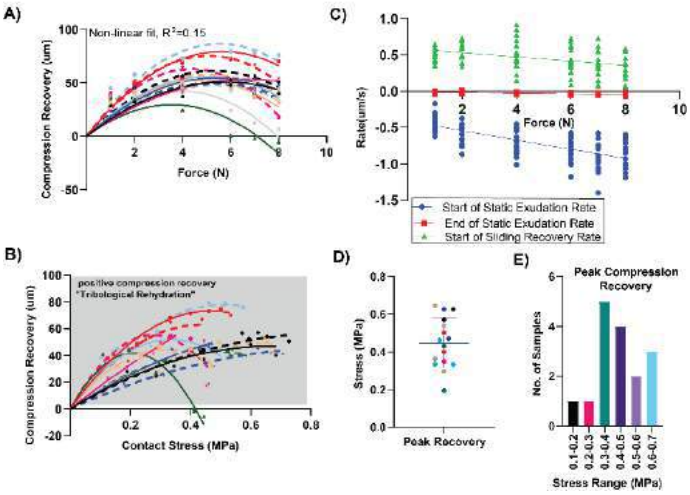

Figure 2: Compression recovery as a function of applied A) Load and B) Stress. C) Fluid exudation and recovery rates plotted against applied load. D&E) Compressive stresses at which each specimen exhibited peak compression recovery magnitudes.

observed (Figure 2B), with peak compression recovery (i.e., maximum tribological rehydration) being observed at a mean compressive stress of 0.45 MPa (ranging from 0.2-0.7 MPa, Figure 2D&E).

Apart from a few explants, all specimens showed qualitatively similar friction vs. applied load and friction vs. applied stress behaviors. While 'initial' start-of-sliding, and 'equilibrium' end-of-sliding friction coefficients increased in proportion to applied loads/stresses (Figure 3 A-B) nearly all cSCA specimens experienced rather rapid reductions in friction upon the initiation of high-speed sliding (i.e., friction recovery/suppression observed; Fig. 1C); apart from two explants at their highest contact stresses.

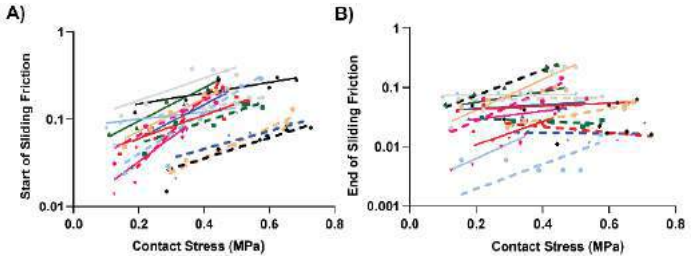

Figure 3: A) Start-of-sliding, and B) End-of-sliding friction coefficients as a function of applied stress in the cSCA under high-speed sliding (80mm/s).

DISCUSSION: Sliding-induced tribological rehydration, which represents a potent means of articulation-induced cartilage functional recovery (i.e., compression/strain & lubricity) is underpinned by competitive processes; pressure-induced fluid exudation (which increases with stress) and sliding-driven rehydration (which we assume largely constant for a given sliding speed).[7] Here, we demonstrate that sliding-induced compression recovery (in ovine cSCA explants) is highly contact stress dependent, illuminating several fundamental behaviors of articular cartilage, as well as limitations of the tissue.

At relatively low contact stresses (<0.2MPa), high-speed sliding (80mm/s) effectively recovered most, if not all cartilage compression due to prior static loading. Peak compression recovery occurred at intermediate stresses (mean = 0.45MPa, range 0.2-0.7MPa), followed by clear suppression of tribological rehydration effectiveness at higher contact stresses. Negative/zero compression recovery magnitude at high contact stress was only observed in one specimen (~0.4-0.5MPa); due to limitations with our tribometer's max loading capacity (≤8N). However, based upon extrapolation, we predict similar 'defeat' of tribological rehydration at stresses ≥1MPa more globally. It is interesting that the contact stresses that generate the best tribological rehydration behaviors overlap with the compressive modulus of cartilage (0.5-1MPa);[2] we are presently investigating if predicted relationships exist between cartilage's material properties and sliding-induced tribological rehydration behaviors.

It is also noteworthy that compression recovery, which is required for recovering interstitial rehydration and lubrication, is quite robust in the face of the spatiotemporally averaged contact stresses mammalian joints typically experience *in vivo* (0.1 to 2.0 MPa). However, this also highlights a potential concern. Because cartilage's tribomechanical behaviors are dictated by average applied contact stresses (as opposed to transient peak stresses),[3] there is the concern that modern socio-demographic increases in both body mass and overall inactivity represent significantly concerning and detrimental stressors to the overall tribomechanical function and health of our joints, even in the face of articulation mediated rehydration mechanisms.

REFERENCES: [1] Ateshian, *J Biomech*, 42:1163-76, 2009. [2] Mow, *J Biomech Eng*, 102:73-84, 1980. [3] Krishnan, *J Biomech*, 38:1665-1673, 2005. [4] Brand, *Iowa Orthop J*, 25:82-94, 2005. [5] Chan, *Scientific Reports*, 6:19220, 2016. [6] Burris, *OA&C*, 25:99-107, 2017. [7] Burris, *Tribology Letters*, 67:46, 2019. [8] Farnham, *J. Mech. Behav. Biomed*, 101, 2020.

DAMAGE MODELING OF THE HUMAN MENISCUS: VALIDATING FINITE ELEMENT MODELS WITH DIGITAL IMAGE CORRELATION

Derek Q. Nesbitt, Trevor J. Lujan

Mechanical & Biomedical Engineering
Boise State University
Boise, Idaho, United States

INTRODUCTION

Meniscus tears are one of the most common orthopedic injuries, with more than a half-million surgeries performed annually in the U.S.[1] The healing capacity of meniscus becomes diminished with age,[2] and surgical interventions to remove damaged tissue increase the likelihood of osteoarthritis.[3,4] With the lack of effective treatment options to fully restore meniscus function, preventing meniscus tear injuries is of utmost importance to combat osteoarthritis. The design of preventive therapies can be improved by computational tools like finite element analysis (FEA) to predict tears, similar to what has been done to inform treatments of aortic aneurysms.[5] One way that FEA can be effectively used to predict material failure, is by using Continuum Damage Mechanics (CDM) to model material weakening due to the onset of damage. However, the validation of an appropriate constitutive framework requires model comparisons to experimental data.[6] Our previous experimental work in human meniscus tracked the progression of surface strains in the tear region using high-speed video and digital image correlation (DIC), enabling the onset and progression of material damage to be measured at specific points of interest on the stress-strain curve.[7] This localized data can be used to validate that the appropriate failure behavior is being captured by a predictive CDM model[8], increasing the probability that the model is truly representing physiological behavior.

O**bjective.** The objectives of this work are to (1) fit a CDM model to the anisotropic tensile stress-stretch behavior of human meniscus and (2) validate that the model predicts the localized planar strains in the tear region as measured by DIC. Our hypothesis is that a CDM model using the maximum normal Lagrange strain failure criteria will reproduce the magnitude of the normal strains in the tear region at yield and ultimate strength, while closely matching the stress-stretch profile during quasi-static tensile tests.

METHODS

All models were developed, run, and analyzed using FEBio studio.[9] Model parameters were calibrated to our previous quasi-static tensile tests on the posterior side of the lateral meniscus from five different donors (<40 yrs).[7] Two fiber orientations were analyzed in order to capture the anisotropic character of the human meniscus, with samples from each of the five donors tested along the primary circumferential fiber axis (n=5 longitudinal) and normal to the primary circumferential fiber axis (n=5 transverse).

Mesh and Geometry. A $1/8^{th}$ symmetric dogbone shaped coupon was modeled to reduce computational effort, with geometry determined by the average dimensions of coupons tested in our previous study. The coupon had a clamp to gauge width ratio of 2:1, with a constant 0.5 mm wide gauge section. Longitudinal models were 5.67 mm long with a 2.5mm gauge length. Transverse models were 4.47 mm long with a 1.5mm gauge length. The clamp was modeled as a rigid body with an irrotational sliding elastic tension contact at the top of the gauge width of the coupon. The models were meshed with a 10 x 4 x 2 element 3D hexahedral mesh.

Model Formulation and Optimization. The selected model was a Veronda-Westmann ground substance[10] reinforced by a transversely isotropic fiber matrix.[11] The damage evolution was modeled using a quintic polynomial cumulative distribution function using the maximum normal Lagrange strain as the failure criteria. Ground substance parameters were fit first by optimizing the model to transverse data in the linear elastic region prior to ultimate tensile strength (UTS; Figure 1B). This was done since the fiber matrix does not contribute to the stress when stretched in this direction. The fiber matrix parameters were then fit to data in the linear elastic region prior to UTS in the longitudinal data (Figure 1A). Material parameters were optimized with the Levenberg-Marquardt algorithm in FEBio. Specimen specific

damage parameters were then fit manually to each transverse and longitudinal test by adjusting damage parameters until stress dipped near UTS.

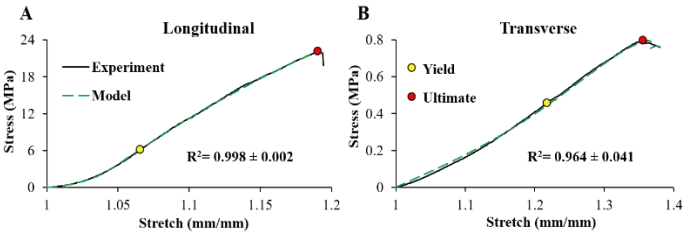

Figure 1: Representative curve fit of model to experimental data for A) longitudinal and B) transverse.

Analysis. Stress-stretch data was output by FEBio and compared to experimental data. Strain from the critical stress element of the model was compared to the tear region strain measured experimentally using DIC at yield and ultimate strength (Figure 3). This element was selected as the element that reached the damage threshold first.

Statistics. Model quality-of-fit to experimental data was determined by calculating the Root Mean Square Error (RMSE) of the stress-stretch data. Experimental and model strain data were compared at yield and UTS using a one-way ANOVA ($p<0.05$).

RESULTS

The average RMSE of model fits to experimental stress-stretch data was 0.01 ± 0.01 and 0.03 ± 0.01 for transverse and longitudinal models, respectively. Both transverse and longitudinal models greatly under predicted the experimental tear region strain, with the model giving a 73% and 40% reduction in strain magnitude at ultimate strength for transverse and longitudinal models, respectively. Additionally the models under predicted the tear region strain at yield strength with approximately 50% reduction in strain magnitude for both longitudinal and transverse models (Figure 2). The average tear region strain was significantly different than the experimentally measured values at both UTS and yield for the longitudinal model ($p < 0.05$), but not for the transverse models (p=0.20 at ultimate and p= 0.33 at yield) (Figure 2).

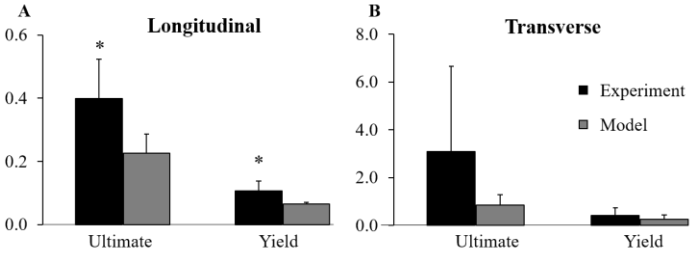

Figure 2: Comparison of the average local strain between experiment and model for A) longitudinal and B) transverse test series. *Significantly greater then model output.

The location of the critical stress element and concentration of greatest strain was the same element in the fillet region for all longitudinal models (Figure 3A). This location of failure initiation is similar to the fillet region type failures seen in 45% of longitudinal coupons from our previous study (Figure 3B).[7] The transverse models failed in the gauge region (Figure 3C), perpendicular to the loading axis, similar to the failures seen in nearly all transverse coupons from our previous experimental study (Figure 3D).

DISCUSSION

This is the first study to successfully model the anisotropic tensile behavior of the human meniscus. It is also the first study to attempt to validate a finite element model for human meniscus using DIC assisted quasi-static tensile experiments. While this model was successful at replicating the general location of failure initiation (Fig. 3), our model was unsuccessful at reproducing the magnitude of the normal strain in the tear region at either yield or UTS (Fig. 2).

The quality of the model fit to experimental stress-stretch data suggests that a Veronda-Westmann ground substance reinforced with a transversely isotropic fiber matrix is an appropriate model formulation for human meniscus. The quintic polynomial cumulative distribution function using maximum normal strain was also successful at re-creating the strain-softening. This is a reduction in modulus with increasing strain, often associated with the onset of damage[12] (Figure 1). However, the inability to reproduce the normal strains in the tear region suggests that our implementation of damage is inadequate for this application. This under prediction of strain indicates that the model tear region is being spread out over a wider area then seen experimentally. Strain concentrations may be improved with changes to the damage evolution model itself, or with a greater mesh density.

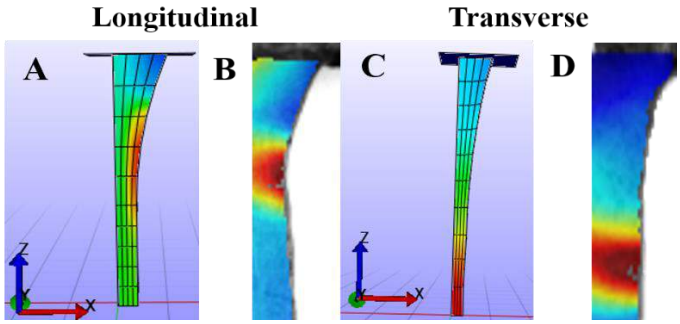

Figure 3: Representative normal strain concentration colormaps comparing the A) longitudinal model to B) experimental, as well as comparing the C) transverse model to D) experimental.

The mesh density used in this study was very coarse to promote model strain-softening, while avoiding the premature model failures due to regions of highly concentrated damage seen with finer mesh resolutions. Strain energy regularization techniques[13] could spread the damage out in a finer mesh to prevent premature failures, while promoting strain-softening. However, by calculating damage from a spatially averaged value as done in regularization, strains could be artificially spread out over this region. This could exacerbate the under prediction of the critical local strains, negating the utility of using a finer mesh resolution while significantly increasing computation time.

In conclusion, this was the first study to model the anisotropic tensile behavior in human meniscus, and to use experimentally measured tear region strain data in attempt to validate a CDM model. Though model improvements need to be made, this study serves to inform model formulation for the human meniscus moving forward.

ACKNOWLEDGEMENTS: Funding support from NSF (1554353).

REFERENCES

[1] Kim et al., J. Bone Jt. Surg Am. 2011. [2] Petersen and Tillman, Acta Orthop. 1995. [3]Feeley et al., Knee. 2016. [4]Han et al., J. Arthro. Rel. Surg. 2010. [5]Martin et al., Am J Phys Heart circ Physiol. 2014. [6]McGregor et al., Comp. Part A. Apl. Sci. & Man. 2017 [7]Nesbitt et al., J. Biomech. 2020.[8]Elruby and Nakhla. Theor & Apl. Fract. Mech. 2019. [9]Maas et al., J. Biomech. Eng. 2012. [10] Veronda and Westmann, J. Biomech. 1970. [11]Weiss et al., Comp. Methods in App. Mech & Eng. 1996. [12]Vignjevic et al., Comp. Meth. Appl. Mech. & Eng. 2018. [13]Pena, Estefania. Comp & Struct. 2014.

TRANSCATHETER HEART VALVE LEAFLET DESIGN AFFECTS LOCAL LEAFLET STRAIN: AN *IN-VITRO* STUDY

Beatrice E. Ncho (1), Katelynne Berland (2), Vahid Sadri(2), Jillian Ortner (2), Ajit P. Yoganathan (1,2)

(1) School of Chemical and Biomolecular Engineering
Georgia Institute of Technology
Atlanta, GA, USA

(2) The Wallace H. Coulter Department of Biomedical Engineering
Georgia Institute of Technology
Atlanta, GA, USA

INTRODUCTION

Transcatheter aortic valve replacement (TAVR) is a minimally invasive treatment for patients with severe symptomatic aortic stenosis [1]. TAVR has historically been reserved for patients deemed to be at intermediate to high-risk for open-heart surgery. In these patients, the valves demonstrated sufficient performance and durability for the remaining life of the patient. Regulatory agencies however have recently expanded indications of TAVR to a low-risk patient population [2]. With these procedures being conducted in a younger patient population, increasing concerns exist for patients outliving the functional lifespan and durability of the valves [3].

Structural valve degeneration such as leaflet deterioration or tearing is a known temporal failure mode of bioprosthetic heart valves. The unique aspects of TAVR technology that include device crimping, asymmetric valve expansion, leaflet/tissue characteristics and valve design factors are recognized to play a role in valve structural damage and affect long-term durability. Leaflet design factors of shorter leaflet length and thinner leaflet material have been shown to improve the valve flow performance [4,5], however the influence of these factors on the leaflet deformation is unknown. The objective of this study was to investigate the effects of TAVR valve leaflet length and material on the leaflet strain as a surrogate measure of valve loading and durability.

METHODS

Creation of transcatheter heart valve designs

Three transcatheter heart valve (THV) models were manufactured with varying leaflet length (15 mm vs 12 mm) and leaflet material (bovine pericardium vs porcine pericardium).

Bovine and porcine pericardium (BP and PP respectively) were treated with 0.6% glutaraldehyde in phosphate buffered saline for approximately 36 hours. The leaflets were laser-cut from uniform sections of treated pericardium using a leaflet template designed for each model, and the leaflets were sewn unto the valve frame. Each valve frame was designed in SolidWorks (Dassault Systemes, Waltham, MA), with locations to account for the native valve leaflet, THV leaflet length, and suture holes.

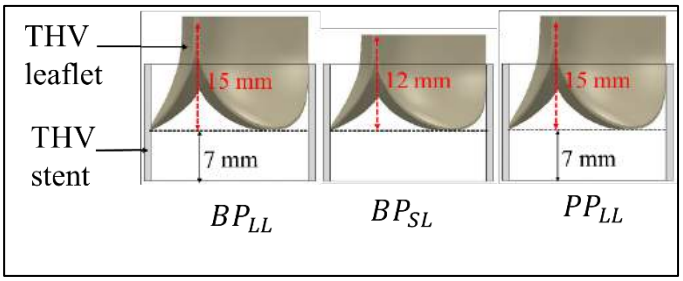

Figure 1. Schematic of THV designs. BP/PP represent bovine and porcine pericardium respectively, and LL/SL represent long and short leaflet length respectively.

In vitro testing of THV designs

Dual camera stereo-photogrammetry was used to measure the *in vitro* THV leaflet strains as demonstrated successfully in previous studies[6]. Tissue marking dye (Richard-Allan Scientific, San Diego, CA) was used to create an array of 56 markers, each approximately 1 x 1 mm^2 on one leaflet for each THV model. Each model was mounted in an idealized, rigid, acrylic aortic chamber and evaluated in a left heart simulator tuned for normotensive flow conditions. All testing was conducted using 3.5 cSt water glycerine at 37°C as the working fluid, mean arterial pressure of 100 mmHg, 5 L/min cardiac output and 70 beats/min heart rate.

The marker positions were tracked throughout the cardiac cycle using two high-speed A504k cameras (Basler Corp, Exton,

PA) and XCAP video acquisition software (EPIX Inc., Buffalo Grove, IL) to record dynamic motion of the leaflets at 200 Hz. Cameras were positioned on tripods approximately 45° relative to each other with the valve as a vertex. External illumination and the camera lenses were adjusted to provide maximum contrast between the markers and the leaflet for both cameras. After image acquisition, image calibration was conducted using a 10 mm steel cube positioned within the volume that was previously occupied by the TAV leaflets such that each camera could image 7 of the cube's corners. A 3D-coordinate system between the two cameras was defined using direct linear transformation.

The displacement and major principal strains in the commissure, coaptation and belly regions between peak systole and mid diastole for THV models were computed over one cardiac cycle using a custom MATLAB code (R2020a, Mathworks, Natick, MA). To assess the influence of leaflet length, displacement and strain fields between BP_{LL} and BP_{SL} were compared in the coaptation region only; and to assess the influence of leaflet material, the displacement and strain fields in the commissure, coaptation and belly regions between BP_{LL} and PP_{LL} were compared.

RESULTS

The results summarized in **Figure 2** and **Table 1** highlight the regional variations in displacement and major principal strain across THV leaflets.

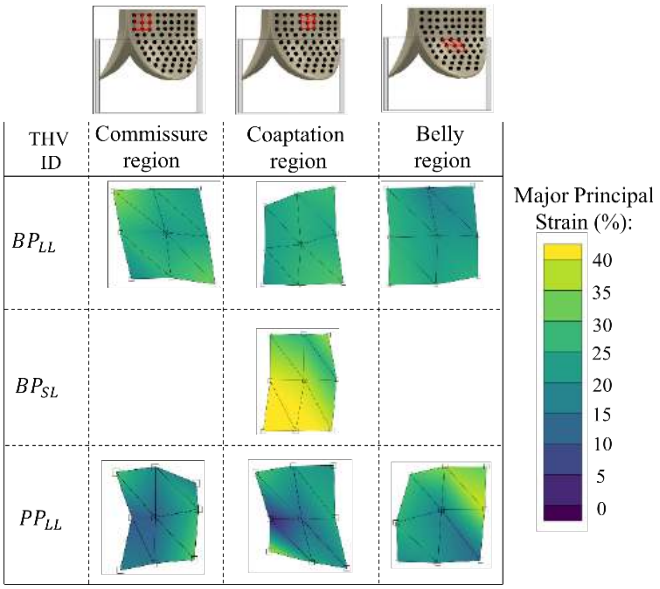

Figure 2. Major principal strain distribution across THV leaflets. BP/PP represent bovine and porcine pericardium respectively, and LL/SL represent long and short leaflet length respectively.

The BP_{LL} valve experienced the highest displacement in the belly region, and highest strain in the commissure region. Comparing the coaptation regions of BP_{LL} and BP_{SL}, BP_{SL} experienced greater displacement and strain. The PP_{LL} valve experienced the highest displacement and strain in the belly region. Comparing BP_{LL} and PP_{LL}, the commissure region of BP_{LL} experienced greater strains than the PP_{LL} valve, however, the coaptation and belly region of PP_{LL} experienced greater strain than the BP_{LL} valve. All three regions of the PP_{LL} valve experienced greater displacements than BP_{LL}. Overall, the coaptation region of BP_{SL} experienced the highest displacement and strain compared to any other model and region.

Table 1. Displacement and strain summary for each THV model at mid diastole.

THV ID	Region	Maximum displacement (mm)	Maximum principal strain (%)
BP_{LL}	Commissure	5.53	33.8
	Coaptation	5.52	29.6
	Belly	9.05	28.5
BP_{SL}	Coaptation	22.2	43.1
PP_{LL}	Commissure	7.80	30.5
	Coaptation	7.70	36.7
	Belly	9.27	37.5

DISCUSSION

The high strains observed in the coaptation region of the shorter leaflet length THV design compared to the longer leaflet length THV designs were due to the larger displacement needed to fully close the valve in diastole. With reduced coaptation length and area in a short leaflet length THV design, the leaflets undergo excessive bending to create a seal and prevent backflow under diastolic pressure. This bending results in higher strains in the coaptation and potentially the belly regions of the leaflet which overtime may lead to premature tissue degeneration. The observations of increased strains in the belly region of the porcine-based THV design compared to the bovine-based THV indicate greater deformations in the porcine-based models, which could be due to the reduced tissue thickness. This reduced thickness could amplify the leaflet stress and its distribution. The increased mechanical stress on THV leaflets may lead to accelerated tissue degeneration and diminished long-term valve durability [7]. As TAVR manufacturers seek to advance device designs, leaflet design characteristics should be optimized for hemodynamics and structural characteristics to ensure further improvement of patient outcomes and long-term durability.

ACKNOWLEDGEMENTS

We will like to acknowledge the financial contributions of the James and Mary Wesley foundation, and Tom & Shirley Gurley for the completion of this study.

REFERENCES

[1] Leon, MB et al., *N Engl J Med*, 363:1597-1607, 2010.
[2] Micheal, F *FDA.gov*, Press Release, 2019.
[3] Egbe, AC et al., *J Am Coll Cardiol* , 66:2285-2294, 2015.
[4] Ncho, B et al., *ABME*, 10.1007/s10439-020-02664-0, 2020.
[5] Ncho, B et al., *ABME*, in revision, 2021
[6] Gunning, P et al., *J.R. Soc. Interface* 12: 20150737
[7] Abbasi, M et al., *The Journal of heart valve disease*, 26(4):386-396, 2017

EFFECT OF POSTURAL ADJUSTMENT AND REPOSITIONING ON CONTACT PENETRATIONS IN HUMAN BODY MODELS

J. M. Caffrey (1), C. Costa (1), B.W. von Kleeck (1), A.A. Weaver (1), J.J. Hallman (2), F. S. Gayzik (1)

(1) Center for Injury Biomechanics
Wake Forest University
Winston-Salem, NC, U.S.

(2) Toyota Motor Eng. & Mfg.
North America, Inc.
Ann Arbor, MI, U.S.

INTRODUCTION

Finite element (FE) human body models (HBMs) are used to simulate various events (vehicle crash, sports impacts, etc.) and research human injury probability. Studies have shown that posture greatly influences the predicted injury[1,2]. HBMs have been developed in standard postures, such as a seated occupant or standing pedestrian, and are repositioned to different postures depending on the application. Repositioning simulations naturally cause deviations from the baseline, which can negatively affect subsequent simulations. The amount of deviation in the HBM can be quantified by measuring aspects of the model, such as contact penetrations. This has become more important with the emergence of autonomous vehicles and the potential for occupants to be in non-traditional seating postures.

A contact penetration occurs when there is an overlap between a node and the shell thickness of an interacting surface; this can be either a node overlapping a segment or two segments overlapping. Repositioning simulations can generate contact penetrations that may persist as initial penetrations in subsequent simulations depending on the contact settings invoked. When running simulations using a model with initial penetrations, the solver attempts to remove all penetrations during the first cycle by applying nodal forces. These forces can be large enough to develop non-physical stresses and strains, which may compromise model stability. Though models can be set to ignore initial penetrations and the solver will not attempt to initially correct penetrations, the presence of initial penetrations also effects the reliability and repeatability across multiple hardware and software combinations[3]. To develop reliable and reproducible results, the effects of repositioning on HBMs must be better understood and quantified. The objective of this study was to quantify how HBM repositioning parameters affect contact penetrations in a state-of-the-art HBM.

METHODS

The chosen model, THUMS v4.1 (Toyota Motor Corporation and Toyota Central R&D Labs, Aichi, Japan), was repositioned using Primer v. 17.0 (Oasys Software, London, United Kingdom) into 4 different realistic postures using volunteer and naturalistic driver and passenger data [UMTRI CITATIONS]. The 4 postures (Figure 1) were selected to cover realistic driver and passenger positions, a full range of positions, and extreme positions that challenged the robustness of the HBM.

Figure 1: The 4 end-state postures used in the study. From left to right: 23º upright posture, relaxed driver, normal driver, and 53º reclined occupant.

For each posture, the model was repositioned over three different Posture Adjustment Times (PATs) of 50ms, 100ms, and 150ms with 3 different levels of mass scaling 1x, 1.5x, and 2.0x of baseline for a total of 36 different combinations of repositioning parameters (4x3x3=36). Mass scaling is a method by which mass is added to the model in order to achieve a greater time step, resulting in a reduction of the simulation computational time.

After the PAT, the model was given 50ms to stabilize while contact penetrations were extracted every 10 ms (+0, +10, +20, +30, +40, and +50 ms). The effects of mass scaling, simulation time, and stabilization time on contact penetrations were assessed using t-tests run using JMP Pro 14.0 (SAS, Cary, NC, USA). All simulations were run using LS-

Dyna R11.0 (Ansys/LST, Canonsburg, PA, USA) using 44 cores on the Wake Forest DEAC computational cluster.

A method to evaluate the presence of contact penetrations in a FE model was developed. This method used Python v. 3.7 to automate the extraction of contact penetrations measured using LS-PrePost v. 4.8.2 (Ansys/LST, Canonsburg, PA, USA). Measurements were obtained using the built-in contact check feature of LS-PrePost and reported as vector components. After calculating the magnitude of each penetration, a threshold value of 0.036 mm, or 1 percent of the average length of the elements in the HBM, was applied. All penetrations below the threshold value were disregarded, as they were not likely to have a significant impact on the model's quality. Reports on the remaining penetrations in the model were output as the total number of penetrations, the total depth of all the penetrations, and the 95th percentile penetration depth.

RESULTS

Contact penetration data were measured as the change from the baseline THUMS model and averaged across all 4 postures for each set of repositioning parameters. Figures 2-4 show the results as three-dimensional bar charts for the total number of penetrations, cumulative depth of penetration, and 95th percentile penetration depth, respectively. Here, 0 ms refers to the end of the PAT, with 10 ms increments plotted thereafter. The 3x3 bar grid shows each of the 9 PAT and mass scaling configurations. The bold time axis labels refer to the stabilization time and the non-bold labels refer to the PAT.

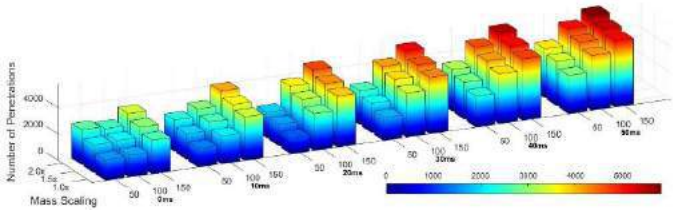

Figure 2: Total number of penetrations for each simulation.

The number of penetrations in the model increased with simulation time ($p<0.001$) and stabilization time (Figure 2), the lone exception being that the number of penetrations in the 50ms simulations decrease from +0 to +20ms of stabilization time. We hypothesize this was due a rebounding of soft tissues from the aggressive motion induced through repositioning the model in a short timeframe. The increase with mass scaling was not statistically significant ($p>0.2$).

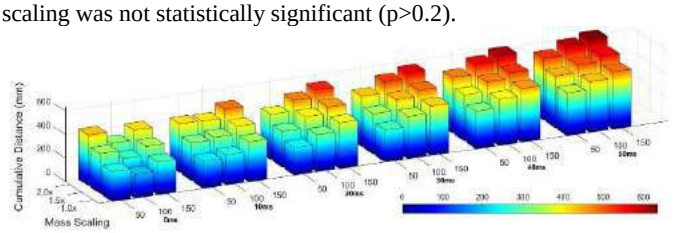

Figure 3: Total depth of all the penetrations for each simulation.

The cumulative penetration depth followed the same trends and exceptions as the total number of penetrations (Figure 3). Mass scaling also caused an increase in cumulative penetration distance for 1.0x to 1.5x ($p=0.002$) and 1.5x to 2.0x ($p=0.006$). Additionally, at +0 ms stabilization time the depth of penetrations for the 50ms simulations was larger than both the 100 and 150 ms PAT simulations.

The decrease in 95th percentile penetration depth grew with simulation time increased (Figure 4). As PAT increased, 95th percentile depth decreased, meaning that, while there were more penetrations, they were very small and receded with time. Mass scaling did not have a consistent effect on the 95th percentile penetration depth.

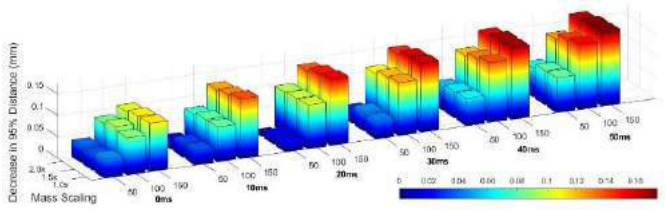

Figure 4: The decrease from baseline in 95th percentile penetration depth for each simulation.

DISCUSSION

The repositioning simulations reviewed here were developed for a larger study that aimed to determine best practices for HBM repositioning. Contact penetrations were just one of the indicators of model quality used for the greater novel study. The repositioning method affects the development of contact penetrations[4], which was seen in this study. It was found that the number of contact penetrations increased with increased simulation time and stabilization time. However, it should be noted that, while penetration count increased, the proportion of small to large penetrations increased shifting the distribution leftward during stabilization. Penetrations with a depth less than the threshold value were ignored, as they were not likely to have a significant impact on model quality. Traditionally, the contact penetrations developed in this process may lead to instability in the simulation. Contact penetrations can be removed manually or upon initialization, however, the practice that leads to the fewest and smallest penetrations should be used. The simulation was set to ignore initial penetrations for the repositioning simulations in this study. Determining the repositioning parameters that produce the fewest contact penetrations will save users a significant amount of time and effort and may serve as the first step to determining standards for repositioning practices. The growing prevalence of HBMs within the injury biomechanics community indicates their impending use in regulatory settings. As such, standard practices should be explored with the goal of reaching a broad consensus.

The results of this study are limited due to a focus on one HBM (THUMS) and a single output measure, contact penetrations. To fully understand the problem other parameters, such as mesh quality, need to be considered. These parameters are being examined in the broader research effort by our group. The strengths of this study are that wide ranges of realistic postures including large ranges of movement and were directly informed by volunteer and naturalistic occupant data were covered. Additionally, many combinations of HBM repositioning parameters were tested. Further work should investigate the initial reduction in contact penetrations of 50 ms simulations. This study found that the number of contact penetrations increase with simulation time and stabilization time while proportion of small to large penetrations increased during stabilization.

ACKNOWLEDGEMENTS

This work was supported by The Toyota Collaborative Safety Research Center (CSRC). The Wake Forest DEAC computational cluster was used for model simulation.

REFERENCES

[1] Meissner, M et al. *SAE Technical Paper*, 01:1608-1627, 2004. [2] Han, Y et al. *Int J Crashworthiness*, 24:2:211-220, 2011. [3] Initial Penetrations, *LS-DYNA Support*, 2006, Livermore Software Technology Corporation [4] Desai, C et al. *IRCOBI*, 12:69:610-621, 2012.

A COMPUTATIONAL FLUID DYNAMICS FORMULATION WITH SOLUTE TRANSPORT DERIVED FROM MIXTURE THEORY AND ITS FINITE ELEMENT IMPLEMENTATION IN FEBIO

Jay J. Shim (1), Steve A. Maas (2), Vijay Vedula (1), Clark T. Hung (3), Jeffrey A. Weiss (2), Gerard A. Ateshian (1)

(1) Department of Mechanical Engineering
Columbia University
New York City, New York, USA

(2) Department of Biomedical Engineering
University of Utah
Salt Lake City, Utah, USA

(3) Department of Biomedical Engineering
Columbia University
New York City, New York, USA

INTRODUCTION

As researchers in the fields of biomechanics and biophysics expand beyond pure fluid and solid mechanics analyses, modeling solute transport and chemical reactions is becoming increasingly necessary in different applications such as cardiovascular mechanics, respiratory mechanics, and mechanobiology, among many others. For example, finite element codes that include solute transport have been used to model thrombosis formation [1], charged solutes in cartilage [2], and drug delivery [3]. Ideally, an open-source FE code that offers both fluid mechanics and solute transport capabilities would be readily available to further facilitate verification and replication of results. However there are few such open-source software, resulting in many biomechanics researchers utilizing their own in-house codes or commercial codes, which may not be sufficiently specialized for all applications.

To model reactive solute transport, the convection-diffusion-reaction (CDR) equation is typically included as one of the governing equations. However, the CDR equation does not converge well when using the standard Galerkin residual method, particularly in high Peclet number flows where convection is dominant. Generally, under physiological conditions, solute transport poses more numerical challenges than fluid flow, as the Peclet number is usually greater than ~10^8 while the Reynolds number is ~10^3. Various methods to overcome this difficulty were proposed, such as upwinding methods [4], discontinuity capturing methods [3], and characteristic methods [5]. Researchers have also considered only steady analyses, or reduced the Peclet number to verify that the solution remains valid [6].

In this study, we formulated a new computational fluid dynamics (CFD) solute formulation derived from mixture theory [7], which was then implemented into FEBio (febio.org) [8], a free and open-source finite element software specialized for modeling biological tissues. Using mixture theory, we coupled solute transport with our previously developed CFD solver [9]. Our CFD-solutes formulation does not require stabilization methods and includes terms typically omitted from the CDR equation, such as body forces for the solutes, and osmotic effects, which include solvent transport driven by solute transport.

METHODS

Our previous CFD formulation assumed that the fluid was compressible and viscous, circumventing the need for upwinding stabilization methods. It used the fluid dilatation as a state variable, from which the pressure may be calculated [9]. Using mixture theory as a framework for the current formulation [7], we accommodate any number of distinct solute species, and include diffusion, convection, chemical reactions, osmotic effects, body forces, and frictional drag between the solvent and the solutes. The solute constituents are assumed to be dilute and intrinsically incompressible, and their respective inertia terms are neglected. The fluid momentum balance is

$$\rho^f \frac{D^f \boldsymbol{v}^f}{Dt} = -\mathrm{grad}\tilde{p} + \mathrm{div}\,\boldsymbol{\tau} + \rho^f \boldsymbol{b}^f + \sum_\gamma \tilde{\kappa}^\gamma(-R\theta\,\mathrm{grad}\tilde{c}^\gamma + M^\gamma \tilde{c}^\gamma \boldsymbol{b}^\gamma) \qquad (1)$$

where ρ^f is the fluid density, $\boldsymbol{v}^f$ is the fluid velocity, $\tilde{p}$ is the effective fluid pressure, $\boldsymbol{\tau}$ is the viscous fluid stress, γ represents each of the solute species, $\boldsymbol{b}^f$ and $\boldsymbol{b}^\gamma$ are the body forces acting on the fluid and solute γ respectively, $\tilde{\kappa}^\gamma$ is the partition coefficient of γ, R is the universal gas constant, θ is the absolute temperature, $\tilde{c}^\gamma$ is the effective concentration of γ, and M^γ is the molar mass of γ. $\frac{D^f \boldsymbol{v}^f}{Dt}$ is the material time derivative following the fluid. The mixture mass balance is

$$\frac{D^f J^f}{Dt} = J^f\left(\mathrm{div}\boldsymbol{v}^f - \hat{\zeta}\sum_\gamma v^\gamma \frac{M^\gamma}{\rho_T^\gamma}\right) \qquad (2)$$

where J^f is the fluid dilatation such that $\rho^f = \rho_r^f / J^f$ where ρ_r^f is the referential fluid density. $\hat{\zeta}$ is the molar production rate of a chemical

reaction, ν^γ is the net stoichiometric coefficient of γ, and ρ_T^γ is the true density of γ. The solute mass balance is

$$\nu^\gamma \hat{\zeta} = \frac{\partial\, \tilde{\kappa}^\gamma \tilde{c}^\gamma}{\partial t} + \mathrm{div}\boldsymbol{j}^\gamma \tag{3}$$

where $\boldsymbol{j}^\gamma$ is the solute flux of γ, given by

$$\boldsymbol{j}^\gamma = d_0^\gamma \left(-\mathrm{grad}\tilde{c}^\gamma + \frac{M^\gamma}{R\theta}\tilde{c}^\gamma \boldsymbol{b}^\gamma\right) + \tilde{c}^\gamma \boldsymbol{v}^f \tag{4}$$

Here, d_0^γ is the free diffusivity of γ. $\tilde{p}$ only depends on J^f according to an equation of state, such as $\tilde{p} = K\left(1 - J^f\right)$ where K is the fluid bulk modulus. The actual concentration is $c^\gamma = \tilde{\kappa}^\gamma \tilde{c}^\gamma$ and the actual pressure is $p = \tilde{p} + R\theta\Phi\sum_\gamma c^\gamma$, where Φ is the osmotic coefficient. This formulation was implemented in FEBio by obtaining the virtual work integrals from Eqs. 1, 2, and 3, linearizing and discretizing them with respect to the nodal degrees of freedom ($\boldsymbol{v}^f$, J^f, and $\tilde{c}^\gamma$'s), and then solving using Newton's method.

RESULTS

The FEBio CFD solutes solver was verified with a variety of test problems. 1D problems were created to ensure that all aspects of the formulation behaved as expected. Here we show the flow past a block in a narrow channel [9], where we are now also prescribing a solute concentration ($\tilde{c}^\gamma = 0.001$ mM) at the inlet in addition to the fluid velocity ($v^f = 1$ m/s). At the outlet, we prescribe $p = 0$ as well as backflow stabilization for the solute and fluid [9], where for the solute, $\tilde{c}^\gamma$ from the previous time point is prescribed in the presence of backflow. The Peclet number is ~10^3. Results at different times for the fluid velocity and concentration are shown in Figure 1. Even with the presence of vortex shedding and backflow at the outlet, the solute flow converged properly in the presence of convection and diffusion.

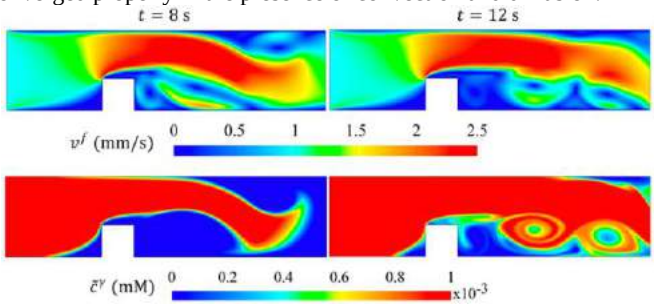

Figure 1: CFD solute flow past a block problem. Both fluid velocity and concentration are shown at different times.

In the next example, we tested the flow of different sized solute species, taking gravitational effects into account. This problem is a simple simulation of a person talking, breathing, or coughing with saliva droplets expelled into a larger domain. The solvent is assumed to be air at 25 °C with three different droplet sizes with properties Table 1.

Table 1: Properties of each of the water droplet solute species

R (μm)	d_0^γ (m²/s)	M^γ (kg/nmol)	$\tilde{c}_0^\gamma$ (pM)	τ_{sed} (s)
1	1.18×10^{-11}	2.51	5.57×10^{-9}	2130
15	7.84×10^{-13}	8490	8.35×10^{-9}	9.44
30	3.92×10^{-13}	67900	5.57×10^{-9}	2.36

The free diffusivity and expected sedimentation time, τ_{sed}, were calculated using Stokes' law using the following equations [10],

$$d_0^\gamma = \frac{k_b T}{6\pi\eta R} \tag{5}$$

$$\tau_{sed} = \frac{k_b T z_0}{d_0^\gamma m g} = \phi\frac{z_0}{R^2} \tag{6}$$

where $k_b T$ is the thermal energy, η is fluid viscosity, R is droplet radius, z_0 is domain height, $m = 4\pi R^3\rho/3$ is droplet mass, g is the gravitational constant, and $\phi = 0.85\times10^{-8}$ m s is a numerical pre-factor. Evaporation effects were ignored. The initial concentration, $\tilde{c}_0^\gamma$, was calculated from size distribution data of expiratory droplets at the mouth opening [11]. The sedimentation time calculated from Eq. 6 was verified separately for different sized droplets in FEBio. Inlet velocity was calculated from respiratory flow values from a ventilator. The Peclet number reached values up to ~10^{11}. Results are shown in Figure 2, where droplet expiration occurred in the first second within a square domain of length 0.5 m (such that $z_0 = 0.25$ m). As expected, for larger solutes, sedimentation dominated over convection.

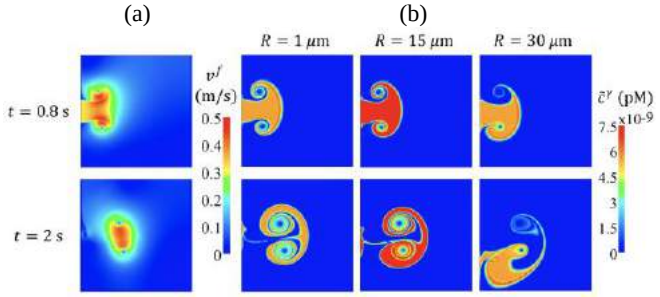

Figure 2: Different sized droplets expelled into a larger domain. (a) The fluid velocity and (b) solute concentrations are shown at two different times for three distinct droplet sizes.

DISCUSSION

In this study, a novel CFD-solutes formulation was implemented in the finite element code FEBio. It was derived from first principles using a mixture framework and is distinct from standard formulations that employed the CDR equation. This new formulation allows for diffusion, convection, chemical reactions, osmotic effects, body forces, and frictional drag between the solvent and the solutes without the need for stabilization methods. The solver behaves as expected in examples shown in Figures 1 and 2. In particular, the second example has potential implications for research in disease transmission and safety protocols, particularly for respiratory infections like COVID-19. More extensive verification and validation problems will be tested, particularly those with chemical reactions. In the future, we will also accommodate charged solutes to account for electrochemical effects. Later, we plan to couple this formulation with our biphasic fluid-structure interaction formulation [12], with the aim of developing a fully general multiphasic-FSI solver that includes all of the features in this study as well as porous media mechanics and fluid-structure interactions.

ACKNOWLEDGEMENTS

This study was supported with funds from NSF GRFP DGE-16-44869 and NIH R01GM083925.

REFERENCES

[1] Biasetti J et al., *Front Physiol*, 3:266, 2012. [2] Yao H et al., *BMMB*, 6(1-2):63-72, 2007. [3] Bazilevs Y et al., *Int J Numer Methods Fluids*, 54(6-8):593-608, 2007. [4] Franca LP et al., *CMAME*, 190(13-14):1785-800, 2000. [5] Kaazempur-Mofrad MR et al., *CMAME*, 192(11-12):1281-98, 2003. [6] Ethier CR et al., *Ann Biomed Eng*, 30(4):461-71, 2002. [7] Ateshian GA, *BMMB*, 6(6):423-45, 2007. [8] Maas SA et al., *J Biomech Eng*, 134(1):011005, 2012. [9] Ateshian GA et al., *J Biomech Eng*, 140(2):021001, 2018. [10] Netz RR et al., *J Phys Chem B*, 124(33):7093-101, 2020. [11] Chao CY et al., *J Aerosol Sci*, 40(2):122-33, 2009. [12] Shim JJ et al., *Arch Appl Mech*, 1-21, 2021.

A HYBRID DISCRETE-CONTINUUM MULTISCALE KINEMATIC GROWTH MODEL

Elizabeth Gacek (1), Ryan R. Mahutga (1), Victor H. Barocas (1)

Department of Biomedical Engineering
University of Minnesota – Twin Cities
Minneapolis, MN, USA

INTRODUCTION

The evolution of biological tissues as they grow and adapt remains of vital importance for understanding disease states from aortic aneurysm to low back pain. Understanding how cells, as the active component of tissues, modulate their environment through the manipulation, addition, and removal of constituents is significant, not only from the aspect of understanding disease progression, but also for creating therapeutics such as tissue-engineered grafts.

Past work in the field of computational modeling of growth and remodeling in biological tissues has focused primarily on the continuum-level tissue growth[1–5]. These models remove the discrete nature of fiber networks with interconnected cells, and instead focus on determining an average behavior for the system. Continuum-level constrained mixture theory presents a valuable tool for understanding tissue growth, yet there exists an entirely different length scale over which the key changes in growth and remodeling actually take place.

Thus, we propose a hybrid discrete-continuum framework where we utilize discrete-fiber networks applying growth laws directly to the fibers and analyzing the growth of the material from the fiber level up through the application of kinematic growth and a fitted continuum-material response. This technique allows us to directly gather discrete information from the fiber network including fiber radii, lengths, and alignment as the remodeling process unfolds.

METHODS

Fiber Network Model: For the following simulations, we utilize a periodic Delaunay network of one fiber type, in this case, collagen, and use the helical fiber constitutive model of Freed & Doehring[6] to model the lockout behavior of the fibers with constitutive model parameters giving transition stretch of 1.145 and a lockout modulus of 20MPa.

After the boundaries have been subjected to an arbitrary deformation gradient tensor, we solve the network nodal positions at equilibrium using Newton's method. We then calculate the network stress using volume averaging as:

$$\sigma_{ij} = \frac{1}{V}\int_{\Omega} \sigma^m n_i^m n_j^m dV = \frac{1}{V}\sum_{m=1}^{M} \sigma^m n_i^m n_j^m V^m = \frac{1}{V}\sum_{m=1}^{M} f^m l^m n_i^m n_j^m \quad (1)$$

where σ_{ij} is the network averaged Cauchy stress, V is the network volume, σ^m is the fiber stress of fiber, m, n_i^m is the fiber direction vector, f^m is fiber force, and l^m is the fiber current length.

The collagen fibers are further allowed to remodel to approach a target stress state. We use the simple first-order remodeling law, given below, that couples fiber radius changes to fiber lengthening. In this model, collagen remodels according to:

$$\frac{dR}{dt} = \frac{1}{\tau}\left(\frac{\sigma^m}{\sigma_\infty^m} - 1\right); \frac{dL}{dt} = k\left(\frac{dR}{dt}\right) \quad (2a; 2b)$$

where R is the fiber radius, t is time, τ is the remodeling rate constant, σ_∞^m is the target homeostatic fiber stress, L is fiber unloaded length, and k is a constant relating the fiber radius change to the fiber length change. In our model, we use $\tau = 72h$, $\sigma_\infty = 2kPa$, and $k = 120$.

Finite Element Model: To describe kinematic growth, the deformation of a body ($\mathbf{F}$) is defined as the product of the elastic deformation ($\mathbf{F}^e$) and the growth ($\mathbf{F}^g$) at time t = T relative to the reference state at t = 0 and is given by $\mathbf{F} = \mathbf{F}^e\mathbf{F}^g$. Inherent to this decomposition of the deformation into an elastic and growth component is the requirement that the body after growth be compatible (i.e. $\nabla \cdot \sigma = 0$). Thus, even with no *external* load it is possible that $F \neq F^g$, an observation from which arises the residual stress found in many tissues. To solve this compatibility condition, we use *FEBio Studio 1.2*[7] utilizing the *Prestrain* plugin[8].

Hybrid Model Coupling: The fiber network simulations are coupled to the FE simulation by prescribing one fiber network to each element in the FE mesh. The network constitutive behavior is then used in the FE simulation to determine local deformation and stress for each element,

which is fed into the network model allowing the fibers to remodel, adjusting the rest state and changing the constitutive properties. Thus, the fiber network model is coupled to the finite element simulations using (1) Mechanical response of the fiber network and (2) Total growth of the fiber network.

In order to solve the mechanics in the finite element simulations, we use a constitutive model of the HGO-type[9]

$$W = c_1(I_1 - 3) + \frac{K}{2}(ln\ (J))^2 + \sum_{i=1}^{3} \frac{c_2^i}{2c_3^i}\left[exp\ \left(c_3^i(I_4^i - 1)^2\right) - 1\right] \quad (3)$$

where W is strain energy density, c_1 is the modulus of the ground matrix, $I_1 = tr(C_{ij})$ is the first strain invariant of the right Cauchy-Green tensor $C_{ij} = F_{iM}F_{jM}$, K is the bulk modulus, c_2^i is the fiber modulus of family i, c_3^i captures the nonlinearity of fiber family i, $I_4^i = C_{ij}N_iN_j$ is the fourth strain invariant C where N is the fiber direction vector.

The growth tensor is determined by remodeling under load, then removing the load and re-equilibrating the network to determine the new reference configuration. The result, $\mathbf{F}^g$, is combined with constitutive response and the compatibility equation is solved using *FEBio*. We then compute the deformation for the next remodeling iteration.

Model Validation: We recreated the controlled mechano-adaptation of fibroblasts in a collagen gel cruciform[10]. We looked at three scenarios: 1. Initial cruciform geometry (Fig. 1A) to remodeled with arms fixed (Fig. 1B), 2. Remodeled with arms fixed (Fig. 1B), then increase force by 20% in x and remodel (Fig. 1C), and 3. Remodeled with arms fixed (Fig. 1B), then decrease force by 20% in x and remodel (Fig. 1D).

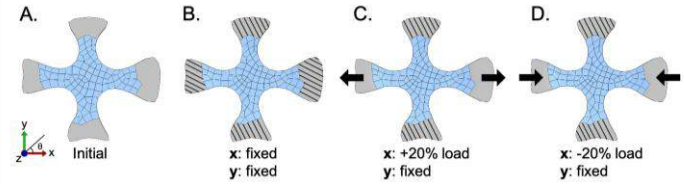

Figure 1: A.) Unconstrained cruciform, B.) Fully constrained cruciform followed by C.) uniaxial stretch of +20% baseline force or by D.) uniaxial compression of 20% baseline force.

RESULTS

To validate our remodeling approach, we compared results to Eichinger and Paukner et al. for grip force with a 20% increase or a 20% decrease in force at hour 28 as shown in Fig. 2 A and B respectively.

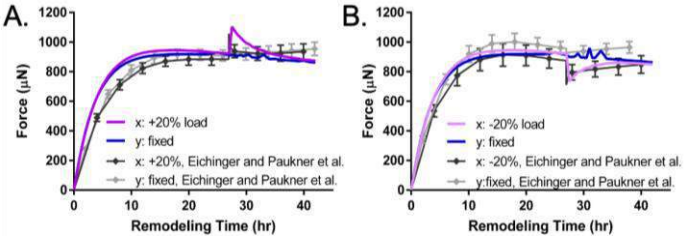

Figure 2: Measured cruciform grip loads over 42 hours with A.) a 20% increase in or B.) a 20% decrease in grip load at 28 hrs.

We further monitored individual elements and networks (Fig. 3). The residual stress in the constrained sample is shown in Fig. 3A and E immediately prior to the 20% load increase (Fig. 3B) or 20% load decrease (Fig. 3F). We also monitored the fiber network directly during remodeling. The network fiber orientations are shown in Fig. 3D and Fig. 3H for 20% increase and 20% in load, respectively. The fiber radii and lengths for networks located in each region (left/right arms, top/bottom arms, and center region) are shown in Fig. 4.

DISCUSSION

Our model recapitulated remodeling of a fixed-arm cruciform (Fig. 2A/B up to 27h). The homeostatic state in the 20% increase in load is more rapidly recovered than the 20% decrease in load in the experiment, which is not captured in our model (Fig. 2A/B after 27h). Our model accurately captures the decay rate, but not the addition rate, likely a result of different time-dependencies in collagen decay and addition.

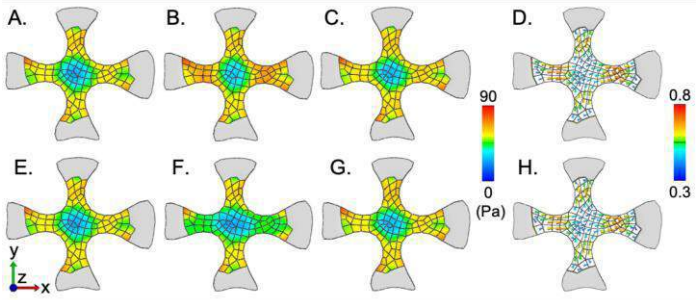

Figure 3: The 1st principal stress at remodeling time of A.) 27h, B.) 28h and C.) 42h with 20% increase in load at hour 28, and the 1st principal stress at time E.) 27h, F.) 28h, and G.) 42h with 20% decrease in load at hour 28. Principal in-plane fiber orientation (theta) at hour 42 for D.) 20% increase in load and H.) 20% decrease in load. Color bar indicates strength of alignment (maximum Eigenvalue of the orientation tensor).

Our allows insight one could not get from continuum-based approaches. We see that the orientations are relatively insensitive to the load changes (Fig 3D/H), which is evidenced by the relatively small differences seen in fiber lengths and radii relative to the +/- 20% load cases (Fig. 4). We do, however, see significant differences from the initial state to the remodeled fixed state (Fig. 4 light blue vs. dark blue bars) where the fibers shorten over time and the radii decrease.

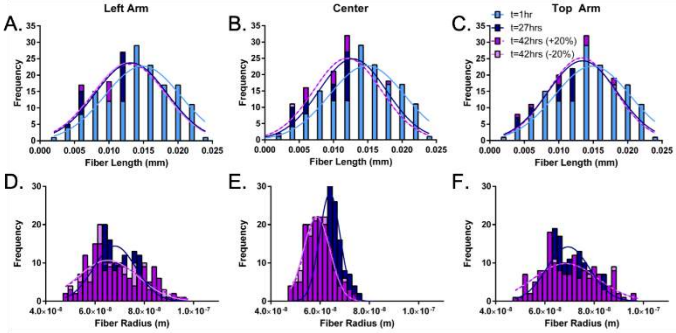

Figure 4: Length of every network fiber within a representative element shown for the A.) left arm, B.) center, and C.) top arm of the cruciform at 1, 27 and 42 hrs of remodeling. Similarly, fiber radii are shown for the D.) left arm, E.) center, and F.) top arm at 27 and 42hrs. The initial fiber radius for all fibers was 8.0 x 10^{-8} m.

This framework demonstrates the ability to capture many macroscopic observables while observing micro-scale phenomena. This framework has applications in many multiscale problems, particularly those that involve the cellular microenvironment such as pain transduction, cellular mechano-adaptation, and the cancer tumor microenvironment.

ACKNOWLEDGEMENTS

The authors acknowledge funding from NIH through NCCIH U01-AT010326, NIAMS T32-AR050938, and NHLBI U01-HL139471.

REFERENCES

[1] Taber LA, *JBME*, 120, 1998. [2] Alford PA et al., *Comp. Methods in Biomech. and Biomed. Eng.*, 11, 2008. [3] Gleason RL et al., *J Biomech*., 38, 2005. [4] Humphrey JD et al., *Math. Models and Methods in Appl. Sci*., 12, 2002.[5] Hariton I et al., *J. Theo. Biol*., 248, 2007. [6] Freed AD et al, *JBME*, 127, 2005. [7] Maas SA, et al. *JBME*, 134, 2012. [8] Maas SA et al., *J. Mech. Behav. Biomed. Mat*., 61, 2016. [9] Gasser TC et al., *J. Royal Soc. Interface*., 3, 2006. [10] Eichinger JF, Paukner D et al., *JBME*, 142, 2020.

ATP UTILIZATION DURING GENERATION AND MAINTENANCE OF CONTRACTILE STRESS IN STRIATED MUSCLE

Andrew A. Schmidt (1,2), Alexander Y. Grosberg (3), Anna Grosberg (1,2,4-7)

(1) Department of Biomedical Engineering, University of California, Irvine, Irvine, California, USA

(2) Edwards Lifesciences Center for Advanced Cardiovascular Technology, University of California, Irvine, Irvine, California, USA

(3) Department of Physics and Center for Soft Matter Research, New York University, New York City, New York, USA

(4) Department of Chemical and Biological Engineering, University of California, Irvine, Irvine, California, USA

(5) Center for Complex Biological Systems, University of California, Irvine, Irvine, California, USA

(6) Stem Cell Research Center, University of California, Irvine, Irvine, California, USA

(7) NSF-Simons Center for Multiscale Cell Fate Research, University of California, Irvine, Irvine, California, USA

INTRODUCTION

The sarcomere is considered the basic contractile unit of striated muscle, however, the actual process responsible for generating force within the sarcomere is the cross-bridge cycle, which involves interactions between a single myosin head and an actin filament. During each cycle, myosin ATPase hydrolyzes one ATP molecule, whose energy is converted into mechanical work (shortening of the sarcomere) during the power stroke. Because each cross-bridge cycle relies on the hydrolysis of one ATP molecule, it follows ATP availability plays an integral role in the potential force generated by each sarcomere, and thus the muscle tissue as a whole. However, existing models of sarcomere contraction do not explicitly consider the free energy contributions of the concentrations of ATP and its hydrolysis products, ADP and inorganic phosphate (P_i), in the states of the cross-bridge cycle at which they are interacting with the actomyosin complex [1-3]. As a result, these models are incapable of simulating the myosin duty ratio as a function of intracellular concentrations of ATP, ADP, and P_i, and therefore cannot predict the rates of ATP consumption needed to produce and maintain certain contractile forces [4,5]. Consequently, existing models are lacking in their ability to dynamically vary ATP concentration to simulate pathological conditions such as hypoxia, i.e. low-oxygen conditions, where tissue may struggle to generate the necessary ATP to maintain the contractile stress required for proper function [1-3].

We therefore aimed to develop a model with a more physiologically relevant distribution of free energy between the various states of the cross-bridge cycle to allow for closer examination of the effects of oxygen presence and ATP availability on sarcomere force generation and maintenance. The construction of such a model will enable an analysis of experimental data that will provide information on ATP consumption for various force generation profiles. Moreover, such a model can include predictions of contractile stress at varying levels of hypoxia and overall ATP utilization required to generate and maintain desired stress levels.

METHODS

The equations that govern the dynamics of the model were formulated analytically. The stochasticity of the cross-bridge cycles was reproduced via Monte Carlo simulations. Random numbers for the Monte Carlo algorithm were generated using MATLAB's internal *rand()* function. The mechanical force balances at each node of the sarcomere model were solved by a system of linear equations. At the end of each time step during a simulation, the mechanical equilibrium of the model, and more specifically the location of each node within the lattice, was calculated using MATLAB's internal system of linear equations solver. In **Fig. 1**, the a_Z and m_M nodes indicate the Z-line and M-line respectively. k_a, k_m, k_{xb}, k_T, and k_e represent the spring constants for the linear spring elements of the actin filament, myosin filament, myosin head/cross-bridge, titin, and the external spring respectively. The dashed red line labeled m_M' indicates a displacement of the M-line that may occur as a result of a contraction i.e. a power-stroke occurring within the system. The contractile force output of the half sarcomere could then be calculated based on the displacement of the M-line from a fixed-point external to the sarcomere (**Fig. 1**).

RESULTS

Model Formulation We developed a stochastic-mechanical half-sarcomere model to predict the amount of ATP required by striated muscle to maintain a specific level of functional force output. The half-sarcomere was modeled as a series of elastic spring elements combined with the biokinetics involved in actin-myosin force generation (**Fig. 1**).

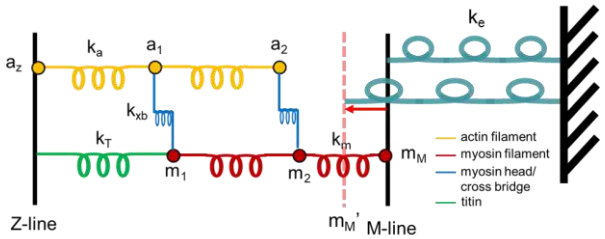

Fig. 1 Schematic of 4-Node Sarcomere Model; 2 actin (a_1 and a_2) and 2 myosin (m_1 and m_2).

The spring elements are connected at nodes, each representing either an actin binding location (on thin filament) or myosin head (on thick filament). Cross-bridges formed between the two filaments were represented by an additional linear spring element between the two attached nodes of the thick and thin filaments.

The stochastic nature of the 3-state cross-bridge cycle and calcium regulation of actin filament availability was modeled using a Monte Carlo algorithm. Actin filament availability governed the number of myosin heads that will bind during contraction and contraction strength. The cross-bridge cycle's states included in the model were (1) unbound myosin head state, (2) bound, pre-power stroke state, and (3) bound, post-power stroke state (**Fig. 2**). Rate constants of transitions from state i to state j are denoted by k_{ij}, which were calculated by defining the free energies of each cross-bridge state (equations 1-4) and the corresponding equilibrium constants K_{ij} (equation 5). Traveling through each cycle required an addition of an ATP from the environment, thus we defined state 1' as the reset energy baseline for each new cross-bridge cycle (equation 4).

$$G_1 = 0 \quad (1)$$

$$G_2 = \Delta G_{bind} + \frac{1}{2}k_{xb}x^2 \quad (2)$$

$$G_3 = \Delta G_{bind} + \Delta G_{stroke} - \Delta G^*_{\text{D,Pi rel.}} + \frac{1}{2}k_{xb}(x+d)^2 + k_B T ln\left(\frac{[ADP][P]}{[ADP]^*[P]^*}\right) \quad (3)$$

$$G_{1'} = -\Delta G^*_{hydr.} - k_B T ln\left(\frac{[ATP]/[ATP]^*}{([ADP]/[ADP]^*)([P]/[P]^*)}\right) \quad (4)$$

$$K_{ij}(x) = \frac{k_{ij}(x)}{k_{ji}(x)} = exp\left(\frac{1}{k_B T}\left(G_i(x) - G_j(x)\right)\right) \quad (5)$$

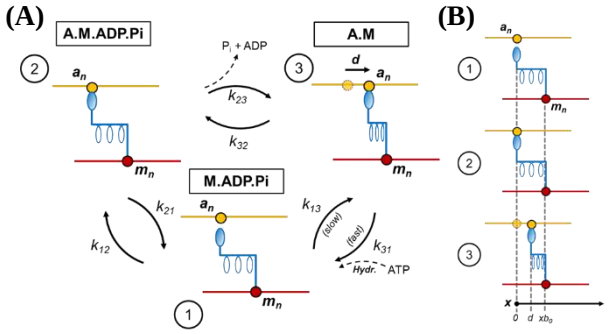

Fig. 2 (A) Schematic of 3-state Cross-Bridge Cycle. (B) Schematic of the change in displacement between a myosin node and actin node during a cross-bridge cycle

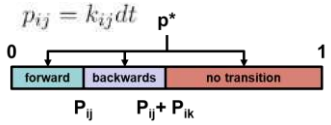

Fig. 3 The p* value determines the state transition chosen for each cross-bridge.

After state transitions are defined by the Monte Carlo algorithm, we assumed mechanical equilibrium is achieved rapidly relative to the time taken to transition between states. Probabilities of state transitions occurring are calculated as the product of the rate constant and time step (**Fig. 3**). Thus, the position of each node within the lattice was calculated by solving a detailed force balance at each node. The formulation of the model is flexible enough to allow for the addition of more actin binding sites (actin nodes) and cross-bridges (myosin nodes).

Simulation Results The model is flexible enough to be modified in accordance with different aspects of the physiology being simulated, and the free energies define fitting parameters that can be adjusted based on experimental data that can be used for validation (for example, ΔG_{bind} and ΔG_{stroke}). Outputs of the model include cardiac force generated at various levels of ATP availability and overall ATP utilization. ATPase activity is quantified by tracking state 3 to state 1 transitions during each simulation. The model is capable of demonstrating the expected step-wise manner of ATP utilization (**Fig. 4**).

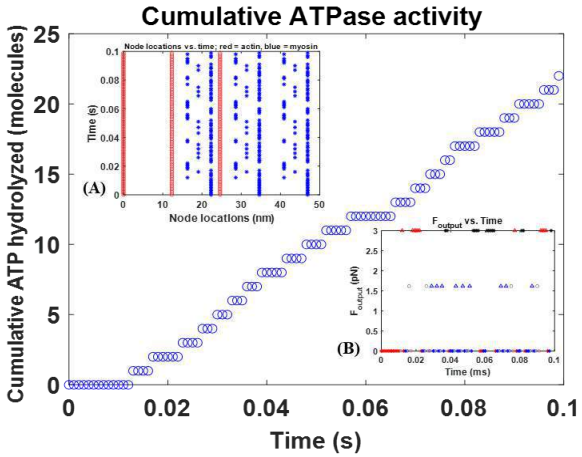

Fig. 4 Cumulative ATP utilization example. (Inset A) Location of actin and myosin nodes during simulation. (Inset B) Force output of the sarcomere and corresponding cross-bridge states of the 4-node system.

DISCUSSION

The results demonstrate that our model is capable of simulating the relationship between ATP availability and sarcomere force generation, which is an important output to investigate the relationship between mitochondrial function, oxidative phosphorylation, and overall cardiac output. Additionally, because ATP utilization persisted even while maintaining certain levels of force, our model is a good representation of the cross-bridge cycling that occurs even when a constant force is applied to a static system. This formulation of this model allows the flexibility to add more nodes and the placement of half-sarcomeres adjacent to each other to simulate larger sarcomeric lattices. Beyond the desired outputs of cardiac stress values at various levels of ATP availability and overall ATP utilization, cardiac stress generation in response to other conditions such as preload and shortening velocity will also be investigated using this model.

ACKNOWLEDGEMENTS

This work was supported by NIH [T32 HL116270 (PI Hughes)] and NSF [CMMI-2035264 (PI Grosberg)].

REFERENCES

[1] Duke, T et al., *PNAS* 96:2770-2775, 1999.
[2] Tanner, B. C. W et al., *Plos Comput Biol* 3:1195-1211, 2007.
[3] Mijailovich, S. M et al., *J Gen. Physiology* 184:459-488, 2016
[4] O'Connell, C. et al., *BBA – Mol. Cell Research* 1773:615-630, 2007
[5] Fitts, R. H. *J Appl. Physiology* 104:551-558, 2008

STIFFNESS AND ANISOTROPY DEPENDENT PROANGIOGENIC POTENTIAL OF MESENCHYMAL STROMAL CELLS

Michael Nguyen-Truong (1), Seungil Kim (2), Courtney Doherty (1,3), Megan Frederes (1,3), Samantha Kaonis (1), Soham Ghosh (1,3), Peiman Hematti (4), William Wagner (2), Zhijie Wang (1,3)

(1) School of Biomedical Engineering
Colorado State University
Fort Collins, CO, USA

(2) McGowan Institute for Regenerative Medicine
University of Pittsburgh
Pittsburgh, PA, USA

(3) Department of Mechanical Engineering
Colorado State University
Fort Collins, CO, USA

(4) School of Medicine and Public Health
University of Wisconsin, Madison
Madison, WI, USA

INTRODUCTION

Right ventricle (RV) dysfunction is common in the advanced stage of pulmonary hypertension, and RV failure is a useful predictor of mortality in these patients [1]. It has been noted that the RV becomes stiffer and more anisotropic with pressure overload [2-4]. We have previously shown that local delivery of mesenchymal stromal cells (MSCs) to failing RVs improved the organ despite persistent pressure overload, suggesting a therapeutic effect of MSCs likely due to the paracrine effects [5]. However, if and how the therapeutic effects are altered by the mechanical environment of the diseased RV is unclear.

It is evident from previous *in vitro* studies that MSC behavior and function depend on substrate stiffness, including the proangiogenic paracrine effect. However, those investigations are limited to a narrow stiffness range (0.5-88 kPa) that does not encompass the range of RV tissue stiffness obtained *ex vivo* [6-8]. Therefore, it remains unknown how MSCs respond to substrate stiffness and anisotropy that mimic RV tissue. We hypothesize that a soft and anisotropic matrix causes an increase in the proangiogenic potential of MSCs. To test the hypothesis, a new class of nanofiber scaffolds was fabricated to mimic healthy and diseased RVs. Then, the effect of the scaffolds' stiffness and anisotropy on MSC angiogenesis function was studied.

METHODS

To fabricate scaffolds, 6% or 12% w/v polyester urethane urea (PEUU) [9] was dissolved in hexafluoro-2-propanol and then electrospun into fibrous scaffolds using a custom electrospinning apparatus with a rotating mandrel (diameter: 7.46 cm). The concentration of PEUU was varied (6 versus 12%) to induce changes in stiffness, and the mandrel speed was varied (100 versus 890 rpm) for production of isotropic and anisotropic fibrous scaffolds (Table 1). Scanning electron microscopy (SEM) was performed to determine the fiber orientations using an ImageJ plugin, and histograms were plotted. The average and standard deviation of fiber angles were determined from three image regions per sample. The elastic moduli (EM) of the scaffolds (n=3 per group) along the fiber and cross-fiber directions were obtained by in-house biaxial testing after 24 hr of phosphate buffered saline soak. Human bone marrow MSCs (hMSCs) at passage 5 were cultured in 24-well plates at 10,000 cells/cm^2 on the sterilized scaffolds. Human vascular endothelial growth factor (VEGF) expression in the condition medium (CM) was determined by ELISA (Invitrogen) after 48 hr culture. DAPI staining elucidated cell counts. Data are presented as mean ± SEM. Unpaired Student's t-test was used to compare between groups and $p<0.05$ was considered statistically significant.

Table 1: Key parameters to adjust scaffold stiffness and anisotropy.

Group	Key spinning parameters
Soft & Isotropic	6% PEUU, 100 rpm
Soft & Anisotropic	6% PEUU, 890 rpm
Stiff & Anisotropic	12% PEUU, 890 rpm

RESULTS

We engineered three groups of scaffolds: a) soft & isotropic PEUU, b) soft & anisotropic PEUU, and c) stiff & anisotropic PEUU. Mechanical tests showed that the soft scaffold groups had significantly lower elastic moduli (EM, $p<0.05$) than the stiff group (Fig. 1), which mimicked the stiffness of healthy and diseased RVs, respectively.

Next, we quantified the scaffold fiber orientation and derived an anisotropy index as the ratio of the EM in the fiber direction to the EM in the cross-fiber direction. The histograms of the fiber orientations showed an even distribution of fiber angles in the isotropic group and

more aligned fibers in the other two anisotropic groups (Fig. 2A-C). The average fiber angles were 0.3±52°, -5.4±45° and -6.4±34° for the soft & isotropic group a, soft & anisotropic group b and stiff & anisotropic group c, respectively. The anisotropic index data showed comparable EM in both directions (ratio ~ 1) in the isotropic group and significantly higher ratio of EM in the other two anisotropic groups (Fig. 2D).

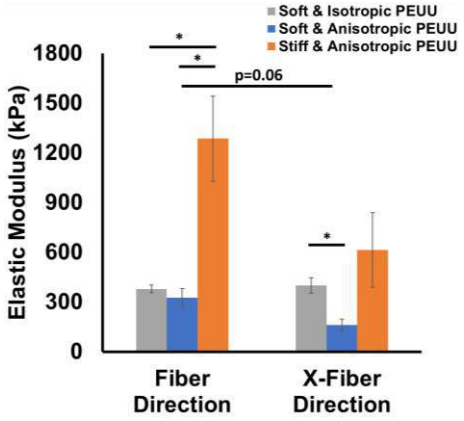

Figure 1: Elastic moduli of the three scaffold groups in the fiber and cross-fiber (X-fiber) directions. *p<0.05.

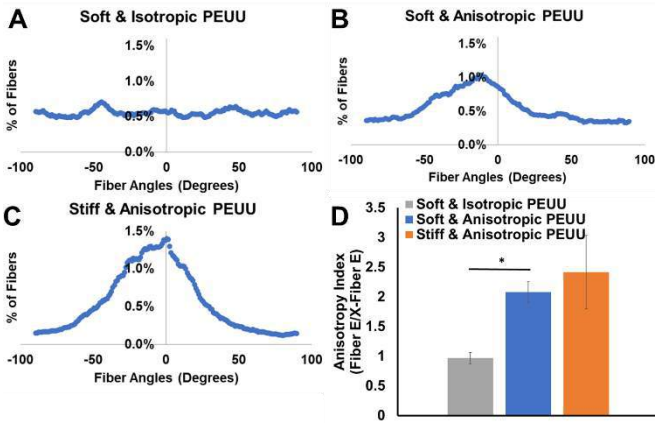

Figure 2: (A-C) Histograms of fiber orientation in the three PEUU scaffolds. (D) Anisotropy indices of the three scaffolds. *p<0.05.

After 48 hr of culture, we found the highest VEGF expression in CM of hMSCs cultured on the soft & anisotropic scaffold (group b). However, when normalized by cell counts, the stiff & anisotropic scaffold (group c) had the highest VEGF production per cell due to the lowest number of cells. Moreover, in the two soft groups, the anisotropic scaffold (group b) had higher production of VEGF per cell (Fig. 3).

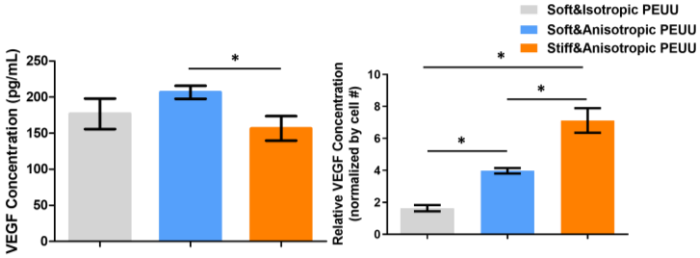

Figure 3: VEGF total concentrations in condition medium (left) and concentration normalized by cell numbers (right) in the three scaffold groups. *p<0.05.

DISCUSSION

In the present study, three different PEUU scaffold groups were engineered with different combinations of stiffness and fiber alignment – soft & isotropic, soft & anisotropic and stiff & anisotropic. The soft and stiff groups had significantly different EM, mimicking that of native healthy and diseased RV tissue. The anisotropy indices from the mechanical tests as well as fiber angle measurements from SEM showed that varying mandrel speed allowed for the production of isotropic or anisotropic scaffolds. Unlike the hydrogel matrix, the cardiac tissue is mechanically anisotropic and the diseased RV had increased anisotropy. Therefore, these electrospun scaffold groups serve as an *in vitro* platform to delineate the effect of stiffness or anisotropy on cells.

To investigate the mechanically regulated MSC proangiogenic function, we first examined the expression of VEGF, a key protein involved in angiogenesis. Our results revealed the highest VEGF production in MSCs cultured on the soft & anisotropic group. We further observed the lowest number of cells in the stiff & anisotropic group (data not shown), which is consistent with prior reports of reduced MSC proliferation on stiffer substrates [10]. The increased anisotropy also led to reduced cells as observed in the two soft groups (data not shown). As a result, when the VEGF production was normalized by cell counts, interestingly, the MSCs cultured on the stiff & anisotropic group showed the highest VEGF production per cell, indicating that higher stiffness promotes VEGF expression. On the other hand, between the two soft groups, the anisotropic group had higher VEGF expression per cell, suggesting that larger anisotropy also promotes VEGF expression. The promotion of MSC angiogenic function by fiber alignment was similarly reported by Su et al. using polycaprolactone (PCL) electrospun scaffolds (with much higher EM), although the scaffold stiffness was not measured and taken into consideration of this paracrine effect [11].

The overall VEGF production is determined by both cell number and production rate per cell. Although the increased stiffness or anisotropy enhanced the VEGF production per cell, they limited cell growth and thus the combined effects led to a maximal VEGF production in the soft & anisotropic group. We speculate that like smooth muscle cells whose contractile and synthetic (proliferative) phenotypes do not co-exist [12], the MSCs with limited proliferation may present higher proangiogenic profiles. Further examination on MSC proliferation, secretion of other growth factors in these groups and at a longer culture period will be needed to confirm our speculation.

In conclusion, the differences among the three scaffold groups showed that the MSC VEGF production was stiffness and anisotropy dependent. Our results suggest that the substrate mechanics similar to healthy RV (soft & anisotropic) may provide the best mechanical environment for MSC proangiogenic function. In general, the mechanical property of the substrate should be a key consideration to optimize MSC paracrine function and therapeutic effect for RV failure.

REFERENCES

[1] Lahm T et al., *Am J Respir Crit Care Med*, 198:15-43, 2018.
[2] Liu W et al., *J Integr Cardiol*, 6:1-6, 2020.
[3] Jang S et al., *J Am Heart Assoc*, 6(9):e0060084, 2017.
[4] Hill M et al., *Ann Biomed Eng*, 42:2451-65, 2014.
[5] Schmuck E, *Am J Physiol Heart Circ Physiol*, 316:1005-13, 2019.
[6] Nguyen-Truong M et al., *Bioengineering*, 7(4): 122, 2020.
[7] Nasser M et al., *Mater Sci Eng C Mater Biol Appl*, 102:75-84, 2019.
[8] Bandaru P et al., *Small*, 16(25):e2001837, 2020.
[9] Gu X et al., *Biomaterials*, 133:132-43, 2017.
[10] Xu J et al., *Differentiation*, 96:30-39, 2017.
[11] Su N et al., *Biomaterials*, 141:74-85, 2017.
[12] Sandison et al., *J Physiol*, 594(21): 6189-6209, 2016.

THREE DIFFERENT OFFICE POSTURES: DETERMINING PELVIC TILT, TORSO OPENNESS, GROUND REACTION FORCES AND BLOOD PERFUSION

Archana Lamsal (1) Garrett Weidig (1), Teresa Bellingar, PhD (2) and Tamara Reid Bush, PhD (1)

(1) Department of Mechanical Engineering
Michigan State University
East Lansing, MI, USA

(2) Haworth
Holland, MI, USA

INTRODUCTION

Prolonged inactivity during work hours is a major factor that leads to various health issues in office workers. Office workers can spend as much as ten to eleven hours in a seated posture, causing prolonged physical inactivity [1]. This can lead to health risks such as poor metabolism, type-two diabetes, and obesity [2]. Kyphotic postures assumed during sitting have been known as a risk factor of intravertebral disc degeneration [3]. Extended times in the seated posture have also been linked to reduced blood flow and blood pooling in the legs [4].

Research indicates that breaks in prolonged sitting reduce these health risks in office workers [2]. Standing desks promote movement, however, keeping workers motivated to use the height adjustable desk has been a challenge because once the novelty of the height adjustable desk wears off, usage diminishes [5]. Also, many individuals find the standing posture problematic. Larger loads through the legs and feet during prolonged standing has been associated with musculoskeletal disorders, pain, and discomfort of the feet and legs [6]. Prolonged standing has also been known to cause blood pooling and swelling in lower legs [7].

Due to the drawbacks of the seated and standing positions, there is a need for other positions which can provide changes in body posture without subjecting the legs to large loads, yet, achieving some of the benefits of standing. The goal of this study was (a) to compare the pelvic tilt, torso openness (a measure of lumbar curvature), and ground reaction forces between seated posture, a new type of mid-seated posture and standing posture (b) to investigate the blood perfusion during posture change from seated to mid-seated as well as mid-seated to standing position (termed, dynamic motions).

METHODS

Twenty consenting participants (ten males and ten females) were recruited in this university approved research study. An 11-camera motion capture system, a six-axis force plate and a laser doppler perfusion monitoring system were used to obtain measurements. Reflective markers were attached on toe, lateral malleolus, lateral epicondyle, greater trochanter, glenohumeral joint, left and right anterior superior iliac spines (ASISs), and left and right posterior superior iliac spines (PSISs). A marker pod with four markers was attached to the sternum. Two rectangular openings were made in the backrest of the chair that allowed the markers on the PSISs to be visible while in the seated and mid-seated postures. The perfusion data was collected on the right lower leg of the participant.

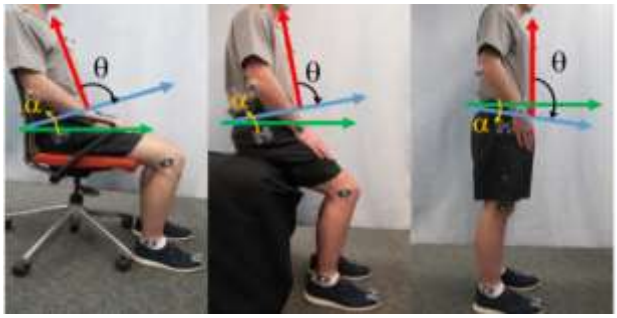

Figure 1 Vector overlay diagram of pelvic tilt angle and openness angle in seated, mid-seated and standing postures. The angle between pelvis plane (blue) and horizontal (green) provides pelvic tilt (α) and the angle between pelvis plane and torso (red) produces the openness angle (θ)

The participants were asked to conduct office tasks (typing and mousing) while assuming three different postures within an hour test period. The postures were: seated, mid-seated, and standing. The mid-seated posture was with a slightly bent knee, in an elevated chair with their feet on the ground (Figure 1). Marker position and force data were collected for every posture and blood perfusion was collected during transitions between seated to mid-seated and mid-seated to standing postures. Pelvic tilt (angle between the pelvic plane and horizontal) and openness angle (angle between the thorax and pelvis) were calculated for all postures. A repeated measures ANOVA followed by a Tukey post-hoc test was used to compare each of the following measures across the three postures: joint angles, ground reaction force and blood perfusion.

RESULTS

The average vertical ground reaction force expressed as the percent of body weight in mid-seated posture (16.41% BW) was larger than in the seated (12.55%) but smaller than in standing (96.54%). The difference in vertical ground reaction was statistically significant across all three postures. The anterior posterior ground reaction forces were largest in the seated posture (1.64%) followed by mid-seated (1.44%) and standing postures (0.03%). The differences in anterior-posterior ground reaction force between the seated and mid-seated postures were not statistically significant ($p=0.4934$). However, there were significant differences ($p<0.001$) between the mid-seated and standing postures as well as seated and standing postures. The medial lateral ground reaction forces were less than 1 percent of body weight in all three postures.

The average pelvic tilt and openness angle during all three postures are presented in Table 1. Both angle values during mid-seated posture were between that of seated and standing postures. The difference in both pelvic tilt and openness were significant for all three pairwise comparisons.

Table 1 Average joint angles and standard deviations in degrees across the subject pool for each posture

Posture	Seated	Mid-seated	Standing
Pelvic Tilt	15.3 (6.6)	6.3 (6.6)	-8.4 (7.6)
Openness Angle	96.7 15.7)	102.1 (14.0)	116.5 (17.1)

The average blood perfusions for the three postures are presented in Table 2. There was no statically significant difference in blood perfusion for three postures (p value for seated vs. mid-seated = 0.6402, p value for mid-seated vs standing= 0.5180, p value for seated vs standing = 0.1238).

Table 2 Average blood perfusion and standard deviation in perfusion unit (PU) across the subject pool for each posture

Posture	Blood Perfusion in PU
Seated	17.2 (9.5)
Mid-seated	15.6 (11.4)
Standing	13.7 (11.9)

An example of the time trace for blood perfusion during the dynamic posture change from seated to mid-seated position is presented in Figure 2. Blood perfusion for both dynamic motions increased to a maximum value during the motion, and after the participant stopped moving, dropped to near the initial value. However, the blood perfusion values did not return to the initial perfusion value immediately after the movement.

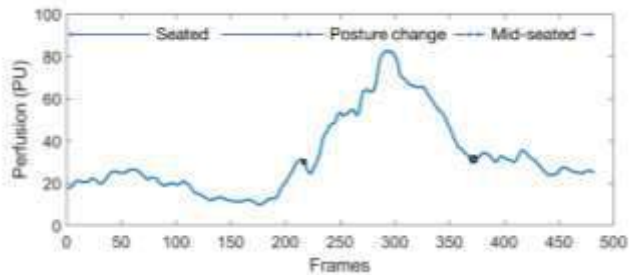

Figure 2 An example of the typical trends seen in blood perfusion during the dynamic movement from seated to mid-seated posture. The blood perfusion increased to maximum during motion then decreased, but not to the same value as before the movement

DISCUSSION

The goal of this study was to investigate the pelvic tilt, openness angle, ground reaction forces and blood perfusion across three working postures.

The difference in the pelvic tilt and openness angles among the three postures suggest that the change in posture permitted additional body movements, especially the pelvis. It is interesting to note that while in the mid-seated posture, the pelvis articulated a point halfway between the seated and standing postures. This is seen as a benefit for this new posture. An increased openness angle is another measure that confirms lumbar articulation is occurring in the mid-seated posture, even though the person is still in a chair. Previous research has shown that a larger openness angle is correlated to an increased lordotic lumbar curvature [8]. This change in lumbar curvature is a positive as posture changes promote blood flow and nutrient transport to the intervertebral discs [9].

Change in posture from seated to mid-seated and mid-seated to standing increased the blood perfusion, which reduces one of the biggest issues for office workers- blood pooling. The blood perfusion data indicated that during the motion, the blood flow increased, and it remained larger than the initial value for a time after the motion. The duration for increased perfusion varied and was subject dependent.

The ground reaction force data indicated that the anterior-posterior or shear loads were smaller in the mid-seated posture than sitting. As expected, the mid-seated posture resulted in smaller vertical loads than the standing posture.

To summarize, the mid-seated posture provided a pelvic orientation and lumbar posture closer to that of standing, while subjecting the legs to a lower vertical loads than in standing. Changing postures from seated to mid-seated as well as from mid-seated to standing increased the blood flow as well as provided motion to the joints. The use of mid-seated posture as an additional working posture could reduce health issues in the office workers.

ACKNOWLEDGEMENTS

This work was supported by Haworth Inc.

REFERENCES

[1] Smith L., et al., *BMC Public Health*, 1-9, 2015
[2] Hamilton MT, et al., *Diabetes*, 2655–2667, 2007
[3] Pynt J., et al., *J Occupational Rehab*, 35-45, 2008
[4] Shvartz E., et al., *J Applied Physiology*, 1673-1680 1983
[5] Garrett G., et al., *Applied Ergonomics*, 17-24 2019
[6] Boussenna, M., et al., *Ergonomics*, 315–322, 1982
[7] Antle et al., *Preventive Medicine Reports*, 117-122, 2018
[8] Leitkam ST., et al. *J Biomechanics*. 117-122, 2011
[9] H Wilke et al., *Spine*, 755-762, 1999

SB³C2021
Summer Biomechanics, Bioengineering and Biotransport Conference
June 14-18, Virtual

EFFECT OF SEAT ORIENTATION ON THE LUMBAR RESPONSE TO FAA-LONGITUDINAL CRASH PULSE: A PARAMETRIC MODELING STUDY

K. Somasundaram (1), J. Humm (2), P. Khandelwal (2), N. Yoganandan (2), F. Pintar (1,2)

(1) Department of Biomedical Engineering
Medical College of Wisconsin
Milwaukee, WI, USA

(2) Department of Neurosurgery
Medical College of Wisconsin
Milwaukee, WI, USA

INTRODUCTION

Aviation safety standards are articulated by the Federal Aviation Administration (FAA) and are used by aircraft manufacturer in the testing of their equipment. In recent decade, there has been increase interest among airline industries to install seats at an oblique orientation to the centerline of the aircraft, in order to maximize seating density and increase comfort. For this novel seating configuration, the current FAA standard only allow seat installation angles ranging from 18º-45º for oblique-facing and 80º-100º for side-facing. However, the existing safety standard in the commercial passenger aircraft were developed based on fore- or aft-facing seats and pure side-facing seats.

The oblique seating configuration put forth unique safety challenges, since the occupant kinematics and loading during emergency landing scenario differ from the traditional fore- or aft-facings and side-facing seats. The human body tolerance to injury in restrained oblique dynamic loading is also unknown and likely different than for pure frontal or pure side loading. Limited work has been done to understand the injury and response of an occupant seated on the aircraft seats installed at different orientation relative to aircraft centerline.

Recently, a series of whole-body Post-Mortem Human Surrogate (PMHS) sled tests were conducted with the aim to assess the gross occupant kinematics and evaluate potential injuries in oblique loading configurations [1]. The test used a survivable crash pulse defined by the FAA [2]. In this test series, two installation angles were investigated, that set the seat centerline at 30° and 45° to primary loading vector. From this testing, multiple injuries were seen throughout the body. However, the complete transection of the vertebral column at L5/S1 level was noteworthy. The authors concluded that these injuries were a combined multi-axial bending and tension. Although, the PMHS tests have shed light on our knowledge of the spinal distraction injury mechanisms, the segment level loads and moments associated with the failure is required for better evaluation of oblique seats in the aircraft environment.

The preliminary test results underscore the need for additional cadaver tests, but physical testing comes with high cost, large data scatter and difficulty in instrumentation. As an alternative, computational modeling can overcome the limitation of physical tests. One such modeling approach was performed in this study using a 75-year-old 50th percentile male Global Human Body Model Consortium (GHBMC) model, with the aim to validate against previous whole-body PMHS oblique impact sled tests and to assess the response and injuries occurring in the lumbar region. The validated model was then simulated with different seating orientations to study the influence of seat configuration on the occupant response.

METHODS

The 75-year-old model was originally developed for automotive crashworthiness applications [3]. The selection of this model was appropriate, as such the actual test used for model validation had male specimens with the age of 65 years and above. The previously conducted PMHS tests comprised of seven instrumented whole-body sled tests, characterized by peak sled acceleration, seat orientation, pelvis restraint, leg constraint, knee angle and presence or absence of armrest. For the purpose of validation in this computational study, a whole-body PMHS test performed with the specimen positioned on a seat installed at 45° orientation relative to the loading vector. In this condition, the specimen's pelvis was restrained using a body-centered belt and traditional lap-belt. Also, the legs were constrained at the thigh and tibiae. The test was performed with no armrest and had a peak sled acceleration of 16 g over 145 ms.

Similar seating and boundary conditions were implemented in the current computational study. Figure 1 shows the simulation setup and the surrogate orientation relative to the primary loading vector. All simulations were completed using LS DYNA 971_R4.2. The model biofidelity was based on the resultant acceleration and angular velocity measured at T6, T12 and S1 levels along the spinal column and was assessed using CORA (CORrelation and Analysis) rating [4]. The test-reported tensile injuries of the spine were validated in the model by measuring the intervertebral distance and comparing the maximum value against the spinal injury threshold obtained from isolated spine tests in tension loading [5]. Parametric simulations were performed with varied seating orientation ranging from 0° to 90° with 15° increment in the angle.

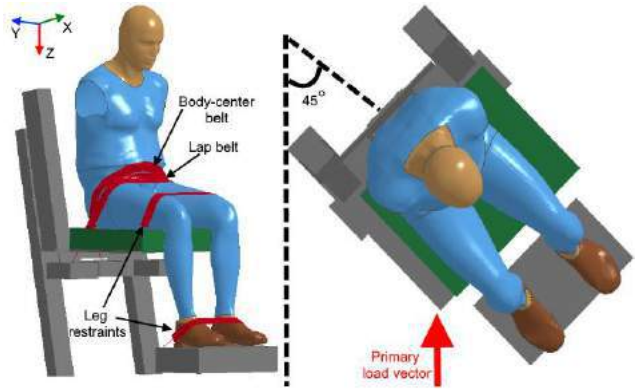

Figure 1: Simulation setup

RESULTS

The overall CORA score ranged from 0.567 to 0.702. The model predicted spinal and pelvis failure locations were consistent with the test reported injury locations. The parametric analysis showed a linear trend among the spine axial loads measured at L5 and T12 levels and it decreased with increase in the seat installation angle. The peak bending moments measured at T12 and L5 levels are shown in Figures 2A and 2B.

It can be observed from the L5 moment plots that the peak lateral moments increased linearly with increase in installation angle, while the peak flexion moments decreased linearly with increase in installation angle. With respect to T12, the peak lateral moments were constant across the installation angle, while the Y moment reversed its bending direction from flexion to extension at 45° orientation onwards. Additionally, the T12 peak moments were relative lower compare to the moments measured at L5 level. This implies the susceptible nature of the lower lumbar spine in aircraft environment.

DISCUSSION/CONCLUSION

The study aimed to evaluate the biofidelity and assess the lumbar spine response to different seat orientation relative to the primary loading vector. The overall biofidelity score for the spinal column ranged from 0.567 to 0.702. The parametric simulations showed a linear trend among the spinal loads with R^2>0.9. The axial force decreases with increase in seat installation angle, consistent with previous modeling study [6]. Additionally, the current study also measured the lateral and forward bending moments, which showed a trend with respect to seat installation angle. The initial data from this study put forth the necessity to develop new lumbar spine injury criterion, comprising of bending moments and axial force for obliquely positioned seats.

Occupant loading in far-side crashes is generally longer in duration than nearside and, hence, more similar to an aircraft emergency pulse, although at a lower delta V. The far-side PMHS studies were performed at 90 and 60 degrees [7, 8]. These studies evaluated gross kinematic of the occupant, with specific interest in head excursion relative to impact direction. Head excursions from the present study matched better with these studies. However, no data was available to compare the model predicted lumbar spine moment.

The preliminary modeling provides the effect of seat orientation on the lumbar spine loads and moments, which will be helpful in designing aircraft seats and countermeasure techniques. The limitation does exist in the current study with respect to the spine model. The selected GHBMC version lacks 3D discs between the lumbar segments, instead they were connected using 1D beam element. Efforts are ongoing to simulate the latest GHBMC with well-developed spine model to evaluate the spine response to FAA crash pulse.

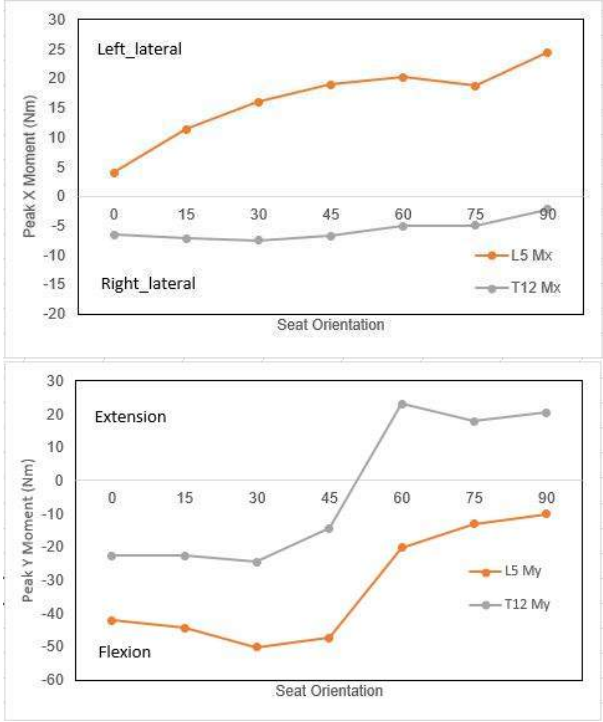

Figure 2: Peak bending moments measured at L5 and T12 levels. along X axis (Above) and Y axis (Below)

ACKNOWLEDGEMENTS

This study was supported under grant #17-G-002, sponsored by the Federal Aviation Administration. Any views expressed in this presentation are those of the authors and are not necessarily representative of the funding organizations.

REFERENCES

[1] Humm, J et al., *Stapp Car Crash*, 58, 2016.
[2] U.S. Code of Federal Regulations. 1988.
[3] Umale et al., *Traffic Inj. Prev*. 1-3, 2020.
[4] Gehre et al., *ESV Conf*, 2007
[5] Pintar, F et al., *ASME Adv Bioeng*, 1986
[6] Moorcroft, D., *DOT/FAA (press)*, 2021
[7] Pintar, F et al., *SAE Tech Pap*, 2007.
[8] Forman, J et al., *SAE Tech Pap*, 2013.

PHYSIOLOGICAL LOADING CONDITIONS TO SIMULATE STANDING

S. Rossman (1,3), E. Meyer (2), J. Isaza (4), S. Rundell (3)

(1) Mechanical Engineering Department
Lawrence Technological University
Southfield, MI, USA

(2) Biomedical Engineering Department
Lawrence Technological University
Southfield, MI, USA

(3) Explico Engineering
Novi, MI, USA

(4) Spine Specialists of Louisiana
Baton Rouge, LA, USA

INTRODUCTION

During standing, the lumbar spine experiences compressive and anterior shear forces. Consequently, the resulting flexion moment causes sagittal imbalance. In order to restore sagittal balance, the posterior muscles of the spine (i.e. posterior chain) must generate sufficient extension. Thus, realistic loading conditions to simulate standing should involve application of posterior muscles to offset the flexion moment that results during standing.

Prior spinal finite element (FE) studies utilize a compressive follower load to represent standing [1,2]. These studies result in no facet contact and inherently cause sagittal balance. While phenomenologically accurate, the lack of appropriate lines of action of muscle force may not represent the load sharing between the disc and facets. Further, these biomechanical models do not provide the ability to investigate alterations in posterior chain strength with respect to the stresses experienced by the disc and facets.

Therefore, the objective of the current study was to establish a set of FE loading conditions that includes the inertial contributions of the upper body as well as the counteracting posterior chain of muscles. We hypothesized that the application of the posterior Erector Spinae (ES) muscles will result in spinal kinematics and disc pressure consistent with experimental studies involving compressive follower loads while also experiencing facet contact forces.

METHODS

A previously developed and validated finite element model of a lumbar motion segment was utilized for the current study [3]. A Three-Dimensional Static Strength Prediction Program (3DSSPP, University of Michigan) was used to determine the loading conditions for the model. Four 3DSSPP analyses were conducted to determine the upper body weight and predicted ES force during an upright standing posture for adult males of heights and weights consistent with a 5th percentile, 50th percentile, and 95th percentile male. An additional run was conducted to represent the male volunteer in a previously published *in vivo* study with a height and weight of 66 inches and 154 pounds, respectively [4].

Axial compression representative of body weight above the L4-5 motion segment, as determined by the 3DSSPP analyses, was applied 15 mm anterior of the center of the L4 superior bony endplate to simulate standing [5]. The inferior bony endplate of L5 was fixed rigidly in space. A surface-to-surface contact was established between the L4 and L5 posterior elements. The ES was simulated by attaching bi-lateral force elements between the spinous processes approximately 5.5 cm posterior of the joint center. The amount of ES force applied for each scenario was based on the results of the 3DSSPP analysis. Table 1 depicts the upper body weight and ES force applied to the FEM (Finite Element Model) for each of the four scenarios. Figure 1 shows the FEM. The lordotic angle, i.e. intersegmental rotations (ISR), facet joint reaction forces, and disc pressures were recorded.

Table 1: Loading conditions for each scenario.

	Wilke 1999	5th Male	50th Male	95th Male
Upper BW	280 N	209 N	347 N	489 N
ES Force	53 N	80 N	116 N	156 N

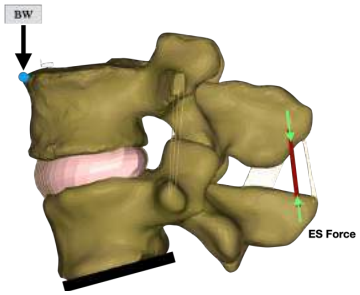

Figure 1: Lateral view of the L4-5 motion segment FEM depicting the boundary conditions utilized to simulate standing.

RESULTS

The 3DSSPP predicted ES muscle loads consistent with *in vitro* data. Specifically, the *in vitro* data demonstrated an estimated ES muscle load of 100 N during standing [6]. The average ES muscle loads predicted by 3DSSPP for all scenarios in the current study was 101 N. For each scenario, results of the current FE study showed peak intervertebral disc pressures and ISRs between L4 and L5 that were consistent with *in vitro* data [4,7-11] (Figure 2 and Figure 3). The peak *in silica* disc pressures were 0.42, 0.26, 0.45, and 0.65 MPa for the 154-lb male, 5th male, 50th male, and 95th male scenarios, respectively. The peak disc pressures agreed well with the *in vivo* data, which showed disc pressures ranging from 0.27 to 0.76 MPa during standing. The ISRs between L4 and L5 also agreed well with *in vivo* data. Wood 1996 demonstrated ISR during standing in the range of 8.8° to 25.6° and Lin 1994 demonstrated ISR during standing of 12.2°±4.4°. The current study resulted in ISRs of 12.6°, 10.6°, 12.2°, and 13.6°, for the 154-lb male, 5th male, 50th male, and 95th male scenarios, respectively.

The facet joints came into contact in all four scenarios. The total facet contact force was 384, 392, 578, and 789 N for the 5th male, 50th male, and 95th male scenarios, respectively. The largest facet contact force was seen in the 95th-percentile male scenario, where the ES muscle load was the largest, while the smallest facet contact force was seen in the Wilke scenario, where the ES muscle load was the smallest (Figure 4).

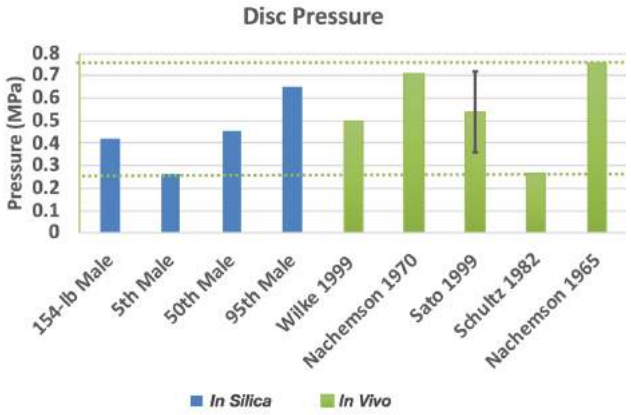

Figure 2: Peak *in silica* disc pressures during standing for each scenario compared to *in vivo* data.

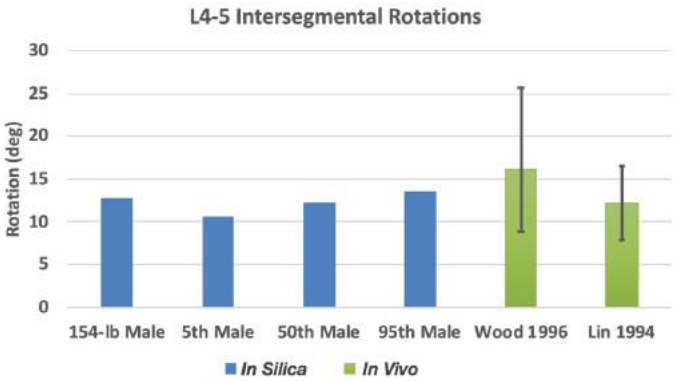

Figure 3: *In silica* L4-5 intersegmental rotations for each scenario compared to *in vivo* data.

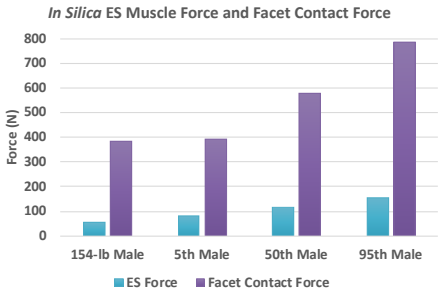

Figure 4: *In silica* ES muscle loads and total facet contact forces for each scenario.

DISCUSSION

The loading conditions for standing utilized in the current study correlate well with published *in vitro* and *in vivo* data. Further, the results demonstrate that the application of upper body weight in conjunction with an offsetting posterior ES muscle load result in disc pressures and intersegmental rotations consistent with published *in vivo* data.

The results of our study confirmed the hypothesis that the application of ES muscle load would result in spinal kinematics and disc pressures consistent with experimental studies while also experiencing facet contact. There was a linear correlation ($R^2 = 0.9407$) between ES muscle load and facet contact reaction force. It is not surprising that greater ES muscle loads resulted in increased facet joint reaction forces. Prior studies in the literature have demonstrated increased facet loads with increased extension moment, which is generated by the activation of the posterior extensor muscles, i.e. ES muscles [12,13].

While the use of a follower load to simulate standing may have undeniable applications, those loading conditions are not fully representative of physiological spinal loads. Studies that have utilized a follower load have resulted in disc pressures and intersegmental rotations that were consistent with *in vivo* data. However, utilizing a follower load does not consider the effects of appropriate muscle action and neglects the contribution of the facets in load sharing, and therefore, has limited clinical application in scenarios where physiological loading conditions are required.

Utilizing loading conditions that mimic physiological spinal loads during standing has many clinical applications. Specifically, the current FEM provides a platform for future studies that involve investigations into the relationship between posterior lumbar muscle strength, facet contact, and disc health. The current model is limited to a single lumbar motion segment and future studies should involve utilizing a full lumbar FE spine to establish physiological loading conditions applicable to the whole lumbar spine. However, we predict that the physiological loading conditions demonstrated in this study will remain applicable to the whole lumbar spine.

REFERENCES

[1] Rohlmann, A et al., *J Biomech*, 42:1520-1526, 2009.
[2] Schmidt, H et al., *J Biomech*, 43:1849-1856, 2010.
[3] Rundell, S et al., *SPINE*, 33:23:2510-2517, 2008.
[4] Wilke, H et al., *SPINE*, 28:8:755-762, 1999.
[5] Bernhardt, M et al., *SPINE*, 14:7:717-721, 1989.
[6] Wilke, H et al., *SPINE*, 28:23:2585-2593, 2003.
[7] Nachemson, A and Elfstrom G, 1970
[8] Sato, K et al., *SPINE*, 24:23:2468-2474, 1999.
[9] Nachemson, A, Acta Ortho Scand, 35:1-4:314-328, 1965.
[10] Wood, K et al., *J of Spine Dis*, 9:2:165-169, 1996.
[11] Lin, R et al., *SPINE*, 19:19:2204-2209, 1994.
[12] Yang, K and King A., *SPINE*, 9:6:557-565, 1984.
[13] El-bohy et al., *J Biomech*, 22:8/9:931-941, 1989.

SB³C2021
Summer Biomechanics, Bioengineering and Biotransport Conference
June 14-18, Virtual

A PROBABILISTIC AND ANISOTROPIC FAILURE METRIC FOR RISK ASSESSMENT OF ASCENDING THORACIC AORTIC ANEURYSM

M. Liu (1), L. Liang (2), Q. Zou (1), Y. Ismail (1), X. Lou (3), G. Iannucci (3), E. Chen (3), B. Leshnower (3), J. Elefteriades (4), W. Sun (1)

(1) Department of Biomedical Engineering
Georgia Institute of Technology
Atlanta, GA, USA

(2) Department of Computer Science
University of Miami
Coral Gables, FL, USA

(3) School of Medicine
Emory University
Atlanta, GA, USA

(4) School of Medicine
Yale University
New Haven, CT, USA

INTRODUCTION

An accurate failure metric plays a critical role for noninvasive assessment of patient-specific rupture/dissection risk of ascending thoracic aortic aneurysm (ATAA). Previously, isotropic material failure metrics were often adopted in biomechanical risk assessment of aortic aneurysms. However, experimental studies [1,2] have revealed that the aortic wall strengths in the circumferential and axial directions are significantly different. Hence, to incorporate direction-dependent failure properties, an anisotropic failure metric needs to be developed and applied.

Patient-specific failure properties (i.e., aortic wall strengths) can only be accurately determined using invasive and destructive tests, and these tests, obviously, cannot be performed for *in vivo* patients whose ATAAs are still intact. Some studies suggested to use deterministic approaches to estimate failure properties [3,4]. However, since the large variability of aortic wall strengths was not considered in the deterministic approaches, the predictive capability is limited.

In this study, we developed a novel probabilistic and anisotropic failure metric for ATAA risk assessment. Uniaxial failure tests were performed using aortic tissue samples from 84 ATAA patients, from which a two-dimensional (2D) joint probability distribution of the anisotropic wall strengths was obtained. Subsequently, an anisotropic failure probability (FP) based on the Tsai-Hill (TH) failure theory was developed from the probability distribution of the circumferential and axial strengths. Using computed aortic wall stresses, the novel FP metric can be used to estimate the risk of an individual ATAA patient. For method validation, "ground-truth" risks of additional 41 ATAA patients were numerically computed from finite element analysis (FEA) using CT images and matching tissue testing data. Using the "ground-truth" data, different risk assessment methods and failure metrics were compared and assessed.

METHODS

Aortic Tissue Samples and CT Image Data. In this study, surgically resected human aortic tissues of 98 ATAA patients (72 males, 26 females, age: 62.57 ± 12.42 years) were obtained from the Emory Saint Joseph's Hospital, GA with IRB approval. In addition, we obtained surgically resected aortic tissue samples and matching CT images of 27 ATAA patients in a previous study [5] from the Yale-New Haven Hospital, CT.

The cohort of 125 (98+27) ATAA patients was divided into two groups: (1) 84 patients without CT images; and (2) 41 patients with CT images (including 27 patients from our previous study [5]). Group 1 was used for method development; and Group 2 was used to compute the "ground-truth" risks for method validation. Hence, there is no overlapping between the two groups.

Uniaxial Tests and Failure Criterion. Uniaxial tensile tests were then performed using the 98 ATAA tissue samples. For each ATAA patient, circumferential and axial specimens were obtained and subjected to uniaxial tensile tests until failure, from which circumferential and axial strengths were extracted.

In this study, the TH criterion was used for modeling failure properties of the aortic tissues. The TH model has demonstrated a good fitting capability with off-axis tension test data of aortic tissues.

Probabilistic and Anisotropic Failure Probability (FP). The anisotropic probabilistic failure metric is developed in the following steps: (1) estimating the joint probability density function (PDF) of the TH model parameters (circumferential strength and axial strength) from uniaxial testing data of Group 1 by using kernel density estimation (KDE); (2) evaluating the KDE-estimated PDFs by performing goodness-of-fit tests using the estimated joint PDF and marginal PDFs; (3) deriving PDF of the TH failure metric, by using the method of random variable transformation (a.k.a. the technique of changing

variables); and (4) calculating the failure probability (FP) using numerical integration.

Validation Using Patient Data in Group 2. In this study, "ground-truth" risks of additional 41 ATAA patients (Group 2) were computationally estimated using matching CT images and tissue testing data from individual patients. Uniaxial failure tests and planar biaxial tests were performed for patients in Group 2 to obtain failure properties and hyperelastic properties, respectively. To estimate ATAA risk, patient-specific geometries were numerically inflated until rupture in FEA using patient-specific hyperelastic and failure properties. For a particular patient, the pressure rupture risk (PRR) [5] is used to quantify the risk revealed by the patient-specific FEA (to compute stresses) and the patient-specific TH model (to determine failure). Using the estimated "ground-truth" data, the following risk assessment methods and failure metrics were compared and assessed: 1) maximum diameter criterion; 2) maximum FP failure metric at systolic blood pressure; 3) maximum TH failure metric at systolic blood pressure using typical deterministic value of circumferential and axial strengths; 4) maximum FP failure metric at elevated pressure (1.5 systolic); and 5) maximum deterministic TH failure metric at 1.5 systolic pressure. Due to static determinacy [6], patient-specific hyperelastic properties are not needed in methods 2) and 3). Patient-specific hyperelastic properties were used in methods 4) and 5). These methods were used to classify high (PRR≥0.6) and low risk (PRR<0.6) patients. The receiver operating characteristic (ROC) curves were used to evaluate the discriminative power of the methods.

RESULTS

FP Metric. The FP metric was developed from failure property data of 84 patients. The value of FP represents the probability of failure. FP can be visualized on a 2D plot of circumferential and axial stresses. In Figure 1, 2D contour plots of FP are generated using representative shear stress $\tau_{\theta z}$ values.

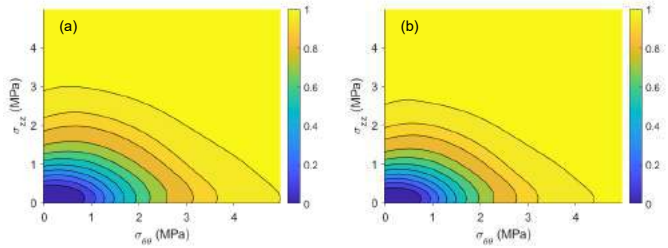

Figure 1. 2D FP contour in the circumferential and axial stress plane ($\sigma_{\theta\theta} - \sigma_{zz}$) with shear stress $\tau_{\theta z}$ (a) 0 and (b) $300kPa$.

Validation. Probabilistic FP and deterministic TH metrics of the 41 ATAA patients (Group 2) were computed by using the patient-specific geometries and blood pressures. Using the maximum diameter criterion, no statistical significance was found between the high and low risk groups (p=0.1677). Difference between high and low risk groups is significant using the maximum FP at systole (p=0.0117), while p=0.0099 when the same method is used with TH. Using patient-specific hyperelastic properties and the maximum TH under elevated pressure, the p-value is low (p=0.0017). The most significant difference was found for FP under elevated pressure (p=0.0001). ROC curves are shown in Figure 2 for failure metrics evaluated at systolic pressure (Figure 2(a)) and 1.5 systolic pressure (Figure 2(b), using patient-specific hyperelastic properties). The plots are generated using false positive rate (FPR) versus true positive rate (TPR). The area under the ROC curve (AUC) is 0.5489 for the diameter criterion. Using the FP and TH under systolic pressure, AUCs are 0.8448 and 0.8017, respectively. Under elevated pressure (1.5 systolic pressure), the AUCs are 0.8621 and 0.8362 for FP and TH, respectively. The results indicate that the probabilistic metric FP has a better discriminative power comparing to the deterministic metric TH.

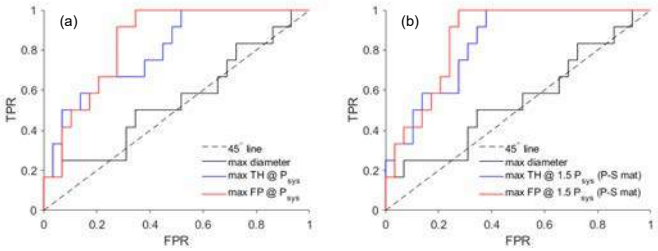

Figure 2. ROC curves of diameter criterion, probabilistic (FP) and deterministic (TH) failure metrics. (a) FP and TH under systolic pressure; (b) FP and TH under 1.5 systolic pressure.

DISCUSSION

In this study, a novel failure metric is developed based on a probabilistic modeling framework, which can be adopted for other types of materials. By employing the TH model, anisotropic failure properties are embedded in FP. Comparing to the deterministic TH metric, FP incorporates uncertainties of wall strengths, i.e., the distribution of the circumferential and axial wall strengths in the ATAA population. With more tissue failure testing data collected, FP can be updated and improved, e.g., a conditional FP can be built based on patient-specific information (age, gender, family history). Using reconstrued risk data, this study demonstrated that the performance of FP metric is superior to the deterministic TH metric with representative failure parameters. To our best knowledge, this is the first study that develops a probabilistic and anisotropic failure metric for aortic aneurysm risk assessment.

Using the estimated risk of the 41 patients, we found that the biomechanical failure metrics (TH and FP) have more discriminative power than the maximum diameter criterion. Using patient-specific hyperelastic properties and FP, the highest AUC is achieved by FP under elevated pressure, which highlights the potential benefit of identifying patient-specific hyperelastic properties for risk assessment. When patient-specific hyperelastic properties are not available, FP can be evaluated on image-derived geometries using static determinacy [6] without the need of patient-specific hyperelastic properties.

In this study, an ideal scenario was assumed, in which the wall thickness can be accurately measured from MRI or high-resolution CT scans. Hence, AUC of the failure metrics could be close to the upper limits. Using an uncertainty quantification (UQ) framework, the wall thickness, which is the input to the FE simulations, can treated as a source of uncertainties. We have recently developed a deep learning model [7] as a fast and accurate surrogate of FE simulation, which can replicate the results of FE simulations instantaneously. To incorporate uncertainties originated from FE inputs such as wall thickness into FP, the DL model can be used to accelerate the UQ framework.

ACKNOWLEDGEMENTS

This study is supported by American Heart Association (AHA) 18TPA34230083.

REFERENCES

[1] Kim, J et al., *Biomech. Model. Mechanobiol.*, 11(6): 841-853, 2012.
[2] Angouras, D et al., *J Mech. Behav. Biomed.*, 98: 58-70, 2019.
[3] Joldes, G et al., *Sci. Rep.*, 7(1): 1-15, 2017.
[4] Geest, J et al., *Ann. Biomed. Eng.*, 34(7): 1098-1106, 2006.
[5] Pham, T et al., *Acta Biomater.*, 9 (8), 7927-7936, 2013.
[6] Liu, M et al., *Biomech. Model. Mechanobiol.*,18: 387–398, 2019.
[7] Liang, L et al., *J. R. Soc. Interface,* 15 (138), 2018.

IMPLEMENTING AN ARTIFICIAL NEURAL NETWORK TO STUDY BRAIN STRAIN AND MILD TRAUMATIC BRAIN INJURY METRICS

L. Patterson (1), Y. Levy (2), H. Mao (1,2)

(1) Mechanical and Materials Engineering
Western University
London, Ontario, Canada

(2) Biomedical Engineering
Western University
London, Ontario, Canada

INTRODUCTION

Helmets are an essential piece of equipment for protection against mild traumatic brain injuries (mTBIs) and other head injuries in sporting activities. The Canadian Journal of Public Health has called mTBIs a "silent epidemic" in Canada. The occurrence of mTBIs has increased by an annual percentage change of 9.6% across all age groups in Canada between 2005 and 2014 [1]. Improving the way a helmet protects the wearer from mTBIs can decrease the occurrence of these injuries.

A mTBI is usually caused by a kinematic impact to the head or upper body, with which there are significant strains in the tissue cells of the brain that may cause damage. Impact severity can be qualified by average maximum principal strain (MPS) and cumulative strain damage measure (CSDM) values, such as $CSDM_{25}$ which is calculated by dividing the volume of elements of MPS over 0.25 by the total volume of the elements in a model. In this case, these elements are finite modelling elements that exist within the Global Human Body Models Consortium (GHBMC) human brain finite element model.

This study intends to specify which kinematic input metric or combination is best able to predict accurate MPS and $CSDM_{25}$ values. We explored various ways to predict these values with an artificial neural network, and how changing the training and test database sizes of the artificial neural network affected the results of the artificial neural network's MPS and $CSDM_{25}$ predictions.

METHODS

The data used in this study was originally collected by *Levy el al.*, in which six helmets were assessed a Hockey STAR rating via experimental tests. [2]. In total, each of the six helmets labelled A to F, were put through an average of 112 tests, resulting in 672 tests in total [2]. The kinematic data of each helmet impact, linear acceleration, rotational acceleration and rotational velocity was collected [2]. Using a custom MATLAB script, LS-DYNA, and LS-PrePost, the MPS and $CSDM_{25}$ values were calculated. Incidence STAR values were output, and subsequently Hockey STAR values were calculated.

The Multilayer Perceptron procedure within SPSS Statistics was used to produce a predictive artificial neural network (ANN) model for which kinematic data was most accurate in predicting real MPS and $CSDM_{25}$ values from the collected data. Different combinations of kinematic inputs were used as covariates. Combinations were tested with a random subset of data used for training and the remainder for testing. The ANN-predicted MPS and $CSDM_{25}$ values were plotted against the actual MPS and $CSDM_{25}$ values from simulations. An R-squared value was generated in Microsoft Excel. The R-squared value of each combination tested was used as the comparator for which combination of kinematic inputs was most accurate, and the combinations were ranked in order.

The ANN was subjected to a sensitivity analysis. This evaluated how sensitive the results generated by the ANN were to different test and training subset breakdowns and showed how well the ANN could predict average MPS and $CSDM_{25}$ values for helmets excluded from the ANN testing and training process. Two test and training subset breakdowns were examined. One divided the data set 70% for training and 30% for testing, and the other 80% training and 20% testing. Over a second series of tests, certain permeations of helmets were excluded from the Multilayer Perceptron ANN creation process. The remaining helmets that were included were used to create the ANN. The created ANN was then used to predict the MPS and $CSDM_{25}$ values for the helmets that were excluded based on the network created from the included helmets. The predicted results were then plotted in Excel against the actual results. Sets of one, two and three helmets were excluded to see if the quality of the prediction dropped below a threshold R-squared value of 0.95.

RESULTS

Fifteen combinations of covariates were used in the analysis. This analysis was completed using 70% of the dataset as a training set and 30% as a testing set. The five strongest correlated kinetic input variable combinations are shown in Table 1. Definitions for the kinematic inputs used in Table 1 are explained in Table 2.

Table 1: Five Strongest Correlated Kinetic Input Variable Combinations, Ranked by R-Squared Value

Case Number	Associated Kinematic Input Variable Combination	R-Squared Value
Case 15	$\boldsymbol{LinA_{x,y,z}} + \boldsymbol{RotV_{x,y,z}} + \boldsymbol{RotA_{x,y,z}}$ + **RPLV** + **RPRV** + **RPRA**	0.988
Case 7	$\boldsymbol{LinA_{x,y,z}} + \boldsymbol{RotV_{x,y,z}} + \boldsymbol{RotA_{x,y,z}}$	0.985
Case 4	$\boldsymbol{LinA_{x,y,z}} + \boldsymbol{RotV_{x,y,z}}$	0.978
Case 5	$\boldsymbol{RotV_{x,y,z}} + \boldsymbol{RotA_{x,y,z}}$	0.955
Case 14	**RPLV** + **RPRV** + **RPRA**	0.955

Table 2: Kinematic Input Variable Definitions

Short Form	Kinematic Input Variable
$LinA_X$, $LinA_Y$, $LinA_Z$	Linear Acceleration in X, Y, and Z Planes
$RotV_X$, $RotV_Y$, $RotV_Z$	Rotational Velocity in X, Y, and Z Planes
$RotA_X$, $RotA_Y$, $RotA_Z$	Rotational Acceleration in X, Y, and Z Planes
RPLA	Resultant Peak Linear Acceleration
RPRV	Resultant Peak Rotational Velocity
RPRA	Resultant Peak Rotational Acceleration

Case 15, which had the greatest number of kinematic inputs, was the variable combination with the highest R-squared value, and subsequently is the best predictor of both average MPS and $CSDM_{25}$ values.

Figure 1 shows how the R-squared value trends as a greater number of helmets are excluded from the ANN generation process.

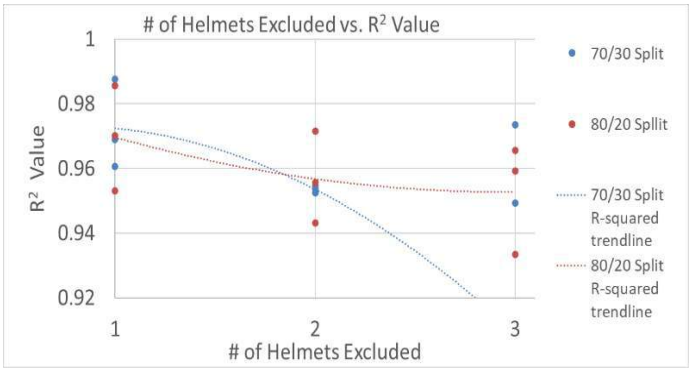

Figure 1: Number of Helmets excluded versus resultant ANN R-Squared Value

DISCUSSION

The prediction combination of kinematic variable inputs with the highest R-squared correlation value was Case 15, which was expected as it contains all twelve potential kinematic input variables. The next three highest cases all contained rotational velocity, which aligns with the current scientific consensus that rotational velocity should be given higher weight than linear or rotational acceleration and is a better predictor of brain strain than other kinematic inputs. The data shows that when rotational velocity is not included in the set of kinematic inputs to the ANN, the ANN's prediction ability decreases significantly.

A kinematic input variable combination of only the peak rotational velocity, linear and rotational accelerations was considered in Case 14. This combination was found to be an unexpectedly efficient way of predicting MPS and $CSDM_{25}$ values. By utilizing the peak kinematic values in the ANN creation, there is a 75% reduction in the amount of data variables that must be collected from the accelerometer, as compared to Case 15. This reduction comes from the kinematic input combination only requiring peak values. The results of using this combination show that high quality predictions of MPS and $CSDM_{25}$ values can still be made with fewer overall data variables collected from each individual test, which may be useful if testing is scaled up significantly.

As more helmets were excluded, the ANN was created based on less data. Consequently, the training and testing sets were smaller and the ANNs ability to accurately predict MPS and $CSDM_{25}$ values was expected to decrease. As the number of helmets involved was decreased from one to three, the R-squared values did decrease, but one half of the trials that were conducted with three helmets excluded still had R-squared values that were greater than 0.95, indicating a high degree of correlation was still possible.

Of the six helmets that data was collected for, three helmets, labelled A, B and C, had good Hockey STAR ratings. The other three helmets, labelled D, E and F, had poor Hockey STAR ratings. A good Hockey STAR rating, for the purposes of this study, was defined as a rating that is less than 6. A poor Hockey STAR rating, for the purposes of this study, was defined as a rating that is greater than 8. None of the six helmets that were assessed had Hockey STAR ratings between 6 and 8. It was determined that using only the helmets with a good Hockey STAR rating or using only helmets with a poor Hockey STAR rating to predict MPS and $CSDM_{25}$ values would result in a less precise prediction than a mixture of good and poor Hockey STAR rated helmets. This was particularly noticeable when there was less data to train and test the ANN that will be used for prediction (e.g. when the data of only three helmets was used).

Having more test data and testing a greater number of helmets would further reduce the error in the ANN prediction process. Having a greater selection of helmets would allow more exclusion and prediction options. Additionally, it was noted that when comparing predicted versus actual MPS and $CSDM_{25}$ values, there were gaps between clusters of data because there were no actual MPS and $CSDM_{25}$ values available for those ranges. The location of these gaps varied for each helmet. Eliminating these gaps and having a more equal spread of data would also further reduce the overall error.

In conclusion, as long as an appropriate training and data exclusion strategy is selected to ensure accuracy, ANNs are an effective tool to use in the study and prediction of brain strain, and in predicting the risk of mTBI occurrence.

ACKNOWLEDGEMENTS

We acknowledge Bauer Hockey for their support in providing testing data. We also acknowledge NSERC and Canada Research Chairs program for their support.

REFERENCES

[1] Feinstein, A et al., *Can. J. Public Health*, 91:325-326, 2000

[2] Levy, Y et al., *Electronic Thesis and Dissertation Repository*, 1:1-153, 2020

EVIDENCE OF SEX BIAS IN FINITE ELEMENT MODELING OF HIP ARTHROPLASTY

Syeda N. Lamia (1,3), Chien-Yu Lin (2), Richard E. Hughes (3), Elizabeth A. Dailey (3), Megan L. Killian (3)

(1) Department of Mechanical Engineering
University of Michigan
Ann Arbor, Michigan, USA

(2) Department of Biomedical Engineering
University of Texas
Austin, Texas, USA

(3) Department of Orthopaedic Surgery
University of Michigan
Ann Arbor, Michigan, USA

INTRODUCTION

Inadequate inclusion of females in medical research has been a matter of concern for a long time. In 1993, the US National Institute of Health (NIH) Revitalization Act was issued, which mandated the inclusion of women in federally supported phase III clinical trials and appropriate reporting of sex effects [1]. Though these policies increased the number of female clinical-research participants, sex bias was still persistent in preclinical studies [2]. In 2014, NIH issued additional guidelines to ensure the inclusion of both sexes in preclinical research [3], yet the success of these policies is mostly unknown, except for a few fields [4].

A recent study found that less than 50% of biomechanical studies had balanced sex distribution in their samples [5], while another identified sex bias in orthopaedic research [6]. We opted to investigate a more specific field in our current study: finite element analysis in hip arthroplasty. Hip fracture is nearly twice as common in women compared to men in the US [7], as are total hip arthroplasty (THA) surgeries. Yet, surprisingly, sex-dependent characteristics are not always considered in design, modeling, and analyses of THA viability. A common method for comparing the viability of THA implants is finite element (FE) modeling because of the accessibility and low-cost operation of computation approaches compared to benchtop experiments. FE modeling is also useful for estimating and analyzing the biomechanical behavior of implanted prostheses. This tool can offer subject-specific insights when modeled accordingly.

In the current study, we first asked if and how FE modeling has been systematically used for comparing sex differences in FE modeling of THA implants. As FE modeling lays the groundwork for clinical research, it is important to understand sex-based differences in models. We performed a systematic review of the literature in 5-year increments to determine if sex bias exists in FE modeling and if and how demographic reporting in FE modeling of hip implants has changed over time.

METHODS

The study design is shown in Figure 1. In brief, PubMed database was systematically searched for eight different years from 1984 to 2019 at discrete 5-year intervals (1984, 1989, 1994, 1999, 2004, 2009, 2014, and 2019). The search keyword was 'Hip and Finite Element'. A total of 432 records appeared in the search; from these, reviews and non-English articles were removed. The remaining records were requested through the University of Michigan Library to obtain the full text. Some articles requested via inter-library loan were excluded due to loan delay of greater than 7 days. 410 full-text articles were acquired and read in total. Articles were excluded from this study if they: (1) were on animal models; (2) did not include FE modeling; (3) were not on hip implants; (4) did not have bony geometry; and (5) were studied in non-physiological conditions. This approach reduced the included articles to n = 122. Demographic data (sex, race, and age) of the following data were noted from the included articles: (1) geometry; (2) Young's moduli; (3) Poisson's ratio; (4) bone density; (5) loading; and (6) model validation. Data were analyzed in Prism v9.0 (GraphPad, LaJolla, CA). The number of studies that used male, female, or other bony geometric models was compared between discrete publication years. If a study used the geometry, Young's moduli, and bone density of the same subject, we identified it as 'subject-specific model,' and their percentage at respective years was plotted. The percentage of studies using experimental model validation was also calculated.

RESULTS

The number of studies that passed the eligibility criteria each year gradually increased and reached steady-state around 2009, ranging from 3 to 32 per year. We found that, generally, researchers model male geometries more frequently than females in the FE analysis of hip

implants (Figure 2). Most articles did not state the sex of the geometry they used (referred to as 'unknown', 25%-100% in earlier years), though this number reduced over time. In more recent years (e.g., 2009 onward), the use of female geometry increased; nonetheless, it was still less common compared with males. Up to 25% of studies annually were based on geometry obtained from surrogate or composite bones (e.g., Sawbone). Some studies did not describe their model; however, that number is relatively low (3 out of 122, not shown in Figure 2). Of all the articles included in this review, fewer than 10% reported geometries from both sexes.

As expected, the percentage of articles that used subject-specific FE modeling increased over time (Figure 3a). In general, the number of studies with male subject-specific models or models of unknown sex were higher than that of female. Surrogates were sometimes used to develop a 'subject-specific' model (e.g., < 5% in 2014 and 2019).

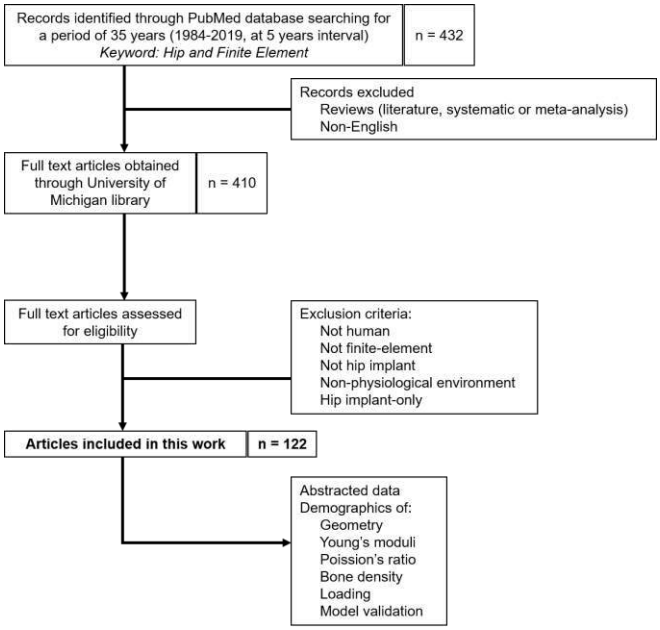

Figure 1: Study flow diagram.

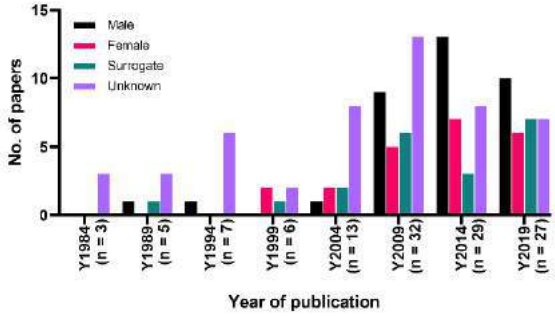

Figure 2: Sex distribution of geometric models in FE analysis of hip implant studies. Most analyses reviewed in this study relied on male geometries. n denotes the total number of articles each year.

The FE model validation rate was less than 50% in all eight years that have been studied (Figure 3b). Besides cadavers, surrogates were also a common option to validate the FE model experimentally, and an upward trend is observed. In recent years (2014 and 2019), almost 50% of the validation studies were completed with surrogates.

Of the demographics included in the studies reviewed systematically, race was the least reported. Fewer than 10% of the articles included in this study stated the race of the subject's geometry.

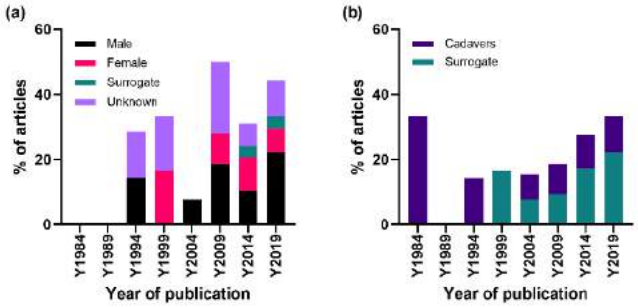

Figure 3: Percentage of articles that included (a) subject-specific models and (b) experimental model validation. Both show an upward trend for increased prevalence over time.

DISCUSSION

We reviewed 122 articles published over 35 years and found convincing evidence that sex bias exists in FE studies of hip implants. We found that male subjects or characteristics are modeled more often than females. Though the number of studies including female geometries has increased recently, we have not yet reached sex equity in FE modeling of hip implants, especially given the increased rate of women undergoing THA compared to men [8].

Bony pelvic geometries are significantly different between men and women. The mature female hip has a greater width to height ratio, anterior pelvic tilt, femoral anteversion, quadriceps angle, acetabular socket depth, and femoral head width compared with the male [9-10]. Such geometric dissimilarities are also observed across different races [11]. Thus, hip joint loading vectors may not be the same between sexes or among races. Moreover, even in the same age group, bone density is different in men and women and can also vary between race [12]. As bone density and strength are directly correlated [13], it is important to consider sex and race while defining the model in FE analysis.

The use of bone surrogates has increased in recent years. Surrogates generally have properties similar to human bones but do not possess inter-specimen variability. However, when it comes to subject-specific FE modeling, surrogates cannot be considered an alternative to the patient-specific bones. As surrogates are designed around a particular age group, these bone analogs may fail to represent aged bone properties.

Subject-specific FE models provide precise information about individuals and help make more informed decisions about patients. However, studies based on only one subject provides information specific to only that subject. We recommend inclusion of multisubject patient-specific models which correspond to different ages, sexes, and/or races so that the results can be applied to a wide range of demographics.

ACKNOWLEDGEMENTS

NSF CAREER (1944448).

REFERENCES

[1] NIH, *Am J Ther*, 1993. [2] Zucker, I et al., *Nature*, 465:690, 2010. [3] Clayton, J et al., *Nature*, 509:282–283, 2014. [4] Beery, A et al., *Neuro Bio Reviews*, 35:565-572, 2011. [5] Bach, S et al., *PLoS One*, 10:1–6, 2015. [6] Bryant, J et al., *J Bone Joint Sur*, 100:124-130, 2018. [7] Dhanwal, D et al., *In J Ortho*, 45:15–22, 2011. [8] Kremers, H et al., *J Bone Joint Sur*, 97:1386–1397, 2015. [9] Shultz, S et al., *J Orthop Sports Phys Ther*, 38:137–149, 2008. [10] Wang, S et al., *Annu Proc AAAM*, 48:287–301, 2004. [11] Jun, Y et al., *Adv Engg Soft*, 41:537-547, 2010. [12] Peacock, M et al., *Bone*, 45:218–225, 2009. [13] Morgan, E et al., *J Biomech*, 36:897–904, 2003.

STRESS ANALYSIS OF INTRACRANIAL ANEURYSM BASED ON *IN VIVO* 3D MODEL AND INTRAOPERATIVE IMAGE: A CASE STUDY

Y. Luo (1), X. Zhai (2), P. Hu (2), H. Zhang (2), Y. Wang (2), L. Cao (3), J. Lu (1)

(1) Department of Mechanical Engineering
The University of Iowa
Iowa City, Iowa, USA

(2) Department of Neurosurgery
Xuanwu Hospital Capital Medical
University, Beijing, China

(3) Boea Wisdom (Hangzhou) Network
Technology Co., Ltd.
Hangzhou, Zhejiang, China

INTRODUCTION

Majority of nontraumatic subarachnoid hemorrhage, which is a devastating condition that carries high rates of mortality, morbidity, and disability, is caused by intracranial aneurysms (IAs) rupture (or called cerebral aneurysms). IAs have an estimated prevalence of 2% - 3%, but most of them stay unruptured [1][2][3][4]. Although medical image technology facilitates detection of unruptured IAs, distinguishing high rupture risk aneurysms remains challenging since the rupture mechanism is not well understood. Mechanically, the wall stress plays a key role in aneurysm rupturing. To accurately obtain local stress results, the thickness of the wall must be known. However, it is impossible to obtain the wall thickness *in vivo* with current medical image technology. Recently, aneurysm wall thickness distribution based on color translucence of intraoperative images are studied [5,6]. The study suggested that the relative wall thickness can be estimated from the pixel intensity. The relative thickness, in conjunction with an inverse method of stress analysis which can effectively determine the wall tension, may open a way to estimate the relative stress level in IAs, and thus locate the high stress region.

To explore the idea, we conduct a pilot study. A patient specific aneurysm 3D model is segmented from computed tomography angiography image, and inverse stress analysis is performed to predict the tension distribution in the wall. The aneurysm is further sub-divided into dome, neck and bleb regions based on their geometric locations; and average tensions in these regions are computed. Later, color intensities of the three regions are computed. Based on Beer-Lambert Law, the relative color intensity level is considered to be a relative thickness level. The relative stress is then computed.

METHODS

The lumen of aneurysm is segmented from CTA medical images and then the 3D geometry is reconstructed using Insight Toolkit (ITK). The wall thickness was set to 0.3 mm uniformly in both parent artery and aneurysm region. The inlet and outlet of the models were fixed. The inner surface of the model was loaded with a uniform pressure 85 mmHg. The inverse finite element method developed by Lu's group was applied on 3D aneurysm models. The method takes the imaged geometry as the current configuration and solves the wall stress by means of finding the reference configuration. For thin walled, sack-like structures, the method enables to determine the stress using hypothetical material models. In the analysis, we used a 5-parameter Mooney-Rivlin type strain energy density function as in [7], which writes as:

$$W = C_{10}(\bar{I}_1 - 3) + C_{01}(\bar{I}_2 - 3) + C_{20}(\bar{I}_1 - 3)^2 + C_{11}(\bar{I}_1 - 3)(\bar{I}_2 - 3) + C_{02}(\bar{I}_2 - 3)^2$$

where $\bar{I}_1$ and $\bar{I}_2$ are the first and second invariants of a normalized deformation gradient $\mathbf{F}$. The material coefficients C_{ij} were obtained from published experimental data [8]. Specifically, C_{10}, C_{01}, C_{02}, C_{20}, and C_{11} are set to 0.42, -0.12, 0.56, 0.58 and 0.585 MPa respectively for all cases computation in this paper. Note that since the uniform wall thickness is assumed, the 'stress' so obtained is in fact the wall tension scaled by the assumed thickness.

To obtain relative thickness information, Beer-Lambert law is employed. The law writes in:

$$A = \varepsilon l c$$

where A is the absorbance, ε is the absorptivity of the attenuating species, l is the optical path length and c is the concentration of the attenuating species. In this study, we assume ε and c are constant for the aneurysm tissue. Absorbance A can be computed by $\log(\frac{I_{out}}{I_{in}})$, where I_{in} and I_{out} are color intensities of incident and transmitted lights respectively. According to Anderson et al., to linearize the intensity, intensity I can be computed with:

$$I = 0.2126\,R + 0.7152\,G + 0.0722B$$

where R, G, B are red, green, blue color value within a pixel [9]. Noted that the image was taken in a surgery room illuminated by white light, $I_{in} \approx 1$. Therefore, color intensity ratio between two locations can be estimated by

$$\frac{Log(I_1)}{Log(I_2)} \approx \frac{I_1}{I_2} \quad (1)$$

RESULTS

As shown in Figure 1, an aneurysm sac is sub-divided into three different regions: bleb, which is a rounded outgrowth on the sac; neck is a annular band connected the sac and its parent artery, and dome is the region between the bleb and neck area. Average tension in bleb, dome and neck regions are 0.13, 0.18 and 0.27 MPa·m respectively. Tension ratio values between dome and neck, bleb and neck are 0.67 and 0.48.

(a) Bleb (b) Dome (c) Neck

Figure 1: Sub-divided regions demonstration.

Rupture site of the aneurysm is carefully observed by doctors during traumatic surgery and scrupulously marked out in the 3D models as shown in Figure 2.

(a) Rupture site (b) Intraoperative image

Figure 2: Rupture site identification and intraoperative image.

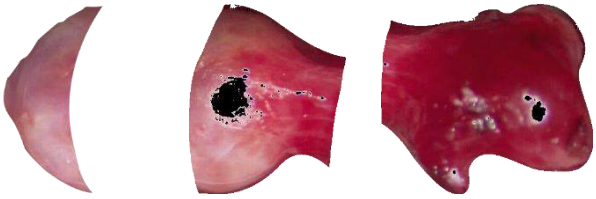

(a) Neck (b) Dome (c) Bleb

Figure 3: Image sub-divided regions demonstration.

The intraoperative image is sub-divided into three regions correspondingly as presented in Figure 3. Glary spots on the image are excluded in intensity calculation. Average intensity in bleb, dome, and neck regions are 0.15, 0.43 and 0.49 respectively. Thickness ratio between dome and neck is 0.88, bleb and neck is 0.31. By definition, stress is equal to tension divided by thickness. Consequently, stress ratio between dome and neck is 0.76, between bleb and neck is 1.55. Stress level of bleb region is the highest in the three. Ratio calculations are summarized in Table 1.

Table 1: Relative ratios of tension, thickness and stress

Ratio	Bleb/Neck	Dome/Neck	Neck/Neck
Tension	0.48	0.67	1.00
Thickness	0.31	0.88	1.00
Stress	1.55	0.76	1.00

With the thickness ratio, regional stress level distribution is calculated. Since thickness information of the parent artery is missing, we assume it is the same as the thickness of neck. To compare, tension and stress distribution are plot side by side in Figure 4. As can be seen in Figure 4 (b), most of the high stresses concentrate at the bleb region. Based on the rupture site identified on 3D model (Figure 2 (a)), the region is coincident with the rupture location.

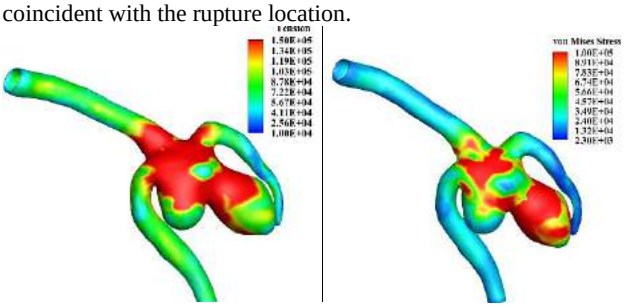

(a) Tension (b) Stress level

Figure 4: Tension and stress results

DISCUSSION

The current medical technology is not able to measure the thickness *in vivo* and this hinders the prediction of wall stress. Under this condition, estimating relative thickness, and thus to estimate the relative stress level, merits investigation. In this abstract, a new method that integrates *in vivo* tension analysis and relative thickness estimation from intraoperative image is explored. Relative thickness ratio between dome and bleb (also rupture location) regions is found to be about 2.87. MacDonald et al., used polarized light microscopy to estimate the thickness and found a ruptured wall-thickness ranges between 16 – 212 μm [10]. By taking average value 114 um and considering the aneurysm dome thickness is about 300 μm [11], dome over bleb ratio is about 2.63 which is close to our findings. Also, thickness of dome and neck regions are roughly the same which agrees with the conclusion by Sherif et al. [12]. In conclusion, our case study shows that relative thickness level of an aneurysm sac can be reasonably estimated, and the results indicate that the rupture site may have the highest relative stress level.

REFERENCES

[1] Rinkel G. J., Djibuti M., Algra A., Van Gijn J., Stroke 29(1998) 251{256}.

[2] Muller T. B., Sandvei M. S., Kvistad K. A., Rydland J., Haberg A., Vik A., Garseth M., Stovner L. J., Neurosurgery 73 (2013) 256{261}.

[3] Vernooij M. W., et al., New England Journal of Medicine 357.18 (2007): 1821-1828.

[4] Etminan N., Rinkel G. J., Nature Reviews Neurology, 12 (2016) 699.

[5] Kadasi L. M., Walter C. D., Adel M. M., Journal of neurointerventional surgery, 5.3 (2013): 201-206.

[6] Song J., Park J.E., Kim H.R., Shin Y.S., Neurological Sciences. 2015 Jun 1;36(6):907-12.

[7] Razaghi, R., Biglari, H., & Karimi, A., Computer methods and programs in biomedicine, 176, 9-16.

[8] Monson, K.L., 2001. Mechanical and failure properties of human cerebral blood vessels (Doctoral dissertation, University of California, Berkeley).

[9] Anderson M., et al., Color and imaging conference. Vol. 1996. No. 1. Society for Imaging Science and Technology, 1996.

[10] MacDonald D. J., et al., Annals of biomedical engineering 28.5 (2000): 533-542.

[11] Torii, Ryo, et al., International Journal for Numerical Methods in Biomedical Engineering 26.3 - 4 (2010): 336-347.

[12] Sherif C., et al., Acta neurochirurgica 156.1 (2014): 27-34.

THE CURVATURE AND COLLAGEN NETWORK OF THE HUMAN LAMINA CRIBROSA IN GLAUCOMA AND CONTROL EYES

Cameron A. Czerpak (1), Yik Tung Tracy Ling (1), Joan L. Jefferys (2), Harry A. Quigley (2), Thao D. Nguyen (1)

(1) Department of Mechanical Engineering
Johns Hopkins University
Baltimore, MD, United States

(2) Wilmer Eye Institute
Johns Hopkins University
Baltimore, MD, United States

INTRODUCTION

The lamina cribrosa (LC) is a connective tissue that forms part of the eye wall in the optic nerve head (ONH). The human LC is formed from cribriform plates composed of elastin, collagen types I and III, and various proteoglycans [1]. When viewed *en face*, the plates resemble a beam and pore network. The LC functions to support the capillaries, cells, and axonal structures of the optic nerve head from the various loading conditions imposed by the intraocular pressure (IOP), intracranial pressure, and extraocular muscles [2]. RGC axon injury has been shown to occur at the LC in human glaucoma and in animal models of glaucoma with increasing IOP [3]. The severity of axon damage in glaucoma is strongly associated with IOP, and higher IOP is associated with increased prevalence [4-5]. The LC has been shown to remodel with glaucoma. The plate-like structure thins and becomes more curved with progressive axonal damage [6]. The collagen, elastin, and proteoglycan composition also change, and the pores may become smaller [1,7-8]. Therefore, the structure, curvature, and biomechanics of the LC are important aspects of glaucoma that may differ between diagnosed glaucoma eyes and normal eyes.

Previous work by Ling et al. [9] examined the LC network microstructure of eyes with no known history of glaucoma and found that lower pressure-induced LC strains were associated with structural features that indicated greater collagen density and beam connectivity. Midgett et al. [10] compared the strain response of normal eyes to glaucoma eyes and found that the stiffness of the LC pressure-strain response was greater in diagnosed glaucoma eyes. The objective of this study is to measure the curvature and features of the collagen beam-network structure of the LC of post-mortem human glaucoma eyes and analyze for differences between diagnosed glaucoma and age-matched normal eyes.

METHODS

We received 10 normal human eyes and 16 diagnosed glaucoma eyes with an age range of 76-93 years and average ages of 83.8 ± 6.1 years and 87.3 ± 5.4 years, respectively [10]. The optic nerves of the enucleated eyes were cut flush to the sclera to remove the post-LC myelinated optic nerve and to reveal the trabecular structure of the LC. The posterior scleral cups were subjected to inflation testing at 5 and 45 mmHg. At each pressure, the LC was imaged using laser scanning second harmonic generation (SHG) imaging as described in Midgett et al. [11]. SHG image volumes were analyzed using digital volume correlation (DVC) to calculate the strain field caused by inflation from 5-45 mmHg [11].

The maximum intensity Z projection of the SHG image Z stack was enhanced using Frangi filter and masked before being analyzed by a custom algorithm developed by Ling et al. [9] for ten structural features including pore area fraction, beam aspect ratio (length/width), and tortuosity (contour length/straight-line distance) of the LC beams (Fig 1) [9]. Average pore size was calculated with a modified version of this method where each image of the SHG image Z stack, instead of the maximum Z projection, was enhanced and masked. Each layer was processed by the algorithm and pore size from each z-slice was averaged to obtain the overall average pore size for the LC.

Curvature was calculated by creating a point cloud of the anterior surface of the DVC-correlated LC volume and fitting a 5th order polynomial to the point cloud using Matlab curve fitting toolbox. Curvature of the surface was determined using the Matlab *surfature* function [12].

To investigate the regional variation of the strain response in the inflation test and structural features, the LC was divided into eight regions centered about the central retinal artery and vein (CRAV), resulting in 80 total regions across the 10 normal eyes and 128 total

regions across the 16 glaucoma eyes. The structural and strain outcomes were averaged over all the LCs and regionally. Preliminary analysis comparing normal eyes to glaucoma eyes are reported using linear regression and unpaired t-tests.

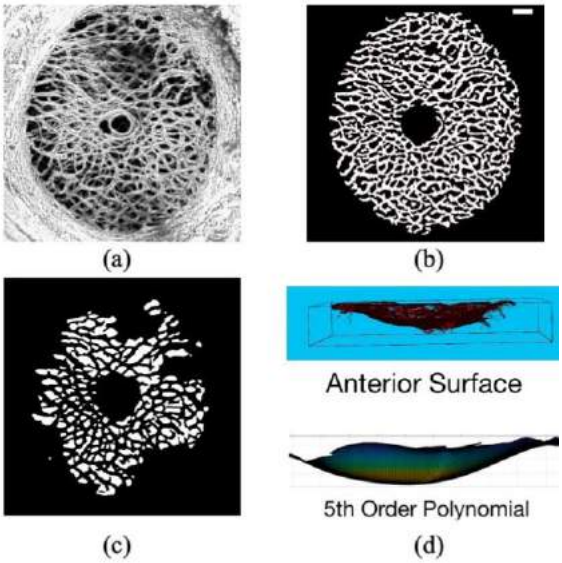

Figure 1: Morphological analysis of the SHG imaged volume of a human LC showing: (a) the maximum projection of the SHG volume, (b) a binary mask of the LC collagen network (scale bar = 200 µm) (c) pores in one slice of the SHG volume, (d) anterior-most points of the SHG volume, and a 5th order polynomial surface fit.

RESULTS

Preliminary results showed the specimen averaged mean curvature (p=0.023) and Gaussian curvature (p=0.015) were significantly greater in the 16 diagnosed glaucoma LCs compared to 10 age-matched normal eyes (Fig 2a). The beam tortuosity was significantly greater in diagnosed glaucoma eyes than age-matched normal eyes (p=0.002) (Fig 2b), while the averaged pore size (p=0.016) and beam aspect ratio (length/width) (p=0.04) were significantly smaller in 16 glaucoma eyes than 10 normal eyes (Fig 2c & d).

Comparisons of the regionally averaged outcomes (n=80 for normal and n=128 for glaucoma eyes) showed that the mean curvature (p<0.001), gaussian curvature (p<0.001), maximum curvature (p=0.004), and tortuosity (p<0.001) were significantly greater in glaucoma eyes than normal eyes, which were consistent with the analysis for the specimen-averaged outcomes. The beam length was significantly shorter (p=0.006), and the beam width was significantly wider (p=0.013) in glaucoma eyes than normal eyes, which were consistent with the finding of a smaller specimen-averaged beam aspect ratio in glaucoma eyes.

Linear regression analysis for the regionally averaged strains in glaucoma eyes showed that the regionally averaged principal strain increased with an increase in principal curvature (n=120, p=0.04). Additionally, principal strain increased with increasing pore area fraction (n=120, p=0.001). The regionally averaged shear strain increased with an increase in pore area fraction for glaucoma eyes (n=120, p≤0.001) and normal eyes (n=74, p=0.03). However, glaucoma eye shear strain increased at a higher rate than normal eye shear strain.

DISCUSSION

The results described glaucoma eye LC microstructure as having

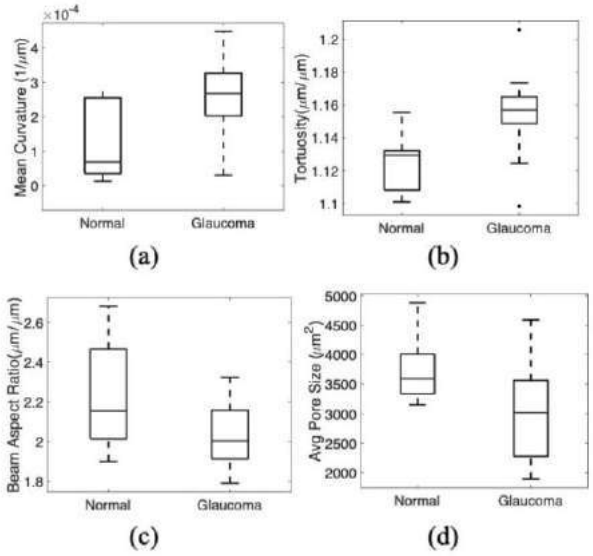

Figure 2: Comparing the specimen averaged (a) mean curvature, (b) tortuosity, (c) beam aspect ratio, and (d) average pore size of the LC of normal (n=10) and glaucoma eyes (n=16) using unpaired t-tests. The mean curvature and tortuosity were higher in glaucoma eyes than normal eyes (p≤0.04), while beam aspect ratio and average pore size were lower in glaucoma eyes than in normal eyes (p≤0.04).

curvier, shorter, and wider beams with smaller pores and higher LC curvature than normal eyes. Some of these features, such as the smaller average pore size and beam aspect ratio in glaucoma eyes may contribute to a stiffer pressure-induced strain response of the LC found in early glaucoma eyes. In contrast, the greater curvature and beam tortuosity should produce a more compliant strain response. Results will be verified using generalized estimating equation models and linear mixed models.

The work demonstrated the need for computational modeling to estimate the effects of the curvature and LC network structure on the strain response.

ACKNOWLEDGEMENTS

Supported by National Institutes of Health Grants EY01765 and EY02120, National Science Foundation CMMI Award 1727104, Brightfocus Foundation G2015132, Public Health Service Research Grants EY021500 and EY001765, Microscopy and Imaging Core Module, Wilmer Core Grant for Vision Research and the Croucher Foundation.

REFERENCES

[1] Albon, J et al., Br J Ophthalmol. 79:368–375, 1995
[2] Burgoyne, CF et al., J neuroophthalmol, 35:S8–S21, 2015.
[3] Quigley, H.A, et al., Ophthalmology. 86:1803–1827, 1979
[4] Quigley, H.A. et al., J. Ophthalmol. 107 453-464, 1989
[5] Nouri-Mahdavi, K et al., Ophthalmol. 111 1627–1635, 2004
[6] Quigley, H.A. et al., J. Glaucoma, 8(6):347–52, 1999.
[7] Rada, JA, et al., Exp Eye Res. 82: 185–200, 2006
[8] Wang, B, et al., Invest Ophthalmol. Vis Sci. 54:8270–827, 2013
[9] Ling, YTT et al., Invest. Ophthalmol.Vis.Sci.60(7):2406-2422, 2019
[10] Midgett, DE. et al., Invest. Ophthalmol. Vis. Sci.;61(4):41, 2020
[11] Midgett, DE. et al., Acta Biomater. 53:123–139, 2017
[12] Claxton, D, Surface Curvature MATLAB File Exchange, 2006

ASSESSMENT OF SEX DIFFERENCES IN VENTRICULAR-VASCULAR COUPLING OF LEFT VENTRICULAR AND AORTIC FLOW DERIVED FROM 4D FLOW MRI IN HEALTHY, YOUNG ADULTS

Cody J. Johnson (1), Ryan J. Pewowaruk (2), David Rutkowski (1), Amanda Wolfinger (1), and Alejandro Roldán-Alzate (1,2,3)

(1) Radiology
University of Wisconsin-Madison
Madison, WI, USA

(2) Biomedical Engineering
University of Wisconsin-Madison
Madison, WI, USA

(3) Mechanical Engineering
University of Wisconsin-Madison
Madison, WI, USA

INTRODUCTION

Males and females have been found to respond differently to cardiovascular disease (CVD)[1]. Prior studies[2-3] have investigated cardiovascular sex differences in healthy subjects to better understand sex differences in CVD. 4D Flow MRI is an increasingly used tool to study cardiac function by non-invasively measuring time-resolved velocity fields in the heart and large vessels[4], and previous studies using 4D Flow MRI have shown kinetic energy (KE) and vortexes to be altered in a variety of CVDs[5-6].

The 4D Flow MRI literature has neglected that cardiovascular function is a combination of both the heart and vasculature's status. The first conceptual framework of the cardiac and vascular interactions was formulated as ventricular vascular coupling (VVC)[7]. The purpose of this study was to apply the concept of VVC to define a novel metric 4D Flow MRI VVC based on the hypothesis that elevated kinetic energy in the left ventricle (LV) is not necessarily inefficient if LV KE is successfully transferred to aortic KE.

METHODS

In this IRB-approved and HIPPA-compliant study, 20 subjects with no history of heart disease (10 male and 10 female) were recruited. MRI was performed on a 3.0T imaging system using bSSFP sequence and the 4D Flow MRI sequence PC-VIPR[8]. Ventricular volumes were segmented and quantified calculated from bSSFP images, and the LV and aorta were segmented from time-averaged 4D Flow MRI, using the Mimics (Materialise, Leuven, Belgium).

Kinetic energy at peak systole and peak diastole for the LV and peak systole for aorta, along with vorticity (ω), and viscous energy loss (EL) for both the LV and aorta were calculated from equations 1, 2, & 3,

$$KE(t) = \int_V \frac{\rho}{2} u_i(t)^2 dV \quad (1)$$

$$\omega = \frac{1}{V\,T_{HB}} \int_{T_{HB}} \int_V \boldsymbol{\nabla} \times u_i dV\, dt \quad (2)$$

$$EL = \int_{T_{HB}} \int_V \mu \mathbf{S_{ij}^2} dV\, dt \quad (3)$$

where ρ is density (1060 kg/m3), ui is the velocity vector, V is the segmented LV or aortic volume, ∇× is the curl operator, THB is the heartbeat duration, and Sij is the strain rate tensor. The results were normalized by stroke volume and normalized by mask volume, in dimensionless form for the LV and aorta, respectively. VVC for both KE and vorticity was calculated by calculating the LV-to-aorta value ratio. Aorta wall shear stress (WSS) was calculated from triangulated surface meshes by taking the cross product of the velocity vector and the surface normal vector and then averaged over the aorta surface, as shown in equation 4.

$$\tau_w = \frac{1}{A} \int_A \mu \frac{\partial u_i}{\partial n_i} dA \quad (4)$$

where μ is viscosity (4 centipoise), and ni is the surface normal vector. WSS was reported as a raw measurement and in dimensionless form. The Male and female groups were compared using the non-parametric Mann-Whitney U test. Figure 1 displays the velocity across the LV and aorta, and the WSS of the aorta.

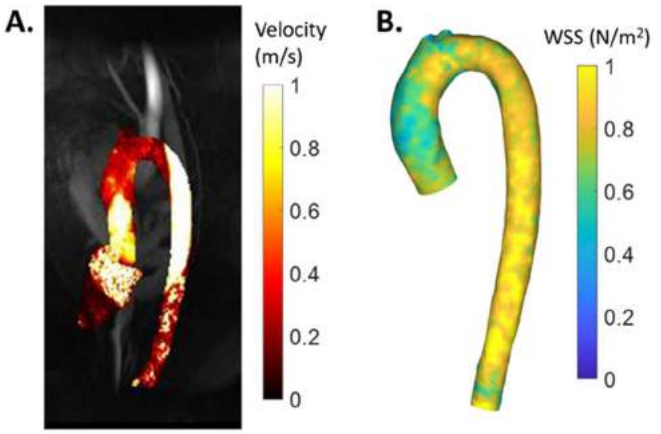

Figure1: A. LV and aorta velocity overlaid on the complex difference angiogram, B. contours of aorta wall shear stress.

RESULTS

Systolic LV KE normalized by stroke volume was significantly larger in male participants (p=0.04), and diastolic LV KE normalized by stroke volume trended towards being greater in male participants (p=0.07). When LV KE was normalized by EDV, it was similar for both groups. Average LV vorticity when normalized SV and EDV was significantly larger in females (p=0.02 and p=0.04). LV EL trended towards being greater in female participants when normalized by EDV (p=0.13). Dimensionless LV flow parameters were similar between male and female participants (systolic p=0.81, diastolic p=0.42). For aortic (Ao) flow, when normalized by either SV or Ao volume, Ao KE, EL, and WSS were all similar between both groups, while vorticity trended towards being smaller in males (p=0.08 & p=0.12 respectively).

Differences in KE VVC and vorticity VVC were not found between male and female participants. KE and vorticity were consistently greater in the aorta giving KE VVC values less than 0.25 and vorticity VVC values less than 1.0 (Figure2).

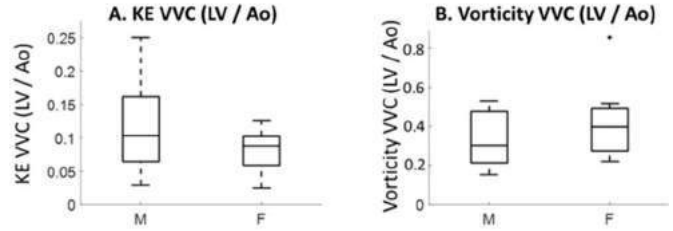

Figure2: A. Kinetic energy ventricular vascular coupling (VVC), B. Vorticity ventricular vascular coupling.

DISCUSSION

By applying the concept of VVC to 4D Flow MRI, it was found that males have greater kinetic energy and females have greater vorticity in the left ventricle; aortic flow was similar between the two groups. No differences in VVC were found between male and female participants suggesting that both flow patterns equally transfer transported flow variables from LV flow to aortic flow. This dimensional analysis suggests that previously identified sex differences in LV flow[9] were largely due to men having greater cardiac output and ventricular volumes than women.

In our results, dimensional analysis accounted for differences in cardiac output and ventricular volume explaining the differences found in LV flow showing the utility of dimensional to accounts for the anatomic differences between healthy men and women when comparing healthy and diseased populations. The advantages of presenting results in dimensionless form, as shown in this study, including that the impacts of SV, EDV, and HR are accounted for in addition to being the proper way to normalize variables from a fluid dynamics perspective.

Our concept of 4D Flow MRI-based VVC is not attempting to non-invasively calculate the traditional VVC like other approaches based on ventricular volumes[10]. Instead, we applied a similar conceptual framework to develop a novel metric of the coupling of aorta flow and LV flow. The analysis methods and results of this study may be of further use in understanding ventricular vascular coupling of transported flow variables in healthy sex differences, healthy aging, and various CV conditions.

ACKNOWLEDGEMENTS

We acknowledge GE Healthcare, which provides research support to the University of Wisconsin.

REFERENCES

[1] Aggarwal, N.R., Patel, H.N., Mehta, L.S., Sanghani, R.M., Lundberg, G.P., Lewis, S.J., Mendelson, M.A., Wood, M.J., Volgman, A.S., Mieres, J.H., 2018. Sex Differences in Ischemic Heart Disease: Advances, Obstacles, and Next Steps. Circ. Cardiovasc. Qual. Outcomes 11.

[2] Andre, F., Steen, H., Matheis, P., Westkott, M., Breuninger, K., Sander, Y., Kammerer, R., Galuschky, C., Giannitsis, E., Korosoglou, G., Katus, H.A., Buss, S.J., 2015. Age- and gender-related normal left ventricular deformation assessed by cardiovascular magnetic resonance feature tracking. J. Cardiovasc. Magn. Reson. 17.

[3] Kolar, F., Ostadal, B., 2013. Sex differences in cardiovascular function. Acta Physiol. 207, 584–587.

[4] Francois, C.J., Srinivasan, S., Landgraf, B.R., Niespodzany, E., Wieben, O., Frydrychowicz, A., 2011. Analysis of right heart flow patterns in repaired Tetralogy of Fallot with 4D flow-sensitive MRI. J. Cardiovasc. Magn. Reson. 13, 1–2.

[5] N. Al-Wakeel, J. F. Fernandes, A. Amiri, H. Siniawski, L. Goubergrits, F. Berger, and T. Kuehne, "Hemodynamic and Energetic Aspects of the Left Ventricle in Patients With Mitral Regurgitation Before and After Mitral Valve Surgery."

[6] Q. J. Han, W. R. T. Witschey, C. M. Fang-Yen, J. S. Arkles, A. J. Barker, P. R. Forfia, and Y. Han, "Altered Right Ventricular Kinetic Energy Work Density and Viscous Energy Dissipation in Patients with Pulmonary Arterial Hypertension: A Pilot Study Using 4D Flow MRI," PLoS One, vol. 10, no. 9, p. e0138365, Sep. 2015.

[7] Sagawa, K., 1981. The end-systolic pressure-volume relation of the ventricle: Definition, modifications and clinical use. Circulation.

[8] Johnson, K.M., Lum, D.P., Turski, P.A., Block, W.F., Mistretta, C.A., Wieben, O., 2008. Improved 3D phase contrast MRI with off-resonance corrected dual echo VIPR. Magn. Reson. Med. 60, 1329–1336.

[9] Rutkowski, D.R., Barton, G.P., François, C.J., Aggarwal, N., Roldán-Alzate, A., 2020. Sex Differences in Cardiac Flow Dynamics of Healthy Volunteers. Radiol. Cardiothorac. Imaging 2, e190058.

[10] Sanz, J., García-Alvarez, A., Fernández-Friera, L., Nair, A., Mirelis, J.G., Sawit, S.T., Pinney, S., Fuster, V., 2012. Right ventriculo-arterial coupling in pulmonary hypertension: A magnetic resonance study. Heart 98, 238–243.

SUSTAINED IL-10 DELIVERY ENHANCES RECOVERY FROM VOLUMETRIC MUSCLE LOSS INJURY THROUGH IMMUNOREGULATORY FACTORS

T. Huynh (1), C. Cassandra (1), Z. Blackwell (1), D. Zaharoff (2), J. Wolchok (1)

(1) Biomedical Engineering
University of Arkansas
Fayetteville, AR, USA

(2) Biomedical Engineering
University of North Carolina
Chapel Hill, NC, USA

INTRODUCTION

Volumetric muscle loss (VML) overwhelms skeletal muscle's regenerative machinery and dysregulates skeletal muscle regeneration. Tissue healing following VML is characterized by a prolonged pro-inflammatory response that is thought to contribute to the substantial fibrosis that occurs at the site of injury [1]. Pre-clinical research suggests that autologous minced muscle (MM) is a promising VML treatment strategy that has been shown to promote functional recovery, but the results do not yet warrant progression to the clinic [2]. What we believe has been overlooked is the importance of reestablishing a pro-myogenic immune environment as part of the regenerative repair strategy. Evidence from our preliminary efforts as well as published evidence from others suggest that VML injury decreases endogenous IL-10 which is a critical cytokine produced by immune cells driving tissue repair and regeneration as well as promoting the transition from the pro-inflammatory / proliferative to the anti-inflammatory / regenerative stage of muscle healing [3, 4]. The objective of this study was to determine if treatment using combined minced muscle and delayed sustained IL-10 injection (immunotherapy) can improve functional muscle recovery following VML injury.

METHODS

Sprague Dawley rats were subjected to ablation of the middle third of the left tibialis anterior followed by repair with autologous minced muscle. To create the VML defect, an 8mm biopsy punch was inserted to a depth of 3mm to create a circular defect in the tibialis anterior muscle (TA). The resulting muscle plug was removed and weighed (defect mass =20% of total TA mass). The MM was prepared by hand-mincing the muscle plug with scalpel and scissors. All of the collected MM was implanted back into the defect site. The contralateral limb remained untreated to serve as an uninjured control. Animals were assigned to receive either IL-10 (2000 ng/ml) or PBS injection (IM at site of repair) beginning 7 days after injury + repair and continuing until day 14 (100ul every other day = 4 injections total) (**Fig 1a-b**). At 14 and 56 days post injury + repair (DPI), muscle contractile torque (N mm/ kg body weight) was measured and TA muscles (treated and contralateral) were collected (n=8/group/ (timepoint). TA tissues samples analyzed using RNA-Seq, multiplexed ELISA, and semi-quantitative histology with a focus on early cellular and genetic responses at 14 DPI and longer term structural muscle recovery at 56 DPI (**Fig 1a**).

RESULTS

At 14 days DPI, mean muscle torque values remained significantly below uninjured values for both PBS controls and IL-10 delivery groups (35%). However, at 56 days DPI, IL-10 delivery torque values had recovered to 68% of uninjured, yet PBS injection controls showed little recovery (**Fig 1c**). The statistically significant increase in contractile torque with IL-10 delivery was accompanied by a significant increase (22% compared to PBS) in normalized TA mass (**Fig 1d**). Whole transcriptome analysis of tissues collected at 14 days revealed activation of several key wound healing signaling pathways in response to IL-10 delivery, most notably IL-10 and muscle hypertrophy signaling (**Fig 2a**). In additional to pathway activation, IL-10 delivery resulted in pro-regenerative changes to several critical genes related to immune cell dynamics, matrix remodeling, and inflammation, but surprisingly little effect on genes associated with satellite cell dynamics / myogenesis were observed (**Fig 2b**).

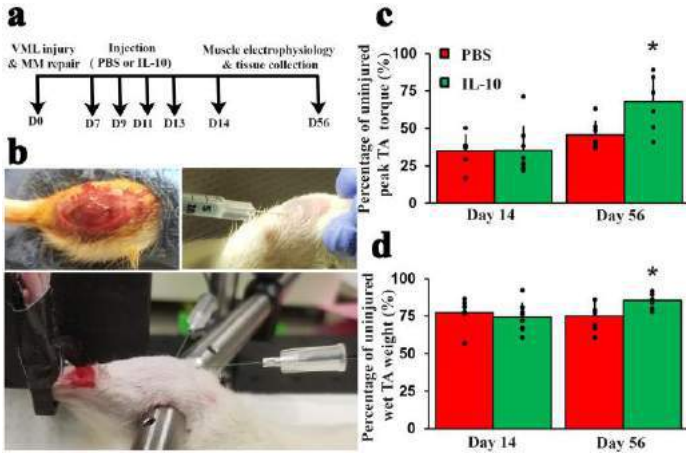

Figure 1. (a) VML injury, repair, and IL-10 delivery experimental timeline. (b) VML injuries (TA muscle) were created and repaired using minced muscle implants. Starting seven days following repair, IL-10 (or PBS control) was administered every other day at the repair site (injection) for a duration of one week. (c) The percentage of normalized peak contractile torque (%) and (d) of muscle wet weight (%) comparing to uninjured internal control were assessed in both IL-10 treated and PBS controls at 14 and 56 DPI. Group means + SD are presented; n=8/group. * denotes statistically significant ($p<0.05$) differences between groups.

Overall, the histological findings were consistent with the RNA-Seq data and detected little effect of IL-10 delivery on myogenesis, but revealed a marked increase in the presence of T-cells and improvements to repair site muscle structure in response to sustained IL-10 delivery. At 14 days DPI VML repair site immunoreactivity to

embryonic myosin heavy chain (eMHC is a protein present in de novo myofibers) (**Fig 3a and e**) was similar in both IL-10 treated and PBS controls, suggesting a similar myogenic response for both groups. However, CD3e (a pan-T cell marker) immunoreactivity (**Fig 3b and f**) was markedly increased within IL-10 treated repair sties (128% compared to PBS) suggesting an IL-10 mediated increase in T cell infiltration during the early of muscle healing.

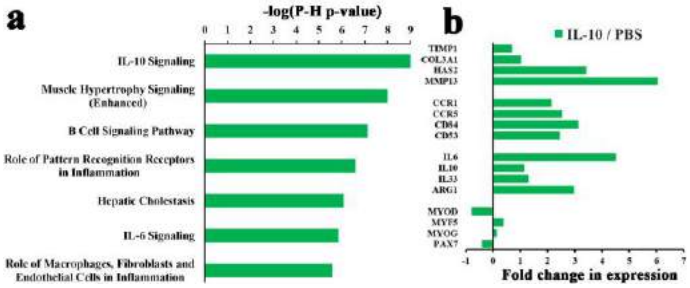

Figure 2: IL-10 delivery repair site RNA-Seq data showing (a) top enriched pathways associated with IL-10 delivery and (b) log fold expression changes for key matrix remodeling, immune cell marker, immune signaling molecules, and myogenesis genes (normalized to PBS controls)

At 56 days DPI some notable structural changes at the site of VML repair were observed. Specifically, while IL-10 did not improve/decrease repair site muscle tissue fibrosis (Col I+ tissue area), both IL-10 treated and PBS controls were marked by extensive Col I immuno-reactivity at the site of repair (**Fig 3c and g),** the sustained delivery of Il-10 did nearly double the size (97%) of repair site muscle fibers measured at the site of repair (**Fig 3d and h**). A finding that is consistent with increase in contractile force that was observed with IL-10 delivery.

Multiplexed analysis of protein concentration at the VML repair site revealed significant increases to key wound healing cytokines in response to IL-10 delivery. When compared to PBS controls, the sustained delivery of IL-10 increased tissue levels of the anti-inflammatory cytokine IL-4 (+207%), the myokine IL-6 (+52%), and the pro-angiogenic growth factor VEGF (+34%). All increases were statistically significant.

DISCUSSION

These *in-vivo* findings suggest that properly timed and sustained IL-10 delivery can have a positive effect on skeletal muscle recovery following VML injury, improving both muscle function (torque) and structure (fiber size). Previous studies investigating the effect of exogenous IL-10 in muscle showed that early delivery (during the first few days following injury) has a negative effect on muscle regeneration [5]. However, a more holistic appreciation of endogenous IL-10 production would suggest that early post injury delivery was unlikely to produce much benefit. It is well accepted that the increase in endogenous IL-10 production during tissue healing is delayed and timed to trigger the transition from the early proliferative to the later differentiation and growth stage, and as such elevated IL-10 levels may be detrimental when delivered too early. Our data is the first to confirm that the timing of IL-10 delivery is critical and specifically indicates that a delayed IL-10 delivery window timed to the biology of muscle healing is necessary to enhance muscle recovery.

Lastly, the early transcriptome, histology, and cytokine data suggests that IL-10 may improve muscle recovery from VML injury through its anti-inflammatory effect on both immune system cell dynamics, most notably T cells, rather than through direct enhancement of early satellite cell dynamics. The important role of T-cells, and more specifically T regulatory cells during the later stages of muscle healing, is known. However, this data appears to be the first to find that the T-cell population at the VML repair site can be enhanced to improve muscle recovery from VML injury. More broadly these finding suggest that immuno-regulation of the muscle wound healing environment can be employed to enhance muscle recovery.

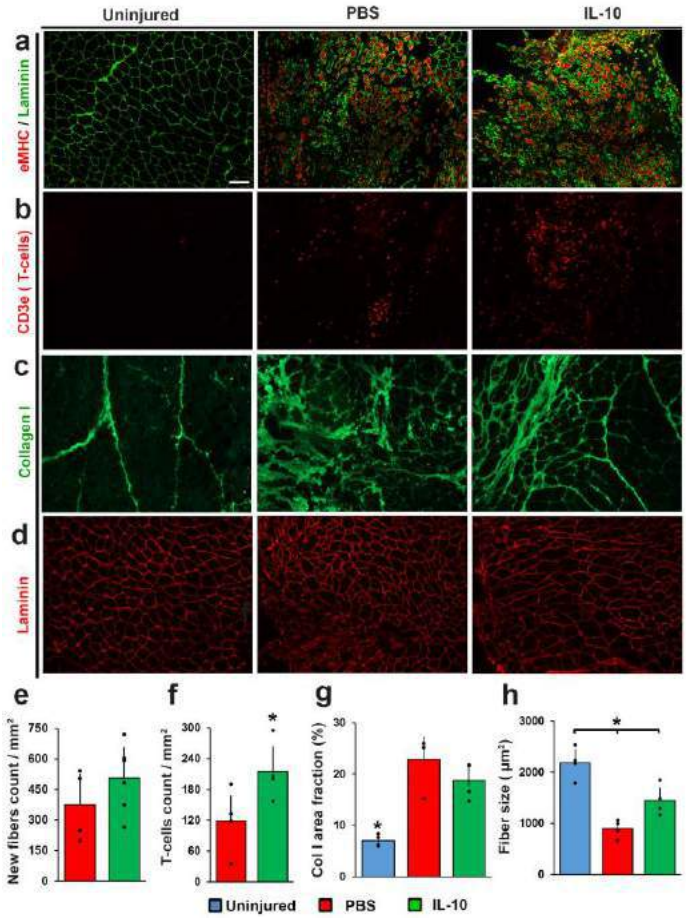

Figure 3: TA muscle cross-sections were stained using immuno-markers targeted against (a) eMHC (red) co-stain with laminin (green) (b) and CD3e (red) at 14 days DPI, as well as (c) collagen I (green), (d) laminin (red) at 56 days DPI. Scale bar = 100µm. Sections were imaged and analyzed to quantify (e) new fiber formation, (f) T-cell infiltration (g) fibrosis / non-contractile tissue area, and (h) muscle fiber cross-sectional area. Group means + SD are presented; n=4-6/group. * denotes statistically significant ($p<0.05$) differences between groups.

ACKNOWLEDGEMENTS

This research was supported by the National Institute of Arthritis And Musculoskeletal And Skin Diseases of the National Institutes of Health under Award Number R15AR064481.

REFERENCES

1. Aguilar, C.A., et al., Cell Death Discov, 2018. **4**: 33.
2. Greising, S.M., et al., Tissue Eng Part B Rev, 2019. **25**(6): 510-525.
3. Hurtgen, B.J., et al., Physiol Rep, 2017. **5**(14).
4. Wynn, T.A. and K.M.. Immunity, 2016. **44**(3): 450-462.
5. Perdiguero, E., et al.,. J Cell Biol, 2011. **195**(2): 307-22.

ENGINEERING ANALYSIS OF AORTIC WALL STRESS AND ROOT DILATION IN THE V-SHAPE SURGERY FOR ASCENDING AORTIC ANEURYSMS

H. Dong (1), M. Liu (1), T. Qin (1), L. Liang (2), B. Ziganshin (3), H. Ellauzi (3), M. Zafar (3), S. Jang (3), J. Elefteriades (3), W. Sun (1)

(1) Tissue Mechanics Laboratory, The Wallace H. Coulter Department of Biomedical Engineering, Georgia Institute of Technology and Emory University, Atlanta, GA, USA

(2) Department of Computer Science, University of Miami, Coral Gables, FL, USA

(3) Aortic Institute at Yale-New Haven Hospital, Yale University School of Medicine, New Haven, CT, USA

INTRODUCTION

Aortic aneurysm could claim lives without any premonitory symptoms or signs [1]. Ascending aortic aneurysms (AsAA) often include the dilatation of sinotubular junction (STJ) and extend into the root part of the aortas, which could lead to aortic insufficiency [2]. The pathologies of the root, valve and ascending aorta can be eradicated by traditional surgeries such as full aortic root replacement. However, this kind of surgery may represent excessive surgical intervention for infirm or elderly patients. The novel surgery [3] of the V-shape resection of the noncoronary sinus has been shown to be a simpler procedure, comparing with the traditional surgeries. The V-shape surgery could reduce the diameter and cross-sectional area of the aortic root aneurysm [3]. However, its detailed effect on the stress field and rupture risk of the aorta has not been fully investigated. Moreover, it is also essential to estimate the growth and dilation of the root post-surgery for evaluation of the outcomes of the surgery. In this study, we performed patient-specific finite element (FE) simulation of the aorta pre- and post-surgery of patients who underwent the V-shape surgery. We obtained the aortic wall stress and investigated the influence of the V-shape surgery on the stress field and rupture risk of the aortic root, ascending aortic aneurysm and aortic arch. Moreover, we also studied the growth and dilation of the aortic root post-surgery by estimating the temporal evolution of the enclosed volume of the aortic root.

METHODS

Patient Data: Deidentified cardiac CT images were obtained for a total of 14 patients (P1-P14) who underwent the surgery of V-shape noncoronary sinus resection at Yale-New Haven Hospital. For 10 patients (P1-P10) among the total 14 patients, the CT images of the thoracic and abdominal aorta pre- and post-surgery were obtained. We used these 10 patients to investigate the effect of the V-shape surgery on the stress of the aorta. For 6 patients (P1, P8, and P11-P14) among the total 14 patients, the CT images of the aortic root at two follow-up time points post-surgery (Post1 and Post2) were obtained. We used these 6 patients to study the growth and dilation of the root post-surgery.

Finite Element Analysis: For each patient of P1-P10, the three dimensional (3D) surface geometry of the aorta was reconstructed from the CT images using 3D Slicer (www.slicer.org). The aortic root, ascending aorta, aortic arch together with the three branches around it, and the descending aorta were obtained. The surface geometry was exported from 3D Slicer and imported into Altair HyperMesh 2017 (Altair Engineering) to generate the finite element model for the aorta. We performed finite element (FE) simulation of the aorta by the Abaqus/Standard 2019 (SIMULIA, Providence, RI) based on the static determinacy approach [4]. The analysis of mesh size independence was performed. The stress field of the aorta pre- and post-surgery was extracted and analyzed.

Dilation of the Aortic Root Post-Surgery: For the 6 patients of P1, P8, and P11-P14, 3D geometries of the aortic root post-surgery at Post1 and Post2 were reconstructed from the CT images by the same method as that in last subsection. Figure 1 shows the 3D geometries of the inner surface of the aortic root (from STJ to aortic annulus) of a representative patient (P13), with Post1 (blue) at the time point about 4 months after the surgery and Post2 (red) at the time point about 20 months from Post1. The geometries in Fig. 1 indicate that the aortic root grew and dilated after the surgery.

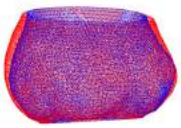

Fig 1. 3D geometries of the aortic root of a representative patient (P13) post-surgery at Post 1 (blue) and Post2 (red).

We calculated the enclosed volumes of the aortic root of Post1 and Post2 for the 6 patients to quantitatively estimate the root dilation post-surgery. We also performed finite element (FE) simulation of aortic root only of Post1 and Post2 for the 6 patients based on the static determinacy approach and obtained the stress of the aortic root.

RESULTS

Wall Stress of the Aorta Pre- and Post-Surgery: The wall stress of the aorta of the 10 patients (P1-P10) pre- and post-surgery was obtained from the FE simulation. Figure 2 shows the max-principal (MP) stress field of the aorta of a representative patient (P1) pre- and post-surgery. We extracted the MP stress field of four ring-bands of the aorta of each patient, with band-1 at the operated aortic root (from STJ to sinus), band-2 at the ascending aneurysm position with the maximum diameter pre-surgery, band-3 at the ascending aneurysm position with diameter affected little by the surgery and band-4 at the position right distal to the aortic arch. The width of the four ring bands is approximately the same for pre- and post-surgery.

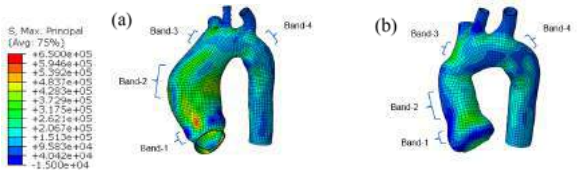

Fig 2. Max-principal stress field of the aorta of a representative patient (P1): (a) pre- and (b) post-surgery.

Figure 3 shows a statistic analysis based on the two-sample T-test of the MP stress between pre- and post-surgery for the 10 patients. The label "mean" on the horizontal axis denotes the mean value of the MP stress within one band of one single patient, while the bar chart represents the mean+standard error (SE) of the 10 patients. For example, the first bar chart in Fig. 3a represents the mean+SE of the 10 patients for mean MP stress within band-1 of each patient pre-surgery. The two "mean" should not be mixed.

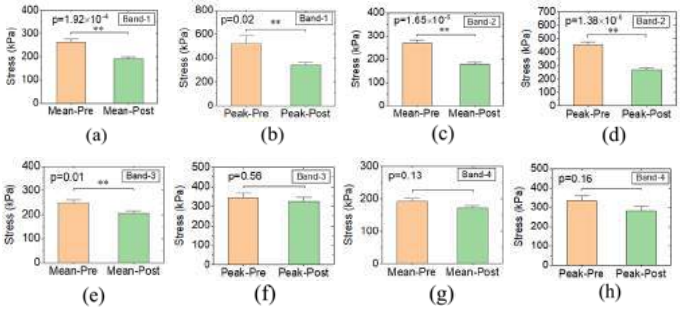

Fig 3. The mean+standard error (SE) for the 10 patients of the mean and peak MP stress of the band1-4. **: p value less than or equal to 0.02.

Dilation of the Aortic Root Post-Surgery: Table 1 presents he enclosed volume of the aortic root of Post1 and Post2 for the 6 patients (P1, P8, and P11-P14), which shows that the enclosed volume of the aortic root increased after the surgery, with a minimum increase of 6.35% for P12 and a maximum increase of 13.69% for P14. Figure 4 shows the relation between the volume change from Post1 to Post2 and the mean MP stress of the aortic root (from around STJ to aortic annulus) of Post1 and Post2.

Table 1. Enclosed volume of Post1 and Post2. Chg: volume change from Post1 to Post2; Chg (%): percentage change of the volume; ΔT: time interval of Post1 and Post2 in month (Mon).

	P1	P8	P11	P12	P13	P14
Post1/cm³	11.58	32.71	34.50	28.18	20.88	36.37
Post2/cm³	13.06	36.64	38.09	29.97	22.34	41.35
Chg/cm³	1.48	3.93	3.59	1.79	1.46	4.98
Chg (%)	12.78%	12.01%	10.41%	6.35%	6.99%	13.69%
ΔT	23 Mon	24 Mon	43 Mon	22 Mon	20 Mon	52 Mon

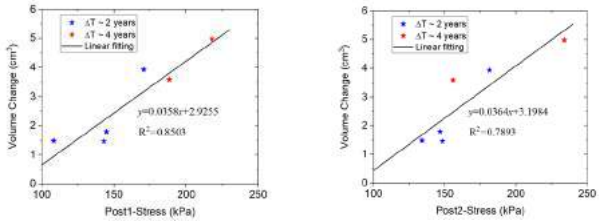

Fig 4. Relation between the mean MP stress and volume change of the aortic root of Post1 and Post2 for patients in Table 1.

DISCUSSION

The V-shape surgery significantly reduces the mean and peak wall stress of the root (Fig. 3a,b). The reason could be that it reduces the diameter of the root [3]. If the rupture strength of the wall is assumed to be unchanged post-surgery, the rupture risk will decrease with the decreasing wall stress. The major portion of the ascending aneurysm (band-2 in Fig. 2a) was replaced by an ascending aortic graft (band-2 in Fig. 2b). The diameter of the graft is much smaller than that of the ascending aneurysm pre-surgery and thus the stress of band-2 (Fig. 3c,d) also reduces significantly. Although the tough graft post-surgery has no rupture issue, the reduction of the diameter of band-2 may contribute to the stress reduction (Fig. 3e) of the adjacent band-3 (live aortic tissue).

The 6 patients in Table 1 are classified into two groups with the first group (P1, P8, P12 and P13, blue stars in Fig. 4) having about 2 years interval between Post1 and Post2, and the second group (P11 and P14, red stars in Fig. 4) having about 4 years interval between Post1 and Post2. Figure 4 indicates that the dilation of the root post-surgery may be induced by the root stress, since larger root stress results in larger volume increase within both groups. The patient-specific dilation rate could be also affected by other factors including sex, age, weight, height, hypertension, diabetes, complications, etc. In the future study, we will identify the critical factors that influence the dilation rate of the aortic root post-surgery and further stratify the patients who may or may not benefit from the V-shape surgery per long-term outcomes, with follow-up CT images for more patients and longer time period being obtained.

ACKNOWLEDGEMENTS

This study is in part supported by American Heart Association (AHA) 18TPA34230083.

REFERENCES

[1] C. Martin, W. Sun, T. Pham, J. Elefteriades, Acta Biomater. 9(12) (2013) 9392-9400.

[2] T.E. David, C.M. Feindel, G.D. Webb, J.M. Colman, S. Armstrong, M. Maganti, J. Thorac. Cardiovasc. Surg. 132(2) (2006) 347-354.

[3] J.A. Elefteriades, S. Peterss, N. Nezami, G. Gluck, W. Sun, M. Tranquilli, B.A. Ziganshin, J. Thorac. Cardiovasc. Surg. 154(1) (2017) 72-76.

[4] M. Liu, L. Liang, H. Liu, M. Zhang, C. Martin, W. Sun, Biomech Model Mechanobiol 18(2) (2019) 387-398.

CROSSLINKING OF CARTILAGE COLLAGEN VIA NONLINEAR FEMTOSECOND LASER ACTIVATION OF RIBOFLAVIN

Jiashuai Fan (1), C.V. Sise (2), Kimberly R. Kroupa (1), Clark T. Hung (2), Gerard A. Ateshian (1,2), Sinisa Vukelic (1)

(1) Mechanical Engineering
Columbia University
New York City, New York, United States of America

(2) Biomedical Engineering
Columbia University
New York City, New York, United States of America

INTRODUCTION

Osteoarthritis (OA) is a progressive, multi-tissue joint disease with degenerative changes in articular cartilage and subchondral bone [1]. It is characterized by an asymptomatic early stage and a debilitating late stage progression. At present, there are no early treatment modalities that provide conclusive relief, whereas late-stage treatment options mostly involve major surgical interventions. Although the nature of OA is complex, the degradation of extracellular matrix (ECM) of cartilage is one of the key parameters for disease progression [2,3]. In particular, crosslinks (CxLs) stabilize the collagen (COL) fibril network, and their disruption results in the loss of tensile strength and structural integrity [3,4]. Therefore, introducing CxLs to OA-afflicted cartilage offers the potential to stabilize the degrading ECM network and impede progression of OA. Similarly, induction of COL CxLs to increase the mechanical strength of structurally compromised corneas has been established as a module to treat keratoconus. Crosslinking of corneal stroma with 365 nm ultraviolet-A (UVA) lamp irradiation, while using riboflavin as photosensitizer has been widely studied and recently approved for treating keratoconus in the U.S. [5-6]. However, the same approach has not translated to cartilage, due to its significant linear absorption of 365 nm light and greater opacity compared to cornea [7].

Our previous work has demonstrated that, in both cartilage [8] and cornea [9], a femtosecond laser can be used to ionize interstitial water and induce a photochemical reaction, which results in CxL formation, and thus increased stiffness and wear resistance [8]. CxLs were induced in the absence of a photosensitizer, providing promise that the proposed treatment modality could be clinically relevant. In this study, we hypothesize that application of a photosensitizer may result in a more efficacious CxL process, which can be more readily imaged to reveal the spatial distribution of imparted CxLs and the penetration depth of the laser treatment. Further, we examine if riboflavin may be activated in cartilage using an infrared (IR) femtosecond laser as an excitation source [10], effectively relying on the second harmonic generation (SHG) effect to actuate it. The study presented here provides valuable insight into the laser treatment characteristics and, in the future, comparison between crosslinking mechanisms.

METHODS

Sample Preparation. Cartilage tissue was harvested from the knees of immature bovine calves (2-3 months old, Green Village Packing Co., New Jersey, USA). Explants (∅3 mm × 2 mm) were biopsy-punched from the femoral condyle and cut to a final thickness of 2.0±0.2 mm. Samples were stored frozen and thawed before treatment.

Crosslinking Treatment. Before laser irradiation, cartilage plugs were soaked overnight in 0.2% Riboflavin 5'-monophosphate (Sigma-Aldrich Inc., USA) with 20% Dextran (Sigma-Aldrich Inc., USA). Wavelength tunable (680-1080 nm) Ti: Sapphire laser Chameleon Ultra II (Coherent Inc., Santa Clara, USA) with out-of-cavity beam waist of 1.2 mm was used to produce 760 nm laser irradiation with 120 fs temporal pulse length at 80 MHz repetition rate. The average power of the light source was adjustable. The laser beam was focused using a ZEISS LD plan-Neofluar 40x/0.6 Corr objective with Numerical Aperture of 0.1463. The focal plane position at the surface of the superficial zone of cartilage was found by identifying a spark on the bottom of a 0.15 mm coverslip pressed against the sample. Lasing was rasterized into the specimen with a hexapod (H-840.D2A-AXIS_X, Physik Instrumente, USA), moving at 1.2 mm/s. Four groups of samples (Groups A, B, C and D) were tested. Groups A, B and C

were subjected to average laser power of 165 mW. Group A had a zigzag grid pattern in the XY-plane, with a spacing of 50 μm between parallel laser paths; the treatment was repeated for 5 layers, 50 μm apart in the Z-direction. Group B had the same treatment pattern in the XY-plane, with 11 layers along Z, 20 μm apart; Group C had a denser zigzag grid with 25um spacing in the XY-plane, and 5 layers along Z, 50 μm apart. Demonstrative Group D had the same in-plane zigzag treatment pattern as Group A, with 3 layers along Z, 50 μm apart, each having a different average laser power: 165 mW, 330 mW, and 495 mW at the 1st, 2nd and 3rd layer, respectively. For Group A, B and C, 5 samples were treated and paired with untreated control samples under similar experimental conditions but not irradiated by the laser.

Multiphoton Confocal Microscopy. Multiphoton confocal imaging is known to reveal the presence of CxLs in collagenous tissues and gels [11,12]. Imaging was performed with a Nikon Ti Eclipse inverted microscope using a Ti: Sapphire laser Chameleon Ultra II at 860 nm as the light source and a Nikon Apo LWD 25x gel immersion objective for focusing. The emission filter was set at FITC channel for autofluorescence signal collection. The XY scanning area was 516 μm by 516 μm, and Z scanning was 250 μm deep with 5 μm increments.

RESULTS

For Group A (Figure 1a1 and 1a2), the XY zigzag pattern and increments along Z are clearly distinguishable compared to the background signal. For Group B (Figure 1b1 and 1b2), the 20 μm increments along Z produce connected sheets across the 11 treatment layers. For Group C (Figure 1c1 and 1c2), the narrower 25 μm XY distance is evident. With a uniform average power of 165 mW for all Z depths, as the laser focal plane delves deeper into the superficial zone, the fluorescence signal intensity of all samples clearly decreases. The autofluorescence signal in Group D is shown in Figure 1d1 in the XZ plane and 1d2 in 3D. With 2-fold power at the 2nd plane and 3-fold power at the 3rd plane, autofluorescence signal intensity increases down to a depth of 200 μm, whereas the signal in groups A, B, C generally decreases to the background level at approximately 150 μm.

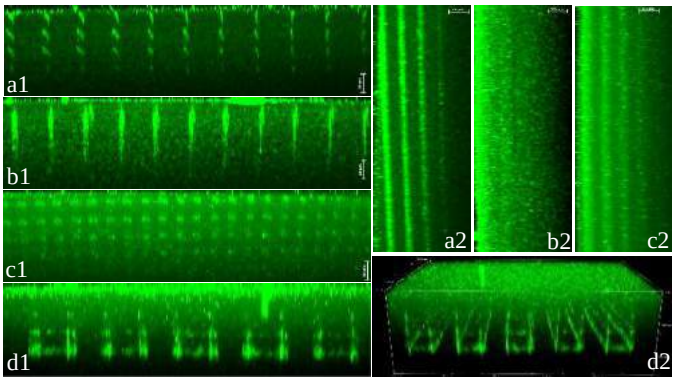

Figure 1. Autofluorescence signal of the treated superficial zone of cartilage. XZ views for Group A, B, C, D shown in a1, b1, c1, d1. YZ views for Group A, B, C shown in a2, b2, c2. Volumetric 3D view for Group D shown in d2. All scale bars are 50μm. XYZ size is 516×516×250 μm. Intensity and size are adjusted for clarity.

The size of the crosslinked regions mostly agreed with the focal volume (FV) estimated from the laser treatment path lines, approximated as a cylinder with radius $W_{xy} = 0.32\lambda/\sqrt{2NA}$, where λ =laser wavelength, and NA =objective numerical aperture [13], and height $2Z_R$, where $Z_R = 2\pi n W_{xy}^2/\lambda$ is the Rayleigh range, n =tissue refractive index [14]. We calculated W_{xy} =1.18 μm and Z_R =7.98 μm.

DISCUSSION

Tightly focused ultrafast laser pulses at 760 nm excite riboflavin via a non-linear, two-photon process [10] and enable CxLs to form in the cartilage. Compared to the single photon process using a UVA light source at 365 nm, it is assumed that the multiphoton laser-photochemical reaction only occurs within the focal volume region where the light intensity is at its highest. This feature provides spatial precision of the crosslinking treatment with a relatively low average power. However, the tissue's depth-dependent light absorption (A) still plays a role and may be governed by the Beer-Lambert Law, $A(\lambda) = \varepsilon(\lambda)c\ell$, where c is concentration, ε absorptivity, and ℓ optical path length. As light penetrates deeper into the tissue, assuming negligible changes in c and ε of attenuating species, absorption increases [15], thus decreasing the efficacy of the crosslinking process. Simultaneously, due to the non-uniform spatial distribution of the native components of the superficial zone of articular cartilage, heterogeneity of the optical refractive index causes a mixture of Rayleigh and Mie elastic scattering of light [16]. While scattering effect decreases with wavelength, absorption is the lowest at near-IR ranges in biological tissues [17]. The superficial zone also introduces optical aberrations as an extension of the focusing lens, including spherical aberration due to its inherent curvature, and chromatic aberration due to group velocity dispersion. The resulting temporal and spatial anomalies of the pulse shape are proportional to the optical path length inside the medium and cannot be neglected for femtosecond pulses [18]. Optical aberrations, together with the absorption and scattering of light, induces loss of crosslinking efficacy in deeper zones of the tissue. This loss can be corrected by raising the focal plane irradiation intensity by adjusting the average power in the deeper treatment plane, as shown here.

In this study, we investigated CxL of COL in articular cartilage. To the best of our knowledge, this was the first time that riboflavin was activated in cartilage with an ultrafast laser through a non-linear excitation process. The process is spatially resolved and allows for precise control of the induction of CxLs. The density of imparted CxLs is a function of focusing and lasing parameters. While the crosslinking mechanism presented in this study is different from the laser-based treatment in the absence of photosensitizers reported in our earlier studies [8, 9], it is likely that the conclusions related to the CxL spatial distribution and laser attenuation can be translated to it.

ACKNOWLEDGEMENTS

This study was supported by NIH grant 5 R01 AR073289-03.

REFERENCES

[1] Bijlsma, J et al., *Lancet*, 377:2115-26, 2011.
[2] Li, Y et al., *BioMed Research International*, 2013.
[3] Bastiaansen-J, YM et al., *OA Cartilage*, 16:359-366, 2008.
[4] Setton, LA et al., *OA Cartilage*, 7:2-14, 1999.
[5] Wollensak, G et al., *Am J Ophthalmol*, 135(5):620-627, 2003.
[6] Lim, L. and Hafezi, F. *Cornea*, 37(10):1218-1225, 2018.
[7] Finch, AJ et al., *Cartilage*, 10(1):82-93, 2019.
[8] Wang, C et al., *Annual Meeting of ORS*, #0563. 2017.
[9] Wang, C et al., *Nature Photonics*, 12: 416–422, 2018.
[10] Bradford, SM et al., *Biomed Opt*, 8(10): 4788-4797, 2017.
[11] Chai, D et al., *IOVS*, 52(7):4242-4238, 2011.
[12] Raub, CB et al., *Biophysical J*, 92:2212-2222, 2007.
[13] Zipfel, W et al., *Nat Biotechnol* 21, 1369-1377, 2003.
[14] Noack, J. and Vogel, A. *IEEE J Quant E*, 35(8):1156-1167, 1999.
[15] Ball, D.W., *Field guide to Spectroscopy*, *SPIE press*, 2006.
[16] Feuchtinger, A et al., *Histochem Cell Biol*, 146(6):781-806, 2016.
[17] Muller, MG et al., *Appl.Opt*, 40, 4633-4646, 2001.
[18] Bor. Z. *Optics Letters*, 14(2):119-121. 1989.

BENT BUCKLING OF ARTERIES WITH NON-CIRCULAR CROSS SECTION

Yasamin Seddighi (1), Hai-Chao Han (1)

(1) Department of Mechanical Engineering
The University of Texas at San Antonio
San Antonio, TX 78249, USA

INTRODUCTION

Mechanical stability of arteries is important for normal arterial functioning. Artery buckling may impede blood flow and result in ischemic attack to the distal organ and other pathologic changes [1]. Axial tension and lumen pressure provide mechanical stability for blood vessels which prevent curling, bending and collapse of the artery [1].

Many arteries do not have ideal uniform circular cross section, but instead having noncircular, such as oval shape or eccentric cross sections [2]. It is unclear how these noncircular cross section shapes will affect the stability of arteries.

Therefore, the objective of this study was to investigate the effect of oval shape cross section on the critical buckling pressure of the arteries.

METHODS

Arteries are modeled as cylindrical tubes with an elliptical cross section. The major lumen diameter, length and uniform thickness are 3.27, 52, and 1.86 mm, respectively [3]. A lumen aspect ratio (AR), defined as the minor to major diameter ratio, of 0.8-1.0 (with corresponding outer wall aspect ratio of 0.91-1.00) were analyzed. The arterial wall is assumed to be a homogeneous, anisotropic, incompressible material with Fung strain energy function [4] in the form of

$$\mathrm{w} = \frac{C}{2} e^{Q} \tag{1}$$

with

$$\mathrm{Q} = b_1 E_\theta^2 + b_2 E_z^2 + b_3 E_r^2 + 2 b_4 E_\theta E_z + 2 b_5 E_z E_r + 2 b_6 E_\theta E_r \tag{2}$$

Where b_1, b_2, b_3, b_4, b_5, b_6 and C are material constants obtained from experimental measurements and are provided in Table 1. E_r, E_θ and E_z are components of Green strain tensor and subscripts r, θ and z represent radial, circumferential and axial direction, respectively.

Table 1: Convex material constants of porcine carotid artery used in Fung strain energy function [5]

b_1	b_2	b_3	b_4	b_5	b_6	C(kPa)
0.679	0.751	0.228	0.0519	0.033	0.051	20.42

Commercial FEA package ABAQUS® was used to simulate bent buckling behavior of arteries. Arteries of elliptic cross sections of different aspect ratio were created and meshed using 8-node linear hybrid hexahedral element with constant pressure (C3D8H). A mesh size of 0.2 mm was used after pilot convergence study. A 1-degree initial curvature along the longitudinal axis was included in the models to facilitate vessel buckling. Arteries were first stretched axially to the length of 67.6 mm (1.3 times of initial length) to mimic the in vivo axial stretch in the arteries [5]. Then, a uniform static pressure (up to 50 kPa) was applied to the vessel lumen. Both ends of the artery were restrained from rotations or axial move but allowed for radial displacement (i.e., had only one degree of freedom).

The displacement of the four points located on the minor and major diameters of the outer wall in the middle section of the artery were monitored to determine the changes in aspect ratio and central axis. The onset of buckling is the time when the central axis starts deflection.

RESULTS

Change of lumen shape under axial stretch and lumen pressure

Changes in the aspect ratio of the middle cross section of the arteries were observed due to the applied axial stretch (time=0-1s) and pressurized inflation (time=1-2s) (Fig.1). The cross-sectional shape of

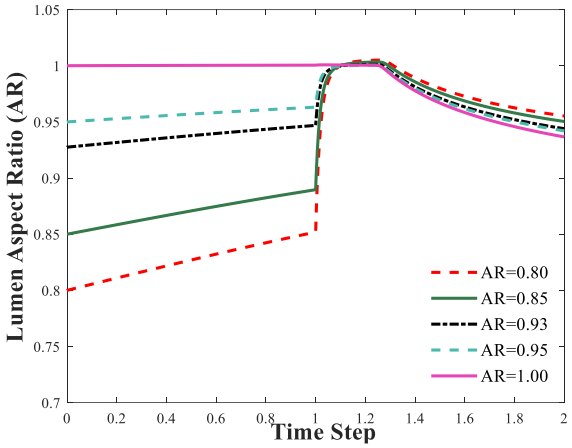

Figure 1. Change of lumen aspect ratio (AR) of the middle cross section of the vessel under axial stretch (time steps 0 - 1) and lumen pressure (time steps 1-2). The vessel buckles in the direction of the minor diameter. Buckling occurred at time step around 1.2 where the aspect ratio starts to decrease.

the elliptic arteries tend to deform into circular shape under increasing lumen pressure and then become elliptic after buckling.

On the other hand, arteries of initially circular lumen but with eccentricity tends to become elliptic at low pressure but then become circular at high pressures.

Effect of aspect ratio on the critical pressure

All arteries buckled when the lumen pressure reached a critical pressure. The maximum deflections (at the middle point of the axial length) for arteries with different lumen aspect ratios are plotted with lumen pressure as shown in Fig.2.

The initial lumen aspect ratio has a small effect on mechanical stability of the arteries. For arteries with lumen aspect ratio in the range of 0.8-1.0, the critical pressure, which is defined by the pressure at which the maximum deflection of the central axis at the middle of the vessel length reaches 0.1mm, decreases with decreasing aspect ratio (Fig.3). The mean critical pressure is 9.32 ± 0.16 kPa for these arteries with lumen aspect ratio in the range of 0.8-1.0.

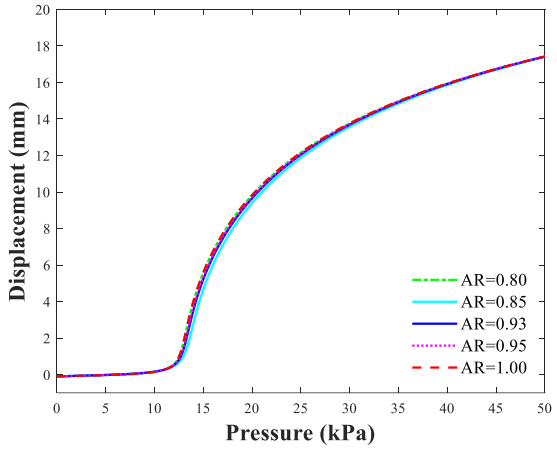

Figure 2. Deflection at the middle section of the vessel plotted as function of lumen pressure.

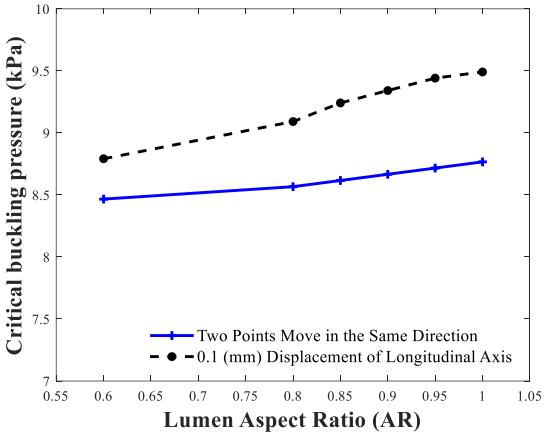

Figure 3. Critical buckling pressure of the artery plotted with the initial lumen aspect ratio

DISCUSSION

Critical pressure of arteries with oval shape cross section has been investigated and compared with the results of the artery with circular cross section which was validated by experimental results of [5].

Our results demonstrated that arteries with elliptical cross section buckle in the direction of minor axis. While increasing lumen pressure initially deforms the elliptic vessel towards circular shape, the vessel lumen become elliptical post buckling. The aspect ratio of the initial lumen has little effect on the critical pressure of the vessels. A possible reason is that all these vessels of different initial AR become very close to circular at high pressure right before buckling occurs.

There are a few limitations in this study. First, static pressure was applied to the lumen and pulsatile pressure was not considered. Secondly, a homogenous material was used for the three-layered arterial wall. Further studies are needed to fully consider the combination of eccentricity and ellipticity of the vessels. Despite of these limitations, current study increases our understanding of the stability of arteries with elliptical cross section.

REFERENCES

[1] Han HC, J Vasc Res, 49(3): 185-197 2012
[2] Datir P et al., *Int J Appl Mech*, 3(2): 385-406, 2011.
[3] Lee AY, et al., *Am. J Physiol. Heart. Circ. Physiol*, 302(4): H873-H884, 2012.
[4] Chuong CJ, et al., *J Biomech*, 108(2): 189-192, 1986.
[5] Lee AY, et al., *J Biomech*, 47(16): 3868-3875, 2014.

MODELING WOUND HEALING MECHANOBIOLOGY: MULTI-SCALE COUPLING OF A CELL ADHESION MODEL TO A FINITE ELEMENT MODEL OF TISSUE

Y. Guo (1), J. Jimenez (2), S. Calve (2,3), A. Buganza Tepole (1,2)

(1) School of Mechanical Engineering
Purdue University
West Lafayette, Indiana, USA

(2) Weldon School of Biomedical Engineering
Purdue University
West Lafayette, Indiana, USA

(3) Department of Mechanical Engineering
University of Colorado Boulder
Boulder, Colorado, USA

INTRODUCTION

Wound healing is a key process that restores mechanical function after injury [1]. Though there is a general understanding of this process that has resulted in existing theoretical and computational models [2], current mathematical descriptions of wound healing ignore the complex mechanical response of the extracellular matrix (ECM) and its coupling with cell mechanobiology. Here, we explicitly model the adhesion of cells to the underlying ECM with a modified version of the well-established model by Bell [3] in order to account for nonlinear mechanics of the ECM. This updated model of cell-ECM interaction is then coupled through an integration point subroutine to a tissue-scale finite element model. Thus, our work addresses existing gaps in wound healing models by explicitly coupling microscale mechanobiology to the macroscale mechanical behavior of tissues.

In previous work, we proposed a computational model of wound healing at the tissue level coupled with a systems-based approach for mechanobiology [2]. However, this model used a phenomenological equation to relate cell density to active tissue contraction. Here, we include Bell's adhesion model [3] to describe the interaction between fibroblasts and the ECM. A key modification of [3] we propose here is to consider nonlinear ECM mechanics. This extension of Bell's model naturally captures cell mechanosensing; as the ECM deforms, changes in the tangent stiffness lead to changes in cell adhesion and traction.

To complete the representation of cell-ECM coupling, an accurate strain energy for the passive material response of the ECM is needed. In previous work, we used the model by Gasser et al. (GHO) [4]; however, after further consideration of the literature [5,6] and our own data, we propose here a new constitutive equation that better describes the mechanical response of collagen and fibrin fibers. We analyze existing fibrin and collagen single fiber data, as well that from fibrin and collagen gels, to describe mechanics at the cell and tissue scales.

METHODS

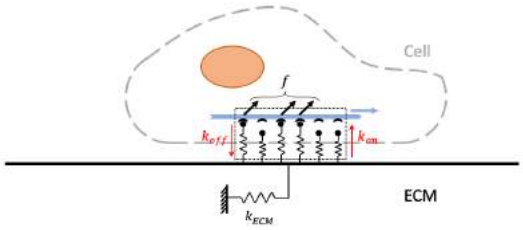

Figure 1: Adhesion model schematic.

Adhesion model. The adhesion process of fibroblasts to the ECM is illustrated in Figure 1. The mathematical form can be written by

$$\dot{\phi}_b = k_{on}(1-\phi_b) - k_{off}\phi_b \quad (1)$$

where ϕ_b denotes the density of integrin-ligand bonds, and k_{on} and k_{off} characterize the association and dissociation rate of integrin - ligand pairs. The association process is spontaneous, so we choose this intrinsic parameter, k_{on}, as a constant. The dissociation rate, k_{off}, is proportional to the energy stored in the adhesion according to [3],

$$k_{off} = \hat{k}_{off}\, e^{\frac{\Delta E}{k_B T}} \quad (2)$$

where $\hat{k}_{off}$ is a constant, k_B is the Boltzmann constant, T is the temperature in Kelvin, and ΔE is the stored energy of adhesion. For a purely elastic adhesion model, $\Delta E = f^2/(2k_{ECM})$, where f denotes the intra-cellular contractile force and k_{ECM} is the stiffness of the ECM. In [3] and most derived work, k_{ECM} is a constant. By considering the nonlinear mechanics of the ECM, the energy in the adhesion becomes a

function of the stretch in the ECM fibers,

$$\Delta E = \frac{f^2}{2k_{ECM}(\lambda)}. \quad (3)$$

From Eq. (1), we solve the ODE and obtain ϕ_b at the equilibrium state to get the relationship between the equilibrium density of bonds and the stretch of the ECM. We also adopt a Monte-Carlo simulation to verify the results.

Mechanical equilibrium at the tissue level. At every point of the tissue domain, we require the vanishing of the stress divergence

$$\nabla_{\mathbf{x}} \cdot \boldsymbol{\sigma} = \mathbf{0}. \quad (4)$$

We split the total stress into three parts, which include a pressure term, the passive isochoric contribution, and the active contribution. The mathematical form of the total stress can be written as

$$\boldsymbol{\sigma} = \mathrm{p}\mathbf{I} + \boldsymbol{\sigma}^{\mathrm{pas}} + \boldsymbol{\sigma}^{act} \quad (5)$$

where p denotes the pressure Lagrange multiplier, $\boldsymbol{I}$ is the identity matrix, and $\boldsymbol{\sigma}^{pas}$ and $\boldsymbol{\sigma}^{act}$ are the passive and active contributions. For the passive contribution of the stress, we assume hyperelastic behavior and we propose the strain energy

$$\psi = k_0\big(I_1 - 3\big) + \phi\,\psi^f \quad (6)$$

$$\psi^f = \frac{k_1}{2k_2}\Big(\mathrm{e}^{k_2\,(\boldsymbol{A_0}:\boldsymbol{C}-1)} - k_2(\boldsymbol{A_0}:\boldsymbol{C}-1) - 1\Big) \quad (7)$$

where k_0, k_1, k_2 are parameters, ϕ is the volume fraction of fibers, I_1 is the first invariant of the deformation, $\boldsymbol{C}$ is the right Cauchy-Green tensor, $\boldsymbol{A_0} = \kappa\boldsymbol{I} + (1-2\kappa)\boldsymbol{a_0}\otimes\boldsymbol{a_0}$ is the structural tensor with $\boldsymbol{a_0}$ the fiber direction and κ the fiber dispersion in the reference configuration. We fit experimental data of single collagen and fibrin fibers [5,6] to obtain two sets of k_1 and k_2. The volume fraction is estimated by comparing experimental data of gels and single fibers as well as computed the approximate value from fiber densities of collagen and fibrin. The pressure p is computed using a plane-stress assumption. The active contribution in current configuration is written as

$$\boldsymbol{\sigma}^{\mathrm{act}} = \phi\, t_\rho \frac{\boldsymbol{A}}{tr(\boldsymbol{A})} \quad (8)$$

$$t_\rho = f \cdot \rho_i \cdot \phi_b(\lambda) \quad (9)$$

where f, ρ_i are contractile force per adhesion and density of integrins on a fibroblast, and $\boldsymbol{A}$ is the structural tensor pushed to the current configuration. The coupled mechanics-mechanobiology problem is solved using a custom finite element implementation.

RESULTS

We simulated uniaxial and biaxial tests for both collagen and fibrin fibers and gels using the strain energy function proposed here. The results of the stress, σ_{xx}, of both fiber types with different dispersions were simulated (Figure 2). When there is no dispersion ($\kappa = 0$), the stress shows large nonlinearity in the case of collagen, while fibrin mechanics are less nonlinear. Increasing dispersion (larger κ) results in lower stress under uniaxial loading for the same fiber density, which reflects that not all the fibers are under tension, only the ones in the direction of loading.

Next, we computed the active contribution of cells to the total stress when interacting with collagen or fibrin fibers. In the absence of deformation ($\lambda = 1$), the difference in cell active stress between collagen and fibrin substrates is entirely defined by the different initial stiffness of these two substrates. Stretching the substrate increases the active cell stress due to the coupling in Eq. (3) (Figure 3). Higher dispersion results in a decrease of the active stress, but it will not influence the maximum value of σ^{act}. Finally, we constructed a wound

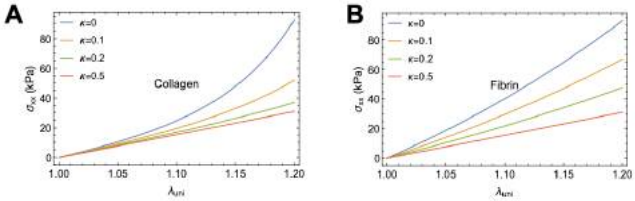

Figure 1: Uniaxial tests of (a) collagen and (b) fibrin fibers. Four different dispersions were tested. The stress components in the x direction, σ_{xx}, is plotted as a function of fiber stretch, λ_{uni}.

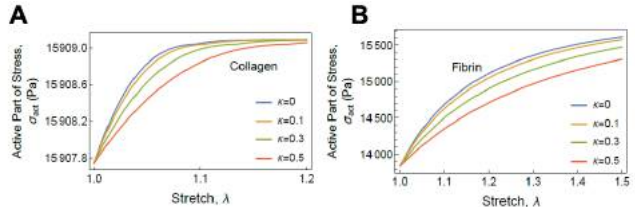

Figure 2: Influence of stretch, λ, on the active contribution, σ^{act} on (a) collagen and (b) fibrin substrates for various dispersions κ.

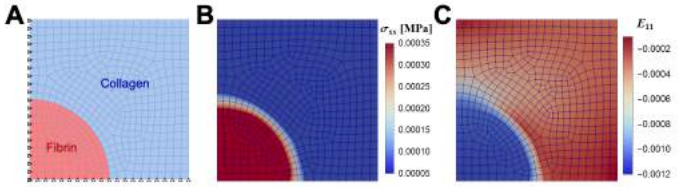

Figure 4: Simulation of a sample wound. (a) x- and y-symmetry boundary conditions were applied on the left and bottom; no tractions were applied. (b) Stress and (c) Green-Lagrange strain contours in response to the active stress produced by a uniform cell density field.

domain to simulate the contraction process [1] (Figure 4). The total stress vanished due to equilibrium; passive stress balances active stress. The strains are not uniform due to the heterogeneity of the material properties, which leads to heterogeneous contraction predicted by Eq. (3) even in the absence of any external forces.

DISCUSSION

To address existing gaps in understanding how tissue-level mechanics influence cell mechanobiology, we coupled a cell adhesion model to a finite element model of tissue. Incorporating the nonlinear behavior of the ECM with Bell's model of adhesion [3], we show that increasing ECM stretch increases cell adhesion, which in turn feeds back to the mechanical equilibrium by affecting the cell active stress. Other works [7] also considered active stress; however, they ignored the underlying mechanism of cell-ECM interaction. Limitations of our model include lack of viscoelastic behavior as well as growth and remodeling, which are being incorporating in our ongoing work.

ACKNOWLEDGEMENT: Supported by NSF CMMI #1911346.

REFERENCES

[1] Tepole A B, Kuhl E., Pediatr Res, 73(2): 553-563, 2013.
[2] Tepole A B, Comput Methods Appl Mech Eng, 314: 46-70, 2017.
[3] Bell G I, Science, 200(4342): 618-627, 1978.
[4] Gasser T C et al. J R Soc Interface, 3(6): 15-35, 2006.
[5] Seliktar D, et al., Ann Biomed Eng, 28(4): 351-362, 2000.
[6] Liu W et al., J Thromb Haemost, 8(5): 1030-1036, 2010.
[7] Loerakker et al., Biomech Model Mechanobiol, 13(5): 985-01, 2014.

DEVELOPMENT OF A COMPUTATIONAL PLATFORM TO EVALUATE A POSITIVE END-EXPIRATORY PRESSURE IN PATIENTS WITH TRACHEOSTOMY

S. Kageyama (1), N. Takeishi (1), H. Taenaka (2), T. Yoshida (2), S. Wada (1)

(1) Department of Mechanical Science and Bioengineering, Graduate School of Engineering Science, Osaka University, 1-3 Machikaneyamacho, Toyonaka, Osaka, Japan
(2) Intensive Care Unit, Osaka University Hospital, 2-15 Yamadaoka, Suita, Osaka, Japan

INTRODUCTION

A tracheostomy tube is used for almost 90% of patients who need long-duration (2-3 weeks) of the ventilator. Since it is also known that there is a correlation between high survival rates and short-duration of the ventilator [1], precise oxygen supply with a tracheostomy tube (Fig. 1(a)) is necessary for postoperative patients with tracheostomy to early removal of the ventilator. Although there is a common sense that a positive end-expiratory pressure (PEEP) should be preserved to prevent the pulmonary collapse [2], much is still unknown about inflow rates of oxygenated air to achieve the PEEP in the patients supported by tracheostomy tube. Numerical approach is useful to investigate mechanical parameters for PEEP considering the flow field of the tracheostomy tube. Therefore, the objective of this study is to develop a computational platform to evaluate PEEP based on the flow filed in 3-dimensional (3D) space of tracheostomy tube. Calculated tracheal pressure, which is the outlet pressure in the tube, will be compared with animal experiments. In this abstract, we report a computational framework, where computational fluid dynamics in 3D, is coupled with a 0-dimensional (0D) lung model. Using developed model, we evaluated the tracheal pressure as a function of inflow rates of the air.

METHODS

To evaluate PEEP, 3D fluid dynamics of the airflow in the tube is coupled with 0D lung model. Each model explanation and coupling method are described follows.

Flow model. The air is modeled as an incompressible, Newtonian fluid, and is governed by the continuum and Navier-Stokes equations. A realizable k-ε turbulence model [3] is also applied. For each boundary shown in Fig. 1(b), constant velocity U_{in} and pressure P_{out} (= 0) are given in the inlet and outlet, respectively, where U_{in} is determined based on the flow rate Q_{in} (= $A_{in}U_{in}$ = 10, 30 and 50 L/min). The velocity on the boundary attached to the trachea U_{tr} is given by 0D lung model, which is described below. A no-slip condition is applied to all walls. The fluid mesh size is set at 1.0 mm (a polyhedral mesh), and an adaptive meshing (prismatic layers) is considered to be lining the walls. CFD is performed by STAR-CCM++ (Version 15.04.010; SIEMENS, Germany). More detail computational descriptions are referred to [4].

0D lung model. Alveoli pressure P_{al} is balanced with pleural pressure P_{pl} driven by respiratory muscle change and elastic stress σ acting on the lung tissue, i.e.,

$$P_{al} = P_{pl} + \sigma. \tag{1}$$

Here, P_{pl} is given as a sinusoidal function such that $P_{pl} = -P_0 \sin(\pi t/T) - P_{base}$, where T = 5 [s], P_0 = 250 [Pa] and P_{base} = 750 [Pa]. The lung tissue is modeled as an isotropic and hyperelastic material. The strain energy function W per unit volume of the lung tissue is given as [5]:

$$W = C_1\left(\widehat{I_c} - 3\right)^2 + C_2\left(\widehat{I_c} - 3\right)^3 + C_3(-2\ln J + J^2 - 1) \tag{2}$$

where C_i (i = 1-3) is the model parameter, $\widehat{I_c}$ is the modified first invariant of right Cauchy-Green deformation tensor $\mathbf{C}$, and J is the volumetric Jacobian defined as the determinant of the determinant of the deformation gradient tensor $\mathbf{F}$ (i.e., J = det($\mathbf{F}$)). Assuming isotropic deformation, the Cauchy stress tensor $\boldsymbol{\sigma}$ can be described as:

$$\boldsymbol{\sigma} = \frac{1}{\det(\mathbf{F})}\mathbf{F}\cdot\mathbf{S}\cdot\mathbf{F}^{\mathrm{T}} = 2C_3\left(J - \frac{1}{J}\right)\mathbf{I} \tag{3}$$

where $\mathbf{S}$ (= $2\partial W/\partial \mathbf{C}$) is the second Piola-kirchhoff stress tensor and $\mathbf{I}$ is the unit tensor. Tracheal velocity U_{tr}, which is a boundary condition in flow model, can be obtained with a linear equation of the flow resistance R and with the assumption of isotropic deformation, i.e.,

$$P_{tr} - P_{al} = \mathrm{R}\dot{V}_{lung}, \tag{4}$$

$$\dot{V}_{lung} = \mathrm{U}_{tr}\pi r^2, \tag{5}$$

where P_{al} is the alveoli pressure, which is given by Eq. (1), and r is the radius of the boundary attached to the trachea (Fig.1(a)). C_3 is determined based on physiological relevant lung deformation such that dV_{lung} = 500 cm^3 and dP_{pl} = 500 Pa [6].

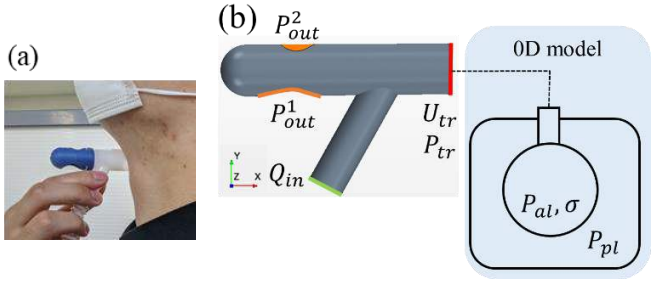

Fig. 1. (a) Tracheostomy tube (Fisher&Paykel Healthcare, New Zealand) . (b) Tube model for 3D CFD and schematics of 0D lung model. For the tube model, each boundary condition set at an inlet velocity U_{in} (green), outlet pressure P_{out} (orange), and tracheal velocity U_{tr} (red) obtained with 0D lung model.

RESULTS AND DISCUSSION

Response of 0D model. Fig. 2(a) shows time histories of calculated alveoli pressure P_{al}, tracheal velocity U_{tr}, and given pleural pressure P_{pl}. The result is obtained with $Q_{in} = 30$[L/min]. The amplitudes of P_{al} and U_{tr} were approximately 100 Pa and 1.7 m/s, respectively. Fig. 2(b) shows the time average of mean P_{al} during a cycle for different $Q_{in}(= 10, 30, 50$ [L/min]), where P_{al} and Q_{in} are normalized by $2A_{pl}$ (here, A_{pl} is the amplitude of P_{pl}) and Q_{in} = 10 L/min (Q_{in_10}), respectively. The time average of maximal and minimal P_{al} are also displayed in Fig.2(b). Since the lung volume increases with Q_{in} resulting in large stress to assist the exhalation, P_{al} increases while its amplitude decreases with Q_{in}. Hence, our developed 0D model qualitatively represents a characteristic response of the lung driven by the lung tissue elasticity [6].

3-dimensional (3D) fluid simulation. Considering outlet velocity U_{tr} obtained with 0D lung model, the airflow in 3D space of tracheostomy tube was simulated. Figs. 3(a) and 3(b) show the pressure and velocity field at Q_{in} = 30 L/min, respectively. Fig. 3(c) shows the time average of mean, maximal and minimal P_{tr} normalized by $2A_{pl}$ as a function of $Q_{in}/Q_{in,10}$. The results of P_{tr} increases with Q_{in} as well as its amplitude. Although model validation has not been fully completed, we are planning to compare calculated P_{oral} with those in animal experiments. Based on these results, we will discuss whether PEEP can be evaluated based on P_{tr}. Our developed model may be useful to estimate minimal Q_{in} to achieve PEEP for individual postoperative patients with tracheostomy.

SUMMARY

We developed a computational platform to evaluate PEEP in the postoperative patients with tracheostomy. The tracheal pressure, which is outlet pressure of the tracheostomy tube, was calculated by 3D CFD analysis coupled with 0D lung model. In the future study, calculated tracheal pressure will be compared with those in animal experiments. We hope that developed model will be applied to evaluate PEEP and minimal inflow rates for individual patients.

ACKNOWLEDGEMENTS

This research was supported by JSPS KAKENHI Grant Numbers JP19H01175, JP20H04504 and by the Keihanshin Consortium for Fostering the Next Generation of Global Leaders in Research (K-CONNEX), established by Human Resource Development Program for Science and Technology.

REFERENCES

[1] Engoren et al., *Chest*, 125(1), pp. 220–7, 2004.
[2] Milési et al., *Intensive Care Medicine*, 39(6), pp.1088–1094, 2013.
[3] Shih et al., *NASA Technical Memorandum* 106721, 1994.
[4] Takeishi et al., *Med. Biol. Eng. Comput.*, 57, pp. 837-847, 2019.
[5] Rausch et al., *J. Mech. Behav. Biomed. Mater.*, 4, pp.583-592, 2011.
[6] Mead et al., *J Appl. Physol.*, 28(5), pp. 596-608, 1970.

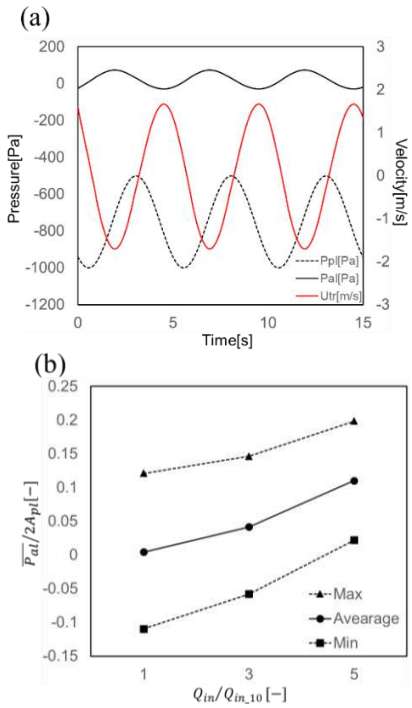

Fig. 2. (a) Time history of alveoli pressure P_{al}, pleural pressure P_{pl} (left *y*-axis), and tracheal velocity U_{tr} (right *y*-axis). The result is obtained with $Q_{in} = 30$ [L/min]. (b) The time average of mean P_{al} during a cycle as a function of Q_{in}, where normalized by P_{al} and Q_{in} are normalized by $2A_{pl}$ *and* Q_{in} = 10 L/min (Q_{in_10}), respectively.

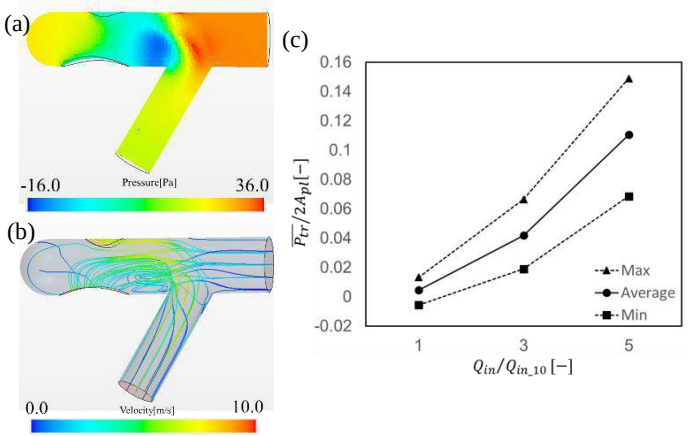

Fig. 3. Snapshots of (a) pressure and (b) velocity for Q_{in} = 30 L/min. (c) Time average of mean, maximal and minimal P_{tr} normalized by $2A_{pl}$ as a function of Q_{in}/Q_{in_10}.

PASSIVE LEG RAISE AS A SIMPLE AND ROBUST MANEUVER TO MEASURE PULMONARY VASCULAR DISTENSIBILITY

Callyn J. Kozitza (1), Farhan Raza (2), Naga L. Dharmavaram (2), Diana M. Tabima (1), Naomi C. Chesler (3)

(1) Department of Biomedical Engineering
University of Wisconsin – Madison
Madison, WI, USA

(2) Department of Medicine/Cardiology
University of Wisconsin - Madison
Madison, WI, USA

(3) Edwards Lifesciences Center for Advanced Cardiovascular Technology
and Department of Biomedical Engineering
University of California, Irvine
Irvine, CA, USA

INTRODUCTION

An important predictor of mortality of all forms of pulmonary hypertension (PH) is right ventricular (RV) function, which in turn depends on RV afterload. RV afterload has two components: a steady (mean) component described by pulmonary vascular resistance (PVR) and an unsteady component dependent on proximal artery compliance and distal arteriolar distensibility (α). Distensibility reflects the ability of the smallest pulmonary arteries to dilate in response to an increase in blood pressure [1]. This increase in diameter, which is ~2% per mmHg in healthy subjects [Reeves], helps to maintain a low PVR during exercise [2]. However, in the settings of chronic hypoxia [3] and PH [4] α decreases significantly, which can impair exercise capacity and contribute to increased RV afterload.

Typically, α is determined using multipoint pressure-flow data [1], which can be collected from an invasive exercise test. Single-point methods have also been used [4]. However, patients with PH may not be able or willing to exercise. A passive leg raise is a simple, easy-to-perform maneuver that works to shift blood from the venous system back towards the heart to increase cardiac preload and has been reported to increase pulmonary artery wedge pressure (PAWP) [5]. Here we sought to determine whether α calculated with a passive leg raise (PLR) maneuver was similar to α calculated with exercise in three different phenotypes of PH: pre-capillary PH (PAH), isolated post-capillary PH (Ipc-PH), and mixed pre-/post-capillary PH (Cpc-PH).

METHODS

Invasive cardiopulmonary exercise testing (CPET), consisting of a right heart catheterization (RHC) and simultaneous expired gas analysis during graded exercise, was performed in patients with suspected PH (n = 46). Hemodynamic evaluation was performed under three conditions: rest (supine), PLR (semi-recumbent) and peak exercise (semi-recumbent). In the semi-recumbent position, the subject's upper body was supported with a wedge-shaped pillow at a 45-degree angle. The PLR maneuver was performed with the subject's feet resting in the pedals of the exercise bike for five minutes. Exercise was performed on a semi-recumbent cycle ergometer at 60 rpm. The workload was increased in increments of 10-20 Watts/min until exhaustion. The study was approved by the UW-Madison institutional review board (2019-0535).

Hemodynamic evaluation consisted of PAWP, cardiac output (CO) by direct Fick method, and pulmonary artery (PA) pressure. These data were recorded at the conclusion of each condition using a balloon-tipped, double-lumen, fluid-filled 7 Fr PA catheter via an internal jugular vein approach. PVR was calculated as:

$$PVR = \frac{mPAP - PAWP}{CO} \tag{1}$$

where mPAP is the mean PA pressure.

Subjects were classified into one of four groups (PAH, n = 10; Ipc-PH, n = 19; Cpc-PH, n = 12; or No PH, n = 5) based on mPAP, PAWP and PVR per 2019 ESC/ERS guidelines [6]. Subjects with No PH had mPAP/CO slope<3.0 and rest mPAP<20 mmHg.

Assuming that the pulmonary arteries are fully recruited, dilated and homogeneously distensible, α can be determined using the governing equation [1]:

$$mPAP = \frac{[(1 + \alpha PAWP)^5 + 5\alpha R_o CO]^{\frac{1}{5}} - 1}{\alpha} \tag{2}$$

where R_0 is the total pulmonary vascular resistance at rest, calculated as:

$$R_0 = \frac{mPAP}{CO} \quad (3)$$

Using the method of successive iterations [1], α was fit to two conditions: rest and peak exercise or rest and PLR.

Results were analyzed with a 2-way ANOVA for condition (peak exercise vs. PLR) and group (PH phenotype or No PH). Two-way interaction effects were evaluated between PH-phenotype and condition but were not found to be significant. Tukey's honestly significant difference test was used as a post hoc test of significance. $p<0.05$ was considered significant and results are presented as mean ± standard deviation.

RESULTS

Table 1 shows the hemodynamic parameters measured at rest, PLR and peak exercise in each subject group.

Table 1: Hemodynamic evaluation of subjects from RHC

PH-Phenotype	No PH	Ipc-PH	Cpc-PH	PAH
mPAP, mmHg				
Rest	19±2	28±7	39±8	38±10
PLR	22±2	34±9	47±8	44±12
Exercise	27±8	44±11	56±8	55±10
CO, L/min				
Rest	6.2±1.1	5.3±1.3	4.7±1.4	4.1±1.0
PLR	6.2±1.2	5.0±1.4	4.2±1.3	4.0±1.3
Exercise	14.1±5.1	8.5±2.9	7.1±2.5	6.4±1.7
PAWP, mmHg				
Rest	13±2	18±4	18±4	13±2
PLR	15±2	24±6	26±6	17±4
Exercise	18±3	31±7	32±6	21±2
PVR, Wood Units				
Rest	0.8±0.6	2.0±0.7	4.9±2.2	6.0±2.1
PLR	1.1±0.5	2.3±1.1	5.1±1.8	6.7±2.1
Exercise	0.8±0.8	1.7±1.0	3.7±1.0	5.8±2.6

There was no significant difference ($p = 0.513$) in α between the two conditions: peak exercise (1.02 ± 0.94% per mmHg) and PLR (0.95 ± 0.71% per mmHg) (Figure 1). The PLR-based measure of α was significantly lower in the Ipc-PH (1.17 ± 0.60% per mmHg), Cpc-PH (0.51 ± 0.22% per mmHg) and PAH (0.44 ± 0.29% per mmHg) groups compared to the No PH group (2.18 ± 0.69% per mmHg) (Figure 2). In addition, α was significantly lower in the groups characterized by a significant pre-capillary PH component (Cpc-PH and PAH) compared to the Ipc-PH group (Figure 2).

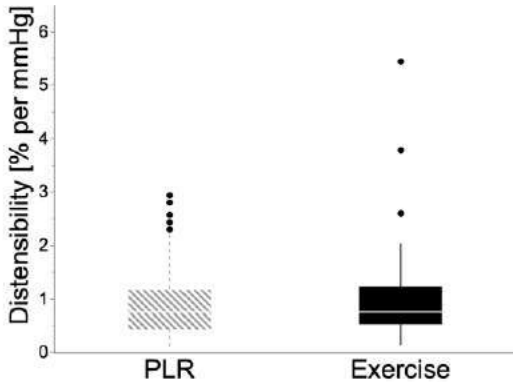

Figure 1: Pulmonary vascular distensibility comparison between the two conditions: PLR and peak exercise (n = 46). P=0.513.

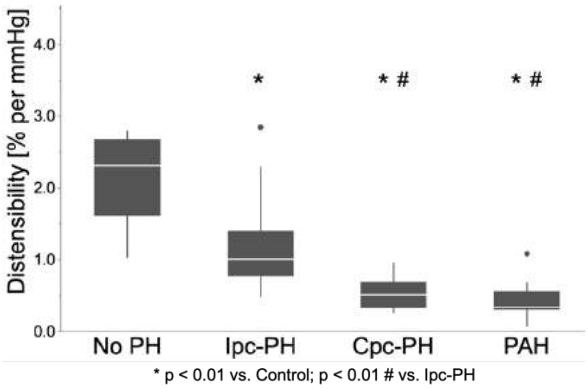

Figure 2: PLR-based measure of pulmonary vascular distensibility for the four groups: No PH (n = 5), Ipc-PH (n = 19), Cpc-PH (n = 12) and PAH (n = 10).

DISCUSSION

RV function depends on RV afterload. The pulmonary arteries dilate to protect the afterload-sensitive RV from excessive increases in pressure. Thus, α acts to help limit the afterload that the RV confronts in conditions of increased pressure (e.g., disease and exercise). Here we show that in subjects with and without PH, pulmonary vascular α can be measured via PLR, which is clinically important for subjects with contraindications to exercise and subjects with severe PH whose exercise capacity is essentially nil.

The present calculations of α for the No PH group agree with prior studies in which a value of 2% per mmHg was observed [3, 8, 9]. Distensibility was significantly decreased in all PH phenotypes, with the lowest values obtained in the groups with a significant pre-capillary component. Reduced α was also observed in a study with PAH [4] and heart failure subjects compared to control [9]. An important limitation to this study is that data were not disaggregated or analyzed for sex or age differences in α, both of which have been reported [10]. In addition, the No PH group cannot be considered healthy as they had dyspnea and suspicion of PH.

In conclusion, we present a clinically simple and robust alternative to exercise for measuring pulmonary vascular distensibility. Broader use of this metric of pulmonary vascular function may shed light on the origins of exercise intolerance in a range of pulmonary vascular diseases and the hemodynamic mechanisms by which PH causes RV failure.

ACKNOWLEDGEMENTS

Funding from NIH R01HL147590-01 (NCC) as well as the UW-Madison Department of Medicine pilot fund (FH) is gratefully acknowledged.

REFERENCES

[1] Linehan, J et al., *J. Appl. Physiol.*, 73(3):987–994, 1992.
[2] Naeije, R *et al.*, *Am. J. Respir. Crit. Care Med.*, 187(6):576–583, 2013.
[3] Reeves, J et al., *Am. J. Physiol. - Lung Cell. Mol. Physiol.*, 288(3):419–425, 2005.
[4] Blyth, K et al., *Respir. Med.*, 101(12):2495–2501, 2007.
[5] Arunachalam, A et al., *Respir. Med. X*, 2:100015, 2020.
[6] Simonneau, G et al., *Eur. Respir. J.*, 53(1), 2019.
[7] Chesler, N et al., *Conf. Proc. IEEE Eng. Med. Biol. Soc.*, 177–180, 2009.
[8] Bellofiore, A et al., *J. Biomech. Eng.*, 137(4), 2015.
[9] Malhotra, R et al., *Circ. Heart Fail.*, 9(6):139–148, 2016.
[10] Argiento, P et al., *Chest*, 142(5):1158–1165, 2012.

QUANTITATIVE ASSESSMENT OF THE EFFECTS OF INTERSTITIAL FLOWS, MACROPHAGE POLARIZATION AND IMMUNOTHERAPY ON TUMOR IMMUNE CELL INFILTRATION

Huu Tuan Nguyen[1], Nadia Gurvich[2], Christie Zhang[2], Giovanni Offeddu[1], Mark R. Gillrie[1], Sharon W.L. Lee[1], Seng-Lai Tan[2], Jonathan Hsu[2], Roger D. Kamm[1]

1. Massachusetts Institute of Technology, Department of Mechanical Engineering and Department of Biological Engineering, Massachusetts Institute of Technology, Cambridge, MA, 02139 USA
2. Elstar Therapeutics, 840 Memorial Dr, Cambridge, MA 02139 USA

INTRODUCTION

Monoclonal and multi-specific antibody-based immunotherapies constitute an expanding therapeutic armamentarium against various diseases, including cancer and viral infection. Due to the complex mechanism of therapeutic antibodies, and often times, their lack of cross-reactivity to murine counterparts of their intended targets, drug testing using animal models or conventional 2D human cell cultures are not sufficient to predict patient drug efficacy. Moreover, in vivo quantification of immune cell infiltration in real-time is challenging. Many previous in vitro models do not recapitulate immune cell extravasation and migration at the same time. New 3D organotypic models that employ 3D cell culture of human cells within a microfluidic device allow detailed characterization of critical biological interactions (1,2). In particular, microfluidic chips that have the capability to create a perfusable microvascular network can deliver signaling molecules and immune cells using microfluidic flow (1–3). Compared to 2D cell culture, spheroids and organoids are better representations of the structure of an organ where each cell is in contact with other cells and the extracellular matrix. Integrating 3D structures such as spheroids and organoids into microfluidic systems not only recapitulate the physiological state of the cells within a body but also allow interactions between cells in a tissue and peripheral cells or circulating immune cells. In this project, we describe a new 3D cell culture model consisting of an in-vitro human perfusable vascularized tissue with cylindrical wells for the insertion of tumor spheroids. We use this system to characterize the effect of interstitial flows and macrophage polarization on monocyte recruitment and establish a model for therapeutic antibody testing. Using the new microfluidic model, we demonstrate the efficacy of UniTI102, a therapeutic multi-specific antibody targeting CSF-R, CCR2 and TGFb, in blocking monocyte recruitment by a tumor spheroid.

METHODS

Microfluidic device fabrication, and cell culture methods for normal human lung fibroblasts (NHLFs), and human umbilical vein endothelial cells (HUVECs) have been previously reported (4,5). Briefly, vascular networks are created by seeding NHLFs (1 M/ml NHLFs) and HUVECs (11 M/ml) in thrombin (2 U/mL) and fibrinogen (6mg/ml) gel solution. Gel holes are created by pushing a bubble into the gel solution or removing spacers from the gel chamber before the gel solution polymerizes. Open channels on both sides of the gel chamber are then filled with media. 3 days later, HUVEC suspension (1M/ml) is added into the two media channels. Primary monocytes (CD14+CD16-) are isolated from human's whole blood from healthy donors. M0 macrophages are differentiated from CD14+CD16- monocytes by culturing with M-CSF (100ng/ml) using 6 well or 12 well plates (1M cells/1.5ml). M2 macrophages are obtained by culturing M0 macrophages in RPMI media supplemented with 10% FBS, IL4 (20 ng/ml) and IL10 (10 ng/ml) overnight. Tumor spheroid composition is 40,000 NHLFs, 13,000 tumor cells (MDA-MB-468), with the presence or absence of 13,000 macrophages per spheroid. Cells are mixed and cultured in low adhesion round-bottom 96-well plates in 5%CO2 at 37C with RPMI media. 6 d after the vascular network is seeded, a tumor spheroid is inserted into the cylindrical well and embedded in rat tail collagen (final concentration is 2mg/ml when the gel solution is mixed). Monocytes are freshly isolated from blood or thawed from frozen vials and are stained with far red cell tracker (3µM, 30 min) at 37°C 5% CO2. 160,000 monocytes are suspended in 100 µl Vasculife (VEGF supplement kit without Heparin sulfate and VEGF, 10% FBS) and perfused into the vascular networks. By generating a pressure difference between two media channels, monocytes are perfused into the vasculatures. 3mmx3mm ROI of the tumor spheroid and the surrounding microvasculature are acquired using FV1000 Laser Scanning Confocal Microscope (Olympus, PA, USA). A Fiji plugin is used to count the number of monocytes in the device. By quantifying the number of immune cells that are inside the central hole and the total number of cells in the ROI, we can characterize the percentage of the cells that are recruited by the tumor spheroid, i.e. both extravasate from the vasculature and migrate through the gel. UniTI102 drug is provided by Elstar Therapeutics (MA, USA). Unpaired Student's t-tests were applied between two groups (significance indicated as $p<0.05$). The analysis was performed by Prism 7 (GraphPad, San Diego, CA).

RESULTS

A polydimethylsiloxane device with several vertical holes on top of the gel channel is used to create the host microvascular endothelial (HOME) network (Fig. 1A). A fibrin gel solution that has HUVECs and NHLFs in suspension is injected into the device. Later, these form a blood-vessel-like network that is also perfusable (Fig. 1B). Tumor spheroids are formed by coculturing MDA-MB-468 tumor cells (T), NHLFs (F), and macrophages with different polarizations: either non-polarized (M0) or polarized toward M2, denoted by TFM0 and TFM2 respectively (Fig. 1C). One day after inserting a tumor spheroid into the HOME networks through the hole together with collagen, freshly-isolated monocytes are perfused into the networks by luminal flow. We observe that after 2 d, majority of the monocytes remain either within the vasculature or extravasate but stay inside the fibrin gel outside of the hole containing the tumor spheroid (Fig. 1Di). On day 2, interstitial flows from the tumor spheroid toward the vasculature are generated by the application of a hydrostatic pressure from a column of media contained in a pipette tip placed on top of the hole containing a spheroid (see Fig. 1C).

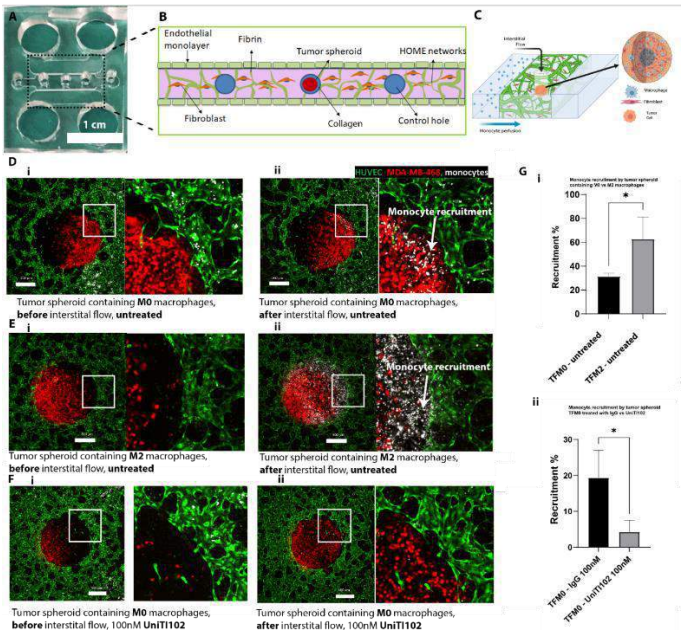

Figure 1: Design and use of the microfluidic chip containing chambers for studying tumor vascularization and immunotherapy. A) Microfluidic chip (transparent) without cells. Gel channel is flanked by two media channels. **B)** Schematic of microfluidic chip in (A) after a few days in culture. A tumor spheroid is placed in holes surrounded by endothelial networks. **C)** Generation of interstitial flow and immune cell recruitment assay. Fluid flow is applied from the opening of the device, passing through the extracellular matrix surrounding the spheroid and directed toward the vascular network. Right: schematic presentation of a tumor spheroid. **D-E)** Effect of interstitial flows and macrophage phenotype on monocyte recruitment. Panels display the top view of a region of a device that has one well containing a tumor spheroid with MDA-MB-468 tumor cells (red), fibroblasts, and macrophages (either M0 or M2 phenotype, in Fig. D and E respectively) surrounded by vascular networks that contain monocytes, before (i) and after (ii) interstitial flows are applied. **Di)** Monocytes (white) still stay inside vascular networks 2 d after perfusing them into the device that has a tumor spheroid containing tumor cells, fibroblast and M0 macrophages (denote TFM0). **Dii)** After applying interstitial flows from the top of the well through the tumor spheroid and toward the vasculature, monocytes within the vascular networks leave the vasculature more readily and migrate toward the spheroid inside the well. **Ei)** Device with a spheroid containing M2 macrophages (TFM2). Before interstitial flow, monocytes also do not migrate into the well. **Eii)** Monocytes in the TFM2 device migrate into the tumor spheroid after an overnight application of interstitial flow. **F)** Device containing TFM0 treated with 100nM UniTI102 for 2 days display less monocyte migration both before (Fi) and after (Fii) applying interstitial flows. Due to the drug that blocks monocyte migration, far fewer monocytes are recruited by the tumor spheroid in (Fig. Fii) compared to (Fig. Dii). In D-F, tumor cells express RFP (red); HUVECs express GFP (green). Scale bars: 500µm. **Gi.** Quantification of monocytes recruited by TFM0 (N=4) versus TFM2 (N=4). **Gii.** Quantification of recruited monocytes in TFM0 devices treated with 100nM IgG (N=4) or with 100nM UniTI102 (N=4).

The device is then imaged on the next day, and we observe that monocytes migrate from the vascular networks and the gel outside of the vascular networks into the hole containing the tumor spheroid (Fig. 1Dii). When a TFM2 spheroid is inserted into the HOME networks, it recruits more monocytes than the TFM0 spheroid (Fig. Ei and Eii), under the same interstitial pressure applied 2 d after perfusing monocytes. Recruited monocytes are the population that leaves the blood vessel and migrate into the hole. The pooled experimental results from 2 different batches showing monocytes are recruited better by the TFM2 spheroid than the TFM0 spheroid (Fig. 1Gi). These data demonstrate that interstitial flow from the tumor spheroid to the vascular networks is essential for monocyte recruitment. In addition, they highlight the importance of macrophage polarization in monocyte recruitment.

UniTI102 is a bispecific antibody targeting CCR2, and CSF-1R, and contains a TGFβ trap (Elstar Therapeutics, MA, USA). It is designed to selectively binds to CCR2+ and CSF-1R+ myeloid cells and is capable of functionally inhibit both CSF-1/CSF-1R and CCL2/CCR2 signaling pathways. Thus, we characterize the ability of UniTI102 to suppress monocyte recruitment. We compared devices having a TFM0 spheroid that are untreated (Fig. 1D) or treated with UniTI102 (Fig. 1F) and observed fewer monocytes migrating into the hole in the presence of 100nM UniTI102. Quantitative data showed that fewer monocytes are recruited when devices are treated with 100nM UniTI102 than 100nM IgG (Fig. 1Gii).

DISCUSSION

We describe here a newly engineered tumor model that has functional perfusable vasculature to study immune cell recruitment and use the platform to screen a new therapeutic antibody. This system is unique in terms of the method used to create an empty space surrounded by a perfusable vascular network. Immune cell trafficking across blood vessels and migrating toward the tumor are characterized in real-time and high resolution using confocal microscopy. Compared with the methodology used for other *in vitro* cell culture systems (2), this technique could better reproduce the complexity of a tumor by incorporating a perfusable vasculature. Furthermore, we employ the open-top hole to generate interstitial flows from the tumor spheroid toward the vasculature, mimicking the physiological interstitial flow emanating from a tumor, and show that interstitial flows help support immune cell recruitment. Moreover, we show that when tumor spheroids have mature M2 macrophages, they recruit more monocytes. Using this new platform, we demonstrate the effect of a therapeutic multi-functional antibody candidate in preventing monocyte recruitment to the tumor spheroid. We believe that immune-competent physiological models, such as the work described here, will play a central role in immunotherapy drug screening in the future.

ACKNOWLEDGEMENTS

This study was supported by National Institute of Health through grant U01CA214381 and Elstar Therapeutics (Cambridge, MA, USA). HTN is supported by a Swiss National Science Foundation postdoctoral fellowship (SNSF-P400PB_186779). RDK discloses that he is co-founder and board member of AIM Biotech, and has research support from Amgen, Biogen, and Elstar.

REFERENCES

1. Boussommier-Calleja A. Trends in Cancer. 2(1):6–19,2016.
2. Sontheimer-Phelps A. Nat Rev Cancer. :1,2019.
3. Chen MB. Nat Protoc. 12(5):865–80,2017.
4. Offeddu GS. Biomaterials. 212:115–25,2019.
5. Haase K. Adv Funct Mater. 30(48):2002444,2020.

MODEL-DIRECTED DESIGN OF KINK-RESISTANT VASCULAR GRAFTS WITH HIGH COMPLIANCE

**David Jiang (1), Andrew J. Robinson (2),
Elizabeth M. Cosgriff-Hernandez (2), Lucas H. Timmins (1,3)**

(1) Department of Biomedical Engineering
University of Utah
Salt Lake City, Utah, U.S.A

(2) Department of Biomedical Engineering
University of Texas at Austin
Austin, Texas, U.S.A

(3) Scientific Computing and Imaging Institute
University of Utah
Salt Lake City, Utah, U.S.A

INTRODUCTION

Each year ~1.4 million patients require arterial grafts in the US. Synthetic vascular grafts are required in ~10-20% of patients when autografts are unavailable; however, synthetic vascular grafts in small diameter applications (ID < 6 mm) have high failure rates. Synthetic grafts are associated with a 40-50% reduction in patency after 2 years and a 40% failure rate at 5 years [2]. This loss of patency due to intimal hyperplasia has been attributed, in part, to poor compliance-matching with native arterial tissue [1]. Data demonstrate that the high compliance of native vessels (e.g., coronary artery, 10-15 %/mmHg*10^{-2}) permits expansion and contraction during the cardiac cycle, whereas commercially available synthetic grafts have limited deformation at these pressure loads (e.g., ePTFE, 1-2 %/mmHg*10^{-2}). Notwithstanding the role of altered hemodynamics at the graft-tissue interface leading to neointimal hyperplasia, improved compliance matching between the graft and arterial tissue has been identified as a key determinant of long-term patency and graft success.

Advances in material chemistry and microfabrication strategies have allowed the manufacturing of polyurethane-based small diameter vascular graft with improved compliance matching [3]. Indeed, these grafts have been shown to reduce cellular markers for intimal hyperplasia, however, the increased compliance resulted in grafts that were prone to kinking, occlusion, and failure. To improve kink-resistance, a polymeric coil was added, but the addition negatively impacted compliance [4]. Due to the nearly infinite combinations of coil geometric properties, optimization strategies can be integrated to balance offsetting graft properties (e.g., kink resistance vs. compliance) and aid fabrication. Herein, we highlight the development and experimental validation of a computationally-informed design process to tune the mechanical properties of synthetic vascular grafts and aid compliance matching with vascular tissue.

METHODS

Vascular Graft Fabrication and Experimental Testing: A 24% Bionate® segmented polyurethane (DSM Biomedical) in dimethylacetamide solution was utilized for electrospinning. A 5 mm mandrel was coated in a polyethylene glycol (Mn = 35 kDa) sacrificial layer (5% in dichloromethane). An initial electrospun layer was deposited via a flow rate of 0.5 ml/hr and charges of +15-16.5 kV and -5 kV were applied to the 20G needle and mandrel, respectively, with a working distance of 50 cm. An 18 wt% solution of Bionate®55D in hexafluoroisopropanol was subsequently deposited on the initial layer forming a kink-resistant coil [outer diameter (d_o) = 0.38 mm]. Finally, a second electrospun layer was deposited on top of the coil forming the final tri-layer kink-resistant graft (Fig. 1A).

Graft compliance was calculated by measuring the change in inner diameter (d_i) of the vascular grafts, as measured via a laser micrometer, from lumen pressures of 80 mmHg to 120 mmHg via the following equation,

$$C = \frac{d_{i,120\ mmHg} - d_{i,80\ mmHg}}{d_{i,80\ mmHg} * 40\ mmHg} \quad (1)$$

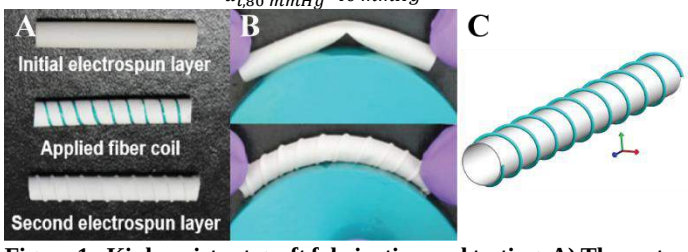

Figure 1: Kink resistant graft fabrication and testing. A) Three step fabrication process. B) Measurement of kink radius of control (no coil) and reinforced graft. C) CAD model of reinforced graft.

The radius of curvature that initiates graft kinking (i.e., kink radius) was examined by bending the graft around a tapered mandrel until a kink was visually observed (~50% reduction in diameter, Fig. 1B). Compliance and kink radius were determined in a control (no coil) and coil reinforced graft. Data are reported as mean±SD.

Computational Modeling: The tri-layer graft was modeled as an axisymmetric cylinder ($l = 40$ mm, $d_i = 4.74$ mm, $d_o = 4.94$ mm) with a reinforced coil wrapped around the other surface (pitch = 0.4 mm, Fig. 1C). Two fiber coil diameters were evaluated ($d_o = 0.19$ and 0.38 mm).

The graft and spiral coil were discretized with hexahedral and tetrahedral elements, respectively. Both the mesh and fiber coil were described as a nearly incompressible neo-Hookean solid with material properties derived from mechanical testing of the fabricated graft (μ =1.315 MPa) and spiral coil (μ =8.13 MPa) constituents. Two computational simulations were performed on a control (no coil) and each coil reinforced geometry to quantify compliance and kink resistance. To quantify compliance (Eq. 1), a lumen pressure from 0 to 120 mmHg to predict changes in diameter. To quantify kink-resistance, a 1° bend was applied to the central axis of the graft and the lumen was pressurized to 120 mmHg, as previously established to evaluate artery buckling [5]. Bending displacement was quantified as the deviation of the central graft axis in the central region under pressurization. For all models, symmetry boundary conditions were enforced on the graft to restrict rigid body motions in the circumferential and axial directions. A tied-elastic contact formulation was implemented between the outer graft surface and the spiral coil. Finite element analysis was performed using open-source finite element software package FEBio [6].

RESULTS

Experiments demonstrated that the presence of the fiber coil ($d_o =$ 0.38 mm) reduced graft compliance and bending displacement when compared to the control graft (no coil). For example, addition of the reinforcing coil resulted in a reduction in compliance from 8.0 ± 0.9 %/mmHg*10^{-2} to 1.5 ± 0.4 %/mmHg*10^{-2} (Fig. 2A). Kink radius measurements indicated an improvement in the kink resistance of the coil (a reduction in kink radius indicates improved kink resistance), as the value decreased from 99 ± 5 mm (control) to 63 ± 3 mm (Fig. 2B). Comparison of the computational and experimental data revealed strong agreement between measures of compliance and kink resistance. Modelling data showed that the addition of the coil decreased compliance from 8.0 %/mmHg*10^{-2} (control) to 1.5 %/mmHg*10^{-2} (Fig. 2A,D) in good agreement with the experimental compliance measurements. Furthermore, the model-predicted bending displacement decreased from 0.15 mm to 0.12 mm for the control and coil reinforced grafts, respectively, correlated with the improved kink-resistance (a reduction in bending displacement indicates improved kink resistance, Fig. 2C,E).

To demonstrate the utility of computational modeling to inform graft fabrication, we examined the impact of changes in coil geometry on predicted graft properties. Modeling data demonstrated that reducing the coil diameter from 0.38 to 0.19 mm resulted in an increase in compliance from 1.5 %/mmHg*10^{-2} to 4.1 %/mmHg*10^{-2}; however, kink resistance was maintained, as a minimal decrease in bending displacement was observed (0.12 to 0.11 mm). These graft fabrication parameters will be used in the next iterative of graft testing.

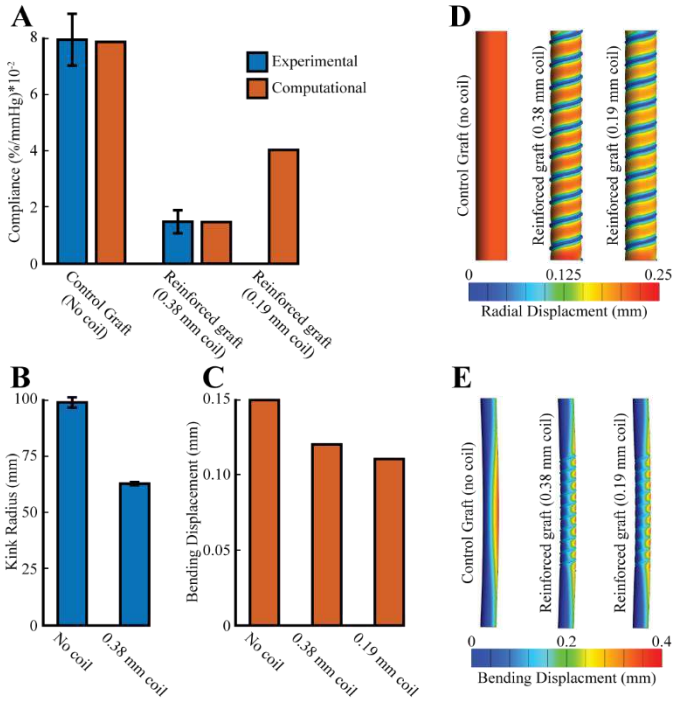

Figure 2: Compliance and kinking resistance data for fabricated and modeled grafts. A) Reduction of compliance with reinforcing coil. B) Reduction of kink radius with reinforcing coil. C) Model-predicted reduction in bending displacement with reinforcing coil. D) Model-predicted radial displacement and E) bending displacement at 120 mmHg.

DISCUSSION

Our investigation demonstrates the potential of computational modeling to inform synthetic vascular graft design, particularly when mechanical properties run counter to each other (e.g., high compliance, kink-resistance). We report that initial computational results agree well with experimental data evaluating the compliance and kink-resistance in a novel graft with a reinforcing polymeric coil. Data show that addition of the coil improves kink-resistance of the graft, but reduces compliance. As a proof-of-concept, we highlight how the computational modeling framework can identify a modified coil geometry (reduced coil diameter) that maintained kink-resistance while improving compliance. Such efforts illustrate the capability of computational modelling to optimize graft design and accelerate testing. We anticipate that the combination of precise material fabrication and model-directed design is expected to provide a kink-resistant graft with high compliance for small diameter vascular graft applications. Ultimately, these unique grafts have potential to improve clinical outcomes by addressing failures of current synthetic grafts.

ACKNOWLEDGEMENTS

This research was supported, in part, by the National Institutes of Health (R01 HL150608)

REFERENCES

[1] Burkel, W. E., *Med Prog Technol*, 14(3-4):165-175, 1989.
[2] Salacinski, HJ et al., *J Biomater Appl*, 15(3):241-278, 2001.
[3] Post, A et al., *Acta biomater*, 89:84-94, 2019.
[4] Li, X., MS Thesis, University of California Los Angeles, 2018.
[5] Sanyal, A et al., *Biomed Eng Online*, 14(Suppl 1): S4, 2015.
[6] Maas, SA et al., *J Biomech Eng*, 134(1):011005, 2012.

SB³C2021
Summer Biomechanics, Bioengineering and Biotransport Conference
June 14-18, Virtual

COLLAGEN DAMAGE IN ARTERIES – CHOICE OF ANALYSIS TECHNIQUE MATTERS IN IDENTIFYING RATE DEPENDENCE

William J. Anderl (1), Noah R. Pearson (1), S. Michael Yu (2), Kenneth L. Monson (1,2)

(1) Mechanical Engineering
University of Utah
Salt Lake City, UT, USA

(2) Biomedical Engineering
University of Utah
Salt Lake City, UT, USA

INTRODUCTION

Since the 1970s, researchers have sought to define tissue damage and failure. Damage occurs across the entire hierarchy of tissue structure but is, to date, poorly understood. The recent use of collagen hybridizing peptide (CHP) to identify damage in mechanically overloaded cerebral arteries [1] and tendon [2] confirmed the delamination theory of tropocollagen damage. We previously reported that CHP does not significantly bind to tissue failed at high strain rates [3]; however, our work was limited to a layer-specific analysis using confocal microscopy. Recent research shows that an alternative digestion-based microplate assay improves the quantification of damage in the highly aligned fibers of tendon [4]. It is less clear if such global quantification of tropocollagen damage is preferred in arteries, where collagen fiber directions vary dramatically through different layers, and baseline collagen remodeling activity is likely higher [1]. To address this knowledge gap, we stretched arteries axially to failure, both quasi-statically and at high strain rate, and compared CHP quantification using confocal analysis of the adventitial layer (where collagen fibers are largely aligned with the axial direction) with quantification using a global microplate assay. We find that the microplate assay does not identify any rate dependence in collagen delamination, while the confocal analysis shows a statistical difference between the two experimental groups. This shows that the choice of CHP analysis technique is critical in identifying damage phenomena in the multi-layer environment of arteries.

METHODS

Brains were removed from Göttingen minipigs, and the middle cerebral arteries (MCAs) were removed and placed in calcium-free phosphate-buffered saline (PBS). The pia-arachnoid complex was removed from the tissue, branches were ligated, and the vessels were stored at 4°C until mechanical testing. All mechanical testing was done within 48 hrs of death. Vessels were mounted onto a previously described tester [5] and preconditioned via pressure cycles at increasing axial stretch levels [1]. The MCAs were then pulled to failure either quasi-statically (0.01 s^{-1}) or at a high strain rate (>150 s^{-1}) as described in [3]. Seven vessels were selected for analysis from the quasi-static group and five from the high-rate group.

Following mechanical failure, the selected arteries were removed from the tester and stained with 20 µm F-CHP (fluorophore tagged CHP; 3Helix #FLU300, Salt Lake City) for at least 12 hours, and rinsed three times in PBS. Samples were then cut longitudinally and laid flat on a glass slide, using Fluormount (Fluoromount G; Southern Biotech) as the mounting medium. Image stacks were acquired with a confocal microscope (Fluoview FV1000, Olympus) at 2 µm slice increments. Following imaging, the image slice having the greatest brightness in axially oriented fibers was selected to represent the adventitial layer of the artery. The selected adventitia image was then normalized by undamaged control samples from the same animal to eliminate contributions from auto-fluorescence and remodeling. CHP attachment was calculated as the percent of pixels having a brightness greater than a threshold of four times the average control brightness.

The use of enzymatic digestion to evaluate CHP attachment largely followed previously established protocols [4]. After confocal imaging, each vessel was removed from its slide and rinsed in deionized water. It was assumed that the total quantity of collagen in the vessels was directly proportional to the dry weight. To evaluate dry weight, vessels were briefly dehydrated and weighed on a microbalance (UMX2 ultra-

microbalance, Mettler Toledo), after which the average of three measurements was recorded. Following weighing, vessels were rehydrated in deionized water and placed in a 100 µL solution of 1 mg/mL proteinase K (in deionized water) for 24 hours at 60° C. Each sample volume was then split into 50 µL segments and placed in an opaque microplate. Fluorescence was evaluated using a microplate reader (SpectraMax Gemini XPS, Molecular Devices, Sunnyvale, CA) with an excitation wavelength of 485 nm and an emission wavelength of 525 nm. The signals from the duplicates were averaged and divided by the dry weight previously obtained to normalize results. CHP attachment was reported as a multiple of control brightness.

Student's *t*-test was used to compare quasi-static and high-rate results for both methods. Significance was concluded for $p<0.05$.

RESULTS

As previously shown [3], vessels tested at quasi-static rates displayed notably higher levels of microstructural damage than those tested at high strain rates (Figure 1; p=0.015). However, this difference in observed damage levels with strain rate disappeared when the same vessels were evaluated using the microplate assay (Figure 2; p=0.35).

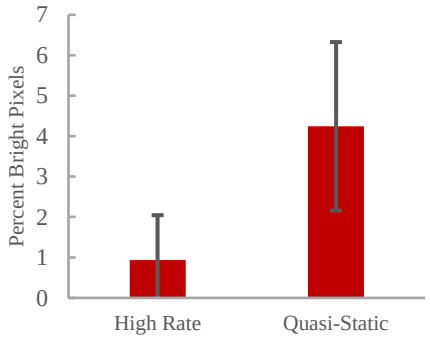

Figure 1: Local CHP quantification using the confocal microscopy technique shows a dramatic reduction in collagen delamination in vessels stretched dynamically compared to those stretched quasi-statically (p=0.015). Mean ± std dev.

DISCUSSION

Our results indicate that the selection of CHP damage quantification technique in the reported experiments has a dramatic effect on conclusions that can be drawn regarding the influence of strain rate on collagen delamination. This provides an interesting case study on the broad significance of method selection in science.

In comparing the two methods, it is clear that tropocollagen delamination differences with strain rate are significant at the local level but are not detectable at the global scale. One factor that seems to be important in this discrepancy is the complexity of the tissue. When used in fiber-aligned rat tail fascicle, the proteinase K assay is clearly accurate in indicating levels of collagen damage [4]. However, when used in cerebral arteries, sensitivity to layer-specific fiber orientation [1] is largely lost. It is interesting, though, that overall indication of damage to the tropocollagen structure is maintained in the microplate assay. While this is under investigation, it seems most likely that there is lower-intensity damage (that is not rate dependent) in layers other than the one chosen for analysis for its greatest fiber brightness, and that the sum of the fluorescence of these other layers overwhelms the specificity of the brightest adventitial damage signal.

Several limitations are inherent to the confocal imaging approach, perhaps the most impactful being the heavy dependence on the operator's ability to interpret collagen fiber orientation and positioning within the vessel wall. Additionally, researcher bias may be introduced while masking out artificial artifacts such as debris or suture. These limitations, together with the time investment required to image each vessel in entirety, demands a relatively large time commitment. Furthermore, the quantification algorithm is complicated and sensitive to the chosen steps. The confocal image analysis and quantification is an ongoing area of advancement but will remain challenging as the complexity level of the examined tissue increases.

The proteinase K assay is limited in its usefulness by its destructive nature. After tissue decomposition, it is impossible to extract fiber direction or other histological landmarks that may increase understanding of damage development. Drawbacks also exist for normalizing the proteinase K assay. Here, the dry weight was obtained using a highly precise microbalance (readability 0.1 µg) where the weight of each vessel ranged from approximately 10 to 50 µg. An alternative is proposed by Lin [4] in which a trypsin-hydroxyproline assay is used to estimate total collagen content. This process, while applicable to a wide range of tissues, is time consuming and carries its own risks of data loss during assay processing.

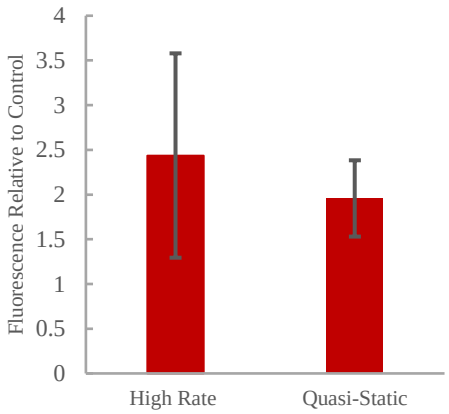

Figure 2: Global CHP quantification using the proteinase K microplate assay technique suggests no difference in extent of collagen delamination with strain rate. Mean ± std dev.

In conclusion, we find a disparity in rate dependent damage shown by CHP attachment when quantified using confocal microscopy compared with a microplate assay. This indicates that the rate-dependent CHP signal, while locally significant, is likely overwhelmed by global CHP attachment elsewhere in the vessel. Future work will further examine this phenomenon, but we expect that proteinase K will continue to be useful for general examination of vessel damage, while a microscopy approach will be required for microstructure-focused examination.

ACKNOWLEDGEMENTS

Funding for this project was provided by DOD grant #W81XWH-14-20134. Access to the UMX2 microbalance graciously provided by the Institute for Clean and Secure Energy at the University of Utah.

REFERENCES

[1] Converse *et al*., *Acta Biomater*, vol. 67, pp. 307-318, Feb 2018
[2] Zitnay *et al.*, *Nat Commun*, vol. 8, p. 14913, Mar 22 2017
[3] Pearson *et al.*, *SB3C* 2020.
[4] Lin *et al*., *J Orthopaedic Research*, vol. 37 pp. 431-438, Feb 2019
[5] Bell *et al*., *J Biomech Eng*, Jul 2018, 140(7): 071004

STUDY ON HEATING CAPABILITY OF NEW RADIOFREQUENCY ANGIOPLASTY BALLOON

Hongying Wang, Shiqing Zhao, Jincheng Zou and Aili Zhang

Department of Biomedical Engineering
Shanghai Jiao Tong University
Shanghai, China

INTRODUCTION

Percutaneous transluminal angioplasty (PTA) based on balloon and stents is widely used to dilate the artery narrowed by atherosclerotic plaque and restore blood flow[1]. However, restenosis often occurred after six months[2]. The main factor of restenosis is endothelial injury brought by the mechanical force in the PTA, which triggered a serial of inflammation process and caused vascular smooth muscle cell (VSMCs) proliferation and migration into the endothelial layer[3]. To inhibit the proliferation of VSMCs while protecting the endothelium may obtain a better therapeutic outcome.

Recently, Zhao et al proposed a novel treatment for atherosclerosis, in which the electrodes on the outer surface of balloon heat the plaque while the cooling water circulating in the balloon to lower the temperature of endothelium [4]. The numerical and phantom heating experiment results demonstrated that the novel treatment could heat the deep region and maintain the lower temperature in the endothelium. However, the conformal heating in the depth direction was not realized, in other words, the depth of heating cannot be adjusted based on the morphology of plaque, which varies with each other[5]. Herein， in order to realize the conformal heating in the depth direction, an experimental system, in which the temperature and velocity of cooling water could be adjusted, was established. Besides, the negative feedback regulation of output voltage on the electrodes was implemented via a temperature control algorithm, in which the setting temperature and voltage was the input and output variable. To investigate the effect of three parameters (the temperature, the velocity of water, the setting temperature) on the heating capability, several phantom heating experiments were conduct and computational model were established.

METHODS

Experiment setup: The experiment setup was similar with the previous study[6]. The cooling water flowed through a polyimide tube as a substitute for the balloon, which was connected with an adjusted water pump and a temperature adjustable thermostat bath. The electrodes were adhered on the outer surface and controlled by the radiofrequency system. The tube with electrodes was inserted into the tissue-mimicking phantom (see Fig.1A). In order to monitor the temperature evolution, three small thermocouples were unilaterally inserted into the phantom (see Fig.1A). Besides, one thermocouple as a control point was located between the two electrodes and the temperature was the input in the control algorithm (see Fig.1B and C, the red point). The intervals between the thermocouples (TC0, TC1, TC2, TC3) were 0.854, 1.61, 1.62mm, respectively. Phantom heating experiment was conducted with different parameters (the temperature and velocity of cooling water, the setting temperature) and duplicated three times. The cooling water pump was switch on 45s before the heating. The heating was lasted for 2 minutes. The temperature of the phantom and water, the voltages were recorded for further analysis.

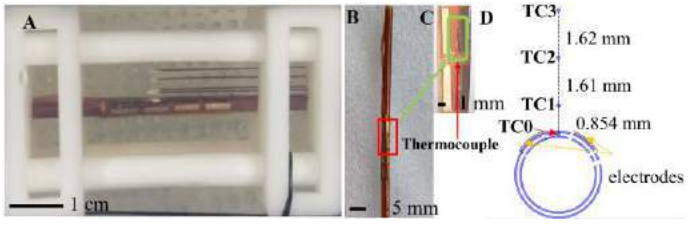

Figure 1: (A) picture of the phantom, electrodes and inserted with five thermocouples, (B) The polyimide tube pasted with microelectrodes and thermocouples, (C) Sectional view of polyimide tube with thermocouple and electrodes.

Temperature control algorithm: A temperature-controlled algorithm, PID control algorithm of integral limit (see Eq.1 ~ 3), was implemented by C# language. The voltage on the electrode and the temperature measured by TC0 were output and input variables. The coefficients in algorithm were determined manually.

$$RFVoltage(\mathrm{k}) = \begin{cases} 35\ (V);\ e(k) > 4\ ;\ e(k) < 4, PID(k) > 200 \\ 0.187 * PID(k) - 2.25\ (V); e(k) < 4, 100 < PID(k) < 200 \\ 16.5\ (V);\ PID(k) < 100 \end{cases} \quad (1)$$

$$e(k) = Tset(k) - T(k) \quad (2)$$

$$PID(k) = Kp * e(k) + Ki * \sum_{j=0}^{k} e(j) + Kd * \big(e(k) - e(k-1)\big) \quad (3)$$

Numerical modeling: In order to obtain the 3D temperature distribution, a finite element model (FEM) with the realistic experimental parameters was established in COMSOL Multiphysics (COMSOL, Inc., Burlington, MA, USA) to quantitatively assess the relationship between ablation zone and the parameters. The model setting details were same with the study[6].

RESULTS

With the fast response of the hardware circuit and the high sampling frequency of the data acquisition card, the temperature of control point reached the setting temperature (40℃) within 10s and the fluctuation was only ±0.5℃. The final temperature of point 0.845 mm away from the electrodes was about 60℃ and far higher than the inner surface temperature.

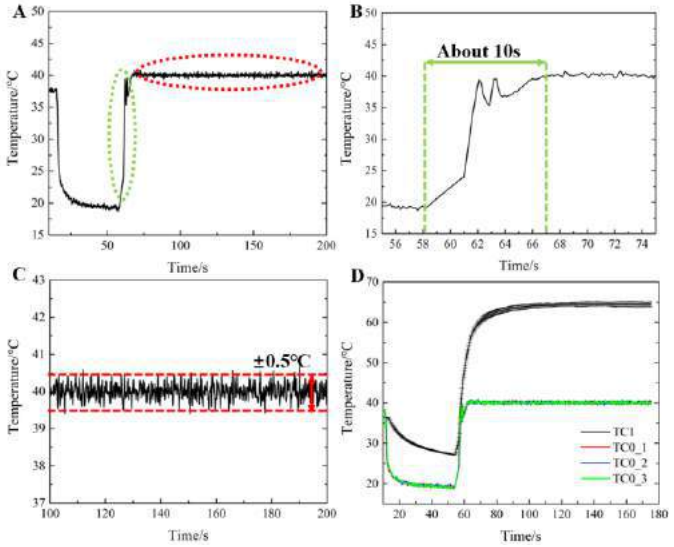

Figure 2: (A) The evolution of control point temperature (TC0), (B~C) The magnified view of the temperature increasing stage and equilibrium stage, (D) TC0 and TC1 temperature evolution (n=3).

The temperature in the phantom (TC1~TC3) increased dramatically as the setting temperature increased and showed a linear relationship, and TC1~TC3 temperature increased by 2.11℃, 1.06℃, and 0.49℃ respectively for every 1℃ increment of TC0. On the contrary, TC1~TC3 temperature decreased as the cooling water temperature increased and the decreasing trend gradually slowed down. The temperature in the phantom stayed almost the same as the velocity increase, especially when the velocity exceeded 3.5m/s.

The ablation area and depth on the middle plane of electrode (see Fig.4A) were calculated in the computational model. Here, we take 50℃ as the threshold of ablation temperature for the tissue[7]. The area and depth linearly increase by 1.001mm² and 0.092mm as the setting temperature increase 1℃ (see Fig.4B), and decreased with the temperature of cooling water. Moreover, the decreasing rate decreased as the cooling water temperature increased. The area and depth drop approximately linearly when the cooling water temperature is lower 20℃, and almost undiminished when the cooling water temperature was higher 25℃ (see Fig.4C). The average ablation area and depth are about 15mm² and 2.5mm, which is close to the size of cardiovascular plaque[8].

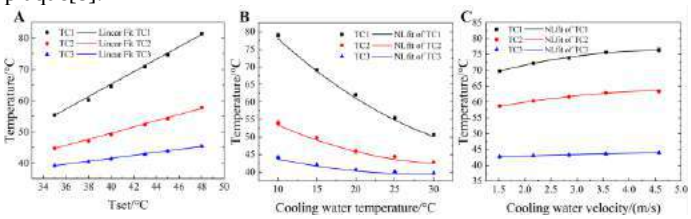

Figure 3: The final temperature in the phantom (TC1~TC3) varied with different parameters: (A) the setting temperature, (B) The cooling water temperature, (C) The cooling water velocity.

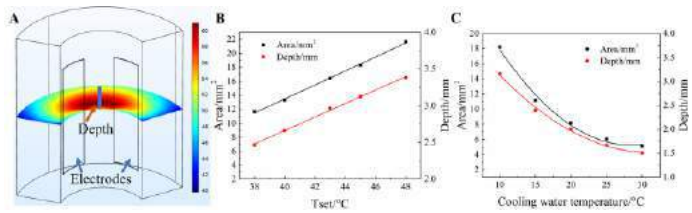

Figure 4: (A) The cross section and the definition of depth, (B~C) The ablation area and depth change as the control point temperature and the cooling water temperature increased.

DISCUSSION

The experimental results demonstrated the temperature control algorithm had a good precision and fast response time. With the algorithm, higher temperature focus on the areas about 0.4mm from the electrode surface and maintain lower temperature on the inner surface of lumen, which may ablate the plaque, inhibit the smooth muscle cell proliferation and protect the endothelium.

Moreover, the setting temperature in the PID algorithm and cooling water temperature had a significant impact on the temperature in the phantom. The effect of water velocity on the temperature was limited. The relationship between the parameters and the heating depth and area would be used to establish a conformal heating algorithm in future. With the help of intravascular imaging, a precise morphology of plaque could be obtained before treatment. Through tuning the setting temperature and the temperature of cooling water, a conformal heating in the depth direction may be realized.

ACKNOWLEDGEMENTS

This work was supported by the National Science Foundation of China under Grants 51890892.

REFERENCES

[1] Perkins, L. E. L. *et al.*,*Toxicol Pathol*, 47:297-310, 2019.
[2] Byrne, R. A. *et al.*,*Eur Heart J*, 36:3320-31, 2015.
[3] Buccheri, D. *et al.*,*J Thorac Dis*, 8:E1150-E1162, 2016.
[4] Zhao, S. *et al.*,*IEEE Trans Biomed Eng*, 2019.
[5] Myredal, A. *et al.*,*Vasc Med*, 15:33-7, 2010.
[6] Zhao, S. *et al.*,*Biomed Eng Online*, 19:44, 2020.
[7] Tian, Z. *et al.*,*Biomed Eng Online*, 15:124, 2016.
[8] Vos, J. *et al.*,*European Heart Journal*, 18:1081-1089, 1997.

WAVY FIBER STRUCTURE IMPROVES CONTRACTILE PHENOTYPE OF VASCULAR SMOOTH MUSCLE CELLS

Chun-Yu Lin and Pen-hsiu Grace Chao

Department of Biomedical Engineering
National Taiwan University
Taipei, Taiwan

INTRODUCTION

Elastic lamellae of arterial media forms three-dimensional network with circumferential wavy microstructure that contributes to mechanical functionality of the vessel (Figure 1A, [1]). With aging, the lamellar structure fragments and flattens due to mechanical damage and proteolytic activity [2]. At the same time, the resident vascular smooth muscle cells (VSMCs) change from a more quiescent and contractile phenotype to proliferate and synthesize matrices, resulting in arterial stiffening, a significant risk factor for cardiovascular health. Although regulation of VSMC phenotype by biochemical factors has been widely investigated [3], the effects of age-associated architectural changes remain unknown. Using electrospun straight and wavy fibrous scaffolds, we examine the topographical regulation of primary VSMC phenotype.

METHODS

Material Fabrication Poly-L-lactide solution (PLLA, 6% w/v in hexafluoropropylene) and polyethylene oxide solution (PEO,13.5%w/v in 80% ethanol) were electrospun based on previously reported parameters [4]. After PEO removal, the remaining PLLA fibers were heated at 85℃ for 15 minutes to induce crimp formation [5]. Fiber morphology was confirmed with SEM. Scaffolds were sterilized and treated with dopamine hydrochloride to facilitate collagen I coating (100 μg/ml). Fiber crimpness was assessed from the SEM images and was defined as the normalized difference of fiber path length and end-to-end distance.

VSMC Culture Primary VSMCs were isolated from explant cultures of thoracic aortae from 8 to 10-week-old mice. Isolated VSMCs were cultured in DMEM/F-12 supplemented with 10% FBS and GlutaMax. Cells from passages 2 and 5 were seeded at 600 cells/cm^2 on glass coverslips for one week for immunofluorescence assessment. Cells from passages 3 and 6 were seeded at 15000 cells per scaffold (1x2 cm^2) for 3 weeks for proliferation and immunofluorescence assays.

Proliferation Assay Alamar Blue dye was used to access cell activity during culture according to the manufacturer's protocol (Thermo Fischer Scientific). Briefly, VSMCs on the fibrous scaffolds were cultured in 10% Alamar Blue dye for three hours and the medium was read at 590 nm.

Immunofluorescence Assessment Samples were fixed in formalin, permeablized, and blocked in 1% BSA. Primary antibodies included anti-alpha smooth muscle actin (αSMA, Sigma), anti-transgelin (SM22, Abcam), and anti-calponin-1 (Abcam). Secondary antibodies (Alexa Flour-conjugated), DAPI, and phalloidin were used to fluorescently label the respective primary antibody, DNA, and f-actin targets. Images were acquired using a Nikon Ti-E2 wide field microscope (2D cultures) or a Leica SP-8 confocal microscope (3D scaffolds).

Data Analysis Statistical tests (student's t test, ANOVA with Tukey's HSD post hoc tests, or Fisher's exact test with Bonferroni corrections) and data figures were generated using R.

RESULTS

To investigate the topographical regulation of VSMC phenotype, scaffolds recapitulating wavy microstructure of native arterial wall were fabricated as previously described (Figure 1B, [4]). Compared to the control group (straight scaffolds), crimp fibers had significantly higher crimpness (Figure 1B). Primary VSMCs cultured on the fibrous scaffolds had elongated morphology with linear actin filaments through the length of the cell, while cells in crimp scaffold had discontinuous and wavy stress fibers at the cell periphery (Figure 1C). To confirm VSMC identity, they were immune-characterized with contractile phenotypic markers. Approximately 80% of cultured cells at passage 2 expressed α-SMA and SM22 (Figure 2A and B). Both markers

decreased significantly with passage, where less than 5% of the cells express SM22 at passage 5. Together with the concomitant decrease in population doubling time (Figure 2C), these results indicated that VSMCs switched from the differentiated contractile phenotype to the synthetic phenotype with subcultures. When the late passage VSMCs (P6) were cultured on fibrous scaffolds, the 3D structure improved expression of the contractile markers, which is further enhanced on the crimp scaffolds (Figure 3A). The crimp fibers also suppressed cell proliferation compared with the straight scaffold (Figure 3B, $p<10^{-4}$), indicating fiber morphology regulates VSMC phenotypic switch.

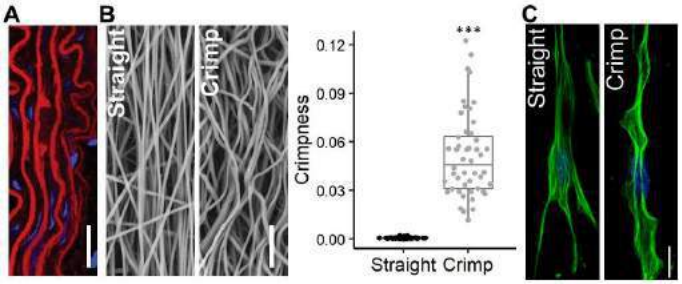

Figure 1 (A) Cross-section of mouse aorta (red-elastin, blue-nuclei, bar: 20μm [6]) (B) SEM images of scaffolds and quantification of fiber structure (bar = 20μm, ***$p<10^{-5}$) (C) Representative VSMC morphology on fibrous scaffolds (blue-nuclei, green-αSMA, bar = 20μm)

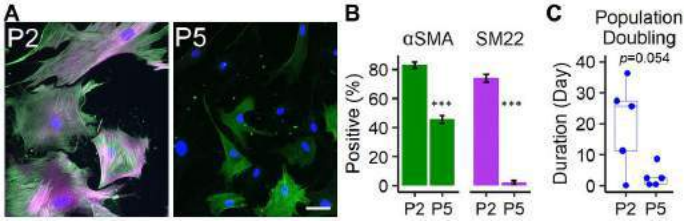

Figure 2 (A) VSMCs at passages 2 and 5 on tissue culture plastic (green-α-SMA, magenta-SM22, blue-nuclei, bar = 50μm) (B) Effects of passaging on the proportion of VSMCs expressing α-SMA or SM22, and (C) population doubling time (***$p<10^{-5}$).

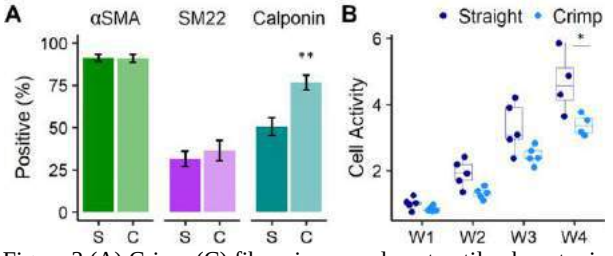

Figure 3 (A) Crimp (C) fibers improved contractile phenotypic expression of late passage VSMCs, compared with straight (S) fibers (**$p<0.001$) (B) Crimp fibers suppressed normalized VSMC activity in culture (W-week, *$p<0.05$).

DISCUSSION

Environmental factors play critical roles in modulating VSMC. Previous studies have found linear topographies control VSMC contact guidance and phenotype [7, 8]. We have also reported that wavy microgrooves regulate nuclear structure and DNA synthesis in VSMC cell lines [9]. In this study, we establish primary VSMC cultures and examine VSMC phenotype in three-dimensional biomimetic crimp fibers. Despite the loss of contractile markers with subculture (Figure 2), 3D scaffolds recover the differentiated phenotype, characterized by decreased proliferation and enhanced calponin-1 expression. In addition to mechanical functionalities [10, 11], our results point to an instructive role of vascular ECM structure on VSMC phenotype. Future studies will investigate the transcriptomic effects of scaffold structure, as well as the interactions of fiber structure and mechanical stimulation on VSMC regulation. As the crimp structure is lost with aging and disease, our findings provide new insights in the maintenance and pathology of vascular homeostasis and health.

ACKNOWLEDGEMENTS

This work was supported by National Taiwan University (JP-110L7214), the National Health Research Institute (EX110-10910EI), and the Ministry of Science and Technology (107-2221-E-002 -071-MY2).

REFERENCES

[1] K.P. Dingemans, Teeling, Peter, Lagendijk, Jaap H., A.E. Becker, Extracellular matrix of the human aortic media: An ultrastructural histochemical and immunohistochemical study of the adult aortic media, The Anatomical Record 258(1) (2000) 1-14.

[2] L. Duca, S. Blaise, B. Romier, M. Laffargue, S. Gayral, H. El Btaouri, C. Kawecki, A. Guillot, L. Martiny, L. Debelle, P. Maurice, Matrix ageing and vascular impacts: focus on elastin fragmentation, Cardiovascular Research 110(3) (2016) 298-308.

[3] M.R. Alexander, G.K. Owens, Epigenetic Control of Smooth Muscle Cell Differentiation and Phenotypic Switching in Vascular Development and Disease, Annu. Rev. Physiol. 74(1) (2012) 13-40.

[4] S.E. Szczesny, T.P. Driscoll, H.-Y. Tseng, P.-C. Liu, S.-J. Heo, R.L. Mauck, P.-H.G. Chao, Crimped Nanofibrous Biomaterials Mimic Microstructure and Mechanics of Native Tissue and Alter Strain Transfer to Cells, ACS Biomaterials Science & Engineering 3(11) (2017) 2869-2876.

[5] P.-h.G. Chao, H.-Y. Hsu, H.-Y. Tseng, Electrospun microcrimped fibers with nonlinear mechanical properties enhance ligament fibroblast phenotype, Biofabrication 6(3) (2014) 035008.

[6] A.J. Cocciolone, J.Z. Hawes, M.C. Staiculescu, E.O. Johnson, M. Murshed, J.E. Wagenseil, Elastin, arterial mechanics, and cardiovascular disease, American Journal of Physiology-Heart and Circulatory Physiology 315(2) (2018) H189-H205.

[7] E.K.F. Yim, R.M. Reano, S.W. Pang, A.F. Yee, C.S. Chen, K.W. Leong, Nanopattern-induced changes in morphology and motility of smooth muscle cells, Biomaterials 26(26) (2005) 5405-5413.

[8] S. Chang, S. Song, J. Lee, J. Yoon, J. Park, S. Choi, J.-K. Park, K. Choi, C. Choi, Phenotypic modulation of primary vascular smooth muscle cells by short-term culture on micropatterned substrate, PLoS One 9(2) (2014) e88089-e88089.

[9] B.-L. Huang, C.-H. Huang, R.K. Assoian, P.G. Chao, Myosin-independent regulation of cell and nuclear structures in wavy patterns, SB3C, Seven Springs, PA, 2019.

[10] H. Wolinsky, S. Glagov, Structural Basis for the Static Mechanical Properties of the Aortic Media, Circul. Res. 14(5) (1964) 400-413.

[11] X. Yu, R. Turcotte, F. Seta, Y. Zhang, Micromechanics of elastic lamellae: unravelling the role of structural inhomogeneity in multi-scale arterial mechanics, Journal of The Royal Society Interface 15(147) (2018) 20180492.

EFFECT OF ECM HETEROGENEITY ON CELL MECHANOSENSING

Maria Proestaki (1), Jacob Notbohm (1)

(1) Department of Engineering Physics
University of Wisconsin-Madison
Madison, Wisconsin, USA

INTRODUCTION

Cells sense mechanical signals within the extracellular matrix, the most familiar being stiffness, but matrix stiffness cannot be simply described by a single value. Randomness in matrix structure can cause stiffness at the scale of a cell to vary by a factor of 3 or greater. Additionally, the extracellular matrix contains stiff and compliant features such as ducts, glands and vessels. Diseased tissues may also contain features of abnormally high stiffness, such as fibrotic scars, stiff arterial walls and tumors. As these various stiff and compliant features alter the matrix stiffness, they could potentially affect the stiffness sensed by a cell. How the features of different stiffness and matrix heterogeneity together affect cell sensing remains unclear. Here we use a combination of experiments and modeling to establish a method to quantify the critical distance over which a cell can sense a locally stiff feature. This method is then used to sort out the effect of matrix heterogeneity on this critical distance.

METHODS

To identify the critical distance over which cells can sense a stiff feature, we conducted experiments using the migratory human breast cancer cell line MDA-MBA-231. Using a 3D Petri dish micro-mold (MicroTissues, Inc.) we formed cell spheroids with an average diameter of 500 μm. A thick layer of rat tail collagen I (Corning) with final concentration 3 mg/mL was polymerized at the bottom of a glass bottom dish, and then a second 3 mg/mL collagen layer was polymerized on top of the first with one cell spheroid and a stiff inclusion embedded into it, as shown in Fig. 1a. Stiff inclusions were introduced by embedding PMMA spheres of 3.5 mm diameter at a distance in the range of 0.5-3 mm from the centroid of each cell spheroid. After 96 hours, images of the cell spheroids were captured, and the area of cell migration toward and away from the stiff inclusion was computed (Fig. 1b). A ratio equal to 1 indicates no preference of cells migrating towards or away from the stiff inclusion, whereas a ratio larger than 1 indicates that cells preferentially migrated towards the stiff inclusion.

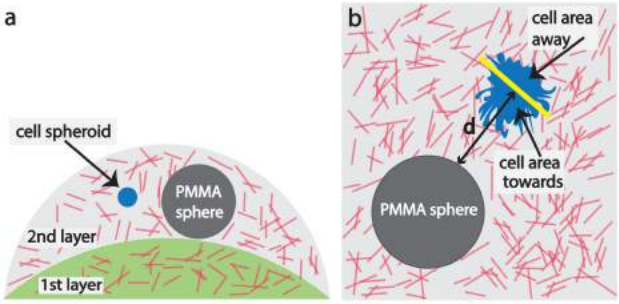

Figure 1: Cell spheroids and stiff inclusions embedded in collagen gels. (a) Schematic of a cell spheroid and a stiff inclusion (PMMA sphere) embedded in a 2-layered collagen gel. (b) Schematic of a collagen matrix with a PMMA sphere located at a distance d from a cell spheroid. Areas of cell migration toward and away from the PMMA sphere are shown.

Additionally, we created a 2D finite element model of a fibrous matrix, that mimics the structure and properties of collagen networks[1]. Each fiber is modeled as a Timoshenko beam that can stretch, bend and buckle and has a stretching, bending and shear stiffness. The important ratio $\kappa = EI/EAL^2$ defines the dimensionless ratio of bending to stretching stiffness, where E is the fiber's Young's modulus, I is the fiber's moment of inertia, A is the fiber's cross sectional area and L is fiber length. For fibrous materials κ is around 10^{-3}, indicating a low resistance to bending compared to stretching[2]. Under compression,

buckling occurs, resulting from bending instability. To match the experiments, a contracting inclusion of radius r and a stiff inclusion located at a distance d from contracting inclusion's centroid were embedded in the fiber network. We quantified the potential for sensing the stiff inclusion by finding the apparent stiffness sensed by the contracting inclusion by applying a nonlinear continuum model for fibrous materials[3]. Because fibers buckle under compression, the stiffness in compression is far smaller than in extension, a phenomenon referred to as compression weakening. The continuum model accounts for compression weakening by introducing a compression weakening factor ρ, which represents the ratio of stiffness in compression to tension, with $0 \le \rho \le 1$. To represent the apparent stiffness sensed by the inclusion, we followed the method of our previous paper[4] to derive an expression for the Young's modulus of the fiber network in the local region surrounding the inclusion, E^n,

$$E^n = \frac{E^i}{g(\nu,\rho)}\left(\frac{\varepsilon^T}{\varepsilon} - 1\right) \qquad (1)$$

where E^i is the Young's modulus of the contracting inclusion, $g(\nu,\rho)$ is a function of Poisson's ratio ν and compression weakening factor ρ, ε^T is the contracting inclusion's strain if it were not in the fiber network and ε is the contracting inclusion's strain in the fiber network. In the results, we express the apparent stiffness as the product of Young's modulus E and function $g(\nu,\rho)$. To determine how the mechanical properties of the fiber network such as fiber density and fiber length can affect the potential for sensing the stiff inclusion, we tested various fiber networks of different density and fiber length.

RESULTS

Results from experiments using cell spheroids and PMMA inclusions showed that the median ratio of the cell migration areas toward the inclusion to away from the inclusion was statistically different than 1 for the cell spheroids located at a distance less than 1.1 mm from the inclusions. Specifically, for the ratios of the spheroids located at a distance less than 1.1 mm from PMMA (Fig. 2 red dots), the sign test rejected the null hypothesis that the median of the data equaled to 1, giving a p-value of 0.02. However, for the ratios of the spheroids located greater than 1.1 mm from PMMA (Fig. 2 black dots), the sign test failed to reject the null hypothesis, with a p-value of 1. The dimensionless ratio of distance d = 1.1 mm to spheroid radius r = 250 μm is 4.4.

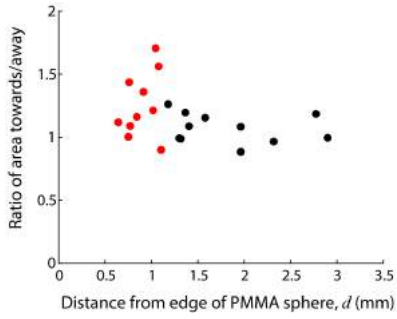

Figure 2: Ratio of cell migration areas towards and away from the PMMA sphere. Each dot represents one cell spheroid. The initial radius r of cell spheroids was approximately 250 μm. Spheroids at distance < 1.1 from the inclusion (red dots) had area ratios significantly greater than 1 (p = 0.02, sign test), whereas spheroids at distance > 1.1 (black dots) had area ratios not significantly greater than 1 (p = 1, sign test).

Results from the fiber network simulations are shown in Fig. 3 for various fiber networks of different fiber density and fiber length. Heterogeneity in stiffness in networks with high density and short fiber length is less than in networks with low fiber density and long fiber length.

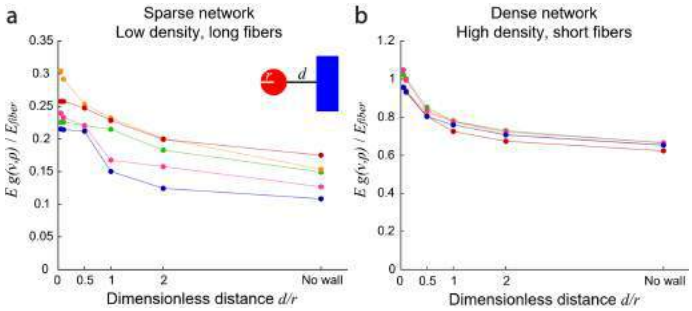

Figure 3: Stiffness expressed as the product of Young's modulus E and function $g(\nu,\rho)$ sensed by the contracting inclusion in different fiber networks in the presence of a rigid wall located at different distances. (a) Product of Young's modulus E and function $g(\nu,\rho)$ for 5 different fiber networks of low fiber density and long fiber length for 15% strain. Young's modulus E is made dimensionless by dividing with the Young's modulus of individual fibers, E_{fiber}. Each line represents a different fiber network. The horizontal axis gives the dimensionless distance d/r, where d is the distance from the contracting inclusion to the stiff inclusion and r is the radius of the contracting inclusion, as shown in the schematic in panel a. The last point in the horizontal axis gives the case of absence of a rigid wall. (b) Product of Young's modulus E and function $g(\nu,\rho)$ for 5 different fiber networks of high fiber density and short fiber length for 15% strain.

DISCUSSION

Our results from simulations showed a large degree of heterogeneity in fiber networks of low fiber density and long fiber length, in which the ratio of inclusion size to fiber length is small. This randomness due to different fiber networks (or, equivalently, different positions in the same fiber network) has a greater effect on local modulus than the presence of a wall. Hence, a cell in a network with low fiber density and long fibers has no chance of sensing the stiff region. In the fiber networks of high density and short fiber length, in which the ratio of inclusion size to fiber length is greater, there is a lower degree of heterogeneity. Thus, in such fiber networks the critical distance increases and a cell may potentially sense the stiff region.

In the experiments, the ratio of cell spheroid size to fiber length is big. Hence the experiments are conducted in fiber networks having short fiber length. Consistent with the theory, the cells sense and respond to the presence of the rigid boundary for small and moderate distances between spheroid and boundary.

ACKNOWLEDGEMENTS

This work is supported in part by NSF CMMI-1749400.

REFERENCES

[1] Grimmer, P et al., *J Biomech Eng* 140 (4), 041011, 2018.
[2] Licup A J et al., *Proc Natl Acad Sci USA*, 112 (31) 9573-9578, 2015.
[3] Rosakis P et al., *J Mech Phys Solids* 85:18–32, 2015.
[4] Proestaki, M et al., *Exp Mech* 59, 1323–1334, 2019.

FORCE TRANSMISSION WITHIN THE MIGRATING ENDOTHELIUM REGULATES SHUNT FORMATION DURING ANGIOGENIC REMODELLING

Lowell T. Edgar **Miguel O. Bernabeu**

Usher Institute
College of Medicine and Veterinary Medicine
University of Edinburgh
Edinburgh, United Kingdom

INTRODUCTION

Developmental angiogenesis occurs in distinct phases: an initial spouting phase followed by a later remodelling phase in which endothelial cells (ECs) composing blood vessels rearrange in response to shear stress signals from blood flow [1]. Some time ago, Pries et. al. proposed "The Shunt Problem" in which they demonstrated that remodelling driven by shear stress signals alone results in the dominance of short proximal pathways at the expense of longer distal pathways, thereby "shunting" blood flow away from downstream regions of the vascular tree [2]. In their hallmark work they proposed that additional "upstream" signalling is required to maintain both proximal and distal paths. We have since demonstrated that these signals may originate from collective migration of ECs during remodelling, possibly in the form of force transmission between cells at adherens junctions [3].

The cellular mechanisms of vascular shunting remain poorly understood despite being highly relevant in the context of arteriovenous malformations (AVMs), a leading cause of stroke and neurodegeneration [4]. To elucidate and demonstrate the role of force transmission during collective migration in shunt formation, we have designed an agent-based model of flow-mediated migration and angiogenic remodelling. We represent individual cells as discrete entities which interact with one another via transmitting force. With this model we can vary the parameters that control the levels of force transmission and will attempt to identify which factors push the system towards shunt formation.

METHODS

We simulated EC migration within an idealised capillary plexus consisting of vessels arranged in a "honeycomb" configuration. Vessels were discretised into cylindrical segments representing the lumen. We prescribed pressure at the inlet and outlet and use the Poiseuille approximation to solve for blood flow. EC agents, confined to the surfaces of the luminal segments, consisted of a pair of nested ellipses. The inner ellipse (semi-major A, semi-minor B) represents the undeformed "stress-free" configuration of the cell, while the outer ellipse (semi-major ΓA, semi-minor ΓB) represents the "yield surface" of junction connections. ECs experiencing tension at their junctions will deform up to a stretch ratio of Γ, after which they will release the junctional connection and attempt to return to the stress-free configuration. Agents also polarise along their major axis against the direction of flow.

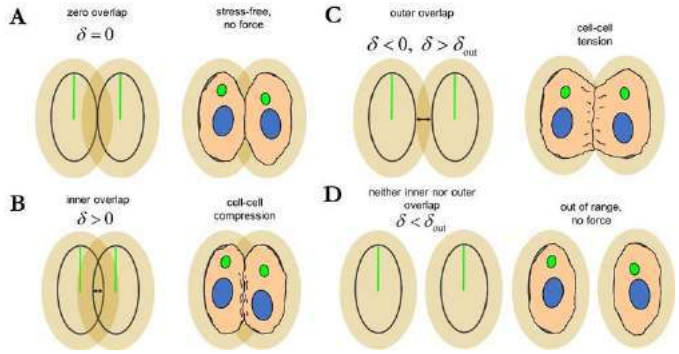

Figure 1: ECs represented as nested ellipses. Overlap between the ellipses produces various modes of cellular mechanics: (A) adjacent inner ellipses with no overlap represents the stress-free configuration with no force transmission. (B) overlap of the inner ellipses produces an extrusive force and represents compression. (C) overlap of the outer ellipses produces a cohesive force and represents tension. (D) cells with no overlap are out of range and transmit no force between one another.

ECs transmit force to one another depending on the overlap, δ, of adjacent ellipses (Figure 1). When considered two agents, i and j with

distance vector $\boldsymbol{r}_{ij}$ between them, the overlap between the agents is defined as

$$\delta_{ij} = \frac{\lambda_i + \lambda_j - \|\boldsymbol{r}_{ij}\|}{2A}, \quad (1)$$

where λ_i and λ_j are the radius of intersection for each agent. The outer boundary of overlap is similarly defined as

$$\delta_{\text{out}} = \frac{(1-\Gamma)(\lambda_i + \lambda_j)}{2A}. \quad (2)$$

The force transmitted between the two agents is then calculated as

$$\boldsymbol{f}_{ij} = \begin{cases} -k_{\text{ext}}\delta_{ij}^2 \hat{\boldsymbol{r}}_{ij}, & \text{if } \delta_{ij} \geq 0 \\ k_{\text{coh}}\delta_{ij}^2 \hat{\boldsymbol{r}}_{ij}, & \text{if } \delta_{\text{out}} \leq \delta_{ij} < 0. \\ \boldsymbol{0}, & \text{if } \delta_{ij} < \delta_{\text{out}} \end{cases} \quad (3)$$

If the inner ellipses of the agents overlap ($\delta_{ij} \geq 0$) the agents transmit an *extrusive force* (scaled by k_{ext}) to push the agents back to the stress-free configuration. If the outer ellipses of the agents overlap ($\delta_{\text{out}} \leq \delta_{ij} < 0$) the agents transmit a *cohesive force* (scaled by k_{coh}) to pull the agents back to the stress-free configuration. The agents are out of range from each other if $\delta_{ij} < \delta_{\text{out}}$ and thus transmit no force. Additionally, each agent produces a migratory force along their polarity vector $\hat{\boldsymbol{p}}_i$ scaled by the parameter k_{mig} which causes them to migrate against the direction of flow. The force transmission parameters can be expressed as two energetic parameters: the work to push cells together and the work to pull cells apart,

$$W^*_{\text{push}} = \frac{k_{\text{ext}}}{k_{\text{mig}}}, \quad (4)$$

$$W^*_{\text{pull}} = \frac{k_{\text{coh}}|1-\Gamma|^3}{k_{\text{mig}}}. \quad (5)$$

Lastly, we implement an overdamped dynamic model (assuming quasi-static equilibrium) to calculate the migration speed $\boldsymbol{v}_i$ of each agent via the summation of all transmitted forces and the migratory force,

$$\eta \boldsymbol{v}_i = \sum_j \boldsymbol{f}_{ij} + k_{\text{mig}}\hat{\boldsymbol{p}}_i, \quad (6)$$

and use Euler's method to update the position of each agent across each step in time. ECs migrate upstream until the encounter a vessel bifurcation: at flow-divergent bifurcations, ECs simple combine at the parent vessel. At flow-convergent bifurcations, ECs are evenly split amongst the two child branches. Additionally, periodic cell boundary conditions were prescribed such that cells exiting via the inlet re-enter at the outlet.

To interrogate the role of force transmission during remodelling, we ran the model with 50 different random seeds (randomising initial cell position each time) at various values of W^*_{push} (0, 1, 3, 5) and W^*_{pull} (0, 1/9, 2/9, 3/9) and collected various network-level features associated with shunt formation for which to perform our analysis.

RESULTS

We found that we could push our system from stable perfusion to shunt formation via control of a single parameter, the amount of cohesion within the system W^*_{pull} (Figure 2). Simulations with little to no cohesion resulted in cells evenly distributed across the plexus and perfusion maintained throughout. However, simulations with high levels of cohesion resulted in aggregations of cells along a minority of the flow pathways, depleting cells and flow from other regions of the plexus.

Increased extrusion within the system allowed the cells to intercalate and reduce stress within the endothelium whilst increased cohesion inhibited this intercalation and created tension. Increased cohesion also produced more prolonged flow reversals and the time vessels spent with reversed flow increased (Figure 3 A). Flow reversals exert a critical behaviour change within the system as they switch the direction of cell migration and flow convergence/divergence at bifurcations. Lastly, the aggregation of cells disrupted perfusion within the plexus, and the time-integrated percentage of flow pathways which lost flow increased with cohesion (Figure 3 B).

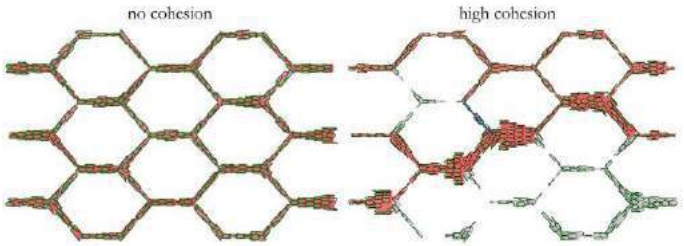

Figure 2: Excessive cohesion produced shunt formation. (Left) Simulations with littler to no cohesion resulted in a stable plexus during remodelling, with cells well distributed and flow uninterrupted. (Right) High levels of cohesion resulted in cells aggregating along a small percentage of flow paths, robbing the remainder of the plexus of cells and perfusion. Vessels with forward flow are coloured in red, reversed flow in blue, and flow loss in grey.

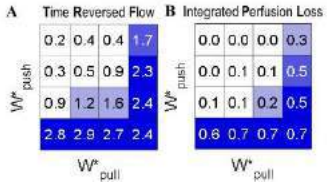

Figure 3: Excess cohesion disrupts flow and perfusion whilst extrusion stabilizes. (A) Time vessel spent with reversed flow decreased with extrusion and increased with cohesion. (B) Perfusion loss similarly increased as cohesion increased.

DISCUSSION

With our model we have demonstrated how excess cohesion between migrating ECs can promote shunt formation by creating large cell aggregates, diverting cells and perfusion away from other regions of the plexus. We believe the primary mechanism of these shunt formations comes in the form of prolonged flow reversals that occur in simulations with high cohesion. In simulations without cohesion, flow reversals that develop are quickly resolved as the cells intercalate to reduce stress and smooth out any aggregates that begin to form. High levels of cohesion disrupt this intercalation and allow flow reversals to persist. Flow reversals lead to a critical switch in EC migration behaviour at vessel bifurcations, switching flow-divergent bifurcations where ECs once split apart to flow-convergent bifurcations where cells now combine (Figure 4). Prolonged switching of bifurcation behaviour causes cells to aggregate along a small percentage of flow paths, creating vascular shunts. These results provide valuable insight into the mechanisms of shunt formation in vivo, implicating cohesion and flow reversals as critical mechanisms and may provide additional targets for vascular normalization strategies in the future.

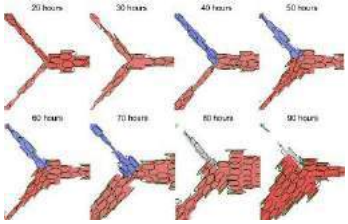

Figure 4: Flow reversals switch flow-divergent bifurcations to flow-convergent bifurcations, and prolonged flow disruptions have a dramatic impact on cell distribution and producing cell aggregates which lead to shunt formation.

ACKNOWLEDGEMENTS

We would like to graciously acknowledge our funding as part of a Foundation Leducq Transatlantic Network of Excellence (17 CVD 03, https://www.mdc-berlin.de/leducq-attract).

REFERENCES

[1] Georgieva PB, et. al. Circ Res. 2019; 125: 262–264.
[2] Pries AR, et. al. Nat Rev Cancer. 2010; 10: 587–593.
[3] Edgar LT, et. al. PLoS Comp Biol. 2021; In Press.
[4] Derdeyna, et. al. Stroke 2017; 48(8): e200-e224.

BONE BIOMECHANICS ADVANCES ANIMAL WELFARE IN EGG-LAYING HENS

Glynn E. Gallaway (1), Brittney J. Emmert (2), Darrin Karcher (2), Thomas H. Siegmund (1),

(1) School of Mechanical Engineering
Purdue University
West Lafayette, IN, USA

(2) Department of Animal Sciences
Purdue University
West Lafayette, IN, USA

INTRODUCTION

While cage-free housing of egg-laying enhances hen natural behavior it leads to increased incidence of fractures to the keel bone. Figure 1 depicts an image of keel bone with a visible fractures and healed fractures. Observed by dissection, one observes a line on the underside of the keel bone (inside the body cavity) and rarely sees any indication of a fracture on the outside where the breast muscle is attached.

Figure 1: Tip of a keel bone with fracture and healed fractures.

The biomechanics of keel bone fracture is poorly understood. This lack of foundational biomechanics knowledge limits efforts to reduce fracture incidence and leaves interventions through housing changes, nutrition, lighting etc. to mostly trial and error. There are very limited publications on the assessment of the biomechanics of the keel bone [1-5] and none have considered detailed computational models of the keel bone and keel bone fracture initiation and propagation during the egg-laying processes. Advances in the understanding of the biomechanics of keel bone fractures are of significance The US egg industry is moving toward cage-free egg production. Currently, 23.3% of the egg industry is in cage-free housing but to meet commitments by retailers, food service and fast-food businesses 71% would need to be cage-free by January 1, 2026 [6]. Bone fracture simulations can be conducted as shown in [7] by the use of the extended finite element method. Here, this approach is applied to investigate keel bone fracture.

METHODS

We obtain a CT-scan of an egg-laying hen without visible fracture. The CT scan data were reconstructed and converted into a finite element mesh using the code Synopsys' Simpleware™ software. The keel is segmented into bone and cartilage components. The finite element discretization was constructed and employed 10-node tetrahedra elements. The total number of finite elements is defined 26,884 in the specific keel bone model considered here. The keel bone was endowed with elastic properties for bone (E_{bone}= 1.96 GPa, ν_{bone}=0.37) and cartilage (E_{cart}=1.0 GPa, ν_{cart}=0.37). Furthermore, a maximum principal stress failure criterion is considered for the onset of fracture formation. The strength of bone is s_{bone}=3.92 MPa for bone and that of cartilage s_{cart}=1.0 MPa. Past the initiation of failure, the material separation to a full loss of load transfer across the propagating fracture process zone is given as 0.1 mm for both bone and cartilage. Bone and cartilage are considered as fully bonded to each other and no interface failure is considered to occur. The keel bone is fixed in space at its fulcrum-near

termination and is free at the opposite end, mimicking anatomical boundary conditions. A rigid body is ascribed a displacement in order to mimic the path an egg would take. The computational model is solved using a finite element code (ABAQUS) with the extended finite element method for material failure. Figure 2 depicts the model with boundary condition and a representation of the loading process.

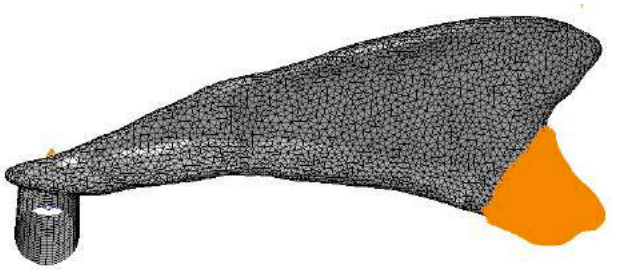

Figure 2: FE model of a keel bone as loaded simulating an egg-laying process.

RESULTS

The finite element simulation of the egg-laying processes predicts a crack initiation site close the tip of the keep bone with the crack initiating from the broad size of the keel bone. Figure 2 depicts the deformed keel bone under the simulated egg-laying load with the as-computed crack visualized. The comparison of Figures 1 and 3 indicates a validation of the simulation model regarding the approximate fracture location. From a biomechanics perspective, the keel bone is found to be a T-shaped cantilevered beam with a graded cross section geometry and a graded effective material property. The stiffness of the keel bone/cartilage combination declines towards the keel tip. As such the location of the fracture is determined by a combination of all such factors in combination. Aging and calcification, i.e. replacement of cartilage by bone, will result in a relocation of the fracture and to potentially increased fracture risk. An increase in egg-size increases the applied displacement on the keel bone and will as well have the potential to increase fracture risk.

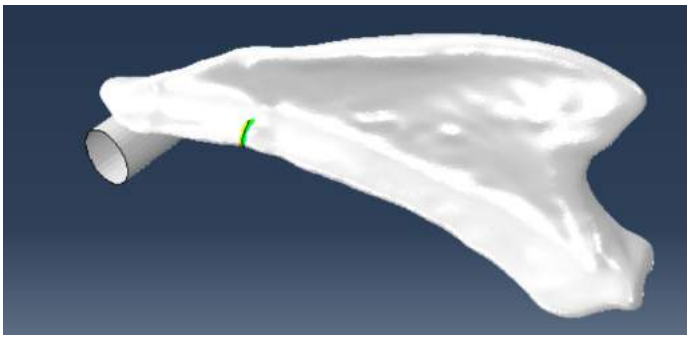

Figure 3: FE model with computed crack following a loading process simulating the egg-laying processes.

DISCUSSION

Keel bone fracture is considered as problem of significance to the poultry industry. If such fractures can be avoided, benefits to both animal welfare and egg production would be realized. Computational simulations of the keel bone fracture by use of an extended finite element approach are demonstrated to allow for the analysis of the interaction effects of geometry, tissue biomechanical properties and egg-laying processes related biomechanical loading scenarios. The present model only considers the keel bone and none of the muscle and additional bones. Models under the consideration of these components, Figure 4, will improve the predictive capability of the computational analysis.

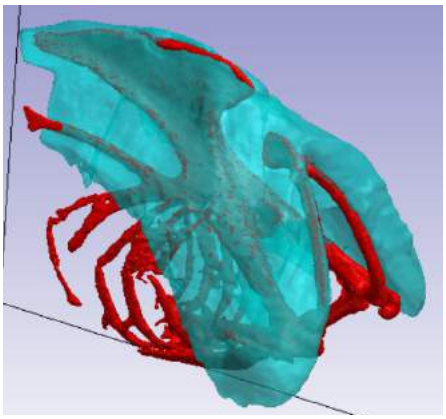

Figure 4: Keel bone with surrounding muscle and bone structure

ACKNOWLEDGEMENTS

This work is supported by the AG-ENG Interdisciplinary Collaboration at Purdue University.

REFERENCES

[1] Fleming, R. H., H. A. McCormack, L. McTeir, and C. C. Whitehead. 2004. Incidence, pathology and prevention of keel bone deformities in the laying hen. Br. Poult. Sci. 45:320–330.

[2] Tarlton, J. F., L. J. Wilkins, M. J. Toscano, N. C. Avery, and L. Knott. 2013. Reduced bone breakage and increased bone strength in free range laying hens fed omega-3 polyunsaturated fatty acid supplemented diets. Bone 52:578–586

[3] Toscano, M., F. Booth, G. Richards, S. Brown, D. Karcher, and J. Tarlton. 2018. Modeling collisions in laying hens as a tool to identify causative factors for keel bone fractures and means to reduce their occurrence and severity. PLoS One 13:1–21.

[4] Toscano, M. J., F. Booth, L. J. Wilkins, N. C. Avery, S. B. Brown, G. Richards, and J. F. Tarlton. 2015. The effects of long (C20/22) and short (C18) chain omega-3 fatty acids on keel bone. Poult. Sci. 94(5):823-835

fractures, bone biomechanics, behavior, and egg production in free-range laying hens. Poult. Sci. 94:823–835.

[5] Toscano, M. J., L. J. Wilkins, G. Millburn, K. Thorpe, and J. F. Tarlton. 2013. Development of an ex vivo protocol to model bone fracture in laying hens resulting from collisions. PLoS One 8(6): e66215.

[6] King, Deven. 2020. Cage-free transition financially and logistically impossible. WattPoultry.com. Accessed Jan. 2021. https://www.wattagnet.com/articles/40818-cage-free-transition-financially-and-logistically-impossible.

[7] Hammond, M.A., Wallace, J.M., Allen, M.R. and Siegmund, T., 2019. Mechanics of linear microcracking in trabecular bone. J. Biomech. 83:34-42.

SB³C2021
Summer Biomechanics, Bioengineering and Biotransport Conference
June 14-18, Virtual

A MICROFLUIDIC APPROACH TO CREATE GRADIENTS IN COLLAGEN FIBER ANISOTROPY

Indranil M. Joshi (1), Mehran Mansouri (2), Adeel Ahmed (2), Steven W. Day (1,2), and Vinay V. Abhyankar (1,2)

(1) Biomedical Engineering
Rochester Institute of Technology
Rochester, NY, USA

(2) Microsystems Engineering
Rochester Institute of Technology
Rochester, NY, USA

INTRODUCTION

Collagens are found in nearly every tissue in the human body. Close to 30 different types of collagens have been identified in vivo, and type I collagen (COL1) is one of the primary structural components found in the extracellular matrix (ECM). Fibrous COL1 plays a vital role in providing mechanical and structural support to bones, tendons, muscles, and other tissues. Over the past several decades, in vitro models have been established to systematically study the relationship between COL1 properties and cell responses. For example, in the tumor microenvironment, bulk matrix stiffness, density, and fiber alignment have been found to influence cell motility and have provided unique approaches to study guidance cues that can direct tumor cells through the ECM. The COL1 microarchitecture is rapidly remodeled in response to both traction forces and biochemical stimuli, resulting in spatial variations (gradients) in matrix properties. More recently, techniques to engineering gradients of matrix properties have emerged. These "taxis" cues include continuous gradients in stiffness (durotaxis) [1], local cues (ratchetaxis) [2], and tethered biomolecules (haptotaxis) [3] have all been shown to influence cell motility.

The reorganization of COL1 fibers can have clinical significance, where the presence of anisotropic (aligned) fiber domains orthogonal to a tumor boundary can predict poor prognosis in breast cancer patients [4]. *In vitro* models to study tumor cell motility on anisotropic fiber domains have been established by several groups [5,6] but exploring the effects of gradients in collagen anisotropy have not been demonstrated within 3D gel environments. To explore cell motility on aligned fiber gradients (gradient alignotaxis), we introduce a microfluidic system that can create controlled gradients in COL1 fiber anisotropy using controlled extensional strain rates (i.e., the velocity gradient along the direction of flow). Leveraging our experience relating extensional strain rate and fiber anisotropy, we create gradients in fiber anisotropy by flowing neutralized collagen solutions through non-uniform channel networks. Under a constant flow rate Q, changes in the cross-sectional area (A) introduces a change in average velocity (V) according to the relationship ($V = QA^{-1}$). Thus, a rapid increase in A produces a drop in velocity along the flow direction and result in a rapid drop off in extensional strain rate and translates to defined gradients in fiber anisotropy.

METHODS

Microfluidic channels: Channels were fabricated via standard soft lithography techniques using a mold with 60 µm tall features. After replica molding, the PDMS channels were cut out, and access ports were cored with a 1mm diameter biopsy punch. Devices were then sequentially cleaned in ethanol followed by water. They were dried and plasma bonded to a glass coverslip. As shown in Figure 1A, the geometry consisted of an inlet region with two access ports (ports 1 and 2), a well region with one access port (port 3). The two regions were connected with a constriction.

Collagen injection: Bovine type I atelocollagen (Advanced Biomatrix) was neutralized using 1M NaOH and diluted down to 2.5 mg/ml using ultrapure water and 10X PBS. The channel was prefilled using 2.5 mg/ml collagen with all access ports open. Then, access port 2 was blocked and 2.5 mg/ml collagen was injected along the path 1-3 at Q = 0.5 ml/min using a syringe pump. (Figure 1B). After injection, the remaining access ports were blocked to prevent evaporation and the microfluidic chip was then incubated to promote COL1 gelation.

Particle Image Velocimetry (PIV) and COMSOL: 5 µm fluorescent beads were added to the collagen solution to measure the velocity field using PIV. PIV data is presented as a mean of 3 individual replicates.

The COMSOL simulation was then validated using the PIV results, and the values matched to within 10%.

Imaging and processing: Collagen fibers were imaged under confocal reflectance microscopy (CRM) using a 40x objective water immersion lens. 2 µm stacks (0.13µm/slice) were obtained 30µm above the coverslip. LOCI CT-FIRE was used to obtain the angle of individual fibers. The coefficient of alignment (CoA) is calculated as the number of fibers within 15˚ of mode of fiber angle to total number of fibers.

RESULTS

As shown in Figure 1, we use microfluidic channels with varying cross-sectional areas to control change in strain rate. COL1 was injected at a flow rate of 0.5 ml/min in a prefilled microchannel as shown in figure 1B, following a path from port 1 to port 3. The velocity of the COL1 solution increased as it passed through the constriction to a maximum of 1.6 m/s and dropped to 0.6 m/s within 200µm of exiting the constriction, as measured using COMSOL and verified by PIV.

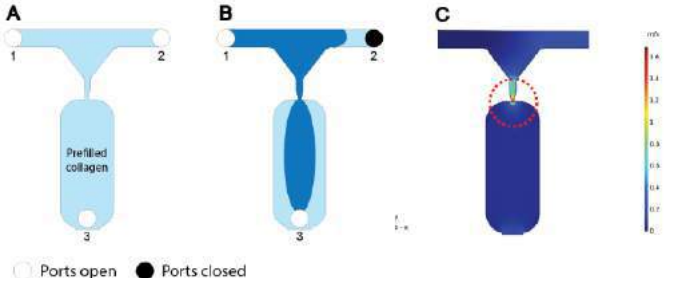

Figure 1: A) Shows the schematic of chip prefilled with collagen with three ports. B) Schematic of second collagen injection with port 2 closed. C) Shows the velocity contour plot of collagen injection at 0.5 ml/min

In figure 2A we show a micrograph of collagen fibers with varying degree of CoA in the ROI (red circle shown in figure 1C). The CoA was plotted for four regions as shown in 2A. The change in CoA was plotted as a function of distance from the constriction as shown in figure 2B. CoA falls from 0.9 to 0. 57 across 200 µm. A polynomial curve was best fitted to the data set with an R^2 of 0.903.

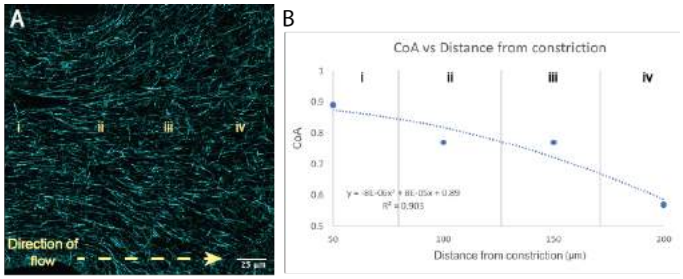

Figure 2: A) Shows the micrograph of collagen fibers in ROI. B) Shows the graph of CoA as a function of strain rate

DISCUSSION

Our results demonstrate the ability to generate gradients in collagen fiber anisotropy, over cellular length scales (100s of micrometers). We created a microfluidic channel network with varying cross section to impose controlled extensional strain on the COL1 solution. With our current design, we can generate a rapid drop in fluid velocity over hundreds of micrometers. Using this system, we leveraged the rapid change in velocity to yield rapid changes in extensional strain rate, which created gradients in fiber anisotropy.

This work builds upon our previous work [7] where we have demonstrated the use of extensional strain rate for controlling fiber direction and anisotropy. Furthermore, we allow access to micro engineered collagen gel by reversibly bonding PDMS to glass coverslips using surface functionalization. Thus, this platform allows to combine the ability to create defined cell length scale anisotropic fiber gradients while providing unrestricted access to engineered microgels. Future development of this technique will establish design rules to create defined gradients in CoA to investigate the effects of gradient alignotaxis on cell motility within a 3D micro engineered gel.

ACKNOWLEDGEMENTS

This work was supported by NIH GM137651 and the RIT New Faculty Startup funds.

REFERENCES

[1] Miroshnikova YA et al., Nature Cell Biology, 18:1336–45, 2016
[2] Caballero D et al., Trends Cell Biol, 25:815-27, 2015
[3] Oudin MJ et al., Cancer Discov, 6:516-31, 2016
[4] Provenzano PP et al., BMC Medicine, 4:38, 2006
[5] Shi Q et al., PNAS, 111:658-63, 2014
[6] Riching KM et al,. Biophysical Journal, 107:2546-58, 2014
[7] Ahmed A et al,. BioRxiv, 2020:2020.06.12.148346, 2020

TENSIONAL HOMEOSTASIS REGULATES CHROMATIN ACCESSIBILITY AND REPRESSES MATRIX DEGRADATION PATHWAYS THROUGH YAP/TAZ

Dakota L. Jones (1), Xi Jiang (1), Eddie D. Bonnevie (1), Elisabeth A. Lemmon (1), Mary Kate Evans (1), Su-Jin Heo (1), Nathaniel A. Dyment (1), Robert L. Mauck (1)

(1) Department of Orthopaedic Surgery
University of Pennsylvania
Philadelphia, PA, USA

INTRODUCTION

Tendinopathies are a progressive pathology associated with a chronic degenerative tissue state. Current surgical, material, and cell-based strategies for tendon repair are limited and re-injury is frequent resulting in loss of mobility and quality of life[1]. Chronic tendinopathies result in altered tensile loading of tendon cell populations[1]. Tensile cues are central to the homeostatic function of tendon fibroblasts and loss of these cues induces aberrant cell behavior[2]. Both normal and aberrant phenotypes in tendon fibroblasts are defined by their current transcriptional activity, which in turn is controlled by accessibility of genomic loci. How tension regulates tendon fibroblast transcriptional and chromatin profiles, the transcriptional pathways involved, and how these play a role in degenerative tendinopathies has yet to be explored. Understanding these mechanisms could lead to therapeutic treatments for tendinopathies.

METHODS

Isolation and culture of tendon fibroblasts: All animals and procedures were approved by the UPenn IACUC. CD1 mice (4-6 weeks old) were sacrificed and tail tendons were extracted. Tendons were digested in an enzymatic cocktail of Liberase and DNase I for 1 hour at 37 ºC. Cells were filtered through a 70 μm strainer and plated in DMEM supplemented with 10% FBS and antibiotics. Blebbistatin (10 μM), a myosin contractile inhibitor, was administered for 6 hours in low-serum (0.1% FBS) DMEM. All cells were used between passage 2 and 3. *ATACseq*: 50,000 cells were subjected to Assay for Transposase Accessible sequencing (ATACseq) following the published protocol[3]. DNA fragment size was analyzed using a Fragment Analyzer. Libraries were sequenced to 50 base pairs from both ends using an Illumina NovaSeq. Raw reads were aligned to the mm10 genome using Bowtie2. Picard and Samtools were used to generate bam files and to filter out duplicates and mitochondrial reads. Peaks were called using MACS2 using the following options: ““--keep-dup all -q 0.01 -no model”. Diffbind was used to identify differentially accessible chromatin loci between groups (n=3 biological replicates/group). Motif analysis was completed using the findMotifsGenome.pl command within Homer. *RNA isolation and sequencing:* RNA was isolated using the Qiagen RNeasy Plus Mini kit following the manufacturer's protocol. RNA quality was evaluated using a BioAnalyzer. RNA libraries were prepared using the Ilumina truSeq stranded poly-A library prep kit and single-end reads were sequenced to 100 base pairs using an Illumina NovaSeq. Reads were aligned to the mm10 genome using Hisat2. Picard was used to generate bam files and sort by chromosomal coordinates. FeatureCounts was used to generate count files. Deseq2 was used for differential expression analysis between groups (n=3 biological replicates/group). Gene ontology analysis was completed using Panther. *siRNA*: siRNA for mouse Yap1 and Wwtr1 (Taz) were administered to primary mouse tendon fibroblasts. Scramble siRNA was used as a control. After 3 days, RNA was isolated as described above. cDNA was synthesized using SuperScript IV Vilo according to manufacturer's protocol. qRT-PCR was performed using Fast SYBR on a QuantStudio6 machine. Statistical evaluation was performed using unpaired t-test.

RESULTS

To investigate the role of tensile cues in regulating chromatin accessibility, we cultured primary mouse tendon fibroblasts in the presence of blebbistatin for 6 hours and performed ATACseq, a fast and efficient next-generation sequencing method to identify active DNA regulatory elements (enhancers and promoters) across the genome. Using an FDR ≤ 0.05 and a log2 fold-change of +/- 1, we observed that blebbistatin treatment reduced accessibility of 954 chromatin loci and increased accessibility at only 17 chromatin loci (**Fig. 1a**). These findings suggest that cytoskeletal tension positively regulates chromatin accessibility. In addition, these accessibility changes were in close

genomic proximity to established mechano-responsive genes (e.g. *Acta2*, *Cyr61*) (**Fig. 1b**). Given that chromatin accessibility is a proxy for transcription factor occupancy, we next performed *de novo* DNA motif enrichment analysis on the 971 differentially regulated accessibility loci to identify putative transcriptional regulators facilitating these accessibility changes. Ranked by ascending P-value, the top predicted transcriptional regulator was Tead (**Fig. 1c**), the transcriptional co-activator for Yap and Taz, major mechano-responsive transcription regulators of the cell[4]. Taken together, these observations demonstrate cytoskeletal tension positively regulates chromatin accessibility potentially through Yap and Taz.

To better understand how these tension-regulated chromatin alterations relate to transcriptional changes, we performed RNA sequencing of mouse primary tendon fibroblasts following blebbistatin treatment for 6 hours. Using an FDR ≤ 0.05 and a log2 fold-change of +/- 1, we identified that inhibition of cytoskeletal tension downregulated the expression of 462 genes while also upregulating expression of 570 genes (**Fig. 2a**). We next performed gene ontology analysis on the gene sets that were downregulated and upregulated by blebbistatin treatment to identify pathways which are activated and repressed, respectively, by cytoskeletal tension in an unbiased fashion. Interestingly, we identified collagen catabolism as being repressed by cytoskeletal tension (**Fig. 2b**). Within this gene set we noted a number of matrix metalloproteinases (MMPs), enzymes involved in matrix degradation, which significantly increase expression following blebbistatin treatment (**Fig. 2c**). Together, these results suggest active tensile cues and cell contractility repress matrix degradation pathways in tendon fibroblasts.

To test whether Yap/Taz facilitate the repression of the same genes which were regulated under blebbistatin treatment, we performed siRNA-mediated knockdown of Yap and Taz in mouse primary tendon fibroblasts. Knockdown of Yap and Taz resulted in upregulation of these same genes (**Fig. 3**), demonstrating Yap and Taz play an active role in repression of matrix degradation pathways.

DISCUSSION

Matrix degradation is an early event in progressive degenerative tendinopathies. MMP expression is also elevated in de-tensioned three-dimensional tendon explant models[5]. However, the mechanistic basis defining what pathways regulate this pathogenic activity in tendon fibroblasts is not known. Here, we demonstrate a cytoskeleton/Yap/Taz axis which is central to the transcriptional regulation of these matrix degradation pathways. Ongoing work is exploring the functional effect of Yap/Taz in matrix degradation models *in vitro* and *in vivo*. Together, this work supports a potential therapeutic avenue of targeting Yap/Taz to thwart the onset of progressive degenerative tendinopathies.

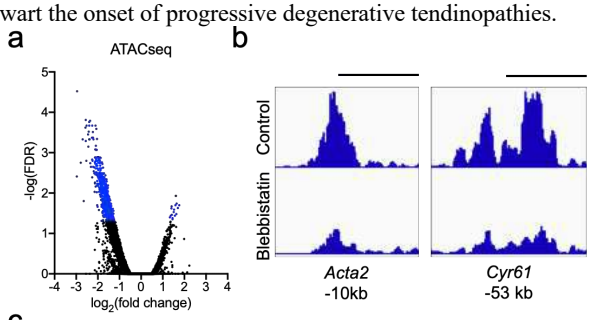

c

Rank	Motif	P-value	% of targets	Best Match
1		1e-254	58.71	TEAD
2		1e-44	31.30	SOX5
3		1e-29	20.71	FOSL2

Figure 1: Cytoskeletal tension is a positive regulator of chromatin accessibility. (a) Volcano plot of differential chromatin accessibility sites following blebbistatin treatment for 6 hours. Each dot represents a single accessibility loci. Blue denotes loci with significantly different accessibility. (b) Genomic views of differential accessibile loci in close proximity to known mechanoresponsive genes. Scale bar is 1kb. (c) *De novo* DNA motif enrichment analysis of differential chromatin accessibility loci ranked by P-value. % of targets represents % of total input ATAC sites which contain that respective motif.

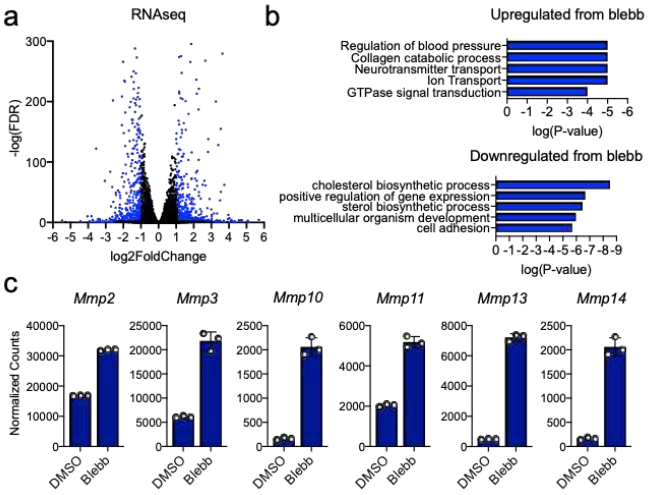

Figure 2: Cytoskeletal tension represses transcription of matrix degradation pathways. (a) Volcano plot of differentially expressed genes following blebbistatin treatment. Each dot represents a single gene. Blue denotes genes with significantly differential expression. (b) Gene ontology of genes upregulated or downregulated following blebbistatin treatment. (c) RNAseq data of candidate differentially expressed genes involved in matrix degradation. Each dot represents an independent biological replicate. Error bars represent standard deviation.

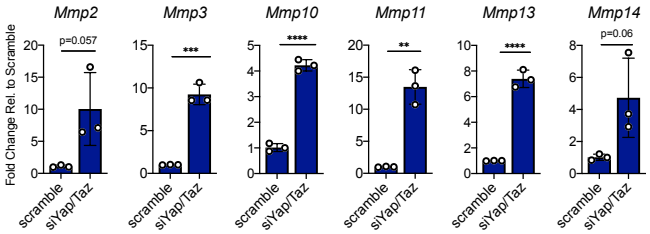

Figure 3: Yap/Taz repress transcription of matrix degradation pathways. qRT-PCR of the candidate genes from Fig. 2c with simultaneous siRNA-mediated knockdown of Yap and Taz. Data normalized to scramble control. Error bars represent standard deviation. **P<0.01, ***P<0.001, ****P<0.0001, evaluated by unpaired t-test.

ACKNOWLEDGEMENTS

Support was provided by the NIH (R00AR067283 and R01AR075418) and the VA (IK6 RX003416).

REFERENCES

[1] Millar, NL et al., *Nat Reviews Disease Primers*, 7, 2021.
[2] Howell, K et al, *Sci Rep*, 7, 2017.
[3] Corces, MR, et al. *Nat Methods*, 10:959-962 2017
[4] Dupont, S, et al. *Nature*, 474:179-183, 2011.
[5] Garder, K, et al. *Disabil Rehabil*, 30:20-22, 2008.

EXPLORING THE LINK BETWEEN WALL SHEAR STRESS TOPOLOGICAL SKELETON AND NEAR-WALL MASS TRANSPORT IN CARDIOVASCULAR FLOWS USING A EULERIAN-BASED METHOD

Giuseppe De Nisco (1), Valentina Mazzi (1), Karol Calò (1), Maurizio Lodi Rizzini (1), Claudio Chiastra (1), Jolanda J. Wentzel (2), David A. Steinman (3), Diego Gallo (1), Umberto Morbiducci (1)

(1) PoliTo*BIO*Med Lab, Department of Mechanical and Aerospace Engineering, Politecnico di Torino, Turin, Italy

(2) Department of Cardiology, Biomedical Engineering, Erasmus MC, Rotterdam, Netherlands

(3) Biomedical Simulation Laboratory, Department of Mechanical & Industrial Engineering, University of Toronto, Toronto, Canada

INTRODUCTION

Mass transport plays a key role in vascular disease. Several studies have suggested that, e.g., high plasma levels of low-density lipoproteins (LDL) are involved in the atherosclerosis process [1]. In this context, in the last decade, computational fluid dynamics (CFD) has been adopted to elucidate the links (if any) among disturbed shear, atherogenesis and mass transport in human arteries [2][3]. However, modelling mass transfer in cardiovascular flows requires the detailed, computationally expensive solution of the advection-diffusion equations [4]. To overcome this limitation, a marked interest has recently emerged on the Lagrangian-based features of the WSS topological skeleton, which have demonstrated to provide a reliable template for near-wall transport [5]. Briefly, the WSS topological skeleton is composed by fixed points, points where WSS vanishes, and stable/unstable connection lines (manifolds), identifying WSS expansion/contraction regions. Moving from the proven effectiveness of WSS Lagrangian Coherent Structures as a template of near-wall mass transport in cardiovascular flows, here a Eulerian-based method [6] recently proposed to analyze the WSS topological skeleton, whose features recently emerged as clear indicator of wall degradation in aortic aneurysm [7] and carotid restenosis risk [8], is applied. The final aim is to test its capability to provide a reliable template of the near-wall mass transport in patient-specific computational hemodynamic models of three distinct arterial district, i.e. the aorta, the carotid bifurcation and the right coronary artery.

METHODS

A scheme of the methods applied in this study is provided in Fig. 1. The 3D geometries of a human thoracic aorta, a carotid bifurcation, and a right coronary artery were reconstructed from medical images as extensively described elsewhere [4,9,10].

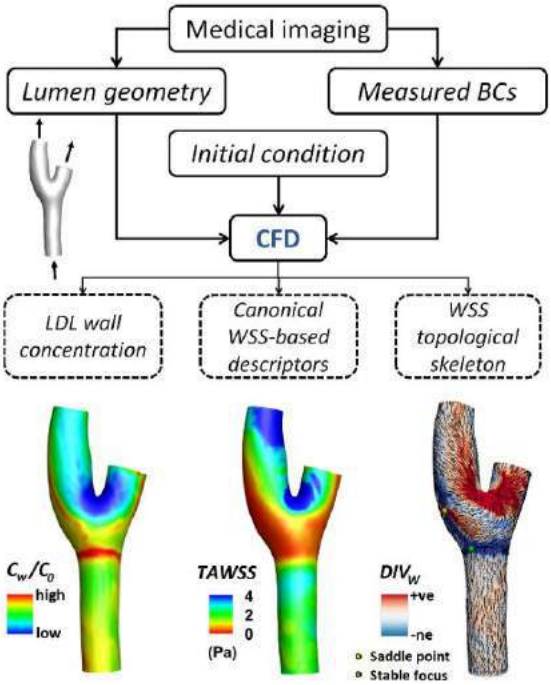

Figure 1: Overview of the proposed approach.

Computational hemodynamics. To model the transport of low-density lipoprotein (LDL), the finite volume method was applied to solve the coupled Navier-Stokes (NS) and advection-diffusion (AD) equations in their discretized form, using Fluent (ANSYS Inc., USA) on computational mesh-grids with 30 boundary layers of high-quality

prismatic cells near the wall [4]. Subject-specific boundary conditions (BCs) were prescribed to solve the NS equations [4,9,10]. A constant LDL concentration C_0 (equal to the average LDL concentration in whole blood) was applied at the inflow section, and the stress-free condition at the outflow sections, to solve AD equation [4]. The LDL blood-to-wall transfer was modelled as follows:

$$C_W v_W - D_{LDL} \frac{\partial C}{\partial n}\Big|_W = 0 \quad (1)$$

where C_W is the LDL concentration at the vessel wall, v_W the water filtration velocity through the wall, D_{LDL} is the diffusivity of LDL in blood, $\frac{\partial C}{\partial n}$ is the concentration gradient normal to the wall. Details on the applied numerical schemes are extensively provided elsewhere [4,9,10].

WSS topological skeleton. A recently proposed Eulerian method to analyze the WSS topological skeleton [6] was here considered. Briefly, based on Volume Contraction theory, it was demonstrated that the divergence of the WSS unit vector field $\boldsymbol{\tau}_u$, defined as:

$$DIV_W = \nabla \cdot \left(\frac{\tau}{\|\tau\|_2}\right) = \nabla \cdot \boldsymbol{\tau}_u \quad (2)$$

represents a template of the WSS vector field manifolds, identifying the WSS expansion/contraction regions on the arterial luminal surface. To complete the WSS topological skeleton analysis, the Poincarè index and the Jacobian analysis were carried out to identify and classify fixed points, according to the scheme proposed in [6]. Here, the Eulerian-based WSS topological skeleton analysis was applied to the cycle-average WSS vector field.

To complement the analysis, the luminal distribution of three well-established descriptors of flow disturbances, i.e., the time-average WSS (*TAWSS*), the oscillatory shear index (*OSI*), and the relative residence time (*RRT*), were also evaluated.

Co-localization analysis. The analysis of the co-localization between WSS manifolds as identified by DIV_W, and local LDL uptake, was carried out according to schemes proposed elsewhere [4]. Briefly, (1) the surface area (SA) exposed to normalized LDL concentration values (C_W/C_0) higher than the 90th percentile was quantified and denoted as LDL90, and (2) the SA exposed to DIV_W values lower than 10th percentile was identified and denoted as DIV10. Similarly, luminal SAs exposed to altered hemodynamics were identified by the lower 10th percentile for *TAWSS* (TAWSS10), and upper 90th for *OSI* and *RRT* (OSI90 and RRT90, respectively), and their co-localization with LDL90 was investigated.

RESULTS

The luminal surface distributions of DIV_W and normalized LDL are provided in Fig. 2 for the three analyzed vascular districts (panel A and B, respectively). WSS contraction regions are coloured in blue (negative DIV_W), while WSS expansion regions are presented in red colour (positive DIV_W, Fig. 2-A). It clearly emerges by visual inspection that contraction regions of the WSS vector field co-localize with LDL concentration polarization on the vessels wall. The observed co-localization is evident: (1) at the inner wall of the aortic arch and in the descending aorta for the thoracic aorta; (2) in the proximal carotid sinus where the bulb expansion starts to occur, and at the outer wall of the internal and external carotid artery; (3) along the inner curvature of the right coronary artery. A direct co-localization analysis between LDL concentration polarization and WSS contraction regions is provided in Fig. 2-C, where LDL90 and DIV10 (black contour lines) luminal SAs are displayed. A marked spatial overlap between LDL90 and DIV10 emerges, with the contour lines of DIV10 mostly encasing luminal regions with high LDL luminal concentration. The co-localization of LDL polarization concentration with WSS contraction regions is less pronounced only locally in the proximal part of the right coronary artery. From a quantitative analysis, it emerged that WSS contraction regions co-localize with high LDL concentration regions at least the 40% more than canonical WSS-based descriptors, with an increase from 20% to 35% (the 75% more) in the right coronary artery (Table 1).

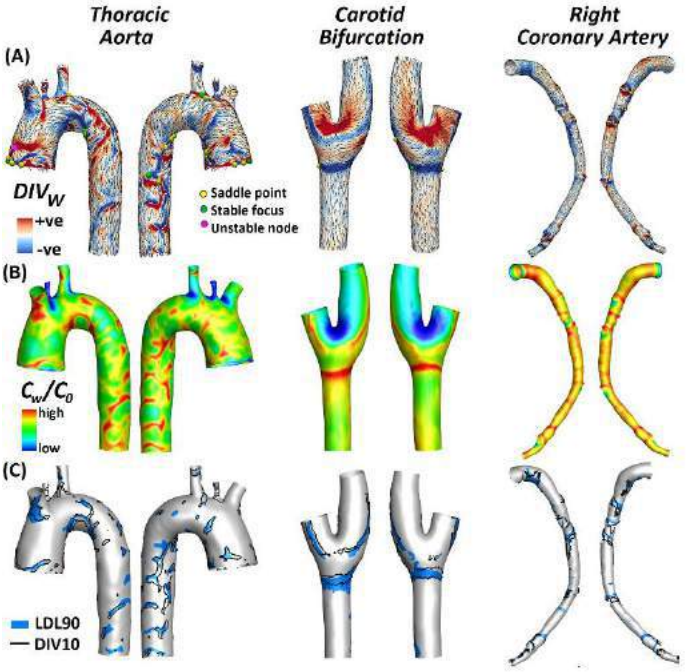

Figure 2: (A) Cycle-average WSS topological skeleton. (B) LDL wall concentration. (C) Distributions of LDL90 an DIV10.

Table 1: Percentage overlap with LDL90

	TAWSS10	OSI90	RRT90	DIV10
Thoracic Aorta	33%	27%	34%	46%
Carotid Bifurcation	30%	28%	29%	48%
Right Coronary Artery	21%	19%	20%	35%

DISCUSSION

The findings of this study: (1) confirm that WSS manifolds can be used as reliable templates of near-wall mass transport in cardiovascular flows [5]; (2) demonstrate that the recently proposed Eulerian-based method for analysing the WSS topological skeleton [6] efficiently provides a template of the LDL blood-to-wall transfer. The methodology, requiring less computational efforts with respect to a fully 3D simulation of mass transport in cardiovascular flows, candidates as an effective tool enriching the analysis of cardiovascular flows, avoiding solving AD equation to identify near-wall regions where mass transport is more pronounced [4]. Moreover, the co-localization of the LDL luminal polarization distribution with the WSS vector field contraction regions is higher than canonical WSS-based descriptors of flow disturbances.

Reference:

[1] Nielsen, LB et al., *Atherosclerosis*, 123: 1-15, 1996.
[2] Lantz, J et al., *J Biomech*, 45: 537-542, 2012.
[3] Li, X et al., *J. R. Soc. Interface*,14: pii20170140, 2017.
[4] De Nisco, G et al., *J Biomech*, 68:33-42, 2018.
[5] Arzani, A et al., *Biomech Model Mechanobiol*,16(3):787–803, 2017.
[6] Mazzi, V. et al., *Biomech Model Mechanobiol*,19:1403-1423, 2020.
[7] Morbiducci, U et al., *Ann Biomed Eng*, 48: 2936–2949, 2020.
[8] De Nisco, G. et al., *Med Eng Phys*, 82:119-129, 2020.
[9] Gallo et al., *J. R. Soc. Interface*, 15(147):20180352, 2018
[10] De Nisco et al., *Ann Biomed Eng*, 47(2):425-438, 2019.

DEVELOPMENT OF AN ANATOMICALLY ACCURATE NON-HUMAN PRIMATE FINITE ELEMENT HEAD MODEL

Tyler F. Rooks, John Humm, Jamie L. Baisden, Narayan Yoganandan

Department of Neurosurgery
Medical College of Wisconsin
8701 Watertown Plank Road
Milwaukee, WI 53226

INTRODUCTION

A considerable amount of historical research was performed using nonhuman primates (NHP) to investigate brain injuries [1]–[4]. Recent advancements in computational processing and power, finite element methods, and neuroimaging methods enable the development of advanced, high-fidelity computational models of the brain. These data provide a valuable resource to investigate the regional response of the brain to different severities and vectors of exposure. Research has shown that the regions brain are susceptible to loading with varied localized response [5]–[7]. While it is known that the regional brain-strain response is affected by exposure; little research has been performed to develop injury risk functions using regional strain response metrics as input criteria [5], [7]. Few finite element (FE) models of non-human primate (NHP) brains exist in the literature. Two recent studies have described the development and use of NHP FE brain models and efforts to investigate scaling relationships from NHP to human models [8], [9]. This objective of this study is to describe the development of a generalized, anatomically accurate, NHP brain model and demonstrate its feasibility with initial results.

METHODS

The NHP model was developed using a structural and anatomical atlas of the Rhesus Macaque [10]. The structural atlas includes basic identification of the cerebral spinal fluid (CSF), grey matter, and white matter. Additional granularity in anatomical structures is provided by an anatomical atlas (NeuroMaps Rhesus Macaque) that includes the cortical and sub-cortical anatomy of the brain (grey and white matter, thalamus, basal ganglia, corpus callosum, and other components) [10], [11].

The first step for creating the model was to generate the anatomical regions of interest using the NHP brain atlas and anatomical labels. The atlas and associated anatomical label information were imported into 3DSlicer and STL files were created for each structure (Figure 1). Subsequent review of the anatomical structures by a practicing clinical neurosurgeon aided with the grouping of multiple anatomical components from the atlas into larger regions of interest (Figure 2). For comparisons with current and developmental human brain models, the anatomical regions of interest for the NHP model included the grey and white matter for the cerebrum, cerebellum, thalamus, pallidum, midbrain, hippocampus, corpus callosum, basal ganglia, brain stem, and third, fourth and lateral ventricles. Comparable regions of interest are included in the latest version of the Global Human Body Model (GHBMC) head/brain model. Similar regions exist in a human model currently being developed and validated by the authors.

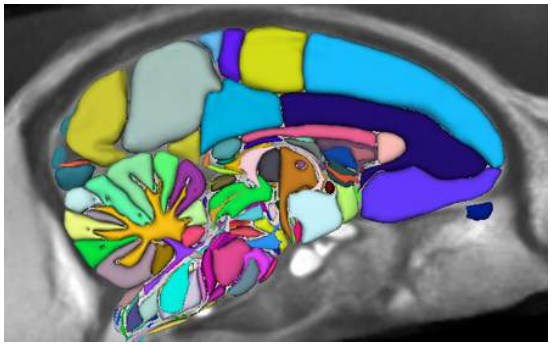

Figure 1: MRI-based brain atlas and regions of interest definition

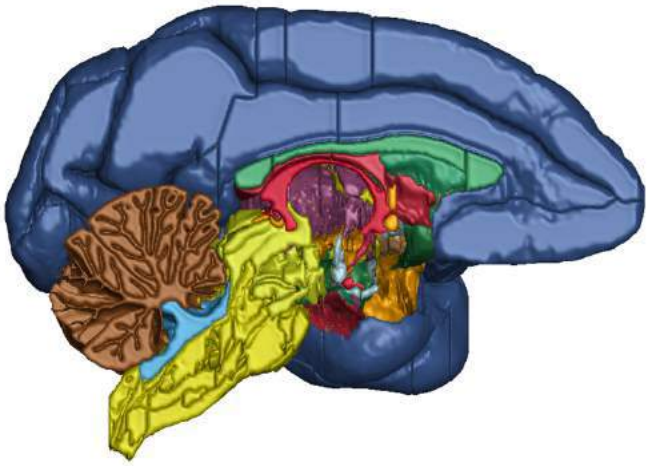

Figure 2: Combined regions of interest based on clinical input

Second, a mask of the cerebral spinal fluid identified in the atlas was created in 3DSlicer and then exported as an STL file. The cerebral spinal fluid surface STL (representing the exterior surface of the brain) was then imported into ANSA and was used to develop a global mesh using the multi-blocking method and hexahedral elements (Figure 3). The ANSA-generated brain mesh was imported in HyperMesh to check element quality (aspect ratio, warpage, Jacobian, etc.).

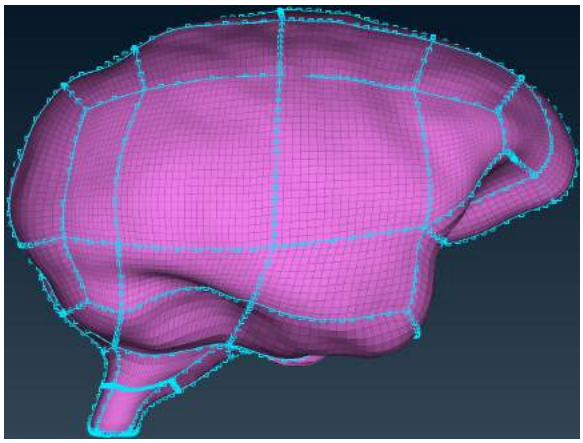

Figure 3: Initial mesh box pattern

RESULTS

There were a total of 378 separate anatomical structures identified in the NeuroMaps labels, 321 were used to generate the 13 brain regions of interest. The 67 anatomical structures left out of the regions of interest consisted of structures that were either very small (e.g., less than the size of 2 elements in the mesh), spanned multiple regions of interest as defined, or defined recesses within the brain that were not feasible for inclusion in a computational model.

For the global mesh, total of 52 hex boxes, including 203 box edges, 177 box faces, and 1340 control points, were created during the multi-blocking process to capture the brain's left hemisphere (brain is symmetrical about the midsagittal plane). The thresholds used to evaluate hexahedral mesh quality were an aspect ratio below 8, warpage below 50, and Jacobian below 0.3. Less than one percent of elements failed the element quality check.

DISCUSSION

Methods for the development an anatomically accurate NHP model were identified, and a multidisciplinary team approach was used for the finite element model. Additionally, element quality checks for the surface mesh were completed. The model has a high-quality mesh with less than 1% of elements failing the quality check.

The development of an anatomically accurate, high-quality NHP model has applications in the automotive, sports, aviation, and military environments, as traumatic brain injuries continue to be a burden on the individual and society, albeit with different mitigation strategies and safety standards. Previous efforts have focused on developing and evaluating scaling relationships between NHP and human for the prediction of injury. An additional application is to analyze historical datasets to develop new metrics for the prediction of injury that can be scaled. With recent advancements in computational power, finite element methods, and imaging capabilities, there may be significant gaps that can be answered using the wealth of historical experimental data collected. For example, recent injury risk curves developed for different accelerative loading vectors from NHP experiments could be updated to provide component-based and overall/global brain response metrics for the prediction of injury using head kinematic data [1]. These updated metrics and injury risk curves can then be scaled to human models to predict human injury from match pair human brain finite elements models that have paralleling component definitions.

ACKNOWLEDGEMENTS

The authors would like to thank Dr. Carol Chancey of the U.S. Army Aeromedical Research Laboratory for her support. This work was supported by the Office of the Assistant Secretary of Defense for Health Affairs, through the Broad Agency Announcement under Award No. W81XWH-16-1-0010, and by the Department of Veterans Affairs Medical Research. The authors thank the computational modeling team at the Medical College of Wisconsin for their assistance. The opinions, interpretations, conclusions, and recommendations are those of the authors and are not necessarily endorsed by the Department of Defense or other sponsors.

REFERENCES

[1] A. V. Olszko *et al.*, *Traffic Inj. Prev.*, 19: sup1:S44–S49, 2018.
[2] L. E. Thibault, et al, 1990.
[3] T. A. Gennarelli, et al, SAE Technical Paper, 1972.
[4] A. K. Ommaya, et al, 1967.
[5] A. A. Weaver, et al, *Ann. Biomed. Eng.*, 40: 9: 2005–2018. 2012,
[6] N. Yoganandan, et al, *J. Biomech.*, 41:10:2253–2262, 2008.
[7] M. Hajiaghamemar, et al, *Biomech. Model. Mechanobiol.*, 2019.
[8] T. Arora, et al, SAE Technical Paper 2019-22–0003, 2020.
[9] T. Wu, et al, *J. Neurotrauma*, 37:2:410–422, 2019.
[10] T. Rohlfing *et al.*, *Front. Neuroinformatics*, vol. 6, 2012.
[11] M. F. Dubach and D. M. Bowden, *Society for Neuroscience Annual Meeting*, 2009, pp. 17–21.

SB³C2021
Summer Biomechanics, Bioengineering and Biotransport Conference
June 14-18, Virtual

SIZE-DEPENDENT SOLUTE DIFFUSIVITY IN SYNOVIAL EXPLANTS PARALLELS SOLUTE TRANSPORT FOLLOWING INTRA-ARTICULAR DELIVERY IN VIVO

Alexandra L. Davis (1), Young Guang (1), Thomas M. McGrath (1), Benjamin B. Johnston (1), Christine T.N. Pham (2), James A.J. Fitzpatrick (1,3), Lori A. Setton (1)

(1) Department of Biomedical Engineering
Washington University in St. Louis
St. Louis, MO, United States

(2) Division of Rheumatology
Washington University School of Medicine
St. Louis, MO, United States

(3) Center for Cellular Imaging
Washington University School of Medicine
St. Louis, MO, United States

INTRODUCTION

Benefits of intra-articular (IA) drug delivery are hindered by rapid drug clearance from the synovial joint space [1]. The synovium is a thin, multi-layered tissue separating the avascular IA space from vascularized tissues surrounding the joint [2]. IA pressure and a solute's concentration gradient drive drug transport through the synovium, whose draining lymphatic and blood vessels limit drug residence time. Although drug clearance has been studied in pre-clinical models and human subjects, comparing quantitative parameters such as half-life ($t_{1/2}$) and diffusivity remains challenging due to unknown boundary conditions and geometries [3,4]. We and others have studied drug transport in synovial explants, but presented parameters such as diffusivity may vary in dimensions and magnitudes across studies [5,6].

Previously, we developed a computational model of synovium as a porous, multi-phasic tissue and used an inverse method to determine urea's effective diffusivity (D_{eff}) through devitalized human and porcine explants [7]. This experimental-computational approach was used in the current study to determine the D_{eff} for uncharged solutes of varying MW in synovial explants as well as to estimate their $t_{1/2}$ that could be compared with *in vivo* transport properties.

METHODS

Synovial explants were harvested from healthy pig or human knees after sacrifice. Tissues were harvested from the medial, lateral, and posterior regions of pig joints. Human donor tissues were similarly obtained via an agreement with the Mid-America Transplant Foundation. All samples were cryoprotected in 15% and 30% sucrose solutions for 24 hours. To ensure devitalization, explants were snap frozen in liquid nitrogen and stored at −80 °C for at least 48 hours. Explants were then trimmed to under 1 mm thickness on a sledge microtome (Leica SM2400, Allendale NJ) and hydrated in phosphate buffer solution (PBS) overnight.

Explant thickness was estimated with a laser-scanning profilometer (Keyence LJ-V7080, Itasca IL) prior to unsteady diffusion experiments. Each explant was placed in a custom-built diffusion chamber between two baths: an upstream "donor" bath containing a finite amount of model solute, and a downstream "sink" bath that was continuously drained with PBS to mimic the draining lymphatics. At time $t = 0$, a model solute (urea, mannitol, or 3 kDa, 10 kDa, or 70 kDa fluorophore-conjugated dextran) of known concentration (C_0) was added to the donor bath; 5 µL aliquots were collected from the donor bath to measure solute concentration over 72 hours using colorimetric assays (urea and mannitol) or fluorescent emission (dextrans).

Following diffusion experiments, desorption of select solutes (3 kDa and 10 kDa dextrans) was assessed in a subset of tissues ($n = 7$). These explants were suspended in a volume of PBS 3x the sample's volume and placed atop a nutating shaker at 37 °C. At 24, 48, and 72 hours, the PBS was removed and replaced with fresh PBS. After 72 hours, solute concentration in the overlying media taken at all three time points was measured as described.

Finite element modeling (FEM) was used to construct a specimen-specific mesh of thickness L in contact with a well-mixed donor bath containing uncharged solute at $t = 0$ [$C_{bath}(x=0, t=0) = C_0$]. At the subintimal face, boundary conditions were set to zero [$C(x=L, t) = 0$] (Fig. 1). Explants were modeled as multi-phasic tissues of fixed permeability, porosity, and material properties (Table 1). A built-in optimization module in the software suite FEBio (University of Utah, Salt Lake City UT) was used to predict solute D_{eff} in the synovium [8]. To compare with *in vivo* data, $t_{1/2}$ was determined by fitting a single exponential decay in C/C_0 against time for each experiment. Differences in D_{eff} and $t_{1/2}$ were evaluated across solutes via one-factor ANOVA

with Tukey's post-hoc test in GraphPad Prism 8.0 (GraphPad Software, La Jolla, CA).

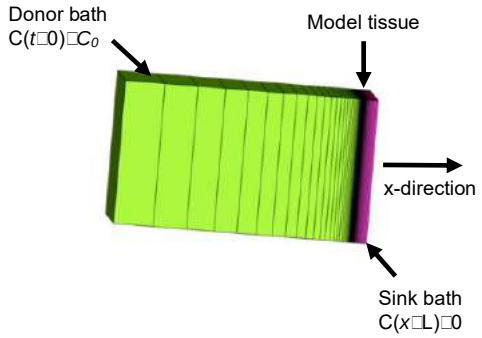

Figure 1. Explant-specific FEM mesh used to model solute diffusivity through synovium.

Table 1. Material properties used in synovium FEM optimization: solid volume fraction (ϕ_s), elastic modulus (E), Poisson's ratio (ν), and hydraulic permeability (k).

ϕ_s	E	ν	k
0.19	100 kPa	0.4	10^{-9} mm^4/μN s

RESULTS

Molecular transport through n = 51 porcine and n = 31 human synovial explants was described well by first-order exponential fitting ($R^2 \geq 0.897$), with the exception of 10 kDa ($R^2 = 0.749$) and 70 kDa ($R^2 = 0.519$) dextrans in human tissue; larger solutes cleared from the donor bath more slowly than smaller solutes. Clearance of 3 kDa and 10 kDa dextrans from n = 7 synovial explants was confirmed by the end of desorption experiments, where concentrations in overlying media were less than 12% of those measured at the final time point of diffusion experiments in all cases.

FEBio predictions of solute clearance showed good agreement with concentration data from unsteady diffusion experiments as evaluated by nonlinear regression fit statistics (RSS < 0.06) normalized by C_0. Solute D_{eff} trended downward as MW increased (Fig. 2), and significant differences were found between solutes below and above 3 kDa MW ($p < 0.05$).

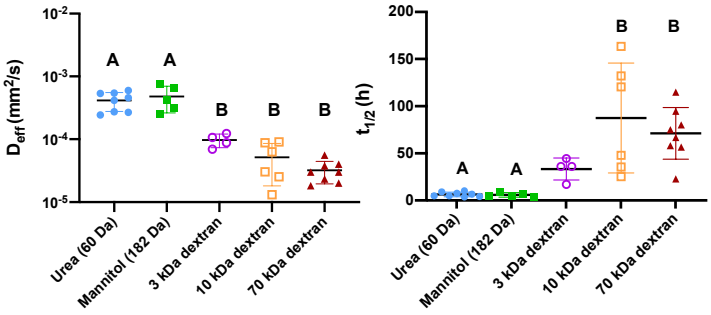

Figure 2. Mean D_{eff} and $t_{1/2}$ for 5 solutes in human synovial explants. Statistical differences are indicated between groups of different letters ($p < 0.01$).

Data for time-varying concentration in the donor bath was also well-described by a single exponential term used to determine solute $t_{1/2}$. Solute $t_{1/2}$ in the donor bath generally increased with MW, as urea and mannitol's values were lower when compared to larger solutes ($p <$ 0.0001). The $t_{1/2}$ for these solutes were compared to those previously measured *in vivo* using radiolabeled probes (Table 2). While *in vitro* half-lives were larger than *in vivo*, that solute $t_{1/2}$ in the joint space increases with MW was nevertheless consistent in both cases.

Table 2. Comparisons of $t_{1/2}$ in synovial explants to *in vivo* IA clearances reported in pre-clinical and human studies, organized by MW. Shaded, italicized rows represent data acquired in the current study in porcine explants.

Solute	MW (Da)	$t_{1/2}$ (h)	Reference
^{24}Na	24	0.23	Scholer 1959
Urea	*60*	*5.01*	—
^{133}Xe	133	0.57-1.3	Phelps 1972
Mannitol	*182*	*3.79*	—
Ceftiofur	524	5.1	Mills 2000
Texas Red	*3×10^3*	*11.9*	—
D-Rho	*1×10^4*	*22.8*	—
I-Albumin	6.7×10^4	12.2	Simkin 1990
D-Rho	*7×10^4*	*66.7*	—
Hyaluronan	~3×10^6	21.8-26.3	Coleman 1997

DISCUSSION

Contrary to previous works that have documented solute clearance but not reported intrinsic diffusivity parameters, we determined D_{eff} through porcine and human synovium using a multi-phasic modeling approach supported by FEBio. Experimental and computational results agreed well, together confirming that MW governs transport of uncharged solutes across synovial explants of known surface area and thickness. Importantly, this work complements *in vivo* drug clearance studies, which also find that solute $t_{1/2}$ increases with MW. For similar MW, however, the $t_{1/2}$ *in vivo* tended to be less than half of $t_{1/2}$ quantified here. This discrepancy can be attributed to active transport rejecting solute retention in vivo, as well as poorer sensitivity when detecting drug within the fluid cavity (e.g. synovial fluid or serum) in living subjects. Nevertheless, general agreement suggests that *in vitro* studies in synovial tissue could predict some aspects of drug transport *in vivo*. The current model is prerequisite to incorporating more complex features, such as charged solute-matrix interactions and pathological contributions such as increased IA pressure.

ACKNOWLEDGEMENTS

Supported by NIH AR070975 and The Foundation for Barnes-Jewish Hospital (3770 and 4642). Use of open-source FEBio was supported in part by a grant from the NIH. We thank Dr. Michael Talcott (WUSM) and Mid-America Transplant Center for providing porcine and human samples, respectively.

REFERENCES

[1] Evans, CH et al., *Nat Rev Rheumatol*, 10:11-22, 2014.
[2] Levick, JR & McDonald, JN, *Ann Rheum Dis*, 54:417-423, 1995.
[3] Singh, A et al., *Adv Healthc Mater*, 3:1562-1567, 2014.
[4] Tellier, LE et al., *Biomater Sci*, 6:1159-1167, 2018.
[5] Sterner, B et al., *Eur J Pharm Biopharm*, 101:126-136, 2016.
[6] Stefani, RM et al., *Tissue Eng - Pt A*, 25:538-553, 2019.
[7] Guang Y et al., *J Biomech Eng*, 142:0410101–8, 2019.
[8] Maas, SA et al., *J Biomech Eng*, 134:011005, 2012.

FACTORS INFLUENCING MINIMUM LAMINA CRIBROSA OXYGEN CONCENTRATION

Yi Hua (1), Jason Walker (2), Po-Yi Lee (1,3), Fengting Ji (1,3), Haiden McDonald (2), Pedro Pallares (2), Bryn Brazile (1), Ian A. Sigal (1,3)

(1) Department of Ophthalmology
University of Pittsburgh
Pittsburgh, PA, USA

(2) Department of Biological Sciences
University of Pittsburgh
Pittsburgh, PA, USA

(3) Department of Bioengineering
University of Pittsburgh
Pittsburgh, PA, USA

INTRODUCTION

Millions of people worldwide are blind or have reduced vision due to damage to the retinal ganglion cell axons that carry visual information from the retina to the brain (Figure 1). [1] In many pathologies, including glaucoma, axonal damage starts within the optic nerve head, specifically within the lamina cribrosa (LC). Although the mechanisms of axonal damage vary between pathologies, it has long been thought that a primary contributor is an insufficient oxygen supply within the LC due to compromised blood perfusion. [2, 3] Measuring LC oxygen experimentally is not yet possible and thus it is usually studied using numerical models. LC oxygen models have been highly simplified and generic, [3] or eye-specific but 2D. [4] Our goal was to leverage novel 3D eye-specific models of the LC microvessel network to identify the factors with the largest influence on the LC oxygen. Specifically, we focused on the minimum (10^{th} percentile) oxygen concentration as potentially indicative of hypoxic conditions.

METHODS

3D reconstruction of the microvessel network. Serial histological sections (thickness: 16 µm) were obtained from a normal monkey optic nerve head, in which the blood vessels had been labeled with a fluorescent dye. The sections were imaged with fluorescence microscopy at a resolution of 0.73 µm per pixel and registered to one another to create a 3D stack. The vessels were identified using a semi-automated algorithm based on a Hessian filter. The result was then skeletonized and converted into a graph, and any isolated branches were removed to ensure that all vessels were connected except at the model periphery (Figure 1). The region modeled was larger than the LC. Microvessels in the LC region were identified based on the LC collagenous beams. The skeleton was converted into a mesh of vasculature for solving flow numerically.

Modeling blood flow and oxygen concentration. Blood was considered as an incompressible Newtonian fluid, and its flow behavior was described by the Hagen-Poiseuille equation. [5] Arteriole pressure of 50 mmHg was applied at the periphery to simulate blood flow from the circle of Zinn-Haller. [3] Venous outlet pressure of 15 mmHg was applied at the center to simulate blood drainage through the central retinal vein. [6] Pressures of 20 mmHg and 16 mmHg were applied at the pre and retrolaminar boundaries, respectively, to simulate the effects of intraocular and cerebrospinal fluid pressures. [7] The oxygen consumption rate of neural tissues was assumed as 5e-4 $cm^3/cm^3/s$. [8] A Green's function method was employed to estimate LC neural tissue oxygen concentration. [9]

Statistical analysis. Using a Monte Carlo approach, 500 models were generated with varying (baseline ± 20%) microvessel diameter, pressures (arteriole, venule, prelaminar, and retrolaminar), inflow hematocrit, and oxygen consumption rate (Table 1). ANOVA was used to determine factor influences on the minimum LC oxygen.

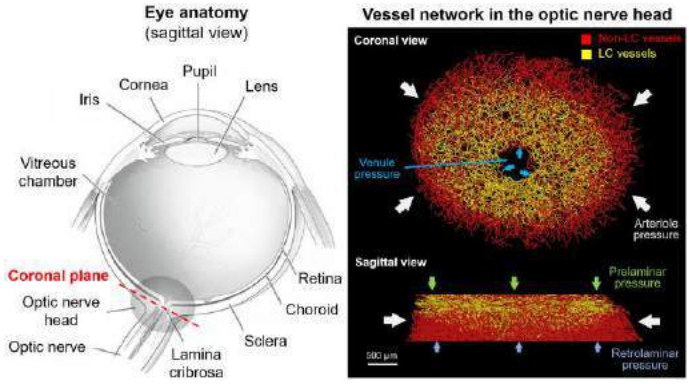

Figure 1: (Left) Anatomy of the eye in sagittal cross-section. Adapted from a diagram by the NEI. (Right) Hemodynamics boundary conditions for the microvessel network in the optic nerve head. We applied boundary conditions at the model edges (periphery for inflow, center for outflow, and pressure-based at the prelaminar and retrolaminar boundaries).

Table 1: Factor baseline values and ranges in sensitivity analysis.

Input parameters	Units	Baseline	Low	High
Microvessel diameter	μm	8	6.4	9.6
Arteriole pressure	mmHg	50	40	60
Venule pressure	mmHg	15	12	18
Prelaminar pressure	mmHg	20	16	24
Retrolaminar pressure	mmHg	16	12.8	19.2
Inflow hematocrit	/	0.45	0.36	0.54
O_2 consumption rate	$cm^3/cm^3/s$	5e-4	4e-4	6e-4

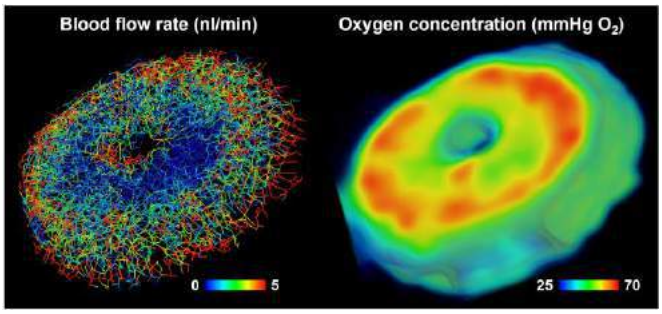

Figure 2: Example microvessel network colored by blood flow rate (left) and contour plots of oxygen concentration in the neural tissues (right), for a model with baseline values of all input parameters. Notice that there are similarities in the regional distribution of high/low blood flow rate and oxygen concentration, but there are also regions of disagreement.

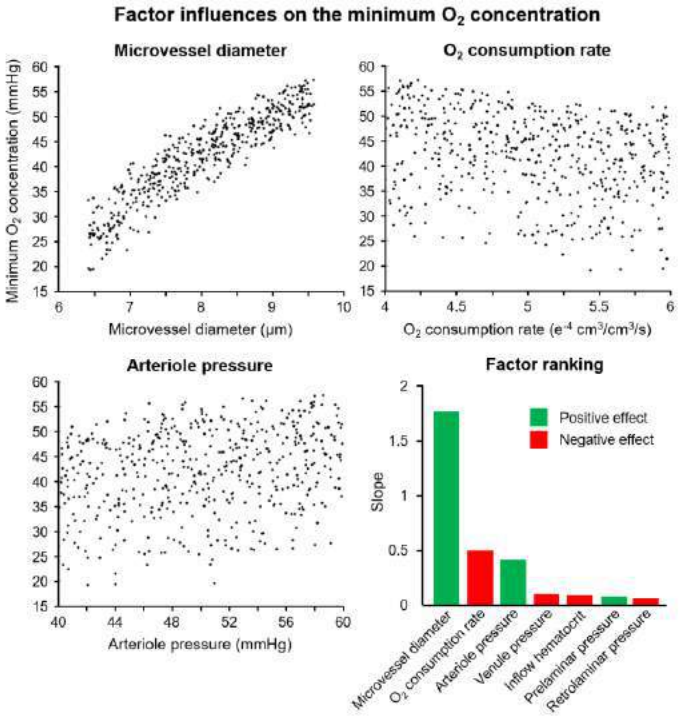

Figure 3: Minimum LC oxygen concentration as a function of the three most influential factors: microvessel diameter, oxygen consumption rate, and arteriole pressure. Each dot is one model. Bar chart of factor influences (ANOVA).

RESULTS

The 3D LC microvessel architecture and its blood flow were quite complex, and the oxygen concentration was heterogeneous (Figure 2). The factors influencing the minimum oxygen concentration the most were: the microvessel diameter ($p<0.001$), oxygen consumption rate ($p<0.001$), and arteriole pressure ($p<0.001$); and to a less extent: the venule pressure ($p<0.001$), inflow hematocrit ($p<0.001$), and prelaminar ($p<0.001$) and retrolaminar ($p<0.003$) pressures (Figure 3).

DISCUSSION

Our goal was to leverage novel 3D eye-specific models of the LC vessel network to identify the factors with the largest influence on the LC oxygen. Our models predicted that the microvessel diameter, oxygen consumption rate, and arteriole pressure have the largest influence on the oxygen concentration in the LC. Below we discuss each of the influential factors in detail.

Microvessel diameter. The minimum oxygen concentration in the LC was positively associated with the microvessel diameter. This is because an increase in microvessel diameter decreased the flow resistance, increasing the blood flow rate, resulting in more efficient oxygen transport and higher oxygen concentrations in the LC.

Oxygen consumption rate. The minimum oxygen concentration in the LC was negatively associated with the oxygen consumption rate of the neural tissues. Note that we assumed the neural tissue consumption rate to be constant and uniform. Early glaucomatous neural tissue degeneration is often localized to specific regions of the optic nerve head [10, 11]. Future studies could consider region-dependent or pressure-dependent oxygen consumption rates.

Arteriole pressure. The minimum oxygen concentration in the LC was positively associated with the arteriole pressure. Arteriole pressure is related to systemic blood pressure. Low systemic blood pressure has been associated with a higher risk of glaucoma, [12] which is consistent with our findings.

The complexity of LC microvessel architecture makes this a difficult region to understand blood flow and oxygenation. However, if as reported herein, relatively few factors account for the oxygenation state of the LC, this may allow for better prediction of LC hemodynamics. With advances in imaging techniques, particularly in optical coherence tomography angiography and super-resolution ultrasound, accurate in vivo measurement of oxygen concentration and blood flow in the LC will be possible in the future.

ACKNOWLEDGEMENTS

Supported in part by NIH R01-EY023966, R01-EY028662, P30-EY008098 and T32-EY017271 (Bethesda, MD), the Eye and Ear Foundation (Pittsburgh, PA), and Research to Prevent Blindness.

REFERENCES

[1] Quigley, H.A., Lancet. 2011; 377: 1367-1377.
[2] Carichino, L. et al., IOVS. 2012; 53: 2836.
[3] Chuangsuwanich, T. et al., IOVS. 2016; 57: 6167-6179.
[4] Walker, J. et al., IOVS. 2020; 61: 632.
[5] Guidoboni, G. et al., JCSMD. 2013; 1: 1-21.
[6] Mozaffarieh, M. et al., Graefes Arch Clin Exp Ophthalmol. 2014; 252: 1569-1571.
[7] Hua, Y., IOVS. 2018; 59: 154-165.
[8] Secomb, T.W. et al., Microcirculation. 2000; 7: 237-247.
[9] Secomb, T.W. et al., Ann Biomed Eng. 2004; 32: 1519-1529.
[10] Quigley, H.A. et al., IOVS. 1984; 25: 918-931.
[11] Sanchez R.M. et al., IOVS. 1986; 27: 1342-1350.
[12] Caprioli, J. et al., Am J Ophthalmol. 2010; 149: 704-712.

DEVELOPMENT ON A COMPUTATIONAL FRAMEWORK TO EXPRESS PATIENT-SPECIFIC INTRACRNICAL CEREBROSPINAL FLUID FLOW BASED ON PHASE-CONTRAST MAGNETIC RESONANCE IMAGES

S. Maeda (1), T. Otani (1), S. Yamada (2), Y. Watanabe (3), S. Ilik (1), N. Takeishi (1), S. Wada (1)

(1) Department of Mechanical Science and Bioengineering,
Graduate School of Engineering Science, Osaka University,
1-3 Machikaneyamacho, Toyonaka,
Osaka, Japan

(2) Department of Neurosurgery,
Shiga University of Medical Science,
Setatsukinowacho, Otsu,
Shiga, Japan

(3) Department of Radiology,
Shiga University of Medical Science,
Setatsukinowacho, Otsu,
Shiga, Japan

INTRODUCTION

Cerebrospinal fluid (CSF) is the fluid in the brain ventricular space and subarachnoid space (SAC) covering the central nervous system (CNS). Abnormal CSF circulation closely associates with CNS diseases such as normal pressure hydrocephalus (NPH), and thus underlying mechanism of the intracranial CSF circulation has been much attracted [1]. In previous experiments, pulsatile flow of the CSF driven by the motions of the SAC and brain ventricles was observed in a phase contrast magnetic resonance imaging (PC-MRI). However, much is still unknown especially about the effect of the boundary movements on the pulsatile flow of the CSF in a whole intracranial space, consisting of complex and narrow pathways [2].

To address this issue, computational fluid dynamics (CFD) simulation is a promising approach. Previous numerical studies proposed various computational modeling of the CSF with considering elastic deformation of the brain parenchyma [3, 4], or with flux exchanges between the CSF and interstitial fluid [5]. Although these novel studies have gained insights into some of underlying mechanism of the CSF circulation in whole brain system, it is still uncertain whether characteristic pulsatile flow of the CSF can be formulated in the same context independently of subjects.

The objective of this study, therefore, we develop a computational framework to investigate patient-specific CSF flow. Using a patient-specific geometry of the CSF domain and pulsatile flux measured based on the PC-MRI data, we conduct a CFD simulation of the intracranial CSF with prescribed moving-wall boundary conditions.

METHODS

MRI image acquisition

Brain MRI images of the normal subject was acquired in Shiga University of Medical Science hospital. Computational domain was set in the brain ventricles and SAC domain geometry, which were reconstructed from MRI images (Fig. 1 (a)). Since the intracranial, the SAC space is geometrically separated by Liliequist's membrane [6], we did not consider the top of intracranial SAC space in the computational domain.

Based on the CSF velocity measured in PC-MRI, we calculated the flux in the cerebral aqueduct (CA), which is a pathway between third and fourth ventricles, and in the foramen magnum (FM) during a cardiac cycle (see Fig. 2). In the PC-MRI images, image resolution is $0.5\times0.781\times0.781$ mm^3 and the velocity encoding of PC-MRI is 10 cm/s.

CFD simulation

The computational domain was discretized as a set of first order tetrahedral elements using Netgen (https://ngsolve.org). The number of nodes and elements of the constructed computational grid is 52,115 and 228,491, respectively. The CSF flow was modeled as Newtonian fluid, and driven by moving-wall boundaries was expressed by the equation of continuity and incompressible Navier-Stokes equations in Arbitrary Lagrangian-Eulerian (ALE) form, given by

$$\nabla \cdot \mathbf{u} = 0, \tag{1}$$

$$\rho\left(\frac{\partial \mathbf{u}}{\partial t} + \tilde{\mathbf{u}} \cdot \nabla \mathbf{u}\right) = -\nabla p + \mu \nabla^2 \mathbf{u}, \tag{2}$$

where ρ is density, μ is viscosity, p is pressure, $\mathbf{u}$ is velocity vector, $\tilde{\mathbf{u}}$ is advection velocity in the ALE coordinates. Eqs. (1) and (2) were spatially discretized by streamline-upwind Galerkin method (c.f., [7]) and updated by the fractional step method iteratively. The displacement field of the computational nodes by the moving-wall boundary condition was expressed by solving the Laplace equation for the entire computational domain at each time step.

Boundary condition and physical properties

We gave the displacements in the upper wall of the lateral ventricles (MW1) and the medial wall of the subarachnoid space (MW2) based on [4] (Fig. 1(b)). We assumed that the volume change of the lateral ventricles was equivalent to the in/out flux in the CA, and also that the volume change in whole computational domain except the lateral ventricle was equivalent to the in/out-flux in the FM subtracted by the flux in the CA. Prescribed displacements were assigned on each node on the moving-wall boundaries and its direction was set to unit surface normal. Magnitudes of these displacements were assumed to be uniform, for simplicity.

Pressure boundary condition of 0 Pa was set at the FM, and no-slip wall boundary condition was imposed. Physical properties of the CSF were set to be equivalent with water (density of $\rho = 998.2$ kg/m^3 and viscosity of $\mu = 1.0 \times 10^{-3}$ Pa · s). Time increment in computation was set to 1.0×10^{-3} s and computed totally four cardiac cycles.

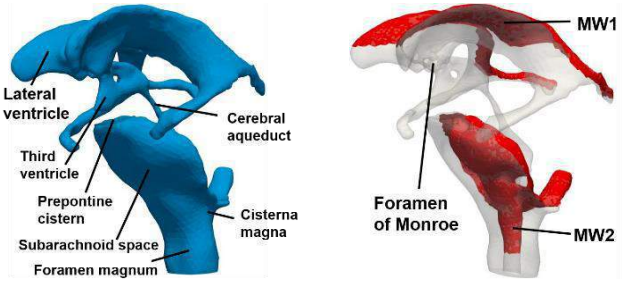

Fig. 1 (a) Computational domain consisting of ventricular constructed based on MRI images. (b) Moving boundaries are represented in red (upper wall of lateral ventricle, inner wall of subarachnoid space).

RESULTS & DISCUSSION

Figure 3 shows representative snapshots of the CSF velocity distribution in the third ventricle at t = 0 s and 0.5 s, respectively. Our numerical results successfully demonstrated characteristic pulsatile flow of the CSF, which was observed in previous experimental observations [8]. Although the effect of the displacement of LV on CSF flow was investigated in [4] considering with fluid-structure interaction problem, the magnitude of the displacement remains to be arbitrary. In our numerical analysis, on the other hands, we gave the displacement of the LV based on the PC-MRI data, and the order of the magnitude of the peak velocity O(vmax)$\cong 10^1$ mm/s agree with the experimental observations [8]. Furthermore, the simulations clearly exhibited the CSF velocity distribution in narrow pathways in the foramen of Luschka and Magendie as shown in Fig. 4. According to Fig.4, the influx (or efflux) in the foramen of Luschka was approximately 85% against total influx (or efflux). Since the CSF flow in such narrow pathways cannot be always detected by PC-MRI measurement due to resolution, our numerical model can be useful not only to investigate the spatiotemporal flux of the CSF but also to quantify the effect of the moving-walls and pulsatile flow of the CSF.

SUMMARY & FUTURE STUDIES

We developed a computational framework to investigate a patient-specific CSF flow. The patient-specific geometry of CSF was constructed based on the MRI data, and the displacement of moving-wall boundaries were determined based on the flux in the CA and FM during a cardiac cycle, which was measured by PC-MRI techniques. Although this study is a first step to clarify the CSF circulation in whole brain, there are several physiological conditions to be considered. For instance, the non-uniform displacements on the brain tissue may be considered to represent more physiologically reasonable ventricle wall movements. It is also necessarily to strictly compare between the CSF flow velocity obtained with simulation and that obtained with PC-MRI data. In the future study, we will gain insights into CSF circulation in whole brain system, and also into mechanics background of NPH.

ACKNOWLEDGEMENTS

This work was supported by research grants from JSPS Grants-in-Aid for Scientific Research (19H01175) and program for accelerating the creation of new result from the supercomputer Fugaku (hp200136).

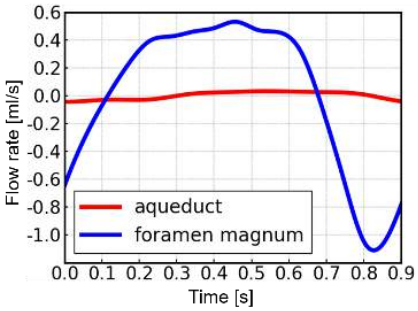

Fig. 2 CSF flow rate in a cardiac cycle calculated from PC-MRI measurements (red: Cerebral aqueduct, blue: foramen magnum).

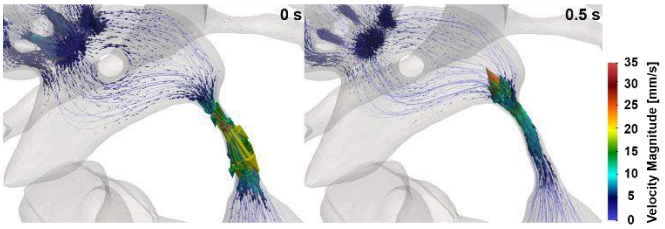

Fig. 3 CSF velocity around the third ventricle when the volume averaged velocity in the Cerebral aqueduct has reached to be minimum (left, t = 0 s) and maximum (right, t = 0.5 s).

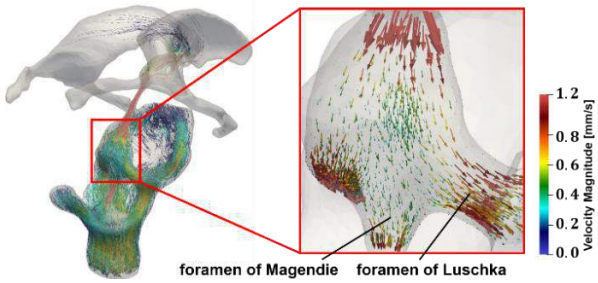

Fig. 4 CSF streamline around the forth ventricle when the volume averaged velocity in the Cerebral aqueduct has reached to be maximum (t = 0.5 s).

REFERENCES

[1] Khani, M et al., *J Biomech Eng*, 139:1-12, 2017.
[2] Orešković, D et al., *Fluids Barriers CNS*, 11:1-3, 2014.
[3] Gholampour, S., *PLoS ONE*, 13:1-20, 2018.
[4] Sweetman, B et al., *Comput. Biol. Med*, 41:67-75, 2011.
[5] Linninger, A et al., *IEEE. Trans. Biomed. Eng*, 54:291-302, 2007.
[6] Mortazavi, M et al., *Child's Nervous System*, 31:15-28, 2014.
[7] Bazilevs, Y et al., (2013), Computational fluid-structure interaction: methods and applications., A John Wiley & Sons, Ltd.
[8] Bapuraj, J et al., *Magn Reson Imaging*, 44:463-470, 2016.

WALL SHEAR STRESS (WSS) VALUES IN A PIG MODEL OF CAROTID STENOSIS BASED ON FREE-RUNNING 5D MRI AND CFD

Yinghan Xu (1), Keshav Kohli (2), Murali Padala (3), Zhenglun Alan Wei (4) John N. Oshinski (1,2)

(1) Department of Radiology and Imaging Sciences
Emory University School of Medicine
Atlanta, Georgia, USA

(2) Department of Biomedical Engineering
Georgia Institute of Technology and
Emory University School of Medicine
Atlanta, Georgia, USA

(3) Department of Surgery
Emory University School of Medicine
Atlanta, GA, USA

(4) Department of Biomedical Engineering
University of Massachusetts Lowell
Lowell, MA, USA

INTRODUCTION

Atherosclerosis is the leading cause of morbidity and mortality in the Western world, and it is the number one cause of death in the US. Vessel wall thickening and formation of plaques associated with atherosclerosis can be detected using noninvasive imaging techniques such as MRI, CT, and PET. Hemodynamics, and specifically, low and oscillatory wall shear in the carotids have been implicated in localization and development of atherosclerotic lesions [1].

Computational Fluid Dynamics (CFD) technique has been used for decades to simulate the blood flow hemodynamics and determine wall shear stress in arteries [2]. CFD uses computational processing to perform numerical analysis on fluid flow inside a 3D models of vessels. The 3D models can come from the reconstruction of the vessel segmentation from images acquired with magnetic resonance angiography (MRA). Three issues which hamper the use of MRA for creating CFD geometries are: 1) the inadequate spatial resolution to create a realistic geometry, 2) flow artifacts that reduce contrast in areas of very high or very low velocity, and 3) respiratory and cardiac motion which cause blurring in the images [3].

Free-running 5D MRA uses signals inherent in the acquisition data to resolve cardiac and respiratory phases on the 3D MRI. Reconstruction uses compressed sensing to reconstruct up to 60 sparsely sampled 3D data sets at different respiratory and cardiac positions. This technique is capable of visualizing arteries high-resolution at multiple cardiac phases without respiratory motion correction [4]. The technique requires an iron-based contrast agent (Fereheme, AMG pharmaceuticals) to shorter the blood T1 values so adequate signal between the blood and static tissue is present.

In this study, we examined a pig model that had undergone a balloon catheter injury on one of the carotid arteries, causing the artery wall thickening and formation of stenosis. *The aim of this study* was to use CFD simulations to calculate velocity distribution and WSS in the diseased and healthy carotid using image data acquired from the free-running 5D MRA to determine the vessel wall geometry. *We hypothesized* that WSS would the equivalent in the healthy artery and the non-diseased section of the injured artery, and that WSS would be elevated in the area of the stenosis.

METHODS

Pig Model: Data were acquired in three hypercholesterolemic Wisconsin mini-pigs who underwent a catheter-based balloon injury on one of the carotid arteries. Institutional Animal Care and Use Committee approval was obtained for the study.

MRI acquisition: The pigs were placed in a 3T scanner (MAGNETOM Prismafit, Siemens Healthcare) in a head-first and supine position. A 20-channel body coil was placed over the heart. Data was acquired with a continuous, ungated, golden-angle spoiled GRE sequence over a 192 x 192 x 192 mm^3 field-of-view (FOV) with 192 samples per readout, giving an isotropic spatial resolution of 1 mm^3. Following acquisition, the raw data were exported offline for reconstruction [5]. To provide velocity boundary conditions, a phase-contrast magnetic resonance (PCMR) scan was performed in the proximal and/or distal carotid. The PCMR scan had a velocity encoding (VENC) value of 80 cm/s and 25 timeframes were acquired over the cardiac cycle. The velocity information was extracted by converting the voxel values into velocity using the defined VENC value. The velocity information extraction is done through the software Segment (http://segment.heiberg.se)

Image Processing: The vessel segmentation is done through Mimics (Materialise NV, Leuven, Belgium). To segment the carotid geometry, vessel segmentation started at the acquisition slice as the PCMR was taken. 3D reconstructions were generated in the software,

manually smoothing was performed, and mesh generation was done in 3-Matic (Materialise NV, Leuven, Belgium). To reduce the computational complicity, the adaptive mesh was used when meshing the 3D models. The maximum mesh size is 2mm and the minimum mesh size is 0.7mm. Extensions on both inlets and outlets was added to the mesh for fully developed flow and numerical stability, respectively.

CFD simulation: For all simulations, Fluent 2019R1 (Ansys, Inc., Canonsburg, PA, USA) was used. All the inlets and outlets enforced mass flow rates. If two outlets were present, their flow weights were calculated based on the ratio of their areas. The fluid was modeled as blood with a density of 1060 kg/m^3 and viscosity of 0.0034 kg/m^{-1}s. Steady flow simulation used the time-averaged flow rate derived from PCMR and transient simulation adopted the time-varying flow waveform from PCMR with a time step size of 0.001s. The duration of a cardiac cycle was 0.49s. The convergence criteria was residual decrease to 10^{-3}.

RESULTS

The segmentation and simulation was successful in both the healthy and injured carotid in two pigs. In one pig, the PCMR was not successful so a subject-specific simulation could not be performed. We generated 3D models of steady and time-dependent velocity and WSS, figure 1, 2. We examined the cross-sectional mean velocity and velocity profile of each carotid at five different locations: near the inlet, proximal to the stenosis, at the narrowest portion of the stenosis, distal to the stenosis, and near the outlet.

In figure 1 and 2, we can see that the two carotids have a similar velocity at the inlets. Velocity differences become more significant at the center of the stenosis, peak velocity is approximately three times larger in the stenosis carotid.

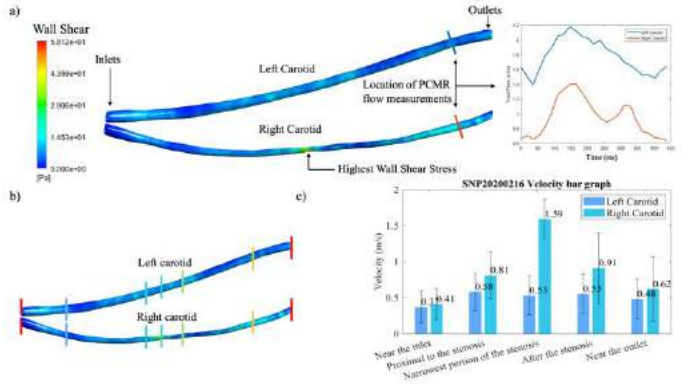

Figure 1 SNP20200216 WSS and Velocity Profile

In the transient flow simulation. From figure 3, normal carotid has similar time mean WSS across the all locations in one of the pigs. WSS increases at the stenosis.

DISCUSSION

Our investigation showed that wall shear stress is the similar at the inlets and outlets in both the injured and health carotids despite the changes in vessel size and flow rate. As expected, CFD simulation results show that WSS and velocity are higher at stenosis. Our hypothesis was that the WSS would be equivalent upstream and downstream of the stenosis, and be similar in both carotids. Furthermore, WSS would be elevated near the stenosis. The data supports this hypothesis, but the number of animals was insufficient to provide statistical significance. WSS has been shown to regulate vessel diameter and wall thickness [6] and this model and these measurements support that mechanism.

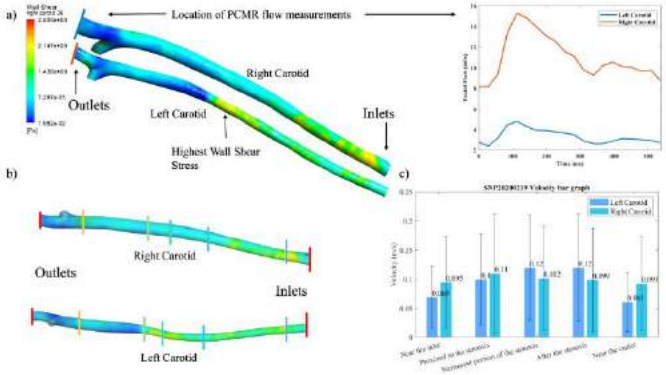

Figure 2 SNP20200219 WSS and Velocity Profile

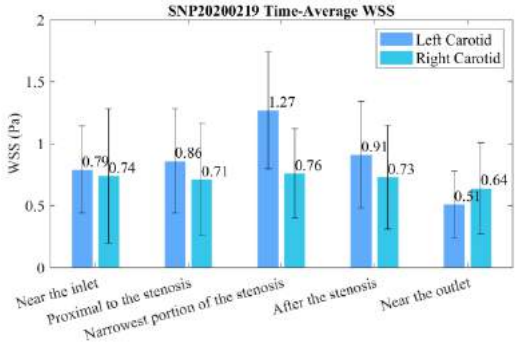

Figure 3. Time-average WSS

The image quality of the 5D free-running MRA sequence with the Fereheme contrast agent was excellent. The high contrast between the blood pool and the static tissue allowed for simplified segmentation of the vessels geometry.

A limitation in this project is that we only have 3 pig models. Our future goals include doing more pig scans and CFD simulation and comparing our simulation data with the histology results.

REFERENCES

[1] Shaaban, Akram M., and André J. Duerinckx. "Wall shear stress and early atherosclerosis: a review." American Journal of Roentgenology 174.6 (2000): 1657-1665.

[2] Szajer, Jeremy, and Kevin Ho-Shon. "A comparison of 4D flow MRI-derived wall shear stress with computational fluid dynamics methods for intracranial aneurysms and carotid bifurcations—a review." Magnetic resonance imaging 48 (2018): 62-69.

[3] Stroud, Robert E., et al. "Correcting versus resolving respiratory motion in free-breathing whole-heart MRA: a comparison in patients with thoracic aortic disease." European radiology 3.1 (2019): 29.

[4] Feng, L. I., et al. "5D whole-heart sparse MRI." Magnetic resonance in medicine 79.2 (2018): 826-838.

[5] Di Sopra, L., et al., An automated approach to fully self-gated free-running cardiac and respiratory motion-resolved 5D whole-heart MRI. Magn Reson Med, 2019. 82(6): p. 2118-2132.

[6] Peiffer, Veronique, Spencer J. Sherwin, and Peter D. Weinberg. "Does low and oscillatory wall shear stress correlate spatially with early atherosclerosis? A systematic review." Cardiovascular research 99.2 (2013): 242-250.

DIFFERENTIAL PROPENSITY OF DISSECTION ALONG THE AORTA

Ehsan Ban (1), Cristina Cavinato (1), Jay D. Humphrey (1)

(1) Department of Biomedical Engineering
Yale University
New Haven, CT, USA

INTRODUCTION

Aortic dissections are typically characterized by intramural tears of the aorta that communicate with the true lumen and allow the entry and accumulation of blood within the vessel wall. Such dissections may be life-threatening events, especially if occurring in the ascending aorta. Margot Roach and colleagues presented experimental studies that addressed the greater propensity of aortic dissection in the thoracic than in the abdominal region [1]. They inserted a needle into the wall of excised porcine aortas and injected pressurized India ink to measure the possible delamination of the wall. They reported drastically different behaviors in the thoracic and abdominal regions. A sudden mode of tearing was observed in the thoracic region, where the wall tore at about 70 kPa, followed by a monotonic decrease of pressure (Fig. 1). In the abdominal region, the aorta started tearing at a smaller pressure. The pressure, however, increased in a stepwise fashion at increasing volumes of injection, which requires more energy. In this work, we utilized computational modeling and microscopy to study the characteristics of tearing in the abdominal and thoracic aortic samples by the intramural injection of fluid.

METHODS

We used a finite element phase-field model of fracture combined with a Fung-type four-fiber family model of wall deformation and a hydrostatic model of the pressurized intramural fluid. Increments of the volume of the intramurally injected fluid were prescribed by a global Lagrange multiplier, similar to the pressure-like field employed to enforce the incompressible deformation of tissue. A homogeneous model was used for the tearing of the thoracic aorta, whereas a microstructural model was used for the abdominal aorta. The microstructural model was motivated by multiphoton microscopy of the structure of the arterial wall.

Microscopy was performed using aortas harvested from three adult female C57BL/6J mice using protocols approved by the Institutional Animal Care and Use Committee of Yale University. The three-dimensional microstructure of elastin within the aortic wall was captured in a stable in vivo-equivalent mechanical configuration through the entire thickness.

RESULTS

In the thoracic region, as the volume of injection increased, pressure increasing accompanied by the rising of the portion of the wall above the injection. The wall subsequently tore, with the tear extending horizontally in the opening mode. Parametric computations demonstrated that the square of the critical pressure of tearing followed the relation

$$P_{\text{tear}}^2 \propto G_c K_t / \sqrt{A_{\text{torn}}}, \tag{1}$$

where G_c and K_t are the characteristic energy of tearing and tissue tangent stiffness. A_{torn} is the torn area of the tissue in the plane of propagation. The change of pressure with increasing injection volume agreed with the experiments in the thoracic region (Fig. 1C).

Multiphoton microscopy demonstrated the higher frequency of radially oriented elastin struts in the abdominal aorta compared with the thoracic aorta (Fig. 2). Informed by multiphoton microscopy, a model with multiple elastic lamellae and radial struts was tested (Fig. 1A). The sequential tearing of the interlamellar medium and radial struts resulted in the stepwise increase of pressure as injection progressed,

qualitatively similar to the experiments of abdominal aortic tissue (Fig. 1B). The struts stiffened the tissue by holding the adjacent lamellae together and increased the tissue characteristic energy of tearing by forming obstacles to the propagation of the pressurized fluid.

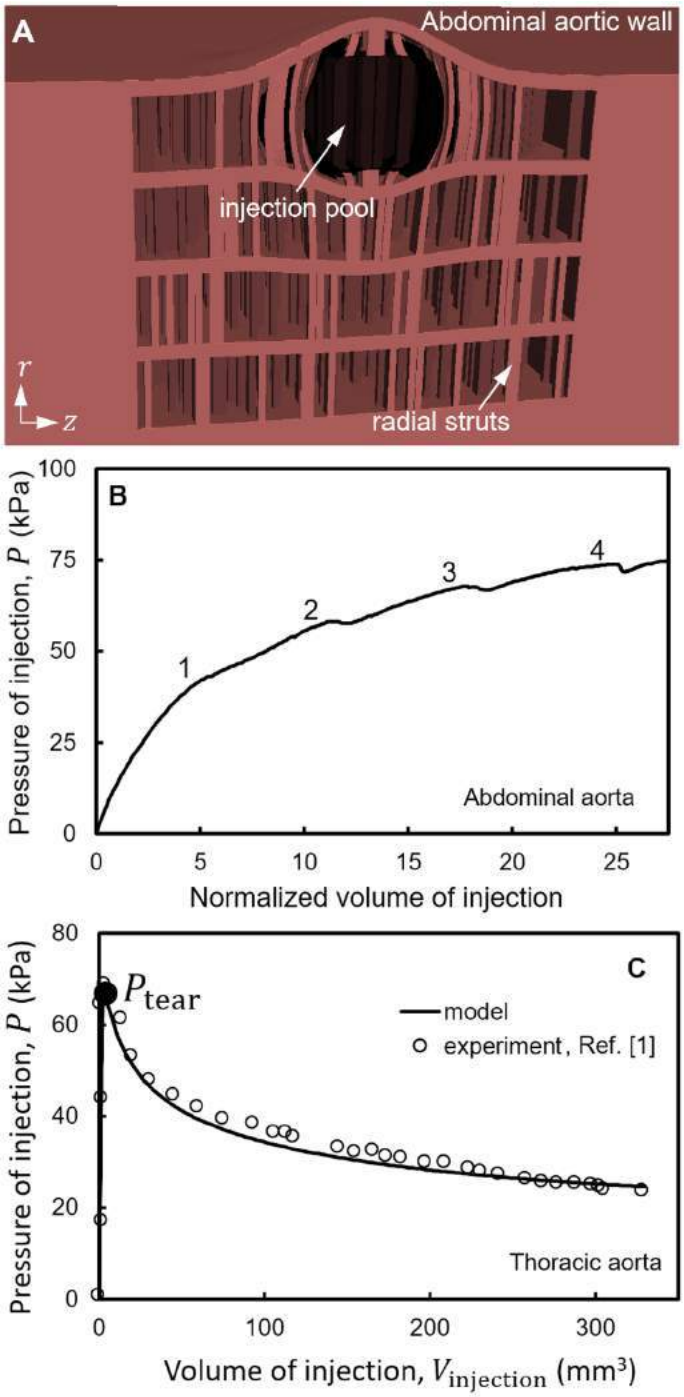

Figure 1: (A) Model of fluid injection into the abdominal aortic wall. The pressure of the injected fluid as a function of volume in (B) the stepwise tearing, observed in abdominal samples, and (C) sudden tearing observed in the thoracic samples that can manifest in other regions. In panel C, 1 refers to the pressure, where the matrix starts tearing; 2, 3, and 4 each correspond to the snapping of a radial strut.

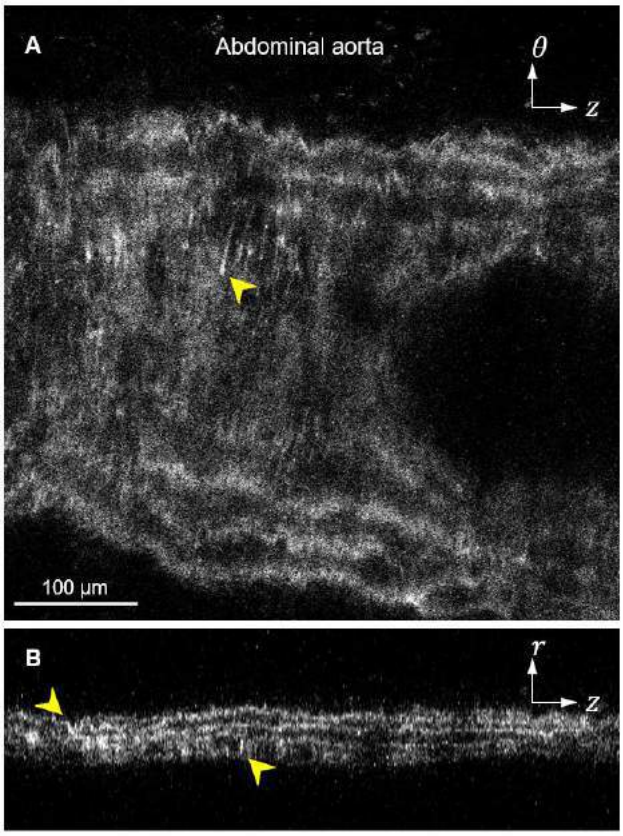

Figure 2: Representative two-photon fluorescence microscopy images of elastin within the aortic wall in the suprarenal abdominal aorta. The yellow arrows point to interlamellar struts.

DISCUSSION

The present work provides computational support for the seminal observations of Roach and colleagues that sites of intramural swelling can lead to propagating delaminations within the aortic wall. Furthermore, the inverse relationship reported between the square of the pressure of tearing and the square root of the torn area of the tissue implies that given a large enough initial tear, the normal pressure of blood can propagate dissections even in healthy aortas. Finally, this work confirms the importance of the radially oriented structural constituents within the wall in allowing or arresting dissection (cf. Ref. [2]).

ACKNOWLEDGEMENTS

This work was supported, in part, by a grant from the US National Institutes of Health (U01 HL142518).

REFERENCES

[1] Roach MR, et al., *Clin Invest Med*, 17:308–318, 1994.
[2] Tsamis A, et al., *J Biomech*, 47:3820–3824, 2014.

DEVELOPMENT AND VALIDATION OF AN ULTRA-HIGH FIELD COMPATIBLE MR ELASTOGRAPHY ACTUATOR

E. Triolo (1), A. Pionteck (1), A. Alipour (2), O. Khegai (2), P. Kennedy (2), P. Balchandani (2), M. Kurt (1,2)

(1) Mechanical Engineering
Stevens Institute of Technology
Hoboken, New Jersey, USA

(2) The Biomedical Engineering and Imaging Institute
Icahn School of Medicine at Mount Sinai
New York City, New York, USA

INTRODUCTION

Historically, pathologies such as tumors or lesions have been identified by physicians by manually palpating soft tissue to compare mechanical properties of healthy tissue to potentially malignant tissues. However, for organs such as the brain, this technique is not feasible, although the mechanical properties of the brain can elucidate significant information about its health and development, such as cell density, myelination, and inflammation [1]. This information can be used to diagnose injuries and diseases, such as Alzheimer's disease, Frontotemporal dementia, or Parkinson's disease [2,3]. Magnetic resonance elastography (MRE) is a technique for determining the mechanical response of tissue using applied harmonic deformation of the tissue and motion sensitive magnetic resonance imaging (MRI) [4]. Currently, studies investigating the mechanical properties of the human brain using MRE are performed at conventional clinical MRI scanner with magnetic field strengths of 3 Tesla (3T) and 1.5T.

More recently, there have been a few attempts at performing MRE on the human brain at the ultra-high field strength at 7T [5]. This ultra-high field strength allows for higher resolution images and higher signal-to-noise ratio (SNR), potentially allowing for the determination of the properties of smaller brain-substructures that have been suggested at 3T MRE [6, 7]. In order to perform MRE at 7T, however, a novel actuator that is ultra-high field compatible and approved needs to be developed and validated due to the size, material, and T2 relaxation constraints imposed by moving to 7T.

In MRE, mechanical waves generated by the actuator, usually transmitted in a burst of specified duration, must be synchronized with the MR signal excitation [8]. The vibration frequency, dependent on the application, is generally in the range of 40-120 Hz [8]. Additionally, since this actuator must be used in an ultra-high MR setting, the tissue-contacting portion of the actuator must contain only ultra-high MR-safe materials. Common electromagnetic and piezoelectric actuators are inherently made of metals and may not be ultra-high field MR-safe. Specifically, electromagnetic actuators can cause electromagnetic interference during MR signal acquisition, while 7T-safe versions of piezoelectric actuators are cost-prohibitive and can cause distortions due to eddy currents. With a pneumatic design, the active metallic components can be stored in the equipment room, while all of the tissue-contacting components used in the scanner room can therefore be made entirely of plastics. However, both acoustic wave attenuation and synchronization with the scanner can present an issue with this type of design due to the time delay of the acoustic waveform moving from the active pneumatic driver to the end-effector.

Therefore, the purpose of this investigation is to develop a 7T MR-compatible actuator for MRE data acquisition, quantify the frequency response using laser doppler vibrometry, and perform a 3T validation scan on a phantom of known mechanical properties.

METHODS

The proposed pneumatic actuator design consists of a modified dual 12" cone subwoofer (MTX 1200 W max, 2 Ω impedance) as an active driver to provide harmonic vibration in the form of pressure waves through flexible PVC tubing (1" ID, 1-1/4" OD) to a pillow-like passive driver as the tissue-contacting end effector. Both cones have acrylic sheets mounted to the front with custom hose attachments to direct the acoustic waves into the tubing and to the passive driver. The passive driver is constructed from heat-sealed polyurethane and compressible foam. The modified subwoofer is driven by a function generator (RIGOL DG-1022) through an audio amplifier (300 W), which provides a harmonic signal to the active driver and a TTL signal synchronized with that signal to the MRI control PC to trigger the MRE acquisition sequence. The schematic of the design is shown in Figure 1.

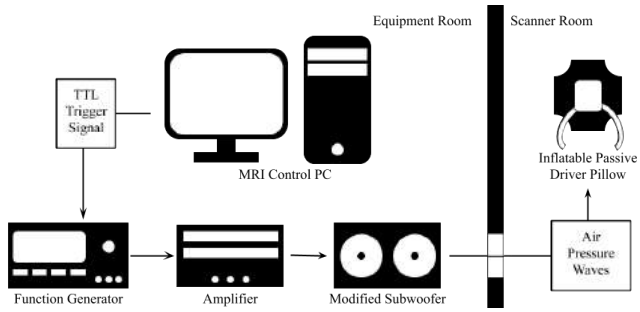

Figure 1: MRE hardware and sequence triggering setup.

To address the time delay from the active driver to the passive driver and the frequency response of the actuator, a laser doppler vibrometer (LDV) was used to capture the harmonic motion of the passive driver. A small square of reflective material was attached to the center of the passive driver, and the laser was aligned with the square. Both the output of the LDV and the signal generator driving the modified subwoofer were visualized in an oscilloscope, and both the amplitude of vibration of the pillow and the time delay (ms) between peaks was measured for driving frequencies 50-100 Hz (5 Hz increments). These data were then phase-unwrapped, and a linear regression was developed to quantify the time delay as a function of driving frequency to be used in that driving frequency range.

To validate that the actuator functions as intended, a custom silicone MRE phantom (CIRS 049) of dimensions 21.0×15.0×10.7 cm was acquired with a background Young's modulus of 5±1 kPa and spherical inclusions of 3, 8, 12, and 20 kPa, ±1 kPa. The passive driver was attached to the surface of the phantom using compression bandages, and while performing MRE imaging, the MRE sequence provided TTL triggering to drive the modified subwoofer in sync with the motion encoding gradients. MRE data was acquired for 24 slices with 3D motion encoding gradients using an echo planar spin echo 2D pulse sequence [9] with vibration frequency 60 Hz, 8 phase offsets, 90-degree flip angle, FOV 300x300mm, resolution of 3.125×3.125 mm, and slice thickness of 2.5 mm. This was performed inside of a 3T Siemens Skyra scanner with a 16-channel head coil (Siemens Healthineers).

Acquiring special mapping of displacement patterns under the external harmonic loading [4], curl filtering was used to capture wave propagation fields (Fig. 3), and an algebraic inversion algorithm without phase wrapping [10, 11] and Romano filtering was utilized to acquire shear stiffness maps of the phantom's cross section.

RESULTS

The linear regression developed from the LDV testing (Fig. 2) to calculate time delay from trigger signal to pillow movement, where f is the driving frequency and n is any positive integer, is shown as equation 1. The R^2 value of this linear regression was 0.9986.

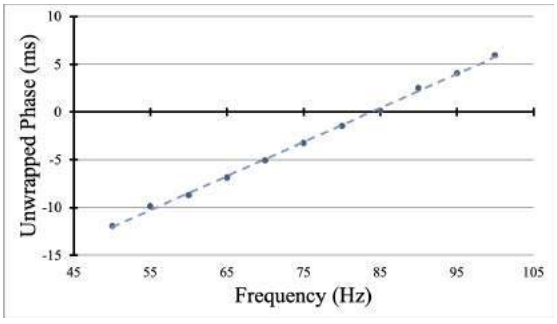

Figure 2: LDV testing time delay linear regression.

$$timedelay = \frac{0.3565f - 29.882}{2\pi f} - \frac{n}{f} \quad (1)$$

The peak-to-peak amplitude of the pillow ranged from 0.6 mm to 0.3 mm, dependent on the frequency of actuation.

Shear wave propagation (from the top of the phantom down) due to the actuator are shown in Figure 3 in units of mm/mm. This algorithm was able to distinguish shear wave propagation in homogeneous slices (Fig. 3a) and those with a spherical inclusion (Fig. 3b). The shear stiffness estimates of the background ranged generally from 1.4-1.6 kPa, which, assuming a Poisson's ratio of 0.5, is equivalent to a Young's modulus of 4.2-4.8 kPa. The shear stiffness estimates for the inclusion ranged from 0.7-0.9 kPa, or a Young's modulus of 2.1-2.7 kPa.

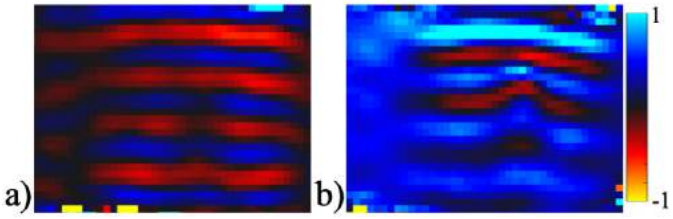

Figure 3: Shear wave propagation in MRE phantom, without an inclusion (a) and with a spherical inclusion (b).

DISCUSSION

While wavefield images and stiffness maps were successfully obtained, there is attenuation as the shear waves propagate farther from the actuator attached to the top surface of the phantom, therefore, the shear stiffness estimate is not as homogenous as we assume the custom phantom is. These estimates are, however, within the ranges of the custom phantom's specifications, indicating that the actuator and inversion algorithm result in accurate stiffness estimates.

In order to generate a more accurate and homogenous stiffness estimate, a more powerful amplifier can be used in the actuator setup to generate higher amplitude acoustic waves, and stiffer and shorter tubing can be used to decrease wave attenuation. Additionally, in the future, this actuator will be tested using a 7T human MRI scanner as well as with human subjects in order to estimate the shear stiffness of the human brain. For this future work at 7T, ultra-high-resolution MRE data of 1.1 mm isotropic resolution will be acquired using a custom (under development) single-shot spin-echo EPI (echo planar imaging) sequence with three orthogonal trapezoidal flow-compensated motion-encoding gradients.

ACKNOWLEDGEMENTS

We acknowledge support from NSF funding 1953323 and NIH funding R21AG071179. We would also like to thank Dr. Curtis Johnson (University of Delaware) for providing the MRE sequence.

REFERENCES

[1] Sack, I. et al., *PLoS ONE*, 6(9):e23451, 2011.
[2] ElSheikh, M. et al., *AJR Am J Roentgenol*, 209(2):403-408, 2017.
[3] Lipp, A. et al., *Neuroimage Clin*., 3:381-387, 2013.
[4] Manduca, A. et al., *Medical image analysis*, 5:237-254, 2001.
[5] Fehlner, A. et al., J. *Magn. Reson. Imaging*, 46:134-141, 2017
[6] Johnson, C. L. et al., *NeuroImage*, 79, 2013.
[7] Vaughan, J. T. et al., *Magn. Reson, in Med*., 46:24-30, 2001.
[8] Latta, P. et al., *Magn. Reson. Imag*., 29:147-152, 2011.
[9] Chaze, C. A. et al., *NeuroImage: Clinical*, 22:101750, 2019.
[10] Oliphant, T. E. et al., *Mag. Reson. in Med.*, 45:299-310, 2001.
[11] Glaser, K. J. et al., *Proc. Intl. Soc. Mag. Reson. Med*., 17, 2009.

DEVELOPMENT OF A METHOD TO QUANTIFY ELASTIN CONTENT IN LARGE DATASETS OF BLADDER TISSUE HISTOLOGY WITH MACHINE LEARNING ALGORITHM

Eli Broemer (1), Sara Roccabianca (1)

(1) Mechanical Engineering
Michigan State University
East Lansing, MI, USA

INTRODUCTION

Extracellular matrix remodeling in which the structure and/or distribution of collagen and elastin fibers in the urinary bladder wall are modified has been associated with dysfunction [1]. Histological images are useful in studying microstructural changes, however, quantifying elastin content in these images is challenging. Specifically, the Verhoeff-van Gieson's (VVG) stain is known to effectively differentiate elastin fibers with sharp intense contrast, although it also stains cell nuclei and other connective tissue [2]. Despite having limitations, the stain is relatively easy, and elastin has high affinity to the dye, making VVG one of the most common elastic tissue stains [3].

Analyzing amounts of elastin in bladder tissue with VVG histologies has long been done qualitatively [4, 5]. Yet, quantitative attempts with VVG micrographs are less common, and may include visually scoring fiber density [6, 7], or estimating area fraction in a region of interest by thresholding the dark fibers from the light background [8, 9]. The primary limitation with the simple thresholding scheme is that cell nuclei and other noise are not removed by the cutoff value, or more strict cutoffs significantly erode the elastin fibers. To solve this issue, prior studies relied on substantial manual postprocessing and homogenization of connective tissue [8, 10]. Alternatively, computationally intense methods have been proposed, however limitations of these are that they either use proprietary software [10] or unsupervised image transforms to segment fibers [11]. Our goal is to improve on the latter approach by simplifying the segmentation procedure and by adding a machine learning postprocessing step to reduce the manual processing of large data sets.

Random forest [12] is a type of machine learning algorithm, and is regarded one of the best overall for prediction problems [13]. In short, the model fits an output dataset by building a decision tree used to interpret the input parameters [14]. Then, bootstrapping the data produces a forest of decision trees, and its final prediction is typically the average or most frequent result from the forest. This makes the algorithm robust to outliers, missing data, and irrelevant parameters. Random forest is easy to implement, fast to train, and has been applied to histology problems before [15]. Yet, its application to identify elastin in bladder tissue is novel and presents unique challenges.

The current work was initiated with a proof-of-concept by training a random forest algorithm on a pseudo dataset representative of VVG stained bladder tissue after simple thresholding to ensure feasibility. Then, we developed a software for processing true histology specimens. The software is used to, first, segment histology images and, second, to label the segments as elastin fibers or not. A segmenting protocol as simple as thresholding was enhanced by preprocessing more powerful image transforms. Then, the labelling process allows for multiple researchers to easily train a new elastin classification algorithm. When the random forest is sufficiently trained by showing reliable accuracy, it can automatize the quantification of elastin area fractions in large data sets, which will significantly improve the time needed for analysis.

METHODS

A set of 35 VVG stained rat bladder wall microscopy images was contributed from a separate study for use. Image preprocessing starts when images are uploaded to the custom-made software. Each image is treated with a combination of transformations that were found to be generally successful at isolating the specific components of interest and masking the background noise. For every image, a set of 50 masks with varying levels of strictness is obtained by tweaking the combination of image transforms. Then, segmentation is done by a researcher choosing the strictness of the final mask with a slider to best capture elastin and remove noise, as shown in **Figure 1**. Combining varying image transforms (i.e., thresholding, contrast normalization, dilation, noise

reduction) and then sorting the resulting image masks by the number of pixels masked allows the researcher to leverage these powerful techniques. This protocol was implemented into a web application using the python Bottle library. The software is hosted locally in the research lab, and lab members can login to easily segment images with this enhanced thresholding method, or label objects extracted from images.

Once an image is segmented, each object isolated by the mask is extracted, and on a different screen, shown in **Figure 2**, a researcher can label the objects based on their expertise. Furthermore, objects may carry labels from multiple researchers, and this is in fact encouraged as some objects are ambiguous and multiple opinions will reduce bias.

RESULTS

The segmentation screen (**Figure 1**) allows quick masking of cells and elastin by utilizing preprocessed image transformations that are more powerful than simple thresholding. The mentally taxing process of tweaking the image transformations is supplanted with simply selecting more/less masking from the set of preprocessed transforms. Segmentation is faster and requires less image analysis intuition.

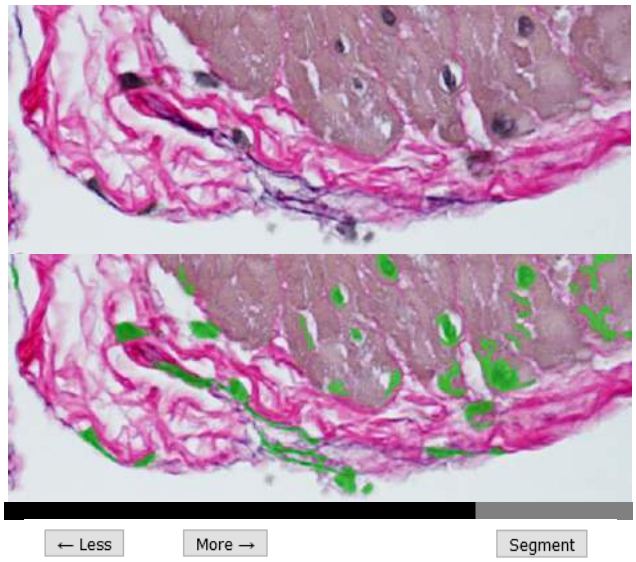

Figure 1: Segmentation screen utilizing enhanced thresholding method. Black/gray slider at the bottom has been adjusted so that cells and elastin are masked (green highlights) as best possible.

The labelling screen (**Figure 2**) presents individual microstructure for the researcher to identify. A given histology image may have between 50 – 200 objects isolated after segmentation, and it can take a time near 5 – 10 minutes to fully label an image. Since the software is hosted locally, loading and saving times are often near instant. This approach is faster and easier than the proof-of-concept method in which image files of isolated objects were labelled correspondingly in a spreadsheet. Data labels are used to train random forest predictions.

DISCUSSION

This histological elastin extraction software shows promise for estimating area fraction of elastic fibers in VVG stained tissues. Other means of quantifying elastin in tissues include commercial assays or Western blots. However, these procedures consume the sample and so the tissue morphology cannot be assessed from the same sample. Scanning electron and confocal microscopy are also used to capture images of elastin, although these technologies are more cost prohibitive.

Figure 2: Labelling screen prompts user to identify if an object is elastin. Extracted object is shown with context (left) and also magnified with outline (right) for clarity.

Current limitations of this study are microstructure components that are not fully separated during segmentation. For example, an elastin fiber intersecting a cell are both joined as one object and cannot be labelled accurately. Next steps include solving this limitation by developing a secondary segmentation option when a researcher encounters this scenario during labelling.

As the development dataset is small, more histology images from bladder tissue are to be added. Then, a new random forest algorithm will be trained and tested on the data using this software. Fully labelled data is to be split 80/20 for tuning algorithm hyperparameters. That is, 80% of the data is used to train and 20% is used to test the algorithm. Random forest parameters including number of trees and branch splitting criteria will be optimized with 5-fold cross validation to assess accuracy. The model will also be tested on new data to further validate.

Later steps include implementing and comparing the accuracy of other machine learning schemes such as Support Vector Machine and Naïve Bayes classifiers.

ACKNOWLEDGEMENTS

We thank fellow lab member Tyler Tuttle for the histology images, and the MSU Investigative Histopathology Lab for staining tissues. This research was inspired by Miguel Contreras' work at SB3C 2020 [16].

REFERENCES

[1] Wognum, S et al., *J Biomech Eng*, 131(10):101018, 2009.
[2] Verhoeff, FH, *JAMA*, L(11):876-877, 1908.
[3] Carson, F & Cappellana CH, Histotechnology 4th ed., 2014.
[4] Ji, P et al., *World J Urol*, 13:191-94, 1995.
[5] Lemack, GE et al., *Neurourol Urodynam*, 18:55-68, 1999.
[6] Kullmann, FA et al., *Front Syst Neurosci*, 2018.
[7] Cantiello, F et al., *Urology*, 81(5):1018-23, 2013.
[8] Jinrok, O et al., *J Orthop Res*, 22:1310-15, 2004.
[9] Johal, N et al., *J Pediatr Urol*, 2020.
[10] Karam, JA et al., *BJU Int*, 100(2):346-350, 2007.
[11] Paul, K et al., *Appl Mater Today*, 22:100890, 2021.
[12] Breiman, L, *Mach Learn*, 45:5-32, 2001.
[13] Caruana, R & Niculescu-Mizil, A, *ICML 2006*, 161-168, 2006.
[14] Zhang, C & Ma, Y, Ensemble Machine Learning, 2012.
[15] Ikeda, T et al., *J Hepato-Bil Pan Sci*, 2020.
[16] Contreras, M, Bachman, W & Long, D, *SB3C*, Abstract 466, 2020.

A COMPUTATIOAL DIGITAL TWIN METHODOLOGY FOR UNDERSTANDING BIOMECHANICS OF VERTEBROPLASTY

H. Ahmadian (1), P. Mageswaran (1), D. Blakaj (2), E. Mendel (3), S. Soghrati (4), W Marras (1)

(1) Spine Research Institute
The Ohio State University
Columbus, OH, US

(2) Department of Radiation Oncology
The Ohio State University Wexner Medical Center
Columbus, OH, US

(3) Department of Neurological Surgery
The Ohio State University Wexner Medical Center
Columbus, OH, US

(4) Department of Mechanical and Aerospace Engineering
The Ohio State University
Columbus, OH, US

INTRODUCTION

Vertebral compression fracture (VCF) is a major clinical concern in treatment of cancer patients with metastatic disease to the spine. These sudden fractures often lead to persistent back pain in patients, who may not be able to perform normal daily activities, and some of them develop into kyphosis, seriously affecting their quality of life. Vertebroplasty is a common treatment modality used to help stabilize VCF in patients[1]. This procedure is usually associated with injection of a polymeric material (e.g. PMMA bone cement) to reinforce the vertebral structure. However, injection of PMMA imposes risks such as intra-spinal cement leakage[2] and development of new fractures. These complications pose a significant challenge to clinicians in the medical treatment of high-risk patients. Therefore, prospective data on the optimal use of Vertebroplasty is vital for the management of high-risk VCF patients.

While biomechanical loads are believed to play a major role in the initiation of VCF injury mechanisms, very little is known on the progression of microstructural damage in the bone. It remains unclear how the underlying relationship between spinal loads and the morphological changes to the vertebral bodies (because of disease and treatment) may contribute towards the initiation of microstructural damage and consequent fracture. Computational methods (e.g., finite element) and machine learning algorithms provide a viable non-invasive scheme to elucidate mechanisms that lead to vertebral instability, failure and eventual fracture. Further, leveraging Computational Fluid Dynamics (CFD) tools in the simulation of vertebroplasty enables surgeons to virtually control and evaluate various parameters such as the needle position and injection flow rate virtually. Here, we will present an AI-assisted computational framework that involves constructing a *digital-twin*[3] of the patient's vertebra, to assess the risk of VCF in cancer patients with spinal metastasis. The concept of digital twin is borrowed from engineering principles, where *in-silico* representations of a complex system (e.g., vertebral body) are used as virtual models to analyze current condition and predict future performance with real-time connection between the physical system and the model

METHODS

In this effort, micro-Quantitative Computer Tomography (micro-QCT) imaging datasets will be utilized to train a Deep Learning (DL) network for creating patient's vertebral digital twins. These surrogate models will then be transformed into an in-house high-fidelity FE mesh for biomechanical analysis. A level-set method is then utilized within a CFD framework to track the displacement of the interface between injected cement and bone marrow. Next, a nonlinear damage model is utilized to simulate the initiation and progression of damage in the vertebra under various loading conditions.

RESULTS

In this section, we have provided a feasibility study to understand failure mechanism of the vertebra subjected to various loading conditions. Morphology of vertebra and tumor lesion is extracted from CT and MR images of a 51 years-old female patient with lung cancer admitted to the Ohio state university comprehensive cancer center (OSUCCC). To conduct high-fidelity FE simulations, the reconstructed vertebral models are first transformed into FE meshes with BMD-dependent elastic properties using an in-house FE modeling framework. The failure behavior of each model is quantified as the force-displacement curves resulted from the FE solver. Such measurement provides us with a good estimate of the vertebral fracture strength as the peak force in the aforementioned curve. Furthermore, the crack propagation is tracked

through visualization of damage initiation and progression patterns projected on the deformed geometry of the vertebra.

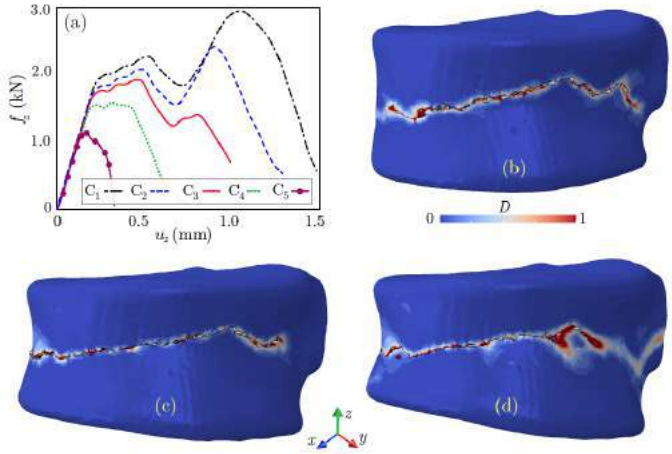

Figure 1: (a) Force-displacement curves. Note that C1-C5 corresponds to loading case scenarios with 0.0, 0.1, 0.2, 0.4, 0.5 °/sec applied rotations. (b-d) Failure pattern after the failure point for the studied vertebra subject to multi-axial loading with compression and (b) 0.0, (c) 0.2, and (d) 0.4 °/sec flexion angle.

In order to investigate the effect of flexion on the failure response, force-displacement curves are quantified for the studied lytic vertebra subjected to multi-axial loading with compression (0.05 mm/sec) and bending (0.0, 0.1, 0.2, 0.4, 0.5 °/sec). Figure 1a illustrates that deformation begins with an elastic region followed by strain hardening, which is associated with trabecular yielding. However, as the flexion angle increases, strain hardening modulus decreases. Under smaller flexion angles i.e. 0.1, 0.2 °/sec, trabecular yield accompanied by initiation and propagation of multiple micro-cracks in regions of trabeculae with higher stress concentrations. Such localized failure mechanism is generally observed as a softening response within the force-displacement curve. As the internal micro-cracks propagate and coalesce to find the path of least resistance, the cortical bone starts to provide mechanical support for the vertebral body. This observation can be explained by stress redistribution after trabecular failure, which activates cortical damage under higher displacements. Such failure mechanism is not observed for the vertebra under higher flexion angles i.e. 0.4, 0.5 °/sec. Therefore, under these loading cases, the catastrophic vertebral failure happens at lower displacements, which explains the importance of anterior height calculations in the clinical assessment of VCF[4]. Note that fracture behavior under flexion, is strongly influenced by the strength of vertebra at the periphery i.e., farthest regions from neutral axis of vertebral body. Therefore, the trabecular microstructure is expected to have lower involvement in load bearing capacity and energy absorption under higher flexion angles. This leads to more brittle failure (limited nonlinearity) with lower vertebral strength as flexion angle increases. These observations justify the prevalence of wedge-shaped fractures in osteoporotic patients, particularly in the thoracic spine, which are subjected to high flexions.

These fractured vertebrae can easily be augmented by virtually embedding the injected cement geometry within the microstructure to re-estimate the risk of fracture after performing vertebroplasty. However, since determination of cement distributions pre-operatively is not feasible, a computational tool allowing surgeons to predict the cement morphology based on injection pressure, location and local tissue micro-architecture could significantly reduce the risk of cement leakage or re-fractures. For this reason, a two-phase level-set method is utilized within a CFD framework to track the displacement of interface between injected cement and bone marrow during the vertebroplasty. Figure 2 shows the vertebroplasty results for three scenarios: (1) cement injection within an intact vertebra with no lesion (injection rate=0.5 mL/sec) (2) cement injection within a lytic vertebra (injection rate=0.1 mL/sec) (3) cement injection within a lytic vertebra (injection rate=0.5 mL/sec). For the intact vertebra a uniform cement distribution is observed, which qualitatively matches clinical observations of vertebroplasty in patients with osteoporosis. However, for the vertebral model with lytic metastasis, risk of cement leakage increases as the injection flow rate increases, which matches with observations from literature[5]. This phenomenon can be explained by the higher viscosity of cement under lower injection flow rates. Finally, a biomechanical damage analysis could be performed to re-evaluate risk of fracture in the vertebral body.

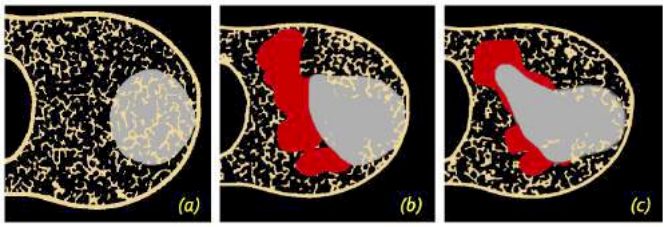

Figure 2: cement morphology (gray color) for (a) intact vertebra (b) lytic vertebra with injection rate of 0.1 mL/sec, and (c) lytic vertebra with injection rate of 0.5 mL/sec. tumor lesion is demonstrated with red color.

DISCUSSION

The computational framework proposed in this is the promising step towards providing a quantitative metric for predicting VCF thresholds in vertebral bodies. Although, achieving its full potential would require further developments beyond the scope of this manuscript, the digital twin concept could potentially translate to innovative clinical applications such as personalized treatment patients with bone diseases (e.g., osteoporosis and cancer metastasis). Note that an accurate prediction of VCF requires a real-time estimate of external stimuli i.e. the spinal loadings applied on the vertebral body during daily life activities. Therefore, the next step is to incorporate the proposed computational framework within our personalized musculoskeletal model.

The parameters used in the biomechanical damage model and estimation of the bone elastic modulus based on BMD are adopted from literature. However, adopting generic parameters from literature for the real subjects without carefully assessing the FE model could undermine the fidelity of predictions. Therefore, a direct and effective comparison with in-vitro (e.g., cadaveric mechanical testing) and in-vivo (e.g., MR Elastography) measurements is of great importance.

ACKNOWLEDGEMENTS

The abstract is based upon work partially supported by the Center for Cancer Engineering at the Ohio State University.

REFERENCES

[1] Mendel, E et al., *Spine,* 34:93-100, 2009.
[2] Baumann C et al*, Cardiovasc Intevent Radiol,* 30:161-168, 2007.
[3] Tao, F et al, *Int. J. Adv. Manuf. Technol.,* 94:3563-3576, 2018.
[4] Diacinti D et al., *Bone*, 46:768-773, 2010.
[5] Baroud G et al., *Biomed. Mater. Eng.*, 14:487-504, 2004.

THE EFFECTS OF FETAL HEAD SIZE ON MATERNAL COCCYX ROTATION DURING A VAGINAL DELIVERY

S. Chen (1), M. Routzong (2), S. Abramowitch (2), M. Grimm (1)

(1) Department of Mechanical Engineering
Michigan State University
East Lansing, MI, USA

(2) Department of Bioengineering
University of Pittsburgh
Pittsburgh, PA, USA

INTRODUCTION

Childbirth is a complex mechanical process that puts both the mother and the infant under a risk of injury. The coccyx, despite its small size, serves a big role during the childbirth process. It provides crucial support to the structural integrity of pelvic floor muscles during childbirth. Its mobility also helps the fetus negotiate through the maternal pelvis. Therefore, the coccyx is a key factor in understanding both maternal and fetal injuries.

The goal of this study is to develop a computational model of vaginal delivery that includes the maternal bony pelvis, a complete maternal pelvic floor, and most importantly, a coccyx that can rotate around the sacrococcygeal joint. This model allows the effects of fetal head size on coccyx rotation during a vaginal delivery to be quantified.

METHODS

A series of three-dimensional (3D) computational models of vaginal delivery were developed including both the mother and the fetus. Three spherical fetal head models with diameters of 74 mm, 80mm, and 86 mm, representing the 3rd, 50th, and 97th percentile head circumferences of newborns [1], were constructed, after considering a 20% reduction in circumferences due to molding. The mechanical properties of the fetal head were set to be nearly rigid. The maternal geometric model was based on the *in vivo* MRI images of a 21-year-old nulliparous woman at the gestational stage of 35 weeks and 6 days. The 3D maternal geometric model includes the bony pelvis (i.e., hip bones, sacrum, pubic symphysis, and coccyx), and soft tissues (i.e., levator ani, coccygeus, and the superficial perineal muscles and perineal membrane). A finite element mesh of the maternal model was constructed in Hypermesh (version 2020, Altair). The maternal bony pelvis was meshed using first-order triangular shell elements, with an average element size of 5 mm and a thickness of 1 mm. The pubic symphysis was added to the maternal pelvis during the meshing process, using the same shell elements. All maternal soft tissues were meshed using first order tetrahedral elements, with an average size of 4 mm. The finite element mesh model was composed of 28379 first order tetrahedral elements, 15077 first order triangular elements, and 14130 nodes, as shown in Figure 1.

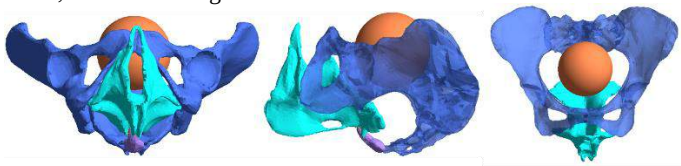

Figure 1: Overview of the childbirth finite element model, from (a) caudal to cranial direction, (b) left to right direction, and (c) ventral to dorsal direction. The fetal head with the 50th percentile circumference is presented in the picture.

The material properties of the maternal bony pelvis were described as rigid. The material properties of the maternal soft tissues were described using a Mooney-Rivlin material, the strain energy density function of which is written as

$$W = C_1(\bar{I}_1 - 3) + C_2(\bar{I}_2 - 3) \quad (1)$$

where $C_1 = 26kPa$, $C_2 = 14\ kPa$ [2]. The density of the pelvic floor soft tissues was $1060\,\frac{kg}{m^3}$ [3]. Rayleigh damping ($\alpha = 0.1$) and material damping ($d = 0.5$) were added to filter out low frequency and high frequency vibration of the soft tissues, respectively.

The maternal pelvis was positioned with a 45° angle between the pubic symphysis and the ground. All degrees of freedom of the following locations were fixed: (1) levator ani's insertion points at the pubic bone; (2) levator ani's insertion points at the ischial spines; (3) the

ends of the ischiocavernosus that join the bulbocavernosus near the pubic symphysis; and (4) the ends of the ischiocavernosus that join the superficial transverse perineal muscle near the ischial tuberosities. Displacement of the following locations were fixed in certain directions: (1) nodes around the anus were restricted from moving in the left - right direction; (2) nodes on the anococcygeal raphe were restricted from moving in the left–right and the cranial–caudal direction; and (3) nodes on the ischiocavernosus along the inferior pubic rami were restricted from moving in the ventral–dorsal and the cranial–caudal direction. The pelvic floor was connected to the coccyx using 11 belt elements that had nearly rigid tensional strength but zero compressive strength.

The descent trajectory of the fetal head followed the Curve of Carus. It consisted of six points described as follows: Point 1- the middle point of the pelvic inlet; Point 2 - the middle point of the mid pelvic cavity; Point 3 - the middle point of pelvic outlet; Point 4 - the projection of the pubic symphysis' lower end on the ground surface at the level of Point 3; Point 5 - the lower one quarter point of the vaginal hiatus; and Point 6 - a point on the extended line of Point 4 and Point 5 that is at a distance of 60 mm from Point 5.

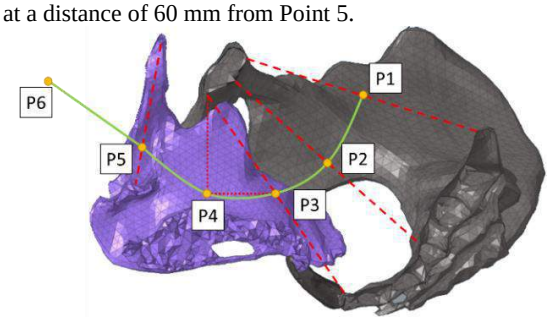

Figure 2: Landmark points and the descent trajectory of the fetal head during the second stage of labor. Points 1 – 6 are marked using yellow dots and labeled as P 1 – 6 in the picture.

The descent trajectory was represented by a spline interpolation going through the five landmark points, fitted by XMADgic (version 7.7, Siemens) using a series of 5th degree polynomials. The delivery time was set to be 1 hour, which is the median time duration of the second stage of labor for nulliparous women without epidural. During the delivery, the fetal head moved along the trajectory in constant speed This dynamic model system was solved in MADYMO (version 7.7, Siemens).

RESULTS

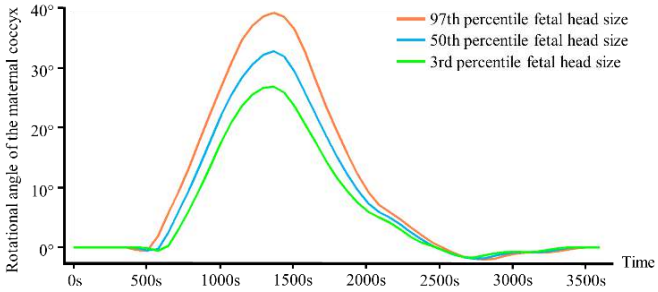

Figure 3: Rotational angle of the coccyx corresponding the delivery of the 3rd, 50th, and 97th percentile fetal head during the second stage of labor.

The rotational angles of the maternal coccyx were recorded at 50 evenly distributed time points. The coccyx rotated around the sacrococcygeal joint and moved in the dorsal, caudal direction as the fetal head went through the pelvis. As shown in Figure 3, different fetal head sizes contributed to different peak angles, but the peak time and the general trend were the same: the maximum angles were all reached at 1368s, when the center of the fetal head is between Point 3 and Point 4. After the peak angle, the coccyx rotation decreased and overshot slightly in the ventral, cranial direction before it returned to its original position from the beginning of the second stage of labor. The peak angles are 39.1°, 32.8°, and 26.8° for the 97th, 50th, and 3rd percentile fetal head size, respectively.

DISCUSSION

This study simulated the second stage of labor using a computational model that included the complete pelvic floor soft tissues and a coccyx with the sacrococcygeal joint. The increased coccyx rotational angle due to a larger fetal head was as expected. Since the descent trajectory was prescribed, the rotation of the coccyx is the only way that fetal head can negotiate through the pelvis. This also explains why certain obstetrical maneuvers are effective at resolving difficult labors. For example, by hyperflexing the mother's legs during a McRoberts' maneuver, the pelvis will be tilted, which leaves room for the coccyx to rotate.

Although the childbirth process has been extensively studied computationally, the rotation of the coccyx has not gained the attention it deserves. Researchers have long acknowledged the rotation of coccyx during the second stage of labor. However, very limited quantitative data can be found in the literature. Bø and colleagues [4] measured the rotational angle of the coccyx during contraction and straining of the pelvic floor in an upright sitting position using dynamic MRI. They reported a ventral, cranial rotation of $15° \pm 10.2°$, and a dorsal, caudal rotational degree of $12.9° \pm 10.9°$. Their angles are much lower that what is reported in the current study because these data were achieved merely through participants' voluntary efforts without passage of a fetus through the pelvic floor. In a computational model for the second stage of labor from Jing and colleges, a rotating coccyx was included, but no rotational angles were reported [5]. In another study that addressed the importance of the coccyx during labor, the coccyx provided extra supporting boundary condition for the pelvic floor but was not allowed to rotate [6]. In a recent study, Borges and colleagues reported a 15.7° rotation of the coccyx in their childbirth computational model [7]. The main factor contributing to the rotational angle difference between their study and the current one is likely to be the different initial position of the coccyx. In Borges's study, the coccyx was positioned along the curvature of sacrum, while in the current study the coccyx was positioned pointing anteriorly based on *in vivo* MRI images.

By addressing the mobility of the coccyx at the sacrococcygeal joint, the current study provides a valuable platform through which more accurate childbirth processes may be simulated. By including more detailed muscle and internal organ representation, along with articulated fetal models, a better understanding of childbirth mechanisms and fetal and maternal injuries can be achieved.

ACKNOWLEDGEMENTS

The authors would like to thank the National Science Foundation (CBET – 2028474) for funding this research.

REFERENCES

[1] Chitty, L et al., An Intl J of Obste & Gynaecology, **101**(1):35–43.
[2] Silva, M et al., Cmp Mthds in Biomch & Biomd Eng **20**(8):842–852.
[3] Urbanchek, M et al., The J of Gerontology: A, **56**(5): B191–B197.
[4] Bø, K et al., Neurourology and Urodynamics, **20**(2):167–174, 2001.
[5] Jing, D et al., J of Biomechanics, **45**(3):455–460, 2012.
[6] Berardi, M et al., Proc Inst Mech Eng H, **228**(5):501–508, 2014.
[7] Borges, M et al., Cmp Mthds & Prog in Biomdcn, **200**:105921, 2021.

STUDYING THE VARIATION OF BIOMECHANICS DURING MYELINATION USING AN IN VITRO NEURON-OLIGODENDROCYTE CO-CULTURE MODEL

Ya-Chen Chuang (1), Ace Alcantara (2), Carmen V. Melendez-Vasquez (2), Mehmet Kurt (1,3)

(1) Dept. of Mechanical Engineering,
Stevens Institute of Technology,
Hoboken, NJ, USA.

(2) Biological Sciences,
Hunter College,
New York, NY, USA.

(3) Translational and Molecular Imaging Institute (TMII),
Mount Sinai Hospital,
New York, NY, USA.

INTRODUCTION

The brain development is among the most complex biological phenomena, including dynamical changes of biochemical and mechanical cues. Myelination is an important process taking place during the brain development, which has shown to be related to the brain tissue stiffening [1]. Even though numerous non-invasive elastographic techniques are able to precisely predict the response of brain tissue to specific strain rates *in vivo* [2, 3], there is still limited understanding between biochemical cues and mechanical response during myelination. Therefore, an *in vitro* dorsal root ganglia (DRG) neuron-oligodendrocytes (OL) co-culture system was designed to mimic the neuron myelination process in developing brain, with controlling different neuronal alignments which represents different anisotropic levels observed in grey and white matters. Despite the fact that *in vitro* culture is not capable of fully mimicking the dynamic environment of the brain, the system provides a simplified and controlled environment, allowing us to investigate the variation of mechanics and biochemical behaviors in cellular level during the myelin development. We hypothesized that the stiffening effect starts occurring at cellular scale after myelin sheath wrapping around axons, which may further serve as mechanical cues to trigger downstream biochemical behaviors.

METHODS

DRG neurons were isolated following a well-established protocol [4] and either dissociated or directly plated as explants on matrigel coated glass substrates. Neurons were allowed to extend axons for 2-3 weeks in either anisotropic (highly aligned axons in DRG explants) or isotropic (non-aligned axons in dissociated DRG neurons) patterns prior to their use in myelinating co-culture experiments. Primary oligodendrocyte progenitor cells (OPC) were purified from mixed glial cultures of postnatal day 1 rat cerebral cortices using immunopanning [4, 5]. Freshly purified OPC (Ran2-, A2B5+) were seeded directly onto DRG neurons for co-cultures (50,000-100,000 cells). OPC alone cultures were maintained in Sato media with 10 ng/ml PDGF and 10 ng/ml bFGF for proliferation, or induced to differentiate into mature oligodendrocytes (OL) in Sato containing T3 (30 ng/ml) for 1-3 days. All animal work was with IACUC regulations and under approved animal protocols.

Myelination was induced by changing DRG-OL co-cultures to MEM media containing 10% FBS, 2 mM L- glutamine, and 4 mg/mL glucose. Cultures were fixed at different time points (3, 7, 14 and 21 days) and confocal microscopy was used to check for the extent of myelination using antibodies to myelin basic protein (MBP), in combination with Olig2 (oligodendrocyte) and NF (neurofilament).

For mechanical characterization, atomic force microscopy (AFM, Bruker BioScan Resolve coupled with an Olympus fluorescent microscope) Peakforce measurement was performed on different tissue cultures at the microscale, coupled with live cell imaging using SiR-Tubulin, Sir-Actin (Cytoskeleton) and FluromyelinTM (Invitrogen) to enable visualization of the cellular structures and myelination level. Bruker PFQNM-LC-CAL pre-calibrated probe was used with spring constant k~0.08 N/m and tip radius R~70 nm in order to reveal microstructure of neurons. Axons moduli were measured at different time points (3, 7, 14 and 21 days) to investigate its variation during the myelination process. Furthermore, we probed into the differences of microstructure and cellular components, performing Peakforce scanning along the axon with and without myelination. Finally, we aimed to build a relationship between axonal myelination, mechanics and fiber orientation, where fiber alignment and myelination level were quantified by ImageJ.

RESULTS

The DRG-OL co-culture system showing the myelination progression with time, as shown in Figure 1. OL started to extend

myelin sheath and wrapped around axons at day 3, and clear myelinated axons were observed by day 7. Local variation of myelination stages originated from the same OL of making myelin in several axons were observed on day 3: non-myelinated axon (white arrow), thin myelin (yellow), and thin MBP+ projections with granulated-like structure (magenta). The amount of myelination, represented by MBP expression, increased significantly from week 1 up to week 3.

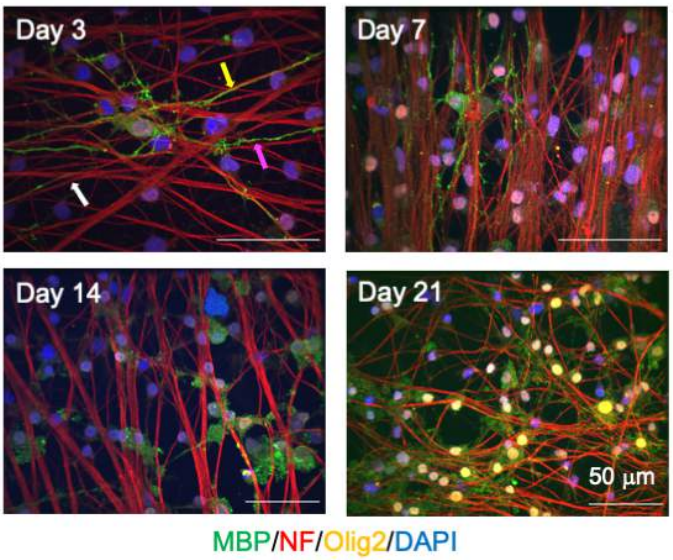

Figure 1: Confocal images of DRG-OL explants co-culture at different time points. Representative images showing increasing MBP expression over time, indicating myelin formation. (Green: myelin basic protein (MBP). Red: neurofilament (NF). Yellow: Olig2. Blue: DAPI)

In order to investigate whether DRG neurons were stiffened during the myelin development, AFM Peakforce measurements were mapping on individual axons to obtain force curves at nanoscale. 3 selected axons were measured at day 14 and 21, respectively, as shown in Figure 2. Increasing modulus were observed from day 14 (mean = 3.4±1.8 kPa, $p<0.0001$) to day 21 (mean = 6.8±2.8 kPa), indicating the axonal stiffening correlates with myelin progression over time.

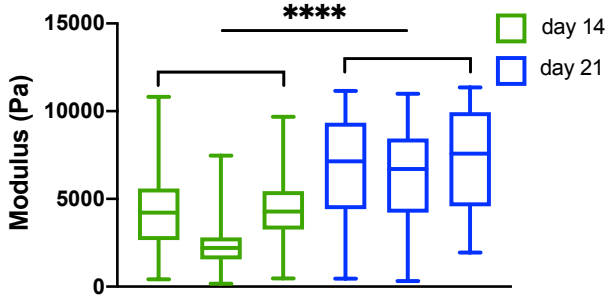

Figure 2: AFM Peakforce mapping on 3 selected axons in DRG-OL explants co-culture at day 14 and 21, respectively. After determination of the contact point, an Ogden fit was applied to the force curve to obtain Young's modulus E. 500 force curves from each axon mapping were used for analysis.

However, myelination was not homogeneous throughout the whole culture up to day 21. Therefore, we probed into a single axon, comparing the modulus on myelinated and un-myelinated segments, respectively, as shown in Figure 3. We found that at an early, pre-myelinating stage (day 3 in culture), when fine MBP+ OL processes begin to align and extend along axons, local heterogeneity of the modulus was already observed between pre-myelinated and un-myelinated axon segments. The pre-myelinated area showing significantly higher modulus (1.83±0.87 kPa, $p<0.01$) compared to the area without myelin sheath wrapped (MBP-, 1.64±0.60 kPa).

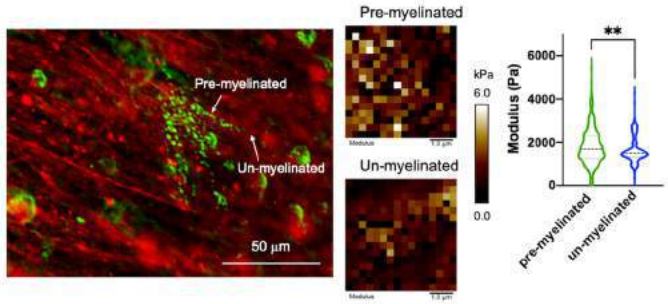

Figure 3: AFM Peakforce mapping on pre-myelinated and un-myelinated axons, respectively, in DRG-OL explants co-culture at day 3. Higher modulus was observed on pre-myelinated area along the axon. 250 force curves from each mapping area were used for analysis. (Green: MBP. Red: NF. Yellow: Olig2.)

DISCUSSION

In this work, an *in vitro* DRG-OL co-culture system was developed to study myelin progression, mimicking the pediatric brain development. Different culturing methods – explants or dissociated DRG, providing various axonal anisotropy models, which represents the variations observed in grey and white matters. We hypothesized that the microstructure of tissue will cause mechanical differences in elasticity and viscoelastic relaxation, and also affect myelin progression. Therefore, quantifications of myelination and fiber alignment will be analyzed, along with mechanical measurements, where we hope further experiments would demonstrate a relationship between these three properties.

AFM results of axonal modulus in the explant co-culture, along with confocal images showing increasing myelination over time, confirming our hypothesis that DRG neuron tissue stiffened during the myelination process existed at cellular level. The increasing moduli of axons were observed over time, however, local heterogeneity of myelination and moduli along axons persisted during myelin development. We find the stiffening effect correlated with myelination at cellular scale which showed heterogeneity along the axon, even though day 3 might be at early pre-myelinating stage. The spatial and temporal mechanical variation during myelination existed in cellular scale which could be revealed by an *in vitro* co-culture model. Furthermore, due to the mechanosensitivity of neurons and oligodendrocytes [6, 7], local stiffening of axons causing from myelination may trigger certain biochemical behaviors, which could be explored in further studies.

REFERENCES

[1] Weickenmeier, J et al., *Acta Biomaterialia*, 42:265-272, 2016.
[2] Lv, H et al., *European Radiology*, 30:6614-6623, 2020.
[3] Ozkaya, E et al., *Journal of the Mechanical Behavior of Biomedical Materials*, 115:104229, 2021.
[4] Wang, H et al., *Journal of Cell Biology*, 182:1171-1184, 2008.
[5] Wang, H et al., *Journal of Neuroscience Research*, 90:1547-1556, 2012.
[6] Jagielska, A et al., *Frontiers in Cellular Neuroscience*, 11, 2017.
[7] Franze, K, *Annual Review of Cell and Developmental Biology*, 36:61-83, 2020.

A VISCODAMAGE MODEL TO SIMULATE BOTH FATIGUE AND STATIC FAILURES IN SOFT FIBROUS TISSUE

Bradley S. Henderson (1), Katelyn F. Cudworth (1), Danielle N. Siegel (1), Madison E. Krentz (1), Estefanía Peña, Ph.D. (2), Trevor J. Lujan, Ph.D. (1)

(1) Department of Mechanical and Biomedical Engineering
Boise State University
Boise, ID, USA

(2) Department of Mechanical Engineering
University of Zaragoza
Zaragoza, Aragon, Spain

INTRODUCTION

Musculoskeletal soft tissues in joints, including ligament, tendon, and meniscus, are frequently torn, leading to pain, joint instability, and increased risk of osteoarthritis. Tissue tears are most commonly associated with single high-magnitude loading events, known as static failures; but tears may also develop from repeated exposure to low-magnitude loads, known as fatigue failures [1]. The risk of fatigue failures in conventional materials (e.g. polymers, composites) has been greatly reduced by the development of failure models that accurately predict fatigue damage, yet comparable fatigue models currently do not exist for soft fibrous tissues.

Fatigue damage can be mathematically described and predicted through constitutive models. Constitutive frameworks that have had success in simulating the damage processes of soft biological tissue include continuum damage mechanics (CDM) [2,3], pseudoelasticity [4], and elasto-viscoplasticity [5] where most of these models have been validated with experiments that use displacement control loading. A loading condition that is more physiological to fatigue injury is repeated application of a targeted stress (force-control), which results in three characteristic stages of cyclic creep (stages I, II, III). However, to our knowledge, no study has modeled force-control fatigue data in any soft tissue. Moreover, no study has used the same constitutive model to simulate both fatigue and static failures in soft tissues.

A novel and elegant solution for modeling cyclic creep behavior in soft tissue may be possible using discontinuous CDM with viscoelasticity. Previous work has determined that discontinuous CDM with strain energy-based failure criteria can model static failure in soft tissue [6] but has intrinsic limitations in modeling steady state creep since damage evolution is restricted under a constant load. Conversely, viscoelastic models can represent steady state creep [7], but not damage propagation to rupture. We hypothesize that by pairing a discontinuous CDM model with a viscoelastic model, damage will evolve in response to viscoelastic creep during fatigue loading.

The objective of this study is to determine the feasibility of using a viscodamage model to simulate high-cycle tensile loading in human meniscus. A validation study was performed to determine if the viscodamage model is also predictive of static failure.

METHODS

This study combined experimental and computational methods.

Fatigue experiment: Prior to fatigue testing, quasi-static uniaxial tensile tests to failure were performed on 8 dumbbell shaped meniscus specimens from 5 human knees to generate a correlation between tangent modulus and ultimate tensile strength (UTS). This allowed for the non-destructive prediction of UTS from modulus data. Tensile fatigue tests were then performed on eight dumbbell shaped specimens from the same set of human menisci used for UTS tests. Force-control loading was applied at 30% (n=3), 50% (n=3), and 70% (n=2) of UTS using the tangent modulus from the last cycle of a 20-cycle triangular waveform to 8% strain. A 4 Hz tensile-tensile sinusoidal waveform was applied to the targeted stress [8] until failure or one-million cycles was reached. All specimens were tested in a 0.9% saline tank at 37 C, and no failures occurred at or near the grips.

Constitutive Model Comparison: Three constitutive models were investigated: viscodamage, visco-only, and damage-only. The cyclic creep curves from the fatigue experiments were used to calibrate the material parameters for each model and NRMSE calculations were used to determine the efficacy of each model.

Viscodamage Model: The viscodamage model used a convolution integral and discontinuous, CDM formulation, where 2nd PK stress **S** was modulated by a damage variable *D* that ranged from zero to one, with one representing complete rupture (Eq. 1). A viscoelastic

relaxation function G was comprised of six material parameters that regulated material relaxation at time t, accounting for all prior times s [9]. An energy-based Weibull cumulative distribution function (CDF) was used for the damage evolution model where damage D is a function of the Simo damage criteria and the Neo-Hookean strain energy density.

$$\mathbf{S}(t) = \int_0^t G(t-s)(1-D(t))\frac{\mathrm{d}\mathbf{S}^e}{\mathrm{d}s}\mathrm{d}s \qquad (1)$$

Visco-only Model: A viscoelastic model, with no damage, was created by setting the CDF parameters in Eq. 1 to high values, effectively making damage 0 for all stretches used in this study.

Damage-only Model: A damage model, with no viscoelasticity, was created by setting all six viscoelastic parameters of the relaxation function in Eq. 1 to 0, effectively eliminating the viscoelastic response.

Curve Fitting Using a Single Element Model: To overcome the inherit limitations of FE solvers when modeling force-controlled damage, a three-dimensional single element material model was developed in MATLAB (Fig. 1A). This custom optimization program consisted of two nested loops. The inner loop used the Levenberg-

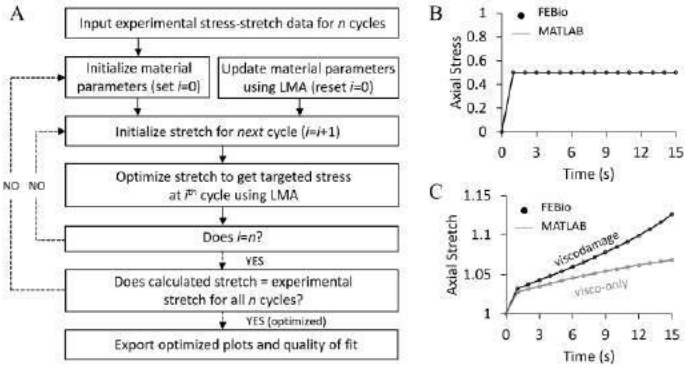

Fig. 1: Force-control single element simulation. A) The MATLAB logic was verified by comparing A) input and B) output to FEBio.

Marquardt algorithm (LMA) to calculate axial and lateral stretches at each time point for a targeted loading profile (force-control) while the outer loop applied LMA to the entire stretch-time profile to optimize the fit of specimen specific material parameters.

Verification and Validation: For verification, axial stretches calculated with our MATLAB program and the finite element (FE) solver FEBio [9] where compared using the same viscodamage model and parameter values (Fig. 1B-C). For validation, the viscodamage material parameters that were curvefit to the fatigue data were used to produce quasi-static pull to failure curves, which were compared to the mean quasi-static tensile results from the same set of five knees.

RESULTS

In general, the viscodamage model resulted in excellent fits for all three stages of fatigue for all experiments (Fig. 2). In comparison, the damage-only model was unable to simulate steady-state creep behavior (stage II), and the visco-only model was unable to simulate failure propagation (stage III). On average, the resulting NRMSE values for stretch at all fatigue stages were 0.22%, 0.45%, and 2.03% for the viscodamage, visco-only, and damage-only models, respectively. The NRMSE values for all creep stages were significantly less for both the viscodamage and visco-only models than the damage-only model ($p=0.004$, $p=0.009$), respectively. When examining each stage of fatigue separately, compared to the visco-only model, the viscodamage model had less than half the NRMSE in stage II and III, but this difference was not significant ($p=0.09$, $p=0.25$, respectively).

The predicted pull to failure results using a viscodamage model resulted in characteristic stress-strain curves when using parameters fit to fatigue tests run at 50% and 70% of UTS (Fig. 3; red and blue lines). For these five tests, the average predicted UTS was 13.6±9.2 MPa, compared to the 14.9±9.9 MPa experimental results; and the average predicted failure stretch was 1.31±0.06, compared to the 1.19±0.04 experimental results. Material parameters used to fit fatigue tests run to 30% were poor predictors of pull to failure experiments (Fig. 3; black lines).

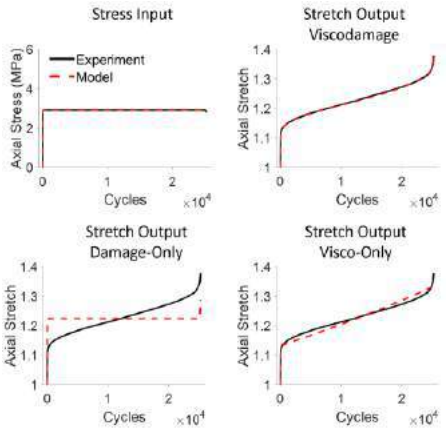

Fig. 2: Model fits to a fatigue experiment. The viscodamage model had the best fit.

DISCUSSION

This study demonstrates for the first time the feasibility of using a viscodamage model to simulate the cyclic creep of soft fibrous tissue during force-control fatigue loading. These results support our hypothesis and highlight the importance of pairing both viscoelasticity and damage formulations when modeling fatigue behavior. This suggests that fatigue injuries in meniscus, ligament and tendon are linked to the intrinsic viscoelasticity of these tissues.

The viscodamage model also reasonably predicted modulus and UTS values from quasi-static pull to failure experiments using parameters fit to fatigue tests, except when using parameters fit to fatigue tests with low stress input (Fig. 3; 30%). To our knowledge, this is the first study to have success simulating both fatigue and static failure with the same model, which could have major implication in future computational studies of musculoskeletal injury mechanisms.

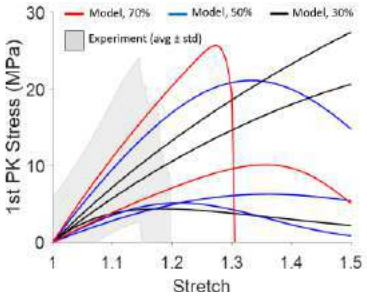

Fig. 3: Prediction of static failure using viscodamage model with parameters fit to fatigue tests.

For this study, a custom MATLAB code was developed to overcome limitations of FE solvers related to parameter optimization in force-control. This code logic (Fig. 1A) could be implemented with a FE solver to examine problems with more complex geometries.

ACKNOWLEDGEMENTS

Support from NSF (CMMI-1554353) and NIGMS (P20GM109095).

REFERENCES

[1] Demange et al., *Int Orthop*, 2015 [2] Martin et al., *BMMB*, 2012 [3] Pena et al., *JMPSA*, 2011 [4] Franceschini et al., *JMPS*, 2006 [5] Zhu et al., *BMMB*, 2018 [6] Martin et al., *JLTEMI*, 2017 [7] Sopakayang et al., *Med Eng Phys*, 2011 [8] Creechley et al., 2017 [9] Maas et al., J. Biomech. Eng., 2012.

PRESENCE OF GREATER TUBEROSITY FACETS SIGNIFICANTLY ALTERED IN SUBJECTS WITH SYMPTOMATIC ISOLATED SUPRASPINATUS TENDON TEARS

Luke T. Mattar (1), Rachel C. Martello (1), Adam J. Popchak (3), Volker Musahl (1,2), James J. Irrgang (2,3), Richard E. Debski (1,2)

(1) Department of Bioengineering, University of Pittsburgh, Pittsburgh, PA, USA

(2) Department of Orthopaedic Surgery, University of Pittsburgh, Pittsburgh, PA, USA

(3) Department of Physical Therapy, University of Pittsburgh, Pittsburgh, PA, USA

INTRODUCTION

Three of the rotator cuff muscles, the supraspinatus, infraspinatus, and teres minor insert on the greater tuberosity of the humerus. Specifically, the greater tuberosity is morphologically comprised of three distinct flat surfaces termed the superior, middle, and inferior facets[1,2] (Figure 1). The supraspinatus inserts on the superior facet and superior half of the middle facet, the infraspinatus on the entire middle facet, and the teres minor on the entire inferior facet[1]. It has been shown that each facet can be easily identified in cadavers that did not exhibit any glenohumeral joint pathology[3]. However, it is unclear if there are boney morphologic changes of the facets in subjects with symptomatic isolated supraspinatus tendon tears.

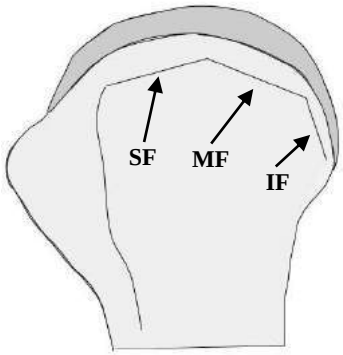

Figure 1: Normal anatomy of the greater tuberosity facets (SF, Superior Facet; MF, Middle Facet; IF, Inferior Facet). Adapted from White E.A. et al., *Emergency Radiology*, 2018.

In the presence of a tear, force is no longer being applied at the insertion cite through the tendon where the tear is located, and in the case of impingement, there may be bone on bone contact. Both mechanisms may lead to boney morphological changes due to resorption or mechanical impact. If the boney morphology of the facets has changed, it may be difficult for surgeons to properly anchor the repaired tendon in the correct location due to the altered anatomy. Therefore, the objectives of the study were: 1) To determine if the superior, middle, and inferior facets are present in-vivo in subjects with symptomatic isolated supraspinatus tendon tears, 2) Determine the association between tear location and presence of the superior, middle, and inferior facet.

METHODS

Forty subjects (mean age 61.1 ± 9.0 years, mean BMI 27.1 ± 4.5, 18 males and 22 females) with a symptomatic rotator cuff tear isolated to the supraspinatus tendon were recruited for the study and provided IRB-approved written informed consent prior to all research procedures. Main exclusion criteria included asymptomatic tears, previous shoulder injury, or presence of severe capsule tightness. Each subject underwent computed tomography (CT, slice thickness of 0.625mm) of the affected shoulder and the images were segmented to create a 3-dimensional (3D) subject specific surface model of the humerus using Mimics 20 software package. The humeri models were then imported into MATLAB, and vertices comprising each facet were identified using the naming convention of a previous study[2]. If a single vertex comprising the facet was missing, the facet was considered unidentifiable.

Ultrasound was used to quantify tear location within the supraspinatus tendon. Assessments utilized a 6-15 MHz linear array transducer and was measured by a musculoskeletal radiologist. Subjects were seated with the glenohumeral joint in extension, and the involved

side hand on the iliac wing to expose the supraspinatus tendon. The transducer was positioned transversely to the supraspinatus tendon, and a short-axis image was acquired. Tear location was quantified as the distance from the posterior edge of the long head of the biceps tendon to the most anterior edge of the tear.

Percentages were calculated for the number of subjects in which each facet could be identified. Furthermore, a Point-Biserial Correlation was used to determine the association between tear location and presence of the superior, middle, and inferior facets. Significance was set at $p < 0.05$.

RESULTS

All variables were successfully collected in 37 subjects (three subjects ultrasound images were not measurable). There were no associations between tear location and presence of the superior, middle, or inferior facet ($p > 0.05$, Table 1). Overall, the superior, middle, and inferior facet were identifiable in 22.5%, 30.0%, and 50% of subjects, respectively. Seventy percent of subjects had tear locations immediately posterior to the biceps tendon and tear location ranged from 0.0mm to 19.0mm.

Qualitatively, rounding of the greater tuberosity was observed in 59.5% of subjects (Figure 2). Five subjects showed rounding of the entire tuberosity and nine subjects showed rounding of the transition between the superior and middle facets. The remaining observations occurred at individual facets (3 superior, 2 middle, 3 inferior).

Table 1: Associations between tear location and presence of the superior, middle, and inferior facets.

Facet	Tear Location	
	r	p
Superior	-0.06	> 0.05
Middle	-0.09	> 0.05
Inferior	-0.14	> 0.05

Figure 2: Lateral view of a subject specific humerus with a "rounded" greater tuberosity. The highlighted region demonstrates the inability to directly identify the distinct facets compared to a "healthy" example shown in Figure 1.

DISCUSSION

Our data demonstrates that symptomatic isolated supraspinatus tendon tears significantly impact the boney morphology of the superior, middle, and inferior facets of the greater tuberosity without respect to the tear location. The inability to identify each facet in the majority of subjects is indicative of changes in boney morphology that are likely due to reductions in force applied to the bone due to the tear. Furthermore, this study demonstrates that even in the presence of relatively small rotator cuff tears, there are also alterations in the middle and inferior facets as well. Inability to identify the superior facet in 77.5% of subjects is important information for orthopaedic surgeons as it may influence the effectiveness of surgical repair of the torn tendon. Changes in the boney morphology of the facet may result in incorrect placement of the bone screw used to reattach the torn tendon since they are not observing the normal anatomy.

A previous study investigating the orientation and inclination of the rotator cuff footprint was able to identify the superior, middle, and inferior facets in all 28 "healthy" cadaveric humeri studied[3]. Average age of the cadavers was 78.0 ± 12.9 years. Therefore, even though subjects in the present study were younger, the presence of a relatively small rotator cuff tear results in significant boney morphological changes. Additionally, a study in cadavers has shown that there is overlap between the tendinous junctions of the supraspinatus and infraspinatus on the middle facet[1]. This overlap is likely why changes were observed throughout the facets due to the rotator cuffs inherent mechanical interactions.

The majority of subjects had tear locations immediately posterior to the biceps tendon and reflects what is most commonly seen clinically, resulting in translational conclusions to the clinic. Therefore, we were able to show that small rotator cuff tears isolated to the supraspinatus tendon result in significant changes to the greater tuberosity's boney morphology. This information is useful for orthopaedic surgeons as it may impact decision making when placing anchors during arthroscopic rotator cuff repair due to altered anatomy.

ACKNOWLEDGEMENTS

Support from the National Institutes of Health grant 5R01AR069503 is gratefully acknowledged.

REFERENCES

[1] Minagawa H. et al., *Arthroscopy*, 14: 302-306, 1998.
[2] White E.A. et al., *Emergency Radiology*, 25: 235-246, 2018.
[3] Berghs B.M. et al., *J Shoulder Elbow Surg*, 20: 637-645, 2011.

PROTEIN SPREADING PATTERNS IN ALZHEIMER'S DISEASE: EXPLORING THE DIFFERENCE BETWEEN A CONNECTIVITY-BASED AND PROXIMITY-BASED CONNECTOME MODEL

Shima Jalalian (1), Johannes Weickenmeier (1)

(1) Department of Mechanical Engineering
Stevens Institute of Technology
Hoboken, New Jersey 07030, US

INTRODUCTION

Alzheimer's disease (AD) is the most prevalent form of dementia and is a significant health burden on our aging society. There are two primary proteins associated with disease progression in AD: amyloid-beta (Aß) and tau [1]. It has been hypothesized that these two proteins spread in a prion-like manner where toxic, misfolded proteins recruit proximal healthy proteins to turn toxic as well [2].

There is growing evidence from postmortem and PET imaging studies that neurotoxic Aß-plaques and tau tangles spread through the brain in a characteristic progression pattern [2]. Strikingly, there seem to be two competing mechanisms, however, by which plaques and tangles spread: PET [3] and in vivo mouse studies [4] have shown that neurofibrillary tangles spread along axonal pathways, i.e., intracellular transport, while Aß-plaques appear to spread by proximity, i.e., diffusion through surrounding tissue [5]. Several computational progression models have been proposed thus far. Typically, protein spread is modeled as a (reaction-)diffusion equation that is solved on either an anatomically accurate brain finite element model [6] or a graph theory-based discrete connectome model [7].

In the present work, we use the connectome data provided by the Budapest Reference Connectome (BRC) [8] to construct two models, a connectivity model, and a proximity model, in order to systematically study the effect on protein spreading behavior.

METHODS

We pose that the prion-like protein spread of Aß-plaques and tau tangles is best described by the Fisher-Kolmogorov reaction-diffusion equation, where toxic protein concentration, or also referred to as biomarker concentration, c, is governed by the following equation:

$$\frac{\partial c}{\partial t} = D\frac{\partial^2 c}{\partial x^2} + \alpha c[1-c]. \qquad (1)$$

Parameter D controls diffusivity of the biomarker, and parameter α characterizes the growth rate, i.e., the conversion rate of healthy into toxic protein. We discretize equation (1) on two graphs G^{con} and G^{dist}. Introducing nodal biomarker levels c_I, we obtain protein spread as:

$$\frac{dc_I}{dt} = \mathrm{k}\sum_{J=1}^{N} L_{IJ}c_J + \alpha c_I[1-c_I], \qquad (2)$$

where k controls the diffusion between two nodes. Using connectome data from 100 BRC subjects, we construct two different weighted Laplacians, L_{IJ}^{con} and L_{IJ}^{dist}. The Laplacian is the difference between the degree matrix, D_{IJ}, and the adjacency matrix, A_{IJ}, as follows:

$$L_{IJ} = D_{IJ} - A_{IJ} \text{ with } D_{IJ} = \mathrm{diag}\sum_{J=1,I\neq J}^{N} A_{IJ}. \qquad (3)$$

The connectivity graph is based on the adjacency matrix A_{IJ}^{con} that incorporates the number of fibers, n_{IJ}, and mean fiber length between two nodes, l_{IJ}. The proximity graph is based on the adjacency matrix A_{IJ}^{dist} that is constructed from the inverse Euclidian distance between two neighboring nodes. That is:

$$A_{IJ}^{con} = \frac{n_{IJ}}{l_{IJ}} \; and \; A_{IJ}^{dist} = \frac{1}{\sqrt{(x_I - x_J)^2 + (y_I - y_J)^2 + (z_I - z_J)^2}}, \qquad (4)$$

where $\{x_I, y_I, z_I\}$ are the coordinates of node I.

RESULTS

Figure 1 shows the normalized adjacency matrix for the proximity and connectivity graph, respectively. It can be seen that there are more connections in the connectivity-based connectome than in the proximity connectome, indicative of a more complex structural network.

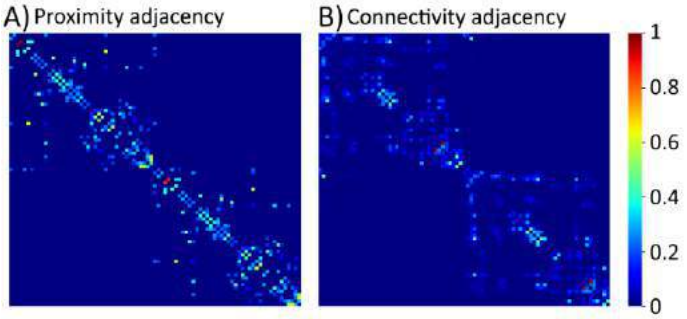

Figure 1 Normalized adjacency matrix for the A) proximity-based and B) connectivity-based graphs

Figure 2 shows the spatial distribution of biomarker concentration for six time points determined via the connectivity and proximity graphs. In both models, proteins originate from the seeding location in the entorhinal cortex and spread throughout the brain. On the one hand, the connectivity-based simulation shows that biomarker concentration appears in dispersed locations in the parietal and frontal lobe as AD progresses; the proximity-based simulation, on the other hand, demonstrates a characteristic diffusive pattern where the biomarker gradually spreads through the brain, reaching the occipital lobe first, then the parietal lobe, and ultimately reaching the frontal lobe.

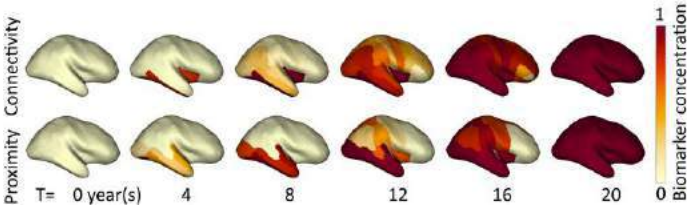

Figure 2: Spatial distribution of the biomarker concentration based on connectivity and proximity at multiple time points.

Figure 3 shows the temporal evolution of biomarker concentration in five specific nodes, i.e., brain regions, that are linked to hallmark symptoms in AD. Based on our model, hippocampus and amygdala, both associated with short term memory loss, are affected first, followed by the posterior cingulate and pars triangularis, which are linked to behavioral changes and speech impediments [9], respectively, and lastly, the frontal pole which contributes to emotional regulations [10].

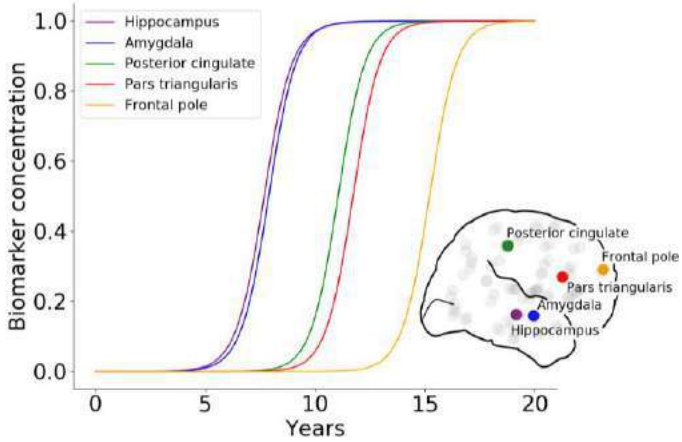

Figure 3: Biomarker concentrations in five nodes associated with hallmark symptoms of AD. The temporal pattern is consistent with the onset of symptoms such as memory loss, behavioral changes, and ultimately loss of speech and motor control.

DISCUSSION

In this work, we built a physics-driven diffusion model to observe protein progression patterns in AD. We specifically aim at exploring the difference between proximity-based and connectivity-based spreading along the brain's connectome network.

Figure 4 shows the dependence biomarker concentration on model parameters D, α, and initial seeding concentration c_0. Higher diffusivity leads to faster spreading; higher growth factor causes more rapid production of toxic proteins and higher initial concentration, c_0, accelerates infection time across the network. These parameters may be treated as patient-specific indicators for disease severity, and the variation in AD progression observed in clinical practice.

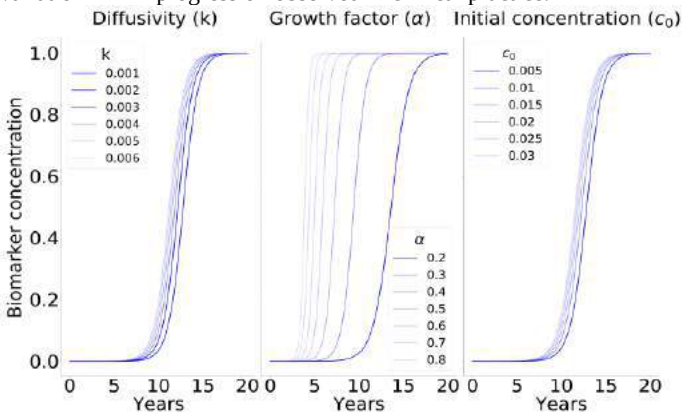

Figure 4: Biomarker concentration in the amygdala as a function of critical model parameters in Equation (2).

The well-established Braak stages of AD indicate that toxic tau is first found in the entorhinal cortex and then appears in the hippocampus and amygdala. From there, it spreads out into the structurally connected inferior regions of the temporal and occipital lobe and the pre- and post-central gyrus. Our connection-based tau model, derived from structural connectome data, replicates this pattern very well, as shown in Figure 2. The results from our proximity graph demonstrate remarkable agreement with the spreading patterns observed for Aß-plaques that are characterized by a homogeneous increase in Aß-concentration across the entire brain [2]. As a next step, we will investigate spatiotemporal correlations with structural brain shape changes associated with AD, including cerebral atrophy and cortical thinning.

In summary, our work supports the notion that Aß and tau follow distinctly different progression patterns. Although it has been shown that tau is a strong biomarker for AD severity, we lack a proper understanding of the coupling between Aß and tau to rationalize the variation in clinically observed AD progression patterns.

ACKNOWLEDGEMENTS

This research was supported by the National Institutes of Health's National Institute on Aging, grant R21AG067442.

REFERENCES

[1] Braak, H. *et al.*, *Acta Neuropathol.*, 82, (1991).
[2] Jucker, M. *et al.*, *Nature*, 501, (2013).
[3] Franzmeier, N. *et al.*, *Sci. Adv.*, 6, (2020).
[4] Ahmed, Z. *et al.*, *Acta Neuropathol.*, 127, (2014).
[5] Mezias, C. *et al.*, *Front. Neurol.*, 8, (2017).
[6] Weickenmeier, J. *et al.*, *Phys. Rev. Lett.*, 121, (2018).
[7] Raj, A. *et al.*, *Neuron*, 73, (2012).
[8] Szalkai, B. *et al.*, *Cogn. Neurodyn.*, 11, (2017).
[9] Nakaaki, S. *et al.*, *Neuropsychiatr. Dis. Treat.*, 9, (2012).
[10] Kenner, N. M. *et al.*, *J. Neurosci.*, 30, (2010).

FABRICATION OF 3D PRINTER ASSOCCIATED ROTATORY BIOREACTOR FOR VASCULAR TISSUE ENGINEERED STRUCTURES

Khemraj Deshmukh (1), Arindam Bit (1), Esther Beltran (2), Kunal Mitra (3)

((1) Biomedical Engineering Department
National Institute of Technology
Raipur, India

(2) Florida Space Institute
University of Central Florida
Orlando, FL, USA

(3) Biomedical Engineering
Florida Institute of Technology
Melbourne, FL, USA

INTRODUCTION

A significant challenge faced by 3D bioprinting technology is to develop a way to supply cells with nutrients and drain their waste products simultaneously [1]. It requires vascularization of bio-printed tissue constructs embedded with blood vessels [2]. Until now, most methods didn't involve any regulated exchange of metabolites - instead, they relied on the simple diffusion process that occurs spontaneously in a cell culture medium. 3D bio-printer based bioreactor acts as a robotic device, which can print any tissue, organs, and blood vessels layer by layer according to the respective CAD model [3]. After printing, the entire bio-printed structure is cultured within a bioreactor. However, this approach of regeneration of organ/tissue is not similar to the natural process for the same phenomena under in vivo conditions [4]. The purpose of the proposed model is to match in vivo and in vitro conditions of blood vessel formation and provide precise control on all the parameters during printing, such as the thickness of blood vessels, media transportation, shear stress, etc. The model development involves the following steps:

❑ Designing of a functional bioprinter for replicating the actual micro-environment for human tissue and organs.

❑ Identification of certain cell-types and extracellular matrix (ECM) components for 3D bio-printing.

❑ Designing of artificial blood vessels by 3D bio-printer.

METHODS

The system uses an extrusion-based co-axial 3D bio-printer, and the printed layer is cultured by a modified rotatory bioreactor (Figure 1). A co-axial nozzle is used to make printing on the printing bed, and it will be located inside a closed chamber housing. The temperature of housing is maintained at 36°C to 40°C. Cellular media (media + CO_2 + O_2) will be fed to the reservoir for cell culture of the printed layer. Regulatory control of each component like media pressure, temperature, valve, pH and CO_2 and N_2 delivery, etc., are managed by a Programmable Logic Controller (PLC). Simulation of the electronic circuit is conducted by LabView Software. A decision-based logic circuit is used to improve the utilization factor of media. $CaCl_2$ is used as a chemical cross-linker during printing using GelMA as a bioink. The corresponding CFD analysis of flow segments of media within the system drainage section is evaluated using ANSYS. Induction of media to the housing is made using a pulsatile pump. It creates pulsatile hydrostatic pressure to the printed bioink. The flow of media is controlled by passing it through the rotating tube, which consists of an array of pores on the lateral wall of the inner concentric cylinder of the housing. The drained-out media from the housing is checked for conductivity. Based on the result of conductivity of the outlet media, PLC operates the valve to direct the flow into a waste reservoir or media reservoir. Some parts of the internal fluid of the printed layer are collected within a microfluidic chamber for real-time analysis of biochemical properties of the media. A pressure sensor, temperature sensor, flow sensor, pH sensor, and dissolved oxygen measurement sensor will be used to sense and regulate all respective variable values using PLC.

RESULTS

The simulation result performed using PLC and LabVIEW indicates that all the logic and circuits are working properly. A signal conditional circuit is used for pH control, waste product, rotational speed control, media stem rod, co-axial nozzle temperature, and pressure. The results show that the proposed algorithm/logic maintains the variable values at the desired range. In our model, shear stress near the wall of the cylindrical hollow housing where bioprinting materials are getting stacked up is altered by three variables - pressure, velocity (v), and strain rate (y). The influence of pressure on shear stress is evaluated by altering one variable while other variables are kept constant. Figure 2

represents the relationship between shear stress and pressure at different points. First, shear stress is calculated for different values of pressure under constant velocity while varying strain rates. It can be concluded that the shear stress is constant for the entire range of applied pressure.

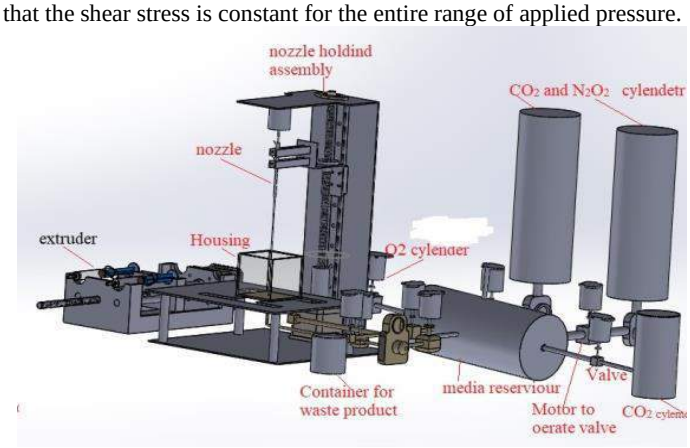

Figure 1: Implemented 3D model of integrated system.

The strain rate variation produces a small change in shear stress for different pressures. Thereafter, shear stress is calculated for different values of pressure under constant strain rate but varying velocity. A linear relationship between the shear stress and pressure for different velocity is observed.

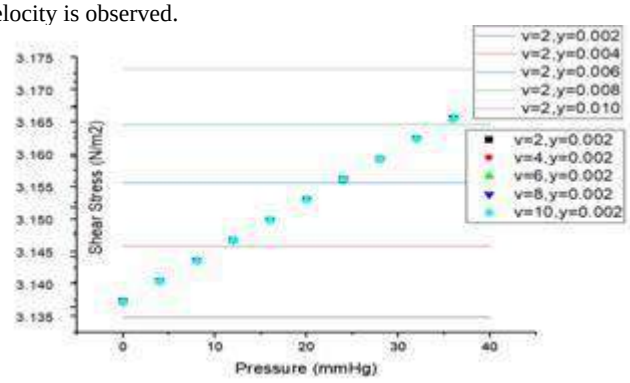

Figure 2: Relationship between shear stress and pressure under constant velocity (all horizontal lines) and constant strain rate (dotted line).

Effective implementation of simulator programming code in hardware has been confirmed by uncertainty analysis. Uncertainty analysis of shear stress and pores height has been performed. The uncertainty of pore height is 7.60 x 10-4 m (minimum). Similarly, the uncertainty of stress was found to be 179.36501 N/m^2. Real-time shear stress generated on the printed structure is also derived. CFD analysis has been performed on the proposed model having three segments: (1) mixing of media, O_2, and CO_2 inside a reservoir; (2) transportation of media from the reservoir to housing; and (3) microfluidic chamber. The velocity profile of module 3 (containing the drained fluid on a microfluidic platform for conductivity evaluation) is shown in Figure 3. Flow path lines inside the micro-channel of the chip represent the velocity vector, as determined by ANSYS. It is observed that the region of the mixture provides better homogeneity of the velocity field.

Figure 4 shows the CAD model and printed geometry of a network of channels simulating blood vessels embedded in GelMA ECM. The channel walls are embedded with Human Umbilical Vein Endothelial cells (HUVECs). Live-Dead Assay will be performed over 14 days to ascertain the cell viability maintained in the bioreactor.

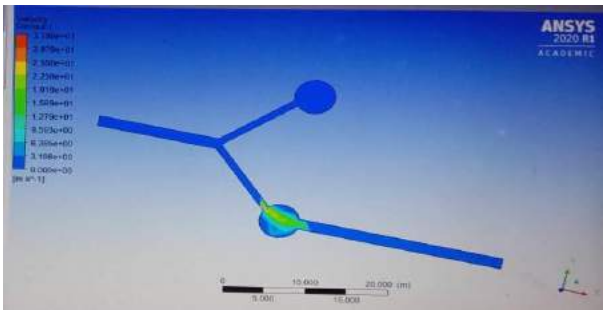

Figure 3: Velocity profile inside the micro channel of microfluidic chip

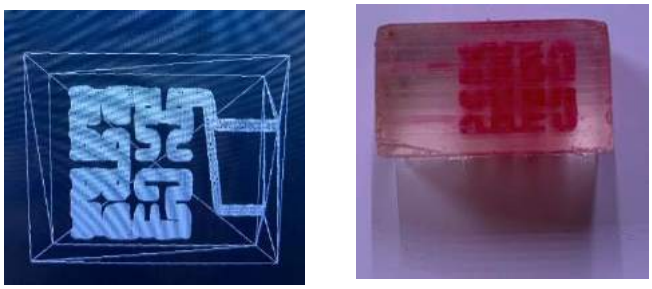

Figure 4: Sample bioprinted tissue construct using GelMA constructs and embedded channels seeded with HUVECs.

DISCUSSION

A unique 3D bio-printing system using a rotary forming device has been developed to fabricate vessel-like structures that will provide precise control over-proliferation of cells within the tubular scaffold. In vivo environmental conditions are mimicked to follow blood vessel generation. The novel concept of conductivity circuit used in our model enhances the utilization of the media. This advanced version of the rotatory bioreactor overcomes the limitations of scaffold size. This model provides a better environment for extrusion based coaxial nozzle printed structure along with rotatory bioreactor for maintaining vascularization in bioprinted constructs.

ACKNOWLEDGEMENTS

KM acknowledge partial funding from NASA Florida Space Grant Program.

REFERENCES

[1] Sharda Gupta, Akalabya Bissoyi and Arindam Bit (2018), A Review on 3D Printable Techniques for Tissue Engineering, BioNanoScience, Springer.

[2] MD Sarker, Saman Naghieh, N.K. Sharma, Xiongbiao Chen (26 August 2018 Cite this article as: MD Sarker, Saman), 3D biofabrication of vascular networks for tissue regeneration: A report on recent advances, Journal of Pharmaceutical Analysis.

[3] M. D. Sarker , Saman Naghieh, N. K. Sharma, Liqun Ning, and Xiongbiao Chen1,2 (2019), Bioprinting of Vascularized Tissue Scaffolds: Influence of Biopolymer, Cells, Growth Factors, and Gene Delivery, volume 2019 edn., Hindawi Journal of Healthcare Engineering.

[4] Fatah N. Habib, Mostafa Nikzad, Syed Hasan Masood, and Abul Bashar M. Saifullah (2016), Design and Development of Scaffolds for Tissue Engineering Using Three-Dimensional Printing for Bio-Based Applications, Volume 3, Number 2 edn.,3D Printing and Additive Manufacturing.

ACCELERATED ACQUISITION OF DISPLACEMENTS AND STRAIN IN TIBIOFEMORAL JOINT CARTILAGE BY SPIRAL DENSE MRI AND COMPRESSED SENSING

Woowon Lee (1), Emily Y. Miller (1), Corey P. Neu (1)

(1) Paul M. Rady Department of Mechanical Engineering
University of Colorado Boulder
Boulder, CO, USA

INTRODUCTION

Soft tissue degeneration such as osteoarthritis (OA) is a severe medical and socioeconomic burden afflicting more than 10% of adults over 60 worldwide [1]. The pathogenesis of cartilage degeneration is largely unknown, as is the impact of daily activities such as walking. Currently, OA can only be detected in the late stage using techniques like radiography. To probe early OA pathogenesis, MR-based imaging methods have been advanced to investigate the structure-function relationship of soft joint tissues such as cartilage. We previously used displacement encoding with stimulated echoes (DENSE) MRI to calculate heterogenous cartilage displacement and strain during cyclic compressive load [2]. In an effort to accelerate image acquisitions suitable for human imaging *in vivo*, we explore the use of spiral acquisitions on DENSE MRI [3] and collect images with a 40 ms temporal resolution on a bovine joint. We also adapt compressed sensing (CS) on low signal-to-noise ratio (SNR) images. We find spiral *k*-space trajectory allows high temporal resolution images and CS reduces imaging time to approximately 2 minutes while having similar magnitude and phase data with high SNR images which takes 7 minutes to acquire.

METHODS

Specimen Preparation: For a proof-of-concept demonstration, a single bovine joint (1-month-old) was obtained from an abattoir. The joint was prepared and mounted by securing both the tibia and femur to a sample holder using bone cement. The sample was placed in a pneumatic loading device (Figure 1A) ready for imaging within a clinical MRI system (3T; Siemens Prisma^{fit}).

Spiral DENSE MRI with Exogenous Cyclic Loading: To mimic gait, the joint underwent cyclic loading (400 N for 1 second, within a 2 second cycle) along the superior-inferior axis. Two spiral interleaves were timed to loading using triggering to allow for cine image acquisition [3], with a total of 22 images (frames) collected within the loading time frame. Each image frame was equivalent to 40 ms. Echo time (TE) and relaxation time (TR) were 2.5 and 20 ms, respectively. The spiral sequence completed when all 22 images had total ten interleaves each. Images were averaged one, four, and eight times to control the SNR. Image acquisition parameters were: field of view = 125×125 mm^2, matrix = 350×350 pixels^2, slice thickness = 1.7 mm, displacement encoding gradient = 1.28 cycles/mm. Prior to spiral DENSE MRI acquisition, the loading cycle was applied for 15 minutes to achieve a quasi-steady state response, and high SNR double echo steady state (DESS) images were collected for segmentation and to confirm that joint tissues were responding to load.

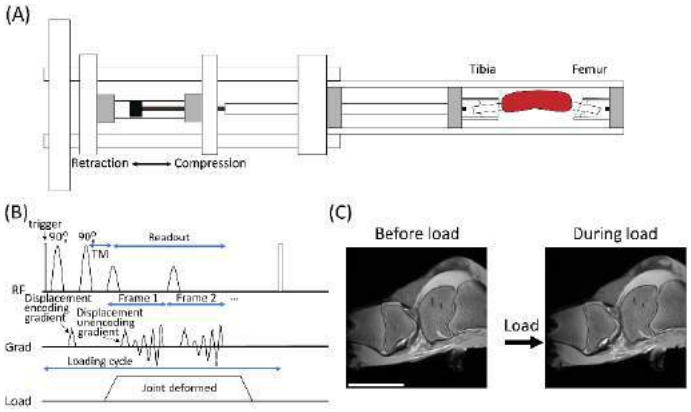

Figure 1: MRI compatible knee loading device for measuring tissue deformation. (A) Pneumatic cyclic loading device with bovine joint placed at the isocenter of a 3T MRI system. (B) Spiral DENSE MRI pulse sequence diagram. DENSE encoding and unencoding gradients are applied before sinusoidal gradients for readout. Three-point phase cycling (θ = 0, 2/3π, 4/3 π) is used to reduce artefacts. (C) Magnitude images of bovine joints obtained of the sagittal plane before and during loading (400 N). Scale bar = 50 mm.

Displacement and strain calculation: Articular cartilage regions of interest (ROIs) were manually segmented using custom software (MATLAB) and binary masks were created to represent the tibial and femoral articular cartilage regions. Displacements for each pixel within the ROIs were determined from phase data as previously described [4]. Displacements were manually phase unwrapped followed by smoothing with a locally weighted scatterplot smoothing (LOWESS) filter and then

the smoothed displacements were used to calculate in-plane Green-Lagrange strains and principal strains.

Compressed Sensing: We used Berkeley Advanced Reconstruction Toolbox [5] PICS command to reconstruct the images where the inputs were the spiral trajectory, channel sensitivity map, and acquired *k*-space data along the interleaves. The regulation parameter was 0.01 and all processes go through five iterations.

RESULTS

Displacement and strain maps were acquired on 22 time-lapse images during loading (Figure 2). A higher number of averages resulted in higher SNR with the cost of longer acquisition time. The acquisition time was two, seven, and fourteen minutes for one averaged (SNR = 1.39), four averaged (SNR = 2.57), and eight averaged (SNR = 4.16) DENSE images, respectively. DENSE images showed heterogeneous patterns of the displacement and strain across cartilage. The 0 to 280 ms time period showed the maximum change of displacement and strain. As seen in previous work, the predominant displacements of the tibial and femoral cartilage regions indicated both compression and shear occurred between the tibia and the femur [2]. Average displacements along the direction compressive load in the femoral cartilage were 0.256 mm. As compressive load is applied, the knee joint bends and moves towards the left which is reflected on the displacement values.

CS enhances the SNR and reduces the number of discontinuous pixels on the displacement map before manual phase unwrapping (Figure 3). Also, the root mean square error (RMSE) of the displacement maps before phase unwrapping with respect to the average 8 images drops substantially after applying CS.

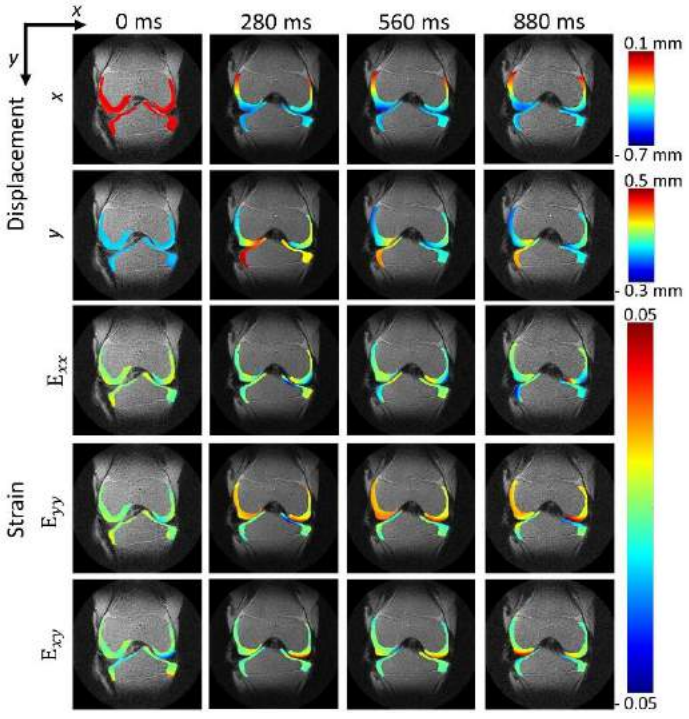

Figure 2: Displacements and strain in tibiofemoral joint cartilage acquired at defined time points within a cyclic loading cycle by displacement-encoded MRI. Spiral acquisition of *k*-space enables rapid and cine collection of image data.

DISCUSSION

Understanding intratissue tissue mechanics under physiologically relevant motion is crucial for OA early detection. In this study we were able to collect DENSE MR images during compressive loading with a temporal resolution of 40 ms by taking advantage of accelerated spiral acquisition and 0.5 Hz cyclic loading of the knee joint. Spiral scanning was able to improve the temporal resolution since high-density *k*-space data are collected in the center of the frequency space, allowing for acquisition of critical displacement-sensitive information. We also verified that CS significantly improves the SNR, while reducing the number of discontinuous displacement pixels and minimizing artefacts. Thus, CS shortens the total acquisition and data processing time without sacrificing data quality. Total acquisition time in this study is significantly shorter than our previous study [2] using single-shot fast spin echo which takes over 30 minutes. Our acquisition scheme is not exclusive, and can additionally be combined with other useful analyses (e.g. relaxometry).

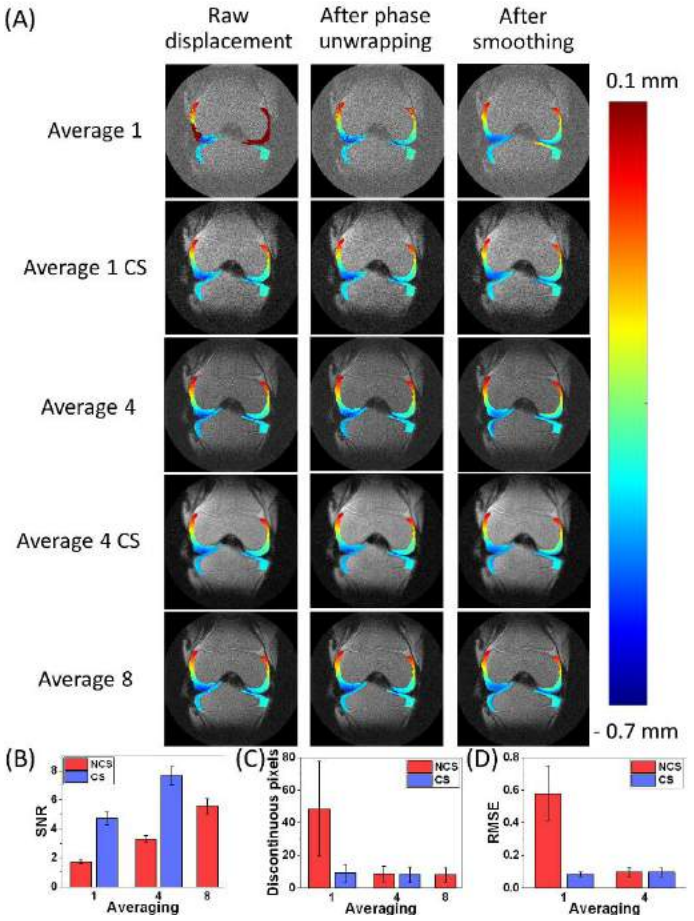

Figure 3: CS improves the image SNR and reduces error of MRI acquisitions. (A) Displacement (*x*) maps of frame 22 (t = 880 ms) after each process. (B-D) Quantitative analysis of CS and NCS (non-CS) on DENSE MRI. Error bars are the standard errors for four frames.

ACKNOWLEDGEMENTS

NIH 5R01AR063712-08.

REFERENCES

[1] WHO Department of Chronic Diseases and Health Promotion. Available at: http://www.who.int/chp/topics/rheumatic/en/

[2] Chan DD. et al., *Sci Rep* 6, 19220, 2016

[3] Zhong X, et al., *Med. Phys.* 36, 3413–3419, 2009

[4] Chan, DD, et al., *Magn Reson Med*, 71, 1231–1237, 2013

[5] Tamir JI, et al., *ISMRM Workshop*, 2016

ELUCIDATING THE ROLE OF WALL SHEAR STRESS IN AORTIC WALL REMODELING IN ASCENDING THORACIC AORTIC ANEURYSMS

S. Pirola(1), M.Y. Salmasi(2), S.M. Fisichella(1), S. Sasidharan(3), O.A. Jarral(2), D.P. O'Regan(4), J.E. Moore Jr(3), T. Athanasiou(2), X.Y. Xu(1)

(1) Department of Chemical Engineering
Imperial College London
London, UK

(2) Department of Surgery and Cancer
Imperial College London
London, UK

(3) Department of Biomedical Engineering
Imperial College London
London, UK

(4) Institute of Clinical Science
Imperial College London
London, UK

INTRODUCTION

Aortic aneurysm is the most common cause of death amongst conditions requiring emergency surgery in high-income countries [1]. Many patients suffering from ascending thoracic aortic aneurysm (ATAA) remain asymptomatic until sudden acute rupture or dissection, which carry a mortality rate of 50% within the first 48 hours. There is an unmet clinical need in the management of ATAA due to a lack of understanding of the mechanisms leading to growth and dissection. Currently, risk stratification relies on size criteria. Intervention is recommended in patients who have a maximal aortic diameter ≥55mm, with lower thresholds for those with bicuspid aortic valves or connective tissue disease. This is clearly inadequate as the incidence of dissection in ATAA below the size threshold is being increasingly reported, with up to 60% occurring below 55mm [2].

The degradation of extracellular matrix (ECM) structures in ATAA is well reported and several studies have linked abnormal wall shear stress (WSS) to disruption of the aortic wall microarchitecture [3], but detailed flow-to-tissue patient-specific mapping that incorporates the whole aneurysm is lacking.

In this work, we integrated imaging, computational fluid dynamics (CFD) and computational pathology to study ATAA in a patient-specific fashion. Our study aims to understand the underlying pathogenic factors associated with aortic medial degeneration in order to develop better risk prediction criteria.

METHODS

10 patients undergoing proximal aortic surgery to treat ATAA were recruited as part of this study. The main exclusion criteria were connective tissue disease, bicuspid aortic valve and redo-aortic surgery. Pre-operative magnetic resonance imaging (MRI) and 4D flow data were collected. Central aortic pressure was measured prior to the scan.

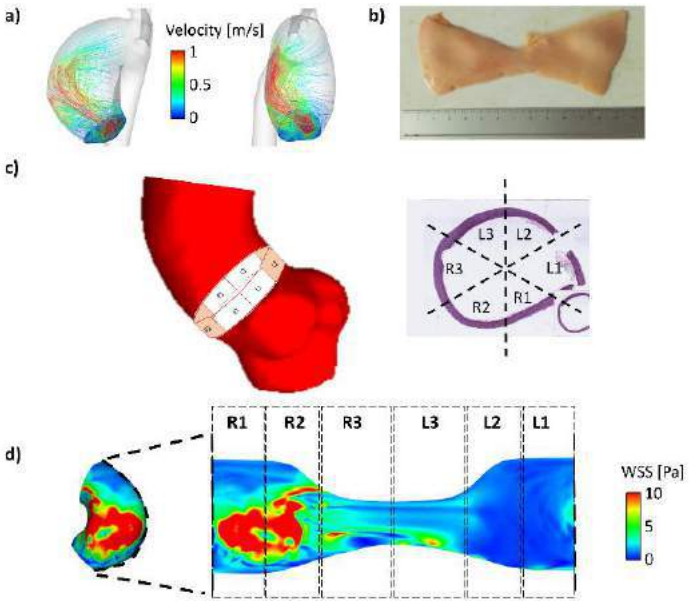

Figure 1: Study methodology: a) Patient-specific CFD analysis of ATAA were conducted for each patient; b) Patients' aortic tissue sample were collected at the time of surgery; c) Each sample was processed for computational histology and subdivided into 6 equal circumferential regions - R1, R2, R3, L1, L2, L3; d) Computational results post-processing: the aneurysmal region was unwrapped from the outer wall (dashed line) and was segmented to obtain 6 circumferential regions (dashed squares) matching the regions used for histological analysis.

MRI data were used to reconstruct patients' aortic geometry. 4D flow images and pressure measurements were used to extract patient-specific boundary conditions for computational fluid dynamic (CFD) analysis, as previously described [4, 5, 6] (Fig. 1a). 3D patient-specific time-varying velocity profiles were imposed at the model inlet, which was located in the aortic root, upstream of the ATAA region. 3-element Windkessel models were used at the aortic outlets, located at the supra aortic branches and thoracic descending aorta. CFD simulations were performed using Ansys CFX.

Aortic specimens (Fig. 1b) were collected immediately after surgical excision. 5mm circumferential portions of the tissue were removed and used for computational histology. Whole slide imaging of full circumferential rings of ATAA samples were obtained using a high-resolution digital optical system (Hamamatsu TM) and uploaded onto a digital processing software (QuPath) for further analysis in ImageJ. Images of each ATAA were divided into six equal circumferential regions (Fig. 1c). Microstructural density calculation of smooth muscle cells (SMCs) and elastin (from slides stained with Elastin Van Gieson) and collagen (slides stained with picrosirius red) was conducted.

Computational results were processed in Ansys EnSight. The aneurysmal region was unwrapped from the outer wall and each patient aorta was segmented to obtain six circumferential regions matching the regions used for histological analysis (Fig. 1d). For each region time-averaged WSS (TAWSS) was calculated.

RESULTS

Maximal WSS levels were significantly higher on the outer curvature of the aorta (24.98 ± 7.79 Pa) compared to the inner curvature (10.18 ± 4.14 Pa). TAWSS values were also considerably higher on the outer curvature (4.85 ± 2.07 Pa) compared to the inner curvature (2.67 ± 0.81 Pa). Asymmetric medial degeneration was observed, with the outer curvature more affected than the inner curvature.

To assess the influence of WSS, linear regression models (Fig. 2) were constructed, finding a statistically significant (p=0.035) negative effect of the maximum value of TAWSS ($TAWSS_{max}$) on elastin abundance. Higher levels of WSS were also associated with higher levels of collagen in the aortic media. However, results of linear regression analysis were non-significant.

The influence of $TAWSS_{max}$ on SMC count was also found to be significant (p=0.021), with higher levels of $TAWSS_{max}$ linked to lower counts of SMCs. A multilevel mixed effects model was used to assess the effect of WSS parameters on elastin and SMC count while also accounting for patient differences. WSS was found to have a persistently negative influence on SMC count (p=0.03).

DISCUSSION

Through segmental analyses using a robust ATAA flow-to-tissue patient-specific mapping approach, we found a co-localization of areas of elevated WSS with regions of the aortic wall presenting enhanced medial degeneration, the hallmark of ATAA disease. This suggests a negative remodeling process of the aortic wall in response to chronic exposure to high shear forces exerted on the wall by the blood.

Higher TAWSS levels were found to be associated with a reduction in both elastin abundance and smooth muscle cell count. Also, albeit not statistically significant, collagen abundance was higher in areas of higher TAWSS. The observed reduction in SMC count suggests a process of mechanodysregulation in response to elevated WSS. Dysfunctional mechanosensing can lead to cellular apoptosis and/or an atrophic remodeling [7], thus disturbing the structural integrity of the aortic wall.

Our findings agree with several previous computational studies assessing flow in TAA, which found asymmetric WSS distribution, highest on the outer curvature [3]. This loss of elastin integrity and relative increase in collagen match the reduced compliance and increased stiffness of the aorta observed in older subjects. Enhanced collagen deposition has also been previously reported in ATAA and linked to compensatory fibrotic changes resulting from the disease process [8]. Elastin fiber thinning in the aortic wall has also been previously linked to increased WSS in BAV patients [3], thus supporting a flow mediated pathogenesis in ATAA, increasing the likelihood of acute dissection.

Aortic samples have also been mechanically tested to evaluate key mechanical parameters (e.g. maximum tangential stiffness, tensile strength, dissection energy). Further statistical analyses assessing the link between WSS and wall mechanical properties are currently ongoing.

Larger sample sizes and the incorporation of patient-specific finite element modelling will form the basis of future work.

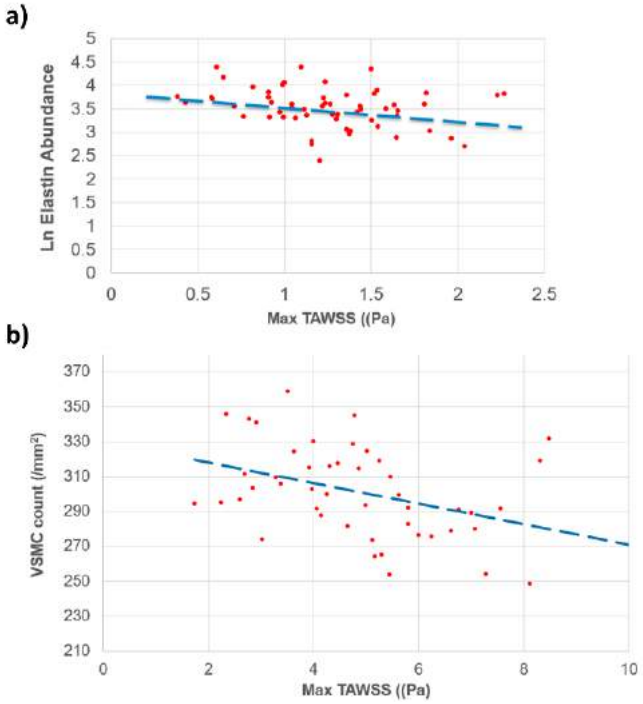

Figure 2: Linear regression analysis results for a) Elastin abundance and b) Smooth muscle cells (VSMC) vs $TAWSS_{max}$. Each data point (N=60) corresponds to a single aortic segment arising from the 10 analyzed patients (6 segments for each patient).

ACKNOWLEDGEMENTS

This work was supported by NIHR Imperial College BRC (grant number P74143) and BHF Centre of Research Excellence (RE/18/4/34215).

REFERENCES

[1] Stewart, B et al., *Br J Surg*, 101:e9-e22, 2014
[2] Paper, L et al., *Circulation*, 116:1120-1127, 2007
[3] Bollache, E et al., *JTCVS*, 156:2112-2120.e2, 2018
[4] Pirola, S et al., *JBiomech*, 60:15-21, 2017
[5] Pirola, S et al., *APL Bioengineering*, 2: 02610, 2018
[6] Pirola, S et al., *IEEE TBME*, 66:3411-3419, 2019
[7] Humphrey, JD et al., *Science*, 344:477-479 2014
[8] Wagsater, D et al., *J Am Heart Assoc*, 2: e000034, 2013

EFFECT OF STENT ORIENTATION ON AORTIC ROOT STRESS DURING TRANSCATHETER AORTIC VALVE DEPLOYMENT: A COMPUTATIONAL STUDY

A. Razavi (1), S.K. Sivakumar (1), B. Yeats (1), V. Thourani (2), V. Polsani (2), P. Yadav (2), L.P. Dasi (1)

(1) Department of Biomedical Engineering Georgia Institute of Technology, Atlanta, GA, USA

(2) Department of Cardiovascular Surgery, Piedmont Heart Institute, Atlanta, GA, USA

INTRODUCTION

Transcatheter aortic valve replacement (TAVR) has evolved into a routine clinical practice to treat patients with aortic valve stenosis. There have been numerous computational and experimental studies on the design, implantation, and post-procedural complications since the advent of TAVs [1-6]. These studies have provided valuable information on the effect of valve shape, deployment configuration, and balloon inflation volume on paravalvular leakage (PVL) and thrombogenic events [1, 2]. Also, the impact of TAVR on mitral valve regurgitation [3], pressure recovery in balloon and self-expandable valves [4], as well as the role of TAVR and BASCLICA on the sinus and non-sinus hemodynamics [5, 6] have been investigated. There are a few computational studies that have considered valve positionings [1, 2, 7, 8], and there is still lack of data on all possible valve configurations and their potential post-procedural effects.

The objective of this study is to develop a computational framework to assess effect of the TAV orientation on the aortic root stresses that may ultimately allow us to predict post-TAVR complications including root rupture, coronary obstruction as well as the PVL. Findings from this study may be ultimately used for surgical planning to notify clinicians on the optimal deployment configuration for a specific patient. Moreover, the methods employed, when applied on a larger cohort, will provide training data for future predictive modeling using machine learning algorithms.

METHODS

MODEL CREATION AND MATERIAL ASSIGNMENT

Pre-procedural computed tomography (CT) images of a 55-year-old male patient with aortic stenosis who received a SAPIEN 3 TAV at Piedmont Atlanta Hospital were obtained after Institutional Review Broad approval. Aortic wall and leaflets of the patient were segmented from pre-TAVR CT images and meshed using Materialize MIS (Leuven, Belgium). We did not include the calcium nodules as it was out of the scope of the current study. The 3D geometry of the aortic wall and leaflets were discretized using explicit 4-node linear tetrahedron elements. Neo-Hookean hyper-elastic constitutive equation was used to represent the aortic material properties with shear modulus, μ=1 MPa, bulk modulus, κ=10 MPa, and density, ρ=1000 kg/m^3 [9]. Stent model employed was SAPIEN 3 29mm which meshed into modified quadratic tetrahedral elements. The SAPIEN material, used an elasto-plastic model with Young's modulus, E=193 GPa, σ_Y (0.2%) =340 MPa, σ_U (48%) =670 MPa, Poisson's ratio, ν =0.29 and, density, ρ =7760 kg/m^3 [10]. The balloon was modeled with quadrilateral shell elements as a linear elastic material with E=600 MPa, ν =0.45 and ρ=1100 kg/m^3 [10].

TAV POSITIONING AND DEPLOYMENT

The balloon and stent models of the TAV were crimped using a cylindrical crimper in ABAQUS (Dassault Systèmes, Johnston, RI, US). The crimped balloon and stent were positioned coaxially inside the aortic root (Z-axis). Rotation boundary conditions (around the X-axis) were applied to the balloon-stent assembly with three degrees of rotation, i.e., 4°, 8° and 12° (Figure 1). Output data for each configuration was used as an initial condition for the deployment step. Fluid-cavity based approach was employed to inflate the balloon and deploy the stent [1]. The aortic side of the aortic root was constrained in its translational and rotational degrees of freedom. Scaled penalty contact was employed for the stent-balloon and stent-AV interactions. Rotation simulations were completed approximately 1.5h and deployment simulations were solved in about 3h on 22 processors. Results were visualized and analyzed in ABAQUS output database.

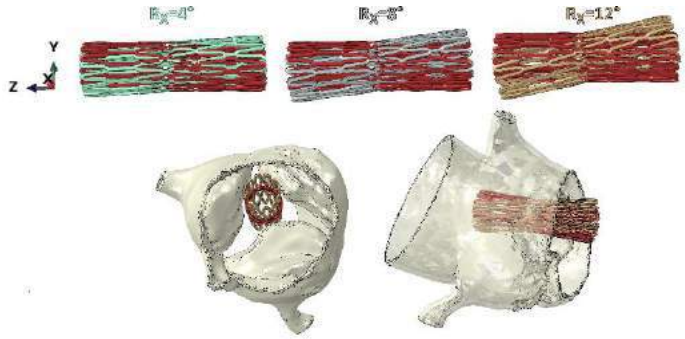

Figure 1. Stent rotation pre-deployment. Top: stent orientation in the aligned (red) and three misaligned states rotated around the X axis by 4°, 8° and 12°. Bottom: stent configuration of the aligned and 12° misaligned states in the aortic root.

RESULTS

Contour plots of stress within the aortic leaflets and wall are indicated in Figure 2 for the aligned state of the stent and for rotation of the stent around the X axis by 4°, 8° and 12° respectively. Top row shows stress distribution on the right and non-coronary AV leaflets of the aortic root and bottom row shows the distribution on the left and right AV leaflets. There is a decrease in stress with increasing in stent rotation on the aortic wall above the leaflets.

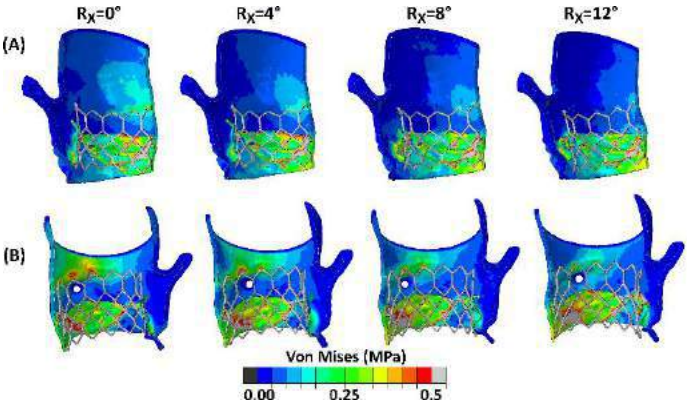

Figure 2. Stress distribution on the aortic root including (A) right and non-coronary sinuses (B) left and right coronary sinuses

Contact pressure distribution on the aortic root is depicted in Figure 3. Higher contact pressure is more concentrated on the non-coronary leaflet. There are some local differences observed on the leaflets with an increasing trend in contact pressure with increase in stent rotation on the left coronary leaflet.

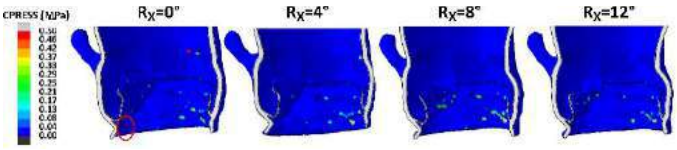

Figure 3. Contact pressure distribution on the aortic root. Red ellipse indicates approximate location of the membranous septum.

DISCUSSION

In this study, effect of the TAV orientation was investigated in a patient specific geometry through computational finite element analysis. The accuracy of the deployment method has been successfully verified previously through comparison of the final configuration obtained from simulation with post-procedural CT imaging of the patient.

As it can be appreciated from Figure 2, during deployment of the stent, there is a strong dependency of valve orientation with respect to the stresses on the root above the leaflets which can be attributed to the contact between the balloon and aortic wall. There is also a trend noticeable for this region: as the angle of rotation increases, the stress values decrease. This shows that the higher 12° orientation is most beneficial for this specific root and the risk of root rupture might be higher for lower angles of rotation. In a study by [7], the stent orientation was determined based on the angle between the native leaflets and prosthetic leaflets (0°-105°). They reported a trend for stress alterations with respect to the angle of orientation and showed that at 0° and 60°, the leaflets experienced lowest and highest stress. In another study by [2], two orientation states were defined similar to [7] and it was shown that when the prosthetic and native valve leaflets are aligned, the PVL is less. The findings from these studies emphasize the impact of the device orientation on structural and hemodynamic parameters.

Contours of the contact pressure in Figure 3 indicated an overall similar distribution within the leaflets. However, there were still some local differences observed which were more defined on the left coronary sinuses. Contact pressure on the membranous septum is negligible showing no abnormality of the atrioventricular conduction system. Our data were consistent with [8] where they showed that the contact pressure did not change for three stent orientations.

Some of the modeling considerations and limitations of the current study are described as the following: (1) We did not include the TAV prosthetic leaflets as it has been shown it has a minimal effect on deformed configurations of the stent [11], (2) Material properties of the aortic valve tissue are not patient-specific. The paucity of data on material properties of the healthy and pathologic aortic valves is a common limitation of the valve studies. Nonetheless, the literature derived material properties used in the current study still meet the objective of the work, (3) Calcific plaques were not included in the modeling. The influence of calcific nodules in combination with degree of rotation of the stent on the deployment results and stress of aortic root will be analyzed to further improve our understanding of the TAV performance and deterioration under these deployment scenarios.

In conclusion, the findings of this study indicate that: (1) the orientation of the stent should be considered when there is a concern for root rupture and (2) optimal TAV configuration can be characterized in a patient-specific manner. Furthermore, similar studies on a larger patient population that include other possible TAV deployment orientations and depths will provide a database for use in predictive algorithms which allow for an improved and more rapid decision making.

REFERENCES

[1] Bianchi, M et al., *Artif Organs*, 40-12:E292-E304, 2016.
[2] Mao, W et al., *J Biomech Eng*, 140-10, 2018.
[3] Caballero, A et al., *J R Soc Interface*, 16-157:20190355, 2019.
[4] Hatoum, H et.al, *Ann Biomed Eng*, 48-2:860-867, 2020.
[5] Hatoum, H et.al, *Ann Thorac Surg*, 110- 4:1348-1356, 2020.
[6] Hatoum, H et.al,*Cardiovasc Revasc Med*, 21-3: 271-276, 2020.
[7] Bailey, J et al., *J Biomech*, 53: 22-28, 2017.
[8] Rocatello, G *et al.*, *Circ Cardiovasc Interv*, 11-2:e005344, 2018.
[9] Bosmans, B et al., *J Biomech*, 49-13: 2824-2830, 2016.
[10] Tzamtzis, J et al., *Med Eng Phys*, 35-1:125-30, 2013.
[11] Bailey, J et al., *Comput Methods Biomech Biomed Engin*, 19-7:733-44, 2016.

DECOUPLING HYDROSTATIC AND DEVIATORIC STRAIN ENERGY DENSITY IN BIOMATERIALS WITH POISSON'S RATIO LARGER THAN 0.5

Amevi M. Semodji, Katherine A. Hollar, Gunes Uzer, Ph.D., Trevor J. Lujan, Ph.D.

Department of Mechanical & Biomedical Engineering
Boise State University
Boise, ID, USA

INTRODUCTION

Strain energy density is a scalar measure of deformation in nonbiological and biological materials. It represents the energy stored in the material during deformation and can be decomposed into two components: hydrostatic energy, responsible for volume change, and deviatoric energy, responsible for shape change (distortion). Decoupling strain energy density is a common engineering practice as each component guides different responses in the material. For example, hydrostatic energy is predictive of cortical bone remodeling [1], while deviatoric energy theory is an excellent predictor of failure in ductile materials [2]. Deviatoric energy may also be a key predictor of damage, growth, and remodeling in soft fibrous tissues (e.g. ligament), but large Poisson's ratios in soft tissue have made this analysis difficult.

The Poisson's ratio is a fundamental metric that defines a material's resistance to distortion or volume change. Several biological materials exhibit a large Poisson's ratio under uniaxial tension (3.0 for tendon [3], 1.7 for collagen constructs [4]), indicating volume loss. Previous studies have investigated the structural origins for these large Poisson's ratios [5,6], but little interest has been given to their strain energy. Finite element (FE) solvers can output strain energy values for deformed materials; yet several solvers, including ABAQUS, lack the energy decoupling feature. FEBio [7] is one of the rare FE solvers that can decouple strain energy, but only for uncoupled materials with Poisson's ratios less than 0.5. A need thus exists to develop a technique to decouple strain energy in materials with a large Poisson's ratio.

The objective of this work is to present a numerical approach to decoupling strain energy density in materials with a large Poisson's ratio. The method will be validated using a FE solver for a material with small Poisson's ratio and will be used to decouple strain energy in type-I collagen constructs, known to have large Poisson's ratios, under simple and complex loading.

METHODS

Strain energy density can be described as the area under the characteristic stress-strain curve of a material (Fig. 1). The integral form of this relationship is defined by equation (1), where $\boldsymbol{\sigma}(\boldsymbol{\varepsilon})$ denotes the engineering stress tensor, and $\boldsymbol{\varepsilon}$ represents the engineering strain tensor.

$$W = \int \boldsymbol{\sigma}(\boldsymbol{\varepsilon}) : \boldsymbol{d\varepsilon} \tag{1}$$

The integral can be numerically computed using a technique similar to the trapezoidal numerical integration. The total area can be subdivided into small intervals, and for each interval, the stress and strain tensors can be formed. For each interval, the stress tensor $\boldsymbol{\sigma}$ can be decomposed into its hydrostatic and deviatoric components $\boldsymbol{\sigma^{HYD}}$ and $\tilde{\boldsymbol{\sigma}}$ respectively (Eq. 2). $\boldsymbol{I}$ denotes the identity tensor, and tr is the tensor trace operator.

$$\boldsymbol{\sigma^{HYD}} = \frac{1}{3} tr(\boldsymbol{\sigma})\boldsymbol{I} \quad \text{and} \quad \tilde{\boldsymbol{\sigma}} = \boldsymbol{\sigma} - \boldsymbol{\sigma^{HYD}} \tag{2}$$

Similarly, the strain tensor can be decoupled. The energy components can be computed by approximating each one with a pair of triangular and rectangular areas (Fig. 1).

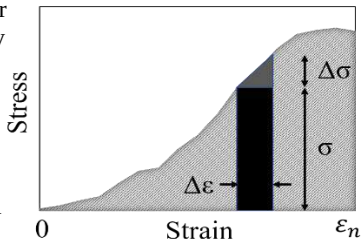

Figure 1: Decomposition into rectangular and triangular

The total hydrostatic energy, W^{HYD} and the total deviatoric energy, $\widetilde{W}$ are found by summing all the area pairs over the entire strain interval (Eq. 3&4).

$$W^{HYD} = \sum \left(\frac{1}{2} \Delta\boldsymbol{\sigma}^{HYD} : \Delta\boldsymbol{\varepsilon}^{HYD} + \boldsymbol{\sigma}^{HYD} : \Delta\boldsymbol{\varepsilon}^{HYD} \right) \tag{3}$$

$$\widetilde{W} = \sum \left(\frac{1}{2} \Delta\tilde{\boldsymbol{\sigma}} : \Delta\tilde{\boldsymbol{\varepsilon}} + \tilde{\boldsymbol{\sigma}} : \Delta\tilde{\boldsymbol{\varepsilon}} \right) \tag{4}$$

The total strain energy density W is computed as the sum of the hydrostatic and the deviatoric energies. A custom MATLAB function was developed to implement this numerical method.

Method validation. To verify our numerical approach: three test cases (based on experimental results using collagen constructs) were set up in FEBio: uniaxial tension (T), uniaxial compression (C), and biaxial tension-compression in equal magnitudes (CT). A single element cube model was designed to represent the material, and displacement was prescribed through a rigid body. A sliding-elastic contact was defined between the cube and the rigid body. The cube was assigned a Mooney-Rivlin material in the T and C loading conditions, and an orthotropic elastic material in the CT loading condition.

The stress and strain values obtained from FEBio were imported into the custom MATLAB function to compute the hydrostatic and deviatoric energies as well as the total energy. The total energy results were compared to the results outputted by FEBio. Additionally, the deviatoric energies were compared to the FEBio results for the C loading condition, which was the only condition that displayed a Poisson's ratio less than 0.5 in our test cases.

Application to uniaxial and biaxial loading. The developed method was used to decouple energy in 3D collagen constructs subjected to different loading configurations. Experiments applied simple and complex loads at a single targeted total energy on collagen specimens (N=5) in a biaxial bioreactor. Type-I collagen sponges were speckled with water insoluble black ink, cut into dog-bone shapes, and hydrated in water overnight. The dog-bone shaped specimen was then placed in the culture chamber of the bioreactor (Fig. 2A). A camera was placed underneath the culture chamber to track displacements in a region of interest (ROI) of the specimen. Each specimen was subjected to the same three tests described in the previous section. Images obtained from the camera were processed via digital image correlation (DIC) to obtain a strain distribution over the 2D surface of the specimen (Fig. 2B).

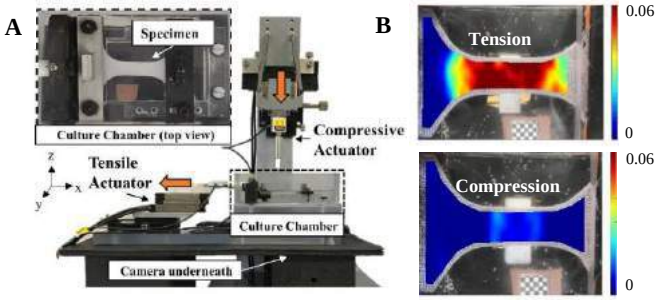

Figure 2: A) Biaxial bioreactor. B) Strain maps for (T) and (C)

A custom LABVIEW program attached to the bioreactor was used to extract load and displacement data, which, added to the strain distribution obtained via DIC, were used to compute the stress and strain tensors in the ROI. The custom MATLAB function was used to compute the hydrostatic, deviatoric, and total strain energy density values. A one-way ANOVA and Tukey-HSD post-hoc was performed to detect differences in energies between the three loading configurations.

RESULTS

FEBio validation. The custom MATLAB function accurately predicted the total energies in all three loading conditions with a percent difference less than 0.03% (Table 1). It also predicted the decoupling of the strain energy density in the uniaxial compression FEBio model with 0.4% difference in deviatoric energy (Table 1).

Table 1: Total (W) and deviatoric ($\widetilde{W}$) strain energy density comparison between MATLAB and FEBio

	W (J/m^3)			$\widetilde{W}$ (J/m^3)		
	FEBio	MATLAB	% Diff	FEBio	MATLAB	% Diff
T	*277.17*	*277.17*	*0.00*	-	*333.98*	-
C	*230.74*	*230.72*	*0.00*	*142.25*	*141.68*	*0.40*
CT	*248.54*	*248.48*	*0.02*	-	*482.84*	-

Uniaxial and biaxial experiments. The experiments hit the target total energy in all three loading conditions (Fig. 3). Additionally, the MATLAB function revealed a significant difference in hydrostatic and deviatoric energies between loading conditions (Fig. 3).

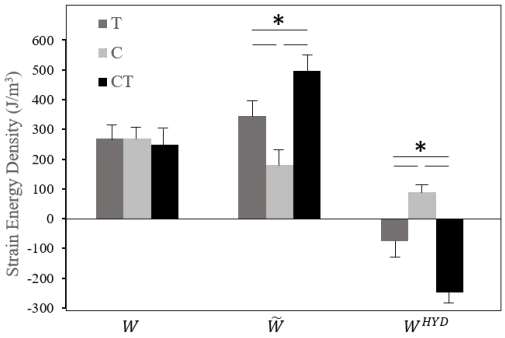

Figure 3: Total (W), hydrostatic (W^{HYD}), and deviatoric ($\widetilde{W}$) strain energy density per loading condition (* p<0.05)

DISCUSSION

This work presented a numerical approach to decoupling hydrostatic and deviatoric strain energy density in materials with large Poisson's ratio. The decoupling computation was validated using FEBio, which could only decouple energy in our C loading condition where Poisson's ratio was less than 0.5 (Table 1). Our method successfully decoupled strain energy density in type-I collagen gels, that experienced similar total strain energy densities but significantly different hydrostatic and deviatoric energies (Fig. 3).

Interestingly, a negative hydrostatic energy was revealed in the T and CT loading conditions (large Poisson's ratios, Fig. 3). To our knowledge, this is the first time a negative hydrostatic energy has been explicitly reported for a biomaterial. Mathematically, a negative hydrostatic energy can be explained as a sign contradiction between the change in hydrostatic strain and the applied hydrostatic stress. Physically, a negative hydrostatic energy occurs from a volume loss due to exudation of fluid from the material [5,6]. One can describe the negative energy as energy loss in the material via the leaving fluid. It's worth noting that fluid exudation leads to significantly greater deviatoric energies, as observed in the CT loading condition (Fig. 3).

This numerical method will finally allow us and others to investigate whether specific energies drive the mechanobiology of soft tissue and, more specifically, whether deviatoric energy can predict damage, growth, and remodeling in native and surrogate soft tissue.

ACKNOWLEDGEMENTS

Funding kindly provided by grant NIGMS #P20GM109095.

REFERENCES

[1] Mercuri, E et al., *Med Eng & Phys*, 38:904-910, 2016. [2] Von Mises, R, *News from Societies of Sciences*, 1:582-592, 1913. [3] Lynch, A et al., *J Biomech Eng*, 125:726-31, 2003. [4] Reese, S et al., *Biomech Model Mechanobiol*, 12:1195-1204, 2013. [5] Swedberg, A et al., *J Biomech*, 47:3201-3209, 2014. [6] Reese, S et al., *J Biomech*, 43:1394-1400, 2010. [7] Maas, S et al., *J Biomech Eng*, 134:1, 2012.

MYOFIBRIL DISARRAY DECREASES PEAK STRESS & EFFICIENCY IN A FINITE ELEMENT MODEL OF MUSCLE FIBER

Charles K. Mann (1), Hossein Sharifi (1), Alexus Rockward (1), Joy Mojumder (2), Lik Chuan Lee (2), Kenneth S. Campbell (3), Jonathan F. Wenk (1,4)

(1) Department of Mechanical Engineering
University of Kentucky
Lexington, KY, USA

(2) Department of Mechanical Engineering
Michigan State University
East Lansing, MI, USA

(3) Department of Physiology & Division of Cardiovascular Medicine
University of Kentucky
Lexington, KY, USA

(4) Department of Surgery
University of Kentucky
Lexington, KY, USA

INTRODUCTION

In healthy muscle fibers, myofibrils are arranged uniformly in parallel. In many muscle diseases myofibril disarray is present and studies show a correlation between this disorganization and impaired function. This study utilizes a Huxley-based cross-bridge distribution model of half-sarcomeres embedded in an implicit finite-element (FE) model of contractile tissue to investigate the effect of myofibril disarray in a muscle fiber. Specifically, this multiscale model is used to simulate isometric twitches and loaded shortening conditions. It is shown that in twitch simulations, peak stress and time to half-relaxation decrease as disarray increases. Furthermore, loaded shortening simulations show that efficiency is also decreased.

METHODS

Cell Contraction Half-sarcomeres were simulated using MyoSim [1]. The kinetics scheme used to describe the states of binding sites on the thin filament and myosin heads on the thick filament is shown in Figure 1. Transitions between these states have been previously described [2]. Briefly, binding sites can be described as OFF or ON and are activated in the presence of intracellular calcium and include a cooperative effect from the binding/unbinding of myosin heads. Myosin heads can exist in one of three states: super relaxed (M_SRX), disordered relaxed (M_DRX) or force-generating (M_FG(x)). The force-generating state is discretized over the working range of a cross-bridge (-10 to 10 nm) and thus has a spatial dependence. The transition from M_SRX to M_DRX is force-dependent and the transition from M_FG to M_DRX includes strain-sensitive detachment of cross-bridges. This yields a system of ODEs whose solution is the relative populations in each state. Active stress for a half-sarcomere T is calculated from the population in M_FG as

$$T = k_{cb} \sum_{i=1}^{n} M_{FG}(x_i) * (x_i + x_{ps}) \quad (1)$$

where k_{cb} is the spring stiffness of a cross-bridge and x_{ps} is the power-stroke distance.

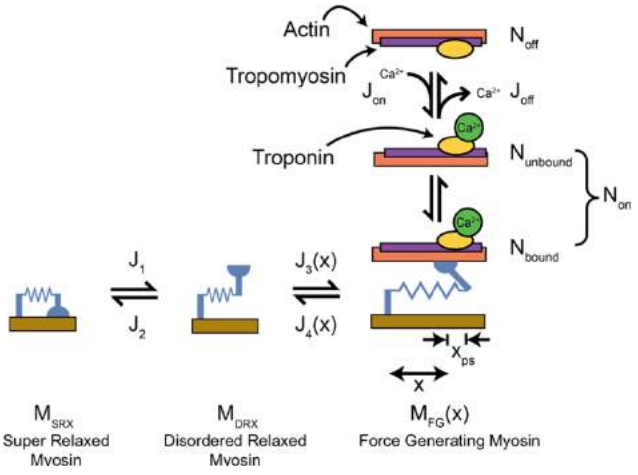

Figure 1: Cell contraction kinetic scheme

Constitutive Equations The contractile tissue is considered a hyperelastic, incompressible material. A local orthogonal coordinate system $\{\mathbf{f}_0, \mathbf{s}_0, \mathbf{n}_0\}$ is defined using the prevailing fiber, sheet, and sheet-normal directions respectively. An element of contractile tissue has a stress state that is additively decomposed into an active contraction stress tensor ($\mathbf{S_a}$) and passive response stress tensor ($\mathbf{S_p}$):

$$\boldsymbol{S}_a = T(\boldsymbol{f_0} \otimes \boldsymbol{f_0}) \quad (2)$$

$$\boldsymbol{S}_p = \frac{\partial W_{bulk}}{\partial \boldsymbol{E}} + \frac{\partial W_{myofibril}}{\partial \boldsymbol{E}} \quad (3)$$

$\mathbf{S}_p$ is further decomposed into contributions from the myofibril and the remaining bulk tissue. The strain energy functions for bulk [3] and myofibrils [4] are

$$W_{bulk} = \frac{C}{2}\left(e^{\left(b_f E_{ff}^2 + b_t\left(E_{ss}^2 + E_{nn}^2 + E_{sn}^2 + E_{ns}^2\right) + b_{fs}\left(E_{fs}^2 + E_{sf}^2 + E_{fn}^2 + E_{nf}^2\right) - 1\right)}\right) \quad (4)$$

$$W_{myofibril} = \begin{cases} C_2\left[e^{C_3(\alpha-1)^2} - 1\right] & \alpha > 1 \\ 0 & \alpha \leq 1 \end{cases} \quad (5)$$

where E_{ab} represent the components of the Green-Lagrange strain tensor with respect to the local fiber coordinate system and α represents the stretch of the myofibril.

Simulation Protocols A series of simulations were performed to simulate an isometric twitch response and a loaded shortening response of the muscle fiber at various degrees of disarray. Disarray was introduced by selecting the cartesian components of the f0 vector at each integration point from a gaussian distribution of varying widths (w) and normalizing the resulting vector. For the isometric twitch simulations, the fiber was stretched 10% to elicit an initial passive stress response and an approximation of a twitch calcium transient [5] was used to drive contraction. The elements within 10% of the ends of the fiber were set as non-contracting tissue to allow the contractile elements to shorten against compliance. Parameters for the contraction model were chosen to mimic a force twitch response [6] and the passive material parameters chosen to obtain an average myofibril shortening of ~8%. For loaded shortening simulations, the twitch protocol was used except for a traction boundary of 30 kPa being applied to the right end once the resultant forced was high enough to satisfy this condition. This allowed the fiber to shorten and subsequently re-lengthen as active force generation declined. Efficiency was calculated using the work done by the fiber during shortening and the energy consumption of the fiber:

$$Total\ Energy = \frac{\pi\rho\left(L_{fiber}\right) * \Delta G' * \sum_{N_G} \sum_{i=1}^{21} J_4(x_i)}{L_0 N_A N_G} \quad (7)$$

where ρ is the density of half-sarcomeres in contractile tissue, $\Delta G'$is the free energy produced by ATP hydrolysis, L_{fiber} is the length of the fiber, L_0 is the reference half-sarcomere length, N_A is Avogadro's number, N_G is the number of integration points, and the summation is the sum of fluxes out of M_FG(x) over N_G.

RESULTS

The muscle stress, peak stress, and time to half-relaxation for twitch simulations were calculated for varying amounts of disarray. Both quantities decrease as disarray increases (Figure 2).

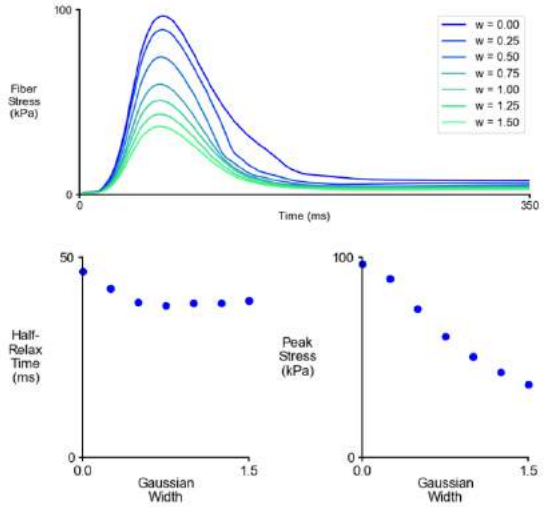

Figure 2: Twitch Simulation Data

The loaded shortening relative length profiles show the magnitude of shortening and also how the duration of shortening is affected. As disarray increases, fiber efficiency decreases (Figure 3).

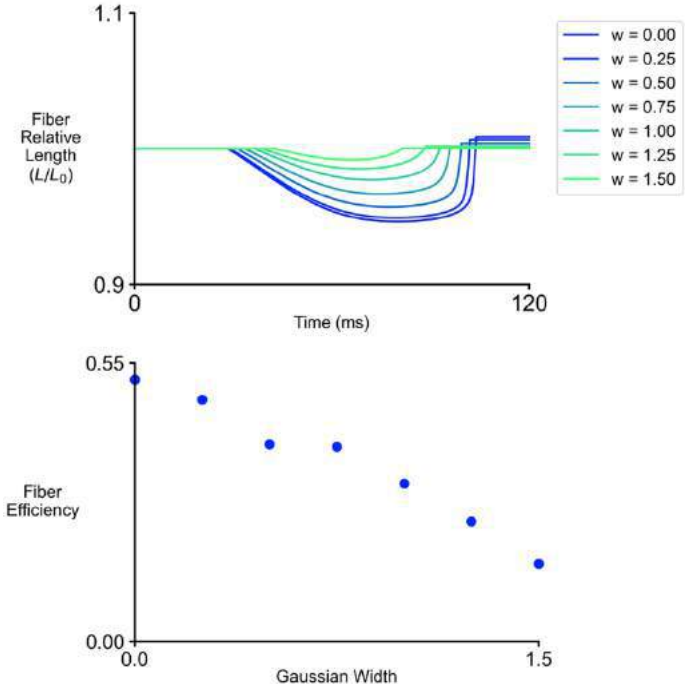

Figure 3: Loaded Shortening Simulation Data

DISCUSSION

This study uses a multiscale finite element framework driven by a physiologically motivated cell contraction model to simulate physiologically relevant experiments. The embedded cell contraction model also allows for the calculation of ATPase, showing that form influences function. Specifically, this study shows that disorganization in myofibrils results in muscle fibers that produce less force and require more energy to do the same amount of work as an organized cell. This example of testing hypotheses linking form to function and energetics will be carried forward in future work regarding growth and remodeling.

ACKNOWLEDGEMENTS

This study was supported by grants from the National Institutes of Health (U01HL133359 and S10RR029541), as well the Halcomb Fellowship in Medicine and Engineering from the University of Kentucky.

REFERENCES

[1] Campbell, KS, *J Gen Physiology*, 143(3):387-99, 2014
[2] Campbell, KS et al., *Biophys J.*, 115(3):543-553, 2018
[3] Guccione, J. M. et al., *J of Biomechanical Eng.* 113:42-55, 1991
[4] Xi, C et al., *Acta Biomaterialia,* 90:241-253, 2019
[5] Baylor, S. M. et al., *J Physiol.*, 551(1):125-138, 2003
[6] Gonzalez, E. et al., *J. Membrane Biol.*, 178:175-183, 2000

PRE-SURGICAL PLANNING OF FEMOROPOPLITEAL BYPASS OPERATION BASED ON PATIENT SPECIFIC IN SILICO SIMULATION

K. B. Kose (1), M. Bayram (2), C. Topel (3), S. Piskin (4)

(1) Department of Biomedical Engineering
Istanbul Medipol University
Istanbul, Turkey

(2) Department of Radiology
Istanbul MAE Thor. & Car. Surgery
University of Health Sciences
Istanbul, Turkey

(3) Department of Cardiovascular Surgery
Istanbul MAE Thor. & Car. Surgery
University of Health Sciences
Istanbul, Turkey

(4) Department of Mechanical Engineering
Istinye University
Istanbul, Turkey

INTRODUCTION

Nearly half (%40) of the patients with symptomatic peripheral arterial disease have aortoiliac occlusive disease (AOID) [1]. Currently guidelines favor open surgical of AOID [2,3]. No consensus is achieved on the management of multilevel occlusive disease, except to treat the inflow (i.e., aortoiliac lesion) first. There is controversial data about Aorta femoral graft (AFB) patency in the presence of Superficial femoral artery (SFA) occlusion [4,5]. The standard procedure is to take inflow from aorta to common femoral artery above the bifurcation of profunda femoral artery and SFA. In this case, while performing endarterectomy to the femoral bifurcation in a patient with total occluded iliac arteries and SFA, the common femoral artery severely got damaged and we had to anastomose the graft to the profunda femoral artery in an end-to-end anastomosis technique. We ligated the common femoral artery, and the ostium of SFA. This way of anastomosis might provide a more stable flow into the main target vessel -profunda femoral artery. Thus, we think it requires to be investigated by engineering methods [6-8].

METHODS

In the present work, aorta femoral by-pass graft operation has been assessed from the haemodynamic point of view [9]. A 55-year-old male patient was selected with an occluded iliac artery on the right leg and the iliac artery and superficial femoral artery was occluded on the left leg. The patient had diabetes mellitus type 2 and dislipidemia comorbidities. There was flow in profunda lumens on both sides. Aortic bypass operation was performed on the right side of the aorta and femoral bypass on the left side to the femoral junction. Pre-operative and post-operative computed tomography angiography (CTA) images were obtained with Toshiba Aquilion Helical CT (Asteion; Toshiba Medical Systems, Tokyo, Japan). The three-dimensional (3D) models for region of interests are obtained from multi-sliced DICOM images with image processing and segmentation tools by Mimics Innovation Suite 19.0 (Materialise, Leuven, Belgium) Figure 1.

The models were optimized with computer–aided design tools (Geomagic Studio (Geomagic Software, 3D Systems, Rockhill, SC, USA).

Approved software ANSYS was used to simulate the blood flow in both models with the computational fluid dynamics (CFD) method (ANSYS Inc, Somerset, PA, USA). The simulation model was governed by Navier-Stokes equations under the assumptions of laminar flow or turbulent flow:

$$\boldsymbol{\nabla} \cdot \boldsymbol{u} = 0 \tag{1}$$

$$\rho \boldsymbol{u} \cdot \boldsymbol{\nabla} \boldsymbol{u} = -\boldsymbol{\nabla} p + \boldsymbol{\nabla} \cdot [\mu(\boldsymbol{\nabla} \boldsymbol{u} + (\boldsymbol{\nabla} \boldsymbol{u})^T)] \tag{2}$$

where $\boldsymbol{u}$ is the velocity vector, p the pressure, t the time, ρ and μ the density and the dynamic viscosity of the blood, respectively. Besides NS equations, the SST k – ω model was included to simulate the turbulence.

The inlet boundary condition has been assigned a plug velocity profile and the outlet boundaries has been assigned a pressure outlet. Results were considered as guiding parameters in the comparison.

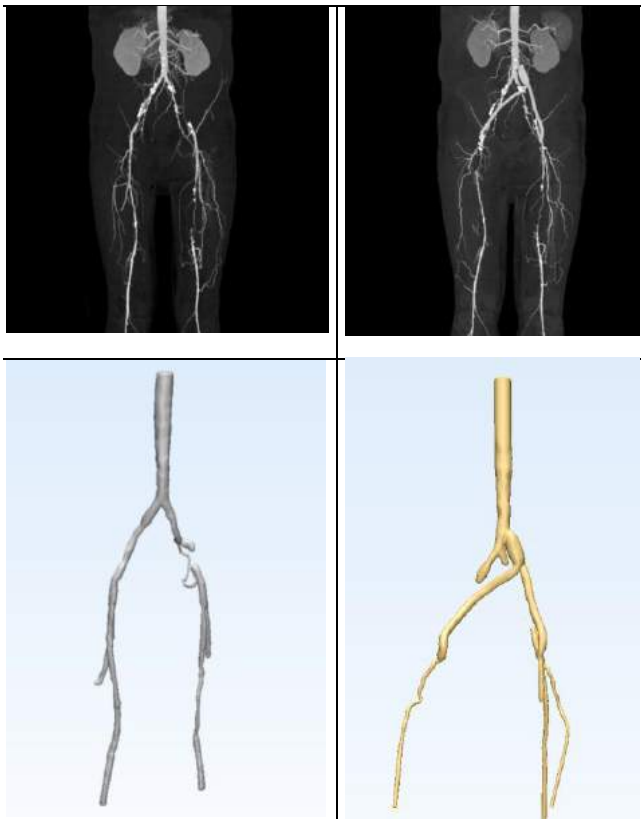

Figure 1: Top: Pre-op (left) and post-op CTA images, Below: Pre-op (left) and post-op three-dimensional virtual models.

RESULTS

The preliminary results are presented in this section for pre- and post-op stages of the surgery. The pressure distribution of both stages is presented in Figure 2. The decrease of pressure from the inlet to the outlets are observed as expected for steady state blood flow. The narrowing regions (obstructions) decrease the pressure substantially for especially the post-op stage.

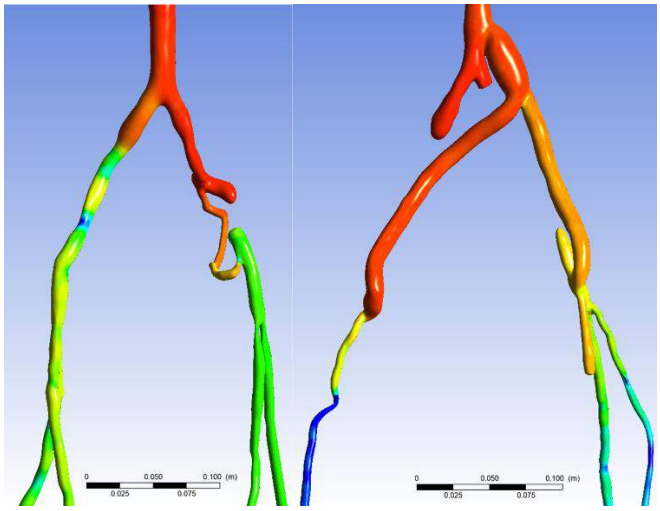

Figure 2: Pressure distribution at pre-op (left) and post-op (right) stages.

Figure 3 shows the wall shear stress (WSS) for both stages. WSS is calculated since it is correlated with re-stenosis and plaque formation. The stenosis or sharp lumen diameter changes cause severe WSS value increases due to high velocity and shear rates. This is valid for both pre- and post-op stages. The larger inlet zones have relatively low WSS due to undisturbed flow profile and low velocity. Also, the pre-op stage has non-symmetric distribution due to flow differences at the branches.

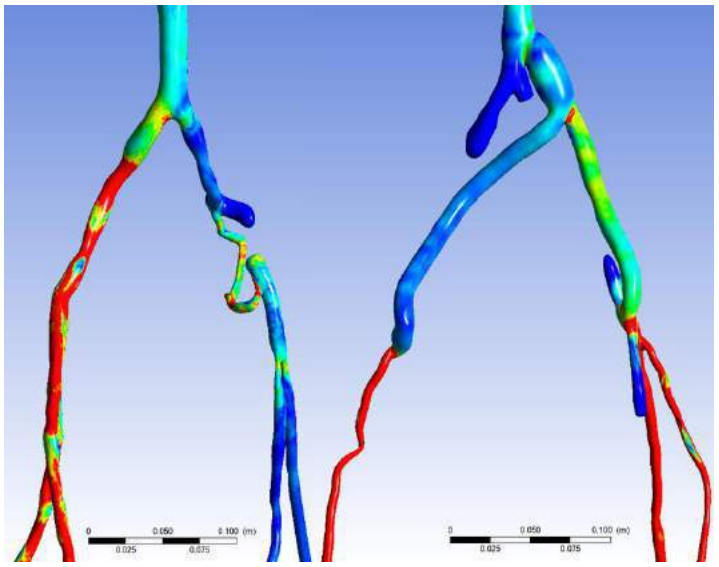

Figure 3: WSS distribution at pre-op (left) and post-op (right) stages.

DISCUSSION

Here, we have presented the first results of our study on pre surgical planning of profunda bypass operation. Early results show the insight of hemodynamics which would otherwise would not be possible by routine clinical investigations. The results show that the location of anastomosis and its configuration are critical as well as the diverging location of the bypass graft. Since we have pre-op and post-op images of the same patient, the analysis of the simulation data are comparable to each other without using any assumptions. The boundary conditions do not belong to the patient since they were not available at the time of the simulation. Also, the walls of the arteries are assumed to be rigid. We are now collecting patient specific boundary conditions for future work. The proposed framework is promising regarding the optimization of the aorta femoral bypass graft placement.

ACKNOWLEDGEMENTS

We would like to acknowledge Istinye University BAP project funding with ID 2019/B1.

REFERENCES

[1] Diehm N. et al, Eur J Vasc Endovasc Surg. 2006 Jan;31(1):59-63.
[2] Aboyans V. et al, Eur Heart J. 2018 Mar 1;39(9):763-816.
[3] Norgren L. et al, Eur J Vasc Endovasc Surg. 2007;33 Suppl 1
[4] Madiba T.E. et al, J R Coll Surg Edinb. 1998 Oct;43(5):310-3.
[5] Nevelsteen A. et al, Surgery. 1980 Nov;88(5):642-53.
[6] Piskin, S et al., *CVET*, 8:107-119, 2017.
[7] Piskin, S et al., *J. Biomech.*, 50:166-171, 2017.
[8] Lashkarinia, S. et al, ABME, 46:9, 2018
[9] Skopalik, S. et al., International Journal for Numerical Methods in Biomedical Engineering, 2021

SB³C2021
Summer Biomechanics, Bioengineering and Biotransport Conference
June 14-18, Virtual

INCORPORATING ENGINEERING STANDARDS INTO A BIOMECHANICS LABORATORY COURSE

Kristen L. Billiar

Department of Biomedical Engineering
Worcester Polytechnic Institute
Worcester, Massachusetts, USA

INTRODUCTION

Engineering standards are critical in the design process for efficiency of the process, uniformity in validation, product safety, and market acceptance.[1] Although ABET has dropped the explicit requirement of "incorporating appropriate engineering standards" in the Criterion 4: Professional Component section, the need for safe and effective medical devices is clear. Further, the FDA requires testing according to published standards, thus the importance for biomedical engineering students to understand how to find and adhere to engineering standards remains.

But where do engineering students learn about engineering standards? Requiring senior capstone design students to list the standards their product would have to adhere to if produced neither aids in their learning nor assesses their understanding. Yet an entire course on engineering standards is difficult to fit within an already packed curriculum. Further, discussion of standards outside of their theoretical underpinnings loses the opportunity to demonstrate the application of engineering theories in real world context. There is a continuing need to implement engineering standards within technical courses in curricula.

The goal of this work is to describe the implementation of engineering standards for mechanical testing of medical implants into a junior-level biomechanics laboratory course. Students were presented lectures on why standards are needed, who develops standards, and the (long) process for such development. They then utilize the standards for characterizing specific aspects of the mechanical performance of various medical devices and report out the required metrics. This work is a work in progress: no statistical analyses of student learning were performed, and the student outcomes were not compared to a control group.

METHODS

Engineering standards were incorporated into a junior-level biomechanics laboratory course focused on characterization of the mechanical behavior of biological tissues and biomaterials. Characterization of metal fracture fixation plates and screws was added to align with accessible ASTM test standards in the fall semesters of 2019 and 2020, with enrollments of 45 and 36 students, respectively.

General lecture materials highlighted the benefits of standards in the design and manufacture of medical implants. These include demonstrating safety and integrity of devices, uniformity of test methods, consistency of data reporting across the industry for valid comparisons, avoiding development and validation of methods by individual companies, and market acceptance. Who develops standards and the standards setting process were also discussed so that the aspiring engineers could understand that they can change and create standards in the future. Additional lectures covered the specific metrics in a few engineering standards including: burst strength and suture pull-out for blood vessel grafts;[2] proof load, bending stiffness, and flexural rigidity of metallic fracture fixation plates;[3] and screw pull-out strength of metallic medical bone screws.[4]

After two preliminary projects involving uniaxial testing of leather and flexure testing of wood and bone through which they students gained the skills to safely perform mechanical testing using an Instron 5544 and to analyze the data using Matlab, the student teams were then challenged to characterize the mechanical performance of metallic plates and screws following ASTM standards (e.g., refs [3] and [4]). As standards often do not specify specific values for test parameters (e.g., sample or fixture dimensions, rate of test, temperature), the students were also asked to assess the effects of one test parameter on each metric and perform statistical analysis (t-test on the slope of the regression line).

RESULTS

From the point of view of the instructor, the standards are helpful in that they provide for the students clear diagrams of the test configurations with dimensions indicated, e.g., Figure 1 for 4-point bending of a metallic plate showing the center span distance, a, and the loading span distance, h. They also provide unequivocal definitions for test variables and equations for calculating the device properties (with units), e.g., bending stiffness (K, N/mm) and bending structural stiffness (EI, N-m^2, Equation 1).

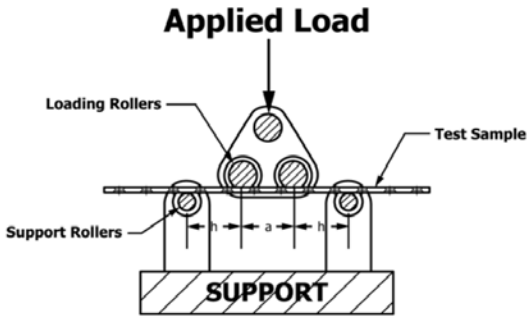

Figure 1: 4-point bending test configuration from [3].

$$EI_e = \frac{(2h+3a)Kh^2}{12} \quad (1)$$

The students were at first confused by the difference in nomenclature between their stress analysis textbook and the standards; however, upon watching the lectures which provided the derivation of the equations from basic stress analysis, they were able to clearly see the connection. In their lab reports, they were also able to demonstrate an understanding of the limitations of their analyses, e.g., often not being able to have a sufficient support span/sample thickness ratio to neglect shear stress.

Through their parametric tests, many groups demonstrated that certain test parameters have little effect on the results, e.g., intrinsic properties such as material modulus or rate of test on the bending stiffness of a fixation plate since it is metal (Figure 2), whereas other test parameters must be controlled carefully, e.g., the span ratio (center/support) for functional properties such as the bending stiffness and for the depth of insertion of a bone screw into a Sawbones polyurethane foam test block (Figure 3).

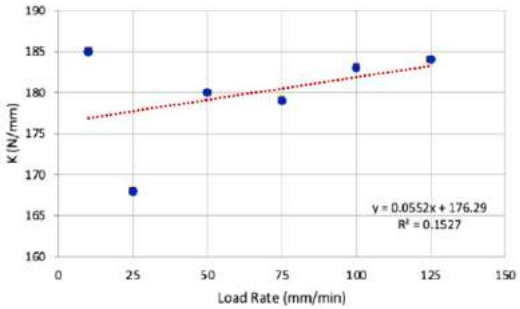

Figure 2: Plot of bending stiffness, K, as a function of load rate with regression showing lack of significant effect of rate (p= 0.44 for t-test on slope); data and plot from team e4.

One group commented in their report: "…this result signifies the importance of a universal standard. This is the reason for the ASTM bone screw standards. The ASTM standard for bone screw pullout testing states the screws should be a depth of 20mm, or 60% of the screw length for smaller screws [4]. Changing just [insertion depth] yields dramatically different maximum loads, proving that the standards are necessary to make data uniform and analyzable."

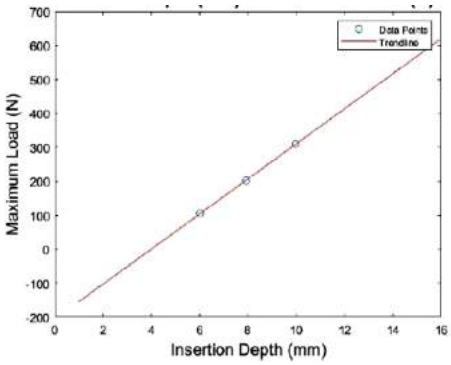

Figure 3: Plot of maximum load from screw pull-out test as a function showing strong linear correlation (p=0.008 for t-test on slope); data and plot from team 1f.

The overall grades on the final project in which they used standards to guide their mechanical characterization were 91% ±7% in 2019 and 86%±11% in 2020, indicating good overall following of the standards for their methods, analysis, and data reporting.

DISCUSSION

Overall, based on lab report content, instructor observations, and student feedback, use of engineering test standards helped students learn how to perform high quality mechanical tests and analyze and report the resulting data in a uniform manner.

The parametric studies demonstrated to the students the need to control critical parameters very tightly, and why standards allow variation in other parameters (e.g., due to vastly different sizes of fixation plates for different applications). This exercise also helped them understand how an engineer goes about choosing value of certain parameters e.g., rate of testing.

Use of standards helped the students draw connections between academic lab exercises and actual industry practice. Standards also showed them first-hand how their coursework (e.g., stress analysis) applies to the mechanical characterization tests completed in industry and required by the FDA.

ACKNOWLEDGEMENTS

I would like to acknowledge William DeMaria, teaching assistant extraordinaire, and the hard work of the students taking BME3505 during the COVID19 pandemic.

REFERENCES

[1] Schultz, Daniel, Standards in the Classroom, accessed January 20, 2021, https://www.astm.org/SNEWS/JULY_2005/schultz_jul05.html
[2] ISO 7198, Cardiovascular implants and extracorporeal systems - Vascular prostheses - Tubular vascular grafts and vascular patches, 2016.
[3] ASTM F382-17 Standard Specification and Test Method for Metallic Bone Plates, 2017
[4] ASTM F 543-17 Standard Specification and Test Methods for Metallic Medical Bone Screws, 2017

EFFECTS OF AGGRESSIVENESS, CONFIDENCE, AND PERCEIVED COACH SUPPORT ON HEAD IMPACT EXPOSURE METRICS IN YOUTH FOOTBALL

Madison E. Marks (1,2), William C. Flood (3,4), Joel D. Stitzel (1,2), Jillian E. Urban (1,2)

(1) School of Biomedical Engineering and Sciences
Virginia Tech - Wake Forest University
Winston-Salem, NC, USA

(2) Department of Biomedical Engineering
Wake Forest University
Winston-Salem, NC, USA

(3) Department of Radiology
Wake Forest University
Winston-Salem, NC, USA

(4) Department of Neuroscience
Wake Forest University
Winston-Salem, NC, USA

INTRODUCTION

Concussions continue to be a prevalent safety concern in contact sports due to their potential short-term and long-term neurodegenerative effects. Studies suggest that repetitive, non-concussive head impact exposure may lead to similar pathologies as those caused by concussion.[1,2] With approximately 3.5 million youth athletes (age 6-13) participating in football each year, it is essential to minimize head impact exposure to prevent future brain injury.[3-6] There is limited information on how individual-level determinants (i.e., characteristics internal to the individual) affect an athlete's head impact exposure.[7,8] Therefore, the objective of this study was to examine the effect of confidence in sports, perceived coach support, and competitive aggressiveness and anger in relation to head impact exposure in football.

METHODS

Thirteen (n=13) middle school level (ages 12-14) and 21 high school level (ages 14 -18) football players were enrolled in this study. Using the Head Impact Telemetry (HIT) System, head impact exposure data was collected from the participating athletes over the span of one season. Each athlete completed the Trait-Robustness of Self-Confidence Inventory (TROSCI)[9], the Sports Climate Questionnaire (SCQ)[10], and the Competitive Aggressiveness and Anger Scale (CAAS)[11] during the season. Head impact exposure was quantified in terms of total number of impacts as well as the median and 95th percentile linear and rotational acceleration. Risk Weighted Exposure (RWE), a cumulative exposure metric encompassing frequency and magnitude of impacts was calculated. Each metric was evaluated for the entire season and separately by exposure attributed to practices and games.

Data analysis was completed using SAS statistical software. The survey results (e.g., TROSCI, SCQ, CAAS) were compared against the biomechanical parameters using linear regression analysis to determine whether survey scores influenced the biomechanical data. Cook's distance was computed to remove outliers from each regression. Data were grouped for the entire sample (youth + high school) and stratified by level of play.

RESULTS

Combined Sample

The means and standard deviations for each survey score for the combined and individual teams are provided in Table 1, below. The TROSCI and SCQ scores for the entire sample were not significantly associated with any biomechanical parameter. The CAAS score for the entire sample was significantly positively associated with the number of impacts overall ($p=0.014$, $R^2=0.236$), number of impacts at practice ($p=0.015$, $R^2=0.198$), RWE overall ($p=0.035$, $R^2=0.145$), and RWE at practice ($p=0.026$, $R^2=0.183$). The CAAS score for the entire sample was negatively associated with the 95th percentile rotational acceleration at practice ($p=0.015$, $R^2=0.232$).

Table 1: Mean and standard deviation values for the teams.

Parameter	Team	Mean	Std. Dev.
TROSCI	Combined	43.09	10.20
	Middle School	42.31	12.05
	High School	43.57	9.150
SCQ	Combined	86.74	17.87
	Middle School	87.46	17.00
	High School	86.29	18.79
CAAS	Combined	29.88	10.86
	Middle School	26.69	9.437
	High School	31.86	11.42

Middle School Sample

The TROSCI score for the middle school team was significantly negatively associated with number of impacts during competition ($p=0.027$, $R^2=0.508$) and significantly positively associated with the linear acceleration during practices ($p=0.009$, $R^2=0.783$). The SCQ score for the middle school team was also significantly positively associated with the linear acceleration during practice ($p=0.008$, $R^2=0.800$); however, the SCQ score for the middle school team was significantly negatively associated with the number of impacts overall ($p=0.008$, $R^2=0.656$) and during practice ($p=0.042$, $R^2=0.542$), and RWE during practice ($p=0.037$, $R^2=0.553$). The CAAS score for the middle school team was significantly positively associated with the number of impacts overall ($p=0.006$, $R^2=0.687$) and RWE at practices ($p=0.021$, $R^2=0.572$).

High School Sample

The TROSCI and SCQ scores for the high school sample were not significantly associated with any biomechanical parameter. The CAAS score for the high-school-level team was significantly positively associated with the number of impacts overall ($p=0.036$, $R^2=0.574$) and significantly negatively associated with the 95th percentile rotational acceleration at practice ($p=0.023$, $R^2=0.284$).

Figure 1: Strong correlations observed for each team. (A) Linear acceleration at practice versus SCQ at the middle school level. (B) Number of impacts overall versus CAAS at the high school level.

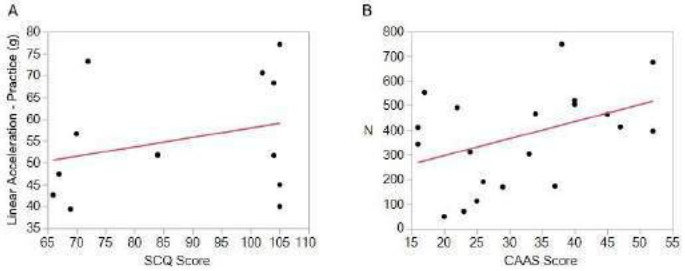

Differences Between the Samples

In evaluating the differences between the separate high school and middle school teams, the only significant parameters were the 95th percentile linear acceleration during practice ($p = 0.020$) and the 95th percentile rotational acceleration during competition ($p=0.005$). The middle school athletes had significantly higher linear acceleration at practice than their high school counterparts. The high school athletes had significantly higher rotational acceleration at competition than the middle school athletes.

DISCUSSION

This study examined the effect of confidence in sports, perceived coach support, and competitive aggressiveness and anger in relation to head impact exposure metrics for youth football. Trends were seen among all survey measures and many biomechanical metrics.

The CAAS score was positively correlated and the number of impacts (overall, practice) and RWE (overall, practice) for the entire sample. Among the high school sample, a significant positive association between CAAS score and the overall number of impacts was observed. Among the middle school athletes, overall number of impacts and RWE in practices were significantly positively correlated to the CAAS score. These results support that players with more aggressive tendencies may not only be more willing to engage in contact more frequently, but also involve themselves in riskier collisions, in general. The negative relationships between the CAAS score and rotational acceleration at practice was not expected. This implies that more aggressive and angry players might have less rotational acceleration at practice.

The positive relationship between TROSCI score and linear acceleration at practice, for the middle school team, may imply that athletes in this age range were more likely to quickly accelerate and engage in contact with greater force if they were more confident. The negative association between TROSCI score and number of impacts at competition could result from confident players engaging in less hits, possibly by outrunning or dodging opponents.

Linear acceleration at practice was found to be positively associated with SCQ score. Middle-school-level athletes have a lot of interaction with their coaches during practice; therefore, greater perceived coach support may indicate trust among the athletes and their coach. If harder hits are celebrated by the coaching staff, this may further encourage risky behavior to impress their coaches; however, the contrary may be true of athletes striving for more coach support. SCQ score was negatively associated with number of impacts, overall and during practice, and RWE during practice. Athletes who feel unsupported by their coaches might try to engage in more collisions in an attempt to earn support. In the same way, players with little perceived support might attempt to hit harder and subsequently experience more cumulative exposure over the season.

The significant difference between the rotational acceleration at competitions in high school and middle school samples is congruent with what was expected. High school athletes likely hit with more force and have more advanced skills which allow for them to better anticipate other players' moves and tackle from side positions. The significant difference between the linear acceleration at practices in high school and middle school samples could be explained by practice structure. High school practices might involve more advanced technical drills and focus less on head-on impacts, therefore causing those athletes to have less linear acceleration at practice. Both of the aforementioned differences could also be explained by player position. In high school, athletes have a dedicated position that they practice and compete in. This could lead to a specialization in tackling or dodging that increases the rotational acceleration as compared to middle school athletes. In middle school, athletes rotate through positions. They might have less position-specialized practice which would allow for players to experience the same high linear acceleration drills.

ACKNOWLEDGEMENTS

The authors thank the youth and high school football organizations who participated in this research. National Institutes of Health (NINDS R01NS094410, R01NS082453, and R01 NS091602). The National Center for Advancing Translational Sciences, (NIH KL2TR001421) supported Dr. Jillian Urban.

REFERENCES

[1] Stern, RA et al., *PM&R*, 3:S460-S467, 2011. [2] Stamm, JM et al., *Neurology*, 84(11): 1114-1120, 2015. [3] Guskiewicz, KM et al., *Am J Sports Med*, 28(5):643-650, 2000. [4] Powell, JW et al., *JAMA*, 282(10):958-963, 1999. [5] Daniel, RW et al., *Ann Biomed Eng*, 40(4):976-981, 2012. [6] Cobb, BR et al., *Ann Biomed Eng*, 41(12):2463-2473, 2013. [7] Schmidt, JD et al., *J Athl Train*, 51(5):366-372, 2016. [8] Sallis J, et al. In: Glanz K, et al, editors. Heal Behav Heal Educ Theory, Res Pract. 2015. p. 465–485. [9] Beattie, S et al., *Psychology of Sport and Exercise*, 12(2):184-191, 2011. [10] Deci, EL, et al., Sport Climate Questionnaire [Measurement instrument]. Retrieved from http://selfdeterminationtheory.org/pas-sport-climate/ [11] Maxwell, JP et al., *Psychology of Sport and Exercise* 8(2):179-193, 2006.

DEVELOPMENT AND MULTI-LEVEL VALIDATION OF A HUMAN AORTA MODEL FOR TRAUMATIC INJURY

W. Zeng, A. Caudillo, S. Mukherjee, M. Panzer

Center for Applied Biomechanics, University of Virginia, Charlottesville, VA, USA

INTRODUCTION

As one of the leading causes of fatalities in blunt impact, traumatic aortic injury (TAI) is only less prevalent than brain trauma [1]. However, there is no consensus on the injury mechanism of TAI in traffic accidents, mainly due to the complexity of occurrence scenarios, limited field data, and difficulty of reproducing testing conditions for TAI.

About 10 to 14% of traumatic aortic rupture (TAR) occurred at the ascending aorta according to a study on autopsy of victims [1]. Nevertheless, the most frequent site of fatal blunt TAR in traffic accidents, accounting for more than 50% deaths, was found to be at the aortic arch and peri-isthmic region, which is located on the junction between the aortic arch and the descending aorta [2]. Several hypotheses have been proposed to anatomically and/or mechanically explain the mechanisms underlying this injury during nonpenetrating thoracic trauma, e.g., the tethering by ligamentum arteriosum [3], deceleration of the thoracic aorta [4], "shoveling effect" theory [5], "water hammer" effect [6]. Based on testing using nine human cadaver thoraces, Forman et al. (2008) found that the posteriorly directed acceleration alone was not sufficient to generate TAR [7]. Otte et al. (2017) analyzed occurrence, frequencies and mechanisms of TAR in Germany during a 40 years' period (1973-2014), and found that the aortic rupture in most cases was caused by high compression force directly on the thorax [8]. In this work, a computational model of the aorta with nonlinear mechanical characteristics and accurate morphology was developed and integrated within a thorax finite element (FE) model that included all major anatomical structures. To maximize the model's capability for predicting TAI, a multi-level process was presented to validate the model comprehensively.

METHODS

The baseline model of the thorax used in this study was the GHBMC detailed mid-sized male occupant model (M50-O v4.5, by LS-DYNA), which included all major components that form the ribcage and internal organs. Fig. 1 displayed the FE model of the aorta and associated regions. The aortic wall model was created to include nonlinear behavior with a single mean thickness of t=2 mm [9]. The mechanical properties of the aortic wall in published studies exhibited a very large discrepancy [10–14]. Most of these investigations showed that the anisotropy of aorta tissue along longitudinal and circumferential directions was not significant [12,14], or even showed as isotropic without directional dependence [11,13]. As such, in this study we adopted *MAT_Simplified_Rubber (*MAT_181) constitutive model to characterize nonlinear aorta tissue behavior, and the input material response was defined by the mean stress-strain curve averaged from dynamic responses reported in Ref. [10] using fresh aorta tissues.

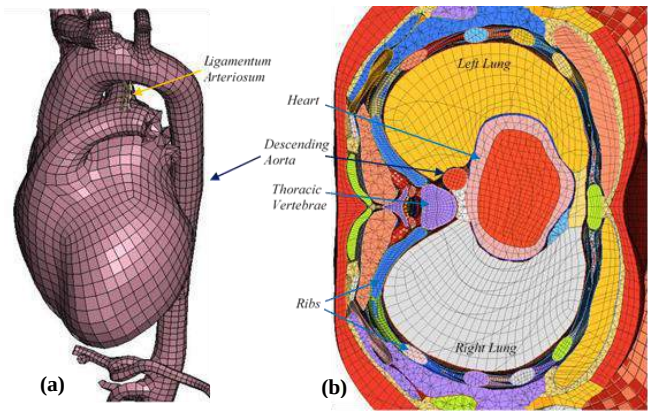

Figure 1: FE model of aorta and thorax: (a) aorta, ligamentum arteriosum and associated heart, and (b) cross-sectional view of the thorax model at T7 level.

Three different sets of experimental data were utilized to validate the developed aorta model. At component level, the *in vitro* aortic pressurization testing was simulated to mimic the aortic burst pressure before rupture [15]. Then, a sled test of a truncated cadaver was modeled

to evaluate aorta response under posterior acceleration [7]. The frontal chest pendulum impact was utilized to validate the performance of the aorta within full body model under direct chest compression [16]. A parametric study was implemented to determine a proper injury tolerance for the aorta under these different loading conditions.

RESULTS

For aortic pressurization, the simulated peak pressure before aorta rupture was 79.5 kPa (the failure threshold was set as MPS=55%), which was within the range of the experimental results [15]. For sled tests under posterior acceleration, the chest deflection and aorta pressure were examined and compared with the experimental data [7]. Fig. 2 compared the cross-sectional aorta pressure between simulation and experimental results. Following the validation by sled test, a validation case involving a chest pendulum impact was simulated. The overall thoracic model performance was evaluated by the force-deflection response under frontal chest pendulum impact. The simulated force vs. deflection response agreed well with the experimental corridor [16].

Our parametric study of aorta failure thresholds showed that when the MPS=50% was adopted as failure strain, several elements exceeded this failure threshold and were deleted on the aortic arch under both sled test and chest pendulum impact. However, the strains (MPS) of these elements were all less than 55%, so a failure threshold of MPS=55% ensured no injury on the thoracic aorta, which matched the results that no aortic injury was observed in the cadavers tested [7,16].

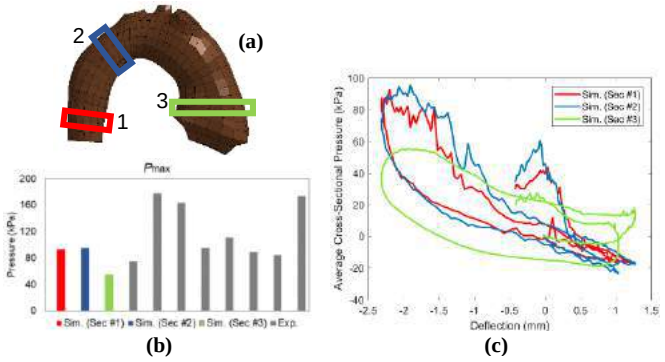

Figure 2: Cross-sectional aorta pressure: (a) three cross-sections selected for pressure measurement, (b) comparison of peak value of the averaged cross-sectional pressure between simulation and experimental data, (c) the cross-sectional pressure-deflection relationship.

DISCUSSION

The mechanism of traumatic aortic injuries remains controversial. Mechanically, major potential mechanisms of TAR associated with loading include excessive intra-aortic pressure, high thoracic acceleration, large stretching and tearing due to chest compression, etc. The primary goal of this study was to develop a computational model of the aorta for blunt traumatic injury prediction, focusing on accurate material and structural representation. To the authors' knowledge, the model developed in this work represents the first effort to provide a multi-level validated computational model capable of predicting traumatic aortic injury. At thorax level, the overall chest deflection was validated against sled testing subjected to posterior acceleration, and the force vs. deflection response of the model subjected to pendulum impact was validated against associated experimental corridor. At the component level of aorta, the peak intraluminal pressure before aortic rupture was validated by the burst pressure obtained from *in vitro* aortic pressurization data, and the cross-sectional pressure of thoracic aorta was validated against the measured pressure due to posterior acceleration. At aortic tissue level, the injury tolerance of aortic wall tissue was determined by the parametric study of tissue failure under all three different experimental testing conditions. Nevertheless, similar to developing other human body models, there are some limitations of this study which can be enhanced in future research. For example, the aorta rupture was not validated by impact loading along the lateral direction due to a lack of experimental data or details, as well as the difficulty to duplicate boundary and loading conditions from the tests [17]. It is expected that this work will encourage additional modeling, validation and biomechanical studies of aortic injuries. The developed aorta model integrated with the thorax FE model will serve as a valuable tool for safety researchers and automobile designers to predict, prevent, and mitigate aortic injuries due to vehicle crashes. In a larger scope, this study provides a framework to improve and validate the biofidelity of future computational human body models for injury prediction and prevention.

ACKNOWLEDGEMENTS

This work was supported by the Global Human Body Models Consortium (GHBMC).

REFERENCES

[1] Watanabe K, et al., *Surg Today* 43: 1339–1346, 2013.
[2] Burkhart HM, et al., *J Trauma* 50: 113–115, 2001.
[3] Cavanaugh J, et al., *SAE Tech Paper* 2005-01-0304, 2005.
[4] Cammack K, et al., *AMA Arch Surg* 79: 244–251, 1959.
[5] Voigt EG, & Wilfert K, *SAE Tech Paper* 690811, 1969.
[6] Lundevall J, *Acta Pathol Microbiol Scand* 62: 34–46, 1964.
[7] Forman J, et al., *J Biomech* 41: 1359–1364, 2008.
[8] Otte D, et al., *J Forensic Biomech* 8: 132, 2017.
[9] Mensel B, et al., *Acad Radiol* 20: 1004–1008, 2013.
[10] Mohan D, & Melvin JW, *J Biomech* 15: 887–902, 1982
[11] Okamoto RJ, et al., *Ann Biomed Eng* 30: 624–635, 2002.
[12] Matsumoto T, et al., *J Biomech Sci Eng* 4: 518–529, 2009.
[13] Azadani AN, et al., *Ann Thorac Surg* 93: 87–94, 2012.
[14] Martin C, et al., *Acta Biomater* 9: 9392–9400, 2013.
[15] Bass CR, et al., *Stapp Car Crash J* 45: 143–160, 2001.
[16] Kroell C, et al., *SAE Tech Paper* 741187, 1974.
[17] Viano DC, *Stapp Car Crash J* 33, 113–142, 1989.

ALTERATION OF INTRINSIC BRAIN MOTION AFTER ENDOSCOPIC THIRD VENTRICULOSTOMY TREATMENT IN NEONATAL HYDROCEPHALUS

A. Pionteck (1), M. Rao (2), P. Morgenstern (3), M. Kurt (1,4)

(1) Dept. of Mechanical Engineering, Stevens Institute of Technology, Hoboken, NJ, USA

(2) Icahn School of Medicine at Mount Sinai, New York, NY, USA

(3) Dept. of Neurosurgery, Icahn School of Medicine at Mount Sinai, New York, NY, USA

(4) BioMedical Engineering and Imaging Institute, Icahn School of Medicine at Mount Sinai, New York, NY, USA

INTRODUCTION

Pediatric hydrocephalus (PHC) has a significant human and economic cost making it a national and international public health problem. Complications such as permanent neurological deficits, worsening of neurocognitive outcomes and even death can occur with or without treatment [1]. Post-hemorrhagic hydrocephalus (PHH), with its long-term repercussions, is one of the most serious complications associated with prematurity. 8-38% of low birth weight infants who developed germinal matrix-intraventricular hemorrhage (IVH) during their NICU stay (approximately 20% [2]) will develop hydrocephalus requiring surgical intervention [3]. A combination of clinical and radiographic measures is currently used to diagnose hydrocephalus. In infants, clinical signs include cardiopulmonary instability, rapid head growth, a bulging fontanelle, splaying calvarial sutures and, sometimes, lethargy or vomiting in the most severe cases. Hydrocephalus is diagnosed in association with brain imaging demonstrating enlarged ventricles. Current standard of care for the management of PHC is cerebrospinal fluid (CSF) diversion in the form of ventriculoperitoneal shunt (VPS) placement. Recent studies have analyzed the biochemical profiles of CSF in hydrocephalus, to better understand the pathophysiology of the disease and identify candidate biomarkers of diagnostic and therapeutic value [4]. Despite advances in the field, for example concerning soluble amyloid precursors proteins [5] or markers of extracellular matrix upregulation [6], there is a need for additional tools and strategies for the management of neonatal PHC patients. Since intrinsic brain motion, driven by cardiac pulsatility, is directly coupled with the CSF dynamics, it appears as a potential candidate biomarker for PHC. It has been well established in prior studies that brain dynamics and movement patterns are altered in brain pathologies such as Chiari Malformation type 1 (CM1) [7] and cerebral aneurysms [8]. However, the periodic deformation and movement of the brain associated with hydrodynamic pulsatility are subtle, making them difficult to visualize and quantify on traditional cine MRI images such as phase-contrast cine MRI [9] or DENSE MRI [10]. Recently, we have applied the amplified MRI (aMRI) processing method [11], [12] to Chiari malformation Type I. Using this technique, sub-voxel motion of the brain can be quantified through video amplification and denoising [13]. Considering the pathophysiological variations in CSF dynamics in neonatal hydrocephalus patients, changes in intracranial pressure and CSF flow during the development of hydrocephalus are likely to change brain motion. In this study, we analyzed aMRI scans of a neonate hydrocephalus patient before and after surgery, thereby demonstrating the perturbations in brain motion induced by the pathophysiologic state of pediatric hydrocephalus. By comparing pre-surgery and post-surgery brain motion, we will identify potential markers that could aid in the initial diagnosis of pediatric hydrocephalus.

METHODS

Neonatal patient: The patient is an infant born at 31 weeks gestation by planned Caesarian section for progressive fetal ventriculomegaly. He underwent brain MRI on day of life 1 and was diagnosed with congenital aqueductal stenosis (AS). He was monitored in the neonatal intensive care unit (NICU). His ventriculomegaly progressed and he experienced increasing bulging of his fontanelle with apneic and bradycardic events, prompting surgical treatment with endoscopic third ventriculostomy with choroid plexus cauterization (ETV-CPC) on day of life 22. After surgery he underwent repeat MRI on day of life 30 to demonstrate patent ETV and reduced ventriculomegaly. His post-operative course was uncomplicated.

Imaging protocol: With IRB approval and informed consent, scans were performed on the hydrocephalus patient using a 3T MR imaging system (Skyra, Siemens Healthcare AG, Germany) with a 16-channel

head coil at Icahn School of Medicine at Mount Sinai. 3D cine MRI were acquired using the following imaging parameters: acquisition matrix = 256 x 246, flip angle = 25-26◦, FOV = 180×180 mm^2, TR/TE=17.52/1.82 ms, pixel bandwidth = ±700 kHz, 17-19 cardiac phases, and 14 slices with 2 mm thickness.

3D aMRI algorithm and motion tracking: The aMRI method first applies a spatial decomposition through a complex steerable pyramid [14] to retrospective cardiac-gated cine MRI data. This is followed by temporal filtering and amplification of the MRI cardiac-gated frames with a specific amplification factor ($\alpha = 20$) before synthesizing a motion-amplified cine data set. As a result, aMRI enables subtle motion of the brain to be visualized. To perform the motion tracking of amplified displacement, we used a non-parametric diffeomorphic image registration based on the Demons algorithm. The original Demons algorithm could be considered as an optimization procedure over the whole displacement field space. This optimization procedure was adapted to a diffeomorphic transformation space, to achieve transformations smoother and closer to reality. The final output of this function is a volumetric displacement field which gives a 3D direction and magnitude for each voxel.

RESULTS

After amplification, pre-surgery and post-surgery displacement fields were acquired with Demons registration algorithm (Fig. 1). Ventricles were masked and excluded from the registration algorithm, since these regions showed flickering due to high CSF flow, creating artifacts that interfered with the measurement of displacement. In post-surgery brain volume, a cavity in the forehead was also excluded (Fig. 1b).

In pre-surgery data, a maximum displacement of 0.56 pixels was observed in the top of the brain, between frontal and parietal lobes. The distribution of displacement in the rest of the brain was inhomogeneous, with a mean displacement around 0.30 pixels and localized regions of higher displacement. The density of these higher displacement spots was lower in the occipital lobe region. In post-surgery data, a maximum displacement of 0.98 pixels was observed in the pons region. High displacement spots were located in the pons and cerebellum area. Displacement is the rest of the brain was low and homogeneous, with an average displacement of 0.10 pixel, except for a high displacement spot located in the occipital lobe where the displacement reaches 0.62 pixels.

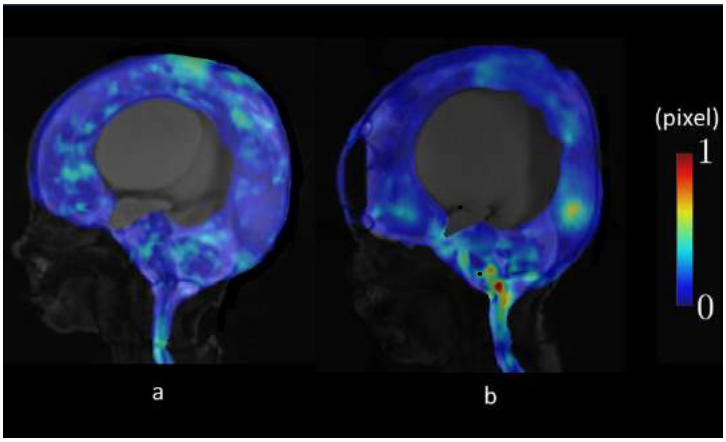

Figure 1: Comparison between pre-surgery (a) and post-surgery (b) amplified displacement fields.

DISCUSSION

In this work, 3D aMRI method was used to compare pre-surgery and post-surgery brain motion in pediatric hydrocephalus patient. Qualitatively, we observed that the brain motion pattern was considerably modified by the surgery. After surgery, high displacement spots were located in pons and cerebellum, when they were located at the top parietal lobe before. Maximum displacement value was also noticeably increased post-surgery, while the displacement field in the rest of the brain is more homogeneous with a lower average value. We hypothesized that changes in intracranial pressure and CSF flow during the development of hydrocephalus were likely to change brain motion. We observed with this case that before surgery, abnormal CSF flow led to unusual high displacement in the parietal lobe and low motion in pons, cerebellum and other hindbrain structures. Then, the surgery has restored normal CSF circulation. This resulted in a motion pattern similar to that observed in healthy subjects [15], with higher displacement located in pons and cerebellum. These results confirmed our hypothesis by showing that, for this case, the abnormal CSF circulation resulted in a measurable change in the brain motion. Absence of high displacement in pons and cerebellum could then be identified as a potential marker for the diagnosis of pediatric hydrocephalus.

Our results showed 3D aMRI's capability as a potential diagnostic tool for pediatric hydrocephalus. With this tool, we demonstrated the differences in brain motion pattern of a pediatric hydrocephalus patient, before and after surgery. This first case seems to confirm that the analysis of brain movements with 3D aMRI is a valid tool to help for the diagnosis, but also to evaluate the success of a surgery and to give proper indications on the prognosis. As a future work, we would recruit more neonatal hydrocephalus patients to assess if the marker identified in this study is generalizable and to confirm that motion analysis with 3D aMRI is feasible and useful in a clinical context.

ACKNOWLEDGEMENTS

This research was partially supported by NSF CMMI 1953323 and NIH Grant No. 1R21NS111415.

REFERENCES

[1] Gupta N., *Journal of Neurosurgery*, 2007, doi: 10.3171/ped.2007.106.5.334.
[2] Inder T. E., *Volpe's Neurology of the Newborn*, Elsevier, 2017, pp. 637–698.
[3] Chen Q., *Journal of the Neurological Sciences*. 2017, doi: 10.1016/j.jns.2017.01.072.
[4] Merhar S., *Neonatology*. 2011, doi: 10.1159/000323498.
[5] Limbrick D. D., *PLoS ONE*, 2017, doi: 10.1371/journal.pone.0172353.
[6] Limbrick D. D., *Pediatric Neurosurgery*. 2017, doi: 10.1159/000477175.
[7] Pujol J., *Neurology*, 1995, doi: 10.1212/WNL.45.9.1746.
[8] Oubel E., 2007, doi: 10.1117/12.708937.
[9] Enzmann D. R., *Radiology*, 1992, doi: 10.1148/radiology.185.3.1438741.
[10] Aletras A. H., *Journal of Magnetic Resonance*. 1999
[11] Holdsworth S. J., *Magnetic Resonance in Medicine*, 2016, doi: 10.1002/mrm.26142.
[12] Terem I., *Magnetic Resonance in Medicine*, vol. 80, no. 6, pp. 2549–2559, Dec. 2018, doi: 10.1002/mrm.27236.
[13] Wadhwa N., *ACM Transactions on Graphics*, 2013, doi: 10.1145/2461912.2461966.
[14] Simoncelli E. P., 1995, doi: 10.1109/icip.1995.537667.
[15] Abderezaei J., *BMES*, 2020, Virtual

EVALUATION OF THE SEEDING EFFICIENCY OF A CUSTOM-DESIGNED SEED-AND-CULTURE PERFUSION BIOREACTOR FOR ENGINEERED TISSUE VASCULAR GRAFTS

Sarah K. Saunders (1), Joao S. Soares (1)

(1) Department of Mechanical and Nuclear Engineering
Virginia Commonwealth University
Richmond, VA, USA

INTRODUCTION

Tissue engineering aims to create viable and functional engineered tissues via biodegradable scaffolds and autologous cells. Scaffolds play an essential part in organizing the architecture of developing tissues and aid in the proper function of implants acutely by serving as mechanical support and long-term by degrading and undergoing absorption as *de novo* tissue is produced. Typically, isolated autologous cells are seeded onto the polymer scaffold to begin forming viable three-dimensional tissues *in vitro*. These 3-D tissue structures are then deployed *in vivo* where they trigger biological mechanisms for repair, remodeling, and growth to continue developing over time. Biodegradable polymers are preferred as they are easy to manipulate in terms of mechanical strength, degradation rate, and permeability and the porous scaffolds will degrade as new tissue forms resulting in a fully functioning replacement [1]. However, some cases require the seeding of cells onto irregular constructs, which can prove challenging.

Engineered tissue vascular grafts (ETVGs) requires cell seeding onto small diameter tubular scaffolds. The tubular geometry makes it difficult to efficiently deliver cells onto the scaffold surface evenly. Many existing techniques are hampered by the length of time required and complexity of the procedure; however, continued investigation and improvement of methods is essential. Optimizing seeding efficiency relieves current research constraints related to cell availability, prolonged culture protocols, and mechanical and physiological performance. Here, we compare a bioreactor mediated perfusion-seeding method against traditional drip seeding in seeding efficiency. We aim to establish perfusion-seeding as a reliable method for creating engineered tissue vascular grafts for further experiments.

METHODS

A solution of polycaprolactone (PCL; Mn = 80,000) at 14 wt% (w/w) in 1/1 DMF/THF was used for electrospinning of tubular scaffolds suitable for small diameter ETVGs. Resulting scaffolds where approximately 40 mm long, 2 mm in diameter, and 200 µm thick. SV40LT-SMC cells were cultured and expanded in DMEM containing 10% FBS and 200 mcg/mL G418. Between passages 4-6 cells were lifted, isolated and seeded onto scaffolds at a density of approximately 15,000 cells/mm^2 with three distinct methods (Figure 1).

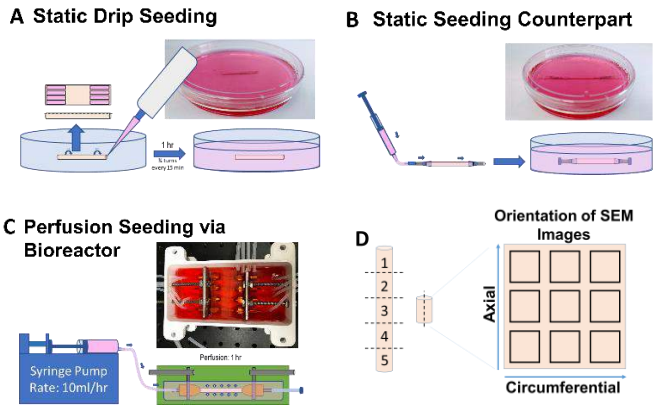

Figure 1: A) Drip seeding method. B) Static counterpart method. C) Perfusion seeding method. D) diagram of scaffold sample orientation for SEM analysis.

A. Static Drip Seeding: using standard seeding procedures, a concentrated cell suspension is carefully pipetted directly onto the lumen of each scaffold. Seeded scaffolds were placed in separate wells, incubated for 1 hour at 37°C, and rotated every 15 minutes. Then the ETVGs were submerged in media with 15% FBS and left in the incubator overnight.

B. Static Seeding Counterpart: Scaffolds were mounted onto shortened cannulas and filled with cell suspension. Scaffolds were then submerged in cell media and left overnight.

C. Perfusion-Seeding: Scaffolds were mounted into our custom bioreactor and seeded via transmural perfusion for 1 hour. After initial seeding the pressure is released and cells are allowed to rest overnight.

After the incubation period (24 hr) is complete, ETVGs are collected and split into 5 sections to be evaluated individually with the goal of characterizing the seeding efficiency of each method across the full length of the scaffold (Figure 1D). We use SEM imaging to evaluate surface coverage over the entire length of the scaffold. We verify cell viability via alamarblue assays. Transmural penetration of cells into the scaffold and phenotype after seeding is evaluated via histology and immunofluorescence. We assessed gross morphology with H&E; collagen with picrosirius red and collagen I and III antibodies; VSMC viability, density, shape, orientation (DAPI), and phenotype with α-SMA and SM-MHC.

RESULTS

Our custom-made bioreactor houses 4 scaffolds for perfusion-seeding and subsequent culture. To test its performance as a perfusion-seeding method, we first mounted scaffolds and perfused dyed fluid through them while taking transluminal pressure readings. Throughout the experiment, dye perfused evenly along the length of the scaffold, and transmural pressure differential never reached over 1 psi through the course of the 1-hour perfusion seeding period at a rate of 10ml/hr. We have verified with SEM imaging that perfusion seeding caused no damage to the microstructure of the luminal surface of the PCL scaffold.

We compared perfusion-seeding against more traditional methods and analyzed seeding efficiency with qualitative and quantitative imaging methods. For SEM imaging, each section was imaged in a 3x3 grid to give an approximate view of the total cell coverage of the luminal surface of the entire scaffold (Figure 1D). SEM only provides a topographical view of the scaffold surface, so individual cells are difficult to pick out, and thick layers of cell aggregates appear as "sheets" covering the scaffold surface (Figure 2). Static seeding methods lead to a concentration of cells along the "bottom" of the scaffold due to gravitational forces. Static seeding methods resulted in a "sheet" of cells forming along the surface of the scaffold, while perfusion methods showed cells penetrating the first luminal layer of scaffold fibers. Drip seeding showed the least amount of cell coverage, mostly restricted to the bottom and both ends of the scaffolds. Histology and immunofluorescence results have corroborated with the those obtained via SEM. Results of viability assays with alamarblue to verify that our perfusion seeding does not impair cell function and they remain viable are currently in progress.

DISCUSSION

The challenges of developing any engineered tissue construct include: (1) determining the appropriate/necessary functional requirements; (2) finding how to engineer an implant meeting them; and (3) predicting its performance after implantation. For ETVGs, a robust cell layer in luminal surface could be beneficial for the continued remodeling of *de novo* tissue after implantation, and relieve problems associated with the development of impenetrable interstitial thrombus [2]. The favored

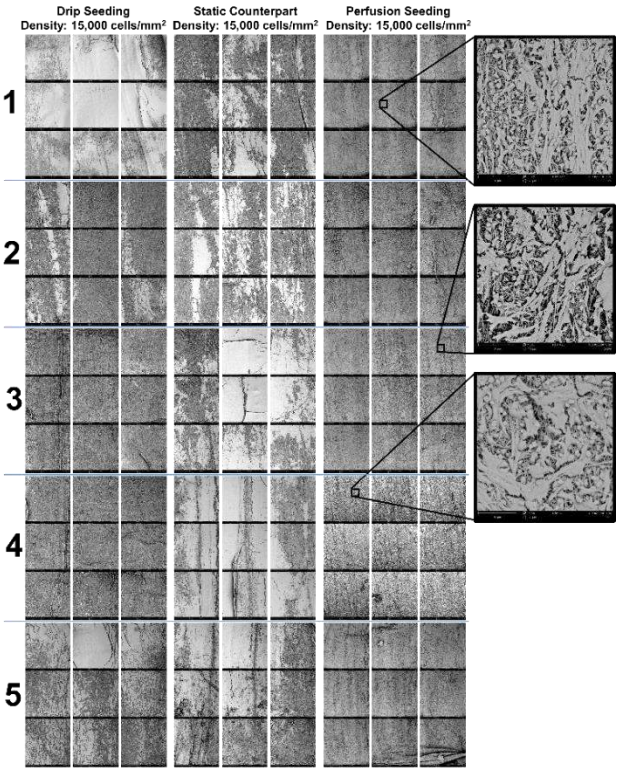

Figure 2: The luminal surface of each scaffold captured with SEM imaging.

methodology to obtain ETVGs is functionalized acellular scaffolds with morphogenic cues to stimulate the regeneration of vascular tissue *in situ* [3]. While this method conceptually shows great promise, the lack of transanastomotic outgrowth of endothelial cells in humans compared to animals and resultant lack of cells in the medial section of ETVGs *in vivo* still poses a serious issue [2].

Our method, like many others, involves bioreactor-mediated *in vitro* culture of ETVGs. However, perfusion-seeding methods are used sparingly, and even fewer attempt to seed ETVG scaffolds on their luminal surface. We believe that creating luminal VSMC layers may serve as a precursor for a basement membrane and help shield the blood-contacting surface from possible inflammatory response initiated by the foreign body response to the implant. We also hypothesize that a confluent VSMC layer will aid in the retention and proliferation of endothelial cells and regulate gene and protein expression essential for native vascular function. The next steps of our research would include extended *in vitro* culture studies, characterization of the mechanical properties of the ETVGs after full term *in vitro* incubation, and pilot studies with small animal models to investigate the host *in vivo* response.

ACKNOWLEDGEMENTS

This research was funded in part by the American Heart Association Predoctoral Fellowship Award 20PRE35210730 to SKS, 2017 VCU Pauley Heart Center Pilot Grant, and 2018 Virginia Commonwealth University Presidential Research Quest Fund.

REFERENCES

[1] Wu, J et al., *Colloids Interface Sci. Commun.*,23:34-44,2018.
[2] Zilla, P et al., *Biomaterials*, 28:5009-5027, 2007.
[3] Lawson, J et al., Lancet, 387:2026-2034, 2016.

COMPARATIVE ANKLE-FOOT ROLLOVER SHAPE ANALYSIS OF POWERED AND UNPOWERED PROSTHETIC FEET IN INDIVIDUALS WITH TRANSFEMORAL AMPUTATION

M. Poppo (1), A. Hansen (2,3), J. Chomack (1), J. Maikos (1)

(1) Veterans Affairs New York Harbor Healthcare System
New York, NY, USA

(2) Minneapolis Department of Veterans Affairs Health Care System
Minneapolis, MN, USA

(3) Rehabilitation Science & Biomedical Engineering
University of Minnesota
Minneapolis, MN, USA

INTRODUCTION

As prosthetic technology evolves, advanced devices for individuals with lower extremity amputation strive to offer more biomimetic features and benefits to users. The Empower (Ottobock, Germany) is one of the most advanced ankle-foot devices currently on the market offering powered push-off at terminal stance. As this technology becomes more widely available, it is important to understand how these devices affect critical gait parameters, such as ankle-foot roll-over shape characteristics. The objective of this preliminary analysis was to determine the effects of using an Empower ankle-foot device (PWR), as well as a device-specific PT intervention, on dynamic function (effective foot length ratio (EFLR), instantaneous radius of curvature (IROC), and radius of curvature (ROC)) for individuals with transfemoral amputation (TFA) compared to traditional energy storing and returning (ESR) prosthetic feet.

Ankle-foot roll-over shape characteristics may be critical in advancing our understanding of the most effective prosthetic designs, which can aid in evidence-based clinical practice and prosthesis prescription guidelines. We hypothesized that the PWR foot would generate roll-over shape characteristics that would suggest improved dynamic functionality compared to ESR feet. We also hypothesized that the PT group would generate improved roll-over shape characteristics at 4 and 8 weeks compared to the non-PT group.

METHODS

Motion capture and kinetic data were captured for 5 people with unilateral TFA during overground walking at the Veterans Affairs New York Harbor Healthcare System (VA NYHHS). Participants were biomechanically assessed at baseline on their current ESR foot and then fit with the Empower device. Participants were then randomized to two different groups during the initial 4 weeks of acclimation to the PWR foot. One group received the standard of care (non-PT group), which included training on the proper use and care of the foot by the study prosthetist and physical therapist (2 participants). The second group also received standard of care, but additionally underwent twice weekly, device-specific PT sessions with the study physical therapist (3 participants) (PT group). The PT program specifically targeted strengthening muscle groups to potentially improve the effectiveness of the PWR foot. Each patient completed a baseline data collection using their ESR foot as well as data collections after acclimating to the PWR foot for 4 and 8 weeks. Center of pressure (COP) data were transformed into the shank coordinate system during single limb stance. EFLR, a measure of the percentage of the foot that is effectively used during a step, was calculated as the distance from the prosthetic heel to the most anterior point of the COP progression divided by the overall length of the foot. Circular arcs of best fit were also applied to the COP data to determine roll-over shape characteristics, such as height-normalized ROC [1]. The IROC was calculated by evaluating the first derivative of COP forward travel with respect to shank angle. The peak IROC is representative of the fastest COP forward travel.

RESULTS

Figure 1 shows that EFLR of the ESR foot at baseline had a value of 0.67±0.04. The PWR foot at 4- and 8-weeks had EFLR values of -0.61±0.04 and 0.60±0.05, respectively for all subjects (n=5). A one-way between subjects Analysis of Variance (ANOVA) suggested a trend toward lower EFLR values of the PWR foot at 4- and 8- weeks compared to the ESR foot ($p=0.07$). Furthermore, the PWR foot at 4- and 8- weeks had peak IROC values of 25.8±7.9 cm and 23.8±4.0 cm, respectively, while the ESR foot at baseline had an average peak IROC value of 31.5±10.7 cm, although differences were not significantly different ($p=0.37$ and $p=0.17$ for 4- and 8- weeks respectively). The

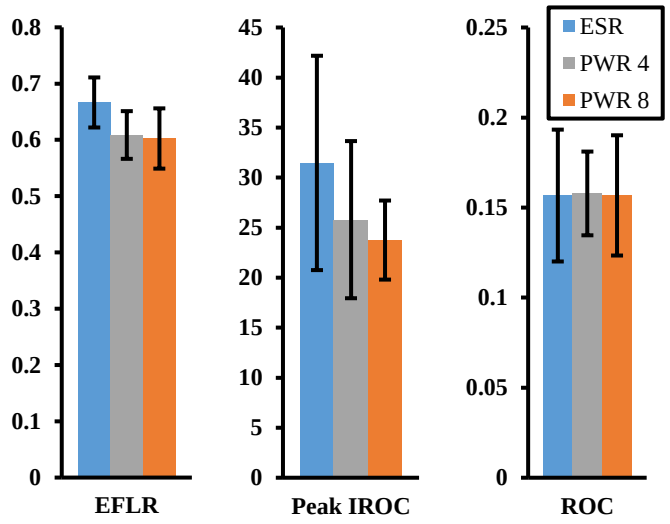

Figure 1: Average EFLR, Peak IROC (cm), and height-normalized ROC for ESR, PWR 4, and PWR 8.

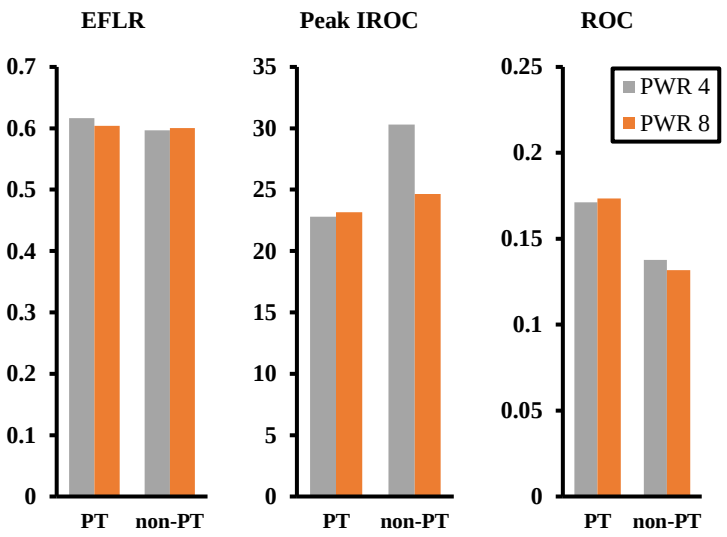

Figure 2: Comparison of PT and non-PT groups average EFLR, Peak IROC (cm), and height-normalized ROC.

height-normalized ROC of the ESR and PWR feet at 4- and 8- weeks were nearly identical (0.16±0.04 ESR; 0.16±0.02 PWR 4; 0.16±0.03 PWR 8).

Figure 2 represents a comparison of ankle-foot rollover shape characteristics between the PT and non-PT PWR groups, though statistical analysis between these groups was not conducted due to the small sample size. Figure 2 shows that the EFLR for the PT group after 4 weeks had a value of 0.62±0.05, while the non-PT group after 4 weeks had an EFLR value of 0.60±0.05. The EFLR of the PT and non-PT groups was similar at 8 weeks (0.60±0.07 and 0.60±0.06, respectively). After 4 weeks, the PT group averaged peak IROC values of 22.8±4.4 cm compared to the non-PT group 30.3±11.9 cm, however peak IROC results may be skewed by an outlier. Finally, the height-normalized ROC for the PT group at 4- and 8- weeks were both 0.17±0.01. The non-PT group had height-normalized ROC values of 0.14±0.03 at 4 weeks and 0.13±0.05 at 8 weeks.

DISCUSSION

The ELFR of the PWR foot at both 4- and 8-weeks showed a trend of being reduced in comparison to the ESR foot. This indicates that the COP did not progress as far anteriorly during single leg stance, which may correlate to a reduced ankle lever arm in late stance, decreasing walking efficiency. Reduced EFLR effectively shrinks the lever arm, potentially limiting the transmission of joint power that the PWR foot is designed to produce. This could highlight an area of improvement for the PWR foot as ESR foot designs may emulate more efficient passive mechanical properties. Although currently only 3 subjects, the PT intervention may slightly improve EFLR after the 4-week PT intervention compared to the non-PT group. This may indicate that a device-specific PT intervention can improve anterior progression of the COP during single-leg stance, improving the walking efficiency of the PWR foot. However, the acute effects were not sustained beyond the PT intervention as shown by the lower EFLR at 8-weeks in Figure 2. This suggests the need for a more-focused home exercise program to help sustain the long-term EFLR improvements. As more participants complete the protocol, EFLR may become a key parameter that shows improvement from a PT intervention.

The PWR foot also demonstrated decreased forward travel, as indicated by lower peak IROC compared to ESR feet, which suggests reduced stability [2]. Figure 2 shows that the non-PT group showed slightly higher peak IROC compared to the PT group however, the non-PT group saw a reduction in peak IROC from 4 to 8 weeks. PT training focused on initiating pelvis movement may have promoted a smoother transition from heel to toe rocker.

This preliminary data set showed no overall differences in ROC between the ESR and PWR feet. Potential differences in ROC can be seen between the PT and non-PT groups, though ROC values did not change from 4 to 8 weeks for either group. The non-PT group showed reduced ROC compared to the PT group. This result could suggest improved stability for the PT group during single leg stance because the foot is rotating about a larger rocker which may be resultant from focused muscle strengthening over the 4-week intensive PT program.

Although large changes in roll-over shape parameters have been shown to affect aspects of gait, it is unclear if the changes seen in this study are clinically relevant. Of note, the PWR foot is specifically designed to provide powered plantarflexion at terminal stance and is therefore not active during the single limb stance phase in which this analysis was conducted. This preliminary analysis of ankle rollover shape characteristics suggests that overall, the PWR foot may exhibit less efficient passive mechanical properties than the ESR feet. The PT group is showing trends of improvement in some parameters and may generate benefits over the standard of care. These results can inform clinicians of the benefits of prescribing the PWR foot along with a device-specific treatment. Additionally, manufacturers can design new componentry and devices to improve the current design with more attention to the passive components.

ACKNOWLEDGEMENTS

This work was supported by a DoD Orthotics and Prosthetics Outcomes Research Program grant (W81XWH-17-1-0568). We would also like to acknowledge our collaborators at Walter Reed National Military Medical Center.

REFERENCES

[1] Hansen, A. et al. *Clinical biomechanics (Bristol, Avon)*, *19*(4), 407–414, 2003.

[2] Curtze, C. et al. *Journal of biomechanics*, *42*(11), 1746–1753, 2009.

THE EFFECT OF HEMATOCRIT ON THE VISCOELASTIC BEHAVIOR OF EMBOLUS ANALOGS

Bryan C. Good (1)

(1) Mechanical, Aerospace, and Biomedical Engineering
University of Tennessee
Knoxville, TN, USA

INTRODUCTION

An estimated 700,000 acute ischemic strokes (AIS) occur each year in the Unites States, as a result of embolic occlusion of a cerebral artery. In spite of the improved recanalization rates of cerebral arteries, by means of novel stent retriever devices, 15% of patients' arteries still cannot be recanalized. In addition, 17% of patients with successful arterial recanalization die within 90 days [1]. Currently there is little understanding as to why some thromboemboli are successfully removed, and others are not. In order to improve our understanding of thromboemboli adhesion and removal in AIS, we must first be able to characterize their mechanical properties and accurately model their behavior. Therefore, we are developing embolus analogs (EAs) from bovine whole blood to mimic the properties of human thromboemboli in AIS patients and experimentally measuring their complex viscoelastic properties.

METHODS

EAs were created from bovine blood collected in CPDA-1 anti-coagulated bags (LAMPRE Biological Laboratories, Pipersville, PA). The whole blood was then separated into its components using a centrifugation protocol and reconstituted to maintain consistent concentrations of red blood cells (RBCs) and platelet-rich plasma (PRP). Coagulation of the reconstituted blood was initiated with the introduction of $CaCl_2$ at a concentration of 20 mMol in blood and allowed to clot for four hours in one of two methods: 1) statically in 50 ml falcon tubes or 2) dynamically on an orbital shaker in 6-well plates. The cylindrical falcon tube clots were cut with a scalpel into disk shapes that were less than half as thick as they were wide to avoid buckling during compressive loading (approximately 20 mm diameter and 10 mm thickness). The well plate clots were removed from their individual wells and tested as is (approximately 30 mm diameter and 12 mm thickness). The exact thickness and diameter of each individual sample was measured prior to testing using digital calipers.

Figure 1: Cyclic compression testing of dynamically formed EAs to measure their viscoelastic behavior.

To investigate the effect of hematocrit on EA mechanical properties, the separated RBCs and PRP were recombined at varying ratios from 0% to 60% hematocrit in 10% increments to represent the range of clot compositions seen clinically. Two different cyclic compression testing protocols were used with a Single Column Materials Testing System and a 50N load cell (Instron, Norwood, MA). All samples were pre-loaded to 0.01 N and then cyclically compressed for four cycles to allow for preconditioning [1]. The first protocol, applied to the static EAs, consisted of compressing the clots to 50% of their original thickness at a rate of 0.1 Hz, while the second protocol was conducted at 1 Hz. These protocols were chosen to investigate any differences in loading frequency and with the 1 Hz frequency to closely mimic the expected loading conditions of lodged thromboemboli in cerebral arteries under 60bpm pulsatile blood flow. A total of eight samples were tested and averaged for each composition and loading condition, with blood coming from two separate donor animals (n = 4 for each).

RESULTS

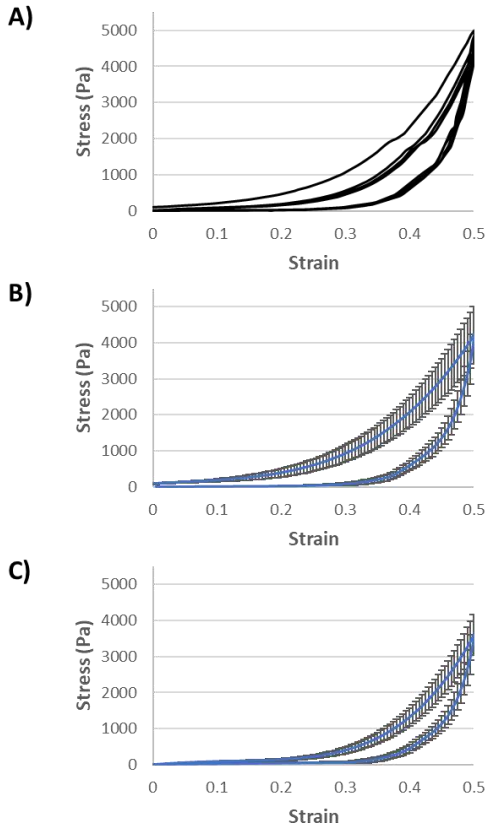

Figure 2: A) An example stress-strain cyclic loading curve for a single 50% hematocrit EA loaded at 0.1 Hz. Averaged data of the B) first cycle and C) fourth converged loading cycles for eight 50% hematocrit EAs.

As observed in **Fig. 2**, the bovine EAs exhibited hyperelasticity, hysteresis (an indication of viscoelasticity [2-4]), and cyclic softening. Example stress versus strain data for a single EA is shown in **Fig. 2A**. Cyclic softening is also clearly observed over the initial loading cycles, but an approximately cyclic steady state was achieved by the third cycle. The averaged stress-strain response from both the first and final (converged) loading cycles for the 50% hematocrit EAs loaded at 0.1 Hz are shown in **Figs. 2B** and **2C**, respectively. Peak stresses at 50% compression were measured to be 6302 ± 1203 Pa during the first loading cycle and 5395 ± 828 Pa in the final converged loading cycle. Under monotonic compressive loading, the EAs behaved linearly up to a strain of approximately 10% with an elastic modulus of 979 ± 157 Pa.

In **Fig. 3**, stress-strain data is shown for EAs of varying hematocrit under 1 Hz compressive loading conditions during the fourth converged loading cycle. As hematocrit increased, from 0-60%, there was a drop in maximum applied stress (19,500 Pa to 11,700 Pa, respectively). Additionally, large differences were observed in the results from **Fig. 2** to **Fig. 3**, with the higher loading frequency (1 vs. 0.1 Hz) leading to larger applied stresses.

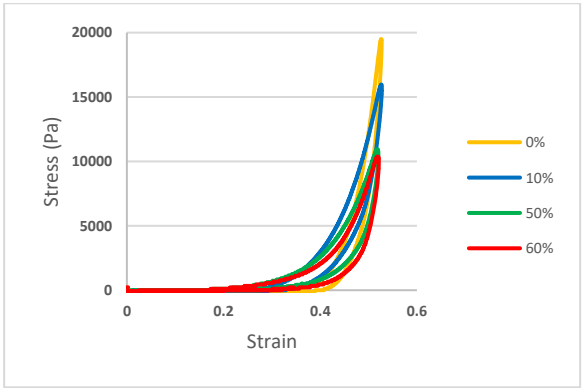

Figure 3: Stress-strain cyclic loading curves for 0, 10, 50 and 60% hematocrit EAs loaded at 1 Hz.

DISCUSSION

These results clearly display a viscoelastic behavior of EAs that is highly dependent on both the amount of RBCs and plasma in their composition as well as the cyclic loading conditions used for mechanical testing. Both higher frequency loading and decreased levels of RBCs both led to larger peak stresses.

Future work will further elucidate the effects of cyclic frequency to determine how clots could behave differently *in vivo* depending on how they are loaded during mechanical thrombectomy procedures. Additionally, EA compositions will be further investigated histologically to determine if the distribution of RBCs, platelets, and fibrin within the EA structure has an influence over their mechanical behaviors.

REFERENCES

[1] Grech, *et al.* 2015. The Neuroradiology Journal.
[2] Humphrey *et al.* 2003. Mathematical, Physical, and Engineering Sciences.
[3] Fung and Cowin. 1993.
[4] Holzapfel *et al.* 2002. Eur J of Mech A-Solid.

DEVELOPING COMMUNITY TO SUPPORT FIRST GENERATION FRESHMAN IN AN ENGINEERING PROGRAMMING COURSE

Sara E Wilson (1,2), Molly A McVey (1), Nolan M Norton (2)

(1) Mechanical Engineering
University of Kansas
Lawrence, Kansas, USA

(2) Bioengineering
University of Kansas
Lawrence, Kansas, USA

INTRODUCTION

First generation students, typically defined as students for whom neither parent received a 4-year college degree, face unique challenges in college. It is estimated that 15 to 40% of college students in the US are first generation students (1-3). First generation students have been found to have an achievement gap when measured by degree completion and time to degree (2). In Mechanical Engineering at the University of Kansas, we observed in a sophomore course that first generation students, who made up 6.5% of the course population, had an average grade substantially lower than the overall classroom population (2.20 versus 2.83). By the subsequent junior level course, first generation students only made up 4.5% of the population.

First generation students are, on average, from lower income households (2,4). These students are also disproportionally from underrepresented racial and ethnic groups (2,5). But more importantly, these students as a whole may lack the "cultural capital" or inside knowledge of how to succeed in college that many of their continuing generation peers may have (2-3). These students may suffer from many of the challenges that other underrepresented groups face such as stereotype threat and imposter syndrome. These challenges have been exacerbated by the COVID pandemic and the move to online and hybrid courses.

In Galina's work, a number of methods are proposed to tackle the challenges first generation students face (2). These include 1. increasing transparency of expectations, 2. teaching study skills that may be missing due to the limited inside knowledge of these students, 3. organizing study groups to build social network, 4. using rubrics to communicate expectation, and 5. developing personal relationships with students to improve dialog.

In this abstract, we will examine one course, a freshman programming course for engineers, and the use of several proposed mechanisms to support first-generation students in hybrid/online learning.

METHODS

ME 208 is an introductory programming course in Mechanical Engineering at the University of Kansas. This course is typically taken in the freshman year. The course was transitioned to a hybrid/online course in Fall of 2020 in response to the COVID pandemic. Students have the option to attend entirely online or in a hybrid mode with online instruction and in person laboratories. One hundred students took the course. The course covers Arduino (C++) programming for the first half of the course and Matlab programming for the second half of the course. The Arduino component required students to program, wire, and instrument microcontroller boards. For this portion of the course, students purchased a Sparkfun Inventor's Kit which included a Arduino-compatible board (Redboard), a breadboard, jumper wire, sensors, LEDs, and motors (https://www.sparkfun.com/products/15267, Sparkfun, Niwon, CO).

The course had 4 major elements each week:
1. Weekly prerecorded tutorial videos on concepts for the week with a comprehension quiz
2. A Monday, 45 minute, live, online class in which students were oriented towards the tasks of the week
3. A 15 minute project online group meeting with the instructor and/or graduate teaching assistants in which groups worked on two course projects (one in Arduino and one in Matlab) and
4. A 45 minute in person or online laboratory with a follow on homework assignment.

The course also had 4 exams, two on Arduino topics and two on Matlab topics.

To tackle the issues of social isolation and help all students (including first generation students) develop networks, project groups were created with 6-7 students in each group. The teams were given a channel within Microsoft Teams to facilitate communication, share files, and organize group meetings. These project groups met with an instructor each week to work on two projects over the course of the semester. For the first project (Arduino), the groups needed to come up with a device that used at least one sensor and one motor. The group was expected to write the code together, but each student was expected to build a prototype from their own kit. Examples of projects created for this first project include an automated toilet flusher and a temperature sensitive fan. The second project in Matlab was to design a STEM related game for second grade children. The game needed to include a variety of programming elements including a graphical display, functions, loops, and if/else conditions.

With approval of the University of Kansas human subjects committee, students were invited to participate in an anonymous survey at the end of the semester. This survey included questions about obstacles faced and questions about the usefulness and importance of different elements of the course in learning.

RESULTS

Thirty-one students completed the survey (31% response rate), but one did not answer the question about being a first-generation student, so only thirty responses were analyzed for this data. Six of the thirty (20%) self-identified as first-generation college students. Consistent with previous studies, first generation students reported finding work and family responsibilities more of an obstacle to learning (Figure 1). These students also were more likely to identify a lack of in person coursework as an obstacle to learning.

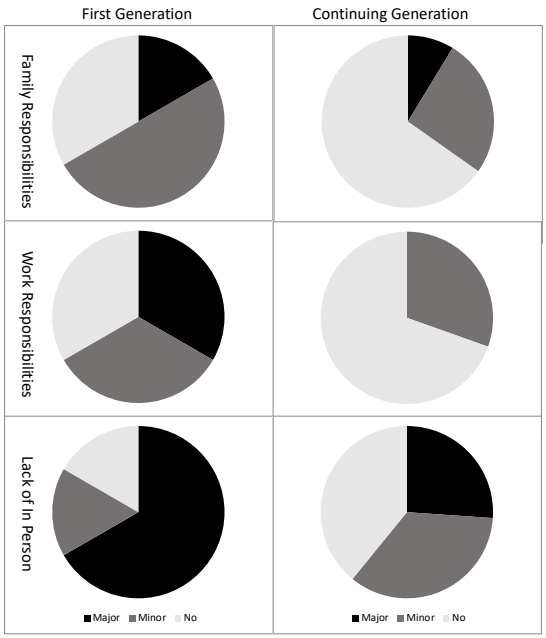

Figure 1. These charts illustrate the obstacles to learning. First generations students were more likely to say family and work responsibilities were a major or minor obstacle to learning.

The project groups were designed to encourage students to connect with each other and facilitate learning teams. The vast majority of students found their project group members to be slightly or very important sources of assistance outside the classroom (Figure 2). However, first generation students were more likely to rely on faculty or teaching assistant office hours and less on other students and outside materials (such as from the Mathworks and Arduino websites) for assistance. First generation students also rated provided materials and exercises (weekly videos, labs, homework, and exams) as more useful to their learning.

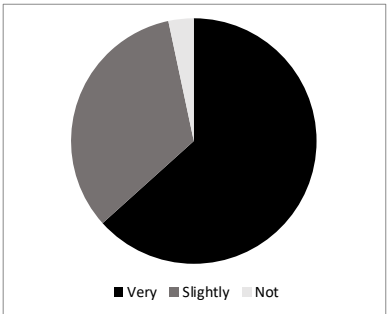

Figure 2. Students found project team members to be an important source of support outside the classroom.

DISCUSSION

The results from this first semester have indicated that having project work that brings students together but also requires individual contributions is effective in developing networks for students to succeed, particularly during the hybrid and online course models of a pandemic. For first generation students, this may be particularly important. However, it was found they did not utilize these networks as much as continuing generation students. In the Spring 2021, the course will be again run as a hybrid/online course. Some modifications will be made to increase the effectiveness of the teams. In particular, group active learning exercises with the teams will be added to the Monday online orientation session to further develop the group. The survey will be repeated with this cohort to examine change in how students utilize resources.

ACKNOWLEDGEMENTS

The authors would like to acknowledge the Center for Teaching Excellence at the University of Kansas for their support of this work.

REFERENCES

[1] Galina, B. Teaching First-Generation College Students, https://cft.vanderbilt.edu/guides-sub-pages/teaching-first-generation-college-students, accessed 1/21/2021.
[2] Nuñez, A., Cuccaro-Alamin, S. First-generation students: Undergraduates whose parents never enrolled in postsecondary education. Washington, DC: U.S. Department of Education, National Center for Educational Statistics (NCES), 1998.
[3] Davis, J. The first-generation student experience: Implications for Campus Practice, and Strategies for Improving Persistence and Success. Sterling, VA: Stylus, 2010.
[4] Lohfink, M. M., Paulsen, M. B. Comparing the determinants of persistence for continuing-generation students. Journal of College Student Development, 46, 409-428, 2005.
[5] Terenzini, P., Springer, L., Yaeger, P., Pascarella, E., Nora, A. First-generation college students: Characteristics, experiences, and cognitive development. Research in Higher Education, 37, 1-22, 1996.

BIOMECHANICAL EFFECTS OF CYCLING CRANK LENGTH ON RESULTANT HIP AND KNEE JOINT FORCES AND RANGE OF MOTION

Avery M. Newman *(1), Abigail L. Fisk *(1), Christiane R. O'Hara, MS (1), Reymil Fernandez, BS (2), Robert D. Clark, PhD (1)

(1) Department of Kinesiology & Public Health
California Polytechnic State University
San Luis Obispo, CA, USA

(2) Department of Mechanical Engineering
California Polytechnic State University
San Luis Obispo, CA, USA

INTRODUCTION

As cycling increases in popularity both as a sport and as a rehabilitation activity, its effects on overall joint health have become an area of interest. The relationship between knee joint forces, moments, and range of motion (ROM) can influence hip and knee joint health (i.e., osteoarthritis, patellofemoral disorder, ligament damage, etc.). Reducing hip and knee joint forces has been seen to result in reduced lower limb injury risk [1]. Hip and knee joint compressive forces and ROM may differ based on varying crank lengths (CL) on a bicycle. Increases in crank length has been shown to have increased peak hip extension and flexion joint powers [2]. Currently, no studies have analyzed the effects of crank length on resultant forces in cycling. The purpose of this study was to examine the effects of four different CL (155, 165, 175, and 185mm) on ROM and resultant compressive forces on the hip and knee.

METHODS

Participants. Twenty-six non-cyclists (12M, 14F, aged 18-55) participated in a single blind randomized cross-over experiment with four CL. Participant characteristics are shown in Table 1. Seven of the participants were excluded from the kinetic data analysis due to error, but all were used for kinematic data for corresponding ROM.

Table 1. Participant Characteristics, Mean ± SD shown.

Participants	N = 26
Age (years)	29.2 ± 11.4
Height (cm)	174.0 ± 8.2
Weight (kg)	69.9 ± 13.0
BMI (kg/m^2)	23.0 ± 3.3
Weekly Training (hrs/week)	6.9 ± 4.3

Equipment. A 12-camera 3D motion analysis system with Cortex software (Motion Analysis Corp., CA, USA) was used to capture kinematic data. Kinetic data was collected using a stationary bike (SRM IndoorTrainer, Germany) retrofitted with custom pedals containing 6-axis load cells (AMTI, MA, USA).

Protocol. An Enhanced Helen Hayes marker protocol was used to place 32 retroreflective markers on anatomical landmarks to track kinematic data (Figure 1). A 3-minute warm-up for each CL was performed at 1.5 W/kg and 70 rpm. 4x1 minute trials were conducted at 2 W/kg. The first two trials were at a constant cadence of 70 rpm and the second two trials were at a constant pedal speed (PS) of 1.47 m/s (RPM = 90, 85, 80, 76 rpm respectively). This value was determined by Equation (1). There were 10 seconds of rest between trials and 5 minutes of recovery between each condition. Saddle and handlebar height was adjusted for each condition to maintain the same height for corresponding crank length.

Data Analysis. Kinematic data was processed using Cortex software and filtered (4th order Butterworth, cutoff 6 Hz) (Figure 2). Kinetic data was filtered using MATLab (MathWorks, MA, USA). All data was averaged from 30 seconds of each trial. A repeated measure ANOVA was performed with Tukey post hoc comparisons.

Equations

$$RPM = (1.47 \text{ m/s} \times 60)\,(2\pi \times CL)^{-1} \quad (1)$$

Figure 1. Experimental Setup

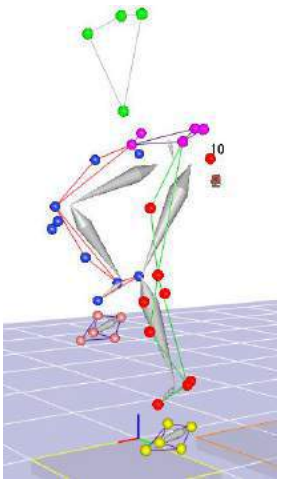

Figure 2. Cortex Processing

RESULTS

During submaximal cycling, the 155 and 165mm CL had a significantly smaller hip ROM compared to the 185mm CL (42.20 & 44.22 degrees vs. 48.34 degrees, p= 0.000 & 0.028 respectively) (Figure 3). ROM at the knee was also significantly smaller between the 155mm CL and the 185mm CL (72.67 degrees vs. 79.52 degrees, p= 0.008) (Figure 4).

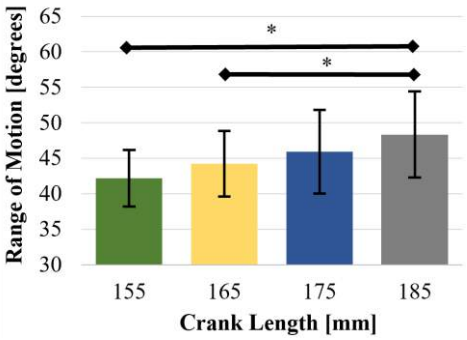

Figure 3. Hip ROM Across the CL. Mean ± SD shown.
*** = significant difference (p<0.05)**

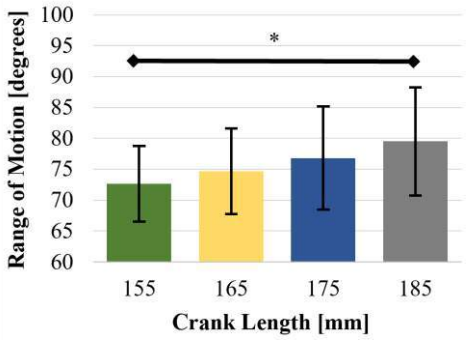

Figure 4. Knee ROM Across the CL. Mean ± SD shown.
*** = significant difference (p<0.05)**

The maximum compressive forces on the knee and the hip at 70 RPM and at a constant pedal speed of 1.47m/s showed no significant difference between CL (p>0.05). Maximum compressive force values for each CL are shown below for the hip (Table 2) and knee (Table 3). The constant pedal speed trials produced lower peak knee and hip compressive forces across all CL (Table 2 & 3) compared to the 70 RPM trials.

Table 2. Maximum Compressive Forces on the Hip, Mean ± SD

CL (mm)	70 RPM (N/kg)	1.47 m/s (N/kg)
155	1.35 ± 0.37	0.82 ± 0.33
165	1.26 ± 0.41	0.84 ± 0.33
175	1.15 ± 0.39	0.84 ± 0.31
185	1.03 ± 0.34	0.85 ± 0.31

Table 3. Maximum Compressive Forces on the Knee, Mean ± SD

CL (mm)	70 RPM (N/kg)	1.47 m/s (N/kg)
155	2.88 ± 0.38	2.50 ± 0.33
165	2.82 ± 0.42	2.57 ± 0.32
175	2.74 ± 0.40	2.57 ± 0.30
185	2.66 ± 0.37	2.54 ± 0.32

DISCUSSION

Hip and knee ROM were significantly greater with a longer CL. Cycling is a useful tool to help restore range of motion during rehabilitation without increasing strain when a person is recovering from an injury to their hip or knee. Using a shorter crank arm would allow for a reduced ROM to assist in rehab efforts.

The constant pedal speed trials at 1.47 m/s produced lower peak knee and hip compressive forces across all crank lengths compared to the 70 RPM trials. If your goal is to lower peak compressive forces, at any CL, picking a higher cadence may be ideal. However, further statistical analysis needs to be conducted.

There were no significant differences in either knee or hip compressive forces across the various CL. The lack of a significant difference reveals that a change in crank length would reduce concerns about any adverse effects it may have on the hip or knee joints. 25% of the population will experience anterior knee pain sometime during their life and for cyclists, the knee joint is one of the most affected by overuse injuries [1]. Whether you are changing crank length for fit, comfort, advantage, etc., you should be able to do so without developing concerns regarding any adverse effects. This finding is beneficial to the countless people who are prescribed cycling has a rehabilitation activity after injury.

These findings add to previous research that found that CL on a bicycle may affect knee and hip joint compressive forces and ROM [2]. Barrett concluded that increases in CL will increase peak hip extension and flexion joint powers. Our findings took these results one step further to show that different CL effect ROM, but do not significantly affect compression forces. No other studies had yet analyzed the effects of crank length on resultant forces in cycling.

Some limitations faced during this study included excessive sweating and loose clothing that may have altered placement of the retro-active markers, software complications that limited the data pool for analysis (some data had to be excluded), and that our pedal configuration did not allow for the foot to be locked in place, therefore possibly altering our results.

During future analysis of our study, trials will be processed through OpenSim along with EMG data to better analyze direct bone to bone contact forces of knee joints.

ACKNOWLEDGMENTS

This research project was supported by the Bill and Linda Frost Fund. *Students are Frost Research Fellows and are recipients of the Bill and Linda Frost Undergraduate Student Research Award. The authors acknowledge Melodie Leroudier, Michael Liang, and Chaitanya Adiga for their contributions to this research study.

REFERENCES

[1] Bini, R., Hume, A. P., Croft, L. J. *Sports Med*, 41(6):463-476, 2011.

[2] Barratt, P. R., Martin, J. C., Elmer, S. J., & Korff, T. *Medicine & Science in Sports & Exercise*, 48(4):705-713, 2016.

INVESTIGATION OF ELASTIC MODULI OF MINERALIZED COLLAGEN FIBRIL AND EXTRAFIBRILLAR MATRIX IN BOVINE CORTICAL BONE USING PEAKFORCE TAPPING ATOMIC FORCE MICROSCOPY

Y. Zhou (1), J. Du (1)

(1) Department of Mechanical Engineering
Pennsylvania State University
State College, PA, USA

INTRODUCTION

An important function of bone is its load-bearing capacity. Bone is a bio-composite that consists of organic and inorganic components. The strength and toughness of bone arises from assembly of these components at multiple scales. Understanding the elastic properties of bone at micro- and nano- scales is important because it can help understand the strengthening and toughening mechanisms of bone; generate inputs for the computational models at micro- and nano- scales; and inspire the design of manmade materials.

The elastic properties of the mineralized collagen fibril (MCF) and the extrafibrillar matrix (EFM) have not been thoroughly characterized. Atomic force microscopy (AFM) has been used in AFM-based tension test of single collagen fibrils[1,2] and AFM-based nanoindentation of bone and cartilage[3,4].

In this work, PeakForce Tapping AFM was used to scan the surface of cut and polished surfaces of bovine cortical bone, when they were submerged in water. The elastic modulus maps were obtained for scans in micro-meter scales. The elastic moduli of mineralized collagen fibrils and the surrounding matrix were extracted and calculated, respectively. The structural and compositional variations that may underly the variations in the measure elastic moduli were discussed.

METHODS

The fresh bovine femur of a 20-month-old cow was obtained from Pennsylvania State University Meat lab. The soft tissues and bone marrow were removed mechanically. Several strips in the mid-diaphysis portion at the posterior side was cut. They were dominated by the haversian bone. They were sectioned into thin slices with its surfaces perpendicular to the longitudinal axis of the femur by a precision saw with diamond blade (Isomet 1000 Precision Cutter, Buehler, Lake Bluff, IL). The size of each specimen was about 10 mm × 10 mm × 1.5 mm.

The specimens were polished by a grinder polisher (EcoMet 30, Buehler, Lake Bluff, IL) using silicon carbide grinding papers with progressively finer grit of 800 and 1200 and then using diamond suspension with grades of 6, 3, 1, 0.5 and 0.1 μm on silk polishing cloths (South Bay Technologies, San Clemente, CA and SMS Labs, Sturbridge, MA). After each round of polishing, they were cleaned in an ultrasonic cleaner (Branson Ultrasonics, Danbury, CT) in deionized (DI) water for 2 minutes. The polished and cleaned specimens were glued onto petri dish using epoxy resin, and was kept moisturized in modified Hanks' Balanced Salt Solution (HBSS) (Sigma Aldrich, St. Louis, MO) until testing.

The elastic modulus map of the polished surfaces on the bone specimens were measured using an AFM (BioScope Resolve, Bruker, Billerica, MA) under PeakForce Tapping mode. Etched silicon AFM probe (RTESPA-525, Bruker, Billerica, MA) was used to scan the polished surface of the bone specimens submerged in DI water. The deflection sensitivity of the probe was calibrated on a sapphire sample (SAPPHIRE-12M, Bruker, Billerica, MA). The setpoint was 400 nN; the peak force frequency was 1kHz; the scan rate was 0.5 Hz. Several scans with size small than 10-μm were obtained at different locations of the specimens. The number of points being tapped in each scan was 256×256.

At each tapping point, cantilever deflection and the vertical position of the AFM tip were recorded. The load-separation relationship was given by the Derjaguin-Muller-Toporov (DMT) model, which has a Hertzian contact profile. The AFM probe was calibrated on a highly oriented pyrolytic graphite sample (HOPG-12M, Bruker, Billerica, MA) with a known nominal elastic modulus of 18 GPa. The elastic modulus of the specimens at each tapping point was be obtained by fitting the load-deformation curves during tip retraction in NanoScope analysis software (Bruker, Billerica, MA).

The elastic moduli measured from the mineralized collagen fibril and the extrafibrillar matrix regions were extracted and compared using t-test using Minitab software (Minitab, LLC, State College, PA). The histograms of the elastic moduli of MCF and EFM were modeled the sum of general normal distributions, respectively, using OriginLab software (OriginLab Corporation, Northampton, MA).

RESULTS

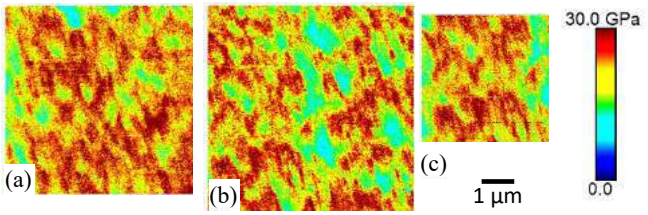

Figure 1: Elastic modulus map of bovine cortical bone showing the mineralized collagen fibril bundles and surrounding matrix (scan size: 6, 6.6 and 4 µm, respectively)

Structures of softer fibril bundles surrounded by harder matrix were observed in both the osteons and the interstitial bone in the scans. Representative scans at three different locations are presented in Fig. 1. The elliptical shape cross sections of the MCF bundles had 0.58 – 1.25 µm major axis and 0.22 – 0.49 µm minor axis. In spite of variations in major and minor axes, the aspect ratio is relatively consistent between different bundles, ranging from 2.34 to 2.72. The elastic moduli for the MCF bundles and EFM, were measured to be 12.94 ± 2.71GPa (n = 4,200) and 28.39 ± 5.75 GPa (n = 7,564), respectively. The difference was statistically significant ($p < 0.05$).

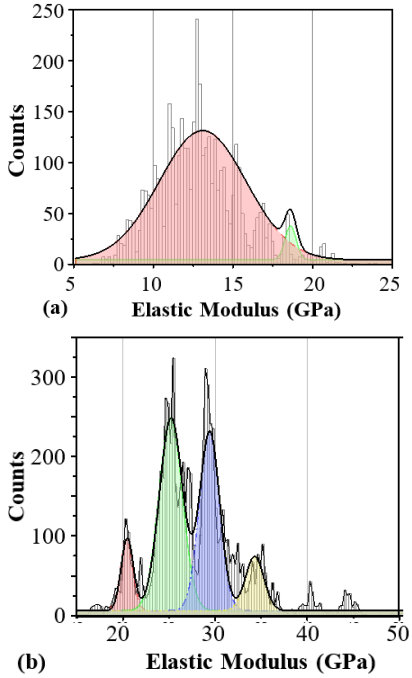

Figure 2: Histograms of elastic moduli for (a) mineralized collagen fibril bundles and (b) extrafibrillar matrix.

Fig. 2 present the histograms of elastic moduli measured in the MCF bundles and the matrix, respectively. The histograms for MCF bundles were modeled by summations of 2 general normal distribution functions with the mean values of 12.48 GPa and 16.90 GPa. The histograms for the matrix were modeled by summations of 4 general normal distribution functions with the mean values of 20.52 GPa, 25.27 GPa, 29.46 GPa and 34.33 GPa. The coefficients of determination, R2, of the curve fittings were 0.8 and 0.87, respectively.

DISCUSSION

In prior works, the elastic modulus of collagen fibrils and MCFs was calculated to be 1.3 - 6.23 GPa by molecular dynamics [5,6]; the elastic modulus of collagen fibrils in air-dried bovine Achilles tendon and MCFs in deer antler was measured to be 2-7 GPa by AFM-based tensile test of single fibrils[1,2]. These are lower than the elastic modulus of MCF measured in this work. The higher values measured in the current work may be attributed to the testing condition in which the specimen was fully submerged in water or to the different species and anatomic locations of the specimens. Harley et al. reported that collagen fibres in NaCl solution have a higher elastic modulus than the elastic moduli of air-dried and dry collagen fibres[7].

Moreover, in this study, the elastic modulus of MCF bundles were measured to lower than that of the matrix. It indicates that the MCF bundles have less mineral content than the matrix.

The histogram for the elastic modulus of MCF bundles (Fig. 2a) was dominated by one general normal distribution. It indicates one dominating angle between the fibrils long-axis and the AFM tapping direction, which is also the long axis of bone. It is consistent with the rope-like twisting fibril structures inside the bundles[8], in which the angle between each single fibril and the long axis of the MCF bundle is the same. In contrast, the 4 general normal distributions in the histogram for EFM (Fig. 2b) can be attributed to the random orientations of fibrils, substantial ground substance, and sub-micron voids[9].

ACKNOWLEDGEMENTS

The authors would like to thank Dr. Markus J. Kastner and Dr. Timothy B. Tighe at the Materials Research Institute at Penn State University for their technical support.

REFERENCES

1. van der Rijt, J. A. J., van der Werf, K. O., Bennink, M. L., Dijkstra, P. J. & Feijen, J. Micromechanical Testing of Individual Collagen Fibrils. *Macromol. Biosci.* **6**, 697–702 (2006).
2. Hang, F. & Barber, A. H. Nano-mechanical properties of individual mineralized collagen fibrils from bone tissue. *J. R. Soc. Interface* **8**, 500–505 (2011).
3. Stolz, M. *et al.* Dynamic Elastic Modulus of Porcine Articular Cartilage Determined at Two Different Levels of Tissue Organization by Indentation-Type Atomic Force Microscopy. *Biophys. J.* **86**, 3269–3283 (2004).
4. Tai, K., Dao, M., Suresh, S., Palazoglu, A. & Ortiz, C. Nanoscale heterogeneity promotes energy dissipation in bone. *Nat. Mater.* **6**, 454–462 (2007).
5. Buehler, M. J. Molecular nanomechanics of nascent bone: fibrillar toughening by mineralization. *Nanotechnology* **18**, 295102 (2007).
6. Nair, A. K., Gautieri, A., Chang, S.-W. & Buehler, M. J. Molecular mechanics of mineralized collagen fibrils in bone. *Nat. Commun.* **4**, 1724 (2013).
7. HARLEY, R., JAMES, D., MILLER, A. & WHITE, J. W. Phonons and the elastic moduli of collagen and muscle. *Nature* **267**, 285–287 (1977).
8. Reznikov, N., Shahar, R. & Weiner, S. Bone hierarchical structure in three dimensions. *Acta Biomater.* **10**, 3815–3826 (2014).
9. Reznikov, N., Shahar, R. & Weiner, S. Three-dimensional structure of human lamellar bone: The presence of two different materials and new insights into the hierarchical organization. *Bone* **59**, 93–104 (2014).

DEEP LEARNING-ENABLED LABEL-FREE ON-CHIP DETECTION AND SELECTIVE EXTRACTION OF CELL AGGREGATE-LADEN MICROCAPSULES

Alisa M. White (1), Yuntian Zhang (1), James G. Shamul (1), Xiaoming He (1,2,3)

(1) Fischell Department of Bioengineering
University of Maryland
College Park, Maryland, United States

(2) Robert E. Fischell Institute for Biomedical Devices
University of Maryland
College Park, Maryland, United States

(3) Marlene and Stewart Greenbaum Comprehensive Cancer Center
University of Maryland
Baltimore, Maryland, United States

INTRODUCTION

Microfluidic encapsulation of cells/tissues in hydrogel microcapsules has attracted tremendous attention in the field of cell-based medicine [1,2]. However, when encapsulating rare cells and tissues (e.g., pancreatic islets and ovarian follicles), the majority of the resultant hydrogel microcapsules are empty[3,4]. Empty capsules should be excluded from the sample because it makes downstream processing difficult and is undesirable for cell/tissue transplantation because *in vivo* space is limited[5]. Furthermore, the cell-laden hydrogel microcapsules are usually suspended in an oil phase after microfluidic generation, while the microencapsulated cells require an aqueous phase for culture/ transplantation and long-term suspension in oil could compromise the tissues[6]. Therefore, an effective method for selective extraction of cell-laden microcapsules from oil into an isotonic aqueous phase timely on-chip can be very important to maintain the cell quality for use in clinical settings. Contemporary extraction methods either require labeling of cells for their identification which can be detrimental for downstream processing and expensive detection systems or have a low extraction purity (< ~30%)[7-9]. Here, we utilize a deep learning neural network system to detect cell aggregates present in microcapsules and sort them on-chip into cell-laden and empty microcapsules and report high efficiency of detection (~100%) and extraction (~97%), high purity of extraction (~90%), and high cell viability (>95%).

METHODS

Experimental Setup. As illustrated in Figure 1a, the system consists of a microfluidic device for microcapsule generation, a cell phone camera for imaging the on-chip detection area, a deep learning model for detection via analyzing the video frames from the camera in real-time, and a microcontroller that receives the output from the deep learning model and controls the switch to activate/deactivate the DEP-based extraction. The workflow of our approach is illustrated in Figure 1b. In the microfluidic device, an aqueous solution of sodium alginate containing cell aggregates is connected to inlet 1 (I1), the oil emulsion containing $CaCl_2$ for gelling the sodium alginate solution into calcium alginate hydrogel is connected to I2, and the isotonic aqueous extraction solution is connected to I3. The microcapsules further flow into the detection region (ii) where images are taken by a cell phone camera via the objective of a bright-field light microscope. An iPhone 7 cell phone is attached to the microscope eyepiece, streaming video to the computer. The deep learning model on the computer analyzes the input images in

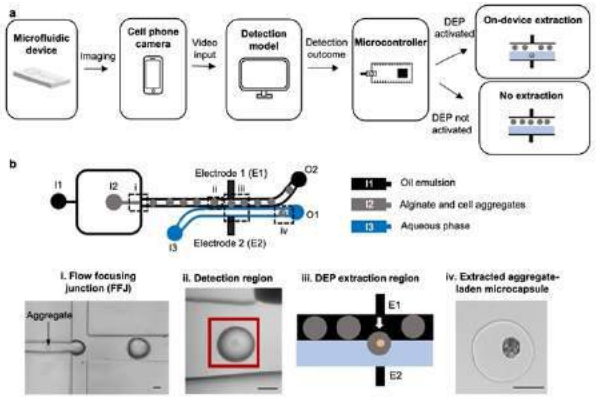

Figure 1. Overview of the deep learning-based detection and extraction system. (a) Flow chart of the overall system design and order of operations. (b) A diagram of the microfluidic device showing its use for generating microcapsules and the deep learning-based label-free on-chip selective extraction of the cell aggregate-laden microcapsules. Scale bar: 100 µm.

real-time to determine if the microcapsule currently in the detection region contains a cell aggregate or is empty. A microcontroller controls a switch that turns on when the model determines there is a microcapsule containing a cell aggregate in the detection region. When the switch is turned on, an electric field is applied across the microchannel via the two electrodes (E1 and E2) to generate DEP force for selectively extracting the cell aggregate- laden microcapsule from the oil emulsion into the isotonic aqueous extraction solution (iii). The extracted microcapsules then flow to outlet 1 (O1, iv) and non-extracted capsuled are collected at outlet 2 (O2).

Deep Learning Model. A deep learning model is utilized to enable label-free detection of cell aggregate-laden microcapsules in real time in this study. This is achieved through training the deep learning neural network model using pre-labeled (i.e., with or without a cell-laden microcapsule) images of the detection region. The detection model is based on the single shot multibox detector (SSD), a current state-of-the-art model for object detection[10]. Three backend models that are first pre-trained on the COCO dataset, an open source dataset of labeled images used for model training, are compared[11].

Purity and Efficiency. To determine the detection efficiency, videos of the detection region are analyzed, and the number of cell aggregates is counted. The detection efficiency is defined as the percent of cell aggregate-laden microcapsules that the deep learning program detects out of all the cell aggregate-laden microcapsules passing through the detection region. To determine the selective extraction efficiency and purity as well as cell viability, microcapsules are collected from both the aqueous outlet O1 and oil outlet O2 (Figure 1b). Extraction efficiency is defined as the percent of cell aggregate-laden microcapsules that were collected containing aggregates out of all aggregates collected from both channels. Extraction purity is the percent of cell-aggregate laden capsules out of the capsules collected from O1.

RESULTS

Based on the speed needed for real-time detection and the imaging rate of the iPhone 7 camera, an acquisition speed of 30 frames per second (fps) is chosen. MobileNet was chosen as the backend structure based on the need for real-time application at 30 ms determined after running a model time comparison[12]. A video frame breakdown of the deep learning-based detection and selective extraction is shown in Figure 2a. The detection region is indicated by a green box (Figure 2a.1) that turns red when the model detects a cell aggregate-laden. If a cell aggregate-laden microcapsule appears in the detection region (Figure 2a.2-3), the computer program sends a corresponding signal to the microcontroller which activates DEP to extract the cell aggregate-laden microcapsule from oil emulsion into the aqueous phase (Figure 2a.4-6). If no cell aggregate-laden microcapsule is detected, DEP stays off and the microcapsule continues to flow down the oil channel (Figure 2a.7-9). It is determined that the deep learning-based label-free method can detect cell aggregates (50-250 µm in diameter) with an ~100% detection efficiency (Figure 2b). The extraction efficiency and purity of the cell aggregate-laden microcapsules in the selectively extracted sample are ~97% (Figure 2b) and ~90 % (Figure 2c), respectively. The purity of the selectively extracted micro-capsules is significantly much higher than that (~2%) without selective extraction. Typical images of the samples without and with selective extraction showing the difference in their purity are given in Figure 2d. Quantitative analysis of live/dead aggregate staining shows more than 95% of cells in the selectively extracted microcapsules (n=3) are viable (Figure 2e), which is not significantly different from that of fresh cells (control) in the cell aggregates without micro-encapsulation or extraction.

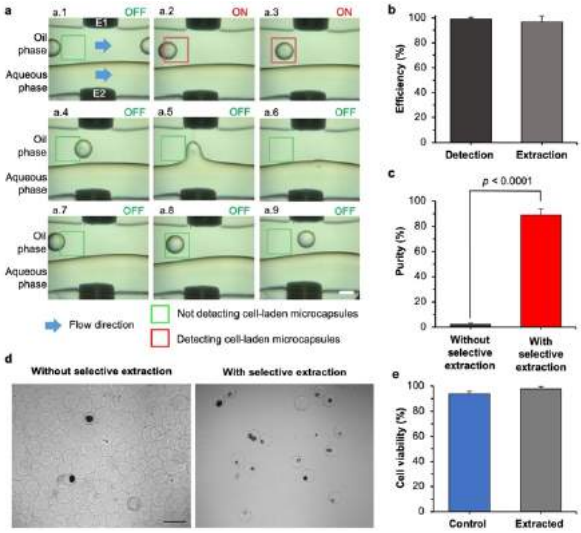

Figure 2. Characterization of the deep learning-enabled detection and selective extraction of cell aggregate-laden microcapsules. (a) Image sequence showing selective extraction of a cell aggregate-laden microcapsule from oil into the aqueous extraction solution. Scale bar: 200 µm. (b) Extraction Efficiency. (c) Extraction purity. (d) Microcapsules collected with and without selective extraction. Scale bar: 500 µm. (e) Aggregate viability.

DISCUSSION

The deep learning-based label-free method can detect cell aggregates of 50-250 µm in diameter with an ~100% detection efficiency, which enables selective extraction of the cell aggregate-laden microcapsules via DEP force with a ~97% extraction efficiency. This is much better than a previously reported optical sensor-based approach that is unable to detect or extract any cell aggregates less than 82 µm[9]. This is important for biomedical applications, for instance for islet microencapsulation, because islets can be as small as 50 µm[13]. The purity (~90%) of the deep learning-based extraction is also much higher than that (~30%) achieved with an optical sensor-based detection method for DEP-based extraction[9]. However, the purity is lower than the extraction efficiency. The oil-water interface in the extraction area is destabilized slightly during extraction of a cell-laden microcapsule, which may cause an upstream neighboring microcapsule (either empty or cell-laden) to be extracted. This issue may be overcome by using an extraction method faster than DEP. Similarly, a more precise extraction method could further improve the extraction efficiency to ~100%, since the efficiency for the deep learning-based detection is ~100%. This technology may find many potential applications including microencapsulating pancreatic islets, ovarian follicles, and stem cell aggregates for the treatment of diabetes and infertility and stem cell-based therapy of many diseases.

ACKNOWLEDGEMENTS

This work was supported by the National Institute of Health R01EB023632.

REFERENCES

[1] Zhang, J. *et al., Science*, 335:690–694, 2012. [2] Mao, A. S. *et al., Proc. Natl. Acad. Sci.,* 116:15392–15397, 2019. [3] Vegas, A. J. *et al., Nat. Med,* 22:306–311, 2016. [4] He, X., *ACS Biomater. Sci. Eng*, 3:2692–2701, 2017. [5] White, A. M. *et al. ACS Biomater. Sci. Eng*, 6:2543–2562, 2020. [6] Huang, H. et al., *Small,* 11:5369-5374, 2015. [7] Agresti, J. J. *et al., Proc. Natl. Acad. Sci.*, 107:4004–4009, 2010. [8] Cao, Z. et al., *Lab on a Chip*, 13:171–178, 2013. [9] Sun, M., et al., *ACS Sensors*, 3:410–417, 2018. [10] Huang, J. et al., *30th Ieee Conference Cvpr*, 3296–3305, 2017. [11] Lin T. et al., *Lect Notes Comput Sc*, 8693:740-755, 2014. [12] Howard, A et al., arXiv preprint,1704.04861, 2017. [13] Jo, J. et al., *Biophys. J.*, 93:2655–2666, 2007.

TOWARD THE TRANSLATION OF 3D-PRINTED FLEXIBLE-PLA INTERVERTERBAL DISCS IN SMALL ANIMAL RODENT MODELS

Samantha L. Marshall (1), Jennifer Pilamunga (2), Joseph M. Lombardi (1), Nadeen O. Chahine (1,2)

(1) Department of Orthopedic Surgery
Columbia University
New York, NY, USA

(2) Department of Biomedical Engineering
Columbia University
New York, NY, USA

INTRODUCTION

Back pain, one of the most common reasons for doctor visits and the leading cause of disability, has been associated with degeneration of the intervertebral discs (IVD) [1–3]. The IVD, the connective tissue between vertebral bodies, is a complex load-bearing composite tissue populated by a relatively low density of mechanosensitive cells (Fig. 1a) [4]. In advanced painful disc degeneration, the current treatment paradigm includes spinal fusion or total disc replacements [5,6]. In both approaches, the native disc tissue is removed and replaced with either a metal cage containing bone grafts to promote fusion or with a motion-preserving artificial disc implant. Despite the vast differences in how these surgical treatments work, both are associated with complications in the surrounding tissues, namely adjacent segment disease, due to disruption of the mechanics of the spine [6,7]. To address this limitation, we have begun to optimize a 3D printing approach of flexible and biocompatible polymer, FPLA, to create a replacement disc insert that has mechanical properties that mimic native IVD properties.

In a previous study, we optimized the mechanical properties of 3D-printed FPLA mesh scaffolds to mimic equilibrium and dynamic moduli of IVD motion segments in tension and compression (Fig. 1b) [8]. These mesh scaffolds, which were optimized by varying the fiber spacing, are also scalable for mimicking idealized geometry of a large animal or human IVD. However, evaluating these scaffolds in a small animal model proved to be more complex, as scaling down the fiber spacing of 3D printed mesh scaffold to suit the geometry of a rodent IVD was limited. Based on literature studies, the rat IVD height is around 1 mm, has a lateral width of 3-6 mm and a total area of 9-20 mm^2, limiting the scaling down of 3D printed FPLA mesh scaffold to this dimension [11].

To overcome the limitation of printing FPLA mesh scaffolds for rat anatomy, this study evaluated two different 3D printed FPLA replacement disc inserts for their biomechanical properties, specifically comparing hollow (0% infill density) shells versus solid (100% infill density) FPLA samples (Fig 1c). To determine an idealized geometry for printing, rat caudal motion segments were also analyzed using µCT, and resulting dimensions were used in generating rat caudal IVD replacement inserts.

Figure 1: a) Schematic of IVD loading, b) 3D printed FPLA meshes, c) 3D printed FPLA IVD disks for rat and 2X scaled up dimensions.

METHODS

Caudal motion segments were dissected from three mature, male Sprague-Dawley rats ranging from 300-500g after freezing. Full bone-disc-bone segments were isolated by cutting through the adjacent disc on either side with a scalpel blade. Motion segments were placed in a tube and packed with PBS soaked KimWipes to retain hydration and prevent motion during the scan. Scans were performed on a SkyScan 1272 (Bruker) with a pixel size of 12.8 µm, power of 70 kV, image size of 1344 x 2016, and a Al 0.5mm filter. Frames were averaged 2 times to remove any background. Reconstructions were performed using SkyScan NRecon.

To measure the segments and make 3D models, the reconstructed scans were imported into DataViewer and converted into coronal image slices. CTAn software was used to select an ROI, despeckle, fill holes to create a solid shape (Fig. 2 center) and binarize the images. CTAn software was used to export the image files to an STL file and CTVox

software was used to visualize the implant. To generate dimensional estimates of the IVD, 2D images from the center of the coronal plane were used to measure width, inner, and outer height based on boney anatomy (Fig. 2). 3D idealized cylinder disks were designed based on these measurements.

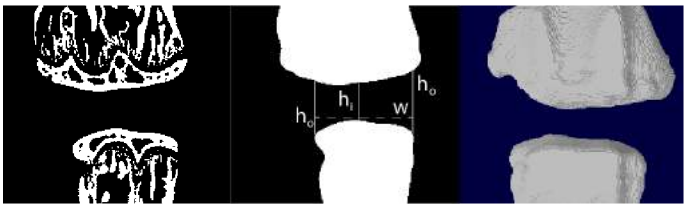

Figure 2: (left) binarized µCT scan (center) outer height, inner height, and width measurements (right) 3D model

Cylinders were printed from FlexiFil PLA (FPLA), a thermoplastic co-polyester elastomer/polymer blend (FormFutura) using a Makerbot Replicator plus 3D printer (Makerbot) and a Makerbot Experimental Extruder with 0.4 mm print nozzle. Tape was used to adhere the scaffold to the bed of the printer during printing to avoid warping of the structure. Printing parameters included extrusion speed of 90 mm/s, extruder temperature of 245 °C, and 0.2 mm layer height. Hollow structures (0% infill) were printed with one shell and solid structures were printed with two shells, and 100% circular pattern infill. Two sizes were printed, rat caudal (1.5 mm height and 4 mm diameter) dimension and 2x the rat caudal dimensions, for characterization of a potential oversized implant as a press fit approach (Fig. 1c).

Unconfined compression tests were performed on a TA Electroforce DMA 3200 Mechanical Tester with a 100lb load cell. Samples were loaded between two stainless steel platens and the top platen was brought into contact with the sample before initiating a displacement ramp of 0.2 mm/min until failure was observed. Elastic modulus was measured from the linear segment of calculated stress-strain curves using Matlab.

RESULTS

The average width of the rat caudal disc was measured to be 4.3 ± 0.9 mm (n=3). The inner IVD height was measured at the narrowest point between the two caudal bones to be 1.04 ± 0.34 mm (n=3) and the outer height was measured on both sides of the outer edge of the caudal bones to be 1.78 ± 0.11 mm (n=3, 2 measurements per sample). An overview of measurement locations is shown in Figure 2.

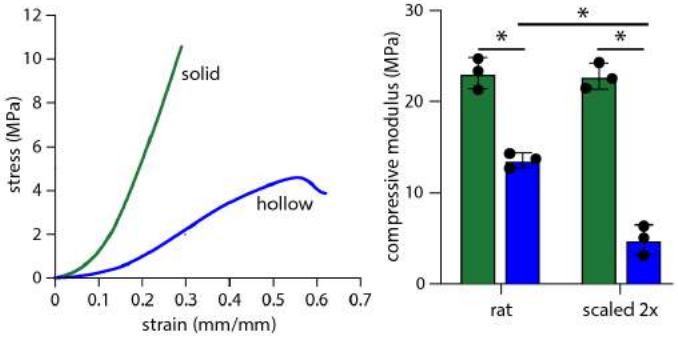

Figure 3: (left) stress-strain curve of hollow and solid 2x printed replacements (right) equilibrium modulus of printed replacements.

Compression testing showed that the solid disks had a significantly larger modulus than the hollow replacements ($p < 0.001$) (Fig. 3). The compressive modulus of rat sized disks was 4.84 ± 1.64 MPa (hollow) and 22.78 ± 1.42 MPa (solid). The scaled up (2x) disks had a compressive modulus of 13.59 ± 0.83 MPa (hollow) and 23.14 ± 1.70 MPa (solid). The solid elastic moduli were similar in the rat sized and scaled up dimensions, indicating no geometric scaling factor ($p = 0.8$), while the hollow elastic moduli were significantly different ($p = 0.0012$) between sizes, indicating that the mechanics of the hollow structures scale with size.

DISCUSSION

Mechanical characterization of 3D printed solid FPLA samples yielded compressive moduli that ranged from 5-23MPa. The hollow (0% infill) structures exhibited a compressive modulus that was within the benchmarks for IVD motion segments in compression (3-10 MPa) [10]. Not surprising, the moduli of the hollow disks changed with width dimension, while solid disks did not have a dependence on dimensions. While the solid printed replacements were significantly stiffer than the hollow, the ~20 MPa is much closer to the native benchmark mechanics than the metals that are currently used in surgical treatment. These results also demonstrate that µCT scans can be used to determine the geometry of individual rat discs as well as create idealized 3D models of specific rat IVD. Our geometric measurements were consistent with literature values [11], confirming the method, while variations can be attributed to the size and age of animals or spinal level.

Future studies will use the µCT reconstructions to perform a 3D volumetric analysis, and to create a customized IVD implant for *in vivo* evaluation in the rat. These disks will be used to drive *in vivo* studies in Sprague Dawley rats, beginning first with subcutaneous implantation to determine the *in vivo* compatibility of the FPLA material and then with implantation in the caudal disc of a rat to observe integration and behavior of the adjacent segments to implantation.

ACKNOWLEDGEMENTS

Funded in part by NIH R01AR069668 and NYSTEM Training grant.

REFERENCES

[1] Serra, T. et al., *Biofabrication*. 8:35001, 2016.
[2] Adams, M.A., *Acupunct. Med.* 22:178-188, 2004.
[3] Bogduk, N., *Neurosurgery*. 2:791-806, 1991.
[4] Urban, J.P.G. et al., *Arthritis Res. Ther.* 5:120–30, 2003.
[5] Freeman, B.J.C. et al., *Spine.* 15:439-447, 2006.
[6] Martin, B.I. et al., *Spine*. 32:382-387, 2007.
[7] Turner, J.A., *Lumbar Spinal Fusions*, 1991.
[8] Marshall, S.M. et al., *SB3C Abstract,* 2019.
[9] Nerurkar, N.L. et al., *J Biomech,* 43:1017-1030, 2010.
[10] Newell, J.P., et al. *J Mech Behav Biomed Mater,* 69:42-434, 2017.
[11] O'Connell, G.D. et al., *Spine,* 32(3):328-333, 2007.

EVOLVING STRUCTURE-FUNCTION RELATIONS IN AORTIC MATURATION AND AGING

Cristina Cavinato (1), Sae-Il Murtada (1), Alexia Rojas (1), Jay D. Humphrey (1, 2)

(1) Department of Biomedical Engineering
Yale University, New Haven, CT, USA

(2) Vascular Biology and Therapeutics Program
Yale School of Medicine, New Haven, CT, USA

INTRODUCTION

Microstructural and mechanical changes that promote homeostasis during aortic maturation and aging are crucial in age-specific adaptations and disease evolution. To ensure sufficient mechanical strength under hemodynamic loads, the aorta consists of a multi-layered composite wall, with collagen and elastic lamellae dominating the passive mechanical behavior and strength. Aortic microstructure, mechanical properties and structural integrity are regulated by arterial cells, in large part via mechanosensing of extracellular matrix, with smooth muscle cells (SMCs) and fibroblasts responsible for its continued mechanoregulation to promote mechanical homeostasis [1]. Notwithstanding the importance of traditional analyses of the global properties of the wall, each aortic region exhibits different local characteristics [2]. Two-photon imaging is a nondestructive method suitable for *ex vivo* 3D assessment of regional microstructural properties of aortic wall components in loaded conditions, and this applies especially for small model organisms such as mice that allow representative observations through the entire aortic thickness. However, there are few studies comparing multiple wall constituents properties across maturation and aging at age-specific loading conditions despite the important role age plays in medicine [3]. Mice are intensively studied for their marked age-related similarity with humans in the patterns of many vascular diseases, but an essential aspect is that the age relationship between mice and humans changes drastically at different stages of their lives. Recent analyses oriented to the age-specific arterial tissue mechanics are insightful [4,5] but there is still a significant need for consistent microstructural and mechanical information across a sufficient number of age stages. In this work, we combined *ex vivo* multiphoton microscopy and computer-controlled biaxial testing to analyze aortic microstructural and mechanical properties in mice as a function of normal postnatal maturation and aging, at 5 age stages from weaning up to one year. For this purpose, a methodology was developed to quantify multiple microstructural parameters of the primary extracellular components – fibrillar collagen and elastic lamellae – and three fundamental cell types – endothelial cells (ECs), SMCs, adventitial cells – locally, in 3D, and as a function of biaxial loading.

METHODS

Samples. Segments of descending thoracic aorta (DTA) were collected from female C57BL/6J mice at postnatal ages of 21 days (P21, n = 4), 42 days (P42, n = 4), 98 days (P98, n = 4) 230 days (P230, n = 4) and 1 year (P365, n = 4).

Biomechanical characterization. Following preconditioning, passive distension-extension protocols consisted of: (i) 3 cycles of pressure-diameter testing cycled between 10 mmHg and age-specific maximum pressure at three different fixed values of axial stretch (*in vivo* value ±5%); (ii) 4 axial force-length cycles with axial force varied from 0 to the maximum load reached at the maximum pressure and *in vivo* +5% axial stretch at a fixed age specific luminal pressure measured *in vivo*. The nonlinear passive mechanical behavior was described by mean axial and circumferential (circ) stress, axial and circumferential material stiffness, elastic stored energy (best fit for an independently validated four fiber family model) and distensibility [6].

Microstructural characterization. Following biomechanical testing, multiphoton microscopy delineated simultaneously multiple components of the aortic wall: collagen fibers, elastic lamellae, and cell nuclei subdivided in EC, SMC, and adventitia cell nuclei. Acquisitions were made at systole, diastole, and half diastole *ex vivo* equivalent blood pressures and sample-specific in vivo axial stretch ± 5%. Dorsal and ventral regions were analyzed consistently. Due to the near cylindrical shape of the samples, analysis of separate wall layers was allowed by

transformation from Cartesian to polar coordinates. A systematic analysis was developed to quantify the following microstructural parameters from 3D images at all different configurations and regions: layer specific thickness and volume fractions, collagen fiber straightness, alignment and bundle width, cell densities and cell alignment, elastic lamella number and inter-lamellar distance.

RESULTS

Several microstructural changes were quantified (Figure 1a) during late stages of maturation (P21-P98) and aging in adulthood (P98-P365). The media was characterized by a progressive decrease in smooth muscle cell density and alignment though with inter-lamellar widening from intermediate to older ages, suggesting cell hypertrophy, matrix accumulation, or both. The endothelium showed progressive reductions in cell density and altered cellular orientation. Despite not changing in tissue thickness, the aging adventitia exhibited a marked thickening and straightening of collagen fiber bundles and reduction in cell density, suggestive of age-related remodeling not growth. Multiple microstructural changes correlated with age-related increases in diameter and material stiffness, among other mechanical metrics (Figure 1b).

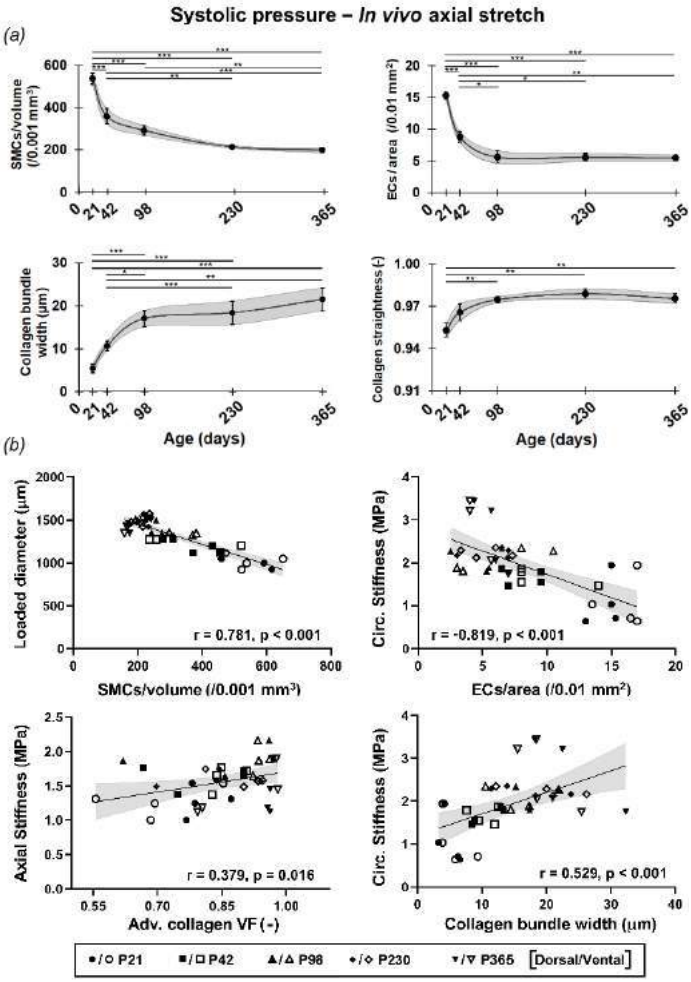

Figure 1: (a) Evolution of selected microstructural parameters (Mean ± SEM) reveal distinct time courses of maturation and aging. * p<0.05, ** p<0.01, *** p<0.001. (b) Sample-specific microstructural and mechanical parameters in statistical correlation for pooled age groups.

These significant correlations indicated the fundamental role of cells and deposited extracellular proteins, including reductions in endothelial and smooth muscle cell densities as well as increases in straightness and thickness of collagen bundles in relation to the increase in circumferential stiffness of the aortic wall.

DISCUSSION

Introducing a continuity between postnatal maturation and aging, our study complemented but extended prior studies via consistent analysis of sample-specific structure-function. Importantly, in maturation and aging, circumferential stiffness associated with collagen morphology as well as SMC density and morphology, supporting the discussions about interactions between SMCs and ECM and ECM-driven SMC modulation which leads to pathologies in aged arteries [7]; axial material stiffness seemed to be governed by the fibrillar collagen fraction. Interestingly, while EC density appeared to be correlated to circumferential stiffness throughout aging, flow-mediated shear stress, seems to have a large influence on EC orientation.

In conclusion, some correlations of fundamental importance highlight relationships between the microstructural organization of collagen and intramural cells and the passive biomechanical metrics in both circumferential and axial directions. The present data show how recent advances of imaging can help to better understand microstructure and mechanics of the aging aorta, providing critical comparators for future studies of diverse diseases that may have different ages of onset.

ACKNOWLEDGEMENTS

This work was supported by grants from the US National Institutes of Health (R01 HL105297, U01 HL142518).

REFERENCES

[1] Humphrey, JD, et al., *Nat Rev Mol Cell Biol*, 15:802-812, 2014.
[2] Roccabianca, S, et al., *J Mech Behav Biomed Mater*, 29, 2014.
[3] Wan, W, Gleason, RL, *Am J Physiol*, 304: H674-H686, 2013.
[4] Murtada, S-I, et al., *Dev Dyn*, 2020.
[5] Hawes, JZ, et al., *Am J Physiol*, 319: H1398-H1408, 2020.
[6] Ferruzzi, J, et al., *Ann Biomed Eng*, 41:1311-1330, 2013.
[7] Sazonova, OV, et al., *Matrix Biol*, 41:36-43, 2015.

LAMINA CRIBROSA DEFORMATIONS INDUCED IN VIVO BY ACUTELY AND CHRONICALLY ELEVATED INTRAOCULAR PRESSURE

Fuqiang Zhong (1), Yi Hua (1), Junchao Wei (1), Manik Bansal (1), Juan Reynaud (3), Brad Fortune (3), Ziyi Zhu (1), Ian A. Sigal (1,2)

(1) Department of Ophthalmology
University of Pittsburgh
Pittsburgh, PA, USA

(2) Department of Bioengineering
University of Pittsburgh
Pittsburgh, PA, USA

(3) Devers Eye Institute
Legacy Health Research
Portland, OR, USA

INTRODUCTION

Elevated intraocular pressure (IOP) is a primary factor for the development and progression of glaucoma [1]. However, the mechanism(s) by which the elevated IOP leads to the biological effect of neural tissue damage remains not well understood and controversial [2]. A leading hypothesis is that the elevated IOP causes deformations of the lamina cribrosa (LC), such as stretch, compression, and shear, and that these deformations act as mechanical insult on the astrocytes and retinal ganglion cell axons at the LC, triggering or contributing to axon damage and death, and thus loss of vision [3, 4]. Glaucoma, however, is a chronic disease. Glaucomatous neural tissue damage does not occur after a few seconds or even minutes of elevated IOP [5]. Glaucoma results from chronically elevated IOP. As a living biological structure, an eye under chronically elevated IOP has the opportunity to remodel, ostensibly to adapt to increased mechanical load. [6]. If this were the case, the effects of an acute increase in IOP would be smaller after an eye has been subjected to chronically elevated IOP. Nevertheless, studies analyzing overall morphometric features of the optic nerve head suggest that in the early stages of glaucoma it is the opposite effect, namely that acutely elevated IOP has a larger effect in an eye that has been under chronically elevated IOP [7]. This intriguing effect is still not well characterized or understood, in part because it has not been measured precisely in vivo.

Our goal was to measure the in vivo LC deformations caused by acutely elevated IOP in an eye when healthy, and after experimentally induced chronically elevated IOP.

METHODS

The optic nerve head (Figure 1) of four eyes of four rhesus macaque monkeys were imaged using optical coherence tomography (OCT, Spectralis) in several imaging sessions. Herein, we analyze three sessions, two before (baselines 1 and 2) and one at the onset of laser-

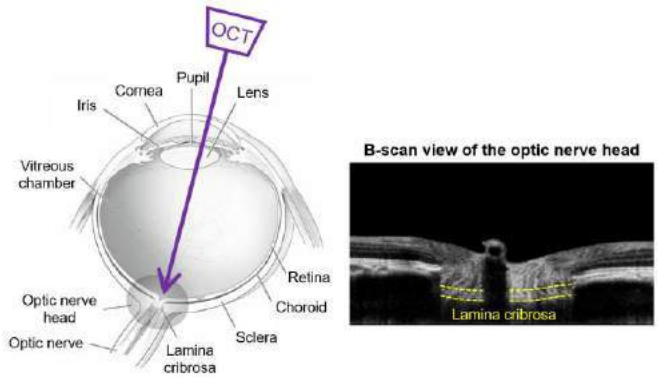

Figure 1. (Left) Anatomy of the eye in longitudinal cross-section. Adapted from a diagram by the NEI. (Right) Example OCT B-scan with manual marks indicating the lamina cribrosa (yellow dashed line) spanning across the scleral canal.

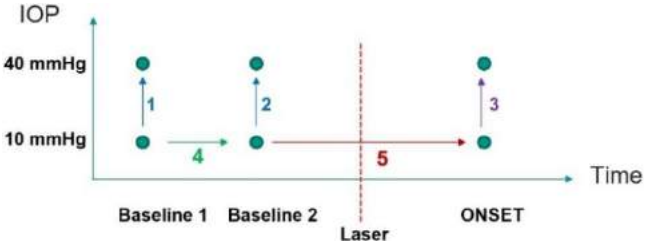

Figure 2: Experiment design with 5 steps comparisons: 1 acute at baseline; 2 acute at baseline repeated; 3 acute at onset; 4 chronic baseline-to-baseline; 5 chronic baseline-to-onset.

induced early glaucoma (EG). Onset was defined as confirmed peripapillary RNFL loss detected using OCT. In each session, the optic nerve heads were scanned after IOP was set for 10 minutes to 10 mmHg and then to 40 mmHg.

Digital volume correlation (DVC) analysis was then used to determine the LC changes between scans. LC changes represent either acute (between IOP levels) or chronic deformations (between sessions at same IOP, Figure 2).

RESULTS

LC deformations between baseline 1 and baseline 2 at low IOP (10 mmHg) were the smallest changes (compression 2-3%) in all four eyes, indicating good repeatability (Figure 3, Step 4). When the eyes were normal, comparing baselines at different IOPs, acute IOP-induced LC deformations were substantially larger (8-12%) and consistent in all four eyes at both tests (Figure 2, Steps 1 and 2), indicating a stable LC compliance in a given eye. Compliance varied between eyes.

Compared with the acute IOP effects at baseline, the acute IOP effects at EG onset (Figure 3, Step 3) were larger in three monkeys (up to 17%) and smaller in one monkey (5%). This indicates that chronically elevated IOP led three eyes to soften and one eye to stiffen.

Interestingly, at onset of EG, the LC changes induced by chronically elevated IOP were larger than the acute IOP-induced LC deformations at baseline (Figure 3, Step 5, 8-15%).

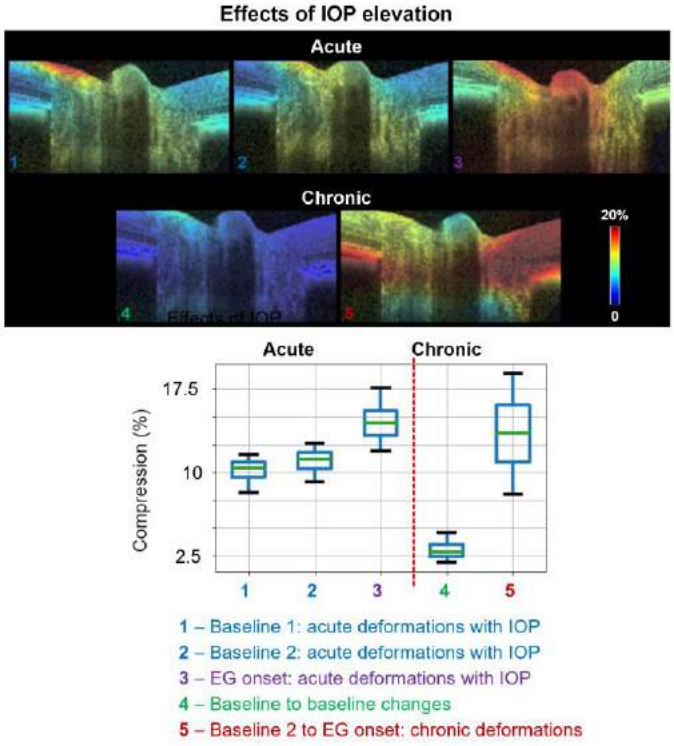

Figure 3: (Top) Example central optic nerve head B scans colored according to the compression magnitude. (Bottom) Distribution of LC compression measurements of a monkey eye using standard box plots (green line: median, box: quartiles, whiskers, 95th percentiles). The differences between any two steps were significant ($p<0.001$).

DISCUSSION

Our goal was to measure LC deformations induced by acutely and chronically elevated IOP when healthy and at onset of experimental glaucoma. Our results first demonstrate that our experimental and computational pipeline allows direct, repeatable measurement of these deformations in vivo in a non-human primate model. At EG onset, three of four monkeys exhibited substantial changes in the LC and increased LC compliance, suggesting that the damage and remodeling processes are already advanced. The fourth monkey exhibited smaller in the LC and slightly decreased compliance.

It is important to note that what is being measured by DVC between time points (steps 4 and 5) are not displacements or strains per se, but instead chronic changes through the development and progression of glaucoma. These could include, among others, neural tissue loss and remodeling of the LC.

Our results support and extend previous results obtained using gross optic nerve head morphology [7]. This demonstrates the great value of the carefully controlled model of chronically elevated IOP possible with the non-human primate. The tools developed in this project enable us to interpret the data and to understand the pathophysiology of glaucoma. Studies using similar OCT/DVC techniques [8] did not find a significant difference in the optic nerve head deformations caused by an acutely elevated IOP between healthy humans and patients with glaucoma. A potential explanation could be that we focused here in the LC region at EG onset. The loss of soft neural tissues and abundant “scars” suggest that in more advanced glaucoma the tissues are likely less compliant [9].

ACKNOWLEDGEMENTS

Supported in part by National Institutes of Health R01-EY023966, R01-EY028662, R01-EY030590, P30-EY008098 and T32-EY017271 (Bethesda, MD), the Eye and Ear Foundation (Pittsburgh, PA), Research to prevent blindness, BrightFocus Foundation, and Legacy Good Samaritan Foundation.

REFERENCES

[1] Quigley, Harry A. Glaucoma: macrocosm to microcosm the Friedenwald lecture. Investigative ophthalmology & visual science 46.8 (2005): 2663-2670.

[2] Yang, Hongli, et al. The connective tissue phenotype of glaucomatous cupping in the monkey eye-clinical and research implications. Progress in retinal and eye research 59 (2017): 1-52.

[3] Sigal, Ian A., et al. Eye-specific IOP-induced displacements and deformations of human lamina cribrosa. Investigative ophthalmology & visual science 55.1 (2014): 1-15.

[4] Campbell, Ian C., Baptiste Coudrillier, and C. Ross Ethier. Biomechanics of the posterior eye: a critical role in health and disease. Journal of biomechanical engineering 136.2 (2014).

[5] Abbott, Carla J, et al. Evaluation of retinal nerve fiber layer thickness and axonal transport 1 and 2 weeks after 8 hours of acute intraocular pressure elevation in rats. Investigative Ophthalmology & Visual Science 55.2 (2014): 674-687.

[6] Grytz R, et al. Lamina cribrosa thickening in early glaucoma predicted by a microstructure motivated growth and remodeling approach. Mechanics of Materials 44 (2012): 99-109.

[7] Yang, Hongli, et al. Spectral-domain optical coherence tomography enhanced depth imaging of the normal and glaucomatous nonhuman primate optic nerve head." Investigative ophthalmology & visual science 53.1 (2012): 394-405.

[8] Wang, Bo, et al. In-vivo effects of intraocular and intracranial pressures on the lamina cribrosa microstructure. PloS one 12.11 (2017): e0188302.

[9] Boote, Craig, et al. Scleral structure and biomechanics. Progress in Retinal and Eye Research 74 (2020): 100773.

EFFECT OF TOTAL ANKLE ARTHROPLASTY IMPLANTATION AND ADAPTIVE GAIT ON ANKLE AND ADJACENT JOINT KINEMATICS DURING SIMULATED GAIT

Jeffrey W. Hoffman (1), Jaeyoung Kim (2), Brett D. Steineman (1), Rogerio Bitar (2), Daniel Sturnick (1), Jonathan Deland (2), Constantine Demetracopoulos (2)

(1) Department of Biomechanics
Hospital for Special Surgery
New York, NY, USA

(2) Foot and Ankle Service
Hospital for Special Surgery
New York, NY, USA

INTRODUCTION

Total ankle arthroplasty (TAA) is developing as an effective treatment to restore function in patients with end-stage ankle arthritis [1,2]. However, due to inferior performance in comparison to hip and knee replacements, a need exists to improve the design of patient specific instrumentation for more accurate placement. Biomechanically, a contemporary TAA implant has been shown to nearly restore functional kinematics of the ankle and adjacent joints during simulations of healthy stance in level walking [3]. Despite this, patients with end-stage arthritis could develop compensatory gait abnormalities that persist after surgery. Patients who adopt abnormal walking patterns may be implanted with devices designed to restore normative walking patterns, potentially exacerbating further gait abnormalities [4]. Therefore, our objective in this study is to isolate the individual and combined effects of TAA implantation and gait adaption from ankle arthritis on foot and ankle kinematics during simulated level walking. We hypothesized that foot and ankle kinematics would primarily be altered through adaptations in gait resulting from ankle arthritis and that the combined effect of the implantation and adaption would further deviate kinematics from normative values

METHODS

An adaptive robotic gait trajectory was formulated through collection of *in vivo* level walking data from 10 post-surgical TAA subjects (Age 62-76; 7M, 3 F; Follow up time 26-77 months) who had incurred ankle arthritis prior to surgery. All subjects were implanted with the Salto Talaris TAA (Salto; Integra LifeSciences; Plainsboro Township, NJ). Three-dimensional gait analysis was performed using a 12-camera motion capture system which tracked retroreflective markers attached to the tibia and foot. Subjects completed three level walking trials over an embedded force plate (Bertec Corp.; Columbus, OH) while tibial kinematics, electromyography of the gastrocnemius and tibialis anterior muscles, and ground reaction forces were collected. The data was then converted into force plate trajectory and muscle inputs to be used for gait simulation.

Twelve mid-tibia cadaveric specimens (5L, 7R; 9M, 3F; Age at time of death: 28-80) were used in this study with Institutional Review Board approval. A validated six-degree of freedom robotic gait simulator was used to simulate stance phase (Baxter, 2016). The simulator recreates kinematics and loading incurred through gait through rotating a force plate around a stationary tibia while muscle forces are applied by eight linear actuators. For each specimen a fuzzy logic controller is used to iteratively converge the *in vivo* ground reaction force profile from the human subject data collection. Reflective markers attached to intracortical bone pins were attached to the tibia, talus, navicular, calcaneus, and first metatarsal. Motion was then tracked by an 8-camera motion capture system during simulations.

In testing, the specimen was first placed on the simulator in the intact condition, where it was simulated in both healthy and adaptive gait simulations. The specimen was then implanted with a Salto Talaris TAA (Integra LifeSciences) by a surgically trained orthopaedic fellow and then loaded back onto the simulator, where adaptive and healthy gait trials were again conducted in the implanted condition. In total, four conditions were collected on each specimen: intact with a healthy walking trajectory (intact-healthy), intact with an adaptive walking trajectory (intact-adaptive), implanted with TAA with a healthy walking trajectory (TAA-healthy), and implanted with TAA with an adaptive gait trajectory (TAA-adaptive).

Ankle, subtalar, and talonavicular joint kinematics in each condition were compared to intact-healthy to isolate the effects of implantation and adaptive gait on kinematics. Although all kinematics were recorded and processed, the results reported in this abstract correspond with joint rotations in the primary anatomic plane for each joint: ankle sagittal rotation, subtalar coronal rotation, and talonavicular transverse rotation. Bias-corrected 95% confidence intervals were calculated of the repeated-measures difference between each condition and intact-healthy. Significant differences were noted in instances in which the confidence intervals did not cross zero.

RESULTS

In the comparison of foot and ankle kinematics between the intact-healthy and intact-adaptive conditions, significant differences were noted in the ankle, subtalar and talonavicular joint (Figure 1). In isolating adaptive gait, ankle dorsiflexion significantly increased in

mid-to-late stance. In the subalar joint, adaptive gait significantly increased in eversion at toe-off, near the end of the stance phase. In the talonavicular joint, adaptive gait significantly increased in abduction for a short period of time in early and late stance.

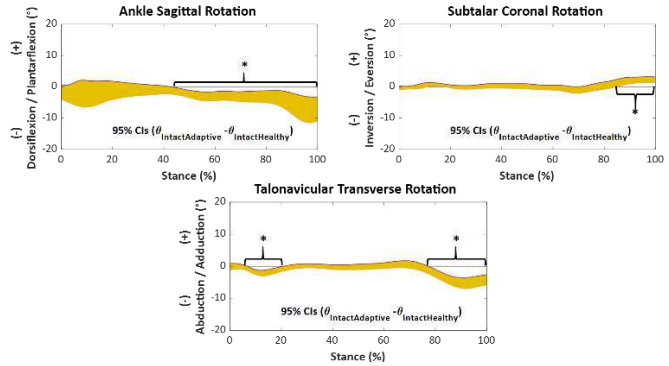

Figure 1: Bootstrapped 95% confidence intervals for the difference between joint kinematics of the intact-healthy condition and the intact-adaptive condition during simulations of level walking. {*} denotes periods of stance which significantly deviates from normative values

In the comparison of foot and ankle kinematics between the intact-healthy and TAA-healthy conditions, significant differences were noted in the ankle, subtalar and talonavicular joint which occurred at different instances of gait than the differences found in isolating gait adaptation (Figure 2). In isolating ankle implantation, the specimens demonstrated increased ankle plantarflexion, increased subtalar eversion, and increased talonavicular abduction compared to intact-healthy stance in mid-stance.

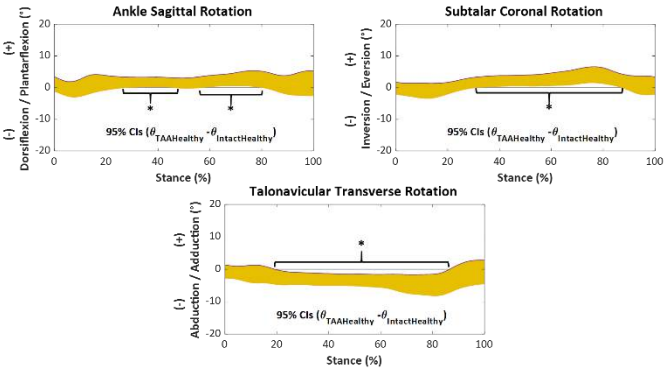

Figure 2: Bootstrapped 95% confidence intervals for the difference between joint kinematics of the intact-healthy condition and the TAA-healthy condition during simulations of level walking. {*} denotes periods of stance which significantly deviates from normative values

In the comparison of foot and ankle kinematics between the intact-healthy and TAA-adaptive conditions, in looking at the combined effects of gait adaptation and implantation, significant differences were amplified in the subtalar and talonavicular joints (Figure 3). In the ankle joint, plantarflexion increased in early stance and dorsiflexion increased in late stance compared to the intact-healthy condition. In the subtalar joint, significant increases in dorsiflexion occurred throughout much of the stance phase with adaptive gait and implantation. In the talonavicular joint, abduction also significantly increased throughout most of the stance phase.

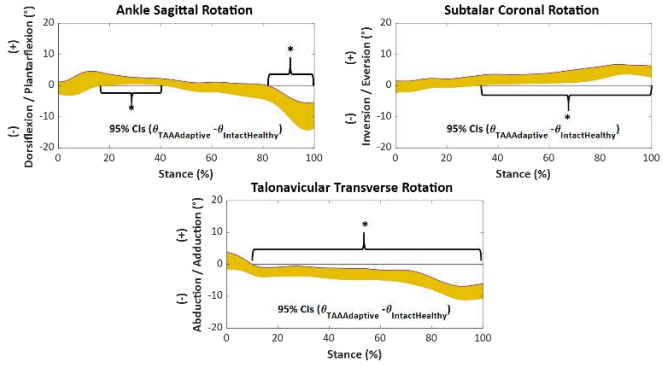

Figure 3: Bootstrapped 95% confidence intervals for the difference between joint kinematics of the intact-healthy condition and the TAA-adaptive condition during simulations of level walking. {*} denotes periods of stance which significantly deviates from normative values

DISCUSSION

Our results suggest that gait adaptation and implant constraint both contributed to changes in ankle and adjacent joint kinematics. The two factors also appear to influence two different regions of the stance phase. For the most part, isolation of gait adaptation demonstrated significant changes to joint kinematics in late stance. Isolation of the effects due to implantation revealed significant differences primarily within mid-stance. The combined influence of gait adaptation and implantation appears to amplify or negate deviations from normal kinematics at times throughout stance. For instance, adaptive gait increased subtalar eversion and talonavicular abduction in late stance and implantation increased them in midstance, which resulted in an amplification of these changes when looking at their combined influence. In contrast, adaptive gait increased dorsiflexion in mid-to-late stance but implantation increased plantarflexion in mid-stance, which resulted in less changes in ankle sagittal rotation from intact with healthy gait in mid-stance when considering both gait adaptation and implantation. Our findings have important implications for the future of development in total ankle arthroplasty. Oftentimes, ankle implants are evaluated or designed based on information derived from healthy kinematics and loading [1,6], which is the ideal scenario but may not be the best case to consider during development. Instead, a more realistic scenario is that patients maintain gait adaptations long after implantation [7]. Therefore, kinematic and loading differences from gait adaptations that remain after implantation may need to be considered in the development process of future devices along with implant constraints.

ACKNOWLEDGEMENTS

Aided by a grant from the Orthopaedic Research and Education Foundation with funding made possible by Wright Medical Technology, Inc. Robotic gait simulator made possible by funding from American Iron and Metal Inc.

REFERENCES

[1] Lefrancois T et al, J Bone Joint Surg Am, 99:342-348, 2017
[2] Gramlich, Y et al, Int Orthop, 42:2375-2381, 2018.
[3] Saito G et al, Foot Ankle Int, 40: 873-879, 2019.
[4] Singer, S et al, J Bone Joint Surg Am, 95:e191(1-10), 2013.
[5] Baxter, J et al, J Orthop Res, 34: 1663-1668, 2016.
[6] Sopher et al., Med Eng Phys, 42: 80-90, 2017.
[7] Valderrabano et al., Clin Biomech, 22: 894-904, 2007.

ESTIMATION OF CLINICAL SIZE OF BREAST TUMOUR LESIONS USING CONTRAST ENHANCED MAGNETIC RESONANCE IMAGING: DELINEATION OF TUMOUR BOUNDARIES

Manpreet Singh (1), Manjesh Dalal (2), Gurasis Singh Sodhi (2)

(1) Department of Mechanical Engineering, University of Maryland Baltimore County, Baltimore, MD, USA

(2) Government Medical College and Hospital, Sector-32B, Chandigarh, India

INTRODUCTION

Breast Imaging-Reporting and Data System (BI-RADS) classifies breasts into four categories in the order of radiographic breast density composition namely extremely dense (ED)-10% (type-D), heterogeneously dense (HD)-40% (type-C), scattered fibroglandular (SF)-40% (type-B) and predominantly fatty (PF) is reported in about 10% of women (type-A) [1]. Under such classification BI-RADS defines tumour into namely six assessment categories[2]. TNM (Tumour-Node-Metastasis) tool is widely used to describe the stage of tumour. T refers to size of the tumour, N relates to primary inspection whether cancerous cells spread to lymphatic nodes and M explains whether it invades to other organs of the patient. Clinically, the staging of the tumour in the breast may be defined as T1 (size≤20 mm): T1mi (≤ 1 mm), T1a (1 mm < size ≤ 5 mm), T1b (5 mm < size ≤ 10 mm), T1c (10 mm < size ≤ 20 mm); T2 (20 mm < size ≤ 50 mm); T3 (≥ 50 mm); T4a (tumour has grown into chest wall), T4b (tumour has grown into skin), T4c (grown into chest wall and skin), T4d (inflammatory).

The delineation of tumour is defined using three fundamental axioms i.e. tumour volumes[3] namely gross tumour volume (GTV), clinical target volume (CTV), planning target volume (PTV) is critical to design an effective radiotherapy planning or thermal ablation treatment therapy (Radiofrequency Ablation) etc. Hence, the accurate tumour boundaries needs clear demarcation in order to ensure the safety of organs at risk (ORs) considering that the organs must not receive higher-than-safe-dose. Therefore, clinical size of tumour holds a great significance for the tumours such as glioblastoma multiforme (GBM), CWR (Chest Wall Recurrence) etc. where damage to healthy anatomical structures such as spinal cord, chest wall etc., produces a severe clinical manifestation[4].

METHODS

Clinical breast MRI examination was performed at Government Medical College and Hospital, Chandigarh, India in the department of Radiodiagnosis & Imaging with Phillips at magnetic field of 1.5T using a standard and consistent contrast enhanced injections following a clinical breast MRI protocol. MRI uses magnetic fields instead of x-rays to produce very detailed and refined cross-sectional images of the cancerous lesion of breast organ. Six Woman were imaged in the prone position using a dedicated multichannel surface array breast coil. After the native scan was obtained, Contrast Enhanced sequences (CE) were acquired in axial plane employing 3D T1-weighed fast gradient echo-based DCE series with one pre and three post-gadolinium contrast-enhanced sequences. MRI exams for breast imaging use a contrast material (usually gadolinium-DTPA) that was injected into a vein in the arm before or during the exam to improve the ability to capture detailed images of breast tissue. The DICOM format information about both breasts including other organs was captured. The nearest neighbor of tumour (subpart node T) node corresponds to the node *i* in the breast (object) mesh having the minimum Euclidean distance (ED) to the tumour node via eq. 1 as:

$$ED = \sqrt{(x_{nodeT} - x_i)^2 + (y_{nodeT} - y_i)^2 + (z_{nodeT} - z_i)^2} \quad (1)$$

where, *x, y, z* represents the nodal coordinates. It is ensured that tumour offers a higher level of refinement compared with the mesh for the breast anatomy as a single unit.

RESULTS

Fig. 1 illustrates one slice from a set of 1051 images of DCE-MRI acquisition. In the first case scenario, the breast composition is found to resemble a case of type-A predominantly or entirely fatty breast anatomy. A relatively well defined irregular mass lesion with spiculated

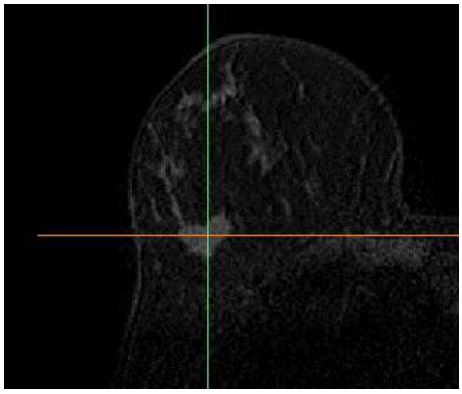

(a)

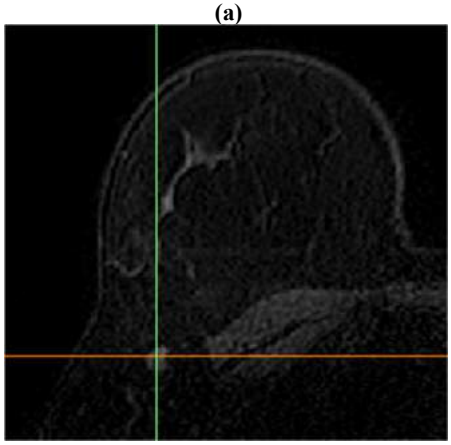

(b)

Figure 1: Case Scenario-1: a) DCE-MRI slice of type-A breast cancerous lesion in axial plane, b) spicule is approaching chest wall.

margins measuring 19 ×17×14 mm in size and appearing isointense to glandular tissue on T2W images and hyperintense on STIR images is noted in the upper outer quadrant of the right breast. The cancerous lesion is reported at a distance of 1.5 cm from the skin at the lateral border of the breast and 1.8 cm from the chest wall. It can be followed from fig. 1b that one of the spicule appears mildly bulky and pulled up and is seen reaching upto the pectoralis muscle. A lymph node measuring 10 × 6.3 mm is also noted in the axillia along the chest wall. Hence, first case is assessed as BI-RADS V (malignant case). Referring to fig. 2, the second case scenario, the breast composition is a case of type-B scattered fibroglandular breast anatomy. STIR hyperintense diffuse subcutaneous thickening thickening measuring 1.3 cm with corresponding mild linear non-mass enhancement curves. It can be coined as a case of BI-RADS IVa. Fig. 3 shows a well circumscribed homogeneously enhancing STIR hyperintense mass lesion measuring 1.4 × 0.8 cm and appearing isointense to glandular tissue on T2W images is noted in retro areolar location in midline with type II enhancement and is a case of BI-RADS IV C. The distance from the skin at anterior surface of the breast is 2.1 cm. Homogeneous internal enhancement is found on post contrast images.

DISCUSSION

This study covers an extended spectrum of clinical cases (1) to analyze the accurate tumour size, (2) to demarcate accurate tumour boundaries in order to plan an effective target volumes for radiotherapy, thermal ablation including radiofrequency ablation and nanoparticles induced thermal ablation. Once the clinical size of the tumour is established, realistic three-dimensional volume of the tumour can be calculated with its realistic shape and irregular nodal features with the available computational imaging platforms such as MIMICS, 3-matic, Simplewa-

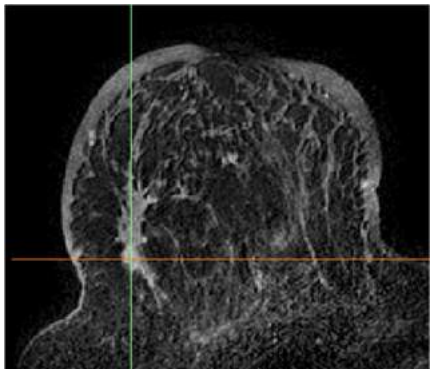

Figure 2: Case Scenario-2: Illustration of DCE-MRI slice of type-B breast carcinoma in axial plane.

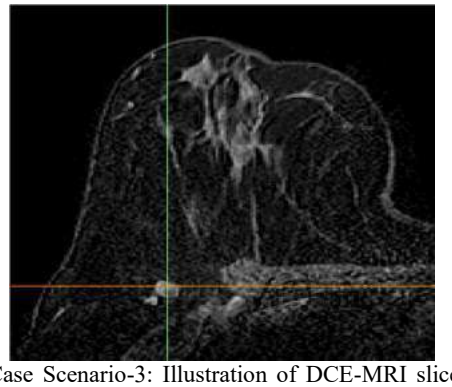

Figure 3: Case Scenario-3: Illustration of DCE-MRI slice of type-B breast carcinoma in axial plane.

-re etc. Such domains can be successfully imported into ABAQUS, Comsol-Multiphysics, ANSYS etc. as mesh files to do heat transfer analysis or run Monte-carlo simulations for effective radiation planning. Accurate margins (0.5 cm-1 cm) can only be sacrificed if true tumour boundaries with irregular spread can be retrieved. Hence, this study helps in enhancing the treatment efficacy of cancer treatments and thereby designing protocols for radiation, thermal ablation and hyperthermia therapies. As used in first case scenario, the high resolution data with slice thickness equivalent to 0.5 mm or lesser must be used in order to capture the detailed anatomical features and pathology of tumour. The future effort in this direction would be to capture the blood supplying vessels to the tumour using MRI-Angiogram although not commonly used in imaging.

ACKNOWLEDGEMENTS

Manpreet Singh is appreciative of the Graduate School, University of Maryland, Baltimore County for conferring the award of Dissertation Fellowship towards the progress of Doctorate degree. M. Dalal and G. S. Sodhi are thankful to the GMCH Sec-32B, Chandigarh for sharing the patient's data following institutional approval. It is also ensured that the details of the patients used for this primary analysis is kept highly confidential and will not be disclosed in any forum except using it for analysis, research and computational purpose.

REFERENCES

[1] https://www.cancer.gov/types/breast/breast-changes/dense-breasts

[2] https://radiopaedia.org/articles/breast-imaging-reporting-and-data-system-bi-rads-assessment-category-6.

[3] Burnet, N.G. et al., *Cancer Imaging,* 4:153-161, 2004.

[4] Vaupel, P et al., Pathophysiol. of solid tumour, *Springer* 51-92, 2009

INVESTIGATING THE EFFECT OF SPORTS HELMETS ON THE FREQUENCY RESPONSE OF THE HUMAN BRAIN

Fargol Rezayaraghi (R. Araghi) (1), Javid Abderezaei (1), Efe Ozkaya (1), Colleen E Shea (1), Mehmet Kurt (1,2)

(1) Dept. of Mechanical Engineering, Stevens Institute of Technology, Hoboken, NJ, USA.

(2) Biomedical Engineering and Imaging Institute, Mount Sinai Icahn School of Medicine, New York, NY, USA.

INTRODUCTION

Sport-related mild traumatic brain injury (mTBI) is one of the causes of mortality and morbidity in athletes, which can be prevented or reduced in severity by wearing protective headgears such as helmets. These protective helmets are often designed to mitigate the head kinematics during an impact [1, 2] and their efficacy is evaluated by analyzing their effect on linear and rotational kinematics of the head [1, 3]. While recent studies have shown that brain substructure dynamics plays an important role in concussion mechanism, these dynamic characteristics are currently not considered in helmet designs. Investigation of the brain substructure biomechanics during impacts has revealed crucial frequency dependent and localized phenomena that have been associated with the injury outcome [4, 5]. Characterizing the dynamics of the brain during impacts has shown the existence of localized modes and multi-modal behavior in the brain [4]. Also, by using modal analysis and Finite Element (FE) simulations a strain concentration in deep regions of the white matter, and distinct modal frequency in corpus callosum have been reported [4, 5]. Specifically, the brain has been shown to be sensitive to displacement frequencies around 30Hz, which exacerbated the observed deformation [4, 5]. Despite the importance of brain substructures in mTBI mechanism, most of the helmet designs have only focused on mitigating the head kinematics. Helmet performance still needs to be improved by including the effect of the dynamics of the brain substructures, along with the mitigation of head kinematics. Here, in this work, our aim was to evaluate the effect of different helmets on dynamic frequency response of the brain substructures during impacts. We performed impact pendulum experiments and then conducted brain FE simulations. Finally, we investigated the dynamic frequency response of different brain substructures by a modal analysis technique.

METHODS

Impact Pendulum Tests: We used an impact pendulum test setup to apply impacts to a Hybrid III anthropomorphic head-neck system (Figure 1(a)). Impact pendulum was released at a 60° angle for each test, with approximate impact velocity of 4.3 m/s. Three different commercially available helmets including a hockey helmet (Figure 1(b)), a football helmet (Figure 1(c)) and a ski helmet (Figure 1(d)) were tested three times to compare their effectiveness on mitigating the head kinematics, and the resultant dynamic response of the brain. Head kinematics were measured using a 6DOF sensor package (DTS, Seal Beach, CA), consisting of one tri-axial accelerometer (ACC3 PRO) and three angular rate sensors (ARS PRO-8K 2000 Hz), which were located at the center of gravity (CoG) of the dummy headform. We applied side impacts to induce coronal rotation, since it has been reported that rotations in the coronal direction can cause large strains in certain vulnerable regions such as corpus callosum [6,7].

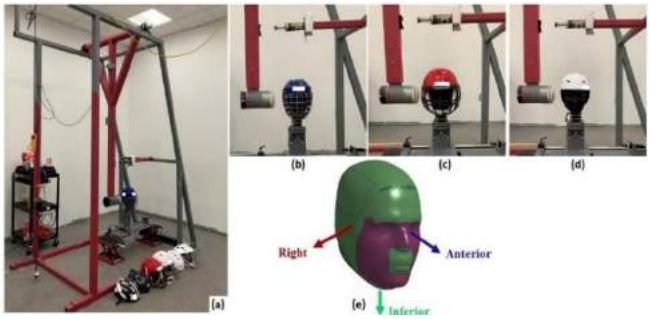

Figure 1. Helmet tests through an impact pendulum: (a) Impact pendulum test setup. (b) Hockey helmet. (c) Football helmet. (d) Ski helmet. (e) Coordinate system in FE model.

Finite Element Analysis: The Global Human Body Models Consortium (GHBMC) skull-brain model was used in this study (Figure 1(e)) to simulate head impacts in the LS-Dyna environment [8]. The purpose of these simulations was to observe the effects of different helmets on the dynamic response of the brain substructures. To this end, we extracted nodal coordinates from brain substructures to calculate their relative displacement to the skull.

Dynamic Mode Decomposition: Dynamic Mode Decomposition (DMD), is a multivariate method that we used for extracting the modal behavior of the brain tissue. It allows analyzing the spatiotemporal differences within the brain substructures as a function of modal frequency [4].

RESULTS

Extracted kinematics datasets from the impact pendulum tests were used as inputs to the finite element model to observe the deformation of each brain region during an impact. Figure 2 (a-c) shows the rotational velocity in three directions for the mentioned helmets. The average maximum rotational velocity was 32.3 rad/s for the hockey helmet, 31.2 rad/s for the ski helmet and 30.9 rad/s for the football helmet.

In the next step, our aim was to study the dynamic response of the brain substructures. Nodal displacements of the corpus callosum, brainstem and cerebellum were extracted to calculate relative displacement of the brain-skull system. We performed DMD analysis on these data to find temporal modes of the corpus callosum, cerebellum and the brainstem (Figure 2 (d-f)). In the corpus callosum, the first frequency was around 10 Hz for all helmets (Figure 2 (d)). At this frequency, the ski helmet had a lower modal amplitude compared to other helmets. The second harmonic appeared at a frequency regime around 40 Hz for the football and ski helmets. For the hockey helmet, the second harmonic was at a frequency of 30 Hz with a higher modal amplitude compared to other helmets. In the brainstem, the main frequency of motion was around 6-10 Hz and the second one was around 35-40 Hz for all helmets (Figure 2 (e)). At the second harmonic, higher amplitude was observed in hockey helmet, which was two times higher than the modal amplitudes of the ski and football helmets. In the cerebellum, while the main frequency of motion for the ski and football helmets was observed around 10 Hz, the first harmonic for the hockey helmet occurred at the frequency of 50 Hz, in which the second harmonic of the ski and football helmets was observed (Figure 2 (f)).

DISCUSSION

Protective helmets are usually designed to mitigate the kinematics of the head during an impact [1]. To improve the performance of the helmets, it is crucial to also investigate the dynamic characteristics of the brain as well as the kinematics of the head. Here, we studied the effect of different helmets on head kinematics and the dynamic response of the brain substructures. When only analyzing the head kinematics, we observed that the football helmet performed better compared to the other helmets. Looking into dynamic frequency response of the brain, our results showed that in the corpus callosum and the brainstem, which have been reported as vulnerable regions in injury, the modal amplitude around the frequency regime of 20-30 Hz was higher in hockey helmet compared to ski and football helmets. This range of frequency was important to us, since in previous studies, it was reported that the brain is more susceptible to injury for vibrations within the frequency regime of 20–40 Hz [4]. Our results suggested that the tested hockey helmet cannot dissipate frequency components of the brain around 35-45 Hz compared to football and ski helmets which is troubling, since it has been shown that the brain is sensitive to these frequency regimes, and such harmonics might lead to strain concentration in corpus callosum [9]. In the future, we will focus on testing these helmets in other impact loading conditions to provide a holistic view between helmet properties and frequency-dependent brain substructure response.

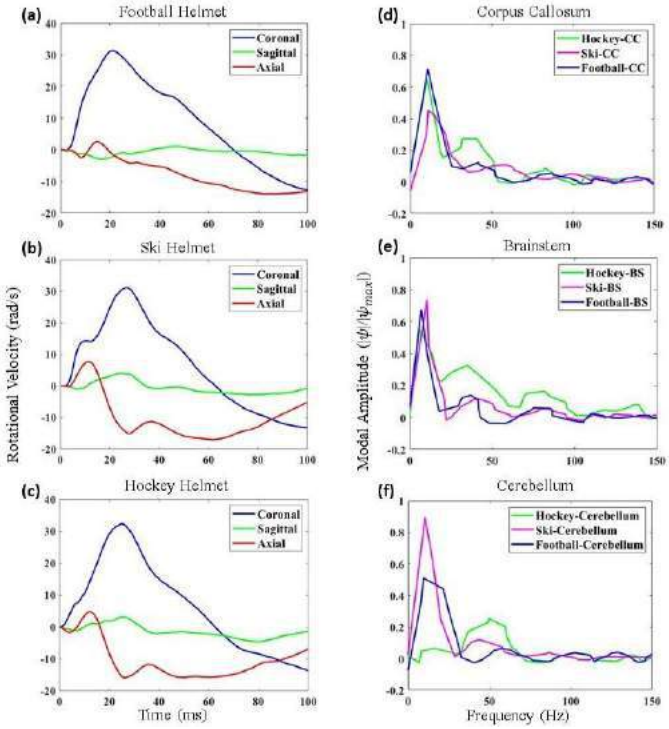

Figure 2. The effect of different helmets on rotational kinematics and modal amplitudes: The rotational velocity of the head for (a) Football helmet, (b) Ski helmet and (c) Hockey helmet. Modal amplitudes of (d) Corpus callosum, (e) Brainstem and (f) Cerebellum for different helmets.

ACKNOWLEDGEMENTS

This research was partially supported by NSF Grant No. CMMI-1728186 and New Jersey Health Foundation Grant No. PC 86-20.

REFERENCES

[1] Hoshizaki, T. B, & Brien, S. E, *Neurosurgery*, 55(4):956–967, 2004.

[2] Allison, M. A, "The performance of helmet-based kinematic measurement systems:Importance for mild traumatic brain injury prevention.", 2015.

[3] Ito, D et al., *International Journal of Crashworthiness*, pp. 1–8, 2020.

[4] Laksari, K, et al., Physical Review Letters, 120(13), p.138101, 2018.

[5] Abderezaei, J, et al., Physical Review Applied,12(1), p.014058, 2019.

[6] Kleiven, S. *International Journal of Crashworthiness*, 11(1), 65-79, 2006.

[7] Zhou, Z, et al., *Journal of Neurotrauma*, 37(8), 1074-1090, 2020.

[8] Tiernan, S, et al., Computer methods in biomechanics and biomedical engineering, pp. 1–1, 2020.

[9] Mojahed, A., et al., *Journal of Biomechanical Engineering*, 142(9), 2020.

EFFECT OF REGION AND DIRECTION ON MENISCUS ELASTICITY AS MEASURED BY ATOMIC FORCE MICROSCOPY

Kevin Orton (1), Wyndham Batchelor (1), Nöel M. Ziebarth (1), Francesco Travascio (2,3,4), Alicia R. Jackson (1)

(1) Department of Biomedical Engineering
University of Miami
Coral Gables, FL USA

(2) Department of Mechanical and Aerospace Engineering
University of Miami
Coral Gables, FL USA

(3) Department of Orthopaedic Surgery
University of Miami
Miami, FL USA

(4) Max Biedermann Institute for Biomechanics
Mount Sinai Medical Center
Miami Beach, FL USA

INTRODUCTION

The meniscus plays an integral role in the mechanical functioning of the knee joint, offering load support and congruency while also providing lubrication [1]. The presence of a healthy meniscus is essential for protecting the underlying articular cartilage against osteoarthritis, a serious condition affecting millions of people each year. To perform its function, the meniscus has a highly organized extracellular matrix composed of parallel collagen fiber bundles that run along the circumferential direction, imparting the tissue with the strength to withstand complex loading [1]. Understanding the structure-function relations for mechanical properties of the meniscus can provide important insight into the tissue physiology and pathology. Such quantitative information is valuable for developing new strategies for treating meniscus defects and/or degeneration, either by way of tissue engineered substitutes or via computational modeling. Atomic force microscopy (AFM) is a state-of-the-art method that can be employed to measure the Young's (elastic) modulus of soft tissues such as the meniscus. The AFM technique allows for measurement of distinct tissue regions, making it suitable for investigating mechanical inhomogeneities in the meniscus.

The objective of this study was to determine the effect of region and direction/orientation on the micromechanical properties of porcine meniscus. We hypothesized that both anisotropic and inhomogeneous properties would be determined, based on our knowledge of the structure of the meniscus. Thus, we used AFM to measure the Young's modulus of porcine meniscus in medial and lateral meniscus from the inner and outer regions and in the axial and circumferential directions.

METHODS

Specimen Preparation: Fresh porcine knees were obtained from a local abattoir. Menisci were harvested, wrapped in saline soaked gauze, and stored in plastic bags at -20ºC. On the day of the experiment, two slabs of tissue were isolated from the central region of a meniscus: one in the circumferential direction and one in the axial direction, see Figure 1. Samples were cut to 1.5mm thickness using a Compresstome® (VF-200-0Z, Precisionary, Natick, MA). The samples were then divided into the outer one-third and the inner two-thirds for 4 total samples per meniscus: axial inner (AI), axial outer (AO), circumferential inner (CI), and circumferential outer (CO), see Figure 1. Samples were also divided into medial and lateral groups, for a total of 8 sample sets. Prior to AFM measurements, each sample was secured to its own petri dish using super glue and then immersed in phosphate buffered saline (PBS) solution supplemented with Protease Inhibitor (Roche) to prevent degradation of the tissue during experimentation.

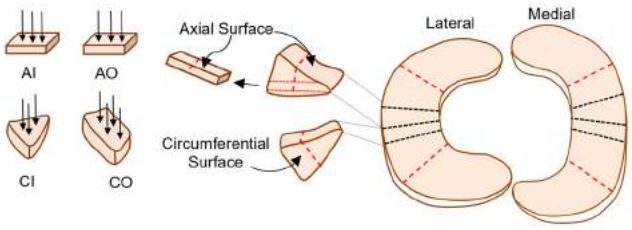

Figure 1: Schematic of locations and orientations of test specimens

AFM Measurements: A custom AFM fitted with a silicon nitride cantilever (k=5.4 N/m) with a 5µm diameter borosilicate glass particle tip (Novascan, Ames, IA) was used to perform indentation tests on the meniscus samples [2]. All tests were performed at room temperature (~22ºC) on fully hydrated tissues. Measurements were repeated 10 times at 3 different locations on each sample to account for normal variations in measurements. Force-indentation data was curve-fit to the

Hertz model using a custom MATLAB code, yielding measurements for the Young's (elastic) modulus of the specimens [2]. The goodness of fit for each was visually assessed to ensure accurate model fitting.

Statistical Analysis: All measurements from each sample set were pooled together. Outliers (more that 2 standard deviations from the mean) were excluded from statistical analysis, resulting in a different total number of measurements in each group. ANOVA analysis of variance followed by Tukey post-hoc testing was used to determine statistically differences between groups; significance was set at α=0.05.

RESULTS

The results for Young's modulus of elasticity for the 8 groups investigated are shown in Figure 2. For each group, n=5. ANOVA showed a significant effect of all factors on the tissue elastic modulus. For outer medial menisci, elasticity was higher in the circumferential direction then the axial direction (i.e., MCO>MAO, p=0.001), but no significant difference was found for corresponding lateral samples. Also in medial menisci, the modulus in circumferential specimens was higher in the outer region than in the inner region (i.e., MCO>MCI, p=0.001). The opposite trend was found for lateral samples (LCO<LCI), although the difference was not significant (p=0.082).

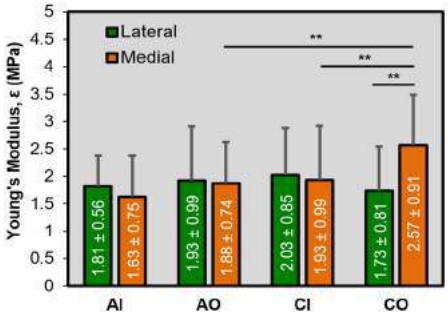

Figure 2: Results (mean ± standard deviation) for modulus of elasticity measurements for all 8 groups. n=5 for each. **: p<0.01

For the circumferentially oriented specimens in the outer region of the tissue, the elastic modulus of medial samples was significantly higher than that of lateral samples (i.e., MCO>LCO, p=0.001). There were no other significant differences between medial and lateral for corresponding specimen groups tested. Therefore, to further investigate correlations with a larger sample size, we pooled medial and lateral specimens into the 4 groups noted (AO, AI, CO, CI), for a total of n=10 for each group, and completed a second ANOVA with Tukey post-hoc testing. The results are shown in Figure 3. There was a significant effect of direction on the Young's modulus. For both inner and outer regions, the modulus in the circumferential direction was higher than in the axial direction (AI<CI, p=0.004; AO<CO, p=0.02). There was no significant difference comparing inner and outer specimens with the same orientation, although for both axial and circumferential groups, the elasticity was higher in the outer region compared to the inner region (p=0.086 for axial and p=0.24 for circumferential).

DISCUSSION

In this study, we investigated the effect of region and orientation on the micromechanical properties of porcine meniscus tissues. Our results, which averaged 1.93 ± 0.88 MPa across all specimens, are within the range of nanoindentation and AFM studies in the literature for meniscus tissues [3-9]. It should be noted that our results are higher than those determined in some other AFM studies; however, these discrepancies are likely the result of important differences in specimen

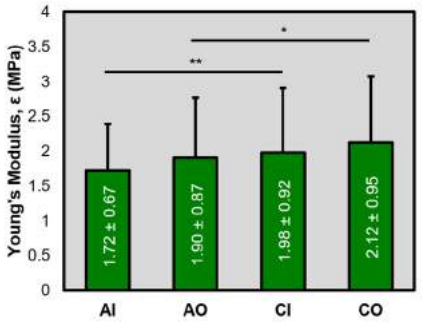

Figure 3: Results (mean ± standard deviation) for modulus of elasticity when pooling medial and lateral groups. n=10 for each. *: p<0.05; **: p<0.01

preparation techniques. That is, our samples were thicker and were fully hydrated during testing. Differences may also be due to species types.

The anisotropic trend for elastic modulus was expected based on the collagen fiber arrangement in the tissue, which includes parallel bundles organized in the circumferential direction of the tissue, allowing the meniscus to withstand hoop stresses upon loading [1]. Previous studies have shown a similar trend as that shown in Figure 3, with elasticity being higher in the circumferential direction [4].

Results also indicated that the region of the tissue (inner vs. outer) affected the mechanical properties, particularly for circumferentially oriented specimens. Region-dependent elasticity in the meniscus has been found previously [4-7]. This is again likely the result of the structural organization of the tissue: an earlier imaging study showed that the fiber bundles become less organized moving from outer to inner regions [10]. This relates with the function of the different tissue regions, with the outer zone bearing tensile forces and the inner zone bearing more compressive forces [1].

Only limited significant differences between medial and lateral meniscus biomechanical properties were found here. While some studies have found that mechanical properties differ between these two tissue types [8-9], others have failed to find differences [3]. The lack of significance here may be due to a small sample size (n=5); more extensive studies are warranted to better understand this effect.

Taken together, the results of this study provide important insight into the inhomogeneous and anisotropic micromechanical properties of the meniscus. This information can be employed to develop site specific tissue scaffolds for tissue repair, which have properties that appropriately mimic the native tissue. Future studies will address study limitations, including small sample size and use of porcine, rather than human tissues, in order to more fully understand tissue micromechanics and related function and pathology.

ACKNOWLEDGEMENTS

This study was supported by NIH/NIAMS (R01AR073222).

REFERENCES

[1] Makris EA et al., *Biomaterials,* 32:7411-7431, 2011.
[2] Ziebarth NM et al., *Molecular Vision*, 13:504-510, 2007.
[3] Li Q et al., *J Biomechanics* 48: 1364-70, 2015.
[4] Li Q et al., *Acta Biomaterialia*, 54: 356-66, 2017.
[5] Li Q et al, *J Biomechanics*, 72: 252-7, 2018.
[6] Sanchez-Adams J et al., *J Orthopaedic Research* 31: 1218-25, 2013.
[7] Kwok J et al., *Nanomedicine* 10(8):1777-1785, 2014.
[8] Moyer JT et al., *J Biomechanics* 45: 2230-5, 2012.
[9] Moyer JT et al., *Acta Biomaterialia* 9(5):6624-9, 2013
[10] Andrews et al., *BMC Medical Imaging* 13: 21, 2013.

EXAMINATION OF PROSPECTIVE AND RETROSPECTIVE GATED 4D FLOW MRI ACQUISITIONS TO EVALUATE FLUID VELOCITIES IN THE CAROTID BIFURCATION

Elliott R. Hurd (1), Jason K. Mendes (2), Edward V.R. DiBella (1,2), John N. Oshinski (3,4), Lucas H. Timmins (1,5)

(1) Department of Biomedical Engineering
University of Utah
Salt Lake City, Utah, USA

(2) Department of Radiology and Imaging Sciences
University of Utah
Salt Lake City, Utah, USA

(3) Department of Radiology and Imaging Sciences
Emory University School of Medicine
Atlanta, Georgia, USA

(4) Department of Biomedical Engineering
Georgia Institute of Technology and Emory University School of Medicine
Atlanta, Georgia, USA

(5) Scientific Computing and Imaging Institute
University of Utah
Salt Lake City, Utah, USA

INTRODUCTION

Four-dimensional flow cardiovascular magnetic resonance imaging (4D flow cMRI) provides a non-invasive, non-ionizing radiation-based technique to evaluate the *in vivo* blood flow environment [1]. The ability of 4D flow cMRI to capture multidimensional flow fields provides a more comprehensive evaluation of the hemodynamic environment over 2D-based techniques (e.g., ultrasound). In addition to continued developments to improve image quality, recent advances in 4D flow cMRI pulse sequences now afford flexibility in the acquisition gating strategy. With prospective gating, MR data acquisition begins after detection of a physiologic "trigger" (e.g., an R-wave), and data are acquired across a finite time window that is set far lower than the cardiac cycle period (Fig. 1). As a result, a gap in acquisition at the end of the cardiac cycle occurs to avoid a missed trigger. With retrospective gating, data are acquired continuously across the complete cardiac cycle and later grouped based on a physiologic measure (e.g., EKG) collected simultaneously with the MR data. Notably, retrospective gating can lead to changes in image quality due to potential temporal smoothing. Thus, the selection of gating techniques is a compromise that ultimately depends on the clinical application of 4D flow and data of interest.

Hemodynamics in the carotid bifurcation are of considerable clinical interest due to the association of complex flow patterns in the carotid bulb and atherosclerosis [2]. In this anatomic region, low fluid velocity and flow reversal occur in late systole and throughout diastole in the carotid bulb, and suggests that retrospective gated 4D flow acquisitions may offer increased prognostic value in the clinical management of stroke. Thus, the aim of this investigation was to quantitatively compare the 4D flow cMRI-derived hemodynamic environment in the carotid bifurcation between prospective and retrospective gated acquisitions.

METHODS

Image data were independently acquired in the left and right carotid bifurcation from two healthy volunteers using a 3T MRI scanner (PRISMA, Siemens, Erlangen, Germany) and bi-lateral carotid coil (Fig. 1). Prospective and retrospective EKG gating techniques were utilized to acquire data at each anatomic location with identical volume coverage. Data were collected across a field of view of 200×163×160 mm with 12 slices, resulting in a voxel size of approximately 1.5×1.5×1.8 mm^3. A velocity encoding (VENC) value of 70 cm/s was used in all spatial directions. Temporal resolution was approximately 49 and 35 ms for prospective and retrospective scans, respectively, and temporal coverage was approximately 85% and 100%, respectively, of the cardiac cycle. To allow evaluation of intra-scan variability, two prospective and retrospective gating acquisitions were performed in one volunteer during the same imaging session.

Acquired image data were segmented with semi-automatic techniques (Seg3D, SCI Institute, Univ. of Utah) to define the fluid (blood) volume (Fig. 1). Raw voxel values were converted to velocities using the defined VENC, and volumetric data were processed to provide interactive visualization of the flow fields and focal quantification of kinematic quantities. For flow visualization, image data were imported into ParaView, which included the OSPRay ray tracing framework plugin for high-quality renderings [3]. The velocity values were used to create streamlines which were encoded with velocity magnitude values for visualization. For quantitative analysis, velocity data were extracted in cross-sections perpendicular to the vessel centerline at locations ~3.5 mm from the carotid bifurcation in the common carotid, internal carotid (i.e., carotid bulb), and external carotid arteries (Fig. 1).

To evaluate the inter-scan (prospective vs. retrospective) and intra-scan variability in acquired data, through-plane velocity values (i.e., v_z) in corresponding anatomic planes (Fig. 1) and time points in the cardiac

cycle were examined. Data were compared at peak systole, as well as temporal average values across the complete (cycle time-average) or diastolic portion (diastolic time-average) of the cardiac cycle. Agreement was evaluated by calculating the concordance correlation coefficient (CCC) and with Bland-Altman analysis. Data are presented as mean±SD.

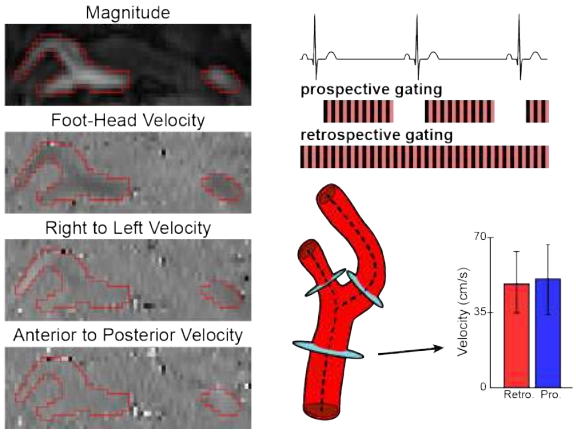

Figure 1: Schematic of image acquisition and quantitative analysis, including MR images (left), gating techniques (top right), and quantification of velocity data (bottom right).

RESULTS

Evaluation of the hemodynamic data revealed similarities between visualizations of flow streamlines encoded with velocity magnitude whether the data were collected with prospective or retrospective gating. For example, streamlines encoded with velocity at peak systole in the right carotid bifurcation of volunteer 1 demonstrated flow pattern similarities, including parabolic flow profile in the common carotid artery and multidirectional flow in the carotid bulb, and high velocities in the distal internal carotid artery (Fig. 2). Similar observations were also observed in the left carotid bifurcation of volunteer 2.

Quantitative examination of velocity data complemented the observed similarities in flow streamline data between the prospective and retrospective gated acquisitions. For example, strong agreement was observed between prospective and retrospective gated scans when comparing velocity values across both volunteers, all anatomic locations, and evaluated time points evaluated (CCC = 0.96; Fig. 3). In addition, Bland-Altman analysis revealed minimal bias (1.42 cm/s) in

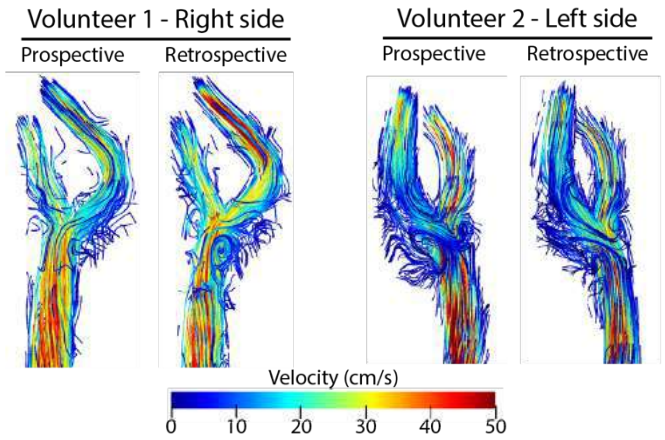

Figure 2: Flow streamlines in carotid bifurcations at peak systole from prospective and retrospective gated acquisitions.

velocity values between the prospective and retrospective gated acquisitions. A voxel-by-voxel comparison across gating techniques demonstrated an average difference of 0.33±4.41, 0.67±8.67, and 0.14±3.66 cm/s from cycle time-averaged, peak systole, and diastolic time-averaged velocity values, respectively. Finally, ~75% of the voxels had a difference of < 5 cm/s.

Evaluation of intra-scan variability (i.e., repeatability) demonstrated similar agreement and bias when compared to inter-scan variability (Fig. 3). For example, strong agreement (CCC = 0.93) and minimal bias (1.15 cm/s) was observed when comparing prospectively gated data independently acquired across two acquisitions. Similar values were seen when examining intra-scan variability with retrospectively gated techniques (CCC = 0.99; bias = 0.87 cm/s).

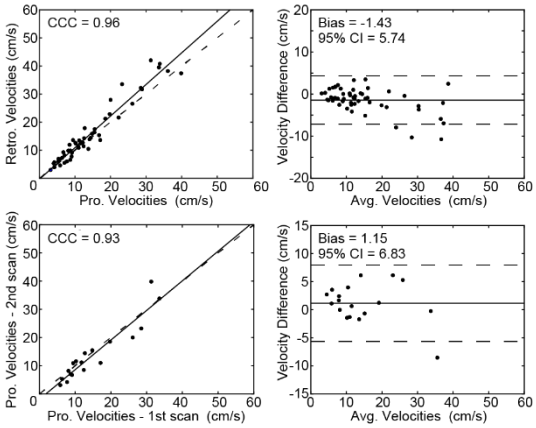

Figure 3: Linear regression (left) and Bland-Altman (right) analysis demonstrating strong agreement between the prospective and retrospective gated acquired velocities (top row) that is comparable to intra-scan agreement with prospective (bottom row) and retrospective (data not shown) gated acquisitions.

DISCUSSION

Our investigation demonstrates strong agreement in fluid velocities acquired with either prospective or retrospective gated 4D flow cMRI in the carotid bifurcation of healthy volunteers. We report qualitative similarities in flow patterns extracted from image data acquired with the two gating techniques with supporting quantitative data highlighting strong agreement and minimal bias in fluid velocities between the gating techniques. Furthermore, the inter-scan variability in velocity values was within the range of differences observed across intra-scan variability for each gating technique. Importantly, there is a clear advantage with the retrospective gated sequence as it covers 100% of the cardiac cycle, whereas the prospective gated sequence only covered 84%. Future studies that utilize 4D flow cMRI with retrospective gating may provide increase prognostic value in the clinical management of patients with stroke.

ACKNOWLEDGEMENTS

This work utilized equipment that was purchased with funding from the National Institutes of Health (S10 D018482).

REFERENCES

[1] Dyverfeldt, P et al., *J Cardiovasc. Magn. Reson.*,17:1-19, 2015.
[2] Ku, D.N. et al., *Arteriosclerosis*, 5:293-302, 1985.
[3] Wald, I et al., *IEEE Trans. Vis. Comput. Graph*, 23:931-940, 2017.

RAPID FORMATION OF 3D TUMOR MODEL WITH TUMOR-STROMA INTERFACE AT EXTREMELY HIGH CELL DENSITY

Cih Cheng, George T.-C. Chiu, and Bumsoo Han

Mechanical Engineering
Purdue University
West Lafayette, IN, USA

INTRODUCTION

Three-dimensional (3D) cell culture systems are becoming increasingly popular due to their ability to more closely mimic the in vivo microenvironment than the traditional 2D cultures. These 3D cultures present both structural and chemical ECM environment and recapitulate various aspects of the interactions between cell-cell and cell-matrix. Recent advances in cell biology, microfabrication, and tissue engineering enable a wide variety of 3D cell culture techniques. These include multicellular spheroids, organoids, hydrogel scaffolds, organs-on-chips, and 3D bioprinting [1]. These models have been developed and adopted for drug discovery, cancer cell biology, stem cell study, engineered functional tissues for implantation, and other cell-based analysis [2]. Among these applications, 3D cell culture models were mostly developed for oncology research. Numerous 3D tumor models have been reported [3], such as multicellular layers on porous membranes, scaffold-embedded cultures, multicellular spheroids, and tumor organoids. These 3D in vitro tumor models simulate the in vivo physiological microenvironment and may be useful platforms for preclinical studies [4].

Recent advances in biomaterials and microfabrication (e.g., microfluidics and microprinting) offered great opportunities to recreate 3D models in a controlled manner. Several groups have attempted to utilize hydrogels as biomimetic matrices [5]. These hydrogels have been tailored into different compositions with flexible properties to support 3D culture. Despite these contributions, challenges remain. The ability to construct functional organs/tissue for therapeutic use remains a challenge, which requires millions of cells to be organized into functional units. However, the typical seeding density of cells on the 3D engineered models is around 10^6 to 10^7 cells/ ml, and it would take several weeks to achieve the cell density of $\sim 10^8$ for the highest cell density to mimic the native tissues. Therefore, two most critical challenges are low cell density and time-consuming fabrication.

In the study, we report a novel method to generate tumor-stroma 3D cultures rapidly. The 3D structures could be formed within one day with a high cell density of $\sim 10^8$ cells/ml.

METHODS

The rapid fabrication of tumor-stroma 3D cultures was developed by inkjet printing of cell-laden hydrogels. The collagen-based hydrogel ink is prepared by mixing 3 mg ml/L rat tail collagen type-I (Corning Inc., NY) solution with 1% w/v poly(N-isopropyl acrylamide-co-methyl methacrylate) (P(NIPAM-AM), PolySciTech, IN) solution. Human pancreatic cancer cells (Panc10.05) with red fluorescence protein and pancreatic cancer-associated fibroblast (CAF19) with green fluorescence protein were used in this study. The cell-laden inks were prepared by mixing the collagen-based hydrogel solution with harvested cells, which are Panc10.05 and CAF19.

The process is illustrated in Figure 1. Firstly, Panc10.05-laden ink drops were deposited on a glass well-plate by a Pipejet system to form a line array. Then, the well-plate was placed in an incubator for 3 minutes for the gelation of the polymer matrix. Next, CAF19-laden ink drops were deposited on the glass well-plate to form a line array adjacent to the first line. Again, the well-plate was placed in the incubator to gelate the polymer matrix. After printing and curing, we added the medium into the well and put the well-plate in an incubation stage for time-lapse imaging. The behavior of the cell-containing matrix was recorded. Due to the cells' contraction force, the matrix will start to shrink and finally form a tumor-stroma 3D aggregate within one day.

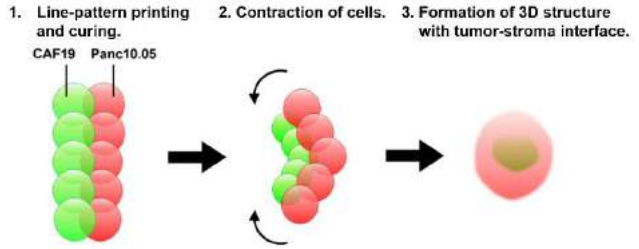

Figure 1. Illustration of the process of the rapid formation for 3D tumor-stroma culture.

RESULTS

The rapid formation of a 3D tumor-stroma culture after printing and curing is illustrated in Figure 2. The fluorescent time-lapse images showing the formation process are displayed in Figure 2(A). The volumetric strain of the matrix, the cell density, and the collagen concentration during the formation process are shown in Figure 2(B).

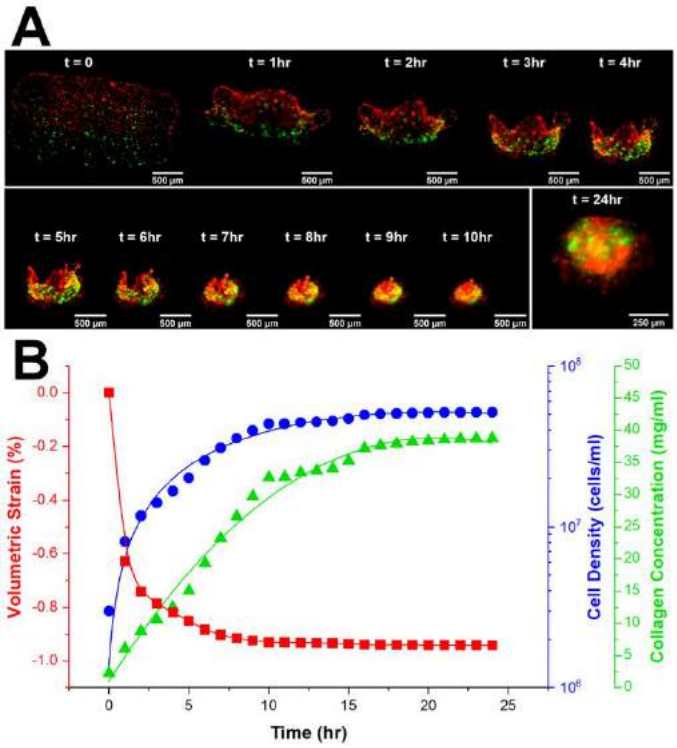

Figure 2. The rapid formation of 3D tumor-stroma culture. (A) Fluorescent time-lapsed images at different time points during the formation (B) the matrix's volumetric strain, the cell density, and the collagen concentration during the formation.

After being printed and cured, the cell-laden hydrogel matrix would detach from the glass surface and float in the culture medium when adding the medium. The matrix will then experience shrinkage due to the cells' contraction force and eventually form a 3D cellular aggregate. It is noted that the 3D aggregate could be quickly formed in 10 hr, which can be seen in Figure 2(A) that the size changed fast initially while it slowed down after ~10hr. In Figure 2(B), the volumetric strain also shows that the size reduced rapidly in the first 10 hr. The formed 3D culture possessed a structure that the CAF19s (green) assemble at the central region, surrounded by the Panc10.05s (red), as shown in Figure 2(A) at t = 24hr. This is because of the contractility difference between CAF19 and Panc10.05 (CAF19 has a strong contraction force while Panc10.05 is less contractile). The change of cell density and the collagen concentration during the formation are quantified. As seen in Figure 2(B), the initial seeding density is $\sim 10^6$ cells/ml. During the formation, the cell density would increase with the decrease in size. The formed structure's final cell density can reach near 10^8 cells/ml. However, the cell density is underestimated since we neglect the cell growth in the first-day culture. It means that the final cell density could be higher, close to cell densities in human tissues. Similarly, the collagen concentration would increase as the size decreases. The collagen concentration is also a conservative estimation since the collagen would degrade and be synthesized by the fibroblast, which is not considered. Nevertheless, Figure 2(B) demonstrates a high cell density and high collagen concentration in the formed structure, comparable to human tissues.

The 3D tumor-stroma aggregates prepared by the proposed method could be further co-cultured to speed up the culturing process and lead to a larger structure. As shown in Figure 3, six tumor-stroma aggregates are co-cultured in a U-bottom shape well-plate. After co-culturing for two days, a 3D model with a size of ~1mm can be obtained.

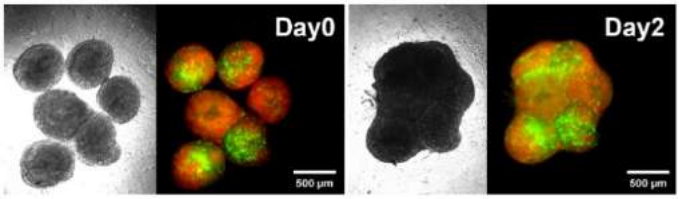

Figure 3. Bright-field and fluorescent images of six 3D tumor-stroma structures at Day0 and Day2 after co-culturing.

DISCUSSION

3D cell culture systems have shown great potential to replicate physiologically relevant cell and tumor models. These 3D constructs can be used as 3D models for human cancers and support diverse cancer research applications. However, current fabrication technologies are limited by the time-consuming and high-cost production, low cell density, and lack of a standardized protocol for any given cell type.

This study reports a rapid formation method to create a 3D structure with the tumor-stroma interface by inkjet-printing of cell-laden hydrogels. The printed collagen-based hydrogel shrinks and self-assembles to a 3D system within one day due to the cells' contraction force. The formed 3D structures could be cultured for more than two weeks. The results demonstrate that the proposed method is a fast and versatile way to create 3D tumor models with high cell density, similar to native human tissues. Moreover, it is applicable to multiple cell lines.

The underlying mechanism of the formation is the force balance between the cell's contraction force and the matrix stiffness. Therefore, the shape of the formed structures can be further controlled by manipulating the cell type, matrix stiffness, and cell density. In the future, when combined with immune cells and fibroblasts, this could be a 3D tumor model for immune-oncology applications.

ACKNOWLEDGEMENTS

This study was partially supported by a Program Grant from Purdue Institute of Drug Discovery, and a grant from NSF (CMMI-1449358).

REFERENCES

[1] Gitschier, BH et al., *Future Oncology*, 55-63, 2017.
[2] Edmondson, R et al., *Assay Drug Dev Technol*, 12(4):207-218, 2014.
[3] Benien, P et al., *Futur Oncol*. 10(7):1311-1327, 2014.
[4] Lv, D et al., *Oncol Lett*, 14(6):6999-7010, 2017.
[5] Tam, RY et al., *Acc Chem Res*, 50(4):703-713, 2017.

EFFECT OF OSMOTIC LOADING ON VAGINAL VISCOELASTIC MECHANICAL PROPERTIES

Gabrielle L. Clark-Patterson (1), Laurephile Desrosiers (2), Leise R. Knoepp (2), Raffaella De Vita (3), Kristin S. Miller (1)

(1) Biomedical Engineering
Tulane University
New Orleans, LA, USA

(2) Female Pelvic Medicine and Reconstructive Surgery
Ochsner Clinical School
New Orleans, LA, USA

(3) Biomedical Engineering and Mechanics
Virginia Polytechnic Institute and State University
Blacksburg, VA, USA

INTRODUCTION

The vagina provides support to the pelvic organs and is critical for facilitating normal physiological activities such as menstruation, intercourse, and childbirth. The vagina is comprised of various glycosaminoglycans (GAGs) which are negatively charged molecules that sequester water, and vaginal GAG and water content increase during pregnancy.[1,2] GAGs play a significant role in tissue repair due to damage or injury, therefore, GAG may also play a role in the vagina with vaginal birth injuries and in the development of pelvic floor disorders.[3,4] Osmotic loading experiments demonstrate that GAG and water content correlate to viscoelastic function in other soft tissues.[5] However, it is unknown how GAGs contribute to the viscoelastic response of the vagina, which is critical to maintain pelvic support. Therefore, the objective of this study was to quantify the effect of hypo- and hyper-osmotic loading on vaginal creep. It is hypothesized that hypo-osmotic loading induces swelling, increasing vaginal wall thickness and subsequently increasing creep. Further, we posit that hyper-osmotic loading decreases both vaginal thickness and creep.

METHODS

Female nulliparous wildtype C57BL6 x 129SvEv mice 3-6 months of age at estrus (n=9) were used in this IACUC approved study. Carbon dioxide inhalation euthanized all mice. The vaginas were explanted, snap-frozen with liquid nitrogen, and stored at -80ºC until mechanical testing. Sutures secured each vagina onto 3.75-mm cannulas within a biaxial extension-inflation system (Biodynamic 5170 System, TA Instruments Electroforce, New Castle, DE; Fig 1A) in room temperature Hanks Balanced Salt Solution (HBSS).[6] A laser micrometer (Mitutoyo 6200 Laser Scan Micrometer, 2 µm resolution; Mitutoyo Corporation, Kanagawa, Japan) optically tracked the outer diameter and a load cell (1000 g; 0.03 g resolution) measured axial load. The experimental physiologic length was determined wherein axial load remained constant over a physiologic range of increasing pressures.[7] Cyclic pressurization preconditioned the vaginal tissue (10 cycles from 0 to 15 mmHg at 1.5 mmHg/s), followed by 10 minutes of equilibration. At the physiologic length, a constant *in vivo* vaginal pressure was applied (7 mmHg; 1.5mmHg/s) for 100 seconds and the laser micrometer recorded the dynamic outer diameter (Fig. 1A).[8-10] Pressure was then removed for 1000 seconds of recovery.[10] At the physiologic length and 7 mmHg pressure, short-axis B-mode ultrasound (40MHz transducer) imaged the vagina (Fig. 1B).[9] ImageJ was used to measure vaginal thickness to calculate volume.[9]

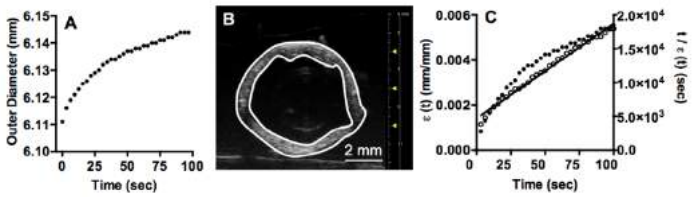

Figure 1: Representative outer diameter over 100 seconds creep curve (A). Representative B-mode ultrasound image of the vagina (B). Peleg's equation linearly (open circle right axis) transformed the strain (filled circle left axis) versus time curve (C). A linear regression determined the slope and intercept of the linear line (black line).

The vagina was randomly placed in either normo-osmotic (134 mM sodium chloride; n=3), hypo-osmotic (46 mM sodium chloride; n=3), or hyper-osmotic (300 mM sodium chloride; n=3) HBSS for 1-hour.[11,10] After osmotic loading, ultrasound imaging was repeated,

followed by preconditioning and equilibration. At the physiologic length, a constant 7 mmHg pressure was applied for 100 seconds.

To analyze the creep data, the outer diameter was normalized by calculating strain with reference to the original outer diameter (i.e. at 0 seconds; Fig 1C). Peleg's equation linearized the nonlinear creep data (equation 1; Fig 1C).[13] A linear regression determined Peleg's constants k_1 (intercept) and k_2 (slope).[13] Peleg's constants were used to calculate the rate of creep (equation 2).

$$t/\varepsilon(t) = k_1 + k_2 t \quad (1)$$

$$b = k_2/k_1 \quad (2)$$

The thickness, volume, Peleg's constants, creep rate, and creep strain at 100 seconds were calculated pre- and post- osmotic loading for all conditions (normo-, hyper, and hypo). To compare the hyper- and hypo-osmotic response to the normo-osmotic control the post-osmotic value for thickness, volume, Peleg's constants, creep rate, and creep strain at 100 seconds were normalized to the pre-osmotic value.[11] A normalized value of 1 indicated no change between the pre- and post-osmotic response. A value greater than 1 indicated an increase, and a value less than 1 a decrease. Multiple unpaired t-tests with Bonferroni correction ($p<0.05/2=0.025$) evaluated the normalized normo-osmotic thickness, volume, Peleg's constants, creep rate, and creep strain to the normalized hyper- and hypo-osmotic values.

RESULTS

Hypo- and hyper- osmotic loading did not significantly affect normalized thickness (Fig. 2A) and volume (Fig. 2B) when compared to the normo-osmotic control. The vagina displayed a similar creep response pre- and post- normo- (Fig. 3A), hyper- (Fig. 3C), and hypo- (Fig. 3E) osmotic loading. Hyper- and hypo- osmotic loading did not significantly affect normalized Peleg's constants (Fig. 3B), creep rate (Fig. 3D), and creep strain at 100 seconds (Fig. 3F) when compared to the normo-osmotic control.

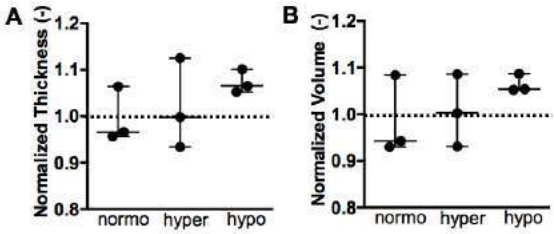

Figure 2: Normalized thickness for normo-, hyper-, and hypo-osmotic loading (A). Normalized volume for normo-, hyper-, and hypo-osmotic loading (B).

DISCUSSION

This study evaluated the effect of osmotic loading on the murine vaginal viscoelastic behavior. Hypo- and hyper-osmotic loading did not significantly affect vaginal wall thickness and volume compared to the normo-osmotic control. This is consistent with previous findings in the murine vagina where hypo-osmotic loading did not significantly affect thickness or volume.[12] The lack of geometrical differences with hyper- and hypo- osmotic loading may be a result of treatment time. In the intervertebral disc, the cross-sectional area and water content significantly decreased after 12 hours of hyper-osmotic loading.[14] Thus, within this study 1 hour may be insufficient time to observe significant changes. Contrastingly, the lack of significance may be due to the vagina lacking a significant number of GAGs to sequester water in the non-pregnant state, as vaginal GAGs, water content, and creep significantly increase during pregnancy.[2] Similarly, this may contribute to lack of significant differences observed in this study.

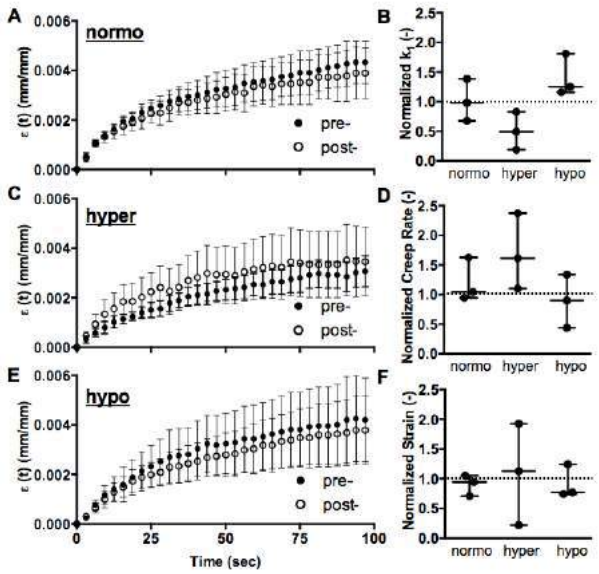

Figure 3: Creep strain verse time pre- (filled) and post- (open) normo- (A), hyper- (C), and hypo- (E) osmotic loading. Data reported as mean and standard error of mean. Normalized Peleg's constant k_1 (B), creep rate (D), and strain at 100 seconds (F) of normo-, hyper-, and hypo- osmotic loading.

Likewise, osmotic loading did not significantly affect creep in the colon.[15] Activation of the colonic smooth muscle cells, however, significantly increased creep suggesting they may significantly contribute to the viscoelastic response.[15] Additionally, previous studies in the knee medial collateral ligament suggest that collagen fiber recruitment dominates the creep phenomenon.[16,17] Future work evaluating changes in GAGs, water, smooth muscle content, and collagen fiber architecture, throughout pregnancy, may improve our understanding of how these components contribute to vaginal creep and subsequently pelvic organ support. Elucidating the key microstructural processes that dictate vaginal creep behavior is critical to understand how and why failures in pelvic organ support may occur during or following pregnancy, as well as changes that may occur following the onset of menopause.

ACKNOWLEDGEMENTS

We acknowledge funding from the NSF CAREER Award Program (CMMI-1751050; KSM).

REFERENCES

[1] Nunes, J et al., *Climacteric*, 14:121-5, 2011. [2] Weli, H et al., *Eur J Obstet Gynecol Reprod Biol*, 214:78-85, 2017. [3] Hurst, R. et al., *J Urol*, 138:433-7, 1987. [4] Plaas, A et al., *Arch Biochem Biophys*, 374:35-41, 2000. [5] Thornton, G et al., *J Orthop Res,* 19: 845-851, 2001. [6] Robison, K et al., *J Biomech Eng*, 139:1045041–1045048, 2017. [7] Van Loon, P, *Biorheology*, 14: 181–201, 1976. [8] Carniel, E et al., *Proc Inst Mech Eng H,* 229:794-803, 2015. [9] Clark, G et al., *Interface Focus*, 9:20190025, 2019. [10] Provenzano, *J et al., Appl Physiol,* 92: 362-371, 2002. [11] Sorrentino, T et al., *J Biomech Eng-Trans ASME,* 137:041008, 2015. [12] Capone, D et al., *J Biomech*, 82: 299–306, 2019. [13] Peleg, M, *Mater Sci Eng*, 40: 197-205, 1976. [14] Han, W et al., *Ann Biomed Eng*, 40:1610-21, 2012. [15] Greven, K et al., *Pflugers Arch*, 362:255-60, 1976. [16] Thornton, G et al., *J Orthop Res,* 20:967-974, 2002. [17] Ali., A et al., *J Biomech Eng*, 127: 484-492, 2005.

CONTACT GUIDANCE DURING BREAST CANCER DISSEMINATION

Kristen E. Loesel (1), Harrison L. Hiraki (2), Brendon M. Baker (2), Carole A. Parent (1,3)

(1) Cancer Biology Graduate Program, University of Michigan, Ann Arbor, MI, USA

(2) Department of Biomedical Engineering, University of Michigan, Ann Arbor, MI, USA

(3) Department of Pharmacology, University of Michigan, Ann Arbor, MI, USA

INTRODUCTION

Metastasis is the leading cause of cancer-related death, yet the metastatic process is poorly understood due to its complexity and tumor heterogeneity [1]. In the initial steps of metastasis, tumor cells acquire the ability to migrate out of the primary tumor into adjacent tissue due to alterations in signaling pathways or changes in the extracellular matrix (ECM) [2,3]. The physical cues provided by the tumor ECM influence the behavior and migration of cells [4]. Contact guidance is the process through which cells sense and respond to substrate anisotropies, ultimately altering cell adhesion formation, directionality, and migration [5,6]. However, the structural features that dictate invasive cell migration and the mechanisms by which cancer cells sense topographic features remain unclear.

While *in vivo* models are extremely useful for studying tumor development and growth, the sheer complexity of the tumor microenvironment makes it impossible to use them to dissect the mechanisms that regulate cell-ECM interactions during invasive migration. Therefore, many *in vitro* approaches have been used to deconstruct the complex ECM and understand the mechanisms by which cells sense the fibrous architectures of the ECM [7-9]. To understand the role of fibrous structures during invasive cell migration, here we used synthetic, electrospun fibrous extracellular matrices and live cell imaging to characterize the collective cell migration pattern of the highly invasive MDA-MB-231 breast cancer cell line.

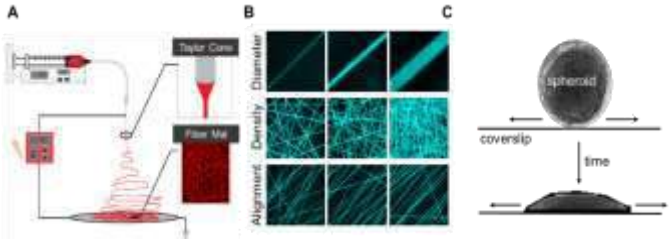

Figure 1: (A) Electrospinning is a voltage-driven process where a synthetic polymer is drawn to a coverslip creating fiber networks. (B) Representative images of synthetic fibrous networks designed to mimic *in vivo* structures. (C) Cancer cell spheroids adhere to the fiber-coated coverslip, and over time cells collectively migrate onto the fibers. (electrospinning figure adapted from Zagho, M.M. et al. *Electrospinning-Material, Techniques, and Biomedical Applications*. 2016).

METHODS

Fabrication of fibrous matrices: To create DexVS, dextran was reacted with divinyl sulfone in a previously described procedure [10]. Electrospinning solution was created by dissolving lyophilized DexVS in a 1:1 solution of water and dimethylformamide with 0.6% (w/v) LAP photoinitiator. DexVS solution was then electrospun onto 25 mm diameter coverslips and rhodamine-labeled fibers were crosslinked with UV light and LAP photoinitiator (**Fig 1A&B**). Cell Culture: MDA-MB-231 cells were cultured in DMEM supplemented with 10% FBS. Spheroids were formed by depositing cells into a 1.2% poly-HEMA coated v-bottomed 96 well plate. 96 well plates were spun on day 0 at 300G for 10 minutes and incubated for 6 days. Cell Migration Assay: Spheroids were plated onto DexVS fiber mats coated with 100ug/mL

type I bovine collagen. Spheroids were allowed to adhere to fibers for 2 hours before imaging. Spheroids and fiber mats were imaged every 10 minutes for 22 hours by fluorescent cell microscopy using a Zeiss Observer 2.1 microscope with an automated stage and incubation chamber (**Fig 1C**). The fibers were functionalized with rhodamine to enable visualization, and the cells are labeled with the nuclear dye, Hoechst 33342 (**Fig. 2**). The migration patterns of the cells were analyzed by automated FIJI tracking plugin, TrackMate, and a custom MATLAB script which extracts cell migration parameters such as cell speed, directionality, persistence, and the prevalence of single cell dissemination [12]. The approximate geometry of the fiber mats is determined using a fluorescent image of the fibers and a MATLAB code which utilizes the Fourier transform (designed by the Barocas Lab at University of Minnesota) [13].

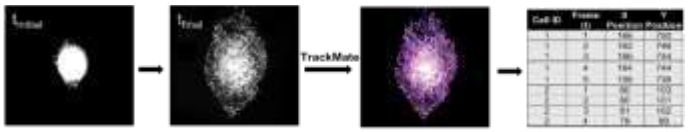

Figure 2: Workflow for tracking cell migration over time where cells are labeled with a nuclear dye. TrackMate identifies nuclei in each frame based on nuclear diameter. Each nucleus/cell is given a unique ID and its corresponding location for each frame.

RESULTS

In our previous studies, we employed nanoscale surfaces with aligned ridges or asymmetric sawteeth to mimic ECM fibers [7]. We discovered that breast cancer cell lines exhibit the ability to sense and respond to physical asymmetric guidance cues in a cell type-dependent manner. Using scanning electron microscopy and fluorescence live cell imaging, we discovered that two breast cancer cell lines with opposite migration behaviors on nanosawteeth exhibit distinct cell cortical plasticity and focal adhesion patterns.

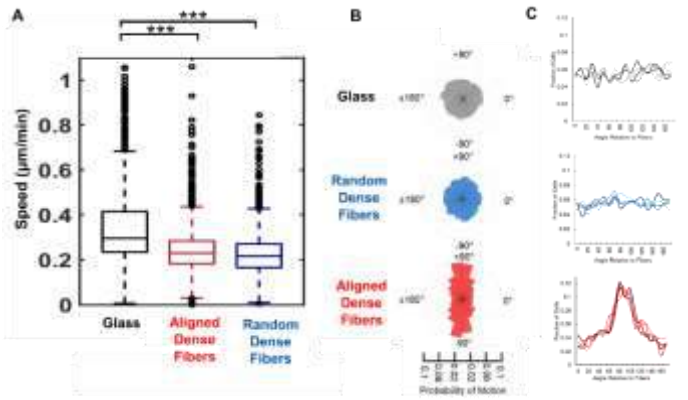

Figure 2: MDA-MB-231 cell migration metrics. (A) Mean cell speed distribution. (B) Probability distribution of cell motion direction. (C) Level of biased cell migration correlated with cell speed where darker colored lines indicate faster binned cells. * = p<0.05 ** = p<0.01 ***= p<0.001

To determine if fibrous architectures also bias collective cell migration, we assessed the group migration phenotype for the MDA-MB-231 invasive breast epithelial cell line. We found that the MDA-MB-231 breast cancer cell line can sense and respond to aligned fiber mats, displaying evidence of contact guidance. In addition, the MDA-MB-231 cells show a decreased mean cell speed when migrating on dense fiber mats, compared to glass surfaces (**Fig. 3A**). Our data indicate that the MDA-MB-231 cell line shows a strong contact guidance response on aligned dense fiber mats (**Fig. 3B**). In addition, we found that the contact guidance response was not dependent on cell speed (**Fig. 3C**).

DISCUSSION

Based on our preliminary findings, we anticipate that invasive breast cancer cell lines will migrate more directionally on aligned fibrous surfaces compared to less invasive breast cancer cell lines, suggesting that invasive breast carcinoma cell lines have more developed contact guidance capabilities. We are currently working on identifying the signaling mechanisms that regulate the distinct migration phenotypes observed. We envision that the spatiotemporal recruitment of Rho GTPases and subsequent focal adhesion distribution are responsible for the distinct migration phenotypes of breast cancer cell lines on similar fibrous surfaces. In conclusion, since cells migrating *in vivo* encounter fibers ubiquitously, our studies will lead to a better understanding of the mechanisms regulating cancer cell invasion.

ACKNOWLEDGEMENTS

K.E.L. acknowledges financial support from the University of Michigan Rogel Cancer Center and University of Michigan Nancy Newton Loeb Fund).

REFERENCES

[1] Hanahan, D. & Weinberg, R. A. *Cell* 144, 646–674 (2011).
[2] Eble, J. A. & Niland, S. *Clin. Exp. Metastasis* 36, 171–198, (2019).
[3] Yamaguchi, H., Wyckoff, J. & Condeelis. *Current Opinion in Cell Biology* (2005).
[4] Jansen, K. A. et al. *Biochim. Biophys. Acta - Mol. Cell Res.* 1853, 3043–3052 (2015).
[5] Doyle, A. D. et al. *Nat. Commun.* 6, (2015).
[6] Kim, D. H. et al. *Cell Biol.* 197, 351–360 (2012).
[7] Chen, S. et al. *ACS Nano* 13, 1454–1468 (2019).
[8] Baker, B. M. et al. *Nat. Mater.* 14, 1262–1268 (2015).
[9] Davidson, M. D. et al. (2019).
[10] Yu, Y. et al., *Biomacromolecules*, 13:937-942, 2012.
[11] Soule, H. D. et al. *Cancer Res.* 50, 6075–6086 (1990).
[12] Tinevez, J. Y. et al. *Methods* 115, 80–90 (2017).
[13] Sander, E. A. & Barocas, V. H. J. *Biomed. Mater. Res.* - Part A 88, 322–331 (2009).

ADHESION STRENGTH IN VIVO IS A PREDICTIVE MARKER OF METASTATIC POTENTIAL

K. Birmingham (1), P. Beri (1), J. Tuler (1), B. Yeoman (1,2), A. Engler (1,3)

(1) Department of Bioengineering
University of California San Diego
La Jolla, CA, USA

(2) Department of Mechanical Engineering
San Diego State University
San Diego, CA, USA

(3) Sanford Consortium for Regenerative Medicine
University of California San Diego
La Jolla, CA, USA

INTRODUCTION

While breast cancer has high rates of early stage detection (ranging from 47% at ages 15-39 to 68% at ages 65+), metastasis of the primary tumor can reduce the patient's 5-year survival rate by 73% (1). Even regional invasion of the cancer can reduce 5-year survival rates by 14%; recurrence rates are even worse for other solid tumors (1). Thus, it is essential to determine tumor aggressiveness when disease is local or regional in order to effectively predict the likelihood of recurrence. However, it is difficult to determine tumor outcomes due to a lack of universal molecular prognostic markers (2, 3).

Prior evidence strongly supports weak cellular adhesion strength to the ECM as a biophysical marker of aggressive and/or metastatic cells, due to an increase in focal adhesion turnover and contractility that stems from intrinsic transcriptomic differences in proteins involved in the microtubule cytoskeleton and vesicular transport (4,5). This transcriptomic profile, when present in triple negative breast cancer patients, correlated with shorter disease-free intervals (5). Despite the strong evidence, the assays were performed in vitro and thus cannot truly mimic the tumor microenvironment. Therefore, it is essential to demonstrate the link between decreased adhesion strength and increased invasive and metastatic behavior in vivo. Using a murine mammary tumor model, we have observed that cells that have locally invaded into the stroma have a decreased adhesion strength in comparison to cells that have remained in the tumor bolus.

METHODS

Isolation of MDA-MB 231 Cells by Adhesion Strength

1×10^6 MDA-MB 231 cells, expressing GFP and Luciferase, were suspended in 40 μL of Matrigel-PBS (1:1) mixture and were injected bilaterally into the inguinal mammary fat pads of 11-week-old female NOD/SCIDγ mice. Tumor growth was monitored at 2-week intervals and the mice were sacrificed at 6 weeks post-injection. Mice were dissected and the fat pads were surgically removed. Using an inverted fluorescent microscope, the stiffened tumor bolus was manually separated from the surrounding stroma. GFP-positive cells in tumor and stroma sections were sorted via FACS.

Sorting and Injection of MDA-MB 231 Cells for Lung Metastases Study

GFP+ Luc+ MDA-MB 231 cells were seeded (~5000 cells/cm^2) overnight onto fibronectin-coated glass slides. Using the parallel-plate flow chamber, the slides were exposed to 25 dynes/cm^2 shear stress for 2 minutes to collect the weakly adherent cells, then exposed to 90 dyn/cm^2 shear stress for 2 minutes. Any cells that remained on the slide were removed via 0.25% trypsin and collected as the strongly adherent cells. The weakly adherent and strongly adherent cell fractions were cultured separately for 48 hours, as well as a perfused but unsorted control population. 1×10^6 GFP+ LUC+ MDA-MB 231 cells from the strongly adherent fraction, weakly adherent fraction, or the unsorted control were suspended in 40 μL of Matrigel-PBS (1:1) mixture and were injected into the inguinal mammary fat pad of 11-week-old female NOD/SCIDγ mice. Tumor growth was monitored at 2-week intervals and the mice were sacrificed at 6 weeks post-injection. At time of sacrifice, the lungs and primary tumors were harvested, frozen in optimal cutting temperature compound, and stored at -80° C.

RESULTS

Invaded Cells Have Decreased Adhesion Strength Compared to Cells in the Tumor Bolus

Our previous findings have shown that within metastatic cell lines, weakly adherent cells isolated using a microfluidic shear assay were

more migratory, more contractile, and had more labile focal adhesions than strongly adherent cells (5). Since decreased adhesion correlated with an increase in behaviors associated with more aggressive cancer cells, we wanted to investigate if these findings could be recapitulated *in vivo*. We injected GFP+ Luc+ MDA-MB231 cells into the mammary fat pads of 11-week-old NOD/SCIDγ mice and resected the tumor 6 weeks post injection. GFP+ cells were isolated from the tumor bolus and surrounding stroma, separated manually, and sorted using FACS (Fig. 1A). The percentage of stroma GFP+ cells was less than those present in the tumor (Fig. 1B). Using a spinning disk shear assay, we observed that the invading GFP+ cells in tumor-adjacent stroma had significantly decreased adhesion strength compared to cells that remained in the tumor (Fig. 1C); when assessing paired samples, we found that tumor adhesion strength was 60% higher than for GFP+ cells isolated from the stromal region (Fig. 1D). These data are consistent with *in vitro* findings that link decreased adhesion to increased metastatic potential.

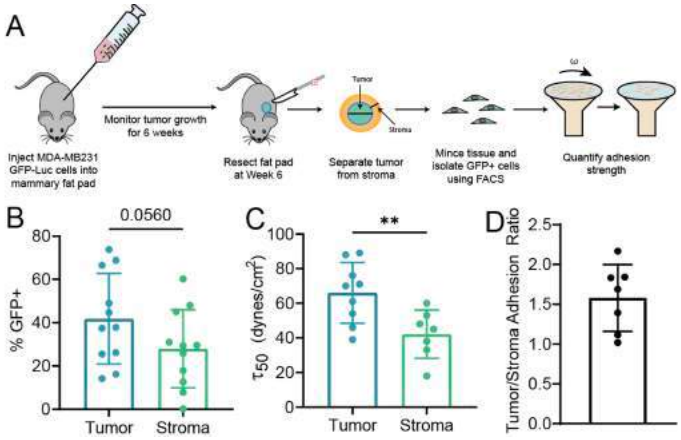

Figure 1: Invaded cells exhibit decreased cell adhesion strength. (A) Timeline of tumor resection study. (B) There are fewer GFP-positive cells present in the stroma versus the tumor. (C,D) Invaded MDA-MB231 cells have decreased adhesion strength compared to MDA-MB231 cells that remain in the tumor. (B,C) Statistical analysis via unpaired t-test. ** represents p<0.01.

Mice Injected with Strongly Adherent Cells Exhibit Fewer Lung Metastases

We next hypothesized that mice injected with pre-sorted weakly or strongly adherent cells would have more or fewer incidences of lung metastases, respectively; thus, weakly or strongly adherent cells should be more or less able to migrate out of the primary tumor microenvironment and enter distant locations in the body, respectively. To test this hypothesis, we injected 11-week-old NOD/SCIDγ mice with unsorted, weakly adherent, or strongly adherent GFP+ Luc+ MDA-MB231 cells into the mammary fat pad, monitored their tumor growth biweekly for 6 weeks using IVIS imaging, then sacrificed the mice and quantified primary tumor size and the number of lung metastases (Fig. 2A,B). While there was no difference in the primary tumor weight among three groups of mice (Fig. 2C), there were notable differences in the number of lung metastases, with the strongly adherent mice having the least number of lung metastases, and the weakly adherent mice having the greatest number of lung metastases (Fig. 2B,D,E). These results are consistent with invading or migratory cancer cells having decreased adhesion strength, exhibiting this weakly adherent phenotype.

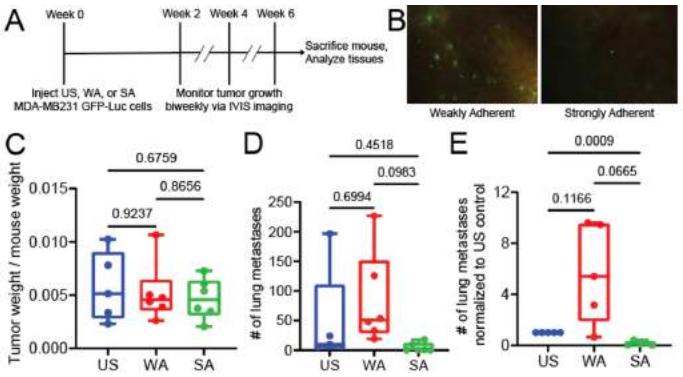

Figure 2: Mice injected with weakly adherent cells have few lung metastases. (A) Timeline of metastasis study. (B) Representative images of GFP+ lung metastases. (C) There is no difference in the tumor size among groups. (D,E) Weakly adherent mice have the most lung metastases and strongly adherent mice have the fewest. (C-D) Statistical analysis via unpaired t-test.

DISCUSSION

Despite a rise in early-stage detection of certain cancers, particularly breast cancer, local or regional invasion can reduce the 5-year survival rate of patients (1). Due to heterogeneity within the tumor and across tumors from different patients, there are no universal biological markers that can predict disease outcome. Adhesion strength has emerged as potential biophysical marker, but its links to cancer cell aggression and metastatic potential have only been demonstrated in vitro (5). It is essential to show that weak cellular adhesion correlates with more aggressive cells vivo to demonstrate the clinical relevance of adhesion strength as a prognostic marker. As such, we sought to correlate in vitro findings of aggressiveness of weakly adherent cells to increased invasion and metastatic tumor formation in vivo.

We observed, in a murine mammary tumor model, that invaded cells within the mammary stroma have lower cellular adhesion strength than cells that remain in the stiff tumor, observation consistent with in vitro findings. Further, we found that mice that were injected with strongly adherent cells exhibited fewer metastases than mice injected with either weakly adherent cells or an unsorted control population. Moreover, these mice injected with strongly adherent cells consistently showed the development of minimal metastatic tumors, which is in stark contrast to the broad range and greater of metastatic lung tumors in mice that received unsorted or weakly adherent cells. These results suggest that strongly adherent cells lack the ability to migrate out of the primary tumor microenvironment, therefore, tumors that are composed of only strongly adherent cells lack the ability to form metastatic tumors. Broadly, these data suggest that adhesion strength can serve as a marker of metastatic potential and can be utilized in a prognostic fashion to screen patient samples.

REFERENCES

[1] A. C. Society, *Cancer Facts & Figures 2020,* 2020.
[2] Polyak, K et al., *J Clin Invest*, 121:3786-3788, 2011.
[3] Liu, Y et al., *BJC*, 110:2063, 2014.
[4] Ridley, A et al., *Science,* 302:1704, 2003.
[5] Beri, P *et al.*, *Cancer Res,* 80:901-911, 2020.

AN *IN SILICO* MODEL OF HUMAN CORNEA SUBJECTED TO PHYSIOLOGICAL AND NON-PHYSIOLOGICAL LOADING: INVESTIGATION OF THE MECHANICAL ENVIRONMENT OF CORNEAL KERATOCYTES

A. Pant (1), E. Paul (1), A. Vahdati (1)

(1) Department of Engineering
East Carolina University
Greenville, NC, USA

INTRODUCTION

Multiscale computer models of the cell-tissue-organ units offer the potential to improve our understanding of various disease pathogenesis. Experimental studies have shown that keratocytes, the predominant corneal cells, although normally quiescent, respond to injury by transitioning into repair phenotypes [1]. Therefore, developing a multiscale computer model of the cornea incorporating the keratocytes may allow us to better understand the cellular causes and responses to injury, which in turn may offer avenues in understanding and preventing the corneal pathologies in the early stages. Therefore, in this study, we developed a computational model of the cornea comprising of the underlying ground matrix and the keratocytes. We then utilized a computational approach to simulate the effect of different loading conditions in the immediate vicinity of the cells located throughout the thickness of the cornea, under physiological intraocular pressure (IOP) loading, and under non-physiological conditions such as IOP spike and eye-poking [2].

METHODS

A finite element model of the cornea, including the limbus, was constructed based on the geometry described by Grytz et al. [3]. We fixed the limbus edge and applied a pressure load to the posterior surface of the cornea and the limbus. To obtain the stress-free geometry of the cornea, we implemented an iterative approach, as proposed by Pandolfi et al. [4].

To study the mechanical response of the cells and to develop the multiscale model of the keratocytes, Ansys software (Ansys Inc, Canonsburg, PA, USA) was used. The solution from the macroscale model of the cornea-limbus was applied as the boundary condition for our microscale cell model. Since keratocytes are flat-shaped cells, we constructed the geometry of the keratocytes to be a nearly flat ellipsoid with dimensions 2 μm for the shorter semi-axis and 7.5 μm for the longer semi-axis. We then ran the simulations for three different cases, with the location of keratocytes changed along the thickness of the cornea (Figure 3). The keratocytes were placed:

i. Near the anterior surface of the stroma
ii. In the middle of the stroma, and
iii. Near the posterior surface of the stroma

We applied two different cases of non-physiological loading conditions in the simulation. For the first case, we considered the effect of elevated IOP. Additionally, eye-rubbing is one of the risk factors for keratoconus, hence, for the second type of loading condition, we simulated the poking effect caused by eye-rubbing by pushing the anterior surface of the cornea to a defined displacement using an idealized indenter representing the second base knuckle bone.

RESULTS

Figure 1 shows the total deformation distribution in the cornea when the cornea is subjected to three different loading conditions respectively: physiological IOP, a moderate IOP spike of 5 mmHg and an indentation (poking) of -0.3 mm. Under the load of 15 mm Hg IOP, IOP spike of 5 mm Hg, and 10 mm Hg, the averaged magnitude of the maximum principal stress in the immediate vicinity of the cell was largest in the cell located near the anterior surface of the stroma and lowest in the cell located near the posterior surface of the stroma.

The magnitude of the maximum principal stress increased as the IOP increased from a physiological loading to an IOP spike of 5 mm Hg to an IOP spike of 10 mm Hg for all the cells located at different locations. For the cell located in the middle of the stroma, the direction of the averaged minimum principal stress changed from a tensile one to

a compressive one as the IOP increased. For the cell located near the posterior surface of the stroma, the averaged minimal principal stress was compressive for all different cases of IOP (Figure 2).

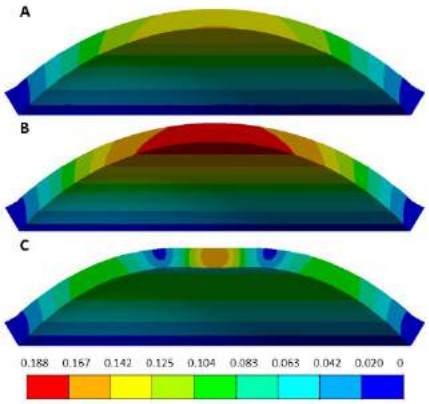

Figure 1: Magnitude of the total deformation (mm) in the cornea (compared to the undeformed configuration) when the cornea is subjected to (A) physiological IOP, (B) IOP spike of 5 mm Hg, and (C) eye-poking loading condition using 0.3 mm downward displacement [2]**.**

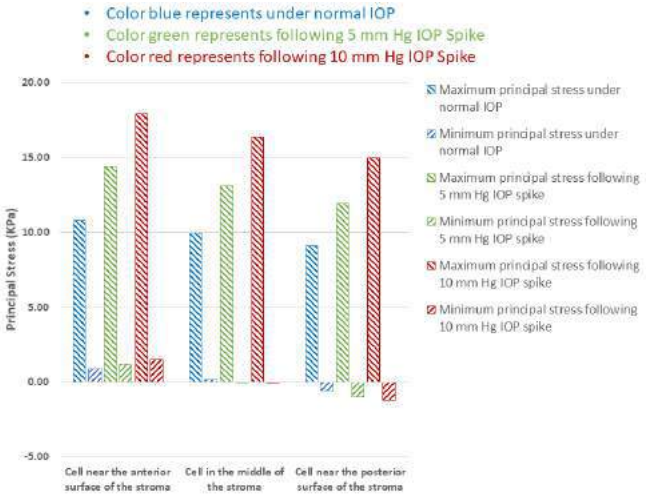

Figure 2: Averaged values of maximum and minimum principal stress developed in the cell's immediate vicinity in different locations following normal (physiological) IOP loading, IOP spike of 5 mm Hg, and IOP spike of 10 mm Hg [2].

Interestingly, under normal IOP, the averaged maximum and the minimum principal strain in the immediate vicinity of the cell did not change significantly irrespective of the location of the cells in the corneal stroma. Similar observations were made under IOP spikes of 5 mm Hg and 10 mm Hg. Results obtained from the progressive eye-poking loading conditions are distinct from the results obtained from IOP loading patterns. The pattern of stress and strain distribution in the immediate vicinity of the cell changed with different displacements used for simulating the poking effect. For all different indentation levels, the cell located near the anterior surface of the stroma experienced on average a large compressive stress state, whereas the cell located near the posterior surface experienced on average tensile stress states (Figure 3).

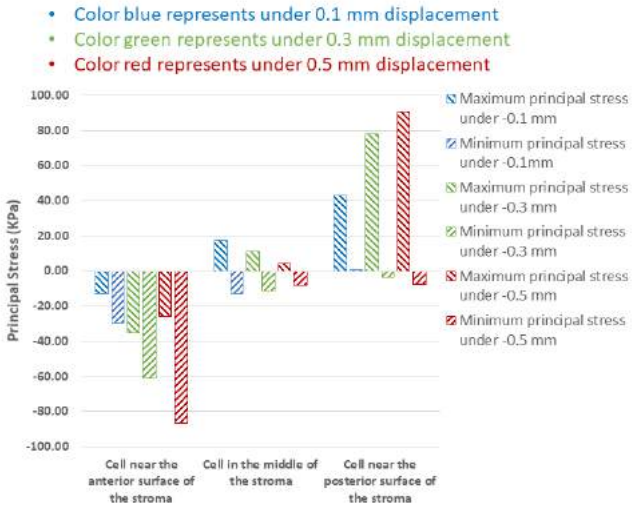

Figure 3: Averaged values of maximum and minimum principal stress developed in the cell's immediate vicinity in different locations following different levels of eye-poking [2].

DISCUSSION

Our study showed that the differences in location of the cell in stroma and the loading condition applied to the cornea can noticeably affect the stress and strain distribution in the surrounding extracellular matrix of the keratocytes. Furthermore, our results demonstrated that while increased IOP can cause large changes in strain and stress magnitude sensed by the cells in a depth-dependent manner, changing the loading mode from IOP to simulated eye-poking can dramatically alter both the direction and magnitude of the stress and strain in corneal keratocytes. From a mechanobiological point of view, it is expected that such large changes in the stresses and strains magnitude and distribution under different loading conditions could have implications for the keratocytes fate and may disrupt the normal corneal homeostasis. While changes in the stress and strain could be induced by either eye-poking or increased IOP, the severity of alterations in loading patterns of keratocytes was more pronounced in the case of simulated eye-poking.

Simulated eye-poking caused inwards bending of the cornea in our simulations, which not only altered the stress and strain magnitudes at different depths but also produced significant changes in the direction of stress and strain and their overall distribution pattern. Our *in silico* findings indicate that the cells near the anterior and posterior surface of the cornea may experience larger strains when compared to the cells present in the middle of the stroma under severe eye-poking.

REFERENCES

[1] J. A. West-Mays and D. J. Dwivedi, *Int. J. Biochem. Cell Biol.*, vol. 38, no. 10, p. 1625, 2006.

[2] A. Pant, E. Paul, and A. Vahdati, *Biocybern. Biomed. Eng.*, vol. 40, no. 4, pp. 1369–1377, Oct. 2020. (The abstract is reprinted in part from this article, Copyright 2020, with permission from Elsevier. License # 4994380212881)

[3] R. Grytz and G. Meschke, *Biomech. Model. Mechanobiol.*, vol. 9, no. 2, pp. 225–235, 2010.

[4] A. Pandolfi and G. A. Holzapfel, *J. Biomech. Eng.*, vol. 130, no. 6, 2008.

MEASURING PROSTHETIC FOOT USE BY ACTIVITY LEVEL WITH STEP ACTIVITY MONITORING

John M. Chomack (1), Alexis N. Sidiropoulos (1), Michael N. Poppo (1), Jason T. Maikos (1)

(1) Veteran Affairs New York Harbor
Healthcare System
New York, NY, USA

INTRODUCTION

As prosthetic foot technology advances and becomes more readily available, patients will have increased opportunities to access a range of energy storing, articulating, and powered devices. Therefore, it is critical to use objective measures for prosthetic prescription to meet the biomechanical and functional needs of each patient outside of the clinic. Capturing a patient's prosthetic performance while navigating his/her everyday environment is a key piece of information that has yet to be effectively utilized in the prescription process [1].

Step activity monitoring for individuals with lower extremity amputation has been previously studied to determine compliance and reporting of community ambulation activity in the prosthetic population. Activity monitoring devices, such as the Modus™, StepWatch 3™ used in this study, have been utilized in over 360 peer reviewed publications. The StepWatch 3™ device boasts a 99.7% accuracy for those walking at low speeds and a 92% accuracy for those ambulating with a prosthesis [2]. This study sought to capture the community ambulation activity levels for individuals with transtibial amputation (TTA) while using three different types of prosthetic feet over four weeks. The purpose of the investigation was to determine if a specific foot type promoted higher activity levels as determined through cadence; and if the activity per level correlated with the outcome measures used in this study.

METHODS:

Fifty-one individuals living with TTA age 56.1±12.8 years, height 1.79±0.08 m, and weight 94.7±18.4 kg with at least 1 year of experience with their prosthesis have completed the study protocol to date. These participants were recruited from the Veteran Affairs (VA) New York Harbor Healthcare System (NYHHS), the James A. Haley VA Medical Center, VA Puget Sound Healthcare System, and Walter Reed National Military Medical Center. All procedures were approved by their respective Institutional Review Boards. Participants within this study were randomized to use 3 types of prosthetic feet: energy storing and return foot (ESR), an ESR with articulation (ART), and a powered articulating foot (PWR). Each study device was attached with duplicated, well-fitting below knee sockets.

Study participants wore each foot for a 1-week acclimation period and then completed a series of functional outcomes (FO), questionnaires, and a biomechanical assessment. Participants repeated this process for each subsequent foot type. After wearing each foot for 1 week, participants were instructed to take all study feet home for 4 weeks and to wear the feet as desired. Modus™, StepWatch 3™ step activity monitors (SAMs) were fixed to each prosthesis to track daily steps and activity levels. At the conclusion of the 4-week at home portion, the study devices were returned, and a close-out survey of the participant's device preference was conducted.

Of the 51 participants to complete the study, 38 used 2 or more feet during the at-home portion. Only these 38 participants were included in this analysis. The SAMs were programmed to record the number of steps taken at each minute for 30 consecutive days. Cadence was calculated for each minute, which was then categorized into activity levels: low (1-15 steps/min), moderate (16-40 steps/min), and high (>40 steps/min). Percent of steps taken while active at each activity level was then calculated. At each activity level, we determined the frequencies of the feet with the greatest percent of steps, and, if these feet corresponded to the subject's foot preference. A one-way between subjects Analysis of Variance (ANOVA) was conducted to compare the effects of prosthetic device type to percent steps taken in low, moderate, and high activity levels. Additionally, a simple linear regression was calculated to predict percent steps based on the following FOs: Orthotics Prosthetics User Survey Functional Status, Prosthesis Evaluation Questionnaire Ambulation section, Timed Up-And-Go, 6-

Minute Walk Test, Amputee Mobility Predictor, Stair Assessment Index, and Hill Assessment Index.

RESULTS

Figure 1 represents the frequency of greatest percentage of steps taken at low, moderate, and high activity levels for each foot type as determined through cadence. Results of the ANOVA indicated that there were no significant effects of prosthetic device type on percent steps taken in any of the 3 activity levels ($p>0.05$ in all cases). However, a trend towards significance was observed for the PWR foot at the high activity level ($p=0.06$), with a frequency of 18 of 37 subjects utilizing the PWR for the greatest percent of steps at the high activity level.

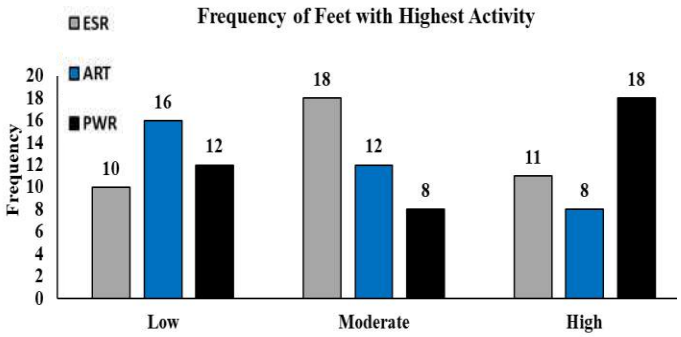

Figure 1:Frequncy of greatest percentage of steps at low, moderate and high activity levels by foot type. (Low, Moderate: N=38)(High: N=37)

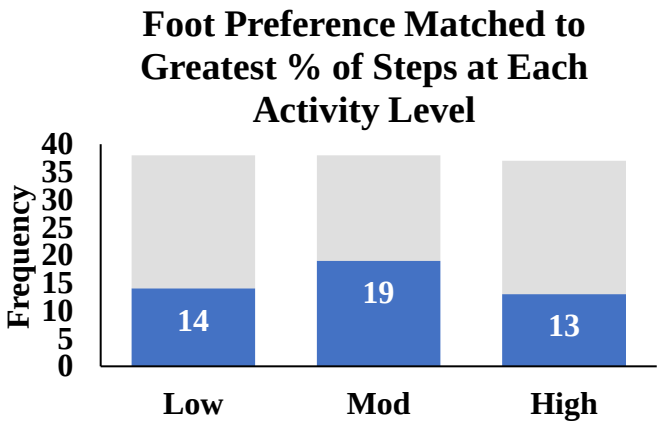

Figure 2: Frequency of subjective foot preference when matched to greatest percentage of steps at low, moderate, and high activity.

Figure 2 represents the frequency of subjective foot preference that matched to the greatest percent of steps taken at each activity level (preference determined by the close-out survey). At high activity 13 of 37 participant (35%) chose the foot that accounted for the greatest percentage of steps. Of the 18 occurrences that the PWR foot provided the greatest percent of steps at high activity, only 6 participants preferred the PWR foot (33%). We observed at low and moderate activity, 37% and 50% of subjects preferred the device that provided the greatest percent of steps. Regression analysis indicated that none of the functional outcome measures were able to predict the percent steps at any of the activity levels ($p>0.05$ in all cases).

DISCUSSION

Step activity monitoring can be a valuable tool to use as part of the prosthetic prescription process since it can help evaluate community ambulation activities. Currently, this key information has been underutilized for this process [1]. This investigation sought to determine if a foot type (ESR, ART, PWR) promoted higher activity levels, and if those associated values correlated to objective metrics. SAM data was recorded for participants using 3 different types of prosthetic feet within their home and community environments over a 4-week period. Percent of steps performed at low-, moderate-, and high-activity were determined and frequencies of prosthetic devices that resulted in the greatest activity at each level were reported.

This preliminary analysis of activity levels for 38 participants showed no significant differences between prosthetic device and percent steps taken at the 3 activity levels. The regression analysis between the objective testing criteria and high activity percent steps taken yielded weak correlative values, suggesting the FO may not be indicative of a subject's activity outside the clinic. However, a trend towards significance was observed for the PWR foot at the high activity level. This trend may be attributed to the powered plantarflexion at terminal stance, which aims to replicate the function of the gastroc-soleus complex. This may allow the user to walk at a consistently higher cadence (>40 steps/min), reducing overall energy expenditure.

Of note, only 35% of users preferred the prosthetic device that promoted the greatest percent of steps taken at high activity (regardless of foot type). Furthermore, of the 18 occurrences in which the PWR foot showed the greatest percent of steps at high activity, only 33% of subjects (n=6) preferred the PWR foot. Participants may not have consistently preferred the PWR foot due to inherent drawbacks of the device, such as heavier weight, increased noise, and the need for daily battery charging. There was an increased percentage of participants who preferred the foot that provided the greatest percent of steps at moderate (50%) activity levels. Because the majority of daily steps were taken at moderate activity levels, these findings suggests that participants may prefer to walk at moderate cadences and select/prefer the prosthetic device that matches the greatest percent of steps at these activity levels.

As more participants complete the protocol, they will be added to this analysis to determine if significance levels can be achieved. Factors such as the number of days of use or accounts of a foot being used specifically for high level activities will need further investigation.

ACKNOWLEDGEMENTS

This work was supported by a DoD Orthotics and Prosthetics Outcomes Research Program grant (W81XWH-17-2-0014). We also acknowledge our co-investigators at the James Haley VA Medical Center, VA Puget Sound Healthcare System, and Walter Reed National Military Medical Center for their work and compliance.

REFERENCES

[1] Halsne, E et al. *JRRD*, 30(4):515-530. (2013).
[2] Coleman, D et al. *JRRD*, 36(1):8-18. (1999).
[3] Stepien, J et al. *Arch. PM&R*, 88(7):896-900. (2007).

BIOMECHANICAL PROPERTIES OF POST-MENOPAUSAL VAGINAL SAMPLES IN RELATION TO PELVIC ORGAN PROLAPSE

E. Danso (1), L. Desrosiers (2), L. Knoepp (2), K. Miller (1)

(1) Biomedical Engineering
Tulane University
New Orleans, LA, USA

(2) Female Pelvic Medicine and Reconstruction Surgery
Ochsner Clinical School
New Orleans, LA, USA

INTRODUCTION

Weakening of the pelvic floor supporting structures could likely lead to the descent of pelvic organs (uterus, rectum, bladder) into the vaginal canal; a condition known as pelvic organ prolapse (POP). Ten percent of women in the United States undergo surgical intervention related to POP [1], and 4 out of 10 women experience reoccurrence of prolapse symptoms 2 years after surgery [2]. There is a huge economic burden associated with this condition, with over $1 billion incurred annually for POP associated interventions in the United States alone [3]. The underlying mechanisms of POP are not understood, but some risk factors include obesity, vaginal delivery, age, race, and mechanical injury [2,4].

The vagina provides pelvic organ support [5,6,7]. It is primarily composed of collagen fibers, smooth muscle, and elastin [8,9]. Biaxial properties which are assessed from two axes simultaneously, provide a more physiologically-relevant biomechanical properties than the widely used uniaxial approach, which only provide a limited information in a single direction. Despite this importance of biaxial properties, including obtaining vital biomechanical properties like anisotropy, no study has reported the biaxial properties of human vaginal samples from women affected by POP. Therefore, the aim of the study was to quantify and compare the biaxial biomechanical properties of vaginal samples from post-menopausal women with or without POP.

METHODS

Vaginal samples were obtained (Ochsner Clinical School IRB approved: 2017.016A) from post-menopausal women with either non-POP (n=9, 62.7±1.7 years old, 32.3±1.6 kg/m^2 BMI), POP I/II (n=6, 60.8±2.5 years old, 29.9±2.9 kg/m^2 BMI) or POP III/IV (n=7, 67.2±2.6 years old, 31.8±3.1 kg/m^2 BMI) condition following transvaginal hysterectomy surgeries (Figure 1). Samples were snap-frozen following surgery and stored at -80°C until the day of biomechanical assessment. Most samples were from Europeans/White women. Five samples were from African-Americans/Black women (non-POP controls only) and two were from Middle-Eastern women (1 non-POP control and 1 POP I/II group). POP III/IV group comprised samples from only Europeans/White women. **Biaxial testing**. Samples were thawed at room temperature, cut into squares, and then speckle coated with alcohol ink for strain tracking (Figure 1) [10]. Using a non-contacting laser micrometer, tissue thickness was measured across multiple locations and averaged. Four fishhooks were used to mount each sample side into a custom planar biaxial test device equipped with load cells (22 N) in both axes, and a camera (Figure 1) [2,11]. The samples were fully submerged in Hank's balance saline solution throughout the experiment. A tare load of 0.1N was applied in the circumferential and longitudinal loading directions, followed by 10 equibiaxial preconditioning cycles to 0.1MPa, after which the samples were allowed to equilibrate for 10 minutes. Next, samples were loaded in the circumferential and longitudinal loading directions to different circumferential:longitudinal loading ratios [12, 13] of 1:0.5, 1:0.75, 1:1, 0.75:1 and 0.5:1 at 0.2%/sec. For each of the loading ratios, 5 preconditioning cycles were applied. **Statistical Analysis.** All data are presented as Mean±SD. Independent samples t-tests were used to assess differences in age, body mass index (BMI), parity, and gravidity between non-POP and POP groups. Statistical significance was set to $p<0.05$. All statistical analyses were performed using SPSS software.

RESULTS

The measured unloaded thicknesses were 1.9±0.2 mm, 2.8±0.4 mm and 2.5±0.2 mm for the non-POP, POP I/II and POP III/IV specimens, respectively. No statistically significant differences were identified with respect to age (p=0.17), BMI (p=0.20), parity (p=0.38), and gravidity (p=0.46), between the non-POP, POP I/II and POP III/IV groups. All vaginal samples exhibited a nonlinear behavior in both the circumferential and longitudinal loading directions (Figure 2), and tissues demonstrated anisotropic behavior. Vaginal samples from POP III/IV groups were most extensible, as compared to samples from the non-POP and POP I/II groups, particularly in the circumferential loading direction (Figure 2A). There were no differences in the

extensibilities between the non-POP and POP I/II in both the circumferential and longitudinal loading directions (Figure 2A,2B).

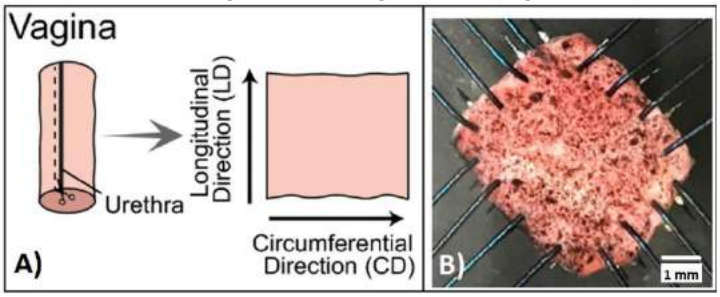

Figure 1: (A) Figure of the vaginal sample showing before and after cutting into a square shape for the biomechanical testing [9]. (B) Samples were speckle-coated and mounted in a planar device via fishhooks for biomechanical testing.

DISCUSSION

Direction-dependent biomechanical properties and nonlinear stress-strain relationships were observed for the vaginal samples. Similar nonlinear behavior has been determined earlier for uniaxial properties of POP vaginal samples [14,15]. The increased extensibility observed in the POP III/IV group may suggest changes in the circumference of the vaginal wall with the progression of POP because of a decreased ability to withstand loads in that direction. This information is useful for reconstructive surgical planning and development of new graft materials for POP repair [2]. A previous human study [16] showed that vaginal biomechanical properties were significantly lower with POP compared to controls. Hence, degeneration of the biomechanical properties in pelvic support may lead to POP development. Further, the POP III/IV uterosacral ligament exhibited the largest extensibility for the main in *vivo* loading direction in a prior study [10], similar to the vaginal response in the circumferential direction herein. Additionally, the perpendicular loading direction did not exhibit differences between the different POP groups in the previous study (uterosacral ligament) and this study (vaginal samples). Perhaps similar biomechanical/structural changes occur with the progression of POP for these two pelvic organs. However, it is important to note that the study herein and the prior study in uterosacral ligament [10] tested samples obtained from the same patient population. Contrary to these results, prior studies leveraging uniaxial tests in the longitudinal direction reported that POP vaginal tissues are significantly stiffer compared to non-POP [17]. Future work is needed to determine if the discrepancies in results are due to differences in biomechanical testing protocols, or whether the POP group was separated into different stages as performed in this study.

Changes in the biomechanical properties exhibited in this study may be caused by changes in the underlying vaginal microstructural composition with respect to the different POP groups. In future, histological analyses will be conducted to determine the composition of the main load-bearing constituents (e.g., collagen fibers, smooth muscle, and elastin) of vaginal samples in each group. The obtained information will subsequently be correlated to the biomechanical properties obtained herein. Prior work, however, reports contradictions in vaginal tissue compositional changes with POP. Some studies report increased [18] levels of collagen III as POP progresses, while others [19] report decreases. Collagen III is the predominant collagen throughout the vaginal wall. Also, some studies report decreased amount of smooth muscle in vaginal tissue with POP, however, the contractile properties of vaginal smooth muscle were not examined in the current study [20,21,22,23,24].

One limitation of the study is the lack of racial diversity in the patient population. Current patient recruitment seeks to improve diversity. Noting, however, that the rate of POP in the African Americans/Blacks population is much lower than other racioethnic groups [19].

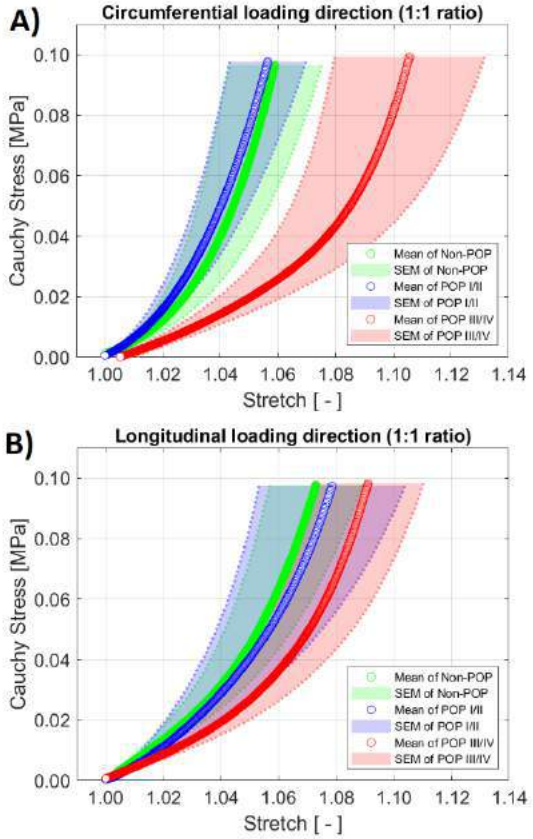

Figure 2: Mean (SEM) of Cauchy stress-stretch plots of vaginal samples loaded at 1:1 ratio for non-POP and various POP stages (I-IV), in the circumferential (A) and longitudinal (B) loading directions.

ACKNOWLEDGEMENTS

This work was supported, in part, by NIHP20-GM103629 (Miller) and the Ochsner Translational Medicine Research Initiative (Miller, Knoepp).

REFERENCES

[1] Olsen, A et al., *Obstet Gynecol*, 89:501-506, 1997 [2] Baah-Dwomoh, A et al., *Ann Biomed Eng*, 46:2036-2047, 2018 [3] Subak, A et al., *Obstet Gynecol*, 98:646-651, 2001 [4] Doshani, A et al., *BMJ*,2007:335-819, 2007 [5] Delancey, L., *Am. J. Obstet. Gynecol.* 166:1717-1728, 1992 [6] Liu X et al., Am. J. Pathol 168:519-528, 2006 [7] Wieslander, C et al., Biol. Reprod. 80:407-414, 2009 [8] Ramanah R et al., *Int. Urogynecol. J*, 23:1483-1494 2012 [9] Huntington, A et al., Ann Biomed Eng, 47:272-281, 2019 [10] Danso, E et al., *Sci Rep*, 10:7386, 2020 [11] Tan, T et al., Ann. Biomed. Eng. 44:3225-3237, 2016 [12] Bellini, C et al., *J. Mech. Behav. Biomed. Mater*. 4:1727-1740, 2011 [13] Vande Geest, J et al., *J. Biomech*. 39:1324-1334, 2006 [14] Rubod, C et al., *Int. Urogynecol. J*. 19:811-816, 2008 [15] Landsheere, L et al., *Int. Urogynecol. J*. 27:629-635, 2016 [16] Lingling L et al., *Int. Urogynecol. J*, 18:603-607, 2007 [17] Jean-Charles, C et al., *Int. Urogynecol. J*. 21:1535-1538, 2010 [18] Moalli, P et al., *Obstet. Gynecol*. 106:95-963, 2005 [19] Lin, S-Y et al., *Int. Urogynecol. J*. 18:43-48, 2007 [20] Badiou, W et al., *Int. Urogynecol. J* 19:723-729, 2008 [21] Boreham, M et al., *Am. J. Obstet. Gynecol*. 187:56-63, 2002 [22] Inal, H et al., *Neurourol. Urodyn*. 29:458-463, 2010 [23] Takacs, P et al., *Int. Urogynrcol. J*. 19:1559, 2008 [24] Whitcomb E et al., *Obstet Gynecol*, 114:1271-1277, 2009.

SB³C2021
Summer Biomechanics, Bioengineering and Biotransport Conference
June 14-18, Virtual

TENDON ENTHESIS TOUGHNESS RELIES ON POSITION-DEPENDENT FIBER RECRUITMENT AND BONY ATTACHMENT GEOMETRY

Mikhail Golman (1), Victor Birman (2), *Stavros Thomopoulos (1,3), *Guy M. Genin (4)

(1) Biomedical Engineering
(3) Orthopedic Surgery
Columbia University
New York, NY, USA

(2) Professor Emeritus of Mechanical Engineering
Missouri University of Science and Technology, St. Louis, Missouri, USA

(4) NSF Science and Technology Center for Engineering Mechanobiology
McKelvey School of Engineering
Washington University in St. Louis, Missouri, USA

INTRODUCTION

The effective transfer of muscle forces across the tendon-to-bone attachment ("enthesis"), is critical for joint stability and mobility. Recent advancements in high-resolution imaging revealed that the fibrous architecture of the tendon enthesis may be key to enabling the attachment to withstand multimodal and multidirectional loadings [1]. Nevertheless, many painful and physically debilitating conditions occur at or near this interface when this architecture is compromised [2].

Tendons present different fibrous architecture depending upon their function within joints. Positional tendons, such as flexor tendons of a hand, function primarily to move joints with precision [3], while energy storing tendon, such as the Achilles and patellar tendons, enable efficient locomotion by stretching and recoiling to store and release energy during joint movement [3]. The excursion and deformation of these tendon groups differ significantly, and range of motion (ROM) varies greatly from joint to joint. For the supraspinatus tendon in the shoulder, loading angles range from 0° to 120°; for the Achilles tendon in the ankle, these range from –40° to 20° [4]. Technologies to repair these tendons and their entheses are very similar, but it is unknown what aspects of these govern and enable their unique function, and what aspects of the entheses provide toughness to protect the tendon-bone interface from injury.

Therefore, our aim was to determine the roles of architectural and positional factors on enthesis toughness in a previously validated positional-recruitment model [5]. We hypothesized that energy storing tendons prioritize toughness over strength relative to positional tendons, regardless of loading direction. Furthermore, we hypothesized that the bony anatomy of each enthesis dictates the toughness profile with changing loading direction.

METHODS

Samples: All animal procedures were approved by the Columbia University IACUC. Supraspinatus, patellar, and Achilles tendon-to-bone attachment units were harvested from healthy adult (>12 weeks) C57BL6/J mice (n=15).

Imaging: Samples were submerged in a 5% mercury chloride ($HgCl_2$, Sigma-Aldrich) for 24 hours fixed at appropriate positions (flexion, straight, and extension; n=3-4 per position). $HgCl_2$ solution was used as a contrast agent to enhance enthesis visualization using high resolution x-ray computed tomography (microCT, Bruker Skyscan 1272, 60kVp, 166uA, 5µm resolution).

Positional-recruitment model: We consider N linear elastic fibers of thickness t, each spaced a distance s apart, beginning with a fiber that is immediately to the left of an elliptical bone ridge with a long axis A and the short axis B. We take the initial (unloaded) length of the inner most fiber (a fiber that is immediately to the left of a bone ridge) to be the shortest; fiber length increases with the distance from the bone ridge of fiber n, $A_o^n = R + 0.5t + (n-1)s$. During loading, fibers engage and contact their neighbors or the bone ridge (**Fig. 1**) at a point:

$$\vec{r}_1^n = -A^n \cos\phi_1^n \,\hat{\imath} + B^n \sin\phi_1^n \,\hat{\jmath} \qquad (1)$$

where the long axis and short axis of the centerline of the wrapped fiber (when the curvature takes an effect) is $A^n = A + (n-0.5)t$; $B^n = B + (n-0.5)t$ and the contact angle is $\cos\phi_1^n = R^n/x_0^n$. A rigid grip at the distal end holds all fibers. When the grip is turned at an angle θ to represent postural change, fibers are stretched in a direction $\hat{e}$. The angle ϕ_2^n at which contact is lost is determined by the innermost fiber, which always stays in tension. Contact is lost at the point $\vec{r}_2^n(t)$ at which the unit vector between $\vec{r}_2^n(t)$ and the connection point on the grip for the strand, $\vec{r}_3^n(t)$, is tangent to the ellipsoid formed by the midline of fiber n. Using this we can determine the maximum length of a fiber when it is engaged and contacts the bone ridge:

$$L_{en}^{n}(t) = \|\vec{r}_1^{\,n} - \vec{r}_0^{\,n}\| + Arc_{L_{en}}^{n}\Big|_{\phi_1^n}^{\phi_2^n(t)} + \|\vec{r}_3^{\,n}(t) - \vec{r}_2^{\,n}(t)\| \quad (2)$$

The $Arc_{L_{en}}^{n}$ is the arc length of an ellipse from ϕ_1^n to $\phi_2^n(t)$ with the long axis A^n and the short axis B^n, computed using the Ramanujan formula.

$$L_{en}^{n}(t) = \|\vec{r}_3^{\,n}(t) - \vec{r}_0^{\,n}\| \quad (3)$$

Load-displacement curves were generated from this position-dependent fiber kinematic model by assuming elastic, brittle fibers.

Initial conditions: To model positional tendons, initial lengths of each enthesis fiber were kept constant for all pull directions simulated. To model energy storing tendons, gauge lengths for all pull directions simulated were kept constant, making initial length of each enthesis fiber change with pull directions simulated. To evaluate effect of bone ridge flattening, energy-storing tendons were simulated with constant long axis (A=1) and changes to the short axis (B=0.2 to 1).

RESULTS

The positional-recruitment simulation, run with 20 fibers, revealed that strength, stiffness, and toughness depended on loading directions and were significantly different between positional tendons (i.e., supraspinatus model) and energy storing tendons (i.e., Achilles model) (**Fig. 2**). The strength of energy storing tendons peaked when the tendon enthesis was pulled straight (i.e., at 90°), decreased rapidly at higher loading angles, and decreased gradually at lower loading angles. In contrast, the strength of positional tendons was highest at -30° and decreased monotonically with increasing loading angles. The stiffness profile for energy storing tendons followed its strength profile. In contrast, the stiffness of positional tendons was relatively constant for all loading angles. When examining toughness, energy storing tendons absorbed more energy before failure at all angles compared to positional tendons, with gradual decreases in toughness with increasing loading angles.

Contrast enhanced images of rotator cuff, ankle, and knee joints at flexion, straight, and extension positions showed that the bone ridge anatomy where tendon attaches to bone (circular, B=1; flat, B=0.2) significantly affected the orientation and engagement of tendon enthesis fibers (**Fig. 3**). The effect of bone ridge flattening on the position-dependent load-sharing of the tendon enthesis was evaluated using the initial conditions for energy storing tendons. The simulation revealed that strength and stiffness increased with bone ridge flattening (**Fig. 4**). There were only modest changes in toughness with bone ridge flattening. Notably, toughness was highest for perfectly circular bone ridge (B=1) for all angles simulated.

DISCUSSION

Our novel fiber recruitment model enables simulation of position-dependent mechanical behavior of tendons for joints with varying bone ridge geometries. Simulated mechanical behaviors of positional and energy storing tendons depended strongly upon the initial loading conditions and bony anatomy of enthesis fiber attachment. These factors also affected responses over the physiologic ranges of loading angles. Consistent with our hypothesis, energy storing tendons appeared optimized for toughness: a small tradeoff in strength gave rise to a large gain in toughness throughout all loading angles. The trade-off was particularly apparent at lower loading angles, where, for instance, rotator cuff muscles would be most engaged and enthesis loads would be highest [6], allowing the enthesis fibers to optimize energy absorption (i.e., protect against onset of injury). Interestingly, the stiffness of positional tendons was constant throughout all loading angles. Positional tendons function to move joints with a precision; a constant stiffness likely allows for better muscle control of these precise motions across a wide range of motion.

The simulations provided insights into why thresholds for injury differ with loading angles for each joint. Acute rotator cuff tears often occur at high abduction angles (110°) [6], while Achilles tendon ruptures occur with a sudden plantar flexion of the foot (–30°) [7] and patellar tendon ruptures with the knee flexed (60°) [8]. These positions coincide with the lowest respective strengths in the simulations (**Fig. 2**). Although factors such as post-yield resistance certainly also contribute, the simulation results showed a clear role for bony anatomy and fiber recruitment in tendon enthesis mechanics.

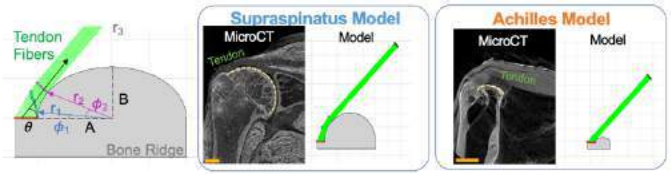

Fig. 1: Positional-recruitment model. Scale 500 µm.

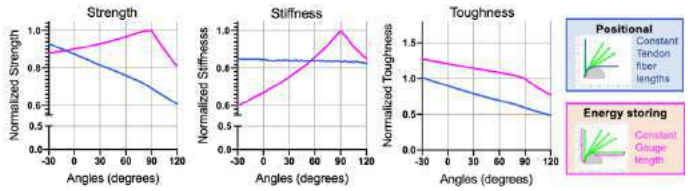

Fig. 2: Results for positional and energy storing tendons simulated to be loaded in range of loading directions.

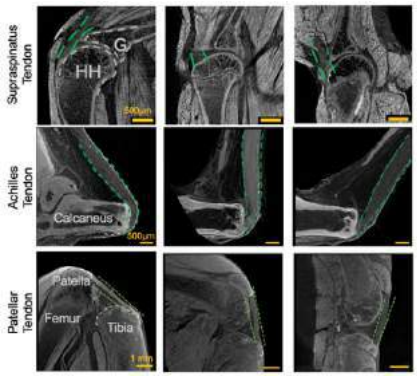

Fig. 3: Contrast enhanced images of rotator cuff, ankle, and knee joints at flexion, straight, and extension. Green outline tendons.

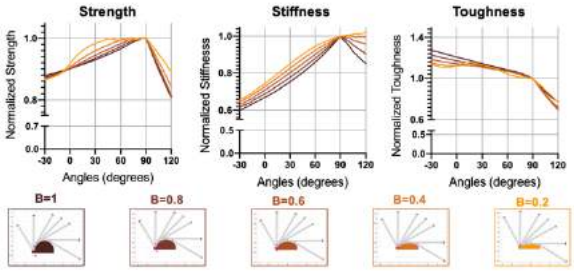

Fig. 4: Simulation results to see effect of anatomical bone-ridge flattening on tendon enthesis mechanics.

ACKNOWLEDGEMENTS

This work was supported by NIH (U01-EB016422, R01-AR055580).

REFERENCES: [1] Rossetti et al., *Nature Materials* 16(6), 664-670; [2] Kim *et al*., *J Bone Joint Surg Am*. 2010 Apr;92(4):829-39; [3] Alexander R.M., *J. Exp. Biol.*1991;160:55–69;[4] El Hawary et al., *Egp. Rheumat. Rehab.* 2019;46(4):237-243; [5] Golman et al., SB³C2020; [6] Gerber et al., *J. Orthop. Res.* 2014; [7] Shamrock AG et al, *StatPearls* 2020; [8] Dan et al., *J Orthop Res*. 2018, 36(12):3105-3112

COMPUTATIONALLY ENHANCED 4D FLOW MRI FOR THE ASSESSMENT OF PRE- AND POST-COARCTATION REPAIR AORTA FLOW DYNAMICS

Labib A. Shahid (1), James Rice (1), Haben Berhane (2), Cynthia K. Rigsby (2), Joshua D. Robinson (2), Lindsay M. Griffin (2), Michael Markl (3,4), Alejandro Roldán-Alzate (1,5,6)

(1) Department of Mechanical Engineering
University of Wisconsin-Madison
Madison, WI, USA

(2) Department of Medical Imaging
Ann & Robert H. Lurie Children's Hospital of Chicago
Chicago, IL, USA

(3) Department of Radiology
Northwestern University
Chicago, IL, USA

(4) Department of Biomedical Engineering
Northwestern University
Chicago, IL, USA

(5) Department of Biomedical Engineering
University of Wisconsin-Madison
Madison, WI, USA

(6) Department of Radiology
University of Wisconsin-Madison
Madison, WI, USA

INTRODUCTION

Coarctation of the aorta (COA) is a congenital heart disease characterized by a narrowing in the aortic arch or proximal descending aorta [1]. COA results in altered aortic flow dynamics (elevated pressure gradient, deranged flow) and subsequent complications such as post-stenotic aneurysms or insufficient blood supply to the periphery. Interventional treatment such as surgery, stent placement, and balloon angioplasty are often performed to restore normal aortic hemodynamics [2]. Diagnostic imaging, such as echocardiogram and cardiovascular magnetic resonance (CMR), for aortic hemodynamics is important for intervention planning and assessment of treatment success. Despite advances in CMR such as 4D flow MRI [3] for in-vivo analysis of cardiovascular flow dynamics, current techniques have limitations in phase offset errors, insufficient spatio-temporal resolution, and distortion of images due to stent (metal artifact), and thus unreliable quantification of flow metrics. Methods have been developed to better predict hemodynamic outcomes using patient specific CMR data supplemented by computational models of cardiovascular fluid dynamics. The purpose of this study was to evaluate the feasibility of patient specific MRI-based computational models using a novel method called adaptive mesh refinement (AMR) for improved quantitative flow dynamics analysis in patients with different types of COA repair.

METHODS

In-vivo 4D flow MRI was performed on three pediatric subjects following an IRB-approved protocol. Patient 1, a pediatric patient with COA and an associated mycotic aneurysm, was scanned before and after surgical repair with interposition graft (at ages 6 and 8). Patient 2 presented with COA and severe aortic kinking in the proximal descending aorta and underwent 4D flow MRI before and after repair by stent placement (at ages 13 and 16). The third subject was a healthy control (age 10). For all subjects, 3D segmentation of the aorta was performed (MIMICs) based on contrast enhanced MR angiography (CE-MRA) or CT scans, and a total of 5 models of the aorta (2 patients pre- and post-COA repair, 1 healthy control) were generated for numerical simulations. Flow velocities derived from in-vivo 4D flow MRI studies (EnSight, CEI) were used to define patient specific boundary conditions. Computational fluid dynamics (CFD) simulations were conducted on Converge CFD software using AMR. AMR refines the local computational grid size based on previously calculated discretization errors [4]. Implementing AMR reduces the computational resources required for the CFD simulations while maintaining high accuracy in the numerical results. Figure 1 shows the schematic of this computational method enhancing 4D flow MRI for cardiovascular flow dynamics analysis for patient 2 before stent placement. Velocities from CFD simulations were compared with 4D flow MRI derived in-vivo velocities.

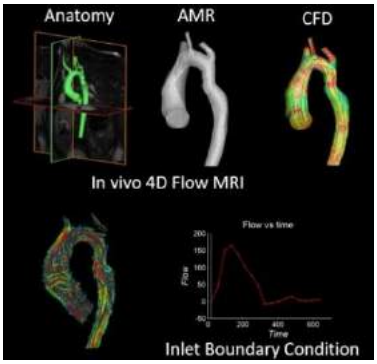

Figure 1: Schematic of computational method enhancing 4D Flow MRI for patient 2 pre-repair. Top (left to right): Patient anatomy

from CE-MRA, autonomously changing computational mesh grid due to AMR, CFD simulation results showing flow information. Bottom (left to right): 4D flow MRI study, flow information extracted from in vivo study used for inlet boundary condition for numerical simulation.

RESULTS

A total of five CFD simulations were successfully executed using patient specific anatomical geometries and flow conditions. For patient 1, the differences in mean velocities (at systole and diastole) between CFD and 4D flow studies were 5.4% and 13.3% in the ascending and descending regions, respectively. For patient 2, differences (at systole and diastole) were 0.3% and 1.8% in the ascending and descending regions, respectively. The locations of vortical flow from CFD simulations matched those from 4D flow MRI data. Figure 2 shows in-vivo 4D flow MRI and CFD results for patient 1 before intervention. CFD simulations revealed flow inside the aneurysm previously not captured by 4D flow MRI due to low flow velocities relative to the velocity encoding (VENC). Figure 3 shows in-vivo 4D flow MRI and CFD results for patient 2 after stent placement. 4D flow MRI results were clearly distorted due to metal artifact of the stent. Notably, numerical simulations could recover flow dynamics inside and distal to the tendered region that could not be resolved by in-vivo 4D flow MRI. The temporal resolution of enhanced CFD method was higher with a timestep size of 10 ms, compared to 38.5 ms for 4D flow MRI. The computationally enhanced technique showed better spatial resolution as well, resulting in visualization of flow in the aneurysm (Figure 2) and stent (Figure 3). The post-intervention cases were compared with the in-vivo 4D flow MRI and CFD results of the healthy control. Qualitative analysis of in-vivo and CFD flow dynamics show that post repair cases had residual complexities in the hemodynamic flow with larger vortices in the ascending region.

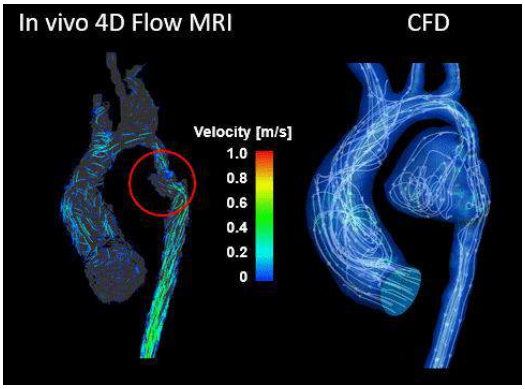

Figure 2: Comparison between in-vivo 4D flow MRI and CFD results for patient 1 pre-repair. Good agreement in velocity magnitudes at acceleration regions and vortical locations can be seen. The VENC used for the acquisition was too high for the low aneurysmal velocities and could not be detected in-vivo (red circle).

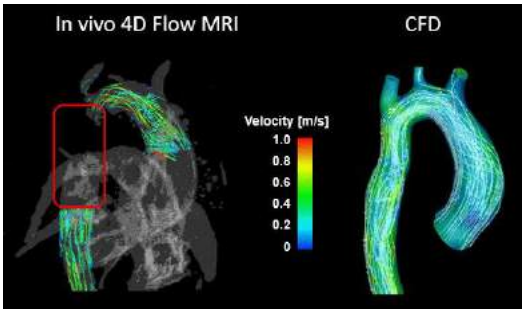

Figure 3: Comparison between in-vivo 4D flow MRI and CFD results for patient 2 post-repair (viewed from the posterior). Good agreement in velocity magnitudes at acceleration regions and vortical locations can be seen. In-vivo results does not show blood flow inside stent (red rectangle) due to distortion of image due to stent (metal artifact).

DISCUSSION

Computationally enhanced 4D flow MRI with AMR improved the spatio-temporal resolution across variable COA anatomy. AMR based CFD successfully restored flow metrics in regions of low velocity in patient 1's aneurysm, likely due to low aneurysmal velocities relative to the VENC. This method also predicted cardiovascular flow inside and surrounding the stent in patient 2 and demonstrated hemodynamic differences between post-operative and normal anatomy. Further, CFD provided flow information with good qualitative agreement with in-vivo results. In addition, mean velocities at ascending and descending aortic regions (at systole and diastole) using this method showed agreement with in-vivo data to within 15% difference.

CONCLUSION

The goal of COA repair is to restore normal hemodynamics. Despite improvements, CFD shows residual complex flow regions post-repair when compared to the healthy case. The novel AMR-augmented 4D flow MRI is feasible to derive quantitative flow metrics. This image-based modeling method can be used as a predictive tool for treatment planning and post-intervention assessment in patient specific clinical applications.

ACKNOWLEDGEMENTS

Grant support by American Heart Association (AHA) 19TPA34850066.

GE Healthcare, which provides research support to the University of Wisconsin-Madison.

REFERENCES

[1] P. S. Rao, "Coarctation of the Aorta," *Curr. Cardiol. Rep.*, vol. 7, pp. 425–434, 2005.

[2] A. Saxena, "Proceedings of the Fourth Scientific Meeting of the World Society for Pediatric and Congenital Heart Surgery Recurrent Coarctation: Interventional Techniques and Results," doi: 10.1177/2150135114566099.

[3] M. Markl, A. Frydrychowicz, S. Kozerke, M. Hope, and O. Wieben, "4D flow MRI," *J. Magn. Reson. Imaging*, vol. 36, no. 5, pp. 1015–1036, Nov. 2012, doi: 10.1002/jmri.23632.

[4] O. Sahni, K. E. Jansen, C. A. Taylor, and M. S. Shephard, "Automated adaptive cardiovascular flow simulations," *Eng. Comput.*, vol. 25, no. 1, pp. 25–36, 2009, doi: 10.1007/s00366-008-0110-5.

POLYMERIC TAVR DURABILITY AND HYDRODYNAMICS TESTING, ENHANCED BY MACHINE LEARNING FOR TRACKING LEAFLETS MOTION

B. Kovarovic (1), S. Crimarco (1), Z. Zhang (2), O.M. Rotman (1), M. Slepian (3) D. Bluestein (1)

(1) Biomedical Engineering
Stony Brook University
Stony Brook, NY

(2) Applied Mathematics & Statistics
Stony Brook University
Stony Brook, NY

(3) Sarver Heart Center
University of Arizona
Tucson, AZ, USA

INTRODUCTION

Polymeric surgical valve designs have been attempted since the 1960s with failures due to the demanding valve performance *in vivo* and the necessary fatigue life of the valve, with continuous functioning for up to 25 years inside the patient [1]. Still, polymeric technology offers benefits beyond the current bioprosthetic valves and mechanical valves, with the promise of reduced thrombogenic response due to the selection of hemocompatible materials and the resistance of structural valve degeneration due to the resistance of regrowth of calcific masses from the inflammatory response. The recent surge in popularity of transcatheter aortic valve replacement (TAVR), which is a minimally invasive percutaneous approach to replace a stenotic aortic valve with a stented bioprosthetic valve, offers additional benefits to the polymeric leaflet technologies. Polymeric TAVR devices can be designed to resist the damage and high stresses during the crimping and expansion of the stent as well as be designed to maintain leaflet performance in eccentric or under-deployment scenarios.

A novel polymeric valve, PolyV1 (PolyNova Cardiovascular Inc, Stony Brook, NY), has shown performance comparable to the gold standard surgical valves in idealized geometries and comparable to commercial TAVR devices in extreme patient-specific anatomies [2]. The PolyV1 utilizes a hemocompatible thermoset polymer and is cast with compression molding, in contrast to dipcoating used in other polymeric valves [3], to achieve a variable leaflet thickness profile that is optimized to reduce stresses in the leaflet [4]. The casting process allows the creation of leaflets with optimal geometries and thinner profiles to achieve the needed durability and performance.

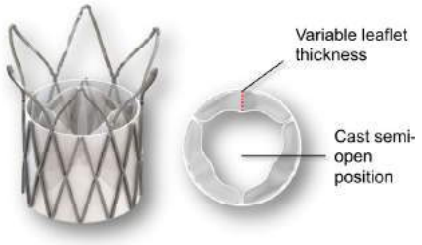

Figure 1 – Rendering of PolyV1 20mm device (left) and top-view of leaflet opening (right).

METHODS

Accelerated wear testing (AWT) was performed with the HiCycle (Vivitro Labs, Victoria, BC, Canada) according to the guidelines outlined in the ISO 5840-3. The (n=4) PolyV1 valves were affixed 3D rigid sleeve and tested with 0.9% saline solution at 37°C. The valves are tested according to the ISO guidelines maintaining a peak differential pressure of 100 mmHg across the closed valve for 95% of the cycles and that 100mmHg is experienced for more than 5% of the cycle. The valves are cycled at 10 Hz and were confirmed to completely open and close at that frequency. The valves were removed from the AWT and the hydrodynamic performance was tested every 50 million cycles. Currently the valves have been tested to 800M cycles (Figure 2) which far exceeds the 200M benchmark (5 year *in vivo* equivalent) defined by the FDA and ISO standard for the minimal valve leaflet durability.

The hydrodynamic performance was evaluated in a Vivitro left heart simulator (LHS) testing for critical valve performance targets of average systolic pressure drop (ΔP), effective orifice area (EOA, Bernoulli derived estimation of opening area), closing flow (backflow during leaflet closure) and leak flows. The valves were tested with a blood analog (50.3/48.8 by weight glycerol/ddH_2O). The valves are tested at various cardiac outputs (2, 3.5, 5, and 7 L/min) at 70 BPM and normotensive of conditions.

Valve imaging: During the hydrodynamic evaluation the valve was imaged with a high-speed camera (1057 FPS HD, Cronos 1.4, Krontech Burnaby, BC, Canada). The valves are imaged perpendicular to the

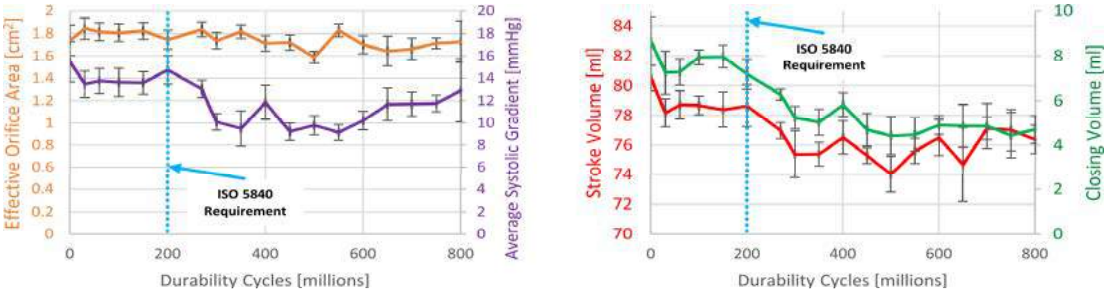

Figure 2 – Progression of EOA (orange), pressure gradient (purple), stroke volume to achieve cardiac output of 5 L/min @ 70 BPM (red), and closing volume (green) over the 800M cycles.

commissural plane with the focus placed upon the commissure attachment. The valves were lit from the aortic side attempting to highlight the leaflet edges. Due to transparent leaflets in the polymeric valve, conventional image processing methods yield poor/noisy segmentation results so a machine learning (ML) approach was adapted. Images were adjusted to increase contrast and then fed into a deep learning-based model that leverages fully convolutional neural networks and Holistically-Nested Edge Detection (HED) algorithm. The model was implemented in Python and was trained using around 200 human-annotated labels to detect the leaflet free edge. Binary images are outputted in which the leaflet edges are predicted and segmented in white. Post-processing in MATLAB is used to close any gaps in the leaflet edges by connecting the endpoints of incomplete segments (Figure 3). The geometric orifice area (GOA, physical opening area) was calculated from the flooded area between the open leaflets and scaled to the commissural diameter.

RESULTS

Initial hydrodynamic results of the valves showed performance meeting or exceeding traditional valves and surgical valves. Over the course of the testing (Figure 2), fatigue characteristics of the valve performance with a drop in the pressure gradient (from 16mmHg to 12mmHg) was seen over the course of the testing and appears to have stabilized. The effective orifice area remained relatively stable (1.7-1.9 cm^2) throughout the entire duration of the testing. Additionally, a drop in the closing volume (9-5 ml/beat) as the semi-open position of the leaflets fatigue into a more closed position. This reduction in closing flow resulted in smaller stroke volumes needed to reach the cardiac output and therefore a stable and higher performance valve is seen over the entire duration of the testing.

The machine learning results were compared to a reference valve (not subject to any fatigue) and shows that the typical leaflet durability behavior is observed, with the reduction in stroke volume, increase in GOA, and shorter period of the leaflet opening. As the leaflets form a more closed morphology, the leaflet opening and closing occurs slower (Figure 3, bottom). Individual analysis of each leaflet shows that a single leaflet can open slower or faster with increasing fatigue cycles, although this does not appear to impact the performance or the fatigue strength of the valve nor is it consistent among the tested valves.

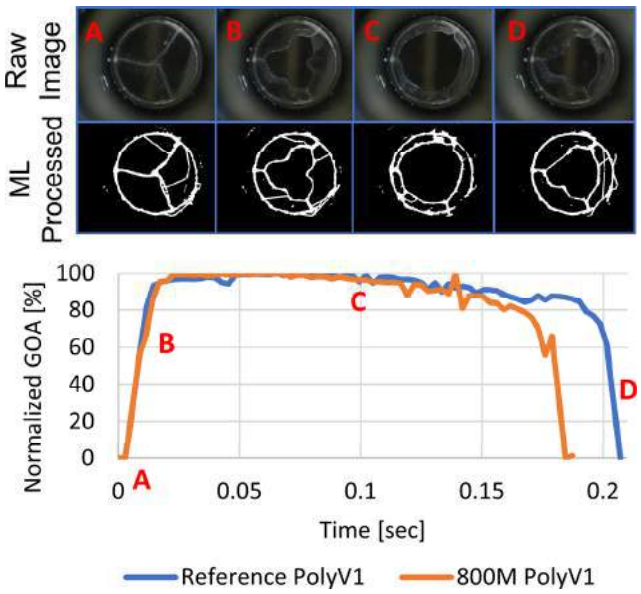

Figure 3 – High speed images of the reference valve (top row) opening and closing (A-D), binary image generated from ML algorithm (middle), and opening profile comparing the opening of one 800M valve to the reference valve (bottom).

DISCUSSION

Increased durability for polymeric valve has been one of the primary pitfalls for adoption of polymeric valve technology and these results are promising. There is no observable wear and tear or catastrophic failure in the four samples tested in the study. The ability to cast a valve in the semi-open position, along with the variable thickness of the leaflet profile to reduce stresses, yields a stable EOA over the expected clinical leaflet fatigue life (5-25 years) as well as the improvement the performance with the reduction of closing flow. With extended leaflet durability testing there are expected changes of the leaflet structure resulting in the changes of the performance as well as the morphology change of a closing leaflet profile.

The generation of a machine learning algorithm will allow further exploration of these fatigue characteristics to the leaflet deformations with minor concern for the changes to the test lighting and exposure over this multi-year study. One limitation of this study is that high-speed imaging the valve was only adopted recently (≥700M cycles) and therefore the machine learning algorithm can only be utilized at the endpoints of the durability study and can only be compared to the reference valve. The machine learning algorithm is also being refined to yield the curvature of the leaflet profile during opening and to track each leaflet individually.

With the initial promise of these results, the cast polymeric technology can be adapted into studying the effects of various semi-open positions of the leaflets as well as more advanced designs such as eccentric valve technologies. The ability to cast a valve with any leaflet profile morphology and design allows the refinement of this durability profile and better success in the clinic and for better patient outcomes.

ACKNOWLEDGEMENTS

This project was supported by NIH-NIBIB 1U01EB026414-01 (DB), NHLBI STTR R41-HL134418 (DB) and the Center for Biotechnology: a New York State Center for Advanced Technology, New York State Department of Economic Development, and corporate support.

Disclosure: Author OMR and BK are consultants for PolyNova Cardiovascular Inc. Author DB has an equity interest in PolyNova Cardiovascular Inc.

REFERENCES

[1] Rotman, O.M. et al., *Expert Rev of Med Devices.* 15:11, 771-79, 2018

[2] Kovarovic, B. et al., *Artif Organs.* 2020; 00: 1– 12.

[3] Jenney, C. et al., *Adv Nanobiomed Res.* 200032, 2021.

[4] Rotman, O.M. et al., *Ann Biomed Eng.* 47, 113–125 (2019).

OPTIMIZING TRANSCATHETER HEART VALVE USE IN MITRAL ANNULAR CALCIFICATION

Breandan Yeats (1), Huang Chen (1), Pradeep Yadav (2), Venkateshwar Polsani (2), Vinod Thourani (2), and Lakshmi Dasi (1)

(1) Department of Biomedical Engineering
Georgia Institute of Technology
Atlanta, Georgia, United States

(2) Department of Cardiology
Piedmont Hospital
Atlanta, Georgia, United States

INTRODUCTION

Mitral annular calcification (MAC) is a degenerative fatal disease which impairs mitral valve function. It is often associated with calcific aortic stenosis (AS) and is present in roughly half of patients with severe AS. [1]. MAC normally occurs in the elderly population thus many patients are deemed high risk of surgical intervention. An alternative is the use of a transcatheter aortic valve replacement (TAVR), specifically the Edwards SAPIEN 3. However, this procedure has low success rate and high 30-day mortality with the most concerning issues being 7% valve embolization rate and 40% rate of left ventricular outflow tract (LVOT) obstruction [2]. This is likely due to the difficulties of anchoring with the complexity of calcium nodule distribution and lack of clinical trials. A recent technique involving laceration of the anterior mitral leaflet to prevent left ventricular outflow tract obstruction (LAMPOON) has shown promise [3]. However, its use in valve in MAC can be difficult with the presence of extensive calcium and has not been thoroughly investigated. Thus clinical guidance optimizing valve sizing and positioning to better device outcome is highly valuable. The goal of this study is to better understand and optimize the valve in MAC procedure through iterative computational techniques.

METHODS

A 60 year old female with severe MAC was analyzed. A cardiac CT scan was obtained under IRB approved protocol. The left atrium, mitral valve, left ventricle, LVOT, and aortic valve were segmented and meshed using Materialize MIS (Leuven, Belgium) (**Figure 1A**).

The SAPIEN 3 29 mm stent was generated in Solidworks (Waltham, MA, USA) based on a microCT performed on the valve. The 23 mm sized valve was also generated through scaling. Both stents were meshed in MIS. Material models were based on those used in previous studies [4-7]. Finite element analysis was then performed in Abaqus

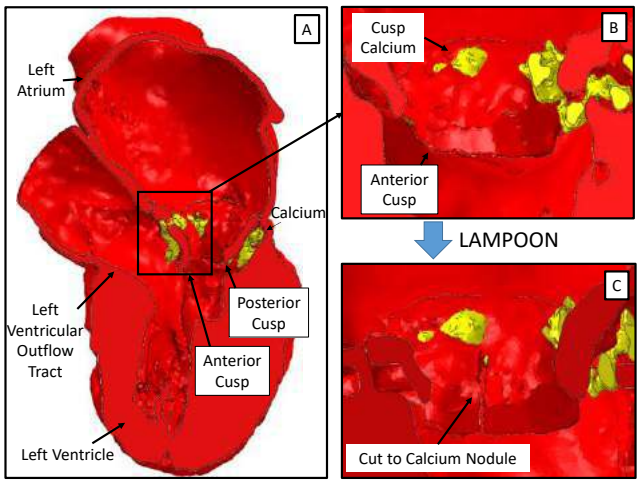

Figure 1: patient segmentation including the mitral anterior and posterior cusps, left ventricle, left atrium, LVOT, and calcium nodules (**A**), anterior cusp and a large calcium nodule at its base (**B**), and LAMPOON procedure cut along the anterior leaflet to the calcium nodule (**C**).

(Johnston, RI, USA). A balloon with the corresponding diameter was generated and computationally deflated for each stent. The stents were then crimped onto their respective balloons. Each stent was positioned in the mitral position and deployed with the bottom of the stent aligned with the annulus after expansion. The LAMPOON procedure was then simulated by making a laceration from the free edge of the anterior cusp to the large calcium nodule embedded at the base of the cusp (**Figure 1B and C**). Both valve procedures were then performed with the LAMPOON geometry. The area of the opening between the mitral

anterior cusp and LVOT wall was measured to analyze LVOT obstruction in each case. Realistically, the SAPIEN valve is designed with an inner skirt covering all cells below the top layer, any of these cells we considered to block flow and subtracted from the opening area calculation. Stent area in contact with the mitral valve surface and calcium nodules was measured to asses stent embolization risk. Contact area was defined as the sum of all element areas where contact force was present.

RESULTS

SAPIEN stent expansion with LAMPOON increased the opening into the LVOT (**Figure 2**).

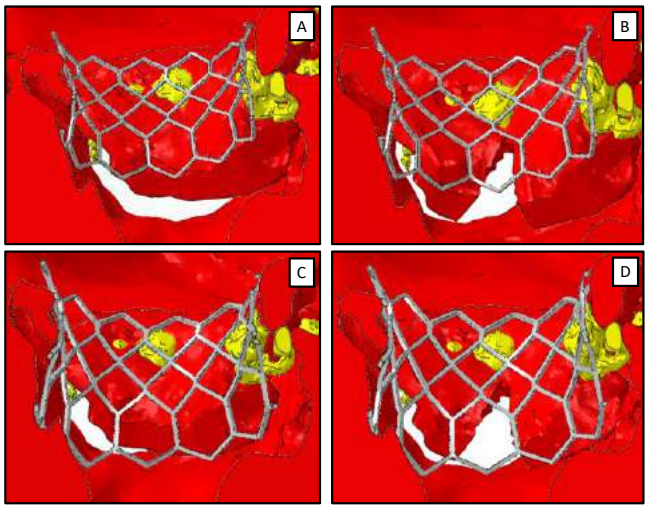

Figure 2: simulation results of the SAPIEN 23 mm without LAMPOON (**A**), with LAMPOON (**B**), SAPIEN 29 mm without LAMPOON (**C**), and with LAMPOON (**D**).

Without LAMPOON the 23 mm stent resulted in a 42% larger opening compared to the 29 mm stent. This was due to the larger diameter causing the stent to push the anterior leaflet closer to the LVOT wall thus limiting the opening area. The LAMPOON procedure increased the opening area by 13% for the 23 mm stent and by 38% for the 29 mm stent. This resulted in only a 16% larger opening after the 23 mm stent deployment compared with the 29 mm stent. The much larger increase in opening for the 29 mm stent deployment was caused by an increased spread of the cut leaflets creating a larger opening specifically where the laceration was located. However, a portion of this opening (13%) was blocked by a closed cell.

The contact area between the stent and tissues is plotted based on balloon expansion percent for each deployment (**Figure 3**).

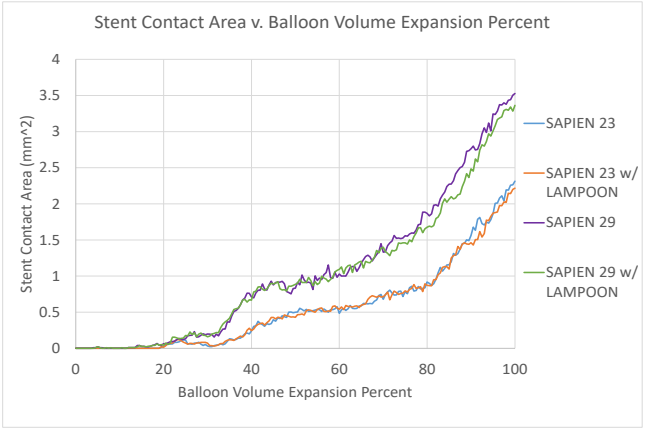

Figure 3: stent contact area plotted against balloon volume expansion percent for each deployment.

The LAMPOON procedure resulted in slightly smaller contact area for both stent sizes. There may have been an increased difference if the calcium nodule was absent thus allowing the cut to be longer. The SAPIEN 23 mm resulted in roughly 50% smaller contact area compared to the SAPIEN 29 mm. This much smaller contact area could be problematic with respect to valve embolization.

DISCUSSION

TAVR implantation in MAC remains to be a complex procedure with high failure rates and limited clinical guidance. This study offers to provide initial patient specific analysis which gives insight into how these procedures may be optimized. When LAMPOON was performed, the larger stent increased the opening of the lacerated leaflet more than the smaller stent. However, when LAMPOON was not performed, the larger stent pushed the anterior leaflet further towards the LVOT wall resulting in a smaller opening compared with the smaller stent. In each case, the large stent had much more contact area which may reduce embolization risk. Lastly, LAMPOON did not significantly lower overall contact area for small or large stents. Further studies should be performed including analyzing additional anatomies, performing computational fluid dynamics to better quantify LVOT obstruction, and deploying more size variations of the SAPIEN stent.

References

[1] Abramowitz, Y et al., *European heart journal*, 38.16: 1194-1203, 2017
[2] Maisano, F et al., *European heart journal*, 40: 452-455, 2019.
[3] Babaliaros, Vasilis C., et al. *JACC: Cardiovascular Interventions*, 10.8: 798-809, 2017
[4] Tzamtzis, S., et al., *Medical engineering & physics*, 35(1): 125-130, 2013
[5] Emendi, M., et al., *Annals of Biomedical Engineering*, 1-15, 2020
[6] Holzapfel, G.A., et al., *J. Biomech. Eng.*, 126(5): 657-665, 2004
[7] Pham, Thuy, and Wei Sun, *Journal of Biomedical Materials Research Part A*, 102.8: 2692-2703 (2014)

SB³C2020
Summer Biomechanics, Bioengineering and Biotransport Conference
June 17-20, Vail, CO, USA

ESCAPING THE STIFFNESS TRAP: ADHESION STRENGTH AND CONTRACTILITY ENABLE METASTATIC CELLS TO BECOME ADUROTACTIC

Benjamin M. Yeoman (1,2), Gabe Shatkin (1), Pranjali Beri (1), Afsheen Banisadr (1), Adam J. Engler (1,3), Parag Katira (2,4)

(1) Department of Bioengineering
University of California
San Diego La Jolla, CA, USA

(2) Department of Mechanical Engineering
San Diego State University
San Diego, CA, USA

(3) Sanford Consortium for Regenerative Medicine
La Jolla, CA, USA

(4) Computational Sciences Research Center
San Diego State University
San Diego, CA, USA

INTRODUCTION

Cancer mortality is the result of the metastatic process where tumor cells migrate from a stiff primary tumor through softer adjacent stroma. While there is limited overlap in biomarkers between cancer types, all solid tumor cells must detach, migrate, and invade the surrounding tissue in order to metastasize. Durotaxis, i.e. migration in the direction of an increasing stiffness, has been observed in the majority of migratory cells [1,2]. However as many tumors progress, the surrounding microenvironment gradually becomes stiffer than the adjacent stroma [3,4], requiring a cancer cell to undergo "reverse durotaxis" in order to metastasize. This suggests there may be a breakdown of the normal processes regulating durotaxis that allows cancer cells to become insensitive to stiffness gradients.

We hypothesize that mechanotypic heterogeneity across and within cell populations might be responsible for differential durotactic behavior in these populations. In recent work, we found that adhesion strength acted as a physical marker that sorted isogenic cells into weakly and strongly adhesive cell groups that were more versus less contractile and migratory [5], respectively. RNA sequencing further showed transcriptional differences characteristic of distinct mechanotypes that sorted patient outcomes in The Cancer Genome Atlas (TCGA); patients with the weakly adhesive gene signatures relapsed at a rate 2-fold higher than the strongly adhesive gene signatures. Such differences could contribute to durotactic differences not previously observed, and here we show that mechanotypic differences are the proximate driver for differential rigidity sensing and adurotactic behavior.

METHODS

Sorting, time-lapse, and traction force microscopy: Weakly and strongly adherent tumorigenic breast (MDA-MB-231), prostate (PC-3), and lung (NCI-H1299) cancer cells were isolated using a microfluidic adhesion-based sorting device. Migration and traction force experiments were conducted with isolated cells seeded on polyacrylamide (PA) gels of elasticity that match both healthy and diseased tissue for each type of cancer. Photopatterned gels containing alternating soft and stiff elasticity profiles were used to observe the durotactic behaviors of WA and SA cells (Fig. 1a). In migration experiments, cell positions were captured every 15 minutes for 24 hours using time-lapse microscopy and then tracked using a custom MATLAB script. Traction forces were captured every minute for 30 minutes on stiff gels containing 0.2 μm fluorescent beads. Traction stresses were then calculated using a custom MATLAB routine and used to determine the strain energy, which was then normalized to cell area.

Model description: In our model, the cell is comprised of a number of focal adhesion (FA) initiation sites that move away or towards the cell's centroid based on actin polymerization or depolymerization. Each site is assumed to contain the adapter proteins necessary to bind a stress fiber (SF). The model loops through the following steps, with each loop completing a single timestep. First, an initiation site will begin to form a FA if an integrin-SF complex binds to an external extracellular matrix (ECM) protein. Bound integrins will have a certain probability of binding or unbinding according to,

$$P_{on} = 1 - e^{-\Delta t k_{on}} \quad (1a)$$

$$P_{off} = 1 - e^{-\Delta t k_{off}} \quad (1b)$$

where Δt is the time step, k_{on} is the integrin binding rate, and k_{off} is the breaking rate based on the catch bond dynamics measured experimentally [6]. Next, the SF applies a force to any bound integrins and associated proteins according to the following equation,

$$F = F_s(1 - e^{-tv_o k_{eff}/F_s}) \quad (2)$$

where F_s is the myosin motor stall force, t is the length of time of the applied force, v_o is the maximal motor velocity, and k_{eff} the effective stiffness of the substrate. If the complex contains a tension sensor protein, which experiences a sufficiently large force, it will expose actin binding sites for recruiting new SFs and integrins, leading to FA growth and maturation. Growth is limited by a finite number of SFs available in the cell. Finally, the forces at all initiation sites are then summed to get the net force on the cell, which is divided by the drag to calculate the velocity and distance the cell will move before the next time step. The positions of the unbound initiation sites are updated and the next iteration begins. We simulate 24 hours of cell migration, and track the cells position relative to the soft/stiff boundary as in the time-lapse microscopy images.

RESULTS

We compared the average speed of cells migrating on stiff or soft regions of the PA gel (Fig. 1a) and found that WA cells migrate faster than SA cells on the same substrate, suggesting that WA cells may have a higher metastatic potential. This is consistent with what has been seen previously [5], and shows that these cells respond differently based on their adherence and local environment. Increased migration speed in WA cells is in part due to greater cell contractility (Fig. 1b), which suggests that migration differences are not solely due to friction from cell-ECM adhesion. Moreover after 24 hours, SA breast and prostate cancer cells preferred to migrate into the stiffer regions whereas the WA cells had no preference (Fig. 1c-d).

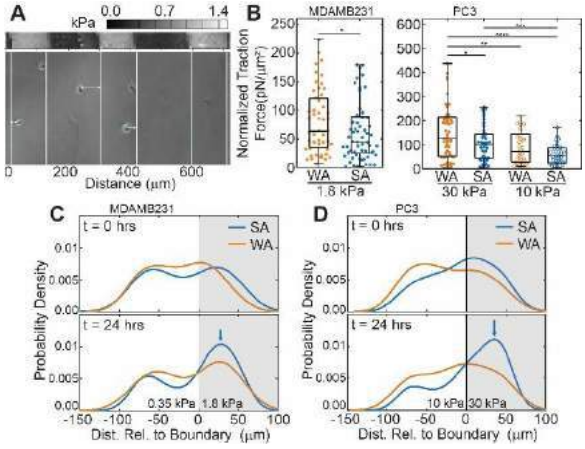

Figure 1: A) Brightfield image of MDA-MB-231 cells (dots) with lines to indicate transitions between soft and stiff substrate regions of step-gradient hydrogels (bottom). Arrows show the distance relative to the closest boundary. Atomic force microscopy (AFM) map is also shown (center) with corresponding color map (top). B) MDA-MB-231 cell speed on step-gradient hydrogels for cells far away from the step-gradient. C-D) At 0 and 24 hours, MDA-MB-231 or PC-3 probability density versus hydrogel position. Blue arrow indicates a peak in the strongly adherent cell distribution at 24 hours. *p<0.05, **p<10^{-2}, ****p<10^{-4}, *****p<10^{-5}.

To test the plausibility of durotaxis occurring due to differing traction forces applied to the substrate through integrin catch bonds, we built a computational model that incorporates cell adhesion, stress fiber (SF) mediated force generation, and catch bond dynamics. Because the load on a catch bond is dependent on the contractility of a cell and the stiffness of the cell's substrate, the bond lifetime can be prolonged under an intermediate load. In our model, cells that were able to exert an intermediate force on stiff substrates exhibited durotaxis, since their adhesions lasted longer than they would on soft substrates. This requires a cell to be optimally contractile, as increasing contractility shifts the load past the catch bond's ideal force. To validate such control in our system, we reduced the number of active myosin motors within a cell, i.e. SF force, finding that it increases the durotactic tendency of cells as predicted by the model between 30 and 45 pN (Fig. 2a). We tested this experimentally by inhibiting the myosin II activity of WA mammary cells with blebbistatin, and found myosin inhibition restored durotactic behavior in these cells (Fig. 2b). Conversely, SA mammary cells also showed a dose dependent response to lysophophatidic acid treatment, wherein the SA phenotype became less durotactic, resembling the adurotactic behavior of WA cells (Fig. 2c).

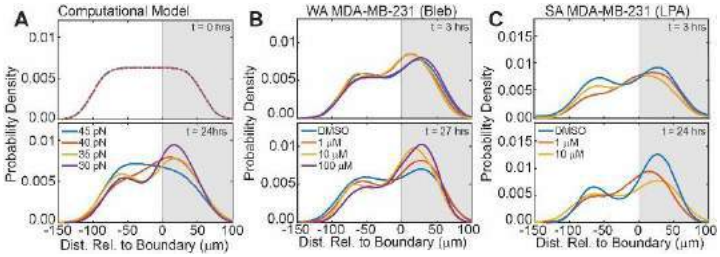

Figure 2: A) Model probability density versus simulated hydrogel position as predicted for 30 (purple), 35 (yellow), 40 (red), and 45 pN (blue) max SF forces at t=0 and t=24 hours. B) Weakly adherent MDA-MB-231 probability density versus hydrogel position for blebbistatin treatment. C) Strongly adherent MDA-MB-231 probability density versus hydrogel position for LPA treatment.

DISCUSSION

The findings of this work help explain how a metastatic cell's distinct mechanotype correlates to the paradoxical migration down a stiffness gradient that occurs during cancer metastasis. Cancer cells isolated by their adhesion strength from a seemingly isogenic population exhibit consistent behavior across different cell lines from vastly different cancer types; moreover, each cancer type exhibits adurotaxis in their tumor-specific niche, which change dramatically for step gradient strength (between 3- and 5-fold) and gradient range (from 0.3 to 30 kPa). Despite these differences, greater contractility in weakly adherent cells is conserved and led to decreased durotactic behavior that is not directly governed by lack of rigidity sensing. From previous work, RNA sequencing shows a distinct underlying phenotype for weakly vs. strongly adherent cells with differences in cytoskeletal protein expression, which relates to decreased progression-free and disease-free intervals when compared to the gene expression signatures of human patients [5]. A weakly adherent cell's ability to migrate against stiffness gradients connects this observation to the material properties of the niche, which contribute to its increased metastatic potential.

ACKNOWLEDGEMENTS

The authors acknowledge grant support from the National Institutes of Health (R01CA206880 and R21CA217735) and National Science Foundation (1763139 and 1763132), and the Army Research Office (W911NF-17-1-0413).

REFERENCES

[1] DuChez, J et al., *Biophys J*, 116: 670–683, 2019.
[2] Joaquin, D et al., *Biotech and Bioeng*, 113:2496–2506, 2016.
[3] Lachowski, D et al., *Sci Rep*, 7:1–12, 2017.
[4] McKenzie, A et al., *Sci Rep*, 8:1–20, 2018.
[5] Beri, P et al., *Cancer Research*, CAN-19-1794, 2019.
[6] Kong, F et al., *J Cell Biol*, 185:1275–1284, 2009.

UNDERSTANDING MECHANISMS OF LOAD TRANSFER IN THE TENDON-TO-BONE ATTACHMENT

Mikhail Golam (1), Jonathan D Almer (2), Stavros Thomopoulos (1), Alix Deymier (3)

(1) Dept. Orthopedic Surgery
Columbia University
New York, NY, USA

(2) Advanced Photon Source
Argonne National Laboratory
Argonne, IL, USA

(3) Dept. Biomedical Engineering
UConn Health
Farmington, CT, USA

INTRODUCTION

Rotator cuff injuries are extremely prevalent and are present in 50% of the population over the age of 80 [1]. Healing of these injuries is poor, with repair failure rates of up to 94% after massive tears [2]. These high failure rates are caused by the body's inability to recreate the multiscale load transfer mechanisms of the healthy tendon-to-bone attachment.

Healthy tendon-to-bone attachments exhibit a number of hierarchical structures that are theorized to decrease stress concentrations. At the millimeter length scale, tendon attaches to bone with a splayed geometry that increases the attachment area, decreasing stress [3]. At the micrometer length scale, an interdigitating interface is seen with gradients in mineral and collagen content, strengthening and toughening the interface [4]. At the nanometer length scale, the mineral crystal size and orientation changes along the attachment[5]. Although we can theorize and model the mechanical roles that these structures play during loading of the tendon-to-bone attachment, there is little to no experimental work measuring their individual contributions.

The small size and complex arrangement of collagen and mineral structures across the attachment have made it difficult to measure their mechanical behavior within the larger attachment tissue during loading. In the current study, we employed *in situ* tissue loading along with high energy synchrotron X-ray diffraction to simultaneously measure whole tissue, collagen fibril, and mineral deformation across the tendon-to-bone attachment. This technique allowed us to identify, for the first time, the mechanisms by which load is transferred across the complex attachment structure.

METHODS

Supraspinatus-humerus complexes were collected from adult canines in accordance with Washington University in St Louis Animal Research Protocols. The complexes were cut along the coronal plane to obtain sections of the supraspinatus-humerus tendon-to-bone attachments measuring ~1 cm in thickness. Samples were wrapped in phosphate buffered saline (PBS) soaked gauze and frozen at -20°C until the time of testing.

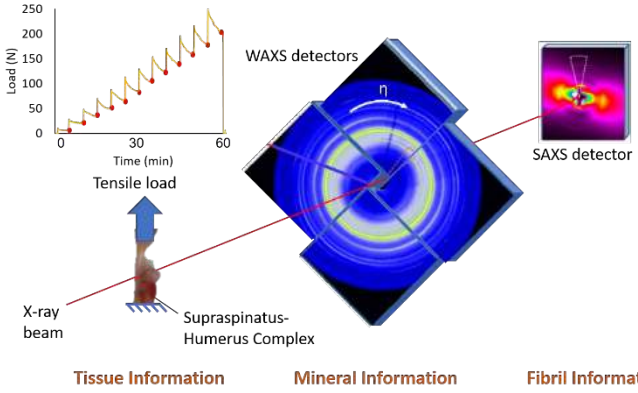

Figure 1: Schematic of experimental set up showing simultaneous collection of tissue, mineral, and fibrillar information.

Samples were brought to hutch 1-ID-E of the Advanced Photon Source (APS) at Argonne National Lab for testing. There, the samples were mounted in liquid nitrogen-cooled freeze clamps in a MTS model 858 hydraulic load frame. Samples (n=2) underwent quasi-static loading up to 250 N in increments of 25 N (**Fig. 1**). Samples were allowed to relax for 5 min after each incremental load after which both Wide and Small angle X-ray scattering (WAXS and SAXS) were recorded. X-ray diffraction patterns were collected simultaneously on 4 GE-41RT detectors in the "hydra" configuration in the case of WAXS and a ScintX DXI-11000R detector in the case of SAXS (**Fig. 1**).

Measurements were made at 10 locations spanning the tendon, enthesis, and bone in intervals of 200 μm with a beam energy of 71.7 keV and a spot size of 30 x 30 μm^2. Whole tissue deformation was measured from the grip displacement.

SAXS and WAXS patterns were analyzed using custom programs in MATLAB as previously described [5, 6]. Mineral d-spacing was calculated from the location of the (002) apatite peak in the WAXS data while fibrillar D-spacing was determined from the location of the 3rd order peak in the SAXS data. Mineral and collagen strain (ε) were calculated according to the equation $\varepsilon=\Delta d/d_o$ where d_o is the d-spacing before loading and Δd is the change is d-spacing with applied load. The mineral and collagen alignment were determined from the FWHM of the intensity peaks as a function η, where a decrease in FWHM represents an increase in alignment. Collagen microstrain (ε_{RMS}) was determined from the width of the 3rd order SAXS peak. Mineral coherent domain size and ε_{RMS} were calculated using the Halder-Wagner method from the width of the (002), (210), and (310) peaks[7].

RESULTS

Tissue scale mechanics exhibited an initial non-linear toe region followed by a linear increase in strain with increasing load.

Fibrillar strain was dependent on both location and applied load (**Fig. 2**). The fibrils in the tendon exhibited very little strain. These fibrils also showed no change in alignment with loading, although there was an increase in fibrillar microstrain. In contrast, the fibrils in the enthesis exhibited very high strains that decreased beyond loads of ~125 N. Despite these high strains, the enthesis fibrils showed no changes in alignment and only small increases in microstrain. Bone fibril strain did not increase until loads >100N and showed no change in alignment or microstrain with loading.

The mineral in both the enthesis and the bone exhibited an increase in strain with increasing applied loads (**Fig. 2**). This increase was immediate in the enthesis, while bone mineral required loads >20N to undergo straining. Neither the size, microstrain, nor alignment of the mineral changed with increasing load.

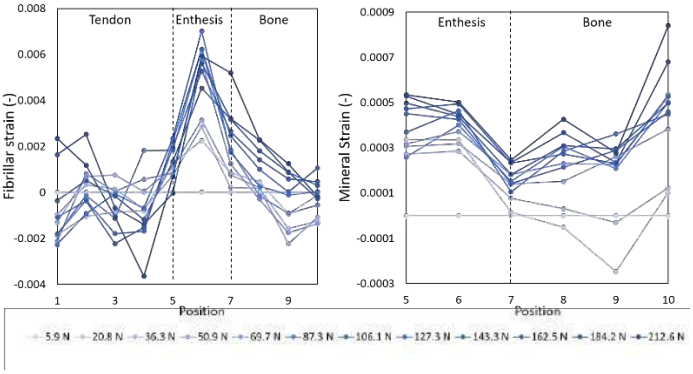

Figure 2: Plots of fibrillar and mineral strain as a function of position and applied load (legend).

DISCUSSION

Tissue-level strain increased linearly with load, indicating that all experiments were performed within the elastic region of supraspinatus-humerus mechanical behavior. This suggests that there was no significant plastic deformation or damage to the tissue during loading.

Strain at the collagen fibril level was far lower than strain at the tissue level during the early portion of loading (i.e., <35 N) (**Fig. 3**). This is indicative of collagen fibril sliding or uncoiling [8, 9]. These changes in the higher order structure of the collagen, likely in the tendon, as indicated by a lack of fibril-level strain at all loads, allows the tissue to deform without stretching the collagen fibrils themselves.

At intermediate levels of loading (i.e., 20-125 N), there was significant accumulation of strain in the fibrils and in the mineral of the enthesis (**Fig. 2**). Unlike the unmineralized tendon, where fiber-fiber sliding dominated, the enthesis exhibited high levels of fibrillar and mineral strain. This is in agreement with other studies that have identified the presence of a compliant zone within the enthesis [10, 11]. The rotation or realignment of collagen and mineral has been suggested as a mechanism for the increased deformation/strain seen in this area [5, 12]. However, the lack of change in mineral and collagen alignment with loading suggests that this is not the cause of the compliant zone. Instead, compositional changes such as the presence of proteoglycans may be responsible for these mechanical behaviors.

At higher levels of load, there was increased strain in the bone mineral and fibrils and a decrease in enthesis fibrillar strain (**Fig. 2**). This suggests that that load sharing was transferred from the enthesis, which may have reached maximum deformation, to the bone. The continued increase in mineral strain with increasing load across the tissues also indicates that collagen is transferring load to the reinforcing mineral.

In conclusion, canine supraspinatus-humerus complexes employed a number of multi-tissue and multi-scale mechanisms to transfer load. At low loads, tissue deformation was mainly dictated by collagen sliding/uncoiling in the tendon. At intermediate loads, there was a transfer of load to the enthesis, which underwent large deformations. Finally, at high loads, the enthesis reached maximum elastic deformation, at which point load was transferred to the bone. These complex mechanisms of load transfer provide the tendon-to-bone attachment with its robust mechanics.

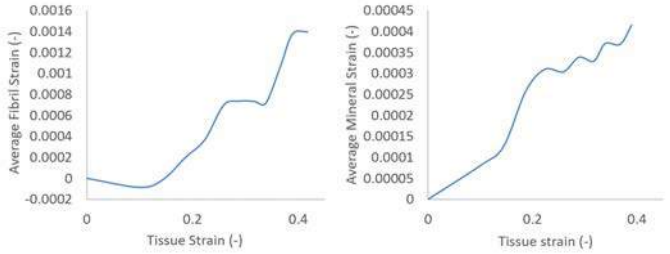

Figure 3: Plots of Average fibrillar strain and mineral strain vs. tissue strain.

ACKNOWLEDGEMENTS

Funding was provided by AD's Startup package and ST's NIH U01 AR063632. This research used resources of the Advanced Photon Source, a U.S. Department of Energy (DOE) Office of Science User Facility, operated for the DOE Office of Science by Argonne National Laboratory under Contract No. DE-AC02-06CH11357. Ali Mashayekhi assisted with all experimental setup.

REFERENCES

[1] S. Tempelhof, et al., Journal of Shoulder and Elbow Surgery 8(4) 296-299.
[2] L.M. Galatz, et al., J Bone Joint Surg Am (2004) 219-24.
[3] Y.X. Liu, et al., Mech Mater 44(10) (2012) 005.
[4] A.G. Schwartz, et al., PLoS One 7(11) (2012) 9.
[5] A.C. Deymier, et al., Acta Biomater 83 (2019) 302-313.
[6] A.C. Deymier-Black, et al., Acta Biomater. 6(6) (2010) 2172-2180.
[7] D. Nath, et al., Mater. Chem. Phys. 239 (2020) 122021.
[8] H.S. Gupta, et al., PNAS 103(47) (2006) 17741-17746.
[9] N. Sasaki, S. Odajima, J. Biomech. 29(9) (1996) 1131-1136.
[10] A.C. Deymier, et al., Acta Biomater 56 (2017) 25-35.
[11] S. Thomopoulos, et al., J Biomech Eng 125(1) (2003) 106-13.
[12] G.M. Genin, et al., Biophys J 97(4) (2009) 976-85.

THE PRIMARY CILIUM REGULATES MECHANORESPONSIVE PATHWAYS IN TENOCYTES

McKenzie E. Sup (1), Fei Fang (2), Thomopoulos Stavros (1,3)

(1) Department of Biomedical Engineering
Columbia University
New York, NY, USA

(2) Department of Orthopedic Surgery
Columbia University
New York, NY, USA

(3) Department of Orthopedic Surgery
Columbia University
New York, NY, USA

INTRODUCTION

Mechanical forces are necessary for tendon and enthesis (tendon-to-bone attachment) homeostasis and development [1]. Studies in other musculoskeletal tissues have shown that an organelle known as the primary cilium plays a role in sensing and transducing applied mechanical signals [2]. Tenocyte cilia numbers in mice increase following loading deprivation and decrease after treadmill running [3]. In response to *in vitro* cyclical tensile stretching, tenocyte primary cilia disassemble, and the expression of *Ift88* (necessary for cilia assembly) decreases [4]. Furthermore, *in vitro* loading leads to a decrease, and *in vivo* unloading leads to increase, in expression of *Smoothened (Smo),* a component of Hedgehog (Hh) signaling that drives the formation of the tendon enthesis and is regulated by the primary cilium[1,3,5,6]. However, it remains unknown whether the primary cilium is necessary for mechanotransduction in tendon, and whether Hh signaling in tendon and the enthesis is dependent on the function of the primary cilium. Therefore, we investigated the role of primary cilia in the response of tenocytes to mechanical stimulus using an *in vitro* loading model. We hypothesized that tenocyte cilia regulate mechanosensory pathways in tendon and thereby affect Hh signaling.

METHODS

In Vitro Loading Model: Tenocytes were isolated from the tail tendons of adult C57BL/6 mice by collagenase digestion in a shaking incubator. The cells were cultured to passage 3 and then seeded on fibronectin-coated PDMS scaffolds. The next day, cells were serum starved with 1% fetal bovine serum (FBS) media to synchronize cell cycle phase and induce primary cilia formation, or treated with transection reagent in 1% FBS for siRNA knockdown experiments. 24 hours later, PDMS scaffolds were loaded into a custom-built bioreactor and allowed to equilibrate for 1 hr prior to beginning the loading protocol. Control scaffolds underwent a mock protocol of preparation for loading prior to being returned to static culture in the same incubator. All loading groups were subjected to 9% cyclical tensile strain at 1 Hz for 1 hr of loading followed by 1 hr of rest, to best simulate physiological conditions of loading and allow sufficient rest periods for transcriptional changes to occur. The hour on/hour off protocol was repeated for a total of 24 hours to evaluate cellular responses over time. For gene expression analysis, cells were lysed and RNA was isolated immediately after the completion of loading. RT-qPCR was then performed for genes related to primary cilia, Hh signaling, and tenogenesis. For imaging experiments, cells were fixed with 10% formalin for 10 minutes prior to immunostaining with phalloidin (actin cytoskeleton), acetylated alpha tubulin (primary cilia), and DAPI (nuclei). Images were taken at 20x magnification.

Ift88 Knockdown: To investigate the role of the primary cilium in tenocyte mechanotransduction *in vitro,* bioreactor loading experiments were performed on tenocytes with dysfunctional *Ift88*, a ciliary trafficking protein necessary for proper cilia function. To disrupt *Ift88,* tail tenocytes were first isolated from adult C57BL/6 mice and seeded on scaffolds as described above. On passage 3, 24 hours after cells were seeded onto scaffolds, cells were serum starved, and *Ift88* siRNA or scramble RNA (negative control) was added to the low serum media along with Transit-TKO Transfection Reagent (Mirus Bio). After 24 hours, the media was

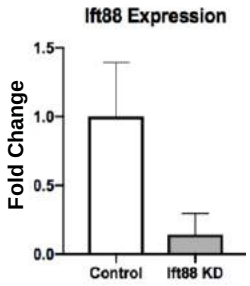

Figure 1: *Ift88* was reduced to 14% of that in scramble siRNA control tenocytes after siRNA knockdown.

replaced with fresh low serum media immediately prior to the initiation of the tensile loading protocol. Changes in the transcriptional and response to loading between tenocytes of *Ift88* knockout and control tenoctyes were compared via RT-qPCR, and qualitative changes in cytoskeletal organization were assessed using immunofluorescence staining.

RESULTS

Primary cilia were mechanoresponsive in tenocytes and disassembled in response to cyclical tensile loading *in vitro* (Fig. 2B and 2C) [10]. Concurrently, the expression of *Ift88* and *Smo* decreased as a result of tensile stretching (Fig. 2A) [4].

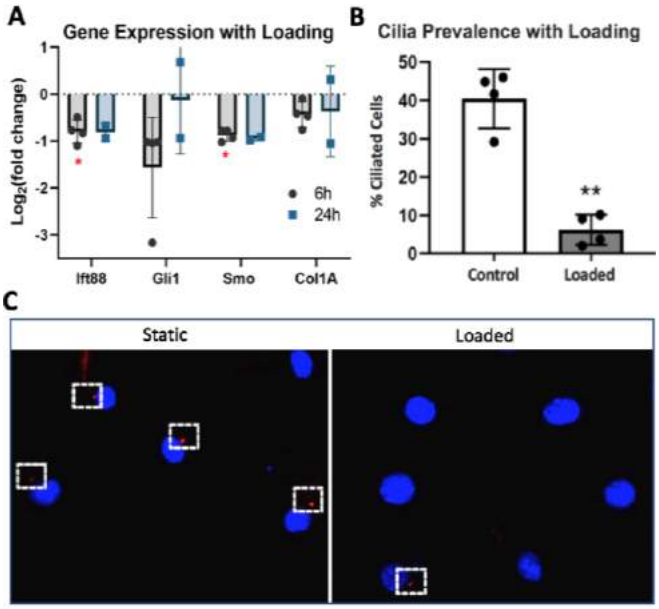

Figure 2: Primary cilia and hedgehog signaling are mechanoresponsive *in vitro*. A) Gene expression related to primary cilia and hedgehog signaling decreased with cyclical tensile loading. B and C) Cilia disassemble after 24 hours of loading (blue: DAPI, red: primary cilia). *indicates p<0.05, **indicates p<0.01.

As a general readout for cell mechanoresponsiveness, the expression of cyclooxygenase-2 (COX-2) was assessed (Fig. 3). COX-2 is upregulated in a variety of cell types in response to loading, and its expression has been tied to primary cilia function in osteocytes [7]. In tendon, it has been shown to play a role in inflammation and in healing [8]. Disruption of cilia function through the knockdown of *Ift88* resulted in a reduction of COX-2 expression in unloaded tenocytes compared to unloaded controls with functional *Ift88 (*Fig. 3). *Ift88* knockdown tenocytes also had lower COX-2 expression after 24 hours of loading compared to loaded controls ($p<0.05$, Tukey's post hoc). Relative abundance was calculated by taking the fold change from COX-2 to GAPDH expression.

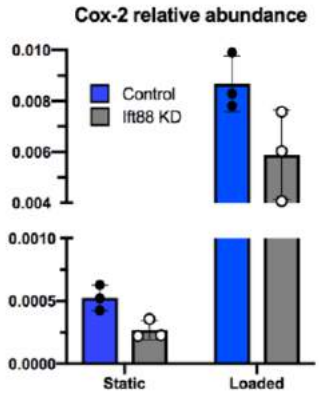

Figure 3: Cox-2 expression was lower in *Ift88* knockdown cells both before and after loading.

To investigate the response of extracellular matrix production and reorganization in the loaded tenocytes, *Col1a1* was also assessed (Fig. 4). *Col1a1* expression was not affected by loading in *Ift88* knockdown and control tenocytes. To investigate the crosstalk between primary cilia and the Hh signaling pathway, the expression levels of *Smo* and *Gli1* (a transcription factor activated by hedgehog signaling) were also assessed [9]. As demonstrated previously and shown in Fig. 2A, *Smo* expression decreased as a result of cyclical tensile loading in control tenocytes. However, in *Ift88* knockdown tenocytes, the expression of *Smo* did not change after 24 hours of loading, demonstrating a loss of mechanoresponsiveness for this gene. Expression of *Gli1* was lower in both static and loaded cells in the absence of *Ift88* compared to control tenocytes.

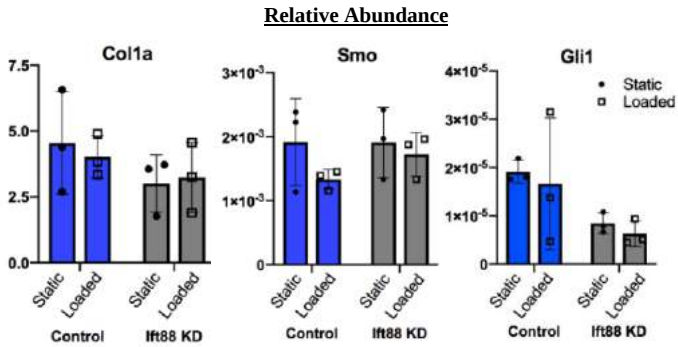

Figure 4: Disruption of primary cilia function via *Ift88* knockdown resulted in changes in the expression of genes related to the hedgehog signaling pathway (*Smo* and *Gli1)*.

DISCUSSION

This study established the involvement of primary cilia in tenocyte mechanosensory pathways *in vitro*. Interestingly, COX-2 expression decreased in tenocytes as a result of the *Ift88* knockdown in static conditions and after 24 hours of cyclical tensile loading. This suggests that primary cilia may play a role in regulating the function of mechanotransduction pathways by regulating the expression of mechanoresponsive genes. Primary cilia also appear to regulate components of the hedgehog signaling pathway, as gene expression levels of *Smo* and *Gli1* were affected by the absence of functional *Ift88* protein in tenocytes. Future studies will explore the effects of primary cilia and Hh agonists on the mechanoresponsiveness of tenocytes. In addition, potential regulation of the inflammatory response to loading through the primary cilium and the Hh pathway will be further investigated.

ACKNOWLEDGEMENTS

The study was supported by NIH R01 AR055580.

REFERENCES

[1] Schwartz, A et al., *Development*, 144:1159-1164, 2015.
[2] Spasic, M et al., *Semin Cell Dev Biol*, 71:42-52, 2017.
[3] Fang, et al. *Sci Adv*, 6(44):eabc1799, 2020.
[4] Sup, M et al., *SB3C*, 1056-1057, 2020
[5] Kopinke, D et al., *Cell*, 170:340-351, 2017.
[6] Rimkus, TK et al. *Cancers*, 8(2):22, 2016.
[7] Delaine-Smith, R. M. et al. *FASEB*, 28(1), 430-439, 2014.
[8] Gilroy DW et al., *Inflamm Res.* 47:79–85, 1998.
[9] Ahn, Sohyun et al., *Cell*, 118.4:505-516, 2004.

MULTISCALE MODELING OF LV GROWTH UNDER AUTONOMIC REGULATION OF BAROREFLEX FEEDBACK LOOP

Hossein Sharifi (1), Charles K. Mann (1), Alexus L. Rockward (1), Kenneth S. Campbell (2), Jonathan F. Wenk (1,3)

(1) Department of Mechanical Engineering
University of Kentucky
Lexington, KY, USA

(2) Department of Physiology & Division of Cardiovascular Medicine
University of Kentucky
Lexington, KY, USA

(3) Department of Surgery
University of Kentucky
Lexington, KY, USA

INTRODUCTION

Cardiac hypertrophy related diseases can occur due to either altered ventricular loading or mutations in sarcomeric protein regulation of cardiomyocytes. Cardiac hypertrophy can be categorized into two groups: 1) Concentric growth, where the ventricular wall mass and wall thickness increase in response to pressure overload condition with small or no change in the ventricular chamber volume. 2) Eccentric growth, in which the ventricular chamber volume dilates due to volume overloading with small change in the wall thickness

Several computational models on cardiac hypertrophy have been developed and provided insight on alterations in mechanics. Although most of these models have yielded stable growth results, many of them did not capture the influence of baroreflex feedback loop and hence they resulted in an alteration in arterial pressure and cardiac output that were not compatible with the published literature.

In this study we extended our previous multiscale model of cardiovascular function via a growth sub-model. The new model was able to capture both types of cardiac hypertrophy in response to any alteration in the ventricular loading (e.g. valvular diseases), while the arterial pressure and cardiac output were maintained with the baroreflex feedback loop. The new model was also able to predict the reverse growth due to partial or proper treatment of valves.

METHODS

The current work extends the multiscale model of cardiovascular function that is presented in Campbell et al. [1] by adding a growth sub-model. The original framework was essentially built on five sub-models that represent different length and time scales, from molecular to organ levels. These sub-models were 1) electrophysiology model of myocardial cell, 2) contraction model of half-sarcomere (MyoSim), 3) hemispherical model of the left ventricle, 4) systemic model of circulation, 5) baroreceptor model of baroreflex feedback loop. The new model is able to capture the evolution of cardiac hypertrophy in response to various changes in ventricular loading.

Both growth laws are stress-driven, in which the active and passive stresses in half-sarcomeres drive the concentric and eccentric cardiac hypertrophies, respectively.

Essentially, a deviation in sarcomeric stresses from their homeostatic levels (set-points) sends a growth signal, g, within the cardiomyocytes. The growth signal g is driven with the following system of ODEs (equation 1) that can be varied between 0 and 1.

$$\frac{dg_i}{dt} = \begin{cases} k_{drive}\dfrac{(S_i - S_{i,set})}{S_{i,set}}(1-g_i) & \text{if} \quad S_i - S_{i,set} \geq 0 \\ k_{drive}\dfrac{(S_i - S_{i,set})}{S_{i,set}}(g_i) & \text{if} \quad S_i - S_{i,set} < 0 \end{cases} \tag{1}$$

where i represents the growth type (i.e. concentric or eccentric). k_{drive} is a constant rate factor. S_i is the driving sarcomeric stress, $S_{i,set}$ is the homeostatic level of driving signal and g_i is the growth signal for growth type i.

When the driving signal (half-sarcomere stress, S_i) is above the set-point, the firing growth signal g_i increases. Whereas, when it drops below the setpoint, the growth signal decreases. The growth signal then transmits into a controller parameter, C_i, via a linear relationship (equation 2). C_i is essentially a proportional gain factor for the output parameter of the growth type i per second.

$$C_i = \begin{cases} m_i(g_i - 0.5) & \text{if} \quad g_i \geq 0.5 \\ -m_i(0.5 - g_i) & \text{if} \quad g_i < 0.5 \end{cases} \tag{2}$$

where, $m_i = 2G_i$ and G_i is the gain factor for growth pattern i. C_i then drives the change in the output parameter θ_i defined as follows. Where

$\theta_{i,n}$ is the output parameter for growth type i at the given time of n and dt is the time step.

$$\theta_{i,n} = \theta_{i,n-1} + \Delta\theta_i$$
$$\Delta\theta_i = \theta_i C_i dt \quad (3)$$

where, θ for concentric and eccentric growth configurations are ventricular wall volume W_{vent} and number of half-sarcomeres in series embedded circumferentially at the basal level of the ventricle n_{hs}, respectively.

RESULTS

The ability of the model in responding to different ventricular loading was assessed by simulating two different cases. First, we tested how the growth law can change the ventricular dimensions in response to a perturbation in the set-point for concentric growth law. Second, we tested a ventricular volume overload case via simulating mitral regurgitation condition and then compared the model predictions with measurements form real patients[2]. Additionally, the ability of the model to predict reverse growth was evaluated by then removing the volume overload condition. All simulations were under continuous regulation of baroreflex feedback loop to maintain the arterial pressure within the range of 110/70 mm Hg.

Perturbed set-point for growth law: Figure 1 shows the model prediction in response to a 50% acute increase of the set-point for active stress. The simulation was initially at steady state for the given set-points for both growth laws, prior to perturbation. The model responded to the perturbed condition by increasing LV chamber volume at end-diastole by 31.2%, LV mass by 2.3%, and stroke volume by 8.4%. The LV wall volume did not change significantly, and hence the maximum wall thickness reduced by 22.5%. Thus, both eccentric and concentric growth of the LV were occurring simultaneously.

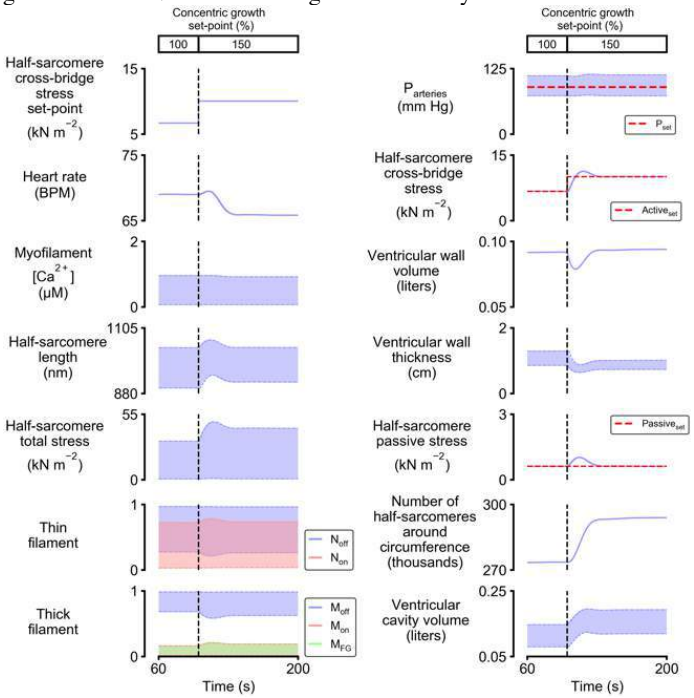

Figure 1: Model prediction in response to perturbed set-point for concentric growth law

Volume overload condition: Mitral valve regurgitation was simulated by allowing a portion of blood volume to flow backward through the mitral valve during systole in the model. The "leakage factor" in the model was tuned to have a consistent regurgitant volume of 40 ml with the measured data from patients in the study by Edward et al. [2]. Figure 2 illustrates the model prediction due to volume overload. The growth module essentially increased the LV chamber volume by 43.9% at end diastole, LV mass volume by 32.5%, and stoke volume by 58.5%. These numbers were quite comparable to those measured data by Edwards et al., where they reported increased LV chamber volume by 41.9% at end diastole, LV mass by 17%, and stroke volume by 31.4%. With respect to the chamber volume, the predicted change in wall thickness was small, representing eccentric growth. When the dilated ventricle was at steady state, the volume overload condition was removed to simulate repair of the mitral valve. The model appropriately predicted the revere growth and changed the ventricular size and shape back to the initial size, before perturbation.

DISCUSSION

For both studied cases, the changes in ventricular size and shape occurred while the arterial pressure was being maintained at the range of 110/70 mm Hg via continuous regulation of chronotropism, Ca^{2+} transient binding to thin filament, myofilament contractility, and vascular tone.

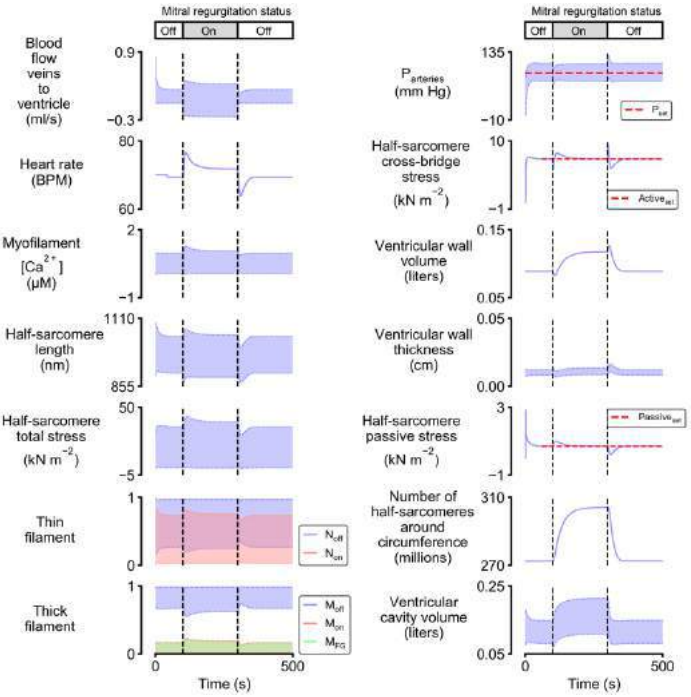

Figure 2: Model prediction in response to volume overload condition and then repair of mitral valve (Mitral Regurgitation)

In conclusion, we introduced a new capability to a multiscale model of cardiovascular function to capture different forms of cardiac hypertrophy simultaneously in response to altered ventricular loading and set-point levels. In addition, the new model is able to predict reverse growth once the perturbations are removed. This framework can be used as an ideal test-bed for exploring different hypotheses before implementing them into more sophisticated models, such as the finite element method.

ACKNOWLEDGEMENT

This study was supported by National Institutes of Health grant U01HL133359.

REFERENCES

[1] Campbell, K.S. et al., *Front Physiol*, 11:1043, 2020.

[2] Edwards, N.C., et al., *Circ Cardiovasc Imaging*, 7(6):946-53, 2014.

THE EFFECT OF HEADER CHARACTERISTICS ON HEAD KINEMATICS OF WOMEN'S SOCCER PLAYERS

Gabriella M. Milef (1,2), Tanner M. Filben (1,2), Jordan M. Hemmen (1,2,3), Jillian E. Urban (1,2), Joel D. Stitzel (1,2)

(1) Department of Biomedical Engineering
Wake Forest School of Medicine
Winston-Salem, NC, USA

(2) School of Biomedical Engineering and Sciences
Virginia Tech – Wake Forest University
Winston-Salem, NC, USA

(3) Department of Biological Systems Engineering
Virginia Tech
Blacksburg, VA, USA

INTRODUCTION

With over 265 million participants, soccer is the most popular sport in the world.[1] Concussion rates for female soccer players are 1.5-2.4 times higher than males soccer players.[2] Although football tends to garner the most attention when it comes to concussions, women collegiate soccer players have a higher incidence of concussion than American football players.[3,4] Concussions in soccer are often caused by player to player contact;[5] however, most subconcussive head impacts in soccer are headers, a fundamental component of the sport.[6] It has been estimated that soccer players make contact with the ball with their head around 6-16 times per game. [7] Acute heading events are associated with alterations in neurocognition and postural control.[8,9] Exposure to repetitive subconcussive head impacts has been associated with short- and long-term changes to the brain;[10] therefore, understanding the biomechanics of headers is critically important. Specifically, this study aims to evaluate the effect of extrinsic factors related to ball delivery on head kinematics. The results of this study will inform strategies to improve header safety.

METHODS

Eight women's soccer players (ages 18-22) were enrolled in this study approved by the Wake Forest School of Medicine Institutional Review Board. Athletes participated at the collegiate and collegiate club levels of play were instrumented with a custom mouthpiece sensor to measure head kinematics. A KWIK soccer ball launcher was used to simulate four common delivery types observed in live game play: throw-ins, corner kicks, and defensive and offensive goal kicks. Each delivery type was defined by adjusting initial ball launch speed, landing distance, and launch angle.[11] Ball pressure was varied in increments of 3 PSI across the range of 6-15 PSI for throw-ins and 6-12 PSI for corner kicks and goal kicks, according to FIFA ball pressure recommendations.[12] Players performed a total of 13 headers with a Nike size five soccer ball in each session. The order of delivery type was randomized and players had the choice of not performing a header if they felt uncomfortable doing so. After each header, players rated perceived success and comfort on a Likert scale of 1-5, with 5 being most comfortable and successful. Time-synchronized video was collected to allow for pairing of header characteristics observed from video to the associated head impact data. Header characteristics, including incoming and exiting ball speed and incoming ball angle relative to the player's upright position (i.e., vertical), were measured from the video using Kinovea v8.25. The coefficient of restitution, representing the ratio of exiting to incoming velocity of the ball, was also determined.

RESULTS

Kinematic data from 114 headers were collected from eight women's soccer players. Most headers were from throw-ins, followed by corner kicks, offensive goal kicks, and defensive goal kicks (Table 1). Balls delivered from defensive and offensive goal kicks approached the player with the greatest mean incoming velocity and steepest angle, while throw-ins had the greatest coefficient of restitution, on average.

Table 1: Incoming Speed, Angle and Coefficient of Restitution for Ball Delivery Types

Delivery Method	N	Mean Incoming Ball Speed (m/s)	Mean Incoming Ball Angle (degree)	Coefficient of Restitution
Throw-In	46	10.7 ± 1.6	59.5 ± 5.10	0.97 ± 0.20
Corner Kick	32	13.7± 1.7	57.9 ± 6.94	0.68 ± 0.13
Defensive GK	17	14.2 ±1.8	52.5 ± 5.00	0.80 ± 0.20
Offensive GK	19	14.4 ± 1.8	53.5 ± 3.56	0.83 ± 0.10

Kick type, ball pressure, and incoming ball speed each had a significant effect on linear acceleration (all $p<0.05$). Kick type also had a significant effect on rotational acceleration and rotational velocity (both $p<0.05$). Defensive goal kicks resulted in greater mean linear and rotational acceleration than corner kicks ($p=0.0013$, $p=0.0434$, respectively) (Figure 1). Additionally, defensive and offensive goal kicks had greater rotational velocity compared to corner kicks (both $p<0.05$). Offensive goal kicks had greater mean linear acceleration than defensive goal kicks ($p=0.0048$). Throw-ins resulted in lower mean rotational acceleration compared to corner kicks ($p=0.0280$), defensive goal kicks ($p=0.0018$), and offensive goal kicks ($p=0.0089$). Throw-ins also resulted in lower rotational velocity compared to defensive and offensive goal kicks (both $p<0.05$).

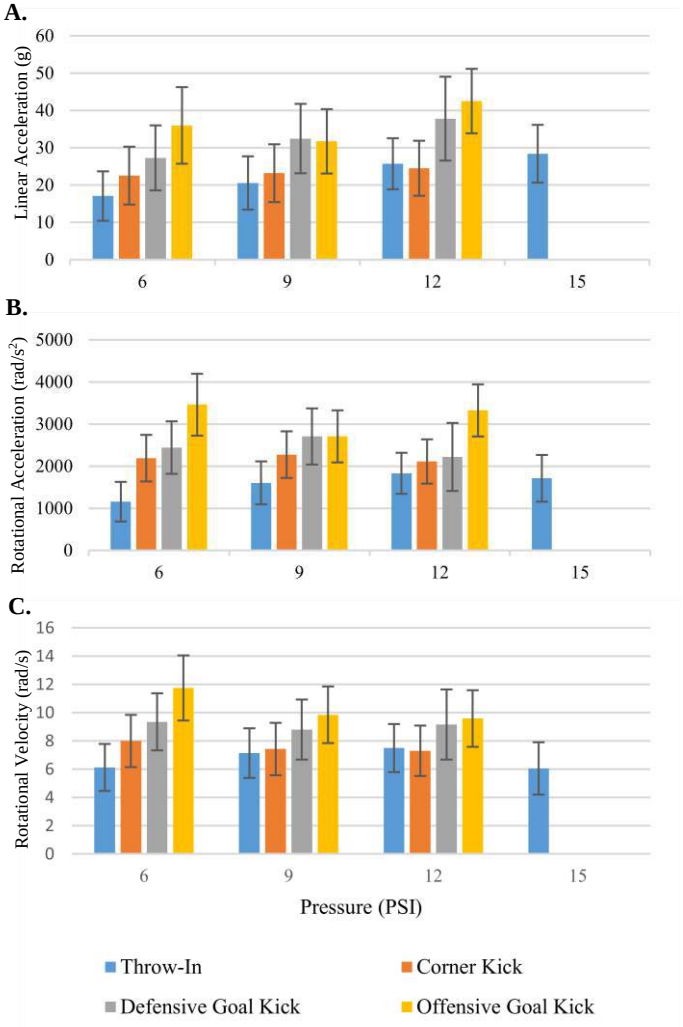

Figure 1: Mean Kinematics and 95th% Confidence Intervals for Varying Ball Pressures and Ball Delivery Types. A. Linear Acceleration and Ball Pressure B. Rotational Acceleration and Ball Pressure C. Rotational Velocity and Ball Pressure

Regarding pressure, headers from balls inflated at 6 PSI and 9 PSI resulted in significantly lower mean linear acceleration than headers from balls inflated at 12 and 15 PSI (6 PSI: both $p<0.005$, 9 PSI: both $p<0.05$). Incoming ball speed was significantly positively associated with all peak kinematics when balls were inflated at 6 PSI and 9 PSI (all $p<0.05$). The strongest correlation between kinematics and incoming ball speed was observed at 6 PSI; rotational acceleration was most strongly correlated ($R^2=0.411$), followed by linear acceleration ($R^2=0.240$), and rotational velocity ($R^2=0.170$).

Kick type had a significant effect on perceived comfort. Throw-ins and corner kicks resulted in higher mean comfort compared to offensive and defensive goal kicks (all $p<0.05$). Overall, headers from throw-ins at 6 PSI were rated most comfortable (4.25 ± 1.14) and offensive goal kicks with balls at 12 PSI were rated lowest comfort (2.5 ± 1.12). No apparent trends were observed among the header characteristics, kinematics, and/or perceived success of the header.

DISCUSSION

This study evaluated head kinematics of headers performed by women's soccer players. This study is novel in identifying the importance of ball delivery characteristics on the magnitude of subconcussive head impacts. Results demonstrate kick type and ball pressure affect head kinematics during headers. Specifically, headers in response to offensive and defensive goal kicks at greater pressures generally resulted in greater peak head kinematics. FIFA law states that ball pressure must be between 8.5 and 15.6 PSI.[12] Results from our study show that balls filled at 6 and 9 PSI have significantly lower linear acceleration compared to balls at 12 and 15 PSI. These trends correlate with findings from similar studies that found reduced accelerations with reduced ball pressures.[13,14] Furthermore, these results provide important insight into future regulatory guidelines related to allowable pressure ranges for soccer balls. One area of study in need of study is use of trainer balls of different material properties to potentially minimize impact magnitude.

Understanding the relationship between peak kinematics and header types can inform future interventions to reduce header magnitude and/or concussion risk. As heading the ball in response to offensive and defensive goal kicks resulted in significantly higher kinematics compared to throw-ins and corner kicks, it may be worthwhile for players to consider chesting the ball in response to these kick types instead. This research is vital to improving player safety and will help to inform efforts to reduce concussion risk and long-term damage from cumulative subconcussive exposure to headers in soccer players.

ACKNOWLEDGEMENTS

We would like to thank the Wake Forest women's soccer players for their participation in this study as well as Virginia Tech-Wake Forest University for providing the resources to conduct this research.

REFERENCES

[1] Fe´de´ration Internationale de Football Association (FIFA) (2008) Web page: http://www.fifa.com/mm/document/fifafacts/bcoffsurv/bigcount.statspackage_7024.pdf.
[2] Zuckerman, S. L. et al. *Am. J. Sports Med.* 43: 2654–2662, 2015.
[3] Gessel, L. M. et al. *J. Athl. Train.* 42: 495–503, 2007.
[4] Spiotta, A. M. et al. *Neurosurgery* 70: 1–11, 2012.
[5] DiStefano, L. J. et al. *J. Athl. Train.* 53: 880–892. 2018.
[6] Hanlon, E. M. et al. *Med. Sci. Sports Exerc.* 44: 1102–1108, 2012.
[7] Smirl, J. D. et al. *Front. Neurol.* 11:, 2020.
[8] Haran, F. J. et al. *Int. J. Sports Med.* 34: 350–354, 2013.
[9] Nowak, M. K. et al. *JAMA Ophthalmol.* 138: 350–357, 2020.
[10] Lipton, M. L. et al. *Radiology* 268: 850–857, 2013.
[11] Lees, A. et al. *J. Sports Sci.* 28: 805–817, 2010.
[12] Laws of the Game. https://www.ussoccer.com/referee-program/laws-of-the-game.
[13] Armstrong, C.W. et al. *Science and Football* 394–398, 1987.
[14] Shewchenko, N. et al. *Br. J. Sports Med.* 39: i33–i39, 2005.

STRESS AND STRAIN DISTRIBUTION ANALYSIS OF SPECIMEN-SPECIFIC INTERWEAVED FIBER SCLERA MODEL UNDER EQUI-BIAXIAL STRAIN

Manik Bansal (1), Fengting Ji(1, 2), Yi Hua (1), Fuqiang Zhong (1), Ian A. Sigal (1,2)

(1) Department of Ophthalmology
University of Pittsburgh
Pittsburgh, PA, USA

(2) Department of Bioengineering
University of Pittsburgh
Pittsburgh, PA, USA

INTRODUCTION

Collagen fibers are the primary load-bearing constituent in the sclera [1], and thus there are many mechanical models of sclera that account for the fibers in some way. However, to the best of our knowledge, current models [2] do not incorporate important aspects of the fiber microarchitecture and mechanics, such as fiber interweaving [3] and fiber-fiber interactions. This is potentially crucial as these characteristics are likely to affect the distribution of stresses and strains at the fiber level, in-turn affecting tissue strength and remodeling.

We have recently developed fiber-based models of the sclera that incorporate fiber interweaving and fiber-fiber interactions [4]. Our goal in this project was to leverage those models to determine the distribution of fiber-level stresses and strains in scleral collagen fibers when the sclera is subjected to a relatively simple equi-biaxial stretch.

METHODS

Fiber structure construction and optimization: The details of the procedure used for constructing and optimizing fiber structure are described elsewhere [4]. Briefly, a rectangular region (484×464 μm) from the coronal section (Figure 1C) was considered for constructing the fiber structure. The fiber orientation distribution obtained from polarized light microscopy (PLM) (Figure 1) was used to assign a direction to the fibers (diameter, $d = 2$ μm). An iterative optimization of fiber architecture was done to introduce interweaving and avoid collisions among the fibers. Later, a pre-stretch equivalent to 2.5% equi-biaxial strain was applied to remove excess fiber undulations introduced during the construction process (Figure 2).

Element type and boundary condition: Fibers were meshed using linear truss elements (T3D2) [4] to avoid any influence of bending stiffness over the results. A displacement boundary condition shown in Figure 2 was implemented to represent equi-biaxial stretch. For the analysis, 2.18% of equi-biaxial strain was applied in agreement with the experimental study [6].

Fiber material properties: The non-linear material behavior of fiber [5] was modelled using a Mooney-Rivlin material model. We then used an inverse-modeling process based on matching the experimental tests of Eilaghi et al [6] to obtain the value of Mooney-Rivlin material constants C_{10} and C_{01}: 5746.9 MPa and -5002.6 MPa, respectively.

Fiber-fiber Interaction: To incorporate the effect of interactions between fibers, a general contact algorithm with no friction was activated in ABAQUS.

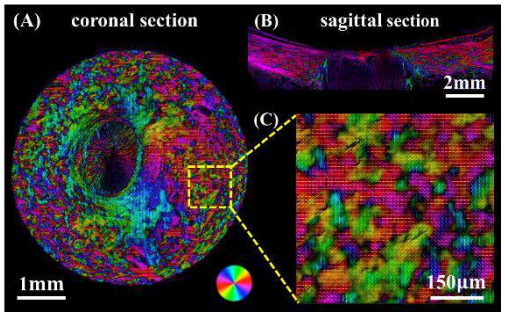

Figure 1. PLM images of (A) Coronal and (B) Sagittal sections of pig and sheep optic nerve head, respectively. Colors represent the local fiber orientation in the section plane. Collagen fiber density was considered directly proportional to the pixel intensity (1 pixel ≈ 1 μm). (C) Close-up of modeled region.

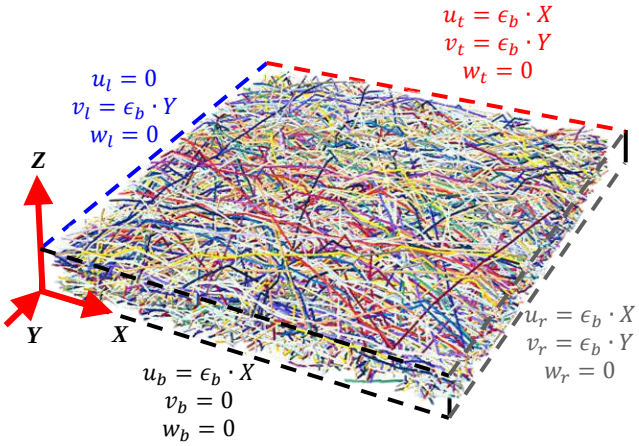

Figure 2. Schematic of displacement boundary condition implemented over fiber structure to imitate equi-biaxial stretch. u, v & w is the displacement in X, Y and Z direction respectively. b, r, t & l represent faces attached to bottom, right, top and left edges of the rectangular domain. ϵ_b is equi-biaxial strain.

RESULTS

The results show a wide range of fiber principal stress and strains (Figure 3). At 2.18% equi-biaxial strain, the value of principal strains varies from 0 to 2.56% and principal stresses vary from 0 to 132.5 MPa at element level (Figure 4). The principal stresses are not directly proportional to the principal strain due to the non-linear material properties. We noticed that fibers with small undulations, the strain could reach levels larger than the applied equi-biaxial strain (Figure 4). Increasing the equi-biaxial strain from 0.55% to 2.18%, approximately 60% of elements transitioned from zero stretch to stretch greater than 0.1% (Figure 5). At 2.18% equi-biaxial strain, approximately 20% of the fiber elements had principal strain lower than 0.1% and the majority of these elements belong to fibers with high undulations (Figure 5B).

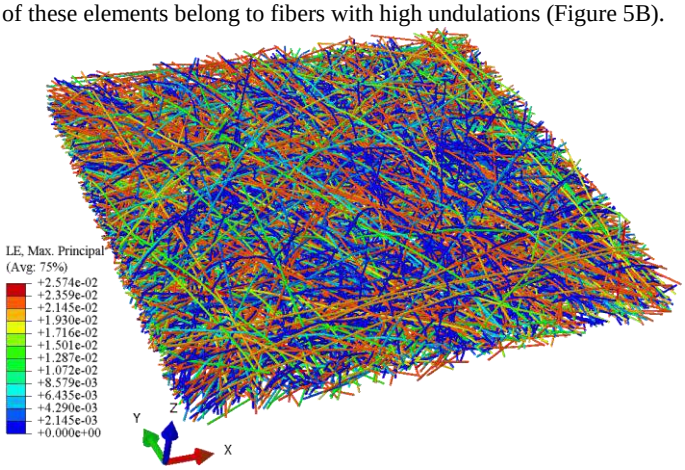

Figure 3. Contour plot illustrating heterogeneous distribution of principal strain in the fiber structure at 2.18% of equi-biaxial strain. The principal strain varied from 0 to 2.56%.

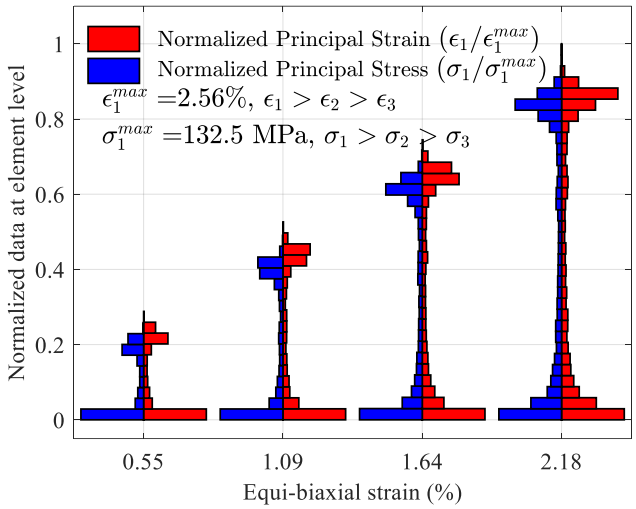

Figure 4. Normalized principal stresses and strains distribution at element level for four different equi-biaxial strains. At 2.18% equi-biaxial strain, the maximum principal stress (σ_1^{max}) and strain (ϵ_1^{max}) among all elements were 132.5 MPa and 2.56% respectively.

DISCUSSION

We simulated a specimen-specific fiber model representing sclera at a micro-scale to determine the heterogeneous distribution of stresses and strains. The results show a wide range of stress and strain due to the presence of fibers with low and high undulations, consistent with the conventional process of fiber recruitment. Fibers with low undulation experienced high stresses and strains. The stresses and strains were low in the fibers with high undulation. The stresses are not directly proportional to strains due to the non-linear material behavior of fiber. The analysis shows the heterogeneous distribution of stresses and strains in the fiber structure. Accounting for this heterogeneity is essential for developing accurate models of structure-function. This type of model provides a much more detailed understanding of the fundamental role of tissue architecture and composition in its biomechanical behavior. The models provide a framework for the study of stress and strain-induced fiber remodeling and failure [7].

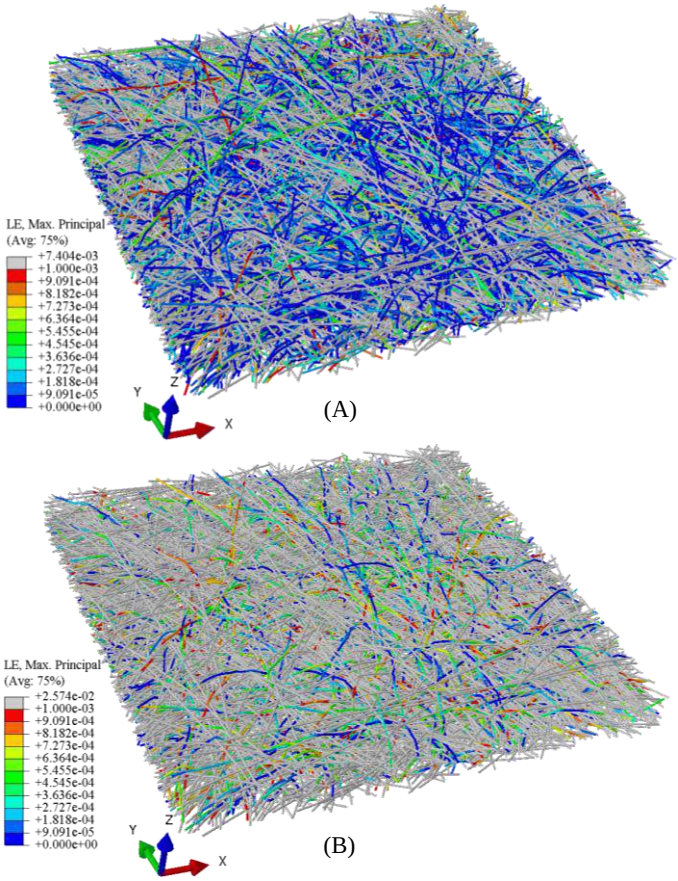

Figure 5. Contour plot showing approximately 60% fiber element transitioned from zero stretch to stretch greater than 0.1% with the increase in equi-biaxial strain from (A) 0.55% to (B) 2.18%. Rainbow color spectrum indicates variation of principal strain (0 to 0.1%) in fiber elements. Grey color indicates principal strain value above 0.1% in fiber elements. Principal strains along the length of fiber were non-uniform.

ACKNOWLEDGEMENTS

Supported in part by NIH R01-EY023966, R01-EY028662, P30-EY008098 and T32-EY017271 (Bethesda, MD), the Eye and Ear Foundation (Pittsburgh, PA), and Research to prevent blindness.

REFERENCES

[1] Boote, C et al., *Prog. Retin. Eye Res.*, 74: 100773, 2020.
[2] Grytz, R et al., *Biomech. Model Mechano*. 10(3): 371-382, 2011.
[3] Wang, B et al., *Acta Biomater.*, 113: 429-437, 2020.
[4] Ji, F et al., *SB3C*, 2021, Abstract ID 109
[5] Holzapfel, G A, *Handb. Mater. Behav. Models*, 3:1049-1063, 2001.
[6] Eilaghi, A et al., *J Biomech*, 43(9): 1696-1701, 2010.
[7] Hadi, M F et al., *J. Biomech. Eng*. 134(9), 2012.

RHEOLOGICAL ANLAYSIS OF THE MECHANICAL PROPERTIES OF MURINE LUNGS OVER THE LIFESPAN

O. Harrison (1), H. Rozycki (2), R.L. Heise (1)

1. Biomedical Engineering Department
2. Children's Hospital of Richmond

Virginia Commonwealth University
Richmond, Virginia, United States of America

INTRODUCTION

The development of the lungs happens in three main periods: the embryonic, fetal, and postnatal period. The embryonic stage happens at week 4-7 post conception. This is when the anlage of the right and left lungs presents as two independents outpouchings of the ventral wall of the primitive foregut. Both of these buds will begin to elongate and create a cycle of growth in the mesenchyme and branching. The fetal period is when the formation of the bronchial tree begins and differentiation of the epithelia allow the morphological distinction between conducting and respiratory airways. Lastly, the terminal airways grow in length and in width. This forms clusters of larger airways. As early as 36 weeks gestation, true alveoli start to develop in the postnatal stage. These infant lungs are significantly different from adults because they contain a double capillary bed, whereas, adults only have a singly capillary bed. Lungs continue to grow to adulthood and the tissue expands proportionality to the increase body weight as we age [1]. Various morphological and tissues parameter of lungs will change due to aging. After the age of 30, there is a 1% decline per year in respirator mechanics and lung. Between ages 50 to 80 years of age, lung tissue will become about 7% less compliant[2].

The mechanical properties of the lung demonstrate a tensegrity dynamic that displays a balance of physical forces, stress, and strain which aids in determining the lung function and structure [3]. In addition, the lungs are constantly experiencing large cyclic mechanical stress and deformation with breath as well as cardiac contraction.

Variations of the elastic properties located in the lung linked with aging are crucial in determining lung function [4]. Rheometry can be a tool used to determine the storage and loss moduli of a material. The elastic and viscous components are important in defining the mechanical behavior of a material. The time dependent-properties or viscoelasticity of a material is associated with stiffness [5].

Analyzing the mechanical properties of the lungs over the lifespan is crucial in correlating lung structure, elasticity, and compliance with organ, tissue, and cell-scale behaviors [6]. Current studies looking into the mechanical properties of the intact lung of different species have used: Uniaxial testing [7], atomic force microscopy (AFM) [4,7], and microfluidic system [8]. Rheometry has been shown to be advantageous for its ability to encompass boarder measurement ranges and closely control the testing environment [9].

In this study, our goal was to characterize the mechanical properties of the murine lung. We accomplished the goal by using a TA Instruments DHR-2 Rheometer and testing the lungs from neonatal to old age. The objective of our study was to analyze the effects of age on rheological lung properties.

METHODS

Murine lungs were collected upon euthanization of C57Bl6j mice (neonatal-23 months old). Lungs were then snap frozen immediately and kept at -80◦C until rheological testing. Murine lungs were categorized into four groups: neonatal (0-10days), young adult (3-6 months), mature/middle adult (10-14 months), and old adult (18-24 months). The age samples were broken into two groups: Young Mice (YM) and Middle Age/Old Age Mice (MOM). The YM group included the neonatal and 6-10week. The MOM group included 7-, 10- and 22–24-month-old mice.

Before testing, murine lungs were kept on ice. The testing was then performed using a TA Instruments DHR-2 Rheometer with a 20-mm parallel- plate fixture and a gap of 0.8-1.0mm under frequency sweep conditions. The lower Peltier cell was set to 25 C for sample loading as well as after lowering the measuring system. The system was enclosed within a solvent trap PBS to prevent the lungs from dehydration during testing. The frequency sweeps, had a soak time of 30.0 seconds, 0.5%

strain, and angular frequency 0.1 to 100rad/s. All the sweep were run in triplicate.

RESULTS

Since the lung is both structurally and mechanically heterogeneous tissue, it is difficult to obtain a comprehensive test. To address this, for each age group we tried to get five separate lung samples to test. This gave us a more complete look at the storage and loss modulus of each specific age group.

As the age of the mice increased in the YM group, we saw an increase in the storage and loss modulus. However, the MOM group did not have a strong correlation of increased age with the storage and loss modulus.

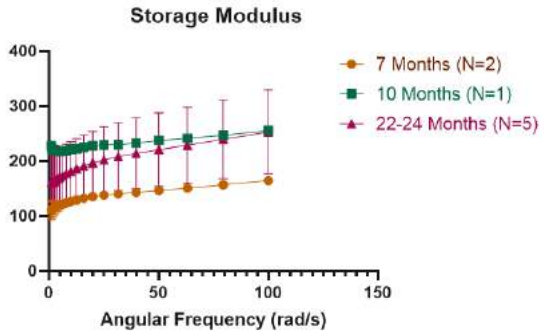

Figure 1: Storage Modulus of MOM group: 7(N=2) ,10(N=1), and 22–24-month-old(N=5) mice.

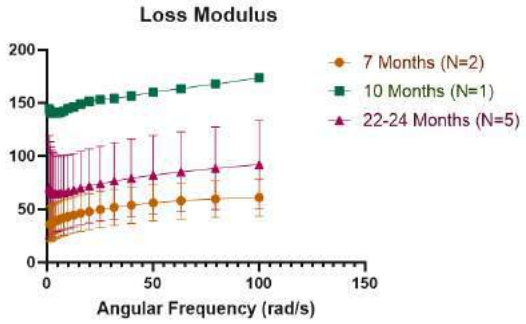

Figure 2: Loss Modulus of MOM group: 7(N=2) ,10(N=1), and 22–24-month-old(N=5) mice.

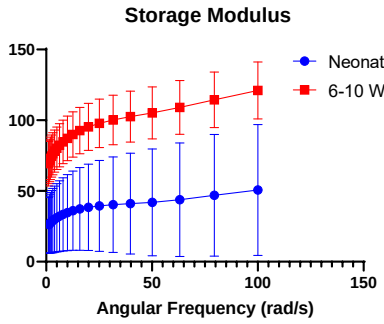

Figure 3: Storage Modulus of YM group: neonatal(N=3) and 6–10-week(N=5) mice.

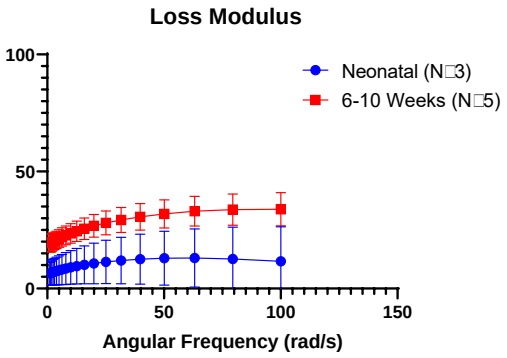

Figure 4: Storage Modulus of YM group: neonatal(N=3) and 6–10-week (N=5) mice.

DISUSSION

Decreased lung function is a common occurrence that happens as we age. This decrease is linked the structural changes that take place on the macro and micro level of the lung. Lung tissue that aid in keeping airways open can lose elasticity as it ages, resulting in smaller and stiffer lung tissue [3]. Using the rheometer, we collected data on the storage and loss moduli of the murine lung. The results displayed that the storage modulus was always greater than the loss modulus, this indicated to us that our lungs were more elastic than viscous. The results also presented an increase in storage modulus which gave the indication that as age increased, the ability for the lungs to deform became more difficult. This indicated that lungs were become stiffer over time.

Our results showed that using rheometer technique can be advantageous in quantifying age impact on the lungs. This study showed similar trend with a previous study done with different human lung compartments which also displayed an increase in Young's modulus as age increased [4]. Some of the limitations we faced during the study is varied number of samples per group. Freezing the sample may have caused some reduction in modulus as shown previously [7].

For future studies, we will gather more samples at different age groups to have a more comprehensive look at the lifespan. These values may be added to develop a more comprehensive computational model of lung mechanics across lifespan. In addition, we plan to decellularize the collected tissue for mass spectrometry to understand the composition of the extracellular matrix at the specific age groups.

ACKNOWLEDGEMENTS

Funding from the Little Giraffe Foundation. We want to thank Tang lab at VCU for letting us use the rheometer.

REFERENCES

[1]NP;, Mullassery D;Smith. "Lung Development."
[2] RE;, Lai-Fook SJ;Hyatt. "Effects of Age on Elastic Moduli of
[3] Hsia, Connie C W. "Comparative Analysis of the Mechanical.".
[4] Sicard, Delphine, et al. "Aging and Anatomical Variations in Lung
[5] Guimarães, Carlos F., et al. "The Stiffness of Living Tissues and Its
[6] Mitzner, Wayne. "Mechanics of the Lung in the 20th Century.".
[7] Polio, Samuel R, et al. "Cross-Platform Mechanical Characterization
[8] Schappell, Laurel E., et al. "A Microfluidic System to Measure Neonatal Lung Compliance Over Late Stage Development as a
[9] B;, Bates JH;Maksym GN;Navajas D;Suki. "Lung Tissue Rheology

PATIENT-SPECIFIC, *IN-VITRO* MODELING OF AORTIC COARCTATION USING 4D FLOW MRI AND PARTICLE IMAGE VELOCIMETRY

James P. Rice (1,6), Labib A. Shahid (1,6), Haben Berhane (2), Cynthia K. Rigsby (2), Joshua D. Robinson (2), Lindsay M. Griffin (2), Michael Markl (3,4), Alejandro Roldán-Alzate (1,5,6)

(1) Department of Mechanical Engineering
University of Wisconsin-Madison
Madison, WI, USA

(2) Department of Medical Imaging
Ann & Robert H. Lurie Children's Hospital of Chicago
Chicago, IL, USA

(3) Department of Radiology
Northwestern University
Chicago, IL, USA

(4) Department of Biomedical Engineering
Northwestern University
Chicago, IL, USA

(5) Department of Biomedical Engineering
University of Wisconsin-Madison
Madison, WI, USA

(6) Department of Radiology
University of Wisconsin-Madison
Madison, WI, USA

INTRODUCTION

Coarctation of the aorta (COA) is one of the most common congenital heart defects (5-8%), presenting as narrowing of the proximal descending aorta. COA can be discrete or more complex and associated with severe complications such as diffuse arch hypoplasia and mycotic aneurysm. Regardless of clinical presentation, the most common therapy is intervention to restore normal aortic blood flow thus, understanding COA-specific hemodynamics is crucial [1-2]. Four-dimensional (4D) flow MRI has shown promise as a tool to assess the hemodynamics of COA in-vivo. However, 4D flow MRI data are acquired with a predefined velocity encoding (V_{enc}), set above the maximum expected velocity to avoid velocity aliasing, and issues can arise when acquiring data in complex flow regions with both high and low flow velocities, e.g. in patients with COA (high velocity flow jets) and mycotic aneurysm (slow vortex flow velocities) distal to the location of the narrowing [3-4]. Pulsatile in-vitro models have proved useful for systematic evaluation of 4D flow performance in complex flow cases by providing a way to produce physiologically realistic geometries and flow conditions that can also be analyzed with higher resolution flow methods, like particle image velocimetry (PIV) [5]. The goal of this study was to: (1) develop a framework for in-vitro modeling of COA hemodynamics using patient-specific aorta COA models and 4D flow MRI and (2) preliminary validation of 4D flow MRI for COA using PIV.

METHODS

The study included a pediatric patient with COA and a mycotic aneurysm who underwent in-vivo 4D flow MRI, following an IRB-approved protocol pre- and post-repair.

Aortic Model Construction: 3D contrast-enhanced magnetic resonance angiography (CE-MRA) was used for segmentation of the aortic anatomy. Following a fabrication process outlined by Ruedinger et. al., two in-vitro, patient-specific silicone models were created representing the pre- and post-repair anatomies [6]. The segmented geometries were 3D-printed in polyvinyl alcohol (PVA), cast in silicone, and then dissolved with water, leaving the aortic cavity in a silicone block. Figure 1 outlines the construction process for the COA models.

4D Flow MRI & PIV Experimentation: The in vitro models were connected to an MRI compatible pulsatile flow circuit and scanned on a 3.0T MRI scanner (Signa Premier, GE, Waukesha, WI) using 4D flow MRI (PC-VIPR technique). Scan parameters were 1.3mm isotropic spatial resolution, 320mm field of view, 150 cm/s velocity encoding and cardiac gaiting. Flow conditions were controlled to match mean aortic flow obtained from in-vivo 4D flow MRI data.

PIV was performed on the pre- and post-repair cases using a solution, seeded with PMMA fluorescent particles (diameter = 10 μm), of 58% glycerol and 42% water (RI = 1.41) to match the index of refraction of the silicone model, minimizing optical distortions. PIV data were acquired using a Flowmaster system (LaVision, Göttingen, Germany), consisting of a dual-pulse 527 nm Nd:YLF laser opposite three high-speed cameras (Vision Research, NJ), oriented at -25, 0, and 25 degrees. The light sheet thickness was 5-mm. Data analysis was performed in Ensight (ANSYS Inc, PA).

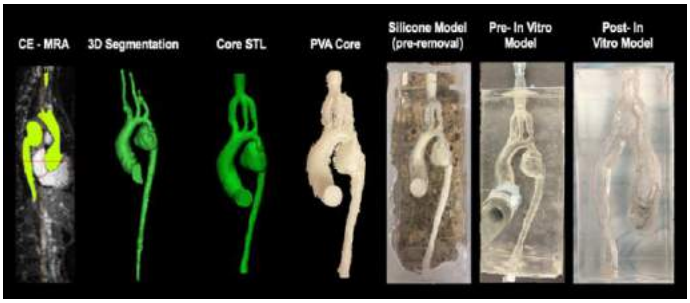

Figure 1: Pipeline for constructing pre- and post- patient-specific, MRI compatible in vitro flow models. Left-to- right: CE-MRA pre-intervention COA dataset. Raw 3D segmentation. STL of post-processed segmentation altered to enhance compatibility with pulsatile flow loop. PVA core cast in silicone block before dissolving step. Fully dissolved core produces patient-specific pre-intervention COA "ow cavity inside the clear silicone block and connectors are placed at the inlet and outlets of the model. Post-intervention in vitro model.

RESULTS

Figure 2 shows the in-vitro 4D flow MRI results pre- and post-repair during the cardiac cycle. Peak pre- and post- repair velocities at the location of the stenosis were recorded as 1.89 and 0.630 m/s, respectively. A high velocity jet was observed for the pre- case upstream of the stenosis and extending to descending aorta. Enhanced flow visualization was achieved in the aneurysm, where vortical flow regions are seen. Post-repair reduction in peak velocity at the location of the coarctation was also observed.

Figure 3 depicts the pre- and post-repair velocity fields at a plane through the center of the in vitro aorta for both 4D flow MRI (left) and PIV (right). For the pre-repair case, the high velocity jet is shown to accelerate in the aortic arch and extend through the aneurysm with PIV showing initialization of the jet earlier in the aortic arch when compared to 4D Flow MRI revealing a displacement artifact. Flow visualization at the stenosis location shows unrealistic disturbances potentially induced by imperfections in the model surface. Post-repair PIV velocity fields are qualitatively consistent with results obtained from 4D flow MRI as both show similar velocity patterns near the inlet and at the COA-repair site, where the velocity jet appears to extend from the arch along the outer wall of the descending aorta and leaving a region of slower, recirculating flow at the inner wall.

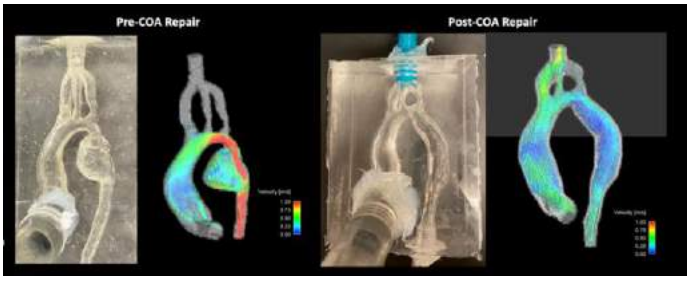

Figure 2: Pre- and post- COA repair in vitro flow models (left) used to generate 4D Flow MRI results (right). 4D Flow MRI derived velocity fields are depicted during peak systole. Clear reduction in pre-operative peak systolic velocities is observed for the post-repair case.

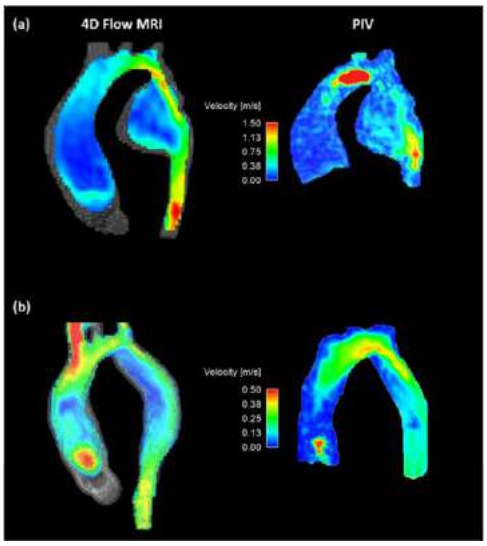

Figure 3: 4D Flow MRI (left) and PIV (right) derived velocity fields for COA in vitro models. (a) Pre-repair case (b) Post-repair case.

DISCUSSION

In this study patient-specific models were fabricated for in-vitro 4D flow MRI experiments to evaluate the blood flow dynamics of COA. The post-repair model showed lower velocities near the stenosis when compared to the pre- case for both 4D flow MRI and PIV. This agrees with clinical expectation, suggesting 4D flow MRI can be employed to characterize COA hemodynamics, however, future comparisons to actual in-vivo datasets must be made. PIV analysis demonstrated feasibility as a validation framework for COA cases. Velocity maps at the center of the aorta show flow features qualitatively consistent with 4D flow measurements, especially for the post-repair case, however, a more robust quantitative analysis is needed. Future direction will concentrate on improving model surface quality and incorporating 3D velocity quantification that can be directly compared to 4D flow MRI results while deriving clinically relevant complex flow metrics such as vorticity and wall shear stress. PIV will also allow for cycle-to-cycle assessment of velocity information, which can account for blood flow dynamics variations not captured with 4D flow MRI [7].

ACKNOWLEDGEMENTS

Grant support by American Heart Association (AHA) 19TPA34850066.

GE Healthcare, which provides research support to the University of Wisconsin-Madison.

REFERENCES

[1] Rao P. *Curr Cardiol Rep.* 2005; 7(6):425-434.
[2] Hope M, et al. *J Magn Reson Imaging.* 2005;31(3):711-718.
[3] Dyverfeldt P, et al. *J Cardiovasc Magn Reson.* 2015;17(72).
[4] Markl M, et al. *J Magn Reson Imaging.* 2021;36(5):1015-1036.
[5] Rutkowski D, et al. *J Biomech Eng.* 2019; 141(12):121004.
[6] Ruedinger K, et al. *Cardiovasc Eng Technol*, 10(3):500-507, 2019
[7] Medero R, et al. *Ann Biomech Eng.* 2020;48:2484-2493.

IN VIVO QUANTIFICATION OF BRAIN MORPHOLOGIES VIA MECHANICS-INFORMED DEEP LEARNING APPROACH

Shuolun Wang[1], Nagehan Demirci[2], Vicente Castro Solar[3], Maria A. Holland[1,2], Francisco Sahli Costabal[3]

[1]Department of Aerospace & Mechanical Engineering
University of Notre Dame
Notre Dame, IN 46556, USA

[2]Bioengineering Graduate Program
University of Notre Dame
Notre Dame, IN 46556, USA

[3]Department of Mechanical and Metallurgical Engineering, School of Engineering
Institute for Biological and Medical Engineering, School of Engineering
Medicine and Biological Sciences
Pontificia Universidad Catolica de Chile, Santiago, Chile

INTRODUCTION

It has long been known that the cortex is thicker in outer folds (gyri) than in inner folds (sulci). The cortical thickness, in particular, serves as an essential biomarker for diagnosing many neurological disorders such as lissencephaly, polymicrogyria, and Autism Spectrum Disorder. Thus, it is imperative to understand the drivers of cortical thickness variations and to be able to account for them in comparisons. Our recent work has suggested that the interactions between mechanics and biology plays a vital role in shaping the thickness variations, as seen in the measurements [5].

However, in the current work, we aim to distinguish between spatial variations that are artifacts of brain folding and those that are due to biological phenomena. As a novel metric of brain morphology, the modified cortical thickness -- or the thickness the cortex would have if it were unfolded and free of the mechanical forces involved in brain folding -- is introduced. Such a metric preserves biologically relevant information that holds great potential for identifying subtle brain morphology changes in heterogeneous disorders such as ASD. The challenge of calculating this new metric from MRI scans is only possible thanks to the rapid advancements of deep learning technology over the past few years, which have revolutionized many sciences and engineering areas. Instead of relying on hundreds of thousands of examples, our investigation is based on our knowledge of the underlying physics of the problem in the form of large deformation mechanics. In particular, we will learn to "undeform" the brain's cortex using a graph neural network, which operates and learns from physics-based simulations of cortical folding.

This work opens the door for precise cortical thickness analysis in neurological disorders, leading to new early diagnosis pathways and effective treatment.

METHODS

In vivo measurements The geometry of N = 564 human brains is measured using software suite Freesurfer [6], which performs automatic reconstruction and segmentation from MRI images (see Figure 1).

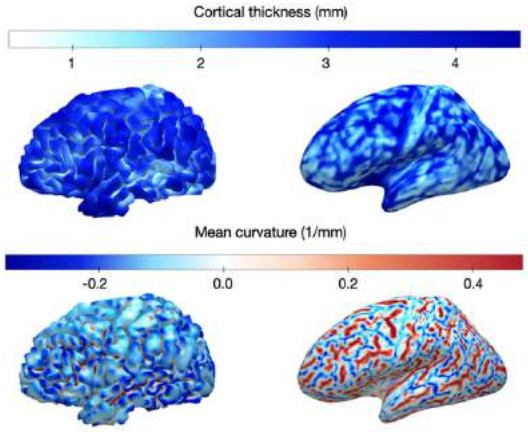

Fig 1. Patterns of cortical thickness and mean curvature in one of N=564 human brains studied. Top: cortical thickness. Bottom: mean curvature. Images to the left represent the anatomical cortical surfaces, while images on the right have been artificially inflated for improved visualization of sulcal values. (Adopted from our recent work [5].)

Constitutive model The cortical folding process undergoes large deformation as well as changes in biological properties. Following Rodriguez et al., 1994 [3], we split the deformation gradient into reversible elastic and irreversible growth counterparts. We model the brain as a bi-layer system consisting of an in-plane growing cortical layer with n_R denoted as its surface out-normal, and an elastic subcortical region underneath. Both tissues are modeled as compressible neo-Hookean material with similar stiffness ($\mu_c/\mu_s = 1$), which is in line with many mechanical testing results [4]. The details of our constitutive model are briefly summarized in Table 1.

We hypothesize that growth is sensitive to mechanical forces, with heterogeneous growth occurring in sulci and gyri after the onset of cortical folding [5]. More specifically, we take the mean curvature κ as a macroscopic evaluation of the local mechanical environment. This is not intended to suggest that cells respond to surface curvature directly, but rather that surface curvature is a convenient proxy for the differing mechanical state between gyri and sulci. Thus, the mean curvature is linked to the cortical growth rate to model preferential growth in either gyri or sulci. The evolution equation of cortical growth parameter ϑ^g is found in Table 1, where G_{ctx} is the homogeneous baseline cortical growth rate constant, $\kappa^* = \kappa t_i$ is the dimensionless mean curvature normalized by the initial cortical thickness t_i, and r^{cur} serves as a curvature sensitivity parameter. As a simplification, we assume that the subcortex does not grow.

Our model is implemented in a commercial non-linear finite element software Abaqus/Explicit [2] by writing user-defined material subroutines. Simulations of cortical folding in 2-D plane-strain and 3-D settings are performed.

Table 1. Summary of our constitutive model

	Gray matter	White matter
Kinematics	$\mathbf{F}^g = \sqrt{\vartheta^g}\mathbf{I} + (1-\sqrt{\vartheta^g})\mathbf{n}_R \otimes \mathbf{n}_R$	$\mathbf{F}^g = \mathbf{I}$
Cauchy stress	$\mathbf{T} = \left[\mu\mathbf{B}^e + (\lambda \ln(J^e) - \mu)\mathbf{I}\right]/J^e$	
Growth evolution	$\dot{\vartheta}^g = G_{ctx}\left[1 - r^{\text{cur}} \tanh(\kappa^*)\right]$	$\dot{\vartheta}^g = 0$

Deep learning Our ultimate goal is to make a meaningful comparison of cortical thickness across human brains from in vivo medical images and investigate the possible correlations between local thickness variations with various neurological disorders. To do that, we seek the *modified cortical thickness,* or the thickness the cortex would have if it were unfolded and free of the mechanical forces involved in brain folding. We assume that the thickness from our finite element simulations is the sum of the uniform normalized thickness and a mechanically driven thickness change, $t_{sim} = t_{norm} + t_{mech}$.

To obtain the modified cortical thickness in neuroimaging data, we use a graph neural network trained on data from the 3-D finite element simulations. It is worth noting that the training data contain the known modified cortical thickness t_{norm} from simulations across all growth modes. In essence, the graph neural network will learn the mapping between the thickness resulting from the combined effects of growth and deformation, and the thickness remaining after elastic forces are released. In the long run, these modified thickness values will then be used at a larger scale to compare typically developing (TD) and Autism Spectrum Disorder (ASD) individuals in an extensive database [7,8].

RESULTS

The measured morphology, including cortical thickness and mean curvature from one of N=564 human brains we studied, is shown in Fig 1. We can quickly tell that the cortical thickness is generally thicker at the gyral peak (negative mean curvature) while thinner at the sulcal fundus (positive mean curvature). Previous literature has shown that the mechanics alone is sufficient to explain such thickness variation [1]. Furthermore, building upon the same foundation, our recent work suggests that a small amount of gyral growth may contribute to the observed thickness difference in addition to the mechanics, suggesting that biological growth and mechanical forces closely interact in the process of cortical folding [5].

Our novel simulations use a randomly assigned initial cortical thickness that varies spatially according to a bivariate normal distribution (Fig. 2). This ensures that the training data for the neural network covers as much thickness variation as possible (the left in Fig. 2).

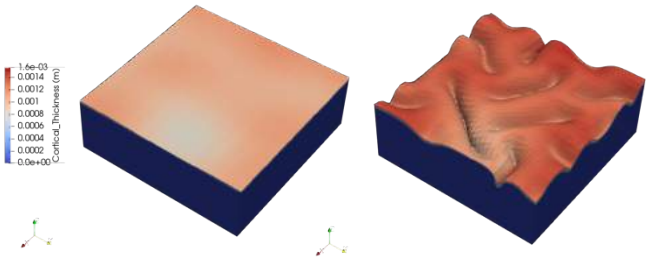

Fig 2. The simulated contour of cortical thickness at the pial surface. Left: the referential state. Right: the deformed state.

DISCUSSION

Cortical thickness serves as an essential biomarker for a wide variety of neurological disorders. Our previous work [1,5] showed the importance of mechanics, biology, and their couplings in predicting the physiological cortical thickness pattern. As an extension, the current work allows a meaningful comparison across human brains via modified cortical thickness. A graph neural network is trained with mechanics-based information to "unfold" the brain and obtain the modified cortical thickness from in vivo medical images.

Looking towards the future, when combined with in vivo medical images at a large scale, our work has the potential to provide a better correlation between cortical thickness variations with various neurological disorders.

ACKNOWLEDGEMENTS

This work was supported by NSF Grant No. IIS 1850102.

REFERENCES

[1] Holland MA, Budday S, Goriely A, Kuhl E. 2018. *Phys. Rev. Lett.* 121:228002.
[2] Abaqus/Explicit. Abaqus Reference Manuals.
[3] Rodrigues EK, Hoger A, McCulloch AD. 1994. *J. Biomech.* 27(4):455-467.
[4] Budday S, Nay R, de Rooij R, Steinmann P, Wyrobek T, et al. 2015. *J. Mech. Behav. Biomed. Mater.* 46:318-30.
[5] Wang S, Demirci N, Holland MA. 2020. *Biomechanics and Modeling in Mechanobiology.* (in press)
[6] B. Fischl, ``FreeSurfer,'' *Neuroimage*, vol. 62, no. 2, pp. 774-781, 2012.
[7] Arya, D., Olij, R., Gupta, D. K., El Gazzar, A., van Wingen, G., Worring, M., & Thomas, R. M. *Medical Imaging with Deep Learning.* 2020.
[8] Parisot, S., Ktena, S. I., Ferrante, E., Lee, M., Guerrero, R., Glocker, B., & Rueckert, D. (2018). *Medical image analysis*. 48, 117-130.

MACROSCALE MECHANICAL CHARACTERIZATION OF HETEROGENEOUS FIBRIN GELS WITH VARYING DENSITY

Julian Jimenez (1), Yifan Guo (2), Adrian Buganza-Tepole (1,2) Sarah Calve (1,3)

(1) Weldon School of Biomedical Engineering
Purdue University
West Lafayette, IN, USA

(2) School of Mechanical Engineering
Purdue University
West Lafayette, IN, USA

(3) Paul M. Rady Department of Mechanical Engineering
University of Colorado, Boulder
Boulder, Colorado, USA

INTRODUCTION

A major aim of bioengineering is to develop scaffolds that mimic properties of the extracellular matrix (ECM) to investigate mechanisms of tissue growth and remodeling. While homogeneous scaffolds are commonly used to support tissue constructs, these do not entirely recapitulate the variable characteristics of the ECM that are observed *in vivo* [1], particularly, tissues near interfacial boundaries where ECM composition, organization, and density can differ drastically [2]. For example, ECM heterogeneities between a tumor and the surrounding stroma [2], or a wound surrounded by healthy tissue [3]. Scaffolds that combine various materials have been engineered to achieve mechanical and biological properties that more closely resemble the tumor and wound microenvironments [1,2,3]. Characterizing the non-uniform mechanics of these scaffolds is critical to understanding how variations in material properties influence cellular behavior.

Fibrin is a naturally occurring protein that is polymerized from fibrinogen and thrombin following injury and provides a temporary structure for remodeling during wound healing [4]. It is a common tissue engineering scaffold because fibrin is biocompatible and its structural properties can be controlled by modulating fibrinogen and thrombin concentrations [4]. Here, we propose a method to characterize the non-uniform mechanical behavior of heterogeneous fibrin gels with varying density by leveraging a finite element (FE) model informed by empirical data. This approach can be adapted to predict and characterize the stress-strain distribution of novel engineered scaffolds that are variable in both geometric complexity and material composition.

METHODS

Porous polyethylene (PE) blocks were used as anchor points for fibrin constructs. PE blocks were bonded onto laser cut polyethylene terephthalate frames using Loctite Super Glue. A 3D printed 2.5mm x 6.6mm x 0.75mm (w x l x h) mold was used to control fibrin geometry as it polymerized between two PE blocks (Fig. 1A).

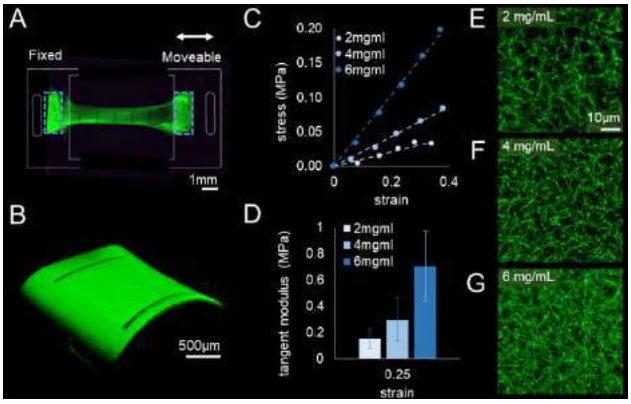

Figure 1: (A) Fibrin on tensile testing frame. PE blocks outlined in blue. (B) 3D rendering of fibrin. (C) Representative stress-strain curves for 2, 4, and 6mg/mL fibrin. (D) Comparison of tangent moduli at ε=0.25 (n=2-4). Error bars=S.D. Microscale structure of 2mg/mL (E), 4mg/mL (F), and 6mg/mL (G) fibrin.

Fibrin concentrations of 2, 4, and 6mg/mL were prepared by combining human fibrinogen and Alexa Fluor (AF) 488 conjugated human fibrinogen at a 1:10 fluorescent to non-fluorescent fibrinogen ratio, 2M $CaCl_2$, and 0.002 U thrombin per mg fibrinogen, in PBS.

Heterogeneous fibrin constructs were made by first pipetting 2mg/mL AF 488-labeled fibrin into a 4mm x 6.6mm x 0.75mm mold, as described above, and then pipetting 4mg/mL AF 546-labeled fibrin into the center of the 2mg/mL fibrin as it polymerized (Fig. 2A).

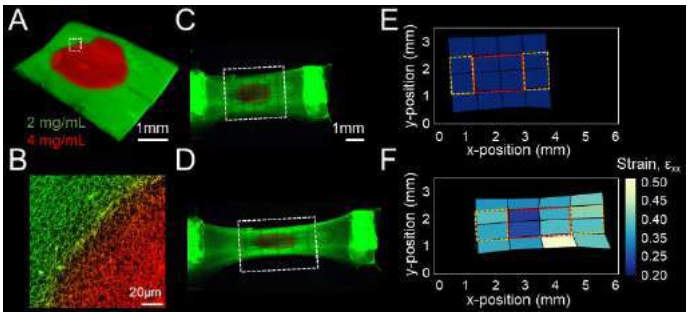

Figure 2: (A) 3D rendering and (B) microscale structure of 2mg/mL fibrin (green) with a 4mg/mL fibrin inclusion (red). Gel before (C) and during (D) tensile testing. Strain field before (E) and during (F) tensile testing. Voxels encompassing and adjacent to the 4mg/mL fibrin outlined in red and yellow, respectively.

Fiducial lines were photobleached onto fibrin in a vertical pattern (Fig. 1A) or a 5x5 grid pattern (Fig. 2C) using a Leica STELLARIS 5 confocal microscope and a 10x objective. Z-stacks were acquired to visualize the macroscale geometry, and FIJI was used to measure cross-sectional areas. The microscale structure of fibrin was imaged using a 63x objective.

A FemtoTools micromanipulator system, microforce sensor probe, custom 3D printed spring, and a Leica microscope camera were used to collect force data and to acquire video of sample deformation, as previously described [5]. Tensile tests were conducted at a strain rate of $0.01s^{-1}$ up to a 6000μm displacement, equivalent to ε=0.91.

For homogeneous fibrin, strain was calculated from the vertical fiducial lines through video analysis using a custom FIJI macro and MATLAB algorithm, as previously described [5]. Stress was calculated by dividing force data by regional cross-sectional area.

For the heterogeneous fibrin gel, FIJI was used to analyze videos and manually track the position of each vertex on the fiducial 5x5 grid. A custom Python code was used to plot the position of the vertices and calculate the strain of each voxel (Fig. 2E, F). A FE model was created in Abaqus to simulate the heterogeneous fibrin gel (Fig. 3).

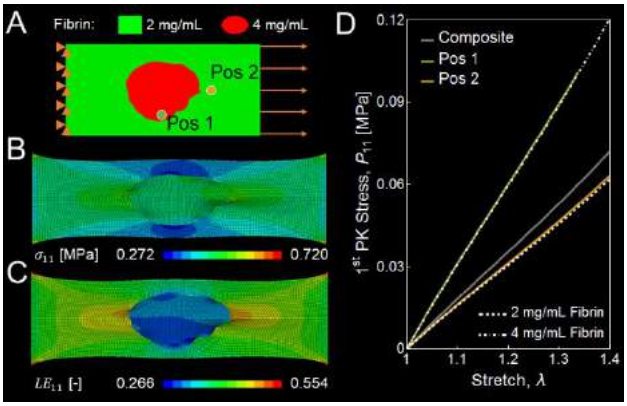

Figure 3: (A) FE model of heterogeneous fibrin gel. Stress (B) and logarithmic strain (C) fields from FE model. (D) Local stress-strain response within (1) and adjacent (2) to 4mg/mL inclusion.

The geometry of the FE model was based on measurements taken from confocal images of the heterogeneous fibrin. Clamped boundary conditions were imposed on the left side of the geometry, and the right side was stretched to 1.5x the original length (Fig. 3A). The model by Gasser et al. [6] was used in Abaqus to simulate the material, with parameters obtained by fitting the bulk material response for 2mg/mL and 4mg/mL fibrin (Fig. 1). Stress-strain data from different locations on the heterogeneous fibrin, encompassing and adjacent to the 4mg/mL fibrin inclusion, were isolated for comparison.

RESULTS

Confocal imaging of homogenous fibrin showed that fibril density increased with higher fibrinogen concentration (Fig. 1E-G). A positive correlation between fibrinogen concentration and stiffness was observed. The average tangent moduli and standard deviations of the 2, 4, and 6mg/mL fibrin at ε=0.25 were 0.15±0.08MPa, 0.30±0.16MPa, and 0.71±0.26MPa, respectively (Fig. 1D).

Confocal imaging of the heterogeneous fibrin gel showed a cohesive interface between the 2mg/mL and 4mg/mL fibrin (Fig. 2B). Different local strains were observed during tensile testing of this gel (Fig. 2C-F). For the displacement shown, voxels encompassing the 4mg/mL fibrin experienced an average strain (±S.D.) of 0.29±0.06. Notably, voxels in the 2mg/mL fibrin region, adjacent to the 4mg/mL fibrin inclusion, experienced a higher average strain of 0.36±0.02.

The FE model showed consistent results with what was observed experimentally. The stress was nearly constant in the 4mg/mL inclusion and the regions adjacent to it on the left and right side (Fig. 3B). However, because the inclusion was made out of a stiffer material, the strain in the inclusion was smaller compared to the adjacent regions (Fig. 3C), as observed experimentally. Position 1, within the 4mg/mL fibrin, had a tangent modulus of 0.29MPa at ε=0.25. Position 2, within the 2mg/mL fibrin had a tangent modulus of 0.15MPa at ε=0.25. The curves of the bulk 2mg/mL and 4mg/mL material are plotted for comparison (Fig. 3D). The homogenized modulus of the heterogeneous fibrin gel was 0.18MPa at ε=0.25.

DISCUSSION

The observed trends of higher fibril density and gel stiffness with increasing fibrinogen concentration matched previously reported findings [4]. For the heterogeneous fibrin gel, strain varied by region upon tensile testing. As expected, regions within higher concentration, 4mg/mL fibrin, experienced a lower strain than regions composed of the lower concentration, 2mg/mL fibrin. This is supported by both the empirical (Fig. 2F) and FE model simulated (Fig. 3C) strain fields.

Creating an FE model based on the mechanical properties of homogenous fibrin allowed us to simulate the stress-strain response of heterogeneous gels that was verified experimentally. The overall stress-strain response of the heterogeneous gel falls in between the bulk response for the 2mg/mL and 4mg/mL fibrin (Fig. 3D). Notably, the strain field for the heterogeneous gel was measured experimentally by imaging the deformation of a fiducial grid (Fig. 2F). These results aligned with the FE model (Fig. 3B, C). This approach can be applied to design and characterize novel biomaterial combinations that seek to recapitulate *in vivo* mechanics to elucidate the mechanisms of tissue formation and to guide regenerative therapies.

ACKNOWLEDGEMENTS

This work is supported by NSF CMMI 1911346. The authors would like to thank Dr. Robert MacCurdy and Brandon Hayes for assistance with 3D printing gel molds.

REFERENCES

[1] Moutos, F et al., *Biorheology*, 45: 501-512, 2008.
[2] Bordeleau, F et al., *Phys Biol*, 10: 065004, 2013.
[3] Miron-Mendoza, M et al., *Matrix Biol*, 64: 69-80, 2017.
[4] Janmey, P et al., *J R Soc Interface*, 6: 1-10, 2009.
[5] Enríquez, A et al., *Adv Funct Mater*, 31:2005021, 2021.
[6] Gasser, TC et al., *J R Soc Interface*, 3: 15-35, 2006.

MECHANOSENSING AS A THERAPEUTIC TARGET IN SYNOVIAL FIBROSIS

Edward D. Bonnevie (1,2), Carla R. Scanzello (2,3), Robert L. Mauck (1,3,4)

(1) Department of Orthopaedic Surgery
University of Pennsylvania
Philadelphia, PA, USA

(2) Translational Musculoskeletal Research
CMC VA Medical Center
Philadelphia, PA, USA

(3) Division of Rheumatology
University of Pennsylvania
Philadelphia, PA, USA

(4) Department of Bioengineering
University of Pennsylvania
Philadelphia, PA, USA

INTRODUCTION

Osteoarthritis is a leading cause of severe disability in the United States, characterized by changes to a joint as an organ system. One tissue of the joint that is emerging as a key mediator of degeneration, pain, and stiffness is the soft tissue lining the joint, the synovium[1]. It is hypothesized that fibrotic changes in this tissue not only cause joint stiffness and loss of mobility, but may disrupt cartilage homeostasis by altered lubricant expression, such as lubricin (PRG4)[2]. Loss of lubricin expression may increase cartilage friction, resulting in cell and matrix damage that further the cascade of disease[3]. As such, targeting synovial fibrosis during arthritis progression emerges as a treatment strategy.

In the context of many other tissues (e.g., lung, liver, kidney), fibrosis leads to organ failure. Fibrosis is characterized by excessive matrix deposition by fibroblasts that have differentiated towards a myofibroblastic phenotype. Both biophysical and biochemical cues are potent regulators of this differentiation process through increased matrix stiffness and transforming growth factor-β (TGFβ) signaling, respectively[4]. While TGFβ signaling is essential for many biologic functions, targeting cellular sensing of biophysical cues emerges as a potential therapeutic target to inhibit fibrotic cascades. Here, we connect fibrotic signaling and altered lubricant expression by synovial fibroblasts to mechanosensing. Additionally, we assess a potential small molecule inhibitor to rescue synoviocyte function.

METHODS

Human synovium samples were collected from organ donors (OD) and patients undergoing total knee arthroplasty (TKA). Hematoxylin and Eosin (H&E), alpha smooth muscle actin (αSMA), and lubricin staining were conducted and quantified for each donor (n = 4 OD, 8 TKA). In vitro models were conducted on bovine synoviocytes with altered biophysical (matrix stiffness) and biochemical cues (TGFβ at 10 ng/mL). Cells were assessed via immunofluorescence and RT-qPCR, and conditioned media were assessed for their lubricating ability of cartilage explants via confocal elastography. Two small molecule inhibitors of ROCK (Fasudil) and YAP/TAZ (Verteporfin) were tested

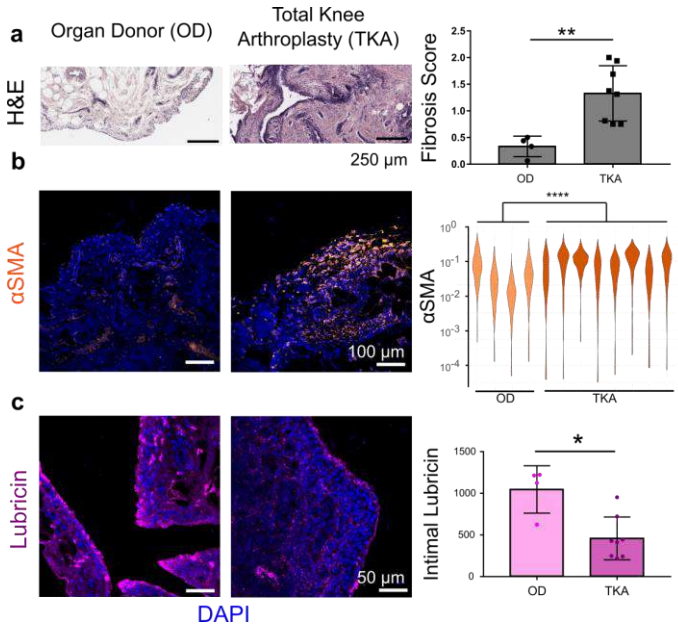

Figure 1. Synovia from TKA patients exhibited (a) higher fibrosis scores, (b) increased αSMA localization, and (c) decreased lubricin at the synovial intima (p < *0.05, **0.01, ****0.0001)

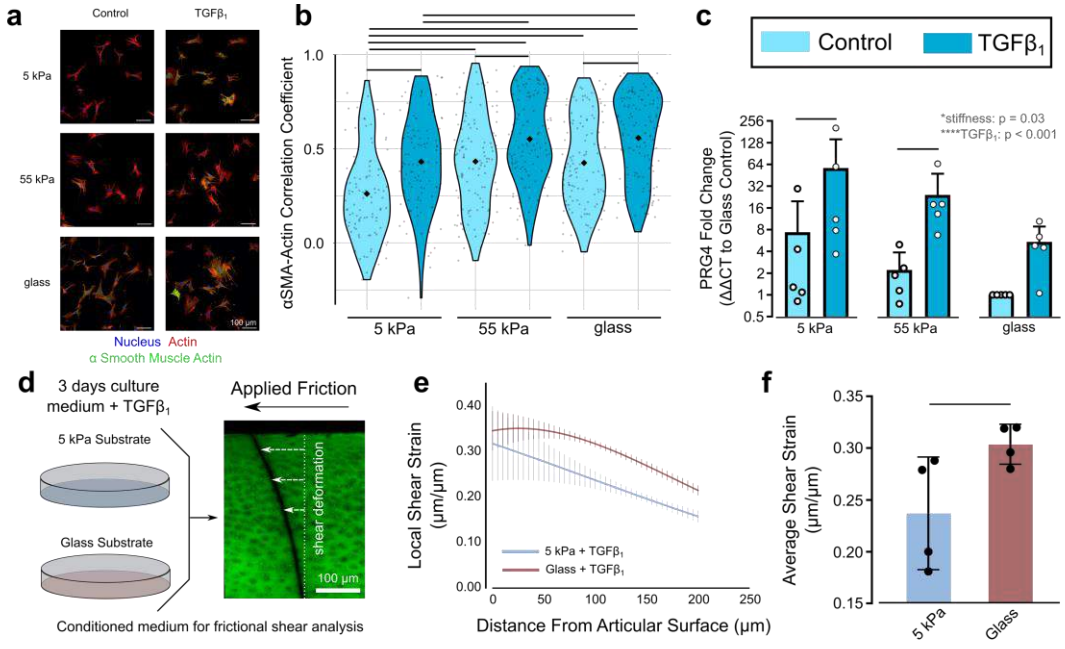

Figure 2. (a) Synoviocytes were seeded on substrates of varying stiffness with or without TGFβ and viewed via confocal microscopy. (b) Both increased stiffness and TGFβ increased αSMA incorporation into stress fibers. (c) Increased stiffness decreased PRG4 (lubricin) expression, while TGFβ increased expression. (d) Conditioned media were assessed for lubricating ability. (e) Confocal microscopy was used to determined depth-dependent deformations due to surface friction. (f) Cells grown on soft substrates secreted biomolecules that reduced cartilage friction deformations. (bars denote p < 0.05)

in cells on glass with TGFβ for their ability to reduce myofibroblast differentiation and restore lubricant expression. Statistical analyses were conducted in R and Prism via one-way or two-way ANOVA with Tukey post hoc, or via t-tests. Sample sizes are denoted by individual dots in plots.

RESULTS

Human synovium samples from TKA patients exhibited consistently increased fibrosis scores compared to organ donors (**Fig 1a**). Additionally, markers of myofibroblast differentiation (αSMA, **Fig 1b**) and increased mechano-signaling (YAP/TAZ, data not shown) were observed in TKA patients. Concomitantly, decreased lubricin localization was observed in TKA patients (**Fig 1c**).

To understand the cues leading to this altered phenotype, both stiffness and TGFβ signaling were assessed in vitro (**Fig 2a**). Both increased stiffness and TGFβ signaling increased myofibroblast differentiation as quantified by αSMA incorporation into stress fibers (via correlation with f-actin fluorescence. **Fig 2b**). In terms of lubricant expression, TGFβ increased PRG4 expression, which is the gene encoding the lubricating molecule, lubricin (**Fig 2c**). To determine change in lubricant function, conditioned media were assessed for their lubricating ability as a function of matrix stiffness via confocal elastography (**Fig 2d**). By quantifying the local shear strains propagating from the articular surface (**Fig 2e**), we observed an enhanced ability of synoviocytes seeded on a soft matrix to secrete lubricating biomolecules (**Fig 2f**). This finding is in agreement with increased lubricin expression in soft environments (**Fig 2c**).

Since substrate stiffness mediates functional lubricant expression, we tested two small molecule inhibitors that target mechanosensing. Fasudil is a ROCK inhibitor that decreases cell contractility and subsequent biophysical cue interpretation, and Verteporfin is a YAP/TAZ inhibitor that inhibits gene expression instigated by stiff substrates. Immunofluorescence imaging revealed decreased cell spreading and decreased αSMA incorporation into stress fibers for both molecules (data not shown). Additionally, RT-qPCR revealed decreased expression of αSMA for both inhibitors (**Fig 3, left**). However, only Fasudil was able to rescue PRG4 (lubricin) expression (**Fig 3, right**).

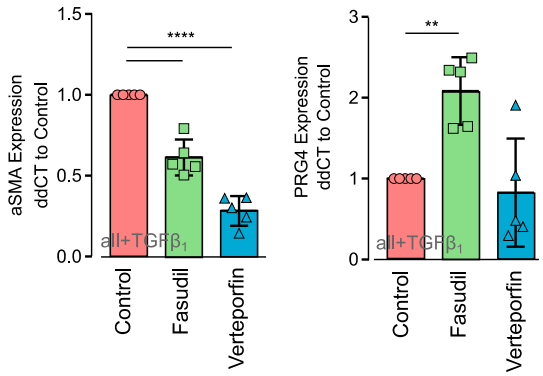

Figure 3. RT-qPCR revealed that both small molecule inhibitors decreased αSMA expression (left), but only Fasudil rescued lubricin (PRG4) expression (p< **0.01, ****0.0001).

DISCUSSION

This study reveals the role that matrix stiffness can play in the emergence or persistence of synovial fibrosis. As such, we revealed the possibility of targeting cellular mechanosensing via ROCK inhibition to alter synoviocyte behavior. Not only does Fasudil decrease myofibroblast differentiation and synoviocyte contractility, but it may rescue lubricant expression to provide chondroprotection.

ACKNOWLEDGEMENTS

This study was supported by the NIH, NSF, and Department of Veterans' Affairs.

REFERENCES

[1] Remst DFG, et al., *Rheumatology*, 54(11):1954–1963, 2015.
[2] Qadri MM, et al., *Am J Physiol Cell Physiol*, 315:432–443, 2018
[3] Bonnevie ED, et al., *J Biomech*, 74:72-78, 2018.
[4] Hinz, B, *Curr Rheumatol Rep*, 11(2):120-126, 2009

EFFECT OF ELASTASE DIGESTION AND MATERNAL AGE ON MURINE VAGINA WALL BIAXIAL MECHANICS

Shelby White (1), Laurephile Desrosiers (2), Leise R. Knoepp (2), Kristin S. Miller (1)

(1) Biomedical Engineering
Tulane University
New Orleans, LA, USA

(2) Female Pelvic Medicine and
Reconstructive Surgery
Ochsner Clinical School
New Orleans, LA, USA

INTRODUCTION

Women who give birth for the first time over the age of 35 have a 350% greater risk of obstetric injury compared to 25-year-old women[1]. While the etiology of the increased risk for trauma is not defined, remodeling of extracellular matrix (ECM) with age may contribute[2] Disruption of elastic fibers is associated with aging and contributes to pelvic floor disorders such as pelvic organ prolapse[3,4] Elastic fibers provide compliance, constrain collagen undulation, and dictate smooth muscle cell (SMC) phenotypes.[5-7] SMCs provide structural and functional integrity to the vaginal wall.[8] Alterations in ECM may include remodeling of the passive contributions, as well as the active responses in the organization and contractility of SMCs.[9,10] The relationship between vaginal elastic fiber composition, SMC contractility and passive mechanical function, however, are not fully understood. Further, alterations in vaginal elastic fibers and SMC phenotype with increasing maternal age is not known. Biaxial extension-inflation protocols are useful tools to evaluate SMC responses, including the baseline contractile potential in the absence of external stimuli (basal tone).[6,11,] Therefore, the objective of this study is to quantify biaxial relationships and SMC contractility as a function of age. Further, elastase digestion will be used to observe potential interactions between elastic fibers and SMC contractility. We hypothesized that elastase treatment will decrease changes in axial force during maximum contraction and increase material stiffness. Additionally, we hypothesized that material stiffness with increase following removal of SMC tone. Further, we hypothesized that vaginal contractile function decreases with age, but that material stiffness increases.

METHODS

A total of $n = 24$ (2-3-month $n=13$; 4-6-month $n=11$) nulliparous female CD-1 mice at estrus were utilized within this study (IACUC approved). **In Vivo Vaginal Pressure Measurements** ($n = 5$/group) To inform the appropriate loading environment for mechanical testing, intravaginal pressure was measured utilizing balloon catheter at the estrus stage.[11-14] The balloon catheter was inserted into the vaginal canal and the software recorded pressure (PowerLab and LabChart8; AD Instrument). **Specimen preparation** A separate cohort of CD-1 mice at estrus (2-3 months n=8; 4-6 months n=6) were euthanized by guillotine without anesthesia to preserve SMC viability.[11] The vagina was immediately dissected and cannulated within a biaxial inflation-extension device. The unloaded configuration was identified, followed by determining the physiologic length[6,11,14] Vaginal SMCs were preconditioned with isobaric- axially isometric contractions induced by 40 mM potassium chloride (KCl) above and below the measured *in vivo* pressure—8 mmHg and 4 mmHg, respectively.[11] Following SMC preconditioning, the vagina was preconditioned circumferentially with 5 cycles pressurization (P= 0-15 mmHg) as well as axially by extending the tissue from -2% to +2% the physiologic length. **Maximum contraction** Maximum contraction was induced with 40 mM of KCl at the physiologic length and mean *in vivo* measured pressure for a total of 5 mins.[11] Changes in outer diameter and axial force were recorded (Figure 1). **Basal tone** Following equilibration, 5 cycles of pressure-inflation tests were performed at isometric stretches of the physiologic length wherein the pressure was increased cyclically from P =0 mmHg-15 mmHg.[5] **Elastase treatment** Vaginal samples were randomly allocated to either a control (n=4 for 2-3 months; n=3 for 4-6 months) or elastase treatment group (n=4 for 2-3 months; n=3 for 4-6 months). Samples were exposed to 15 U elastase digestion for 45 mins, and then the maximum contraction and basal tone assessments were repeated. [6,11] **Passive treatment** Control and elastase groups were subjected to 2 mM of Egtazic acid for 30 mins to remove SMC contraction potential.[11] The protocols for pressure-inflation and axial-extension cycles were repeated. **Data Analysis** The change in axial force and outer diameter was measured from the force and outer diameter prior to KCl addition to the peak values over the 5-minute time period (Figure 1). For control and elastase groups, vaginal material stiffness was quantified by taking the slope of the stress-stretch curve over the range of measured

physiologic pressures (4 mmHg- 8 mmHg). The net changes in material stiffness were calculated by subtracting the untreated response from the elastase treated (Figure 2). **Statistical analysis** To determine if aging and elastase treatment decreased maximum SMC contractility, a 2-way ANOVA (age, treatment) evaluated the changes in axial force and outer diameter. A 3-way ANOVA (tone, age, treatment) evaluated if SMC tone, age, and elastase treatment increased material stiffness. Data reported herein as mean +/- SEM.

RESULTS

Maximum contractility A 2-way ANOVA identified significant differences in the change in axial force with respect to elastase treatment ($p=0.005$) and a trend among the age groups ($p=0.09$). No significant interactions were identified. Elastase treatment significantly decreased the change in axial force in the 2-3 months age group ($p=0.003$) as well as the 4-6 months age group ($p=0.04$; Figure 1A). A 2-way ANOVA (treatment, age) identified significant differences in the change in outer diameter with respect to elastase treatment ($p=0.005$) and age ($p<0.001$) as well as an interaction between age and treatment ($p=0.03$; Figure 1B). **Material stiffness** A 3-way ANOVA identified significant differences in circumferential material stiffness with respect to elastase treatment ($p<0.001$) and tone ($p<0.001$), however, age was not significant ($p=0.74$). The interaction between tone and treatment was significant ($p=0.009$). The 3-way ANOVA identified significant differences in axial material stiffness with respect to elastase treatment ($p=0.007$) and tone ($p=0.03$), however, age was not significant ($p=0.39$). **Changes in material stiffness following elastase** A 3-way ANOVA (direction, age, tone) for change material stiffness in the axial direction showed significant differences in both treatment ($p=0.007$) and tone ($p=0.001$), however, age was not significant ($p=0.69$) (Figure 2). The interaction between tone and direction was significant ($p=0.03$).

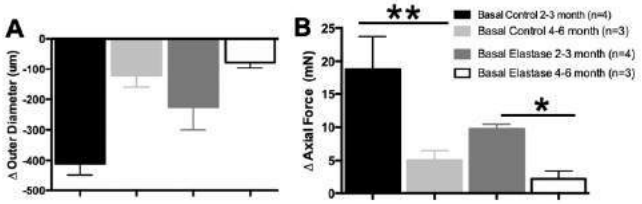

Figure 1: Change in outer diameter (A) and axial force (B) Elastase decreased the force in both age groups (*p<0.05, **p<0.01. Significance was noted in diameter among treatment and tone. Posthoc tests were not performed due to interactions between treatment:tone (p=0.009). Differences among the force were noted in treatment from the basal control 2-3 months (black) to the basal elastase 2-3 months (dark gray) and basal elastase at 2-3 months to basal elastase 4-6 months (white).

DISCUSSION

Maximum contractility Elastase reduced vaginal contractility in both the circumferential and axial directions, as evidenced by the decreased changes in outer diameter and axial force. This decrease is likely due to the disrupted physical interactions between elastic fibers and vaginal SMCs. The diminished contractility has been noted in prior work including the canine trachea and C57BL/6 mouse vagina at 4-6 months of age.[15, 16] However, the previous mouse studies observed significant differences in only the axial direction and was performed in an inbred strain (C57BL/6).[16] Changes in both circumferential and axial directions as a function of ECM composition may suggest SMCs oriented in both directions may be influenced by the ECM structure. Further, performing the experiment in the outbred CD-1 strain provides the benefit of genetic diversity.[18] Maximum contraction of the vagina decreased with age in the circumferential direction and a trend was observed in the axial direction. A statistically significant interaction between age and SMC tone was observed in the circumferential direction. It is possible that the SMC are more prominent or easily influenced by increasing maternal age and elastase disruption compared to the axial direction. This is supported by prior literature finding that the C57BL/6 mouse contains SMC oriented primarily in the circumferential direction.[11] However, the lack of significant changes in the axial direction may be due to the sample size, as a power analysis indicated a required sample size of 14/ group to obtain statistical significance. Future investigations include expanding the age ranges from 6 months to 14 months, which would be comparable to extending the study from 35 human years to 62 years to further elucidate potential changes with maternal age.[17] **Material stiffness** A significant interaction was noted in the circumferential material stiffness between treatment and SMC, however, no significant interactions were noted in the axial direction. This observation further supports the hypothesis that circumferentially oriented SMC may be influenced more by ECM changes. While elastase further increased the material stiffness of the vagina in both basal and passive smooth muscle tone, the difference was exacerbated under passive conditions. This phenomenon is noted in other soft tissues, such as the carotid artery, where the loss of elastic fibers subsequently decreases collagen undulation and alters the stiffness of the tissue.[5] This may be due to smooth muscle tone minimizing the changes in outer diameter following elastase treatment, which would preserve some degree of the native collagen architecture and result in less dramatic changes in material stiffness. Future work to integrate second harmonic generation (SHG) imaging is required to investigate collagen undulation and architecture regarding smooth muscle tone, elastase treatment, and age. Characterizing the mechanical properties of the vagina as a function of increasing age and SMC contractility may provide insight to how structural changes alter the functional integrity of the vagina.

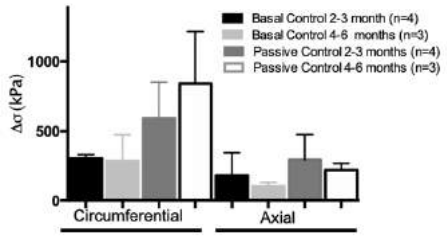

Figure 2: Change in material stiffness along each direction. The 3-way ANOVA showed differences with direction (p=0.007) and tone (p=0.03). The difference was further enhanced by passive induction (2-3 months dark grey, 4-6 months white). Posthoc tests were not performed due to interactions of direction:tone (p=0.03).

ACKNOWLEDGEMENTS

We acknowledge funding from the NSF (CMMI-#1947770; KSM)

REFERENCES

[1]Rahmanou et al Am J Obstet 215(4) pp451-457, 2016 [2]Collins et al J Biomech 45(4) pp 660-665, 2012 [3]Liu et al., Am J Pathol 168(2) pp519-528, 2006 [4]Drewes et al., Am J Pathol 170 (2) pp 578-589 [5]Murtada, etal., J of biomechanical engineering, 128(5) [6]Ferruzzi et al., Cardiovasc Res 92 (2) pp 287-295, 2011 [7]Akintunde et al., *J Biomech Eng* 2018. [8]Chen et al., *Int J Mole Med* 25(93) pp 95-104, 2016. [9]Feola et al., Am J Obstet Gynecol 203(6) pp 595e591-598 [10]Mei et al., Female Pelvic Med Reconstru Surg 19(5) pp 254-259 [11] Clark et al., *Interface Focus*, 9(4), p. 20190025, 2019. [12] Robuck et al., *Society for Reproduction and Fertility* 155(5) pp 10-15, 2018 [13] Byers, S et al., *PloS ONE*, 7(4), pp-13-17, 2012 [14]. Van loon et al., *Biorheology* 14(4), pp181-201, 1997. [15] Lockett, A et al., *American J of Phys* (Consolidated), Vol.314(4), p.L626(9), 2018. [16] Clark et al., SB3C (abstract) 2019. [17] Dutta et al., *Life Sci*, 152, pp. 244-248, 2016. [18] Dubé Biocompare 2017.

THE TRICUSPID VALVE (MAL)ADAPTS IN OVINE MODELS OF VENTRICULAR HEART DISEASE

William D. Meador (1), Artur J. Iwasieczko (2), Tomasz Jazwiec (2), Mrudang Mathur (3), Marcin Malinowski (2), Tomasz A. Timek (2), Manuel K. Rausch (1,3,4)

(1) Department of Biomedical Engineering
University of Texas at Austin
Austin, TX, USA

(2) Cardiothoracic Surgery
Spectrum Health
Grand Rapids, MI, USA

(3) Department of Mechanical Engineering
University of Texas at Austin
Austin, TX, USA

(4) Department of Aerospace Engineering and Engineering Mechanics
University of Texas at Austin
Austin, TX, USA

INTRODUCTION

The tricuspid valve regulates blood flow between the right atrium and the right ventricle. During ventricular systole, its three leaflets coapt and seal the right atrioventricular orifice to prevent the backflow of blood. In diastole, the leaflets passively allow for ventricular filling. This function, repeated with every heartbeat, relies heavily on the interplay between the tissues of the leaflets, the dynamic tricuspid annulus, and the contracting papillary muscles that prevent leaflet prolapse through chordae tendineae attachment. In a dysfunctional valve, leaflet coaptation is incomplete resulting in retrograde blood leakage through the valve, or tricuspid regurgitation (TR).

Clinically significant TR is an independent predictor of mortality and affects more than 1.6 million Americans [1,2]. Generally, TR is considered secondary or functional, meaning that extrinsic factors result in valvular dysfunction, while the valve tissue itself is intact and healthy [1]. For example, a dilated right ventricle can result in chordal tethering of the leaflets, preventing proper coaptation. However, we have recently challenged this paradigm with evidence of leaflet (mal)adaptation which may suggest a primary contribution to valvular dysfunction. In a tachycardia-induced cardiomyopathy (TIC) ovine model, we found that tricuspid anterior leaflets actively respond to heart disease on all functional scales: protein, cell, matrix, and tissue [3]. This active leaflet response resulted in larger and thicker leaflets, increased and reorganized collagen, and increased leaflet stiffness. While larger leaflets may improve leaflet coaptation (i.e. adaptation), stiffer and thicker leaflets may hinder coaptation (i.e. maladaptation). Thus, leaflet (mal)adaptation may play a diametrical role, both in addressing and contributing to TR.

Our previous study's TIC ovine model developed all salient signs of biventricular heart failure with concomitant TR as it presents clinically. However, due to the rapid development of the model (2-3 weeks) and the exaggerated nature of tachycardic hemodynamics, our results were naturally limited. Firstly, we likely only reported on the early response of the leaflets to disease. Secondly, the TIC model prohibited the ability to isolate the effects of mechanical stimulation (i.e. annular dilation and chordal tethering) from hemodynamic stimulation. In this study, we address these limitations by investigating the tricuspid leaflet (mal)adaptive response in a pulmonary hypertension (PH) ovine model. Our PH ovine model incubates for 8 weeks, extending the time window with a more gradual onset than previously reported on. Additionally, with our PH model we impart hypertensive hemodynamics, while still reliably producing annular and ventricular dilation. As such, we expect this model to better isolate the effects of mechanical stimulation on leaflet (mal)adaptation. The objective of our study is to evaluate and compare the (mal)adaptive response between the TIC and PH ovine models.

METHODS

For this study we utilized TIC and PH ovine models. For our TIC study, in brief, we randomly assigned 50 healthy male Dorset sheep to either control (CTL, n=17) or TIC groups (n=33). We anesthetized and monitored TIC subjects as we implanted a pacemaker. For 2-3 weeks post-surgery, we over-paced at 180-260 bpm until TIC subjects developed all salient signs of ventricular disease including ventricular and annular dilation, and atrioventricular regurgitation. For our PH study, in brief, we randomly assigned 29 healthy male Dorset sheep to either control (CTL, n=12) or PH groups (n=19). We anesthetized and monitored PH subjects as we partially occluded the pulmonary artery through banding. Within 8 weeks post-surgery, PH subjects developed all salient signs of ventricular disease including ventricular and annular dilation, and atrioventricular regurgitation. We euthanized all subjects and harvested the tricuspid valves for evaluation.

Immediately post-harvest, we photographed the tricuspid valves from a floating configuration on a calibrated grid. We digitized the anterior leaflets to determine metrics of leaflet size and shape. We then stored the tissues at -80°C. After thawing the anterior leaflets, we isolated a 7x7mm sample of the leaflet for tensile biaxial testing, aligning the major axis with the circumferential and radial directions. We applied four dots to each sample and photographed the stress-free reference configuration. We then mounted, preconditioned, and tested each sample in force-controlled equibiaxial tension. To analyze these data, we informed deformation gradients via strain tracking, and calculated membrane tensions from raw force and displacement data. To summarize our data, we determined four metrics of each sample curve: calf stiffness (i.e. upper region), toe stiffness (i.e. lower region), transition stretch, and degree of anisotropy.

RESULTS

All TIC and PH animals recovered well from their respective procedures and developed clinically accurate ventricular heart disease.

Morphologically, we observed a 1.2x significant increase in anterior leaflet area for PH subjects when compared to CTL subjects ($p = 0.024$) (Figure 1b). In comparison, we observed a 1.3x significant increase in leaflet area between TIC and CTL subjects ($p = 0.002$) (Figure 1a).

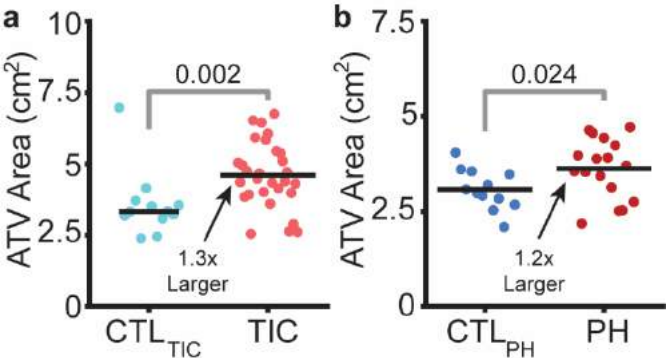

Figure 1: Anterior leaflet areas for (a) tachycardia-induced cardiomyopathy (TIC), and (b) pulmonary hypertension (PH)

From mechanical characterization, we observed a classic J-shaped curve for all samples (Figure 2a,b). Moreover, we found a significant 1.3x increase in circumferential calf region stiffness for PH samples when compared to CTL samples ($p = 0.019$) (Figure 2d). No other metrics for PH resulted in significant findings. Interestingly, in our previous study, we similarly found a significant 1.3x increase in TIC sample calf region stiffness ($p = 0.006$), but instead found this increase in the radial direction (Figure 2c).

DISCUSSION

We set out to compare the (mal)adaptive response of tricuspid valve leaflets between two ovine models: a previously reported TIC model and a newly presented PH model. To this end, we compare the leaflet morphology and the mechanical characterization of each group to healthy control leaflets.

We found that TIC leaflets and PH leaflets each had similar increases in anterior leaflet area. As these measurements were performed under explanted stress-free configurations, we are confident that growth, and not elastic stretch, is responsible for this difference. Interestingly, both TIC and PH leaflets had increased calf region stiffnesses when compared to CTL leaflets, but in opposite directions. The direction of calf region stiffening between animal models may suggest that different stimuli in each model are responsible for the maladaptive stiffening. In TIC we observed radial stiffening, which

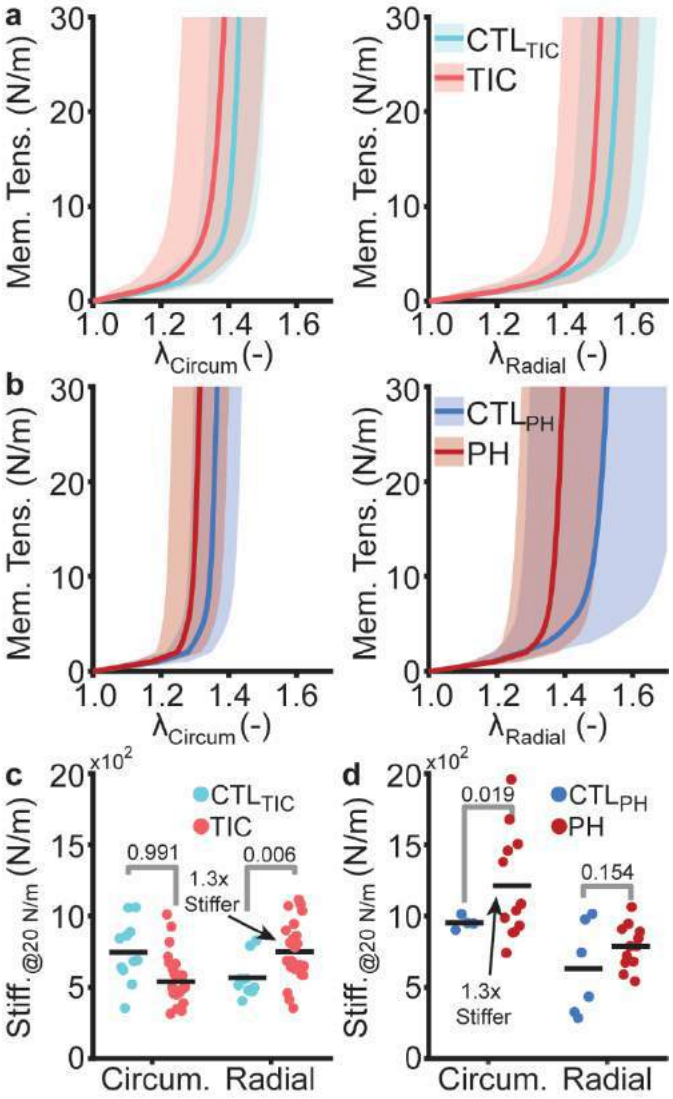

Figure 2: Average equibiaxial curves for (a) tachycardia-induced cardiomyopathy (TIC) and (b) pulmonary hypertension in circumferential and radial directions. (c-d) Calf region stiffness summaries for (c) TIC and (d) PH subjects

may be initiated by either hemodynamic shearing or radial tethering. In PH leaflets, we observed circumferential stiffening, possibly initiated by increased annular dilation stimulation.

In conclusion, the PH ovine model induced (mal)adaptive changes, i.e., growth and stiffening, to the tricuspid valve anterior leaflet, as we observed in our TIC model. As we expand the timeline of TR development, we may continue to understand the underlying mechanisms of maladaptation with promise of future interventions.

ACKNOWLEDGEMENTS

We acknowledge our funding sources: National Institutes of Health (F31HL145976) – WDM, and American Heart Association (18CDA34120028) – MKR.

REFERENCES

[1] Mangieri A, et al. *Circ Cardiovasc Interv*, 10:e005043, 2017.
[2] Nath, J et al. *J Am Coll Cardiol*, 43:405-409, 2004.
[3] Meador, W et al. *eLife*, 9:e63855, 2020.

WEARABLE SENSOR VALIDATION FOR TASKS REQUIRING HIGH ACCELERATION

Sarah C. Moudy (1), Yein Lee (1), Shelby Alfred (1), Rita M. Patterson (1)

(1) Department of Family Medicine
University of North Texas Health Science Center
Fort Worth, TX, USA

INTRODUCTION

Marker-based optical motion capture is the most commonly used method in biomechanics research to examine human movement as it is considered the most accurate, precise, and repeatable approach. Inertial measurement units (IMUs) are a wearable sensor technology that have gained popularity in recent years to analyze human movement as an alternative to motion capture systems. IMUs are portable and cost-effective wearable sensors that gather segment acceleration data to examine human movement. Previous studies have suggested that IMU-derived temporal-spatial parameters, such as step length, are comparable to motion capture data [1]. Further, one case-study on a transfemoral amputee found a 1-3° error between IMU and motion capture knee and ankle joint flexion angles during walking in which greater IMU error was found due to skin and muscle artefact [2]. As skin and muscle artefact increase with tasks requiring greater accelerations [3], it is possible that IMU-derived data during these tasks may be increasingly different from motion capture data. As far as the authors are aware, this has not yet been examined.

IMUs have the potential for clinic and at-home monitoring of daily activities to detect if an individual is at risk for falls. However, it is unclear if IMUs can provide valid data, as compared to motion capture, for tasks that require higher acceleration of a limb, such as recovering from a trip. In particular, the ability of the limb to swing through quickly following a trip event by use of knee and hip flexion [4, 5] is crucial for recovery to avoid a fall to the ground possibly causing subsequent injury.

Therefore, the purpose of this study was to validate IMU-derived knee and hip joint kinematic data on tasks requiring higher acceleration as compared to walking. It was hypothesized that no significant differences would be found between IMU-derived data and motion capture derived data.

METHODS

Five healthy young adults (3 males, 2 females) participated in this study (Age (years): 23.4 ± 2.9, Mass (kg): 69.2 ± 24, Height (cm): 172 ± 11). Kinematic and kinetic data were captured using an 18-camera motion capture system (100 Hz; Motion Analysis Corp., Santa Rosa, CA) synchronized with a dual-belt treadmill (1000 Hz; V-Gait Motekforce Link, Culemburg, Netherlands) and five IMUs (100 Hz; STT Systems, San Sebastián, Spain). Motion capture reflective markers (diameter: 14 mm) were placed bilaterally on the lower-limbs and trunk in accordance with the V-Gait marker set. IMUs were attached bilaterally using a flexible strap on the following body segments: lower-back on the spine, lateral placement on mid-thigh, and anterior placement directly below the knee. These placements are the recommended IMU placements by STT Systems and confirmed through testing of various tibia sensor placements compared to motion capture data.

Participants performed three tasks: treadmill walking, perturbation at small acceleration (2 m/s^2), perturbation at large acceleration (5 m/s^2). Walking data were collected for 30 seconds at the participant preferred habitual walking speed. Perturbations were elicited via treadmill acceleration to occur around toe-off of the right limb as the participant was walking at their preferred speed. A short break (<2 min) was taken between tasks.

IMU-derived joint angle data were calculated within STT Systems proprietary software, iSen. In brief, 3-dimensional vectors from each IMU are transformed into a local reference frame, representative of the bone reference frame, in line with the rotation axis of the joint. Joint angles are calculated as the angle formed by two local vectors (i.e., thigh IMU and tibia IMU generate knee joint angle data). Motion capture data

were exported to visual3D (v6, C-motion, Inc., Germantown, MD, USA) to perform kinematic calculations.

Knee and hip flexion angles were extracted for each task. For walking, data were extracted for twenty gait cycles from heel contact to heel contact. For perturbation tasks, a total of 5 perturbations trials were extracted for each acceleration from the heel contact prior to the elicited perturbation through to the toe-off following the stance after the perturbation. This is representative of the gait cycle in which the perturbation occurred and the stance phase in which recovery from perturbation occurred. Trials were averaged for each participant and time-normalized to 100%.

Statistical Analysis: Paired *t*-tests were performed between IMU and motion capture derived knee and hip flexion angles for each task individually. Statistical parametric mapping, a type of waveform analysis, was utilized to perform the analysis in order to examine the dynamic nature of the waveform. Statistical significance was set at $p<0.05$. Root mean square error (RMSE) was also calculated for each comparison at each data point in the waveform.

RESULTS

No significant differences were found between IMU and motion capture derived knee and hip joint flexion angles (Figure 1) for any task. RMSE values suggest that hip data tended to have greater differences between IMU and motion capture data compared to the knee (Figure 2). Further, RMSE values during stance (~1-60% of time for walking, ~1-50% and 75-100% of time for perturbations) tended to be greater for all tasks than during swing (61-100% of time for walking, and 50-75% of time for perturbations).

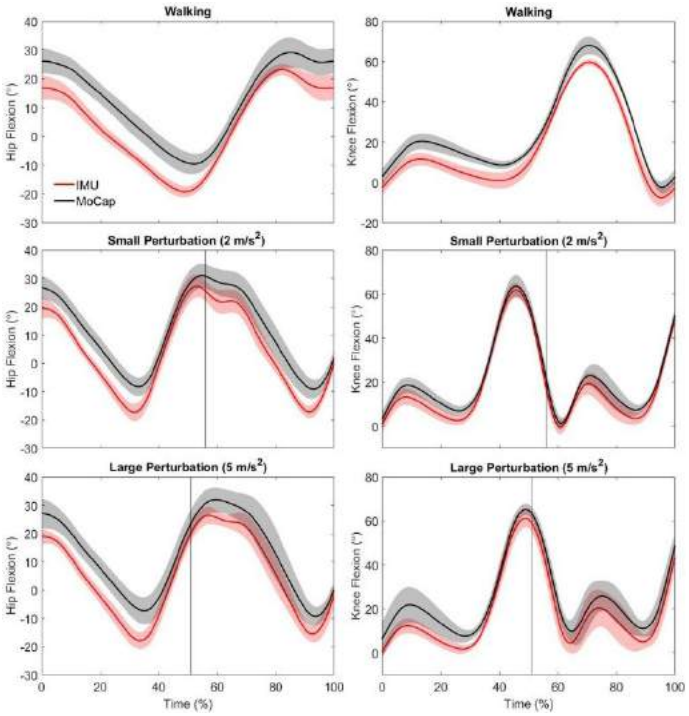

Figure 1: Hip and knee flexion angles from IMU (red) and motion capture (black) data for each task. Vertical solid line represents the average time at which the perturbation occurred.

DISCUSSION

The main finding from this study was that IMU-derived knee and hip joint kinematic data is comparable to that of motion capture data for habitual speeds and higher acceleration tasks. The overall waveform pattern and magnitude was not significantly different between IMU and motion capture joint angles for any task.

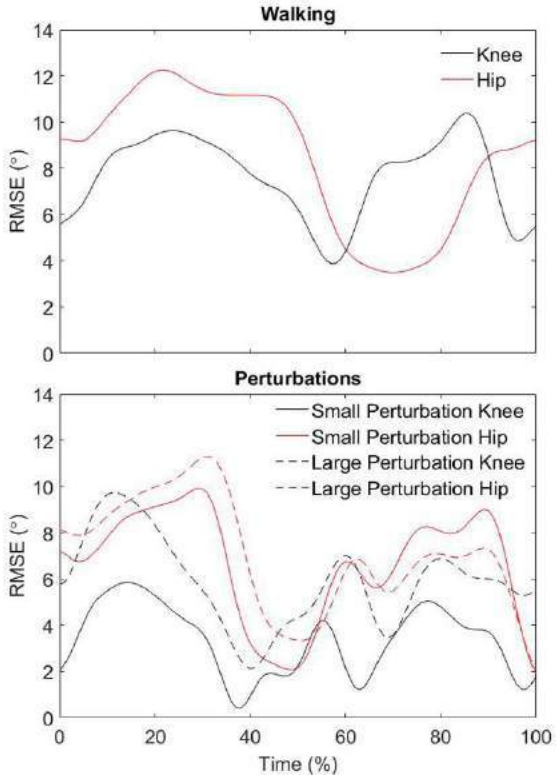

Figure 2: RMSE values between IMU and motion capture knee and hip flexion data for the specified time period of each task

RMSE results found that IMU-derived joint angles were consistently reduced in magnitude (<12° at any given time) compared to motion capture. Further, this magnitude offset was greatest during stance phases of each task (Figure 2). This would suggest clinical significance during phases above 10°, yet, the magnitude offset is most likely a result of the calibration process of the IMUs. Calibration requires the participant to stand in the anatomical standard position at the start of each trial which defines the knee and hip in full extension to 0°. However, if the participant stands with slight flexion at the moment of IMU calibration, this could result in the magnitude offset as presented in Figure 1 at 0% time.

Overall, these data present promising findings for the use of IMUs as a portable and cost-effective alternative to motion capture systems for a variety of task speeds. Further verification is necessary for other tasks and movement features before implementation into clinical settings.

ACKNOWLEDGEMENTS

This project was supported through an intramural seed grant from UNTHSC Texas College of Osteopathic Medicine.

REFERENCES

[1] Teufl et al., *Sensors*, 19(1):38, 2019.
[2] Seel et al., *Sensors*, 14:6891-6909, 2014.
[3] Benoit et al., *Gait & Posture*, 24:152-64, 2006.
[4] Grabiner et al., *J Gerontology*, 48:M91-M102, 1993.
[5] Yoo et al., *Gait & Posture*, 71:98-104, 2019

3D IMAGE CORRELATION OF PORCINE ADIPOSE TISSUE UNDER COMPRESSION

D. Samson (1), B. Chapman (2), B. Burke (2), L. Williams (2)

(1) Mechanical and Aerospace Engineering
University of Florida
Gainesville, FL, USA

(2) Biomedical Engineering
University of Florida
Gainesville, FL, USA

INTRODUCTION

Adipose Tissue (AT) has a unique composition and function. It is composed of 60-80% lipids (mainly triglyceride lipids), 5-30% water, and 2-3% collagen proteins [1]. Compositional variations occur due to different types of AT [2, 3]. The four types of AT are subcutaneous AT (SAT) [2], visceral AT (VAT) [2], white AT (WAT) [2, 3], and brown AT (BAT) [2, 3]. Despite there being various types of AT, they all share similar anatomy [1, 2], as shown in Figure 1. AT's unique anatomical characteristics allow for the storage of energy (in the form of lipids) [1, 2, 4], heat insulation [1, 2, 4], the ability to protect underlying organs by absorbing energy from high impacting forces [1, 2, 4, 5, 6], and the ability for AT to act as an endocrine organ [7, 3].

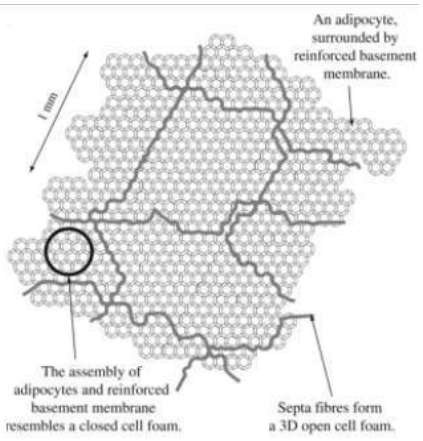

Figure 1: Adipose tissue anatomy

There are very few studies [1, 4, 6, 7, 8] that can be found which seek to analyze the mechanical response of AT. Information on AT's response to mechanical forces can be used for many different purposes. AT's cushion effect [9, 10, 11, 12] could be utilized by car manufacturers to develop safer cars when analyzing injuries obtained in car crashes. During car crashes, AT is known to cushion internal organs in the abdomen by absorbing high impacting forces [9, 10, 11, 12]. Manufacturers of hernia meshes [13, 14] could benefit from a mechanical understanding of AT, especially considering that one-third of patients who receive hernia meshes must undergo revisional surgery [13]. Part of the reason hernia meshes fail is that they do not match the surrounding abdominal tissues' responses to mechanical stimuli [13, 14]. Plastic surgeons could enhance patient outcomes by using a finite element analysis model of AT to stimulate the soft tissue deformation of patients undergoing surgery in preoperative planning [7]. Furthermore, mechanical characterization of AT could also improve the safety profile of high impact sports.

Experimental data on AT's responses to axial compressive loading must be gathered to develop mathematical models of AT [7], simulations of AT responses to various loading conditions [7], and to better tissue-engineer substitutes [13, 14, 15] that respond similarly to native AT under different types of mechanical stresses. In this study, Digital Imaging Correlation (DIC) is used to measure the surface deformation resulting from compressed porcine adipose tissue. The surface deformation is then compared to the engineering strain on the sample and the strain rate.

METHODS

Porcine adipose tissue was sourced from the University of Florida Animal Care Services (ACS). Subcutaneous adipose samples were extracted from the back of each pig. Samples were transported to Williams lab on ice to maintain integrity. They were then hydrated with gauze presoaked in phosphate-buffered saline (PBS). PBS was used to mimic in vivo pH and osmolarity conditions [16]. Samples were cut using a custom-made die tool. The custom die tool was used to slice samples into cylindrical specimens of 9-13 millimeters (mm) in height and 25 mm in diameter. The samples were then sprayed with a random speckling pattern using an airbrush gun (Paasche TG-300R). Compression testing on these samples was performed at 1%/s with the Instron 5942 (Instron, Norwood, MA). True stress and true strain were calculated using equations (1) and (2). Surface deformation was measured using a Digital Image Correlation (DIC) system (Correlated Solutions, Irmo, SC). DIC data was then exported to MATLAB where the strain was compared to surface deformation using equation (3), Poisson's ratio. Figure 2 represents the experimental set-up in the stages before compression (left) and immediately following the application of compressive axial loads (right).

$$\varepsilon = \delta/L \quad (1)$$

$$\sigma = F/A \quad (2)$$

$$\upsilon = -d\varepsilon_{trans/d}\varepsilon_{axial} \quad (3)$$

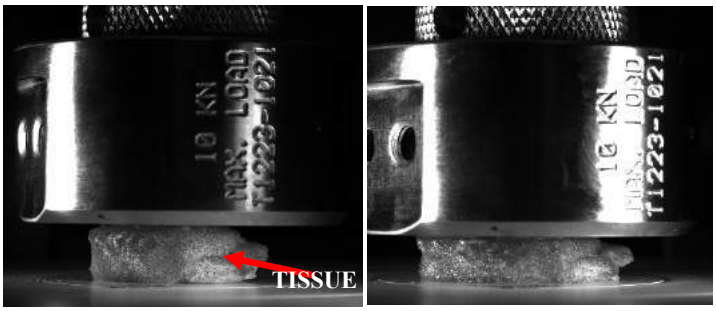

Figure 2: Adipose tissue immediately preceding compression (left), adipose tissue immediately following compression (right)

RESULTS

Early data suggests that the Lagrange number is highest near the center of the specimen and lowers near the top and bottom, as displayed in Figure 3. Table 1 is a presentation of the mechanical properties of four tests. These are calculated using the extension length of the sample and cross-sectional area, respectively. It reveals that compressive strain (as calculated using the extension of the sample) is directly proportional to stress.

Table 1: Stress and strain relationship of porcine AT

	Maximum Load	Compressive extension at Maximum Load [mm]	Modulus (Automatic Young's)	Compressive stress a Maximum Load
1	0.93169	80.95570	0.07633	0.00245
2	20.39441	85.17818	0.35994	0.05365
3	20.39442	85.49871	1.19500	0.05365
4	19.95819	85.80356	1.23527	0.05250

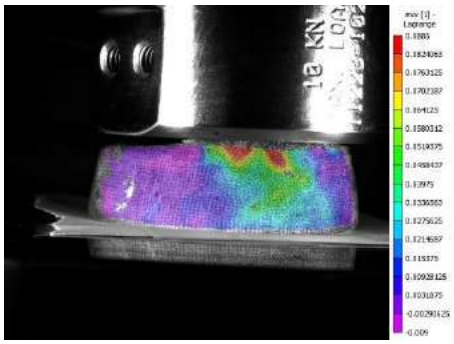

Figure 3: Lagrange distribution of compressed porcine AT

DISCUSSION

Early findings suggest that data obtained during this experiment does align with the suggestions of soft tissue mechanics literature. There is a non-linear stress-strain response and a correlation between stress and strain. Future work on this project will further characterize the mechanics of porcine adipose tissue as it relates to surface deformation and will provide insight into AT's response across low and high strain rates.

ACKNOWLEDGEMENTS

The team would like to thank the University of Florida Animal Care Services for the tissue donation.

REFERENCES

[1] Comley K., *International Journal of Impact Engineering*, vol. 46, pp. 1–10, 2012.
[2] Schoettl T., *The Journal of Experimental Biology*, vol. 221, no. Suppl 1, 2018.
[3] Coelho M., *Archives of Medical Science*, vol. 2, pp. 191–200, 2013.
[4] Comley K., *International Journal of Solids and Structures*, vol. 47, no. 21, pp. 2982–2990, 2010.
[5] Zwick R. Z., *Cell Metabolism*, vol. 27, no. 1, pp. 68–83, 2018.
[6] Alkhouli N., *American Journal of Physiology-Endocrinology and Metabolism*, vol. 305, no. 12, 2013.
[7] Sommer G., *Acta Biomaterialia*, vol. 9, no. 11, pp. 9036–9048, 2013.
[8] Geerligs M., *Journal of Biomechanics*, vol. 43, no. 6, pp. 1153–1159, 2010.
[9] Harbaugh C. M., *Journal of Pediatric Surgery*, vol. 53, no. 5, pp. 1033–1036, 2018.
[10] Homaie-Rada E., *Journal of Injury and Violence Research*, vol. 12, no. 1, pp. 85–1-2, Jan. 2020.
[11] Kim J. E., *Computer Methods in Biomechanics and Biomedical Engineering*, vol. 17, no. 9, pp. 965–977, 2012.
[12] Wang S. C., *Increased depth of subcutaneous fat is protective against abdominal injuries in motor vehicle collisions*, 2003, pp. 545–559.
[13] Deeken C. R., *Journal of the Mechanical Behavior of Biomedical Materials*, vol. 74, pp. 411–427, 2017.
[14] Deeken C. R., *Journal of the Mechanical Behavior of Biomedical Materials*, vol. 38, pp. 6–16, 2014.
[15] Babaei B., *Journal of the Mechanical Behavior of Biomedical Materials*, vol. 84, pp. 198–207, 2018.[16] García M. M., *Journal of Functional Biomaterials, 8*(4), 48. doi:10.3390/jfb8040048

3D VISUALIZATION OF THE PODOCYTE ACTIN NETWORK USING INTEGRATED MEMBRANE EXTRACTION, ELECTRON MICROSCROPY, AND DEEP LEARNING

Chengqing Qu (1),

Shumeng Jiang (1), Robyn Roth (2), Charles Loitman (2), Dina Hammad (2), Andrey S. Shaw (3), Guy M. Genin (1), Jeffrey H. Miner (2) and Hani Y. Suleiman (2)

(1) NSF Science and Technology Center of Engineering Mechanobiology, Washington University in St. Louis, MO, US

(2) Division of Nephrology, Department of Medicine, Washington University in St. Louis, MO, US

(3) Genentech, South San Francisco, CA, US

INTRODUCTION

End stage kidney disease (ESKD) is a major public health burden that can arise when specialized kidney epithelial cells called podocytes lose their ability to filter blood [1]. Although this is known to be associated with shape changes and eventual effacement of podocyte foot processes, the cytoskeletal structures that regulate podocyte shape have not been fully characterized [2]. A challenge is that these cells should be studied in the natural environment of the kidney's glomerular filtration barrier (GFB), which comprises an intricate epithelial layer of podocytes lying atop the thick glomerular basement membrane (GBM) and the endothelial layer of the glomerular capillary on the opposite side of the GBM [3]. Additionally, the nanoscale features of the slit diaphragms that filter blood are too small to be resolved optically. When injured, podocytes undergo foot process effacement (FPE), a massive change in shape including loss of the intricate foot processes and the replacement of these with a sheet of cell membrane covering the GBM. Although a role of the actin cytoskeleton in these processes is evident from the large list of actin-associated genes whose mutation leads to FPE, the pathways leading to FPE in injury remain unclear, and targets for a cure to ESKD have yet to be identified.

The critical need to identify the mechanobiological structures underlying podocyte shape regulation, structures we hope can one day form the targets for ESKD therapies, motivated us to develop a technique to image these. We hypothesized that the actin cytoskeleton had direct connections to the slit diaphragms, and that these connections and the cytoskeleton itself would be compromised in kidney disease.

METHODS

Overview: We isolated glomeruli from kidneys of healthy mice as well as from three different mouse injury models: *Cd2ap*$^{-/-}$, *laminin beta 2* KO (*Lamb2*$^{-/-}$) and a mouse model of Alport syndrome. We applied a new imaging technique that integrates membrane extraction, focused ion bean scanning electron microscopy (FIB-SEM), and deep learning image segmentation. After actin stabilization and a membrane extraction technique to these glomeruli, they were imaged after sequential layer ablation using FIB-SEM to create a 3D dataset. We applied deep learning segmentation to convert these FIB-SEM datasets into 3D models of the podocyte actin networks.

Image segmentation: To segment the GBM and podocyte actin cytoskeleton from FIB-SEM image stacks of glomeruli of WT control, *Cd2ap*$^{-/-}$, *Lamb2*$^{-/-}$ and Alport syndrome mice, Fiji/ImageJ (version 1.53C) was utilized with the Waikato Environment for Knowledge Analysis (Weka) trainable segmentation plugin (version 3.2.34) [3, 4, 5]. Before training the model, features were selected. For edge detection features, the *Sobel filter*, *Hessian* and *Difference of Gaussian* options were selected. For texture description features, the *Structure* and *Neighbors* options were selected. For noise removal and edges detection features, *Gaussian blur* and *Membrane projections* were utilized [4].

Deep learning: To train deep learning models, we generated independent trained classifier for each dataset: WT control, *Cd2ap*$^{-/-}$, *Lamb2*$^{-/-}$ and Alport syndrome. For each classifier, five elements were classified and assigned to the selected region on the image stack via the graphic user panel. These five elements represented "actin", "GBM", "background", "microtubules" and "gaps", where "gaps" indicated the peripheral fading boundary between the podocyte actin cytoskeleton and the "background" in the image. The development and training of deep learning models for each of the four conditions was based on a region of interest (ROI) within FIB-SEM image stacks. The training ROI was 251 slices at 587 x 218 pixels for WT control, 251 slices at 252 x 676 pixels for *Cd2ap*$^{-/-}$, 201 slices at 378 x 484 pixels for *Lamb2*$^{-/-}$, and 150 slices at 286 x 172 pixels for Alport syndrome. The classifiers were trained based on the ROI and the selected features, one

for each of the image stacks, except for Alport syndrome. The classifiers were then applied to the ROI to generating probability maps.

Image visualization All probability maps were projected into 3D models using Amira software (Thermo Fisher Scientific, Version 2019.4), with each probability map having one channel for each class. The final channels used for 3D visualization were the "GBM" and "actin" channels, resulting in low 3D visualizations of the structures of the GBM and podocyte actin network.

RESULTS

The healthy podocyte cytoskeleton in 3D has direct connections between actin and slit diaphragms: After generating the probability maps of all four types of kidney glomeruli, the segmented regions were projected by using Amira software (Thermo Fisher Scientific, Version 2019.4). For the first time, we were able to view the GBM and the actin assembly in the foot process areas in 3D (Fig. 1). These results supported our hypothesis that the actin cytoskeleton in the foot processes are connected to the slit diaphragms structures.

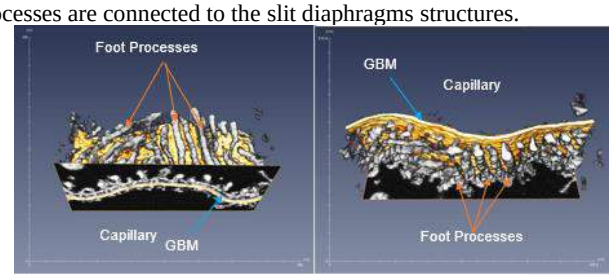

Figure 1: Deep learning segmented model of healthy podocyte FIB-SEM images showing interdigitating foot processes.

The actin-slit diaphragm connections are compromised in injured kidneys: Glomeruli from *Cd2ap*$^{-/-}$ (Fig. 2) *Lamb2*$^{-/-}$ (Fig. 3) and Alport syndrome (Fig. 4) mice showed a disruption in the cytoskeleton integrity and actin condensation, supporting our hypothesis. GBM disruption was evident in the latter two.

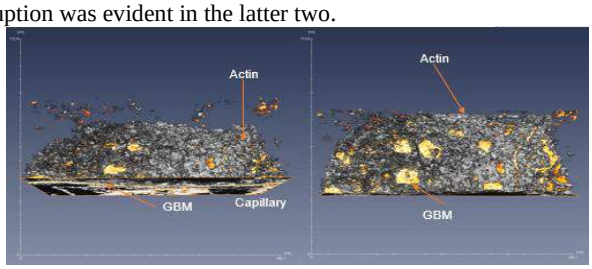

Figure 2: Deep learning segmented model of *Cd2ap*$^{-/-}$ podocyte showing actin condensation in the effaced areas juxtaposing to the GBM.

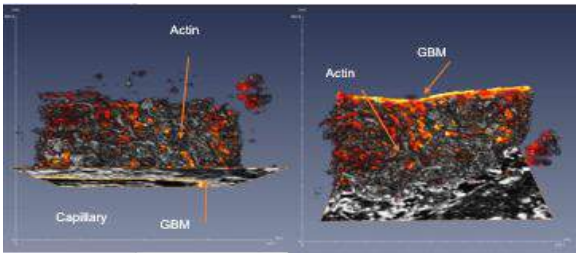

Figure 3: Deep learning segmented model of *Lamb2*$^{-/-}$ podocyte showing occasional GBM splitting and extensive actin condensation in the effaced areas juxtaposing the GBM.

Finally, 3D image segmentation of Alport Syndrome glomeruli showed the irregularly thickened GBM, consistent with the disease features. Our data also the extensive actin condensation similar to the other two injury models (Fig. 4).

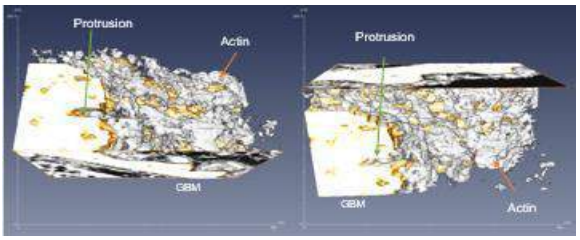

Figure 4: Deep learning segmentation of Alport syndrome podocytes showing irregularly thickened GBM and extensive actin condensation juxtaposing the GBM**.**

DISCUSSION

Results uncovered connections between the actin cytoskeleton and slit diaphragms. This enables construction of a free body diagram showing how filtration and cell contraction combine to provide physiological levels of tension to the cytoskeleton (Fig. 5). The new visualization method enabled us, for the first time, to observe the detailed 3D organization of actin networks in both healthy and injured kidney glomerular podocytes. Data supported the hypothesis of an actin-based underpinning to morphological changes in injury. Similarities between the presentation of actin condensations across all three injury models further suggested common mechanobiological pathways that govern changes to podocyte morphology after injury.

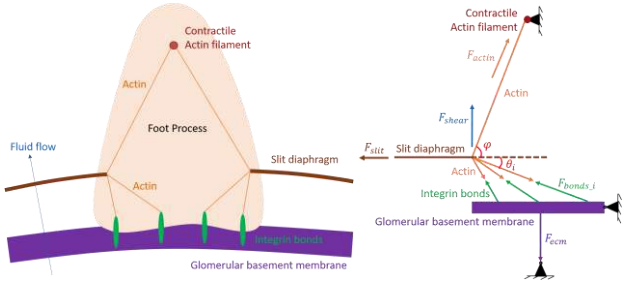

Figure 5: Free body diagram for cytoskeletal resistance, as supported by the new imaging and 3D deep learning reconstructions.

ACKNOWLEDGEMENTS. We acknowledge the assistance of M. Joens, D. Oakley, S. Sviben, P. Krishnamoorthy, and J. Fitzpatrick for microscopy at the Wash. Univ. Center for Cellular Imaging (Wash. Univ. School of Medicine, Children's Discovery Institute (CDI-CORE-2015-505, CDI-CORE-2019-813), Foundation for Barnes-Jewish Hospital (3770, 4642), and the Wash. Univ. Diabetes Research Center (NIH P30 DK020579), Vice Chancellor for Research and Div. of Nephrology. This work was also supported by AHA (17SDG33420069), NIH (P30DK020579, R01DK058366, R01DK078314), NSF (CMMI 1548571).

REFERENCES

[1] Burridge, K. and E.S. Wittchen, *The tension mounts: Stress fibers as force-generating mechanotransducers.* The Journal of Cell Biology, 2013. **200**(1): p. 9-19.

[2] Melak, M., M. Plessner, and R. Grosse, *Actin visualization at a glance.* Journal of Cell Science, 2017. **130**(3): p. 525-530.

[3] Schindelin, J., et al., *Fiji: an open-source platform for biological-image analysis.* Nat Methods, 2012. **9**(7): p. 676-82.

[4] Arganda-Carreras, I., et al., *Trainable Weka Segmentation: a machine learning tool for microscopy pixel classification.* Bioinformatics, 2017. **33**(15): p. 2424-2426.

[5] Moen, E., et al., Deep learning for cellular image analysis. Nat Methods, 2019. 16(12): p. 1233-1246.

EFFECT OF TEMPERATURE ON EQUILIBRIUM COMPRESSIVE MODULUS OF IMMATURE BOVINE ARTICULAR CARTILAGE

C.V. Sise (1), Kimberly R. Kroupa (2), Jiashuai Fan (2), Clark T. Hung (1), Sinisa Vukelic (2), Gerard A. Ateshian (1,2)

(1) Biomedical Engineering
Columbia University
New York City, New York, United States of America

(2) Mechanical Engineering
Columbia University
New York City, New York, United States of America

INTRODUCTION

Osteoarthritis (OA) is a multi-tissue disease characterized by degeneration of articular cartilage. Current late-stage clinical treatment methods require invasive surgical intervention and can fail to provide long term pain relief to patients. Despite the pervasive nature of the disease and significant effort dedicated to OA research, there is no existing clinical method that successfully delays the progression of osteoarthritis through repair of diseased cartilage.

The extracellular matrix (ECM) is the primary structural component of cartilage tissue and contains the collagen (COL) fibril network and the proteoglycans (PGs). Tissue integrity depends on the homeostasis between the COL and PGs, as the COL fibril network, maintained with crosslinks (CxLs), counteracts swelling pressure of the PGs. Correspondingly, loss of CxLs results in increased swelling due to the osmotic pressure of PGs, and loss of compressive stiffness in the tissue [1]. Thus, induction of cross-links to restore the COL fibril matrix may impede OA progression and repair damage to the bulk tissue.

The induction of CxLs may be achieved with a non-invasive low-level femtosecond laser. Our preliminary work has demonstrated the efficacy of femtosecond laser treatment for cartilage CxL induction and the corresponding enhancement of tissue mechanical properties [2]. The low-level pulse energy of the laser is below the optical breakdown threshold and thus is able to mimic the effect achieved with higher laser power without damage to surrounding tissue. However, to realize the potential of laser treatment and delineate CxL induction as the source of modulus stiffening, the structural modification of tissue due to thermal effects must be fully understood.

It has been previously shown that thermal exposure of immature bovine articular cartilage to temperatures ranging from 24 to 60 ℃ leads to 8% stiffening to the equilibrium modulus [3] and reduction in relaxation time. However, exposure of human cartilage to 70 °C led to a substantial decrease in its shear modulus [8]. Since articular cartilage is a complex heterogenous structure, the exact effect thermal exposure has on the individual components providing structural integrity to the ECM over a range of temperatures has yet to be elucidated. In this study, we exposed devitalized immature bovine cartilage explants to a range of temperatures from 40 ℃ to 85 ℃, spanning the denaturation temperature of COL (58-65 °C [4]), in an effort to understand structural modification of cartilage due to thermal heating. To distinguish the effect of heating on the COL fibril matrix from PGs, in one sample group we also perform a PG digestion prior to thermal heating. In studying the modification of the cartilage structure during thermal exposure, we aim to better understand changes in cartilage stiffness through modification of the ECM, as well as further identify an envelope of safe treatment parameters for femtosecond laser CxLing.

METHODS

Sample Preparation: Cartilage tissue was harvested from the knees of immature bovine calves (2-3 months old, Green Village Packing Co., New Jersey, USA). Explants (∅3 mm × 2±0.2 mm) were biopsy-punched from the femoral condyle. Samples were stored frozen in phosphate buffered saline containing protease inhibitors (PBSPI) and thawed before treatments.

Intact Thermal Experiment: The equilibrium modulus from unconfined compression was assessed using a custom mechanical testing device under a creep tare load (0.1 N, 600 s) and a subsequent stress-relaxation test to 10% strain (0.5 μm/s ramp, 1800 s). Following the unconfined compression test, the devitalized explants were suspended in PBSPI and heated at a consistent temperature on a hot plate for 12 minutes. Samples were divided into 7 groups for thermal treatments from 40 to 85 °C. The unconfined compression test was repeated after thermal exposure.

PG-Digested Thermal Experiment: The equilibrium compressive modulus of 10 additional explants was assessed using the method described above. Then, 5 explants were sequentially digested of GAG to remove PGs while keeping the COL fibril network intact, following the protocol outlined by Schmidt et al. [5]. The digestion consisted of three sequential 24-hour treatments with chondroitinase ABC, trypsin, and hyaluronidase. Samples were kept at 37 °C under gentle agitation during the 72-hour digestion. The equilibrium compressive modulus of the digested samples was measured directly after digestion. Then, the 10 explants (5 digested samples and 5 control samples) were suspended in PBSPI and heated at 74.0 ± 2.5 °C on a hot plate for 12 minutes. The compressive modulus was reassessed after thermal exposure.

RESULTS

Intact Cartilage Thermal Experiment: Explants exposed to temperatures above 65 °C showed an increase in compressive modulus, whereas samples exposed to temperatures below 65 °C did not show a significant change in modulus (Fig. 1). On average, explants with thermal treatment between 40 and 64 °C (n=24) had a modulus of 662±190 kPa before treatment, and 653±196 kPa after treatment. Samples with thermal treatment between 65 and 85 °C (n=25) had a modulus of 570±247 kPa before treatment, and 733±321 kPa after treatment, representing a significant enhancement of 28.7±17.9% in the compressive modulus due to thermal treatment ($p<0.001$). Statistical analysis using a one-way ANOVA test with Bonferroni correction (NCSS Statistical Software, Kaysville, Utah) confirmed that the change in modulus for samples exposed to temperatures above 65 °C was statistically higher from samples exposed to temperatures below 65 °C ($p<0.05$).

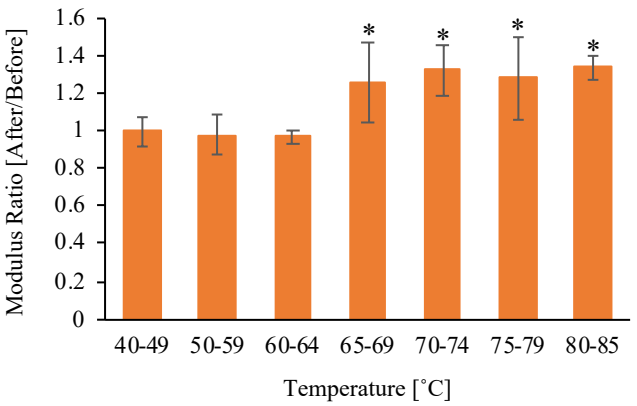

Figure 1: Ratio of bovine sample modulus (After/Before) for different cartilage thermal exposure groups. Thermal exposure produced stiffening in temperature exposure ranges from 65 – 69 °C, 70 – 74 °C, 75 – 79 °C, and 80-85 °C ($p<0.05$*)

PG-Digested Cartilage Thermal Experiment: PG digestion decreased the compressive modulus of articular cartilage samples (n=5) from 665±168 kPa to 27±3 kPa, consistent with results from our prior study [6]. Upon thermal exposure, PG-digested samples stiffened to 303±49 kPa, representing more than a tenfold increase (Figure 2). Statistical analysis using a repeated measures ANOVA test with Tukey-Kramer multiple-comparison (NCSS Statistical Software, Kaysville, Utah) confirmed that the PG-digested samples stiffened significantly after thermal exposure ($p<0.001$). The sample thicknesses averaged 2.03±0.09 mm before digestion, 2.11±0.14 mm after digestion, and 1.95±0.11 mm after thermal treatment. The corresponding undigested control group (n=5) had a modulus of 1070±169 kPa before thermal treatment (thickness 2.18±0.07 mm), and 1289±209 kPa after thermal treatment (thickness 2.24±0.10 mm), representing a significant enhancement of 20.5±5.1% in the compressive modulus ($p<0.002$).

DISCUSSION

Results of the current study showed that heating immature bovine articular cartilage from 40-64 °C to 65-85 °C, spanning the denaturation temperature of COL, caused an increase in its equilibrium compressive modulus by ~20 to 30%. This finding does not contradict prior literature reports of tissue equilibrium modulus stiffening by 8% from 24 to 60 °C [3], as these tests spanned significantly different temperature ranges. The current results indicate an abrupt change in cartilage mechanical properties over a narrow range of temperatures (Fig. 1).

We considered the possibility that PGs could shield COL from the effect of heating. Hypothetically, since the superficial zone (SZ) of articular cartilage is softer than the middle (MZ) and deep (DZ) zones [7], we were concerned that further softening of the SZ due to thermal treatment would manifest itself as an apparent stiffening during compressive testing of the full-thickness cartilage plugs, as the SZ might get compacted under a very low tare load, such that the full-thickness modulus would now reflect the higher modulus of the MZ and DZ. To address this possibility, we digested the PGs and exposed the (mostly-) COL II matrix to heating. Those results demonstrated that thermal treatment considerably enhanced the compressive modulus of the COL II matrix (more than tenfold), in the absence of PGs. Therefore, we can conclude that COL II stiffening with thermal treatment above 65 °C significantly contributed to the increase in compressive equilibrium modulus of intact cartilage explants.

We may also speculate that PGs either provided some measure of protection to COL in explants heated above 65 °C, or thermal effects on PGs led to ECM softening, since the enhancement in tissue modulus was smaller in intact versus PG-digested tissue samples. In fact, Marshall et al. reported that thermal exposure of human articular cartilage to a temperature change from 24 to 70°C reduced its shear modulus significantly [8]. Since articular cartilage shear properties are significantly influenced by PGs [9], we may combine those earlier findings with the results of the current study to hypothesize that thermal exposure of articular cartilage above 65°C has opposite effects on the COL and PG in the ECM, producing a net stiffening of ~20 to 30% in compressive modulus at COL denaturation temperatures (Fig. 1).

In the context of our ongoing investigations of femtosecond laser crosslinking of articular cartilage, we may conclude that our previously reported enhancement in compressive modulus induced by the femtosecond laser treatment [2] was not caused by structural modification of cartilage through thermal heating, since those experiments maintained the temperature of tissue samples below 36 °C. Future studies will investigate the depth-dependent compressive modulus of bovine cartilage explants before and after thermal exposure.

ACKNOWLEDGEMENTS

This study was supported by NIH grant 5 R01 AR073289.

REFERENCES

[1] Dijkgraaf, L et al., J. Oral Maxillofac. Surg., 53(8):924–29, 1995. [2] Wang C et al., Annual Meeting of the ORS. 2017 [3] June, R. et al., J. Exp. Biol, 213(22):3934–40, 2010. [4] Bozec L. et al., Biophys J, 101(1), 228-236, 2011 [5] Schmidt, M.B. et al., J. Orthop. Res. 8:353–363, 1990. [6] Canal-Guterl C et al., J. Biomech., 43(7):1343-1350, 2010. [7] Wang C et al., J Biomech Eng., 124(5):557-67, 2002. [8] Marshall, L et al., J Mech Behav Biomed, 103:103595, 2020 [9] Zhu, W et al., J Orthop Res, 11(6):771–81, 1993.

BIOFLUID MECHANICS OF SURFACTANT DELIVERY IN A BIOENGINEERED THREE-DIMENSIONAL LUNG AIRWAY MODEL

Hannah M. Combs (1), Hossein Tavana (1)

(1) Department of Biomedical Engineering
The University of Akron
Akron, Ohio, USA

INTRODUCTION

Pulmonary surfactant is produced by the type II alveolar cells in the lungs and is responsible for the reduction of surface tension at the air-liquid interface of respiratory airways (1). Dysfunctional or insufficient surfactant can result in high surface tension, leading to blockage and collapse of airways and alveoli. Pre-term infants born prior to 29 weeks are at a greater risk for insufficient surfactant production, due to their immature alveolar cells, and may develop a condition known as Neonatal Respiratory Distress Syndrome (NRDS), where lungs tend to collapse. Re-inflating the lungs requires substantial force beyond the infants' ability. Surfactant replacement therapy (SRT) is a critical treatment for infants suffering from NRDS to facilitate breathing (2). SRT involves intratracheal delivery of a plug of surfactant followed by mechanical ventilation to distribute the instilled surfactant in the lungs. Despite benefits of SRT, there is a large non-response rate of up to ~35% among infants. Considering large variations in the administration methods in terms of positioning of infants with respect to the gravitational field and the ventilation flow, we postulate that optimizing delivery conditions is critical to ensure a uniform distribution of administered surfactant in the lungs and improves the SRT outcomes. Our overarching goal is to approach this problem from a fluid mechanics viewpoint to define specific orientations of the lung airway tree and flow that result in a uniform surfactant distribution. To that end, we have developed a bioengineering approach to construct 3D models of the lung airway tree of infants and study fluid dynamics of the surfactant delivery process in terms of surfactant film deposition, plug splitting at airway bifurcations, and distribution in the airways.

METHODS

The computational lung model was created in Solidworks, beginning with a single tube representing the trachea (generation z=0). The dimensions used for modeling the trachea were a diameter of 3.5 mm and a length of 17.5 mm. Following this, a bifurcation zone was added to the end of the tracheal tube followed by a pair of daughter tubes (z=1 airways) at an angle of $\theta = 80°$, representing the bifurcation angle. The dimensions of these airways and those in subsequent generations (z=1-7) followed the equations below that represent airway dimensions in the lungs of a preterm infant.

$$\text{Diameter, } d_z = d_0 \text{ x } 2^{-\frac{z}{3}} \quad (1)$$

$$\text{Length, } \; l_z \cong 3d_z \quad (2)$$

To account for the rotation of airways in 3D space in the lungs, at the level of z=3 and after, the airways were rotated 90° with respect to their parent generation. At the end of this process, a 3D, eight-generation computational model of the lung airway tree was constructed (Figure 1a). The computational model was used to 3D-print a semi-transparent physical model for studies of intratracheal surfactant delivery (Figure 1b) (1).

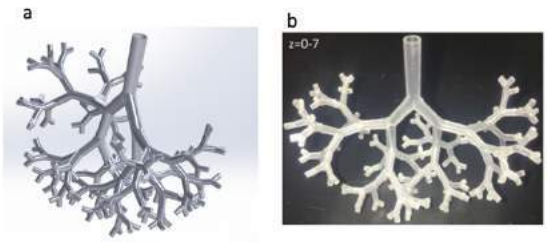

Figure 1: (a) Computational model of z=0-7 airways of preterm infants, (b) 3D printed semi-transparent lung model.

To study fluid mechanics of surfactant delivery, Infasurf (ONY, Inc) surfactant was used at a concentration of 35 mg/ml. Infasurf was heated in a water bath at a temperature of 37℃ and prior to the surfactant plug being inserted, the model was placed in a plasma cleaner (Harrick Plasma) to render it hydrophilic, as in native airways. Once the plug was inserted into the trachea, air pressure from a syringe pump was used to propagate the plug downstream into the airway tree.

RESULTS

We quantified surfactant distribution using a plug split ratio that defines the volume ratio of two daughter plugs formed at a bifurcation. The evaluation of the split ratio was completed by securing the model to a plexiglass platform allowing for adjustment of roll angle (α), which defines relative gravitational orientation of daughter tubes in a bifurcating airway unit. Figure 2 shows a typical result of surfactant plug dynamics. With $\alpha = 0°$, the plug split evenly between the two daughter airways at z=0-1 (Figure 2b) but when α increased to 30°, the plug split asymmetrically, and more solution drained into the gravitationally favored daughter airway (Figure 2c). The daughter plugs propagated into subsequent airways to further split and distribute in downstream airways (e.g., Figure 2d-e for $\alpha = 30°$).

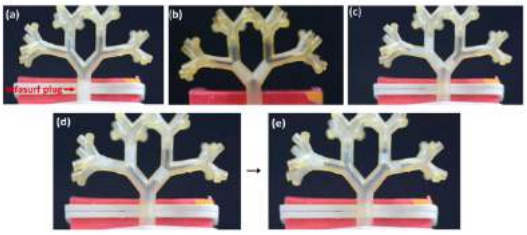

Figure 2: (a) shows an Infasurf plug located in the trachea tube with a roll angle of $\alpha = 0°$, (b) the plug has passed the first bifurcation occupying z=1. (c) the plug passes bifurcation z=1-2 with a roll angle of $\alpha = 30°$ to occupy (d) the left lung, and (e) the right lung (1).

We conducted experiments at $\alpha = 0°, 30°, 60°,$ and $90°$ to determine effects of orientation on the plug splitting. These angles respectively represent an infant receiving SRT laying on their backs or being rolled onto their sides. We also used flow rates to result in a physiologically relevant capillary number of Ca=0.030 at z=0 and Ca=0.024 at z=1. At the z=0-1 bifurcation and an increasing roll angle from $\alpha = 0°$ to $\alpha = 30°$ caused asymmetric splitting with a split ratio of R=0.31 $\pm$ 0.11. As the roll angle was increased to $\alpha = 60°$ and $\alpha = 90°$, there is further reduction in the split ratio from 0.08 $\pm$ 0.04 and 0.07 $\pm$ 0.03 (Figure 3).

Evaluating further into the model, the z=1-2 bifurcation showed a large variation in split ratio from the left and right side of the lung. As the model roll angle was increased from $\alpha = 0°$ to $\alpha = 30°$, there was a 70% greater amount of Infasurf that drained into the lower left daughter tube providing a split ratio of 0.04 $\pm$ 0.07. Following a similar pattern to the z=0-1 bifurcation, there was a decrease in split ratio when the model was increased to $\alpha = 60°$ and $\alpha = 90°$, with the ratio of R=0.24 $\pm$ 0.05 and R=0.18 $\pm$ 0.06 (Figure 3).

The bifurcation (z=1-2) of the right lung once again followed a similar pattern to the previously mentioned split ratios. Increasing the roll angle was from $\alpha = 0°$ to $\alpha = 30°$ resulted in a split ratio of R=0.95$\pm$ 0.11. Further increase in the roll angle to $\alpha = 60°$ and $\alpha = 90°$ gave further reduction in the split ratio to 0.77 $\pm$ 0.08 and 0.83 $\pm$ 0.05 (Figure 3).

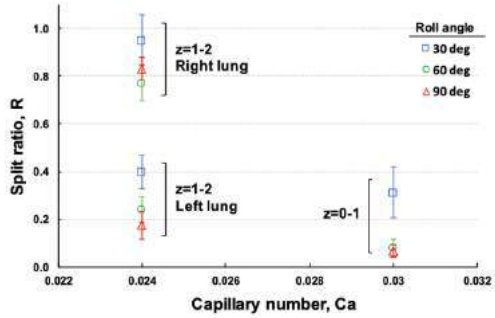

Figure 3: Split ratios using varying roll angles and vs. the Capillary number for bifurcations z=0-1, z=1-2 right lung, and z=1-2 left lung.

At the z=1-2 bifurcation, the upper daughter tube in the left lung was almost horizontal, while the z=0-1 bifurcation is directed farther from the horizontal plane, allowing 75-95% drainage into the lower daughter of z=1-2. The right lung presented less than 30% of plug drainage, due to the roll angle moving z=1 farther from the horizontal plane.

DISCUSSION

We developed a bioengineering approach to computationally design and fabricate biomimetic models of the tracheobronchial tree. This model enabled us to study transport of a surfactant solution in airways and evaluate how orientation of the airway tree in the gravitational field affects distribution of surfactant between left and right lungs. Importantly, results from our empirical approach are consistent with previous computational studies of plug splitting in bifurcations (2). However, unlike previous studies that mainly used 2D numerical models or planar physical models, our study presents the first 3D, multi-generation airway tree model to investigate surfactant transport in airways as in SRT. This ongoing study will help gain a fundamental understanding of fluid mechanics of the SRT and design strategies to uniformly distribute surfactant in airways, either with a single dose or multiple doses at different orientations. This approach may also be used to model and study other respiratory disorders.

ACKNOWLEDGEMENTS

This study was supported by a grant 1904210 from the National Science Foundation (NSF).

REFERENCES

[1] Copploe, A et al., *A Three-Dimensional Model of Human Lung Airway Tree to Study Therapeutics Delivery in the Lungs,* 47:1435-1445, 2019.

[2] Grotberg. J et al., *Three-dimenstional model of surfactant replacement therapy*, 112:9287-9292, 2015.

FINITE ELEMENT MODELING OF THE LONG HEAD OF THE BICEPS TENDON

Miles F. Wing (1), Arin M. Ellingson, PHD (2), Paula M. Ludewig, PHD (2), Aaron Hellem (2), Victor H. Barocas, PHD (1), S. Cyrus Rezvanifar, PHD (2)

(1) Department of Biomedical Engineering
University of Minnesota – Twin Cities
Minneapolis, MN, USA

(2) Department of Rehabilitation Medicine
University of Minnesota
Minneapolis, MN, USA

INTRODUCTION

The long head of the biceps tendon (LHBT) is the site of numerous pathologies associated with debilitating symptoms. The LHBT originates at the superior glenoid and labrum, extends laterally over the humeral head and through the bicipital groove. Its distal end inserts into the long head of the biceps (Figure 1). Pathologies affecting this tendon include but are not limited to tendon rupture, hypertrophy, and superior labrum anterior and posterior (SLAP) lesions or tears. A previous study on 544 patients who were prescribed shoulder arthroscopy found that 35 patients (6.4%) had Type II or IV SLAP tears, which include damage to the LHBT,[2] with symptoms reported as shoulder pain and a 10-20 degree loss in arm elevation range of motion.[3] An ongoing concern with these injuries is the variety of contributors and thus the varying success rate of injury treatment methods.[4] Therefore, a deeper understanding of the LHBT mechanical environment and underlying mechanisms of its pathologies is of great importance. A finite element (FE) model was developed to investigate the mechanical behavior of the LHBT during arm elevation.

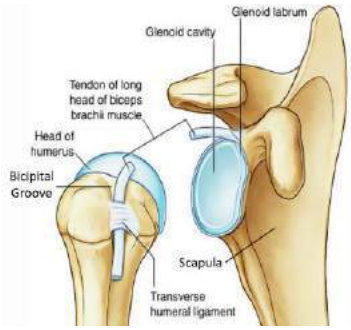

Figure 1: Relevant anatomy of the shoulder.[1]

METHODS

MRI scans of a right shoulder (48-year-old female) were reconstructed using *Mimics* (Materialise, Leuven, Belgium) to create the 3D model of the shoulder joint. An initial 3D mesh was assigned to the 3D models using *HyperMesh* (Altair, Troy, MI) and the humerus, scapula, LHBT, and transverse humeral ligament (THL) were imported into *FEBio*.[5] Four-node tetrahedral elements (TET4) were used for all bony and soft tissue components of the model (Figure 2).

The humerus and scapula were defined as rigid bodies, and the THL and LHBT were given an isotropic, compressible, Neo-Hookean base material with a Young's modulus of 600 and 50 MPa, respectively. The Poisson's ratio for both the THL and LHBT was 0.478.[6] The LHBT was also reinforced with one group of longitudinal power-linear fibers with a Young's modulus of 600 MPa.[7-9] Power-linear fibers are defined by a piecewise function that makes stress increase exponentially while the fibers are crimped and linearly when they are uncrimped. The exponent value for the LHBT fibers was set to 5, and the fibers became uncrimped at 3% strain based on previous experimental data.[7,9] Before implementing motion into the model, these material properties were

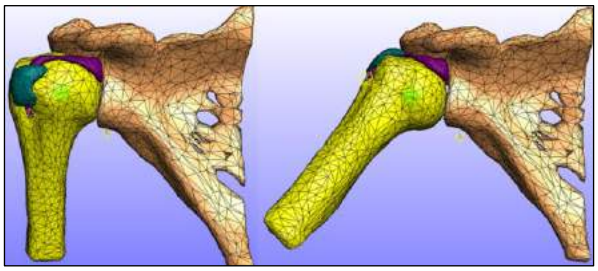

Figure 2: The start and end positions of the shoulder model in the FEBio workspace with meshes applied.

evaluated by performing a uniaxial tensile test simulation on the LHBT and comparing the results to previous experimental data.[9]

Rigid contacts were used to fix the THL and proximal LHBT to the humerus and scapula, respectively. Frictionless sliding contacts were defined between the LHBT and humerus, as well as between the LHBT and THL. In vivo joint kinematics during arm elevation, acquired with bone-fixed sensors through our previous experimental study,[10] were used to drive the simulation. With the scapula fixed to a global reference frame, humeral motion started with an inferior translation to align with the initial neutral position, followed by combined rotations about all three axes to move from the coronal plane with 0° of abduction to the scapular plane with about 45° of abduction (Figure 2). The implemented motion also caused the humerus to undergo external rotation. Forces ranging from 20N to 60N[11] were applied to the distal end of the LHBT during different trials of the simulation to represent the force applied by the biceps muscle during arm elevation. The force pointed toward the distal end of the humerus and was a constant magnitude for the duration of each trial. Since the LHBT is most resistant to tensile loads, the 1st principal stress (i.e., the maximum tensile stress) was exported for comparison across different arm elevation angles and locations in the LHBT.

RESULTS

The initial uniaxial tension study compared favorably with published data on LHBT mechanics, as shown in Figure 3. The stress-strain curves from the model and the literature had similar shapes and stresses. Figure 4 (A) shows the 1st principal stress plotted against arm elevation angle for three different locations in the LHBT. Each location is represented by a single element in the model. Figure 4 (B) shows where each of the three locations are on the LHBT, and it shows a 1st principal stress map on the LHBT.

Qualitatively, the model showed that LHBT geometry and the load on the distal end of the LHBT have a significant impact on LHBT behavior. Only one tendon geometry was used, but observations could be made about how its physical characteristics affected its behavior. The characteristic that had the biggest impact on the LHBT behavior was its thickness. Thick sections of the tendon were less susceptible to deformation and struggled to slide under the THL. The thin section on the distal LHBT slid under the THL with much smaller stresses. Comparing the varying geometries within a single tendon helped form generalized observations on tendon geometry. The loads on the distal LHBT directly impacted its deformation and stresses. Large loads (40-60 N) on the distal LHBT compressed its intra-articular portion to a narrower state as it was pulled against the THL. Narrowing the LHBT with reaction forces from the THL helped the LHBT slide through the bicipital groove, and the entire tendon was primarily under tension. Small loads (20-40 N) on the distal LHBT couldn't cause the intra-articular portion to narrow, which made it difficult for the tendon to slide through the bicipital groove. The result of the LHBT being unable to slide through the bicipital groove was compression and buckling in the proximal LHBT during arm elevation.

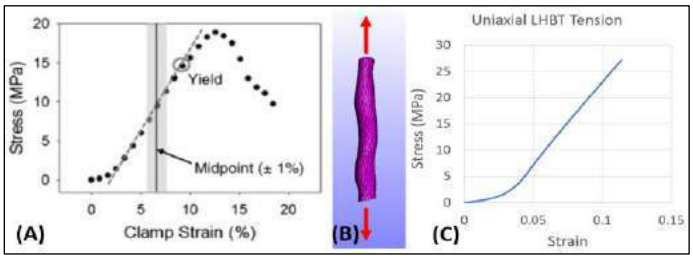

Figure 3: (A) Experimental data by Kolz et al.[9], and (B) and (C) show the FEBio setup and stress-strain data.

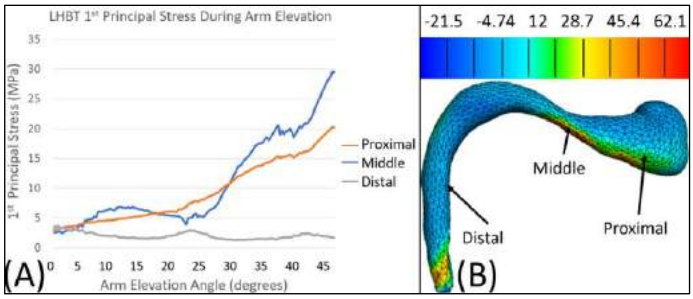

Figure 4: (A) Stresses in the LHBT during arm elevation and (B) the corresponding locations and a 1st principal stress Map (MPa).

DISCUSSION

An important output of the model was how tensile stress varies throughout the tendon. Graphing 1st principal stress shows that the narrow "Middle" section experiences the highest stress, followed by the "Proximal" section and then the "Distal" section (Figure 4). The regional differences suggest either the need for structural differences throughout the tendon, or relative injury susceptibility. The reason for the stress differences could be from varying cross-sectional areas or varying types of loads applied (bending or pure tension). This information along with further enhancement of the model can play a significant role in identifying failure mechanisms of the LHBT. Another important output of the model was the qualitative observation of how the tendon's geometry and biceps loads affect the behavior of the tendon, which can help in identifying patients who are at an increased risk of LHBT injury. Ongoing development of this model will expand upon the quantitative and qualitative findings for improving clinical treatment of LHBT pathologies and more accurately assessing the risk of LHBT injury within overhead athletes and individuals with repetitive overhead shoulder movements.[12]

While the FE model provided promising preliminary results, future work will more meticulously investigate the specific material properties of the THL. Sensitivity analyses will be performed to study the effect of implemented material properties on the stress/strain values and overall behavior of the LHBT. Lastly, more structures and movements will be added to the model to represent native anatomy more realistically.

ACKNOWLEDGEMENTS

The authors acknowledge funding from the National Institutes of Health under Grant No. K01HD042491 and Grant No. R03HD070871-02. The authors acknowledge technical assistance from Elizabeth Gacek and Dr. Justin Staker.

REFERENCES

[1] Earth's Lab, *Earth's Lab*, 2019. [2] Kim, TK et al., *J Bone Joint Surg Am*, 85(1):66-71, 2003. [3] Boileau, P et al., *J Shoulder Elbow Surg*, 13(3):249-57, 2004. [4] Krupp, R et al., *J Orthop Sports Phys Ther*, 39(2):55-70, 2009. [5] Maas, SA et al., *J Biomech Eng*, 134(1):011005, 2012. [6] Jang, SW et al., *Arthroscopy*, 31(11):2073-2081, 2015. [7] McGough, RL et al, *Knee Surg, Sports Traumatol, Arthroscopy*, 3:226-229, 1996. [8] Carpenter, JE et al., *Clin Biomech*, 20(2):162-165, 2005. [9] Kolz, CW et al., *Clin Biomech*, 30(9); 940-945, 2015. [10] Ludewig, PM et al., *J Bone Joint Surg*, 91(2):378, 2009. [11] Gramstad, GG et al., *Int J Shoulder Surg*, 4(1): 8–14, 2010. [12] Chalmers, PN et al., *Clin Sports Med*, 35(1):163-179, 2016.

COUPLING NO-CGMP-PKG CHEMICAL PATHWAY WITH HEMODYNAMICS MODEL TO UNDERSTAND REGULATION OF VASCULAR TONE IN THE PULMONARY VASCULAR TREE

Haritha N. Mullagura (1), Vasilina Filonova (2), Hamidreza Gharahi (2), C. Alberto Figueroa (2,3) Seungik Baek (1)

(1) Department of Mechanical Engineering
Michigan State University
East Lansing, Michigan, USA

(2) Department of Surgery
University of Michigan
Ann Arbor, Michigan, USA

(3) Department of Biomedical Engineering
University of Michigan
Ann Arbor, Michigan, USA

INTRODUCTION

Pulmonary arterial hypertension (PAH) is a disease associated with an elevated mean pulmonary arterial pressure. Sustained vasoconstriction is one of the hallmarks of PAH. Thus, the treatments of PAH include arterial vasodilators such as PDE5 inhibitors, soluble guanalyte cyclase stimulators, calcium channel blockers along with inhalation of nitrous oxide (NO). To understand the mechanics and degree of effectiveness of these pharmacological treatments, it is necessary to quantitatively estimate the impact of various chemical pathways on modulation of active tone of vascular smooth muscle cells (VSMC). To do so, we aim to develop a biochemo-mechanical model that couples the NO-cGMP-PKG chemical pathway with a hemodynamics model.

The NO-cGMP-PKG chemical pathway has been extensively studied in the last couple of decades. The nitric oxide in the NO-cGMP-PKG pathway is an important cellular signaling system for the regulation of VSMC relaxation. Several mathematical models have been developed to represent the chemical kinetics of this pathway. These models predict the concentrations of different signaling compounds over a time period for a NO-driven signal transduction. [Klinger et al 2007].

Although there have been extensive efforts to model either the hemodynamics or the NO-cGMP-PKG pathway, little attention has been paid to the coupling between the two. There are still many unanswered questions regarding the PAH treatment such as why only some patients respond to inhaled NO treatment, why infants respond differently than adults, etc. To be able to tackle these questions, we need quantitative model and coupling chemical pathway and hemodynamics.

With previous knowledge about change in smooth muscle tone with different concentrations of signaling compounds and quantitative knowledge on the chemical pathway, we aim to develop an integrated model to estimate the mechanical response of vessels in a pulmonary arterial tree. We use our model to study short-term adaptations of pulmonary arteries following pressure fluctuations and NO inhalation. A better understanding of chemical pathways of VSMC and their impact on hemodynamic responses will lead to improved therapies for PAH.

METHODS

A homeostatic optimization framework was used to establish the baseline characteristics of a healthy pulmonary arterial tree [Filonova et al 2020]. In the model, a homeostatic state in the distal arterial tree was determined based on an extension of Murray's law and steady state hemodynamics. Then, each vessel was equipped with a chemical kinetic model of the NO-cGMP-PKG pathway.

Homeostatic Baseline for Pulmonary Vasculature: The homeostatic optimization is a framework to estimate the homeostatic morphometric (e.g, diameters), structural (e.g, thickness), and hemodynamics (e.g., wall shear stress) properties of an arterial tree by minimizing the energy dissipation under the constraint of mechanical equilibrium. In this framework, the mechanics of each vessel are represented using a constrained mixture model, which accounts for the response of individual constituents: elastin, collagen, and VSMCs [Filonova et al 2020]. The homeostatic optimization in the distal arterial tree is determined at steady state hemodynamics and chemical equilibrium of the NO-cGMP-PKG pathway.

Hemodynamics: We consider the pulmonary arterial tree as a 1D bifurcating network, where each vessel is characterized by its radius and length. The steady state hemodynamics in the arterial tree are computed using Poiseuille flow for each vessel, flow conservation and pressure continuity for each bifurcation, and boundary conditions at the tree inlet and outlets.

NO-cGMP-PKG Pathway Model: We extend Yang's model [Yang et al 2005] to quantify blood flow through the pulmonary tree, resulting from a step change of inlet pressure or inhaled NO. This kinetic chemical model is connected to the mechanical model through a linear relation between [NO] concentration and stress in the blood vessels as shown in Figure 1b. In summary, change in [NO] concentration causes a reduction in $[Ca]^{2+}$ concentration in the SMCs, which further induces change in active tone (Figure 1).

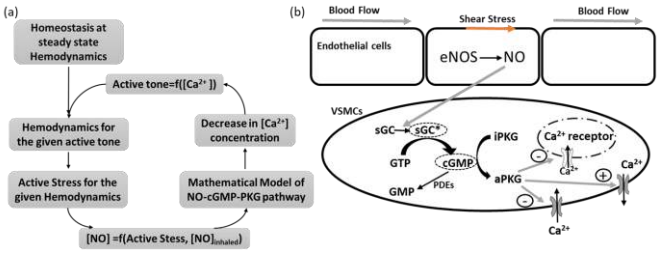

Figure 1. a) Information exchange inside biochemo-mechanical model that account for hemodynamics, tissue homeostasis and NO-CGMP-PKG pathway. b) Series of chemical reactions that occur inside VSMCs to an external stimuli.

The hemodynamics and chemical pathway models are solved iteratively until convergence of chemical and mechanical parameters. The entire system is solved marching forward in time to describe responses to different stimuli.

RESULTS

The results of biochemical part of the model were compared with the Yang's model as shown in Figure 2. The plots in Figure 2 give concentrations of chemical compounds involved in NO-cGMP-PKG pathway changing with time following a step change in the input flux of nitrous oxide at time t=0s. Panel (a) and (b) represents [cGMP] concentration and its rate of production (v_p) and decomposition (v_d). Panel (c) and (d) represents concentration of different sGC forms. The model is in agreement with the previously verified mathematical model.

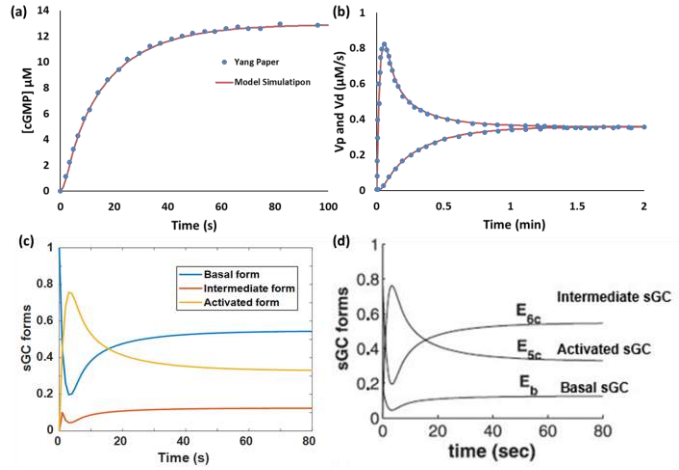

Figure 2. Comparison of Biochemical part of the model with Yang's model [Yang et al 2005] for similar [NO] stimuli. a) Change in concentration of cGMP and b) Rate of production and decomposition of cGMP. Change in concentration of different forms of sGC: c) in the current model d) in the Yang's model.

Figure 3 shows the relative change in the diameter and active tone as a result of a step change in pressure (a) and (b) and nitrous oxide concentration (c) and (d). Vessel diameter across different generations increased by 5-15% when pressure was increased 1.5 times. Similar trend was observed when the inlet [NO] was 200nM, although the maximum diameter change was 5% as shown in panel (d). Active tone changed from the homeostatic value (~70%) by almost 40% and 30% for change in pressure and inlet [NO] concentration respectively.

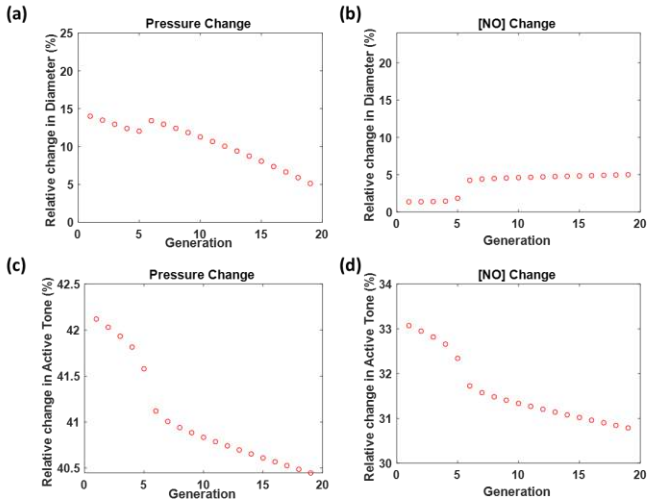

Figure 3: Relative change in the diameter and active tone of blood vessels for different generations of arterial tree: a) & c) when inlet pressure is changed to 1.5 times the initial pressure: b) & d) when there is a step change in [NO] concentration of 200nM.

DISCUSSION

As Figure 2 suggests, our model accurately replicates a previously verified mathematical model to represent the NO-cGMP-PKG chemical pathway. Therefore, this model can be further extended to study biochemo-mechanical coupling in the pulmonary circulation.

From Figure 3 we observe that with changes in inlet pressure, the diameter in each blood vessel increases as expected response by the blood vessels. In the case of spike in the [NO] concentration (200 nM) in the pulmonary blood vessels, a very small dilatory response is observed from the pulmonary vasculature.

As this biochemo-mechanical model has shown promising preliminary results and is a good representative of the actual pulmonary vasculature, we plan to extend this model to study responses in PAH in the near future.

ACKNOWLEDGEMENTS

This work was supported by the National Institute of Health under Grant U01 HL135842.

REFERENCES

[1] Klinger JR, 'The nitric oxide/cGMP signaling pathway in pulmonary hypertension', Clin Chest Med, 2007.

[2] Filonova et al, 'A Multiscale Framework for Defining Homeostasis in Distal Vascular Trees: Applications to the Pulmonary Circulation', arXiv preprint arXiv:2001.04880, 2020.

[3] Yang et al, 'Mathematical modeling of the nitric oxide/cGMP pathway in the vascular smooth muscle cell', Am J Physiol Heart Circ Physiol, 2005.

TRANSCRIPTIONAL REGULATION OF CONNEXIN 40 AND THE ROLE OF GAP JUNCTIONS IN THE ANTI-INFLAMMATORY EFFECT OF EMPAGLIFLOZIN TO GLYCOCALYX DEGRADATION

Marc-Antoine Campeau (1), Richard Leask (1,2)

(1) Department of Chemical Engineering
McGill University
Montreal, QC, Canada

(2) Montreal Heart Institute
Montreal, QC, Canada

INTRODUCTION

Following the EMPA-REG OUTCOME trial, sodium-glucose cotransporter 2 inhibitors (SGLT2i), a class of drug in the treatment of type 2 diabetes, rapidly gained interest as the treatment with empagliflozin (Jardiance™) showed significant reductions in the rate of hospitalization for heart failure and cardiovascular deaths, suggesting a cardiovascular protective effect provided by SGLT2i [1]. Subsequent studies and clinical trials demonstrated protective effects against the complications associated with atherosclerosis [2], heart failure [3] and ischemia-reperfusion injury [4] in non-diabetic conditions, indicating a possible pleiotropic effect independent of glycosuria. The onset of the observed effects suggests the implication of underlying cellular mechanisms preventing vascular dysfunction [5].

In recent years, the endothelial glycocalyx (GCX) has been recognized as a marker of vascular health with its disruption resulting in increased inflammation and impaired vasodilation response to flow, hallmarks of endothelial dysfunction [6]. Hyperglycemia has been shown to damage the endothelial GCX [7]. Heparan sulfate (HS) being one of the main components of the endothelial GCX, plays a crucial role in the shear-mediated regulation of endothelial cell (EC) functions.

We previously showed that treatment with EMPA alleviate the EC dysfunction caused by the enzymatic degradation of HS [8]. The present study aims at better understating the effects of EMPA on ECs and if the GCX acts as a mediator in the response through mechanotransduction.

METHODS

Cell culture and shear experiment. Human abdominal aortic ECs were cultured statically or under flow (10 dyn/cm^2) in 3D tubular cell culture models for 24h. Cells were stimulated with TNF-α (10 ng/mL) and treated simultaneously or not with empagliflozin (50 uM). Heparinase III (0.1 U/mL) was used to enzymatically degrade HS before (preDEG) or during flow exposure (DEG).

Adhesion assay. Leukocyte-like inflammatory cells (NB4) were cultured in suspension and stimulated with all-trans retinoic acid 48h prior to the assay. Inflammation of the TNF-α-treated ECs was assessed following 24h of flow culture by exposing the monolayer to circulating NB4 cells under low shear (1 dyn/cm^2). The firm adhesion of NB4 to the ECs were visualized and numbered under light microscopy.

Permeability assay. Paracellular permeability was quantified with a modified XPerT assay [9]. µ-Slide VI 0.4 plates were coated with biotinylated collagen and seeded with ECs to form a confluent monolayer. Following TNF-α/EMPA treatment, ECs were incubated with avidin Alexa 488. The paracellular permeability was quantified by measuring the covered area of the green channel signal.

Protein quantification. Quantification of the protein levels of phospho-eNOS (Ser1177), eNOS and ICAM-1 was performed through immunoblotting to characterize the endothelial inflammatory response. Following static or flow culture, ECs were lysed *in situ* to collect proteins. Protein samples were separated and transferred on nitrocellulose membranes. Chemiluminescent signal was used to evaluate the relative expression by densitometry.

Global transcriptional regulation study. The transcriptional changes after 24h was examined with a transcriptome analysis. RNA was extracted *in situ* with QIAGEN RNeasy Plus Micro kit. The concentration and RIN of each sample was verified prior to hybridization on a Clariom™ S human microarray chip. Results were analyzed with the Transcriptome Analysis Console software 4.0.2.

RESULTS

EMPA normalized the increased adhesion caused by HS degradation. Adhesion of NB4 cells was significantly reduced by

empagliflozin after 24h (Fig. 1). HS degradation (preDEG and DEG) resulted in significantly more NB4 cell adhesions. In both cases, treatment with EMPA normalized the adhesion, indicating a decreased inflammatory response from the TNF-α-treated ECs. The effect observed under sustained HS degradation suggests that HS integrity does not play a role in the anti-inflammatory effect provided by EMPA.

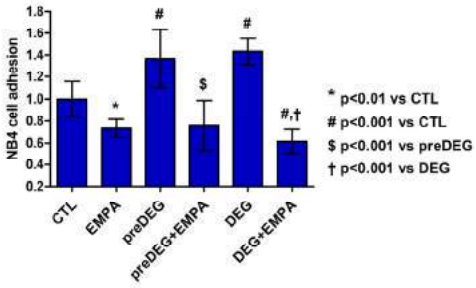

Figure 1: NB4 cell adhesion assay. EMPA reduced the number of adhered NB4 cells to TNF-α treated ECs under HS degradation.

EMPA had no impact on the TNF-α induced increase of permeability *in vitro.* TNF-α significantly increased the avidin 488 signal at cell-cell junctions indicating increased paracellular permeability in both static and flow culture after 24h. The increased level of permeability was unaffected by EMPA.

EMPA does not restore shear-induced eNOS activation or reduce ICAM-1 expression. TNF-α reduced eNOS expression in all conditions while EMPA nor HS degradation had an impact. Phospho-eNOS levels were similarly reduced suggesting impaired eNOS activation. Again, no significant changes were induced by EMPA or HS degradation (Fig. 2A). TNF-α induced the expression of ICAM-1 to similar levels in all conditions tested (Fig. 2B).

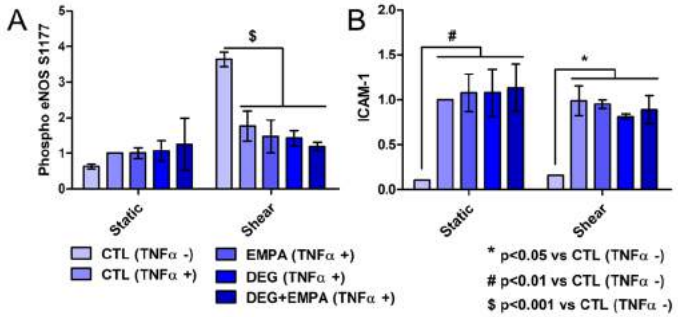

Figure 2: Phospho-eNOS (A) and ICAM-1 (B) protein levels. HS degradation and EMPA had no effect on the impairment of phospho-eNOS and the increase of ICAM-1 induced by TNF-α.

The shear-induced GJA5 expression is partially restored by EMPA under HS degradation. HS degradation and EMPA treatment significantly affected the expression of GJA5 (gap junction alpha 5; connexin 40). Shear induced an upregulation of GJA5 (CTL vs CTL S). HS degradation impaired the shear-induced regulation of GJA5 while EMPA partially restored normal expression, resulting in a 5-fold increase between DEG and DEG-EMPA (Fig. 3).

DISCUSSION

Evidence from *in vitro* and *in vivo* studies suggest that vascular mechanisms would be in part involved in the protective effect of SGLT2i. As EC dysfunction is pivotal in the early progression of cardiovascular diseases, we previously hypothesized and showed that endothelial dysfunction caused by a degraded glycocalyx can be restored by EMPA [8]. The results of this work offer more information

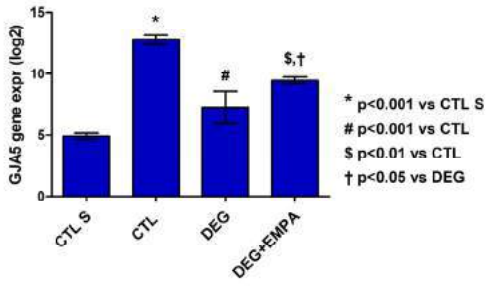

Figure 3: Transcriptional level of GJA5. HS degradation decreased the expression of GJA5 while EMPA partially restored the normal expression compared to the shear control (CTL).

regarding the possible cellular mechanisms involved.

HS degradation triggers a pro-inflammatory response with impaired nitric oxide (NO) regulation, increased adhesion molecule expression, vascular permeability and inflammatory cell migration. It remains unclear if SGLT2i can impact the regulation of adhesion molecules. Ortega et al. [10] showed an attenuation of ICAM-1 expression, NF-kB signaling and leukocyte adhesion in EMPA-treated ECs whereas others reported no significant changes in expression of adhesion molecules [11]. Our results suggest that the reduction in NB4 cells caused by EMPA cannot be attributable to a reduction in ICAM-1 expression or a reduction in permeability.

Normal EC-dependent vasodilation through NO release has been shown to be restored by SGLT2i treatment in *ex vivo* experiments [12]. Although NO bioavailability appeared to be partially restored by EMPA *in vitro* [11], the recovery of the shear-induced eNOS Ser1177 activation may not be involved in the reduction of EC inflammation.

Taken together, our results suggest that the reduced inflammatory response provided by EMPA may stem from different cellular mechanisms than the recovery of the shear-induced NO release and the regulation of immune cell migration associated with an intact GCX.

Interestingly, gap junction intercellular communication (GJIC) has been related to the GCX integrity [13] and to the regulation of eNOS [14] and leukocyte adhesion [15]. Further experiments will aim at characterizing the GJIC of EMPA-treated cells and to better understand how changes in the expression or function of connexin 40 can result in the reduction of EC inflammation.

ACKNOWLEDGEMENTS

We would like to thank Boehringer Ingelheim who kindly provided the empagliflozin and Genome Quebec for their expression analysis services. This study is supported by NSERC 2018-06161.

REFERENCES

[1] Zinman B, et al. New England Journal of Medicine. 2015;373:2117. [2] Han JH, et al. Diabetologia. 2017;60:364. [3] Connelly KA, et al. JACC Basic to translational science. 2019;4:27. [4] Andreadou I, et al. Frontiers in physiology. 2017;8:1077. [5] Uthman L, et al. Frontiers in Physiology. 2018;9:1575. [6] Tarbell JM, et al. Annual Review of Biomedical Engineering. 2014;16:505. [7] Nieuwdorp M, et al. Diabetes. 2006;55:480. [8] Cooper S, et al. Molecular and Cellular Biochemistry. 2019;459:121. [9] Dubrovskyi O, et al. Laboratory investigation; a journal of technical methods and pathology. 2013;93:254. [10] Ortega R, et al. Arteriosclerosis, Thrombosis, and Vascular Biology. 2019;39:1614. [11] Uthman L, et al. Cellular physiology and biochemistry. 2019;53,5:865. [12] Steven S, et al. Redox biology. 2017;13:370. [13] Mensah SA, et al. PloS one. 2017;12:e0186116. [14] Ebong EE, et al. Pflügers Archiv - European Journal of Physiology. 2013;465:1293. [15] Chadjichristos CE, et al. Circulation. 2010;121:123.

PID CONTROLLED, FINITE-ELEMENT SIMULATION OF BIPOLAR RADIOFREQUENCY ABLATION OF PORCINE SPINAL MUSCLE

Hanife Tugba Kumru (1), Anilchandra Attaluri (2), Daniel H. Cortes (3)

(1) Department of Mechanical Engineering, The Pennsylvania State University, State College, PA, USA

(2) Department of Mechanical Engineering, School of Science, Engineering, and Technology, Penn State, Harrisburg, PA, USA

(3) Department of Mechanical Engineering, The Pennsylvania State University, State College, PA, USA

INTRODUCTION

Approximately 15% to 45% of the chronic back pain cases involve facet joints [1]. Monopolar radiofrequency ablation (RFA) of the medial branch of the dorsal rami is widely used and effective to reduce facet joint pain. In this procedure, an electrode is placed near or at the medial branch and a radiofrequency current is applied to the tissue. Thermocoagulation of the medial branch blocks pain signals originating from the facet joint [2]. Unfortunately, this procedure also denervates the multifidus muscle. Denervation causes atrophy and fat infiltration of the multifidus muscle, and accelerated intervertebral disc degeneration, which are of great concerns [3]. Therefore, monopolar RFA is beneficial in the short time, but multifidus dysfunction may contribute to the degeneration cascade of other structures of the spine and may lead to other pain mechanisms in the long term. To avoid multifidus muscle denervation, RFA can potentially be applied down-stream at the articular branch instead of the medial branch. However, articular nerves are smaller and a new RFA procedure would require a more precise control of the lesion size. Bipolar RFA, in which two electrodes are placed into the tissue, is preferred over monopolar RFA. In bipolar RFA, radiofrequency current runs from one electrode to the other. Therefore, the size and shape of the ablated region can be controlled by the location and distance between electrodes. Bipolar RFA has other advantages in terms of minimal energy loss which causes faster ablation process, and decreased risks of skin burns from ground pads [4]. Clinical RFA devices (radiofrequency generators) keep the temperature of the electrodes constant during the ablation procedure by dynamically controlling the voltage applied to the electrodes [5]. The objective of this study is to develop a multiphysics finite element model of the bipolar ablation process of ex-vivo tissues with a dynamic-controlled feedback loop for temperature of the electrodes to simulate clinical RFA procedures.

METHODS

a. FEM Analysis-COMSOL

Bioheat Transfer and Electric Current modules of COMSOL Multiphysics® were used to couple the thermal and electrical effects of the RFA process. The model consisted of a cylinder of homogeneous muscle tissue (5 mm in diameter, 15 mm in height) with bipolar electrodes with an active length of 10 mm and diameter of 0.8 mm. The initial temperature of the muscle tissue was set to 37 °C and the initial voltage of the entire model was set to zero. One of the electrodes was modeled as ground (V=0) while voltage of the other electrode was controlled by using a PID controller to keep the electrode temperature ($T_{electrode}$) at a target value (T_{target}). Lastly, the temperature error

$$e(t) = T_{target} - T_{electrode} \tag{1}$$

was used to control the voltage of the active electrode by the following governing equation:

$$V(t) = K_P\, e(t) + K_i \int_0^t e(\tau) d\tau + K_d \frac{d}{dt} e(t), \tag{2}$$

where V is the applied voltage (V). For this simulation, the optimal PID parameters were found as K_p=2, K_i=1 and K_d=0 by parametric sweeping. In this study, the average domain temperature of the electrode (T_{target}) was set to 60 °C. Only an active tip of the electrode was modeled to make the model simpler and faster in solving the bioheat equation. Blood perfusion rate (w_b) in the bioheat equation was not considered since model is focused on simulating the ablation process ex-vivo. A finer mesh comprising tetrahedral elements was generated to get more sensitive temperature change around the electrodes (Figure 1).

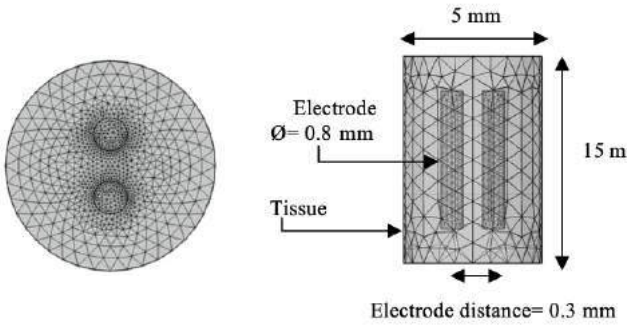

Figure 1: Model dimensions and mesh distribution.

b. Electrical Conductivity Measurements

The electrical conductivity of the tissue has been shown to play a critical role on the simulation of the RFA. The electrical conductivity of porcine spinal muscle was measured with an impedance analyzer (Agilent 4294A). Muscle tissues was obtained from a local abattoir. A sample from the multifidus muscle of with an approximate thickness of 0.3 cm, length of 4.3 cm and width of 4.8 cm was dissected. Copper electrodes were placed on each side of the sample in a vacuum sealed bag, then the bag was placed in a water bath. Measurements of electrical conductivity were performed at several temperatures from room temperature to 80 °C for and a frequency 460 kHz.

c. Other material properties and parameters

Other material properties needed for the simulation of the RFA process were obtained from the literature [7-9]. To determine the optimal parameters of the PID controller, a parametric analysis was performed.

Table 1. Material Properties Used in FEM Model

Region	Material	k[W/mK]	σ[S/m]	c[J/kgK]	ρ[kg/m^3]
Tissue	Muscle	tc(T)	ec(T)	3421	1090
Electrode	Ni-Ti	18	10^8	840	6450

RESULTS

The electrical conductivity of the tissue sample linearly increased from room temperature up to 70 °C and was followed by a decreasing trend for higher temperatures. The measurement readings were fitted into a 5th order polynomial model with R squared value of 0.9997 (Figure 2). The 5th order polynomial describing the conductivity dependency is:

$$ec(T) = -1.31\times10^{-10}\,T^5 + 2.18\times10^{-7}T^4 - 1.48\times10^{-4}\,T^3 + 5.12\times10^{-2}T^2 - 8.92\,T + 627. \quad (3)$$

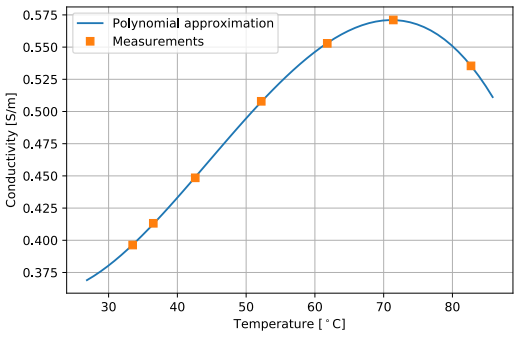

Figure 2: Electrical conductivity change of a muscle tissue at different temperatures at 460 kHz.

An example of the temperature distribution around the electrode can be seen in Figure 3a. The time passed to reach the target temperature of 60 °C has been found to be less than 10 seconds (Figure 3b). During this time, the applied voltage increases initially and reaches a maximum value then starts decreasing to keep the electrode temperature constant. The electrode domain temperature for various PID parameters can be seen in Figure 3b.

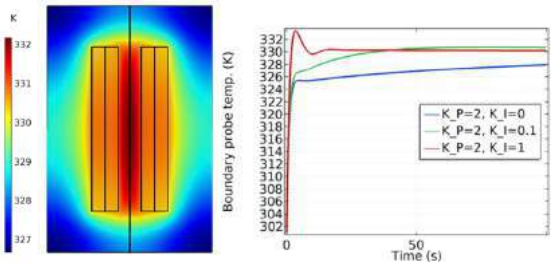

Figure 3: (a) Temperature distribution around the electrode, (b) probe temperature change for different PI parameters.

DISCUSSION

A FEM model of the PID-controlled simulation of the bipolar RFA procedure was developed. The values of electrical conductivity measurements are similar to those reported in [7] and references therein. The linear increase and subsequent drop in electrical conductivity has also been reported for muscle tissue [10]. COMSOL Multiphysics modules have been used to accurately simulate RFA process in several tissues including liver, muscle and kidney. However, to the best of our knowledge, this is the first report of bipolar RFA simulation that includes a PID controller for the voltage of the electrodes. Adding active control of electrode voltage is necessary to accurately simulate the RFA performed by clinical systems. Most RFA systems maintain a constant electrode temperature for a period of time. During this time, the surrounding tissues experience an increased temperature for a period of time that causes the desired targeted tissue damage. Following the same process as clinical devices is extremely important to accurately estimate the size of the ablated region. This is expected to be a critical step for future studies exploring new methods RFA of spinal nerves. As our ongoing work, the proposed method will be applied in vivo in a porcine animal model and to perform clinical trials to evaluate its effectiveness to reduce pain and decrease muscle dysfunction.

REFERENCES

[1] Kavita, N., et al., Pain physician, 11(1), 67-75, 2008.
[2] Smuck, M., et al., The Spine Journal, 15(6), 1415-1421, 2015.
[3] Dreyfuss, P., et al., PM&R, 1(8), 719-722, 2009.
[4] Osaki, Y., et al., Journal of gastroenterology, 48(7), 874-883, 2013.
[5] Kandala, S. K., et al., International Journal of Hyperthermia, 2018.
[6] Singh, S., & Repaka, R., Int. J. of Hyperthermia, 33, 122-34, 2017.
[7] Gabriel C., AL/OE-TR-1996-0037, 1996.
[8] Shao, Y. L., et al., Appl. Thermal Engineering, 116, 623-35, 2017.
[9] Duck, F. A., Academic press, 2013.
[10] Ryan, T. P., et al., S., ASME-Publications-HTD, 355, 167-172, 1997.

A NOVEL DYNAMIC BLALOCK–TAUSIG SHUNT REGULATOR: AN IN VITRO STUDY

Milad Samaee (1), Subhadhara Shashidharan (2,3), Kevin O. Maher (3), Ajit Yoganathan (1), Lakshmi Prasad Dasi (1)

(1) Biomedical Engineering
Georgia Institute of Technology
Atlanta, GA, USA

(2) Department of Surgery
Emory University School of Medicine
Atlanta, GA, USA

(3) Children's Healthcare of Atlanta (CHOA)
Atlanta, GA, USA

INTRODUCTION

The modified Blalock–Tausig shunt (BTS) is an aortic to pulmonary shunt, which is implanted as part of a palliative procedure for neonates with congenital heart disease to supply blood flow to the pulmonary arteries [1]. The size selection of the shunt is based on the patient's weight, which is in the range of 3-5 mm [2]. Although the outcomes of congenital heart disease surgery have improved, the rate of mortality is still excessive, and those with the BTS remain at high risk for sudden death. Imbalances in blood flow to the body or lungs contributes to this [3], with blood flow during diastole compromising coronary perfusion, referred to diastolic run-off. The BTS has been in use for over 40 years with no significant change or improvement in the technology to date.

The main goal of this study is to develop a novel device to dynamically control shunt flow by expanding a soft balloon around the shunt to restrict excessive flow to the pulmonary artery in a dynamic and programmable manner. The device will control diastolic run-off by closing the shunt during diastole. The future goal is developing a device as a sub-cutaneous implant that is wirelessly chargeable and programmable for better clinical management of patients with BTS.

METHODS

The developed device consists of an expandable balloon with a pre-existing resistance to a 5 mm PTFE vascular graft, extension tubing, and a controllable linear actuator. The balloon is a two-layer hollow cylinder with soft silicone-based material for the inner surface and a stiff (but bendable) material for the outer side. The space between the inner and outer faces is filled with water and is connected to a controllable linear actuator through a semi-rigid extension tubing. In such a way, the cylinder can only expand from the inner layer, which is in contact with a PTFE vascular graft and can control the shunt's cross-section area. As proof of concept, the device prototype is tested on a shunt in an *in vitro* circulation simulator setup (heart rate = 60 bpm), as shown in Figure 1.

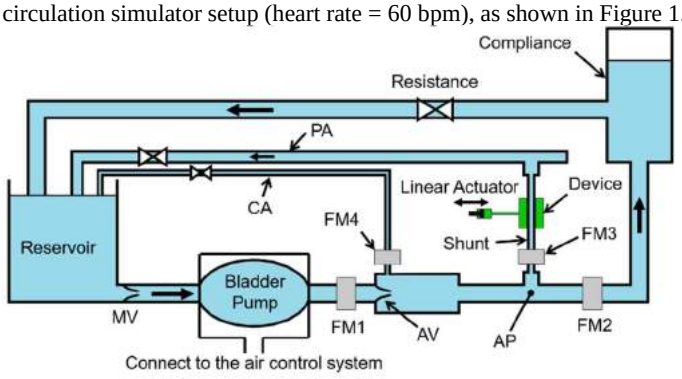

Figure 1: Flow setup. AV: Aortic valve, MV: Mitral valve, PA: pulmonary artery, CA: Coronary artery, FM: Flowmeter.

The controllable linear actuator pressurizes the balloon hence the amount of fluid in the balloon dictates a certain level of resistance to the shunt. This device's concept is very similar to an on/off valve. It allows shunt flow during systole and minimizes blood flow through the shunt during diastole to maintain diastolic and hence coronary perfusion pressure. Instantaneous aortic pressures is recorded as a function of balloon resistance. Dynamic aortic flow, coronary flow, and shunt flow are measured. The system response of the linear actuator coupled with the shunt is characterized. The balloon dynamically controls the shunt resistance hence the orifice diameter of the shunt, d, is changing during the cardiac cycle. Therefore, the balloon to shunt diameter ratio, d/D, can be varied from 0 (fully occluded) to 1 (fully open). The waveform of the d/D ratio in the cardiac cycle will be determined.

We can derive optimum shunt resistance values by having a target aortic flow and the actual aortic flow after shunt implantation. **Figure 2** shows an ideal d/D ratio curve (yellow curve) and the optimum d/D ratio curve (green curve) versus time. A pre-existent resistance is applied to the shunt to control the maximum flow (the horizontal dash line in Figure 3, where d/D < 1) and regulate an appropriate Q_P/Q_S. In reality, as infants grow, the shunt flow needs to increase to satisfy the normal Q_P/Q_S. As a result, we propose to have a larger shunt, and physicians adjusts Q_P/Q_S by changing the pre-existent resistance in patient checkups.

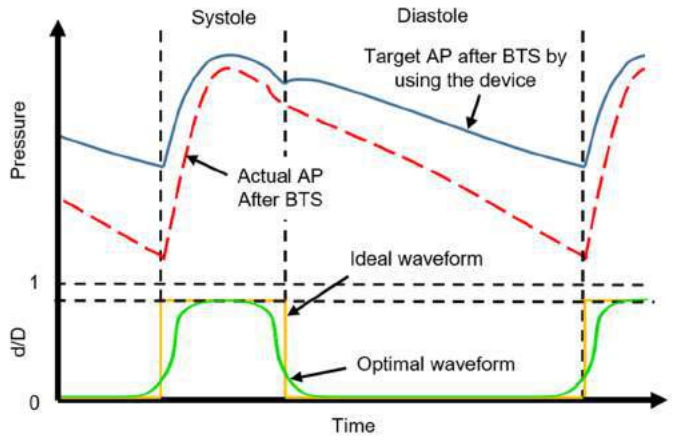

Figure 2: Achieving optimal device input waveform. AP: Aortic pressure

In this study, we applied an ideal waveform (yellow curve in **Figure 2**) and further optimization will be investigated.

RESULTS

All the pressure and flow rate results are displayed in **Figure 3**. Mean Aortic pressure was 78.83±0.92 mmHg and 72.51±0.60 mmHg for the cases with and without using the device. Peak flow rate was 11.19±0.15 L/min and 12.85±0.15 L/min for the cases with and without using the device. Mean right coronary flow rate was 11.59±0.09 mL/s and 10.84±0.07 mL/s for the cases with and without using the device. Mean shunt flow rate was 5.75±1.19 mL/s and 12.63±0.07 mL/s for the cases with and without using the device.

DISCUSSION

This study was conducted as a proof of concept for developing a novel flow regulator device to help BTS patients. Results show that pinching the shunt by the device during diastole leads to drastically drop in shunt flow (**Figure 3D**). As a consequence, the aortic pressure increases during diastole (**Figure 3A**) as we expected in **Figure 2**. Increase in aortic pressure during diastole results in having higher mean coronary perfusion up to 7% as shown in **Figure 3C**. This preliminary data shows a significant improvement in coronary perfusion by using the device on the BTS. However, in this study we used an ideal square waveform to control the shunt flow (yellow waveform in **Figure 2**). As a future work, the actuator's cyclic behavior will be determined for optimal flow control defined as therapeutic pulmonary to system flow ratio with minimal diastolic run-off.

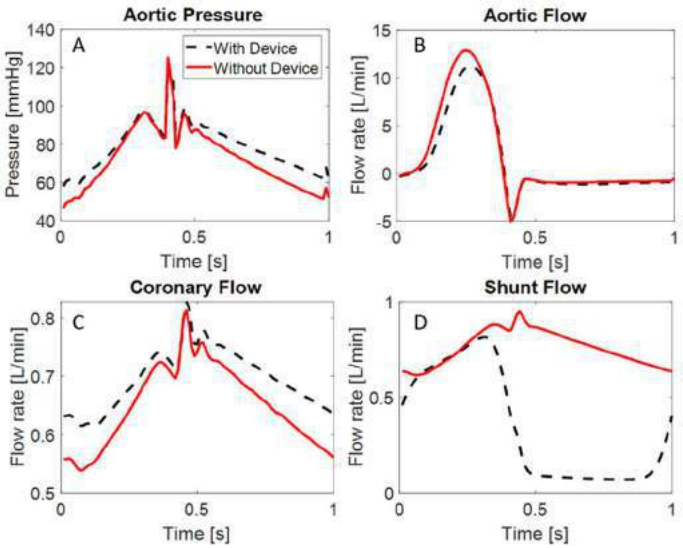

Figure 3: Pressure and flow curves before and after using the device on the BTS graft

Ideally, the shunt should be closed during diastole to avoid run-off; however, this will not be achievable due to possible damage to the shunt and possible rupture. Moreover, the risk of blood clotting will be increased due to stop and start the blood flow. As a result, the maximum possible resistance (d_{min}) needs to be investigated. During systole, the device needs to be open, and the shunt must have a minimum resistance. According to that, we will develop a simple *in vitro* loop and run pulsatile pig blood flow in the shunt to investigate the shunt thrombosis. By having the device around the shunt, we will apply dynamic resistance to the shunt. The amount of resistance and duration of pinching will be characterized by thrombosis formation. The maximum resistance and the optimum duration of resistance (without damaging to the blood) will be documented.

In this study, we used a 5 mm PTFE vascular graft and we used the device on it. As a result, by using the device we will end up with less shunt flow (**as shown in Figure 3D**) compared to the shunt without using the device. The future goal of this study is using a 3-3.5 mm shunt without using the device and compare the results with a 5 mm shunt with using the device. In this case the shunt flow will be reserved to keep the Q_P/Q_S.

REFERENCES

[1] Kiran, U., et al., *Ann Card Anaesth*, 20(3): 323-330, 2017.
[2] Guzzetta, N.A., et al., *Ann Thorac Surg*, 96(1): 176-82., 2013.
[3] Dirks, V., et al., *Eur J Cardiothorac Surg*, 44(6): 1096-102, 2013.

EFFECT OF STIMULUS WAVEFORM ON TRANSCRANIAL MAGNETIC STIMULATION METRICS IN PROXIMAL AND DISTAL ARM MUSCLES

Christopher S. Lynch (1), Thibault Roumengous (1), Carrie L. Peterson (1)

(1) Department of Biomedical Engineering
Virginia Commonwealth University
Richmond, VA, USA

INTRODUCTION

Transcranial magnetic stimulation (TMS) is useful for modulating neural activity when applied repetitively or assessing neural pathway excitability when applied in single or dual pulse paradigms [1]. TMS devices generate one of two types of stimulus waveforms, monophasic or biphasic, which have dissimilar neuronal activation and therefore different impacts on stimulation characteristics [2]. To date, research on the effects of waveform has been conducted on upper limb distal muscles, such as the first dorsal interosseous (FDI). Research in the FDI has shown greater efficacy in the monophasic stimuli (when the induced brain current is in the posterior-anterior direction) demonstrated via reduced motor threshold's (MTs) [2]. This is likely a result of the 2nd phase in biphasic stimulation as the 2nd phase not only reduces the activation time and thus the effectiveness of the initial phase, but activates different neurons that have different sensitivity to each current direction [2]. Additionally, FDI research has shown that MTs and motor evoked potential's (MEPs) are inversely correlated due to their role in measuring intrinsic and synaptic plasticity, respectively [3]. However, the FDI has more available motor neurons than the biceps brachii (BB) at equivalent force levels [4]. Therefore, conclusions regarding neuroplastic effects drawn from the numerous TMS studies using upper limb distal muscles may not necessarily apply to other muscle groups, particularly upper limb proximal muscles. This presents a clinical need as TMS is increasingly being utilized for neurorehabilitation as an adjunct to conventional physical therapy, especially spinal cord injury (SCI) which affects entire extremities [5].

The purpose of this study is to determine the effect of TMS waveforms (monophasic vs biphasic) on important TMS metrics and determine if muscle groups (i.e. upper limb proximal vs distal) have any effect on these outcome metrics. We hypothesize that monophasic stimulation will result in lower MTs, both resting MT (RMT) and active MT (AMT), compared to biphasic [2], however the opposite will occur for normalized MEPs (nMEPs) resulting in greater nMEPs for monophasic compared to biphasic stimulation, for both muscles [3]. Furthermore, we hypothesize that an upper limb proximal muscle (BB) will have statistically different MTs, RMT and AMT, as well as nMEPs compared to the upper limb distal muscle (FDI) for both waveforms.

METHODS

Experimental Set-up: Ten individuals aged 25.0 ± 3.22 years (3 female, 7 male) were recruited for this study which was approved by the Institutional Review Board (IRB) at Virginia Commonwealth University. Surface electromyogram (EMG) electrodes were located over the primary target muscles (BB and FDI) before determining the cortical hotspot, maximum voluntary contraction (MVC), RMT, and AMT. TMS stimulation was applied via a Magstim® BiStim^2 stimulator (monophasic) and Magstim® Super Rapid^2 Plus^1 stimulator (biphasic), both via a Magstim® D70 Alpha flat (uncoated) figure-eight coil. The coil was oriented similarly for each waveform (i.e. perpendicular to the central sulcus) as to induce a biphasic posterior-anterior/anterior-posterior (PA/AP) current and a monophasic PA current in the motor cortex. RMT was determined as the lowest stimulus intensity that induced MEPs of ≥ 50 μV in at least 5 of 10 consecutive stimuli with the target muscle fully relaxed. With visual feedback provided, participants sustained an isometric contraction of 20 ± 2.5% MVC of the target muscle during which the AMT was determined as the stimulus intensity that elicited a MEP ≥ 200μV in at least 5 of 10 consecutive stimuli. Lastly, 10 single pulse MEPs were recorded at 120% RMT for each waveform.

Data and Statistical Analysis: Statistical analyses were performed using MATLAB (MathWorks (2020)) and GraphPad Prism. RMT, AMT, and nMEPs were compared between monophasic and biphasic waveforms using a two sampled t-test with unequal variance. Additionally, RMT, AMT, and nMEPs were compared between BB and FDI using an ANOVA with interactions.

RESULTS

BB RMTs were significantly lower for monophasic (60.1±9.06 %MSO) than for biphasic (84.4±11.02 %MSO) ($p<0.01$). FDI RMTs were also significantly lower for monophasic (48.4±8.2 %MSO) than for biphasic (67.9±11.94 %MSO) ($p<0.01$). BB AMTs were significantly lower for monophasic (39.2±9.3 %MSO) than for biphasic (60.9±11.4 %MSO) ($p<0.01$). FDI AMTs were also significantly lower for monophasic (34.1±11.7 %MSO) than for biphasic (55.5±14.7 %MSO) ($p<0.01$) (Figure 1).

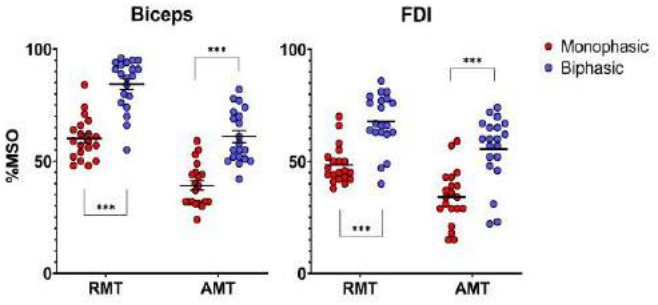

Figure 1: Left: Biceps MTs, are significantly greater for biphasic compared to monophasic. Right: FDI MTs, are significantly greater for biphasic compared to monophasic. Asterisks represent statistical difference ($p<0.01$) and error bars represent standard the error of the mean (SEM).

BB nMEPs present no significant difference between monophasic (6.20±19.55 μV%MVC) and biphasic (6.56±21.38 μV%MVC) ($p=0.88$). However, FDI nMEPs were significantly greater for monophasic (3.02±2.37 μV%MVC) compared to biphasic (2.36±1.91 μV%MVC) ($p=0.01$) (Figure 2).

An ANOVA revealed a statistical difference between BB and FDI for RMT ($p<0.01$) and nMEP ($p<0.01$), however, there was no significant difference for AMT ($p<0.01$). Additionally, there was no significant interaction amongst waveform and muscle for RMT ($p=0.31$), AMT ($p=0.95$), and nMEP ($p=0.65$).

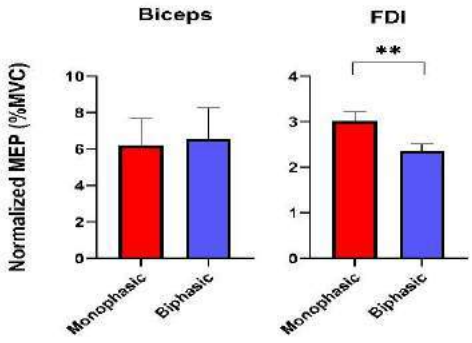

Figure 2: Left: Biceps nMEPs are not significantly different between monophasic and biphasic. Right: FDI nMEPs are significantly greater for monophasic compared to biphasic. Asterisks represent statistical difference ($p<0.01$) and error bars represent standard the error of the mean (SEM).

DISCUSSION

There were two key outcomes of this study. First, in agreement with the literature [2], using a monophasic stimulus led to lower MTs, both RMT and AMT, for the FDI and the BB. The difference in MT is likely related to the general organization of inhibitory and facilitatory corticospinal pyramidal tract neurons and the facilitatory neurons having higher sensitivity to the PA current direction [6]. However, this also contributes to the increased MT of the biphasic PA/AP stimulation. The 2nd AP phase not only reduces the activation time and thus the effectiveness of the initial phase, but activates different neurons that have different sensitivity to each current direction [2]. Additionally, the 2nd AP phase hyperpolarizes the membrane and reduces the number of sodium ion-channels available for depolarization [6]. While MTs reflect sodium ion-channels activity which may indicate intrinsic plasticity due to long-lasting changes in neuronal excitability, analyzing MEPs provides information about synaptic plasticity, caused by long-lasting attenuation of synaptic transmission [3].

Second, while we found a significant difference in FDI nMEP amplitude between waveforms, with monophasic having greater nMEPs than biphasic [3], we did not find a significant difference in BB nMEP amplitudes between waveforms. A possible explanation of this finding could be that more distal muscles not only have larger cortical areas, but the cortical areas are also denser than proximal muscles [7]. This, in combination with proximal muscles having weaker monosynaptic input [8], could lead to relatively greater biphasic nMEPs in the BB compared to the FDI. Furthermore, Turton, et al., discovered that at lower force levels a larger number of available motor neurons are recruited for upper limb distal muscles compared to proximal muscles where greater force levels were required for the same level of neuronal activation [4]. Being that our MEPs were recorded while at rest, this is another potential reasoning for the unexpected lack of significant difference between waveforms for BB nMEPs.

One limitation of our study is the small sample size. In order to fully understand these effects for the purpose of neurorehabilitation, this study would need to be further investigated in individuals with neurological impairment. However, our preliminary data suggests that regardless of the waveform, the neuroplasticity findings from FDI research, may not necessarily be applicable to all muscles, specifically the BB. This is rationale that further investigation needs to be conducted on the intrinsic and synaptic plasticity effects on additional muscles where TMS neurorehabilitation could be advantageous.

REFERENCES

[1] Delvendahl, I et al., *PloS ONE*, 9(12): e115247, 2014.
[2] Sommer, M et al., *Brain Stimulation*, 11:558-565, 2018.
[3] Delvendahl, I et al., *Brain Stimulation*, 5:586-593, 2012.
[4] Turton, A et al., *Experimental Brain Research*, 129:559-572, 1999.
[5] Dionísio, A et al., *Journal of Stroke and Cerebrovascular Diseases*, 27:1-31, 2018.
[6] Pell, G et al., *Progress in Neurobiology*, 93:59-98, 2011.
[7] Malcolm, M et al., *Clinical Neurophysiology*, 117:1037-1046, 2006.
[8] Taylor, J et al., *Journal of Physiology*, 541:949-958, 2002.

SB³C2021
Summer Biomechanics, Bioengineering and Biotransport Conference
June 14-18, Virtual

A HIGH PERFORMANCE, LOW-COST APPROACH TO VENTILATION TO INCREASE GLOBAL CAPACITY FOR COVID 19

D.J. Watson (1), J. Frattolin (1), M. Madekurozwa (1), W. Bonneuil (1), A.C. Moore (1), J.E. Moore Jr. (1), J. Mathiszig-Lee (2,3), J. van Batenburg-Sherwood (1)

(1) Department of Bioengineering
Imperial College London
London, United Kingdom

(2) Department of Surgery and Cancer
Imperial College London
London, United Kingdom

(3) Department of Anaesthesia and Perioperative Medicine
Royal Marsden Hospital
London, United Kingdom

INTRODUCTION

There is an established global demand for ventilators, for which the supply has been restricted due to the high cost and complexity of existing ventilator designs. The onset of the COVID-19 pandemic increased demand for critical care ventilators, resulting in an unprecedented strain on the global ventilator market. The intricate design and fabrication of traditional ventilators restricted the ability of manufacturers to accelerate production to meet the increased demand triggered by COVID-19. Therefore, there is a critical need for high performance, low-cost ventilators. This demand could be met by producing designs that achieve traditional methods of ventilation with fewer components or developing new approaches to the fundamental tasks of pressure and flow regulation to inherently reduce design complexity.

We propose a novel ventilator design that performs the essential functions of a traditional ICU ventilator, while utilizing simple components outside of the ventilator supply chain. The proposed design implements the clinically preferred ventilation method, pressure-regulated volume-control (PRVC), in addition to spontaneous and suction modes. With the PRVC method, a fixed volume of gas is delivered to the patient for each breath. This flow is constrained such that airway pressure does not fall below a positive end-expiratory pressure (PEEP). Classically, proportional solenoid valves mediate the patient's connection to high pressure gas supplies but are currently in extremely short supply. Instead, we implemented the design with on-off solenoids valves, which are widely available off-the-shelf worldwide and are cheaper than their proportional counterparts.

In the following study, an overview of the novel approach to ventilation is presented, as well as results from benchtop testing.

METHODS

Two on-off Valves (A and B) are used to load each breath from high pressure air and oxygen supplies into a 2L reservoir (Figure 1). A pressure sensor is used to determine when the reservoir has been sufficiently filled, after which Valves A and B are closed. The breath is delivered to the patient through the opening of another on-off valve, Valve C. A second pressure sensor measures the pressure delivered to the patient. When the inhalation has finished, Valve C is closed, and Valve D opens to allow exhalation. During exhalation, Valves A and B are reopened, and the next breath is loaded into the reservoir.

The system dynamics of the ventilator are dictated by the flow-pressure characteristics of the valves. The selection of the valve flow coefficients was informed by a numerical model of the ventilator system. With these properties known, the two pressure sensors can be used to estimate the flow rate during inhalation and exhalation, removing the requirement for a dedicated flow sensor. Patient-specific lung parameters can be estimated at each breath and used to inform the next breath, allowing a control system to meet ISO guidelines and UK MHRA requirements. A commercially available ventilator testing device (Citrex H5) was used to assess the performance of the ventilator over a range of tidal volumes (V_T), PEEP values, and timing conditions. Durability testing of the prototype was conducted over 14 days to evaluate system stability. In addition, the ventilator prototype was tested with a portable oxygen concentrator, in place of a compressed oxygen source, to evaluate if any change in system performance occurred.

RESULTS

Benchtop testing was performed to evaluate the performance and response time of the proposed design. A parametric sweep of target PEEP and V_T was performed. The system performed consistently across a clinically relevant parameter space (Figure 2), with cases omitted

where the peak inspiratory pressure would exceed the maximum allowable airway pressure. The achieved PEEP and V_T are shown against the target values for a test lung with a compliance of 20 ml/cmH_2O and a resistance of 20 cmH_2O/l/s. Good agreement was observed between values reported by the prototype system and the commercially available ventilator testing machine, Citrex H5. In response to changes in ventilation settings, PEEP and V_T stabilized to target values within 1-2 breaths. When run for 14 days, the system maintained performance with no change in key ventilation parameters. In addition, no significant change in performance was identified when the system was used with compressed air and an oxygen concentrator.

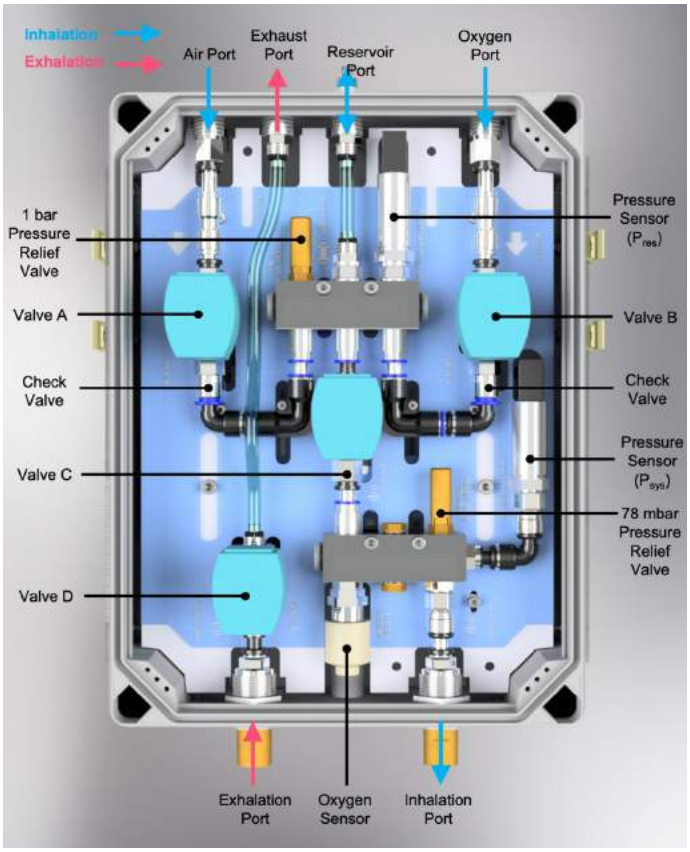

Figure 1: Annotated schematic of pneumatic components of the proposed ventilator design.

DISCUSSION

The proposed design constitutes a new approach to achieve ICU-level ventilation performance with components that do not interfere with the existing supply chain, specifically, specialist proportional control valves and flow meters. Employing only standard components increases the robustness of the design, allowing for alternative sourcing of parts for repairs. Furthermore, implementation of standard, 'off-the-shelf' components significantly decreases ventilator cost to manufacture and maintain, increasing access for resource-poor countries. This is critical for low- and middle- income countries where respiratory conditions such as pneumonia, influenza, and tuberculosis remain major causes of mortality. The ability to combine the proposed design with oxygen concentrators, when hospital grade gas supplies are not available, increases the ventilator's functionality and portability. Despite its low-cost, the proposed ventilator design meets performance standards and metrics identified by both international and national governing bodies. For these reasons, it has the potential to answer the unmet global need for increased ventilator capacity.

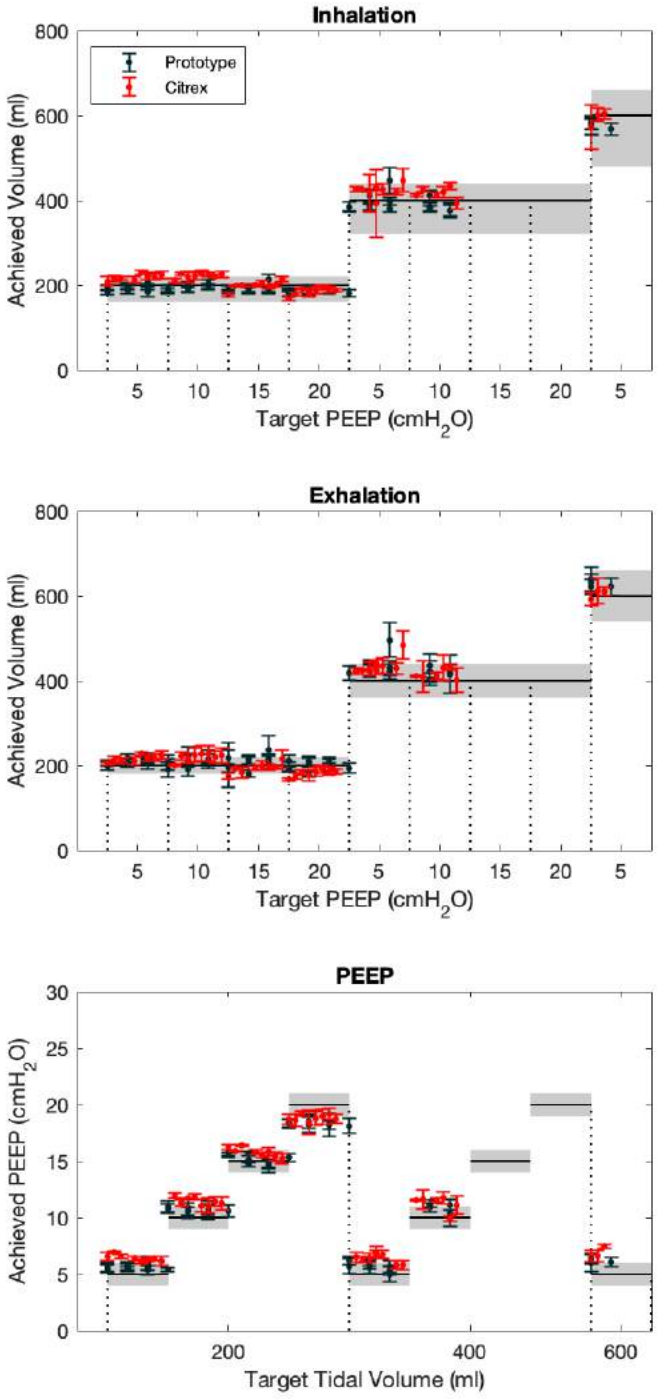

Figure 2: Example plots of achieved V_T and PEEP against target values from the parameter sweep, utilizing a high compliance, low resistance test lung.

ACKNOWLEDGEMENTS

The authors acknowledge financial support from the Royal Academy of Engineers and Imperial College London. The authors also wish to thank all those who supported and contributed to this project.

SB³C2021
Summer Biomechanics, Bioengineering and Biotransport Conference
June 14-18, Virtual

DIFFERENTIAL NANOPOARTICLE ACCUMULATION IN A MOUSE MODEL OF ATHEROSCLEROSIS MAY BE DRIVEN BY SMOOTH MUSCLE CELLS

Morgan A. Schake (1), Ian McCue (1), Hunter A. Miller (2), Badrul Alam Bony (2), Evan T. Curtis (2), Connor C. Gee (2), Forrest M. Kievit (2), Ryan M. Pedrigi (1)

(1) Department of Mechanical and Materials Engineering
University of Nebraska-Lincoln
Lincoln, NE, U.S.A.

(2) Department of Biological Systems Engineering
University of Nebraska-Lincoln
Lincoln, NE, U.S.A.

INTRODUCTION

Atherosclerosis is the fundamental pathology of heart attack and stroke, and the leading cause of death globally [1]. This disease is characterized by lipid-rich and immune cell-dense plaques localized to areas of disturbed wall shear stress (WSS); namely, in areas of the vasculature that produce low or multidirectional WSS. Studies in animal models have demonstrated that low WSS conditions cause development of an unstable plaque phenotype, whereas multidirectional, including oscillatory, WSS produces a more stable phenotype. High WSS, found in straight arterial segments, does not induce atherosclerosis and is recognized to be protective against disease formation. Presently, no diagnostic modality or therapeutic exists that leverages the flow-induced nature of plaque formation. Targeted nanoparticles present an opportunity to address this shortcoming for both diagnostics and therapeutics. Previous work has demonstrated achievable uptake in atherosclerotic plaques, but no such work has shown this uptake as a function of WSS.

To address this need, we aim to (1) identify differential accumulation of nanoparticles as a function of the WSS environment and, in turn, plaque phenotype, and (2) assess what components of plaque may contribute to differential accumulation. We used an ApoE$^{-/-}$ atherogenic mouse model instrumented with a blood flow-modifying cuff, which has been previously shown to induce both low and multidirectional WSS blood flow profiles and, in turn, plaque development [2]. Nanoparticles were developed to passively accumulate within the vasculature, with accumulation kinetics measured via dynamic contrast-enhanced Magnetic Resonance Imaging (DCE-MRI). To assess features of plaque phenotype, smooth muscle intensity was determined via histological analysis.

METHODS

Nanoparticles. Gadolinium-based small molecule contrast agents are common in clinical evaluation of vascular permeability. Here, we used a gadolinium paramagnetic NP-based contrast agent. To be useful in DCE-MRI, these nanoparticles were coated in folic acid. Using a modified polyol synthesis method, [3] we achieved synthesis of folic acid-coated gadolinium (FA-Gd) nanoparticles.

Mouse Model and Nanoparticle Imaging. Five female ApoE$^{-/-}$ mice (Jackson Labs) at 11 weeks of age were placed on an atherogenic diet (Envigo) for two weeks and then instrumented with a tapered blood flow-modifying cuff (Promolding) around the left carotid artery. This cuff induces three WSS profiles: low WSS upstream, high WSS within, and multidirectional WSS downstream of the cuff. At 5 and 9 weeks after cuff placement, the mice were injected with FA-Gd nanoparticles and imaged with DCE-MRI. DCE-MRI was performed using a 2-D gradient echo sequence with two flip angles for calculation of R_1 and generation of K^{trans} maps, which indicate NP permeation into the arterial wall. Two baseline scans were performed to calculate T_1 values prior to injection with the following parameters: TR = 138 milliseconds, TE = 3.48 milliseconds, flip angles of 10° and 30° respectively, 2 averages, 256x256 data matrix, 20 slices each with a 23x23x0.5 mm^3 FOV for a total scan time of 53 seconds. Post-contrast scans all used a flip angle of 30° with the same parameters as above. After completion of baseline scans, NPs were injected through the tail vein catheter, followed by 1 hour of post-contrast image collection. The K^{trans} maps were then generated and readouts were analyzed using a custom MATLAB program.

Histology. To assess features of different plaque phenotypes, histology was performed on all five mice. After imaging at 9 weeks, mice were anesthetized, and perfusion fixed with saline and 4%

paraformaldehyde at mean arterial pressure. The carotid arteries were then excised, embedded in OCT, and snap frozen in -80°C isopentane. Serial cryosections at a thickness of 8 µm were obtained from the aortic arch to the carotid bifurcation of each artery. Co-registration of the histology to the DCE-MRI images and K^{trans} maps was achieved using the aortic arch, cuff region, and carotid bifurcation. Sections were stained for smooth muscle cells using smooth muscle α-actin (ABCAM). Fluorescence imaging of the smooth muscle stain was performed using a Zeiss confocal microscope at 20X magnification. Images were quantified using a custom MATLAB program that employed a grey scale conversion to calculate stain intensity. Histology sections were co-registered to MRI slices using the cuff as a landmark.

Data Analysis. To evaluate NP accumulation in the different WSS regions, NP accumulation was obtained by using maximum K^{trans} values in both the low and multidirectional WSS regions of each mouse at 5 and 9 weeks after cuff placement; K^{trans} from the contralateral carotid artery served as a control. To assess how smooth muscle in each plaque region might influence NP accumulation, stain intensity was averaged over all histology sections for a given co-registered MRI slice (typically four) and correlated with K^{trans}. One to two histology-MRI pairs were identified per plaque region per mouse. All reported values are mean±SD. Correlation was calculated using a Pearson's coefficient. Significance was set at a p-value of 0.05.

RESULTS

K^{trans} maps indicated a higher accumulation of nanoparticles in both diseased segments of the cuffed artery at 5 and 9 weeks (Figure 1) compared to the control artery. Further, there was a significantly higher passive accumulation of nanoparticles in the low WSS region of the instrumented artery at 5 weeks compared to 9 weeks with K^{trans} values of 0.067±0.009 min^{-1} versus 0.046±0.013 min^{-1}, respectively. In the region of multidirectional WSS, K^{trans} demonstrated a nearly identical nanoparticle accumulation between 5 and 9 weeks with mean values of 0.066±0.016 min^{-1} and 0.067±0.0025 min^{-1}. Interestingly, smooth muscle intensity in the inner-most part of the plaques (the "plaque cap") in the low WSS region exhibited a strong inverse relationship with Ktrans (ρ = -0.95, p<0.01), which was not observed in the downstream segment (ρ = -0.03, p=0.95) (Figure 2). In addition, there is an overall lower intensity of smooth muscle in the low WSS region compared to the multidirectional WSS region with intensity values of 0.016±0.010 versus 0.026±0.015, respectively.

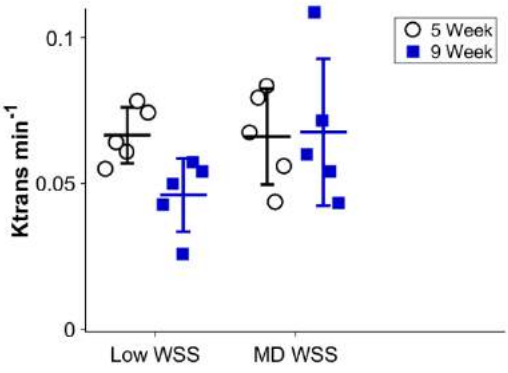

Figure 1: NP accumulation as determined from K^{trans} in the low (upstream) and multidirectional (MD; downstream) WSS regions of the instrumented carotid artery at 5 and 9 weeks after cuff placement. Each point represents the max K^{trans} from one mouse (n=5 mice) and bars are mean±SD.

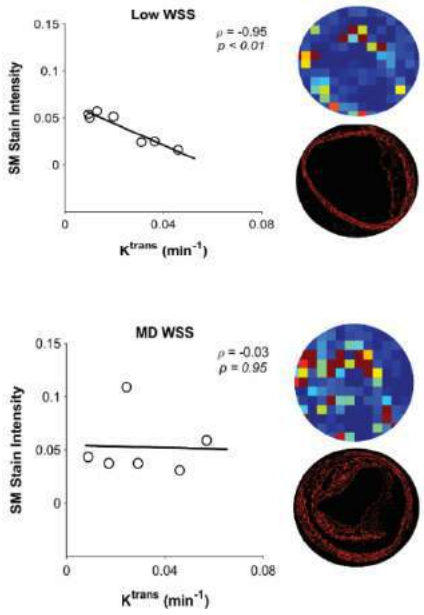

Figure 2: Smooth muscle intensity as a function of K^{trans} in the low and multidirectional WSS regions. Best-fit lines are given in black. Pearson's correlation coefficient (ρ) and p-value are given in the upper-right coroner of the plots. A representative K^{trans} map and smooth muscle histology section for each artery region is also shown.

DISCUSSION

To our knowledge, this is the first study to examine the accumulation of nanoparticles in different regions of atherogenic WSS. We did not see a difference in NP accumulation between the low and multidirectional WSS regions at 5 weeks when plaques are at an intermediate stage, suggesting no direct effect of the flow environment. However, at 9 weeks when plaques are considered fully developed in this model, there was lesser accumulation in the upstream (low WSS) unstable plaque region compared to the downstream stable plaque region. This suggests that plaque phenotype is the principal driver of NP accumulation, although the flow environment is an important determinant of plaque phenotype. Furthermore, we found a negative correlation between nanoparticle accumulation and smooth muscle in the fibrous cap region of the unstable plaque, but not the stable plaque. This may indicate a difference in smooth muscle organizing in the unstable plaque that may physically inhibit the NPs from entering the plaque compared to the stable plaque region, which had smooth muscle diffuse throughout the plaque. Another possibility is that this inverse correlation of smooth muscle with K^{trans} somehow relates to endothelial function. A decline in smooth muscle, particularly in the plaque cap, is indicative of a more unstable plaque that might correspond with a more dysfunctional endothelium. Additional work is needed to evaluate endothelial function and other constituents in these plaques that may determine differential NP accumulation.

ACKNOWLEDGEMENTS

We gratefully acknowledge support for this work from the AHA (grant number 19CDA34660218) and NIH (grant R21EB028960).

REFERENCES

[1] Virani, S. et al., *Circulation,* 141:139-596, 2020.
[2] Pedrigi R.M. et al., *Royal Society Open Science,* 3, 2016.
[3] Bony, B.A. et al., *ACS Omega*, 5, 2020.

INVERSE FINITE ELEMENT MODELING OF EX-VIVO ORGAN-SCALE PORCINE LUNG BASED ON 3D DIGITAL IMAGE CORRELATION AND CONTROLLED PRESSURE-VOLUME LOADING

M. Maghsoudi-Ganjeh (1), C. Mariano (1), S. Sattari (1), M. Eskandari (1,2,3)

(1) Department of Mechanical Engineering
University of California
Riverside, CA, United States

(2) BREATHE Center, School of Medicine
University of California
Riverside, CA, United States

(3) Department of Bioengineering
University of California
Riverside, CA, United States

INTRODUCTION

Pulmonary diseases are responsible for significant socioeconomic strains, affecting millions and costing billions in the U.S. alone. Research efforts focused on the understudied subject of lung mechanics are more indispensable than ever before, especially given the respiratory-damaging nature of pandemics, as seen with the COVID-19 virus. Restrictive and obstructive pulmonary diseases remodel the structure of tissue and alter function [1]. Inverse finite element modeling has proven to be a promising approach for investigating the relationships between loads and deformations, and can offer insights to understand how deviations in diseased states affect respiratory function [2]. To date, however, inverse pulmonary models have either been too simplistic and lacking in local-level resolutions (i.e., zero-order/compartment-based models) [3], or too complex and expensive (e.g., 4D computed tomography) [4], prohibiting systematic conclusions to analyze fundamental mechanical variations, such as positive-pressure versus physiologically-relevant negative-pressure respiration.

To address these limitations, we introduce an inverse finite element (FE) lung model based on local 3D digital image correlation (DIC) measurements of the inflating organ, dynamically interfaced with synchronous global pressure-volume data. The resulting material parameters, calibrated through experimental testing, represent the compound contributions of the parenchyma, visceral pleura, and airways by employing a simplified reduced order surface model of the lung. The resulting physiologically-relevant in-silico lung model can be used to optimize ventilation strategies for the clinic through comprehensive parametric studies, assess the degenerated mechanics in diseased states, and guide better physics-based designs of compliant lung-replicating ventilator components that are in unprecedented high demand.

METHODS

In this experimental-computational proof-of-concept study, a freshly excised porcine lung was inflated with 900ml of air at 15 breaths-per-minute using a validated custom-developed pressure-volume controller and data acquisition setup [5]. Following the 3D-DIC procedure previously described [6], several preconditioning inflation-deflation cycles were performed, and the real-time deformation of the lung was recorded (Figure 1a). A finite element model was generated from the visceral pleura surface geometry of the right lung lobe in the uninflated configuration. Discretization and 3D membrane element formulation was implemented in the commercial FE-package Abaqus (~5,000 M3D3 elements). The organ-level pressure data was applied as a dynamic load to the model (Figure 1b). The DIC displacement field, probed at 1mm evenly distributed point clouds on the parenchymal surface, was interpolated using the k-nearest neighbor algorithm [7]. The interpolated DIC displacements were imposed as boundary conditions in the FE model and used to evaluate the root mean square error between experimental and simulation-based displacement predictions.

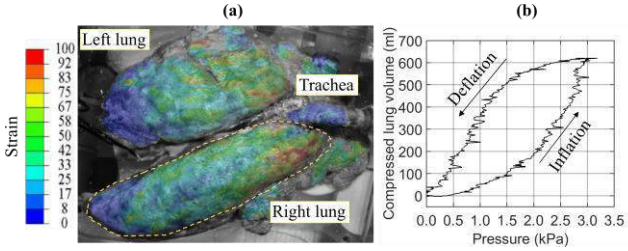

Figure 1: Experimental setup using air-inflated porcine lung interfaced with synchronous Digital Image Correlation (a) and pressure-volume measurements (b).

The compressible Mooney-Rivlin hyperelastic constitutive response was used as the material model of the lung. The strain energy density was defined as $W = C_{10}(\bar{I}_1 - 3) + C_{01}(\bar{I}_2 - 3) + \frac{1}{D_1}(J-1)^2$, where $\bar{I}_1$, $\bar{I}_2$ are the first and second invariants of the deviatoric deformation tensor, J is the Jacobian of deformation gradient, and C_{10}, C_{01}, and D_1 are the unknown composite material parameters. The optimal value of these material parameters was estimated with a fully automated optimization pipeline linking Matlab, Abaqus, and Python. Two broad classes of gradient-based and gradient-free optimization algorithms were studied (trust-region-reflective and particle-swarm-optimization). To avoid local optima, the optimization algorithm was run from multiple initial estimate points, randomly selected from the search space $C_{10}, C_{01} \in [1,200]$ kPa and $D_1 \in [10^{-2}, 10^{-4}]$1/kPa.

RESULTS

Table 1 lists the resulting optimal material parameters. The displacements, maximum in-plane principal strains and stresses obtained from characterizing DIC were contrasted with the calibrated model (Figure 2). The aerated lung's anterior portion exhibited the greatest deformation with a maximum of 25mm (Figure 2a). The experimental stress plot was obtained by running the DIC displacements through the FE model with the parameters listed in Table 1. The compressibility parameter D_1=13.4×10^{-4}1/kPa corresponded to a bulk modulus of 1.5 MPa and the small displacement shear modulus was μ_0=2C_{10}=272 kPa. The parameter C_{10} (controlling the contribution of the $\bar{I}_1$) was two orders of magnitude greater than C_{01} (linked to $\bar{I}_2$). The average error between experimental DIC and the optimized inverse FE model displacement was 2.3 mm, less than 10% of the maximum lung distension. To compare the validity of the resulting optimal material properties, a generic balloon made of the same predicted material was compared against the classic single-compartment lung model [2], where the elastance values predicted by these two methods were in close agreement.

Table 1: The optimal material properties and the averaged error

C_{10} (kPa)	C_{01} (kPa)	D_1 (×10^{-4}/kPa)	Error (mm)
136.5±0.3	1.0±0.01	13.4±0.16	2.3

DISCUSSION

This study investigated, for the first time, an inverse FE modeling approach to generate the compound elastic properties of the whole lung organ using DIC measurements. The proposed reduced order surface model of the lung is more practical than computationally demanding 4D CT-based works [4,8], and is more insightful than simple compartment-based inverse modeling studies [2, 3]; compared to the latter, our approach predicts a similar shear modulus while enabling evaluation of regional pulmonary behaviors previously unaccounted for. We find that while assuming a homogeneous isotropic hyperelastic constitutive response can represent the overinflated behavior of the lobes, it is not as successful in resolving complex strain and stress regional heterogeneities. While this current study yields a new advancement for pulmonary biomechanics research, we will examine a heterogenous and/or anisotropic material behavior to improve model performance and acknowledge that this method may come with at a higher computational cost.

The preliminary results obtained here offer promise to improve the design of bladder/balloon shaped components prevalent in novel didactic and clinical ventilator systems [9,10]. Currently, the material properties of these lung-replicating components are not selected based on rigorous physiological calculations. This may significantly hinder the effectiveness of these ventilators once applied to actual patients in need of respiratory support. Our inverse analysis framework can effectively produce pulmonary-based material properties for ventilator design.

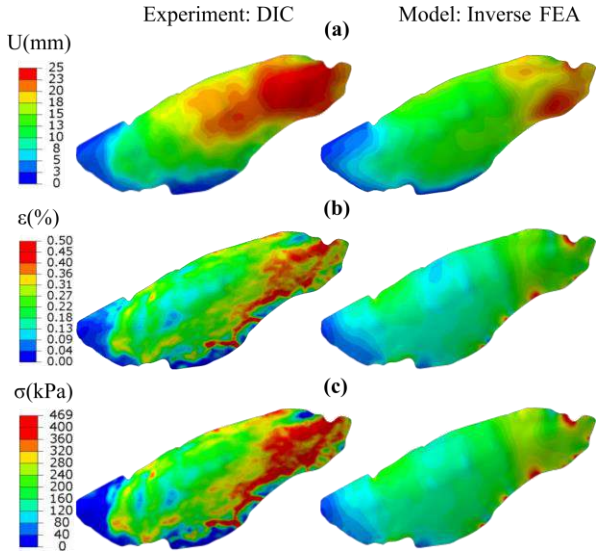

Figure 2: Experiment and inverse FE modeling displacements (a), major strains (b), and major stresses (c).

A limitation of this study is the use of one lung to formulate this pipeline, restricting the conclusive statistical relevance of predicted material properties and average error. Nonetheless, this novel proof-of-concept study demonstrates the advantages and pitfalls in pulmonary inverse modeling based on DIC data.

Future simulations are aimed at applying the developed inverse modeling framework to systematically establish the regional behavior and governing physiology of the lung. This DIC-informed computational framework can be used to evaluate potential differences in respiratory mechanics and function in healthy versus diseased states. Altering inflation volumes in-silico will enable us to assess how ventilation methods effect pulmonary deformations and stretches, facilitating clinical strategies to minimize ventilation induced lung injury.

In summary, this study introduces inverse FE modeling for the complex organ-level deformations during the breathing cycle. While the results are indicative of promising applications for the method, further investigations calibrating the constitutive response will improve the accuracy and efficacy of the model to enable clinical applications and benefit patient care.

ACKNOWLEDGEMENTS

Authors gratefully acknowledge funding support from Dassault Systèmes U.S. Foundation Grant.

REFERENCES

[1] Eskandari, M et al., *Acta Biomaterialia*, 97: 513-523, 2019
[2] Bates, J.H , Lung mechanics: an inverse modeling apprach, 2009
[3] Hantoz, Z et al., *J Appl Physiol*, 52:955-963, 1982
[4] Li, M (et al.), *Med Phys*, 40: 081902, 2013
[5] Sattari, S et al., *Front. Bioeng. Biotechnol*, 8:1183, 2020.
[6] Mariano, C et al., *Front Physiol*, 11:1536, 2020
[7] Altman, N et al., *Am Stat*, 46:175-185, 1992
[8] Risholm, P et al., *Inf Process Med Imaging*, 22:699-710, 2011
[9] Zuckerber, J et al., *Life Sci*, 257:118113, 2020
[10] DiCarlo, S, *Adv Physiol Educ*, 32:185-191, 2008

AN *IN VITRO* MODEL OF BONE INGROWTH IN A POROUS TITANIUM SCAFFOLD

Alyssa G. Oberman (1), Brett English (2), Weidong Tong (2), Glen L. Niebur (1)

(1) Department of Aerospace and Mechanical Engineering
University of Notre Dame
Notre Dame, IN, United States

(2) Front End R&D
DePuy Synthes
Warsaw, IN, United States

INTRODUCTION

Over 90% of total hip arthroplasties (THAs) in the U.S. are fixed by osseointegration. Osseointegrated implants offer a significant reduction in revision risk and an extended implant lifetime [1]. This reduction of risk is critical, because the average age of implant recipients is decreasing [2]. However, the use of osseointegration in knee implants, where the majority of the implant surface interacts with cancellous bone, is less common. Efficient and inexpensive methods to evaluate osseointegration of new scaffold designs is important.

The goal of this study was to evaluate the potential of bioreactors as a platform to evaluate bone ingrowth into osseointegrated scaffolds. Scaffolds with and without mesenchymal stromal cells were implanted into trabecular bone implants and cultured for six weeks to quantify bone ingrowth and interface stiffness mechanics between the bone and the scaffold.

METHODS

Medical grade porous Ti6Al4V (Ti64) scaffolds, approximately 5 mm diameter and 10 mm long, were additively manufactured using a selective laser melting powder bed process and subsequently treated by hot isostatic pressing (HIP), cleaned, gamma sterilized, and autoclaved.

Bone formation into the porous scaffolds in a bioreactor was quantified. Twenty-one cylindrical bone explants were prepared from porcine cervical vertebrae (C2-C4) with an 8 mm diamond tipped coring bit. A 5 mm hole was drilled into the center. Explants were then cut to a length of 10 mm with flat, parallel ends.

Eight scaffolds were placed in a 12-well low attachment plate with media added to the depth of the scaffold. Each scaffold was seeded with 250,000 porcine mesenchymal stromal cells (MSCs) pipetted dropwise on the top surface and incubated overnight to allow attachment. Thirteen scaffolds were used without cell seeding. Each prepared scaffold was inserted into the inner hole of a trabecular bone explant. Once prepared, five explants were immediately fixed to provide a non-cultured control group. The remaining sixteen explant-scaffold constructs were cultured in a bioreactor for 6 weeks. The constructs were subjected to sinusoidal vibration at a frequency of 50 Hz and peak acceleration of ±0.3 g for 30 minutes twice daily, 5 days/week. At the end of the first, third, and fifth weeks of culture, media was supplemented with 0.5 mM alizarin complexone, 0.05 mM xylenol orange, and 0.08 mM Calcein, respectively, for 24 hours to label forming bone for dynamic histomorphometry.

Following culture, the explants and scaffolds were cut in half transversely using a diamond wafering saw. One half was stored at -20° C for later mechanical testing, while the other half was fixed in formalin and embedded for histology. Multiple thick sections (200-500 μm) prepared from each fixed sample were polished stepwise ending with 0.25 μm diamond paste. Eight locations around the perimeter of the scaffold were imaged with confocal microscopy (Nikon C2+) to visualize fluorochrome labels. The area of the bone within the scaffold pores was quantified using ImageJ (NIH) by manual tracing.

Mechanical properties of the interface were evaluated using a push-out test. Displacement was applied to the titanium scaffold at 3 mm/min (Bose Electroforce 3300, Eden Prairie, MN). The force and displacement were recorded continuously. Interface stiffness was calculated as the slope between 25% and 90% of the maximum force divided by the total surface area of the bone-implant interface. The push-out strength was determined by dividing the maximum force applied during the test by the surface area of the interface.

Groups were compared using a Kruskal-Wallis test due to non-normal distributions of the data. Improper embedding prior to mechanical testing reduced each group from eight to five samples. Two samples were excluded from image analysis due to over-polishing of the slides. One of the samples that was used for ingrowth image analysis

was unable to be paired to mechanical testing data due to improper embedding.

RESULTS

New bone was present in the scaffold following six weeks of culture. Fluorochrome stained tissue was visible under confocal microscopy, indicating bone formation was occurring during the culture period (Fig. 1). Fluorochrome staining was present in every section viewed for cultured samples, but none was present in uncultured controls. Staining was most common along cut surfaces of the bone, however, fluorochromes were also detected along the surfaces of trabeculae. Triple labels were found within the trabeculae, indicating active bone formation for all six weeks (Fig. 1). Within the scaffold pore space, staining was diffuse rather than linear, indicative of a woven bone morphology. No differences in ingrowth area were seen for the no cell and pre-seeded culture groups (Fig. 1).

The interface stiffness and push-out strength were compared between groups and correlated to ingrowth area. No significant differences were seen between groups for either interface stiffness or strength (Fig. 2A and 2B). The interface stiffness increased with the total area of bone ingrowth ($p = 0.03$) (Fig. 2C). In contrast, there was no correlation between strength and ingrowth area (Fig. 2D).

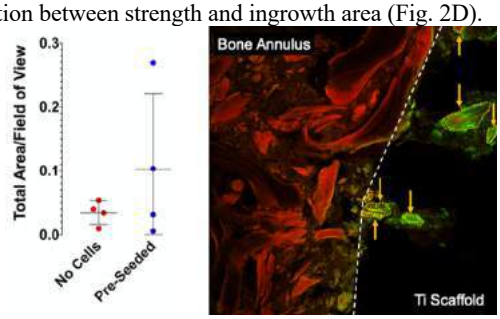

Figure 1. New bone was stained using calcium-chelating fluorochromes at weeks 1, 3, and 5. These fluorochromes were used to determine when bone formed within the porous scaffold over the 6-week culture period. Ingrowth area was measured by outlining regions manually in ImageJ.

DISCUSSION

We developed a method to investigate osseointegration of porous scaffolds using *in vitro* culture in a bioreactor. We found that bone formed in the pores of additively manufactured Ti64 scaffolds during a six-week culture period, as verified by dynamic histomorphometry. To our knowledge, this is the first demonstration of osseointegration in a bioreactor system.

Fluorochrome labeling showed new bone formation in the pores along the outer surface of the scaffold. Normal bone marrow morphology was maintained within the bone explant, providing a source of mesenchymal stromal cells for bone to form within the scaffold pores. Bone formation in the bioreactor was less robust than in *in vivo* experiments. The depth of bone formation from the surface was limited to the first 500 μm of the pore space. In contrast, *in vivo* studies found bone ingrowth up to 5 mm into the scaffold in eight-week studies [3]. These differences are likely due to differences in bone behavior *in vivo* vs. *in vitro* as well as the absence of mechanical loading. While the inertial loading applied to this bioreactor has been shown to induce bone formation [4,5], it relies on the stimulation of the marrow compartment rather than osteocytes. In contrast, compressive and shear loading across the bone-scaffold interface could induce damage and osteocyte signaling in order to prompt a localized bone remodeling cascade.

In the absence of the normal fracture healing response, it is unclear if a sufficient number of cells would migrate from the bone marrow to achieve osseointegration. We tested whether the presence of MSCs prior to culture would improve bone ingrowth by providing a chemokine gradient or small bone deposits on the scaffold surface. MSCs showed no impact on bone ingrowth, possibly due to the limited number of cells present in the scaffold space at the start of the experiment or due to inability of cells to migrate freely in the scaffold pore space. In fracture healing, an initial hematoma forms providing both a chemokine-rich fibrin clot and a matrix for 3-D cell migration from the native bone. Providing a similar physical junction between the bone and scaffold could provide better insight as to the benefit of using MSCs for pre-seeding.

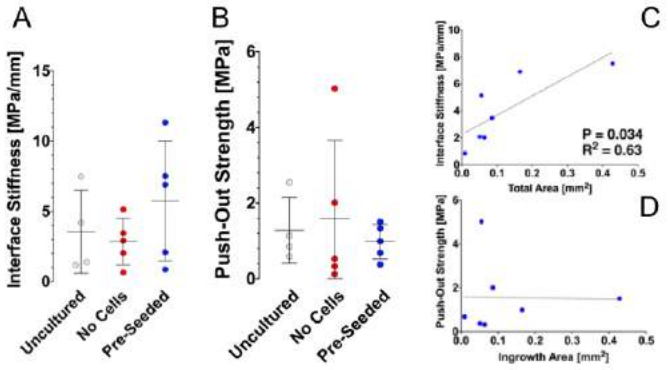

Figure 2. Push-out testing was used to determine interface stiffness (A) and push-out strength (B) of the bone at the bone-scaffold interface. Interface stiffness correlated with the total bone area measured within the pore space ($p = 0.03$) (C). Pushout strength showed no correlation (D).

This analysis shows that interface stiffness increased with ingrowth area, confirming that more bone within the scaffold space results in a stiffer interface. Further mechanical analysis could help to determine how the depth of bone in the pores impacts this relationship, as bone in the scaffold pores was not always directly abutting the original bone annulus. Mechanical properties for the uncultured control were likely a result of interference fit. Total area did not have an impact on strength, but this could be a result of the quality of the new bone volumes rather than their size alone.

Our results demonstrate that bioreactor culture has potential to be used as an assay to assess biological and mechanical factors that affect osseointegration. Relatively large numbers of scaffolds can be evaluated in an *in vitro* experiment without the expense of animal husbandry and with greater control over mechanical loading. As such, this *in vitro* method could improve screening of scaffold designs prior to animal testing, providing more precise control over external variables in order to extrapolate interactions between scaffold morphology and loading.

ACKNOWLEDGMENTS

This research was supported by DePuy Synthes, a Johnson&Johnson company.

REFERENCES

[1] Karuppal, R., J Orthop. 13:190–2, 2016.
[2] 2019 Annual Report, American Academy of Orthopaedic Surgeons, 2019.
[3] Taniguchi, N, et al., Mater Sci Eng C Mater Biol Appl. 59:690–701, 2016.
[4] Birmingham, E, et al., Ann. Biomed. Eng. 43:1036–1050, 2014.
[5] Curtis, K.J, et al., Bone. 107:78–87, 2018.

ANALYZING SUTURE FIXATION TECHNIQUES FOR TIBIAL EMINENCE AVULSION FRACTURES

Yulia A. Yatsenko (1), Calvin K. Chan (1), Nyaluma Wagala (2), Volker Musahl (2,1), Richard E. Debski (1,2)

(1) Department of Bioengineering
University of Pittsburgh
Pittsburgh, PA, USA

(2) Department of Orthopaedic Surgery
University of Pittsburgh
Pittsburgh, PA, USA

INTRODUCTION

Tibial avulsion fractures occur as a result from high tension within the anterior cruciate ligament (ACL) which can be seen in adults and children in similar proportions [1]. These injuries result in knee joint instability often requiring internal surgical fixations to regain normal knee biomechanics such as extension and flexion [2]. Treatment depends on the severity of the tibial eminence avulsion fracture. Type III fractures are generally managed with surgical fixation. Two main suture types exist for surgical fixation: UltraTape, a suture tape and UltraBraid, a cord-like suture. Two different suture configurations, the bridge and sling, are used with the suture fixation techniques. (Figure 1) UltraTape exhibits greater stiffness while UltraBraid has greater material recovery three minutes after removing a load [3]. The objective of this study was to quantify tibial avulsion fragment motion based on the repair suture type and configuration to provide the optimal knee stability following treatment.

METHODS

Twenty-eight intact fresh-frozen unpaired mature porcine knees (Hampshire, 7-8 months) were used for testing. Knees with congenital anomalies or arthritis were excluded. All knees were frozen at -20°C and thawed the night before testing. A type III tibial eminence avulsion fracture was created with the remaining soft tissue removed, creating a femur-ACL-tibia complex (FATC). UltraTape (Smith & Nephew) and UltraBraid (Smith & Nephew) were used for suture types. The fracture was fixed using one of the suture fixation construct groups: UltraBraid Bridge, UltraBraid Sling, UltraTape Bridge, and UltraTape Sling. Seventeen markers were placed on the tibia and femur of the porcine knee and on the materials testing machine (Model 5965; Instron Corp., Norwood, MA, USA) that underwent tensile cyclic loading. Two cameras were set up so that the digital motion tracking system (Spica Technology, Kihei, Maui HI) could capture all markers. The three-dimensional marker coordinates on the specimen were determined using DMAS7. The specimens were kept moist with physiologic saline solution during testing to prevent desiccation of the soft tissues.

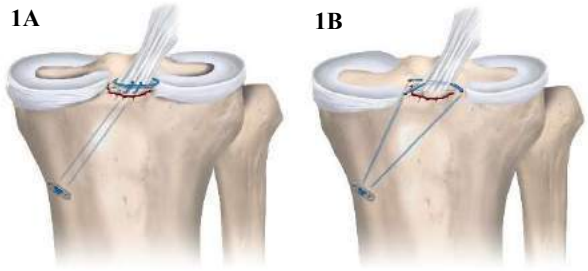

Figure 1: The bridge (1A) allows for the suture to wrap around the ACL and cross over the fracture whereas the sling (1B) utilized a 4-point fixation that goes through the ACL [4][5].

For each suture fixation technique, seven specimens underwent 2 Newtons (N) preload, 2-10 N preconditioning (30 cycles), and 10-50N cyclic loading for 500 cycles. The marker data was then run through a custom MATLAB program that calculates the translational and rotational data in the coronal, sagittal, and transverse planes of the tibia throughout the cyclic loading. Positive axes were defined as a vector pointed in the medial direction, a vector pointed in the posterior direction, and the cross product of the first two vectors pointed in the distal direction.

The translational and rotational data was tested for normality for each of the specimens at the last loading cycle at 50 N. Normal

distribution was assessed using a Shapiro-Wilk goodness of fit test in JMP (SAS, Cary, NC). A one-way ANOVA was utilized with a post-hoc Tukey-Kramer HSD test. Statistical significance was set at $p < 0.05$.

RESULTS

The UltraBraid Bridge group displayed a difference of 189% in vertical displacement compared to both the UltraTape Sling and UltraBraid Sling groups at the last cycle of 50 N. A 115% difference exists between the UltraTape Bridge group and the UltraTape Sling group. Lastly, a 116% difference is found between the UltraBraid Sling group and the UltraTape Bridge group. Three of the seven specimens in the UltraBraid Sling group failed before reaching cycle 500. For this group, data was taken from the last cycle at 50 N and combined with specimens that did not fail at cycle 500. For this reason, specimens with insufficient data could not be used. A significant difference exists between the UltraBraid Sling and UltraBraid Bridge groups, the UltraTape Sling and UltraBraid Bridge groups, the UltraBraid Sling and UltraTape Bridge groups, and the UltraTape Sling and UltraTape Bridge groups. (Figure 2)

For all construct groups, rotational data was, also, assessed. (Figure 3) No significant difference exists for sagittal rotation. However, a significant difference is found in coronal rotation of the tibial eminence fragment. From the post-hoc test, a significant difference exists in the same construct group pairs as in vertical displacement. The UltraBraid Bridge and UltraBraid Sling groups exhibit a 123% difference in coronal rotation. A 115% difference in coronal rotation is seen between the UltraBraid Bridge group and the UltraTape Sling group. The UltraTape Bridge group and the UltraTape Sling group showed a 99% difference in coronal rotation. Lastly, a 108% difference is found between the UltraBraid Sling group and the UltraTape Bridge group in coronal rotation.

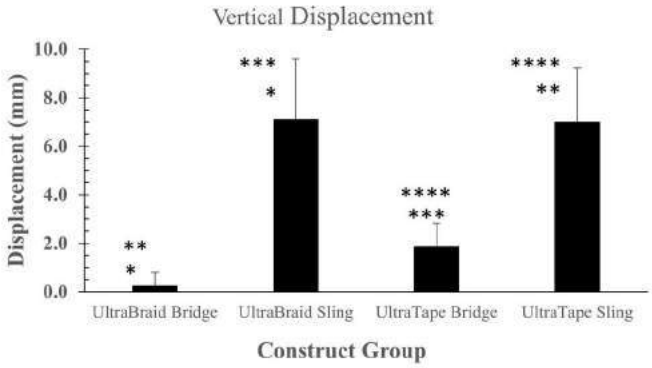

Figure 2: Mean ± S.D vertical displacement of each construct group at the last cyclic loading cycle of 50 N. Significance found at $p \leq 0.001$ between marked groups.

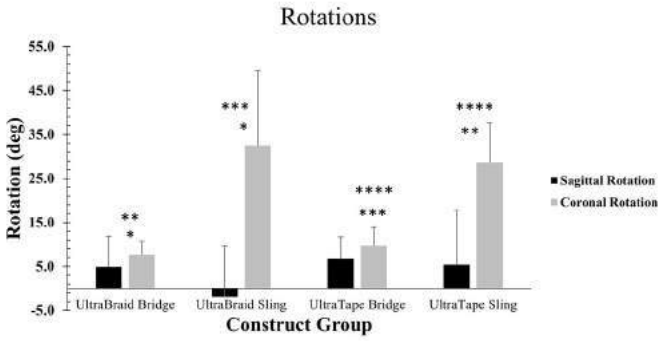

Figure 3: Mean ± S.D sagittal and coronal rotations shown at the last cyclic loading cycle at 50 N. Significance found at $p \leq .007$ between marked groups.

DISCUSSION

Vertical displacement shows a significant difference between the suture sling and the suture bridge construct groups. The suture bridge configuration reduces motion of the FATC more than the suture sling configurations, as expected. There is no significant difference in sagittal rotation for any construct groups because the bridge configuration goes over the superior surface of the fragment to prevent rotation. The sling configuration goes through the fragment body and thus contributes less of a moment to restrict fragment rotation. In the clinical setting, the suture sling or suture bridge setup limits inferior or superior rotation of the FATC. Suture slings exhibit greater movement, specifically in coronal rotation. As more force is applied, the FATC shifts medially which may interfere with the ACL's ability to properly heal and regain full functionality of knee extension and flexion.

When comparing suture types, no significant differences are seen between UltraBraid or UltraTape configurations for any movements. It can be concluded that UltraTape provides slightly more stability than UltraBraid as none of the UltraTape Sling specimens failed during cyclic loading while some UltraBraid Sling specimens did.

Bridge suture techniques should be considered over sling techniques during arthroscopic surgeries for tibial eminence fractures. Clinicians can use this tibial eminence fragment tracking using other imaging modalities, such as MRIs, to evaluate future fragment fixations focusing on vertical displacements and medial movements.

ACKNOWLEDGEMENTS

Support from the University of Pittsburgh Swanson School of Engineering, Department of Bioengineering, and Orthopaedic Surgery is gratefully acknowledged.

REFERENCES

[1] Bong, M et al., *Arthroscopy,* 21:1172-1176, 2005.
[2] Eggers, A et al., *AJSM*, 35:404-410, 2007.
[3] Taha, M et al., *Arthroscopy,* 36 :708-713, 2020.
[4] Sawyer, G et al., *Arthrosc Tech*, 2:315-318, 2013.
[5] Aboalata, M et al., *Arthrosc Tech,* 7:491-497, 2018.

SB³C2021
Summer Biomechanics, Bioengineering and Biotransport Conference
June 14-18, Virtual

EFFECT OF HELMET ON GENDER-BASED CERVICAL SPINE SEGMENTAL RESPONSES IN REAR IMPACT

Yuvaraj Purushothaman, John Humm, Hoon Choi, Deepak Rajasekaran, Narayan Yoganandan

Department of Neurosurgery
Medical College of Wisconsin
Milwaukee, WI

INTRODUCTION

Studies have reported the susceptibility of females to Whiplash Associated Disorders [1] [2]. It is known that morphological differences exist between female and male cervical necks [3]. While the use of the head supported mass is less common in the civilian populations, military personnel use the head mounted devices (helmet, night vision goggles, etc.) in their activities. Any added head supported mass from the helmet and its attached devices adds to the in vivo head mass. This additional weight on the human head-neck system alters the load path, affects load-sharing, changes the internal forces and moments and kinematics on the osteoligamentous cervical spine column under accelerative and chronic loads [4]. While many studies have been conducted to delineate the role of gender in whiplash injury via experiments, clinical investigations, modeling and epidemiological research, the effect of the added head mass on segmental motions have received less attention. This study was conducted to quantify the differences in kinematic responses, as defined by the range of motion metric, between mid-sized male and female models with and without the helmet using three-dimensional finite element modeling under rear impact accelerative whiplash loading.

METHODS

A mid-size male head-neck finite element model was developed and validated using experimental data [5][6]. It simulated the human head integrated with a detailed cervical spinal column model, developed with cervical and first thoracic vertebrae, intervertebral discs, endplates, facets, ligaments, and musculature. The skull, cortical bones, endplates and ligaments were modeled using shell elements, and the cancellous bone, annulus, nucleus and facets were modeled using solid elements. The neck muscles were simulated using anatomical origin-insertion locations as one-dimensional beam elements. The material properties for each of these components were obtained from literature studies [7][8]. The mid-size female model was developed by morphing the male model using respective anatomical ratios of male and female head and cervical spines [9]. The mapping block-based mesh morphing approach was used for the development of female model [5].

A coordinate measuring machine was used to describe the geometry of the helmet. A collection of coordinates was registered at each point of contact of the probe with the external part surface. The inner part of the helmet was lined with seven foam pads. The helmet and inner foam were modeled as solid hexahedral elements, and the material properties were based on literature studies [10][11]. The mass of the helmet was 1.47 kg. The helmet model was strapped to the male and female head-neck finite element models using a chinstrap, modeled using solid elements. Automatic surface-to-surface contact was defined between the head and helmet. The models were exercised under rear impact (G_x loading) by inputting a velocity pulse of 2.6 m/sec to the T1 vertebra, similar to field input. A total of four cases were simulated for male and female anthropometry, with and without helmet. The male model without helmet were validated with the experimental data [3]. The segmental motions were obtained from all subaxial cervical spinal levels, and the effects of gender and helmet mass were investigated. The segmental range of motion data from the helmeted models were normalized with respect to the respective models without the helmet to quantify the effect of helmet, motions from the female model was normalized with respect to the male model to determine the role of gender. These data and validation are given in the results section.

RESULTS

Model validation: The male head-neck model without helmet was validated using whole body human cadaver sled tests conducted in our laboratory [3]. The acceleration profiles of the T1 vertebra along the x, y, and z axes from the sled experiments were used as input to the model. The segmental kinematic response from the simulation was compared to the experimental data. The model-predicted ranges of motion were within mean ±1 standard deviation corridors of experimental motions (Figure 1).

Gender-based variations: The female model compared with the male model showed an increase in the range of motion at all segmental levels for both the cases of without and with helmet; however, the maximum increase occurred in case of the helmeted condition. In the

case of with helmet, the female model showed an increase of 11.6%, 9.4%, 11%, 10.1%, and 8.2% at the C3-C4, C4-C5, C5-C6, C6-C7, and C7-T1 levels, respectively.

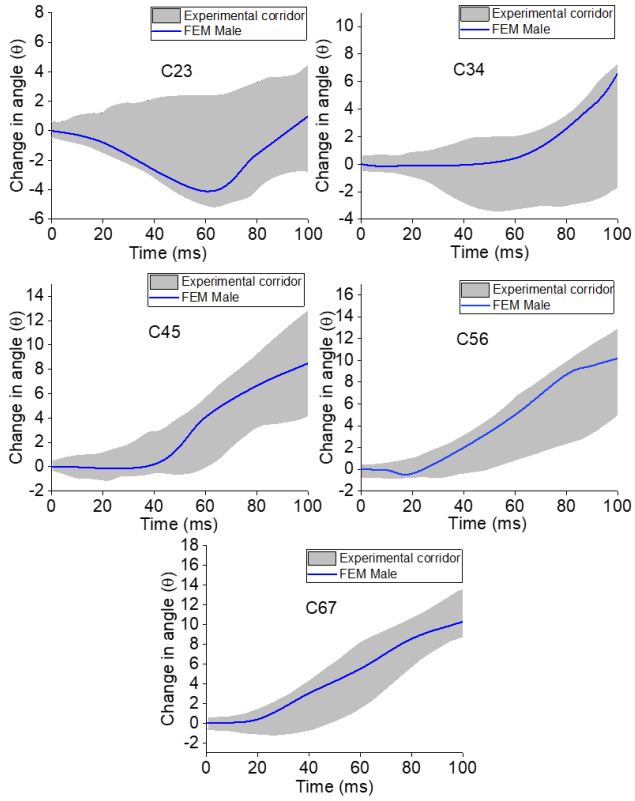

Figure 1: Model validation for segmental angulations response from C2–C3 through C6–C7 levels. The shaded region represents the experimental corridors from human cadaver sled tests.

Helmet-based variations: The segmental motion of the helmeted model increased when compared to the case without helmet model. In the male model, the increases were 12.2%, 12.4%, 29.2%, 19.6% and 13.8% at the C3-C4, C4-C5, C5-C6, C6-C7, and C7-T1 levels, respectively, whereas the increases in the female model were 14.1%, 13.8%, 30.1%, 20.5% and 14.9% at the corresponding levels of C3-C4, C4-C5, C5-C6, C6-C7, and C7-T1 levels, respectively (Figure 2).

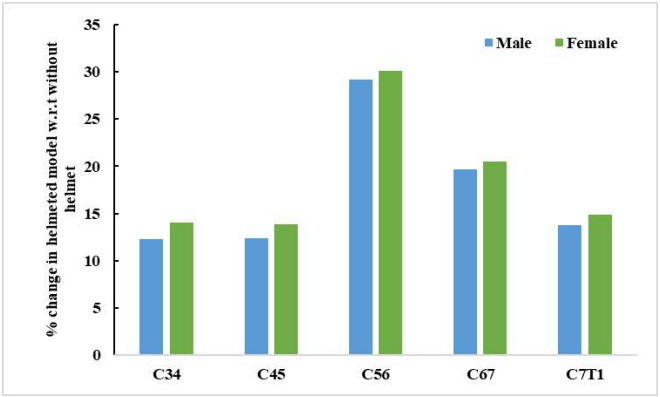

Figure 2: Segmental range of motion comparison between without and with helmet for male and female models

DISCUSSION

The objective of the study was to determine the segmental responses to elicit the role of gender and helmet on the segmental responses of the cervical spine from rear impact. The acceleration pulse was applied to the T1 vertebra, a process used in other modeling and isolated head-neck complex human cadaver studies. The segmental response in the form of the range of motion is a clinical measure for assessing the mobility of the spine, and hence, it was selected as a parameter for the assessment of gender and head supported mass. While not described here, in the initial stage of the pulse, the upper and lower cervical spines sustained flexion and extension. This combination representing a reverse curvature within the lordosis of the cervical column is attributed to the inertia of the human head and the transmission of the accelerative pulse from the distal end of the neck. Compared to all the spinal levels, the C5-C6 and C6-C7 regions experienced greater segmental ranges of motion. This is attributed to the local curvature of the cervical spine. These lower spinal levels are known to be the affected segments in whiplash patients from low severity impacts, similar to the velocity of the pulse used in the present study. In the case of gender response comparison, the female spine responded with a greater segmental range of motion than the male spine, a phenomenon observed in human cadaver studies and attributed to increased susceptibility of females to WADs [12]. This is attributed to the due to the differences in the morphology of the female spine from the male spine, a variable included in the present study. It should be noted that the female model was not a scaled-down version of the male model; instead actual level geometrical variations were included in the present female head-neck model. Thus, the results are more realistic than a simple male-to-female modeling approach, commonly adopted to study biomechanics of female spines. In the case of the helmet-based variations, the helmeted condition resulted in increased segmental motions compared to without helmet, and this is attributed to the center of mass shifting anteriorly and inferiorly with the added head mass. Any increase to the in vivo head mass and shift in its center of gravity away from its natural center of rotation elevates the kinematics and may predispose to injury in females. In summary, the present modeling study provides data on the role of gender and helmet on segmental kinematics rear impact.

ACKNOWLEDGEMENTS

This research was supported by the Department of Veterans Affairs Medical Research, Department of Neurosurgery at the Medical College of Wisconsin, and W81XWH-16-01-0010. This material is the result of work supported with the resources and use of facilities at the Zablocki VA Medical Center, Milwaukee, Wisconsin. The last author (NY) is an employee of the VA Medical Center, Milwaukee, WI.

REFERENCES

[1] Schmitt et al., *Trauma biomechanics*, Berlin: Springer, 2010.
[2] Spitzer Wo et al., Spine, 20 (April Suppl.): S1-73, 1995.
[3] Stemper, Brian D et al., AAAM, vol. 48, p. 149., 2004.
[4] Van den Oord et al., *Appl Ergon*, vol. 43, no. 5, pp. 958-64, 2012.
[5] John J. D. et al., 54th RMBS, pp 1-12, 2017,
[6] John J. D. et al., *Journal of biomechanical engineering*. 2019.
[7] Osth J, *J. biomechanical engineering*, vol. 138(6), no. 061005, 2016.
[8] Panzer and Cronin, *J Biomech*, vol. 42, no. 4, pp. 480-90, 2009.
[9] Vasavada, A. et al., J Biomech, vol. 41, no. 1, pp. 114-21, 2008.
[10] Palta E. et al., *International J. Impact Eng.*, pp. 125-143, 2018
[11] Li X.G. et al., *International J. Impact Eng*, vol. 91, pp. 56-67, 2016.
[12] Stemper, B. D. et al., *J. biomechanics*, 36(9), 1281-1289, 2003.

DEVELOPMENT OF PREDICTIVE MODEL OF ISCHEMIA IN ANOMALOUS AORTIC ORIGIN OF CORONARY ARTERY

Y. Farsiani (1,2), J. Parthasarathy (1), S. Molossi (3), C. Mery (4), R. Krishnamurthy (1), L.P. Dasi (2)

(1) Department of Radiology
Nationwide Children's Hospital
The Ohio State University College of Medicine
Columbus, Ohio, USA

(2) Department of Biomedical Engineering
Georgia Institute of Technology
Atlanta, Georgia, USA

(3) Department of Pediatrics,
Texas Children's Hospital,
Baylor College of Medicine
Houston, Texas, USA

(4) Dept. of Cardiothoracic Surgery,
Dell's Children's Medical Center
The University of Texas at Austin
Austin, Texas, USA

INTRODUCTION

Potential mechanisms of sudden cardiac death (SCD) in the anomalous aortic origin of coronary artery (AAOCA) are indeed dynamic and complex. Among these mechanisms are proximal coronary hypoplasia, dynamic ostial narrowing, intussusception of the intimal wall of the intramural segment, and interarterial compression during exercise. However, lack of understanding and inaccurate evaluation of the exact mechanism leading to ischemia and/ SCD has been the critical barrier to risk stratification. The clinical data has shown that the decision to operate and the type of surgery performed for the same condition in AAOCA patients can vary due to a lack of clarity on surgical approaches that target the offending mechanism. Among the morphological variables derived from advanced imaging in AAOCA patients, the main substrates are ostial stenosis, longer intramural length, and high origin of the ostium that correlate with ischemia[1]. To better understand these correlations, in the current study, we leverage large advanced imaging data of patient-specific morphological biomarkers to create a predictive model by quantifying the correlations and severity of each morphological variables to ischemic burdens. This model can potentially be a validated source for risk stratification, need for surgery, and type of surgery. This will be done using patient-specific 3D-printed models and subject them to the flow study, developing a mathematical model from fluid dynamics that matches the experimental measurement, and establish and validate the predictive model in a separate group of patient models.

METHODS

In this progressing study, we use the largest single-institutional patient and advanced imaging registry on AAOCA to identify a representative subset of AAOCA patients with and without clinically documented ischemia. IRB approval was obtained for case studies in a patient with AAOCA-L presented with repeat SCD after initial unroofing, and a second surgical intervention, translocation related to the pillar with the subsequent resolution if ischemia. Patient-specific biomechanical 3D-printed models were connected to a left heart flow simulator detailed in the previous study[2]. Temporal and spatial variation of flow rates and dynamic pressure are obtained at different locations along the proximal anomalous coronary artery throughout the cardiac cycle using catheter-based pressure measurement and transonic flowmeters. Details of the in vitro flow study can be found in our previous work [2]. The cumulative effect of all risk variables is shown in pressure drop along the proximal coronary. However, to investigate and quantify the contribution of each morphological or physiological risk factor to the ischemic burden and specific impact on fractional flow reserve (FFR), and instantaneous flow rate (IFR) a mathematical model for sensitivity analysis is being developed.

Using static and dynamic data acquired from in vitro flow study, a mathematical model is being built from fundamental fluid dynamics concepts and will be validated with clinical in vivo and in vitro data. The weight of morphological variables and their interactions on FFR and total pressure drop are represented by coefficients which is derived using regression analysis and machine learning application.

FFR is the main parameter to quantify the severity of ischemic burden in AAOCA and is essentially normalized pressure given as either the averaged or instantaneous ratio P_d/P_a where P_d is the distal pressure and P_a is the aortic pressure measured simultaneously along the aortocoronary path to capture pressure losses as blood flows through the lesion. From fundamental fluid dynamics, it is known that the pressure drop is associated with three major

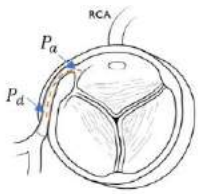

Figure 1 AAOCA-L ischematic

components including the viscous friction effects, the blockage effect (stenosis), and the flow unsteadiness effect[5]. This is generally captured with the unsteady Bernoulli's equation.

$$P_d(t) - P_a(t) = \frac{1}{2}\rho\left({V_a}^2(t) - {V_d}^2(t)\right) - \int_a^d \rho\left(\frac{dV}{dt} + k_f\frac{V}{D}(t)\right)ds - k_s\rho{V_o}^2(t) \quad (1)$$

In Equation (1) The first term on the right side accounts for dynamic pressure difference between points (a) and (b) in Figure 1, the second term accounts for losses due to unsteadiness in the flow and friction losses and the last term is losses from stenosis. Different flow features, including the blood viscosity, flow rate, and flow profile as well as the blockage morphology, are essential. In Equation 1, t is time, D is the internal diameter of the artery, ρ is the fluid density, V is instantaneous velocity throughout the cardiac cycle and k_f and k_s derived empirically. The effect of each variable or combination of them is identified using regression analysis to calculate α, β, and γ presented in Equation 2. By finding these coefficients by matching pressure drop measured from the experiment on different AAOCA models and theory, the mathematical model will be ready to get validated.

$$\Delta P(t) = \boldsymbol{\alpha}\Delta p(t)_{friction} + \boldsymbol{\beta}\Delta p(t)_{stenosis} + \boldsymbol{\gamma}\Delta p(t)_{unsteadiness} \quad (2)$$

RESULTS

Flow study was performed for the patient with AAOCA-L, and 3.5 mm intramural course, passing through a thickened intercoronary pillar (1A-D in figure 2), presented with repeat SCD after initial unroofing (2A-D), and coronary translocation to resolve recurrent ischemia related to the pillar with the subsequent resolution if ischemia (3A-D). Patient 3D-printed models were connected to a left heart flow simulator detailed in the previous study[2]. Flow studies showed FFR of 0.7 in the distal intramural segment preoperatively consistent with ischemia (1D), FFR less than 0.8 in the proximal mediastinal segment after unroofing (2D), consistent with persistent ischemia related to compression by the thickened pillar, and normal FFR at all locations after translocation (3D). From this preliminary data, the importance of resolving patient-specific mechanism of ischemia during surgery for AAOCA is illustrated using biomechanical flow-modeling. This methodology is the basis for the mathematical modeling and sensitivity analysis.

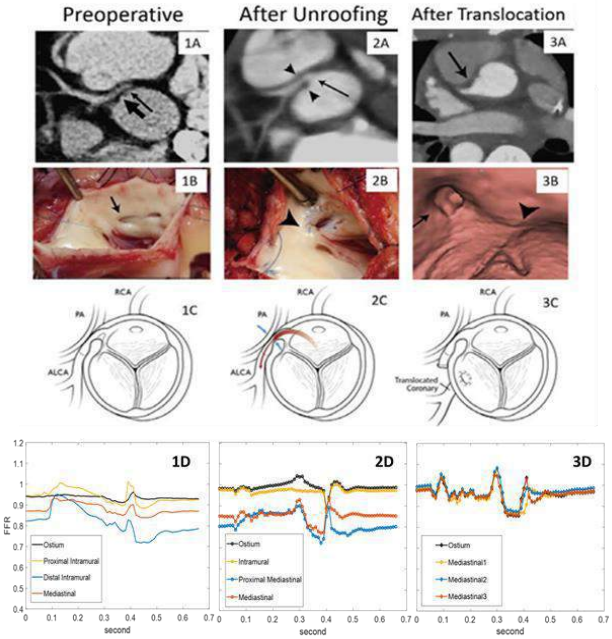

Figure 2 Importance of resolving patient-specific mechanism of ischemia after surgery

for the pre-operative case, the mathematical model was created using Equations 1 and 2. Pressure drop for stenosis, friction, and unsteady flow was calculated using measured flow rate along the anomalous coronary artery covering ostium to the distal intramural course. Coefficients $(\alpha,\ \beta,\ \gamma)$, was achieved by matching the pressure drops with the pressure drop acquired from in vitro flow study for point (a) to (d). In Figure 2, the pressure drop of the theoretical model and experiment is plotted in black, the FFR pair are also shown in purple, they show good agreement throughout most of the cycle. This is an ongoing experiment, and these empirically derived coefficients for the effect of stenosis, friction, and flow unsteadiness will be derived for other AAOCA models including postop unroofing and postop translocation to then be applied for regression analysis.

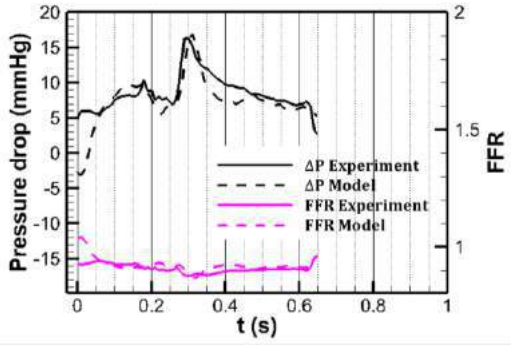

Figure 3 Pressure drop and FFR from in vitro study and mathematical modeling

In continuing this study, AAOCA patient's registry will be used to categorize models based on the main morphological variables; intramural lengths and ostial stenosis. A linear mixed model will be applied with 1) outcome being FFR; 2) exposures being intramural length, ostium configuration, location of FFR measure, and interactions between a pair of these three variables. Technically, the model can be expressed as

FFR = b0 + b1 x intramural length + b2 x ostial configuration + b3 x intramural length x ostial configuration + b3 x location of FFR measure + random effect + error term

DISCUSSION

Studies have been done on establishing a physics-based model of pressure drop and myocardial FFR for coronary stenosis[3,4]. However, this study is unique in using patients specific AAOCA models to develop a predictive theoretical model for FFR. This preliminary data shows promising results with the presented terms to capture the flow behavior in the experiment, predicting pressure gradient over the cardiac cycle and matching the model and experimentally derived FFR. Although it is showing the gradients over the cardiac cycle, by incorporating FFR from dynamic data related to exercise or hyperemia, prediction will be enhanced for impact of exercise which is a critical measure in AAOCA. We anticipate that creating a dataset input using all the categorized ischemic and non-ischemic models utilizing a machine learning algorithm will result in a robust predictive model of FFR from CT images.

ACKNOWLEDGEMENTS

We acknowledge Nationwide Children's Hospital and Georgia Tech discretionary funds. LPD and RK shared senior authorship.

REFERENCES

[2] Molossi, S., *Circ CV Imaging*, 13:e008445, 2020.
[1] Hatoum, G et al., *S. in thoracic and cardiovascular surgery*, 2020.
[3] Hou et al., *J. The Royal Society Interface, 9(71), 1325-1338*. 2011.
[4] Young, D.F. et al., *Circulation research*, 36(6), 735-743, 1975.

ADDITIONAL DISTAL FEMORAL RESECTION INCREASES MID-FLEXION LAXITY OF POSTERIOR STABILIZED TKA WITH FLEXION CONTRACTURE: A COMPUTATIONAL MODEL

S. Elmasry (1), B. Chalmers (2), C. Kahlenberg (2), P. Sculco (2), T. Wright (1), M. Cross (2), D. Mayman (2), G. Westrich (2), C. Imhauser (1)

(1) Department of Biomechanics
Hospital for Special Surgery
NYC, NY, USA

(2) Adult Reconstruction and Joint Replacement Service
Hospital for Special Surgery
NYC, NY, USA

INTRODUCTION

In Total Knee Arthroplasty (TKA), improper correction of preoperative flexion contracture can lead to a restricted range of motion and diminished knee function [1]. A common surgical approach to correct flexion contracture and achieve full knee extension is the additional bone resection of the distal femur. However, previous studies linked this approach to mid-flexion instability [2]. Mid-flexion instability is defined as symptomatic coronal laxity in the mid-ranges of knee flexion with clinically acceptable laxity at both 0° and 90° of flexion [3]. Previous clinical and cadaveric studies investigated the relationship between additional distal resection and midflexion stability [2, 4, 5]. However, these studies may not control for potential confounding factors such as variability in bony cuts, implant placement, and ligament properties. In contrast, computational models enable systematic comparison among surgical techniques while controlling the confounding factors [6]. Therefore, the purpose of this study was to develop a computational model of TKA with preoperative flexion contracture to quantify the effect of additional femoral resection on the midflexion coronal laxity.

METHODS

Six computational knee models were constructed based on cadaveric CT scans [7]. Twenty nonlinear springs representing the capsular and collateral ligament were added and the slack length of each ligament was calibrated using reference data from a cadaveric experiment (Fig.1) [8]. The models were implanted with a contemporary posterior stabilized TKA using the measured resection technique [6]. A subject-specific 2D static equilibrium model of a passive extension exam, a common exam to clinically evaluate flexion contracture, was developed and solved to estimate the knee extension moment (Fig. 2). The extension moments were used to calibrate the slack lengths of the posterior capsule to simulate a flexion contracture of 10°.

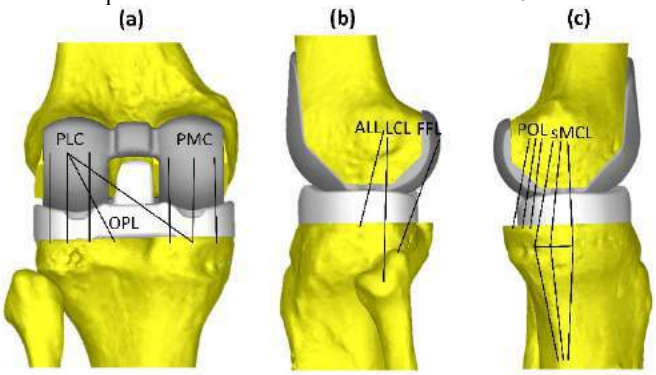

Figure 1: Six knee models were implanted with posterior stabilized TKA. The model included a total of 20 ligament fibers representing: (a) Posterior capsule, (b) lateral ligaments, and (c) medial ligaments. PMC: posterior medial capsule, PLC: posterior lateral capsule, OPL: oblique popliteal ligament, LCL: lateral collateral ligament, ALL: anterolateral ligament, FFL: fabellofibular ligament, sMCL: superficial medial collateral ligament, POL: posterior oblique ligament.

To evaluate the model's credibility, distal femoral resections of 2 mm and 4 mm were simulated (Fig. 3). The knees were then extended by applying the same extension moment estimated in the static equilibrium model of the clinical exam of passive extension and measuring the respective extension angle. The extension angle was compared with previous studies using a two-sample, two-tailed t-test ($p<0.05$) [2, 4, 5]. Subsequently, the knee was flexed to 30° and 45°; then, varus and valgus moments of ±10 Nm were applied for the baseline position of the femoral component and then after distal resections of 2 and 4 mm.

Coronal laxity, defined as the sum of varus and valgus angulation was measured at 30° and 45°of flexion and compared for each femoral component position using repeated measure ANOVA.

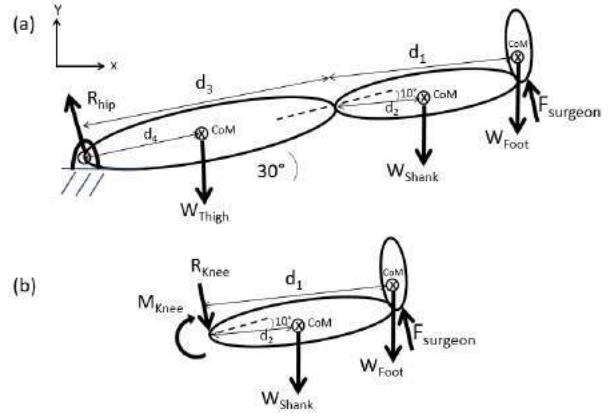

Figure. 2: Two-dimensional free body diagrams representing forces applied in the clinical exam of passive extension. (a) diagram of the full leg to determine the force applied by the surgeon at the foot. (b) diagram of the shank and foot segment to determine the internal knee moment. R_{hip}: ground reaction force at the hip; W_{thigh}: thigh weight; W_{shank}: shank weight; W_{foot}: foot weight; and $F_{surgeon}$: surgeon's lifting force; d_1: shank length; d_2: distance between the knee joint and shank center of mass (CoM); d_3: thigh length; d4a: distance between the center of hip joint and thigh center of mass.

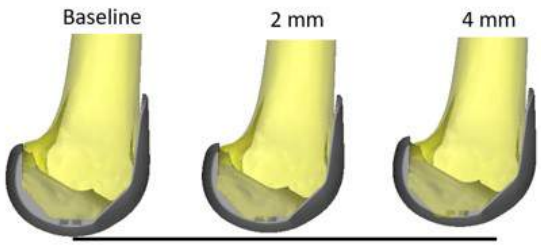

Figure. 3: Proximalizing the femoral component to simulate additional 2- and 4-mm bone resection of the distal femoral.

Table 1: Mean increase in knee extension of the six knee models after recutting the distal femur by 2 and 4 mm compared to three previous studies

	Increase in Knee Extension (°)			
	2 mm	**P value**	**4 mm**	**P value**
Knee models	4.6° ± 0.6°		8.3° ± 0.9°	
Cross 2012 [2]	3.6° ± 2.5°	0.36	8.6° ± 1.8°	0.72
Liu 2016 [4]	3.4° ± 2.9	0.32	6.7° ± 3.1	0.25
Kim 2017 [5]	4.8° ± 2.1	0.82	-	

RESULTS

With 2 and 4 mm of distal femoral resection, the knee extended an additional 4.6 ± 0.6° and 8.3± 0.9°, respectively (Table 1). Model predictions of the maximum extension angle after resecting the femur by 2 and 4 mm were within 1.2° ($p \geq 0.32$) and 1.6° ($p \geq 0.25$), respectively, compared to previous cadaveric and clinical studies (Table 1). After resecting 2 mm, the mean coronal laxity increased by 3.1° and 2.7° at 30 and 45°of flexion, respectively. At 30° of flexion, distal resections of 2 and 4 mm increased coronal laxity by 3.1±0.2° ($p<0.001$) and 6.5±0.6° ($p<0.001$), respectively, compared to baseline. At 45° of flexion, distal resections of 2 and 4 mm increased coronal laxity by 2.7±0.3° ($p<0.001$) and 5.5±0.7° ($p<0.001$), respectively, compared to baseline (Fig. 4).

DISCUSSION

A computational model of posterior stabilized TKA representing a knee with preoperative flexion contracture was developed. The model predictions corroborated previous cadaveric and clinical studies in measuring knee extension following additional femoral bone resection of 2 and 4 mm (Table 1) [2, 4, 5], suggesting that this model could be a credible method of representing TKA patients with preoperative flexion contracture. Additional distal resection was associated with increased coronal laxity at 30 and 45° of flexion ($P<0.001$). Elevated midflexion laxity could contribute to midflexion instability; a condition that may require revision surgery [5]. Therefore, surgeons should avoid additional distal resection if possible and attempt to use other surgical interventions to first address a flexion contracture such as removal of all posterior femoral osteophytes and release of the posterior capsule. If a flexion contracture persists, then additional distal femoral resection is warranted. It is important to examine the knee intraoperatively in extension and in flexion and between 30 and 45° of flexion to have the greatest chance of detecting increased coronal laxity. Further studies are warranted to understand the relationship between midflexion laxity and symptomatic instability.

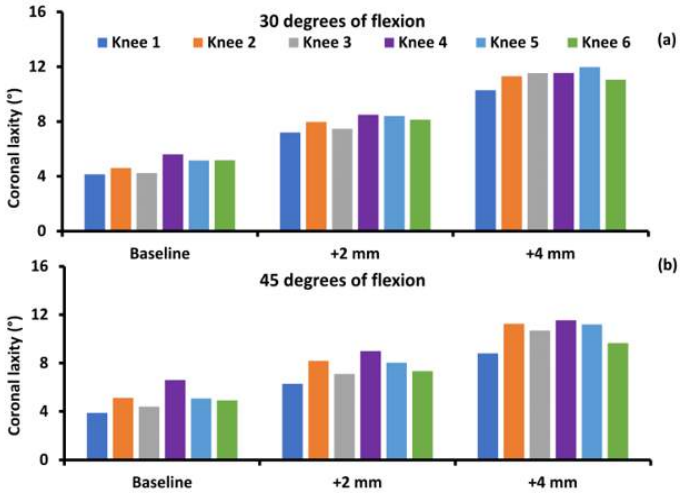

Figure. 4: Coronal laxity at (a) 30° and (b) 45° of flexion with the initial bone resection (baseline), and +2 mm, and +4 mm of additional bone resection of the distal femur.

ACKNOWLEDGEMENTS

Shady Elmasry was supported by a training award from the National Center for Advancing Translational Sciences of the NIH under Award Number TL1TR002386.

REFERENCES

[1] Anania, A et al., *International Orthopaedics* 37, 1917–1923(2013)
[2] Cross, M et al., *Knee*, 9(6): 875-79, 2012
[3] Nagle, M et al., *J Knee Surg*, 33(5):713-17, 2020
[4] Liu DW et al., *J Arthroplasty*, 31:98-102, 2016
[5] Kim, SH et al, *Sports Traum Arthr*, 25: 3501-07, 2017
[6] Elmasry. S et al., *J Arthroplasty*, 34(5): 981-86, 2019
[7] Elmasry, S et al., *J Orth Res*, 38(7):1637-45, 2020
[8] Kia, M et al., *J Biomech Eng*, 138(5): 051010, 2016

HISTO-MECHANICS OF THE PASSIVE RIGHT VENTRICULAR MYOCARDIUM

Sotirios Kakaletsis (1), Gabriella P. Sugerman (2), Tomasz Jazwiec (3), Marcin Malinowski (3), Tomasz A. Timek (3), Manuel K. Rausch (1,2,4)

(1) Department of Aerospace Engineering and Engineering Mechanics
University of Texas at Austin
Austin, TX, USA

(2) Department of Biomedical Engineering
University of Texas at Austin
Austin, TX, USA

(3) Cardiothoracic Surgery
Spectrum Health
Grand Rapids, MI, USA

(4) Department of Mechanical Engineering
University of Texas at Austin
Austin, TX, USA

INTRODUCTION

The right ventricle has been referred to as the "forgotten", the "dispensable", the "neglected", and the "unnecessary" side of the heart. Today, we know that of course the right ventricle is necessary. Nonetheless, it remains the "ignored" ventricle. That is, very little research has focused on investigating its microstructure and mechanics. This is a significant shortcoming as the right ventricle is a source of many devastating diseases and conditions. For example, this current pandemic affects the right ventricle disproportionately [1]. We currently do not understand why that is. Similarly, many patients with left ventricular assist devices, develop right heart failure for currently unknown reasons [2].

The goal of the current work was to fill many of the existing gaps in our knowledge about right ventricular mechanics. Specifically, we set out to characterize the complex, three-dimensional constitutive behavior of right ventricular myocardium and its microstructure.

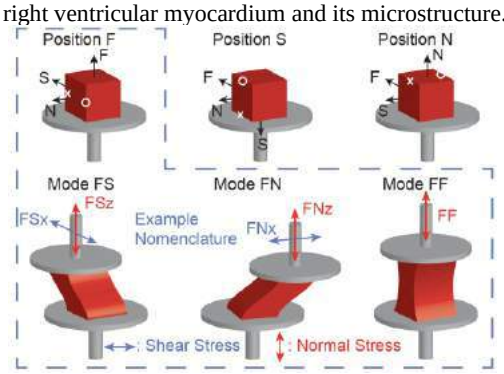

Figure 1: Myocardial shear testing modes and directional nomenclature

METHODS

To study and understand right ventricular myocardial mechanics, we used an ovine animal model. Specifically, we sacrificed 12 adult, male Dorsett sheep and excised their hearts. From these hearts, we extracted cube-shaped myocardial samples of approximately 10x10x10 mm with a surgical scalpel. Next, we tested these cubes under six different simple shear modes and three uniaxial extension and compression modes (Figure 1). For these tests we used our custom triaxial simple shear testing device that recorded both shear forces as well as normal forces. We performed all tests in a 37C physiological solution. After testing, we fixed the tissue in formaldehyde, and stored them in 70% alcohol before submitting them to a commercial histology service. There, our samples were cut at 1mm intervals in both

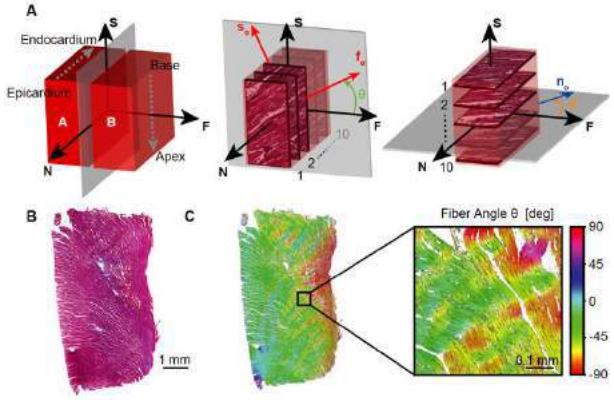

Figure 2: A) Tissue separation for radial and longitudinal histological investigation. B) Example Masson's trichrome stain, C) OrientationJ analysis

longitudinal and radial direction and subsequently stained via Masson's Trichrome. Once returned to our laboratory, we imaged the stained slides and characterized the tissue's microstructure via an ImageJ plugin, OrientationJ [3] (Figure2). From these microstructural maps, we informed probability density functions describing the tissue's major anisotropy axis. With gross cube dimensions and microstructural data at hand, we built custom 3D finite element meshes of each cube. Specifically, we discretized each cube with 1000 linear hexahedral elements. Using the open-source finite element software FEBio in combination with Matlab, we conducted inverse finite element analysis that iteratively identified the material parameters of a Holzapfel-type hyperelastic constitutive law by fitting simulation predictions to experimental mechanical data.

RESULTS

Figure 3 summarizes the mechanical data from our study. Specifically, it illustrates the mean and the standard error for all 6 individual shear modes (shear and normal stress) as well as the 3 uniaxial tensile/compression modes. Via a linear mixed model in which we compared the peak stresses at +/-30 strain (for shear modes) and +/-10% strain (for uniaxial modes) we found that right ventricular myocardium shows anisotropy, shear-stiffening, negative Poynting effect, and tension compression nonlinearity. Thus, right ventricular myocardium behaves very similarly to left ventricular myocardium.

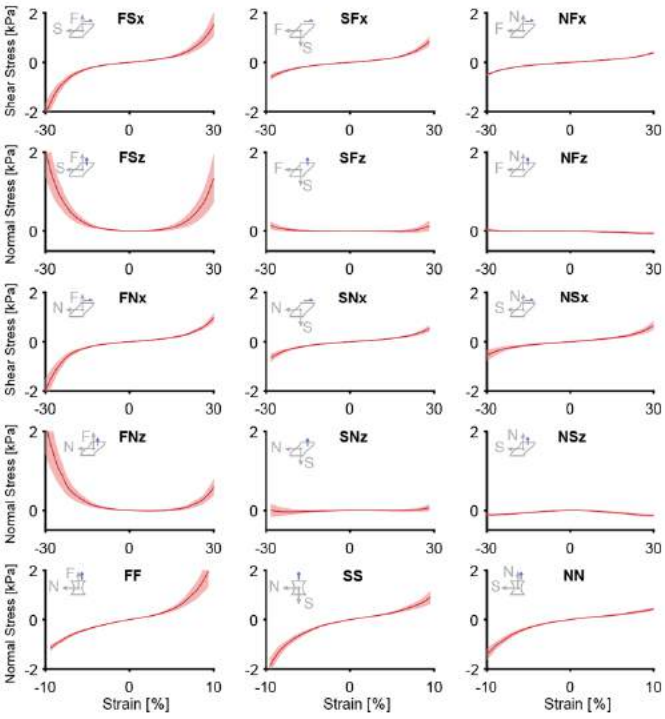

Figure 3: Mechanical test data for 12 right ventricular myocardial samples

Additionally, we analyzed the microstructure of right ventricular myocardium and found that its orientation varies significantly along the radial direction, but does not vary in longitudinal direction. Moreover, within each histological image, fibers are not perfectly aligned but are dispersed. This is true for radial and longitudinal sections. We found that this dispersion can be well captured via von Mises probability density functions (Figure 4).

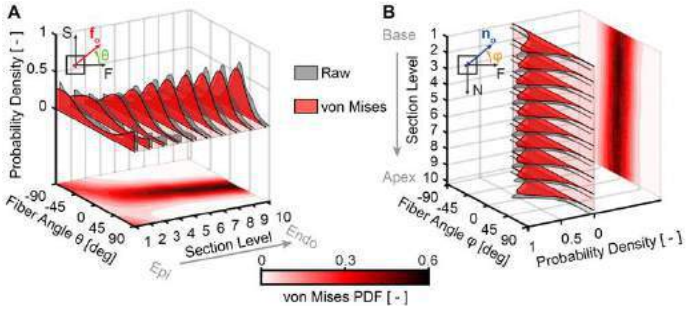

Figure 4: Histology-based microstructure of right ventricular myocardium in (A) radial direction, and (B) longitudinal direction.

Finally, we implemented and tested a hyperelastic constitutive law originally developed for left ventricular myocardium by Holzapfel [4]. Through our inverse approach, we identified its material parameters using different microstructural-inclusion strategies. We found that the material model fits our data excellently and is insensitive to different microstructural inclusion strategies. Figure 5 shows one example mode fit with this model.

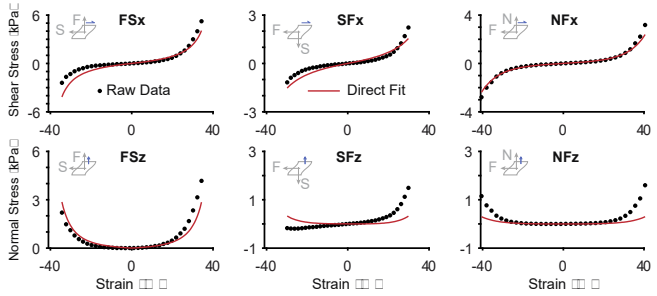

Figure 5: Holzapfel constitutive law fit to three shear modes (both normal and shear stress) of a representative sample

DISCUSSION

We presented mechanical data on ovine right ventricular myocardium and supplemented these data with histology-derived microstructural information. Combining these data, we also tested a hyperelastic constitutive law to represent the behavior of right ventricular myocardium. We found that myocardium behaves qualitatively very similar to left ventricular myocardium [5]. We also for the first time reported on radial and longitudinal organization of its microstructure and found that its organization is complex with distributions changing in radial direction, but not longitudinal direction. However, we found that even relatively simple inclusion strategies (using a single fiber direction vector for example) can achieve high quality constitutive fits with the Holzapfel constitutive law. Future work should now focus on the active properties of right ventricular myocardium that we have entirely ignored in our current work. Additionally, we tested samples from only a narrow region of the free wall. Future studies should also explore mechanical and microstructural heterogeneity through the right ventricular free wall.

REFERENCES

[1] Argulian, E et al., *JACC Imag*, 13:2459-2461, 2020.
[2] Bellavia, D et al., *Euro J Heart Fail*, 19:926-946, 2017.
[3] Meador, W et al., *Acta Biomaterialia*, 102:100-113, 2020.
[4] Holzapfel, G et al., *Phil Trans Royal Soc A*, 367:3445-3475, 2009.
[5] Sommer, G et al., *Acta Biomaterialia*, 24:172-192, 2015.

IN VIVO INJURY THRESHOLDS OF NEONATAL BRAHCIAL PLEXUS NERVES WHEN SUBJECTED TO STRETCH

V. Orozco, MS (1), R. Magee, MS (1), M. Sahni, MD (2), S. Balasubramanian, PhD (1), A. Singh, PhD (3)

(1) School of Biomedical Engineering, Sciences and Health Systems
Drexel University
Philadelphia, PA, USA

(2) Department of Pediatrics
Colle of Medicine, Drexel University
Philadelphia, PA, USA

(3) Department of Biomedical Engineering
Widener University
Philadelphia, PA, USA

INTRODUCTION

Neonatal brachial plexus palsy (NBPP) is a stretch injury to an infant's brachial plexus (BP) during complicated birthing scenarios, resulting in varying degrees of upper extremity paralysis. Despite improvements in obstetric care, NBPP continues to occur in about 1 to 4 per 1000 live births and has not decreased in recent years [1]. No *in vivo* data exists on the biomechanical responses of the anatomically complex neonatal BP when subjected to stretch. This study reports *in vivo* injury thresholds at each level and segment of the neonatal BP subjected to stretch using a neonatal large animal model.

METHODS

Fourteen neonatal piglets (3-5 days old) were anesthetized and BP exposed using an axillary approach per preapproved procedures by Institutional Animal Care and Use Committee (IACUC). Bifurcations of the divisions were located and BP segments above these bifurcations were labeled as root/trunk (i.e., proximal segment) and those below were labeled as cord followed by terminal nerve branch (i.e., distal segment). A custom-built mechanical testing device was used to perform *in vivo* stretch of BP (Fig. 1A). BP nerve segments were distally cut was cut and anchored (Fig. 1B). To measure real-time strain, three to five black acrylic paint markers were placed along BP nerve segment length (Fig. 1B, C). A stereo-camera (StereoLabs, San Francisco, CA, USA) was positioned above for strain analysis. BP segments were stretched at 500 mm/min. Load and displacement data was acquired at a sampling rate of 1000 Hz. Images were captured at 100 frames/s.

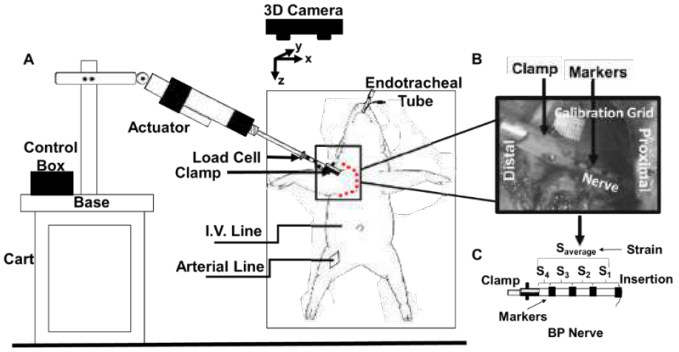

Figure 1. (A) *In vivo* biomechanical testing apparatus. (B) Clamped BP nerve with black markers along length. (C) Strain measured between adjacent makers of BP nerve.

DLTdv Digitizing Tool [2] was used to track marker displacements in 2D image plane of left and right videos. Stereo-camera was calibrated using Direct linear transformation (DLT). DLT calibration coefficients and 2D image points from left and right videos were used to obtained 3D points of marker displacement. Using a custom MATLAB (MathWorks, Natick, MA, USA) program 3D points were imported and length (l) of nerve segment and between each pair of adjacent markers at each time point was calculated using the distance formula (Eq. 1).

$$l_i = \sqrt{\left(x_{2_i} - x_{1_i}\right)^2 + \left(y_{2_i} - y_{1_i}\right)^2 + \left(z_{2_i} - z_{1_i}\right)^2} \quad (1)$$

Displacement (Δl) at each time point was calculated (Eq. 2).

$$\Delta l_i = l_i - l_o \quad (2)$$

Precent strain was determined at each time point (Eq 3).

$$perent\ strain_i = \frac{\Delta l_i}{l_o} * 100 \quad (3)$$

Camera data were used to track changes in structural integrity of BP nerve segments.

RESULTS

In vivo biomechanical response at failure of each BP terminal nerves (i.e., musculocutaneous (MSC), median, ulnar, and radial) are reported in table 1.

Table 1. Average *in vivo* biomechanical response of BP nerves (mean ± SD). MSC = musculocutaneous.

	MSC	Ulnar	Median	Radial
n	14	7	8	14
Average Diameter [cm]	0.11 ± 0.04	0.15 ± 0.03	0.21 ± 0.03	0.23 ± 0.04
Average Failure Load [N]	9.8 ± 3.9	15.8 ± 1.6	21.7 ± 3.6	23.7 ± 3.1
Average Failure Strain [%]	29.5 ± 7.6	27.3 ± 10.5	32.2 ± 19.8	39.8 ± 15.4

Differences were found in average diameter and average failure load ($p < 0.05$, Mann-Whitney U test, Figure 2A, B, respectively) between the BP nerves. No significant differences were found in the average failure strain between the four BP nerves ($p = 0.174$, Figure 2C).

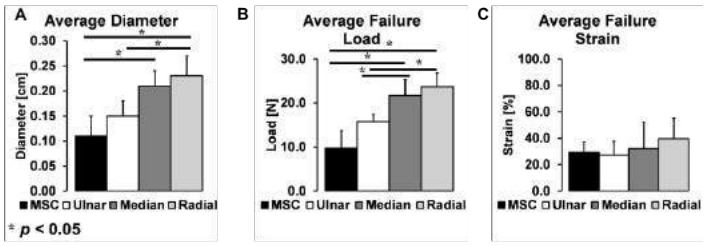

Figure 2. Bar graphs of the average (A) diameter, (B) failure load, and (C) failure strain of the BP nerves stretched to failure at 500 mm/min. MSC = musculocutaneous.

Maximum failure strain of proximal and distal segments (Figure 3A) of the BP complex was also examined. Figure 3B details the average maximum segmental failure strain of BP segments located proximally (root/trunk) and distally (chord/nerve). A total of 43 BP complexes were examined. It was found that 77% (33/43) failure site corresponded with the observed maximum failure strain location, while 23% (10/43) did not.

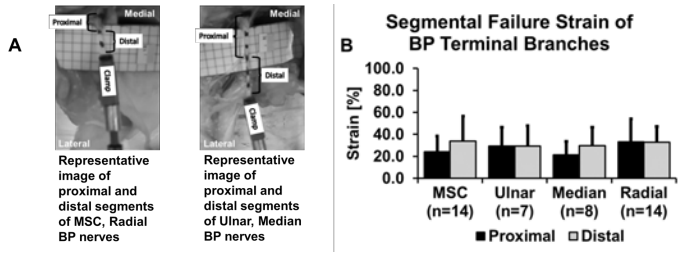

Figure 3. (A) Representative schematic defining the proximal and distal ends of BP terminal branches. (B) Bar graph detailing the average segmental failure strain of the BP terminal branches proximal and distal segments.

The average failure strain of the proximal and distal segments for each BP terminal branch is reported in Table 2.

Table 2. Average failure strain of proximal and distal segments of BP complex (mean ± SD). MSC = musculocutaneous.

	MSC		Ulnar		Median		Radial	
n	14		7		8		14	
Segment	Proximal	Distal	Proximal	Distal	Proximal	Distal	Proximal	Distal
Average Failure Strain [%]	24.1 ± 14.3	34.0 ± 22.4	29.5 ± 17.0	29.2 ± 18.8	21.3 ± 12.2	29.6 ± 16.8	33.2 ± 20.8	32.8 ± 14.2

DISCUSSION

Currently adult human cadaveric studies and adult small animal model studies are the ones that report the effect of stretch on the BP, however, due to ethical limitations, no studies have reported the stretch-injury response of the human neonatal BP. As a result, there is a need for neonatal large animal models to study the *in vivo* injury response of the neonatal BP subjected to stretch. Piglet animal models have been previously used to study functional deficit following injury to the BP as seen in NBPP [3].

This study is the first to report *in vivo* biomechanical response at each level and segment (i.e., proximal and distal) of the neonatal BP using a neonatal large animal model. Such biomechanical response data can be used to help characterize the mechanism of injury to allow clinicians to develop strategies to minimize occurrence of NBPP and guide treatment strategies.

ACKNOWLEDGEMENTS

This study was supported by the Eunice Kennedy Shriver National Institute of Child Health and Human Development of the National Institutes of Health (R15HD093024).

REFERENCES

[1] Addas, B. M., *Neurosciences* 15:136–137, 2010.
[2] Hedrick, T. L., *Bioinspir. Biomim.* 13:034001, 2008.
[3] Gonik, B., *Am. J. Obstet. Gynecol.* 178:688-695, 1998.

COMPARISON OF NONLINEAR MEMBRANE, SHELL, AND 3D FORMULATIONS FOR VASCULAR BIOMECHANICS

N. Nama (1), M. Aguirre (2), R. Ortigosa (3), A. J. Gil (4), J. D. Humphrey (5), C. A. Figueroa (1,6)

(1) Department of Surgery
University of Michigan
Ann Arbor, MI, USA

(2) Mines Saint-Etienne
Saint-Etienne, France

(3) Applied Mathematics and Statistics
Technical University of Cartagena
Cartagena, Murcia, Spain

(4) Zienkiewicz Centre for Computational Eng.
Swansea University
Swansea, United Kingdom

(5) Department of Biomedical Engineering
Yale University
New Haven. CT, USA

(6) Department of Biomedical Engineering
University of Michigan
Ann Arbor, MI, USA

INTRODUCTION

Computational techniques to simulate cardiovascular biomechanics have attracted significant interest owing to their applications in disease research, medical device design, and surgical planning [1]. Depending on the specific application, computational models of varying degree of mathematical sophistication have been employed to model the vessel wall. Typically, the vessel wall is represented either via membrane, shell, or 3D solid elements. Each of these formulations involves inherent assumptions and presents with its own advantages and disadvantages concerning accuracy, ease of implementation, and computational costs. Despite the widespread use of these elements for vascular biomechanics, there is little information on the precise physical regimes where these elements are applicable and the errors that may be induced due to the use of an inappropriate formulation. Consequently, the decision regarding the choice of the optimal element often relies on intuition or previous experience, with unclear consequences of choosing one approach over the others.

The primary objective of this work is to assess the impact of modeling element choice on solution accuracy via a systematic comparison of the commonly employed formulations for vascular biomechanics. We present comparison results to assess the accuracy of these approaches in both idealized and mouse-specific arterial models.

METHODS

We consider four different formulations to represent the vessel wall: (i) a nonlinear membrane model [2], (ii) a rotation-free shell model [3], (iii) a 3D solid formulation employing linear interpolation (referred as P1 wedge), and (iv) a 3D solid formulation employing quadratic interpolation (referred as P2 wedge). We present comparison results in three geometries with increasing degree of complexity: (a) a cylindrical tube, (b) an idealized bifurcation model, and (c) a mouse-specific geometry featuring multiple branches. The solid mesh for all comparisons is generated via an extrusion of the surface mesh used for 2D formulations with a single element across the thickness. The resulting number of degrees of freedom for each geometry is listed in Table 1. Figure 1 shows a representative example of the surface mesh and the corresponding volume mesh for the inflation of a cylinder.

Table 1: Degrees of freedom for different formulations

Geometry	Membrane	Shell	P1 wedge	P2 wedge
Cylinder	8601	8601	17202	102420
Bifurcation	--	48945	97890	586134
Mouse-specific	--	63843	127686	764865

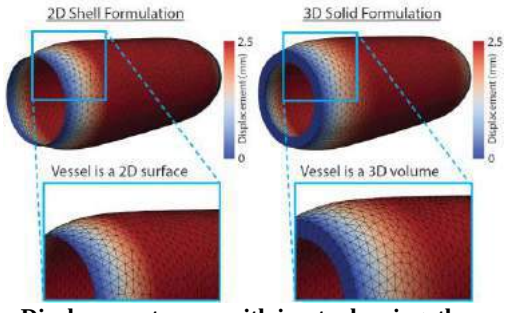

Figure 1: Displacement maps with insets showing the surface and volume mesh for 2D and 3D formulations, respectively.

RESULTS

Figure 2 compares the performance of all four formulations against the well-known axisymmetric solution [4] for the inflation of a cylindrical tube (radius, R=8.5 mm) with two different thickness-to-radius ratios (h/R). For the thin wall case (h/R=0.05), all the formulations agree very well with the axisymmetric solution with no significant errors. However, as the wall thickness is increased relative to the radius, the P1 wedge solution starts to deviate significantly from the axisymmetric solution. In contrast, the membrane and shell formulations exhibit smaller deviation. As expected, the P2 wedge formulation, with the largest computational expense, accurately captured the axisymmetric solution. These results indicate that, in the absence of the availability of an axisymmetric solution, P2 wedge solution can be taken as the true solution.

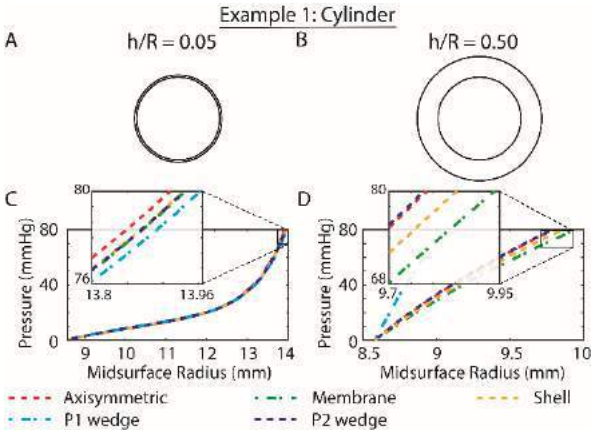

Figure 2: Comparison of different formulations against the axisymmetric solution for two values of thickness-to-radius ratio.

Next, we consider the inflation of an idealized bifurcation model comprising a main artery (R=0.6 mm) and a branch artery (R=0.2 mm) with wall thickness taken to be 10% of local radius. Due to significant bending in the bifurcation region, the membrane formulation fails to converge for this geometry, rendering it inappropriate for general vascular biomechanical analyses. Figure 3 compares the shell and P1 wedge results against the P2 wedge results. It is observed that the shell formulation captures the P2 wedge solution with superior accuracy compared to the P1 wedge solution, despite using fewer degrees of freedom (see Table 1).

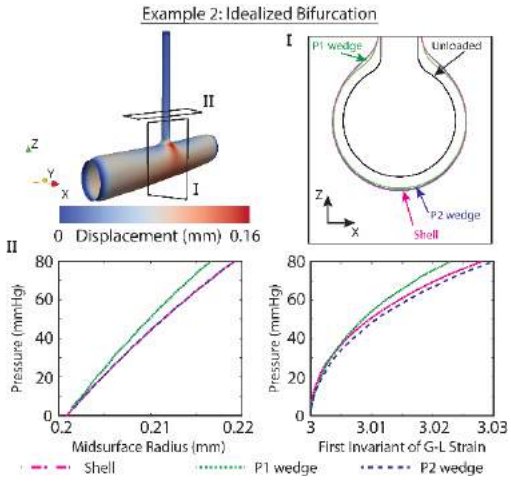

Figure 3: Comparison of shell and P1 wedge formulation against P2 wedge results for an idealized bifurcation model.

Figure 4 compares the performance of shell and P1 wedge formulation against P2 wedge results in a mouse-specific arterial model featuring multiple branches. The material parameters and wall thickness values were obtained via in vitro biaxial tests. Both P1 wedge and shell formulation yielded results virtually identical to P2 wedge solution, despite the shell formulation using 50% and 92% fewer degrees of freedom than P1 wedge and P2 wedge, respectively (see Table 1).

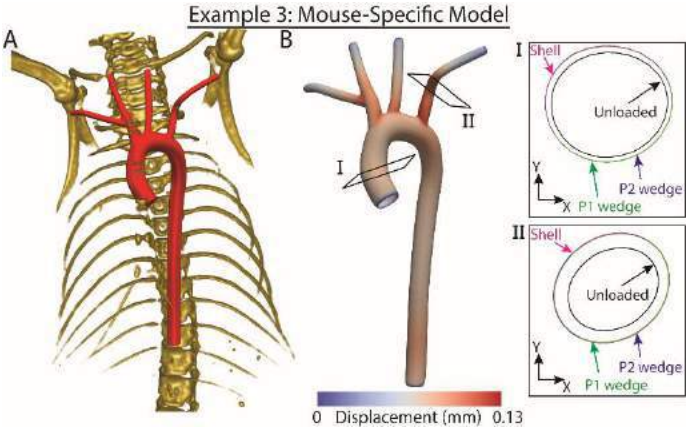

Figure 4: Comparison of shell and P1 wedge formulation against P2 wedge results for a subject-specific mouse geometry.

DISCUSSION

This work presented a comparison of different nonlinear formulations for vascular biomechanics. For thin geometries (h/R<0.05), all formulations (membrane, shell, P1 wedge, and P2 wedge) provided virtually identical results. As wall thickness increased relative to the radius, results started to differ. The primary findings of this work are: (a) the nonlinear membrane formulation is unable to handle bending mode deformations in bifurcating vascular structures, and (b) For relatively thicker vessel walls (h/R>0.05) and geometries including bifurcations, the rotation-free shell formulation, provides more accurate solution than P1 wedge formulation, despite using fewer degrees of freedom (see Table 1), and produces maximum errors of less than 6% relative to the P2 wedge formulation in all cases, while requiring only 8.3% of the degrees of freedom. Since typical vascular geometries exhibit wall thickness ratios in the range (h/R=0.05 to h/R=0.25), these results suggest that the shell formulation represents a computationally superior alternative, considering a balance between cost and accuracy, to the solid element formulations.

Future work aims to incorporate the rotation-free shell formulation within the CRIMSON software (www.crimson.software) to provide a computationally efficient, monolithic, fluid-structure interaction framework for cardiovascular hemodynamics.

ACKNOWLEDGEMENTS

This work was supported by grants from National Institute of Health (R01 HL105297) and American Heart Association postdoctoral fellowship (AHA 20POST35220004).

REFERENCES

[1] Taylor, C. A. and Figueroa C. A., *Annu Rev Biomed Eng.*, 11:109-134, 2009.

[2] Lu, J. et al., *Biomech. Model. Mechanbiol.*, 7: 477-486, 2008.

[3] Nama, N. et al., *Scientific Reports*, 10:1-17, 2020.

[4] Humphrey, J. D., Cardiovascular solid mechanics: cells, tissues, and organs. *Springer Science & Business Media*, 2013.

SPATIOTEMPORAL PROGRESSION AND MODULATION OF THE BLOOD-BRAIN-TUMOR BARRIER

Qi Cai (1), Xiaoqing Li (2), Hejian Xiong (1), Xiaofei Gao (3), Robert Bachoo (3,4), Zhenpeng Qin* (1,2,5,6)

(1) Department of Bioengineering, University of Texas at Dallas, Richardson, TX, USA

(2) Department of Bioengineering, University of Texas at Dallas, Richardson, TX, USA

(3) Department of Internal Medicine, University of Texas Southwestern Medical Center Dallas, TX, USA

(4) Department of Neurology, University of Texas Southwestern Medical Center, Dallas, TX, USA

(5) Department of Surgery, University of Texas Southwestern Medical Center, Dallas, TX, USA

(6) Center for advanced pain study, University of Texas at Dallas, Richardson, TX, USA

INTRODUCTION

Entry of circulating molecules into the brain is strictly limited by the blood-brain barrier (BBB) that includes the endothelial tight-junction (TJ) complex and low rates of transcytosis. In glioblastoma (GBM), the most common and deadly primary brain tumor in adults, the BBB displays heterogeneous permeability to circulating drugs [1] and raises a challenge for drug delivery across this barrier. The standard of care for GBM is maximal safe resection followed by radiation and chemotherapy [2]. However, since the properties of the blood-brain-tumor barrier (BBTB) has been poorly understood, the treatment efficacy and the development of new drug delivery platform are significantly limited. Therefore, a better understanding of the GBM microenvironment, particularly the BBTB and new avenues to enhance drug delivery into the brain are of great importance.

To safely and reversibily increase the BBB permeability, we have developed a method that non-invasively modulates the BBB with picosecond laser excitation of TJ-targeted plasmonic gold nanoparticles (AuNPs) [3]. In this approach, AuNPs were conjugated with the antibody BV11 (AuNP-BV11) to target JAM-A, which is a part of the TJ complex. Then the picosecond laser pulse excitation of AuNPs leads to the generation of mechanical wave that perturbs the TJ, increasing the BBB permeability without compromising normal brain function. This method allows the delivery of immunoglobulins, adeno-associated viral vectors, and liposomes to the brain parenchyma. However, it remains unclear whether this strategy can be applied for the BBTB.

In this work, we analyzed the progression of BBTB in terms of permeability and BBB-related key biomarkers as the tumor grows in a mouse GBM model. We found that the BBTB remains intact at early stage (7 days) while starting to break down at later time points (14 and 21 days). We then showed that the BBTB permeability can be modulated to allow dye accumulation by using the optical approach introduced above. This BBTB modulation approach paves a new way of drug delivery for the treatment of glioma.

METHODS

Glioma model: 73C glioma cells were used, which were generated in primary astrocyte cultures from neonatal mice and carried conditional mutations for $Pten^{f/f}$, $p53^{f/f}$, and $LSLBraf^{V600E}$. 370 μL of the cell suspension (2×10^5 cells/mL) was transplanted into the left hemisphere of the mice (Nu/J, stock no.002019, 7 weeks) at 500 μm depth.

Glioma microenvironment study: To study the BBTB integrity, EZ-link biotin (Biotin, 660 Da) and Evans blue (EB, 66 kDa, binds to albumin) were intravenously injected into two mice at 7, 14 and 21 dpi (days post injection). Coronal brain slices (20 μm thickness) were cut using cryostat for imaging. To study the IF alterations of BBB-related proteins, coronal brain slices (20 μm thickness) were stained with vascular biomarker (CD31) and tight junction proteins (i.e. Claudin-5, ZO-1 and VE-cadherin) using the reported method [3].

Modulating the BBTB in vivo: The molecular targeting nanoparticles AuNP-BV11 are prepared as reported [3]. At 7 dpi, the glioma-bearing mouse was intravenously injected with AuNP-BV11 (18.5 μg/g). Picosecond laser pulse (532 nm, 45 mJ/cm^2) was then applied through the intact mouse skull. EB dye was intravenously injected to visualize the BBB disruption. The animal was perfused after 30 min. Then coronal brain slices (40 μm thickness) were cut using cryostat for imaging.

RESULTS

BBTB integrity study on 73C glioma model: As shown in Figure 1A, the BBTB remains intact at the tumor core (i) and tumor margin (ii) compared to the contralateral side (iii) at 7 dpi. In this case, the tracers are confined in blood vessels. The permeability of the tumor core

increases at 14 dpi and 21 dpi (Figure 1 B, C), indicates by an increased background fluorescent intensity due to the extravasation of the fluorescent dye from blood vessels, while the BBTB in the tumor margin is not disrupted.

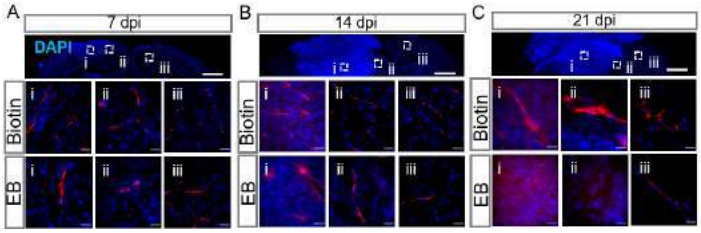

Figure 1: Dye permeability in 73C glioma model at (A) 7, (B) 14, and (C) 21 dpi. Scale bar represents 1 mm in the upper panels and 20 µm in the lower zoom in panels.

To understand the mechanism of the BBTB disruption, immunohistochemistry (IHC) is used to stain on BBB-related proteins (Figure 2). No significant differences of the IF intensities of TJ protein Claudin-5 and adherens junction protein VE-Cadherin were observed. However, the loss of the IF intensity of TJ-associated protein ZO-1 was discovered at 14 and 21 dpi.

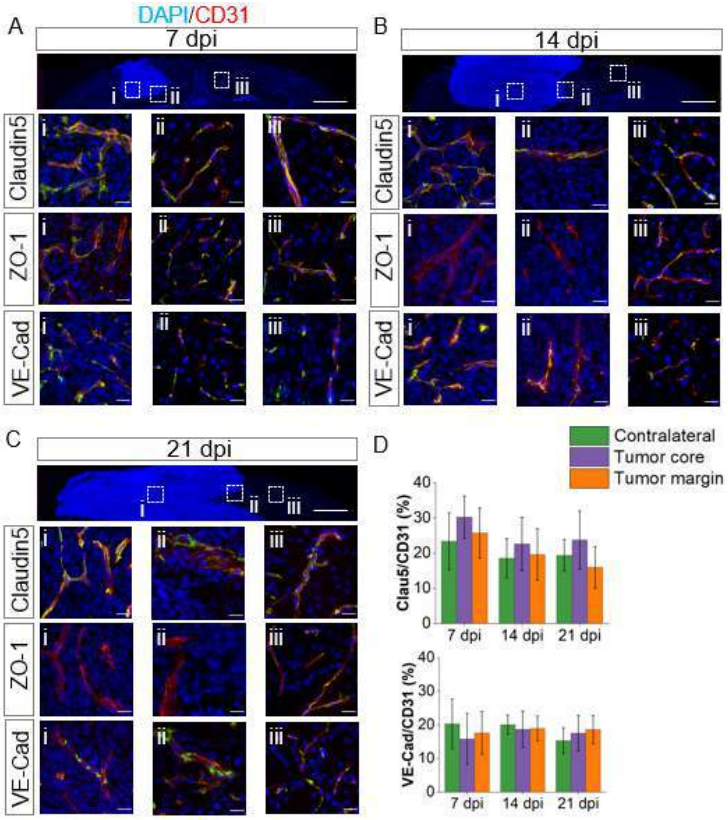

Figure 2: IHC staining of BBB-related proteins (green color) at (A) 7 dpi, (B) 14 dpi and (C) 21 dpi. Scale bar represents 1 mm in the upper panels and 20 µm in the lower zoom in panels. (D) Analysis of protein coverage ratio over CD31. No significant difference was detected. One-way Anova, n=8.

BBTB modulation: To modulate the BBTB in 73C glioma model, TJ-targeted AuNP-BV11 was injected via tail vein and picosecond laser was applied on both the tumor side (left hemisphere) and the contralateral side (right hemisphere) of the brain. Figure 3A shows that extravasation of EB is observed in both tumor side and contralateral side. Successful BBTB modulation was confirmed by the leakage of EB into the tumor area as shown in the fluorescent images (Figure 3B and C). Although both sides show an increase in permeability, the contralateral brain side has a stronger tracer leakage.

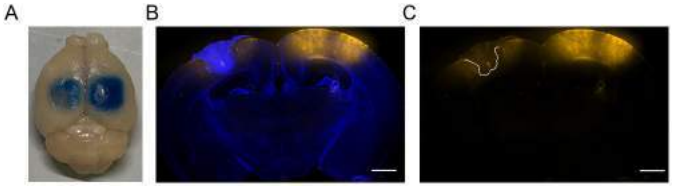

Figure 3. BBTB modulation at 7 dpi using picosecond laser excitation of AuNP-BV11. (A) Visualization of the EB extravasation after BBTB modulation. (B) Hoechst staining indicates the tumor area. (C) fluorescent imaging of the EB signal in the brain parenchyma. Scale bar represents 5 mm.

DISCUSSION

A better understanding of the glioma microenvironment facilitates the design of novel drug delivery platform to enhance the treatment efficacy. A heterogenous permeability of the BBTB in the glioma has been reported to circulating drugs [1]. Yet, detailed understanding of BBTB permeability progression is missing and limits the capability to design effective strategies for GBM treatment. In this study, BBTB integrity in glioma bearing mice was studied by analyzing the fluorescent dye permeability and BBB-related proteins by IHC staining at three different time points. The results reveal that the BBTB in 73C glioma core remains intact at 7 dpi, but it is disrupted at 14 and 21 dpi. The BBTB dysfunction is probably due to the loss of TJ-associated protein ZO-1, since the ZO proteins are essential for assembly of functional TJs by binding to and cross-linking a wide range of TJ proteins and tethering them to the actin cytoskeleton [4].

The standard of care for GBM is maximal safe resection followed by radiation and chemotherapy. However, since gliomas infiltrate into surrounding healthy brain tissue, unresected tumor margin is the primary cause of recurrence. Moreover, since the BBTB remains intact at the tumor margin, chemotherapy drug concentration is much lower within the tumor margin than at the tumor core [5]. Therefore, GBM always results in poor patient prognosis, and there is an imperative need for the development of novel, targeted, and effective therapies for GBM. This study shows that the BBTB permeability can be enhanced by using picosecond laser excitation of TJ-targeted AuNPs. This technique has several advantages, such as non-invasive, entirely reversible and has minimal influence on the normal brain structures and functions [3]. Future work will be focused on the delivery of anti-cancer drugs into the glioma model using the optical BBTB modulation approach and study the treatment efficacy *in vivo*.

ACKNOWLEDGEMENTS

We acknowledge funding support from Cancer Prevention & Research Institution of Texas (RP190728).

REFERENCES

[1] Arvanitis, C et al., *Nature Reviews Cancer*, 20:26-41, 2020.
[2] Harder, B et al., *Front Oncol*, 8:462, 2018.
[3] Li, X et al., *BioRxiv*, 2020.
[4] Lochhead, J et al., *Front. Physiol*, 11:914, 2020.
[5] Mainprize, T et al.,. *Sci Rep*, 9:321, 2019.

SB³C2021
Summer Biomechanics, Bioengineering and Biotransport Conference
June 14-18, Virtual

NOTOCHORD ECCENTRICITY AND ITS RELATION TO CELL PACKING

Emma L. Sorrell (1), Sharon R. Lubkin (1)

(1) Department of Mathematics
North Carolina State University
Raleigh, NC, USA

INTRODUCTION

We previously categorized and quantified the packing patterns of the vacuolated interior cells in the zebrafish notochord [1]. We showed, in wild type and in mutants, as well as in a model system of gel beads, that the local packing patterns are determined by the local ratio λ of vacuolated cells per unit length. We also observed that the zebrafish notochords were not necessarily circular in cross section [1]. The local eccentricity e of the wild-type notochord correlated with regions along its length that were in the staircase configuration, where $e = 0.4$; in regions packed in other patterns, the cross section was more circular ($e = 0$). Since the staircase pattern of the zebrafish WT notochord is associated with normal spinal development, and the absence of staircase patterning in various mutants appears to be correlated with defects in spine morphogenesis such as scoliosis [2]–[5], and since the variety of packing metrics seen in the zebrafish notochord hold equally in a nonliving system, we would like to better understand the relationship between the mechanics of packing and the cross-sectional ovaling of the arrangement.

To better understand the relationship between cell packing pattern and notochord eccentricity, and how these may relate to morphogenesis, function, and evolution, we developed and analyzed three models of the regular packing of cells in a sheath. Because eccentricity is associated with the staircase pattern, and because notochords are seen to have a small number of cells per unit length, we focus specifically on the lowest-order regular packing patterns, bamboo and staircase.

METHODS

Following the principle of parsimony, our models of cell packing mechanics in the notochord are based on simplifying assumptions:

- The notochord is infinitely long, without taper.
- The notochord consists of a sheath and interior cells, with no space between them.
- Interior cells are of a uniform constant volume, have equal internal pressures, and are packed in regular patterns.
- There is a uniform distribution of cells, with a constant count λ of cells per unit length.
- The sheath is thin relative to the notochord diameter, and of uniform material properties. We neglect individual sheath cells and sheath thickness.
- The mechanics of internal vacuolated cells are dominated by surface forces. Cells have a uniform surface tension γ_c.

The remaining assumption is the mechanics of the sheath. We used three different models of the notochord sheath, of increasing generality:

- The rigid sheath is an elliptic cylinder of fixed eccentricity.
- The semi-flexible sheath is rigid longitudinally, but flexible in cross section. We restrict the semi-flexible sheath to have elliptic cross section; its eccentricity is the result of the packing of cells inside it. It has uniform surface tension γ_s.
- The flexible sheath is of uniform surface tension γ_s. Its shape is determined by the packing of cells inside it.

The models reveal the relationship between packing pattern and three key dimensionless ratios:

- cells per unit length λ
- sheath eccentricity e
- surface tension ratio $\Gamma = \gamma_s/\gamma_c$.

RESULTS

Rigid sheath A simple analysis shows that the surface energy of the bamboo pattern in a rigid elliptic cylinder does not depend on the eccentricity. We verified that minimal-energy simulations for bamboo fit this solution at a wide distribution of eccentricities.

We determined the surface energy of the staircase pattern at a variety of fixed sheath eccentricities, and determined the bifurcation values of λ, at which one pattern became a lower-energy configuration.

As observed in bubble experiments [6][7], there is some overlap of the range of λ in which the patterns are observable.

For a circular cylinder, the bamboo-staircase bifurcation is at λ = 1.13; as eccentricity increases, this λ value decreases, increasing the range of λ for which staircase is the more optimal pattern. That is, tube eccentricity shifts the packing patterns away from bamboo, towards staircase.

Semiflexible sheath In this model, e is not predetermined, but is adjusted by the energy minimization. A simple analysis shows that the minimal energy cylinder for bamboo pattern has $e = 0$. We verify that all bamboo patterns in this model converge to circular in cross-section.

The bamboo-staircase bifurcation was at approximately λ = 1.13, independent of Γ.

The staircase pattern was never observed to have $e = 0$, though as the sheath tension increased relative to the cell tension (as Γ increased), e decreased. As Γ decreased (sheath softening), e increased. Statistical analysis of the eccentricity of staircase patterns' dependence on λ and Γ revealed insignificant λ dependence.

Flexible sheath The flexible sheath, like spandex, reveals the shapes of the vacuolated cells within (**Fig 1**). In the limit of infinite Γ, the sheath is straight, but as Γ decreases, the sheath shows cusps at the cell-cell junctions, of angle $\cos\theta = 1/(1+\Gamma)$.

As with the semiflexible model, for Γ > 0.7, the lowest-energy pattern was bamboo for λ < 1.13, and staircase for λ > 1.13 (**Fig 2**). The bamboo pattern never showed eccentricity; the staircase pattern had eccentricity which depended strongly on Γ and insignificantly on λ, fitting best to the same biexponential function as in the semiflexible model.

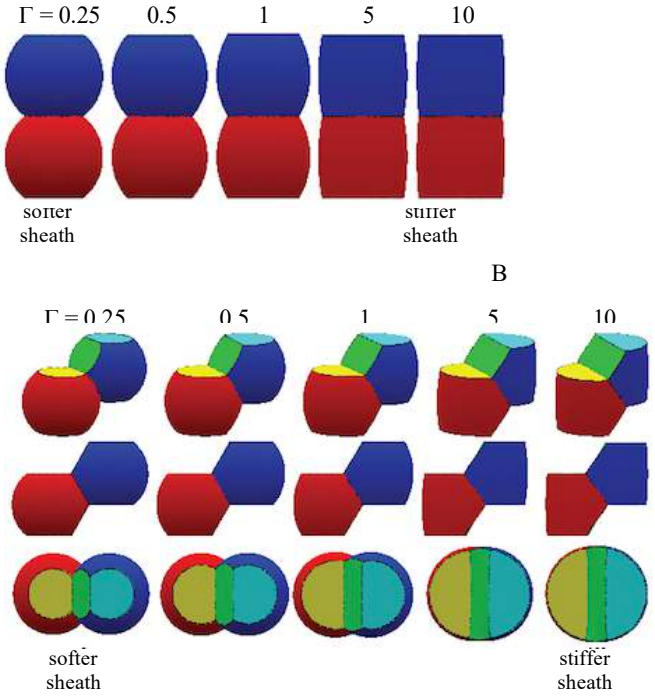

Figure 1: Flexible sheath morphology. Sheath has fixed surface tension ratio Γ, and λ cells per unit length, but eccentricity e and sheath shape are determined by energy minimization of cell packing. Bamboo (A, λ = 0.96) and staircase (B, λ = 1.39) patterns show that sheath straightness increases with Γ.

For Γ < 0.7, a new pattern was seen at intermediate λ, with some of the properties of bamboo (each cell having two neighbors) and some of the properties of staircase (zigzag geometry). We call this pattern "serpentine".

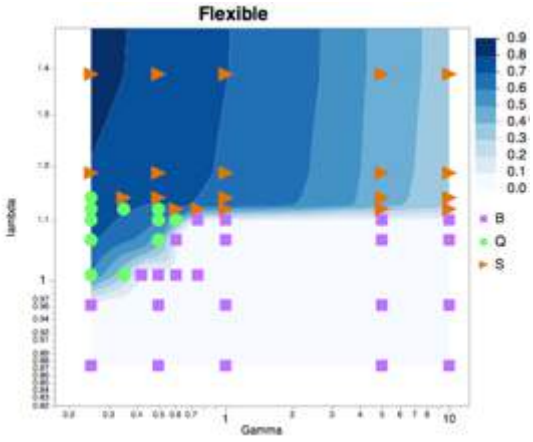

Figure 2: Bifurcation diagram for flexible sheath. For Γ > 0.7, and λ < 1.1, pattern is bamboo with $e = 0$ (purple). Above λ ~ 1.1, pattern is staircase (orange), with e determined by tension ratio Γ. At low Γ, novel serpentine pattern (green) is seen.

DISCUSSION

The consistency of the results of the three models, despite different assumptions, coupled with the agreement between these results for regular patterns and the previously analyzed irregular patterns in gel beads and zebrafish notochords [1], suggest that the bidirectional relationship between staircase and eccentricity is a *generic phenomenon*, at most weakly dependent on the mechanical details of the tubes/sheaths and their contents, but dependent on the two ratios λ (cells per unit length) and Γ (sheath tension/cell tension).

The results suggest inferences regarding the mechanics of vacuolated notochords. For a notochord in a staircase packing, the eccentricity of the cross section corresponds to a specific tension ratio Γ, for which we found a formula. For example WT zebrafish notochords in staircase have $e = 0.4$ [1], suggesting that the sheath is under 6-7 times greater tension than the vacuolated cells within it.

The zebrafish has several mechanisms ensuring the formation of an eccentric notochord packed in staircase pattern at a particular developmental stage, the failure of which leads to spine malformation [2]–[5][8]. What might be the functional significance of the eccentric staircase notochord, which makes it worth controlling for? That is the subject of another study.

ACKNOWLEDGEMENTS

SRL was partially supported by grant 524764 from the Simons Foundation.

REFERENCES

[1] Norman, J., E.L. Sorrell, Y. Hu, et al., *Phil Trans Roy Soc B: Biol Sci* **2018**, *373*, 20170320.
[2] Bagnat, M., R.S. Gray, *Development* **2020**, *147*.
[3] Bagwell, J., J. Norman, K. Ellis, et al., *ELife* **2020**.
[4] Ellis, K., J. Bagwell, M. Bagnat, *J Cell Biol* **2013**, *200*, 667.
[5] Ellis, K., B.D. Hoffman, M. Bagnat, *Bioarchitecture* **2013**, *3*, 64.
[6] Pittet, N., N. Rivier, D. Weaire, *Forma* **1995**, *10*, 65.
[7] Hutzler, S., D. Weaire, R. Crawford, *Phil Mag B* **1997**, *75*, 845.
[8] Garcia, J., J. Bagwell, B. Njaine, et al., *Curr Biol* **2017**, *27*, 1982.

PATIENT-SPECIFIC ARTERY GEOMETRY AND ABM/FEA/CFD COMPUTATIONAL FRAMEWORK

[a] John E. Yoo, [a] Jeremy L. Warren, [b] Habib Samady, [b] David Molony, [a] Clark A. Meyer, [a] Heather N. Hayenga

[a] Department of Bioengineering
The University of Texas at Dallas
Richardson, Texas, U.S.A.

[b] School of Medicine
Emory University
Atlanta, Georgia, U.S.A.

INTRODUCTION

Cardiovascular disease has long been one of the leading causes of death across the world. In this study we explore the development and application of an automated method to computationally model patient-specific arteries using a trifecta of finite element analysis (FEA), computational fluid dynamics (CFD) and agent-based modeling (ABM). FEA has commonly been used in 2D modeling per VH-IVUS slice or linear 3D modeling [1][2] to determine stress and strain within arteries, yet its lone application is limited. Similarly, CFD and ABM have been used to understand artery wall shear stress (WSS) [6], however both fall short of a fully comprehensive model. The framework driving our system takes the best of all three disciplines and uses patient-specific virtual histology intravascular ultrasound imaging (VH-IVUS) and angiogram data to create a 3D model and separate IVUS images by tissue composition to understand plaque deposition and growth. The overarching objective is to produce an open-source tool to advance the research community's innovative agenda and provide a tool that can be used to predict growth and remodeling of an atherosclerotic artery.

METHODS

To align ourselves with an open-source mentality the program utilizes open-source python libraries, java tools (Repast Simphony), a custom in-house CFD script, FEA software (FEBio 3.0) [7], and GIBBON code [4] to maintain accuracy while also addressing each angle of the project. Figure 3 displays the framework our tool is based around. In stage one, IVUS images and angiogram are taken of a suspected atherosclerotic artery (Figure 1). This data is passed to stage two where the VH-IVUS slices, catheter centerline, co-registration data, and angular rotational references for the VH-IVUS slices were utilized. The stated information including necessary angiogram data between baseline and follow-up (collected 6 months apart) were provided by an Emory University clinical study [3]. Out of the 27 patients with VH-IVUS and angiogram data at baseline and 6-month follow-up, we only used data from patient 26 in this study.

The raw VH-IVUS slices were filtered to only keep the fibrofatty tissue, fibrous tissue, necrotic core, arterial vessel wall, and dense calcium. We then extracted the catheter centerline from the angiogram data. The filtered VH-IVUS images were then plotted orthogonally along the extracted catheter centerline data and along a straight centerline for a comparison study discussed in the results. Marking bifurcations helped to align the tilt between slices. The surface mesh of the outer wall and inner lumen were created with inner and outer contours. The volumetric mesh was created utilizing GIBBON [4] where a 2x2 filter was applied to simplify the geometry.

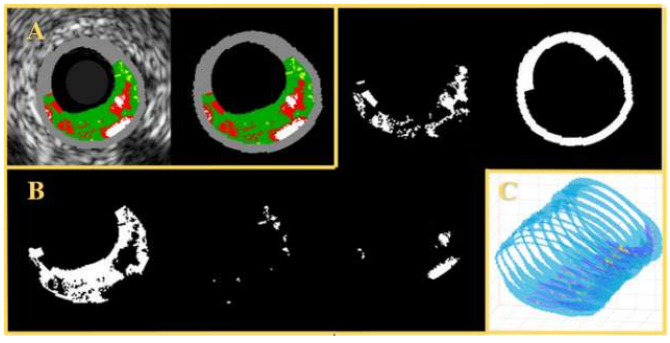

Figure 1. Filtering, Separation, and Plotting along 3D Centerline. **A**: Pre and post filtering **B**: Splitting of materials from image **C**: Plotting materials along 3D centerline.

Once the patient-specific geometry has been generated, FEA and CFD simulation is run to compute the initial wall strains/stresses and wall shear stresses (WSS) respectively. To do so, each element from the volumetric mesh is given a unique material property based on the nearest material data in the same space (Figure 2). The Mooney Rivlin equation was used to apply material properties, which was predefined by FEBio (Equation 1).

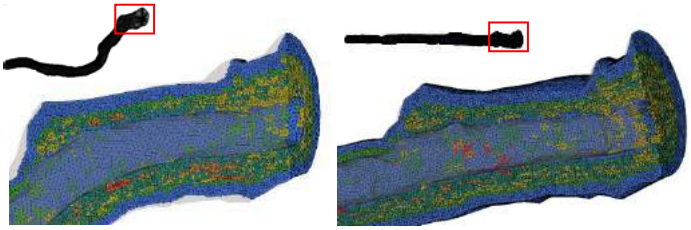

Figure 2. Cut View of Meshed Artery with Materials Assigned The material data along each centerline was used to accurately assign material values to elements in the volumetric mesh.

From here the third stage starts and the looping scheme begins running the ABM where rules derived from literature simulate the biological interactions between the various leukocytes and tissue types present in the artery wall [6]. To maintain spatial-temporal accuracy the ABM pauses at fixed time steps or changes in geometry to run FEA and CFD simulations and compute new WSS and strain values that are passed back into the ABM.

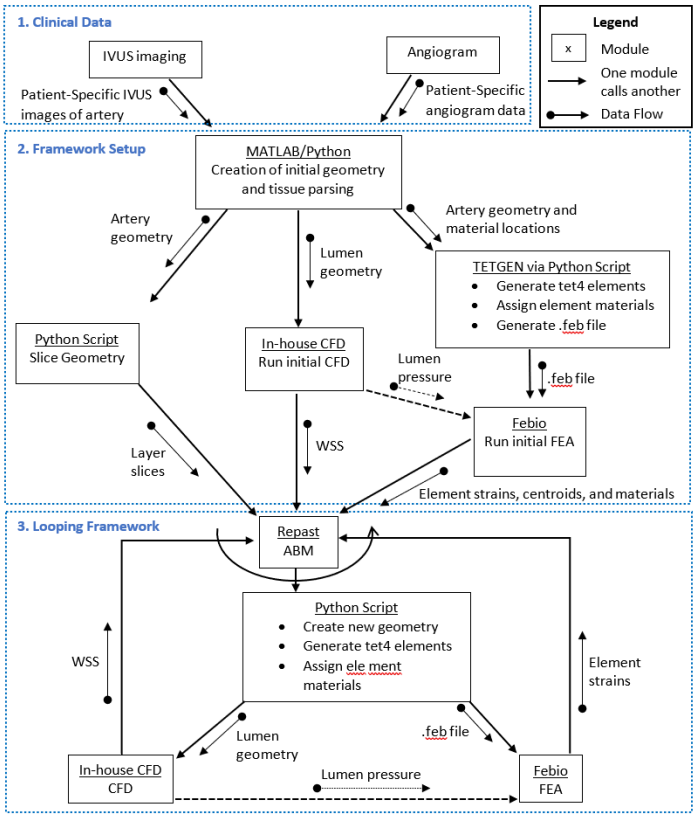

Figure 3. Computational Framework: Framework is divided into 3 sections; Clinical data; Framework setup; Looping framework.

$$W = C_1(I_1 - 3) + C_2(I2 - 3) + \frac{1}{2}K(lnJ)^2$$

Equation 1. FEBio Mooney-Rivlin strain energy density function The given coefficients and variables represent exchangeable material value parameters.

RESULTS

Utilizing this framework, we are able to handshake Repast with FEBio and our in-house CFD code automatically. The iterative handshaking will inform biologically and mechanically inspired remodeling. In patient 26, the relative volumes of the material constituents are 52.48% buffer material, 17.78% fibrotic/fibrous cap, 18.34% arterial wall, 6.47% fibrofatty, 3.21% necrotic core, and 1.71% dense calcium in the straight centerline artery reconstruction and 52.02% buffer material, 17.95% fibrotic/fibrous cap, 18.49% arterial wall, 6.57% fibrofatty, 3.24% necrotic core, and 1.73% dense calcium in the curved centerline artery reconstruction. The values for both centerlines are within 2.5% of each other suggesting the methods are similar but not exactly equivalent. The 2.5% difference is owed to the non-linear change in distance between each slice of the VH-IVUS slices orthogonal to the curved centerline, resulting in slightly larger elements.

DISCUSSION

The usage of the new model created from this research will be able to determine the impact that wall mechanics and biological factors have on plaque remodeling and atherosclerotic development. A better understanding of these underlying elements and how they affect each other will validate previous models and drive future research on other ABM, FEA, and CFD frameworks. Owing to the data available from Emory University, we hope to utilize our model and validate the results for all other 26 patients in the data set. Depending on the outcome of our model on the remaining patient data, we hope to optimize our ABM rules, looping framework and produce a model that could even lead to applications in other areas of the body.

The biggest limitations present in our model present themselves as the assumptions made on the material assignment in the empty space between IVUS slices. With respect to our IVUS to 3D geometry methods, the spacing between image slices is minimal and makes no assumptions. However, creating a nonlinear 3D model always creates small gaps between slices and material assignments must be normalized for the space between them. This may cause some deviation in CFD and FEA outputs when comparing to data from other studies. In future works, we will build on previous experiences to build a fully intuitive, applicable, and data-driven model for atherosclerosis remodeling.

ACKNOWLEDGEMENTS

Authors gratefully acknowledge funding for this work provided by the American Heart Association (17SDG33400239) and by the National Heart, Lung, And Blood Institute of the National Institutes of Health under Award Number R01HL136776. The content is solely the responsibility of the authors and does not necessarily represent the official views of the National Institutes of Health.

REFERENCES

[1] Timmins, Int J Cardiovasc Imaging, 33:13-24, 2017
[2] Teng, AHA Journals: Cardiovascular Imaging, 7: 461-470, 2014
[3] Samady, AHA Journals: Circulation, 124:779-788, 2011
[4] Moerman, JOSS, 3(22), 506, 2018
[5] Noble, et al, J Mesh Behav Biomed Mater, 10.1016, 2019
[6] Rita, et al, PLOS Computational Biology, 13: 5, 2017
[7] Maas SA, Ellis BJ, Ateshian GA, Weiss JA: FEBio: Finite elements for biomechanics. Journal of Biomechanical Engineering, 134(1) 2012.

FUNCTIONAL MECHANICS OF THE MURINE PULMONARY HEART VALVE

X. Feng (1), Y. Liu (2), H. Liu (1,3), C. Breuer (2,4), D. McComb (2), M. Sacks (1,3)

(1) Willerson Center for Cardiovascular Modeling and Simulation
Oden Institute for Computational Engineering and Sciences
University of Texas at Austin
Austin, TX, USA

(2) Center for Electron Microscopy and Analysis
The Ohio State University
Columbus, OH, USA

(3) Department of Biomedical Engineering
University of Texas at Austin
Austin, TX, USA

(4) Center for Regenerative Medicine
Nationwide Children's Hospital
Columbus, OH, USA

INTRODUCTION

Murine models provide an efficient platform to study heart valve diseases compared to other mammalian animals due to the low maintenance cost and high turn-over rate of mice. Moreover, since mice share more than 85% protein-coding genome as human, it is often possible to use readily available techniques for manipulating murine genome to mimic human valvular diseases [1]. These grant genetically modified murine models a relevant animal model for investigating the genetic cause and pathological development of valvular diseases, and for testing potential therapeutical treatment as well.

However, the functional mechanics of murine heart valves is still under-studied. This is mainly due to lack of high-resolution real-time imaging and *ex vivo* mechanical testing methods given the small size of murine heart valves (~1mm). Indeed, many scientific questions remain largely unknown regarding, e.g., the structural-mechanical properties of a murine heart valve and its shape adaptation in a cardiac cycle. Few studies on quantifying the stiffness of murine heart valves utilized the atomic force microscopy or micropipette aspiration experiments, and hence limited by the assumption of linear elasticity [2-3].

To address this gap in heart valve research, we and our collaborators have proposed an integrated imaging/computational framework to quantify the nonlinear mechanical properties of murine pulmonary valves (PVs) based on a series of µCT-derived geometries. From the µCT images, we have previously obtained a set of geometric characteristics of murine PVs at multiple physiological transvalvular pressure (TVP) levels. In this study, our aim is to extend the work and use mechanical simulation to provide, for the first time, an estimate of the functional elastic parameters for murine PVs and the unloaded shape.

METHODS

Experiments and Image Analysis

We excised the PVs from eleven healthy one-year old C57BL/6J mice (n=3 at 10mmHg, n=5 at 20mmHg, n=3 at 30mmHg). Each PV was pressurized hydrostatically, chemically fixed, and then imaged using a Heliscan µCT instrument (Thermo Fisher Scientific, resolution ~5µm). From the µCT images, we obtained a set of geometric characteristics of the murine PVs including geometric quantities of interest such as the valve height (H), free edge (FE) and basal attachment (BA) length of different leaflets, tilt angle between the annulus (ANL) and sino-tubular-junction (STJ) planes, β, as well as the representative profiles of central cross sections in the circumferential and radial directions of each leaflet (see Figure 1). Additionally, we developed a correlative workflow to map local collagen fiber structure acquired by serial block face imaging scanning electron microscopy (SBF-SEM) onto the segmented PV surface, allowing us to validate the collagen fiber orientation in the mechanical model.

Theoretical Framework and Simulation

We modeled the PV leaflet as a Kirchhoff-Love thin shell. Given the transvalvular pressure P, the equilibrium displacement $\boldsymbol{u}$ for a single leaflet is defined by the principle of virtual work, i.e.,

$$D_{\delta \boldsymbol{u}} W^{int}(\boldsymbol{u}) - D_{\delta \boldsymbol{u}} W^{ext}(\boldsymbol{u}) = 0 \tag{1}$$

for any compatible virtual displacement $\delta\boldsymbol{u}$ in which the variations of the internal and external virtual works are given, respectively, by

$$D_{\delta \boldsymbol{u}} W^{int}(\boldsymbol{u}) = \int_{M^0} \left(\int_{-\frac{h}{2}}^{\frac{h}{2}} D_{\delta \mathbf{u}} \psi \, dh' \right) dS, \tag{2}$$

$$D_{\delta \boldsymbol{u}} W^{ext}(\boldsymbol{u}) = \int_{M^0} P \boldsymbol{e}_n \cdot \delta \boldsymbol{u} J dS. \quad (3)$$

Here, M^0 represents the undeformed mid-surface, ψ is the strain energy density of the PV, h is the leaflet thickness, $\boldsymbol{e}_n$ is the unit normal vector of the deformed mid-surface, and J is the Jacobian. Leaflet-leaflet contact during coaptation was simulated by incorporating a volumetric contact potential [4]. Particularly, the contact potential between two neighboring leaflets is defined as

$$E_c = \int_{M_1^0} \int_{M_2^0} \varphi(r_{12}) d\boldsymbol{X}_1 d\boldsymbol{X}_2 \quad (4)$$

where M_1^0 and M_2^0 are the undeformed mid-surfaces of the two leaflets, r_{12} is the distance between two material points $\boldsymbol{X}_1$ and $\boldsymbol{X}_2$ in the deformed configuration and φ is a univariate nonnegative function which rapidly increases as r_{12} is less than a threshold.

Overall, the simulation of PV deformation under hydrostatic pressure solves the following nonlinear variational problem:

$$\sum_{\text{all leaflets}} \left[D_{\delta \boldsymbol{u}} W^{int}(\boldsymbol{u}) - D_{\delta \boldsymbol{u}} W^{ext}(\boldsymbol{u}) \right] + \sum_{\text{all leaflet pairs}} D_{\delta \boldsymbol{u}} E_c = 0, \forall \delta \boldsymbol{u}. \quad (5)$$

which is implemented using the state-of-the-art finite element libraries FEniCS and ShNAPr [5]. Experimentally estimated root distention is applied linearly on the basal attachment as TVP increases.

We modeled the PV as a Fung-type hyperelastic material with additional fiber contribution along the circumferential direction consistent with the SBF-SEM measurement (see Figures 1 and 2). The strain energy density ψ is given by:

$$\psi = \frac{1}{2} c_1 \left[\exp\left(c_2 (I_1 - 3)^2 \right) - 1 \right] + \frac{1}{2} c_3 \left[\exp\left(c_4 (I_4 - 1)^2 \right) - 1 \right] \quad (6)$$

in which $I_1 = \mathrm{tr}(\boldsymbol{C})$ and $I_4 = \boldsymbol{e}_f \cdot \boldsymbol{C} \boldsymbol{e}_f$ are two invariants of the right Cauchy Green's deformation tensor $\boldsymbol{C}$ and $\boldsymbol{e}_f$ is the unit fiber direction.

Geometric Model of Murine PVs

We developed a geometric model for the unloaded PV mid-surfaces based on the nonuniform rational B-splines (NURBS), which is integrated seamlessly with the finite element solver using the technique of isogeometric analysis. This allowed us to optimize the PV geometry on the fly without remeshing. The geometric model captures key features of the segmented PV geometries including left-right symmetry, a nonzero tilt angle between ANL and STJ planes, etc., with the total number of parameters equal to 16.

Optimization Scheme

We used SBPLX, a global simplex-based algorithm from the NLOPT package, to optimize the parameters for both the mechanical and geometric models (n_{params}=12). For each set of trial parameters, we obtained the central cross-sectional profiles of the simulated PV in both circumferential and radial directions at 10, 20 and 30 mmHg. The profiles were then compared with the µCT-derived representative cross sections and used to define the cost function. By iteratively minimizing the cost function, we were able to obtain the optimal unloaded PV geometry and mechanical parameters at the same time.

RESULTS

From the µCT images, we obtained geometric characteristics for murine PVs at 10, 20 and 30mm Hg, all of which had high consistency among different PVs at the same TVP (see Figure 1). By matching the extrapolated values of geometric quantities of interest at 0mmHg, we were able to partially constrain the unloaded PV geometry. The rest of the geometric parameters, which characterize the belly profile ($\mathbf{r}_2$) of the leaflets, were determined by the optimization scheme, together with

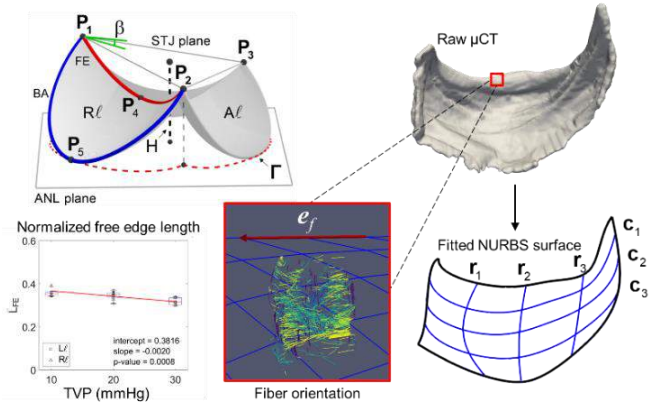

Figure 1: Geometric quantities of interest, local collagen fiber orientation and leaflet cross sectional profiles of the PVs are obtained using µCT and SBF-SEM imaging at multiple TVPs.

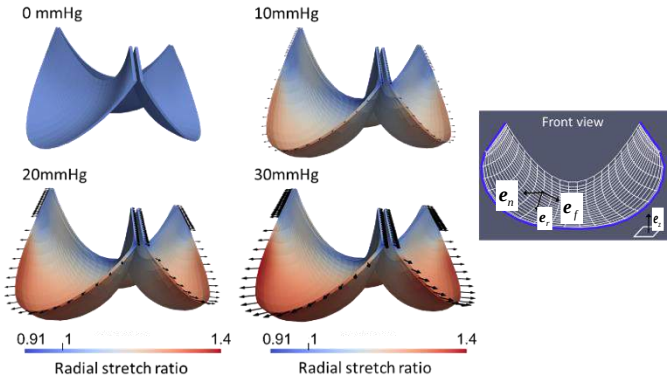

Figure 2: Simulated valvular deformation. The surface of the PV is color coded by the stretch ratio in the radial direction $\boldsymbol{e}_r$. Arrows indicate the Dirichlet boundary condition which mimics the root distention under increasing TVP.

the four mechanical parameters. With estimate root distention and proper mechanical parameters, we were able to match the representative cross-sectional profiles accurately (see Figure 2).

DISCUSSION

Using our imaging/computational approach, we were able to obtain, for the first time, the functional nonlinear mechanical properties of murine PVs. Since each murine PV needs to be fixed before imaging, only one pressure measurement is available per PV. To remedy the issue, we developed representative geometric characteristics from multiple PVs at the same TVP. Additionally, due to distortion of PVs at 0mmHg, we were not able to obtain accurate unloaded PV geometry directly from experiment. We resolved the problem by developing a data-constrained geometric model at 0mmHg and using optimization to fully determine the model parameters. Our future direction is to combine the numerical method with *in vivo* imaging techniques (e.g., the high frequency 4D ultrasound imaging) and apply the approach to study aortic valves of diseased mouse models.

REFERENCES

[1] Cheek, J., et al., *J. Mol. Cell. Cardiol.*, 52(3): 689-700, 2012.
[2] Krishnamurthy, V. K., et al., *J Biomech*, 44(1): 77-83, 2011.
[3] Sewell-Loftin, M. K., et al., *J Heart Valve Dis*, 21(4): 513, 2012.
[4] Kamensky, D., et al., *CMAME*, 330:522-546, 2018.
[5] Kamensky, D., *Comput. Math. with Appl.*, 2020 (in press).

SB³C2021
Summer Biomechanics, Bioengineering and Biotransport Conference
June 14-18, Virtual

Energy dissipation in the meniscus: a parametric study on tissue properties and mechanical loading conditions

Massimiliano De Rosa (1), Alicia R. Jackson (2), Francesco Travascio (1,3,4)

(1) Department of Mechanical and Aerospace Engineering
University of Miami
Coral Gables, Florida, USA

(2) Department of Biomedical Engineering
University of Miami
Coral Gables, FL, USA

(3) Department of Orthopaedic Surgery
University of Miami
Coral Gables, FL, USA

(4) Max Biedermann Institute for Biomechanics
Mount Sinai Medical Center
Miami Beach, FL, USA

INTRODUCTION

The meniscus is a fibrocartilaginous structure mostly made of a proteoglycan and collagen matrix immersed into a fluid phase [1]. Such a structure plays a fundamental role in the knee function, offering protection to the cartilage of the femur and tibia during joint motion [2]. Every movement of the knee results in the mechanical loading of each individual part of its structure. In particular, the meniscus plays the essential role of dissipating the mechanical energy transferred to the knee during motion [3]. This dissipative mechanism is fundamental to protect the underlying articular cartilage [3].

The way the meniscus dissipates energy is through the friction developed by the relative motion between the fluid phase and the porous solid matrix.[3] This particular mechanism of dissipating energy is regulated by two physical parameters: the aggregate modulus (H), responsible of the elastic deformation of the solid matrix; and the hydraulic permeability (K), regulating the ease of fluid motion within the tissue. Both H and K are material parameters whose magnitude depends on tissue composition [4]. Accordingly, degenerative phenomena affecting the composition of the meniscus may also cause changes in the magnitudes of H and K and, consequently, alter the capability of the meniscus to dissipate mechanical energy.

To date, the effect of degeneration on the dissipating capability of the meniscus has not been determined. The goal of this work was to quantitatively investigate how energy dissipation is affected by the values of the parameters H and K. This was conducted via computer simulated experiments of meniscal energy dissipation during cyclic loading at different values of H and K. We hypothesized that energy dissipation would be directly related to the magnitude of H and inversely related to the magnitude of K.

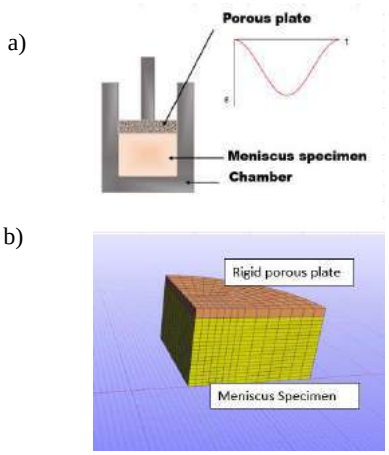

Figure 1: (a) Schematic representation of the confined compression of the meniscus sample. (b) Computatioanl model of the confined compression of the specimen.

METHODS

A finite element model was developed to simulate a meniscus cylindrical specimen undergoing cyclic confined compression at control of displacement, see Figure 1. In the simulations, the specimen was compressed by a rigid porous plate. The presence of pores in the plate allowed the fluid naturally contained in the tissue to flow outside the meniscus during the compression. As previously reported [5,6], the meniscus was modeled as a biphasic material with neo-Hookean solid phase and constant hydraulic permeability. As boundary conditions, the displacement of the bottom of the sample was fixed in all the directions,

while the displacement of its lateral surface was fixed in the plane orthogonal to the line of compression. Due to the axisymmetric geometry, only a quarter of the cylinder was simulated (Figure 1b), and symmetry conditions were imposed on the internal faces of the simulated sample. Because of the porosity of the compressing plate, the gauge pressure on the top surface of the sample was set to zero. A sliding, frictionless, elastic contact was assumed between the tissue and the compressing plate.

Simulations were conducted at several values of K and H to investigate the effects of these physical parameters on the capability of the meniscus to dissipate energy. Previous studies have shown that healthy meniscal permeability is in the order of 10^{-3} mm^4/Ns [5]. Therefore, in the simulations, K ranged from $1*10^{-4}$ mm^4/Ns and $1*10^{-2}$ mm^4/Ns. Similarly, it has been reported that, for healthy menisci, the magnitude of H is 0.2 MPa [5]. Accordingly, in the simulations, H varied from 0.1 MPa to 1 MPa. In addition, variations in the amplitude and frequency of the cyclic compressions were investigated to account for a broader range of knee movements. Specifically, the frequencies considered ranged between 0.01 Hz and 0.5 Hz, whereas the compressive strain amplitude ranged between 1% and 5%.

The dimensions of the modeled cylindrical sample were 2.5mm radius and 1.5mm height. The number of elements in the mesh (2686 elements) was chosen as the result of a mesh convergence study (data not shown), and the type of element was an 8-node trilinear hexahedral 'brick' element. The model was developed in FEBio Studio version 1.0.0.[6]

For each simulated case, the stress-strain data over the entire cycle were computed. The energy dissipation was computed via numerical algorithm as the area under the stress-strain curves, see Figure 2.

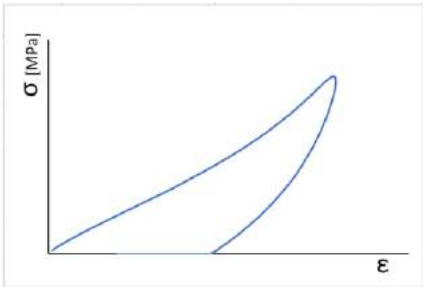

Figure 2: Sample of Stress-Strain curve for the simulated compressive single-cycle on the meniscus sample.

RESULTS

The sensitivity of the energy dissipation to changes in H and K is reported in Figure 3a. For all the cases simulated, the amplitude of the compressive strain was 1% and the frequency was 0.5 Hz. It was observed that increasing the H modulus increases the energy dissipation. The opposite effect was observed for K.

The trends of variation of energy dissipation with extent of compressive strain and frequency of compression are reported in Figure 3b. For all the cases simulated, the value of H was 0.25 MPa and that of K was $1*10^{-3}$ mm^4/Ns. Data show that energy dissipation increases with the magnitude of the compressive strain and the frequency of loading.

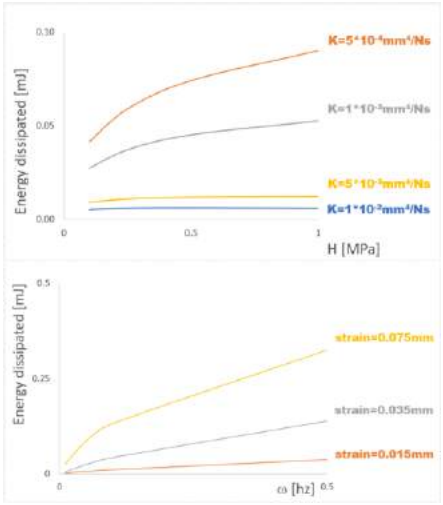

Figure 3: (a) Energy dissipated as a function of H, parametric with K. (b) Energy dissipated as a function of the loading frequency, parametric with the compressive strain magnitude.

DISCUSSION

This study investigated the mechanism of meniscal energy dissipation as a function of two physical parameters, H and K, that regulate the poromechanics of this unique tissue. Such an analysis is significant since both H and K may change with the meniscal composition which, in its turn, depends of the health status of the meniscus. Degenerated menisci exhibit higher water content and lower proteoglycan content when compared to healthy ones [7]. The magnitudes of K and H are positively related to water and proteoglycan content, respectively [8]. Our simulations indicate that increase of K and reduction of H, as one may expect to observe in a degenerated meniscus, reduce the capability of the tissue to dissipate mechanical energy. This may directly affect the health status of the underlying knee cartilage, which would be subjected to a more aggressive mechanical environment.

It was also found that larger compressive strains and higher loading frequencies increase the amount of energy dissipated. This was expected since the energy dissipated in a cycle is proportional to the applied strain. In addition, larger frequencies increase the fluid pressure, which is responsible for dissipating phenomena in a poroelastic system.

In summary, investigating the mechanisms of energy dissipation in the relation to meniscal composition and mechanical environment provides new knowledge on the pathophysiology of the tissue, which can be leveraged to elaborate strategies for the treatment of meniscus degeneration.

ACKNOWLEDGEMENTS

Study supported by NIH/NIAMS grant number 1R01AR073222.

REFERENCES

[1] Pereira, H et al., *Meniscal Transplantation*, 1:7-14, 2013.
[2] Athanasiou, K et al., *Engineering the Knee Meniscus*, 10-12, 2009.
[3] Andrews, S et al., *Journal of Biomechanics*, 1, 2011.
[4] Bursac, P et al., *Biorheology*, 1, 2009.
[5] Morejon, A et al., *Frontiers*, 1, 2021.
[6] Maas, SA et al., *Journal of Biomechanical Engineering*, 134(1):011005, 2012
[7] Herwig, J et al., *Annals of the Rheumatic diseases,1, 1984.*
[8] Joshi, M et al., *Journal of Biomedical Materials Research,1, 1995.*

CELL-CELL ADHESION MODULATES TISSUE FLUIDITY DURING EPITHELIAL MORPHOGENESIS

Xun Wang (1), Christian M. Cupo (1), Karen E. Kasza (1)

(1) Department of Mechanical Engineering
Columbia University
New York, NY, USA

INTRODUCTION

Biological tissues behave as remarkable materials that can actively change shape and structure in a process known as morphogenesis [1]. During embryonic development, tissues can reorganize and flow dramatically on timescales as short as minutes during embryonic development [2,3]. In *Drosophila* embryos, for instance, the germband epithelium extends to rapidly double the length of the body axis in just 30 minutes (Fig. 1a) [3-6]. Anisotropies in internal and external forces are thought to drive tissue remodeling [4-6]. Recent experimental studies and theoretical models have highlighted the linkage between tissue remodeling and tissue fluidity [2, 7, 8]. We recently showed that body axis elongation in *Drosophila* (Fig. 1a) is associated with a transition of the epithelial tissue from solid-like to more fluid-like behavior, where tissue fluidity can be read-out from two experimentally accessible metrics of cell patterns – cell shape and cell alignment (Fig. 2) [9]. However, how an epithelial tissue regulates its fluidity to allow or prevent tissue reorganization at specific times remains unknown.

Cell-cell adhesion, mediated by junctional proteins such as E-cadherin (E-cad), and contractile tension, mediated by cytoskeletal proteins such as myosin II and F-actin, are thought to be key machineries controlling epithelial tissue behaviors [5,6] and are likely to also regulate tissue fluidity. To gain insight into how an epithelial tissue regulates its fluidity, we systematically modulated cell-cell adhesion levels *in vivo* by using molecular genetics approaches to tune E-cad expression in the *Drosophila* embryo (Fig. 1b). To study the effects of cell-cell adhesion levels, we combined live confocal imaging and quantitative image analysis of cell patterns and tissue behaviors before and during epithelial tissue remodeling in body axis elongation. Prior to the onset of tissue remodeling, we find a biphasic response of cell shapes to cell-cell adhesion levels. This relationship between cell shape and adhesion changes during tissue remodeling, where we find that increased cell-cell adhesion is instead associated with more aligned cells. These findings suggest complex roles for cell-cell adhesion in modulating tissue fluidity. Our quantitative *in vivo* experimental studies are essential to advance fundamental understanding of how cell-level adhesions control tissue-level mechanical behaviors, which is essential to revealing mechanisms underlying epithelial tissue morphogenesis and embryonic development.

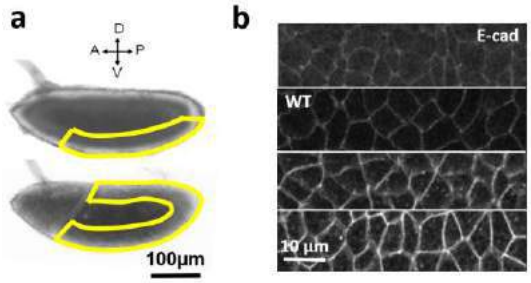

Figure 1. a, Extension of the germband epithelium (*yellow*) contributes to body axis elongation in *Drosophila* embryos. Anterior (*A*), left. Dorsal (*D*), top. **b**, We systematically modulated the levels of the core cell-cell adhesion protein E-cadherin (E-cad) to study how adhesion influences tissue fluidity. Top to bottom: E-cad levels are increased.

METHODS

Fly Stocks and Genetics. Fly stocks are from the Bloomington *Drosophila* Stock Center. Cell outlines and E-cad were visualized with fluorescently-tagged proteins (mCherry [10] or GFP). E-cad levels were decreased by inhibiting expression using RNAi or increased by overexpression using a shg:GFP transgene [11].

Time-Lapse Imaging. Embryos were dechorionated for 2 min in 50% bleach, washed in distilled water, and mounted in halocarbon oil

between a coverslip and an oxygen-permeable membrane. The ventrolateral region of the embryo was imaged on a Zeiss LSM880 laser scanning confocal microscope. Two-color z-stacks were acquired at 1-μm steps and 15-s time intervals. 3 z-slices at the apical side of the tissue at the level of adherens junctions were projected by maximum intensity.

Image Quantification. Time-lapse images were processed in ImageJ [12]. Cells were segmented and analyzed by the semi-automated software SEGGA [13] and customized Python codes [9]. Tissue elongation starts at $t = 0$. Cell patterns were quantified by the cell shape index p and cell alignment index Q, defined in Ref. [9] and schematized in Fig. 2. Mean values from normal distributions were compared by one-way ANOVA and the Tukey HSD *post-hoc* test.

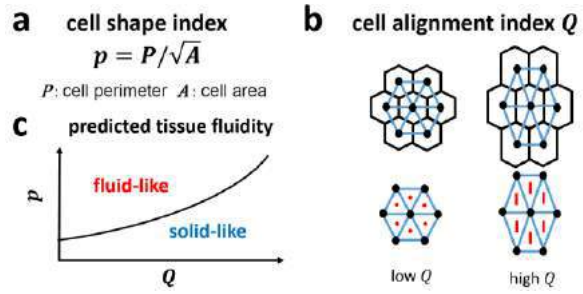

Figure 2. Tissue fluidity can be predicted by two metrics of cell patterns. Cell patterns are quantified by the cell shape index p and cell alignment index Q, following the approach in Ref. [9]. **a**, p is the ratio of the cell perimeter P to the square root of cell area A. Circles have the smallest value of $p = 3.54$. **b**, Q is quantified by the triangle method [9, 14, 15]. Cell centers (black dots) are connected by a triangular network (blue bonds). Q is large when cells are stretched and aligned. **c,** Tissues are predicted to be more fluid-like when cell patterns display high values of p and low values of Q [9].

RESULTS

Cell patterns change dramatically during tissue remodeling. In wild-type *Drosophila* embryos, cells take on nearly isotropic hexagonal shapes at 10 min before tissue remodeling, but change shape dramatically during body axis elongation. Consistent with this, the cell shape index p increases during tissue remodeling [9]. In contrast, the cell alignment index Q peaks 2 min after the onset of tissue remodeling, before returning to low levels again [9].

Prior to tissue remodeling, cell-cell adhesion levels modulate the cell shape index p in a biphasic manner. To test how cell-cell adhesion influences cell patterns and tissue behaviors, we systematically manipulated E-cad levels and analyzed cell shapes in the germband. We first examined p and Q prior to tissue remodeling when the tissue is more static. We find that the cell alignment index Q is low and nearly independent of E-cad levels at $t = -10$ min (data not shown). In contrast, tissues with either increased or decreased E-cad display increased values of p (Fig. 3a). The tissues with altered E-cad levels and elevated values of p (and nearly constant Q) are predicted to have more fluid-like properties (Fig. 2c) [9]. Thus, the cell shape index p shows a biphasic response to adhesion levels in static tissues prior to remodeling, challenging simple models that predict increased adhesion would yield monotonic changes in tissue properties [2, 7].

During tissue remodeling, increased levels of cell-cell adhesion are associated with higher values of the cell alignment index Q. Next, we explored how p and Q vary during tissue remodeling. Interestingly, during tissue remodeling, the differences in p among embryos with different E-cad levels disappear (data not shown). The cell alignment index Q, however, is increased in embryos with increased E-cad (Fig. 3b). More solid-like tissue behavior is predicted for tissues with increased values of Q (and nearly constant p) [9] (Fig. 2c). Thus, increased cell adhesion is associated with increased cell alignment during tissue remodeling associated with body axis elongation.

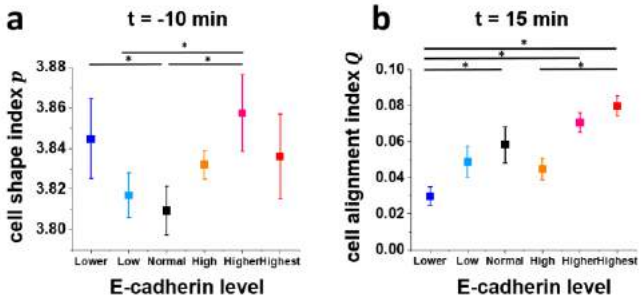

Figure 3. Cell patterns are tuned by cell-cell adhesion. a, The cell shape index p at t = -10 min for embryos expressing varying E-cad levels. Embryos with increased or decreased E-cad compared to wild type (normal) display higher p (*, $P<0.05$). Error bars, standard deviation. n = 4-7 embryos. **a**, The cell alignment index Q at t = +15 min during tissue remodeling. Embryos with increased E-cad display higher Q (*, $P<0.05$). Error bars, standard error. n = 5-8 embryos.

DISCUSSION

Our work systematically studies the effects of cell-cell adhesion on epithelial tissue structure and mechanics *in vivo*. We find that modulation of E-cad levels influences cell patterns in the *Drosophila* embryo. Before tissue remodeling, there is a biphasic dependence of cell shape on E-cad, with either increased or decreased E-cad levels associated with a higher cell shape index p and longer cell-cell contacts and cell perimeters, which is predicated to be associated with more fluid-like tissue properties [9]. We are currently examining the molecular and mechanical mechanisms that contribute to these changes. Interestingly, this relationship between cell shape and adhesion changes during axis elongation when the tissue is more dynamically remodeling. During this time, increased E-cad levels are associated with more aligned cells, suggesting more solid-like tissue behavior [9]. One potential explanation for this is that increased cell-cell adhesion might slow the cell rearrangements that drive tissue remodeling and that are thought to relax tissue stretching resulting from external stresses acting on the germband; we are currently investigating this possibility. Taken together, this work reveals the complex roles of cell-cell adhesion in modulating tissue structure and mechanical behavior during development. Future studies of how adhesion influences cytoskeletal dynamics and cell tension will provide insight into the mechanisms underlying these unexpected effects of adhesion on tissue structure and fluidity.

ACKNOWLEDGEMENTS

This work was supported by the NSF-CMMI-1751841, a Burroughs Wellcome Fund CASI, and a Packard Fellowship to KEK.

REFERENCES

[1] Davies, J, Mechanisms of morphogenesis, 2013. [2] Mongera, A et al., *Nature*, 561:401–405, 2018. [3] Irvine, KD et al., *Development*, 120:827–841, 1994. [4] Butler, L C et al., *Nat Cell Biol*, 11(7):859–864, 2009. [5] Herrera-Perez, RM et al., *Curr Opin Genet Dev*, 51:88–95, 2018. [6] Heisenberg, CP et al., *Cell*, 153(5):948-962, 2013. [7] Bi, D et al., *Nat Phys*, 11(12):1074–1079, 2015. [8] Park, JA et al., *Nat Mater*, 14(10), 1040–1048, 2015. [9] Wang, X et al., *Proc. Natl. Acad. Sci. U.S.A.*, 117 (24):13541-13551, 2020. [10] Fabrowski et al., *Nat Commun*, 4:2244, 2013. [11] Lee JY et al., *PLoS Genet*, 12(5): e1006043, 2016. [12] Schindelin, J et al., *Nat Methods*, 9(7): 676-682, 2012. [13] Farrell DL et al., *Development*, 144:1725, 2017. [14] Merkel, M et al., *Phys Rev E*, 95:032301, 2017. [15] Etournay, R et al., *Elife*, 4:e07090, 2015.

HIGH-SPEED SIMULATION OF THE 3D BEHAVIOR OF MYOCARDIUM USING A NEURAL NETWORK PDE APPROACH

Wenbo Zhang (1), David S. Li (1), Tan Bui-Thanh (2), Michael S. Sacks (1)

(1) Willerson Center for Cardiovascular Modeling and Simulation
Oden Institute for Computational Engineering & Sciences
Department of Biomedical Engineering
The University of Texas at Austin
Austin, TX, USA

(2) Oden Institute for Computational Engineering & Sciences
Department of Aerospace Engineering and Engineering Mechanics
University of Texas at Austin
Austin, TX, USA

INTRODUCTION

The full characterization of three-dimensional (3D) mechanical behavior soft tissues, such as myocardium, is essential in simulating organ function in health and disease. The hierarchical structure of soft tissues dictates their highly anisotropic mechanical behaviors, with the spatial variations in fiber structure also giving rise to heterogeneity. To address these issues in a full 3D context, we have developed a novel numerical-experimental approach to determine the optimal model form and parameter estimation for continuum constitutive models of soft tissues, as applied to the myocardium [1, 2]. This approach utilized optimal experimental design of the full 3D kinematic (triaxial) experiments coupled to an inverse model that incorporated local fibrous structure to perform robust parameter estimation (Figure 1). Due to the natural variations in soft tissue structures (Figure 2), the mechanical behaviors of soft tissues can vary dramatically within the same organ. The set of optimal loading paths for a tissue specimen is shown in Figure 2, including three pure shear and three simple shear loading conditions.

In-silico implementation of such complex 3D continuum soft tissue constitutive models to obtain the responses of varying boundary conditions and fibrous structures requires the solution of the associated hyperelasticity problem, which remains impractical in translational clinical time frames. To alleviate the associated substantial computational costs at the time of simulation, we have developed a neural network-based method that can simulate the 3D mechanical behavior of soft tissues. A physics-informed approach [3] was employed to train the neural network (NN) surrogate model to give physically correct solution for a range of loading conditions by minimizing the potential energy without any training dataset generated by finite element (FE) solver.

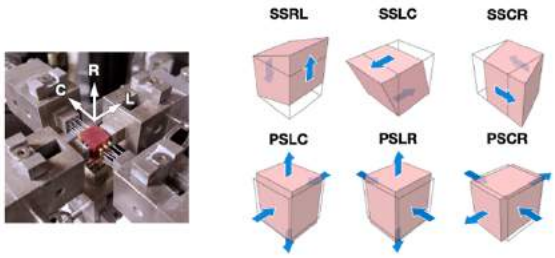

Figure 1: The triaxial testing system (a) for determining the myocardium model parameters using the set of optimal loading (b)

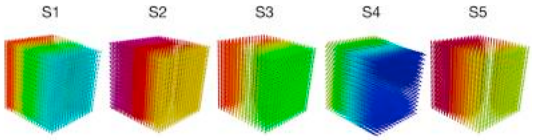

Figure 2: The fiber orientations of five myocardium specimens.

METHODS

We consider the parametric hyperelasticity problem of myocardium on domain Ω with a prescribed displacement $\mathbf{u}_0$ on the Dirichlet boundary Γ_u and a traction term $\mathbf{t}$ the Neumann boundary Γ_t in the reference configuration $\mathbf{X} \in \boldsymbol{\Omega}$. The displacement $\mathbf{u}(\mathbf{X})$ depends on the prescribed Dirichlet boundary condition $\mathbf{m}(\mathbf{X})$ on Γ_u. The displacement $\mathbf{u}(\mathbf{X})$ is parametrized using $\mathbf{u}(\mathbf{X}) = \mathbf{U}\mathbf{N}(\mathbf{X})$ where $\mathbf{N}(\mathbf{X})$ are the finite element basis functions and $\mathbf{U}$ is the nodal displacement values, and the Dirichlet boundary conditions $\mathbf{m}(\mathbf{x})$ is parametrized by a vector $\mathbf{M}$. Thus, solving

parametric PDEs is essentially to find the parameter-to-state map **U**(**M**) that minimize the energy potential of hyperelasticity for all **M**. We use a fully connected neural network f_{FCN} along with a linear term **TM** as the surrogate model to approximate the parameter-to-state map using

$$\mathbf{U}(\mathbf{M};\boldsymbol{\theta}) = f_{\mathrm{FCN}}(\mathbf{M};\mathbf{W},\mathbf{b}) + \mathbf{TM} \quad (1)$$

where $\boldsymbol{\theta}$ includes the weights **W**, the biases **b** for the FCN and the matrix **T** for the linear term as a skip connection which is originally proposed in the residual NN [4]. Thus, the surrogate model represents the solutions for a range of Dirichlet boundary conditions. The FCN is a sequence of composite functions,

$$f_{FCN} = A_L \circ \phi \circ A_{l-1} \circ \cdots \circ \phi \circ A_1 . \quad (2)$$

where ϕ: $\mathbb{R}^{\mathrm{d}} \to \mathbb{R}^{\mathrm{d}}$ is element-wise nonlinear differentiable activation function, A_l: $\mathbb{R}^{\mathrm{d}_{l-1}} \to \mathbb{R}^{\mathrm{d}_l}$ (l = 1, …, L) are affine functions with weights $\mathrm{W}_l \in \mathbb{R}^{\mathrm{d}_l \times \mathrm{d}_{l-1}}$ (l = 1, …, L) and biases $\mathrm{b}_l \in \mathbb{R}^{\mathrm{d}_l}$ (l = 1, …, L), L is the number of hidden layers, d_l is the number of neurons in the l-th hidden layer. The activation function can be discontinuous since the hyperelasticity problem does not involves its derivatives

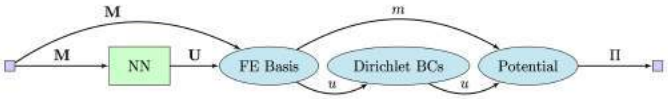

Figure 3: The end-to-end computational graph of the NN surrogate model U(M) integrated with the FE basis functions to compute the corresponding energy potential Π, where automatic differentiation is to back-propagate the derivatives for minimizing the aggregated energy potential for a range of Dirichlet boundary conditions.

To capture the mechanical response of the myocardium, we used [2],

$$\begin{aligned}\Psi = {} & \frac{a}{2b}\left(\exp\left(b(I_1-3)\right)-1\right) \\ & + \sum_{i=\mathrm{f,s}} \frac{a_i}{2b_i}\left(\exp\left(b_i\left(I_{1_i}-1\right)^2\right)-1\right) \\ & + \sum_{i,j=\mathrm{f,s}} \frac{a_i}{2b_i}\left(\exp\left(b_i {I_{8_{ij}}}^2\right)-1\right), \end{aligned} \quad (4)$$

where $\{a, b, a_{\mathrm{f}}, b_{\mathrm{f}}, b_{\mathrm{f}}, b_{\mathrm{s}}, a_{\mathrm{fs}}, b_{\mathrm{fs}}\}$ are eight model parameters, I_1 is the first invariant of the right Cauchy-Green deformation tensor $\mathbf{C} = \mathbf{F}^{\mathrm{T}}\mathbf{F}$ and $\mathbf{F} = \nabla\mathbf{u}$ is the deformation tensor, and I_{4i} are the diagonal components of **C** and I_{8ij} are the off diagonal components of **C**. Next, to make the optimization problem in Equation (3) feasible, we minimized an aggregated potential energy

$$\begin{aligned} & \text{find } \boldsymbol{\theta} \\ & \min \Sigma_i \int_\Omega \Psi\left(\mathbf{u}^{(i)}(\mathbf{X})\right) \mathrm{d}\mathbf{X} + \int_{\Gamma_t} \mathbf{t}\cdot\mathbf{u}\mathrm{d}\mathbf{X} \\ & \text{s.t. } \mathbf{u}^{(i)}(\mathbf{X}) = \mathbf{U}(\mathbf{M}^{(i)})\mathbf{N}(\mathbf{X}). \end{aligned} \quad (4)$$

The Dirichlet boundary condition was parametrized in a fashion of representative volume element by **M**

$$\mathbf{u}^{(i)}(\mathbf{X}) = \mathbf{M}^{(i)}\mathbf{X}$$

The integral in Equation (4) is computed by an element-wise Gauss quadrature. A Markov chain Monte Carlo (MCMC) method using Halton sequence is used sampled **M**. The end-to-end computational graph is shown in the schematic diagram (Figure 3).

RESULTS

We consider a cube of nearly incompressible myocardium with dimensions 1.0 × 1.0 × 1.0. The training range for sampling all components of **M** is [-0.2, 0.2] and we restrict **M** to be symmetric to eliminate rigid rotation. The training range is incrementally expanded in 20 steps. The number of MCMC samples is 100. The NN has 1 hidden layer of 100 neurons. The results obtained with present NN matched closely with the finite element method which has 8000 nodes (20×20×20) (Figure 4). The training process converged and has a good agreement with the FE solutions (Figure 5).

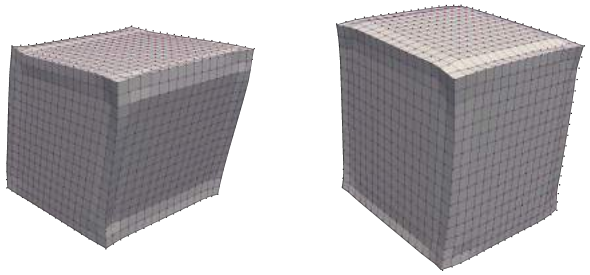

(a) **(b)**

Figure 4: Validation on the deformed configurations of the predictions of the NN surrogate model (blue wireframe) and the FE solutions (red points): (a) shear deformation with relative L2 error of 9.65%; (b) extension in two directions with relative L2 error of 6.48%.

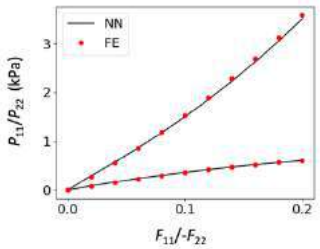

Figure 5: The average first Piola-Kirchhoff stress on the boundary vs the deformation of the FE solutions and NN predictions.

The compute time for one prediction of the NN surrogate model was 0.02236 s, while the FE solver takes 6.5762 s for assembly and solution for one step, which is a speed-up of 294.1. The NN surrogate model can give predictions in parallel while the FE solver needs stepping scheme to incrementally obtain the solution for the fully loaded state which multiplied cost with the number of steps, which is 10 in the present case.

DISCUSSION

In this work, we have developed a high fidelity NN 'surrogate' model that is trained in a physics-informed approach to give a direct solution of 3D soft tissue hyperelasticity in-silico. The present method was found to be an order of 10^2 time faster than the equivalent FE model (using the same mesh on the same machine). With the learnability of the neural networks, the architecture of the NNs can incorporate attributes such as spatially varying fiber structures. By shifting the computation expense from FE problem solving to NN training, The NN surrogate model can be used to give significantly fast predictions of complex 3D deformations in full kinematic space with population-based fiber structures by forward propagation in the neural network. This method will provide efficient and robust computational models for clinical evaluation to improve patient outcomes.

REFERENCES

[1] Avazmohammadi, R et al., *Biomech Model Mechan*, 17(1): 31-53, 2018.
[2] Li, DS et al., *J Mech Behav Biomed Mater*, 103: 103508, 2020.
[3] W. E and B. Yu, *Commun Math Stat*, 6(1): 1-12, 2018.
[4] He, K et al., Proc IEEE Comput Soc Conf Comput Vis Pattern, 770-778, 2016.

THE EFFECT OF ENDOTHELIAL DYSFUNCTION ON AORTIC MECHANICS AND EXTRACELLULAR MATRIX MICROSTRUCTURE DURING AGE-RELATED VASCULAR REMODELING

Liya Du (1), Jeffrey Rodgers (1), Tarek Shazly (1), John F. Eberth (1,2), Susan M. Lessner (1,2)

(1) Biomedical Engineering Program
University of South Carolina
Columbia, SC, USA

(2) School of Medicine
University of South Carolina
Columbia, SC, USA

INTRODUCTION

The endothelium, comprised of a single layer of endothelial cells, is the innermost lining of blood vessels providing the crucial interface between blood and the arterial wall. "Endothelial dysfunction," characterized as a reduction in the bioavailability of the major vasodilator nitric oxide (NO), is associated with abnormal vascular remodeling and correlated with cardiovascular pathologies such as hypertension and atherosclerosis. [1]

Based on previous studies, endothelial dysfunction can lead to arterial wall thickening and arterial stiffening, which involves changes in extracellular matrix (ECM) structure or composition and, consequently, alterations in the passive mechanical properties.[2] [3] Additionally, acute NO deficiency leads to increased contractile tone; but long-term deficiency may reduce the overall contribution of the smooth muscle cells (SMCs) to the mechanical environment. The microstructure of the ECM, especially collagen fiber organization, plays an essential role in aortic mechanics. However, very few studies have been performed on the impact that endothelial dysfunction has on the microstructure of the ECM, especially collagen fiber organization, during age-related vascular remodeling that could be used to decipher changes in macroscopic mechanical properties. Thus, a mouse model of direct genetic deletion of endothelial nitric oxide synthase (NOS3) was used in this project to manifest endothelial dysfunction to study the alterations of collagen fiber organization as well as changes in active and passive biomechanics over the time course of vascular remodeling.

METHODS

We used groups of endothelial NO synthase (NOS3) knockout (KO), NOS3 heterozygous (Het), and wild type (WT) B6 mice (controls) to study the time course of vascular remodeling between 6 wks to 12 mo. Multiphoton second harmonic generation (SHG) microscopy was used to image collagen fibers through the wall of the descending thoracic aorta (DTAo). The axial (0°) direction was defined by the average orientation of endothelial cell nuclei; the corresponding perpendicular direction was defined as circumferential (90°). An image-processing protocol was then developed to reconstruct collagen fibers in 3D space. Reconstructed fibers were classified into three fiber families, with one axially-oriented, one circumferentially-oriented, and helically-oriented families (axial= 0-22.5° and 157.5-180°, circumferential= 67.5-112.5°; helical= 22.5-67.5° and 112.5-157.5°) using a custom MATLAB code. The mean normalized frequency for each fiber family and average undulation associated with the family were calculated.

Active and passive mechanical tests of DTAo taken from mice of each genotype were conducted on a customized murine artery inflation-extension testing apparatus. For active tests, maximal contraction of SMCs was achieved by adding phenylephrine into the bathing medium (Krebs solution) to achieve a final concentration of $2x10^{-5}$ M. The medium was temperature-controlled within 37-38°C and continuously aerated

with 95% O_2/5% CO_2. Arteries were then preconditioned with 5 inflation/deflation cycles to minimize viscoelastic effects. For data acquisition, each DTAo sample was extended and held at three different axial stretch ratios which are 1.5, 1.6 (corresponding to the in-vivo stretch ratio), and 1.7, respectively. At each stretch ratio, the arterial sample was pressurized from 10 to 160mmHg in increments of 10 mmHg using in 3 consecutive quasi-static inflation cycles with the axial force, luminal pressure, and axial stretch recorded. The passive mechanical response was assessed by exchanging the perfusion and test chamber medium with phosphate buffered saline (PBS) containing 10^{-5} M sodium nitroprusside (SNP) to fully relax the SMCs. Passive mechanical preconditioning and inflation-extension testing were performed in an identical manner to that described above.

RESULTS

As shown in Figure 1 (a.), there is a slight, non-significant increase in the relative number of circumferentially oriented fibers (p value = 0.116) and a similarly small decrease in axially oriented fibers with age in WT mice (p=0.128). There are no obvious trends in heterozygotes (b.), while in KO (c.) there is a significant increase in the number of circumferentially oriented fibers with age (p=0.035). The trend in KO mice indicates that more dramatic collagen fiber reorganization occurs with endothelial dysfunction during age-related vascular remodeling.

The active and passive mechanical responses of different genotypes at 12 mo are compared in Figure 2. In both (a.) and (b.), the mechanical responses of DTAo from all genotypes exhibit J shaped stress-stretch behavior in the circumferential direction. In (a.), the active mechanical response shows slight difference between genotypes, while in (b.) there is very little variation among genotypes under SMC relaxed state. Based on (c.), the SMC active stress generation in circumferential direction at common circumferential stretch 1.6 in KO is lower than both WT and Het which suggests diminished SMC contraction in KO at 12mo. In addition, corresponding lumen area compliance at a common loading condition (100 mmHg) of KO vessels is lower than WT and Het under SMC relaxed states in (d.), indicating increased aortic stiffness in KO for passive mechanical property. However, the sample size is only two, so more data is required to determine whether these differences are statistically significant.

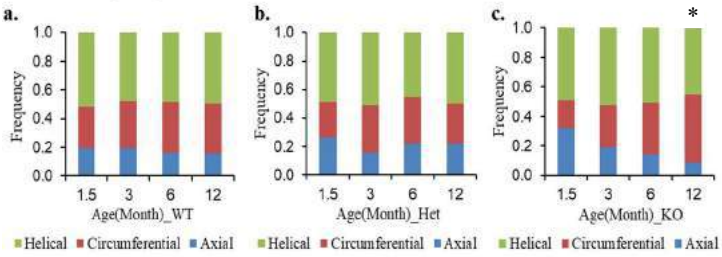

Fig 1. Changes in distribution of collagen fiber families with age in each genotype. WT mice shown in (a.), Het in (b.) and KO in (c.). The mean frequency of three fiber families is represented using different colored bars in the graph. N=3-6 for each group. * indicates significant difference (p<0.05) between age groups in KO mice.

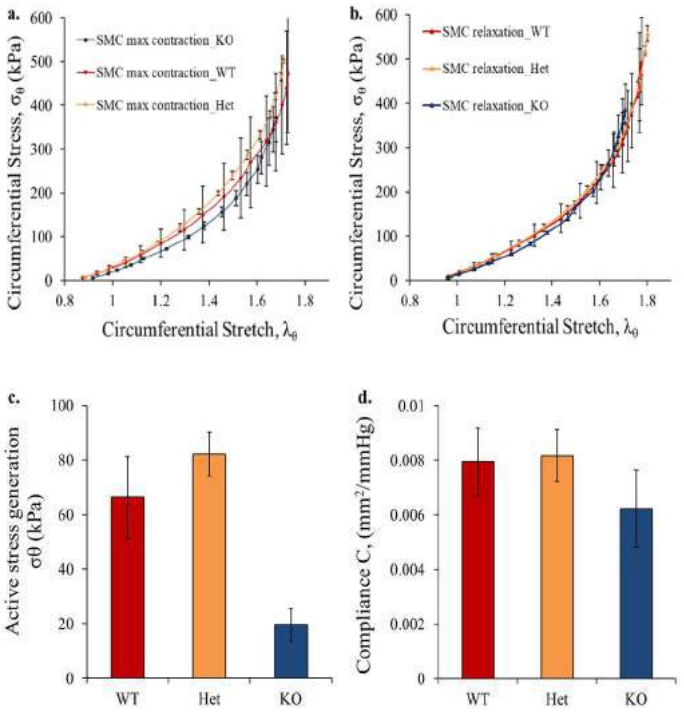

Fig 2. Comparison of circumferential stress-stretch relationships at in-vivo axial stretch, 1.6, for different genotype groups (n=2) at 12 mo under SMC maximally contracted state in (a.) and under SMC relaxed state in (b.). Corresponding SMC active stress generation at common circumferential stretch λθ=1.6 in (c.). Lumen area compliance (C, mm²/mmHg) at common loading condition (100 mmHg) under SMC relaxed state in (d.)

DISCUSSION

Preliminary results demonstrate that there is a trend in collagen fibers shifting towards circumferential from axial orientation with age in KO mice compared to the other two genotypes. However, the sample size for active and passive mechanical study is currently too small, so the effect of endothelial dysfunction on mechanical properties is still uncertain. Thus, active and passive biaxial mechanical tests of all genotypes will be completed in the future to compare mechanical properties between genotypes and time points.

ACKNOWLEDGEMENTS

This work was funded in part by NSF CMMI-1760906, NIH R01 HL133662 and NIH R01 HL145064.

REFERENCES

[1] Gradinaru, D., et al., *Oxidized LDL and NO synthesis--Biomarkers of endothelial dysfunction and ageing.* Mech Ageing Dev, 2015. **151**: 101-13.

[2] Watson, S. R. et al. *Diet alters age-related remodeling of aortic collagen in mice susceptible to atherosclerosis*." Am J Physiol. Heart Circ Physiol, 2021. **320**(1): H52-H65.

[3] Leloup, A.J.A., et al., *Ex vivo aortic stiffness in mice with different eNOS activity.* Am J Physiol Heart Circ Physiol, 2020. **318**(5): H1233-H1244.

NANOPARTICLE-MEDIATED CONTROLLED MYOCARDIAL DELIVERY FOR HYPERTROPHIC CARDIOMYOPATHY

Katherine M. Copeland (1), Uday Chintapula (1), Isha Parab (1), Yi Hong (1), Matthias Peltz (3), Pietro Bajona (2,3), Kytai T. Nguyen (1), Jun Liao (1)

(1) Department of Bioengineering,
University of Texas at Arlington,
Arlington, TX 76010

(2) Hypertrophic Cardiomyopathy Program,
Allegheny Health Network,
Pittsburgh, PA 15212

(3) Department of Cardiovascular and Thoracic Surgery,
University of Texas Southwestern Medical Center,
Dallas, TX 75390

INTRODUCTION

Hypertrophic cardiomyopathy (HCM) is a genetic disease caused by mutations in contractile sarcomeric proteins that result in abnormal thickening of ventricular heart muscle, particularly the septum that separates that left and right ventricles [1]. The current gold standard, septal myectomy, is commonly performed to remove excess, thickened tissue. However, many patients are poor surgical candidates and require another, less invasive, treatment option. In these cases, cardiologists use the alcohol septal ablation (ASA) technique to kill the overgrown tissue. Although ASA is a relatively common procedure for non-surgical patients, it has many downfalls including atrioventricular blockage and considerable myocardial necrosis [2]. To overcome ASA limitations, we have designed a new nanoparticle-mediated system to replace the pure alcohol in ASA and achieve a controllable, localized septal tissue shrinkage and a safe ablation.

METHODS

Doxorubicin-loaded PLGA NPs were created using a double emulsion method developed in-house Nanoparticles were characterized by size, charge, conjugation efficiency, cytocompatibility, and cell uptake. HL1 cells were seeded onto collagen coated plates to mimic the fibrotic environment associated with HCM. Hypertrophy was induced in HL1 cardiomyocytes by stimulating them with endothelin-1 (ET-1). Following ET-1 treatment, cells were treated with various concentrations of collagenase coated, Doxorubicin-loaded PLGA (COL-PLGA-DOX) nanoparticles.

RESULTS

COL-PLGA-DOX NPs were fabricated using a double emulsion technique and were then fully characterized. The drug release profile showed that within 48 hours, ~50% of the drug was released. The nanostructure, presence of Doxorubicin, and collagenase conjugation was confirmed by FTIR. Cytocompatibility studies were performed to show that PLGA NPs had no negative effects on the viability of the cells. PLGA NPs had excellent cytocompatibility with HL1 cardiomyocytes. Cell uptake of COL-PLGA-DOX NPs showed a dose-dependent response, with more NPs taken up by the cell at higher NP concentrations. COL-PLGA-DOX NPs were tested in 2D culture on collagen coated plates to determine the effectiveness of the NPs to kill hypertrophied cardiomyocytes in a mimicked collagenous (fibrotic) environment. Within 48 hours of treatment with the IC50 and IC75 of COL-PLGA-DOX (Figure 3.8 C) ~80-85% of cells were killed, similar to the rate of death caused by free, untargeted Doxorubicin, showing the success of these NPs in killing hypertrophied cells in a collagenous environment.

DISCUSSION

We have developed a COL-PLGA-DOX NP drug delivery system, with an ultimate goal to replace the ASA procedure with a more effective therapeutic option for HCM. PLGA NPs showed excellent cytocompatibility with HL1 cells, as well as a concentration-dependent uptake into hypertrophic HL1 cardiomyocytes. COL-PLGA-DOX successfully killed hypertrophic cells in vitro. Our ongoing ex vivo study, using a fresh pig heart model, has showed that our new system had a better localized delivery capability when compared with alcohol.

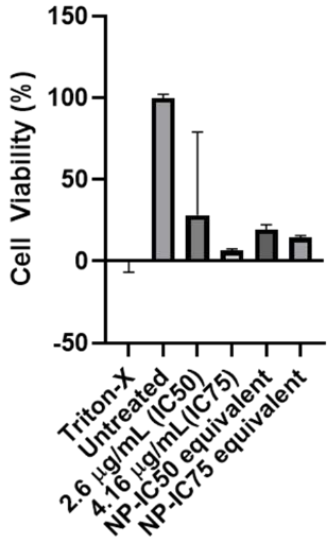

Figure 1: Cell viability after treatment with IC50 and IC75 of free doxorubicin and IC50 and IC75 of COL-PLGA-DOX

ACKNOWLEDGEMENTS
NIH 1R15HL140503; T32 HL134613.

REFERENCES

[1] A.J.Marian, R.R. The Molecular Genetic Basis for Hypertrophic Cardiomyopathy J Mol Cell Cardiol 33, 655-670 (2001).
[2] Spirito, P., Rossi, J. & Maron, B.J. Alcohol septal ablation: in which patients and why? Ann Cardiothorac Surg 6, 369-375 (2017).

PATIENT-SPECIFIC PREDICTION OF IMR RECURRENCE AFTER MITRAL VALVE SURGICAL REPAIR

Harshita Narang (1), Bruno V. Rego (1), Robert C. Gorman (2), Joseph H. Gorman III (2), Michael S. Sacks (1)

(1) J.T. Willerson Center for Cardiovascular Modeling and Simulation
Oden Institute for Computational Engineering and Sciences
Department of Biomedical Engineering
The University of Texas at Austin
Austin, TX, USA

(2) Gorman Cardiovascular Research Group
Department of Surgery
Perelman School of Medicine
University of Pennsylvania
Philadelphia, PA, USA

INTRODUCTION

Ischemic mitral regurgitation (IMR), also known as functional or secondary mitral regurgitation, is an especially prevalent and dangerous form of mitral valve (MV) incompetence in which a myocardial infarction (MI) causes maladaptive remodeling of the left ventricle (LV). MI-induced LV dilation stretches the MV annulus and tethers down the MV leaflets via the chordae tendinae, causing backflow through the left atrioventricular junction. The condition afflicts up to half of the population that has suffered a MI, and this number is expected to grow substantially as the population ages [1]. Current treatments, including surgical repair and replacement of the MV, continue to have high rates of failure, with moderate to severe IMR recurring within the first two years post-surgery in over 30% of patients [2]. It is believed that surgical outcomes can be substantially improved through the use of personalized diagnostics and treatments that account for patient-specific variations in MV structure and infarct kinematics.

A previous study by Bouma et al. [3] utilized clinical real-time 3D echocardiographic (rt-3DE) images of surgical repair for IMR to quantify the patient-specific risk of MR recurrence at six months post-surgery and found that metrics including the preoperative MV leaflet tethering angle in the P3 Carpentier segment were significantly different between MVs with and without IMR recurrence and that P3 tethering angle was predictive of 6-month IMR recurrence. This exciting result suggested that there are detectable pre-surgical differences in the functional state of regurgitant MVs in patients that respond well to URA and suggests that patient-specific pre-surgical assessment could be used to guide MV repair methods for improved outcomes.

We have previously developed a completely noninvasive method to produce open and closed MV geometries and compute MV leaflet deformation patterns from 3D in vivo images. We have previously applied this approach to large animal (ovine) post-IMR MVs and determined that the kinematic behavior of the MV changes progressively and substantially in the period immediately following an MI and that IMR progression induces plastic effects in the leaflet tissue which may affect its ability to fully recover after surgical intervention [3]. Each of these results strongly suggests that there is a relationship between pre-surgical MV state and post-surgical outcomes. To investigate this relationship, we have developed models of 21 human MVs and investigated leaflet strains and deformations. Deriving factors that play a role in predicting repair success could help elucidate underlying mechanisms of disease progression, lay the basis for more advanced models of surgical repair, and improve surgical techniques and planning on a patient-specific basis.

METHODS

Clinical rt-3DE images of the MV were obtained from 18 patients with IMR (11 without recurrence of IMR and 7 with recurrence) and 3 normal human MVs. These images were processed to obtain 3D midsurface representations of each valve in the fully open (end-diastolic) and fully closed (end-systolic) states, immediately pre- and post-surgery. In order to establish material point correspondence between the open and closed states of each valve, we applied a hyperelastic shape morphing technique in a finite element (FE) framework, where the open state geometry of the valve was morphed to match the closed state shape using globally applied pressure as well as a level-set penalization (Figure 1). The method is described in detail by Rego et al. [4]. Metrics including in-plane circumferential and radial strain, leaflet area, coaptation area, and orifice dimensions were then computed and compared between MVs with and without recurrence of MR at 6 months post-repair.

RESULTS

We found that MVs with IMR had significantly lower magnitudes of

compressive circumferential strain in the posterior leaflet and significantly higher radial strains across the whole MV than MVs

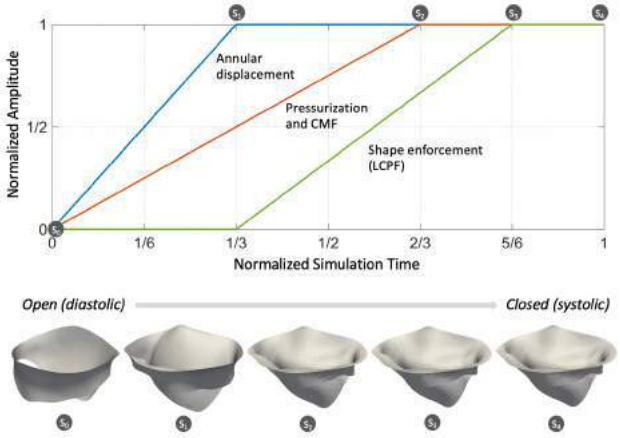

Figure 1. Time course of the FE simulation used to morph the open state MV mesh to the closed state shape.

without IMR (Figure 2). Patients who would later exhibit IMR recurrence were found to have significantly higher circumferential leaflet strain in the anterior commissure prior to surgery than those without recurrence ($p = 0.0228$). Pre-surgical circumferential strain in the A1 segment is likely predictive of patient-specific repair success through a logistic regression model ($p=0.0362$), as shown by a high area under the associated ROC curve of 0.832—in other words, a high rate of correctly identified recurrent MVs (Figure 3). The recurrent MVs also had significantly larger leaflet areas and annuli than the non-recurrent MVs and had reduced annular contraction at systole.

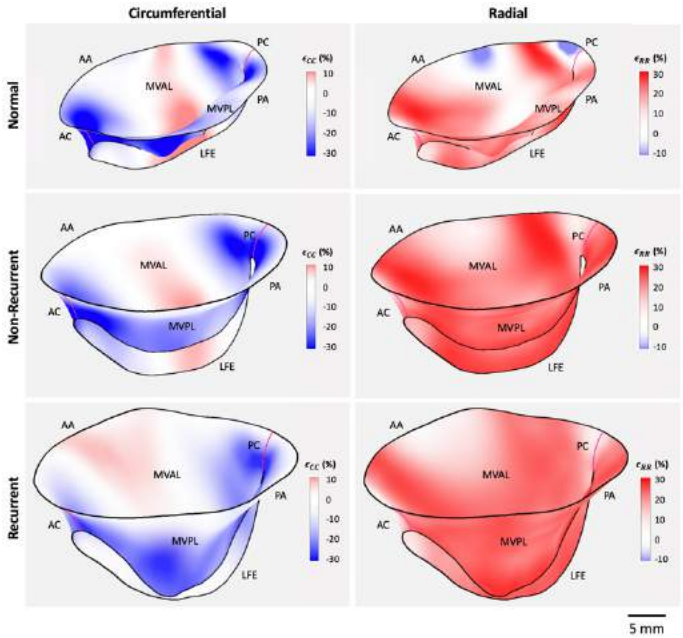

Figure 2. Average directional strains plotted on the corresponding averaged 3D geometries for MVs without IMR and those with non-recurrent or recurrent MR.

DISCUSSION

The analyses performed in our study show that while the patterns of MV leaflet deformation are complex, they consistently display statistical differences between MVs with and without of recurrence of IMR at 6 months post-surgery, especially in strain at the commissural segments and in MV size. There are also consistently significant differences between MVs with IMR and normal MVs.

Key features of IMR including reduced annular contraction and increased downward leaflet tethering correspond directly to the reduced circumferential leaflet strains, increased radial strains, and increased size observed in MVs with IMR as compared to the normal MVs. Similarly, we observed significantly larger leaflet surface area and orifice area as well as significantly reduced compressive strains in recurrent MVs as compared to non-recurrent MVs. The reduction in compressive circumferential strains in the recurrent MVs may indicate a MI located closer to the mitral annulus or increased LV dilation due to further progression of IMR. It may also be caused by an effective stiffening of the MV due to plastic deformations. Furthermore, the differences in size in the groups of MVs may again indicate differences in the degree of IMR progression, where the progression of IMR leads to larger MVs that have undergone plastic changes and are more difficult to repair. In order to fully understand how differences in deformation manifest during MV closure and how the MV interacts with the infarcted LV, it is necessary to have a full model of the MV.

We believe that the modeling technique we used, in conjunction with functionally equivalent chordae tendinae [8], can be used to help develop a predictive surgical planning tool to assist surgeons in quantitatively assessing repair performance prior to surgery. The altered pattern of strains we observed have been shown to trigger cell biosynthetic pathways toward deleterious remodeling of MV tissue [6,7]. A model such as ours could identify such patterns and quantify the risk of surgical methods for a patient prior to surgery. The model may also be extended to optimizing other repair methods such as minimally invasive leaflet clipping or augmentation.

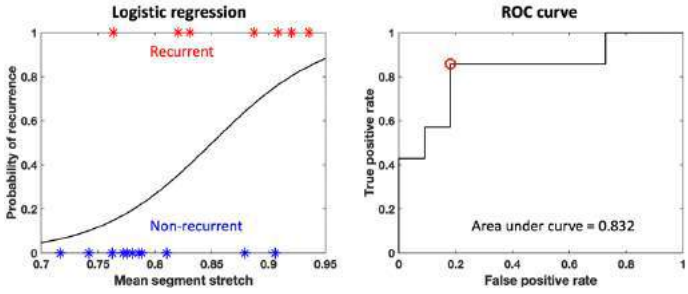

Figure 3. Logistic regression curve (left) and ROC curve (right) show that segment-averaged pre-surgical circumferential strains in the A1 segment of individual MVs may be predictive of long-term outcomes of surgical MV repair.

ACKNOWLEDGEMENTS

This material is based upon work supported by the National Institutes of Health (grant no. R01-HL119297 and R01-HL073021), the Harry S. Moss Heart Trust, and the Cain Foundation-Seton-Dell Medical School Endowment for Collaborative Research.

REFERENCES

[1] Borger MA et al., *Ann Thorac Surg*, 81(3):1153-61, 2006.
[2] Perrault L et al., *J Thorac Cardiovasc Surg*, 143(6):1396-1403, 2012.
[3] Rego BV et al., *Sci Rep*, In Press.
[4] Bouma W et al., *Ann Thorac Surg*, 101(2):567-75, 2016.
[5] Rego BV et al., *Int J Numer Meth Biomed Eng*, 34(12):e3142, 2018.
[6] Merryman et al., *Am J Physiol Heart Circ Physiol*, 290(1):H224-31, 2006.
[7] Howsmon DP et al., *J R Soc Interface*, 17(166):20200098, 2020.
[8] Khalighi AH et al., *Ann Biomed Eng*, 47:60-74, 2019.

EFFICACY OF TEACHING BIOMEDICAL ENGINEERING LABORATORIES USING VIRTUAL REALITY

Anita Singh (1), Arun Ramakrishnan (2), Sriram Balasubramanian (3)

(1) Biomedical Engineering
Widener University
Chester, PA, USA

(2) College of Nursing & Health Professions
Drexel University
Philadelphia, PA, USA

(3) School of Biomedical Engineering, Sciences and Health Systems
Drexel University
Philadelphia, PA, USA

INTRODUCTION

Biomedical Engineering laboratories are designed to create connections that bridge gaps between theory and practice [1,2]. Hands-on experience during lab sessions help attain student learning outcomes including the ability to design an experiment to solve a problem, apply engineering principles, perform data acquisition, perform analysis, consider safety aspects, apply required engineering standards, apply modern technical skills, perform teamwork, and develop communication skills. While the attainment of these outcomes in the lab courses is widely reported, recent challenges with the COVID-19 pandemic have created serious limitations in immersive learning and hands-on training of engineers enrolled in these courses. Innovative approaches are warranted to enhance student learning and engagement to best attain the student outcomes relevant to these courses during the pandemic. We employed virtual reality (VR) videos of lab procedures to enhance student learning of experimental protocol and steps involved in data acquisition.

METHODS

A total of 14 Junior-level biomedical engineering (BME) students enrolled in BME 303: Biomedical Engineering Lab 1 participated in this study. They were asked to provide feedback on the use of VR to assess its efficacy in teaching the steps involved in the six experiments (Electromyography, Electrocardiograph, Kinetic, Bone Compression, Three-point bending, Tension) that are typically performed for the lab course. The lab instructor recorded themself performing the steps of six different experiments using an Insta360 EVO 3D-180° VR camera (www.insta360.com/). This VR camera captured the scene using two adjacent lenses, each with a horizontal and vertical field of view of 180°, giving a fully immersive view of the scene. Further, the separation of the two lenses enabled depth perception using the principles of stereophotogrammetry. Each student was asked to watch this video during the synchronous offering of the lab using VR glasses (Funsparks, VR glasses, Google, WA), provided by the instructor to standardize their VR experience. An in-class quiz related to the lab procedures and related-technical details was administered at the end of the VR video-watching session. This allowed for active student engagement and direct assessment of student learning (Figure 1). Students were then asked to fill an anonymous survey that allowed assessing the efficacy of VR in teaching labs. All surveys were approved by the Institutional Review Board and were anonymously collected using online Qualtrics forms (Qualtrics Inc., UT).

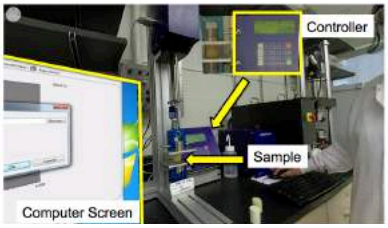

Figure 1: Bone compression lab with zoomed controller and computer screen display in VR.

RESULTS

After watching the VR videos, students answered questions that were directly related to the use of VR and the learning objectives of the labs. All students reported VR glasses to be user-friendly, and the average score on the in-class quiz was 95%. Overall student learning was improved with VR immersion and students were able to feel more immersed than just reviewing the written lab protocol (Figure 2). Students also reported more confidence in performing these experiments, if needed, for their senior design project or in the real world. All students agreed that incorporating a review of lab VR videos prior to the in-person lab will help attain better preparedness of students for the labs.

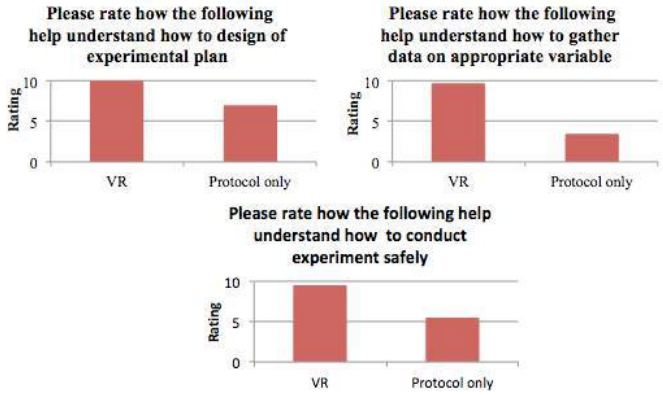

Figure 2: Student responses on utilizing VR videos versus written protocol only in EKG Lab (n=10).

Table 1: Mean Student rating of VR experience for EKG lab based on a 0 (Strongly Disagree)-10 (Strongly Agree) Likert scale (n=10)

Question	Rating
How do your rate your overall VR experience for this Lab module that covers physiological recordings?	8.2±1.8
How would you rate the EKG VR videos in understanding the steps involved in performing this experiment?	9.2±0.8
Should these videos be used in future offerings of the course?	10
Can VR videos replace in-person labs?	
Yes	7
No	3

DISCUSSION

The benefits of using VR technology in teaching biomedical engineering labs were evident and appeared very timely as an alternative to in-person lab teaching during the pandemic. While there were a few limitations to using VR, including limited availability of the desired VR videos, the expertise required for developing the desired videos into effective learning modules, and the costs associated with VR cameras and glasses, our efforts to create these videos were worthwhile and enhanced learning experience for BME students. Our future studies will employ VR in teaching biomechanics and graduate labs. It is noteworthy that extended learning in graduate school can greatly benefit from VR technology.

ACKNOWLEDGEMENTS

The research reported in this publication was supported by the National Institute of Biomedical Imaging and Bioengineering of the National Institutes of Health under Award Number R25EB023857.

REFERENCES

[1] Trumbower, R.D et al., IEEE EMBS, 101-110, 2003.
[2] Foulds, R.A et al., IEEE EMBS, 92-100, 2003.

DEVELOPMENT OF A FULLY DEGRADABLE FETAL HEART VALVE FOR IMPLANTATION *IN UTERO*

Hieu T. Bui (1), Sanchita S. Bhat (1), Christopher K. Breuer (2), Aimee Armstrong (2), Martin Bocks (3), Ajit P. Yoganathan (1), Lakshmi Prasad Dasi (1)

(1) The Wallace H. Coulter Department of Biomedical Engineering
Georgia Institute of Technology
Atlanta, GA, USA

(2) Department of Pediatric Surgery
Nationwide Children's Hospital
Columbus, Ohio

(3) Pediatric Cardiology
UH Rainbow Babies & Children's Hospital
Case Western Reserve University School of Medicine
Cleveland, Ohio

INTRODUCTION

Single ventricle physiology has presented challenges particularly related to cures and treatment. The available treatment methods comprise interventions that are currently palliative and not curative. Recently, prenatal intervention success rates have improved, and prenatal cardiac interventions such as fetal aortic valvuloplasty and other minimally-invasive procedures seem to be promising treatment options to avoid single ventricle physiology [1]. Unfortunately, even if intervention results in biventricular physiology, almost all go on to require postnatal valvuloplasty or repair and eventual valve replacement, which is limited by poor durability and somatic outgrowth in children.

The central hypothesis driving this project is that a biodegradable heart valve will normalize the fetal hemodynamics in a way that the complexity and severity of the congenital heart defect formation may be mitigated or even eliminated. Further the highly regenerative potential of fetuses may serve as the perfect host and timing for intervention such that the neovalve takes over the function as a normal heart valve with the capacity to grow. Recently, our group has demonstrated the feasibility of replacing the pulmonary valve with a fully biodegradable tissue engineered heart valve (TEHV) in a fetal lamb model using endovascular techniques [2]. Fetal valve replacement with a TEHV provides the opportunity to restore flow and heart valve function with a living neovalve created from an individual's own cells.

Towards this goal, this pilot project will focus on two goals: one, to manufacture and characterize the performance and degradation profile of synthetic biodegradable valves *in vitro*, using a pulse duplicator and two, to perform proof of concept delivery and performance of these valves *in vivo* using a fetal lamb pulmonary valve replacement model.

METHODS

Valve design optimization. In order to primarily understand the fundamental loading conditions on the valve, and prevent subsequent mechanical wear and tear, we conducted computational simulations to evaluate the efficacy of our previously established design [2]. We simulated two computer aided designs (CAD) with the first being from our published work consisting of a closed-cell stent made of Zn-Al4 (Michigan Tech University, Houghton, Michigan) and a tubular film of polycaprolactone (PCL) (Mn = 80,000 Da) (Sigma-Aldrich, St. Louis, MO). The PCL film was anchored onto the stent by three sutures on the commissures, and circumferentially around the bottom of the film (toward annular anchor region). The second design consisted of in-house designed 3D leaflets fit into the same stent and anchored all around the commissures and bottom region. The purpose of this design modification was to assess the loading conditions on each, and therefore establish the most optimum design. The stent was not simulated to save computational time and isolate loading on the leaflets. Across all simulations, we used material properties for PCL for the leaflets and applied a load of 25mmHg (peak fetal pulmonic pressure). For benchtop experiments, we are developing the PCL film using a solvent based technique [3].

Stent fabrication. As we have already shown in our previous publication [2], ZnAl4 possesses exceptional mechanical properties to serve as an alloy for endovascular stenting and as a scaffold for fetal valve implantation. Issues with elemental aluminum in the developing fetus may limit the use for this application going forward. However, the mechanical properties, stent design, low crossing profile, and optimal dimensions (7mm diameter, 10mm height) allows the ZnAl4 stents to serve as an excellent scaffold for this preclinical model.

RESULTS

Valve design optimization. From the first design, we observed that the peak stresses were located at the sutured points, possibly due to the valve being balloon-expanded during implantation. The leaflets being anchored to those three points experienced the greatest loads. However, as the leaflets were designed as a tubular film, they did not coapt completely. We attribute these results to the material properties of PCL; hence, we are also simultaneously optimizing leaflet material.

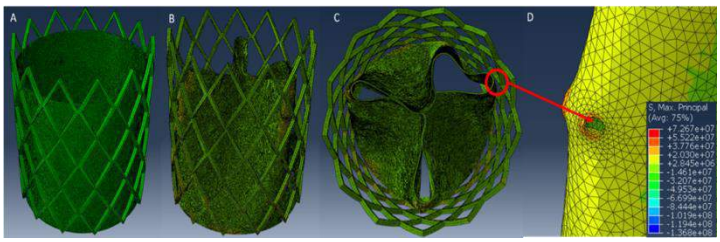

Figure 1: Simulation results from design 1 with tubular PCL film showing A) initial time point B) Final time point and C) *En face* view of final time point and D) Area of maximum stress with magnitude

From the second design, we observed the stresses to be substantially lowered by ~95% in the commissural region (as shown in Figure 2), indicating that the 3D leaflet design may yield better experimental results than the tubular film.

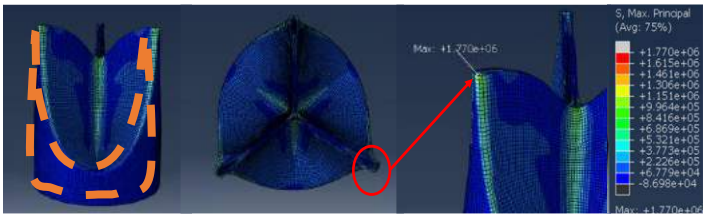

Figure 2: Simulation results from design 2 with 3D leaflets showing A) Final time point (region shown in orange was fixed during simulations) B) *En face* view of final time point C) Area of maximum stress with magnitude

Stent fabrication. As such, we have currently designed a metal jig (as shown in Figure 3) to aid in braiding the valve stent. The closely braided cross links will provide structural integrity to the overall valve. Once we have the assembled prototypes, we will begin *in vitro* work on the project. To date, we have the supplies needed for the benchtop work including valve deployment and crimping devices.

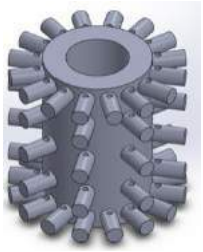

Figure 3: CAD model of metal jig designed for braiding the valve stent

DISCUSSION

This project will be a first step to overcome the current drawback of the lack of biodegradable neovalves that results in the need for repeat interventions and valve replacements. The neovalve has the potential to grow, repair, and remodel as the valve recipient grows, and restoration of normal flow in the fetus could enable reversal of ventricular hypoplasia and restoration of biventricular anatomy. Thus, the ability to replace a stenotic fetal heart valve with a living autologous TEHV would, for the first time, enable the creation of a truly curative strategy for the complex cardiac anomalies that cause single ventricle physiology.

ACKNOWLEDGEMENT

Funding is provided by Additional Ventures.
Zinc stents provided by Mr. Tim Moran, President PediaStent, LLC.

REFERENCES

[1] Graupner O. et al., *Geburtshilfe Frauenheilkd.*, 79(8):863-872. 2019.
[2] Zakko J. et al., *JACC Basic Transl*, 5(8):815-828, 2020.
[3] Tang Z.G. et al., *Biomaterials*, 25(19):4741-8, 2004.

A COMPARATIVE BIOMECHANICAL STUDY OF PORCINE EPICARDIAL LAYER AND ENDOCARDIAL LAYER

Sara R. McMahan, Alan M. Taylor, Katherine M. Copeland, Xiaodan Shi, Aneetta E. Kuriakose, Karla L. Perez, Yi Hong, Kytai T. Nguyen, Jun Liao

Department of Bioengineering, University of Texas at Arlington, Arlington, TX 76010

INTRODUCTION

To better understand the cardiac biomechanical behavior, the knowledge of each individual layer of the ventricular wall is needed. Recently, we reported an important phenomenon of the outmost layer of the ventricular wall: the epicardial layer, rich in elastin, acts like a prestrained "balloon" that wraps around the heart and functions as an extra confinement and protection interface [1]. This new observation points out the importance of a full biomechanical assessment of the epicardial layer and endocardial layer, which have not been characterized as well as the myocardial layer.

METHODS

Porcine hearts from ~6 month-old pigs were obtained from a local abattoir. The epicardial layer was dissected from the anterior middle region of the left ventricle. The heart muscles were gently removed, and the resulting samples were trimmed into a dogbone-shape (~12 mm x 4 mm). The endocardial layer was dissected similarly, while also avoiding the rugged trabecula. Both the circumferentially and longitudinally oriented samples were subjected to uniaxial mechanical characterizations. All mechanical tests were carried out in a 1X PBS bath using a TestResources uniaxial tensile testing machine. After 15 cycles of preconditioning, tissue samples were subjected to a loading-unloading protocol, stress relaxation, and failure testing. For stress relaxation, the sample was pulled to the designated load and held at that constant strain to monitor the stress decay for 15 minutes. Movat's pentachrome histology was also performed to assess the ultrastructure of the epicardium and endocardium. The histological slices were imaged with a bright field microscope (Nikon EC600).

RESULTS

The epicardial layer and endocardial layer show a stress relaxation behavior similar to that of other soft tissues; approximately 50% stress decay was observed. Failure stress-strain curves indicated that the longitudinal direction had a higher failure stress in both the endocardium and epicardium compared to the circumferential direction (Figure 1). The failure strain for the endocardium in the longitudinal direction is much larger than that of the circumferential direction, and overall the longitudinal direction was more extensible; for the epicardium, however, the failure strain of the longitudinal direction was similar to the circumferential direction. Moreover, we found that the endocardial elastin fibers were finer and denser, as well as more wavy than the epicardial elastin fibers. Those ultrastructural difference might be the underlying mechanism of various biomechanical behavior between epicardial layer and endocardial layer.

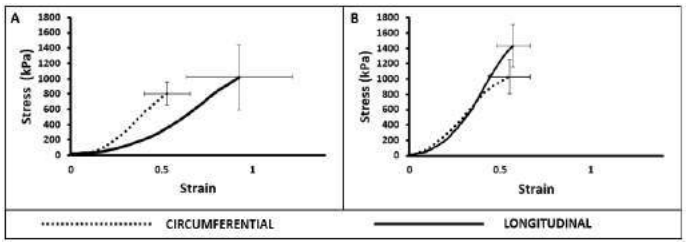

Figure 1: Average failure stress-strain curves for (A) the endocardium and (B) epicardium, where dotted lines signify the circumferential orientation and the solid lines signify the longitudinal direction.

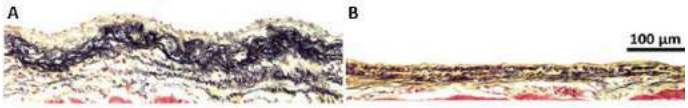

Figure 2: Histological images of (A) the endocardium and (B) epicardium imaged longitudinally, or parallel to the heart's surface.

DISCUSSION

We found that the epicardial layer and endocardial layer behaved differently, and the biomechanical differences were likely caused by their various ultrastructure. This study will provide a better understanding of the biomechanical behavior of the epicardial layer and endocardial layer, as well as provides essential data for high-fidelity computational modeling and simulation.

ACKNOWLEDGEMENTS

NIH 1R15HL140503; T32 HL134613.

REFERENCES

[1] X Shi, et al. Journal of the Royal Society Interface: 16 (152) 20190028, 2019

BIOMECHANICAL CHARACTERIZATIONS OF ACELLULAR NEONATAL PORCINE VENTRICLES

Karla Perez (1), Sadia Naz (1), Sara R. McMahan (1), Rachel Claus (4), J. Ryan Butler (4), Matthias Peltz (3), Yi Hong (1), Kytai T. Nguyen (1), Pietro Bajona (2), Jun Liao (1)

(1) Department of Bioengineering, University of Texas at Arlington, Arlington, TX 76010

(2) Hypertrophic Cardiomyopathy Program, Allegheny Health Network, Pittsburgh, PA 15212

(3) Cardiovascular and Thoracic Surgery, University of Texas Southwestern Medical Center, Dallas, TX 75390

(4) College of Veterinary Medicine, Mississippi State University, Mississippi State, MS 39762

INTRODUCTION

Approximately 8 out of a 1000 people suffer congenital heart disease (CHD) around the world, and some of the pediatric patients need surgical intervention to correct their severe defects [1]. However, not many studies have been carried out to understand the biomechanical properties of the neonatal hearts, which have unique mechanical properties that evolve quickly to adapt to the increasing working load of the hearts along with the growth of the infants. Recently, biomechanical properties of neonatal porcine ventricles were assessed [2]. The obtained data provided a solid basis for surgical intervention planning, implant design, and computational simulation in CHD. In this study, we deepen the understanding of neonatal hearts by distinguishing the biomechanical contribution of neonatal heart ECM and report the biomechanical properties of decellularized neonatal left ventricle tissue and right ventricle tissue.

METHODS

Neonatal porcine hearts were obtained from one day old piglets from a local farm. Each ventricle was visually inspected to avoid any anomalies prior to dissection and decellularization. The neonatal heart ventricles were dissected as longitudinally-oriented strips and marked by placing a suture on the upper left corner (Fig. 1A). Four groups were compared: left anterior ventricle (LAV), left posterior ventricle (LPV), right anterior ventricle (RAV), and right posterior ventricle (RPV). After dissection samples were placed in a 50 ml tube filled with 1% SDS solution. The tubes were placed in a rotational shaker continuously until the heart tissue appeared completely white color (Fig. 1B). Acellular ventricle scaffold samples were then subjected to uniaxial mechanical testing (TestResources universal machine). Tensile test and stress relaxation were performed. Histology was assessed with H&E staining and imaged with a bright field microscope (Nikon EC600).

RESULTS

Thorough decellularization was achieved and confirmed by histology (Fig. 1C, D). Preliminary testing results showed that (i) the acellular LAV was stiffer than the acellular RAV; (ii) the failure stress and strain of the acellular LAV were significantly higher than the acellular RAV (Fig. 1E). Both acellular LAV and RAV were much stiffer and the stress-strain showed a linear trend when compared with the native neonatal porcine ventricle, which showed a typical nonlinear behavior2. This difference was likely due to the removal of cardiomyocytes, and the left acellular scaffolds consisted of collagen fibers that experienced cardiomyocyte lacunae collapse. We also noticed that stress relaxation in the acellular LAV took place faster with a greater amount when compared with the acellular RAV (Fig. 1F).

DISCUSSION

A series of mechanical tests have been performed to characterize the biomechanical behavior of acellular neonatal porcine ventricles. The obtained knowledge will help better understanding cardiac biomechanics and multiscale tissue behavior of the newborn hearts.

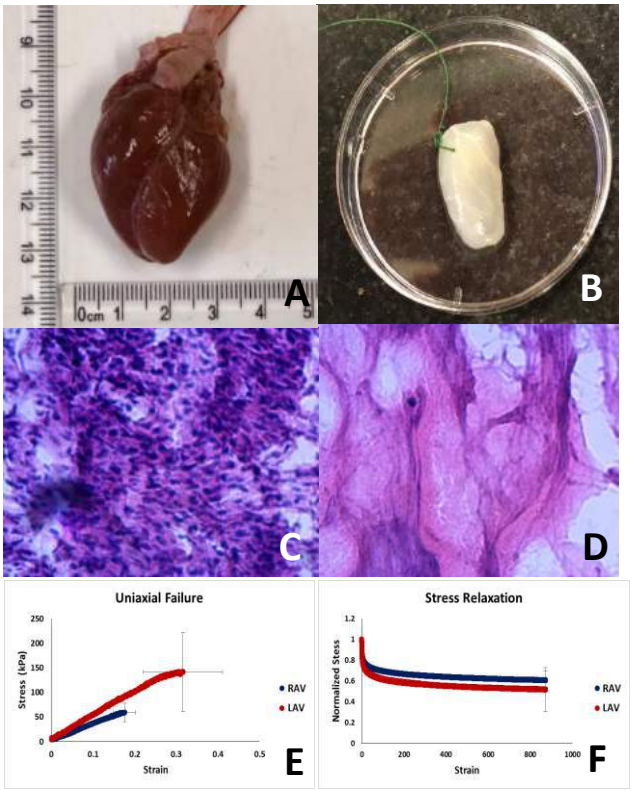

Figure 1: (A) Neonatal porcine heart. (B) Neonatal ventricle strip after decellularization. H&E staining of (C) neonatal ventricle and (D) acellular neonatal ventricle. (E) Failure test results. (F) Stress relaxation results.

ACKNOWLEDGEMENTS
NIH 1R15HL140503; T32 HL134613.

REFERENCES

[1] van der Linde D, et al. Birth prevalence of congenital heart disease worldwide: a systematic review and meta-analysis. Journal of the American College of Cardiology. 58:2241, 2011

[2] Ahmad F, et al. Biomechanical properties and microstructure of neonatal porcine ventricles. Journal of the Mechanical Behavior of Biomedical Materials, 88, p18-28, 2018

THUMB AND INDEX FINGER MOTIONS COUPLED WITH PILOT WORK ON AN OCTOPUS TOWARD THE DEVLOPMENT OF SMART PROSTHETICS

Garrett Weidig , Chris Sadler , Tamara Reid Bush PhD

Department of Mechanical Engineering
Michigan State University
East Lansing, MI, USA

INTRODUCTION

Loss of limb is accompanied by loss of independence, financial burden, and other traumatic effects [1]. The most common form of treatment is a prosthetic device. However, prosthetic limbs are not able to restore the entire function to the individual. Additionally, use of a prosthetic may provide residual problems such as long adjustment periods and increased skin irritation on the contact surface [2].

Up to 56% of individuals with upper limb loss use some sort of prosthetic [3]. Many upper extremity prosthetics, especially distal to the elbow, are passive prosthetics- they are aesthetically similar to the hand, but provide little hand function, other than stabilizing abilities [4]. Prosthetics that do focus on function are typically able to provide only part of the lost function.

In nerve driven prosthetics, neurons' action potentials are responsible for controlling the assigned movement in the prosthetic. This can lead to complications such as the misreading or crossing of neurological signals into the prosthetic. This is because a movement is usually thought of as a process of the brain sending signals to the body- but there is a need for prosthetics to be more intuitive. There is one animal that is able to act before it thinks- the octopus.

The octopus is a boneless, muscular hydrostat which allows for infinite degrees of freedom of the arms. The octopus is also equipped with an axial nerve in each of the arms that allows each arm to act without the brain's input. Studying this 'disconnect' between the limbs and brain could be crucial to the development of new, smarter robotics.

Therefore, the goals of this work were twofold 1) to determine the operational finger space for specific every-day tasks and 2) to initiate a study of octopus reach and grasp movements. Together, these unique studies have the potential to aid in the design of future smart prosthetics that parallel some natural components found in the octopus.

METHODS

Human: Five male participants (average age 20.2 years standard deviation 1.3 years) were tested using a motion capture system. Participants wore reflective markers (two individual markers and 16 pods) to track the movements of their dominant hand (Figure 1). Participants completed four experiments related to daily living: *typing, mousing, swiping on a phone, and moving a game controller*.

Motion data were analyzed and plotted on planes to accent differences in motion for both the task and specific finger. Ranges of motion were mapped for the thumb and the index finger.

Octopus: Preliminary work occurred with the octopus; species *Octopus bimaculoides.* The first step of this research was to evaluate the feasibility of obtaining movement of an octopus leg using a motion capture system (i.e. marker size, marker placement, adherence of markers, capturing movement type and speed of movements). Four marker pods and one singular marker were glued, using a human skin glue, along the length of the arm. Stereotypical arm movements were simulated out of water. Position profiles and curvature patterns were obtained.

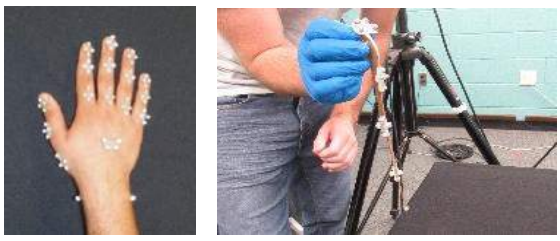

Figure 1: Hand marker setup for tasks of daily living experiment (left). Octopus marker setup (right)

RESULTS

Human Data: Figure 2 provides the visual results from the index finger space and the thumb space for the four tasks.

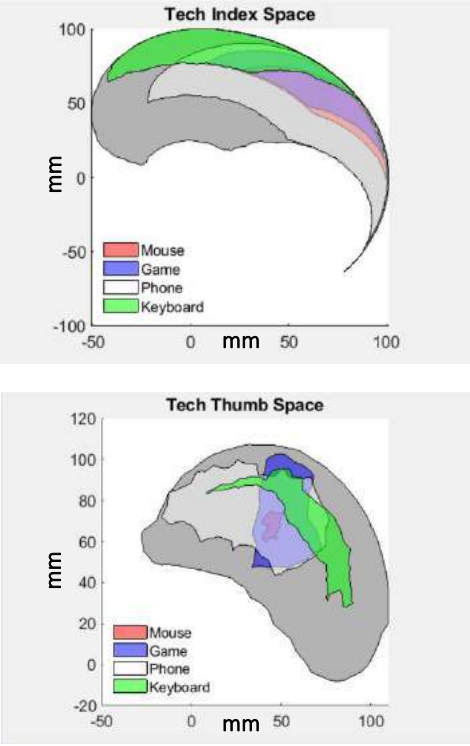

Figure 2: Range of motion for tasks of daily living involved in grasping for the index finger (top) and the thumb (bottom). Mousing can be seen in red, gaming in blue, phone swiping in white, and typing in green. The dark gray area describes the maximum range of motion of the index finger.

The index finger motion largely focused on the combined flexion of the interphalangeal joints whereas the thumb range of motion is reflected on the plane perpendicular to the proximal part of the hand.

The second piece of this experiment revolves around the position data associated with the octopus leg. Figure 3 (left) shows the unstretched length of the octopus' leg. The leg was whipped, being held at the most proximal part of the leg (peach-colored markers, top right) and a wave was produced, similar to that of a real octopus reaching motion in dry conditions.

DISCUSSION

In this experiment, human grasping tasks along with approaches to gathering data from an octopus leg were investigated. The end goal of this work is to link the two to the development of new, smart prosthetics.

For index finger data, the phone task used the greatest percentage of the maximum range of motion area, whereas the mousing task used the least. During both mousing and gaming, simple flexion actions dominated the movement strategies. The keyboard task involved greater extension of the fingers, especially to move to the letters higher on the keyboard (when the wrist is in a fixed location).

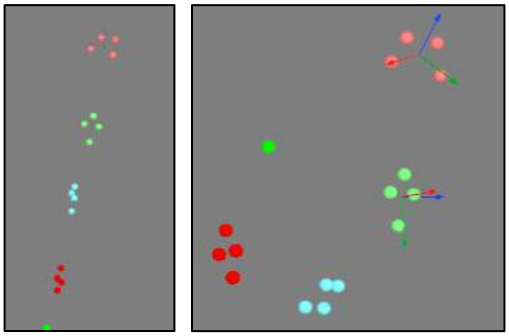

Figure 3: Motion capture visualization for a fully extended octopus' arm (left) and an octopus arm during the whip-like motion (right). Four marker pods and one single marker (at the tip) were glued onto the octopus' arm. Together, the 17 markers on the arm produced numerical data which define velocity profiles, curvature, and torsion.

The thumb data demonstrated a different story. Although one would think that the thumb always operated in the center of maximum boundaries, our data indicated that the tasks utilize different spaces. This may be because the thumb is in charge of stability and the space in which the thumb operates must accommodate both the movement and maintain stability.

The differences in the thumb and finger ranges of motion provide insight on how grasping and actions around activities occur. Clearly, based on the different movement spaces, different activities vary the postures of the index and thumb. Understanding these working spaces and the relative movements between the index finger and thumb are crucial to functional prosthetic hand designs.

The pilot octopus data also showed success with the initial steps. We were able to successfully adhere marker sets to an octopus' arms and gather movement data of a simulated motion. The whip-like motion of the octopus' arm successfully replicated a wave that moved distally along the arm. There is one parameter that was not included during this above water testing which is the torsional ability of the octopus' arm. Other than this, it is expected that similar data will be collected underwater, first with a detached leg, and then on a leg of a live octopus. We expect that further octopus reach and grasp data paired with the human hand data will indicate ways that the octopus' arm can be a better model for a prosthetic.

REFERENCES

[1] Bowrey, S et al., *Disability and Rehabilitation*, 26:831-836, 2009.
[2] Meulenbelt, H et al., *Disibility and Rehabilitation*, 28:603-608, 2005.
[3] Raiche, K et a., *Journal of Rehabilitation Research & Development*, 45:961-972, 2008.
[4] Maat, B et al., *Prosthetics and Orthotics International*, 42:66-74, 2018.

INTERACTION MECHANISMS OF PEPTOID AND NEURONAL CELL RECEPTORS AND ITS DEPENDENCE ON PEPTOID SPHERE SIZE AND CHAIN LENGTH

Mohan Yasodharababu (1), Shannon Servoss (2), Arun K. Nair (1, 3)

(1) Multiscale Materials Modeling Lab, Department of Mechanical Engineering, University of Arkansas, Fayetteville, AR, USA.

(2) Ralph E. Martin Department of Chemical Engineering, University of Arkansas Fayetteville, Arkansas.

(3) Institute for Nanoscience and Engineering, 731 W, Dickson Street, University of Arkansas, Fayetteville, AR, USA.

INTRODUCTION

Neuronal cells interacts with extracellular matrix (ECM) to detect the microenvironment to influence the cell functions such as differentiation, migration, and proliferation [1]. The two important transmembrane proteins that transmit signals between ECM and cell are integrin and neural cellular adhesion molecules (NCAM). They play an important role in sensing the ECM properties [2]. Neuronal cell differentiation is sensitive to the properties of natural or synthetic ECMs, which include biochemical composition, biomechanical properties, and structural/ topographical features [3]. *In vitro* study of neuronal cell differentiation uses mostly synthetic ECM; since it can be tuned for the desired mechanical properties such as stiffness and topography [4]. Biocompatible synthetic materials such as polyelectrolyte multilayers (PEMs), polyacrylamide hydrogels, Matrigel®, and peptoids are utilized to achieve the desired ECM stiffness and topography. Peptoids have gained importance due to its self-assembling structure as microsphere [5] and nanosheets [6]. Peptoids are biopolymers that have a backbone similar to that of peptides with the side chains attached to the amide group rather than the α-carbons [7]. The number of monomers addition to peptoid by solid-phase synthesis enables to control the chain length and the desired size of secondary structure [8]. Peptoids have the ability to form a microsphere when it is exposed to organic solvents [5]. The number of monomer addition to peptoid by solid-phase synthesis enables to control the chain length and the desired size of secondary structure [5]. Peptoids exhibit self-assembling and increased cellular permeability as compared to the corresponding peptide, thus enhancing the potential as an ECM [5]. Besides, peptoids have better biocompatibility compared to other synthetic ECM material while retaining the ability to interact with neuronal cell receptors [9]. Together, these characteristics render peptoids an attractive, novel ECM material for *in vitro* neuronal cell differentiation. Peptoids as an ECM ligands form a bond with the receptors; this physical linkage transfers the forces from receptors to the cell nucleus. Several experiments have proved the number of receptors binding with ligands and their strength determines the fate of cell growth [10]. However, in literature, there is a lack of understanding about the interaction mechanisms between the peptoids and neuronal cell receptors such as integrin and NCAM [5]. In this study, we specifically examine the peptoids 3 chemical structure extracted from the Bakovic et al., 2019 [11]. Since they have observed that peptoids 3 has the ability to form a uniform microsphere in solvent (water) concentration by varying the number of monomers (chain length). Hence, we plan to perform molecular dynamics study to investigate the peptoid as an ECM, and their interaction with neuronal cell receptors (integrin and NCAM). In addition, we plan to study the peptoid sphere size and number of monomer influence on the interaction energy between self-assembling peptoids and neuronal cell receptors.

METHODS

Peptoid 3 chemical structure extracted from the Bakovic et al., 2019 [5] is composed of nonstandard amino acid sequence $(NSPE_4 - NLYS_1 – NSPE_1)_n$, where n is the number of monomers in the chain. Modeling this non-standard amino acid is a challenging task. However, a recent study using density functional theory have proved that substituting the equivalent standard amino acid parameters (PHE and LYS) have yielded comparable results with the experiments[12].

The diameters of the peptoids sphere is chosen based on the normal distribution of microsphere observed in experimental results [11]. Due to the challenge in modeling microns range in MD, we model the peptoids sphere at the nanometers scale. Also, our focus in this study is to understand the number of monomers and sphere size influence on the interaction energy between peptoids and receptors. We build the peptoids sphere using a packmol open-source software [13] with n equal to 12 and 24 (refer Figure 1), and with different sphere diameter ≈ 25Å and 35Å respectively (refer Figure 2). These peptoid spheres will be equilibrated with integrin α1β1 and NCAM, to study the interaction energy between the peptoids sphere and neuronal cell receptors.

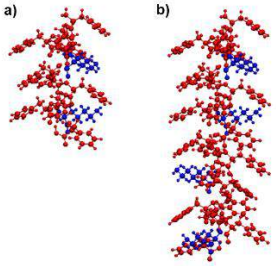

Figure 1: Shows the α-helix secondary structure of peptoid with the different number of monomers a) 12 mer and b) 24 mer.

The protein structure of receptors such as integrin α1β1 (1CK4 pdb) and NCAM Ig 1-2-3 (1QZ1 pdb) of Rattus norvegicus are extracted from the protein database [14]. CHARMM 22 [15] and MFTOID [16] force fields are used to analyze the peptoid and receptor interactions. First step of energy minimization is performed on the peptoid sphere-receptor mixture to reduce instabilities in the initial conformation. Next, the minimized mixture is equilibrated using NPT ensemble at a temperature of 300 K for 2ns. For all MD simulations, a time step of Δt= 2 fs is used. Constant temperature and pressure were maintained with the Berendsen algorithm using a barostatic time

constant of τ_p = 5.0 ps atm^{-1} and a thermostatic time constant of τ_t = 1.0 ps. To find the position and velocity of atoms at each time step, we use the Nose-Hoover method. The equilibration of proteins are carried out until the root mean square deviation is less than 1 Å. We used LAMMPS [17] (Large-scale Atomic/Molecular Massively Parallel Simulator) for all our MD simulations, which is an open-source code.

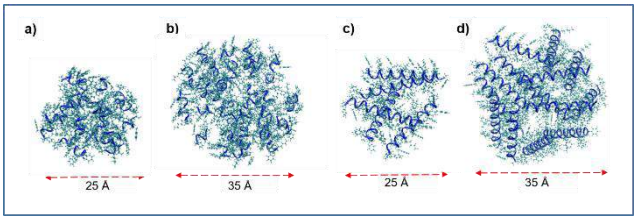

Figure 2: Molecular structure of the peptoid sphere with 25 Å (a,c) and 35 Å(b,d) diameters created from the random distribution of 12mer and 24 mer respectively.

RESULTS

After equilibration, we analyze the peptoid-integrin α1β1 structure to evaluate the pair interaction energy (*epair* = van der Waals (*evwdl*) + Coulombic energy (ecoul)). Preliminary results of peptoid-integrin α1β1structure show that increasing the peptoid sphere size the interaction energy increases; refer Figure 3a. This may be due to the increase in the number of peptoid molecules at the interface between peptoid-integrin. However, varying the number of monomers from 12 to 24 shows that interaction energy is higher for 12 mer when compared to 24 mer even though the number of molecules are equal in both cases; refer Figure 3b. To examine the reason for higher interaction energy in 12 mer peptoid sphere, we perform contact surface analysis on the peptoid-integrin structure using the solvent-accessible surface area (SASA) technique[18]. A previous study on collagen-integrin and laminin-integrin has shown that receptors are more attracted to hydrophilic surface molecules [19]. Hence, we evaluate the hydrophilic contact surface area between integrin and peptoid sphere with 25Å diameter; refer Figure 4. It shows that 12 mer peptoid sphere has a higher hydrophilic contact surface area, which explains the reason for higher interaction energy in 12 mer peptoid sphere.

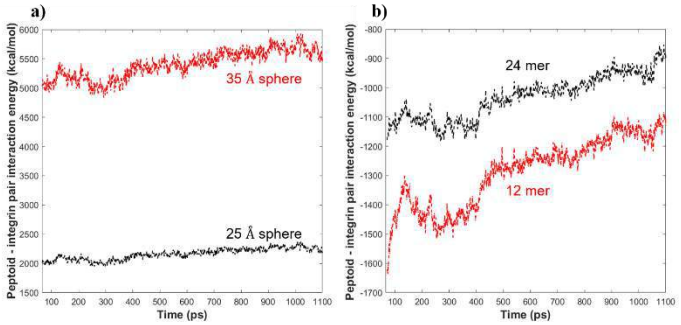

Figure 3: a) Shows the effect of varying sphere size (25 and 35Å) on pair interaction energy of peptoid – integrin for n=12 mer. b) Shows the effect of a varying number of monomers (n = 12 and 24) on pair interaction energy of peptoid – integrin.

DISCUSSION

We performed molecular dynamics studies to investigate the peptoid sphere size and chain length (number of monomers) influence on the interaction energies between peptoid and neuronal cell receptors. Preliminary results suggest that the peptoid sphere with 12 mer have better adhesion with integrin α1β1; since the number of hydrophilic contact surface area is higher in 12 mer when compared to 24 mer. This effect could be due to the flexibility of a smaller chain (12 mer) to accommodate a larger surface area at the peptoid –integrin interface. These findings will enhance the understanding of the interaction mechanism of peptoid- neuronal cell receptors and also aid *in vitro* studies to select the optimal peptoid sphere size and the number of monomers.

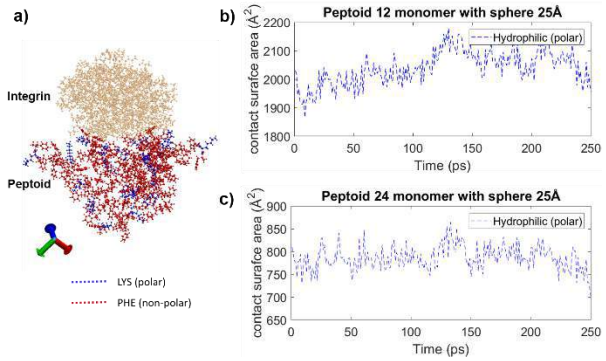

Figure 4: a) Shows the snapshot of integrin α1β1 - peptoids equilibrated structure along with the distribution of polar and non-polar molecules in the peptoid chain. Calculated hydrophilic surface area for different numbers of monomers 12 mer and 24 mer is plotted in b) and c), respectively.

ACKNOWLEDGEMENTS

We would like to acknowledge the support provided by the Center for Advanced Surface Engineering (CASE) from National Science Foundation [No. OIA 1457888], and the EPSCoR Arkansas Program. AKN would like to acknowledge the support from 21st century professorship grant from University of Arkansas.

REFERENCES

[1] Sonam, S., et al. *Sci Rep*, 6: 20415.2016.
[2] Katsumi, A., et al. *J Biol Chem*, 279, 13: 12001-12004.2004.
[3] Nguyen, A. T., et al. *J Phys Condens Matter*, 28, 18: 183001.2016.
[4] Mammadov, B., et al. *Biomaterials Science*, 1, 11: 1119.2013.
[5] Hebert, M. L., et al. *Org Biomol Chem*, 11, 27: 4459-4464.2013.
[6] Edison, J. R., et al. *Proceedings of the National Academy of Sciences*, 115, 22: 5647.2018.
[7] Renfrew, P. D., et al. *J Am Chem Soc*, 136, 24: 8772-8782.2014.
[8] Mukherjee, S., et al. *J Phys Chem B*, 119, 50: 15407-15417.2015.
[9] Montolio, M., et al. *Chem Biol*, 16, 7: 691-701.2009.
[10] Li, Z., et al. *Experimental cell research*, 349, 1: 85-94.2016.
[11] Perez Bakovic, G. R., et al. *Biopolymers*, 110, 6: e23283.2019.
[12] Lin, H., et al. *Journal of Chemometrics*, 30, 7: 369-376.2016.
[13] Martinez, L., et al. *J Comput Chem*, 30, 13: 2157-2164.2009.
[14] Berman, H. M., et al. *Journal of computer-aided molecular design*, 28, 10: 1009-1014.2014.
[15] MacKerell, A. D., et al. *The Journal of Physical Chemistry B*, 102, 18: 3586-3616.1998.
[16] Mirijanian, D. T., et al. *Journal of Computational Chemistry*, 35, 5: 360-370.2014.
[17] Plimpton, S. *Journal of Computational Physics*, 117, 1: 1-19.1995.
[18] Durham, E., et al. *J Mol Model*, 15, 9: 1093-1108.2009.
[19] Chen, L., et al. *PLoS One*, 7, 7: e40202.2012.

OPTIMIZATION OF PERIVASCULAR REGION GEOMETRY AND MATERIAL PROPERTIES FOR APPLICATION IN PATIENT-SPECIFIC MODEL OF A CORONARY ARTERY

Caleb C. Berggren (1), David S. Molony (2,3), Habib Samady (2,3), Lucas H. Timmins (1,4)

(1) Department of Biomedical Engineering
University of Utah
Salt Lake City, Utah, USA

(2) The Heart Center of Northeast Georgia
Medical Center
Gainesville, Georgia, USA

(3) Division of Cardiology
Department of Medicine
Emory University School of Medicine
Atlanta, Georgia, USA

(4) Scientific Computing and Imaging Institute
University of Utah
Salt Lake City, Utah, USA

INTRODUCTION

Acute coronary syndromes (ACS), characterized by reduced blood flow to the heart, remain the highest cause of mortalities worldwide with ~9 million deaths annually [1]. An ACS event is caused by the rupture of an atherosclerotic plaque and is the primary origin of major adverse cardiac events (MACE). Prior work has shown that rapid transition from stable to unstable plaque phenotypes precedes ACS [2], so there is great interest in establishing prognostication strategies to identify rapidly progressing coronary atherosclerosis. Indeed, virtual-histology intravascular ultrasound (VH-IVUS) has emerged as a clinical imaging tool to identify tissue composition, plaque phenotype, and disease progression; however, current image-based methods for predicting future MACE remain insufficient.

As mechanical loads have been postulated to play a central role in coronary atherosclerosis and plaque rupture, efforts have been directed at developing computational techniques to predict the *in vivo* biomechanical environment towards advancing prognostic capabilities. Recent investigations have shown that increased plaque structural stress is observed in vulnerable and ruptured coronary plaques when compared to stable and non-ruptures lesions [3,4]. It is important to note, however, that these image-based studies assumed plane strain (i.e., models were 2D). A primary challenge in the development of 3D patient-specific computational models is the application of boundary conditions to keep the curved vessel fixed in space while still permitting deformation under the application of a lumen pressure.

Therefore, this study aimed to optimize a perivascular (PV) support structure, including structure geometry and material properties, that prevents coronary tissue rigid body motions and prohibits impact upon tissue deformation under loading.

METHODS

Model Geometries Two computational geometries were created – idealized and patient-specific coronary geometry – and each included models with or without PV support (Fig. 1). The idealized geometry, created in the FEBio software suite [5], consisted of a quarter-cylinder with a 2-layer coronary artery model whose dimensions were derived from the literature (inner radius = 1.5 mm, medial thickness = 0.43 mm, adventitial thickness = 0.48 mm) (Fig. 1A) [6]. A PV support was added with a thickness of 5 or 10 mm. The patient-specific coronary geometry was created from VH-IVUS image data [7]. Briefly, ECG-gated (end-diastolic) VH-IVUS images acquired from a 71-year-old Caucasian female were segmented, boundaries were stacked along the VH-IVUS catheter centerline, and volume surfaces were generated and smoothed (Geomagic, 3D Systems, Rock Hill, SC). To aid study goals and modeling efforts, the centerline was straightened and the model only included data from 50% of the geometry circumference (Fig. 1B). Adventitial and PV support layers with thickness values of 0.48 and 10

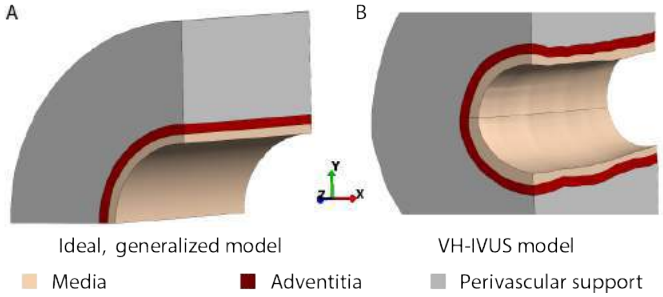

Figure 1: Coronary artery geometries with PV support for (A) an ideal, generalized quarter-symmetry model and (B) a VH-IVUS model.

mm, respectively, were added in ANSA (Beta CAE Systems, Thessaloniki, GD).

Computational Modeling Geometries were imported into ANSA and discretized with hexahedral elements. Each coronary geometry had an identical mesh regardless of whether the PV was present or not, and the arterial layers were meshed at 20× the density of the PV support.

Across both computational geometries, the medial and adventitial layers were defined as fiber-reinforced materials (i.e., an isotropic ground matrix with fiber reinforcements). Material coefficients for each layer were extracted from prior experiments [6]. Bulk moduli for the medial and adventitial layers were 50 and 90 MPa, respectively, to enforce incompressibility. The sensitivity of tissue deformation to PV support parameters in the idealized geometry was evaluated using combinations of Young's modulus (E) and thickness (h) (Table 1).

Across all computational models, the ends of the vessel and PV support structure, if present, were fixed in the z-direction. Furthermore, symmetry planes (i.e., θ-faces) were only allowed to deform in the radial direction. In the patient-specific model, the nodes lying at half the vessel circumference were not allowed to deform in the θ-direction. When the PV support structure was present, nodes on the outer PV surface were fixed in all directions. A pressure of 40 mmHg was applied to the vessel lumen. All computational simulations were performed in the FEBio software suite [5].

Data Analysis Following model convergence, element kinematic data and principal stresses were evaluated. An element-by-element comparison of total displacement was performed to evaluate the impact of the PV support structure on artery deformations and the sensitivity of deformations to PV support geometry and material properties. In addition, differences in transmural stress distributions in the presence or absence of the PV support structure were examined.

RESULTS

Table 1: Effects of varying PV parameters upon vessel displacement and 1st principal stress.

PV Parameters		Total Displacement [mm]		
h [mm]	E [kPa]	Min	Max	Avg.
no PV	-	0.781	0.930	0.854
5	1.0	0.779	0.928	0.852
5	0.1	0.781	0.930	0.854
5	0.01	0.781	0.930	0.854
10	1.0	0.779	0.928	0.852
10	0.01	0.781	0.930	0.854

Examination of tissue displacements in the idealized geometry demonstrated that deformations were not sensitive to variations in the thickness (h) or Young's modulus (E) of the PV support structure. Without the PV support, the minimum and maximum total displacements were 0.781 and 0.930 mm, respectively (Table 1). The addition of PV support with h and E values of 5 mm and 1.0 kPa, respectively, resulted in minimum and maximum tissue displacements of 0.779 and 0.928 mm, respectively. Furthermore, an element-by-element comparison revealed an average difference in total displacement of 2.25e-3 mm and ~96% of elements had a change of <2.4e-3 mm. Similar minute changes in total displacement were observed across other variations in h and E. Notably, h and E values of 10 mm and 0.01 kPa had nearly identical values of total displacement compared to the model with no PV support as 100% of elements had a total displacement change of <1.9e-5 mm.

The inclusion of a PV region with a thickness and Young's modulus of 10 mm and 0.01 kPa had a minimal effect upon arterial deformation in the VH-IVUS-derived model. Compared to the model without a PV region, the average and maximum differences in total displacement were 4.1e-5 and 1.52e-4 mm, respectively. Also, ~99% of elements had a displacement change of <1.3e-4 mm. Evaluation of the transmural distribution of 1st principal Cauchy stress further highlights the minimal impact that the PV structure had on the artery mechanical environment (Fig. 2A). At a location near the central region of the vessel, a nearly identical decrease of stress from the medial to the adventitial surface was observed in models with the presence or absence of the PV region (Fig. 2B). An element-by-element comparison revealed an average stress difference of 0.2% between the models, and ~97% of elements had a difference in stress of <0.04%.

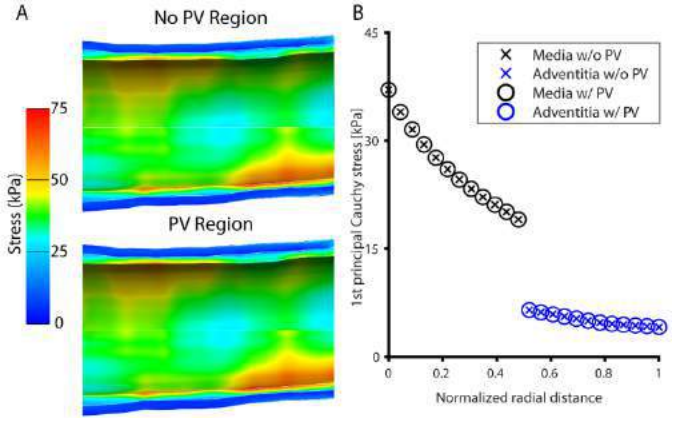

Figure 2: Impact of a PV region upon VH-IVUS model stresses (A) over the whole model and (B) at a central region of the vessel.

DISCUSSION

These results illustrate the minimal impact that an optimized PV support structure can have on the coronary artery mechanical environment during lumen pressurization. Data demonstrated that the identified PV geometry and material properties have minimal impact upon vessel distensibility in an ideal, generalized model (Table 1) and prevented rigid body motions in a straightened, patient-specific 3D coronary artery model (Fig. 2). Importantly, inclusion of a PV region allows application of boundary conditions in future 3D patient-specific coronary models with complex geometries, including multi-planar curvature and branching vessels. We acknowledge the limitation of using a straightened model cut in half. However, such a model was necessary to enable application of boundary conditions to an asymmetric coronary model without a PV region for comparative purposes. We anticipate the addition of a PV region will enable the establishment of 3D patient-specific coronary artery computational frameworks to more accurately predict the *in vivo* mechanical environment and enhance prognostic capabilities for plaque progression and ACS events.

ACKNOWLEDGEMENTS

This research was supported by the National Institutes of Health (R01 HL150608).

REFERENCES

[1] WHO, "Disease Burden and Mortality Estimates", 2018.
[2] Motoyama, S et al., *JACC*, 66(4): 337-46, 2015.
[3] Costopoulos, C et al., *JACC: Cardiovasc Imaging*, 10(12):1472-1483, 2017.
[4] Costopoulos, C et al., *Eur Heart J*, 40(18):1411-1422, 2019.
[5] Maas, S et al., *J Biomech Eng*, 134(1):011005, 2012.
[6] Holzapfel, G et al., *Am J Physiol Heart Circ Physiol,* 289: H2048 – H2058, 2005.
[7] Timmins, LH et al., *Ann Biomed Eng*, 43(1):94-106, 2015.

CROSSLINKING OF COLLAGEN ACROSS CARTILAGE TEARS FOR IMPROVED INTERFACE STRENGTH

Kimberly R. Kroupa (1), C.V. Sise (2), Clark T. Hung (2), Sinisa Vukelic (1), Gerard A. Ateshian (1,2)

(1) Department of Mechanical Engineering
Columbia University
New York, NY, USA

(2) Department of Biomedical Engineering
Columbia University
New York, NY, USA

INTRODUCTION

Articular cartilage is a connective tissue found at the joints of long bones in the body, where it serves to reduce friction while sustaining contact forces under intense mechanical stresses. Over time cartilage may degrade, leading to the formation of defects and lesions, and resulting in a painful, debilitating condition called osteoarthritis (OA). Despite being the leading cause of disability among older Americans and affecting 27 million people in the US alone [1], few early-stage treatment options are available for OA, in part because the disease is largely asymptomatic until degradation has become severe enough to cause pain and immobility. OA frequently progresses, until the only viable treatment option is total joint replacement.

Articular cartilage has a hydrated extracellular matrix (ECM) sparsely populated by chondrocytes. The ECM structure consists of negatively charged proteoglycans that produce an osmotic pressure, which contribute to its compressive stiffness, and an interwoven collagen network, which counteracts this swelling and provides tensile strength. A key pathogenic pathway of OA is the disruption or unraveling of this collagen network, which results in instability of the ECM and swelling of the tissue [2]. Therefore, methods of repairing this damaged collagen network have been studied as treatment strategies for combating the progression of OA.

Crosslinking by femtosecond laser treatment has been shown to strengthen cartilage tissue that has begun to wear in the superficial zone, by reconnecting the fragmented collagen pieces [3]. For large cartilage defects where an implant is used for repair, it has been shown that promoting collagen crosslinking at the interface can promote the integration of this implant with the native tissue [4]. Fibrin glues are also used clinically to aid in the repair of musculoskeletal tissue tears, like in the meniscus, by acting as an adhesive [5]. In this study, we examine the feasibility of repairing tears in cartilage and other collagenous tissues, by crosslinking collagen fibers across the interface to 'glue' and strengthen the bond. A collagen hydrogel can also be used to coat the surface of the interface, to increase the proximity of collagen fibrils and fibers at this junction and provide more sites for the broken collagen fragments to bind with. To address these aims, we measured the interface strength of cartilage explants bonded with and without a collagen gel and crosslinked with glutaraldehyde (GTA), a common crosslinking agent for cartilage tissue research [6].

METHODS

Cylindrical cartilage explants were harvested from the femoropatellar grooves of four immature bovine knee joints (∅10 mm). The superficial and middle zones were removed by sledge microtome resulting in a uniform thickness of 3.79 ± 0.1 mm. A ∅4 mm plug was cored out from the center of the explant. For six samples (Gel/GTA group), the hole of the annulus was filled with collagen type I liquid hydrogel (ThermoFisher Scientific A1064401), prepared at 4 mg/mL with 10X phosphate buffer saline (PBS) and 1N NaCl. The plug was then placed back into the hole. These samples were placed in a 37 °C incubator for 1 hour to allow the hydrogel to coagulate, then removed, wrapped in parafilm, and allowed to set for 12 hours at 25 °C. For six additional samples (GTA group), the plug was placed back into the hole without hydrogel. Six other samples (CTRL group) were separated so that the center plug was left outside of the annulus as a negative control, to isolate the effect of GTA on the interface strength. All samples were then exposed to 0.6% GTA, prepared in PBS, 6 mL per sample at 8 °C for 24 hours [7].

A standard push-out test was performed [8], conducted on mechanical testing devices with a modified platen. Each sample was stained with India ink to locate the top of the inner plug, placed on an aluminum support plate with a ∅6 mm hole to allow the inner plug to

be pushed out, and submerged in 1X PBS. A ∅3 mm rigid flat indenter parallel to the cartilage surface was pressed against the inner plug, concentric with the stained circle, and displacement was prescribed in the form of a linear ramp at a rate of 0.5 μm-s^{1}, until failure (Fig. 1, left). A 45 N load cell and LVDT recorded force and displacement data throughout the test.

The interface strength was reported as the failure stress, evaluated as the maximum load normalized by the lateral area of the interface, and energy to failure, evaluated as the area under the force-displacement curve from onset to maximum force. A one-way ANOVA with post hoc testing of the means was performed to analyze statistical significance.

RESULTS

For each sample, force-displacement curves were obtained, and converted to stress-displacement curves using the interface area of each sample, equal to the lateral area of the inner plug (Fig. 1, right). One outlier was removed from the GTA group, due to its very low failure stress of 8.3 kPa, when compared to other samples in that group (Fig. 2, left).

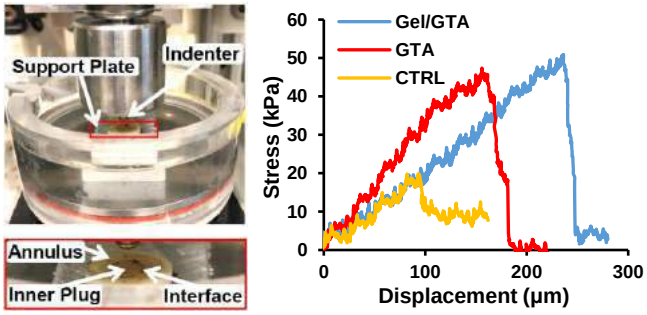

Figure 1: (Left) An image of the push-out test, cylindrical inner plugs were dislodged from an annulus via an indenter descending at a constant rate. (Right) Representative stress-displacement curves for push-out tests.

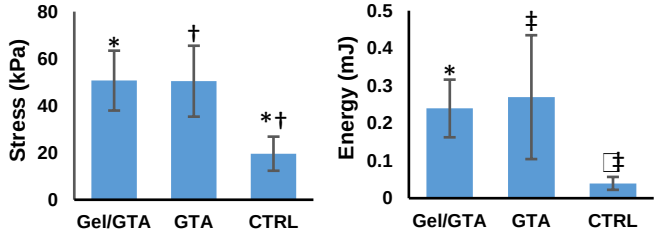

Figure 2: (Left) Average failure stress across each group (Right) Average energy to failure across each group. * p<0.0005, † p<0.005, ‡ p<0.05: statistical difference between mean value of two groups.

The failure stress for each sample was averaged across each group (Fig. 2, left). The Gel/GTA group had an average failure stress of 50.7 ± 12.7 kPa. The GTA group had a failure stress of 50.4 ± 15.1 kPa, which was not statistically different from the Gel/GTA group (p=0.98). The failure stress of the CTRL group, at 19.6 ± 7.2 kPa, was statistically lower than the Gel/GTA (p<0.0005) and GTA (p<0.005) groups.

The energy to failure for each sample was evaluated using units of mJ (Fig 2, right). This quantity was also similar between the treated groups, 0.24 ± 08 mJ for the Gel/GTA, and 0.27 ± 0.17 mJ for the GTA group. In contrast, the energy to failure in the CTRL group, 0.40 ± 0.02 mJ, was significantly lower than Gel/GRA (p<0.0005) and GTA (p<0.05) groups.

DISCUSSION

The results of this study indicate that collagen crosslinking can occur by simply fitting a cartilage plug within a cartilage annular ring and exposing it to a crosslinker (GTA in this study). Evidence in support of crosslinking was presented as an improvement in the mechanical strength of the interface. The higher failure stress in the treated groups compared to the control group suggests that collagen crosslinks did form at the interface, and contributed to increasing the interface strength. The lower failure stress of the control group provides support for the hypothesis that this increased mechanical strength was due to crosslinking, and not due to the presence of GTA-induced differential swelling of the plug and annulus, which might increase the frictional forces at the interface and consequently increase the failure stress. To further verify this finding, we have initiated additional tests where we place back the inner plug of the GTA group in its annulus and test the sample a second time, to see if the failure stress and energy to failure reproduce those of the CTRL group. Preliminary findings (not shown here) suggest that the crosslinks were indeed ruptured during the primary test, and were no longer contributing to mechanical strength.

The addition of collagen I gel to the interface (Gel/GTA group) did not significantly affect the failure stress or energy to failure of the samples when compared to the GTA group. This result indicates that solubilized collagen I fragments, when exposed to a crosslinker, may not form a matrix with significant mechanical integrity to enhance the interface strength. Nevertheless, since defects in OA joints may not present with a sufficiently smooth interface to crosslink with an allograft, we may continue exploring alternative collagenous gels to enhance the interfacial strength between allograft and native tissue. In particular, the primary collagen type found in articular cartilage is type II, not type I, which could affect the ability of these fragments to bind with the fragments native to the tissue. Collagen gel also has the advantage of being able to conform to the shape of irregular defects, and could be beneficial in bonding other geometries, where the two pieces of tissue do not fit together perfectly.

This study represents a proof of concept that crosslinking is a suitable repair strategy for collagenous tissue repair. In modifying this technique for the clinical setting, the use of glutaraldehyde would not be suitable, as it is toxic and can lead to cell apoptosis [9]. Therefore, other crosslinking methods should be investigated. UV light paired with a riboflavin photosensitizer has been successful in crosslinking corneal tissue, and could be an appropriate alternative if properly adapted to cartilage [10]. Another promising technique is femtosecond laser crosslinking, which has been successful in cornea and cartilage tissue [3]. This would be an advantageous technique, as unlike most other methods, it doesn't require use of any additional chemicals.

ACKNOWLEDGEMENTS

The authors acknowledge support from NIH 5R01AR073289-03.

REFERENCES

[1] Neogi et al., *Osteoarthritis Cartilage*, 21:1145-1153, 2013. [2] Mobasheri et al., *Nat Rev Rheumatol*, 13:302-311, 2017. [3] Wang et al., *ORS*, 0563, 2017. [4] Athens et al., *PLoS ONE*, 8 2013. [5] Ishimura et al., *Arth. J. of* arth. & Rel. Surg. 7:177-181, 1991. [6] Englert et al., *Arthritis Res Ther*, 9 2007. [7] Oungoulian et al., *J Biomech*, 47:694-701, 2015. [8] Shirazi-Adl, *J. Biomech Eng*. 114: 111-118, 1992. [9] Gough et al., *J Biomed. Mater. Res*, 61:121-130, 2002. [10] Raiskup et al., *TOS*, 11:65-74, 2013.

A MECHANISTIC STUDY OF THE INTERSTITIAL TRANSPORT OF COLLAGENASE-SECRETING TUMOR-TARGETING *SALMONELLA* TYPHIMURIUM TOWARD IMPROVING TUMOR COLONIZATION

Eric J. Leaman (1), Bahareh Behkam (1,2)

(1) Department of Mechanical Engineering
Virginia Tech
Blacksburg, VA, USA

(2) School of Biomedical Engineering and Sciences
Virginia Tech
Blacksburg, VA, USA

INTRODUCTION

One of the principal impediments to the broad success of conventional chemotherapy is poor delivery to and transport within the tumor microenvironment (TME), caused by irregular and leaky vasculature, the lack of functional lymphatics, and underscored by the overproduction of extracellular matrix (ECM) proteins such as collagen. Co-administration of proteases that degrade the ECM with chemotherapeutics has been shown to significantly enhance their transport in murine tumor models [1]. However, systemic administration of proteases causes collateral damage to normal tissue and has been suggested to increase the risk of tumor metastasis, necessitating targeted delivery. An innovative approach is to use engineered bacteria-based cancer therapy (BBCT), wherein microbes such as *Salmonella* Typhimurium, which preferentially replicate in the TME, are programmed to locally degrade the ECM. Not only would this target ECM degradation to tumors, but such an approach would augment the intrinsic benefits of BBCT over passive modalities such as active translocation and the ability to transport drug-loaded cargo. In this work, we engineered attenuated tumor-targeting *S.* Typhimurium VNP20009 [2] to express and secrete a recombinant collagenase to locally degrade the ECM. We then developed innovative microfluidic assays to systematically and quantitatively characterize the engineered bacteria transport in tissue-mimicking reductionist collagen models with and without interstitial flow. Our results demonstrate significant improvement of bacterial interstitial transport when advection dominates. To investigate the mechanism behind the observed enhanced transport, we tuned the collagenase expression rate and conducted swim plate assays in collagen. We show that besides collagenase secretion, bacterial fitness plays a strong role in self-actuation scenarios. Altogether, we show the vast potential of this approach for augmenting BBCT while highlighting the critical importance of balancing the overall metabolic load.

METHODS

Cloning of a Heterologous Collagenase – A bacterial matrix metalloproteinase gene, *mmpG*, was cloned into a plasmid vector and expressed constitutively along with mRFP1 to enable fluorescence imaging of the bacteria. Collagen degradation was quantified using a dye-quenched (DQ) collagen type I assay.

Microfluidic Assay – A microfluidic device with 7 parallel channels separated by pillars was designed to study interstitial transport of non-motile strains (Fig. 1a). The central channel was filled with 5 mg/mL collagen type I, while phosphate buffered saline (PBS) filled the adjacent channels. Polyethylene glycol diacrylate (PED-DA; 700 Da) was used between the outermost channels to create permeable barriers separating media flow from adjacent channels.

Microfluidic Experiments and Data Collection – Non-motile *S.* Typhimurium VNP20009Δ*fliF* expressing *mmpG*, at 5×10^7 CFU/mL,

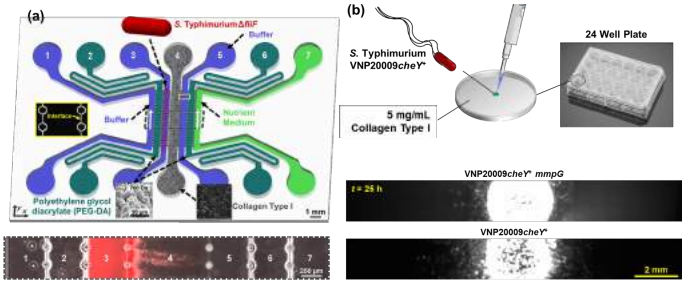

Figure 1: (a) Microfluidic assay and composite bright-field and fluorescent micrograph after 26 hr, and (b) collagen swim plate assay and fluorescent micrographs after 25 hr

were introduced into channel 3 (Fig. 1a). Nutrient medium and PBS were flowed through the outermost channels (1 and 7).

Swim Plate Assays – The chemotactic strain *S.* Typhimurium VNP20009*cheY*$^{+}$ [3] was used for swim plate experiments. Nutrient collagen was polymerized in the wells of a 24-well plate at 5 mg/mL, and 1 µL of bacterial suspension at 10^6 CFU/mL was introduced onto the center of the gel surface in each well (Fig. 1b). High and low frame rate movies were recorded for single-bacterium scale and population-scale transport characterization, respectively. From the single-cell tracking, we calculated the average squared displacement,

$$\mathrm{ASD}(t_{n_0}) = \frac{1}{\Delta t(N_t - 1)} \sum_{i=n_0-N_t}^{n_0} \|\vec{r}_i - \vec{r}_{i-1}\|^2 , \qquad (1)$$

where Δt is the time step, N_t is the number time steps used to define bin size (4), and $\vec{r}$ is bacterium position between each frame during 0.2 s bins. *Sticking* periods were defined as ASD < 20 µm^2/s, while a bacterium was *running* if ASD ≥ 20 µm^2/s.

RESULTS

We first performed microfluidic assays using the non-flagellated VNP20009Δ*fliF* to decouple the effects of motility and collagenase expression on transport in collagen hydrogel. Analogous to the aberrant nature of the TME, low rates of stochastic interstitial flow were present. Penetration of the *mmpG* strain was significantly greater than control, reaching an average of 171% greater depth between the 11th and 20th hour (Fig. 2a). We developed a mathematical model of transport:

$$\frac{\partial B}{\partial t} = D\frac{\partial^2 B}{\partial x^2} - v\frac{\partial B}{\partial x} + k_g B(1 - B), \qquad (2)$$

where B is bacterial concentration, D is bacterial diffusivity, v is the effective advection coefficient, and k_g is growth rate [4]. Fitting the model using time-lapse fluorescence data suggests that diffusion was negligible; advection was the primary driver of bacterial transport. The effective advection coefficient was significantly higher for the *mmpG* strain between 7 and 14 hr after bacterial introduction (Fig. 2b).

To further investigate the mechanisms behind enhanced *mmpG* transport, we developed a swim plate assay devoid of interstitial flow and engineered a ribosomal binding site (RBS) library to modulate the rate of collagenase secretion in motile, chemotactic VNP20009*cheY*$^{+}$ strains. Our original RBS design (RBS O) had the highest collagenase production rates, and we achieved good gradation amongst the other designs (Fig. 2c). Experiments with RBS O, RBS 1, RBS 2, and control strains revealed better colonization (*i.e.* greater radial penetration) of the swim plates by the RBS O strain on average (Fig. 2d,e).

We characterized each strain's growth rate and motility to elucidate differences at the single-cell scale. Bacterial fitness was

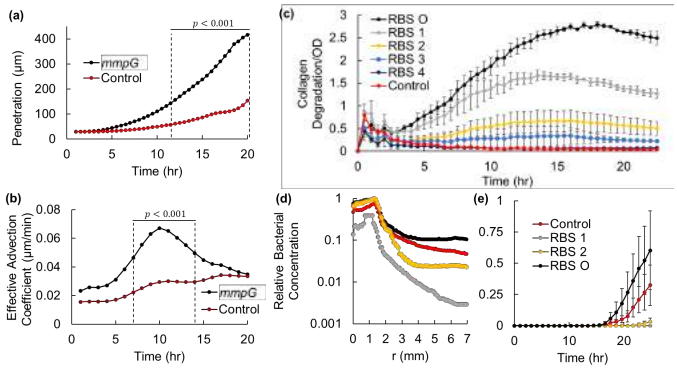

Figure 2: Average penetration (a) and effective advection coefficient (b) of bacteria in microfluidic collagen assay, (c) bulk collagen degradation normalized to bacterial optical density vs. time, and average relative bacterial concentrations in collagen swim plates vs. radial location (d) and vs. time at *r* = 6 mm (e)

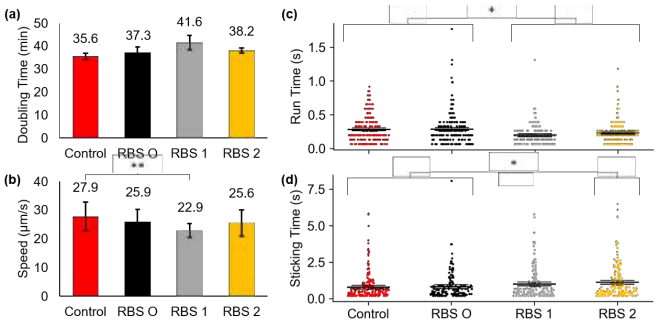

Figure 3: (a) doubling time of motile strains, (b) speed during run periods, (c) run duration, and (d) stick duration. Error bars show standard deviation (a,b) or 95% confidence intervals (c,d).

affected by collagenase expression, with the RBS 1 strain having the longest doubling time (Fig. 3a) and lowest swimming speed (Fig. 3b). Each of the other strains had similar swimming speeds, but the control strain had the highest growth rate. Bacterial swimming in collagen consisted of a series of "run" (smooth translation in space) and "stick" periods (collision with collagen, remaining fixed in space for at least 0.2 s). On average, the durations of runs were similar between RBS O and control, each being significantly higher than those of RBS 1 and 2 (Fig. 3c). Conversely, sticking periods were found to be lowest for the RBS O and control strains, while they were highest for RBS 2 (Fig. 3d).

DISCUSSION

Our work illustrates that bacterial collagenase secretion can improve the efficacy of transport by advection or by self-propulsion. In presence of advective flow, collagenase is particularly effective because bacteria may "clog" their local porous environment if daughter cells are not effectively transported away after proliferation. Our findings with motile strains in no-flow environments suggest that rates of "sticking" to collagen play a role in transport, but interpretation is complex due to differences in bacterial fitness. The RBS 1 strain harbored the greatest metabolic load, as its growth rate was lowest and swimming speed was significantly lower than that of the control strain. Stark differences existed between RBS O and RBS 2, which had nearly identical growth rates and swimming speeds, but the latter had a lower rate of collagenase expression, suggesting a clear role for collagenase in reducing bacteria sticking time. Moreover, RBS O also outperformed the control strain on average, despite the control bacteria having the best overall fitness.

Taken together, our findings suggest that collagenase secretion can enhance transport, but fitness plays a major role and must be balanced when engineering such strains, especially for applications where swimming motility is possible. Our results demonstrate strong overall potential for *in vivo* BBCT applications. The small pore size of the TME will likely preclude motility, and transport will be driven by coupled growth and advection. In the future, the collagenase-secreting strains will be further engineered for tumor-specific expression and will be evaluated using *in vitro* and *in vivo* tumor models.

ACKNOWLEDGEMENTS

We gratefully acknowledge support from the National Science Foundation (CAREER award, CBET-1454226), the Virginia Tech Institute for Critical Technology and Applied Science (ICTAS), 2020 Charles C. Walts Fellowship, and 2021 J. R. Jones III Fellowship.

REFERENCES

[1] Dolor, A and Szoka, F C, *Mol Pharm*, 15:2069-2083, 2018.
[2] Low et al., *Nat Biotechnol*, 17:37-41, 1999.
[3] Broadway et al., *J Biotech,* 211:117-120, 2015.
[4] Suh, S et al., In *40th Ann Int Conf IEEE EMBC*, 6162-6165, 2018.

ALTERING SURFACE CURVATURE OF PATELLAR OSTEOCHONDRAL ALLOGRAFTS THROUGH SUBJECT-SPECIFIC MODIFICATION OF SUBCHONDRAL BONE

Katherine A. Spack (1), Courtney A. Shaeffer (2), Peter T. Shyu (1), James L. Cook (3), Clark T. Hung (1), Melvin P. Rosenwasser (4), Gerard A. Ateshian (1,2)

(1) Biomedical Engineering
Columbia University
New York, New York, USA

(2) Mechanical Engineering
Columbia University
New York, New York, USA

(3) Orthopedic Surgery
University of Missouri
Columbia, Missouri, USA

(4) Orthopedic Surgery
Columbia University
New York, New York, USA

INTRODUCTION

Osteoarthritis is the leading global cause of disability, and the most common form of arthritis in adults, impacting 27 million Americans age 25 and older [1]. Osteoarthritis is characterized by the degradation of articular cartilage in diarthrodial joints. This damage impacts the ability of cartilage to evenly cushion the joint and protect the underlying bone during normal daily activities. Approximately 10% of all cases of osteoarthritis in the knee are post-traumatic osteoarthritis (PTOA), initiated by a traumatic injury to the joint such as intraarticular fractures, acute ligament sprain, damage to subchondral bone, joint dislocation, meniscal tears, or any combination of these injuries [2]. Currently, the relatively limited lifespan of artificial joint replacement technologies is a major obstacle for treatment of younger patients with PTOA who are expected to outlive any orthopedic implants.

Osteochondral allografts provide a promising avenue for treatment of PTOA. Advancements in the capabilities of tissue banks to maintain tissue samples for longer periods of time have paved the way for the use of osteochondral allografts in replacing regions of damaged articular cartilage. Tissue banks can harvest fresh human donor tissue and preserve live articular cartilage and underlying subchondral bone prior to the transplantation process. Though osteochondral allografts have demonstrated positive clinical results in the knee, the technique is limited in surgical settings due to the difficulty of ensuring that joint congruence is not reduced in the patient. This is an important consideration, as a reduction in joint contact area causes increased localized contract stresses that can instigate degenerative changes in the transplanted allograft.

One of the primary limitations to osteochondral allografts in surgical settings is the difficulty of matching donor allograft size and curvature to the recipient's joint anatomy. Fresh donor allografts have a limited shelf life in the tissue bank, so the ability to alter the articular curvature of available donor tissue to match that of the recipient considerably expands the use of fresh allografts.

In our prior report, in silico models demonstrated that grooving the underlying bone in donor osteochondral patellar allografts increases their ability to conform to recipient femoral grooves [3]. Following up on these computational results, the objective of this study was to develop a robust experimental method for creating bendable osteochondral allografts (BOCAs) from canine patellae, and to demonstrate the ability to modify the surface curvature of these BOCAs in vitro, in advance of anticipated animal studies.

METHODS

Four canine patellae harvested from non-arthritic stifles were sourced from the Thompson Laboratory for Regenerative Orthopedics (University of Missouri, MO). Samples were shipped frozen to the Musculoskeletal Biomechanics Lab (Columbia University, NY) where they were thawed and dissected free of adherent soft tissue. The canine patellae were secured in a custom-built fixation rig for μCT scanning and machining. The rig was designed to allow complete processing of the patellae under sterile conditions, to enable future processing of live allografts. The articular surface of each patella was covered with hydrated gauze and submerged in a phosphate buffered saline bath, while the apical surface of the patella was fixed using soft fit clamps cast in Adafruit low temperature fixation thermoplastic (Adafruit Industries, New York, NY). Once fully suspended in the rig, the patella was scanned in a vivaCT 80 (ScanCo, Wangen-Brüttisellen, Switzerland) scanner to generate corresponding DICOM models with a voxel size of 78 μm. The DICOM was processed using the opensource imaging software 3D Slicer (Harvard, Boston MA) to create a volume scan of the subject-specific bony structure of the patella in relation to fiducial markers embedded in the scanning rig. The generated model and corresponding spatial data were used to create tailored CNC cutting

paths using the HSM Works application in SOLIDWORKS (Dassault Systèmes, Waltham, MA)

Prior finite element analyses on human knee models determined that enhancing congruence along the medial-lateral direction offered the best strategy for increasing surface conformity between patellar BOCAs and recipient femoral grooves. This has been achieved by milling grooves in the underlying bone of the patella. Each patella was first milled to plane the anterior surface before two 2.5 mm wide grooves were machined in the proximal-distal direction through the full depth of the subchondral bone (Fig. 1). Each groove in the patella was separated by a 6 mm wide bone strut. All machining was done in a custom-built sterile field cabinet using a Sherline 5400 CNC milling machine (Sherline, Vista, CA) using Flashcut CNC software (Flashcut, Deerfield, IL). The cuts were made using a 1/16" ball end mill and speeds and feeds were optimized for surface smoothness [4]. All four patellae were successfully grooved without visible damage to the articular surface.

Fig. 1: Canine patella following groove milling

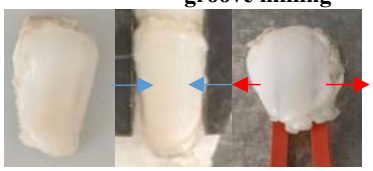

Fig. 2: Scanning configurations; arrows indicate direction of force applied to bone struts

After machining the osteochondral allografts, scans of the articular surface were acquired with a laser scanner, with the grooved bony struts placed in relaxed, compressed, and expanded states (Fig. 2). The relaxed, or reference, state representing the natural curvature of the patella, was obtained by scanning the surface of the grooved patellae without modification. Scanning of the compressed state was accomplished by clamping the bone struts of the sample together prior to scanning in order to minimize the radius of curvature to simulate conformity to a narrow femoral groove. The expanded state was created by expanding the space between bone with strips of 3.2 mm thick rubber to flatten the articular surface to simulate conformity to a wide femoral groove. The scanned point cloud data were reconstructed to form 3D models of the articular surface using custom C++ code and the SOLIDWORKS CAD software.

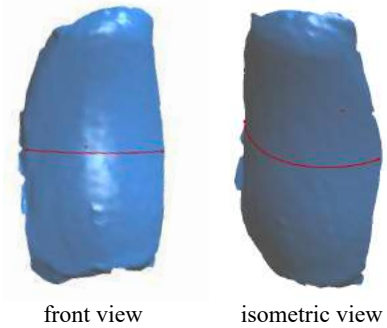

Fig. 3: Measuring surface curvature with 3 point curve fitting

Curvature was measured using CAD surface models fitted to the laser scan data by fitting a circular arc using a three-point circle fit method at the median antero-posterior surface of the patellae (Fig. 3). This result was further validated by fitting 4th degree B-spline surfaces to the scanned point cloud [5] and evaluating the surface-wide average of the maximum curvature (Fig. 4). These curvature results are displayed in Fig. 5.

RESULTS

Using the 3-point curve fitting method, the compression produced an average reduction of the radius of curvature by 70% ± 5.4% ($p = 1.59 \times 10^{-3}$), while extension produced 150% ± 19.9% ($p = 1.47 \times 10^{-2}$) increase of the radius of curvature. With the 4th degree B-spline surfaces method, the compression produced an average reduction of the radius of curvature by 71% ± 3.2% ($p = 3.71 \times 10^{-4}$), while extension produced 142% ± 9.8% ($p = 3.41 \times 10^{-3}$) increase of the radius of curvature.

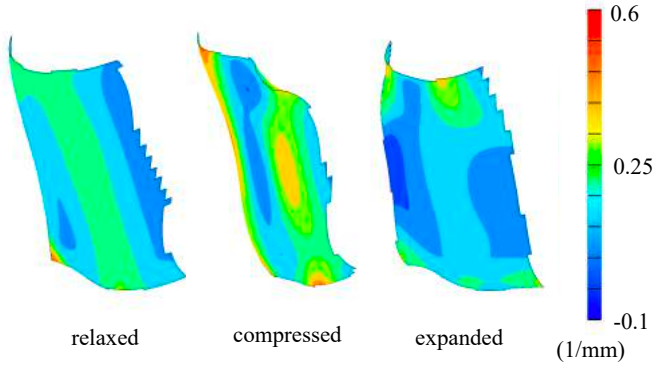

Fig. 4: Representative maps of maximum curvature from B-spline fits of the compressed, relaxed and expanded patellae

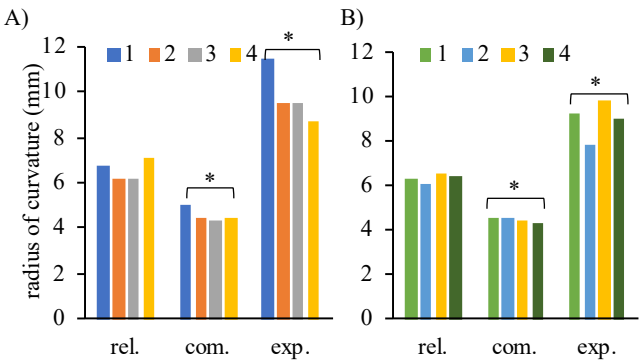

Fig. 5: Curve fit results from (4A) 3-point, (4B) B-Spline methods; * indicates difference compared to relaxed group (p<0.05)

While the 4th order B spline fitting method for measuring average radius is a more comprehensive measurement of curvature over the whole patella surface, both methods produced consistent results and no statistically significant differences for the results in compression ($p = 0.664$) or extension ($p = 0.347$).

DISCUSSION

The fabrication method for developing grooved patellar osteochondral allografts in this study provides a reliable method for altering surface curvature in osteochondral allografts through grooving of the subchondral bone. Follow-up studies are planned to ensure that this method of creating BOCAs does not negatively impact chondrocyte viability in live osteochondral allografts preceding a canine clinical trial.

ACKNOWLEDGEMENTS

We thank X. Edward Guo and the Bone Bioengineering Laboratory (Columbia) for use of their µCT scanner. We also thank Chantelle Boyzinski and Mary Romesburg (Missouri) for providing canine patella samples. This project is funded by U.S Department of Defense (W81XWH-18-1-0361/PR171360).

REFERENCES

[1] Bergmann, G et al., *J Biomech*, 2001. [2] CDC & Arthritis Foundation, National Public Health Agenda for OA, 2010 [3] Shaeffer, C.A., et al., 2020 SB3C [4] Noordin M et al., *Proc Inst Mech Eng H*, 2015 [5] Ateshian, G et al., *J Biomech Eng,* 1993

CHANGES IN VAGINAL SHAPE THROUGHOUT THE LIFESPAN

Liam C. Martin (1), Megan R. Routzong (1), Pamela A. Moalli (2), Ghazaleh Rostaminia (3), Victoria L. Martin (1), Katherine B. Lebrun (1), Steven D. Abramowitch (1)

(1) Department of Bioengineering
University of Pittsburgh
Pittsburgh, PA, USA

(2) Department of Obstetrics, Gynecology & Reproductive Surgery
University of Pittsburgh
Pittsburgh, PA, USA

(3) Division of Urogynecology
University of Chicago
Skokie, IL, USA

INTRODUCTION

In women, the vagina undergoes remarkable structural changes before (puberty and menstruation), during, and following (menopause) the reproductive lifespan[1]. As events linked with reproductive capacity occur at relatively predictable ages, shape changes in the vagina associated with these events should be identifiable within specific age ranges[2].

For example, prior to puberty, the pelvis is not fully developed and likely does not fully mature until the completion of the teenage years. Thus, we should anticipate that the vaginal shape of children (aged 0-19 years) would differ from that of mature, reproductive-aged women over age 20 years. During the prime reproductive years, age 20 to 34 years, the vagina and its supportive tissues likely remain consistent (unless pregnancy and delivery occurs) with only small changes occurring as a result of the menstrual cycle.[3] In the late reproductive and peri-menopausal years, the vagina likely undergoes additional shape changes as evidenced by increased maternal birth injury in women >34 years. Finally, post-reproduction (menopause) the vagina and its supportive tissues thin relative to younger women likely resulting in additional changes in shape.

This study aimed to quantify the average vaginal shape and shape variation across women of varying ages; children (0-19), young adults (20-34), adults (35-49), and seniors (50+). We hypothesized that there would be significant differences consistent with the known effects of aging on the vagina[1,2]. These data are intended to provide a baseline of the variations in shape with aging within the population to build towards better diagnostic tools for the identification of injury and disease.

METHODS

MR images were collected from the University of Pittsburgh Medical Center and Northshore University HealthSystem between 2005 and 2018. Patients underwent MRIs under instruction of their physician for medical indications. This retrospective study consisted of 106 women sorted into 4 groups based on their age. The groups were 0-19 (N=15), 20-34 (N=47; 11 imaged in pregnancy), 35-49 (N=24; 6 imaged in pregnancy), and 50+ (N=20) years old. These groups were chosen to show a range of the physiological changes throughout the life cycle. The young group's age range was chosen based on the majority of secondary ossification occurring by the age of 20, indicating skeletal maturation[4].

The vagina was segmented as one solid object. To decrease computational cost, the vaginal canal was not segmented. Additionally, the apical portion of the vagina (that may include both the vagina and cervix) was segmented as one continuous object.

In order to smooth the vaginal shapes and apply corresponding points, an ellipsoid template was generated. Previous 3D statistical shape models (SSMs) conducted in our lab showed that an ellipsoid model would allow for accurate representation of the structure while also smoothing the aliasing from the MRI scans which could incorrectly influence the SSM. After the corresponding points were determined, the shapes were imported into a Mathematica™ notebook that was previously established in our lab to conduct the rest of the SSM[5]. This process included a Procrustes analysis to scale and align the shapes. Followed by a principal component (PC) analysis to determine modes of variation in each shape and a parallel analysis to determine the variance due to noise. This analysis returns PC scores for each patient for every mode. These scores were then used for statistical analysis.

In order to isolate the effect of age on vaginal shape from that which occurs within pregnancy, pregnant women were excluded from the statistical analyses. To control for the impact of parity, a MANCOVA analysis was performed with total parity of the subject as the covariate followed by univariate ANOVAs with multiple comparisons followed by a Benjamini-Hochberg correction post-hoc[6]

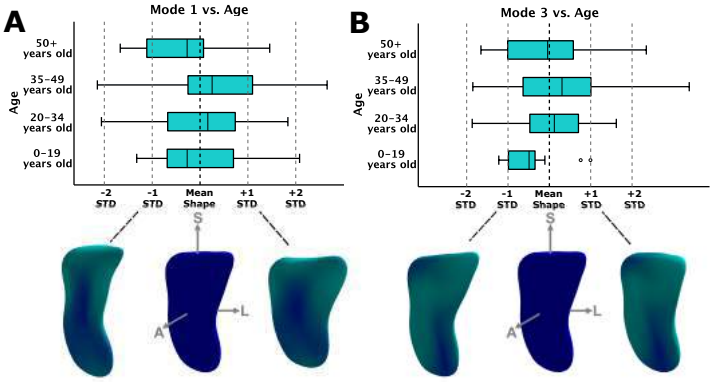

Figure 1: A) Mode 1, B) Mode 3. Top: Mode 1 Age vs. Standard deviations from the mean shape, Bottom: standard deviations of shape, lighter colors show more variation from the mean.

RESULTS

Twelve modes of variation explained 24, 18, 11, 9.2, 8.8 5.9, 2.9, 2.7, 2.2, 1.7, 1.5, and 1.3 percent of the total variance respectively, and were greater than that attributed to noise. For every mode, the average PC scores of all of the age groups fell within one standard deviation from the mean shape.

After the MANCOVA analysis (parity as covariate), we found that age differed significantly across four modes: 1, 3, 6, and 12 ($p=0.012$, $p=0.029$, $p=0.011$, $p=0.021$ respectively). Mode 1 also differed with parity ($p=0.001$). Following the ANOVA, modes 6 and 12 were significantly different between the 0-19 age group and the 20-34 age group ($p=0.006$, and $p=0.013$ respectively).

The top half of Figure 1 shows the standard deviations of modes 1 and 3, significant p-values shown by brackets. The bottom half of Figure 1 shows the average vaginal shape for each mode with ±1 standard deviation from the mean. Figure 2 shows the same for modes 6 and 12. All group averages are within this range.

DISCUSSION

The results showed that there are significant shape differences in the vagina that are due to age. Overall, we saw that there were two different types of variation that may be caused by aging, one that could be tied to maturity, and the other that could be tied to menopause/aging. Modes 3, 6, and 12 represent the changes due to maturation while mode 1 represents changes are suspected to be due to menopause.

In modes 6 and 12, the 0-19 group differs from the 20-34 group, while Mode 3 differs only at the univariate level but not significantly between any individual age groups. The outliers (denoted by empty circles in Figure 1) were infants, suggesting that there might be changes in early development that this study was not powered to detect. In each of these modes, the vaginas in the 0-19 group appear to be straighter and more vertically aligned relative to the older groups. The left shapes of Figure 1B, and Figure 2B, and C more closely represent the shape of the 0-19 group while the middle or right shapes represent the older groups. In all three of these modes, the left shape is more aligned with the frontal plane (plane created by the superior and left arrows in Figure 2) when compared to the average shape which is slightly angled posteriorly. The posterior angle that is observed in the older patients is consistent with literature demonstrating the support of the pelvic floor muscles for the upper portion of the vagina[7]. This support is hypothesized to limit the mobility of the vagina during increases in intrabdominal pressure. Our results seem to indicate that this angulation of the vagina may be related to skeletal maturity.

We hypothesize that the reason for the increased angulation is due the expansion of the pelvis in the anterior-posterior direction. The more posterior movement of the sacrum relative to the vagina has the effect of pulling the uterosacral ligaments and apex of the vagina posteriorly over the iliococcygeus. It could also be a consequence of muscle development within the pelvic floor. However, further analysis is required to test these hypotheses.

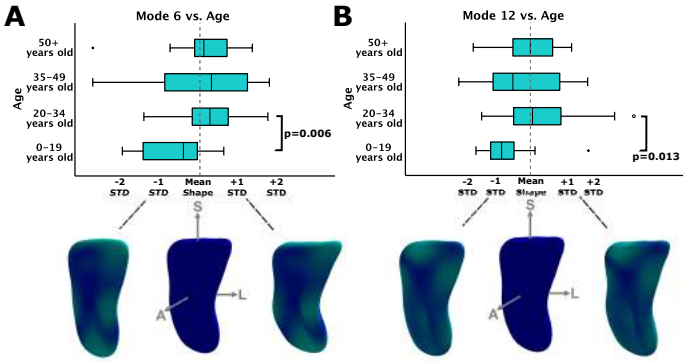

Figure 2: A) Mode 1, B) Mode 3. Top: Mode 1 Age vs. Standard deviations from the mean shape, Bottom: standard deviations of shape standard deviations of shape, lighter colors show more variation from the mean. Significant p-values shown.

Shape variation that may be related to menopause and/or aging is shown in mode 1 (Figure 1A). While only different at the univariate level, older women (50+) had a thinner and longer vaginal shape. This is consistent with prior literature that showed atrophy of many of the structures that support the vagina[1]. Prior research has shown that post-menopausal women (50+ years old) have a significant decrease in the physiologic cross-sectional area of the pelvic floor muscles and the rate at which this occurs substantially outpaces the natural loss of muscle mass in the rest of the body[8]. This loss of pelvic floor musculature allows the distal vagina to fall and become more suspended by the apex; thus, possibly explaining this shape variation.

This study was limited by the shape that was used as the template for the smoothing and corresponding point application did not include a vaginal lumen. Future studies should include a lumen so that resulting shapes can be more aptly used in computational simulations and the addition of a lumen could show shape variation of the interior vagina that would have been excluded by this study. Additionally, the retrospective nature of the study made it so that we only had one scan of each women. A future prospective study could collect scans of women at multiple timepoints throughout their lifespan and shed light on potential mechanisms of vaginal shape changes due to aging.

ACKNOWLEDGEMENTS

We acknowledge use of the University of Pittsburgh Center for Research Computing advanced computing resources.

REFERENCES

1. Farage, M, *Arch Gynecol Obstet*, 273(4): 195-202, 2006.
2. Hale, GE, *Best Pract Res Clin Obstet Gynaecol*, 23(1): 7-23, 2009.
3. Patton, DL, *Am. J. Obstet. Gynecol.*, 183(4):967-73, 2000.
4. Parvaresh, KC, *J Pediatr Orthop*, 38(8), 418-23, 2018.
5. Routzong, MR, *Comput Methods Programs Biomed*. Epub, 2020
6. Benjamini, Y, *J R Stat Soc Ser B*. 57: 289-300, 1995.
7. Petros P. *The Female Pelvic Floor: Function, Dysfunction and Management According to the Integral Theory*, 3:54, 2010
8. Alperin M, *Am. J. Obstet. Gynecol.*, 215(3):312, 2016.

DEVELOPMENT OF AN AUTOMATED, MACHINE LEARNING-BASED METHODOLOGY FOR YIELD POINT IDENTIFICATION FROM TENSILE TESTING DATA OF SOFT TISSUES

Joseph Kim[1], Timothy K. Chung[2], David A. Vorp[2-7], Madhavan L. Raghavan[1]

[1]Biomedical Engineering
University of Iowa
Iowa City, IA, USA

[2]Bioengineering
University of Pittsburgh
Pittsburgh, PA, USA

[3]Department of Surgery
University of Pittsburgh
Pittsburgh, PA, USA

[4]Department of Cardiothoracic Surgery
University of Pittsburgh
Pittsburgh, PA, USA

[5]Department of Chemical and Petroleum Engineering
University of Pittsburgh
Pittsburgh, PA, USA

[6]McGowan Institute for Regenerative Medicine
University of Pittsburgh
Pittsburgh, PA, USA

[7]Center for Vascular Remodeling and Regeneration
University of Pittsburgh
Pittsburgh, PA, USA

INTRODUCTION

The stress/strain curve of a biological soft tissue helps characterize its mechanical behavior. The yield point on this curve is when a specimen breaches its elastic range due to irreversible microstructural damage. This can easily be found in traditional engineering materials using the offset yield method, where a line is drawn parallel to the modulus and offset by a specified amount until the line and curve intersect at a yield point [1]. However, correctly identifying the yield point in soft tissues can be subjective due to its nonlinear material behavior. The typical method for yield point identification is visual inspection, which is investigator-dependent and doesn't lend itself to automation of the analysis pipeline [2]. Machine learning has been a growing field of study in data analytics. Bhandari et al. implements RF regression, a decision tree-based machine learning method, to predict yield strength in metals [3]. This method leverages computer algorithms to iteratively improve and converge to an answer that can be difficult to attain using conventional mathematical techniques. The goal of this study was to analyze data from uniaxial extension testing on biological soft tissue specimens and create a machine learning model to objectively determine a tissue sample's yield point. Developing an automated algorithm to identify the yield point can give researchers an objective assessment of the biomechanical properties of soft tissues, as well as progressing our understanding of elastic tissue behavior in general.

METHODS

Uniaxial extension testing was performed on 280 human soft tissue samples from a previous study [2]. These specimens were harvested from human cadavers and patients ranging in age from 30 to 70 years old. Samples were cut in rectangular strips approximately 4 mm wide and 20 mm long. Stress/strain curves were calculated from force-displacement data for each tissue sample, and ground truth yield point picks were adjudicated and determined by biomechanics experts. A 2% window was created surrounding the pre-determined yield point to indicate relative closeness to improve the model's learning process.

Tissue sample data was stored in individual files and compiled through MATLAB (R2020b, Natick, MA) before training the machine learning model. Extension and force measurements were recorded from extension tests and used to calculate stress and strain values. The datasets were then prepared using features derived from the stress and strain values including localized elastic moduli, strain failure ratio and others for a total of 22 unique parameters. These features were selected to analyze distinct properties of a tissue. Specifically, the elastic modulus analyzes the linear portion of a stress/strain curve and reveals elastic resistance to tension. Another feature, strain failure ratio, calculates the current strain over overall failure strain for each data point in a test case. This can be indicative of how much a specimen can be elongated to failure. A sample with a higher strain failure ratio value indicates higher ductility and lower tensile strength. These features were calculated prior to model training to maximize the model's learning capability and options.

The bulk data was input into MATLAB's Classification Learner toolbox. The machine learning model was trained using multiple algorithms within the toolbox, utilizing a fine tree algorithm with Principal Component Analysis disabled. The model's predictions were pre- and post-processed. Model output gave a small region of interest along the strain axis, and a mean clustering method was implemented to iteratively sweep across strain values using a 3% window to determine a singular point as the model's final pick. The resulting picks were compared to pre-determined, ground truth yield points.

The final model was evaluated using a separate set of test cases. Uniaxial extension testing was performed on 44 different human soft tissue samples, and yield points were again adjudicated and determined

by experts. The 2% window and 20 unique parameters were calculated as input features for evaluating the model. The model's test set results were compared to two rule-based algorithms used in a previous study. The first rule-based pick, the peak yield point (Y_p), designated the yield point as the point where the stress/strain ratio, or the current stress over current strain value, reaches its peak. The second pick, the elastic yield point (Y_e), designated the yield point as the first instance where the stress/strain ratio drops by 3% or more. In cases where this was invalid, the first rule-based pick, Y_p, was chosen. Notably, the rule-based picks Y_e and Y_p were included as features for model training. Evaluation consisted of case-by-case analysis followed by a final statistical assessment. Percent error in strain was calculated from each pick to the ground truth previously determined by experts.

RESULTS

Training consisted of 280 cases. The model was trained, and the cross-validation score had an internal accuracy of 93.9%. A separate dataset of 44 cases reserved for validation (and not used in training) was input into the trained classifier yielding a test accuracy of 97.7%.

Evaluation was done by calculating percent error in strain from the ground truth pick. The machine learning model determined yield point picks with an average percent error in strain of 5.04%. The rule-based picks had average percent errors in strain of 20.6% for Y_e and 5.06% for Y_p. Notably, several successful machine learning picks demonstrated a near-perfect prediction. **Figure 1** shows one of the test cases, where the model's prediction lies close to the actual yield point.

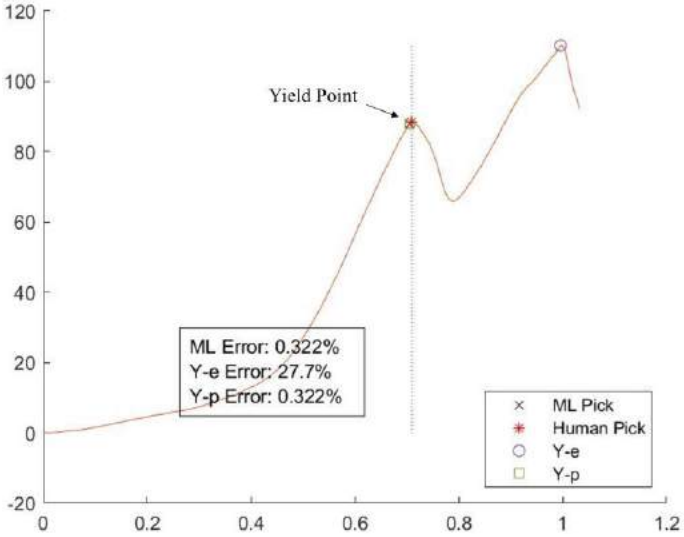

Figure 1. Illustration of yield point picks by rule-based and ML-based algorithm compared against expert-adjudicated picks.

Comparison with each rule-based method indicates the same pick as Y_p and a significantly closer pick than Y_e.

DISCUSSION

The percent error in strain was compared among the three yield points. The elastic yield point (Y_e) method gave several picks far from the ground truth resulting in 20.6% average percent error. The peak yield point (Y_p) method gave significantly lower average percent error with only 5.06%. The machine learning model returned a similar average percent error of 5.04%. A Wilcoxon signed rank test was performed to compare the machine learning model with each rule-based method. The ML-based approach had lower percent error than the Y_e-based approach with statistical significance (5.04% ± 15.8% s.d. versus 20.6% ± 21.4% s.d.; $p < 0.0005$). The ML-based approach had slightly lower percent error than the Y_p-based approach without statistical significance (5.04% ± 15.8% s.d. versus 5.06% ± 6.7% s.d.; $p > 0.5$).

The stress/strain curve obtained from tensile testing is widely used to quantitatively characterize soft tissue behavior. The yield point is often overlooked due to concerns about subjectivity and consistency in its determination. Overcoming this limitation may help to reveal it as a key aspect in biomaterial failure. We evaluated two rule-based approaches to picking yield point on uniaxial extension curve and one ML-based approach by comparing them against adjudicated expert-picked yield point as gold standard. We found that while the ML-based method was significantly improved over one of the rule-based approaches (Y_e), it offered insignificant improvement over the second rule-based approach (Y_p).

ACKNOWLEDGEMENTS

Thanks to Drs. Erasmo Simao da Silva and Otavio Henrique, University of São Paulo for sharing tensile test data.

REFERENCES

[1] Ross, C., *Mechanics of Solids,* 1st ed., 1999.

[2] Raghavan, M.L., et al., *J Biomech,* 13:2501-2507, 2011.

[3] Bhandari, U et al., *Materials Today Communications,* 101871, 2020.

BLOOD FLOW IN A RETINA CAPILLARY VASCULAR NETWORK WITH EXPLICIT BLOOD CELLS

Kacper Ostalowski, Jifu Tan

Department of Mechanical Engineering
Northern Illinois University
DeKalb, IL, 60115, USA

INTRODUCTION

According to the Center for Disease Control and Prevention, cardiovascular diseases is the leading causes of death in the United States [1]. Cardiovascular diseases, including heart attacks and strokes, occur when a clot blocks a blood vessel and leads to a reduction of oxygen supply into downstream tissues. In this work, we study the flow of blood cell suspensions on the local circulation of a capillary network in a realistic retina vascular network.

Blood flow in a vascular network has been studied previously using various methods. The effects of vascular occlusion on local flow rates were studied in Ref. [2]. Similarly, changes to flow characteristics were studied under vascular dilation and occlusion [3]. Simulations of hematocrit distributions throughout a microvascular network were performed [4].A hybrid multiscale model for simulations of large scale networks was introduced and applied to a large realistic vascular configuration [5]. A full pulmonary vascular tree has been reconstructed [6] and the geometry and temporal flow characteristics were studied. A reconstructed model of a rat brain microvascular network [7] was analyzed using the finite volume method, where the flow rates, velocities, and pressures were solved using hematocrit and shear-dependent fluid properties. A set of generalized microvascular networks [8] have been simulated using the finite volume method, with explicitly modeled red blood cells in the suspending fluid. Flow in a tree-like capillary network was simulated [9] using a network model, tracking the hematocrit levels through the capillary network.

In this work, we quantified the flow rate without red blood cells (RBCs) and with RBCs suspended in the fluid to investigate the effect of complex geometry and blood cell suspension on the flow in the complex retina vascular network. The effect of red blood cells on the flow properties in the vascular network was observed and quantified. In the upcoming part of the study, various blood vessels will be blocked off to simulate a microstroke and its effect on flow redistribution in the network. The same analysis will be performed comparing pure fluid flow to the flow of red blood cell suspensions for each microstroke location.

METHODS

The RBCs were modeled as a coarse grained molecular dynamics cell membrane model implemented in LAMMPS (large-scale atomic/molecular massively parallel simulator) [10]. The membrane nodal forces are calculated from potential functions, and the positions are updated based on the Newton's law of motion. Bonds, angles, and dihedrals are defined for the cell membrane. In our implementation, the red blood cell has energy potentials which resist stretching and bending and maintain the red blood cell's equilibrium surface area and volume. The red blood cell coarse grained membrane model (Fig. 1) can react to external forces and restore its equilibrium shape after deformation.

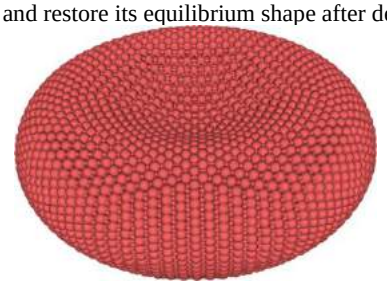

Figure 1: Red blood cell membrane model with particles connected with bonds.

The fluid flow was solved by the Lattice Boltzmann method using PALABOS [11]. The immersed boundary method (IBM) [12] was used to model fluid-cell interactions. The geometry of the retina network was

generated from a stl file obtained from NIH 3D print database (https://3dprint.nih.gov/discover/3dpx-005107). Off-lattice boundary conditions were used in between fluid nodes using linear interpolation for a smooth flow profile. Red blood cells were placed inside the network. Solid wall particles (Fig. 2) were placed at the vertices of the mesh to create a solid boundary for the red blood cells to interact with. The fluid velocity was defined at the inlet and the outlet of the retina network and the flow was developed until steady state was reached.

RESULTS

To analyze the flow in the retina vascular network, a few critical vessels were selected from the network, as labeled in Fig. 2. The diameter was calculated for each vessel of interest. The flow velocities were solved, and the volumetric flow rates were computed once the flow was at steady state. The flow rates of pure fluid and RBC suspensions were compared and are shown in Table 1. The largest difference in flow rates between pure fluid and RBC suspension occur in the main high-flow pathway between inlet and outlet through vessels C, D, and E. Vessels A and B are the only ones that did not see a change in flowrates between pure fluid and RBC suspension flow.

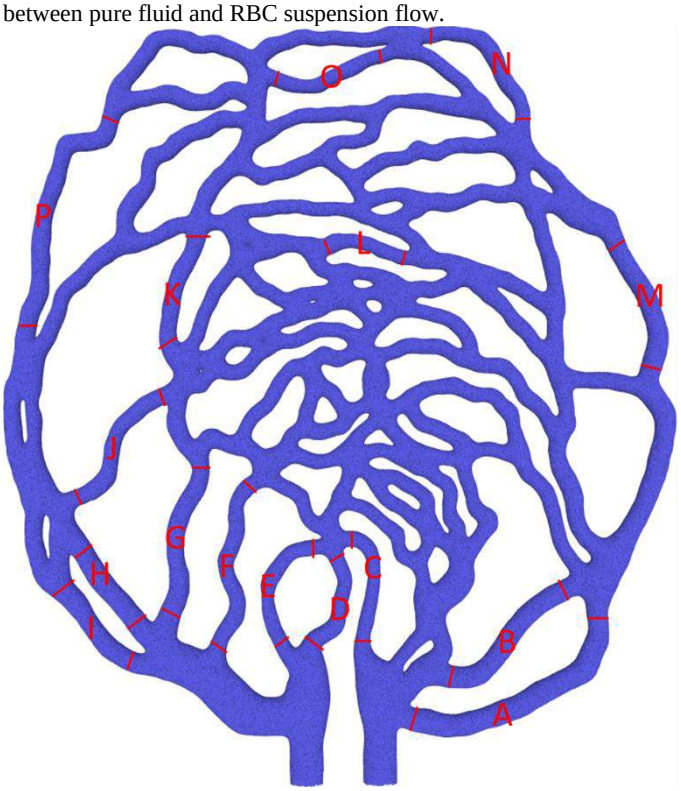

Figure 2: Retina capillary vascular network wall particles. Vessels of interest labeled A-P.

DISCUSSION

The pure fluid simulation shows the main pathways of fluid flow through the network. Vessel C acts as the main inlet into the short loop CDE, with D and E as outlets. Vessel G has the second highest flow rate in the network where it acts as the main outlet from the central region of the retina capillary network. Lowest flow rates were found in vessels K, L, N, and O, which are far from the inlet region. The four vessels also have other parallel vessels nearby which offer alternate fluid flow pathways.

The inclusion of red blood cells resulted in an overall decrease of flow rate through the vessels that were analyzed. The reduction of flow rate may be beneficial to allow for better exchange of oxygen between the red blood cells and the surrounding tissues. Further detailed analysis of the effects of hematocrit levels and microstrokes in the vascular networks will be presented at the conference.

Table 1: Diameters and flowrates of vessels of interest

Vessel	Diameter (μm)	Flow rate (m^3/s) Fluid only	Flow rate (m^3/s) With RBC
A	13.9	1.67E-13	1.67E-13
B	13.9	1.44E-13	1.44E-13
C	8.11	1.86E-13	1.55E-13
D	9.08	2.46E-13	1.78E-13
E	9.08	1.42E-13	1.17E-13
F	10.6	1.57E-13	1.43E-13
G	11.2	2.19E-13	1.89E-13
H	13.6	1.31E-13	1.31E-13
I	12.4	1.03E-13	1.03E-13
J	10.0	1.08E-13	9.16E-14
K	10.8	2.61E-14	2.39E-14
L	8.57	2.88E-14	2.26E-14
M	11.3	1.05E-13	8.99E-14
N	8.15	2.11E-14	1.62E-14
O	7.79	2.13E-14	1.62E-14
P	11.5	5.78E-14	5.00E-14

ACKNOWLEDGEMENTS

The authors acknowledge the startup funding and the high-performance computing support from Gaea at Northern Illinois University.

REFERENCES

[1] J. Xu et al, *NCHS Data Brief no. 355*, 2020.

[2] F. Schmid et al., pp. 15–19, 2020, doi: 10.1101/2020.07.05.188565.

[3] J. Reichold et al., *J. Cereb. Blood Flow Metab.*, vol. 29, no. 8, pp. 1429–1443, 2009, doi: 10.1038/jcbfm.2009.58.

[4] A. R. Pries and T. W. Secomb, *Microcirculation*, pp. 3–36, 2008, doi: 10.1016/B978-0-12-374530-9.00001-2.

[5] M. Peyrounette et al., *PLoS ONE*, vol. 13, no. 1. 2018.

[6] H. Tamaddon et al., *Comput. Methods Biomech. Biomed. Engin.*, vol. 19, no. 6, pp. 673–685, 2016, doi: 10.1080/10255842.2015.1058926.

[7] T.-W. Lee et al., *ISRN Biomath.*, vol. 2014, pp. 1–11, 2014, doi: 10.1155/2014/359327.

[8] P. Balogh and P. Bagchi, *Phys. Fluids*, vol. 30, no. 5, 2018, doi: 10.1063/1.5024783.

[9] J. M. Davis and C. Pozrikidis, *Bull. Math. Biol.*, vol. 73, no. 8, pp. 1857–1880, 2011, doi: 10.1007/s11538-010-9595-3.

[10] S. Plimpton, *J. Comput. Phys.*, vol. 117, no. 1, pp. 1–19, Mar. 1995, doi: 10.1006/jcph.1995.1039.

[11] J. Latt *et al.*, *Palabos: Parallel Lattice Boltzmann Solver*. 2019.

[12] C. S. Peskin, *Acta Numer.*, 2002, doi: 10.1017/S0962492902000077.

EFFICACY OF COMBINATIONAL THERAPY ON BONE RESTORATION AND COMPENSATION AFTER CONTUSION SPINAL CORD INJURY

Valerie Lallo (1), Michael Feeley (1), Anita Singh (1)

(1) Biomedical Engineering
Widener University
Chester, PA, USA

INTRODUCTION

Spinal cord injury (SCI) can be detrimental to the patient's quality of life, and often leads to the loss of sensory and motor function below the injury site. As of 2020, SCI is seen in about 54 people per million residents of the US with approximately 17,810 new cases seen each year (1). Treatment is available in the form of active training rehabilitation techniques, but the effectiveness of combinational treatment, incorporating transplantation therapies along with rehabilitation, needs to be further investigated (2). This study evaluates the microstructural changes in the forelimb and hindlimb bones of adult rats that underwent incomplete SCI followed by combinational treatment, including scaffolds loaded with neurotrophins and body weight supported treadmill training (BWSTT).

METHODS

The Institutional Animal Care & Use Committee approved all procedures. Sprague Dawley rats (n=75) were split into five groups: a control group, a group that received no therapy after SCI, a group that received only active training (BWSTT) after SCI, a group that received only transplantation of neurotrophins after SCI, and a group that received both a transplantation of neurotrophins and active training (BWSTT) after SCI. As can be seen in Table 1, four of the five groups underwent SCI and eight weeks post their last surgery, the forelimb and hindlimb bones from all five groups were harvested. The harvested bones were then scanned using a SkyScan 1172 Micro-CT; these images were reconstructed and the regions of interest were drawn for the diaphyseal areas (Figure 1) of the bones using NRecon and CTan software, respectively. CTan was also used to a perform binary analysis on the reconstructed scans to acquire data.

Table 1: Details of experimental groups.

	Week 0	Week 1	Week 2	...	Week 8	Week 9	Week 10
Group 1	Normal	→			Harvest		
Group 2	Contusion	→			Harvest		
Group 3		BWSTT	→			Harvest	
Group 4		Transplant	→			Harvest	
Group 5		Transplant	BWSTT		→		Harvest

Figure 1: Regions of Tibial, Ulna and Humerus bone studied.

RESULTS

Changes in cortical parameters suggest that a combination of BWSTT and transplantation of a neurotrophin-releasing scaffold shows greater improvement than BWSTT by itself (Figure 2 and 3). This can be seen with Tibial decrease in cortical

BV/TV, when comparing Group 3 and Group 5 (Figure 3). In contrast to the hindlimb, the forelimbs' BV/TV of the cortical bone increased after injury due to compensation as observed commonly after SCI. Additionally in the forelimbs, animals in BWSTT (Group 3) and the combinational group (Group 5) had lower BV/TV when compared to injury (Group 2) and transplant (Group 4) animals, showing a decrease in overcompensation, and an increase in effectiveness of the therapy (Figure 3).

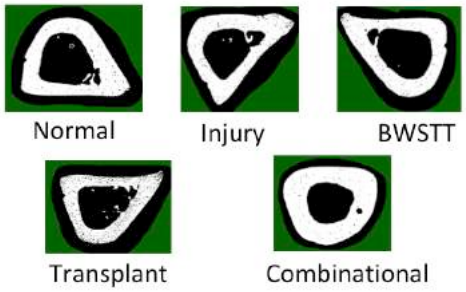

Figure 2: Diaphyseal scans of Tibial bone from all groups.

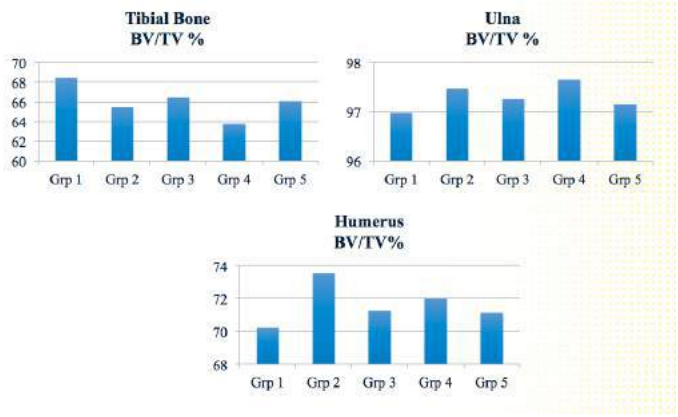

Figure 3: Structural parameters obtained from CT scans in Tibial, Ulnar and Humerus diaphyseal regions. Abbreviations and their respective meanings are as follows: BV/TV – bone volume over total volume.

DISCUSSION

SCI affects both the forelimb and hindlimb bones of rats, and BWSTT greatly helps restore some of the loss. While BWSTT leads to bone structural properties similar to normal rats, combinational treatment using a neurotrophin-releasing scaffold reports further improvement.

ACKNOWLEDGEMENTS

This work was supported by New Jersey State Commission Grant #CSCR14ERG001.

REFERENCES

[1] Spinal Cord Injury Facts and Figures at a Glance, NSCISC

[2] Corcoran et al., *Western Journal of Medicine*. 1991;154(5):536-538.

EFFECT OF SURGERY ON CORONARY FLOW HEMODYNAMICS IN CHILDREN WITH ANOMALOUS AORTIC ORIGIN OF A CORONARY ARTERY (AAOCA): A PATIENT-SPECIFIC COMPUTATIONAL STUDY

A. Razavi. (1), B. Yeats (1), J. Parthasarathy (2), Y. Farsiani (1, 2), S. Molossi (3), C. Mery (4), R. Krishnamurthy (2), L.P. Dasi (1)

(1) Department of Biomedical Engineering Georgia Institute of Technology, Atlanta, GA, USA

(2) Nationwide Children's Hospital, Columbus, OH, USA

(3) Department of Pediatrics, Texas Children's Hospital, Baylor College of Medicine, Houston, Texas, USA

(4) Department of Cardiothoracic Surgery, Dell's Children's Medical Center, The University of Texas at Austin, Austin, Texas, USA

INTRODUCTION

AAOCA is a congenital defect where one coronary artery arises from the opposite sinus of Valsalva. Cross-sectional imaging often shows ostial stenosis, and an intramural course within the aortic wall of the anomalous coronary, which carry an increased risk of myocardial ischemia. AAOCA is the 2nd leading cause of sudden cardiac death (SCD) in children and may require life-long restriction from exercise [1] or surgery. There is controversy over the need for surgery, type of surgery, and residual risk of ischemia after surgery in AAOCA. The intramural course can be addressed by surgical procedures like unroofing of the intramural course or coronary artery reimplantation. While some groups favor unroofing as the primary option, with reimplantation restricted to specific conditions such as with a short intramural course [1], other groups advocate reimplantation as the primary approach [2]. The appropriate indication for each procedure, their effect on coronary morphology and blood flow patterns, and their short-term and long-term risk of residual or recurrent ischemia have not been systematically investigated. Recently it has been suggested that factional flow reserve (FFR) measurements (approximated as the ratio of pressure distal to the stenotic lesion to the pressure measured proximal to the lesion) can be used to identify hemodynamic significance in anomalous coronary arteries with FFR <0.8 as a threshold for ischemia [3]. There is an urgent need to develop physical and computational hemodynamic models of AAOCA in the pre-operative and post-operative period to explore mechanistic questions since hemodynamic assessment is not routinely performed in children with AAOCA. The objective of this work is to create patient-specific computational models of AAOCA, characterize local hemodynamics related to morphological variations in AAOCA pre-/post- operatively and assess hemodynamic effects of surgery using biomechanical flow modeling as well as virtually derived FFR (vFFR). Findings from this study may provide mechanistic insight into the cause of ischemia and eventually lead to improved surgical decision making, and assessment of residual risk after surgery.

METHODS

After Institutional Review Board approval, patient-specific geometries were reconstructed from computed tomography angiography (CTA) in a patient with anomalous left coronary artery (AAOCA-L), with a short 3.5 mm intramural course, who presented with SCD. He was treated with unroofing of the intramural segment and developed recurrent SCD. Repeat surgery demonstrated the intercoronary pillar as the cause of ischemia requiring coronary reimplantation. For computational model development, validity of the image segmentation and reconstruction method has been previously assessed by our group. A set of boundary conditions were assigned at the models' inlet and outlets to solve for the governing blood flow equations. At the inlet, aortic flow waveform was used from the in-vitro set-up of the current work with cardiac output of 5 L/min and heart rate 72 beats/min We used a coupled multi-domain method previously developed [4] in which 0D lumped parameter network (LPN) models are assigned at coronary outlets. Parameters of the LPN model were determined based on a robust protocol to capture physiologic flow and prescribed blood pressures (BP) [5]. Systolic and diastolic aortic BP were set as120mmHg/80mmHg. Geometries were then meshed using tetrahedral elements. Since our geometries include multi-scale dimensions (i.e., the size of the aorta is about one order of magnitude larger than the size of the coronary artery), mesh elements sizes were assigned proportional to the size of the arteries using the "local mesh" option. Regional mesh refinement was also performed to generate more elements for locations with high velocity gradients and expected flow disruptions. A mesh size of (600-800) K elements were used for the simulations. Blood was modeled as an incompressible Newtonian fluid

with a density of 1.06 g/cm^3 and viscosity of 4 cP. The artery walls were modeled as rigid. Solutions were run for (6-8) cardiac cycles until BP and flow at the inlet and outlets did not change more than 1%. Data including flow, pressure and velocity from the last cycle of each simulation were used for visualization and analysis using SimVascular (simtk.org), Paraview (Kitware, Clifton Park, NY), and Tecplot (Tecplot, Inc., Bellevue, WA) software packages and compared pre- vs post-unroofing and reimplantation.

RESULTS

Axial CTA of the aorta and the left coronary artery is depicted in Figure 1(A) for the patient preoperatively (PRE), post-unroofing (POST-1) and post reimplantation (POST-2). The reconstructed 3D model includes aorta, normal right coronary, and anomalous left main coronary artery. Results for the representative flow waveform show that physiologic phasic coronary behavior has been captured by the imposed BCs. Figure 1(B) shows that for the left coronary artery, minimum flow occurs during systole and the peak flow occurs during diastole. Contours of pressure distribution within the reconstructed models are indicated for the peak coronary flow in Figure 1(C). Pressure drop was highest (≅12 mmHg) for PRE in the anomalous artery during maximum coronary flow. This pressure drop was decreased POST-1 (≅8 mmHg) and POST-2 (≅6 mmHg). The pressure recovery was higher POST-2 compared to the POST-1. Therese pressure drops corresponds to vFFR values of 0.9, 0.93 and 0.95 for PRE, POST-1, and POST-2, respectively.

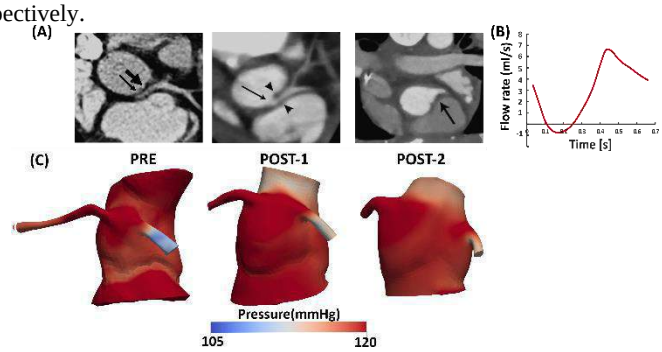

Figure 1: (A) Axial CTA of the aorta and the anomalous left coronary pre-operatively (PRE), post-unroofing (POST-1), and post coronary reimplantation (POST-2), (B) flow waveform at the left coronary outlet, (C) contour distribution of pressure in the patient PRE, POST-1, and POST-2

Contours of the velocity distribution as well as the streamlines are shown at a plane through the length of the anomalous artery for the peak coronary flow. For PRE, a complex flow pattern is observed distal to the coronary ostium. There is local accelerated flow region which forms a neck in the distal intramural segment. Flow recirculation zones are also observed in the anomalous coronary artery as highlighted by the streamlines. For POST-1, the complex flow behavior seen in PRE has been resolved. However, there is a spiral flow observed which is deviated towards the outer wall. For POST-2, streamlines are aligned with the anatomy and there is almost no localized flow acceleration compared to the other two models.

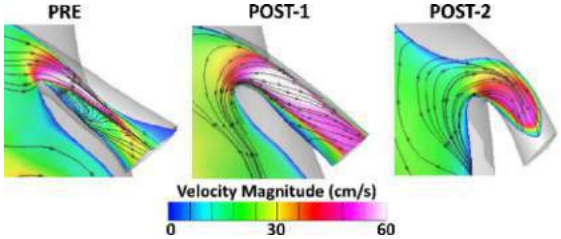

Figure 2: Contour distribution of velocity and streamlines in the patient pre-operatively (PRE), post-unroofing (POST-1), and post coronary reimplantation (POST-2)

DISCUSSION

This computational study is the first one which assesses coronary flow and pressure in an AAOCA patient who had both coronary unroofing (POST-1) and reimplantation (POST-2). We observed that the coronary flow was altered by the surgery and affected by the type of surgery. The jet flow with localized acceleration was observed pre-operatively due to the presence of the intramural segment (Figure 1 (A), PRE) which resulted in recirculation regions with increased energy dissipation. The energy dissipated in the intramural segment caused the pressure to drop and FFR to decrease. The complex flow pattern and wash-out was improved POST-1 but there was a helical flow leaning towards the outer wall that can be attributed to the intercoronary pillar which acted like ostial stenosis (Figure 1 (A), POST-1). The flow behavior was almost fully resolved POST-2 in which there was no residual intramural segment and localized flow acceleration (Figure 1 (A), POST-2). The ostium located in the correct sinus also provided a more streamlined flow similar to the flow patterns observed in normal coronary arteries. The energy dissipation was recovered and FFR increased consequently. Our results are in agreement with [6] where similar flow behavior was observed in the anomalous artery of a representative AAOCA-L model. Our vFFR data showed values >0.8 for the PRE and POST states. However, it should be noted that these calculations were performed for the nominal blood pressures 120 mmHg/80 mmHg which are below the blood pressures under maximum hyperemic conditions for which FFR is commonly calculated [7, 8].

The first limitation of the study is that the aortic valve was not included in the simulations. Nonetheless, the realistic BCs implemented will lead to temporal physiologic pressure gradients within the model, despite absence of the physical valve. We also assumed the walls to be rigid. Although we are aiming at including deformable walls for the future analyses, it is of note that material properties of the coronary arteries will not be patient specific due to limited data regarding coronary artery material properties of the adult or pediatric population in either healthy or diseased conditions. Furthermore, movement of the coronary arteries was not considered in this study since the effect of coronary artery motion has been shown to be secondary as compared to the geometry and BCs [9, 10].

We conclude that the type of surgery influences the local flow hemodynamics and FFR. Finding from the current study, once validated against the ongoing in-vitro experiments in our group, will allow us to design virtual surgical procedures for ultimate use in predicting the need for and type of surgery and residual risk of SCD after surgery.

ACKNOWLEDGEMENTS

We acknowledge Nationwide Children's Hospital and Georgia Tech discretionary funds. LPD and RK shared senior authorship.

REFERENCES

[1] Molossi, S et al., *Methodist Debakey Cardiovasc J*, 15, no. 2: 111-121, 2019.
[2] Law, T et al., *Ann Thorac Surg*,102-1: 192-8, 2016.
[3] Agrawal, H et al., *J Invasive Cardiol*, 33-1:E45-E51, 2021.
[4] Kim, H. J, et al., *Ann Biomed Eng*, 38-10: 3195-209, 2010.
[5] Razavi, A et al., *Biomedical Science Instrumentation*, 55-2:388-98, 2019.
[6] Razavi, A et al., *Semin Thorac Cardiovasc Surg*, 2020.
[7] Pantos, I and Katritsis, D, *Interv Cardiol*, 9-3:145-150, 2014.
[8] Zimmermann, M et al., *Eur Heart J*, 38-33:2569, 2017.
[9] Santamarina, A et al., *Ann Biomed Eng*, 26-6: 944-54,1998.
[10] Zeng, D et al., *J Biomech Eng*, 130-4:041014, 2008.

INTERCELLULAR COUPLING AMONG SMOOTH MUSCLE CELLS CHANGES WHILE UNDERGOING AGONIST-INDUCED CONSTRICTION

Suzanne E. Stasiak (1), Dhananjay T. Tambe (2), Harikrishnan Parameswaran (1)

(1) Department of Bioengineering
Northeastern University
Boston, Massachusetts, USA

(2) Department of Mechanical/Biomedical Engineering
University of South Alabama
Mobile, Alabama, USA

INTRODUCTION

Smooth muscle cells (SMCs) form a connected layer that lines tubular organs in the cardiovascular, respiratory, digestive, and reproductive systems, and are responsible for constricting the lumen and regulating flow. Theoretical and experimental studies have treated smooth muscle as a homogenous ensemble of identically behaved cells, contributing equally to total force generated[1–3]. However, recent studies have shown that not only do SMCs respond to contractile agonist differently when they are isolated cells or part of a connected multicellular ensemble[4], but also that this connectivity between cells can change depending on underlying extracellular matrix (ECM) stiffness. ECM stiffness can cause cells to preferentially connect to each other directly via cell-cell adherens junctions (AJs), or indirectly via cell-matrix focal adhesions (FAs)[5] (**Fig 1**). Therefore, is it impossible to infer the force dynamics of a smooth muscle layer by scaling up the contractile response of a single cell by the number of SMCs present.

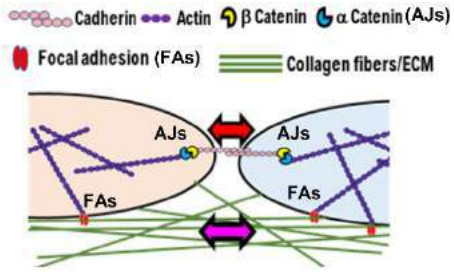

Figure 1: A schematic depicting mechanical connectivity between cells. Cells can connect directly to neighbor cells via cell-cell adherens junctions (AJs) or indirectly through the extracellular matrix (ECM) via focal adhesions (FAs).

In this study, we investigated dynamic intercellular coupling of SMCs undergoing agonist-induced constriction. By measuring traction forces and monolayer stresses within a multicellular ensemble over time, we were able to quantify the contractile moment of each cell as well as the pathway of force transmission between cells. Using this new method will help shed light on the mechanisms regulating the force transfer among a multicellular SMC ensemble, and improve our understanding of how SMCs regulate flow through airways, vasculature, and other organs, *in vivo*.

METHODS

Primary bronchial smooth muscle cells from healthy human donors (passage 3-7) were grown to confluence on collagen-coated silicone substrates with Young's modulus (E) of 13 kPa. The surface of the substrates was coated with fluorescent microspheres for displacement tracking prior to cell culture.

After serum starvation, the cells and microspheres were continuously imaged with a 20x objective at 1Hz for 1 minute at baseline followed by exposure to 10^{-5}M histamine, a contractile agonist, for 5 more minutes. A final phase contrast image of the cells was captured before removing the cells with lysis buffer to record the zero-displacement image of the microspheres.

In order to calculate intercellular coupling between cells, we first tracked microsphere displacements due to cell constriction over the course of the experiment using a particle velocimetry tracking algorithm adapted from Janke et al[6]. The resultant displacements were input into a Fourier transform traction force microscopy method using Bayesian regularization for noise filtering, modified from Huang et al[7]. The resulting traction vectors quantifying the cell stress exerted on the matrix were taken into a monolayer stress microscopy (MSM) code, adopted from our collaborator Dr. Dhananjay Tambe's work[8–10]. The

MSM algorithm uses the TFM inputs in a 2D force-balance equation to solve for mechanical forces within the layer of cells, which are then converted into stresses. Stresses at cell-cell borders were calculated using MSM stresses at points along cell borders demarcated by the phase contract image. Cell-matrix traction forces were calculated using the TFM forces over the area of the cells demarcated by the phase contrast image.

To evaluate the path of force transmission among cells undergoing constriction, we calculated each cell's net contractile moment, μ as well as a dimensionless ratio, Ψ, that varies from 0 to 1, and is defined as the fraction of the total contractile moment that a SMC exerts on its neighboring cells through AJs. As Ψ → 1, the cell's force is transmitted to its neighbors entirely through AJs. As Ψ → 0, the cell's force is transmitted entirely through FAs. This value is calculated for each cell over the course of the experiment.

RESULTS

Upon exposure to contractile agonist, the average net contractile moment of the SMCs increased over a period of approximately 60 seconds, but then held steady for the remaining 4 minutes of agonist exposure (**Fig 2A**). This indicates that there was an increase in SMC force. However, corresponding Ψ measurements show that intercellular coupling was continuously changing. When normalized to baseline, the mean Ψ value across cells decreased significantly over time (N=17, $p<0.05$, One-way ANOVA over time) (**Fig 2B**). This indicates that the cells were losing their direct coupling with neighboring SMCs via AJs, and dynamically switching to transmit force via FAs.

DISCUSSION

Smooth muscle is responsible for regulating flow through tubes in our body by constricting and controlling luminal area. In order to constrict these tubes, the SMC force must be transmitted through a percolating path around the circumference. Cells can communicate mechanically with other cells in two ways; by sending force directly to adjacent cells via adherens junctions, and by sending force to cells nearby and farther away through cell-matrix connections called focal adhesions. A recent study by Polio et al.[5] found that this path of preferred force transfer between cells can switch depending on underlying matrix stiffness. However, these studies were done at baseline, static conditions without addition of contractile agonist. Therefore, we asked if this force transfer pathway can change over time, and how it may change as cells undergo constriction.

To investigate dynamic force transmission, we recorded displacements of surface-adhered microspheres as cells constricted in response to agonist and used these displacements to calculate traction forces that cells exert on the matrix as well as stresses within the confluent monolayer that cells exert on each other. For each cell, we found the moments due to cell force exerted on its border, and therefore directly onto neighboring cells through AJs, and also the moments due to cell force exerted directly on the underlying substrate through FAs. Together, these moments gave the net contractile moment of each cell, μ. We also used a dimensionless metric, Ψ, comparing the moments due to cell-cell and cell-matrix forces, to quantify changes in force transfer pathway over time.

Upon agonist exposure, we found that the SMCs increase force over about 60 seconds, which matches published data on force development in this cell type[11]. The mean net contractile moment remained steady after this period. On the other hand, the psi value changed throughout the course of agonist exposure. While being exposed to histamine, the mean normalized Ψ value decreased significantly, indicating that the force transfer pathway was dynamically changing. Decreasing Ψ values shows that the force transfer pathway is

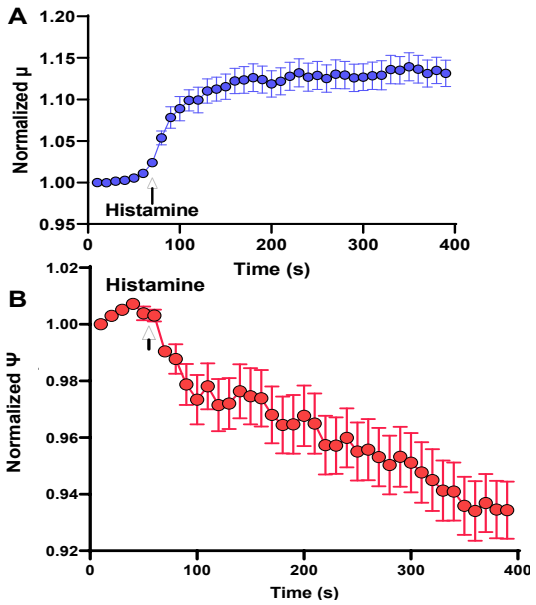

Figure 2: **We measured variations in the (A) contractile moment (μ) and (B) intercellular coupling (Ψ) for N=17 human bronchial SMCs. Symbols indicate mean and error bars indicate standard deviation. As the SMCs start to constrict, their direct cell-cell coupling (AJs) weakens in favor of focal adhesions, and more force is transmitted through the matrix.**

transitioning from cell-cell to cell-matrix as time goes on. These results indicate that cells change their connectivity from one moment to the next, and so we cannot infer dynamics of force transmission among smooth muscle by simply counting number of cells from static histology slices of airways, vasculature, and other organs.

This is the first time a technique has been able to decipher how force flows through a multicellular ensemble while also being able to quantify the contribution of each cell to the total force generated by the ensemble. Further investigation of the mechanisms regulating how cells actively modulate the path of force transmission has implications for understanding basic physiology as well as how constriction goes awry in disease conditions like asthma and hypertension.

ACKNOWLEDGEMENTS

This work was supported by NIH grants HL129468 and HL122513.

REFERENCES

1. Fredberg, J. J. et al., *Am. J. Respir. Crit. Care Med.* **156**, 1752–1759 (1997).
2. Brook, B. S. et al., *Respir. Physiol. Neurobiol.* **170**, 44–58 (2010).
3. Donovan, G. M. et al., *J. Theor. Biol.* **501**, 110337 (2020).
4. Stasiak, S. E. et al., *Sci. Adv.* **6**, eaba1149 (2020).
5. Polio, S. R. et al., *Sci. Rep.* **9**, 9564 (2019).
6. Janke, T. et al., *SoftwareX* **11**, 100413 (2020).
7. Huang, Y. et al., *Comput. Phys. Commun.* **256**, 107313 (2020).
8. Tambe, D. T. et al., *Nat. Mater.* **10**, 469–475 (2011).
9. Patel, N. G. et al., *Biochem. Biophys. Res. Commun.* **522**, 279–285 (2020).
10. Tambe, D. T. et al., *PLoS One* **8**, (2013).
11. An, S. S. et al., *Biochem Biophys Res Commun* **382**, 697–703 (2010).

THE ROLE OF GLYCOSAMINOGLYCANS IN ANTERIOR AND POSTERIOR SCLERAL SWELLING AND TENSILE BEHAVIOR

Mohammad Pachenari, Hamed Hatami-Marbini

Department of Mechanical and Industrial Engineering
University of Illinois at Chicago
Chicago, Illinois, USA, Email. hatami@uic.edu

INTRODUCTION

Many investigations have observed that scleral stiffness had the most dominance on ONH biomechanics [1,2]. The sclera is a hydrated tissue comprised of collagen fibers, elastin, proteoglycans, glycosaminoglycans (GAGs), and water molecules [3]. The assessment of scleral biomechanical properties is essential for better understanding the progression of a number of ocular diseases. For example, alteration in scleral biomechanical properties has been associated with the onset and further progression of pathological conditions such as myopia and glaucoma. It has also been shown that the content of scleral GAGs changes during normal growth, contributing to the regional alterations in scleral biomechanical properties [4]. Previous reports mainly examined the changes in the mechanical response and/or hydration-of the posterior sclera [5,6], and possible regional dependent structural roles of GAGs on sclera mechanics were not well characterized. In the present study, we investigated how GAG removal affects the tensile and swelling behavior of anterior and posterior porcine sclera. To this end, we meticulously tracked the hydration changes over time for anterior and posterior porcine sclera specimens before and after GAG removal treatment. The biochemical assay was also used to confirm the GAGs digestion method and measure the anterior- and posterior-GAG content of porcine samples. Followed by the hydration study, we performed uniaxial tensile stress-relaxation tests to characterize the mechanical behavior of the scleral strips after and before GAG removal. The findings characterized the regional differences in the scleral swelling and tensile properties in addition to clarifying the role of GAGs in hydration and mechanical response of sclera.

METHODS

The strip of size 4×12 mm^2 were dissected from anterior and posterior porcine sclera (Figure 1). The anterior/posterior samples were divided into two groups: buffer group and enzyme group. Following the protocol described in our recent studies [7,8], the samples in the enzyme group were treated enzymatically in 0.125 U/ml Chondroitinase ABC (ChABC) to remove the GAGs. We used the biochemical assay to measure the GAG content in the anterior and posterior by using scleral disks and confirm the GAG removal procedure was successful.

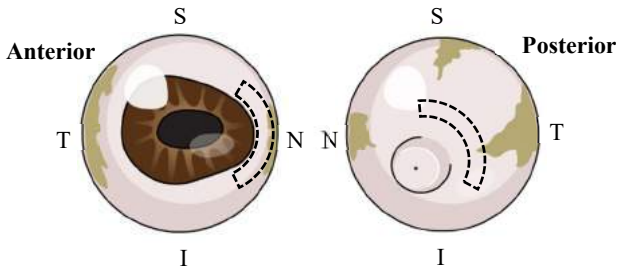

Figure 1: The dissection site of the anterior and posterior strip. S: Superior, I: Inferior, T: Temporal and N: Nasal.

We first let all samples after dissection to be dried in a desiccator for 24 hours in order to obtain their dry weight. The dry weight of samples is required to determine their hydration knowing their wet weight. Then, we soaked all samples in the buffer solution (containing no enzyme) for 24 hours and allowed them to rehydrate. During the rehydration period, we measured the wet weight of samples at certain time intervals in order to determine the hydration as a function of time. Then, the samples in the buffer group were allowed to stay in buffer for another 18 hours while the samples in the enzyme groups were immersed in the enzyme solution to deplete the GAGs from these samples. After measuring the weight of samples in both groups, they

were immersed in buffer solution (containing no enzyme) for four hours and their hydration was found as a function of time by measuring their wet weight. Then, all samples were dried again for 24 hours in a desiccator and later soaked in the buffer solution for 24 hours to measure the changes in the sclera hydration because of GAG removal. Finally, the strips were mechanically tested using a stress relaxation uniaxial experiment to determine the possible effects of GAGs removal on the sclera mechanical properties. Here, the strips were pulled with a displacement rate of 2 mm/min until an engineering strain of 5% was reached and were then allowed to relax for 20 minutes. The tensile stress was found from dividing the force by the initial cross-section of the samples. The stress at the end of the ramp period was denoted as the peak stress and the stress at the end of the relaxation time was called equilibrium stress.

RESULTS

The scleral GAGs content was obtained for the buffer-enzyme comparison in the anterior and posterior sclera (Table 1). Regional GAG content was significantly different, as the posterior specimens have, on average, 101.5% higher content of GAGs than anterior. The GAGs content was significantly different between buffer- and enzyme-treated groups in both anterior and posterior. The scleral hydration was obtained for buffer-enzyme comparisons in the anterior and posterior sclera (Figure 2). Hydration was the same for the buffer and enzyme groups before treatments. In the anterior and posterior specimens, enzyme digestion decreased the hydration immediately after the treatment. We compared the peak and equilibrium stress from the stress relaxation experiment between buffer and enzyme-treated, the results showed a significantly stiffer peak and equilibrium stress for anterior and posterior (Table 2).

	Buffer group	Enzyme group
Anterior	3.21 ± 0.34	0.1 ± 0.02
Posterior	6.46 ± 0.24	0.69 ± 0.2

Table 1: GAG content in µg/mg dry tissue weight, comparing the buffer-treated to the enzyme-treated specimens.

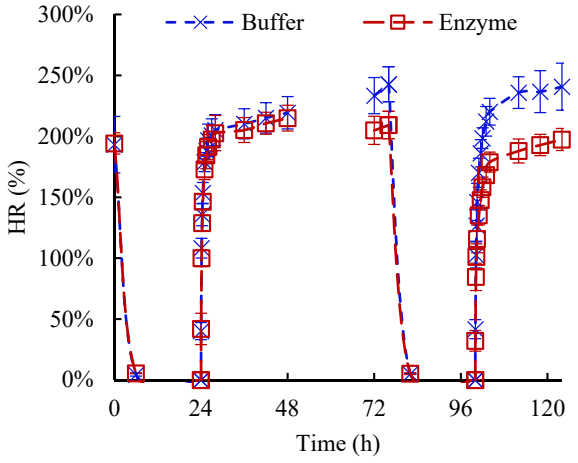

Figure 2: The average results of the hydration study on anterior strips; the plot shows the sample's water content in percentage during the experiment. The bars represent the standard deviations.

	Anterior		Posterior	
	Buffer	Enzyme	Buffer	Enzyme
Peak stress	54.2 ± 28.5	143.5 ± 51.6	85.3 ± 13.5	121.1 ± 13
Equilibrium stress	7.2 ± 3.2	21.6 ± 9.4	28 ± 8.4	45 ± 7.7

Table 2: Comparison of the peak and equilibrium stress (KPa) between the buffer- and enzyme-treated groups.

DISCUSSION

In the present study, anterior-posterior GAGs content and hydration, in addition to tensile properties, were characterized to explore how GAGs contribute to the sclera microstructural and biomechanical integrity. In our study, the posterior porcine specimens have a higher content of GAGs compared to anterior ones. These GAGs contents agree with in the human sclera, which showed a relatively same difference, comparing anterior to posterior. The results of this study suggest that GAGs are responsible for the hydration and swelling properties of sclera. Although a few studies in the past have suggested contradictory results for GAGs depletion in the sclera, this study is novel because it measured hydration changes and viscoelastic behavior simultaneously in order to identify the effects of GAGs in sclera properties. The present study also characterized the sclera swelling and mechanical properties in the posterior and anterior region. Despite its important findings, we should note that uniaxial tensile experiments do not measure the mechanical response of sclera in physiological conditions and experimental methods such as inflation tests can be used in future studies to see if they also give similar results.

ACKNOWLEDGEMENTS

The authors would like to acknowledge the support in part by National Science Foundation: Grant No. 1636659 and NIH R21 EY030264.

REFERENCES

1. Sigal, I.A., J.G. Flanagan, and C.R. Ethier, Factors influencing optic nerve head biomechanics. Investigative ophthalmology & visual science, 2005. 46(11): p. 4189-4199.
2. Mehr, J.A., Moss, H.E., Hatami-Marbini, H. Numerical Investigation on the Role of Mechanical Factors Contributing to Globe Flattening in States of Elevated Intracranial Pressure, Life, 2020 10(12): 316, 1-12.
3. Hatami-Marbini, H. and M. Pachenari, Hydration related changes in tensile response of posterior porcine sclera. Journal of the Mechanical Behavior of Biomedical Materials, 2020. 104: p. 103562
4. Rada, J.A., et al., Proteoglycan composition in the human sclera during growth and aging. Investigative ophthalmology & visual science, 2000. 41(7): p. 1639-1648.
5. Boubriak, O., J. Urban, and A. Bron, Differential effects of aging on transport properties of anterior and posterior human sclera. Experimental eye research, 2003. 76(6): p. 701-713.
6. Murienne, B.J., et al., The effects of glycosaminoglycan degradation on the mechanical behavior of the posterior porcine sclera. Acta biomaterialia, 2015. 12: p. 195-206.
7. Hatami-Marbini, H. and M. Pachenari, The contribution of sGAGs to stress-controlled tensile response of posterior porcine sclera. Plos one, 2020. 15(2): p. e0227856.
8. Hatami-Marbini, H. and M. Pachenari, On influence of sulfated glycosaminoglycans on tensile properties of posterior sclera. Mechanics of Soft Materials, 2020. **2**(1): p. 1-10.

SB^{3}C2021
Summer Biomechanics, Bioengineering and Biotransport Conference
June 14-18. Virtual

EFFECT OF CURVATURE ON THE THERMAL INTERFACE CONDUCTANCE BETWEEN NANOSCALE GOLD AND WATER

Blake A. Wilson (1), Jaona H. Randrianalisoa (2), Steven O. Nielsen (3), Zhenpeng Qin (1)

(1) Department of Mechanical Engineering
The University of Texas at Dallas
Richardson, Texas, United States of America

(2) Institut de Thermique, Meanique Materiaux
University of Reims Champagne-Ardenne
Reims, France

(3) Department of Chemistry and Biochemistry,
The University of Texas at Dallas
Richardson, Texas, United States of America

INTRODUCTION

Upon laser stimulation plasmonic gold nanoparticles (AuNPs) can absorb light and convert that energy into heat [1], allowing AuNPs to serve as effective nanoheaters for applications such as hyperthermia-based cancer treatments [2] and selective inactivation of proteins via Molecular Hyperthermia [3,4]. However, pulsed laser induced heating of AuNPs can result in elevated lattice temperatures which promote particle degradation via melting and fragmentation [5]. Understanding how key thermal transport properties relate to AuNP structure and particle size, may allow for better rational tuning of nanoparticle properties in order to reduce or avoid unwanted particle degradation during laser stimulation.

Under laser stimulation AuNPs dissipate heat with a finite thermal interface conductance into the surrounding solvent [5]. This thermal interface conductance (or its inverse the Kapitza resistance) is a key parameter affecting the kinetics of heat dissipation from the nanoparticle [1], and it is a principal regulator of nanoparticle temperature during laser heating. We hypothesized that smaller AuNPs with larger particle-solvent interface curvature would have more efficient heat dissipation as measured by their thermal interface conductance. The objective of this work was therefore to use atomistic Molecular Dynamics simulation to investigate the effects of curvature on the heat transfer through the nanoscale gold-water interface. Our key finding thus far was that nanoscale gold-water interfaces with higher curvature had higher thermal interface conductance. In the case of spherical AuNPs, this meant that smaller particles had higher thermal interface conductance, corresponding to more efficient heat dissipation and thus lower AuNP temperatures for comparative heating power densities during steady-state heating.

METHODS

We constructed four atomistic models of nanoscale gold immersed in water. The first system was composed with a planar gold slab which was periodic in the x and y dimensions. The other three systems were composed with spherical AuNPs with diameters 3 nm, 5 nm, and 10 nm (Figure 1). Spherical AuNPs were cut from a block of Au(111).

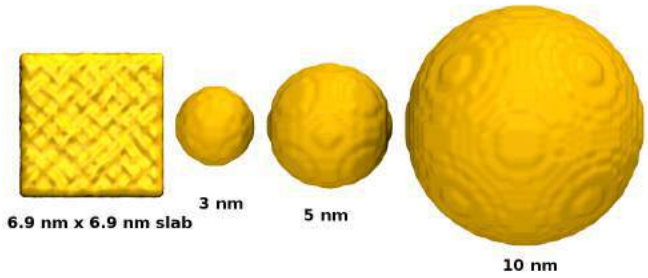

Figure 1: Nanoscale gold structures used in the simulated gold-water systems.

Gold-gold interactions were modeled using the Embedded Atom Model [6]. Water was modeled using the flexible SPCE-

F potential [7]. Gold-water interactions were modeled using 12-6 Lennard-Jones potential with parameters from Chen et al. [8]. All simulations were carried out with the LAMMPS software [9] using periodic boundary conditions. Nanoscale gold-water systems were first equilibrated for 1 nanosecond at 300 K under NVT conditions and then further equilibrated for 1 nanosecond at 300 K and 1 atm under NPT conditions. Laser stimulation was modeled using nonequilibrium molecular dynamics simulation at 1 atm under NPH conditions with continuous uniform heating of gold while a surrounding water pool (heat sink) was maintained at 300 K. Laser heating simulations were run for a total of 4 nanoseconds – the first 1 nanosecond was used to establish a steady-state and was not included in subsequent analysis. Analysis was carried out using custom Python code.

RESULTS

Our key finding thus far was that the thermal interface conductance of the nanoscale gold-water interface scaled linearly with interface curvature, so smaller AuNPs (curvature = 1/R) had higher thermal interface conductance (Figure 2 A).

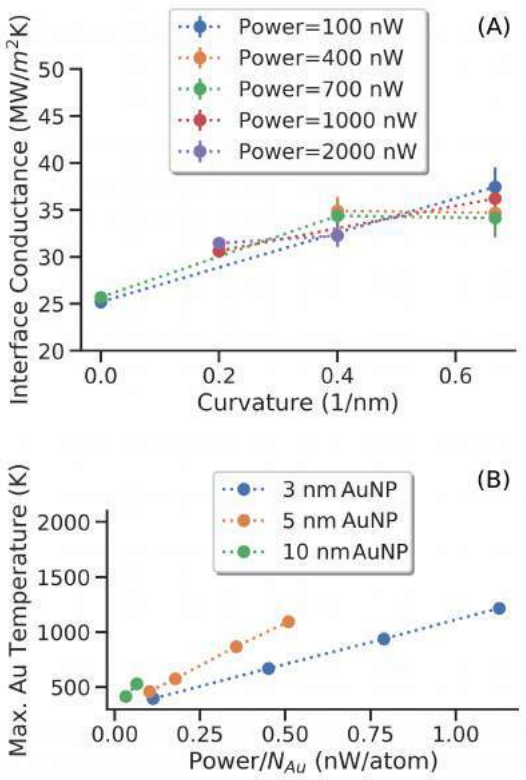

Figure 2: (A) Interface conductance versus nanoscale gold surface curvature at various total heating powers. (B) Maximum gold temperature versus heating power density for the three spherical AuNPs.

As a result, under similar heating power densities (power per gold atom) the smaller AuNPs with fewer gold atoms experienced lower gold lattice temperatures (Figure 2 B) which was consistent with more efficient heat dissipation.

DISCUSSION

We have constructed four atomistic models of nanoscale gold in water which were subjected to steady-state heating in order to estimate the effects of curvature on the gold-water heat transfer. Our results thus far have indicated that the thermal interface conductance between nanoscale gold and water increases with interface curvature. This trend is consistent with that reported by Tascini et al. [10] for nanospheres in liquid. However, it is in contrast to the results reported for molecular dynamics simulations of AuNPs in hexane [11] in which the thermal interface conductance between nanoscale gold and hexane decreased with interface curvature. Overall, previous molecular dynamics simulations [8, 10-12] suggest that the thermal interface conductance of nanoparticles is largely governed by two interrelated factors: i) overlap between the vibrational density of states of the nanoparticle lattice and solvent, and ii) adsorption of the solvent onto the surface of the nanoparticle. As such, we are currently investigating the role of these two factors in the curvature dependence of thermal interface conductance between nanoscale gold and water.

ACKNOWLEDGMENTS

Research reported in this work was supported by the National Institutes of Health under award number R35GM133653. The authors also acknowledge the Texas Advanced Computing Center (TACC) at The University of Texas at Austin for providing HPC resources that have contributed to these research results. URL: http://www.tacc.utexas.edu

REFERENCES

1. Baffou, G et al., Laser Photonics Rev, 7:2:171-187, 2013
2. Hirsch, L. R et al., Proc. Natl. Acad. Sci., 84:4023-4032, 2003
3. Kang, P et al. Small, 13:1700841, 2017
4. Kang, P et al. ACS Nano, 13:12487-12499, 2019
5. Plech, A et al. Physical Review B, 70:195423, 2004
6. Foiles, S. M et al., Physical Review B, 33:7983-7991, 1986
7. Lopez-Lemus, J et al., J. Chem. Phys., 128:174703, 2008
8. Chen, X et al., J. Phys. Chem. C, 118:1285-1293, 2014
9. Plimpton, S, J. Comp. Phys., 117:1-19, 1995
10. Tascini, A et al., Phys. Chem. Chem. Phys., 19:3244-3253, 2017
11. Neidhart, M. S et al., J. Phys. Chem. C, 122:1430-1436, 2017
12. Merabia, S et al., Proc. Natl. Acad. Sci., 106:15113-15118

QUANTIFICATION OF NEURON MORPHOLOGICAL DEVELOPMENT USING THE CHANGE POINT TEST

Ashlee S. Liao (1), Victoria A. Webster-Wood (1,2,3), Yongjie J. Zhang (1,2)

(1) Mechanical Engineering
Carnegie Mellon University
Pittsburgh, PA, USA

(2) Biomedical Engineering
Carnegie Mellon University
Pittsburgh, PA, USA

(3) McGowan Institute for Regenerative Medicine
University of Pittsburgh
Pittsburgh, PA, USA

INTRODUCTION

Neurite polarization and arborization give rise to the distinct morphology of neurons and development of functional networks. Dotti et al. were among the first to characterize the morphology as the neurites develop into axons and dendrites [1]. The growth of these processes was qualitatively described into distinct stages for different neurons (e.g., hippocampal [1] and cerebellar granule [2]) [3]. With only qualitative characteristics, it is challenging for non-experts to identify the growth stage of an individual cell and determine when it has fully transitioned to a subsequent stage. Quantitative representations defining each growth phase are needed to accurately describe the neurite development process and for validation of neuron growth simulations in the future. In addition, neurite growth directions are influenced by various extracellular and intracellular factors to form functional networks. Thus, when observing the morphological development, it is crucial to identify locations at which the neurite redirected the direction of growth.

To identify locations of redirection in meandering paths, the change-point test (CPT) was previously developed to study animal travel [4]. This is analogous to identifying points along a neurite trajectory to determine when the path changed direction due to potential extracellular and intracellular sensory cues. However, to our knowledge, this approach has not yet been assessed for applicability in quantifying and comparing neuron growth stages. By identifying these points, further studies on neurite development can quantifiably determine whether a potential cue directed the change in neurite growth.

Additionally, morphological features, such as tortuosity and number of neurites, have been compared to distinguish different neuron types [5]. However, quantitative metrics have not been identified for defining neurite developmental stages. Therefore, this work compares CPT and morphological feature metrics from primary rat hippocampal neurons to characterize neurite morphogenesis.

METHODS

To assess neurite development, rat hippocampal neurons (A36513, Gibco, USA) were cultured (Figure 1A) per the manufacturer's protocol [6] at 10,000 and 20,000 cells/cm^2 on cell-culture-treated 48-well plates (150687, Nunc, USA). Prior to plating, the wells were incubated for 1 hour at room temperature with a poly-D-lysine (A3890401, Gibco, USA) solution, diluted to 50 µg/mL with 0.5 M borate buffer (PI28341, ThermoScientific, USA). Subsequently, the solution was aspirated, and the plate was rinsed with Dulbecco's phosphate buffered saline (14190144, Gibco, USA). Plated cells were imaged with phase contrast and brightfield microscopy (Echo Revolve 4, inverted) under 20X and 40X magnification at 0.5, 1, and 2 days *in vitro* (DIV) (Figure 1B-C), which correspond with Stages 2-3 in neurite growth.

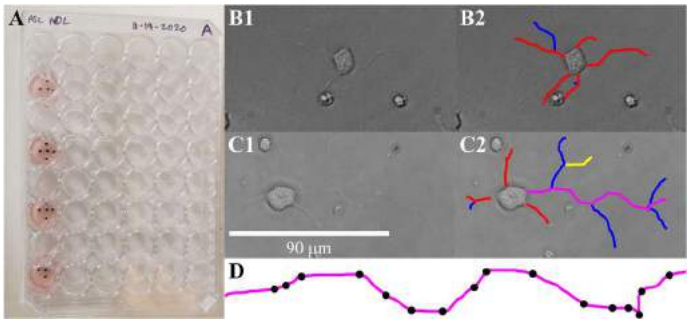

Figure 1: (A) Neurons were cultured per manufacturer protocols. Dots were drawn on the bottom of the plate prior to culture to facilitate neuron location. (B-C) Cells were imaged and traced at 0.5 (not shown), 1 (B1-2), and 2 (C1-2) DIV. (D) The CPT identified change points. The trace in D is the fuchsia trace in C2.

Neurites were semi-automatically traced with NeuronJ [7] in the Fiji [8] distribution of ImageJ [9] (Figure 1B-C). Length, tortuosity, number of neurite end points (degree) per cell, and number of neurites per cell were measured from the traces. Additionally, locations of significant direction changes in each trace were identified using the CPT (Figure 1D) [4]. The CPT decomposes tortuosity into growth length before a direction change (segment length) and the neurite growth direction (turning angle) for each segment. The CPT was applied 10 times to each trace with a significance level (α) of 0.5, while varying the number (q) of vectors prior to a change point from 1 to 10. The smallest q with the most points was selected to measure the segment length between direction changes. Relative turning angles were also measured for each neurite segment.

For all morphological features, the distributions were assessed for normality using the Anderson-Darling test. The distributions were found to be not normal; thus, the nonparametric Mann-Whitney test was used to determine whether there were statistically important differences between the medians of each feature between different culture ages.

RESULTS

The distributions of the morphological features were overall skewed to the left (Figure 2 for segment length as a characteristic example). The features were significantly different between 1 and 2 DIV, except for the relative turning angle at a density of 20,000 cells/cm^2 and for the number of neurites at a density of 10,000 cells/cm^2 (Table 1). Trace length at 20,000 cells/cm^2, segment length, degree, and number of neurites were significantly different between 0.5 and 2 DIV (Table 1). Only degree and number of neurites, both at a density of 10,000 cells/cm^2, were significantly different between 0.5 and 1 DIV.

DISCUSSION

For the time frame monitored for this study, the morphological features quantified were expected to have less change from 0.5 to 1 DIV and to change significantly by 2 DIV. Hippocampal neurons are expected to reach Stage 2 at around 0.5 DIV, with about half of them reaching Stage 3 by 1 DIV [1,10]. By 2 DIV, over 80% of the neurons should have transitioned from Stage 2 to 3 [1,10]. Several features investigated exhibited significant changes between 1 and 2 DIV. However, turning angle and tortuosity were not able to distinguish between 0.5 and 2 DIV, but still captured a significant difference between 1 and 2 DIV. This could indicate these features do not strongly correspond with the developmental stages.

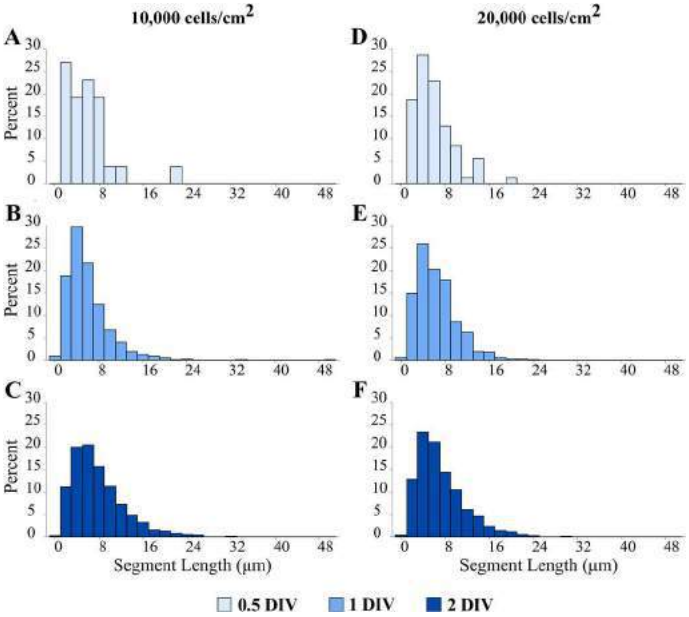

Figure 2: Distribution of segment length measured for neurites at a density of (A-C) 10,000 cells/cm^2 and (D-F) 20,000 cells/cm^2 at a culture age of (A, D) 0.5 DIV, (B, E) 1 DIV, and (C, F) 2 DIV.

In addition to standard morphological features investigated, potential new characteristics to quantify the neurite development process were identified using the CPT [4]. Additional studies manipulating neurite direction should be implemented to determine if the CPT can capture intentional directional changes. Overall, the CPT has potential use for identifying directional changes, but only segment length could distinguish neurons at 2 DIV from those at 0.5 and 1 DIV.

Complementing the qualitative descriptions of neurite growth stages with the CPT and quantitative metrics, particularly segment length, degree, and number of neurites can more clearly describe neurite morphogenesis. However, more studies at additional developmental stages are needed to fully characterize the process. Identifying relevant metrics simplifies tracking of neurite development and exhibits potential for direct comparison of experiments with mathematical neuron growth models, thereby supporting model validation.

ACKNOWLEDGEMENTS

This material is based upon work supported by the National Science Foundation (NSF) Graduate Research Fellowship Program under Grant No. DGE1745016. Any opinions, findings, and conclusions or recommendations expressed in this material are those of the author(s) and do not necessarily reflect the views of the NSF.

REFERENCES

[1] Dotti, CG et al., *J Neurosci*, 8:1454-1468, 1988.
[2] Powell, SK et al., *J Neurobio*, 32:223-236, 1997.
[3] Tahirovic, S et al., *Cold Spring Harb Per Biol*, 1:a001644, 2009.
[4] Byrne, RW et al., *Anim Behav*, 77:619-631, 2009.
[5] Laturnus S et al., *Neuroinform*, 18:591-609, 2020.
[6] B-27 Plus Neuronal Culture System User Guide, Rev. 4.0, *ThermoFisher*, 2018.
[7] Meijering, E et al., *Cytometry*, 58A: 167-176, 2004.
[8] Schindelin, J et al., *Nat Methods*, 9: 676-682, 2012.
[9] Rueden, CT et al., *BMC Bioinformatics*, 18: 529, 2017.
[10] Kaech, S et al., *Nat Protoc*, 1:2406-2415, 2006.

Table 1: The *p*-values from pairwise Mann-Whitney tests to identify significant differences between culture ages.

Morphological Feature	Density (cells/cm^2)	*p*-Values per DIV Pair		
		0.5 - 1	0.5 - 2	1 - 2
Segment Length (μm)	10,000	0.899	**0.021**	**<0.001**
	20,000	0.174	**0.017**	**0.001**
Turning Angle (°)	10,000	0.438	0.147	**0.008**
	20,000	0.449	0.308	0.449
Total Trace Length (μm)	10,000	0.105	0.896	**<0.001**
	20,000	0.493	**0.009**	**<0.001**
Degree	10,000	**0.04**	**0.008**	**0.003**
	20,000	0.254	**0.027**	**0.001**
Number of Neurites	10,000	**0.021**	**0.02**	0.459
	20,000	0.103	**0.013**	**0.006**
Tortuosity	10,000	0.218	0.573	**0.007**
	20,000	0.082	0.94	**<0.001**

WAVE TRANSMISSION AND BONE GROWTH IN BIOINSPIRED SCAFFOLDS

Marco A. Fielder (1, 2), Arun K. Nair (1, 2)

(1) Materials Science and Engineering
University of Arkansas
Fayetteville, AR, USA

(2) Institute for Nanoscience and Engineering
University of Arkansas
Fayetteville, AR, USA

INTRODUCTION

Current research has begun to investigate combining the techniques of tissue scaffolds and ultrasound stimulation to enhance bone growth [1-4]. However, these studies have mainly focused on how ultrasound interacts with the tissue and a lack of understanding remains in how the ultrasound wave energy distribution occurs within the scaffold, which will also affect the response of tissue to mechanical stimulation. This study hypothesizes that different pore shapes can cause higher or lower wave transmission at constant porosity. It is also hypothesized that the bioinspired scaffold from Gu et al., which is shown to be more resistant to deformation compared to scaffolds with uniform square or hexagonal pores [5], can maintain a high ultrasound transmission to enhance cell growth compared to pore geometries of uniform shape. This would be useful for addressing the issue of designing a scaffold structure with a high structural integrity that also does not impede tissue growth.

METHODS

In this study, we use finite element method (FEM) simulations and experiments with 3D-printed scaffolds composed of Acrylonitrile butadiene styrene (ABS) as a proof of concept to predict the effect of pore shape and wave signal frequency on acoustic wave scattering and transmission in porous scaffolds at constant porosity. The pore shapes studied are solid, square, hexagon, and a bioinspired geometry as shown in Figure 1.

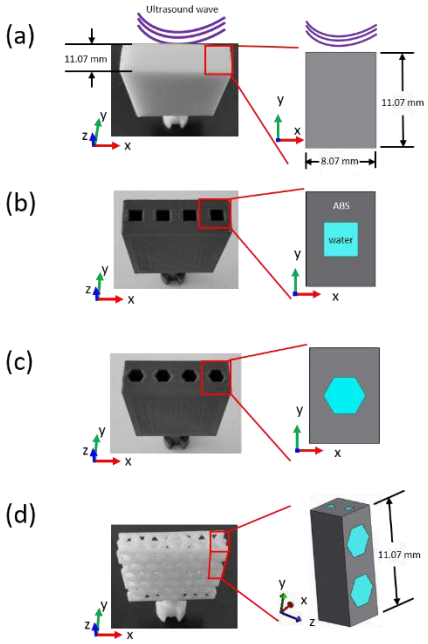

Figure 1: The scaffold structures studied are shown in the center of the figure. On the left side of the figure are the experimental scaffolds made from the unit cell, and on the right side of the figure are the finite element models made from the scaffold unit cell. The scaffold pore structures are (a) solid, (b) square, (c) hexagonal, (d) and bioinspired.

We predict the ultrasonic transmission and visualize solid displacements as the wave propagates, with the simulations performed using FEBio [6]. The ultrasound signal is a single sinusoidal pulse at frequencies of 1, 2.25, 5, 7, and 10 MHz with an amplitude of 1 μm. The transmission T is calculated as the amplitude of the transmitted wave divided by the amplitude of the input wave. An exponential curve is fitted to the transmission data points using Equation 1, which experiments has shown to be the relationship between transmission and frequency [7]. In Equation 1, α_o and η are fitting coefficients, f is the wave frequency, and d is the distance the wave travels and is 11.07 mm.

$$T = e^{-[\alpha_o d(2\pi)^{\eta}]f^{\eta}} \quad (1)$$

For the experiments the ABS scaffold fabrication is carried out using the 3D printing capabilities of the University of Arkansas Mechanical Engineering Department while the ultrasonic testing is conducted using Olympus Immersion ultrasonic transducers connected to a JSR DPR500 DUALPulser/Receiver and a Tektronix TBS 1000B oscilloscope.

The bone cell growth algorithm used is from Byrne et al. [8] and is written in MATLAB. For the growth simulations, the pores of the scaffold are filled with granulation tissue and the structure undergoes compression at 2 MPa. The simulations are also performed on the scaffold structures while also receiving compression and ultrasound stimulation at a frequency of 1 MHz. The scaffold is modeled as an isotropic solid while the granulation tissue is modeled as a biphasic material of an isotropic solid and Newtonian fluid. Initially, the granulation tissue is randomly seeded at 1% with mesenchymal stem cells (MSCs). These stem cells can then proliferate or differentiate into fibroblasts (fibrous tissue), chondrocytes (cartilage), or osteoblasts (bone) based on the mechanical stimulus.

RESULTS

First we performed FEM simulations of ultrasound waves propagating in the scaffolds to choose an appropriate scaffold structure, which was then confirmed by experiments. From Figure 2 (a), we find in both simulations (solid lines) and experiment (dashed lines) the hexagonal pore and bioinspired scaffolds show a significantly larger wave transmission compared to the square pore shapes. Figure 2 (b) shows the color plots of the normalized solid displacements as a wave propagates through the scaffolds and shows that the angle of the pore surfaces allows a higher transmission of the ultrasound wave and produces a more nonuniform wavefront in the hexagonal and bioinspired scaffolds compared to the square scaffolds.

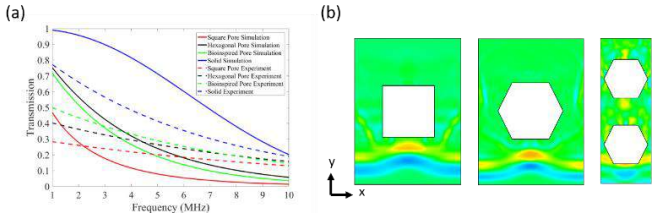

Figure 2: (a) Transmission versus frequency in different porous samples in simulations and experiments. (b) Normalized solid displacements in the pore shapes studied at a time of 6 μs. The wave signal frequency is 1 MHz.

Next we performed the cell growth simulations on the porous scaffolds. From Figure 3 we find the square scaffolds show the fastest bone growth while the bioinspired scaffolds show the slowest. Ultrasound waves have a negligible effect (less than 1%) on the bone growth in the hexagonal and bioinspired scaffolds since their higher wave transmission means that less wave energy is transferred to the cells to stimulate differentiation. In contrast, the lower wave transmission in the square scaffolds means more wave energy is transferred to the stem cells to produce approximately 2% more bone tissue after 60 days as seen in Figure 4. Some shortcomings of the cell growth model are that it does not account for variables such as nutrient transfer, scaffold degradation, or cell apoptosis.

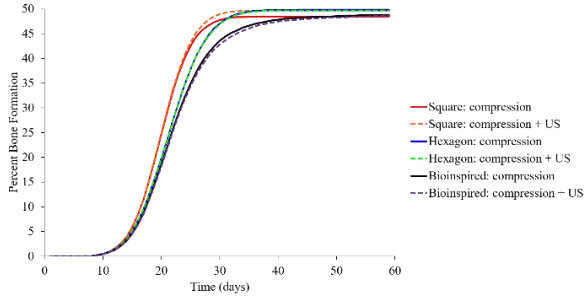

Figure 3: Percent bone formation over time for different scaffold geometries with and without ultrasound (US) stimulation.

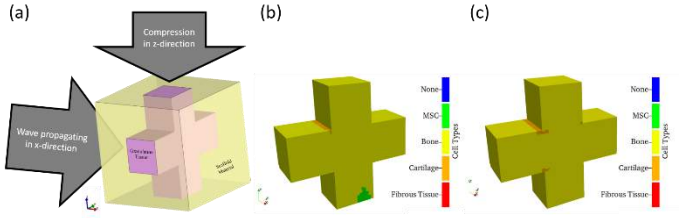

Figure 4: (a) Square pore scaffold with mechanical stimulation. Also shown is the cell distribution in the granulation tissue at day 60 while: (b) under compression, (c) under compression and ultrasound stimulation.

DISCUSSION

The results of this study show that the pore shape of the scaffold affects the ultrasound transmission even when porosity is constant, and that the bioinspired scaffolds can allow as much as 67% greater ultrasound wave transmission at 1 MHz wave frequency when compared to scaffolds with square pores. Additionally, finite element simulations give insight into how pore shape affects the ultrasonic transmission. The cell growth simulations in this study further show that while the bone tissue growth in the bioinspired scaffolds is slow, it can produce amounts of bone tissue comparable to the square and hexagonal scaffolds. The results of this study are important for designing bioinspired tissue scaffold geometries to maximize ultrasound wave penetration to enhance mechanical stimulation for tissue growth.

ACKNOWLEDGEMENTS

MF and AKN would like to thank support from 21st Century Professorship grant from Department of Mechanical Engineering, University of Arkansas and the resources from the Arkansas High Performance Computing Center.

REFERENCES

[1] Loving, J., Fielder, et al., *J Nondestructive Eval*, 37:43, 2018.
[2] Zhao, L., et al., *Applied Acoustics*, 153:102-109, 2019.
[3] Grabec, T., et al., *Wave Motion*, 92:102417, 2020.
[4] Aliabouzar, M., et al., *Biomed Mater*, 13. 2018.
[5] Gu, Y., et al., *Comp Methods in Biomech and Biomed Eng*, 21:703-711. 2018.
[6] Maas, S.A. et al., *J Biomech Eng-T Asme*, 134:011005, 2012.
[7] Chen, W et al., *J Acoust Soc Am*, 114:2570-2574, 2003.
[8] Byrne, D.P., et al., *Biomaterials*, 28:5544-5554, 2007

DO GLYCOSAMINOGLYCANS ACT AS A STRUCTURAL CONSTITUENT OF THE SCLERAL TISSUE?

Hamed Hatami-Marbini, Mohammad Pachenari

Department of Mechanical and Industrial Engineering
University of Illinois at Chicago
Chicago, Illinois, USA, Email. hatami@uic.edu

INTRODUCTION

The sclera delivers stable support to keep the optical process unaffected during intraocular pressure (IOP) variations and eye movements [1]. The microstructural components in the extracellular matrix (ECM) are accountable for scleral macroscopic behavior [2]. Fibrillar collagen is a significant load-bearing constituent of the extracellular matrix (ECM) of the sclera. Several studies of the structural components and mechanics of scleral ECM have explored collagen fiber effects, however, there have been fewer studies about the role of glycosaminoglycans (GAGs) [3]. GAGs are of pivotal importance because of their multiple biological functions and pathological processes [4]. The changes in the posterior sclera ultrastructure, arrangement, and biomechanical properties increase vulnerability to vision diseases, especially in elderlies [5].

The goal of this study was to perform a set of the experiments, including the effects of preconditioning, displacement rate, and stress relaxation, to thoroughly examine how GAGs contribute to sclera viscoelasticity. We treated scleral specimens by chondroitinase ABC enzyme and removed chondroitin/dermatan sulfate GAGs. Then, we studied whether the tensile mechanical behavior of the strips was affected because of GAG depletion. The sclera strips were divided into four control/no-GAG comparison group based upon applying two displacement rates and the presence or absence of the preconditioning step in the experimental protocol. Four-step stress-relaxation testing with 5% strain increments was used to characterize the posterior porcine sclera mechanical response. The experimental results indicated that a significant alteration in the sclera tensile stress-relaxation characteristics after the enzymatic modification, i.e. the GAGs play a significant role in the mechanical response of the sclera.

METHODS

The strip specimens (5 mm × 20 mm) were dissected from the posterior region (nasal-temporal direction) of fresh porcine eyeballs, obtained daily from a slaughterhouse. To remove all the sulfated GAGs, specimens in no-GAG groups were treated enzymatically in 0.125 U ml-1 Chondroitinase ABC [6]. The buffer solution contains 50 mM Trizma base, pH 8.0, with 60 mM sodium acetate and 0.02% BSA. The treatment process lasted for 18 hours and the samples were gently agitated during this period. Another group of specimens, represented as the control group, treated in the buffer solution but without the enzyme. Alcian Blue staining with a pH of 1.0 was employed to validate the successful removal of the sulfated GAGs.

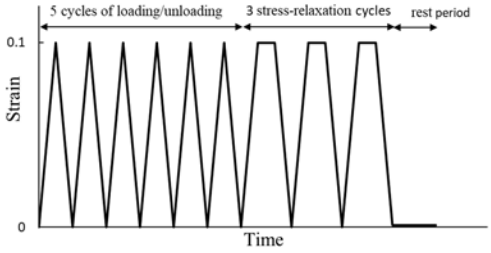

Figure 1: Precondition scheme before running final stress relaxation for 1 mm/min displacement rate.

We used two different displacement rates (0.2 mm/min and 1 mm/min) and performed the mechanical experiments with and without preconditioning of the samples. Thus, four sets of No GAG and control groups were considered, i.e. 1) displacement rate of 0.2 mm/min without preconditioning, 2) displacement rate of 1 mm/min without preconditioning, 3) displacement rate of 0.2 mm/min with

preconditioning and 4) displacement rate of 1 mm/min without preconditioning. The specimens in the preconditioned groups were initially preconditioned with five cycles of loading/unloading followed by three one-minute long relaxation cycles as shown in Figure 1. For the stepwise stress-relaxation tests, strains were applied to the scleral samples in 5% strain increments and were held for 30 minutes after each increment. The process was repeated four times and until the total applied strain as 20%. The stress was calculated by dividing the measured force by the initial cross-sectional area and the strain was defined as the ratio of the length change in each loading step and the reference length. The equilibrium modulus was defined as the variation in two successive relaxed stress to the strain increment.

RESULTS

The histochemical staining images, Figure 2, confirmed that GAGs were successfully removed from the samples. In the displacement rate effect comparisons, the higher rates exhibited higher stresses, especially at higher strains. In comparing the preconditioning load on the scleral biomechanical properties at two different displacement rates, the preconditioning caused a significant increase in the elastic modulus of the sclera in the control and No GAG groups.

Figure 3 shows the effect of GAG removal on the tensile response of porcine sclera. This figure also shows the effects of the loading displacement rate effect on the experimental results. It is seen that without preconditioning and independent of displacement rates and strain levels, scleral strips in the control group had significantly lower elastic modulus than samples in the No GAG group. The GAG removal did not have any significant effect on the elastic modulus of preconditioned specimens.

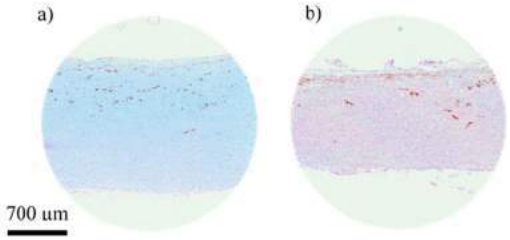

Figure 2: Alcian blue stain representing sulfated GAGs, indicating the successful removal of the GAG after enzyme treatment; a) a scleral sample immersed in buffer solution; b) a scleral sample digested in Chondroitinase ABC solution.

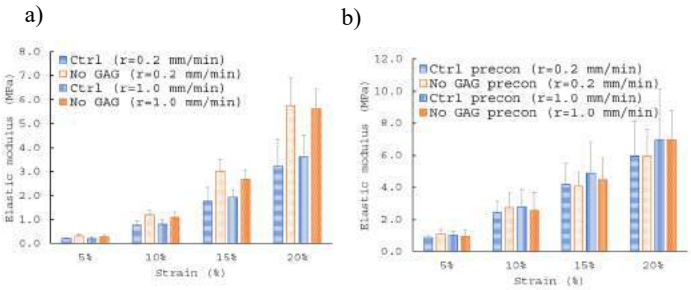

Figure 3: The variation of equilibrium elastic modulus following GAG removal for a) not preconditioned and b) preconditioned scleral samples. The bars represent the standard deviations.

DISCUSSION

The posterior sclera is an important load-bearing tissue around the optic nerve head (ONH). It is known that the majority of the lamina cribrosa (LC) displacement occurs in the ONH peripheral region, which may affect the signal transmission to the brain and subsequently the vision [7]. Therefore, it is essential to explore if there is a significant alteration to the scleral stiffness if there is a change in the GAG content of the tissue. In the present work, we characterized the scleral mechanical behavior after GAG depletion and investigated the displacement loading rate and the sample preconditioning effects by performing the uniaxial tensile experiments.

The difference in the stepwise relaxation behavior between control and no-GAG groups (set 1 and 2) was a function of the applied displacement rate and appeared to reduce as the displacement rate increased. Removing GAGs caused stronger tensile properties in experiments that did not initially preconditioned the samples. This is because the absence of GAGs from the tissue increases the friction between collagen fibers and allows them to fuse together forming bigger collagen fibers. In contrast, when the preconditioning step was used, the tensile stress values did not significantly change because of GAG removal. This is because an earlier stiffening of samples would occur during the precondition step because of significant fiber recruitment and reorientation. Considering the in-vivo loading condition of the sclera, using uniaxial tensile tests was a limitation of this study since we did not characterize scleral material properties under a physiological condition. We also note that, although our results showed that the majority of GAGs were removed, some residual GAGs still existed in the samples; these remaining GAGs might have affected the experimental results. Despite these limitations, our results showed that GAGs as a non-collagenous component of the tissue significantly contribute to the mechanical response of the sclera in tension. Improving the current knowledge about the complex GAG-collagen interaction in the sclera ECM may further help researchers recognize the underlying mechanisms causing significant damage to the ONH.

ACKNOWLEDGEMENTS

The authors would like to acknowledge the support in part by National Science Foundation: Grant No. 1636659 and NIH R21 EY030264.

REFERENCES

[1. Boote, C., et al., *Scleral structure and biomechanics.* Progress in retinal and eye research, 2019: p. 100773.
2. Myers, K.M., et al., *The in vitro inflation response of mouse sclera.* Experimental eye research, 2010. **91**(6): p. 866-875.
3. Hatami-Marbini, H. and M. Pachenari, *The contribution of sGAGs to stress-controlled tensile response of posterior porcine sclera.* Plos one, 2020. **15**(2): p. e0227856.
4. Clark, S.J., et al., *Mapping the differential distribution of glycosaminoglycans in the adult human retina, choroid, and sclera.* Investigative ophthalmology & visual science, 2011. **52**(9): p. 6511-6521.
5. Coudrillier, B., et al., *Effects of peripapillary scleral stiffening on the deformation of the lamina cribrosa.* Investigative ophthalmology & visual science, 2016. **57**(6): p. 2666-2677.
6. Hatami-Marbini, H. and M. Pachenari, *On influence of sulfated glycosaminoglycans on tensile properties of posterior sclera.* Mechanics of Soft Materials, 2020. **2**(1): p. 1-10.
7. Sigal, I.A., J.G. Flanagan, and C.R. Ethier, *Factors influencing optic nerve head biomechanics.* Investigative ophthalmology & visual science, 2005. **46**(11): p. 4189-4199.

HETEROGENOUS EXPRESSION OF LONG NON-CODING RNA REGULATES VASCULAR SMOOTH MUSCLE ADHESION STRENGTH AND PHENOTYPE

J. Mayner (1), A. Kumar (1), P. Beri (1), V. Lo Sardo (2), A. Torkamani (2), K. Baldwin, A.J. Engler (1,3)

(1) Bioengineering,
University of CA San Diego
La Jolla, CA, USA

(2) The Scripps Research Institute
La Jolla, CA, USA

(3) Sanford Consortium for Regenerative Medicine
La Jolla, CA, USA

INTRODUCTION

Single nucleotide polymorphisms (SNPs) within the 9p21 locus have the strongest correlation with coronary artery disease (CAD) [1]. However, the 9p21 locus is a non-coding region, making its connection to CAD enigmatic. 9p21 SNPs affect vascular smooth muscle cells (VSMCs) contractility [2], which during CAD switch from a contractile phenotype, responsible for regulating vascular tone, to one more synthetic, which is more proliferative and migratory. Using induced pluripotent stem cells (iPSCs) derived from patients homozygous for risk (R/R) or non-risk (N/N) variants along with knock out cells (R/R KO), iPSCs are differentiated into VSMCs **(Figure 1A)** to study how variants alter phenotype. We have designed a microfluidic device with the aim of separating VSMCs into synthetic and contractile phenotypes to study the mechanism through which 9p21 variants alter phenotype. We hypothesize variable expression of lncRNA within a patient population drives heterogeneous gene expression resulting in variable penetrance of a synthetic phenotype that can be identified by adhesion strength.

METHODS

RNA Sequencing was performed on iPSC derived VSMCs from R/R and N/N patients as well as R/R KO and N/N KO and hierarchical clustering was performed to group cell lines based on similarity in integrin expression **(Figure 1B).** Microfluidic channels were designed **(Figure 1C)** to expose cells to an acute shear stress varied by adjusting the volumetric flow rate, following Equation 1. VSMCs were seeded in the device, allowed to adhere, and then exposed to acute shear stress, with the population that detach collected at the outlet (weakly adherent population, WA) and the cells that did not detach (strongly adherent population, SA) collected after disassociation with TrypLE. The percentage of cells that detached were subsequently analyzed. Post sorting, WA and SA populations were seeded onto gelatin for morphological analysis or onto gelatin coated polyacrylamide gels for traction force microscopy (TFM).

Equation 1: Shear Stress in Microfluidic Device

$$\tau = \frac{6\mu Q}{wh^2} \qquad (1)$$

$\tau = shear\ stress$
$\mu = viscocity$
$Q = volumetric\ flow\ rate$
$w = channel\ width$
$h = channel\ height$

RESULTS

All differentiated VSMCs stained positive for smooth muscle cell markers, calponin and SM22α **(Figure 1A),** but there were significant differences in size and morphology between R/R and non-risk patients as well as within a R/R population. RNA sequencing analysis revealed R/R VSMCs had reduced collagen binding integrin expression compared to other genotypes **(Figure 1B).** Fluid flow in the device is laminar and shear stress across the surface of the device is uniform, as confirmed by COMSOL simulations **(Figure 1D).** When cells are exposed to uniform shear stress, a greater percentage detached for both R/R patients compared to R/R KO and N/N **(Figure 1E)** which correlated with genotypic differences in size, specifically R/R cells are smaller than both R/R KO and N/N **(Figure 1F)**. When VSMCs are sorted using the microfluidic device, we found the WA are smaller and more circular than SA, for all genotypes, and there were fewer cells populating the WA fraction for the R/R Patient 1 KO line compared to the R/R Patient 1 **(Figure 2A).** TFM revealed differences in contractility between the WA and SA populations, with SA exerting greater tangential strain energy **(Figure 2B).** RNA Sequencing of WA and SA

populations will reveal differential gene expression and potential mechanisms through which these phenotypic differences arise.

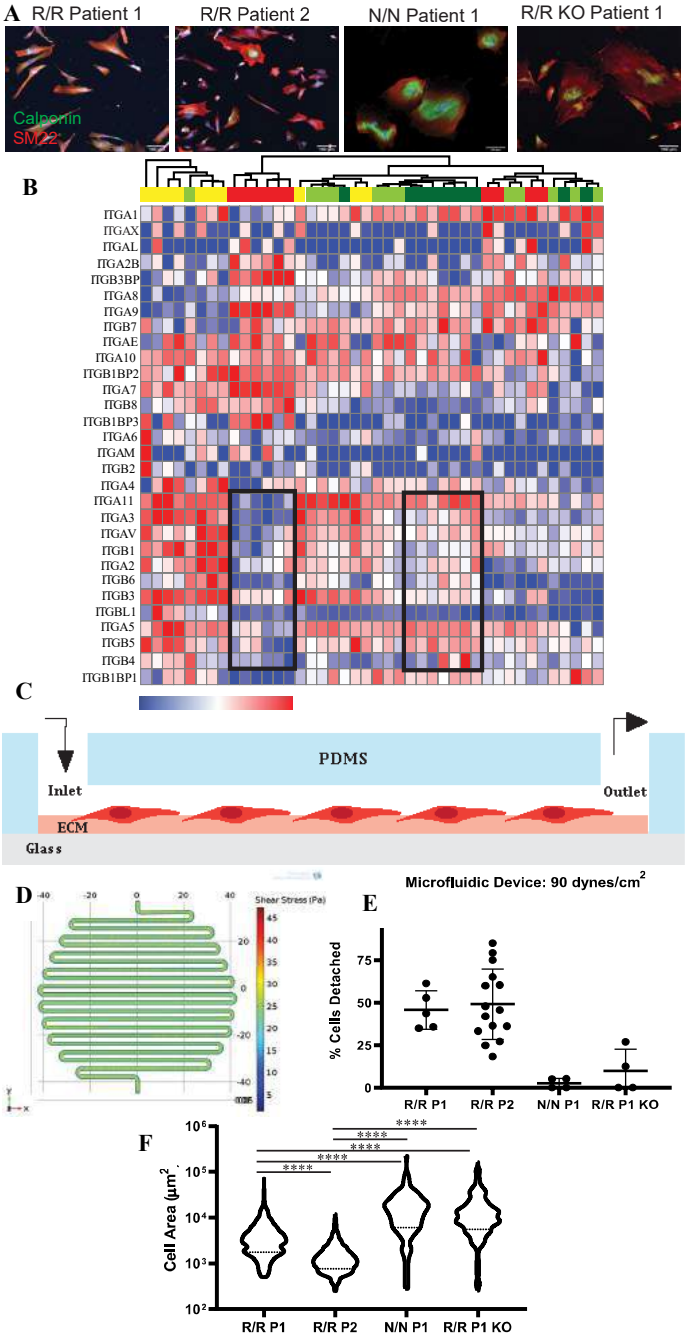

Figure 1: (A) Immunofluorescent staining for VSMC markers of cells differentiated from R/R, N/N and R/R KO iPSCs. **(B)** RNA sequencing of VSMCs clustered by similarity in integrin gene expression. **(C)** Schematic of the microfluidic device used to sort cells into WA and SA populations using shear stress. **(D)** Heatmap of shear stress across the channel's surface generated using a COMSOL simulation. **(E)** Percentage of cells that detach when exposed to a shear stress of 90 dynes/cm^2. **(F)** Cell area measurements of VMSCs for all cell lines.

In preliminary qPCR data, the WA also express more ANRIL, an associated lncRNA, compared to SA, suggesting that it plays a role in regulating VSMC adhesion and promotes a synthetic phenotype.

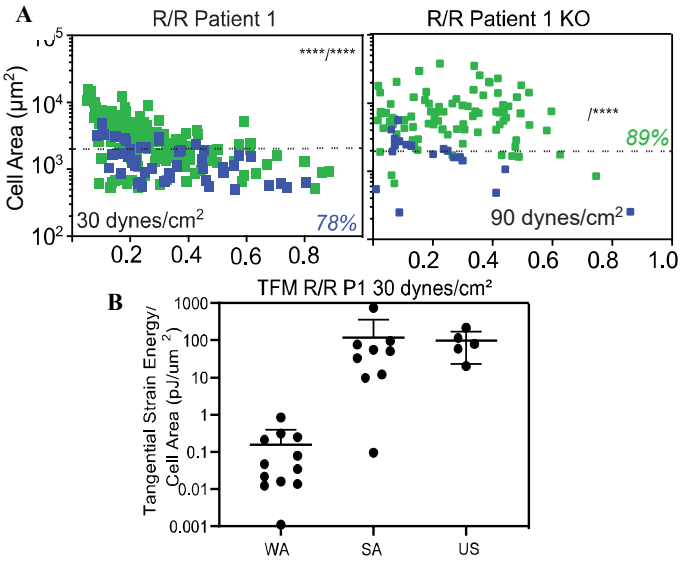

Figure 2: (A) Cell area and circularity of WA and SA populations for R/R Patient 1 sorted at 30 dynes/cm^2 and R/R Patient 1 KO sorted at 90 dynes/cm^2. **(B)** TFM contractility measurements for WA, SA, and unsorted R/R cells.

DISCUSSION

While VSMCs differentiated from every genotype expressed SMC markers **(Figure 1A)**, the differences in size and morphology between patients **(Figure 1A, F)** as well within a risk population suggested the presence of synthetic and contractile phenotypes. The differences in collagen binding integrin gene expression between genotypes **(Figure 1B)** were accompanied by functional differences in adhesion strength, with a greater percentage of cells detaching for R/R patient derived VSMCs **(Figure 1E)**. Such differences in adhesion suggest the R/R patients possess a less prevalent contractile phenotype population and more prominent synthetic population. The microfluidic device was able to sort patient iPSC derived VSMCs into distinct subpopulations, with WA cells being smaller and more circular, morphology indicative of synthetic phenotype, while SA are larger and more spread, indicative of a contractile phenotype **(Figure 2A).** TFM also revealed the SA are more contractile than WA **(Figure 2B)**. With contractile and synthetic phenotypes sorted from a single patient population, the mechanism through which VSMC phenotype is regulated can be more precisely studied using RNA sequencing and biochemical assays such as PCR. This work provides new perspectives on VSMC phenotype heterogeneity regulated by non-coding loci that contribute to CAD.

ACKNOWLEDGEMENTS

National Institutes of Health (NIH) grants R01AG045428 (A.J.E.), UL1RR025774 and U01HL107436 (K.K.B.), and U54GM114833 (A.T.). NIH grants T32HL105373 (J.M) and T32AR060712 (A.K.) and the ARCS/Roche Foundation Scholar Award Program in the Life Science (A.K.) provided trainee support. National Science Foundation grant 1763139 (A.J.E.) and graduate fellowship program (A.K., P.B.) also provided support.

REFERENCES

[1] Schaub, M. et al. *Genome Res*. 22, 1748-1759, 2012. [2] Lo Sardo, V., et al. *Cell*, 175,1796-1810, 2018.

CONTRACTILE PERPENDICULAR LATERAL PROTRUSIONS FACILITATE MYOFIBROBLASTIC EXPANSION

Abinash Padhi (1), Edna Cukierman (2), Klaus M. Hahn (3), Rakesh K. Kapania (4), Amrinder S. Nain (1)

(1) Department of Mechanical Engineering
Virginia Tech
Blacksburg, VA, USA

(2) Cancer Biology Program
Fox Chase Centre
Philadelphia, PA, USA

(3) Department of Pharmacology
University of North Carolina Chapel Hill
Chapel Hill, NC, USA

(4) Department of Aerospace and Ocean Engineering
Virginia Tech
Blacksburg, VA, USA

INTRODUCTION

Fibroblasts get activated into myofibroblasts during acute wound healing and this is accompanied with the inward deformation of collagenous rich extracellular matrix (ECM) by application of contractile forces. This myofibroblastic activation process is pivotal to physiological instances such as developmental process, wound healing. However, this process is also key to pathological instances such as chronic inflammation and fibrosis-related diseases such as the solid epithelial cancer[1,2]. The contractile tumor like microenvironment observed in such cases, known as desmoplasia, are characterized by aligned ECM fibers which are shown to be detrimental for patient outcomes. Cancer associated fibroblasts (CAFs) are activated fibroblasts and are responsible for the remodeling of the ECM fibers into aligned configuration. This expansion of desmoplasia can further activate the naïve fibroblastic cells into CAFs thereby perpetuating a cyclic process of desmoplastic expansion. However, it is still unclear as to how cells polarized along anisotropic fibers can exert these contractile forces as the commonly understood notion suggests restricted probing in lateral direction[3]. In this study[4], we thus use anisotropic fibers generated through STEP technique (Spinneret based Tunable Engineered Parameters) to identify the formation of a new structure we termed perpendicular lateral protrusions (PLPs) and also report the forces exerted by them. We demonstrate that cell spreading across multiple fiber configuration is facilitated by these contractile structures that deflect the fibrous ECM inwards.

METHODS

Human mesenchymal stem cells (hMSCs i.e. fibroblastic naïve) derived from human bone marrow (Lonza) were used in this study and cultured at 37˚C and 5% CO_2. Polystyrene nanofiber scaffolds (~250nm) were generated using the previously established STEP technique[5]. Immunostaining was performed using rhodamine phalloidin for actin and primary antibodies mouse total paxillin and rabbit anti-phospho FAK. Cell forces were computed using Nanonet Force Microscopy (NFM). Graphpad PRISM was used for ANOVA statistical tests.

RESULTS

As cells are suspended on anisotropic fibers, they stretch onto multiple fibers by extension of lateral protrusions. We observed this structure initiate from thin filamentous filopodia resembling structure which we termed as twine and is it matures, it becomes a force exerting structure as can be seen (Fig 1i). We also observed that these PLPs form not only in the planar geometry but also are capable of forming in 3D, which we captured by creating a 3D scaffold stack (Fig 1ii).

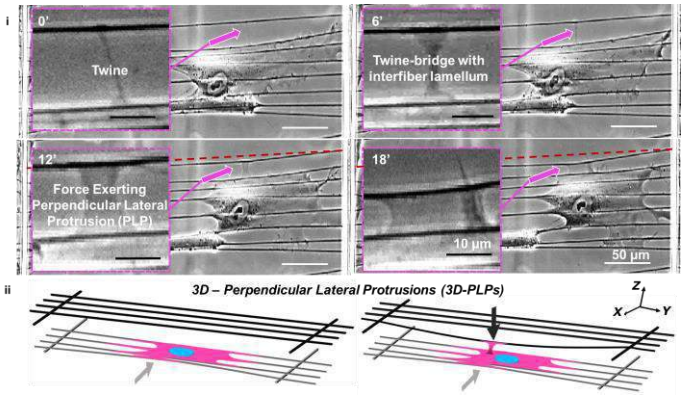

Figure 1: (i) Example case of cell forming PLP through the initiation of twine on anisotropic fibers (ii) Cartoon exhibiting the 3D nature of the PLPs. Adapted from Ref [4].

Our observations suggest 7 distinct steps involved in the formation of a force exerting perpendicular lateral protrusion (PLPs) (Fig 2i). As cells are suspended on anisotropic fibers, actin ruffles along the side of cell body give rise to filamentous twines that swing freely in 3D (i) to attach to neighboring fibers. After engagement to adjacent fiber in a matter of seconds (ii), a lamellum grows from the base of twines (iii). This gives rise to secondary twines (iv) one of which attaches to the neighboring fiber establishing a twine bridge (v). Interfiber lamellum grows along the railings of this bridge (vi) and the majority of these structures that attach perpendicularly initially, develop into force exerting PLPs that deflect the neighboring fiber inwards (vii). Interestingly, the force exerting PLPs are mostly perpendicular while the twines that do not form PLPs have a wider angle of attachment to neighboring fiber. Two example cases using phase contrast images of PLP formation are shown (Fig 2ii).

To investigate the role of fiber architecture in perpetuating the formation of these force exerting PLPs, we constructed fiber scaffolds of different architectures: anisotropic, hexagonal, angled and crosshatch. While higher aspect ratio of cells resulted in greater number of twines formed per cells, it was seen that only the anisotropic fiber arrangement was the most conducive to PLP formation, thereby suggesting the importance of fiber architecture.

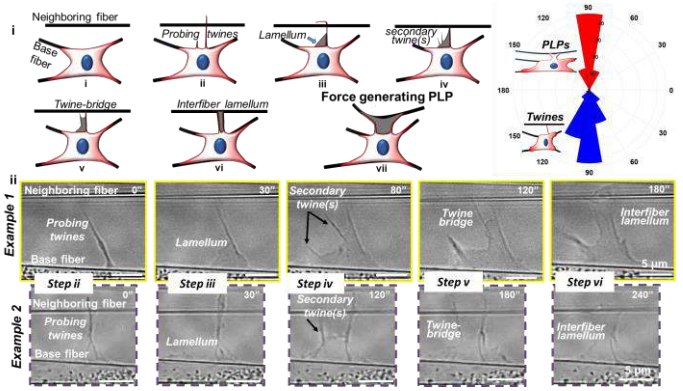

Figure 2: (i) Discreet steps in formation of force exerting perpendicular lateral protrusions shown by cartoons. Polar histogram shows that lateral protrusions are majorly perpendicular as opposed to twines with a wider distribution of angle of attachment (ii) Two example cases of the various steps involved in PLP formation. Adapted from Ref [4].

We next quantified the forces exerted by twines and PLPs using NFM. We observed that twines exert low forces and the mature PLPs exert high forces with sharp increase observed at 10µm width of the PLPs. The forces are computed by assuming the force vectors along the curvature of the PLPs as shown (Fig 3) and by modeling the fibers as beams with fixed-fixed boundary condition. The difference between a finite element model prediction and the experimentally observed fiber deflection is minimized to compute the forces.

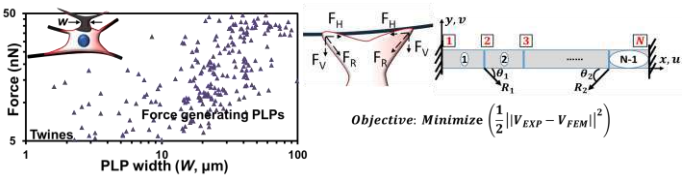

Figure 3: Forces exerted by twines and PLPs measured using NFM. Forces increase with increase in PLP width with a sharp increase observed around 10 µm width. Schematic representation of the mechanics model of NFM. Adapted from Ref [4].

Similarly, we utilize NFM to study the forces exerted by cells attached to different number of fibers. Through fixed staining, we observed the cytoskeletal arrangement of actin stress fibers and compute the average angles subtended. From paxillin staining, it is observed that the focal adhesion clusters are located at either ends of cell, so NFM uses forces originating at the ends of cells along the stress fibers (Fig 4i-iii). With increase in number of fibers a cell is attached to, the total forces exerted increases (Fig 4iv) while the migration velocity decreases (Fig 4v).

DISCUSSION

We demonstrate for the first time, fibroblastic cells form contractile force-generating 3D-PLPs originating all along the cell body. Our experimental observations suggest a new role of anisotropic environments in activating naïve fibroblasts into contractile activated myofibroblastic cells through 3D-PLP formation. We achieve this by generation of different fiber architectures and show that cellular polarity is not the governing factor in such activation. Further, these activated cells can remodel the microenvironment through extending the 3D PLP structures thereby providing the necessary contractile forces necessary for desmoplastic expansion.

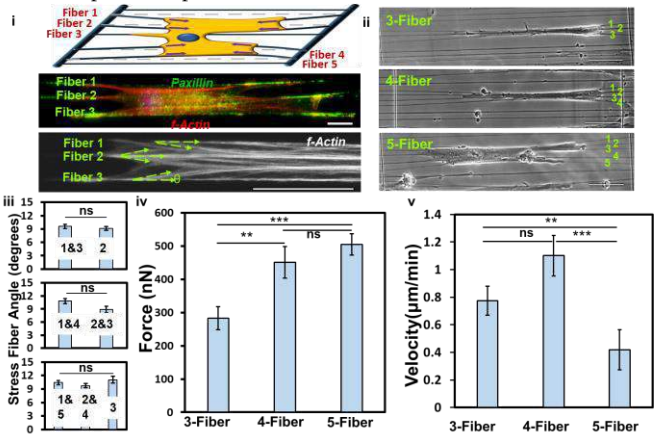

Figure 4: (i) Cell suspended on multiple fibers. Actin (red) and paxillin (green) is observed through immunostaining (ii) Example phase images of cells suspended on 3 fibers, 4 fibers and 5 fibers (iii) Actin stress fiber angles formed by cells on different fiber categories. Force vectors are along these stress fibers (iv) Magnitude of forces exerted by cells increase with the number of fibers, as computed using NFM (v) Increase in number of fiber attachments lead to decrease in migration velocity of cells. Adapted from Ref [4].

ACKNOWLEDGEMENTS

This work is supported by National Science Foundation (1762634) to ASN.

Reference:

[1] B. Hinz, G. Gabbiani, *Curr. Opin. Biotechnol.* **2003**, *14*, 538.

[2] B. Hinz, D. Mastrangelo, C. E. Iselin, C. Chaponnier, G. Gabbiani, *Am. J. Pathol.* **2001**, *159*, 1009.

[3] K. M. Riching, B. L. Cox, M. R. Salick, C. Pehlke, A. S. Riching, S. M. Ponik, B. R. Bass, W. C. Crone, Y. Jiang, A. M. Weaver, K. W. Eliceiri, P. J. Keely, *Biophys. J.* **2015**, *107*, 2546.

[4] A. Padhi, K. Singh, J. Franco-Barraza, D. J. Marston, E. Cukierman, K. M. Hahn, R. K. Kapania, A. S. Nain, *Commun. Biol.* **2020**, *3*, 1.

[5] A. S. Nain, M. Sitti, A. Jacobson, T. Kowalewski, C. Amon, *Macromol. Rapid Commun.* **2009**, *30*, DOI 10.1002/marc.200900204.

TARGETED HEATING OF MITOCHONDRIA GREATLY AUGMENTS NANOPARTICLE-MEDIATED CANCER CHEMOTHERAPY

Jiangsheng Xu[1,2], Xiaoming He[1,2*]

(1) Fischell Department of Bioengineering,
University of Maryland
College Park, MD, USA

(2) Department of Biomedical Engineering,
The Ohio State University,
Columbus, OH, USA

INTRODUCTION

Cancer is the second leading cause of mortality globally[1,2]. Various nanoparticles have been developed to improve the efficacy and safety of chemotherapy, photothermal therapy, and their combination for treating cancer. However, most of the existing nanoparticles are low in both subcellular precision and drug loading content (< ~5%), and the effect of targeted heating of subcellular organelles on the enhancement of chemotherapy has not been well explored. Here, we report a hybrid Py@Si-TH nanoparticle to first target cancer cells overexpressed with the variant CD44 via its natural ligand HA on the outermost surface of the nanoparticle before cellular uptake, and then target mitochondria after they are taken up inside cells. In addition, the nanoparticle is ultra-efficient for encapsulating doxorubicin hydrochloride (DOX) to form Py@Si-TH-DOX nanoparticle. The encapsulation efficiency is ~100% at the commonly used low feeding ratio of 1:20 (DOX:empty nanoparticle), and >80% at an ultrahigh feeding ratio of 1:1. In combination with near infrared (NIR, 808 nm) laser irradiation, the tumor weight in the Py@Si-TH-DOX treatment group is 8.5 times less than that in the Py@Si-H-DOX (i.e., DOX-laden nanoparticles without mitochondrial targeting) group, suggesting targeted heating of mitochondria is a valuable strategy for enhancing chemotherapy to combat cancer.

METHODS

Synthesis of Nanoparticles. Polypyrrole (Py) conductive polymer was encapsulated inside silica nanoparticles by a modified reverse microemulsion method. First, Triton X-100 (2 mL), hexanol (10 mL), and cyclohexane (2.4 mL) were mixed together for 30 min. A total of 600 μL of Py in DI water (5 mg/mL) was then added into the mixture and stirred at room temperature for 1 hour. Afterward, 120 μL of ammonium hydroxide (28 wt%) and 200 μL of TEOS were added consecutively and the sample was stirred at room temperature for 24 h to form the Py-embedded silica (Py@Si) nanoparticles. Then, 40 μL of APTMS and 10 μL of TEOS were added and stirred overnight. Lastly, the sample was added into 30 mL of ethanol to terminate the reaction. The resultant Py@Si-NH_2 nanoparticles were cleaned and collected by centrifuging at 13,000g for 10 min and washing with ethanol and DI water for 3 times, respectively. To further modify the nanoparticles, the mitochondria-targeting ligand TPP-COOH ((3-carboxyethyl)triphenylphosphonium bromide was prepared according to previously reported procedure [3]. Then, 167 mg of the TPP-COOH was treated with EDC·HCl (120 mg) and sulfo-NHS (120 mg) in 5 mL of DMSO and stirred at room temperature for 1 h before being added to the solution of Py@Si-NH_2 (150 mg) in 15 mL of DI water and 30 μL of triethylamine (TEA). The mixture was stirred at room temperature for 24 h and the resultant Py@Si-T nanoparticles were cleaned and collected by centrifuging at 13,000g for 10 min and washed with ethanol and DI water 3 times, respectively. Finally, the Py@Si-TH nanoparticle was synthesized by mixing the Py@Si-T nanoparticles (5 mg/mL) with HA (1 mg/mL) and stirring at room temperature for 3 h, and collected by centrifuging at 13,000g for 10 min. DOX-laden nanoparticles were made by mixing DOX and empty nanoparticles at various ratios in weight. The ratio of 1:10 (DOX:empty nanoparticles) was used for cell and animal studies.

All data was reported as mean ± standard deviation (s.d.) from at least three independent experiments. Student's t-test (unpaired and two-tailed) was used to compare two groups of independent samples. One-way analysis of variance (ANOVA) with Dunnett's post hoc analysis was used for multiple comparison (when more than two groups compared). In all cases, a p value less than 0.05 was considered to be statistically significant. All statistical analyses were carried out with Graphpad Prism 7.0.

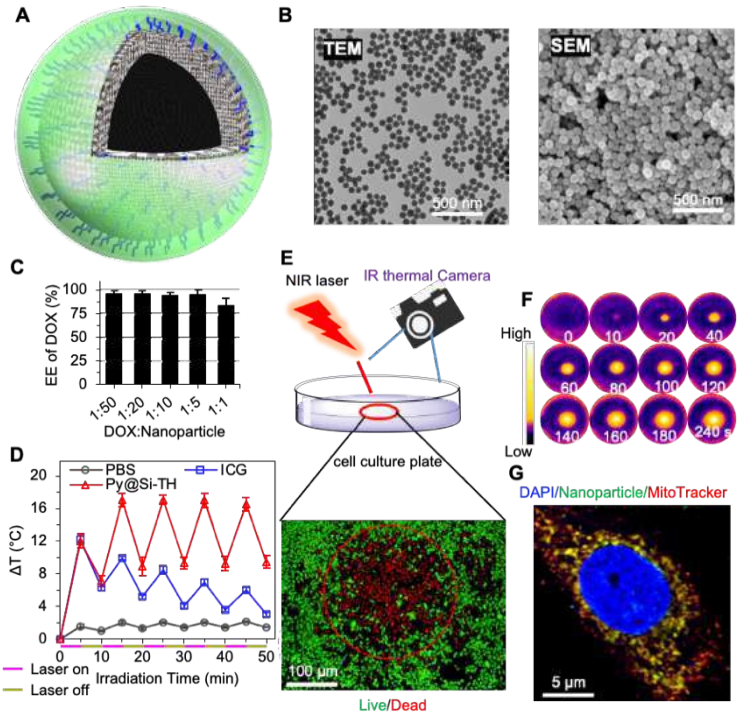

Fig. 1. Nanoparticles enabled ultra-efficient drug encapsulation and targeted heating of mitochondria.

RESULTS

The multi-functional nanoparticle is synthesized using polypyrrole (Py) conductive polymer and mesoporous silica, and further modified with triphenylphosphonium (TPP) and hyaluronic acid (HA) sequentially on the surface (**Fig. 1A**), exhibiting spherical morphology with ~70 nm in diameter (**Fig. 1B**). The nanoparticles can be used to encapsulate DOX in an ultra-efficient manner with simply mixing, ~100% of the DOX could be encapsulated in the nanoparticle when the feeding ratio is from 1:50 to 1:5 (DOX:nanoparticle) (**Fig. 1C**). **Fig. 1D** shows the photothermal effect of nanoparticles. The nanoparticle is highly stable compared with that of indocyanine green (ICG) within 5 cycles of NIR laser irradiation. The cells attached on Petri dish were first treated with nanoparticles for 4 h and washed with pure medium, then irradiated with NIR laser. The temperature of the cells was monitored by infrared thermal camera (**Fig. 1E,F**) and followed with live/dead staining (**Fig. 1E**), demonstrating the photothermal effect of the nanoparticle after taking up inside cells. The subcellular co-localization study, shown in **Fig. 1G,** indicate the targeted accumulation of the nanoparticles in mitochondria. The ivis imaging (**Fig. 2A,B**) and the NIR-mediated thermal imaging (**Fig. 2C**) studies demonstrate the tumor targeting capability and photothermal effect of nanoparticles *in vivo*. Interestingly, the combination of Py@Si-H-DOX nanoparticles (with no mitochondria targeting capability) and NIR laser irradiation (*i.e.*, the Py@Si-H-DOX+L treatment) is not as effective as the Py@Si-TH-DOX+L treatment; tumors from the Py@Si-H-DOX+L group is ~8.5 times more than that from the Py@Si-TH-DOX+L group on average (**Fig. 2D,E**). These data indicate that targeted heating of mitochondria significantly enhances the *in vivo* antitumor efficacy of the nanoparticle-mediated chemotherapy.

DISCUSSION

In summary, we demonstrate the ability to augment the effectiveness of chemotherapy using non-toxic, triple (tumor, cell, and mitochondria) targeting Py@Si-TH-DOX nanoparticles in combination with NIR laser irradiation. By embedding polypyrrole (Py) inside silica and decorating on the surface sequentially with triphenylphosphonium (TPP) and hyaluronic acid (HA), we fabricated a nanostructure with superb anticancer effect through precisely targeted heating of the mitochondria of cancer cells upon NIR laser irradiation. In addition, the nanoparticle is ultra-efficient for encapsulating doxorubicin hydrochloride (DOX) because of the π-π stacking interaction between Py and DOX. The encapsulation efficiency is ~100% at the commonly used low feeding ratio (in weight) of 1:20 (DOX:nanoparticle), and >80% at an ultrahigh feeding ratio of 1:1. Upon NIR laser irradiation, the temperature of both *in vitro* cancer cells and *in vivo* tumors loaded with Py@Si-TH nanoparticles can be elevated by ~10 °C within 1 min for mild hyperthermia. When combined with NIR laser irradiation, our Py@Si-TH-DOX nanoplatform can reduce tumor weight by 8.5 times compared to the Py@Si-H-DOX nanoplatform that is devoid of TPP, indicating the crucial role of the mitochondria-targeted heating for enhancing nanoparticle-mediated chemotherapy. This study suggests that targeted heating of subcellular organelles (*e.g.*, mitochondria) is a valuable strategy to enhance cancer chemotherapy.

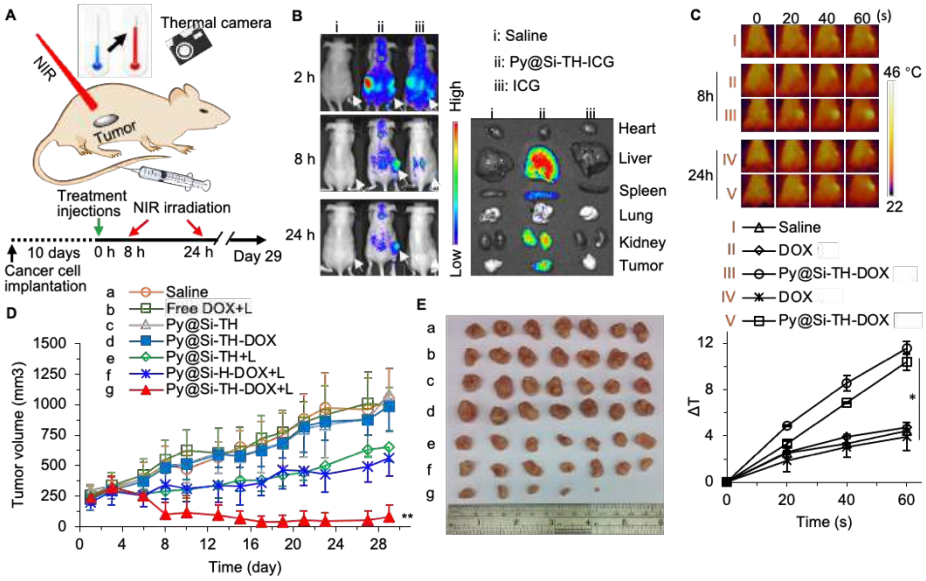

Fig. 2. Nanoparticle-mediated targeted heating of mitochondria is a valuable strategy to enhance chemotherapy *in vivo*.

ACKNOWLEDGEMENTS

This work was partially supported by grants from American Cancer Society (ACS #120936-RSG-11-109-01-CDD) and NIH (R01CA206366) to X.H., and Pelotonia post-doctoral Fellowship to J.X.

REFERENCES

[1] Mayer, E. L. et al., *J. Clin. Oncol.,* 34. 3369, 2016.
[2] Xu, J. et al., *Nature Nanotech*., 14. 388, 2019.
[3] Xu, J. et al., *Small,* 10. 3750, 2014.

SB³C2021
Summer Biomechanics, Bioengineering and Biotransport Conference
June 14-18, Virtual

IMPACT OF FLOW RATE ON HIGH FREQUENCY FLOW INSTABILITIES IN INTRACRANIAL ANEURYSMS, WITH IMPLICATIONS FOR WALL VIBRATION

David A. Bruneau (1), Mehdi Najafi (1), Thangam Natarajan (2), Kristian Valen-Sendstad (2), David A. Steinman (1)

(1) Department of Mechanical & Industrial Engineering
University of Toronto
Toronto, Ontario, Canada

(2) Department of Computational Physiology
Simula Research Laboratory
Oslo, Norway

INTRODUCTION

Intracranial aneurysms (IAs) are present in over 3% of the human population [1,2], and those with IAs have approximately a 30% lifetime risk of rupture [3]. While some general risk factors are established, such as aneurysm size and family history [3], there is a need for more specific rupture risk predictors based on the actual mechanics of rupture [4][5].

IAs are known to produce sound [6] at frequencies in the range of 150-800 Hz [6,7] which is thought to be caused by vibration of the aneurysm wall [7]. Aneurysm wall vibration could be a harbinger of deleterious wall remodeling, leading eventually to rupture [7,8]. However, such vibration has not been examined with modern fluid structure interaction (FSI) simulations, possibly because previous FSI software was unable to simulate high-frequency vibration, or previous thinking that blood flow in aneurysms is laminar. Recently, high-fidelity CFD has made it clear that high-frequency flow instabilities can exist in brain aneurysms [9,10]. In addition, new FSI tools are emerging which are capable of modelling aneurysm wall vibration [11].

It is uncertain what type of flow instability may cause aneurysm wall vibration. It is possible that vibration is driven by increasing turbulent kinetic energy, or by vortex-shedding at Reynolds numbers (Re) close to the onset of instability [12]. Previous studies have measured wall vibration in IAs at discrete flow rates [5]; however, it is possible that resonant frequency peaks could be missed by considering discrete flow rates. It is thought that a slowly increasing flow rate in an aneurysm CFD model may show all types of flow instability possible in a specific aneurysm geometry, and that the wall may vibrate most, not necessarily at the highest flow rates, but at the flow rates which induce more spectral power at frequencies close to a certain mechanical resonance frequency of the wall. Therefore, the objective of this preliminary study was to subject three aneurysm geometries to a slowly increasing flow rate to generate all possible types of flow instability, as a precursor to FSI simulation of the aneurysm wall vibration.

METHODS

We considered three aneurysm geometries in the current study, which have previously been shown to exhibit stable flow (Case 8), mildly unstable flow (Case 9) and highly unstable flow (Case 16) [10]. The computational fluid dynamics (CFD) meshes were generated using the Vascular Modelling Toolkit, with roughly 70,000 tetrahedral elements in each case (Figure 1a). Blood kinematic viscosity and density were 0.035 mPa-s and 1 g/cm^3 respectively. The simulations were run using a high-fidelity, finite-element CFD solver [13]. A medium temporal resolution of 5600 steps per cardiac cycle (~5888 steps per second), which has been shown in previous studies to be adequate to capture the main features of the flow [10].

A parabolic velocity profile was specified at the inlet, and zero pressure at the outlets. A linearly increasing flow rate (i.e., a "ramp") was applied to the inlet for a total physical simulation time of 6.7s, with a maximum spatial average inlet velocity of 0.8 m/s for all cases (Figure 1b), or a maximum flow rate of 2.21ml/s, 3.96 ml/s and 4.24 ml/s for Case 8, 9 and 16 respectively, representing twice the cycle-averaged flow rates reported in a previous study [10]. The slope of the ramp, and therefore the length of the simulation, was chosen to result in a maximum variation of 25% in flow rate for the 0.95s interval (the length of a cardiac cycle) required to calculate the spectrograms, at the onset of flow instability. Simulations at steady flow rates of 0.4, 0.5, 0.6, 0.7 m/s with a total simulation time of 1.9s (twice the length of a cardiac cycle) were compared to the ramp simulations.

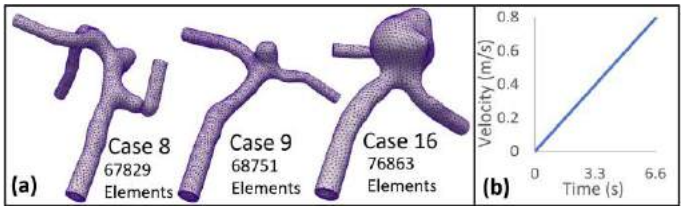

Figure 1: Model inputs: (a) mesh for Case 8, Case 9, Case 16, (b) spatial average inlet velocity as a function of time, for all cases.

Spectrograms of the fluid velocity magnitude were generated to demonstrate the onset and nature of flow instability in the three aneurysm cases, following methods presented previously [9]. Every fourth timestep was used to generate the spectrograms, resulting in a maximum frequency of ~750 Hz (the Nyquist limit). For steady flow, the last 0.95s of the simulation were analyzed, to eliminate the initial transient response.

RESULTS

The spectrograms for Case 9 and Case 16 both exhibited flow instability (Figure 2), while the spectrograms for Case 8 did not display any flow instability during the simulation. In Case 9, stable flow (no frequency content) was observed until Re = 310, with a rapid onset of flow instability after this time and frequencies exceeding 750 Hz observed at Re = 350 (Figure 2a). Prominent bands of power were present at 25-35 and 100-150 Hz, respectively, which rose in frequency with increasing Re. At ~5.25s, the prominent frequency band at 150 Hz widened and remained prominent for the remainder of the simulation. In Case 16, a slightly later onset of flow instability was observed at Re = 340, where very distinct bands appeared until Re = 400 (Figure 2b). Subsequently, the bands became broader and eventually blended, suggesting, as expected, a transition from periodic or near periodic flow (similar to laminar vortex shedding) to more disordered or turbulent-like flow. The ramp spectrograms captured similar spectral qualities to the steady flow spectrograms (Figure 3), however, the ramp slightly delayed the onset of instability due to the positive pressure gradient.

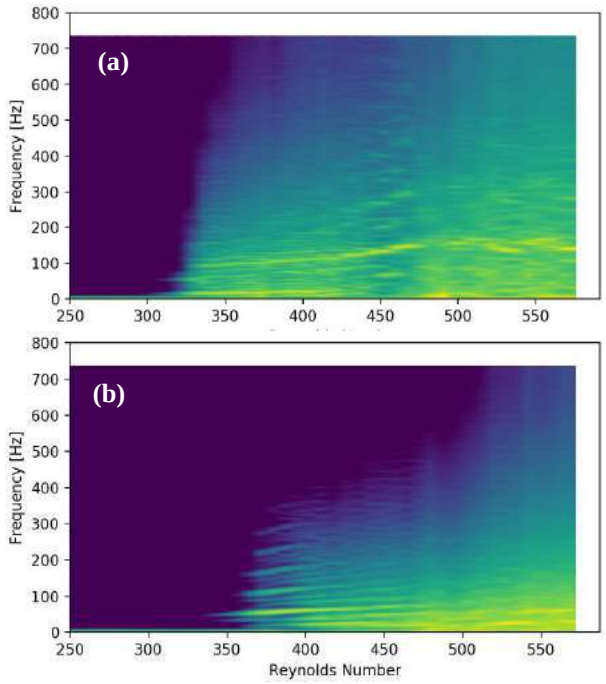

Figure 2: Spectrograms for (a) Case 9 and (b) Case 16, plotted against inlet Reynolds Number, which increased linearly in time.

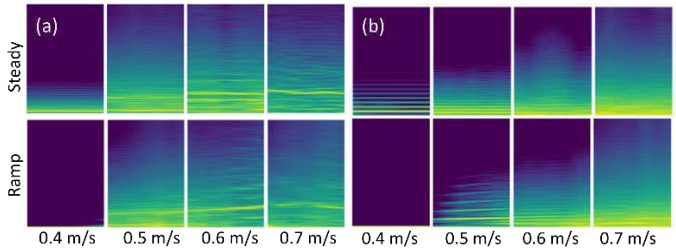

Figure 3: Steady Flow (top row) and Ramp (bottom row) Spectrograms for (a) Case 9 and (b) Case 16, with average velocity indicated. Spectrograms are the length of a cardiac cycle (0.95s).

DISCUSSION

In both Case 9 and 16, the ramped flow rate was found to induce the three major flow phenotypes commonly observed in high-fidelity CFD of aneurysm models: (1) stable flow with no high frequency content, (2) mildly unstable flow with periodic behavior and (3) highly unstable (turbulent-like) flow. While no flow instability was observed in Case 8, instability could of course be induced by prescribing higher, albeit non-physiological, flow rates.

Prominent frequency bands observed in both Case 9 and 16 were both within the range of frequencies of sounds recorded in aneurysm patients (150-800 Hz) [6,7]. Of course, not all aneurysms produce sound, consistent with Case 8 in the current study, which had stable flow. Balasso et al. used an experimental reconstruction of an IA to measure wall vibration and found that flow rate had little influence on the frequency content of the wall response. It was found that the wall vibrated at frequencies of 40-60Hz and 255–265Hz [5]. Intermediate flow rates (1.4 ml/s) were found to have high frequency vibration (260 Hz) at higher amplitudes than higher or lower flow rates [5].

The mechanism of vibration in aneurysm sounds is not clear. Additionally, the exact type of flow which causes aneurysm sounds is also not clear. The results of Balasso et al. suggest that higher flow rate does not necessarily cause higher amplitude of high-frequency wall vibration, suggesting that wall vibration is increased by flow with increased frequency content close to the high-frequency mode of the wall. Therefore, Case 16 in the current study could experience a higher amplitude of vibration at flow velocities immediately after the onset of flow instability, if the wall has a resonant frequency close to one of the prominent frequency bands and those bands have higher power than the more broadband turbulent-like flow near the end of the simulation. In Case 9, it is possible that strong vibration could occur if one of the wall resonant frequencies is close to the single prominent band at 100-150 Hz. However, if one of the main wall resonant frequencies is higher in either case (400 – 800 Hz), wall vibration may simply increase with flow rate, due to the increase in broad-band high frequency content in both cases.

To help characterize the influence of flow rate on wall vibration amplitude, we are currently repeating these Ramp simulations using a monolithic fluid structure interaction (FSI) solver, which was previously shown to predict the presence of wall vibration under steady flow conditions [11].

ACKNOWLEDGEMENTS

This work was supported by a doctoral fellowship (to DAB) and grant (to DAS) from the Natural Sciences and Engineering Research Council of Canada. Simulations were supported by priority core hours granted by Compute Canada for their Niagara HPC cluster.

REFERENCES

[1] Vlak MHM et al. Lancet Neurol 2011;10:626–36.
[2] Li M et al. Ann Intern Med 2013;519:514–21.
[3] Korja M et al. Stroke 2014;45:1958–63.
[4] Valen-Sendstad K et al. Am J Neuroradiol 2014;35:536–43.
[5] Balasso A et al. Biomed Tech 2019;64:275–84.
[6] Kurokawa Y et al. Stroke 1994;25:397–402.
[7] Ferguson GG. J Neurosurg 1970;33:485–97.
[8] Kosugi Y et al. Stroke 1983;14:37–42.
[9] Natarajan T et al. J Biomech 2020;110:109977.
[10] Khan MO et al. Am J Neuroradiol 2015;36:1310–6.
[11] Souche A et al. 6th International Conference on Computational and Mathematical Biomedical Engineering: 2019, p. 714–7.
[12] Foreman JEK et al. Circ Res 1970;XXVI:583–90.
[13] Mortensen M et al. Comput Phys Commun 2015;188:177–88.

BIOINSPIRED 3D CULTURE IN NANOLITER CORE-SHELL HYDROGEL MICROCAPSULES ISOLATES HIGHLY PLURIPOTENT HUMAN IPSCS

Jiangsheng Xu, James G Shamul, Xiaoming He*

Fischell Department of Bioengineering,
University of Maryland
College Park, MD, USA

INTRODUCTION

Human induced pluripotent stem cells (iPSCs) are ideal for developing personalized medicine[1]. However, the spontaneous differentiation of human iPSCs under conventional 2D and 3D cultures for expansion, may compromise their quality for further use. Therefore, strategies to isolate and expand high-quality human iPSCs is critically needed. Here, we developed a biomimetic microencapsulation method to isolate and culture high-quality human iPSCs. This is inspired by the natural proliferation and development of blastomeres into early blastocyst where the pluripotent embryonic stem cells-containing inner cell mass (ICM) are enclosed in a semipermeable hydrogel shell known as the zona pellucida (Zona) during early embryonic development. Blastomere cluster-like human iPSC clusters were encapsulated in the core of microcapsules with a semipermeable Zona-like hydrogel shell and subsequently cultured to form the pluripotent ICM-like cell spheroids. This microencapsulation provides a biomimetic, miniaturized, and proliferation-only microenvironment for expanding iPSCs, which significantly improves their quality as indicated by the high expression of pluripotent markers Nanog, OCT4, SOX2, and SSEA-4. The ICM-like iPSC spheroids are capable of maintaining high pluripotency even after transferred into 2D culture. Collectively, our bioinspired approach has great potential for generating high-quality human iPSCs, which are essential for human iPSC-based personalized disease modeling and regenerative medicine.

METHODS

Human iPSC culture. Human iPSCs (DF19-9-11T.H) from WiCell (Madison, WI, USA) were used in this work. For 2D culture, the iPSCs were maintained in StemFlex medium (ThermoFisher Scientific, Waltham, MA, USA) in Matrigel (Corning, Corning, NY, USA)-coated 6-well plates (1×10^6 cells in 1.5 mL of medium per well) with medium being changed daily. For 3D suspension culture, uncoated petri dish and StemFlex medium with 10 μM Rock inhibitor (RI, Selleck Chemicals, Houston, TX, USA) were used.

Microfluidic devices. The non-planar PDMS-based microfluidic device was fabricated as described previously[2]. The 2% alginate and 1% HA solutions were made by dissolving the purified alginate and HA in 0.9% saline, respectively, followed by filtering through a 0.22 μm filter (Merck Millipore, Cork, IRL). The 2% alginate solution was used as the shell fluid. The fluid in the core (1% alginate + 0.5% HA) was made by mixing an equal volume of 2% alginate and 1% HA solutions. A mixture of mineral oil (15 mL), aqueous $CaCl_2$ solution (1.0 g/mL, 1.5 mL), and SPAN80 (93.3 μL) was sonicated for 1 min using a Branson 450 sonifier (22% power) to make the oil emulsion.

Microencapsulation of iPSC clusters. The 2D cultured iPSC colonies were treated with Versene, gathered with gentle washing of the well bottom, and centrifuged for 45 s at 300g. Then, the cells were gently pipetted 5 times into clusters and resuspended in the core solution at 3×10^5 clusters mL^{-1}. All the solutions were injected into the microfluidic device using syringe pumps (Harvard Apparatus, Holliston, MA, USA) to generate microcapsules. Flow rates for core, shell, and oil emulsion fluids were 250 μL h^{-1}, 500 μL h^{-1}, and 5 mL h^{-1}, respectively. The device outlet was submerged in a 50 mL tube containing 30 mL DMEM/F12 medium (ThermoFisher Scientific) to collect the microcapsules on ice. After collecting for 1 h, the microcapsules naturally sunk down to the bottom of the tube. After aspirating the supernatant including oil and 25 mL of medium, the remaining 5 mL of medium with microcapsules was transferred to a new 50 mL tube by pipetting. Thereafter, an equal volume (5 mL) of $CaCl_2$ (200 mM) was added to the tube to further gel alginate in the microcapsule for 45 s. The microcapsules were then rinsed using 25 mL

of DMED/F12 three times and further transferred into a 6-well plate for culture as aforementioned.

Statistical analysis. Each experiment was independently repeated at least three times. All data are presented as mean ± standard deviation (s.d.). One-way analysis of variance (ANOVA) with Turkey's post hoc analysis was used to compare between different groups. All statistical analyses were carried out with the Prism GraphPad Software. A p value less than 0.05 was considered statistically significant.

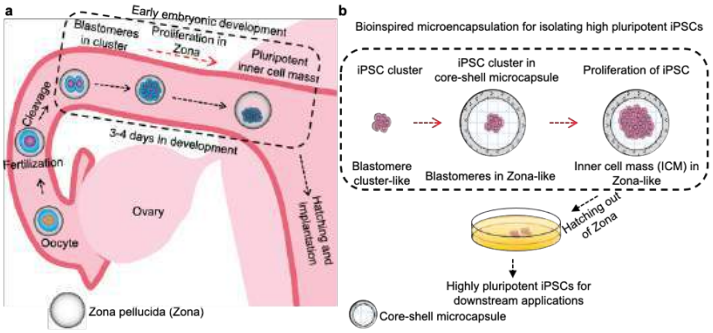

Fig. 1. A bioinspired microencapsulation approach for isolation and culture of high-quality human iPSCs.

RESULTS AND DISCUSSION

As schematically illustrated in **Fig. 1a**, in nature, the ESCs contained in the ICM are developed from blastomeres (e.g., at the 2- to 16-cell stages) via growth/proliferation without aggregation/fusion with blastomeres in any other early embryos[3]. This procedure includes the following key features: 1) encapsulation of a cluster of multiple blastomeres in a nanoliter core that is enclosed in a semipermeable Zona shell, and 2) proliferation of the blastomeres in the miniaturized core for 3-4 days to produce the ESC-containing ICM before hatching out of the Zona shell for implantation. Thus, we hypothesize that a strategy that shares some similarities with the basic steps of the aforementioned procedure in ICM development can be used to isolate/culture the highly pluripotent iPSCs among the conventionally cultured heterogeneous iPSCs (**Fig. 1b**). To test this hypothesis, we generated "blastomere cluster-like" human iPSC clusters and fabricated "Zona-like" core-shell microcapsules with a nanoliter-scale hydrogel core enclosed in a semipermeable alginate hydrogel shell. The non-planar microfluidic device for the bioinspired microencapsulation of human iPSC clusters, together with a schematic illustration of the formation of an iPSC cluster-laden core-shell microcapsule at the flow focusing junction, is shown in **Fig. 2a**. The iPSC clusters are suspended in aqueous core solution containing 0.5% (in weight, by default) hyaluronic acid (HA) and 1% alginate in saline, and the suspension is introduced into the device through Inlet 1 (In1). The microencapsulation of the iPSC clusters in the core enclosed in the semipermeable alginate shell is illustrated in **Fig. 2b**. The "Blastomere cluster-like" iPSC clusters with mostly 3-13 cells per cluster (**Fig. 2c**) were generated by detaching 2D cultured iPSCs and gently pipetting into iPSC clusters. These iPSC clusters were then encapsulated in the "Zona-like" core-shell microcapsules (Figure 2c) using the aforementioned microfluidic device. The microchannel dimensions and flow rates used in this study are given in **Fig. 2d**, which were chosen to achieve a high throughput of the microencapsulation (~150 microcapsules per minute) with

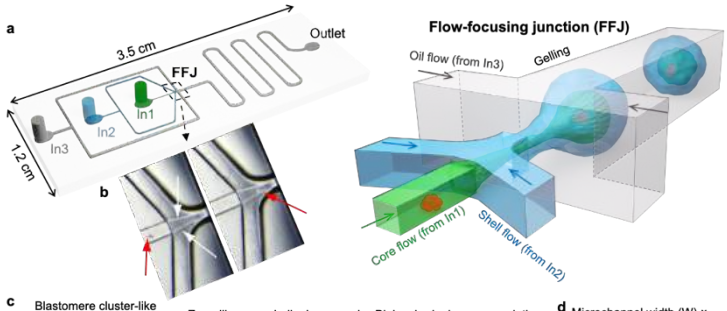

	W×D	Flow rate
Core	100×100	250
Shell	150×150	500
Oil	300×400	5000
gelling	400×400	5000

Fig. 2. Microencapsulation of human iPSC cluster in a Zona-like core-shell microcapsule.

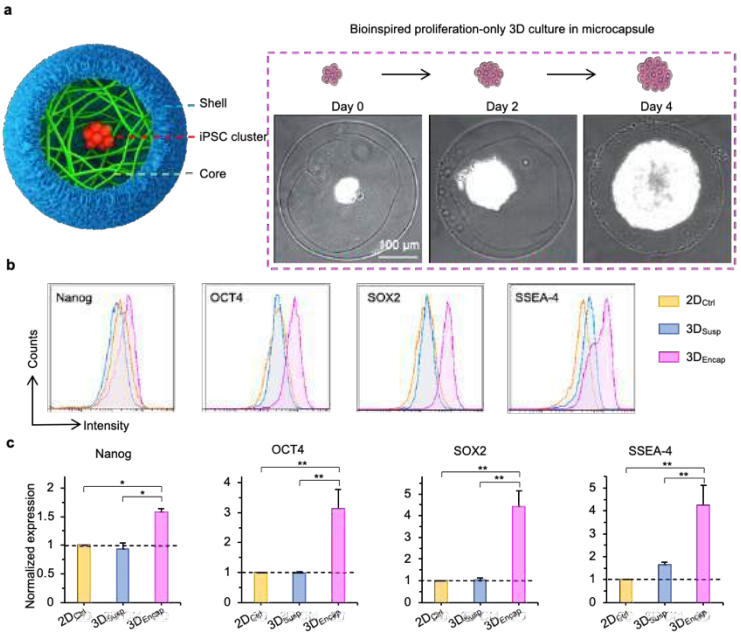

Fig. 3. Bioinspired culture isolates and produces highly pluripotent human iPSC spheroids.

microcapsules less than 400 μm in outer diameter. The microencapsulation approach creates a miniaturized 3D microenvironment for the iPSC clusters to proliferate into "ICM-like" iPSC spheroids. After 4 days of culture, only highly pluripotent iPSCs (20%) can proliferate into spheroids (**Fig. 3a**). The high pluripotency of the iPSCs is further confirmed using flow cytometry analyses (**Fig. 3b**), iPSCs from our bioinspired microencapsulation culture ($3D_{Encap}$) have significantly higher expression of Nanog, OCT4, SOX2, and SSEA-4 than the cells from both conventional 2D and 3D suspension culture methods ($2D_{Ctrl}$ and $3D_{Susp}$). Quantitative analyses showing that expression of in our microencapsulation iPSCs are 1.6-fold, 3.1-fold, 4.4-fold, and 4.2-fold higher than that in 2D iPSCs (**Fig. 3c**).

ACKNOWLEDGEMENTS

This work was partially supported by grants from National Science Foundation (NSF CBET- 1831019) and National Institutes of Health (NIH R01EB023632).

REFERENCES

[1] Rowe, R. G. et al., *Nature Reviews Genetics* 20. 377, 2019.
[2] Agarwal, P. et al., ACS Nano 11. 6691, 2017.
[3] Zhao, S. et al., *Nature Communications* 7. 13306, 2016.

FIBER-GEL COUPLING IN COATED ELASTOMERIC SCAFFOLDS FOR REPLACEMENT HEART VALVES

Shruti Motiwale (1, 2), Madeleine Russell (1,3), Megan Wancura (3), Andrew Robinson (3), Elizabeth Cosgriff-Hernandez (3), Michael S. Sacks (1,2,3)

(1) James T. Willerson Center for Cardiovascular Modeling and Simulation, Oden Institute, University of Texas at Austin, TX, USA

(2) Department of Mechanical Engineering, University of Texas at Austin, TX, USA

(3) Department of Biomedical Engineering, University of Texas at Austin, TX, USA

INTRODUCTION

Gluteraldehyde-treated pericardium has been the most common material for prosthetic heart valves for the past decade. However, it faces several problems, including durability and inconsistent material properties due to biological origins, just to name a few. To address these issues, we are developing a synthetic material for heart valves, consisting of electrospun polycarbonate urethane (ES-PCU) coated with a poly(ethylene glycol) diacrylate (PEGDA) hydrogel. The ES-PCU provides the mechanical structure and function, while the hydrogel helps with biocompatibility. In order to assist with future developmental efforts, we are developing a material modeling approach to predict the mechanical behavior of these materials. Here, we present material models for the fiber mesh, the gel and the composites. Our goal is to identify if there are any interactions between the fiber and the gel.

METHODS

The composite biomaterial was fabricated in two distinct groups: a) aligned fiber meshes, which had a strongly aligned preferred direction, and b) randomly oriented. A comprehensive set of strain-controlled experiments consisting of 9 deformation protocols (Table 1) were conducted using a novel biaxial testing device [1] capable of independent control of all components of the in-plane deformation gradient tensor, including in-plane shear. A maximum extensional deformation of 20% was used for aligned specimens and 37.5% for random specimens. To assist with modeling efforts, similar tests were also performed on the uncoated fiber meshes. Hydrogel isotropic properties were quantified using uniaxial tests. To model the composite biomaterial, we assumed a hyperelastic material model. The total strain energy of the composite was assumed to be given by algebraic sum of the strain energies of its constituents:

$$\Psi = \phi^{g}\Psi^{g} + \phi^{m}\Psi^{m} \quad (1)$$

where, Ψ, Ψ^{g} and Ψ^{m} are the strain energies of the composite, gel and fiber respectively, and Φ^{g} and ϕ^{m} are the volume fractions of the gel and the mesh. Any stress contributions from fiber-gel interactions were ignored at this stage.

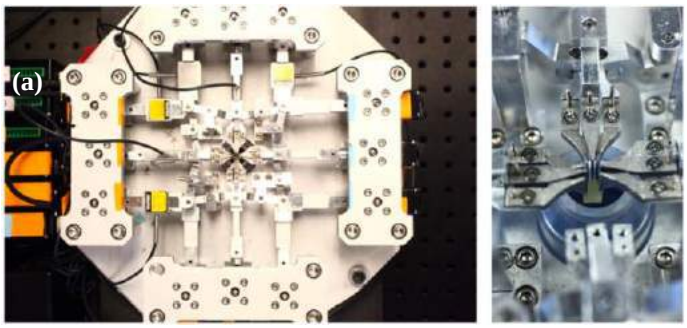

Figure 1 (a): Top view of the testing device showing specimen test area. (b) Close-up view of the mounted specimen.

Table 1: List of experimental protocols and corresponding deformation gradients for aligned specimens.

Extensional Protocols	$\begin{bmatrix}1.2 & 0\\ 0 & 1.2\end{bmatrix}$	$\begin{bmatrix}1.067 & 0\\ 0 & 1.2\end{bmatrix}$	$\begin{bmatrix}1.04 & 0\\ 0 & 1.2\end{bmatrix}$
		$\begin{bmatrix}1.2 & 0\\ 0 & 1.067\end{bmatrix}$	$\begin{bmatrix}1.2 & 0\\ 0 & 1.04\end{bmatrix}$
Shear Protocols	$\begin{bmatrix}1 & 0.3\\ 0 & 1\end{bmatrix}$	$\begin{bmatrix}1 & 0\\ 0.3 & 1\end{bmatrix}$	$\begin{bmatrix}1 & 0.3\\ 0.3 & 1\end{bmatrix}$
Extension and Shear	$F = \begin{bmatrix}1.2 & 0.3\\ 0.3 & 1.2\end{bmatrix}$		

Gel Model: The gel was assumed incompressible and was modeled with a neo-Hookean material model:

$$\Psi^{g} = C_1(I_1 - 3)$$
$$\mathbf{S}^{g} = 2C_1(I_1 - C_{33}\mathbf{C}^{-1}) \quad (2)$$

where, C_1 is a material constant and I_1 is the first invariant of right Cauchy-Green deformation tensor, **C**.

Mesh Model: The mesh model was developed by first modeling the response of a single fiber. We assumed the mesh to be hyperelastic and modeled the uniaxial response of a fiber with an Ogden model:

$$\Psi^f = G\left(\lambda_f{}^a + 2\lambda_f{}^{-\frac{a}{2}} - 3\right) \quad (3)$$

where Ψ^f is the strain energy function, λ_f is the fiber stretch, and G and a are model parameters. Next, the orientation of fibers spread throughout the scaffold was modeled with an orientation distribution function (ODF). The ODF was assumed to be a linear combination of beta distribution and uniform distribution, so that

$$\Gamma(\theta;\ \mu,\sigma,d) = (1-d) * \beta(\theta;\ \mu,\sigma) + \frac{d}{\pi} \quad (4)$$

$$\beta(\theta;\ \mu,\sigma) = \frac{[\omega^{\alpha-1}(1-\omega)^{\alpha-1}]}{\pi B(\alpha,\alpha)},\ \omega = \frac{\theta-\mu+\pi/2}{\pi},\ \sigma = \frac{\pi^2}{4(2\alpha+1)}$$

where, μ,σ are mean and standard deviation of the beta distribution and d is the random distribution parameter, and $B(a,b) = \int_0^1 t^{a-1}(1-t)^{b-1}\,dt$. Finally, the bulk level mesh response was obtained by integrating the fiber response with the ODF for all fiber orientations:

$$\mathbf{S^m} = \int_{-\frac{\pi}{2}}^{\frac{\pi}{2}} \Gamma(\theta) S^f \mathbf{n}\otimes\mathbf{n}\,d\theta \quad (5)$$

where, $\mathbf{S^m}$ is the second Piola-Kirchhoff stress tensor of the mesh, S^f is the fiber stress, $\mathbf{n} = \mathbf{n}(\boldsymbol{\theta})$ denotes the fiber direction and $\lambda_n = \sqrt{\mathbf{n}(\mathbf{Cn})}$, is the stretch along $\mathbf{n}$. This equation has 5 parameters, $G, a, \mu, \sigma,$ and d. These parameters were determined by fitting the model to data from 3 specimens for 5 extensional protocols with varying ratios of maximum stretch along the preferred (PD) and cross-preferred (XD) directions.

Composite Model: The composite model response was obtained by combining Eq. 1 with Eq. 2 and Eq. 4:

$$\mathbf{S} = \phi^g \mathbf{S}^g + \phi^m \mathbf{S}^m \quad (6)$$

$$= 2\phi^g C_1(I_1 - C_{33}\mathbf{C}^{-1}) + \phi^m \int_{-\frac{\pi}{2}}^{\frac{\pi}{2}} \Gamma(\theta) G\left(\lambda_f{}^{a-2} - \lambda_f{}^{-\frac{a}{2}-2}\right)\mathbf{n}\otimes\mathbf{n}\,d\theta$$

We evaluated the validity of Eq. 6 by comparing the model prediction against experimental data for composites for extension and shear protocols. In the absence of interactions, it is expected that the model predictions should match experimental data, whereas if interactions are present, the model is expected to underpredict the data.

RESULTS

The gel response was captured very well by the neo-Hookean model with r^2=0.9809 (Fig. 2).

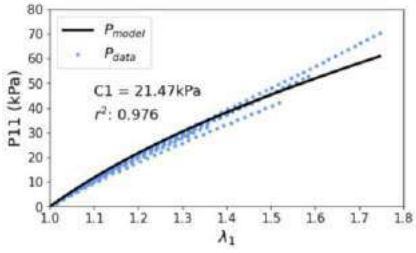

Figure 2: Gel model fit to uniaxial tension data

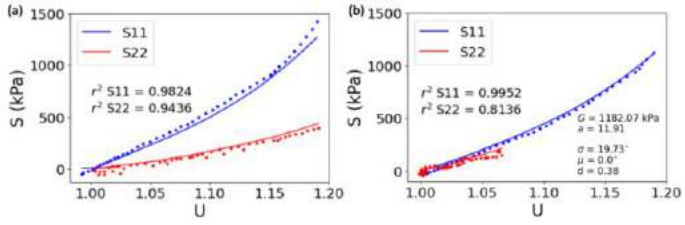

Figure 3: Mesh model fit to extensional protocols for (a) $\lambda_1{:}\lambda_2 = 1{:}1$, (b) $\lambda_1{:}\lambda_2 = 3{:}1$. Dotted line denotes the data, solid line denotes the model fit.

The mesh model was able to accurately capture the response of all mesh specimens for all the extensional protocols (Fig. 3), and yielded the following values for model parameters, $G = 1182.07$ kPa, $a = 11.91$, $\sigma = 19.73°$, $d = 0.38$, and μ was fixed to 0°.

The composite model was able to predict the results for all the extensional protocols with remarkable accuracy (Fig. 4). We also utilized the composite model to predict the results for shear protocols (Fig. 5). The model prediction seemed to slightly underestimate the experimental data implying strong evidence of fiber-gel interactions under these modes.

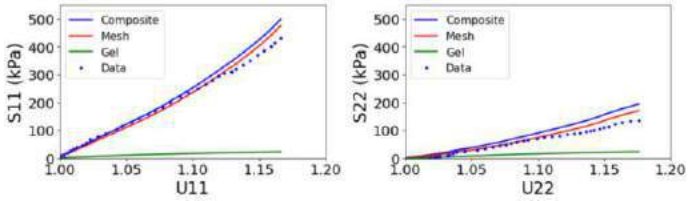

Figure 4: Model prediction for aligned composites for equibiaxial extension. Predicted stress closely matches experimental data, implying that there are no interactions between fiber and gel under extension. The gel contribution is to the total stress is very low.

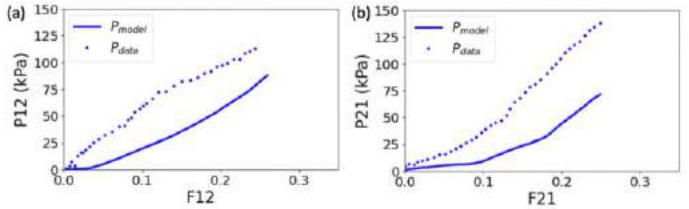

Figure 5: Model prediction for aligned composites for shear protocols (a) F12=0.3, F21=0, (b) F12=0, F21=0.3. The model underpredicts shear stresses, implying strong evidence of fiber-gel interactions under shear modes.

DISCUSSION

The primary goal of this project was to develop a material model that can predict the mechanical behavior of the ES fiber-gel composites under varying loading conditions and to determine if there is any evidence of interactions between the fiber and the gel. Our modeling results suggested that the properties of the mesh can be captured accurately. Furthermore, the composite model predictions under extensional stretches suggested that there is no evidence of interactions under pure extension. However, for shear protocols, the stresses were underpredicted by the model (Fig. 5). This suggested that there are stress contributions from interactions between the mesh and the gel under shear modes. Our assumption is that these interactions are primarily due to fiber rotation and coupling, since we do not see any conclusive evidence of interactions under biaxial extension. Thus, the pseudo-invariant $I_8 = (\mathbf{n}_\alpha.\mathbf{n}_\beta)\mathbf{n}_\alpha.\mathbf{C}\mathbf{n}_\beta$, appears to be a good candidate to capture the coupling phenomenon between fibers oriented at angles α and β. We are currently working on a model with a modified form of I_8 to capture these interactions, based on the model presented in [2].

ACKNOWLEDGEMENTS

NIH/NHLBI R01 HL129077.

REFERENCES

[1] Potter S, et al. J Biomech Eng. 2018;140-5.
[2] Sacks et al., Interface Focus (6.1). 2016; p.20150090.

MIGRATION PATTERNS OF CONTRACTILE CELL FRAGMENTS ON ECM MIMICKING SUSPENDED FIBERS

Abinash Padhi (1), Brooke E. Danielson (2), Deema S. Alabduljabbar (3), Ji Wang (4), Daniel E. Conway (2), Rakesh K. Kapania (5), Amrinder S. Nain (1)

(1) Department of Mechanical Engineering
Virginia Tech
Blacksburg, VA, USA

(2) Department of Biomedical Engineering
Virginia Commonwealth University
Richmond, VA, USA

(3) Department of Biomedical Engineering
University of California, Davis
Davis, CA, USA

(4) Department of Engineering Science and Mechanics
Virginia Tech
Blacksburg, VA, USA

(5) Department of Aerospace and Ocean Engineering
Virginia Tech
Blacksburg, VA, USA

INTRODUCTION

Cytoplasmic fragments or cellular fragments are independent bodies devoid of nucleus capable of exerting forces and sustaining migration long after separation from the parent cell body. Often understood as waste disposal mechanisms, their vital role in intercellular communication based on the cargo enclosed within their membranes such as proteins and RNA transcripts have been recently realized[1]. Their spontaneous emergence as cells migrate through the complex extracellular matrix (ECM) which is fibrous in nature, have also been implicated to be vital in pathological conditions such as in cancer biology[2]. Their potential as important diagnostic and therapeutic tool have been recognized, as for instance, their uptake in murine fibroblasts have led to loss of tumorigenic phenotype[2]. Biophysically, they have also been used as model systems to deduce the role of nucleus in guiding cellular polarity, migration as well as contractility. However, current understanding on fragment mechanobiology is derived from studies on flat, featureless substrates while the native ECM is fibrous. To quantitatively describe fragment biophysics in a more physiologically relevant ECM, we used non-electrospinning Spinneret-based Tunable Engineered Parameters (STEP) technique to generate various fiber architectures: crosshatch, hexagonal and parallel, with each fibrous geometry representing a subset of the in vivo ECM observed under different conditions. Using Nanonet Force Microscopy (NFM)[3,4], we estimate single fragment forces of varying shapes and sizes. On all fiber networks, we document a peculiar oscillatory migration mode, not readily observed on flat. Interestingly, these fragments remain contractile for several hours. Pharmacological ROCK inhibition drastically reduces the oscillatory behavior as well as the contractility. Overall, contextual fiber networks reveal new fragment behaviors, not observed on flat 2D.

METHODS

Suspended fiber networks were generated using our previously established STEP technique[5]. Parallel, crosshatch and hexagonal fiber networks were generated out of 220nm polystyrene fibers. Human mesenchymal stem cells (hMSCs) used were cultured in growth medium at 37˚C and 5% CO_2. Imaging was done in a Zeiss AxioObserver Z1 microscope equipped with incubation. 20x and 63x objectives were used for phase contrast imaging and fluorescent imaging respectively. Immunostaining was performed to stain actin, paxillin and microtubules. Fragment forces were evaluated using customized MATLAB code that minimizes error between computed and experimental fiber deflections. ROCK inhibition was performed by using the drug Y27632.

RESULTS

We observe spontaneous formation of fragments on fibers. Cells suspended on parallel fibers assume a polarized shape and as they stretch along the fibers, the lamellipodial extension pinches off to form a fragment (Fig 1A). Similar mechanism is demonstrated by cells on hexagonal as well as crosshatch fibers to generate fragments (Fig 1B,C). Fragments formed are of different shapes and sizes. We classified them into three main shapes: circular, blob-like and rectangular. Circular fragments are near spherical bodies (AR~1) while blob-like fragments are marked by characteristic blebbing (AR~4). Rectangular fragments are elongated fragments with high aspect ratio (AR~12).

The fragments formed mostly remained stationary. However, the motile fragments demonstrate majorly two main migratory modes: oscillatory and persistent (Fig 2A). In general, fragments move faster on fibers than on flat (Fig 2B). The fragments that moved back and forth about a mean position for at least one cycle were termed as oscillatory

fragments. This oscillatory behavior was conserved across the fiber categories but was not observed on flat. On quantification of time periods of their oscillations, we found them to be independent of fiber architecture (Fig 2C). This behavior is sometimes observed for hours and one example case is shown (Fig 2D). Interestingly, these fragments also extend lateral protrusions that helps them to transition across fibers (Fig 2E). Over time, these fragments rupture reminiscent of cells undergoing apoptosis (Fig 2F).

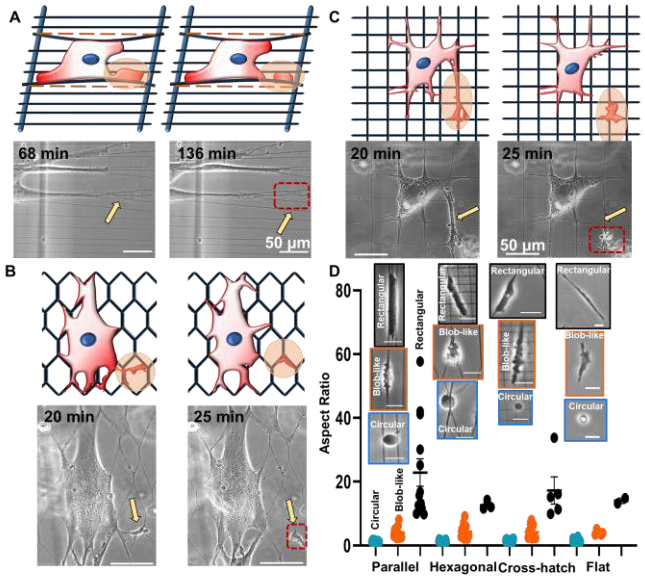

Figure 1: (A-C) Fragment formation by pinching on parallel, crosshatch, and hexagonal scaffolds (D) Aspect ratio of the different shapes (circular, blob-like and rectangular) of fragments formed on all fiber networks as well as flat. Adapted from Ref [6]

On inspection of the cytoskeletal and adhesion components, we found stark differences between fragments and intact cells. The f-actin distribution was diffusive without any dominant stress fibers. Further, the paxillin signal was found distributed across the entire length of fragment as opposed to concentration at the poles of intact cells (Fig 3A). Based on these observations, we modified our previously established NFM technique to measure the forces of contractile fragments (Fig 3B). We introduced distributed loading represented by 10 force vectors. It was found that fragment forces were not correlated with fragment sizes. Furthermore, the maximum force a fragment exerts does not necessarily occur immediately after its separation from the main cell body (Fig 3B inset). On inhibiting the contractility by introducing Y27632, a ROCK inhibitor, we observed reduction in number of small size fragments (Fig 3Ci). It was confirmed with shape analysis that circular fragments were reduced in number whereas the large rectangular fragments were higher in percentage of fragments formed (Fig 3D). Surprisingly, we observed that the oscillatory behavior is completely inhibited in presence of the drug which suggests that the origin of this peculiar motion is driven by the contractility driven changes in polarity.

DISCUSSION

In conclusion, for the first time to the best of our knowledge, we report precise force measurements as well as the migratory behavior of individual fragments of varying sizes and shapes on fiber architectures. The fragments undergo an oscillatory motion exclusive to fibrous environments, which we find to be driven by ROCK based contractility.

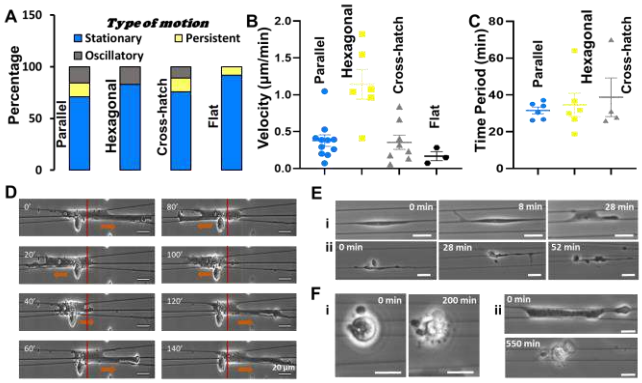

Figure 2: (A) Percentage of fragments exhibiting different migratory modes on the fibers as well as on flat (B) Velocity of the motile fragments on different fibers and on flat (C) Time period of oscillations observed in case of the oscillatory fragments (D) Example case of fragment undergoing oscillations on parallel fibers (E)i,ii Fragments forming lateral protrusions on fibers (F)i,ii Fragments undergoing apoptosis on fibers. Adapted from Ref [6]

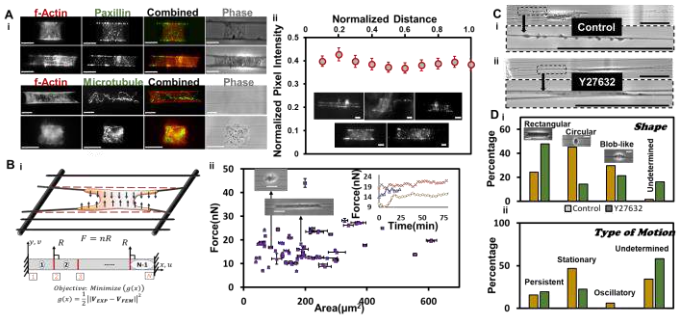

Figure 3: (A)i. Fluorescent images of fragments showing actin, paxillin and microtubules. ii. Intensity analysis shows uniform distribution of paxillin along fragment length (B) NFM used to compute forces exerted by fragments. Distributed loading is utilized in the model. Forces exerted are independent of sizes of fragments. (C) Example cases of fragments formed in control condition as well as in presence of Y27632 (D) ROCK inhibition reduces percentage of smaller fragments formed. Oscillatory motion is completely absent in cases of Y27632 treatment. Adapted from Ref [6]

ACKNOWLEDGEMENTS

This work is supported by National Science Foundation (1762634) to ASN.

Reference:

[1] C. Tricarico, J. Clancy, C. D'Souza-Schorey, *Small GTPases* **2017**, *8*, 220.

[2] P. Vader, X. O. Breakefield, M. J. A. Wood, *Trends Mol. Med.* **2014**, *20*, 385.

[3] A. Padhi, K. Singh, J. Franco-Barraza, D. J. Marston, E. Cukierman, K. M. Hahn, R. K. Kapania, A. S. Nain, *Commun. Biol.* **2020**, *3*, 1.

[4] K. Sheets, J. Wang, W. Zhao, R. Kapania, A. S. Nain, *Biophys. J.* **2016**, *111*, 197.

[5] A. S. Nain, M. Sitti, A. Jacobson, T. Kowalewski, C. Amon, *Macromol. Rapid Commun.* **2009**, *30*, 1406.

[6] A. Padhi, B. E. Daneilson, D. S. Alabduljabbar, J. Wang, D. E. Conway, R. K. Kapania, A. S. Nain, (Under Review)

DEVELOPMENT OF A NOVEL TESTING SYSTEM TO EVALUATE MICROSCALE MECHANICS AT THE VITREORETINAL INTERFACE

Joseph D. Phillips (1), Brittany Coats (1)

(1) Mechanical Engineering
University of Utah
Salt Lake City, Utah, USA

INTRODUCTION

Posterior vitreous detachment (PVD) is a natural process that occurs in 87% of people by 80-89 years of age [1]. PVD results from vitreous liquefaction concurrent with interfacial weakening between the gel-like vitreous and the thin, delicate retina [2]. Complete PVD is typically harmless; however, partial PVD can lead to strong, localized adhesions at the vitreoretinal interface. These lingering adhesions exert traction forces that can cause retinal disruption and vision loss. Despite the critical role of vitreoretinal mechanics in PVD, the mechanical nature of PVD remains unclear. To date, few mechanical studies have been performed at the vitreoretinal interface, and no micromechanical studies exist. In this study, we aim to elucidate mechanisms of PVD by developing a novel magnetic-based micromechanical testing system and protocol that can be used to measure adhesion variability across localized regions of the retina.

METHODS

Whole vitreous with intact retina was dissected from fresh porcine eyes (n=2). Following dissection, a 17.5 mm wide specimen of vitreous and retina was cut from the equatorial region and fixed to a plastic tab using a thin layer of cyanoacrylate adhesive. The tab and specimen were then placed into a 3D-printed fixture with a #0 coverslip glued to the bottom (Figure 1).

Following specimen preparation, 25 µL of 5 mg/mL magnetic microbeads (BM551, Bangs Laboratories, Fishers, Indiana) were injected into the vitreous near the vitreoretinal interface. The microbeads are coated in streptavidin, a protein with an Arg-Tyr-Asp amino acid sequence that mimics the Arg-Gly-Asp receptor domain of fibronectin [3], a common adhesive protein to collagen. Therefore, the surface-modified streptavidin-coated beads can form covalent bonds with vitreous collagen, resulting in tight binding between beads and fibers. Specimens were incubated for 10 minutes following injection to facilitate bead-fiber binding.

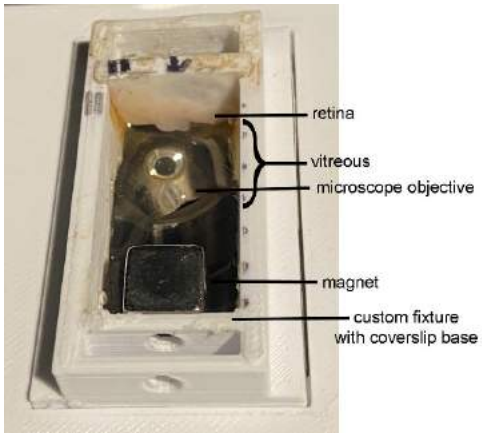

Figure 1: Image of testing system. Retina is fixed to a removable tab and placed inside a custom fixture for imaging.

Vitreous collagen fibers and beads were observed by confocal reflectance microscopy (Olympus FV1000, Olympus Corporation, Tokyo, Japan). Time-series images were captured prior to placement of a 9.51 mm cuboid magnet and every 10 seconds for two minutes after magnet placement. Bead and fiber displacement were tracked using a custom segmentation code in MATLAB (Figure 2). Prior to applying the magnet, a constant linear drift was observed. This linear drift was quantified and subtracted from displacement (Figure 3). The number of bound beads in each image was quantified and defined as beads with <10% relative displacement to adjacent collagen fibers.

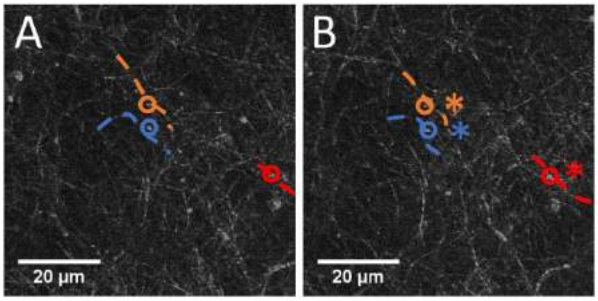

Figure 2: Confocal reflectance microscopy image of beads (circles) and collagen II (dashed lines) displaced 5.49 µm before (A) and after (B) magnet placement (*original bead location). 180X magnification.

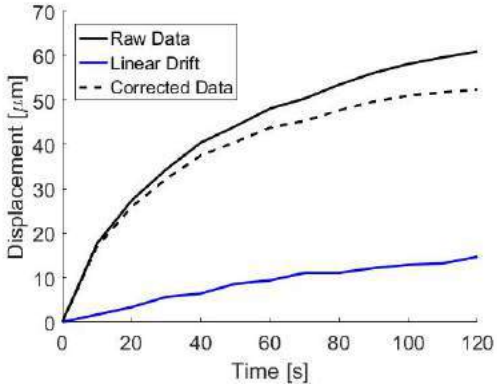

Figure 3: Magnetic displacement data were corrected for linear drift occurring without magnet placement.

The magnetic force exerted on one bead is given by [4]

$$F = \nabla(m_{Sat} \cdot B) \quad (1)$$

where m_{Sat} is the magnetic moment and B is the magnetic field at the bead. The magnetic field for a cuboid permanent magnet is given by

$$B(x) = \frac{B_r}{\pi}\left[\tan^{-1}\left(\frac{ab}{2x\sqrt{4x^2+\phi}}\right) - \tan^{-1}\left(\frac{ab}{2\varphi\sqrt{4\varphi^2+\phi}}\right)\right] \quad (2)$$

where $\phi = a^2 + b^2$, $\varphi = c + x$, and a, b, and c are the height, width, and thickness of the magnet, respectively. B_r, the residual magnetic field of the magnet, is 1.32 T (or 13,200 G) based on manufacturer data. The magnet was placed at an average distance of 26.00 mm from the center of the specimen, giving an approximate magnetic field of 62 G at the center of the specimen and a range of 23-131 G across the specimen. Using the field at the center of the specimen results in a magnetic moment of 8.975 emu/g. The estimated force on a bead at the center of the specimen is 1.03 pN and the potential bead force range is 0.38-2.18 pN, depending on bead location.

RESULTS

Approximately 34.9±8.0% of the beads successfully bound to collagen fibers and were displaced up to 70 µm during application of the magnetic field. The displacement was nonlinear and started to reach equilibrium at two minutes with a percent change of 0.87±0.41% from the previous time point (Figure 4). Within each image, bead displacement variation was small (2.52±1.05 µm), but displacement across image locations varied greatly (47.48±25.57 µm). Variation between specimens was 6.81-25.98 µm, depending on location.

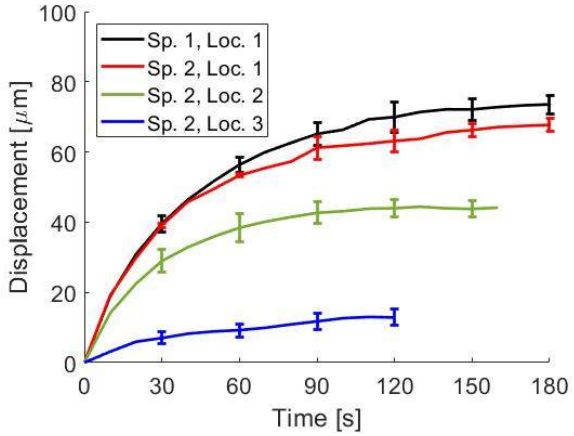

Figure 4: Displacement curves for four locations from two specimens. Error bars represent ±1 standard deviation.

DISCUSSION

In this study, we developed a testing system and procedure to perform micromechanical tests at the vitreoretinal interface. By binding magnetic microbeads to collagen fibers, the localized mechanics of the vitreous and vitreoretinal interface can be elucidated. The system and procedures were successful in binding 35% of the beads to collagen, resulting in approximately 9.21-28.9 pN of force in the imaging window and 0.889 µN of force in the volume of vitreous for beads injected at the center of the specimen. Parameters for confocal reflectance microscopy were carefully optimized to illuminate the highly reflective beads simultaneously with low autofluorescence collagen fibers. Natural linear drift was present in specimens, but this was overcome with application of a sufficiently strong magnet and linear correction of the data.

Bead displacement within an image was minimal, but displacement across imaging locations varied greatly. We observed distinct difference in displacement with visually different densities of collagen. This relationship will be quantified in future experiments. Timing of imaging may also contribute to the differences in displacement. All image locations were captured within 30 minutes of dissection, but as time passes, fluid may disperse across the coverslip, reducing the ease of collagen displacement. To evaluate this, we plan to implement an electromagnet to carefully control the application and magnitude of the magnetic field, and evaluate hysteresis curves over time within single location. While still in the preliminary stages, this novel test system has the potential to provide micromechanical data critical to closing gaps in our knowledge of the mechanisms of PVD. These data will aid in the development of pre-surgical methods to correct imbalances in vitreous liquefaction and interfacial weakening leading to partial PVD and vision loss.

ACKNOWLEDGEMENTS

Support for this work was provided by the University of Utah's 1U4U Innovation Funding Initiative. We acknowledge the Cell Imaging Core at the University of Utah for use of the Olympus FV1000 confocal microscope.

REFERENCES

[1] Hollands et al., *JAMA*, 302:2243–2249, 2009.
[2] Johnson, *Trans. Am. Ophthalmol. Soc.*, 103:537–567, 2005.
[3] Guo and Kaufman, *Biomaterials*, 28:1105–1114, 2007.
[4] Lipfert et al. *Biophys J*, 96:5040-5049, 2009.

PROBING NEUROPEPTIDE VOLUME TRANSMISSION IN VIVO BY A NOVEL ALL-OPTICAL APPROACH

H. Xiong (1), H. Ouyang (1), X. Xu (1), E. Lacin (2), T. Kern (2), D. Kircher (2), X. Li (1), C. Matéo (3), D. Kleinfeld (3), P.A. Slesinger (2), Z. Qin (1,4,5,6)

(1) Department of Mechanical Engineering, University of Texas at Dallas, Richardson, TX, USA

(2) Nash Family Department of Neuroscience, Icahn School of Medicine at Mount Sinai, New York, NY, USA

(3) Department of Physics, University of California, San Diego, San Diego, CA, USA

(4) Department of Bioengineering, University of Texas at Dallas, Richardson, TX, USA

(5) Department of Surgery, University of Texas Southwestern Medical Center, Dallas, TX, USA

(6) Center for Advanced Pain Studies, University of Texas at Dallas, Richardson, TX, USA

INTRODUCTION

Neuropeptides are the most diverse class of signaling molecules in nervous system and play important roles in regulating neuronal activity and a wide range of physiological processes. In contrast to fast amino acid synaptic transmission, neuropeptides may diffuse from the release sites and exert their actions through G-protein coupled receptors (GPCRs) at relatively long distances. This diffusion-driven distribution is referred to as volume transmission, a nonsynaptic dispersion in the extracellular space (ECS).[1-2] Where a particular neuropeptide acts relative to its release site is a fundamental and critical question to elucidating its functional role in neural circuits, but less understood. While some neuropeptides travel long distances from a few micrometers to millimeters, several factors affect their diffusion, including the degradation by extracellular proteases and the narrow and diverse ECS in the brain.[3] Furthermore, neuropeptides can typically activate GPCRs at low endogenous concentrations, up to 1000-fold or lower than classical neurotransmitters.[2] These make it challenging to characterize neuropeptide and quantitatively measure the neuropeptide diffusion in the local brain environment by using traditional methods such as mass spectrometry or bioassays. To date, there are limited tools available to study the properties of neuropeptide released *in vivo*.

In this study, we developed an all-optical approach to probe neuropeptide diffusion *in vivo* by integrating two new neuropeptide release and sensing techniques. Photosensitive nanovesicles can be packaged with biomolecules (e.g., dyes, peptides) and provide a way to use near-infrared light to photorelease under tight temporal and spatial control *in vivo*. For detection, we developed a new cell-based neurotransmitter fluorescent engineered reporter (CNiFER) that is sensitive to nM concentrations of somatostatin (SST). By stimulating nanovesicle release and imaging under two-photon microscopy, we demonstrate, for the first time, *in vivo* measurement of neuropeptide local diffusion that contributes to volume transmission and determine the maximal diffusion distance. We further demonstrate that, the diffusion of fluorescent molecules and neuropeptide is altered in hyaluronan-deficient mouse, a disease condition indicated in various neurodegenerative diseases including Parkinson's disease.

METHODS

Nanovesicles preparation: Gold-coated calcein or somatostatin-14 (SST)-loaded liposomes were prepared by the thin-film rehydration method reported before.[4]

SST2 CNiFERs: We created a new SST2 CNiFER based on the design of previous CNiFERs,[5] but with the following changes: we increased the brightness and sensitivity by replacing the TN-XXL with Twitch 2B;[6] we coexpressed a chimeric G Protein Gqi5 that redirects Gi/o receptors to the Gq signaling pathway; we performed CRISPR to knockout the endogenous human muscarinic M4 receptor. We then expressed the hSSTR2 receptor in this modified HEK293 cell (clone #128C3) and isolated a single clone #5F3, which is referred to as SST2 CNiFER.

Diffusion measurement in mouse cortex: Gold-coated calcein-loaded nanovesicles (Au-nV-Cal) were stereotaxically injected to the somatosensory neocortex of C57BL/6 mice at depth of 400-500 μm through the open-skull cranial window. Nanovesicles were imaged at 920 nm and stimulated at 720 nm to trigger calcein release by a multi-photon laser scanning microscope (FVMPE-RS, Olympus). To measure SST diffusion, gold-coated SST-loaded nanovesicles (Au-nV-SST) were mixed with SST2 CNiFERs (core implant) and injected into mouse neocortex. Photo-stimulations at 720 nm were performed on the core implant. Several clusters of SST2 CNiFERs without nanovesicles were implanted into adjacent sites to detect the release of SST from the core implant. Fluorescence of CNiFERs was collected in cyan (460-500 nm) and yellow (520-560 nm) fluorescence channels when excited at 900 nm, and the ration change (ΔR/R) was calculated for each ROI. For calcein diffusion, the following equation was derived from the point source diffusion model:[7]

$$t = \left(\frac{1}{6D^*}\right) r^2 \quad (1)$$

where r represents the diffusion distance, and t is the time that the diffusion takes to reach the maximum concentration for a given r.

To develop a hyaluronan-deficient brain model, approximately 4 µL of 20 mg/mL hyaluronidase from bovine testes in PBS was injected intraventricularly at a depth of 2 mm two days before the diffusion measurement.

RESULTS AND DISCUSSION

As a proof of concept, we first demonstrate the feasibility of the all-optical approach by measuring the diffusion of a fluorescent dye in mouse cortex. As shown in Fig. 1a, near-infrared (720 nm) femtosecond laser scans on Au-nV-Cal implanted in the cortical layer II/III triggered the instantaneous release of calcein from the nanovesicles. In the nanovesicles, calcien fluorescence is quenched but upon photostimulation, a large increase in F is observed, which decreases as the dye diffuses through the ECS. Thus, the stimulated nanovesicles could be considered as the point source for calcein diffusion. The distribution of calcein was analyzed by a ring-analysis method (Fig. 1b). In addition to a decrease in F with distance, the time to reach the maximal intensity is longer. We considered the interval between these peak times to reflect the diffusion time at the corresponding distance. The relationship is fit well by a mathematical model for diffusion (Fig. 1c). Based on the equation (1), we calculated the calcein diffusion coefficient (D^*) *in vivo* (Fig. 1d). We predicted that this coefficient would increase if we increased the ECS. To test this, we treated brains with hyaluronidase (hyase) and found that D^* is 1.8-fold higher than that in normal brain, consistent with faster diffusion in this condition. The tortuosity (λ) was calculated as 73% lower after comparing D^* with free diffusion coefficient (D) in 0.2% agarose gel (Fig. 1e).

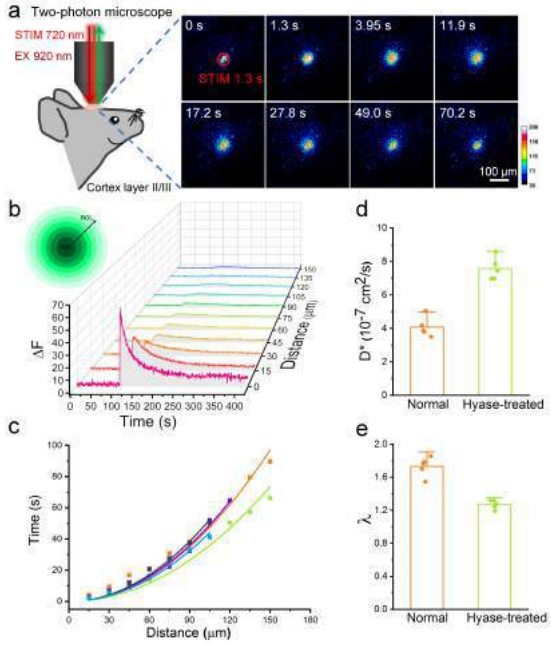

Fig. 1. Diffusion measurement of fluorescent dye in mouse cortex. (a) Calcein fluorescent images over time in mouse cortex measured by a two-photon microscope. Scale bar: 100 µm. (b) Calcein fluorescent intensity changes in different ring-ROIs. (c) The time intervals between the peaks in (b) and the corresponding distance were fitted by the equation (1). (d) Calcein effective diffusion coefficient D* and (e) the tortuosity (λ) in normal and hyase-treated mouse brains. Data were expressed as Mean ± SD (n = 5 independent implants in c, d, e).

To measure neuropeptide release *in vivo*, we developed a new CNiFER for detecting SST. SST2 CNiFERs have an EC_{50} of ~ 4 nM for SST, and little or no response to other peptides and neurotransmitters. Integrating the CNiFER technology with the ultrafast photorelease method provided us with the tools to measure neuropeptide diffusion and volume transmission *in vivo*. SST2 CNiFERs were mixed with Au-nV-SST and implanted in the cortical layer II/III (Fig. 2). In addition, two other CNiFER clusters without nanovesicles were implanted (ROI-2, ROI-3). Photo-stimulation of Au-nV-SST in the core implant (ROI-1) triggered the release of SST, which was detected first by SST2 CNiFERs in ROI-1 and then by SST2 CNiFERs in ROI-2 and ROI-3 (Fig. 2b). As with calcein, the peak was smaller and occurred after a delay in the SST2 CNiFERs in ROI-2 and ROI-3, reflecting the diffusion time for the peptide. We carried out several experiments varying the distances between core and satellite SST2 CNiFER implants to quantatively determine the diffusion time over these distances (within 250 µm). In the hyase-treated brain, the diffustion time is faster than that in normal brain, which is consistent with the results of calcien diffusion.

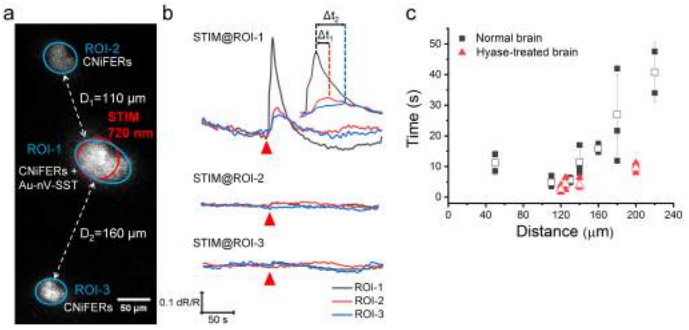

Fig. 2. Diffusion measurement of neuropeptide in mouse cortex. (a) Fluorescent image of SST2 CNiFERs implanted in the layer II/III of mouse cortex. The implant in the center (ROI-1) was mixed with Au-nV-SST, while the other two implants (ROI-2, ROI-3) were just SST2 CNiFERs alone. (b) The response curves of CNiFERs when stimulating at different regions (720 nm, 100 mW, 2.6 s). The enlarged curve shows the time intervals between the peaks of response. (c) Summary of SST diffusion distance and corresponding time measured in normal mice and hyase-treated mice. The blank squares and triangles indicate the mean values.

CONCLUSION

We developed a new all-optical approach to monitor the hindered diffusion of fluorescent dyes to neuropeptides in mouse cortex. We quantitatively determined the neuropeptide diffusion time over a certain distance for the first time. We also demonstrate that change of ECS matrix would affect the molecular diffusion. The mapping of neuropeptide spatial signaling provides more opportunity to elucidate the function of neuropeptides in regulating neural circuits.

ACKNOWLEDGEMENTS

We acknowledge funding support from NIH under award number RF1NS110499 (Z.Q., P.A.S.) and R01MH111499 (P.A.S., D.K.).

REFERENCES

1. Van Den Pol, A N. *Neuron*, 76: 98-115, 2012.
2. Russo, A F. *Headache*, 57: 37-46, 2017.
3. Godin, A G et al., *Nat Nanotechnol*, 12: 238-243, 2017.
4. Xiong, H et al., *Angew Chem*, 132: 8686-8693, 2020.
5. Muller, A et al., *Nat Methods*, 11: 1245-1252, 2014.
6. Thestrup T et al., *Nat Methods*, 11: 175-182, 2014.
7. Syková, E et al., *Physiol Rev*, 88: 1277-1340, 2008.

THE EFFECT OF AGE-RELATED ADVANCED GLYCATION END-PRODUCTS ON TISSUE MECHANICS DEPENDS ON UNDERLYING COLLAGEN ORGANIZATION

Austin G. Gouldin (1), Jennifer L. Puetzer (1,2)

(1) Biomedical Engineering
Virginia Commonwealth University
Richmond, VA, USA

(2) Orthopaedic Surgery
Virginia Commonwealth University
Richmond, VA, USA

INTRODUCTION

In musculoskeletal menisci, tendons, and ligaments there is a clear link between increasing age and injuries. Many mechanisms have been suggested to contribute; however due to the high reliance on collagen fibers in these tissues, the most prominent mechanism is believed to be advanced glycation end-products (AGEs).[1-2] AGEs accumulate in collagen with age, producing non-enzymatic crosslinks that alter tissue mechanics, leading to more injuries. Specifically, AGEs are thought to stiffen tissues making them more prone to injury. However, *in vivo* studies have shown inconsistent results, with AGE crosslinks increasing, decreasing, or not effecting mechanical properties in tendons and ligaments throughout the body.[1,3-4] Despite correlative evidence linking collagen glycation to age-related injury, little is known about how AGEs impact matrix mechanics and cell-matrix interactions, resulting in limited therapeutic options.[1-2] We hypothesize that these inconsistences in mechanics are primarily due to differences in collagen organization, with musculoskeletal tissues having varying degrees and sizes of collagen fibrils, fibers, and fascicles throughout the body. Recently, we developed a novel cell-seeded culture device that guides cells using mechanical restraints to produce native-sized hierarchically organized collagen fibers over 6 weeks of culture (Fig 1A).[5] Further, we recently developed a method for inducing physiological AGEs, which match AGE levels of 21-23 month old mice tail tendons and human 60-70 year old menisci,[2] without effecting cell viability or metabolism.[6] The objective of this study is to combine these two systems and induce AGEs temporally, as cells align fibrils and develop them into fibers and fascicles. We will evaluate the effect of AGEs on mechanics at each hierarchical level to better predict the impact of AGEs on different tissues throughout the body. We hypothesis AGEs will increase stiffness in fibrils but decrease viscoelasticity in fibers and fascicles.

METHODS

Rat type I collagen was extracted and reconstituted as previously described.[5,6] Isolated bovine meniscal fibrochondrocytes were mixed with collagen, injected between glass sheets, and gelled at 37°C for 1 hour to obtain 20 mg/ml collagen gels at $5x10^6$ cells/ml. Rectangles (8x30mm) were cut from sheet gels and cultured in our clamping device for up to 6 weeks in basic DMEM to drive the formation of fibrils, fibers and fascicles (Fig 1A).[5] Meniscal fibrochondrocytes were used since previously they produced the largest range.[5] At 0, 2, 4, or 6 weeks AGEs were induced with the addition of 100 mM ribose to the media for 3 days to induce AGE levels that match human 60-70 year old menisci (Fig 1B),[2,6] while control constructs remain in DMEM. Time points were collected after 3 days of induction at day 3, 17, 31, and 45 (labeled 0, 2, 4 and 6 weeks for simplicity) to evaluate the effect of AGEs in unorganized collagen, and at the fibril, fiber, and fascicle length scale, respectively. Samples were imaged with confocal reflectance to evaluate collagen organization, with auto-fluorescence of cells and AGEs captured together at 400-470 nm. DNA, collagen, total AGEs, and AGE specific crosslink pentosidine, were determined via PicoGreen, hydroxyproline (hypro), AGE fluorescence (360/460 nm, quinine standards), and pentosidine fluorescence (328/378 nm) assays, respectively.[6] Mechanical properties were determined by ramping to 5% strain at 5% strain/sec and holding for 180 seconds to measure stress relaxation.[5,7] Constructs were then returned to 0% strain for 60 seconds and ramped to failure at 0.5% strain/sec.[5] All data are expressed as mean±SD. Significance determined by 1- and 2-way ANOVA with Tukey post-hoc ($p<0.05$).

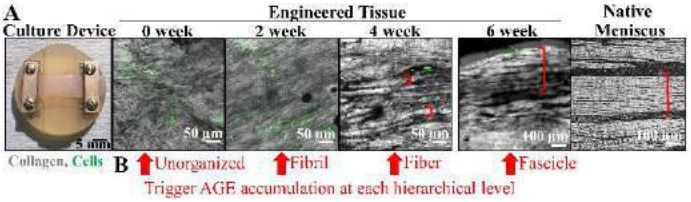

Figure 1: A) Culture device that guides cells to form aligned collagen fibrils, fibers, & fascicles at 2, 4 and 6 weeks, respectively. Brackets denote fibers and fascicles. B) AGEs induced at 0, 2, 4 or 6 weeks to evaluate how AGEs effect each level of organization

RESULTS

Constructs developed aligned fibrils by 2 weeks, native size fibers

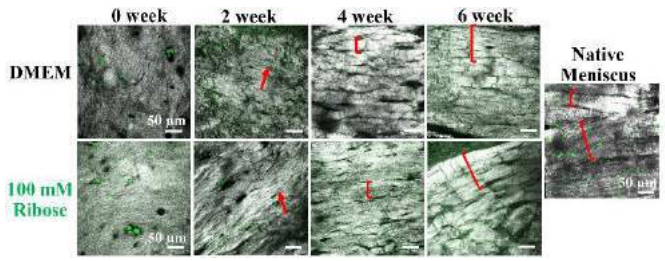

Figure 2: Confocal reflectance. Grey = collagen, Green = auto-fluorescent cells and fluorescent AGE crosslinks. Arrows denote fibrils and brackets denote fibers and fascicles.

by 4 weeks, and larger fascicles by 6 weeks (Fig 2), matching previous studies.[5] Induction of AGEs for 3 days with 100 mM ribose did not disrupt collagen organization and resulted in increased AGE fluorescence (Fig 2). As expected, DNA (not shown), and collagen content (Fig 3A) did not significantly change throughout culture. As cells form aligned fibrils in the first 2 weeks, there was a significant decrease in weight for all constructs (Fig 3B). However, interestingly, AGEs induced at 2 weeks resulted in a significantly higher percent weight then the controls at 2 weeks, while all other time points maintained similar weight to controls (Fig 3B). Three days of ribose induced a significant amount of total AGEs and AGE specific crosslink, pentosidine, at 0, 2, and 4 weeks of culture, with unorganized collagen accumulating the most amount of pentosidine crosslinks (Fig 3C-D). However, once fascicles formed at 6 weeks, 3 days of ribose did not induce a significant increase in AGE crosslinks (Fig 3C-D).

Generally, AGE induction resulted in reduced stress relaxation, with a trending decrease at 2 weeks, and a significant decrease at 6 weeks (Fig 4A). AGE induction also significantly increased the tensile and toe modulus compared to controls when induced at the fascicle level (6 weeks), but had no significant change in modulus when induced in unorganized (0 week) or fibril level organizations (2 weeks, Fig 4B-C). AGE induction at the fiber level (4 weeks), increased the tensile modulus over 0 week samples, but was not significantly different to controls at 4 weeks (Fig 4B). AGE induction had little effect on ultimate tensile strength, strain at failure, or strain at toe region transition (Fig 4D-F), expect for when AGEs were induced at the fiber level (4 weeks), which resulted in a significant decrease in strain at failure and transition (Fig 4E-F). Overall, the results show that the degree of collagen organization will alter AGE's effect on the mechanics of the tissue.

DISCUSSION

In this study we demonstrated that the degree of collagen organization has a significant effect on the amount of AGEs

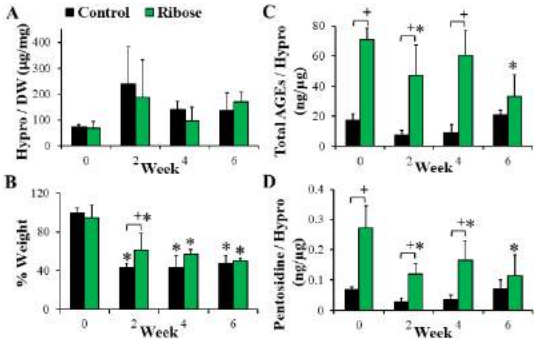

Figure 3: A) Hydroxyproline (hypro) normalized to dry weight, B) % weight compared to 0 week control, C) Total AGEs / hypro and D) AGE specific crosslink pentosidine / hypro. Significance compared to *0 week and +brackets (p<0.05), N = 4.

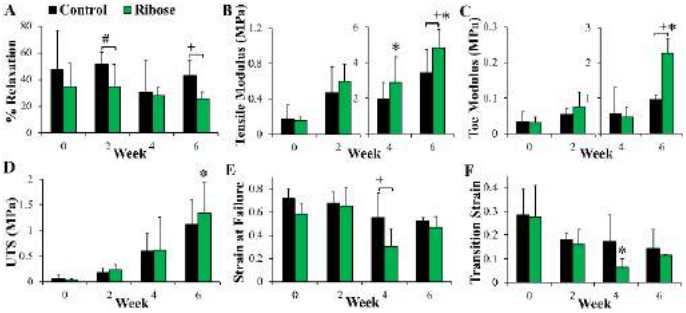

Figure 4: A) % relaxation, B) tensile and C) toe modulus, D) ultimate tensile strength (UTS), E) strain at failure, and F) strain at transition from toe to linear region. Significance compared to *0 week and +brackets (p<0.05). #trending (p<0.1). N = 3-4.

accumulated and the effect those AGEs have on tissue mechanics. At 0 weeks, with no collagen organization, the most AGEs were induced, however this had no effect on tissue mechanics. Once fascicles formed at 6 weeks, 3 days of ribose no longer induced a significant amount of AGEs, however this reduced amount of AGEs still showed a significant increase in both the tensile and toe modulus. At 2 weeks, once aligned fibrils had formed, AGEs did not affect tissue strength or strain properties, however it did decrease viscoelastic stress relaxation. Additionally, at 2 weeks ribose treated constructs had a significantly higher weight (Fig 3B), most likely due to AGE crosslinks having a great affinity for water;[8] however interestingly this was not observed at any other levels of organization. Overall, our work is in contrast to the general belief that crosslinking, both enzymatic and non-enzymatic, increases stiffness and modulus at the fibril level.[1,9] However, our findings support recent work which reported AGEs restrict fibril sliding, resulting in reduced viscoelasticity, but no change in fibril stiffness of rat tail tendons.[3,10] Together these results suggest AGEs occur primarily on the outside of fibrils, unlike enzymatic crosslinks which occur within fibrils and result in increased stiffness. Additionally, AGEs have been shown to effect fiber-fiber sliding at the fiber level,[3] which our work also supports with limited changes in stiffness at the fiber level, but significant changes in strain properties at 4 weeks.

Overall, we found AGEs induced at the fibril level effect viscoelastic properties but not stiffness, while AGEs at the fascicle level effecting both stiffness and viscoelasticity, demonstrating a complex relationship between collagen organization and AGE crosslinking. Our inducible glycation and culture system provides a means to investigate the mechanism of AGEs and their effect on tissue mechanics and cellular function at multiple levels of organization. This system will provide a better understanding of the effects of AGEs at each hierarchical level of collagen, helping to predict the impact of AGEs in tissues throughout the body, in an effort to produce new therapeutic options to reduce age-related injuries.

ACKNOWLEDGEMENTS

We acknowledge the VCU Nanomaterials Characterization Core and the Laboratory for Musculoskeletal Research and Innovation.

REFERENCES

[1]Eekhoff et al., *Conn Tiss Res*, 59(5):410-422, 2018. [2]Takahashi et al., *Arthroscopy*, 4:366-372, 1998. [3]Gautieri et al., *Matrix Biology*, 59:95-108, 2017. [4]Snedeker et al., *MLTJ*, 4(3):303-308, 2014. [5]Puetzer et al., *Biomat*, 2020. [6]Gouldin et al., BioRxiv, 2020. [7]Ansorge et al., *Biomed Eng*, 39(7):1904-1913, 2011. [8]Rich et al., *JOMS*,25(1):11-21, 2014. [9]Reddy et al., *JOR*, 21(4):738-743, 2003. [10]Fessel et al., *PLoS One*, 9(11):e110948, 2014.

FIBRIL STRAIN PROMOTES ADDITION OF TYPE I COLLAGEN MOLECULES TO SINGLE, NATIVE COLLAGEN FIBRILS *IN VITRO*

Seyed Mohammad Siadat (1), Jeffrey W. Ruberti (1)

(1) Department of Bioengineering
Northeastern University
Boston, MA, USA

INTRODUCTION

How organized collagenous fibrils can arise and grow from a cluster of cells remains one of the most important basic science questions associated with connective tissue research. The assembly of collagen network is concomitant with integrin expression to transmit compulsory biomechanical information from intracellular space to ECM [1]. Cultures of human dermal fibroblasts and tenocytes under static strain generate tendon-like structures where mechanical loading is required for formation of parallel collagen fibers, tissue maturation, and growth of fibrils' diameter [2]. While tension is part of the collagenous tissue niche and plays a critical role in formation and maintenance of collagen fibrils [3], the manner in which mechanical forces affect the addition of molecules or fibril segments to the growing fibril is not fully understood.

Fibril diameter may be limited by other extracellular matrix residence such as proteoglycans [4], hyaluronate [5], collagen propeptides [6], and minor types of collagen [7]. Nonetheless, failure to maintain tissue homeostasis and fibril diameter after a period of tissue unloading, points to the critical role of mechanics. Whether the association and dissociation rates of collagen monomers with fibrils are directly guided by mechanical load on fibrils or cells indirectly control fibril growth by sensing and processing mechanical information from the ECM is not clear. We hypothesize that local mechanical signals not only control fibril formation and alignment [8], they also directly govern the mechanism of fibril growth and remodeling. It has been suggested that collagen monomers and enzymes are in a dynamic equilibrium with existing fibrils [9]. Tensile forces on fibrils can shift this equilibrium and change the balance between molecular association and dissociation. Here, we sought to answer the question: Does fibril strain promote the molecular assembly of collagen?

METHODS

Bovine sclera fibrils Extraction. Collagen fibrils were extracted from 1-10-day old bovine scleras. Shallow cuts were made on each scleral piece and then placed into 20 mL of pH 7.5-8.0 extraction medium containing: >1000 BAEE unit/mL trypsin, 4 mM ethylenediaminetraacetic acid, 0.1 M tris-HCl, and 0.05% sodium azide. Samples were shaken for ~5 minutes until the sclera pieces swelled and fibrils could be removed.

Fluorescent Labeling of Collagen Molecules. Type I bovine collagen solution was mixed 1:1 with 0.2 M sodium carbonate–bicarbonate buffer containing 1 M sodium chloride. Alexa Fluor 488 TFP ester was added to collagen solution in 1:1 molar ratio. The reaction mixture was stirred for 3 hours at room temperature.

Fibril Stretching and Incubation with Labeled Monomers. Fibrils were attached between microneedles using two Eppendorf Transferman NK2 micromanipulators. Fibrils were kept under 0%, 4%, or 6% static strain at 35°C in a temperature controlled open dish. Labeled monomers were added to the dish at a final concentration of 0.5 µg/mL. DIC and fluorescent images were captured every 1 minute.

Image Analysis of Fluorescent Fibrils. The association rate was calculated based on the fibril fluorescent intensity and photobleaching of labeled monomers.

RESULTS

Monomer/Fibril Association is Fibril Strain-Dependent. For all tested fibrils, the fibril intensity increased rapidly and reached a plateau during the first 30 minutes. Figure 1 shows a representative fibril before and 30 minutes after adding labeled monomers.

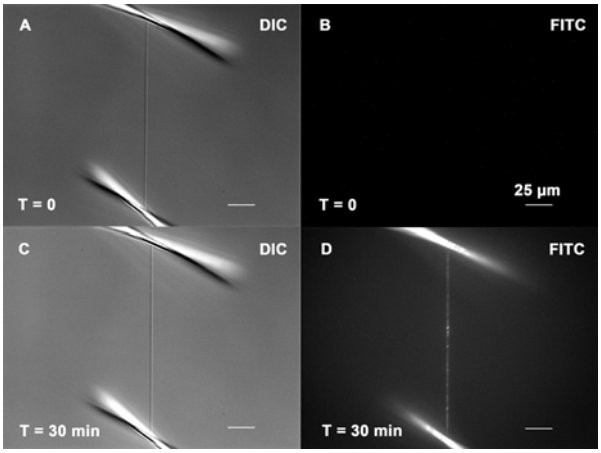

Figure 1: DIC and fluorescent images of a representative fibril stretched to 6% strain between needles. Panel A (DIC) and B (fluorescent) show the fibril at time 0, right before adding the labeled monomers. Panel C (DIC) and D (fluorescent) show the fibril at 30 minutes after adding the labeled monomers.

Normalizing each fibril's intensity by its maximum intensity at the plateau (Figure 2) showed that fibrils which were under 4% or 6% strain reached their plateau faster than the 0% strain fibrils. The plateau times (time to reach 90% of the maximum intensity) were 15.6 ± 5.3, 7.0 ± 1.7, and 6.0 ± 2.4 for fibrils under 0%, 4%, and 6% strain, respectively. Data are presented as mean ± standard deviation (n=3 replicates per group). Post-hoc Tukey HSD test showed a significant difference between 0% and 4% groups (p-value = 0.0234099; * $p<0.05$) and 0% and 6% groups (p-value = 0.0086839; ** $p<0.01$).

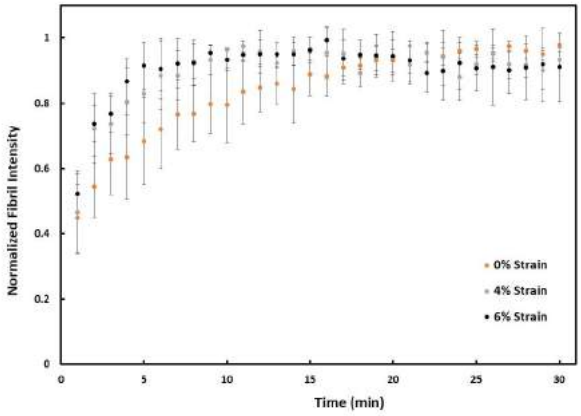

Figure 2: Normalized fibril intensity. The fibrils' intensity rapidly increased and reached a plateau during the first 30 minutes.

Monomers Associate with 6% Strained Fibrils with a Significantly Higher Rate compared with 0% and 4% Strained Fibrils. For all tested fibrils, the highest monomer association rate was immediately after addition of labeled monomers (Figure 3). Association rate rapidly decreased during the first 10 minutes, and remained rather constant afterward until 30 minutes. Remarkably, the fibrils under 6% strain maintained a higher association rate. Normalized association remained fairly constant after 10 minutes at 0.26 ± 0.03, 0.25 ± 0.04, and 0.49 ± 0.15 for fibrils under 0%, 4%, and 6% strain, respectively. Data are presented as mean ± standard deviation (n=3 replicates per group). Post-hoc Tukey HSD test showed a significant difference between 0% and 6% groups (p-value = 0.0122180; * $p<0.05$) and 4% and 6% groups (p-value = 0.0143004; ** $p<0.05$).

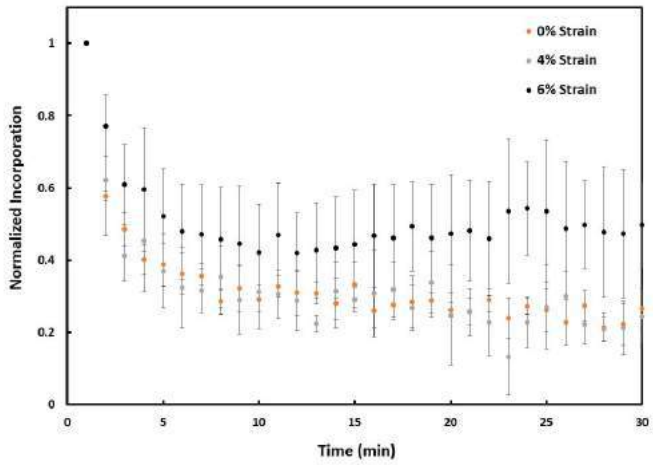

Figure 3: Labeled monomers incorporation onto fibrils.

DISCUSSION

A simple method was developed to mechanically stretch single native fibrils using microneedles and micromanipulators. Analysis of fibrils' fluorescent intensity showed that labeled monomers rapidly associated with fibrils with no lag time and that mechanical stretching of fibrils promoted monomer association with fibrils. Specifically, monomer association rate was significantly higher with fibrils under 6% strain compared with fibrils under 0% and 4% strain.

The higher association rate of fibrils under 6% strain supports a structural limited growth model, where mechanical strain stimulates monomers association and fibrils growth. It has been shown that 1) tension can directly drive initial fibrillogenesis and structures into the path of force [10], 2) applied mechanical strain preferentially preserves type I collagen against enzymatic degradation [11], and 3) in the absence of cells, unloading of collagen fibers can increase fiber disassociation [10]. Here we showed that stresses and strains on collagen fibrils can promote the molecular assembly and fibril growth. The results elucidate the role that mechanics could play in the collagen fibril growth mechanism and provide new opportunities to develop treatments for variety of pathological conditions by promoting growth or degradation when/where needed.

ACKNOWLEDGEMENTS

This work was funded by NIH R21 EY029167-01.

REFERENCES

[1] Li, S., et al., Am J Pathol, 163(3): p. 1045-56, 2003.
[2] Deng, D., et al., Biomaterials, 30(35): p. 6724-30, 2009.
[3] Kalson, N.S., et al., Proc Natl Acad Sci USA, 110(49): p. E4743-52, 2013.
[4] Vogel, K.G., Biochem J, 223(3): p. 587-97, 1984.
[5] Scott, J.E., Biochem J, 195(3): p. 573-81, 1981.
[6] Fleischmajer, R., et al., Proc Natl Acad Sci USA, 78(12): p. 7360-4, 1981.
[7] Romanic, A.M., et al., J Biol Chem, 266(19): p. 12703-9, 1991.
[8] Bayer, M.L., et al., Biomaterials, 31(18): p. 4889-97, 2010.
[9] Ruberti, J.W. and N.J. Hallab, Biochem Biophys Res Commun, 336(2): p. 483-9, 2005.
[10] Paten, J.A., et al., ACS Nano, 10(5): p. 5027-40, 2016.
[11] Flynn, B.P., et al., Biomech Model Mechanobiol, 12(2): p. 291-300, 2013.

SB^{3}C2021
Summer Bioengineering and Biotransport Conference
June 14-18, Virtual

Microfluidics Layout Design for Improved Circulating Tumor Cell Capture Efficiency

Michael C. Hood (1), Jifu Tan (2)

(1,2) Department of Mechanical Engineering
Northern Illinois University
Dekalb, IL, USA

INTRODUCTION

Microfluidics is a promising technique in isolation of circulating tumor cells (CTCs) from patient derived blood samples in early cancer diagnostics, and exhibit several advantages over traditional tissue biopsies [1]–[3]. One challenge for early cancer diagnostics is that CTCs are exceedingly rare in samples [4]. Thus, devices should be able to capture CTCs at very low concentrations. Various capture mechanisms and device designs for CTC isolation can be found in the literature [4], [5]. However, study of device design on the performance of the immunoaffinity-based positive enrichment technique is limited. In this application, CTCs are intended to adhere to microposts coated with desired antibodies and placed throughout the device. Adhesion is accomplished through binding of ligand-receptor antibody pairs. Device performance can be characterized by capture efficiency, which quantifies how many cells out of the total available are captured. Because of the capture mechanism, device performance is highly influenced by the exposure of cells to microposts, as adhesion cannot occur without exposure.

Previous studies [6] found that cells follow streamlines throughout the device closely for low cell concentrations, and showed some deviation at higher cell concentrations. Streamlines in the device are determined by the device configuration, which can be characterized by micropost shape, size, and distribution. The distribution of the microposts defines what fraction of the domain they occupy, as well as how they are placed. The placement of microposts can take many styles, such as a grid, lattice, or algorithmic placement style. It is not well known how these layouts will affect the device performance. It is suspected that devices with a regular post layout would be outperformed by those with irregular post layouts due to greater likelihood of cells being exposed to microposts caused by transport along irregular and non-repeating streamlines. Of particular interest are disordered hyperuniform post layouts, due to their structural similarity with packed beds which are used in filtration processes [7], [8]. Disordered hyperuniform layouts suppress density fluctuations in the placement of posts on large length scales, similar to regular post placements, but allow for irregular flow patterns to arise. An example of prelimary cell trajectories obtained in a disordered hyperuniform device can be seen in Fig.(1). Additionally, cell trajectories obtained from a regular layout device can be seen in Fig.(2).

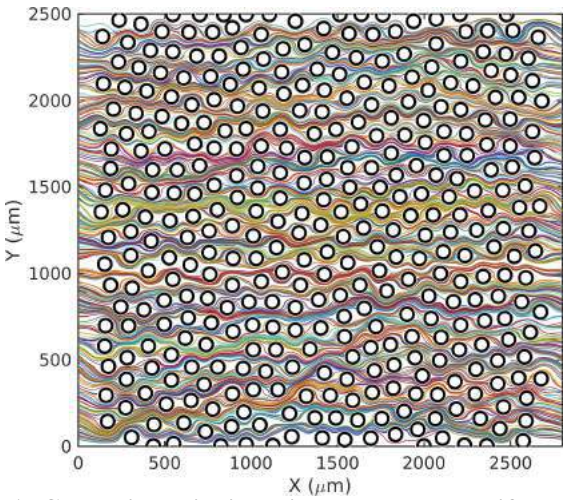

Figure 1: Cell trajectories in a disordered hyperuniform layout device. Microposts are indicated by circles.

METHODS

Because microfluidic devices typically have many thousands of microposts in these applications, it was decided to use a 2D simulation domain for computational efficiency. The fluid flow is solved by the lattice Boltzmann method through the Palabos [9] software library. The cells in the system are modeled using coarse-grained molecular dynamics through the LAMMPS [10] software library. Coupling of the fluid and solid is handled by the immersed boundary method. To model ligand-antibody binding, a probabilistic bond creation and breaking model was implemented based on the work of [11] for the purpose of analysing when adhesion occurs in the ongoing studies. The advantage of the use of a discrete bond

model is that it mimics the physical phenomenon of bond formation to impart forces on cells within the flow. This is in contrast to a pairwise interaction potential, where any particles within the cutoff distance from one another impart a force.

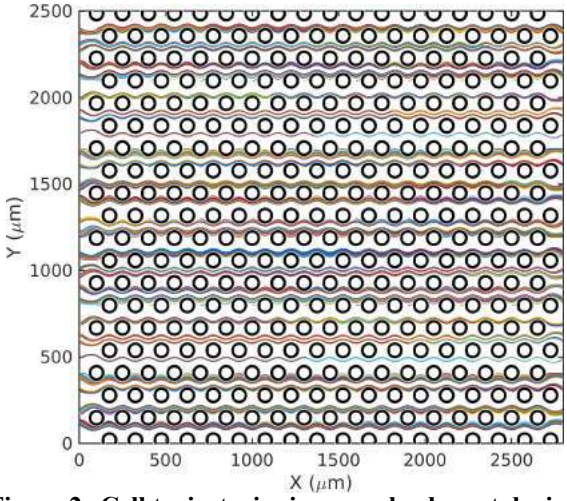

Figure 2: Cell trajectories in a regular layout device.

Device performance is measured by finding probabilities for cell exposure and capture with respect to different device configurations (e.g., micropost size, shape, layout) and operating conditions (e.g., shear rate, cell stiffness, and cell concentrations). An important metric for this application is the amount of time that CTCs spend near posts with reference to total time in the device. We call this the *normalized exposure time* of the CTCs, and it is calculated as:

$$\epsilon = \frac{T_{near}}{T_{total}} \tag{1}$$

The normalized exposure times for each cell are found via post-processing of the simulation data. T_{near} is calculated by summing the total time where the given cell is within a desired distance of a micropost.

RESULTS

Preliminary results show some evidence that disordered hyper-uniform layouts are superior to regular layouts. One can clearly see the qualitative differences in the trajectories between Fig.(1) and Fig.(2). Cases with different flow velocities were also conducted, which showed some indication that higher flow velocities introduced more exposure time to microposts for cells, however this result may not lead to better capture efficiency due to higher shear rates around microposts. Examples of the normalized exposure time can be seen in the distributions in Fig.(3). It is important to note that the regular layout creates a population of exposure times that are concentrated around a time fraction of 0 to 0.05, indicating that the design would not be ideal. It is intended to conduct these same analyses on a larger population of layouts to gain more comprehensive results. Of particular interest are the use of triangular posts, and providing more examples of these different layout classes for their comparison.

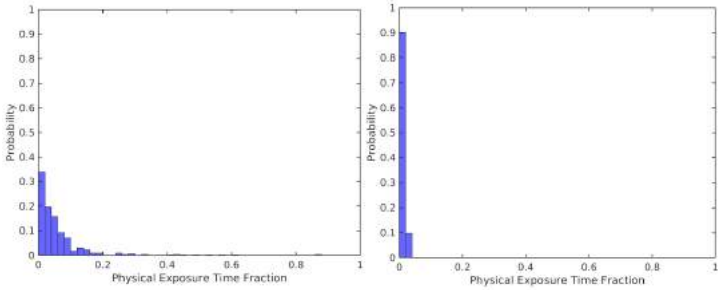

Figure 3: Normalized exposure times for the given device layouts using the same driving pressure, with the disordered layout on the left, and the regular layout on the right.

DISCUSSION

Results collected indicate very different behavior of a regular and disordered type device, as the regular device obtains very little exposure time and the disordered device obtains a much larger number of cells exposed to microposts for a significant amount of time. This shows some indication that disordered designs will generally outperform regular ones. Further studies are being conducted to develop a more in depth understanding of design principles for microfluidics in this application. To study the relationship of flow velocities and shear rates on the performance of these device, tests to find a range of when adhesion can occur are also underway. If a superior class of device designs can be found, it could lead to more efficient and smaller devices, as well as faster processing times. Informing design decisions for microfluidic devices is indispensable in creating more effective solutions for clinical and research settings.

ACKNOWLEDGEMENTS

The authors acknowledge the startup funding and the high performance computing support from Gaea at Northern Illinois University.

REFERENCES

[1] A. Alba-Bernal *et al.*, *EBioMedicine*, 62: 103100, 2020.
[2] C. Wu *et al.*, *Clinical Biochemistry*, 2020.
[3] E. Geeurickx *et al.*, *Molecular aspects of medicine*, 72: 100828, 2020.
[4] S.-B. Cheng *et al.*, *TrAC Trends in Analytical Chemistry*, 117: 116–127, 2019.
[5] M. M. Ferreira *et al.*, *Molecular oncology*, 10: 374–394, 2016.
[6] J. Tan *et al.*, *Biomicrofluidics*, 13: 064105, 2019.
[7] R. Dreyfus *et al.*, *Physical Review E*, 91: 012302, 2015.
[8] S. Torquato, *Advances in Water Resources*, 140: 103565, 2020.
[9] J. Latt *et al.*, *FlowKit, Lausanne, Switzerland*, 2009.
[10] S. Plimpton, *Journal of computational physics*, 117: 1–19, 1995.
[11] D. A. Fedosov *et al.*, *Biophysical journal*, 98: 2215–2225, 2010.

SB³C2021
Summer Biomechanics, Bioengineering and Biotransport Conference
June 14-18, Virtual

DIRECTIONAL CELL MIGRATION GUIDED BY A STRAIN GRADIENT

Feiyu. Yang (1), Yubing. Sun (1)

Department of Mechanical and Industrial Engineering
University of Massachusetts Amherst
Amherst, MA 01003, USA

INTRODUCTION

Directional cell migration is critically involved in various physiological and pathological processes, including embryonic development, wound healing, and immune responses [1-3]. It is well-known that directional cell migration can be guided by a chemical gradient (chemotaxis) or a stiffness gradient (durotaxis). In this study, we prove directional cell migration by a strain gradient on the extracellular matrix using rat embryonic fibroblast (REF). We designed a low-cost, easily modified, programmable biaxial cell stretching device and corresponding cell culture samples. By adjusting the design, various strain fields on the extracellular matrix were generated. We proved by tracking the single-cell migration that about 60% to 70% of cells would prefer to migrate towards the lower strain direction in both static and 0.1Hz cyclic stretch experiments. The control experiment was conducted to exclude the potential effect of durotaxis and haptotaxis in directing cell migrations. Live-cell focal adhesion dynamic was quantified to investigate the mechanism. We found that focal adhesion size was relatively increased, coupled with more protrusion formations in the lower strain direction.

METHODS

We developed a low-cost, flexible cell stretching device using the Arduino interface. It had the unique feature of generating a strain gradient field on the cell culture area with biaxial stretching. The sample was fabricated by bonding a PDMS membrane to a silicon rubber base with specific geometries design generated by laser cutting (Fig.1a). A well-controlled 4% per mm strain gradient was established on the cell culture area. The sample strain fields were quantified experimentally with micro-contact printing techniques（ Fig.1b ）. During the experiment, rat embryonic fibroblast (REF) cells were cultured on top of the PDMS membrane with a density lower than 80 cells/mm^2. After cells were fully attached 15 hrs later, we started the cell stretching and image the cells for the next 6 hours. The sample was stretched once and kept at the stretched status for 6 hours for live-cell imaging for the static experiment group. For the cyclic experiment group, the sample was cyclic stretched at 0.1 Hz for 3 hrs. The cells were imaged at the same time for 6 hours. Durotaxis, a directional cell migration signal caused by the stiffness gradient, could coexist with the strain gradient on the extracellular matrix. To solve this problem, we design a control experiment, where REF cells were seeded after the cell culture sample was held at the stretched status. Therefore, cells were not exposed to the strain gradient without being stretched. As a result, only the potential durotaxis signals exist in the environment, and the condition of the cell culture substrate was not changed. However, unlike the gradient groups, the pre-stretched control group had no directional cell migration preferences.

To investigate the mechanisms, we analyzed the focal adhesion dynamics, the size of protrusion, and retraction. Two images were taken for each cell before and after stretching was applied, respectively (Fig 2.a). The cell was divided in half by the line passing the nucleus's center and perpendicular to the maximum gradient direction. One half was in the direction of the lower strain, and the other half was in the direction of the higher strain. Focal adhesion total size and the protrusion percentage at the lower and higher strain directions were compared.

RESULTS

When experiencing a strain gradient of 4% per mm, for the static group, approximately 60% of cells migrated towards the direction with the lower strain (Fig.1c). For the cyclic group, 65% of cells migrated towards the direction of lower strain (Fig.1d). No directional migration preferences have been observed for the pre-stretched control group (Fig.1. e). Rayleigh tests were applied to determine whether a single directional preference exists for all three groups. We further evaluate the efficacy of the strain gradient signaling in the migration preferences

using the Forward Migration Index (FMI) (Fig1.f). Both static and cyclic gradient groups were significantly different from the pre-stretched control group. Such preference of migration directionality is also correlated with the magnitude of the strain, albeit with the same strain gradient. It was found that a higher percentage of cells migrated along the decreasing strain direction in the regions with larger strain magnitude (data not shown).

We quantified the focal adhesion dynamics and the protrusion at the lower and higher strain direction to investigate the mechanism. Sixteen cells were analyzed from three experiment batches. The size of focal adhesion and protrusion were relatively increased at the lower strain direction after stretching (Fig 2).

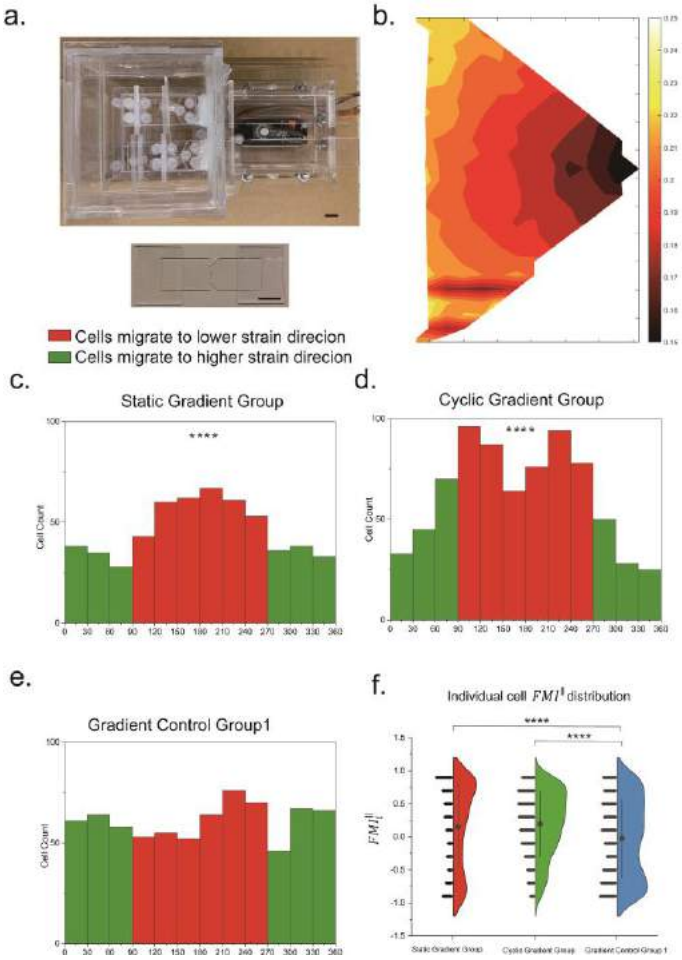

Figure 1. a. Photo of cell stretch device (top) and cell culture sample (bottom). Scale bar, 10mm. b. Gradient of strain field. c. Cell migration distribution of static gradient group from N samples and M cells. N=7, M=554. e. Cell migration direction distribution of the cyclic gradient group from N samples and M cells. N=8, M=746. f. Cell migration direction distribution of the gradient control group 1 from N samples and M cells. N=7, M=732. g. Individual cell's FMI distribution. Mann-Whitney test was run to determine the significance.

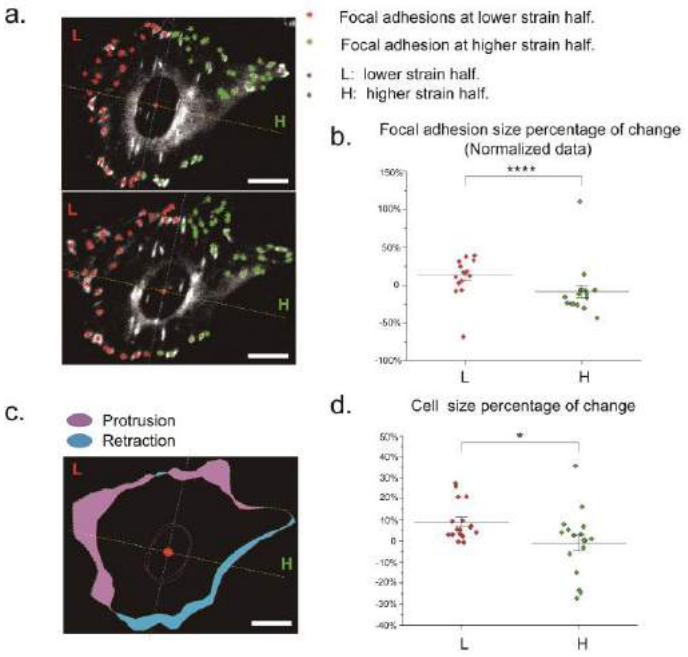

Figure 2. a. Marking a REF cell's focal adhesions that were analyzed before (up) and after (down) stretching. Scale bar 20 um. B. Normalized focal adhesion size change percentage before and after stretching in the lower and higher strain half. N=16. c. Overlap the cell before and after stretching. The protrusion and retraction after stretching were highlighted. d. Percentage of cell size change in the lower and higher strain half. N=17.

DISCUSSION

In this work, we uncover that REF cells can sense a subtle change in local strain gradient and migrate towards the direction of lower strains. We excluded the potential effect of durotaxis with a pre-stretching control group. Without sensing a strain gradient, no directional cell migration was observed. This highlights the possibility that during embryo development and wound healing processes, a local strain gradient generated due to tissue-generated forces may facilitate the directed cell migration. The strain gradient generation device can be broadly applied for further studies of cellular strain sensing.

ACKNOWLEDGEMENTS

This work is supported in part by the National Science Foundation (CMMI 1662835 and CMMI 1846866 to Y.S.) and the Department of Mechanical and Industrial Engineering at the University of Massachusetts Amherst. We acknowledge the support from the Institute for Applied Life Sciences at UMass, Amherst.

REFERENCES

[1] Reig G,et al., *Development* 141(10) 2014..

[2] Friedl P, et al., *Nature Reviews Molecular Cell Biology* 10(7):445–457, 2009.

[3] Luster AD, et al., *Nature Immunology* 6(12):1182–1190, 2005

SB³C2021
Summer Biomechanics, Bioengineering and Biotransport Conference
June 14-18, Virtual

MEAN AND TRANSVERSE WALL SHEAR STRESS CORRELATE WITH ENOS EXPRESSION IN ENDOTHELIAL CELLS UNDER ORBITAL FLOW

Jaideep Sahni, Glenn T. Richardson, Ryan M. Pedrigi

Department of Mechanical and Materials Engineering
University of Nebraska-Lincoln
Lincoln, NE, USA

INTRODUCTION

Atherosclerosis is the primary pathology of coronary heart disease and ischemic stroke, and, thus, is the leading cause of death in the world [1]. Despite the systemic risk factors, such as age, obesity, and high LDL, atherosclerotic plaques localize to curvatures and branches of the arterial vasculature. These regions are dominated by disturbed flow, typically characterized by using metrics that quantify the magnitude or directionality of wall shear stress (WSS) over the cardiac cycle. WSS acts on the endothelium, which is a key regulator in the initiation and progression of the atherosclerotic pathology [2]. WSS metrics of disturbed flow have been strongly correlated to markers of endothelial cell dysfunction, primarily using microfluidics, orbital shakers, and step flow chambers *in vitro*, wherein high values of these metrics have been associated with an atherogenic phenotype and low values (indicating normal laminar flow) with an atheroprotective phenotype. To our knowledge, none of these studies have evaluated how markers of endothelial cell function change over a continuous degree of disturbed flow.

In this study, we used an orbital shaker, a machine with a platform moving in a circular motion that causes circumferential motion of the media contained within cell culture well plates placed atop the shaker platform. At the center of each well, media flow is highly multidirectional, mimicking an atherogenic flow condition, which transitions incrementally to unidirectional laminar (atheroprotective) flow with increasing radial position to the outer portion of the well [3]. We used the potential theory (PT)-Stokes method to compute WSS in the well and then computed two WSS metrics of disturbed flow as a function of radial position. We then evaluated the correlation between these WSS metrics and an established marker of endothelial cell function, endothelial nitric oxide synthase (eNOS).

METHODS

Computation of shear stress. We used a previously reported analytical approach called PT-Stokes to compute the instantaneous WSS vectors for a given point in the well of a 6-well plate over an orbital shaker cycle [4,5]. The input parameters were as follows: 2.5 mm fluid height at rest; 17.5 mm cylinder radius; 5 mm orbital radius; 200 rpm angular velocity; 0.76 mm^2/s fluid kinematic viscosity; 1000 kg/m^3 fluid density; and a 9.81 m/s^2 gravitational acceleration constant [6]. We then computed two WSS metrics, including magnitude of the mean wall shear stress over one orbital cycle (MagMeanWSS) and transverse wall shear stress (transWSS), which is the magnitude of the components of the instantaneous WSS vectors perpendicular to the mean WSS direction averaged over one orbital cycle that characterizes the multidirectionality of WSS [6]. The formulations of these two metrics are

$$MagMeanWSS = |\tau_{mean}|, \text{ where } \tau_{mean} = \frac{1}{T}\int_0^T \tau_w \, dt \quad \textbf{(1)}$$

$$transWSS = \frac{1}{T}\int_0^T \left| \overrightarrow{\tau_w} \cdot \left(\vec{n} \times \frac{\int_0^T \overrightarrow{\tau_w} \, dt}{\left| \int_0^T \overrightarrow{\tau_w} \, dt \right|} \right) \right| dt \quad \textbf{(2)}$$

where τ_w is the instantaneous WSS, T is the period of the cycle, and $\vec{n}$ is the unit normal vector to the flow. Bars represent magnitude.

Cell Culture. Primary human umbilical vein endothelial cells (HUVECs) pooled from 10 donors (ATCC), were used for all experiments at passages 4 to 7. HUVECs were maintained with vascular cell basal medium, supplemented with endothelial cell growth kit-BBE (ATCC) and 0.1% Penicillin-Streptomycin-Amphotericin B solution (ATCC) within a humidified incubator at 37°C and 5% CO_2, as per the supplier's protocol. Cells were sub-cultured and seeded into the wells

of 6-well plates at a density of 15,000 cells/cm^2. Prior to cell seeding, wells were coated with rat tail type I collagen (Corning) in 1% 17.5 mM of acetic acid and distilled water overnight in a humidified incubator at 37°C and 5% CO_2. After, collagen-coated wells were carefully washed three times with PBS and then seeded immediately.

Experiment Setup. Experiments were run two days after seeding with 2.41ml of media in each well to give a resting media height of 2.5 mm. PBS was put in the spaces between the wells to minimize the effects of media evaporation. One covered well plate was placed on an orbital shaker (Grant Instruments) and run for 24 hrs at 200 RPM within a humidified incubator at 37°C and 5% CO_2. As a control, a second cell-seeded well plate was placed in the same incubator as the orbital shaker.

Staining and Imaging. After 24 hrs of flow, cells were incubated in 4% paraformaldehyde in PBS for 10 mins and then stained for eNOS. Briefly, cells were permeabilized with 0.1% Triton X100 in PBS for 15 mins and incubated with blocking buffer (1% W/V bovine serum albumin, 22.52 mg/ml glycine, in PBST) for 30 mins to prevent nonspecific binding. Cell layers were then incubated with mouse-eNOS primary antibody at 1:100 (ab76198, Abcam) and Alexa Fluor secondary antibody (ab150117, Abcam) at 1:750, both of which were diluted in blocking buffer and incubated for 1 hr. All incubation steps were conducted on a rocker at room temperature.

Imaging and Analysis. Cells were imaged with Zeiss LSM 800 confocal microscope at 10x magnification. All confocal settings were kept constant over all cell layers. A tile scan of 30-by-2 was taken to capture the cells from the center to the periphery of the well with 16 focus points. The center of each well was identified by finding the left and upper most tangent of the well. Images were analyzed using a custom MATLAB script that computed the average pixel intensity for each image.

Outputs and Statistics. Fluorescence intensity of eNOS as a function of radial position in the well was quantified and a linear regression was performed for each cell layer. The slopes of these lines from experimental versus control cell layers were compared using a one-tailed, two-sample *t*-test. A Pearson's correlation coefficient was computed for eNOS intensity versus the WSS metrics.

RESULTS

Fluorescence intensity of cell layers under flow at the center of the well was 32.9% higher than the same location in cell layers under static culture. This ratio continually increased moving towards the periphery to 141% at 12.7 mm radially. Regressions showed a mean slope of 1.02 ±0.12 (eNOS intensity/mm) for the orbital shaker layers, which was significantly different from controls, 0.10±0.11, $p < 0.009$ (Figure 1).

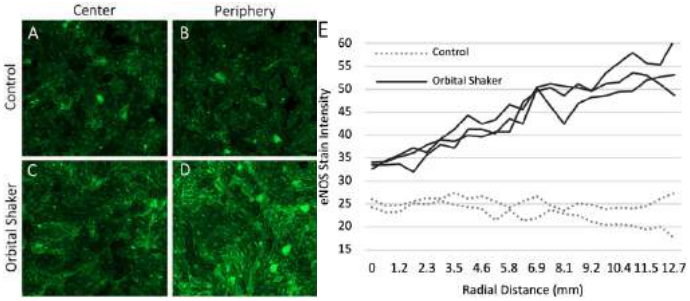

Figure 1: Representative eNOS fluorescence images at the center and periphery (12.7 mm from center) for the control (A and B) and orbital flow cell layers (C and D). (E) Plot shows comparison of average fluorescence intensity where all flow values are greater than control.

The fluorescence intensity of eNOS exhibited a statistically significant correlation with the two computed WSS metrics, wherein the relationship with MagMeanWSS had a Pearson's rho coefficient of 0.94 ($p < 0.001$) and that for transWSS had a coefficient of -0.93 ($p < 0.001$).

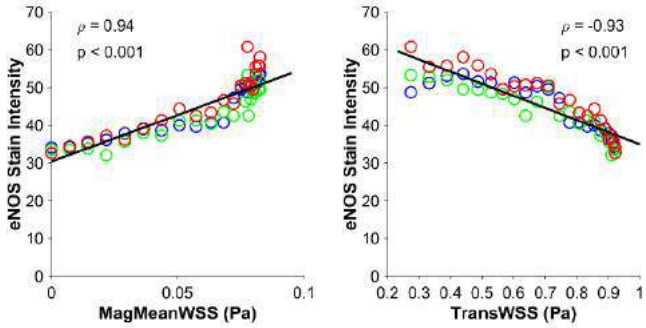

Figure 2: eNOS fluorescence intensity of endothelial cell layers under orbital flow (n=3, each given by red, blue, and green circles, respectively) as a function of two WSS metrics, magnitude of the mean WSS vector (left) and transverse WSS (right). Linear regression lines are in black.

DISCUSSION

Shear stress due to blood flow is an important determinant of endothelial cell function/dysfunction and the development of atherosclerosis. Numerous studies have characterized relationships between WSS metrics of disturbed flow and (patho-)biological readouts, but typically without consideration of the biological response over a continuous range of WSS [3]. The orbital shaker is a convenient tool that can address this deficiency because WSS in a well plate continuously varies from the center to the periphery. Using this approach herein, we found a nearly constant increase in eNOS expression over the well radius from the center to the periphery. In addition, eNOS was higher in cells at the center of the wells exposed to orbital flow compared to cells in static media, which suggests that some flow, even if disturbed, is better than none. These increases in eNOS expression as a function of well radius were highly significantly correlated with the computed WSS metrics, wherein a positive correlation was seen versus magmeanWSS (atheroprotective flow) and a negative correlation was seen with transWSS (atherogenic flow). Defining such relationships over a continuous range of WSS may improve our understanding of endothelial cell function and ability to predict atherosclerosis development.

ACKNOWLEDGEMENTS

We gratefully acknowledge support for this work from the American Heart Association (19CDA34660218), the National Science Foundation (CMMI1944131), and the National Institutes of Health (R21EB028960).

REFERENCES

[1] Roger V.L. et al., *Circulation*, 125(1):e2-e220, 2012.
[2] Davies P.F., et al., Cardiovasc Res., 99(2):315-27, 2013.
[3] Warboys C.M., et al., *Atherosclerosis*. 285:170-177. 2019
[4] Paola A., et al., *Physics of Fluids*, 30(3):032107, 2018.
[5] Paola A., et al., *Physics of Fluids*, 30(3):032108, 2018.
[6] Arshad M., et al., *J. R. Soc. Interface*, 18(174):20200772, 2021.

SB3C
biomechanics.
bioengineering.
biotransport.

PI Attestation

Student Paper Competition
Summer Biomechanics, Bioengineering and Biotransport Conference 2021

This form must be completed and submitted via the SB3C website before a BS or MS-level Student Paper Competition abstract can be submitted. The form is not necessary for PhD-level abstracts.

Student name: Olivia Kight

Student institution: Mercer University

Competition level (MS or BS): BS

Advisor name: Sinjae Hyun

Advisor institution (if different):

Advisor signature:

Date signed: 1/23/20

By signing above, I attest to the following:

1. I serve as an advisor/PI of this student, and I consent to the submission.
2. The student conducted this work while they were registered in the BS/MS level for which they compete.
3. The student completed the majority of the work presented.
4. The student will submit as the first and presenting author, without co-first authors.
5. The student will not submit more than one entry to the competition.
6. The student has not won a student paper competition award in the same level in which they will participate this year.
7. The work is unpublished at the time of submission.
8. The same work will not be submitted for consideration in any other session at the meeting.
9. The student will be available during the conference to answer questions about this work independently (e.g., without assistance from research advisor(s) or peers).

ROLE OF MUSCLE ACTIVATION ON LUMBAR SPINE FORCE IN FRONTAL IMPACT LOADING

Sagar Umale, John Humm, Narayan Yoganandan

Medical College of Wisconsin
Milwaukee, WI, USA

INTRODUCTION

Anthropomorphic test devices (Hybrid III) are used for crashworthiness studies in automotive, military, aviation, and athletic environments [1-3]. These infrangible physical devices have been used for frontal and rear impacts, i.e., $G_{\pm X}$ accelerative loading, to protect civilian motor vehicle and mounted military occupants. The recorded data from load cells (e.g., femur and upper neck) and accelerometers (chest) are used in the injury criteria (femur force, upper neck axial force and sagittal moment, and head injury criterion) in Federal standards [2], whereas, loads on the lumbar spine are not a part of the assessment. While such studies are underway, human body models have been developed to understand the response of the various body regions with a better representation of the human anatomy, especially from a musculoskeletal perspective. Examples are the Global Human Body Models Consortium (GHBMC) and Toyota Model for Human Safety (THUMS), and others [4-6]. The GHBMC model has been widely used for analyzing loads on the spine and neck and kinematics under different load vectors ($G_{\pm X}$, $G_{\pm y}$, and $G_{\pm z}$) [7, 8]. The model currently does not include the effects of muscles on spinal loads. As muscles contribute to spine stability, posture, internal spinal load paths and load sharing, a better representation of the human musculature is necessary to obtain realistic estimates of the forces. As studies suggest bracing to be a contributor to kinematic variation and injury outcome [9], it is important to investigate the effect of muscle activation on spinal loads using a model that better represents the human muscular anatomy and material properties. The objective of the study, therefore, was to incorporate the thoracic musculature to the GHBMCv5 model and determine the segmental forces on the lumbar spine from frontal impact in a vehicle environment.

METHODS

The anatomy and the origin-insertion locations of muscle were identified [10]. Eleven muscle groups, consisting of 210 one-dimensional elements were incorporated (Figure 1 - left): erector spinae iliocostalis lumborum pars thoracis; erector spinae iliocostalis lumborum pars lumborum; erector spinae longissimus thoracis pars lumborum; erector spinae-longissimus thoracis pars thoracis; multifidus lumborum; multifidus thoracis, quadratus lumborum muscles; rectus abdominus; external oblique muscles, internal oblique muscles, and psoas major. The material properties (cross-sectional areas, density, stress-strain relationship, strain rate) [10-13] were used from the literature to define the Hill-type model for the muscles. The effect of the musculature on occupant kinematic response was verified using human volunteer (three males) sled test experimental data [14]. The setup included a volunteer placed on a rigid seat attached to a sled which was accelerated at 1g and decelerated by collision with a damper setup. The muscle activities were measured using EMG electrodes attached to the skin. The synchronized volunteer kinematics was measured using a motion capturing system. The model was simulated under same experimental boundary conditions (Figure 1 - center). It was positioned on a rigid seat and restrained using a two-point seatbelt to constrain the lower limbs. Three simulations were performed: model without muscles, model with no muscle activation, and muscle activation. The normalized (with respect to peak muscle activation) EMG curves reported in the tests were used for muscle activation.

The models were simulated for 500 ms, and each simulation took approximately 90 hours to solve on a high-performance computing cluster. The head and thoracic excursions from the simulations were compared with the experimental excursions.

Figure 1: Left – the thoracic musculature incorporated into the model, Center – the setup to reconstruct experiments, Right – the setup to simulate frontal impact.

To investigate the effect of bracing during frontal impacts, a Toyota Yaris vehicle environment was used (Figure 1 - right). The occupant was positioned in the seat and restrained with a 3-point seatbelt with pretensioner and retractor. The seatbelt pretensioner was activated as the impact started, the retractor was activated at 12 ms, and the steering wheel-mounted airbag was deployed at 20 ms [15]. Occupant contact with the vehicle environment was modeled using automatic surface-to-surface contact. The entire setup was given an initial velocity of 15.6 m/s, and the vehicle environment was decelerated using a 50 g pulse. Muscles activation was varied: no activation, 50% activation and 100% activation. Cross-section planes were defined at L1, L3 and L5 levels to obtain the lumbar spine forces. The models were simulated for 150 ms, and each simulation took approximately 27 hours to solve on a high-performance computing cluster.

RESULTS

The peak frontal head excursion from the volunteer tests was compared with the excursions from the three simulations. The simulation without muscles and with no activation of muscles showed larger head excursion compared to the volunteers. Whereas, the head excursion in the simulation with muscle activation, was within the range of volunteer excursions reported in the tests (Figure 2 - left). The thoracic excursions at T1 and T10 vertebrae were also within the experimental excursion range for muscle activation case.

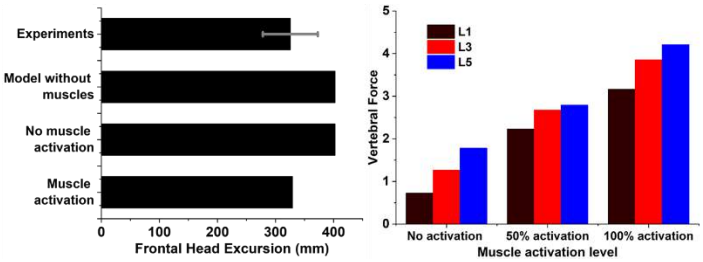

Figure 2: Left – comparison of model head excrusion with the volunteer head excursions, Right – the lumbar spine forces for different thoracic muscle activation levels.

The lumbar spine forces at the L1, L3 and L5 levels extracted using cross-sectional planes were, 0.7, 1.3 and 1.8 kN for no muscle activation, 2.2, 2.7 and 2.8 kN for 50% muscle activation, and 3.2, 3.8 and 4.2 kN for 100% muscle activation. They increased for the higher muscle activation levels and were greater at the inferior level for all activation levels. The timing of the peak forces for all three activation levels was between 80 and 90 ms.

DISCUSSION

The incorporation of the musculature improved the kinematic response of the occupant model for the low speed human volunteer impact tests. The EMG data in the tests was reported for superficial muscles and the same activation curves were used for the deep musculature activation. These results show that the occupant response in finite element human body models can be improved with muscle activation data from volunteer experiments.

The increase in the peak compressive force was more pronounced at the proximal levels of the spine with increased levels of activation. The upper lumbar spine injuries reported in literature [16, 17] under the $G_{\pm X}$ accelerative vector may be attributed to the muscle activation process, although the exact profile of activation for each muscle is not known. It should be noted that European studies have also reported the upper lumbar level bias in the injury, while the environment (belt restraints, seat and vehicle stiffness) is different [18, 19]. In the present study, muscle anatomical-geometrical data was used from literature in supine and upright postures. It is known that the morphologies of the human lumbar and cervical spine muscles are dependent on posture [20, 21]. From this perspective, it is important to obtain sitting posture muscle geometry data from radiographic or MRI scans, and develop volunteer-specific models to study the loading pattern of lumbar spine. The updated models can be used to determine the segmental or vertebral level loads due to the added personal protective equipment (PPE) for soldiers. These future studies will be helpful to delineate the role of muscles for civilian and military populations.

ACKNOWLEDGEMENTS

This research study was supported in part by the Office of the Assistant Secretary of Defense for Health Affairs, through the Broad Agency Announcement under Award No. W81XWH-16-01-0010, Department of Transportation DTNH22-13-D-00290L, and Department of Veterans Affairs Medical Research. The authors thank the Global Human Body Models Consortium and Argonne National Laboratory. The Opinions, interpretations, conclusions, and recommendations herein are those of the authors and are not necessarily endorsed by the US Department of Defense or other sponsors.

REFERENCES

[1] Elgy, I.D., et al J Biomech, 2020. 101: p. 109618.
[2] Beeman, S.M., et al., Accid Anal Prev, 2012. 47: p. 128-39.
[3] Kent, R., et al., J Biomech, 2020. 99: p. 109551.
[4] Vavalle, N.A., et al., Ann Biomed Eng, 2015. 43(9): p. 2163-74.
[5] Iwamoto, M., et al., Traffic Inj Prev, 2015. 16 Suppl 1: p. S36-48.
[6] Kent, R., et al., Stapp Car Crash J, 2005. 49: p. 231-49.
[7] White, N.A., et al., J Biomech Eng, 2014. 136(11).
[8] Gayzik, F.S., et al., Traffic Inj Prev, 2018. 19(sup1): p. S183-S186.
[9] Iwamoto, M., et al., Enhanced Safety of Vehicles (ESV), 2015.
[10] Östh, J., 2010, Chalmers University of Technology: Sweden.
[11] Winters, J.M., Springer, New York, 1990.
[12] Winters, J.M., Human Movement Sci, 1995. 14(4): p. 401-442.
[13] Ward, S.R. and R.L. Lieber, J Biomech, 2005. 38(11): p. 2317-20.
[14] Ejima, S., et al., IRCOBI Conference 2007.
[15] Phen, R.L., et al. Advanced air bag technology assessment, 1998.
[16] Pintar, F.A., et al., Ann Adv Automot Med, 2012. 56: p. 277-83.
[17] Kaufman, R.P., et al., Accid Anal Prev, 2013. 59: p. 153-63.
[18] Thorsten Adolph, et al., IRCOBI Conference 2013, 2013.
[19] Lotta Jakobsson, et al., IRCOBI Conference, 2016.
[20] Shaikh, N., et al., The European Spine Society, 2020. 29(9): p. 2306-2318.
[21] Hoon Choi, et al., Mil Med (in Press), 2020.

ENHANCEMENT OF DRUG DELIVERY TO PANCREATIC CANCER TARGETING FIBRIN MATRIX

Sae Rome Choi (1), Hye-ran Moon (1), Yi Yang (2), Matthew J. Flick (2), Bumsoo Han (1)

(1) School of Mechanical Engineering
Purdue University
West Lafayette, IN, USA

(2) Dept. of Pathology & Laboratory Medicine
University of North Carolina
Chapel Hill, NC, USA

INTRODUCTION

Pancreatic ductal adenocarcinoma (PDAC) is one of the most-deadly cancers with a dismal 10% five-year survival rate [1]. Current treatment is primarily limited to chemotherapy but is largely ineffective due to chemoresistance and poor drug delivery to the cancer cells. A dense desmoplastic stroma is a hallmark of PDAC, including cancer-associated fibroblasts (CAFs) and substantial extracellular matrix (ECM) [2]. In order to enhance the treatment outcomes, it is essential to devise strategies for improving drug delivery through the PDAC tumor microenvironment (TME).

Therapeutic strategies targeting the tumor stroma have been proposed to address the poor drug delivery. Since the PDAC stroma matrix is abundant in type I collagen and hyaluronan (HA), depletion of HA is being pursued to improve drug delivery [3,4]. Despite recent advances, it is still extremely challenging to achieve effective drug delivery to PDAC due to the complex stromal microenvironment. Recently, it was reported that fibrin is another major component of the PDAC ECM [5]. Fibrin is the primary matrix component found in a blood clot, but it is also found to be abundant in the PDAC stroma because of leaky vasculature leading to coagulation in the PDAC TME. The coagulation cascade is amplified through conversion of prothrombin to active protease thrombin by Tissue Factor (TF), which is highly expressed by pancreatic cancer cells [5]. In turn, thrombin converts fibrinogen into fibrin in the ECM as illustrated in Figure 1.

The objective of this study is to investigate the effects of fibrin matrix on the drug delivery in PDAC. It is hypothesized that (i) blood coagulation and fibrin formation within the PDAC TME restricts drugs from reaching the tumor cells, and (ii) drug delivery to PDAC cells can be improved by reducing fibrin in the stromal matrix. To test this hypothesis, transport properties of FITC-labeled dextran was measured in a collagen-fibrin matrix using the integrated optical imaging (IOI) method. Moreover, doxorubicin accumulation and penetration in collagen-fibrin matrix was measured in the microfluidic model tumor-microenvironment-on-chip (T-MOC) which mimics *in vivo* transport dynamics.

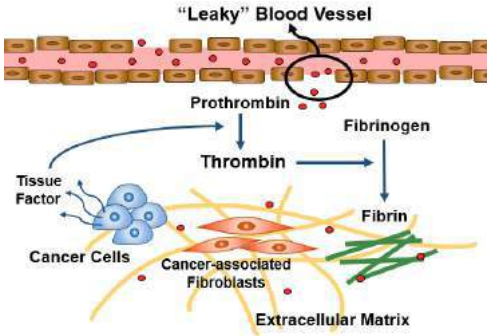

Figure 1. Thrombin mediated PDAC coagulation pathway and fibrin deposition in the extracellular matrix.

METHODS

Preparation of collagen-fibrin matrix

6 mg/ml type I collagen matrix was prepared with 10x PBS, NaOH, HEPES solution, FBS, Glu, P/S, and cell-culture grade distilled water. 6 mg/ml fibrinogen from bovine plasma (Sigma-Aldrich, St. Louis, MO) was dissolved in 0.9% NaCl at 37°C for 3 hours and sterile filtered with 0.2 μm polyethersulfone (PES) filter. Collagen and fibrinogen solutions were mixed in 1:1 ratio to reach a final concentration of 3mg/ml:3mg/ml collagen:fibrinogen. 500 μl of solution was suspended in PDMS mold with 12mm diameter and allowed to polymerize at 37°C for 1 hour 15 minutes. Subsequently, 1 U/ml thrombin was suspended above the gel and incubated for additional 1 hour for fibrin polymerization. The gel was thoroughly washed with distilled water before microinjection experiment.

Integrative optical imaging (IOI)

The diffusivity of the collagen-fibrin(ogen) matrix was measured using an integrative optical imaging (IOI) method [6]. A small volume (25-50 pL) of fluorescent probes with known sizes were injected into the tissue constructs using a microinjection system (MINJ-D-BDCI, Tritech). In this study, FITC-labeled dextran with molecular weight of 4 kDa (hydrodynamic radius = 1.3 nm) and 40 kDa (5.1nm) were used. After the injection, fluorescent images were taken at a 2-second interval for 120 seconds. The fluorescence intensity of the images was quantified using image processing software (MATLAB, Mathworks). The intensity profiles were curve-fit to the analytic solution of diffusion from a point source to obtain an estimated value of diffusivity.

Drug Delivery Assay using T-MOC

The T-MOC device was prepared with murine pancreatic cancer line, eKIC, as reported previously [7]. Briefly, cells mixed in 3 mg/mL collagen-fibrinogen solution at 1×10^7 cells/mL concentration was loaded through the interstitial channel and incubated at 37ºC for 1 hour 15 minutes. Afterward, 1 U/mL thrombin diluted in RPMI 1640 with 2.05 mM L-glutamine and 100 µg ml–1 penicillin/streptomycin was perfused through the lymphatic channels and incubated for 1 hour. 2 µM doxorubicin diluted in supplemented culture medium was perfused through the capillary channel and fluorescent images were taken at a 30-minute interval for 24 hours. Drug accumulation and penetration by cellular uptake were analyzed as developed previously [8].

RESULTS AND DISCUSSION

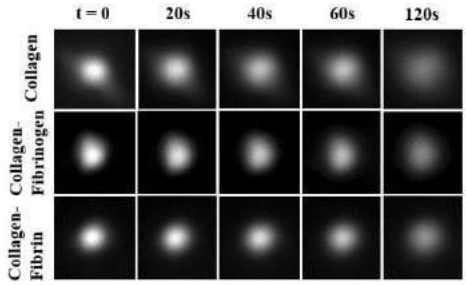

Figure 2. Fluorescent images of 4 kDa dextran diffusion in collagen and collagen-fibrin(ogen) matrices.

Sequential fluorescent images of 4 kDa dextran particle diffusion in different tissue constructs are shown in Figure 2. Even at early time point (20s), the radial diffusion of dextran in collagen-fibrin(ogen) matrices is notably reduced compared with collagen matrix. This difference is further intensified at the end of the experiment at 120s. The measured fluorescent intensity from above images is proportional to the spatiotemporal dextran concentration. The resulting relative decrease in the intensity at t = 120s normalized to t = 0s are 0.48, 0.5, and 0.51 for collagen, collagen-fibrinogen, and collagen-fibrin, respectively. The slowest decay of intensity in collagen-fibrin matrix reflects the reduced matrix transport properties due to the presence of fibrin.

The results from fluorescent images also correlate with the calculated diffusivity in Figure 3. For both 4 kDa and 40 kDa dextran, a significant decrease in diffusivity was observed with the introduction of fibrin(ogen) matrix compared with collagen matrix ($P < 0.05$). This phenomenon is likely due to the more clustered and finer mean fiber diameter when collagen is formed with fibrin [9]. Moreover, fibrin matrix has a reported smaller pore size and fiber radius compared with collagen [10]. Taken together, these findings suggest that mechanical properties of fibrin imposes physical hindrances for particle diffusion. The decrease in diffusivity with fibrin(ogen) is more evident with 40 kDa dextran compared with 4 kDa dextran. However, the saturation of matrix pores with 40 kDa dextran resulting from greater particle size likely contributes to the no meaningful difference between diffusion in fibrinogen and fibrin.

To more accurately model what may be happening the *in vivo*, pancreatic cancer cells were cultured in collagen-fibrin matrix in microfluidic device, known as tumor-microenvironment-on-chip (T-MOC).

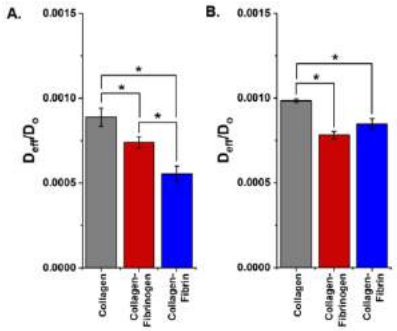

Figure 3. A. 4 kDa and B. 40 kDa dextran diffusivities normalized to free diffusivity, D_o, at 37ºC.

Doxorubicin transport was measured from capillary into the interstitial channel (Figure 4). Pancreatic cancer cells demonstrated a notable decrease in accumulation and penetration of doxorubicin in collagen-fibrin compared with collagen matrix alone. The concentration of collagen-fibrin was 3 mg/ml and that of collagen control was 6 mg/ml. Even at lower concentrations, collagen-fibrin significantly deterred doxorubicin transport.

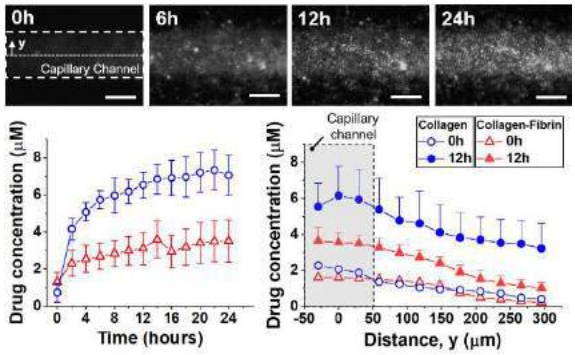

Figure 4. Doxorubicin accumulation by cellular uptake and penetration are hindered with fibrin deposition with collagen.

The results from this study demonstrated significantly reduced matrix transport properties within a fibrin matrix by measuring the diffusivity of varying sizes of dextran and doxorubicin transport in T-MOC. These results further provide convincing evidence for fibrin as a novel target for enhancing drug delivery to PDAC tissue. Additional studies are necessary to demonstrate the improved drug transport after fibrin degradation.

ACKNOWLEDGEMENTS

This work is partially supported by Grants from National Institutes of Health (U01 HL143403, UL1 TR002529 to BH, and R01 CA211098, U01 HL 143404, R01 DK112778 to MJF).

REFERENCES

[1] Siegel, R. L. et al., *CA A Cancer J Clin*, 69:7–34, 2020.
[2] Han, B. et al., *Cancer Letter,s* 380:319–329, 2016.
[3] Wong, K.M. et al., *Curr Oncol Rep*, 19:47, 2017.
[4] Provenzano, P. P. et al., *Cancer Cell*, 21(3):418-429, 2012.
[5] Yang, Y. et al. *Cancer Res*, 79:3417–3430, 2019.
[6] Nicholson, C. et al., *Biophysical Journal*, 65:2277-2290, 1993.
[7] Moon, H. et al., *Lab Chip*, 20:3720-3732, 2020
[8] Ozcelikkale, A. et al., *J Control Release*, 266:129-139, 2017
[9] Lai, V.K. et al., *Acta Biomater*, 8(11):4031-42, 2012
[10] Moreno-Arotzena, O. et al., *Materials*, 8(4):1636-51, 2015

MODULATING EPITHELIAL FLUID SECRETION AND TRANSMURAL FLUID PRESSURE TO REGULATE PROLIFERATION AND BRANCHING MORPHOGENESIS IN THE EMBRYONIC LUNG

Shelby R. Mohr-Allen (1), Victor D. Varner (1)

(1) Department of Bioengineering
The University of Texas at Dallas
Richardson, TX, USA

INTRODUCTION

The development of several organs in the body, including the lung, kidney, and salivary gland, involves a series of recursive branching events that are referred to collectively as branching morphogenesis. In the embryonic lung, this process builds the bronchial tree, which facilitates the transport of air to the distal alveoli where gas exchange occurs [1]. Normal airway branching depends crucially on cell proliferation, as well as on reciprocal interactions between the branching airway epithelium and the adjacent pulmonary mesenchyme. Several signaling pathways, including those downstream of sonic hedgehog (Shh), Wnt, as well as various fibroblast growth factors (FGFs), have been shown to regulate airway branching, but recent work has shown that mechanical forces can also influence this process. The embryonic airways are fluid-filled, and changes in luminal fluid pressure can modulate rates of branching morphogenesis in cultured embryonic lung explants [2]. It is unclear, however, how these changes in pressure impact the patterns of proliferation that sculpt the bronchial tree.

Here, we used different pharmacological activators and inhibitors of epithelial fluid secretion to modulate the transmural fluid pressure in cultured embryonic chicken lungs. These experiments were then combined with quantitative fluorescence microscopy to determine how changes in fluid secretion impact the patterns of proliferation in the developing lung. We also microinjected a small volume of biologically-inert oil into the lumen of other embryonic lungs to locally dilate the embryonic airway. These explants were then cultured and quantified for changes in proliferation in the neighborhood of the distended airway.

METHODS

Fertilized White Leghorn chicken eggs were incubated at 37°C in a forced-draft incubator to Hamburger and Hamilton stage 26. Embryonic lungs were dissected in phosphate-buffered saline (PBS) using fine forceps and cultured for 24 hr on Nucleopore membranes at the air/liquid interface in DMEM/F12 medium supplemented with 5% fetal bovine serum (FBS) and antibiotics. The culture medium was supplemented with either an agonist (1-10 μM forskolin, or 100 μM CPT-cAMP) or antagonist (100 μM CFTR inhibitor-172 or 100 μM bumetanide) of epithelial fluid secretion. In order to directly dilate the airway epithelium in some experiments, a pulled glass micropipette was filled with mineral oil and inserted it into the lumen of the embryonic airway. A small amount of mineral oil was then injected into the lumen with the use of a pneumatic pump.

Bright-field images of cultured explants were captured at 0 and 24 hr. We used the Click-iT EdU Imaging Kit to quantify rates of epithelial proliferation. Samples were pulsed with EdU 20 min prior to fixation. Fixed explants were then co-stained with LCAM (E-Cadherin) immunofluorescence and DAPI, to label the airway epithelium and nuclei, respectively, and then optically cleared. Confocal fluorescence images of whole-mount explants were then captured using a laser scanning confocal microscope. Quantitative image analysis was performed using ImageJ. Briefly, individual nuclei were counted on high resolution confocal images of both EdU and DAPI fluorescence and used to compute the fraction of proliferating cells along both bud-forming and non-bud-forming regions of the airway epithelium.

RESULTS

We used pharmacological modulators of epithelial fluid secretion to modulate the transmural fluid pressure in cultured embryonic chicken lungs. Treatment with forskolin, an activator of cAMP and agonist of fluid secretion, caused the embryonic airways to dilate dramatically and produced a significant decrease in the formation of new branches after 24 hrs of culture (Fig. 1). (Similar results were also obtained using

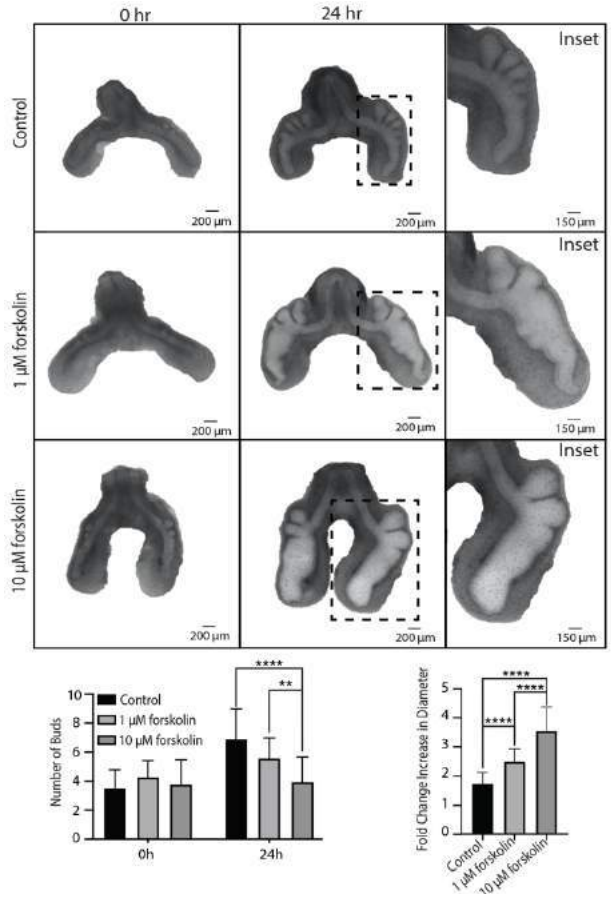

Figure 1: Embryonic chick lungs treated with forskolin, an agonist of fluid secretion, show decreased branching morphogenesis.

explants treated with 100 µM CPT-cAMP, another activator of cAMP and agonist of fluid secretion.) To determine if the observed decreases in branching were associated with a concomitant change in epithelial proliferation, we quantified rates of EdU incorporation in explants cultured in the presence of forskolin. Increased levels of fluid secretion modified the patterns of proliferation observed along the embryonic airway epithelium (Fig. 2). In control explants, we detected elevated

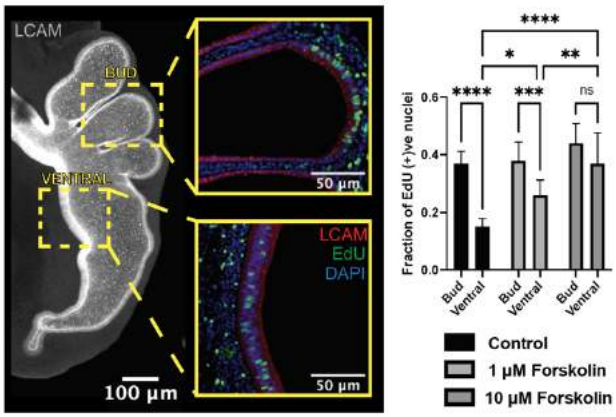

Figure 2: Increased luminal pressure promotes proliferation in a non-bud forming region of the embryonic chick airway epithelium

levels of proliferation in new epithelial buds, but low levels along non-branching regions of the ventral airway epithelium. Treatment with forskolin, however, increased proliferation in this non-bud-forming region of the airway to levels on par with those observed in epithelial buds (Fig. 2).

To perturb the transmural pressure in other embryonic lungs, we microinjected a small volume of mineral oil into the lumen to locally distend the embryonic airway (Fig. 3). This purely physical perturbation eliminates the possibility of off-target molecular effects due to pharmacological modulators of fluid secretion, allowing us to attribute any changes in branching and proliferation to localized changes in transmural pressure. Preliminary experiments have suggested that each localized distension of the airway inhibits the formation of nearby epithelial buds (Fig. 3) and leads to a localized increase in proliferation, as revealed by EdU incorporation.

Lastly, we also cultured some explants in the presence of either 100 µM CFTR inhibitor-172 or 100 µM bumetanide, which inhibit epithelial fluid secretion via the inactivation of either the CFTR or NKCC1/2 ion channels, respectively, to determine if decreases in transmural pressure elicit a branching phenotype. Indeed, explants treated with either of these inhibitors developed collapsed airways and increased numbers of new epithelial buds. Taken together, these data suggest that changes in transmural pressure can modulate the branching and proliferation of cultured embryonic lung explants.

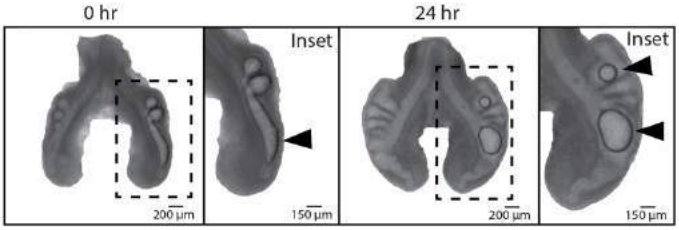

Figure 3: Microinjection with mineral oil produces local dilation of airway epithelium leading to disrupted branching morphogenesis.

DISCUSSION

Many congenital lung conditions, including pulmonary hypoplasia and congenital diaphragmatic hernia, can be attributed to defects in the mechanical environment surrounding the lung [3]. It is unclear, however, if the changes in transmural fluid pressure associated with these conditions can regulate the patterns of proliferation that underlie airway branching morphogenesis. Our experiments suggest that increases in epithelial fluid secretion, and thus transmural pressure, can inhibit branching and alter the spatial distribution of proliferating cells in cultured avian lungs. These results were somewhat suprising, since previous work has suggested that increases in pressure promote branching morphogenesis in the embryonic mouse lung. The reason for these species-specific differences remains unclear. Future work will use similar experimental approaches to modulate transmural pressure in cultured mammalian lung explants to resolve this apparent contradiction.

ACKNOWLEDGMENTS

This work was supported, in part, by the NIH grant R01HL145147 to VDV.

REFERENCES

[1] Cardoso WV, Lü J, *Development*, 133:1611-1624, 2006.
[2] Nelson CM, et al., *Development*, 144:4328-4335, 2017.3
[3] Smith NP, et al., *Arch. Dis. Childh,* 90**:**426-428, 2005

RAPID AUTOMATIC RECONSTRUCTION OF HEART VALVES AND CARDIAC STRUCTURES FROM CT IMAGES FOR PRE-TAVR EVALUATIONS USING A PARAMETRIC LEAFLET MODEL

Huang Chen (1), Beom Jun Lee (1), Sri Krishna Sivakumar (1), Breandan A. Yeats(1), Vinod H. Thourani (2), Venkateshwar Polsani (2), Lakshmi P. Dasi (1)

(1) Department of Biomedical Engineering
Georgia Institute of Technology
Atlanta, GA

(2) Department of Cardiovascular Surgery
Marcus Valve Center, Piedmont Heart Institute, Atlanta, GA

INTRODUCTION

As an alternative option to the highly invasive surgical aortic valve replacement (SAVR), transcatheter aortic valve replacement (TAVR) has become more popular in recent years [1, 2], even among low-risk patients [3]. Unlike SAVR, whose size and implantation location can be precisely determined during surgery, TAVR relies on more thorough pre-surgery evaluations to determine the valve type, size, and deployment strategies with the help of advanced medical imaging techniques [4]. A sub-optimal valve deployment has been associated with various adverse effects including elevated transvalvular pressure gradient, paravalvular leakage, aortic root rupture during implantation [5], coronary obstructions [6], etc. To minimize these adverse effects, pre-TAVR evaluations may involve accurately reconstructing the patient's anatomy, generating a computational mesh, and using it for Finite Element Analysis (FEA) or/and Computational Fluid Dynamics (CFD) simulations. These state-of-the-art approaches based on patient-specific geometries have proven to have high predictive capabilities for TAVR outcomes and to prevent severe adverse events from happening in high-risk patients. However, conducting such evaluations requires reconstructing a patient's anatomy from CT or MRI data, which is a tedious and time-consuming manual process (3-6 hours per case). To address this problem, we have developed an automatic method to build patient-specific geometries based on a parametric leaflet model and generate meshes for *in-silico* studies with just a few manual inputs (about 5-10 minutes per case).

METHODS and RESULTS

To start the automatic mesh generation from imaging data, one needs to pick several landmark points related to the aortic valve. A parametric leaflet model is used to fit the valve geometry, followed by an automatic aortic root reconstruction algorithm that extracts the shape of the aorta. Later, the coronary arteries and calcium deposits are obtained automatically using a region-growing algorithm. Finally, a mesh for computational studies is generated by combining all the components. A visual inspection and possible manual clean-up are performed to ensure the accuracy and quality of the mesh. A detailed illustration of the process is shown in Fig.1.

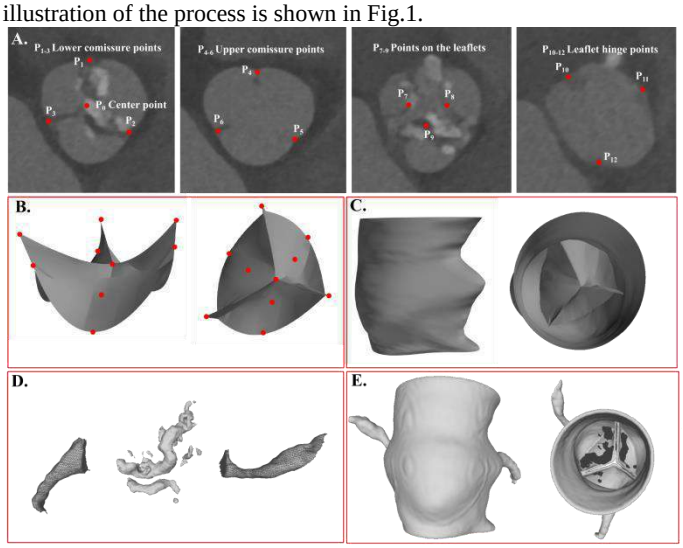

Figure 1: A detailed illustration of the auto segmentation process. (A) The locations of the thirteen landmark points; (B) The parametric leaflet model with landmarks shown; (C) Aortic root with parametric leaflets; (D) Coronary arteries and calcium deposits; (E) The final mesh output.

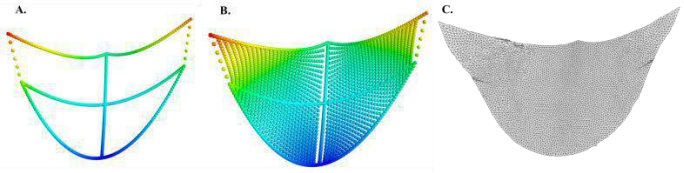

Figure 2: The parametric leaflet generation process. (A) A skeleton connecting the landmarks using second-order polynomials; (B) Multiple second-order polynomials are used to fit the leaflet surface; (C) The final triangular mesh.

Parametric leaflet model:

The parametric leaflet model is constructed based on thirteen landmark points (shown in Figs.1A&B: P_0 at the center coaptation point of the three leaflets; P_{1-3} and P_{4-6} are the six commissural points. P_{7-9} are three surface points on the leaflets, and P_{10-12} are the three leaflet hinges). First, a leaflet skeleton is generated using second-order polynomials connecting these landmarks (Fig.2A). Then, multiple second-order polynomials are fitted to the skeleton to create a surface (Fig.2B). Finally, triangular meshes are used to represent the leaflet (Fig.3C). This parametric leaflet model can handle complex surface geometries and capture individual leaflet's irregular shape. A parametric aortic valve sample is shown in Figs.1B &D.

Aortic root/aorta extraction algorithm:

The extraction of the aortic root/aorta geometry is based on an intensity-based, slice-by-slice, multi-point ray-casting edge detection algorithm (Fig.3). Slices parallel to the aortic annulus are extracted from the original 3D data. Starting with one point in the blood domain and casting rays in all directions, one can extract the intensity variations along the rays. A sudden jump of the intensity value from high (blood) to low (tissue) indicates the location of the aortic wall (Fig.3A). The boundary of the aorta is defined by connecting all the detected edge points. However, errors may occur in this process due to noise or poor image quality (Fig.3A). A modified method that casts rays from a series of origins is introduced to address this issue. Since most rays from different origins should converge at specific points on the actual aortic wall, and if there is a detection error for one ray, it is unlikely for rays from other origins to repeat the same error. Thus by comparing the detected edges from all origins, one can filter out the ambiguous points if they are too far away from the mean location. The mean value of the remaining points should accurately determine the aorta wall (Fig. 3B). Figures 3A&B have shown clearly that this multi-point approach can accurately capture the aortic root's shape. Finally, a cubic spline is fitted to all the detected points. This algorithm works from the left ventricular outflow graft to the ascending aorta. A reconstructed root geometry is shown in Fig.1C.

Coronary artery and calcium deposit segmentation:

Both coronary artery and calcium deposit geometries are segmented by an intensity-based region-growing algorithm. The coordinates of the two coronary ostia need to be specified (human input) as starting points for the algorithm. A global threshold of 850 Hounsfield Units (HU) is applied for the calcium as suggested in the literature [7], followed by a cleaning process that discards blobs smaller than 20 voxels or located outside the aorta.

Final mesh generation:

The final mesh assembling process is based on Boolean operations in the intensity space. First, the surface meshes of the aorta and the leaflets are thickened based on physiological values and voxelized. Later the coronary arteries and calcium deposits are added to the domain using Boolean operations. Finally, a marching cubes algorithm converts the voxel data into an STL mesh. The final mesh will be visually inspected and corrected for any problems before using it in computational simulation.

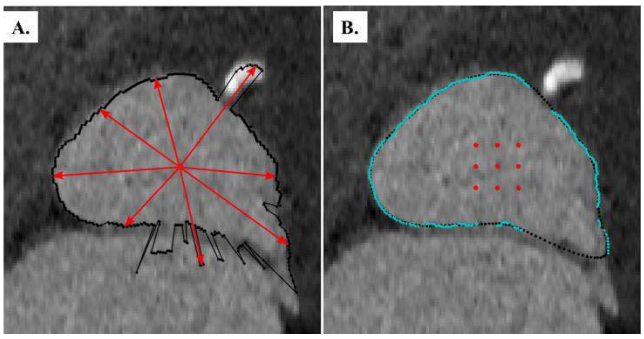

Figure 3: Aorta reconstruction process. (A) Detected aortic wall using a single-point ray-casting algorithm. (B) Detected aortic wall using the multi-point ray-casting algorithm.

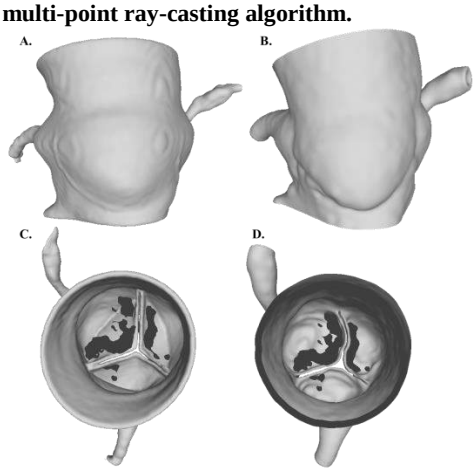

Figure 4: Comparisons between the automatic (left) and manual (right) segmentation results.

DISCUSSION

Comparisons with the manual segmentation results were carried out (Fig.4) to ensure the accuracy of this method. For the aorta, the auto-generated geometry (Fig.4A) was very similar to that from the manual segmentation process (Fig.4B). However, the manual result had more fine details due to less smoothing. In the en face views between the models (Figs.4C&D), they showed similar aortic leaflet geometries and calcium distributions. However, the current parametric leaflet model could not resolve the curved coaptation line between the leaflets, since only three landmark points were used for this line. If an extra landmark point along the coaptation line was added or a local deformation algorithm was applied, the edge of the leaflet would be captured more accurately. This improvement will be implemented and tested in our future work.

REFERENCES

[1] Makkar, Raj R., et al. *N Engl J Med*, 2012, 366(18): 1696-1704.
[2] Reardon, M. J., et al., *N Engl J Med*, 2017, 376(14): 1321-1331.
[3] Mack, M.J., et al., *N Engl J Med*, 2019. 380(18): 1695-1705.
[4] Litmanovich, D.E., et al., *Insights Imaging*, 2014. 5(1): 123-45.
[5] Pislaru, S.V., et al., JACC Cardiovasc Imaging, 2016. 9(2):193-206.
[6] Jabbour, R.J., et al., J Am Coll Cardiol. 2018. 71(14): 1513-1524.
[7] Jilaihawi, H., et al., Eur Heart J Cardiovasc Imaging, 2014. 15(12): 1324-32.

PRESSURE DROP AND RECOVERY WITH MITRACLIP: AN IN VITRO STUDY

S. Gooden (1), B. Yeats (1), V. Thourani (2), K. Boudoulas (3), L. Dasi (1)

(1) Department of Biomedical Engineering
Georgia Institute of Technology
Atlanta, Georgia, US

(2) Department of Cardiovascular Surgery
Marcus Valve Center
Piedmont Heart Institute
Atlanta, Georgia, US

(3) Division of Cardiac Surgery
The Ohio State University Wexner
Medical Center
Columbus, Ohio, US

INTRODUCTION

Mitral regurgitation is a prevalent disease which occurs when the two leaflets of the mitral valve (MV) do not close properly during systole. For treatment of symptomatic moderate-to-severe or severe MR in patients deemed high-risk for surgical treatment, Abbott's MitraClip may be used. MitraClip is the only FDA approved transcatheter device and one of two transcatheter devices with CE mark. The device clips the two leaflets together to reduce MR, creating a double orifice. The clipping scheme, i.e., placement of the device, depends on MR characteristics of the individual patient.

Analyzing mitral valve (MV) pressure gradient (MVPG) during the MitraClip procedure is important, as gradients of 5 mmHg or more are undesirable and can lead to iatrogenic mitral stenosis, worsening patient prognosis [1-2]. However, MVPG through the MV and the vena contracta can differ based on the clipping scheme. The objective of the study is to assess the pressure drop through a single and symmetric and asymmetric double orifice mitral valve analog.

METHODS

A rigid MV model was created for the unclipped single orifice (Figure 1a), symmetrically clipped (Figure 1b), and asymmetrically clipped (Figure 1c) cases, where the clipped cases mimic the MitraClip NT MV repair. The models were created using ABAQUS, where the MV was approximated as a tube, and opposing areas of 5 mm x 9 mm (the MitraClip footprint) were brought together while transvalvular pressure (30 mmHg) was imposed for the clipped cases. The inlet and total outlet areas were approximately 6.47 cm^2 and 1.82 cm^2, respectively.

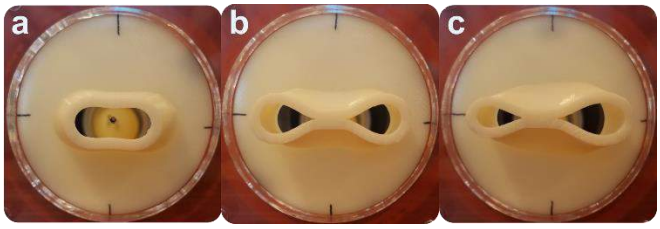

Figure 1: a) Single Orifice, and b) Symmetric and c) Asymmetric Double Orifice Models

Each model was placed upstream a bioprosthetic mitral valve in an *in vitro* left heart simulator, shown in Figure 2, that allows for high fidelity pressure and flow measurements. Hemodynamic conditions imposed include: 60 bpm heart rate; 3 and 5 L/min cardiac output (CO); 120 mmHg peak ventricular pressure. A 60-40 water-glycerin mixture was used to mimic the density (1060 kg/m^3) and kinematic viscosity (3.88 cSt) of blood. A Millar catheter was dragged through the orifice for pressure measurements, and data was collected at 100 Hz for 200 cycles at 19 positions, starting 4 mm upstream the annulus and ending 3 cm downstream the leaflet tip; volumetric flow rate was recorded simultaneously. MVPG was calculated.

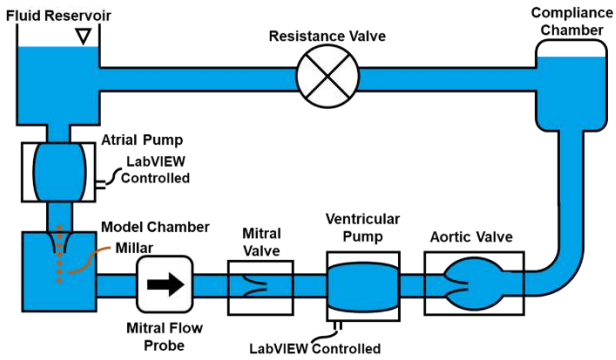

Figure 2: Mitral Flow Loop Schematic

RESULTS

MVPG for each model and CO is shown in Figures 3 and 4 for the peak of the E and A waves of mitral flow, respectively.

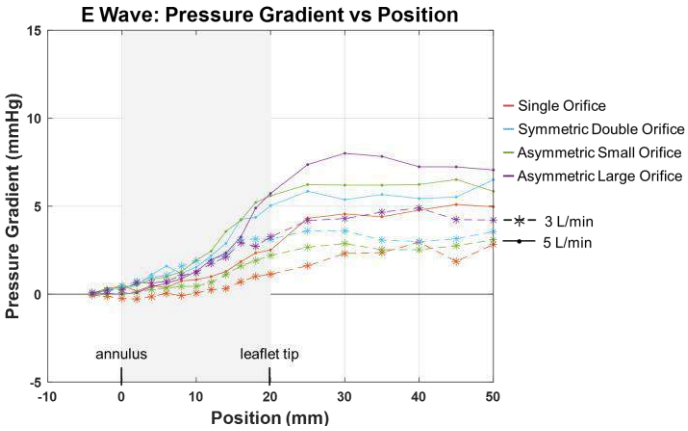

Figure 3: Pressure Gradient vs Position at the E Wave

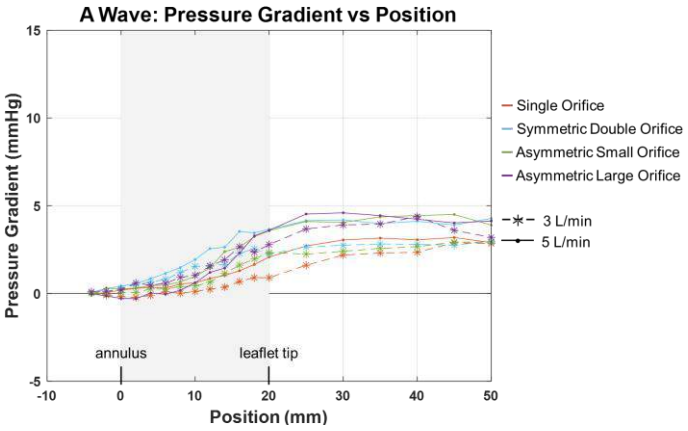

Figure 4: Pressure Gradient vs Position at the A Wave

For each orifice, the MVPG curve followed the same trend of increasing rapidly through the model followed by a slight further increase through the vena contracta before remaining approximately constant further downstream the model.

Overall, MVPG did not exceed 5 mmHg, except for the double orifice cases at a CO of 5 L/min. The E-wave had higher MVPG than A-wave, and 5 L/min had higher MVPG than 3 L/min.

Focusing on the vena contracta, which is just downstream the leaflet tip, MVPG was higher for the clipped cases compared to the unclipped case. The large orifice of the asymmetric model had higher MVPG than the small orifice, and both were higher than the symmetric case.

DISCUSSION

Focusing on the vena contracta, MVPG was higher for the clipped cases compared to the unclipped case. This shows that a single orifice is most efficient.

Comparing the large and small orifices of the asymmetric case, the MVPG of the large orifice is higher than the small orifice. This may be due to flow diverting to the large orifice as a result of increased flow resistance through the small orifice. This can be further explained by applying mass conservation and the inviscid flow theory to the orifice. Equation 1 shows the total fluid velocity, V_T, as a function of the large and small orifice velocities, V_L and V_S, respectively, and β, which is the ratio of the small orifice area to the total area and is less than 0.50 for the asymmetric case.

$$V_T = V_L(1-\beta) + V_S\beta \tag{1}$$

Applying the inviscid flow theory to each orifice, the relation between V_S and V_L can be obtained, as shown in Equation 2.

$$\frac{V_S}{V_L} = \sqrt{\frac{2\beta-\beta^2}{1-\beta^2}} \tag{2}$$

By solving the system of equations, the normalized velocities for the large and small orifices can be obtained, as shown in Equations 3 and 4, respectively.

$$\frac{V_L}{V_T} = \left[1-\beta+\beta\sqrt{\frac{2\beta-\beta^2}{1-\beta^2}}\right]^{-1} \tag{3}$$

$$\frac{V_S}{V_T} = \left[\beta+(1-\beta)\sqrt{\frac{1-\beta^2}{2\beta-\beta^2}}\right]^{-1} \tag{4}$$

With $\beta < 0.50$, the V_L is higher than V_S. This accounts for the higher pressure gradient across the large orifice due to turbulent losses past the vena contracta.

Among the clipped orifices, focusing on the 5 L/min CO cases, the symmetric model had lowest MVPG, indicating that the symmetric clipping scheme is more efficient than the asymmetric clip placement chosen in this study.

In conclusion, analysis of MVPG through the MV can be used to characterize efficiency of transcatheter edge-to-edge repair, which varies based clipping scheme. Overall, a double orifice has higher MVPG. Since the asymmetric clipping scheme had higher MVPG, a central clipping scheme is more efficient.

Future work includes improvement of models to better match MV leaflet geometry, further exploration of the effect of device location on MVPG, and exploration of different device generations.

ACKNOWLEDGEMENTS

This research was supported by National Institutes of Health (NIH) under Award Number R01HL119824.

REFERENCES

[1] Itabashi, Y et al., *J Cardiol*, 71:336-345, 2018.
[2] Nishimura, R et al., *J Am Cardiol*, 63:e57-e185, 2014.

CHANGE IN KNEE JOINT MECHANICS AFTER ACL TRANSECTION DURING SIMULATED GAIT: A HUMAN CADAVERIC MODEL

Amanda Wach (1), Joseph Ruzbarsky (2), Ashley Pekmezian (1), Tony Chen (1), Russell F Warren (2), Peter A Torzilli (3), Suzanne A Maher (1)

(1) Department of Biomechanics
(2) Sports Medicine
(3) Research Division
Hospital for Special Surgery
New York, NY, USA

INTRODUCTION

Anterior cruciate ligament (ACL) rupture predisposes patients to developing post-traumatic osteoarthritis (PTOA) [1]. While many causative factors have been suggested, for example the magnitude of the impact and continued unresolved inflammation, a central concept has been that after ACL rupture the distribution of forces across the joint change, and cartilage cannot respond quickly to those changes.

Our objective was to quantify changes in joint kinematics and tibiofemoral contact mechanics after ACL rupture during simulated gait. We hypothesized that the location of peak contact stress would change, and that those changes would concur with kinematic changes including increased anterior translation.

METHODS

Following IRB approval, six intact, freshly frozen human cadaveric knees were stripped of bulk soft tissue and patella, leaving the remaining joint capsule, ligaments and menisci intact. A Kirshner wire was drilled through the femur flexion axis, using fluoroscopic guidance to determine the epicondylar axis. Knees were then potted in custom fixtures, such that the knee was in full extension with the flexion axis aligned with the six degree of freedom VIVO joint simulator (AMTI, Watertown, MA), Fig 1. Once mounted on the simulator, each knee was subjected to 200N axial load in full extension, with other off-axes loads left floating for 30 seconds. The position of the joint after this loading was set as the zero position for that knee.

Simulated gait testing consisted of 12 cycles of ISO standard gait input waveforms, normalized to specimen specific bodyweight, at 0.2 Hz. The simulator's iterative learning control adjusted all axes control parameters every 3rd cycle, to correct measured differences between applied load and the ISO standard. All data presented is from the 11th tested gait cycle for each specimen.

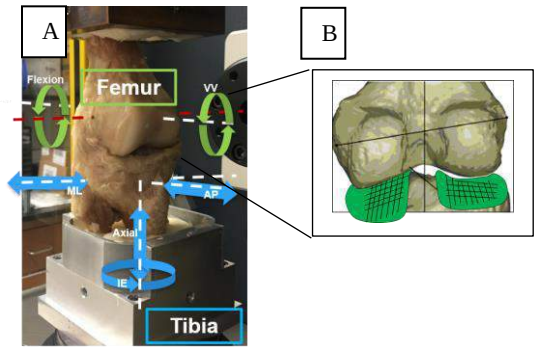

Figure 1: (A) A cadaveric knee fixed in the VIVO knee simulator (AMTI) with six degrees of control. (B) A schematic of the positioning of the sensor, which was prepared with tabs for easier insertion.

Knee joint kinematics were quantified by encoded sensors on each axis of control. Kinematics are reported in the Grood and Suntay [3] coordinate system. Contact mechanics were measured using a Tekscan 4011 pressure sensor (Tekscan, Boston, MA) placed along the tibial plateaus, under the meniscus and secured to the ACL and posterior capsule.

Kinematics and contact mechanics were compared between intact and ACL deficient knees at specific instances: 0%, 4%, 8%, 14%, 20%, 45%, and 60% of the gait cycle. Contact mechanics measures included in the analysis were maximum force, total force, and contact area for the entire tibial plateau, and individually for the medial and lateral plateaus. Additionally, the position of the weighted center of contact for the

medial and lateral plateaus were analyzed. One-way repeated measures ANOVA with Holm-Sidak method for multiple comparisons was conducted ($p<0.05$ considered significant).

RESULTS

We successfully quantified kinematics and contact mechanics throughout simulated gait for all knees, see **Fig 1,** for representative contact mechanics.

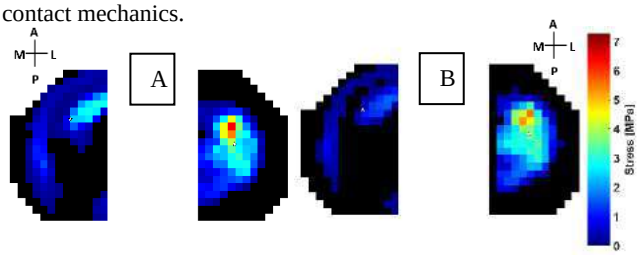

Figure 1: Sample contact maps of a representative specimen (A) intact and (B) after ACL transection, both at 4% gait. Maps are oriented with anterior at the top and the medial plateau on the right of each map.

The total force across the tibial plateau decreased after ACL transection at 4%, 14%, and 45% gait ($p=0.007$, $p=0.020$, $p=0.002$, respectively) (**Fig 2**). The decrease in total force after ACL transection was also observed when considering each plateau individually, with the medial plateau showing differences at 4% and 45% gait ($p=0.008$, $p=0.046$), and the lateral plateau at 8%, 14%, 20%, and 45% gait ($p=0.031$, $p<0.001$, $p=0.035$, $p=0.001$).

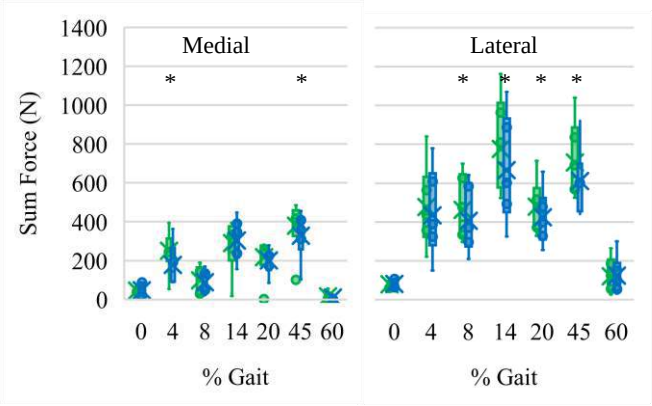

Figure 2: Intact (green) and ACL-transected (blue) medial and lateral plateau sum force.

Total contact area decreased after ACL transection at 4%, 8%, 14%, 20%, and 45% gait ($p<0.001$, $p=0.032$, $p=0.035$, $p=0.036$, $p=0.020$). Similarly, lateral plateau contact area decreased at 4%, 8%, 14%, 20%, and 45% gait ($p=0.003$, $p=0.003$, $p=0.007$, $p=0.020$, $p=0.003$). The medial plateau showed a decrease in contact area at 4% gait ($p=0.004$).

The weighted center of contact on the medial plateau moved posteriorly after ACL transection at 0%, 20%, and 45% gait ($p<0.001$, $p=0.045$, $p=0.034$) and peripherally, at 60% gait ($p<0.001$). The weighted center of contact on the lateral plateau also moved posteriorly at 0% gait ($p<0.001$). No differences in maximum force were determined across the total tibial plateau, medial plateau, or lateral plateau after ACL transection.

Kinematic differences between intact and ACL transected knees were minimal. At 0% and 45% gait, ACL transected knees showed increased anterior transection ($p<0.001$ at 0%; $p=0.03$ at 45%) and lateral translation ($p<0.001$ at 0%; $p=0.03$ at 45%), **Figure 3**.

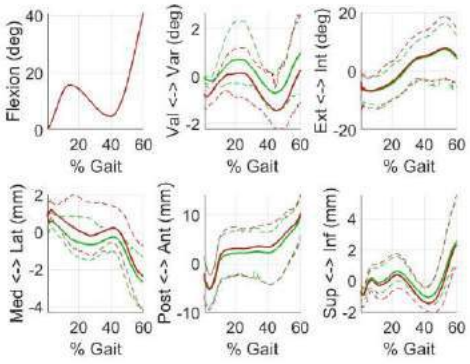

Figure 3: Intact (green) and ACL-transected (red) average gait anterior-posterior (A) and medial-lateral (B) translations with 95% confidence intervals included (dashed).

DISCUSSION

We successfully developed a protocol to simulate gait in cadaveric knees before and after ACL transection. As seen clinically [2, 4], anterior translation increased after ACL injury, with significant differences observed at heel strike (0% gait) and in late stance (45% gait). These kinematic changes corresponded to movement of the weighted center of contact on each plateau – which moved posteriorly at heel strike - and which moved posteriorly on the medial plateau at 45% gait.

Total force and contact area decreased after ACL transection. These changes in contact could indicate altered loading of the meniscus as it behaves as a secondary stabilizer after ACL injury [5]. These results warrant further investigation, particularly in changes of loads distributed along tibial cartilage directly or through the meniscus.

We accepted our hypothesis that there exists a relationship between the change in tibial kinematics during simulated gait and the posterior shift in contact forces after ACL rupture. The alteration in force location will require that cartilage can respond adequately, to avoid degeneration. We plan to input the quantified contact mechanics data generated in this study into bioreactors, so that we can explore the effect of changes in force on the response of chondrocytes, thereby allowing us to investigate at least one hypothesized mechanism of the development of PTOA.

ACKNOWLEDGEMENTS

We acknowledge the National Institutes of Health (ROI AR066635), the Clark Foundation, the Kirby Foundation, the Russell Warren Chair in Tissue Engineering, and the Stryker/ORS Women's Research Fellowship.

REFERENCES

[1] Lohmander, LS et al., *Am J Sports Med*, 35:1756-69, 2007.
[2] Kaur, M et al., *Sports Med*, 46:1869-95, 2016.
[3] Grood and Suntay, *ASME*, 105:136-44, 1983.
[4] Andriacchi, T et al., *J Biomech*, 38:293-8, 2005.
[5] Kent, R et al., *Am J Sports Med*, 48:109-16, 2020.

IN-VIVO ESTIMATION OF MYOCARDIAL ELASTICITY IN HFPEF USING FOUR-DIMENSIONAL ULTRASOUND IMAGING

Maziyar Keshavarzian (1), Sunder Neelakantan (1), Lilly McAllister (2), Carl Tong (2), Reza Avazmohammadi (1,3)

(1) Computational Cardiovascular Bioengineering Lab, Department of Biomedical Engineering, Texas A&M University, College Station, USA

(2) Department of Medical Physiology, Texas A&M University Health Science Center, College Station, USA

(3) Department of Mechanical Engineering, Texas A&M University, College Station, USA

INTRODUCTION

Heart failure with preserved ejection fraction (HFpEF) is a major public health problem in the United States and its prevalence is increasing [1]. Left ventricular diastolic dysfunction (LVDD) remains to be the predominant characteristic of impaired cardiac function in HFpEF [2] which indicates a need for better understanding and characterizing diastolic abnormalities. Indeed, strong pathophysiological heterogeneity of LVDD remains a key impeding factor for developing effective treatments for HFpEF patients [3]. Typical organ-level manifestations of LVDD includes slow and incomplete relaxation and/or a stiff end-diastolic pressure–volume relationship (EDPVR) [4]. In particular, myocardial stiffening is a major tissue-level mechanism contributing to LVDD, here, referred to as *passive remodeling*. Imaging-based methods that can non-invasively identify the presence and severity of myocardial passive remodeling and its contribution to LVDD is essential for treatment planning for HFpEF patients.

The estimation of *intrinsic* changes in mechanical properties of myocardium through medical imaging serves as an important step to quantify the contribution of passive remodeling. The current technique to estimate LV passive remodeling is limited to the measurement of LV-EDPVR through left heart catheterization. However, the LV-EDPVR provides a confounded picture of myocardial *tissue-level* stiffening as it is influenced by chamber anatomy and loading. Therefore, an integrated in-silico-imaging method that allows us to estimate myocardial stiffening independent of LV anatomy and loading will be of high significance. Our objective in this work is to use four-dimensional ultrasound (4DUS) imaging in mice models of HFpEF and estimate myocardial stiffness from a collection of hemodynamic and image-based data including chamber volume and pressure and myocardial wall strain. 4DUS is an advanced imaging modality that can be used to fully capture cardiac motion (in space and time) in small animals as well as in humans. The estimation of intrinsic myocardial stiffening promotes the development of personalized treatment for HFpEF.

METHODS

Animal model. We have established a transgenic murine model of HFpEF based on the studies of the phosphorylation of cardiac myosin binding protein (cMyBP)-C and its important role in actin-myosin cross-bridge mechanism [5,6]. Briefly, the model expresses deficient phosphorylation of cMyBP-C causing diastolic dysfunction and phenotypes resembling HFpEF.

Our study includes a total of 21 male mice which will be divided into three groups labeled as: t3SA, t3SD, and tWT described below [5,6]:

t3SA: cMyBP-C is readily phosphorylated by protein kinase A (PKA). Three PKA phosphorylation sites in mouse cMyBP-C are Ser273, Ser282, and Ser 302 in the M-domain. In this model, all 3 residues were mutated to alanine by expressing non–PKA-phosphorylatable cMyBP-C in the FVB/N mouse strain. FVB/N mice expressing this transgene were then bred with the cMyBP-C knockout mouse to produce t3SA mouse.

t3SD: This model restores phosphorylation at PKA sites and is generated by expressing phosphorylation-mimetic transgene on the cMyBP-C knockout mouse.

tWT: This model serves as the control and is generated by expressing wild-type transgene on the cMyBP-C knockout mouse.

In-vivo imaging and hemodynamic measurements. The gated 4DUS imaging is performed for all the mice at the terminal point using FUJIFILM/Visualsonics Vevo3100 rodent ultrasound system. These images provide a 4D representation of cardiac motion enabling the reconstruction of full left ventricle at multiple time points within a cardiac cycle. The imaging will be followed by the catheter-based intraventricular pressure measurement in the LV. After sacrifice, the hearts will be harvested and the ex-vivo studies are followed.

Ex-vivo studies. After organ-level in-vivo measurements, hearts will be used to characterize biomechanical adaptations of LVFW (Fig. 1):

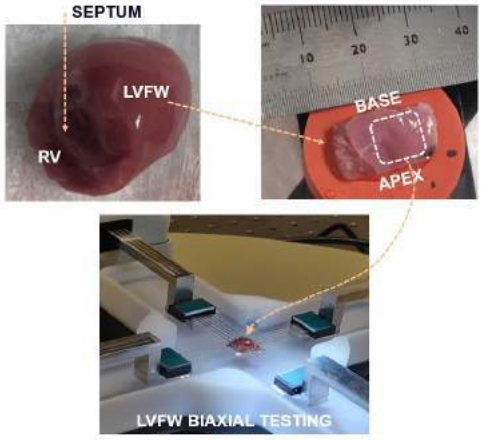

Figure 1: Tissue-level biomechanical testing of LVFW specimens.

Biaxial tests. LVFW excised tissues are placed in BDM-enriched cardioplegic solution and tested under multiple strain ratios to quantify the passive response.

Histology. A total of 10 sections is taken of each LVFW specimen after biaxial tests and stained using Gomori Trichrome. Structural analysis is performed to reconstruct transmural fiber architecture for myo- and collagen fibers.

Inverse modeling to estimate myocardial stiffness and its contribution to LVDD. The inverse model consists of four majors steps:

(i) Extracting myocardial strains. Regional radial, circumferential, and longitudinal strains is estimated and contrasted using speckle tracking (Fig. 2).

(ii) FE model development. A FE model of the LV at the beginning of filling will be created using 3D Dicom images generated from 4DUS. Helical fiber distribution and structural stress-strain model will be incorporated into the FE model for each mouse.

(iii) Matching the strains. The regional strains calculated from the FE model and the strains calculated directly from 4DUS in (i) will be used in an objective function.

(iv) Estimate tissue-level properties. The minimization of the objective function will lead to the estimation of myocardium mechanical properties.

Estimate the contributions of remodeling mechanisms resulting in LVFW stiffening. We will integrate the data from tissue mechanical tests, together with fiber-specific stress-strain model, within an inverse model framework, to estimate unknown myofiber and collagen mechanical properties.

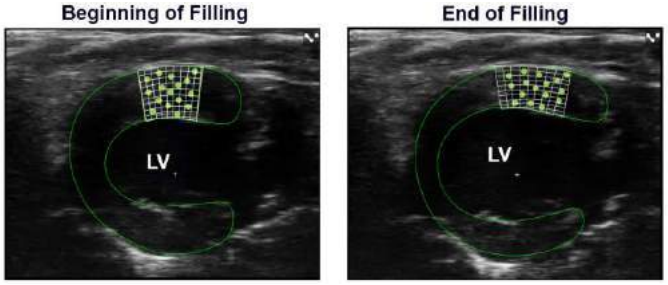

Figure 2: Speckle tracking technique to estimate 3-D strains during diastole.

RESULTS

Our central hypothesis is that 4DUS, integrated with computational modeling of cardiac motion, can provide a load-independent biomarker that reflects intrinsic stiffness of myocardium.

We are currently conducting 4DUS imaging, ex-vivo experiments, and modeling. We expect that the multiscale tissue-level measurements will provide us with a unique set of data to quantify the relations between LV stiffening and the alterations in myofiber and collagen characteristics.

Further, we expect that the 4DUS-based animal-specific computational inverse model provides similar estimates for overall LVFW stiffness. These findings will serve as an important step towards facilitating the clinical use of the integrated 4DUS-computational modeling approach in the patient-specific diagnosis and treatment of HFpEF patients.

DISCUSSION

In this work, we are taking an essential step towards multiscale modeling of the LVDD in HFpEF. The final product of this research offers an impactful and highly translational toolset for a feasible determination of LVDD phenotype in HFpEF that serves as an essential step towards individualizing therapeutic strategies for HFpEF.

ACKNOWLEDGMENTS

RA was partially supported by R00HL138288.

REFERENCES

[1] Oktay, AA et al, *Cur Heart Fail Reports*, 10:401-10, 2013.
[2] Borlaug, BA et al, *Nat Rev Cardiol* 11:507-15, 2014.
[3] Abhayaratna, TH et al, *Heart*, 92:1259-64, 2006.
[4] Rosaa, PC. et al, *Circ Heart Fail*, 8:582-94, 2015.
[5] Tong, CW. et al, *Circ Res*, 103:974-82, 2008.

POLYMERIC PEDIATRIC HEART VALVE REPLACEMENTS

Sanchita S. Bhat (1), Hieu T. Bui (1), Milad Samaee (1), Subhadra Shashidharan (2), Susan P. James (3), Ajit P. Yoganathan (1), Lakshmi Prasad Dasi (1)

(1) The Wallace H. Coulter Department of Biomedical Engineering
Georgia Institute of Technology
Atlanta, GA, USA

(2) Department of Congenital Cardiac Surgery
Emory University School of Medicine
Atlanta, GA, USA

(3) School of Biomedical Engineering
Colorado State University
Fort Collins, CO, USA

INTRODUCTION

Congenital heart defects such as aortic valve stenosis and ventricular outflow tract dysfunctions often require heart valve replacements in pediatric patients [1]. Optimal valve substitutes would constitute a valve that is the right patient size, has potential to grow, has minimal susceptibility to thrombosis and demonstrates excellent prosthesis longevity. Currently the standard of care for pediatric valve replacement is mechanical prosthesis or a smaller sized adult tissue prosthesis which requires lifelong anticoagulation or risks limited longevity due to increasing patient-prosthesis mismatch [2]. The only expandable valve prostheses for accommodating growth are off-label products that were not designed for pediatric patients, and therefore, they are not available in sizes less than 19mm [3]. Common complications involving off-label pediatric valves include valve dislodgement, stent fracturing, recurrent stenosis, and regurgitation. Assuming the pediatric patient survives after a successful heart valve replacement, the medical procedure is still expensive due to their elaborate manufacturing, quality control and storage requirements. The additional surgical intervention caused by the above complications only exacerbates the medical cost. Therefore, a critical need exists for a safe, durable, and cost-effective pediatric valve.

The objective of this study is to develop a pediatric polymeric heart valve (PPHV), based on our hyaluronan (HA) enhanced and biomechanically designed polymeric transcatheter heart valve (HAPTAV) technology [4], and furthermore develop a testing paradigm to investigate the function of the valve. The material has the a unique features such as (1) flexible leaflets made from an interpenetrating polymer network (IPN) between linear low density polyethylene (LLDPE) and hyaluronan (HA) and (2) advanced valve design with unique three-dimensional leaflets and stent frame configuration to provide optimal hemodynamic performance while minimizing the stresses and strains in the leaflet to maximize durability.

The hypothesis is that the HA enhanced pediatric valve will not need anticoagulant therapy, will have comparable hemodynamic and durability compared to commercially available valves, and will be capable of expanding to accommodate growth and development of the pediatric patients' hearts. This advanced valve design with unique three-dimensional leaflets and stent frame configuration provide optimal hemodynamic performance while minimizing the stresses and strains in the leaflet to maximize durability.

METHODS

In order to test the efficacy of our design, we created valve models in Solidworks (Dassault Systèmes, Concord, Massachusetts, USA) and then meshed these geometries using Altair Hypermesh (Altair Engineering, Troy, Michigan, USA). We then conducted simulations using ABAQUS (ABAQUS Inc., Johnston, Rhode Island, USA) to determine areas of high stresses on the stents and leaflets, to identify candidate designs that we can implement in the experimental growth model.

To identify stresses on the stent, we crimped our adult HATAV model to a pediatric size. We conducted additional simulations to identify stresses on leaflets. Since this is a self-expandable valve that is expected to grow with the patient, we wanted to identify loading condition on the leaflets in the initial and fully deployed conditions. As such, we simulated one in the completely deployed position (16mm sized valve) and one in the initial underexpanded condition as shown in Figure 1. The leaflets consisted of approximately 19,000 meshed elements. They were modelled to be of LLDPE material and a diastolic load of 60mmHg was applied to the leaflets. A displacement type boundary condition was used to compress the leaflets radially and a loading type boundary condition was used to apply uniform pressure on the leaflets.

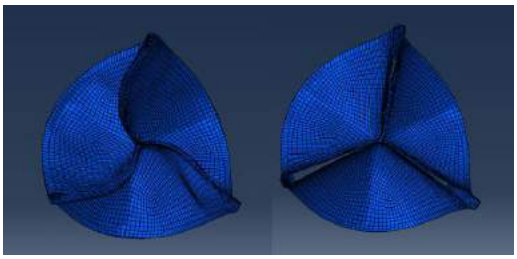

Figure 1: Simulated leaflets shown in the initial crimped and final fully deployed conditions

In order to simulate a benchtop growth scenario, we developed a compliant 'growth' model made of silicone (Silicones Inc., High Point, North Carolina) to test a valve in a left heart simulator, for demonstration purposes. The valve was sutured inside the model and it was used with an in-house designed crimper to allow manipulation of 'growth' in vitro. The crimper was designed especially for the manufactured mold with dimensions that allow valve size adjustment from a pediatric to an adult size. The buttons around the crimper were used to manually reduce the orifice area and crimp or expand the valve. It was fit on the outside allowing for control during the experiment. The pulse duplicator was run at varied flow rates (3.5 to 5 L/min) and pressure (90/60mmHg) to test the silicone prototype.

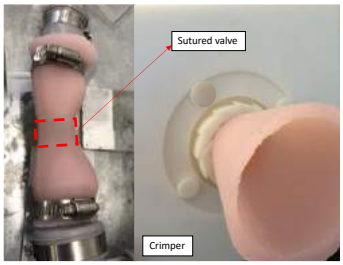

Figure 2: Silicone 'growth' model with implanted valve and crimper shown here during preliminary tests

RESULTS

Upon simulation of the experiment, the compliant model expanded and contracted, successfully withstanding the pressure in the setup and mimicking pulsatile motion.

From our stent simulation it was observed that finite element modeling demonstrated that the valve can be crimped to the pediatric size of 15 mm diameter while maintaining symmetry and the structural integrity of the stent, as shown in Figure 3.

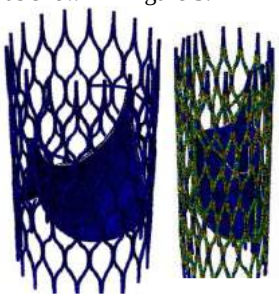

Figure 3: Our HATAV from previous work was be used as the basis for our pediatric valve design.

Preliminary results for the crimped valve prototype from ABAQUS simulations are shown in Figure 3. The maximum loads were seen at the commissures and at the center of the coaptation zone of the leaflets and as they were compressed progressively, the principal stresses got larger. As shown in Figure 4 for example, between two time steps, the maximum principal stresses increased from 2.18 to 2.44 MPa. The stent was not simulated for computational time optimization and due to the fact that the main goal was to observe loading conditions on the leaflets.

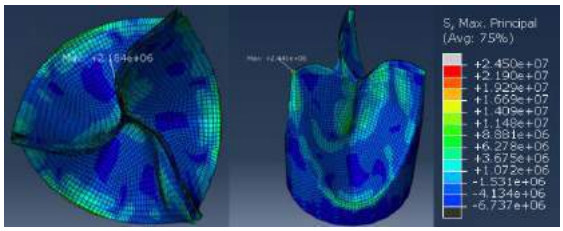

Figure 4: Our in house 3D leaflet design evaluated at the crimped or initial state of pediatric loading conditions. Highest loads are observed at the commissures and leaflet free edges

In the fully expanded state, the maximum principal loads were observed on the commissural regions in the order of 1.67MPa.

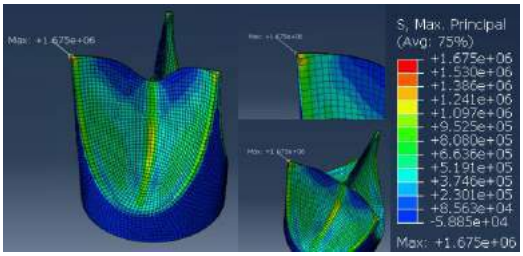

Figure 5: Our in house 3D leaflet design evaluated in its final fully expanded form. Highest loads are observed at the commissures

DISCUSSION

We have seen excellent hemodynamic performance in our preliminary work for adult polymeric heart valves [4] and expect similar conclusions. The loads we currently see in our simulations are comparable to those described in literature [5-6]. In the crimped state, the leaflets tend to pinwheel possibly due to the overall taller profile of the valve. As the valve starts to expand with growth, the leaflets will automatically assume their natural 3D shape. Optimizing the leaflet design will reduce the free edge length and reduce effects of pinwheeling. In the fully expanded state, the loads on the leaflets are lower. However, these commissural stresses are expected as the leaflets are anchored to the stent in that region.

Our results are expected to have positive impact because it lays the foundation for potentially solving the long-standing problems that plague all pediatric heart valves – patient-prosthesis mismatch, need for lifelong anticoagulation and long term durability.

REFERENCES

[1] Singh G.K., *Cong. Aortic Valve Stenosis. Children (Basel).* 13;6(5):69, 2019.
[2] Henaine R. et al, *Arch Cardiovasc* Dis. 517-28. 2012.
[3] Pluchinotta F.R. et al, *Circ. Interventions.* 2018.
[4] Heitkemper M. et al., *J Mech Behav Biomed Mater.*, 98:163-171. 2019
[5] Xuan et. al., *JTCVS*, 153(5):1065-1073, 2017.
[6] Zhu G et.al., *PLoS One*, 4(1):e0210780., 2019.

DEVELOPMENT OF AN ABDOMINAL AORTIC ANEURYSM PROGNOSIS CLASSIFIER TO PREDICT PATIENT OUTCOMES

Timothy K. Chung[1], Nathan L. Liang[2], David A. Vorp[1,3-7]

[1]Department of Bioengineering
University of Pittsburgh
Pittsburgh, PA, United States

[2]Division of Vascular Surgery
University of Pittsburgh Medical Center
Pittsburgh, PA, United States

[3]Department of Surgery
University of Pittsburgh
Pittsburgh, PA, United States

[4]Department of Cardiothoracic Surgery
University of Pittsburgh
Pittsburgh, PA, United States

[5]Department of Chemical and Petroleum Engineering
University of Pittsburgh
Pittsburgh, PA, United States

[6]McGowan Institute for Regenerative Medicine
University of Pittsburgh
Pittsburgh, PA, United States

[7]Center for Vascular Remodeling and Regeneration
University of Pittsburgh
Pittsburgh, PA, United States

INTRODUCTION

Abdominal aortic aneurysm (AAA) is an irreversible localized dilatation of the aorta and if left untreated may lead to rupture, the 15th leading cause of death in the United States[1]. Upon diagnosis of AAA a clinician will intervene using the maximum diameter criteria of 5.5 cm, when the risk of intervention is thought to be lower than the risk of rupture. However, it has been reported that up to 23.4% of smaller sized aneurysms between 4.1 and 5.5 cm rupture adding complexity to the clinical management of AAA[2,3] and highlighting the deficiencies of a one-size-fits-all maximum diameter criterion.

The biomechanics of AAA has been extensively studied to experimentally measure the material properties of the degenerated wall and intraluminal thrombus towards the development of representative patient-specific computational finite element models[4–7]. In addition to stress analysis of AAA, morphological indices have yielded multi-dimensional (one, two, and three-dimensional) measurements to provide rigorous interrogation of reconstructed patient-specific aneurysm geometries[3,8]. In addition, the rupture potential index was introduced as a mathematical model to provide a ratio of wall stress to wall strength based on experimental uniaxial extension tests and clinical indices[9,10]. However, the major limitation of these studies include a low number of aneurysms studies for clinical relevance (n = 348 Khosla et al.), variations in the finite element model and the fact that nearly all of the aneurysms analyzed were clinical size or greater than 5.0 cm in diameter[11].

Machine learning (ML) algorithms have improved over time and has been implemented in clinical datasets to aid in diagnosis and predict patient prognosis[12,13]. In this study we present a novel aneurysm prognosis classifier that trains a ML classification model using clinical, biomechanical and morphological indices to predict patient outcomes with the aim of highly informed clinical decision support.

METHODS

An anonymized dataset of clinical and imaging data was delivered via Globus cloud services (Argonne National Laboratory, Chicago, IL) by the Health Record Research Request in collaboration with the University of Pittsburgh Medical Center and the Department of Biomedical Informatics at the University of Pittsburgh. A total of 778 patients that were diagnosed with AAA were identified to extract clinical and imaging data at each follow up visit. Clinical data included demographics, pharmaceutical use, and co-morbidities (diabetes, peripheral vascular disease, coronary artery disease, renal failure and other conditions). A total of 32,067 images were collected that included both 2D and 3D images but were filtered to include only CT images that totaled 11,040 for the cohort. For the preliminary proof-of-concept study, 385 unique patients were chosen at a single time point. There was a total of 356 stable aneurysms, 16 clinical interventions and 13 rupture events in the cohort.

Image segmentation was performed using two primary approaches: A U-NET convolutional neural network was trained using Amazon Web Services (Amazon, Seattle, WA) Elastic Compute Cloud and local machines using multiple graphics processing units for automated segmentation and semi-automated segmentation using in-house code in MATLAB (Mathworks, Natwick, MA). The segmented CT images were then imported into an automated pipeline that converted the 3D point cloud to a surface reconstruction, converted the surface reconstruction of the wall/lumen/ILT into a computational mesh with ANSYS (ANSYS, Canonsburg, PA), and assembled of a final Abaqus (Dassault Systemés, Johnston, Rhode Island) input file. The computational model consisted of shell elements (S3R) for the wall that were defined with a uniform thickness of 1.3 mm and anisotropic material properties[6] and tetrahedral elements (C3D4H) for the ILT defined as an isotropic hyperelastic material under compression[7]. Biomechanical indices were extracted that included mean wall stress, peak wall stress, tension, and additional stress values (25th, 50th, 75th percentile). Further geometric quantification was performed using in-house code to measure one, two, and three-dimensional indices that included maximum diameter, surface area, tortuosity, vessel asymmetry, non-sphericity index, ILT volume, and other morphological indices[3,8,14,15].

A tabulated dataset was created using a finalized list of clinical, biomechanical, and morphological indices that included a final column for patient outcome (0 for stable, 1 for clinical intervention and 2 for

rupture). There were three levels of training performed, the first level was performed using each category and patient outcomes, the second level paired clinical/biomechanical, clinical/morphological, and biomechanical/morphological categories, and the third level included all three categories for training. The ML classification algorithms were trained using Tree-based optimization pipeline (TPOT) and the MATLAB Classification libraries.

RESULTS

Confusion matrices (CM) and receiver operator characteristic (ROC) curves were generated for each training level and the area under the curve (AUC) was calculated to inform the classifiers ability to discriminate patient outcomes. The AUC for the first level when predicting clinical intervention or repair was 0.57 for clinical data training, 0.78 for biomechanical data training and 0.80 for morphological data training. The AUC for the second level when predicting clinical intervention or repair was 0.87 for clinical and biomechanical data training, 0.89 for clinical and morphological data training and 0.87 for biomechanical and morphological data training. Finally, the AUC when predicting clinical intervention was 0.87 when trained with all categories, 0.88 for predicting stable aneurysms and 0.79 when predicting for rupture (**Fig. 1**). The confusion matrix

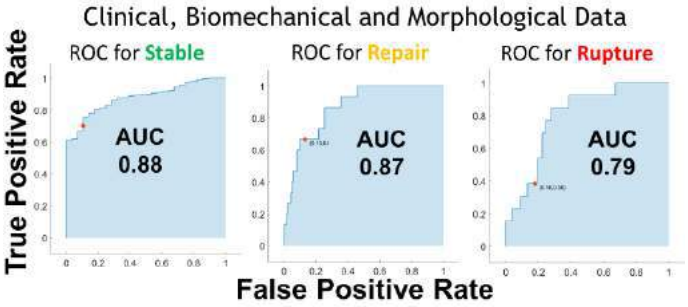

Fig. 1: Output from the APC trained with clinical, biomechanical, and morphological data. These are the ROC curves for each patient outcome (stable, repaired, and ruptured).

displayed in **Fig. 2** reports the predictions of APC and their true outcomes.

DISCUSSION

The trained ML classifiers based on individual categories, paired categories and all categories resulted in varying degrees of accuracy and discriminability of patient outcomes. When training a classifier with clinical data alone, it was found that the discriminability of patient outcomes remained poor (0.57 for clinical intervention). When incorporating image-based studies (biomechanics and morphological indices) there was a significant improvement, an indication that aneurysm progression towards intervention and rupture is driven by shape and biomechanical wall stresses. Although not shown, the CMs for the first level and second level failed to predict clinical intervention/repair and rupture events. However, the third level of training that incorporated all categorical indices was able to accurately predict clinical intervention/repair and rupture events. It is important to note that the CM (**Fig. 2**) predicted 0.78% of AAA as stable when in fact they ruptured, but this is a considerable improvement over the maximum diameter criterion (where up to 23.4% smaller sized aneurysm were found to rupture). There are several limitations to the study including the reliance on internal cross-validation and using a single data point rather than incorporating longitudinal forecasting models. In future studies, external cross validation will be performed with additional clinical and imaging datasets. This body of work demonstrates that rigorous biomechanical and morphological assessment along with clinical data may better inform clinical decision making and, to our knowledge, represents the single largest study to predict patient outcome.

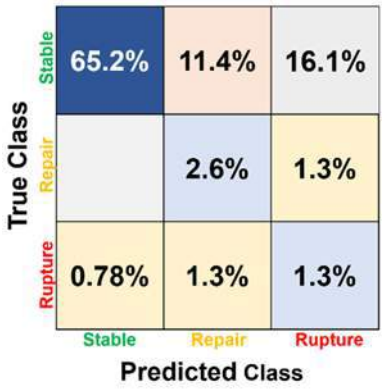

Fig. 2: Confusion matrix of the APC trained with clinical, biomechanical, and morphological indices.

ACKNOWLEDGEMENTS

The APC project was funded by the Center for Commercial Applications of Healthcare Data (CCA), an arm of the Pittsburgh Health Data Alliance (PHDA). We would also like to acknowledge Amazon Web Services (AWS) for providing credits to train the U-NET.

REFERENCES

1. Vorp, D. A. Biomechanics of abdominal aortic aneurysms. *J. Biomech.* **40**, 1887–1902 (2009).
2. Darling, R. C. Autopsy study of unoperated abdominal aortic aneurysms. The case for early resection. *Circulation* **56**, II161-4 (1977).
3. Doyle, B. J. Vessel asymmetry as an additional diagnostic tool in the assessment of abdominal aortic aneurysms. *J. Vasc. Surg.* **49**, 443–454 (2009).
4. Raghavan, M. L. Ex vivo biomechanical behavior of abdominal aortic aneurysm: assessment using a new mathematical model. *Ann Biomed Eng* **24**, 573–582 (1996).
5. Raghavan, M. L. Wall stress distribution on three-dimensionally reconstructed models of human abdominal aortic aneurysm. *J. Vasc. Surg.* **31**, 760–769 (2000).
6. Vande Geest, J. P. The effects of anisotropy on the stress analyses of patient-specific abdominal aortic aneurysms. *Ann. Biomed. Eng.* **36**, 921–932 (2008).
7. Wang, D. H. J. Effect of intraluminal thrombus on wall stress in patient-specific models of abdominal aortic aneurysm. *Journal of Vascular Surgery* vol. 36 598–604 (2002).
8. Shum, J. Quantitative assessment of abdominal aortic aneurysm geometry. *Ann. Biomed. Eng.* **39**, 277–286 (2011).
9. Vande Geest, J. P. Towards an Improved Rupture Potential Index for Abdominal Aaneurysms: Anisotropic Constitutive Modeling and NonInvasive Wall Strength Estimation. 317 (2005).
10. Vande Geest, J. P. A biomechanics-based rupture potential index for abdominal aortic aneurysm risk assessment: Demonstrative application. *Ann. N. Y. Acad. Sci.* **1085**, 11–21 (2006).
11. Khosla, S. Meta-Analysis of Peak Wall Stress in Ruptured, Symptomatic, and Intact Abdominal Aortic Aneurysms. *J. Vasc. Surg.* **61**, 836–837 (2015).
12. Ogunleye, A. XGBoost Model for Chronic Kidney Disease Diagnosis. **5963**, 1–10 (2019).
13. Olson, R. S. Automating biomedical data science through tree-based pipeline optimization. in *Lecture Notes in Computer Science (including subseries Lecture Notes in Artificial Intelligence and Lecture Notes in Bioinformatics)* (2016). doi:10.1007/978-3-319-31204-0_9.
14. Sacks, M. S. In Vivo Three-Dimensional Surface Geometry of Abdominal Aortic Aneurysms. *Ann. Biomed. Eng.* **27**, 469–479 (1999).
15. Vorp, D. A. Mechanical wall stress in abdominal aortic aneurysm: Influence of diameter and asymmetry. *J. Vasc. Surg.* **27**, 632–639 (1998).

D_{33} CHARACTERIZATION OF POROUS POLVINYLIDENE FLUORIDE POLYMER FOR BIOSENSOR APPLICATIONS

Matthew J. Danley (1), Jack T. Kloster (2), Zhaolin Gao (3), Ping Zhao (3), Victor K Lai (4)

(1) Department of Chemistry & Biochemistry
University of Minnesota Duluth
Duluth, Minnesota, United States

(2) Advanced Material Sciences
University of Minnesota Duluth
Duluth, Minnesota, United States

(3) Department of Mechanical & Industrial Engineering
University of Minnesota Duluth
Duluth, Minnesota, United States

(4) Department of Chemical Engineering
University of Minnesota Duluth
Duluth, Minnesota, United States

INTRODUCTION

The Transcatheter Aortic Valve Replacement (TAVR) procedure is a common surgery performed in adults, and the amount of procedures is increasing [1]. The TAVR procedure does have complications, and underlying mechanisms of the complications have not been well studied [1]. It is unknown if the complications due to the procedure are from wear and tear of the heart tissue or due to changes in mechanical forces due to the implant. To study the underlying mechanisms, a small sensor that can detect changes in localized stresses and pressures before and after implant is required. One possible material that is promising is Polyvinylidene Fluoride (PVDF).

PVDF is a piezoelectric material that has applications as a nanogenerator of electricity [2]. PVDF has also been used as a biosensor in other applications. For example, McLaughlin used PVDF to study arterial pulse wave velocity of peripheral arterial blood vessels, to detect pressure changes associated with pulse of the blood vessels and to calculate the flow of blood through the arteries [3]. Although PVDF is a piezoelectric material and it can produce electrical signals in pure bulk strips, it was found that porous strips produce a larger signal likely due to larger deformations to the material due to the porous structure [2].

While many piezoelectric sensors have been characterized under a tensile load, there are few studies that have measured piezoelectric properties under compression, which is necessary for our application. For example, Bernard et al determined the d_{31} value of PVDF, which is the piezoelectric coefficient under strain [4]. Bernard reported the d_{31} to be 3.98 $pC.N^{-1}$, when used as a sensor and actuator[4]. However, d_{31} is determine by stress applied as tension on the piezoelectric material, not from compressive loads or pressures. Hence the overall goal of this study is to investigate the effect of porosity on the d_{33} piezoelectric coefficient of PVDF membranes.

METHODS

PVDF Synthesis:

PVDF powder (Sigma Aldrich, St. Louis MO) was dissolved in 2-butanone solvent at 75° C, then mixed with Zinc Oxide (ZnO) nanoparticles (35-45 nm, US Research Nanomaterials INC, Houston TX.). The mass ratio between ZnO nanoparticles and PVDF were adjusted to 10%, 20%, 30% and 40% wt ZnO to create differences in porosity. The mixture was treated in ultrasonic bath for 30 minutes to create a uniformly mixed PVDF and ZnO nanoparticle suspension. The suspension was cast into films in petri dishes and dried at 75° C. The dried strips then were placed in an acid bath of 10molar HCl for three hours to remove the ZnO nanoparticles from the structure. The films were then washed in deionized (DI) water before testing.

Compression tests:

A Test Resources Newton 100 series Tensile Tester was used to apply loads of 30, 60 and 100lb_f at a rate of 3in/min to the PVDF samples. Copper tape was placed on both sides of the PVDF membrane as electrodes to detect any voltage produced by the samples.

The PVDF membranes with copper tape electrodes was connected to a modified Sawyer-Tower Circuit in parallel to the capacitor (Figure 1). The voltage generated from the PVDF samples were collected over the 0.01 μF capacitor using a National Instruments cDAQ-917 and 9215 Voltage Input Modules at a rate of 1,000Hz for 10 seconds.

Theory:

To measure the piezoelectric output of the PVDF, the d_{33} coefficient was calculated. d_{33} is calculated by

$$d_{33} = \frac{D}{\sigma} \quad (1)$$

In which D is the electric displacement given by equation 2.

$$D = \frac{CV}{A} \quad (2)$$

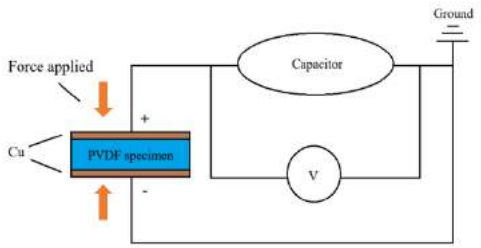

Figure 1: Modified Sawyer-Tower Circuit. The porous PVDF membrane with Copper tape electrodes was connected to a 0.01 µ F capacitor. The voltage acquired was measured across the capacitor.

C is defined as the capacitance of the capacitor, V is the voltage generated from the PVDF membranes, A is the area of the electrode. The applied compressive stress is $\sigma = \frac{F}{A}$, where F is the force applied to the membranes and A is the area of the PVDF under stress. Since the area of the electrode is the same as the area of PVDF under stress, and equation 1 becomes

$$d_{33} = \frac{CV}{F} \qquad (3)$$

This means that the slope of the voltage (V) versus load (F) graph for each membrane can be used to calculate the d_{33} coefficient.

RESULTS

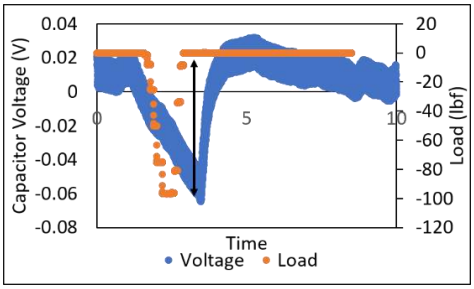

Figure 2: Sample Voltage and Load Data of 40% Wt ZnO at 100lbf. This figure shows the filtered voltage from the PVDF membrane, using a 5point Savitzy Golay fit, and the load applied to the membrane. The black arrow shows where the peak voltage is collected.

Figure 2 shows that there is a change in voltage occurring while the compressive load is applied. The voltage peak of each trial was calculated by finding the voltage values at the peak and valley during the compressed load application.

Once the voltage values were determined, the relationship between voltage and force was plotted. An example for the 40% wt ZnO sample is shown in figure 3.

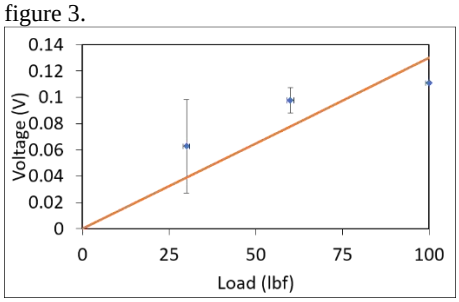

Figure 3: Linear Regression of 40% Wt ZnO Membranes The figure shows the average voltage values from 5 replicates compared to the line of best fit.

Figure 3 shows that as the compressive force increased, the voltage generated increased. The slope from the linear regression was used to calculate the d_{33} values according to equation (3).

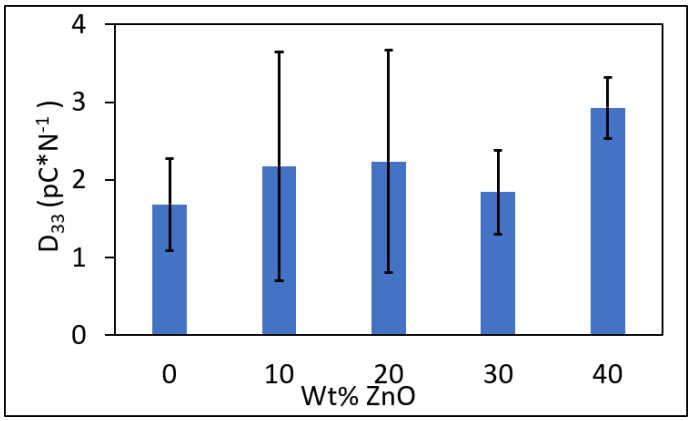

Figure 4: d_{33} values for Porous PVDF Membranes. The graph above shows the d_{33} values as the porosity changes. Error bars represent the standard error of the slope obtained from linear regression.

Figure 4 shoes the d_{33} values for the different PVDF samples tested. The pure, or 0% wt ZnO, 10%, 20% and 30% wt ZnO samples all have similar d_{33} values. The 40% wt ZnO membrane shows larger average d_{33} values, however, this larger value is not statistically significant due to the large deviations in d_{33} values.

DISCUSSION

The d_{33} values for 0% through 30% porosity vary and do not seem to follow a trend, but once the porosity is increased up to 40% wt ZnO, the d_{33} value increases. This suggests that porosity can affect the d_{33} values of PVDF. Mao reported a linear increase in voltage generated from increasing porosity of PVDF membranes up to 50% wt ZnO, but those experiments involved looking at the voltage generated under surface oscillations, where these d_{33} experiments look at how PVDF reacts under single compressive forces [2].

Even though the d_{33} values do not increase with increasing loads as expected, these results are still promising. Mao suggested that the increase in voltage was a result from the pores which allowed great deformation of the PVDF polymer chain [2]. This is likely the reason the d_{33} value for the 40% wt ZnO increased compared to the other porous membranes.

Although the d_{33} values calculated are not significantly different due to large deviations, there is potential that increasing the porosity of the membranes could result in larger piezoelectric coefficients. This means further studies on the porous PVDF membranes are warranted, including increasing the porosity past 40% Wt ZnO to values of 50%, 60% or even 70% wt ZnO.

REFERENCES

[1] Culler, S et al., *The Annals of Thoracic Surgery*, 34:859-871, 2001.
[2] Mao, Y et al., *Adv. Energy Mater.* 4:1301624, 2014
[3] McLaughlin, J et al., *Physiol. Meas*. 24:693–702, 2003.
[4] Bernard, F.et al, . (2017). Direct Piezoelectric Coefficient

DEVELOPING A REDUCED ORDER MODELLING METHODOLOGY FOR SIMULATING TRANSCATHETER AORTIC VALVE REPLACEMENT PROCEDURES

Imran A. Shah (1), Milad Samaee (1), Atefeh Razavi (1), Alessandro Veneziani (2), Lakshmi P. Dasi (1)

(1) Wallace H. Coulter Department of Biomedical Engineering
Georgia Institute of Technology
Atlanta, Georgia, USA

(2) Department of Mathematics
Emory University
Atlanta, Georgia, USA

INTRODUCTION

Transcatheter aortic valve replacement (TAVR) has become a viable alternative to tackle severe aortic stenosis, especially for high surgical risk patients that are unable to undergo traditional surgical procedures. Computational modeling is a critical tool that can be used to visualize and predict deployment behavior for patient-specific TAVR procedures, and identify potential complications including coronary obstruction, paravalvular leakage, and thrombosis. Within this modeling pipeline, the key component is simulating the structural dynamics of the valve frame, native valve leaflets, and aortic root. However, due to the intrinsic complexity of the geometrical and mechanical aspects of the problem, the computational simulations of TAVR deployment becomes extremely expensive.

For systems that are heavily structured, reduced order models (ROMs) can be used to decrease the computational costs of the full order model (FOM) by orders of magnitude [1]. ROMs are low dimensional versions of the FOM that are created using available data; typically, there are two stages in the development of the ROM. In the *offline* stage, the FOM is run for a specific set of parameters from which a low-dimensional basis is formed. In the *online* stage, the ROM is then used for parameters different from the original parameters to rapidly obtain new solutions [2]. ROMs have been employed in various biomedical engineering applications, including fluid-structure interaction problems and computational electrocardiology [3]. However, the application of ROMs in TAVR deployment has not yet been studied.

The primary objective of this study is to develop a model reduction methodology for the structural deformation of a 29 mm Medtronic Evolut R valve. Specifically, a series of linear elastic simulations were performed with an idealized Evolut stent to obtain a databank of deformed states, which are called *snapshots*. From this, a singular value decomposition (SVD) procedure was performed to identify the principle components of the mechanical problem. A Proper Orthogonal Decomposition (POD) approach can then be taken to create the ROM. The ultimate goal of this work is to use this model reduction approach to significantly reduce the computational costs associated with simulating TAVR deployment procedures.

METHODS

An idealized geometry of the Evolut stent frame was created in *SolidWorks*. The geometry was meshed and refined using a combination of *Netgen* and *Mmg Platform*, resulting in a final mesh size of 257,000 tetrahedral elements. Snapshots were obtained by defining five nodes across three planes of the stent geometry (top, middle, and bottom planes), for a total of fifteen nodes, all of which are shown in Fig. 1.

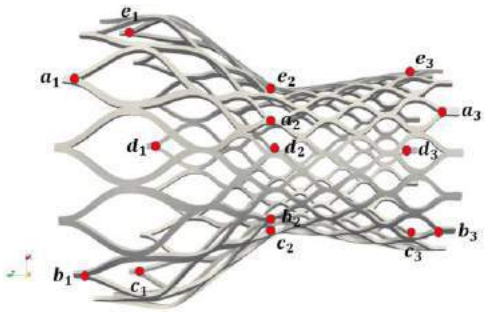

Figure 1. Evolut valve stent frame with all defined nodes.

Coordinates for each node were extracted from the mesh using *Autodesk Netfabb™*. Each snapshot consisted of defining an equal and opposite displacement (with a magnitude of 2.0 mm) between two nodes and simulating a linear elastic problem over the entire stent geometry. Each

of these displacement pair simulations represents the different effects of the forces from the aorta and aortic valve onto the Evolut stent. Material parameters defined include the Young's modulus (50,000 MPa) and the Poisson ratio (0.33). Simulations were performed in *FEniCS*, an open source Finite Elements library. In total, 105 node pairs were simulated. Displacement fields at all fifteen nodes were extracted from each simulation and placed into a 45 by 105 matrix. The rows of the matrix are the *x*, *y*, and *z* components of the displacement for each node, while the columns show all possible combinations with the fifteen nodes.

The SVD analysis was performed using *MATLAB*. Singular values of the individual *x*, *y*, and *z* components of displacement are plotted to determine if there is a significant exponential decay. A sharp and fast decay in the singular values suggests that the data can be well approximated by a linear combination of a small number of vectors, given by the eigenvectors associated with the largest singular values. Using the POD approach, the solution $\underline{x}$ to the differential problem is

$$\underline{x} = W\underline{c} \quad (1)$$

where, W is the rectangular matrix of the chosen eigenvectors, and $\underline{c}$ is a vector of unknown coefficients. Generally, $\underline{c}$ is a much lower dimensional vector than $\underline{x}$ (tens vs hundreds of thousands), yielding the model reduction. Plugging (1) into the original elasticity problem to solve in a least-squares sense, one obtains the ROM. Having to solve tens or hundreds of unknowns, as opposed to hundreds of thousands in the FOM is anticipated to reduce the computational costs significantly. More precisely, let

$$A\underline{x} = f \quad (2)$$

be the FOM represented by a linear system obtained after a finite element discretization of the elasticity problem in the stent. Here, f is the applied force. The square matrix A depends on the finite element mesh and is generally hundreds of thousands of rows. The ROM model on the other hand reads as follows, where W^TAW is a matrix that generally features a size in the range of tens or hundreds of rows [4].

$$W^TAW\underline{c} = W^Tf \quad (3)$$

RESULTS

All 105 node pair simulations were analyzed in terms of the resulting displacement field along the stent geometry. Displacement field vectors for one specific node pair simulation (nodes $a_1 - d_3$) are shown in Fig. 2. Maximum displacement of approximately 7.6 mm is seen near the top left edge nodes of the stent, while the remaining portions of the stent deformed within a range of 0.6 to 5.0 mm. At the nodes themselves, a displacement of 2.0 mm is seen, which matches the prescribed boundary conditions.

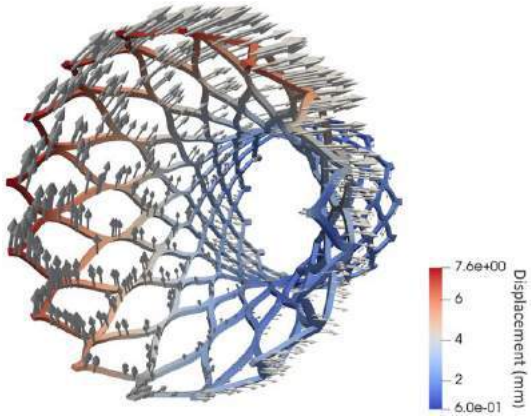

Figure 2. Resultant displacement field (mm) for simulating the $a_1 - d_3$ node pair.

Displacement data is extracted for each of the fifteen nodes over all 105 simulations. From this data set, the individual *x*, *y*, and *z* displacement vectors are separated, and the SVD analysis is performed. The resulting singular values are plotted and shown in Fig. 3. The *x*-axis here represents the total number of nodes (fifteen), and the *y*-axis represents the singular values. A sharp and rapid decline in the singular values is seen at approximately five nodes.

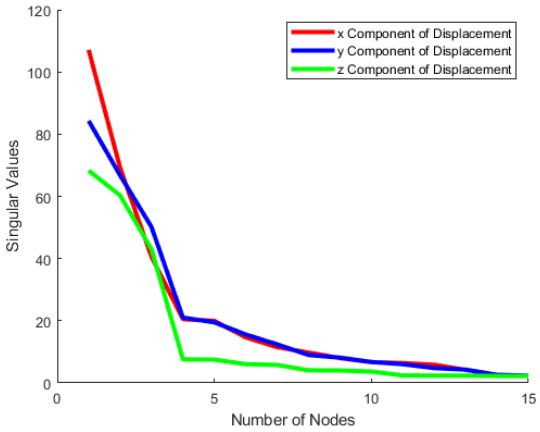

Figure 3. Singular values of the displacement snapshots.

DISCUSSION

In this study, a model reduction approach is introduced to reduce the computational costs associated with simulating TAVR deployment. Specifically, the aim was to determine if the snapshot data obtained from the linear elastic simulations with the Evolut stent was reduceable. To this end, an SVD analysis was performed as the initial steps towards creating the ROM. From the SVD analysis (Fig. 3), a significant decay in the singular values is apparent. This suggests that a combination of only five displacements is enough to represent the entire FOM and reduce the problem. This conclusion will be tested on several linearly elastic test cases. However, in reality the self-expanding nitinol frame of the Evolut valve would be more accurately modeled as a superelastic alloy. Thus, a constitutive model for superelasticity is needed to capture all material properties of the nitinol stent and provide more reliable results from which the ROM can be constructed. The basic POD approach, however, also requires linear differential operators. To extend the approach to more practical superelastic cases, the Empirical Interpolation Method (EIM) will be applied. In addition, these findings will be further corroborated with a mesh independence study, showing the importance of ROMs for reliable and efficient solutions.

In conclusion, this study shows that POD is a viable method for reducing the computational costs for predicting the structural deformation of the Evolut stent. The rapid decay of the singular values suggests room for a significant reduction of the computational costs that may, in turn, enable the use of computational mechanics in optimization problems or real-time settings.

ACKNOWLEDGEMENTS

A.V. wishes to acknowledge the NSF Project DMS 2012686

REFERENCES

[1] Hesthaven, J. et al.. *Certified Reduced Basis Methods for Parametrized Partial Differential Equations*, Vol. 590. Springer, 2016.
[2] Bertagna, L., Veneziani, A., *Inverse Problems*, 30:055006, 2014
[3] Barone A., et al. *J of Comp Physics*, 423:109810, 2020
[4] Barrault, M., et al. *Comptes Rendus Mathematique*, 339(9):667-672, 2004.

SB³C2021
Summer Biomechanics, Bioengineering and Biotransport Conference
June 14-18, Virtual

COMPUTATIONAL MODELING OF BORDERLINE LEFT VENTRICULAR CIRCULATION FOR CLINICAL DECISION-MAKING

Yurui Chen (1), Isao Anzai (2), David Kalfa (2), Vijay Vedula (1)

(1) Department of Mechanical Engineering
Columbia University
New York, NY, USA

(2) Pediatric & Congenital Cardiac Surgery
Columbia University Irving Medical Center
New York, NY, USA

INTRODUCTION

Borderline left ventricle (BLV) patients are neonates born with an undersized left ventricle, possibly concomitant with aortic valve stenosis, hypoplastic aortic arch, hypoplastic left heart complex, and right ventricular pressure overload. [1] A critical dilemma facing pediatric heart surgeons is to choose between a biventricular repair (BiVR) or a single ventricle palliation procedure (SVPP) for BLV patients. While BiVR is aimed at creating two functioning ventricles in a single surgery, SVPP involves multiple staged open-heart surgeries resulting in a single functional ventricle. Typically, SVPP has high inter-stage mortality, especially after the first stage (Norwood procedure) performed as neonates, and has poor long-term outcomes with only 70% reaching adulthood. [2] On the other hand, patients undergoing BiVR may exhibit reduced heart function post-surgery and may have to be subsequently switched to SVPP. [3] There is a need to better stratify BLV patients based on functional data and predicted outcomes for different surgical pathways.

While tremendous progress has been made in applying computational modeling for SVPP, modeling the circulation of BLV patients has not received much attention to date. We present a computational model of the preoperative BLV circulation using lumped parameter network (LPN) and modify the layout to simulate BiVR and Norwood surgical procedures. The LPN models have been independently verified with previously published data, although we aim to personalize the model by tuning the preoperative LPN to match actual patient data. Model predictions will be correlated with patient outcomes retrospectively using available clinical data at the New York-Presbyterian (NYP) Morgan-Stanley Children's hospital and the database at the Society of Thoracic Surgeons (STS), to assess the viability of using simulations to guide surgical decision-making.

METHODS

We have developed an LPN-based computational model of preoperative BLV circulation for neonates (Figure 1). Our model is derived from Corsini et al. [4], originally developed for Norwood procedure, with the following modifications: (a) we reintroduce the undersized left heart into the network and model atrial and ventricular septal defects using resistances; (b) we model the aortic arch hypoplasia by including an additional resistive element in the ascending aorta; (c) we employ a versatile valve model for all four cardiac valves, which accounts for stenosis and regurgitation effects [5]; (d) we also retain the patent ductus arteriosus (PDA) between the pulmonary artery (PA) and ascending aorta supporting neonatal systemic circulation.

We further modified the preoperative LPN layout to simulate BiVR and Norwood procedures. For BiVR, we close all the septal defects, lower the resistance and compliance of the aortic arch mimicking its reconstruction with a homograft patch, and lower the degree of valvular stenoses. For the Norwood procedure, the LPN layout is the same as that of Corsini et al. [4] with a 3.5mm Blalock-Taussig shunt between the aorta and PA. The PDA is assumed to be closed post-surgery in both procedures. The LPN parameters are extracted from Corsini et al. [4] tuned for a Norwood patient with BSA = $0.34\ m^2$ and PVR = $6\ WU \cdot m^2$. [6, 7] For the preoperative BLV model, we have reduced the unloaded volume of the ventricle to 50% of its nominal value and assumed that the mitral and aortic orifices are 70% stenosed.

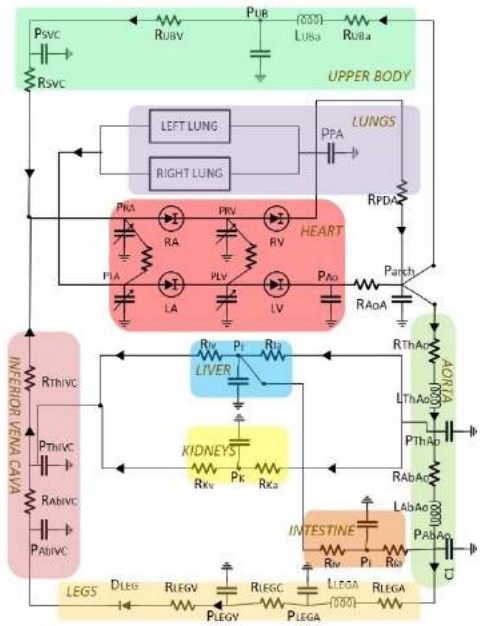

Figure 1: Layout of the preoperative LPN-based circulation model of a borderline left ventricle (BLV).

Our LPN model provides functional hemodynamic variables including atrial and ventricular pressure-volume (PV) loops, cardiac stroke work (SW), cardiac index (CI), the ratio of pulmonary (Qp) to systemic (Qs) flow rates, and other key pressures and flow rates of the circulation system. We also perform O_2 calculations including O_2 saturations of the systemic arteries (S_{ART}) and veins (S_{VEN}), and oxygen delivery (OD). [8]

RESULTS

In Figure 2, we compare the LPN results between BiVR and Norwood procedures for a BLV patient, including PV loops for both left and right ventricles, aortic and pulmonary flow rates and pressures, and flow through upper (UB) and lower body (LB) during the cardiac cycle. A quantitative comparison of the hemodynamic indices is shown in Table 1.

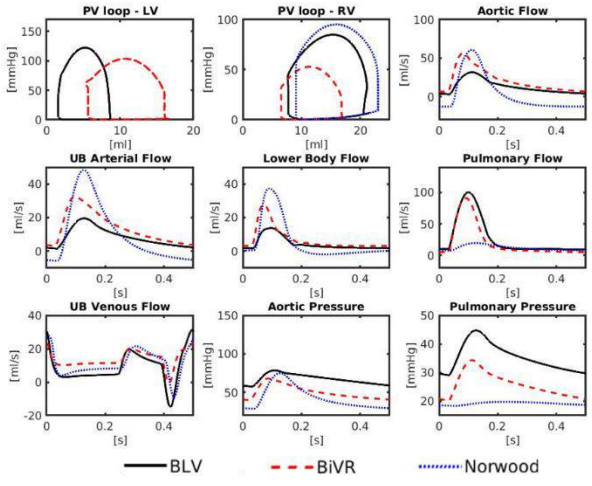

Figure 2: Model predicted hemodynamic quantities during the cardiac cycle for a BLV patient before and after surgery.

Table 1: Comparison of hemodynamic indices before and after surgical procedures. (Qp/Qs: ratio of pulmonary to systemic flows; SW: stroke work; LV: left ventricle; RV: right ventricle; CI: cardiac index; S_{ART}, S_{VEN}: arterial and venous saturations; OD: O_2 delivery)

	Qp/Qs	SW (LV)	SW (RV)	CI	S_{ART}	S_{VEN}	OD
BLV	2.05	646	807	2.28	82.0	51.1	407
BiVR	1.00	835	404	3.65	98.0	77.5	749
Norwood	0.74	-	1023	4.34	64.7	39.9	416

Units: SW [mmHg·ml], CI [l/min/m^2], S_{art}, S_{ven} [%], OD [ml/min/m^2]

Our results indicate that performing a BiVR on the current BLV patient leads to an equal distribution of pulmonary and systemic flows (Qp/Qs=1), reduction in RV SW (~50%), and an increase in CI (~60%). On the contrary, performing a Norwood would increase RV SW (~27%) although CI increases by 90%. A BiVR leads to higher S_{ART} and S_{VEN} while performing Norwood would lead to a substantial reduction in both the saturations. OD is substantially elevated (80%) after a BiVR compared to only a marginal increase from Norwood.

DISCUSSION

We have demonstrated a proof-of-concept application of computational modeling to predict the post-operative outcomes of a BLV patient. Typically, these patients undergo a binary evaluation between BiVR and SVPP, primarily based on anatomical markers. Computational modeling provides functional data that could be of critical importance to surgical decision-making. In this study, our preoperative BLV model with an undersized LV and valvular stenosis, correctly predicts insufficient OD and higher RV SW. Functional data from post-operative models indicate that BiVR is the optimal choice of surgery for this patient that restores bi-ventricular circulation with a substantial increase in OD and reduced RV SW.

There are several limitations in the current study that we plan to overcome in the future. While the current study involves only one patient, whose LPN parameters have been tuned for Norwood circulation, we plan to perform patient-specific modeling by tuning the preoperative LPN to match BLV patient data. We also plan to demonstrate statistical significance by recruiting more patients (20+) from NYP and STS databases and perform validation of the preop and postop LPN models. Our novel framework will also allow us to investigate outliers such as those BLV patients who had to be switched from one surgical procedure to another. We hope that our pilot study will pave way for the development of personalized multiscale finite element models of BLV circulation to address the important clinical question, `how small is too small?'

ACKNOWLEDGEMENTS

Y.C. would like to acknowledge a fellowship received through SEAS of Columbia University.

REFERENCES

[1] Corno, A.F., et al., Euro. J. Card Surg., 27(1), 67-73, 2005. [2] Feinstein JA, et al., J Am Coll Cardiol., 59(5), 544, 2012. [3] Delius, R.E. et al., J. Thor. Cardi. Surg., 112(6), 1561-1569, 1996. [4] Corsini, C., et al., Comp. Biomed. Eng., 17(14), 1572-1589, 2014. [5] Mynard, J. P., et al., Int. J. Num. Bio. Eng., 28(6-7), 626-641, 2012. [6] Snyder, et al., IEEE Trans. on Biomed. Eng., (4), 325-334, 1969. [7] Baretta A., et al., Phys. and Eng. Sci., 369(1954), 4316-4330, 2011. [8] Mahdi, et al., J Biomech. Eng., 134(5), 051002, 2012.

SB³C2021
Summer Biomechanics, Bioengineering and Biotransport Conference
June 14-18, Virtual

THE EFFECT OF AORTA SHAPE ON TYPE A DISSECTION RISK

Jessica G. Williams (1,2), David Marlevi (2), Marie Billaud (1), Thomas G. Gleason (1), Elazer R. Edelman (2)

(1) Cardiac Surgery
Brigham and Women's Hospital
75 Francis St.
Boston, MA 02115

(2) Harvard-MIT Biomedical Engineering Center
Massachusetts Institute of Technology
77 Massachusetts Ave
Cambridge, MA 02139

INTRODUCTION

In patients with ascending thoracic aortic aneurysm, an enlarged maximum aortic diameter is correlated with increased risk of clinical events (ATAA)[1], and maximum diameter is often used as a predictor of potential tearing of the inner layer of the aorta, or thoracic ascending aortic dissection (TAAD). However, assessment of maximum diameter alone fails to capture the multifaceted geometric structure of the aorta, and in fact, it has been shown that maximum diameter serves as an imperfect indicator of dissection risk[2]. Instead, the three-dimensional structure of the aorta serves as a better predictor of functional aortic characteristics (flow, stiffness, remodelling) and could hence be superior in dissection risk stratification. Statistical shape analysis (SSA) enables identification of key modes of shape variation, or particular shape changes that capture the majority of geometric dissimilarities among a cohort of individual geometric structures. Application of SSA to the aorta has revealed differences between principal modes of aortic variability among asymptomatic patients[3], but has not previously been used to identify shape features associated with risk of TAAD.

METHODS

SSA reduces a complex geometric structure to single, discrete shape scores, describing the structure's associations with particular shape features extracted from a larger population. Our retrospective study explores the correlations between SSA-derived shape feature and TAAD occurrence on a dataset of 31 patients with ATAA, 12 of which dissected and 19 of which did not dissect. Using clinical thoracic computed tomography (CT) images, we extracted aortic geometries for all patients using standard image segmentation techniques, truncating the carotid arteries and smoothening the resulting geometries using VMTK[4]. We utilized open-source software, Deformetrica[5], to perform SSA on the cohort of aorta shapes and performed principal component analysis (PCA) to extract principal shape features. Furthermore, we utilized partial least-squares (PLS) regression to identify the shape mode most correlated with dissection outcome.

RESULTS

In Figure 1, a visual representation of the first three PCA modes of the full dataset is provided. Figure 1 (a)-(c) displays PCA 1 (corresponding visually with aortic size), (d)-(e) shows PCA 2 (corresponding visually to cubic[6] – rectangular arch with reduced inner curvature in comparison to outer curvature – or gothic arch shape[6] – acute angulation between the ascending and descending portions of the aorta), and (f)-(g) demonstrates PCA 3 (corresponding visually to aortic arch angle). The middle column shows the mean (template) shape, which corresponds to a shape score of zero along any mode, and the left and right columns display the shapes corresponding to shape scores -2σ and $+2\sigma$, respectively, where σ is the standard deviation of shape scores along each particular mode. The aortas are colored corresponding to the distance from the template shape. Quantifying the percent shape variation captured by each mode, PCA 1 represents 26.4% of the total shape variation, PCA 2 14.7%, and PCA 13.2%, respectively.

The results of the PLS analysis are provided in Figure 2, where aortas which dissect are more associated with negative scores and those which do not dissect associated with positive scores. This shape mode explains

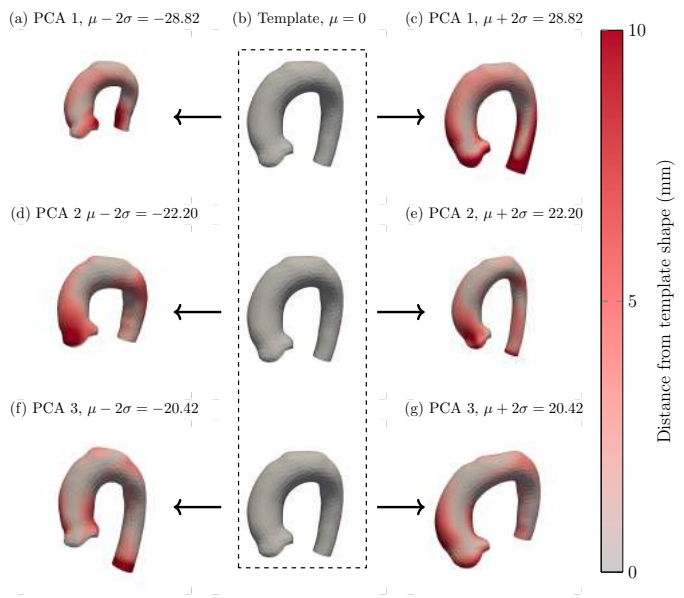

Figure 1: The first three shape modes: (a)-(c) PCA 1, (d)-(e) PCA 2, and (f)-(g) PCA 3. The mean shape (middle column) corresponds with a shape score of zero, left column shows each mode at -2σ, where σ is the standard deviation of shape scores along the mode, and right column at $+2\sigma$. The aorta surfaces are colored according to distance between each point and the corresponding point on the template surface.

10.6% of the total shape variation in the entire cohort. The shape scores for all four modes are summarized in Figure 3, with boxplots splitting the cohort into aortas which dissect (red) and don't dissect (blue). Comparing the dissection and no dissection populations with a Wilcoxon rank-sum test, there is a strong statistically significant difference between shape scores for the two groups along the PLS mode ($p = 1e-3$), a slight difference along PCA 2 ($p = 9e-2$), and no significant difference ($p > 0.1$) between shape scores for the two groups along PCA 1 or 3.

DISCUSSION

We have explored shape variation amongst a cohort of 31 aneurysmal aortas, using SSA techniques, and compared the shape scores for extracted shape modes with dissection outcome. We have found that the first three shape modes correlate visually with aortic size, arch shape (cubic vs. gothic), and aortic arch angle, and that these three together account for almost half of the total shape variations within the evaluated cohort. Furthermore, out of these three, PCA 2 showed weak, but

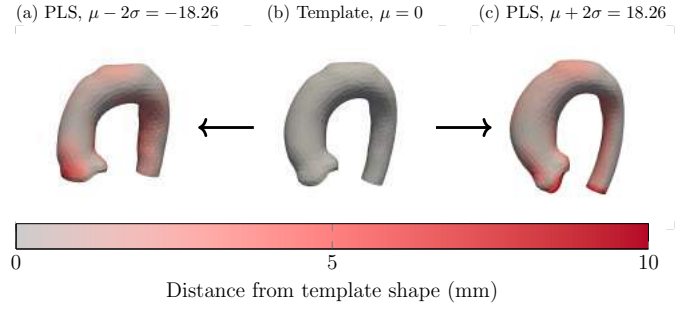

Figure 2: The shape mode resulting from a PLS analysis of the dataset with dissection outcome. Negative scores are more associated with dissection and positive scores with no dissection.

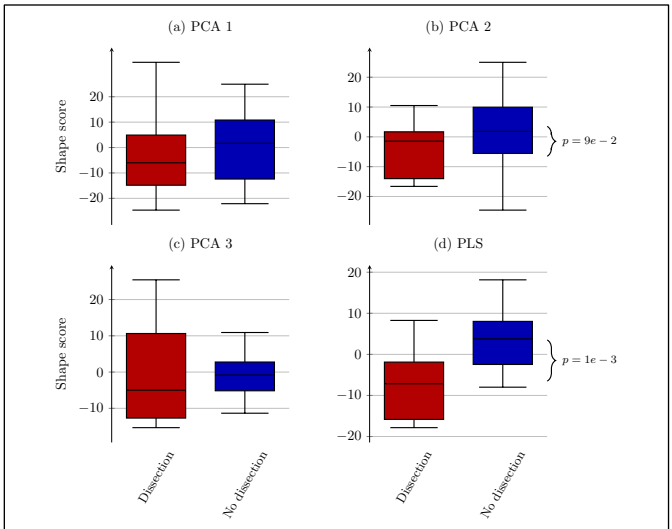

Figure 3: Shape scores for all 31 aortas along (a) PCA 1, (b) PCA 2, (c) PCA 3, and (d) the PLS mode correlated with dissection outcome. The red boxplots are for aortas which dissect and the blue boxplots for aortas which do not dissect. The p-values are shown next to (b) and (d) as the results hold statistical significance.

significant, correlation with dissection outcome. We used PLS regression to identify a shape mode most correlated with dissection outcome, and found that shape scores along this mode do separate statistically significantly with dissection outcome. The work presented here demonstrates the capacity for SSA techniques to quantify three-dimensional shape features for use in dissection risk assessment. Further work in fluid and structural analysis of blood flow through shapes correlated with dissection occurrence is required to mechanistically understand why particular aorta shape features may contribute to dissection risk.

REFERENCES

[1] M. A. Coady, J. A. Rizzo, G. L. Hammond, G. S. Kopf, and J. A. Elefteriades, "Surgical intervention criteria for thoracic aortic aneurysms: A study of growth rates and complications," *Ann. Thorac. Surg.*, vol. 67, no. 6, pp. 1922–1926, 1999.

[2] L. A. Pape *et al.*, "Aortic diameter ≥5.5 cm is not a good predictor of type A aortic dissection: Observations from the International Registry of Acute Aortic Dissection (IRAD)," *Circulation*, vol. 116, no. 10, pp. 1120–1127, 2007.

[3] J. B. Kim, M. Spotnitz, M. E. Lindsay, T. E. MacGillivray, E. M. Isselbacher, and T. M. Sundt, "Risk of Aortic Dissection in the Moderately Dilated Ascending Aorta," *J. Am. Coll. Cardiol.*, vol. 68, no. 11, pp. 1209–1219, 2016.

[4] L. Antiga, M. Piccinelli, L. Botti, B. Ene-Iordache, A. Remuzzi, and D. A. Steinman, "An image-based modeling framework for patient-specific computational hemodynamics," *Med. Biol. Eng. Comput.*, vol. 46, no. 11, pp. 1097–1112, 2008.

[5] A. Bône, M. Louis, B. Martin, and S. Durrleman, "Deformetrica 4: An Open-Source Software for Statistical Shape Analysis," *Lect. Notes Comput. Sci. (including Subser. Lect. Notes Artif. Intell. Lect. Notes Bioinformatics)*, vol. 11167 LNCS, pp. 3–13, 2018.

[6] S. Schnell *et al.*, "Altered aortic shape in bicuspid aortic valve relatives influences blood flow patterns," *Eur. Heart J. Cardiovasc. Imaging*, vol. 17, no. 11, pp. 1239–1247, 2016.

MECHANO-TRANSCRIPTOMIC ANALYSIS OF MIGRATORY PHENOTYPES OF GLIOBLASTOMA PATIENT CELLS

J. Hou (1), M. McMahon (1), J. Sarkaria (2), D. Odde (1)

(1) Department of Biomedical Engineering
University of Minnesota
Minneapolis, Minnesota, USA

(2) Department of Radiation Oncology
Mayo Clinic
Rochester, Minnesota, USA

INTRODUCTION

Glioblastoma (GBM) preclinical cancer models with primarily cultured GBM cells such as in vivo xenografts could recapitulate parental tumor invasiveness, proliferation index, microvessel density, genomic alterations, and patient GBM subtypes [1]. With consensus clustering of RNA-seq data of freshly isolated GBM patient cells, GBM cells were classified into three subtypes, Mesenchymal (MES), Proneural (PN), and Classical (CL), and MES and PN became dominant for recurrent tumor [2]. Since GBM cell invasion and migration is the key factor for GBM recurrence and poor survival [3], it is critical to understand the migratory phenotypes of GBMS cells with different subtypes using GBM preclinical models.

In a typical cell migration cycle, the first step is the protrusion of the leading edge driven by actin polymerization into self-assembled actin filaments (F-actin). F-actin undergoes retrograde flow driven by myosin II (motor)-mediated contraction, while binding and stretching actin-adhesion linkage proteins (clutch). These adhesion proteins form focal adhesions and allow the cell to transmit traction forces onto compliant substrates. This system is referred to as a motor-clutch mechanism [4], and was implemented and simulated by the motor-clutch model [5]. In addition, the cell nucleates multiple protrusions via F-actin polymerization, each of which can be modeled as a motor-clutch system, with traction forces balancing across the different protrusions. Stochastic perturbations to the force balance due to adhesion bond rupture enable larger scale cell movements and can define the front and the rear of the cell. This force-driven cell motion was described and simulated in the cell migration simulation (CMS) developed by [6] (Figure 1a).

In this study, the cell migratory mechanics was measured for GBM patient cells derived from in vivo xenografts in adherent culture. Migratory mechanisms were studied by fitting the CMS predictions to patient cell migration data in order to parameterize patient cells. Highly correlated genes to CMS parameters were investigated using patient cell RNA-seq data derived from mRNA sequencing.

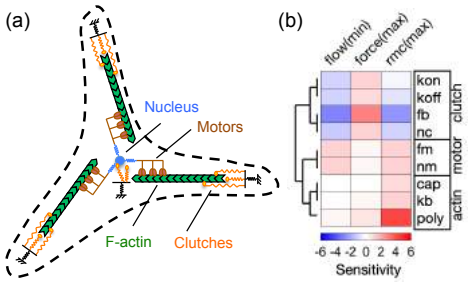

Figure 1: (a) The cell migration simulator (CMS). (b) Sensitivity analysis of CMS.

METHODS

6 GBM patient cell lines (3 MES, 3PN subtype) were derived from Mayo PDX lines developed in Mayo Clinic Sarkaria Lab with adherent culture [7] (Figure 2a). Cells were cryopreserved and cultured adherently with Neural Stem Cell (NSC) media before experiments. GBM cells were then plated on polyacrylamide (PA) gels coated with laminin. Cell migration speed, traction force, and F-actin flow speed were measured following previous protocols [6] (Figure 2b,c).

The C++ version of the CMS was compiled and simulated using High Performance Computing system at the Minnesota Supercomputing Institute. Based the base parameter values described in [6], the parameter sensitivity analysis was studied on the minimum

F-actin flow, maximum traction force, and maximum migration speed for different substrate stiffness (Figure 1b). Three parameter groups were classified using unsupervised hierarchical clustering (Figure 1b).

We found three principal parameters, one from each parameter group, can be variable to different cells and can predict their migratory mechanics. The three principal parameters include motor number (nm), clutch number (nc), and F-actin polymerization rate (poly), which represent cell myosin motor level, adhesion protein level, and actin polymerization activity, respectively. The specific CMS parameter values for each patient cell line were further determined by fitting CMS predictions with adjustable principal parameters (nc,nm,poly) to patient cell migration data (Figure 3).

Mayo cell RNA-seq data was derived from www.cbioportal.org, and verified using NovaSeq at UMN Genomics Center. Cell migration gene list was derived from Gene Ontology (http://geneontology.org).

RESULTS

Based on GBM cells derived by Mayo PDX lines, we found that GBM MES cells had significantly faster migration speed and higher F-actin flow rate compared to PN cells, while traction forces were similar to both subtypes (Figure 2c).

The CMS parameter values for each patient cell lines were derived by fitting CMS predictions with adjustable principal parameters (nc,nm,poly) to patient cell migration data (Figure 3). We found that GBM MES cells generally have higher nm and poly compared to PN cells, indicating higher myosin II level and enhanced actin polymerization activity. The CMS predicted that higher nm and poly result in faster migration and higher F-actin flow [6], which is consistent with the patient cell migration data (Figure 2c).

Based on the RNA-seq data of GBM patient cells, and using the migration gene list derived from Gene Ontology, we found the most correlated migration genes to CMS principal parameters (nm, nc, poly) for GBM patient cells ($R > 0.6$, $p < 0.05$, Figure 4a). We recognized that, for example, the motor-correlated genes, RHOG and RRAS, and the poly-correlated genes, CD2AP, have higher expressions in MES cells than in PN cells (Figure 4b). RHOG belongs to Rho family, which regulates myosin activity by affecting myosin light chain via ROCKs [8]. RRAS regulates Rac and Rho activity, and further effects myosin activity [9]. CD2AP directly associates with actin filament formation [10].

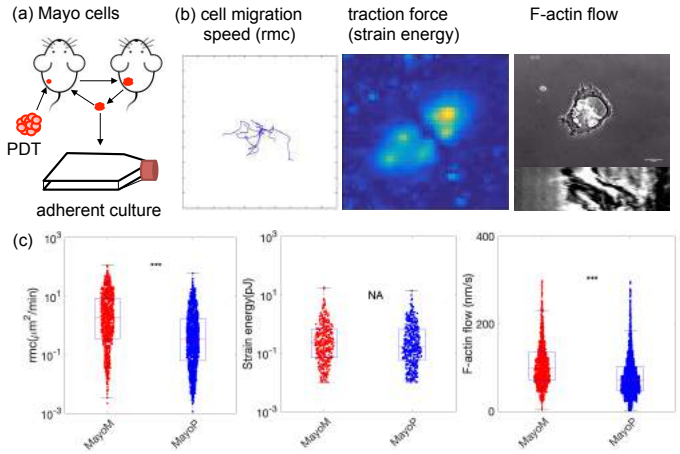

Figure 2: Cells derived from Mayo PDX lines (a). Cell migration speed, traction force, and F-actin flow rate were measured for MES(red) and PN(blue) cells (c), using previous protocols (b) [6].

ACKNOWLEDGEMENTS NIH U54 CA210190

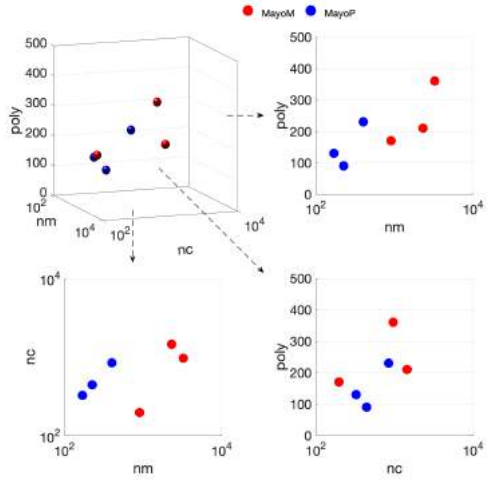

Figure 3: The CMS parameter values for GBM patient cells.

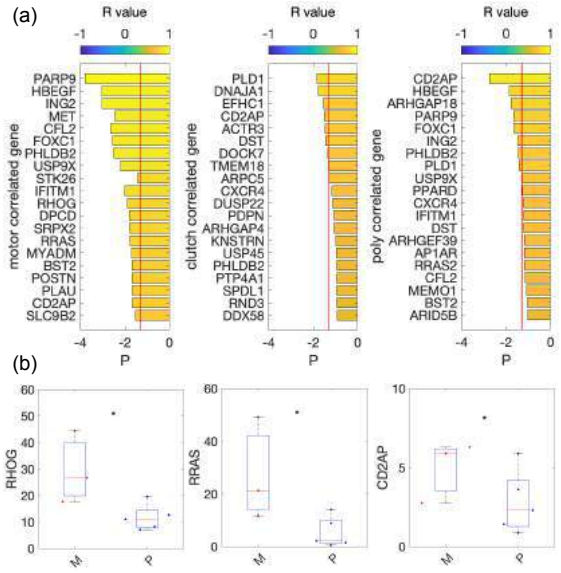

Figure 4: (a) Most correlated genes within migration gene list (geneontology.org) to CMS principal parameters based on patient cell RNA-seq data. (b) Three example correlated genes.

DISCUSSION

In this study, we used the CMS framework to understand the biophysical mechanisms of the heterogeneity of GBM patient cell migration with MES and PN subtypes (Figure 3), and to link migratory mechanics to cell transcriptomic information (Figure 4).

In order to have better statistical significance, more patient cell lines could be studied, including in vitro freshly isolated GBM cells from patient tumors, which can also retain tumorigenic and infiltration potentials in vivo, and similar gene profiles as to parental tumors [11].

REFERENCES [1] Joo, Cell Rep, 3(1), 260--273, 2013. [2] Wang, Cancer Cell, 32(1), 42--56, 2017. [3] De Vleeschouwer, Glioblastoma, 2017. [4] Hu, Science, 315(5808), 111—115, 2007. [5] Chan, Science, 322(5908), 2008. [6] Bangasser, Nat Commun, 8(15313), 2017. [7] Carlson, Curr Protoc Pharmacol, 52(1), 14--16, 2011. [8] Ridley, J Cell Sci, 114(15), 2713--2722, 2001. [9] Wozniak, Mol Biol Cell, 16(1), 84--96, 2005. [10] Lehtonen, Am J Physiol Renal Physiol, 283(4), F734--F743, 2002. [11] Pollard, S. M., Cell Stem Cell, 4(6), 568--580, 2009.

T CELLS FROM CADHERIN-11 DEFICIENT MICE PROMOTE NEOINTIMA FORMATION FOLLOWING VASCULAR INJURY

Matthew R. Bersi (1,4), Matthew Z. Madden (2), Tessa M. Huffstater (1), Lance A. Riley (1), J. Ethan Joll (1), Michael A. Raddatz (1), Victoria Le (3), Aaron B. Baker (3), Jeffrey C. Rathmell (2), W. David Merryman (1)

(1) Department of Biomedical Engineering
Vanderbilt University
Nashville, Tennessee, USA

(2) Department of Pathology, Microbiology, and Immunology
Vanderbilt University Medical Center
Nashville, Tennessee, USA

(3) Department of Biomedical Engineering
University of Texas at Austin
Austin, Texas, USA

(4) Department of Mechanical Engineering and Materials Science
Washington University in St. Louis
St. Louis, Missouri, USA

INTRODUCTION

Coronary heart disease (CHD) accounts for the majority of all cardiovascular disease related mortality in the United States. CHD is often characterized by persistent narrowing of the coronary vasculature which leads to the formation of cardiac ischemic events. Patients with severe CHD often undergo percutaneous coronary intervention (PCI) to deploy intravascular stents intended to restore coronary blood flow. However, the process of stenting can lead to injury of the vascular wall which promotes cellular ingrowth and in-stent restenosis. Therefore, patients often present with common comorbidities of myocardial infarction (MI) and neointimal hyperplasia (NH) formation. Though drug-eluting stents have shown efficacy at mitigating NH formation, the overall impact of novel therapeutic strategies targeting cardiac fibrosis after MI should also be investigated in the context of vascular injury.

Toward this end, cadherin-11 (CDH11) is a cell-cell adhesion protein known to regulate inflammation and fibrosis in multiple conditions ranging from rheumatoid arthritis to pulmonary fibrosis and calcific aortic valve disease [1]. Recently, we have shown that inhibition of CDH11 following MI preserves cardiac function and reduces scar burden in the left ventricle [2] due to a reduction in immune cell recruitment immediately following injury that attenuates myofibroblast activation and collagen deposition at later times.

Though CDH11 blockade has shown a beneficial effect in the heart, this treatment strategy has yet to be evaluated in the context of vascular injury. Preliminary data shows that CDH11-deficiency promotes neointima formation, though the cellular source responsible for these changes is not currently known. Thus, the objective of this study was to investigate the role of CDH11-deficient T cells in the remodeling response of the murine femoral artery following mechanical wire injury. Our findings reveal that T cells from CDH11-deficient animals promote NH formation in immune-compromised recipients.

METHODS

Animal Models. CDH11 transgenic mice (*Cdh11*$^{+/+}$, *Cdh11*$^{+/-}$, and *Cdh11*$^{-/-}$) were used in all vascular injury studies. Additionally, to investigate the specific role of CDH11-deficient T cells, immuno-compromised *Rag1*$^{-/-}$ mice lacking mature T and B lymphocytes were reconstituted with purified *Cdh11* transgenic splenic T cells by adoptive transfer. For all cell transplantation studies, a total of $3x10^6$ donor cells were delivered to each recipient mouse retro-orbitally.

Femoral Artery Wire Injury. Mice were anesthetized by isoflurane and the femoral artery was exposed and gently dissected away from the femoral vein. Proximal blood flow was temporarily ligated and a small transverse arteriotomy was introduced in the muscular branch of the femoral artery. A straight spring wire (0.38 mm in diameter) was then inserted into the arteriotomy and advanced toward the iliac artery. The wire was left in place for 1 minute prior to removal, closure of the arteriotomy by cautery, and restoration of blood flow [3]. Injured animals were maintained for 28 days after surgery.

Histology and Immunohistochemistry. Injured animals were perfusion fixed with cold formalin to maintain tissue architecture, and femoral arteries and spleens were gently dissected and placed in formalin overnight. Fixed samples were then embedded, frozen, and sectioned at a thickness of 8 μm. Slides were stained with either Elastica van Gieson to visualize the elastic lamellae of the femoral artery or fluorescent antibodies to visualize specific markers of interest. Custom image processing algorithms were developed to quantify neointima area (defined by tissue inside of the continuous internal elastic lamina) and media area of femoral artery sections, as well as immunofluorescent staining from all tissues.

Migration Assay. Spleens from *Cdh11*$^{+/+}$ and *Cdh11*$^{-/-}$ mice were excised and digested into a single cell suspension. T lymphocytes were isolated from all splenocytes by negative selection magnetic assisted

cell sorting (MACS). Following isolation, cells were plated into a 5 μm pore 96-well plate and allowed to migrate toward gradients of potent T cell chemokines CCL21, CXCL10, 11 and 12 [4]. Cells were allowed to migrate at 37°C and 5% CO_2 for 3 hours prior to staining with calcein; the number of migrated cells was calculated based on the formation of a calcein standard curve.

Bulk RNA-sequencing. Injured femoral arteries with isolated and frozen prior to homogenization and RNA isolation. The Vanderbilt Technologies for Advanced Genomics (VANTAGE) center performed library preparation, sequencing, and read alignment. Differential gene expression analysis was performed using the R package DEseq2 using Cook's outliers to filter low gene counts and $\alpha = 0.05$. Gene sets were considered over-represented if $p_{adj} < 0.05$.

Statistical Analysis. Comparisons between groups were assessed by one-way ANOVA followed by a post-hoc Tukey HSD test for multiple comparisons. Nonparametric statistics were used where appropriate based on normality and equal variance tests.

RESULTS

Following wire injury, the extent of vascular remodeling – as defined by the ratio of neointima to media area – increased with loss of CDH11. Indeed, *Cdh11*$^{-/-}$ mice were found to have a roughly 2-fold increase in the intima/media ratio, relative to *Cdh11*$^{+/+}$ (Fig. 1).

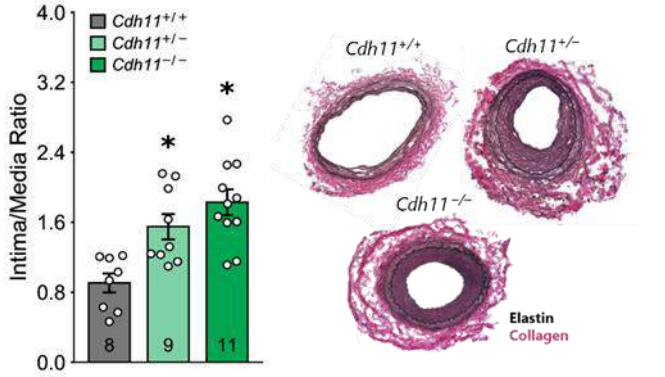

Figure 1: NH formation is increased in *Cdh11*$^{-/-}$ mice after injury

To examine the transcriptional differences between the injury response of *Cdh11*$^{+/+}$ and *Cdh11*$^{-/-}$ mice, bulk RNA-sequencing was performed. Following RNA isolation, library preparation, sequencing, and read alignment, differential gene expression analysis identified a total of 95 differentially expressed genes (Fig. 2A). Of these, 43 genes were downregulated and 52 genes were upregulated in *Cdh11*$^{-/-}$ mice, relative to *Cdh11*$^{+/+}$. Gene set enrichment analysis (GSEA) revealed multiple enriched gene sets. Notably, we observed a positive enrichment in genes associated with mesenchymal cell proliferation and a negative enrichment in genes associated with leukocyte proliferation (Fig. 2B). The former is consistent with our observation of increased NH formation and the latter would suggest an altered immune response to vascular injury. Further analysis revealed a downregulation of genes set related to T cell activation, proliferation, and migration. This would suggest an altered T cell phenotype in *Cdh11*$^{-/-}$ mice, relative to *Cdh11*$^{+/+}$. To investigate this further, we performed adoptive transfer of T cells from *Cdh11* mutant donors into *Rag1*$^{-/-}$ mice lacking mature lymphocytes. Indeed, we observed a similar level of injury in *Rag1*$^{-/-}$ mice with *Cdh11*$^{-/-}$ T cells and global *Cdh11*$^{-/-}$ mice as well as in *Rag1*$^{-/-}$ mice with *Cdh11*$^{+/+}$ T cells and global *Cdh11*$^{+/+}$ mice (Fig. 3A). Further, analysis of immunofluorescence images revealed a decrease in CD3+ T cell expression in the neointimal layer of injured femoral arteries from *Cdh11*$^{-/-}$ mice, relative to *Cdh11*$^{+/+}$ (Fig. 3B).

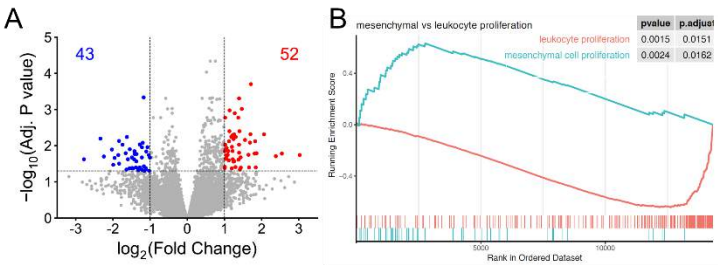

Figure 2: (A) Volcano plot showing differentially expressed genes and (B) GSEA plot of positively and negatively enriched gene sets

Given the observation of reduced T cell expression, we hypothesized this may be due to altered migratory potential of *Cdh11*$^{-/-}$ T cells. Using a transwell migration assay, we confirmed that *Cdh11*$^{-/-}$ T cells were less migratory than *Cdh11*$^{+/+}$ T cells to multiple potent chemoattractants (Fig. 3C). In particular, the chemotaxis in responses to CXCL10 and CXCL12 stimulation are likely the most relevant in this disease context. Altogether, this may provide insight into a potential mechanism and suggests that altered T cell recruitment is contributing to the excessive NH observed with CDH11 deletion.

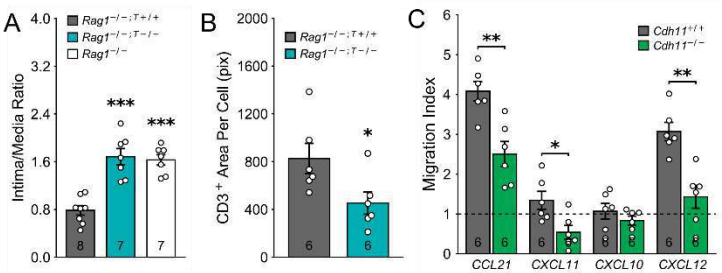

Figure 3: (A) *Cdh11*$^{-/-}$ T cells promote NH in *Rag1*$^{-/-}$ mice. (B) *Cdh11*$^{-/-}$ T cells are less expressed in the neointima after injury and are (C) less migratory to chemokine stimuli than *Cdh11*$^{+/+}$ T cells

DISCUSSION

Using transgenic animals, RNA-sequencing, and adoptive transfer, we show that the exacerbated NH response observed in *Cdh11-/-* mice is due to an altered T cell. While the specific effect of CDH11 in T cells is yet unknown, findings from this work suggest it may be involved in either T cell recruitment or may modulate another secreted factor to promote excessive cell proliferation. For example, altered levels of T cell cytokines – such as IFN-γ and IL-17a, among others – are known to contribute to altered vascular smooth muscle cells responses in conditions such as atherosclerotic plaque formation [5]. Altogether, the findings from this work highlights the role of the immune system in regulating cardiovascular disease progression and importance of evaluating the effect of novel treatment strategies for CHD in both cardiac and vascular disease models.

ACKNOWLEDGEMENTS

This work was supported, in part, by NIH grants R35 (HL135790), T32 (HL007411), and K99 (HL146951)

REFERENCES

[1] Bowler MA et al., *AJP Heart Circ Phys* 315(6): 1614-26, 2018. [2] Schroer AK et al., *JCI Insight*, 4(18), 2019. [3] Sata M et al., *J Mol Cell Cardiol*, 11:2097-104, 2000. [4] Yagawa Y et al., *Sci Rep* 7(1):1-16, 2017. [5] Eid R et al., *Circulation* 119:1424-32, 2009.

STROMA AFFECTS THE INTRATUMORAL TRANSPORT OF BACTERIA-BASED DRUG DELIVERY AGENTS

Y. Zhan (1), RM. Davis (2), B. Behkam (1,3)

(1) Department of Mechanical Engineering
Virginia Tech
Blacksburg, VA, USA

(2) Department of Chemical Engineering
Virginia Tech
Blacksburg, VA, USA

(3) School of Biomedical Engineering & Sciences
Virginia Tech
Blacksburg, VA, USA

INTRODUCTION

In the U.S., cancer is the second leading cause of death, responsible for over 600,000 deaths per year. Nanomedicine has immense potential in cancer treatment due to unique properties such as preserving therapeutics' bioavailability and reduced systemic toxicity via improved targeting. However, only ~0.7% of the systemically administered dose of nanomedicine accumulates in solid tumors[1]. Furthermore, the transport of nanoparticles (NPs) from blood to tumor cells is impeded due to the irregular tumor vasculature structure as well as increased interstitial pressure, dense stroma, and compressive tissue stress within the tumor microenvironment. The tumor microenvironment consists of stromal cells, including cancer-associated fibroblasts (CAFs) and the extracellular matrix (ECM). CAFs play a crucial role in tumor growth, progression, and metastasis in part by producing the physical scaffold of the tumor microenvironment - the ECM[2]. Collagen, a primary component of ECM, promotes the elevation of tumor interstitial pressure, collapse of blood vessels, and increase of hypoxia, which all limit the delivery of anticancer drugs.

Microbe-based drug delivery systems are a potential strategy to overcome the intratumoral transport challenge and significantly enhance drug delivery efficacy in cancer through improved targeted transport. Attenuated bacteria are promising candidates with advantages of self-propulsion and targeted accumulation, which enable deep penetration to overcome the transport limitation of nanomedicine. However, the effect of ECM content on the distribution of bacteria-based drug delivery agents remains largely unexplored. Here, we use a breast cancer organoid model comprising mammary CAFs (mCAFs) and epithelial breast cancer cells to assess the role of ECM production by mCAFs in the penetration of bacteria and bacteria-nanoparticle assemblies, known as NanoBEADS[3,4]. We introduce a new generation of our Nanoscale Bacteria-Enabled Autonomous Drug Delivery System (NanoBEADS) constructed by linking maleimide-activated gold nanoparticles to the thiol groups on the outer membrane of the tumor-targeting *S.* Typhimurium VNP20009 *cheY*$^+$ bacteria. First, we evaluated the nanoparticle loading capacity of the NanoBEADS. Then, we investigated the impact matrix production by mCAFs on the penetration of bacteria and NanoBEADS into breast cancer organoid models *in vitro*. We found that high ECM content significantly hinders the intratumoral transport of bacteria and NanoBEADS in tumor organoids and limits the tumor killing potential of bacteria. This model could be used to evaluate the tumor colonization and delivery efficacy of microbial-based drug delivery agents with different bacterial strains.

METHODS

Salmonella Typhimurium VNP20009 *cheY*$^+$ RFP were cultured in MSB medium[5] supplemented with 35 μg/mL of chloramphenicol at 37 °C and 100 rpm. Bacterial culture at OD_{600} = 1.0 was washed with motility media (MM)[5] twice and concentrated to OD_{600} = 2.0. The bacterial suspension was mixed with 40 nm maleimide-activated gold nanoparticles at 1:100 bacteria/NP ratio and incubated for 60 mins at 15 rpm on an end-over-end shaker at room temperature to facilitate NanoBEADS formation. Subsequently, the NanoBEADS were incubated with mPEG-thiol (Mw: 5000 g/mol) at 0.8 μg/mL for 30 min to quench the remaining maleimide binding sites.

Tumor organoids were formed with 4T1 murine mammary carcinoma cells and mCAFs murine cancer-associated fibroblasts[6]. 4T1 cells or 4T1 cells with mCAFs (1:5 ratio) were seeded in ultra-low adhesion 96 well plates. Once tumor diameters reached 600 μm, up to 6 tumor spheroids were transferred into Eppendorf tubes and incubated with bacteria or NanoBEADS at OD_{600} = 1.0 in L15 media supplemented with 10% calf serum on an end-over-end shaker at 37 ºC. After an hour, tumor spheroids were washed twice with fresh culture

media and put back on the shaker. After 12 h, 18 h, and 24 h incubation period, the tumor spheroids were assayed for viability and also were frozen to evaluate the spatial distribution of bacteria. A minimum of 3 independent experiments and 3 tumors for each experiment category were used.

RESULTS

We developed a new class of NanoBEADS by conjugating 40 nm maleimide-activated gold nanoparticles to the thiol groups on the surfaces of bacteria (**Fig 1a**). This nanoparticle size was selected due to its well-known performance for drug delivery applications[7] and its lack of adverse influence on bacteria growth and motility[8]. First, we investigated the role of the bacteria/NP ratio on conjugation outcome. The attachment number was quantified using scanning electron microscopy (SEM) images (**Fig 1b**). At 1:50 bacteria/NP assembly ratio, an average of 46 ± 17 nanoparticles per bacteria was achieved, whereas the 1:100 bacteria/NP assembly ratio resulted an average of 26 ± 15 attached (**Fig 1c**). The distribution of NP loading, shown in **Fig 1d**, demonstrates that the 1:50 bacteria/NP ratio produced NanoBEADS with not only high average NP load but also small variation across the samples. Thus, this preparation of NanoBEADS was used for the tumor studies.

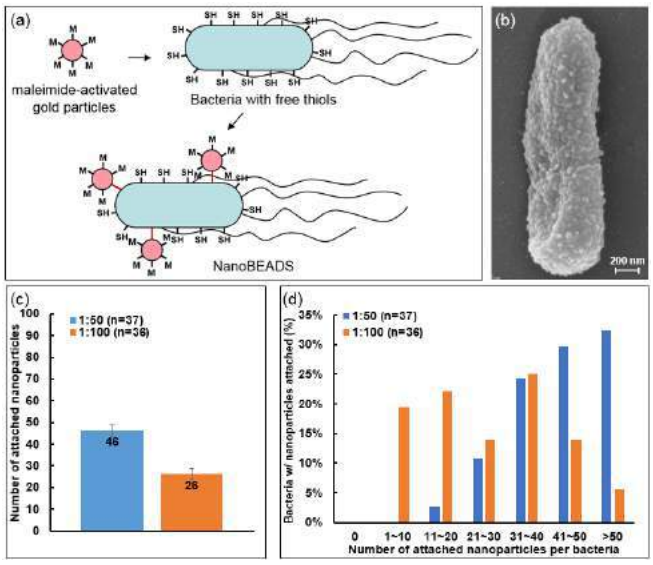

Figure 1: a) Schematic of the conjugation chemistry and b) representative SEM images of a NanoBEADS agent. c) The average nanoparticle loading of NanoBEADS agents constructed at different bacteria/NP assembly ratios. d) The distribution of number of nanoparticles on NanoBEADS agents as a function of assembly ratio.

Before tumor experiments, NanoBEADS were incubated with mPEG-thiol to quench residual maleimide groups on the nanoparticles. The 4T1 and co-culture tumor organoids were incubated with bacteria or PEGylated NanoBEADS for the specified durations. Bacteria were used as a control to determine the effect of nanoparticle conjugation on intratumoral transport. The 4T1 tumor organoids and the 4T1-mCAF organoids were used to investigate the influence of mCAFs on bacteria and NanoBEADS colonization and penetration. Using immunofluorescence staining, it is shown that the collagen content of co-culture tumor organoids is significantly higher than the 4T1 tumor organoids (**Fig 2a**). After 12 h, bacteria self-propelled into the tumor, in some cases reaching the tumor center. Over time, the number of accumulated bacteria increased, primarily due to growth (**Fig 2b**). At 24 h, 4T1 tumor organoids completely disintegrated, and only 9% of the cells were alive (**Fig. 2c**). In contrast, the co-culture tumors contained very few bacteria at 12 h, which were all limited to 20% of the radial distance from the tumor's surface (**Fig 2d**). Even after 18 h, bacteria were primarily limited to 30% of the radial distance, although their number increased due to growth. At 24 h, the bacteria finally reached the core of the co-culture tumors; however, the tumors remained intact and viable (**Fig 2c-d**).

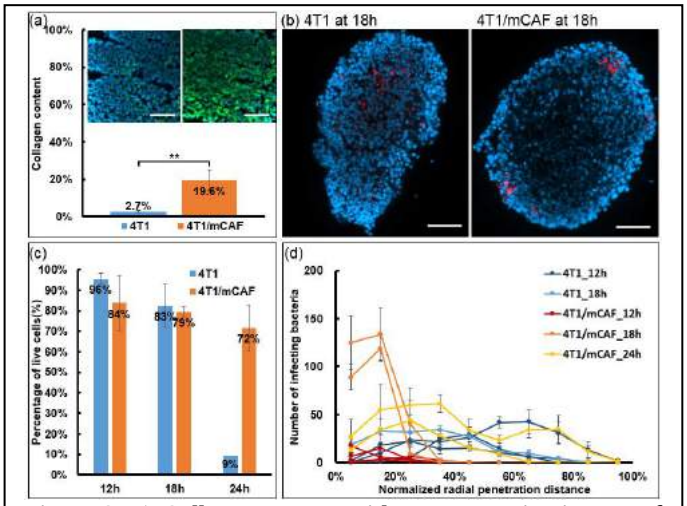

Figure 2: a) Collagen content with representative images of collagen type I immunofluorescence staining in co-culture and 4T1 tumor slices. **p value < 0.01. All scale bars are 50 µm. b) Intratumoral distribution of bacteria in 4T1 and co-culture tumor slices at 18 h. Blue, DAPI; red, bacteria; green, collagen I. All scale bars are 50 µm. c) Viability of tumor cells after tumor incubation with bacteria. d) Radial distribution of bacteria in 4T1 and co-culture tumor organoids.

DISCUSSION

A new class of NanoBEADS, which uses thiol-maleimide linkage to achieve high nanoparticle loading on the bacterial cell, is reported. This one-step conjugation method does not require the use of an antibody, precluding immune stimulation. Furthermore, the attachment chemistry is specific to the membrane and will not interfere with bacterial flagellar motility.

In the breast cancer organoid model with mCAFs, the higher collagen content inhibits bacteria's intratumoral transport and limits bacteria tumor-cell killing effects. We expect that the NanoBEADS will have similar trends to bacteria and is currently being investigated. In the future, we will develop a nano-bio-based approach to overcome the ECM barrier to drug delivery in high-collagen content solid tumors.

ACKNOWLEDGEMENTS

We gratefully acknowledge support from the National Science Foundation (CAREER award, CBET-1454226) to BB.

REFERENCES

[1] Wilhelm, S et al., Nat. Rev. Mater., 1.5:1-12, 2016.
[2] Alkasalias, T et al., Int. J. Mol. Sci., 19.5:1532, 2018.
[3] Traore, A et al., Appl. Phys. Lett., 105.17: 173702, 2014.
[4] Suh, S, et al., Adv. Sci., 6.3:1801309, 2019.
[5] Broadway, K et al., J. Biotechnol., 251:76-83, 2017.
[6] Ivascu, A et al., J. Biomol. Screen., 11.8:922-932, 2006.
[7] Hoshyar, N et al., Nanomedicine, 11.6:673-692, 2016.
[8] Y. Zhan, Y et al., bioRxiv, 867101, 2019.

COMPARISON OF ANABOLIC OSTEOPOROSIS TREATMENTS: PTH *VS*. PTHRP ON THE ACTIVATION OF NEW BONE FORMATION AND IMPROVEMENTS IN BONE MICROARCHITECTURE

Tala Azar (1), Wenzheng Wang (1), Wei-Ju Tseng (1), Hongbo Zhao (1), Jing Du (2) Nathaniel Dyment (1), X. Sherry Liu (1)

(1) McKay Orthopaedic Research Laboratory
University of Pennsylvania
Philadelphia, PA, United States

(2) Department of Mechanical Engineering
The Pennsylvania State University
University Park, PA, United States

INTRODUCTION

Postmenopausal osteoporosis is a chronic condition that leads to deterioration of trabecular microarchitecture and reduced bone mass. Current osteoporosis treatments are categorized as either anticatabolic, which reduce bone resorption, or anabolic, which increase new bone formation. Intermittent parathyroid hormone (PTH, teriparatide) was the first and only FDA-approved anabolic treatment for postmenopausal osteoporosis since 2002 and until 2017, when PTH-related peptide analogue (PTHrP, abaloparatide) was approved by the FDA. Like PTH, PTHrP exerts its anabolic effects by activating the PTH 1 receptor (PTH1R), which subsequently activates multiple downstream pathways. However, the effects of PTHrP on bone microarchitecture, activation of new bone formation, and how these effects compare to those of PTH remain unclear.

It has been widely known that remodeling-based bone formation (RBF – bone formation coupled with resorption by osteoclasts) plays an important role in maintaining healthy skeletal homeostasis. Recently, modeling-based bone formation (MBF – *de novo* bone formation on quiescent surfaces without prior bone resorption) has been identified as an important mechanism by which anabolic agents improve bone mass. MBF is an intrinsically rare cellular mechanism that only naturally occurs during growth, healing, and with external mechanical loading in the adult skeleton [1]. However, recent studies demonstrated that both MBF and RBF can be activated by PTH/PTHrP and are critical to their anabolic effects [2, 3]. Therefore, the objective of this study was to compare the efficacy of PTH and PTHrP by assessing their effects on trabecular bone microarchitecture and their ability to induce MBF and RBF. We hypothesized that different levels of MBF and RBF induced by PTHrP *vs.* PTH may lead to different degrees of improvement in trabecular bone microarchitecture.

METHODS

Animal protocol and treatment: All animal experiments were IACUC approved. Female Sprague-Dawley (SD) rats received bilateral ovariectomy (OVX) surgery at 4 months of age to simulate post-menopause estrogen deficiency and they developed osteopenia after 4 weeks. All animals received treatment 5x/wk for 3 wks (40 μg/kg/day for μCT and 20 μg/kg/day for histomorphometry). Animals were assigned to μCT or histomorphometry. Within each set of animals, there were three groups: (1) Vehicle: saline treated (n=15 for μCT, n=6 for histomorphometry), (2) PTH (n=36 for μCT, n=6 for histomorphometry), and (3) PTHrP (n=17 for μCT, n=6 for histomorphometry). *In vivo* μCT imaging: At wks 0 and 3, μCT scans of the metaphysis of the right proximal tibia were performed (Fig. 1A) using the VivaCT40 (Scanco Medical AG, 10.5 μm voxel size). Trabecular bone microarchitectural parameters were obtained. Mineral label injections, cryohistomorphometry, and imaging: Calcein (green, G), alizarin complexone (red, R), and tetracycline (yellow, Y) fluorochrome labels were injected in a G-R-Y-G sequence on days -2, 5, 12, and 19 (treatment initiated on day 0) with euthanasia on day 21. Cryosections (8μm thick) of the proximal tibia underwent imaging using darkfield and fluorescent microscopy to obtain the trabecular structure and visualize multi-fluorochrome labels (Fig. 2A-C). These same sections were then decalcified and viewed under a polarizing microscope to visualize the cement line and surrounding collagen fibers. Identification of MBF and RBF sites: MBF sites were identified as having a smooth cement line and uniform surrounding collagen fibers (Fig. 2D). RBF sites were identified as having a scalloped cement line with interrupted collagen fibers (Fig. 2E). Dynamic histomorphometry: Mineral labels were used to calculate dynamic histomorphometry parameters. Statistics: Data from μCT are reported as percent change from wk 0, except for structural model index (SMI -

ranging from -3 to 3, reported as absolute change). A one-way ANOVA with Bonferroni post-hoc tests was used to compare responses between treatments. For all analyses, $p \leq 0.05$ was considered to indicate statistical significance.

RESULTS

In vivo μCT (Fig. 1B-G): Without anabolic treatment, OVX led to a deteriorated trabecular bone microarchitecture. This is indicated by a reduction in bone volume fraction (BV/TV), trabecular number (Tb.N), trabecular thickness (Tb.Th), connectivity density (Conn.D), and plate-like trabeculae (indicated by SMI), and an increase in trabecular separation (Tb.Sp) in the VEH group. However, with both PTH and PTHrP treatment, there were improvements in trabecular bone microarchitecture compared to VEH. This is indicated by improvements in BV/TV, Tb.Th, and more plate like trabeculae. PTH and PTHrP lessened the reduction in Tb.N and Conn.D and attenuated the increase in Tb.Sp. Interestingly, we found greater improvements in trabecular bone microarchitecture with PTHrP than with PTH, including BV/TV (68% *vs*. 44%), Tb.Th (54% *vs*. 45%), plate-like trabeculae (-0.9 *vs*. -0.6 in SMI), and greater connectivity (-12% *vs*. -14% in Conn.D). However, no difference was detected between the percent change of Tb.N between PTHrP (-14%) and PTH (-9%).

Histomorphometry (Fig. 2F-H): PTH and PTHrP resulted in greater MBF- and RBF-induced mineralizing surface (MS/BS), mineral apposition rate (MAR), and bone formation rate (BFR/BS) compared to VEH. No difference was found in MAR between PTH and PTHrP groups in both MBF and RBF. However, PTHrP led to a greater MS/BS and BFR/BS compared to PTH at MBF sites (0.33 *vs*. 0.22 for MS/BS, 0.53 *vs*. 0.35 for BFR/BS), but not RBF sites.

DISCUSSION

This was the first study to compare PTH and PTHrP in a rat model. It also provided valuable longitudinal tracking of trabecular bone microarchitecture using *in vivo* imaging. Lastly, using a novel cryohistology imaging platform coupled with sequential mineral labels, we were able to distinguish the effects of MBF *vs*. RBF.

PTH and PTHrP enhanced trabecular bone microarchitecture through the induction of a higher MAR and greater MBF and RBF surfaces compared to VEH treatment. PTHrP was more efficient at improving trabecular bone volume and microarchitecture than PTH due to the formation of more MBF surfaces that may improve trabecular bone microarchitecture.

Here, we studied both PTH and PTHrP at the same dose to compare the efficacy of the drugs. In a clinical trial that tested the efficacy of abaloparatide (PTHrP), abaloparatide was administered at a clinically relevant dose, which is four times (4x) that of teriparatide (PTH) [4]. In human trans-iliac bone biopsies from that trial, compared to teriparatide, the 4x dose of abaloparatide resulted in a greater MS/BS at the periosteal envelope [5]. MAR did not differ between the two treatments. Arlt *et al*. compared equal doses, like in our study, and clinically relevant doses of PTHrP *vs*. PTH in 8-week-old female B6 mice [6]. PTHrP at both doses resulted in a higher osteoblast surface at the proximal tibia than PTH and VEH. These studies and our results suggest that the greater benefit observed with PTHrP *vs*. PTH exists between both equal and clinically relevant doses. PTHrP incurred greater benefits to bone than PTH, although MAR did not contribute to this improvement. Furthermore, the benefits of PTHrP that we see here may be further amplified if this drug were administered at a higher dose.

In summary, our study suggests that MBF and RBF are important contributing factors to the improved trabecular bone microarchitecture by anabolic agents and that PTHrP may be a more efficient anabolic agent than PTH, although more work is needed to confirm this result.

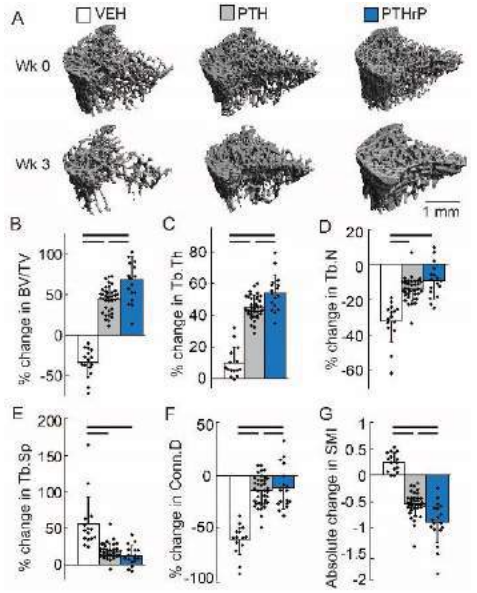

Figure 1: (A) Representative 3D images of trabecular bone microarchitecture of the proximal tibia at baseline (wk 0) and end of treatment regimen (wk 3). (B-F) % change in (B) BV/TV, (C) Tb.Th, (D) Tb.N, (E) Tb.Sp, and (F) Conn.D. (G) Absolute change in SMI. Bar: p<0.05 by one-way ANOVA.

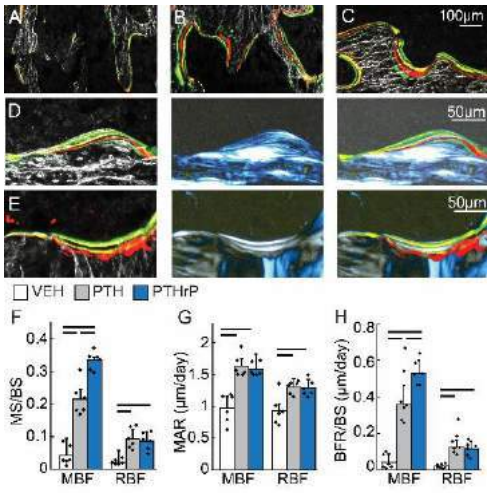

Figure 2: (A-C) Representative images of bone dynamics of (A) VEH, (B) PTH, and (C) PTHrP groups. (D-E) Representative images of (D) MBF sites and (E) RBF sites where MBF sites were identified by smooth cement lines and uniform collagen fiber alignment indicated by polarized images while RBF sites were identified by scalloped cement lines with interrupted collagen fiber alignment. (F) MS/BS, (G) MAR, and (H) BFR/BS of MBF and RBF bone surfaces (BS) in response to VEH, PTH, and PTHrP. Bar: p< 0.05 by one-way ANOVA.

ACKNOWLEDGEMENTS

NIH/NIAMS K01-AR066743 and T32-AR007132, NSF #1661858, Penn Center for Musculoskeletal Disorders (P30-AR069619).

REFERENCES

[1] Jee, W et al., *J Musculoskelet Neuronal Interact*, 7(3):232-9, 2007.
[2] Lindsay, R et al., *J Bone Miner Res*, 21(3):366-73, 2006.
[3] Dempster, D et al., ACR Convergence, Abstract 0107, 2020.
[4] Leder, B et al., *J Clin Endocrinol Metab*, 100(2):697-706, 2015.
[5] Dempster, D et al., Virtual ASBMR Annual Meeting, 2020.
[6] Arlt, H et al., *Bone Rep*, 13:100291, 2020.

DESIGN, CONSTRUCTION, AND TESTING OF A DIFFERENTIAL RESISTANCE ELLIPTICAL EXERCISE MACHINE

John D. Easton (1), Christopher P. Hurt (2) David A. Brown (3), Alan W. Eberhardt (4)

(1) Department of Biomedical Engineering
University of Alabama at Birmingham
Birmingham, Alabama, US

(2) Department of Physical Therapy
University of Alabama at Birmingham
Birmingham, Alabama, US

(3) School of Health Professions
The University of Texas Medical Branch
Galveston, Texas, US

(4) Department of Biomedical Engineering
University of Alabama at Birmingham
Birmingham, Alabama, US

INTRODUCTION

A prominent symptom of hemiparesis is an imbalance of muscular strength between the left and right leg, resulting in gait abnormalities. The individual develops compensatory motor patterns, causing overuse and pain. Secondary symptoms associated with sedentary lifestyle emerge, including heart disease and obesity. While the simple answer to such problems is "exercise", it is consistently more difficult for individuals with mobility impairments to access the proper equipment due to physical, social, psychological, and/or financial reasons. A home-based exercise system would bypass transportation limitations by default while providing privacy for the user, and a more affordable device would ameliorate financial concerns, increasing the potential to reach more users.

Significance. Every 40 seconds someone has a stroke, and every year in the United States alone, nearly 800,000 people will have a stroke [1]. Depression, anxiety, and reduced gait stability conspire to keep survivors of stroke off their feet, thus increasing the rate of health decline [2, 3]. Meanwhile, faster gait velocity and better appearance of gait are regarded as ultimate goals of rehabilitation in the post stroke population [4, 5].

Role of Resistance Training and Aerobic Exercise. The accomplishment of rehabilitation goals often entails the use of technologies such as specialized treadmills and ellipticals. There exists an array of commercial gait trainers for users with hemiparesis. Unfortunately, either high cost or sub-optimal functionality seem to be yet unavoidable compromises. There are more basic, less expensive models without motor assistance and more expensive models such as the Innowalk-Pro and Lokomat. Ellipticals have been investigated as rehabilitation devices for more than a decade, producing devices such as the iCARE, a device which is marketed as affordable yet costs approximately $30,000.

Specific Aims. Elliptical exercise machines provide a low impact alternative for users with limited aerobic capacity or injury in fitness improvement. A motorized elliptical device (the Motogaitor) was created for a child with level IV cerebral palsy by a team of students under the guidance of the senior author. User testing produced an enthusiastic reception, and feedback indicated a number of new design constraints, including:

1. The need for freewheeling capability such that a user could bypass motor assistance and encounter resistance;
2. The ability for device access while using a walker;
3. Price tag less than $3000.

It has been demonstrated that the application of horizontal resistance to the user while walking on a treadmill at self-selected velocity can be scaled to produce strength adaptations in post stroke individuals [6, 7, 8]. Critically, Brown et al. found that increasing posteriorly directed forces while post-stroke users walked on a split belt treadmill resulted in the paretic limb producing more propulsive force [9]. This finding has been a primary impetus for development of an elliptical with differential resistance capability that targets adults post stroke.

Therefore, the goal of this master's thesis was to design, construct, and test an elliptical exercise machine with adjustable differential resistance, a freewheeling motor drive mechanism, and compatibility with a Rifton walker, all with a budget of less than $2000 so that the resultant device could be sold commercially for $3000.

METHODS

In order to verify compatibility with a Rifton walker, it was necessary to create a CAD model of the walker. A front-drive elliptical configuration was chosen to allow ease of access from rear. Interferences were eliminated throughout the range of motion.

Figure 1: Clearances were verified using CAD model.

Freewheeling allows the user to rely on motor assistance for startup of the device. This removes the contribution of static friction, preventing the need to overcome these greater force values. Once the device is moving at a baseline velocity chosen by the user via the control panel, they are free to "out-pedal" the motor.

This function was achieved by attaching a freewheeling sprocket to the main axle about which the flywheel and crank arms rotate. An ANSI 41 chain couples this rotating assembly to the motor output. Due to the unidirectional engagement of the freewheeling sprocket, the motor only applies assistive force when the user's RPM falls below that of the motor. Conversely, when the user's RPM is greater than the motor RPM, the motor only experiences the load of the chain itself. This relationship is functionally identical to a ratcheting socket wrench.

Figure 2: Differential resistance was implemented.

Differential resistance will be achieved by adjusting the length of the moment arm for each leg independently. The crank arm was drilled at 0.5" increments to allow consistency between uses and ease of adjustment.

To save cost, the final device was constructed using mild steel, a relatively inexpensive material. Parts were ordered when necessary and fabricated when possible.

RESULTS

The resultant device, dubbed the Motogaitor Elite, is fully compatible with the Rifton walker, features a freewheeling mechanism that incorporates a motor with variable speed control, implements differential resistance at the crank arm with adjustable friction resistance at the flywheel, and was produced at a final cost of $1748.67. Additionally, it has been estimated that larger scale production could reduce this production cost to $1200-$1400.

The prototype occupies a floor space of 60"x25" which means it would likely fit comfortably in most living spaces. Height adjustable handles, full-sized flywheel for smooth operation, and readily accessible controls are also prominent features of this design.

Figure 3: The Motogaitor Elite is pictured here.

DISCUSSION

Ongoing work includes safety testing, which will utilize motion analysis and collection of pedal force data for inverse dynamics calculations to compare joint torques experienced during use of the device with those seen in overground walking. Future work will ultimately prove whether this model produces a differential training effect, but regardless of the outcome, its creation will provide further insight into ways exercise can combat the secondary effects of stroke.

ACKNOWLEDGEMENTS

The authors gratefully acknowledge the following personnel: Steve Thompson, Director of the UAB Design & Fabrication Center for his consultations and expertise in building; Andres Guerrero, MEng, who designed and constructed the original Motogaitor; and Dr. David Brown, who provided the funding for this project.

REFERENCES

[1] S. Virani Salim et al., *Circulation*, 141:e139-e596, 2020.
[2] S. Barker-Collo et al., *Stroke*, 43:50-55, 2012.
[3] T. Krasovsky et al., *Journal of Neurophysiology*, 109:77-88, 2013.
[4] R. W. Bohannon et al., *The Occupational Therapy Journal of Research*, 11:73-79, 1991.
[5] R. W. Bohannon et al., *The Occupational Therapy Journal of Research*, 14:246-250, 1991.
[6] J. Wang et al., *Clinical Biomechanics*, 30:40-45, 2015
[7] C.P. Hurt et al., *Journal of NeuroEngineering and Rehabilitation*, 12:12, 2014.
[8] C. P. Hurt et al., *J Strength Cond Res*, 34:3569-3576, 2020.
[9] D. A. Brown, "Unpublished," 2021.

DETERMINING TIBIAL STRESS AND STRAIN DURING THE STANCE PHASE WITH 3D FINITE ELEMENT MODELING IN A HEALTHY RUNNING POPULATION

Patricia M. Butler (1), Ali Vahdati (1), Stacey A. Meardon (2), Stephanie M. George (1)

(1) Engineering
East Carolina University
Greenville, North Carolina, United States

(2) Physical Therapy
East Carolina University
Greenville, North Carolina, United States

INTRODUCTION

There are numerous benefits associated with running; however, the tibia is subjected to repeating forces and can develop bone stress injuries (BSIs) [1]. BSIs begin with a mild pain that can progress with continued exercise [2]. Studies have suggested that, each year, more than 20% of runners develop BSIs and 40-60% of those BSIs occur in the tibia [3, 4, 5]. In order to develop and propose interventions for BSIs, a better understanding of the mechanisms for BSIs is needed. To obtain a better understanding of BSIs, computational methods like 3D finite element (FE) analysis are used. The objective of this study was to develop a workflow to create 3D tibia FE models using personalized running force data from the stance phase and magnetic resonance (MR)-derived subject-specific tibia geometries in both male and female runners.

METHODS

Data were previously collected from 40 volunteers, who were aged 18-35, healthy, non-injured, and frequently ran more than 16 kilometers weekly. As producing personalized 3D models is a very time-intensive process, four females and four males were used in this study. All the participants warmed up on an instrumented force treadmill (Bertec, Columbia, Ohio, USA). 3D kinetic and kinematic data (100 and 200 Hz respectively) was collected using a real-time motion capture acquisition and processing software (TheMotionMonitor, Innovative Sports Training, Chicago, Illinois, USA) and a 10-camera 3D motion capture system was used to track reflective markers (Qualysis Corporation™, Gothenburg, Sweden). Ground reaction forces were filtered, and kinetic and kinematic data of the stance phase were isolated and input to a musculoskeletal model to estimate muscle forces of the muscles that span the tibial region of interest [6, 7]. Static optimization and vector summation of the muscle forces with distal tibia reaction forces were further used to approximate the forces acting at the distal tibia.

Each subject's right tibia was imaged using a 1.5-T scanner with a torso coil. Sagittal and Coronal T1 weighted turbo spin echoes (4mm thick/1mm gap, 480 FOV) and axial T1-weighted turbo spin echoes (7mm thick/2mm gap, 220 FOV) were acquired. Vitamin E capsules were placed on anatomical landmarks to aid in coordinate system alignment. Each MR image was imported into Mimics (Materialise, Belgium) where semi-automatic thresholding was used to segment the entire bone (cortical and inner bone), and the inner bone (trabecular bone, bone marrow, etc.).

The entire tibia was rotated about the longitudinal axis to align the MRI and force coordinate systems. Due to low trabecular bone resolution, the distal and proximal ends were cropped resulting in a tibial model comprised of the middle 70% of the tibia shaft. The distal and proximal centroid locations were identified and imported into 3-Matic (Materialise, Belgium). The longitudinal axis of the tibial model, defined as a line from the distal to proximal centroid locations, was aligned with the 3-Matic coordinate system. Volumetric meshes were created from the 3D models using tetrahedral (10-node) elements.

A preliminary mesh sensitivity analysis was performed. For this initial analysis, 1.2 mm was selected to ensure a uniform edge length across all subjects. The volumetric meshes were exported into ANSYS (ANSYS, Canonsburg PA). A Young's Modulus of 17.19 GPa and a Poisson's ratio of 0.3 was defined for the cortical bone [8]. Previously determined distal tibial forces for the 10 increments of the stance phase were used for FE analysis and the distal end was fixed. For each subject the maximum equivalent stresses and equivalent elastic strains were extracted at each 10% interval of stance phase and analyzed descriptively.

RESULTS

Subject demographics and maximum equivalent stress and strain are reported in Table 1. The maximum equivalent stress and equivalent elastic strain occurred at 50-60% of the stance phase and are visualized in Figure 1. The maximum stress across the entire stance phase is shown in Figure 2.

Table 1: Subject Information and FE Outputs.

Parameter	All	Males	Females
Age	23.75 ± 3.53	24.0 ± 4.42	23.50 ± 2.29
Mass (kg)	70.56 ± 13.3	82.79 ± 6.72	58.34 ± 2.96
Preferred Run Speed (m/s)	2.94 ± 0.13	3.00 ± 0.07	2.87 ± 0.14
Max. Equivalent stress (MPa)	149.6 ± 39.6	143.5 ± 29.5	155.8 ± 46.8
Max. Principal Strain (με)	7616 ± 2032	7478 ± 1423	7752 ± 2489

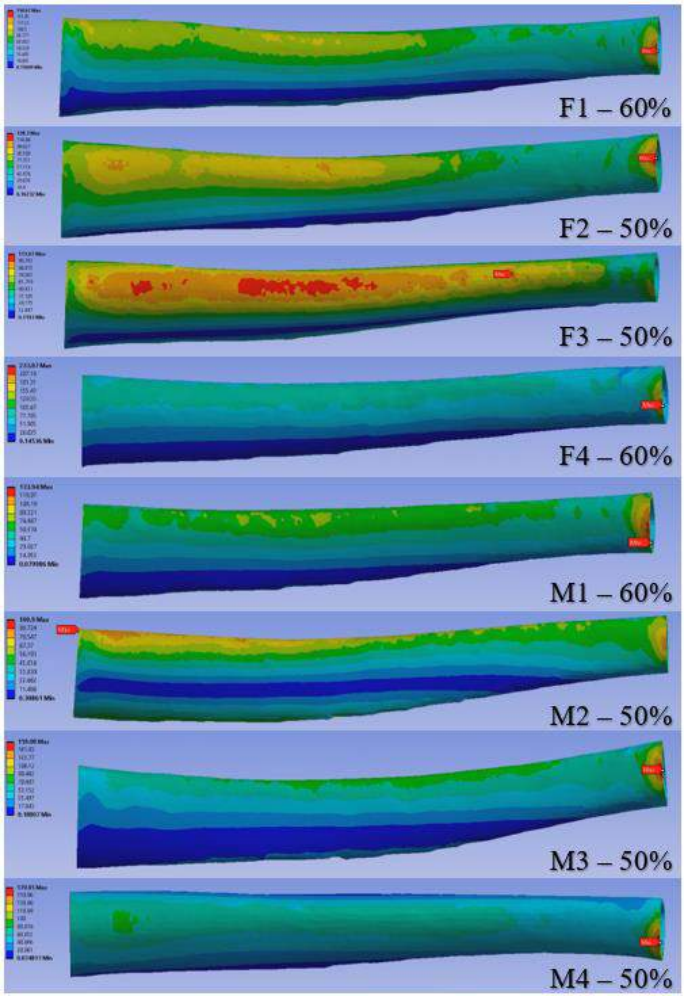

Figure 1: Equivalent Stress at the time point corresponding to maximum equivalent stress and strain for each subject. (Note the scales vary across subjects; M-male and F-female)

DISCUSSION

This study demonstrates a workflow for MR-reconstruction of the tibia to FEM utilizing subject specific running forces across the stance phase in young healthy female and male runners. Past studies have utilized CT scans to acquire tibia geometry and estimate mechanical properties [9]; however, subjects are exposed to radiation. Furthermore, we have combined subject specific geometry with subject specific forces; whereas other studies have used generalize geometries [8, 10] or estimated forces [9].

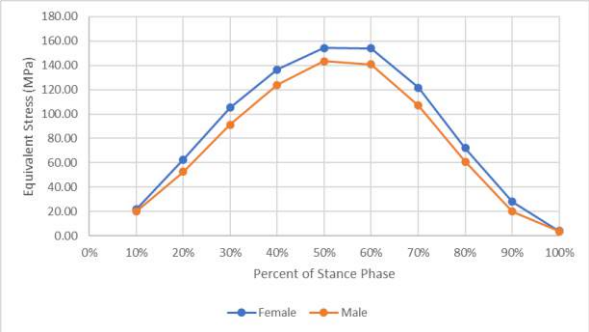

Figure 2: Subject averaged maximum equivalent stress across 10% intervals of the stance phase.

The values for Maximum Equivalent von Mises stresses found in this study (149.6 ± 39.6 MPa) are similar to those from [9]: 102.1MPa and 120.24 MPa for one male and one female respectively. The minor difference may be explained by the inclusion of both trabecular and cortical bone versus just cortical bone as in this study. Trabecular bone is not captured well with MRI. Furthermore, the subjects were older, and the applied forces were estimated based on the subject's body weight. The location of maximum stress and strain, as seen here in the posterior middle of the tibia, is similar to other studies [8-10].

In this study the maximum equivalent strain was 7616 ± 2032 με. Other studies have reported similar values during running such as 7939.79 ± 1588.74 με for rear foot-strike [8]. Edwards et al, reported maximum compressive strains between 2800 and 4800 με during running conditions [10]. Here, the maximum normal strains were 5782 ± 1895 με. However, the subjects from Edwards et al. were all male and the inclusion of female runners may increase the subject-averaged maximum strain.

There were limitations of this study such as a small population size, cortical bone-only hollow models, not accounting for the contribution of the fibula, and use of a generalized Young's modulus instead of personalized values. However, this work demonstrates a successful workflow to build personalized FEMs from MR images and running data. As 3D modeling is time intensive, future work will compare these results to that of simpler 2D cross-sectional analyses. Ultimately, these data can improve understanding of BSI and risk-mitigating strategies.

ACKNOWLEDGEMENTS

Funding from the National Science Foundation EEC-1359183 and the ECU Graduate School; John Wilson, PhD, MPT; Richard Willy, PhD, PT, OCS; Mara Thompson.

REFERENCES

[1] Meardon, S et al., *Clinical Biomechanics*, 30:895-902, 2015.
[2] Harrast, M, *Clinical Care of the Runner E-Book*. Philadelphia: Elsevier, 2019.
[3] Tenforde, A et al., *Medicine & Science In Sports & Exercise*, 47:905, 2015.
[4] Tenforde, A et al., *Physical Med and Rehab Clinics of N. America*, 27:139-149, 2016.
[5] Jerban, S et al., *NMR In Biomedicine*, 31: e3994, 2018.
[6] Arnold, E et al., *Annals of biomedical engineering*, 38:269–279, 2009.
[7] Derrick, T et al., *J. Biomechanics*, 49(3), 429-435, 2016.
[8] Chen, T et al., *Clinical Biomechanics*, 33:49-54, 2016.
[9] Tarapoom, W et al., *Engineering Journal*, 20:155-167, 2016.
[10] Edwards et al., *Med & Science in Sports & Exer.*, 41(12):2177-2184, 2009.

SITTING MRI STUDY OF LUMBAR SPINAL MUSCULATURE

Vicky Varghese (1), Hoon Choi (1), Jamie Baisden (1), Anjishnu Banerjee (2), Ulrich Kemmo (2)
Sagar Umale (1), John Humm (1), Narayan Yoganandan (1)

(1) Center for NeuroTrauma Research,
Department of Neurosurgery
Medical College of Wisconsin
Milwaukee, WI, USA

(2) Department of Biostatistics
Medical College of Wisconsin
Milwaukee, WI, USA

INTRODUCTION

Studies have reported a high prevalence of back pain (lumbar spine) and neck pain in the military population [1-4]. Low back pain has been attributed to mechanical loading (vibrations), constrained posture, or simultaneous exposures to both these factors in civilian and military populations [5-7]. Similar variables are attributed to neck pain. Painful conditions can have consequences in the work environment. They may lead to compromised mission efficiency, and or early termination from the original mission or occupation (e.g., truck driving population) [8]. A study on F-16 pilots found that flight duration and sitting posture were the main causes of back pain [9]. From a physiological perspective, muscles undergo morphological alterations including alignment or curvature to accommodate loading and or age-related changes in both neck and spine structures. From a bioengineering perspective, such changes can be accommodated in finite element models to determine the internal loads in the various joints of the spine.

Supine magnetic resonance imaging (MRI) is routinely performed for diagnostic purposes; however, they are not effective to quantify the potential geometrical changes in the spine musculature for the in vivo situation as the axial loading is not included in this posture [10]. For example, in the upright sitting posture, increased extension of the upper lumbar spine is not captured in the supine imaging mode [11]. There is a lack of human morphological studies for spinal musculature in the upright position as it is not the most common mode for patient screening. The present study was conducted determine the changes the lumbar musculature in the upright position for females with the following two purposes. The first purpose was to obtain the morphology of lumbar muscles in the upright position, and the second purpose was to develop cross-sectional area scaling factors from the supine to upright posture.

METHODS

Ten healthy female civilian volunteers participated in the study according to the approved protocols from the Institutional Review Board and sponsor. The inclusion criteria for the subject selection were: Females under the age of 40 years, asymptomatic individuals, no history of low back pain or injuries or congenital spinal abnormalities or spinal surgeries. The demographics of the volunteers were age 31±4.8 years, stature 163.6±7.1 cm, and BMI 25.6±4.2 kg/m^2.

An upright MRI scanner (Fonar Corporation, Melville, NY, USA) was used to image the volunteers in a seated posture. A custom seat was used. Image data were stored in Digital Imaging and Communication in Medicine (DICOM) format for analysis. All scans were obtained in the neutral position defined as the horizontal Frankfort plane with volunteer facing forward. T1 and T2 weighted MRIs were used in the analysis. The morphology of the psoas, multifidus and erector spinae muscles were measured using a commercial software (OSIRIX, Bernex, Switzerland). The cross-sectional area of each muscle was measured at the cranial surface of each vertebra from L1 to L5 levels by a practicing and board-certified neurosurgeon and a trained biomedical engineer. The reliability of the observations by the observers were measured using inter-class correlation coefficient (3,1), and coefficients of < 0.40 were categorized as poor, 0.40 to 0.60, as fair, 0.60 to 0.75 as good, and >0.75 as excellent [12].

A systematic review was performed to obtain the muscle cross-sectional areas of asymptomatic and symptomatic subjects in supine and upright positions. Literature data were normalized to the upright position to

compare the differences in morphology. The weighted average technique was used to obtain the aggregated mean effect size for muscle morphology of asymptomatic and symptomatic subjects [13]. The effect size was calculated by dividing the mean by standard deviation. The mean of the effect size from an individual study was used to obtain the aggregated effect size in the present analysis.

RESULTS

The muscle cross-sectional areas were measured from the MRI images (Figure 1). The psoas muscle and multifidus muscles cross-sectional areas increased from the cephalad to caudal levels. The erector spinae cross-sectional area was the greatest in the middle region and reduced towards both cephalad and caudal ends. The range for the psoas muscles cross-sectional was from 1.9 cm^2 to 12.1 cm^2. For the erector spinae, it ranged from 8.8 cm^2 to 13.9 cm^2, and for the multifidus it ranged from 1.8 to 5.7 cm^2. (Table 1).

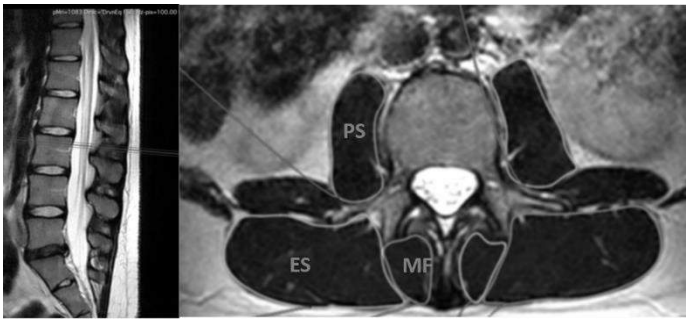

Figure 1: Lumbar muscle cross-sectional area measured at the L3 level. The areas of psoas (PS), erector spinae (ES) and multifidus (MF) are marked in the MRI image.

Table 1: Area (cm^2) data

Level	Psoas		Erector spinae		Multifidus	
	Mean	SD	Mean	SD	Mean	SD
L1	1.9	1.1	8.8	3.4	1.8	0.3
L2	4.3	1.9	12.9	2.6	2.4	0.5
L3	7.2	2.0	13.9	2.2	3.1	0.6
L4	11.1	2.3	13.0	2.4	4.2	0.9
L5	12.1	2.5	11.4	2.9	5.7	1.4

The inter-class correlation analysis showed that all coefficients in excellent category except for the multifidus muscles (inter-class: good at L2 and L3, intra class: L1 and L5 good and fair at L3). Female volunteer psoas muscle cross-sectional areas at the L3-L5 levels ranged from 12.08 to 11.9 cm^2, and the cross-sectional areas of the combined multifidus and erector spinae ranged from 19.5 to 20.7 cm^2 [14]. The scaling factor from the supine to upright data was obtained as the ratio of upright to the supine cross-sectional areas at each level. The scaling factors for the psoas muscles were: L3-L4: 1.34, L4-L5: 1.10, and L5-S1:0.93 and multifidus-erector spinae muscles were: L3-L4: 0.94, L4-L5: 0.88, and L5-S1:0.87. These scaling factors were used to convert the literature data of muscle cross-sectional areas in the supine to upright position. Similar muscle cross-section areas were obtained from other studies [15], [14], [16]. The effect size of the psoas muscle cross-sectional area for the asymptomatic subjects at L3 and L4 was 5.05 and 5.13, whereas for symptomatic back pain patients, they were 3.58 and 3.97. There was a 25% reduction at the L3 level, and 24% reduction at L4 level.

DISCUSSION

The upright muscle cross-sectional areas from the current study are comparable with those in the literature [14]. The scaling factors showed an increase in cross-sectional area for flexors (psoas muscle, except at L5-S1), and a decrease in the cross-sectional area for the extensors, i.e., combined multifidus and erector spinae muscles. This can be attributed to the shortening of the psoas muscles with flexion in the sitting posture. Lengthening may occur for the extensor muscles in the siting posture. The scaled literature data showed a decrease in psoas muscle cross-sectional area in patients with low back pain. Additional data such as muscle centroid location (radius and angle) are needed to better quantify the muscle geometry due to posture and pain. As muscles locate closer to the spine in back pain patients, muscle radii and angle decreases. These changes alter the internal load paths and load (re)distributions within the osteoligamentous lumbar column. It should be possible to determine segmental loads by inputting the data from present study into isolated thoracolumbar column or total human body models [17]. The present results may have application in biomedical, automotive, and military scenarios. The limitation of the current study is the small sample size although the comparison of effect size with similar studies in literature shows comparable results. Additional studies are needed to determine these parameters for the male spine.

ACKNOWLEDGEMENTS

This research was supported by the Department of Veterans Affairs Medical Research, Department of Neurosurgery at the Medical College of Wisconsin, and W81XWH-16-01-0010. This material is the result of work supported with the resources and use of facilities at the Zablocki VA Medical Center, Milwaukee, Wisconsin. The last author (NY) is a part time employee of the VA Medical Center, Milwaukee, WI.

REFERENCES

[1] Grossman, A et al.,*Aviat Space Environ Med,* 83, 7: 702-5, 2012.
[2] Gaydos, S et al., *Aviat Space Environ Med,* 83, 9: 879-89, 2012.
[3] de Oliveira,C et al., *J Biomech,* 34, 10: 1309-15, 2001.
[4] de Oliveira, C et al., *Aviat Space Environ Med,* 75, 4:317-22, 2004.
[5] Bongers, P et al., *Ergonomics,* 33, 8: 1007-26, 1990.
[6] Burstrom, L et al., *Int Arch Occup Environ Health,* 88,4,03-18,2015.
[7] Pelham, T et al.,*Work,*24,2:101-10, 2005.
[8] McCrary, B et al., *Aviat Space Environ Med,* 73, 11 :1117-21,2002.
[9] Thoolen, S et al., *Aerosp Med Hum Perform,* 86, 11: 936-41, 2015.
[10] Alyas, F et al., *Clin Radiol,* 63, 9:1035-48, 2008.
[11] Jinkins, J et al., *Eur Radiol,* 15,9:1815-25,2005.
[12] Cicchetti, D et al., *Am J Ment Defic,* 86, 2:127-37,1981.
[13] Cumpston, M et al., *Cochrane Database Syst Rev,* 10:142, 2019.
[14] Shaikh, N et al., *Eur Spine J,* 29, 9:2306-2318, 2020.
[15] Marras, W et al., *Clin Biomech (Bristol, Avon),* 16, 1: 38-46, 2001.
[16] Jang, H et al., *World Neurosurg,* 131:e88-e95,2019.
[17] Umale S et al., *J. Biomech Behav Biomater (In Press).*

HEAD IMPACT BIOMECHANICS BY ICE ZONE AND ATHLETE INTENT IN YOUTH ICE HOCKEY

Abigail G. Swenson (1), N. Stewart Pritchard (2, 3), Logan E. Miller (2, 3), Jillian E. Urban (2, 3), Joel D. Stitzel (2, 3)

(1) Department of Neuroscience
Wake Forest School of Medicine
Winston Salem, NC, USA

(2) Department of Biomedical Engineering
Wake Forest School of Medicine
Winston Salem, NC, USA

(3) Virginia Tech-Wake Forest University
School of Biomedical Engineering and Sciences
Winston Salem, NC, USA

INTRODUCTION

Ice hockey is an increasingly popular sport, with nearly 1 million registered athletes under the age of 20 worldwide [1]. Boys' and men's hockey is considered a collision sport, as athletes use body checking (intentionally colliding with an opponent) to control the flow of gameplay. Ice hockey has a high rate of concussions. Additionally, athletes are frequently exposed to subconcussive impacts which do result in overt signs and symptoms of concussion, but are of rising concern due to their association with neurocognitive and microstructural brain changes [2-4]. Prior research has demonstrated that apparent player anticipation of contact affects head kinematics, while player position does not [5,6]. However, positioning in hockey is dynamic during play, as such, zone location on the ice during an impact may be an additional exposure measure of interest. Additionally, athlete awareness during impacts does not differentiate between different roles athletes may play during a checking scenario and their impact on head kinematics. As greater understanding of sport-specific determinants of head impact exposure is necessary to inform safety measures in the sport, the objective of this study was to evaluate the effect of ice zone and athlete intent on peak head kinematics in youth boys' ice hockey.

METHODS

This study enrolled male athletes (n=18, ages 12-14) participating in a local 14U hockey team over two seasons of play. Athletes were fit with a custom instrumented mouthpiece to wear during all games and practices. Mouthpieces featured a tri-axial accelerometer and gyroscope embedded within a rigid retainer material bonded to a soft elastomer overlay and have been previously validated for sport-related impacts [7,8].

On-ice impact data were collected during 127 sessions. Data acquisition was triggered when the linear acceleration exceeded 5 g for at least 3 ms; when triggered, mouthpieces collected 60 ms of linear acceleration and rotational velocity data. Kinematic data from the mouthpiece were paired with time-synchronized video of each corresponding session to identify characteristics of contact scenarios experienced on-ice using a custom MATLAB graphical user interface (MathWorks, Natick, MA).

Contact scenarios were coded by type, including board checks, mid-ice collisions, falls, fights, unintentional collisions with the boards, and other head impacts. For this study, board checks and mid-ice collisions (i.e., body checks) were further categorized by ice zone (location on the ice the contact occurred): offensive, neutral, and defensive zones on the ice. Intent of the instrumented athlete (i.e., athlete intent) was coded as target (i.e., the instrumented athlete is intentionally contacted by an opponent), initiator (i.e., the instrumented athlete intentionally contacts the opponent), and incidental contact (the instrumented athlete and opponent collide unintentionally) based on criteria in table 1.

Table 1: Criteria to evaluate athlete intent during body checking.

1.	Does instrumented athlete approach opponent?
2.	Does the instrumented athlete keep knees bent?
3.	Does the instrumented athlete lead into the collision with their shoulders?
4.	Does the instrumented athlete keep their head up?
5.	Does the instrumented athlete have control of the puck?
6.	Is the instrumented athlete pinned between the boards and their opponent during a board check?

Post-processing of the mouthpiece data follows the methodology detailed by Rich et al. (2019) [8]. Following data transformation, resultant time histories and summary statistics associated with peak

resultant kinematics were calculated and compared by ice zone and athlete intent.

RESULTS

A total of 892 visually verified contact scenarios were recorded by the mouthpiece; of which, 235 were board checks and 350 were mid-ice collisions, resulting in 585 body checks for the present analysis. Most body checks occurred in games (n=533, 91%) compared to practices (n=52, 8.9%). The median (95th percentile) peak linear acceleration, rotational velocity, and rotational acceleration for all body checking impacts was 7.30 (27.8) g, 8.62 (19.2) rad/s, and 610 (2147) rad/s^2 respectively.

Among the body checks, 213 (36.4%) occurred in the offensive zone, 220 (37.6%) in the defensive zone, and 103 (17.6%) in the neutral zone; 49 (8.3%) impacts were not coded for zone, as they occurred during practice drills in which zone type could not be defined. Additionally, 197 (33.6%) body checks involved the instrumented athlete as the initiator, 350 (59.8%) involved the instrumented athlete as the target, and 38 (6.5%) were deemed incidental contact. There was little variation in medial and 95th percentile peak kinematics between ice zones; however, intentional body checks (initiator and target type contacts) had greater peak kinematics than incidental contact, with the exception of 95th percentile accelerations.

Table 2: Median (95th percentile) peak head kinematics by ice zone and athlete intent.

		N	*Linear Accel.(g)*	*Rotational Vel. (rad/s)*	*Rotational Accel.(rad/s^2)*
Ice Zone	Offensive	213	7.26 (28.57)	8.77 (18.95)	616 (2585)
	Neutral	103	6.91 (23.15)	8.43 (22.76)	585 (1980)
	Defensive	220	7.68 (32.96)	8.93 (19.50)	629 (2337)
Athlete Intent	Initiator	197	7.31 (27.28)	8.33 (17.67)	597 (2092)
	Target	350	7.40 (27.93)	9.08 (19.89)	635 (2404)
	Incidental	38	5.58 (38.19)	4.61 (12.44)	419 (3245)

DISCUSSION

This study evaluated head kinematics during body checking by two novel determinants of exposure: ice zone and athlete intent. We found that athletes experienced more impacts in defensive and offensive zones compared to the neutral zone, and that intentional contact types (target, initiator) had greater median and 95th percentile peak kinematics than incidental contact, with the exception of 95th percentile accelerations.

Previous studies revealed no significant differences in kinematics experienced by player position [6]; positioning is relatively fluid in ice hockey compared to sports such as football, and with the exception of goaltenders, athletes will spend time in each of the three ice zones. This study found that there was little variation in median and 95th percentile peak head kinematics experienced across ice zones. However, we observed that among mouthpiece-recorded impacts, impacts occurred in the offensive and defensive zones 2.06 to 2.13 times as in the neutral zone. This is could be influenced by the relative size of the zone, as the offensive and defensive zones are larger compared to the neutral zone. Additionally, due to the competitive nature of the sport, more gameplay occurs in defensive and offensive zones, where athletes are likely to attempt to disrupt plays than in the neutral zone, where athletes primarily carry the puck to set up a play.

We observed that intentional body checks (target and initiator contact types) had higher median and 95th percentile peak kinematics than incidental contact, except for 95th percentile linear and rotational acceleration. Higher magnitude incidental contacts were observed to occur when athletes were unintentionally involved in an impact between other players, or when athletes appeared less aware of their surroundings on the ice (e.g., skating backwards or with their head down). This is consistent with findings from Mihalik et al., who reported athletes with poor anticipation of collisions experienced more severe impacts compared to well-anticipated collisions, particularly for impacts in the 50th-75th percentile severity range [5]. Among our sample, the instrument athlete was most often involved in contact in which they were the target during the impact. Among body checks resulting in a mouthpiece recording, the instrumented athlete was the target 1.77 times more often than the initiator. However, it is possible that not all contact scenarios experienced on-ice were recorded by the mouthpiece. For example, if an instrumented athlete delivered a check without contacting his head, the mouthpiece linear acceleration may not have crossed the 5 g threshold to trigger recording. Additional video review of all contact scenarios, not just mouthpiece-recorded events may provide insight on differences in intent and the frequencies at which different types of impacts occur.

This study was limited by several factors. Firstly, the sample size for this study was small, with 18 athletes over 2 seasons of play. Future studies within this population aim to include a larger sample size. Similarly, to judging athlete anticipation of an impact, objective characterization of athlete intent from video is challenging [5]. Other objective measurements of factors affecting head impact exposure, such as player speed and angle of approach should be explored to better understand how characteristics of contact influence head kinematics and head impact exposure in ice hockey [9].

The goal of this study was to compare head kinematics to ice zone and athlete intent. This adds to a limited, but growing body of knowledge on determinants of head impact exposure in the sport. Results of this study and of future studies of head impact exposure may be used to drive sport-specific interventions and regulations, reducing athlete head impact exposure and improving sport safety.

ACKNOWLEDGEMENTS

The authors extend their gratitude to the Childress Institute for Pediatric Trauma for funding this study and thank the Triad Alliance Hockey Association for participation in this study. Special thanks Konstantina Strates for her efforts in project management and study coordination, as well as Autumn Knight, Jordan Rahm, Nicole Rogers, and Richard Metzler Jr. for their assistance in data collection and video review. The mouthpiece technology presented herein is patent pending.

REFERENCES

[1] International Ice Hockey Federation, *Survey of Players*, 2019.
[2] Davenport EM, et al., *J Neurotrauma* 1624(19):1617-1624, 2014.
[3] Bahrami N, et al., *Radiology* 281(3), 919-926, 2016.
[4] Talavage TM, et al., *J Neurotrauma* 31(4), 327-338, 2014.
[5] Mihalik JP, et al., *Pediatrics* 125(6), 2015.
[6] Mihalik JP, et al., *Ann Biomed Eng* 40(1): 141-149, 2012.
[7] Miller LE, et al., *J Biomech Eng* 140(5), 2018.
[8] Rich A, et al., *Ann Biomed Eng* 47(10):2109-2121, 2019.
[9] Campolettano ET, et al. *IRCOBI* (Vol. 2018, p. 326), 2018.

PATIENT SPECIFIC MODELING AND 3-DIMENSIONAL PRINTING FOR PLANNING OF REDO TRANSCATHETER AORTIC VALVE REPLACEMENT

Sri Krishna Sivakumar[1], Huang Chen[2], Breandan Yeats[2], Sarah Tucker[2], Scott Hollister[2], Pradeep Yadav[3], Venkat Polsani[3], Vinod Thourani[3], Lakshmi Prasad Dasi[2]

(1) Department of Mechanical Engineering,
Georgia Institute of Technology,
Atlanta, Georgia, USA

(2) Department of Biomedical Engineering,
Georgia Institute of Technology,
Atlanta, Georgia, USA

(3) Department of Cardiology,
Piedmont Atlanta Hospital,
Atlanta, Georgia, USA

INTRODUCTION

Transcatheter aortic valve replacement (TAVR) has quickly evolved into the preferred mode of aortic valve replacement in patients diagnosed with aortic valve stenosis. However, as TAVR is still a developing method of treatment, there are some complications associated with it that could affect success of the valve replacement namely coronary obstruction, root rupture, paravalvular leak etc. emphasizing the need for procedural planning. Many computational studies on the design, implantation, and post-procedural complications have been published since the beginning of TAVR [1-3]. Recently, patients who received TAVR have presented to the hospital with degenerated prostheses needing another intervention to help with the elevated transvalvular gradients. In such cases, a second TAV is deployed inside of the degenerated transcatheter valve, called redo-TAVR, to treat the aortic stenosis. Computational modeling and 3-dimensional (3D) printing allows us to predict and plan for post-TAVR complications including root rupture, coronary obstruction, paravalvular leak etc. The objective of this study is to develop a computational framework to model redo-TAVR accurately and predict the risk of coronary obstruction to help with optimization of placement of TAV in redo-TAVR for best outcomes.

METHODS

Pre-procedural computed tomography (CT) images of a 63-year-old patient with a pre-existing Evolut 26mm TAV (Medtronic, Dublin, Ireland) were obtained through an IRB approved protocol. Aortic root, TAV stent and calcification of the patient were segmented from CT images and lofted using Mimics 22.0 (Materialise, Leuven, Belgium). Segmenting the Evolut stent geometry and accurately reconstructing the valve geometry without artifacts from pre-procedural cardiac CT scans has always been a challenge due to artifacts caused by the metal stents and the leaflets' poor visibly [4,5]. As illustrated in Figure 1, we have developed a registration-based valve geometry reconstruction method to address this issue. First, a high-quality valve geometry file (29mm Evolut R) was obtained from high-resolution micro CT scans (Figure 1A). Contrast agent was sprayed onto the leaflets to increase their signal strength during scanning. The stent segmented from the patient's pre-procedural CT images (Figure 1B) showed a significant increase in stent thickness due to blooming artifacts. The deviation from the original stent geometry would cause problems in evaluating the effectiveness of the treatment. The registration started with manually picking several corresponding points between the two geometries. After an initial pass of 3D rigid transformation, a spline-based non-rigid transform [6] accurately aligned the high-quality stent to match the patient's CT scan results. As shown in Figure 1C, good agreement between the two geometries was achieved. The last step was to apply the same transformations to the leaflets and combine them with the deformed stent to generate the final valve model for 3D printing (Figure 1D).

Aorta vessel anatomy with an embedded stent structure was 3D printed using a Stratasys Digital Anatomy (DAP) J750 polyjet printer (https://www.stratasys.com/3d-printers/j750-digital-anatomy). The .STL file created from the patient CT scan was loaded into GrabCAD (https://grabcad.com/print) and assigned specific anatomical presets to appropriate structures within the assembly. The aortic wall was assigned the “blood vessel wall” preset with a compliance preset of “moderately compliant”, the stent was assigned a rigid Vero material and the leaflets were assigned the “valve leaflet” preset with a stiffness preset of “stiffened.” The J750 Polyjet printer jets small liquid resin droplets that are cured by a UV lamp layer by layer. It is able to achieve a variety of textures, colors, and compliances due to a six-material capacity allowing for multi-material prototypes. After printing is completed, the prototypes were Post processed using the Forti by Post Process which

includes a support-removal submersion bath that dissolves support material.

The 3D geometry of the aortic wall and TAV stent and leaflets were then discretized in ABAQUS (Dassault Systèmes, Johnston, RI, US) using explicit 4-node linear tetrahedron elements. Neo-Hookean hyper-elastic constitutive equation was used to represent the aortic material properties with shear modulus, μ=1 MPa, bulk modulus, κ=10 MPa, and density, ρ=1000 kg/m^3 [7]. Stent model of a SAPIEN 3 23mm valve was employed after meshing with quadratic tetrahedral elements in ABAQUS. The SAPIEN stent was modeled using an elasto-plastic model with Young's modulus, E=193 GPa, σ_y (0.2%) =340 MPa, σ_u (48%) =670 MPa, Poisson's ratio, ν = 0.29 and, density, ρ =7760 kg/m^3[8]. The balloon was modeled with shell elements as a linear elastic material with E=600 MPa, ν =0.45 and ρ=1100 kg/m^3 [8]. The crimped balloon and stent were positioned coaxially inside the aortic root (Z-axis). Fluid-cavity based approach was employed to inflate the balloon and deploy the stent. The ends of the aortic root were constrained in translational and rotational degrees of freedom about Z-axis. Scaled penalty contact was employed for the stent-balloon and stent-AV interactions. Results were visualized and analyzed in ABAQUS.

RESULTS

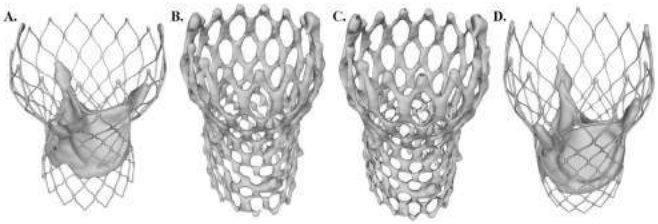

Figure 1. (A) Stent and leaflet geometry reconstructed from high-resolution micro CT scans. (B) Manually segmented stent from the patient's pre-procedural cardiac CT scan. (C) Comparison between the registered high-resolution stent (shown in a darker color) and the patient's stent. (D) The final valve geometry with deformed leaflets

As seen in Fig. 1, the use of image registration algorithm resulted in a precise transcatheter valve geometry free of artifacts and captured the deformed state of the valve inside the patient anatomy accurately. The segmented aortic root geometry was combined with the TAV model to 3-D print the geometry of the patient (Fig. 2) for subsequent inspection by clinicians to decide the optimal deployment position that gave minimal risk of coronary obstruction. The deployment in the nominal showed very high risk of coronary occlusion whereas deployment of the SAPIEN stent below the leaflets of the Evolut resulted in no obstruction (Fig. 4). Comparison of the simulation result with post-procedural CT

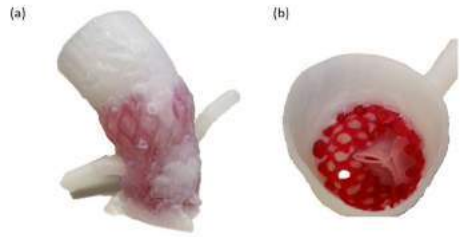

Figure 2. Pictures of the 3D-printed geometry provided to clinicians for decision making in (a) lateral and (b) axial views.

imaging showed very good agreement (Fig. 4).

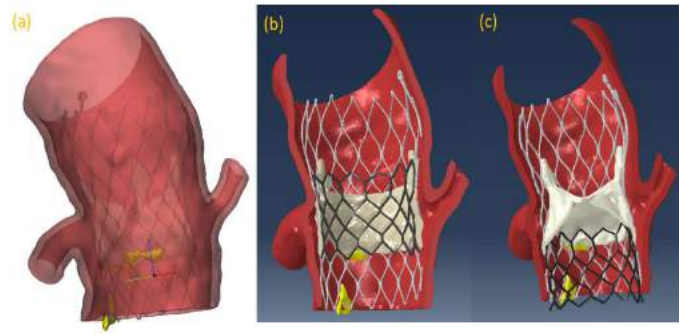

Figure 3. (a) Geometry of the aortic root, TAV and calcification after segmentation and image registration (b) Result of simulation of SAPIEN 23mm valve deployment in nominal position and (c) below the leaflets of the Evolut THV

DISCUSSION

In this case study, clinicians at Piedmont Hospital were provided with 3-D printed models of the patient anatomy to plan the redo-TAVR procedure. In conjunction, simulations were run with two deployment configurations to assess obstruction risk. The patient underwent TAVR similar to Fig. 3(b). Redo-TAVR is expected to increase in volume as TAVs currently being implanted in patients have limited durability. Computational modeling and 3-D printing can play a major role in improving the understanding of redo TAVR and ensuring successful outcomes. Further computational fluid dynamic studies and experiments with 3-D printed geometry are planned for this case.

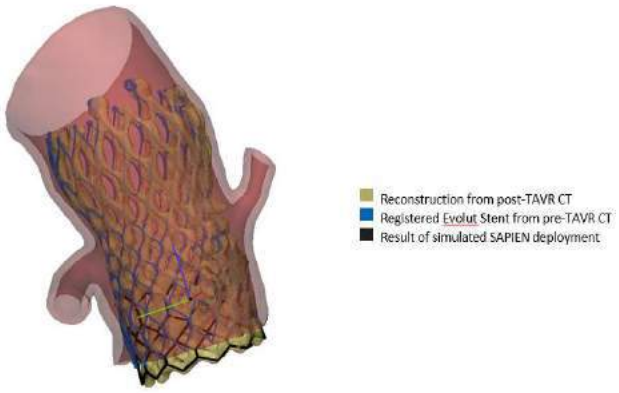

Figure 4. Validation of simulated TAV deployment with post-procedure CT imaging

REFERENCES

[1] M. Bianchi et al., Artif Organs, pp. E292-E304, 2016

[2] W. Mao et. al., J Biomech Eng, 140(10): 1010071–10100711, 2018.

[3] Caballero et. al., J R Soc Interface, vol. 16, no. 157, p. 20190355, 2019.

[4] Jilaihawi, Hasan, et al. *JACC: Cardiovascular Imaging* 10.4 (2017): 461-470.

[5] Blanke, Philipp, et al. *JACC: Cardiovascular Imaging* 12.1 (2019): 1-24.

[6] Szeliski, Richard, and James Coughlan. International Journal of Computer Vision 22.3 (1997): 199-218.

[7] B. Bosmans, et.al, J Biomech, vol. 49, no. 13, pp. 2824-2830, 2016.

[8] S. Tzamtzis et. al, Med Eng Phys, vol. 35, no. 1, pp. 125-30, Jan 2013.

TOLL-LIKE RECEPTOR-4 MODULATES INFLAMMATORY RESPONSE OF INTERVERTERBAL DISC TO STATIC BUT NOT DYNAMIC INJURIOUS LOADING

Hagar M. Kenawy (1,2), Samantha Marshall (2), James Rogot (1,2), Clark T. Hung (1,2), Nadeen O. Chahine (1,2).

(1) Department of Biomedical Engineering
Columbia University
New York, New York, USA

(2) Department of Orthopedic Surgery
Columbia University
New York, New York, USA

INTRODUCTION

Intervertebral disc degeneration (DD), a debilitating condition that is a leading cause of low back and neck pain, is estimated to affect 403 million individuals worldwide and costs at least $100 billion annually in healthcare[1–3]. Common occupations that are associated with higher prevalence of DD include large vehicle operators, flying aircraft personnel, and those working on vibrating surfaces[4]. Pro-inflammatory cytokines, such as TNFα and nitric oxide (NO), have been shown to be catabolic mediators of DD, promoting matrix degradation and fibrosis [6–10]. It is well established that loading profiles regulate the biological responses of IVD cells in a magnitude and frequency dependent manner. While prolonged static loading or dynamic loading above 0.5 Hz promote matrix degradation, changes in inflammatory cytokine profiles in response to loading are less well understood[11–13]. The goal of this study was to characterize the inflammatory signaling changes in response to static and dynamic loading. Recent studies of human DD suggest that the innate immune receptor toll-like receptor-4 (TLR4) regulates inflammatory signaling in the IVD[10]. Therefore, this study also investigated the contributions of TLR4 to inflammatory signaling induced by mechanical loading. We hypothesize that inflammatory responses of the IVD will depend on loading frequency and amplitude, and that blocking TLR4 signaling reduces pro-inflammatory signaling in loaded discs.

METHODS

Caudal (Co) motion segments from 14 mature male Sprague-Dawley rats ranging from 300-500g were dissected from the Co9 to Co13 vertebral levels. Samples were loaded for 3 hours using a custom-made displacement control mechanical loader to mimic static, low frequency dynamic, high frequency dynamic, and physiologic loading conditions. A static tare displacement of 1.75 mm (~20% of segment height) was applied to the static, low dynamic and high dynamic groups, followed by an additional 0.35 mm displacement at 0.5 Hz for low dynamic, or a 0.7 mm displacement at 3 Hz for high dynamic, or a 0.1 mm displacement at 0.125 Hz for the physiologic loading groups. Unloaded motion segments were also cultured as a control group. Change in IVD height was measured from pre- to post loading using fluoroscopy images, serving as an estimate of effective compressive strain magnitude in each loading group. Three discs were loaded at a time in the bioreactor with ~25 mL of chemically modified phenol-free media. At the end of 3 hours of loading, the culture media was collected, and volume was recorded. Motion segments were then cultured in fresh phenol-free chemically defined media for 9 hours to allow a period for biological responses to loading to play out (**Figure 1**). In some groups, TAK-242, a drug known to block TLR4 signaling, was added to the organ culture model at a dose of 1.0 µM to examine the potential downstream effects during the 3-hour loading period as well as 9 hours post-loading. Outcome measures: Media was analyzed for NO release. Motion segments were snap-frozen and prepared for qPCR. Gene expression of TLR4 and TNFα in motion segments post loading was

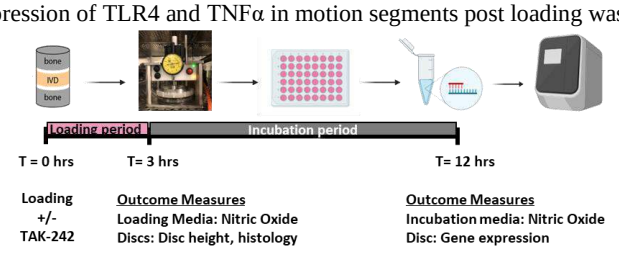

Figure 1: Experimental Setup

also measured, with GAPDH as the housekeeping gene. Gene expression results were normalized to the unloaded controls without the

TAK-242 drug using the $2^{-\Delta\Delta Ct}$ method. Statistics: One-way ANOVA followed by Holm-Sidak post hoc tests were conducted for NO release into loading media. Individual student t-tests were conducted to compare loading groups ± TAK-242. Kruskal-Wallis and Mann-Whitney tests were used for non-normal data distributions. Statistical significance was set at $p < 0.05$.

RESULTS

Loading profile had a significant effect on average disc height change (unloaded: 8.5±9.3%, static: -17.3±12.3%, physiologic: -8.9± 8.0%, low dynamic: -36.0±21.5%, and high dynamic: -61.3±13.3%). Static, physiologic, low dynamic, and high dynamic loading profiles were all significantly different compared to unloaded discs resulting in greater height changes ($p<0.032$ for all comparisons). Static, physiologic, and low dynamic loading profiles were also statistically significant compared to the high dynamic loading profile ($p\leq0.014$). Disc height change in static loading was also significantly lower than low dynamic loading (p=0.032) but not physiologic loading (p=0.23). In addition, low dynamic loading was statistically significant compared to physiologic loading ($p=6.8\times10^{-3}$) (**Figure 2i**). Nitric oxide (NO) release into the loading media of low dynamic (p=0.019) and high dynamic ($p<1.0\times10^{-4}$) loading was statistically greater compared to media of unloaded discs. NO release in loading media of unloaded, static (p=0.98) and physiologic loading (p=0.98) groups were comparable. NO in low (p=0.022) and high dynamic ($p<1.0\times10^{-4}$) loading groups was significantly greater than static, physiologic, and unloaded groups. NO in high dynamic loading was significantly greater compared to low dynamic loading (p=0.030). NO release of low dynamic loading was also trending upwards compared to the media of physiologic loading (p=0.052) (**Figure 2ii**).

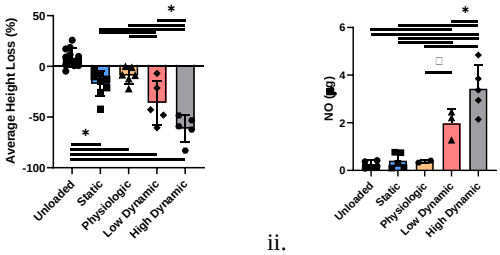

i. ii.

Figure 2: i. Average height loss experienced under each loading profile ii. Nitric oxide release into loading media

There was no difference in NO release from individual discs during the 9 hrs post loading incubation period (p=0.67). When incubated for 9 hrs with TAK-242, the discs had a significant decrease in NO release into the media (**Figure 3**).

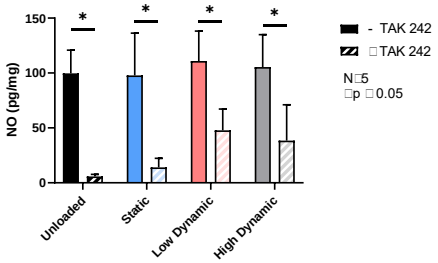

Figure 3: Nitric oxide release from individual motion segments 9 hours post loading ± TAK-242.

Among loading groups, TLR4 gene expression in the disc was significantly greater in static (p=0.012) and high dynamic conditions (p=0.028) compared to unloaded discs. Co-culture with TAK-242 significantly decreased the gene expression of TLR4 in static loading (p=0.018) but not high dynamic loading groups (**Figure 4i**). In addition, when examining the expression of the proinflammatory cytokine TNFα, expression was significantly higher in static ($p=2.6\times10^{-3}$) and high dynamic ($p<1.0\times10^{-4}$) discs compared to unloaded discs. TNFα expression in low dynamic discs exhibited a moderate increase compared to unloaded discs (p=0.051). Co-culture with TAK-242 mitigated the expression of TNFα in the static (p=0.020) but not high dynamic loading group (**Figure 4ii**).

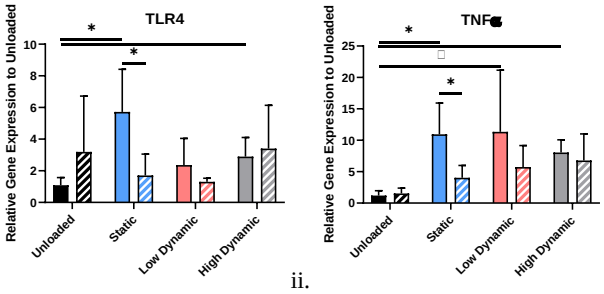

i. ii.

Figure 4: i. TLR4 and ii. TNFα gene expression of loaded motion segments cultured for 9 hours in ± TAK-242 media.

DISCUSSION

The loading organ culture system used in this study produced varying degrees of disc height loss and inflammatory responses that depended on loading magnitude and frequency. Magnitudes of disc height loss in low and high dynamic loading were clearly hyper physiologic, and NO release was also elevated under these conditions. Expression of TNFα was moderately elevated in low dynamic loading and significantly elevated in high dynamic loading. In addition, only the high dynamic group exhibited a significant increase in TLR4 expression. On the other hand, static loading, which had a lower disc height change magnitude, exhibited upregulation of both TNFα and TLR4, but not NO release. Addition of the TLR4 inhibitor, TAK-242, reduced TLR4 and TNFα expression only under static loading. These results suggest that dynamic and injurious static loading both promote pro-inflammatory signaling though through distinct pathways and temporal profiles. Dynamic loading led to more pro-inflammatory activation by NO signaling during loading, whereas static loading led to pro-inflammatory activation of TNFα. TLR4 appears to play a greater role on static loading response, compared to dynamic loading, as indicated by the greater protective effects of the TAK-242 drug on static loaded groups. Future studies will evaluate the temporal response of inflammation and therapeutic strategies to mitigate inflammatory responses to loading via cell based anti-inflammatory strategies.

ACKNOWLEDGEMENTS

This study was supported by NIH R01AR069668.

REFERENCES

[1] Frymoyer, J et al., *Orthop Clin North Am*, 22:263-71, 1991; [2] Maidhof, R et al., *Discov Med*, 14:401-411, 2012; [3] Ravindra, V et al., *Global Spine J*, 8:784-94, 2018; [4] Sandover, J et al., *Spine*, 8:652-8, 1983; [5] Kepler, C et al., *J Am Acad Orthop Surg*, 19:543-53, 2011; [6] Kang, J et al., *Spine*, 21:271-7, 1996; [7] Risbud. M et al., *Nat Rev Rheumatol*, 10:44-56, 2014; [8] Kazezian, Z et al., *Sci Rep*, 5:156-62, 2015; [9] Fang, F et al., *Biosci Rep*, 35:1-10, 2016; [10] Shah, B et al., *J Orthop Res*, 37:220-31, 2019; [11] MacLean, J et al., *J Orthop Res*, 22:1193-200, 2004; [12] MacLean, J et al., *Spine*, 28:973-81, 2003; [13] Wuertz, K et al., *J Orthop Res*, 27:1235-42, 2009.

MODELLING COLLOGEN FIBER RECRUITMENT IN AORTIC TISSUE USING KINEMATIC AVERAGE

Xuehuan He, Jia Lu

Department of Mechanical Engineering
The University of Iowa
Iowa City, Iowa, United States

INTRODUCTION

The gradual recruitment of wavy collagen fibers is an important feature of the aortic tissue. In this work, we introduce a framework for incorporating the fiber recruitment in hyperelastic modeling of aortic tissues by means of kinematic average approach. An effective stretch, which is a response variable representing the true stretch at the tissue-scale, is introduced. The waviness distribution of collagen fibers is quantified using a beta distribution function [1], which enables the effective stretch to be expressed in a closed form. Incorporating fiber recruitment amounts to replacing the strain values in a structurally motivated strain energy function with modified invariants. This construction is investigated in conjunction with the Holzapfel-Gasser-Ogden (HGO) strain energy function (SEF) and its variants [2].
In this talk, we present the theoretical framework of the proposed method, and investigate the predictive capability of the constitutive construction using experimental data.

METHODS

Consider a single fiber whose curved length is L_f and the end-to-end length is L, the straightness parameter p (defined as the ratio of L to L_f) is assumed to distribute in the tissue level following a beta distribution as

$$\psi(p;\alpha,\beta) = \frac{p^{\alpha-1}(1-p)^{\beta-1}}{B(\alpha,\beta)}, \quad p \in [0,1], \tag{1}$$

where (α,β) are shape parameters, both positive and $B(\alpha,\beta)$ is the beta function. For a single wavy fiber with straightness p, the recruitment stretch spent to uncrimp the fiber is $\frac{L_f}{L} = \frac{1}{p}$. The following piecewise response holds for the true stretch λ_t (a portion of stretch responsible for stress generation)

$$\begin{aligned} \lambda_t &= \lambda \cdot p; \qquad if\ \lambda > p^{-1}\left(p \geq \frac{1}{\lambda}\right) \\ \lambda_t &= 1; \qquad if\ \lambda \leq p^{-1}\left(p < \frac{1}{\lambda}\right) \end{aligned} \tag{3}$$

Consider now an ensemble of fibers or fiber bundles on the tissue-level, taking into account the straightness distribution, the effective stretch $\bar{\lambda}$ is

$$\bar{\lambda} = \int_0^{\frac{1}{\lambda}} \psi(p)\ dp + \int_{\frac{1}{\lambda}}^1 \lambda p\, \psi(p)\, dp \tag{4}$$

Upon using the beta distribution $\psi(p,\alpha,\beta)$, the effective stretch reduces to a closed-form expression of λ as.

$$\bar{\lambda} = F(\lambda^{-1},\alpha,\beta) + \frac{\alpha}{\alpha+\beta}\lambda F(\lambda^{-1},\alpha+1,\beta,\text{upper}) \tag{5}$$

where $F(x;\alpha,\beta) = \frac{\int_0^x p^{\alpha-1}(1-p)^{\beta-1}\,dp}{B(\alpha,\beta)}$ is the cumulative distribution function and $F(x;\alpha,\beta,upper) = 1 - F(x;\alpha,\beta)$ is its tail.

The Gasser-Ogden-Holzapfel (GOH) model (Equation 6) has been broadly adopted to describe the vascular tissue response [3]. The first term accounts for the isotropic response of ground substance and the second term represents the contribution of the collagen fiber network.

$$W = \frac{\mu_1}{2}(\mathrm{I}_1 - 3) + \sum_{i=1}^{2}\frac{\mu_2}{4\gamma}\left(e^{\gamma(\mathrm{I}_{ki}-1)^2} - 1\right) \tag{6}$$

Without considering the recruitment, the 2nd Piola-Kirchhoff stress is

$$\begin{aligned} S = \mu_1(I - I_2^{-1}C^{-1}) + \\ \mu_2 e^{\gamma(I_{ki}-1)^2}(I_{ki}-1)(\kappa I + (1-2\kappa)\boldsymbol{M_i}\otimes\boldsymbol{M_i}) \end{aligned} \tag{7}$$

Here invariant I_{ki} is a weighted average of squared stretches in the *i-th* family considering the orientation density. $\boldsymbol{M_i}$ is the preferred direction of the *i-th* family. The parameter *ki* represents the dispersion. Considering fiber recruitment, we define

$$\bar{\mathrm{I}}_{ki} = \frac{1}{4\pi}\int_{S^2}\rho(\phi,\theta)\overline{\lambda^2}\ da \quad \text{with} \quad \frac{1}{4\pi}\int_{S^2}\rho(\phi,\theta)\ da = 1 \tag{8}$$

Where ρ is the orientation density function. The integral is approximated using the six-point Lebedev quadrature. To this end we choose a local basis $\{\boldsymbol{E}_I'\}_{I=1}^3$ (called the fiber basis hereafter) such that

$\boldsymbol{E_3'}$ aligns with the fiber direction $\boldsymbol{M}_i$ and other two basis vectors are in the transverse plane. The integration points are taken to be the vertices of the local basis vectors $\{\pm\boldsymbol{E_1'}, \pm\boldsymbol{E_2'}, \pm\boldsymbol{M}_i\}$. The weights are uniform and equal to $4\pi/6$. This gives

$$\bar{\mathrm{I}}_{\kappa i} = \frac{1}{3}\left(\rho(\boldsymbol{E_1'})\bar{\lambda^2}(\boldsymbol{E_1'}) + \rho(\boldsymbol{E_2'})\bar{\lambda^2}(\boldsymbol{E_2'}) + \rho(\boldsymbol{M}_i)\bar{\lambda^2}(\boldsymbol{M}_i)\right) \quad (9)$$

Under the same normalization scheme as shown in Equation 6. We have $\frac{1}{3}\left(\rho(\boldsymbol{E_1'}) + \rho(\boldsymbol{E_2'}) + \rho(\boldsymbol{M}_i)\right) = 1$. Let $\frac{\rho(\boldsymbol{E_1'})}{3} = \kappa$. We obtain

$$\bar{\mathrm{I}}_{\kappa i} = \kappa\left(\bar{\lambda^2}(\boldsymbol{E_1'}) + \bar{\lambda^2}(\boldsymbol{E_2'})\right) + (1-2\kappa)\bar{\lambda^2}(\boldsymbol{M}_i) \quad (10)$$

With the new invariant (Equation 9), the energy function becomes

$$W = \frac{\mu_1}{2}(I_1 - 3) + \sum_{i=1}^{2}\frac{\mu_2}{4\gamma}\left(e^{\gamma(\bar{\mathrm{I}}_{\kappa i}-1)^2} - 1\right) \quad (11)$$

The fiber stress $\boldsymbol{S_f} = 2\frac{dW_f}{d\,\boldsymbol{C}}$ is

$$\boldsymbol{S_f} = \sum_{i=1}^{2}\mu_2 e^{\gamma(\bar{\mathrm{I}}_{\kappa i}-1)^2}(\bar{\mathrm{I}}_{\kappa i} - 1) * \left(\kappa_i\left(\sum_{I=1}^{2}\frac{d\left(\bar{\lambda^2}(\boldsymbol{E_I'})\right)}{d\left(\lambda^2(\boldsymbol{E_I'})\right)}\boldsymbol{E_I'}\otimes\boldsymbol{E_I'}\right) + (1-2\kappa_i)\frac{d\bar{J_i}}{dJ_i}\boldsymbol{M_i}\otimes\boldsymbol{M_i}\right) \quad (12)$$

To investigate the descriptive capability of the proposed recruitment models, they are fitted to two groups of experimental data. The first group consists of 157 uniaxial stress-stretch data from human ascending thoracic aortic aneurysm (ATAA) tissues collected at Dr. Auricchio's laboratory [4]. We elect to describe the uniaxial response of ATAA tissue using a 1D HGO SEF, which is a special case of GOH model .

$$W = \frac{\mu_1}{2}\left(\lambda^2 + \frac{2}{\lambda} - 3\right) + \frac{\mu_2}{4\gamma}\left\{e^{\gamma(\lambda^2-1)^2} - 1\right) \quad (13)$$

$$\sigma = \mu_1(\lambda^2 - \lambda^{-1}) + \mu_2 e^{\gamma(\lambda^2-1)^2}(\lambda^4 - \lambda^2) \quad (14)$$

Considering the fiber recruitment, we replace λ the second term in SEF (Equation 13) with $\bar{\lambda}$ to arrive at

$$\sigma = \mu_1(\lambda^2 - \lambda^{-1}) + \mu_2 e^{\gamma(\bar{\lambda}^2-1)^2}\left(\bar{\lambda^3} - \bar{\lambda}\right)\lambda\bar{\lambda}'(\lambda) \quad (15)$$

The performance of 2D model with (Equation 12) and without fiber recruitment (Equation 7) are examined using bi-axial response data of ATAA tissues collected from bulge inflation test [5]. There are 2304 data points for each specimen.

Optimized material parameters were determined by minimizing the sum of square difference between the experimental stress values and the model predictions. For the recruitment model, the parameters include the elastic properties and the straightness parameters. The latter are absent in the original model. In our work, elastic parameters were constrained such that $(u_1, u_2, \gamma) > 0$ for 1D model and $(u_1, u_2, \gamma) > 0, 0 \le \theta \le \pi, 0 \le \kappa \le 0.5$ for 2D model. As for the straightness parameters (α, β), the density function is unbounded when p approaches 0 or 1 if α <1 or β <1. Therefore, the straightness parameters are constrained as α >1 and β >1.

RESULTS

Figure 1 illustrates the fitting result for the uniaxial response data. Figure 1 (left) presents the fitted curve with and without recruitment for one sample. It is a good representation of the majority of cases. The improvement is garnered in the toe region. This is the region where the graduate fiber recruitment takes place. The original model categorically over-predicts the stress, resulting a curve that lies above the experimental data points. The over-stress is rectified by using the effective stretch, with R^2 increasing from 0.932 to 0.99. The R^2 values of all 157 samples are compared in Figure 1 (right). The percentage of points (PP) which show improvement in the R^2 value reaches 99%. Clearly, the fitting quality are universally improved when the recruitment is considered.

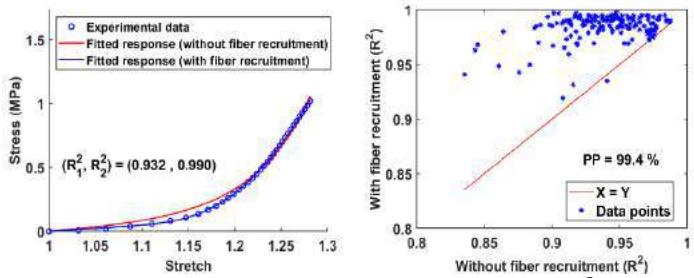

Figure 1: Fitted response curves (left). Comparison of R^2 values with and without fiber recruitment in all 157 samples (right). (R_1^2, R_2^2): R^2 values without and with considering the fiber recruitment, respectively.

Figure 2 depicts the pointwise fitting behavior with and without considering the fiber recruitment in specimens 1 and 2. Each subfigure represents a specimen. The mean R^2 values (R_2^2 with fiber recruitment , R_1^2: without) and the PP values are also presented. Overall the fitting quality are improved when taking into account the fiber recruitment, with PP values greater than 90% for both specimens.

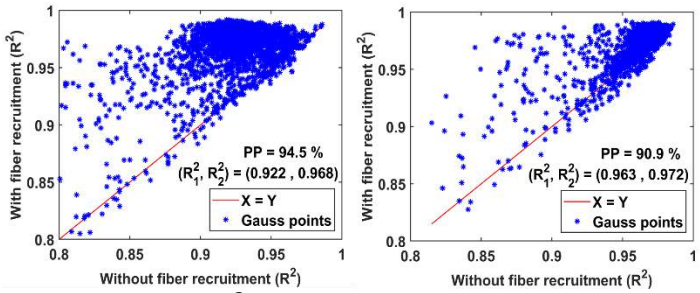

Figure 2: Pointwise R^2 values with and without considering the fiber recruitment. (R_1^2, R_2^2): R^2 values without and with considering the fiber recruitment, respectively.

DISCUSSION

In this study, we presented a framework for considering the graduate recruitment of collagen fibers in hypereslastic modeling of aortic tissues. We have examined the descriptive capability of this constitutive construction against experiments. Models incorporated the fiber recruitment significantly improve the fitting quality. Although not reported here, we also assessed the predictive capability using finite element simulation. The model incorporated fiber recruitment overwhelmingly outperformed the model without recruitment in reproducing the experimental results.

REFERENCES

[1] Rezakhaniha, R. et al., Biomech. Model. Mechanobiol. 11(3-4) (2012) 461-73.

[2] Holzapfel et al., Proc. Math. Phys. Eng. Sci. 466(2118) (2010) 1551-1597.

[3] Gasser, T. et al., J R SOC INTERFACE. 3(2006) 15-35.

[4] Ferrara et al., J. Mech. Behav. Biomed. Mater. 77 (2018) 1-11.

[5] Davis, FM. Et al., Biomech. Model. Mechanobiol. 14(2015) 967-978.

FLOW VISUALIZATION AND AEROSOLS IN PERFORMANCE

Abhishek Kumar (1), Tehya Stockman (1), Jean Hertzberg (1), Shelly Miller (1), Don Milton (2), Jelena Srebric (2), Shengwei Zhu (2), Lingzhe Wang (2), Marina Vance (1), Darin Toohey (1), Sameer Patel (1)

(1) Mechanical Engineering
University of Colorado Boulder
Boulder, CO, USA

(2) Mechanical Engineering
University of Maryland
College Park, MD, USA

INTRODUCTION

The COVID-19 pandemic has created a great deal of fear and uncertainty around whether aerosols from singers and musical instruments can transmit the virus. The World Health Organization has recognized that SARS-COV-2 is transmissible through aerosols[1]. Additionally, outbreaks from singing have resulted in superspreader events leading to many infections and deaths[2]. Hence, aerosol generation in performance (playing brass and woodwind instruments, singing, and theatre speech delivery) should be quantified, monitored, and mitigated. Notable work in this area includes Becher et al.[3] who used the Background Oriented Schlieren (BOS) technique to determine the extent of jets generated while playing musical instruments and singing[4]. Abkarian and Stone made particle counts using visible light images and documented the stretching and breakup of saliva filaments during speech delivery[5].The present work incorporates imaging, aerosol measurements and CFD to address the following research questions: (i) What is the aerosol generation rate? (ii) How does air flow from the performer's mouth/instrument and how does it disseminate into the environment? and (iii) What control methods can be employed to mitigate risk?

METHODS

This study consisted of 3 methods: (i) flow visualization and characterization, (ii) aerosol measurements, and (iii) computational fluid dynamics modeling. We first characterized the flow visually using schlieren imaging (Figure 1) and laser sheet imaging (Figure 2).

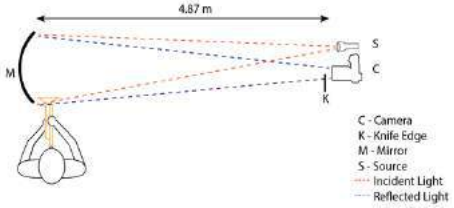

Figure 1: The Schlieren Method

The mentioned techniques provided a general sense of the extent and velocities of the plumes/ jets of air emanating from the instrument/performer, and provided sampling location data for aerosol measurements. Hot wire anemometry was also used to measure maximum velocities in the near field. Aerosol and CO_2 measurements were then made using a LICOR 7000 and UHSAS Aerosol Spectrometer to measure aerosols with sizes ranging from 60-1000 nm. The chosen sampling time was 1 second.

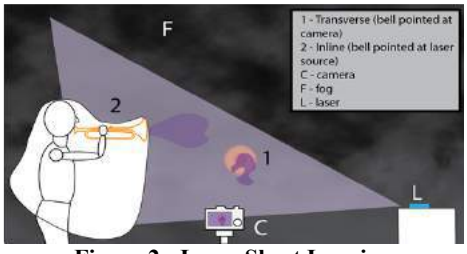

Figure 2: Laser Sheet Imaging

An Aerodynamic Particle Sizer (APS) was also used to measure aerosols with sizes ranging from 0.5-20 um, with a sampling time of 50 seconds and 10 seconds between each sample. The study included singers, actors and a variety of woodwind and brass instrument performances, with and without surgical masks. Results from imaging and aerosol measurements are presented here.

RESULTS

Bell velocity data obtained from schlieren, laser sheet imaging, and anemometry are provided below (see Figure 3).

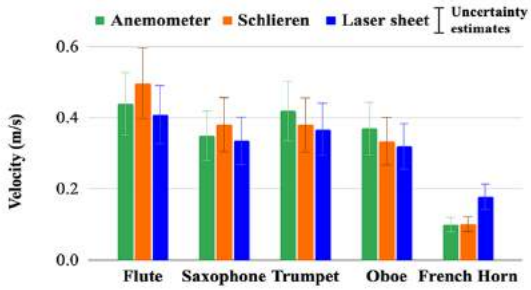

Figure 3: Maximum bell velocities

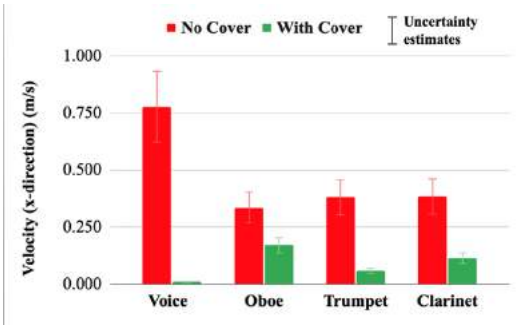

Figure 4: Horizontal velocity comparison with and without cover

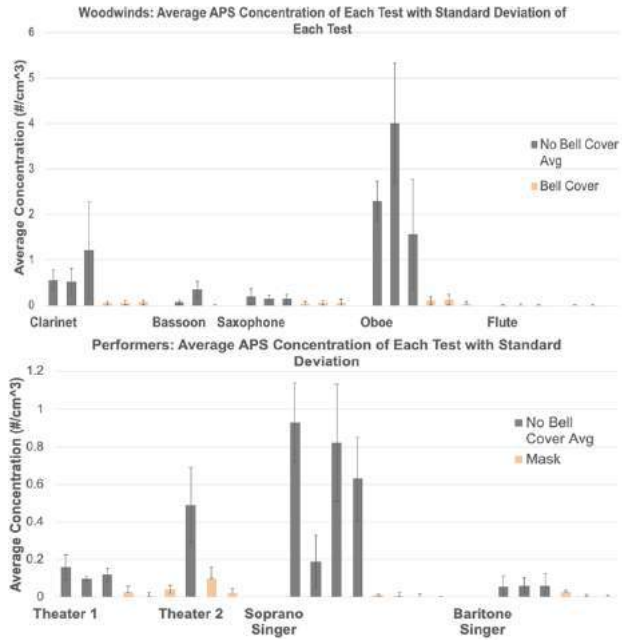

Figure 5: APS total aerosol concentration for woodwinds (above) and voice (below)

Velocity measurements were also made with and without bell covers/ masks (Figure 4). Uncertainty was estimated at 20%, or 0.10 m/s. For both instrument and voice performers, aerosol concentrations near the bell of the instrument or in front of the mouth were lower when a mitigation strategy was used compared to when it was not used. Surgical masks were used as bell covers and masks for voice performers with the exception of the flute, which instead utilized a piece of high density woven cotton fabric. The error bars in figure 5 show the standard deviation of each test.

DISCUSSION

Preliminary flow visualization results suggest that musicians and performers produce prominent jets, particularly when specific notes throughout the range are played. The jets are complex, unsteady, and highly three-dimensional. For example, the clarinet produces higher velocity jets from its bell compared to most notes in the lower register, which have higher velocities out of the keyholes. The direction of jets produced by a singer varies dramatically depending on the consonant or vowel sounds.

The preliminary velocity measurements clearly indicate that covers are effective in significantly diffusing the jet velocities, by more than half in most cases (Figure 4). Leakage flows (for singing, theatre performances, and from keyholes) can still occur when covers are used, depending on the fit. The anemometry data agrees with the flow visualization analyses.

These aerosol results show that playing musical instruments generate micron-sized aerosols similar in number concentration and size to singing, over 100x increase in aerosols compared to breathing (from previous studies[6]). Aerosols measured from keyholes were minimal, and hence negligible. Wearing masks when singing reduces aerosol emissions. Although aerosol emissions from these activities are generally low and must be measured in a controlled environment, disease transmission may occur at low concentrations as well especially if allowed to build up in low ventilation settings.

Tests to determine volume flow rates for different instruments, and estimation of generation rates for CFD modeling applications are currently underway. Our conclusions to date include: (i) activities including singing and playing brass and woodwinds produce 100x more aerosols compared to a quiet, inactive human, (ii) proper masking with quality materials and minimized leaks reduce these higher emissions to normal conversation levels. Our recommendations to minimize the risk of SARS-COV-2 transmission are to play instruments/perform outside or in well-ventilated spaces, use HEPA filter air cleaners, reduce occupancy, limit rehearsal time to 30 minutes, socially distance, maintain hand hygiene, and use masks and bell covers.

ACKNOWLEDGEMENTS

We would like to thank the NAMM Foundation, NFHS, D'Addario Foundation, CBDNA, and all other contributing organizations.

REFERENCES

[1] World Health Organization. July 9, 2020
[2] Miller, S. L., *Indoor Air.* Sep 26, 2020
[3] Becher, L., et al*, Optics and Lasers in Engineering,* Vol. 134, 2020
[4] Becher, L., Völker, C., et al, *Experiment Findings,* July 2020
[5] Abkarian, M., Stone, H. A., *Physical Review Fluids*, Vol. 5, 2020
[6] Papineni, R., S., *J Aerosol Medicine*, Vol. 10, No. 2, 2009

LINKS TO ADDITIONAL RESULTS:

[1] Active Conclusions, [2] Singing with mask comparison, [3] Oboe laser sheet, [4] Trumpet laser sheet, [5] Schlieren alphabet test

PATIENT SPECIFIC COMPUTATIONAL MODELING TOWARDS PLANNING OF VALVE IN VALVE TRANSCATHETER AORTIC VALVE REPLACEMENT

Sri Krishna Sivakumar (1), Breandan Yeats (2), Venkateshwar Polsani (3), Pradeep Yadav (3), Vinod Thourani (3), Lakshmi Prasad Dasi (2)

(1) Department of Mechanical Engineering, Georgia Institute of Technology, Atlanta, Georgia, USA
City, State, Country

(2) Department of Biomedical Engineering, Georgia Institute of Technology, Atlanta, Georgia, USA

(3) Department of Cardiology, Piedmont Atlanta Hospital, Atlanta, Georgia, USA

INTRODUCTION

Aortic valve stenosis (AS) is caused by valve degeneration and affects 3% of all adults over 65 years of age. Based on the severity, the aortic valve is replaced by an artificial bioprosthetic valve device. Currently, transcatheter based approaches to valve replacement are being widely adopted, especially in patients with comorbidities. However, there are many risks associated with transcatheter aortic valve replacement (TAVR), such as coronary obstruction, that are associated with high mortality rates. Bioprosthetic valve degeneration is a commonly known issue with aortic valve replacement, with patients receiving a TAV inside a degenerated surgical aortic valve, known as valve-in-valve (ViV) TAVR. Occurrence of coronary obstruction in ViV TAVR is specifically of concern as the coronary arteries are positioned low with respect to the bioprosthetic aortic valve (BAV) whose leaflets possess a high risk of obstruction after TAVR. Bioprosthetic Aortic Scallop Intentional Laceration to prevent Iatrogenic Coronary Artery obstruction (BASILICA) is a technique that is adopted in ViV TAVR cases to mitigate the risk of coronary obstruction. Due to the limitations of current imaging techniques in visualizing the risk of complications post-TAVR, computational patient specific modeling has proven to be extremely valuable in the procedural planning for TAVR [1-3]. The objective of this study is to utilize patient specific computational modeling of TAVR to simulate the risk of coronary obstruction in ViV TAVR with and without BASILICA and assess the obstruction risk with change in laceration location to aid in pre-procedural planning.

METHODS

Pre-procedural computed tomography (CT) images of a 78-year-old female patient who had a degenerated surgical bioprosthetic aortic valve and diagnosed with aortic stenosis were obtained through an IRB approved protocol. After discussion with the clinical team at Piedmont Atlanta Hospital, the patient was modeled for valve-in-valve TAVR for planning the procedure. Aortic root, bioprosthetic valve stent and leaflets of the patient were segmented from CT images using Mimics 22.0 (Materialise, Leuven, Belgium) (Fig. 1 a-b). Lacerations were made in the leaflet geometry (Fig. 1c-d) in both aligned and misaligned configurations with respect to the coronaries to simulate the effectiveness of the BASILICA procedure. The 3D geometry of the aortic wall and BAV stent and leaflets were then discretized in ABAQUS (Dassault Systèmes, Johnston, RI, US) using explicit 4-node linear tetrahedron elements. Neo-Hookean hyper-elastic constitutive equation was used to represent the aortic material properties with shear modulus, μ=1 MPa, bulk modulus, κ=10 MPa, and density, ρ=1000 kg/m^3 [4]. Stent model of SAPIEN 3 23mm was employed after meshing with quadratic tetrahedral elements in ABAQUS. The SAPIEN stent was modeled using an elasto-plastic model with Young's modulus, E=193 GPa, σ_y (0.2%) =340 MPa, σ_u (48%) =670 MPa, Poisson's ratio, ν = 0.29 and, density, ρ =7760 kg/m^3[5]. The balloon was modeled with quadrilateral shell elements as a linear elastic material with E=600 MPa, ν =0.45

and ρ=1100 kg/m^3 [5]. The CoreValve stent was modeled using superelastic nitinol properties and employed as beam elements in ABAQUS using VUMAT subroutine. The crimped balloon and stent were positioned coaxially inside the aortic root (Z-axis). The CoreValve was crimped and released inside the BAV as it is modeled as a self-expandable stent. Fluid-cavity based approach was employed to inflate the balloon and deploy the stent. The ends of the aortic root were constrained in translational and rotational degrees of freedom about Z-axis. Scaled penalty contact was employed for the stent-balloon and stent-AV interactions. Results were visualized and analyzed in ABAQUS.

RESULTS

Geometries of the aortic root and bioprosthetic valve are shown in Fig. 1 along with lacerations tested for mitigating coronary obstruction. Simulation of an idealized TAV expanded to 20mm inside the BAV showed a high risk of obstruction for both coronary arteries (Fig. 2). Deployment of the SAPIEN 20mm stent inside the bioprosthetic valve with aligned and misaligned lacerations on the leaflets is shown in Fig. 3. Deployment of the CoreValve 23mm TAV inside BAV with aligned lacerations is shown in Fig. 4.

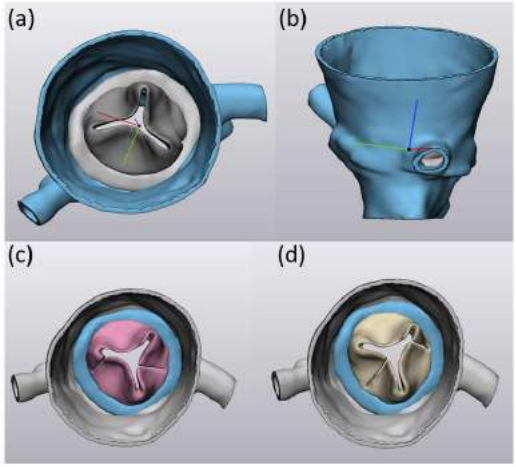

Figure 1. Geometry of the aortic root and bioprosthetic stent and leaflets in axial (a) and lateral (b) views. En-face view of aligned (c) and misaligned (d) lacerations of the bioprosthetic leaflets.

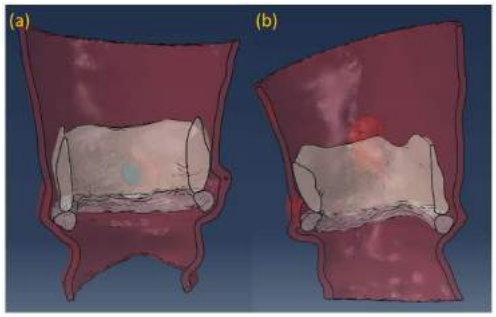

Figure 2. Cross sectional views of the left (a) and right (b) coronary arteries after idealized TAV deployment without BASILICA show high degree of obstruction.

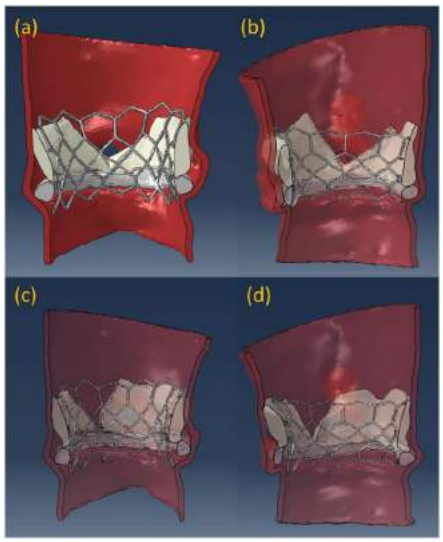

Figure 3. Cross-sectional views of the left (a) and right (b) coronary arteries after SAPIEN deployment with aligned (top) and misaligned (bottom) lacerations

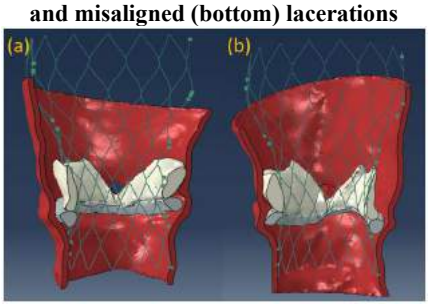

Figure 4. Cross-sectional views of the left (a) and right (b) coronary arteries after CoreValve deployment with aligned lacerations

DISCUSSION

Coronary obstruction is a rare but deadly procedural complication of TAVR that plays an important role in decision making during procedural planning. As shown in Fig. 2, ViV TAVR elevates the risk of obstruction due to relatively low heights of coronaries from the bioprosthetic valve stent. Lacerations made to mitigate obstruction may or may not be effective depending on the location of laceration relative to the coronary ostium as seen in Fig. 3. Precise computational modeling of ViV TAVR allows for optimization of outcomes ensuring the success of the procedure. In conclusion, computational modeling plays a very important role in TAVR planning specifically in the mitigation of coronary obstruction. Further computational fluid dynamic studies could provide a better insight into the degree of obstruction of flow as pressure gradients.

REFERENCES

[1] Heitkemper M. et.al, JTCVS, 2020, 159(3):829-838.e3
[2] W. Mao et. al., J Biomech Eng, 2018.
[3] Caballero et. al., J R Soc Interface, vol. 16, no. 157, p. 20190355, 2019.
[4] B. Bosmans et. al, J Biomech, vol. 49, no. 13, pp. 2824-2830, 2016.
[5] S. Tzamtzis et. al, Med Eng Phys, vol. 35, no. 1, pp. 125-30, 2013.

MECHANICAL ENVIRONMENT OF SUPRASPINATUS TENDON DURING FUNCTIONAL REACH: A FINITE ELEMENT STUDY

S. Cyrus Rezvanifar, PhD (1), John M. Looft, PhD (2), Anna Spracklin (3), Mohab M. Eid (4), Justin L. Staker, PhD, PT (1), Arin M. Ellingson, PhD (1), Paula M. Ludewig, PhD, PT (1)

(1) Department of Rehabilitation Medicine
University of Minnesota – Twin Cities
Minneapolis, MN, USA

(2) Minneapolis VA Health Care System
Minneapolis, MN, USA

(3) Department of Biomedical Engineering
Northwestern University
Evanston, IL, USA

(4) Medical School
University of Minnesota – Twin Cities
Minneapolis, MN, USA

INTRODUCTION

Shoulder pain is the second most common musculoskeletal condition [1], accounting for nearly 4.5 million annual visits to physicians in the United States [2]. Rotator cuff (RC) pathology has been recognized as the predominant factor underlying shoulder pain. RC pathology has been linked with chronic, repetitive deformation and compression of the RC tendons, particularly within the supraspinatus tendon (SST). Current standard clinical care mainly focuses on a static magnetic resonance (MR) scan to diagnose RC pathology. While an MRI would allow identification of soft tissue damage, it only provides a static view of the joint, typically in a supine position, and does not consider combinatory effects of individual-specific anatomical and movement-based abnormalities causing excessive RC deformation. Therefore, using computational techniques to simulate and analyze in vivo mechanical environment of the SST during functional activities and across the range of motion would provide a deeper insight about the underlying factors of SST pain and injury. The purpose of this study was to develop a finite element model with individual-specific anatomy and in vivo joint kinematics to computationally simulate functional reach task and study the consequent stress/strain measures.

METHODS

A 3T MRI scan of a right shoulder (48-year-old female) was used for 3D reconstruction of the shoulder joint model. Humerus, scapula and supraspinatus muscle and tendon were manually segmented using Mimics software (Materialise, Leuven, Belgium). The 3D models were meshed using HyperMesh software (Altair, Troy, MI) and imported into FEBio software [3]. Four-noded tetrahedral elements (TET4) were used for all bony and soft tissue structures. Figure 1 demonstrates the components of the developed finite element model.

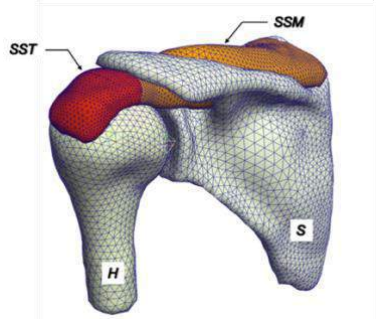

Figure 1: Depiction of the developed finite element model of the shoulder joint with scapula (S), humerus (H), supraspinatus muscle (SSM) and tendon (SST).

Scapula and humerus were modeled as rigid bodies, with supraspinatus muscle (SSM) defined as incompressible, hyper-elastic material with Mooney-Rivlin constitutive model. SST was defined with the same base material reinforced by fibers aligned with a semi-circular von Mises distribution. The main fiber orientation was defined along the medial-lateral axis of the SST, with fibers distributed up to 90° posterior and anterior to this orientation. A fiber concentration factor of k_f = 4 was used to represent highly aligned fibers along the main orientation, based on previous literature [4,5]. The constitutive model parameters used for the SST material properties are as follows: C_1 = 1 (MPa); C_2 = 1 (MPa); C_3 = 0.1 (MPa); C_4 = 25; C_5 = 98.7 (MPa); bulk modulus = 10,000; and *lam_max* = 1.06. It should be noted that bulk modulus is in fact a penalty parameter that, when set as a large number, enforces incompressibility of the represented material. Prior to simulating functional reach, these material parameters were evaluated

through a uniaxial tensile test simulation and comparison of the results with previous experimental and computational data [4,8].

The scapula was fixed to the global reference frame, and the glenohumeral joint was represented with a spherical joint about the center of the humeral head. The SST was attached to the humerus at the insertion via a "rigid" contact. Frictionless sliding contacts were defined between the bony structures and the soft tissues. Average joint kinematics of healthy participants during functional reach movement were acquired from our previous in vivo study [6] and were used to drive the simulation following International Society of Biomechanics (ISB) recommendation for the glenohumeral joint [7]. A 70N uniaxial force was simultaneously applied to the proximal end of the SSM throughout the simulated motion to represent muscle activation and contraction during the arm movement. Relative volume output was used to inspect the incompressibility of the soft tissue. Maximum principal Green-Lagrange strain was extracted throughout the simulated motion to investigate the strain distribution, as well as the magnitude and location of the peak strain values.

RESULTS

A maximum volume change of 3% was found within the SST, verifying acceptable incompressibility of the defined material properties. The results demonstrated a maximum principal strain of 13% with 180N of uniaxial tensile load (Fig.2), consistent with previous studies on the mechanical properties of the SST [8,9]. During simulated functional reach task, the maximum principal strain was found to be 0.99 occurring at the posterior joint surface of the SST at nearly 90° of glenohumeral abduction (Fig.3).

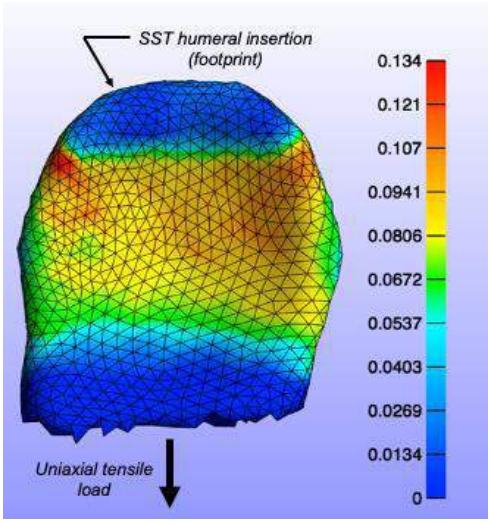

Figure 2: Demonstration of maximum principal strain on the joint surface of the SST under 180N uniaxial tensile load.

DISCUSSION

In this study, a finite element model was developed to investigate SST strains during a functional reach task. The results were in agreement with previous literature on the average magnitude and location of highest strains on the joint (articular) side of the SST under uniaxial tensile loading [8]. Multiple experimental and computational studies have previously studied in vitro mechanical properties of SST [5,8,9] under uniaxial loading conditions. However, the developed model provides the unique advantage of combining subject-specific anatomy and in vivo joint kinematics to study the mechanical environment of SST within the shoulder range of motion.

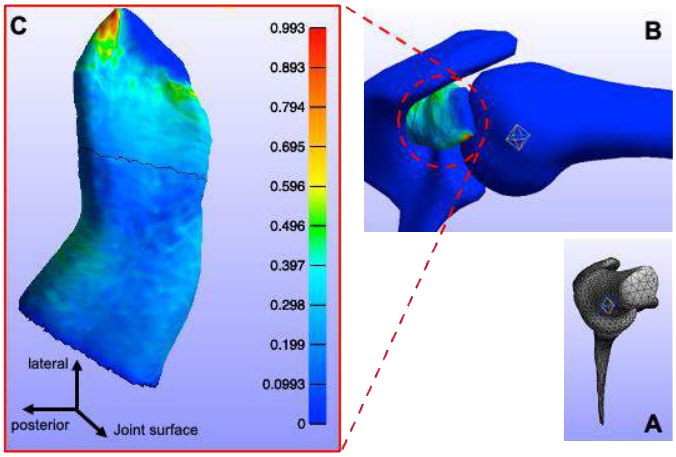

Figure 3: Depiction of end-range simulated glenohumeral abduction (A), colormap of 1st principal Lagrange strain within the SST (B), and a magnified view of strain distribution on SST joint surface

Future work will address certain limitations of the current model. First, we speculate that the excessively large strain magnitudes found in some areas might be due to stress concentration near the footprint rigid contact or material properties with inappropriate formulation for larger strains. Further computational and experimental work will be performed to ensure the validity of the results. Additionally, SST material properties will be varied along anterior/posterior and superior/inferior sections to reflect findings of previous literature [5]. Second, a mesh study will be performed to ensure the accuracy and reliability of the computational output measures irrespective of the mesh size. Third, SSM was simulated with the same material properties as SST (Mooney-Rivlin constitutive model) without fiber reinforcements. Future work will improve upon the material properties of the SSM to more realistically simulate in vivo functions. While the foregoing alterations may affect the magnitude of observed strain values within the SST, the overall strain distribution and location of critical spots are expected to remain generally the same. The developed model lays the groundwork for investigating the effect of various anatomical features as well as different athletic and daily activities on the mechanical behavior of SST and enables a more accurate prediction of risk and location of rotator cuff injuries.

ACKNOWLEDGEMENTS

This study was partially supported by National Institute of Health (NIH) K01HD042491 and R03HD070871-02 grants.

REFERENCES

[1] Picavet, HSJ and Schouten, JSAG, *Pain*, 102(1-2),167-178, 2003.
[2] Oh, LS et al., *Clin. Orth. Rel. Res.*, 455, 52-63, 2007.
[3] Maas, SA et al., *J Biomech. Eng.*, 134(1): 011005, 2012.
[4] Szczesny, SE et al., 2012. *J of Biomech. Eng.*, 134(2), 2012.
[5] Lake, SP et al., *J Ortho. Res.*, 27(12), pp.1596-1602, 2009.
[6] Braman, JP et al., *J Shoulder Elbow Surg.* 18, 960–967, 2009.
[7] Wu, G et al., *J Biomech.*, 38(5), pp.981-992, 2005.
[8] Miller, MR et al., *J of Biomech. Eng.*, 141(11), 2019.
[9] Mesiha, MM et al., *JBJS*, 95(20), pp.1817-1824, 2013.
[10] Kim, HM et al., *JBJS.* Am. 92, 1088–1096, 2010.

"HANDS-ON, MINDS-ON, AND SCIENCE-UP": A CONCEPT-BASED LEARNING LABORATORY WITH A TASTE OF RESEARCH EXPERIENCE FOR AN UNDERGRADUATE BIOMEDICAL ENGINEERING COURSE

Cyrus J.B.M. Fiori (1), Taisiya Sigaeva (2), Maria J. Pino Alban (3,4), Youssef Beauferris (3,4), Donovan Stagg (3,5), Elena S. Di Martino (3,6)

(1) Department of Chemical Engineering
(2) Department of Systems Design Engineering
University of Waterloo
Waterloo, Ontario, Canada

(3) Centre for Bioengineering Research and Education
(4) Department of Mechanical Engineering
(5) Department of Chemical Engineering
(6) Department of Civil Engineering
University of Calgary
Calgary, Alberta, Canada

INTRODUCTION

While the field of biomedical engineering is set to cultivate future breakthroughs in biology, medicine, and engineering, a clear strategy for empowering undergraduate students to develop skills in solving complex problems at the interface between engineering and biology has yet not been established [1]. Education in this area is supported by two main pillars: research and up-to-date learning strategies [2, 3]. Undergraduate research experiences commonly include course laboratories, however, laboratories that fail to connect the course content with hands-on application in a meaningful way result in poor conceptual learning outcomes [4,5]. Designing hands-on laboratories specifically to clarify challenging concepts and highlight connections between topics introduced in lectures (the "minds-on" approach) has been shown to be more effective [6]. Additionally, incorporating faculty members' own research into these laboratories can provide a more authentic and engaging research experience for students, effectively "science-ing them up". In this work, we linked faculty research expertise with concept-based teaching strategies to design and implement a novel laboratory experience for an undergraduate biomechanics of tissues course at the University of Calgary.

METHODS

In our designed laboratory activity, we related mathematically heavy nonlinear continuum mechanics to its practical applications in the experimental analysis of cardiovascular tissues, the area of research expertise of the faculty member instructing the course.

We designed and built a miniaturized version of a planar-biaxial tensile testing device typically used for soft anisotropic tissues and biomaterials (Fig. 1). Miniaturization was done to reduce equipment cost and overcome accessibility barriers that students often face to gaining hands-on experience with expensive and sophisticated laboratory equipment.

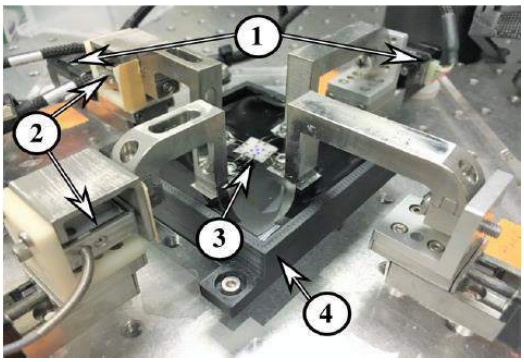

Figure 1: The mini-biaxial testing device: ① linear actuators, ② load cells, ③ specimen, ④ tissue bath

The laboratory itself was optimized into a "storyline" format by partially completing some steps of the experiment ahead of time to facilitate student engagement and conceptual learning without the stress of executing complex laboratory procedures correctly. Four stations were assembled. Stations 1 and 4 took place in a conference room and described the required pre- and post-lab information, respectively. Station 2 gave students hands on experience with a porcine aorta ring opening angle experiment and with hooking mini-biaxial specimens. Station 3 featured the mini-biaxial experiment with a pre-attached specimen. Following the laboratory session, students completed a lab report which required them to analyze data using a wide variety of the

techniques and concepts introduced during lectures, including using stress-strain curves to judge the tissue's behaviour.

Students were surveyed twice, once immediately following the laboratory activity and again following their completion of the laboratory report to gather data on their level of engagement and their overall experience. The survey was prepared and utilized in accordance with the regulations for human research at the University of Calgary, and this study was approved by the Conjoint Faculties Research Ethics Board. The survey included both Likert Scale-based and open-ended questions.

RESULTS

16 out of 18 students volunteered to take part in the survey. Overall, student feedback suggested that the students found the laboratory fun, easy, and worthy of their attention. Strong evidence was present in survey responses of students acknowledging the "storyline" format and wishing for it to be adopted more widely. A large portion of students expressed appreciation that their "hands-on" experiences with human tissues were intended for training purposes only and that the actual experimental samples for data collection had been prepared by lab instructors ahead of time. Students actively engaged in discussions of research with lab facilitators, demonstrating the "scienced-up" laboratory environment. Several students reported that this activity reinforced the concepts from the course by relating theory to application and helped them deepen their understanding. A few students were dissatisfied with either the report or the lab session timing.

Examining historical grade point average (GPA) and universal student rating of instruction (URSI) scores for students (University of Calgary scoring schemes) seemed to suggest small increases in student academic performance and course satisfaction the year of the laboratory. While the instructor was the same in the years examined, these gains may have resulted from other factors unrelated to the lab.

DISCUSSION

The positive attitude exhibited by the students involved in this laboratory can be attributed chiefly to the format of this experience. Our activity injected research into their undergraduate coursework by adding a relatively less demanding "scienced-up" activity to capture their attention while still holding true to the related course content. This matches other studies which have shown that the introduction of research activities promotes high levels of student engagement and can also be useful for accommodating different learning styles [7, 8].

Qualitative survey responses indicated that students found it easier to focus and openly communicate with instructors and facilitators while working in small groups during the "storyline" exercise. This setup may help better engage passive students – those who are resistant to active learning approaches – in a nonconfrontational way [7]. The format of our laboratory also empowered students to think critically, as evidenced by the questions they raised regarding the limitations of our testing machine.

Several students specifically mentioned that they appreciated the pre- and post-lab presentations at stations 1 and 4, which is congruent with previous findings that most students complete little or no preparation for laboratory sessions [9 – 11]. Effective pre-lab sessions are known to reduce students' stress-levels, increase their engagement and confidence, and decrease their resistance to active learning [7, 11]. Similar increases in levels of student comfort related to working with specimens purely for the sake of practice have also been reported elsewhere [6]. It is noted that this laboratory was not without its flaws, as evidenced by facilitators and feedback from some students.

A key limitation of this laboratory activity is its scale-up potential. The work presented took place in a course with small enrolment (15 – 25 senior undergraduates). In this study, two options were presented for scale-up to a 100-student class with the ability to host minimum 4 hour-long laboratory sessions. Both options required that for a larger and more junior audience, the content presented would have to be simplified (i.e. simplified linear elasticity) at the cost of its related accuracy in predicting tissue biomechanical behaviour.

Facilitator and instructor hours for activity preparation and execution would also scale appropriately. In the first option, three laboratory sessions would occur, group sizes would remain at three to four students each, and groups would circulate between four stations analogous to those presented. Each facilitator would need to spend approximately 15 hours running the lab. In the second option, the group sizes would be increased to 11 – 12 students, and experimental stations would be modified to accommodate larger space requirements. As a result, students would most likely experience less direct interaction with the instructors and facilitators. This second option would be more time efficient, and could be performed in a single laboratory session, requiring 5 hours from each facilitator. Other areas of concern for scale-up include access to sufficient amounts of tissue and monitoring safety.

In summary, we bridged faculty research expertise with concept-based learning pedagogy to design and implement a unique laboratory experience for biomedical engineering undergraduate students enrolled in a biomechanics of tissues course at the University of Calgary. By designing custom equipment and using a "storyline" format, students were able to focus on the conceptual understanding underlying the experiment. This approach resulted in an overall valuable and positive learning experience for students.

ACKNOWLEDGEMENTS

The authors would like to thank Adam Laser and Richard Beddoes for their contributions to tissue mechanical testing and software development. They would also like to thank Jolene Phelps for her help with facilitating the educational study. T.S. and E.S.D.M. acknowledge funding from Canada Foundation for Innovation (CFI), the Alberta Economic Development, Trade and Tourism (EDTT), the Heart and Stroke Foundation of Canada Grant in Aid G-17-0019141 and from NSERC Discovery Grant Nos. RGPIN04043 and RGPIN07178. C.J.B.M.F. acknowledges funding from the AIHS Summer Studentship. M.J.P.A. and Y.B. acknowledge funding from the NSERC USRA.

REFERENCES

[1] Abu-Faraj, Z., *Int. J. Eng. Educ.*, 24:990-1011, 2008.

[2] Clyne, A. M., et al., *ASME J. Biomech. Eng.*, 138:70804, 2016.

[3] Weed, H. R., *IEEE Trans. Biomed. Eng.*, BME-22:110-114, 1975.

[4] Abdulwahed, M., et al., *J. Eng. Educ.*, 98:283-294, 2009.

[5] Mackechnie, J. R., et al., *J. Prof. Issues Eng. Educ. Pract.*, 138:55-61, 2012.

[6] Halme, D. et al., *CBELife Sci. Educ.*, 5:41-51, 2006.

[7] Shekhar, P., et al., *Int. J. Eng. Educ*., 31:597–609, 2015.

[8] Felder, R.M., et al., *Engr. Educ.*, 78:674-681, 1988

[9] Abdulwahed, M., et al., *J. Eng. Educ.*, 98:283-294, 2009.

[10] Edward, N.S., *Int. J. Elect. Eng. Educ.*, 39:11-19, 2002.

[11] Abdulwahed, M., et al., *Comput. Appl. Eng. Educ.*, 22:110-119, 2014.

SB³C 2021
Summer Biomechanics, Bioengineering, and Biotransport Conference
June 14 – 18, Virtual

TUNABLE PHYSICAL AND SOLUBLE MICROENVIRONMENTAL CUES SYNERGISTICALLY ENHANCE TENOCYTE MIGRATION

Robert N. Kent[1], Mohamed Said[1], Megan E. Busch[1], Daniel L. Matera[1], William Y. Wang[1], Samuel J. DePalma[1], Harrison L. Hiraki[1], Megan L. Killian[2], Adam C. Abraham[2], Jae-Won Shin[3], Ariella Shikanov[1], Brendon M. Baker[1]

(1) Department of Biomedical Engineering
University of Michigan
Ann Arbor, MI, USA

(2) Department of Orthopedic Surgery
University of Michigan
Ann Arbor, MI, USA

(3) Department of Biomedical Engineering
University of Illinois Chicago
Chicago, IL, USA

INTRODUCTION

Poor clinical outcomes following Achilles tendon (AT) rupture are largely attributed to the generation of disorganized, hypervascularized, hypercellular scar tissue lacking the architecture necessary to meet the mechanical demands of the tendon.[1,2] Regenerative tendon healing that restores its densely aligned architecture would dramatically improve outcomes and reduce the significant socioeconomic burden of these injuries. Tendon healing relies on the timed recruitment of cellular mediators of tissue repair.[2] Thus, therapies that can regulate the identity and number of repair cells entering the wound site are likely required for the regeneration of functional tendon in lieu of dysfunctional scar tissue. While injection and suture-based delivery of drugs and biologics have shown promise, these approaches lack the spatiotemporal control required for regenerating the tendon's native architecture.[3,4] To address this problem, efforts have shifted toward tissue constructs engineered to recapitulate the biochemical and mechanical properties of tendon.[5,6]

Synthetic hydrogels represent an exciting avenue in the field of regenerative biomaterials given their injectability, orthogonally tunable mechanical properties, and potential for modular inclusion of cellular cues. However, optimizing physical cues to permit cell infiltration while still maintaining sufficient mechanical properties required of a musculoskeletal implant remains challenging. Analogous to rebar-reinforced concrete, synthetic fibers can mechanically reinforce bulk hydrogels with the added benefit of providing topographical cues to guide cell migration and spreading in a 3D hydrogel network.[7] Separately, recent advances in soluble factor release technology have demonstrated microparticle-mediated, sustained release of growth factors.[8] A composite hydrogel incorporating both of these components could robustly mediate tendon healing with a single injection. Therefore, we sought to assess whether 3D migration of cells involved in tendon healing can be enhanced via combined mechanical, topographical, and microparticle-delivered soluble cues.

METHODS

Cell Isolation and Spheroid Formation: All cells used in this work were harvested from C57BL/6J mice. Tendon stem/progenitor cells (TSPCs) and mesenchymal stem cells (MSCs) were isolated using established methods.[9,10] Spheroids were formed using AggreWells™.

Chemokine Screening: A 3D migration assay that generates chemokine gradients across hydrogels was microfabricated as in previous work.[11]

Microgel Fabrication and Loading: To achieve the monodispersity required for precise control of soluble factor release,[12] a droplet-based microfluidic device was used to fabricate dextran vinyl sulfone (DexVS) microgels with either 1 or 10 wt/vol% heparin methacrylate (HepMA) (**Fig. 1**). Water-in-oil droplets 107±5 μm in diameter were formed and crosslinked (**Fig. 1C**). UV exposure and emulsion breaking yielded an aqueous suspension of DexVS/HepMA microgels, which absorbed PDGF-BB at 250 ng/mL overnight. Loaded microgels were washed twice with HEPES buffer before use in cell experiments.

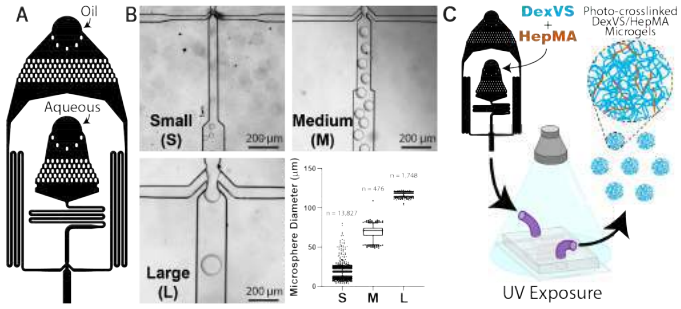

Fig. 1: A) Microfluidic device design for generating monodisperse water-in-oil droplets. B) Images and quantification of droplet radii as a function of channel geometry. C) DexVS/HepMA microgel fabrication scheme.

Composite Hydrogel Fabrication: Fiber segments were fabricated by crosslinking electrospun DexVS fibers with UV light through a photomask followed by functionalization with RGD in HEPES buffer.[7] Fibers, spheroids, and microgels were added to a mixture of DexVS, RGD, heparin binding peptide, and a cell degradable peptide crosslinker (VPMS) to encapsulate them together in a hydrogel bulk. Bulk stiffnesses of 0.5 and 2.0 kPa were respectively achieved by adding 12.5 mM and 20.0 mM VPMS.[7] Importantly, varying fiber density does not influence cell-scale bulk stiffness in this material system.[7]

Immunostaining and Microscopy: Samples were fixed, permeabilized, and stained with Hoechst dye and phalloidin. Z-stacks of microfluidic channels and spheroids were collected via confocal microscopy. Data

Analysis and Statistics: Custom MATLAB software either quantified migration distance for the chemokine screen or the increase in cell spreading area outside of the original boundary of a spheroid (presented as mean ± SD). Statistical significance was determined by one- or two-way ANOVA with Tukey's post-hoc analysis ($\alpha = 0.05$).

RESULTS

We used a 3D migration assay to screen a panel of chemokines for their ability to enhance TSPC migration into type I collagen matrices (**Fig. 2A**). For each chemokine, concentrations were screened over a range of 0 to 1 μg/mL to find an optimum with respect to cell migration. Then, comparison of these optima revealed that PDGF-BB and SDF-1α are relatively potent inducers of 3D TSPC migration (**Fig. 2B, C**).

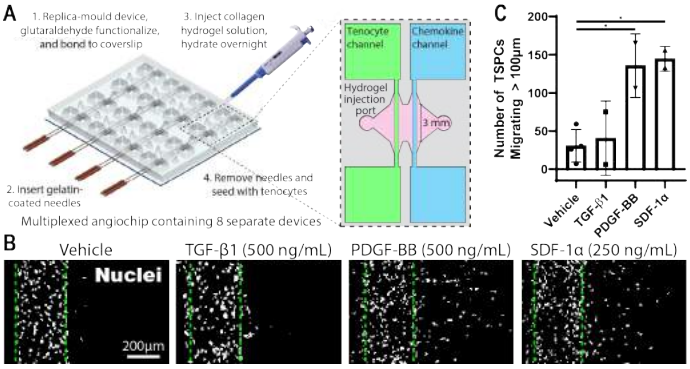

Fig. 2: A) Schematic of chemokine assay. B) Confocal fluorescent images of migrating tenocytes (channel in green). C) #cells invading >100μm. *p<0.05.

Synthetic hydrogels afford increased tunability of mechanical and topographical properties, which are known to impact cell spreading and migration in 3D microenvironments.[7,11] Therefore, we explored the combined effect of PDGF-BB and fiber density on outgrowth of tendon MSC spheroids in a composite DexVS hydrogel (**Fig. 3A**). This assay only required 10 ng/mL of chemokine in the media, as there is no need to establish a persistent gradient like in the case of the chemokine screen. Comparison of spheroid outgrowth areas confirmed that PDGF-BB enhances 3D MSC migration in DexVS and showed that fiber density can synergistically increase migration but can potentially hinder outgrowth above 2.5 vol% (**Fig. 3B**).

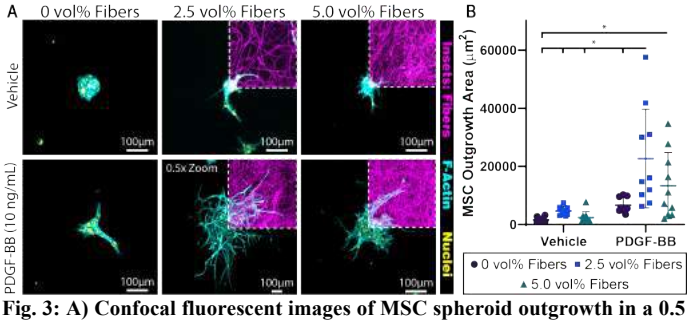

Fig. 3: A) Confocal fluorescent images of MSC spheroid outgrowth in a 0.5 kPa DexVS gel, varying fiber density and PDGF-BB concentration. B) Outgrowth area. *p<0.05.

Heparin affinity-based delivery vehicles can prolong the presence of soluble factors in cellular microenvironments through sustained release.[8,12] Therefore, we investigated the effect of sustained release of PDGF-BB from co-encapsulated DexVS/HepMA microgels on TSPC and MSC migration in fibrous DexVS matrices (**Fig. 4A**). Fibers were included at 2.5 vol% per the optimum determined previously, and HepMA wt/vol% was varied in the microgels to alter their loading capacity and release rate.[12] Given its dual implications for scaffold durability and cell spreading/migration, we also examined the effect of bulk matrix stiffness. Both TSPCs and tendon MSCs exhibited increased spheroid outgrowth in response to microgel-delivered PDGF-BB. Moreover, we found that these trends persist at a higher bulk matrix stiffness, albeit with an attenuated response (**Fig. 4B-D**).

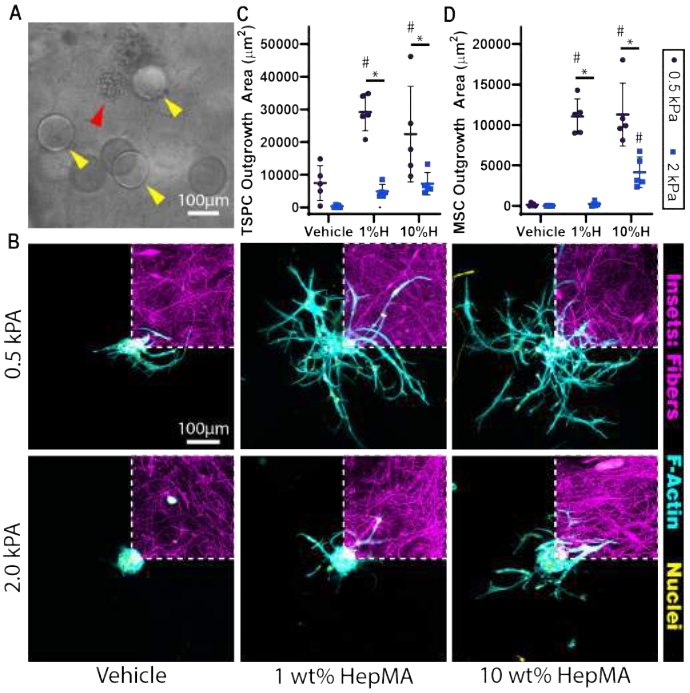

Fig. 4: A) Brightfield image of spheroids (red arrowheads) and microgels (yellow arrowheads) encapsulated in a fibrous DexVS hydrogel. B) Confocal fluorescent images of TSPC spheroid outgrowth in fibrous DexVS hydrogels in response to empty microgels (Vehicle) or PDGF-BB-loaded microgels with 1 wt/vol% (1%H) or 10 wt/vol% (10%H) HepMA. C) Quantification of TSPC outgrowth area shown in 4B. D) MSC outgrowth area. *p<0.05, #compared to vehicle.

DISCUSSION

In this work, we investigated the role of physical and soluble microenvironmental cues in regulating migration of tendon repair cells through fabrication of hydrogel composites with orthogonally tunable mechanical and biochemical properties. Our results show that multiple chemokines are capable of encouraging tenocyte infiltration into 3D hydrogel matrices, and that this effect exhibits synergy with fibrous topographical cues. Moreover, we demonstrate a method for high-throughput generation of monodisperse microgels capable of heparin affinity-based release of growth factors and chemokines,[8] and we apply this technology to elicit cell migration over a range of bulk matrix stiffnesses. These studies strongly suggest that modular, composite DexVS hydrogels meet fundamental criteria for an injectable musculoskeletal scaffold:[13] (1) mechanical durability via fiber reinforcement over a range of bulk moduli permissive to migration and (2) programmed regulation of the soluble milieu following a single administration. Thus, this biomaterial approach could likely be generalized to a range of connective tissue injuries, including skin, ligaments, and bone. Future studies will examine how cell recruitment impacts tenogenesis and tendon repair *in vitro* and in a murine tendon injury model.

ACKNOWLEDGEMENTS

This work was supported in part by the University of Michigan Endowment for Basic Sciences and the NIH (HL124322). DLM acknowledges financial support from the NSF GRFP (DGE1256260).

REFERENCES

[1] Killian, ML et al., *J Shoulder Elbow Surg*, 2012. [2] Wu, F et al., *EFORT Open Rev*, 2017. [3] de Vos, RJ et al., *JAMA*, 2010. [4] Efird, WM et al., *Orthop J Sports Med*, 2018. [5] Tarafder, S et al., *Biofabrication*, 2019. [6] Yoon, JP et al., *Am J Sports Med*, 2018. [7] Matera, DL et al., *ACS Biomat Sci Eng*, 2019. [8] Hettiaratchi, MH et al., *Tiss Eng Part A*, 2019. [9] Shimada, A et al., *Histiochem Cell Biol*, 2014. [10] Huber, AK et al., *J Clin Invest*, 2020. [11] Trappmann, B et al., *Nat Commun*, 2017. [12] Sakiyama-Elbert, SE et al., *J Control Rel*, 2000. [13] Tatara, AM et al., *J Bone Joint Surg Am*, 2016.

WHOLE BRAIN PERIVASCULAR SPACE NETWORK REDUCES MEAN TRANSPORT DISTANCE BETWEEN PARENCHYMA AND CEREBROSPINAL FLUID

Julian A. Rey (1), Uzair M. Farid (1), Christopher M. Najjoum (1), Kulam N. Magdoom (1,2), Thomas H. Mareci (3), Malisa Sarntinoranont (1)

(1) Department of Mechanical and Aerospace Engineering
University of Florida
Gainesville, Florida, U.S.A.

(2) National Institute of Child Health and Human Development
National Institutes of Health
Bethesda, Maryland, U.S.A

(3) Department of Biochemistry and Molecular Biology
University of Florida
Gainesville, Florida, U.S.A

INTRODUCTION

Blood vessels in the brain are surrounded by slender perivascular spaces (PVS) that are involved in the clearance of waste from brain tissue by enabling fluid exchange between interstitial fluid and cerebrospinal fluid (CSF) compartments [1]. The clearance function of PVS may be related to accumulation of harmful proteins in Alzheimer's and Parkinson's disease [2]. While a number of studies have demonstrated uptake of imaging tracers into PVS near the brain surface [1], few have examined deeper PVS and their connections to the ventricular CSF channels [3]. Histological sections following tracer uptake suggest an intricate and extensive network of PVS throughout the brain, but the resolution of whole brain imaging *in vivo* has limited analysis of the intact network to only the largest vessels [4]. There is a need for a 3D map of PVS to better understand their waste clearance function and create more accurate mechanical models of drug delivery in the brain. Magdoom et. al. [5] presents a set of *ex vivo* whole rodent brain images, at the highest resolution to date, following intraventricular contrast agent infusion, revealing numerous connections between the PVS network and the cerebral ventricles. In the present study, these images were newly processed to produce clearer visualizations of the PVS that facilitate identification of major blood vessel groups surrounded by functional PVS structures. A custom segmentation workflow was developed to create 3D maps of the PVS network containing contrast agent following intraventricular infusion. The resulting maps revealed continuous PVS segments several millimeters in length and the portions of the network directly connected to the ventricles by numerous PVS segments. Further analysis shows the PVS network greatly reduces the transport distance from the parenchyma to CSF, a condition which may be central to their waste clearance function.

METHODS

In a previous study from our group [5], high-resolution magnetic resonance images (40 μm isotropic voxels) were acquired from seven excised whole rat brains. In five of the animals, gadolinium-labeled human serum albumin (Gd-DTPA-albumin) was infused into the lateral ventricle for 40 min to allow distribution into the PVS. The remaining animals served as naïve controls. The animals were sacrificed via vascular perfusion with a 4% formaldehyde fixative solution to crosslink the contrast agent to the brain tissue. Each brain was subsequently excised and imaged at 17.6 T with a T1-weighted 3D gradient echo imaging sequence lasting approximately 24 hrs. This high-resolution scan was acquired with TR = 100 ms, TE = 0.2 ms, flip angle = 50°, an FOV of 20 x 16 x 12 mm^3, a matrix size of 500 x 400 x 300, and 7 averages.

The ventricles and PVS appear bright in the T1-weigted 3D images because of a reduction in T1 caused by Gd-DTPA-albumin [5]. Computing a maximum intensity projection of the data resulted in a set of projection images in which the brightest PVS and the ventricles were more apparent. However, smaller, dimmer PVS were not projected and many PVS were occluded by the bright ventricles in the center of the brain. To overcome these limitations, partial projections (pMIPs) through a subset of planar images spanning 30-voxels were produced.

Because the PVS surround blood vessels, they appeared like slender, tube-like, bright structures in many brain regions having a range of mean intensity values. To better distinguish the PVS, a measure of the tube-like nature, or *tubeness*, of the intensity field surrounding each voxel was computed. The tubeness metric for a given voxel is defined as the geometric mean of the two most negative eigenvalues of the Hessian matrix for that voxel [6]. The Hessian matrix elements are the second spatial derivatives of the intensity field, I:

$$H_{ij} = \frac{\partial^2 I}{\partial x_i \partial x_j} \qquad (1)$$

The PVS segmentation was generated by computing the tubeness of the 3D image and selecting voxels with tubeness values greater than 99 percent of the voxels in the naïve control brains. The ventricles were segmented separately. The connectivity between the PVS and ventricle networks was examined with a custom region grow algorithm that iteratively expanded the ventricle segmentation into the PVS segmentation. The extent to which the PVS network facilitates clearance from parenchyma was quantified by calculating the minimum distance, d, between parenchyma voxels and the nearest CSF voxel with and without the PVS network. Time scales for diffusion, t_D, and advection, t_a, were computed for bovine serum albumin (D^*= 1.63 × 10^{-7} cm^2/s [7]) as in Eq 2. The assumed parenchyma interstitial velocity, u, was 1 μm/s.

$$t_D = d^2/D^* \qquad (2a)$$
$$t_a = d/u \qquad (2b)$$

RESULTS

Extensive PVS uptake of Gd-DTPA-albumin throughout the brain was observed following intraventricular infusion. Long PVS segments, some over several millimeters in length, extended from the surface of the brain into the deep tissues surrounding the ventricular system (Fig 1 a-c). PVS surrounding subcortical penetrating arteries (scop) traversed the cortex and appeared to provide a pathway for tracer between the dorsal subarachnoid space and the lateral ventricles (Fig 1 a-c). Branches from large ventral surface vessels extended dorsally into the midbrain and include the anterior (astr), medial (mstr), and posterior striate arteries (pstr), as well as the anterior choroidal arteries (ach) (Fig 1 a-c). Image segmentation revealed a dense network of PVS throughout the brain (Fig 1 d-f). Isolating the portion of the PVS network that approaches the ventricles within 120 μm revealed connections between the lateral ventricles and major ventral and dorsal surface vessels via the scop, ach, and the striate arteries (Fig 1 g-i)

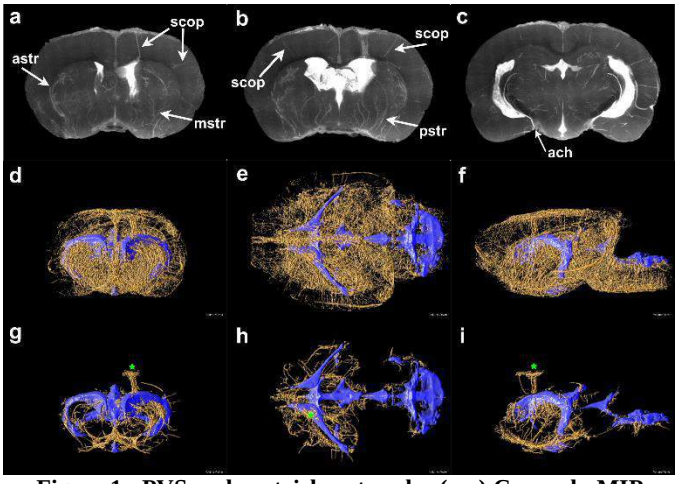

Figure 1: PVS and ventricle networks. (a-c) Coronal pMIPs proceeding caudally. See text for notable vessel group names. (d-f) Solid renderings of the PVS segmentation (gold) and ventricle segmentation (blue). (g-i) Solid rendering of the portion of the PVS network (gold) most closely connected to the ventricles (blue). The needle track is indicated by a green star.

To quantify the extent to which the PVS network may improve waste clearance from parenchyma to CSF spaces, the distance between each parenchyma voxel and the nearest CSF voxel was computed. In the absence of PVS, the parenchyma was on average 0.78 ± 0.52 mm away from the nearest CSF space with some parenchymal regions located over 2 mm away from the nearest CSF space (Fig 2 a-c, g and h). When PVS was considered part of the CSF spaces, the minimum distance between parenchyma and the CSF was reduced to 0.17 ± 0.10 mm and all parenchyma voxels were within approximately 1 mm of a CSF space (Fig 2 d-f, g and h). This reduction in minimum distance represents a nearly 22 fold reduction in the time scale for diffusive clearance from the parenchyma (Fig 2 h). Assuming an interstitial flow is present in parenchyma as posited by the glymphatic hypothesis [1], the presence of PVS affords a nearly 5 fold reduction in advective clearance time from the parenchyma (Fig 2 h).

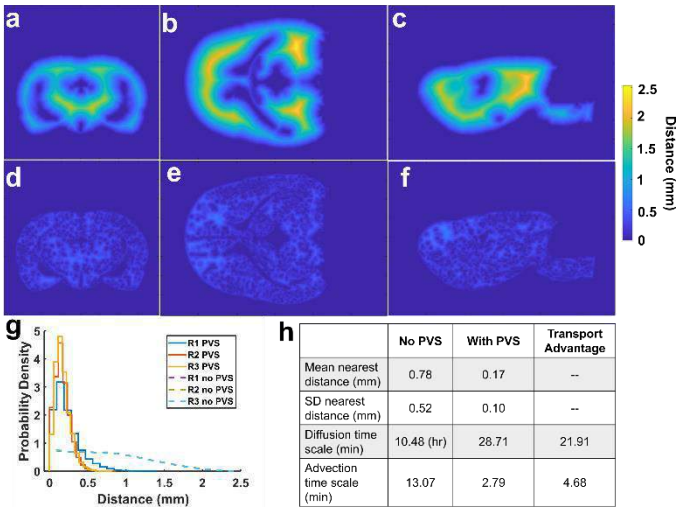

	No PVS	With PVS	Transport Advantage
Mean nearest distance (mm)	0.78	0.17	--
SD nearest distance (mm)	0.52	0.10	--
Diffusion time scale (min)	10.48 (hr)	28.71	21.91
Advection time scale (min)	13.07	2.79	4.68

Figure 2: Minimum distance between parenchyma and CSF. The distances between parenchyma voxels and the nearest CSF fluid voxel without PVS (a-c) and including PVS (d-f) presented as coronal (a and d), horizontal (b and e), and sagittal (c and f) planar color images. (g) Minimum distance distributions with and without PVS. (h) Table of transport parameters with and without PVS. The transport advantage is the factor by which the transport time scales are reduced due to the presence of PVS.

DISCUSSION

Growing evidence suggests that PVS are central to the clearance of dissolved compounds from brain tissue [2]. However, little is known about the 3D arrangement of the PVS available for transport, especially their connections to the ventricles and cisterns. The PVS segmentation presented here includes continuous PVS segments several millimeters in length that traverse the parenchyma and link distant CSF spaces. Moreover, the PVS form a dense and extensive network, substantially reducing the distance between parenchyma and low resistance clearance pathways that exchange fluid with larger CSF spaces. Irrespective of the main transport mode within the parenchyma itself, our results suggest PVS substantially enhance parenchyma clearance rates.

REFERENCES

[1] Iliff, J. J. et al., *Science Trans Med*, 4(47), 2012.
[2] Wardlaw J. M. et al. *Nat Rev Neurol*, 16:137-153, 2020
[3] Bedussi, B, et al., *Fluids and Barriers of the CNS*, 12(23), 2015
[4] Pizzo, M. E., et al., *J Physiol*, 596(3), 2018
[5] Magdoom, K. N, et al., *J Magn Resn*, 299:49-58, 2019
[6] Sato, Y. et al., *Med Image Anal* 2(2):143-168, 1998
[7] Tao L. and Nicholson C., *Neuroscience*, 75(3):839-847, 1996

SEGMENTAL LOADS IN MALE AND FEMALE NECKS UNDER HELMETED CONDITION IN FRONTAL (G-X) IMPACTS

Yuvaraj Purushothaman, Sagar Umale, John Humm, Narayan Yoganandan

Medical College of Wisconsin
Milwaukee, WI, USA

INTRODUCTION

The cervical spine is flexible and holds the head and bears the weight of the head [1]. Its motion is facilitated by the deformations of intervertebral discs and facets. The anatomical and structural characteristics of spine differ based on sex [2, 3]. Any head supported mass such as the helmet adds to the in-vivo head mass. This additional mass increases load on the cervical spine, in both civilian and military training and operational activities [4]. From a biomechanical perspective, it is important to understand the effect of the added head mass on the responses of the human cervical spine during these types of events. Therefore, the objectives of the present study were to investigate the forces and moments at each vertebral level using three-dimensional finite element models (FEM) of male and female models with and without the helmet, and determine the role of gender and head mass under G_X loading.

METHODS

A mid-size male head-neck finite element model was developed in house and validated using experimental data [5, 6]. The head model was integrated with a detailed cervical spine that consisted of the intervertebral discs, endplates, facets, ligaments, and musculature. The head, vertebral cortical bones, endplates and ligaments were modeled using shell elements. The cancellous bone, annulus, nucleus and facets were modeled using solid elements. The musculature was incorporated using anatomical origin-insertion locations as 1D beam elements. The material properties were based on the literature [7, 8]. The mid-size female model was developed by morphing the male model using anatomical ratios between male and females for the cervical spine and head mass [2]. The mapping block morphing approach was used for the development of female model [5]. The morphing process incorporated the variations in the shape and size of each vertebral body and overall spinal column length [2].

An advanced combat helmet model was developed inhouse by scanning the geometry of helmet using a coordinate measurement system. The inner part of the helmet was lined with seven foam pads. The helmet and inner foam were modeled as solid hexahedral elements and the material properties were assigned based on the literature [9, 10]. The mass of the helmet was 1.47 kg. The helmet was strapped to the male and female models using a chinstrap modeled using solid elements.

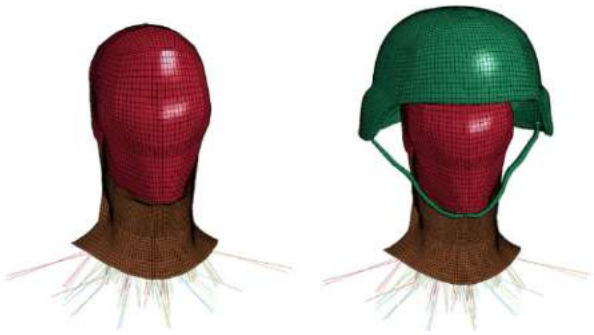

Figure 1: Left - the head neck model without helmet, and right the head neck model with helmeted condition.

The finite element models were exercised under a frontal impact scenario by inputting the acceleration pulse (velocity 6.5 m/s) to the T1 vertebra [11]. A total of 4 models were simulated for male and female anthropometry, with and without helmet. The results of male model without helmet were used to validate the model (kinematics of the head,

forces at the lower spine C7- T1, and time signal morphologies) with the experimental data. The forces and moments at the vertebral bodies were analyzed for male and female models with and without helmet, to delineate the effect of sex and the added helmet mass. The forces and moments at each disc level were determined along the local axis using cross-section planes in the model. The axial forces (along longitudinal axis), shear forces (along sagittal axis) and moments (along frontal axis) for male and female models were extracted.

RESULTS

The male model was validated using in-house PMHS sled test data. The input was acceleration pulse to the T1 vertebra in x, y, and z axes. The kinematic head response from the simulation was within the experimental corridors (average ± one standard deviation).

For the male model without helmet, the segmental axial forces at the C2-C3, C3-C4. C4-C5, C5-C6, C6-C7 and C7-T1 were 1.10, 0.89, 0.99, 0.97, 0.87 and 0.93 kN, respectively. The segmental shear forces were 0.5, 0.29, 0.37, 0.22, 0.45, and 0.53 kN, respectively. The moments at these intervertebral joints were 12.0, 21.1, 29.8, 43.8, 41.2, and 42.6 Nm, respectively. The axial forces with helmet at C2-C3, C3-C4. C4-C5, C5-C6, C6-C7 and C7-T1 were 1.21, 0.95, 1.12, 1.11, 0.97 and 0.99 kN, respectively. The segmental shear forces were 0.54, 0.31, 0.41, 0.24, 0.50, and 0.58 kN, respectively. The moments at these intervertebral joints were 12.7, 23.1, 32.8, 49.7, 45.5, and 45.4 Nm, respectively.

For the female model without helmet, the segmental axial forces at the C2-C3, C3-C4. C4-C5, C5-C6, C6-C7 and C7-T1 were 1.18, 0.93, 1.07, 1.09, 0.95 and 0.97 kN, respectively. The segmental shear forces were 0.55, 0.31, 0.40, 0.25, 0.49, and 0.57 kN, respectively. The moments at these intervertebral joints were 12.7, 23.0, 32.8, 49.7, 45.6, and 45.4 Nm, respectively. The axial forces with helmet at C2-C3, C3-C4. C4-C5, C5-C6, C6-C7 and C7-T1 were 1.31, 1.02, 1.23, 1.27, 1.10 and 1.04 kN, respectively. The segmental shear forces were 0.59, 0.35, 0.47, 0.28, 0.57, and 0.65 kN, respectively. The moments at these intervertebral joints were 14.3, 25.1, 37.4, 61.2, 54.6, and 51 Nm, respectively.

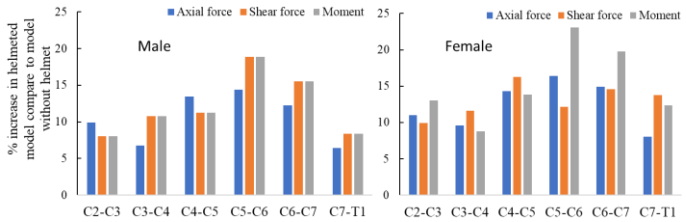

Figure 2: Percentage increase in force and moment responses for female model with respect of male model

The percentage increase in the peak force and moment responses in the male model with helmet, the axial forces, shear forces and moment increased by an average of 10.5%, 9.3% and 12.1%. In the female model with helmet, the axial forces, shear forces and moment increased by an average of 12.4%, 13% and 15.1%.

The force and moment responses were higher in female spine compared to male. The axial forces, shear forces and moments were higher by an average of 7.6%, 9.6%, and 9.2% (Figure 3), for model without helmet. In helmeted condition, the axial forces, shear forces and moments were higher by an average of 9.5%, 12.6%, and 12.3%, for helmeted condition.

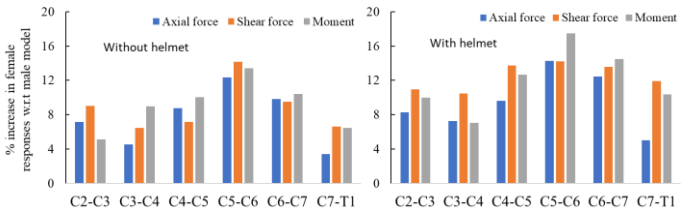

Figure 3: Percentage increase in force and moment responses for male and female model in helmeted condition

DISCUSSION

In the current study, head neck models of male and females were simulated in helmeted and without helmet condition. The helmet resulted in an increase in spinal loads (force and moments) for both males and females. The ratio of increase in shear force and moment was greater at the C5-C6 and C6-C7 discs in the male model. Whereas for females, the ratio of increase in axial force and moment was greater at C5-C6 and C6-C7 discs. Thus, the risk of injury may be higher at the lower cervical spine due to head supported mass.

The female model had greater load compared to the male model in both helmeted and without helmet condition. Thus, the females are at greater risk of neck injury compared to the males. The female cervical spine is also regarded weaker compared to males [2].

ACKNOWLEDGEMENTS

This research was supported by the Department of Veterans Affairs Medical Research, Department of Neurosurgery at the Medical College of Wisconsin, and W81XWH-16-01-0010. This material is the result of work supported with the resources and use of facilities at the Zablocki VA Medical Center, Milwaukee, Wisconsin. The last author (NY) is a part time employee of the VA Medical Center, Milwaukee, WI.

REFERENCES

[1] Rahman, S. and M.D. J, StatPearls. 2020: Treasure Island (FL).
[2] Vasavada, A.N., et al., J Biomech, 2008. 41(1): p. 114-21.
[3] Yoganandan, N., et al., J Biomech Eng, 2017. 139(5).
[4] Van den Oord, M.H., et al., Appl Ergon, 2012. 43(5): p. 958-64.
[5] John, J.D., et al., Annual Rocky Mountain Bioengineering SymposiumAt: Denver, Colorado, 2017.
[6] Yuvaraj, P., et al., Military Medicine (In press), 2020.
[7] Osth J, et al., J Biomech Eng. , 2016. 138(6)(061005).
[8] Panzer, M.B. and D.S. Cronin, J Biomech, 2009. 42(4): p. 480-90.
[9] Palta, E., et al., International Journal of Impact Engineering, 2018. 112: p. 125-143.
[10] Li, X.G., et al., International Journal of Impact Engineering, 2016. 91: p. 56-67.
[11] Pintar, F.A., et al., Stapp Car Crash J, 2010. 54: p. 133-66.

POLARIZED SPATIAL DOMAIN IMAGING FOR SIMULTANEOUS TISSUE STRAIN AND FIBER ORIENTATION MEASUREMENTS

Coinneach M. Mackenzie Dover (1), Will Goth (2), James W. Tunnell (2), Michael S. Sacks (1)

(1) Willerson Center for Cardiovascular Modeling and Simulation
Institute for Computational Engineering and Sciences
Department of Biomedical Engineering
The University of Texas at Austin
Austin, TX USA

(2) Biophotonics Laboratory
Department of Biomedical Engineering
The University of Texas at Austin
Austin, TX USA

INTRODUCTION

Collagen fibers are the primary structural element of many soft-tissues [1], so that fiber morphology dictates macroscopic behavior in health and disease. Moreover, cross-linked soft-tissues are used in bioprosthetic heart valves (BHVs), and are intimately related to their limited durability [2]. Extant methods to quantify collagen structure are typically either restricted to thin tissues or histological sections, or requires optical clearing. Additionally, the local tissue deformation field is often required, and the ability to obtain both dynamic fiber structure and tissue deformation is thus highly desirable. Polarized Spatial Frequency Domain Imaging (pSFDI) is a recently developed non-contacting, wide-field, light scattering-based technique that can rapidly obtain fiber architecture without requiring sample preparation [1]. In addition to structural quantification, it is also possible to exploit pSFDI structural information, which is at the individual pixel level, as a texture source for digital image correlation (DIC) [3] to track local deformation. We present a method that combines pSFDI and DIC analyses in a single system that can rapidly collect soft tissue specimen structure, strain, and stress information. We also investigated the role of measurement length scale on strain measurements, with an aim to inform soft tissue material modeling.

METHODS

A detailed description of the pSFDI technique has been previously presented [1]. Briefly, a spatial frequency pattern is projected on to a soft-tissue specimen (Figure 1). There is an anisotropic scattering of the light by the fibrous microstructure and the measured scattering yield is dependent on the rotation of the polarization of the input beam relative the fiber orientation. Therefore, the output contains information about the fiber orientation. The signal is then captured by a CMOS camera after passing again through the linear polarizer and post-processing produces spatial 2D maps of fiber preferred direction, θ_p.

The pSFDI was integrated with our biaxial testing device (BTD) [4]. Native bovine pericardium (BP) samples were pre-sorted by their preferred direction (PD) and mounted on to the BTD and testing carried out by stretching the sample along perpendicular loading directions parallel to the plane of the tissue sample. Equibiaxial stress up to 225 kPa was applied to the specimens over several steps under the pSFDI device. The technique was confirmed via the agreement of the deformation gradient tensor **F** derived from physical markers and non-contacting pSFDI 'virtual' markers derived from the DIC analysis of the images.

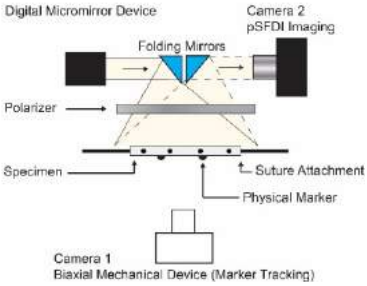

Figure 1: Schematic of the pSFDI device

This analysis was carried out using the μDIC package [3], a finite-element based software that utilizes bicubic spline interpolation. The software compares a 'reference' image (the unloaded, mounted specimen) with subsequent deformed images and by tracking the changing position of local surface texture, the software quantifies the local deformation.

The measured $I_{pSFDI}(\theta)$ signal is a convolution of the single fiber scattering function, $I_{fiber}(\theta)$ and the orientation distribution function $\Gamma(\theta)$.

$$I_{pSFDI}(\theta) = \int_{-\pi}^{\pi} \Gamma(\theta) I_{fiber}(\theta) \tag{1}$$

$\Gamma(\theta)$ was fitted to a wrapped normal distribution [5]

$$\Gamma(\theta; \mu, \sigma) = d\left\{\frac{1}{\sigma\sqrt{2\pi}} \sum_{k=1}^{1} exp\left[\frac{-(\theta-\mu+\pi k)^2}{2\sigma^2}\right]\right\} + \frac{1-d}{2\pi} \tag{2}$$

Where μ, σ, and d are the mean, standard deviation, and isotropic component fraction. μ was set to θ_p, so only σ and d were fit. The following transformation was used to determine Γ in the deformed state [5]

$$\Gamma(\beta) = \Gamma\left(\theta, \theta_p; \mu, \sigma\right) \frac{\boldsymbol{n}(\theta)(C_n(\theta))}{J_{2D}}$$
$$\beta = tan^{-1}\left[\frac{F_{21}\cos(\theta) + F_{22}\sin(\theta)}{F_{11}\cos(\theta) + F_{12}\sin(\theta)}\right] \tag{3}$$

Where $C=F^TF$, $J_{2D}=\|C\|$, and β is the θ fiber orientation in the deformed state.

RESULTS

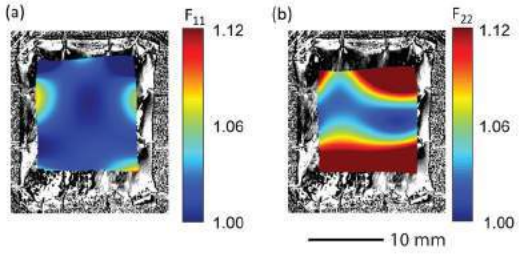

Figure 2: (a) F_{11} and (b) F_{22} fields calculated using pSFDI measurements as a texture source for DIC analysis.

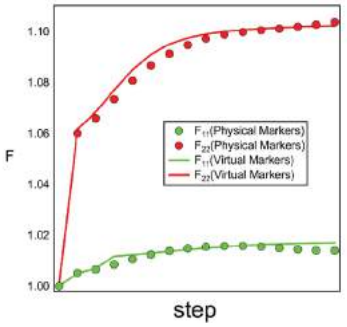

Figure 3: F_{11} (green) and (b) F_{22} (red) calculated from physical (circles) and virtual (solid lines) markers.

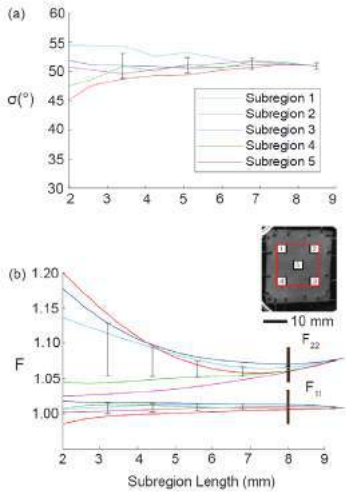

Figure 4: sub–regions selected within the ROI (inset: red box). (a) Associated fiber splay results. and (b) the F_{11} and F_{22} values determined by expanding each sub–region. The vertical black line indicates the approximate length scale where local variations become negligible.

The deformation field of the central ROI was tracked successfully using DIC analysis to an accuracy of a single pixel (~40μm). The resulting displacement field complex and heterogenous (Figure 2). The resulting spatial maps of **F**(**X**) were predictably complex. This can be best seen in the fully loaded state, where **F**(**X**) demonstrated complex, spatially varying behavior. We compared **F**(**X**) derived from physical markers (Figure 3) with the virtual **F**(**X**) from the tracked ROI region corners to confirm equivalence and an excellent agreement was established. Substantial regional

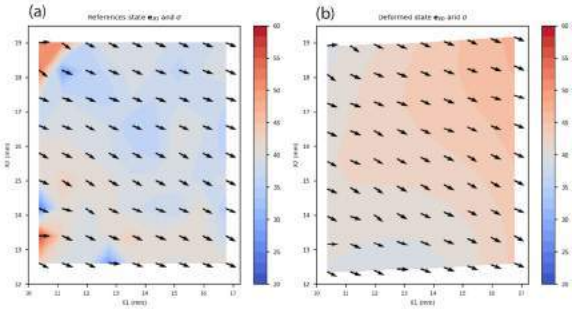

Figure 5: Mapped n(θp) (black vectors) and σ (color scale in degrees) for the ROI region of specimen 2 in the (a) referential and (b) peak equibiaxial stress state of 225 kPa.

variation was observed for the smallest size of ~2 mm for **F**, which converged to a common value as the distinct sub–regions were increased in size (Figure 4). Similar trends were observed in the σ, but with less overall initial variation (Figure 4). Collectively, these results indicate that there is a critical length (conservatively ~8 mm) at which the strain measurements become more representative of the bulk (i.e. homogenized) tissue.

Γ(β) was computed and mapped (Figure 5). Results for specimen 2 exhibited changes in both **n**(θp) and σ with deformation (Figure 5). Although the preferred directions **n**(θp) had small rotation, the σ values increased due to preferential stretch in the cross-preferred direction, which increases the Γ splay.

DISCUSSION

The aim of this study was to demonstrate that pSFDI texture (θ_p) can be utilized as a texture source for DIC in a manner equivalent to particle-based speckle patterns. This facilitated the simultaneous measurement of the tissue level deformation and collagen structure behavior. We demonstrated a step towards addressing this problem with a non-contact, non-destructive approach. The deformation behavior of distinct subregions within the ROI were examined and it was found that at the critical length of ~8 mm the data homogenizes. This has immediate potential in discerning what are local and global effects of soft-tissue behavior and structure. This is *vital* to correctly assigning the role of data in the overall picture. Moreover, it allows the role of suturing and structural defects (in both healthy and diseased specimens) on tissue-level behavior to be correctly characterized, improving the applicability of *in-vitro* measurements to *in-vivo* processes.

ACKNOWLEDGEMENTS

Supported by NIH NHLBI R01 HL142504, R01HL129077.

REFERENCES

[1] Goth, W et al, *Ann Biomed Eng*, 47(5) 1250-1264, 2019.

[2] Goth, W et al, *Proc SPIE Int Soc Opt Eng*, 9710 2016.

[3] Olufsen, S N et al, *SoftwareX*, 11 100391, 2020.

[4] Zhang, W et al, *Annu Rev Biomed Eng*, 11 289-313 2009.

[5] Fan, R and Sacks, M S et al, *J.Biomech*, 47, 2043–2054, 2014

REMODELING OF THE THORACIC AORTA DUE TO AGEING IN MICE

Yasmeen M. Farra (1), Jacqueline Matz (1), Chiara Bellini (1)

(1) Bioengineering Department
Northeastern University
Boston, MA, USA

INTRODUCTION

Cardiovascular disease is the leading cause of death in older adults [1]. Age-related remodeling of the human vasculature features dilatation and thickening of central arteries [2-3], which contribute to the doubling of pulse wave velocity (a measure of structural stiffness) between 20 and 80 years of age [4]. Critically, aortic stiffening is a known, independent predictor of cardiovascular disease mortality [5].

Preclinical studies in mice are often used to elucidate underlying mechanisms of cardiovascular disease, yet whether mouse models can recapitulate aging processes observed in humans remains unclear. Moreover, longitudinal studies in mice necessitate a baseline understanding of the interactions between disease-inducing treatment and natural ageing. Allometric scaling laws, which correlate physiological parameters with body mass [6-7, 10], may further illuminate the effects of ageing on vascular morphology. To address these questions, we characterized here the age-related structural and functional remodeling of the thoracic aorta in female C57BL/6 mice.

METHODS

Natural ageing. Adult, female C57BL/6 mice (N=48) were randomly assigned to groups that were aged naturally to 26 ± 1 weeks (shown as "0.5 year", blue), 48 ± 2 weeks ("1 year", purple), 68 ± 1 weeks ("1.5 year", red), and 84 ± 4 weeks ("2 year", gold), respectively.

Aorta mechanics. Mice were euthanized and descending thoracic aortas (DTA) were dissected. Passive biaxial inflation-extension tests were conducted using a computer-controlled custom device that measured luminal pressure, outer diameter, axial force, and axial length. Aortic rings were imaged using a dissection microscope to obtain unloaded wall thickness. A microstructurally-motivated constitutive model was fit to experimental data using a nonlinear regression algorithm. Estimated material parameters were used to predict biaxial Cauchy stresses, linearized material stiffness, distensibility, and energy storage at physiological systolic pressure and axial length. A Pearson correlation was used to determine if there was a significant relationship between estimated parameters and age, with significance set to $p<0.005$.

Allometric scaling. Allometric scaling was used to describe how aortic geometry (luminal diameter, d) changes with body mass (M), according to the relationship $d = \alpha * M^{\beta}$, where constant α and scaling exponent β relating inner diameter to body mass were estimated via linear regression on the experimental data.

RESULTS

Biaxial data revealed changes in the material response of the thoracic aorta across age groups. In the circumferential direction, the tissue experienced a progressive decrease in distensibility, accompanied by a decline in stress (Fig. 1A, red arrow). A similar behavior was observed in the axial direction up to 1.5 years of age (Fig. 1B, green arrow), followed by a stark leftward shift of the stress / stretch curve at 2 years (Fig. 1B, black arrow).

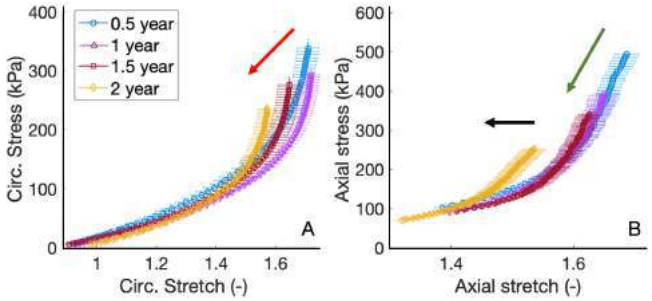

Figure 1: DTA biaxial stresses across four age groups. A) Circumferential and B) Axial stress / stretch curves.

The thickness of the DTA increased significantly and linearly with age, from 32 ± 1 μm at 0.5 years to 54 ± 2 μm at 2 years (Pearson's correlation coefficient r=0.748, p<0.001, Fig. 2A). Consistently, the stretch of the tissue declined linearly in the circumferential (r=-0.647, p<0.001, data not shown) and axial (r=-0.551, p<0.001, data not shown) directions, from 1.68 ± 0.02 to 1.54 ± 0.02 and from 1.57 ± 0.02 to 1.45 ± 0.02, respectively. The circumferential (r=-0.721, p<0.001, Fig. 2B) and axial (r=-0.769, p<0.001, data not shown) components of the Cauchy stress exhibited a similar behavior, decreasing linearly with age, from 294 ± 12 to 201 ± 7 kPa and from 268 ± 14 to 171 ± 7 kPa, respectively. While material stiffness was negatively correlated with age in the axial direction, declining from 2.94 ± 0.19 MPa at 0.5 years to 2.09 ± 0.09 MPa at 2 years of age (r=-0.579, p<0.001, data not shown), circumferential stiffness and age were not significantly correlated (r=-0.320, p=0.034, data not shown). Nonetheless, structural stiffness (distensibility) decreased steadily from 22 ± 1 $mmHg^{-1}$ at 0.5 years to 16 ± 1 $mmHg^{-1}$ at 2 years of age (r=-0.698, p<0.001, Fig. 2D). Finally, the stored elastic energy declined linearly with age, from 73 ± 4 to 40 ± 2 kPa (r=-0.834, p<0.001, Fig. 2C).

Allometric analysis estimated a scaling exponent β = 0.3835 and a constant α = 361.27 $m * g^{-0.3835}$ for the exponential relationship between the luminal diameter of the DTA and the mouse body mass (Fig. 3).

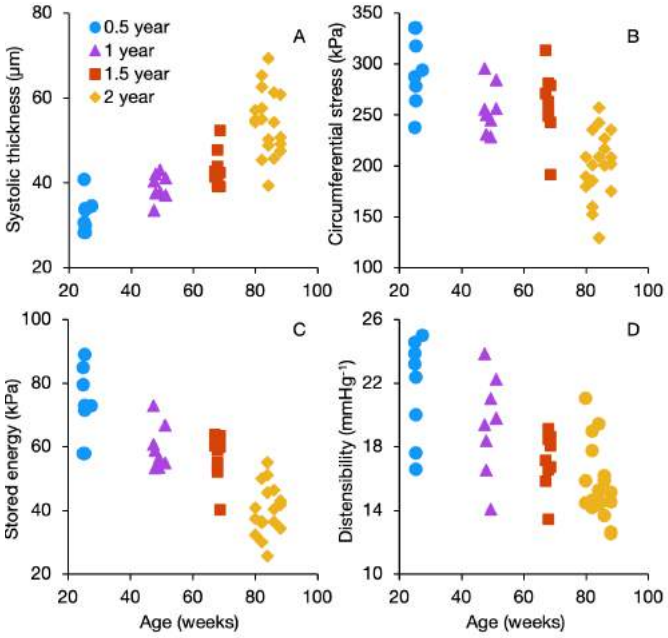

Figure 2: Mechanical parameters at systolic pressure in the DTA across four age groups. A) Wall thickness, B) Circumferential stress, C) Stored energy W, and D) Structural distensibility.

DISCUSSION

Motivated by the need to elucidate age-induced vascular remodeling, we monitored changes in the passive structure and function of the descending thoracic aorta at 4 equally spaced timepoints throughout the life of female wild-type mice.

The wall of the aorta became progressively thicker (Fig. 2A), leading to a decline in estimated biaxial Cauchy stresses (Fig. 2B). Aortic specimens exhibited a progressive loss of both circumferential and axial stretch with ageing, which caused the stored elastic energy to decline (Fig. 2C). Coupled with the increased structural stiffness (Fig. 2D), the loss of energy storage capability indicates that ageing may promote a gradual functional loss in the thoracic aorta, possibly rendering the vessel vulnerable to cardiovascular disease.

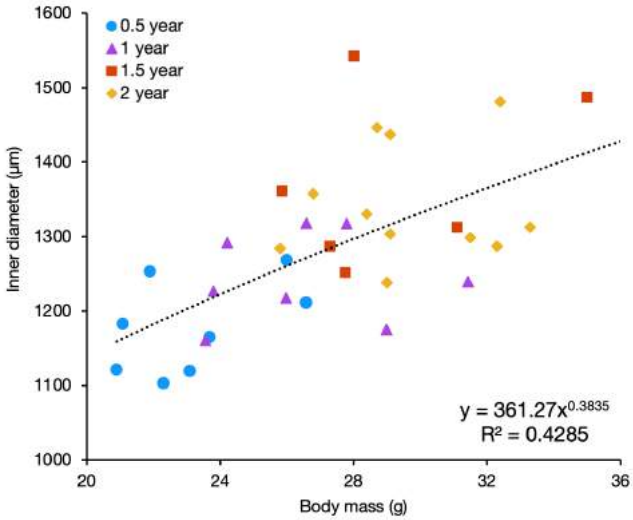

Figure 3: Allometric scaling using an exponential relationship to relate systolic inner diameter of the DTA to body mass.

In agreement with our findings (Fig. 2A), Ferruzzi *et al.* [8] and Wheeler *et al.* [9] also reported thickening of the thoracic aorta in aged (100 weeks and 21 months old, respectively) mice, driven by collagen deposition and increased medial interlamellar spacing, as shown by histological analysis [8-9]. Using stress relaxation tests, Wheeler *et al.* further observed structural stiffening of the thoracic aorta at 21 months of age when compared with 6-month-old mice [9], consistent with our results of decreased distensibility (Fig. 2D). Finally, past studies have established the need to use allometric scaling laws for the purpose of relating aortic geometry to body mass [6-7, 10]. The value of the allometric exponent (β = 0.3835) that we estimated from our experimental data falls within the range of previously reported allometric coefficients (β ≅ 0.375) between mammalian aortic diameter and body mass [7, 10].

In conclusion, our data suggest that the mouse thoracic aorta undergoes a natural process of age-related remodeling, which leads to dilatation, thickening, structural stiffening, and loss of energy storage capability. These features recapitulate salient aspects of human vascular ageing [2-4] and may provide insights on the interaction between the natural ageing process and the progression of cardiovascular disease.

ACKNOWLEDGEMENTS

Sincere thanks to our funding sources, in particular the NSF GRFP.

REFERENCES

[1] Jaul, E *et al.*, *Front. Public Health*, 5:1-7, 2017.
[2] Mao, S *et al.*, *Acad. Radiol.*, 15:827-834, 2008.
[3] Lakatta, E *et al., Med. Clin. N. Am.,* 93:583-604, 2009.
[4] O'Rourke, M *et al., JACC,* 50:1-13, 2007.
[5] Laurent, S *et al., Hypertension,* 37:1236-1241, 2001.
[6] Korneva, A *et al.*, *Biomech. Model. Mech.*, 18:261-273, 2019.
[7] Goergen, C *et al.*, *J. Endovasc. Ther.*, 14:574-584, 2007.
[8] Ferruzzi, J *et al.*, *Biomech. Model. Mech.*, 17:1281-1295, 2018.
[9] Wheeler, J *et al.*, *JAMA,* 4:1-9, 2015.
[10] West, G *et al.*, *Science*, 276:122-126, 1997.

ROLE OF MITRAL VALVE LEAFLET PRE-STRAIN IN AN INTEGRATED LEFT VENTRICLE-MITRAL VALVE MODEL

Hao Liu (1), Harshita Narang (1), Joseph H. Gorman (2), Robert C. Gorman (2), Michael S. Sacks (1)

(1) Department of Biomedical Engineering
University of Texas at Austin
Austin, Texas, USA

(2) Department of Surgery
University of Pennsylvania
Philadelphia, Pennsylvania, USA

INTRODUCTION

The first integrated left ventricle-mitral valve (LV-MV) computational model was developed in 2010 which is based on MRI data from a sheep with moderate ischemic MR [1]. In the following study, living heart project model, as the first one modeling the whole heart with four chambers and four valves [2], was capable of capturing electrical potential, mechanical deformation, and strain in fiber from finite element model which had an agreement with clinical observation. In a recent study on LV-MV model with fluid-structure interaction had been investigated [3]. However, detailed LV-MV interactions, especially in the post-infarcted state, have yet to be achieved.

When strain is relieved when an organ is excised from the body, it is defined as a form of residual or pre-strain. It was firstly found to exit in living organ or tissue dating back to two decades ago by opening angle analysis of arteries [4][5]. Along these lines, we discovered mitral valve tissues also exhibited pre-strain in a novel in-vivo study [7]. We determined that a unit square of leaflet's area decreased by 17% when heart was excised from the body, and by 43% when MV leaflets were excised from the heart. More recently, we explored the micro-mechanical mechanisms in a nonlinear material model was used to investigate the effect of pre-strains on MV leaflets [8] . However, this effect has never been explored as part of LV function.

The goals of the present study were to 1) investigate the role of MV leaflet prestrain on model predictions and 2) study the role of regional myocardial infarction patterns on MV function and strain. We first developed a pipeline of creating an anatomically accurate LV-MV model. Then parametric studies were conducted to explore the role of pre-strain and infarct location and extent to MV function.

METHODS

A biventricular LV/MV ovine model was developed, with all data collected in a single living heart to facilitate model integration of the various model components. The geometry of biventricular model was obtained by MRI and local myofiber orientation obtained from diffusion tensor MRI after the animal is sacrificed. Dynamic heart cavity pressure and volume data were captured using in-vivo catherization and sonomicrometry, respectively. With respect to mitral valve, we processed real-time 3D echocardiographic (rt-3DE) images of another animal to obtain geometry of leaflets [Figure 1, top line] and the MV plane. These two annular traces were represented as 3D spline curves parameterized by arc length and point-wise mapping between the curves was optimized by minimization of total displacement [Figure 1 bottom left]. Finally, we used functionally equivalent chordal structure [9] to capture the native chordal behavior [Figure 1 bottom right].

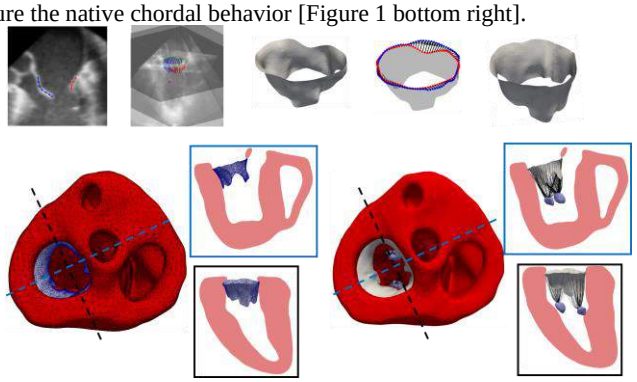

Figure 1: Pipeline of how we built the anatomically accurate LV-MV model: MV geometry segmented from rt-3d echo (top); insertion of mitral valve in left ventricle (bottom left); insertion of papillary muscle and chordae tendineae in left ventricle

MV closure was simulated under pressure. From previous findings of constitutive model of MV leaflets, accurate MV closure and strain

analysis could be obtained with an incompressible nonlinear isotropic material model [10]

$$S = \frac{1}{\pi}\int_{-\pi/2}^{\pi/2} S_{ens}[E_{ens}(\theta)]\hat{n}(\theta)\otimes\hat{n}(\theta)d\theta + \mu_m(\mathbf{I} - C_{33}\boldsymbol{C}^{-1}) \quad (1)$$

Where S is the second Piola-kirchhoff stress tensor with contribution of collagen fibers oriented along local coordinates and neo-Hookean ground matrix.

After the LV-MV computational model was established, we moved on to next step of looking into pre-strain of mitral valve leaflets. Adding prestrain into MV leaflets was performed by updating deformation matrix $F^{new} = F^{old}F^{pre-strain}$ where the amount of pre-strain applied in circumferential and radial direction were introduced. First trial has been made with uniform pre-strain applied on MV leaflets. Then, actual in-vivo pre-strain measured from sonocrystal study of MV was obtained and it was used as input for in-silico model.

RESULTS

Substantial pre-strain was first observed along loading path from unloaded state to end-diastolic state [Figure 2], with fiber stretch defined as $\lambda = \sqrt{N^T F^T F N}$ (F is deformation matrix and N means local direction). These results show the extensive effects of incorporating the MV in the ED deformation state.

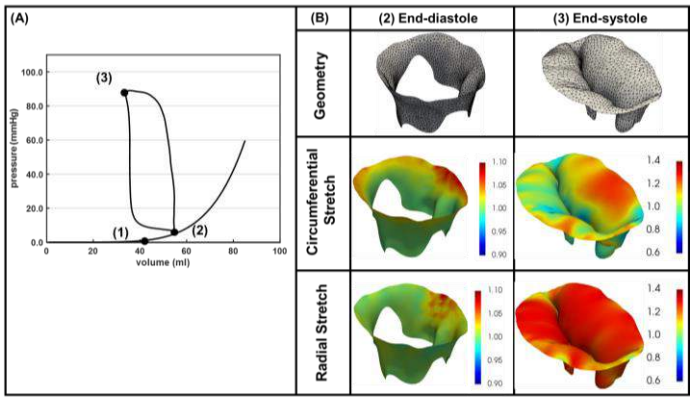

Figure 2: [A] The simulation was following pressure-volume loop with three critical states (1) unloaded state (2) end-diastolic state (3) end-systolic state; [B] Fiber strain mapping with respect to unload state as reference state

In our previous MV in-vivo strain mapping study [11], we developed a computational method to morph MV leaflets in constructed from in-vivo images of the open-state geometry to enforce MV close-state geometry, which resulted in accurate strain maps of the MV leaflets. The results of these strain maps for the ovine MV are shown in the last column of Figure 3. We then compared the open and close state of MV geometries from LV-MV in-silico model to this result, using various pre-strain values [First column of Figure 3]. When compared to the in-vivo strain maps, some differences have been observed including less compression ($\lambda < 1$) along free edge in circumferential direction and larger fiber extension ($\lambda > 1$) in radial direction. Uniform prestrain as $\lambda_1 = \lambda_2 = 0.9$ was prescribed in the MV leaflets which results in strain increase while uniform pre-strain of $\lambda_1 = \lambda_2 = 1.1$ leads to strain reduction due to material stiffening. Interestingly, when the actual observed in-vivo pre-strain was used, the strain maps agreed most closely [fourth column, Figure 3].

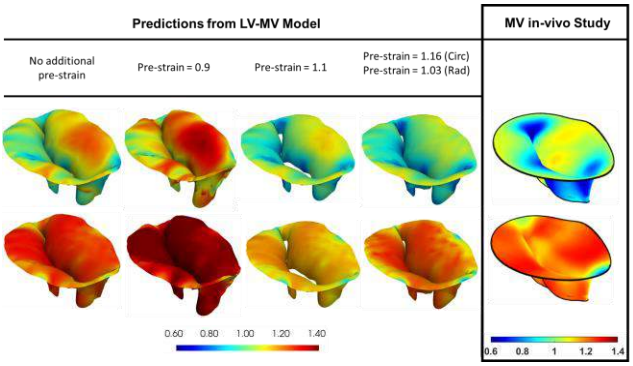

Figure 3: Role of prestrain in prediction of strain analysis from simulation with comparison of in-vivo MV strain analysis. Actual in-vivo MV strain mapping was shown in the last column

In a final step, we the explored various infarct locations and simulated them in the LV-MV model by shutting down local contraction. Simulation results indicated that the posterobasal infarction location induced the largest regurgitation orifice area, consistent with largest IMR grade reported from related animal studies [Table 1].

	ROA (In-silico Model)	IMR Grade Prediction	IMR Grade (Enomoto, et al. 2005)
Posterobasal	23.52 mm²	2.0	1.98 ± 0.20
Laterobasal	11.40 mm²	1.0	0.28 ± 0.22
Anterobasal	13.79 mm²	1.0	1.06 ± 0.25
Anteroapical	6.63 mm²	1.0	0.96 ± 0.25

Table 1: Predicted IMR grade from in-silico model of different infarct locations, with the value reported an in-vivo animal study. Our LV-MV model accurately predicted that the posterobasal infarct location induced the greatest IMR grade.

DISCUSSION

This study established a connection between MV in-vivo functional state and in-vitro reference state through applying pre-strain. The importance of this role has been emphasized by comparing with in-vivo stain mapping and it should be included in the future LV-MV modeling. However, uniform pre-strains in both circumferential and radial directions were introduced into the model which had spatial variation in reality. We then demonstrated the that this modeling approach was able to accurately predict the severity IMR grade in an initial study of myocardial infarction location and extent. We thus conclude that the incorporation of MV pre-strain of MV in FE model presented in this work contributes to a more accurate physiological picture of MV function in health and disease.

ACKNOWLEDGEMENTS

NIH R01-HL108330 and NIH R01-HL119297

REFERENCES

[1] Wenk et al. Ann Thorac Surg
[2] Baillargeon et al. Eur J Mech A Solids; [3] Gao et al. Med Eng Phys
[4] Fung et al. Circ Res; [5] Fung. Ann Biomed Eng
[6] Rausch et al. J Mech Phys Solids; [7] Amini et al. Ann Biomed Eng
[8] Lee et al. Biomech Model Mechan;
[9Khalighi et al. Ann Biomed Eng;][10] Zhang et al. Acta Biomater
[11] Rego et al. Int J Numer Method Biomed Eng

A SEMI-AUTOMATIC APPROACH FOR AORTIC WALL SEGMENTATION TO IMPROVE RAPID AND REPEATABLE ASSESSMENTS OF REGIONAL WALL STRAIN USING DENSE MRI

Patrick A. Jones (1), John S. Wilson (1,2)

(1) Department of Biomedical Engineering
Virginia Commonwealth University
Richmond, VA, USA

(2) VCU Health Pauley Heart Center
Virginia Commonwealth University
Richmond, VA, USA

INTRODUCTION

Aortic mechanics plays a significant role in a large number of aortopathies, including aneurysms, dissections, and hypertension; however, a reliable method for non-invasively assessing patient-specific regional mechanical data of the aortic wall has been lacking. Recently, a novel method for quantifying heterogeneous *in vivo* distributions of circumferential strain in the aortic wall using 2D Displacement Encoding with Stimulated Echoes (DENSE) MRI has shown promise [1-3]. However, a limitation of this approach has been reliance on manual segmentation of the cross-section of the aortic wall. Due to the thinness of the wall and limits on the resolution of aortic DENSE MRI for generating adequate signal, these masks are generally only two pixels thick. Thus, the inclusion or exclusion of only a few pixels in a mask can result in differences in calculated regional strain [3]. Additionally, this manual segmentation is time-intensive and subject to interuser variation, currently limiting the turnaround and reliability of this unique strain imaging modality for clinical analysis.

Similar to previous work to automate cardiac DENSE imaging segmentation [4], we aimed to develop an iterative semi-automated segmentation approach to improve repeatability and dramatically reduce processing time by utilizing the unique DENSE-derived displacement data for each voxel of the wall through time rather than relying solely on traditional image processing techniques for thresholding or edge detection.

METHODS

For this study, we re-analyzed previously acquired 2D spiral cine DENSE data (voxel size 1.3 x 1.3 x 8 mm, TE 1.21 ms, TR 16 ms, ω=0.17-0.25 cyc/mm, 4 signal averages) from a transverse cross-section of three *in vitro* cylindrical polymer phantoms connected to a pulsatile flow pump and from six healthy volunteers at either the infrarenal abdominal aorta (IAA, n=2), descending thoracic aorta (DTA, n=2), or distal aortic arch (DAA, n=2) [1]. Aortic wall masks were manually segmented from the *in vivo* DENSE images by two readers for the 'manual' strain calculations, and the results were averaged. Manual segmentation and analysis of the DENSE images from the *in vitro* phantoms was performed by one reader. The new semi-automatic method was conducted by a third reader to generate the 'automated' strain calculations for both the *in vivo* and *in vitro* images.

For the semiautomatic segmentation approach, MATLAB (Mathworks, Natick, MA) was utilized to manually select an initial rough region of interest that fully encompassed the aortic wall and surrounding periaortic and luminal regions in all timepoints for each scan. Note that with 2D DENSE imaging, each voxel in each serial image is phase-encoded to allow quantitative assessment of *x* and *y*-direction displacement since the encoding time. By 'back-projecting' these displacement vectors from each consecutive image to their common reference state (immediately before timepoint 1) tracked position vectors for each voxel in the mask at timepoint 1 can be interpolated for all subsequent timepoints [5]. Notably, the DENSE-derived displacements for luminal and some periaortic voxels are often random, unlike voxels from the aortic wall that tend to follow a stable path through each timepoint.

To establish the best reference mask at timepoint 1, the back-projected displacement vectors from the initial masks at each subsequent timepoint were used to create an originating point density map at the reference time. The point density map was divided into 16 sectors and used to calculate a centerline and standard deviation for the estimated position of the aortic wall at reference. Voxels outside of one standard deviation away from the centerline were then excluded from an updated mask. The voxels included in this new reference mask were

then tracked through each subsequent timepoint to generate updated masks for the full cine series. This process was repeated iteratively until termination criteria of three iterations or a minimum mask wall thickness of two voxels were met. Additional weighting was also applied as a function of path linearity and overall spatial variability for the tracked voxels to further filter out voxels representing areas that were stationary or moving erratically and therefore less likely to represent aortic wall (with the notable exception of limited displacements for points along the aorto-vertebral interface). The final automated aortic wall masks and manually segmented masks (**Figure 1**) were used in previously described custom post-processing algorithms to generate a 16-sector regional circumferential strain map [1-3].

Finally, quantitative comparisons of the processing time and the regional strain distributions (both in absolute values and normalized values relative to the mean circumferential strain of each cross-section) were performed between the original manual segmentation method and the new automated method. Strain results of the automated segmentation were considered reasonable in this pilot study if they were within 33% difference of normalized circumferential strain compared to the manual method.

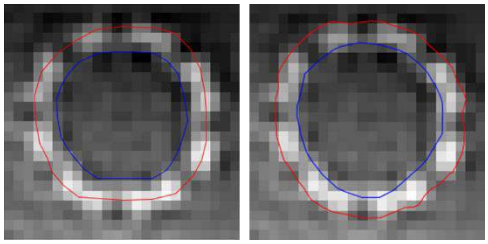

Figure 1: Comparison of a manually drawn (*left*) and automatically generated (*right*) aortic phantom wall mask.

RESULTS

Aortic DENSE strain analysis using the new semi-automatic segmentation approach took <10 minutes per phantom/volunteer, compared to ~2 hours for the standard manual method. Mean absolute differences in sector-wise circumferential wall strain between the manual and automated methods averaged ~2% for the phantoms, and 3-5% for the *in vivo* scans (**Table 1**).

Table 1: Mean circumferential strain, mean absolute difference in strain, and coefficient of variation (CoV) of the differences in strain calculated using manual vs. automated masks, and the percentage of total sectors with a normalized circumferential strain (NCS) difference between the methods below 33%.

	Phantom	IAA	DTA	DAA
Mean Strain (Manual)	0.08	0.15	0.10	0.10
Mean Abs. Diff.	0.023 ± 0.01	0.031 ± 0.01	0.047 ± 0.03	0.042 ± 0.01
CoV (Mean Diff.)	0.193 ± 0.07	0.182 ± 0.05	0.387 ± 0.07	0.376 ± 0.20
Sectors <33% NCS diff.	75%	81%	47%	56%

For the phantoms, 75% of total sectors differed by less than 33% normalized circumferential strain (i.e., 1/3 of the mean circumferential strain, ~3% strain) between the manual and automatic methods, with the most notable differences occurring in the left lateral wall region of Phantom 2 (**Figure 2**). For the *in vivo* scans, the automated method performed better in the IAA than the DTA and DAA (81% of sectors with a reasonable match compared to 47% and 56%). For the IAA & DTA, when the sectors bordering the aorta-vertebral interface were excluded from the analysis, the percent of sectors below the 33% normalized strain threshold increased to 88% and 50%, respectively.

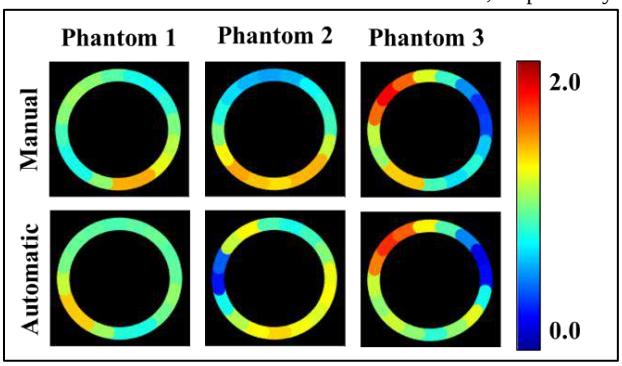

Figure 2: Normalized circumferential strain maps for three phantoms comparing strain results calculated using the manual and semi-automatic methods.

DISCUSSION

The new semi-automatic segmentation method reduced the time required to quantify patient-specific aortic circumferential wall strain using DENSE MRI by an order of magnitude (from ~120 minutes to <10 minutes); however, the reliability of the automated strain results suggests the need for further improvement to the semi-automatic segmentation. In comparison to the manual DENSE analysis, the new automated method performed reasonably in the majority of sectors in the *in vitro* phantoms and IAA, but only half of the sectors in the DTA and DAA. Notably, the motion of the thoracic aorta is more complex than the abdominal aorta due to the large motions of the heart that can displace and twist the aorta at these locations. In addition, wall segments along the aorto-vertebral interface in the IAA & DTA undergo little displacement (possibly due to local tethering), making them difficult to distinguish from non-moving periaortic structures like the vertebra and adjacent connective tissue. This may explain the slight improvement in results when excluding these regions.

Finally, the semi-automatic method currently uses initial voxel displacement data before phase unwrapping has been performed and is therefore sensitive to phase-wrap artifacts. Closer inspection revealed this was likely a major contributor to the elevated circumferential strain difference along the left lateral wall of Phantom 2, and may have also played a role in the *in vivo* data. Future efforts will be focused towards increasing the robustness of the elimination processes for outlying voxels on the adventitial surface of the masks (particularly along the aorto-vertebral interface) and incorporating phase unwrapping into the iterative processing. With these improvements, a rapid and reliable semi-automatic method for processing clinical aortic DENSE MRI may be attainable in the future.

ACKNOWLEDGEMENTS

The authors thank John Oshinski for sharing DENSE data collected under an Emory Dept. of Radiology & Imaging Sciences seed grant. Funding for this project was provided by the VCU Department of Biomedical Engineering.

REFERENCES

[1] Wilson JS, et al., *J Biomech Eng*, 141(6), 2018.
[2] Wilson JS, et al., *J Cardiovasc Magn Reson*, 21(1), 2019.
[3] Jones PA and Wilson JS, *J Biomech Eng*, 2021 [accepted]
[4] Spottiswoode BS et al., *Med Image Anal*, 13(1), 2009.
[5] Spottiswoode BS et al., *Trans Med Img*, 26(1), 2007.

FLUID-STRUCTURE INTERACTION MODELING OF PATIENT-SPECIFIC BICUSPID AORTIC VALVES

T. Qin (1), A. Caballero (1), W. Mao (2), B. Barrett (1), N. Kamioka (3), S. Lerakis (3,4), W. Sun (1)

(1) Department of Biomedical Engineering Georgia Institute of Technology and Emory University Atlanta, GA, USA

(2) University of South Florida, Tampa, FL, USA

(3) School of Medicine Emory University Atlanta, GA, USA

(4) Icahn School of Medicine Mount Sinai New York, NY, USA

INTRODUCTION

Bicuspid aortic valve (BAV) disease is considered the most common congenital heart disease, occurring in 0.5–2% of the population [1], where the aortic valve (AV) has only two rather than the normal three leaflets. Compared with patients with a tricuspid AV (TAV), BAV patients are more prone to develop ascending aortic dilation, or bicuspid aortopathy [2]. The exact cause of BAV aortopathy remains unclear, as both the genetic factors and biomechanical factors can play a role. Recent studies have found strong evidence that BAV aortopathy is different than Marfan patients which have proven genetic aortopathies [3]; on the other hand, there have been growing evidence that the abnormal hemodynamics in BAV could lead to altered regional wall shear stresses [4], the change in aortic wall histology [5], which could contribute to the disease progression.

Detailed investigation of biomechanical factors related with BAV aortopathy disease progression requires computational approaches. However, most of the previous computational models have been significantly limited by their inability to simultaneously solve the soft tissue mechanics and the fluid dynamics. Moreover, most studies were limited to idealized or simplified geometries of the leaflets, and did not considered the calcification in their analysis. Fully-coupled patient-specific fluid-structure interaction (FSI) models of BAV patients that solve the 3D time-dependent flow and large deformation of the valve tissue are not yet available.

With these challenges in mind, this study aimed to: 1) develop patient-specific BAV models, and validate the coupled function of the valve and hemodynamics with clinical imaging and echocardiography (echo) data, 2) investigate the relationship between the flow patterns in the ascending aorta and the BAV phenotypes, 3) compare the results between the rigid and flexible aorta, and evaluate the effect of the aortic wall elasticity on the hemodynamics in the ascending aorta.

METHODS

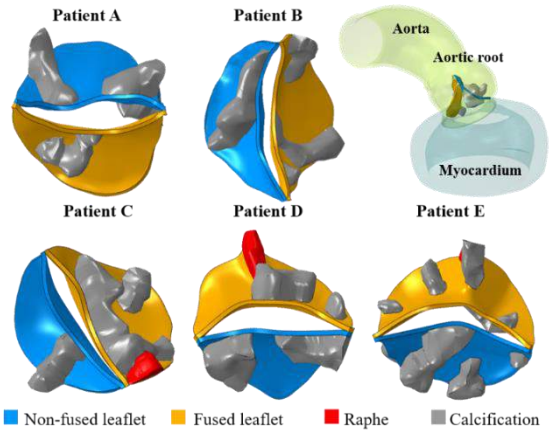

Figure 1: Patient-specific BAV models.

This retrospective study consisted of 5 BAV patients that underwent successful transcatheter aortic valve replacement (TAVR). BAV was classified using the Sievers system, based on the number of functional leaflets and presence of raphe: type 0, pure BAV with 2 leaflets and no raphe; and type 1, presence of one raphe [6]. The cardiac multislice computed tomography (MSCT) images, as well as the transthoracic echo examination were collected from Emory University Hospital (Atlanta, GA). The use of de-identified patient data for this study was approved by the Institutional Review Board. Patient-specific 3D models containing the BAV leaflets, raphe (if present), calcification, sinuses, ascending aorta, left ventricular outflow tract (LVOT) and proximal myocardium were constructed from the MSCT images using 3D solid elements (HyperMesh, Altair Engineering, Inc., MI), as seen

in Figure 1. Soft tissue mechanical behavior was characterized using the anisotropic hyperelastic modified Holzapfel-Gasser-Ogden model. Material properties were obtained in-house by fitting multiprotocol biaxial testing data of human cardiac tissues.

A previously validated FSI framework that combines smoothed particle hydrodynamics (SPH) for the blood flow, and nonlinear FE analysis for the tissue deformation [7, 8] was used to simulate the dynamics throughout the cardiac cycle. Time-dependent pressure boundary conditions were applied at the LV myocardium inlet and ascending aorta outlet. These waveforms were fitted to match the pressure values clinically measured for each patient. To evaluate the effect of aortic wall elasticity on the flow patterns, both fixed aorta and flexible aorta were used to developed the BAV model. For fixed aorta, the aortic root geometries were directly segmented from the MSCT images and were assumed static throughout the cardiac cycle. For flexible aorta, the unpressurized (stress-free) aortic root geometries were obtained using the generalized pre-stressing algorithm based on the MSCT images at mid-systole [9], and used as the initial geometries. Abaqus/Explicit (SIMULIA, Providence, RI) was used for all FSI simulations presented in this study.

RESULTS

Patients were between 57 and 82 years old. Sievers classification was type 0 in two patients and type 1 in three patients. The patient-specific FSI models were validated by comparing: 1) the deformed BAV leaflet geometries with the MSCT images (ground truth) at mid-diastole, and 2) the computed hemodynamic parameters with the clinical echo measurements. The average point-to-mesh error distance between the simulated and ground truth geometries was < 1.8 mm for all patients. Differences in the simulated and *in vivo* aortic peak velocity were < 10%.

For each BAV patient, systolic flow patterns were identified and analyzed using the 3D velocity field obtained from the FSI models. The streamlines at peak systole (Figure 2) showed two asymmetric recirculation rolls above the two BAV leaflets; in addition, helical flows were observed in the ascending aorta. The flow at the different cross-sections along the aortic root (Figure 3) showed eccentric jets at the level of sinotubular junction (STJ), and the counterclockwise secondary flow in the cross-sections which were associated with the right-handed helical flow structure. The flow patterns between the fixed aorta and the flexible aorta were qualitatively similar. The recirculation rolls within the fused sinuses were larger with the fixed aorta. In addition, the helical flow was stronger in the fixed aorta, which a higher peak velocity, and a more pronounced secondary flow.

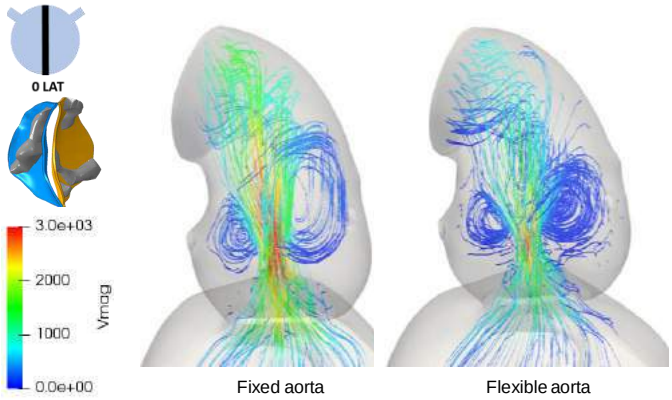

Figure 2: Representative BAV model (Patient B) showing streamlines at peak systole with a) fixed aorta, b) flexible aorta.

DISCUSSION

In this study, patient-specific FSI modeling in 5 BAV patients under various anatomic scenarios provided novel quantitative data about the 3D flow patterns in the aortic root. The accuracy and predictability of our FSI modeling framework were confirmed with pre-operative echo and imaging data. Additionally, this work provided mechanistic insights that led to better understanding of BAV aortopathy disease progression. While helical flow structures have been associated with ascending aortic aneurysms [11], it was found that even though all the five BAV patients in this study had normal size of aorta, abnormal eccentric jets and helical flows were still observed. This suggests that the abnormal flow patterns in BAV might not be secondary to dilated aorta, but could be the contributing factor to BAV aortopathy. In addition, the jet structures at peak systole were qualitatively similar between the fixed and flexible aorta, while the size and location of the recirculation flow above the sinuses, and the velocity magnitude showed some difference.

This study was small and retrospective, and would be enhanced through a larger, prospective evaluation of BAV patients, which is required to definitively establish the power of the computational simulations.

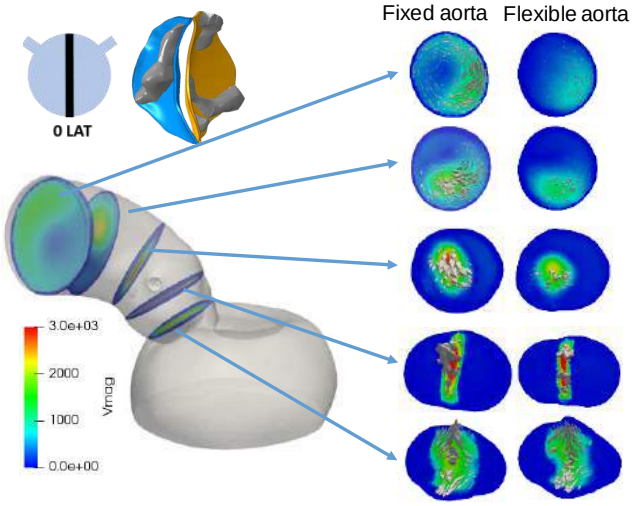

Figure 3: Representative BAV model (Patient B) showing the flow at peak systole on five cross-sections in fixed and flexible aorta.

ACKNOWLEDGEMENTS

This study was supported in part by the Marvin H. and Nita S. Floyd Research Fund and NIH HL142036. Dr. Tongran Qin was in part supported by an American Heart Association Postdoctoral Fellowship 19POST34450161. Dr. Andrés Caballero was in part supported by a Fulbright-Colciencias Fellowship.

REFERENCES

[1] Phan, K et al., Heart, Lung and Circulation 24, 649-659 (2015).
[2] Ward C, Heart. 83:81–85 (2000).
[3] Itagaki S et al., J Am Coll Cardiol 65, 2363-9 (2008).
[4] Barker AJ et al. Circ Cardiovasc Imaging, 5, 457–66 (2012).
[5] Mahadevia R et al., Circulation, 129, 673–82 (2014).
[6] Sievers, H. & Schmidtke, C., J Thorac Cardiovasc Surg 133, 1226-1233 (2007).
[7] Caballero, A et al., J R Soc Interface 16, 20190355 (2019).
[8] Mao, W et al., PloS one 12, e0184729 (2017).
[9] Weisbecker, H et al., Int J Numer Method Biomed Eng 30, 857-872 (2014).
[10] Hope TA et al., J Magn Reson Imaging, 26 (6): 1471 – 1479 (2007)

CONSTANT PRESSURE CED INFUSIONS WITH CONTROLLED CATHETER MOVEMENT IN AGAROSE GEL BRAIN TISSUE PHANTOMS

Jason N. Mehta (1), Brianna E. Morales (2), Christopher G. Rylander (1)

(1) Walker Department of Mechanical Engineering
The University of Texas at Austin
Austin, TX, USA

(2) Department of Biomedical Engineering
The University of Texas at Austin
Austin, TX, USA

INTRODUCTION

Convection-enhanced delivery (CED) is a drug delivery technique that can be used to effectively bypass the blood-brain barrier and can be used in the treatment of brain tumors such as Glioblastoma. While this technique shows promise, the Phase III clinical trial (PRECISE) failed to show an advantage with CED treatment compared to the control arm [1]. A retrospective study found that the failure could be partially explained by an inability of catheters to distribute therapeutics in high enough quantities to treat the entire tumor and its margins [2]. To combat this we proposed the use of controlled catheter movement which was shown to increase the volume dispersed (V_d) of indigo carmine dye in an agarose gel brain tissue phantom by about 50% when catheters were continuously retracted [3]. This work along with most clinical trials relied on the use of syringe pumps that create a constant flow rate. But, one cause of the increase in V_d with controlled catheter retraction is a constantly growing surface area over which advection can occur. Since this surface area is growing, an increase in flow rate may be achievable throughout the infusion without causing reflux, a common occurrence with increased flow rate [4]. In the present work, we develop a controller to allow a syringe pump to be used as a constant pressure source and test the ability of constant pressure infusions coupled with controlled catheter movement to increase the V_d in agarose gel brain tissue phantoms.

METHODS

Controller: A PID controller was implemented to control infusion line pressure, measured at the needle inlet (P_N in Figure 1) by updating the flow rate of a programmable syringe pump. In the absence of a reliable plant model, the system was tuned experimentally using data obtained from the stationary, constant flow rate experimental group. The mean of 5 pressure response curves were used to determine a plant model using the system identification toolbox in Matlab (version R2018a, MathWorks Inc., Natick, MA). This model was then used to tune a PID controller with a design focus toward reference tracking. This focus was chosen in order to limit overshoot as excessive overshoot could result in the creation of reflux. The resulting controller was then implemented in a custom LabView program to control the flow rate of a programmable syringe pump. Pressure measurements were recorded once a second and flow rate was updated on the same interval.

Experimental Setup: A 23.5 cm catheter was fabricated by gluing a fused silica capillary tube (150 µm ID/ 350 µm OD) into a 20 G plastic dispensing needle. As shown in Figure 1, the catheter was then clamped to a deployment mechanism driven by a leadscrew attached to a stepper motor. Next, the catheter was connected to a t-connector, one end of which was attached to a pressure sensor, the other end was attached to

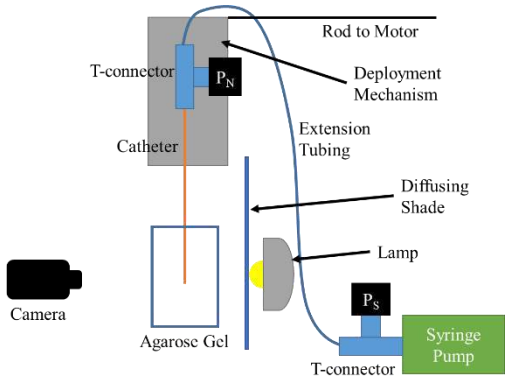

Figure 1: Schematic of experimental setup with P_N and P_S representing the locations of the pressure sensors.

a micro bore extension tubing which was connected to another t-connector with a second pressure sensor (P_s) on one arm and a 3 mL syringe on the third arm. Finally, the syringe was inserted into the syringe pump which was used to create the desired flow rate.

Infusions of 1% (wt./wt.) indigo carmine dye were performed in 0.6% (wt./wt.) agarose gel brain tissue phantoms for a total of 100 minutes per infusion. Optical images were acquired once per minute and were used to measure the V_d of each infusion in a similar fashion to previous work [3, 5]. In addition, infusion line pressure was sampled at 2 kHz and the mean pressure was recorded once per second. Four experimental groups with 5 replicates were evaluated: 1) stationary, constant flow rate (Sta. CF), 2) controlled retraction, constant flow rate (Ret CF), 3) stationary, constant pressure (Sta. CP), and 4) controlled retraction, constant pressure (Sta. CP). The constant flow rate was chosen to be 1 µL/min and the constant pressure was chosen to be the average pressure of the stationary, constant flow rate infusions, 977 Pa. Finally, the controlled retraction rate was 0.25 mm/min resulting in a total retraction distance of 25 mm.

RESULTS

As shown in **Table 1**, the controlled retraction catheter with a constant infusion line pressure of 977 Pa resulted in a nearly 130% increase in V_d compared to both the constant pressure and constant flow rate stationary catheters and an over 50% increase in V_d compared to the controlled retraction constant flow rate catheter. Further, the controlled retraction constant flow rate catheter had a 46% increase in V_d compared to the stationary constant flow rate catheter. Finally, the stationary constant pressure catheter resulted in nearly the same V_d as its constant flow rate counterpart, but was about 1.6% lower. Figure 2 shows the average pressure (**a**) and average flow rates (**b**) of all four groups, and reveals the decrease in pressure and subsequent increase in flow rate over time with the constant flow rate controlled retraction catheter.

Table 1: Results from infusions in agarose gel (n=5).

Group	V_d (mL)	V_i (mL)	V_d:V_i	Avg. Pressure (Pa)	Avg. Flow Rate (µL/min)
Sta. CF	1.0 ± 0.04	0.1	10.4 ± 0.4	976.7 ± 160.3	1
Ret. CF	1.5 ± 0.11	0.1	15.1 ± 1.1	309.7 ± 196.5	1
Sta. CP	1.0 ± 0.09	0.11 ± 0.01	9.3 ± 1.4	967.1 ± 93.1	1.1 ± 0.1
Ret. CP	2.4 ± 0.17	0.24 ± 0.01	9.8 ± 0.8	945.7 ± 89.4	2.4 ± 0.4

DISCUSSION

While the addition of controlled catheter retraction results in a significant increase in V_d of 46-50% [3] compared to a stationary catheter, the addition of constant pressure with the controlled retraction appears to more than double this advantage. What is more, the use of constant pressure infusions allows for time varying infusion flow rates which not only could increase the amount of drug infused (and likely the V_d) but it can also be used to minimize reflux of the infusate up the needle tract. Commonly, the magnitude of flow rate has been used as the metric to predict whether reflux would occur as flow rate is the usual controllable parameter for CED infusions [4]. However, it is most likely that a critical infusion pressure resulting in tissue deformation would result in reflux, as reflux is believed to be the result of the creation of an annular gap between the catheter and the tissue due to tissue deformation [6-8]. While infusion line pressure is not a perfect representation of actual infusion pressure, prescribing infusion line

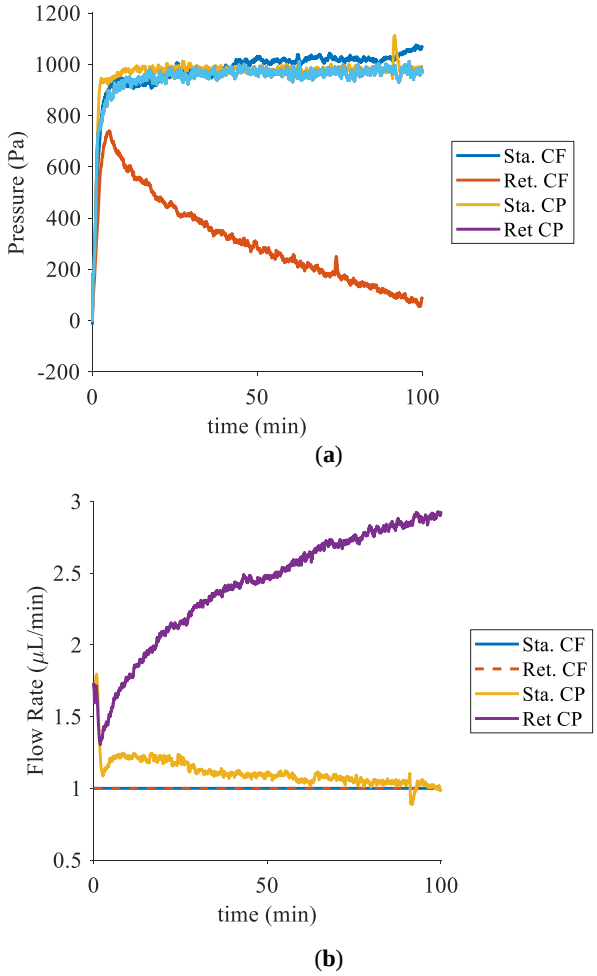

Figure 2: Plot of (a) average pressure over time and (b) average flow rate over time for Sta. CF, Ret. CF, Sta. CP, and Ret. CP (n=5 each).

pressure near but below a critical reflux inducing pressure may have significant benefits in increasing the overall V_d, especially when catheter movement or other catheter control is used. It should be noted however, that real time imaging will be an extremely important component in these systems as reflux could also result in a drop in measured pressure which would have negative consequences in a constant pressure system if intervention does not occur. Lastly, the limitations of agarose gel brain tissue phantoms should be acknowledged as it is a homogeneous material and does not fully replicate infusions in tissue.

ACKNOWLEDGEMENTS

This research was funded by the National Institutes of Health/ National Cancer Institute, grant number P01 CA207206-01.

REFERENCES

[1] Kunwar, S., et al., Neuro-oncology, 12:871-81, 2010.
[2] Sampson, J. H., et al., J Neurosurg, 113:301-9, 2010.
[3] Mehta, J. N., et al., Pharmaceutics, 12:753, 2020.
[4] Chen, M. Y., et al., Journal of Neurosurgery, 90:315-320, 1999.
[5] Elenes, E. Y., et al., Glioblastoma, 359-372, 2017.
[6] Morrison, P. F., et al., Am J Physiol, 46:1999.
[7] Raghavan, R., et al., Physics in Medicine & Biology, 55:281, 2009.
[8] Orozco, G. A., et al., Med Biol Eng Comput, 52:841-9, 2014.

COMPUTATIONAL ANALYSIS OF QUANTITATIVE ECHOCARDIOGRAPHIC ASSESSMENTS OF FUNCTIONAL MITRAL REGURGITATION: VENA CONTRACTA AREA (VCA) METHOD

T. Qin (1), A. Caballero (1), R. Hahn (2), R. McKay (3), and W. Sun (1)

(1) Department of Biomedical Engineering Georgia Institute of Technology and Emory University Atlanta, GA, USA

(2) Division of Cardiology Columbia University Medical Center New York, NY, USA

(3) Cardiology Department The Hartford Hospital Hartford, CT, USA

INTRODUCTION

Mitral regurgitation (MR) is the most common valvular heart disease, with a prevalence of 9.3% in the US population aged 75 and above [1]. Although Doppler echocardiography (echo) is the primary clinical tool to evaluate MR severity, MR quantification remains challenging, and a true gold standard technique is still missing [2]. With the recent advent of 3D color Doppler imaging, vena contracta area or VCA method has drawn more attention in MR quantification [3,4], however, there still lacks an in-depth analysis based on the fundamental theoretical background of VCA. The clinical studies are often limited by the lack of a robust reference value (gold standard) for MR quantification. *Ex vivo* bench experimental studies are also challenging due to the complexity of experimental setups (e.g., beating heart conditions) and the difficulty to obtain the detailed interrogation of the MR flow field crossing the mitral valve (MV).

Recent advances in patient image-based computational modeling, on the other hand, have substantially enhanced the investigation of patient-specific cardiac dynamics. In particular, a patient specific fluid-structure interaction (FSI) computer framework has been applied to study valvular functions under a variety of physiologic, pathologic states, including the echo measurement for MR [5], where the FSI models were able to replicate the patient-specific flow field inside the left heart, and can be treated as a phantom model for systematical quantification of different sources of errors in echo measurements.

Therefore, in this study we will investigate the accuracy and reliability of VCA in functional MR (FMR) using FSI models, from which the reference values of mitral regurgitation flow rate and regurgitant volume can be directly obtained. The virtual VCA measurements were then performed on the same phantom models assuming optimal echo probe angulation and positioning. By comparing the results obtained using VCA methods with the reference values, the accuracy of different VCA methods will be evaluated, and the multiple sources of errors in VCA method will be analyzed and quantified.

METHODS

FSI models: Five FSI models for FMR patients were created, validated and treated as phantom models. The first model was a previously validated patient-specific left heart FMR computer model based on a 71-year-old male patient [6, 7] (data collected under the Institutional Review Broad approvals). The other four FMR models were computationally created from the first model by displacing the papillary muscles (PM) apically and laterally, replicating a type IIIb lesion with restricted leaflet motion [8].

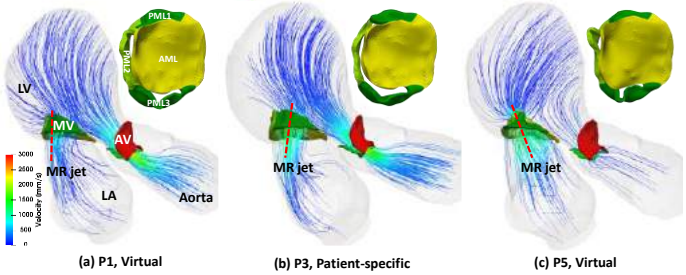

Figure 1. The velocity field of three representative FMR computer models (P1, P3, and P5) ranging from mild to severe MR.

Reference values: The phantom models have fully resolved and detailed flow fields (Figure 1) in the left atrium (LA), left ventricle (LV) and cross the mitral valve, from which the reference values of mitral regurgitant flow rate and regurgitant volume can be obtained. Specifically, the reference MV regurgitant volume RV_{MV} was obtained by integrating the negative MV flow rate over systole. The regurgitant

fraction $RF_{MV} = RV_{MV}/SV_{LV}$ was used to grade MR severity, where $SV_{LV} = SV_{AV} + RV_{MV}$ is the total stroke volume (SV) of the LV.

Virtual echo acquisition and VCA measurement: The velocity field obtained directly from FSI models (Figure 1) is referred to as the "true velocity", while the velocity field used for virtual echocardiographic data acquisition is referred to as the "Doppler velocity". Due to the Doppler angle effect [2], the virtual echo only measures the velocity component aligned with the ultrasound beam. Therefore, the Doppler velocity field was obtained by projecting the true velocity field along the direction of the ultrasound beam. To emulate VCA method, we will identify the narrowest location of the regurgitant jet at peak systole on color Doppler with aliasing velocity V_a (Figure 2a), then rotate the third cropping plane normal to the jet orientation, and measure the effective regurgitant orifice area (S_{VCA}) directly on the cropping VCA plane (Figure 2b). The regurgitant volume RV_{MV} can then be calculated as $RV_{MV} = S_{VCA} \times VTI_{MR}$. The velocity time integral VTI_{MR} of the regurgitant jet were obtained by emulating continuous wave Doppler (CWD) measurements with the virtual ultrasonic probe parallel to the jet in an optimal position.

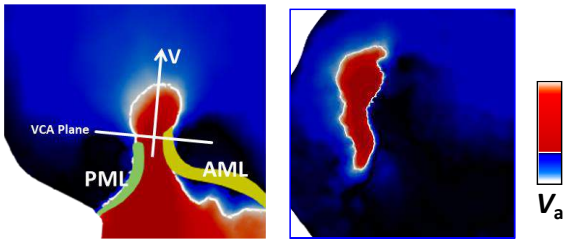

(a) (b)

Figure 2. Schematic showing (a) MR jet of velocity V across VCA plane; (b) measurement of VCA area (in red) on VCA plane. AML-anterior mitral leaflet, PML-posterior mitral leaflet

RESULTS

The reference values were obtained directly from FSI models. Patient 1 (P1) and P2 have mild-moderate MR, P3 has moderate-severe MR, while P4 and P5 have severe MR (Table 1). To evaluate the accuracy of the VCA method, the regurgitant volumes obtained with VCA measured at peak MR were compared with the reference values using Bland-Altman analysis (Table 2). For comparison, the same analysis was performed for the 3D PISA method on the same FSI models [9], which was found to be the most accurate PISA method. The VCA method showed a significantly smaller bias (-1.3 ± 3.3 ml) than that of the 3D PISA method (-12.7 ± 7.8 ml) for the quantification of regurgitant volume.

Table 1. Patient (FMR FSI model) information.

Patient	P1	P2	P3	P4	P5
SV_{AV} (ml)	55.65	51.02	46.28	33.71	21.52
SV_{MV} (ml)	74.59	75.58	74.64	77.26	75.61
RV_{MV} (ml)	27.68	32.61	37.59	51.62	62.69
RF_{MV} (%)	33.22	38.99	44.82	60.50	74.45
MR Severity (Based on RF_{MV})	Mild-moderate	Mild-moderate	Moderate-severe	Severe	Severe

Table 2. Results of Bland-Altman analysis for RV_{MV} quantification using both VCA method and 3D PISA method.

Method	Mean bias (ml)	Limits of agreement (ml)
VCA	-1.3	[-4.6, 2.0]
3D PISA [9]	-12.7	[-20.4,-4.9]

DISCUSSION

In this study, five FSI models of FMR were used to evaluate the accuracy of VCA method for MR quantification. Based on fundamental fluid mechanics principles, the instantaneous regurgitant flow rate through VCA is $Q_{MR} = \int_s V_n dS$, where V_n is the *normal* component of the true velocity V across VCA. The simplified expression $Q_{MR} = V_{MR} S_{VCA}$ used in VCA method will therefore only be accurate when $V_{MR} = V_n$ over the entire VCA plane, which is not always the case. Due to the Doppler angle effect, the velocity of the MR jet detected by echo $V_{MR} = V\cos\theta$ underestimates the true velocity V, where θ is the "Doppler angle" between the direction of flow and the ultrasound beam. On the other hand, only the normal component $V_n = V\cos\gamma$ will contribute to the flow rate across VCA, where γ is the angle between the flow direction across VCA and the normal direction of VCA plane. As $V_{MR} = V_n\left(\frac{\cos\theta}{\cos\gamma}\right)$, the underestimation due to the Doppler angle θ, and the overestimation due to the flow direction angle γ compensate each other. In addition, since the ultrasound beam is aligned with the MR jet, and the VCA plane is cropped normal to the MR jet, both θ and γ are close to zero. This is why VCA method tend to be more accurate than PISA method, as θ and γ could deviate significantly from zero in PISA method. However, the accuracy of VCA method is directly affected by the selection of the aliasing velocity V_a, as the VCA area will increase (or decreases) with a smaller (or larger) aliasing velocity. In this study, the aliasing velocity is selected as one third of the peak MR velocity.

For the quantification of regurgitant volume, an additional source of error is due to the dynamic feature of the regurgitant orifice, especially in FMR [10,11]. The calculation based on a single measurement at peak MR ignores the dynamic variation of the regurgitant orifice, therefore can lead to either over- or underestimation of MR.

This study focused on FMR of type IIIb lesion with restricted leaflet motion. Other types of FMR such as type I MR with normal leaflet motion have not been investigated. Additionally, the effect of the aliasing velocity settings on the VCA method was not investigated. These warrant a future study. Virtual echo represents an ideal measurement with optimal positioning and angle of the echo probe, hence certain sources of error for clinical echo such as reverberation artifacts and shadowing were not incorporated.

ACKNOWLEDGEMENTS

Dr. Tongran Qin was in part supported by an American Heart Association Postdoctoral Fellowship 19POST34450161. Dr. Andrés Caballero was in part supported by a Fulbright-Colciencias Fellowship.

REFERENCES

[1] Benjamin EJ, et al., Circulation, 135(10):e146-e603 (2017).
[2] Little SH, J Am Soc Echocardiogr. 25(8):824-6 (2012).
[3] Marsan A. et al., JACC:Cardiovasc. Imaging, 2(11)1245-52 (2009)
[4] Iwakura K, et al. Am J Cardiol, 97:1630-1637 (2006).
[5] Mao W, et al., Am J Physiol Heart Circ Physiol. 318(3):H547-H57 (2020).
[6] Caballero A, et. al., J R Soc Interface. 16(157):20190355 (2019).
[7] Caballero A, et. al., Structural Heart. 1-13 (2020).
[8] Jaworek M, et. al., Ann Biomed Eng. 45(10):2324-34 (2017).
[9] Qin, T. et al., J Am Soc Echocardiogr, under review
[10] Hung J, J Am Coll Cardiol. 33(2):538-45 (1999).
[11] Francis DP, Int. J. Cardiol. 73(3):237-42 (2000).

LIVE-CELL, DYNAMIC IMAGING OF MATRIX ASSEMBLY IN AN IN VITRO MODEL OF HUMAN CORNEAL DEVELOPMENT

Alexandra A. Silverman (1), Seyed Mohammad Siadat (1), Jeffrey W. Ruberti (1)

(1) Department of Bioengineering
Northeastern University
Boston, MA, USA

INTRODUCTION

Despite more than a century of research, one of the most fundamental questions in biology: "How is tissue built? [1]" remains unanswered. Understanding extracellular matrix (ECM) assembly is critical for connective tissue engineers who are trying to produce or induce load-bearing structures but cannot point to a viable mechanistic model of organized matrix morphogenesis. Collagen, the principal structural molecule in vertebrates, is generally produced and secreted by fibroblasts, and then assembles to form fibrils through a process known as fibrillogenesis [2]. Collagen fibrils are further processed into fibrillar structures and organized into macroscale tissues by mechanisms that are not well-understood.

Our current understanding of collagen assembly is derived primarily from electron microscopy images of ECM formation. Based on interpretations of these static images, it has been suggested that fibrillogenesis occurs within cell surface crypts or invaginations and that fibrils are then released from the cell into the ECM [2],[3],[4]. Recent revisions to this concept suggest that tensional forces are critical to formation of fibrils in these putative fibril depositors [4] and that, for the cornea in particular, fibrils form on the outside of cell extensions or keratopodia [5]. However, it is difficult to confirm or reject any hypothesis of matrix assembly using static images alone. Indeed, recent data suggests that fibrillogenesis is a highly dynamic process [6]. Even sophisticated, high-resolution serial block face SEM imaging tells us little of the dynamics of fibril formation. To access fibril assembly dynamics requires live cell dynamic imaging at high resolution and the ability to resolve the formation of nanometer scale fibrils, without affecting their formation kinetics. No study to date has combined all of these requirements to expose collagen fibrillogenesis in real-time. In this study we have examined a model of human corneal development during the critical period of matrix production to elucidate the dynamics of collagen fibril formation for the first time.

METHODS

Primary Human Corneal Fibroblast (PHCF) cultures were established from 74yr donor corneas as described in Bueno *et al*. [7]. Briefly, donor corneas were cut into 2x2 mm pieces, adhered to 6well dishes, and were cultured in Dulbecco's modified eagle medium containing 10% fetal bovine serum and 1% antibiotic/antimycotic until PHCF migrated off and were expanded. PHCF were seeded on temperature-controlled dishes at passage 3 at a concentration of 30,000 cells/cm^2. Once confluent on Day 3, 0.5mM L-Ascorbic Acid was added to permit the culture to construct a 3D matrix of orthogonal cell layers.

Acid soluble type I bovine collagen (TeloCol, #5225, Advanced BioMatrix) was labeled with Alexa Fluor 488 (AF488) to be added exogenously to the PHCF culture. Briefly, 2 mg/mL TeloCol was adjusted to pH 7.5 and mixed with AF488 in a 1:2 collagen:dye molar ratio. The degree of labeling (moles of AF488 per mole of collagen monomer) was measured as 0.9.

1.5 mL of CO_2 infused media containing 0.5 mM L-ascorbic acid and 1 µg/mL AF488-col was added to the cells at timepoints ranging from day 3 to day 8. The culture was imaged using 600x differential interference contrast microscopy by taking a photo every 5 seconds.

To analyze the live cell images, the following equations were used:

PHCF Velocity of Cellular Contraction Calculation:

$$v_{cellular\ contraction} = \frac{\Delta L}{\Delta t} \quad (1)$$

PHCF Filament Extensional Strain Rate Calculation:

$$\dot{\varepsilon} = \frac{\Delta L / L_o}{\Delta t} \quad (2)$$

Where *Lo* is the initial length of the filament and *ΔL* is the change in filament length. 42 filaments were measured, and were assumed to have cylindrical geometry, constant volume, and experience radial thinning.

RESULTS

Fibrillar Network Evolution: Within 5 minutes after the addition of AF488-col, AF488 was primarily concentrated in vesicles within the cell, trafficked through the cell in a parallel direction to ECM fibers, and also associated with the pre-existing fibril network (Figure 1). Vesicles containing AF488-col moved constantly within cell body and keratopodia, with the highest recorded vesicle velocity being 7.28 µm/min. Over a period of 48 hours, there was an evolution of the fibrillar network containing AF488-col (Figure 1). Overall, there appears to be a transfer of labeled collagen from cell vesicles to the extracellular fibrillar network.

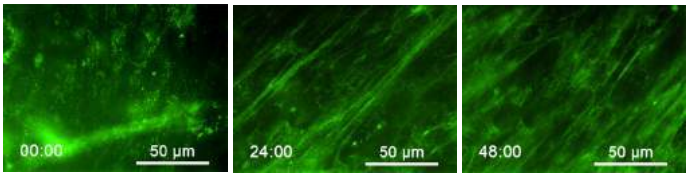

Figure 1: 74yr PHCF, 1.5µg AF488-col added D6 at T=0HRS

Rapid Cellular Contraction Events: Cells and cell processes were continually connecting between cells and rapidly contracting, often forming trailing and persistent filaments. These contraction events were categorized as bubbling keratopodia, non-bubbling keratopodia, parallel to cell axis, and perpendicular to cell axis (Figure 2).

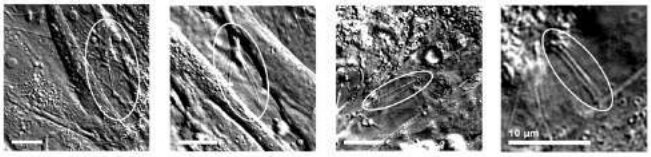

Figure 2: DIC Images of 74yr PHCF Cellular Contraction Events Left to Right: Bubbling Keratopodia, Non-Bubbling Keratopodia, Parallel to Cell Axis, Perpendicular to Cell Axis

Keratopodia, the sites of fibril formation in corneal development [5], were continually connecting one cell to another at multiple adjacent sites in a starburst configuration. Some keratopodia attachment sites also exhibited dynamic bubbling with high velocities and extensional strain rates. Figure 3 shows this event, where bubbling cell material contracts, forming a starburst of keratopodia that are rapidly stretched. The plot shows the corresponding velocity of this contraction, and the extensional strain rate on the thinning keratopodia.

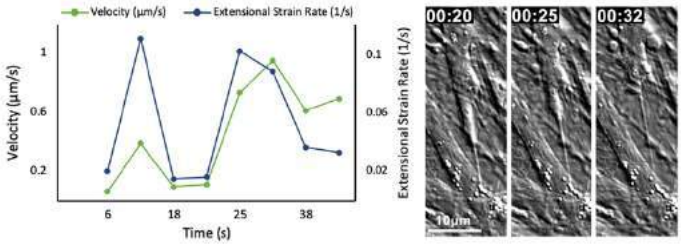

Figure 3: Plot of Cellular Contraction Velocity and Filament Extensional Strain Rate, and DIC Images of 74yr PHCF Bubbling Keratopodia Cellular Contraction

Smaller cell processes and lamellae were also formed between contracting cells in a parallel or perpendicular fashion. The maximum velocities for all pull types were significantly larger than the average cell nucleus velocity ($p<0.05$) (Figure 4). As the cells contracted, the persistent filaments stretched and thinned, with 7 out of 42 exhibiting extensional strain rates within the range of 0.1 and 0.3 s^{-1} (Figure 4), which may be sufficient for collagen fibrillogenesis given a concentrated collagen solution [8].

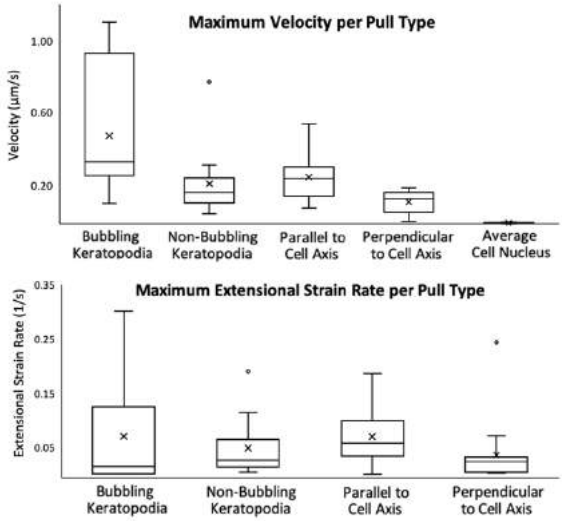

Figure 4: Plots of Velocities and Extensional Strain Rates for Four Types of Cellular Contractions

DISCUSSION

Our investigation has revealed a number of novel phenomena. The first is the near immediate internalization and trafficking of our AF488-col within the cell body and extensions. The second is the association of the label with the extant network, upon introduction and apparently after trafficking within the cell. The third discovery is the continuous application of forces from one cell to another through rapid contractions and the characterization of four distinct cellular contraction types. It is clear that tensile force, applied between cells, is an important part of the process of cell/matrix organization in this model system. Contraction velocities of the cell extensions were often more than 100 times faster than average cell nucleus velocities suggesting a critical function unrelated to locomotion. It is not yet clear if collagen is associated with these persistent filaments, however the contractions cause extensional strain rates sufficient to induce collagen fibrillogenesis [8], [9].

Taken together, our observations support a mechanochemical mechanism of matrix assembly whereby tensile forces produce extensional strains that initiate and sustain the growth of mechanosensitive filaments (perhaps fibronectin/collagen co-fibers [9]) directly in the path of the force that created them.

ACKNOWLEDGEMENTS

This work was funded by NIH R21 EY029167-01.

REFERENCES

[1] Cowin, S, *J. Biomech. Eng.*, 122:553–569, 2000.
[2] Kadler, K et al., *J. Biochem.,* 316:1–11, 1996.
[3] Birk, D et al., *J. Cell Biol.*, 99:2024–2033, 1984.
[4] Canty, E et al., *J. Cell Biol.*, 165:553–563, 2004.
[5] Young, R et al., *Proc. Natl. Acad. Sci. U. S. A.*, 111:687–692, 2014.
[6] Lu, Y et al., *J Bone Min. Res.*, 33:1166–1182, 2018.
[7] Bueno, E et al., *Tissue Eng. - Part A*, 15:3559–3573, 2009.
[8] Paten, J et al., *ACS Nano,* 10:5027-5040, 2016.
[9] Paten, J et al., *Chem,* 5:2126-2145, 2019.

STRESS-DRIVEN FIBER REMODELING IN A FINITE ELEMENT MODEL OF CARDIAC TISSUE

Alexus L. Rockward (1), Charles K. Mann (1), Hossein Sharifi (1), Joy Mojumder (2), Lik Chuan Lee (2), Kenneth S. Campbell (3), Jonathan F. Wenk (1,4)

(1) Department of Mechanical Engineering
University of Kentucky
Lexington, KY, USA

(2) Department of Mechanical Engineering
Michigan State University
East Lansing, MI, USA

(3) Department of Physiology & Division of Cardiovascular Medicine
University of Kentucky
Lexington, KY, USA

(4) Department of Surgery
University of Kentucky
Lexington, KY, USA

INTRODUCTION

Hypertrophic cardiomyopathy (HCM) is a genetic cardiac disease, characterized by the thickening of the left ventricular (LV) walls, fibrosis, and myofiber disarray. A study performed by Tseng et al. suggests that fiber disarray contributes to impaired passive and active cardiac function in HCM patients [1]. Current cardiac models are capable of simulating the mechanical and structural properties of the left ventricle, as well as volumetric growth and remodeling of the cardiac tissue. However, to the knowledge of the authors, none of the current cardiac models simulating HCM incorporate the remodeling of cardiac myofibers.

This omission is partly due to the fact that the mechanisms related to fiber orientation in the heart are yet still unclear, and few adaptative laws have been created to explore these mechanisms. Kroon et al. developed an adaptative orientation law based on stretch to accomplish reorientation [2]. This stretch-based law aimed to reduce circumferential-radial shear strain and achieved realignment in the principal strain directions. However, the strain-based approach is not sufficient to reproduce the fiber orientations found in the human heart. Based on observations of the principal stress and principal strain distributions in a previous LV model from our group, which did not include fiber remodeling, it was shown that the fibers throughout the cardiac cycle are very closely aligned with the direction of maximum principal stress (Figure 1). This is the motivation for implementing and investigating a stress-based remodeling law, which is then compared to the strain-based law from Kroon et al. The goal of this abstract is to present a novel stress-based fiber reorientation law and compare to the previous strain-based law.

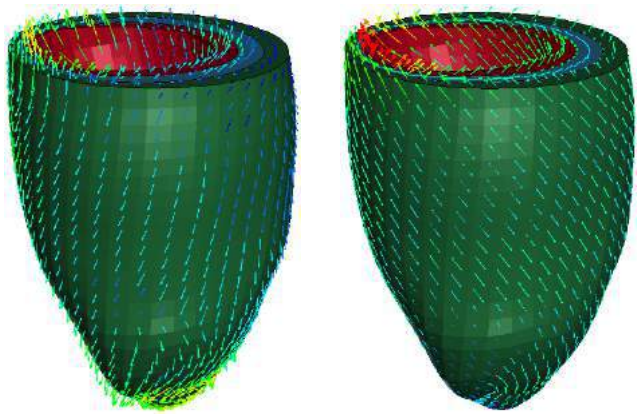

(a) (b)

Figure 1: Finite element model of the left ventricle comparing (a) principal strains and (b) principal stresses at end-systole.

METHODS

Reorientation Laws The reorientation law presented by Kroon et al. [2] uses the right stretch tensor to evolve the fiber orientation:

$$\frac{de_{f,0}}{dt} = \frac{1}{\kappa}\left(e_f(U) - e_{f,0}\right) \quad (1)$$

where $e_{f,0}$ is the fiber orientation in the reference configuration and e_f is the fiber orientation in the current configuration after correction for rigid rotation. The term κ is a rate constant used to adjust the rate of evolution. We developed a stress-based reorientation law which uses the first eigenvector of the second Piola-Kirchhoff stress tensor, e_g, to evolve the fiber orientation:

$$\frac{de_{f,0}}{dt} = \frac{1}{\kappa}\left(e_g(S) - e_{f,0}\right) \qquad (2)$$

where S is the second Piola-Kirchhoff stress tensor.

Uniaxial Simulations The mesh and finite element (FE) analysis were performed using the FEniCS platform. A unit cube mesh consisting of 6 second-order Lagrangian tetrahedrons was generated using built-in functions. The left face normal to the x-axis was constrained to remain in the yz plane, and a displacement boundary condition was applied to the opposite face. One of the faces normal to the z-axis was constrained to remain in the xy plane, in order to avoid rigid body motion. For all cases presented in this abstract, the mesh was subjected to a uniaxial stretch along the x-axis. A local orthogonal coordinate system $\{\mathbf{f}_0, \mathbf{s}_0, \mathbf{n}_0\}$ is defined using the prevailing fiber, sheet, and sheet-normal directions, respectively.

For the initial period of time of the simulation, no deformation is applied, after which uniaxial stretch is incrementally applied over a given interval of time. Once the deformation phase is complete, the appropriate reorientation law is activated, and the simulation is run until the fiber reorientation is completed to steady state. The Guccione transversely isotropic constitutive law is used for material properties of the cube [3]. The weak form of the balance of linear momentum is solved using a built-in Newton solver withing FEniCS.

Two sets of simulations were run to compare the strain-based law and stress-based law. The first set of simulations compare the resulting fiber orientations when each reorientation law is applied to fibers initialized at 0 degrees. The second set of simulations differ from the first set only in regards to the initial fiber orientation being assigned to 70 degrees.

RESULTS

Neither reorientation law resulted in reorientation when the fiber orientation was initialized at 0 degrees, i.e. the fibers remain oriented along the x-axis over the duration of the simulation. The deformation was uniform and uniaxial for both the stress-based law and the strain-based law.

Differences in final reorientation were observed between the stress- and strain-based laws when the fiber orientation is initialized at 70 degrees (Figure 2). The strain-based law results in a final orientation which corresponds with the direction of applied stretch, i.e. along the x-axis. Again, the deformation pattern is uniform and uniaxial along the x-axis. The stress-based law, however, results in a final fiber orientation approximating 45 degrees. The deformation pattern resembles a simple shear deformation.

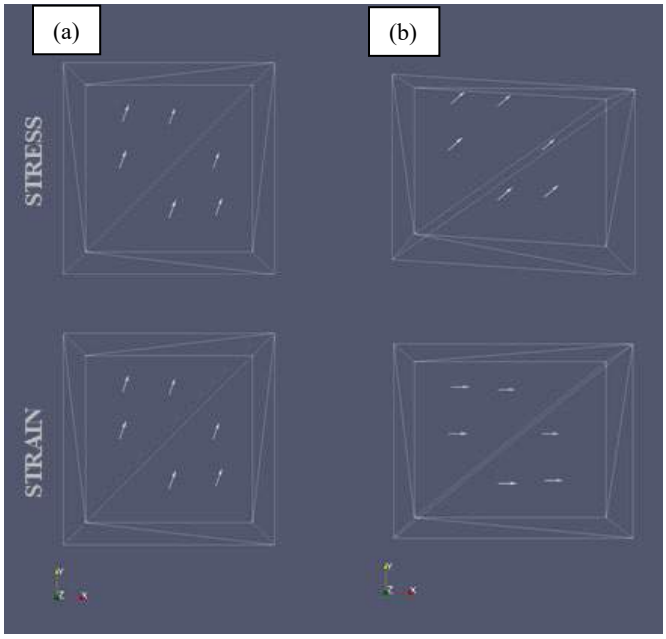

Figure 2: Simulations of uniaxial stretch cases with fibers initialized at 70 degrees (a) before and (b) after the application of the stress and the strain reorientation laws. The arrows represent the fiber orientation in each element.

DISCUSSION

To the best of the authors' knowledge, this preliminary work presents a novel stress-based fiber reorientation law. This work reveals a key difference in the two reorientation laws and demonstrates the potential for the use of stress as a primary signal for fiber remodeling. The difference in fiber reorientation seems to be due, in large part, to the transversely isotropic nature of the material. Since such a material has a direction of maximum stiffness, cases of loading and fiber orientation emerge in which the principal stretch direction and principal stress direction do not coincide. Future work will include a more complex range of loading and geometric cases, which will further elucidate the effect of a stress-based reorientation law. Ultimately, this work confirms the potential for the incorporation of a stress-based law into a LV model to more fully represent the structural state of the HCM heart, and to explore the mechanism behind the development of myofiber disarray.

ACKNOWLEDGEMENTS

This study was supported by grants from the National Institutes of Health (U01HL133359 and S10RR029541)

REFERENCES

[1] Tseng et al., *JMRI*, 23:1-8, 2006.
[2] Kroon et al., *Med Image Anal,* 13:346-353, 2009.
[3] Guccione et al., *J Biomech Eng*, 113:42-55, 1991.

SB^{3}C2021
Summer Biomechanics, Bioengineering and Biotransport Conference
June 14–18, Virtual

ASSESSING THE HEMODYNAMIC INFLUENCE OF PULSE FLOW MODULATION FOR LEFT VENTRICULAR ASSIST DEVICES

Akshita Sahni[1], Jay Pal[2], Debanjan Mukherjee[1]

[1]Department of Mechanical Engineering
University of Colorado Boulder
Boulder, CO, USA

[2]Division of Cardiothoracic Surgery
University of Colorado Anschutz Medical Campus
Aurora, CO, USA

INTRODUCTION

Advanced Heart Failure (HF) affects more than 6 million people over the age of 20 within the United States [1], where the patient's heart is unable to pump blood to support normal circulation. Left Ventricle Assist Device (LVAD) provides mechanical circulation support in HF patients by shunting blood from dysfunctional left ventricle using a pump directly into the aorta. LVADs have emerged as the primary treatment modality for HF - as a *bridge to transplant* when donor heart is not available and also as a *destination therapy* when a patient is ineligible for heart transplantation due to other medical conditions [2]. LVAD therapy is frequently associated with serious complications such as stroke and thrombo-embolic events, gastrointestinal bleeding, and aortic insufficiency. These complications are reckoned to be intimately related to the altered state of hemodynamics as the LVAD bypasses flow into the aorta. Several existing studies have looked into LVAD outflow graft anastomosis as a key determinant for hemodynamic status [3]. However, with continuous flow LVAD designs, the lack of flow pulsation, the physiological benefits of pulsation, and pulse-modulation of LVAD flow could be key hemodynamic drivers [4] which have received lesser attention [5]. Here, we study flow in the aortic arch and abdominal aorta as function of pulsatile LVAD flow modulation, with the aim of elucidating the role of pulsation in LVAD flows.

METHODS

Hemodynamics simulation: A patient-specific model of the aorta from the aortic valve outlet to the ilio-femoral branches was obtained from approved patient CT images [6, 7]. A model LVAD outflow graft (diameter: 1.0 cm) was virtually attached to the ascending aorta at an incident angle 45° towards the aortic valve. Blood was assumed to be a Newtonian fluid with density 1.06 g/cm^3 and dynamic viscosity 0.04 $g/(cm \cdot s^2)$. The incompressible Newtonian fluid mass and momentum balance equations were numerically solved using a stabilized finite element method implemented in SimVascular [7]. Baseline flow simulations without an implanted LVAD were driven by a pulsatile flow imposed at the aortic inlet with a Womersley-type profile. Corresponding LVAD flow simulations imposed a specified profile at the outflow graft inlet, keeping the aortic inlet sealed. All remaining outflow boundary conditions were specified as three-element Windkessel conditions, with resistance and capacitances held the same between baseline and LVAD flow computations. Three LVAD inflow profiles with successively increasing extent of pulse modulation were chosen for this study [8] (see Fig: 1). All flow profiles have a mean of 5.0 L/min equivalent to the normal cardiac output for the baseline model.

Flow descriptor quantification: Based on the resultant flow velocity field, the extent of helical flow was quantified using Local Normalized Helicity (LNH), described as a scaled version (ranging between -1 and $+1$) of the pointwise flow helicity value as follows:

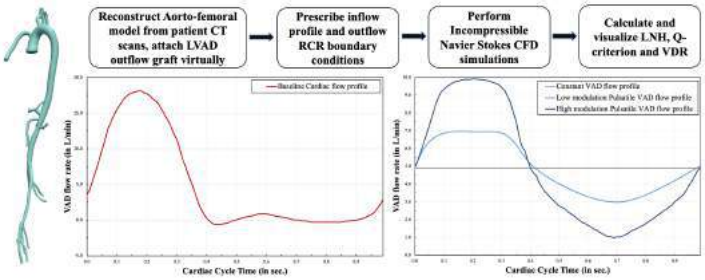

Figure 1: Hemodynamics modelling workflow (top); Baseline(natural) flow profile and LVAD flow profiles used in simulation (bottom); Virtual Aorto-femoral Model with LVAD outflow graft towards aortic valve (left corner).

$$LNH = \frac{\boldsymbol{u} \cdot (\nabla \times \boldsymbol{u})}{\| \boldsymbol{u} \| \| \nabla \times \boldsymbol{u} \|} \tag{1}$$

In addition, the extent of vortex generation in the flow was quantified using isosurfaces of the Q-criterion to identify vortical structures in the flow.

Estimation of viscous dissipation: Viscous dissipation rate is estimated using the localized fluid energy balance equation stated as follows:

$$\rho \frac{De}{Dt} = \underbrace{\boldsymbol{\tau} : \boldsymbol{\nabla u}}_{\text{Stress power}} + \underbrace{\boldsymbol{\nabla} \cdot \boldsymbol{q}}_{\text{Surface heat flux}} + \underbrace{\rho \phi_h}_{\text{Heat sources/sinks}} \tag{2}$$

The stress power term above incorporates contribution from all internal mechanical forces, and is the basis for estimating viscous dissipation. The stress power for a Newtonian constitutive relation can be written as a combination of volumetric deformation and viscous contributions - where the former is zero for incompressible flows, and the latter yields the viscous dissipation rate (VDR) as stated below:

$$\tau_{ij} \frac{\partial u_i}{\partial x_j} = \tau_{ij} \epsilon_{ij} = \underbrace{-p \boldsymbol{\nabla} \cdot \boldsymbol{u}}_{\text{volume deformation}} + \underbrace{2\mu \epsilon_{ij} \epsilon_{ij} - \frac{2}{3} \mu (\boldsymbol{\nabla} \cdot \boldsymbol{u})^2}_{\text{viscous effects}} \tag{3}$$

$$\boldsymbol{\nabla} \cdot \boldsymbol{u} = 0 \Rightarrow \tau_{ij} \epsilon_{ij} = VDR = 2\mu \epsilon_{ij} \epsilon_{ij} \tag{4}$$

where μ is the dynamic viscosity of blood, and ϵ_{ij} are the components of the rate of strain tensor: $\boldsymbol{\epsilon} = 0.5 \left(\nabla \boldsymbol{u} + \nabla \boldsymbol{u}^T \right)$. For this study, we computed the pointwise VDR estimate, as well as computed a volume integrated VDR for the aortic arch and branching vessels; and the abdominal aorta and branching vessels.

RESULTS

Influence of pulsation on flow features: In Figure 2 panel a, isosurfaces at ± 0.20 of LNH values averaged over one cardiac cycle are shown for *constant*, *low-pulsation*, and *high-pulsation* cases. Panel b presents the instantaneous LNH isosurfaces at ± 0.80, taken at $t = 0.18\ sec$ (peak systole) respectively. These are compared against the corresponding baseline values, and we observed that pulse-modulation retains a helical flow in the aortic arch but the spatial variation of helical flow patterns show differences with increasing pulsation. This is a consequence of the impingement of the jet flow emanating from the LVAD outflow graft onto the aorta wall. This is further illustrated via the Q-criterion isosurfaces in the aortic arch at peak systole shown in Figure 2 panel c. The Q-criterion values are normalized by the peak Q-value for the baseline case. The illustration clearly shows a significant increase in the extent of vortical structures with pulse-modulation, as the increased pulsation with fixed mean flow leads to a faster LVAD jet impinging on the wall. Further, reduced vorticity near aortic inlet in constant and low-pulsation cases indicate presence of a region of flow stasis, which was observed to reduce with increase in pulsatility.

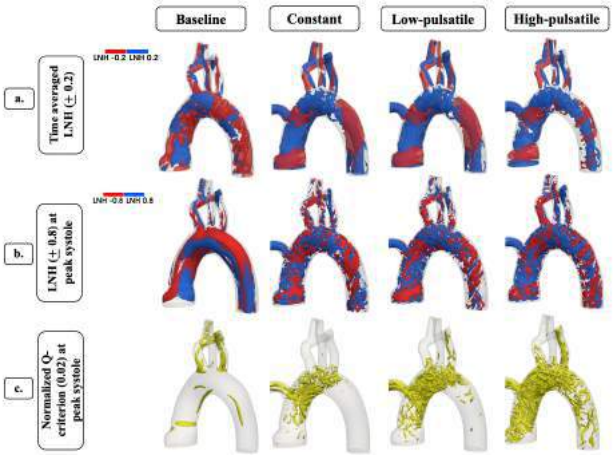

Figure 2: Time averaged LNH isosurfaces at ± 0.2(a); Peak systole LNH isosurfaces at ± 0.8(b); Normalized systole Q-criterion isosurfaces at 0.02(c).

Influence of pulsation on energy dissipation: Volumetric visualization of VDR iso-surfaces in the range 2×10^4 to 10^5 $g/(cm \cdot s^3)$ for varying extent of pulse-modulation are presented for the aortic arch in Figure 3, panel a. Panel b represents similar VDR iso-surfaces viewed for the abdominal aorta (until immediately after the renal arteries). For each of these vascular regions, the corresponding VDR isosurfaces for the baseline case are also provided for comparison. Volume integrated values of the time-averaged VDR for the entire aortic arch region, and the abdominal region (including the branching vessels) are provided in Figure 3 panel c. These results indicate that all LVAD induced flows have significantly higher dissipation in the aortic arch, and significantly lower dissipation in the abdominal aorta region, as compared to the baseline case. It is also observed that viscous dissipation increases with an increase in pulsation of LVAD flow, with the changes in dissipation in the aortic arch being more pronounced. This can be also attributed to the jet impingement from the LVAD outflow graft, where higher pulsation increases the extent of dissipative vortical structures in the aortic arch which contribute to the net viscous dissipation. This aspect is further illustrated in Figure 4, where time-averaged VDR values normalized with those for the baseline case, are plotted along the centerline of the aortic arch (panel a) and the abdominal aorta (panel b) for *constant*, *low-pulsation*, and *high-pulsation* cases. We observe that within the ascending aorta and aortic arch region, the VDR values peak in the LVAD jet impingement zone, with the maximum values being around 1000 times higher than corresponding baseline case. At locations away from the impingement zone, the VDR values become comparable to those of the baseline case - including in the abdominal aorta (deviating within a factor of $0.1 - 10.0$ of the baseline VDR values). Data in Figure 4 also support the observation that, generally, increased pulsation increases the extent of dissipation.

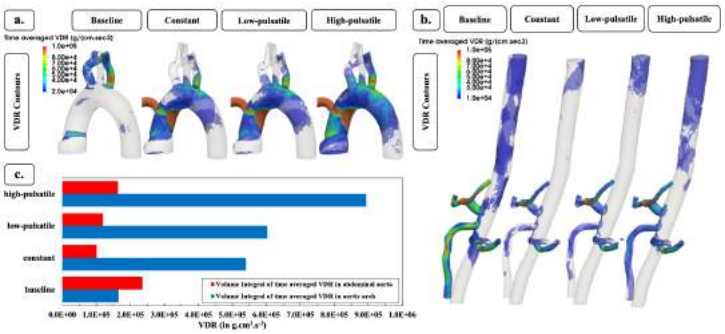

Figure 3: Isosurfaces of Viscous Dissipation Rate(VDR) in the Aortic arch(a) and Abdominal Aorta(b); Comparison of Volume integrated values of time averaged VDR for aortic arch and abdominal aorta(c).

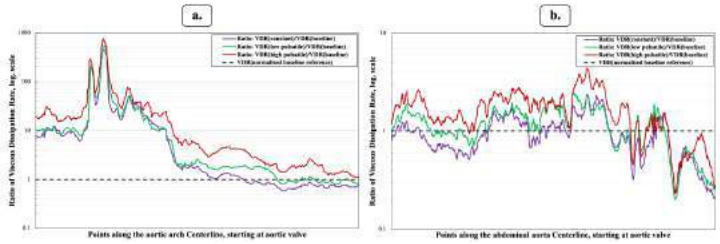

Figure 4: Plot of Time averaged Viscous Dissipation Rate(VDR) along the center-line of Aortic Arch(a); Abdominal Aorta(b).

DISCUSSION

Data obtained from our study indicate a multi-faceted role that pulse-modulation of LVAD flow can play. Hemodynamically, pulsation influences helical flow and vortex generation, which in turn are intimately connected to mixing, flow stasis, and thrombogenic potential. Simultaneously, pulsation influences energy dissipation, which can further influence LVAD pump operational efficiency, and associated complications in HF patients. Specifically, for each oscillatory frequency component of the pulse, it can be shown that in a cycle-averaged sense the energy expenditure to drive the flow is solely due to viscous dissipation [9]. Additionally, our observations highlight the flow physics significance of the impingement of LVAD jet flow onto the aorta wall. This unsteady jet impingement is the defining feature of the altered state of hemodynamics in LVAD patients, even in the presence of pulse-modulation. We note that, while the impingement and subsequent vortex generation can affect mixing (and thereby thrombogenicity) and energy dissipation (and thereby flow efficiency); arbitrarily raising the outflow graft angle towards the arch to negate the impingement is not advisable due to increased stroke risks as the flow gets directed towards the cervical vessels. This motivates our ongoing investigations on comprehensive characterization of hemodynamics and stroke risks in patients with LVAD, towards obtaining optimal guidelines for LVAD surgical therapy for HF - specifically with regards to optimizing the LVAD outflow graft surgical anastomosis.

ACKNOWLEDGMENTS

This research was supported by a University of Colorado Anchutz-Boulder (AB) Nexus Research Collaboration grant. This work utilized resources from the CU Boulder Research Computing Group, which is supported by NSF (awards ACI-1532235 and ACI-1532236), CU Boulder, and Colorado State University.

REFERENCES

[1] Virani, S.S. et al., *Circulation*, 141(9):e139-e596,2020.
[2] Stevenson , L. W. et al., *Circulation*, 108(4):492-497,2003.
[3] Prisco, A. R. et al., *ASAIO Jour*, 63(4):392–400,2017.
[4] Purohit , S. N. et al., *Circ-Heart Fail*, 11(6):e004670,2018.
[5] Zhang, P.H. et al., *Curr Cardiol Rep*, 20(10):1-7,2018.
[6] OSMSC Model Repository. *www.vascularmodel.com*. 2020.
[7] Simvascular. *http://simvascular.github.io/*. 2020.
[8] Ising M. et al., *Cardiovasc Eng Techn*, 2(2):90,2011.
[9] Zamir, M. et al., *Appl Mech Rev*, 55(2):B35-B35,2002.

SIGNIFICANCE OF GAGS IN UNCONFINED COMPRESSION RESPONSE OF POSTERIOR PORCINE SCLERA

Anshul Bhardwaj and Hamed Hatami-Marbini

Department of Mechanical and Industrial Engineering
University of Illinois at Chicago
Chicago, Illinois, USA Email. hatami@uic.edu

INTRODUCTION

The sclera is the enveloping soft tissue layer that forms the outer shell of the eyeball and is continuous with the cornea. The sclera resists against stresses caused by the intraocular pressure (IOP), maintains the shape of an eyeball, and protects the eye from the external trauma such as laceration and rupture. The alternation in the normal mechanical properties of the posterior sclera could lead to Glaucoma, the second leading cause of irreversible blindness worldwide affecting 60 million people [1,2]. Thus, it is important to fully understand the mechanical response of the posterior sclera and investigate how it is related to the microstructure and mechanical properties of its constituents.

The mechanical properties of the sclera originate from its extracellular matrix, which is primarily composed of collagen fibrils, proteoglycans (PGs), and elastin [3]. Various researchers have contributed and demystified the mechanical properties of sclera using uniaxial tensile, inflation, and biaxial tensile testing methods among others [1,3,4,5]. However, only a few researchers have conducted compression studies on the posterior porcine sclera. In the present work, we investigated the compressive mechanical response of scleral tissue and determined the possible structural roles of sulfated glycosaminoglycans (GAGs). GAGs are composed of repeating negatively charged disaccharide units. We have recently shown that they play an important role in tensile mechanical properties of the sclera [3]. In these studies, we compared the tensile response of sclera after and before digesting the GAGs using the chondroitinase ABC enzyme. This paper discusses our recent study on the mechanical response of posterior porcine sclera under unconfined compression (UCC) in order to determine the structural roles of GAGs in compressive response of posterior sclera.

METHODS

The porcine eyeballs were obtained and transported from the local butcher shop to the UIC CBRL laboratory within 4 to 6 hours of post-mortem at a regulated temperature of 4˚C. The specimens were carefully operated and dissected with the help of scalpels and micro-dissecting scissors from the surrounding extraocular muscles to obtain eyeballs. A trephine biopsy punch was used to dissect an 8mm disc from the superior temporal (ST) section of the sclera as shown in Figure 1.

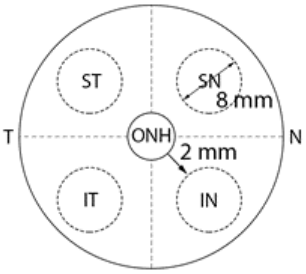

Figure 1. Sclera tissue's region-based nomenclature (right-eye). The samples were obtained from ST section.

Three groups were considered, Table 1. a) control group: here the samples were incubated in PBS solution Then samples were placed in the PBS bath for 3 hours prior to the mechanical experiments, b) buffer group: the samples were placed in the buffer solution composed of 50mM Trizma Base, 60 mM Sodium Acetate, and bovine serum albumin at pH 8 for 18 hours prior to mechanical tests, and c) enzyme group: the samples were placed in the buffer solution which includes the 0.125 U/ml ChondroitinaseABC for 18 hours. Alcian Blue staining

with a pH of 1.0 was employed to validate the successful removal of the sulfated GAGs. The thickness and weight of all sample were recorded after the incubation period, as shown in Table 1, and before subjecting to unconfined compression.

Table 1. different groups considered in the present work

Group name	Treatment	Incubation Period
Control	Phosphate Buffered Saline	3 hours
Buffer	Triz and Sodium Acetate Buffer	18 hours
Enzyme	ChABC in Buffer	18 hours

The mechanical tests were done by a RSA-G2 rheology equipment (TA instruments) using the protocol that we have previously used to test corneal samples [6,7]. After determining the initial thickness of the disks, the upper head of the machine was displaced such that the tissue was compressed by 5%. Then, the samples were allowed to relax until the compressive stress reached equilibrium. The above procedure was repeated five times until the total compressive strain reached 25%. The data acquisition was enabled for every half a second for compressive axial reaction force. The stress was found from dividing the compressive force by the initial cross-sectional area of the samples, and the stress-time behavior of the samples was plotted. The stress at the end of each ramp period was referred to as the peak stress and the stress at the end of each relaxation period was denoted by the equilibrium stress.

RESULTS

No significant difference was observed in the thickness of samples from the different control groups following their incubation in their respective solution and prior to the mechanical experiments. Figure 2 shows a typical mechanical response of samples in the present study. It is seen that the stress increased during the ramp period and then relaxed to an equilibrium stress during the relaxation period.

Figure 3 shows the variation of the peak stress as a function of applied compressive strain in different groups. It is seen that although the samples in the buffer and control groups had an almost similar response, there was a significant reduction in the peak compressive stress of the scleral samples from the enzyme group.

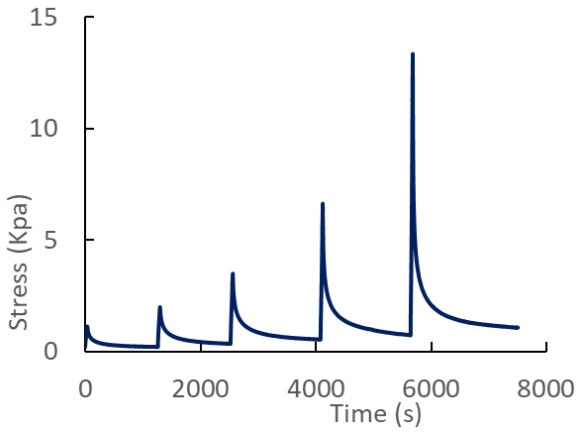

Figure 2. The compressive stress variation as a function of time during successive unconfined compression experiments on a typical sclera samples.

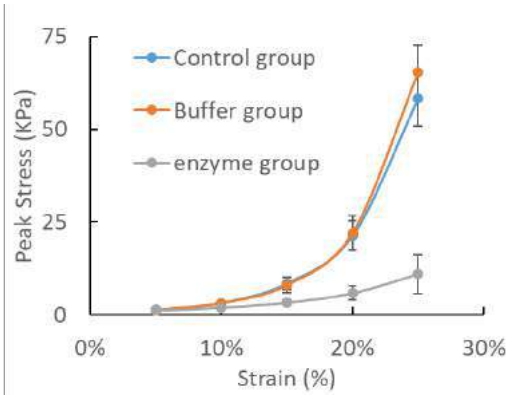

Figure 3. The effect of GAGs on the maximum compressive stress-strain behavior of the posterior sclera.

DISCUSSION

The objective of the study was to investigate the role of GAGs on the compressive mechanical response of posterior sclera. To this end, we removed GAGs from the scleral disks obtained from the posterior porcine sclera. We then conducted unconfined compression experiments to compare the mechanical response of samples with and without GAGs. It was found that GAGs had a significant effect on the compressive properties of the sclera. This is because GAGs are negatively charged and their presence in the soft tissues, including the sclera, induces a tendency for the tissue to absorb water when immersed in the tissue [6,7]. The presence of the water and its interaction with GAGs are important in defining the mechanical response in compression. With removal of the GAGs (a complete removal was not achievable, we observed a reduction of about 90%), water still will be absorbed inside the tissue (we saw an insignificant difference in the thickness of samples in all groups). However, this water was removed easily from these samples because the pore size inside the tissue was larger (because the GAG density was significantly reduced).

ACKNOWLEDGEMENTS

The authors would like to acknowledge the support in part by NIH R21 EY030264

REFERENCES

[1] Mortazavi, A. M., Simon, B. R., Stamer, W. D. & Vande Geest, J. P. Drained secant modulus for human and porcine peripapillary sclera using unconfined compression testing. Exp. Eye Res. 89, 892–897 (2009).

[2] Quigley, H. & Broman, A. T. The number of people with glaucoma worldwide in 2010 and 2020. Br. J. Ophthalmol. 90, 262–267 (2006).

[3] Hatami-Marbini, H. & Pachenari, M. The contribution of sGAGs to stress-controlled tensile response of posterior porcine sclera. PLoS One 15, 1–16 (2020).

[4] Wang, B., Hua, Y., Brazile, B. L., Yang, B. & Sigal, I. A. Collagen fiber interweaving is central to sclera stiffness. Acta Biomater. 113, 429–437 (2020).

[5] Murienne, B., Quigley, H. & Nguyen, T. The role of glycosaminoglycans in the mechanical behavior of the posterior sclera. Invest. Ophthalmol. Vis. Sci. 54, 52 (2013).

[6] Hatami-Marbini, H. & Etebu, E. Hydration dependent biomechanical properties of the corneal stroma. Exp Eye Res 116, 47–54 (2013).

[7] Hatami-Marbini, H. & Etebu, E. An experimental and theoretical analysis of unconfined compression of corneal stroma. J Biomech 46, 1752–1758 (2013).

DEVELOPMENT OF A 3D *IN VITRO* VASCULARIZED HUMAN SKIN EQUIVALENT UTILIZING COLLAGEN/KERATEINE HYDROGELS

K. Zuniga (1), N. Ghousifam (2), M. Van Dyke (3), M.N. Rylander (1,2)

(1) Department of Biomedical Engineering
The University of Texas at Austin
Austin, TX, United States

(2) Department of Mechanical Engineering
The University of Texas at Austin
Austin, TX, United States

(3) College of Biomedical Engineering
The University of Arizona
Tucson, AZ, United States

INTRODUCTION

Human skin is a complex tissue, consisting of multiple layers, vascular networks, and cell types to create a barrier against environmental factors. As the largest organ in the body, skin covers $2m^2$ for the average human and makes up about 15% of total adult body weight [1]. Therefore, many studies have been conducted to develop the most effective and representative model for human skin to study skin diseases and wound inflammation and develop regenerative therapies for skin wounds.

Existing skin models employ animal models, ex vivo models of human tissue, two-dimensional (2D) cell monolayers, or simple three-dimensional (3D) skin platforms lacking vasculature and immune components typically composed of only a single layer or without the addition of any 3D ECM. Without robust biomimetic in vitro testing platforms, a number of false-positive therapeutics are being studied in vivo. Although pig models provide the most complete and physiologic microenvironment for studying burn injury and testing therapeutics, the dynamics and spatial kinetics of burn injury cannot be easily studied without significant time and expense. We have created a first-of-its-kind vascularized human skin equivalent (VHSE) platform, consisting of an epidermis with differentiated keratinocytes cultured on top of collagen type I mixed with equal weight of dry keratin powder. This unique collagen/keratin (C/KTN) composition of our epidermis was used to better mimic the ECM of the native epidermis, which is made of approximately 80-90% keratin. Below the epidermis resides the vascularized dermis composed of normal human dermal fibroblasts (NHDFs) cultured in 100% collagen type I, the main type of ECM protein found in the native human dermis. The major innovation of the VHSE is the presence of an aligned, endothelialized fully functional vessel, enabling perfusion of media/blood, immune cells, therapeutics, and growth factors.

METHODS

To initially determine whether KTN itself increased keratinocyte differentiation, 100% collagen, 50/50 C/KTN (w%/w%), and 30/70 C/KTN hydrogels were prepared Ker-CT (TERT-immortalized keratinocytes) were seeded on to the hydrogels and cultured with calcium-free media and once 80% confluent, was cultured with the same media or switched to an increased calcium concentration differentiation media to increase differentiation (Figure 1A). Lysosomal activity, an indication of keratinocyte differentiation [2], was measured by the glucocerebrosidase (GBA) activity at 12, 24 and 48 hours post-media change. Samples were also fixed at day 4 and 10 post-media change and stained for caspase 14, a keratinocyte differentiation marker.

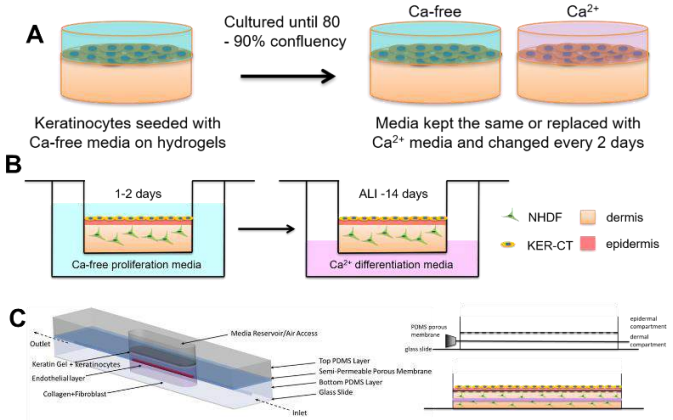

Figure 1: Schematics of 2D keratintocyte model (A), organotypic transwell skin model (B), and vascularized human skin equivalent model (C).

Organotypic skin platforms were prepared using a transwell system to further determine the effect of increased KTN on differentiation (B). The dermis was composed of fibroblast (NHDF)-seeded collagen and the epidermal layer was composed of either pure collagen or the C/KTN blend seeded on top if Ker-CT cells. Transwells were lifted to the air-liquid interface (ALI) and cultured in Ca^{2+} media for 14-21 days until they were fixed for staining of diffentiation markers, used for transepithelial electrical resistance (TEER) measurements, or for permeability assays employing 70 kDa dextran.

The VHSE housed within a PDMS was fabricated by inserting a 22 G needle through the dermal layer to create a 700 µm diameter microchannel vessel and removed after polymerization (Figure 1C). The platform was cultured in Ca^{2+} differentiation media on a rocker at the ALI to allow differentiation for 2 weeks. The vessel was injected with telomerase-immortalized microvascular endothelial (TIME) cells and cultured for 3 days on a rocker with endothelial media. The VHSE was stained for CD90 (NHDFs) and CK14 (keratinocytes).

RESULTS

As shown in Figure 2A, the increase in KTN increased the GBA/lysosomal activity of keratinocytes in both calcium-free and Ca^{2+} (differentiation) media when compared to pure 100% collagen hydrogels. This indicates that there is an increase in differentiation with increase in KTN concentration of the hydrogel. In addition, keratinocytes showed higher expression of caspase 14, both with and without the presence of calcium. (Figure 2B). Keratinocytes were able to differentiate on their own with calcium-free media, with even higher expression of caspase 14 when calcium+ media was used.

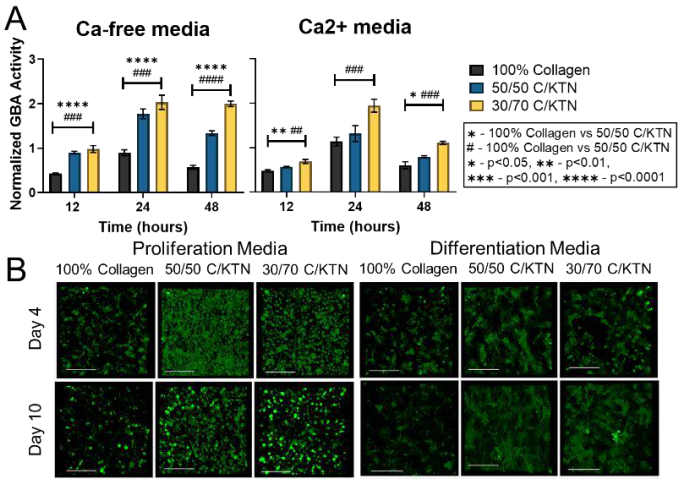

Figure 2: 2D hydrogel studies analyzing GBA activity (A) and caspase 14 expression (B) of keratinocytes. Scale bar = 200 µm.

Transwell studies were conducted to analyze the permeability of the stratum corneum layer of differentiated keratinocytes. As shown in Figure 3A, no significant differences in permeability between pure collagen and C/KTN hydrogels after 2 weeks of differentiation were observed. Significantly lower permeability was observed between NHDF-only hydrogels and 50/50 C/KTN hydrogels after 2 weeks of differentiation. Significant decrease in permeability between weeks 2 and 3 were only observed with 30/70 C/KTN hydrogels. TEER measurements demonstrated there was significant increase in resistance with 50/50 C/KTN hydrogels when compared to 100% collagen hydrogels (Figure 3B). CK14 (proliferation marker) and involucrin (differentiation marker) was also expressed in all samples with similar expression to 100% collagen (Figure 3C). H&E staining showed a well-stratified stratum corneum layer after 2 weeks of differentiation. C/KTN hydrogels showed similar stratification to 100% collagen (Figure 3C).

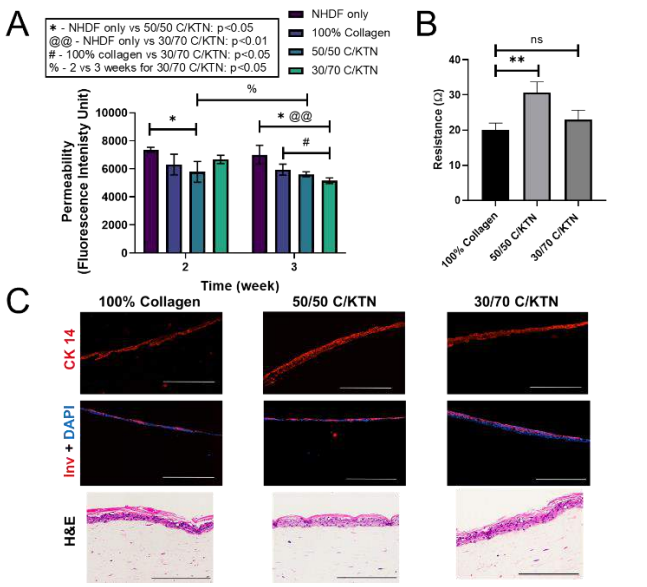

Figure 3: Skin barrier function was analyzed by measuring permeability of 70 kDa dextran perfused through the skin barrier (A) and resistance (B). Expression of CK14 and involucrin with a well-developed stratum corneum (C). Scale bar = 100 µm.

We were also able to develop a functional vessel within our skin platform. By placing the platform on a rocker, a confluent lumen of endothelial cells was created to form a functional vessel surrounded by dermal fibroblasts (Figure 4). 2 distinct layers of the dermis and epidermis was developed with the vessel in the dermal layer and keratinocytes in the epidermal layer.

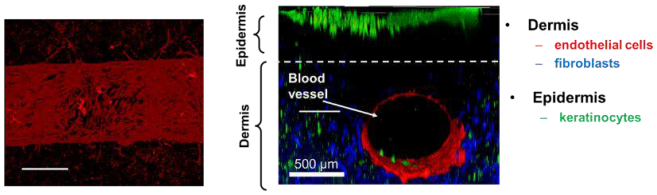

Figure 4: VHSE platform with a fully developed vessel (left) and distinct layers of the dermis and epidermis (right).

DISCUSSION

In this study, we demonstrated that keratin promoted the differentiation of keratinocytes with increased GBA activity and increased caspase 14 expression when seeded on top of C/KTN hydrogels. The addition of keratin serving as the epidermal layer led to a trend of decreasing permeability, indicating that keratin promotes increased barrier function with a stratified stratum corneum similar to that of 100% collagen. Creation of a vascularized skin model better recapitulates in vivo skin with a functional vessel.

By providing an affordable high-throughput VHSE system which can be used to down-select therapeutics before in vivo testing with the presence of a vessel, the use of the VHSE will reduce the time and cost of product development. Developing and testing therapeutic strategies in the VHSE will significantly decrease the product translation time of drugs and therapeutics for skin.

ACKNOWLEDGEMENTS

This work was made possible due to generous funding from Battelle Institute Grant US001-0000544452 and the Oak Ridge Institute for Science and Education (ORISE).

REFERENCES

[1] McGrath, JA et al, *Rook's Textb. Deramatology*, 8:1- 53, 2010. [2] Mahanty, S et al, *Cell Death*, 10:1-17, 2019.

MICROENVIRONMENTAL DETERMINANTS OF ORGANIZED STEM CELL DERIVED CARDIOMYCOYTE TISSUES ON SYNTHETIC FIBROUS MATRICES

Samuel J. DePalma[1], Christopher D. Davidson,[1] Austin E. Stis[1], Adam S. Helms[2], Brendon M. Baker[1]

(1) Department of Biomedical Engineering
University of Michigan
Ann Arbor, MI, USA

(2) Division of Cardiology
University of Michigan
Ann Arbor, MI, USA

INTRODUCTION

The mechanical function of the myocardium is in part defined by a highly organized network of fibrous extracellular matrix (ECM) proteins that surround cardiomyocytes (CMs) and facilitate anisotropic contraction of the tissue [1]. The importance of this structure-function relationship is particularly evident in disease states such as fibrosis, where fibroblasts deposit excessive amounts of disorganized matrix in the perimysial space and impair tissue function [2]. Because of the critical role that microenvironmental cues play in driving proper tissue organization and function, a number of material platforms have been developed to recapitulate these cell-instructive cues to drive structural and functional maturation of engineered induced pluripotent stem cell (iPSC) derived cardiac tissue [3-5]. Despite the success of these and other culture platforms in improving iPSC-CM tissue function, each of these approaches only mimics certain aspects of the cardiac ECM. As such, a comprehensive, multiparameter understanding of the physical environmental cues necessary to form high-functioning CM tissues is currently lacking. Thus, new biomaterial approaches are needed that can accurately and orthogonally recapitulate fibrous, biochemical, and mechanical attributes of the cardiac ECM to promote cardiac tissue assembly. Previously, our lab developed a cell-adhesive, mechanically tunable synthetic fibrous ECM consisting of electrospun dextran vinyl sulfone (DVS) fiber matrices that support long term cell culture [6]. Here, we employ this platform to create a robust culture system for iPSC-CMs and examine how architectural and mechanical properties of the ECM impact cardiac tissue assembly and function [7].

METHODS

Substrate Fabrication: DVS dissolved at 0.7 g/ml in 1:1 milli-Q water and dimethylformamide with 0.6% w/v lithium phenyl-2,4,6-trimethylbenzoyl phosphinate (LAP), 2.5% v/v 25 mM methacrylated rhodamine, and 5.0% v/v glycidyl methacrylate was electrospun on coverslips affixed to a rotating mandrel, stabilized by UV crosslinking (20 s at 100 mW/cm^2), hydrated in LAP photoinitiator solution, and UV crosslinked again. Heparin methacrylate was covalently attached during photocrosslinking and fibronectin (FN) (100 µg/ml) was then adsorbed to fibers at RT for 1 h. CM Differentiation: Induced pluripotent stem cells containing a GFP-titin reporter or a connexin43 (Cxn43) reporter (Allen Institute) were expanded in mTeSR1 media and differentiated in RPMI 1640 with B27 lacking insulin. Differentiation was initiated on d0 with 12 µM CHIR99021 for 24 h and then 5 µM IWP4 on d3 for 48 h. On d9, insulin was introduced. CMs were purified by culturing in RPMI lacking glucose and glutamine supplemented with 4 mM DL-lactate on d11-15. CMs were seeded on substrates on d30. Staining and Microscopy: Calcium handling analysis was performed by incubating cells for 1 h with 5 uM Cal520, AM and imaging cells at 37 °C and 5% CO_2. For immunostaining, samples were fixed, permeabilized, blocked in 2% BSA, incubated for 1 h at RT with anti-vinculin antibody (1:1000; Sigma), and counterstained with Alex Fluor 647 (1:1000; Sigma) and DAPI. Sarcomeres were visualized by GFP-titin. All calcium imaging and staining was conducted on d7 after seeding. Data analysis: Sarcomere alignment, calcium tracings, and focal adhesion data were analyzed using custom MATLAB scripts. Statistics: Statistical significance was determined by one-way ANOVA with Tukey's post-hoc analysis or Student's t-test where appropriate, with significance indicated by $*p < 0.05$. All data presented as mean $\pm$ std.

RESULTS

We first modulated matrix alignment by altering the speed of the rotating collection mandrel (**Fig. 1a,b**). With alignment of matrix fibers, sarcomere alignment increased and calcium flux rise time and decay time decreased, suggesting more functional subcellular calcium

handling machinery (**Fig. 1c,d**). Next, we altered matrix stiffness by controlling LAP photoinitiator concentration during the crosslinking of aligned matrices (**Fig. 1e**). While sarcomeres remained highly aligned on matrices of all stiffness conditions, calcium flux decay time and peak-to-peak irregularity increased on stiffer matrices, suggesting decreased function at supraphysiologic stiffnesses (**Fig. 1f,g**).

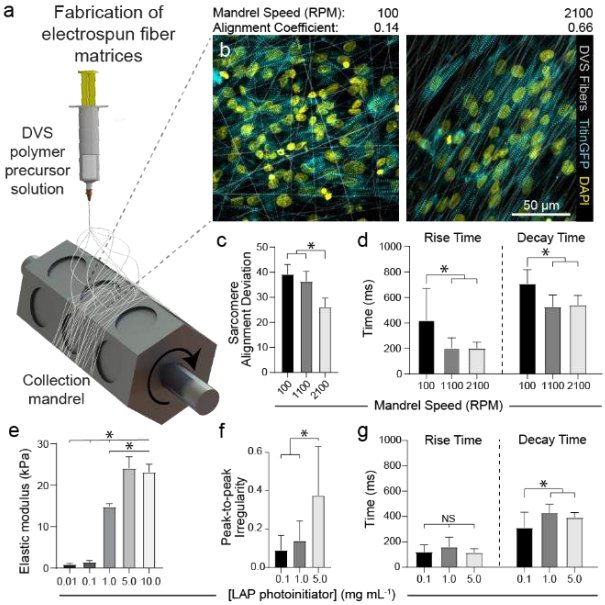

Fig. 1: a) Electrospinning setup for fabrication DVS matrices. b) CMs cultured on DVS aligned/non-aligned DVS matrices. c) Sarcomere alignment and d) calcium dynamics of CMs on matrices of varied alignment. e) Elastic modulus of DVS matrices. f-g) Calcium flux dynamics of CMs on matrices of varied stiffness. n ≥ 12 fields.

Because changes in matrix architecture and mechanics have been noted in numerous disease states, we next took advantage of the tunability of DVS matrices to examine how matrix alignment and mechanics affect CM tissue formation. Given the role of cell-matrix adhesions in CM mechanotransduction and function, we immunostained for the focal adhesion (FA) protein vinculin and found that both alignment and stiffness of matrix fibers influenced adhesion morphometrics (**Fig. 2a-d**). CMs on aligned/soft matrices had the most adhesions with higher aspect ratios, in contrast to cells on stiff/aligned matrices (**Fig. 2b**).

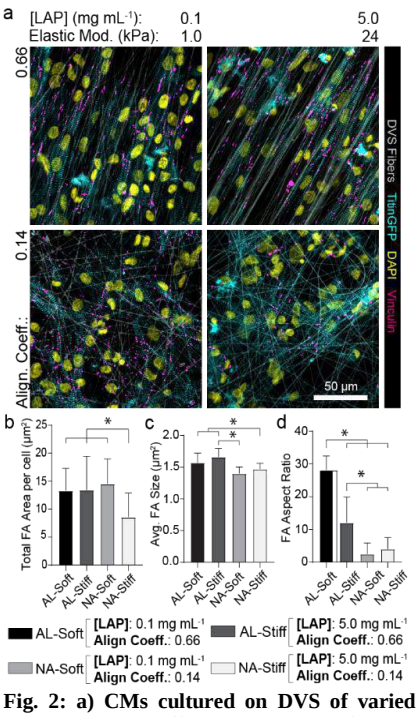

Fig. 2: a) CMs cultured on DVS of varied alignment and stiffness. b-d) Quantification of FA formation in CM tissues. n ≥ 18.

Lastly, we found that DVS matrices afford greater stability of iPSC-CM tissues over long-term culture as compared to other commonly used culture platforms including microcontact FN lines and FN coated glass, where CMs detach after ~10 days [7]. As it has previously been indicated that extended culture of non-confluent iPSC-CMs facilitates further structural organization [8], we examined Cxn43 expression of iPSC-CMs on aligned DVS matrices over time and observed a marked increase in expression after 7 days in culture as compared to FN-coated glass and non-aligned DVS (**Fig. 3a,b**). On day 14, Cxn43 expression increased further on both aligned and non-aligned matrices, with aligned matrices driving significantly more expression.

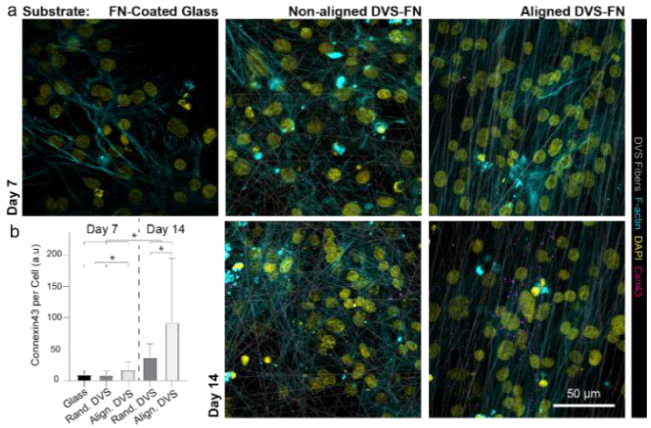

Fig. 3: a) CMs cultured on various substrates expressing Cxn43-GFP for 7 and 14 days. b) Quantification of Cxn43 expression. n ≥ 18.

DISCUSSION

In this work, we examined how matrix structural anisotropy and mechanics affect iPSC-CM tissue formation by generating CM tissue on tunable, synthetic fibrous DVS matrices. Our results indicate that iPSC-CMs sense and respond to architectural and nano-scale mechanical cues from the matrix as characterized by changes in sarcomere organization and calcium handling dynamics. By examining FAs, we found that matrix architecture and mechanics exert a synergistic effect on iPSC-CM tissue formation. It has been noted that cell-matrix adhesions drive myofibrillogenesis, further supporting the use of soft aligned matrices in creating functional CM tissues [9]. Additionally, iPSC-CMs cultured on soft, aligned DVS matrices for 14 days indicated higher levels of structural organization as evidenced by Cxn43 expression. As limitations in long-term culture on substrates that introduce physiologic anisotropic cues to drive significant maturation have been suggested [10], ongoing work is focused on taking advantage of the long-term stability of CMs on DVS to examine how metabolic factors can drive further tissue maturation. Additionally, this platform has great potential for studying how pathologic microenvironmental changes affect CM functionality.

ACKNOWLEDGEMENTS

This work was supported in part by the National Science Foundation (1647837) and the NIH (HL124322). S.J.D acknowledges financial support from NIDCR of the NIH under Award Number T32DE007057. C.D.D acknowledges funding from the Ruth L. Kirschstein National Research Service Award (F31HL152501).

REFERENCES

[1] Weber, KT *J Am Coll Cardiol*, 13:1637-1652, 1989. [2] Frangogiannis NG, *Circ Res* 110:159-173, 2012. [3] Ribeiro, AJS et al., *Proc Natl Acad Sci*, 112:12705-12710, 2015. [4] Allen, ACD et al., *J Tissue Eng*, 25:1426-1437, 2019. [5] Carson, D et al., *ACS Appl Mater Interfaces*, 8:21923-21932, 2016. [6] Davidson, CD et al., *Acta Biomater*, 105:78-86, 2020. [7] DePalma, SJ et al., *Biomater Sci*, 9:93-107, 2021. [8] Lundy, SD et al., *Stem Cells Dev*, 22:1991-2002, 2013. [9] Chopra, A et al. *Dev Cell*, 44:87-96, 2018. [10] Karbassi, E et al., *Nat Rev Cardiol*, 17:341-359, 2020.

A 3D MACROMOLECULAR MODELING FRAMEWORK FOR COLLAGEN FIBRIL MECHANICS AND PLASTICITY

Lauren M. Bersie-Larson (1), Paolo P. Provenzano (1), Victor H. Barocas (1)

(1) Department of Biomedical Engineering
University of Minnesota – Twin Cities
Minneapolis, MN, USA

INTRODUCTION

Collagen fibers are present in all tissues within the body and provide the main source of mechanical strength within the extracellular matrix [1]. Connected by chemical crosslinks and physical entanglements, collagen fibers form interconnected fibrous matrices that are in a constant state of flux, dynamically rearranging and remodeling in response to cellular forces [2].

The concept of plasticity has recently been invoked to describe collagen rearrangement (e.g., [3-5]). Although classically defined in terms of crystalline dislocations [SOURCE], plasticity in the collagen fiber network context refers to deformation that results in lasting changes_to network topology and/or inter-fibrillar connections upon unloading. Such plasticity in collagen networks has been widely observed in both developmental and pathological processes, but it remains poorly understood. Previous models of this behavior thus far have only been in 2D and simplify assumptions of these bonds.

To address the limitations of existing models, we used the Large-scale Atomic/Molecular Massively Parallel Simulator (LAMMPS), an open-source molecular dynamics software [6], to construct a collagen fiber network model that accounts for fiber-fiber bonding in 3D. LAMMPS has been used previously in studies of fiber network mechanics [7].

METHODS

Model Creation Networks were created in MATLAB as previously described [8]. Briefly, random seed points were generated in 3D, and a Voronoi diagram was constructed to create the fiber network with a volume fraction of approximately 2%. Fibers were discretized into segments 0.1 um long, and the resulting geometry was imported into LAMMPS; each fiber junction was modeled as an "atom," and each fiber was modeled as a "bond" (Figure 1).

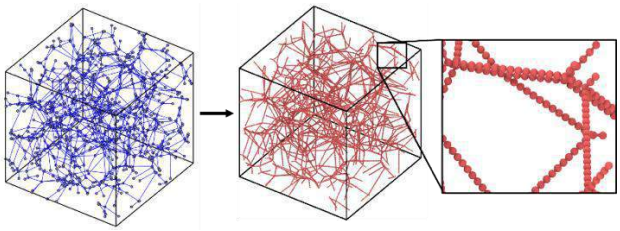

Figure 1. a) A Voronoi network created in MATLAB. b) The same network input into LAMMPS as bonds and atoms. c) A close-up of the atoms and bonds making up the fibers of the network.

Simulation Setup Atoms were modeled as point particles of unit mass, and harmonic bonds were used to model fibers as linear springs:

$$f = -K(r - r_0) \quad (1)$$

Where K is the spring stiffness (200 nN/μm), r is the current bond length, and r_0 is the equilibrium bond length (~ 0.1 μm). To model the new inter-fibrillar connections that drive plasticity, fibers were bonded together when within 0.1 to 0.25 microns of each other. New bonds were as in Eqn. (1), but with a spring stiffness of 400 nN.

Simulations were run using the *minimize* command in LAMMPS, utilizing a conjugate gradient solver with the *forcezero* style line search.

Uniaxial Tensile Loading To simulate uniaxial tensile loading of networks with and without plasticity, networks were stretched in the x-direction incrementally to a stretch of 150%, and then incrementally unloaded. Atoms on the x-faces were fixed in x but allowed to slide in-plane, while atoms on the transverse faces were left free. The resulting fiber orientation tensor in the direction of loading, Ω_{xx}, was measured for each load and unload step as follows:

$$\boldsymbol{\Omega}_{xx} = \frac{1}{l^{f,total}} \sum l^f n_x^f n_x^f \qquad (2)$$

where $l^{f,\,total}$ is total length of fibers, l^f is length of each fiber, and n_x^f is the x-component of a unit vector in the fiber direction. For a highly aligned network, Ω_{xx} goes to one; for an isotropic network, Ω_{xx} is 0.33.

Cell Contraction Cell contraction in a 3D collagen gel was simulated in both networks with and without plasticity. Two spherical particles representing cells were placed in the networks 1 micron apart, and contractile force was modeled using a cut-off Lennard-Jones potential:

$$f = -24\epsilon \left[\frac{2}{r}\left(\frac{\sigma}{r}\right)^{12} - \frac{1}{r}\left(\frac{\sigma}{r}\right)^{6}\right] \; for\; r < r_{cut} \qquad (3)$$

where f is the force exerted on an atom in a fiber, ϵ corresponds to the energy minimum of the pair potential ($1x10^{-1}$), σ the distance between two atoms where the energy minimum exists (2 μm), r is the distance between the cells and atoms in the fibers, and r_{cut} (3.5 μm) is the maximum distance over which two atoms can interact. Sigma was chosen to match the radius of the cells, such that the repulsive force term represented steric interactions of any fibers with the cell and prevented overlapping. After cell contraction, cell lysis was simulated by turning off the pair potential in Eqn. (3).

RESULTS

Uniaxial Tensile Loading Results from the uniaxial simulations are shown in Fig. 2. Network x-orientation, Ω_{xx}, is plotted against network stretch ratio for the loading and unloading portions of the test, for the same network without plasticity and with plasticity.

The network without plastic fiber interactions (Fig. 2a) reaches a maximum fiber orientation value of approximately 0.35, which is still close to isotropic, and follows the same path during unloading, resulting in no difference in fiber orientation once the test is complete.

When plastic fiber interactions are added (Fig. 2b), fiber orientation in the x-direction becomes more pronounced with stretch, and a slight hysteresis appears, with Ω_{xx} increased at the end of the simulation relative to the start.

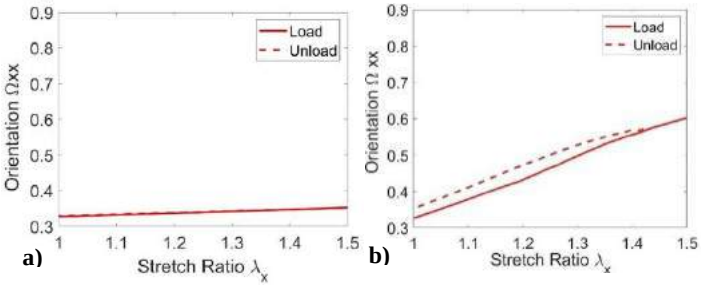

Figure 2: (a) Network orientation in the stretch direction (Ω_{xx}) for all load-unload steps of the uniaxial tensile test, without plasticity. (b) Network orientation in the stretch direction (Ω_{xx}) for all load-unload steps of the uniaxial tensile test, with plasticity.

Cell Contraction Figure 3 shows the results of the simulated cell contraction experiments. In Fig. 3a-c, the network (with no plastic fiber interactions) and cells are shown before and during contraction, and after simulated cell lysing. In this instance, no difference in the network architecture is observed before and after cell contraction.

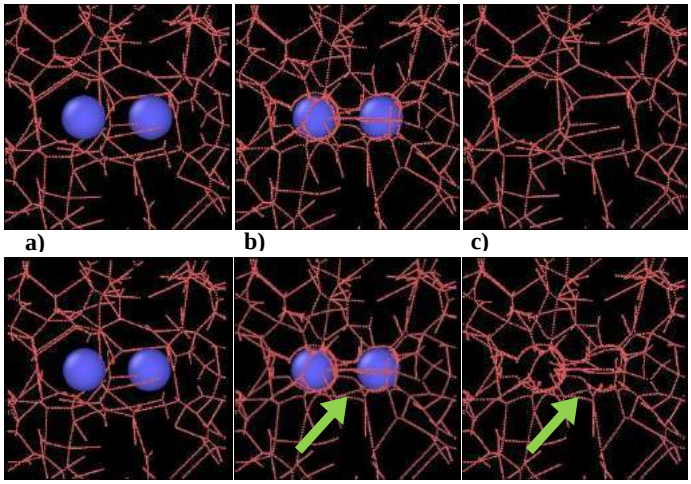

Figure 3: Cells in a network without plasticity a) before contraction, b) during contraction (middle), c) and after lysis; cells in a network with plasticity d) before contraction, e) during contraction, and f) after lysis. Densified fibers are marked by an arrow.

In contrast, in Fig. 3d-f, the fiber network does not return to its original state after cell contraction. After lysis, as shown in Fig. 3f panel, fibers have remained densified where the cells once were, and a cord of fibers has been created in between the two cells.

DISCUSSION

In this work, we present a modeling framework for simulating plasticity in 3D fiber networks. We simulated both uniaxial tensile testing and cellular contraction within a collagen gel and examined how modeling plastic fiber interactions in each case affected the resulting fiber architecture. For both the uniaxial and cell contractility cases, with plasticity, we found permanent fiber rearrangement, consistent with both our expectations and existing literature [3].

Although the fiber mesh in this study was fairly coarse, and the model of cell contraction was a considerable simplification of the actual interactions that occur between a cell and the surrounding fibrous matrix, the model nevertheless gave promising qualitative results and appears to be capable of describing at least some of the plastic-like effects observed experimentally. Other observations, such as network collapse during confined compression [8, 9], remain to be simulated and will provide additional tests for the new framework.

ACKNOWLEDGEMENTS

This research was made possible by the University of Minnesota Supercomputing Institute, a University of Minnesota Doctoral Dissertation Fellowship, and NIH grant U54 CA210190.

REFERENCES

[1] P. Fratzl, Collagen: Structure and Mechanics, an Introduction. Springer, 2008. [2] F. Spill, et al., *Curr. Op. in Biotech*. 40. 2016. [3] J. Kim et al., *Nat. Commun*. 8(842), 2017. [4] Ban et al., *Biophys J* 114:450, 2018. [5] Wisdom et al., *Nat. Commun*. 9:4144, 2018. [6] S. Plimpton, *J Comp Phys*, 117:1-19, 1995. [7] Picu and Sengab, *Soft Matter*, 14, 2254-2266 .2018. [8] Chandran and Barocas, *JBME*, 2007. [9] J. Ferruzzi et al., *Scientific Reports*, 9:17151, 2019.

MECHANICAL CUES DRIVE THE ROBUST ASSEMBLY OF MICROFABRICATED STEM CELL-DERIVED CARDIAC TISSUES

Samuel J. DePalma[1], Austin E. Stis[1], Domenica Passariello[1], Christopher D. Davidson[1], Adam S. Helms[2], Brendon M. Baker[1]

(1) Department of Biomedical Engineering
University of Michigan
Ann Arbor, MI, USA

(2) Division of Cardiology
University of Michigan
Ann Arbor, MI, USA

INTRODUCTION

The mechanical function of the myocardium is dictated by contractile cardiomyocytes (CMs) and the fibrous extracellular matrix (ECM) that surrounds, orients, and groups CM bundles [1]. Aberrations to the architectural or mechanical properties of the cardiac microenvironment common in numerous cardiomyopathies often result in cardiac dysfunction [2]. However, due to limitations in existing models of cardiac disease, how CMs and other cells in the myocardium sense and respond to these mechanical microenvironmental changes is largely unknown. *In vivo* models lack control over matrix architecture and mechanics, with confounding factors limiting the ability to parse the signaling and behavior of individual cell types within the tissue [3]. Current *in vitro* models leverage natural materials to generate 3D microtissues but lack the mechanical control required to accurately model fibrotic ECM changes and require the inclusion of stromal cells [4-6]. Therefore, improved *in vitro* models of the cardiac microenvironment are necessary to advance our understanding of how fibrosis initiated changes to the ECM alter tissue function and propagate disease progression.

Here, we establish a robust method for creating well-defined fibrous cardiac microtissues composed of photocrosslinkable dextran vinyl sulfone (DVS) suspended between two elastomeric cantilevers (termed fibroTUGs). Previous work from our lab has shown the ability to create organized and functional cardiac tissues on DVS matrices [7]. Expanding on these findings, we present a novel system to generate highly tunable pure CM tissues that enables tissue fractional shortening and real-time contractile force measurments. Additionally, we report on the effects of pathogenic microenvironmental cues on induced pluripotent stem cell derived-CM (iPSC-CMs) tissue function by tuning boundary stiffness, DVS matrix stiffness, and fiber alignment and analyzing tissue contractile output and cellular organization.

METHODS

Microfabrication: DVS was synthesized and electrospun as previously described [7]. Fibers were collected on poly(dimethylsiloxane) (PDMS) post arrays fabricated by soft lithography affixed to a rotating mandrel. Fibers were then crosslinked through a chrome mask such that only fibers suspended between two posts were exposed to UV light (**Fig. 1a**). Uncrosslinked fibers were dissolved upon hydration (**Fig. 1b**). Matrices were then crosslinked further to define matrix stiffness and functionalized with cRGD. Mechanical Testing: PDMS cantilever mechanics were characterized by deflecting individual cantilevers with a tungsten rod of known elastic modulus (**Fig. 2a**). Bending stiffness was calculated by measuring the cantilever deflection and the force applied by the tungsten rod using custom Matlab scripts. Matrix modulus was determined by pressing a microfabricated SU8 rectangle across the center of the fiber matrices to apply a tension on the matrix (**Fig. 2b**). Using custom Matlab scripts, matrix modulus was extrapolated from measured cantilever deflection. CM Differentiation: iPSCs were differentiated into cardiomyocytes as previously described via temporal modulation of the Wnt signaling pathway [7]. After differentiation, iPSC-CMs were seeded on substrates on after d25. Seeding: PDMS seeding masks were cast from 3D printed molds and aligned with suspended fibers (**Fig. 1a**). 125k pure CMs were then added through the mask and allowed to adhere for 18h. Immunostaining and Microscopy: Contractile stress analysis was conducted via brightfield, time lapse imaging (>30 Hz) at 37 °C and 5% CO_2. Fixed samples were then stained for anti-α-actinin and DAPI. All analysis was conducted on d10 after seeding and quantified using custom MATLAB scripts [7]. Statistics: Statistical significance was determined by one-way ANOVA or Student's t-test where appropriate, with significance indicated by $*p < 0.05$. All data presented as mean ± std.

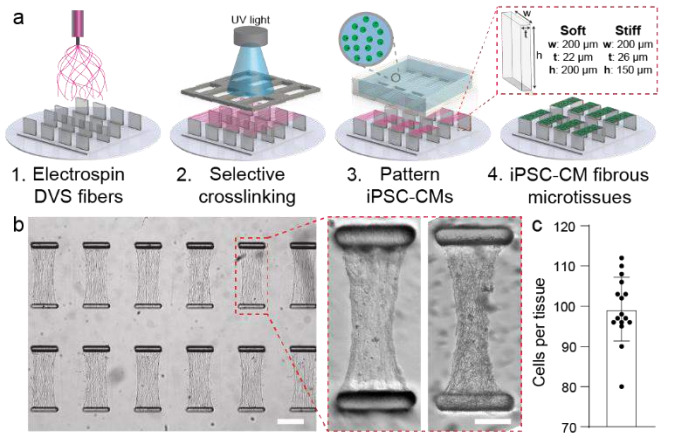

Fig. 1: a) fibroTUG fabrication scheme. b) Array of suspended matrices (scale bar: 200 µm) and example tissues on aligned and random suspended matrices (scale bar: 100 µm). c) Distribution of CM seeding densities.

RESULTS

Fibrous matrices were fabricated by electrospinning DVS on to an array of microfabricated PDMS posts affixed to a rotating mandrel [7] (**Fig. 1a**). Post arrays consisted of 98 pairs of posts spaced 500 µm apart. Fibers were then selectively crosslinked through a chrome mask and iPSC-CMs patterned on matrices through a microfabricated seeding mask (**Fig. 1a,b**). Reproducibility of fibroTUG fabrication and seeding protocol was quantified to confirm consistant tissue formation (**Fig. 1c**).

As this culture platform affords precise mechanical tunability, we preformed mechanical characterization of the PDMS cantilevers and suspended fiber matrices using custom analysis techniques (**Fig. 2a,b**). Alterations to post dimensions (**Fig 1a**) defined boundary stiffnesses with relevance to healthy and diseased cardiac tissue (**Fig. 2c**) [8,9]. DVS matrix modulus was determined via microindentation and increased with higher photoinitiator concentration (**Fig. 2d**).

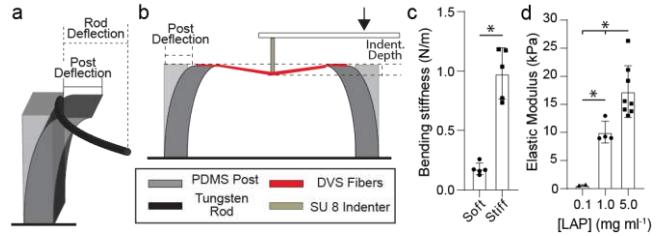

Fig.2: Schematics of PDMS cantilever (a) and DVS matrix (b) mechanical characterization methods. c) Bending stiffness of soft and stiff cantilever. d) Elastic modulus of DVS matrices.

Lastly, we examined how iPSC-CMs respond to alterations in boundary stiffness, matrix stiffness and alignment. When keeping matrix alignment and stiffness constant, we observed an increase in iPSC-CM tissue contractile stress on stiffer cantilevers (**Fig. 3a,b**). Additionally, we found that iPSC-CMs cultured on soft matrices (~1 kPa) contracted with a higher stress than iPSC-CMs cultured on stiff matrices (>20 kPa) (**Fig. 3c**). To our surprise, we observed no difference in tissue contractile stress between aligned and non-aligned soft matrices (**Fig 3f**). In line with this finding, sarcomere alignment was consistent regardless of the underlying matrix organization (**Fig. 3d,e**).

DISCUSSION

In this work, we developed a new microfabrication strategy to create fibrous cardiac microtissues of pure iPSC-CMs to examine how alterations in the mechanical cues affect cardiac tissue function. Mechanical characterization of this platform indicated an ability to orthogonally define boundary mechanics, matrix stiffness, and matrix architecture, enabling precise exploration of the role that the ECM plays in cardiac mechanosensing and contractile function. Additionally, this platform facilitates tissue fractional shortening, which has been shown to be critical for myofibrillar development and maintenance [4]. Previously established platforms used to study cardiac fibrosis have a variety of limitations including a lack of control over fibrous elements that induce iPSC-CM organization, limited mechanical control over the matrix, and the necessary inclusion of stromal cells for tissue formation which may confound studies focused on CM biology [5,6,8,9]. Using the fibroTUG platform, we highlight the importance of orthogonal mechanical and architectural control in creating *in vitro* models of cardiac tissue. Specifically, we find that altered boundary stiffness, matrix stiffness, and matrix architecture have distinct effects on iPSC-CM function, potentially due to the activation of distinct mechanosensing pathways. Intriguingly, we find that decreased matrix alignment does not result in decreased contractile stress in the platform. A possible explanation for this could be that only aligned fibers that span the entire distance between the two PDMS cantilevers remain in tension in contrast to those oriented perpendicularly. High myofibril alignment on both matrices suggests that CMs develop strong cell-matrix interaction only with tensed fibers, consistant with previous studies on focal adhesion formation of CMs in various mechanical environments 10,11]. Future experiments will assess how iPSC-CM tissues respond to pathologic alteration in their physical environment. Additionally, this platform could be useful in examining how physical cues and tissue forces affect iPSC-CM maturation.

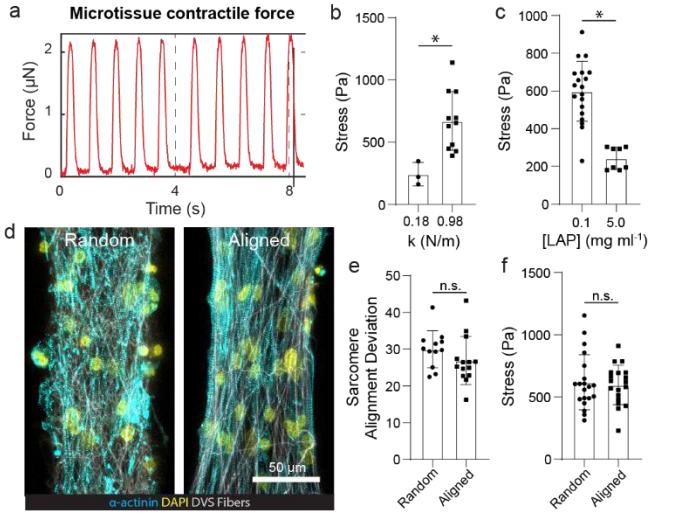

Fig. 3: a) Sample plot of tissue contractile force over time. Contractile stress of tissues with varying (b) boundary stiffness, (c) DVS matrix modulus, and (f) matrix alignment. d) Confocal fluorescent images of fibroTUG tissues of varying alignment. e) Quantification of sarcomere alignment.

ACKNOWLEDGEMENTS

This work was supported by the NSF (EEC-1647837, CBET-2033654) and the NIH (HL124322). S.J.D acknowledges financial support from NIDCR of the NIH under T32DE007057. C.D.D acknowledges funding from the NSF Graduate Research Fellowships Program (DGE1256260).

REFERENCES

[1] Weber, KT *J Am Coll Cardiol*, 13:1637-1652, 1989. [2] Kong, P et al., *Cell Mol Life Sci*, 71:549-472, 2014. [3] Mathur, A et al., *Avd Drug Deliv Rev*, 96:203-213, 2016. [4] Ribeiro, AJS et al., *Proc Natl Acad Sci*, 112:12705-12710, 2015. [5] Ronaldson-Bouchard et al., *Nature*, 556:239-243, 2018. [6] Wang, EY et al., *ACS Cent Sci*, 5:1146-1158, 2019. [7] DePalma, SJ et al., *Biomater Sci*, 9:93-107, 2021. [8] Boudou, T et al., *J Tissue Eng*, 18:910-919, 2011. [9] Leonard, A et al., *J Mol Cell Cardiol*, 118:147-158, 2018. [10] McCain et al. *Proc Natl Acad Sci*, 109:9881-9886, 2012. [11] Chopra, A et al. *Dev Cell*, 44:87-96, 2018.

SB³C2021
Summer Biomechanics, Bioengineering and Biotransport Conference
June 14-18, Virtual

DEVELOPMENT AND UTILIZATION OF A VASCULARIZED 3D PRINTED *IN VITRO* PHYSIOLOGICALLY REPRESENTATIVE SKIN TISSUE PLATFORM FOR BURN INJURY INVESTIGATION

S. Brocklehurst (1), N. Ghousafim (2), K. Isaac (1), D. Stolley (2), M. N. Rylander (2)

(1) Biomedical Engineering
University of Texas
Austin, Texas, USA

(2) Mechanical Engineering
University of Texas
Austin, Texas, USA

INTRODUCTION

There is a lack of burn studies using *in vitro* and *in vivo* models that quantify both time-temperature history and tissue response for short-duration, high-temperature burns, both of which are needed to elucidate mechanisms of burn injury and to develop predictive models [1, 2]. The influence of vasculature embedded within skin on resulting burn injuries has not been adequately investigated. Engineered *in vitro* tissue platforms provide a great system for evaluating burn injury mechanisms [1, 3]. Some previous studies have created skin platforms with embedded vascular networks, however to the best of our knowledge none have been used as models for burn or wound healing research [4]. 3D bioprinting allows for the creation of complex skin platforms with more representative branching vascular networks to better understand the influence of blood vessel structure and perfusion on burn injury. This paper presents a multilayer vascularized *in vitro* human skin platform to conduct quantitative burn experiments for investigation into the influence of vasculature on burn injuries.

$$\Omega(\tau) = \ln\left(\frac{C(0)}{C(\tau)}\right) = \int_0^{\tau} A\, e^{\left(\frac{-Ea}{R\,T(t)}\right)} dt \quad (1)$$

The Arrhenius model (equation 1) has been widely used for modelling burn injuries to account for the temperature-dependence of damage rates, with the common form assuming irreversible first-order kinetics [cc]. Use of this model allows tissue damage and cell response to be predicted from time/temperature data, assisting heat-based therapies to achieve successful outcomes while minimizing complications due to damage to surrounding tissue [2]. $C(0)/C(\tau)$ is the ratio of the initial cell concentration or tissue strength over that at time τ, the logarithm of which gives the damage parameter Ω. Two process coefficients determine the behavior of the common form of the Arrhenius model (Equation 1), frequency factor A (Hz) and activation energy Ea (kJ/mol). Each type of tissue damage and cell response is modelled by its own set of coefficients, which must be determined for the temperature range of interest due to the domination of different mechanisms at different temperatures [5]. Results from quantitative burn experiments using *in vitro* skin models can be applied to the Arrhenius model to facilitate better understanding of the underlying mechanisms of burn injury and enable prediction of burns using time and temperature.

METHODS

In vitro skin tissue platforms were created by 3D printing collagen I hydrogels bearing human dermal keratinocytes and fibroblasts into a layered structure using a BioX bioprinter. Using a narrow-gauge needle, collagen solution was extruded into a gelatin microbead slurry serving as a support scaffold. The shear-thinning behavior of this microbead slurry allows for it to be readily displaced at the point of collagen extrusion and as the needle passes through the upper portion of the support scaffold. After completion of the bioprinting process, the support scaffold with its embedded skin platform was placed into an incubator at 37 ˚C to complete the polymerization of the collagen matrix and to melt the surrounding gelatin microbeads into a thin liquid that is readily washed off. This approach allows use of the same collagen I solution used in our previous skin burn studies, without modification to facilitate printing [6]. Larger skin platforms with more complex configurations can be created without loss of shape at larger heights, and without being restricted to a 2D printing surface.

In order to create vascular networks within printed skin platforms, a sacrificial Pluronic bioink was extruded into the shape of the desired

vasculature within the dermis layer and surrounded with collagen hydrogel. Removal of this sacrificial bioink by rinsing after polymerization of the collagen left behind channels in the shape of the extruded Pluronic filaments, forming the foundation for the vascular network. Holders for skin platforms were created by 3D printing bottomless wells out of PLA, which were then adhered to the top of glass slides using polydimethylsiloxame (PDMS). Inlet and outlet ports incorporated into the holder allowed connection to hoses and a pump for perfusion through the platforms. Vascular networks within skin platforms were gradually perfused with a suspension of microvascular endothelial cells in a ramping flow scheme. After creation, platforms were sustained by the perfusion of culture media through their vascular networks, with exposure to air on the top surface facilitating differentiation of keratinocytes.

Platforms were created with variable distances between parallel channels, and variable media perfusion rates. They were subjected to contact burn injury to characterize both extracellular matrix damage and the response of cells to thermal stress. A contact burn apparatus was made with a 3 mm diameter cylindrical copper burn tip and a motor with a microcontroller for consistent control of tip position and contact duration. Burn tests were performed with the burn tip heated to 50-100 ^{o}C for 3 seconds of contact with the platforms. Platforms were treated with a variety of fluorescent stains and imaged with z-stack confocal microscopy 24 hours after exposure. The resulting 3D images show the spatial distribution of this damage throughout the platforms and were used to measure the volumes of damaged regions.

Temperature distributions within platforms during contact burns were modeled computationally in Comsol Multiphysics (5.4a) to obtain a much higher temporal and spatial resolution than could be directly measured. Experimentally determined thermal characteristics of skin platforms and perfused media were used as inputs for this model. The resulting time/temperature histories were correlated with the experimentally determined distributions of tissue damage and cell response to determine which temperature conditions caused which level of damage. Arrhenius process coefficients A and E_a were determined for cell death and collagen ablation that closely predict the experimentally observed tissue damage using the computational temperature model.

RESULTS

Vascularized skin platforms were successfully created using a bioprinting methodology designed in our lab. Cells are stratified within their respective layers and retain their viability. Endothelial cells form monolayers adhered to the channel walls similar to *in vivo* vessels. Bioprinting methodology allowed for rapid creation of vascularized platforms without the need for specialized molds for each channel.

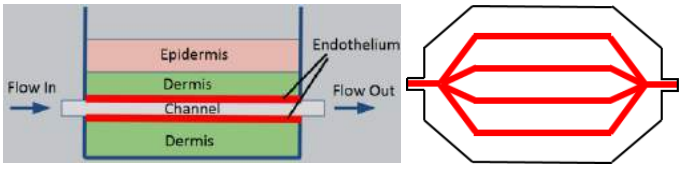

Figure 1 - Configuration of vascularized skin platforms. Left: cross-section of endothelialized channel within skin platforms. Right: Top-down layout of branching channels

Figure 2 – Demonstration of 3D printed networks

Contact burn injuries resulted in consistent injury to the skin platforms, which were quantified by the volume of damaged regions. Close to the contact point collagen was completely ablated, whereas further out the damage is progressively less severe as evaluated by different stains. The different measurements taken show a range of severities of cell response, and provide a potential means to study how cell fate is determined after burn exposure. Further work is in progress to collect burn injury data using variants of vascularized skin platforms.

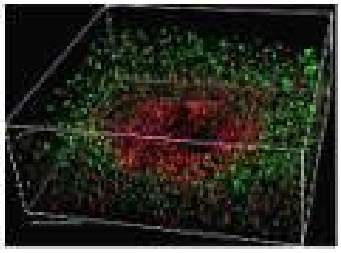

Figure 3 - Live/dead (green/red) staining of skin platform 24 hours after contact burning with a 75 ^{O}C copper cylinder.

DISCUSSION

The *in vitro* multilayer vascularized skin tissue platforms created in this project provide a means of quantitatively evaluating the as-of-yet unknown influence of vasculature on burn injury response. Platforms can be created in large quantities with minimal specialized equipment and maintained with minimal labor due to the perfusion of media – essential for the large sample sizes required to determine mechanisms of burn injury. Knowledge of these parameters is needed to elucidate mechanisms of burn injuries and to help drive the parameters of predictive therapeutic models.

ACKNOWLEDGEMENTS

We would like to thank Nicholas Fuselier, Alican Ozkan, Danielle Stolley, Leslie Schroder, and Steven Pugliese for their assistance.

REFERENCES

[1] Ryan, C. M., Parry, I., & Richard, R. (2017). Functional outcomes following burn injury. Journal of Burn Care and Research, 38(3), e614–e617. https://doi.org/10.1097/BCR.0000000000000537

[2] Kollias, S., Stampolidis, N., Kourakos, P., Mantzari, E., Koupidis, S., Tsaousi, S., … Castana, O. (2015). Abdominal compartment syndrome (ACS) in a severely burned patient. Annals of Burns and Fire Disasters, 28(1), 5–8.

[3] Sen, S., Palmieri, T., & Greenhalgh, D. (2015). Review of burn research for year 2014. Journal of Burn Care and Research, 36(6), 587–594. https://doi.org/10.1097/BCR.0000000000000289

[4] Kolesky, D. B., Homan, K. A., Skylar-Scott, M. A., & Lewis, J. A. (2016). Three-dimensional bioprinting of thick vascularized tissues. Proceedings of the National Academy of Sciences of the United States of America, 113(12), 3179–3184.

[5] Viglianti, B. L., & Dewhirst, M. W. (2013). Thresholds for thermal damage to normal tissues : An update, 27(4), 320–343.

[6] Yang, X., Lu, Z., Wu, H., Li, W., Zheng, L., & Zhao, J. (2018). Collagen-alginate as bioink for three-dimensional (3D) cell printing based cartilage tissue engineering. Materials Science and Engineering C, 83, 195–201.

EFFECTS OF IMPACT POSITION, MUSCLE ACTIVATION, AND POSTURE ON HEAD INJURY RISK

Jonathan Mortensen (1), Nikolaus Benko (1), Britany Coats (1), Andrew Merryweather (1)

(1) Mechanical Engineering
University of Utah
Salt Lake City, UT, USA

INTRODUCTION

Musculoskeletal modeling has been proposed as an ethical tool for studying risk mitigation strategies in contact sports such as American football [1]. To date, these models have been used to study the effect of impact location, muscle strength, muscle activation, and posture on head accelerations caused by head-to-head collisions. These studies have quantified the risk of concussion using traditional kinematic-based injury metrics such as HIC, HIP, and BRIC. However, strain-based methods of injury prediction are thought to be more accurate at predicting concussion because they account for complex brain geometry and the directional dependency of injury. Strain-based injury metrics have not been adopted for use in conjunction with musculoskeletal models due to the large computational time required to compute brain strain. In this study, we incorporate a recently developed method for rapid brain strain estimation with a musculoskeletal model of head-to-head impact to quantify the effect of impact direction, muscle activation, and posture on brain strain.

METHODS

An OpenSim musculoskeletal model of the head and neck was previously used to investigate the effects of several parameters, including posture, impact location, and muscle activation on head accelerations [1]. This model is composed of rigid bodies connected by rotational joints which are constrained by realistic kinematic relationships. The model includes 72 Hill-Type muscle actuators and additional force elements which provide passive resistance.

To determine the effect of neck posture and impact location on brain strain, the kinematic outputs of 76 musculoskeletal simulations were analyzed. These simulations incorporated 5 impact directions (frontal, occipital, lateral, lateral off-center) and 5 postures (neutral, extended, flexed, toward and away from lateral impact, Figure 1).

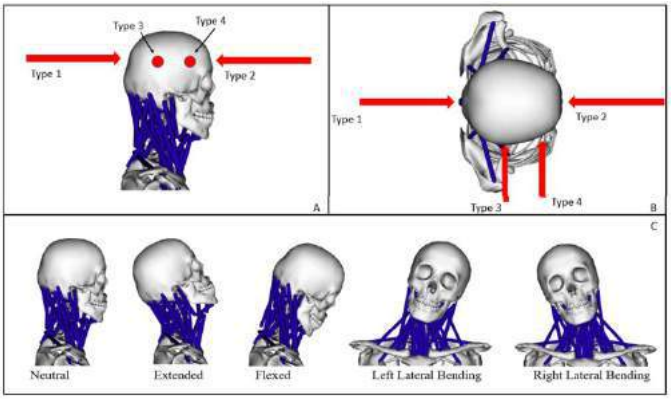

Figure 1. Impact directions (top) and postures (bottom) simulated with stiff or loose neck muscle activation at low (2914 N) and high (6800 N) head impacts.

'Stiff' neck muscle activation represented anticipation of the impact and a 'loose' response to represent unanticipated impact. The stiff response coactivates neck muscles and generates maximum muscle forces to resist impacts. The loose response involves no muscle activation. Each simulation was initiated with a low (2914 N) or high (6800 N) head impact force.

To estimate brain strain, we fit a second-order response surface concussion [2]. Briefly, a central composite design with circumscribed axial points was used to generate simplified acceleration inputs for the finite element model. Seven degrees of freedom were used to define the duration and 3D linear and angular accelerations for each finite element simulation. model to brain strain outputs from a finite element model of adult A total of 79 finite element simulations spanning a range of

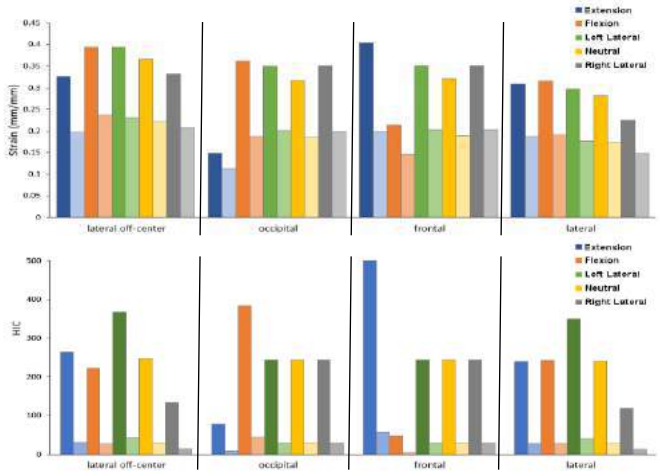

Figure 2. Strain (top) and HIC (bottom) calculated from head kinematic data following musculoskeletal simulation of head impact from multiple directions and postures. Darker shades indicate high impact and lighter shades indicate lower impact.

Table 1. Summary of kinematic parameters used to generate response surface model

Parameter	$A_x\,(g)$	A_y (g)	A_z (g)	$\alpha_x\left(\frac{rad}{s^2}\right)$	$\alpha_y\left(\frac{rad}{s^2}\right)$	$\alpha_z\left(\frac{rad}{s^2}\right)$	$\Delta t\,(ms)$
Minimum	5	5	2	800	200	300	6
Maximum	60	90	42	5000	3400	7300	24

kinematic parameters (Table 1) informed the model.

Using methods similar to the finite element model, a simplified triangular acceleration pulse was fit to the kinematic data from the musculoskeletal model simulations. These acceleration parameters were then input into the response surface model to estimate brain strain associated with each musculoskeletal simulation.

Two-way ANOVAs were performed to determine the effects of posture and impact direction on strain for each activation method and each impact force. A type I error of 0.5 was considered significant.

RESULTS

Stiff muscle activation had a minimal average reduction of 0.00237±0.00318 brain strain. Based on this finding, the remainder of the analysis combined data from both muscle activation configurations. Impact direction, posture, and the interaction between the two effects significantly affected brain strain ($p<0.001$). Lateral off-center impacts resulted in the largest average brain strains (0.290±0.077) and lateral impacts resulted in the lowest average brain strains (0.231±0.062). The effect of posture on brain strain was significantly related to the impact direction. Specifically, an extension posture associated with a frontal impact had the worst effect on brain strain (0.406), while an extension posture with occipital impacts resulted in the lowest brain strain (0.145). During lateral impacts, angling the head toward the impacts resulted in larger strains (0.073±0.005) than angling the head away from the impact. Low impacts (light colors in Figure 2) had similar trends to higher impacts (dark colors in Figure 2), but the distinctions between all the impact direction/posture combinations was more muted.

The strain-based trends were compared to calculations of HIC to compare the effect of strain-based metrics to kinematics-based head injury metrics. HIC lowest and highest values corresponded to those from strain, but values in between were not well correlated with strain.

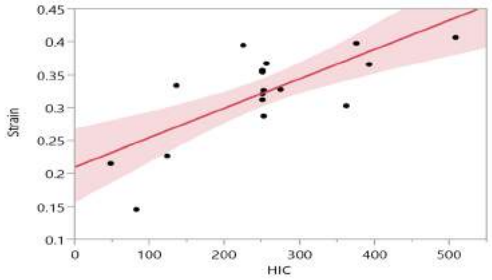

Figure 3. Correlation of HIC to brain strain for all high-impact simulations with loose neck muscle activation.

Specifically, HIC values were less sensitive to subtle changes in posture and direction with the majority of values near 245 (Figure 3).

DISCUSSION

Posture, impact direction, and the interaction between the two affects brain strain and can be explained by the change in moment arm of the applied force with either a change in impact direction or posture. Applying a force to the same location on the skull can result in a dramatically different applied moment about the base of the neck as posture changes. For example, applying a lateral force to the center of the head in a neutral posture will result in mostly lateral bending, but applying a lateral force to the center of the head in a flexed posture will result in both lateral bending and axial rotation of the neck. The increased moment arm allows the same magnitude of force to result in higher linear and rotational accelerations.

Overall, the brain strain followed the same trends as the HIC as posture, impact location/direction, and muscle activation were altered. Notably, frontal impacts and an extended posture both resulted in higher relative HIC than brain strain. This difference highlights the need for additional research on the potential insights of strain-based injury metrics. The results of HIC and brain strain in this study may lead to different conclusions. The results suggest that even while frontal impacts or extended postures result in higher linear accelerations than other directions or postures, the anatomy of the brain allows for lower strain than other directions or postures.

This study demonstrates how the limitations of both kinematic-based and strain-based methods can be addressed using musculoskeletal modeling and rapid brain strain estimation. The musculoskeletal modeling has allowed for estimation of head kinematics for a broad range of impact scenarios. These kinematics can directly be used to calculate kinematic-based injury metrics, such as the HIC. However, the results of this study indicate strain-based methods may lead to different conclusions. This is likely due to neglecting the effects of brain geometry and impact direction. Previously, strain-based methods required finite element simulations. The limitations of finite element models, including simulation time, prohibit simulating a broad range of impact scenarios. Using rapid strain estimation methods accounts for complex brain geometry and the directional dependency of injury, while using the musculoskeletal model allows for investigating a large range of impact parameters.

ACKNOWLEDGEMENTS

This work was supported by the National Science Foundation (#1622741).

REFERENCES

[1] Mortensen et al. *J Biomech* 100:109411, 2020
[2] Benko. *PhD Dissertation.* University of Utah, 2020

EFFECTS OF COVID-19 INFLAMMATION ON THE REGIONAL BEHAVIOR OF THE LUNG: A COMPUTATIONAL STUDY

Sunder Neelakantan (1), Hamed Babaei (1), Reza Avazmohammadi (1,2)

(1) Department of Biomedical Engineering
Texas A&M University
College Station, Texas, United States

(2) Department of Mechanical Engineering
Texas A&M University
College Station, Texas, United States

INTRODUCTION

Lung biomechanics has gained significant attention in recent years, and particularly very recently due to the COVID-19 pandemic. The outbreak has indicated the need for a better understanding of the structure-function relationship in the lungs and its computational modeling. Acute respiratory distress syndrome (ARDS) is a frequent complication in COVID-19 and is manifested by mild to severe hypoxemia. Patient with ARDS often require to be mechanically ventilated and poor ventilation protocols can lead to further complications such as ventilator induced lung injury (VILI).

Existing physical models of lung parenchyma involve approximating the acinar structure into a cluster of spheres or dodecahedrons (1). These models may require simulating a large number of clusters to statistically represent the lungs containing over a million alveolar sacs. Alternatively, phenomenological models treating the lung parenchyma as a poroelastic isotropic material can be sought to reduce computational complexity for whole organ modeling. Berger et al. (2) is an example of such models that studies the effect of a spherical blockage on lung function.

In this study, we developed a patient-specific computational model of the lungs for a covid-19 patient. The model is based on thoracic CT scans indicating inflamed regions in the lungs. Our primary objective was to study the effect of inflammation on the regional kinematics and stress distribution in the lung. This study serves as an initial step to understand and predict the mechanical behavior of lung parenchyma with inflammation to improve mechanical ventilation protocols to reduce patients suffering from ARDS and VILI.

METHODS

The patient thoracic CT scans were obtained from St. Joseph Health Regional Hospital. Presence of inflamed regions (indicated by opaque regions in the CT scan) was clear in the scan and was identifiable for image segmentation and reconstruction. The lungs, airways, and the inflamed regions were segmented and reconstructed. The generated mesh was used in ABAQUS to simulate the ventilation of the left lung.

Image reconstruction

The lungs, airways and inflamed region were segmented using the CT scan images. The segmentation of the airways is sensitive to the resolution and number of images in a CT stack. In the current work, 7-8 generations of airways were segmented using the CT images. A representative image from the CT scans is shown in Fig. 1 with inflamed regions being shown with red arrows.

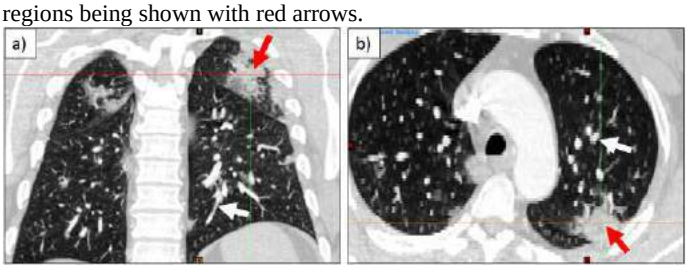

Figure 1: CT scan of patient lungs with inflammation. The inflamed region is marked by the red arrows and the airways are marked by the white arrow. (a) the coronal view, (b) the axial view.

Meshing

The airways were subtracted from the lobes and the resulting part was meshed, i.e., the solid domain is the whole lung with the airways removed. A volumetric mesh was generated for the lungs using quadratic tetrahedral elements. Representative surface/volumetric mesh have been shown in Fig. 2.

Material Model

We developed a poroelastic material model in ABAQUS that relates the alveolar pressure to volumetric deformation. The stress-strain relationship accounts for the changes in local porosity and permeability of the tissue with deformation which leading to a non-linear behavior between pressure and deformation.

Similar stress-strain relationships were used for healthy and inflamed regions. The permeability and compressibility values were altered in the inflamed region to represent the change in the biomechanical behavior of parenchymal tissue due to inflammation.

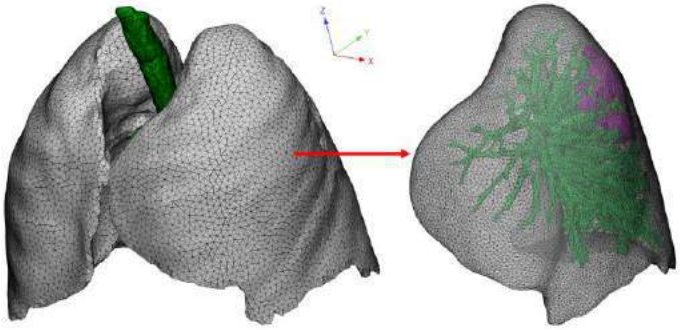

Figure 2: The surface mesh of the lungs. The left lung has been shown separately with transparency with the airways (in green) and inflamed regions (in purple).

Forward model

We conducted several forward simulations to study the effect of inflammation on the regional mechanical behavior. We used pore-pressure elements in ABAQUS for the simulations. The soils solver was used designated for boundary value problems for porous material with fluid pressure in the pores.

The primary bronchus was fixed, and the fluid pressure of 2 cmH_2O was applied in the airways. The initial pressure in the lungs was set to atmospheric pressure and initial porosity was set to 75%. The local stress and strain in the deformed configuration were investigated.

RESULTS

Representative Cauchy stress and logarithmic strain contours in the deformed configuration of the lung with inflammation are shown in fig. 3. Changes in the permeability and compressibility of the inflamed regions led to reductions in stress and strain in the region close to the inflammation.

The initial volume of the lung, 1.61 liters, increased by 250 ml when pressurized to 2cmH_2O. These volume and pressure values are consistent with those reported in Ben-Tal (3). In the healthy regions, strain values of around 5% were observed on the surface of the lungs along with stress values of around 160 Pa.

DISCUSSION

Our results suggest that the inflamed regions sustain a lower strain when compared to the healthy region due to a lower compressibility and permeability. Therefore, compared to a fully healthy lung, when the same volume of air is pumped into a patient with regions of inflammation, the remaining healthy tissue needs to expand further to compensate for reduced deformation in the inflamed regions. This larger strain may lead to damage in the alveoli of the healthy tissue leading to VILI.

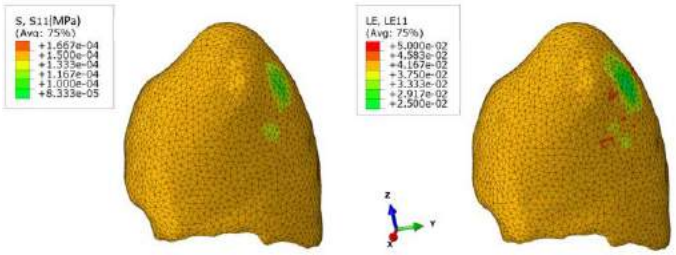

Figure 3: Strain and stress contour plots of the left lung with inflammation. The left figure shows the Cauchy stress where the x-axis is the normal to the sagittal plane.

Our poroelastic lung model serves as a proof-of-concept effort to study the biomechanics of the lungs affected under inflammation. Similar models can be developed for animal models of lung diseases where a variety of experimental measurements and imaging can be conducted. Animal models allow measuring relevant tissue properties in ex-vivo mechanical testing of excised parenchymal tissues. Such integrated models can be used to improve mechanical ventilation protocols.

One limitation of the current study is the absence of the effect of surface tension caused by the thin liquid film present on the inner surface of the alveoli. The surface tension is a function of surfactant concentration which are secreted by the epithelial cells and prevent the alveoli from collapse at low volumes (4, 5). Inclusion of the effect of surface tension will eliminate the need for artificial stresses to keep the lungs inflated in simulations.

Another limitation is the absence of forces acting on the lungs as a result of pleural pressure, the rib cage, diaphragm, and inspiratory muscles. While replicating such forces could be complex, they improve the model towards the representation of patient-specific in-vivo lung function and potential validations with plethysmography data. These limitations are currently being addressed.

ACKNOWLEDGEMENTS

This work was partially supported by NIH R00HL138288.

REFERENCES

[1] Concha, F et al. *J Mech Phys Solids*, 112 126–144, 2018.
[2] Berger, L. et al. *Int. J. Numer. Meth. Biomed. Engng.*, 32, 2016.
[3] Ben-Tal A. *J Theor Biol.* ;238(2):474-95, 2006.
[4] Wall, W.A. et al. *Int. J. Numer. Meth. Biomed. Engng.*, 26: 807-827, 2010.
[5] Suki, B. et al, *Comprehensive Physiology*, 2011.

MODELLING MECHANICAL FEEDBACK MECHANISMS IN MULTISCALE SLIDING FILAMENT MODEL OF LYMPHATIC MUSCLE PUMPING

Peter Y. Xie (1), Christopher J. Morris (1), James E. Moore (1)

(1) Department of Bioengineering
Imperial College London
London, United Kingdom

INTRODUCTION

The lymphatic system is responsible for returning interstitial fluid back into the venous circulation to maintain fluid homeostasis. Lymph flow can occur via extrinsic and intrinsic pumping mechanisms, although the relative contributions of these mechanisms to flow is poorly understood. The intrinsic pumping mechanisms are intricately regulated by mechanical forces acting on the lymphatic vessel [1]. The ability of the lymphatic vessel to respond to local mechanical forces allows it to respond to transient changes in interstitial fluid volume or local pressure/flow conditions [2]. Although multiple studies and experiments have explored the effects of varying pressure gradients and transmural pressures on lymphatic pumping [3,4], little is understood of the sub-cellular/molecular mechanisms underlying this behavior [5].

From existing research, we understand that the two most significant biomechanical signals that affects lymphatic contractile activity are flow-induced shear stress and pressure-induced stretch. Flow-induced shear stress induces the production of the chemical substance Nitric Oxide (NO), produced by eNOS in the lymphatic endothelial cells and diffuses rapidly into nearby lymphatic muscle cells. NO is a well-known vasodilator which inhibits Ca^{2+} entry from internal stores, resulting in negative inotropic and chronotropic effects [5]. Pressure-induced stretch results in clear elevations in both basal and peak calcium levels as pressure in the lymphatics is increased. This results in intrinsic positive inotropic and chronotropic effects [1]. The increase in phasic contractile force occurs up to a maximum level of stretch, when the amount of stroke work required to compress the lumen surpasses the increase in phasic contractile force [6]. It is speculated that stretch-activated ion channels undergo conformational changes in response to stretch, allowing more calcium entry from outside the cell [5].

The overarching aim of this research is to develop a more accurate and representative model of a single lymphangion at the sub-cellular level, to improve our understanding of lymphatic pumping on multiple scales and find ways to improve lymphedema treatments.

METHODS

An existing sub-cellular muscle model developed by our research group [7] was updated to incorporate biomechanical feedback mechanisms, modelled and trained to replicate experimental results exploring the effects of varying pressures on lymphatic pumping [3,4]. We used experimental results obtained from rat mesenteric vessels as a basis for parameter values in the model. The performance of the model with the incorporation of biomechanical feedback mechanisms is verified using afterload experiments [8].

In the implementation of biomechanical feedback mechanisms, wall shear stress imposed on the lymphatic vessel is calculated assuming Poiseuille flow:

$$\tau = \frac{32\mu Q}{\pi D^3} \quad (1)$$

and the magnitude of pressure-induced stretch of the lymphatic vessel is defined by the stretch_ratio (ratio of diastolic diameter to the diameter at 0cmH2O transmural pressure).

The average value of wall shear stress across the whole contractile cycle and the average stretch_ratio across the diastolic period of a contractile cycle are used as variables to modulate sub-cellular mechanisms in the next contractile cycle. These control signals are then processed to modify a) the systolic calcium amplitude concentration and b) frequency of action potentials.

The 3D representation of the functions modulating a) and b) (Fig 1,2.), represents the computational function, and the line plots represent experimental data from Gashev [3,4].

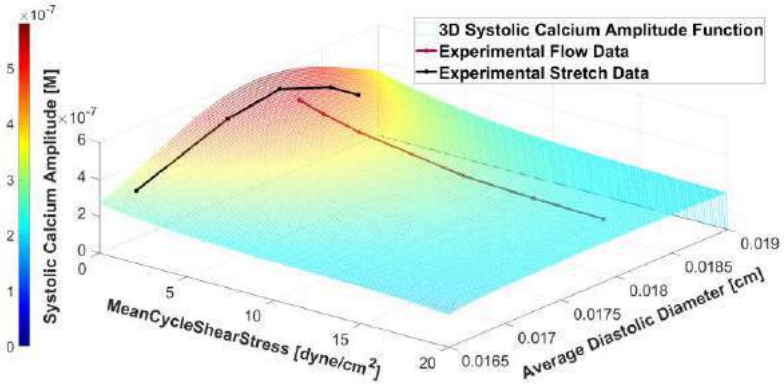

Figure 1. 3D Plot of Systolic Calcium Amplitude Modulation. Function postulated by considering experimental flow data (red) [3] and experimental stretch data (black) [4].

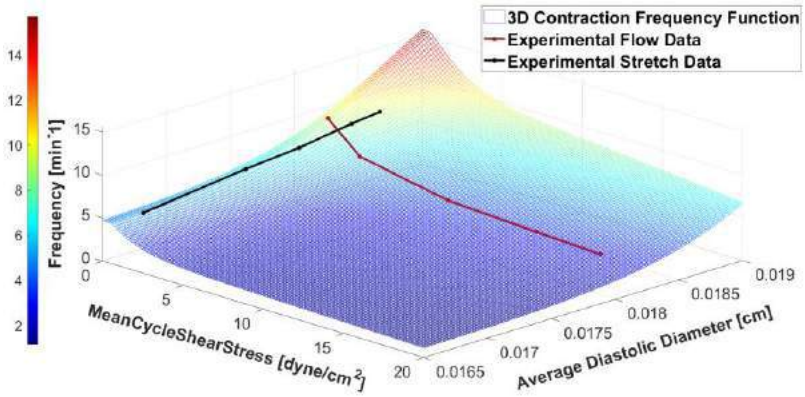

Figure 2. 3D Plot of Frequency Modulation Function. Function postulated by considering experimental flow data (red) [3] and experimental stretch data (black) [4].

RESULTS

The performance of the model with the incorporation of biomechanical feedback mechanisms was tested by comparing to afterload experiments on isolated rat mesenteric lymphatics from the literature [8].

Elevation of outlet pressure tests the response of the lymphangion to increases in pressure that could result from a gravitational load, outflow obstruction, or tissue compression [8]. In the model, Diameter response to elevated outlet pressure shows a gradual increase in systolic diameter (Fig 3B), due to a combination of the increase mid-lymphangion pressure, as well as inhibition of the intracellular systolic calcium amplitude during the pressure ramp.

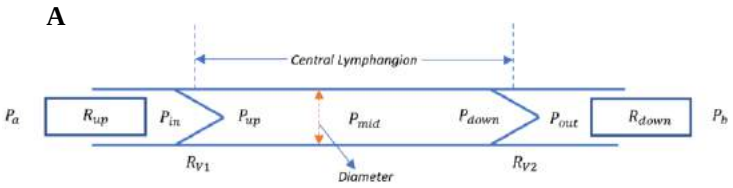

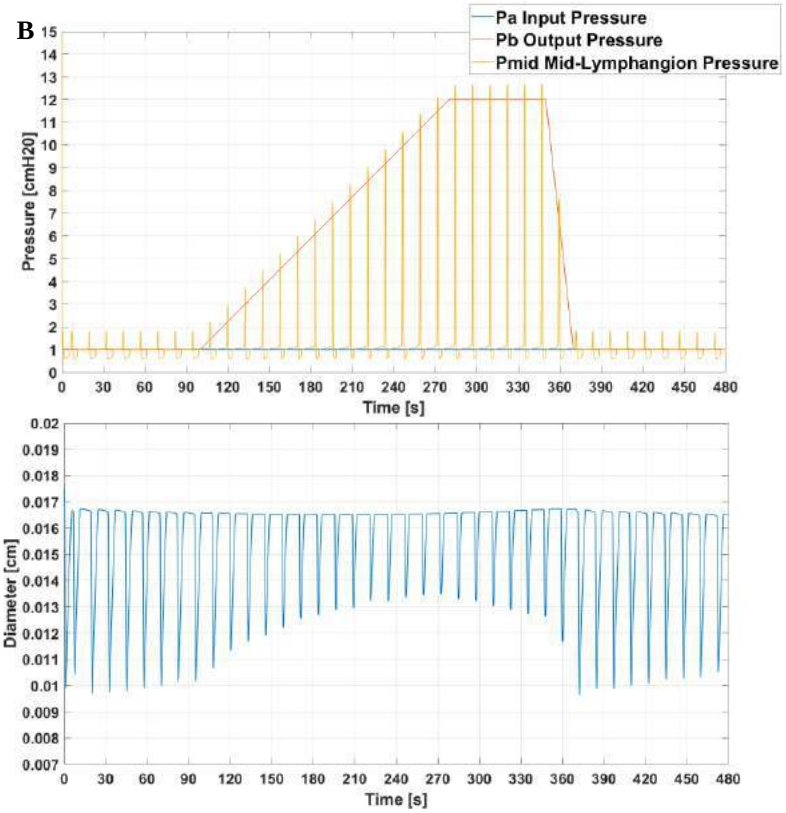

Figure 3. Response of single lymphangion to an output pressure ramp. A: Schematic of the single lymphangion with associated pressure values. B: Diameter response of Lymphangion to ramp-wise elevation in outlet pressure.

DISCUSSION

Stroke volume comparison show there is close replication between the response of the computational model and the experimental results from Davis [8]. The addition of biomechanical feedback mechanisms is a first step to quantitatively understand the relationship between mechanical signals acting in lymphatic vessels and its effect on the subcellular response of lymphatic muscle cells.

Further validation with experimental results, as well as extending this model to multiple lymphangions in series will further progress our understanding of lymphatic pumping to help find better treatments for lymphedema.

REFERENCES

[1] Muthuchamy M, Zawieja D. Ann N Y Acad Sci. 2008; 1131:89-99.
[2] Gashev AA. Ann N Y Acad Sci. 2008;1131:100-109.
[3] Gashev AA et al., J Physiol. 2002;540(Pt 3):1023-1037.
[4] Gashev AA et al., Microcirculation. 2004;11(6):477-492.
[5] Munn LL. Semin Cell Dev Biol. 2015;38:67-74.
[6] Rahbar E et al., PaLymphat Res Biol. 2012;10(4):152-163.
[7] Morris C.J., Zawieja D.C. and Moore Jr J.E. (2021) A multiscale sliding filament model of lymphatic muscle pumping. Manuscript submitted for publication.
[8] Davis MJ et al., Am J Physiol Heart Circ Physiol. 2012;303(7):H795-H808.

IT TAKES BOTH: ON THE PROTEIN INTERACTIONS OF NEUROFIBRILLARY TANGLES AND AMYLOID BETA PLAQUES IN ALZHEIMER'S DISEASE

Trisha Gollamudi (1), Shima Jalalian (2), Johannes Weickenmeier (2)

(1) Biomedical Engineering
Stevens Institute of Technology
Hoboken, New Jersey, 07030, US

(2) Mechanical Engineering
Stevens Institute of Technology
Hoboken, New Jersey, 07030, US

INTRODUCTION

Alzheimer's Disease (AD) is a progressive neurodegenerative disorder and the most prevalent form of dementia [1]. AD is known for extreme memory loss, cognitive decline, and ultimately death. The two primary biomarkers of AD are amyloid-beta (Aβ) peptides and neurofibrillary tangles (NFT) of tau. These proteins and their interactions lead to disruptions in neuronal activity and eventually neuronal death. Corresponding cerebral atrophy, which manifests as cortical thinning and ventricular enlargement, follows a spatiotemporal pattern that is incongruous with each biomarker's spreading pathways. This study aims to formalize the relationship between neurofibrillary tangles and Aβ plaques progression. To date, it has been shown that Aβ plaques, which precede tau, spread by proximity, while NFTs spread based on the structural network form by axons and are typically referred to as the connectome. Our proposed model incorporates these distinct differences and forms a unifying theory of atrophy progression in AD patients.

METHODS

We review the literature on experimental methods and medical imaging that investigate the initiation, progression, interaction, and neurodegenerative effect of the two misfolded proteins involved in AD: Aβ and NFT. We summarize our findings in schematic pathways and propose a tissue damage model that couples Aβ and NFTs and can be used to predict cerebral atrophy.

RESULTS

Aβ plaques. The Aβ monomer is formed when the amyloid precursor protein (APP) misfolds. This changes Aβ's conformation, which proceeds to form low (dimer/trimer) oligomers [2]. These oligomers accumulate in intraneuronal pathways and exhibit prion-like behavior [3]. As shown in Figure 1, these oligomers convert normal APP into Aβ oligomers. These oligomers are then released outside the cell via exocytosis, where they form Aβ fibrils that ultimately form Aβ plaques. In AD, these Aβ plaques are first found in the neocortex, from where they progress into subcortical regions, medulla oblongata, and finally, appear in the cerebellum [4].

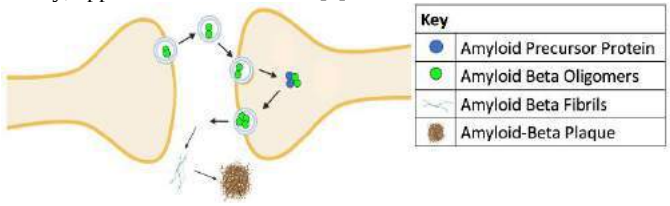

Figure 1: Schematic of Aβ pathway from precursor protein to plaque. Aβ infiltrates proximal neurons via trans-synaptic spread.

Neurofibrillary tangles. Tau protein appears primarily in axons and stabilizes microtubules. In AD, tau is hyperphosphorylated, which causes it to misfold and form fibrils. Fibrils then aggregate as neurofibrillary tangles that substantially disrupt normal axon function due to the destabilization of microtubules. As shown in Figure 2, tau travels intercellularly through tunneling nanotube structures (TNT's) or via the release of exosomes [5]. Tau pathology is first observed in the transentorhinal cortex from where it spreads into the hippocampus. The subsequent stages are well known and based on the work of Braak et al. [6]. Following the hippocampus, NFTS begin to appear in structurally connected regions in the neocortex via the axonal connections of the brain [6]. This spreading pattern is markedly different from Aβ and plays a critical role in formulating a model that couples Aβ and NFT concentrations to form a tissue damage model.

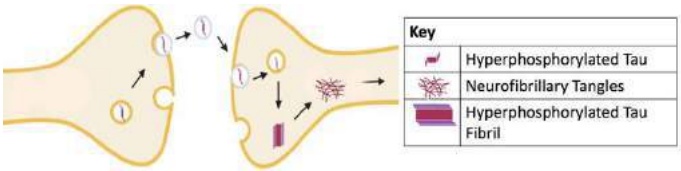

Figure 2: Schematic of intracellular spreading of NFTs.

Aβ and NFT coupling. Besides the independent pathways described above, we identified pathways in which Aβ oligomers directly contribute to tau's hyperphosphorylation in various pathways. As illustrated in Figure 3, there are three main interaction pathways: In the first pathway (black arrows), Aβ peptides bind to the NMDAR receptor. This leads to calcium ion dysregulation and drives calcium ion influx, which activates another kinase named calmodulin-dependent protein kinase (CAMKKB). CAMKKB, in turn, phosphorylates adenosine monophosphate protein kinase (AMPK), which is known to phosphorylate tau [7]. In the second pathway (red and green arrows), Aβ oligomers bind to insulin receptors and subsequently inhibit the Akt pathway (shown in red arrows) [8]. Akt is a serine/threonine kinase that inhibits GSK3beta through the activation of P13k. However, since the Akt pathway is inhibited, P13k cannot inactivate GSK3beta, leading to tau's hyperphosphorylation [8]. Finally, the third pathway (blue arrows) shows how Aβ oligomers inhibit Wnt signaling, leading to the overactivation of GSK3beta [8]. In this case, Aβ oligomers activate the kinase DKK1, which internalizes LRP6 receptors. This inhibits Wnt signaling and leads to GSK3beta overactivation [8]. This then leads to hyperphosphorylation of tau.

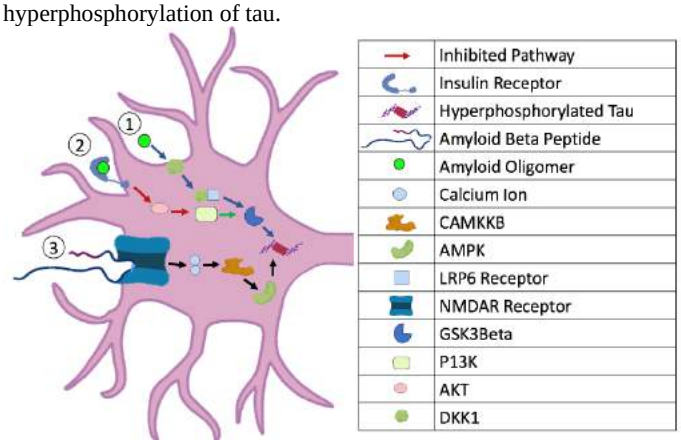

Figure 3: Schematic of Aβ-facilitated hyperphosphorylation of tau. We identified three relevant pathways (black/red/blue arrows).

Framework for a mathematical atrophy model. Aβ plaques damage neuronal synapses and induce neuron cell death based on the amyloid cascade hypothesis [2]. Hyperphosphorylated tau is implicated in disrupting microtubule dynamics, which can lead to apoptosis [5]. Additionally, Aβ is also known to precede and contribute to tau's hyperphosphorylation, such that there is an intricate coupling that leads to spatially heterogeneous neurodegeneration. We schematically show our Aβ-NFTS-apoptosis model in Figure 4. We pose that the production of Aβ leads to the creation of Aβ plaques that cause apoptosis. In a similar process, and not necessarily in the same place, tau protein is converted into neurotoxic NFTs. Coupling takes place in the form of Aβ plaques accelerating the production of neurotoxic NFTs. The result is a positive feedback loop that triggers progressive neurodegeneration that spreads through the brain by distinct spatial mechanisms.

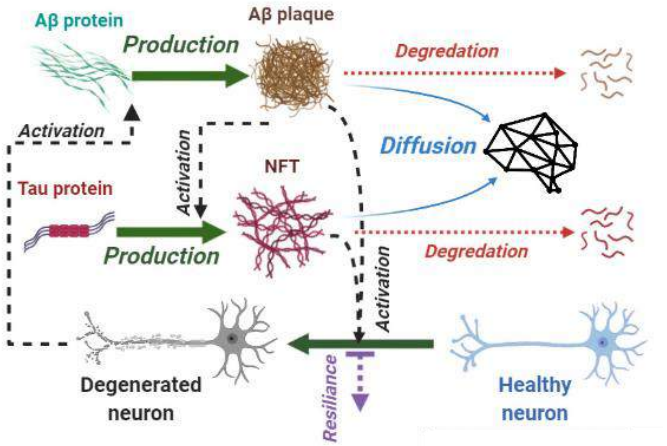

Figure 4: Schematic of our atrophy model that couples Aβ and tau to make predictions of spatiotemporal AD progression patterns.

DISCUSSION

Two biomarkers characterize AD: Aβ plaques and hyperphosphorylated tau. Tau spreads through neuronal connectivity, whereas Aβ spreads by proximity. There are structural changes in AD that can be correlated to Aβ and hyperphosphorylated tau progression. In AD patients, the earliest atrophy occurs within the hippocampus and the entorhinal cortex, where neurofibrillary tangles pathology is initially detected [9]. The atrophy spreads into the neocortical regions, where Aβ plaques are first detected, and neurofibrillary tangles are later found [8]. Aβ pathology is widespread in early disease stages, while tau pathology develops considerably later. This observation is in line with the amyloid cascade hypothesis, which predicts that changes in Aβ are the initial driving force behind tau pathology [10].

Symptoms of AD begin to appear when tau pathology spreads into the hippocampus, and the symptoms become more severe when tau pathology reaches the neocortex's primary and secondary areas [10]. This suggests that AD pathology is driven by a coupling between tau pathology and Aβ pathology [10]. The presence of Aβ plaques in non-demented brains is further evidence that AD is characterized by a distinct interaction between these two biomarkers [9]. Using the information provided in this study, we will be able to formulate the corresponding mathematical in order to simulate the spatiotemporal progression of cerebral atrophy. We will validate our simulations by comparing longitudinal structural and functional PET imaging data from the Alzheimer's Disease Neuroimaging Initiative.

ACKNOWLEDGMENTS

This research was supported by the National Institutes of Health's National Institute on Aging, grant R21AG067442.

REFERENCES

[1] Karantzoulis, S. *et al., Expert Rev Neurother*,11:1579-1591 (2011)
[2] Kayed, R. *et al., J of Alzheimer's Disease*, 33:S67-S78, (2013)
[3] Sinha, M.S. *et al., Acta Neuropathol Commun* .136:41-56, (2018)
[4] D.R.Thal, *Front. Aging Neurosci.*, 7:25, (2015)
[5] Laurent, C. *et al., Biomedical Journal*, 41:21-33, (2018)
[6] Braak H *et al., Acta Neuropathol Commun*, 82:239-259, (1991)
[7] Thornton, C. *et al., Biochemical Journal*, 434:503-512, (2011)
[8] Tello, P. *et al., Int J Alzheimer's Dis*,2011:1-12, (2011)
[9] Thompson *et al., J Neuroimage*,22:1754-1766, (2004)
[10] Kant *et al., Nat. Rev. Neurosci*, 21:21-35, (2020)

ENGAGING BIOMEDICAL ENGINEERING STUDENTS WITH GAMIFICATION IN ONLINE LEARNING

N. Dorfner (1), R. Zakerzadeh (1)

(1) Department of Engineering,
Rangos School of Health Sciences,
Duquesne University
Pittsburgh, PA, US

INTRODUCTION

In the past year, remote education has become much more prevalent due to the COVID-19 pandemic. Within online learning environments, students have fewer opportunities to engage with peers, which requires instructors to adjust their teaching approaches and strategies [1]. This study offers evaluation of gamification in remote teaching of a third-year level biomedical engineering core course. The course teaches introductory concepts of cardiovascular fluid mechanics and flow characteristics of biological systems.

While gamification in pedagogy is not new, procedures must be altered for a remote classroom in order to improve lecture engagement. In both in-person and remote environments, the same approach can be utilized to employ games, however, the benefits of increasing attentiveness and inducing motivation are more advantageous in an apathetic online setting [2]. In this work, we present a roadmap for creating a more engaged environment in BME classrooms by using academic games for teaching. The incorporation of BME concepts is in the "preparation" stage of gamification, regardless of the type of game. Various game ideas with BME integration are suggested, as well as a preliminary analysis of student engagement while playing Bingo with cardiovascular biofluid terminology.

METHODS

Several key steps must be followed in creating an academic game: definition of learning objectives, game design, preparation of tools, implementation, and assessment [3]. This process is illustrated in **Figure 1.** When following these stages to create a BME Bingo game, we first define the learning goal as practicing cardiovascular mechanics concepts. For game design and preparation, a list of keywords is composed and input into an online Bingo card generator. The preparation step is unique in its incorporation of the fluid mechanics course concepts. The selected keywords should reflect course material to fulfill the learning objective of practicing and reviewing the terminology. For example, the keyword list can include but is not limited to density, artery, viscosity, Bernoulli, stent, stenosis, blood flow, velocity profile, pressure gradient, laminar flow, diffusion, aneurysm, and cardiac cycle. Bingo cards are then distributed to students in an online link or downloadable PDF via email or a file sharing service, such as Blackboard or Canvas.

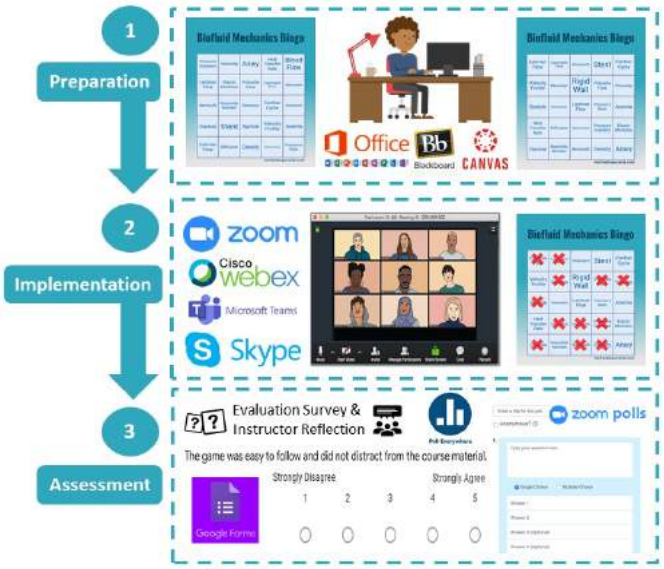

Figure 1: Steps to implement Bingo as an academic game.

In the virtual classroom on Zoom, instructors ask students to select a random Bingo card to play. The instructor solves problems and students mark keywords as they notice definitions, formulas, or concepts applied in the problem set. Students who mark 5 keywords in the same horizontal, vertical, or diagonal row send the word "Bingo" in the chat box. A reward or incentive can be offered to induce motivation and participation. However, this reward must be carefully selected [4]. All 38 students enrolled in the course were given the option to participate in the game activity. We played Bingo twice in the Fall 2020 semester as exam review. Participation was voluntary and no reward was offered to ensure authentic student motivation and engagement in the game. 35 students participated in Bingo and responded to a post-game questionnaire (92% of the course enrollment).

RESULTS

Through instructor observations and interpretation of the gameplay, students responded positively to the game and were motivated to play. Students asked more questions during the game and sent more In the post-game survey distributed after the second Bingo game, students were asked to rank their perception of engagement with the Likert Scale, where 1 represents "strongly disagree" and 5 represents "strongly agree." The statements on the survey and results are presented in **Figure 2.**

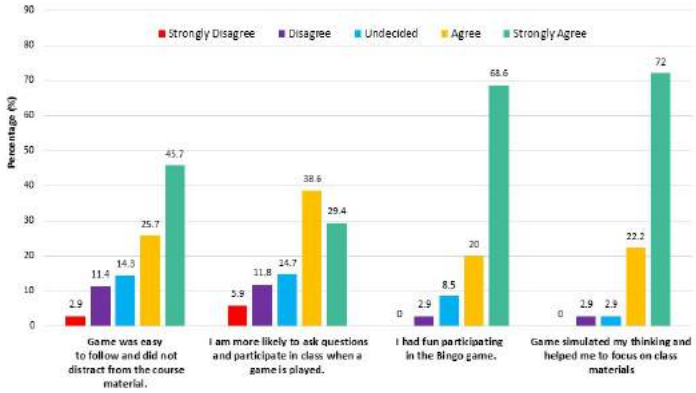

Figure 2: Results of the survey showing the percentage of students participating in the game and responding in each category to the statements.

Based on the survey results, students agreed that they were more engaged in class while playing Bingo. Students felt comfortable and relaxed while playing the game, as they enjoyed Bingo and were more likely to ask questions. The game also stimulated their thinking, and students said they were attentive to the problem solving. Due to ethical and logistical concerns, student marks were not used to evaluate comprehension or engagement in material. Only four survey statements were used to generate high student participation in the post-game questionnaire. The survey was not designed to be strenuous or time consuming for students, as that negates the simple, entertaining, and engaging intention of playing Bingo. We also employed the anonymous polling feature on Google Forms, so students could leave honest responses about the game without fear of bias or concern of their grades.

DISCUSSION

Our results demonstrate that this instance of gamification successfully engaged students during course review of biofluid mechanics concepts. However, the study is limited to the small sample size, time, and resources dedicated to preparation and implementation of Bingo. Games are recommended when instructors need to break their typical classroom routine and make teaching fun. Remote gamification proved to be more difficult than anticipated. One challenge experienced was the lack of emotional and social interaction during the game. Students absorb energy from the social aspect of education, and instructors respond accordingly with dynamic teaching. The absence of this exchange made game play engagement uninspiring and more demanding. Another challenge was finding game materials that can be easily distributed virtually.

Despite these inconveniences, the adaptation of Bingo to encompass biomedical engineering concepts was rather simple. Additional examples of biomedical engineering academic games are shown in **Figure 3**. In Pictionary, instructors present a picture, such as a diagram of laminar flow, and students explain the meaning and application of the picture. Similarly, in "the one-minute paper," students read a paper for homework and explain the significance and application of course concepts the next class period. Execution of a trivia game, like Jeopardy, involves instructors making questions relating to course material and vocabulary with teams of students answering for points. Students in an online environment may benefit from an interactive picture or experiment of the day, where the instructor performs a demonstration relating to a course concept. In biofluid mechanics, the definition of viscosity would be explained by showing that honey has a higher viscosity than water or blood.

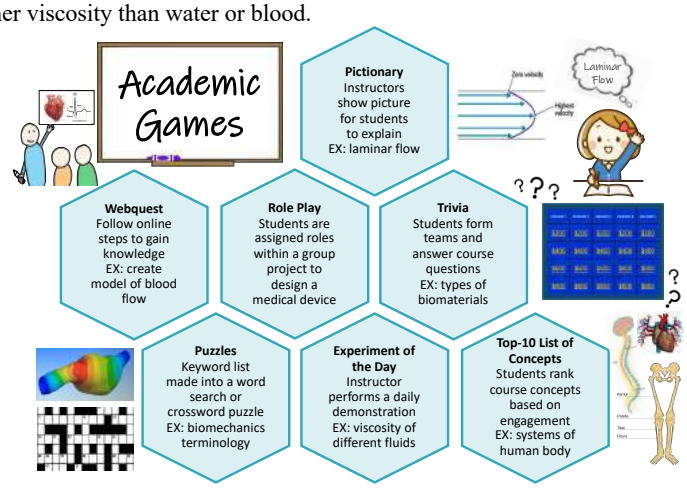

Figure 3: Examples of academic games for online biomedical engineering implementation.

In the future, we would like to investigate gamification using course marks, lecture attendance, and more detailed student feedback. This can be achieved using reflection assignments, blog posts, and activity evaluation rubrics to enhance our perception of students' thought process, suggestions, and improvements for games. Gamification is not appropriate in all educational setting or classes. Games can make concepts seem less serious to students, and the time-consuming nature of the gamification process may outweigh the potential benefits. Games cannot be used to replace pedagogy, but rather should be integrated into course delivery to enhance the overall learning experience.

ACKNOWLEDGEMENTS

Funding for this work was provided by the Faculty Development Fund and the Duquesne University Departmental Support.

REFERENCES

[1] Barata, G., et al. VS-GAMES, 2013. IEEE.
[2] Gary, J.A., et al. J Ed Leadership Preparation, 2016. 11(1): p. n1.
[3] Barkley, E.F., et al. John Wiley & Sons, 2014.
[4] Richter, G., et al. Springer, 2015. p. 21-46.

SIMULATION OF OXYGEN MASS TRANSPORT IN A COMPLIANT ABDOMINAL AORTIC ANEURYSM MODEL

A. Throop (1), B. Carbino (1), A. Guy (1), N. Dorfner (1), R. Zakerzadeh (1)

(1) Department of Engineering, Rangos School of Health Sciences, Duquesne University, Pittsburgh, PA, USA

INTRODUCTION

Abdominal aortic aneurysm (AAA) is a cardiovascular disorder that affects more than 3 million Americans per year. Ruptured aneurysms of this type are up to 80% fatal in clinical cases [1], and detection of symptoms is particularly challenging. Little is understood about the mechanisms of AAA formation in the body and the progression towards AAA rupture. Consequently, a proper understanding of AAA behavior can lead to diagnostic tools that can simulate and assess patient-specific cases. The use of computational models has been employed on a number of AAA problems, but most lack interactions between arterial components and blood. This study will model and examine patient-specific AAA using a fluid-structure interaction approach with coupling of blood flow and wall deformation. Observations of total deformation, blood velocity, and maximum principal stress are made on a fully coupled, ANSYS Workbench model. In addition to analyzing hemodynamics and wall deformation, we will also present findings of the oxygen concentration in the vessel. Unlike existing literature, combining a coupled hemodynamic and wall deformation model with oxygen transport is addressed in this study.

METHODS

The patient specific geometry is provided by the NIH repository in an STL (STereoLithography) file format [2]. It is constructed from CT scans visualizing the lumen and arterial wall but lacks the ILT due to its complex nature [3]. This model includes one inlet, with diameter of 1.5 cm and wall thickness of 0.1 cm, and four outlets. The discretized model consists of 2367337 elements, while the fluidic domain is comprised of 843879 tetrahedral cells. To account for the dynamic fluid-structure interactions between blood and AAA wall, a fully-coupled multiphysics model was created in ANSYS 2020 R2. Blood dynamics are defined in ANSYS CFX, arterial wall mechanics are modeled in ANSYS Mechanical, and the fluid and solid components interact directly through a fully coupled Fluid-Structure Interaction (FSI) method.

With regard to hemodynamics, blood is modeled as a steady state, incompressible, Newtonian, laminar fluid with the Navier-Stokes equations. The blood flow is coupled with the oxygen transfer in the lumen and accounted for by the convection-diffusion equation. The diffusion-reaction equation is used to model the oxygen transport in the AAA wall. The inlet boundary condition is described as a uniform velocity profile of U_f^{in} = 0.3 m/s and an oxygen concentration of C_f^{in} = 5.2×10^{-3} kg/cm^3, while the outlet has a pressure of 0 Pa [4]. These equations and conditions are implemented in a fully coupled system with the arterial wall treated as an impermeable structure. The fluid and structure are solved simultaneously in a monolithic linear system (Figure 1).

Table 1: Physical material properties and values

Material Name	Parameter Description	Parameter Value
Blood	Density	1050 kg/m^3
	Dynamic Viscosity	0.0035 kg/m.s
Arterial Wall	Density	2000 kg/m^3
	Poisson Ratio	0.49
	Oxygen Diffusivity	1.08×10^{-9} m^2/s
	Young's Modulus	1.08 MPa

The arterial wall is assumed to be elastic, isotropic, incompressible and homogeneous. Concerning structural interactions, the material properties shown in Table 1 are input into the Engineering Data widget of Static Structural. The static AAA mesh is then assigned elastic fixed supports at the inlet and outlet boundaries, and a fluid-solid interface was defined on the inside of the lumen to act as the system coupling region.

The two models are joined along a single FSI boundary. The simulation is carried out using ANSYS' system coupling feature included with the ANSYS Workbench product. The System Coupling component solves fluid and solid domains separately to obtain the pressure loads from the blood flow in ANSYS CFX. These pressure loads are applied to the solid arterial wall through the fluid-solid interface and the wall displacement is solved in ANSYS Mechanical. This process of the System Coupling algorithm in ANSYS is illustrated in Figure 1.

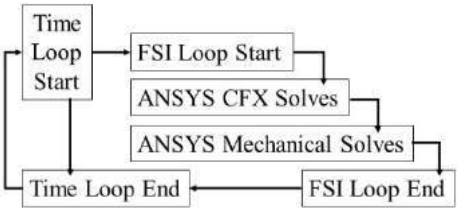

Figure 1: FSI algorithm in ANSYS.

RESULTS

Figure 2 demonstrates the results of the system coupling's CFX component. The plot on the left shows colored streamlines to demonstrate the velocity magnitude. The pattern shown expresses a three-dimensional helical shape at the bulge which uncoils further down the lumen. The blood velocity at different cross-sectional slices are also shown on the right plot of Figure 2. As expected, the blood velocity is observed to be the smallest at the bulge.

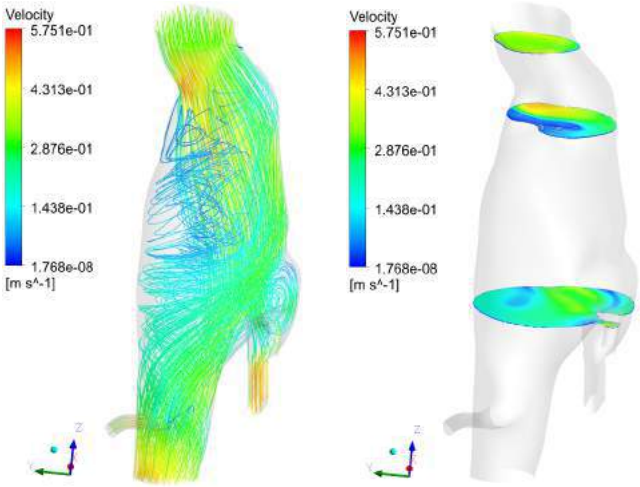

Figure 2: Stream traces colored by the velocity (left) and velocity contours of steady flow on cross-sectional slices (right).

The results of the structural component are shown in Figure 3. On the left of the figure, the plot shows the total wall deformation from the stress of the blood. The greatest point of deformation is found at the bulge. This correlates with the plot of the maximum principal stress on the right of Figure 3 which indicates the maximum stress to be at the bulge.

In Figure 4, the oxygen concentration is plotted on the top view of the cross-sectional slices from Figure 2. The smallest concentration is indicated to be on the outer portion of the wall and the largest on the interior. These results are expected due to the oxygen transport from the blood in the lumen.

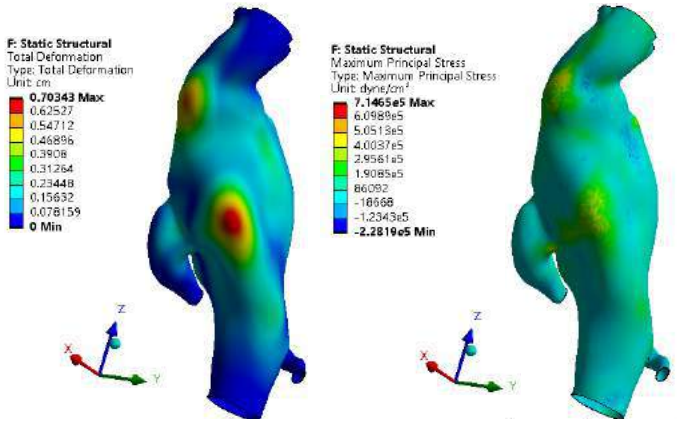

Figure 3: Total deformation (left) and maximum principal stress (right) on the arterial wall.

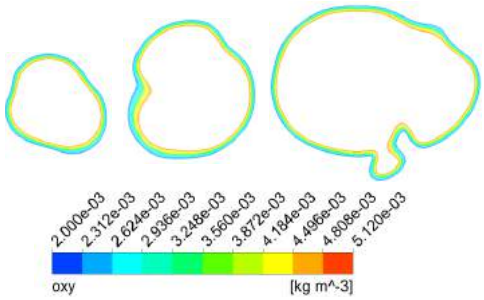

Figure 4: Oxygen concentration profiles of cross-sectional slices shown in Figure 2.

DISCUSSION

In this study, a patient-specific AAA case was modeled using the fluid-structure interaction (FSI) method on ANSYS. The finite element solver accounted for blood flow, oxygen concentration, and arterial wall deformation. The displacement of the wall was taken into consideration through the implementation of the static structural component. This allows for a better representation of the stress from the blood on the arterial wall. Our goal is to further investigate the effects of wall compliance of oxygen transport in the model.

Our approach, however, has some limitations: the geometry does not include the ILT. We have previously explored the effect of a porous arterial wall on oxygen transport [3] using a rigid wall model, and we plan to investigate how the wall deformation affects the flow-driven mass transport. Additionally, although we believe that the steady-state assumption is reasonable for the current stages of our study; we would like to analyze the effect of transient behavior and pulsatile simulation in our future studies. This consideration, combined with the shift towards accounting for ILT and arterial wall permeability could generate high computational costs, so alternative computing methods may be required.

ACKNOWLEDGEMENTS

Funding for this study was provided by the Faculty Development Fund and the Duquesne University departmental support.

REFERENCES

[1] Kuivaniemi, H, et al. Exp Rev. Cardiovasc. Therapy. 13(9): 975-987
[2] Coakley, M.F, et al. 3D Print Addit Manuf. (2014): 137-140.
[3] Zakerzadeh, R., et al. Comput Method Biomech, (2020): 1-15.
[4] Zakerzadeh, R., et al. Cardiovasc Eng Techn, (2021): 1-17.

THE EFFECT OF STENOSIS SEVERITY AND ARTERIAL WALL MECHANICS ON FUNCTIONAL DIAGNOSTIC PARAMETERS

A. Alday (1), T. Lone (1), R. Zakerzadeh (1)

(1) Department of Engineering, Rangos School of Health Sciences, Duquesne University, Pittsburgh, PA, USA

INTRODUCTION

Vascular stenosis is the hardening of arteries caused by a buildup of fat and cells. This can cause narrowing of vessels and ultimately cause difficulty in fluid flow, indicated by a pressure gradient that occurs across the stenosed region (**Figure 1**).

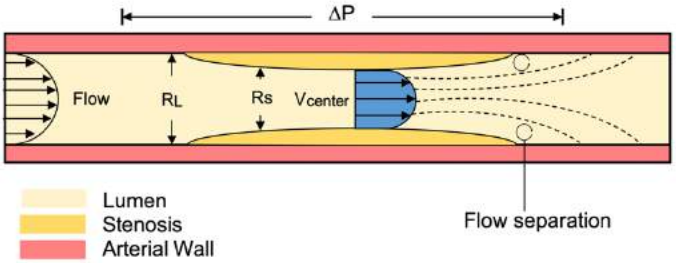

Figure 1. Schematic of a stenosed blood vessel.

This is indicative of the energy loss of the fluid flow which inhibits the distribution of nutrients throughout the body. Depending on the severity of the stenosis, it is possible for the condition to occur undiagnosed until a fatality occurs. The most common method to assess this condition is through routine clinical testing. Doppler echocardiography is a widely used, non-invasive method that often provides inaccurate information regarding pressure and blood flow [1]. This is due to the conversion of velocity to pressure drop by means of the Bernoulli equation, which can lead to premature surgical treatment. Another option frequently utilized is an invasive catheter operation that provides direct pressure values but can be hazardous to a patient's health [1]. In order to minimize clinical risk and ensure the safety of the patient, it is necessary to develop a reproducible, non-invasive, and comprehensive method. A computational model is more suitable than the Doppler measurement as it can simulate functional assessment factors, such as pressure gradient, more accurately by taking into account the viscous losses resulting from resistance of the fluid flow.

The purpose of this study is to assist with the assessment method of an arterial stenosis by analyzing the effect of stenosis severity and arterial wall stiffness on pressure gradient and diagnostic parameters across the stenosed region. We hypothesize that the computational model will sufficiently measure invasive parameters in a vascular stenosis without the risks of invasive clinical assessment methods.

METHODS

Our objective is to identify the relation between arterial wall motion and pressure drop in a model of a stenosed vessel. In order to approximate this problem, we use a partitioned, loosely coupled finite element solver developed in our previous work (see [2] for details). Our fluid-structure interaction (FSI) solver is based on the weak enforcement of interface conditions using Nitsche's method, allowing us to independently solve the equations in different regions. The computational method allows us to simulate propagation of pressure waves and the related arterial wall deformation into an arterial segment. Blood is modeled as an incompressible, viscous fluid and the arterial wall consists of a thick material, accounting for its multilayer structure.

We created finite element geometric models using FreeFem++, an open-source software package, for the FSI simulations. Our solver used Navier-Stokes equations to model blood flow and a hyperelastic material was employed to model a deformable arterial wall. An Arbitrary Lagrangian-Eulerian mesh was generated to perform the FSI simulations. To simulate the response to stenosis, we modified the geometry to exhibit a defined degree of narrowing. Wall mechanical properties in the geometrical models were tuned to account for the wide range of stenotic wall features reported in literature. Using this model, Fractional Flow Reserve (FFR), Pressure Drop Coefficient (CDP), and fluid pressure across the stenosed region are measured. FFR is a ratio of pressure values measured in dyne/cm^2 determined using equation (1):

$$FFR = \frac{Pressure_{distal}}{Pressure_{proximal}} . \quad (1)$$

FFR measures trans-stenotic pressure difference to assess severity of

arterial damage. CDP is a non-dimensional index that combines stenotic pressure, proximal velocity flow, and blood density. It is determined by the following equation (2), where ρ is the density of blood (1 g/cm^3) and $\mathcal{V}$ is the velocity proximal to the stenosis measured in cm/s:

$$CDP = \frac{\Delta P}{0.5\rho\mathcal{V}^2}\ . \quad (2)$$

This parameter can be utilized to further evaluate a stenosis because it takes into account the viscous energy lost to friction and the change in momentum across a stenosed region. These techniques are used in invasive catheterization, whereas non-invasive Doppler echo-cardiography assesses stenosis severity using a simplified Bernoulli principle. This equation (3) relates pressure difference to maximum velocity at the neck of the stenosis, represented by V_{max} in cm/s:

$$\Delta P_{Doppler} = 4V_{max}^2. \quad (3)$$

RESULTS

The computational model was executed at seven different stenosis severity percentages (10, 30, 50, 70, 80, 90, 95) and with four different arterial wall elasticity measurements in MPa (0.5, 1, 4 10). In order to confirm the functionality of the model, fluid pressure was analyzed. The peak fluid pressure gradient was found to occur prior to the completion of half of a cardiac cycle **(Figure 2**). Further, FFR nonlinearly decreased with increased stenosis severity in the cases with varying wall elasticity (**Figure 3**). We found at the greatest wall stiffness, the FFR value decreased the most among all stenosis severities. **Figure 4** showed a nonlinear increase in CDP with increased stenosis severity for all arterial wall elasticity values. We found the greatest increase in CDP occurred in the case of most extreme stenosis severity. Finally, in **Figure 5** a nonlinear increase in P-Doppler with an increase in stenosis severity for varing values of wall compliance is observed.

DISCUSSION

Our computational model is a sound approach because the trans-stenotic pressure over two cardiac cycles confirmed physiological hemodynamics, visualized by the increased pressure proximal to the stenosis and the slight decrease distal to the stenosis (**Figure 2**). Doppler echocardiography does not account for this pressure gradient, thus overestimating stenosis severity [3]. Therefore, surgical correction is often premature and unnecessarily risky. Furthermore, clinical literature states that FFR<0.75 requires surgical correction; this was determined to fall in the range of 78.7-82.7% stenosis severity [4]. Our data is in agreeance with this conclusion, as **Figure 3** demonstrated that stenosis cases greater than 80% severity, across all arterial wall stiffnesses, indicate FFR>0.75. Thus, the computational model successfully simulated parameters from invasive stenosis assessments as opposed to the non-invasive Doppler echocardiography approach.

Figure 3 and **Figure 4** demonstrated that FFR and CDP are inversely related. As stenosis severity increased, blood flow velocity increased across the stenosis which caused a decrease in distal pressure and increase in viscous energy loss. This can be attributed to frictional forces and change in momentum [4]. **Figure 3** also demonstrated that pressure drops proximal to the stenosis are minor in mild stenosis cases (<30% severity level). Therefore, we can conclude that mild stenoses maintain relatively consistent velocity across the stenosis for all arterial wall stiffness levels.

Although a standardized cut-off value for CDP has yet to be determined, we observed that the nonlinear increase in CDP values began to rapidly increase at stenosis severity levels greater than 80%. In the future, patient-specific geometries can be used to create a higher fidelity framework, as well as expand on parameteric knowledge like that of CDP. Also, using heterogenous material properties for the arterial wall may result in more realistic physics of the lesion.

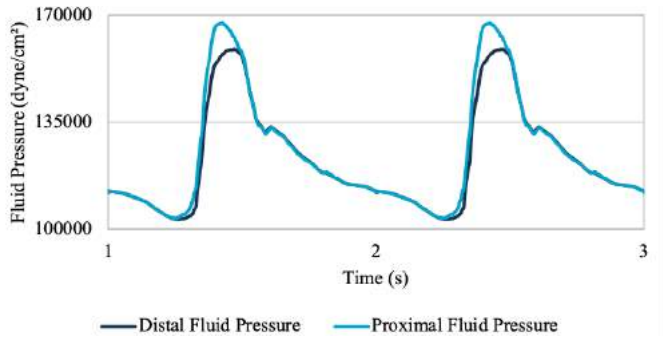

Figure 2. Fluid pressure for two cardiac cycles with time.

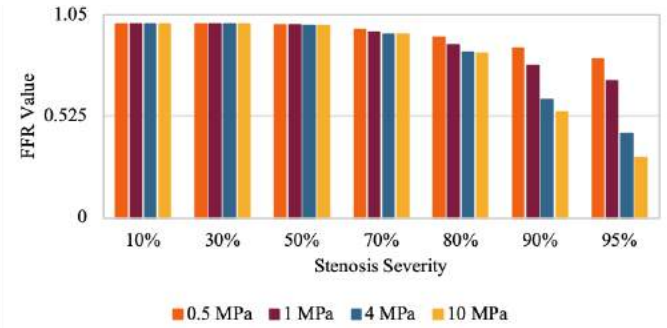

Figure 3. Variation of FFR with stenosis severity elasticity values.

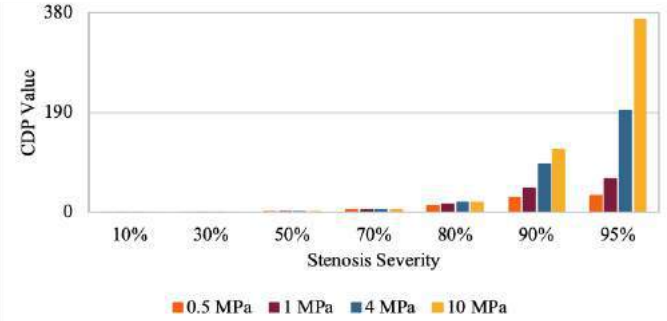

Figure 4. Variation of CDP with stenosis severity.

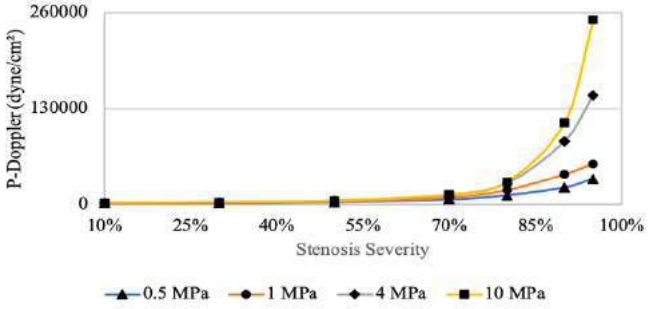

Figure 5. Variation of P-Doppler with Stenosis Severity.

ACKNOWLEDGEMENTS

Funding for this work was provided by the Faculty Development Fund and the Duquesne University departmental support.

REFERENCES

[1] Saikrishnan, N, et al. Circulation AHA 2014, **130**(15), p. 244-253.
[2] Zakerzadeh, R, et al. Meccanica 2019, **54**(1), p. 101-121.
[3] Paul, A, et al. Journal of Computational Medicine 2014, 419689.
[4] Konala, B, et al. Journal of Biomechanics 2010, **44**(5), p. 842-847.

SB³C2021
Summer Biomechanics, Bioengineering and Biotransport Conference
June 14-18, Virtual

A PRELIMINARY FRAMEWORK FOR COMPUTATIONAL FLOW DIVERTER DESIGN OPTIMIZATION AT SCALE

M. Gunther (1), B. Chong (2), D. Frakes (1,3)

(1) Wallace H. Coulter Department of Biomedical Engineering
Georgia Institute of Technology and Emory University
Atlanta, Georgia, USA

(2) Division of Neuroradiology and
Department of Neurological Surgery
Mayo Clinic Arizona
Phoenix, Arizona, USA

(3) School of Electrical and
Computer Engineering
Georgia Institute of Technology
Atlanta, Georgia, USA

INTRODUCTION

Benchtop design is a longstanding cornerstone of medical device design. One upside of benchtop design is its inherent reality. That is, because it is carried out in the physical world on the benchtop, numerous factors that affect use of a device in its intended environment (which of course is also in the physical world) are inherent. One downside of benchtop design in the context of medical devices, however, is lack of scalability. That is, only so many benchtop models of anatomical and physiological environments can be explored. This lack of scalability is particularly problematic when a single device is intended for use across a highly variable patient population.

Computational modeling and simulation on the other hand have historically played a very different role in medical device design. In fact, only over the past decades has it become more common for the FDA to consider (and now recommend) computational modeling and simulation in the design of certain devices. One downside of simulation is that that unlike benchtop work it is not rooted in reality. That is, the result of a simulation will only be as realistic as the underlying model that is employed and the assumptions that inform it. But there is also a massive upside to simulation – scalability. That is, simulations can be performed to explore countless scenarios bounded only by computing power and input data, both of which continue to grow.

One device that may benefit greatly from computational design practices is the flow diverter (FD). In fact, computational components are already common to applications to the FDA involving new FD designs. FDs are braided stents composed of many wires that can be deployed across the neck of a cerebral aneurysm (CA), which is a localized ballooning of a blood vessel in the brain. One objective of deploying an FD is to limit flow of blood into the aneurysm, thereby promoting clotting in the aneurysm and eventual exclusion of the lesion from circulation over time. Like most, if not all, medical devices, many design inputs affect FD performance, and performance can be quantified based on many different interventional outputs.

Although patient-specific FD design and manufacture may be on the horizon given the advent of 3D printing, we still live in a world of "one device for many patients." In this paper, we propose a preliminary framework for FD design at scale. Specifically, computational modeling and simulation are used to identify the optimal wire count design input across a population of five anatomies based on interventional outputs including apposition proximity and post-deployment pore density.

METHODS

DICOM format CT images of five sidewall CA anatomies with similar parent vessel diameters were segmented in Mimics (Materialise, Lueven, Belgium) to create STL models. The centerline of each CA geometry was computed, smoothed, and resampled using the Vascular Modeling Toolkit (VMTK) in Python. All further computation and processing was done in Python, using the Visualization Toolkit (VTK) for visualization. Unique planes were ascribed to each centerline point defined by the vector pointing to the subsequent centerline point as the normal. A coordinate system was created on each plane for raycasting and visualization of FD models. By raycasting vectors at increments of ¼ degree through every plane, the in-plane vessel wall contours were approximated and used to locate the aneurysm and its neck.

To model the aggregate behavior of the FD wires, circular stent contours were expanded along vectors every ¼ degree using active contour modeling. Contours were bounded spatially by the vessel wall. Curvature parameters constrained the ovalization of the stent contour to model FD compliance as informed by prior studies of physically deployed FDs [1]. The rate of change of the distance from a centerline point to a stent contour was constrained by adjacent stent contours to maintain gradual expansion of the FD mesh along the main vessel axis.

The landing zone of each deployment simulation spanned 4 mm proximally from the aneurysm neck to 4 mm distally from the aneurysm neck. Beginning from the distal end of the landing zone, a modified form of the Jedwab et al. [2] equations describing geometric stent properties was employed to determine wire position on the stent contours. The resulting deployments are shown in Figure 1.

Apposition proximity was defined as the inverse of the distance from a stent wire point to the blood vessel wall and only measured on the landing zone portions outside of the aneurysm neck. Pore density was defined as the number of pores per mm^2 and calculated by dividing the number of pores in one pitch of the FD by the surface area of one pitch of the FD. The number of pores (P) in one pitch is given by:

$$P = \frac{n^2}{2}, \quad (1)$$

where n is the number of wires in the FD. The surface area (SA) of one pitch of the FD is given by:

$$SA = 4\,R^2\,\pi^2 \tan\left(\arccos\left(\frac{2\,R\cos(\beta_0)}{D_0}\right)\right), \quad (2)$$

where R is the distance from the centerline point to the stent contour point, β_0 is the on-mandrel pitch angle, and D_0 is the on-mandrel diameter. Pore density (PD) is given by:

$$PD = \frac{P}{SA}. \quad (3)$$

FDs with wire counts of 40, 44, 48, 52, and 56 were deployed in each CA geometry. The percent metal coverage as defined by Jedwab et al. [2] was kept constant across all deployments at 30%. An FD of 4.5 mm fully-extended diameter was appropriate for all five geometries according to standard FD Instructions for Use. The landing zone was consistent for all five deployments.

To approximate pore density, the pore density values calculated at each stent contour point at the aneurysm neck were averaged across all five cases then normalized. Apposition proximity was calculated as the inverse of wire-to-vessel wall distance outside of the aneurysm neck. Values were again averaged across all five cases then normalized.

RESULTS

As wire count increased, the pore density increased approximately linearly while the apposition proximity decreased less linearly, as shown in Figure 2. High pore density is favorable because it reduces velocity of blood flow inside of aneurysms [3]. High apposition proximity is also favorable because it keeps the FD in position and has been found to indicate aneurysm occlusion [4, 5].

The optimal FD, based on the summative value of normalized pore density and apposition proximity, was the 48-wire FD, which exhibited the best overall performance given the assignment of equal importance weightings to the two output parameters. However, a recent study by Aquarius et al. [6] indicated that wall apposition is more important than pore density. The optimal FD could then be either the 40-wire or 44-wire version, both of which exhibited higher apposition proximity at the expense of lower pore density.

DISCUSSION

This paper demonstrated a preliminary framework for flow diverter design optimization at scale. While the framework considered only several aneurysm geometries, the goal is to extend application to several hundred geometries, then several thousand, etc. A few shortcomings of the specific approach presented here are noteworthy. First, there are more sophisticated methods of combining the deployment outputs than normalization and averaging to appropriately consider the impact of outliers on design efficacy. Second, the spatial regions over which deployment outputs are calculated can be further improved to focus where those outputs are most relevant. Lastly, the weightings of the outputs themselves in identifying optimal designs should be adjusted to reflect clinical importance as defined by expert physicians. Nevertheless, the results revealed a key design tradeoff between apposition and pore density with respect to wire count. Although a wire count of 48 appeared optimal in this case, weighting the outputs differently within the proposed framework could point to different optimal wire counts. The framework thus affords designers the opportunity to make informed decisions about design performance based on quantitative data that transcend the scale of the benchtop.

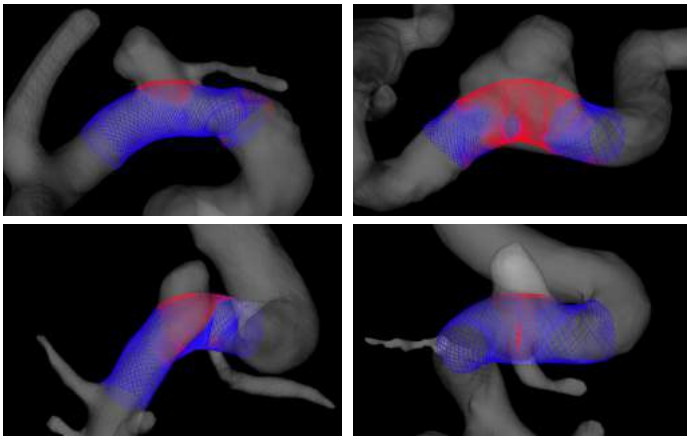

Figure 1: 48-wire FD deployments in four sidewall aneurysm models. Blue indicates regions of high apposition proximity. Red indicates regions of low apposition proximity. (Additional models and wire counts are omitted due to space constraints.)

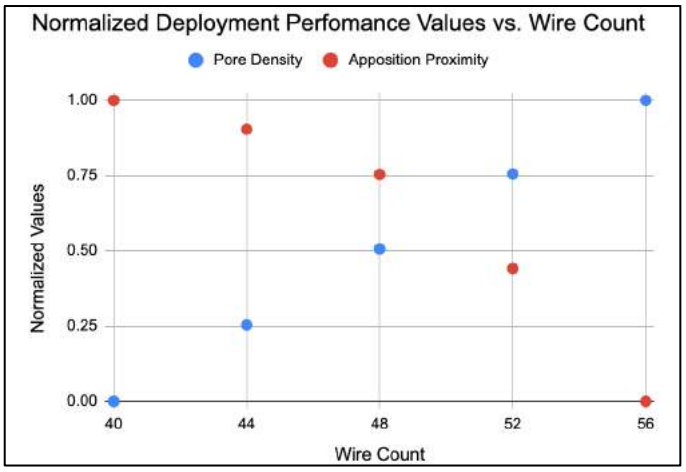

Figure 2: Normalized values of pore density (blue) and apposition proximity (red) plotted versus various wire counts.

ACKNOWLEDGEMENTS

The authors acknowledge the consultation of Haithem Babiker regarding medical device design and computational modeling.

REFERENCES

[1] Chong, B. et al., *Am J of Neuroradiol*, 40:1759-1765, 2019.
[2] Jedwab, M.R. et al., *J of Applied Biomaterials*, 4:77-85, 1993.
[3] Yu, C.H. et al., *Bio-Med Mat and Engineering*, 24:2417-2424, 2014.
[4] Kühn, A.L. et al., *Interventional Neuroradiol*, 23:129-136, 2017.
[5] Rouchad, A. et al., *Am J of Neuroradiol*, 37:2087-2091, 2016.
[6] Aquarius, R. et al., *Neurosurgery*, 84:804-810, 2019.

WHITEWATER HELMET STAR: EVALUATING THE BIOMECHANICAL PERFORMANCE AND RISK OF HEAD INJURY FOR WHITEWATER HELMETS

Brock G. Duma, Mark T. Begonia, Stefan M. Duma

Institute for Critical Technology and Applied Science
Virginia Tech
Blacksburg, Virginia, USA

INTRODUCTION

There are more than 6 million people who participate in whitewater kayaking and rafting in the United States each year (Figure 1).[1] Of these 6 million participants, there are over 50 whitewater related deaths each year, which makes it have one of the highest fatality risks of all sports. As the popularity in whitewater activities grows, the number of injuries, including concussions, also increases. The objective of this study was to create a rating system for whitewater helmets by evaluating the biomechanical performance and risk of head injury of whitewater helmets using the STAR system.

Figure 1: Whitewater rafting is one of the most dangerous sports in the U.S with over 50 fatalities each year.

METHODS

All watersport helmets that passed the EN: 1385: 2012 standard and that were clearly marketed for whitewater use were selected for this study. A total of 21 helmets models were selected, and 2 samples of each model were tested. A custom pendulum impactor was used to test the helmets under conditions which are known to be associated with the highest risk of head injury and death. The struck head consisted of a NOCSAE head and Hybrid III 50th percentile neck, with the head instrumented with three linear accelerometers, and a triaxial angular rate sensor. For this study, 126 tests were performed at six different configurations. The helmets were tested at 3.1 m/s and 4.9 m/s with impacts to the front, side, and rear for each speed (Figures 2-4). The velocities were chosen given that the highest recorded flow rate in a whitewater river is 5 m/s, which implies that any underwater head impact is unlikely to occur at a speed greater than 5 m/s.[2] Each helmet's Summation of Tests for the Analysis of Risk (*STAR*) value was calculated using the combination of exposure and injury risk that was determined by the linear and rotational accelerations (Eq. 1).[3-7]

$$Whitewater\ STAR = \sum_{L=1}^{3}\sum_{V=1}^{2} E(L,V) * R(a,\alpha)$$

Equation 1: Whitewater *STAR* equation where *L* = location, *V* = Velocity, *E* = exposure, *R* = risk, *a* = linear acceleration, and *α* = rotational acceleration.

Figures 2-4: (left) Front impact location, (Center) side impact location, (right) rear impact location.

RESULTS

In the 3.1 m/s front impact condition the 21 helmeted tests resulted in a range of 30.2 – 131.2 (g), and 1601 - 5036 (rad/sec^2). In the 3.1 m/s side impact condition the 21 helmeted tests resulted in a range of 35.7 – 129.7 (g), and 2500 - 3678 (rad/sec^2). In the 3.1 m/s rear impact condition the 21 helmeted tests resulted in a range of 24.7 - 152.6 (g), and 1759 – 6889 (rad/sec^2). In the 4.9 m/s front impact condition the 21 helmeted tests resulted in a range of 82.0 – 282.5 (g), and 4024 - 13069 (rad/sec^2) (Figure 5 and 6). In the 4.9 m/s side impact condition the 21 helmeted tests resulted in a range of 88.1 – 316.4 (g), and 5609 - 24563 (rad/sec^2). In the 4.9 m/s rear impact condition the 21 helmeted tests resulted in a range of 82.9 – 332.0 (g), and 3336 - 14381 (rad/sec^2). The helmets' star values resulted in a range of 0.2518 - 4.8634 (Figure 7).

Higher linear acceleration values were observed for the front impact conditions, and higher rotational acceleration values were observed for the side impact conditions. The linear regression relating linear and rotational acceleration was strongly correlated (r^2=0.71). However, there was a low correlation between helmet price and STAR value (r^2=0.11), and there was also a low correlation between helmet mass and STAR value (r^2=0.03).

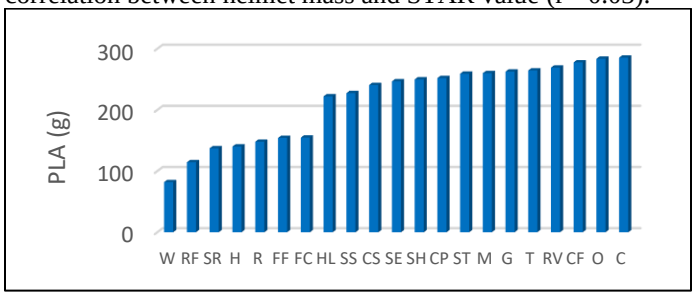

Figure 5: Peak resultant linear acceleration values (g) for the high speed of 4.9 m/s in the front impact direction.

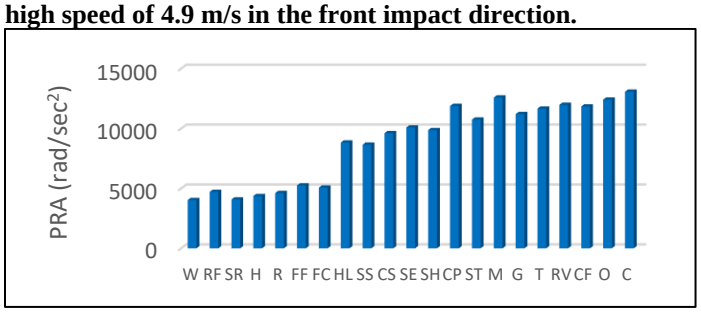

Figure 6: Peak resultant rotational acceleration values (rad/sec^2) for the high speed of 4.9 m/s, front impact direction.

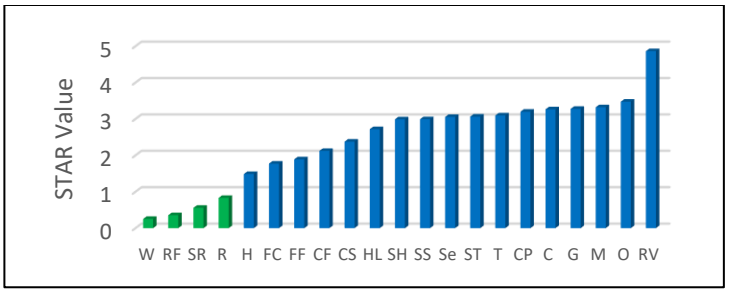

Figure 7: STAR values for each helmet, lower values indicating lower risk of concussion on the left.

DISCUSSION

The majority of the whitewater helmets are not recommended given that the STAR values observed for the helmets indicate an extremely high probability of concussion for each impact. The helmets should reduce head accelerations by a far greater margin for lower concussion risks. For example, the STAR values over three indicate that for the six impact conditions over three concussions would be predicted. In contrast, the best helmets can reduce this value below one. The whitewater helmets should be able to reduce the head impact accelerations much more across all helmets. One method to accomplish this would be to mirror some of the technologies utilized to design newer and more advanced football helmets.

Higher acceleration values for both linear and rotational acceleration were observed at higher impact speeds, with linear and rotational acceleration being strongly correlated (r^2 =0.72). Linear acceleration was observed to be higher in the front impact conditions, whereas rotational acceleration was observed to be higher in the side condition. A possible cause for this observation is the difference in centric and non-centric aspects for each impact location.

Helmet performance did not correlate well with other factors such as weight (r^2=0.03) and price (r^2=0.11). This highlights the necessity of a helmet rating system, because consumers cannot always use these factors as an indication of helmet performance. When comparing the 21 total helmet models tested by brand, the top four best performing helmets (W, RF, SR, and R) were all manufactured by "Sweet Protection."

ACKNOWLEDGEMENTS

Funding for this study was provided by the Institute for Critical Technology and Applied Science (ICTAS). The authors thank our good friend Brett Stoner and his unfortunate water sport head injury for motivating this study.

REFERENCES

[1] Spittler, J et al., *Sports-Specific Ill Injury*. 19, 422-429, 2020.
[2] EN 1385: 2012, *BSI Standards Publication* 2013.
[3] Rowson, S et al., *J of Neurosurgery*. 120, 919-922, 2014.
[4] Bland, M et al., *Ann Bio Eng*. 48, 47-57, 2020.
[5] Rowson, S et al., *Ann Bio Eng*., 39, 2130-2140, 2011.
[6] Rowson, B et al., *Ann Bio Eng*. 43, 2429-2443, 2015.
[7] Campolettano, E et al., *Ann Bio Eng*. 48, 1640-1650, 2020.

ENHANCING TRANSSCLERAL DELIVERY OF A DRUG SURROGATE USING ULTRASOUND IN PORCINE EYES

Grayson N. Bockman (1), Jr-Jiun Liou (1), Jonathan P. Vande Geest (1,2,3)

(1) Bioengineering Department
Swanson School of Engineering
University of Pittsburgh
Pittsburgh, PA, USA

(2) McGowan Institute for Regenerative Medicine
Louis J. Fox Center for Vision Restoration
University of Pittsburgh
Pittsburgh, PA, USA

(3) Louis J. Fox Center for Vision Restoration
University of Pittsburgh
Pittsburgh, PA, USA

INTRODUCTION

Globally, glaucoma is the leading cause of irreversible blindness, and disproportionally impacts people of African and Asian descent [1]. To investigate the effect of scleral stiffness on the susceptibility to glaucoma, Kimball treated mouse eyes with glyceraldehyde via subconjunctival injections but found no effect on the structure or function of the retina. However, in mice with experimentally-induced glaucoma, it was found that glyceraldehyde significantly increased intraocular pressure (IOP) and axon loss after 6 weeks [2]. It can therefore be hypothesized that de-stiffening of the sclera can halt glaucomatous damage, but we want to ensure that de-stiffening agents are delivered through the sclera. Therefore, we will enhance scleral permeability in porcine eyes via ultrasound and deliver Texas Red Dextran, a fluorophore with similar molecular weight to certain de-stiffening agents at 70 kDa.

METHODS

Twenty fresh porcine eyes and Texas Red Dextran (D1864, Thermo Fisher) were purchased commercially. Porcine whole globes were submerged in either 1X PBS or Texas Red Dextran solution. Half of the globes (n=5 eyes per group, see **Table 1**) from each solution were treated with or without 1 MHz ultrasound (0.250 MPa, spatial temporal peak intensity 2.0 W/cm^2, 40% duty cycle [40 ms on, 60 ms off, 10 Hz PRF] spatial peak temporal average intensity 0.8 W/cm^2, TI 1.2) via a flat disk transducer for 3 minutes, after which the eyes were fixed in 10% formalin (see **Figure 1** for transducer set up).

Table 1: Experimental Setup

	Without Ultrasound	With Ultrasound (1 MHz)
PBS	n = 5 pig eyes; Expected Outcome: no fluorescent signal	n = 5 pig eyes; Expected Outcome: no fluorescent signal
Texas Red Dextran	n = 5 pig eyes; Expected Outcome: fluorescent signal observed on the outer surface of the sclera	n = 5 pig eyes; Expected Outcome: fluorescent signal penetrated through the sclera

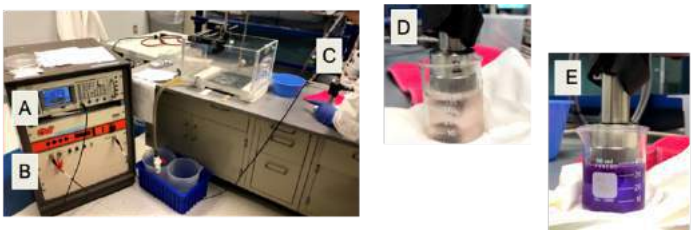

Figure 1: [A] Generator, [B] Amplifier, [C] Transducer, [D] Whole globe in PBS, and [E] Whole globe in Texas Red Dextran.

The porcine optic nerve heads (pONHs) were isolated, embedded in paraffin, and sectioned for imaging. A Cy3 filter and 4x objective on the fluorescent microscope were utilized to visualize the Texas Red Dextran signals

After obtaining the microscopy images, a MATLAB open-source code was used to calculate the porosity of the Texas Red Dextran-treated eyes. The images were also processed by MATLAB with a line

intensity program that demonstrates the fluorescent intensity of the Texas Red Dextran shown from the external side of the sclera into the thickness of the sclera.

RESULTS

All eyes were imaged under fluorescence microscopy and some representative samples of each group can be seen in **Figure 2**. All of the PBS-treated eyes showed no fluorescence in their images.

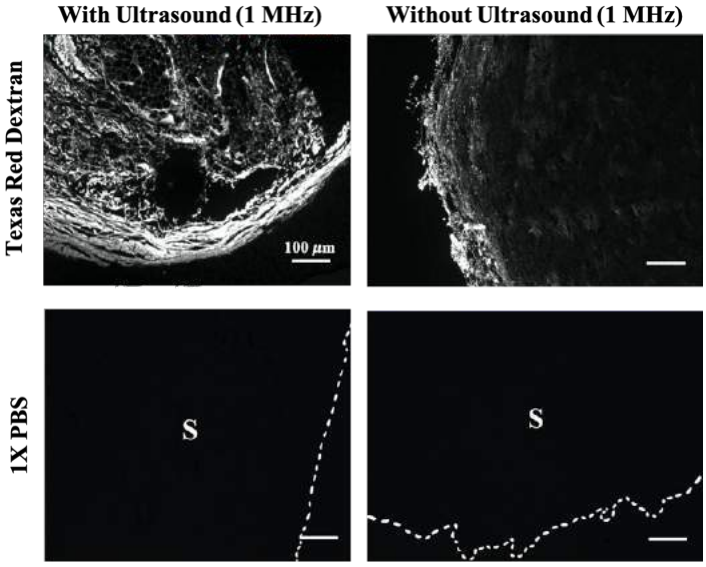

Figure 2: Fluorescent microscope images of pONH sclera (S depicting sclera not emitting fluorescence).

The results of the porosity calculation showed a 54.1% mean porosity for the ultrasound-treated eyes (SD = 15.5%) and a 60.3% mean porosity for the untreated eyes (SD = 17.2%) (see **Figure 3**).

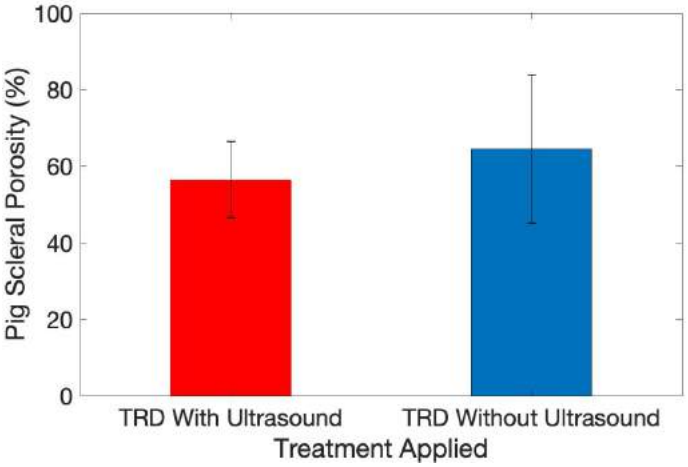

Figure 3: pONH head porosity between Texas Red Dextran (TRD) groups treated with or without ultrasound.

The graphs for the ultrasound-treated porcine eyes are shown to have a sustained intensity through the sclera, while the untreated eyes show an intensity localized to the external sclera lacking penetrance throughout (see **Figure 4**).

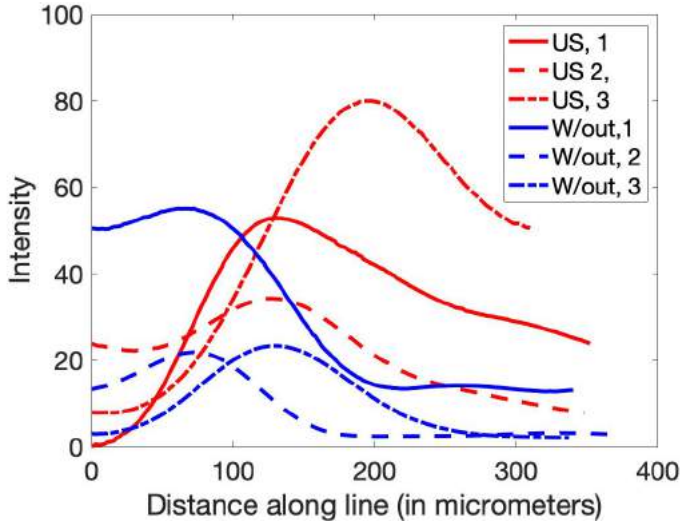

Figure 4: Graph depicting the intensity of fluorescent signal going from the outer sclera into the sclera of both ultrasound treated (US) and untreated (W/out) pONHs.

DISCUSSION

A two-sample t-test showed no statistical significance between the porosity of ultrasound-treated and untreated porcine eyes ($p = 0.15$). The results of the intensity study showed that the intensity of the Texas Red Dextran fluorescence in the untreated porcine eyes was limited to the outer surface of the sclera, while the ultrasound-treated eyes showed fluorescent permeance throughout the sclera, suggesting that diffusion of the fluorophore was enhanced by the application of ultrasound. The increased intensity does not appear to correspond with an increased porosity of the tissue, however this could relate to a change in porosity on a smaller scale that allowed for the diffusion of the Texas Red Dextran. This work leads us to believe that the application of ultrasound to eyes during treatment for glaucoma may help facilitate an increased responsivity of the sclera and therefore better outcomes, but we also must continue research to ensure this ultrasound is not causing any additional damage to the eyes.

ACKNOWLEDGEMENTS

I would like to thank my lab mates Kenneth Furdella, Ali Behrangzade, Hirut Kollech, Gloriani Sanchez, Lucy Jones, and Hannah Keeney for their collaboration and assistance with all challenges I faced. In addition, I would like to thank Hirut Kollech for advising me through some difficult programming.

REFERENCES

[1] Tham, YC et al., *American Academy of Opthamology,* 121:2081-2090, 2014.
[2] Kimball, EC et al., *Experimental Eye Research,* 128:129-140, 2014.

DATA ACQUISITION SYSTEM TO QUANTIFY BONE VISCOELASTICITY IN HINDFOOT AND MIDFOOT ARTHRODESIS

Melissa R Requist (1), Amanda L Rugg (2), Brooks W Johnson (2), Michelle M Son (2), Alicia Alvarez (3), L Daniel Latt (1,2)

(1) Department of Biomedical Engineering
University of Arizona College of Engineering
Tucson, AZ, USA

(2) Department of Orthopaedic Surgery
University of Arizona College of Medicine
Tucson, AZ, USA

(3) Department of Physiology
University of Arizona College of Medicine
Tucson, AZ, USA

INTRODUCTION

Obtaining and maintaining compression between bone surfaces is critical for successful healing in fixing fractures and fusing joints because bone remodeling is highly dependent on mechanical loading [1]. Bone, like other biologic tissues, is viscoelastic, meaning that stress on the bone dissipates over time [2]. An understanding of how and when compressive stress is lost is critical to the design of surgical devices and techniques created to maintain bone compression for optimized healing. While many sensors exist to study compressive forces, few are optimized to the demands of screw implantation, which is a key component to many orthopaedic surgical techniques, including joint arthrodesis [3]. Here we present a simple and cost-effective sensor and data acquisition system that quantifies bone compression over time and to demonstrate the viability of this model in cadaveric models for hindfoot and midfoot arthrodesis.

METHODS

The key component of this system is a Futek LTH 300 donut load cell, since the hole in the center of the sensor allows for screw placement through the device. This sensor was connected to a Futek IAA 100 amplifier and MEGA 2560 Arduino board. This amplifier is designed to work with the sensor's existing wiring, but custom gain and shunt settings were used to adjust for the voltage outputs of the Arduino board. The Arduino was connected to the computer via USB, and data collection and processing was done in a custom MATLAB app (Figure 1). Key features of this program include the real-time data visualization, embedded filtering, continuous autosaving (so raw and filtered data are not lost if there is an interruption in data collection), calibration and check calibration features, and flexibility to modify filter parameters or data collection frequency. The system was calibrated from 0 to 2000N using an MTS machine, and calibration was checked in the lab prior to each data collection using handheld weights. Data were collected at 10 Hz and filtered with a 6th order Butterworth lowpass filter with a 0.075 normalized frequency cutoff.

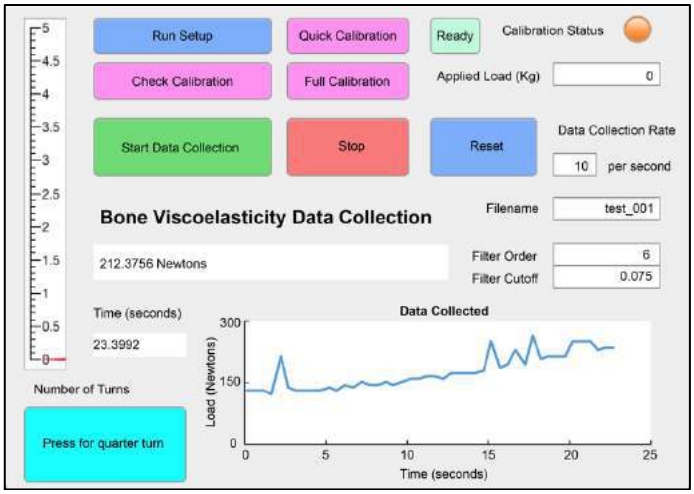

Figure 1: Graphic User Interface for custom MATLAB program

Hindfoot Arthrodesis Model: 25 mm diameter bone cylinders were cut from cadaveric talus and calcaneal pairs. The bone cylinders were prepared for simulated arthrodesis by removing the cartilage and flattening the subchondral bone surface. The sensor was placed between the two cylinders with a washer on each side to contact the loading surface, and additional washers were added as spacers when needed (Figure 2). A partially threaded cannulated lag screw was placed from the posterior-inferior aspect of the calcaneus cylinder to the anterior-superior aspect of the talus cylinder to simulate subtalar arthrodesis. The complex was left to rest for three minutes before screw retightening, then left untouched for 30 minutes with compression data collected throughout the trial.

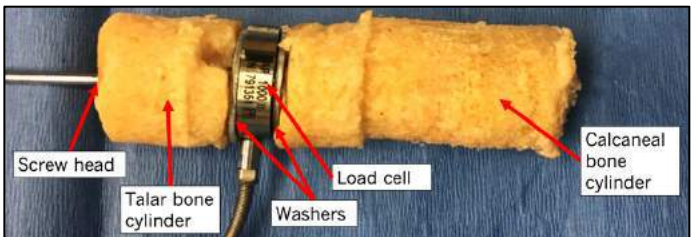

Figure 2: Hindfoot arthrodesis model

Midfoot Arthrodesis Model: A guide pin was placed along the optimal trajectory for medial column beaming from the center of the first metatarsal head along the first ray to the center of the dome of the talus. The middle 12 mm of the medial and intermediate cuneiforms was excised to create space for the compression sensor, leaving in place the articular surfaces of the naviculocuneiform and 1st tarso-metatarsal joints. Using the guide pin for alignment, the load cell was placed in this space with two or three washers on each side to contact the loading surfaces (Figure 3). A drill was used to prepare the screw track and a cannulated screw was inserted over the guide pin. Compression data was collected starting when the threads at the head of the screw entered the metatarsal head and recorded until the head of the screw was buried 10mm deep in the metatarsal head and then allowed to sit untouched for 150 seconds.

Figure 3: Midfoot arthrodesis model

RESULTS

This system was able to accurately collect data in both hindfoot and midfoot arthrodesis cadaveric models. An example of this data is shown in Figure 4, which gives data from the retightening lag screw trials in the hindfoot arthrodesis model. Data output includes raw, calibrated, and filtered values.

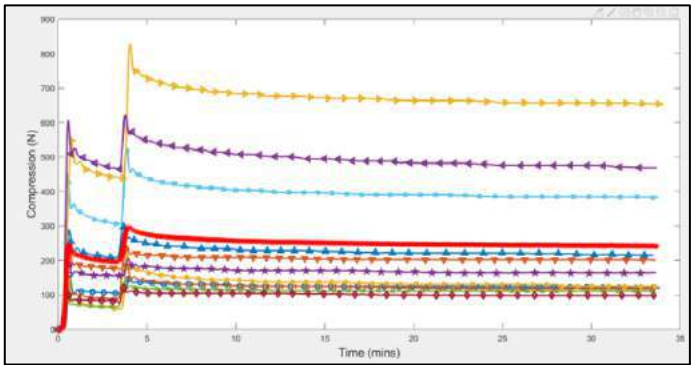

Figure 4: Example data from screw retightening trials for simulated hindfoot arthrodesis model

In addition to functioning satisfactorily, the sensor system is also cost-effective, in large part due to the use of an Arduino board and a custom MATLAB data acquisition program. Prices for all components of this system are given in Table 1. The MATLAB and Arduino based setup further allow adaptability for use of this system in a variety of applications and transferability to be used by different researchers and computers.

Table 1: Cost for components of the data acquisition system

Component	Cost
Futek LTH 300	$598.00
Futek IAA 100	$450.00
Elegoo MEGA 2560 Arduino	$17.99
MATLAB*	$0.00
Flat washers**	$0.74
Wiring**	$0.48

*MATLAB subscriptions are covered by many academic institutions, hence why $0 is listed. The annual student license is $49, the annual academic license is $250 and the annual standard license if $860.
**Price reflects components used, even if they are not purchasable in that small of a quantity.

DISCUSSION

This data acquisition system represents a cost-effective and easily adaptable strategy for studying longitudinal compressive stress response in bones with screw implantation. The Arduino and MATLAB base allow the system to be easily used by different operators and computers, and give flexibility for modifications to adapt this system to many applications. We demonstrated to applications, with cadaveric models of hindfoot and midfoot fusion, and further work with focus on using these models to answer clinical questions and adding additional sensor inputs to the system for more complex models.

ACKNOWLEDGEMENTS

This research was supported in part by a grant from the University of Arizona Graduate & Professional Student Council.

REFERENCES

[1] Frost HM. Angle Orthod. 1994; 64(3)
[2] Manda K et al. Biomech Model Mechanobiol. 2017; 16(1)
[3] Nihal A et al. Foot Ankle Surg. 2008; 14(1)

LOCATION DEPENDENT MECHANICAL BEHAVIOR OF APONEUROSIS TISSUE UNDER UNIAXIAL TENSILE STRETCH

Emily E. Tully (1), Benjamin B. Wheatley (1)

(1) Department of Mechanical Engineering
Bucknell University
Lewisburg, PA, USA

INTRODUCTION

Aponeurosis is a connective tissue that attaches muscle fibers to tendon [1]. The aponeurosis covers the surface of a muscle in a sheath-like manner and fans out with decreasing thickness away from tendon [2]. Although aponeurosis is commonly found in muscle-tendon units throughout the body, there have been comparably few studies on the mechanical role of aponeurosis and fewer still on the material properties of aponeurosis. Specifically, there are no reported investigations on the interaction of aponeurosis thickness, distance from the tendon, and mechanical response to load. Previous studies measured material properties of aponeurosis samples assuming that there is a constant thickness throughout the tissue, when it is known to be variable [2-5].

This unknown relationship between aponeurosis regional structure and function makes aponeurosis tissue a poorly understood component of muscle-tendon units. For example, it remains unclear if aponeurosis acts as a material extension of tendon, or if it transitions from a higher or lower stiffness near the tendon to a different stiffness near the muscle midbelly. Computational models regularly neglect aponeurosis tissue or aponeurosis variability due to lack of information, rather than confidence in assumptions. The goal of this work is to perform uniaxial tensile testing and digital image correlation analysis to measure the mechanical response of aponeurosis tissue as a function of thickness and location from tendon to muscle. We hypothesize that aponeurosis tissue maintains consistent material properties, as measured by stress-strain curves, as it transitions from tendon to muscle.

METHODS

Triceps brachii tissue was extracted from porcine shoulder for testing (Figure 1A). The aponeurosis was separated from the muscle tissue using standard dissection tools such as scalpel and forceps. Ten (n=10) samples were then cut into rectangular strips measuring ~60 mm in length and ten mm in width with custom dissection equipment, with fibers oriented longitudinally. Five mm increments were marked on each sample with permanent marker. Each sample was placed under a dissection microscope with the marked edge facing up. Four evenly spaced thickness measurements were taken between each marking in the middle 40 mm, for a total of 32 total thickness measurements for each sample (Figure 1B).

Uniaxial tensile testing was completed on a custom planar biaxial material testing system (ADMET, Inc., Norwood, MA). Ten mm sections at both ends of the sample were clamped with serrated grips and the strain rate for the tensile test was set to 0.03 min^{-1} elongation to failure. A charcoal powder was lightly dusted onto the sample through a sifter for digital image correlation (DIC) (Figure 1C).

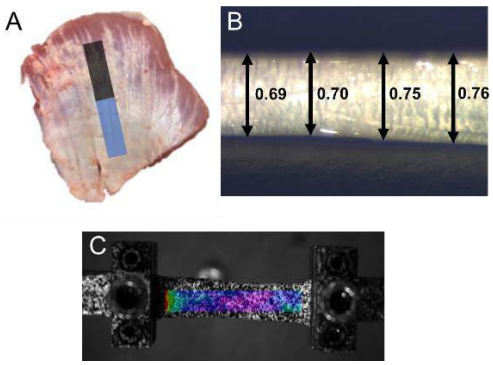

Figure 1. A) Triceps brachii muscle with attached aponeurosis and representative sample regions (black – transition region, blue – insertion region) [2] B) dissection light microscope image for

measuring thickness [mm] C) rectangular sample used for tensile testing, including charcoal speckle pattern and representative DIC analysis strain color contour plot.

Image capture rate was at an interval of 0.5 seconds. Using the uniaxial force data, inhomogeneous 2D DIC data, and thickness measurements, the average nominal (engineering) stress and Lagrange strain values were determined for two sections of each sample, one considered the 'transition region', where the aponeurosis tissue connects to muscle fibers and is thinner, and the other considered the 'insertion region', where the aponeurosis tissue connects to the tendon tissue and is thicker. Linearized moduli were determined at each time point by dividing nominal stress by Lagrange strain of both regions. Paired t-tests ($p<0.05$) were performed on the Lagrange strain and linearized modulus at each time point to determine any statistically significant differences in the material behavior of tissue of varying thickness and location.

RESULTS

The average nominal stress and Lagrange strain data for both regions showed a nonlinear response, with an initial toe-region, a linear region, and a softening region (Figure 2). The transition region had an average thickness of 0.703 ± 0.073 mm, and the insertion region had an average thickness of 0.952 ± 0.061 mm. The Lagrange strain t-tests remained above $p=0.05$ for each data point. At 131 seconds, indicated by a red asterisk in Figure 2, the p-value of the linearize modulus t-test drops below $p=0.05$ and remains below that threshold until the test is complete at 200 seconds (Figure 3).

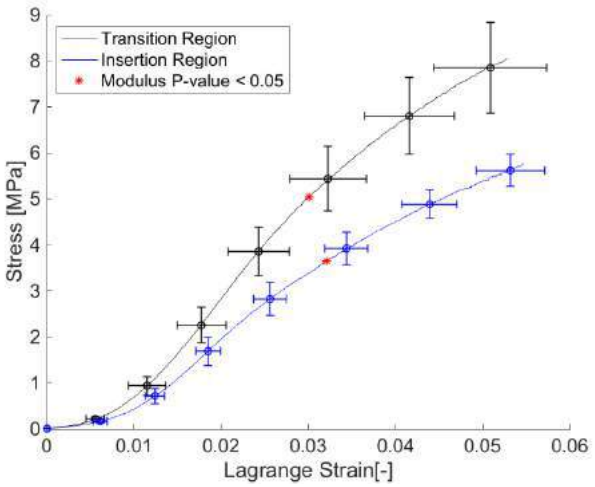

Figure 2. Average stress-strain curves for each quarter of aponeurosis tissue samples. Error bars in Figure 2 are shown at time points with intervals of 55 seconds.

DISCUSSION

Previous studies have investigated the material properties of aponeurosis tissue assuming an average thickness across samples, while this study investigated how variations in thickness may affect stress-strain behavior. Aponeurosis thickness measurements from this study showed a decrease in thickness from the tendon insertion region to the muscle transition region. This varying thickness may be a function of the inhomogeneous load the aponeurosis bears *in vivo*. A paired t-test of the strain of the two regions indicated that there is no significant difference in the strain of an aponeurosis sample at different thicknesses. However, a paired t-test of the linearized modulus shows that the moduli of the regions may diverge as the stress increases over time (Figure 3). Specifically, the transition (thinner) region exhibited a stiffer stress-strain response than the insertion (thicker) region, disproving our hypothesis. This suggests that under load, aponeurosis may exhibit higher moduli in thinner sections.

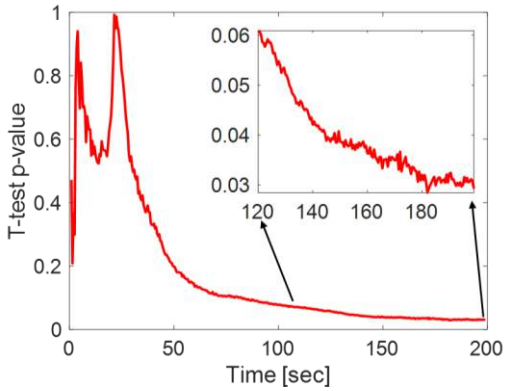

Figure 3. P-values of t-test comparing insertion and transition region linearized modulus (stress/strain) versus time.

When working with and analyzing the mechanical properties of many biological materials, including aponeurosis tissue, it is important to consider how natural variations in the material may affect the observed behavior. The collagen fibers in aponeurosis are likely to have some inhomogeneous alignment and/or crimping, which is shown in the existence of a toe region at the beginning of stress-strain curves (Figure 2). Additionally, individual collagen bundles are likely to have varying geometry, meaning they experience different stresses under the same force or uncrimp and fail at different loads and strains, and may naturally have different stiffness. This study assumed that there were consistent material properties and thicknesses across the width and thickness of the sample, with variations only occurring lengthwise, when the DIC imaging showed varying strain measurements in both directions (Figure 1C). Future work to better characterize the stress-strain response of the two regions, such as with tangent moduli or hyperelastic modeling would benefit this work.

CONCLUSIONS

Variations in aponeurosis tissue thickness and material properties are likely to affect muscle-tendon unit mechanics and subsequent modeling efforts [3]. This work suggests thinner aponeurosis regions near the muscle midbelly may exhibit a stiffer stress-strain response than regions closer to the tendon. The mechanical consequences of this are not known but could impact the function of muscle-tendon units. These data help to create a more complete understanding of the material properties of aponeurosis, with the goal of improving future computational studies of muscle-tendon unit mechanics.

ACKNOWLEDGEMENTS

This material is based upon work supported by the National Science Foundation under Grant No. 1828082.

REFERENCES

[1] Eng, C. J. Appl Physiol., 125: 513-519, 2018.
[2] Grega, KL. J. Mech Behav Biomed Mater., 110:1-3, 2020.
[3] Oda, T. ABE., 4:12-14, 2014.
[4] Azizi, E. Integr Comp Biol 49.1: 51-58, 2009
[5] Shan, X. PLoS ONE 14.2: 1-18, 2019

LOSS OF ENDOTHELIN-1 MAY OFFER PULMONARY VASCULAR PROTECTION AFTER MYOCARDIAL INFARCTION

Hailey H. Frye (1), Diana M. Tabima (1), David J. McCulley (2), Naomi C. Chesler (3)

(1) Department of Biomedical Engineering
University of Wisconsin – Madison
Madison, WI, USA

(2) Department of Pediatrics
University of California, San Diego
San Diego, CA, USA

(3) Edwards Lifesciences Center for
Advanced Cardiovascular Technology and
Department of Biomedical Engineering
University of California, Irvine
Irvine, CA, USA

INTRODUCTION

Left heart failure (LHF) burdens an estimated 6.2 million American adults and appeared on 379,800 death certificates in 2018 [1]. Pulmonary hypertension occurs in 60-80% of patients with LHF (PH-LHF) leading to a two-fold increase in mortality compared to isolated LHF [2,3]. Initial PH-LHF, termed isolated post-capillary PH (Ipc-PH), develops due to a passive one-to-one increase in pressure throughout the pulmonary vasculature. Classified by elevated mean pulmonary arterial pressure (mPAP) with normal pulmonary vascular resistance (PVR), the effects of Ipc-PH can be reversed [4]. However, Ipc-PH progresses to combined pre- and post – capillary PH (Cpc-PH) in 12-38% of the patient population [5]. Cpc-PH patients demonstrate increased vascular resistance and diastolic pressure gradient (DPG), both contributing to the irreversibility of this disease and the increased prevalence of right heart failure, a key predictor of decreased survival [6].

The mechanisms associated with Ipc-PH progressing to Cpc-PH remain unknown. We sought to investigate the contributions of mechanobiological pathways to disease progression. Worsening LHF leads to increased left atrial pressure (LAP) and decreased cardiac index (CI), which should decrease venous shear stress. Low shear stress has been observed in PH patients and is associated with pathologic changes including pulmonary remodeling [7,8]. Endothelial cells sense changes to mechanical stimuli, including decreased shear stress, and respond through mechanotransduction signaling. These pathways lead to decreased endothelial nitric oxide synthase (eNOS) phosphorylation and increased vasoconstrictor endothelin-1 (ET-1) release [9]. Clinical studies observed increased ET-1 levels in PH-LHF patients [10,11]. We hypothesized that LHF leads to decreased shear stress and increased ET-1, promoting increased total PVR (TPVR) and thus RV remodeling. To test this hypothesis, we generated myocardial infarction (MI) in control mice (Ctrl) and those with a mutation of ET-1 in pulmonary artery endothelial cells (Mut).

METHODS

Mice with disrupted ET-1 expression in pulmonary endothelial cells were bred using the flox allele of ET-1 and an inducible Cre-recombinase directed by the Tbx4 lung enhancer which is active in the pulmonary vascular endothelium [12,13]. Litter mate controls and Mut mice were randomly assigned into myocardial infarction (MI) and sham groups. Initial anaesthetization used 5% isoflurane followed by a maintained dosage of 1-2% during the procedure. We performed left anterior descending coronary artery ligation on a heated platform to produce an MI and thus, LHF. Operational complications resulted in an n=2 for each group with no animals in the mutant sham group.

At week 0, 4, 10, and 20, animals underwent echocardiography using previously established M-Mode, mitral valve, tricuspid valve, and pulmonary valve protocols. Values were averaged over three consecutive cardiac cycles.

Terminal studies at week 20 began with urethane anesthetization followed by intubation. To obtain *in vivo* hemodynamic measurements, the thoracic cavity was exposed, and a calibrated 1.2-Fr admittance catheter was inserted into the right ventricle (RV). We monitored heart rate and systemic pressure throughout the procedure. After baseline pressure-volume data was obtained, brief occlusions of the inferior vena cava allowed measurement of end-systolic and end-diastolic pressures to assess alterations in venous return. Commercial software (Notocord; Croissy Sur Seine, France) recorded pressure volume data for analysis. A minimum of three steady state timepoints and two occlusions were averaged for each hemodynamic metric.

After right heart catheterization, animals were euthanized, and the RV free wall was separated from the left ventricle and septum (LV+S)

for weights and preservation in liquid N_2 or formalin. All animal procedures were approved by the University of Wisconsin – Madison Institutional Animal Care and Use Committee.

All values presented as mean ± SD. With n=2 per group, statistical analysis could not be conducted. Evaluations of results were based on observable trends to inform future studies.

RESULTS

Echo, morphology, and RHC data demonstrate possible differences in PH-LHF progression in control mice compared to Mut mice. Echo data indicates the systolic LV volume normalized to bodyweight was greater for control MI group compared to Mut MI and control sham (Figure 1A). Additionally, LV ejection fraction (LVEF) was decreased in control MI animals compared to Mut MI animals with an increased difference at week 20 compared to week 10 (Figure 1B).

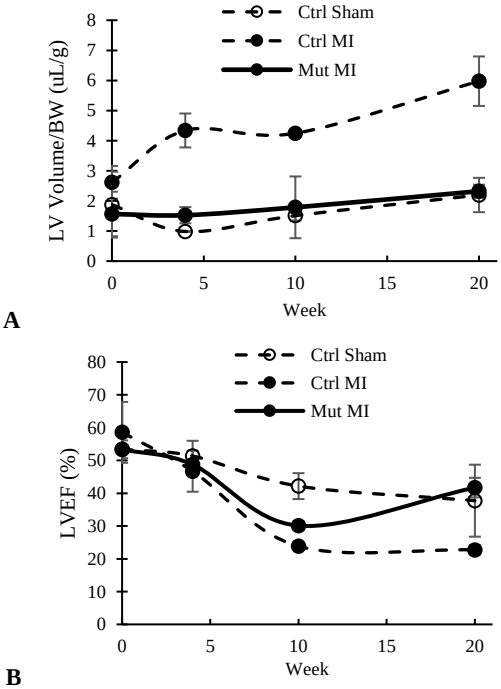

Figure 1 A: Systolic LV volume normalized to BW and B: LVEF throughout experimental time course.

Control MI mice developed greater ventricular remodeling compared to Mut MI mice and control sham animals as evident in LV+S and RV weights normalized to bodyweight (Figure 2 A&B).

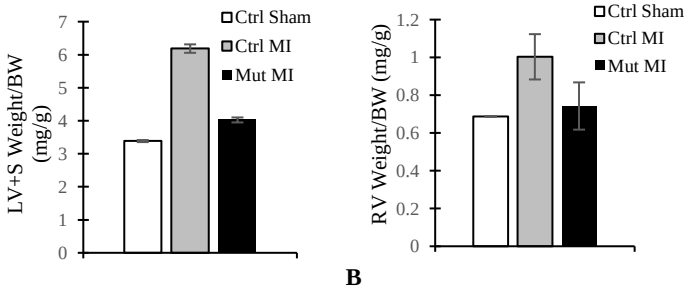

Figure 2 A: LV and septum weight normalized to bodyweight. B: RV weight normalized to bodyweight.

Cardiac index was lowest in the control MI animals followed by Mut MI animals and highest in the control sham (Figure 3A). TPVR, calculated by dividing RV end-diastolic pressure by cardiac output, was generally increased for control MI animals compared to control sham and Mut MI animals (Figure 3B).

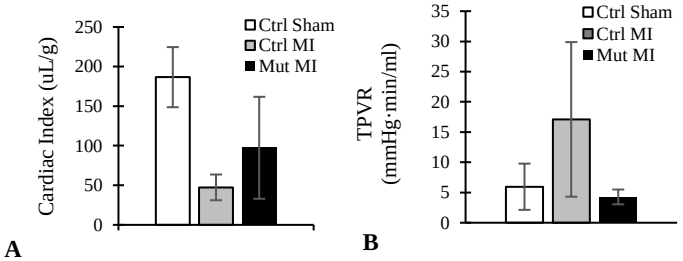

Figure 3 A: Cardiac index and B: TPVR values from RHC analysis 20 weeks after MI surgery.

DISCUSSION

As PH-LHF progresses from Ipc-PH to Cpc-PH, biventricular remodeling occurs (Figure 2) and cardiac function decreases (Figure 1B and 3A). ET-1 mutant mice appear to have less remodeling and dysfunction 20 weeks after MI surgery compared to control MI mice. The time course of LVEF suggest mice with ET-1 mutation recovered LV function after week 10 (Figure 1A). We propose the lack of pulmonary ET-1 prevents both the pulmonary arterial vasoconstriction and remodeling that leads to increased TPVR observed in control MI animals. This inhibition may prevent RV remodeling by maintaining a low RV afterload.

The current study has three main limitations. First, the sample size prevented statistical analysis and definitive conclusions. Second, the original study design included both male and female mice, but early mortality after MI surgeries generated a Mut MI group with only male mice and a control MI group with only female mice. Finally, there were no Mut sham animals.

The results from this initial study justify future experiments investigating the role of ET-1 in progression of Ipc-PH to Cpc-PH. Discerning the mechanism contributing to PH progression and RV failure secondary to LHF may provide a targetable pathway for pharmacological treatment in the future.

ACKNOWLEDGEMENTS

We would like to thank Dr. Tim Hacker for performing MI and RHC procedures and Allison Brodbeck for performing echocardiography. Funding from NIH 5R01HL147590-02 is gratefully acknowledged.

REFERENCES

[1] Virani, S et al., *Circulation*, 141(9):139-596, 2020.
[2] Guglin, M et al., *J Card Fail*, 16(6): 461-474, 2010.
[3] Guazzi, M et al., *Circulation*, 126(8): 975-990, 2012.
[4] Ghio, S et al., *PLoS ONE*, 12(11), 2017.
[5] Rosenkranz, S et al., *European Heart Journal*, 37: 942-954, 2016.
[6] Gaeli, N et al., *European Heart Journal*, 37: 67-119, 2016
[7] Barker, A et al., *Magnetic Resonance in Medicine*, 73(5): 1904-1913, 2015.
[8] Shafer, M et al., *Pulmonary Circulation*, 6(1): 37-35, 2016.
[9] Chatzizisis, Y et al., *Journal of American College of Cardiology*, 49(25): 2379-2393, 2007.
[10] Moraes, D et al., *Circulation*, 102(14): 1718-1723, 2000.
[11] Cunningham, K et al., *Laboratory Investigation*, 85(1): 9, 2005.
[12] Kisanuki, Y et al., *Hypertension*, 56(1):121-8, 2010.
[13] Zhang, W et al., *BMC Biology*, 11:111, 2013.

THE SYNOVIOCYTE RESPONSE TO PHYSIOLOGIC SHEAR UNDER CULTURE CONDITIONS SIMULATING DIABETIC INSULIN RESISTANCE AND OSTEOARTHRITIS JOINT INFLAMMATION

Neeraj Sakhrani[1], Lance A. Murphy[1], Andy J. Lee[1], Eric J. Semler[2], Roshan P. Shah[3], Gerard A. Ateshian[1,4], Clark T. Hung[1,3]

(1) Department of Biomedical Engineering
Columbia University
New York, NY, USA

(2) MTF Biologics
Edison, NJ, USA

(3) Department of Orthopedic Surgery
Columbia University
New York, NY, USA

(4) Department of Mechanical Engineering
Columbia University
New York, NY, USA

INTRODUCTION: Osteoarthritis (OA) is a degenerative joint disease characterized by articular cartilage degradation and inflammation of the synovium, the specialized connective tissue that envelops the diarthrodial joint.[1] The prevalence of type 2 diabetes (DM) is linked with OA progression.[2] DM is characterized by chronic hyperglycemia that results from insulin resistance or defects in insulin secretion.[3,4] The correlation between OA and DM are associated with shared risk factors, including age and joint loading from obesity.[2] Fluid-induced shear stress from joint articulation is a relevant stimulus for fibroblast-like synoviocytes (FLS).[5] It is known that insulin resistance contributes to decreased cellular response[6], but FLS respond to mechanical cues to support joint health and modulate inflammation.[7,8] We hypothesized that synoviocyte mechanotransduction is modulated by glycemic and cytokine exposure. To simulate OA and DM in the synovial joint, we subjected healthy fibroblast-like synoviocytes (FLS) to varying glycemic and cytokine culture treatments to induce the biological response of the diseased phenotype. By exposing healthy FLS to hyperglycemic conditions and interleukin-1 (IL), a pro-inflammatory cytokine elevated in OA, we could model diabetic insulin resistance and OA pathogenesis, in order to overcome challenges associated with age and/or disease state.[9] It is known that patients with DM can suffer compromised synovium function as the development of synovial insulin resistance leads to the production of inflammatory mediators linked with OA.[1,10] In OA, pro-inflammatory cytokines, including IL, are known to stimulate the synthesis and release of nitric oxide (NO), which contributes to joint pathology.[11] In DM, the AKT signaling pathway is involved in the regulation of insulin and glucose uptake in adipose tissue[3], where AKT phosphorylation stimulates translocation of glucose transporters to cell surface insulin receptors.[12] Study 1 characterized concurrent changes in AKT phosphorylation and NO release of synovial explants (healthy, OA±DM) in response to hyperglycemic, IL, and insulin culture conditions as an indicator of diabetic insulin resistance and OA inflammatory response, respectively. While the AKT pathway and NO secretion are separate downstream markers of DM and OA, both are regulated by upstream calcium influxes, an ubiquitous measure of cellular activity.[13,14,15,16] By investigating synovial explants under glycemic and cytokine treatments, we optimized preconditioning conditions to confer the diabetic and OA phenotype in healthy tissue, from which we derived cells to monitor the intracellular calcium response ($[Ca^{2+}]_i$) to shear. Study 2 characterized mechanotransduction of FLS cultured in glucose (low: euglycemic, high: hyperglycemic) ± IL by observing the $[Ca^{2+}]_i$ response to fluid-induced shear stress.

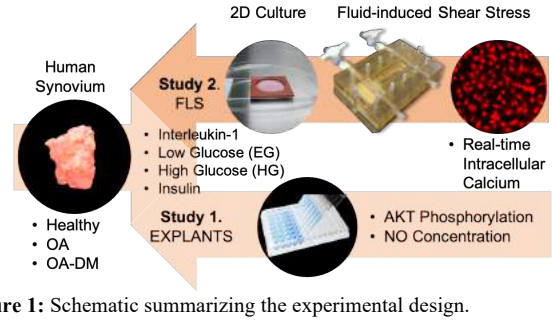

Figure 1: Schematic summarizing the experimental design.

METHODS: *Explant Preparation*. OA human synovia were harvested from diabetic and non-diabetic patients during total knee arthroplasty (IRB#AAAQ2703) and healthy synovium was obtained from the Musculoskeletal Transplant Foundation (Edison, NJ). Synovial explants were pre-conditioned in varying glucose and insulin levels for 5 days to detect levels of AKT (Ser 473) phosphorylation (n = 3 donors per group, 2 explants/donor). Synovial explants were treated in euglycemic (EG;

5.56 mM D-glucose) and hyperglycemic (HG; 12.5 mM D-glucose) culture conditions.[3] Physiologic levels of human recombinant insulin (6.25 µg/mL) were added to both EG and HG groups (EGI and HGI respectively).[3] *AKT Phosphorylation*. Synovial explants were lysed, homogenized, and quantified for relative levels of phospho- and pan-AKT using an ELISA (RayBiotech, Inc.). *Nitric Oxide*. NO released into the glucose and cytokine treated media was quantified using Griess Reagent for nitrite quantification (Life Technologies). *Cell Isolation and Culture*. FLS were isolated from healthy and OA±DM synovial explants using 1mg/mL of type II collagenase digestion. Cells were expanded in αMEM supplemented with 10% FBS, 1% PSAM and 5 ng/mL FGF (Life Technologies) for two passages.[13] *Calcium Imaging*. FLS were plated in silicone wells (Grace Bio-Labs) on 5 µg/cm^2 collagen type 1 coated glass slides at 5.3 x 10^4 cells/cm^2.[13] Cells were pre-conditioned in the same glucose groups with 10 ng/mL IL-1 for an additional 24 h prior to imaging, with parallel untreated controls (EG, HG, EG+IL, HG+IL). An osmotic control consisted of EG medium supplemented with sucrose (EGS). Changes in $[Ca^{2+}]_i$ were tracked via Fura Red-AM (Life Technologies).[13] Fluid flow using HBSS with 0.1% FBS was applied in a parallel plate flow chamber at 0.1 Pa shear stress (N=100 cells/slide,5 slides/group).[13,17] FLS were considered responders for $[Ca^{2+}]_i \geq 20\%$ above baseline level.[13] *Statistical Analysis*. Non-parametric data was analyzed via Fisher's Exact Test with Holms-Sidak correction for multiple comparisons ($\alpha = 0.05$). Healthy and OA±DM donor groups were analyzed using a three-way ANOVA with Tukey's post-hoc test ($\alpha<0.05$) to determine significant differences between disease states, glycemic conditions, and cytokine treatment **(Fig. 1)**.

RESULTS: *Study 1*. Phospho-AKT levels were significantly elevated in baseline EG compared to HG groups across explants (healthy, OA±DM; p<0.0001) **(Fig. 2A-C)**. OA+DM synovium exhibited greater decrease in AKT phosphorylation for the HG group, possibly indicative of a more insulin resistant environment **(Fig. 2C)**. For the healthy and non-diabetic phenotype, insulin treatment increased phospho-AKT levels compared to the respective non-insulin treated EG and HG groups (p<0.001) **(Fig. 2A, B)**. The EGI group in the OA+DM phenotype exhibited increased levels of phospho-AKT compared to control (p=0.004), but no significant changes were observed between the insulin and non-insulin treated HG groups (p=0.2182). Hyperglycemic treatment led to decreased release of nitric oxide in media compared to the control EG group in both the healthy and non-diabetic OA cells (p<0.0001) **(Fig. 2D, E)**. No significant differences in NO secretion were observed between the EG and HG treated groups in the diabetic OA group **(Fig. 2F)**. IL significantly increased NO release compared to the non-cytokine treated groups across all three phenotypes and both glycemic conditions. *Study 2*. The $[Ca^{2+}]_i$ response for healthy FLS was significantly elevated in the control EG group compared to HG treated cells, 73.3 ± 7.3% responders vs. 14.0 ± 6.7%, p<0.001 **(Fig. 2G)**. While the OA±DM FLS response to shear was elevated in the EG treated cells (p<0.001), the HG group for both diseased phenotypes had a greater response to shear compared to healthy FLS with 53.7 ± 2.1% and 34.0 ± 12.5% responders respectively **(Fig. 2H, I)**. The response of EGS and EG groups suggest no osmolarity effects. FLS response to IL treatment was significantly greater in the EG compared to the HG group for both the healthy and diseased cells. (p=0.0032 healthy, p=0.0813 OA-DM, p=0.0012 OA+DM) **(Fig. 2G-I)**. However, compared to non-cytokine treated FLS, IL exposure significantly increased the percentile response across all control groups. Specifically, the HG+IL group for the healthy FLS exhibited a significant increase in response that yielded similar behaviors to those of native OA cells, with 44.7 ± 12.7% responders for the heathy HG-IL group vs. 53.6 ± 4.1% and 34.0 ± 12.5% for the OA non-diabetic and diabetic hyperglycemic groups respectively.

DISCUSSION: Under conditions of the current study, healthy synoviocytes exhibited biological behavior consistent with a disease phenotype associated with OA and DM. Study 1 demonstrated that hyperglycemic treatment for both healthy and diseased synovial explants led to decreased phospho-AKT levels compared to the control EG groups, characteristic of the diabetic disease state. Lower levels of AKT phosphorylation are indicative of more insulin resistant environments.[18] The explants also exhibited elevated NO secretion in media supplemented with IL compared to groups without cytokine treatment, characteristic of OA.[19] As recognized downstream markers of DM and OA pathogenesis, both AKT and NO concentrations exhibited consistent changes in cell behavior between healthy and diseased tissue, suggesting a potential link between glycemic conditions, insulin resistance, and joint inflammation. Studies of shear-induced calcium signaling (Study 2) suggest that cells from healthy (young) synovium can be cultured to exhibit the biologic response of diseased (aged) synovium, providing a model system to support basic science and translational studies towards developing therapies to mitigate diabetic insulin resistance and OA pathogenesis.

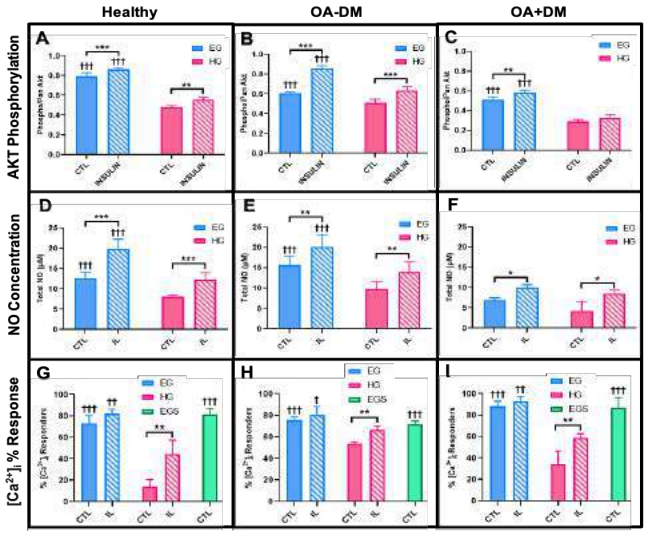

Figure 2: Healthy and OA±DM synovial explants **(A-C)** relative phospho-AKT levels in insulin and non-insulin treated groups, and **(D-F)** NO secretion with glycemic and IL-1 treatment. **(G-I)** Shear-induced $[Ca^{2+}]_i$ response with glucose, sucrose, and cytokine treatment for healthy and OA±DM FLS. *p<0.05, **p<0.01, ***p<0.0001 (control vs. insulin or IL). †p<0.01, ††p<0.002, †††p<0.0001 (EG vs. HG and EGI vs. HGI).

ACKNOWLEDGEMENTS: OSRF, MTF, NIH. **REFERENCES:**
[1] King, K.B. et al. *Osteoarthritis Cartilage*, 23: 841–850, 2015. [2] Piva, S.R. et al. *Clin Geriatr Med*, 31: 67-87, 2015. [3] Hamada, D. et al. *Arthritis Rheumatol*, 68: 1392-1402, 2016. [4] Röder, P.V. et al. *Exp Mol Med*, 48: 219, 2016. [5] Schett, G. *Arthritis Res*, 3: 80-86, 2001. [6] Wilcox, G. *Clin Biochem Rev*, 26: 19–39, 2005. [7] Sun, H.B. et al. *Connect Tissue Res*, 44: 42–49, 2003. [8] Yanagida-Suekawa, T. et al. *Eur J Oral Sci*. 121: 566-572, 2013. [9] Wang, P. et al. *FASEB J*, 27: 4664–4467, 2013. [10] Griffin, T. M. et al. *Arthritis Rheumatol*, 68: 1330–1333, 2016. [11] Zhong, L. et al. *Int J Mol Sci*, 18: 2491, 2017. [12] Mackenzie, R. et al. *Diabetes Metab Syndr Obes*, 7: 55–64, 2014. [13] Estell, E.G. et al. *J Biomech*, 60: 91-99, 2017. [14] Nicholson-Fish, J.C. et al. *Neurochem Res*, 41: 534–43, 2016. [15] Ebner, J. et al. *Pflugers Arch*, 472: 61-74, 2020. [16] Sears, C.E. et al. *Circ Res*, 92: 52-59, 2003. [17] Hung, C.T. et al. *Cell Signal*, 9: 587–94, 1997. [18] Tonks, K. T. et al. *Diabetologia*, 56: 875–885, 2013. [19] André, M.C. *Arthritis Res Ther*, 15: 115, 2013.

THE IMPACT OF PREGNANCY AND CHILDBIRTH ON VAGINAL DIMENSIONS AND CURVATURE

Victoria L. Martin (1), Megan R. Routzong (1), Liam C. Martin (1), Pamela A. Moalli (2), Ghazaleh Rostaminia (3), Steven D. Abramowitch (1)

(1) Department of Bioengineering
University of Pittsburgh
Pittsburgh, PA, USA

(2) Department of Obstetrics, Gynecology & Reproductive Surgery
University of Pittsburgh
Pittsburgh, PA, USA

(3) Division of Urogynecology
University of Chicago
Skokie, IL, USA

INTRODUCTION

Pelvic organ prolapse (POP) occurs when the pelvic muscles or connective tissues that support the vagina are weakened or injured, allowing for descent of pelvic organs into the vagina. POP often has a negative impact on a woman's reproductive health and overall quality of life. Thirteen percent of all women will undergo surgery for POP in their lifetime [1]. Vaginal delivery is the greatest epidemiologic risk factor for the development of pelvic floor disorders, yet the exact cause remains unclear [2,3]. One hypothesis is that delivery causes injury to the musculature and/or connective tissue that supports the vagina which leads to maladaptive remodeling and eventually symptoms of POP. If true, changes in vaginal shape could serve as a proxy for injury.

As a first step towards testing this hypothesis, we aimed to quantify the impact of pregnancy and vaginal delivery on vaginal shape by comparing measurements between nulliparous (have never given birth), currently pregnant, and vaginally parous (have given birth) women. Because pregnancy and delivery are the greatest risk factors for the development of POP, we expected that the vaginas of nulliparous women would be longer and more curved than those of pregnant and parous women.

METHODS

This retrospective study was approved by the Institutional Review Board at the University of Pittsburgh and considered exempt at Northshore University HealthSystem. The study included the pelvic magnetic resonance imaging (MRI) scans of 43 women between the ages of 20 and 49 acquired at Magee-Womens Hospital or Northshore University HealthSystem between 2005 and 2018 at their physician's request. For this analysis, pregnant women were only included if they were in their third trimester. Patients were sorted into three Groups: nulliparous (N=19), pregnant (N=9), and parous (N=15).

Utilizing Seg3D2 (University of Utah), MRI slices of the vagina were identified and segmented to form the 3D geometry. These models were then imported into Blender (v.2.91, blender.org) where curves were traced along the objects' anterior vaginal wall, posterior vaginal wall, and lines traced along the largest transverse width (Figure 1). Mathematica (Wolfram, Inc) was used to measure the arc length (in mm) of the anterior and posterior curves. These lengths are referred to as the anterior and posterior vaginal wall curved lengths. Those traces were also used to calculate three other measures: straight length, curvature index, and width height.

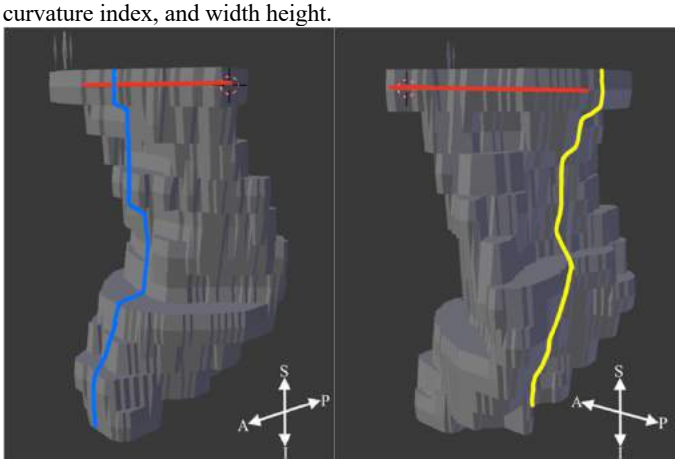

Figure 1: Anterior curved length (blue), posterior curved length (yellow), and the largest transverse width (red) used to calculate straight length, curvature index, and width height. Anterior (A), posterior (P), superior (S), and inferior (I) directions are denoted.

The straight length was defined as the distance from the midpoint of the most superior point to the midpoint of the most inferior point on the anterior and posterior curves, respectively. The curvature index was defined as the ratio of the straight length to the average of the anterior and posterior curved lengths multiplied by 100. This means a value of 100 indicates a completely straight object, while smaller values represent more curved objects. The width height was defined as the normalized height along the vaginal straight length where the largest transverse width was located, where a value of 1 and 0 would indicate the most superior and inferior point along the vagina, respectively.

Statistical analyses were conducted in SPSS™. Correlations were performed to choose which variables to include in subsequent analyses. The analyses consisted of a One-Way Independent MANOVA followed by Bonferroni test post hoc with multiple comparisons. Independent variables included vaginal measures not correlated with one another. Group (nulliparous vs. pregnant vs. parous) was the dependent variable. A p-value < 0.05 was considered statistically significant.

RESULTS

Due to significant correlations between anterior curved, posterior curved, and straight lengths, only curvature index and straight length were included in the MANOVA. Also, due to significant correlations between width and width height, only width height was included in the MANOVA.

According to the univariate ANOVAs, Group had a statistically significant effect on curvature index (p=0.010), whereas its effect on straight length (p=0.252) and width height (p=0.482) were not significant (Figure 2). The difference in curvature index between the nulliparous (88.7 ± 5.8) and pregnant (93.8 ± 3.2) groups were statistically significant (p=0.020). With pregnant women having a straighter vagina (Figure 2A). The curvature index of parous (92.4 ± 2.5) women remained statistically similar to both the nulliparous (p=0.056) and pregnant (p=1.000) groups.

DISCUSSION

Overall, these results support the idea that pregnancy affects the shape of the vagina, specifically its curvature. The fact that the curvature index of parous women did not differ from either group suggests that in some parous women the vagina maintains its straightness after childbirth, while in others it may return to its nulliparous curvature. Nonetheless, the similarities between the pregnant and parous groups from Figure 2A suggest that for most women the straightening observed during pregnancy does not revert to the nulliparous curvature postpartum.

Later in pregnancy, the levator ani muscles remodel, allowing for descent of the vaginal introitus (opening). If the vaginal apex remains supported, this would explain the straightening observed in this study. This mechanism – straightening that fails to recover postpartum – could reflect a persistent change in the muscles that support the vagina caused by pregnancy/delivery. However, further work is necessary to determine if this change reflects injury or weakness to the muscles and, if so, what degree of curvature change might be associated with the future development of POP.

This study was limited by the number of patients, and its retrospective, cross-sectional study design. This meant that the power of the statistics performed were lowered and that pregnant and parous women were not compared to their own nulliparous geometries. Nevertheless, this study demonstrates that the vaginal shape is straighter during late pregnancy, and, because of this, provides a motivation to further investigate the changes in vaginal shape during pregnancy while also evaluating recoverable vs. unrecoverable postpartum shape attributes in future prospective studies.

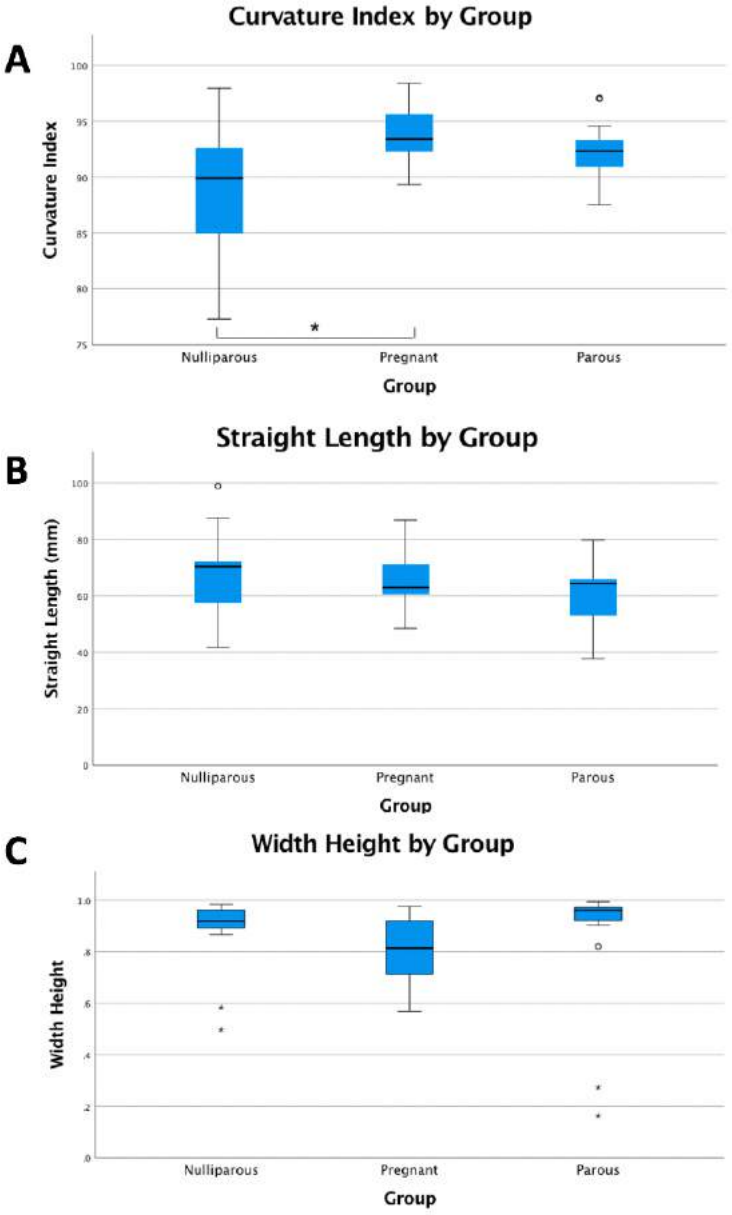

Figure 2: Compares A) curvature index, B) straight length, and C) width height across the three groups of interest (nulliparous, pregnant, and parous).

ACKNOWLEDGEMENTS

This material is based upon work supported by the National Science Foundation Graduate Research Fellowship Program under Grant #1747452.

REFERENCES

[1] J.M Wu, et al., *Obstet. Gynecol.,* 123:141-148, 2014.
[2] Routzong M, et al. *Comput. Meth. Prog. Bio.,* 194:105516, 2020.
[3] Oliphant, S, et al. *Am. J. Obstet. Gynecol,* 218:242.e1-242e7, 2018.

Pharmaceutical Intervention Helps but Does Not Prevent Proteoglycan Loss in the Meniscus Following Traumatic Knee Injury

A. Herrick (1) G.E. Narez (1), L. Dejardin (2), F. Wei (3, 4), R.C. Haut (3, 4), T.L. Haut Donahue (1)

(1) Department of Biomedical Engineering
University of Massachusetts
Amherst, MA, USA

(2) Department of Small Animal Clinical Sciences
Michigan State University
East Lansing, MI, USA

(3) Orthopaedic Biomechanics Laboratories
Michigan State University
East Lansing, MI, USA

(4) Department of Mechanical Engineering
Michigan State University
East Lansing, MI, USA

INTRODUCTION

The meniscus is a crescent shaped cartilaginous tissue found between the femoral condyles and tibial plateau of the knee joint. It functions to provide stability and distribute joint forces, which can be attributed impart to its high water content due to presence of proteoglycans [1]. Proteoglycans are composed of a core protein and 1 or more glycosaminoglycan (GAG) chains. Injuries to the anterior cruciate ligament (ACL) and meniscus can result in a loss of GAGs which is associated with the onset and progression of post-traumatic osteoarthritis (PTOA) in the knee [2].

It has been demonstrated that ACL reconstructive surgery alone does not prevent the development of PTOA [3]. Hence, additional treatment is likely necessary to treat potential occult damage to the joint tissues such as the meniscus, which is likely exposed to large joint loads during traumatic injury [4]. This study is designed to determine the efficacy of injecting a surfactant drug Poloxamer 188 (P188) into the impact area at several time points. P188 is known to increase cell viability, and therefore may prevent degenerative GAG loss within the meniscus.

METHODS

With IACUC approval, the right knees of ninety skeletally mature Flemish Giant rabbits were impacted to generate ACL tear and meniscal damage, leaving the left knee as a contralateral control group. Animals were then randomly assigned to one of four treatment groups; reconstruction only (Recon), reconstruction and P188 administration following impact (P188 D0), reconstruction and P188 administration following impact and 24 hours after (P188 D1), and reconstruction and P188 administration following impact, 24 hours after, and 7 days after (P188 D7). Two weeks following impact, ACL reconstructive surgery was performed. Animals were then euthanized one, three, or six months following impact. Menisci were harvested and prepped for histology using the Safranin-O/ Fast Green stain. Stained slides were then imaged using a microscope and CellSens GAG coverage was determined using ImageJ by isolating the area covered in red stain compared to total tissue area. Finally, the tissues were blindly graded by four trained individuals for GAG intensity using a 0-3 scoring method. A fixed effects model was used to determine statistical significance between treated samples and contralateral control. A p-value < 0.05 was deemed significant.

RESULTS

Analyzing GAG coverage concluded in a significant difference in the lateral menisci between all P188 treatment groups and their control limbs at the 1-month time point. At 3 months, P188 D0 saw a significant increase in GAG coverage from Recon. At the 6-month time point all groups saw a significant decrease from their control limb except for P188 D0.

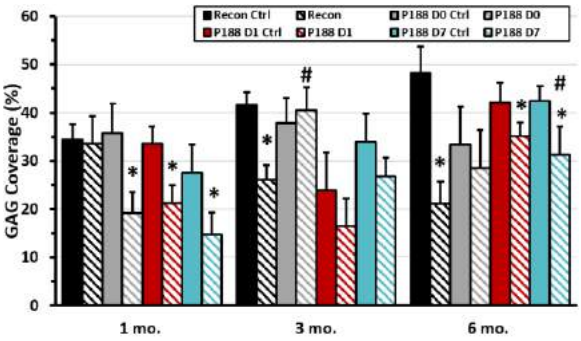

Figure 1. GAG coverage of lateral menisci across all time points and treatment groups * denotes significant differences from control # denotes significant differences from reconstruction only

Additionally, P188 D7 had a significant increase in GAG coverage from Recon (Fig 1).

In the medial menisci at 1- month, all groups saw a decrease compared to their control groups. However, P188 D7 at 3 months saw an increase in GAG coverage from Recon, and P188 D0 at 6-months also saw a significant increase from reconstruction. At 6 months, all other treatment groups saw an increase in GAG coverage from their controls, but it was not significant (Fig. 2).

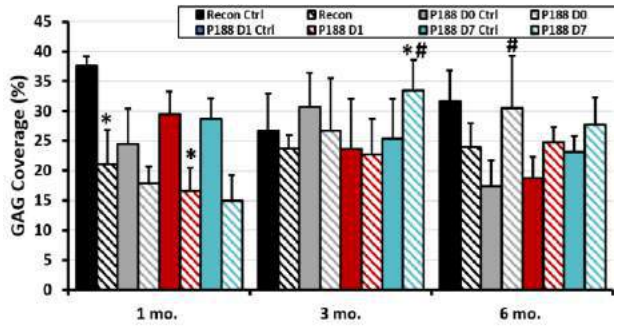

Figure 2. GAG coverage of medial menisci across all time points and treatment groups * denotes significant differences from control # denotes significant differences from reconstruction only

GAG intensity grading resulted in a significant difference in the lateral menisci between all P188 treatment groups and their control limbs at the 1-month time point. P188 D0 and D7 showed a significant decrease from Recon at the 1-month time point (Fig 3).

In the medial menisci, there was a significant decrease in GAG intensity at P188 D1 from its control and Recon. However, at the 3-month time point, there are no significant decreases in intensity. Additionally, at 6 months, there is an increase between all treatment groups and their controls, but it is not statistically significant (Fig 4).

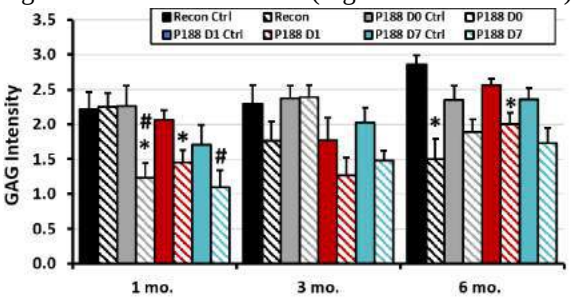

Figure 3. GAG intensity of lateral menisci across all time points and treatment groups * denotes significant differences from control # denotes significant differences from reconstruction only

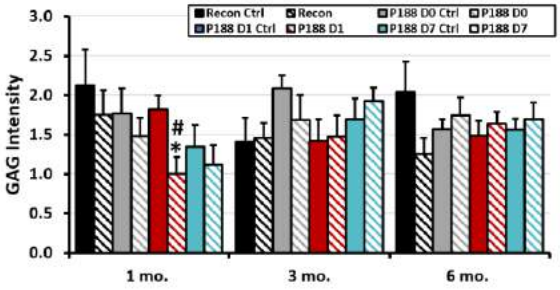

Figure 4. GAG intensity of medial menisci across all time points and treatment groups * denotes significant differences from control # denotes significant differences from reconstruction only

DISCUSSION

Injection of surfactant drug P188 helps but does not prevent degradation of menisci at later time points following traumatic knee injury. While there are not significant increases in GAG coverage or intensity across all treatments and time points, it is clear that P188 is more effective in maintaining GAG content at 3 and 6 months in medial menisci, in comparison to the 1-month time point.

Future directions include delivery of P188 into the meniscus directly. Relying on diffusion during intra-articular injection may not be sufficient enough for P188 to target the meniscus.

ACKNOWLEDGEMENTS

The study is funded by DOD grants W81XWH-16-1-0735 and W81XWH-16-1-0734.

REFERENCES

[1] Mow, VC et al., *Basic Orthopaedic Biomechanics and Mechano-Biology*, 3, 2015. [2] Felson, DT, *Radiol Clin North Am*, 42(1):1-9, 2004. [3] Fink, C et al., *J SportsMed*, 22: 304-309, 2001. [4] Fischenich, KM et al., *J Biomech*, 48(2):246-253, 2015.

SB³C2021
Summer Biomechanics, Bioengineering and Biotransport Conference
June 14-18, Virtual

EVALUATING FLEXOR DIGITORUM SUPERFICIALIS TENDON FATIGUE USING HIGH-FREQUENCY ULTRASOUND BASED STRAIN ALGORITHMS

Andrew J. Darling (1), Conner C. Earl (1), Fredrick W. Damen (1), Nan Chen (2), Travis Mendoza (3), Denny Yu (2), Grace D. O'Connell (3), Carisa Harris Adamson (4), Craig J. Goergen (1)

(1) Weldon School of Biomedical Engineering
Purdue University
West Lafayette, IN, USA

(2) School of Industrial Engineering
Purdue University
West Lafayette, IN, USA

(3) Department of Mechanical Engineering
University of California, Berkeley
Berkeley, CA, USA

(4) Occupational and Environmental Medicine
University of California, San Francisco
San Francisco, CA, USA

INTRODUCTION

Ultrasound speckle tracking can be used to study the movement of the Flexor Digitorum Superficialis (FDS), which is the tendon primarily responsible for finger flexion at the proximal interphalangeal joints. The FDS tendon is frequently engaged when fingers are involved in forceful flexion, where long term usage has been known to cause serious damage, including rupture of the tendon due to continuous manual labor [1].

Here, we present a method for calculating FDS tendon strain using high-frequency ultrasound imaging and speckle tracking. We utilized a custom-built image analysis script that allows us to calculate the strain measurements over a predetermined contraction and relaxation cycle and estimate observed strain over a period of FDS tendon stress. We hypothesize that reliable strain estimates can be determined using this high-frequency ultrasound imaging technique. Several groups have published papers on measuring tendon displacement and measuring strain in different tendons using techniques such as texture correlation [2-4], yet this study is the first to our knowledge to quantify strain values in the FDS tendon *in vivo* using speckle tracking.

METHODS

Seven participants aged 19 to 50 volunteered to have their wrists imaged during various cycles of contraction and relaxation in this initial study. All protocols were performed with Purdue Institutional Review Board Approval. Prior to imaging, each participant was familiarized with the data collection method. Each participant rested their arm on a platform near the ultrasound machine that allowed their elbow to rest at a 120-degree angle while standing (Figure 1a). The arm was then secured, and the ultrasound probe lowered into place against the skin on the anterior side of the wrist parallel to the FDS tendon.

The subject was given a hand grip Dynamometer probe (MicroFET, Hoggan Scientific, Salt Lake City, UT, United States) that can wirelessly measure grip force. A baseline test of maximum force was measured three times and averaged for each participant. This averaged max force was then used to find the target force of each duty cycle. Based on the maximal acceptable effort equation, there was a total of five conditions that varied duty cycles and force exertions which ranged from 3% to 70% of cycle time (30 seconds) and 8% to 57% of maximum force, respectively [5]. The participants performed three cycles of ramp up, hold, ramp down, and rest, which represented one cycle. This was repeated for each condition with each cycle being 30 seconds total where larger force exertions had shorter hold and longer break periods, while small force exertions had longer hold and shorter break periods. During the entire cycle, we used a Vevo3100 system (FUJIFILM VisualSonics Inc., Toronto, Ontario Canada) with a 40 MHz center frequency linear array ultrasound transducer (25-55 MHz bandwidth; MX550D) to acquire continuous B-Mode images throughout the experiment.

Using a custom-built MATLAB graphical user interface (MathWorks, Inc., Natick, Massachusetts, United States) that allowed us to manually define tendon borders and track displacement throughout each duty cycle, we were able to estimate the 2D Green-Lagrange full strain tensor using the upper and lower boundaries of the FDS tendon. For each frame of the ultrasound, the 2D version of the deformation gradient tensor (***F***) was used to estimate the Green-Lagrange strain tensor (***E; eq 1***) using the following equation:

$$\boldsymbol{E} = \frac{1}{2}(\boldsymbol{F^T F} - \boldsymbol{I}), \quad \boldsymbol{E} = \begin{bmatrix} \mathrm{E_{xx}} & \mathrm{E}_{xy} \\ \mathrm{E}_{yx} & \mathrm{E}_{yy} \end{bmatrix} \tag{1}$$

where $\boldsymbol{I}$ represents the identity matrix, $\boldsymbol{E_{xx}}$ is the component of the strain tensor corresponding to the longitudinal strain, $\boldsymbol{E_{yy}}$ is the component corresponding to the radial strain, and the $\boldsymbol{E_{xy}}$ and $\boldsymbol{E_{yx}}$ are components

corresponding to shear strain [6-7]. For the purpose of our analysis, we were primarily interested in the $\boldsymbol{E_{xx}}$ (i.e., longitudinal strain).

RESULTS

Initial analysis of strain in one subject has shown that we can estimate the longitudinal component (E_{xx}) of the 2D Green Lagrange strain tensor over a duty cycle. A representative graphical depiction of strain over 600 frames (1 duty cycle or ~30 seconds) for a 50% duty cycle is shown in Figure 1c. As the tendon begins to perform work by squeezing the force probe, the average longitudinal strain value decreases and then returns to baseline with relaxation. While preliminary results have been obtained from subject seven, a complete set of results has not yet been obtained that would allow for a meaningful comparison between all seven subjects.

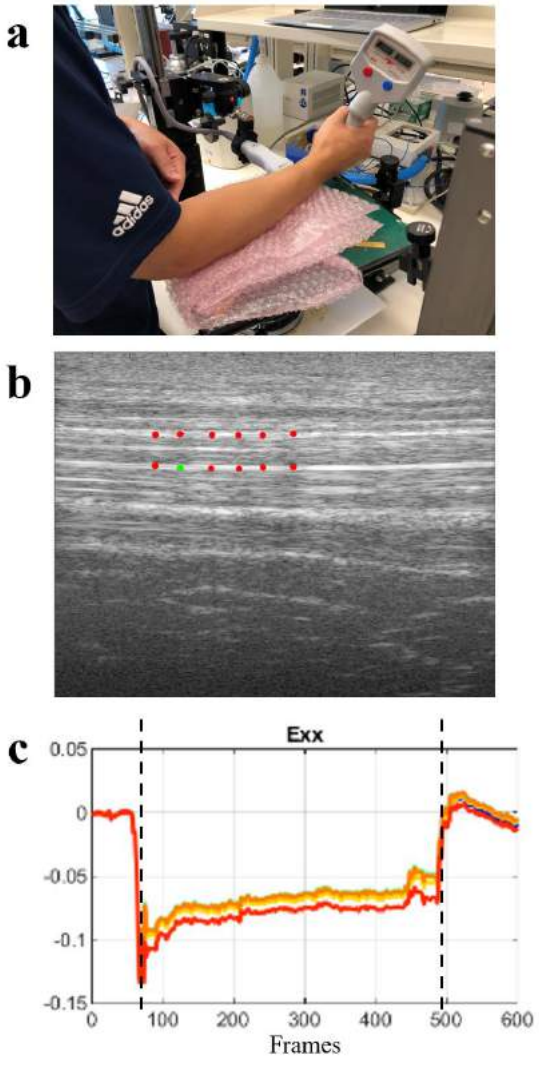

Figure 1: (a) Image of subject's wrist position when performing data collection. The angle of the elbow was positioned in approximately a 120° angle, while the hand holds the force probe off the edge of the elevated resting platform. (b) Example of manual point segmentation along the edge of the FDS tendon. (c) Longitudinal strain output for frames 1-600 from participant seven. Frames 1-600 collected at 25 frames per second represent the brief rest to start, ramp up to goal force, hold, and ramp down to rest. Dotted lines indicate the start and end of the hold period.

DISCUSSION

Based on these preliminary results, we can estimate the longitudinal strain in the flexor digitorum superficialis tendon in *vivo* using high-frequency ultrasound imaging and speckle tracking. Additionally, we found that the strain pattern during a duty cycle from our analysis occurs as a negative value that returns to baseline with relaxation, suggesting that the observed strain is the result of tendon shortening. While we continue to work on refining our methods in order to reduce intra- and inter-user variability, observing general trends are a positive start in demonstrating the efficacy of using the MATLAB graphical user interface to track manually assigned boundaries aligned along the top and bottom of the FDS tendon.

Although our results are promising, further refinement of our methods is still required. While images as shown in Figure 1c are common for one cycle, all three cycles have yet to be pieced together to find a total longitudinal strain over the entire duty cycle, and we are still refining our method to improve the sensitivity and repeatability of our estimations. We are also working to remove ultrasound artifacts from the images that that will hopefully increase the signal to noise ratio. We believe we can do this by averaging multiple frames together in an effort to reduce noise and improve speckle tracking [8]. We also hope that averaging frames will eliminate human error that occurs when manually assigning focal points for the MATLAB algorithm to track.

The results obtained in this research study are unique and can provide clarity into FDS tendon longitudinal strain. Currently there are multiple papers published that have attempted similar methods with various other tendons yet have not reported consistent results [2-4, 6-7, 9-10]. One paper found that there is a high degree of variability in strain estimation when analyzing tendon tissue with commercial ultrasound speckle tracking algorithms [3]. We found inconsistencies within our pool of strain results, but we are confident in results collected to date due to similarities in results across participants.

Our method of finding strain values opens the door to look at the long-term effects of strain on a tendon without invasive procedures. Additionally, we anticipate these results can be applied to study settings like assembly lines, where intensive wrist work is a common practice. We hope that the data obtained from this research allows recommendations to be made concerning the rest periods for workers and for improved working conditions that allow for a less strenuous use of wrist and underlying tendons.

REFERENCES

[1] Imai S., et al., *J Hand Surg Am*. 2004;29(4):587-590. doi:10.1016/j.jhsa.2004.03.005.

[2] Korstanje JWH., et al., *J Biomech*. 2010;43(7):1373-1379. doi:10.1016/j.jbiomech.2010.01.001.

[3] Fröberg Å., et al., *Acta radiol*. 2016;57(10):1223-1229. doi:10.1177/0284185115626471.

[4] Okotie G., et al., *J Biomech Eng*. 2012;134(2):24504. doi:10.1115/1.4006116

[5] Potvin JR., *Hum Factors*. 2012;54(2):175-188. doi:10.1177/0018720811424269

[6] Ligas, M., M. Banaś, and A. Szafarczyk, *Reports on Geodesy and Geoinformatics*, 10.2478/rgg-2019-0007, 2019.

[7] Humphrey, J.D., et al., *Journal of Biomechanical Engineering*, 10.1115/1.2891193, 1990.

[8] Toulemonde MEG., et al., *JACC Cardiovasc Imaging*. 2018;11(6):923-924. doi:10.1016/j.jcmg.2017.09.011

[9] Chernak LA., et al., *J Biomech*. 2012;45(15):2618-2623. doi:10.1016/j.jbiomech.2012.08.001.

[10] Svensson RB., et al., *J Appl Physiol*. Published online December 17, 2020. doi:10.1152/japplphysiol.00654.2020.

SB³C2021
Summer Biomechanics, Bioengineering and Biotransport Conference
June 14-18, Virtual

RELATIVE DISPLACEMENTS BETWEEN THE BRAIN AND SKULL IN THE MINI-PIG: EFFECTS OF AGE AND MOTION DIRECTION

Keshav A. Kailash (1), Charlotte A. Guertler (2), Ruth J. Okamoto (2) Philip V. Bayly (1,2)

(1) Biomedical Engineering
Washington University in St. Louis
St. Louis, MO, USA

(2) Mechanical Engineering
Washington University in St. Louis
St. Louis, MO, USA

INTRODUCTION

Understanding the role of the skull and brain interface is critical to illuminating the pathology of concussion and traumatic brain injury (TBI). Here we characterize the skull-brain interface by inducing low-amplitude, harmonic motion of the head using external pneumatic actuators and measuring the resulting motion of the skull and brain using magnetic resonance elastography (MRE).

The mini-pig, which has a gyrencephalic brain with white matter tracts analogous to those in humans, has been established as a powerful animal model for TBI in humans [1,2]. In both mini-pig and human TBI, skull motion transmitted into the brain induces shear deformations in the brain [1,2]. However, the similarities and differences between mini-pigs and humans must be understood quantitatively in order to interpret research findings.

In the current study, MRE studies were performed in the Yucatan mini-pig *in vivo* with three different pneumatic vibrations applied to the mini-pig brain and skull using a jaw actuator. This induced both translation and rotation of the head. The goal was to quantitatively characterize skull-brain interactions, specifically the relative motion between the skull and brain in the mini-pig at various ages.

METHODS

Imaging: Yucatan mini-pigs (n=2) were imaged at ages 3, 4, 5, and 6 months (avg. mass = 14.06, 19.91, 24.31, 26.76 kg). Each animal underwent T1-weighted MRI and MR elastography head scans using a custom EPI pulse sequence [3] on 3T MRI scanner (Prisma^{TM}, Siemens). MRE parameters provided field of view 180 mm and voxel size 2 mm (Fig. 1). Three pneumatic actuator configurations were used to induce harmonic motion of the skull and brain at 100 Hz using a custom multi-directional jaw actuator fabricated from two flexible bottles [4]. The actuator configurations were: (1) both bottles actuated in-phase ("BA"); (2) only the left side active ("LA"); (3) only the right side active ("RA"). BA provided symmetric loading; RA and LA provided asymmetric forces on the skull. Excitation was applied by a pneumatic driver (Resoundant^{TM}, Rochester, MN) at 60% amplitude.

Image analysis: Three-dimensional (3D) harmonic motion of each voxel was estimated from MRE. Voxels in the skull and the brain were manually segmented using ITK-Snap (ITK-Snap^{TM} ,Yushkevich and Geric) in T1W image volumes. Voxels with insufficient MRE signal-to-noise (SNR) were identified from non-harmonic spectra and removed from analysis. Rigid-body ("bulk") components of skull and brain displacement were estimated by fitting these 3D displacement fields in skull and brain regions, respectively, to equations of rigid-body motion. Dynamic deformation ("wave motion") in the brain was obtained by subtracting bulk motion from total displacement in brain voxels. [5]

Because of the inherent water content in the tissue, harmonic motion was able to be measured by MRE throughout the entire brain but only in a small fraction (~12-15%) of skull voxels. Since the skull is effectively rigid (6 degrees of freedom), even this small fraction of voxels is enough to estimate skull motion. To characterize relative skull-brain displacement at the brain surface, we first constructed the virtual motion of a "skull-fixed" brain: the motion that a rigid brain would exhibit if it were rigidly attached to the skull. This skull-fixed brain motion was then compared to the total motion of the brain, specifically in voxels at the surface of the brain, to calculate relative displacement of the brain with respect to the skull

RESULTS

Fig. 2 shows translation and rotation of the skull and brain from one scan in a single mini-pig (MP2; 4 months, 17.2 kg), using actuator

configuration BA. Qualitatively both skull and brain exhibit similar harmonic translation and rotation. Fig. 3A shows the amplitude of the difference between skull-fixed brain displacement and total brain displacement on the brain surface (our estimate of relative skull-brain displacement). Fig. 3B shows the difference between skull-fixed brain motion and the bulk motion (only) of the brain.

Fig. 4A shows the mean amplitude of relative displacement between brain and skull in animals MP1 and MP2. Fig. 4B shows the mean amplitude of displacement in the skull-fixed brains. Fig. 4C shows relative brain-skull displacement normalized by the skull-fixed brain displacement. While the amplitude of skull displacement and relative skull-brain displacement both decrease with age (likely due to the increase in head mass), the ratio of relative skull-brain displacement to skull displacement remains stable over this period. This ratio is also similar for all three actuator configurations.

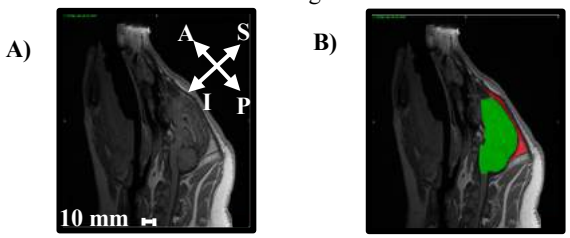

Figure 1: (A) T1-weighted sagittal slice. (B) T1-weighted sagittal slice with brain (green) and skull (red). A – Anterior, P – Posterior, S – Superior, I – Inferior, R – Right, L – Left (in and out of page).

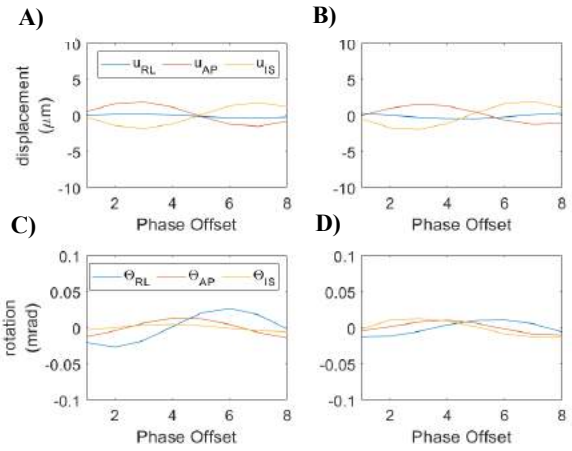

Figure 2: Components of rigid-body translation and rotation (u_{AP}, u_{RL}, u_{IS} and $\theta_{RL}, \theta_{AP}, \theta_{IS}$) of (A,C) mini-pig brain and (B,D) skull. Minipig MP2, 4 mos. Actuator BA.

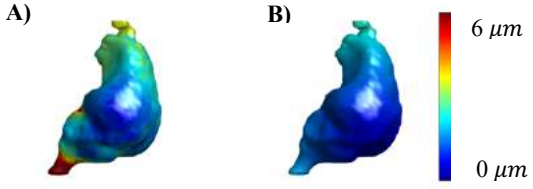

Figure 3: (A) Amplitude of the difference between the displacement of the skull-fixed brain and total brain displacement (i.e., relative skull-brain displacement) mapped on the brain surface; (B) Amplitude of the difference between skull-fixed brain displacement and brain bulk displacement. Minipig MP2, 4 mos. Actuator BA.

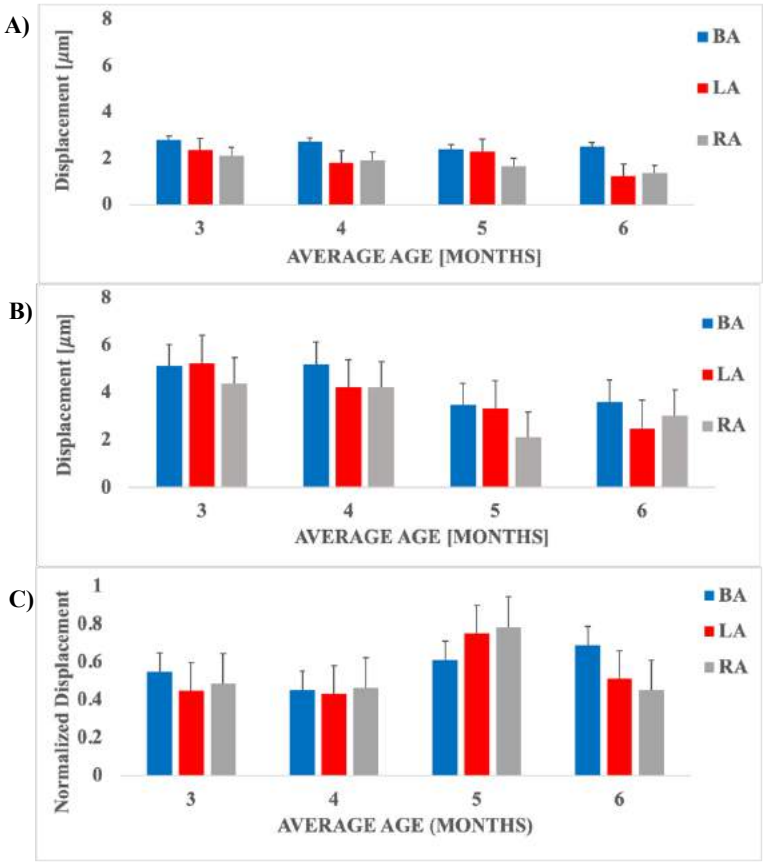

Figure 4: (A) Mean amplitude of relative displacement between the brain and skull-fixed brain; (B) Mean displacement amplitude of skull-fixed brain. (C) Mean ratio of relative brain-skull displacement to mean skull displacement. (Averages over minipigs MP1 and MP2).

DISCUSSION

Displacement fields and relative displacement between the skull and brain were measured by MRE in two mini-pigs aged 3-6 mos. Amplitude of brain and skull motion decreased with age, likely due to increasing head mass, but the amplitude of relative skull-brain displacement was consistently between 50-80% of skull displacement and exhibited no clear trend with age. This ratio did not depend on whether force was applied symmetrically (actuator configuration BA) or asymmetrically (configurations RA and LA).

These data will inform computer models of TBI and enable quantitative comparison of skull-brain interface mechanics in the mini-pig and human. Future work will investigate relative skull-brain motion in human volunteers, and in specific brain regions like the cerebellum.

ACKNOWLEDGEMENTS

This study was supported by NIH Grant R01EB027577.

REFERENCES

[1] Cullen DK et al., *Methods Mol Bio*, 1462:289-324, 2016
[2] Ibrahim NG et al., *J. Neurotrauma*, 27: 1021-1035, 2010
[3] Johnson CL et al., ISMRM, 325, 2014
[4] Guertler CA et al., *SB3C*, 2020
[5] Badachhape AA et al., J Biomech. 17;73:40-49. 2018
[5] Smith DH et al, *J. Neuropath Exp Neurol,* 58: 982-999, 1999
[6] Johnson VE et al, *Acta Neuropatholigca,* 135:711-7256, 2017

METABOLISM OF CHONDROCYTES AFTER TRAUMATIC OVERLOADING DETERMINED BY CLICK CHEMISTRY TECHNIQUES

Annie Porter, Liyun Wang, X. Lucas Lu

Department of Mechanical Engineering
University of Delaware
Newark, DE, USA

INTRODUCTION

Traumatic joint injuries often induce inflammation in the joint cavity with elevated levels of pro-inflammatory cytokines, such as TNF-α and IL-1β. The cytokines act on chondrocytes, causing aberrant cell hypertrophy, over-proliferation, apoptosis, and imbalanced metabolic activities [1]. Treatment varies, given individual physician's clinical impressions and preferences, which include a non-pharmaceutical option, R.I.C.E. (rest, ice, compression, and elevation), oral or topical use of nonsteroidal anti-inflammatory drugs (NSAIDs), and intra-articular cortisone injections [2].

The objective of this study was to quantify the combined effects of traumatic overloading and inflammatory challenge on chondrocytes to inform clinical decisions on the treatment of joint inflammation after traumatic injuries. To evaluate the responses of *in situ* chondrocytes, new click-chemistry based techniques were developed to visualize and quantify cell proliferation and metabolic activities. The copper-free click chemistry reactions are bioorthogonal, *i.e.*, not interfering with native cellular processes [3]. The two aims of this study were (1) to develop new click-chemistry techniques to quantify the proliferation and metabolic activities of *in situ* chondrocytes in cartilage explants, and (2) to investigate the effects of IL-1β on chondrocytes in the trauma-damaged cartilage.

METHODS

Cartilage explants (3 mm in diameter and 2 mm in thickness) were harvested from fresh calf knee joints (1-2 months old) and cultured in chondrogenic media [4]. Four experimental groups were tested: control, overloading (OL), IL-1β (1ng/ml), and OL+IL-1β (overloading followed by IL-1β challenge). Overloading was applied to cartilage explants in an unconfined compression setup with a 50% strain in 1 second (~6-10 MPa/s in stress rate) and held for 15 seconds. Cell viability was imaged using Live/Dead™ staining 24 hours after overloading (n=3).

Proliferation Assay. Proliferation of *in situ* chondrocytes was determined using a copper-free click chemistry-based assay. Post overloading, explants were treated for 24 hours with an azide modified nucleoside AmdU (10 μM), which can be incorporated into DNA of proliferating cells by endogenous enzymes (Fig. 2a). Afterwards, samples were fixed with cellular permeabilization, and a fluorescent dye, AF488 DBCO, was "clicked" to the azide groups on the DNA of the proliferating cells. All cell nuclei were counterstained with a red tracker. Chondrocytes in explants were imaged on a confocal microscope and counted in ImageJ (n=6).

Protein Synthesis. After traumatic overloading, new GAG (in 24 hrs) and collagen (in 48 hrs) synthesized in the explant was fluorescent-labelled using click chemistry methods (Fig. 3a). To label newly synthesized GAG or collagen, a "clickable" modified monosaccharide (Gal) or methionine (AHA) with an azide functional group was supplied in the culture media, which can be used by cells and incorporated into the newly synthesized GAGs and collagens, respectively. The newly synthesized molecules were conjugated with AF488 DBCO via a click chemistry reaction. By enzymatically digesting the labeled tissue and normalizing the fluorescent intensity of the digested solution to the explant weight, the synthesis rate of GAG or collagen content can be quantified and compared between the groups (n=8).

ECM Degradation. The GAG or collagen content synthesized in each explant in 2-day culture was first fluorescent-labelled with the click chemistry methods (Fig. 3a). The explants then underwent overloading damage and/or IL-1β challenge. In the following explant culture, the longitudinal loss of GAG or collagen contents from the cartilage can be quantified by reading the fluorescent intensity of culture media every other day (n=8).

RESULTS

Chondrocyte Viability. Limited cell death (red) was observed along the explant surface in the top zone cartilage (ctrl), which was not significantly affected by 24-hour IL-1β challenge. One day after overloading, significant cell death was observed in top zone and the neighboring middle zone tissue (Fig. 1).

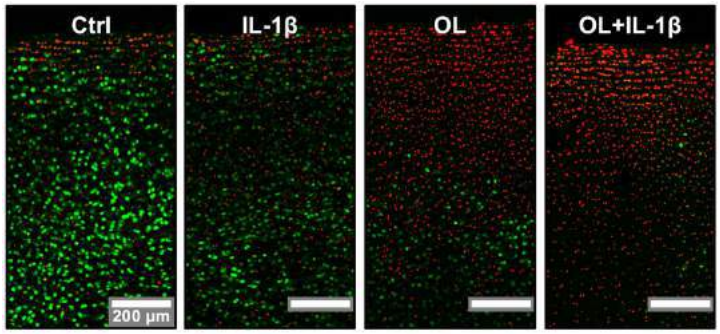

Figure 1: Cell viability in cartilage by Live/Dead™ staining.

Chondrocyte Proliferation. In the ctrl group, proliferation rate in the top zone cartilage from 2-4 month calf joints is 47.7 ± 5.7%, which is further increased to 55.9 ± 4.6% for 1-day IL-1β treated samples, and decreased to 24.7 ± 12.7% and 24.3 ± 7.6% for the OL and OL+IL-1β treated samples, respectively ($p < 0.001$, Fig. 2c,d). The proliferation of chondrocytes in the middle zone cartilage was not affected by any treatments (Fig. 2c).

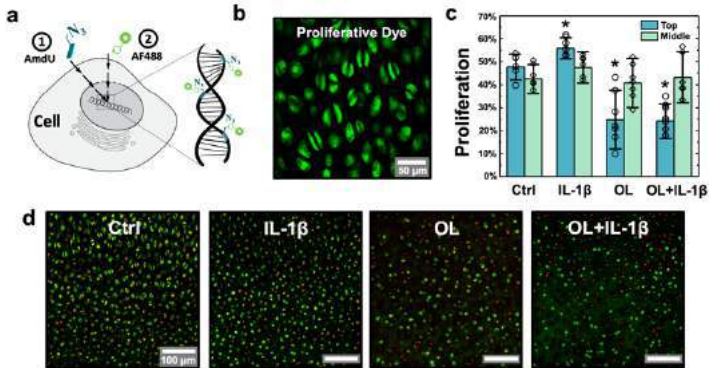

Figure 2: Chondrocyte proliferation. (a) AmdU with azide groups are embedded into proliferating DNA, on which fluorescent dye AF488 can be "clicked". (b) Confocal image of proliferative cells. (c) Proliferation rates in top and middle zones (n=6) (*: $p < 0.001$). (d) Confocal images of proliferative cells (green) in top zone cartilage with all cell nuclei stained in red.

Effects on ECM Synthesis. One-day exposure to IL-1β alone had no significant effects on GAG (in 24 hrs) or collagen (in 48 hrs) synthesis in explants (Fig. 3b). In contrast, overloading reduced both the GAG and collagen synthesis rates significantly ($p < 0.015$), as many cells dyed in the top zone. No significant difference was detected between the OL and OL+IL-1β samples (Fig. 3b).

Effects on ECM Degradation. In contrast to its prominent effects on proliferation and ECM synthesis, overloading alone had no effect on the loss of GAG or collagen content from the explant in the following long-term culture. Exposure to IL-1β caused 39.9 ± 6.2% GAG loss in 10 days and 55.6 ± 10.9% collagen loss in 44 days. For samples with overloading damage, subsequent IL-1β exposure exacerbated the loss of both GAG (67.9 ± 7.9%, $p < 0.01$) and collagen (62.6 ± 10.1%, $p < 0.01$), significantly higher than the IL-1β alone group (Fig. 3c).

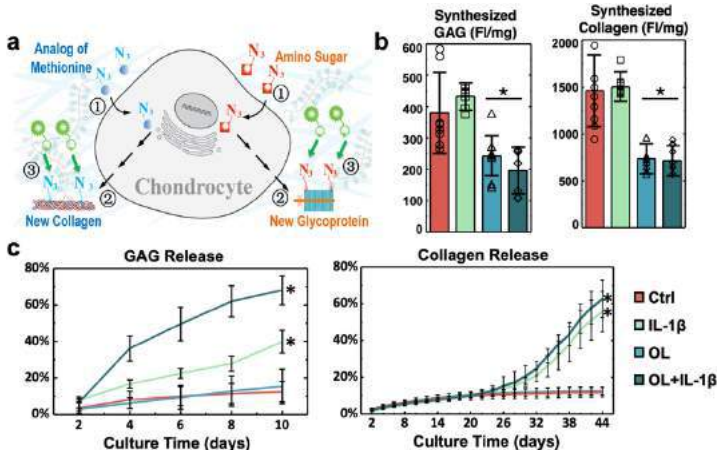

Figure 3: Effects of overloading and IL-1β on cell metabolic activities. (a) Click chemistry method to label new GAG and collagen within explant. (b) GAG (24 hrs) and collagen (48 hrs) synthesis. (c) Longitudinal GAG and collagen loss (%) from cartilage explants into culture media. (n=8) (*: $p < 0.015$)

DISCUSSION

The newly developed click chemistry methods are accurate, sensitive, and cost-effective in quantifying the proliferation and metabolic activities of *in situ* chondrocytes in cartilage. GAG and collagen measurements with click chemistry have been verified by traditional hydroxyproline and BMMB assays (data not shown). The click chemistry proliferation assay results were affirmed by known chondrocyte responses. IL-1β treatment induced chondrocyte over-proliferation, and the decrease in top zone proliferation after overloading is consistent with cell viability data [5]. These new methods represent useful tools for *in vitro* studies in osteoarthritis and regenerative medicine related research.

Chondrocyte proliferation measured at the top and middle zones in the control group were consistent with reports in literature [6]. IL-1β challenge caused chondrocyte over-proliferation. Impact overloading induced cell death in the top zone cartilage, as the top zone has a compressive modulus ~10% of the middle zone, causing large deformations resulting in damaged cells [7]. Overloading alone reduced the GAG and collagen synthesis in cartilage, possibly due to extensive cell death. Overloading, followed by IL-1β treatment, caused more severe ECM degradation than the IL-1β alone group or overloading alone group. These results indicate that while the initial traumatic overloading causes chondrocyte death and reduces new ECM synthesis, the combination of overloading and inflammation induces more damage to the cartilage. Our results support the fast ease of joint inflammation, *i.e.,* pharmaceutical treatment such as NSAIDs, after trauma injuries to avoid or mitigate the occurrence of irreversible degradation of cartilage.

ACKNOWLEDGEMENTS

Undergraduate Summer Scholarship at University of Delaware; NIH R01AR074472 (Lu).

REFERENCES

[1] Lv, M. et al., *Sci Rep.*, 9:93, 2019. [2] Buckwalter, J.A. et al., *Cartilage,* 4(4):286-294, 2013. [3] Eunha K., et al., *Chem. Sci.,* 10:7835-7851, 2019. [4] Lv, M. et al., *J Ortho Res.*, 36:730-738, 2018. [5] Simsa-Maziel, S. et al., *Endocrinology*, 153(5):2296-2310, 2021. [6] Bartell, L.R. et al., *J Biomech.*, 48(12):3440-3446, 2015. [7] Wang, C.C.B, et al., *J Biomech*., 36(3):339-353, 2003.

CAN EXERCISE-BASED LOAD PREVENT OR REDUCE AGE-RELATED ADVANCED GLYCATION END-PRODUCT ACCUMULATION IN TENDONS?

Panth Doshi (1), Kelly Ott (1), Jennifer L. Puetzer (1,2)

(1) Department of Biomedical Engineering
Virginia Commonwealth University
Richmond, VA, USA

(2) Department of Orthopaedic Surgery
Virginia Commonwealth University
Richmond, VA, USA

INTRODUCTION

There is a clear link between increasing age and injuries in tendons. In a growing aging population, there is a need to understand these age-related changes in order to treat and reduce such injuries. Many mechanisms have been suggested to contribute; however, one of the most predominant mechanisms is believed to be advanced glycation end-products (AGEs) [1-2] due to the dominance of collagen in tendons. AGEs accumulate in tendons with age, producing non-enzymatic crosslinks in collagen that alter the mechanics of the tissue and lead to more injuries [1-2]. Exercise may combat AGE accumulation and reduce tendon injuries; however, *in vivo* investigations have yielded variable results [3-5]. It is unknown whether exercise loading reduces AGEs by increasing matrix turnover, thereby preventing AGE crosslink formation, or whether loading stimulates the breakdown of existing AGEs. To determine optimal exercise regimes, the mechanism by which loading affects AGE accumulation and tendon homeostasis must be understood. The objective of this study was to investigate how tensile loading affects AGE accumulation, breakdown, and tissue homeostasis in *ex vivo* tendons, in an effort to reduce AGEs and age-related injuries.

METHODS

Tail tendons were harvested from 2-4-month-old freshly sacrificed Sprague Dawley rats. Extracted tendon bundles were separated into individual fibers and cut into approximately 30 mm long segments. Separated tendon segments were cultured in a custom clamping device [6], to maintain viability and phenotype, for up to 4 weeks in standard media (DMEM), with or without 100 mM ribose to induce AGE formation and artificially age the tissue [1,2,7]. Tendons with and without ribose exposure were loaded with an established cyclic tensile load (5% strain at 1 Hz for 1 hour on-1 hr off-1 hr on) three times weekly for up to two weeks in a CellScale tensile bioreactor [8]. Two experiments were performed to investigate whether cyclic tensile load can prevent AGE accumulation (Fig 1A) and/or 2) can reduce existing AGEs (Fig 2A). DNA, glycosaminoglycan (GAG), collagen, total AGEs, and specific AGE crosslink pentosidine were determined via PicoGreen, DMMB, hydroxyproline (hypro), AGE fluorescence, and pentosidine assays respectively [6-7]. Confocal reflectance and fluorescence imaging were performed to observe collagen fiber organization in response to induced AGEs and tensile load. Autofluorescence of cells and AGEs were captured together at 400-470 nm (green, Fig 3). Statistical analysis was performed by 2-way ANOVA with Tukey's post-hoc (p<0.05 significant). All data are mean ± SD.

RESULTS

To investigate if loading prevents AGE formation, tendons were mechanically stimulated while AGEs were induced with ribose (Fig 1A). Weight, GAG (data not shown), and collagen (Fig 1B) of all groups remained steady or increased over 2 weeks, suggesting cells remained viable and produced matrix. Loaded tendons in DMEM increased GAG and collagen (Fig 1B) after one week before returning to baseline values, suggesting loading increases matrix turnover. Interestingly, loaded tendons in ribose did not have this increase in matrix at 1 week. Ribose treatment significantly increased total AGEs and AGE specific crosslink, pentosidine, throughout culture when normalized to wet

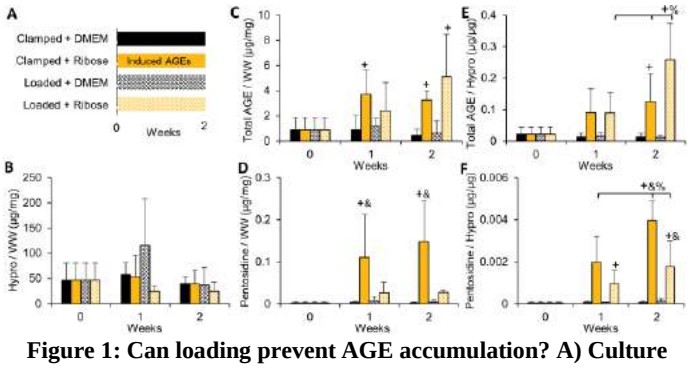

Figure 1: Can loading prevent AGE accumulation? A) Culture conditions, B) Collagen (hypro) / wet weight (WW), C-D) Total AGEs and pentosidine / WW, and E-F) Total AGEs and pentosidine / collagen. N = 4-7, Significance (p<0.05) compared to +0wk, %bracket, &all other groups within week

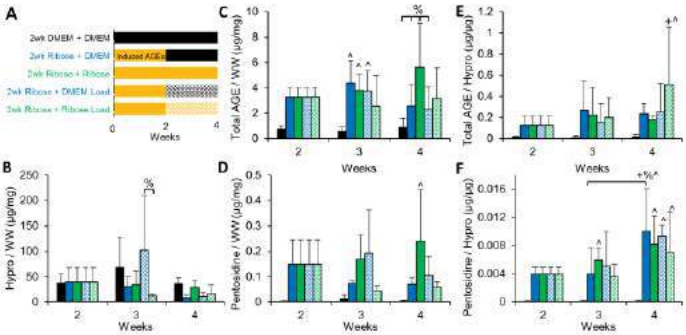

Figure 2: Can loading reduce existing AGEs? A) Culture conditions, B) Collagen (hypro) / wet weight (WW), C-D) Total AGEs and pentosidine / WW, and E-F) Total AGEs and pentosidine / collagen. N = 4-7, Significance (p<0.05) compared to +2wk, %bracket, ^DMEM control (2wk DMEM +DMEM)

weight or collagen content (Fig 1C-F). Addition of tensile load over 2 weeks reduced formation of specific AGE crosslink, pentosidine (Fig 1D&F), but had no effect on reducing total AGEs (Fig 1C&E).

When investigating if loading is capable of driving cells to reduce existing AGEs, AGEs were induced for 2 weeks prior to loading tendons with and without ribose (Fig 2A). Again, GAG (data not shown) and collagen content (Fig 2B) increased after 1 week of loading in DMEM suggesting turnover of the matrix with load, however loaded tendons in ribose did not have this increase in matrix at 1 week. Loading of AGE induced tendons in DMEM (patterned blue bars) did not significantly reduce total AGEs or pentosidine crosslinks in comparison to control AGE induced tendons cultured in DMEM (solid blue bars), suggesting loading is not capable of reducing existing AGEs (Fig 2C-D). Interestingly, AGE induced tendons loaded while still in ribose (patterned green bars) did have reduced pentosidine levels when normalized to wet weight (Fig 2D), suggesting loading may reduce pentosidine crosslinks or at least mitigate formation of additional crosslinks. However, total AGEs and pentosidine levels in all loaded tendon, whether in DMEM or ribose, did not decrease when normalized to collagen (Fig 2E-F).

Confocal reflectance revealed tendons exposed to ribose had greater fluorescence than tendons not exposed to ribose, suggesting an increase in AGEs (Fig 3). Tendons loaded while inducing AGEs revealed reduced AGE fluorescence at 2 weeks, however, injurious kinking was also observed (Fig 3A). Tendons which had AGEs induced for two weeks and were then loaded with or without additional AGE induction revealed little reduction in AGE fluorescence, but significant injurious kinking at 3 and 4 weeks (Fig 3B).

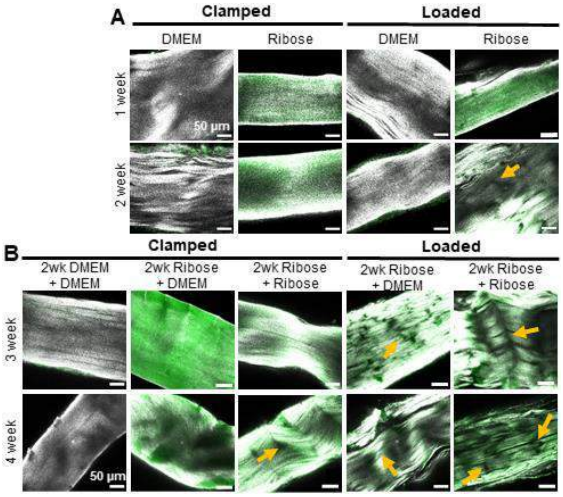

Figure 3: Confocal of tendons loaded A) during or B) after ribose induction of AGEs; Grey = collagen, Green = auto-fluorescent cells and AGEs, arrows point to injurious kink

DISCUSSION

AGEs accumulate with age and diabetes. They crosslink collagen, disrupting cellular function and altering tendon mechanics, ultimately resulting in increased injuries [1-2]. In this study we have shown that loading decreases formation of specific AGE crosslink, pentosidine, but does not mitigate formation of overall total AGEs and that the loading regime for optimal collagen turnover still needs to be determined. Specifically, control tendons maintained DNA with increasing weight in all groups (data not shown), indicating cells remained viable and produced matrix. This suggests our *ex vivo* system is not detrimental to tendon homeostasis. Further, 100 mM ribose treatment produced a significant increase in total AGEs and pentosidine, matching and exceeding AGE levels for various tissues and ages [4,7,9]. GAG and collagen concentration increased with 1 week of loading but returned to pre-load values by 2 weeks, suggesting the loading regime increases the metabolism of cells, resulting in anabolic, catabolic tissue turnover [8]. However, when loaded in the presence of ribose, there was no increase in GAG or collagen, suggesting ribose may alter cellular response to load or affect the timing of this response. Loading while inducing AGE crosslinks was capable of mitigating pentosidine formation, but not total AGE formation. Pentosidine crosslinks take longer to form than many other AGEs, including adducts which often form more quickly [7]. Thus, loading may prevent pentosidine formation by stimulating quicker cellular turnover of the matrix, providing less time for pentosidine crosslinking.

Loading after AGE induction did not reduce AGEs when compared to induced tendons cultured in DMEM, suggesting loading is not capable of reducing existing AGEs. However, when compared to induced tendons culture in ribose, loading did decrease AGEs normalized to wet weight, suggesting loading may reduce AGE crosslinks or at least mitigate formation of additional crosslinks in the continued presence of ribose. This reduction in AGEs with load was lost when normalized to collagen, suggestisng cells are turning over non-crosslinked collagen more than AGE-crosslinked collagen. Loading after induction also induced increased injurious response. This work demonstrates loading can reduce certain types of AGEs, but loading regimes need to be optimized to drive healthy matrix turnover instead of injurious response in cells. More loading regimes are currently being investigated. This study provides new insight into how cells of AGE crosslinked tendons respond to cyclic tensile load and begins to shed light on a mechanism for reduced AGEs *in vivo*. This *ex vivo* system is a valuable model for investigating effects of AGEs and methods of reducing them for treatment of age-related musculoskeletal injuries.

ACKNOWLEDGEMENTS

We thank the VCU Pulmonary Mechanobiology Lab for providing aged rat tails, and the Nanocharacterization Core (NCC) at VCU. This work was funded by the VCU Mechanobiology REU Site and the VCU Center for Clinical and Translational Research (CCTR).

REFERENCES

[1] Gautieri, A et al., *Matix Biol*, 14:366, 2017. [2] Snedeker, J et al., *MLTJ*, 4:304, 2014. [3] Eriksen, C et al., *BMC Geriatr*, 2019. [4] Wood, L et al., *J Orthop Res*, 2015. [5] Svennson, R et al., *J Appl Physiol*, 121:1357, 2016. [6] Puetzer, J et al., *Biomaterials*, 2020. [7] Gouldin, A et al., *BioRx*, 2030. [8] Puetzer, J et al., *Tiss Eng*, 22:910, 2016. [9] Takahasi, M et al., *Arthroscopy*, 1998.

PARAMETRIC PATIENT-SPECIFIC MODEL SIMULATING HUMAN CERVIX DEFORMATION DURING THE FIRST STAGE OF LABOR

Arielle D. Feder (1), Erin M. Louwagie (1), Joy Y. Vink (2), Kristin M. Myers (1)

(1) Department of Mechanical Engineering
Columbia University
New York, NY, USA

(2) Department of Obstetrics and Gynecology
Columbia University Irving Medical Center
New York, NY, USA

INTRODUCTION

Despite World Health Organization reported estimates that only 10-15% of births pose a medical necessity for caesarian section (CS) [1], about 1 in 3 babies born in the United States are delivered via CS [2]. CS is a major surgery that increases the cost of delivery and places the mother at greater risk of infection [2]. Birth is a complex process, typically split into three stages of labor. Arrest of the first stage of labor, characterized by the effacement (shortening) and dilation (opening) of the cervix, is the primary motivation for CS, cited in 15-30% of cases [2]. The mechanical function of the cervix in pregnancy is two-fold: it must be robust enough to stay closed as the fetus grows, but flexible enough to allow for the fetus's passage at the time of delivery. Given the ethical constraints to researching human tissue during delivery *in vivo*, it is convenient to use computational models to study the biomechanics of birth.

Computational research in birth simulation has shed light on many birthing complications. The work done thus far has primarily focused on the pelvic floor and related injuries, and on fetal head deformation during vaginal delivery [3,4]. These models lack attention on the uterus and cervix during delivery, and typically rely on imaging modalities which are not common in obstetric clinical care. To address this, parametric patient-specific modeling frameworks based on 2D ultrasound images have been proposed to study pregnancy biomechanics throughout gestation [5,6]. However, the resulting models were not designed to capture uterine and cervical geometry at the time of delivery, nor do they include fetal geometry. Therefore, we have developed a method to simulate the first stage of labor based on a 2D ultrasound measurement method.

MRIs of pregnant patients scheduled for CS were taken at 38-39 weeks gestation, segmented, and converted into 3D models [7]. From these models, 2D ultrasound measurements (as proposed by Louwagie et al.) were taken, and 3D parametric patient-specific models were built. Using these models, this research aims to simulate birth in order to deduce the principal strains of the cervix during the first stage of labor, potentially aiding in determining which deliveries necessitate CS.

METHODS

The geometry of the uterus, cervix, fetal head and abdomen were created in Solidworks (Dassault Systemes, Vélizy-Villacoublay, France), based on an existing 2D ultrasound measurement method. The uterine and cervical geometry build was based on an existing modeling method [6]. Because this method assumes an elliptical coronal shape, which is inaccurate for late gestation, the model was adjusted by taking 15 transverse intrauterine diameters and wall thicknesses from MRI-derived solid models and incorporating them as parameters of the coronal shape [8]. The cervix was separated from the uterus at the uterocervical junction fillet, and a surrounding supporting abdomen with a hollowed out vaginal canal was built around the uterus and cervix (Fig. 1). Given a dataset of 5 pregnant patients at term [7], the model was built using the shortest measured cervical length and widest measured cervical diameter as parametric dimensions.

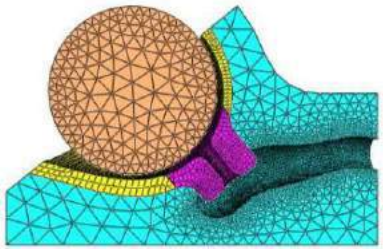

Figure 1: Meshed model viewed from the sagittal plane. The model includes the fetal head, cervix, uterus and abdomen.

The models were meshed in HyperMesh (Altair Engineering Inc., Troy, MI), using tetrahedral elements in the fetal head and abdomen. Hexahedral elements were used for the uterus and cervix. Finite element analysis (FEA) was done in FEBio Studio (v1.1.0) [9]. Within FEBio, the head was modeled as a spherical rigid body, with the diameter measured from MRI, and it followed a prescribed birthing trajectory. The cervix, uterus and abdomen were modeled as neo-Hookean materials because we are only analyzing kinematics. Sliding contact was defined between the head and the cervix/uterus. Tied elastic contact was defined between the cervix and uterus, abdomen and cervix, and abdomen and uterus. The following boundary conditions were applied: the entire system was fixed in the normal direction in the mid-sagittal plane, and the abdomen was fixed in the normal direction at the posterior and inferior ends. A contraction was simulated by pulling the faces of the uterus and abdomen perpendicular to the cervical canal, opposite the motion of the head. An image of the FEBio setup is shown in Figure 1. Symmetry across the sagittal plane was assumed, and a half model was used for computational efficiency.

RESULTS

This research is ongoing, and therefore limited comparisons between cervical geometries can be made. However, looking at a single model, several insights into the deformation of the cervix during the first stage of labor can be drawn. The simulation demonstrates effacement of the cervix, and only after effacement does dilation begin.

The maximum 1st principal Lagrange strain is 6.24, the range of the 2nd principal Lagrange strain is between -0.198 and 2.1, and the minimum 3rd principal strain is -0.494. As illustrated in Figure 2, most of the tensile strain appears concentrated as a ring at the uterocervical junction. The undeformed cervix in Figure 2 illustrates the stretch of the cervix during labor.

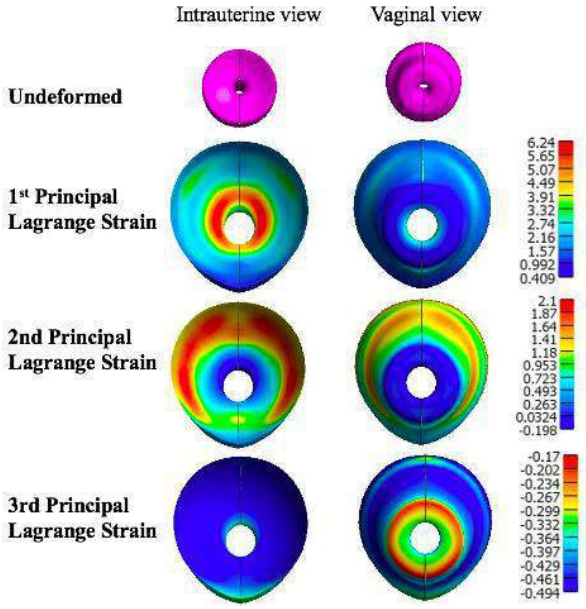

Figure 2: 1st, 2nd, and 3rd principal Lagrange strain maps of the cervix at the final time step, as well as the undeformed cervix for reference. Models are to scale. The result is mirrored over the sagittal plane for a full cervix view. The head is hidden for clarity. Views specify the vantage point from which the cervix is viewed.

Principal strain directions are consistent with expectations. The 1st principal Lagrange strain, aligned circumferentially, shows hoop strain at the internal os (uterine cervical canal opening) of the cervix as it stretches around the fetal head. The 3rd principal Lagrange strain is near minimum throughout most of the cervix, demonstrating compression of the entire cervix as it is pushed by the fetal head and pulled by the uterus.

This simulation only shows the beginning of the first stage of labor for a patient with a comparatively short and wide cervix. As we simulate more geometries, we can draw comparisons between different cervical shapes. With our current simulation metrics, the external os (vaginal cervical canal opening) dilates to 2.2cm. The simulation currently models most of the latent phase of the first stage of labor (3-6 cm dilation), and does not include the active phase, when the cervix is considered to be completely dilated at 10cm [10,11]. Future iterations of this model will aim to allow for more advanced cervical dilation, thereby modeling the process to the end of the first stage of labor.

DISCUSSION

This research simulates the latent phase of the first stage of labor and reports cervical strain during this period. The strain is most concentrated at the uterocervical junction, and is intuitively patterned with circumferential tension dominating at the internal os and compression present throughout the cervical body. The magnitude of the 1st principal strain exhibits the tension of the cervix as it is stretched around the head, and the 3rd principal strain shows large amounts of compression due to the displacement of the head onto the cervix. As we implement further geometries using this FEA method, we will compare deformation as well as strain pattern and magnitude for different cervical sizes during the first stage of labor. This research is limited by the omission of specific active and supporting pelvic structures, such as the pelvic bone and pelvic floor anatomy, whose omission required an imposed fetal head trajectory. The simulated contraction was also simplistic, acting on a single plane of the uterus rather than throughout the entire body. Also, physiologically relevant fiber-based material models were not used, and the material properties were not patient-specific. Although measurements from the model were taken from an MRI-derived model, this measurement process can be done using 2D ultrasound images. The success of a patient-specific birthing model could greatly improve patient care in labor by predicting success in the first stage of labor, the necessity of cervical ripening, or if a CS is needed. Such patient-specific modeling would allow for a more individualized and efficient approach to labor interventions.

ACKNOWLEDGEMENTS

This work is supported by the Eunice Kennedy Shriver National Institute of Child Health & Human Development of the National Institutes of Health under award number R01HD091153. The content is solely the responsibility of the authors and does not necessarily represent the official views of the National Institutes of Health. We would also like to thank Alicia Dagle for help editing.

REFERENCES

[1] World Health Organization, “Statement on Cesarean Section Rates”, 2015.
[2] Spong, C et al., *Obstetrics and gynecology*, 120(5):1181-93, 2012.
[3] Lapeer, R. et al., *Biomech Model Mechanobiol*, 18:681–700, 2019.
[4] Bailet, M et al., *SURGETICA*, 116–119, 2014.
[5] Westervelt, A et al., *J Biomed Eng*, 139(5):051004, 2017.
[6] Louwagie, E et al., *PLoS ONE*, 16(1): e0242118, 2021.
[7] Fang, S. et al., 2020. doi:10.7916/d8-gxv7-2z02.
[8] Rajasekharan, D. et al., 2020. doi:10.7916/d8-p164-vg61.
[9] Maas, S, et al., *J Biomech Eng*, 134(1):011005, 2012.
[10] Mayo Clinic, “Labor and delivery, postpartum care”, 2020.
[11] American Pregnancy Association, “First Stage of Labor”, 2020.

LAYER-SPECIFIC MECHANICAL AND COLLAGEN MICROSTRUCTURAL CHARACTERIZATIONS OF TRICUSPID VALVE LEAFLETS

Katherine M. Casey (1), Mulan Tang (1), Devin W. Laurence (1), Chung-Hao Lee (1,2)

(1) Biomechanics and Biomaterials Design Laboratory
School of Aerospace and Mechanical Engineering
The University of Oklahoma
Norman, OK, USA

(2) Institute for Biomedical Engineering, Science, and Technology
The University of Oklahoma
Norman, OK, USA

INTRODUCTION

The tricuspid valve (TV) regulates the unidirectional blood flow from the right atrium to the right ventricle of the heart via the cyclic opening and closing of three leaflets – the anterior leaflet (TVAL), the posterior leaflet (TVPL), and the septal leaflet (TVSL). Each leaflet has four distinct anatomical layers, which are, from the atrium to the ventricle, the atrialis (A), spongiosa (S), fibrosa (F), and ventricularis (V). Each tissue layer is hypothesized to serve a particular role in the leaflet function based on their microstructural constituents. For example, the fibrosa contains a dense network of crimped collagen fibers that contribute to the load bearing capacity of the TV leaflets.

A detailed knowledge of the characteristics of individual tissue layers and the variations among the TV leaflet types is essential to understand the *in vivo* behavior of the TV. A prior study used high-fidelity *in-silico* simulations to elucidate how the layer-specific properties of the mitral valve leaflets can influence the cellular deformations, which has implications for the leaflet's mechanobiological response to pathological stimuli [1].

Our lab previously characterized the mechanical responses of the four tissue layers for the TVAL [2]; however, we did not characterize the TVPL and TVSL (each has unique microstructural morphologies), or directly compare the mechanical responses between the individual layers and the intact leaflet – a key inter-layer relationship. Further, our lab recently developed a polarized spatial frequency domain imaging (pSFDI) system [3] to quantify the load-dependent changes in the leaflet collagen fiber architecture (CFA). This system can help provide additional insight into the layer-specific CFAs. Hence, the objective of this study is to characterize the mechanical and CFA properties of the three TV leaflets and their respective tissue layers.

METHODS

• **Tissue Preparation and Characterization Overview.** To collect the intact leaflet, tricuspid valve leaflets were dissected from porcine hearts (Animal Technologies, TX), then cut into 12x12 mm specimens. Before testing was performed, the thickness of all tissue samples was determined by averaging three measurements made via a laser displacement sensor (Keyence, IL). The overall experimental protocol was as follows: (i) biaxial mechanical testing and pSFDI of the intact TV leaflets (n=10 for each TV leaflet type), (ii) microdissection of the leaflets, (iii) step (i) procedures applied to the microdissected layers.

• **Layer Microdissection.** The intact leaflet was dissected to separate the tissue into two composite layers: (i) the A/S composite layer, containing the atrialis and spongiosa layers, and (ii) the F/V composite layer, containing the fibrosa and ventricularis layers. First, the square of tissue was pulled taut, pinned to a wax board, and covered with deionized (DI) water to ensure tissue hydration. A scalpel was then used to gently cut along the edge of the tissue, penetrating the atrialis while avoiding the fibrosa underneath. Following the incision, tweezers were used to grasp the A/S and pull it away from the F/V (**Fig. 1a**). The largest sample possible of each layer was collected; however, the A/S composite layer was very thin and elastin rich, which resulted in notable planar tissue shrinkage and smaller A/S specimens.

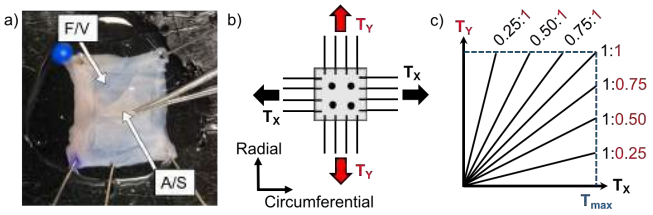

Figure 1: (a) Layer microdissection, (b) mounted tissue, and (c) biaxial testing protocols.

• **Biaxial Mechanical Testing.** The tissue was mounted on a BioTester (CellScale, Canada) using four sets of tines (**Fig 1b**). The intact tissue had a testing region of 10x10 mm while the A/S and F/V layers had

testing regions ranging from 3.3x3.3 mm to 6.6x6.6 mm. Four glass beads were glued to the surface of the tissue in an array for digital image correlation to compute tissue stretches. The tissue was then submerged in a 37 °C DI water bath for the duration of mechanical testing.

Briefly, six cycles of equibiaxial preconditioning were performed with a target peak membrane tension of 40 N/m to restore the approximate *in vivo* configuration [4]. For the thinner A/S composite layer, the targeted membrane tension was adjusted to correspond with a 200 kPa stress since stresses >200 kPa would likely tear the tissue. Following preconditioning, the specimen was biaxially characterized using a series of seven loading ratios (**Fig. 1c**), and the data from the final (third) cycle of each biaxial tension protocol was used for the stress/strain analyses [5].

• **pSFDI Collagen Imaging.** After mechanical testing, the tissue remained mounted and submerged in the DI water bath. Light was shone through a rotating polarizer lens onto the tissue. Images of the reflected light were captured at angles from 0° to 180° with 5° increments for the deformation associated with each biaxial tension ratio. The images were processed to determine the fiber orientation angle θ_{fiber} and the degree of optical anisotropy (DOA) -- indicating the collagen fiber alignment along the predicted fiber angle. Further details of the pSFDI system can be found in [3].

RESULTS

The intact tissue and microdissected layers of the representative TV leaflets exhibited nonlinear and anisotropic mechanical responses (**Fig. 2**). The F/V of the TVAL was more compliant in the circumferential direction, but stiffest in the radial direction. For the TVPL, the F/V was stiffer than the A/S for both the circumferential and radial direction. The TVSL also displayed a consistently stiffer F/V. In both directions, the F/V layer was the stiffest and the intact tissue was the most compliant. Across the three TV leaflets, the intact issue generally exhibited more distinct high-tension and low-tension regimes compared to the A/S and F/V layers. Importantly, the intact leaflet's response does not appear to be the summation of the individual layers, indicating the intrinsic contribution of layer interactions to the tissue mechanics of the intact leaflet.

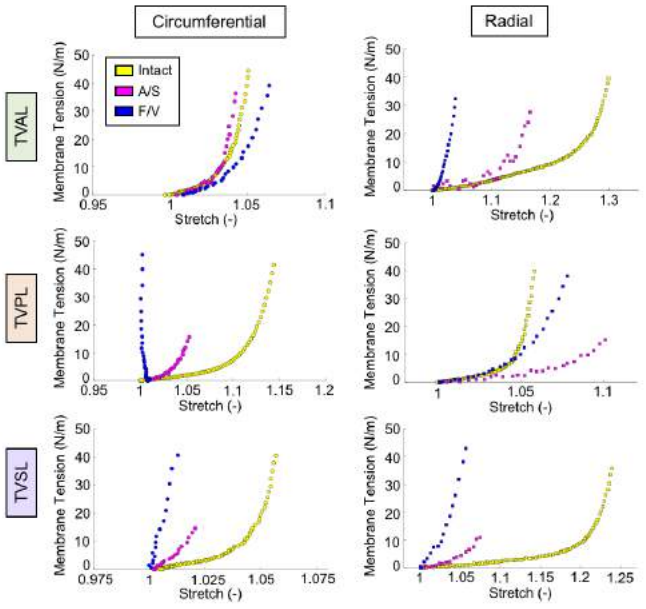

Figure 2: Representative equibiaxial results for the TV leaflets.

The results of pSFDI imaging reinforce the trends seen in the mechanical responses of the TV leaflets (**Fig. 3**). Collagen fibers in the F/V are highly aligned in the circumferential direction compared to the A/S and the intact specimens, supporting the stiffer F/V circumferential responses observed in the biaxial testing (**Fig. 2**). The DOA values across the three TV leaflets indicate notable local changes in the fiber alignment for both the intact and the F/V tissues, while these shifts were not observed in the A/S.

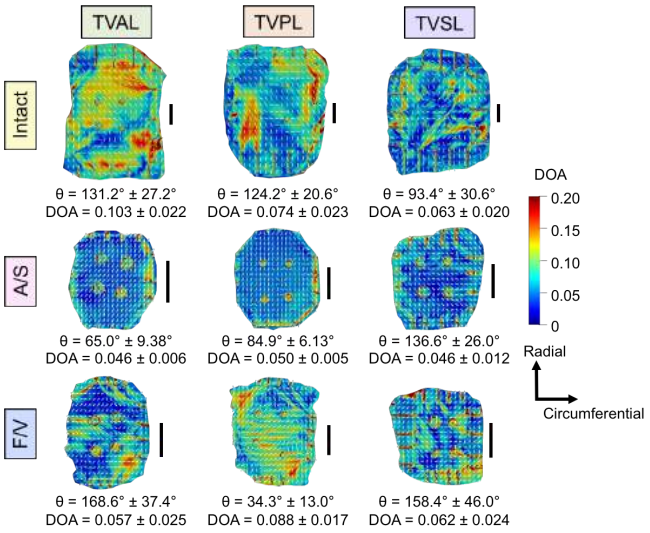

Figure 3: Collagen fiber orientation vector maps overlaid on DOA colormaps for representative specimens under equibiaxial loading. Scale bars are 3 mm. Values are in mean ± SD.

DISCUSSION

This study has provided the *first-of-its-kind* characterization of the biaxial mechanical and CFA properties for the tissue layers of the three TV leaflets. The biaxial mechanical characterization results showed the presence of influential inter-layer interactions, as supported by the quantified mechanical behavior of the A/S and F/V layers not simply summing to the mechanical response of the *intact* leaflet. Moreover, the sharper transition from the low- to high-tension regime of the mechanical response curves for the intact leaflet compared to the composite layers indicates an altered recruitment of collagen fibers. The insight into the CFA architecture as quantified by pSFDI revealed the preferential orientation of collagen fibers in the circumferential direction for the F/V composite layer. More circumferentially oriented collagen fibers within the leaflet suggested a greater resistance to stretching along this direction, generating its stiffer mechanical response. Additionally, the local variations in the fiber alignment of the intact and F/V tissues demonstrate the complex nature of the collagen network and its primary presence in the F/V layer. Overall, our comparisons of the composite layers and the original leaflet provide a better understanding of how the tissue components and inter-layer interactions influence the overall function of the TV leaflets, which can aid in future developments of microstructurally informed constitutive models. The developed models can then be incorporated into accurate finite element simulations to improve the current clinical understanding of the healthy and diseased TV function.

ACKNOWLEDGEMENTS

This work was funded by the American Heart Association Scientist Development Grant (16SDG27760143), the Presbyterian Health Foundation, and OU's Undergraduate Research Opportunities Program.

REFERENCES

[1] Lee, C.-H., *et al*., *J Theor Biol*, 373:26-39, 2015.
[2] Kramer, K., *et al*., *Acta Biomater*, 96:368–384, 2019.
[3] Jett, S., *et al*., *Acta Biomater*, 102:149–168, 2020.
[4] Chuong, C.-J., Fung, Y.-C., *Front Biomech*, pp. 117-129, 1986.
[5] Jett, S., *et al., J Mech Behav Biomed Mater*, 87:155-171, 2018.

MR IMAGE-BASED CHARACTERIZATION OF MEDIAL AND LATERAL MENISCAL GEOMETRIES FOR PATIENT-SPECIFIC FINITE ELEMENT MODELING

Kathryn H. Colone (1), Madison L. Lang (1), Kate E. Lindsey (1), Sofia L. Guarnieri (1), Amy L. Lerner (1)

(1) Biomedical Engineering
University of Rochester
Rochester, NY, USA

INTRODUCTION

The menisci serve an essential biomechanical role, with their circumferential fibers converting compressive stresses on the knee joint into hoop stresses that reduce contact forces on the tibial articular cartilage [1]. Partial meniscectomy is a common surgical treatment for meniscal tears, however, this intervention may reduce the effectiveness of the menisci in dissipating stresses, leading to increased contact forces on the tibial cartilage and development of osteoarthritis.

Knowledge of meniscal geometries is important for allograft and implant sizing, and for patient-specific finite element modeling [2,3]. Some studies have quantified meniscal geometries for only the medial meniscus, as it is more prone to injury [2], and others have quantified different sets of geometries of the menisci, such as slope or height [3,4]. Non-MRI based approaches have also been used including laser-based non-contacting 3-D coordinate digitizing systems and calipers [5,6]. Few studies have provided a comprehensive set of both lateral and medial meniscus geometries of living subjects in the anterior-posterior (AP), medial-lateral (ML), and radial directions, and examined relationships with other patient-specific geometries.

Regional material property variations across the tibial cartilages are reported to be related to which areas of the cartilage are covered by the menisci [7,8]. Our current work is motivated by a goal to develop efficient patient-specific finite element (FE) models of the tibiofemoral joint to investigate risks for developing osteoarthritis after partial meniscectomy. Mapping these regional material properties across the tibial cartilages using the meniscal footprint, however, may be time consuming or difficult due to lack of images of the intact menisci. Information on meniscal geometry relationships may therefore be advantageous for recovering the intact meniscal footprint. Our main objectives include (1) performing MR Image-based meniscal measurements, (2) assessing the interobserver reproducibility and intraobserver repeatability of these measurements, and (3) identifying a systematic approach to make predictions of intact meniscal geometry.

METHODS

We characterized meniscal geometries by performing MR Image-based measurements on both the medial and lateral menisci of 20 subjects using 3D Slicer [9]. The subjects included 10 men and 10 women (27.9 ± 6.46 years; height: 1.68 ± 0.10 m) with normal, healthy, uninjured knees. MR Images from a previous study were used, specifically 3DGRE, acquired from a 1.5 T scanner in the sagittal plane. The field of view was 140 mm with an in-plane resolution of 0.273 mm and 1.2 mm slice thickness. Tibial plateau width (TPW) and height were also quantified [10].

Key geometries characterized in this work include (a) anterior length, (b) posterior length, (c) total meniscus length, (d) midbody width, (e) anterior radial width, and (f) posterior radial width (Figure 1). Each dimension was measured for both medial and lateral menisci.

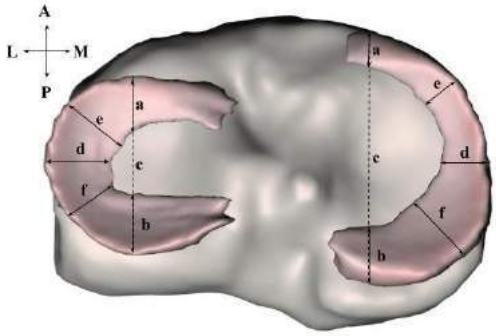

Figure 1: Diagram of meniscus geometry measurements

Knees were oriented in 3D slicer along the epicondylar axis, as previously defined for TPW measurement [10]. Anterior, posterior, and total meniscus length measurements were performed in the sagittal plane. The slice used for AP measurements was selected by locating the sagittal slice with the widest horizontal span, while maintaining the characteristic wedge-shape of the meniscus. In the coronal plane, the slice that approximately bisected each meniscus in the AP direction was used to obtain midbody widths. Measurements were made as the greatest horizontal distances to the outer edges of each geometry.

Anterior and posterior radial width measurements were performed on oblique views, obtained by rotating the MR Images 45 degrees about the inferior-superior (IS) axis, predefined by 3D Slicer. The slices used for these measurements were determined by relocating the pixel locations where the sagittal and coronal plane slices intersected from the previous AP and ML meniscus measurements.

Independent measurements were performed by two observers with similar training. Interobserver reproducibility and intraobserver repeatability of measurements were analyzed by performing linear regression analyses for each of the six parameters, for both medial and lateral menisci. Intraclass correlation coefficient (ICC) and root mean square difference (RMSD) values were also calculated to assess the reproducibility and repeatability of these measurements. Linear

regressions were performed to identify significant relationships between measurements, using Bonferroni correction ($p<0.05$). The standard error of the estimate (SEE) was used to quantify uncertainty in the meniscal relationship predictions.

RESULTS

ICC and RMSD values for reproducibility and repeatability indicated strong agreement for interobserver measurements (Table 1). Based on a grading system proposed by Koo and Li [11], 8 measurements had excellent reproducibility (ICC> 0.9), while 2 were in the good range (0.9>ICC>0.75) and 2 were in the moderate range (0.75>ICC>0.5). Results for repeatability were similar.

Table 1: Interobserver reproducibility of meniscal geometry

	Medial		Lateral	
Meniscal Geometry	**ICC**	**RMSD (mm)**	**ICC**	**RMSD (mm)**
Total Length	0.940	1.133	0.971	0.533
Anterior Length	0.774	0.747	0.909	0.578
Anterior Radial Width	0.636	0.923	0.908	0.734
Midbody Width	0.918	0.899	0.903	0.755
Posterior Radial Width	0.843	1.295	0.925	0.438
Posterior Length	0.920	0.969	0.743	0.844

Table 2: Meniscal geometries (mean ± standard deviation)

Meniscal Geometry	**Medial (mm)**	**Lateral (mm)**
Total Length	41.88 ± 3.19	33.22 ± 2.59
Anterior Length	8.64 ± 1.24	10.45 ± 1.35
Anterior Radial Width	7.14 ± 1.25	9.26 ± 1.63
Midbody Width	7.84 ± 2.09	8.36 ± 1.64
Posterior Radial Width	12.12 ± 2.39	9.12 ± 1.05
Posterior Length	15.74 ± 2.43	9.05 ± 1.16

We found only the medial total length to be significantly correlated to TPW ($p<0.05$), indicated by the bolded Pearson correlation coefficient (Table 3).

Table 3: Relationships between meniscal geometries and tibial plateau width

	Medial		Lateral	
Meniscal Geometry	**r**	**SEE (mm)**	**r**	**SEE (mm)**
Total Length	**0.674**	2.424	0.618	2.096
Anterior Length	0.090	1.269	0.413	1.260
Anterior Radial Width	0.473	1.155	0.390	1.540
Midbody Width	0.282	2.058	0.446	1.505
Posterior Radial Width	0.375	2.275	0.417	0.982
Posterior Length	0.558	2.073	0.416	1.083

Intrameniscal relationships were also investigated for the medial and lateral menisci relative to the medial and lateral midbody widths, respectively, indicating significant relationships ($p<0.05$) for 3 medial and 2 lateral meniscus geometries (Table 4).

DISCUSSION

Based on an approximate element length of 1.2 to 1.6 mm in our FE models, our SEE values for reproducibility and repeatability suggest our measurements are comparable to the size of one element on the tibial plateau (Table 1). Our average medial and lateral total length measurements were 41.88 and 33.22 mm, respectively, consistent with the average lengths reported by Elsner [2] and Stone [12], and about 3 mm less than the averages reported by Haen [13]. Similarly, our midbody width and total length measurements were 2 to 3 mm lower than those reported by McDermott, who used digital calipers to quantify meniscal geometries [6].

Table 4: Relationships between medial and lateral midbody width and other meniscal geometries

	Medial		Lateral	
Meniscal Geometry	**r**	**SEE (mm)**	**r**	**SEE (mm)**
Total Length	0.270	3.157	0.026	2.664
Anterior Length	0.479	1.119	0.520	1.182
Anterior Radial Width	**0.710**	0.904	**0.759**	1.088
Posterior Radial Width	**0.898**	1.082	**0.722**	0.748
Posterior Length	**0.746**	1.662	0.441	1.069

While total meniscus lengths were found to be significantly correlated to TPW, other dimensions did not exhibit these relationships (Table 3). In contrast, half the measured geometries were shown to be significantly related to the midbody widths (Table 4). Although some relationships were found to be statistically significant, the Pearson correlation coefficient values suggest some relationships may not indicate clinically meaningful findings. Our results show midbody width measurements could potentially serve as predictors to estimate other meniscus measurements and may be more suitable than average lengths to predict sizing, however, the weak meniscus-to-TPW relationships indicate that subject-specific FE modeling may be necessary. Only 20 knees were measured in this preliminary study, however, our data set of 100 knees may offer the opportunity to increase the confidence of our meniscus geometries and relationships. Future efforts may include considerations of covariates such as height and sex. A potential limitation of our work is that the 45-degree rotations for the radial measurements were performed about the IS axis predefined by 3D Slicer, rather than about an established and consistent coordinate system.

Our study demonstrated our ability to reproducibly measure key meniscal dimensions. Considerable variations were found between subjects with limited potential for prediction of meniscal geometries from bone measurements or midbody widths. Since posterior horn tears are most common [14], it may be helpful to be able to use intact midbody width geometries as predictors to estimate posterior horn geometries and therefore approximate the meniscal footprint.

ACKNOWLEDGEMENTS

DePuy Orthopaedics, Inc., a Johnson & Johnson Company (Warsaw, IN), provided support for the original MR Image acquisition. Support was also provided by NIH R01AR075523-02 (PI: S. Maher / Sub: A. Lerner).

REFERENCES

[1] Feeley, BT et al., *J Am Acad Orthop Surg*, 26: 853-863, 2018.
[2] Elsner, JJ et al., *J Biomech Eng*,123:101008-11, 2010.
[3] Erbagci, H et al., *Surg Radiol Anat*, 26:28-32, 2004.
[4] Haut TL et al., *J Orthop Res*, 18:228-237, 2000.
[5] Haut Donahue, TL et al., *J Orthop Res*, 24:1535-1543, 2006.
[6] McDermott, LD et al, *Knee Surg Sports Traumatol Arthrosc*, 12: 130-135, 2004.
[7] Deneweth, J et al., *J Orthop Res*, 31(3), 2013.
[8] Chaudhari, AM et al., *Med Sci Sports Exerc*, 40(2), 2008.
[9] Fedorov, A et al., *Magn Reason Imaging*, 30:1323-41, 2012.
[10] Hovinga, KR and Lerner, AL, *J Orthop Res*, 27:1191-1196, 2009.
[11] Koo, TK and Li, MY, *J Chiropr Med*, 15:155-163, 2016.
[12] Stone, KR et al., *J Arthroscopy*, 23: 503-508, 2007.
[13] Haen, TX et al., *The Knee*, 25: 841-848, 2018.
[14] Metcalf, MH and Barrett, GR, *Am J Sports Med*, 32(3), 2004.

CARBON NANO-ONION-MEDIATED DUAL TARGETING OF P-SELECTIN AND P-GLYCOPROTEIN TO OVERCOME CANCER DRUG RESISTANCE

Y. Liang (1), H. Wang (1), X. He (1)

(1) Fischell Department of Bioengineering
University of Maryland
College Park, MD, USA

INTRODUCTION

The drug efflux pump is a major mechanism of cancer drug resistance that results in cancer recurrence. An important element of drug efflux pumps is the transmembrane P-glycoprotein (P-gp), which is an ATP-binding cassette (ABC) transport protein that is commonly located in the plasma membrane of multidrug-resistant cancer cells.[1] Inhibiting the function of P-gp could serve as an effective approach to hindering MDR within cancer cells. However, the P-gp multidrug transporter protein also plays a crucial physiological role in protecting tissues from poisonous xenobiotics and endogenous metabolites and is widely distributed throughout the body.[2] As cellular processes within the body are also dependent on the protection of P-gp, non-targeted systemic administration of P-gp raises concerns of significant systemic toxicity.[3]

To address the challenges associated with non-targeted administration of P-gp inhibitor, this study reports on a nanovesicle-mediated delivery system targeting tumor vasculature to co-deliver P-gp inhibitor and chemotherapeutic molecules. The designed fucoidan-decorated silica-carbon nano-onion (FSCNO) hybrid nanoparticle specifically targets and binds to P-selectin that is overexpressed in tumor vasculature.[4] Furthermore, based on the properties of this designed platform, the release of P-gp inhibitor and chemotherapeutic drugs can be triggered and precisely controlled with low-power near-infrared (NIR, 800 nm) laser irradiation at tumor sites to overcome the multidrug resistant capability of tumor cells, with no evident impact on the function of P-gp in non-cancerous tissues.

METHODS

For the preparation of fucoidan-decorated silica-carbon nano-onion (FSCNO) hybrid nanoparticles, carbon nano-onions (CNOs) were utilized and treated with tetraethyl orthosilicate (TEOS) to form silica-CNO (SCNO) nanoparticles that improve solubility in organic solvents and increase drug-loading capacity. To attach the fucoidan for targeting tumor vasculature, SCNO was further then reacted with (3-Aminopropyl) trimethoxysilane (APTMS) to produce ASCNO intermediates, which were coated with fucoidan through electrostatic interaction to form the resulting FSCNO nanoparticles. Transmission electron microscopy (TEM) images of the CNOs were also recorded.

To confirm the tumor targeting and antitumor capacity of the FSCNO nanoparticles, they are encapsulated with the chemotherapy drug doxorubicin chloride (DOX or D) and the P-gp inhibitor HM30181A (HM or H) to form the FSCNO-DH nanoparticles. Furthermore, two drug-resistant (NCI/ADR-RES and A2780ADR) and one nondrug resistant (OVCAR-8) tumor models were used for growing tumor at the dorsal side of the upper hindlimb of 6-week female NU/NU nude mice. The NCI/ADR-RES, A2780ADR, and OVCAR-8 cells were incubated in medium containing various drug formulations, irradiated with laser for 1 min at 0.2 W cm^{-2}, fixed with 4% PFA, washed and analyzed using flow cytometry.

RESULTS

CNOs were treated with tetraethyl orthosilicate (TEOS) to form silica-CNO (SCNO) nanoparticles (**Figure 1a**). In order to decorate them with fucoidan for targeting tumor vasculature, the SCNO nanoparticles were further reacted with (3-Aminopropyl) trimethoxysilane (APTMS) to produce the ASCNO intermediates. Fucoidan was then coated on the surface of the ASCNO intermediates through its electrostatic interaction with APTMS to form the resultant FSCNO nanoparticles. Transmission electron microscopy (TEM) images of CNOs are given in **Figure 1b**. After coating the SCNO nanoparticles with fucoidan, the FSCNO

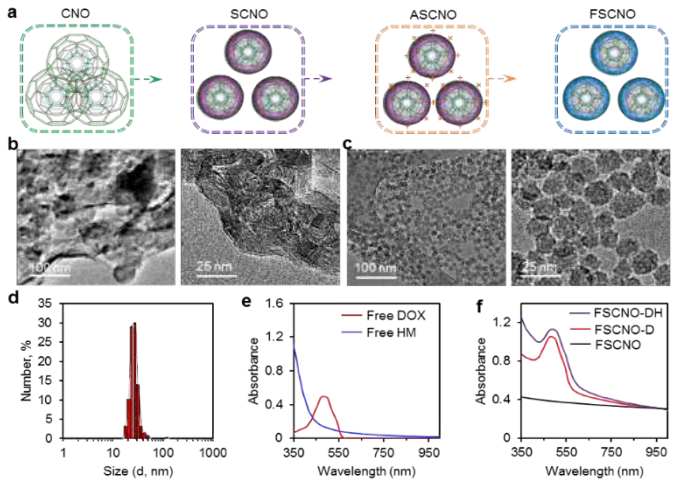

Figure 1: A schematic illustration and characterizations of the FSCNO-DH nanoparticles.

nanoparticles of ~20nm with clear nanostructure and little aggregation can be obtained (**Figure 1c-d**). Both the hydrophobic HM and hydrophilic doxorubicin hydrochloride were encapsulated in the FSCNO nanoparticles to form FSCNO-DH nanoparticles. The successful encapsulation of HM and DOX was further confirmed with UV-Vis absorbance and fluorescence spectrometry (**Figure 1e-f**).

Absorbance measurements of the FSCNO nanoparticles in the NIR region indicated that they were is 2–3 times higher than that of the FSCNT and FSGO nanoparticles when the concentration is more than 0.25 mg ml−1, implicating the superior photothermal property of the FSCNO nanoparticles (**Figure 2**).

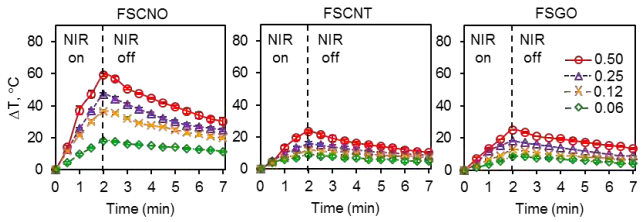

Figure 2: Photothermal effect of FSCNO nanoparticles.

Two types of multidrug-resistant human cancer (NCI/ADR-RES and A2780ADR) cells were used in this study together with a nondrug resistant type of human cancer (OVCAR-8) cells for control. Compared with OVCAR-8 cells, free DOX is inefficient in killing NCI/ADR-RES and A2780ADR cells due to the drug-resistant nature of the cells. However, the efficacy of DOX in killing NCI/ADR-RES and A2780ADR cells is significantly enhanced when administered with 1–10 μg ml^{-1} HM (dissolved with DMSO at 1 mg ml^{-1} in stock. The 1W cm^{-2} IR laser combined with FSCNO-D nanoparticles was able to effectively kill all the three different types of cancer cells due to the superior photothermal effect of the FSCNO nanoparticles (**Figure 3**).

The expression of P-selectin is evident in activated HUVECs (aHUVECs, **Figure 3a**) while it is negligible in the HUVECs without activation. FSCNO-DH nanoparticles could efficiently bind with P-selectin on the aHUVECs while the binding between SCNODH nanoparticles and aHUVECs was not observable, showing the crucial role of the fucoidan on the surface of the FSCNO-DH nanoparticles in targeting aHUVECs (**Figure 3b**).

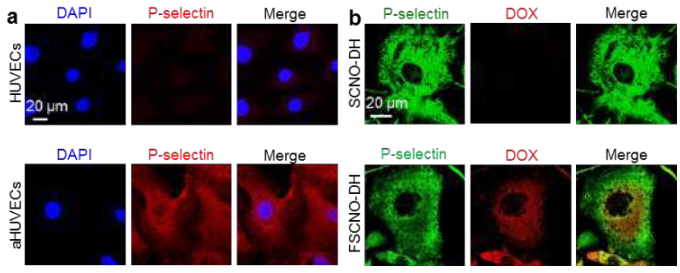

Figure 3: Tumor vasculature targeting.

In vivo whole animal imaging indicates that the FSCNO nanoparticles can efficiently target the tumor as shown in **Figure 4a**. The treatment of FSCNO-DH nanoparticles combined with NIR laser irradiation (FSCNO-DH+L) demonstrated the best antitumor efficacy, as indicated by tumor weights (**Figure 4b**). This result further confirms that controlled release of P-gp inhibitor is crucial to overcoming the multidrug-resistant capability of NCI/ADR-RES cells and for killing them in vivo. Similarly, the FSCNO-DH+L treatment is more effective in killing tumors with EC, confirming the importance of tumor vasculature targeting for enhancing the efficacy of nanoparticle-mediated cancer therapy.

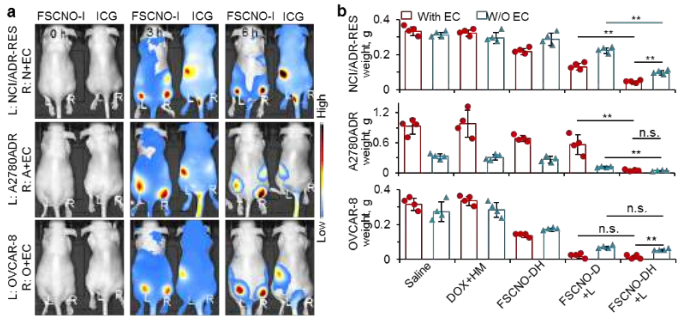

Figure 4: In vivo tumor targeting and antitumor capacity.

DISCUSSION

In this study, the sequence of encapsulating DOX and HM was further developed and investigated. The encapsulation efficiency of HM is only ~24% if mixing HM with the FSCNO nanoparticles first, which is much lower than that (~69%) of the optimized method of mixing DOX with the nanoparticle first. One possible mechanism for this is the electrostatic interaction between the negatively charged silica and the local positive charges within the HM molecule.[5]

When controlling the drug release, HM and DOX are triggered to release simultaneously from the FSCNO nanoparticles during the NIR irradiation. As a result, although some DOX may be pumped out of cells before the function of all the P-gp is inhibited, it could re-enter the cells after the HM binds with all the P-gp quickly. Data from the multidrug resistance cells (NCI/ADR-RES and A2780ADR) either pre-treated with HM (HM-DOX) or without any pre-treatment confirmed that releasing HM and DOX simultaneously from the FSCNO nanoparticles is of significance for overcoming cancer drug resistance.

In summary, this study aimed to synthesize a fucoidan-decorated silica and CNO hybrid (FSCNO) nanoparticle for targeting tumor vasculature and P-gp overexpressed on drug-resistant cancer cells. Through NIR laser irradiation, controlled release of P-gp inhibitors and chemotherapeutic drugs can be achieved. Furthermore, the FSCNO-DH nanoparticles can precisely compromise the function of P-gp pumps in multi-drug resistant cancer cells. This study holds promise in laying the foundation for further developing nanotechnology-based strategies in overcoming multidrug-resistance in cancer.

ACKNOWLEDGMENTS

This work was supported by grants from the National Institutes of Health (NIH R01CA206366 and R01CA243023).

REFERENCES

[1] Lambert, A. W., Pattabiraman, D. R. & Weinberg, R. A. Cell 168, 670–691 (2017).
[2] Bajaj, P., Chowdhury, S. K., Yucha, R., Kelly, E. J. & Xiao, G. Drug Metab. Dispos. 46, 1692–1702 (2018).
[3] Glaeser, Handb. Exp. Pharmacol. 201, 285–297 (2011).
[4] Natoni, A., Macauley, M. S. & O'Dwyer, M. E. Front. Oncol. 6, 93–93 (2016).
[5] Vallet-Regi, M., Balas, F. & Arcos, D. Angew. Chem. Int. Ed. Engl. 46, 7548–7558 (2007).

MACHINE LEARNING SEGMENTATION FOR DENSITOMETRIC PHANTOM CT DATA

Ashley N. Pernsteiner (1), Carla Winsor (1), Heidi-Lynn Ploeg (2), Corinne R. Henak (1)

(1) Department of Mechanical Engineering
University of Wisconsin - Madison
Madison, Wisconsin, USA

(2) Department of Mechanical and Materials Engineering
Queen's University
Kingston, Ontario, CAN

INTRODUCTION

CT-based patient-specific finite element analysis (FEA) is a proposed clinical method to identify osteoporotic patients who could benefit from pharmacological intervention[1]. The largest barrier to implementing this method in the clinic is segmentation. Segmentation is used to isolate phantom plugs in CT scans and create digital geometries. Manual segmentation (MS), the current clinical standard, is time-consuming and only repeatable for skilled operators carefully following a detailed protocol. Thus, there exists a need to improve efficiency and repeatability of segmentation. Alternatively, automated segmentation can be carried out using machine learning (ML) or deep learning (DL) techniques. The aim of this study was to compare the results of ML, DL, and MS in terms contour mesh geometry and density calibration slope.

METHODS

A $Ca_5(PO_4)_5$ calibration phantom (CIRS, Inc, Norfolk, VA, USA) including custom plug densities [mg/cc] of 100 (part: RDH357Y-23) and 400 (part: RDH362Y-24) and stock plugs of 1000 (part: 06217) and 1750 (part: 06221) were CT scanned in air. Data were captured on GE CT scanner models Discovery CT 750HD and Optima 660 (GE Healthcare, Waukesha, WI, USA) with a standard reconstruction kernel. Scan parameters were consistent with established clinical protocols[2] (slice spacing [mm]: 0.325, 0.625; slice thickness [mm]: 0.625, 1.25; voltage [kVp]: 120; current [mA]:105, 120). Phantom plugs were chosen to be the subjects of this study due to their simple geometry. An overview of the study elements and segmentation methods are detailed in Figure 1.

In Dragonfly v. 2020.1 (Object Research Systems Inc., Montreal CAN), multiple ML and DL algorithms were trained to segment plugs from a training dataset of 15 to 20 segmented frames.

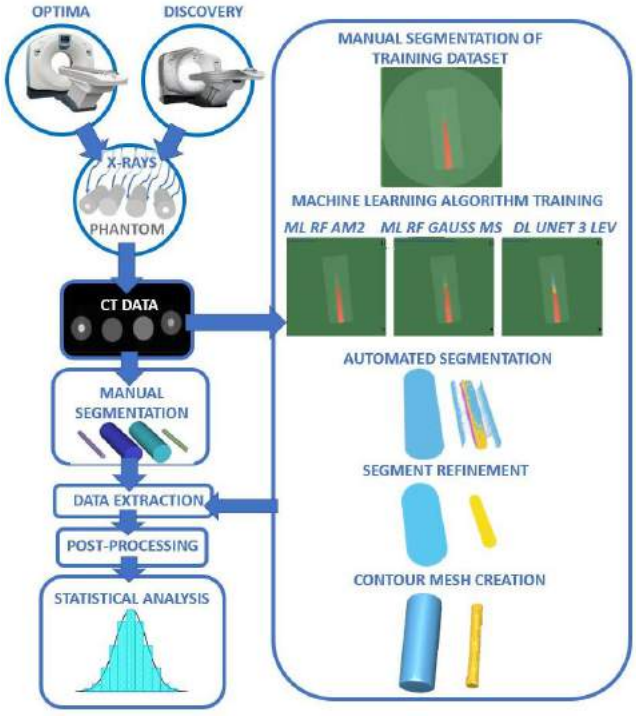

Figure 1: An overview schematic of study elements and parallel segmentation methods. Manual segmentation (MS) (Left), machine learning (ML) and deep learning (DL) segmentation (Right) are detailed.

Algorithm training and related segmentations were performed on a laptop equipped with an NVIDIA GeForce MX 230 GPU. Training was stopped when there were no changes to the loss function monitoring the performance for five iterations. Model performance was assessed based on the percentage of correctly segmented pixels in each training frame and visually by the quality of segments created by each ML segmentation model for an entire CT image stack. The most accurate ML algorithm, *Random Forest Activation Map 2 (ML: RAM)*, was applied to the CT data, to automatically segment a CT image stack of four plugs. Individual plug segments were extracted and artifacts outside of the plug were removed manually. A contour surface mesh of each plug was created from the refined meshes.

3-D geometry and volumetric statistics including standard deviation of CT Number and mean CT Number, were extracted from contour surface meshes for statistical analysis. For comparison purposes, the same types of data were extracted from MS in both Mimics v. 23 (Materialise, Leuven, BE) and Slicer v. 4.10.2 (Slicer, Boston, MA, USA). Geometrical differences in contour surface meshes were compared for results produced by ML, DL and MS using quantiative difference maps in Dragonfly. Density calibration slopes which linearly relate extracted mean CT Numbers [HU] to plug densities [mg/cc] were tested for significant differences between ML, DL, and MS using Mann-Whitney (α= 0.01).

RESULTS

ML segmentation outperformed DL and produced similar results to MS in commercial software. Both ML algorithms had higher pixel accuracy than DL with all algorithms having pixel accuracies greater than 95% (Figure 2). Despite having high pixel accuracies, ML: RGM and DL: U3 failed to correctly segment entire CT image stacks (Figure 3). The ML: RAM and MS in Mimics methods did not produce significantly different slopes (p = 0.097). The ML: RAM and MS in Slicer methods did produce significantly different slopes (p = 0.001).

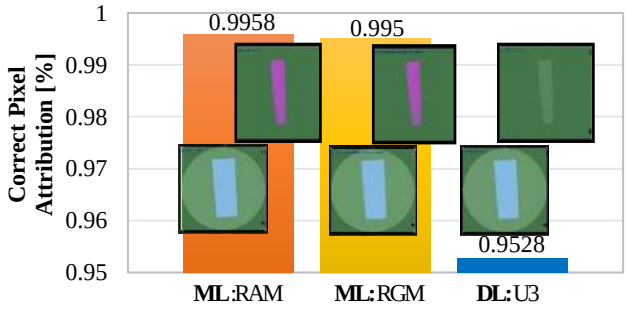

Figure 2: Accuracy measured as correct pixels are plotted for each algorithm. Overlaid are segments of two different plugs produced by machine learning (ML) and deep learning (DL); Random Forest Activation Map 2 (RAM), Random Forest Gaussian-MS (RGM), and 3-level U-Net (U3). These plugs show the varying accuracy of segmentation for each algorithm.

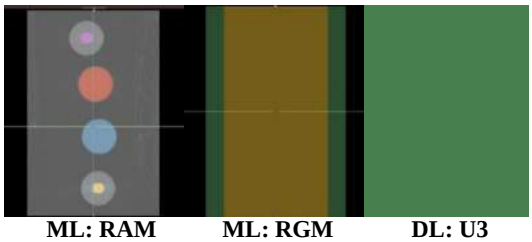

Figure 3: Only ML: RAM accurately performed segmentation on the phantom plugs. A trained operator can discern that ML: RGM and DL: U3 failed to correctly segment the plugs despite high pixel accuracy.

Surface contour meshes created by ML and by MS in Slicer were highly similar for low density plugs (<5% different) as shown in Table 1. Additionally, contour meshes created by ML and by MS in Mimics were very similar (<5% different) for plugs with densities 400 mg/cc or greater. When ML was compared to MS in Slicer and MS in Mimics, standard deviations of geometrical difference were smaller for high density plugs.

Table 1: Plug densities [mg/cc], mean difference, the distance between points [mm], and standard deviation are tabulated. Percent difference is difference normalized by plug diameter.

	Mimics - Dragonfly				Slicer - Dragonfly			
Plug Dens. [mg/cc]	100	400	1000	1750	100	400	1000	1750
Mesh Mean Dif. [mm] *(%)*	7.6 *(19)*	-1.7 *(-4.2)*	-0.3 *(-2.6)*	-0.2 *(-1.5)*	0.5 *(1.2)*	-1.69 *(-4.2)*	-1.7 *(-17)*	-1.8 *(-18)*
Dif. St. Dev. [mm]	10	12	6.8	3.1	13	0.7	0.6	0.8

It took 40 minutes to run ML: RAM for 5mm slice thickness, two hours for 1.25 mm slice thickness, and over four hours at 0.625 mm slice thickness. After which, ten minutes of operator input was necessary to finalize results. Comparatively, trained operators using established protocols for MS in Mimics and MS in Slicer took ten and twelve minutes respectively to complete segmentation.

DISCUSSION

The aim of this study was to compare the results of ML, DL, and MS in terms contour mesh geometry and density calibration slope. ML: RAM performs accurate segmentation with little user input, only requiring ten minutes of trained operator time compared to twelve minutes for an experienced operator to perform MS. However, ML: RAM required up to four hour of run time to segment one image stack of plugs. Higher power workstations intended for research or clinical use will likely perform segmentation tasks more quickly. Additionally, the current time investment for training and running is expected to reduce as technology develops. When compared to ML: RAM, DL: U3 models produced less accurate results, as noted by a trained operator. The poor performance of DL in this setting may be the result of using a small training dataset of 20 or less segmented images. DL is expected to perform better with more training data, which should be tested in future work. Future works should continue to examine the potential error introduced by ML segmentation. A potential follow-up study would be to calculate and compare the impact of ML: RAM and MS in a clinical context such as CT-based patient-specific finite element analysis.

ACKNOWLEDGEMENTS

The authors acknowledge Emily Cameron for prior segmentation used for comparison. We acknowledge the support of the UW-Madison Sophomore Research Fund, Natural Sciences and Engineering Research Council of Canada (NSERC), Ploeg's Research Initiation, and the Human Mobility Research Centre, Queen's University, Kingston, ON, Canada. Thanks to Dr. P.J. Pickhardt and Carrie Bartels for help capturing the image data used.

REFERENCES

[1] Imai K. *World J Exp Med.* 5(3):182-187. (2015)

[2] Lee SJ, *Am J Roentgenol*.;209(2):395-402. (2017)

ACCELERATED DEGRADATION OF ELECTROPUN POLYCAPROLACTONE TISSUE ENGINEERING SCAFFOLDS UNDER DYNAMIC LOADING

Emily C. Clement (1), Johane Bracamonte (2), Joao S. Soares (2)

(1) Department of Biomedical Engineering
Virginia Commonwealth University
Richmond, VA, United States

(2) Department of Mechanical and Nuclear Engineering
Virginia Commonwealth University
Richmond, VA, United States

INTRODUCTION

Engineered tissue vascular grafts (ETVGs) are composed of cells seeded on a biodegradable scaffold. These scaffold-cell constructs are created with the intention of producing a viable implant with mechanical properties similar to the damaged native tissue the graft is replacing. The scaffold is meant to provide a proper mechanical environment and structural support to the maturing tissue as the extracellular matrix develops.[1] If the scaffold degrades too rapidly, the forming engineered tissue will lose its integrity; if the scaffold degrades slowly, it may provide adverse developmental cues to the tissue and promote fibrosis.

In the body, the degradation of polycaprolactone (PCL) can take from 12 to 18 months to occur depending on scaffold properties and its design. Accelerated-degradation techniques are therefore necessary to make the study of electrospun PCL scaffolds more reasonable by decreasing its degradation time. The *in vitro* and *in vivo* degradation of PCL occurs mainly through hydrolysis of the ester bonds, which can be catalyzed by a pH increase in an alkaline NaOH liquid media.[2]

However, studies have shown that mechanical forces, in particular cyclic loads, increases the degradation rate of polymers by introducing additional mechanisms of polymer degradation. At the same time, it is generally desired to include dynamic training during incubation of engineered tissues because those are known to enhance cell proliferation, the rate of synthesis of *de novo* engineered tissue, and improve its resulting stiffness and microstructure.[3]

Therefore, it is key to study the effects of mechanical loading in the degradation profiles of tissue engineering scaffolds. In order to increase the throughput of these experimental investigations, those should be performed under accelerated-degradation conditions. Previous works have studied the degradation of polymers under static and constant loading,[4] while degradation under cyclical loading on degradation dynamics is mainly conducted for electromechanical applications.[5] Thus, there is a gap of knowledge on the characterization of polymer degradation of under physiological cyclic loading for tissue engineering applications.

The goal of this study is to characterize the accelerated-degradation profiles for PCL scaffolds under both static and dynamic loading conditions. This accelerated degradation profile can then be correlated to the behavior of a scaffold degrading in physiological conditions. This goal is achieved by first developing an accelerated-degradation chamber with both static and dynamic conditions. Ultimately, this information can be used to improve the design of biodegradable scaffolds by predicting scaffold behavior.

METHODS

Scaffold Manufacture. The degradation experiments conducted in this study utilized electrospun polycaprolactone (PCL 80,000 g/mol) scaffolds. Our manufacturing process results in tubular scaffolds with 3 mm diameter, and 160 ± 30 μm thickness. These tubular scaffolds were cut and flattened out to produce testing samples with 3 cm in length. Each sample was weighed on a high precision scale and the thickness was measured using micrometers.

Mechanical Testing. Scaffold membrane stiffness was tested using a custom-designed uniaxial-extension stretcher. The samples underwent 10 preconditioning cycles followed by one cycle mechanical test carried out up to 10% strain over the course of 720s. The deformation of the sample was measured by tracking four dots placed at the center of the scaffold. Stress vs. strain graph are generated, and the membrane stiffness is calculated as the slope of the linear region.

Microstructural Analysis. Scanning Electron Microscopy (SEM) imaging was used to characterize the scaffold microstructure: fiber diameter, fiber orientation distribution, and % porosity. SEM is taken at 3,000x magnification, and analyzed using ImageJ and DiameterJ.

Degradation Protocol. Each degradation chamber is able to hold 6 rectangular samples clamped at both ends. Accelerated-degradation conditions were produced by submerging the scaffolds in NaOH solutions at varying concentrations and pH. Preliminary results have shown that pH of 12.45 produced weight loss of 16.4% and membrane stiffness reduction of 57.6% under static conditions after 42 days, which was deemed appropriate for the accelerated-degradation on this study.

Degradation under dynamic conditions is produced by stretching the samples to 1, 2 and 5% uniaxial strain in linear ramp cycles with period of 2 seconds. Static vs. dynamic degradation is compared after several timepoints up to two weeks (3, 7 and 14 days). After undergoing static or dynamic degradation, samples are collected and dried in a vacuum oven at 40 °C and 2.06 bar vacuum for 24 hours. The samples are again weighed, their thickness measured, and then undergo destructive mechanical testing or microstructural analysis.

Statistical Analysis. We used the software JMP, Version 15.1.0 (AS Institute Inc., Cary, NC, 1989-2019.) to carry a Dunnett's test with a significance level of 5% to compare the weight, thickness, and membrane stiffness of the degraded samples (static and dynamic) to the untreated virgin scaffolds as the standard controls

RESULTS

Degradation Chamber Design and Construction. The design of pH resistant degradation chambers that are able to impose dynamic strains is challenging. The design of both the static and dynamic degradation chamber were built to withstand the highly alkaline liquid media solution required to produce adequately accelerated degradation while holding 6 samples at a time and having only the imposition of dynamic training as the only difference. The container box was machined from a PP slab to assure hermiticity. The brackets and sample holders were 3D printed on ABS. One linear actuator is driven with an Arduino board with custom-designed user interface to control the experiment during its course.

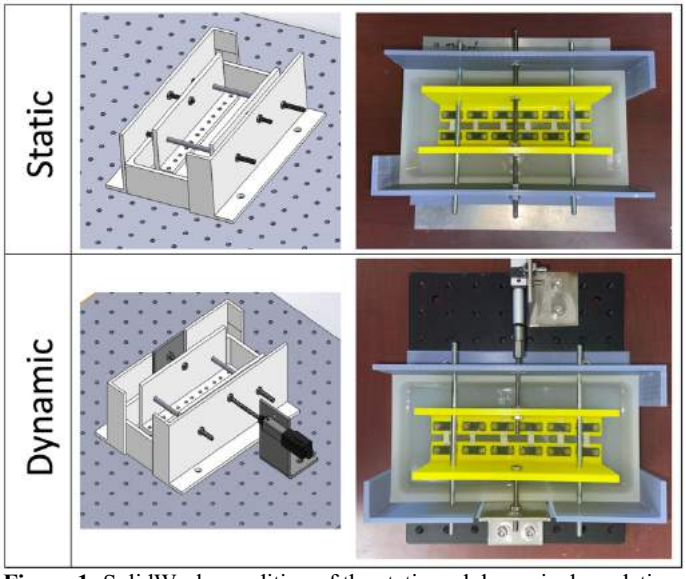

Figure 1: SolidWorks rendition of the static and dynamic degradation chambers (left) and their built instances (right).

Static vs. Dynamic Degradation under Accelerated Conditions. There appeared to be no significant change in the weight or thicknesses of the scaffolds over the course of two days of degradation. Results shown dynamic loading produced a significant decrease in scaffold membrane stiffness when compared with virgin scaffolds ($p^* = 0.041$). The membrane stiffness of the dynamic degradation samples was on average 52% lower than the stiffness of untreated samples, whereas the static group showed only difference of 31% (Figure 2). This suggest that the cyclical loads accelerate the decline of mechanical properties, nevertheless more replications are needed to gain statistical significance.

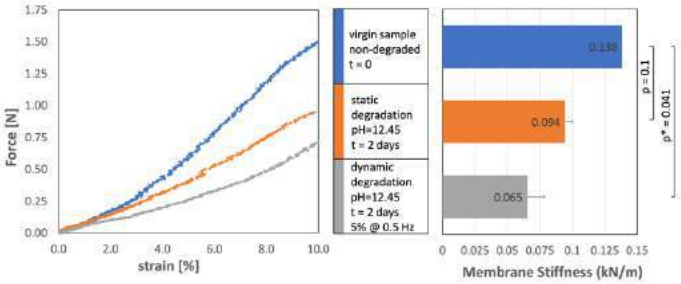

Figure 2: (left) representative load vs. strain curves for virgin and degraded scaffolds; (right) statistical comparison of membrane stiffness (force per unit length)

DISCUSSION

At physiological pH and under static conditions, it takes several months to years for PCL scaffolds to demonstrate significant mass loss, degradation, and loss of mechanical integrity. These are typically the conditions tested at the benchtop to design tissue engineering scaffolds; however, very often these are intended to function *in vivo* in a complex dynamic mechanical environment, and possibly, will be subjected beforehand to mechanically-stimulated in vitro incubation. The introduction of chemically-accelerated degradation and cyclic dynamic loading induced substantial differences in scaffold degradation profiles. The employment of accelerated-degradation conditions allowed us to observe significant differences due to the mechanical environment in a matter of days. In order to obtain insight and calibrate predictive models of mechanical properties depreciation and mass loss, the accelerated-degradation time-scale is matched with a long-term experiment (up to 2 years) we are conducting at physiological pH under static conditions.

Future work includes more thorough investigations on the influence of mechanically-induced degradation on the evolving microstructure of the PCL scaffolds and a direct quantification of the degradation scale with molecular weight determination with gel permeation chromatography. In conclusion, the employment of accelerated-degradation techniques to investigate the effects of mechanically-induced degradation of tissue engineering scaffolds allows for a decreased turnaround time in R&D applications for tissue engineering, and further insight into the degradation profile of scaffolds allows for improved tissue engineering methods.

ACKNOWLEDGEMENTS

This research was funded in part by VCU Summer Fellowship for Undergraduate Research.

REFERENCES

[1] Thottappillil and Nair, Vasc Health Risk Manag. 2015;11:79-91.
[2] Sailema-Palate et al., Polym. Degrad. Stab.. 2016; 130:118-125.
[3] Soares and Sacks, Biomech Model Mechanobiol. 2016;15:293–316.
[4] Fan et al., Polymer Degradation and Stability. 2008; 93: 677-683.
[5] Garcia-Sanchez et al., Applied Energy 259 (2020): 114210.

COMPUTATIONAL MODELING OF ARTERIAL HEMODYNAMICS IN PEDIATRIC PULMONARY ARTERIAL HYPERTENSION

Nathan Y. Li (1), Christopher Tossas-Betancourt (2), C. Alberto Figueroa (2,3)

(1) Department of Pharmaceutical Sciences
University of Michigan
Ann Arbor, MI, USA

(2) Department of Biomedical Engineering
University of Michigan
Ann Arbor, MI, USA

(3) Department of Surgery
University of Michigan
Ann Arbor, MI, USA

INTRODUCTION

Pulmonary arterial hypertension (PAH) is a complex disease defined by a mean pulmonary arterial pressure > 20 mmHg [1] which causes anatomical and physiological alterations in the pulmonary vasculature, leading to drastic changes in hemodynamics and wall mechanics. Because of the intricate nature of PAH, there is a pressing need to identify metrics to aid in early non-invasive PAH diagnosis.

Due to the current lack of prospective pediatric PAH trials, clinical diagnostic metrics are often extrapolated from adult patients [2]. Extrapolating adult data to the pediatric population can be problematic as younger subjects have significant differences in hemodynamics [3], and lower survival rates [4]. In addition, age-specific symptoms like impaired lung development and comorbidities such as congenital heart defects are found at a higher rate in pediatric populations [5]. Due to the aforementioned discrepancies in PAH pathophysiology between adults and children, there is a critical need for clinical trials focused on pediatric PAH patients to derive diagnostic metrics.

Computational models informed by patient-specific data can be used to complement clinical data and establish additional metrics of the overall pathology and progression of PAH. Computational models can provide useful quantities of interest (i.e. pressure, flow, wall shear stress, cardiac work, stiffness, contractility, etc.) at higher temporal and spatial resolutions than current diagnostic tools.

In this work, we combine prospective clinical data on anatomy, flow, and pressure with computational tools to provide a description of arterial hemodynamics in pediatric PAH. Inconsistencies were present in the acquired data due to temporal gaps between data acquisition studies, sedation, and tolerances in diagnostic tools. Mitigation strategies were developed and implemented to correct the prospective clinical data, ensuring physiologically consistent computational results. The purpose of this work is to develop a strategy to calibrate the boundary conditions and material parameters of the computational models for each PAH patient, using open-source software tools, and the physiologically consistent patient data.

METHODS

Clinical data were prospectively acquired in seven pediatric PAH patients as part of an ongoing clinical trial [6] conducted at C.S. Mott Children's Hospital at the University of Michigan. This study was approved by the University of Michigan Institutional Review Board (HUM 00117706), and informed consent was obtained from the subjects or parents.

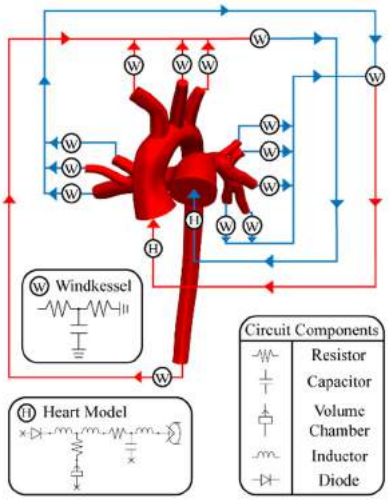

Figure 1. Modeling framework of arterial hemodynamics. (W) indicates a Windkessel model and (H) indicates a heart model.

Clinical Data. Three-dimensional (3D) vascular anatomy was acquired using a 3D steady-state free precession sequence with a magnetic resonance imaging (MRI) scanner. Phase-contrast MRI (PC-MRI) was performed to obtain dynamic data of luminal area and blood flow velocity at the ascending (AAo) and descending thoracic aorta (DTA), and the main (MPA), left (LPA), and right (RPA) pulmonary arteries. Invasive right heart catherization was performed to obtain pressure waveforms.

3D Arterial Modeling. Patient-specific 3D fluid-structure-interaction (FSI) models [7] were built using the blood flow modeling software CRIMSON [8]. Each model required specification of patient-specific arterial wall mechanical properties and inflow and outflow boundary conditions. Spatially-varying arterial wall stiffness and thickness were calculated using dynamic luminal area and pressure waveforms [9,10]. Lumped-parameter Windkessel models were coupled to each outlet of the 3D model [11] to represent the resistance and compliance of the distal vasculature. The heart was represented by a lumped-parameter network of circuits that was coupled to the Windkessel models to form a closed-loop network, resembling the cardiopulmonary circulation (**Figure 1**).

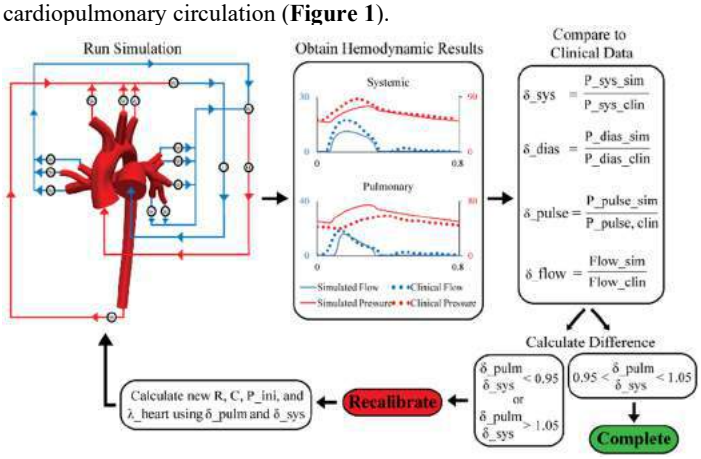

Figure 2. Workflow for calibration. Resistance (R), capacitance (C), and initial pressures (P_ini) of the circulatory Windkessel models, and heart model parameters (λ_heart), were calibrated until simulation results matched clinical data within 5%.

Windkessel parameters (resistance, capacitance, initial pressure) and heart model parameters (elastance waveform) were iteratively calibrated to match clinical data (**Figure 2**) within 5%. Reference metrics such as systolic, diastolic, and pulse pressure, and mean flow were used to compare simulated results to clinical data (**Figure 3**).

RESULTS

Following model calibration, the contributions from the 3D image-based models of the large pulmonary arteries and lumped-parameter models of the pulmonary microcirculation to the total resistance (driving mean pressure) and total compliance (driving pulse pressure) were derived (**Figure 4**). The average contributions of the large pulmonary arteries to the total resistance and compliance of the pulmonary circulation were 4% and 58%, respectively.

DISCUSSION

We established a modeling workflow to combine advanced computational analyses with prospectively acquired clinical data, including strategies to mitigate inconsistences in clinical data to ensure consistent computational results. Our results show an interesting finding: the pulmonary microcirculation contributes most to the total resistance, which mainly affects mean pressure. The large pulmonary arteries contribute most of the total compliance of the pulmonary circulation, which primarily influences pulse pressure. Assuming that, in PAH, the wall properties of the pulmonary microcirculation remodel before those of the large pulmonary arteries, our results would suggest that rises in mean pressure precede rises in pulse pressure. The combination of prospective clinical data and the proposed computational framework provides a comprehensive description of PAH pathology and can help uncover metrics to improve early PAH diagnosis.

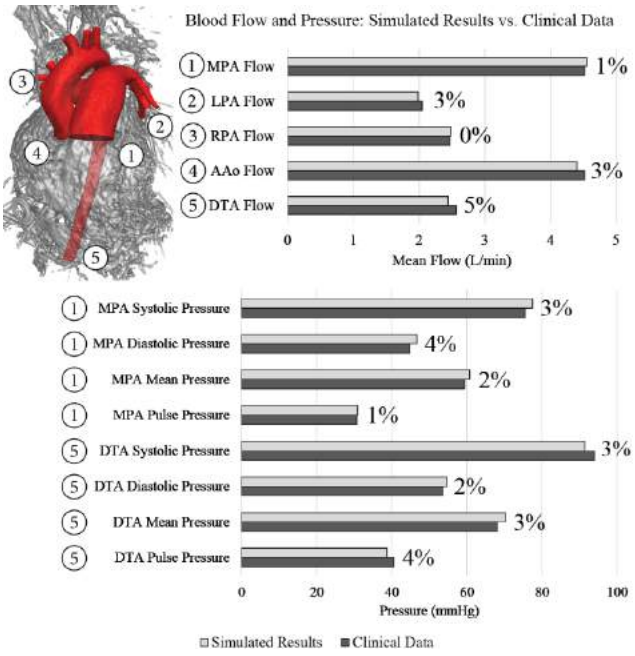

Figure 3. Calibrated arterial model simulated flows at (1) MPA, (2) LPA, (3) RPA, (4) AAo, and (5) DTA, and simulated pressures at (1) MPA and (5) DTA were matched to clinical data within 5%.

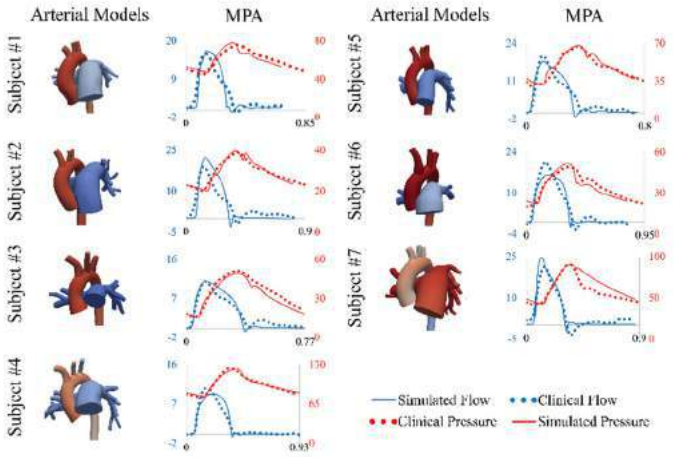

Figure 4. Hemodynamic results for the seven patients included in the prospective clinical trial.

ACKNOWLEDGEMENTS

This work was supported by the NIH (U01 HL135842), and the NSF (Grant 1531752) Acquisition of Conflux.

REFERENCES

[1] Simonneau, G et al., *Eur Respir J*, 1:1913-2018, 2019.
[2] Ivy, D et al., *Am J Cardiol*, 9:1332–38, 2010.
[3] Cuomo, F et al., *PLoS One,* 3:1–21, 2017.
[4] Douwes, JM et al., *Int J Cardiol* , 2:1370–77, 2013.
[5] Berger, RMF, et al., *Eur Respir Rev,* 19(118):321-330, 2010.
[6] NIH. https://clinicaltrials.gov/ct2/show/NCT03564522
[7] Figueroa, CA et al., *CMAME,* 195:5685–706, 2006.
[8] Arthurs, CJ et al., *bioRxiv*, 2020.10.14.339960.
[9] Hirai, T. et al., *Circulation,* 80: 78-86, 1989.
[10] Roccabianca, S. et al., *J Mech Behav Biomed,* 29: 618-634, 2014.
[11] Vignon-Clementel, IE et al., *CMAME*, 195: 3776–96, 2006.

Efficacy of Poloxamer 188 in Mitigating Changes to Subchondral Bone Composition and Architecture Following Traumatic ACL Injury and Reconstruction

G. Brown[1], G. Narez[1], L. De□ardin[2], F. Wei[3,4,5], R.C. Haut[3,4], T.L. Haut Donahue[1]

(1) Department of Biomedical Engineering
University of Massachusetts
Amherst, MA, USA

(2) Department of Small Animal Clinical Sciences
Michigan State University
East Lansing, MI, USA

(3) Orthopaedic Biomechanics Laboratories
Michigan State University
East Lansing, MI, USA

(4) Department of Mechanical Engineering
Michigan State University
East Lansing, MI, USA

(5) Department of Biomedical Engineering
Michigan State University
East Lansing, MI, USA

Introduction: Previously, our lab evaluated the efficacy of ACL reconstruction surgery in preventing changes to subchondral bone architecture and composition following traumatic knee injury. We found the surgery to be helpful in preventing changes to the subchondral bone, but not completely effective in eliminating all degradation of the bone. This is consistent with previous work that suggests reconstruction surgery does not decrease the risk of developing post traumatic osteoarthritis (PTOA) [1]. We are now evaluating the use of an FDA approved nonionic surfactant, poloxamer 188 (P188), in preventing changes to subchondral bone quality and quantity. It is hypothesized that P188 delivered to the joint at three separate time points will be the most effective in mitigating changes to subchondral bone architecture and composition following traumatic injury to the knee joint.

Methods: 90 skeletally mature Flemish Giant rabbits (6.81 ± 0.34 kg) were used for this study. With IACUC approval and under general anesthesia, the right knee and paw of each rabbit was secured into a custom fixture and a controlled impact was delivered using a servo-hydraulic actuator (Instron, Norwood, MA), until ACL failure was observed. Within 2 minutes of impact, each rabbit received an intra-articular injection of either 1.5 mL of phosphate buffered saline (PBS) or 1.5 mL of 8mg/ml P188. Animals were randomly assigned to treatment groups: no P188, P188 following impact (P188 D0), P188 following impact and 24 hours post-impact (P188 D0,1), and P188 following impact, 24 hours post-impact, and 7 days post-impact (P188 D0,1,7). Surgical reconstruction of the torn ACL was performed by a licensed veterinarian 2-3 weeks post-impact. The semitendinosus (ST) tendon was transected at the musculotendinous junction while its tibial insertion was left intact. The tendons free end was rerouted through tibial and tunnel femurs (3.2mm in diameter), which overlapped the ACL footprint. The ST tendon was tensioned and then secured into the femoral tunnel using an interference fit screw and periosteal sutures. An anterior drawer test was performed to assess postoperative joint stability prior to routine closure. The left knee of each animal served as a contralateral control. Animals were euthanized one (n=30), three (n=30), and six months (n=30) post-surgery. Following mechanical testing of the articular cartilage, tibias and femurs were fixed in 10% formalin. uCT imaging and reconstruction were performed using a Skyscan 1276 (Bruker, Billerica, MA). Similar to a previous study, regions of interest were chosen to coincide with the location of mechanical testing

of the articular cartilage on the lateral and medial hemijoints [2]. CTAn software (Bruker, Billerica, MA) was used to determine bone volume/tissue volume (BV/TV), trabecular thickness (Tb.Th), trabecular separation (Tb.Sp), trabecular number (Tb.N) and volumetric bone mineral density (vBMD). Cortical volumetric bone mineral density (Co.BMD), cortical thickness (Co.Th), and osteophyte volume were also determined. A fixed effect model was used to determine significant differences between treatment groups with a p-value of < .05 deemed significant.

Results: Mid-substance ACL tears were documented in all animals. ACL failure force was 868.2 ± 69.9 N. Statistically significant changes in osteophyte volume observed in both femurs and tibias. Significant changes in BMD of femurs also observed between treatment and control groups.

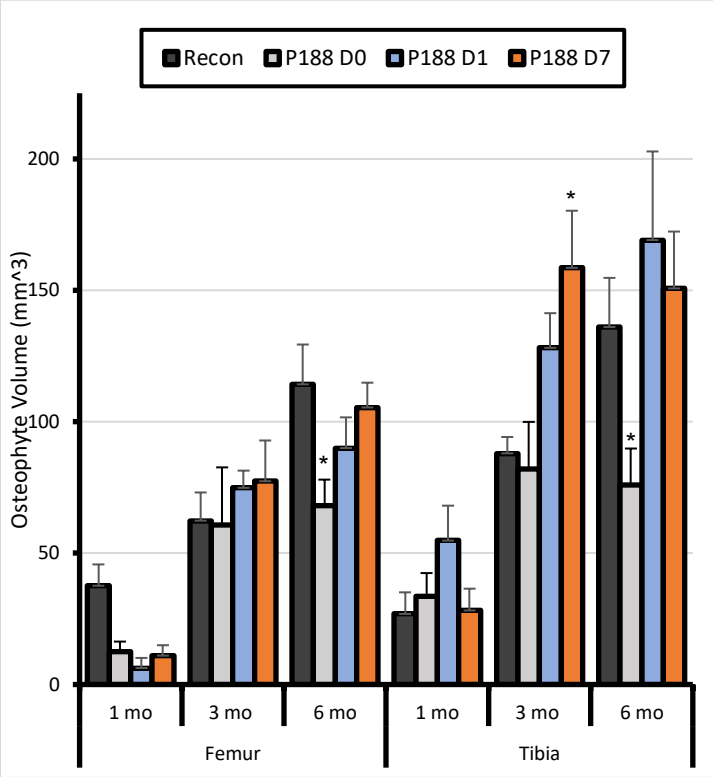

Figure 1. Osteophyte formation in tibias and femurs across all time points

Discussion: Results showed that intra-articular injections of P188 were not effective in mitigating damage to the bone. This being said, P188 delivered only at the day 0 time point showed considerably decreased osteophyte volume at almost all time points. This reduced osteophyte formation suggests less degeneration of the underlying natural bone. Multiple injections to the joint may cause increased inflammation and osteophyte formation. A limitation of this study is that the P188 was injected intra-articularly and relied on diffusion to reach the bone. Future work could investigate the effects of targeted delivery of P188 directly to the bone.

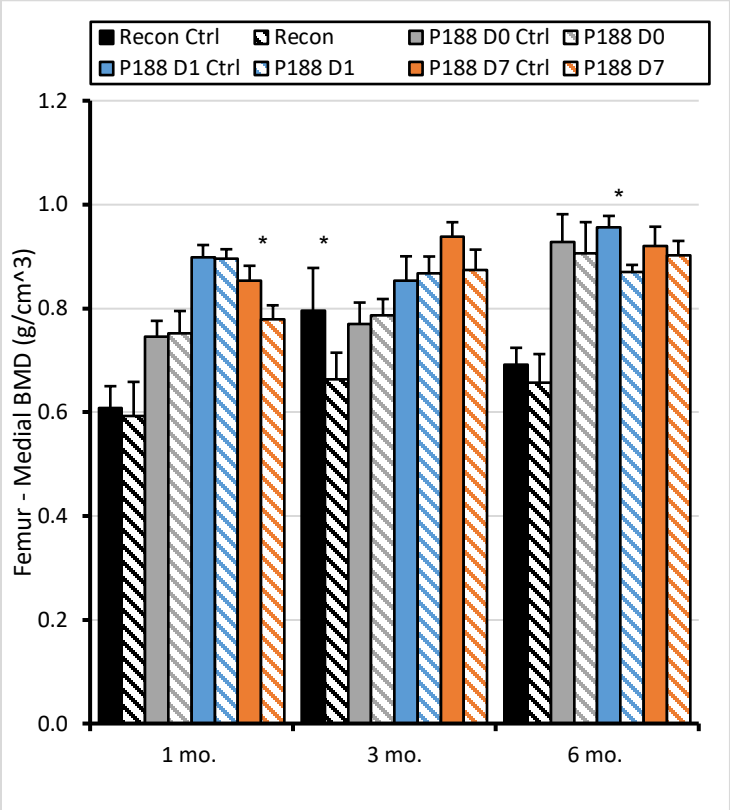

Figure 2. Comparison of volumetric bone mineral density in medial hemijoint of femurs

Conclusions: The novel closed-joint traumatic impact model was able to successfully generate ACL tears and meniscal damage comparable to what is observed in the clinical setting. Surgical repair of the damaged ACL and meniscal debridement was successfully performed as well, which replicates the current clinical gold standard. The surgical intervention proved effective in reducing changes in composition and architecture of the subchondral bone. The addition of P188 resulted in bone composition that was more comparable to the control limb than the reconstruction only animals, albeit not statistically significant. In fact, the bone quality was sometimes better than control in the P188 groups (Fig 2). Hence, P188 shows promise as a potential treatment for PTOA. Intra-articular injections of P188 may not significantly affect the bone due to the method of delivery. Targeted delivery of P188 to specific tissues may be necessary to truly access the effects of this pharmaceutical intervention.

Acknowledgements: The study is funded by DOD grants W81XWH-16-1-0735 and W81XWH-16-1-0734.

References: [1] Felson, DT, Radial Clin North AM, 42(1): 1-9, 2004. [2] Pauly, H.M., et al., *J Orth Res*, 33(12):1835-1845, 2015

A COMPUTATIONAL MODEL OF THE IMPACT OF CEREBRAL AMYLOID ANGIOPATHY ON VASO-RESPONSIVENESS OF CEBEBRAL ARTERIES

Cole T. Theobald (1), Ryan R. Mahutga (1), Patrick W. Alford (1), Victor H. Barocas (1)

(1) Department of Biomedical Engineering
University of Minnesota – Twin Cities
Minneapolis, Minnesota, USA

INTRODUCTION

Alzheimer's disease (AD) is a progressive, degenerative brain disease that results in dementia. Cerebral amyloid angiopathy (CAA) is present in over 80% of patients that have AD[1]. CAA is the result of amyloid beta, which can form plaques that surround and integrate into the small arteries. Patients that have CAA have a greater chance of intracranial hemorrhage (ICH)[2]. This elevated risk connects to AD as AD patients who have an ICH are almost twice as likely to develop dementia than AD patients who don't have an ICH[3]. While it is known that CAA can lead to the vascular dysfunction and result in an ICH, the mechanism by which CAA causes vascular dysfunction remains relatively unknown.

There are two main components of the vascular dysfunction caused by CAA: (1) loss of vaso-responsiveness and (2) loss of vaso-integrity. This study focused on understanding the mechanisms driving the loss of vaso-responsiveness in intercranial vessels due to CAA. It has been shown in animal studies that insoluble amyloid beta plaques can reduce the functional dilation of the vessel, as the plaque places a physical restriction on the dilation[4]. The plaque can exist in two forms: circumferential (surrounding the vessel) and intramural (integrating within the vessel). It has also been shown that soluble amyloid beta can lead to loss of vascular smooth muscle (vSMC) contractility[5]. The goal of this computational study was to show how circumferential plaque contributes to the overall loss in vaso-dynamics, and how the plaque formation can further exacerbate arterial loss-of-function when combined with lower vSMC contractility.

In this study, we construct a computational model of a cerebral artery with CAA to analyze the role of amyloid beta in vascular disease. The percent coverage of the circumferential plaque was varied, and the impact of both the circumferential plaque and the soluble plaque on vasodynamic dysfunction of the vessel measured. This model offers a unique perspective on the role of amyloid beta plaque on vascular mechanics.

METHODS

A finite-element model of the cerebral artery with CAA was generated using FEBio[6]. The initial model was created with 100% circumferential coverage of the amyloid beta plaque (Fig. 1A). Two tangent cylindrical constructs were generated and attached to each other, with the inner construct representing the vessel and the outer construct representing the plaque. The inner diameter of the vessel was 58.3 μm, the outer diameter of the vessel was 65.8 μm, and the outer diameter of the amyloid plaque was 67.9 μm[7]. The passive four-fiber family strain energy density model was used for the vessel with the nonfibrillar matrix defined using a Neo-Hookean model, and the fibers defined with an exponential power law:

$$W = c_1(I1 - 3) + \sum_{i=1}^{4} \frac{k_i}{2\alpha_i}(\exp(\alpha_i(I4_i - 1)^2) - 1) \qquad (1)$$

where c_1 is the Neo-Hookean modulus, $I1$ is the first strain invariant, k_i is the fiber modulus parameter for fiber family i, α_i is the fiber nonlinearity parameter for fiber family i, and $I4_i$ is the fourth strain invariant for fiber family i, dictated by the in-plane circumferential-axial fiber angle, θ and the out-of-plane radial fiber angle, ϕ. The parameters for the fibers can be seen in Table 1. The nonfibrillar component had a bulk modulus of 0.6 MPa and coefficients of 0.015 MPa. In addition, an active contraction was added to the vessel to simulate the contractility of the vessel. The material for the amyloid beta plaque was defined as a Neo-Hookean material with a bulk modulus of 0.6 MPa and coefficients of 0.25 MPa. We also modeled contractility using the prescribed active contraction model in FEBio, where we define the active contraction stress for the material.

Table 1: Parameters for the Fibers used in the Vessel Material[8]

Fiber Family #	Fiber Nonlinearity (α_i)	Fiber Modulus (k_i)	Circumferential-Axial Angle (θ)	Radial Angle (ϕ)
1	1	0.009 MPa	0°	90°
2	1	0.009 MPa	90°	90°
3	0.325	0.0018 MPa	68.6°	90°
4	0.325	0.0018 MPa	68.6°	90°

Once the FEBio model had been created for the 100% coverage scenario, the associated FEBio input file was modified to reduce the coverage to a value in the range from 0% to 100% with intervals of 10%. A set of elements from the plaque was randomly selected via a MATLAB script with the number of elements selected determined by the desired percent coverage and was used to create a new input file. A model with 50% is shown in Fig. 1B.

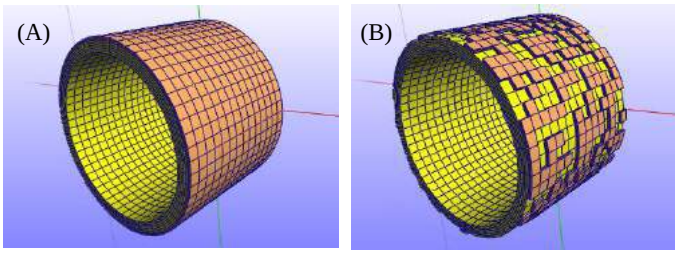

Figure 1: Computer model of vessel with (a) 100% and (b) 50% plaque coverage

For each simulation, the vessel was stretched axially to 1.17[8]. A luminal pressure load was added to the vessel and increased linearly to 80 mmHg[7]. Next, we reduced the luminal pressure to 64 mmHg, representative of mean cerebral artery pressure, and we linearly ramped the active contraction within the vessel to 0.150 MPa[5]. In this model, we use the different contractility levels to compare the insoluble plaque effects to the effects of soluble amyloid beta. The position of each of the nodes on the inside of the vessel were exported at each time step to measure the average diameter of the vessel.

RESULTS

To see how different plaque coverages affect the vessel's ability to dilate, the average inner diameter of the vessel was plotted versus the pressure load (Fig. 2A). In the healthy case (0% coverage), we see the typical lockout behavior of blood vessels. Further, as the plaque coverage is increased, we see stiffer material behavior and the material becoming more linear.

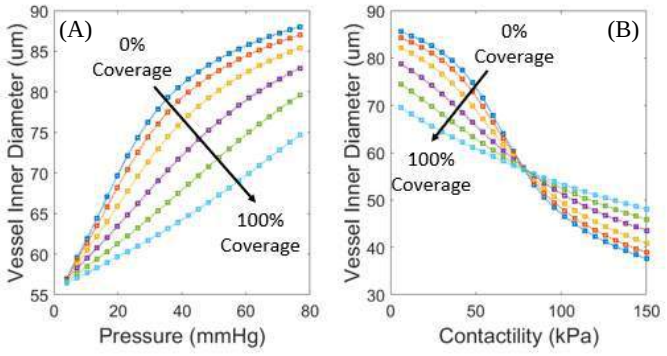

Figure 2: The average inner diameter of the vessel as the pressure load was increased (a) and the contractility was increased (b) for plaque coverages ranging from 0% to 100% with intervals of 20%

The effect of plaque coverage was also analyzed for varied contractility (Fig. 2B). We see in this figure that the shape of the contractility curve starts as a sigmoid with 0% coverage and becomes more linear as we add more stiff, non-contractile plaque. Additionally, we see an inflection point in the contractility vs diameter plot that seems to appear at the same contractility level for all plaque coverage scenarios. We also note that this inflection point occurs at the vessel undeformed diameter. Thus, the vessel contractility at this point exactly counters the internal pressure meaning the vessel stays in its undeformed configuration.

To see how the change in vascular stiffness changed as the plaque coverage was increased, the normalized vasodilation, or increase of the diameter of the vessel from its original diameter, was calculated for each of the amyloid plaque coverages with the pressure load at 80 mmHg and the contractility at 0 kPa. Fig. 3 shows a nonlinear decrease in vasodilation with increasing plaque coverage.

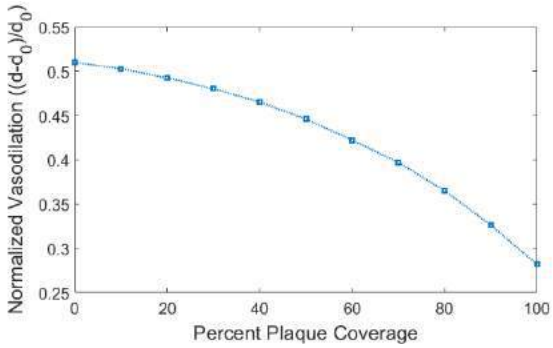

Figure 3: The normalized vasodilation when the pressure load was at maximum for the plaque coverages ranging from 0 to 100%

DISCUSSION

The impact of the circumferential plaque on the vasodynamic function of the vessel is clearly demonstrated in Figs. 2-3. The circumferential plaque makes the vessel stiffer, restricting its ability to dilate (Fig. 2A) and contract (Fig. 2B). The magnitude of loss of passive vasodynamic function specifically due to the circumferential plaque is displayed in Fig. 3, where 100% coverage reduced the normalized vasodilation of the vessel from 0.51 to 0.28 and the general trend showed nonlinear decrease in vasodilation with plaque coverage. By varying the contractility, we show that the soluble amyloid beta limits the minimum diameter that the vessel can reach, as soluble amyloid beta reduces the contractility of the smooth muscle cells.

This study is among the first computational models demonstrating both the structural and biological impacts of amyloid beta on the function of cerebral arteries. The model created presents an opportunity to continue studying various arrangements of amyloid beta plaques and their impact on the loss of vasodynamic function in vessels with CAA. Further, we can use this model as a springboard for understanding how this type of loss-of-function might impact the perfusion of the brain, and lead to long-term damage.

ACKNOWLEDGMENTS

The authors acknowledge funding from the National Institutes of Health under Grant No. U01-HL139471.

REFERENCES

[1] Jellinger, KA (2002). *J Neural Transm* 109:813-836; **[2]** Biffi, A, et al (2011). *J Clin. Neurol.* 7(1):1-9; **[3]** Snowdon DA (1997). *J Am. Med. Assoc.* 277(10):813; **[4]** Han BH, et al. (2008). *J Neurosci.* 28:13542-13550; **[5]** Hald ES, et al (2016). *J Biomech Eng.* 138(11):111007; **[6]** Maas SA, et al. (2012). *J. Biomech. Eng.* 134(1):1-10; **[7]** Baumbach GL, et al. (1993). *Hypertension* 21:816-826; **[8]** Hu JJ, et al. (2007). *J Biomech* 40(11):2559-2563

USING 4D-FLOW MRI TO QUANTIFY LEFT ATRIAL FLOW AND WSS TO BETTER UNDERSTAND ATRIAL REMODELING AND STRETCH IN ATRIAL FIBRILLIATION PATIENTS

Cody Johnson (1), Morgan Parks (1), Riley Parks (1), Matthew Kalscheur (2), Alexey Glukhov (2), Alejandro Roldán-Alzate (1,3,4)

(1) Radiology
University of Wisconsin-Madison
Madison, WI, USA

(2) Cardiology
University of Wisconsin-Madison
Madison, WI, USA

(3) Mechanical Engineering
University of Wisconsin-Madison
Madison, WI, USA

(4) Biomedical Engineering
University of Wisconsin-Madison
Madison, WI, USA

INTRODUCTION

Atrial fibrillation (AF) is the most common cardiac rhythm disorder worldwide and a major public health burden due to its impact on the risk of stroke, dementia, and heart failure [1]. It is estimated that the number of people diagnosed with AF will increase about three-fold by 2050 due to population aging and the rising prevalence of risk factors [2]. The Hemodynamic impairment related to AF have resulted in significant morbidity, mortality, and cost [3]. 4D Flow MRI allows the non-invasive quantification of time-resolved velocity fields in the heart and large vessels, and as a result, has increasingly been used to study cardiac flow dynamics and function [4].

Previous studies have used 4D-Flow to assess atrial hemodynamics in AF patients and compare that to healthy subjects finding a correlation between AF burdens and differences in blood flow dynamics [5-6]. However, the literature has neglected the use of 4D-Flow MRI to obtain wall shear stress (WSS) in patients with AF. Therefore, the purpose of this study is to investigate the correlation between blood flow dynamics and atrial WSS in patients with AF using 4D Flow MRI.

METHODS

In this IRB-approved and HIPAA-compliant study, 10 subjects (5 AF and 5 Healthy) were recruited. An MRI was performed on a 3.0T imaging system using bSSFP sequence and the 4D flow MRI sequence PC-VIPR [7]. The Left atria (LA) and pulmonary veins (Left Superior: LSPV, Left Inferior: LIPV, Right Superior: RSPV, and Right Inferior: RIPV) were segmented from time-averaged phase-contrast (PC) MR angiogram, using the software Mimics (Materialise, Leuven, Belgium). These segmentations provided a virtual 3D model of the LA and pulmonary veins.

Using the software Ensight, the peak velocity, net flow, and percent regurgitation were all quantified at each pulmonary vein. Figure 1A displays the 3D construction of the LA and its pulmonary veins, and 1B displays the velocity path lines calculated by Ensight.

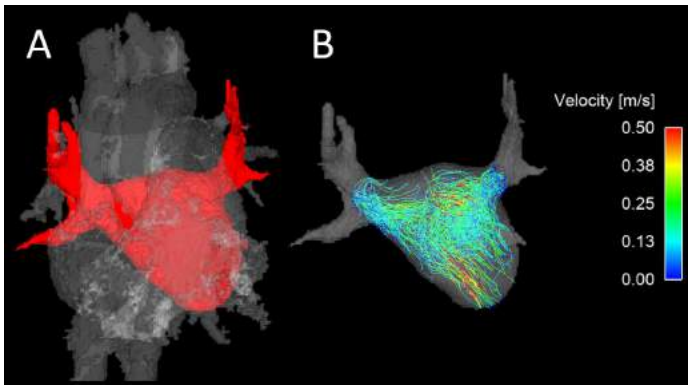

Figure 1: A. 3D construction of LA and Pulmonary veins embedded in the blood flow. B. Velocity streamlines from the pulmonary vein inlets.

LA average velocity and wall shear stress (WSS) was calculated using MATLAB. WSS was calculated from triangulated surface meshes and taking the cross product of the velocity vector and the surface normal vector and then averaged over the LA surface, as shown in equation 1,

$$\tau_w = \frac{1}{A}\int_A \mu \frac{\partial u_i}{\partial n_i} dA \quad (1)$$

where μ is viscosity (4 centipoise), and n_i is the surface normal vector. The AF and Healthy groups were compared using the student's T-Tests.

RESULTS

Peak velocity in the inferior pulmonary veins was lower in patients with AF than in healthy subjects (LIPV: 0.98 vs. 1.26 m/s, RIPV: 0.88 vs. 1.19 m/s). However, only the difference between the RIPV was significant (LIPV: p=0.129, RIPV: p=0.047). The peak velocity was not different in the LSPV (0.97 vs 0.97 m/s) and RSPV (0.94 vs 0.83 m/s). Average velocity within the atria was found to be lower in AF patients (29.70 m/s) than in healthy subjects (48.81 m/s). These results were found to be significant (p=0.012).

AF patients had lower net flow in all the pulmonary veins except the RSPV. The net flow at each of the pulmonary veins for the AF patients and controls were LSPV: 12.87 vs 19.13 ml/cycle, LIPV: 10.01 vs 21.70 ml/cycle, RSPV: 17.27 vs 16.06 ml/cycle, and RIPV: 10.786 vs 19.816 ml/cycle, respectively. The LSPV, LIPV, and RIPV differences were all significant (p<0.015), however, RSPV was not (p = 0.575). Regurgitation fraction into the pulmonary veins was higher in AF patients than healthy subjects (LSPV: 7.27 vs 0.65 %, LIPV: 6.24 vs 0.3 %, RSPV: 5.658 vs 1.39 %, and RIPV: 5.94 vs 5.24 %, respectively). Only the LSPV (p=0.006) and RSPV (p=0.011) were significant. However, both LIPV and RIPV have low p-values (p<0.135).

When analyzing the WSS maps, there is a noticeable increase in WSS around the pulmonary veins, as seen in Figure 2. This will be the area of specific interest in the more detailed analysis of WSS. Further analysis will compare the differences in WSS with the different flow parameters collected in the LA.

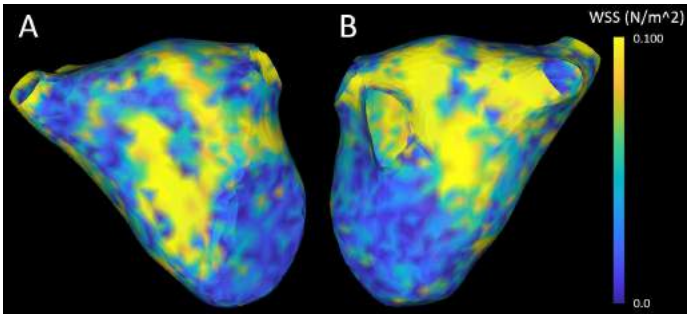

Figure 2: A. Anterior contours of left atria wall shear stress, B. Posterior contours of left atria wall shear stress

DISCUSSION

By using 4D-Flow MRI, our preliminary results indicate that AF patients have lower peak velocities in their inferior pulmonary veins, lower net flow in the LSPV, LIPV, and RIPV, and higher regurgitation fraction into all four pulmonary veins. WSS was also highest around the pulmonary veins, suggesting different regional fluid structure interactions.

Previous 4D-Flow MRI studies reported in the literature confirms most of our findings, especially the fact that velocity in the atria decreases in individuals with AF [5-6,8]. This lower velocity in the LA is likely attributed to the lower velocity in the pulmonary veins. A previously preliminary study done by our group also found that WSS was greatest in the area next to the pulmonary veins [9].

4D-Flow MRI is a comprehensive and diverse tool that has many functions, including its use to analyze quantitative blood flow dynamics metrics such as WSS. Most studies reported in the literature have only looked at how AF has affected the atrial blood flow. However, this study looks to use of 4D-Flow MRI to analyze trends in flow and WSS and correlate that to atria remodeling in AF patients.

Intra atrial flow is important when investigating the potential for thrombus formation in patients with AF. On the other hand, a comprehensive analysis of flow and structure is important because it can signal which regions are undergoing the most stress, which can then be assessed against the remodeling of the atria. Therefore, the future direction of this project is to determine in vivo patterns of regionalized WSS and flow parameters in order to understand the different regional fluid structure interactions.

ACKNOWLEDGEMENTS

We acknowledge GE Healthcare, which provides research support to the University of Wisconsin.

REFERENCES

[1] Fuster, V., et al. (2006). ACC/AHA/ESC 2006 guidelines for the management of patients with Atrial Fibrillation—Executive Summary. *Circulation*, *114*(7), 700–715.

[2] Go, A. S., Hylek, E. M., Phillips, K. A., Chang, Y., Henault, L. E., Selby, J. V., & Singer, D. E. (2001). Prevalence of diagnosed atrial fibrillation in adults: national implications for rhythm management and stroke prevention: the AnTicoagulation and Risk Factors in Atrial Fibrillation (ATRIA) Study. JAMA, 285(18), 2370–2375.

[3] Kannel, W. B., Wolf, P. A., Benjamin, E. J., & Levy, D. (1998). Prevalence, incidence, prognosis, and predisposing conditions for atrial fibrillation: population-based estimates. *The American journal of cardiology*, *82*(8A), 2N–9N.

[4] Francois, C.J., Srinivasan, S., Landgraf, B.R., Niespodzany, E., Wieben, O., Frydrychowicz, A., 2011. Analysis of right heart flow patterns in repaired Tetralogy of Fallot with 4D flow-sensitive MRI. J. Cardiovasc. Magn. Reson. 13, 1–2.

[5] Garcia, J., Sheitt, H., Bristow, M. S., Lydell, C., Howarth, A. G., Heydari, B., Prato, F. S., Drangova, M., Thornhill, R. E., Nery, P., Wilton, S. B., Skanes, A., & White, J. A. (2020). Left atrial vortex size and velocity distributions by 4D flow MRI in patients with paroxysmal atrial fibrillation: Associations with age and CHA2 DS2 -VASc risk score. Journal of magnetic resonance imaging : JMRI, 51(3), 871–884.

[6] Lee, D. C., Markl, M., Ng, J., Carr, M., Benefield, B., Carr, J. C., & Goldberger, J. J. (2016). Three-dimensional left atrial blood flow characteristics in patients with atrial fibrillation assessed by 4D flow CMR. *European heart journal cardiovascular Imaging*, *17*(11), 1259–1268.

[7] Johnson, K.M., Lum, D.P., Turski, P.A., Block, W.F., Mistretta, C.A., Wieben, O., 2008. Improved 3D phase contrast MRI with off-resonance corrected dual echo VIPR. Magn. Reson. Med. 60, 1329–1336.

[8] Ma, L., Yerly, J., Di Sopra, L., Piccini, D., Lee, J., DiCarlo, A., Passman, R., Greenland, P., Kim, D., Stuber, M., & Markl, M. (2021). Using 5D flow MRI to decode the effects of rhythm on left atrial 3D flow dynamics in patients with atrial fibrillation. *Magnetic resonance in medicine*, 10.1002/mrm.28642. Advance online publication.

[9] Rutkowski, D. R., Glukhov, A., & Roldán-Alzate, A. (2020). Abstract 15940: Wall shear stress AND VORTICITY in atrial Fibrillation, pulmonary hypertension, and Normal ATRIAL Anatomy Models. *Circulation*, *142*(Suppl_3).

SIMULATING STRUCTURAL COVARIANCE NETWORKS IN SCHIZOPHRENIA PATIENTS

Katherine M. Dash (1), Brendan M. Muldoon (2), Konasale M. Prasad (1,2,3)

(1) Department of Bioengineering
University of Pittsburgh
Pittsburgh, PA, USA

(2) Department of Psychiatry
University of Pittsburgh
Pittsburgh, PA, USA

(3) VA Pittsburgh Healthcare System
Pittsburgh, PA, USA

INTRODUCTION

According to the global burden of disease studies, schizophrenia affects 21 million people worldwide and is one of the top 25 causes of disability [1]. Schizophrenia costs about $125 billion per year to the US economy. Existing medications are symptomatic and full recovery for sustained periods can be achieved in about 14% of patients [2]. Precise understanding of the underlying pathophysiology of schizophrenia could provide avenues to design novel treatments.

Schizophrenia is increasingly considered a "dysconnection disorder" where single regional anomaly is less important relative to the network across the brain. Structural covariance networks (SCN) that represent shared variation among brain regions is known to largely reflect the white matter connections. SCNs are represented by correlations between pairs of regions' volumes or other morphometric measures for all subjects in a group. Characteristic differences in SCNs have been found between schizophrenia patients and healthy controls (HC) [3]. In this study, our goal was to simulate targeted and systematic modification of nodal values to explore whether such simulations decrease the dissimilarity between the patient and HC SCNs so that these SCNs are statistically similar, providing information on the resilience/robustness of the patient SCN. Such findings could be of use in identifying critical network features as treatment targets.

METHODS

We generated the SCNs of first-episode antipsychotic-naïve psychosis (FEAP) patients and HC from gray matter volumes derived from the regions that were computationally parcellated using the Desikan-Killiany-Tourville atlas within the FreeSurfer V6 program. MATLAB was used to simulate "removal" and "partial removal" of the nodes by setting the correlation coefficients to 0 or by proportional reduction of correlation coefficients to mimic that of the HC nodes. We used 4 different simulation approaches to test the resilience of the schizophrenia SCN.

Simulation 1 involved "removal" of one region at a time in the FEAP group by setting correlations of all edges for a given node to zero. This was repeated for every node, one node at a time. Simulation 2: The nodes were grouped on percentile ranking of the clustering coefficient. Top 20% of the nodes (the top 18.5th percentile) were successively "removed" one at a time by setting the correlations to 0 for each node. Followed by this, correlations of these nodes were set back to the actual correlations as they were originally. Then, we selected the next set of nodes between the 18.6th and 37th percentile, and the process was repeated until all nodes were dealt with. After each step in simulations 1 and 2, graph metrics -- clustering coefficient, transitivity, strength and assortativity, were recalculated for the modified network. Results were then compared to the unmodified HC metrics. These measurements were chosen because they characterized the network on a nodal (clustering coefficient and strength) and global level (transitivity and assortativity), and reflect the integration, segregation and centrality measures of the network.

Simulation 3: Complete "removal" of a brain region has little clinical application because it does not reliably reflect biological networks, and not feasible for therapeutic development. For these reasons, similar simulations as in 1 and 2 were implemented by reducing the edge weight by 25%, 50%, and 75%. Results were again compared to the HC group's metrics.

Simulation 4: Using a different algorithm in which the volume data for FEAP nodes were altered such that the volume correlations were brought closer to that of HC. The graph metrics were again calculated following each node's volume was modified. The DeltaCon metric [4] was then used to examine the similarity between the two networks more directly. Since in the unthresholded networks, all nodes are directly

connected to all other nodes, making their similarity 1, i.e., 100%. Therefore, threshold values were determined using both intensity (values from 0 to 1) and density (values from 0.01 to 1) thresholds (both with increments of 0.01). The respective threshold value at which the networks were least similar was used (0.61 for intensity, 0.65 for density). The networks were then thresholded using these values, and FEAP nodes were replaced with data similar to the HC's. After each replacement, the FB network was thresholded again, and the DeltaCon metric between the two networks was recalculated.

RESULTS

Simulation 1: Complete "removal" of one node at a time did not make the FEAP SCN's mean clustering coefficient similar to that of the HC (Fig 1).

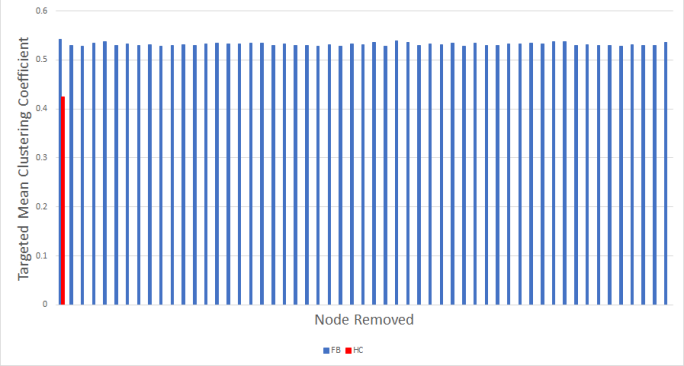

Figure 1: FEAP mean clustering coefficient after "removal" of one node at a time.

Simulation 2: "Removal" of most of the nodes in the top 18.5th percentile or all the nodes in the 18.6th to 37th percentile resulted in SCNs similar in mean clustering coefficient and mean strength but not of assortativity or transitivity of the HC SCN. "Removal" of nodes in the lower percentile ranking did not have the same influence (Fig. 2).

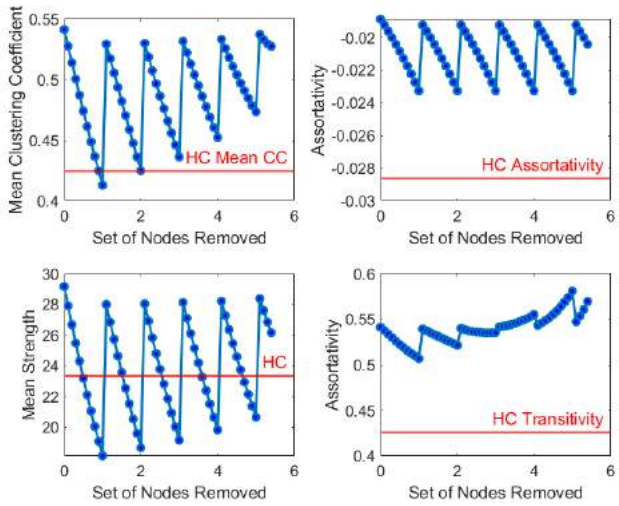

Figure 2: FEAP mean clustering coefficient, assortativity, mean strength and transitivity after targeted removal of nodes grouped by percentile ranking of the clustering coefficient.

Simulation 3: Similar to simulation 1, "partial removal" of any one node in the FEAP group did not make the FEAP SCN's mean clustering coefficient similar to that of the HC (Fig. 3).

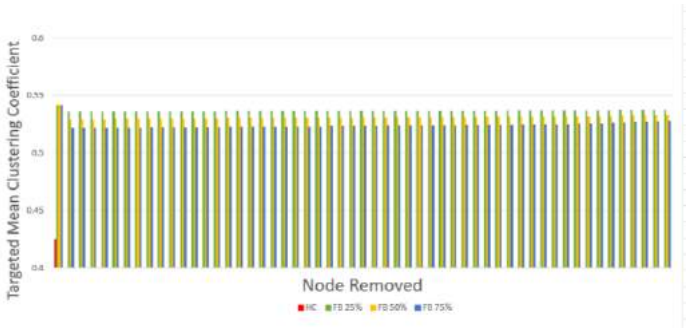

Figure 3: First Break mean clustering coefficient after partial removal of one node by 25%, 50%, and 75%.

Simulation 4: Using the volume alteration algorithm and DeltaCon metric, over 70% similarity was observed between the FEAP and HC SCNs with both intensity and density thresholding (Fig. 4). With intensity thresholding, successive replacement of FEAP nodes caused similarity to increase in almost a linear fashion.

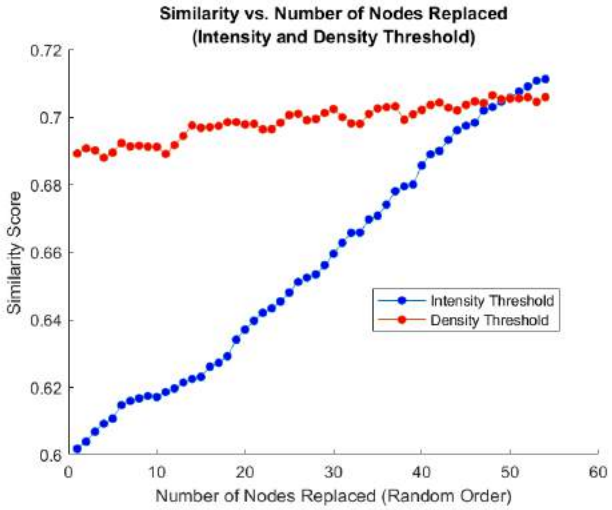

Figure 4: DeltaCon similarity scores after nodes were cumulatively replaced in random order with intensity and density thresholding.

DISCUSSION

Our overall goal was to test the resilience/robustness of the first break SCN network compared to unaltered HC network. Our first and third simulations showed that no single node had overarching influence on the patient SCN, supporting the existing neurobiological findings. Instead, "removal" of multiple regions is necessary to make the patient SCN characteristics to be more similar to the HC. Manipulation of multiple nodes may be needed to alter FEAP network to be more similar to HC's. Potential applications of our results include targeting specific groups of regions to make treatment for patients and preventive measures for high-risk individuals more effective.

REFERENCES

[1] Charlson, F et al., *Schizophrenia Bull.*, 44:1195-1203, 2018.
[2] Jääskeläinen, E et al., *Schizophrenia Bull.*, 39: 1296-1306, 2013.
[3] Palaniyappan, L et al., *Brain Structure and Function*, 220: 2059–2071, 2015.
[4] Koutra, D et al., *ACM Transactions on Knowledge Discovery from Data*, 10:1-43, 2016.

IN VITRO VALIDATION OF A REAL-TIME 3D MRI URODYNAMICS PROTOCOL

Colin Kim (1,2), Cody Johnson (1,2), James Rice (1,2,3), Alejandro Roldán-Alzate (1,2,3)

(1) Medical Physics
University of Wisconsin-Madison
Madison, WI, USA

(2) Radiology
University of Wisconsin-Madison
Madison, WI, USA

(3) Mechanical Engineering
University of Wisconsin-Madison
Madison, WI, USA

INTRODUCTION

Lower urinary tract symptoms (LUTS) and changes in bladder function occur frequently as individuals age. Patients with LUTS are commonly evaluated through multi-channel urodynamic studies that determine bladder pressure and flow during voiding, however, these studies are invasive and provide little insight into the changes in bladder anatomy and detrusor muscle function that occur with aging and obstruction. Non-invasive methods of imaging the bladder are useful but can be limited by motion and chemical shift artifacts[1,2]. Although a combination of MRI and computational fluid dynamics has been used to analyze the movement of the bladder during voiding, 3D MRI acquisition has not yet been performed[3]. This study analyzes 3D MRI protocols during the voiding of an in vitro bladder model and validates them with high-speed optical imaging using different vitro models. These novel methods serve to confirm adequate spatial and temporal resolution of this 3D MRI protocol and bring us closer to utilizing this technique for regular in vivo diagnostic imaging.

METHODS

In this IRB-approved and HIPPA-compliant study, a healthy, 37-year old subject was recruited to void in the scanner during 3D MRI acquisition. Using this data, an in vitro bladder model was fabricated. The bladder was segmented from the MRI images and an STL was exported (Mimics, Materialize, Leuven, Belgium). The bladder was 3D printed using poly-vinyl alcohol (PVA) (Ultimaker, Geldermalsen, Netherlands). The bladder was then coated in silicone (SYLGARD™ 184 Silicone Elastomer, DOW Silicones Corporation, Midland, MI, USA) followed by latex (AeroMarine, Keyport, NJ). The inner PVA core was dissolved out and the remaining latex mold served as the in vitro bladder model. A ¼" diameter tube was then attached to the latex model to represent the urethra and used to fill the model with H_2O until full (approximately 300 mL). The void time of the bladder model was calibrated to approximately 35 seconds.

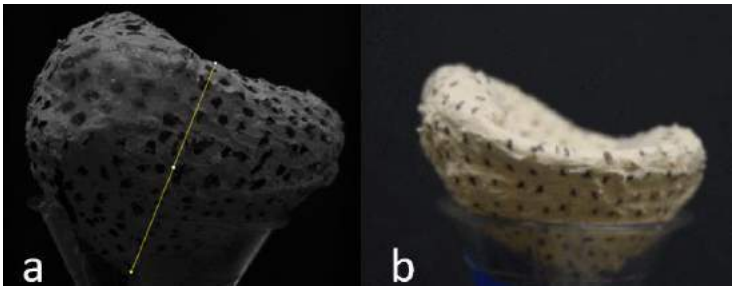

Figure 1 a) single frame from the phantom camera footage with measured segment. b) static capture from SLR footage of voiding bladder.

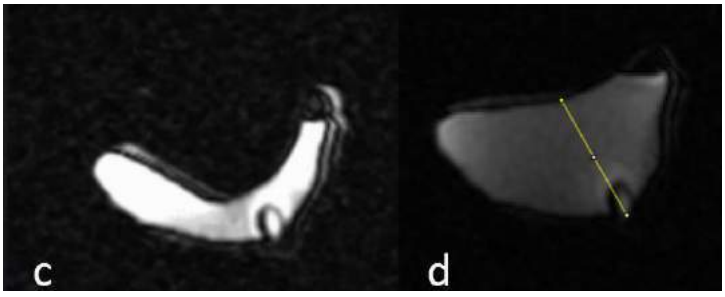

Figure 2 c) static capture from MRI sequence of voiding. d) single frame from MRI sequence with measured segment.

3D sagittal DISCO Flex images were used to analyze both in vitro and in vivo deformation over the voiding period. The in vitro MRI protocol was compared to hi-speed phantom cameras capturing deformation during identical voiding conditions. Additional hi-speed footage was acquired using an SLR camera. The MRI and phantom camera footage deformation were analyzed frame-by-frame using ImageJ (NIH, Maryland, USA) and the percent deformation rate using line segments was calculated (Figure 1a & b).

RESULTS

Figure 1 shows the side-by-side comparison of the deformation measured by the MRI sagittal 3D volumes and the SLR camera footage of the in vitro latex bladder model and the approximate line segments used to calculate percent deformation. Table 1 shows the deformation rate of both the MRI and optical imaging modalities**.** The calculated rates of deformation in both the MRI and phantom camera were 6.2% deformation per second and 5.3% deformation per second, respectively (Table 1). There was a 15% difference in the two deformation rates relative to the phantom camera value. Qualitative analysis of both methods showed similar patterns of deformation. The rate of volume decrease was also measured (Table 1).

Time elapsed (s)	MRI deformation (%)	Phantom camera deformation (%)
0	0	0
1.5	3.992	6.232
3	17.122	13.865
4.5	29.544	19.876
6	36.243	29.557
7.5	42.744	39.5507
	6.2% deform./sec	**5.3% deform./sec**

Table 1. Quantitative analysis results.

DISCUSSION

Assessment of bladder wall movement during voiding proves difficult due to various artifacts during imaging. This study utilized optical imaging and an anatomically realistic in vitro bladder model to verify the accuracy of this 3D MRI acquisition protocol. Comparison between in vitro optical imaging and MRI experiments, proved useful for studying deformation patterns and to validate our MRI approach. Further in vivo results obtained in the healthy subject demonstrated feasibility of this approach for non-invasive in vivo evaluation of bladder wall deformation during voiding.

There are many factors that differentiate the in vitro experiments conducted in this study from the in vivo bladder analysis. Although the rate of the in vitro bladder model voiding was kept similar to that of the subject trial, the pattern of bladder deformation in vivo varies greatly due to the assistance of the surrounding detrusor muscle[4]. Another limitation of the study is that the rate of the high-speed footage was only analyzed to the point at which the posterior wall of the bladder deformed below the anterior wall, making it impossible to track subsequent deformation.

To address this problem, efforts have begun towards fabricating a transparent thin-wall model to overcome this visibility limitation. For the prototype, a thin-walled mold was created (Figure 4a) in 3Matic (Materialize, Leuven, Belgium) and printed in ABS plastic (Ultimaker, Geldermalsen, Netherlands). A clear model was then created by pouring clear, flexible silicone in the mold (Solaris Clear Silicone Rubber, Smooth-on, Macungie, PA) (Figure 4b). With this model, particle image velocimetry (PIV) will be utilized to analyze fluid vorticity during the bladder voiding process. By tracking the movement of fluorescent particles in a plane of flow using PIV, instantaneous velocity vectors will be acquired within the transparent bladder[5]. We expect these measurements to provide insight into the behavior of fluid during the in vitro bladder voiding and can further validate 3D MRI imaging protocols.

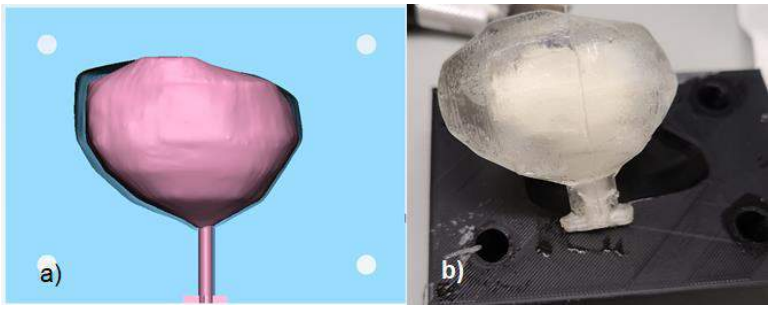

Figure 3 a) Capture from 3Matic of the designed thin-walled bladder mold STL file. b) An initial scaled-down prototype of the model using the clear, flexible silicone.

ACKNOWLEDGEMENTS

We acknowledge GE Healthcare, which provides research support to the University of Wisconsin.

REFERENCES

[1] NIH (2020) Urinary Tract Imaging. National Institute of Diabetes and Digestive and Kidney Diseases. https://www.niddk.nih.gov/health-information/diagnostic-tests/urinary-tract-imaging

[2] Verma, S., Rajesh, A., Prasad, S. R., Gaitonde, K., Lall, C. G., Mouraviev, V., Sandrasegaran, K. (2012). Urinary Bladder Cancer: Role of MR Imaging. RadioGraphics, 32(2), 371-387. doi:10.1148/rg.322115125

[3] Pewowaruk R, Rutkowski D, Hernando D, Kumapayi BB, Bushman W, Roldán-Alzate A (2020). A pilot study of bladder voiding with real-time MRI and computational fluid dynamics. PloS ONE 15(11): e0238404. https://doi.org/10.1371/journal.pone.0238404

[4] Sam P, Nassereddin A, LaGrange CA. Anatomy, Abdomen and Pelvis, Bladder Detrusor Muscle. [Updated 2020 Aug 10]. In: StatPearls [Internet]. Treasure Island (FL): StatPearls Publishing; 2020 Jan-. Available from: https://www.ncbi.nlm.nih.gov/books/NBK482181/

[5] Ionita, C. N., Hoi, Y., Meng, H., & Rudin, S. (2004). Particle image velocimetry (PIV) evaluation of flow modification in aneurysm phantoms using asymmetric stents. Proceedings of SPIE--the International Society for Optical Engineering, 5369, 295. https://doi.org/10.1117/12.534274

MAGNETIC RESONANCE IMAGING (MRI) OF BRAIN MOTION: PHASE CONTRAST VELOCITY VERSUS DISPLACEMENT ENCODING

David Bat (1), Blaise Simplice Talla Nwotchouang (2), Maggie S. Eppelheimer (2), Daniel Barrow (3), Francis Loth (2), John Oshinski (1,4)

(1) Department of Biomedical Engineering
Georgia Institute of Technology
Atlanta, GA, US

(2) Con□uer Chiari Research Center,
Department of Biomedical Engineering
The University of Akron
Akron, OH, U.S.

(3) Department of Neurosurgery,
Emory University
Atlanta, GA, U.S.

(4) Department of Radiology & Imaging Sciences and Biomedical Engineering
Emory University
Atlanta, GA, U.S.

INTRODUCTION

Brain tissue undergoes motion in response to blood pressure and blood flow over the cardiac cycle [1]. This cardiac-driven brain tissue motion has been previously quantified within the cerebellum and brainstem by using phase contrast magnetic resonance (PCMR) tissue velocity mapping with a low velocity encoding value [2], or by using displacement encoding with stimulated echoes (DENSE) MRI [3]. The DENSE technique directly measures displacement at multiple time points over the cardiac cycle compared to a reference location after the cardiac trigger signal (R-wave or pulse peak). To determine displacement values from PCMR measurements, velocity must be calculated using a 'tracking' algorithm to determine position.

Chiari malformation type I (CMI) is a neurological syndrome classified as the elongation of the cerebellar tonsils five millimeters below the foramen magnum, identified on static structural MRI. Patients with CMI experience symptoms including sub-occipital headaches, neck pain, and cognitive/neurological deficits [4]. In addition to altered brain morphology, CMI patients demonstrate increased tissue motion [1-3] which may be the underlying cause of CMI symptoms due to repeated compression of the cerebellum, brainstem, and upper cervical cord.

The purpose of this study was to compare brain tissue motion from PCMR-derived displacement measurements to DENSE displacement measurements in a series of patients with CMI. *We hypothesized that the displacement measurements by PCMR and DENSE would be highly correlated, but the DENSE measurements would have a lower standard deviation than PCMR as DENSE directly measures displacement.*

METHODS

Magnetic Resonance Imaging (MRI) exams were conducted in 10 CMI patients with an average age of 37.7 and consisting of 8 women and 2 men in a study approved by Emory University. Patients had CMI diagnostic criteria, including greater than 5 mm tonsillar descent below the foramen magnum and the presence of CMI symptoms. These CMI patients were referred by single neurosurgeon (Daniel Barrow, MD).

Using a 3T MRI scanner (Siemens PrismaFit, Erlangen, Germany), cardiac-gated spiral cine DENSE sequences were evaluated at the mid-sagittal plane [5]. Acquisition parameters included: two directions of in-plane motion encoding, an encoding frequency of 0.6 cycles/mm, two spiral interleaves per heartbeat, pixel size of 1.2 x 1.2 mm, slice thickness of 7 mm, four signal averages, and 16-27 frames over the cardiac cycle, depending on the heart rate. PCMR measurements were acquired in the same anatomical location and with the same field of view and spatial resolution as the DENSE measurements. Twenty-five frames were acquired over the cardiac cycle depending on heart rate, and retrospective cardiac gating was used. The velocity encoding value (VENC value) was 2 cm/sec.

Two programs developed in MATLAB (Mathworks, Natick, MA) were used to quantify brain tissue motion. One program (DENSEPro) used DENSE phase images to calculate the average displacement of the brain tissue as a function of time over the cardiac cycle; the second program (PhasePro) used PCMR images to calculate the average brain tissue velocity. The brain tissue velocity values from PhasePro were corrected to ensure there is no net displacement of the soft tissue in the brain over the cardiac cycle. These corrected velocity values were then integrated over time to calculate the brain tissue displacement at every time point.

PCMR derived displacement values, and DENSE displacement values were plotted at each cardiac cycle for each patient. In *figure* 3, all data points from all patients were combined onto one correlation plot to examine the relationship between the PCMR derived displacement and the DENSE displacement measurements.

Two regions of interest (ROIs) were identified by a single observer (David Bat) on each patient. One ROI was a 1.14 x 1.14 cm square within the brainstem, and the second ROI outlined the cerebellum for each patient, *figure 1*. The small square ROI in the brainstem was chosen to have a region where the velocity was nearly uniform (bulk motion only) and where CSF was not present. The cerebellum ROI was chosen as the cerebellum has significant motion in CMI patients. The cerebellum ROIs were drawn to conservatively stay within the cerebellum tissue such to reduce potential artifacts by unintentionally capturing CSF motion.

In order to compare the standard deviation of the displacement values from the two methods, the standard deviation of each patient was obtained at the timepoint at which maximum displacement occurs. These standard deviation values were then compared using paired sample t-test, where $p < 0.05$ was considered statistical significant.

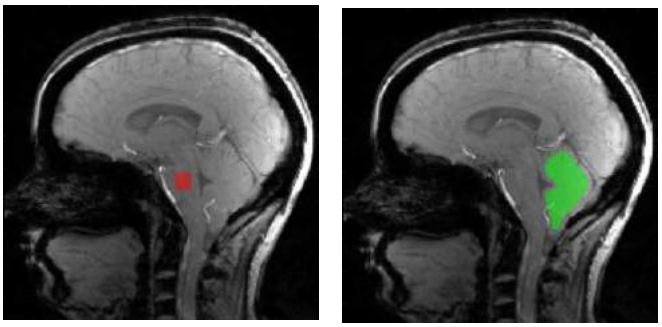

Figure 1**:** *The regions of interest (ROI) are shown on PCMR magnitude images of a patient. The brainstem ROI (red, left) is a small square located in the center of the brainstem. The cerebellum ROI (green, right) is a conservative shape of the cerebellum.*

RESULTS

Figure 2 presents an example of the results for one patient using the brainstem ROI (left) and one patient in the cerebellum ROI (right). Displacement values from DENSE and PCMR and the standard deviation of values from within the ROI are plotted as a function of time. The error bars represent the respective standard deviations at each time point. The displacement values between the two methods are similar; however, the standard deviation of the PCMR derived displacement is cumulative because of the integration and is much larger than the standard deviation of the DENSE.

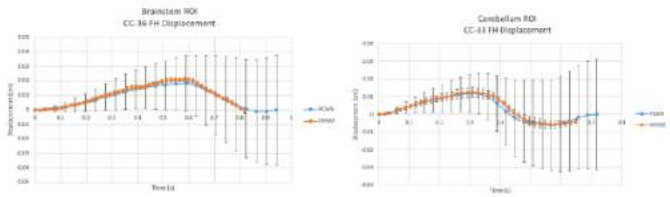

Figure 2: *The displacement of the brainstem ROI (left) and cerebellum ROI (right) is shown for both PCMR derived displacement,* and DENSE *derived displacement as a function of time across the cardiac cycle.*

Figure 3 shows correlation plots with the DENSE-derived displacement on the y-axis and PCMR-derived displacement on the x-axis for each ROI with a linear trendline to fit the data. The trendline presents relatively high R^2 values, and a slope of 0.86 and 0.92 for the brainstem and cerebellum ROI, respectively.

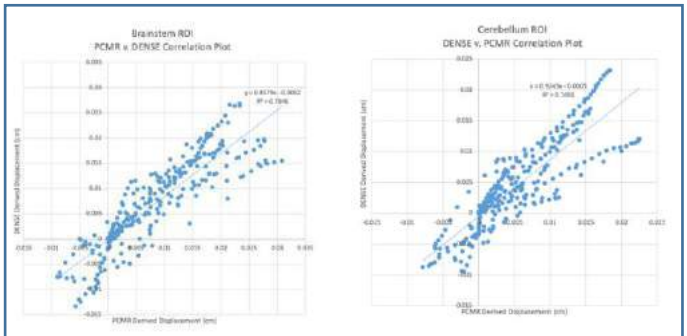

Figure 3: *Correlation plots for the brainstem ROI (left) and cerebellum ROI (right) with DENSE-derived displacement on the y-axis and PCMR derived displacement on the x-axis. A linear trendline with the R^2 value and equation is shown additionally.*

The two methods' displacement values have a relatively high correlation; however, the standard deviations within the ROI's at peak displacement between the two methods are significantly different. In the brainstem ROI, the standard deviations were 180 microns, and 10 microns for the PCMR and DENSE derived displacements, respectively. In the cerebellum, the standard deviations were 160 cm, and 40 microns for the PCMR and DENSE derived displacements, respectively. A paired t-test resulted in a $p = 2.7 \times 10^{-8}$ and $p = 6.5 \times 10^{-5}$ for the brainstem and cerebellum ROIs, respectively. This rejects the null hypothesis and shows a statistically significant difference between the standard deviations of the two methods.

DISCUSSION

The major findings of this study were that PCMR derived displacement measurements were highly correlated with the DENSE displacement measurements in both the brainstem and cerebellum ROI. This implies that PCMR images can be a valid method of measuring the displacement of soft tissue in the brain. However, the standard deviation of PCMR derived displacement measurements is significantly larger than the standard deviation of DENSE displacement measurements, which shows that using PCMR images increases the error in the measured displacement. This is likely because DENSE measurements directly measures the displacement, while PCMR velocity values are integrated over time to calculate the displacement, which leads to a cumulative standard error over time. In conclusion, PCMR derived displacement is accurate for mean displacement, but caution must be given to the results due to the high standard deviation of the results.

ACKNOWLEDGEMENTS

This work was funded by a grant from Conquer Chiari and a grant from the National Institutes of Health (R15 NS109957 to Frank Loth).

REFERENCES

[1] Leung, et al., Journal of Neurosurgery: Spine, 24: 546-555, 2016.
[2] Lawrence BJ, et al, World Neurosurg. 2018.
[3] Pahlavian, et al., Journal of Biomechanical Engineering, 140: 2018.
[4] Allen, et al., *PloS one*, 9: e94844, 2014.
[5] Zhong X, Med Phys. 2009.

YOUTH PITCHING KINEMATICS: ASSOCIATIONS WITH BODY OVERWEIGHT PARAMETERS

Christina K. Fong (1), Ryan C. Sax (1), Rafael Escamilla (3), Arnel Aguinaldo (4), Scott J. Hazelwood (1,2), Stephen M. Klisch (1,2)

(1) Mechanical Engineering Department
California Polytechnic State University
San Luis Obispo, CA, USA

(2) Biomedical Engineering Department
California Polytechnic State University
San Luis Obispo, CA, USA

(3) Physical Therapy Department
California State University
Sacramento, CA, USA

(4) Kinesiology Department
Point Loma Nazarene University
San Diego, CA, USA

INTRODUCTION

Prevalence of youth baseball pitching injuries has not decreased despite adoption of safety guidelines, pitch count recommendations, and increased media coverage [1]. Strong evidence shows that high and repetitive joint kinetics (i.e., forces, torques) are a biomechanical mechanism for pitching injuries [2-3]. Further evidence suggests that flaws in pitching kinematics lead to an increase in joint kinetics and pitching injuries [4]. Studies aimed at correcting flaws in several kinematic parameters have been conducted for adults [4]. However, similar studies do not exist for youth baseball pitchers. Also, previous studies have shown that body mass index (BMI) has been linked to increased injury-related kinetic parameters [5]. However, there are no studies that have investigated relations between BMI and injury-related kinematic parameters.

The goal of this study was to investigate associations between injury-related kinematic parameters and overweight measures for youth baseball pitchers. The hypothesis was that injury-related kinematic parameters would be associated with BMI. The injury-related kinematic parameters considered were 1) measurements at foot contact (FC): stride length (SL), front foot position (FFP), shoulder external rotation (SER), shoulder abduction (SAFC), and elbow flexion (EF); 2) measurements between FC and ball release (BR): peak knee extension (KE); and 3) measurements at BR: shoulder abduction (SABR) [4].

METHODS

Participant Recruitment. Motion analysis and anthropometric data were available from three studies: 1) a published study with 18 10- to 11-year-old male baseball players [6] and unpublished studies with 2) 11 14- to 16-year-old male baseball players [7], and 3). 104 16- to 18-year-old male baseball players [8].

Details are provided below for methods used in the 1st study; generally, methods were similar in the 2nd and 3rd studies (see [6-8] for more details).

Experiments. In the 1st study [6], participants completed pre-game tests to measure body weight and height using a scale/stadiometer (LW Measurements LLC, Rohnert Park, CA, USA). Participant BMI was calculated as body mass divided by height squared (kg/m^2). In addition, participants underwent a DXA scan using a Lunar iDXA scanner (GE Healthcare, Madison, WI, USA) to determine body composition. Pitching kinematics data were captured using a motion analysis system. 12 motion analysis cameras (Motion Analysis, Santa Rosa, CA, USA) were used to track 38 retroreflective markers placed on anatomical landmarks based on the PitchTrak (Motion Analysis) software marker set. Participants pitched off a portable mound into a net 25 feet away with a scaled strike zone. Marker trajectories were recorded in Cortex analysis software (Version 7.4.6, Motion Analysis) at 200 Hz, interpolated (third-order spline), and filtered (4th order Butterworth filter, cutoff frequency 12 Hz) [9]. 10 pitches were recorded for each participant.

Analysis. In the 1st study [6], kinematic parameters were obtained using PitchTrak (a subset of Cortex). The last three pitches with usable data were analyzed independently and averaged for each participant. This study considered eight kinematic parameters that were analyzed at different parts of the pitch cycle, which is defined from FC to BR. FC was determined when the front foot segment stopped moving, and BR was determined based on how the wrist pronated during the pitch. The pitch cycle time was then normalized such that 0% and 100% represented times of FC and BR, respectively.

SL was calculated by measuring the distance between left and right toe markers at front-FC in the direction of the axis parallel to the pitching mound to home plate vector, expressed as a percent of body height (BH). FFP was calculated by taking the distance, in the lateral direction (perpendicular to the pitching mound to home plate vector), between the front ankle's position at the instant of front FC and back ankle's position at maximum knee height [4]. FFP was deemed positive when the front foot landed closed (i.e., towards the third base side for a right-handed pitcher) [4]. Both absolute and normalized (by BH) values were considered. SER (Figure 1, left) at FC, measured in degrees, was the external rotation angle of the throwing shoulder, SAFC (Figure 1, middle), also measured in degrees, was the abduction angle of the throwing shoulder at FC. EF (Figure 1, right) was the elbow flexion angle at FC measured in degrees. KE was calculated by taking knee flexion at FC minus knee flexion at BR [4]. Finally, SABR was the shoulder abduction at BR and calculated the same way as at FC.

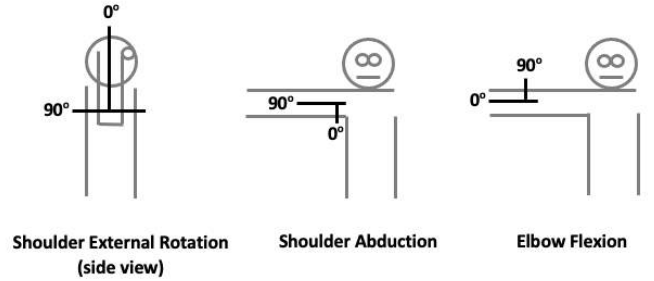

Figure 1: Anatomical shoulder and elbow angles used in analysis.

Statistics. Data were separated into three groups based on data collection site to prevent possible analysis errors from different lab environments and procedures. Linear regression analyses were performed to determine significant correlations between kinematic parameters and BMI. Statistical significance was defined by $p<0.05$.

RESULTS

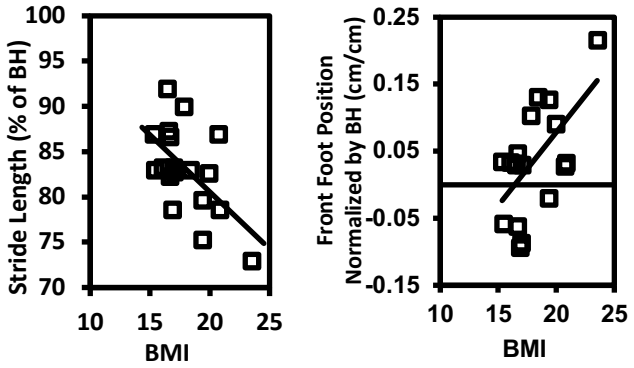

Figure 2: Correlations between stride length (SL) and front foot position (FFP) normalized by body height (BH) and BMI for 10-11-year-old participants.

A significant negative correlation was found between normalized SL and BMI for the pitchers in the 10- 11-year-old age group (p=0.013). Pitchers in the 14-16- and 16–18-year-old studies had no significant correlation between SL and BMI (p=0.532 and p=0.437 respectively) (Table 1). A significant positive correlation was found between normalized FFP and BMI for the pitchers in the 10- 11-year-old age group (p=0.009). Pitchers in the 14-16- and 16–18-year-old studies had no significant correlation between FFP and BMI (p=0.211 and p=0.421 respectively) (Table 1). Significant correlations were not found for any of the other kinematic parameters.

Table 1. Single linear regression results of stride length (SL) and front foot position (FFP) normalized by body height vs BMI. * = significant correlation with BMI; $p < 0.050$.

Population	SL	FFP
	R^2 (p)	R^2 (p)
10- to 11-year-olds	0.36 (0.013*)	0.36 (0.009*)
14- to 16-year-olds	0.045 (0.532)	.17 (0.211)
16- to 18-year-olds	0.0059 (0.437)	.0064 (0.421)

DISCUSSION

The correlations between two of the seven kinematics parameters (SL and FFP) and BMI support the hypothesis that injury-related kinematics parameters are associated with overweight measures. However, those associations were significant for only the youngest age group. The difference in SL and FFP trends between the age groups suggest that pitchers in the 10- to 11-year-old range with a higher BMI have more difficulty stabilizing their body during the pitching motion. With age, these difficulties may be resolved as prior studies have shown that pitching kinematics improve rapidly from 9-12 years [10]. Another possible explanation is that 10- to 11-year-old pitchers with flawed pitching kinematics are no longer pitching at the 14+ age range. While it is difficult to make a definitive conclusion, both arguments are in favor of placing emphasis on proper pitching kinematics at a younger age when pitching injuries begin to develop [11].

There were several limitations in the 1st study. First, the pitching distance was limited to 25 feet due to lab size constraints. Second, the total numbers of overweight and obese participants (16.6% and 5.5%) were comparable for overweight but not for obese youth baseball players [12]. Third, there is an error of approximately 3% that may occur from visually selecting frames associated with FC and wrist pronation, which signified BR. Fourth, the data came from three different experimental sites. A future recommendation would be to perform all experiments for the different age groups in one lab.

A key clinical implication of this study is that select kinematic parameters have been identified that could guide coaches and trainers when working with overweight pitchers. Also, the results suggest that future work should investigate if a coaching intervention for overweight youth pitchers can correct flaws in injury-related pitching kinematics.

REFERENCES

[1] Melugin, H. et al., *Curr Rev Musculoskelet Med,* 11:26-34, 2018.
[2] Sabick, MB. et al., *J Shoulder Elb Surg*, 13:349-355, 2004.
[3] Fleisig, G. et al., *J Biomech,* 32:1371-1375, 1999.
[4] Fleisig, G. et al., *Sports Biom*, 17:3, 314-321, 2018.
[5] Darke, J. et al., *Orthop J of Sports Med*, 6(4):1-10, 2018.
[6] Jennings DJ, et al., *Congress of the Internat Soc of Biomech and Annual Meeting of the Amer Soc of Biomech*, 2019.
[7] Aguinaldo, A. et al., *Orthop J of Sports Med,* 2019.
[8] Escamilla, R. et al., *J of Appl Biomech,* 2018.
[9] Matsuo, T. et al., *17th Int Symp Biomech Sport*, 389-392, 1999.
[10] Fleisig, G. et al., *Amer J of Sports Med*, 2017.
[11] Fleisig, G. et al., *Sports Health,* 4.5:419-424, 2012.
[12] Choate, N. et al*., J Adolesc Health*, 2007.

CHARACTERIZATION OF GLYCOCALYX CORE PROTEINS IN HUMAN ENDOTHELIAL CELLS

J. Mwangi (1), T. Stanley (2), S. Banerjee (3), R. Mitra (3), E. Ebong (3,4)

(1) Department of Biology
Northeastern University
Boston, MA, USA

(2) Department of Health Sciences
Northeastern University
Boston, MA, USA

(3) Department of Chemical Engineering
Northeastern University
Boston, MA, USA

(4) Department of Bioengineering
Northeastern University
Boston, MA, USA

INTRODUCTION

The endothelial cell glycocalyx (EC GCX) is a sugar-rich layer lining the endothelium which consists of glycosaminoglycan (GAG) chains, such as heparan sulfate (HS) and hyaluronic acid (HA)[1]. These chains are attached to core proteins such as syndecan-1 (sdc1), glypican-1 (gpc1), and CD44 and which line the endothelial cell membrane (**Figure 1**)[1]. Research has shown that EC GCX degradation can lead to atherosclerosis, which is one of the precursors to strokes, as well as other serious cardiovascular events[1,2]. Studies conducted by our lab and others have shown the presence of a degraded EC GCX in the early stages of vascular diseases, particularly in atherosclerosis[1].

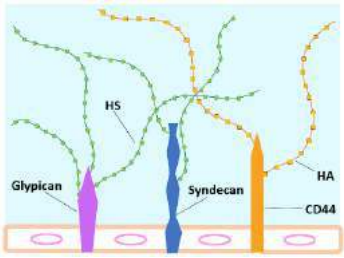

Figure 1- GAG and core protein components of the EC GCX

Because cardiovascular disease is the leading cause of death worldwide, affecting over 126 million adults in the United States alone, there is incentive to develop treatment strategies which target this structure[2]. Previous research has specifically targeted the HA and HS components of the EC GCX due to their significant composition within this structure[3]. Given that HA and HS are closely associated with their respective core proteins, understanding how these core proteins respond to flow conditions allows a crucial secondary confirmation of HA/HS presence. In this study we aim to establish the presence of the core proteins CD44 and sdc1 in Human Umbilical Vein Endothelial Cells (HUVECs) in static and uniform flow conditions. We plan to use HUVECs because they are an established and commonly used cell line when studying endothelial cells *in vitro*. In addition to HUVECs, we plan to use Human Coronary Arterial Endothelial Cells (HCAECs), a cell line more geographically relevant (within the body) in the progression of atherosclerosis.

METHODS

HUVECs were plated at a density of 62,000 cells/cm^2 on 2.2 cm x 2.2 cm fibronectin-coated glass coverslips until 100% confluency. These cells were then exposed to a uniform flow environment and static environment for 0 or 24 hours. The flow environment was modeled using a custom parallel plate flow chamber[1] (**Figure 2**).

Figure 2- A diagram of the parallel flow chamber apparatus used to simulate uniform flow.

Following exposure to the static or flow environment, the cells were then fixed and stained for CD44, sdc1 and gpc1 via immunocytochemical staining (ICC) (**Table 1**).

Component	Primary Antibody	Secondary Antibody
CD44	CD44 Rabbit anti-Human	AF488 Goat anti-rabbit IgG
Sdc1	Sdc1 Rabbit anti-Human	AF488 Goat anti-rabbit IgG
Gpc1	Gpc1 Rabbit anti-Human	AF488 Goat anti-Rabbit IgG

Table 1- Primary and secondary antibodies used for ICC

Confocal microscopy was ultimately used to image the fluorescently labeled HUVECs, and ImageJ, an Adobe-based image processor, was used to quantify fluorescence intensity. Fluorescence

intensity was assumed to be indicative of GCX component expression. GCX expression levels were then displayed as mean ± standard error of mean (SEM) and statistical significance was determined using Mann-Whitney t-tests for $\alpha = 0.05$ through GraphPad Prism software. All flow or static values (n=4) were normalized to the zero-hour static expression (Equation 1). This model, as well as its protocols, will then be translated to other future cell types, such as HCAECs.

$$Fold\ change\ in\ GCX\ Intensity = \frac{Flow\ or\ Static\ \ Intensity\ at\ x\ Hours}{Static\ Intensity\ at\ Zero\ Hours}$$

Equation 1- Method of normalization for analysis and comparison.

RESULTS

Our analysis of HUVECs found that at 24 hours, the expression of sdc1 in flow and static conditions was not statistically different (p= 0.343) (**Figure 3**). Expression of CD44 was also observed at 24 hours and was shown to significantly increase in the flow condition (p = 0.0286) (**Figure 3**).

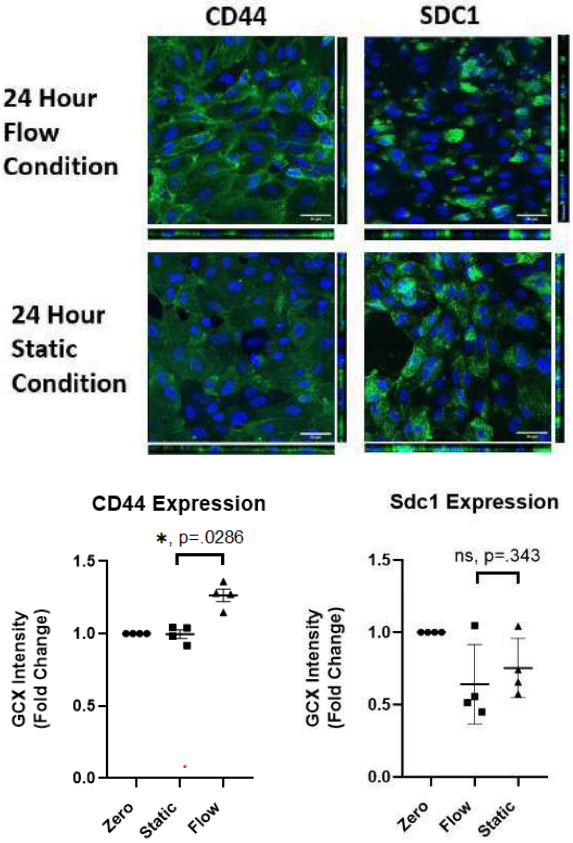

Figure 3 - Confocal images and graphs of the fold change intensities of core proteins CD44 and sdc1 in HUVECs at the 24-hour time point in uniform flow and static conditions. At 24 hours the difference between static and flow is found to be significant for CD44 but not significant for sdc1. Blue = DAPI (cell nuclei), Green = AF488 (core protein)

DISCUSSION

Our studies allowed us to confirm previous findings of sdc1 at the protein level[3], and to establish CD44 protein expression in HUVECs. We also present the novel characterization of how these core proteins respond to the uniform flow environment found in the human vasculature. Studies on CD44 expression in a context relevant to CVDs are limited, and to our knowledge only one group has investigated CD44 expression in flow[4]. However, this study was in S12NL1 cancer cells and is not comparable for understanding the role of CD44 in EC GCX mechanobiology[4]. Conversely, our observation of unchanged sdc1 protein expression in flow follows the results seen by Liu et al., where sdc1 mRNA expression in HUVECs remained unchanged after 24 hours, compared to the control[3]. These trends may be explained by differences in how the core proteins themselves interact with the surrounding EC GCX[5,6]. CD44 does not covalently bind to components of the GCX whereas sdc1 *does* interact via covalent binding[5]. Thus, it is possible that CD44 expression changes can be observed due to the simple fact that it is more accessible to antibody binding[5]. Sdc1 expression changes may not be detectable if the core protein is obstructed by covalently bound GCX components[6]. A potential study which may confirm this hypothesis would be to enzymatically degrade or silence surrounding EC GCX components to explore these core proteins free of surrounding obstruction. We also note that in our current *in vitro* model, the use of HUVECs are inherently a limitation because they are found in regions of the vasculature that are not often associated with atherosclerotic CVD. Rather, atheroprone regions are found in the coronary arteries and aortic arch, due to their branched and curved nature, respectively, and due to the associated disturbed flow. Thus, a more beneficial model would be the use of Human Aortic Endothelial Cells (HAECs) or HCAECs along with a disturbed flow environment to simulate GCX degradation. Mirroring the same methods performed with HUVECs, we plan to use HCAECs to study the effects of disturbed flow in addition to uniform flow on the GCX. In doing so, we hope to gather a more relevant understanding of core protein behavior in the diseased GCX condition.

ACKNOWLEDGEMENTS

We thank the Undergraduate Research and Fellowships office at Northeastern University for their funding of this work and support of Selena Banerjee, John Mwangi, and Theodora Stanley. We also acknowledge the NSF for providing REU funding to supplement CMMI-1846962 (awarded to E. Ebong) and support John Mwangi and Theodora Stanley. We also thank our mentors in the laboratory, and we thank the Institute for Chemical Imaging of Living Systems at Northeastern University for consultation and imaging support.

REFERENCES

1. Harding, I.C., et al., *Pro-atherosclerotic disturbed flow disrupts caveolin-1 expression, localization, and function via glycocalyx degradation.* Journal of Translational Medicine, 2018.
2. Benjamin Emelia, J., et al., *Heart Disease and Stroke Statistics—2019 Update: A Report From the American Heart Association.* Circulation, 2019. 139
3. Liu JX, et al. *Hemodynamic shear stress regulates the transcriptional expression of heparan sulfate proteoglycans in human umbilical vein endothelial cell*. Cell Mol Biol (Noisy-le-grand). 2016 Jul 31;62(8):28-34.
4. Qazi, H., et al.*Cancer cell glycocalyx mediates mechanotransduction and flow-regulated invasion.* Integrative biology : quantitative biosciences from nano to macro, 5(11), 1334–1343. (2013).
5. Nandi A, et al. *Hyaluronan anchoring and regulation on the surface of vascular endothelial cells is mediated through the functionally active form of CD44*. J Biol Chem. 2000 May 19;275(20):14939-48.
6. Zhang L, et al. *Repetitive Ser-Gly sequences enhance heparan sulfate assembly in proteoglycans.* The Journal of Biological Chemistry. 1995 Nov;270(45):27127-27135.

A METHODOLOGY TO MEASURE THE TRUE FLEXURAL STRENGTH OF BRITTLE CYLINDERS

Michael P. MacIsaac (1), Ghatu Subhash (1), Salil Bavdekar (1)

(1) Mechanical & Aerospace Engineering
University of Florida
Gainesville, FL, USA

INTRODUCTION

Four-point bend tests are used to experimentally obtain the flexural strength of ductile materials. As plastic deformation is the primary mode of failure in ductile cylindrical samples, failure always occurs at the point under maximum tension. However, this is not always the case with brittle samples, as their failure is governed by the growth of microstructural flaws [1]. These flaws, being randomly distributed, can lead to orientation-dependance of the measured flexural strength. If the point under maximum tension contains the critical flaw in the sample, the measured flexural strength will be its true value. However, if the cylinder is rotated to any other orientation, this critical flaw will be under a lower tensile stress, resulting in a higher measurement of flexural strength, due to the brittle materials strength in compression.

In this study, the goal is to measure the true flexural strength of the sample by ensuring that failure occurs at its weakest point. This can be achieved by loading a solid or hollow cylindrical sample as it rotates along its longitudinal axis, thereby activating its critical flaw during a four-point bending test. This allows every point on the sample's surface to experience a state of maximum tension at any given load.

METHODS

The materials tested using the develop methodology are borosilicate glass rods, ceramic (alumina) tubes, and 3D printed tubes. The glass rods and ceramic tubes were chosen because they are typical brittle materials with well-established material properties. 3D printed tubes were chosen because, although the majority of printing filaments are plastics, the printing process can produce tubes that fail in a brittle manner. Their brittle behavior can be attributed to failure due to delamination between filament layers. The 3D printed materials selected were Z-HIPS, Z-ULTRAT, and Z-GLASS.

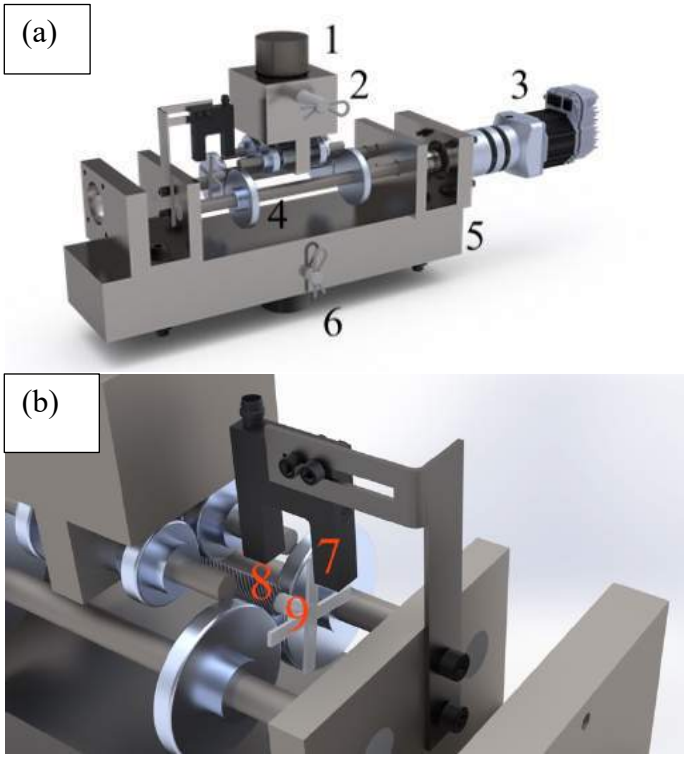

Figure 1. (a) CAD rendering of flexural test fixture. 1. top post, 2. head, 3. motor, 4. roller, 5. base, 6. bottom post. (b) Close up CAD rendering of fork sensor. 7. fork sensor, 8. sample, 9. propeller

Z-HIPS was selected because it is a commonly used filament, Z-ULTRAT was selected because it is the strongest filament offered by Zortrax™, and Z-GLASS was selected because it is a transparent filament. The 3D printed samples were printed vertically to obtain a circular cross-sections, whereas horizontal printing would result in a polygonal cross-section, due to limitations of the 3D printing process.

CAD renderings of the fixture developed to determine a sample's true flexural strength are shown in Figure 1. The fixture was developed for use with an Instron™ 5900 series Universal Testing System. Like a standard four-point bend fixture the base (part 5 in Figure 1) remains stationary as the head (part 2 in Figure 1) travels down (at a rate of 5 - 15 x10^{-3} mm/s to achieve quasi static loading) to apply the bending load. Unlike a standard four-point bend fixture, where the sample (part 8 in Figure 1) rests on two support anvils and load is applied via two loading anvils, the sample here is cradled between eight rollers (part 4 in Figure 1). The sample is rotated (at consistent rates ranging from 80-125 rpm) via a driveshaft connected to a Teknic™ servo motor (part 3 in Figure 1), model #CPM-MVC_2311S_RQN. In order to reduce undesired force concentrations, it is important that sample rotation speed remain consistent. Consistent rotation is accomplished by attaching a lightweight 3D printed propeller (part 9 in Figure 1) to the end of the sample where propeller blade passes can be recorded by an Automation Direct fork sensor (part 7 in Figure 1), model #PSUR-0N-3F. The speed of the sample is calculated and autonomously adjusted by an Arduino based controls system that uses fork sensor readings and elapsed time as key inputs.

The bending moment applied by the head onto the sample at failure is given by

$$M = Fd \tag{1}$$

where F is half of the load applied by the head and d is the distance between a lower roller and an upper roller (40.9375 mm in this case).

The resulting bending strength of each sample is given by

$$\sigma_{bending} = \frac{My}{I} \tag{2}$$

where y is the radial distance, and I is the second area moment of inertia of the sample, given by

$$I = \frac{\pi}{4}(r_o^4 - r_i^4) \tag{3}$$

where, r_i is the inner radius of the sample and r_o is the outer radius of the sample.

RESULTS

Preliminary tests were conducted on the Z-HIPS samples and the borosilicate samples. These results are shown in Table 1.

Table 1: Flexural strengths of glass rods and 3D printed tubes

Material	Measured	Literature
Z-HIPS	19.20±0.842 MPa	29.30 MPa [2]
Borosilicate	64.12±3.05 MPa	150 MPa [3]

DISCUSSION

As discussed earlier, the objective of this experiment was to measure sample's true flexural strength by ensuring failure occurs at the weakest point via critical flaw activation. Comparing the measured flexural strengths of the borosilicate and Z-HIPS to strength values found in literature [2-3], it is seen that the measured flexural strength is lower than the literature value for both materials. This is due to the critical flaws of the samples experiencing maximum states of tensile stress due to sample rotation. The Z-HIPS samples failing at lower stress levels than predicted by literature may be due to the 3D printing manufacturing process. Variables in the tube printing process that could affect strength include: tube printing orientation [4], cooling rate of filament, print quality, and layer thickness. It has been observed that printing orientation affects strength [4], therefore utilizing a vertical printing process may have produced a weaker sample, that fails via delamination. This occurs because the interlayer strength of a 3D printed part is less than its intralayer strength, and the bending stress is oriented perpendicular to the printed layers in a vertically-printed sample. Additionally, two factors of the printing process that were adjusted for greater print speed (i.e., layer thickness and print quality) may have also affected the strength. The borosilicate samples also failed at lower stress levels than predicted by literature, likely due to surface defects. Surface defects would result in stress concentrations, damaging the samples and reducing their strength.

The advantage of this methodology lies in the activation of the critical flaw in each sample, causing it to experience a maximum state of tensile stress. Hence, the true flexural strength of the samples can be measured. However, there are limitations to this methodology that must be mentioned. Principally, this methodology is applicable to cylindrical samples that fail in a brittle manner. Ductile samples cannot be used, because upon plastic deformation rotation ceases. Secondly, due to the rotation of the specimen, the specimen may endure fatigue effects as each point on the surface is cycled between a stage of max tension and max compression per revolution. Thirdly, there is rolling fatigue at the roller/sample interfaces. Issues that may present are crushing effects and sample surface degradation. These issues may contribute to sample failure at a contact point, which would result in a lower than actual flexural strength value. The findings of this developed methodology are applicable to where understanding a material's true flexural strength is paramount.

ACKNOWLEDGEMENTS

This research was performed under the Department of Energy (DOE) Nuclear Energy University Programs (NEUP) grant No. DE-NE0008773 to University of Florida.

REFERENCES

[1] W.F. Brace, E.G. Bombolakis, A note on brittle crack growth in compression, J. Geophys. Res. 68 (1963) 3709–3713. https://doi.org/10.1029/JZ068i012p03709.

[2] "Zortrax.com," 12-Dec-2014. [Online]. Available: https://cf.zortrax.com/wp-content/uploads/2019/01/Z-HIPS_Technical_Data_Sheet_eng.pdf. [Accessed: 18-Feb-2021].

[3] *BOROFLOAT 33-Mechanical Properties* [PDF]. (n.d.). Jena, Germany: Schott Technical Glass Solutions GmbH.

[4] Cantrell, J. T., Rohde, S., Damiani, D., Gurnani, R., DiSandro, L., Anton, J., . . . Ifju, P. G. (2017). Experimental characterization of the mechanical properties of 3d-printed abs and polycarbonate parts. *Rapid Prototyping Journal, 23*(4), 811-824. doi:10.1108/rpj-03-2016-0042

KNEE CONTACT FORCES IN TRANSTIBIAL AMPUTEES: IMPLICATIONS FOR REHABILITATION AND LIFELONG FITNESS EXERCISES

Reymil Fernandez (1), Shaida Biglari (2), Scott J. Hazelwood (1,2), Stephen M. Klisch (1,2)

(1) Mechanical Engineering Department
California Polytechnic University
San Luis Obispo, CA, USA

(2) Biomedical Engineering Department
California Polytechnic University
San Luis Obispo, CA, USA

INTRODUCTION

Osteoarthritis (OA) is a degenerative disease affecting joint cartilage and bone tissues. Transtibial (TT) amputees are at high risk for knee OA due to their abnormal knee biomechanics and high prevalence of overweight/obesity [1-3], both of which likely lead to increased knee joint contact compressive forces (KJCCFs) [4]. While one study suggested that regular participation in exercise may lead to better physical and mental well-being [5], most previous studies of TT amputee knee biomechanics were focused on gait, while few studies have considered non-impact exercises such as cycling and elliptical training [6,7]. Thus, there is a need to better characterize OA-related TT amputee knee biomechanics among different exercises in an effort to provide evidence-based guidelines for rehabilitation and lifelong fitness sustainment exercises that mitigate knee OA in TT amputees.

Thus, the objective of this study was to calculate KJCCFs during gait, cycling, and elliptical exercises for TT amputee and control participants. Hypotheses were (H1) KJCCF would differ due to exercise type (gait, cycling, and elliptical) for the amputee group, (H2) KJCCF would differ due to exercise type (gait, cycling, and elliptical) for the control group, and (H3) KJCCF would differ due to participant status (amputee, control) for the same exercise (gait, cycling, and elliptical).

METHODS

Experimental Procedure. Experimental data were available from a prior study [6]. All protocols were approved by our Institutional Review Board. Control and amputee participants were in good health with no history of cardiovascular/respiratory diseases, diagnosis of psychiatric illnesses, restrictions in physical activities, or extreme weight loss/gain in the past six months. Women who were pregnant or were trying to conceive were excluded from this study. Ten unilateral transtibial amputees (7 males and 3 females, aged 32.2±6.7, BMI 25.2±2.6) and ten control participants (8 males and 2 females, aged 22.1±1.8, BMI 24.4±3.1) performed a minimum of three trials for gait, cycling, and elliptical exercises. Amputee participants performed these three exercises with an Energy Storage and Release (ESAR) prosthesis (Vari-Flex, Ossur, Reykjavik, Iceland) fitted by a certified prosthetist. An enhanced Helen Hayes marker set with 32 markers was used to identify anatomical landmarks. Kinematic data were recorded with 12 cameras at 150 Hz using Cortex (Motion Analysis Corp., Santa Rosa, CA, USA). Kinematic data were processed and filtered (4th order Butterworth, 6 Hz cutoff frequency) in Cortex. Gait trials were conducted at self-selected speeds with 4 force plates (AccuGait AMTI, Watertown, MA, USA). Cycling and elliptical trials were performed at a cadence of 70 RPM at moderate machine resistance levels for 30 seconds using a stationary bike (Lifecycle GX, Life Fitness, Schiller Park, IL, USA) and elliptical machine (XE-795, Spirit Fitness, AR, USA). Experimental setups for gait, cycling, and elliptical exercises are shown in Figure 1.

Figure 1. Experimental setups for gait (left), cycling (middle), and elliptical (right) experiments for control and amputee participants.

Both cycling and elliptical pedals were instrumented with 6-axis load cells (AD2.5D, AMTI) and fitted with a custom marker configuration to track pedal position and orientation relative to a global coordinate system [6]. MATLAB (MathWorks, Natick, MA, USA) was used to filter force plate and load cell data (4th order Butterworth, 10 Hz cutoff frequency) and to format kinematic and kinetic data for use in OpenSim (Stanford University, Palo Alto, CA, USA).

OpenSim Analyses. An OpenSim musculoskeletal model [8] developed for relatively large knee flexion angles (as observed for cycling and, to a lesser extent, elliptical) was used. The OpenSim scaling tool was utilized to scale the model for each participant. The Inverse Kinematics tool was used to calculate joint kinematics. Those results were then loaded into the Residual Reduction Algorithm tool to correct the joint kinematics and optimize the scaled model using ground/pedal reaction force data. The Static Optimization tool predicted muscle forces that were subsequently inputted to the Joint Reaction tool to calculate KJCCFs. Those results were interpolated to one full gait cycle (0% = 1st heel strike, 100% = 2nd heel strike) or one crank revolution for cycling (0% = 1st top dead center [0 deg.], 100% = 2nd top dead center [360 deg.]) and elliptical (0% = 1st pass most anterior position [0 deg.], 100% = 2nd pass most anterior position [360 deg.]). Three trials for each exercise were averaged for each of the control dominant and amputee intact legs. KJCCFs were normalized by body weight.

Statistical Analysis. Maximum normalized KJCCF values that were two standard deviations (SDs) away from the mean were considered outliers and were subsequently removed from statistical analysis. Significant differences were conducted using a two-factor repeated measures of variance (ANOVA) and post-hoc Tukey tests at 95% confidence. A Bonferroni adjustment of three (due to three types of exercise) was applied on the maximum kinetic values for each hypothesis, with statistical significance defined as $p<0.0167$.

RESULTS

Kinetic data from nine controls and eight amputees were included for statistical analysis. Maximum gait KJCCF for one control and elliptical KJCCF for one amputee were 2 SDs higher than average, and another amputee exhibited abnormally low walking speed (2.5 SD below average), so data for those three participants were excluded. Significant differences for maximum KJCCF due to exercise type were found within each population ($p<0.001$) (Figure 2), supporting H1 for amputees and H2 for controls. Specifically, KJCCF was lowest in cycling compared to gait and elliptical for both control and amputee groups (gait>elliptical>cycling). Significant differences were found across control and amputee legs with the KJCCFs of the intact amputee legs higher than the dominant control legs (supporting H3) in gait ($p=0.004$) but not in cycling ($p=0.998$) or elliptical ($p=0.499$).

DISCUSSION

Novel results of this study predicted KJCCFs for TT amputees in gait, cycling, and elliptical exercises using OpenSim. These findings suggest that non-weight bearing and non-impact activities (such as cycling) are preferred exercises for reducing joint contact loading and, consequently, minimizing OA risk for both TT and control populations. Clinical implications of the results indicate that cycling should be emphasized for rehabilitation and fitness to minimize risk of knee OA. This conclusion generally agrees with earlier research [6] which suggested that, for TT amputees, cycling likely produce normal (i.e., similar to controls) cartilage loading patterns due to their non-weight bearing mechanism that constrains the feet with pedals. Because this current study found that KJCCF in elliptical exercise was lower than gait, elliptical exercise should be preferred over gait. This study also demonstrated that ESAR prostheses do not completely restore natural knee biomechanics in gait [9-11]. However, lack of significant differences between controls and amputees for cycling and elliptical exercises suggest that ESAR appears to be suitable for those exercises.

This study has several limitations. First, the number of participants were relatively low, partly due to difficulty recruiting amputee participants that met the exclusion/inclusion criteria. Second, cycling and elliptical experiments were performed with only one resistance level; future work should consider varying resistance levels. Third, only one specific type of ESAR (Vari-Flex) was used. A prior study suggested that prosthetic design may influence biomechanics in TT amputees [12]. Fourth, the Static Optimization tool predicted muscle-tendon forces from published literature; future work should predict KJCCF with EMG data using the Computed Muscle Control tool in OpenSim.

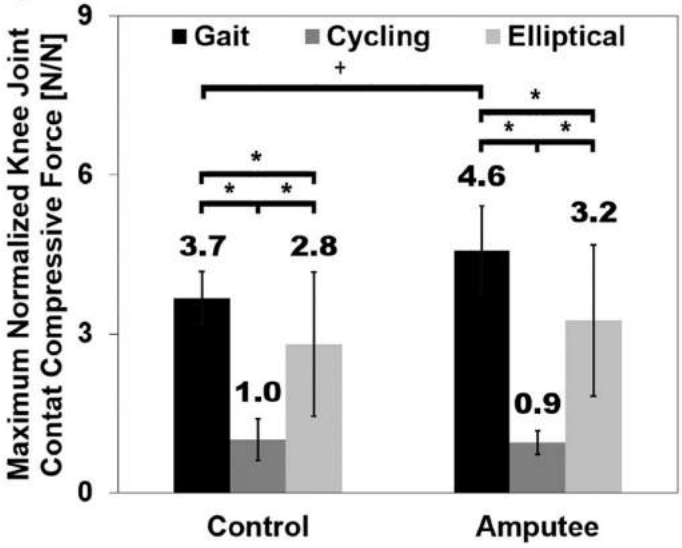

Figure 2. Maximum normalized knee joint contact compressive forces [N/N]. Mean ± 1 standard deviation values shown. * = significance due to exercise type within a group (gait vs. cycling vs. elliptical; $p<0.0167$). + = significance due to participant status within an exercise (amputee vs. control; $p<0.0167$).

ACKNOWLEDGEMENTS

Supported by the Donald E. Bently Center (SMK) and Defense Health Program through the DoD Broad Agency Announcement for Extramural Medical Research Program #W81XWH-BAA-14-1 under Award No. W81XWH-16-1-0051. The authors acknowledge the contributions of A. Matt Robinson, Gregory Orekhov, and Christie O'Hara for help with recruitment and experiments.

REFERENCES

[1] Andriacchi TP et al. *Curr Opin Rheumat*, 18:514-8, 2006.
[2] Ebrahimzadeh MH et al. *Mil Med*, 174:593-7, 2009.
[3] Westerkamp EA et al, *Prosthet Orthot Int*, 43:284-292, 2019.
[4] Silverman AK et al. *J Biomech*, 47:2556-62, 2014.
[5] Royer T et al, *Gait Posture*, 23:303-6, 2006.
[6] Orekhov G et al. *PLoS One*, 14:e0226060, 2019.
[7] Childers WL et al. *Prosthet Orthot Int*, 33:256-71, 2009.
[8] Lai A et al. *Ann Biomed Eng*, 45:2762-2774, 2017.
[9] Ventura JD et al. *Gait Posture*, 33:220-6, 2011.
[10] Versluys R et al. *Disabil Rehabil Assist Technol*, 4:65-75, 2017.
[11] Grimm M et al. *Clin Biomech*, 17:325-344, 2002.
[12] Fey NP et al. *J Biomech*, 46:637-44, 2013.

A REPEATABLE METHOD FOR IN-SITU JOINT ALIGNMENT OF DISARTICULATED HUMAN KNEES DURING IN-VITRO MECHANICAL TESTING

Zachary A. Pinkley (1), Kate J. Benfield (1), Trevor J. Lujan Ph.D. (1)

(1) Department of Mechanical and Biomedical Engineering
Boise State University
Boise, Idaho, USA

INTRODUCTION

Accurate kinematic alignment is crucial for in-vitro biomechanical testing of human joints in a laboratory setting. Misalignment of knee joints leads to significant errors in joint kinematics and resultant forces, with joint alignment variations causing a 2-3 times increase in kinematic errors [1]. For example, minor positional changes due to alterations in testing procedures, such as removing the joint from the testing apparatus, have been shown to cause significantly larger forces during position-control testing [2]. Further, in total knee arthroplasty (TKA), joint misalignment can cause component loosening, increased wear, and early failure [3]. For these reasons, accurate positioning of the knee joint is critical.

While previous in-vitro studies have developed methods to accurately align whole human knee joints prior to biomechanical testing [1,2], no such study has developed a method to re-establish natural alignment for disarticulated knees. Joint disarticulation, where soft tissue restraints are removed prior to testing, can be a necessary step in research that requires early access to the joint capsule [4]. For example, meniscus and cartilage experiments may require imaging of these tissues prior to testing. Therefore, the objective of the current study is to define and quantify a method to repeatedly position disarticulated knees to their natural intact alignment (in-situ position).

METHODS

This study used a surrogate bone model consisting of a cortical foam replica of a human knee joint (Sawbones) to address the study objective. To simulate a natural human knee, the tibia-replica was fitted with foam pads to represent the medial and lateral menisci, and elastic bands were attached with screws on the medial and lateral epicondyles to imitate the medial cruciate ligament and lateral cruciate ligament. Bone replicas were cut 17 cm distal from the joint line using a custom-made cutting guide. Both the femur and the tibia replicas were cut perpendicular to the anatomic axis of the tibia in order to preserve natural joint angles of the leg during testing [3,5]. Anatomical landmarks of the tibia and femur were marked with screws and digitized to embed joint coordinate systems using the Grood-Suntay (G-S) convention [6]. The transformation matrix between embedded coordinate systems was established using intermediate "marker" coordinate systems by attaching kinematic markers on each bone (**Fig 1A**). This simplified the digitizing process during testing [7].

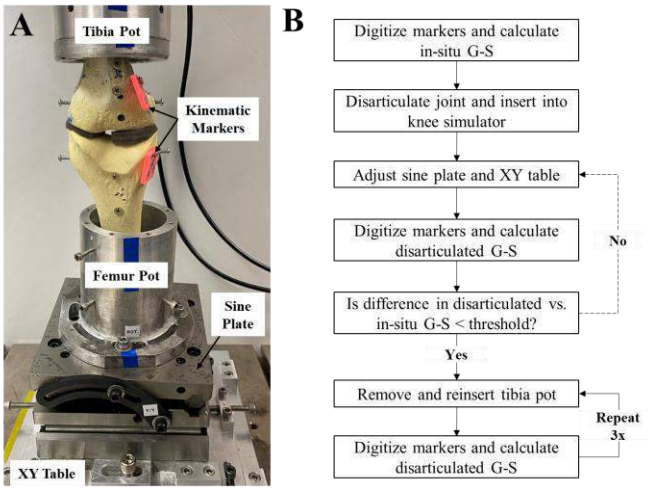

Figure 1: Test methods. A) A Sawbones model was inserted in a knee motion simulator. B) Flowchart of test procedure. In-situ kinematics were calculated, the joint disarticulated, and the kinematics were then re-established and tested for repeatability.

The tibia-replica was potted in a cylindrical mounting pot using a catalyzed polymer resin (Bondo) and inserted into a custom-made knee fixture device attached to an Instron E10000 mechanical test system (**Fig 1A**). The knee fixture device allowed for adjustments to clinical rotations and translations following the G-S convention. Medial/lateral (M/L) and anterior/posterior (A/P) adjustments were made using an XY table while flexion/extension (F/E) and varus/valgus (V/V) rotations were adjusted using a compound sine plate (**Fig 1A**). Axial translations were controlled by the Instron mechanical testing system, and internal/external (I/E) rotation adjustments were measured using a digital angle finder and rotating the femur pot.

An experimental protocol was developed to quantify errors in joint positions after disarticulation (**Fig 1B**). First, the "intact" joint was allowed to freely hang from the tibia pot, and marker locations were digitized (Revware Inc, accuracy ±0.05 mm). These locations were input into a custom MATLAB code that calculated the in-situ G-S data. The joint was then disarticulated and the femur pot was bolted into the testing apparatus. The "disarticulated" kinematic markers were then digitized and adjustments to the femur and tibia were made incrementally until the joint was within ±0.5 degrees for rotations and ±1.0 mm for translations of the in-situ position (this required 5-8 iterations). Once the in-situ position had been re-established, the tibia was removed and reinserted into the test apparatus, and the kinematic markers were re-digitized. The tibia removal-insertion process was done 3 times for each trial. In total, three trials were conducted of the entire protocol (**Fig. 1B**). Differences in G-S rotations and translations at each time point were calculated relative to the in-situ position (i.e. error), and a repeated measures ANOVA test was performed to determine the effect of time points on these errors ($p < 0.05$).

RESULTS

The errors between the in-situ and disarticulated joint positions did not significantly change after repeated removal of the tibia from the test system (**Fig. 2**). Errors in re-establishing the in-situ rotations never exceeded a difference larger than 0.60 degrees, with an average rotational difference of 0.33 degrees. Errors in re-establishing the in-situ translations never exceeded a difference larger than 1.05 mm, with an average translational difference of 0.50 mm.

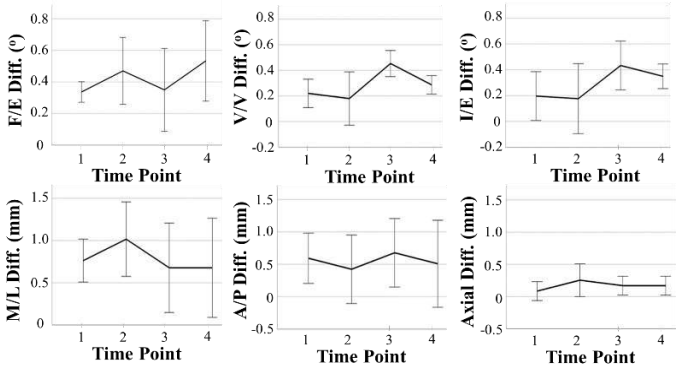

Figure 2: Error in reproducing in-situ knee position (rotations and translations). Errors were less than 1° and 1.05 mm at all time points.

DISCUSSION

For the first time, this study provides a method to re-establish natural joint alignment accurately and repeatedly for disarticulated human knees using G-S clinical rotations and translations. Using this method, the disarticulated femur and tibia were positioned on average to be within ±0.33 degrees and ±0.50 mm of the targeted in-situ rotations and translations respectively. While we saw some relatively high standard deviations, they can be explained in part by the inherent error of using the digitizer, which was found to be ±0.07 degrees for rotations and ±0.13 mm for translations (data not shown).

Future in-vitro mechanical experiments of cadaveric joints can benefit from this developed method. For example, our lab has previously simulated knee motion in whole knee joints to visualize meniscus wear using 3D optical scanning [4]. This requires disarticulating the knee joint prior to testing and then removing the knee joint at various time points, similar to our test protocol (**Fig. 1B**). While this experiment was successful in visualizing meniscus wear (**Fig. 3**), the findings had limited clinical significance due to improper kinematic alignment which led to significant damage on the articular surface of the tibia when subjected to joint loading. This misalignment caused an uneven distribution of force on the joint leading to crack propagation on the lateral region of the tibial surface (**Fig 3B**). This method can therefore be used to ensure that significant force concentrations due to malalignment are avoided. Additionally, this method can benefit in-vitro research and development of TKA implants. Misalignment of TKA implants has been shown to cause increased wear, premature component loosening, and even implant failure in in-vivo cases [3]. This method using G-S kinematics can provide a way to avoid such problems for in-vitro testing or design of TKA devices.

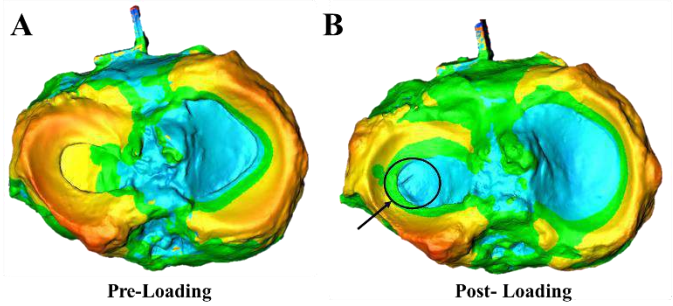

Figure 3: Meniscus wear testing of a disarticulated knee joint using optical 3D imaging A) pre- and B) post loading (1 million cycles). Damage occurred to the tibia due to malalignment [7].

Limitations of this study include the use of foam inserts and rubber bands as substitutes for menisci and ligaments, which led to a significant internal compressive force being applied to the knee joint replica while in-situ. This force was recreated during the digitization of disarticulated marker positions and may have caused slight movements of the potted femur replica when disarticulated. Another limitation is the lack of testing on variable knee geometry. Human knees can vary greatly, which may result in greater variability in error when re-establishing the in-situ joint position in knee cadavers.

In summary, this is the first study to our knowledge to define and quantify a method to re-establish in-situ knee joint alignment accurately and repeatedly for disarticulated human knees. This was accomplished by using the G-S convention to quantify the in-situ position and guide joint positioning after disarticulation. By improving joint alignment, this study can help advance clinically impactful research in knee biomechanics and TKA technology.

ACKNOWLEDGEMENTS: This work was funded by NSF-1154353.

REFERENCES

[1] MacWilliams et al, J Biom, 31, 1998. [2] Goldsmith et al, Eng Phys, 36, 2014. [3] Cherian et al, Curr Rev Muskel Med, 7, 2014. [4] Benfield, Thesis, 2020. [5] Luo et al, Knee, 11 2004. [6] Grood et al. J Biom, 105, 1983. [7] Lujan et al, J Biom, 127, 2005.

CATEGORIZATION BASED ON IN-VIVO IMAGING AND HISTOLOGICAL DATA IMPROVES PREDICTION CAPABILITY OF A STRUCTURE-BASED CONSTITUTIVE MODEL FOR ANEURYSMAL AORTIC TISSUE MECHANICS

Tuan Thinh Tong (1), Miriam Nightingale (2), Michael B. Scott (3), Alex J. Barker (4), Taisiya Sigaeva (5), Paul W.M. Fedak (6), Elena S. Di Martino (7)

(1) Department of Chemical & Petroleum Engineering, University of Calgary, Calgary, Alberta, Canada

(2) Biomedical Engineering Graduate Program, University of Calgary, Calgary, Alberta, Canada

(3) Department of Radiology, Northwestern University, Evanston, Illinois, U.S

(4) Department of Radiology, University of Colorado Anschutz Medical Campus, Aurora, Colorado, U.S

(5) Department of Systems Design Engineering, University of Waterloo, Waterloo, Ontario, Canada

(6) Department of Cardiac Science, Libin Cardiovascular Institute of Alberta, University of Calgary, Calgary, Alberta, Canada

(7) Department of Civil Engineering, Libin Cardiovascular Institute of Alberta, Center for Bioengineering Research and Education, University of Calgary, Calgary, Alberta, Canada

INTRODUCTION

Aortic aneurysms result from structural changes to the aortic wall tissues leading to altered mechanical behavior. Current criterion for aortic aneurysm surgery intervention is based on the size of the aneurysm, with elective surgery recommended for a maximal diameter of 4.2 – 5.5cm [1]. However, mechanical behavior of the aortic wall tissue also plays an important role in predicting the rupture/dissection risks. Structure-based constitutive models can relate changes in structural constituents of aortic wall tissue (elastin and collagen fibers) to altered stresses and deformations. This research focuses on the prediction capabilities of these models in capturing the stress-stretch nonlinear aortic tissue behavior curves, when samples are categorized by structural changes (level of elastin fragmentation, EF – graded by a pathologist) [2] or in vivo imaging parameter (wall shear stress, WSS). Categorizing samples based on non-invasive indices (such as WSS) potentially improves Finite Element Analysis for clinical application as different constitutive models can be used for areas under different state of mechanical loading.

METHODS

Experimental planar biaxial mechanical testing data (3 protocols of controlled stretch ratio, 1:1, 1:05, and 05:1, both circumferential-11 and axial-22 directions) of 46 ascending thoracic aortic tissue samples taken from 12 patients post-surgery (age: 55.5 ± 9 years old, 11:1 male to female, all patients have Bicuspid Aortic Valve) were fitted by a commercial modeling software called HYPERFIT [3] to the Holzapfel-Ogden-Gasser 2005 (shortly, HOG-2005) model [4]. Samples were categorized into Normal and High WSS, 0- (normal) and 1- (mild) graded elastin fragmentation (EF). By randomization, 70% of the behavior curves in each category were used to obtain the average mechanical behavior (see Figure 1). The model parameters of this curves were applied towards the other 30% (named the predictive group). The Normalized Root Mean Square Error (NRMSE) values between the model and experimental data were calculated to assess the predictability of HOG-2005 model for the predictive group. Prediction capabilities were compared between the models constructed on categorized data versus *no categorization* (the average mechanical behavior was determined from 70% of all samples) through paired t-tests. The process was repeated 10 times in each category to ensure good distribution of samples in the predictive group.

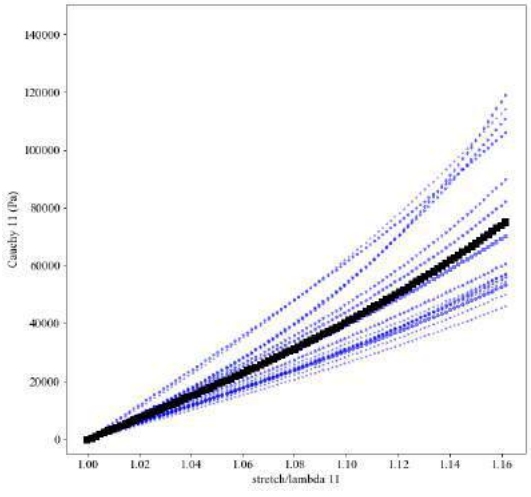

Figure 1. Construction of the Average Mechanical Behavior (black data points) from sample-specific mechanical behaviors (blue data points) by taking average of sample-specific Cauchy stress values at each stretch data point

HOG-2005's Strain Energy function:

$$\psi = \mu(I_1 - 3) + \sum_{i=1,2} \frac{k_1}{2k_2}(e^{k_2(1-\rho)(I_1-3)^2+\rho(I_{4i}-1)^2} - 1) \quad (1)$$

$$I_{4i} = A_{0i} : C \quad (2) \quad \text{and} \quad A_{0i} = a_{0i} \times a_{0i} \quad (3)$$

$$a_{01} = \begin{bmatrix} cos\ \varphi \\ sin\ \varphi \\ 0 \end{bmatrix} \text{ and } a_{02} = \begin{bmatrix} cos\ \varphi \\ -sin\ \varphi \\ 0 \end{bmatrix}$$

where μ is the stress-like material parameter referenced to matrix properties, I_1 is the (pseudo-) invariants of C, C is the right Cauchy-Green tensor, $I_{4i,\ i=1,2}$ are the (pseudo-) invariants of C, $A_{0i,\ i=1,2}$ are the structural tensors referenced to individual family of members, $a_{0i,\ i=1,2}$ are the direction vectors defining the orientation of fiber families, k_1 is the stress-like material parameter referenced to fiber properties, k_2 is the dimensionless material parameter referenced to fiber properties, φ is the structure parameter defining the mean orientation angle of fiber families from circumferential direction in the undeformed configuration, ρ is the dimensionless parameter (weight factor) within [0; 1]. The modeled Cauchy Stresses in circumferential and axial directions are then calculated, respectively, as:

$$\sigma_{11,i} = \left(\lambda_1 \frac{\partial \psi_{11}}{\partial \lambda_1}\right)_i \quad (4) \quad and \quad \sigma_{22,i} = \left(\lambda_2 \frac{\partial \psi_{22}}{\partial \lambda_2}\right)_i \quad (5)$$

where σ is the Cauchy Stress, λ is the stretch, 11 represents circumferential direction while 22 represents axial direction of the aortic wall tissue.

NRMSE values were calculated as:

$$NRMSE = \frac{\sqrt{\frac{1}{n} \times \sum_{i=1}^{n} (y_e - y_m)^2}}{|y_a|} \quad (6)$$

where y_e is the experimental value, y_m is the model value of the fitted function, i is the data-point index, n is the number of data points while y_a is the mean value from experimental values calculated as follows:

$$y_a = \frac{1}{n} \times \sum_{i=1}^{n} y_e \quad (7)$$

RESULTS

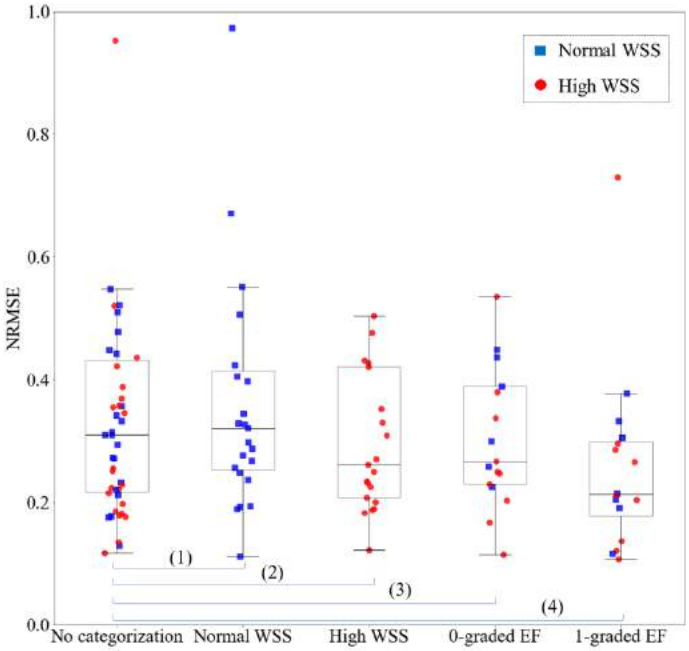

Figure 2. NRMSE comparison (each data point represents the average values of NRMSE for the sample over the 10 iterations)

Table 1. p-values from paired t-tests between No Categorization and respective category

NRMSE comparison (sees Figure 2)				
Test #	(1)	(2)	(3)	(4)
p-value	0.0511	0.0161*	0.6160	0.0220*

**Statistically significant at 0.05*

It can be observed that by categorizing samples into groups such as High WSS or 1-graded EF, the average mechanical behavior can predict better the mechanical behavior of samples that belong to the predictive group (by statistically lowering NRMSE values).

DISCUSSION

This abstract demonstrated the potential of incorporating useful information such as in vivo imaging (WSS) and histological (EF) data to improve the predictability of constitutive model on a new experimental mechanical behavior dataset (see Table 1).

This method of constructing the average material mechanical behavior is also applicable to screen other factors that may contribute to the rupture/dissection risks such as level of Collagen Distribution and Alterations. In-vivo measurable parameters have the added potential of being able to be measured non-invasively through medical imaging. Research on a larger population dataset will further investigate the role of WSS and other mechanics-based parameters that can be estimated in vivo.

ACKNOWLEDGEMENTS

The author thanks the funding of National Institutes of Health (US), the Alberta Innovates, Libin Cardiovascular Institute, Schulich School of Engineering, University of Calgary to support this project.

REFERENCES

[1] M. Boodhwani *et al.*, "Canadian cardiovascular society position statement on the management of thoracic aortic disease," *Can. J. Cardiol.*, vol. 30, no. 6, pp. 577–589, 2014, doi: 10.1016/j.cjca.2014.02.018.

[2] M. K. Halushka *et al.*, "Consensus statement on surgical pathology of the aorta from the Society for Cardiovascular Pathology and the Association for European Cardiovascular Pathology: II. Noninflammatory degenerative diseases - Nomenclature and diagnostic criteria," *Cardiovasc. Pathol.*, vol. 25, no. 3, pp. 247–257, 2016, doi: 10.1016/j.carpath.2016.03.002.

[3] P. Skacel, "HYPERFIT Software." HYPERFIT software, Brno, Czech Republic, 2020, [Online]. Available: www.hyperfit.wz.cz/models.php.

[4] G. A. Holzapfel, G. Sommer, C. T. Gasser, and P. Regitnig, "Determination of layer-specific mechanical properties of human coronary arteries with nonatherosclerotic intimal thickening and related constitutive modeling," *Am. J. Physiol. - Hear. Circ. Physiol.*, vol. 289, no. 5 58-5, pp. 2048–2058, 2005, doi: 10.1152/ajpheart.00934.2004.

THE RELATIONSHIP BETWEEN PERCIEVED CONFIDENCE AND WRITING IN A BIOMEDICAL ENGINEERING REU SITE

Elisabeth C Reed (1), Donna Kain, PhD (2), Stephanie M. George, PhD (3)

(1) Department of Psychology
East Carolina University
Greenville, NC, USA

(2) Department of English
East Carolina University
Greenville, NC, USA

(3) Department of Engineering
East Carolina University
Greenville, NC, USA

INTRODUCTION

The Research Experiences for Undergraduates (REU) Site in Biomedical Engineering in Simulations, Imaging, and Modeling (BME-SIM) at East Carolina University was funded by NSF in 2014 (EEC-1359183), 2017 (EEC-1659796), and 2020 (EEC-1950507). The goal of the BME-SIM REU program is to broaden participation by providing authentic research experiences to students who are traditionally under-represented in engineering. Historically, women have been underrepresented in STEM fields- from 2017-2018, women made up only 21% of those awarded with a BS in Engineering [1]. This underrepresentation is thought to be caused by sexism in the field, a lack of role models, and low self-efficacy beliefs [2]. Self-efficacy is our own perceived ability to perform certain tasks, influenced by our previous mastery experiences, watching others perform the task, or receiving feedback regarding our abilities to perform the task [3].

Research experiences can be vital in developing one's sense of competence within a domain [4]; Interestingly, however, it's been found that mastery experiences, or accomplishments, have a higher influence on males' self-efficacy, while women's self-efficacy is influenced more by vicarious experiences and verbal persuasions [5]. Women may lack this sense of self-efficacy due to a small number of role models in the field and little encouragement due to subtle gendered biases [5].

Women are stereotyped as warm, kind, and nurturing, often having communal goals, whereas men are defined as competitive, logical, and competent, often pursing more agentic goals [5]. STEM fields are characterized with more masculine traits leading women to feel as though the female gender is not as STEM-oriented as male counterparts, thus pursuing lower positions and feeling a lowered sense of confidence and self-efficacy [5]. Moreover, women tend to be modest when discussing their academic achievements, notably in public spaces, whereas men tend to overestimate their achievements [6]. Daubman et al.'s study questions that it is not lack of confidence that influences how one presents their academic achievement, but rather a need to maintain presentation of gender roles [6]. Studies have shown that women who chose to self-promote, thus violating gender norms, were perceived more negatively than male counterparts who behaved in a similar manner [7]. This modesty could potentially be damaging to a woman's career- if she fears social back-lash due to self-promotion and competitiveness or feels she is not as competent as her male counterparts, she may be inadvertently opting out of career-enhancing opportunities [3, 7].

Given that women will alter their self-promotion based on social contexts, this project will investigate gender differences in confidence of research abilities before and after participating in a Biomedical Engineering REU program. Confidence will be assessed by reviewing personal statements, essays that should highlight an applicant's reasons for pursuing a program as well as their past accomplishments, and student self-reported confidence levels.

METHODS

This study was approved by the Institutional Review Board at ECU and informed consent was received by all participants. The BME-SIM program is a 10-week residential summer program that provides students with an authentic research experience, professional development, including writing and communication workshops, and mentoring opportunities [4]. During the application process, students are asked to submit a personal statement. This statement is a critical component of the applicant reviewal process, shedding light on the student's personality, goals, and accomplishments. At the end of the program, students are asked to submit an updated personal statement as if they were applying to graduate school. Student surveys were completed on the first and last day of the program. Students reported

their progress towards mastery of knowledge and skills using a 10-point Likert scale, including confidence in research abilities. These data indicated that women who participate in the program have a significantly lower sense of self-efficacy in research abilities when compared to male counterparts in both pre- and post-program participation, but no differences in actual performance [4]**.** A total of 55 students have participated in the program from 2014-2019.

A sub-set of the students (n=16) were selected for further analysis in this study, with eight being men and eight being women. Pre- and post-program personal statements were evaluated by a group of 11 faculty reviewers of varying gender and STEM disciplines. Each statement was carefully anonymized removing references to gender, home university, and other identifiers. Each personal statement was assigned to three faculty reviewers. Faculty reviewers were asked to highlight portions of statements they found to be good in green, bad in red, and interesting in yellow. Along with highlighting, they were asked to make comments elaborating on why they chose to highlight specific portions of text. Following statement mark-up, reviewers were asked to fill out a survey rating perceived characteristics of students, notably perceived confidence (five-point Likert scale). To enable comparison, student self-reported scores were converted to a five-point scale.

A total of 639 comments from reviewers were categorized by varying themes, garnering an 85% interrater reliability rating; however, this study will focus on only confidence categorizations. Comments categorized as confidence must either include the word "confidence," or mention the student's achievements, strengths, or positive attributes; however, these comments could discuss these characteristics in a positive or negative way. A few examples of how these confidence-related comments can be either positively or negative received are as follows: "the writer shows humility through the word choice --grateful--and therefore described his ability to get scholarships without bragging" coded as green; "This is not for the writer to say, it is boastful and in fact may not be true" as red; and "self-conscious" as yellow. Once all data was collected, faculty survey results, highlights, and commenting were compared to students' self-reported characteristics.

Quantitative data was compared using a Student's *t-test (paired or two-sample unequal variance)* to find if confidence in research skills was statistically different pre- and post- program, and across gender.

RESULTS

Prior REU data found that women's self-reported confidence levels were not as high as male counterpart's when surveyed both pre- and post-program [4]. For this sample of the participants, self-reported confidence was lower both pre- and post-program for women as compared to men (Table 1). Although statistically significant in the total cohort, these differences were not significant in our sub-population. Faculty's perceptions of confidence from the women's writing was lower than their perceptions of the males in the pre-program personal statements; however, the women's faculty-perceived confidence made a leap in the post-program statements, even being higher than the male's faculty-perceived confidence (Table 1). However, none of these differences were statistically significant in our small sample.

Table 1: Comparison of Faculty's Perceived Confidence Compared to Students' Self-Reported Confidence

	Faculty Confidence Rating		Student's Self-Reported Confidence	
	Pre	**Post**	**Pre**	**Post**
Men	4.1 ± 0.87	4.18 ± 0.73	3.0 ± 1.2	4.25 ± 0.89
Women	4.0 ± 1.09	4.35 ± 0.65	2.5 ± 0.76	4.13 ± 0.84

Of all comments between pre- and post-program statements, about 9.4% of comments were categorized as confidence related. Men were found to have the most green confidence comments in both the pre- and the post-program statements (Table 2).

Table 2: Comparison of Confidence Comment Amount by Statement and Gender

	Pre		Post	
	Men	**Women**	**Men**	**Women**
Green	18	9	13	6
Yellow	2	1	1	4
Red	0	4	1	1

DISCUSSION

The increase of faculty-perceived confidence in the women's personal statements seems to correlate with the women's self-reported self-efficacy levels. However, the faculty perceived limited increase in confidence in the men compared to their self-reported increase in self-efficacy. Men had more green coded confidence comments, indicating a possibility that their personal statements are being perceived more positively than their female counterparts. This correlation may reveal that writing could have a role in conveying one's level of confidence in relation to the writing-topic. Moreover, it seemed that faculty reviewers appreciated confident students, but were wary of overly confident students. Comments such as "overly confident" were coded as red, indicating the reviewer saw the comment as negative, whereas comments such as "student is confident without being cocky. they are aware of how they would benefit from the program" were coded as green to indicate the reviewer's positive perception. However, this possible link between highlighting, perception, and comment categorization is still being investigated.

Overall, confidence in research ability did increase following participation in the BME-SIM program. Data found differences between how men and women perceive themselves, and how faculty seem to perceive students based on their writing. This may have further implications of investigating how confidence is displayed between men and women, and possibly have implications for future research regarding how review boards evaluate personal statements; notably, in how confidence is perceived. It is not a question of one being too confident, but how we decide to characterize confident individuals.

ACKNOWLEDGEMENTS

Special thanks to the faculty reviewers who volunteered their time. Funding provided by ECU Undergraduate Creativity and Achievement Award and National Science Foundation (NSF) grants EEC-1359183, EEC- 1659796.

REFERENCES

[1] Society of Women Engineers. https://research.swe.org/wp-content/uploads/sites/2/2020/11/FOR-PRINT-SWE-Fast-Facts_Oct-2020.pdf

[2] American Association of American Women. https://www.aauw.org/resources/research/the-stem-gap/

[3] Rittmayer, A.D. and Beier, M.E. *Assessing Women and Men in Engineering*, 10:1-12, 2009.

[4] George, S. M. and Domire, Z. J. *Journal of Biomechanical Engineering*, 142(11):111012, 2020. https://doi.org/10.1115/1.4047630

[5] Sobieraj, S. and Kramer, N. C. *Frontiers in Psychology*, 1-16, 2019.

[6] Daubman, K. A. et al. *Sex Roles*, 27:187-204, 1992.

[7] Smith, J.L. and Huntoon, M. *Psychology of Women Quarterly*, 38:447-459, 2014.

A COMPUTATIONAL TOOL TO AUTOMATE THE ANALYSIS OF STRESS-STRAIN DATA FROM TENSILE TESTS OF SOFT TISSUE

Miranda L. Nelson, Derek Q. Nesbitt, Trevor J. Lujan

Mechanical & Biomedical Engineering
Boise State University
Boise, Idaho, United States

INTRODUCTION

Stress-strain curves are commonly generated to analyze the mechanical tensile behavior of biological materials. In soft tissue, several key material properties can be calculated from these curves, including ultimate tensile strength (UTS), yield strength, energy to failure, and the transition point. The transition point is at the intersection of the toe region and the linear region, which physically represents the point where the crimped collagen fibers are collectively straightened.[1] The transition point defines a safe strain range below the threshold of microtears,[2] and is explicitly included in some constitutive equations used to model soft tissue. Despite its importance, there is no standard method to find the transition point. While a variety of methods have been used,[3-8] no study has reported the accuracy or robustness of their method. Furthermore, there are currently no software tools available to automate the calculation of the transition point, or other material properties of interest. This lack of standardization makes it difficult to compare results across studies and is time inefficient, as each research group has to create their own method. A need therefore exists to develop a standard, fast, and accurate method to calculate the transition point and other tensile mechanical properties in soft fibrous tissue.

Objective. The objectives of this study are to 1) develop a user-friendly program that automates the calculation of mechanical properties from stress-strain curves, and 2) identify the optimal settings to minimize error when calculating the transition point by using synthetic and experimental data.

METHODS

Program Development. A custom graphical user interface (GUI) was created using Python. This GUI allows users to upload stress-strain data and then automatically generates a stress-strain curve with marked points of interest (**Fig. 1**), as well as a .csv file that appends the following mechanical properties: tangent modulus, energy to failure, and stress and strain at ultimate, yield and transition points. The GUI first finds yield as the point of maximum slope[9] and then calculates tangent modulus as a linear fit to the data from yield to 1% strain below yield.[7] The transition point is found when the slope of the stress-strain curve deviates by a certain percent from the tangent modulus. GUI settings allow for users to customize the slope deviation threshold to determine this point. The UTS is the point of maximum stress and rupture occurs 50% below UTS. Energy to failure was approximated using trapezoidal integration to UTS and to rupture.

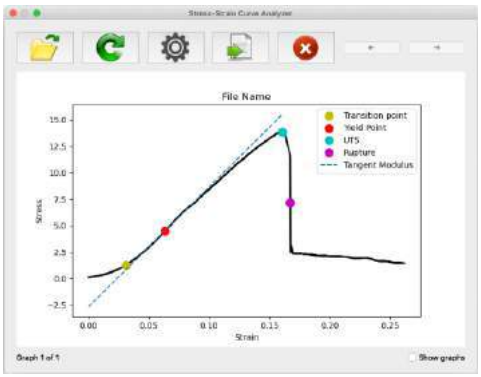

Figure 1: The new GUI automates the generation and analysis of stress-strain curves. Multiple files can be simultaneously uploaded.

Synthetic Data. The software's accuracy was evaluated using synthetic stress-strain curves with known transition points. This data was generated using FEBio studio, a free finite element software program.[10] A single element cube was created with sliding elastic

contact between the cube and the dynamic rigid body. For the constitutive model, a transversely isotropic fiber matrix[11] was selected with a Veronda-Westmann hyperelastic ground substance.[12] Damage evolution was modeled using a quintic polynomial cumulative distribution function. Importantly, one of the user-specified material parameters for this model is the strain at the transition point. This allows for the calculation of error between the stress at the known transition strain predicted by the software (**Fig. 1**) and the actual transition stress being modeled. The effect of modulus slope (low, medium, high) (Fig. 2) and rate-of-damage (low, medium, high) (Figure 2B) on error was analyzed. In addition, the effect of % slope deviation to determine the transition point was tested at 1, 2, 3, 5, 10 and 20%.

Experimental Data. The software's accuracy was also evaluated using tensile test data from our previous study on human meniscus.[8] First, the parameters of the aforementioned constitutive model were calibrated to stress-strain curves from 10 different meniscus specimens pulled to failure along the primary circumferential fiber axis. This resulted in excellent fits for all 10 cases (**Fig. 2**; RMSE = 0.14 ± 0.09). Transition stresses were determined as the stress at the optimized value of transition stretch. The model parameters were optimized with the Levenberg-Marquardt algorithm in FEBio. This experimental data was then analyzed with the GUI (**Fig. 1**) using % slope deviations of 1, 2, 3, 5, 10 and 20%. Error was calculated as the percent difference in the transition point calculated by the GUI and the transition parameter optimized in FEBio.

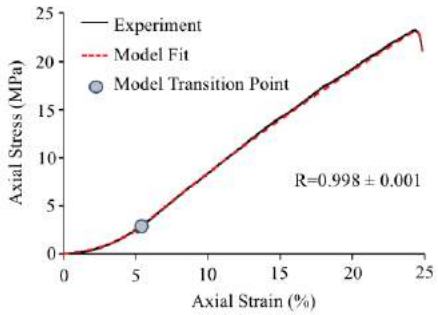

Figure 2: Representative model fit to experimental data.

Statistics. Effect of slope variation on transition error was measured using a one-way ANOVA with Tukey HSD post-hoc for both the experimental and synthetic data. The effect of changing the damage rate and moduli on transition error was measured using a MANOVA with Tukey HSD post-hoc. Significance was set at $p<0.05$.

RESULTS

There were no significant differences in transition stress error due to changing the tangent modulus (**Fig. 3**; $p=0.56$). Similarly, there were no significant differences in transition stress error due to changing the curvature of the stress-strain curve with damage (**Fig. 3**; $p=0.35$). When analyzing synthetic data, the least error in calculating the transition stress was 10.7%, and occurred when using slope deviations of 2% and 3% (**Fig. 4A**). Using slope deviations of 10 and 20% resulted in errors exceeding 72%. When the GUI was used to analyze experimental data, the slope deviation that produced the lowest error for transition stress was 2%, with an error of 3.3% (**Fig. 4B**).

DISCUSSION

A GUI was created that can quickly and accurately find points of interest on a stress-strain curve and calculate material properties. Our GUI was used to identify the optimal settings of a scalar threshold used to find the transition point. Notably, the GUI closely predicted the same transition point calculated using a more complex FE optimization routine. We found that a 3% slope deviation returned the lowest error for transition stress in this study. The error in calculating the transition point was insensitive to changes in the modulus and damage rate of the stress-strain curve (**Fig. 3**). This means that this methodology for calculating the transition point should be relatively robust for the large variations in stress-strain curves typical of soft fibrous tissue.

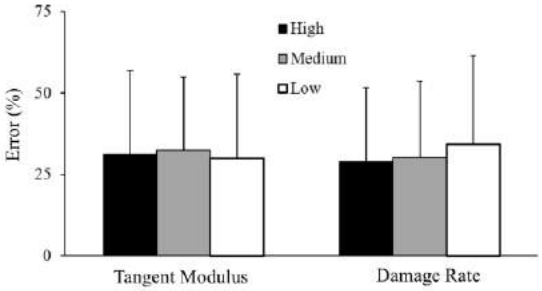

Figure 3: Changes to tangent modulus and damage rate did not affect the error in calculating the transition point (all tests pooled except changing variable; n=18 for each bar).

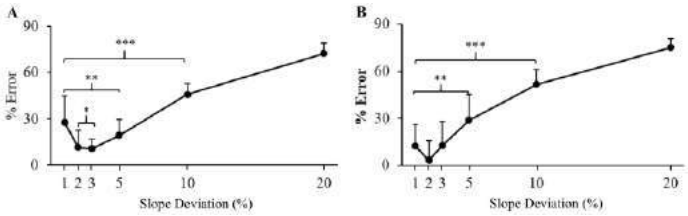

Figure 4: Error in calculating transition stress is lowest when using slope variations between 2% to 3% in A) synthetic and B) experimental data. Significance for all groups under brackets is defined as: *less than 5% group; **less than 10% group; ***less than 20% group ($p < 0.05$).

The material properties calculated by our GUI are typically calculated using custom semi-automated methods that differ between research groups. Our program can help standardize this process and with a runtime under 3 seconds, can dramatically reduce calculation time. In addition, all results can be exported as PDF files (with figures) and .csv files that summarize the material properties of multiple experiments.

The next step for this program is to make it accessible to the biomedical research community be creating a web-based version. We also would like to continue evaluating the accuracy of the software by testing experimental data with more noise. In conclusion, by creating an accurate computational tool to automate the analysis of stress-strain curves, this study can advance the standardization of biomechanical testing in soft fibrous tissue.

ACKNOWLEDGEMENTS: Funding support from NSF (1554353).

REFERENCES:

[1] Holzapfel GA. Academic Press; 2001. pp. 1049–1063. [2] Provenzano, PP et al., *J Appl Physiol* 92(1):362-371, 2002 [3] Danso, EK et al., *J Biomech*, 47(1):200-6, 2014. [4] Ristaniemi, A et al., *J Biomech*, 79:31-38, 2018. [5] Abdelgaied, A et al., *J Biomech*, 48(8):1389-1396, 2015. [6] Lake, S et al., J Orthop Res 27:1596–1602, 2009. [7] Wale, M et al., *J Biomech*, 143(1):110-126, 2021. [8]Nesbitt, D et al., *J Biomech*, 115:110-126, 2020.[9] Peloquin, JM et al., *J Biomech*, 138(2):021002, 2016 [10] Maas et al., J. Biomech. Eng. 2012 [11] Weiss et al., Comp. Methods in App. Mech & Eng. 1996. [12] Veronda and Westmann, J. Biomech. 1970.

SB³C2021
Summer Biomechanics, Bioengineering and Biotransport Conference
June 14-18, Virtual

A LOW-COST, OPEN-SOURCE ROBOT HAND-WRIST SYSTEM FOR TACTILE-ASL BASED COMMUNICATION FOR THE DEAF BLIND

Samantha T. Johnson (1), Gaogeng Gao (2), Minas Liarokapis (2), Chiara Bellini (1)

(1) Department of Bioengineering
Northeastern University
Boston, MA, USA

(2) Department of Mechanical Engineering
The University of Auckland
Auckland, Auckland, NZ

INTRODUCTION

Deaf-blindness refers to concurrent vision/hearing impairments that compromise the ability of ~1.5 million Americans to study, work, and live independently [1]. To communicate, the deaf blind community uses a combination of tactile American Sign Language (ASL) and Braille. Although the former is their primary conversation language, it requires an interpreter – deaf blind individuals place their hands over an interpreter's hands to follow the movements as the interpreter signs ASL. While reading Braille does not necessitate an interpreter, it is ~30% slower than ASL, it requires frequent breaks [2-3], and reliable Braille displays are costly. As a result, there is an urgent need to develop low-cost communication aids for deaf blind users that (1) are efficient and easy to use, (2) can be integrated into mainstream communication devices, and (3) can be used independently (without an interpreter).

ASL grammar and vocabulary are expressed using a combination of facial and hand gestures with bodily positional references for context. The language is also complete with a 26-letter alphabet that is finger spelled with single-hand gestures used to convey proper nouns or pop culture references (brands, songs, movies, etc.). Several attempts have been made to design a robotic device capable of fingerspelling. The first prototype developed by SouthWest Research Institute in 1977 has been progressively refined to complete 24 letters of the ASL alphabet, although with low recognition rates in validation studies [4]. These fingerspelling hands often featured dexterous manipulators made from rigid components. Since tactile ASL requires the deaf blind user's hand to be placed on the robotic device, traditional designs are not safe (e.g., the user's fingers could be pinched between a revolute joint when the robotic hand performs flexion).

The PARLOMA project was the first to develop a robotic hand + wrist system specifically targeted to develop a deaf blind remote communication device. While the authors claimed a 90% recognition rate of the handshapes, validation was based on visual observations alone (without tactile feedback) and did not include hard-to-render letters (e.g., E, G, J, M, N, Q, R, T, U, Z) [5]. Furthermore, their system lacks an anthropomorphic feel, has not been evaluated for tactile ASL with deaf blind participants, and cannot discern between words that share the same handshape and motion but need different spatial positioning (e.g., the handshape for "man" and "woman" are the same, but the former requires placement of the hand on the forehead, the latter on the chin).

In an effort to overcome these drawbacks, the goal of project TATUM (Tactile ASL Translational User Mechanism; powered by Interpres) is to develop, validate, and disseminate a low-cost, open-source, 3D printed anthropomorphic robotic arm capable of signing tactile ASL with required positional references. TATUM can be used independently, which is especially important to prevent the isolation of the deaf blind community in times of social distancing, when close contact between people (e.g., a deaf blind individual and interpreter) is discouraged.

METHODS

Design. The hand (Figure 1) component of the system was designed to achieve an anthropomorphic appearance both by sight (as other existing prototypes) and touch (novel design aspect).

First, the portions of the hand that encounter the user are 3D printed from flexible thermoplastic polyurethane (TPU) instead of rigid polylactic acid (PLA). Furthermore, we based our design on an open-source scan of a human hand, that we modified to include flexure joints and attachment methods (Figure 1). To sign the 26-letter ASL alphabet, the hand features 14 degrees of actuation (DOAs) that are supported by pulley-tendon mechanisms distributed across the fingers. The ring and pinky fingers include 2 DOAs each, the first attached to the flexion of

the metacarpophalangeal (MCP) joint, the second coupled to both the proximal interphalangeal (PIP) and distal interphalangeal (DIP) joints. The index and middle fingers contain an additional DOA each to sign letters like 'R' or 'V', which require abduction of the fingers (Figure 2). The thumb consists of 2 DOAs allocated to the opposition of the finger and the flexion of its MCP and DIP joints. The final 2 DOAs are reserved for flexion and abduction of the wrist.

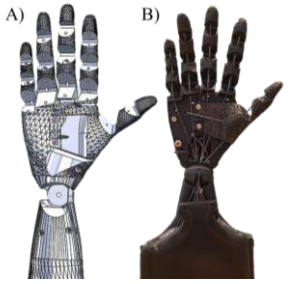

Figure 1: (A) SolidWorks CAD model of the designed hand. (B) 3D printed and actuated hand.

Actuation. The robotic hand includes 14 servo motors. We used 10 Goteck GS-9025MG, 9-gram servos for actuating the fingers and 4 FEETECH FS5103B servos for the wrist and thumb. We selected a microcontroller (Arduino Mega) to control the device in active flexion and passive extension under the contact pressure exerted by the user, while maintaining a signing speed of 1.95 signs per second [3]. TATUM utilizes Interpres (software as a service, SaaS) to translate the communication (e.g., a text input) and send it along to the robotics with the necessary instructions for the motors to produce the desired finger and handshapes.

Validation. To validate the design, we conducted human-subject trials to determine the user's recognition rate of the ASL alphabet. The testing protocol (approved by Northeastern University's IRB) first introduced participants (both deaf blind, n=3 and blind with vision, n=2) to all the letters as signed by TATUM in alphabetical order. Later, participants were asked to recognize the handshapes when presented in a random order. At the end of the session, we solicited feedback from each participant on the speed, feel, and overall ease of use of the device.

RESULTS

Operation of the robotic hand did not cause any harm to the users. Since most deaf blind individuals put their hand on the back of the device, the choice of flexure joints (Figure 2) prevented pinching of the skin. Additionally, the robotic hand transitioned smoothly from one letter to the next, which was achieved by building sufficient compliance into the joints (i.e., they become increasingly thinner more distally, towards the point of flexion to reduce the torque). Furthermore, the robotic hand required a maximum of 6V and 6amps to achieve any handshape. The wrist and thumb motors (which need the most torque to actuate) are current-regulated, preventing overheating of the board.

Overall, we found a 75% recognition rate of the 26-letter ASL alphabet handshapes. Four of the participants struggled differentiating between 'U' and 'V', which have very similar fingerspelling. Secondly, handshapes that need a very precise thumb placement, such as 'M', 'T', and 'O', were often confused. Lastly, participants also failed to recognize the 'R', which requires to move the middle finger behind the index finger by abduction. Since both fingers are acting in the same plane, the movement did not produce a clear enough cross, causing confusion with the letter 'U'.

Nonetheless, the subjects believed the hand 'felt like a woman's hand,' making the device easier to recognize. Also, when the fingers moved into position, the users did not believe that they would be hurt, and they were not concerned about the speed of the movement. This feedback suggests that users can easily acclimate to the device, and minimal design changes could greatly improve the handshapes fingerspelling recognition rates.

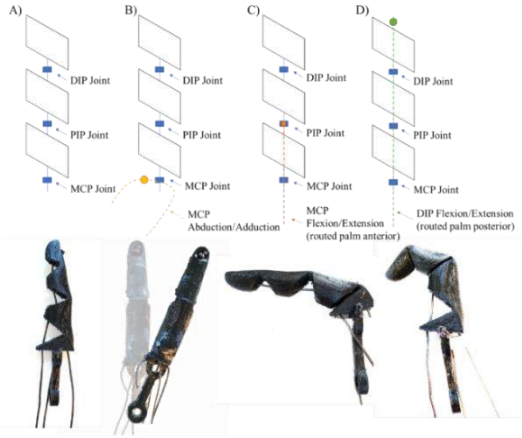

Figure 2: (A) Side-view of the 3D printed finger. (B) Finger abduction at the MCP joint. Finger flexion around the MCP (C) and DIP-PIP (D) joints.

DISCUSSION

Physical restrictions imposed over the past year have emphasized the need for a device that can facilitate independent interactions between deaf blind individuals and their community, while continuing to use their primary conversational language, tactile ASL. To answer this need, we successfully designed a robotic hand with anthropomorphic shape and feel that can sign ASL. While we already achived a recognition rate that is comparable to that of existing solutions, we will leverage the feedback from the users to increase it to at least 90%. We will change the actuation scheme of the thumb to better drive it toward the MCP of the fingers, thus improving the signing of 'M', 'N', and 'T'. Additionally, we will reduce the spacing between the index and middle fingers to better sign bent handshapes ('O', 'C', 'M', 'N', etc.). Finally, we will decrease the size of the proximal phalanx to ensure proper abduction of the middle finger for rendering of the 'R' handshape.

Next, we will develop an elbow platform to perform flexion, abduction, as well as translational motions of the arm, in order to communicate complex words and phrases that require precise spatial references. A body reference platform will also be designed to provide reference points within the body (e.g., forehead and chin). Finally, we will include hybrid Wi-Fi & Bluetooth Chip (ESP32) to connect the system to electronic devices (e.g., computers and cellphones to access documents, emails, and texts). Once these new features are implemented, project TATUM will provide millions of deaf blind individuals with a tool for communicating independently via mainstream communication systems.

ACKNOWLEDGEMENTS

We are grateful for Northeastern University support through the PEAK Summit Award providing preliminary funding for development and validation.

REFERENCES

[1] Swenor, B, et al., *Jama Intern Med*, 173.23:312–313, 2013.
[2] Letson, C, *J. Educ. Res*., 52.2:49–54, 1958.
[3] Wilbur, R, *Lang. Speech*, 52.2–3:245–285, 2009.
[4] Jaffe, D, *J. Rehabil. Res. Dev.*, vol. 31, no. 3, pp. 236–244, 1994.
[5] Bulgarelli, A, et al., *Int. J. Adv. Robot. Syst*.,13.3, 2016.

SB³C2021
Summer Biomechanics, Bioengineering and Biotransport Conference
June 14-18, Virtual

COLLAGEN MICROSTRUCTURAL ORGANIZATION CONTRIBUTES TO NEOVESSEL GUIDANCE DURING ANGIOGENESIS

Jason C. Manning (1,2), Adam Rauff (1,2), Jeffrey A. Weiss (1,2)

(1) Department of Biomedical Engineering
University of Utah
Salt Lake City, Utah, United States

(2) Scientific Computing and Imaging Institute
University of Utah
Salt Lake City, Utah, United States

INTRODUCTION

Angiogenesis, the growth of new blood vessels, provides vascularization to native tissues and is fundamental to engineering new tissues. A limiting factor in tissue engineering is insufficient perfusion across the host-implant interface of tissue grafts [1]. Typically, perfusion is provided through angiogenesis as neovessels sprout and navigate toward regions with insufficient vascular supply. However, interfaces separating distinct tissues have been shown to inhibit neovessel growth between tissues. [2]. Moreover, mechanical factors contribute to limited neovascularization across interfaces [2].

Angiogenic growth is modulated by mechanical factors as sprouting neovessels receive and respond to cues from the surrounding tissue [3]. Advancing neovessel tip cells exert tension on the extracellular matrix (ECM), inducing regions of alignment. Tension-driven realignment of collagen fibrils enables force transmission and cellular mechanosensing over relatively long distances, enabling neovessels to respond to cues from the ECM [3,4]. Previous studies have demonstrated that collagen microstructural organization influences vascular networks, but the underlying mechanisms modulating neovessel guidance remain poorly understood [2,3].

Our objective was to study neovessel guidance by the collagen microstructural organization within the tip cell microenvironment. We developed an image analysis method to quantify the collagen fibril organization adjacent to advancing neovessels and identify regions of tension-driven collagen realignment. We calculated the distance of influence, or the distance from which collagen fibrils were realigned by tension forces. We gained insights into the reach of tip cell tension forces and examined the collagen microstructural organization near an advancing neovessel over time.

METHODS

3D In Vitro Model of Angiogenesis: We used a type I collagen ECM (3 mg/ml) seeded with intact microvessel fragments (30,000 fragments/ml) [5]. This model recapitulates all aspects of the sprouting phase of angiogenesis as neovessels spontaneously sprout from "parent" microvessels, grow over millimeters in length over 3-10 days, and create a perusable vascular network [6].

Multiphoton Time-Series Imaging: After 48 hours of preliminary incubation, a culture was transferred to an incubator on a multiphoton microscope (Bruker Ultima, Billerica, MA). Multi-channel volumetric mosaic images (2 x 2 x 0.9 mm) were acquired every two hours for five days using an excitation wavelength of 780 nm [5]. The collagen ECM and vascular network were imaged using second-harmonic generation (SHG) and autofluorescence signal, respectively.

Analysis of Collagen Microstructural Organization: SHG projections around neovessel tips were divided into rectilinear blocks (30x30 microns) to quantify the preferred collagen fibril orientation, the anisotropy of the orientation distribution, and the relative density. Relative collagen density was determined as the mean intensity of each block normalized to the maximum intensity [2]. A custom program based on the discrete Fourier transform was used to determine the principal fibril direction and fractional anisotropy of the orientation distribution (Matlab, Natick, MA) [5, 7].

Quantifying the Distance of Influence: The distance of influence was determined from the tension-driven realignment of collagen fibrils. Realignment was characterized by collagen fibrils aligned with the neovessel direction with high anisotropy and density (Fig 1). For five independent neovessel tips, data was sampled at five-micron intervals extending 100 microns from the neovessel tip. The distance of influence

was computed as the minimum of the following distances: 1) the average anisotropy dropped below 0.35 or 2) the average angle between the preferred collagen fibril direction and neovessel orientation was greater than 20 degrees.

Neovessel Guidance Analysis: A sprouting neovessel with a well-defined collagen microenvironment was tracked over five time points (Fig 2a). For each time point, the preferred direction was determined from the collagen organization within the tip cell microenvironment. Discretized growth paths spanned +/- 90 degrees from the neovessel's direction at 10-degree increments over a radius of 40 microns (Fig 2b). The path with the highest anisotropy was determined the preferential direction and was compared to the actual growth trajectory (Fig 2c).

RESULTS

Quantifying the collagen microstructural organization around neovessel tips revealed the distance of influence from cellular tension (Fig 1a-b). The following trends were observed with increasing distance from the neovessel tip: 1) decreasing anisotropy and collagen density (Fig 1c) and 2) increasing deviation angle between the neovessel and collagen fibrils (Fig 1d). The average distance of influence was 45 microns (std = 16.6, n=5).

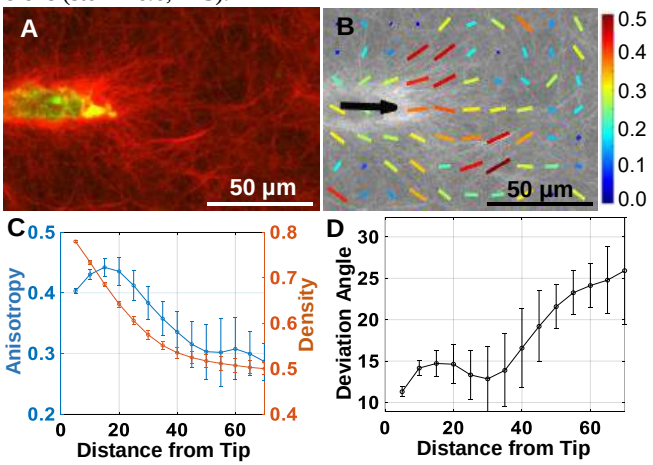

Figure 1. Distance of Influence. (A) Collagen fibril realignment (red) observed in front of a neovessel (green). (B) Collagen around the neovessel tip (grayscale image) with local direction and anisotropy (color). (C-D) Collagen microstructural data from 5 independent neovessels.

The preferred direction of the collagen microenvironment around a sprouting tip cell nearly coincided with the subsequent growth trajectory in 2 of the 5 examined time points. The errors were 10 and 9 degrees at hours 88 and 92, respectively (Fig 3). During this time, the neovessel made a course correction which followed the preferred directions (Fig 3). At hour 94, two filopodia extended from the neovessel tip, possibly contributing to the higher error observed (Fig 3). The average error between the preferred direction and growth trajectory was 17.1 degrees (std = 7.7, n = 5).

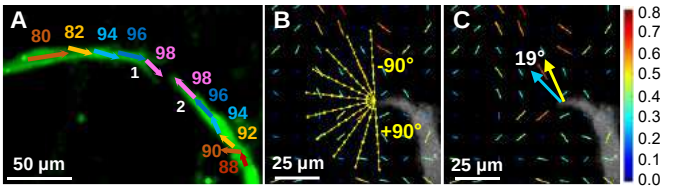

Figure 2. Neovessel Guidance Analysis. (A) Neovessels (green) with superimposed growth trajectories. The collagen microenvironment of neovessel 2 was analyzed. (B) Neovessel 2 at hour 90 (grayscale image) with local ECM directions and anisotropy (color). The discretized growth path (yellow lines) with the highest anisotropy was the preferred direction. (C) The preferred direction (yellow arrow) and growth trajectory (blue arrow) differed by 19 degrees.

DISCUSSION

Using measurements of the ECM anisotropy and density, we quantified the tip cell distance of influence to gain insights into the space from which neovessels sense mechanical cues from the ECM. In fibrous ECM constructs, Rudnicki et al. found that fibroblasts could sense stiff structures from distances over 65 microns [8]. We calculated our distance of influence as the distance over which tension-driven collagen realignment extended. Our distance of influence was more consistent with a study by Abhilash et al. [4]. They found that circular cells interacted via overlapping regions of tension-realigned collagen from distances up to 50 microns [4].

Analysis of time-series data revealed a relationship between the neovessel growth trajectory and the preferred direction of the collagen in the tip cell microenvironment. The larger difference observed between these directions at hour 94 could be due, in part, to the presence of two filopodia. Each presented a path with relatively high anisotropy, and the neovessel growth trajectory followed the filopodium path most oriented towards the nearby neovessel (Fig 3). Like Abhilash et al., we observed overlapping regions of tension-realigned collagen between the tip cells at hours 94 and 96 (Fig 3) [4]. Furthermore, the similarities between the growth trajectories and preferred directions of hours 88 and 92 indicate that that the collagen organization of the tip cell microenvironment contributed to neovessel guidance. Further work is needed to study neovessel guidance by the collagen microstructural organization to improve neovascularization at tissue interfaces.

ACKNOWLEDGEMENTS

Funding from NIH R01AR069297 and F31HL154781.

REFERENCES

[1] Rademakers T, et al, *J Tissue Eng Regen Med*, 13(10), 2019. [2] Strobel, A, et al, *Front Physiol*, 11, 2020. [3] Sieminksi, AL, et al, *Experimental Cell Research*, 297(2), 2004. [4] Abhilash AS, et al, *Biophysical J*, 107(8),2014. [5] Utzinger, U, et al, *Angiogenesis*, 18(3), 2015. [6] Hoying, JB, et al, *In Vitro Cell Dev Biology*, 32(7), 1996. [7] Marquez, JP, et al, *J Solids and Structures*, 43(21), 2006. [8] Rudnicki MS, et al, *Biophysical J*, 105(1), 2013.

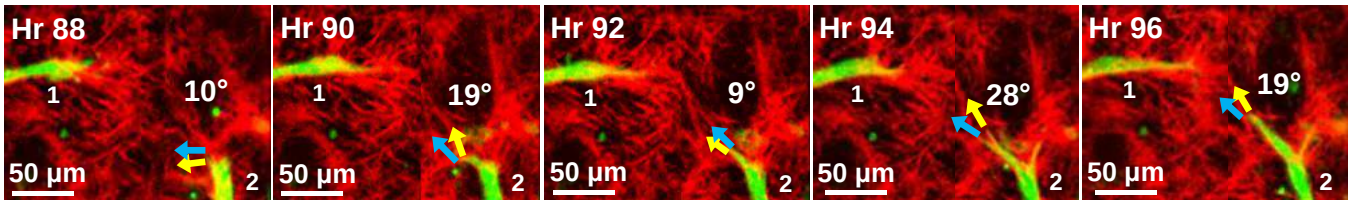

Figure 3. Neovessel Guidance. Comparison of the growth trajectory (blue arrow) and preferred direction (yellow arrow) for neovessel 2. The directions nearly coincided at hours 88 and 92. At hour 94, the neovessel follows the filopodium path most oriented toward neovessel 1. Regions of tension-realigned collagen extending from each neovessel tip overlap between hours 94 and 96.

MEASUREMENT OF MECHANICAL PROPERTIES OF IBERIAN RIBBED NEWT TENDON TOWARD ESTABLISHMENT OF COMPLETE TENDON REGENERATION MODEL

Fumiya Sato (1), Daisuke Suzuki (2), Toshinori Hayashi (3), Takeo Matsumoto (4), Eijiro Maeda (4)

(1) Biomechanics Laboratory, School of Engineering, Nagoya University, Nagoya, Aichi, Japan

(2) Hokkaido Chitose College of Rehabilitation, Chitose, Hokkaido, Japan

(3) Amphibian Research Center, Hiroshima University, Higashi-Hiroshima, Hiroshima, Japan

(4) Biomechanics Laboratory, Graduate School of Engineering, Nagoya University, Nagoya, Aichi, Japan

INTRODUCTION

Mammals such as human or mouse have little ability to regenerate body tissues completely, including tendons and ligaments. On the other hand, amphibians are well known for their remarkable ability to regenerate not only limbs, but also brain, spinal cord, or retina [1]. Therefore, amphibians may be used as the emerging experimental animals to study the mechanisms of the complete regeneration of tendons and ligaments in adult, and the findings would be useful as a roadmap for tendon and ligament regeneration in adult mammals. However, there have been no experimental model for tendon regeneration study of amphibians. In the present study, we aimed to develop a biomechanical study model of tendon regeneration using Iberian ribbed newt (*Pleurodeles waltl*) (Fig. 1) through microscopic observation of regenerated tendon and the establishment of tensile testing system for its functional analysis.

Fig. 1 Experimental model (*Pleurodeles waltl*, female)

METHODS

Animal model

Iberian ribbed newts (9-month-old, female) were purchased from Amphibian Research Center, Hiroshima University, and kept in a water chamber at room temperature in the laboratory. The following experiments were approved in the animal experiment committee of Nagoya University (#20-10). Six newts were used in this work. First, we tried to find which tendon is used for the regeneration study, and determined the digital flexor tendon (DFT) as an experimental material.

Tendon transection surgery

Two types of tendon transections were tested on DFT: partial transection and complete transection. The newt was anesthetized by placed in 0.2% MS-222 solution in water. A straight incision was made on the skin of the ventral side of the digit, and DFT was exposed. The animal, including DFT exposed and its surrounding tissues, was kept moist by dipping Holtfreter's (HF) solution. DFT was either transected half of the tendon width (Fig. 2), or transected completely (Fig. 3). The damaged tendon was returned to its original position, and the skin was closed but not sutured. The newt was kept in the chamber and normal activity was allowed for 6 weeks.

Biomechanical analysis of original DFT

We characterized the mechanical properties of unoperated original newt DFTs as the first step, using a custom-made tensile tester. After DFTs were isolated from newts under anesthesia, their cross-sectional area (CSA) was obtained. They were hung in a clear acrylic chamber filled with HF solution and rotated with a stepping motor, and a photograph of the front view of DFT was captured every 14.4° for 25 times. The width of DFT, measured with ImageJ (NIH), was used to reconstruct the cross-section of the tendon, from which the CSA was calculated.

Fig. 4 shows a schematic of the tensile testing system for newt DFT. The sample was maintained in a reservoir filled with HF solution during the test. A load cell of 5 N and a linear actuator were positioned on the both sides of the reservoir. The actuator was controlled by a LabVIEW program on a PC, which also collected the data from the load cell.

Tensile test was performed on a stereo microscope (M165FC, Leica), so that a movie of the test was recorded by its CCD camera.

To measure tissue strain, either nigrosine or microspheres (UVPMS-BO-1.00, Cospheric) was placed on the surface of the isolated DFT as strain markers. The specimen was held with acrylic jigs and attached to the load cell or the actuator. The specimen was stretched slowly until tensile load of 0.02 N was applied, at which the zero point was defined. This was followed by preconditioning between 0-1% of tensile strain at a rate of 0.17%/s 10 times. Finally, the sample was stretched at the same rate until rupture. Nominal stress was calculated by dividing the load by the CSA. Strain was calculated by the changes in the position of strain markers. Stress at rupture point was defined as tensile strength and elastic modulus was determined as a slope of the stress-strain curve between 20-60% of tensile strength.

Microscopic observation

At 6 weeks after the transection surgery, the animal was sacrificed and healing DFT was isolated. Cell nuclei were fluorescently stained with ethidium homodimer-Ⅲ (Nacalai Tesque). Multiphoton microscopy (A1RMP, Nikon) was performed to observe fluorescence of nuclei and second harmonic generation (SHG) of collagen of the DFT.

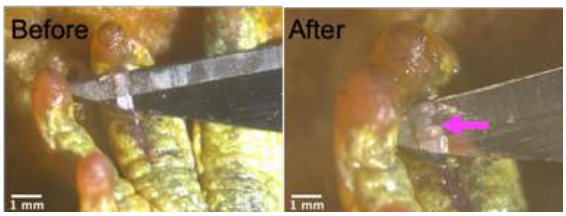

Fig. 2 Partial transection. Arrow indicates the transection.

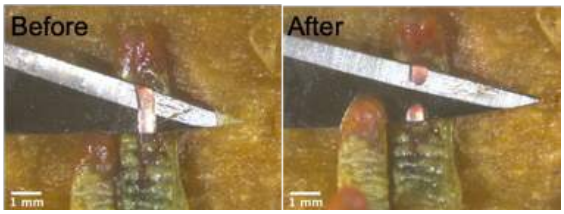

Fig. 3 Complete transection.

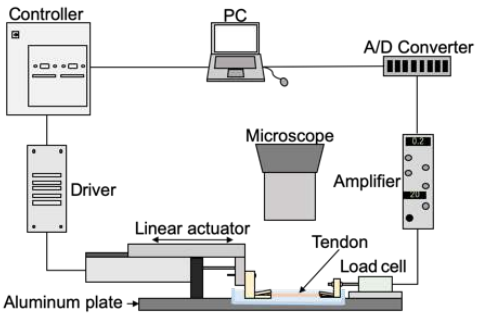

Fig. 4 Schematic of tensile testing system for newt DFT.

RESULTS AND DISCUSSION

Microscopic observation

Original DFT showed a robust SHG signal from the main body of the tendon, in which tendon cell nuclei were aligned longitudinally (Fig. 5(a)). In healing tendons, a similar pattern of SHG signal from collagen was observed at the site of transection in the partial transection model (Fig. 5(b)) as well as the complete transection model (Fig. 5(c)), suggesting that tendon-like collagen structure was regenerated.

Mechanical properties

Fig. 6 shows the stress-strain curves of three original DFTs obtained from two animals. Although there were some variations in tensile strength, tangent modulus and failure strain, these were relatively smaller than those reported in the literature determining mechanical properties of rabbit DFT [2]. Therefore, the variations observed here may present sample-related differences. Tensile strength (MPa), tangent modulus (MPa) and failure strain were 39.5 ± 7.79 (mean ± SD), 227 ± 64.8 and 0.285 ± 0.061, respectively. The strength and the modulus of the newt DFT were 34.7% and 64.7% lower, respectively, than those of rabbit DFTs, which may reflect the differences in the collagen types and/or intensity of animal activity.

In summary, tendon regeneration was suggested in newt DFT after 6 weeks of healing period and mechanical properties of original newt DFT were characterized. In future work, the comparison of mechanical properties between original and regenerated tendon will be performed.

ACKNOWLEDGEMENTS

This work was supported in part by JSPS KAKENHIs (18H03752 for TM and 20K21887 for EM).

REFERENCES

[1] Matsunami, M et al, *DNA Res*, 26 (3): 217-229, 2019.

[2] Chong, A et al, *Plast Reconstr Surg,* 123 (3):1759-1766, 2009.

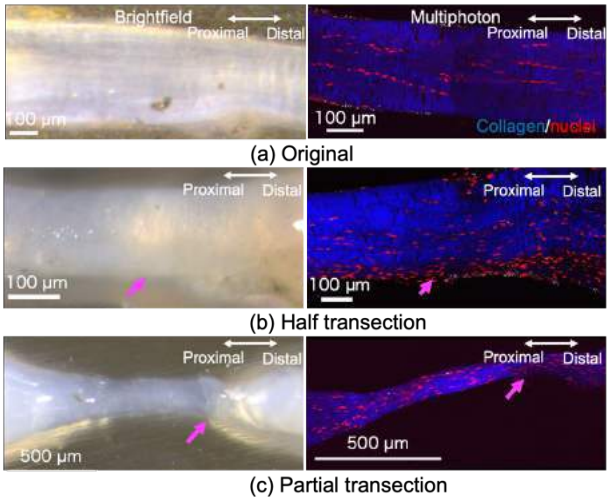

Fig. 5 Brightfield (left) and multiphoton (right) images of the original (a), the partial-transected (b), and the complete transected DFT (c). Arrows indicate the location of the injury.

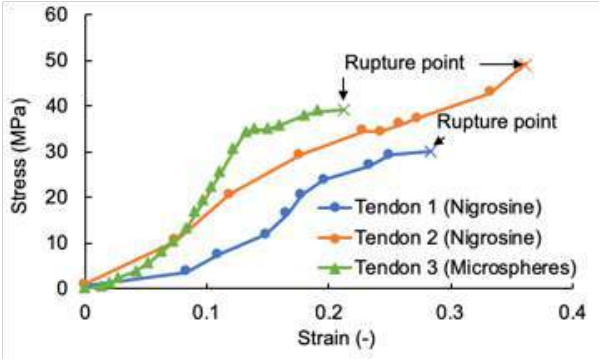

Fig. 6 Stress-strain curves of original newt DFTs.

THE RELATION BETWEEN CORTICAL THICKNESS AND MORPHOLOGY: A STUDY OF NONHUMAN PRIMATE BRAINS

Mia E. Hoffman (1,2), Nagehan Demirci (2), Maria A. Holland (1,2)

(1) Department of Mechanical Engineering
University of Notre Dame
Notre Dame, IN, United States

(2) Department of Bioengineering
University of Notre Dame
Notre Dame, IN, United States

INTRODUCTION

Previous research shows that the functioning of the brain is related to its structure and that mechanical forces are a significant factor in neural growth [1]. Atypical patterns in the thickness of the cerebral cortex, the outer layer of the brain, can be linked to Autism Spectrum Disorder, Alzheimer's disease, Williams syndrome, schizophrenia, and epilepsy [2-4].

In our previous work [5], we found that the gyral regions (on outer folds) are thicker than sulcal regions (in inner folds) in humans. This study showed that physical factors alone could produce the variations found in the gyral and sulcal regions during cortical folding without genetic factors at work. The purpose of the present study is to investigate the thickness of gyral and sulcal cortical areas across different primate species. If we consistently find thick gyri and thin sulci in other mammalian species, then it would support our previous findings and suggest that intrinsic mechanical forces are an important cause of cortical morphogenesis.

METHODS

To calculate the cortical thickness of the cerebral cortex, T1-weighted MRI scans were obtained from University of Utrecht [6] via the International Neuroimaging Data-Sharing Initiative's PRIMatE Data Exchange (INDI PRIME-DE) [7] database and the National Chimpanzee Brain Resource (NCBR) (supported by NIH grant NS092988). We manually segmented the MRI scans using BrainBox (Paris, France) into two masks: one of the entire brain and one of the cortex. After the manual segmentation process, we analyzed the morphology of the brain via our custom Python pipeline. First, a subtraction of the cortex from the complete brain mask resulted in a mask of the subcortex, which was visually validated and edited, as necessary. Next, the binary volumetric masks of the pial surface and the subcortical surface were converted to volumetric meshes using the Marching Cubes algorithm [8], which converts a three-dimensional binary matrix to a tessellated mesh by "marching" through the matrix to determine where there are borders between the ones and zeros.

The cortical thickness was then calculated for each node on the pial surface, or the outer surface of the cortex, as the three-dimensional Euclidean distance to the nearest neighbor on the cortex-subcortex interface.

$$d = \sqrt{(x_2 - x_1)^2 + (y_2 - y_1)^2 + (z_2 - z_1)^2} \quad (1)$$

The topography of the pial surface was then quantified. The gyrification index, or the ratio between the total surface area and the exposed surface area, was calculated as a measure of degree of folding which allows for comparisons between different brains [9]. The exposed surface area of the pial surface was approximated from an alpha shape of the brain's surface. The topography of an individual subject's brain was quantified by the mean curvature, where a positive mean curvature correlates with a gyrus and a negative value indicates a sulcus. These calculations utilize the surface area of the mesh, which is calculated using Heron's formula, and the neighborhood information from the mesh.

RESULTS

Over the course of the present study, we analyzed nine brains, each from a unique primate species (Table 1). The mean thicknesses were found by averaging all calculated cortical thicknesses for the subject. A distribution of the cortical thickness for each subject is shown in Figure 1. The relationship between curvature and the cortical distribution for the brain of *Macaca mulatta* is shown in Figure 2.

Table 1. The mean cortical thickness of the species represented in the present study. The brain volumes were calculated using the binary masks and voxel dimensions.

Common Name	Brain Volume (cm^3)	Mean Cortical Thickness (mm)
Grey Mouse Lemur	0.838	1.215
Prince Demidoff's Bushbaby	1.96	1.661
Squirrel Monkey	9.55	1.233
Ring Tailed Lemur	12.7	1.476
Mongoose Lemur	14.6	1.682
King Colobus	40.7	1.751
Brown Wooly Monkey	49.6	1.897
Green Monkey	53.9	1.436
Rhesus Macaque	78.6	2.127

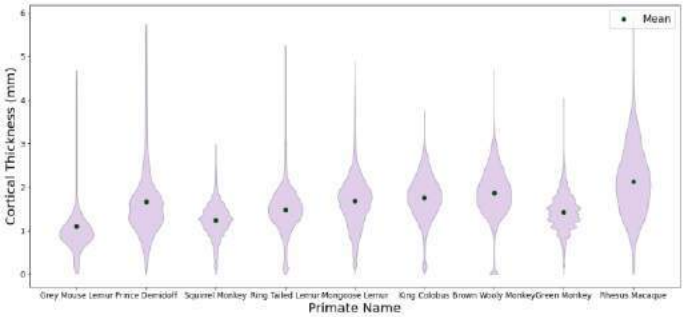

Figure 1. A violin plot of the cortical thickness for each primate where the x-axis is arranged in terms of increasing brain volume.

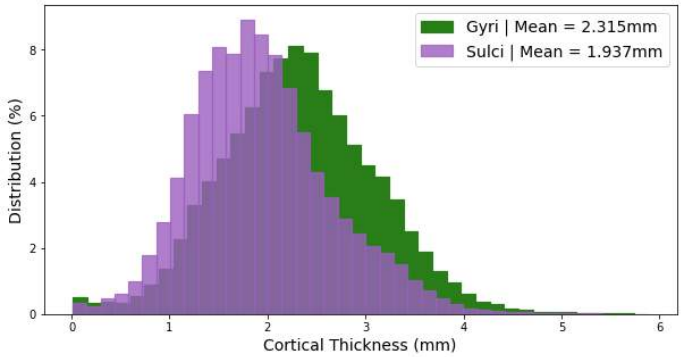

Figure 2. The cortical thickness distributions for the gyral and sulcal regions of a Rhesus Macaque brain, where the curvature differentiation is based on the mean curvature.

DISCUSSION

Figure 1 shows that the cortical thickness tends to increase with brain volume, which aligns with previously held knowledge. However, there are a few subjects for which this trend is not seen and the cause of this is being investigated to determine whether this reflects the true morphology of the subject or is due to an error in the analysis pipeline or manual segmentation.

Holland et al. 2018 [5] found that the gyri are universally thicker than the sulci in human brains. The results from this study here show that above a certain brain volume gyral regions are distinctly thicker than sulcal regions. Our current work has been unable to identify the exact threshold at which this distinction occurs, but it appears to happen between 50 cm^3 and 75 cm^3. A possible future investigation could be into the morphology that is necessary for this phenomenon to occur. This phenomenon may also be related to the degree of folding in the brain.

The work described in the current paper details the development of a Python pipeline that is capable of analyzing mammalian brains at large, human fetal brains, and disorders that result in atypical growth of the human brain, such as microcephaly and macrocephaly. Current automated and semi-automated methods of brain morphological analysis, such as FreeSurfer or AFNI, were developed to study the adult human brain using a brain atlas that helps to map brain regions to a common template. As such, these software are challenged when tasked with analyzing a brain of different morphology. The presently described pipeline of analysis tools aims to provide similar outputs of morphological markers as the human-focused software already in use. Future work will include a study of multiple individuals of the same species to establish standard cortical thicknesses for the species. The inclusion of multiple subjects of the same species will also serve to verify the findings in the present paper at large.

REFERENCES

[1] Goriely, A. et al. *Biomechanics and Modeling in Mechanobiology*, 14.5:931-965, 2015.
[2] Garcia, K., Kroenke C., and Bayly P. *Philosophical Transactions of the Royal Society B: Biological Sciences*, 373.1759, 2018.
[3] Hilgetag, C. and Barbas, H. *PLOS Computational Biology*, 2.3, 2006.
[4] Goriely, A. Budday S., and Kuhl E. *Advances in Applied Mechanics*, 48:79-139, 2015.
[5] Holland, M. et al. *Physical Review Letters*, 121.22:228002, 2018.
[6] Navarrete, A. et al. *Brain, Behavior and Evolution*, 91.2:109-117, 2018.
[7] Milham, M. et al. *Neuron*, 100.1: 61-74, 2018.
[8] Lewiner, T. et al. *Journal of Graphic Tools*, 2003.
[9] Zilles, K et al. "*Brain Behav Evol*, 34.3: 143–150, 1989.

Connexone: A Medical Application for Protection Against Opioid Overdose

Hirschel M. Nambiar

Food and Drug Administration, 10903 New Hampshire Ave, Silver Spring, MD 20993

INTRODUCTION

Opioids are a class of drugs that include the illegal drug heroin as well as powerful pain relievers available legally by prescription, such as oxycodone (OxyContin®), hydrocodone (Vicodin®), codeine, morphine, fentanyl, and many other substances. These drugs are related and interact with opioid receptors on nerve cells in the body and brain to produce pleasurable effect and relieve pain. Opioid overdose is the leading cause of accidental death. Opioid addiction is driving this epidemic. In the US in 2015, there were 52,404 deaths due to opioid abuse which is higher than car crash deaths or gun violence deaths. In the world, almost 207,000 die due to opioid overdose. Nearly 14% high school students use opioid and that is a large number. In Maryland there were 1,259 deaths due to opioid in 2015 and 2,000 deaths in 2016. So opioid overdose now ranks with cancer, stroke, and heart attack among top killers in MD. CDC data clearly show that opioid use is increased among most demographic groups and death rate is also increasing. The main problem is that after overdosing, on an average, 911 is called only 33% (range 10-56%) of the time due to the fear of arrest. The healthcare costs for treating victims are almost 37 billion dollars per year.

I developed a smart lifesaving medical app for opioid, drugs, and substance abuse, called as Connexone. The novel medical app Connexone has features to get help for opioid overdosed victims with a press of a button and much faster than 911 responders. It can also identify the closest naloxone carrier for treatment.

METHODS

After brainstorming the ideas to develop a medical app for protection against opioid overdose, I narrowed down the key features of the app to include a large button in the center for an emergency use. The large help button can make it easier to press once the person is intoxicated (Figure 1). When that is pressed, it triggers other essential features. Including three emergency contact information of the opioid user in the app can alert them once the button is pressed. The press of the help button will alert the three emergency contacts who can come and help the victim. The press of the help button can also trigger a 911 call.

Another important feature of the App included the connection to GPS for identifying location of the victim. The GPS system can also help to identify the closest opioid antidote, naloxone carrier and needle exchange place to obtain the treatment immediately.

I used MIT App Inventor and Java Eclipse to code for the Medical App. After few trial and error, I could design and develop a functional app. This smart lifesaving Mobile Medical App, called as Connexone, can help to solve a current national crisis and major public health issue.

RESULTS

The prototype of the app was functional, and testing did show that it alerts the three pre-considered contacts without any failure. The app also helps to identify the nearest naloxone (opioid antidote) carrier while informing the closest 3 people

identified earlier by the overdose victim to come and administer the drug.

To implement this overdose response, a program is developed with the certified Naloxone carrier. The app notifies the Naloxone career and emergency contacts by SMS messaging. Finally, it contacts the 911 as backup.

The app also has information on opioid. Legal information is also provided. States with Good Samaritan Laws protects the caller or victim from arrest or prosecution for possession and under influence.

Figure 1 Connexone Key App Features

DISCUSSION

I have developed a smart lifesaving app for opioid, drugs, and substance abuse, called as Connexone. Opioids are a class of drugs that include the illegal drug heroin as well as powerful pain relievers available legally by prescription, such as oxycodone (OxyContin®), hydrocodone (Vicodin®), codeine, morphine, fentanyl, and many other substances.

These drugs are related and interact with opioid receptors on nerve cells in the body and brain to produce pleasurable effect and relieve pain. Addition is a chronic brain disease characterized by pursuing substance abuse and dangerous behaviors.

Opioid addiction and overdose are the leading causes of accidental death. Since very few people call the 911 after an overdose, a method such as Connexone app is required to protect these victims. By the switch of a button the app can perform many features to protect an overdose victim. The app also provides legal information to protect the victim from arrest or prosecution for possession or under influence.

My next step is to include coverage for other drugs and make it accessible to consumers.

ACKNOWLEDGEMENTS

Food and Drug Administration for supporting this research work as a part of the digital health program.

REFERENCES

1. Boyer, Edward W., M.D., Ph.D. *PubMed Central*. Web. 29 July 2016.

EFFECT OF STRESS-FIBER CONTRACTION ON THE 3D SHAPE OF THE AORTIC HEART VALVE INTERSTITIAL CELL

Quan Nguyen, Alex Khang, Xinzeng Feng, Michael S. Sacks

James T. Willerson Center for Cardiovascular Modeling and Simulation
The Oden Institute for Computational Engineering and Sciences and the Depart of Biomedical Engineering
The University of Texas at Austin
Austin, TX, USA

INTRODUCTION

Calcification of the aortic valve (AV) affects leaflet stiffness, typically preventing the AV from opening completely. The main treatment for calcific AV disease (CAVD) is valve replacement with prostheses, which continues to suffer from limited durability. Currently, there are no pharmaceutical approaches for CAVD, in part due to our lack of understanding of the role of AV interstitial cells (AVIC). AVICs are known to undergo phenotypic activation in periods of growth or disease. This can result in changes in shape, increases in overall contractility due to expression of alpha smooth muscle actin stress fibers, and lead to an increase in collagen production and matrix remodeling. While it is widely accepted that cell shape is intimately connected to cell function; we have little understanding on how AVIC shape regulates mechanical function. In this study, we quantify the 3D shape of AVICs locally and globally.

METHODS

3D Traction Force Microscopy. 3D traction force microscopy was used to obtain AVIC surfaces. AVICs and fluorescent tracking beads were imbedded within poly (ethylene glycol) hydrogel (PEG) and incubated for 3 days. For the normal state, AVICs were treated with Tyrode's Salt solution. After 40 minutes, we took an image stack of a single AVIC and the surrounding beads. AVICs were then treated with Cytochalasin D for 40 minutes to reach their inactive state. We took a second image stack of the same field of view. To obtain surface meshes of AVICs in their normal and inactive state, we analyzed the image using out custom software FM-track [1].

Local curvatures of AVIC surface. To obtain a quantitative descriptor of the local shape, AVIC local curvatures were computed through a surface patching method [2,3]. First, the method defines a center node and obtains a patch of nodes surrounding the center node. Since the global x, y, z system does not provide a single-valued function, a local coordinate system u, v, n is defined. The local surface curvature of AVIC was described with a reduced biquadric surface

$$S(u,v) = au^2 + 2buv + cv^2, \quad (1)$$

where a, b, and c are fit constants. With the fit constants, the local principal major curvature, k1, and principal minor curvature, k2, were computed [2,4]. This is iterated across all nodes on the surface mesh.

$$k_1 = \mathrm{a} + \mathrm{c} - \sqrt{(a-c)^2 + 4b^2} \quad (2)$$

$$k_2 = \mathrm{a} + \mathrm{c} + \sqrt{(a-c)^2 + 4b^2}. \quad (3)$$

Global shape of AVIC. To analyze the global shape of AVIC, we used Spherical Harmonics (SPHARM) [5,6]. AVIC surface is parameterized onto a unit sphere using a one-to-one mapping to minimize distortion. The mapping results in the transformation from cartesian to spherical coordinates $[\mathrm{x}(\theta,\varphi), \mathrm{y}(\theta,\varphi), \mathrm{z}(\theta,\varphi)]$. The resulting parameters can be expressed with respect to the SPHARM basis function

$$Y_l^m(\theta,\varphi) = \sqrt{\frac{(2l+1)(l-m)!}{4\pi(l+m)!}} P_l^m(cos\theta) e^{im\varphi}, \quad (4)$$

where l and m are the degree and order of SPHARM, and $P_l^m(cos\theta)$ is the following Legendre polynomials

$$P_l^m(x) = \frac{(-1)^m}{(2^l l!)} (1+x^2)^{\frac{m}{2}} \frac{d^{l+m}}{dx^{l+m}} (x^2-1)^l. \quad (5)$$

The SPHARM expansion of the parameterized surface is as follow:

$$\mathbf{v}(\theta,\phi) = \sum_{\mathrm{l}=0}^{L_{max}} \sum_{\mathrm{m}=-\mathrm{l}}^{\mathrm{l}} \mathbf{c}_{\mathrm{l}}^{\mathrm{m}} \mathrm{Y}_{\mathrm{l}}^{\mathrm{m}}(\theta,\phi), \quad (6)$$

where $\mathbf{v}(\theta,\phi) = (\mathrm{x}(\theta,\phi), \mathrm{y}(\theta,\phi), \mathrm{z}(\theta,\phi))^T$, $\mathbf{c}_{\mathrm{l}}^{\mathrm{m}} = (\mathbf{c}_{\mathrm{xl}}^{\mathrm{m}}, \mathbf{c}_{\mathrm{yl}}^{\mathrm{m}}, \mathbf{c}_{\mathrm{zl}}^{\mathrm{m}})^T$ are the SPHARM coefficients. Using a SPHARM software adapted from Shen et al. [6], we can input a maximum degree L_{max} to calculate the

SPHARM coefficients. The power spectra of AVIC can be created by plotting its coefficients against the degrees and orders.

RESULTS

The major principal curvature is a sensitive descriptor of AVIC shape. The magnitude of k_1 (0.01 to 4.92 μm^{-1}) is larger than that of k_2 (-0.98 to 0.89 μm^{-1}) (Fig. 1). Since the values of k2 are miniscule, k_1 can be used to analyze the shape of AVIC.

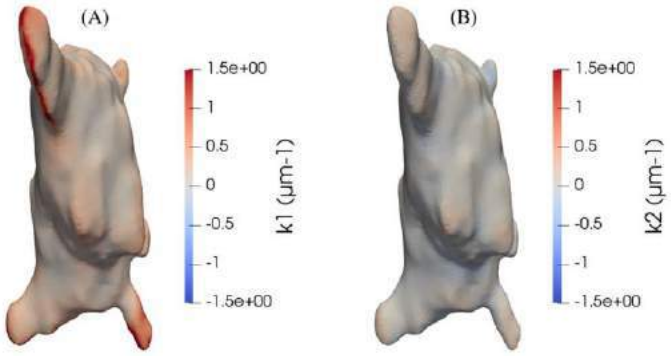

Figure 1: (A) Major principal curvature k_1. (B) Minor principal curvature k_2 for a reconstructed AVIC surface (normal state).

AVIC protrusions have higher k1 values than k2 which suggests that they are cylinder-like (Fig. 1).

As the harmonic degree increases, precision of AVIC fitting increases. An AVIC surface mesh is reconstructed with SPHARM (Fig. 2). A harmonic degree of 47 produces a surface mesh with a mean-squared error of 0.0532 μm^2 relative to the original mesh.

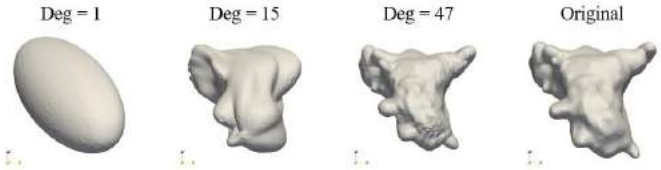

Figure 2: An AVIC surface mesh reconstructed in SPHARM, from degree 1 to degree 47.

AVIC contracts going from its inactive to normal state. The difference between an AVIC inactive and normal state shows mostly contraction (Fig. 3).

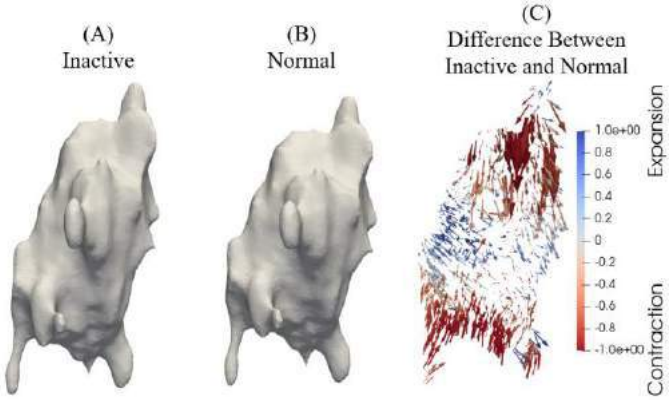

Figure 3: (A) An AVIC inactive state. (B) An AVIC normal state. (C) The difference between inactive and normal state.

Inactive cells are more spherical than normal cells. The SPHARM coefficients for an AVIC's inactive state are much larger than that of the normal state (Fig. 4). A positive difference between the two states suggests that the cell becomes more spherical as it contracts.

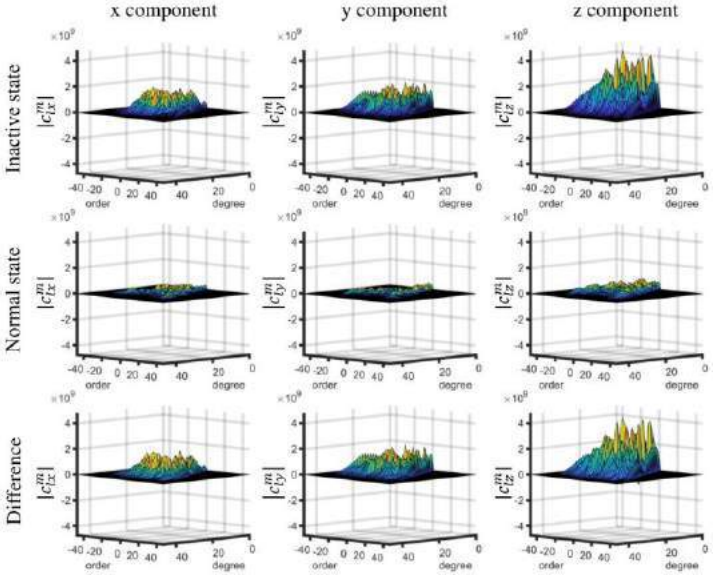

Figure 4: The power spectra of an AVIC in its inactive state, normal state, and the difference between the states. The inactive state power spectrum has higher SPHARM coefficients (0 to 4.71×10^9) compared to the normal state (0 to 6.33×10^7). This results in a positive difference.

DISCUSSION

In this study, we assessed the global shape and local curvatures of AVICs in several states. By displaying the major and minor principal curvatures visually onto the surface mesh, we observed that the major principal curvature is significantly larger and therefore more useful for understanding the shape of the cells. We report that k1 >> k2, particularly at protrusions, which suggests that AVIC protrusions are cylinder-like. When AVICs transition from the inactive to normal state, the cell contracts, wherein the AVIC becomes more spherical overall, and contracts the greatest at its protrusions. Overall, our results suggest that AVIC shape and contractile behaviors are intimately linked. Future work is focused on relating these contraction patterns to 3D subcellular structures through finite element modeling.

ACKNOWLEDGEMENTS

NSF-GRFP grant no. DGE-1610403, NIH grant no. F31HL154654, NIH grant no. R01 HL142504.

REFERENCES

[1] Lejeune, E et al., *Software X*, 2019.
[2] Sacks, M et al., *Ann Biomed Eng.* 21:263-275, 1993.
[3] Sander, P et al., *TPAMI.* 12:833-854, 1990.
[4] Pedregosa, F et al., *J. Mach. Learn. Res.* 12:2825-2830, 2011.
[5] Brechbühler, CH et al., *Comput Vis Image Und*, 61:154-170, 1995.
[6] Shen, L et al., *Evolution*, 63:1003-1016, 2009.

ANALYSIS OF BOUNDARY CONDITIONS IN NUMERICAL ASSESSMENT OF PARAVALULAR LEAKAGE IN TRANSCATHETHER AORTIC VALVE REPLACEMENT

Kyra M. Halbert-Elliott (1), Zhenglun A. Wei (1,2), Huang Chen (1), Sri Krishna Sivakumar **(1)**, Breandan A Yeats **(1), Ajit P. Yoganathan (1), Prasad Dasi (1)**

(1) Wallace H. Coulter School of Biomedical Engineering, Georgia Institute of Technology, Atlanta, GA, USA

(2) Department of Biomedical Engineering University of Massachusetts Lowell Lowell, MA, US

INTRODUCTION

Transcatheter aortic valve replacement (TAVR) is a less invasive alternative to surgical aortic valve replacement (SAVR), principally preferred in patients considered high risk for open heart surgery [1, 2]. Though general outcomes for TAVR are promising, complications - including paravalvular leakage (PVL), aortic rupture, and coronary occlusion - have hindered the expansion of TAVR to wider swaths of patients seeking treatment for aortic stenosis [3].

The use of finite element analysis (FEA) in combination with computational fluid dynamics (CFD) has proved invaluable in advancing TAVR surgical planning, enabling investigation of potential outcomes and means of maximizing beneficence for patients. Previous papers have illustrated the utility of FEA and CFD in modelling TAVR deployment on potential root rupture [4], leaflet calcium displacement [5], and PVL [6].

However, there is no consensus on numerical settings on the FEA and CFD in TAVR modeling. We focused on CFD for studying PVL and found that previous studies employed various boundary conditions (BCs). For example, many studies have used a constant pressure gradient (dP), principally 32 mmHg [6-8] or 90 mmHg [9], in their PVL simulations and provided little physiological justifications. Recently, pulsatile pressure waveforms were prepared from post-TAVR readings in patients' aorta and left ventricle [10]. Though pulsatile BCs are more physiological, they demand more computational time and may not fit the timeline of interventional planning for TAVR.

Therefore, it is worth exploring the impact of using different BCs in TAVR simulation. This study conducts a CFD simulation to investigate the impact of BCs on PVL severity.

METHODS

This study will retrospectively include 15 patients from Cardiovascular Fluid Mechanic Lab's TAVR database, all of whom received 26-mm Edwards Sapien valve and were classified as exhibiting (1) No, (2), Mild, or (3) Moderate PVL. This retrospective, deidentified data analysis was approved by the Georgia Institute of Technology Institutional Review Board ("Transcatheter Heart Valve Imaging and Hemodynamics"). Written informed consent was obtained through the Cedars Sinai Institutional Review Board-approved study.

ITK-Snap was used to segment each patient's aorta, left ventricle, calcifications, and stent from post-deployment CT scans at end-systole with a semi-automatic snake algorithm. Segmentations were further refined manually. The stent and balloon delivery system were constructed from in-house μ-CT scans of a 26 mm Edwards Sapien 3 and Commander Delivery System (Edwards LifeSciences). Mimics was employed to refine the geometry and prepare computational meshes. ABAQUS\Explicit was used to conduct FEA to simulate the valve deployment. The deployment parameters, including deployment angle and depth, were adjusted iteratively until the absolute value of error between the FEA stent and CT stent was less than or equal to twice the stent thickness (approximately 1 mm). Ref 11 further details the FEA simulation methods.

The geometry of the aorta, calcifications, and stent post-deployment were exported from ABAQUS to Mimics for the generation of CFD mesh. The exterior of the stent was sealed to account for the accompanying skirt and native leaflets covering the stent. The left ventricle side of the aortic valve was also sealed to model the effect of the stent leaflets. The calcifications and stent were then merged and exported, along with the aorta geometry, to ANSYS Fluent,which was later used for CFD simulation.

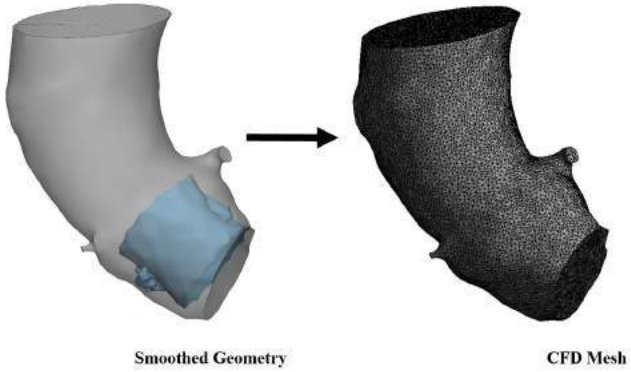

Figure 1: Aorta, Calcifications, and Implanted Stent

Examined BCs inlcude constant dP = 32 mmHg, 63 mmHg and 90 mmHg, as well as time varying dP, as shown in Fig. 2. It is worth noting that the constant dP = 63 is the maximum pressure gradient between the Aorta and LV during diastole in the time-varying dP waveform.

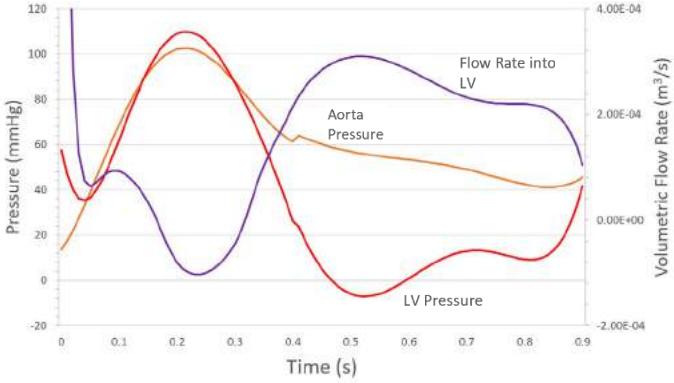

Figure 2: Time-Varying dP and corresponding VFR

Volumetric flow rate (VFR) across the left ventricle end of the aorta was calculated to estimate PVL volume. In pulsatile cases, VFR was integrated across diastole to obtain a time-averaged PVL regurgitation volume.

RESULTS

Fig. 3 tabulates the PVL volume comparison for a sample case between using different BCs. Fig. 4 shows corresponding flow fields. Average regurgitant volume was 63.19% greater in the steady 90 mmHg case than in the pulsatile pressure gradient case (Fig. 3). Streamlines (Fig. 4) showed stark differences in velocity at the LV end of the stent and at the LV-aortic root interface, and that the pressure gradient reversed flow throughout the aorta, not just at the LV-aortic root interface. The remaining cases will be segmented, implanted, and modelled with both pulsatile and steady flow boundary conditions.

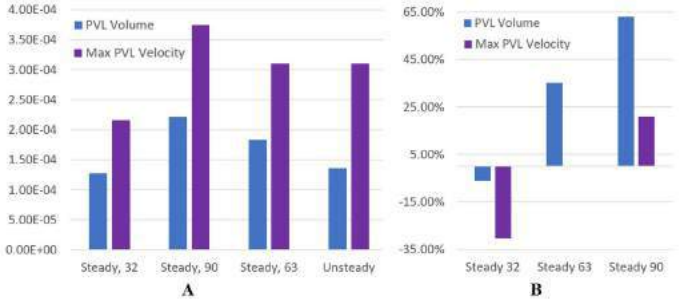

Figure 3: (a) Effect of boundary conditions on PVL volume (m^3) and maximum PVL velocity (m/s) (b) percent difference with respect to unsteady

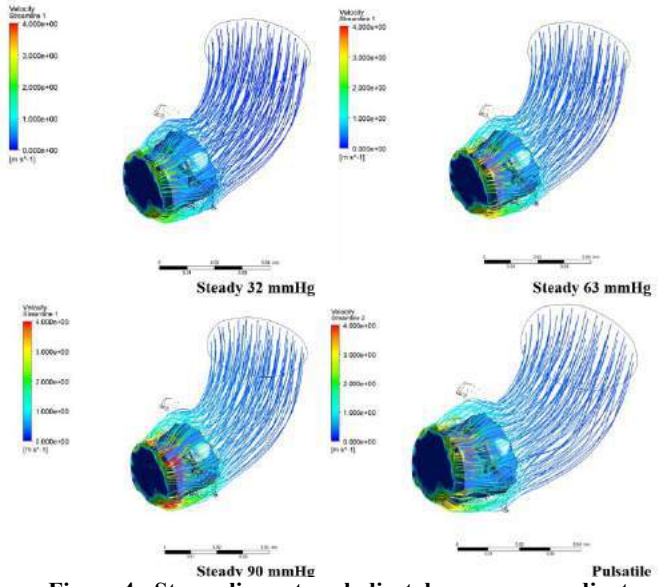

Figure 4: Streamlines at peak diastole pressure gradient

DISCUSSION

The results of the sample case shows that using different BCs has considerable impact on the PVL volume. It may affect shear stress, and other hemodynamics considerations impact clinical decision making. Once we finish CFD simulation for other cases, we will examine the effect of using different BCs on determine the PVL severity (No, Mild, or Moderate PVL).

The authors acknowledge that the Sapien valve leaflets were not included in the simulation. As every case must be consistent, this limitation should not affect the finding of this study.

ACKNOWLEDGEMENTS

The authors acknowledge the use of ANSYS products, which were provided through Academic Partnerships provided by ANSYS, Inc.

REFERENCES

1. Cribier, A., et al., Circulation, 2002. **106**(24): p. 3006-3008.
2. Cribier, A., Glob Cardiol Sci Pract, 2016. **2016**(4): p. e201632.
3. Genereux, P., et al., European Heart Journal, 2012. **33**(19): p. 2388-+.
4. Wang, Q., et al., Biomech Model Mechanobiol, 2015. **14**(1): p. 29-38.
5. Schultz, C., et al., EuroIntervention, 2016. **11**(9): p. 1044-52.
6. Bianchi, M., et al., Biomech Model Mechanobiol, 2019. **18**(2): p. 435-451.
7. de Jaegere, P., et al., JACC Cardiovasc Interv, 2016. **9**(5): p. 508-12.
8. Dowling, C., et al., Circ Cardiovasc Imaging, 2019. **12**(10): p. e009178.
9. Lavon, K., et al., Med Biol Eng Comput, 2019. **57**(10): p. 2129-2143.
10. Sinning, J.M., et al., Journal of the American College of Cardiology, 2013. **62**(1): p. 11-20.
11. Halbert-Elliott, K., et al., Presented at BMES, 2020.

INTERACTIVE PROGRAM DEVELOPMENT FOR ANALYSIS OF HEMODYNAMIC DATA IN PATIENTS WITH PULMONARY HYPERTENSION

Jordan M. Elliott (1), Franz P. Rischard (2), Rebecca R. Vanderpool (3)

(1) Biomedical Engineering
University of Arizona
Tucson, Arizona, United States

(2) Division of Pulmonary, Allergy, Critical Care and Sleep Medicine
University of Arizona
Tucson, Arizona, United States

(3) Biomedical Engineering
University of Arizona
Tucson, Arizona, United States

INTRODUCTION

Right heart catheterization (RHC) is a clinical procedure to measure pulmonary hemodynamic data such as the mPAP mean pulmonary arterial pressure (mPAP), wedge pressure (PW), and cardiac output (CO). In an invasive cardiopulmonary exercise test (iCPET), pulmonary hemodynamics are measured at different workloads. Alpha distensibility, which is a measure of resistance vessel stiffness, is determined from multi-beat exercise pulmonary pressure and flow plots. Alpha distensibility associates with the severity of the clinical outcomes for patients with PAH. Calculation of alpha distensibility requires fitting a non-linear equation to pressure-flow data that can be difficult in clinical settings. The aims of this project were to 1)investigate changes in alpha distensibility from pressure-flow plots in repeat RHCs and 2)develop an interactive application to standardize the analysis of exercise pulmonary hemodynamic data

METHODS

Participants with repeat exercise RHCs and PAH were identified from the University of Arizona (UA) PH Registry (n = 30). Resting and exercise hemodynamics were included in the analysis. Alpha distensibility (α) was computed from exercise pressure-flow plots using the Linehan model [1]:

Linehan Model

$$\mathrm{mPAP} = \left([(1 + \alpha * \mathrm{PW})^5 + \alpha \mathrm{R_0 CO}]^{(1/5)} - 1\right)/\alpha \qquad (1)$$

where mean PA pressure (mPAP) is a function of pulmonary artery wedge pressure (PW), cardiac output (CO), total resting resistance (R_0) and α distensibility. Alpha distensibility is a measure of the percent change in vessel diameter per mmHg increase in pressure. Total Pulmonary Resistance (TPR) was calculated using the ratio of mPAP and CO(Eq. 2)

TPR Equation

$$\mathrm{TPR} = \mathrm{mPAP}/\mathrm{CO} \qquad (2)$$

Statistical Analysis: A p-value < 0.05 was considered significant. A two way ANOVA test with repeated measures was performed to compare the effects of visit and exercise on the mPAP, CO and TPR values. A TukeyHSD test was used to test pairwise comparisons. A paired t-test was performed to assess significant change in the alpha values between visit 1 and visit 2.

Development of Python Based GUI analysis Program:

A Python based GUI program was developed to expand the capabilities as well as improve the speed of analysis compared to the Matlab-based prototype. Requirements for the program included the ability to 1) generate pressure-flow plots from the RHC exercise data, 2) run the analysis to return the α distensibility and Pulmonary Vascular Resistance (PVR) values, and 3) generate a report (pdf) of the graphical outputs and corresponding data tables (csv) for later reference.

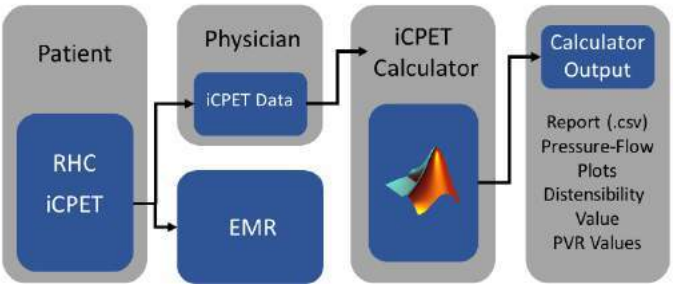

Figure 1: Data workflow from RHC pressure measurements to analysis outputs.

RESULTS

RHC Exercise Data Analysis:

Data from the UA PH Registry (n=30) was analyzed using a custom MATLAB Program to generate pressure-flow plots and calculate the α values for each exercise RHC. Exercise increased mPAP, cardiac output but had no effect on TPR at both the first and second visit (**Figure 2**). Resting mPAP decreased at visit 2 (55 ± 24 mmHg vs 62 ± 23 mmHg, p = 0.0002) but there was no significant change in cardiac output between visits (9.8 ± 3.1 L/min vs. 9.4 ± 4.3 L/min, p = 0.35) . Resting TPR decreased at visit 2 (5.9±3.1 mmg*min/L vs 7.4±5.5 mmg*min/L, p = 0.006). The alpha distensibility values were analyzed between the two visits and the median at visit one was 0.17± 0.27 and 0.2 ± .43 at visit two.

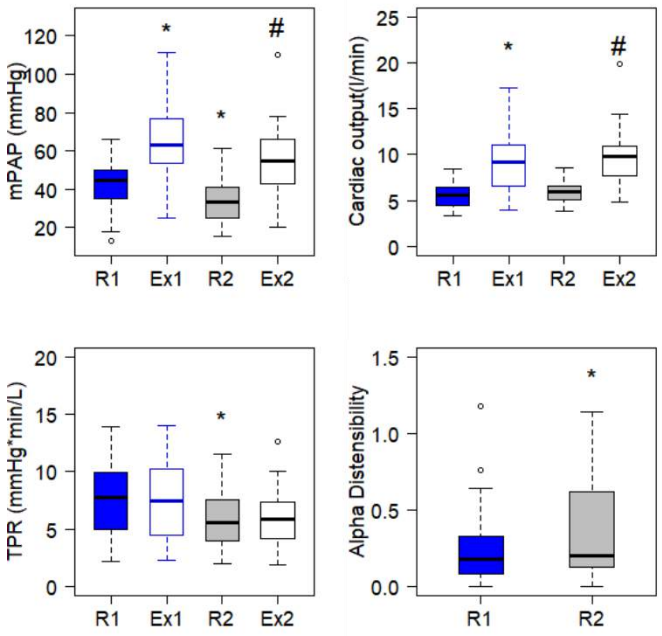

Figure 2: RHC hemodynamics data at rest (R1 and R2) and peak exercise (Ex 1 and Ex 2) for both visits. *p< 0.05 vs R1 and # p<0.05 vs R2

Python GUI Development

The Python program is capable of generating the pressure-flow plots as well as determining the PVR and α distensibility values. In initial testing, the Python program is capable of generating the same outputs as the MATLAB prototype.

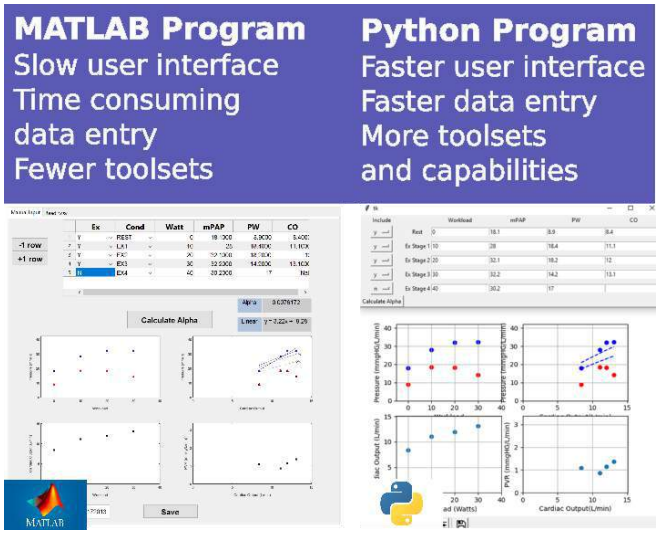

Figure 3: Side by side comparison of the Matlab (left) and Python (right) interfaces.

DISCUSSION

Pulmonary Hypertension (PH) is higher than normal blood pressure in the vessels in the heart and lungs. In pulmonary arterial hypertension (PAH) there is a narrowing of pre-capillary pulmonary blood vessels. As a result, the flow of blood is slowed through the lungs and the blood pressure is increased in the pulmonary arteries and vessels that results in increased pressure, resistance, and vascular stiffness. In response to increased pressure, the right ventricle has to work harder and eventually leads to impaired right ventricular (RV) function and eventually heart failure (HF). In analysis of the RHC exercise data in patients with PAH, there was a significant decrease in mPAP and TPR between the two visits. This indicates the values for visit two are closer to normal range, indicating a decrease in severity. The normal range for the CO is 4 - 8 L/min, both the average CO for visit one and visit two were higher than this range, likely due to the higher mPAP, however there was no significant change in CO at each visit. The analysis also showed a significant increase the α values for each visit, indicating a larger increase in vessel diameter in response to pressure, which could indicate decreased vessel stiffness.

ACKNOWLEDGEMENTS

This research was supported by a Sarver Heart grant from the Archie Clifford and Clara Mabel Rentfrow Heart Disease Fund and Mark and Emma Schiffman Research Fund.

REFERENCES

[1] Linehan, J et al., J Appl Physiol, 73(3):987-94 1192.

RAMAN NEEDLE ARTHROSCOPY TOWARDS IN VIVO MONITORING OF ENGINEERED CARTILAGE GROWTH

Juncheng Zhang (1), Tianbai Wang (1), Magnus Jensen (2), Mark W. Grinstaff (1), Brian D. Snyder (1), Mads S. Bergholt (2), Michael B. Albro (1)

(1) College of Engineering
Boston University
Boston, MA USA

(2) Department of Craniofacial Development & Stem Cell Biology
Kings College London
London, UK

INTRODUCTION

Cartilage tissue engineering (TE) is a promising osteoarthritis treatment strategy whereby cellularized tissue constructs are surgically implanted into cartilage defect sites to promote the generation of hyaline cartilage repair tissue. In current clinical practice, implanted autologous chondrocyte-seeded scaffolds begin to synthesize and elaborate a cartilaginous extracellular matrix (ECM) with the aim of recapitulating the functional mechanical properties required for long-term survival [1]. To date, clinical TE platforms have had limited success, encumbered by fibrocartilage formation and eventual tissue failure. This has led to expansive efforts in recent years to improve clinical outcomes through optimization of cell sources, cell expansion protocols, scaffold biomaterials, and delivered anabolic growth factors agents. However, a major hurdle in the field remains the lack of diagnostic platforms to monitor the growth and stability of implanted engineered tissues *in vivo*. Conventional imaging platforms (e.g., radiographs, CT, MRI) possess poor resolution of cartilage composition assessments, thus limiting the ability to assess the efficacy of TE novel platforms in clinical trials and to monitor regeneration in individual patients.

Raman spectroscopy is an inelastic light scattering technique that provides an optical fingerprint of a tissue specimen that reflects specific molecular building blocks (amides, sulfates, carboxylic acids, hydroxyls) [2]. As such, it has the potential to monitor the composition of engineered cartilage tissues with an exceptional specificity and accuracy. In our recent work, we developed a novel needle-based Raman arthroscopic probe capable of performing intra-articular assessments of articular cartilage composition for diagnostics of degeneration during osteoarthritis [3,4]. Results demonstrated that this platform in conjunction with spectral multivariate analytical models can assess cartilage GAG depletion, swelling, and collagen alignment loss with outstanding accuracy. In the current study, we aim to advance Raman arthroscopy as a novel platform for monitoring the growth of engineered cartilage *in vivo*. Towards this goal, we perform an initial assessment of this platform *ex vivo* by assessing the capability of our Raman arthroscopic probe and spectral analysis to predict the mechanical and biochemical property changes of engineered cartilage constructs during growth in culture. Here we analyze the growth of bovine chondrocyte-seeded agarose constructs with and without growth factor supplementation at different time points to serve as a model system to examine the platform's diagnostic potential.

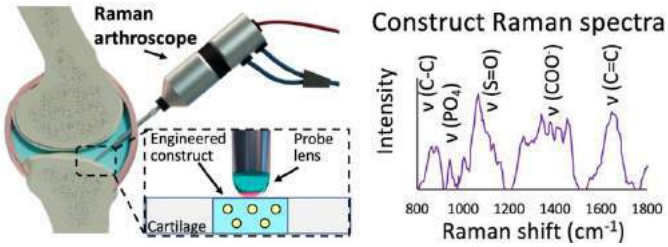

Fig 1: Raman needle arthroscopy platform for intra-articular monitoring of engineered cartilage construct growth *in vivo*.

METHODS

Raman probe: Our custom Raman needle arthroscope was designed for intra-articular entry through a hypodermic needle (Fig.1), consisting of an NIR diode laser (λ_{ex}=785nm, 500mW, B&W Tek) and a fiber-coupled spectrograph (QEPro, Ocean Optics). Laser light is directed through the distal part of the probe and through the needle

probe (ø=2mm, l=50mm), and tightly focused onto the tissue using a 2.0mm sapphire ball lens that achieves a 250μm depth of penetration into the tissue [4].

Tissue constructs: Immature bovine chondrocytes were encapsulated in 2% agarose hydrogel scaffolds at a density of $45x10^6$ cells per mL. Cell seeded constructs (∅4×2mm) were cultured for up to 56 days in high glucose DMEM supplemented with ITS+ premix, dexamethasone, L-proline, antibiotic-antimycotic, ascorbate, and with or without 10ng/mL TGF-β3 for the initial two weeks of culture [5]. **Raman analysis:** After 0, 14, 28, 42, and 56 days of culture, Raman spectra of constructs were acquired (n=4 constructs per each TGF-β group/time point). Raman spectra in the fingerprint range (800-1800 cm^{-1}) were collected and preprocessed, as described [3], and subjected to multivariate linear regression, using the following model:

$$\boldsymbol{Cartilage_{spectra}} = GAG_{score} * \boldsymbol{(GAG_{REF})} + COL_{score} * \boldsymbol{(COL_{REF})} + H_2O_{score} * \boldsymbol{(H_2O_{REF})} + Agarose_{score} * \boldsymbol{(Agarose_{REF})},$$

where GAG_{REF}, COL_{REF}, H_2O_{REF} , $Agarose_{REF}$ are the component spectra of purified reference chemicals (GAG [chondroitin-6-sulfate; Shark cartilage], collagen [type-II; chicken sternal cartilage], water [PBS], agarose [type-VII]) used to extract the corresponding regression coefficient or "score" that reflects the contribution of the spectra of each constituent element [3]. **Mechanical/biochemical analysis**: Following Raman analysis, constructs were analyzed for their equilibrium compressive modulus (E_Y) and GAG content (DMMB assay) [5].

RESULTS

Table 1: Mean values of Raman multivariate regression coefficients (scores) and property measures of construct groups.

		Raman scores				Property Measures		
TGF-β [ng/mL]	Day	Agarose	GAG	COL	H_2O	GAG [%ww]	H_2O [%ww]	E_Y [kPa]
NA	0	0.59	0.01	0.14	0.35	0.3	96.0	3.1
0	14	0.46	0.08	0.18	0.38	0.7	96.3	3.8
0	28	0.42	0.08	0.20	0.40	1.0	97.4	5.6
0	42	0.31	0.18	0.24	0.36	1.0	95.4	7.3
0	56	0.27	0.18	0.30	0.33	1.4	95.0	8.6
10	14	0.26	0.18	0.28	0.38	1.0	95.7	18.2
10	28	0.10	0.36	0.34	0.29	3.6	92.1	77.3
10	42	0.05	0.48	0.32	0.24	4.6	89.7	152
10	56	0.06	0.55	0.23	0.24	8.4	88.3	175

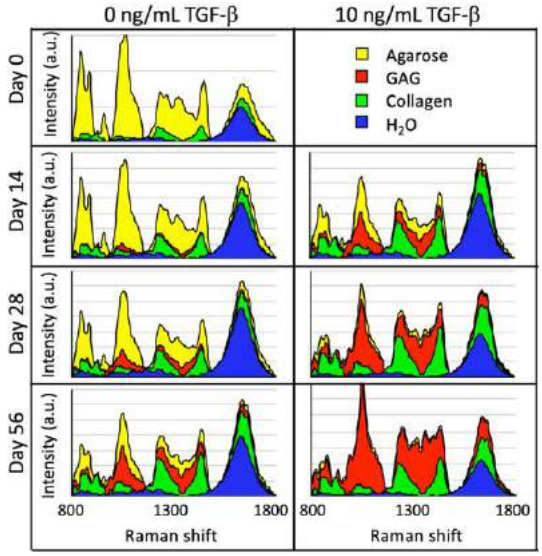

Fig 2: 2D stacked area plot of cumulative contribution of agarose, GAG, collagen, and H_2O spectra to composite Raman spectra of constructs after multivariate linear regression. Contribution of GAG & COL increases with time and TGF-β exposure.

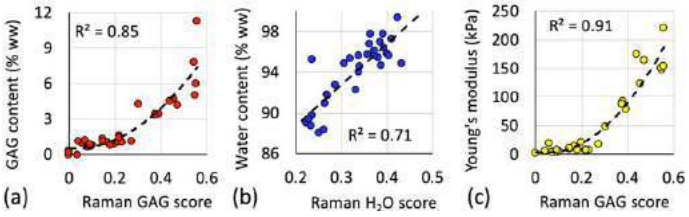

Fig 3: Bi-variate regression between (a) Raman GAG score and GAG content, (b) Raman H_2O score and water content, and (c) Raman GAG score and E_Y in tissue constructs.

Construct GAG content and E_Y increased with culture time and TGF-β supplementation while water content decreased (Table 1). Multivariate regression models were able to describe the measured Raman spectra, as the cumulative contribution of the individual ECM constituents accounted for 75% ± 6% of the variation of the composite construct spectra (Fig 2). Raman GAG and COL scores generally increased with culture duration and TGF-β supplementation while Raman agarose and H_2O scores decreased (Table 1). Linear regression was performed between Raman GAG scores and GAG content, Raman GAG scores and E_Y, and Raman H_2O scores and water content. Raman GAG scores predicted 85% and 91% of the variation in construct GAG content and E_Y, respectively. Raman H_2O scores predicted 81% of the variation in construct water content (Fig 3).

DISCUSSION

Raman spectroscopy represents a promising technology to achieve highly specific diagnostics of the chemical composition of musculoskeletal connective tissues. In the current study, we demonstrate that our newly developed Raman arthroscopic probe, in conjunction with multivariate spectral analysis, can achieve strong predictions of the composition (GAG and water content) and mechanical properties of engineered cartilage tissues. A major strength of this platform is the use of multivariate regression to ascertain the individual contributions of the agarose scaffold, interstitial water, and newly deposited ECM constituents (GAG and COL) to the cumulative Raman spectra, allowing for quantitative assessments of their evolution over time and in response to growth factor treatment. Clinically, we envision that Raman arthroscopy can be performed intra-articularly via a hypodermic needle cannula, allowing for minimally invasive assessments of engineered cartilage growth and stability *in vivo*. Raman arthroscopy can serve as a transformative research tool, evaluating the efficacy of emerging tissue engineering platforms in clinical trials. Further, Raman arthroscopy can evolve into a low cost, minimally invasive, clinical office-based procedure to monitor the growth and stability of engineered cartilage after surgical implantation procedures.

ACKNOWLEDGEMENTS: Supported by the Boston University 2020 Materials Science & Engineering Innovation Grant and Musculoskeletal Transplant Foundation Biologics Grant.

REFERENCES: [1] Huang BJ+ 2016 Biomaterials. 98: 1-22. **[2]** Bergholt MS+ 2019 Frontiers Bioeng Biotech. 7:303. **[3]** Kroupa K+ 2020 ORS Ann Mtg: Abstract No. 0198. **[4]** Jensen M+ 2020 Optics Letters. 45(10):2890-3. **[5]** Byers B+ 2008 Tis Eng A. 14(11): 1821-34.

THE EFFECT OF SHEAR STRESS ON HUMAN LUNG MICROVASCULAR ENDOTHELIAL CELL GLYCOCALYX

Camden Holm (1), Natasha Cruz-Calderon (1), Solomon Mensah (1,2)

(1) Department of Biomedical Engineering
Worcester Polytechnic Institute
Worcester, Massachusetts, USA

(2) Department of Biomedical Engineering
Northeastern University
Boston, Massachusetts, USA

INTRODUCTION

Endothelial Glycocalyx (GCX) is an extremely important determinant in vascular permeability and endothelial integrity [1]. GCX plays a role in mediating blood-cell and plasma and shear stress due to blood flow interactions with the endothelium [1].

The endothelial glycocalyx layer is a structure on the surface of the endothelial cells at the luminal side of the blood vessel. It regulates vascular permeability and molecular interaction with endothelial receptors [4]. This layer is responsible for flow-mediated responses in the endothelial cells.

Vascular endothelial cells form an interface between blood vessel walls and circulating blood, subjecting them to shear stress, and tensile and compressive strain [1]. Morphology, physiology, gene expression and inflammatory responses are regulated by these forces. [2,3] The reliance on these forces can result in pathological responses to an altered mechanical state and lead to various diseases such as atherosclerosis, abdominal aortic aneurysm [2], lack of vasomotion [4], or lack of immune response [5]. It has been shown that mechanotransduction of GCX increases vascular health [3].

When GCX are damaged, the flow-mediated responses are impaired leading to pathological responses from the endothelial cells [5]. Studies have determined that GCX expression is vital for the endothelial layer to properly function and respond to stimuli and serve as a protective barrier to pathogenic molecules [6].

The goal of this project is to understand the role of shear stress in pulmonary endothelial glycocalyx health. We hypothesized that subjecting human lung microvascular endothelial cells (HLMVEC) to shear stress in our flow chamber will result in an increase in expression of the GCX compared to control conditions.

METHODS

To introduce shear stress to HLMVEC on the glycocalyx, a parallel plate flow chamber was developed. Using SolidWorks to run simulations, we confirmed that the cells in the flow region would be exposed to a shear stress of 10 dynes/cm^2 with an average flow velocity of 171.3 mL/min. This flow rate was determined by equation 1 where σ is shear stress, in dynes/cm2, w is the width of the flow chamber, h is the height of the flow chamber, and v is the viscosity of the flow media.

HLMVEC for the experiment were cultured on glass slides, one control and one experimental. The cells were seeded for two days prior and were assessed to ensure confluence. Once confluent, the cells were transferred to the flow chamber. The flow chamber was placed in an incubator to ensure a controlled environment with a temperature at 37 °C and 5% CO2. In the first set of experiments, the cells were exposed to uniform flow for 4 hours. Flow was later increased to 6 hours. This was done to develop a trend for the relationship between GCX expression and time. Following exposure to shear stress, HLMVEC were fixed with a solution of 2% paraformaldehyde (PFA), 0.1% glutaraldehyde in phosphate-buffered saline (PBS) for 30 minutes at room temperature. They were later stained with wheat germ agglutinin (WGA; Vector Labs), for 30 minutes, being incubated at 4°C to label the GCX. For secondary detection Alexa Flour 488-conjugate at a concentration of 1:1000 was used. The GCX samples were covered with VECTASHIELD anti-fade mounting medium (Vector Labs) with 4′,6-diamidino-2-phenylindole, or DAPI, to stain the cell nuclei. The samples were sealed with clear nail polish to prepare them for imaging. The stained cells were imaged using confocal microscopy. This allowed for different planes of the cell layers to be captured. Coverage and thickness of the GCX was quantified using the NIH (National Institutes

of Health) Software ImageJ. The coverage was determined by looking at the composite images of each sample and measuring the percentage of the cell surface that was stained with WGA. The thickness was quantified by measuring the glycocalyx in the orthogonal view using the built-in measuring capabilities in ImageJ. The measurements of the thickness and total coverage from the control and uniform flow experiments were statistically analyzed using an unpaired t-test on the fold change values. This was done to show if the changes were statistically significant.

$$Q = (\sigma * w * (\frac{h^2}{1000 * v})) \quad (1)$$

RESULTS

Simulations revealed that cells in the flow area can be exposed to shear stress of up to 12 dynes/cm^2 (Fig 1). For the purpose of this project the flow area cells were exposed to 10 dynes/cm^2 with an average flow velocity of 171.3 mL/min (Fig 1). The average coverage of GCX for the experimental group was at 79.37% ± 0.02 and the thickness was at 1.25µm ± 0.05 while the control average coverage was at 74.82% ± 0.01 and average thickness at 1.13µm ± 0.03. The coverage and thickness of the GCX between control and experimental groups can be observed visually by changes in cell morphology between control and experimental groups (Fig 2 A-D). The data was found to be statistically significant through statistical analysis with a students *t*-test.

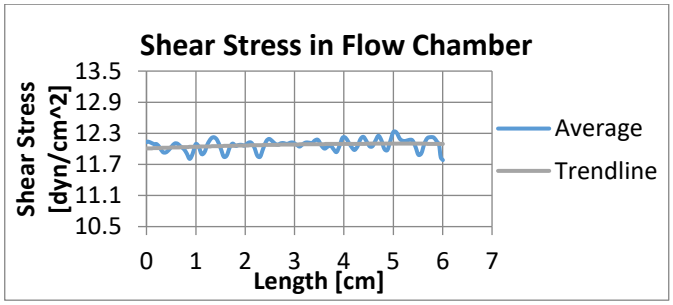

Figure 1: Simulation Data. Graph shows average shear stress along the length of the glass slide.

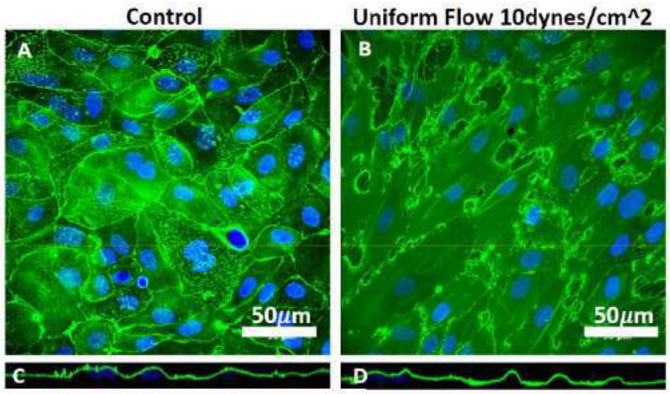

Figure 2: Effect of shear stress on the GCX. A. Coverage and thickness (C) are significantly lower in the no flow experiments (Green is WGA-labeled GCX and blue is DAPI-labeled nuclei.). B. Coverage and thickness (D) of GCX is significantly increased under uniform flow (UF) conditions.

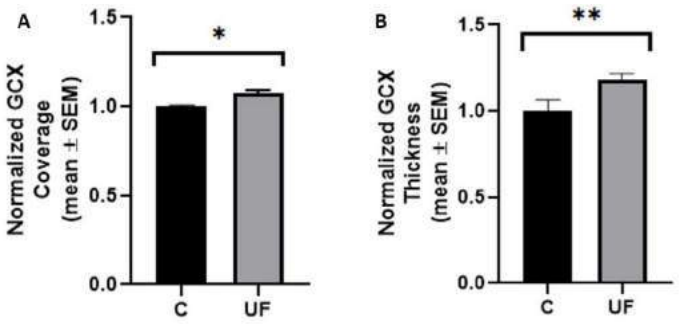

Figure 3: Data quantification for GCX coverage and thickness for control vs UF. All data normalized with control. Students *t*-test was used to compare control vs UF. Sample sizes: control N = 4, UF N = 3. Significance denoted as *P < .05, **P < .01.

DISCUSSION

The results show that HLMVEC GCX expression is shear stress dependent. Our results provide insight into the effect of shear stress on the expression of the GCX, demonstrating that consistent shear stress due to blood flow is important for GCX health. The data trend also implies that increasing the time of exposure to shear stress could correlate to the increase in GCX expression of HLMVEC.

The immediate future direction of this project is to increase the time of exposure. To confirm the relationship between exposure time and GCX expression, we plan to increase the time of exposure of HLMVECs to shear stress to 8 hours and then up to 24 hours. This increase in exposure time will further confirm the trend for the relationship between time and GCX expression.

In the next set of experiments, we will be staining for heparan sulfate, and sialic acid, which are GCX components.

ACKNOWLEDGEMENTS

The authors would like to thank Dr. Solomon Mensah for valuable direction, support and discussions, and WPI for providing laboratory space and funding for the project through the startup package provided to Dr. Solomon Mensah. We would also like to thank Victoria Huntress from the Bioengineering Core Facility for help with confocal imaging.

REFERENCES

[1] Reitsma, S., et al. *Pflugers Arch*. 434:345-359. 2007.
[2] Ramella M., et al. *Int J Mol Sci*. 20:287. 2019.
[3] Russo T. A., et al. *Life Sciences.* 213:214-225. 2018.
[4] Bar, A., et al. *JAHA*. 8. 2019.
[5] Abassi, Z., et al. *Am J Pathol*. 190:752-767. 2020
[6] Koo A., et al. *Am J Physiol Cell Physiol*. 304:C137–C146 2013.
[7] Fraser, D., et al. *Crit Care Ex*. 2:e0194. 2020.

STRESS-RELAXATION RESPONSE OF PORCINE AND HUMAN SYNOVIUM IN CONFINED COMPRESSION

Benjamin B. Johnston (1), Young Guang (1), Alexandra L. Davis (1), Lori A. Setton (1,2)

(1) Department of Biomedical Engineering
Washington University in St. Louis
St. Louis, Missouri, United States

(2) Department of Orthopedic Surgery
Washington University School of Medicine
St. Louis, Missouri, United States

INTRODUCTION

The synovium is a heterogeneous tissue that separates the diarthrodial joint space from systemic circulation. This thin, layered connective tissue consists of a cell dense intimal layer and a loosely connected extracellular matrix (ECM) in the subintimal layer [1]. Previous studies have measured the transport of solutes across synovial tissue both *in vivo* and *in vitro* to determine factors that regulate drug transport following intra-articular delivery [2-5]. In our prior work, we developed a finite element (FE) model of synovium as a fluid-filled, porous, and permeable solid using open source FEBio (University of Utah, Salt Lake City UT) to better study the factors that regulate solute diffusivity in the synovium [6-7]. Given a lack of information on the mechanical properties of native synovium, the model predictions of solute diffusivity depended on assumed values for hydraulic permeability, porosity, modulus, and Poisson's ratio. Here, we perform confined compressions of human and porcine synovial explants in order to quantify an equilibrium compressive modulus and hydraulic permeability through optimization to FE predictions of stress-relaxation testing. Our results provide one of the first-available measures for the modulus and hydraulic permeability of human and porcine synovium from direct compression that can be used to construct models of healthy and diseased tissue.

METHODS

Mechanical Testing: Synovial explants were harvested from the knee joints of human donors and porcine tissues and immediately flash-frozen to devitalize the tissue [6]. Explants were then trimmed to less than 1 mm thickness with a sledge microtome (Leica SM2400, Allendale NJ) and a 0.25" diameter test sample was obtained using a biopsy punch. Stress-relaxation tests were performed on the prepared samples in confined compression using the displacement-controlled features of a materials test system (Enduratec ELF 3200, TA Instruments). The tissue was placed in a confining ring in contact with a stainless-steel porous platen with a pore size of 40 μm (McMaster-Carr 9446T31, Elmhurst IL) to allow fluid flow during compression and in line with a load cell (45N). A solid stainless-steel platen interfaced with the test system actuator was first placed in contact with the tissue surface. The testing chamber was submerged in a 1x PBS bath to maintain hydration throughout testing.

The tissue was seated by applying a tare load of 0.1 N (100s relaxation, 3x), after which unloaded tissue thickness was measured as the distance between the porous platen and actuator positions. Samples underwent cyclic sinusoidal pre-conditioning of 0-1% peak-to-peak strain for 200 seconds at 0.25 Hz with a subsequent hold of 800 seconds at 1% strain. This strain pre-conditioning was followed by application of five successive compressive ramp and hold displacements (strain increments of 2% at 0.01% s^{-1}, 800 s relaxation). An equilibrium stress was calculated from the sample area and force averaged over the last 40s of the 800s relaxation period; linear regression of the equilibrium stress on strain for strains from 4-10% was used to determine an equilibrium compressive modulus.

Model Development: Specimen-specific FE models of synovium tested in confined compression were developed using FEBio. The synovium samples were modeled as a biphasic material with a porous and permeable, deformable Neo-Hookean solid and a constant and isotropic permeability. The Poisson's ratio was assumed to have a value of 0.2, the solid volume fraction was 0.19, and the fluid and solid density were both 1 kg/m^3. Experimentally determined thickness and equilibrium modulus were used to estimate a Young's modulus on a per sample basis. Each cylindrical synovial sample was modeled as a 3° wedge to simplify computational time and intensity (Figure 1).

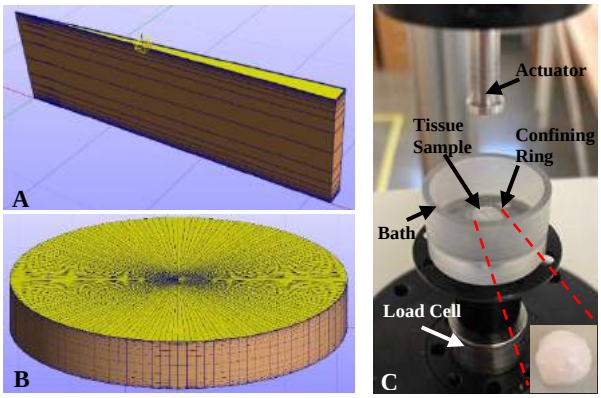

Figure 1: A) Modeled 3° wedge. Horizontal lines in the synovial tissue indicate the FEM mesh. This model was meshed with slices parallel to the xy-plane. B) Full cylindrical model example. C) Mechanical testing chamber with inset of tissue sample.

Boundary conditions in this one-dimensional problem enforced at the bottom face allowed for zero displacement and no resistance to fluid-flow; boundary conditions applied to the top face matched axial displacement to that of the actuator for each successive compressive strain (2% increments). For each sample, model predictions of transient compressive force in the platen were numerically matched to experimental force data following a moving average filter with a window size of 20s, using nonlinear optimization algorithms available within FEBio. In this manner, the FE model was optimized to fit the experimental data in order to determine a single parameter at each strain increment, the hydraulic permeability, *k*. Values of *k* were determined by optimization to the final ramp and hold waveform from 8%-10% strain.

RESULTS

Confined compression experiments were run on *n*=20 porcine samples and *n*=12 human samples. Stress-relaxation data for synovium tissue were matched moderately well by the FEM (Figure 2) as determined by average values for RSS of 0.0159 N^2 and 0.0127 N^2 for porcine and human synovium, respectively.

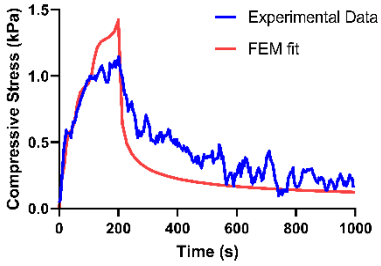

Figure 2: FEM output overlaid on experimental stress data between 8-10% strain. The optimized permeability for the curve shown is 5.41E-19 m^4/N-s while the modulus value is 3.48 kPa and RSS value is 0.00884 N^2.

For each curve fit, the model best matched the experimental stress during the ramp portion of the stress-relaxation curve and at longer times following periods of relaxation. The model often overshot the peak stress and predicted a faster relaxation at the beginning of the hold period than seen in the experimental data.

There was no statistically significant difference between porcine and human results for either equilibrium modulus or *k* (Figure 3, p>0.05, t-test, GraphPad Prism).

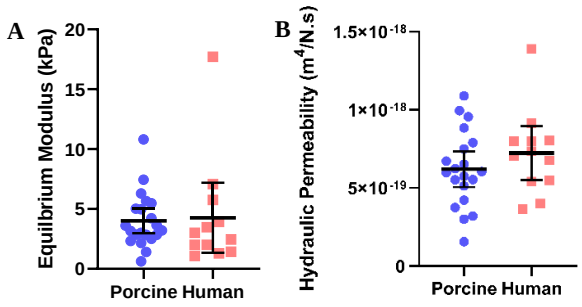

Figure 3: Mean with 95% confidence intervals for A) Equilibrium modulus and B) Hydraulic permeability

For porcine samples, the mean equilibrium modulus was 4.00 kPa (95% CI 2.97 – 5.04 kPa), and the mean *k* was 6.19E-19 m^4/N-s (95% CI 5.05E-19 – 7.33E-19 m^4/N-s). For human samples, the mean equilibrium modulus was 4.27 kPa (95% CI 1.34 – 7.19 kPa), and the mean *k* was 6.188E-19 m^4/N-s (95% CI 5.52E-19 – 8.95E-19 m^4/N-s).

DISCUSSION

This work represents the first study to report multiphasic mechanical properties of human and porcine synovium from direct compressive testing and FE model optimization. Here we report average values for compressive moduli that fall between 1-8 kPa, not unlike those reported in a recent conference paper using AFM testing [8]. The moduli were well-determined by a linear fit to compressive strains between 4-10%, suggesting that our assumption of a constant and linear modulus was appropriate at these strain levels. The values for *k* are among the lowest reported for any connective tissue, with an order of magnitude corresponding to 10^{-19} m^4/N-s.

This finding and our observation of poor model fits at the peak compressive stress may reflect our use of a strain-independent, constant permeability value; this assumption sets the stage for future work incorporating model complexity of strain-dependent permeabilities and possibly tissue viscoelasticity or nonlinear stress-strain behaviors for the synovial tissue.

With new and experimentally determined values for the modulus and permeability of human and porcine tissues, we are able to refine our prior estimations for model solute diffusivity constants in the synovium. Taken together, these studies bring us closer to building models that better predict factors regulating solute clearance and distribution in healthy and pathological synovium.

ACKNOWLEDGEMENTS

Work supported by NIH AR070975 and AR077678. Use of open-source FEBio was supported in part by a grant from the NIH. We would like to thank Dr. Michael Talcott (WUSM) and Mid-America Transplant Center for providing porcine and human samples, and Barbara Semar (WUSTL MEMS) for support of the ELF testing.

REFERENCES

[1] Castor, CW. et al *Arthritis Rheum* 3(2):140-151, 1960.
[2] Mwangi, TK. et al *J Control Release* 283:76-83, 2018.
[3] Doan, TN. et al *Acta Biomater* 93:270-281, 2019.
[4] Bell, RD. et al *Arthritis Res Ther* 21(1):240, 2019.
[5] Levick, JR. et al *Ann Rheum Dis* 54(5): 417-423, 1995.
[6] Guang, Y. et al *J Biomech Eng* 142(4):0410101–8, 2019.
[7] Maas, SA. et al *J Biomech Eng* 134(1):011005, 2012.
[8] Gangi, LR. et al *ORS Annual Meeting* 2021.

DEVELOPMENT OF A SOFTWARE TO COLLECT AND ANALYZE WORLDWIDE COVID-19 CLINICAL DATA AND ANALYSIS

Marshall M. Nambiar

National Institutes of Health
Besthesda, MD

INTRODUCTION

Over the course of the past year, I have worked on gathering, storing, parsing, and analyzing COVID-19 data from all around the world. The emergence of COVID-19 over the past year has changed lives in numerous ways. Not much research has been conducted on the prevalence of the disease and how it has affected individuals. Numerous hospitals in countries all over the world have stored data regarding COVID-19 but to effectively analyze it, we must bring in the data and standardize the format.

METHODS

Over the summer and school year, I worked on creating a questionnaire to help standardize the data received from other countries and parse it. The questionnaire included data regarding patient comorbidities, phenotypes, oxygen treatment received. Since countries send patient data for over one hundred patients, creating scripts to parse the data into a format accepted by the LabKey survey would help efficiency. Python and VBA was used to translate the received questionnaires into English and then parse out certain sections into viable formats for entry into the LabKey survey. To help with this process, we created mappings that showed a mapping process of how each part of the questionnaire is mapped into different sections and which information is captured.

RESULTS

We successfully created the software that is being used across the world to collect covid-19 clinical data, especially with people who have comorbidity conditions such as diabetes, hypertension, smoking, alcohol, opioid use and pregnant women.

We are analyzing the covid-19 clinical data using this software regularly.

DISCUSSION

We are analyzing the covid-19 clinical data using this software regularly.

ACKNOWLEDGEMENTS
National Institutes of Health for supporting this research work.

REFERENCES

QUANTIFICATION OF THE FLEXURAL RIGIDITY OF PERIPHERAL ARTERIAL ENDOVASCULAR CATHETERS AND SHEATHS

Chase M. Hartquist (1-3), Vinay Chandrasekaran (1-3), Halle Lowe (1-3), Eric C. Leuthardt (1,4), Joshua W. Osbun (4), Mohamed Zayed (1,2), Guy M. Genin (1,3,4)

(1) McKelvey School of Engineering
Washington University in St. Louis
St. Louis, Missouri, USA

(2) Department of Surgery
Washington University School of Medicine
St. Louis, Missouri, USA

(3) NSF Science and Technology Center
for Engineering MechanoBiology
Washington University in St. Louis
St. Louis, Missouri, USA

(4) Department of Neurological Surgery
Washington University School of Medicine
St. Louis, Missouri, USA

INTRODUCTION

Although endovascular technology has revolutionized treatment of complex vascular pathology,[1] surgical procedures are complicated by the need to use multiple catheters and guiding sheaths to access distal peripheral arterial networks, as no one device is both highly navigable and supportive.[2,3] Interventionalists rely on these devices to support the transport of therapeutic devices such as balloons, stents, or thrombectomy devices. However, no engineering basis currently exists for determining which devices are best suited for peripheral arterial procedures in the lower extremities and the neurovascular system.[4] We hypothesized that flexural rigidity of catheters can serve as a quantitative metric for device selection.

Mechanical factors have long been considered in the process of catheter design and integration.[5-9] Flexural rigidity is a sensible target in determining a catheter's capacity to navigate tortuosity in the vasculature: a catheter or sheath with low flexural rigidity can buckle during advancement, but one with high flexural rigidity can suffer limited maneuverability and risk injuring the arterial lumen. Small strain, Euler-Bernoulli methods used to characterize the earliest endovascular catheters are not accurate for the more compliant catheters in current use. Therefore, there is a compelling need for protocols to quantify the flexural rigidity of these tools, and to evaluate commercial devices. To test our hypothesis and meet this need, we evaluated the prediction that catheters and sheaths for the treatment of arterial structures in the neurovascular and lower extremity peripheral arterial vasculature would have distinct flexural rigidities. To test this hypothesis, a nonlinear beam theory approach was developed and applied to a range of endovascular devices used for lower extremity peripheral arterial and neurovascular procedures.

METHODS

To characterize flexural rigidity, a nonlinear beam theory solution was developed, and an integrated test was developed. These were applied to a range of commercial endovascular devices.

Device testing procedure: 9 catheters and 12 sheaths used in interventional procedures at Washington University were tested, ranging in diameter from 4-12 French (1.33-4 mm). Devices were cut into 25 cm specimens. The proximal 10 cm of each specimen was placed into a clamp to create a 15 cm fixed-free cantilever beam. Images were taken of the initial position, and as a series of F = 12.3-259 mN loads attached L_0 = 4-8 cm from the fixed end. This was repeated three times for each specimen. The final length L and angle of deflection θ (Fig. 1), were measured as described below from images taken using a calibrated 10-megapixel smartphone camera.

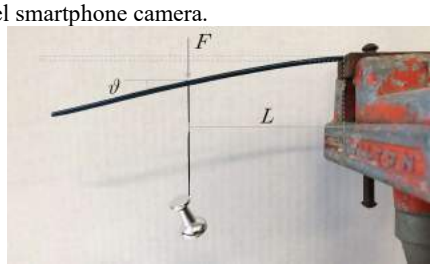

Figure 1: Testing fixture for measuring the flexural rigidity of catheter specimens. For the nonlinear beam theory approach, the method required measuring both the angle of deflection θ and the position L of the applied dead load in the deformed configuration.

Models for flexural rigidity quantification: While linear beam theory is sufficient to analyze cantilevered beams under small deflections, it proved inadequate, as described below. The nonlinear solution started with the standard linear constitutive law[10]:

$$M(x) = -EI\kappa(x) \quad (1)$$

where $M(x)$ is the local moment, E is the elastic modulus, I is the second area moment of the area of the cross section, and $\kappa(x)$ is the local curvature. The combined term EI is defined as flexural rigidity. For small curvature, the usual linearization of slope and curvature applies, and flexural rigidity can be approximated as:

$$EI = (FL^2)/(2\tan\theta) \quad (2)$$

where F and L are defined above, and θ is the rotation angle at the point of the load. Using the exact relation between slope and curvature, the flexural rigidity was derived for nonlinear systems:

$$EI = (FL^2\sqrt{1+\tan^2\theta})/(2\tan\theta) \quad (3)$$

FE validation: To verify the framework, an FE simulation was developed in COMSOL (COMSOL Inc., Burlington, MA). A 450 mm hollow tube was subject to a load applied 420 mm from the fixed end of the fixed-free cantilever beam. The beam was made of a neo-Hookean material, and a finite strain formulation was applied. The angle of deflection θ was derived from trigonometry comparing deflections at the loading point (x = 420 mm) and the end of the beam (x = 450 mm). Gravitational loading was neglected. The measured angle was applied using Eqs. 2-3 to estimate flexural rigidity of the beam under varying loads from 0.25-1.5 mN. The dimensions matched standard 6F catheter models with an elastic modulus of 0.4 GPa. Estimated values were compared to the predetermined input flexural rigidity (EI). Tests were repeated for a short 35 mm beam with the load applied 30 mm from the fixed end. Convergence tests were performed, and all models achieved convergence with between 2238 and 423906 degrees of freedom (DOF).

Image analysis: The FEM simulations and experimental images were examined using ImageJ to obtain the deflection angle θ for Eqs. 2-3. Images were 1024x1024, with at least 512 pixels over the free end length of the device past the loading point. The angle was measured as a difference in angle between initial and final tangents at the load. The length L was measured from the fixed end to the applied point load.

RESULTS

The FEM validation in COMSOL indicated that the nonlinear flexural rigidity calculations are precise and accurate at high angles while linear values are less accurate with increasing deflection angle θ (Fig 1-2). The image analysis technique validation test accurately estimated the flexural rigidity using the nonlinear approach and was less precise for the linear approach at high angles. The validated framework was applied to characterize a range of commercial catheters and sheaths used for endovascular procedures in the neurovascular and lower extremity peripheral arterial systems. Measured values were plotted and clustered based on device type and procedure (Fig. 3).

DISCUSSION

The flexural rigidity values measured revealed key differences between catheters and sheaths used for neurovascular and lower extremity peripheral arterial procedures. First, catheters clustered into a single range of values. This is logical since catheters are commonly employed as the flexible tool used for navigation through the entire the peripheral arterial system. In contrast, sheaths clustered into two distinct groups based on the anatomical destination. Lower extremity peripheral arterial sheaths were measured to be more rigid than neurovascular sheaths. This is justified procedurally since neurovascular sheaths must traverse acute bends across the aortic arch and proximal carotid arteries.[11] Drastic differences between sheaths are justified since they scale with diameter along the trendlines, showing similar elastic moduli.

The methods are simple but have limitations that should be noted. Nonlinear beam theory is valid for the geometric nonlinearity, but not for material nonlinearity.[12] Flexural rigidity measure can evolve with flexure for nonlinear materials, and it is possible for this to change over time if the material is viscoelastic.[13] Precision was limited by image quality, requiring use of megapixel cameras.

The measured flexural rigidity of common sheaths and catheters provide parameters for increased procedural efficiency and future device development. Our technique will enable assessments of endovascular tools to determine suitability for specific interventions. The stiffness ranges identified serve as baselines for evaluating and developing new products within these procedural device ecosystems.

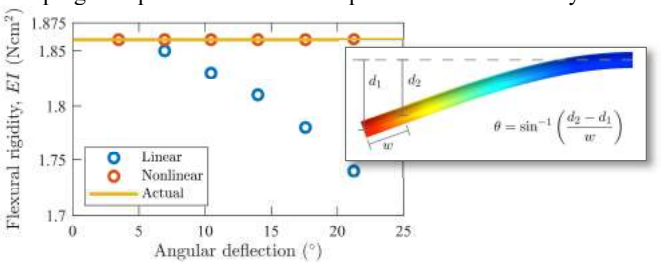

Figure 2: Validation of finite the experimental method using synthetic images generated using finite element analysis. The linear approximation was accurate to within ~5%, while the nonlinear approach was accurate to within a fraction of a percent.

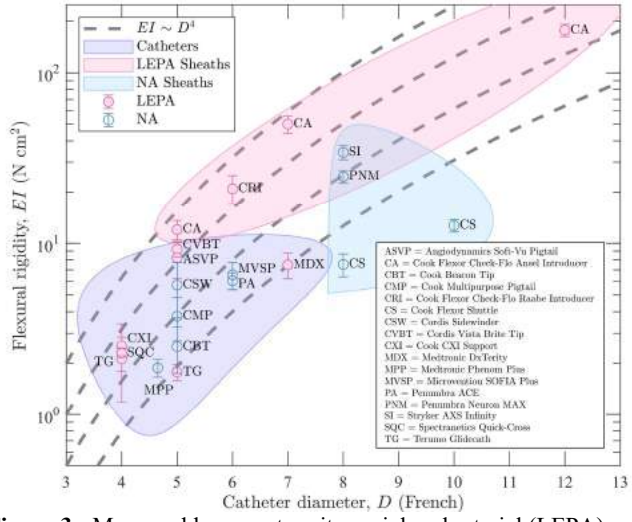

Figure 3: Measured lower extremity peripheral arterial (LEPA) and neurovascular (NA) catheter and sheath flexural rigidity measurements based on diameter are clustered by procedure.

ACKNOWLEDGEMENTS

This work was supported by the Society for Vascular Surgery Foundation, the American Surgical Association, NIH K08HL132060, The Center for Innovation in Neuroscience and Technology, and the NSF Science and Technology Center for Engineering MechanoBiology (CMMI 1548571).

REFERENCES

[1] Starke, et al., *J. Neurointervent. Surg.*, 8:135-144, 2016. [2] Theron, J., et al., *American Journal of Neuroradiology*, 11: 869-874, 1990. [3] Berenstein, A., et al., *Radiology*, 132: 619-630, 1979. [4] Almallouhi, E., et al., *J. Neurointervent. Surg*, 12:176–180, 2020. [5] Alm´en, T., *Acta Radiologica: Diagnosis*, 5:11-21, 1966. [6] Bersten, A, et al., *Anaesthesia and Intensive Care*, 16:342-351, 1988. [7] Abraham, G., et al., *J. Applied Polymer Sci.*, 65:1193-1203, 1997. [8] Braun, U, et al., *J. Mech. Beh. Biomed. Mat.*, 64:281-291, 2016. [9] Busch, J., et al., *J. Mech. Beh. Biomed. Mat.*, 82:183-186, 2018. [10] Fosdick, R., et al., *Amsterdam: Springer*. [11] Rooke, T. W., *John Wiley & Sons*, 2008. [12] Culver, D., et al., *Mechanical Systems and Signal Processing*, 134:106340, 2019. [13] DiTaranto, R. A., *Journal of Applied Mechanics*, 881-886, 1965.

IDENTIFYING HEMODYNAMIC PREDICTORS OF CEREBRAL ANEURYSM GROWTH USING COMPUTATIONAL FLUID DYNAMICS

Allyson J. Weiss (1), Aaron O. Panduro (2), Ingrid S. Lan (3), Erica L. Schwarz (3), Alison L. Marsden (3), Nicholas A. Telischak (4)

(1) Biomechanical Engineering
Stanford University
Stanford, CA, USA

(2) Biochemistry
California State University, Fresno
Fresno, CA, USz

(3) Bioengineering
Stanford University
Stanford, CA, USA

(4) Radiology
Stanford Hospital
Stanford, CA, USA

INTRODUCTION

Cerebral aneurysms are weak or thin sections of the artery wall in the brain that bulge and fill with blood with the potential of placing pressure on nerves or brain tissue[1]. Ruptured aneurysms spill blood into the surrounding tissue and can cause serious health complications or even death. One of the most established risk factors of aneurysm rupture is size[2]; larger aneurysms are typically more likely to rupture. Because of this, many aneurysm management plans and prognoses are assessed by size of the aneurysm. However, smaller aneurysms can and do rupture, demonstrating the need for additional risk assessment[3]. Other risk factors of rupture include location, high blood pressure, smoking, and family history of cerebral aneurysms[1]. While these can improve prediction of rupture, they still do not provide complete accuracy.

Previous studies have identified hemodynamic predictors for aneurysm rupture, including low wall shear stress (WSS), low WSS area, high oscillatory shear index (OSI), lower systolic and mean arterial pressures in the aneurysm, narrow pulse pressures in the aneurysm dome, and high relative residence time in the aneurysm, as well as morphological predictors such as larger size, aspect ratio, size ratio, and height-width ratio[4,5,6,7]. In contrast to the focus of these existing studies on ruptured aneurysms, we aim to identify and assess hemodynamic predictors of cerebral aneurysm *growth* to enable earlier clinical detection and prevention of rupture.

METHODS

From MRA and CTA scans, we will model 15 matched pairs (30 total) of cerebral aneurysms using 3D segmentation tools in the Vascular Modeling Toolkit (www.vmtk.org). Each pair consists of one non-growing cerebral aneurysm and one growing aneurysm of a similar size in the same location. Given the limitations of current 3D segmentation methods, models were manually smoothed in MeshMixer (www.meshmixer.com), and all vessels were truncated normal to the vessel centerline. All models were meshed with linear tetrahedral elements and 3 boundary layers with a layer decreasing ratio of 0.8 in TetGen.

All computational fluid dynamics (CFD) simulations were performed using the open-source software SimVascular (simvascular.org). Clinically measured flow waveforms from published studies were prescribed at the inlets with a parabolic velocity profile, and outflows were distributed proportionally to outlet areas[8,9]. Wall compliance was neglected and no-slip boundary conditions were applied at the walls.

We systematically tuned our outlet boundary conditions to achieve systolic, diastolic, and mean aortic pressures at the inlets as well as the target area-based outflow splits. With steady inflows prescribed, outlet resistances were first tuned to achieve mean aortic pressures. In progressing to pulsatile inflows and outlet RCR Windkessel boundary conditions, these tuned outlet resistances were then distributed, and the proximal:distal resistance ratio and capacitances were tuned to achieve target aortic pulse pressures. Simulations were run for 4-18 cardiac cycles to enable convergence of all inlet and outlet pressures to

a limit cycle. Upon completion of outlet boundary condition tuning, mesh refinement was performed to ensure WSS convergence.

We will compute the temporally and spatially averaged WSS, minimum WSS, maximum WSS, and mean OSI over various spatial regions, including the dome, parent artery, and neck, and further determine the most appropriate means of normalizing these metrics across the patients. These metrics will be statistically compared for the growing and non-growing aneurysms using a non-parametric Wilcoxon signed-rank test to account for the paired samples.

RESULTS

We have constructed anatomical models of two growing aneurysms with smoothed geometries and truncated inlets and outlets (**Figure 1**) and will model the remaining 28 aneurysms over the next few months**.**

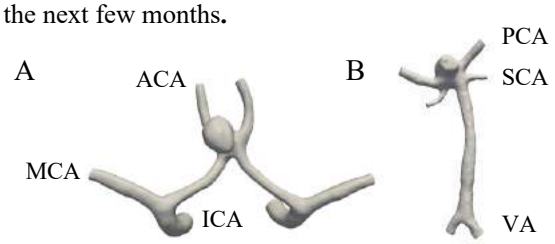

Figure 1: (A) Aneurysm of the anterior communicating artery with internal carotid artery (ICA) inlets and anterior cerebral artery (ACA) and middle cerebral artery (MCA) outlets, and (B) aneurysm of the basilar apex with vertebral artery (VA) inlets and superior cerebral artery (SCA) and posterior cerebral artery (PCA) outlets

Beyond modeling, we have completed boundary condition tuning (see **Figure 2**) and achieved time-averaged WSS (TAWSS) convergence (see **Figure 3**) via mesh refinement for case A, as well as the steady tuning of case B. The target systolic and diastolic pressures of case A were reached within 5% error in the simulation, but the mean pressure is slightly high, likely because the target mean pressure was not patient-specific. The TAWSS spatially averaged over the dome was 3.69 Pa, which was in agreement with previously published values[6]. In case B, the target flow splits and target inlet mean pressures were reached within 5% error.

Statistical analyses comparing hemodynamic quantities of interest between the growing and non-growing cohorts, as well as preliminary observations regarding optimal hemodynamic predictors of growth, will also be presented.

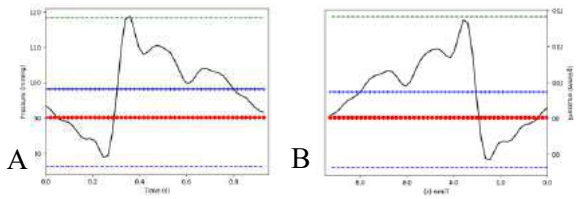

Figure 2: Target inlet pressures were reached for (A) the left ICA and (B) the right ICA in case A. The green and blue dashed, blue crossed, and red dotted lines represent target systolic and diastolic, simulated mean, and target mean pressures, respectively.

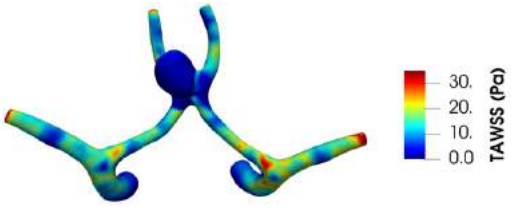

Figure 3: TAWSS distribution for case A

DISCUSSION

While previous studies have investigated hemodynamic predictors of growing cerebral aneurysms, limitations in their sample size and computational methods have precluded any conclusive clinical consensus. A study completed by Brinjikji et al. at Mayo Clinic suggests that the area under low WSS is lower in growing cerebral aneurysms, but the study had a small sample size of only 12 pairs of matching aneurysms[11]. Another study, completed by Sforza et al. at George Mason University, found that growing cerebral aneurysms tend to have complex flow patterns that lead to non-uniform WSS[12]. The growing and non-growing aneurysms in the study, however, were not matched in location or size. Further, both studies neglected to mention pressures in their papers, making the methods for simulation and outflow boundary conditions unclear.

Both studies also computed flow splits using Murray's law, which tends to be more accurate for smaller arteries; however, we found a large variation of flow splits in literature, leading us to believe that an area-based assumption would better match our data set. We also made a point to perform a mesh convergence study for WSS, to include validated pressures to account for pressure pulse in boundary conditions, and to increase the sample size in order to increase the reliability of our results.

CFD simulations have the potential to greatly improve care and treatment for cerebral aneurysms. Knowledge of hemodynamic predictors for growth could provide an opportunity for faster, potentially more preventative treatments without the need for a second imaging scan to detect growth.

ACKNOWLEDGEMENTS

This study is supported by the Bioengineering REU program at Stanford University. CFD simulations were performed using Stanford Research Computing Center's Sherlock cluster.

REFERENCES

[1] Cerebral Aneurysms Fact Sheet, *National Institute of Neurological Disorders and Stroke,* 2019.
[2] Wiebers, D, *The Lancet,* 362:103-110, 2003.
[3] Beck, J et al., *Surg Neurol.,* 65:18-25, 2006.
[4] Fan, J et al., *World Neurosurg.,* 84:114-120, 2015.
[5] Perera, R et al., *Magn Reson Med Sci.,* 19:333-344, 2020.
[6] Suzuki, T et al., *J Neurosurg.,* 132:1116-1122, 2019.
[7] Li, Y et al., *Neurosurgery,* 84:1261-1268, 2019.
[8] Aaslid, R et al., *J Neurosurg.,* 57:769-774, 1982.
[9] Seymour, R et al., *J Anat.,* 236:522-530, 2020.
[11] Brinjikji, W et al. *J Neurointerven Surg.,* 9:376-380, 2017.
[12] Sforza, D et al. *J Neurointerven Surg.,* 8:407-412, 2016.

SB^{3}C2021
Summer Biomechanics, Bioengineering and Biotransport Conference
June 14–18, Virtual

IN SILICO MODELING OF EMBOLIC PARTICLE DRUG DELIVERY FOR LIVER CANCER

Autumn Zemlicka[1], Andrew Beiter[1], Premal Trivedi[2], Debanjan Mukherjee[1]

[1]Department of Mechanical Engineering
University of Colorado Boulder
Boulder, CO, USA

[2]Division of Interventional Radiology
University of Colorado Anschutz Medical Campus
Aurora, CO, USA

INTRODUCTION

Embolization therapy has become an increasingly common approach to treat liver tumors [1]. Catheter directed microparticles are injected into the arterial circulation, which are often loaded with drug (e.g. Trans-arterial Chemo-embolization or TACE) [3] or radiation agents (e.g. Y90 radio-embolization) [2]. The particles perfuse the tumor vasculature, and can lead to ischemic conditions to reduce tumor size, or lead to efficient and targeted local drug or radiation delivery. With a growing utility in treatment, several fundamental questions pertaining to release, transport, and distribution of embolic drug particles in the vascular pathways into the tumor need further exploration. These questions are intimately connected to treatment efficacy and success. However, systematic evaluation of how various drug release and delivery parameters affect the treatment outcomes remains a challenge. With advancements in medical image-based modeling techniques, *in silico* or computational approaches provide a viable alternative to explore these questions. Such platforms can support clinical practice and decision making by enabling pre-treatment virtual simulations of various intervention scenarios. Here, we outline the development of a full-scale patient-specific computational model for intravascular delivery of embolic drug particles into the hepatic vessels for applications in liver cancer (hepatocellular carcinoma).

METHODS

Image-based modeling: A patient-specific model of the abdominal aorta upto the ilio-femoral bifurcation was constructed from abdominal CT scans using SimVascular [4]. Two generations of branches for the celiac trunk, which specifically includes the left and right hepatic arteries and the gastro-duodenal artery, are included in the model (as shown in Figure 1). Pre-procedural Dyna-CT/Cone-beam CT [5] images are used to identify the path taken by the embolic delivery catheter, and a 2 mm (6 French) catheter is segmented out of the arteries along this identified path. The catheter is placed such that the delivery tip is located approximately midway into the common hepatic artery. The final computational model is obtained from a Boolean intersection operation between the segmented catheter and the artery model obtained from CT scans. For comparative evaluation of local hemodynamics at the drug release site, the same arterial network with and without the catheter in place were analyzed.

Hemodynamics: Blood is modeled as an incompressible Newtonian fluid with viscosity 4.0 cP and density 1.06 g/cm^3. The Navier-Stokes equation for fluid momentum balance, and the continuity equation for mass balance, were solved using a stabilized finite element method implemented in SimVascular [4]. A specified physiologically realistic inflow profile was employed at the abdominal aortic inlet face to drive the flow. At all other arterial branch outlets a resistance-based boundary condition was imposed. Resistances were calculated by assuming that approximately 30 percent of incoming flow is routed to the femoral arteries, approximately 34 percent routed to the renal arteries, and the remaining portion of the flow is distributed to all other arterial branches such that $Q_b \propto A_b^3$; with A_b the cross-sectional area of the artery outlet. To mimic the release of particles without any additional fluid injection, the catheter tip was assumed to be a fixed impermeable wall. The fluid flow was simulated for three cardiac cycles with a numerical time-step of 0.001 seconds, and flow velocities and pressures from the third cycle were used for embolic drug particle modeling.

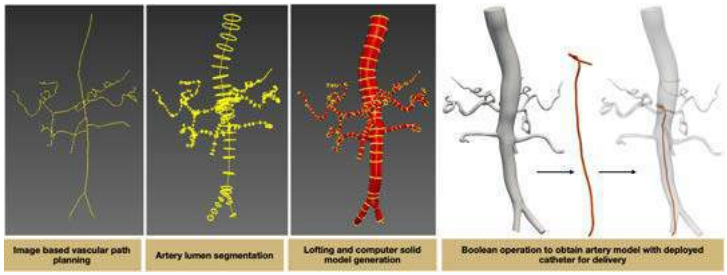

Figure 1: Illustration of the steps involved in image-based modeling of the vascular network of interest with delivery catheter in place.

Drug particle modeling: Embolic drug particles were modelled as spherical inertial particles with diameter 100 µm, using a one-way coupled scheme (that is, particle is influenced by the flow but not vice versa). Fluid-particle interactions are modeled using a custom modified form of the Maxey-Riley equation [6] proposed in prior work for embolic transport through arterial hemodynamics [7]. Briefly, this equation accounts for the dominant forces on the drug particle from the flow including drag, shear-induced lift, fluid stresses and pressure, and added mass effects. Particle interactions with vessel wall were accounted for using a viscoelastic contact mechanics model with model details and parameters as outlined in [7]. A fixed number concentration of drug particles was released at the start of one cycle, and simulated for four successive cycles using a 4'th order Runge-Kutta scheme with numerical time-step 0.0005 seconds. Number fraction of drug particles reaching each hepatic artery branch outlet was computed based on the positions of the particles at the end of the fourth cycle.

RESULTS

Hemodynamics with delivery catheter in place: Flow velocity across the entire arterial model is visualized using streamlines viewed at four instants during the cardiac cycle - mid acceleration, peak systole, mid deceleration, and mid diastole in Figure 2. For the model with catheter in place, a close-up view of the streamlines at these four instances are presented in Figure 3 (where the catheter is highlighted in green). To fur-

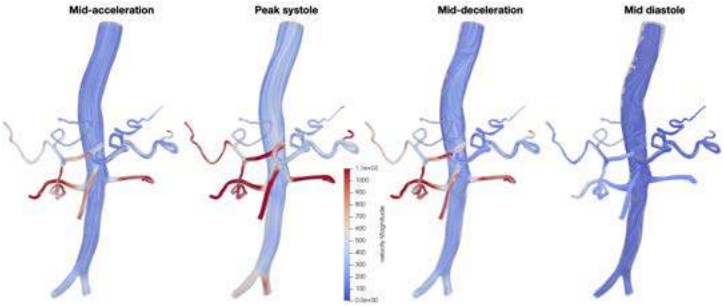

Figure 2: Blood flow streamlines visualized at four successive instants in a cardiac cycle for model with catheter. Velocity units in mm/sec.

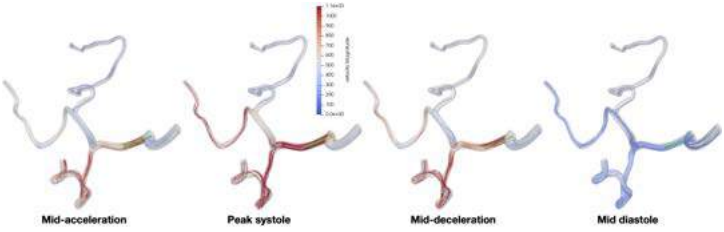

Figure 3: Close-up view of flow velocities (mm/sec) in the hepatic artery network in presence of delivery catheter (marked in green).

ther illustrate local hemodynamic features at the catheter site, slices along the common hepatic artery at three locations (midway along catheter from common hepatic entry, tip of the catheter, and immediately distal to the catheter) are presented for both models at each of the stated instances during the cardiac cycle - as presented in Figure 4. Results indicate that while larger scale flow patterns and velocity regimes between models with and without catheter remain similar, locally around the catheter there are significant hemodynamic differences as indicated in Figure 4, which originates from the catheter-hemodynamics interactions.

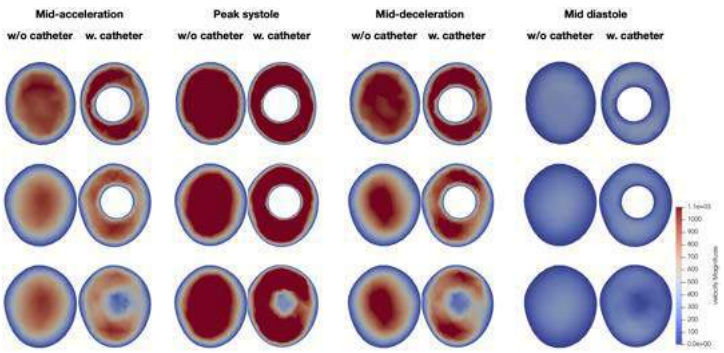

Figure 4: Cross-sections along common hepatic artery for models with and without delivery catheter, illustrating differences in local hemodynamics (units in mm/sec) around the drug release site.

Quantitative analysis of embolic drug delivery: The distribution of the embolic drug particles across the hepatic artery branches are shown in Figure 5. A total of 2126 particles released across the catheter face were tracked. At the end of four cycles, we observed that 30 percent of the drug particles reached a destination vessel. The biggest proportion, around 22 percent, reached the right hepatic artery, while the left hepatic artery received around 0.3 percent, and none reached the gastro-duodenal artery. The embolic drug particle distribution was observed to be dominantly into the right hepatic artery for the simulated case for this study. Analysis of the particle dynamics patterns revealed that as particles traverse the right hepatic vessel, owing to their inertia, the dominant flow direction, and the nearly 90 degree branching angle for the left hepatic artery, the particles predominantly continue their motion along the right hepatic artery. Similar particle inertia effects have been demonstrated in prior works on inertial embolic particles causing a stroke [8].

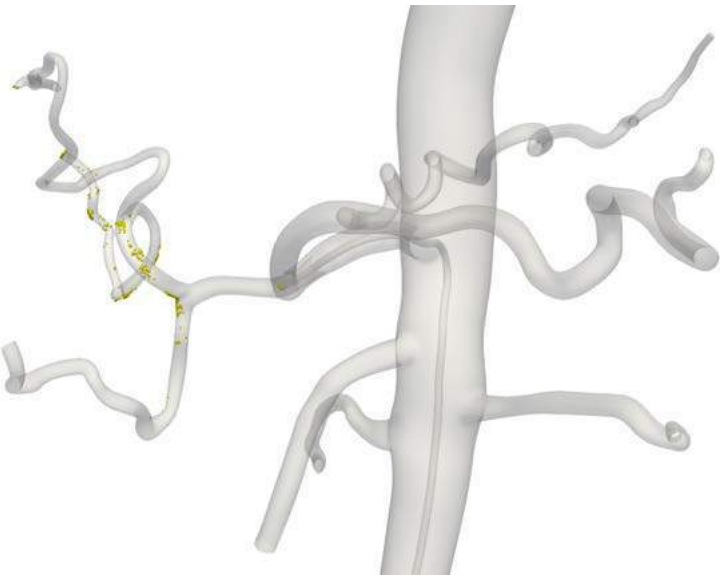

Figure 5: Distribution of 100 micron embolic drug particles (shown in yellow) across hepatic vessels after four cardiac cycles.

DISCUSSION

Implications: We have established a comprehensive *in silico* modeling approach for embolic drug particle delivery, with applications in liver cancer. Results from simulations establish the efficacy of the proposed framework in evaluating extent of drug particle delivery to various vessels of interest. This has broad implications in terms of treatment planning prior to intervention, and assessment of treatment efficacy metrics. Additionally, the results also illustrate the importance of accounting for local hemodynamic environment at particle release site from delivery catheter. For example, over 60 percent of particles remain stuck close to the catheter site for our simulations, mainly because of the local flow separation phenomena around the catheter tip that likely entrains particles and prevents them from migrating towards a destination artery. Hence, specifically, local state of flow at the release site will serve as the initial conditions that ultimately determine the particle trajectories and their distribution. Determining the final particle destination requires consistent characterization of local drug-release hemodynamics.

Assumptions and limitations: The focus of this work was on development of the computational framework. Hence, several aspects have not been accounted for, which are key goals for ongoing and future work. Specific details about the cancer site itself have not been considered here. Similarly, release parameters like drug injection volume, injection flowrate, and injection pressure have not been accounted for at the catheter tip. For the sake of computational costs, we simulated drug particles only for four cycles. We note that particle trajectory computations over a longer duration will provide a more detailed estimation of delivery to various branches, albeit at a higher cost. Finally, interactions between individual drug particles have not been considered here. While for typical number densities of drug particles this may not be a major factor, when number density is increased, we may see an influence of these interactions on particle fate. We remark that, despite these assumptions, the underlying flexibility of the modeling approach we devised here enables easy incorporation of these factors into the computational model - an aspect that we are currently continuing to investigate.

REFERENCES

[1] Kennedy, A. *J. Gastrointest. Oncol.* , 5(3):178–189, 2014.
[2] Braat A.J. et al., *J. Nucl. Med.* , 56(7):1079-1087, 2015.
[3] Gaba, R.C. et.al. *J. Vasc. Interv. Radiol.* , 28:1210–1223, 2017.
[4] Simvascular. *http://simvascular.github.io/*. 2020.
[5] Tacher, V. et.al. *Radiology*, 270(2):321-334, 2015.
[6] Maxey, M.R. et.al. *Phys. Fluids*, 26(4):883-889, 1983.
[7] Mukherjee, D. et.al. *J. Biomech.* , 52:155-164, 2017.
[8] Mukherjee, D. et.al. *Ann. Biomed. Eng.*, 46:1128-1145, 2018.

JUNCTION MODELING IN PATIENT-SPECIFIC BLOOD FLOW SIMULATIONS

Elena S. Martinez (1), Martin R. Pfaller (2,3,4), Jonathan Pham (5), Alison L. Marsden (2,3,4)

(1) Department of Mathematics
Loyola Marymount University
Los Angeles, CA, USA

(2) Department of Pediatrics
Stanford University
Stanford, CA, USA

(3) Depart of Bioengineering
Stanford University
Stanford, CA, USA

(4) Institute for Computational and Mathematical Engineering
Stanford University
Stanford, CA, USA

(5) Department of Mechanical Engineering
Stanford University
Stanford, CA, USA

INTRODUCTION

Knowledge of cardiovascular pathologies relies largely on an understanding of the fluid dynamics of the circulatory system. Fluid dynamics, however, can be difficult, computationally expensive, and sometimes impossible to study through traditional experimental techniques like magnetic resonance imaging. Reduced-order computational models, specifically 0D and 1D models, offer the potential to simulate physical and dynamic systems with significant accuracy while maintaining minimal computational resources. Existing models, on the other hand, do not account for changes of energy at junctions.[1]

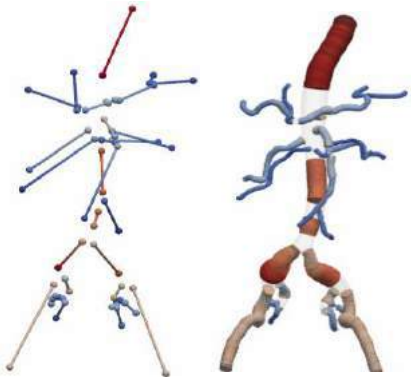

Figure 1: The gaps in the 3D model (left) and 1D model (right) illustrate the lack of junction modeling.

When addressing the accuracy of these models, changes in energy can cause significant discrepancies. Current methods for estimating pressure change employ phenomenological models that are specialized for certain junction geometries and specific blood flow conditions. We compare the performance of such a model for a large database of vascular models from multiple patients. Collectively, these vascular models compose of a total of approximately 3,000 junctions. Such a large comparison has not been done before. Based on our results we suggest improvements of the junction model so that it can be applied to a variety of junction parameters.

METHODS

Constructing reduced-order models from a 3D vascular model requires identifying various blood vessel properties such as vessel lengths, radii, blood viscosity, and flow rates. These parameters can be derived using an image segmentation or a centerline technique. [2,3] We used the open-source SimVascular software (simvascular.org) to extract these characteristics. [4] SimVascular's pipeline takes a 3D model as its input and extracts the geometry's centerlines.

The software generates a 1D solver input file using vessel connectivity, vessel length, and cross-sectional area obtained from the 3D model. The pipeline then maps each anatomical vessel to a corresponding lumped parameter element and computes its value. From this process we derive centerline section normal vectors, flow rate measurements at multiple time steps, area, and a point representation of every branch.

When a blood vessel splits, the original vessel is called the inlet and the resulting blood vessels are referred to as the outlets. Resistance R_k at a given outlet, k, can be calculated by applying the parameters produced by the SimVascular pipeline to

$$R_k = \frac{\rho Q_i}{2\pi^2 r_i^4}\left[\frac{1}{Q_k} + \frac{Q_k r_i^4}{Q_i r_k^4} - \frac{2r_i^2}{Q_i r_k^2}\cos\left(\alpha_{(i,k)}\right)\right] \quad (1)$$

where ρ represents the density of the fluid, blood, Q_i and r_i represent inlet flow rate and inlet radius respectively, Q_k and r_k represent outlet flow rate and outlet radius respectively, and $\alpha_{(i,k)}$ represents the supplementary angle between the inlet and outlet.[5]

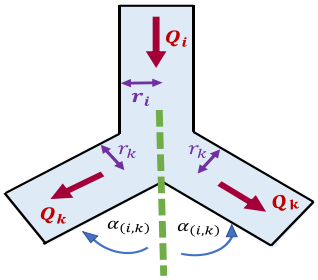

Figure 2: A junction with two outlets and the location of its parameters illustrated.

After solving for resistance, R_k, we can calculate change in pressure, ΔP_k, using the Hagen-Poiseuille equation

$$\Delta P_k = Q_k R_k \tag{2}$$

We programmed the junction model in Python using equations (1) and (2) as its numerical basis. The program outputs the change in pressure at the specified outlet upon being provided with the appropriate inlet and outlet properties as specified above.

RESULTS

We tested the robustness of the junction model using patient-specific data. We used 105 distinct vascular models from an open-source repository (vascularmodel.org). Each model contains pressure and flow data from each model captured at different time steps. The vascular models can be grouped into seven different categories: aorta, cerebrovascular, pulmonary, aortofemoral, congenital heart disease, coronary, and animal and miscellaneous. We calculated the error, e, between the pressure change between inlet and outlet, k, from the repository, ΔR_k, and the change in pressure produced by the junction model from equation (2), using

$$e = \left| \frac{\Delta R_k - \Delta P_k}{\Delta R_k} \right| \tag{3}$$

We calculated error for all the outlets of all the junctions, which produced a total of 3,886 outlets.

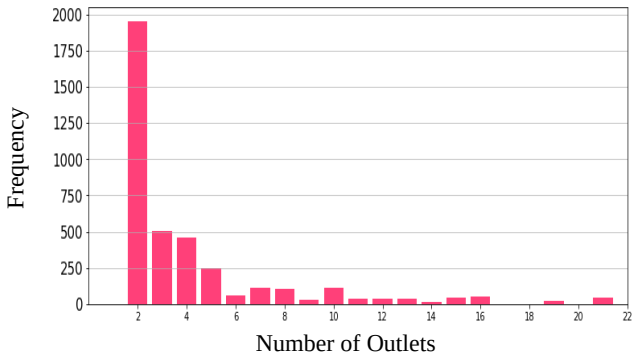

Figure 3: The distribution of outlet counts for every junction of every model in the repository.

In order to determine which vessel parameters produce junction model values closest to the repository values, i.e. which parameters produce the smallest errors, we created our own vascular models using SimVascular. SimVascular provides a complete pipeline from medical image segmentation to patient-specific blood flow simulation and analysis.[6] Creating our own models granted us anatomy of junction bifurcations as well as blood flow conditions. We created models with one inlet and two outlets that have a 45° angle between them and initialized a 50% flow rate between the outlets, meaning half of the inlet's flow traveled through each outlet. We experimented with different flow rates, specifically 8, 16, 24, and 32 cc/s.

Our current results and error analysis demonstrates that the lossy junction model does not accurately predict the pressure loss of the set of over 3,000 patient-specific junction geometries analyzed in our study. There are multiple possible reasons for this behavior. The original lossy junction model that employs formulas (1) and (2) had only been applied to bifurcation junctions simulated under steady flow. Furthermore, prior applications analyzed junctions with only two outlets whereas the anatomies we considered in this study include junctions with outlet counts varying from 2 outlets to 21 outlets. Finally, the vascular models we used were simulated under realistic, unsteady conditions with pulsatile flows.

DISCUSSION

In this work, we used actual patient-specific data and specially designed SimVascular models to test and suggest improvements for a model that measures pressure change at blood vessel junctions. Altering the junction model will aid its application to a variety of junction parameters. After improving the junction model, we can implement it to reduced-order models for cardiovascular blood flow, thereby ensuring that pressure change measurements are not neglected. Its implementation has the potential to improve the accuracy of current blood flow analysis.

We are in the process of creating more SimVascular models to test the junction model. Given the various parameters involved in the junction model, there are various control and experimental variables that we can use. For example, we can control or test the inlet and outlet lengths, the angles between the inlets and outlets, the number of outlets, the amount of blood flow through the inlet, and the distribution of flow between outlets. This lends itself to a further project that involves machine learning. We can use our current and future understanding of the specific effects that these junction parameters have on blood flow measurements to create a network that outputs the best version of the junction model based on the parameters that it is given, such as inlet flow rate, outlet count, and blood flow boundary conditions. Furthermore, the network would possess the potential to learn to differentiate between different vessel anatomy such as the seven categories that the repository vascular models are grouped into.

ACKNOWLEDGEMENTS

This work was supported by Stanford's Summer Undergraduate Research Fellowship and the McNair Scholars Program at Loyola Marymount University.

REFERENCES

[1] Mynard, J et al., *Numerical Methods in Biomedical Eng*, 31, 2015.
[2] Fleeter, C et al. *Computational Methods Appl Mech Eng*, 2019.
[3] Antiga, L et al. *Med Biol Eng Comput*, 46:1097–1112, 2008.
[4] Wilson, N et al. *J Med Devices*, 7: 040923, 2013.
[5] Chnafa, C et al. *Biomechanics*, 51:83 – 88, 2017.
[6] Marsden, A.L et al. *Annuals of Biomedical Eng.* 1 – 17, 2016.

BIAXIAL MECHANICAL PROPETIES OF RIGHT VENTRICULAR MYOCARDIUM IN ADVANCED PULMONARY ARTERIAL HYPERTENSION

Michael Bennington (1), Daniela Valdez-Jasso (1)

(1) Department of Bioengineering
University of California, San Diego
La Jolla, CA, USA

INTRODUCTION

Pulmonary arterial hypertension (PAH) is a progressive vasculopathy characterized by sustained elevated mean pulmonary arterial pressure imposing right-ventricular (RV) afterload.[1] Previous studies in early PAH have shown ventricular remodeling, hypertrophy, and myocardium properties.[1][3]. Here, we extended the disease timeline and investigated how the myocardium properties changed in advanced PAH using a well-established rat model of Sugen-hypoxia (SuHx).

METHODS

Tissue preparation. PAH was induced in the male Sprague-Dawley rats through a 20 mg/kg injection of Sugen 5416 (a vascular endothelial growth factor receptor blocker), followed by three weeks of hypoxia (10% O_2). The animals were then returned to normoxia for an additional 15 to 18 weeks to allow the disease to progress to advance PAH. Control animals were kept at normoxia for the same time period. Hypertension was confirmed in an open-chest surgery. The RV free wall was excised, and a square sample was cut from the middle of the tissue aligning one axis with the apex to outflow-tract (AOT) direction (x_1) and the perpendicular axis ran circumferentially (x_2). Five graphite markers were placed on the center region of the tissue surface to track tissue displacement. Side length and thickness measurements were taken, and four custom-made hooks were attached to each side of the sample. The sample was loaded on the Bose Electro-Force planar biaxial testing device. During the biaxial tests, the tissue kept in a 37°C bath of phosphate-buffered saline.

Mechanical testing. RV samples were pre-stretched with a 3.0 g tare load and subjected to displacement control biaxial testing. The x_1:x_2 stretch ratios were 1:1, 1:0.5, 1:0.25, 1:1, 0.5:1, 0.25:1, 1:1, with a maximum stretch of 10% of the *ex vivo* length. Each block consisted of 15 loading-unloading cycles at 0.5 Hz. The first block was used to ensure the tissue was pre-conditioned and the last 3 cycles of blocks 2-6 were point-wise averaged and used for analysis.

Constitutive equation. Loads measured on each axis were used to calculate the first Piola-Kirchhoff (PK1) stress tensor $\boldsymbol{P}$ using the unloaded dimensions measured before the test. The pixel location of the four exterior markers measured with an overhead camera sampling at 200Hz were used to calculate the deformation gradient tensor $\boldsymbol{F}$ *via* isoparametric mapping to a bilinear finite element. The reference configuration β_1 (**Fig. 1**) was defined to be the tare-loaded configuration, with the Green strain tensor $\boldsymbol{E}$ defined with respect to β_1:

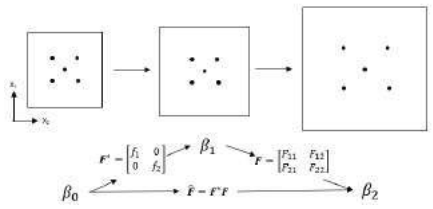

Figure 1: Mapping from stress-free reference state $\boldsymbol{\beta_0}$ to arbitrary test state $\boldsymbol{\beta_2}$.

$$\boldsymbol{E} = \frac{1}{2}(\boldsymbol{F}^T\boldsymbol{F} - I). \quad (1)$$

The second Piola Kirchhoff (PK2) stress tensor $\boldsymbol{S}$ relative to the tare state was calculated as $\boldsymbol{S} = \boldsymbol{F}^{-1}\boldsymbol{P}$.

The myocardium was assumed to be a planar hyperelastic material described by a Fung-type exponential strain-energy function defined as

$$W(\widehat{\boldsymbol{E}}) = C\left(e^{Q(\widehat{\boldsymbol{E}})} - 1\right) \quad (2)$$

where

$$Q(\widehat{\boldsymbol{E}}) = \hat{a}_1\widehat{\boldsymbol{E}}_{11}^2 + \hat{a}_2\widehat{\boldsymbol{E}}_{22}^2 + \hat{a}_3\widehat{\boldsymbol{E}}_{11}\widehat{\boldsymbol{E}}_{22} \quad (3)$$

is the Green strain tensor $\widehat{\boldsymbol{E}}$ referenced to the unloaded state (β_0). The

PK2 stress with respect to β_0 is thus

$$\widehat{\boldsymbol{S}}_{ij} = \widehat{\boldsymbol{F}}^{-1}_{ik}\boldsymbol{P}_{kj} = \frac{\partial W(\widehat{\boldsymbol{E}})}{\partial \widehat{\boldsymbol{E}}_{ij}} = Ce^{Q(\widehat{\boldsymbol{E}})}\frac{\partial Q(\widehat{\boldsymbol{E}})}{\partial \widehat{\boldsymbol{E}}_{ij}} \quad (4)$$

Using the mapping from β_0 to β_1 ($\boldsymbol{F}^*$), the deformation from the unloaded state β_0 to the current configuration β_2 is $\boldsymbol{F}^*\boldsymbol{F}$. Using this total deformation, (4) can be reformulated in terms of the experimental stretches Λ_i (β_1 to β_2):

$$S^M_{ii} = Cf_ie^{Q(\boldsymbol{\Lambda})}\left(4a_i((f_i\Lambda_i)^2-1) + 2a_3\left(\left(f_j\Lambda_j\right)^2-1\right)\right) \quad (5)$$

where

$$Q(\boldsymbol{\Lambda}) = \sum_i^2 a_i((f_i\Lambda_i)^2-1)^2 + a_3((f_i\Lambda_i)^2-1)\left(\left(f_j\Lambda_j\right)^2-1\right), \quad (6)$$

$i \neq j$, $a_k = \hat{a}_k/4$, and S^M_{ii} the PK2 stress with respect to β_1. In (5), f_i are the pre-stretches in the normal direction.

Numerical implementation. Data were then fit to these reformulated model equations using the following objective function:

$$\phi(\theta) = \sum_i^2\sum_j^n\left(S_{ii}(t_j) - S^M_{ii}(t_j;\theta)\right)^2 \quad (7)$$

where θ is the set of parameters $\{C, a_1, a_2, a_3, f_1, f_2\}$ and $S_{ii}(t_j)$ is the experimentally-derived stress tensor. The parameter estimation was carried out in SciPy using the Limited Memory BFGS algorithm. The material parameters were bounded to be positive and the pre-stretches greater or equal to 1. Using the optimal set of parameters, the strain-energy surface for each animal was generated. Within each group, the surfaces were point-wise averaged with their respective upper and lower bounding surfaces. The averaged and bounding surfaces were then fit to the strain-energy function to obtain a set of parameters representative of the control and SuHx RVs. The stresses at equibiaxial strains of 0.06 were compared between axes and groups using two-factor ANOVA. Significance was determined at α of 0.05.

RESULTS

Hypertension was confirmed in the treated group (RV end-systolic pressure of 65±11 mmHg in the disease *vs* 23±6 mmHg in control). RV thickness increased from 1.46±0.16 mm to 1.8±0.6 mm in and RV mass increased from 0.33±0.5 g to 0.64±0.11 g. The mechanical data from the control and treated animals were closely fitted with a coefficient of determination (R^2) ranging from 0.82 to 0.95 (**Fig. 3**). The mean strain energy surface was steeper for the SuHx animals, and the largest change (percent difference) in parameters being the stiffness scaling parameter *C*, and the circumferential exponential coefficient $\hat{a}_2$. The RV myocardium was anisotropic, but the differences between AOT and circumferential stresses were only statistically significant in PAH (**Fig. 2**). The shear components of the strain tensor were negligible throughout the tests for control and treated animals.

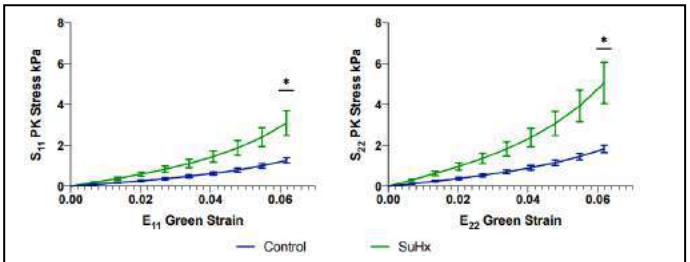

Figure 2: Mean and standard errors of the mean equibiaxial stress-strain relations obtained from normo- and hyper-tensive right-ventricular myocardium.

DISCUSSION

In the advanced stage of PAH, there was a significant increase in stiffness on both axes, which is consistent with previous findings in the early-stage PAH[1]. This study provides evidence that, while the tissue remodels along the fiber and transverse axes, there are larger changes in the circumferential direction, leading to a greater level of anisotropy in the PAH ventricle. In addition, while there was an increase in the free wall thickness from control to PAH, this change was far lower than was seen in the studies of the early stages of PAH. While in those experiments there was a two-fold increase in RV thickness[1], the increase in thickness of these later SuHx animals was ~25%. This indicates that the RV continues to remodel, with a thinning of the wall.

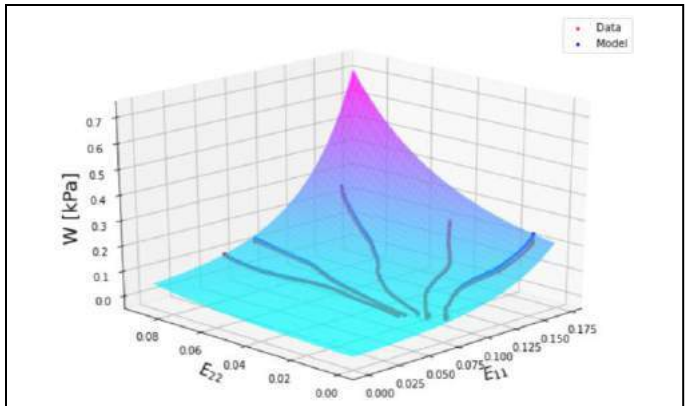

Figure 3: Strain-energy surface generated with biaxial.

The adjusted Fung model used in this study was able to approximate the experimental data well while also taking into consideration the tare applied to the tissue. Given that shear components were negligeable in the tests, the mapping from β_0 to β_1 being only in the normal directions was a valid assumption. By incorporating the preload stretches into the model, we can better back extrapolate the toe region of the tissue within the context of the model and map all the tissues to a common reference configuration, independent of preload stretch, which itself depends on the mass and tissue dimensions. This is critical because a fixed tare load will lead to different levels of initial stretch between axes and between tissues, meaning different regions of the strain-energy surfaces are being compared. With this modification, corresponding regions can be properly compared.

While the model fit well and provided insights about the remodeling in advanced PAH, it was unable to explain the asymmetrical axis coupling that was noticed in both the control and disease state tissues, where the strains in the circumferential direction had a larger contribution to the stress on the AOT axis than the AOT strains had to the circumferential stress. In the current formulation of the Fung-type model only has a single coupling term $\hat{a}_3$, which is not sufficient to explain this phenomenon. This, in addition to the increased thickness in both the control and disease state tissues, suggest that the transverse axis contributions to the planar stress may be more significant in older animals and in the more advanced stages of the PAH.

ACKNOWLEDGEMENTS

This work was funded by the AHA 16SDG29670010, NHLBI 1R25HL145817-01, and NHLBI 1R01HL155945 - 01

REFERENCES

[1] Vélez-Rendón, D et al., *J Biomech Eng*, 141(9):091011, 2019.
[2] Hill, M et al., *Ann Biomed Eng*, 42:2451-2465, 2014
[3] Vélez-Rendón, D et al., *Pulmonary Circulation*, 8(4):1-13, 2018.

CONTRASTING THE MECHANICS OF HEALTHY AND ASTHMATIC AIRWAY DEVELOPMENT USING IN SILICO MODELING

N. Lau (1), M. Maghsoudi-Ganjeh (1), M. Eskandari (1,2,3),

(1) Department of Mechanical Engineering
University of California, Riverside
Riverside, CA, USA

(2) Department of Bioengineering
University of California, Riverside
Riverside, CA, USA

(3) BREATHE Center, School of Medicine
University of California, Riverside
Riverside, CA, USA

INTRODUCTION

The most recent report published by the Global Asthma Report enumerates over 300 million people suffer from asthma, killing an estimated 1000 people daily [1]. Despite existing methods to alleviate asthma related symptoms, such as inhalers and nebulizers, there are still no known cures; lung mechanics is a vastly underexplored area of research, and airway mechanics specifically is misunderstood: recently, our lab disproved the long-standing concept of smaller bronchi being more compliant, sparking reconsideration of the role of distal airways in breathing systems, such as ventilators, which have built on these concepts [2]. Here in this study, we use finite element modeling to investigate the beneficial or harmful effects of remodeling on airway obstruction by comparing the development of healthy versus asthmatic airways.

A 2007 experimental study by Plopper et al. considered the disrupted growth of airways in monkeys by toxin and pollutant exposure [3]. From 1 to 6 months, normal airways grow by one-third in diameter and double in length. In comparison, grown asthmatic airway dimensions were significantly altered (relatively shorter in length and with a narrower diameter), and notable variations in the contractile smooth muscle orientation, responsible for bronchoconstriction and obstruction of the airway lumen, was observed. Here we implement bronchoconstriction via smooth muscle pressure loading using SolidWorks and Abaqus to compare the obstruction in healthy and diseased cases. Additionally, a third theoretical scenario is constructed, where the altered diseased airway dimensions are paired with the healthy smooth muscle orientation to evaluate the extent of the roles of morphology and bronchoconstriction. All analyses are informed by experimental parameters from the literature. We hypothesize this remodeling is a protective mechanism and that the narrowing of the airway will be greatly impacted by the angle of the pressure induced by the smooth muscle, but decreased growth in asthmatic airways may help to maintain structural integrity of the lumen.

METHODS

Bronchial models were constructed using the 6 month old healthy and asthmatic (ozone exposed) airway geometry of infant rhesus monkeys [3]. The third theoretical airway used the dimensions of the asthmatic model and the smooth muscle orientation of the healthy case (detailed below). The standardized diameter (d) as illustrated in Plopper 2007 was set to 0.5mm, based on anthropometric relationships [4], and was used to calculate the airway diameter (D) and length (L) 6 month grown parameters. The thickness of the airway walls (the inner mucosa thickness t_i and outer submucosa thickness t_o) are matched to the dimensionless, experimentally-specified, geometric ratios by airway generation, as shown in Table 1 [3,4]. The inner radius (R_2) refers to the distance from the center of the airway to the submucosa layer, while the innermost radius (R_1) refers to the distance from the center of the airway to the mucosa layer [4].

Bronchoconstriction was implemented by applying pressures via a smooth muscle wrapped around the airway cylinder, either orthogonally oriented relative to the airway axis for the healthy and theoretical case, or at 30 degrees for the diseased case, (with matched surface areas for all three study cases). The maximum contractile load of 0.147 MPa [5] was used and the instance where the lumen collapsed and inner layer self-contacted (in the limiting asthma model only) was analyzed for equivalent comparisons. An elastic modulus of 30 kPa and Poisson's ratio of 0.45 was used, in accordance with the literature [2,3,6]. Hybrid elements are used to account for the near compressible nature of the airways and model parameters are also listed in Table 1 [6]. The extent of obstruction is quantified (as a percent of final to initial lumen cross-

section), and the maximum principal stresses induced due to bronchoconstriction are compared.

Table 1: The geometric, material, and loading parameters used to construct and analyze the healthy and asthmatic airways are listed. The third theoretical airway utilized asthmatic model dimensions and the healthy smooth muscle orientation.

Geometric Parameters		
	6 mo Healthy	6 mo Asthmatic
D (mm)	0.675	0.475
L (mm)	1.2	1.001
t_o (mm)	0.1125	0.0792
t_i (mm)	0.0045	0.00317
R_2 (mm)	0.225	0.1583
R_1 (mm)	0.2205	0.15517
Smooth Muscle Orientation	0 º	30º
Material & Loading Parameters		
Pseudoelastic modulus (Young's Modulus)		30kPa
Poisson's Ratio (Submucosa & Mucosa)		0.45
Maximum Pressure of Smooth Muscle		0.147 MPa
Linear Hybrid Elements		71 – 92K
Nodes		78 – 103K

RESULTS

Figure 1 illustrates the obstruction pattern and stress distribution of the deformed (A) healthy, (B) asthmatic, and (C) theoretical airway configurations. The asthmatic airway is seen to self-contact and greatly obstruct. Maximum principal stress magnitudes, areas and percent obstruction are listed in Table 2.

Table 2: Quantification of obstruction and principal stresses in the healthy, asthmatic, and theoretical airways.

Airway Obstruction			
Model	Original Cross-Sectional Internal Area [mm^2]	Internal Cross-Sectional Area after Deformation [mm^2]	**% Obstruction**
Healthy Airway	0.1527	0.1195	21.7%
Asthmatic Airway	0.0755	0.0091	87.9%
Theoretical Airway	0.0755	0.0556	26.4%
Principal Stresses in Obstructed Region			
Healthy Airway			4.863e-04 MPa
Asthmatic Airway			1.659e-02 MPa
Theoretical Airway			4.672e-04 MPa

DISCUSSION

In this study we characterize obstruction mechanics in silico, comparing experimentally measured airway dimensions and smooth muscle orientations in healthy and asthmatic rhesus monkeys to examine the potential advantages versus disadvantages of pulmonary remodeling. We find that the asthmatic airway with 30 degree smooth muscle results in much greater obstruction (87.9%) compared to orthogonal smooth muscle models (21.7% and 26.4%). This model also buckles into a 2 fold pattern, where reduced folding patterns are known to cause greater obstruction than higher modes [4,5]. Furthermore, the principal stress magnitudes are multiples greater in the asthmatic airway.

The theoretical airway model (with the smooth muscle orientation of the healthy scenario and dimensions of the asthmatic lumen), exhibits slightly greater stresses than the healthy case but much lower stress values than the asthmatic model; this suggests the smooth muscle orientation plays a more notable role in airway mechanics than the geometry. Conversely, the theoretical (asthmatic) dimensioned airway does not obstruct to the same extent as the healthy model, suggesting the narrowed geometry inhibits collapse of the airway under identical loads.

This model has limitations. For instance, here we use a representative length of the airway with a single smooth muscle instead of the physiologically observed stacks of muscle spirals wrapped in series along the length of the bronchi; contractile neighboring effects are not considered [3]. However, models of airway collapse are primarily 2D, and this 3D approach considering the angle of the smooth muscle for the first time yields new insights [4,5]. Additionally, this model does not account for the tethering effects of cartilaginous bronchial scales or the parenchyma, which will enable elastic recoil and resist lumen collapse [3]. While this simplified approach provides new practical considerations to explore further, it is idealized and can benefit from including additional complexities including airway anisotropy [2].

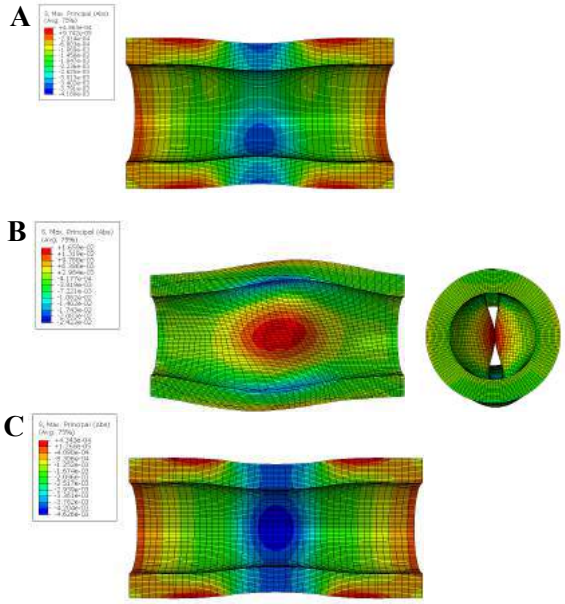

Figure 1: (A) healthy, (B) asthmatic (side and cross-sectional view), and (C) theoretical airway deformations with principal stress illustrations.

We hypothesized bronchial remodeling to have beneficial effects but conclude that while narrowed airway morphology may maintain structural integrity and keep the lumen unobstructed, the orientation of the smooth muscle dominates lumen behavior and resulting stresses. These findings may have implications for clinical interventions aimed at targeting bronchoconstriction and smooth muscle mechanisms, such as bronchial thermoplasty.

REFERENCES

[1] Addo-Yobo, EO, et al. (2018). The Global Asthma Report 2018. Retrieved from http://www.globalasthmareport.org/
[2] Eskandari, M, et al, *J. Appl. Physiol*, 125.3 (2018): 878-888.
[3] Plopper, CG, et al. *Toxicol. Pathol.,* 35.1 (2007): 97-110.
[4] Wiggs, BR, et al. (1997). *J. Appl. Physiol, 83*(6), 1814-1821.
[5] Lambert, RK, et al. (1993). *J. Appl. Physiol, 74*(6), 2771-2781.
[6] Eskandari, M, et al. *Materials* 6.12 (2013): 5639-5658.

MECHANOCHEMICAL COMPARISON BETWEEN HYDROGEL AND SILICONE GEL USED FOR STUDYING STIFFNESS SENSING BY ADHERENT CELLS

Kathleen T. Heusser*, Nikhil Mittal*, Mohanish K. Chandurkar*, Zhongtian Zhang*, Karrar T. Alofari, Jeffrey S. Allen**, Bruce P. Lee*, Fei Long**, Sangyoon J. Han***

*Biomedical Engineering
Michigan Technological University
Houghton, MI, USA

**Mechanical Engineering-Engineering Mechanics
Michigan Technological University
Houghton, MI, USA

INTRODUCTION

Physical characteristics of a cell's environment impact cellular function and development. Rigidity of the extracellular matrix (ECM) is sensed by adherent cells, eliciting multiple protein signaling pathways, which ultimately activate DNA in the nucleus. Force across cell-ECM adhesion molecules induces a conformational change which can accommodate binding or phosphorylation of other cytoskeletal molecules. It is important to comprehend the traction force transmission from cells to the ECM as a function of ECM stiffness, as it determines the force across the adhesion structure. Ultimately, this understanding can lead to better therapeutic strategy in cancer metastasis, atherosclerosis, stem cell differentiation, and other fields[1,2,3].

Investigation of potential mechanisms of the relationship between traction force transmission and substrate stiffness has unearthed some contradictory results. Studies ranging from 2005-2017[2,4,5,6] indicate a monotonic (linear) relationship between stiffness and focal adhesion (traction) force, consistent with current knowledge of mechanotransduction. However, some have shown opposite findings: decreased traction with increasing stiffness[7]. These studies support their data with a molecular clutch mathematical model.

To reproduce either of these findings, a graduate student in Han lab at MTU has measured traction force of 3T3 (mouse fibroblast) cells with varying gel stiffness. The result was consistent not with the monotonic trend but with the biphasic trend; that is, after a short rise until 5kPa, traction decreases with increasing stiffness. This is surprising, as cell types and stiffness range was consistent between this study and Roca-Cusachs et al[1]. After interpretation of the plot and with the understanding about the stiffness-sensing theory, we hypothesized that most-likely cause of this different response is the difference in mechanical and chemical characteristics of the silicone gel used in Han lab (Q-gel, made of two components QGel 920A and 920B) and the polyacrylamide (PAA) hydrogel, formula (C3H5NO)n.

In this study, we show that Qgel and PAA gel differ significantly in hydrophobicity, although they can be similar in stiffness; with an understanding of this data, we propose that hydrophobicity dominates cell spreading and adhesion.

METHODS

Polyacrylamide (PAA) hydrogel was synthesized on acid washed coverslips using a mixture of acrylamide and bisacrylamide at different ratios, yielding different stiffnesses. Qgel920 from Quantum Silicones was synthesized with different ratios of components A and B to manipulate stiffness. Contact angles were photographed using a microscope attached to a camera; the images were analyzed using ImageJ software with the LB-ADSA plugin[8] to quantify the contact angles for each gel. Plasma treatment of Qgel and subsequent contact angle measurement established that the contact angle (hydrophobicity) of Qgel can be easily adjusted. Gels' attractive capabilities (stickiness) and stiffnesses were measured via Atomic Force Microscopy, although first the Qgel had to be coated with 1% Bovine Serum Albumen (BSA) for one hour to minimize the surface charge-induced attractive force to the cantilever (Fig. 3). Storage moduli (G') for Qgel's stiffness spectrum at all mixing ratios was quantified using a DHR-2 hybrid rheometer time sweep program in TRIOS software (Fig. 1).

RESULTS

First, rheometry tests over the range of Qgel mixing ratios (1:1 - 1:2) produced stiffness values within a range similar to that of PAA (Table 1). Gutierrez et al[9] have calculated the stiffness of Qgel by applying a known shear hydrodynamic stress using a microfluidic device and measuring the resulting shear strain, but rheometry experiments have given slightly different values. See Fig. 1 for an example of how storage modulus, G', increases with time, coming nearly to a plateau at 10 hours.

Table 1: Rheological Spectrum of Qgel

Mixing ratio	1:1.0	1:1.1	1:1.2	1:1.5	1:2.0
G' (kPa)	0.7	1.3	2.7	6.0	13.0
G' reported by Gutierrez et al.	0.7	3.7	N/A	N/A	18.0

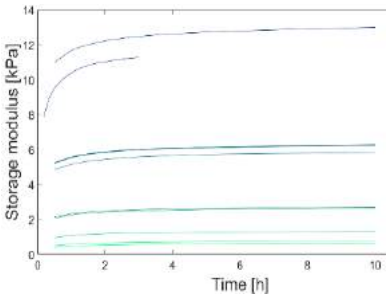

Figure 1. Qgel storage modulus (G', Pa) as a function of time during the curing process. Lines progress from light to dark with increasing amount of Qgel component B added (1:1, 1:1.1, 1:1.2, 1:1.5,1:2).

Secondly, however, contact angle measurement showed that Qgel (120º-130º) was much more hydrophobic than PAA (20º-30º). (Fig. 2A,B,D). This suggests that the effect of surface hydrophobicity on cell adhesion, and thus on spreading, could potentially contribute to inconsistency between literary PAA and laboratory Q gel results.

Interestingly, we also found that while Qgel remained consistently hydrophobic across multiple stiffnesses, PAA showed inverse correlation between stiffness and hydrophobicity; the higher PAA stiffness, the lower its contact angle (Fig. 2D). The effect of stiffness on hydrophobicity was measured for both gels using a Mann-Whitney U-test; the null hypothesis was rejected for PAA gel only.

To make the Qgel surface more hydrophilic, we treated Qgels with plasma for 30 seconds and measured the contact angle. This treatment made the surface successfully hydrophilic, with an average angle of 53º (Fig. 2C,D), again with no stiffness dependency. Longer plasma treatment has been attempted; however, the contact angle did not decrease further.

To further test the surface characteristics of the Qgel, we have performed nano-indentation tests using atomic force microscopy (AFM). Even in PBS, we reproducibly observed that there was a huge attractive force to the AFM cantilever well before actual contact to the gel surface. Treating the gel with a bovine serum albumin (BSA), we were able to remove the attractive force and obtain a flat baseline (Fig. 3, see positions indicated by arrows). We are in the process of estimating Young's moduli from the force-displacement curves.

DISCUSSION

Our data show that the high-refractive silicone gel surface, i.e., Qgel, is extremely hydrophobic compared to a common hydrogel, i.e., PA gel. This hydrophobicity is reduced when treated with plasma. Future experiments will utilize plasma-treated Qgels and untreated Qgels to test how hydrophobicity affects cell adhesion and spreading, independently of stiffness. This will determine whether plasma treatment, by decreasing hydrophobicity, allows cells to mimic the results found using PAA gel: spread increasing with stiffness. We anticipate the result that the substrate hydrophobicity dominates cell spreading and adhesion; this will resolve at least some of the discrepancies between stiffness-sensing studies utilizing silicone and hydrogels.

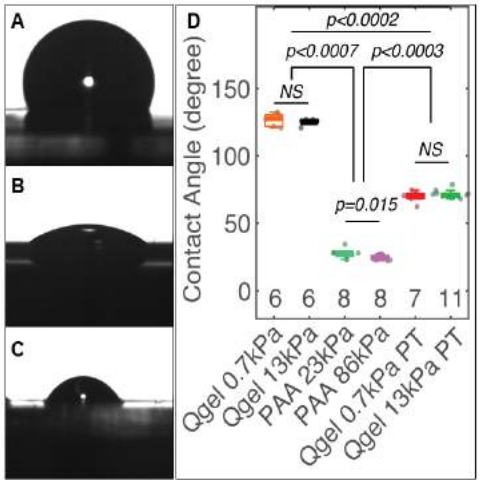

Figure 2. A: 0.7 kPa Qgel ; B: 13.0 kPa Qgel ; C : 13.0kPa Qgel with 30s plasma treatment; D : Box plot of contact angle for each gel type and condition. PT indicates Plasma Treated; numbers on X axis represent sample number *n* for each stiffness.

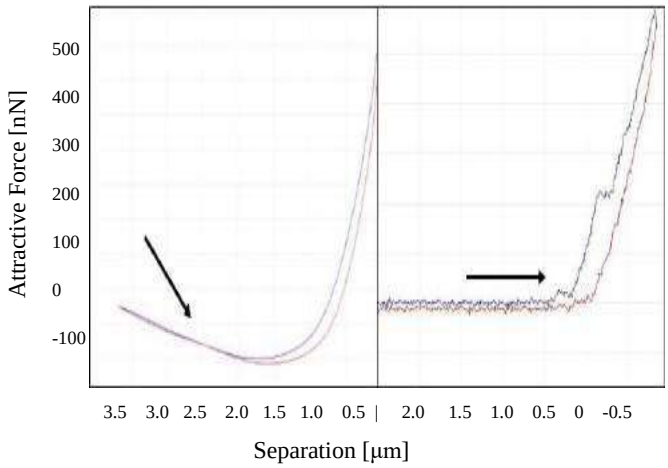

Figure 3. AFM Force-Distance Curve with Qgel before (L) and after (R) BSA coating. Note the large attractive force causing a curved baseline (see direction of arrows), even when the tip is 3 μm away from the gel surface. The blue curve represents the approach of the AFM tip to the gel ("trace"), whereas the red curve shows the "retrace" force as the cantilever leaves the gel's surface.

ACKNOWLEDGEMENTS

We would like to acknowledge Dr. Faith Morrison of the MTU Rheology Lab for assistance with equipment, and the Portage Health Foundation for support. This work was funded by NIH R15GM135806.

REFERENCES

[1] Elosegui-Artola, A. et al. Mechanical regulation of a molecular clutch defines force transmission and transduction in response to matrix rigidity. Nat Cell Biol 18, 540–548 (2016).
[2] Ghibaudo, M. et al. Traction forces and rigidity sensing regulate cell functions. Soft Matter 4, 1836 (2008).
[3] Dupont, S. et al., (2011). Role of YAP/TAZ in mechanotransduction. Nature *474*, 179–183.
[4] Han, S. J., Bielawski, K. S., Ting, L. H., Rodriguez, M. L. & Sniadecki, N. J. Decoupling Substrate Stiffness, Spread Area, and Micropost Density: A Close Spatial Relationship between Traction Forces and Focal Adhesions. Biophysical Journal 103, 640–648 (2012).
[5] du Roure, O. et al. Force mapping in epithelial cell migration. Proc Natl Acad Sci U S A 102, 2390 (2005).
[6] .Oria, R. et al. Force loading explains spatial sensing of ligands by cells. Nature 552, 219–224 (2017).
[7] Elosegui-Artola, A., Trepat, X. & Roca-Cusachs, P. Control of Mechanotransduction by Molecular Clutch Dynamics. Trends in Cell Biology 28, 356–367 (2018).
[8] Stalder, A. F. et al. Low-bond axisymmetric drop shape analysis for surface tension and contact angle measurements of sessile drops. Colloids and Surfaces A: Physicochemical and Engineering Aspects 364, 72–81 (2010).
[9] Gutierrez, E. et al. High Refractive Index Silicone Gels for Simultaneous Total Internal Reflection Fluorescence and Traction Force Microscopy of Adherent Cells. PLoS ONE 6, e23807 (2011).

COLLAGEN V PROMOTES CELL CONTRACTILITY COMPARED TO COLLAGEN I

Shaina P. Royer (1), Nikhil Mittal (1), Sangyoon J. Han (1)

(1) Department of Biomedical Engineering
Michigan Technological University
Houghton, MI 49931, USA

INTRODUCTION

Collagen is the primary structural protein in the human body. Most types of collagen have a fibrillar triple helix structure. Collagen I is by far the most common type of collagen. It is frequently found alongside collagen V whose globular N terminal is thought to play a regulatory role in the formation of collagen fibrils [1]. Yet, collagen type-specific cell behavior has not been fully understood. Differences in the behavior of fibroblast have been observed in fibroblasts cultured on collagen I compared to collagen V. While fibroblasts cultured on collagen V initially display similar levels of proliferation to those cultured on collagen I. This drops off on the 3rd day and by the 5th day there is less coverage of the plate than there was on the 3rd day. Additionally, fibroblasts cultured on collagen V form a ball on the 3rd day with pieces of collagen V from the substrate remaining attached to the cells in the ball [2]. We hypothesized that this behavior is due to an increase in contractility via strong integrin mediated adhesions causing the collagen V to get ripped off from the underlying glass substrate.

To test this hypothesis, we have used traction force microscopy (TFM), a technique used to quantify the contractile force a cell exerts on the deformable substrate, to compare traction transmitted by cells on collagen I vs. collagen V by coating them on a high-refractive silicone gel. Compared to the previous study [2], our bonding of collagen to the gel was covalent, i.e., amine-carboxyl interaction, thus prevents the potential rupture of collagen layer from the gel layer. Thus, the deformation and traction would well represent the contractile state of the cells on each collagen.

METHODS

To fabricate high-refractive index TFM gel with an elastic modulus of 2 kPa, Q-gel 920 (Quantum Silicones) parts A and B were mixed in a 1:1.2 ratio for 2 minutes on a vortex at high speed followed by gentle hand mixing. The gel mixture was pipetted into a glass bottom dish then spin-coated to a thickness of 45 µm and cured in an oven at 80 °C for 2 hours. The cured gel was stored in PBS. Silane coating was performed by liquid deposition using a 5% solution of (3-Aminopropyl) triethoxysilane in absolute ethanol. Bead coating was performed by sonicating a mixture of 50 µL of 100x 1-Ethyl-3-(3-dimethyl aminopropyl)carbodiimide (EDC), and 1 µL of 0.04 µm diameter carboxyl-coated dark-red polystyrene microspheres in DI water for 15 minutes then applying it to the silane coated gel for 10 minutes. To coat the collagen, collagen I or V was diluted in 1% EDC solution in PBS to a concentration of 1 µg/mL. The silicone gel was submerged in the collagen solution for 30 min and rinsed with PBS. NIH 3T3 fibroblasts expressing mRuby-paxillin were cultured in DMEM with 10% fetal bovine serum, 1% Penicillin/Streptomycin, and 1% L-Glutamin and seeded onto the TFM substrate. After incubating the cells at 37 °C for 4 hours, imaging was carried out using total internal reflection with a 60x oil-immersion objective for both beads and mRuby-paxillin. Bead images were taken with Cy5. After imaging, the cells were lysed using 10% bleach and reference images for relaxed gel configuration were taken. From bead images, traction reconstruction was done using MATLAB-based TFM package [3]. From paxillin images, focal adhesion morphologies and populations were analyzed using a custom-built function written in Han Lab [4].

RESULTS

To compare overall contractility of cells on the two collagens, we plated 3T3 fibroblasts on a soft, 2kPa silicone bead-coated gel that were further coated with collagen I or collagen V. Using bead images, we quantified traction distribution (Fig. Overall traction distribution showed that traction magnitude was greater for cells cultured on collagen V (Fig. 1B) than cells cultured on collagen (Fig. 1A1A, C).

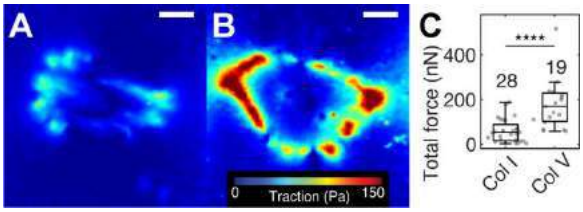

Figure 1: (A-B) Representative traction maps of a cell cultured on collagen I (A) and a cell cultured on collagen V (B). Scale bar = 10 μm. (C) A boxplot of the total force per cell on collagen I vs. on collagen V. ****: p<1e-6 by Mann-Whitney U test.

The measuring total force in cell, which was the integration of traction over whole cell area.

To seek how the force became higher, we performed adhesion imaging and quantified basic morphological parameters and densities using focal adhesion (FA) segmentation and detection of diffraction-limited spots, i.e., nascent adhesions (NAs) (Fig. 2). Qualitatively, we observed that compared to cells on collagen I, which showed lots of adhesions in both perimeter and interior (Fig. 2A), cells on collagen V exhibited primarily only focal adhesions along the perimeter (Fig. 2B). Quantification of FAs showed that there was no significant difference in FA area (Fig. 2C), whereas top 10 percentile of FAs of cells on collagen V were longer than those of cells on collagen I (Fig. 2D). Also, the bottom 30 percentile of FAs in cells, as well as the entire FA population (data not shown) on collagen V were wider than those in cells on collagen I (Fig. 2E). These suggest that collagen V promotes a subset of strong FAs, preferentially at cell perimeter. Quantification of the adhesion density made this interpretation clearer. Traction at all adhesion types is dramatically increased at all types of adhesion types for cells cultured on collagen V as well as a broader distribution of traction per adhesion (Fig. 2I). Densities of both FAs (Fig. 2F) and NAs (Fig. 2G) of cells on collagen V were lower than those on collage I, suggesting that the high force observed on collagen V-coated gel was not from the quantity of adhesions but from strong cytoskeletal tension induced by cells' collagen V binding. Furthermore, cell spreading was much larger for cells on col V than cells on col I (Fig. 2H). By reading traction magnitudes at the locations of identified adhesions from the traction maps, we sampled traction per adhesion type and per collagen type. We found that in general there were increasing amount of traction from NAs to focal complexes (FCs) to FAs regardless of the type of collagen. However, we also found that the increase in force on collagen V per adhesion was much greater than traction at the matching adhesion types (Fig. 2I). This represents that indeed cells, even with fewer adhesions, transfer much larger force through them.

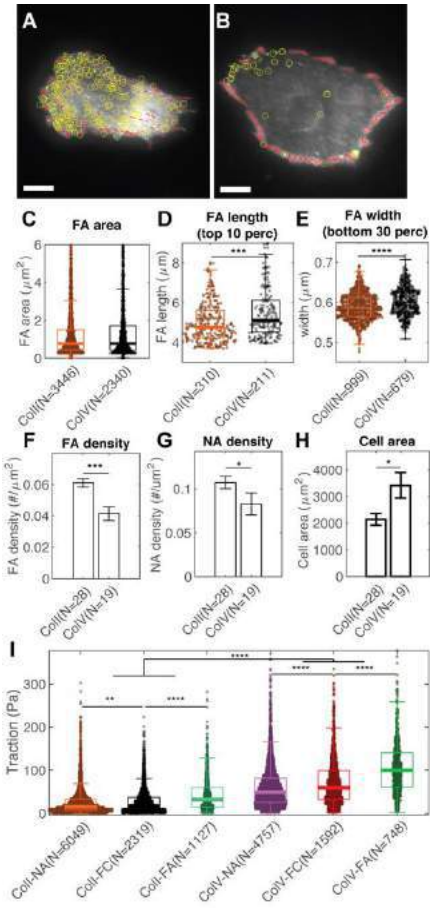

Figure 2: (A,B) Representative paxillin images overlaid with adhesion segmentations (red: focal adhesions (FAs), green: focal complexes (FCs), yellow: nascent adhesions (NAs)) for a cell cultured on Collagen I (A) and on Collagen V (B). Scale bar = 10 μm. (C-E) Box plots of areas (C), lengths (D) and widths (E) of focal adhesions. (F-H) Bar plots of focal adhesion density (F), nascent adhesion density (G), and cell area (H). (I) Average traction magnitude measured from NA, FC and FA. N represents the number of adhesions. The data is from M=25 cells for collagen I and M=28 for collage V condition. *: p<0.05, **: p<1e-3, ***: p<1e-5, ****: p<1e-10 by Man-Whitney U test.

DISCUSSION

Our results on the increased in total force in the cells cultured on collagen V compared to collagen I tentatively confirm our hypothesis that collagen V induces a strong myosin contractility. The exact pathway that leads to myosin contractility remains to be determined. A likely candidate is the integrin heterodimer $\alpha_{11}\beta_1$ that specifically binds to collagen V but not to collagen I [5]. To test this hypothesis, we plan on using anti-integrin α_{11} antibody to block the ability of the integrin $\alpha_{11}\beta_1$ and repeat the TFM experiment outlined in the methods section.

Another possible biomechanical explanation is when the local elasticity of the collagen I coating is significantly lower than that of the collagen V coating and also the underlying gel. If this is true, the displacement would primarily happen in the collagen coating rather than the silicone gel, therefore said displacement would not be recorded via the displacement of the fluorescent beads, resulting in relatively little bead displacement for the contractility of the cell. To investigate this possibility, we plan on performing an atomic force microscopy (AFM) wherein a glass slide is coated with collagen and the AFM tip is chemically bonded to a collagen fibril and retracted. Since this setup will allow for measurement of the local collagen stiffness I and V, we will be able to determine if the experimental data for cells cultured on collagen I is accurate.

Additionally, an increase in cell spread area had been previously reported to cause an increase in cell contractility, therefore the increase in spread area may be involved in the increased contractility of cells cultured on collagen V [6]. In light of the substantial increase in total force the reduction in focal adhesion density in cells cultured on collagen V is surprising given that a decrease in focal adhesion density has been previously correlated with a decrease in contractility [7]. Taken together, out data suggest that collagen V induces mechanoresponses of cells to generate high contractility with fewer focal adhesions.

ACKNOWLEDGEMENTS

I would like to thank Pavlis Honors College for providing funding. This work was funded by NIH R15GM135806.

REFERENCES

[1] Kielty, C et al, *Connective Tissue and Its Heritable Disorders: Molecular, Genetic, and Medical Aspects, Second Edition*, ch. 2.1, 2002
[2] Kihara, T et al., *Cell and Tissue Research*, 318:343–352, 2004
[3] Han, S.J. et al., *Nature Methods*, 12:7:653–6, 2015
[4] Han, S.J. et al., BioRxiv 735183, 2021
[5] Zeltz, Z eta al. *Biochimica et Biophysica Acta (BBA) - General Subjects*, 1840:2533-2548, 2014
[6] Oakes, P et al, *Biophysical Journal*, 107:825-833, 2014
[7] Han, S et al. *Biophysical Journal*, 103:640-848, 2012

EXPLORATION OF THE IMPACT OF BLOOD VISCOSITY IN THE DEVELOPMENT OF EMBOLISMS AT THE PULMONARY ARTERY OF HIGH-RISK COVID-19 PATIENTS

Ifti Hossain (1), Diana L. Alatalo (2), Fatemeh Hassanipour (1,2)

(1) Department of Biomedical Engineering
The University of Texas at Dallas
Richardson, TX, USA

(2) Department of Mechanical Engineering
The University of Texas at Dallas
Richardson, TX, USA

INTRODUCTION

Blood viscosity is often an overlooked aspect when it comes to healthcare. Currently, critically ill patients diagnosed with severe acute respiratory syndrome coronavirus 2 (COVID-19) exhibit elevated levels of fibrinogen and inflammatory indicators, which have been seen to reflect intravascular thrombosis (clot formation). One study found thrombotic incidences were 48% in COVID-19 patients admitted into the ICU [1]. Increases in fibrinogen and inflammatory factors can increase blood viscosity, which can lead to thrombosis and impact perfusion rates. A higher blood viscosity indicates less blood and nutrients being delivered to tissues. Increased blood viscosity decreases cardiac output and tissue perfusion [2]. Decreased perfusion rates coupled with other health problems have been shown to increase the prevalence of cardiovascular events and thrombogenesis [3].

In the context of COVID-19, a high-risk patient could have a history of hypertension, diabetes, inflammation, and respiratory distress. These factors combined with COVID-19 infection could lead to a cascade effect and form a thrombosis due to elevated fibrinogen levels and erythrocyte aggregation. A thrombosis can then break loose and travel to the pulmonary arteries, which impedes gas exchange [4]. To understand how increases in blood viscosity due to COVID-19 infection can affect blood flow, a computational fluid dynamics (CFD) simulation of the pulmonary artery was undertaken.

METHODS

An analysis of vascular behavior was conducted using ANSYS computational fluid dynamics (CFD) software. An open-source geometry model of a carotid artery was augmented to resemble a subsegmental pulmonary artery. The diameters of the arteries were 63 mm for the inlet, 44 mm for the large output, and 3 mm for the small output, which were used to make the mesh. These dimensions are very similar to vessel sizes of the subsegment branches from the pulmonary artery, as initial branches have diameters of 6-7 mm and taper down to even 1.5 mm before the alveoli in the lung [5]. Thus, the mesh can be applied in the context of pulmonary embolism and understand the pulmonary arterial flow. The fluid model used was laminar flow, as it best describes the motion of blood through a vessel. Poiseuille's Equation (1) was used to implement blood viscosity and the dimensions of the mesh model [6]. Other parameters can be seen in Table 1, where the fluid, "Blood", was defined [7,8]. These parameters define the conditions in which blood flows through average human arteries. The velocity was chosen to be 0.6 m/s as it represents a normal peak pulmonary arterial velocity [9].

$$Q = \frac{4\pi r \Delta P}{8\mu l} \quad (1)$$

Table 1: Parameters for circulating blood.

Variable	Value
Density	1060 kg/m^3
Specific heat	3513 J/kg K
Thermal conductivity	0.44 W/mK
Viscosity	0.010; 0.013; 0.020 kg/m*s
Temperature	37°C
Velocity	0.60 m/s

The only fluid property varied was viscosity based on varying fibrinogen levels, *f*. Normal fibrinogen levels in healthy adults are 2-4 g/L, but critically ill COVID-19 patients often present with fibrinogen levels >7 g/L [10]. Three fibrinogen levels were used, 2, 4, and 8 g/L, to calculate viscosity at the shear rate of 0.07 s^{-1} according to Equation 2 [11]. Although blood is non-Newtonian, this study models steady-state flow in vessels >2 mm so Newtonian viscosity was assumed. To

accurately approximate blood viscosity at 1000 s^{-1}, the amplitude, A, of a power law equation reported in [12] was modified for each fibrinogen level used.

$$\mu(\dot{\gamma} = 0.07s^{-1}) = 0.085 \times f + 36.4 \quad (2)$$

$$\mu = A(\dot{\gamma})^{-0.172} \quad (3)$$

RESULTS

Both outlet velocity and pressure changed as viscosity increased. From Figure 1, there is a greater variation of static pressure magnitude as viscosity decreases. The maximum pressure output was nearly 40 Pa at low viscosity. While the outlet pressures at lower viscosity were higher for many points, the contour maps in Figure 2 show that the inlet pressure was higher by over 400 Pa (1449.71 Pa compared to 1031.70 Pa for high and low viscosities, respectively) as well as the pressure at the bifurcation. Given that there was no vascular resistance to account for and the same velocity and model was used, it can be theorized that this increase in pressure can negatively impact endothelial tissue integrity.

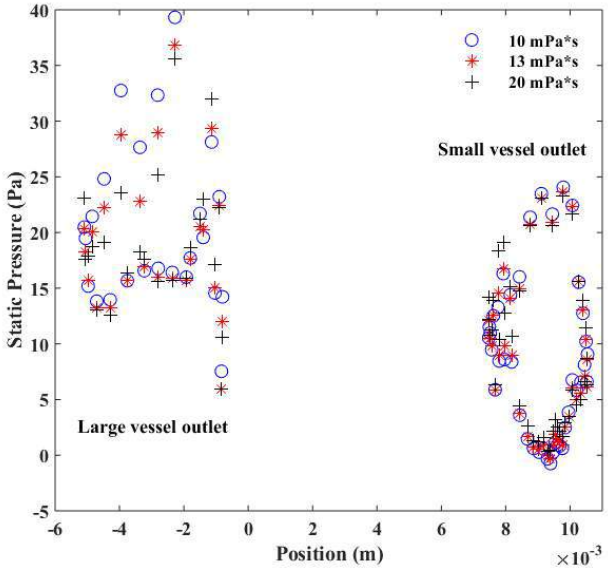

Figure 1: Plot of static pressure on both large (left) and small (right) outlets based on blood viscosity.

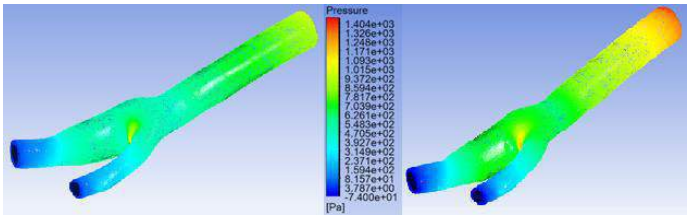

Figure 2: Contour maps of arterial pressure for viscosity at 0.01 kg/m*s (left) and 0.02 kg/m*s (right). The arterial pressure is seen to be greater in the presence of higher viscosity.

Velocity is also known to be a factor in thrombosis formation and is critical for tissue perfusion. The maximum velocity of the large outlet was from the high viscosity model of 20 mPa*s (Figure 3), particularly noticeable in the center of the vessel. However, the small outlet experienced lower velocity as viscosity increased.

DISCUSSION

COVID-19 infections have had a profound effect on both individuals with underlying health conditions and apparently healthy

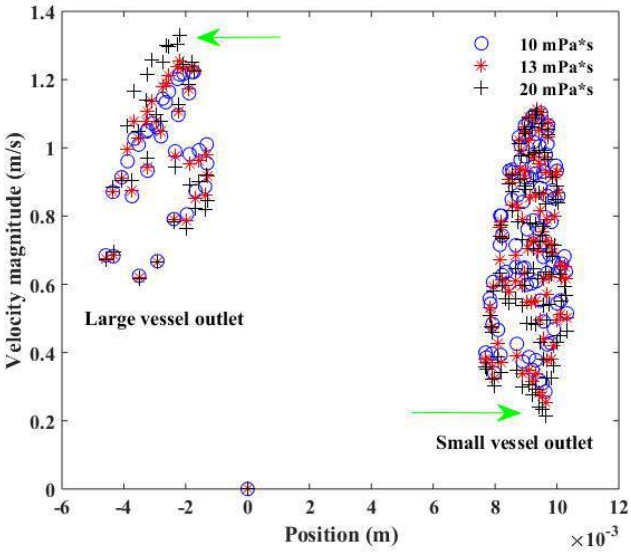

Figure 3: Plot of output velocity based on varying viscosity. Arrows show areas of increased and decreased velocity for high viscosity blood.

populations. The increase in fibrinogen along with other inflammatory factors increases blood viscosity which decreases tissue perfusion and increases the risk of thrombosis formation in vessels throughout the body. From this CFD study, the increase in blood viscosity specifically on the pulmonary artery increased output velocity and pressure that could activate a thrombosis cascade as described by Sloop et al. [4] that can lead to ischemia and compromised tissues.

For the case of COVID-19, further investigation can hope to illustrate blood viscosity as a point-of-care test in mitigating an exacerbation of the pulmonary system. This exploration is very novel but superficial. It lacks the accuracy of differential fluid models and makes a lot of assumptions from the geometry to fluid parameters. Nevertheless, it is unique in its scope and reviews how viscosity can play a role as a potential factor in the development of cardiovascular and pulmonary diseases.

ACKNOWLEDGEMENTS

This work was supervised by Diana Alatalo, supported by the National Science Foundation Graduate Research Fellowship Program under Grant No.1746053 and Eugene McDermott Graduate Fellowship No.201701, and Fatemeh Hassanipour supported by the National Science Foundation under Grant No.1454334.

REFERENCES

[1] Price, L et al. , European Respiratory, 56: 2001608, 2020.
[2] Pop, G et al. , Netherlands Heart Journal, 10:512-6, 2002.
[3] Lowe, G.D. et al. , BJH, 10.1046/j. , Vol 96: 168-173, 2003
[4] Sloop, G et al., Sage Journals, 10.1177/1753944714566427, 2015
[5] den Exter, P et al., RPTH, , DOI: 10.1002/r th2.12422, 2020
[6] Richard, B et al. , Elsevier, 0323429742, 2009
[7] Cutnel, J et al. , Wiley New York, 1119391865, 2018
[8] Gabe, I et al. , AHA Journal, 40:603-613, 1969
[9] Bouhemad, B et al. , ASA Publications, Vol. 108, 55-62, 2008
[10] Wise, J., BMJ, 369:m2058, 2020.
[11] Yilmaz, F et al., Korea-Australia Rheology J, 20:197-211, 2008.
[12] Matsuda, T et al. , Elsevier, 0049-3848(76)90044-X, 1976

DYNACON PLS

Robert Anhalt
University of Florida
Gainesville, FL, US

Brooke Towns
University of Florida
Gainesville, FL, US

Peter DiNapoli
University of Florida
Gainesville, FL, US

Sebastian Moreno
University of Florida
Gainesville, FL, US

Faculty Advisor(s)

Warren Dixon
University of Florida
Gainesville, FL, US

Sean Niemi
University of Florida
Gainesville, FL, US

Kimberly Stubbs
University of Florida
Gainesville, FL. US

INTRODUCTION

Body weight support systems have been widely used in rehabilitative medicine to aid users in improving their motor recovery after suffering from symptoms of neuromuscular disorders as a result of genetics or injury. Gait training can aid users in improving balance [1], however many solutions are expensive [2] and rely on the user to build strength through other physical therapies prior to use.

Alternatively, elliptical training allows patients to both improve strength and gait simultaneously [3]. When elliptical training was used in physical therapy for stroke patients, patients were able to improve endurance, balance, and functional mobility [3]. Functional Electrical Stimulation (FES) has been shown to be more effective in improving patients' balance after stroke than non-actuated exercise [3, 4]. By implementing a body weight support system to be used in conjunction with FES and elliptical training, these results could likely be reproduced while increasing muscle mass in patients with neuromuscular disorders.

The DynaCon PLS solves problems presented by current body weight support systems by providing a controllable weight offset while differentiating the weight supported by each leg. It can be implemented into rehabilitation techniques utilizing elliptical training and FES, saving time, and cost over purchasing multiple systems for strength training and motor recovery. With the added security provided by DynaCon PLS, rehabilitation becomes more efficient both in recovery time as well as reducing the number of therapists needed to assist with the exercise. Investment into the DynaCon PLS body weight support system would facilitate in-home training for a more affordable price compared to the expenses of facility-led physical therapy, although clinics could also benefit from the use of the DynaCon PLS system in their facility for the reasons listed above.

PRODUCT DESIGN

The DynaCon PLS features a Unistrut-based I-beam ceiling mount system, an in-house manufactured trolley capable of one-dimensional powered translation and braking, an energy chain to protect cables that supply power to the system, a dynamic, dual NEMA motor system equipped with an electromagnetic (EM) brake system capable of preventing injury to the patient in the event of power loss, and a series of safety mechanisms and fail-safes to prevent catastrophic failure. DynaCon PLS is equipped with a network of Unistrut adapters which allow it to be mounted to any system of ceiling rafters. Additionally, the unique ceiling mounted design allows for free floor space up until DynaCon PLS is ready to be used. A translational lock mechanism secures the patient in any location along the I-beam during rehabilitation. In the event of an accident or power loss scenario, an electromagnetic braking system ensures that the patient stays supported until proper assistance can be provided. With a spacious layout, simple wiring, and consistent fastener sizes, this design allows maintenance to be quick, easy, and cost effective.

Once the patient is ready to begin therapy, a full body harness will secure them to the DynaCon PLS. Utilizing the servo motors and the dual-axis motion allowed by DynaCon PLS, the user can safely be lifted and transported above any physical therapy equipment. During exercise, the patient's weight is offset using the response from two load cells added in line with the harness supports. The load cells output a voltage to be read by an onboard Arduino that communicates with the motor controller to adjust the voltage being sent to each motor. By controlling the motors in this manner, the weight offset system will respond to only the patient's generated forces. This is important because it provides a fully custom experience that changes based on the ability of each user. An encoder is installed on each motor to get a baseline location when the patient was first lifted prior to operation, so that each motor knows how far to return as weight offset is being applied. The motors respond instantaneously based on the amount of tension or lack thereof read by the force sensors as the patient is using the elliptical and applying forces associated with gait.

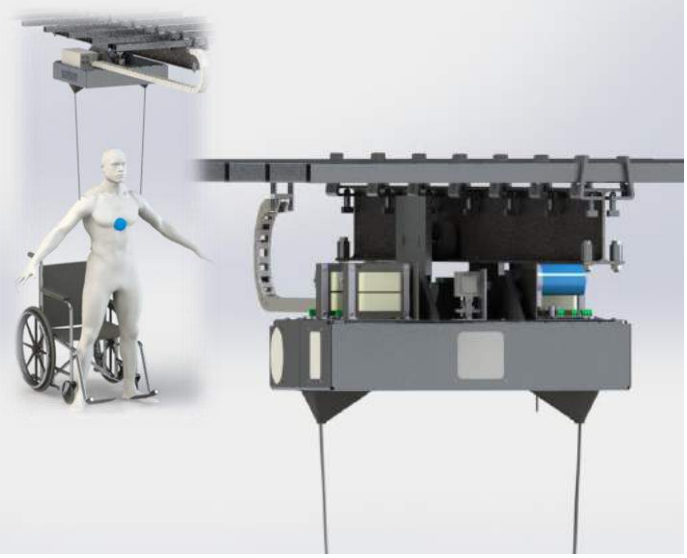

Figure 1: DynaCon PLS rendering with example of patient being lifted from wheelchair.

BUDGET & MARKET ANALYSIS

Budget: The total budget for the design, build, and testing of the prototype is $5,200 which was covered by the University of Florida and the MERGE Laboratory. The design and testing portions of the budget were absorbed by the student participation in senior design courses. Widespread production of the DynaCon PLS would incur additional costs for manufacturing power consumption and assembly.

Market Analysis: To identify the market, the end user of this project must be considered. The end user of this project is someone who has suffered injuries which limit lower body mobility. Our ideal user is an individual who is seeking lower body rehabilitation using functional electric stimulation (FES). The need for FES rehabilitation derives from the following debilitating injuries: paralysis, stroke, spinal cord injuries (SCI). With the end user in mind, the primary market is for at home use. The secondary market for this product is comprised of physical therapy clinics and research institutes.

Every year in the USA there are approximately 17,000 new spinal cord injuries [5] and 610,000 new strokes [6]. Those injured individuals are the targeted users and primary market for the DynaCon PLS. The secondary market for this product includes hospitals, orthopedic institutes, physical therapy centers, and research institutes. The potential market size, based on the total targeted market, is approximately 515,000 clients. The primary market of at-home users is totaled to the fraction of stroke and SCI patients (75%) that could use the DynaCon PLS at home. This is estimated at three quarters of total SCI and stroke patients to 470,000 potential clients. In the United States, there are 6090 hospitals [7], 38,800 physical therapy clinics [8], and 233 physical therapy schools or institutions. The secondary market is totaled to 45,123 potential clients. Totaling the primary and secondary market size creates a final market of 201,123 potential clients.

The expected manufacturing costs (Table 1), per unit, with a market of this magnitude is $4,000.00. The projected sales price of a single unit will be $10,000 including installation. Investments in engineering costs and tooling will be initially absorbed by the University of Florida, though they will be further explored for future fabrication and mass production. The total return on investment, assuming all possible clients purchase a unit, is 350%.

Table 1: Budget for the DynaCon PLS Manufacturing

Type	Price ($)
Off the Shelf Parts	$4250
Raw Materials	$700
Assembly Costs	$250
TOTAL	**$5200**

ACKNOWLEDGEMENTS

We would like to thank the MERGE Lab at the University of Florida, as well as the Nonlinear Controls and Robotics Group for their support and resources provided. We would also like to recognize the work of Mechanical Engineering Design III students that tested and developed the initial prototype of the DynaCon PLS.

REFERENCES

[1] Sharan, D et al., *Journal of Rehabilitation and Assistive Technologies Engineering*, 3:1-12, 2016

[2] Hocoma, Gait and Balance Solutions, DIH Medical Group, 2021.

[3] Jackson, K, PhD et al., *Journal of Neurologic Physical Therapy*, 34:168-174, 2010

[4] Elsner, V et al., *Neural Regeneration Research,* 16:805-812, 2021

[5] National Spinal Cord Injury Statistical Center, Facts and Figures at a Glance. Birmingham, AL: University of Alabama at Birmingham, 2020.

[6] Virani SS et al., Heart disease and stroke statistics – 2020 update: a report from the American Heart Association. *Circulation.* 2020; 141(9): e139 – e596.

[7] American Heart Association, *AHA Hospital Statistics.* 2021.

[8] LaRosa, J, U.S. Physical Therapy Clinics Constitute a Growing $34 Billion Industry, *MarketResearch.* 2019.

PHANTOM LIMB PAIN (PLP) STRAP

Camara L. Casson
Florida Institute of Technology
Melbourne, FL, USA

Angel E. Collins
Florida Institute of Technology
Melbourne, FL, USA

Dina Dragoljic
Florida Institute of Technology
Melbourne, FL, USA

Alexis R. Hopkins
Florida Institute of Technology
Melbourne, FL, USA

Marissa A. Jordan
Florida Institute of Technology
Melbourne, FL, USA

Faculty Advisor(s)

Ted Conway
Florida Institute of Technology
Melbourne, FL, USA

INTRODUCTION

According to the Amputee Coalition, up to 80% of amputee patients worldwide suffer from a condition called phantom limb pain. This condition is characterized as a painful sensation felt in the amputated limb [1]. While the limb is absent, the pain that is felt by the patient is very real.

When an amputation takes place, the nerves leading into the limb are rerouted into the surrounding muscle. This technique is done in order to prevent neuromas (an abnormal growth on the nerve). It is suggested that the cause of PLP is the lack of sensory input from the nerves that were part of the amputated limb.

Fundamentally, the amputated limb's nerves are still present within the body, but are not supplying any sensory input to the brain, causing a disconnect that results in a painful sensation. Very little research has been done pertaining to the cause of PLP, and existing treatments are either expensive or rudimentary. Current treatments are designed to numb the pain and there has been no focus on either tracking the progress of the pathology, or finding a treatment that permanently decreases the presence of PLP.

PRODUCT DESIGN

The PLP Strap's current design will greatly increase the quality of life for each amputee using the device. When an amputee experiences pain near the amputated area, it can be observed as a large spike in the electrical signal that is produced by the musculature; an electromyograph (EMG) can be utilized to collect these electrical signals. In the design for the PLP Strap, the electromyograph (EMG) will be programmed to switch on and off alternately with a transcutaneous electrical stimulation (TENS) unit. The TENS unit will provide electrical stimulation to the amputated limb to quiet the misfiring of the salvaged/local remaining nerves. The new EMG signal, post-TENS stimulation, will then be compared to the initial or baseline EMG signal. The goal is to observe lower levels of neuronal activity after electrical stimulation. If lower levels are observed, then the device can be considered a successful alternative to common TENS units as well as over-the-counter and prescription drugs. The EMG component elevates the design in comparison to generic TENS units because it connects to an online mobile application that is accessible to medical professionals, allowing PLP trends to be monitored more closely for proper diagnosis and long-term personalized treatment. Thus, if the device only abates PLP rather than fully treat it, doctors can provide additional feedback and treatment options catering to a more quantitative pain analysis. The system further allows quantification of pain that will give the medical field useful information on treating individuals with varying degrees of PLP.

The solution is technically feasible as the design includes already existing hardware and software meaning that the design simply combines these mechanisms into a coordinated, efficient system. The Pocket Box iteration is, also, physically possible as existing devices on the market are comparable in size. With the more compact design, the consumer will be able to handle and transport the device easily; thus, lessening the likelihood of damage to the device. All connecting wires in this model are enclosed within the Pocket Box, to reduce the amount of wear on the wires; thus, increasing the longevity of the device's life expectancy. The Pocket Box design iteration prioritizes the customer attributes of comfort, accessibility, saftey, and ease of use, while maintaining a low cost.

Referring to the CAD drawing included in Figure 1, the Pocket Box will be a 3D printed structure composed of plastic and used as housing unit for the electrical components, such as Arduino, Raspberry Pi, EMG, and TENS unit. The Pocket Box design iteration allows for all processors, sensors, electrodes, and the battery to be detached, allowing the strap to be washed and lightweight. The strap portion of the Pocket Box design will be made of polycotton that will have electrodes embedded in the fabric. The consumer will be able to remove the electrodes via the two portholes seen in the auxiliary view (upper right-hand corner) in Figure 1. This design iteration increases the device's safety and effectiveness, which along with its compact design allows ease on the user

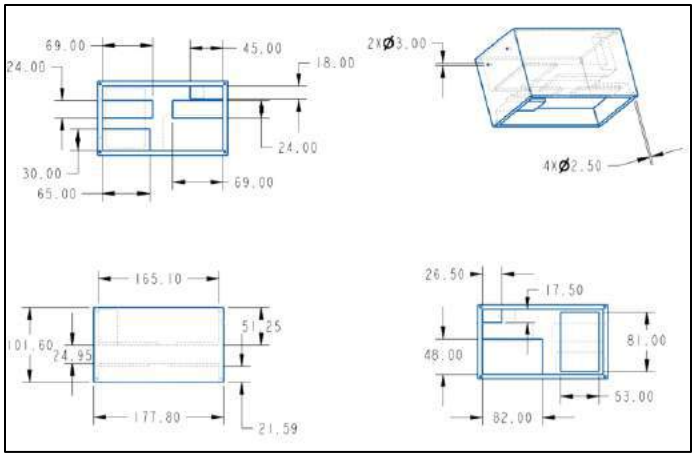

Figure 1: PLP Pocket Box Design. Main portion of the design, housing all electrical components as well as docking ports for EMG electrodes for proper user function. Within the box are 3D representation of the compiled component layout. All dimensions are denoted in millimeters [mm].

BUDGET & MARKET ANALYSIS

The total projected cost of the PLP strap is $355.91 (prototype). This estimate includes the following components necessary for the development of the prototype:

2 - GROVE Relay Unit ($2.84)
2 - TENS 3000 3 Analog TENS Unit with Timer ($18.90)
1 - MFI Medical Bar EMG Electrode ($51.03)
1 - MFI Ground Electrode ($40.16)
1 - Raspberry Pi Zero ($5.00)
2 - Poly Cotton Broadcloth 60” Fabric by the Yard ($7.90)
2 - Arduino Nano 33 BLE Sense with Headers ($33.40)
2 - 9 Volt Lithium Battery GP ($11.99)
2 - Breadboard ($5.00)
2 - LCD Displays ($10.95)
6 - AD620 ($11.26)
2 - Jump Switches ($2.44)
6 - Capacitors ($0.76)
4 - Rectifying Diodes ($0.19)

The above breakdown shows the quantity of each component utilized, the name of the component, and the unit price of each component, respectively. This total projected cost is subject to change due to alterations in the design and/or unforeseen circumstances (i.e., component damage).

Based on the current market for technologies that noninvasively treat peripheral neuropathy, the PLP Strap would be entering a market upwards of 3 million individuals. Of the 30,000 amputations conducted annually in the United States, approximately 6% of amputees report experiencing prolonged phantom limb pain because of the amputation [2]. Utilizing the above total projected cost of production with the addition of manufacturing and labor expenses and then applying a traditional 100% markup, the PLP Strap is estimated to have a market price of approximately $800 per unit. Meaning the expected gross profit, annually, of the Phantom Limb Pain Strap would be $720,000. With the inclusion of just 10% of consumers with pre-existing amputations purchasing the product, the gross profit increases to over $120 million dollars annually.

ACKNOWLEDGEMENTS

Florida Institute of Technology Biomedical Engineering Department

REFERENCES

[1]Hanyu-Deutmeyer, AA et al. Phantom Limb Pain. [Updated 2020 Jul 4]. In: StatPearls [Internet]. Treasure Island (FL): StatPearls Publishing; 2020 Jan.
[2] Chin J Traumatol. 2018 Dec; 21(6): 366–368.
[3] Kaur A et al. Phantom limb pain: A literature review. Chin J Traumatol. 2018;21(6):366-368.
[4] Ortiz-Catalan et al. Phantom motor execution facilitated by machine learning and augmented reality as treatment for phantom limb pain: a single group, clinical trial in patients with chronic intractable phantom limb pain. Lancet. 2016.
[5] Harris AJ. Cortical origin of pathological pain. *Lancet*. 1999; 354: 1464-1466
[6] Pearson B. 2013. Journal of Pain Research 2013:6 459–469

ULTRASONICS – TRACKING FULL THICKNESS SKIN DEFORMATIONS FOR A BIOPHYSICS-BASED EVALUATION OF SKIN HEALTH

Kyra Bednarski
Stevens Institute of Technology
Hoboken, NJ, United States

James Brown
Stevens Institute of Technology
Hoboken, NJ, United States

Edward LaGrassa
Stevens Institute of Technology
Hoboken, NJ, United States

Mary McNeil
Stevens Institute of Technology
Hoboken, NJ, United States

Kyle Shepitka
Stevens Institute of Technology
Hoboken, NJ, United States

Faculty Advisor(s)

Ahsanul Torza
Stevens Institute of Technology
Hoboken, NJ, United States

Johannes Weickenmeier
Stevens Institute of Technology
Hoboken, NJ, United States

INTRODUCTION

According to the American Academy of Dermatology, over 85 million Americans suffer from skin disease [1]. While many skin conditions like acne, rosacea, and atopic dermatitis have minor implications for patients, severe skin diseases such as scleroderma, and systemic sclerosis require medical treatment. The multilayered structure of skin leads to a complex mechanical response to external loads and functional behavior to bio-chemical stimuli. Moreover, skin behavior changes profoundly with age, lifestyle, and disease [2]. Strikingly, to date, no clinical tools exist to reliably assess the biomechanical state of skin, including the thickness of individual skin layers or their relative interactions. Our senior design project seeks to develop an ultrasound video-based software tool to determine a person's mechanical skin properties. The ultimate goal of our software, called Ultrasonics, is to evaluate the subject's skin health and to inform dermatologists or estheticians about possible treatment options. Ultrasonics is a software program that tracks full-thickness skin deformations in ultrasound videos. The deformation profile of full-thickness skin is a reliable indicator for the stiffness of individual layers and the interaction properties between layers. This information can be used to assess skin conditions and recommend possible treatment. The software will provide a user-friendly interface to make this technology available in the clinical setting for the monitoring of severe skin diseases as well as for professionals in the skin care industry.

PRODUCT DESIGN

Ultrasonics will provide a biomechanics-based assessment of a person's skin features. Our software determines the thickness of individual layers, such as the epidermis, dermis, and subcutis, and determines deformability of the full-thickness skin. The deformability of the skin is a reliable indicator for its state of healthy and is dependent on the interaction between individual layers and their respective stiffness. *Figure 1* shows a representative ultrasound image from the forehead region and clearly depicts the three most superficial layers, as well as the thick adipose tissue layer. The forehead region is of particular interest to the cosmetic industry, for example, as it is prone to wrinkle with age.

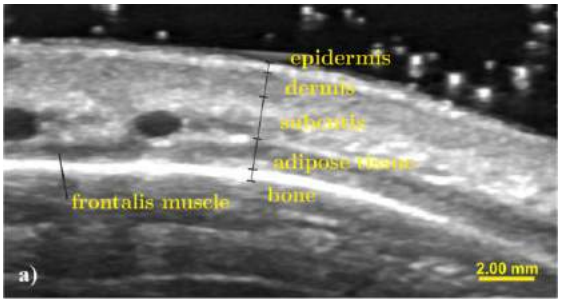

Figure 1: Representative ultrasound image of the forehead showing the multi-layered structure of the skin. Ultrasound is particularly useful to visualize full thickness skin and will be used to obtain video recordings of skin deformations.

As input to Ultrasonics, the operator will apply a small displacement on the skin surface while recording with the ultrasound probe. This is shown in *Figure 2*, in step 1. Ultrasound is a readily available, non-invasive and cost-effective medical imaging technique to visualize soft tissues. This process creates a video that captures the displacement of all skin layers. In step 2, we show a representative 2D image of skin. This video is then imported into Ultrasonics for analysis. The operator manually clicks at the boundary of each layer, to determine the thickness of each layer. Next, the tracking grid is defined, as shown in step 3. Once the grid is defined, Ultrasonics uses OpenCV combined with Optical Flow and the Lucas-Kanade method to track all grid points in each frame. The Lucas-Kanade method takes a 3x3 box around a point constructed of 9 nodes that are all assumed to have similar displacement and outputs the 2D vector field where each vector is a displacement vector showing the movement of points from the first frame to the second. The displacement field of all the points is then derived into a deformation field. Finally, in step 4, we analyze grid deformation in each frame and determine the spatiotemporal evolution of critical mechanical properties. Using standard continuum theory, we will use nodal displacements to determine the element-wise deformation gradient $\mathbf{F}$ and the Green Lagrange strain tensor $\mathbf{E}$ via $\mathbf{E}=1/2*(\mathbf{C}-\mathbf{I})$, where $\mathbf{C}$ is the right Cauchy Green deformation tensor, $\mathbf{C}=\mathbf{F}^T\mathbf{F}$, and $\mathbf{I}$ is

the second order identity tensor. Moreover, we use the deformation of each grid point to construct the full thickness skin deformation profile. We calculate the average horizontal displacement component of all nodes in each row of our grid and generate a deformation profile ranging from the surface to the deepest layer of skin. As output, Ultrasonics will provide thickness of each skin layer, the deformation profile, any abnormalities detected in the deformation profile, and a comparison of the subject's deformation profile to a database of other healthy patient profiles. Since skin properties differ from subject to subject and will be heavily affected by skin disease, we consider these output measures as a diagnostic measure of skin health.

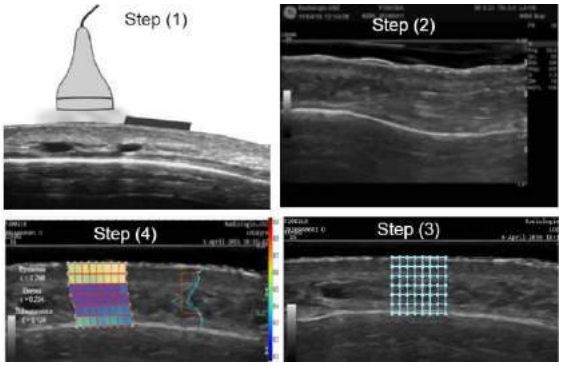

Figure 2: Schematic outline of the skin evaluation process with Ultrasonics. 1) We first record a video showing minor skin displacements, then 2) import that video into Ultrasonics, 3) define a tracking grid to quantify the full thickness skin deformation profile, and 4) derive several skin health measures.

In *Figure 3*, we show preliminary data of our software in the form of a strain map and a deformation profile. We observe that epidermis is rather stiff and shows little strain. The dermis is a softer layer and exhibits increased shear strain, also reflected in the belly in the of the deformation profile. The final version of Ultrasonics will provide a user-friendly output format to allow doctors and users to easily interpret our results. In previous studies on skin deformation, it has been shown that skin deformation is non-uniform across layers [2,3]. Specifically, it has been shown in shear tests of pig skin that the shear modulus varies throughout full thickness skin and is subject to sharp stiffness changes at the epidermis-dermis interface [3]. Each layer will deform differently due to cellular composition and stiffness of each layer. Moreover, skin layers have variable connectivity, all of which leads to a non-uniform deformation profile. This is particularly relevant for our product and requires Ultrasonics to accurately track tissue displacements across all skin layers.

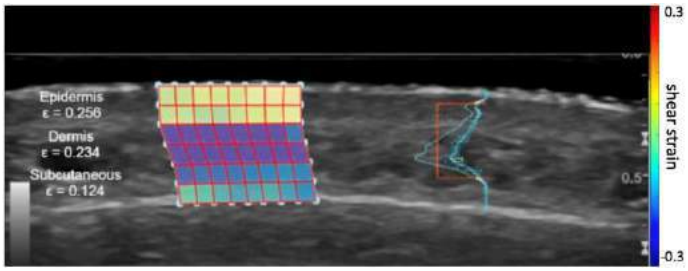

Figure 3: Preliminary results from a volunteer with deformation profile (green line) and strain field (color map).

We are currently in the programming phase and developing the tracking algorithm, data analysis, a user interface, and are implementing a database. Through frequent use of Ultrasonics, we will begin building this database with each patient's skin assessment that includes healthy subjects from a wide age-range, as well as patients in varying states of health, and their treatment plans. Through the collection of this data, we will be able to identify indicators of abnormal skin properties and provide personalized recommendations for treatment.

BUDGET & MARKET ANALYSIS

The team plans to market this project to dermatologists and estheticians. We aim for Ultrasonics to become part of every dermatological checkup in order to reliably and continuously monitor a patient's skin changes over time. Understanding the mechanical properties of skin is also important in the clinical settings to find better plastic surgery techniques, and better treatments for skin diseases. Moreover, we will try to market Ultrasonics as a real-time service for estheticians which would use this software to advise their customers on the right cosmetic products to improve their skin health and prevent typical signs of aging. Our product can be used to test the efficiency of cosmetic products as well as recommend different cosmetic products based on the layer specific properties of each patient's skin.

Under FDA regulations for the Medical Device User Fee Amendments (MDUFA), the Ultrasonics is considered a Class II non-510(k) medical device. The registration cost for our device with the FDA would be $3,108 under the classification of a small business. Revenue for this product prior to launching would not exceed $100 million for the tax year, thus classifying it as a small business product and is not anticipated to reach that following. An annual registration fee of $5,546 is also collected from the FDA to ensure our product can go to market.

According to IBIS World, there are 5,952 dermatology businesses and 151,193 estheticians in the US [3]. The national average cost for a visit to an esthetician is $80, and to see a dermatologist without insurance will cost about $150. We want to ensure that this product can be covered by insurance when it is medically necessary. For example, if a patient is using this product to track the progression of skin disease. However, if a patient simply wants an analysis of their skin, it may not be covered by insurance, but we want to make sure it remains affordable. If we are able to license our software at $600/year, we anticipate a revenue stream of $600,000 per year. Moreover, we will identify a portable ultrasound machine vendor, to offer software and hardware as a package for $1000/year. We expect that 1,000 estheticians will be interested in our product initially, and as the product becomes more refined, it can continue to expand in the market.

Product cost is primarily limited to software development, FDA licensing, and marketing. Once the product is ready to go to market, we will look into working with a consulting company to help us market the product. Also, as the market grows, we will look to hire a software developer in order to improve the user interface for a wider group of dermatologists and estheticians.

ACKNOWLEDGEMENTS

The Mechanical Engineering Department at Stevens is supporting this project with a $700 stipend. Moreover, we thank Ahsanul Torza and Dr. Johannes Weickenmeier for their advice and guidance throughout this project.

REFERENCES

[1] *American Academy of Dermatology* (2017)
[2] Joodaki and Panzer, *Engineering in Medicine,* 232 (2018)
[3] Gerhardt et al., *JMBBM,* 14 (2012)
[4] *IBIS World*, December 29, 2020

THE MULTIFLEX CATHETER – A VARIABLE STIFFNESS ENDOVASCULAR CATHETER

Halle R. Lowe
McKelvey School of Engr.
Washington University
St. Louis, Missouri, USA

Vinay D. Chandrasekaran
McKelvey School of Engr.
Washington University
St. Louis, Missouri, USA

Chase M. Hartquist
McKelvey School of Engr.
Washington University
St. Louis, Missouri, USA

Faculty Advisor(s)

Jin V. Lee
Department of Surgery
Washington University
School of Medicine
St. Louis, Missouri, USA

Mohammed Zayed
Department of Surgery
Washington University
School of Medicine
St. Louis, Missouri, USA

Joshua W. Osbun
Dept. of Neurological Surgery
Washington University
School of Medicine
St. Louis, Missouri, USA

Eric C. Leuthardt
Dept. of Neurological Surgery
Washington University
School of Medicine
St. Louis, Missouri, USA

Michael Talcott
Dept. of Comparative Medicine
Washington University
School of Medicine
St. Louis, Missouri, USA

Guy M. Genin
McKelvey School of Engr.
Washington University
St. Louis, Missouri, USA

INTRODUCTION

Although minimally invasive endovascular catheter surgeries are poised to revolutionize the treatment of neurovascular pathologies such as stroke and aneurysm, adoption has been slow because of two key challenges.[1] First, the classic approach for diagnostic and therapeutic catheterization, a transfemoral approach in which the catheter is inserted at the groin and advanced through the vasculature to the brain, is difficult because it requires catheters with stability over long distances and flexibility around tight bends. Second, for the alternative transradial approach, in which the catheter inserts through the arm, around the aorta, and to the brain, requires stability around the tight bends of the aorta but also flexibility to navigate these same bends.[3] The transradial approach has more favorable patient outcomes,[2] but is also associated with increased vascular tortuosity,[3] and thus with increased risk of adverse events such as catheter kinking or entanglement, and catheter-induced coronary dissection.[4,5] In both cases, there is strong need for a catheter that can navigate to a surgical site, then be stiff enough to maintain stability as surgical tools are advanced to the surgical site.[6]

Therefore, an endovascular catheter of switchable stiffness would be of great utility. Our team has successfully created such a device, which we call the MultiFlex catheter.

PRODUCT DESIGN

Conceptual design and proof of principle calculations. The MultiFlex catheter consists of 3 main layers – an inner layer, a string layer, and an outer layer (Fig. 1). In the flexible state, the string layer does not connect the inner and outer layers, and the flexural rigidity is sum of those of the inner and outer layers. In the stiff state, the application of a vacuum draws the inner and outer layers together into frictional contact, causing what we estimated to be a ten-fold increase in flexural rigidity. In characterizing the range of commercially available tools, as described in a separate paper submitted to this conference,[7] this range would be suitable to shift a device from the stiffness of a guide catheter to that of a stiff sheath (Fig. 2). Proof-of-principle estimates (not shown here) of shear stresses associated with flexure from advancing a tool through the inner catheter indicated that the frictional resistance vacuum applied by a Luer lock syringe or indeflator would be adequate to maintain the increased stiffness during tool advance. We received provisional patent protection for the design of MultiFlex and the use of a vacuum to change a catheter's flexural rigidity.

Figure 1: CAD model of the layered MultiFlex catheter design.

Prototype and benchtop test. A "9 French" (3 mm diameter) prototype of the MultiFlex catheter was developed in partnership with Nordson Medical (Fig. 2). Benchtop testing to measure its change in flexural rigidity. The prototype could shift from compliant to sufficinly stiff to hold a bent shape when vacuum was applied by a Luer lock system (Fig. 3). This prototype achieved a 6.3-fold increase in flexural rigidity (3.9 N cm^2 - 25 N cm^2), a transition that spans the stiffness profiles of both sheaths and catheters (Fig. 2).

Animal testing. To validate that the prototype could sustain sufficient stiffness with the insertion of a surgical tool and with normal blood flow through the vasculature, the prototype was tested in a porcine model. All animal protocols were approved by the Institutional Animal Care and Use Committee at Washington University, and the procedures were performed by a trained vascular surgeon in conjunction with a team of veterinary surgical staff. Results show that the catheter was sufficiently compliant to navigate through the animal's vasculature,

and then, under vacuum, was sufficiently stiff to support medical devices *in vivo* compared to other neurovascular catheters (Figs. 4-5).

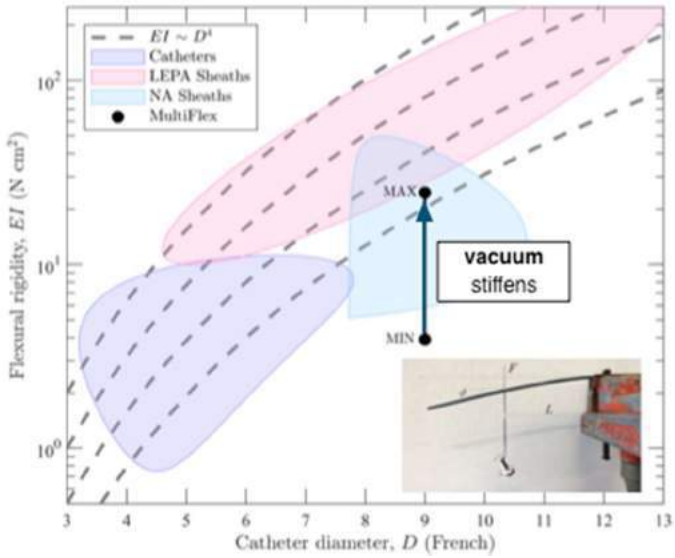

Figure 2: Benchtop tests of vascular catheters, neurovascular (NA) sheaths, and lower extremity (LEPA) sheaths, as well as the MultiFlex catheter. Tests were performed using cantilever loading interpreted via nonlinear beam theory. Application of vacuum to the MultiFlex device stiffened it, reversibly, from the range of catheters to the range of sheaths. 1 French = 3 mm.

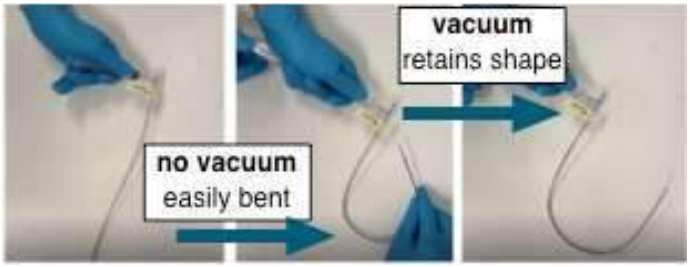

Figure 3: Benchtop testing revealed that the MultiFlex prototype switched from compliant to stiff with the application of vacuum.

BUDGET & MARKET ANALYSIS

Initial investment costs will come from further prototype development, FDA approval, and manufacturing costs totaling an estimated $2 Million. It is estimated that the U.S. accounts for 125,000 embolic strokes each year,[8] representative of $437.5 Million in catheter products used for embolic stroke treatment alone (at $3500 of catheter products used per surgery). With an initial market penetration of 6%, a product price of $2,000, and an average annual market saturation rate of 6%, the return on investment would be $20 Million/year 6 years after initial product release, considering the market for embolic stroke treatment alone. There is potential for utilizing this technology in numerous other neurovascular, peripheral arterial, and cardiovascular procedures, as well as potential for application outside the realm of vascular surgery.

DISCUSSION AND FUTURE WORK

The device shows promise for improving the efficiency of intravascular neurointerventions by meeting a well-defined need for radial-entry specific tools. Future endeavors seek to scale the design down to a 6 French outer diameter which is the maximum allowable catheter size for neurovascular interventions. Going forward, efforts will be made to prototype these to obtain FDA approval via the 510k pathway as the device is substantially similar to predicate devices, despite its novel functionality and its optimization for neurovascular procedures.

Figure 4: An animal test of the MultiFlex prototype in a porcine model showed that the device has sufficient flexibility to navigate through tortuous vasculature to distal sites.

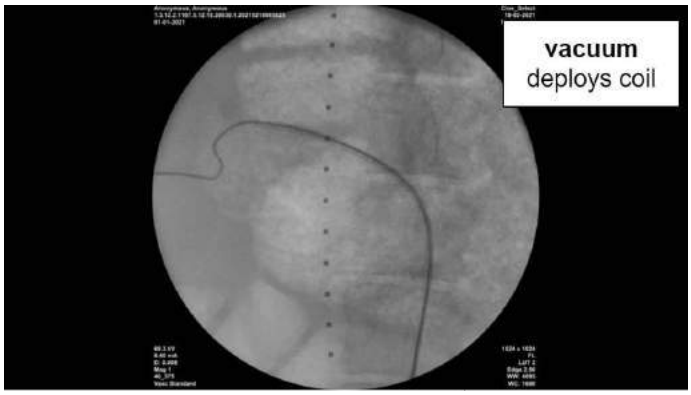

Figure 5: An animal test of the MultiFlex prototype in a porcine model showed that the device, with vacuum applied, was sufficiently stiff for tools to be passed to a distal surgical site.

ACKNOWLEDGEMENTS

This work was supported by the Society for Vascular Surgery Foundation, the American Surgical Association, NIH K08HL132060, The Center for Innovation in Neuroscience and Technology, and the NSF Science and Technology Center for Engineering MechanoBiology (CMMI 1548571). We thank Joseph Calderon of Distal Solutions, Inc. (Boston, MA) for assistance with fabrication of the catheter prototype used for animal testing.

REFERENCES

[1] Starke, et al., *J. Neurointervent. Surg.*, 8:135-144, 2016.
[2] Saiegh, et al., *Operative Neurosurgery,* 2020.
[3] Jhand, et al., *Am J. Cardiol.,* 141:23-30, 2021.
[4] Dangoisse, et al., *EuroIntervention.,* 3:345-352, 2013.
[5] Shahbaz, et al., *J. of Am. College of Cardiol.* 2:1657-1661, 2020.
[6] *Acta Radiologica: Diagnosis,* 4:11-20, 1966.
[7] Hartquist, et al., *Proc. 2021 SB3C*, (submitted).
[8] Reiffel, *Am. J. Med.,* 127:15-16, 2014.

AUTOMATIC RECLINING CAR SEAT

Md Joynal Abedin
The City College of New York
New York, New York, USA

Mohammad Shah Jalal
The City College of New York
New York, New York, USA

Alex Sullivan
The City College of New York
New York, New York, USA

Ahmee Cho
The City College of New York
New York, New York, USA

El Mokhtar Majdoub
The City College of New York
New York, New York, USA

Ahmed Ahmed
The City College of New York
New York, New York, USA

Faculty Advisor
Parisa Saboori
The City College of New York
New York, New York, USA

INTRODUCTION

Children are spending more time in car seats, which increases the possibility that a child will fall asleep in an unsafe position. Sleeping in an unsafe position can then lead to a head slump, which happens when the chin falls onto their chest causing discomfort, difficulty in breathing, and in the worst-case scenario, positional asphyxia which happens when the child cannot inhale enough air to breathe. Positional asphyxia contributes to 48% of non-accident-related car seat deaths. In 2017, 900 deaths were related to scenarios involving accidental suffocation (positional asphyxiation).

The size of the global baby car seat market was valued at USD 7.0 billion in 2018. A rising concern about fatal accidents involving children, has increasing the market across the globe as well as nationwide. In USA, the baby car seat market size was approximately 2.0 billion and the this will increase to 3 billion by 2025, and to 11 billion worldwide.

PRODUCT DESIGN

This design has two bases, a lower base which attaches to the latch anchors in the car, and an upper base to house a mechanism for the translation of the seat (Figure 1 top-left). The upper base also has a mechanism to allow for seat rotation, and to provide attachment points for the baby seat itself (Figure 1 top-right).

The design mechanism consists of a stepper motor, ball screw, two linear slides, connecting rods, and appropriate bearings, along with the necessary structural frame, which contains a curved slot to promote the reclining of the car seat. After the stepper motor receives a signal from the microcontroller, the ball screw rotates, and the two bearing slides translate freely along the slider rods. The slides also serve to support the car seat weight, and are connected via two connecting bars to prevent jamming because of the wide span that exists between the linear slides. This allows only one stepper motor to be required (thereby reducing cost and complexity), and to provide room for the electronic components. The rear bottom of the baby car seat is connected to the two platforms using two small shafts which have a ball bearing on both ends to reduce friction between the car seat connector and the shafts during the rotation. From the front view shown in figure 1 (top-right), there are two fixed small shafts at the front bottom part of the car seat which slide along a curved slot on both sides of the frame. To reduce friction between the slots and the shafts, two flange bearings were added to the end of each sliding rod. Figure 1 shows how the mechanism was attached to the car seat frame. This figure also shows the overall view of the seat in its original and final positions (Figure 1 bottom left and bottom right).

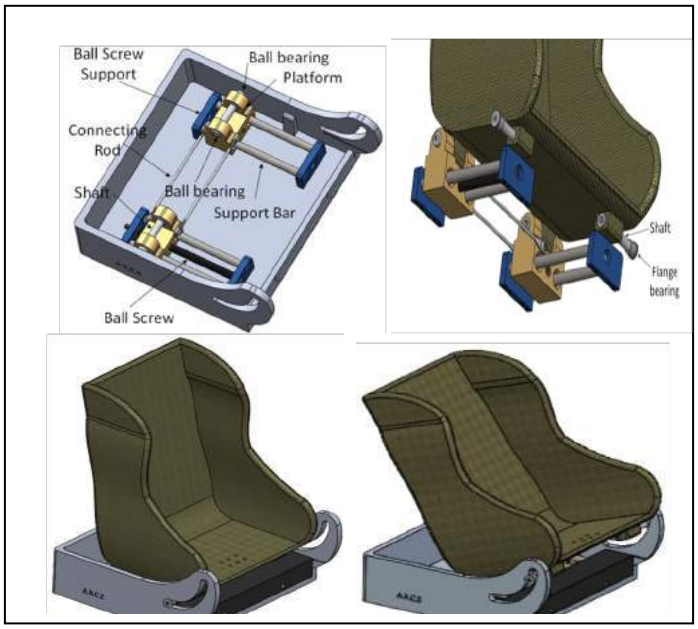

Figure 1: Lower base (top-left), Upper base (top-right), Initial position of seat (bottom-left), final position of seat (bottom-right).

Consequently, for a child to sleep in a safe position the seat should be reclined at an angle of between 30-45 degrees. The arc cut-out of the sides of the base allows for a 39 degrees angle of inclination, which fits well within the required range for the child to be in a safer sleeping

position. Also, in this design, the translation and rotation occur at the same time thereby reducing the total repositioning time, which addresses concerns about the stability of the seat should an accident occur.

Control of the system can be achieved either manually, via a Bluetooth™ interface with a cellphone, or via a built-in controller that employs a heart rate monitor which would be installed on the baby's wrist. This device would constantly capture the baby's heart rate during the time of use, and if a rate associated with sleep is detected an Arduino microcontroller automatically reclines the car seat (Figure 2).

This mode of control is based on the fact that a baby's heart rate falls significantly during sleep. This significant change of heart rate is observed by the microcontroller that processes input signal to initiate the seat motion. The microcontroller sends a signal to the stepper motor which would then rotate at a fixed RPM for a certain period of time. Then once the car seat reaches the desired position, it would lock the system in place. Subsequently, when the baby wakes up, the reverse process takes place, and the car seat is moved to its more upright position.

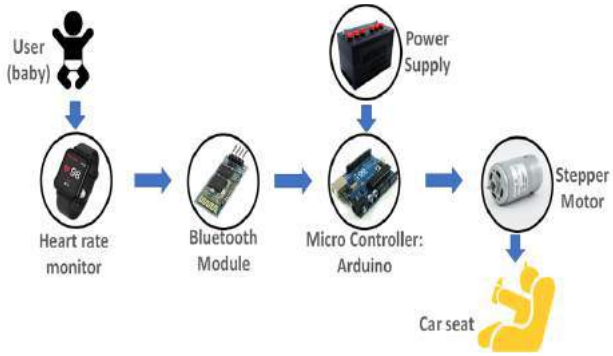

Figure 2: Control elements for the operation of the system

BUDGET & MARKET ANALYSIS

Table 1 is a list of the components used in the design and provides information about the component names, material, dimensions, quantity, costs, and service qualities of the selected materials. The materials have been selected based on a finite element analysis (FEA), that allowed a fatigue, kinematic, and visual analysis of the system to be performed. The price for manufacturing the product seems to be high but mass production would reduce the price by three quarter.

Selected materials and their costs of Automatic Reclining Baby Car seat

Component's name	Types of materials	Dimensions	Qty.	Costs ($)	Service quality
Base of seat	HDPE	18x18x1/2(LxWxH)	1	18.00	Good
Base wall	HDPE	24x12x1/2(LxWxH)	1	17.00	Good
Turnbuckle style connecting rods	6061 Aluminum	12 (L), Ø5,0.197 HØ0.315	2	35.00	Good
Flange sleeve bearing	Stainless steel	OD(0.75), ID(0.59)	2	16.00	Good
Linear ball bearings	Stainless steel	1.42(L), OD(1)	4	24.00	Good
Lead screw end supports	6061 Alloy	12x1/2 (LxD)	2	35.00	Good
Flanged Ball Bearings	Stainless steel	OD(0.91), ID(0.354)	2	12.00	Excellent
Lead screw	1018 Carbon Steel	10.36(L)), M(0.394.1.18)	1	21.00	Excellent
Front seat shaft	6061-T6	3.94(l), Ø0.60	2	40.00	Good
Platform	6061-T6		2	60.00	Excellent
Platform support bars	6061-T6	9.84(L), Ø0.63	4	30.00	Good
Motor	n/a	n/a	1	35.00	n/a
Power supply	n/a	n/a	1	30.00	n/a
Screws	Stainless steel	n/a	#24	22.00	Good
Sit cover	Leather	n/a	1	30.00	n/a
Sensors	n/a	n/a	2	10.00	n/a
Heart rate Monitor	n/a	n/a	1	100.00	n/a
Estimation of total costs				= 535.00	

Table 1: Selected materials and associated costs

The baby car seat market growth CAGR of 6.4% during the period of 2017-2021. Current baby car seat manufacturer making good revenue each year despite the safety concern of the existing car seat. Our redesign product with highest safety and low cost would replace 80-90% of the current car seat market which turns out to be approximately 3 billion dollars every year.

ACKNOWLEDGEMENTS

Rectorship of Grove School of Engineering, The City University of New York, New York, USA.

REFERENCES

[1] Distribution Channel, Market analysis Report,july 2019.

[2] https://www.standinbaby.com/positional-asphyxiation/

[3] https://www.hindawi.com/journals/cmmm/2018/9603451/

[4] https://babybouncerscenter.com/can-baby-sleep-in-bouncer/

[5]https://www.cdc.gov/injury/features/child-passenger-safety/index.html

[6] https://thecarseatlady.com/vehicles/latch/latch-101-the-basics/

[7] https://www.standinbaby.com/positional-asphyxiation/

THE DEVELOPMENT OF A MECHANIZED STEPPED TENSION BRACE FOR TREATMENT OF ACHILLES TENDONITIS IN COLLEGIATE ATHLETES

Sneha Jeevan
University of Pittsburgh
Pittsburgh, PA, US

Jack Latella
University of Pittsburgh
Pittsburgh, PA, US

Faculty Advisor(s)
Dr. Mary Murray
University of Pittsburgh
Pittsburgh, PA, US

INTRODUCTION

According to the American Academy of Family Physicians (AAFP), ankle injury is one of the most common musculoskeletal injuries in athletes and sedentary persons, accounting for an estimated 2 million injuries per year and 20 percent of all sports injuries in the United States [1]. The largest contributor to ankle injury is Achilles tendonitis, the overuse of the tendon at the back of the heel bone. Achilles tendon tears happen mostly in recreational athletes (75%) and over 80 percent of AT ruptures also occur during sport or recreational activities [2]. Achilles tendonitis affects competitive and recreational athletes, specifically collegiate athletes aging between 18-25 years old. There are currently 460,000 NCAA student-athletes, with 170,000 in Division-1 sports. In a 2017 study, the NCAA Injury Surveillance Program found that 63.7% of athletes playing basketball, volleyball and gymnastics faced Achilles tendonitis. Surgery is required in about 25% of athletes with Achilles tendon overuse injuries, with patient age and duration of symptoms causing an increase in the frequency of surgical intervention. However, about 20% of injured athletes require a re-operation for Achilles tendon overuse injuries, and about 3 to 5% are compelled to abandon their sports career because of these injuries [3].

Orthotic devices such as foot orthoses, splints, taping, and bracing are recommended for Achilles tendinopathy (AT) [4]. Current braces used for treatment are bulky, heavily weighted, and prevent the user from walking with a normal gait, while other options such as kinesiology tape do not provide sufficient support to allow for proper rehabilitation. These devices also lack any quantified levels of tension, often leading to patients using more or less tension than is needed, lengthening recovery time. Customer discovery was performed and revealed that clinicians face issues in quantifying the level of pressure that is applied to the patient's ankle to promote healing.

PRODUCT DESIGN

The stepped tension Achilles tendonitis brace (STAT-B) is a lightweight and low form factor ankle brace for the treatment of Achilles tendonitis. The device utilizes a novel stepped tension mechanism to precisely apply stabilizing force to users' ankles and provide support to their Achilles tendon. A clearly marked scale enables different quantified levels of tension to be applied to the user's Achilles tendon, with the level depending on the severity of their injury and stage of the healing process. By clearly delineating different steps of tension and quantifying the levels of force associated with each, we can build a biomechanical profile of how each setting affects the Achilles tendon. This will allow us to design treatment regimens of different force settings over the course of device use in order to speed up healing time.

The device itself provides tension using two elastic bands pulled from the bottom of the foot to different points of a linear scale fixed to a cuff above the ankle. The more the two tension straps are pulled medially along the length of this cuff, the higher the force that will be applied to the Achilles tendon. One benefit of this design is the overall simplicity of the construction and use; it is constructed only of soft and flexible materials and incorporates no complex mechanical parts. A working prototype has already been constructed and experimented with. Efforts are ongoing to identify more innovative and effective methods of ratcheting tension through the elastic bands as well as types of material used in the device in order to enhance comfort, adjustability, and functionality.

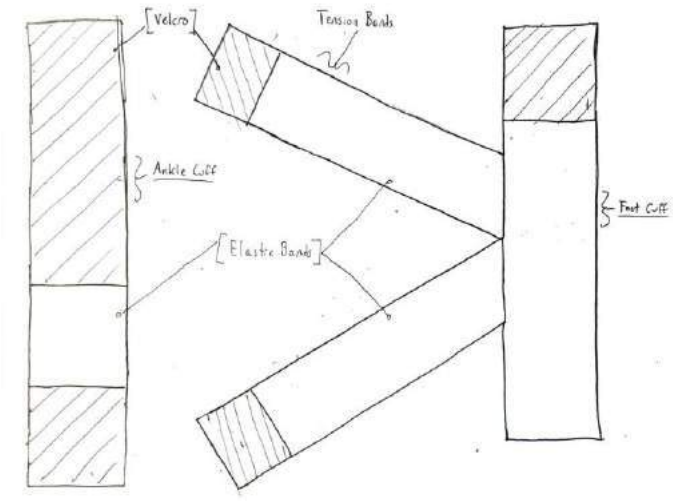

Figure 1: Overview of the three main components of the device, the ankle cuff, the elastic bands, and the foot cuff.

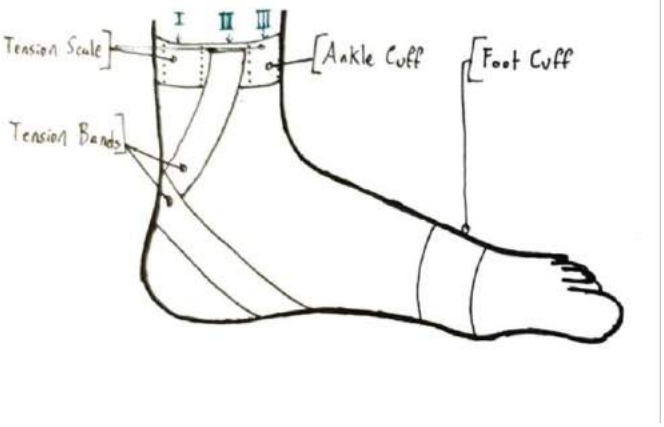

Figure 2: Side view of STAT-B device on human foot, highlighting tension scale and bands for customizable compression.

BUDGET & MARKET ANALYSIS

The global orthopedic braces and support market currently has an estimated value of $3.1B with a CAGR of 5.8% with expected market growth until 2025, with the growth being driven by the prevalence of orthopedic diseases and rising number of sports and accident-related injuries [5]. North America had the largest market share across the globe in 2016 and is expected to maintain its position within the forecast period, with ankle braces being used for a myriad of reasons to immobilize and support the joint. The target current market segment is athletic adults from 18-25 years old, the specific niche market segment for performance-related injury. The product would be marketed to sports medicine therapists who work with collegiate athletes. Leveraging connections to Pittsburgh sports centers and Division I athletes, the focus will be on establishing a foothold with university PTs to gain their trust in the brace.

Given the personalized functionality of the STAT-B brace, the estimated cost of the device is $80, putting the device in the price range of mid- to high-end range of Achilles Tendonitis braces. After revising the final design of the device, the expected manufacturing costs at this volume would be approximately $50 per unit. The Stat-B device will be sold to the 38,800 physical therapy centers across the US. With each center catering to approximately 257 Achilles tendonitis injuries per year, the total available market per year would be 797.7 million dollars. Taking only 5 percent to address the serviceable available market, the target market would be approximately 39.8 million dollars.

Budgetary amounts for development and testing of prototype is listed in Table 1. From Q4 of 2020 to Q1 of 2023, preliminary testing on the current prototype will be performed, including finite element analysis and validation testing with collegiate athletes from the University of Pittsburgh. Clinical trials will occur in Q2 2023 to Q4 of 2025. With the prevalence of Class I orthopedic braces, a similar 510(k) regulatory pathway can be pursued with the same third-party product code ITW. A utility patent will be filed in Q4 of 2025.

Table 1: Budget for STAT-B device development and testing.

Task	Amount	Time Frame
Finite Element Analysis	$10,000	Oct 2020-Aug 2021
Validating Testing	$100,000	Aug 2021-Mar 2023
Phase I Clinical Trial	$500,000	Apr 2023-May 2025
510(k) Submission	$25,000	May 2023-Nov 2025
Utility Patent	$20,000	Dec 2025

ACKNOWLEDGEMENTS

This project originated out of a bioengineering senior design team project at the University of Pittsburgh. Part of the fundamental work for the development of this device came from team members who have opted out of applying to SB^{3}C. These members include Neeshil Patel, Ashlinn Sweeney, Nick Ferchak, Austin Sims and Sean Hartwick. We would also like to thank Dr. Mary Murray of the University of Pittsburgh and Dr. Robroy Martin of Duquesne University for consulting with us on the development of this device.

REFERENCES

[1] Ivins D. Acute ankle sprain: an update. Am Fam Physician. 2006 Nov 15;74(10):1714-20. PMID: 17137000.

[2] Laurent, Didier et al. "Relationship between tendon structure, stiffness, gait patterns and patient reported outcomes during the early stages of recovery after an Achilles tendon rupture." Scientific reports vol. 10,1 20757. 27 Nov. 2020

[3] Kvist M. Achilles tendon injuries in athletes. Sports Med. 1994 Sep;18(3):173-201. doi: 10.2165/00007256-199418030-00004. PMID: 7809555.

[4] Scott LA, Munteanu SE, Menz HB. Effectiveness of orthotic devices in the treatment of Achilles tendinopathy: a systematic review. Sports Med. 2015 Jan;45(1):95-110. doi: 10.1007/s40279-014-0237-z. PMID: 25108348.

[5] "Orthopedic Braces & Supports Market." *Market Research Firm*, Markets and Markets, 2018

WIRELESS INTRACRANIAL PRESSURE SENSING AND MOBILE APPLICATION TRANSMISSION FOR VENTRICULOPERITONEAL SHUNTS

Madison Belyea
Northeastern University
Boston, MA, USA

Erik Jaklitsch
Northeastern University
Boston, MA, USA

Levon Rodriguez
Northeastern University
Boston, MA, USA

Alexandra Silverman
Northeastern University
Boston, MA, USA

Halyn Valley
Northeastern University
Boston, MA, USA

Faculty Advisor(s)

Dr. Michael Jaeggli
Northeastern University
Boston, MA, USA

Dr. Yasmeen Elsawaf
UCF College of Medicine
Orlando, FL, USA

INTRODUCTION

Characterized by excessive accumulation of cerebrospinal fluid (CSF) within the ventricles of the brain, hydrocephalus is a neurological disorder that affects more than one million patients in the United States alone [1]. This build-up may originate from issues of CSF occlusion, absorption, or production due to a range of congenital or developmental conditions; these complications cause an increase in intracranial pressure (ICP) which causes white brain matter atrophy, permanent disability, and death [2]. One treatment option is the implantation of a ventriculoperitoneal (VP) shunt, which allows CSF to drain through a catheter-valve system from the ventricles of the brain to the peritoneum. While this reduces ICP, shunts often malfunction due to obstruction, infection, disconnection, and fracture, or from common activities such as submersion in water or flying on a plane [3]. In fact, about 40% of shunts fail within two years after implantation [3]. Shunt failure causes untreated hydrocephalus, with symptoms that include headaches, vision alteration, nausea, and lethargy [4]. However, some symptoms are identical to symptoms of benign diseases, meaning patients have constant stress about their shunt function and must frequently visit clinics for valve adjustments and check-ups [5], impeding daily life.

Development of an assistive device serving as an ICP monitoring system can obviate unnecessary appointments, relieve emotional distress about symptom origin, and alert the patient of life-threatening pressure levels. There currently exists no device that is fully internal and directly measures ICP, providing accessible and continuous data to the patient and physician [4,6,7,8,9]. Therefore, to address the unmet need for this assistive device, we are prototyping an implantable, continuous, rechargeable ICP-monitoring system that communicates wirelessly with an application on a patient's iOS device. This will provide continuous and reliable readings, alleviating patient stress and permitting physicians to monitor hydrocephalus progression, thereby enhancing the mental and physical health of the patient.

In the US alone, 40,000 hydrocephalus operations are performed annually [11], and the global hydrocephalus shunt market is predicted to reach $322.01 million by 2027 [12], making this device a worthy and profitable area of research and development.

PRODUCT DESIGN

Device Requirements: To permit robust knowledge of the patient's ICP trends, this device must accurately and constantly measure ICP while not interfering with shunt function, and this ICP data must then be accessible to the patient and physician through the iOS application. The device also must be straightforward to implant during VP shunt insertion surgeries, be biocompatible, and have a 10-year longevity to outlast the longevity of over 50% of shunts [3].

Device Design: This device will consist of four main components: the catheter-integrated pressure sensor, electronic components, battery, and iOS app, as seen in Figure 1. The pressure sensor will measure the ICP and transmit that value to the electronic components, which will be powered by the battery. The electrical components will then transmit the value to our iOS app where it can be easily visualized.

To accurately measure ICP, a specialized microelectromechanical system (MEMS) sensor will integrate into the outer sheath of the proximal catheter. This pressure sensor will measure ICP within the range of 0-100 mmHg with an accuracy of ±2 mmHg at a frequency of 2 Hz to allow for near-instant ICP updates for the patient [4]. For our prototype, we will use an off-the-shelf MEMS pressure sensor by Millar. However, for the final device, we will collaborate with Millar engineers to create a custom pressure sensor integrated with an antibiotic-impregnated proximal catheter.

The electrical components consist of a Bluetooth Low Energy (BLE) device to transmit the pressure values to the iOS app, a micro-SD card to provide long-term and backup storage of pressure values,

and a microcontroller to integrate the system. For our prototype, we will use an Arduino Nano 33 BLE microcontroller, 64 GB Micro SD card, and Micro SD card adapter. However, these components will be miniaturized for the final product so they can be stored within the shunt housing. To power the electrical components, we will use an implantable, rechargeable Lithium-Ion battery in tandem with Qi charging. To prevent brain tissue damage due to battery heat, the battery will be stored in the armpit and connected to the device with subcutaneous wires [10]. Using Qi charging will improve the patient's quality of life by eliminating invasive surgeries to replace the battery.

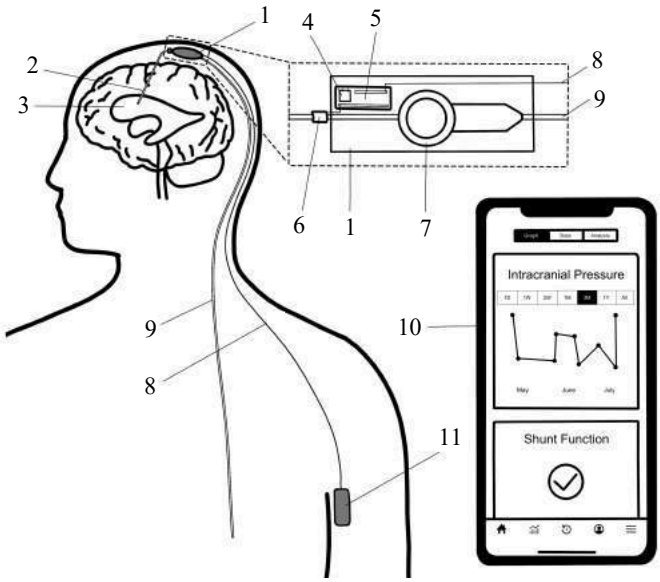

Figure 1: Diagram of Intracranial Pressure Sensing Device
Labels: 1) shunt casing, 2) proximal catheter, 3) enlarged ventricle, 4) micro-SD card, 5) microcontroller with BLE capabilities, 6) catheter-integrated pressure sensor, 7) shunt components, 8) wire connecting microcontroller to battery, 9) distal catheter, 10) iOS app displayed on iPhone, 11) battery

Lastly, the pressure values will be transmitted to our iOS app, which will display a graph of smoothed pressure values in real-time, as the physician needs to visualize the raw data collected to determine if there is a need for repair or adjustment.

Novelty: There are several methods to directly measure ICP including using a catheter with external drainage system or an intraparenchymal device. While these methods are effective, they are noncontinuous, inaccessible, and require neurosurgery to implement. Telemetric devices can also be used to directly measure ICP, but these require extensive external devices, are not continuous, and must be used at a physician's office [4,6,7]. There are also devices that promote accessible and non-invasive ICP measurements, but these require an external measurement device, indirectly measuring ICP by measuring CSF flow, and are non-continuous [8,9]. With our device, we propose a novel idea and method of directly measuring ICP using a fully internal device in which the pressure data is continuous and accessible.

Technical Feasibility: To ensure building the prototype is feasible, we will be using macro-scale components (such as our Arduino microcontroller). These components often come with tutorials and are relatively easy to troubleshoot. Our main technical challenge will be integrating the Millar pressure senser with our Arduino system and eliminating background noise. However, we are in contact with representatives from Millar and are troubleshooting this issue. Once our prototype is built, we will simulate ICP using a water column, and perform robust testing to see how pressure changes when the catheter-shunt system fails, simulating the catheter becoming blocked or disconnected from the shunt *in situ*.

BUDGET & MARKET ANALYSIS

It's estimated that, globally, one of every 770 babies are born with hydrocephalus, which is as common as Down's syndrome [11]. Hydrocephalus can also develop later in life due to tumors, infections, or injuries to the brain and spinal cord, making it a pervasive disease that affects patients of all ages across the globe [11].

The global hydrocephalus shunt market size is predicted to reach $322.01 million by 2027 [12], making shunt optimization a worthy area of research. Since nearly half of shunts experience failure within the first 5 years of implementation, our method of continuous and accurate ICP monitoring would be beneficial to hydrocephalus patients. Our device will have three main groups of patient consumers: infants born with hydrocephalus, infants/children/adults who acquire hydrocephalus, and current hydrocephalus patients with implanted shunts looking to improve their mental and physical health.

Since our device is designed to integrate within the casing of most shunts currently on the market, our product could theoretically be implanted in every new and preexisting hydrocephalus patient. Thus, our market size equals that of the shunt market; in the US alone, if our device were to be implanted during 25% of the annual procedures, we would sell approximately 10,000 units yearly [11].

We estimate that our current budget for prototype design, building, and testing will not exceed $1,000, which includes a microcontroller, Qi charging system, battery, memory card and adapter, and pressure sensors. We were also gifted shunts to use for implementation testing and validation purposes. When developing the final device, we will invest in a custom pressure sensor from Millar and a custom microcontroller from Microchip. We have spoken with representatives from these companies, and the cost for engineering these custom parts would likely be several thousand dollars. However, once created, we will be able to purchase these devices in bulk, paying approximately $20 per microchip and $400 per pressure sensor, making the total cost of our device, including manufacturing costs, approximately $700. By selling this device at $1,000 per unit, we estimate to make $300 per unit, and selling 10,000 units, we will make $3,000,000 in annual profits. The estimated median cost of a programmable shunt is $3,320 [13], and therefore adding our product would increase the price by less than 33%; we believe patients and physicians will deem its positive impact on their mental and physical health worthy of the financial investment.

ACKNOWLEDGEMENTS

This project was funded by the Northeastern University Bioengineering department. Shunts were gifted by Medtronic. This device concept is pending provisional patent, application #63093154.

REFERENCES

[1] Dewan, M et al., *J Neurosurg,* 1:1-15, 2018
[2] Tully, H et al., *J Child Neurol.* 31:309-320, 2016
[3] Soler, G et al., *Yale J Biol Med,* 91:313-321, 2018
[4] Kawoos, U et al., *Int. J Mol. Sci.,* 16:28973-28997, 2015
[5] Dunn, L et al., *J Neurol. Neurosurg. Psychiatry,* 73:23-27, 2002
[6] Zhang, X et al., *Physiol. Meas.,* 38:143-182, 2017
[7] Czosnyka, M, *J Neurol. Neurosurg. Psychiatry,* 75:813-821, 2004
[8] Krishnan, S et al., *Nat. Partn. J. Digit. Med* 3:29, 2020
[9] Swoboda, M et al., Patent: US20150045717A1, 2011
[10] Wolf, P, *CRC Press/Taylor & Francis*, 2008
[11] Hydrocephalus Association, "Facts & Stats," www.hydroassoc.org
[12] Telugunta, R et al., *Allied Mrkt Rsrch,* 2020
[13] Agarwal, A et al., *J Neurosurg* 130:1252-1259, 2019

VENTILATORS FOR THE DEVELOPING WORLD

Grace L. Bugara
Northeastern University
Boston, MA, USA

Taylor A. Corpuz
Northeastern University
Boston, MA, USA

Maeve X. Enright
Northeastern University
Boston, MA, USA

Jay B. Fortescue
Northeastern University
Boston, MA, USA

Laurie A. Trainer
Northeastern University
Boston, MA, USA

Vanessa S. Zighelboim
Northeastern University
Boston, MA, USA

Faculty Advisor(s)

Michael Jaeggli, PhD
Northeastern University
Boston, MA, USA

Lee Makowski, PhD
Northeastern University
Boston, MA, USA

Marc Fuller, PhD
Northeastern University
Boston, MA, USA

INTRODUCTION

The scope of this project is specific to Ghana and arose in response to the COVID-19 pandemic which highlighted many global issues in healthcare, including a world-wide ventilator shortage [1]. As of April 18, 2020, there were only 200 ventilators available in Ghana, meaning that there were more than 145,000 people per ventilator. Of countries in Africa suffering from ventilator shortages, Ghana has been ranked number 22 [2]. For these reasons, Ghana serves as an excellent platform to develop a ventilator design specific to the needs and resources available in that region.

Before the SARS-CoV-2 virus was discovered, Dr. Craig Smallwood already developed the first model of his non-invasive ventilator for Ghana, called the Smallwood Unit. The Smallwood Unit was used on one patient at the Korle Bu Hospital in Accra, Ghana. Before using the Smallwood Unit, the patient had a heart rate near 140bpm and an SpO2 of 87%. After using the Smallwood Unit for an hour, the patient's heart rate dropped to 80-90bpm with an SpO2 of 100%. These improved statistics showed that the Smallwood Unit was a success, however, specific design improvements were required before this ventilator could fully satisfy the needs of developing countries like Ghana.

This project looks to re-engineer the Smallwood Unit to optimize its functionality and features specific to developing areas. This opens the possibility of deploying this device all over Africa. This device will be designed to be used in regional hospitals and to treat adult patients in low resource areas with respiratory issues, COVID-19 or others, that require the use of a non-invasive way to provide EPAP. This target population requires specific constraints to fill the gap in the market including being low in cost (less than $60), electricity free, reusable, and easy to use for treating patients in poor resource areas.

PRODUCT DESIGN

The original design of the Smallwood Unit functions as follows. A mask is placed over the patient's mouth and nose creating an airtight seal. When the patient inhales, the one-way valve opens allowing the patient to breath in air. When the patient exhales the one-way valve closes and the breath is released into the tubing. The opposite end of the tubing is placed in a basin of water to a depth of about 15 cm H_2O to maintain a positive end expiratory pressure (PEEP) in the system to keep the lungs from collapsing during exhalation. When pressure is applied solely during exhalation, it is called expiratory positive airway pressure (EPAP). This breath is then released through the end of the tube in the basin generating bubbles that break the fluid surface and exit the system as aerosols via the expiratory port. The Smallwood unit also allows for an oxygen tube to attach at the facemask should a physician decide that this is something the patient needs.

The main engineering principle that allows for pressure to be maintained in the column is the hydrostatic pressure equation which states:

$$P_h=\rho g h \quad (1)$$

Equation 1: Hydrostatic Formula

Where P_h is the pressure in the liquid, ρ is the density of the liquid, g is the acceleration of gravity and h is the depth in the fluid where the pressure is measured [3]. This equation tells us that only the density of the fluid and the depth that the tube is inserted in the water contribute to the pressure.

Although the Smallwood Unit is a functioning design, the goal of this project is to improve upon the achievements that have already been made by Dr. Smallwood and his team. Potential changes to this system revolve around the expiratory port, bubble diffuser, the basin itself, stability, and the sanitation of the system. The new design for the Smallwood Unit can be seen below in Figure 1. Here, the changes to the design are highlighted with the red circles.

Currently, the expiratory port is a hole in the top of the lid that allows aerosols to leave the system and enter the surrounding environment. This is particularly dangerous if used on patients with infectious diseases such as COVID-19. It is known that aerosol particles between the sizes of 0.5-10 micrometers are the most likely to transmit viral infection [4]. The COVID-19 pandemic has shown it is necessary to capture expired aerosols from the Smallwood Unit in case they are

infectious. To design for this concern, the new iteration of the Smallwood Unit will include a filter at the end of the aerosol tubing that connects to the basin. This will eliminate infectious aerosols before they reach the inside of the basin which will reduce the risk of potential exposure.

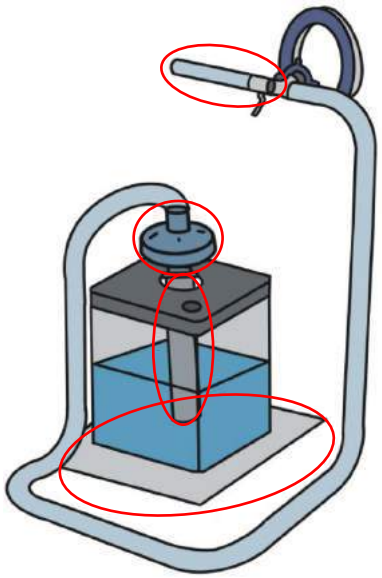

Figure 1: Re-engineered Smallwood Unit

The original design incorporated a bubble diffuser which was designed to reduce the amount of bubbles created upon exhalation. However, the decisions made about the positioning of the filter mitigated these concerns because the aerosols in the basin are no longer infectious. This will end up reducing the overall cost of the system which will help to meet the design requirement of a low-cost ventilator.

Another important change is regarding the basin itself which must be modified to include markings that indicate how far to lower the tube. Equation 1 shows that the most significant variable in ensuring a proper pressure within the system is the depth at which the tubing is inserted in the water. The markings will help to ensure that the tube is at this prescribed height.

Another improvement for the Smallwood Unit is an increase in stability of the basin. If the device tips over during use, all function will be lost. Therefore, a larger piece of plastic will be attached to the bottom of the basin. This uses geometry to increase the surface area of the bottom of the basin to increase the force needed to tip the basin over.

Lastly, improvements involving the reusability and sanitation of the system were made in order to reduce the overall cost of the system. In Ghana and other developing countries, a dilution of household bleach is used to clean medical supplies because it is an accessible and affordable chemical [5],[6]. The basin and base were chosen to be reusable because they are the largest components of the device. This means they must be able to undergo multiple uses while not degrading in the cleaning reagent and still maintain functionality.

The final improvement made to the Smallwood Unit is the addition of an oxygen reservoir at the input valve. This reservoir will help conserve oxygen which will lower the price for the hospitals using the Smallwood Unit.

BUDGET & MARKET ANALYSIS

Cost is a very important element of this project, as making the Smallwood Unit affordable is an essential design requirement for making it available in developing countries. The overall budget for this project to design, build, and test the prototype is $1,000. However, the cost of a single Smallwood unit is broken down in Table 1.

Table 1: Current Smallwood Unit price breakdown

Smallwood Unit Price Estimate			
Component	**Price (USD)**	**Quantity**	**Price per Unit (USD)**
Aerosol Tubing [7]	$3.99	6 feet	$3.99
NIF-Tee Adapter [8]	$68.49	12 adapters	5.70
Oxygen Tubing [9]	$1.13	1 segment	1.13
Anesthesia Mask [10]	$3.59	1 mask	$3.59
Reusable Mask Harness [11]	$56.00	5 harnesses	$11.20
Polycarbonate Container with Lid [12]	$18.99	1 container	$18.99
Rubber Grommet [13]	$12.00	8 pieces	$1.50
CPAP Oxygen Port [14]	$4.95	1 adapter	$4.95
Example Filter [15]	$5.95	1 filter	$5.95
Estimate Cost per Smallwood Unit			**$52.55**

Since low cost is an important design requirement it is expected that each Smallwood Unit is sold for $60. Based off Table 1, this means that a profit of $7.45 will be made off each unit sold. This profit margin is expected to grow as this device is manufactured on a larger scale because the cost per unit will decrease as each component is bought in larger bulk. The rest of the money in the budget will go towards testing equipment such as a pressure transducer, force gauge, Ambu bag, and in-line flow meter. The cost of the testing equipment is still being determined but is not expected to exceed the $1,000 budget.

This project is unique because it will be the only ventilator on the market that is low cost, electricity free, reusable, noninvasive and easy to use. This coupled with the fact that the COVID-19 pandemic has effected developing countries at a higher rate than developed countries makes the market for this device untapped.

ACKNOWLEDGEMENTS

We would like to acknowledge the creator of the Smallwood Unit, Dr. Craig Smallwood, who designed the original model of this device. We would also like to thank our faculty advisors Professor Michael Jaeggli PhD, Professor Lee Makowski PhD and Dr. Mark Fuller PhD along John Thompson who helped guide us through the improvements of this device.

REFERENCES

[1] *MIT E-Vent | MIT Emergency Ventilator*, 2020.
[2] Maclean, R et al, *The New York Times*, 2020.
[3] *ChemistryGod*, 2019.
[4] Umer, F et al, *Int. Endod. J*, 2020.
[5] Fast, O et al, *BMJ Glob. Health*, vol. 2, 2017.
[6] *Stanford Environmental Health & Safety*, 2020.
[7] *IndeMedical.com*, 2020.
[8] *www.cascadehealthcaresolutions.com*, 2020.
[9] https://www.vitalitymedical.com, 2020.
[10] https://www.sasrx.com, 2020.
[11] https://www.sharn.com, 2020.
[12] https://www.target.com, 2020.
[13] https://www.amazon.com, 2020.
[14] https://www.sleepdirect.com, 2020
[15] https://www.cpap.com , 2020.

HAPTIC FEEDBACK TO AID THE VISUALLY IMPAIRED

John C. Tereck
The University of Alabama
Tuscaloosa, AL, USA

Carter M. Roper
The University of Alabama
Tuscaloosa, AL, USA

Peyton D. Duersel
The University of Alabama
Tuscaloosa, AL, USA

Brandon M. Jackson
The University of Alabama
Tuscaloosa, AL, USA

Matthew J. Kamin
The University of Alabama
Tuscaloosa, AL, USA

Faculty Advisor
Dario Martelli
The University of Alabama
Tuscaloosa, AL, USA

INTRODUCTION

The World Blind Union estimates that there are 253 million people worldwide who are fully blind or partially sighted [1]. The blind and visually impaired (BVI) are challenged with independent mobility, especially in public environments. Lack of vision is a vast disadvantage when traversing foreign land, whether it relates to changes in elevation or obstructing objects such as walls, people, trees, etc. The lives of the BVI can be improved through the development of new assistive technologies that could aid their independent mobility.

Historically, the white cane has been the gold standard for assisting locomotion. This device works by giving haptic feedback directly to the user over the length of a 3 to 4-foot aluminum stick. Advantages of the white cane include quick and reliable haptic feedback, ease of use, and higher movement stability through contact with the physical environment. Some notable flaws of the white cane include a lack of verticality, (i.e., the sweeping motion usually only covers the ground plane, lacking sensory feedback for hanging objects) lack of concealability, limited distance of sensing range, and the constant occupation of an entire hand of the user, limiting overall freedom. Also, the sweeping motion could increase energy consumption, create a dual-task interference, and is limited to giving feedback only at the location of the cane at any given moment. Finally, the white cane is designed to be relatively long, making it difficult to conceal or stow in public places; however, the overall length of the cane gives it a finite sensing range for the BVI user. With these limitations in mind, an additional assistive device that can be used in conjunction with the white cane or as a replacement for the white cane would be a major asset for the BVI community.

Currently, there are three categories of electronic walking assistants for the BVI: sensor based, computer vision based, and smartphone based [2]. Each system can be evaluated by five properties: capturing device, feedback, coverage area, weight, and cost. Many types of sensors can be used to detect objects, including ultrasonic, infrared, laser, and radar. Most devices that have already been produced use a complex system of multiple sensors and different outputs such as haptic feedback, audio, or verbal commands to aid the BVI. Some examples of current devices are wearable navigation devices mounted on the head, waist, or chest; specialized canes; and smartphone applications. Many of these solutions result in complicated and expensive devices that would not be affordable to most of the BVI community.

By utilizing modern technology, our team is dedicated to designing a new device that will revolutionize the way the BVI can traverse the unknown at a reasonable price. The device will use ultrasonic sensors in conjunction with vibrotactile haptic feedback to give the BVI user a multidirectional sensory feedback that is proportional to the distance of the obstacles, thus providing a comprehensive scope of the environment.

PRODUCT DESIGN

The team plans to design the device with four ultrasonic sensors enclosed in a 3D-printed case (Figure 1). The case will ensure that the sensors are pointed in the correct directions with the predefined angles of detection. One sensor will be angled upward, encompassing the head and neck area of the BVI user to detect hanging objects such as tree limbs. Two sensors will point in front of the BVI user with one angled slightly to the left and the other slightly to the right. These two sensors will encompass the scope in front of and in the peripheral areas of the BVI user. The sensing ranges of these two sensors are flat cone shapes on the left and right sides in front of BVI users; therefore, objects on the left of the user will produce haptic feedback on the left side of the users' chest, objects on the right side will produce feedback on the right side, and objects in the middle will produce feedback on both sides. The final sensor will be angled downward toward the ground with a shortened sensing range. This sensor will detect changes in elevation in front of the BVI user such as stairs, ramps, or holes in the ground. PING ultrasonic sensors were chosen because they are much cheaper in relation to other considered sensors or radars, and they are simple to program. However, these sensors are still capable of detecting both moving and stationary objects with a resolution of 1 cm and a range of 3 m.

The case will also contain an Arduino Nano, which will be used to process the information gathered from the ultrasonic sensors into haptic feedback. The Arduino Nano is a small and simple processing

board that is relatively inexpensive. However, it processes information quickly enough to convey the objects in front of the BVI user with a resolution of 0.001 seconds. The 3D-printed case will be attached to a vest worn around the chest of the BVI user (Figure 1).

Figure 1. Trimetric View of 3D Printed Case for Sensors (left) and Device Worn on Chest (right)

Sensory feedback will be relayed through vibrating motors attached to the interior of the vest. There will be 4 groups of 2 motors: 2 on the chest slightly below the neck corresponding to the top sensor, 2 on the right pectoral muscle corresponding to the right sensor, 2 on the left pectoral muscle corresponding to the left sensor, and 2 just below the sternum near the rib cage corresponding to the bottom sensor. The motors will vibrate with varying frequency depending on the relative distance of the detected object from the BVI user. When an object is initially detected, the motors will vibrate with a slow frequency. Then, the frequency will increase when the object is sensed between 1 and 2 m. Finally, the motors will vibrate at the maximum frequency when the object is within 1 m of the sensor. Vibration motors were chosen for providing feedback because they are the least intrusive on the senses while also providing consistent feedback.

Considering the design specifications above, the proposed device will sense objects in front of the BVI user at distances of 1 centimeter to 3 meters, whether the objects are moving or stationary. Then, it will convey the locations of the objects through varying frequencies of vibration motors attached to the chest of the BVI user. Therefore, whether the device is used in conjunction with a white cane or without a white cane, it will enhance the ability of the BVI user to traverse unfamiliar territories by yielding more information about surroundings with a comfortable, nonintrusive, and inexpensive solution.

MARKET ANALYSIS & BUDGET

In 2015, 36 million people were fully blind with 217 million people having moderate to severe blindness. The Vision Loss Expert Group projects the number of people with visual impairments to rise over the next 30 years. Accordingly, this figure is projected to rise to 55 and 330 million in the year 2030.[3] According to NORC at the University of Chicago, the average of expected annual expenses related to vision loss is approximately $15,900 and $26,900 for each BVI user [4]. These costs include everything from medical vision aids, vision assistive devices, and medical services. In 2017, the global assistive technologies for the BVI market was valued at approximately $3.40 billion [5]. According to Fior Markets, this market is forecast to grow to $6.57 billion in 2025.

The Perkins School for the Blind reports that only 2 to 8 percent of BVI utilize the white cane. The overwhelming majority of these users use either a guide dog or a sighted dog [6]. The ultrasonic haptic feedback device will provide a modern, economic, sleek solution that is more concealable than the white cane, and will eliminate the need for another conscious guide while providing more effective feedback when supplementing or substituting for the white cane.

The entire cost of the device is covered in a budget of $190 (Table 1). The intended market product will most likely cost less than our prototype budget, as ordering materials and manufacturing in bulk will lower the production cost of a single unit. However, some of the utilities necessary for the construction of this project have been provided by the University of Alabama (e.g. soldering station, 3-D printers, and more).

Table 1. Project Budget

Item Name	Unit Cost	Quantity	Item Subtotal
Vibration Motors	$1	10	$10
PING Ultrasonic Distance Sensor	$30	4	$120
3D Printed Case	$5	1	$5
Battery	$10	1	$10
Vest	$40	1	$40
Arduino Nano	$5	1	$5
Total			**$190**

ACKNOWLEDGEMENTS

The team would like to acknowledge The University of Alabama ME 489/490 course professors and administrators for assistance and budget allowance, in addition to the individual and institutional benefactors of the University that generously provide their resources and monetary contributions. The University has provided $1,000 from the Mildred Hire fund and has donated various critical components necessary for the prototyping of this device.

REFERENCES

[1] "Who We Are." *Who We Are : World Blind Union*, worldblindunion.org/about/.

[2] Islam, Milon, et al. "Developing Walking Assistants for Visually Impaired People: A Review." IEEE Sensors Journal, Vol. 19, No. 8, 15 Apr. 2019.

[3]Ackland, Peter, et al. "World Blindness and Visual Impairment: despite Many Successes, the Problemis Growing ." *Research Gate*, Global Eye Health Data, 2017.

[4]Wittenborn, John. "The Economic Burden of Vision Loss and Eye Disorders in the United States." *Prevent Blindness America*, NORC, 11 June 2013.

[5]D, Avinash. "Global Assistive Technologies for Visually Impaired Market by Product (Educational Devices and Software, Mobility Devices, Low Vision Devices), End User, Region, Global Industry Analysis, Market Size, Share, Growth, Trends, and Forecast 2018 to 2025." *Globe News Wire*, Fior Markets, 30 Jan. 2020

[6] Winter, Bill. "10 Fascinating Facts about the White Cane." *Perkins School for the Blind*

SHEAR, PRESSURE, AND VIBRATION COMFORT SYSTEM

Brittany Wieland
Lawrence Technological University
Southfield, Michigan, United States

Bethany Balint
Lawrence Technological University
Southfield, Michigan, United States

Juan Jaramillo
Lawrence Technological University
Southfield, Michigan, United States

.

Drake Barry
Lawrence Technological University
Southfield, Michigan, United States

Faculty Advisor(s)

Eric G. Meyer, PhD
Lawrence Technological University
Southfield, Michigan, United States

Wu Pan Zagorski, PhD
Lear Corporation
Southfield, Michigan, United States

INTRODUCTION

Comfort is a complex characteristic to quantify, subject to a combination of physical, physiological, and psychological perception. While short-term comfort has been extensively studied in most seat designs, long-term comfort testing has its own set of challenges, including human participant trials. Many drivers experience discomfort when driving for extended periods of time [1]. Drivers who suffer from arthritis, osteoporosis and spinal conditions are even more likely to experience discomfort. Not only can discomfort make traveling difficult, but it can also distract drivers from the road. For these reasons, automotive companies have made comfort a high priority in recent years, with "Comfort Lab", such as the one at Lear Corporation established as part of the Research and Development to pursue this work. In the hopes of reducing the costs and variations associated with using human participants, Lear has tasked our team with developing a testing method for automotive seating that provides quantitative results to indicate occupant comfort for at least 45 minutes in a laboratory setting, without the use of human participants. The Shear, Pressure, and Vibration (SPV) Comfort System is designed to collect data pertaining to the three most important variables regarding seat comfort: Shear, Pressure, and Vibration [1]. The ability to successfully collect data on these variables aids automotive companies in developing seats that provide long-term comfort for passengers.

PRODUCT DESIGN

The first step was to identify if products already existed on the market that would satisfy the needs of the project. We found that there were currently no cost-effective products on the market that could measure seat comfort for an extended period. We brainstormed four variations of how sensors could be attached to the equipment or seat: a simple seat cover, a transparent indentor, only using current Lear equipment, or creating a manikin suit. Our 5th idea was to solely collect enough data to create computer modeling software. The most achievable design with the team's skillset and resources was to make the SPV Comfort system that attaches to the current indentor Lear uses.

The first step in fabricating the SPV Comfort System was the construction of its tissue-mimicking silicone component, which is encapsulated by athletic clothing and can be tightly fit onto butt-form manikin, seen in Figure 1.

This material improved the manikin's ability to simulate loads from a human's own body, by mimicking the mechanical properties of the skin and superficial tissue layers (epidermis, dermis, etc.). This component improved pressure distributions from the manikin, showing more human-like load distributions on the seat. The tissue-mimicking material (Smooth-On Silicone Rubber, Table 1) was cast in a butt-form mold and encapsulated between two layers of athletic shorts.

The second component consists of the sensors that measure shear, pressure, and vibration. For measuring pressure and shear, an array of sensors was integrated superficial to the shorts and tissue-mimicking materials. This array consists of piezoelectric pressure force sensors and stretch force sensors. The pressure force sensors change in resistance due to compressive forces on them, while the stretch sensors change in resistance as they are stretched.

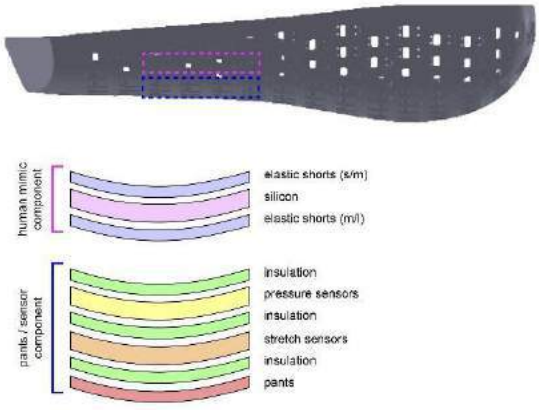

Figure 1: Overall Sensor Suit Design. This demonstrates the primary components of the SPV Comfort System.

Configuring these sensors as variable resistors in a circuit results in voltage/signal changes, which can be converted into force readings. Combining one stretch sensor with one pressure force sensor in a voltage-divider circuit configuration creates a sensor "node", with each node connected to a microprocessor board (Arduino Uno). Multiple nodes of these sensors were combined into an array that covers the areas of interest on the buttocks or back of the manikin's suit (Figure 2). The program running on the microprocessor converts

the sensor outputs into force outputs for display and recording. Each node is representative of a force reading at a "pressure point" on the manikin's buttocks, leg, or tailbone. The combination from the tensile and compression force readings was used to calculate a shear force estimate. Stress transformation principles show that if an object experiences tension and compression in one orientation, then it has to experience pure shear in another orientation. This principle is the route the team took to measure shear between the seat and driver/manikin, as measuring shear is an underdeveloped area of study. A 2-D map of shear and pressure readings were used to determine the highest points of potential discomfort in the buttocks, proximal thigh, and tailbone regions.

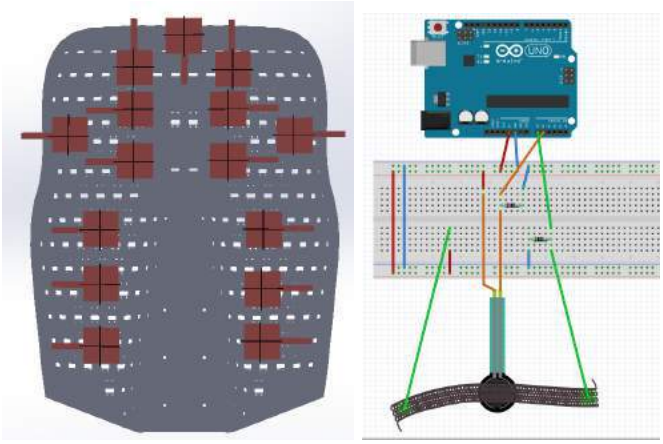

Figure 2: Node Array on Butt-form. This simplified CAD schematic (left) shows the butt-form manikin along with the array of pressure force sensors and stretch cord sensors, forming several nodes. Each node is wired to an Arduino board (right).

As a final addition, two tri-axial accelerometers measured vibration. These sensors were placed according to the ISO 2631 standard, with one on the shaker table in the laboratory, and one was placed on the butt form-seat interface [2]. This setup can give insight into how well the seat absorbs shock/vibration from the road [1]. This accelerometer setup is not directly attached to our manikin suit but part of our overall system measuring these important parameters. The successful combination of these sensors for the collection of data regarding pressure, vibration, and shear allows automotive seat manufacturers to accurately measure the driver's experience. This design and testing process improves the comfort and safety of the driver.

BUDGET & MARKET ANALYSIS

The market for this product includes automotive seating, medical seating, office seating, and can be adapted for the shoe industry. The automotive seat industry alone is an over $50 billion industry with testing facilities around the world [3]. While the other markets available are smaller they still contribute to the available market for the SPV comfort system. The market size allows for an estimated hundreds of devices sold per year.

The focus of the device is shear force reading capabilities. To have a shear force output the device needs to include pressure sensors and piezoelectric stretch sensors. The team ordered various sensors and began testing for the sensors with the lowest drift over time. Once the ideal sensors were chosen, more were bought for the final prototype. The prototype consists of 24 stretch sensors and 14 pressure sensors.

To adjust the pressure distribution of the indentor silicone was added to the device to replicate human tissue. The silicone molding equipment was purchased from Smooth-On. Some silicone molding was bought to run compression tests with. The needed testing equipment was already available in the school laboratories and Lear testing site. Accelerometers used were also available through a previous project at Lear. This allowed for a cost of $621.95. Future material costs to replicate the prototype would cost $234.99 without accelerometers or $2,474.99 with accelerometers, as shown in Table 1.

Table 1: Bill of Materials for One Testing Device.

Product	Company	Quantity	Unit Cost	Cost
P1364 Knit Jersey Conductive Fabric	Adafruit	2	$14.95	$29.90
FSR01CE	OHMITE	14	$8.71	$121.94
Polyester Fabric	Amazon	6	$8.49	$50.94
Ecoflex 00-30 Super Soft Platinum Silicone	Smooth-On	1	$32.21	$32.21
				$234.99

The SPV comfort system can be used to run tests repeatedly, allowing buyers to only purchase one device for years of use. To create a greater profit the SPV comfort system needs to be continuously improved with newer system releases for manufacturers to purchase. Maintenance costs to keep a system running are unknown but can be estimated at around $10 per sensor or $1,000 for the accelerometers that need to be replaced. Other maintenance needs are less likely but could include, silicone replacement, wiring replacement, coding bugs, fabric repairs, and shell replacement.

The estimated number of yearly sales is in the hundreds, based on the industry's number of testing facilities. The manufacturing cost for 100-800 units a year is projected to be $2,177.25 per unit with accelerometers. At this cost, the sales price will be in the range of $3000's for systems with accelerometers and the range of $300's for systems without accelerometers. The profit per unit will be $800+ ($140 without accelerometers), providing for a profit of $300,000+ a year, creating a strong return on the investment.

ACKNOWLEDGEMENTS

We thank Lear Corporation for sponsoring this project through Lawrence Technological University. We would also like to thank Missy Pereny and Steve Gamche from Lear for their support and guidance.

REFERENCES

[1] W. Zagorski, M. Pereny, "Quantitative Investigation on Dynamic Comfort in Automotive Seats: A Ride and Drive Study", 2019.

[2] "ISO 2631-1 Mechanical vibration and shock - Evaluation of human exposure to whole-body vibration Part 1", 1997.

[3] "Top Five Global Automotive Seat Manufacturers: Performance, Strategies, and Competitive Analysis", 2012.

NON-INVASIVE SYSTEM TO SYNCHRONIZE AEROSOL DELIVERY WITH INHALATION IN NEONATES

Franklin Briones
Rice University
Houston, TX, United States

Athena Chien
Rice University
Houston, TX, United States

Hope Fa-Kaji
Rice University
Houston, TX, United States

Samantha McClendon
Rice University
Houston, TX, United States

Pujita Munnangi
Rice University
Houston, TX, United States

Rithika Proddutoor
Rice University
Houston, TX, United States

Faculty Advisor(s)
Dr. Sabia Abidi
Rice University
Houston, TX, United States

INTRODUCTION

Surfactant is a fluid located within the alveoli, small spherical sacs within the lungs that enable gas exchange [1], [2]. The alveoli do this by decreasing in surface tension, preventing lung collapse and allowing expansion [1]. However, underdeveloped Type II alveolar cells of neonatal infants under 35 weeks of gestational age do not produce enough surfactant for sufficient breathing [3]. These preterm neonates are prone to developing respiratory distress syndrome (RDS), which affects approximately 1% of all newborns and is the leading cause of death for preterm infants [3], [4]. Symptoms of RDS include apnea (temporary cessation of breath), shallow breathing, and prolonged gaps between breaths [3]. RDS may lead to asthma, vision problems, neurological issues in other organs, or lifelong breathing problems due to inadequate oxygen and carbon dioxide exchange within the alveoli [5], [6].

The prevailing treatment for RDS is liquid surfactant replacement administered with the INSURE (INtubation-SURfactant-Extubation) method [7], where liquid surfactant is delivered through an endotracheal tube inserted in the neonate's trachea. This invasive method interrupts respiration support (i.e. Continuous Positive Airway Pressure or CPAP) [8]. Large amounts of fluid within neonatal lungs from liquid surfactant can lead to dyspnea (difficulty breathing), pneumothorax, airway obstruction, decreased oxygen levels, or hemorrhage [9]. Aerosolized surfactants, on the other hand, are non-invasive and present the potential for improved pulmonary distribution and oxygenation [8], [10].

Although aerosol delivery systems exist as an alternative, they are inefficient, [11] as jet nebulizers typically have a delivery efficiency below 1% [12], [13]. The most effective nebulizers, including eFlow, can get 20x greater drug delivery compared to the jet nebulizer but are prohibitively expensive ($1,275 for the entire eFlow system) [13],[14]. Thus, there is no optimized aerosol delivery system on the market for neonates receiving respiratory support [8].

We are designing a non-invasive device delivering surfactant through a CPAP interface that synchronizes automatic aerosol delivery with inhalation to increase the amount of surfactant that reaches the alveoli. This proof-of-concept drug delivery system does not interrupt CPAP and provides an efficient alternative to existing treatments for infants with RDS.

PRODUCT DESIGN

The device consists of two major functions: breath synchronization and aerosol delivery. In order to detect inhalation, the device collects the infant's electrocardiogram (ECG) signal, a routine measurement for this population. This is achieved using a 3-lead system and an AD8232 signal conditioning ECG block. The ECG signal is then filtered to acquire a signal corresponding to respiration. The respiratory signal is derived from the change in position of the heart as the chest rises. As the heart moves back in the chest, a low-frequency respiration signal wave is embedded in the ECG signal. A respiratory signal can thus be obtained by filtering the ECG signal within the frequency range of respiration, typically 0.33-1 Hz in a neonate [15]. The onset of inhalation or exhalation can be determined by calculating a derivative to identify the peaks and troughs of this new respiratory signal. In this system specifically, the detection is done by finding the difference between two adjacent data points to determine where the respiratory signal switches from decreasing to increasing, a trough. The information obtained will be used to actuate aerosol propulsion at an appropriate time to maximize drug delivery using the system in **Figure 1**.

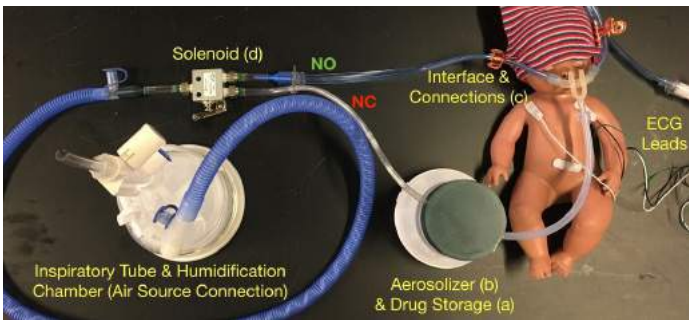

Figure 1: Drug Delivery Configuration

The Aerosol Delivery System in **Figure 1** is comprised of: (a) **drug storage:** a receptacle to hold a dose of liquid surfactant, (b) **aerosol generation:** a high-frequency vibrating piezoelectric that converts liquid to aerosol, (c) **physical connections:** a connection to the infant's cannula interface, and (d) **aerosol propulsion:** a 3/2 solenoid valve that redirects the CPAP flow from its normal route (normally opened position, NO) to push the aerosol into the infant's nose (normally closed, NC). Airflow to the infant is never interrupted and positive pressure is always maintained.

To evaluate the accuracy of inhalation detection, ECG data was first collected from an adult team member, with the described filtering and inhalation detection conducted afterwards. Inhalation start and duration times were compared to those recorded using a button pressed during inhalation and released during exhalation, while the ECG signal was simultaneously acquired. A graph of this test is shown in **Figure 2**, in which RESP data refers to that acquired using the button press.

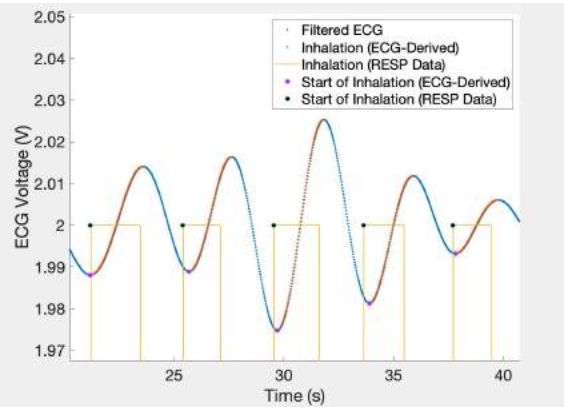

Figure 2: Graphical Evaluation of Inhalation Detection

For this test, the difference between the ECG-derived starting inhalation times and the corresponding button press respiratory times was an average of -0.32 sec, with a standard deviation of 0.44 sec. A two-sample t-test (α = 0.05) to compare the inhalation durations resulted in a p-value of 0.103, indicating that there was no statistical evidence that the means of the ECG and respiratory inhalation durations were unequal. The detection system has also been implemented in real-time, allowing inhalation start times to be displayed within approximately 81 ms of computation time.

A typical CPAP for a preterm infant has a 4-8 lpm flow rate. In initial testing at 8 lpm of crossflow, we propelled over 1.1 mL of aerosolized drug through the interface over an 8-minute treatment window. This successfully coated the entire surface of our test lung with much less drug than the traditional dose of 3 mL/kg infant weight for liquid surfactant. To validate the particles are small enough to reach the alveoli (.5-5 μm), we developed a particle size evaluation method using high speed photo analysis, as seen in **Figure 3**. With this method, we qualitatively compared aerosol particles with larger particles from a nebulizer and preliminarily determined that the particles are in the appropriate size range. Looking forward, we plan to use darkfield microscopy for more accurate size characterization.

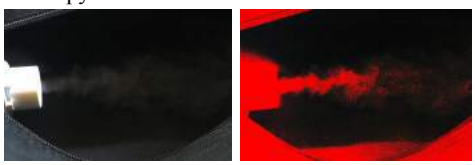

Figure 3: Mesh Nebulizer: Raw (left) and Processed (right) Images

BUDGET & MARKET ANALYSIS

The total budget allocated to the team for designing, building, and testing the prototype is $2500. Our current proof-of-concept prototype costs around $100, split approximately evenly between electronics and physical components. Future testing costs include materials to build a spirometer to verify the breath sensing functionality, as well as costs to buy parts of a CPAP circuit, a compressor if the device is used in a setting without a wall air source, a neonate model, and materials to generate duplicates of the device system for usability testing.

The primary market for the final device is the U.S. preterm infants (400,000/year) [16]. We estimate that over $55.2 million is spent annually on surfactant treatment for this population [17]. Our sponsor projects that the total market reach—including different age ranges and drug types—would move 1 million units/year, reducing the expected manufacturing cost to less than $50, including tooling costs for injection molds. To maintain affordability, the sale price would be $80-100, on par with many commercially available nebulizers. The device's automation and efficient use of surfactant will reduce labor and drug costs, expanding accessibility in non-US markets.

Existing surfactant treatments drastically reduce mortality rates for preterm infants. However, there is an acute need for an optimized, non-invasive neonatal drug delivery system. Our device combines the benefits of breath synchronization, automation, and aerosolized surfactant with a non-invasive, CPAP-integrated design to effectively help the littlest lungs get the breath they need.

ACKNOWLEDGEMENTS

Thank you to our sponsor at Zewski Corp. and to our faculty in the Rice University Bioengineering department for their financial support and mentoring through the Rice University Bioengineering Design course.

REFERENCES

[1] Han, S et al., *Ann Am Thorac Soc*, 12(5):765, 2015.
[2] "How the Lungs Work." [Online]. https://www.nhlbi.nih.gov/
[3] "Neonatal Respiratory Distress Syndrome and Its Treatment with Artificial Surfactant." [Online]. https://embryo.asu.edu
[4] Dyer, J, *Pharmacy and Therapeutics*, 44(1):12, 2019.
[5] "Respiratory Distress Syndrome." [Online]. https://www.nhlbi.nih.gov/
[6] Walther, F et al., *Expert Review of Respiratory Medicine*, 13(6):499–501, 2019.
[7] Bohlin, K et al., *J Perinatol*, 27(7) 2007.
[8] Mazela, J et al., *Eur J Pediatr*, 170(4):433, 2011.
[9] Nouraeyan, N et al., *Can J Respir Ther*, 50(3):91–95, 2014.
[10] Walther, F et al., *PeerJ*, 2, 2014.
[11] Ibrahim, M et al., *Med Devices*, 8:131, 2015.
[12] Longest, P et al., *J Aerosol Med Pulm Drug Deliv*, 27(5):371, 2014.
[13] DiBlasi, R, *Respir. Care*, 60(6):894–916, 2015.
[14] "PARI eRapid Nebulizer System with eFlow Technology." [Online]. nebology.com
[15] Reuter, S et al., *Pediatr Rev*, 35(10):417-429, 2014.
[16] Martin, J et al., *National Vital Statistics Reports*, 68(13), 2019.
[17] Cheah, I, *Transl Pediatr*, 8(3):246–256, 2019.